

Edited by
Zakaria Hossain
Bujang B.K.Huat
Vivi Anggraini
Jim Shiau



GEOMATE

ISBN 978-4-9905958-8-3 C3051



GEOMATE 2018 KUALA LUMPUR, MALAYSIA
GEOTECHNIQUE, CONSTRUCTION MATERIALS AND ENVIRONMENT

PROCEEDINGS OF THE EIGHTH INTERNATIONAL CONFERENCE – GEOMATE 2018
GEOTECHNIQUE, CONSTRUCTION MATERIALS AND ENVIRONMENT, KUALA LUMPUR,
MALAYSIA 20-22 NOVEMBER, 2018

Geotechnique, Construction Materials and Environment

Edited by

Prof. Zakaria Hossain

*Department of Environmental Science and Technology
Graduate School of Bioresources
Mie University, Japan*

Prof. Bujang B.K. Huat

*Department of Civil Engineering
Universiti Putra Malaysia*

Dr. Vivi Anggraini

*School of Engineering
Monash University Malaysia*

Dr. Jim Shiau

*School of Civil Engineering and Surveying
University of Southern Queensland, Australia*



THE GEOMATE INTERNATIONAL SOCIETY

Copyright © 2018 by The GEOMATE International Society

All rights reserved. In principle, no part of this publication or the information contained herein may be reproduced in any form or by any means, translated in any language, stored in any data base or retrieval system, or transmitted in any form or by any means without prior permission in writing from the publisher.

Disclaimer: The editors and the publisher have tried their best effort to ensure the integrity and the quality of this publication and information herein. However, they give no warranty of any kind, expressed or implied with regard to the material contained in this book, and will not be liable in any event for the consequences of its use.

Published by:
The GEOMATE International Society
Tsu city, Mie, Japan
E-mail: society@geomate.org
<http://www.geomate.org/>

ISBN Number: 978-4-909106001 C3051

8116	THE BEHAVIOR OF UNTREATED AND TREATED EXPANSIVE SOIL AS EMBANKMENT OF FLEXIBLE PAVEMENT Yulvi Zaika, Eko Andi Suryo	49
8120	GEOTECHNICAL ASSESSMENT OF MALAYSIAN RESIDUAL SOILS FOR UTILIZATION AS CLAY LINERS IN ENGINEERED LANDFILLS Lee Li Yong , Endene Emmanuel, Ria Purwani and Vivi Anggraini	55
8121	INVESTIGATING THE EFFECT OF GEOTEXTILE AS REINFORCEMENT ON THE BEARING CAPACITY OF GRANULAR SOIL John Carlo R. Samarita, and Mary Ann Q. Adajar	61
8122	A COMPARATIVE STUDY ON THE USE OF WOVEN GEOTEXTILE FOR SETTLEMENT REDUCTION OF SPREAD FOOTING ON GRANULAR SOIL Mary Ann Adajar, Maricris Gudes and Lillibelle Tan	67
8123	INVESTIGATING THE EFFECTIVENESS OF RICE HUSK ASH AS STABILIZING AGENT OF EXPANSIVE SOIL Mary Ann Q. Adajar, Christian James P. Aquino, Joselito D. Dela Cruz II	73
8124	INDUSTRIAL BY-PRODUCT-BASED BINDERS FOR USE IN DEEP SOIL MIXING TECHNIQUE Mohammadjavad Yaghoubi, Arul Arulrajah, Mahdi Miri Disfani, Suksun Horpibulsuk and Stephen Darmawan	79
8128	CYCLIC MECHANICAL PROPERTIES OF SANDY SOILS BY MIXING RECYCLED ASPHALT PAVEMENT MATERIAL Shoji Yokohama and Atsuko Sato	85
8129	QUEZON CITY SOIL PROFILE REFERENCE Joanel G. Galupino and Jonathan R. Dungca	91
8130	GEOTECHNICAL PROPERTIES OF SLUDGE BLENDED WITH CRUSHED CONCRETE AND INCINERATION ASH Muhammad Rashid Iqbal, Kento Hashimoto, Shinya Tachibana, and Ken Kawamoto	98
8132	NUMERICAL ANALYSIS FOR 3D INFLUENCE OF PILE PULLING-OUT HOLES ON SURROUNDING GROUND Shuichi Kuwahara and Shinya Inazumi	105
8133	POSSIBILITY OF NEUTRAL-BASED SOLIDIFYING MATERIALS FOR PREVENTING ELUTION OF RADIOACTIVE SUBSTANCES FROM RESERVOIRS Hiroyuki Hashida, Shinya Inazumi	111
8134	LEAKAGE RISK ASSESSMENT ON SIDE IMPERVIOUS WALLS AT COASTAL LANDFILL SITES Ken-ichi Shishido and Shinya Inazumi	119
8135	DEVELOPMENT OF METAL-INSOLUBILIZING MATERIAL ON SOIL CONTAMINATED WITH HEAVY METALS USING CHEMICAL AND MINERAL ANALYSIS Shinya Inazumi, Ken-ichi Shishido and Hiroyuki Hashida	127
8141	LIQUEFACTION ANALYSIS OF ROAD EMBANKMENT IN PIDIE JAYA DUE TO ACEH EARTHQUAKE IN 2016 M Sofian Asmirza, Anissa Maria Hidayati and Abdul Hakam, M Maisaquddus Hape	134
8143	MEASUREMENT OF CEMENT CONTENT IN CEMENT MIXED SOIL BY HYDROCHLORIC ACID HEAT REACTION METHOD Hiroshi Kubo, Toshihiko Miura and Shinya Inazumi	139
8147	RELATIONSHIP BETWEEN CONSTRUCTION METHOD OF CRUSHED STONE PILE AND BEARING CAPACITY CHARACTERISTICS Seiya Yamazaki, Naoaki Suemasa, Kazuya Ito, Makoto Hotta	145
8148	A STUDY ON INFLUENCE OF PENETRATION DISTANCE ON GEL TIME OF CHEMICAL GROUT Ryota Nakamura, Naoaki Suemasa, Sakamitsu Sasaki, Syunsuke Shimada	151

8149	A STUDY ON STRENGTH DEVELOPMENT OF SUSPENDED TYPE INJECTION MATERIAL USING MICROPARTICLES USED FOR LIQUEFACTION COUNTERMEASURE Takuya MOUE, Kentaro UEMURA , Koichi NAGAO , Naoaki SUEMASA , Kazuya ITO and Shunsuke SHIMADA, Takamitsu SASAKI	157
8150	BIO-INSPIRED STABILIZATION OF EMBANKMENT SOIL MEDIATING PSYCHROBACILLUS SP. AND LOW-GRADE CHEMICALS: PRELIMINARY LABORATORY INVESTIGATION Sivakumar Gowthaman, Shumpei Mitsuyama, Kazunori Nakashima, Masahiro Komatsu and Satoru Kawasaki	163
8152	EFFECTS OF THRUST PROTECTING METHOD FOR BURIED PIPE USING GEOGRID GABION OF DIFFERENT SIZES Hiroyuki Araki and Daiki Hirakawa	169
8154	EXPERIMENTAL STUDY ON RAINFALL INTENSITY AND SHALLOW LANDSLIDES WITH QUASI-SATURATED STATE Kota Okazaki, Keigo Koizumi, Kazuhiro Oda, Katuo Sasahara and Keiji Sakuradani	176
8155	COLLAPSE MECHANISM OF STEEL PILES BELOW HIGH-RISE BUILDING IN LIQUEFIED SOIL Moeko Matoba and Yoshihiro Kimura	179
8156	MODIFIED NATURAL FIBER ON SOIL STABILIZATION WITH LIME AND ALKALINE ACTIVATION TREATED MARINE CLAY Fatin Amirah binti Kamaruddin, Bujang B.K Huat, Vivi Anggraini and Haslinda Nahazanan	185
8159	Soil Stabilized with Geopolymers for Low Cost and Environmentally Friendly Construction Wisam Dheyab, Afshin Asadi, Bujang B.K. Huat, Mohd Saleh Jaafar, and Lokmane Abdeldjouad	192
8160	EFFECT OF CURING TEMPERATURE ON THE DEVELOPMENT OF HARD STRUCTURE OF ALKALI-ACTIVATED SOIL Lokmane Abdeldjouad, Afshin Asadi, Bujang B.K.Huat, Mohd Saleh Jaafar, Wisam Dheyab, and Ahmed Giuma Elkhebu	206
8161	EFFECTS OF ALKALI-ACTIVATED WASTE BINDER IN SOIL STABILIZATION Tan Teing Teing, Bujang B.K. Huat, Sanjay Kumar Shukla, Vivi Anggraini and Haslinda Nahazanan	213
8164	EVALUATION OF FILLER MATERIAL BEHAVIOR IN PRE-BORED PILE FOUNDATION SYSTEM DUE TO SLOW CYCLIC LATERAL LOADING IN SANDY SOIL Adhitya Yoga Purnama, Noriyuki Yasufuku and Ahmad Rifa'i	219
8165	DENSITY DISTRIBUTIONS WITHIN CERAMIC MATERIALS SATURATED FOR USE IN SUCTION MEASUREMENT Katsuyuki KAWAI, Shinya KIKUI, Naoki YOSHIKAWA and Takayuki FUMOTO	226
8169	PREDICTION METHOD FOR LONG-TERM SETTLEMENT OF HIGLY ORGANIC SOIL USING NATURAL STRAIN Shoji KAMAO	232
8170	DIAPHRAGM WALL SUPPORTED BY GROUND ANCHORS AND INCLINED STRUTS: A CASE STUDY Adnan Anwar Malik, Gorkem Dora, Ramy Derar and Majid Naeem	238
8178	AN ANALYSIS OF VERIFICATION ON THE INFLUENCE OF LIQUEFACTION ON UNDERGROUND STRUCTURE Keita Sugito, Tetsuya Okano and Ryoichi Fukagawa	245
8181	CALCULATION FORMULA FOR PULLOUT RESISTANCE EXERTED BY OPEN-WING-TYPE GROUND ANCHOR Kota Kono, Akihisa Nakahashi, and Ryoichi Fukagawa	251
8191	INVESTIGATION OF CYLINDRICAL SPECIMEN COLLAPSE BEHAVIOR USING 3D SMOOTHED-PARTICLE HYDRODYNAMIC ANALYSIS Tetsuya Okano, Yukiko Sumi, Tsutomu Matsuo, and Ryoichi Fukagawa	257
8193	CALIBRATION OF EARTH PRESSURE CELL FOR A SPECIFIED LABORATORY APPLICATION Mohammad Zahidul Islam Bhuiyan, Shanyong Wang, Scott William Sloan, Daichao Sheng and Harry Michel	263

8205	SLOPE STABILITY ANALYSIS OF FRICTIONAL FILL MATERIALS PLACED ON PURELY COHESIVE CLAY Kongkit Yingchaloenkitkhajorn	269
8221	WEST SUMATRA COASTLINE CHANGE DUE TO ABRASION PROTECTION STRUCTURES: PADANG BEACH Abdul Hakam, Junaidi, Bayu M Adji, Shafira Rahmadilla Hape	275
8228	EFFECT OF TUNNEL SIZE AND LINING THICKNESS ON TUNNEL DEFORMATION DUE TO ADJACENT PILE UNDER LOADING Prateep Lueprasert, Pornkasem Jongpradist, Kodchamon Ruangvirrojanakul and Suchatvee Suwansawat	281
8230	DISCRETE PARTICLE SIMULATION MODEL FOR SLAKING OF GEOMATERIALS INCLUDING SWELLING CLAY MINERALS Yutaka Fukumoto and Satoru Ohtsuka	288
8232	EVALUATION OF BEARING CAPACITY ON SOIL-CEMENT MIXING WALL USING PERMANET PILE Koji Watanabe and Minoru Mizumoto	294
8233	FUNDAMENTAL STUDY OF THE EFFECT OF WATER LEVEL LOWERING IN THE GROUNDWATER DRAINAGE WORK UTILIZING SIPHON Takeshi YAMAMOTO, Yuki MINAMIGUCHI, Keigo KOIZUMI, Mitsuru KOMATSU, Kazuhiro ODA, and Adrin THOHARI	300
8237	METHODS TO MEASURE THE INITIAL QUASI-SATURATED VOLUMETRIC WATER CONTENT OF SOIL Miki Nishimura, Hiroshi Kita, Mitsuru Komatsu, Keigo Koizumi, Kazuhiro Oda and Keiji Sakuradani	306
8240	DESIGN CONCEPT FOR AN ANCHORED DIAPHRAGM WALL IN PROJECT ADP ASTANA, KAZAKHSTAN Askar Zhussupbekov, Abdulla Omarov, Gulzhanat Tanyrbergenova and Karlygash Borgekova	311
8241	EVALUATION OF THE CALIBRATION ACCURACY OF SOIL MOISTURE USING A NEW MICROCHIP SENSOR Mitsuru Komatsu, Masato Futagawa and Yasushi Fuwa	317
8247	SLOPE STABILITY ANALYSIS OF INTEGRATED MUNICIPAL DISPOSAL SITE BASED ON ORGANIC CONTENT CHANGE TO OPTIMIZE EMBANKMENT CAPACITY Ahmad Rifa'i, I Wayan Ariyana Basoka and Fikri Faris	323
8258	STABILITY PERFORMANCE OF LOADING TEST FOR SHORT PILED RAFT FOUNDATION SYSTEM ON PEAT Sajiharjo Marto Suro, Adnan Zainorabidin, Agus Sulaeman and Ismail Bakar	329
8259	ASSESSING THE ULTIMATE BEARING CAPACITY OF FOOTING IN A TWO-LAYERED CLAYEY SOIL SYSTEM USING THE RIGID PLASTIC FINITE ELEMENT METHOD Kazuhiro KANEDA, Masamichi AOKI and Satoru OHTSUKA	335
8263	SETTLEMENT BEHAVIOUR OF PARIT NIPAH PEAT UNDER STATIC EMBANKMENT Adnan Zainorabidin, Mohamad Niizar Abdurahman, Azman Kassim, Mohd Firdaus Md DanAzlan and Siti Nooraiin Razali	341
8274	LAND SUBSIDENCE IN SUMATERA PEATLAND FOREST Nurhamidah Nurhamidah, Bujang Rusman, Bambang Istijono, Abdul Hakam, Ahmad Junaidi, Taufika Ophiyandri	346
8277	COMPARISON OF BEARING CAPACITY IMPROVEMENT FOR SOFT CLAY USING SOIL-LIME AND SOIL-CEMENT COLUMNS Satyajit Patel, Amruta Joshi and Shravan Sukumaran	354
8284	THE EFFECT OF L-SHAPED SHEAR WALL ON STUDENT DORMITORY BUILDING OF ANDALAS UNIVERSITY, PADANG, INDONESIA Fauzan, F A Ismail, M W Rizki, I Fikri, and Z A Jauhari	360
8290	STRUCTURAL EVALUATION OF NURUL HAQ SHELTER BUILDING CONSTRUCTED ON LIQUEFACTION PRONE AREA IN PADANG CITY-INDONESIA Rina Yuliet, Fauzan, Abdul Hakam, Helza Riani	366

8293	TESTING OF FOAM CONCRETE FOR DEFINITION OF LAYER INTERACTING WITH SUBSOIL IN GEOTECHNICAL APPLICATIONS Marian Drusa, Jozef Vlcek, Walter Scherfel and Bronislav Sedlar	373
8295	SEDIMENT FLOW CHARACTERISTICS ON SEABED SUBJECTED TO STATIONARY WAVES WITH DIAGONAL INCIDENT WAVE LOADING NEAR LINE STRUCTURES Anh Quang TRAN, Kinya MIURA, Tatsuya MATSUDA and Takahito YOSHINO	379
8306	THE SIMPLE METHOD OF SHEAR WAVE VELOCITY PROFILE FROM EXPLOSION SOURCE IN SURIN, THAILAND Pithan Pairojn	385
8312	LOADED SWELL TESTS TO ESTIMATE THE HEAVE OF THE EXPANSIVE SOIL IN INSTRUMENTED SOIL COLUMN Udukumburage RS, Gallage C and Dawes L	390
8315	MULTI-CHANNEL FIBRE BRAGG GRATING SENSORS (MC-FBGs) FOR UNIAXIAL COMPRESSIVE TEST ON LIMESTONE ELASTICITY BEHAVIOUR Isah B. W., Mohamad H. and Ahmad N. R.	396
8316	VOLUME LOSS CAUSED BY TUNNELLING IN KENNY HILL FORMATION C.M. Khoo, T. Gopalan, N.A. Abdul Rahman and H. Mohamad	402
8320	THE NECESSITY OF EMPLOYING THREE DIMENSIONAL CONCEPTS IN SLOPE STABILITY ANALYSIS Roohollah Kalatehjari, Ahmad Safuan Abdul Rashid, and Mostafa Babaeian Jelodar	408
8323	SEISMIC MICROZONATION OF SEMARANG, INDONESIA, BASED ON PROBABILISTIC AND DETERMINISTIC COMBINATION ANALYSIS W. Partono, M. Irsyam, M. Asrurifak, I.W. Sengara, A. Mulia, M. Ridwan and L. Faizal	415
8325	UNDRAINED RESPONSE OF SILTY SAND UNDER STATIC AND CYCLIC LOADING Akhila M, Dr. K Rangaswamy and Dr. N Sankar	421
8329	CONSTRUCTION OF EARTH FILL STRUCTURE FOR SMALL FARM POND BY USING BHUTANESE TRADITIONAL WALL MAKING METHOD UENO Kazuhiro, NATSUKA Isamu, SATO Shushi, ONJO Norio, Karma Tshethar and Kelzang Tenzin	427
8345	QUANTITATIVE ANALYSIS OF MOISTURE INDUCED ALTERATIONS ON THE DIMENSIONS OF GRAVITY FLOW EXTRACTION ELLIPSOID OF COARSE GRAINED PARTICLES IN A GLASS-BOX MODEL Uziell Boringot and Juan Fidel Calaywan	433
8349	INFLUENCE OF INITIAL CONDITIONS ON UNSATURATED GROUNDWATER FLOW MODELS Aizat Mohd Taib, Mohd Raihan Taha and Dayang Zulaika Abang Hasbollah	437
<i>ID</i>	<i>Construction Materials</i>	444
8114	MECHANICAL PROPERTIES OF CONCRETE WITH RECYCLED COMPOSITE AND PLASTIC AGGREGATES Dan Li and Sakdirat Kaewunruen	445
8117	ASSESSMENT OF QUALITY OF DIFFERENT AGGREGATES FOR ROAD CONSTRUCTION IN THE CENTRAL DIVISION OF FIJI Atinesh Vijay Prasad, Darga N Kumar	451
8127	DEVELOPMENT OF CARBON FIBER REINFORCED THERMOPLASTIC STRAND ROD Y Mochida, Y Imoto	457
8136	QUICK ASSESSMENT PROCEDURES FOR TWO STORIES BUILDING BASED ON NUMERICAL SIMULATION RESULTS Febrin Anas Ismail, Abdul Hakam, M Maisaquddus Hape, M Sofian Asmirza	463

8138	COMPRESSED EARTH BLOCKS WITH POWDERED GREEN MUSSEL SHELL AS PARTIAL BINDER AND PIG HAIR AS FIBER REINFORCEMENT Bernardo A. Lejano, Ram Julian Gabaldon, Patrick Jason Go, Carlos Gabriel Juan, and Michael Wong	467
8139	INVESTIGATION OF THE FLEXURAL STRENGTH OF COLD-FORMED STEEL C-SECTIONS USING COMPUTATIONAL AND EXPERIMENTAL METHOD Bernardo A. Lejano and Eyen James D. Ledesma	473
8151	STUDY ON STRENGTH ESTIMATION OF SOIL CEMENT USED IN THE EMBEDDED PILE METHOD BY ELECTRICAL RESISTIVITY MEASUREMENT Y Mochida, M Matsuura	479
8157	CENTRIFUGE TEST OF SUPERSTRUCTURE-SC PILE-LIQUEFIED SOIL SYSTEM AND SC PILES' DYNAMIC BUCKLING BEHAVIOR Hiroki Goto, Moeko Matoba and Yoshihiro Kimura	486
8171	VOLUME CHANGE BEHAVIOR OF SEA WATER EXPOSED COAL ASH USING HYPERBOLIC MODEL Erica Elice S. Uy, Jonathan R. Dungca and Mary Ann Q. Adajar	492
8172	FINITE DIFFERENCE METHOD FOR SOLVING HEAT CONDUCTION EQUATION OF THE GRANITE Dalal Adnan Maturi	498
8196	REGRESSION MODELING OF BREAKOUT STRENGTH OF AN EXPANSION ANCHOR BOLT AS INFLUENCED BY CONCRETE AGGREGATES Gilford B. Estores, Wyndell A. Almenor and Charity Hope A. Gayatin	502
8198	CORROSION CURRENT DENSITY OF MACROCELL OF HORIZONTAL STEEL BARS IN REINFORCED CONCRETE COLUMN SPECIMEN Nevy Sandra, Keiyu Kawaai and Isao Ujike	508
8213	SIMULATING LUNAR HIGH LAND ROCKS USING JAPANESE IGNEOUS ROCKS Hiroyuki Ii and Hiroshi Kanamori	514
8224	RELIABILITY ASSESSMENT OF WOODEN TRUSSES OF A HISTORICAL SCHOOL Alvin Quizon and Lessandro Estelito Garciano	520
8236	EXPERIMENTAL STUDY ON CHEMICAL GROUTING INTO CALCIUM-CONTAINING SAND Hidetake Matsui, Yusuke Tadano and Hiroyasu Ishii	526
8249	EXPERIMENTAL STUDY ON THE EFFECT OF REBAR CORROSION ON THE MEASUREMENTS OF VARIOUS NONDESTRUCTIVE TESTS Kohei Mishima, Kenichi Kondo, Isao Ujike, Chun Pang-jo and Keiyu Kawaai	531
8250	Basic Study of Cement Solidification Technology for Solidification of Cesium Adsorbed Zeolite Evaluation of Microscopic Structure of Cement Solidification Taisei SAKAI and Kazuhito NIWASE	537
8261	Effect of Chemical Admixture on Cement Solidification of Cesium Adsorbed Zeolite Sora SUTO and Kazuhito NIWASE	543
8264	A FUNDAMENTAL EXPERIMENT ON PNEUMATIC TOMOGRAPHY OF UNSATURATED SOIL GROUND USING A HORIZONTAL ONE-DIMENSIONAL COLUMN Naoya Nishihara and Mitsuru Komatsu	549
8299	PARAMETRIC STUDY OF CES COMPOSITE COLUMNS WITH FRC USING FINITE ELEMENT ANALYSIS Fauzan, Ruddy Kurniawan, Zev Al Jauhari, and Nabila Felicia	555
8324	ASSESSMENT TECHNIQUES FOR ALKALI SILICA REACTION DIAGNOSIS IN MASS CONCRETE STRUCTURE Suvimol Sujjavanich, Thanawat Meesak, Krit Won-in and Viggo Jensen	563

8330	BACK PROPAGATION ARTIFICIAL NEURAL NETWORK MODELING OF FLEXURAL AND COMPRESSIVE STRENGTH OF CONCRETE REINFORCED WITH POLYPROPYLENE FIBERS Stephen John C. Clemente, Edward Caezar D.C. Alimorong and Nolan C. Concha	569
8332	EFFECT OF MANUFACTURED DOLOMITIC LIMESTONE SAND AS ALTERNATIVE FINE AGGREGATES FOR SHOTCRETE WET-MIX APPLICATION Benedicto, Patrizia S., Calaywan, Juan Fidel B. , Ebueng, Rio Jocelle A., and Matba, Ylam Shalev dT.	574
8358	STRENGTH AND FLOWABILITY OF HIGH WATER CONTENT STABILIZED SOIL AT EARLY CURING TIME Vincentius Harry, Luky Handoko, Sumiyati Gunawan, John Tri Hatmoko and Jim Shiau	583
ID	<i>Environment</i>	588
8104	TOPOGRAPHIC CONTROL ON GROUNDWATER FLOW IN CENTRAL OF HARD WATER AREA, WEST PROGO HILLS, INDONESIA T. Listyani R.A., Nana Sulaksana, Boy Yoseph CSSSA and Adjat Sudradjat	589
8118	COMMUNITY EMPOWERMENT IN PLANTING VEGETATION TO REDUCE COASTAL ABRASION IN WEST SUMATRA Taufika Ophiyandri, Bambang Istijono and Abdul Hakam	595
8119	THE EFFECT OF FLOOD TO QUALITY INDEX OF SOIL PHYSICAL PROPERTIES AT THE DOWNSTREAM OF KURANJI RIVER WATERSHED, PADANG CITY Aprisal, Bambang Istijono, Taufika Ophiyandri and Nurhamidah	601
8125	ENVIRONMENTAL PARAMETERS CONTROLLING THE HABITAT OF THE BRACKISH WATER CLAM CORBICULA JAPONICA IDENTIFIED BY PREDICTIVE MODELLING Yukari Sugiyama, Mikio Nakamura , Suguru Senda and Michiko Masuda	608
8131	THE MANAGEMENT OF RIVERBANK MAINTAINS THE DUNE PLANT POPULATION, ESPECIALLY AN ENDANGERED SPECIES, FIMBRISTYLIS SERICEA Michiko Masuda, Sota Yotsuya and Fumitake Nishimura	614
8137	APPROACH TO ASSESSMENT OF SOIL AND WATER CONTAMINATION BY MINING ACTIVITIES IN MANDALAY REGION, MYANMAR Than Htike Oo, Toshiro Hata	619
8140	DEVELOPMENT OF THE MODIFIED EICP FOCUSED ON THE HIGH STRENGTH UNDER LOW CALCITE PRECIPITATION RATE Yusui Murata, Toshiro Hata	625
8142	WATER RETENTION, GAS TRANSPORT PARAMETERS, AND THERMAL PROPERTIES FOR ROADBED MATERIALS UTILIZING CONSTRUCTION DEMOLITION WASTE AND INDUSTRIAL BYPRODUCTS Mohd Redzuan MOHD SAUFI , Takeshi SAITO, Taro UCHIMURA, and Ken KAWAMOTO	630
8145	WATER QUALITY AND SEDIMENTATION MODELING IN SINGKARAK LAKE, WESTERN SUMATRA, INDONESIA Harman Ajiwibowo, R.H.B. Ash-Shiddiq, Munawir B. Pratama	636
8153	INTEGRATED LAND USE – FLOOD MANAGEMENT APPROACH IN URBAN SPRAWL OF LAFIA, NASARAWA STATE OF NIGERIA Danjuma Inarigu, Zakiah Ponrahono, Mohammad Firuz Ramli and ZulfaHanan Ashaari	645
8163	GEOCHEMISTRY ANALYSES OF SEA FLOOR SEDIMENTS FROM THE COASTS OF SHIKINE ISLAND IN JAPAN INDICATE AN INFLUENCE OF CO2 SEEPS TO COASTAL ENVIRONMENTS Hirosuke Hirano, Koetsu Kon, Masa-aki Yoshida, Ben Harvey, Davin H. E. Setiamarga	651
8168	AN ALTERNATIVE INTEGRATED OCCUPATIONAL HEALTH, SAFETY AND ENVIRONMENTAL MANAGEMENT SYSTEM FOR SMALL AND MEDIUM-SIZED ENTERPRISES (SMEs) IN THAILAND Thepporn Jaroenroy, Chutarat Chompunth	659
8176	SOME INSIGHT INTO DIRECT OBSERVATION OF HYDROLOGICAL PARAMETERS IN PEATLAND AREA OF THE SOUTH SUMATERA Muhammad Irfan, Wijaya Mardiansyah, M. Yusup Nur Khakim, Menik Ariani, Albert Sulaiman and Iskhaq Iskandar	665

8179	SHEAR BEHAVIOUR OF CONNECTION BETWEEN STEEL AND REINFORCED CONCRETE MEMBERS ADOPTING A NEW COLUMN BASE SYSTEM ALLOWING THE STEEL MOMENT-RESISTING FRAME TO PERFORM BEAM YIELDING MECHANISM Sachi Furukawa, Yoshihiro Kimura, Katsunori Kaneda and Akira Wada	670
8180	DEVELOPING REHEATED MOTORCYCLE EXHAUST FOR PM2.5 EMISSION Wardoyo, Arinto Y.P. Dharmawan, Hari A	677
8187	THE INFILTRATION CAPACITY OF THREE-DIAMOND PAVER TYPE IN LOW RAINFALL INTENSITY Jeanely Rangkang, Lawalenna Samang, Sakti Adji Adisasmita and Muralia Hustim	685
8189	HYDROLOGICAL CHARACTERISTICS AND WATER MANAGEMENT IN THE AIR SUGIHAN SUB-RIVER BASIN, SOUTH SUMATERA, INDONESIA Wijaya Mardiansyah, M. Yusup Nur Khakim, Dedi Setiabudidaya, Satria J. Priatna and Iskhaq Iskandar	691
8197	CONCENTRATIONS OF METAL(LOID)S IN OUTDOOR AND INDOOR DUST FROM RUSSIAN CITY T.G. Krupnova, I.V. Mashkova, S.V. Gavrilkina, E.D. Scalev and N.O. Egorov	697
8201	EFFICIENT REPAIR SCHEDULING STRATEGY OF A MULTIPLE-SOURCE LIFELINE NETWORK USING CONSTRAINED SPANNING FOREST (CSF) Lessandro Estelito Garciano, Agnes Garciano, Mark Tolentino and Abraham Matthew Carandang	705
8211	PHYSIO-ECOLOGICAL ACTIVITY OF PHRAGMITES JAPONICA AS A GREEN INFRASTRUCTURE PLANT Taizo Uchida, Teruo Arase, Yohei Sato and Daisuke Hayasaka	712
8212	SOIL QUALITY INDEX ANALYSIS UNDER HORTICULTURAL FARMING IN SUMANI UPPER WATERSHED Aprisal, Bambang Istijono, Juniarti and Mimin Harianti	718
8215	THE EFFECT OF REBAR IN A SHORT HEIGHT CONCRETE WALL FOR THE ULTIMATE LATERAL STRENGTH Tetsuya Ohmura, Dong Hesong, Kyouhei Iwasaki and Mamoru Kawasaki	724
8217	FORECAST OF PRODUCTIVE AND BIOLOGICAL EFFECTS OF METAL NANOPARTICLES ACCORDING TO TOLERANCE INDEX Elena Sizova, Sergey Miroshnikov, Nikolai Balakirev	731
8218	3D MODEL-BASED IMAGE REGISTRATION FOR CHANGE DETECTION IN HISTORICAL STRUCTURES VIA UNMANNED AERIAL VEHICLE Apichat Buatik and Krisada Chaiyasarn	739
8220	DEFECT-DRIVEN DEVELOPMENT: A NEW SOFTWARE DEVELOPMENT MODEL FOR BEGINNERS Wacharapong Nachiangmai, Sakgasit Ramingwong and Kenneth Cosh	746
8234	DEVELOPMENT OF ASSESSMENT FOR POTENTIALLY TOXIC ELEMENT CONTAMINATION INDICATOR IN CLOSED LANDFILLS AND PROSPECTIVE GEOSTATISTICAL ANALYSIS Azizi Abu Bakar, Minoru Yoneda, Nguyen Thi Thuong and Noor Zalina Mahmood	753
8238	EVALUATING POSSIBLE AVENUES FOR SOIL IMPROVEMENT BY BIOCEMENTATION IN SRI LANKA: A PRELIMINARY INVESTIGATION P.G.N. Nayanthara, A.B.N. Dassanayake, Kazunori Nakashima and Satoru Kawasaki	759
8242	BUILDING MASS RAIL TRANSIT IN KUALA LUMPUR: IS IT GOOD TRANSPORT ECONOMICS? Hamid AHA, Tabassi AA and Samsurijan MS	765
8243	UNDERSTANDING OF FIRE DISTRIBUTION IN THE SOUTH SUMATRA PEAT AREA DURING THE LAST TWO DECADES Raden Putra, Edy Sutriyono, Sabaruddin and Iskhaq Iskandar	769
8244	PADDY FIELD MAPPING USING UAV MULTI-SPECTRAL IMAGERY Rokhmatuloh, Supriatna, Tjong Giok Pin, Ronni Ardhianto, Oka Setiawan, Iqbal Putut Ash Shidiq, Adi Wibowo and Riza Putera	775

8246	SUITABILITY ANALYSIS OF SEAWEED (<i>Eucheuma cottonii</i>) BASED ON ENSO VARIABILITY IN AMAL COAST, TARAKAN ISLAND, INDONESIA Dewi Susiloningtyas, Tuty Handayani and Della Ayu Lestari	780
8251	SEISMIC RELIABILITY ANALYSIS OF LIFELINE: A CASE STUDY ON THE WATER NETWORK SYSTEM OF BIÑAN CITY, LAGUNA Rainier Lawrence A. Valdez, Lessandro Estelito O. Garciano and Takeshi Koike	787
8253	PASSENGER BEHAVIORAL MAPPING AND STATION FACILITIES DESIGN AT COMMUTER LINE TRAIN STATION (CASE: TANGERANG STATION, INDONESIA) Ahmad Zubair, Lita Sari Barus and Jachrizal Soemabrata	793
8254	PHYSICAL ANALYSIS CONDITIONS AROUND MRT STATION TO BE A TRANSIT ORIENTED DEVELOPMENT AREA BY SOME INDICATORS (CASE STUDY: LEBAK BULUS MRT STATION, SOUTH JAKARTA, INDONESIA) Doddy Apriansyah, Lita Sari Barus, Ahmad Zubair, H. Andi Simarmata, Jachrizal Sumabrata	799
8256	IMPACT OF 2016 WEAK LA NIÑA MODOKI EVENT OVER THE INDONESIAN REGION Deni Okta Lestari, Edy Sutriyono, Sabaruddin, and Iskhaq Iskandar	805
8257	DEVELOPMENT OF RISK EVALUATION METHOD CONSIDERING AFTERSHOCKS Sei'ichiro Fukushima, Hiroyuki Watabe and Harumi Yashiro	811
8260	THE EFFECTS OF TRANSFLUTHRIN AS THE ACTIVE SUBSTANCE OF ONE PUSH AEROSOL REPELLENT ON ORGANS DAMAGE OF MICE (<i>MUS MUSCULUS</i>) (CASE STUDY OF LUNG, LIVER, BLOODS, AND KIDNEY) Unggul P. Juswono, Arinto Y. P. Wardoyo, Chomsin S. Widodo, and Johan A. E. Noor	817
8267	INTEGRATION OF SPATIAL CHARACTERISTIC TO HEALTH SERVICES: A CASE STUDY OF CHILDREN HEALTH IMPROVEMENT COMPARE TO THE ENVIRONMENTAL MANAGEMENT AT DEPOK CITY SCALE- INDONESIA Irene Sondang Fitrinitia, Esty Suyanti, Purnawan Junadi, Hardya Gustada	823
8270	EVALUATION OF DRAINAGE PROCESS IN POROUS MEDIA BY INVADED PERCOLATION PROBABILITY Junichiro Takeuchi and Masayuki Fujihara	829
8272	DAMAGE DETECTION AND LOCALIZATION IN MASONRY STRUCTURE USING FASTER REGION CONVOLUTIONAL NETWORKS Luqman Ali, Wasif Khan and Krisada Chaiyasarn	835
8273	TEMPORAL CHANGES OF SESIMIC LOADS USING PROBABILISTIC SEISMIC HAZARD ANALYSIS WITH A RENEWAL PROCESS Takayuki Hayashi and Harumi Yashiro	842
8281	THE ASSOCIATION AND DISSOCIATION OF ENVIRONMENTALLY SIGNIFICANT MINERALS ON STRENGTH PROPERTIES OF SEDIMENTS IN OCEAN ENVIRONMENT J.Rajaraman, PhD, S.Narasimha Rao, PhD	848
8286	CFD IMPACT OF AIR POLLUTION AND ITS MULTIFARIOUS ADVANTAGES (CASE: SUDIRMAN-THAMRIN STREET, JAKARTA) Heidy Octaviani Rachman and Lita Sari Barus	855
8287	SPATIO-TEMPORAL ANALYSIS OF RICE FIELD PHENOLOGY USING SENTINEL-1 IMAGE IN KARAWANG REGENCY, WEST JAVA, INDONESIA Supriatna, Rokhmatuloh, Adi Wibowo, Iqbal Putut Ash Shidiq, Glen Putra Pratama and Laju Gandharum	860
8297	DEVELOPMENT OF GREEN INFRASTRUCTURE IN URBAN CATCHMENT AREA (CASE STUDY: TANJUNG BARAT SUB-DISTRICT, SOUTH JAKARTA) Dimas Ario Nugroho, Jachrizal Soemabrata, Hendricus Andy Simarmata, Dwinanti Rika Marthanty	865
8300	REMOVAL OF ACID ORANGE II DYE BY GRANITIC NANO-ZERO VALENT IRON (nZVI) COMPOSITE Nur 'Aishah Zarime, Wan Zuhairi Wan Yaacob and Habibah Jamil	871
8301	INFLUENCE OF RAILINGS STIFFNESS ON WHEEL LOAD DISTRIBUTION IN THREE- AND FOUR-LANE CONCRETE SLAB BRIDGES Ghassan Fawaz, Mohammad Abou Nouh, Mounir Mabsout, and Kassim Tarhini	879

8307	INFLUENCE OF DIESEL OIL CONTAMINANTS ON GGBS BLENDED WITH BENTONITE AND LATERITIC SOIL AS LINERS Devarangadi Manikanta, Uma Shankar M, B.R. Phanikumar	885
8313	IS WATER AVAILABLE IN THE PUBLIC PLACES SAFE TO DRINK IN BANGLADESH? Ijj Mahmod Chowdhury, Istiakur Rahman, Sk. Sadman Sakib, Kazi Ismile Hossain and Shoumic Shahid Chowdhury	890
8314	A STUDY TO IMPROVE THE WATER QUALITY PARAMETRS OF THREE MAJOR RIVERS SURROUNDING THE CAPITAL CITY OF BANGLADESH THROUGH COAGULATION Istiakur Rahman, Sk. Sadman Sakib, Md. Rezoan Khan Nafiz, Shadman Alam, Md. Rwanakul Islam Chowdhury	896
8340	EXPERIMENTAL STUDY FOR EVALUATING THE SEISMIC PERFORMANCE OF RC FRAME STRUCTURE WITH PARTIALLY INFILLED BY BRICK MASONRY Jafri Tanjung, Febrin Anas Ismail, Oscar Fithrah Nur, Maidiawati, Hamdeni Medriosa and Mahlil	902
8342	CORAL REEFS DEGRADATION PATTERN AND ITS EXPOSURE TOWARDS CLIMATE CHANGE IN BUNAKEN NATIONAL PARK Nafil Rabbani Attamimi, Ratna Saraswati	908
8162	ROLE DIFFERENCE AMONG RIVERS AFFECTED BY VOLCANIC ACTIVITIES OF MT. ONTAKE FOR WATER QUALITY OF THE NIGORIGAWA RIVER Akiko Usami, Yoshitaka Matsumoto, Megumi Nobori, Akihiko Yagi and Eiji Iwatsuki	914
8183	COMPRESSIVE LOADING TEST OF STEEL PILE TOP FILLED WITH CONCRETE Mutsuki Sato, Toshiharu Hirose and Yoshihiro Kimura	920
8190	INFLUENCE OF FLOODS ON THE INCLINATION OF STUPAS IN AYUTTHAYA, THAILAND Yuko Ishida, Ayaka Oya, Weerakaset Suanpaga, Chalemnchai Trakulphudphong, Chaweewan Denpaiboon and Ryoichi Fukagawa	926
8260	THE EFFECTS OF TRANSLUTHRIN AS THE ACTIVE SUBSTANCE OF ONE PUSH AEROSOL REPELLENT ON ORGANS DAMAGE OF MICE (MUS MUSCULUS) (CASE STUDY OF LUNG, LIVER, BLOODS, AND KIDNEY) Unggul P. Juswono, Arinto Y. P. Wardoyo, Chomsin S. Widodo, and Johan A. E. Noor	932
8227	DEVELOPMENT OF THE DEFORMATION MONITORING SYSTEM WITH WIRELESS SENSOR NETWORK AND EVALUATION OF MECHANICAL STABILITY FOR DAMAGED STONEWALLS BY HUGE EARTHQUAKE IN KUMAMOTO CASTLE Yuuya KATSUDA, Satoshi SUGIMOTO, Yoichi ISHIZUKA, Shohei IWASAKI, Ryoma TAKAESU, Koichiro YAMASHITA, Minoru YAMANAKA	<u>938</u>

Preface

On behalf of the GEOMATE 2018 Organizing Committee, we would like to welcome you in attending the International Conference on Geotechnique, Construction Materials and Environment held at the Istana Hotel, Kuala Lumpur, Malaysia in conjunction with School of Graduate Studies, University Putra Malaysia, Monash University, Malaysia, Mie University Research Center for Environmental Load Reduction, The GEOMATE International Society, Useful Plant Spread Society, Glorious International, AOI Engineering, HOJUN, JCK, CosmoWinds and Beppu Construction, Japan.

On Friday 11 March 2011, at 14:46 Japan Standard Time, the northeast of Japan was struck and severely damaged by a series of powerful earthquakes which also caused a major tsunami. This conference was first dedicated to the tragic victims of the Tohoku-Kanto earthquake and tsunami disasters. The Geomate 2018 conference covers three major themes with 17 specific themes including:

- | | |
|---|---|
| • Advances in Composite Materials | • Ecology and Land Development |
| • Computational Mechanics | • Water Resources Planning |
| • Foundation and Retaining Walls | • Environmental Management |
| • Slope Stability | • Public Health and Rehabilitation |
| • Soil Dynamics | • Earthquake and Tsunami Issues |
| • Soil-Structure Interaction | • Safety and Reliability |
| • Pavement Technology | • Geo-Hazard Mitigation |
| • Tunnels and Anchors | • Case History and Practical Experience |
| • Site Investigation and Rehabilitation | |

Alike earlier conferences, this year we have received many paper submissions from different countries all over the world, including Australia, Bank Receipt, Czech Republic, India, Indonesia, Japan, Malaysia, Oman, Philippines, Russia, Switzerland, Tajikistan, Thailand, Tunisia, United Kingdom, United States, and Vietnam. The technical papers were selected from the vast number of contributions submitted after a review of the abstracts. The final papers in the proceedings have been peer reviewed rigorously and revised as necessary by the authors. It relies on the solid cooperation of numerous people to organize a conference of this size. Hence, we appreciate everyone who supports as well as participate in this joint conferences.

Last but not least, we would like to express our gratitude to all the authors, session chairs, reviewers, participants, institutions and companies for their contribution to GEOMATE 2018. We hope you enjoy the conference and find this experience inspiring and helpful in your professional field. We look forward to seeing you at our upcoming conference next year.

Best regards,

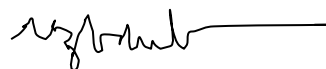
Prof. Bujang B.K. Huat, University Putra Malaysia (Program)



Prof. Zakaria Hossain, Prof. Mie University, Japan (General)



Dr. Vivi Anggraini, Monash University Malaysia (Co-Chair)



Dr. Jim Shiau, University of Southern Queensland, Australia (Assistant to Chairman)



Organization

Conference Honorary Chairmen:

Emeritus Professor Dr. Sohji Inoue, Mie University, Japan
Emeritus Professor Dr. Teruo Nakai, Nagoya Institute of Technology, Japan
Emeritus Professor Dr. Fusao Oka, Kyoto University, Japan

Scientific Committees:

Conference Chairmen:

Prof. Dr. Bujang B.K. Huat, Univ. Putra Malaysia (Program)
Dr. Zakaria Hossain, Prof. Mie University, Japan (General)
Conference General Secretay:
A/Prof. Dr. Shinya Inazumi, Shibaura Ins. of Tech., Japan

Conference Organizing Committee:

Prof. Dr. Bujang B.K. Huat, University Putra Malaysia (Chair)
Prof. Dr. Zakaria Hossain, Mie Univrsity, Japan (Chair)
Dr. Jim Shiau, USQ, Australia (Assiatant to General Chair)
Prof. Dr. Aminaton Marto, UTM, Malaysia (Co-Chair)
Prof. Dr. A.S.M. Abdul Awal, UTHM, Malaysia (Co-Chair)
Prof. Dr. Hj. Ramli Nazir, UTM, Malaysia (Co-Chair)
Prof. Dr. M Ibn Ibrahimy, Prof., Int. Islamic Univ. (Co-Chair)
Prof. Dr. Toshinori Sakai, Mie University, Japan (Co-Chair)
Prof. Dr. Takamitsu Kajisa, Mie University, Japan (Co-Chair)
A/Prof. Dr. Masaaki Kondo, Mie University, Japan (Co-Chair)
Dr. Zainuddin Md. Yusoff, Senior Lecturer, UPM (Co-Chair)
Dr. Haslinda Nahazanan, Senior Lecturer, UPM (Co-Chair)
Dr. Vivi Anggraini, Lecturer, Monash Uni Malaysia (Co-Chair)

National & International Advisory Committee:

Dr. Fumio Tatsuoka, Prof., Tokyo University of Science, Japan
Dr. Junichiro Takeuchi, Prof., Kyoto University, Japan
Dr. Kingshuk Roy, Prof., Nihon University, Japan
Dr. Sai Vanapalli, Prof., University of Ottawa, Canada
Dr. Musharraf Zaman, Prof. Univ. of Oklahama, USA
Dr. Rafiqul Tarefder, Prof. University of New Mexico, USA
Dr. M. Bouassida, Prof., National Sch. of Engg. of Tunis
Dr. L.R. Austriaco, Prof., Angles Univ. Found., Philippines
Dr. A.S.M. Abdul Awal, Prof., UTHM, Malaysia
Dr. M. Ibn Ibrahimy, Prof., Int. Islamic Univ., Malaysia
Dr. Bujang B.K. Huat, Prof., Univ. Putra Malaysia
Dr. Nemy Banthia, Prof., Univ. of British Columbia, Canada

Dr. Ian Jefferson, Prof., Univ. of Birmingham, UK
 Dr. John Bolander, Prof., Univ. of California, USA
 Dr. Shamsul Chowdhury, Prof., Roosevelt Univ., USA
 Dr. Isabel Pinto, Prof., University of Coimbra, Portugal
 Dr. Mark Jaksa, Prof., University of Adelaide, Australia
 Dr. Hj. Ramli Bin Hj. Nazir, A/Prof., UTM, Malaysia
 Dr. M.S. Hossain, Prof., International Islamic Univ. Bangladesh
 Dr. Suksun Horpibulsuk, Prof. Suranaree Uni of Tech, Thailand
 Dr. Muzamir Hasan, Director, CERRM, Univ. Malaysia Pahang
 Dr. Afshin Asadi, S/Lecturer, Int. College of Auckland, New Zealand

International Technical Program Committee:

Prof. Sai Vanapalli, University of Ottawa, Canada
 Prof. Alaa Masoud, Tanta University, Egypt
 Prof. Aly Ahmed, Beni-Suef University, Egypt
 Prof. Aminaton Marto, Universiti Teknologi Malaysia, Malaysia
 Prof. Bandari Shankar, Osmania University, India
 Prof. Bashir Ahmed Mir, National Institute of Technology, India
 Prof. Hamidi Abdul Aziz, Universiti Sains Malaysia (USM), Malaysia
 Prof. Hussein Elarabi, University of Khartoum, Sudan
 Prof. M. Shohidullah Miah, International Univ. of Business Agriculture &Tech., Bangladesh
 Prof. Michele, Casagrande, Pontifical University Catholic of Rio De Janeiro, Brazil
 Prof. Radim Cajka, Technical University of Ostrava, Czech Republic
 Prof. Rajaraman Jambunathan, AMET University, India
 Prof. Reshma Chandran T., Global Institute of Architecture, India
 Prof. Roslan Hashim, University of Malaya, Malaysia
 Prof. Seyed Naser Moghaddas Tafreshi, K.N. Toosi University of Technology, Iran
 Prof. Valeriy Perminov, Tomsk Polytechnic University, Russia
 Prof. Quanmei Gong, Tongji University, China
 A/ Prof. Abdoullah Namdar, Sichuan University, China
 A/ Prof. Abdul Naser Abdul Ghani, Universiti Sains Malaysia, Malaysia
 A/ Prof. Alaeddinne Eljamassi, Islamic University of Gaza, Palestine
 A/ Prof. Alina Paranina, Herzen State Pedagogical University of Russia, Russia
 A/ Prof. Ashraf Elmoustafa, Ain Shams Univeristy, Egypt
 A/ Prof. Bindu C S, Cochin University of Science & Technology, India
 A/ Prof. Chee-Ming Chan, Universiti Tun Hussein Onn Malaysia, Malaysia
 A/ Prof. Chidanand Naik, Anjuman Institute of Technology and Management, India
 A/ Prof. Dahlia Hafez, Cairo University, Egypt
 A/ Prof. Deepa G Nair, Isfahan University of Technology, India
 A/ Prof. Dolrerdee Hormdee, Khon Kaen University, Thailand
 A/ Prof. Farhad Behnamfar, Isfahan University of Technology, Iran
 A/ Prof. Gabriela B. Cazacu, Geotech Dobrogea, Romania
 A/ Prof. Hadi Khabbaz, University of Technology, Sydney (UTS), Australia
 A/ Prof. Homayoon Ganji, Herat Univercity Badghis, Afghanistan
 A/ Prof. Hudson Jackson, US Coast Guard Academy, United States
 A/ Prof. Inazumi Shinya, National Institute of Technology, Akashi, Japan
 A/ Prof. John Smith, RMIT University, Australia
 A/ Prof. Kasinathan Muthukkumaran, National Institute of Technology, India
 A/ Prof. Lindrianasari Lindrianasari, Universitas Lampung, Indonesia
 A/ Prof. Mahdi Karkush, Baghdad University, Iraq
 A/ Prof. Mohamed Redha Menani, Batna University, Algeria
 A/ Prof. Navid Khayat, Ahvaz Branch, Islamic Azad University, Iran
 A/ Prof. Salam, Bash AlMaliky, AlMustansiriya University, Iraq
 A/ Prof. Shailesh Kumar Jha, Indian Institute of Technology, India
 A/Prof. Teodor Lucian Grigorie, University of Craiova, Romania
 A/Prof. Pares Dalal, Shri Vitthalrao Shankarrao Naik Arts, Commerce and Science College, India
 A/Prof. Muhammad Qasim, Abdul Wali Khan University Mardan, Pakistan

A/Prof. R. S. Ajin, GeoVin Solutions Pvt. Ltd., India
 Dr. Abdul Karim M. Zein, University of Khartoum, Sudan
 Dr. Abdull Halim Abdul, Universiti Teknologi MARA, Malaysia
 Dr. Afshin Asadi, University Putra Malaysia, Malaysia
 Dr. Ahmad Safuan A Rashid, Univeristi Teknologi Malaysia, Malaysia
 Dr. Ahmad Safuan Bin A Rashid, Univeristi Teknologi Malaysia, Malaysia
 Dr. Akindele Okewale, Federal University of Petroleum Resources, Nigeria
 Dr. Akinola Johnson Olarewaju, Federal Polytechnic Ilaro, Nigeria
 Dr. Ali Sobhanmanesh, Universiti Teknologi Malaysia (UTM), Malaysia
 Dr. Alireza Bahiraie, Semnan University, Iran
 Dr. Allan Manalo, Centre of Excellence in Engineered Fibre Composites, Australia
 Dr. Aniza Ibrahim, National Defence University of Malaysia, Malaysia
 Dr. Arif Ali Baig Moghal, King Saud University, Saudi Arabia
 Dr. Aslan S. Hokmabadi, University of Technology, Sydney (UTS), Australia
 Dr. Ather Ashraf, PUCIT, Old Campus Punjab University, Pakistan
 Dr. Atsuko Sato, Cical Engineering Research Institute for Cold Region, Japan
 Dr. Ben-Hur Silva, Military Institute of Engineering, United States
 Dr. Choy Soon Tan, Univeristi Teknologi Malaysia, Malaysia
 Dr. David Thorpe, University of Southern Queensland, Australia
 Dr. Delsye Ching Lee Teo, Universiti Malaysia Sarawak, Malaysia
 Dr. Domenico Lombardi, University of Manchester, United Kingdom
 Dr. Ehsan, Jorat Newcastle University, United Kingdom
 Dr. Ganesh Kumar Shanmugam, National Institute of Ocean Technology, India
 Dr. Helsin Wang, Institute of Bridge Engineering, Taiwan
 Dr. Hossein Moayed, Kermanshah University of Technology, Iran
 Dr. Hossein MolaAbasi, Babol University of Technology, Iran
 Dr. James Hambleton, University of Newcastle, Australia
 Dr. James Hambleton, University of Newcastle, Australia
 Dr. Janaka Kumara, Tokyo University of Science, Japan
 Dr. Jirayut, Suebsuk Rajamangala University of Technology Isan, Thailand
 Dr. Juhung Lee, Korea Institute of Civil Engineering and Building Technology, South Korea
 Dr. Jun Sugawara, Advision - WorleyParsons Group, Australia
 Dr. Lamia Touiti Bouebdellah, Ecole Nationale d'Ingénieurs de Gabes, Tunisia
 Dr. Luky Handoko, Universitas Atma Jaya Yogyakarta, Indonesia
 Dr. M. Mohammad Ali, California Public Utilities Commission, United States
 Dr. Marfiah Ab.Wahid, Universiti Teknologi Mara, Malaysia
 Dr. Maryam Naeimi, Semnan University, Iran
 Dr. Mehdi Mokhberi, Islamic Azad University, Shiraz, Iran
 Dr. Mohd Hairy Ibrahim, Sultan Idris Education University, Malaysia
 Dr. Neelima Satyam, International Institute of Information Technology, India
 Dr. Nor Zurairahetty Mohd Yunus, Univeristi Teknologi Malaysia, Malaysia
 Dr. Siavash Zamiran, Southern Illinois University Carbondale, United States
 Dr. Subha Vishnudas, Cochin University of Science and Technology, India
 Dr. Sunggi Jin, SK E&C, South Korea
 Dr. Sunil Pusadkar, Govt. College of Engineering, Amravati, India
 Dr. Teresa Lopez-Lara, Universidad Autonoma De Queretaro, Mexico
 Dr. Usama Juniansyah Fauzi, University of Tokyo, Japan
 Dr. Yusep Muslih Purwana, Sebelas Maret University, Indonesia
 Dr. Ana Almerich-Chulia, Universitat Politècnica de Valencia, Spain
 Dr. Khor Shing Phan, Universiti Malaysia Perlis, Malaysia
 Dr. Afshin Asadi, International College of Auckland, New Zealand

Conference Correspondence:

Prof. Dr. Zakaria Hossain, Conference Chairman,
Dept. of Env. Sci. & Tech., Mie University, Japan,
Dr. Vivi Anggraini, Lecturer, Monash Uni Malaysia (Co-Chair)
Dr. Shinya Inazumi, General Secretary
A/Prof. National Ins. of Tech., Akashi, Japan
E-mail: conference@geomate.org
Tel & Fax: +81-59-231-9578

Editorial Committee and Executive Committee:

Prof. Bujang B.K. Huat, University Putra Malaysia
Prof. Zakaria Hossain, Prof. Mie University, Japan
Dr. Vivi Anggraini, Monash University Malaysia
Dr. Jim Shiau, University of Southern Queensland, Australia
Dr. Sinya Inazumi

Keynote Papers

AN APPLICATION OF SCREW DRIVING SOUNDING TEST TO A SURVEY ON LIQUEFACTION POTENTIAL

Naoaki Suemasa

Department of Civil and Urban Engineering, Tokyo City University, Japan

ABSTRACT:

In geotechnical engineering, ground information is quite important especially for piling works, ground improvement or prevention of disaster. A lack of the information would lead to unsuspected settlement of a structure or increasing the disaster damage. Information from boring logs is provided in many cases of construction. It is quite reliable but always ungratified in volume, and cannot be expected to be added because of the limitation of construction cost. Alternatively, interpolation of their information may be required in some way such as adding sounding tests.

In this presentation, a new sounding method, named Screw Drive Sounding, is introduced. The approach to soil classification is different from other sounding tests such as CPT and SPT. The methods of testing and interpreting the results are explained. As an application of the test, the survey on liquefaction damage is reported.

GEOTECHNICAL CHARACTERIZATION OF PEAT DEPOSIT IN JAPAN

Hirochika Hayashi
Civil Engineering Research Institute for Cold Region (CERI), Japan

ABSTRACT

Peat is a highly organic soil composed of the remains of plants that grew in swamps and remained there without fully decomposing due to low temperatures and wet conditions. Peat is a soft soil with special engineering properties, such as very high compressibility and very low shear strength. When an embankment or a structure is constructed on peat deposit, these special engineering properties cause geotechnical-engineering problems, including failure and settlement of the ground. Peat deposit is widely distributed in the cold regions of North America, Europe and Asia including Japan, as well as in Southeast Asian countries such as Indonesia and Malaysia. In Japan, peat with wide engineering properties are found. .

This keynote talk delivers overview of peat deposit in Japan and its geotechnical characterization. In the overview, peat distribution and some problems of construction project are presented. Next, in the geotechnical characterization, physical index, compressibility, permeability, shear strength and stiffness are described.

Keywords: Peat Physical index Compressibility Permeability Shear strength

Technical Papers

Geotechnique

PULL-OUT RESISTANCE OF SINGLE PILES AND PARAMETRIC STUDY BASED ON NUMERICAL SIMULATION APPROACH(FDM) USING FLAC2D

Alex Otieno Owino¹, Zakaria Hossain¹, Jim Shiau²

¹Dept. of Environmental Science Graduate School of Bioresources, Mie University, Japan

²School of Civil Engineering and Surveying, University of Southern Queensland, Queensland, Australia

ABSTRACT

Many engineering structures both above ground and under the ground surface are subject to forces that create overturning moments upon them. In this study, the structure under consideration is the single pile foundation structure of solar panels. Increasing demand for clean energy is pushing for more economical means of constructing such structures with maximum evaluation focused on the cost of installation and the ultimate strength of the fully loaded structure hence single piles come into place. As studied in the previous paper on the design of the pile element, dimensions of $1.4m$ pile foundation length and $0.26m$ diameter are also employed in this paper to determine the pull-out capacity. Strength evaluation is done through numerical simulation using FLAC2D which use the finite difference method to evaluate the input codes in step by step manner while integrating the input parameters in a stress strain relation as described in the pull-out code. The dimensions of the model mesh are twice the pile foundation depth, $2L$ in the y -direction and $2L$ in the x -direction from the pile vertical axis. Strength evaluation is done on sandy, clay and silty medium to determine the vast array of data for engineering design measures. A parametric study is then done by varying the foundation depth from $0.7m$ to $2.0m$, soil angle of internal friction from 10° to 40° and the inclusivity of gap upon failure. The design dimensions show good bearing capacity with load up to $94kN$, $90kN$ and $80kN$ for dense sand, silty soil and clay soil respectively. The suggested relations for the pull-out capacity of the single pile regarding the axial ability are within design limits.

Keywords: Pull-out capacity, Skin friction, Finite difference method, Stress-strain relation, FLAC2D

INTRODUCTION

Pile foundations are commonly used in support of engineering structures to prevent them from overturning moments produced by winds and earthquakes in most cases. To understand how piles, transmit the loads to the ground, several experiments are necessary before construction. In literature, the pull-out capacity of pile foundations has been carried out in a few studies most of which employ full-scale field experiments. In the previous research [1] it was suggested that static cone penetration test can be used in the estimation of the pile ultimate lifting capacity with the most determining factor being the uplift skin friction. The value obtained however needed some adjustments which led to the introduction of the reduction factor which was highly dependent on the soil type and the type of pile used in the construction and reduction values on the uplift load if the force was oscillating.

A large-scale experimental set up in [2] focused on the analysis of the pull-out loads. Their experiment was mainly based on fixed pile dimension installed in soft moist silty to fine clayey sand. The results obtained were used in the formulation of the equation: $P_u = \pi d L/2 (KL \tan \theta + 2c)$ where K represented the coefficient of lateral earth pressure. However, their approach reflected the effect of type of casing and method of backfilling on the uplift capacity.

In accordance to the fact that the uplift capacity of

the pile is dependent on the relative skin friction on the pile-soil interface, Sowa (1970), analysis on the field tests on cast piles depicted that the coefficient of the earth pressure was considerably less during loading than the ratio of earth pressure at rest and Rankine's active earth pressure coefficient. Due to this variation, it was perverse to set value during the preliminary design [3].

To counter the fluctuation of the earth pressure coefficient, Meyerhof [4], introduced the uplift coefficient in place of the factor of earth pressure. For a pile installed at an angle of shearing resistance θ , the uplift coefficient increased with the increase in the slenderness ratio L/d up to a maximum value, then remained constant. However, the limiting factor was shown to increase with an increase in angle of shearing resistance.

McClelland [5], demonstrated the effects of installation on the uplift capacity of piles by field tests on same steel pipe piles of diameter 508 mm installed to penetration of $14.63m$ in uniform beach sand by four different techniques. The driven pile exhibited net uplift capacity, which was 1.4 times that of a pile installed by jetting with external return flow. He concluded that the ultimate shaft resistance was dependent on the methods of driving/installation.

More research in [6], suggested the evaluation of the ultimate loading capacity of the piles was by the assessment of the skin friction along the pile and soil interface and the bearing pressure along the perimeter

of the pile. Using this proposed approach, the ultimate bearing capacity became a function of the diameter of the pile, d , depth of the center of the first under-reamed bulb, d_1 , thickness of the center of the last under-reamed bulb, d_n , diameter of the under-reamed bulb, B_1 , number of under-reamed bulb, n , coefficient of earth pressure and the bearing capacity depending on the angle in friction. This relationship is as shown in Eqn. 1

$$Q = \pi/2dk_y \tan \theta (d_1^2 + L^2 + d_n^2) + \pi/4(B_1^2 - d^2) (1/2n\gamma B_1 N_\gamma + \gamma N_\gamma + N_q d_1) \quad (1)$$

The effects of pull-out load on piles were further analysed with the coexisting relations to the stress-strain relations [7]. This analysis was done in frozen sandy soils, and the stress-strain relationship proved to be linear. This approach was found to apply to the short pile only installed in moderately to densely over-consolidated clay soils hence a limiting factor in the predesign considering the fluctuating soil layers. The study further showed that during the loading process, the deformation of the earth along the pile perimeter acted similarly as the shearing of concentric cylinders hence the linearity in the stress and strain relations.

In the process of determining the pile failure mechanism, Kulhawy [8], came up with a general analytical model for the drained uplift capacity of drilled pile foundations. The main aim was to establish the main determining variables that will lead to the calculation of the ultimate loading capacity that produced the pile failure pattern. From his study, the uplift capacity, Q_u was a function of the foundation weight, W , pile tip resistance, Q_{tu} , pile side resistance, Q_{su} , length of the pile, D , and the shearing resistance along a general shear surface as shown in Fig.1.

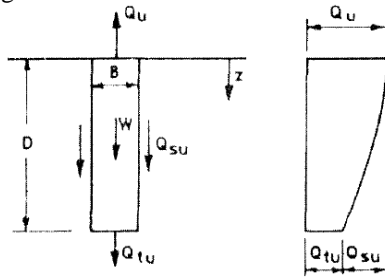


Fig. 1 Uplift capacity function and the failure pattern by Kulhawy

Following these essential researches on the pile foundations, several experimental models have been developed to have an understanding of the pile-soil interaction during loading. These include the effects of repeated loading on the drained uplift capacity of the piles in granular soils [9] so as to examine the influence of the soil density and the pile diameter on the mechanism of the drilled shaft resistance, a study on the effects of straight piles and the piles with

enlarged bases and roughness variation on the uplift capacity [10], and a study on the reaction of single piles embedded in layered sand under inclined pulling loads. The most recent researches have involved the development of scaled physical models [12], to study the responses of pile groups under uplift loads and an analytical method to predict the uplift capacity of the pile under study and, model tests on tabular steel tubes to analyse the effects of compressive load on the uplift capacity [13].

This study engages the use of numerical modelling to establish the foundation reaction concerning the uplift or pull-out loading. The numerical model uses the finite difference method embedded into the FLAC2D software to assess and computes the variation of the different input parameters, to obtain the desired output on pile performance. The reckoning is achieved mainly by the simulation of the stresses and the strains developed in the model grid during deformation by the applied corresponding velocities of the uplift load.

MODELLING TECHNIQUE

A numerical approach is a vital tool in the close examination of soil behaviour under complex ground conditions. To obtain these critical results a finite element analysis mesh to replicate the real problem [14] is necessary as shown in Fig. 2.

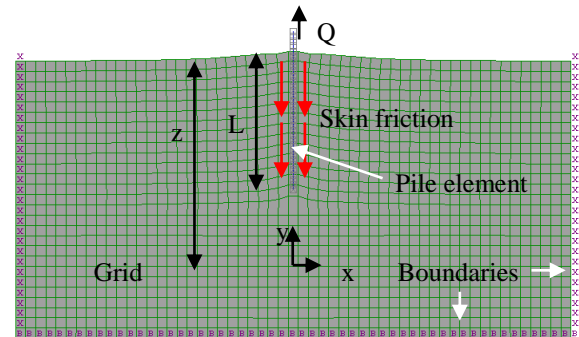


Fig. 2 Generated mesh, boundary conditions and the pile element

This mesh places all the parameters to be input into the FLAC2D domain considering the pile and the soil interaction and the desired output. FLAC2D software then employs the Finite difference codes to provide a step by step integration of the input parameters for time and the set loading velocity. The products of the combination are summed up in the plane-strain mode which places the pile as a wall extending out of the plane of the cross-section (grid). FLAC2D, therefore, calculates the vertical stresses which are representative of the skin friction along the pile and the grid (soil) interface. These stress calculations are computed by the FISH function embedded in FLAC2D within all the zonal centroids in the model grid which is a representative of the soil component. Considering the forces represented in Fig. 1, the calculated vertical stresses, σ_{yy} in the axial

direction, can be described theoretically as shown in Eqn. 2 for $y_y \geq z-L$ and Eqn. 3 for $y_y \leq z-L$. Where y_y is the vertical displacement, z is the depth of the overburden soil layer, L is the length of the pile and x is the horizontal displacement

$$\sigma_{yy} = Q/\pi L \left(\ln \frac{x^2}{(z-y)^2+x^2} + \frac{(z-y)^2}{(z-y)^2+x^2} \right) \quad (2)$$

$$\sigma_{yy} = Q/\pi L \left(\frac{\ln \frac{(z-L-y)^2+x^2}{(z-y)^2+x^2} + \frac{x^2}{(z-L-y)^2+x^2}}{\frac{x^2}{(z-L-y)^2+x^2} + \frac{x^2}{(z-y)^2+x^2}} \right) \quad (3)$$

Ones all the input parameters and coded into the program, numerical stepping is therefore initiated, and the results obtained analysed and plotted to capture the relationship between the axial/pull-out load and the vertical displacement. Also, the deformation of the grid/soil, the stress and strain concentrations and directions on the grid, bending moments on the pile and shear plane of failure as discussed in the next chapter.

RESULTS AND DISCUSSION

In this paper, the finite difference numerical method is used to analyse the interaction of the pile element and the soil element. This analysis is done by the presentation of the corresponding pile head displacement curves during axial loading together with a comprehensive parametric study to show a particular design phenomenon. The analysis, therefore, helps engineers in project optimisation while maintaining good foundation strength.

Figure 3 represents the loading characteristics of the pile element under different grid mediums. The pile element is simulated in three types of soils namely, clay soils, silty soils and dense sandy soils. The pile head displacement curves show that sandy soils bear the most robust load handling capacity with maximum axial loads up to 94kN at minimal axial pile head displacements of 10mm. Silty soils and clay soils attain values of 90kN and 80kN respectively at 10mm axial pile head displacements.

FLAC2D provides a visual display of the soil movements during axial loading as shown in Fig. 4. The deformations on the grid show a high upward movement of the overburden soil around the pile and grid interface and this movement reduces as the distance from the centre of the pile element increases. This upward movement of the media is due to the vertical stress produced around the pile element due to the skin friction. In the process of axial loading, the load is transferred through the specified media by uniform skin friction hence the increment in symmetrical deformation. This symmetry is shown in Fig.5 which represents the contour map of the effective stress on both sides of the pile elements. The stresses recorded in the grid range from -3E04 to

4E04 N with the intensities demarcated by the colour coding, where light blue and red show the areas that experience maximum stresses and minimum stresses respectively.

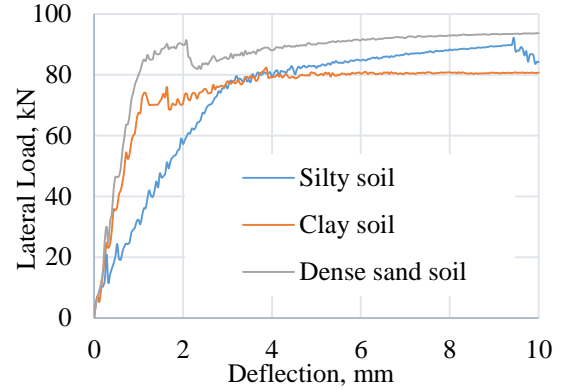


Fig. 3 pile head displacements at different axial loads

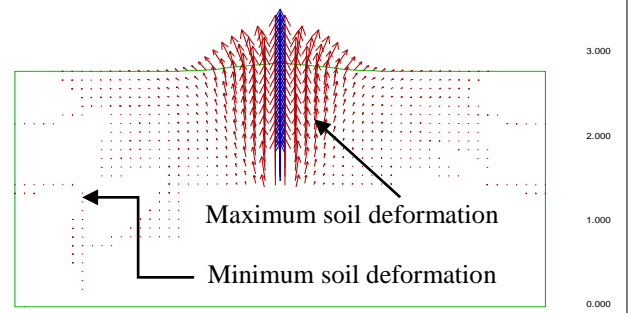


Fig. 4 Ground movements during axial loading

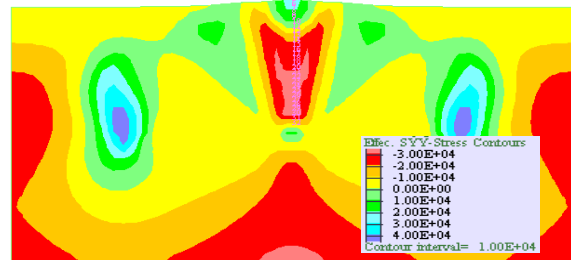


Fig. 5 Contour zone for effective stress distribution on the grid

Figure 6 represents an in-depth view of the distribution of the principal stress tensors in the network during axial loading. It is evident that extreme stresses are felt around the pile/grid interface close to the ground surface and symmetrically deep into the grid at points that act as the hinges to the vacuum created due to the movement of the overburden weight. These high stresses are due to the high rates of grid deformations at these junctions as the pile element is pulled out. In theory, this behaviour is represented by linear springs under the axial force that is dependent on the direction of the pile element movement, in this case along the y-axis.

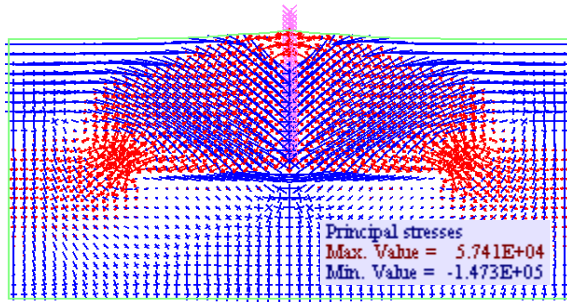


Fig. 6 Effective Principal stress tensor distribution on axial loading

To further understand the pile /grid interface, a contour view of the maximum shear strain shows the areas of high deformations as shown in Figure 7. The shear strain developed along the pile is also dependent on the cohesive strength of the pile/grid interface as well as the frictional resistance on the perimeter of the pile element. As the axial load is applied, the strain at the bottom of the pile increase up to 1.5×10^{-1} which is recorded as the highest due to the high rates of deformations on the grid.

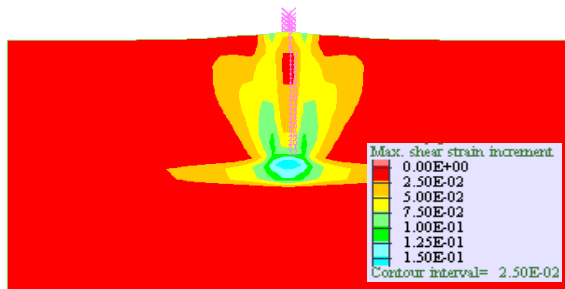
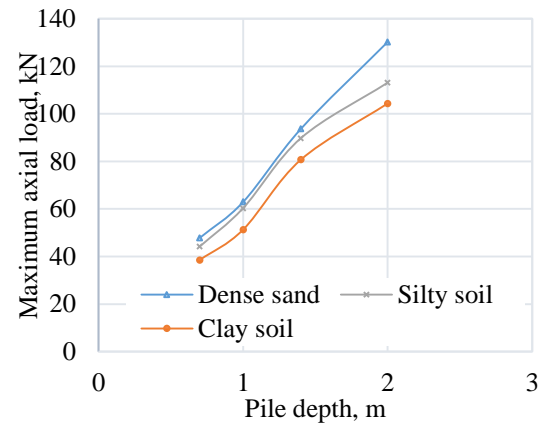


Fig. 7 Maximum shear strain increment around the pile element

PARAMETRIC STUDY

Variation of the pile foundation depth

The depth of the foundation is one of the major components that dictate the strength of the structure upon completion. This strength is due to the ability to transmit all the overburden load into the soil without any fear of structural failure. In this study, the depth of the foundation is varied in steps of 0.7m, 1.0m, 1.4m, 2.0m. From the FLAC2D output, it's evident that there is a linear relationship between the depth of the foundation and the ultimate axial load the pile can withstand before failure point. Considering the three types of soil involved in this model i.e. dense sand, silty soil and clay soil, dense sand has the highest permissible ultimate axial load of 130.22kN at 2.0m depth and the minimum allowable axial load of 38.54kN obtained from the clay soil at 0.7m depth as shown in Fig. 8.



Variation of the Angle of internal friction

The angle of internal friction is an essential parameter in the estimation of the ability of the soil to withstand the shear stresses experienced within the ground during loading. By replicating this into the input parameters of FLAC2D software, the effects of a range of the angle of internal friction gives a corresponding impact on the bearing capacity of the pile foundation. This angle is the angle measured between the normal force and the resultant force that is attained upon failure in response to the shearing stress. In this model, the angle of internal friction is analysed at 10° , 20° , 30° and 40° for silty soil, dense sand and clay soils with increasing sand component. The plot shows a curvilinear relationship with maximum values recorded at the 20° angle in internal friction. The maximum values of the ultimate axial load obtained are 93.67kN and 85.78kN for dense sand and silty soils respectively. Sandy clay depicted a dramatic reduction in bearing capacity as the angle of internal friction increased to 40° where the ultimate axial load fell to 64.23kN as shown in Fig. 9.

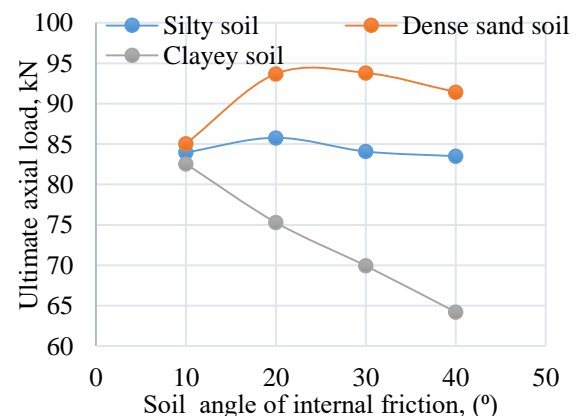


Fig. 9 Influence of the angle of internal friction of the soil

Influence of gap formation during loading

In this FLAC2D model, the interaction between the pile element and the grid can be represented by the normal and the shear coupling springs that tend to

squeeze the grid/soil medium element on to the pile element. The pressing ensures a continuous wall/medium contact. During the application of the axial load, this constant contact may be affected in a way that tends to bring in separation called the gap formation. The gap is mainly evident upon the failure of the structure itself from the ultimate load recorded. From this experiment, two formulations are taken into account that is, analysis with the expectation of gap formation and the other analysis without the gap formation. From the output, it is recorded that for sandy soil, and clay soil, the creation of gap has minimal effects on the ultimate load recorded and the differences in the pile head displacements. On the other hand, silty soils attain a higher final pressure when no gap formation is occurring than when there is no gap. The model with no gap and full gap predicts an ultimate load of 85kN and 80kN respectively as shown in Fig. 10

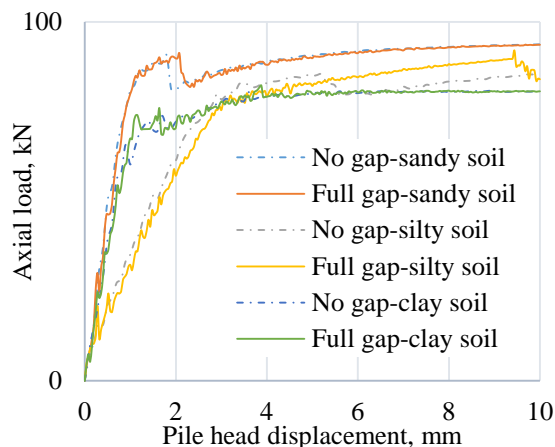


Fig. 10 Effects of the gap on the ultimate axial load

CONCLUSION

This study focused on the analysis of the pile structural element for strength and the ability to resist the axial loads subjected to it. Axial loads are the forces that tend to pull the structure of the soil medium. Such effects are due to earthquakes or winds depending on the area of the basic installation. The approach used in this paper is the numerical simulation approach using FLAC2D which employed the use of finite difference method embedded within the program to determine the shear capacity of the pile during loading. The results are a clear indication of good strength with permissible loads shooting up to slightly above 90kN. The load can withstand external forces that may be subject to the pile foundation. In this study, the pile foundation is focused on supporting the solar panels at a cheaper cost than the existing structures. The aim is also based on the economics with more emphasis on the material costs for the realisation of green energy in the developing countries. The parametric study further portrays an indication of the pile foundation

flexibility for use in a variety of soil mediums with a minimum fluctuation of the strength properties. The result is vital in giving design engineers an in-depth understanding of the new foundation approach for proposed structural developments. Further research is necessary to determine the effects of the variable shape of the piles on the ultimate bearing capacity considering the structure to be constructed.

ACKNOWLEDGEMENTS

Thanks are also to Japan International Cooperation Agency (JICA) for giving the postgraduate scholarship to the first author

REFERENCES

- [1] Begemann, H. K. S, 1965, The Maximum Pulling Force on a Single Tension Pile Calculated on the Basis of Results of the Adhesion Jacket Cone, Proc. 7th International Conference on SMFE
- [2] Downs. D. L and Chieurrzzi, R, 1966, Transmission Tower Foundations, Journal of Power Division, ASCE. Vol.92, No.2, pp. 91-114
- [3] Sowa, V. A, 1970, Pulling Capacity of Concrete Cast-In-Situ Bored Piles, Canadian Geotechnical Journal, Vol.7, pp. 482-493
- [4] Meyerhof, G. G, 1973, Uplift Resistance of Inclined Anchors and Piles, Proceedings 8th International Conference on SMFE, Moscow. Vol.2, pp. 167-173
- [5] McClelland, B, 1974, Design of Deep Penetration Piles for Ocean Structures, Journal of GTE Division, ASCE, Vol.100, pp.709-745
- [6] Sharma, B. V. R, 1988, Uplift Capacity of Anchor Piles in sand Under Axial Pulling Loads, M. Tech Thesis, Kharagpur, India
- [7] Poorooshab, H. B, and Paramesw ARAN, V. R, 1982, Uplift of Rigid Piles in Frozen Sand, Soils and Foundations, Vol.22, No.2, pp. 82-88
- [8] Kulhawy, F. H, Kozera, D. W, and Withium, J. L, 1979, Uplift Testing of Model Drilled shafts in Sand, Journal of GTE Division, ASCE. Vol. 105, pp. 31-47
- [9] Kulhawy, F. H, 1985, Drained Uplift Capacity of Drilled Shafts, 11th International Conference on SMFE, San Francisco. Vol. 3, pp. 1549-1551
- [10] Turner, J. P, and Kulhawy, F. H, 1990, Drained Uplift Capacity of Drilled Shafts Under Repeated Loading, Journal of GTE Division, Vol.116, pp. 470- 491
- [11] Sharma, B.V and PISE, P.J, 1994, Uplift Capacity of Anchor Piles in Sand Under Axial-Pulling Loads, IGJ, Vol. 24, pp. 181-203
- [12] Patra, N. R and Pise, P. J, 2001, Ultimate Lateral Resistance of Pile Groups in Sand, Journal of Geotechnical and Geo-Environmental Engineering Division, ASCE, Vol. 127, pp. 481-487

- [13] Das, B. K and Pise, P. J, 2003, Effect of Compressive Load on Uplift Capacity of Model Piles, Journal of Geotechnical and Geo-Environmental Engineering Division, ASCE, Paper No.023132
- [14] Lysmer J 1970, 'Limit analysis of plane problems in soil mechanics', ASCE Journal of the Soil Mechanics and Foundations Division, vol. 96, pp. 1311–34
- [15] Geddes, J. D, 1969, Boussinesq-Based Approximations to the Vertical Stresses Caused by Pile-Type Subsurface Loadings, Geotechnique 19(4), 509-514
- [16] Cernica, J. N, 1995, Foundation Design, in Geotechnical Engineering. John Wiley

NUMERICAL ANALYSES OF SINKHOLE COLLAPSE

Jim Shiau¹ and Mohammad Mirza Hassan¹

¹School of Civil Engineering and Surveying, University of Southern Queensland, Australia

ABSTRACT

Current sinkhole research has been centered on the use of geophysical techniques to detect underground cavity sizes and the associated depths. With the measured information, it is possible to theoretically predict the extent of a ground surface collapse. In this paper, the failure of a cavity underlying homogeneous clay in an unsupported greenfield condition is examined. Shear strength reduction technique is utilised to study two- and three-dimensional failure mechanisms of a horizontal trapdoor by using the finite difference program, *FLAC*. Stability results are presented in the form of a factor of safety and a failure extent ratio for various dimensionless ratios and verified by using the finite element limit analysis technique with upper and lower bound theorems. A number of practical examples are provided to demonstrate the use of design charts and tables. It is suggested that an early warning system could be developed in the future to save lives and assets based on the failure extent charts and the geophysical tools.

Keywords: Sinkhole, Factor of Safety, *FLAC*, Strength Reduction Method, Surface failure extent

INTRODUCTION

Sinkholes have long been an important problem in geotechnical engineering. Similar to earthquakes, they can present environmental risks through subsidence or sudden ground collapse, leading to a great loss of life and infrastructure. There has been an increase in sinkhole occurrences over the years, particularly in urban areas. Human activities such as mining, piping and underground construction have contributed to this increase in sinkhole occurrences.

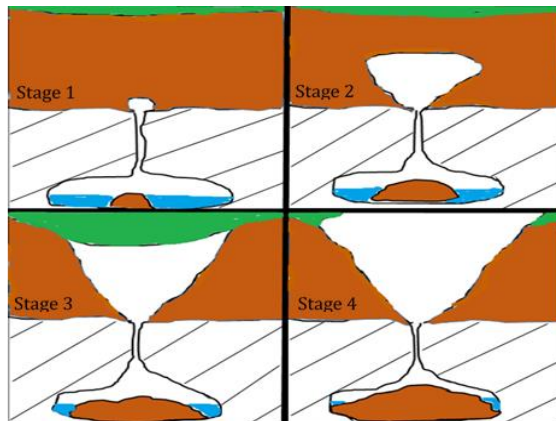


Fig.1 Sinkhole formation for cover collapse

Irrespective of the formation process, sinkholes are characterised by a depression of the soil surface into the underlying cavity. The most catastrophic type is a cover collapse sinkhole, where the failure is often sudden. This type of sinkhole, as shown in Fig.1, occurs mainly in areas where clay is the main type of soil that forms the cover. The cover soil

deposits into the underground cavity and the cavity tends to move toward the surface until a sudden failure occurs. Fig.2 shows an actual sinkhole occurrence. Interestingly, perfect circles are always observed in the real world. It is therefore the aim of this paper to study the stability of cover collapse sinkholes in two- and three-dimensional spaces.



Fig.2 Seffner sinkhole [26]

The stability of trapdoors was originally initiated by [1], who experimentally investigated the stress distribution of a trapdoor opening in sand. A relatively large number of the studies on the stability of trapdoors have since been conducted over the past decades. Stability evaluations of underground openings are most often conducted using the stability number (N) described in Broms and Bennermark [2]. This is shown in the equation (1).

$$N = \frac{\sigma_s - \sigma_t + \gamma H}{S_u} \quad (1)$$

Broms and Bennermark's work [2] was continued by many other researchers such as in [3]-[5] and more recently by [6]-[9]. Furthermore, researchers have been able to investigate the stability of underground openings, such as sinkholes and tunnels, through the use of limit analysis with lower and upper bound theorems. Atkinson & Potts [10] used the bound theory to investigate the stability of an underground tunnel in cohesionless soil. This approach was followed and expanded by other researchers such as [11]-[13] to investigate various types of underground openings. Tharp [14] and [15] also investigated sinkhole generation in homogeneous cohesive soil and rocks due to pore pressure changes or oil extraction.

With the vast development of computer technology, numerical analysis has played a major role in the prediction of sinkhole failures. Many researchers such as [16]-[18] have used computer programs to simulate sinkhole failures. Drumm et al. [19] and [20] developed dimensionless stability charts that can be used to evaluate the stability of soil in karst. Shiau et al. [9] introduced design charts to estimate tunnel heading stability in homogeneous cohesive soil using the finite difference method.

In the past two decades, a large number of stability studies have been presented using the stability number (N) presented in Eq. (1). In this paper, a unique approach to presenting the stability results is presented in the form of factor of safety (FoS), which has been frequently implemented in the analysis of slopes. The well-known Taylor's stability chart is still a popular tool for engineers in the field. Using the limit equilibrium method, Taylor [21] presented the undrained stability number as follow:

$$N_s = \frac{S_u}{\gamma H * FoS} \quad (2)$$

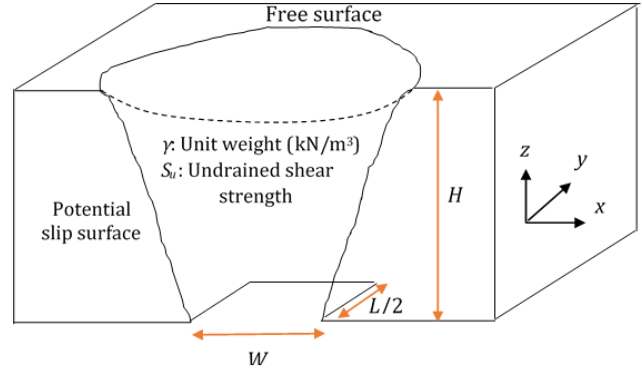
where S_u is the undrained shear strength of soils. γ and H are the soil unit weight and the cover depth respectively. Therefore, the aim of this investigation is to use Taylor's stability number approach to formulate the results for sinkhole stability. Design charts, tables and equations are provided throughout the paper with examples demonstrated.

PROBLEM DEFINITION

The sinkhole propagation process is a complex procedure; therefore, it is not possible to predict the exact behaviour of sinkholes over the time. Hence, this study assumes an idealised three-dimensional horizontal trapdoor and assumes that the propagation process is at the last stage where the cavity is big

enough to cause a collapse failure.

Figure. 3 presents an idealised horizontal trapdoor problem underlying undrained homogeneous clay layer with constant unit weight (γ) and shear strength (S_u). The three-dimensional soil body is modelled as uniform Tresca material, which is the same as Mohr-Coulomb material when the soil friction angle (ϕ) is zero. The opening of the cavity is assumed to be horizontal, with the width represented by (W) in the x direction, the length (L) in the y direction and the height represented by (H)



in the z direction.

Fig.3 An idealised sinkhole problem

To cover a wide range of practical parameters, an extensive range of depth ratios ($H/W = 1$ to 6), width ratios ($L/W = 1$ to 10) and shear strength ratios ($S_u/\gamma W = 0.2$ to 2) were chosen for the parametric studies. Note that the shear strength ratio defined following Taylor's method and the FoS can be defined as a function of the shear strength ratio ($S_u/\gamma W$), the depth ratio (H/W) and the width ratio (L/W). This relationship is shown in Eq. (3).

$$FoS = f\left(\frac{S_u}{\gamma W}, \frac{H}{W}, \frac{L}{W}\right) \quad (3)$$

It is interesting to see that, for a large width ratio such as $L/W = \infty$, the factor of safety is equivalent to a two-dimensional plane strain analysis and the FoS is the function of the strength ratio ($S_u/\gamma W$) and depth ratio (H/W) only.

MODELLING TECHNIQUE

Both the two- and three-dimensional finite difference software and shear strength reduction method (*SSRM*) developed by *ITASCA* [22]-[23] were employed to examine the trapdoor stability in undrained cohesive soil. Built-in *FISH* scripts were also developed for the problem to facilitate the auto mesh generation, and hence allow parametric studies to be conducted efficiently. For the purpose of

validating the model, three different mesh types were established; the full, half and quarter meshes. Internal verification and model validation of the solution revealed that results from full, half or quarter meshes were almost identical. This has greatly enhanced the level of confidence in the current 3D development.

A typical half grid for simulating a trapdoor problem is shown in Fig.4. Although the mesh shows perfect square cubes, *FLAC3D* uses a mixed discretisation technique of various element shapes such as wedges, pyramids, bricks and tetrahedrons to form and solve the problem [24].

A symmetrical boundary condition was employed to reduce the computational time. The faces at the two sides and at the back of the model are restrained in all directions, while the front face is only fixed in the y direction, allowing the soil particles to move in both x and z directions. The lower boundary grid points are fixed in the x , y and z directions except where the trapdoor openings are specified. The other important consideration for 3D numerical studies is the domain size, which could influence the sensitivity and reliability of the results. It is necessary to ensure that the velocity field is not affected by the finite domain size. In general, this can be detected by the output contour plot of the velocity field. This has been carefully checked for all cases, especially for large values of L/W .

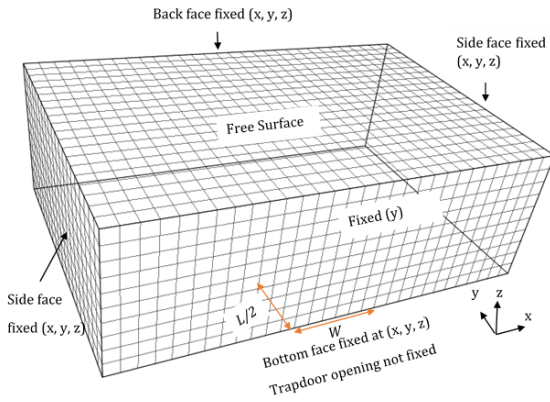


Fig.4 Typical half mesh and boundary condition

Many researchers have used the *SSRM* to analyse slope stability problems, however, this method has not been adopted in determining the stability of underground cavities. This method was first utilised by [25], and it was followed by many others. The *SSRM* is usually applied with the conventional model of Mohr-Coulomb material. For undrained cohesive soil, the factor of safety is defined as the ratio of the undrained shear strength and the critical shear strength.

$$FoS = \frac{S_u}{S_c} \quad (4)$$

Where S_u is undrained shear strength and S_c is critical shear strength. The numerical process involved in the factor of safety calculation is to gradually reduce the shear strength of the material to estimate the point where the system reaches a state of limiting equilibrium.

RESULTS AND DISCUSSION

Figure.5 investigates the effect of the opening size (i.e. the width ratio L/W) on the stability of the trapdoor. It can be seen that an increase in L/W results in a nonlinear decrease in the stability i.e. a decrease in FoS . Further observation reveals that, as L/W increases, the FoS approaches a constant value which is the result of a two-dimensional plain strain analysis ($L/W = \infty$). This observation is for all values of H/W .

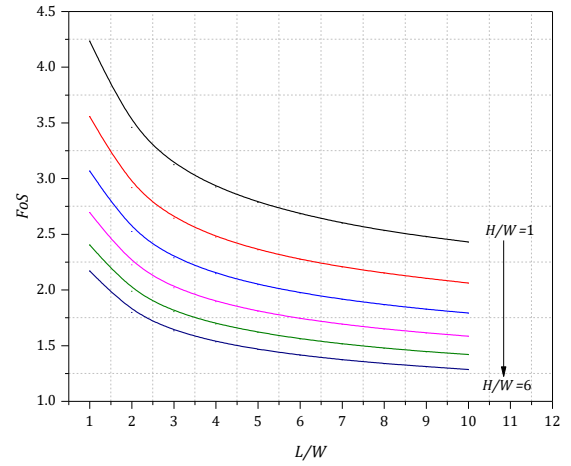


Fig.5. Effect of L/W (for $S_u/\gamma W = 1$)

Fig.6 shows a linear relationship between FoS and shear strength ratio ($S_u/\gamma W$) for all values of L/W . As expected, FoS increases as the shear strength of the soils $S_u/\gamma W$ increases.

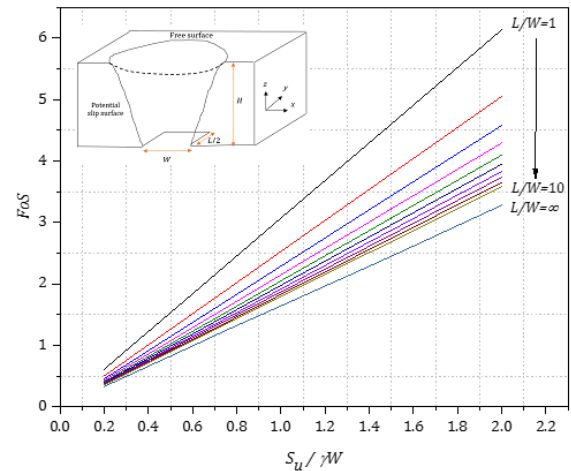


Fig.6 Effect of $S_u/\gamma W$ (for $H/W=3$)

Given the linear relationship in Fig.6, a failure envelope or critical strength ratio ($S_u/\gamma W FoS$) is presented in Fig.7. The shear strength ratio is normalised with respect to FoS , and therefore represents a critical condition where the $FoS = 1$.

Figure 7 is particularly important for designers because it represents the critical value of each parameter. The values above each line indicate a safe working zone ($FoS > 1$), while the values below indicate an unsafe zone ($FoS < 1$). Closer inspection of the figure reveals that the value of ($S_u/\gamma W FoS$) increases as both the depth ratio (H/W) and the width ratio (L/W) increase.

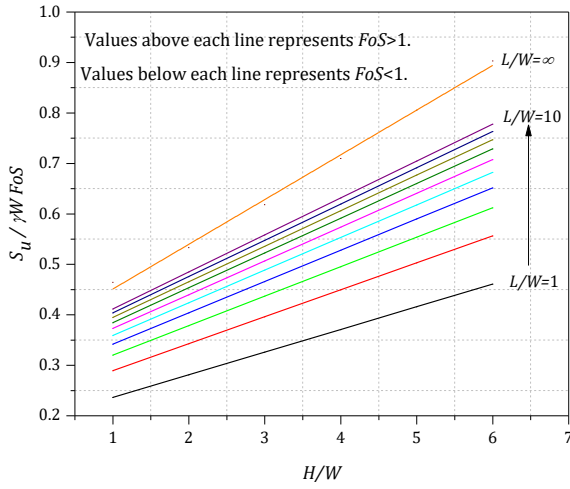


Fig.7 Failure envelope for $L/W=1$ to ∞

A nonlinear regression analysis was employed to develop a practical design equation covering both geometrical parameters L/W and H/W . This is shown in equation (5)

$$\frac{S_u}{\gamma W \times FoS} = \left(\frac{0.045H}{W} + 0.191 \right) + \left(\frac{0.012H}{W} + 0.064 \right) \ln \frac{L}{W} \quad (5)$$

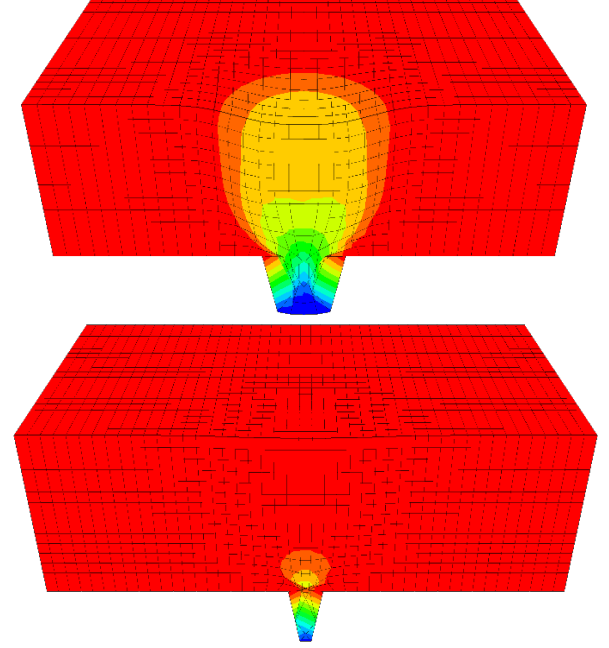
Equation (5) represents a critical condition where the FoS is 1. Hence, it can be used to obtain critical parameters such as undrained shear strength (S_u), depth (H), opening width (W), and in-plane depth (L). It can be further transformed into Eq. (6) to determine FoS for known design parameters such as H/W , L/W and $S_u/\gamma W$. Equation (6) may be particularly useful in the early design stages of an engineering project.

$$FoS = \frac{S_u / \gamma W}{\left[\left(\frac{0.045H}{W} + 0.191 \right) + \left(\frac{0.012H}{W} + 0.064 \right) \ln \frac{L}{W} \right]} \quad (6)$$

Figure 8 presents vertical velocity contours for a shallow ($H/W = 2$) and deep case ($H/W = 5$). It suggests that strong arching support was developed near the cavity in the deep case, possibly resulting in

a local failure. The failure mechanism does not show a slip surface being extended to the ground surface.

Further study of the failure extent on the ground surface indicates a transformation from a perfect circle for $L/W=1$ to a shape of an ellipse when L/W



increases, as shown in Fig. 9.

Fig.8 Plot of vertical velocity contours of $H/W=2$ (above) and $H/W=5$ (below) for $L/W=1$

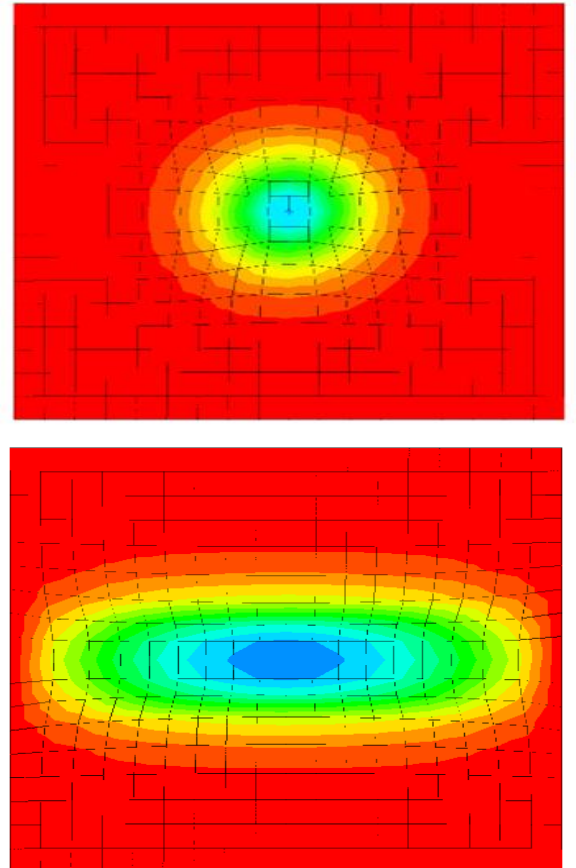


Fig.9 Surface failure for $L/W=1$ (top) and $L/W=5$ (bottom)

RESULTS VERIFICATION

The use of *SSRM* and *FoS* is prevalent in slope stability analyses, however, this process is uncommon when it comes to estimating the stability of underground cavities. The authors were not able to find any published literature for comparison purposes. Hence it was decided that the current 3D results obtained are to be compared with 2D upper bound and lower bound solutions using the finite element limit analysis method. Fig. 10 shows such a comparison.

Two observations can be made from Fig.10. Firstly, the 2D finite difference results (i.e. $L/W=\infty$) are in good agreement with the rigorous lower bound and upper bound results. This has provided some confidence over the current numerical models. Secondly, there is significant variance between the 3D ($L/W=1$) and 2D results ($L/W=\infty$). In the current study, 3D analysis produced results that are two-fold higher than those in the 2D analysis. This is not particularly surprising, as a two-dimensional analysis will always yield conservative results when compared to a three-dimensional analysis.

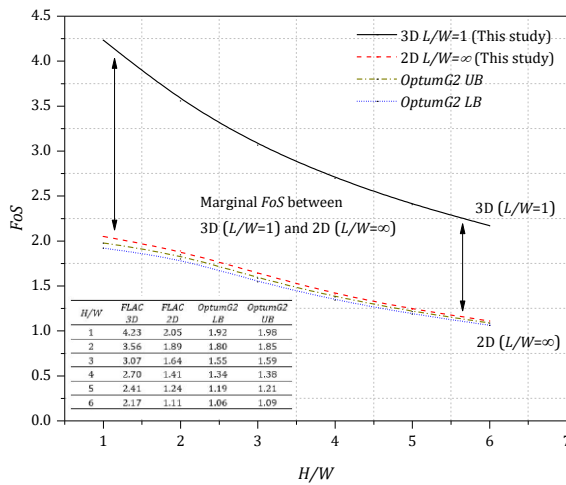


Fig.10 Comparison of results from 2D and 3D analyses (for $S_u/\gamma W=1$)

Further inspection of the comparison with 2D results reveals that the finite difference results are consistently higher than the upper bound results by approximately 3%. Note that the results presented in Fig. 10 were all obtained in this study, including the upper and lower bound solutions.

THE USE OF DESIGN CHARTS AND EQUATIONS

Workability of the stability design chart can be demonstrated through a number of examples, as follows.

Example 1 - determine the factor of safety (*FoS*)

An existing sinkhole has no internal pressure and no surcharge pressure, determine the factor of safety for the cavity. The following data has been provided:

$H=12$ m, $W=4$ m, $L=12$ m, $\gamma= 18$ kN/m³ and $S_u=80$ kPa.

1. Given $H/W=3$ and $S_u/\gamma W = 1.1$, Fig.7 returns a *FoS* value of approximately 2.50.
2. Using Eq.(6), a value of $FoS = 2.52$ is obtained.
3. An actual computer analysis of this case using *FLAC* gives $FoS = 2.518$.

Example 2 - determine the critical depth ratio (H/W)

In the case of a deep sinkhole, what would be the critical depth (H) required to maintain a *FoS* of 1 for the following given parameters:

$S_u= 162$ kPa, $W=30$ m, $L=30$ m, $\gamma= 18$ kN/m³.

1. Given the parameters, $S_u/\gamma W FoS = 0.3$.
2. Using Eq.5, the depth (H) is calculated to be 72.67 m. Converting the results in terms of a dimensionless ratio, $H/W = 2.42$.
3. Using Fig.7 with $S_u/\gamma W FoS = 0.3$, H/W is estimated to be 2.5.

CONCLUSION

A series of 2D and 3D numerical models were established to investigate the stability of trapdoors with various opening sizes in undrained cohesive soil. Numerical results were obtained by utilising the shear strength reduction method in the finite difference method software *FLAC2D* and *FLAC3D*. In order to efficiently perform parametric analyses, a *FISH* script was developed to enable auto mesh generation and solver.

It was noted that strong arching support has been developed for deep trapdoors, and the corresponding failure mechanisms do propagate to the ground surface. Local failure was observed for these deep cases. Furthermore, the study of surface failure extent revealed a transformation from a perfect circle to an ellipse as the value of width ratio L/W increased i.e. changing the opening size from a square to a wide rectangle.

To assist practical designers, numerical results were presented in the form of factor of safety that is a function of the depth ratio and the shear strength

ratio. Examples have demonstrated how to use the design charts and equations practically. It is suggested that future work may include the use of Broms and Bennermark's original stability number to formulate solutions in both 2D and 3D analyses.

REFERENCES

- [1] Terzaghi, K 1936, 'Stress distribution in dry and saturated sand above a yielding trap-door', in Proceedings of the international conference of soil mechanic, Harvard University Press, Cambridge, vol. 1, no. 4, pp. 307-311
- [2] Broms, B.B. & Bennermark, H. (1967), 'Stability of clay at vertical openings', Journal of the Soil Mechanic & Foundations Division, Proceedings of the American Society of Civil Engineers, vol. 93, pp. 71- 93
- [3] Mair, RJ 1979, 'Centrifuge modelling of tunnel construction in soft clay', PhD Thesis, University of Cambridge.
- [4] Craig, W 1990, 'Collapse of cohesive overburden following removal of support', Canadian Geotechnical Journal, vol. 27, no. 3, pp. 355-64.
- [5] Abdulla, WA & Goodings, DJ 1996, 'Modeling of sinkholes in weakly cemented sand', Journal of geotechnical engineering, vol. 122, no. 12, pp. 998-1005.
- [6] Jacobsz, S 2016, 'Trapdoor experiments studying cavity propagation', in Proceedings of the 1st Southern African Geotechnical Conference, Durban, South Africa, 18-19 October 2016, CRC Press, pp. 159-65.
- [7] Shiau, J & Hassan, MM 2017, 'Numerical investigation of two-dimensional trapdoor stability', in Proceedings of 3rd International Conference on Science, Engineering & Environment, The GEOMATE international society, Brisbane, Australia, pp.354-359.
- [8] Shiau, J, Hassan, MM & Hossein, Z 2018, 'Stability charts for unsupported square tunnels in homogeneous undrained clay', International Journal of Geomate, vol. 15, no. 48, pp. 195-201.
- [9] Shiau, J, Sams, M, Al-Asadi, F & Hassan, MM 2018, 'Stability charts for unsupported plane strain tunnel headings in homogeneous undrained clay', International Journal of Geomate, vol. 14, no. 41, pp. 19-26.
- [10] Atkinson, J & Potts, D 1977, 'Stability of a shallow circular tunnel in cohesionless soil', Geotechnique, vol. 27, no. 2, pp. 203-15.
- [11] Davis, E, Gunn, M, Mair, R & Seneviratne, H 1980, 'The stability of shallow tunnels and underground openings in cohesive material', Geotechnique, vol. 30, no. 4, pp. 397-416.
- [12] Mühlhaus, H-B 1985, 'Lower bound solutions for circular tunnels in two and three dimensions', Rock Mechanics and Rock Engineering, vol. 18, no. 1, pp. 37-52.
- [13] Leca, E & Dormieux, L 1990, 'Upper and lower bound solutions for the face stability of shallow circular tunnels in frictional material', Geotechnique, vol. 40, no. 4, pp. 581-606.
- [14] Tharp, TM 2003, 'Cover-collapse sinkhole formation and soil plasticity', in Sinkholes and the Engineering and Environmental Impacts of Karst, pp. 110-23.
- [15] Vaziri, HH, Jalali, JS & Islam, R 2001, 'An analytical model for stability analysis of rock layers over a circular opening', International journal of solids and structures, vol. 38, no. 21, pp. 3735-57.
- [16] Sloan, S, Assadi, A & Purushothaman, N 1990, 'Undrained stability of a trapdoor', Geotechnique, vol. 40, no. 1, pp. 45-62.
- [17] Augarde, CE, Lyamin, AV & Sloan, SW 2003, 'Prediction of undrained sinkhole collapse', Journal of geotechnical and geoenvironmental engineering, vol. 129, no. 3, pp. 197-205.
- [18] Drumm, EC, Aktürk, Ö, Akgün, H & Tutluoğlu, L 2009, 'Stability charts for the collapse of residual soil in karst', Journal of geotechnical and geoenvironmental engineering, vol. 135, no. 7, pp. 925-31.
- [19] Keawsawasvong, S & Ukritchon, B 2017, 'Undrained stability of an active planar trapdoor in non-homogeneous clays with a linear increase of strength with depth', Computers and Geotechnics, vol. 81, pp. 284-93.
- [20] Yang, MZ & Drumm, EC 2002, 'Stability evaluation for the siting of municipal landfills in karst', Engineering Geology, vol. 65, no. 2, pp. 185-95.
- [21] Taylor, DW 1937, Stability of earth slopes, vol. 24, Wright & Potter print.
- [22] Itasca (2002), Fast Lagrangian Analysis of Continua, FLAC3D Version 2.0, Itasca Consulting Group, Minneapolis, Minnesota, USA.
- [23] Itasca (2003), Fast Lagrangian Analysis of Continua, FLAC2D Version 5.0, Itasca Consulting Group, Minneapolis, Minnesota, USA.
- [24] Abbasi, B, Russell, D & Taghavi, R 2013, 'FLAC 3D mesh and zone quality'. Itasca Consulting Group, Minneapolis, Minnesota, USA.
- [25] Zienkiewicz, O, Humpheson, C & Lewis, R 1977, 'Discussion: Associated and non-associated visco-plasticity and plasticity in soil mechanics', Geotechnique, vol. 27, no. 1, pp. 101-2.
- [26] Mettler, K 2015, 'Seffner sinkhole', Tampa Bay Times, Florida, United States, viewed 26 June 2018, <<http://www.tampabay.com/news/publicsafty/report-new-hole-opens-at-site-of-2013-fatal-sinkhole-in-seffner/224>

A STUDY ON LANDSLIDE AND COLLAPSE CAUSED BY THE 2016 KUMAMOTO EARTHQUAKE IN JAPAN

Naomasa Honda¹

¹ Faculty of Regional Environment Science, Tokyo University of Agriculture, Japan

ABSTRACT

The occurrence mechanism for landslides and collapses due to earthquakes is greatly different from rainfall cases. Since earthquakes cause a repeated load and generate excess pore water pressure, they reduce the shear strength near the sliding surface on the slope, and the mountain slope loses stability and collapses rapidly. Kumamoto Prefecture in Japan was struck by two huge earthquakes of Japanese seismic intensity scale 7 in April 2016. Based on a stability analysis, we discuss the landslide and the collapse caused by the 2016 Kumamoto Earthquake. We set both the rainfall and earthquake calculation conditions for semi-infinite slopes and conducted slope stability analyses that focused on the groundwater level rising and the decrease of the shear strength near the sliding surface. According to the analytical results, if we could appropriately estimate the reduction of the shear strength in the slope caused by the earthquake, we could explain a mass movement occurrence on a mountain slope that doesn't collapse from rainfall. In addition, depending on the earthquake's scale, mass movement might not occur. Our result suggests that the huge scale of the 2016 Kumamoto Earthquake was unprecedented.

Keywords: Slope disaster due to earthquakes, Groundwater level rising, Lowering shear strength, Slope stability analysis

INTRODUCTION

In Kumamoto Prefecture in Japan in April 2016, such serious sediment-related disasters as landslides, collapses, and debris flows were caused by huge earthquakes equivalent to Japanese seismic intensity 7.

Kumamoto Prefecture is located in Kyushu, which get a lot of rain and is frequently attacked by typhoons. Its citizens are vigilant about sediment-related disasters. But they were shocked that slopes, which had previously survived large amounts of rain, were destroyed by the earthquake.

The occurrence mechanism for landslides and collapses from earthquakes is very different from rainfall cases. Earthquakes cause a repeated load and generate excess pore water pressure, and since they instantly reduce the shear strength near the sliding surface, the mountain slope loses stability and rapidly collapses [1], [2].

In this paper, we discuss the mass movements caused by the 2016 Kumamoto Earthquake in Japan based on a stability analysis of semi-infinite slopes. We investigated and discussed two actual slope disasters: a landslide and a collapse. Both the rainfall and earthquake calculation conditions for these slopes are set, and the slope stabilities that focused on rising groundwater levels and the decrease in the shear strength near the slope's sliding surface are analyzed.

METHOD AND PROCEDURE FOR STUDY

Stability analysis of semi-infinite slopes

Assuming a straight sliding surface in the semi-infinite slope (Fig.1), the following are Fellenius's formulas on slope stability analysis:

$$F_s = \frac{C' + (W \cos \theta - k_h W \sin \theta - u) \tan \phi'}{W (\sin \theta + k_h \cos \theta)} \quad (1)$$

$$W = \gamma h \cos \theta \quad (2)$$

$$u = \gamma_w h_2 L \quad (3)$$

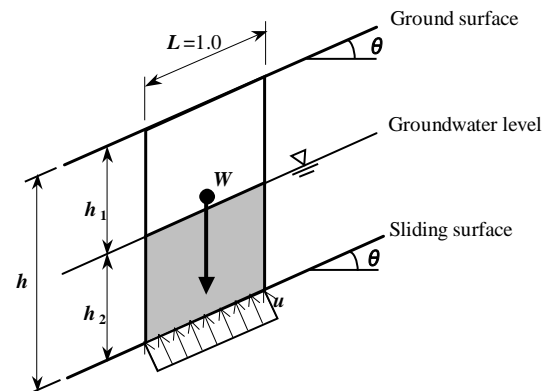


Fig.1 Stability analysis of semi-infinite slopes

where F_s is the slope's safety factor, C' is the soil cohesion, W is the total soil weight, k_h is the design

horizontal seismic coefficient, θ is the slope gradient, u is the pore water pressure, ϕ' is the sediment's internal friction angle, γ is the unit soil weight, h is the collapse depth, h_1 is the soil layer thickness from the groundwater level to the ground surface, h_2 is the soil layer thickness from the sliding surface to the groundwater level (measured from the sliding surface), γ_w is the unit water weight ($\gamma_w = 9.8 \text{ kN/m}^3$), and L is the unit length ($L=1.0$).

In the case of $k_h=0.00$ (rainfall case), Eq.(1) is described as follows:

$$F_s = \frac{C' + (W \cos \theta - u) \tan \phi'}{W \sin \theta} \quad (4)$$

Equation (4) shows that F_s depends on C' regardless of ϕ' when h_2 is a value where $W \cos \theta$ equals u ($W \cos \theta$ is the characteristics of the slope's right angle direction of the soil weight).

Previous studies on decrease in shear strength due to earthquakes

Ohara and Yamamoto [1] performed dynamic triaxial compression tests on the andosol of the Aso district in Kumamoto Prefecture. Their results argued that, most of the soil cohesion was lost and the sediment's internal friction angle was almost halved by the repeated loads. The internal friction angle ranged from 11° to 15° .

Sassa, Fukuoka, and Oh [2] concluded that, due to such repeated loads caused by earthquakes, the increase of the pore water pressure decreased the friction angle, raising the chance that a high-speed, long-distance landslide might occur even if the slope gradient was mild.

Outline of the 2016 Kumamoto Earthquake

Kumamoto Prefecture (Fig. 2) was struck by two huge earthquakes of Japanese seismic intensity scale 7 on April 2016.

The first event's seismic center (the fore shock) occurred near the Kumamoto district (at latitude $32^\circ 44.5'$ north and longitude $130^\circ 48.5'$ east, the seismic center's depth was about 11 km) in April 14 at 21:26 pm and recorded a moment magnitude of 6.5. The second event's seismic center (the main shock) was generated near the Kumamoto district (at latitude $32^\circ 45.2'$ north and longitude $130^\circ 45.7'$ east, the seismic center's depth was about 12 km) on April 16 at 1:25 am and recorded a moment magnitude of 7.3.

These earthquakes killed 50 people died over two days and caused house collapses, road surface cave-ins, and train derailments.



Fig.2 Location of Kumamoto Prefecture

Such sediment-related disaster occurrences as landslides, collapses, and debris flows were concentrated in an area near earthquake faults. Ten people died over two days in sediment-related disasters.

Outline of actual landslide and collapse

In the present study, we focus on two actual slope disasters, both of which were located near the earthquake fault. Neither has collapse recently due to rainfalls.

Case 1: Landslide in Takanodai district [3]

- Soil quality: the andosol
- Maximum slope gradient = 10°
- Maximum collapse width = 150 m
- Maximum collapse depth = 10.0 m
- Landslide length = 250 m
- Sediment erosion volume = $153,000 \text{ m}^3$

Case 2: Collapse in Hinotori spa district [3]

- Soil quality: the pyroclastic fall deposit
- Maximum slope gradient = 35°
- Maximum collapse width = 50 m
- Maximum collapse depth = 5.0 m
- Collapse length = 100 m

Calculation Conditions

The landslide length of Takanodai district's slope ($L=250\text{m}$) and the collapse length of Hinotori spa district's slope ($L=100\text{m}$) are long together. And their sliding surfaces are taken as straight lines roughly. Therefore, we assumed the semi-infinite slopes and analyzed the slope stabilities using Fellenius's formulas.

We set both the rainfall and earthquake calculation conditions for semi-infinite slopes and investigated the relationship among ϕ' , C' and F_s .

There is no detailed data of actual slopes, especially, γ and C' . Therefore, we decided them in references to previous studies that dealt with soils near actual slopes. The following are the calculation conditions:

Case 1: Landslide in Takanodai district

- $\theta = 10^\circ$, $h = 10.0$ m
- $h_2 = h$ (rainfall case), $h_2 = 0$ (earthquake case)
- $\gamma = 11.76$ kN/m³ (1.20 tf/m³) [4]
- Maximum soil cohesion, $C'_{max} = 14.7$ kN/m² (0.15 kgf/cm²) [1]

Case 2: Collapse in Hinotori spa district

- $\theta = 35^\circ$, $h = 5.0$ m
- $h_2 = h$ (rainfall case), $h_2 = 0$ (earthquake case)
- $\gamma = 15.68$ kN/m³ (1.60 tf/m³) [5]
- $C' = 14.7 \sim 58.8$ kN/m² (0.15 ~ 0.60 kgf/cm²) [5]

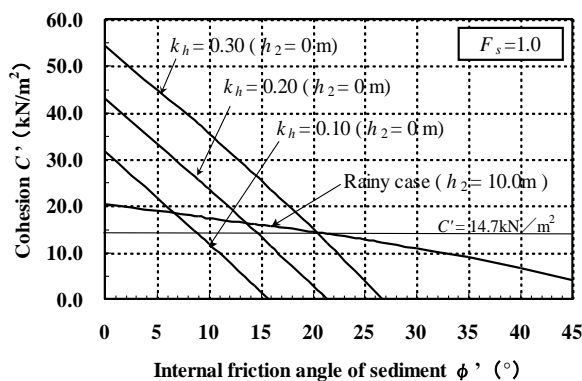
Design horizontal seismic coefficient k_h

The design horizontal seismic coefficients are similar with the next values for all cases [6], [7].

- $k_h = 0.00$ (rainfall case)
- $k_h = 0.10$ (Japanese seismic intensity lower 5)
- $k_h = 0.20$ (Japanese seismic intensity upper 5)
- $k_h = 0.30$ (Japanese seismic intensity 6)

RESULTS AND DISCUSSION

Case 1: Landslide in Takanodai district



(a) Relationship between ϕ' and C' ($F_s=1.0$)

Figure 3(a) shows the relationship between ϕ' and C' when F_s equals 1.0 in Eq. (1) (state of equilibrium). h_2 equals 10.0 m during rainfall and 0 m during the earthquake.

Figure 3(b) shows the change in F_s by the difference in k_h when C' equals 0 and ϕ' is halved by the earthquake in reference to Ohara and Yamamoto [1].

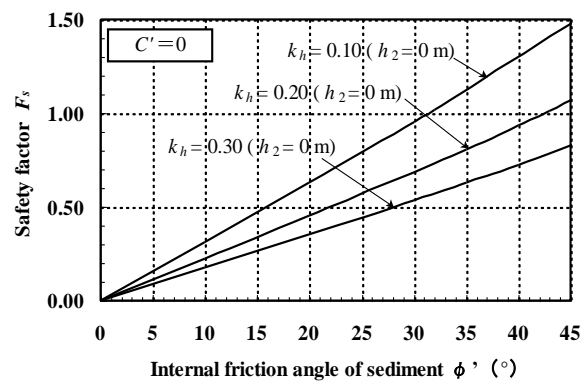
As shown in Fig. 3(a), when C' is kept at 14.7 kN/m² (maximum value of the soil cohesion), the slope stability is equilibrium at ϕ' around 20° even if the ground water level reaches the ground surface due to rainfall. This slope's safety is high for landslides from rain. In Fig. 3(a), when k_h equals 0.30 and h_2 equals 0 m (no influence of the pore water pressure by the groundwater level), the slope is stable at ϕ' around 20° .

In Fig.3(b), when k_h equals 0.30 and h_2 equals 0 m, F_s is less than 1.0 and the slope is unstable even if ϕ' in the normal equals 45° . On the other hand, when k_h equals 0.20 or 0.10, F_s equals 1.0 and the slope is stable at ϕ' around 42° or 31° .

Based on our results, we conclude the following:

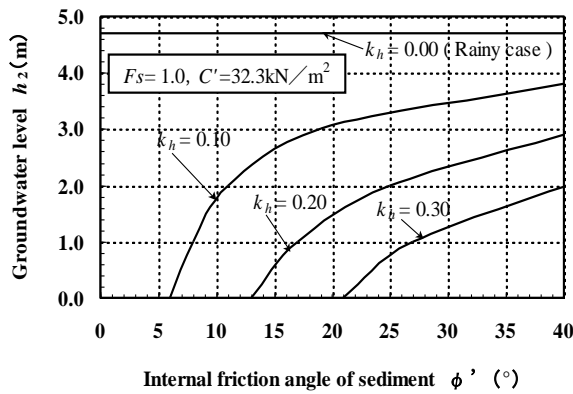
- We assume that this slope's safety from landslides is high due to its rainfall.
- The decrease of ϕ' and C' near the sliding surface occurred instantly during the huge earthquake at least more than Japanese seismic intensity 6, and the mountain slope lost stability and slipped rapidly.
- Depending on the earthquake's scale, no mass movement might occur. Our result suggests that the huge scale of the 2016 Kumamoto Earthquake was unprecedented.

Case 2: Collapse in Hinotori spa district

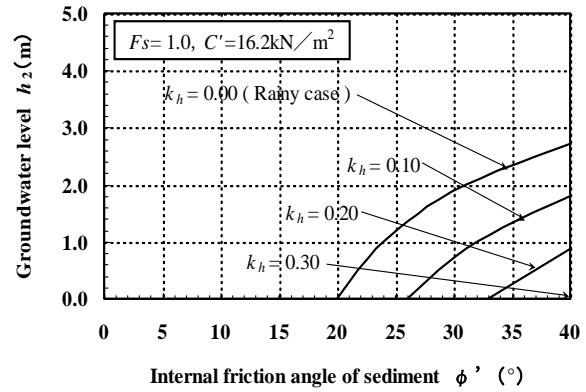


(b) Relationship between ϕ' and $F_s=1.0$ ($C'=0$)

Fig.3 Results of stability analysis (Case 1)



(a) Relationship between ϕ' and h_2
($F_s=1.0$, $C'=32.3\text{kN/m}^2$)



(b) Relationship between ϕ' and h_2
($F_s=1.0$, $C'=16.2\text{kN/m}^2$)

Fig.4 Results of stability analysis (Case 2)

Soil cohesion C' is one of the conditions under which a slope doesn't collapse even if the groundwater level increases to around ground surface ($h_2 = 5.0$ m) by rainfall. Since we assumed this value in the ranges, we investigated the range of h_2 from 0.0 m to 5.0 m.

Figure 4(a) shows the relationship between ϕ' and h_2 when F_s equals 1.0 and C' equals 32.3 kN/m^2 in Eq. (1).

As shown in Fig.4(a), when k_h equals 0.30 and if ϕ' ranges from 30° to 35° , the slope stability is equilibrium for the groundwater level from around 1.3 to 1.6 m. Similarly, when k_h equals 0.20 or 0.10 and if ϕ' ranges from 30° to 35° , the slope stability is equilibrium for the groundwater level from around 2.4 to 2.7 m or 3.5 to 3.7 m.

The dynamic shear strength characteristics of the pyroclastic fall deposit remain unidentified. But the decrease of the shear strength near the sliding surface due to earthquakes probably occurred there in like Case 1. Therefore, we assume that ϕ' is kept at a normal value even if an earthquake occurs and C' is halved ($C'=16.2 \text{ kN/m}^2$) by it.

Figure 4(b) shows the relationship between ϕ' and h_2 when F_s equals 1.0 and C' equals 16.2 kN/m^2 in Eq. (1).

As shown in Fig. 4(b), when k_h equals 0.30, h_2 satisfies the slope stability ($F_s=1.0$) and equals 0 m even if ϕ' equals 40° . For example, even if h_2 is a very small value less than 1.0 m, this slope becomes unstable due to the earthquake. When k_h equals 0.10, a collapse may not occur, depending on the degree of the rise of the groundwater level.

We express caution about the unclear details of the decrease of ϕ' and C' caused by the earthquake. According to the results, this slope has never collapsed from rainfall. But the decrease in the shear

strength near the slope's sliding surface occurred instantly to a huge earthquake at least more than Japanese seismic intensity 6, and the mountain slope lost stability and collapsed rapidly.

CONCLUSIONS

- (1) For the Takanodai district, the slope that the landslide produced by the 2016 Kumamoto Earthquake had resistance for landslides due to rainfall.
- (2) In two cases (the Takanodai district landslide and the Hinotori spa district collapse), the decrease of the shear strength near the slope's sliding surface occurred instantly due to by the huge earthquake at least more than Japanese seismic intensity 6, and the mountain slope lost stability and slipped rapidly.
- (3) Mass movement depend on the earthquake's scale. Our result suggests that the huge scale of the 2016 Kumamoto Earthquake was unprecedented.
- (4) If we could appropriately estimate the decrease of the shear strength near the slope's sliding surface due to earthquakes, we could reasonably explain mass movements.

Most of the sediment-related disaster in the 2016 Kumamoto Earthquake occurred near the earthquake fault, which is different from the areas that haven't collapsed from rainfall for many years. It must be strongly recognized that earthquakes are triggers and inherent factors of sediment-related disasters.

ACKNOWLEDGEMENTS

Part of the present study was supported by Strategic Research Project from Tokyo University of Agriculture.

REFERENCES

- [1] Ohara S. and Yamamoto H., Dynamic Shear Characteristics of Aso Kuroboku. *Memoirs of the Faculty of Engineering, Yamaguchi University*, Vol. 30, Issue 2, 1980, pp.225-231 (in Japanese).
- [2] Sassa K., Fukuoka H. and Fawu W., Mechanism of Rapid Long Runout Motion in the May 1997 Sumikawa Reactivated Landslide in Akita Prefecture and the July 1997 Harihara Landslide-Debris Flow, Kagoshima Prefecture, Japan. *Journal of the Japan Landslide Society*, Vol. 35, Issue 2, 1998, pp.29-37 (in Japanese).
- [3] Japan Society of Erosion Control Engineering, Urgent Investigation Report of the Sediment-related Disasters caused by the 2016 Kumamoto Earthquake, Dec. 2016, 81pp (in Japanese).
- [4] Ohta K., Property of Science and Technology Study of Main Special Soils - Creation Maintenance of Farms in Kyushu -. *Journal of the Agricultural Engineering Society*, Vol. 51, Issue 10, 1983, pp.899-909 (in Japanese).
- [5] Fukutomi M., Kanemitsu K., Egashira Y. and Tanaka H., Properties of Pyroclastic Flow in Kyushu. *OYO Technical Report*, Vol.1, 1979, pp.173-209 (in Japanese).
- [6] Japan Meteorological Agency, Japan Meteorological Agency Seismic Intensity Scale (the old version), 1949 (in Japanese).
- [7] Japan Meteorological Agency, Japan Meteorological Agency Seismic Intensity Scale (the new version), 1996 (in Japanese).

THE COMPARISON BETWEEN SOIL SAMPLING AND UNSATURATED SOIL HYDRAULIC DATABASE (UNSODA)

Chollada Kanjanakul¹

¹Department of Civil Engineering, College of Industrial Technology and Management, Rajamangala
University of Technology Srivijaya, Thailand

ABSTRACT

Analysis of rainfall-induced landslide on unsaturated soil slope is one of the principal problems in geotechnical engineering analysis. Natural soil slope is heterogeneous, that means it's difficult to predict time and location of failure. This uncertainties parameters (problems) lead to many risks in permeability behaviour on slope stability analysis. There are too many that show the special behavior and characteristic of unsaturated soil. In unstandard equipment and procedure to collect natural soil samples it's easy to make mistake in soil data base and waste the time to determine construction in little time for geotechnical engineering. The permeability method for natural soil samples is one of the laboratory testing that determines the soil water characteristic curve (SWCC Curve).

This paper describes a method to solve the problem about the unstandard procedure to collect natural soil samples and uncertainties parameters (problems) by comparison between soil sampling and unsaturated soil hydraulic database which is recognized as a universal standard. The soil water characteristic curve from Unsaturated Soil Database (UNSODA) were used as input parameters to estimate surface infiltration rates for slope stability analysis. SEEP/W was employed to model fluctuations in pore-water pressure during a rainfall, using the computed water infiltration rates as surface boundary conditions. SLOPE/W was then carried out to compute their factors of safety. Slope at the site became unstable (factor of safety less than 1) at 50 hours.

Keywords: Unsaturated Soil Database (UNSODA), Unsaturated soil, Slope stability analysis, Rainfall induced landslides, SWCC Curve

INTRODUCTION

Frequent landslides occur in tropical region countries, causing great harm and costs. Scientists and Engineers have continually tried to find better methods of warning systems to reduce the problem. Thailand is a tropical country that has high rainfall intensity in rainy season. Evaporation and precipitation such as rainfall result in positive pore-water pressures and ground water level fluctuations in unsaturated slope [1].

A complex hydro-mechanical behavior based on the basic physical properties (grainsize distribution and weight-volume relationship of soil) of the unsaturated soil has significant influence on rainfall induced landslide and slope stability analysis. Especially, the relationship between the amount of water in the soil and suction drawn on a curve called Soil Water Characteristic Curve (SWCC).

Determining SWCC curve at a site can be measured directly through various in-situ and laboratory tests. However, it's costly and time-consuming due to high standards equipment, procedural control and limits in testing apparatus [2].

As a result, only a limited number of data points (volumetric water content and matric suction) on SWCC at some values of suction are obtained in

practice [3].

The limited number of data points are then used to estimate the SWCC by fitting them with some parametric SWCC models, such as [4]-[6].

This research is focused to mitigate the problems about unstandard in soil laboratory equipment and the uncertainty in the SWCC data (the hydro-mechanical behavior parameters such as the amount of water in the soil, matric suction etc.) collected from field test by comparison between the basic physical properties data and real data in Unsaturated Soil Database (UNSODA), developed by U.S. Department of Agriculture. After the author can find, UNSODA soil code that have the basic physical properties data similar to the soil sampling. The soil water characteristic curve from UNSODA was used as input parameters to estimate surface infiltration rates for slope stability analysis. In more detail, a finite element analysis in SEEP/W was used to model the fluctuations in pore-water pressure during rainfall, with the computed water infiltration rate as the surface boundary condition. SLOPE/W application of the limit equilibrium Bishop simplified method, using the temporal pore water pressure distributions derived from the seepage analysis. Slope stability analysis with regard to the outcome of Factor of safety (F.S.) was produced for

case study area. These result indicated that unsaturated slope at case study area in Southern part of Thailand will collaps at 50 hours with the average factor of safety (F.S.) = 0.940.

RAINFALL INDUCED UNSATURATED SLOPE IN THE STUDY AREA

Landslide problems are aggravated by high intensity rainfall precipitation and weak natural geological structures. Increasing water content in unsaturated soil by rainfall is the main cause of the landslide, so that the shear strength, matric suction and factor of safety in soil decreases.

The investigated landslide area is Khanom district in the Nakhon-Si-Thammarat province of Thailand, as shown in Fig. 1 The area is rainy across all seasons with exceptionally high rainfall amounts. In terms of geology, the Khanom-slope is mantled with deeply weathered granite regolith.



Fig.1 Study site at Khanom, Nakhon Si Thammarat province, Thailand

The study aims to determine basic physical properties data from in-situ and laboratory tests (Sieve Analysis, Grain Size Distribution, Liquid Limit, Plastic Limit, Shrinkage Limit) in unsaturated slope that will describe in methodology.

UNSATURATED SOIL

Unsaturated soil has three levels. They allow the water to rise at the presence of pore-water pressure u_w and pore-air pressure u_a which resulted in an interface between the water and the air, known as contractile skin [5]. The difference between u_w and u_a called matric suction. In unsaturated slope, the SWCC curve has significant effects in stability matric suction and infiltration characteristics of the soil that are defined as below:

Soil-Water Characteristic Curve

The soil-water characteristic curve (SWCC) describes the amount of water in the soil. It changes in soil matric suction. The amount of water depends on the volumetric water content (θ_w) and the degree of saturation (S_r). But the matric suction is described as the difference between the air and the water pressure. SWCC equations are as shown below.

A. Van Genuchten (1980)

$$\frac{\theta - \theta_r}{\theta_s - \theta_r} = \left(\frac{1}{1 + (\alpha \Psi)^n} \right)^m \quad (1)$$

Where Ψ is soil matric suction, Ψ_a is air entry suction, θ is the volumetric water contents θ_s and θ_r represent the volumetric water contents at the saturated and residual conditions respectively, α is a function of max pore size and m, n, λ are constant parameter in van-genuchten equation and $m = 1 - \frac{1}{n}$

B. Brooks and Corey (1964)

$$\left(\frac{\Psi_a}{\Psi} \right)^\lambda = \frac{\theta - \theta_r}{\theta_s - \theta_r} \quad (2)$$

Where Ψ is soil matric suction, Ψ_a is air entry suction, θ_w is volumetric water content, θ_s and θ_r represent the volumetric water contents at the saturated and residual conditions respectively and λ are constant parameter in brooks and corey equation

C. Fredlund and Xing (1994)

$$\theta = \theta_s \left(\frac{1}{\ln \left[e + \left(\frac{\Psi}{\Psi_a} \right)^n \right]} \right)^m \quad (3)$$

Note: All notations are as earlier detailed for Eq. (1) and (2).

Soil Classification

The basic physical properties of the soil are important parameters for the soil classification that can be used to identify soil characteristics and behaviour such as Sieve Analysis, Grainsize distribution and Atterberg limits.

- Sieve Analysis

The process of grading soil is done in accordance with the Unified Soil Classification system (USCS). In a sieve analysis, a coarse-grained soil sample is shaken through a series of mesh sieves. Each sieve has successively smaller openings so particles larger than the size of each sieve are retained on the sieve. The percentage of each soil size is measured by weighing the amount retained on each sieve and comparing the weight to the total weight of the sample. The results of a sieve analysis are plotted as a grain size distribution curve, which is then analyzed to determine the soil gradation of the particular soil [7].

The coefficient of uniformity, C_u is a crude shape parameter and is calculated using the following equation:

$$C_u = \frac{D_{60}}{D_{10}} \quad (4)$$

where D_{60} is the grain diameter at 60% passing, and D_{10} is the grain diameter at 10% passing.

The coefficient of curvature, C_c is a shape parameter and is calculated using the following equation:

$$C_c = \frac{(D_{30})^2}{D_{10}D_{60}}$$

(5)

Where D_{60} is the grain diameter at 60% passing, D_{30} is the grain diameter at 30% passing, and D_{10} is the grain diameter at 10% passing.

- Atterberg Limits

A. Atterberg defined the boundaries of four states in terms of limits as follows:

- - *Liquid Limit (LL)* is the water content at which soil changes from a plastic to a liquid state, when the soil specimen is just fluid enough for a groove to close when jarred in a specified manner.
- - *Plastic Limit (PL)* is the water content at the change from a plastic to a semisolid state. This test attempts to deform a soil specimen below the moisture by rolling it into a thread, resulting in the soil crumbling.
- - *Shrinkage Limit (SL)* is the water content where further loss of moisture does not cause a decrease in specimen volume.
- - *Plasticity Index (PI)* is calculated as the Plastic Limit subtracted from the Liquid Limit and is an important value when classifying soil types.

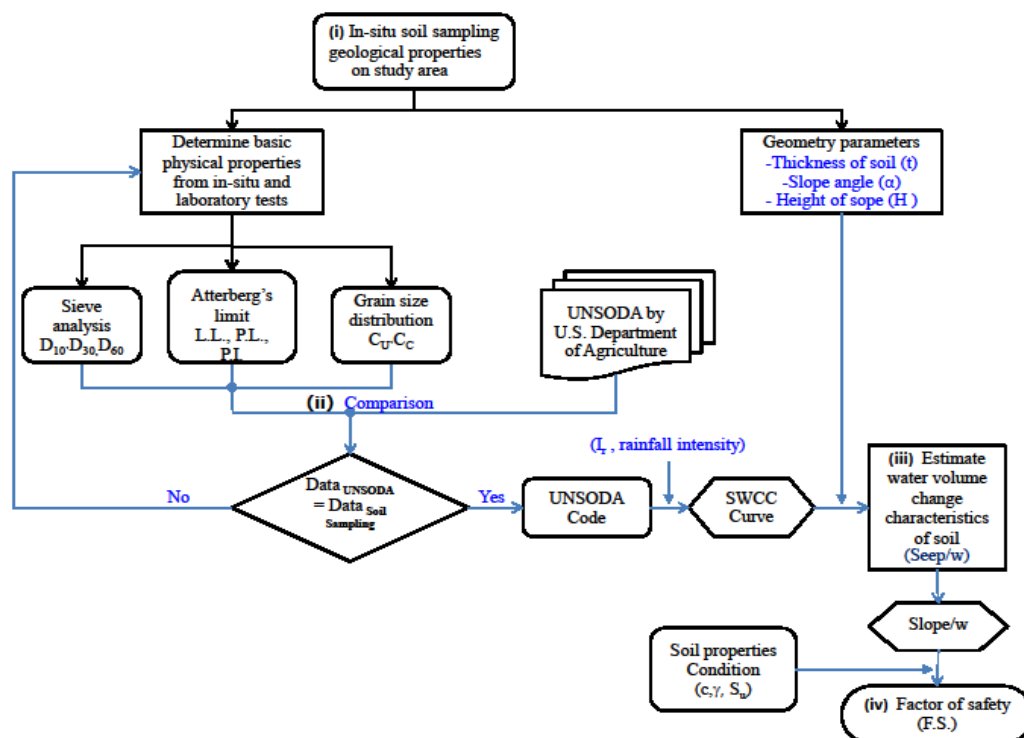


Fig. 2 Methodology.

RESEARCH METHODOLOGY

Fig. 2: Four stages were conducted in this research: (i) Determining physical parameters result from In-situ soil sampling laboratory on study area; (ii) Comparison between the basic physical properties data and real data in Unsaturated Soil Database (UNSODA); (iii) Estimation water volume change characteristics of soil from Seep/w results; (iv) Calculation Factor of safety (F.S.) from SLOPE/W results. These are described in more details in next section, thus:

Determining Physical Parameters

In this topic, both slope geometry of the study area and result from soil sampling are significant on the stability of soil slope

- Result from In-situ soil sampling

As shown in Fig. 3, CL-ML Soil properties Liquid Limit (LL) obtained from Atterberg limits laboratory testing (ASTM D 4318-04) are: 37.01, Plastic limit (PL); 22.6, and 14.44, Plastic Index (PI).

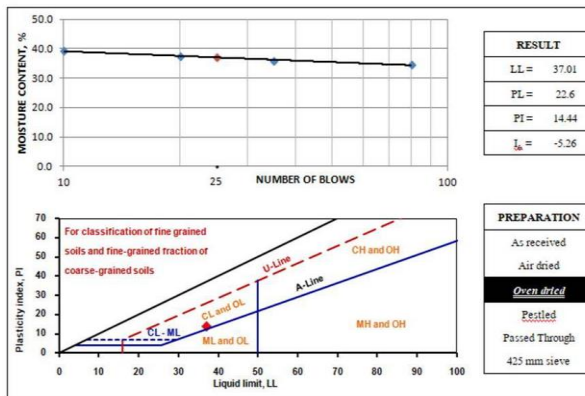


Fig. 3 Atterberg limits laboratory testing.

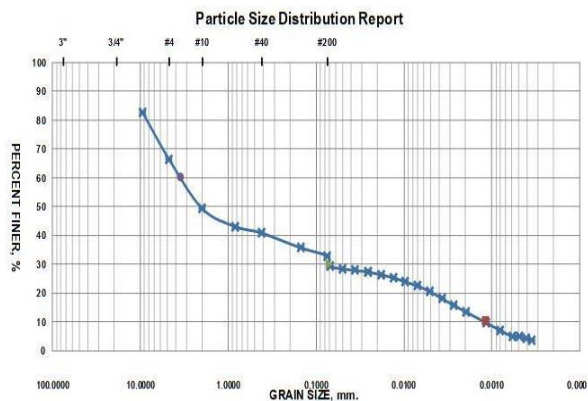


Fig. 4 Grain size distribution curve Analysis.

As shown in Fig. 4, Soil properties size in mm such that 10%, 30% and 60% of particles are finer than this size (D_{10} , D_{30} and D_{60}) from Sieve Analysis laboratory testing are: 0.0012, 0.07 and 3.6. The coefficient of uniformity (C_U) are 3000 and 1.13, the coefficient of curvature (C_C).

- Slope geometry of the study area

Fig. 5 idealizes the study slope to be used in the mathematical models. There is a 80 m thick CL-ML soil layer. The slope height is 80 m and the slope degree 27° . In the finite element analysis, the slope profile was divided into meshes of equal quadrilateral elements with a total number of more than 1,000 elements.

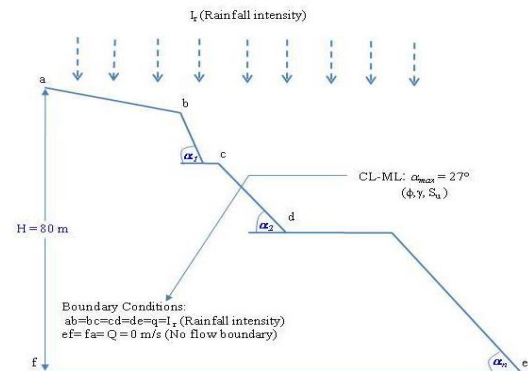


Fig. 5 Slope geometry and soil property of the site.

Boundary conditions utilized for the transient seepage analysis are: Zero flux for the lower horizontal and the left vertical bed boundaries (there is no seepage through the base of the soil slope) and a rainfall intensity I_r for the upper horizontal boundary

Comparison Between The Basic Physical Properties Data and Real Data in Unsaturated Soil Database (UNSODA)

UNSODA is a database with unsaturated soil hydraulic properties and other soil information that consists around 790 soil materials with data measured in the field or basic properties result. In addition, UNSODA is a database with water retention, saturated and unsaturated hydraulic conductivity [8].

Kosugi developed a general conductivity model for soils with lognormal pore-size distribution based on the Mualem-Dagan pore-scale model and two predictive methods reducing the average prediction error more than 77% compared with the Burdine and Mualem predictive models with use of 200 soil

samples in UNSODA [9], [10]. This paper describes a method to determine the UNSODA code by compared basic properties results from soil sampling

laboratory and the UNSODA code's basic physical properties.

RESULT AND DISCUSSION

Two stages were conducted in this topic: (i) Results from the soil sampling laboratory compared to UNSODA code; (ii) Results from slope stability analysis. These are described in more details in the next paragraph:

Results from the soil sampling laboratory compared to UNSODA code

The basic properties results from the soil sampling laboratory (Sieve Analysis, Grain Size Distribution, Liquid Limit, Plastic Limit, Shrinkage Limit) were compared with the UNSODA code's basic physical properties by general report U.S. Department of Agriculture as shown in Table.1, the results from the soil sample test were similar to the UNSODA 3033.

Table 1 Comparison basic soil properties between soil sampling in case study and Clay-Loam UNSODA 3033.

Sample	Case Study	Orenburg region, Russia
Soil Properties	Position	UNSODA Code
	Khanom	UNSODA 3033
Liquid Limit (LL %)	37.01	-
Plastic Limit (PL %)	22.6	-
Plastic Index (PI %)	14.44	-
Soil Classification	CL-ML	CLAY-LOAM
The coefficient of uniformity, Cu	3000	
The coefficient of curvature, Cc	1.13	1.00
D10	10	9
D30	30	25
D60	3.6	4
P200	30.56	42
Bulk-density (g/cm ³)	-	1.32
Porosity (cm ³ /cm ³)	-	0.51

Employing permeability data from UNSODA 3033 in general report U.S. Department of Agriculture, soil water retention curve (SWRC) program was used to calculated principal parameters such as the volumetric water content at saturated and residual conditions and constant parameter (Table 2) Table 2 Result from SWRC program

Model	Equation	Parameters	R ²
Brooks and Corey	$\left(\frac{\Psi_a}{\Psi}\right)^\lambda = \frac{\theta - \theta_r}{\theta_s - \theta_r}$	$\theta_s = 0.571$ $\theta_r = 0.160$ $\lambda = 0.287$	0.991
Van Genuchten	$\frac{\theta - \theta_r}{\theta_s - \theta_r} = \left[\frac{1}{1 + (\alpha \Psi)^n} \right]^m$	$\theta_s = 0.569$ $\theta_r = 0.272$ $\alpha = 0.024$ $n = 1.771$	0.996
Kosugi	$\theta = \theta_s \left[\frac{\ln\left(\frac{h}{h_m}\right)}{\sigma} \right]$	$\theta_s = 0.570$ $\theta_r = 0.298$ $h_m = 79.28$ $\sigma = 1.194$	0.996
Fredlund and Xing	$\theta = \theta_s \left[\frac{1}{\ln\left[e + \left(\frac{\Psi}{\Psi_a}\right)^n \right]} \right]^m$	$\theta_s = 0.569$ $a = 46.82$ $m = 1.149$ $n = 1.551$	0.997

Fig. 7 shows the relationship between matric suction and volumetric water content in different SWCC equation.

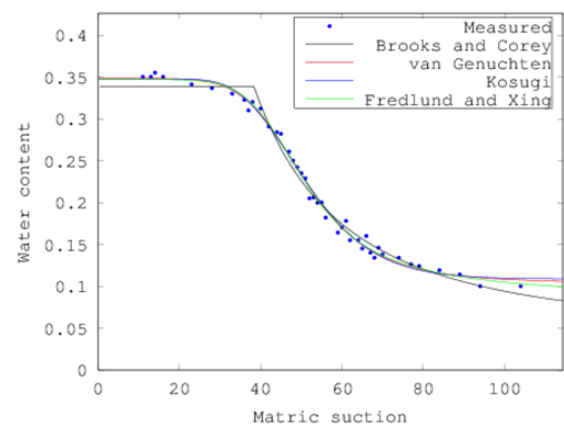


Fig. 7 SWCC curve in different equation [9], [10].

Results and discussion for the Khanom case study

A typical geometry of the Khanom soil slope was earlier shown in Fig 5. SWRC fit curve program was adopted to calculate the important parameters and plot the SWCC graph. Rainfall intensities from the Thailand's intensity-duration-frequency curve were used in SEEP/W and SLOPE/W programs to compute the factors of safety in the soil slope. The results from using SEEP/W and SLOPE/W were showing five separate time-steps (Figure 8) in the developments of factors of safety.

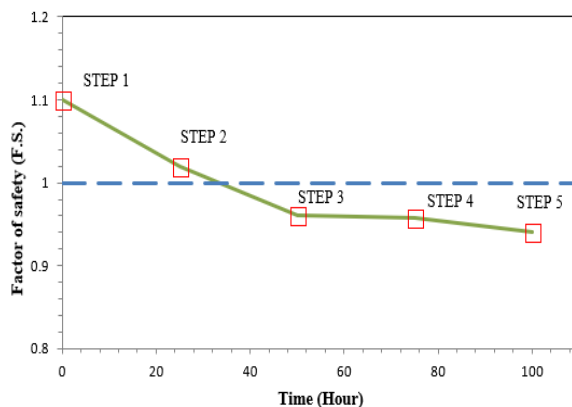


Fig. 8 Time-step versus factor of safety during the rainfall

At the beginning the factor of safety varied from 1.10 to 1.02 (step 1 at 0 h, to step 2 at 25 h). At 100 h, the increase in rainfall intensity lowered the factor of safety down from 1.10 to 0.94 (step 1 to step 5). Thus, the factor of safety declined to the point of the slope became unstable at approx. 50 hours (step 3 at 50 h) after the initiation of the rainfall. Results for the Khanom case study show that increasing rainfall intensity induces increased matric suction and decreased shear strength in soil mass. Increasing amount of moisture from the rainfall leads to reduced slope stability. The F.S. is an inverse relationship with rainfall precipitation, moisture content and coefficient of permeability changes. It can be used as an early warning indicator for landslide.

CONCLUSION

The advantages of a method to calculate the factor of safety by comparison between soil sampling and unsaturated soil hydraulic database in slope stability analysis is important to mitigate the problem in the soil sampling laboratory such as costly and time-consuming due to high standards equipment. The author can find UNSODA soil code and the hydro-mechanical behavior from determine SWCC curve by comparison between the basic physical properties data in soil sampling and real

data in Unsaturated Soil Database (UNSODA). The results from the Khanom soil sample test were similar to the UNSODA 3033. The SWCC from UNSODA were used as input parameters to estimate surface infiltration rates and the F.S. by using SEEP/W and SLOPE/W for an early warning indicator. Khanom slope became unstable at 50 h (F.S. = 0.94). The above findings suggested that the effect of antecedent rainfall is significant in the stability of soil slope, and that SWCC play important roles in Factor of safety.

ACKNOWLEDGEMENTS

I am very grateful to a former PSU Surat Thani lecturer, Miss Andrea Bayer, in rendering helpful reviews and in polishing up somewhat the English of the paper.

REFERENCES

- [1] Sony P., Ahmed R. and Kabul B., Determination of unsaturated soil properties and slope deformation analysis due to the effect of varies rainfall. The 5th International Conference of Euro Asia Civil Engineering Forum (EACEF-5) Proedia Engineering, 125, pp. 376-382 2015.
- [2] Lu N. and Likos W.J., Unsaturated Soil Mechanics. John Wiley & Sons, Inc., Hoboken, New Jersey. 2004.
- [3] Lin W., Zi-Jun C., Dian-Qing L, Kok-Kwang P. and Siu-Kui A., Determination of site-specific soil-water characteristic curve from a limited number of test data-A Bayesian perspective. International Journal of Geoscience Frontiers, 2017, pp.1-13.
- [4] Van Genuchten M. T., A closed-form equation for predicting the hydraulic conductivity of unsaturated soils. Soil Science Society of America Journal 44, 1980, pp. 892-898.
- [5] Fredlund D.G. and Morgenstern N.R., Stress state variable for unsaturated soils. Journal of Geotechnical Engineering Division, Proceedings, American Society of Civil Engineering (GTS), 103, 1997, pp. 447-466.
- [6] Fredlund D.G. and Xing A., Equations for the soil-water characteristic curve. Canadian Geotechnical Journal, 31(3), 1994, pp. 521-532.
- [7] Holtz, R. and Kovacs, W. (1981), An Introduction to Geotechnical Engineering, Prentice-Hall, Inc. ISBN 0-13-484394-0
- [8] Nemes A., Schaap M.G., Leij F.J. and Wösten J.H.M., Description of the unsaturated soil

- hydraulic database UNSODA version 2.0. J. Hydrol, 251, 2001, pp. 151–162.
- [9] Kosugi K., Three-parameter lognormal distribution model for soil water retention. Water Resour. Res., 30, 1994, pp.891–901.
- [10] Kosugi K., General model for unsaturated hydraulic conductivity for soils with lognormal pore-size distribution. Soil Science Society of America Journal., 63, 1999, pp. 270–277

A NEW PRESSUREMETER FOR TESTING STIFF CLAY

Prof. Radhi Alzubaidi

College of Engineering, University of Sharjah, UAE

ABSTRACT

A large size pressuremeter was developed to test stiff fissured clay; the new pressuremeter is suitable for testing glacial till with a constant rate of membrane expansion. It is capable of measuring the pore water pressure of the soil during a test and possesses other features such as, reversals of expansion to permit cyclic load tests, running Menard incremental pressure tests and holding the diameter or the pressure constant at any time during the test. The large size of the pressuremeter in itself is an important aspect of the device, enabling the representative and satisfactory in situ testing of fissured till. One pressuremeter test carried out at in situ, enabling information on the horizontal at rest pressure, elastic modulus, undrained shear strength, limit pressure and the horizontal coefficient of consolidation.

Keywords: New pressuremeter, Glacial till, Constant rate of strain, Pore water pressure, Horizontal coefficient of consolidation

INTRODUCTION

The pressuremeter received great applications in testing the soils at site, the developments were in the methods of manufacturing and others developed the analytical solutions developed a Pressuremeter to operate in Alluvial Soils of Punjab[1] , the pressuremeter possesses a large diameter in order to test representative samples ,there was a need to develop a device in Pakistan that could be used as pre-bored as well as full-displacement pressuremeter for characterizing the alluvial soil deposits of Punjab province. Moreover, the new device should be simple, robust and cost effective and still produces parameters of high quality. A new methodology developed to deduce hyperbolically shaped p-y curves of transversely isotropic rock from pressuremeter test through extensive theoretical and numerical simulation works [2]. The method was validated by four case studies involving both actual full-scale lateral load test data and pressuremeter test data at the test site as well as hypothetical numerical simulation cases. A new analysis for interpreting pressuremeter tests data are developed [3]. The new analysis method based on an energy approach concept. The objectives are to determine the outer radius of the clay hollow cylinder that models a normally consolidated clay medium idealized in undrained conditions and to express the clay behavior by the effective stress path and the stress-strain relationship. At the position of three particles across such a cylinder, the developed excess pore water

pressures were measured during testing. The analysis showed that the development of greater excess pore pressure than the circumferential stress in compression indicates the critical state and that the testing rate has a negligible influence on the deduced critical state. Thus, the undrained shear strength at the level of testing underground can be obtained. Extensive pencil pressuremeter and cone penetrometer tests performed at two sites chosen in Florida[4], from the comparisons between pressuremeter and cone penetrometer data, promising correlations were developed between the pressuremeter initial elastic moduli and cone penetrometer tip resistances, correlations were also developed between pressuremeter limit pressure and cone penetrometer tip resistances. Pressuremeter tests ,standard penetration tests (SPT) and cone penetrometer (CPT), carried out at three different sites [5],also they carried out laboratory testing to deduce the strength parameters of the soil .The sites comprised very soft to medium stiff clays, stiff to very stiff clays and loose to medium dense sands . Their aim was to develop mathematical correlations of pressuremeter testing data with standard penetration tests, cone penetration tests and laboratory tests data.

A new large diameter pressuremeter is developed for testing glacial till with a constant rate of membrane expansion. It is capable of measuring the pore water pressure of the soil during a pressuremeter test and

possesses other features such as, reversals of expansion to permit cyclic load tests, running Menard incremental pressure tests and holding the diameter or pressure constant at any time during the test.

THE SECOND VERSION OF STRATHCLYDE PRESSUREMETER

A new pressuremeter developed by [6], the pressuremeter is designed to pressurize borehole wall, while maintaining a constant rate of strain of expansion the borehole diameter. During the design process of the present pressuremeter, the shortcomings in the first version of Strathclyde pressuremeter been considered and overtaken, and modifications added. The pressuremeter suitable to insert in 152 mm diameter pre-bored hole. The new pressuremeter is built robust enough to face the stiff properties of the glacial till and also to test a relatively large mass of the clay to represent the macrostructure of the deposit. It has also additional attributes to those of the first version like,

- Constant rate of pressure or strain change
- Three levels of diameter monitoring (top, middle and lower level 184 mm apart)
- Capacity to hold a selected pressure or selected diameter at any stage of a test.
- Cyclic loading.
- Manual control enabling Menard type incremental tests to be made.
- Pore water pressure measurement at one location on the membrane surface.

The new pressuremeter consists of:

- (1) The control unit.
- (2) The probe.

The Control Unit

The control unit consists of the pneumatic valve box and the control box which contains the electronic circuits and controlling the operating process of the device.

Description of the Probe

The probe consists of three sets of sensors are provided to monitor the diameter of the device at any stage. Thus circularity and cylindricity of the inflated probe can be noted at any time. Control of inflation referred to (any) one set of sensors. In the first version [7] used one sensor set of six registering feet, while in the second version of Strathclyde pressuremeter three sets of eight feet were

incorporated to assure and control radial strain. The air pressure at any time in the probe is measured by a transducer inside the probe. The pore water pressure at the membrane interface with the soil is also measured by a transducer inside the probe, but the transducer having its ceramic measuring face carried through the membrane to be in contact with the soil under test. The sensor units and the matching end cones are separated and fixed to spacing sections of high strength aluminum tube and the whole strengthened by four steel rods treaded through. The electrical lead from the sensors and transducers are led through the upper end cone and up to the control box.

The rubber membrane, 35 mm wall thickness, is commercially produced from a standard former made and supplied by the author. In use each membrane is carefully slide over the probe and clamped to each end cone. The sensor feet and pore water pressure transducer are then fitted through the membrane and locked to it. Thus when the membrane is inflated or deflated the feet and the transducer move with it. The finished probe diameter is about 142 mm and its cylindrical membrane length 710 mm. An air/ gas connection is made at the upper end cone, the air line extending also to that control unit.

Radial Movement Sensors

The mechanism is based on potentiometers reading attached to the rubber membrane of the probe, where the membrane pulls out the brass rods and turns the potentiometers, the voltage increases giving the diameter increase to a scale

The range of diametrical movement available is about 50 mm. Although the potentiometers may be read individually, the operating arrangement is to sum the voltages from eight potentiometers in any one set to give an average diameter (radius). This average is compared electrically with a master value from a ramped increase in diameter and the inflation adjusted to follow the chosen ramp values.

Regulation of Pressure to the Probe

There are several ways of operating the device but its principal mode is one of constant rate of strain expansion. Each of these ways, it is necessary to regulate the gas pressure to the probe in order that expansion follows the selected mode. Thus instructed on instructions from the control, the pressures of gas to the probe are adjusted by means of electrically operated solenoid inflated and exhaust valves. A further two manual valves are provided in the

housing, with the control knobs. One closes off the gas supply to the stem and the other use only allows the system to be exhausted. These manual valves are for emergency use only. Continual operation of the valves during testing is accompanied by some vibration, for this reason the valve housing was separated from the control unit.

Electronic Control Unit

The detailed circuit is complex but essentially the control unit comprises:

- DVM reading probe diameter
- DVM reading probe pressure
- DVM reading pore water pressure
- Selector for diameter sensor level (upper, middle and lower)
- Selector for test mode (constant rate of strain ,constant rate of pressure increase , manual control of diameter or pressure etc)
- Selector to display individual potentiometer readings
- Signal indicators of activity
- Ramp generator ,as a control device

In an earlier version of the pressuremeter, the constant rate of probe expansion was achieved by a “slave” following a clock motor. In present version an electronic ramp generator provides the “master” control. The ramp is essentially linear with time but its range can be varied from 60 minutes to complete the full expansion. Thus, while the normal operating mode is to test the soil under conditions of constant rate of strain (deformation) , other modes can be selected e.g. Menard type incremental loading manually , cyclic loading pressure , pressure or diameter “ hold” with pore pressure reading.

The Pore Water Pressure Device

The present pressuremeter represents the first version developed at Strathclyde University to be equipped with pore water pressure device. It is essential that any pore water pressure measuring device on the surface of the membrane of the probe meets the following requirements:

- (i) Fast response.
- (ii) The device an integral part of the membrane, moving freely as the membrane is inflated.
- (iii) Satisfactory and easy method of de-airing.
- (iv) Small in comparison to the radius of the probe.
- (v) Easy to replace when a new membrane is fitted.

The diameter of the transducer is 6 mm and its total length is 12 mm. Before placing the pore pressure

device inside the probe, the system is tested by simulating the in situ practical working condition in the laboratory. For this purpose two Rowe cells are incorporated jointed one over the other and divided by aluminum circular partition. The upper Rowe cell is filled with water while the lower Rowe cell is kept empty. The pore water pressure transducer with collar is screwed to the circular partition keeping the sintered bronze filter facing the upper Rowe cell and the aluminum box placed in the lower Rowe cell. The lower Rowe cell is considered to represent the inside of the probe while the upper Rowe cell represents water pressure that comes from the soil. This arrangement is considered to simulate the operation process of the pore water pressure device during the in situ testing. The testing program includes, increasing the water pressure (upper Rowe cell) and at the same time increasing the gas pressure (lower Rowe cell) , during the initial testing ,it was found that the reading of the pore water pressure decrease when the air pressure was increased . After investigation it was discovered that the transducer was being pressurized through the connection between the wires of the transducer and the aluminum box wires namely through the Teflon tube and thus affecting the reading of the transducer. This problem was overcome by gluing the connection of the wires with Perspex liquid cement and in turn gluing the Teflon tube, so forming a seal. It was then possible to increase the air pressure (lower cell) to 1800 Kpa the membrane pulls out the brass rods and turns the potentiometers, the voltage increases giving the diameter increase to a scale kpa with out any change in the reading of the transducer. After calibration the pore water pressure device was fitted to the probe. The method of keeping the pore water pressure transducer saturated is by keeping the sintered bronze filter itself saturated with a detachable reservoir of de-aired water connected to the outside of the membrane. The reservoir is kept connected to the filter during transpiration and also when the pressuremeter is kept in the laboratory. Before the removal of the reservoir from the pore water pressure device, the water in the reservoir is pressurized in order to check if there is any air in the pore water pressure measuring system, and if so to remove it. Occasionally the pore water pressure device is also subjected to a vacuum , As in the pressure transducer ,the readings of the pore water pressure transducer are also arranged to display in KN/m^2 on the digital voltmeter on the control box. The last operation between lowering the probe to its depth is the removal of the reservoir .

The Calibration Testing

Several measurements are made during a pressuremeter test and the observations at any instant displayed on control unit. It is vital to analyses of the observed data that the data themselves are dependable. Several calibration checks are regularly made these are as follows

- 1- Values of probe diameter from potentiometer readings
- 2- Values of probe inflation pressure
- 3- Values of pore water pressure

The calibration of the diameter is achieved by inflating the probe inside steel tubes of different diameters. When all the domed screws are in contact with steel tubes, no further movements of the rotary potentiometers occur with increasing the pressure and the diameter is well defined.

The calibration of the two pressure gauges that housed in the control box achieved by connecting the pressure gauges by plastic tube to air pressure source, the air pressure source been connecting to a pressure gauge. The electrical connection from the pressure transducer is linked to an electronic circuit inside the control box, the object of this circuit being to present output of the pressure transducer directly in KN/m^2 . The check calibration process involves increasing the pressure step by step and to check that the readings are the same readings as on the control pressure gauges in KN/m^2 . The same calibration system is used to calibrate the pore water pressure transducer, but with a water pressure source. Again the readings of the pore water pressure are displayed in KN/m^2 on a digital voltmeter on the control box.

RESULTS OF PRESSUREMETER TESTS

The undrained parameters of Glasgow till are obtained using the new version of pressuremeter, the probe being first inserted into the pre-bored 150 mm diameter boreholes using a pilcon rig for making the holes. The pressuremeter tests were mainly run at a constant rate of strain of about 0.52 %/ min., the duration of the tests is being 7-10 min.

Fig. 1 shows the pressure- volume curve test at one site in Glasgow glacial till. The value of the horizontal at rest pressure (P_o) at the start of linear part and near the point of inflection is equal to 50 KN/m^2 for this particular test. Values of the P_o obtained for different sites are shown in Fig. 2. The new version of the pressuremeter also predicted the undrained shear strength of the glacial till using the analysis of [8], their method developed theoretical relationship to interpret the undrained shear strength from pressuremeter tests. From their analysis they suggest the following equation

$$P = P_L + C_u \ln (\Delta V/V)$$

Where

P = applied pressure

P_L = limit pressure

ΔV = volume change

V = volume of the borehole wall

By plotting the pressure (P) versus $\ln (\Delta V/V)$, the plot consists of a curve and a final linear part,

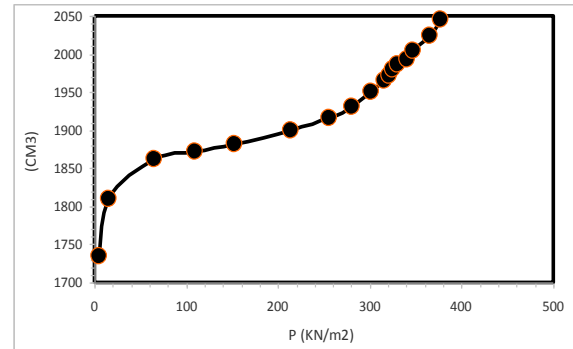


Fig.1 Typical pressure – volume curve for Glasgow till

, the slop of the straight portion represents the undrained strength, (C_u).

Such a plot is shown in Fig.3. The values of the undrained shear strength, C_u derived from Gibson and Anderson [8] method for different sites are shown in Fig.4. The pressuremeter tests also deduced values for the pressuremeter modulus, E , using the analysis introduced by [8], in their method stated that during the elastic phase of the expansion of the borehole at pressures above P_o , the values of the elastic modulus, E can be expressed as follows

$$E = [\Delta P (1+\nu)] / (\rho_o) \quad \text{where}$$

ΔP = change in applied pressure

ν = Poisson's ratio

ρ_o = change in radial displacement at the borehole wall

The values of E expressed for different sites of Glasgow till are drawn with depth can be seen in Fig. 5.

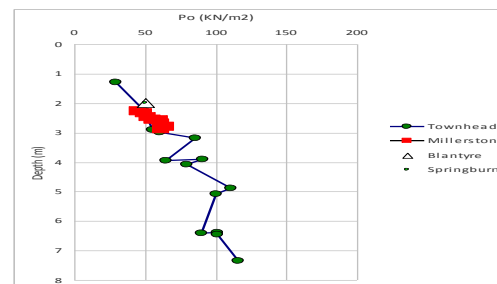


Fig.2 Values of P_o with depth

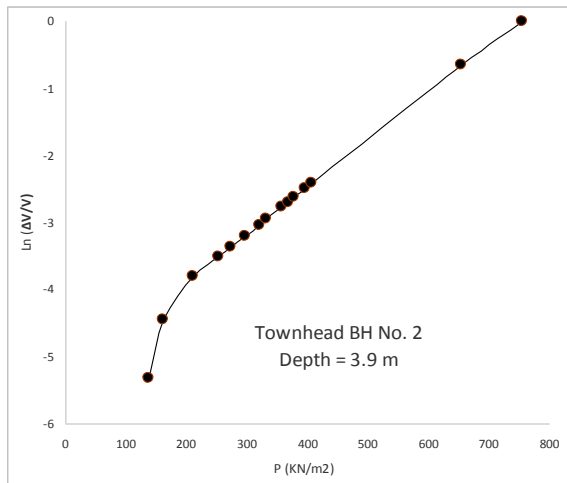


Fig.3 Showing P- $\ln(\Delta V/V)$ curve

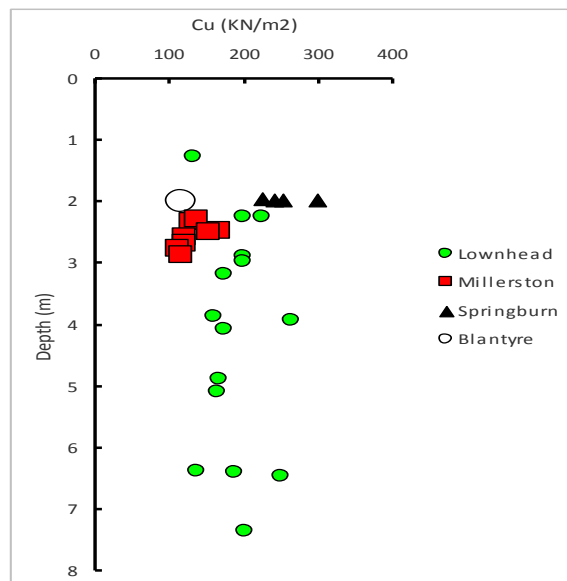


Fig.4 showing the values of undrained shear strength with depths

The values of P_L deduced for different sites are plotted in Fig.7. The conventional limit pressure, P_L , also can be predicted by plotting the pressure, P , versus $\ln(\Delta V/V)$, where ΔV represents the change in volume above V_o , this method developed by [6], to yield by extrapolation the values of the conventional limit pressure as can be seen in Fig.3 and the values of the conventional pressure for different sites with depths can be seen in Fig.8.

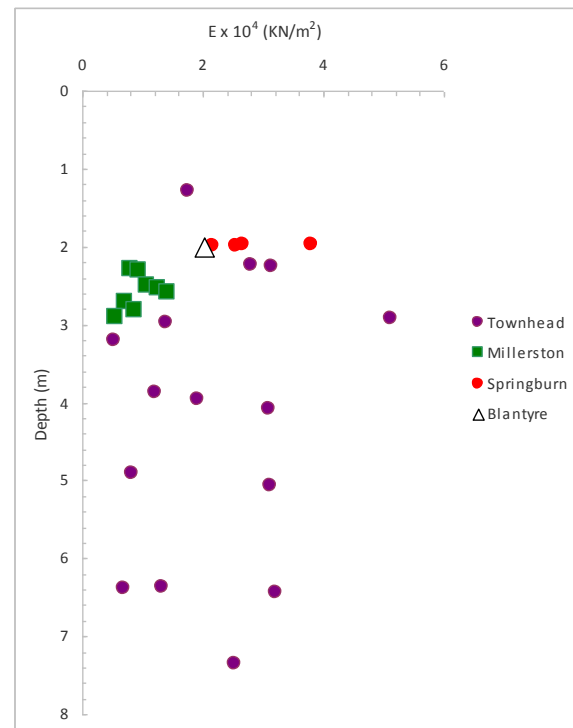


Fig.5 Values of E with depth using Gibson And Anderson Method

The limit pressures also can be detected from the pressuremeter tests, the theoretical limit pressure (P_L) as derived from up-side curve method introduced by [9], involves plotting the pressure (P) versus $(1/\Delta V_i)$, where ΔV_i represents volume change above original volume of the probe, the last linear portion when extrapolated gives P_L at $1/\Delta V_i = 0$, this can be seen at Fig.6.

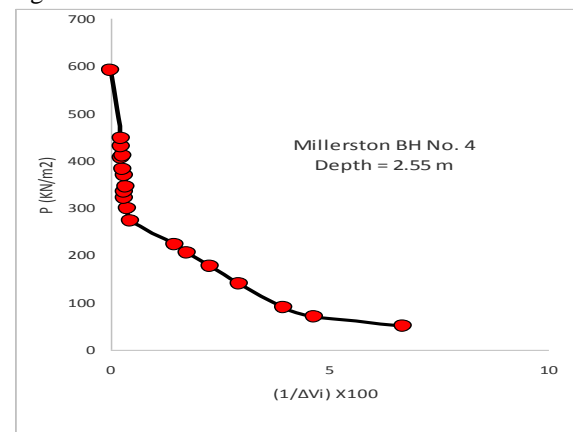


Fig. 6 showing the up- side curve method

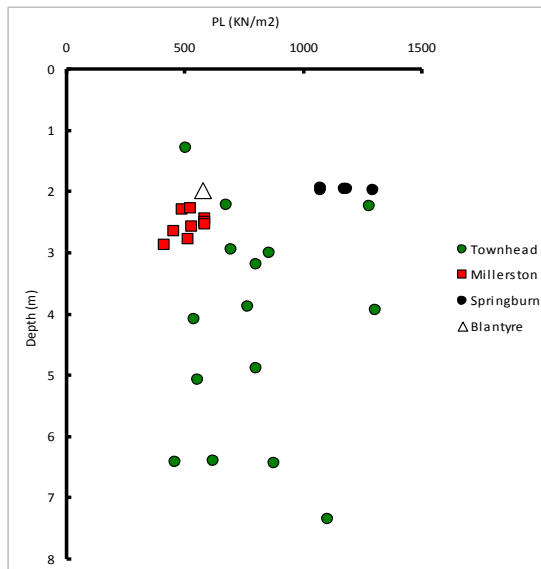


Fig. 7 Values of P_L with depth for different sites

The cyclic loading tests also can be conducted by the new version of pressuremeter, such tests for testing the Glasgow till carried out with constant rate of strain, one test example for Glasgow till is illustrated in Fig.9.

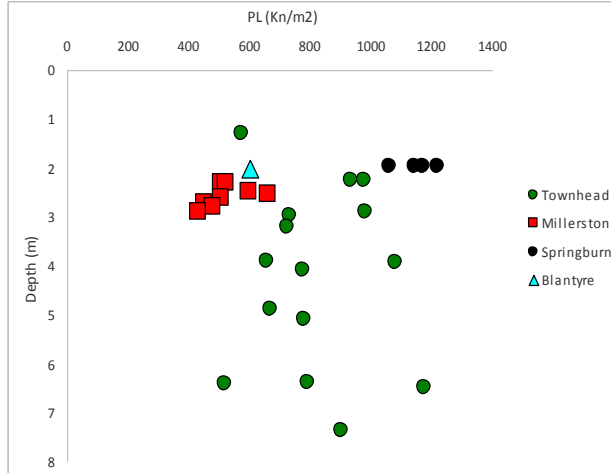


Fig. 8 Showing values of P_L with depth using the conventional limit pressure method

The new version of pressuremeter can also determine the horizontal coefficient of consolidation conducting the “holding tests”, with the direction of pore water pressure drainage sensibly radial. The holding tests as described by [10] involves increasing the total pressure, P at a constant rate of expansion and then holding the diameter constant at a predetermined strain. During the expansion of the borehole, the pore water pressure builds up.

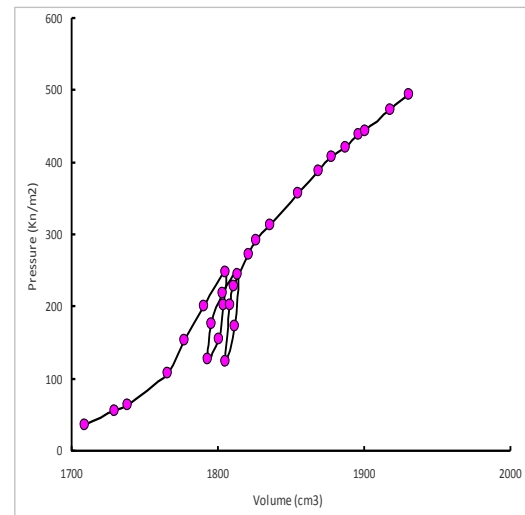


Fig.9 Typical pressure – volume curve for cyclic loading test

When the diameter of the probe is held constant the pore water pressure dissipated as shown in Fig.10 and the total pressure diminishes a little as can be seen in Fig. 11. The first part of the diameter holding test is similar to the conventional pressuremeter tests and the values of P_o , C_u , P_L and E can be determined and from the dissipation of the pore water pressure the values of the horizontal coefficient of consolidation is evaluated.

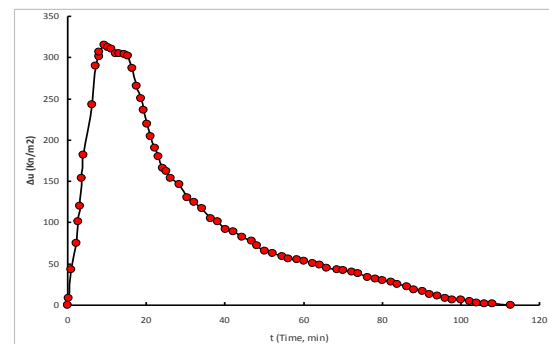


Fig. 10 Variation of pore water pressure with time

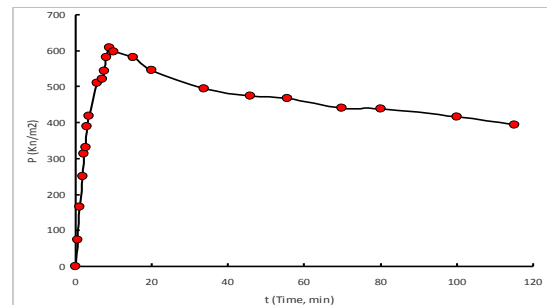


Fig.11 Variation of the total pressure with time

CONCLUSIONS

The new version of pressuremeter so developed with robust enough to test the stiff glacial till, the present paper allows the following conclusions to be drawn

- 1- A new version of pressuremeter developed to test large, representative soil and to test stiff clay, the diameter of the probe was 142 mm and the length 710 mm, the test can be carried out in a borehole with 152 mm.
- 2- The device have three arrays of monitoring the diameter of the borehole, thus the circularity and cylindricity of the inflated probe can be noted at any time.
- 3- The pressuremeter conducted the tests with constant rate of radial expansion of the membrane, this including
 - (a) Constant rate of strain
 - (b) Constant rate of pressure change
- 4- Menard pressuremeter tests also can carry out with new version of pressuremeter.
- 5- The device could also hold the pressure or the diameter of the borehole constant at any instant during pressuremeter tests.
- 6- The new pressuremeter could also conduct cyclic loading tests.
- 7- A small transducer attached to membrane which enables measurement of pore water of the soil during the tests.
- 8- Carrying out one pressuremeter test the following factors can deduced for the soil
 - (a) Horizontal at rest pressure, P_o
 - (b) Undrained shear strength
 - (c) Young modulus
 - (d) Limit pressure
 - (e) Horizontal coefficient of consolidation

REFERENCES

- [1] Rehman Z (2010) Development of a Pressuremeter to Operate in Alluvial Soils of Punjab. Doctoral thesis, University Of Engineering And Technology, Lahore, Pakistan
- [2] Sharo A, A (2009) Pressuremeter Applications in Laterally Loaded Drilled Shaft Socked Into Transversely Isotropic Rock, PhD Thesis, University of Akron, USA
- [3] Iskander K (2013) New Pressuremeter Test Analysis Based on Critical State Mechanics International Journal of Geomechanics, volume 13, issues 5
- [4] Farida M, Abdelkadera H, and Salaha L (2013) Analysis of Correlations between Cone Penetrometer and Pencil Pressuremeter Parameters, Procedia Engineering, Vol. 54, pp 505 – 515
- [5] Rehman Z, Akbar, Khan A and Clarke B (2016) Correlations of Pressuremeter Data with SPT, CPT and Laboratory Tests Data, Pak. J. Engg. & Appl. Sci. Vol. 19 July, 2016 (p. 1–13)
- [6] Alzubaidi R (1984). Pressuremeter Practice in Testing Glacial Till, PhD, Thesis, civil Engineering. Dept, University of Strathclyde, UK
- [7] Anderson, W (1972) The Geotechnical Properties of The Till of The Glasgow Region And The Development Of a Constant Rate of Expansion Pressuremeter Suitable For Measuring the Undrained Strength And Deformation Characteristics Of This Till. Ph.D. Thesis; Univ. of Strathclyde
- [8] Gibson Rand Anderson W (1961). In-situ measurement of soils properties with the pressuremeter. Civ. Engng. Publ. Wks. Rev. 56 : 615-618.
- [9] Van Wambeke, A. and d Hericourt, J (1975) Coubed Pressiometriques inverses: méthode d interpretation de lessai pressiometrique, Soils-soils, Vol.25 pp15-25
- [10] Randolph Mand Wroth C (1979). "An analytical solution for the consolidation around a driven pile". International Journal for Numerical and Analytical Methods in Geomechanics. Vol. 3, pp 217–229.

DYNAMIC BEHAVIOUR OF RAILWAY BALLAST EXPOSED TO FLOODING CONDITION

Sakdirat Kaewunruen^{1,2} and Tao Tang¹

¹Department of Civil Engineering, School of Engineering, The University of Birmingham, U.K,

²Birmingham Centre for Railway Research and Education, The University of Birmingham, U.K

ABSTRACT

Railway ballast is one of the main components in ballasted railway track systems. It is installed under the railway sleeper to absorb dynamic wheel/rail interaction forces, preventing the underlying railway track subgrade from excessive stresses, enabling the interlocking of skeleton track onto the ground and providing lateral track stability. Generally, the dynamic modelling of ballast gravels relies on the available data, which are mostly focused on the condition at a dry condition. Recent findings show that railway track could significantly experience extreme climate such as long-term flooding. This phenomenon gives rise to a concern that the ballast may experience higher level of moisture content than anticipated in the past. On this ground, a test rig for estimating the dynamic properties of rail ballast has been devised at the University of Birmingham. A non-destructive methodology for evaluating and monitoring the dynamic properties of the rail ballast has been developed based on an instrumented hammer impact technique and an equivalent single degree-of-freedom system approximation. This investigation focuses on the dynamic single-degree-of-freedom (SDOF) model of rail ballast submerged under the flood where the dependent effects of frequency can be distinguished. Based on the impact-excitation responses, the analytical state-dependent model was applied to best fit the experimental modal measurements that were performed in a frequency range of 0-500 Hz. The curve fitting gives such dynamic parameters as the modal mass, dynamic stiffness and dynamic damping constant, all of which are required for modern numerical modelling of a railway track.

Keywords: Dynamic properties, railway ballast, flood condition, climate change.

INTRODUCTION

Railway ballast or granular media is a major track component used in ballasted railway tracks worldwide. It is mostly derived from crushed rock-based local materials from various sources such as crushed igneous rocks (granite, rhyolite, decite, basalt, quartzite or latite), crushed metamorphic rocks, crushed sedimentary rocks, crushed gravel (from river, lake), or sometimes even from waste products (such as crushed slag, chitter) [1-4]. Early railways did not place ballast as being highly significant to the makeup of a successful design of the permanent way. This position gradually changed and the performance of the ballast material is now highly regarded in the design process. Ballast is required to fulfil the task of maintaining the track in good alignment both horizontally and vertically. To provide this it must have the following characteristics:

- Durable to be able to absorb the loads imposed by the sleepers and transmit the loads to the sub-grade without undue breakdown.
- Hard wearing with high abrasion resistance in both wet and dry conditions.
- Angular with sufficient bulk density to resist movement of the track both longitudinally

and laterally.

- Particle size to allow packing and transfer of the loads of the track but with sufficient void space to allow free draining to assist shedding of all moisture.

Both the ballast and capping layer material can be seen in Fig. 1.



Fig. 1 Ballast and capping layer [2].

The functions or roles expected of the ballast layer have changed with time and the evolutionary development of railway technology. There is some

discussion of the functions of ballast in the references, “Railroad Engineering” (Ch 21) by WW Hay, “British Rail Track” (Ch 2), by the Permanent Way Institution, “A Review of Track Design Procedures” (Vol 2, Ch 4) by Jeffs and Tew, and “Track Geotechnology and Substructure Management”, by Selig and Waters [1]. The functions of ballast can be divided into two criteria:

- Primary Functions, - the original purpose of ballast; and,
- Secondary Functions, - the characteristics of the material that enable the ballast to fulfil and continue to fulfil its primary function and those functions that have been added with technology improvements and community expectations.

The primary functions of the ballast are to provide a uniform elastic vertical support; to fix the track in position laterally and longitudinally; and to facilitate the correction of the track level and line enhancing constructability and maintainability of railway network [2-4].

The secondary functions of ballast are to allow surface water to drain rapidly; to inhibit the growth of vegetation; to compensate for the presence of fouling material, to reduce noise; to provide electrical insulation of one rail from the other; and, to moderate the effect of frost heave in cold climates and the movement due to climate uncertainties [5-8].

Railway ballast is installed under railway sleepers to transfer the quasi-static stress (already filtered by rail pads and sleepers) from axle loads and wheel loads from both regular and irregular train movements, as shown in Fig. 2. In accordance with the design and analysis, numerical models of a railway track have been employed to aid the track engineers in failure and maintenance predictions [9-12].

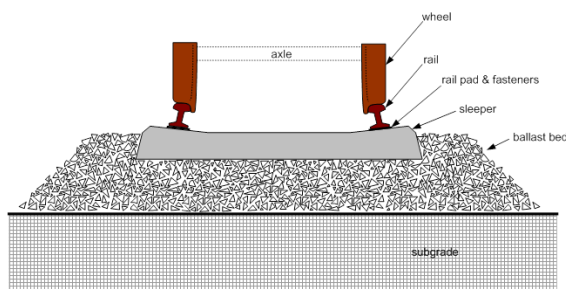


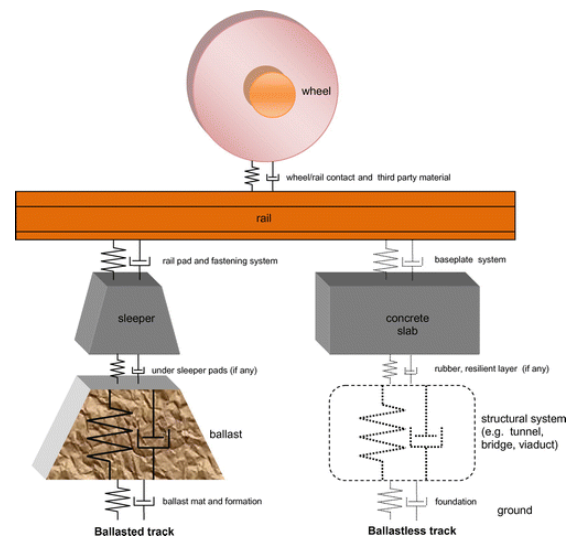
Fig. 2 Typical track structure [9].

The current numerical models or simulations of railway tracks mostly consider the track components in perfect situation or in a normal weather condition. The effect of flooding on the dynamic behaviour of railway ballast has never been investigated, although it is evident that climate uncertainty has a significant influence on railway networks that affect the serviceability and performance of railway tracks [13-20]. The primary reason is due to a lack of

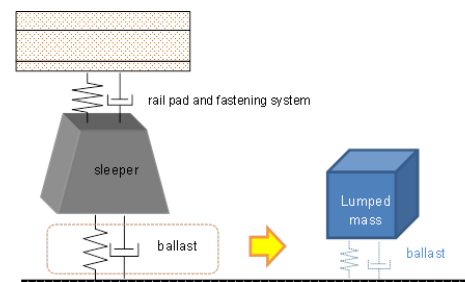
information, either about the dynamic characteristics of railway ballast under variable flooding conditions, or about the dynamic train-track modelling to capture the flooding conditions. This paper is the world first to present dynamic behavior of railway ballast in flooding conditions. It also discusses the experimental results obtained as part of the railway engineering research activities at the University of Birmingham (UoB) aimed at improving the dynamic performance and modelling of railway tracks globally. The proposed relationships could be incorporated into track analysis and design tools for a more realistic representation of the dynamic train-track interaction and load transfer mechanisms.

ANALYTICAL MODELLING

Majority of train-track dynamic simulations adopt a multi-degree-of-freedom system (MDOF) approach for modelling train and track components. MDOF system or so-called ‘multi-body simulation’ idealises the structural and mechanical components into nodes of freedom and string elements (spring and dashpot). This structural idealisation concept is very common in practice and academia in order to reduce computation time and resources. Fig. 3 illustrates the train-track simulation and track idealisation for the numerical simulation [21].



a) Train-track simulation



b) Ballast idealisation

Fig. 3 MDOF train-track idealisation [21]

The dynamics of resilient track have been studied mostly based on a two-degree-of freedom (2DOF) model. In this paper, a SDOF-based method has been developed to help track engineers to evaluate the realistic dynamic behavior of railway ballast required for the design using the numerical simulation. An analytical solution has been used to best fit the vibration responses. Considering the SDOF system in Fig. 3, the dynamic behavior of ballast in the vertical direction can be described by the well-known equation of motion:

$$m\ddot{x} + c_p\dot{x} + k_px = f(t) \quad (1)$$

$$\omega_n^2 = k_p/m_p, \text{ or } 2\zeta\omega_n = c_p/m_p \quad (2a, b, c)$$

$$\zeta = c_p / 2\sqrt{k_pm_p}$$

where m_p , c_p , and k_p generally represent the effective sleeper mass, damping and stiffness of ballast, respectively. By taking the Fourier transformation of (1), the frequency response function can be determined. The magnitude of the frequency response function $H(f)$ can be represented as follows:

$$H(f) = \frac{1}{m_p} \frac{4\pi^2\beta f^2}{\sqrt{\left[1 - 4\pi^2\beta f^2\right]^2 + \left[4\pi^2\beta \left(\frac{c_p^2}{k_pm_p}\right) f^2\right]}} \quad (3)$$

where,

$$\beta = \frac{m_p}{k_p} \quad (4)$$

This expression contains the system parameters m_p , k_p and c_p that will later be used as the curve-fitting parameters.

Considering Eq. (2), the fundamental frequency of railway ballast is relatively low if the track mass is significant. This implies that significant energy is required to excite the vibration of the SDOF system. By lowering the effective mass over a representative area of ballast (similar to a falling weight method with relatively small diameter of proctor, e.g. 50mm), the fundamental frequency of the SDOF system can be lifted to a higher range and it will require relatively lower energy to excite the system in order to obtain a realistic vibration response. In this study, a block of concrete (150mm x 150mm x 150mm) is used to represent the effective mass in the system. This enables the effective use of a modal hammer to excite the system [22-26].

EXPERIMENTAL SETUP

Fig. 4 demonstrates the experimental setup in this study. Pilot studies (over 200 data sets) using a modal hammer (PROSIG) were carried out to evaluate the accuracy and precision of the vibration responses. The modal vibrations show excellent agreement between each test. The resonant frequency of the system is around 50-60 Hz, which are significantly above the minimum requirement for the calibrated, instrumented modal hammer (> 4 Hz). The boundary condition of the box is twice the side of the concrete block to avoid reflected shear wave. Since only vertical vibration is excited and measured, it was found that the boundary condition can be negligible and twisting and Rayleigh modes of vibration cannot be detected (as small-amplitude resonances). This pilot result allows further research into the effect of flooding condition on the dynamic behavior of railway ballast.



Fig. 4 A test setup

To measure the vibration response of the ballast, an accelerometer was placed on the top surface of the upper segment, as illustrated in Fig. 4. The mass of the upper segment is 8.2kg. It should be noted that a test rig was mounted on a “strong” or “isolated” floor, the frequency responses of which are significantly higher than those of interest for the ballast. During the tests, the floor also isolates ground vibration from surrounding sources. To impart an excitation on the upper mass, an impact hammer was employed within a capable frequency range of 0–3,500 Hz. The FRF could then be measured by using the PCB accelerometer connected to the PROSIG modal testing system, and to a computer. Measurement records also included the impact forcing functions and the coherence functions.

DYNAMIC RESPONSES

The aim of this study is to establish a better insight into the dynamic behavior of railway ballast in flooding condition. The insight will help track engineers to develop appropriate models of flooded railway ballast [27-28].

The dynamic responses of railway ballast in flood conditions can be seen in Fig. 5 (in time domain) and in Fig. 6 (in frequency domain). Fig. 5 shows that the vibrational amplitude of the representative mass is reduced with the increased level of water or flooding condition. The level of water also reduces the secondary amplitude of vibration over the time. It is clear that the flood level can also increase the energy dissipation capacity of

the track when stagnant water fills the pore of gravels or clog the ballast.

Fig.6 also confirms the insight into the dynamic behavior of the ballast in flooding conditions. The dynamic receptance (H) decreases with the increment of flood level. Also, the flooding condition can also shift the natural frequency of the ballast layer (of the SDOF system). Considering that the representative mass is relatively constant, it implies that the water level can also reduce the stiffness of the system.

CONCLUSION

Railway ballast is one of the critical components widely used in modern ballasted railway track systems. It is generally installed under

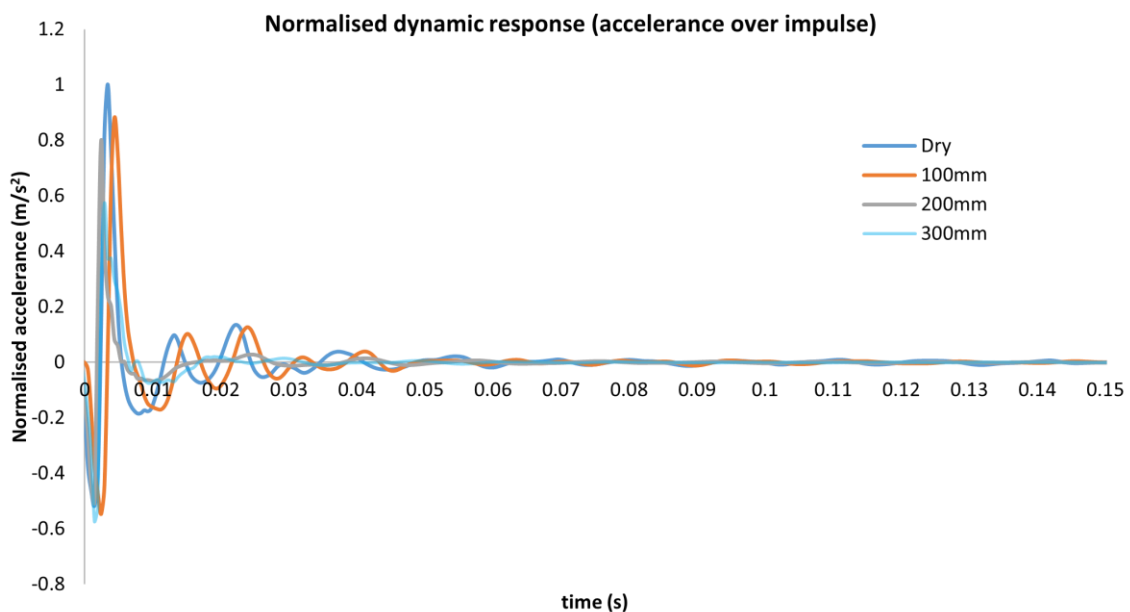


Fig. 5 Dynamic responses to impact hammer loading (normalised by the maximum impulse)

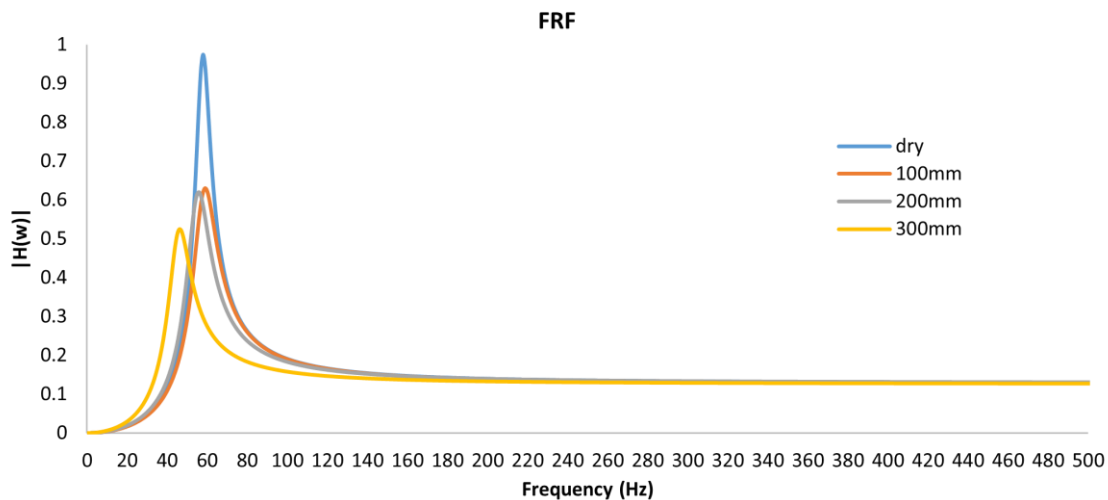


Fig. 6 Frequency response functions of flooded ballast

the railway sleeper to absorb dynamic wheel/rail interaction forces, preventing the underlying railway track subgrade from excessive stresses, enabling the interlocking of skeleton track onto the ground and providing lateral track stability. Current practices in numerical simulations make use of MDOF systems that adopt merely the dry ballast condition. Recent findings show that railway track could significantly experience extreme climate such as long-term flooding. Therefore, there is a need to identify appropriate models as well as to investigate the realistic dynamic behavior of railway ballast exposed to flooding conditions. This study is the world first to highlight such critical effect. Analytical and experimental studies have been carried out to address such the pressing issue. The experimental studies reveal an unprecedented insight into the dynamic behavior of the flooded ballast. The flood condition can reduce the instant stiffness of the track system, whilst also increase the damping or energy dissipation of the track. It is important to note that this study considered a flash flood case only. In reality, the flood condition can also reduce the load carrying capacity and stiffness of the subgrade layer too. Future work will highlight the modal identification and the development of new SDOF model that is more realistic and more capable to define dynamic characteristics of the railway tracks submerged under flood conditions. The influence of impulse energy as well as the track mass will also be investigated in the near future.

ACKNOWLEDGEMENTS

The first author wishes to gratefully acknowledge the Japan Society for Promotion of Science (JSPS) for his JSPS Invitation Research Fellowship (Long-term), Grant No L15701, at Track Dynamics Laboratory, Railway Technical Research Institute and at Concrete Laboratory, the University of Tokyo, Tokyo, Japan. The JSPS financially supports this work as part of the research project, entitled "Smart and reliable railway infrastructure". Special thanks to European Commission for H2020-MSCA-RISE Project No. 691135 "RISEN: Rail Infrastructure Systems Engineering Net-work" (www.risen2rail.eu) [29]. In addition, the sponsorships and assistance from CEMEX, Network Rail, RSSB (Rail Safety and Standard Board, UK) are highly appreciated. Financial support from BRIDGE Grant (Collaboration between University of Birmingham and University of Illinois at Urbana Champaign) is also gratefully acknowledged.

REFERENCES

- [1] Indraratna, B., Rujikiatkarnjorn C., and Salim W., *Advanced Rail Geotechnology – Ballasted Track*, CRC Press, London, UK, 2011
- [2] Kaewunruen S., *Ballast and ballast mat*, Rail Engineering Course Topic 2.8, RailCorp NSW, Sydney, Australia, 2012, pp. 1-13.
- [3] Kaewunruen S., and Remennikov A.M., *Non-destructive testing (NDT): A tool for dynamic health monitoring of railway track structures*. *Materials Australia*, 39(6), 14-16 (invited), 2006.
- [4] Remennikov A.M., and Kaewunruen S., *A review on loading conditions for railway track structures due to train and track vertical interaction*. *Structural Control and Health Monitoring*, 15, 207-234, 2008.
- [5] S. Kaewunruen, A.M. Remennikov, *Experimental simulation of the railway ballast by resilient materials and its verification by modal testing*, *Experimental Techniques*, 32(4): 29-35, 2008.
- [6] S. Kaewunruen, A.M. Remennikov, *Nonlinear finite element modeling of railway prestressed concrete sleeper*, *Proceedings of the 10th East Asia-Pacific Conference on Structural Engineering and Construction*, EASEC 2010, 4, 323-328, 2006.
- [7] M. Vu, S. Kaewunruen, M. Attard, Chapter 6 – *Nonlinear 3D finite-element modeling for structural failure analysis of concrete sleepers/bearers at an urban turnout diamond*, in *Handbook of Materials Failure Analysis with Case Studies from the Chemicals, Concrete and Power Industries*, p.123-160, Elsevier, the Netherlands, 2016. <http://dx.doi.org/10.1016/B978-0-08-100116-5.00006-5>.
- [8] A.M. Remennikov, M.H. Murray, S. Kaewunruen, *Reliability-based conversion of a structural design code for railway prestressed concrete sleepers*. *Proceedings of the Institution of Mechanical Engineers, Part F: Journal of Rail and Rapid Transit* 226, 155-173, 2012.
- [9] Kaewunruen, S., Ishida, T., Remennikov, A.M., "Dynamic performance of concrete turnout bearers and sleepers in Railway Switches and Crossings", *Advances in Civil Engineering Materials* 7 (3), 2018. doi:10.1520/ACEM20170103
- [10] AREMA, *AREMA-Manual for Railway Engineering*, Chapter 30 Ties. American Railway Engineering and Maintenance-of-Way Association, USA, 2012.
- [11] S. Kaewunruen, A.M. Remennikov, *Sensitivity analysis of free vibration characteristics of an in-situ railway concrete sleeper to variations of rail pad parameters*, *Journal of Sound and Vibration* 298(1): 453-461, 2006.
- [12] S. Kaewunruen, S. K. Kimani, *Damped frequencies of precast modular steel-concrete composite railway track slabs*, *Steel & Composite Structures*, An Int J., 25 (4), 427-442, 2017.

- [13] S. K. Kimani, S. Kaewunruen, Free vibrations of precast modular steel-concrete composite railway track slabs, *Steel & Composite Structures, An International Journal* 24 (1), 113-128, 2017.
- [14] S. Kaewunruen, "Impact Damage Mechanism and Mitigation by Ballast Bonding at Railway Bridge Ends", *International Journal of Railway Technology*, 3(4), 1-22, 2014. doi:10.4203/ijrt.3.4.1
- [15] Kaewunruen, S., Lopes, LMC, Papaelias, M.P., "Georisks in railway systems under climate uncertainties by different types of sleeper/crosstie materials", *Lowland Technology International* 20 (1), 67-76, 2018.
- [16] De Man, A.P. DYNATRACK: A survey of dynamic railway track properties and their quality. Ph.D. Thesis, Faculty of Civil Engineering, Delft University of Technology, The Netherlands, 2002.
- [17] Fenander, A. A fractional derivative railpad model included in a railway track model. *Journal of Sound and Vibration* 212(5), 889-903, 1998.
- [18] Cai, Z. Modelling of rail track dynamics and wheel/rail interaction. Ph.D. Thesis, Department of Civil Engineering, Queen's University, Ontario, Canada, 1992.
- [19] Kaewunruen, S., Remennikov, A.M. Effect of improper ballast tamping/packing on dynamic behaviors of on-track railway concrete sleeper. *International Journal of Structural Stability and Dynamics*, 7(1): 167-177, 2007.
- [20] Kaewunruen, S., Remennikov, A.M. Application of experimental modal testing for estimating dynamic properties of structural components, *Proceedings of Australian Structural Engineering Conference 2005*, Sep 11-14, Newcastle, Australia [CD Rom].
- [21] Kaewunruen, S., Remennikov, A.M., Current state of practice in railway track vibration isolation: an Australian overview, *Australian Journal of Civil Engineering* 14 (1), 63-71, 2016.
- [22] Remennikov, A., Kaewunruen, S., Determination of dynamic properties of rail pads using instrumented hammer impact technique. *Acoustics Australia* 33(2): 63-67, 2005.
- [23] Kaewunruen, S., Remennikov, A.M. Field trials for dynamic characteristics of railway track and its components using impact excitation technique. *Ndt & E International* 40 (7), 510-519, 2007.
- [24] Esveld, C. *Modern Railway Track* (2nd edition), MRT-Productions Press, The Netherlands, 653p., 2001
- [25] Setsobhonkul, S., Kaewunruen, S., Sussman, J.M., Lifecycle Assessments of Railway Bridge Transitions Exposed to Extreme Climate Events, *Frontiers in Built Environment* 3, 35, 2017.
- [26] Kaewunruen, S., Remennikov, A.M., Experimental determination of the effect of wet/dry ballast on dynamic railway sleeper/ballast interaction, *ASTM Journal of Testing and Evaluation* 36 (4), 412-415, 2008.
- [27] Dindar, S., Kaewunruen, S., An, M., Identification of appropriate risk analysis techniques for railway turnout systems, *Journal of Risk Research*, 1-22, 2016.
- [28] Dindar, S., Kaewunruen, S., An, M., Sussman, J.M., Bayesian Network-based probability analysis of train derailments caused by various extreme weather patterns on railway turnouts, *Safety Science*, in press, 2017.
- [29] Kaewunruen, S., Sussman, J.M., Matsumoto, A., Grand challenges in transportation and transit systems, *Frontiers in Built Environment*, 2016, 2, 4. doi:10.3389/fbuil.2016.00004

COLLOIDAL SILICA GROUT IN SOIL IMPROVEMENT: AN EXTENSIVE REVIEW

Jiji Krishnan¹, Shruti Shukla²

¹Research Scholar, ²Faculty, Applied Mechanics Department, Sardar Vallabhbhai National Institute of Technology, Surat, Gujarat, 395007, India.

ABSTRACT

The aqueous suspension of silica nanoparticles otherwise called colloidal silica has been gaining recognition as a grout material for use in soil improvement. Colloidal silica particles have the size range from 2 to 100 nanometers. In a given suspension the particle size of the colloidal silica is almost constant. The research on the soil improvement with the addition of colloidal silica is slowly yet increasing day by day due to its mechanical stability with respect to most other chemical grouts. Colloidal silica is also nontoxic, biologically, and chemically inert, and has excellent durability characteristics. The effects of silica grout on modifying the soil improvement properties were observed by different researchers. This review paper is an attempt to summarize the technical benefits and feasibility of applying colloidal silica gel as a grout in soil stabilization. The gel time of colloidal silica depends on various factors such as silica concentration, pH, salt concentration and so on. It also covers the gel characterization and gel time of colloidal silica to improve the soil properties.

Keywords: Colloidal Silica, Grout, Soil, Improvement.

INTRODUCTION

Colloidal silica is an aqueous dispersion of nanosilica particles. This low viscosity liquid is stabilized by changing the pH as well as the ionic strength of the solution. It is chemically and biologically idle, safe to handle with exceptional durability properties [8], [21].

Soil stabilization is nothing but the modification of soils to upgrade their properties. Yonekura and Kaga [22] proposed the new concept of stabilizing sands grouted with colloidal silica as a substitute for sodium silicate. The pioneers in this field are Persoff et al. [13], Gallagher and Mitchell [3] and Liao et al [9]. It has been reported that the treated sand with colloidal silica exhibit liquefaction resistance as well. Many researchers observed liquefiable soils treated with colloidal silica grout have appreciably improved the liquefaction resistance as well as unconfined compression strength. As expected they also noticed a reduction in the settlement as well as hydraulic conductivity.

The research works on Nanoparticles in soil stabilization is still in its blooming stage. So every work irrespective of the quantity of the work is important for the advancement of research in this field. This review focuses only on the use of colloidal silica in soil improvement.

MECHANISM OF COLLOIDAL SILICA STABILIZATION

Colloidal silica particles develop when H_4SiO_2

molecules form siloxane bonds (Si-O-Si) because the surface of the particle has an uncombined silanol (SiOH) group. Silica particles contain negative charge on the surface [16]. The silica sol will stabilize by changing the pH when it reaches to its desired size.

Response and structure of the particles are primarily due to its electrical interparticle forces, a negative surface charge of silica particles as well as its tiny size [15], [16], [17].

During manufacturing colloidal silica is stabilized against gelation i.e. by increasing the double layer thickness. Changing the repulsive forces of silica particles in a controlled manner will lead to gelation in a solution. Colloidal silica gel has a broad range of gel times which in turn related to different properties. The reduction in double layer thickness, as well as ionization, initiates with the help of adding silica sol to the solution which contains alkaline solutions. The other properties that affect gel time are silica concentration, ionic strength, pH, particle size and specific surface area. The longest gel time occurs for a given silica concentration without any salt content. Whereas lowest gel times occurs at pH between 5 and 7 [2]. The greater the ionic charge the lesser the gel time which creates a chance of interparticle conflicts.

Formation of siloxane bonds (Fig. 1) and dissociation of water molecules will occur as a result of the reduction in double layer thickness (I.e. reduction in repulsive forces). Gelation binds the soil particles together thereby restrict the movement of

pore fluid in the soil-silica matrix. The dissociated water caused by multiple bonds remains within the pore space of the gelled silica particle network.

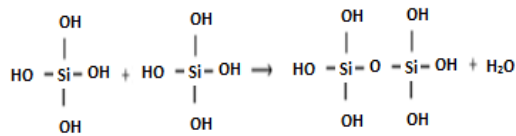


Fig 1. Illustration of siloxane bonding [17].

COLLOIDAL SILICA AS AN ADDITIVE IN SOIL

Noll et al. [12] noticed a decrement in permeability and metal absorption capacity with the addition of colloidal silica in the sand. They noticed a permeability range from 10^{-8} to 10^{-7} cm/s after stabilizing with 5 wt% of colloidal silica.

Yonekora and Miwa [23] studied the unconfined compressive strength of 335 kPa in 32 wt% colloidal silica stabilized sand. They noticed an increment in compressive strength to 1200 kPa in the treated sand I.e. almost 3.5 fold increment after curing the samples for 347 days. They also reported that UCS increased with increase in curing days up to 1000 days.

Persoff et al. [13] determined the one month, three months and one-year compressive strength of sand grouted with colloidal silica. They reported an increment in compressive strength with the addition of colloidal silica (Fig. 2) They engrossed the treated samples in water, water saturated with aniline, CCl_4 , PCE, water saturated with different Non-aqueous phase liquids (NAPLs), HCl diluted to pH-3. They noticed a gain in strength in samples dipped in water whereas samples immersed in aniline enfeebled the bond. They hardly observed any difference in strength with the mixture of NAPLs, HCl diluted to pH-3. They estimated a maximum of 400kPa compressive strength and concluded that the strength of sand grouted with colloidal silica is proportional to the amount of colloidal silica particles. They also noticed that increment in strength continues for one year after treating with colloidal silica. Also, they generalized that the maximum strength occurred in the samples which were cured for four times the gel time. They also studied the hydraulic conductivity of silica treated sand. They calculated a hydraulic conductivity less than 1×10^{-1} cm/s for colloidal silica percentage greater than 7.4.

Towhata and Kabashima [19] investigated the deformation behaviour and liquefaction resistance on Toyoura sand using cyclic triaxial test. They noticed a similarity in both the properties in treated specimens (4.5% colloidal silica by weight) with 40% relative density as well as untreated specimens with 75% relative density and more. This indicates that the

addition of colloidal silica greatly influences the liquefaction properties.

Gallagher and Mitchell [3] prepared colloidal silica grout on the deformation properties of saturated loose sand. They have done the cyclic triaxial test on a total of 31 samples grouted with colloidal silica with various concentrations (5%, 10%, 15% and 20%). Also, unconfined compression tests were performed with the varying concentrations and noticed that the strength gain occurs with the addition of colloidal silica (Fig. 2). In addition to this 25 samples were tested for UCS test after cyclic testing to define the strength reduction due to cyclic loading. They revealed that the untreated samples collapsed in 10-12 cycles whereas the treated samples remained intact for at least 100 cycles. Figure 3 shows the strain during cyclic loading depleted with the addition of colloidal silica %. Thus it is very clear that the colloidal silica stabilized sand consequently increased the deformation resistance of loose sand to cyclic loading. Thus the presence of colloidal silica greatly influence the properties of treated sands.

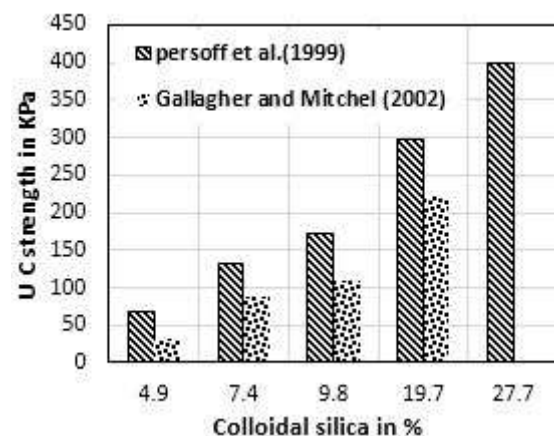


Fig. 2 The unconfined compressive strength of treated samples [3], [13].

Based on the experiment they also noticed that the treated samples UC strength ranged from 32kPa to 222kPa. They also noticed that colloidal silica that experienced less than 1% strain had a reduction of 15% baseline strength whereas samples experienced more than 2% strain had a residual strength that was between $\frac{1}{2}$ and $\frac{2}{3}$ of the baseline strength. The general trend they noticed that the samples which experienced high strains showed the higher reduction in strength. This indicates that colloidal silica bonds weaken with cyclic loading. They concluded that 5% colloidal silica reduces the liquefaction risk and stabilization with acceptable strain levels are also possible with adding more percentage of colloidal silica. Though more than 10 % colloidal silica is not reasonable economically.

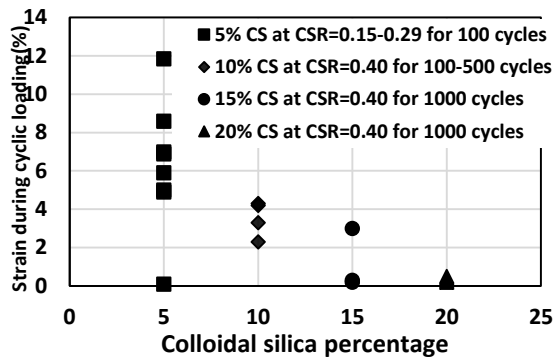


Fig. 3 Variation of strain with the addition of colloidal silica % [3].

Thevanayagam and Jia (2003) conducted an experiment and reported that it is feasible to use colloidal silica grouts into silty soils by means of a dc current.

Gallagher and Lin [4] conducted UCS test on Nevada Sand no: 120 treated with 5 wt % nano-silica. Test results varied from an average strength from 47kPa to 67kPa. From the test results, it was expected to mitigate the liquefaction risk. Though they haven't performed any dynamic tests to validate their conclusion, they have compared the results with test results in which experiment is conducted on the same sand and on the same weight percentage of colloidal silica with the exact same laboratory conditions. They proposed that 5 wt% of colloidal silica treated sand was suitable for mitigating the risk of liquefaction. They justified that liquefaction resistance as well cohesion of sand increases with the addition of colloidal silica. They also noticed that colloidal silica solutions stopped moving when the viscosity increased above 4 cP under low pressures.

Kodaka et al. [8] examined a new method to prevent the liquefaction of sandy ground. They used a 4wt% colloidal silica to study the deformation and strength characteristics. They noticed an effective increase in resistance to liquefaction using monotonic and cyclic torsional shear tests.

Liao et al. [9] estimated the compressive strength and cyclic behaviour of grouted sand. They reported an increment in cyclic resistance with the addition of colloidal silica grout. They also noticed that 4-7 folds increase in stress ratio needed to initiate liquefaction in grouted sands which were cured for 28 days. Also, the liquefaction-induced strain of un-grouted sand was about 1.6 times larger than that of colloid silica grouted sand.

Gallagher et al. [5] conducted a full-scale field testing of colloidal silica grouting for mitigation of liquefaction risk. They identified a recognizable reduction in the settlement after stabilizing 2 m of the liquefiable zone. Whereas they recommended

additional studies to establish new methods to measure the liquefaction improvement of colloidal silica grouted sand. This recommendation is based on the CPT and shear velocity profiles since they didn't provide any significant improvement.

Gallagher et al. [6] conducted centrifuge modelling to estimate the effect of 6% by weight colloidal silica treated loose sand on liquefaction and deformation resistance. They noticed that the measured settlements were reduced up to 25 times in colloidal silica treated sand than in untreated sand. They reported that the optimal amount of colloidal silica used for stabilization of sand was 6%. They reported a reduction in liquefaction potential with an increase in deformation resistance.

Rodriguez et al. [14] noticed that 14.5 wt% of colloidal silica in silty sand caused a reduction in pore pressure as well as shear strain (Fig 4) substantially during cyclic loading at the age of seven days. They also reported a substantial increment in liquefaction resistance of treated sample for a given initial relative density and initial effective vertical stress.

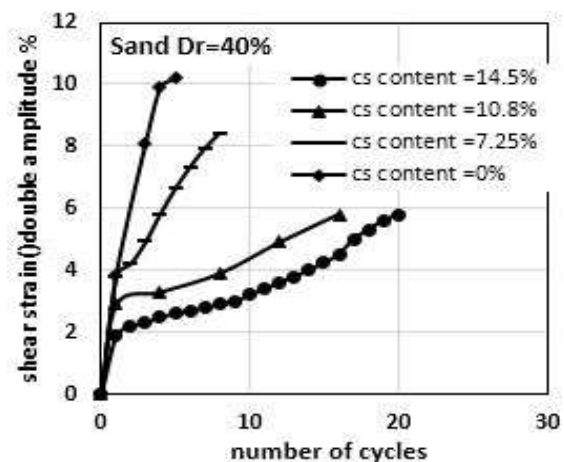


Fig. 4 Shear strain versus the number of cycles at different percentage of colloidal silica [14].

Spencer et al. [17] conducted a resonant column test (5, 7 and 9 wt% of colloidal silica) and he reported that the shear modulus increased approximately 6 MPa over 28 days. According to their experiment, the effect of damping ratio with the addition of colloidal silica was nugatory in the applied strain range.

Mollamahmutoglu and Yilmaz [10] conducted a study to investigate pre and post-cyclic loading strength of silica grouted sand. They observed that hardly any samples treated with colloidal silica (10%, 15%, 20% and 25%) failed after performing cyclic tests. The grouted samples experienced different stress ratios such as 0, 0.013, 0.26, 0.39, and 0.52. Unconfined compressive strength tests showed (Fig. 5) that grouted samples gained strength with time for

all percentage of saline solutions (10%, 15%, 20%, and 25%) and colloidal silica suspensions. Addition of 20% and 25% colloidal silica with salt water ratio 1:12 showed a very close range. This shows that after a specific range (20% colloidal silica suspension), the increase in strength is very minute with the addition of colloidal silica suspension.

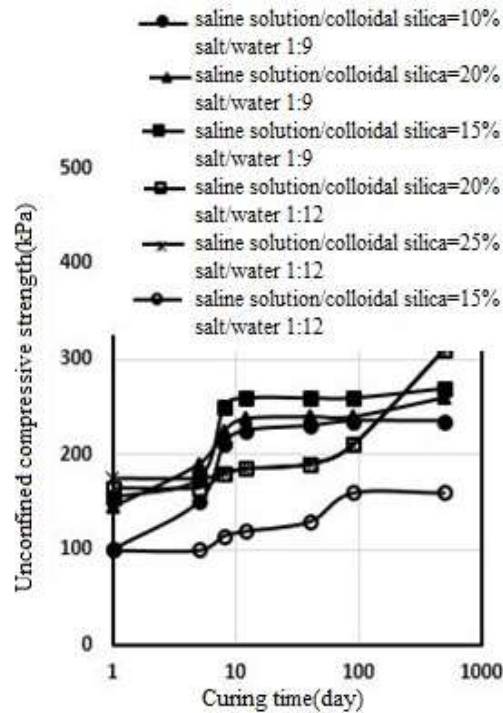


Fig. 5 Unconfined compressive strength results in colloidal silica stabilized sand [10].

Conlee et al. [1] conducted a study to evaluate the liquefaction mitigation of colloidal silica treated sand. They conducted a centrifuge test on 4%, 5% and 9% of colloidal silica stabilized sand. After comparing the results they noticed a decrement in ground deformations in the treated sand. They also evaluated higher cone tip resistance and shear wave velocity as well as a reduction in lateral spreading on treated liquefiable soil layers. Overall they noticed a reduction in CSR and shear strains with the addition of colloidal silica. They reported an increase in cyclic resistance ratios with the increase of colloidal silica concentrations. Fig. 6 shows CSR versus Shear strain for a shake in treated as well as untreated sands at three different depths.

Moradi and Seyedi [11] studied the effect of sampling method on strength of stabilized silty sands with colloidal nano-silica. They prepared various samples with silt content from 0 to 30% prepared by sedimentation method in 4.5 wt% colloidal nano-silica suspensions. They conducted unconfined compressive strength tests after a curing period of 6

weeks. It has been reported an increment in unconfined compressive strength when the silt content was up to 10%, whereas strength decreased with the increment of silt content more than this (Fig. 7). They also examined the Scanning Electron Microscope (SEM) analysis to observe the variations in colloidal silica treated soil (Fig. 8).

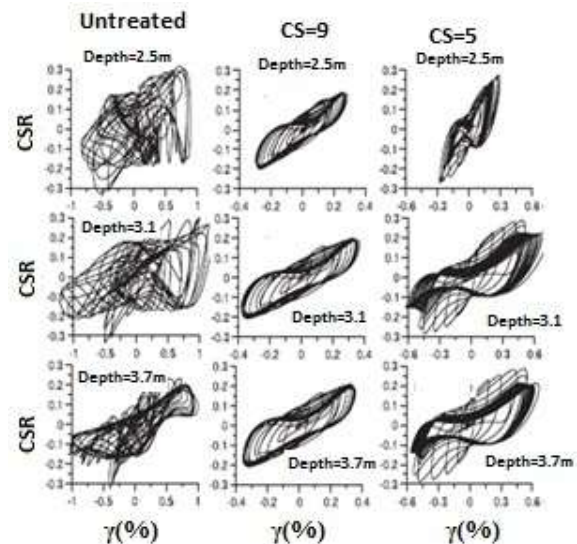


Fig. 6 Stress-strain profiles at specific cycles in the shaking event [1].

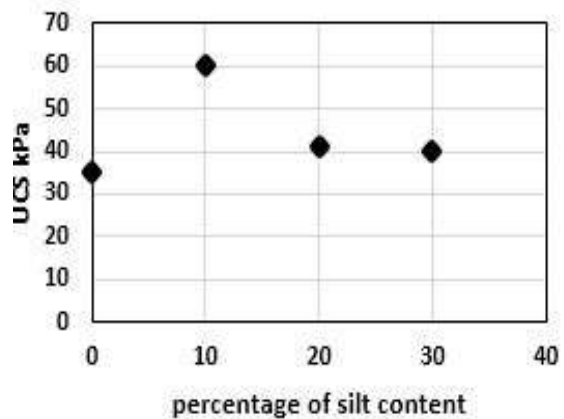


Fig.7. Variations in UCS in colloidal silica sands having various % of silts [11].

The treated grains were angular, of high relief with abundant mechanical texture associated with adherence to colloidal silica including straight and arcuate steps, imbricated blocks, fractured plates, meandering ridges and irregular depressions. The increment in strength and stiffness of treated samples were due to these characteristics. Table 1 shows the results provided by various researchers in a nutshell



Fig. 8 SEM images of untreated and treated soil grains [11].

Table 1 Summary of research considered

Researchers	Remarks
Noll et al. [12]	The decrement in permeability and metal absorption capacity.
Yonekora & Miwa [23]	The gain in compressive strength.
Persoff et al. [13]	Increase in UCS and decrease in hydraulic conductivity.
Towhata & Kabashima [19]	The increment in liquefaction resistance.
Gallagher and Mitchell [3]	UCS tests, as well as cyclic triaxial tests, showed an increment in strength.
Thevanayagam & Jia [18]	Feasible to use colloidal silica grouts in silty soils.
Gallagher & Lin [4]	Mitigate the liquefaction risk.
Kodaka et al. [8]	Resistance to liquefaction.
Liao et al. [9]	Increment in cyclic resistance.
Gallagher et al. [5]	Reduction in the settlement for mitigation of liquefaction risk.
Gallagher et al. [6]	Reduction in liquefaction potential with an increase in deformation resistance.
Rodriguez et al. [14]	Gain in liquefaction resistance. Reduction in pore pressure as well as shear strain.
Spencer et al. [17]	Increase in shear modulus.
Mollamahmutoglu & Yilmaz [10]	The gain in unconfined compressive strength as well as cyclic resistance.
Conlee et al. [1]	Reduction in CSR and shear strains. Increase in cyclic resistance.
Moradi and	Increment in unconfined

Seyedi [11]	compressive strength.
-------------	-----------------------

CONCLUSIONS

This review is an attempt to give a wide knowledge about the mechanism of colloidal silica stabilization as well as the use of colloidal silica as an additive in soil stabilization. Following points can be inferred from this review:

- 1) Addition of colloidal silica suspensions in soil greatly increases the unconfined compressive strengths. While UCS test is an elementary test, it can be considered as an ordinary indicator of the degree of stabilization achieved.
- 2) Ionic strength, pH, silica concentration, particle size and specific surface area are important factors to be considered for the gelling of colloidal silica to initiate strength.
- 3) Cyclic triaxial tests on loose saturated sands treated with colloidal silica showed a dramatic increment in deformation resistance. And increasing treatment levels produced greater cyclic ratios as well.
- 4) Addition of colloidal silica up to 10% is economical.
- 5) Cost-effectiveness of colloidal silica suspensions in soil is inevitable. So more research on this study should be encouraged.
- 6) Permeability reduced with the addition of colloidal silica in the sand.
- 7) More work needs to be done on soil stabilization using different colloidal silica concentrations and soil densities.
- 8) The experimental studies that are specifically based on the effect of viscosity in gelling time as well as curing time of colloidal silica in the soil are limited.
- 9) Further trials should be needed which could exploit more complex base shakings to determine dynamic properties with the addition of colloidal silica

It should be noted that the colloidal silica has some different behaviours on the type of particle proportions. So it is unavoidable to select the exact composition needed for the experiment.

REFERENCES

- [1] Conlee C., Gallagher P.M., Boulanger R.W., and Kamai R, Centrifuge modeling for liquefaction mitigation using colloidal silica stabilizer. J. Geotech. Geoenviron. Eng. Vol.138, Issue 11, 2012, pp.1334–1345.
- [2] Gallagher P.M. and Lin Y., Colloidal silica transport through liquefiable porous media. J. of Geotech. And Geo environmen. Engng. Vol.135,

- Issue 11, 2009, pp.1702–1712.
- [3] Gallagher P.M. & Mitchell J.K., Influence of colloidal silica grout on liquefaction potential and cyclic undrained behavior of loose sand. *Soil Dynamics and Earthquake Engineering*. Vol.22, Issue 9-12, 2002, pp.1017-1026.
 - [4] Gallagher P.M., and Lin Y., Column testing to determine colloidal silica transport mechanisms. *Innovations in grouting and soil improvement, Geotechnical Special Publication*, Vol.136, 2005.
 - [5] Gallagher P.M., Conlee C.T., and Rollins, K.M., Full-scale field testing of colloidal silica grouting for mitigation of liquefaction risk,” *Journal of Geotechnical and Geo environmental Engineering*. Vol.133, Issue 2, 2007, pp.186–196
 - [6] Gallagher P.M., Pamuk A. and Abdun T., Stabilization of liquefiable soils using colloidal silica. *Journal of Materials in Civil Engineering*, Vol.19, Issue 1, 2007, pp. 33-40.
 - [7] Iler R.K., *The chemistry of silica: solubility, polymerization, colloid and surface properties and bio chemistry*. New York: Wiley, 1979, pp.1-866.
 - [8] Kodaka T., Oka, F., Ohno Y., Takyu T., and Yamasaki, N., Modeling of cyclic deformation and strength characteristics of silica treated sand. *Conference proceedings, in Proc. Geomechanics: testing, modeling, and simulation*, 2003, pp.205–216.
 - [9] Liao H. J., Huang C. C., and Chao B.S., Liquefaction resistance of a colloid silica grouted sand. *Conference proceedings, in Proc. 3rd Int. Conf. ASCE*, Reston, 2003, pp.1305–1313.
 - [10] Mollamahmutoglu M. & Yilmaz Y., Pre- and post-cyclic loading strength of silica grouted sand. *Conference proceedings, in Proc. The Institution of Civil Engineers - Geotechnical Engineering Geot. Engineering*, 2010, pp. 343-348.
 - [11] Moradi G, Seyedi S., Effect of Sampling Method on Strength of Stabilized Silty Sands with Colloidal Nano Silica. *Journal of Civil Engineering Research*, Vol.5, Issue 6, 2015, pp. 129-135.
 - [12] Noll M.R., Bartlett C., Dochat T.M., In situ permeability reduction and chemical fixation using colloidal silica, *Conference proceedings, in Proc. of the Sixth National Outdoor Action Conference*, Las Vegas, NV, 1992, pp.443–457.
 - [13] Persoff P., Apps J., Moridis G., and Whang J.M. Effect of dilution and contaminants on sand grouted with colloidal silica. *J. Geotech. Geoenviron. Eng.*, Vol.125, Issue 6, pp. 461–469.
 - [14] Rodriguez Diaz.J.A, Antonio Izarraras.V.M., Bandini Pand Lopez-Molina J.A., Cyclic strength of a natural liquefiable sand stabilized with colloidal silica grout. *Canadian Geotechnical Journal*, Vol.45, Issue 10, 2008, pp.1345–1355.
 - [15] Santamarina J. C., Klein K. A., and Fam M. A., *Soils and Waves*, John Wiley & Sons, New York Publisher, 2001, pp.1-508.
 - [16] Scott R. P. W. , *Silica Gel and Bonded Phases: Their production, properties and use in LC*, John Wiley & Sons, New York Publisher, 1993, 1-2666.
 - [17] Spencer M., Rix G.J., and Gallagher P.M., Colloidal silica gel and sand mixture dynamic properties. *Conference proceedings, in Proc. Geotechnical Earthquake Engineering and Soil Dynamics IV*, 2008, pp.1-8.
 - [18] Thevanayagam S., and Jia W., Electro-osmotic grouting for liquefaction mitigation in silty soils. *Conference proceedings, in Proc. Third International Conference on Grouting and Ground Treatment*, 2003, pp.1507–1517.
 - [19] Towhata I., Kabashima Y., Mitigation of seismically-induced deformation of loose sandy foundation by uniform permeation grouting. *Conference proceedings, in Proc. 15th International Conference on Soil Mechanics and Geotechnical Engineering*, Istanbul, Turkey, 2001, pp.313–318.
 - [20] Vrana A.D., Th. Tika., The mechanical behaviour of a clean sand stabilized with colloidal silica. *Conference proceedings, in Proc. XVI European Conference on Soil Mechanics and Geotechnical Engineering*, 2015, pp-2-7.
 - [21] Whang J.M., *Section 9: chemical based barrier materials*. Springfield Publishers, 1995, pp.211–47.
 - [22] Yonekura R. and Kaga M., Current chemical grout engineering in Japan. *Conference proceedings, in Proc. Grouting, Soil Improvement and Geosynthetics*, 1992, pp.725-736.
 - [23] Yonekura R., Miwa M., Fundamental properties of sodium silicate based grout, *Conference proceedings, in Proc. The Eleventh Southeast Asia Geotechnical Conference*, Singapore, 1993, pp.439–444.

THE BEHAVIOR OF UNTREATED AND TREATED EXPANSIVE SOIL AS EMBANKMENT OF FLEXIBLE PAVEMENT

Yulvi Zaika¹, Eko Andi Suryo²

^{1,2}Faculty of Engineering, Brawijaya University, Indonesia

ABSTRACT

Designing of pavement structures passing through the expansive soil as subgrade areas is inevitable in Ngasem Ngawi, East Java, Indonesia. So it takes a study of the analysis of the structure of the pavement on the expansive soil in static loading. The purpose of this study is to find out how the stresses, strain and deformations that occur when soil expansive or lime stabilized soil in 5 m high as the embankment which are the subgrade layer as natural expansive soil. Laboratory experiments were conducted on characteristic the natural soil (expansive) and assigned the optimal mixture of lime stabilized soil. Stress, strain and deformation analyzes were performed by using FEM program with simulated non linear model : pavement layer including lime stabilized soil as Mohr Column model and soft soil model for expansive soil. From this analysis shows that the effect of lime stabilized soil in embankment can reduce deformation and avoid premature structure failure causing compressive stress on the top pavement and tensile stress at the bottom pavement structure.

Keyword: Expansive l, Non linear, Soft soil, Stress, Deformation

INTRODUCTION

Expansive soil is clay soil that is classified as having high plasticity generally caused by monmorilonite mineral content. This mineral content performed the liquid limit (LL) and Plasticity Index (PI) os soil to increase. Expansive soil is a soil that is known to have a high swelling and shrinking ability. If the soil absorbs large amounts of water, it expands, causing an uplift and will shrink if water loss causes crack. As a result the volume can increase and decrease due to changes in water content. In dry conditions the soil becomes stiff, has a high shear strength and cracks in the vertical and horizontal dirt. This will change if the soil is in wet condition where its shear strength is low.

If expansive soils located in tropical climates are known as black cotton soils in which the area, gravel or aggregate is not available. Most of the tropical black clay (deposit) layer is formed by weathering on basalt and alluvial beds. Currently there are many studies on expansive soil to understand basic mechanisms involved in swelling of expansive soil to avoid the problem in construction. The foundation base of a pavement structure, railway, airfield or light building then the structure will suffer significant damage due to swell potential of the soil. It requires a large of money to maintain and repair structures damaged by expansive soil.

Considerable research has been done to improve behavior of expansive soil such as adding materials likes lime [3], fly ash [10] and

cement [11][7]. This method will obtain optimal results when the mixing of soil and lime or other material are done at the shallow soil surface, although also known Deep Soil Mixing (DSM) method [13] but requires considerable equipment.

The use of computer programs in analyzing slope stability has been widely applied in many cases including the embankment [2][9]. In the case of embankment there is slope stability analyses which is solve by limit equilibrium and finite element method. Other analysis has been performed if the subgrade is soil is a soft soil or expansive soil [6] as consolidation problem. The consolidation analysis was conducted to estimate the settlement of subgrade due to embankment, pavement structure and vehicles.

There was investigated the behavior of flexible pavements on expansive soils consisting mainly of brown clayey silt in Tebessa, Algeria[4]. Computer code Plaxis 8.2 was used for numerical simulation to check the behavior of structure pavement with three models in pavement structure and free expansion test was performed to calibrate the soil sub-grade with Soft-Soil Model. The results showed that the combined model Mohr-Coulomb in the pavement structure and the Soft-Soil in sub-grade accord perfectly with deformations taken on the existing pavement. The prediction of swelling behavior of compacted expansive soils have been analysed [11]. The study is based on a semi-empirical approach in which a model of swelling behavior is developed leading to equations relating swelling potential or swelling pressure of a compacted soil to its

plasticity index, clay content and initial molding water content. The results showed that the predicted values of the swelling potential and swelling pressure based on Plasticity Index, clay content and water content for grundite and bentonite soil and kaolinite and bentonite clay mineral. It was made study to model the behavior of expansive soil in the framework of unsaturated soil mechanics[1]. The proposed model is used then to predict the displacements associated with the changes in soil suction. The elasto-plasticity framework is used for constitutive modeling.

The purpose of this study is to investigate the response of expansive soil, stabilized expansive soil and flexible pavement structure due to different material embankment and traffic passing through the road. Expansive soil data has taken to Ngasem village Bojonegoro East Java, Indonesia. Previously several investigations have been conducted on characteristics in several places in the area and resulted in the same conclusion that the area has potential problems with expansive soil layers deep enough to 20 m. The rocks on the surface of the location are claystone from the Tongue Formation. The clay found in greenish gray, slightly sandy, locally encountered carbonate sandstone lenses. The weathered soil clay is dark gray, with white spots. During the dry season found many fractures with a width of about 5 cm, and during the rainy season is very plastic.

MATERIAL

Embankment Material

The pavement structure model consists of expansive natural soil as subgrade, improved lime soil as embankment and pavement structure that represent a material layer.

Material for embankment construction consist of un frost susceptible earth, sand, gravel, fractured rock or combination thereof containing no muck, peat, root or other deleterious materials, and shall be compatible to the density required by the specification. There are natural material, selected material and selected material on peat for embankment. Selected material for embankment use to improve subgrade by increase bearing capacity or other reasons. The selected material should not include high-exspansive soils classified as A-7-6 according to AASHTO and as CH according to "Unified or Casagrande Soil Classification System". If soil with high-plastic use in the ground is unavoidable, the material should be used only on the bottom of the embankment or on the backfill that does not require high bearing capacity or shear strength. Such plastics should not be used at a 30 cm layer directly below the bottom of the pavement or the

shoulders or the bottom of the shoulder. In addition, the embankment for this layer has CBR value not less than the bearing capacity taken for the design or not less than 6% if otherwise specified soaked CBR.

Very expansive soils that have an active value greater than 1.25, or the degree of expansion classified by AASHTO T 258 as "very high" or "extra high" should not be used as an embankment material. The active value is the comparison between the Plasticity Index / PI - the percentage of clay content. Materials for ordinary embankment should not be content minerals as the following properties:

1. Organic soil such as OL, OH and Pt soils in the system as well as soil containing foliage, grasses, roots, and garbage.
2. Soil with a very high natural moisture content that is not practically dried to meet the moisture tolerance at compaction.
3. Soils that have high and very high shrinkage properties

The soil embankment is consisted compacted layer or lift of suitable material placed on top each other until the level of subgrade surface is reached. Any suitable materials may be used to construct the embankment, although the contractor has to improve the material to make it stable. The component of embankment construction are thickness of layer, material and degree of compaction that represent in CBR value

In general, the soil for embankment usually have soaked CBR at least 10% in maximum dry density. The other characteristics are Atterberg Limit and composition. It respect of the letter for embankment material to be classified as tolerable its degree settlement such as 1% and its swelling potential less than 3%.

The specification can be reached if the type of material as well-graded rock or gravel or a low plasticity silt-clay. The type of material selected and approved by the Engineer will depend on the steepness of the slopes, dumped material and the loading traffic.

The expansive soil does not meet qualification as an embankment material due to high plasticity. The soil with low plasticity could be used as an embankment by so that before being used as an expansive landfill material it must be improved in order to decrease the nature of its swelling.

The material that use in this study has $LL > 60$, $IP > 35$ which classified as high plasticity soil. Further handling is required by:

- a. Soil improvement such with lime or cement; mixed compositions should be based on laboratory test results.
- b. Soil reinforcement, for example geotextile woven.
- c. Soil replacement by replacing expansive soil with selected soil material.

d. Grading slope geometry, where the slope of the embankment is very sloping, at least V: H = 1: 3, and based on slope stability analysis.

The chosen alternative can be a combination of these alternatives and should be based on baseline soil bearing capacity analysis and slope stability analysis.

Soil improved with lime is used as embankment in this study by some reasons such as:

1. Availability material.
2. Lime in optimal content 8% increase unsoaked and soaked CBR 15,5 % and 11,6 % respectively.
3. Swell Potential decrease 4,9% to 0,91%.

Material Model

Design of pavement structure usually need CBR value to determine pavement layer so that swelling effect of expansive soil is not detected. If soil data is obtained in dry season, CBR value will be high which is different to rainy season will

generate in low CBR because the moisture content will influence the soil strength. The investigation assumed expansive soil as soft soil in case in Algeria National Road N16 Tebessa, the experimental test result closed to computer analyses of FEM program was done [5]. The criterion need some parameters as MC and also modified compression index (λ) and modified swelling index (κ) or compression index (C_c), swelling index (C_s) and void ratio (e).

Linear elastic model was applied to pavement structure layer and improved soil as embankment. The elasticity associated Mohr Coulomb (MC) criterion in a linear isotropic Hooke type. The criterion contain five mechanical parameter: modulus elasticity (E), Poisson ratio (ν) are elastic parameter and cohesion (c), friction angle (ϕ) and dilation (ψ) are plastic parameter. The asphalt concrete is dismissed in this study

The laboratory tests carried out to material of pavement structure are given in Table 1.

Table 1 Input parameter of model

Characteristic	Unit	Base	Improved Soil	Subgrade
Model		MC	MC	Soft Soil
Type of behavior		Drained	Undrained	Undrained
Thickness	m	0,5	5	8
Young Modulus	kPa	140000	8000	5000
Poisson ratio		0,35	0,25	-
Unit Weight	kN/m ³	22	17,5	17,4
Cohesion	kPa	5	126	40
Friction angle	°	40	20	8
Dilatation Angle	°	13	6	-
Compression Index				1,034
Swelling Index				0,21
Void ratio				0,5
CBR un-soaked	%	55	15,5	8,5
CBR soaked	%		11,6	4,46

LOADING MODEL

In the case of Bojonegoro area, the classification road is collector in which the line connect to local road, low speed and low serviceable. The access road is passed by Indonesia Petroleum Company transportation so that model of vehicle used as truck with dual tires.

The contact area between the tires and pavement surface to be able to assume the area that axle load will be uniformly distributed. The dual tires contact area could be considered as one large circle. One large circle give more appropriate result in calculations than two separate circle. The size of contact area depend on the contact pressure. The contact pressure is assumed as equal to the tire pressure. The load of dual tire is 40 kN and the tire pressure is 650

kN/m². The pressure of load ia transferred to the pavement in 2D condition is 404 kPa, where length of contact area 0,6m and the area of one large circle is 0,099 m². Thus pressure of load is 404 kPa and then is multiplied by 1,2, which static load is 484,8 kPa. The contact pressure is the tire pressure 650 kPa

GEOMETRIC MODEL

Geometric model can be shown in Fig. 1

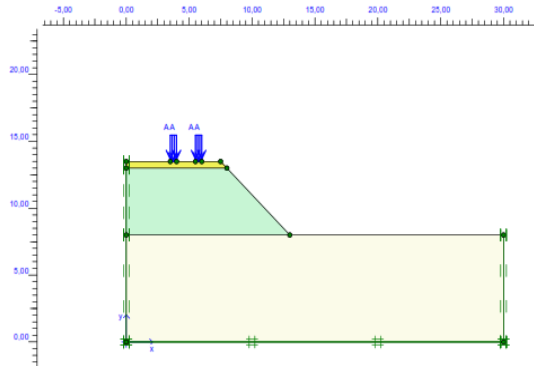


Fig. 1 Geometric condition of numerical model

There are two condition will be compared in this study:

1. Subgrade and embankment are the same material as expansive soil.
2. Subgrade is expansive soil and embankment is improved lime expansive soil.

Boundary conditions

The element of mesh is triangular and will be avoid to rotation for all nodes. Two degree of freedom have to consider in defining the boundary condition are applied such as: the vertical and horizontal displacement of node on the bottom plane is fixed, the horizontal displacement in vertical plane are prevented. The analyses will be done is half cross section are pavement structure which is consider in symmetry plane

RESULT AND DISCUSTION

Natural Expansive Soil as Embankment

The design of pavement structure require maximum high design embankment 5m and approve the soil from excavation activity in the same area. Based on numerical model by using FEM, this condition generated 1,2 m total displacement and 0,13 m increment displacement show in Fig. 2.

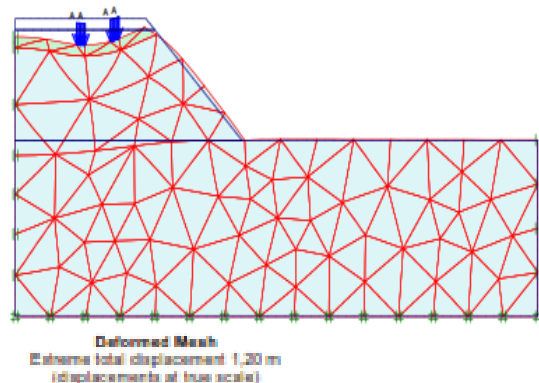


Fig. 2 Deformation mesh of natural expansive soil

The negative excess pore pressure performed the suction in expansive soil layer as shown in Fig. 3.

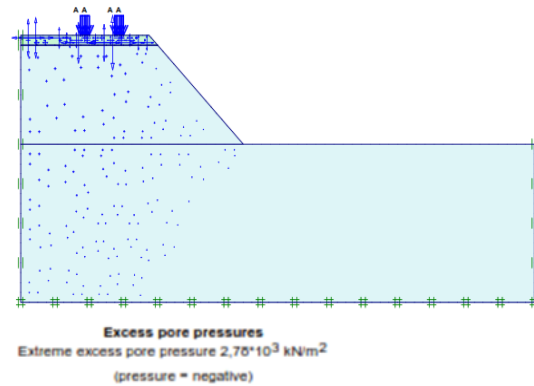


Fig. 3 Excess pore water pressure

Based on the calculation result could be say that it is inappropriate to design abutment with natural expansive soil without improve the soil.

Improved Soil as Embankment

Lime as additive material

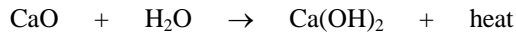
The lime commonly used is lime (CaO) as a mixture of mortar as a building material. Lime (CaO) itself comes from limestone (CaCO_3) which is a sedimentary rock composed of minerals calcite and aragonite. Lime is known as a material that has a function as a binding material in the manufacture of walls and pillars. The properties of lime are not brittle, easy and quick harden, workability, good and have the connectivity for stone or brick (Satrio, 1998). Lime minerals may be calcium hydroxide, calcium oxide, and calcium carbonate so that it can cause chemical reactions with clay soil. This base material is distinguished according to the content of the contaminating material, known as:

- a. Lime high calcium content of lime CaO levels of more than 95%.
- b. Lime of magnesia is lime which is MgO content more than 5%, if MgO level exceed 20% then called dolomite.
- c. Lime of hydrolysis is limestone containing soil oxides (Al_2O_3 , SiO_2 , Fe_2O_3).

In this study soil used lime for improve properties such as plastic properties (not brittle), as a binder that can harden easily and quickly to provide binding strength to clay soil, workability without having to go through a manufacturing process, cheap and easy to obtain.

The phases of chemical processes on soil stabilization using lime are as follows:

- a) water absorption, exothermic reaction and expansive reaction; When the lime is mixed on the ground there is water content, there will be a reaction as follows:



The reacting between water and lime will heat up and at the same time, the volume of lime becomes larger than its original volume, causing a decrease in the water content in the soil.

- b) Ion exchange reactions. Clay in the soil content is smooth and negatively charged. Positive ions such as hydrogen ions (H^+), sodium ions (Na^+), calcium ions (Ca^{2+}), and polarized water all attach to the surface of clay granules. If lime is added to the soil with the above-mentioned conditions, the ion exchange immediately takes place, and the calcium ion derived from the lime solution is absorbed by the surface of the clay grain. Thus, the surface of the clay had lost its repulsion force, and there was cohesion on the grain, resulting in an increase in the consistency of the soil.
- c) pozzolan reaction; With the passage of time, the silica (SiO_2) and alumina (Al_2O_3) contained in clay with reactive mineral content, will react with lime and form calcium silicate hydrate such as: tobermorite, calcium aluminate hydrate $4\text{CaO} \cdot \text{Al}_2\text{O}_3 \cdot 12\text{H}_2\text{O}$ and 2CaO gehlenite hydrate. $\text{Al}_2\text{O}_3 \cdot \text{SiO}_2 \cdot 6\text{H}_2\text{O}$. The formation of these chemical compounds lasts continuously for a long time so that the soil becomes hard and not easily fragile (durable).

Natural expansive soil has been improved by lime use as embankment material and apply in numerical calculation of FEM in which decrease the total displacement to 0,432m (64,75%) as show in Fig. 4.

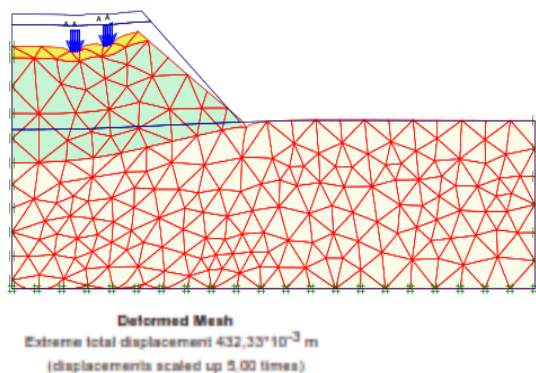


Fig. 4 Total displacement of embankment with lime improved soil

The excess pore water pressure decrease from 2780 kN/m^2 to $96,74 \text{ kN/m}^2$ in the improved layer

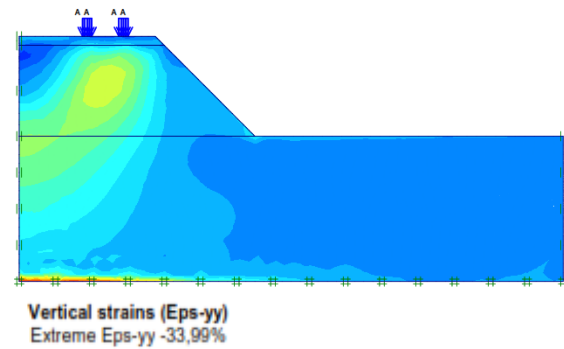


Fig 5 The vertical strain condition in expansive soil embankment

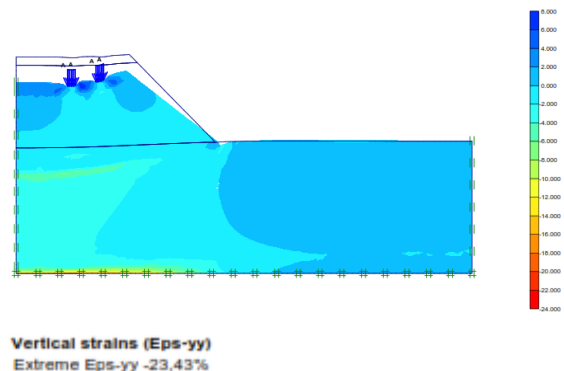


Fig. 6 The vertical strain condition in improved embankment

Fig. 5 depicts the distribution of vertical strain that maximum value in subgrade layer, The higher value is mainly caused by swelling pressure induced by subgrade to the pavement. Under the pavement structure the strain is small, the fact of surcharge due to embankment reduce the effect of swelling pressure. The vertical strain in pavement structure are positive value that impressed compressive stress occur. Because the both sides pavement structure have two stress in opposite value causing premature structure failure. Fig. 6 shows the top and bottom layer pavement under the wheel path is the same value (almost zero) but other area in pavement structure are totally compressive.

CONCLUSIONS

- The use of expansive soil as embankment cause very large displacement.
- Effect of swelling pressure made top and bottom pavement structure have opposite direction strain causing crack in the pavement structure.
- Improved lime soil could avoid crack in pavement structure and decrease total displacement.

REFERENCE

- [1]Abed Ayman A,"Numerical modelling of expansive soil behavior", Ph.d dissertasi Institute of Geotechnical, Stuttgart, Germany 2008.
- [2]Baba K, Bahi L, Ouadif L, Akhssas A," Slope stability evaluation by lilmit equilibrium and finite element method applied to a railway in the Moroccan Rif", JCE, 2, 2012, pp. 27-32.
- [3] Bell.F.G , " Lime stabilization of clays minerals and soils", Engineering Geology, Elsevier, Vol.42,1996, pp 223-237.
- [4]Djellali A, Ounis A, Saghafi.B," Behavior flexible pavement on expansive soil", International Journal of Transportation Engineering, vol 1,2013, pp.1-16.
- [5] Djellali A, Houam A, Saghafi.B, Hamdane A, and Benghazi Z, " Static Analysis of Flexible Favement over Expansive Soil", International Journal of Civil Engineering, DOI 10.1007/s40999-016-0058-6, 2016.
- [6] Deep Hashem M, Abu Bakar, AM," Numerical Modeling of flexible pavement constructed on expansive soil", European International Journal of science and technology, 2.10, 2013,pp. 20-34.
- [7] Khemissa M, Mahamedi A," Cement and lime mixture stabilization of an expansive over consolidated clay", Applied Clay Science, 95,pp.104-110, doi:10.1016/j.clay.2014.03.017
- [8]Liu X, Sheng K, Hua J, Hong B, Zhu J," Utilization of high liquid limit soil as subgrade material with pack and cover method in road embankment construction, IJCE, 13 (3 and 4B),2015, pp. 167-174.
- [9] Maula B A, Zhang L, "Assessment of embankment factor safety using two commercially Available Programs in slope stability analysis", Procedia Engineering, 14, 2011,Elsevier, pp. 559-566.
- [10] Mir BA,"Some studies on the effect of fly ash and lime on the physical and mechanical properties expansive clay", IJCE, 13, 2015, pp.203- 212.
- [11] Mircea A, Irina L and Angel S," Effect of eco-cement (GGBS) on the expansive soil strength", Journal of civil engineering and science, Vol.3. , 2014, pp 74-80.
- [12]Nayak, NV, Chrishtensen RW," Swelling characteristics of compacted expansive soil", Clays and Clay Minerals, vol.19, 1971,pp.251-261.
- [13] Zaika Y, Rachmansyah A,"The estimation of bearing capacity and swell potential od deep soil mixing on expansive soil by small scale model",International Journal of Geomate, 2017,pp. 09-15.

GEOTECHNICAL ASSESSMENT OF MALAYSIAN RESIDUAL SOILS FOR UTILIZATION AS CLAY LINERS IN ENGINEERED LANDFILLS

Lee Li Yong¹, Endene Emmanuel², Ria Purwani³ and Vivi Anggraini⁴
^{1,2,3,4}School of Engineering, Monash University, Malaysia

ABSTRACT

Compacted natural soils are often used as liner materials in sanitary landfills to minimize the environmental impacts attributed to landfill by preventing the migration of leachate and landfill gases into the environment and groundwater. In this study, two residual soil deposits of Kenny Hill rock formation were collected and evaluated for their suitability as liner materials in engineered landfills by conducting physical, mineralogical and geotechnical characterization tests using distilled water and leachate as saturating and permeating liquids. The tropical soil samples collected from Subang and Putrajaya were classified as ferruginous and ferralitic soils respectively. Results of the study indicated that ferruginous soil complied with the requirements of soil liner material in terms of their fines content, plasticity index, hydraulic conductivity and unconfined compressive strength. However, ferralitic soil failed to meet the requirement of landfill liner in terms of their fines content and unconfined compressive strength. When leachate was used as permeating fluid, there was a reduction in the permeability of both soils from 3.927×10^{-8} cm/s to 3.448×10^{-8} cm/s for ferruginous soil and from 1.202×10^{-7} cm/s to 1.461×10^{-8} cm/s for ferralitic soil. Nonetheless, increased compressive strength and reduced Atterberg limit were observed for both soils when saturated with leachate. In general, leachate had effects on the geotechnical properties of the studied soils. Based on the experimental results, it can be concluded that ferruginous soil from Subang is more suitable for soil liner materials compared to ferralitic soil from Putrajaya.

Keywords: Clay liners; Landfill; Leachate; Residual soils; Geotechnical properties

INTRODUCTION

In Malaysia, government effort on waste management was not palpable until the late 1970s when solid waste management began with street cleaning and domestic waste transportation to disposal sites [1]. The management of solid waste then was quite primitive and suited to cater only for the daily municipal solid waste (MSW) generated, and was estimated at about 0.5kg per capita [2]. Moreover, the system of waste collection was only confined to urban areas while the rural communities disposed of by burying or burning within their compounds [3]. Besides, disposal sites then were mere open-dumping grounds with small sizes corresponding to the small communities and were preserved by the local authorities [4].

With the growth in economic development, urbanization, industrialization, population, and improvement in the standard of living, the quantity of waste produced has rapidly increased in recent years with an average daily per capita generation of 1.2kg in 2007 and greater than 1.7kg in 2010 [1], thus making the management of MSW one of Malaysia's most critical environmental issues. As a result, the solid waste management system (SWMS) was required to be upgraded to suit the waste quantity and composition.

Typical SWMS techniques employed to curtail

menace of waste generation included; incineration, well injection, source reduction and reuse, recycling, and composting, among others. Despite these advancements in solid waste management technologies to minimize the environmental impacts attributed to the waste, a safe disposal facility was still necessary for the disposal of the final and/or unusable waste. Therefore, municipal authorities were compelled to impound these waste behind specially designed engineered landfills that utilize bottom liner systems. Bottom liners are primarily used to prevent the migration of leachate and landfill gases from the landfill into the surrounding environment and groundwater and, hence, protect the environment and groundwater from pollution.

Geosynthetic clay liners, geomembranes, and natural soils are commonly used as landfill liner. These liners have their unique advantages and disadvantages over their counterparts. The pros and cons of geosynthetic clay liners are extensively discussed by [5]. On the other hand, the merits of natural soils for liner utilization have been examined by several researchers [6] - [9] and they include; they are naturally occurring and readily available, relatively inexpensive when on site or in close proximity, less vulnerable to mechanical accidents (punctures), good compatibility with the permeating fluid and high attenuation capacity, etc.

Various naturally occurring geomaterials have

been evaluated for their suitability as liner materials for sanitary landfills in Malaysia. For instance, Rahman, Yaacob, Rahim, Lihan, Idris and Mohd [10] investigated the potential of marine clay obtained from Kedah as landfill liners. Taha and Kabir [9] studied the suitability of granite residual soils obtained from a granitic formation at Cheras for their application as liner materials. Taha and Kabir [11], evaluated the potential of sedimentary residual soils as hydraulic barriers in waste containment systems. Zulkifli, Wong, Alia, Ridzuan and Zawawi [12] studied the properties of natural soil from Endau Rompin National Park as compacted soil liner for sanitary landfills. Nik, Mazidah, Soenita and Norazlan [13] investigated the properties of blended lateritic soils for designing soil liners. However, very little is known about the potential of Subang and Putrajaya residual soils for use as hydraulic barriers in engineered landfills. Moreover, previous studies evaluated the suitability of residual soils for liner application using distilled water as the saturating and permeating fluid which is far from being representative of the field conditions. Thus, this study aimed at assessing the geotechnical properties of two Malaysian residual soils which occur in considerable quantities for their usability as liner materials in engineered landfills. Their suitability was investigated using both distilled water and leachate as the saturating and permeating fluids.

MATERIALS AND METHODS

Residual Soils

The residual soils used in the study were obtained from Subang and Putrajaya for soil sample A and B respectively as depicted in Fig.1. The soils were sampled from 0.5m depth below the ground surface and transported to the geotechnical laboratory of Monash University for analysis. The residual soils in both areas are the weathering products of Kenny Hill rock formation consisting of interbedded sandstone, siltstone and shale [14].

The soil samples were oven-dried, crushed and sieved to appropriate size prior to testing. The pulverized soil samples were subjected to physical and geotechnical tests by using distilled water and landfill leachate as saturating and permeating liquids. The physical properties of the soils such as particle size distribution, Atterberg limits, specific gravity were conducted according to British Standard (BS1377:1990) [15]. The oven-dried soil that passed through sieve number 4 (4.75mm) was used for geotechnical tests including compaction, permeability and unconfined compressive strength tests. The compaction characteristics were evaluated by utilizing the standard proctor compaction method as stipulated in British Standard (BS1377:1990) [15]. The unconfined compression strength (UCS) test was

conducted according to standard procedures outlined in the ASTM 2166 method [16] with applied rate of strain of 1% per minute. The hydraulic conductivity was measured by performing a falling head permeability test with rigid wall compaction mould permeameter in accordance with ASTM D5856 method [17]. The mineralogical composition of the soil samples were determined using X-ray fluorescence spectrometer.

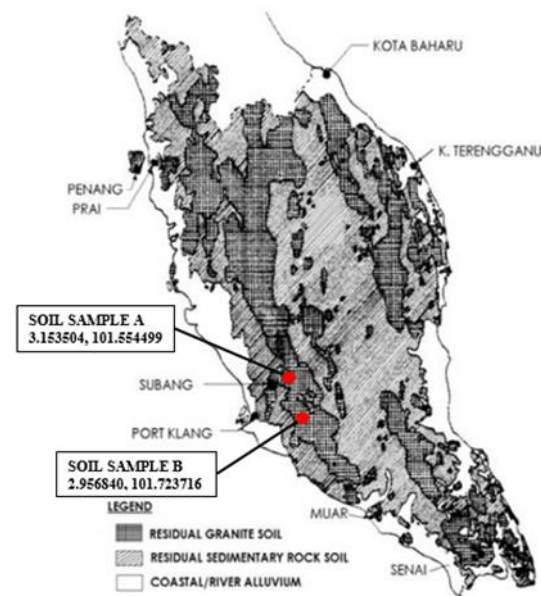


Fig. 1 The location of soil sampling (after Ooi, 1982) [18].

Leachate

Leachates used in the study were collected from Taman Beringin Transfer Station and stored in a refrigerator at 4°C in order to minimize any chemical reactions prior to testing. The physico-chemical composition of the leachate is presented in Table 1.

Table 1 Physico-chemical composition of the leachate.

Parameters	Concentration
Physical and Aggregate Properties	
Total Dissolved Solids (mg/L)	9660
Total Hardness as CaCO ₃ (mg/L)	1900
pH	3.57
Electrical Conductivity (mS/cm)	12.61
Inorganic and Nonmetallic Properties (mg/L)	
Chloride	2370
Sulphate	497
Metals and Major Cations (mg/L)	
Cadmium	0.02
Chromium	0.49
Copper	0.39
Iron	369
Lead	0.08
Manganese	5.11
Nickel	0.36
Zinc	6.1
Environmental Quality (mg/L)	
Biological Oxygen Demand	23800
Chemical Oxygen Demand	61200
Total Suspended Solids	12000
Ammonia as N	462

RESULTS AND DISCUSSIONS

Soil Classification and Properties

The soil samples were classified based on their silica-sesquioxide ratio (SSR). The silica-sesquioxide ratio is defined to differentiate the soil types by their degree of weathering based on their metal oxides composition as shown in Eq. (1) [19].

$$SSR = \frac{\%SiO_2/60}{\left(\frac{\%Al_2O_3}{102}\right) + \left(\frac{\%Fe_2O_3}{160}\right)} \quad (1)$$

Table 2 Metal oxides composition of the residual soil samples.

Metal Oxides (%)	Soil Samples	
	A	B
Al ₂ O ₃	28.683	30.213
SiO ₂	55.35	27.868
Fe ₂ O ₃	5.928	24.715
Silica-sesquioxide ratio, SSR (%)	2.9	1.03

Note : SSR < 2.0 is intensely weathered ferrallitic soil whereas SSR > 2.0 is less intensely weathered ferruginous soil [19].

Soil sample A is categorised as ferruginous soil (SSR=2.9) while soil sample B is classified as ferrallitic soil (SSR=1.03).

The physical and geotechnical properties of soil samples are summarized in Table 3 with their corresponding grading curves presented in Fig.2. Ferruginous soil is dominated by sand (69.25%), clay fraction (15%), silt fraction (13.9%) and gravel (1.85%). Ferrallitic soil contains 84.1% of sand, 10.03 % of silt fraction and 5.87% of clay fraction. Daniel [20] and Benson and Trast [21] suggested the following requirements for soil liner materials: percentage of gravels ≤ 30%, percentage of fines ≥ 20-30% and percentage of clay ≥ 15%. Based on the stated requirement, the grading characteristic of ferruginous soil fulfilled the requirement of recommended materials for landfill liner. However, the percentage of fines and clay fraction presented in ferrallitic soil were not sufficient to meet the requirement.

The fine fractions of ferruginous soil and ferrallitic soil are categorized as inorganic clay of high plasticity (CH) and silt of high plasticity (MH) respectively in accordance with British Standard (BS 5930:1999) [22]. The plasticity index of ferruginous soil and ferrallitic soil are 28.30% and 36.50% respectively. The values of plasticity index for both soil samples met the plasticity index criteria which is ≥ 7-10% for soil liner materials [20], [21]. Soil-leachate samples recorded lower liquid limit and plasticity index relative to soil-water samples. This reduction in Atterberg limits can be attributed to the increased concentration of multivalent cations in leachate that may cause the reduction in the diffusive double layer thickness of soil and lead to an increased amount of free water in the system [23], [24]. Similar findings were also reported by Frempong and Yanful [25], Harun, Ali, Rahim, Lihan and Idris [26] and Yantrapalli, Krishna and Srinivas [27].

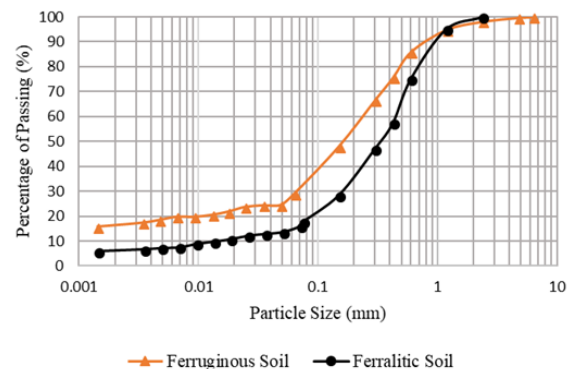


Fig. 2 Grading curves for tropical residual soil samples

Table 3 Geotechnical and physical properties of the tropical soil samples.

Properties	Soil –water Sample		Soil-leachate Sample	
	Ferruginous Soil	Ferralitic Soil	Ferruginous Soil	Ferralitic Soil
Particle Size Distribution, %				
Gravel	1.85	0	-	-
Sand	69.25	84.1	-	-
Silt	13.9	10.03	-	-
Clay	15	5.87	-	-
Fines Fraction	28.90	15.90	-	-
Natural Moisture Content , w (%)	25.35	32.24	-	-
Specific Gravity , G _s	2.70	2.84	-	-
Atterberg Limit, %				
Liquid Limit , w _L	50.10	73	46.20	57.8
Plastic Limit , w _P	21.80	36.5	19.00	25.76
Plasticity Index , I _p	28.30	36.50	27.20	32.04
Classification of fine fraction	CH	MH	-	-
Standard Proctor Compaction Test				
Max. Dry Density , ρ _{dry} (kN/m ³)	17.25	14.95	17.08	15
Optimum Moisture Content, W _{opt} (%)	18	30.5	18	29
Falling Head Permeability Test				
Hydraulic Conductivity (cm/s)	3.927 x 10 ⁻⁸	1.202 x 10 ⁻⁷	3.448 x 10 ⁻⁸	1.461 x 10 ⁻⁸
Unconfined Compressive Strength (kPa)	383.34	164.1	453.75	231.5

Compaction Properties

Soil compaction is normally performed to break down the soil chunk into homogenous mass that results in increased soil density and strength and reduced hydraulic conductivity [9]. The compaction properties and curves for both residual soil samples are shown in Table 3 and Fig. 3 respectively. The differences between the optimum moisture content and maximum dry density recorded before and after leachate saturation for ferruginous soil (0% difference in optimum moisture content, 0.99% difference in maximum dry density) and ferralitic soil (4.92% difference in optimum moisture content, 0.33% difference in maximum dry density) were minimal. Hence, it can be concluded that the leachate has no significant effect on the compaction properties of both soil samples.

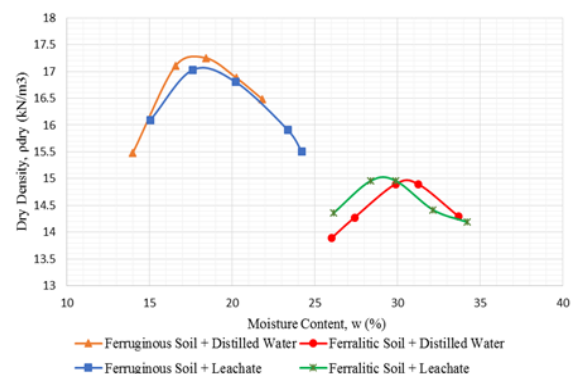


Fig. 3 Compaction curves for tropical residual soil samples saturated with distilled water and leachate.

Hydraulic Conductivity

The hydraulic conductivity of ferruginous and ferralitic soil after permeated with distilled water were found as 3.927×10^{-8} cm/s and 1.202×10^{-7} cm/s respectively. After leachate permeation, it was noticed that the measured hydraulic conductivities for ferruginous and ferralitic soil reduced to 3.448×10^{-8} cm/s and 1.461×10^{-8} cm/s accordingly. The permeability reduction could be due to the presence of suspended particles and microorganism inside the soil pores that cause pore clogging [25], [27], [28]. Similar findings have been reported by Frempong and Yanful [25], Francisca and Glatstein [28] and

Yantrapalli, Krishna and Srinivas [27]. The measured hydraulic conductivities for both soil samples were within the requirement for soil liner materials which was less than 1×10^{-7} cm/s [20], [21]. The lower permeability value recorded for ferruginous soil in comparison to ferralitic soil is attributed to the higher percentage of fines fraction (28.90 %) compared to ferralitic soil (15.90 %).

Unconfined Compressive Strength (UCS)

The unconfined compressive strength for ferruginous soil showed an increment from 383.34kPa to 453.75kPa after leachate application. Similarly, the UCS value for ferralitic soil has increased from 164.1kPa to 231.5kPa after leachate application. This increase in UCS is probably caused by the generation of calcium carbonate through in situ microbial processes that bind the soil particles together [29]. Daniel and Wu [30] recommended a minimum unconfined compressive strength of 200kPa for soil liner materials. The UCS of ferruginous soil for both types of saturation liquids met the requirement whereas for ferralitic soil saturated with distilled water did not fulfill the minimum required strength.

CONCLUSION

The suitability of two tropical residual soils from Kenny Hill rock formation as compacted soil liner material were assessed by conducting a series of physical and geotechnical test with distilled water and leachate as permeating and saturating fluid. The following conclusions can be drawn based on the experimental results.

1. Ferruginous soil from Subang is considered as a potential material for landfill liner compared to ferralitic soil from Putrajaya soil. The properties of ferruginous soil complied with all the requirements for soil liner materials in terms of particle size distribution, Atterberg limit, hydraulic conductivity and unconfined compressive strength whereas ferralitic soil only satisfied the minimum requirement of hydraulic conductivity.
2. After leachate application on both soil samples, it was observed that their Atterberg limits decreased due to increased concentration of multivalent cations in leachate that results in a reduction in the thickness of diffusive double layer which causes an increased amount of free water in the system.
3. The UCS of both soil sample increased due to the formation of particle-binding materials through biocementation.
4. It can be concluded that both soil samples were compatible with leachate as their hydraulic conductivities decreases after permeated with

leachates due to physical and biological clogging.

ACKNOWLEDGEMENTS

Financial support for this study is provided by Ministry of Higher Education in Malaysia with grant number FRGS/1/2017/TK01/MUSM/03/01. This support is gratefully acknowledged.

REFERENCES

- [1] Fauziah S. H. and Agamuthu P., Landfills in Malaysia: Past, Present, and Future, 1st Int. Conf. on Final Sinks, 2010, pp. 1-9.
- [2] Perithamby A., Hamid S.F. and Khidzir K., Evolution of Solid Waste Management in Malaysia: Impacts and Implications of the Solid Waste Bill 2007, *Journal of Material Cycles and Waste Management*, Vol 11, Issue 2, 2009, pp. 96–103.
- [3] Fauziah S. H. and Agamuthu P., Trends in Sustainable Landfilling in Malaysia, a Developing Country, *Waste Management and Research*, Vol 30, Issue 7, 2012, pp. 656 – 663.
- [4] Latifah A. M., Mohd A. A. S. and Nur I. M. Z., Municipal Solid Waste Management in Malaysia: Practices and Challenges, *Waste Management*, Vol 29, Issue 11, 2009, pp. 2902–2906.
- [5] Bouazza A., Geosynthetic Clay Liners, *Review Article, Geotextiles and Geomembranes*, Vol 20, No. 1, 2002, pp 3 -17.
- [6] Manoj K. and DK. S., A Study on the Technique to Improve Desiccation Cracks, *International Journal of Research in Advanced Engineering and Technology*, Vol 1, No. 3, 2015, pp. 24-26.
- [7] Akayuli C. F. A., Gidigas S. S. R. and Gawu S. K.Y., Geotechnical Evaluation of a Ghanaian Black Cotton Soil for use as Clay Liner in Tailings Dam Construction, *Ghana Mining Journal*, Vol 14, 2013, pp. 21 - 26.
- [8] Preeti S. A. and Singh B. K., Instrumental Characterization of Clay by XRD, XRF, and FTIR. *Indian Academy of Science*, Vol 30. No. 3, 2007, pp. 235-238.
- [9] Taha M. R. and Kabir M. H., Tropical Residual Soil as Compacted Soil Liners, *Environmental Geology*, Vol 47, No. 3, 2005, pp. 375–381.
- [10] Rahman Z. A., Yaacob W. Z. W., Rahim S. A., Lihan T., Idris W. M. R. and Mohd W. N. F., Geotechnical Characterization of Marine Clay as Potential Liner Material, *Sains Malaysiana*, Vol 42, No. 8, 2013, pp. 1081 – 1089.
- [11] Taha M. R. and Kabir M. H., Sedimentary Residual Soils as a Hydraulic Barrier in Waste Containment Systems, In: *Proceedings of the 2nd International Conference on Advances in Soft Soil Engineering Technology Putrajaya, Malaysia*, 2003, pp. 895-904.

- [12] Zulkifli A., Wong M. S., Alia D., Ridzuan M. B. and Zawawi D., Study on the Natural Soil Properties of Endau Rompin National Park (PETA) as Compacted Soil Liner for Sanitary Landfill. *International Journal of Integrated Engineering*, Vol 5, No. 1, 2013, pp. 14 – 16.
- [13] Nik N. S., Mazidah M., Soenita H. and Norazlan K., Influence of Compaction Effort for Laterite Soil Mix with Geopolymer in Designing Soil Liner, *Electronic Journal of Geotechnical Engineering*, Vol 20, No. 22, 2015, pp. 12353 – 12364.
- [14] Mohamed Z, Rafek A.G. and Komoo I., Characterisation and Classification of the Physical Deterioration of Tropicallly Weathered Kenny Hill Rock for Civil Works, *Electronic Journal of Geotechnical Engineering*, Vol 12, 2007, 16pp.
- [15] British Standard Institution 1377, Methods of Test for Soils for Civil Engineering Purposes, 1990, 142 pp.
- [16] American Society for Testing and Materials D2166, Standard Test Method for Unconfined Compressive Strength of Cohesive Soil, 2005, 6pp.
- [17] American Society for Testing and Materials D5856, Standard Test Method for Measurement of Hydraulic Conductivity of Porous Material Using a Rigid-wall, Compaction-Mold Permeameter, 2007, 8pp.
- [18] Huat B.K., Gue S.S. and Ali F.H., Country Case Study: Engineering Geology of Tropical Residual Soils in Malaysia, *Tropical Residual Soils Engineering*. 2nd ed. Taylor and Francis Group, London, UK, 2009, pp. 421.
- [19] Engineering Group of the Geological Society, Working Party Report, *Quarterly Journal of Engineering Geology and Hydrogeology*, Vol 23, No 4-101, 1990, 98pp.
- [20] Daniel D.E., *Clay Liners, Geotechnical Practice for Waste Disposal*, 1st ed, Chapman and Hall, UK, 1993, pp. 137-163.
- [21] Benson, C.H. and Trast J.M., Hydraulic conductivity of thirteen compacted clays, *Clays and Clay Minerals*, Vol 43, No. 6, 1995, pp. 669-681.
- [22] British Standard Institution 5930, Code of Practice for Site Investigations, 1999, 207 pp.
- [23] Mitchell J.K. and Soga K., *Soil-Water-Chemical Interactions, Fundamentals of Soil Behavior*, 3rd ed., John Wiley & Sons, Canada, 2005, pp. 143-171.
- [24] Othman M.Z. and Shafii F, The Effects of Electrolytes on Liquid Limit of Clay, *Journal of Civil Engineering*, Vol 11, No. 1, 1998, pp. 7-19.
- [25] Frempong E.M. and Yanful E.K., Interactions between Three Tropical Soils and Municipal Solid Waste Landfill Leachate, *Journal of Geotechnical and Geoenvironmental Engineering*,
- [26] Harun S.N., Ali Rahman Z., Rahim S.A., Lihan T. and Idris W.M.R., *AIP Conference Proceedings*, Vol 1571, No.1, 2014, pp. 530-536.
- [27] Yantrapalli S., P.Krishna Hari and K Srinivas, A Study on Influence of Real Municipal Solid Waste on Properties of Soils in Warangal, India. *Journal of Geoscience, Engineering, Environment and Technology*, Vol 3 No. 1, 2018, pp. 25 -29.
- [28] Francisca F.M. and Glatstein, Long Term Hydraulic Conductivity of Compacted Soils Permeated with Landfill Leachate, *Applied Clay Science*, Vol 49, 2010, pp. 187-193.
- [29] Ivanov V. and Chu J., Applications of Microorganisms to Geotechnical Engineering for Bioclogging and Biocementation of Soil in Situ, *Reviews in Environmental Science and Bio/Technology*, Vol 7, No. 2, 2008, pp. 139-153.
- [30] Daniel. D. E., and Wu. Y. K., Compacted Clay Liners and Covers of Arid Sites. *Journal of Geotechnical Engineering*, Vol 199, No. 2, 1993, pp. 223-237.
- [31] Arasan S., Effect of Chemicals on Geotechnical Properties of Clay Liners: A Review. *Research Journal of Applied Sciences, Engineering and Technology*, Vol 2, No.8, 2010, pp. 765-775.

INVESTIGATING THE EFFECT OF GEOTEXTILE AS REINFORCEMENT ON THE BEARING CAPACITY OF GRANULAR SOIL

John Carlo R. Samarita¹, and Mary Ann Q. Adajar²

¹Graduate Student, De La Salle University, Philippines; ²Faculty, De La Salle University, Philippines

ABSTRACT

Considering that soils in parts of the Philippines, particularly Manila, are characterized as weak and soft, bearing capacity failure becomes a major concern. While many studies dealt with reinforced soil foundation, there are some research gaps in observing ground deformation and explaining the role of geotextile in bearing capacity improvement. This paper addresses these questions through using a concentric static loading test for shallow foundations on granular soils with single layer of geotextile reinforcement placed at different depths relative to the footing base wherein ultimate bearing capacity (q_{ult}) improvement is quantified and verified using Terzaghi's and Vesic's equations using frictional angle (ϕ) from laboratory direct shear tests, optimal depth of geotextile embedment (u) is identified using bearing capacity ratio (BCR), and images of internal deformation of the model ground were obtained using a unique visualization technique. Results indicate that q_{ult} -values are improved for reinforced samples whose u -value lies within the maximum depth of failure zone at 1.00B. The increase in bearing capacity was validated using direct shear test which highlights that ϕ increased by 2.50° between unreinforced and reinforced samples (from 40.70° to 43.20°), leading to good agreement with theoretical q_{ult} using Vesic's formula. This q_{ult} improvement, however, varies with u ; the optimal depth is tallied at 0.25B at BCR of 1.52. Meanwhile, the ground deformations were effectively observed where it was concluded that the unreinforced sample fails under local shear whereas the reinforced sample with maximum BCR undergoes punching shear.

Keywords: Bearing capacity, Interface frictional angle, Ground deformation visualization, Failure modes

INTRODUCTION

Throughout history, major occurrences of bearing capacity failure have been well-documented [1]. Bearing capacity failure is characterized by the shear failure of the soil due to the overwhelming magnitude of the applied bearing pressures [2]. Events such as the collapse of the Transcona Grain Elevator in Winnipeg, Canada in 1913 and Fargo Grain Elevator in North Dakota four decades after are some of the more well-known geotechnical catastrophes of this nature; both had undeniable resemblance in terms of their foundation types and the characteristics of their respective underlying soils which were ultimately reported as incompetent, weak soils [1].

Bearing in mind that the composition of local soils in the Philippines, most especially Manila, is characterized as weak and soft [3], cases of bearing capacity failure become huge concerns.

Fortunately, the risks associated with the use of weak soil can be alleviated through introducing reinforcing elements [4]-[9]; in the forefront of which are geosynthetics such as geotextiles.

However, while many studies [4]-[9] have focused on exploring the field of reinforced soil foundation to improve the soil's bearing capacity and to reduce its corresponding settlement, much is still left to be desired in some facets of these researches.

For the analysis aspect, some were limited to the discussion of BCR values but have not provided an apt explanation as to what soil parameter is being improved when adding reinforcement to the ground.

In terms of the experimental aspect, these same studies were not able to track the internal deformations for the model ground upon loading. This is a significant gap since these said deformations are indicative of the failure mode. Fortunately, a comprehensive method in the form of a visualization technique was developed in a certain study [10], a modification of which is deemed appropriate for the purposes of this research. In the same work, however, no reinforcing medium was present.

As such, this study aimed to extend the domain of knowledge in reinforced soil foundation by improving both its experimental and analytical aspects. Through the adaptation of a visualization technique which allowed for the observation of internal ground deformation and the extension of discussion beyond BCR parameters by using the concept of an interface frictional angle, this study sought to quantify the improvement in the bearing capacity of granular soil reinforced with geotextile, to determine the optimal depth of embedment of the geotextile layer based on BCR values, and to create photo-visualizations of the internal deformations in the model ground.

METHODOLOGY

Materials

The model footing used for this study is made of rigid steel, comprising of a square column and square base with dimensions of 25mm x 25 mm x 200mm and 100mm x 100mm x 5mm, respectively. A square plywood, whose dimensions are 150mm x 150mm x 20mm, is attached on top of the column to facilitate the loading process. The model ground is made of black sand and Ottawa sand. The decision to use two types of sand for the model ground is derived from the concept developed from a reference study [10] wherein color variation of soil layers was used as an instrument to visualize the post-loading deformation. The materials are placed in a glass tank (1000mm x 1000mm x 500mm) designed to accommodate the expected bearing loads. The schematic diagram of the loading setup is shown in Fig. 1.

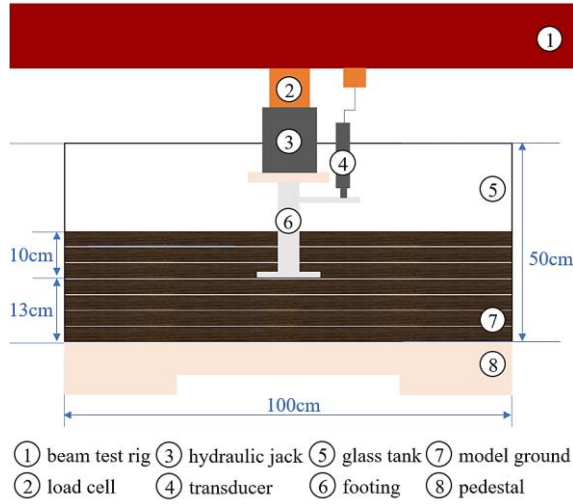


Fig. 1 Schematic diagram of loading system

For the reinforced samples, a single layer of geotextile (PP Woven, AASHTO Class 1) was incorporated in the model ground; its placement in terms of embedment depth varies for each trial. The summary of the samples used is Table 1 (see note).

Table 1 Types of sample used for loading test

Sample	Geotextile Embedment Depth (u)
Sample U	(no geotextile)
Sample R1	0.25B (25% of footing width)
Sample R2	0.50B (50% of footing width)
Sample R3	0.75B (75% of footing width)
Sample R4	1.00B (100% of footing width)
Sample R5	1.25B (125% of footing width)

Note: u refers to the geotextile embedment depth which is the depth relative to the base of the footing; whereas B refers to the footing width, equal to 10cm

Procedure

Index properties were first tested for both sands. The properties of concern are specific gravity (G_s), minimum void ratio (e_{min}), and maximum void ratio (e_{max}); these were obtained using tests based on ASTM standards [11]-[13]. The target unit weight for both sands (set at a relative density of 75%) was resolved using the above-mentioned parameters.

After this, air pluviation technique was applied. In this method, separate series of tests for the two sands was done with each trial having a unique falling height. This, in turn, resulted to a variation in the unit weight of the sample per trial. The target falling height was retrieved by searching for the value of the falling height that results to density equal to the target unit weight. Since consistency of the sample affects the resulting bearing capacity [10], this strategy is important to make sure that the relative density of the model ground is held constant for all samples.

The third phase is the load testing. This process involved the use of a load cell (coupled with a hydraulic jack) and a vertical transducer. These were connected to a data logger which records the values for pressure and settlement during loading. The sets of output were experimental values (q_{ult}) of ultimate bearing capacity of the samples listed in Table 1. After loading, photos of the ground deformations were taken by performing cross-sectional slices on the model ground wherein saturation and drainage of the liquid are prerequisite steps [10].

To validate the results, laboratory direct shear tests were conducted whose aim is to procure the angle of internal friction (ϕ') for both unreinforced [14] and reinforced trials [15]. The data were processed using Microsoft Excel spreadsheets.

$$q_{ult} = 1.3c'N_c + \sigma'_{zD}N_q + 0.4\gamma'BN_\gamma \quad (1)$$

$$q_{ult} = c'N_{cs}d_c + \sigma'_{zD}N_{qs}d_q + 0.5\gamma'BN_{\gamma s}d_\gamma \quad (2)$$

where q_{ult} = ultimate bearing capacity
 c' = effective cohesion of soil
 σ'_{zD} = vertical effective stress at depth D
 γ' = effective unit weight of soil
 B = width of footing
 s_c, s_q, s_γ = shape factors
 d_c, d_q, d_γ = depth factors
 N_c, N_q, N_γ = bearing capacity factors

Using the equations for ultimate bearing capacity [1]-[2], theoretical values of q_{ult} were obtained. For this purpose, Terzaghi's formula, Eq. (1), and Vesic's formula, Eq. (2), were used wherein the different factors are a function of ϕ' . The frictional angle used was based on the results of the direct shear tests.

Ultimately, the research questions were addressed by utilizing these findings from the experiment.

RESULTS AND DISCUSSION

Index Properties

The properties obtained from laboratory tests [11]-[14] are shown in Table 2. At a specified relative density of 75%, the target void ratio of 0.98 and 0.51 for black sand and Ottawa sand, respectively, were garnered. This resulted to target dry unit weights of 13.15 kN/m³ (1.34 g/cm³) for the black sand and 17.22 kN/m³ (1.75 g/cm³) for Ottawa sand.

Table 2 Summary of index properties

Index Property	Black sand	Ottawa sand
Specific gravity, G_s	2.65	2.65
Maximum void ratio, e_{max}	0.93	0.47
Minimum void ratio, e_{min}	1.11	0.62
Target relative density, D_r	0.75	0.75
Target void ratio, e	0.98	0.51
Target dry unit weight, γ_d [kN/m ³ (g/cm ³)]	13.15 (1.34)	17.22 (1.75)

These values for the dry unit weight were used as reference values for the air pluviation technique.

Air Pluviation Technique

This technique used an apparatus composed of a funnel attached to a PVC pipe with a wire mesh whose dimensions are specified below. By regulating the flow of sand, the sample's consistency is ensured to be only influenced by falling height (see Fig. 2).

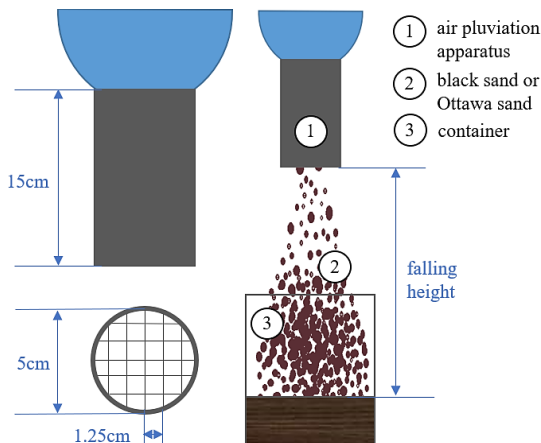


Fig. 2 Air pluviation apparatus and technique

A separate series of tests was conducted on both sands. Several trials with unique falling heights were tested for their dry unit weights; the value that yields the target dry unit weight (see Table 2) was deemed the target falling height: it was found to be at 26cm and 12cm for black and Ottawa sands, respectively. This parameter was then used for soil preparation.

Loading Test Results

Prior to loading, soil preparation was performed by forming the model ground using the target falling height retrieved for both sand types. This was done to ensure that the only parameter being varied for each sample was the (1) the presence of geotextile between unreinforced and reinforced trials and (2) the depth of embedment of geotextile (u) among reinforced trials.

Upon conducting the concentric loading test, values for the bearing pressure at increasing records of settlement were obtained. The summary of these results is listed on Table 3 and is illustrated in Fig. 3.

Table 3 Summary of pressure vs. settlement curves

Settlement (mm)	Bearing Pressure (kPa)					
	R1	R2	R3	R4	R5	U
0	10	10	10	10	10	10
1	60	40	40	40	40	40
2	90	70	60	60	60	60
3	110	90	80	80	80	80
4	140	130	110	110	110	110
5	160	150	130	130	130	130
6	180	170	160	150	150	150
7	230	210	190	180	180	180
8	280	260	230	210	190	190
9	330	290	260	230	220	210
10	350	320	280	250	240	220
11	380	350	310	280	260	260
12	410	380	330	300	290	290
13	430	400	350	310	310	310
14	460	430	380	320	320	320
15	500	450	420	350	340	330

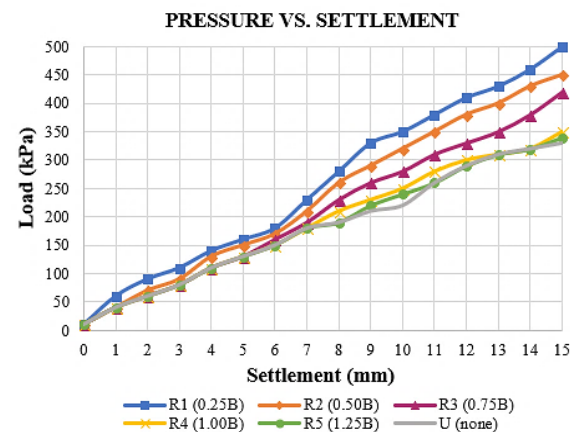


Fig. 3 Pressure vs. settlement curves of samples

From Fig. 3 above, it can be deduced that for all pressure-settlement curves, there is an absence of a peak value for the load from settlements of 0 – 15mm. As such, the bearing pressure at 15% strain (equivalent to 15% of the footing width of 100mm) was considered as the experimental value for ultimate bearing capacity (q_{ult}).

However, the influence of using geotextile as soil reinforcement seems to be insignificant for initial settlement values of up to 6mm. At this juncture, the load (including the overburden pressure) is still relatively minimal that it is unable to mobilize the geotextile. The reinforcement takes into effect once greater stresses are applied and its mobility depends on its relative placement (u) on the model ground.

The unreinforced (control) sample yielded a q_{ult} of 330 kPa. The highest record for q_{ult} is 500kPa which occurred for Sample R1 ($u=0.25B$), followed by Samples R2 ($u=0.50B$) and R3 ($u=0.75B$) at 450kPa and 420kPa, respectively. Samples R4 ($u=1.00B$) and R5 ($u=1.25B$) resulted to marginal q_{ult} improvement.

While this suggests that there is an increase in the q_{ult} when the sample was reinforced, it also highlights the variation in improvement as a function of u . However, it does not address which soil parameter was being refined in the process of reinforcing the model ground. The researchers theorize that there may have been some positive developments for the frictional angle, one of the factors that influence bearing capacity, for reinforced soil foundation. This was verified using laboratory direct shear tests for both unreinforced and reinforced samples.

Direct Shear Test Results

Results from the direct shear test indicate that for the unreinforced sample, a linear failure plane can be projected at an R^2 value of 0.9848, resulting to a slope of 0.8602 (see Fig. 4). This is equal to a ϕ' value of 40.70° . This may be concluded to be a by-product of the intergranular friction among soil particles.

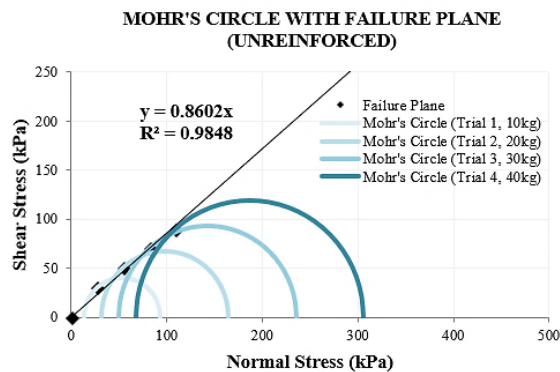


Fig. 4 Mohr's circle with failure plane for the unreinforced sample from direct shear test

As for the reinforced sample, it generated an R^2 value of 0.9391, with a slope of 0.9656 for the failure plane (see Fig. 5). This is equivalent to a ϕ' value of 43.20° having a 2.50° increase relative to the previous sample. This, however, may no longer be due to purely soil particles alone but the interface friction between geotextile and sand – in other terms, this may be taken as the interface frictional angle.

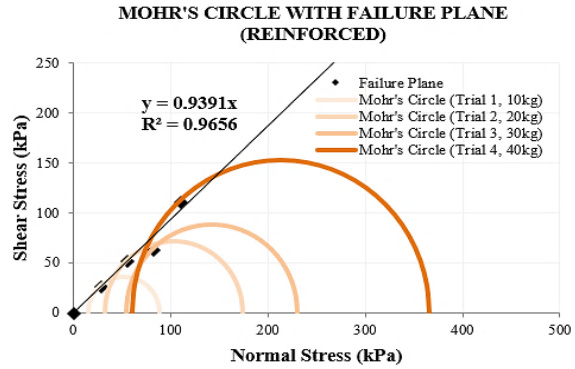


Fig. 5 Mohr's circle with failure plane for the reinforced sample from direct shear test

Theoretical Validation

Using the ϕ' values obtained from the direct shear test, theoretical values for q_{ult} were resolved using Eqs. (1)-(2). For the unreinforced sample, 251.34kPa and 338.39kPa were obtained for the two formulas, respectively. The experimental value for q_{ult} at 330kPa (Sample U) shows good correlation with Vesic's results at around 2.48% error. Meanwhile, for the reinforced sample, the two formulas yield 387.10kPa and 505.14kPa, respectively. The latter theoretical result has good agreement with the experimental value for Sample R1 which had an experimental q_{ult} of 500kPa (1.02% error).

Optimal Geotextile Embedment Depth

Bearing capacity ratio (BCR) refers to the ratio between the q_{ult} of the reinforced and unreinforced samples. It suggests the degree of q_{ult} improvement for reinforced trials. At the 15mm settlement, Sample R1 ($u=0.25B$) registered the highest BCR at around 1.52, followed by R2, R3, and R4 at 1.36, 1.27, and 1.06. However, Sample R5 ($u=1.25B$) yielded a BCR of only 1.03. In addition, an observation of Fig. 6 shows that Sample R5's BCR-settlement curve almost always coincides with that of Sample U. This suggests that placing the geotextile at a depth beyond 1.00B (such as 1.25B) renders the reinforcement ineffective in ameliorating the soil's bearing strength.

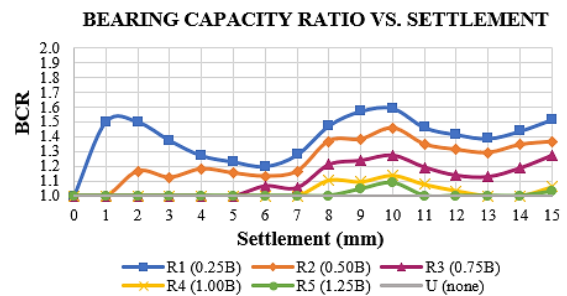


Fig. 6 Bearing capacity ratio vs. settlement curves of samples from concentric loading test

Ground Deformation Visualization

While the failure mode may be predicted through non-intrusive means by evaluating the appearance of the pressure-settlement curve, there seems to be a crucial ambiguity in differentiating the case for a local shear and punching shear failure modes which both have graphical resemblance in that both have curves that continuously increase with no evident peak value and are applicable only for homogeneous soil types [1]-[2]. A novel contribution of this study was exploring the use of a visualization technique in observing ground deformation. By using this method, the failure mode can be ascertained not by relying on the pressure-settlement curve but by using actual photographs of the internal deformations.

This was done through saturating the model ground after the loading test to retain the internal soil displacements. The water was then drained from the model ground in a span of several hours up to a day; consequently, cross-sectional cuts were performed in specific regions such as at distances 30cm and 15cm relative to the center of footing, as well at the edge of the base of footing and at the edge of the column of footing. Due to the use of two sand types that have contrasting colors, the model ground's post-loading deformations can be visualized. These photographs were then used as a basis for concluding the failure mode for the samples. For this section, the findings for the various critical samples are elaborated.

Sample U is deemed as one of the critical samples for it served as the unreinforced, control trial. For this sample, significant findings were obtained from the cut at the edge of the column of footing. As shown in Fig. 7, some relevant physical manifestations were (a) the formation of slight bulging on the ground surface, (b) the presence of evident settlement for the Ottawa Sand layers located underneath the bottom of the footing base, and (c) an estimated length of 3B relative to the edge of the footing base for both its sides representing the horizontal coverage of the failure zone. These characteristics align well with the description for a local shear failure.

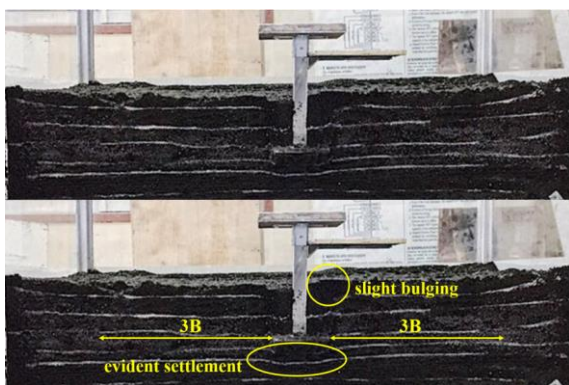


Fig. 7 Ground deformation at edge of the column of footing for Sample U (no geotextile)

Sample R1 ($u=0.25B$) is considered yet another critical sample for it yielded the highest BCR, thus, concluded to be the optimal depth. However, its failure mode does not resemble that of the unreinforced sample. In fact, the soil layers displayed little-to-no difference before and after loading as exemplified by (a) the presence of parallel layers of Ottawa Sand especially on the upper portion of the model ground on the periphery of the column of footing, and (b) the formation of minimal settlement underneath the footing base. In addition, no heaving was found on the ground surface. These are striking features of a punching shear failure mode (see Fig. 8).

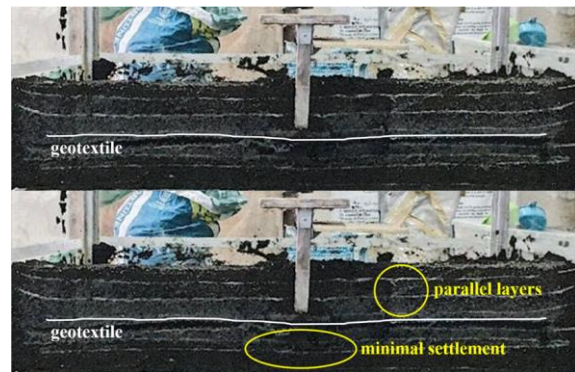


Fig. 8 Ground deformation at edge of the column of footing for Sample R1 ($u=0.25B$)

Finally, Sample R4 ($u=1.00B$) is also taken as critical in that among all samples, excluding Sample R5 ($u=1.25B$) deemed as beyond the maximum failure depth of $1.00B$, it is the reinforced sample with the least BCR. Figure 9 highlights some similitude with the visualization for Sample U. For instance, bulging was also seen although very minimal relative to Sample U's observed heaving. Moreover, (a) minimal settlement was also found underneath the footing base and (b) an approximate length of 3B on the left side of the footing base appeared to be disturbed. This is an example of a local shear failure albeit to a lesser degree than that of Sample U.

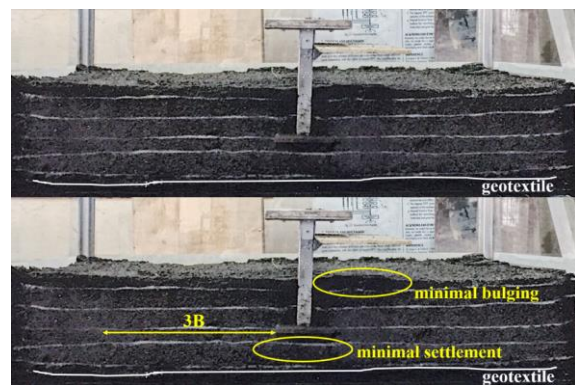


Fig. 9 Ground deformation at edge of the column of footing for Sample R4 ($u=1.00B$)

CONCLUSIONS AND RECOMMENDATIONS

Conclusions crucial to the further understanding of reinforced soil foundation were derived from the study's findings. For instance, it was discovered that reinforced samples whose u -value falls within the maximum depth of failure zone ($1.00B$) yielded marginal to significant improvements for the ultimate bearing capacity. This increase was verified through laboratory direct shear tests which confirmed that an increase of 2.50° was present between the angle of internal friction of the unreinforced and reinforced samples. This had good agreement with theoretical results using Vesic's formula. Furthermore, it was interpreted that this frictional angle is no longer due to the intergranular friction between soil particles but due to the interface between geotextile and sand grains, thus, the term "interface frictional angle".

Meanwhile, the optimal depth of geotextile embedment was observed at Sample R1 ($0.25B$) wherein a BCR of 1.52 was recorded. In addition to this, it was also concluded that due to the relative coincidence of the BCR vs. settlement curves for Sample R5 ($1.25B$) and Sample U, the geotextile may no longer be effective when placed at a depth beyond the value of the footing width itself.

Through the visualization technique, the internal ground deformations were effectively observed. Based on the photos, features of the model ground were highlighted especially in the region near the footing. Failure modes for critical samples were deduced with the unreinforced sample failing under local shear whereas for the reinforced samples: Sample R4 ($1.00B$) also experienced local shear but to a lesser degree and Sample R1 ($0.25B$) suffered punching shear albeit non-excessive.

Considering the tedious process involved in dealing with natural soil types, it is recommended to explore the use of transparent soils. In this manner, a practical, non-intrusive means of visualizing internal ground deformations can be possible. This innovation can lead to the tracking of not only post-loading but also real time displacements of the model ground.

Likewise, there is a limitation to this study due to the use of a static loading setup – the absence of scaling laws. In which case, the authors also recommend pursuing the use of centrifuge technology which allows for the scaling of model dimensions, as well as displacements and forces, to corresponding full scale (or prototype) values.

REFERENCES

- [1] Coduto, D.P., Kitch, W.A., and Yeung, M.R., *Foundation Design: Principles and Practices*, 2nd edition. Upper Saddle River, NJ: Pearson Education, Inc., 2016, pp. 215-258.
- [2] Das, B., and Sobhan, *Principles of Geotechnical Engineering*, 9th edition. Boston, MA: Cengage Learning, 2018, pp. 710-742.
- [3] Dungca, J., Concepcion Jr, I., Limyuen, M., See, T., and Vicencio, M., Soil bearing capacity reference for Metro Manila, Philippines, *International Journal of GEOMATE*, Vol. 12, Issue 32, 2017, pp. 5-11.
- [4] Marto, A., Oghabi, M., and Eisazadeh, A., The effect of geogrid reinforcement on bearing capacity properties of soil under static load; a review, *The Electronic Journal of Geotechnical Engineering*, Vol. 18, 2013, pp. 1881-1898.
- [5] Oghabi, M., Marto, A., and Eisazadeh, A., Effect of geocell reinforcement in sand and its effect on the bearing capacity with experimental test; a review, *The Electronic Journal of Geotechnical Engineering*, Vol. 18, 2013, pp. 3501-3516.
- [6] Kolay, P.K., Kumar, S., and Tiwari, D., Improvement of bearing capacity of shallow foundation on geogrid reinforced silty clay and sand, *Journal of Construction Engineering*, 2013, pp. 1-10.
- [7] Tafreshi, S.M., and Dawson, A., Behaviour of footings on reinforced sand subjected to repeated loading – comparing use of 3D and planar geotextile, *Geotextiles and Geomembranes*, Vol. 28, Issue 5, 2010, pp. 434-447.
- [8] Latha, G., and Somwanshi, A., Effect of reinforcement form on the bearing capacity of square footings on sand, *Geotextiles and Geomembranes*, Vol. 27, Issue 6, 2009, pp. 409-422.
- [9] Ghosh, A., Ghosh, A., and Bera, A.K., Bearing capacity of square footing on pond ash reinforced with geotextile, *Geotextiles and Geomembranes*, Vol. 23, Issue 2, 2005, pp. 144-173.
- [10] Adajar, M.A., Daimon, T., and Kusakabe, O., Embedment effect on the bearing capacity of spread footing in sand, *JSPS Core University Program, Environmental Engineering Bulletin*, Vol. 6, 2005, pp. 1-12.
- [11] American Society for Testing and Materials. Standard test methods for specific gravity of soil solids by water pycnometer. ASTM D854.
- [12] American Society for Testing and Materials. Standard test methods for maximum index density and unit weight of soils. ASTM D4253.
- [13] American Society for Testing and Materials. Standard test methods for minimum index density and unit weights of soils. ASTM D4254.
- [14] American Society for Testing and Materials. Standard test methods for direct shear test of soils under drained conditions. ASTM D3080.
- [15] Anubhav, and Basudhar, P., Modeling of soil-woven geotextile interface behavior from direct shear test results, *Geotextiles and Geomembranes*, Vol. 28, Issue 4, 2010, pp. 403-408.

A COMPARATIVE STUDY ON THE USE OF WOVEN GEOTEXTILE FOR SETTLEMENT REDUCTION OF SPREAD FOOTING ON GRANULAR SOIL

Mary Ann Adajar¹, Maricris Gudes² and Lillibelle Tan²

¹Faculty, De La Salle University, Manila, Philippines

²Civil Engineer, De La Salle University, Manila, Philippines

ABSTRACT

Utilization of geotextiles has been known to reduce the settlement in any kind of soil such as sand. This study seeks to quantify the settlement reduction mentioned. It is done by comparing the settlement data obtained from an isolated footing concentrically loaded on varying depths of geotextiles and a test trial with no geotextile. The varying embedment of the geotextile is related to the depth of the boundary condition, which is equivalent to the width of the footing equal to 10 cm. All experimental setup is identical, aside from the presence of the geotextile, and are comprised of granular soil simulated by Ottawa and black sand with a 75% relative density. From test results, it was concluded that the setup with the geotextile closest to the footing, having a depth that is equal to the quarter of the width of the footing displayed the highest magnitude in terms of settlement reduction consequently having the greatest load-bearing capacity. On the other hand, geotextile at a depth equal to the width of the footing exhibits results similar to the trial with no geotextile supported by the findings that as the depth of geotextile embedment increases further away from the footing, the settlement increases. The variation of geotextile embedment also resulted in a variation in mode of failure. Punching shear failure mode developed for footing with geotextile while local shear failure was observed for footing without geotextile.

Keywords: Woven geotextile, Settlement reduction, Spread footing, Embedment, Failure mode

INTRODUCTION

Problems in construction are very common in the majority of areas in the Philippines due to various conditions of the soil. In such predicaments, polymers are commonly used as a major material to remedy the multiple complications caused by the soil or are used to maintain and preserve the desired soil conditions for impending structures. Polymers are also otherwise known as geosynthetics; a rapidly emerging family of geo-materials used in wide variety of civil engineering application [1]. Akovali [2] states that geotextiles are permeable geosynthetics, which is a part of the oldest and largest group of geosynthetics. Geotextiles are composed of two types: woven and nonwoven. Woven geotextiles made by weaving together fabric on a loom and are relatively high in strength and stiffness but have relatively poor filtration or drainage characteristics. Nonwoven geotextiles, on the other hand, are made by binding the materials through chemical, heat, needle punching or other methods. It has low to medium strength with high elongation at failure but has good filtration or drainage characteristics

Dungca [3] presented that cities near bodies of water in Metro Manila such as Manila, Navotas, and Marikina have low bearing capacities. It is most rational that only shallow foundations may be used

when structures are built on a nearby water source such that only low design loads are expected and settlement reduction is maximized. Moreover, soil on nearby shorelines or bodies of water like sand is still not immune to the adverse effects of erosion, infiltration, compaction, and loss of stability, etc. due to its granular characteristics. In effect, this limits the capacity of the soil to withstand applied loadings and in most cases, structures constructed near these areas experience greater settlement when subjected to extreme loadings. Thus, reinforcing soil in these areas would be beneficial for construction.

In this study, the woven geotextile is used as a component of ground support for the foundation. The main objective of this study is to investigate the effect of using geotextile for soil reinforcement on the settlement of spread footing founded on granular soil like sand under vertical concentric loading. It specifically aims to determine the magnitude of the settlement produced from spread footing on sand reinforced with geotextile and compare it with the settlement of spread footing without geotextile; to recommend the most appropriate location of geotextile beneath a footing that will result to maximum reduction in settlement; to determine and analyze the slip failure surface of the supporting ground with and without geotextile; and to identify the advantages using woven geotextile in settlement reduction of spread footing on granular soil under

concentric loading.

The physical properties of Ottawa sand used in this study are established values [4] and will remain constant throughout all the trials for varying conditions of geotextile usage.

METHODOLOGY

Woven Geotextile Sample

The woven geotextile used for all testing is of the same material and supplier to ensure equality of properties in all test runs. It is commonly made from the woven strands of polypropylene fabric, which is non-biodegradable and high in UV resistance making it ideal for long-term use [5].

Experimental Procedures

A total of six (6) test runs with spread footing on granular soil subjected to vertical loading was done in the experiment. Ottawa sand and black sand were used to simulate granular soil. One (1) test run was made on granular soil without geotextile while five (5) test runs were with geotextile buried underneath the soil with varying depth. The ground was made of alternating layers of Ottawa sand and black sand to visualize the settlement after the application of the vertical concentric load. After loading, the ground was saturated with water in preparation for the slicing at various distances from the center of the footing.

Air Pluviation Technique

The constant relative density of 75% was maintained in the conduct of the experimentation for this study so that it would not be a factor to the results; and to achieve such scenario, a modified air pluviation technique was performed [6]. To execute, a tool called the pluviation apparatus was made. The device is constructed with a plastic funnel, a 6-inch long tube with a 2-inch diameter PVC pipe, a ½ inch opening screen and a funnel. The test is performed by elevating the apparatus above the container at different heights, and then the sand is set free to pass through the tube, beginning from the funnel to the end through the screen. The height of the apparatus above the ground surface that produced the desired density was determined.

Application of Vertical Loading Test

The dimensions of the container used in the experimental set-up were based on the theory of failure surface zone [7]. The friction angle of the sand sample was assumed to be 37 degrees which are the usual friction angle of sand [8]. The width of the footing B is equal to 10 cm, as well as the

assumed boundary condition, in which foundation settlement is expected and limited to this value beneath the area of the footing. With these dimensions, it was computed that the length from the center of the footing to the end of the failure surface at one side is 40.17 cm. The total length of failure zone at the ground surface is equivalent to 80.34 cm as shown in Figure 1. With these computed values, the container used in the experiment was a confined glass box measured with dimensions 100 cm x 100 cm x 50 cm that has an opening on the topside to allow direct contact with the soil to be enclosed. These dimensions are used to allow a 10 cm allowance for each side of the tank horizontally to be able to check if failure surface will reach beyond its computed value. One of its sides is removable and there were taps used to serve as an outlet to drain water introduced into the tank for visualization of settlement.

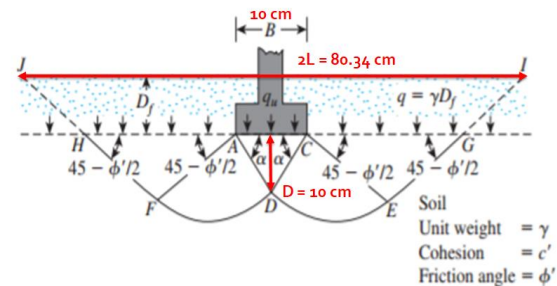


Fig. 1 Computed dimensions of failure surface zone

The miniature reinforced footing made of a steel plate with a base dimension of 10 cm x 10 cm x 0.5 cm, a column dimension of 3 cm x 3 cm x 30 cm with a top plate for loading purpose. It was embedded within the layers of sand and was subjected to loading from the load cell and hydraulic jack. Throughout the application of force, a data logger was attached to the load cell and transducer to keep track of the displacement and the corresponding load that applies. The multi-colored sand is found to have a depth of 22.5 cm and such measurement eliminates the boundary effect of the base of the glass box. Figure 2 shows the schematic diagram of the experimental set-up.

Ground Deformation Visualization

For a visual representation of the ground deformation and settlement, water was introduced into the soil after loading while the outlet valves are closed until the sand is moist. The saturation of the soil was done without disturbing the ground deformation. The outlet valves were then opened to drain excess water so that sand would clump together, preserving the settlement that has occurred. The sample was sliced at various distances from the

center of the footing to expose the area that has settled. These distances were 30 cm and 15 cm from the center of the footing, at the edge of the footing and at the edge of the column.

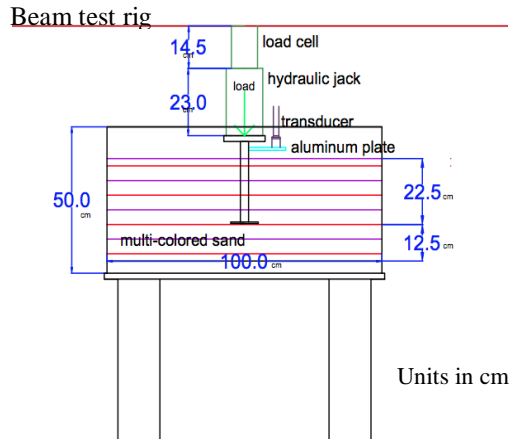


Fig. 2 Schematic diagram of the experimental set-up

RESULTS AND DISCUSSION

Preliminary Data

The specific gravity of the black sand was established to be 2.65 based from ASTM D854. Determination of the maximum and minimum void ratio for both Ottawa and black sand was done based on ASTM D 4254 and ASTM D 4253. The void ratio of black sand and Ottawa sand is calculated to be 0.98 and 0.51, respectively to achieve the target relative density of 75% with a fall height from the air pluviation technique of 12 cm for Ottawa sand and 26 cm for black sand. Table 1 shows the preliminary data.

Table 1 Summary of preliminary data

Property	Black Sand	Ottawa Sand
Specific Gravity, G_s	2.65	2.65
Maximum Void Ratio, e_{max}	1.11	0.62
Minimum Void Ratio, e_{min}	0.93	0.47
Void Ratio, e	0.98	0.51
Dry Unit Weight, γ_d (g/cc)	1.34	1.75
Fall Height (cm)	26	12

Test Results

The intended type of failure for the sample according to a study [9] should not be a general shear failure given that the data of the researchers have a maximum settlement of 15%, which is based

from the width of the footing (B) in relation to the target relative density of 75%. It is, however, expected to have either local shear failure or punching shear failure. Table 2 shows the stress-settlement data obtained from experimentation while Fig. 3 summarizes the stress-settlement curve for all test runs.

Table 2 Stress-settlement data

Settle ment (mm)	Stress (Pa) at Depth (cm) of Geotextile from Base of Footing					
	None	2.5	5	7.5	10	12.5
0	1	1	1	1	1	1
1	6	6	4	4	3	3
2	8	9	7	6	6	6
3	11	11	9	8	8	8
4	14	14	13	11	9	11
5	16	16	15	13	13	13
6	18	18	15	16	14	16
7	23	23	21	19	18	18
8	24	28	26	23	21	19
9	28	33	29	26	23	21
10	29	35	32	28	24	24
11	33	38	35	31	28	26
12	36	41	39	33	30	29
13	36	43	42	35	33	31
14	36	46	45	38	34	33
15	36	49	47	42	36	34

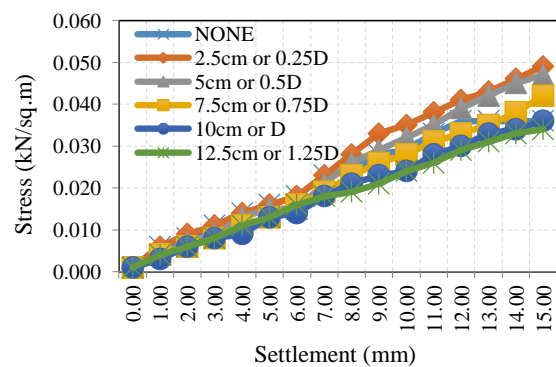


Fig. 3 Data plot of the stress-settlement curve for all samples.

Without geotextile

The sample with no geotextile has the least maximum load bearing capacity with a value equal to 36 Pa as shown in Table 2, which is equal to a

force of 3.6 kN. The value of the maximum concentric load was retained from 12 mm to 15 mm settlement. Moreover, deformation of the soil sample is not present 50 cm outward from the center of the footing. Slicing of the ground at 30 cm and 15 cm from the center of the footing shows no significant change at 12.5 cm depth. However, at the edge of the support and the column, deformation is now visible beneath the footing and adjacent the column. All layers of Ottawa sand except for the 12.5 cm depth are seen to move downward as it approaches the footing as shown in Fig. 4. Therefore, it conforms to the theory that there will be no settlement beyond the boundary condition [7], which is limited to the width of the footing, B that is equal to 10 cm. It was found that settlement occurred at roughly $3.25B$ or 32.5 cm horizontally from the center of the footing. Upon analysis, the graph for the sample with no geotextile holds true for both types of failure which are the local shear or punching shear failure. Since the deformation is found directly below the footing and there is minimal bulging in the ground surface, the type of failure for the sample with no geotextile is a local shear failure.

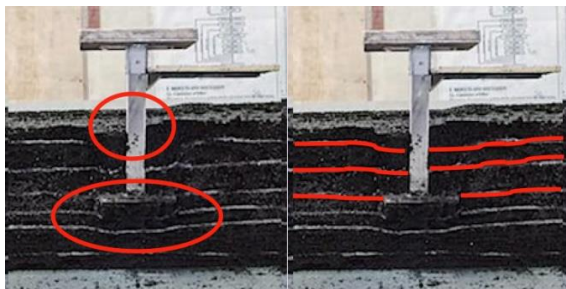


Fig. 4 Slicing at the edge of the column of the sample without geotextile

With geotextile at depth 2.5 cm beneath the footing

Upon the release of hydraulic jack during the experiment, it was found that the footing followed the rise of the jack to a certain height before it permanently becomes motionless allowing for the assumption that the presence of a geotextile causes the soil to become flexible. Although the result is minute, instead of the gradual and continuous downward settlement towards the column, there was an existing inconsistency. The slicing at the edge of the column evidently shows the variability of the second layer whose upward and downward settlement can be roughly measured to 0.5 cm. Upon the measurement of the horizontal distance of the deformation, it was found to have a length of $2.5B$, which is equivalent to 25 cm. In comparison to the visualization found for the sample with no geotextile, the settlement was still only found when the slicing was done at the edge of the footing and at the edge

of the column as shown in Figure 5. Slicing at 30 cm and 15 cm from the center of the footing shows no change in the layers of Ottawa Sand. The effect of the loading did not reach the 12.5 cm depth below the footing as well. Throughout this trial, there is no significant change in the behavior of Ottawa sand below the geotextile which further proves that geotextile alleviates the presence of settlement. Moreover, geotextile at depth 2.5 cm shows the greatest load values among all the depths tested. For this trial, it was found that the settlement performs a punching shear failure because there is no gradual behavior from the Ottawa sand layers adjacent to the column, therefore, no bulging effect on the surface.

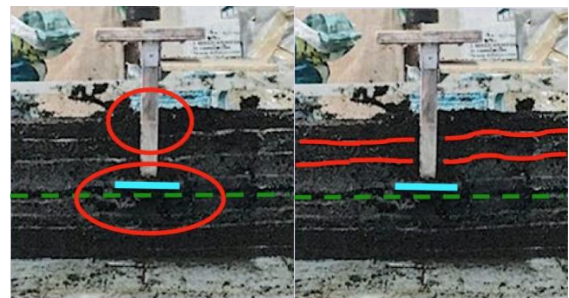


Fig. 5 Slicing at the edge of the column of the sample with geotextile at a depth of 2.5 cm

With geotextile at depth 10 cm beneath the footing

The behavior of the soil at 10 cm depth is different compared to the sample with no geotextile. There is still no alteration in the behavior of Ottawa layers in slicing at 30 cm and 15 cm distance from the center of the footing. No change was also found at the 12.5 cm depth beneath the footing. Slicing at the edge of the footing and at the edge of the column, however, shows a different behavior from the sample with geotextile at depth 2.5 cm; the 10 cm geotextile depth displays a gradual downward behavior with no inconsistencies. This then would set apart the two samples, further supporting that the 2.5 cm depth geotextile experiences punching shear failure, while the 10 cm depth geotextile experiences local shear failure. The failure surface zone of the 10 cm depth geotextile is present at the radial and Rankine surface zones similar to the sample with no geotextile. Additionally, there was a slight bulging on the surface of the sample adjacent to the column. Observing the values at Table 2, the values were relatively close leading to the conclusion that geotextile at a depth of 10 cm no longer bears effect of having a geotextile upon loading compared to other geotextile values in between 2.5 cm to 10 cm. At this sample, the maximum load applied was also found to be 3.6 kN, identical to the maximum load of the sample with no geotextile. Supporting the statement that at a depth equal to B , which is 10 cm in this study, there will be little to no effect on the

settlement reduction.

Another observation shows that when the geotextile is relatively close to the footing, the mode of failure is punching shear failure whereas the distant depth of geotextile reveals the local shear type of failure. Hence, the distance of the geotextile beneath the footing reveals significance not only to the values of the load but also to the behavior of the settlement and the mode of failure.

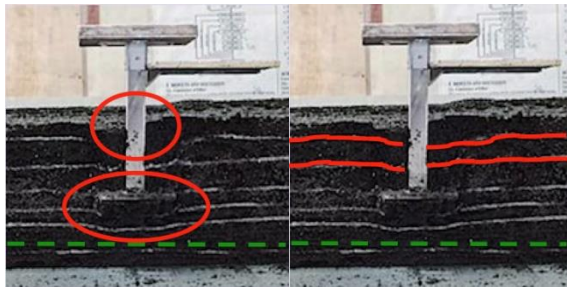


Fig. 6 Slicing at the edge of the column of the sample with geotextile at a depth of 10 cm

With geotextile at depth 12.5 cm beyond boundary condition

The magnitude of the load applied in this trial was lower than that of without the presence of the woven geotextile as shown in Table 2. Therefore, placing the geotextile beyond the boundary condition will not produce a reduction in settlement of granular soil. A factor to consider in such conditions is the distance of the woven geotextile to the bottom of the tank at 1.0 cm. This may prevent the geotextile from performing its use because of the little amount of sand under it or the little gap of the geotextile from a rigid body.

Summary of All Test Trials

The data presented in Table 3 shows the value of settlement achieved at a load of 3.6 kN. This load is obtained at 15 mm in the sample without geotextile and in the varying depths of geotextile, the settlements were found to vary.

Table 3 Settlement reduction of all trials

Depth of Geotextile (cm)	Settlement (mm) at P = 3.6 kN		Settlement Reduction (%)
	Without Geotextile	With Geotextile	
2.5		10.33	31
5		11.25	25
7.5	15	13.33	11
10		15	N/A
12.5		16.33	N/A

Figure 7 shows the relationship between the settlement and placement of geotextile with respect to the base of the footing. The least settlement among all trials is 10.33 mm at 3.6 kN load and is found to be at a depth of 0.25B or D/4 equivalent to 2.5 cm from the base of the footing. At this depth, the geotextile was able to reduce soil settlement by 31% compared to that of without geotextile. On the other hand, the maximum settlement reached within the boundary condition is 13.33 mm, where the soil settlement is reduced by 11%. However, at depth B equal to 10 cm which is known to be the boundary condition itself, the geotextile will not be able to reduce soil settlement.

Loads greater than 3.6 kN cannot be fully analyzed due to limitations. However, for the geotextile depth of 10D/4 equivalent to 12.5 cm from the base of the footing which is known to be beyond the boundary condition, the settlement value of 16.33 mm was not obtained through experiment but calculated instead to enable comparison of all settlement values. With this, placing geotextile beyond boundary condition does not have an effect in the soil.

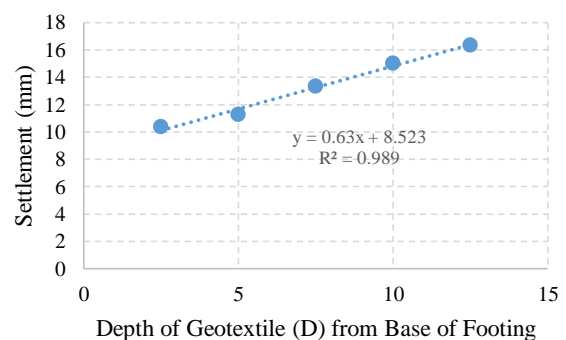


Fig. 7 Graph of settlement vs. depth of geotextile

Noticeably, the displacements are seen to have a directly proportional relationship with the depth of geotextile. When the geotextile is placed further from the base of the footing, the settlement is also seen to increase. Thus, the best depth to reinforce the soil with geotextile is at the depth of D/4 because this is where the soil can withstand greater loads and consequently decreasing greater settlement. Furthermore, it was found that the soil settlement was reduced by 11% to 31%, depending on the depth of geotextile, in comparison to the sample without geotextile upon computation verifying that the use of geotextile improves the strength of soil.

CONCLUSION

In this study, the effect of woven geotextile for soil reinforcement on the settlement of spread

footing founded on granular soil under vertical concentric loading was investigated. Through research, experiments, and analysis, the following results were obtained:

Specific gravity for both Ottawa and black sand were 2.65. A target relative density of 75% density was used all throughout the study. Void ratios were averaged at a value of 0.51 for Ottawa sand and 0.98 for black sand. The target dry unit weight for Ottawa and black sands are 1.75 g/cc and 1.34 g/cc, respectively resulting to a fall height of 12 cm for Ottawa sand and 26 cm for black sand from the modified air pluviation technique done. These values were used as preliminary data for the preparation of the ground sample. The physical properties of black sand were determined through experiments whereas physical properties of Ottawa sand except for void ratio was based from the research literature.

A total of six trials were done: one without woven geotextile and the remaining with woven geotextile at varying depths under the spread footing. The data produced during experiments showed a consistent pattern where the relationship of the settlement is directly proportional to the depth of geotextile. After analyzing the difference in a settlement in terms of its magnitude in the load applied and the failure surface zone of all samples, it was found that the most appropriate location of the woven geotextile is at 0.25B beneath the footing. At this depth, the woven geotextile acted the strongest in terms of the magnitude in the settlement. On the other hand, the magnitude of the settlement was the same without the woven geotextile and when woven geotextile is placed at the boundary condition which is 10.0 cm beneath the spread footing. When geotextile is placed beyond the boundary condition equal to 12.5 cm beneath the footing, the magnitude of the settlement was greatest among all trials therefore woven geotextile does not have an effect anymore as a soil reinforcement material. The greatest depth at which the woven geotextile can be placed to have a minimal reduction settlement will be at 7.5 cm beneath the footing or 0.75B.

Furthermore, the failure mode was found to vary depending on the presence of the geotextile. On the sample without geotextile, it has been established that the mode of failure was local shear failure whereas the sample with geotextile at the depth of 0.25B obtained features that prove it to be a punching shear failure. Throughout the experiment, the mode of failure differs as the depth of embedment of the geotextile increases. The researchers were able to manifest that as the depth of embedment of the geotextile increases to the value equivalent to the dimension of the footing, the mode of failure leans toward a local shear failure whereas the mode of failure is more inclined to punching shear failure when it is closer to 0.25B. Thus, the

advantage of using geotextile is seen through the change in failure mode specifically to the depth that is favorable to punching shear failure. The least amount of settlement was observed and this mode of failure shows the least disturbance in horizontal length, Rankine's passive and triangular zones upon the application of load, which is the preferable result.

The study was able to prove that woven geotextile may be used as a soil reinforcement material in spread footing for settlement reduction on the granular soil.

REFERENCES

- [1] Zoghi, M., Sprague, J., Allen, S., Chapter 3, Emerging Geomaterials for Ground Improvement, Emerging Materials for Civil Infrastructure: State of the Art, American Society of Civil Engineers, 2000, pp. 80.
- [2] Akovali, G., Polymers in Construction, Rapra Technology Limited, 2005, pp. 115-118.
- [3] Dungca, J.R., Concepcion, I., Limyuen, M. C. M., See, T. O., and Vicencio, M. R., Soil Bearing Capacity Reference for Metro Manila, Philippines, International Journal of GEOMATE, Vol. 12, Issue 32, 2017, pp. 5-11.
- [4] Ojuri, O. and Fijabi, D., Standard Sand for Geotechnical Engineering and Geo-Environmental Research in Nigeria: Igbokada Sand, Advances in Environmental Research, Vol. 1, No. 4, 2012, pp. 305-321.
- [5] Rawal, A, Shah, T., and Anand, S., Geotextiles: Production, Properties, and Performance, Textile Progress, Vol. 42, Issue 3, 2010, pp. 181-226.
- [6] Katapa, K., Undisturbed Sampling of Cohesionless Soil for Evaluation of Mechanical Properties and Micro-structure, 2011.
- [7] Das, B., Chapter 4.3, Principles of Foundation Engineering, Eighth Edition, Global Engineering, 2014, pp. 160-165.
- [8] Bareither, C., Edil, T., Benson, C., and Mickelson, D., Geological and Physical Factors Affecting the Friction Angle of Compacted Sands, Journal of Geotechnical and Geo-Environmental Engineering, American Society of Civil Engineers, 2008, pp. 1476-1489.
- [9] Vesic, A. S., Analysis of Ultimate Loads of Shallow Foundations, Journal of Soil Mechanics and Foundations Division, American Society of Civil Engineers, Vol. 99, No. SM1, 1973, pp. 45-73.
- [10] Kumar, S., Solanki, C. H., Patel, J. B., Sudevan, P. B., & Chaudhary, P. M. Study on Square Footing Resting on Prestressed Geotextile Reinforced Sand. Sustainable Civil Infrastructures Advances in Reinforced Soil Structures, 2017, 70-81.

INVESTIGATING THE EFFECTIVENESS OF RICE HUSK ASH AS STABILIZING AGENT OF EXPANSIVE SOIL

Mary Ann Q. Adajar¹, Christian James P. Aquino², Joselito D. Dela Cruz II²,

Clutch Patrick H. Martin², and Denzel Keith G. Urieta²

¹ Faculty, De La Salle University, Manila, Philippines

² Civil Engineer, De La Salle University, Manila, Philippines

ABSTRACT

Expansive soils pose a significant threat to structures due to its ability to cause damage from the footing up to the superstructure. This paper intends to provide an economic and environment-friendly method of mitigating the detrimental effects of expansive soil by replacing a set volume of expansive soil with rice husk ash (RHA) – an abundant waste material produced by biomass power plant. The swelling behavior of the soil mixtures was analyzed through its expansion index obtained via ASTM D4829. Results of the tests revealed that the mixture containing 20% and 25% RHA are considered non-expansive soil. Soil stability parameters were also obtained through the tests specified by ASTM D4609. The tests on the soil stability parameters revealed that soil-RHA mixtures exhibited an improvement in the Atterberg limits which garnered a 36.32% decrease in the liquid limit and 64.75% decrease in the plasticity index; however, a decline was observed in the compaction characteristics and the unconfined compressive strength. Soil-RHA mixtures experienced a maximum decrease of 230 kg/m³ in the maximum dry density and a 40.17% increase in the optimum moisture content. The unconfined compressive strength of treated soils yielded a decrease of as much as 194.2 kPa as well as a decrease in the cohesion development of the soil. The results revealed that while an increase of the RHA content reduces the swelling potential of soil, other strength parameters such as the compaction behavior and the unconfined compressive strength of the soil declines.

Keywords: Expansive soils, Rice husk ash, Soil stability, Expansion index

INTRODUCTION

Expansive soils are abundant in tropical countries and locations where volcanic activity is rampant. These soils have often considered as problematic due to the volume change it exhibits when exposed to moisture [1]. Tropical climate conditions can trigger the shrinking (during extremely hot weather) and swelling (during heavy rainfall) of expansive soil. On the other hand, volcanic activity produces volcanic soils which eventually weather to clay. These clays are rich in kaolinite and montmorillonite, minerals which increases the shrink-swell potential of soils [2]. The shrink-swell behavior of expansive soils caused differential movement of structures in direct contact to it and therefore increases the probability of structural damage. Considering the potential damage expansive soil may induce structures, the National Structural Code of the Philippines (NSCP, 2010) provided solutions when expansive soils are identified in the location of construction. One solution suggested by the NSCP is the replacement of expansive soil with a non-expansive fill [3]. However, this may cause several environmental and economic concerns specifically with regards to its transportation and disposal. In order to prevent this

possible scenario, an alternative solution is through soil stabilization - a type of soil treatment wherein the soil's engineering properties are improved. One form of such is through chemical stabilization which is performed by adding a certain effective material with the pozzolanic property. Waste materials like bagasse ash and hydrated lime have been found to improve the strength and bearing capacity of stabilized expansive soil while reducing its linear shrinkage [4].

Rice husk is considered as the most common agricultural waste in the Philippines. Its properties have been denoted to be highly beneficial specifically when it is incinerated at high temperature and turned into ash. Several studies have recognized rice husk ash (RHA) as an effective pozzolan [5], [6]. RHA contains 85% to 90% amorphous silica plus about 5% alumina, which makes it highly pozzolanic [7] similar to bagasse ash and hydrated lime. Besides its favorable chemical composition, RHA is relatively cheaper and more abundant compared to other chemicals used for engineering purposes. In most cases, RHA has been widely used for concrete production (as cement additives), mine reclamation and soil stabilization.

This study intends to investigate the effectiveness of rice husk ash (RHA) in mitigating

the swelling potential and improving the strength properties of expansive soils. To evaluate its effectiveness, an improvement in the soil's engineering properties, namely Atterberg Limits, Maximum Dry Density (MDD), Optimum Moisture Content (OMC), Unconfined Compressive Strength (UCS), and Expansion Index (EI), must be observed. The study seeks to determine the best proportion of RHA as a stabilizing agent of expansive soil that will yield the best result in controlling the swelling potential and improving the unconfined compressive strength.

The utilization of RHA as a soil stabilizing agent is heavily recommended, considering that about 2 million tons of rice husks are annually produced in the country [8]. This study provides an environmentally-friendly, economical and effective approach to mitigating the swelling potential of expansive soils; therefore, eliminating the numerous hazards it imposes.

MATERIALS AND METHODS

Source of Expansive Soil

The soil used for the study was identified by using the soil map provided by the National Mapping and Resource Information Authority (NAMRIA). From this soil map, it was revealed that soils located around Pulang Lupa, Las Piñas City, Metro Manila contained Guadalupe Clay, a type of clay which is known to exhibit a high shrink-swell behavior [9]. The samples were specifically collected from an on-going construction site at a depth of more than 5 meters to ensure that no organic materials were present. The collected soil exhibited a dark shade of gray when moist, which is a good indicator of a clayey soil. The moist soil samples also exhibited a sticky texture when touched, which signifies that it is cohesive when exposed to moisture. When dry, the soil samples exhibited a significant amount of cracking and its volume significantly decreased - an indication of high shrinking and swelling potential.

Source of Rice Husk Ash

The rice husk ash (RHA) used in this study (Fig. 1) was obtained from Restored Energy Development Corporation - a local Biomass Power Plant located in Muntinlupa City, Metro Manila. Initially, rice husks were delivered from rice plantations in Central Luzon and incinerated in the plant at a constant high temperature to produce Biomass energy. Through this process, RHA is generated as a byproduct. The RHA was sourced from only one power plant to ensure that the properties of the material are consistent. To avoid the deterioration of quality, the material was fully contained and placed away from

moisture and harsh environments.



Fig. 1 Rice husk ash (RHA) used in the study

Experimental Program

Prior to testing the effects of rice husk ash on various soil properties, the extracted soil samples must be classified as expansive. This was done in accordance to the provisions set by Section 303.5 of the NSCP 2010 [3]. Table 1 presents the required parameters to classify the soil as expansive. These parameters were obtained through conducted laboratory experiments in accordance with their respective ASTM standards.

Based on Unified Soil Classification System (USCS) criteria, soils which are classified as CL (Lean Clay) with liquid limit (LL) less than 50 and plasticity index (PI) greater than 7 and soil classified as CH with LL greater than 50 or more and PI plots on or above the "A" line of the plasticity chart are usually considered as potentially expansive.

Table 1 Expansive soil classification summary

Required Parameters	NSCP Criteria
Liquid Limit, LL (%) Plasticity Index, PI (%)	Plasticity Index (PI) of 15 or greater and Liquid Limit greater than 50.
Percentage of soil particles passing the #200 (0.075 mm) sieve opening (%)	More than 10% of the soil particles pass the #200 sieve.
Percentage of soil particles less than 5µm in size (%)	More than 10% of the soil particles are less than 5µm in size.
Expansion Index, EI	An expansion index value greater than 20.

Standard Tests for the Evaluation of RHA as an Admixture

To evaluate the effectiveness of RHA as an admixture, the soil mixtures must be tested as prescribed by ASTM D4609 – Standard Guide for Evaluating Effectiveness of Admixtures for Soil Stabilization, and the criteria that must be met are summarized in Table 2. In addition to the ASTM D4609 criteria, the soil's expansion index (EI) must also be known following the procedure of ASTM

D4829. The RHA will only be deemed as effective if the resulting EI value of the soil mixture is below 20.

Table 2 Criteria to gauge the effectiveness of RHA as an admixture

Parameter	ASTM D4609 Criteria
Liquid Limit, LL (%) Plasticity Index, PI (%)	A significant reduction in the LL and PI
Maximum Dry Density (MDD), (kN/m ³) Optimum Moisture Content (OMC), (%)	A decrease of greater than 15% in OMC or an increase of more than 80 kg/m ³ in MDD.
Unconfined Compressive Strength (UCS), q_u (kPa)	An increase in the UCS of 345 kPa.

Soil – RHA Mixture Preparation

After classifying the soil as expansive, the samples were blended with RHA through dry mixing. Soil mixtures were formed by replacing a percentage of the soil's volume with rice husk ash, which was formulated using the soil and RHA's index properties. The admixture was added at varying amounts ranging from 5% to 25% at 5% intervals. The mixture was allowed to cure for at least 16 hrs. before subjecting to a series of tests.

TESTS RESULTS

Micro-fabric Structure and Chemical Composition

Based on the Scanning Electron Microscopy (SEM) test results of the RHA (Fig. 2a), it can be observed that the particles exhibit a randomly arranged aggregation with large spaces. The presence of a cellular-like structure with the significantly high amount of trans-granular and intra-granular voids was also observed. This is due to the spaces which cut and separate each particle from each other. At greater magnification (Fig. 2b), the results exhibited the presence of extra layers with exceedingly small intra-granular voids from within its structure. These extra layers and microspores contributed to the significantly high specific area of RHA. In particular, this property plays an important role in proving the high water absorption capability of RHA. The area allows water to adhere; thus, increasing its water adsorption capability.

The SEM result for the clay soil was also observed as presented in Fig. 3. The clay particles passing the #200 sieve were considered. The results show that the sample exhibited a highly dense flaky granular arrangement which contains connectors in

between the grains, typical to clay particles. Flaky surfaced clays contribute to the adsorption of water due to the capability of its high surface value to carry small negative charges which attract water molecules.

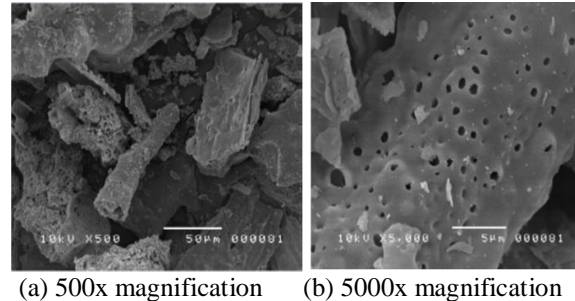


Fig. 2 Micrographs of RHA

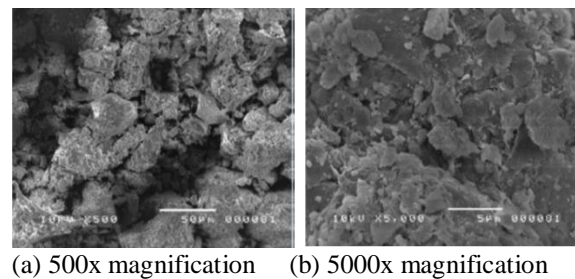


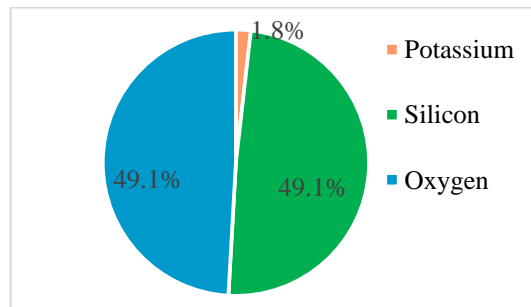
Fig. 3 Micrographs of soil sample

The Energy Dispersive X-ray Spectroscopy (EDX) test results of both the RHA and soil are presented in Fig. 4. Test results revealed that RHA contains a significantly high amount of oxygen and silicon amounting to about 98% of the material and a small amount of Potassium of about 2%. Several studies revealed that the presence of silica improves the strengthening capabilities of cement or other cementitious material; thus, making the material such as RHA as an effective pozzolan [10]. The chemical composition of soil contains a significantly high amount of iron. The high value of iron is an indication that the soil contains montmorillonite - a mineral which increases the shrink-swell potential of soil [2]. In particular, montmorillonite minerals are mainly composed of iron, aluminum, and silicon - elements similarly present in the EDX results of the clay. In addition, the low amount of carbon indicates that the soil is inorganic.

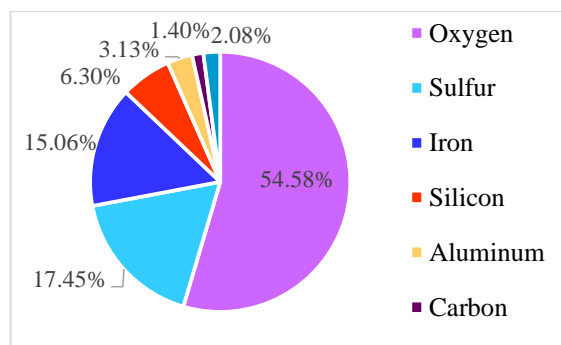
Soil Classification

Table 3 presents the summary of the obtained results for the soil's classification. It can be observed that the criterion for the percentage of particles greater than 5 μ m (ASTM D422) was not satisfied. However, the NSCP section states that a resulting EI value greater than 20 still governs; thus, classifying the soil as expansive. Based on USCS criteria, the

soil was classified as Fat Clay (with group symbol CH). This is an indication that the soil contains a high amount of clay.



(a) RHA



(b) Soil

Fig. 4. The chemical composition of RHA and soil

Table 3 Summary of results on soil classification

Parameter	Required Value	Result	Remarks
Percent Passing #200 Sieve (%)	>10%	55.38	Pass
Percent greater than 5 μ m (%)	>10%	3.15	Fail
Liquid Limit, LL (%)	>50	74.97	Pass
Plasticity Index, PI (%)	>15	52.31	Pass
Expansion Index, EI	>20	111	Pass
USCS Classifications	CH (Fat Clay)		
Specific Gravity, G_s	2.67		

Evaluation of RHA as Stabilizing Agent

Atterberg Limits

The Atterberg Limits are important parameters which determine the amount of water needed to transform the soil's consistency from one state to another. Table 4 presents the mean values for the

Atterberg limits.

Table 4 Atterberg limits test results

RHA Content (%)	Liquid Limit, LL (%)	Plasticity Limit, PL (%)	Plasticity Index, PI (%)
0	75	22	53
5	63	23	40
10	56	25	31
15	53	26	27
20	51	28	23
25	48	30	18

The standard guide for the evaluation of the effectiveness of soil additive (ASTM D4609) states that a decrease in the liquid limit and plasticity index proves that the additive is effective in improving the Atterberg Limits of the soil. Based on test results, the decrease in the soil's LL and PI were observed at increasing amount of added RHA. This is due to the reduction of clay particles present in the soil mixture. Clay minerals such as Montmorillonite, Illite, and Kaolinite are responsible for the clay's high plasticity. Through the introduction of RHA, a non-plastic material, the Atterberg limits of soil mixture were improved.

Moisture-Density Relationship

The moisture-density relationship is an important property which is generally associated with soil compaction - a common practice in improving the strength characteristics and the overall stability of the soil. Table 5 presents the summarized results for the soil's maximum dry density (MDD) at optimum moisture content (OMC) obtained from Standard Compaction Test (Proctor Method). In order to consider RHA as effective in terms of improving the soil's Moisture-Density Relationship, ASTM D4609 states that it must exhibit an increase of 80 kg/m³ in the MDD and a decrease in the OMC by 15%. A decrease in the MDD and an increase in the OMC were observed at increasing amount of RHA added. The decrease in the MDD can be attributed to the presence of RHA, which has a significantly low specific gravity. The high amount of voids present in the RHA contributed to the reduction of the soil's MDD. The increase in the OMC is due to the increased porosity of soil mixtures with RHA [11]. A significant amount of voids are present in RHA which increases the capacity of water a sample can intake. In turn, the increase of the OMC indicates that more water is needed to effectively compact the soil.

Table 5 Summary of moisture-density relationship

Mixture	Maximum Dry Density (MDD) kg/m ³	Optimum Moisture Content (OMC) %
Untreated Soil	13.93	27.3
95% Soil + 5% RHA	13.83	31.8
90% Soil + 10% RHA	13.44	34.4
85% Soil + 15% RHA	12.85	36.0
80% Soil + 20% RHA	12.07	38.5
75% Soil + 25% RHA	11.68	40.2

Unconfined Compressive Strength

The unconfined compressive strength test is a widely performed test to quickly obtain the soil's unconfined compressive strength (UCS), a strength parameter of the soil which does not consider confining pressure. Figure 5 presents the relationship between the unconfined compressive strength and the curing period. It can be observed from the test results that the specimens exhibited an increase in UCS as the curing day progresses. This is due to the presence of water maintained within the samples, allowing its strength through time. A curing period of 35 days was also considered in order to analyze the soil's long-term strength development.

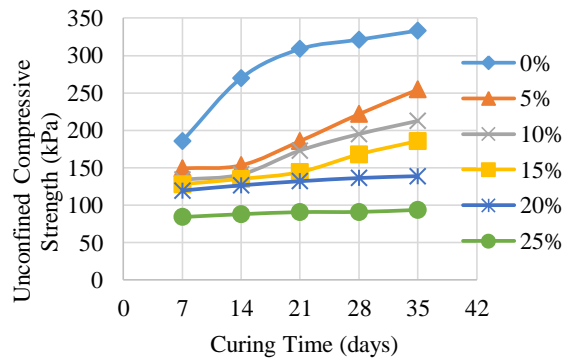


Fig. 5. Unconfined compressive strength vs. curing period

ASTM D4609 states that an increase of 345kPa (50 psi) in the UCS indicates that the additive is effective in improving the soil's UCS. From test results, it can be observed the soil's UCS decreases at increasing amount of RHA added. Figure 6 presents the effect of RHA on the UCS of the soil. Due to the introduction of RHA, a non-cohesive material, the decrease in the soil's UCS was observed. The presence of RHA prevented the soil's strength to develop over time. Though RHA

contains pozzolanic property, its content is not enough to produce cementitious mixture preventing the soil-RHA mixture from developing a strong chemical bond.

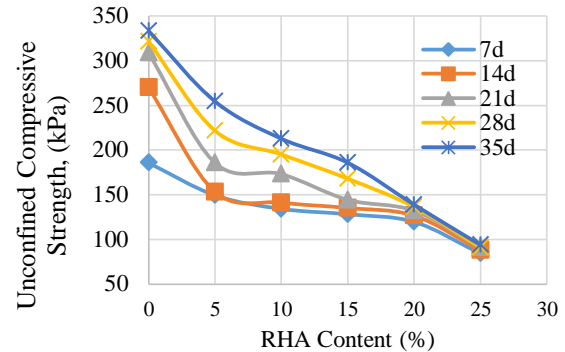


Fig. 6. Unconfined compressive strength vs RHA content

Predicting the Unconfined Compressive Strength

From the normalized plot of unconfined compressive strength against the varying RHA content, an equation was generated as shown in Equation (1) which can be used to predict the unconfined compressive strength of the soil at varying RHA content. Through the use of the formulated equation, the maximum attainable strength of the 25% RHA (35-day curing period) is around 104.97 kPa, which shows a significant drop from the control specimen's 333.25 kPa strength at 35-day curing period.

$$UCS = (474.88x^4 - 329.9x^3 + 75.751x^2 - 8.479x + 1)UCS_o \quad (1)$$

where:

UCS = unconfined compressive strength at a specific $x\%$ RHA, kPa

UCS_o = unconfined compressive strength of the control specimen at any given curing period, kPa

x = RHA content in decimal form

Expansion Index

The expansion index (EI) test is generally performed to reveal the expansion potential of the soil based from ASTM D4829. Table 6 presents the summarized data obtained from performing the EI test.

In order to determine if the RHA is effective in terms of improving the soil's expansion index, the resulting EI value must be less than 20 in order to negate its classification as expansive. Based on test results, a decreasing trend in the soil's EI was observed at an increasing amount of RHA content.

In particular, soil mixtures with 20% and 25% RHA yielded EI values lesser than 20; thus, classifying it as non-expansive. The reduction in the EI value at increasing RHA content can be attributed to the RHA's high water adsorption capabilities and non-plastic behavior. As previously stated from the clay's EDX results, it was evident that it contained montmorillonite and other minerals which are responsible for the soil to swell with the presence of water. The clay's chemical composition can be linked to the soil's high plasticity and expansion index as evidently seen from the conducted test results. Through the presence of RHA, its non-plastic behavior prevented the soil from swelling despite being fully inundated in water. In addition, the RHA's high water adsorption capability was also a factor since it allowed the water to adhere, which limits the water's attraction to the clay particles.

Table 6. Summary of results for expansion index

Percentage of RHA	Mean EI value	Potential Expansion
0	111	High
5	66	Medium
10	49	Low
15	29	Low
20	12	Very Low
25	0	No Expansion

CONCLUSION

Based on the conducted study, the following conclusions were formulated:

A significant decrease of about 27.23% and 33.87% in the soil's Liquid Limit and Plasticity Index respectively were observed when RHA was added in the expansive soil. This classifies RHA as effective in terms of improving the soil's Atterberg limits.

A decrease of as much as 230 kg/m³ in the soil's maximum dry density and an increase of 47.41% in the soil's optimum moisture content were observed. This classifies RHA as ineffective in terms of improving the soil's Moisture-Density relationship.

A decrease of as much as 194.2 kPa in the soil's unconfined compressive strength was observed as the amount of added RHA increases. This classifies RHA as ineffective in terms of improving the soil's Unconfined Compressive Strength.

The addition of RHA reduced the expansion index value of the soil of as low as 0 (no expansion). Only the mixtures with 20% and 25% with EI values of 12 and 0 respectively were not considered expansive as per NSCP Section 303.5. This classifies RHA as effective in improving the

expansion index of the soil specifically with 20% to 25% RHA content only.

It is recommended for future work that a cementitious agent should be added to soil-RHA mixture to improve its compressive strength property.

REFERENCES

- [1] Rezaei M., Ajalloeian R., and Ghafoori M., Geotechnical Properties of Problematic Soils Emphasis on Collapsible Cases. *Int'l. Journal of Geosciences IJG*, 03(01), 2012, pp. 105-110.
- [2] Miranda-Trevino J.C. and Coles C.A., Kaolinite Properties, Structure and Influence of Metal Retention on pH. *Applied Clay Science*, 23(1-4), 2003, pp. 133-139.
- [3] National Structural Code of the Philippines, Vol. 1, Chapter 3: Earthworks and Foundations, Association of Structural Engineers of the Philippines, 2010, pp. 1 – 22.
- [4] Dang L.C., Hasan H., Fatahi B., Jones R. and Khabbaz H., Enhancing the Engineering Properties of Expansive Soil Using Bagasse Ash and Hydrated Lime, *International Journal of GEOMATE*, Sept. 2016, Vol. 11, Issue 25, pp. 2447-2454
- [5] Sarkar G., Islam R., Alamgir M., & Rokonzaman M. (2012). Interpretation of Rice Husk Ash on Geotechnical Properties of Cohesive Soil, *Global Journal of Researches in Engineering Civil and Structural Engineering* 12, 2012, pp. 1-7.
- [6] Pote R., Potential Applications of Rice Husk Ash Waste from Rice Husk Biomass Power Plant, *Renewable and Sustainable Energy Reviews*, 53, 2016, pp. 1468-1485.
- [7] Zareei S.A., Ameri F., Dorostkar F., & Ahm M., Rice Husk Ash as a Partial Replacement of Cement in High Strength Concrete Containing Micro Silica: Evaluating Durability and Mechanical Properties, Elsevier: *Case Studies in Const. Materials*, Vol. 7, Dec. 2017, pp. 73-81.
- [8] Zafar S., *Agricultural Wastes in the Philippines*. Retrieved date: May 12, 2015, from <http://www.bioenergyconsult.com/agricultural-resources-in-philippines/>
- [9] Mokhtari M. and Deghagani M., Swell-shrink Behavior of Expansive Soils, Damage, and Control. *Electric Journal of Geotechnical Engineering*, 17, 2012, pp. 2674-2682.
- [10] Habeeb G.A. and Mahmud H.B., Study on Properties of Rice Husk Ash and its Use as Cement Replacement Material. *Materials Research*, 13(2), 2010, pp. 185-190.
- [11] Lu S., Sun F., and Zong, Y. Effect of Rice Husk Biochar and Coal Fly Ash on Some Physical Properties of Expansive Clayey Soil, *Catena*, 114, 2014, pp.37-44.

INDUSTRIAL BY-PRODUCT-BASED BINDERS FOR USE IN DEEP SOIL MIXING TECHNIQUE

Mohammadjavad Yaghoubi¹, Arul Arulrajah², Mahdi Miri Disfani³, Suksun Horpibulsuk⁴ and Stephen Darmawan⁵

^{1,2}Faculty of Science, Engineering and Technology, Swinburne University of Technology, Australia;

³School of Engineering, The University of Melbourne, Australia; ⁴Faculty of Engineering, Suranaree University of Technology, Thailand; ⁵ Geotesta Pty Ltd., Australia

ABSTRACT

Deep soil mixing (DSM) is one of the most suitable techniques for ground improvement of deep deposits of soft soils with high water content. Traditionally, the common binder being used in DSM is Portland cement. The production of cement is expensive, requires large amounts of natural resources and generates considerable quantities of CO₂. In such situation, utilizing industrial by-products abundantly available, such as fly ash (FA) and slag (S), can be advantageous. This paper investigates the effect of water content and curing temperature and time on the changes in the engineering behavior of a soft marine soil stabilized with alkaline activated FA and S as a binder with much lower carbon footprint compared to Portland cement. Moreover, the changes in the microstructures are studied. The aim is to find an ecologically friendly binder as well as to utilize stockpiled FA and S in landfills. Mixtures with initial water contents of 0.75-1.25 liquid limit (LL) of the soil were prepared, and samples were cured at 10-40 °C for 7 and 28 days. The compressive strength of the soft soil is considerably improved by using these new binders. Furthermore, the strength is enhanced with increasing the curing temperature. An improvement of the strength is observed when water content is increased from 0.75 LL to 1.0 LL. However, the strength decreases by enhancing the water content to 1.25 LL. In addition, the strength requirements specified for DSM using cement are met that means the introduced binders can be a proper replacement for cement.

Keywords: Deep soil mixing, Fly ash, Slag, Geopolymer

INTRODUCTION

The growth of population and need for infrastructure around the world urge researchers and practitioners to find alternative binders with low environmental impacts compared to binders currently in use such as Portland cement. In addition to the consumption of large amounts of natural raw materials and energy for the production of Portland cement, air pollution and CO₂ emission during the production is considerable [1], [2]. Geopolymer, in which wastes with high silica and alumina content such as fly ash (FA) and slag (S) are used, has been proposed as a potential alternative binder [3], [4]. In addition, excellent engineering properties such as high compressive and flexural strength and early strength development have been reported for geopolymer binders [1], [2], [4]-[7].

In geopolymerization, the aluminum and silicon in FA and S is dissolved by an alkaline activator and monomers are formed. Then, the geopolymer gels are generated by polycondensation of the monomers [5], [8], [9]. FA, the by-product of electricity generation in power plants, and S, the by-product of steel production, are plentifully available in landfills. Moreover, FA and S have high reactivity during

alkaline activation because of their larger surface, compared to other sources of silica and alumina such as metakaolin [10].

The use of geopolymers in concrete, brick and ceramic industry has been studied widely [5], [6], [9], [11], [12], but in ground improvement applications, such as deep soil mixing, is fairly recent [1]-[4], [13], [14]. The production conditions are controllable in concrete, brick and ceramic industries. On the contrary, in ground improvement applications, field conditions such as water content and temperature can be varied, especially at areas close to rivers and oceans. Melbourne in Australia is exemplary where the temperature range of air and ground is 10- 40 °C 90% of the year [15], [16], and the water content varies at different locations and depths. Different water contents of around 40-65% is reported for a soft marine clay that covers a wide area in Yarra Delta. This soft soil is locally termed as Coode Island silt (CIS), and deposits of CIS with thicknesses of up to 30 m have been observed, with maximum undrained shear strengths of 80 kPa [13], [17]. Continuous attempt is being made to improve the engineering characteristics of CIS since there is a large demand for infrastructures in this area [13].

This study therefore investigates the effect of

field factors, such as water content and temperature, on the compressive strength improvement and microstructure of FA+S based geopolymer-stabilized CIS. Unconfined compressive strength (UCS) and scanning electron microscopy (SEM) imaging tests were performed. The usage of geopolymers, which consume the stockpiled FA and S in landfills, in the ground improvement of soft soils, under different field conditions would be enabled from the results of this study.

MATERIALS AND METHODS

Materials

The soft marine clay, CIS, used in this study was obtained from depths of around 3-5 m in the Port Melbourne region. The natural water content of CIS was in the range of approximately 40 to 60%. FA and S were obtained from local suppliers in Australia. The particle size distribution and various characteristics of CIS, FA and S, are presented in Fig.1 and Table 1, respectively. The maximum particle diameter (D_{max}) and fine content (particles smaller than 75 μ m) of CIS were 150 μ m and 90%, respectively. The plastic limit (PL) and liquid limit (LL) of CIS were 23.4% and 50.4%, respectively.

Table 1 Properties of CIS, FA and S

Material	D_{max} (μ m)	$75 \mu\text{m} < D^a$ (%)	$2 \mu\text{m} < D < 75 \mu\text{m}^b$ (%)	$D < 2 \mu\text{m}^c$ (%)	LL (%)	PL (%)	PI (%)	G_s	pH
CIS	150	10	59	31	50.4	23.4	27.0	2.61	7.75
FA	106	2	85	13	-	-	-	2.10	7.5
S	63	0	78	22	-	-	-	2.82	9.5

Note: ^a Sand size; ^b Silt size; ^c Clay size.

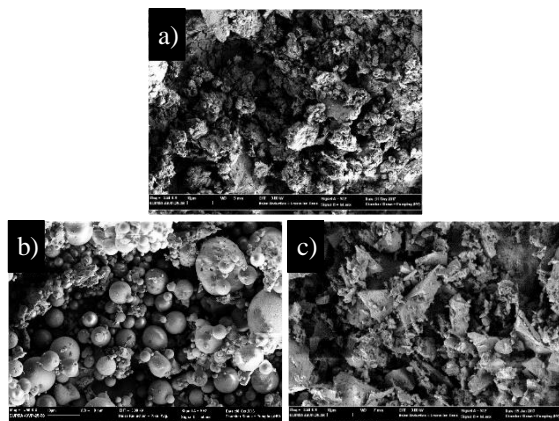


Fig. 2 SEM images of: a) CIS, b) FA and c) S.

The liquid alkaline activator (L) was composed of NaOH, at 8 molarity, and Na_2SiO_3 for proper dissolution of the alumina and silica and accelerated geopolymerization [6], [18]. The L was prepared by

From these results, CIS was classified as a silty clay with high plasticity.

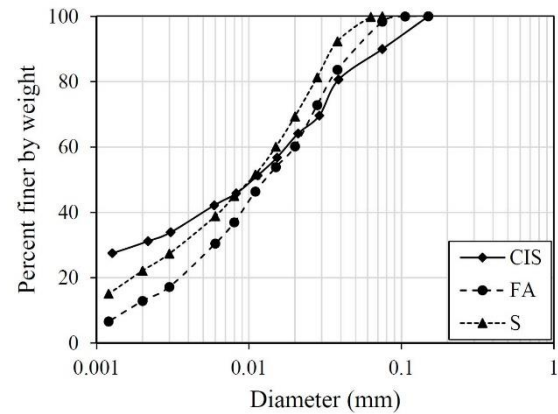


Fig. 1 Particle size distribution of CIS, FA and S.

Figure 2 illustrated the SEM images of CIS, FA and S. Irregular, spherical and semi-polygonal morphology was observed for CIS, FA and S particles, respectively. CIS particles had rough surfaces, whereas smooth surfaces were observed for FA and S.

dissolving the NaOH beads in distilled water first and then blending with Na_2SiO_3 solution. The NaOH: Na_2SiO_3 ratio was 30:70 [4], [6], [13].

Methods

A mix of FA+S at 20% content (by dry mass of CIS) with the FA:S ratio of 25:75 was used in all mixtures as recommended previously [14]. For sample preparation, the water content of CIS was initially adjusted to the target values of 0.75, 1.0 and 1.25 LL, replicating the field water contents. This was achieved by air-drying the soil or adding water, as required. The FA+S were then added and mixed for 2.5 minutes using a mechanical mixer. Afterwards, the L, with L/(FA+S) ratio of 1.0 based on previous findings [3], [10], [13], was added and mixed for another 2.5 minutes, resulting in total mixing time of 5 minutes. Specimens with 38 and 76

mm diameter and height, respectively, were then prepared in PVC split molds for testing. Samples were prepared in two layers, each layer being tapped 25 times to ensure no air bubble remained in the sample. The prepared specimens were sealed in cling wraps and cured at temperatures of 10, 25 (room temperature) and 40 °C for 7 and 28 days.

The UCS tests were conducted after the curing period, on at least three specimens to ensure the consistency of the results. A displacement rate of 1-mm/min (1.32%/min) was selected to conduct the UCS tests, according to AS [19] and ASTM [20]. Small pieces of the samples, after UCS testing, were obtained to investigate the microstructural changes of the mixtures through SEM testing. The obtained pieces needed to be air-dried and then gold-coated prior to being placed in the SEM apparatus. An oven set at 50 °C was thus used for the air-drying based on the requirements of the testing devices. Figure 3 illustrates the methodology of the experiments.

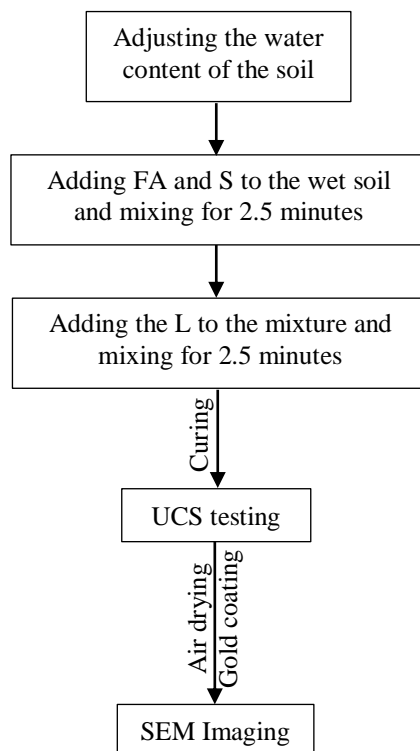


Fig. 3 Flowchart of the testing program.

RESULTS AND DISCUSSION

UCS Tests

Figure 4 illustrates the variation of the UCS of mixtures with changing the initial water contents of 0.75-1.25 LL and cured at 10-40 °C for 7 and 28 days. The 28-day UCS value of 1.034 MPa has been recommended for deep cement mixed columns, under embankments and earth structures, and is

depicted in Fig. 4 for comparison purposes [21]. Figure 4 shows that the compressive strength of CIS stabilized with FA and S based geopolymers was significantly improved. This was due to the dissolution of the amorphous silicon, aluminum and calcium in the FA and S by the L and formation of monomers in the presence of sodium, available in the L. This was then followed by the polycondensation of the monomers, the development of geopolymeric network and stabilization of the CIS that resulted in the UCS enhancement [5], [8].

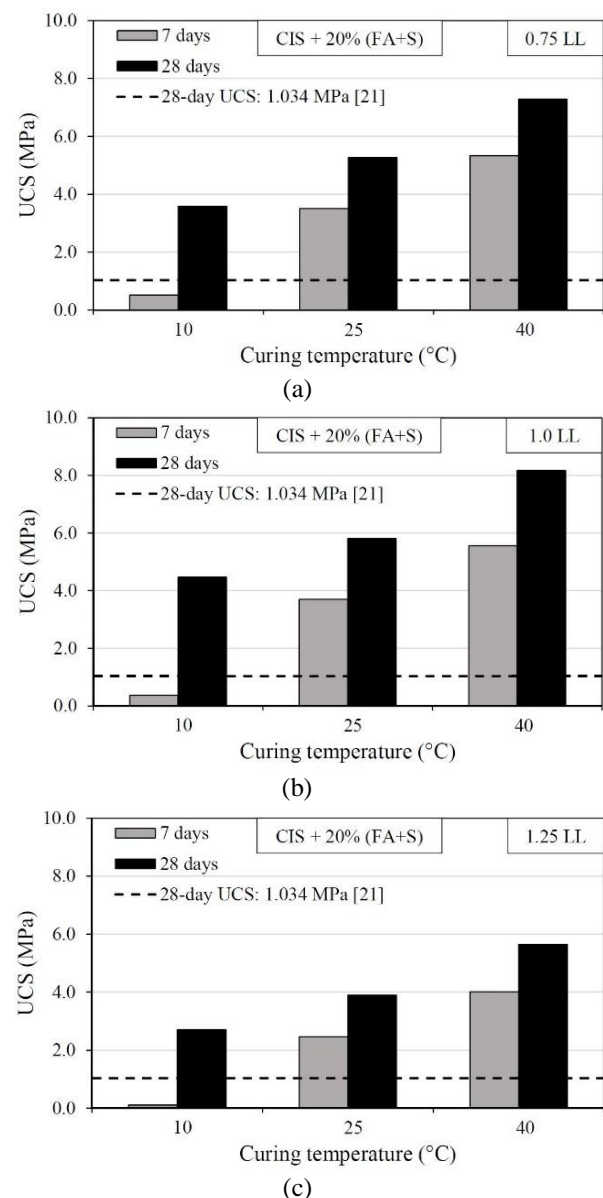


Fig. 4 UCS values for different mixtures cured for 7 and 28 days at various temperatures and water contents of: a) 0.75 LL, b) 1.0 LL and c) 1.25 LL.

In these mixtures, 0.75 LL water content was insufficient to activate the pozzolanic and/or

geopolymeric reactions Furthermore, with increasing the water content to 1.0 LL and 1.25 LL, the UCS was enhanced and decreased, respectively. While at both water contents of 0.75 LL and 1.25 LL notable strength development was achieved, 1.0 LL (of CIS) was found as the ideal water content. At 0.75 LL water content, there was insufficient water in the mixtures for the geopolymeric reactions to occur fully. Moreover, two factors could cause the reduction in the UCS when the water content was increased to 1.25 LL. First, the geopolymerization was decreased due to the molarity of the L being reduced as a result of increasing the water content, and second, voids were created through the matrix of the mixtures because of the excess amount of water in the system [5], [7], [8], [13]. Overall, the minimum 28-day UCS requirement was met for the mixtures prepared at all water contents studied here. This means that with the variation of water content in the field, within the ranges studied here, FA+S based geopolymers can be relied on as a proper binder.

Moreover, the UCS values were increased by enhancing the curing temperature. For the samples cured for 7 days, an insignificant improvement was observed when cured at 10 °C, followed by a significant UCS increase at 25 °C and 40 °C, although the rate of UCS enhancement was lower after 25 °C. On the other hand, for the samples cured for 28 days the increase of UCS with curing temperature was almost linear. This indicated that the geopolymerization and accordingly, strength development were accelerated by increasing the curing temperature [4], [8], [9], [11]-[13], [18]. Although notable compressive strengths could be achieved at low curing temperatures, longer curing times are required [9], [22]. Geopolymers cured at low temperatures were reported to have high qualities as a result of slow development of gels and consequently having less pores [9].

It was also noticed from the results that curing the specimens for 28 days at 25 °C and for 7 days at 40 °C resulted in almost the same UCS values. A similar pattern of strength development was observed for specimens that were cured for 28 days at 10 °C and for 7 days at 25 °C. This further proved that the curing temperature had an accelerating effect on geopolymerization and strength development, as stated earlier. The results indicated that FA+S based geopolymer can be used as a reliable binder for stabilization of CIS, with high water contents. In addition, significant strength development could be achieved even at low temperatures, over the cold seasons of the year.

SEM Tests

Figure 5 illustrates the effect of curing

temperature on the microstructure of FA+S based geopolymer stabilized CIS at water content of 1.0 LL and cured for 28 days at different curing temperatures. In Fig 5 (a) where the curing temperature was 10 °C, non-activated FA and S particles and minimal changes to the CIS matrix are observed. When the curing temperature was increased to 25 °C, the FA and S particles were activated with some semi-activated particles observed in the medium (Fig. 5(b)) that resulted in a denser structure. The UCS value was accordingly increased from 4.47 MPa to 5.81 MPa (around 30% increase). Figure 5 (c) shows that almost all FA and S particles were activated in mixtures cured at 40 °C and a compact matrix with a high UCS value of 8.17 MPa was achieved. This indicated a UCS value increase of around 83% and 41% compared to samples cured at 10 and 25 °C, respectively.

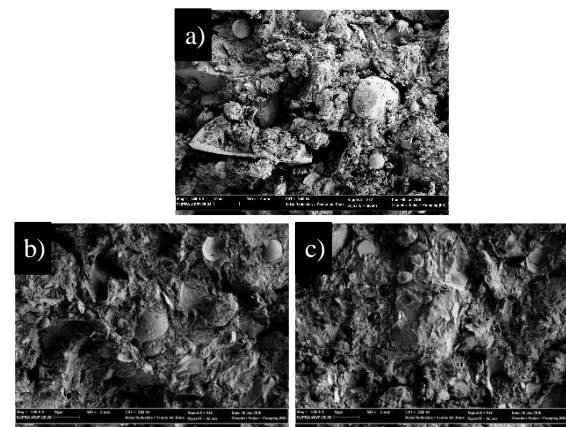


Fig. 5 The SEM images of CIS stabilized with FA+S based geopolymer, at 1.0 LL water content and cured for 28 days at: a) 10 °C, b) 25 °C and c) 40 °C.

CONCLUSION

The stabilization of a soft soil with novel geopolymer binders with low carbon footprint was evaluated in this study. The effect of different water contents and curing temperatures on the strength development and microstructure of the soil stabilized with a FA+S based geopolymer were evaluated.

Results showed that higher UCS was achieved when the water content was increased from 0.75 LL to 1.0 LL, and increasing the water content further to 1.25 LL resulted in the decrease of UCS. Furthermore, enhancing the curing temperature accelerated and improved the strength development.

This study showed that FA+S based geopolymers, considerably enhanced the unconfined compressive strength of the studied soft soil. FA+S based geopolymers, with considerably lower carbon

footprint compared to traditional binders, are a potential green solution for future ground improvement projects on soft soil deposits.

Further study is recommended to study the different engineering characteristics such as compressibility, durability and shear strength of geopolymer stabilized soft soils.

ACKNOWLEDGEMENTS

This research was supported under Australian Research Council's Linkage Projects funding scheme (project number LP150100043). The fourth author is grateful to the financial support from the Thailand Research Fund under the TRF Senior Research Scholar program Grant No. RTA5980005 and Suranaree University of Technology.

REFERENCES

- [1] Zhang M., Guo H., El-Korchi T., Zhang, G., and Tao M., Experimental feasibility study of geopolymer as the next-generation soil stabilizer. *Construction and building materials*, Vol 47, 2013, pp. 1468-1478.
- [2] Du Y. J., Bo Y. L., Jin F., and Liu C.Y., Durability of reactive magnesia-activated slag-stabilized low plasticity clay subjected to drying-wetting cycle. *European Journal of Environmental and Civil Engineering*, Vol 20, Issue 2, 2016, pp. 215-230.
- [3] Cristelo N., Glendinning S., Fernandes L., and Pinto A. T., Effects of alkaline-activated fly ash and Portland cement on soft soil stabilisation. *Acta Geotechnica*, Vol 8, Issue 4, 2013, pp. 395-405.
- [4] Rios S., Ramos C., Viana da Fonseca A., Cruz N., and Rodrigues C., Mechanical and durability properties of a soil stabilised with an alkali-activated cement. *European Journal of Environmental and Civil Engineering*, 2017, pp. 1-23.
- [5] Gao K., Lin K. L., Wang D., Hwang C. L., Tuan B. L. A., Shiu H. S., and Cheng T. W., Effect of nano-SiO₂ on the alkali-activated characteristics of metakaolin-based geopolymers. *Construction and Building Materials*, Vol 48, 2013, pp. 441-447.
- [6] Phoo-ngernkham T., Maegawa A., Mishima N., Hatanaka S., and Chindaprasirt P., Effects of sodium hydroxide and sodium silicate solutions on compressive and shear bond strengths of FA-GBFS geopolymer. *Construction and Building Materials*, Vol 91, 2015, pp. 1-8.
- [7] Nath P., and Sarker P. K., Flexural strength and elastic modulus of ambient-cured blended low-calcium fly ash geopolymer concrete. *Construction and Building Materials*, Vol 130, 2017, pp. 22-31.
- [8] Hardjito D., and Rangan B. V., Development and Properties of Low-Calcium Fly Ash-Based Geopolymer Concrete. 2005, Perth, Australia: Curtin University of Technology.
- [9] Rovnaník P., Effect of curing temperature on the development of hard structure of metakaolin-based geopolymer. *Construction and Building Materials*, Vol 24, Issue 7, 2010, pp. 1176-1183.
- [10] Heah C., Kamarudin H., Al Bakri A. M. M., Bnhussain M., Luqman M., Nizar I. K., Ruzaidi C. M., and Liew Y., Study on solids-to-liquid and alkaline activator ratios on kaolin-based geopolymers. *Construction and Building Materials*, Vol 35, 2012, pp. 912-922.
- [11] Palomo A., Grutzeck M., and Blanco M., Alkali-activated fly ashes: a cement for the future. *Cement and concrete research*, Vol 29, Issue 8, 1999, pp. 1323-1329.
- [12] Ismail I., Bernal S. A., Provis J. L., San Nicolas R., Hamdan S., and van Deventer J. S., Modification of phase evolution in alkali-activated blast furnace slag by the incorporation of fly ash. *Cement and Concrete Composites*, Vol 45, 2014, pp. 125-135.
- [13] Phetchuay C., Horpibulsuk S., Arulrajah A., Suksiripattanapong C., and Udomchai A., Strength development in soft marine clay stabilized by fly ash and calcium carbide residue based geopolymer. *Applied Clay Science*, Vol 127-128, 2016, pp. 134-142.
- [14] Yaghoubi M., Arulrajah A., Disfani M. M., Horpibulsuk S., Bo M., and Darmawan S., Effects of industrial by-product based geopolymers on the strength development of a soft soil. *Soils and Foundations*, Vol 58, Issue 4, (In press, accepted on 5 March 2018).
- [15] Colls S., Johnston I., and Narsilio G., Experimental study of ground energy systems in Melbourne, Australia. *Australian Geomechanics*, Vol 47, Issue 4, 2012, pp. 15-20.
- [16] BM, Climate statistics for Australian locations. Retrieved from http://www.bom.gov.au/climate/averages/tables/cw_086071_All.shtml on 10 June 2016. Bureau of Meteorology (BM).
- [17] Ervin M., Engineering properties of Quaternary age sediments of the Yarra Delta. *Engineering Geology of Melbourne*, 1992, pp. 245-260.
- [18] Suksiripattanapong C., Horpibulsuk S., Chanprasert P., Sukmak P., and Arulrajah A., Compressive strength development in fly ash geopolymer masonry units manufactured from water treatment sludge. *Construction and Building Materials*, Vol 82, 2015, pp. 20-30.
- [19] AS, Methods for preparation and testing of stabilized materials - Unconfined compressive strength of compacted materials, AS 5101.4-

2008. 2008, Sydney, Australia: Standards Australia.
- [20] ASTM, Standard Specification for Unconfined Compressive Strength of Cohesive Soil, D2166/D2166M – 16. 2016, West Conshohocken, PA: American Society for Testing and Materials (ASTM) Internationals.
- [21] Puppala A., Madhyannapu R., and Nazarian S., Special specification for deep soil mixing, 0-5179. 2008, The University of Texas at Arlington, Arlington, TX.
- [22] Heah C., Kamarudin H., Al Bakri A. M. M., Binhussain M., Luqman M., Nizar I. K., Ruzaidi C. M., and Liew Y., Effect of curing profile on kaolin-based geopolymers. *Physics Procedia*, Vol 22, 2011, pp. 305-311.

CYCLIC MECHANICAL PROPERTIES OF SANDY SOILS BY MIXING RECYCLED ASPHALT PAVEMENT MATERIAL

Shoji Yokohama¹ and Atsuko Sato²

¹Faculty of Engineering, Hokkaido University, Civil Engineering Research Institute for Cold Region, PWRI ²

ABSTRACT

Reusing of recycled asphalt pavement material (RAP) as engineering material for ground improvement is important for reducing construction or maintenance costs. Reusing of RAP for ground improvement and ground protection seems available for reduction of construction cost because there are many stock of RAP. In this study, it is indicated that the cyclic mechanical properties of the sandy soil improved by mixing RAP. In order to obtain the fundamental results for the effect of mixing RAP on improvement of cyclic behavior, the series of cyclic undrained triaxial tests were conducted. From the test results, it is shown that the cyclic strength of sandy soil - RAP mixture was greater than the cyclic strength without RAP case. It is also shown that the accumulation speed of excess pore water pressure at sandy soil - RAP mixture is slower than that without RAP mixing. In addition, the mechanism for cyclic mechanical properties of sandy soil - RAP mixture is also suggested.

Keywords: Recycled asphalt pavement material, Cyclic behavior, Sandy soil, Volcanic soil

INTRODUCTION

Recycling of industrial waste materials are actively promoted in the civil engineering work. In order to progress using recycled asphalt material as a construction material, many research for the mechanical properties of recycled asphalt pavement or recycled asphalt shingle have conducted and good performance of recycled asphalt material have pointed out by [1]- [5]. When the road pavement is restored, recycled asphalt pavement gravel material and newly gravel materials are mixed to properly make effective use of construction materials. Therefore, it is difficult to secure the storage space for asphalt waste material because the amount of waste material has been increased.

On the other hand, it is necessary to realize constructing the flexible earth structure or improving seismic mechanical properties of ground for reducing the ground disasters. In this study, the fundamental data for mechanical properties of sandy soil mixed with the recycled asphalt pavement material (RAP) are obtained from the series of laboratory tests. The series of cyclic undrained triaxial tests are conducted. First, the basic data for the cyclic mechanical properties of RAP - fine sand mixture are investigated. Next, the mechanical properties of mixture of RAP and volcanic coarse-grained soil are also discussed. From these results, it is shown that the cyclic undrained strength of the mixture of RAP - fine sand or volcanic coarse-grained soil is higher than those without RAP mixing. In addition, to investigate the influence of specimen temperature on the cyclic strength, the cyclic undrained triaxial tests are conducted at the

temperature of 50 °C. It is also clarified that the specimen temperature and the magnitude of the effective confining pressure affect the cyclic mechanical characteristics of the mixture of RAP - volcanic coarse-grained soil.

FIELD APPLICATION

One example of ground protection works utilizing the recycled asphalt pavement material is introduced in this paper. Fig.1 shows one situation of the ground protection by laying RAP at the site in Hokkaido, Japan. In order to prevent muddy ground due to the rainfall or snow melting, the protection work was performed on June 2009. RAP material was laid on the ground surface with thickness of 100mm. The persons and vehicles for forestry work can easy pass on the protected ground surface. Even if water is provided due to heavy rain and snow melting on the ground, remarkable erosion has not seen for 9 years. The temperature of the ground surface at the site is shown in Fig.2. The ground temperature is monitored since April 2016. As can be seen from Fig.2, the temperature reached about 50 °C in the summer and about -20 °C in the winter. The result indicates that the temperature change behavior of RAP is sensitive.

The soil hardness on the protected ground surface is shown in Fig.3. The soil hardness is measured by the handy soil penetrometer shown in Fig.4. When the soil hardness is measured, the cone of handy soil penetrometer is inserted in the protected ground. The penetration length of the cone of penetrometer is recorded as the soil hardness value. From Fig.3, it is recognized the soil hardness

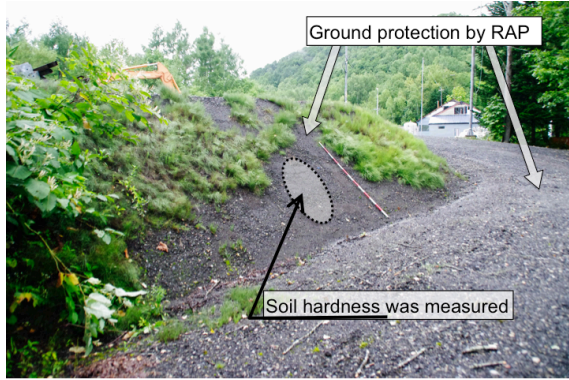


Fig.1 Ground protection by RAP

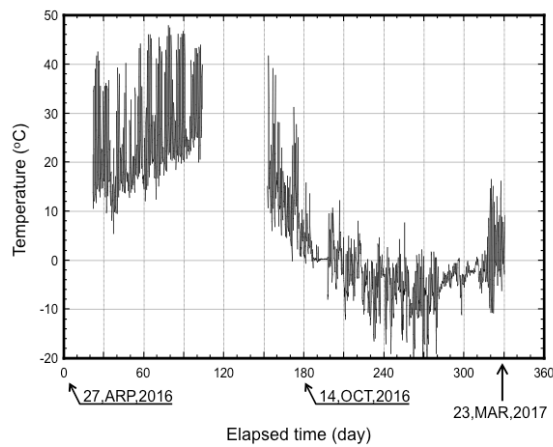


Fig.2 Temperature on ground protected by RAP

is slightly lower in the spring season (April 27, 2016 and March 23, 2017) than the other periods. The soil hardness did not decrease even under high temperature condition such as the summer season. From the obtained data, it is found that the protected ground by RAP can keep its stable state throughout the year.

TESTING MATERIALS

In this study, recycled asphalt pavement material (RAP) and some sandy soils are prepared for testing materials. RAP is the recycled aggregate produced from deteriorated asphalt pavement. RAP is sampled in Sapporo city on August 2014. Fig.5 shows the appearance of RAP particles. The black object on the surface of RAP particle seems as asphalt binder. Toyoura sand (T sand) and one of the volcanic coarse-grained soil (Shikotsu pumice flow deposits, Spfl) are also adopted for the testing materials. Fig.6 shows the external appearance of Spfl particles. Many volcanic soils including Spfl have unique mechanical characteristics such as the many cavities in the soil particles and particles breakage behavior [6], [7]. In order to indicate the effects of RAP mixing on the cyclic mechanical behavior of sandy soils, the cyclic undraind triaxial tests are conducted

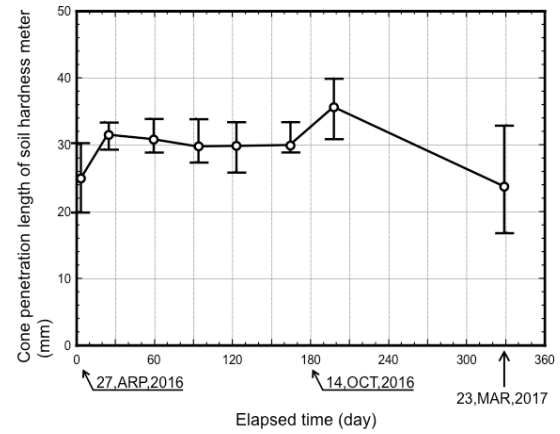


Fig.3 Soil hardness on Protected ground

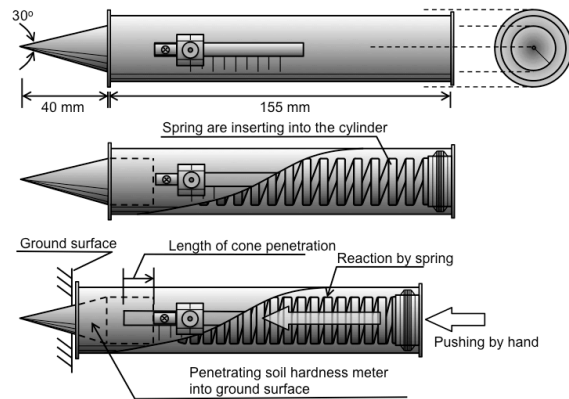


Fig.4 Soil hardness meter (handy type)

by using RAP-T sand mixture (As-T sand) and RAP-Spfl mixture (As-Spfl). The grain size distribution and the list of index properties of the test samples are shown in Fig.7 and Table.1, respectively. For As-T sand and As-Spfl, the mixing ratio of RAP, M_{AS}/M_s is 50%. M_{AS} and M_s are the dry mass of RAP and the dry total mass of specimen, respectively.

TEST PROCEDURE

The specimens for cyclic undraind triaxial tests are prepared by air pluviation of soil particles into the mold. The diameter and height of the specimen are 70 and 150 mm, respectively. Carbon dioxide is percolated and de-aired water is slowly permeated from the bottom to the top of the specimen. Thereafter, backpressure of 200 kPa is applied into the specimen. Application of backpressure is carried out until the pore pressure coefficient B-value reaches 0.95 or above. The isotropic consolidation is conducted under the confining pressure σ'_c of 50 and 100 kPa. The isotropic consolidation is continued until the volumetric strain rate is less than $1.0 \times 10^{-4} \%$ /min. After isotropic consolidation, the cyclic deviator stress is applied to the specimen with 0.1 Hz in frequency.

In order to investigate the effects of specimen temperature on the cyclic mechanical properties, the



Fig.5 RAP particles



Fig.6 Spfl particles

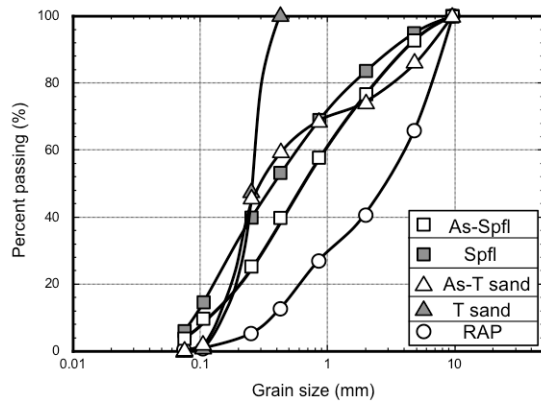


Fig.7 Grain size distribution

series of cyclic undrained triaxial tests are also conducted under high temperature condition. Fig.8 illustrates the test apparatus under high temperature condition. Hot water is poured into the triaxial cell. The specimen temperature is kept by winding the belt-shaped heater round the triaxial cell. Furthermore, the heat-insulation sheet is also wrapped round the triaxial cell. The thermo-sensor shown in Fig.9 is installed into the center of the specimen. The example data for the specimen temperature recorded by the thermo-sensor is shown in Fig.10. The specimen is prepared by As-Spfl at the dry density $\rho_{dc}=1.155\text{Mg/m}^3$. The temperature of belt-shaped heater is set to 65 °C. It can be seen the specimen temperature is kept about 50 °C from start

Table 1 Index properties of testing materials

	ρ_s (Mg/m ³)	ρ_{dmax} (Mg/m ³)	ρ_{dmin} (Mg/m ³)	F_c (%)	M_{As}/M_s (%)
Recycled asphalt pavement material (RAP)	2.366	1.607	1.412	---	100
Volcanic soil (Spfl)	2.453	1.005	0.778	6.15	0
RAP and Spfl mixture (As-Spfl)	2.466	1.306	1.038	3.11	50
Toyoura sand (T sand)	2.649	1.636	1.344	---	0
RAP and T sand mixture (As-T sand)	2.516	1.805	1.462	---	50

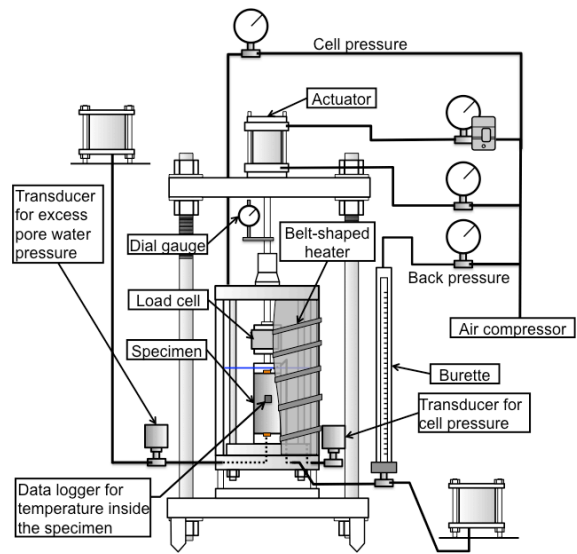


Fig.8 Apparatus for cyclic triaxial test

to end. In this study, the specimen temperature is set to 50 °C by this heating method.

RESULTS AND DISCUSSIONS

The relationship between cyclic stress ratio $\sigma_d/2\sigma'_c$ and number of loading cycles N_c to cause the double amplitude of axial strain DA of 5 % is shown in Fig.11. In order to get the reliable results, the cyclic tests were carried out at least 4 or 5 times per one of the $\sigma_d/2\sigma'_c - N_c$ curve. In order to show the mechanical trend of RAP, the $\sigma_d/2\sigma'_c - N_c$ curve drawn by only 3 data is also plotted in Fig.11. σ_d and σ'_c are amplitude of cyclic deviator stress and effective confining pressure, respectively. These results are obtained at $\sigma'_c = 50$ and 100 kPa under room temperature conditions. It is seen that $\sigma_d/2\sigma'_c$ at As-T sand is higher than that of T sand. The value of $\sigma_d/2\sigma'_c$ for RAP is highest of all. However the effect of the difference of the grain size distribution between RAP and As-T sand cannot be ignored, it is recognized that the cyclic strength is improved by mixing RAP with T sand particles.

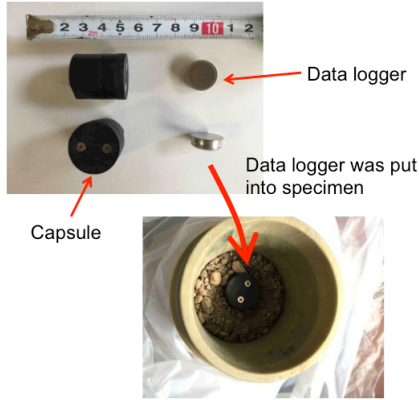


Fig.9 Temperature logger in the specimen

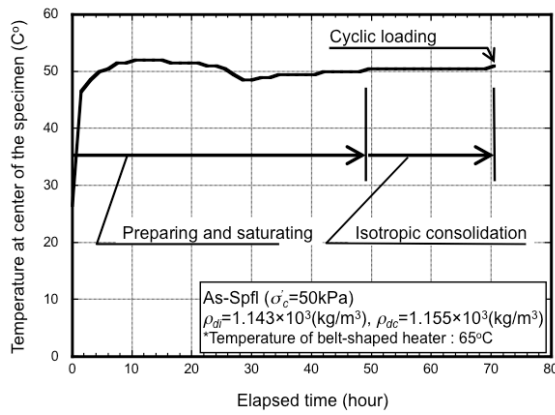


Fig.10 Specimen temperature (As-Spfl)

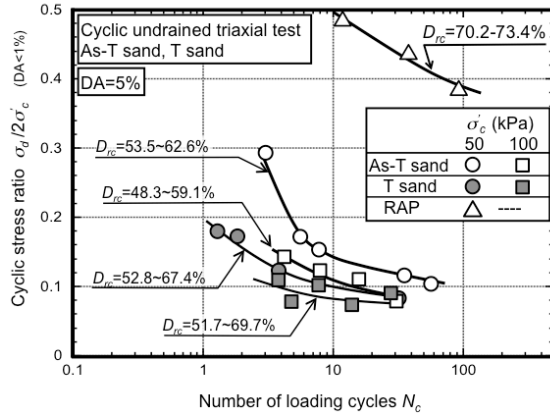


Fig.11 Cyclic strength (T sand, As-T sand)

The excess pore water pressure ratio $\Delta u / \sigma'_c$ and N_c relations at $\sigma'_c = 50$ and 100 kPa are shown in Figs.12 (a) and (b). It can be seen that N_c until reaching $\Delta u / \sigma'_c = 0.95$ for As-T sand specimen is larger than that at T sand specimen. In addition, the accumulation speed of the excess pore water pressure seems slow down due to mixing RAP. Such tendency is remarkable at $\sigma'_c = 50 \text{ kPa}$ than the case at $\sigma'_c = 100 \text{ kPa}$. At $\sigma'_c = 100 \text{ kPa}$ case, the difference of $\Delta u / \sigma'_c$ between As-T sand and T sand is very small. Despite the similarity of excess pore

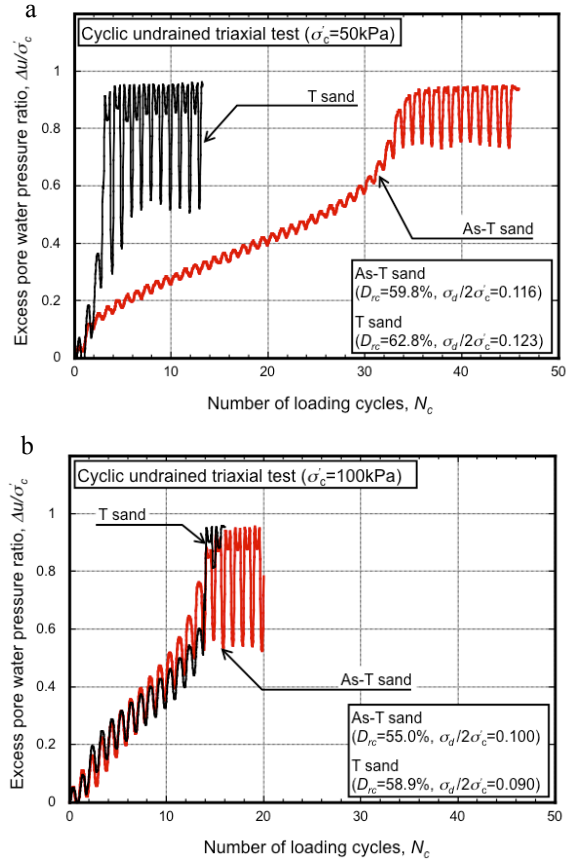


Fig.12 Excess pore water pressure ratio (T sand, As-T sand) : (a) $\sigma'_c = 50 \text{ kPa}$, (b) $\sigma'_c = 100 \text{ kPa}$

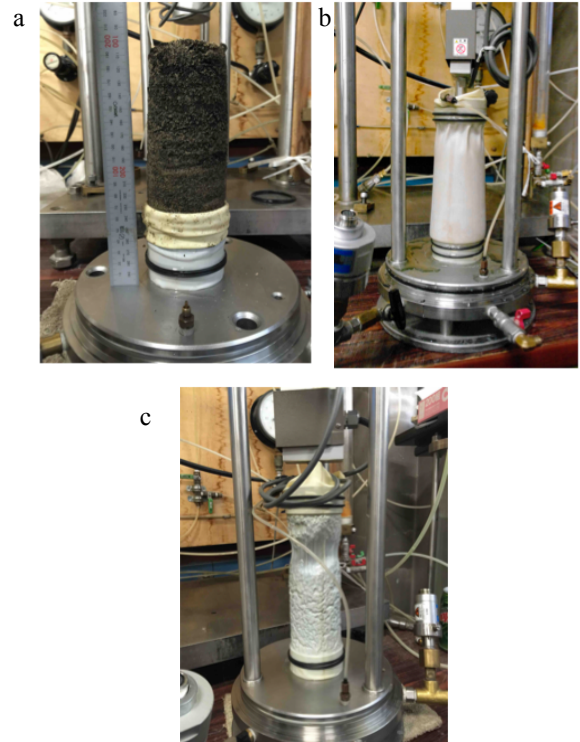


Fig.13 Appearance of specimen after cyclic loading : (a) As-T sand, (b) T sand, (c) RAP

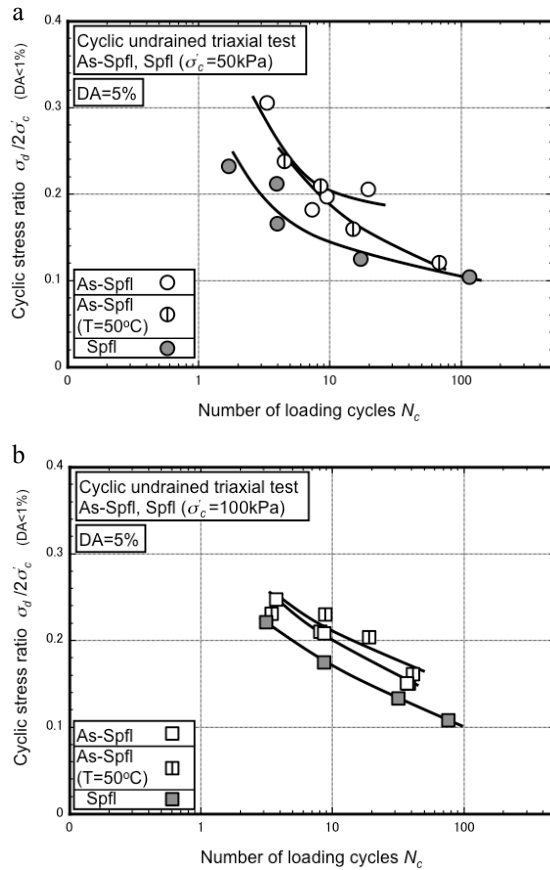


Fig.14 Cyclic strength (As-Spfl, Spfl) :
(a) $\sigma'_c=50\text{kPa}$, (b) $\sigma'_c=100\text{kPa}$

water pressure behavior, the difference in cyclic strength between As-T sand and T sand is recognized in Fig.11. Contacting between RAP and T sand particles may cause the change in cyclic deformation characteristic.

In order to observe the deformation behavior of specimens after cyclic loading, Figs.13 (a), (b) and (c) display the photographs of the specimen for As-T sand, T sand and RAP, respectively. At As-T sand specimen shown in Fig.13 (a), the specimen keeps its cylindrical shape after cyclic loading. The adhesive bonding [8] may lead this behavior. From Fig.13 (b), it is seen that T sand specimen failed to maintain its cylindrical shape and flow deformation is observed after the cyclic loading. From Fig.13 (c), the tensile behavior of RAP specimen is seen after cyclic loading. The pattern of such deformation behavior seems different from the As-T sand and T sand specimens.

The cyclic strength for As-Spfl and Spfl specimens are also verified. The relationships between $\sigma_d/2\sigma'_c$ and N_c to cause the DA value of 5 % are shown in Figs.14 (a) and (b). For each testing case, the cyclic tests are carried out at least 4 times. In these figures, the test results at the specimen temperature of 50 °C at As-Spfl specimen are also included. From these figures, it is found that

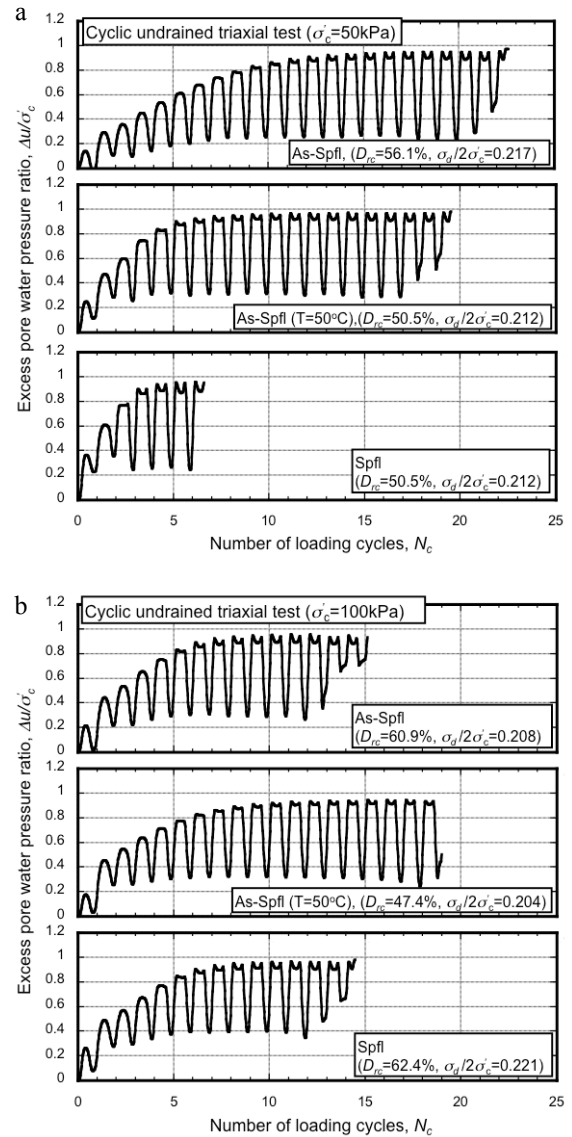


Fig.15 Excess pore water pressure ratio (As-Spfl, Spfl) : (a) $\sigma'_c=50\text{kPa}$, (b) $\sigma'_c=100\text{kPa}$

$\sigma_d/2\sigma'_c$ of As-Spfl are higher than that of Spfl. It is also found that the difference of specimen temperature causes the difference of cyclic stress ratio $\sigma_d/2\sigma'_c$ for As-Spfl. Based on these results, it is revealed that mixing of RAP lead improving the cyclic mechanical properties of volcanic soil and the confining pressure and specimen temperature influenced the cyclic strength.

Figs.15 (a) and (b) show the relationships between $\Delta u/\sigma'_c$ and N_c for As-Spfl and Spfl specimens at $\sigma'_c = 50$ and 100 kPa, respectively. In these figures, the relative density after isotropic consolidation D_{rc} is 47 to 62 %, and the cyclic stress ratio is about 0.22. It is found that the $\Delta u/\sigma'_c$ is accumulated rapidly for Spfl specimen from Fig.15 (a). On the other hand, there is no noticeable difference of $\Delta u/\sigma'_c$ between As-Spfl and Spfl

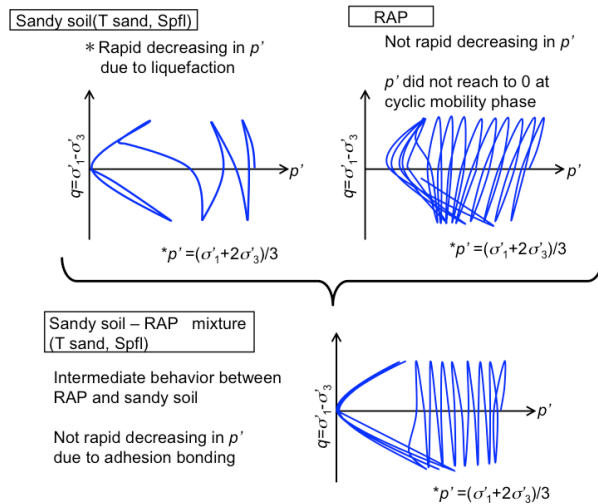


Fig.16 Mechanism of cyclic behavior for sandy soil – RAP mixture

specimens in Fig.15 (b). These results denote that the mixing of RAP makes the liquefaction resistance higher.

The mechanism of cyclic deformation for the sandy soil - RAP mixture is expressed in Fig.16. Fig.16 illustrates the p' - q relationships for the sandy soil. Where, p' and q are effective mean principal stress and deviator stress, respectively. For sandy soil, the effective stress decreased quickly due to accumulation of the excess pore water pressure by cyclic undrained loading. The sandy soil behaves the cyclic mobility when the effective stress reaches to zero. On the other hand, the effective stress is not decreasing so much at RAP specimen. Additionally, the effective stress does not reach to zero due to cyclic loading. Finally, the sandy soil – RAP mixture shows the intermediate behavior between sandy soil and RAP specimen. Many numbers of loading cycles are required until the effective stress reaches zero. The effective stress decreases slowly due to cyclic loading. One of the reasons for delaying effective stress reduction seems the bonding effect between RAP and sandy soil particles.

SUMMARY AND CONCLUSIONS

Improvement of cyclic undrained mechanical properties for sandy soils by RAP mixing is denoted in this study. It is indicated that the cyclic strength of As-T sand and As-Spfl is about 1.3 times to T sand and Spfl, respectively. For As-T sand specimen, the shape-keeping effect is recognized after the cyclic loading as like as adhesion bonding effect shown in the sandy soil.

The effect of specimen temperature on the cyclic

undrained strength for As-Spfl specimen is also discussed. At the confining pressure in 50 kPa, the cyclic strength at 50 °C condition is smaller than that at room temperature condition. On the other hand, at the confining pressure of 100 kPa, the cyclic strength at 50 °C condition is slightly higher than that at room temperature. These experimental results show the cyclic strength for As-Spfl is affected by both confining pressure and specimen temperature.

Accumulation of excess pore water pressure ratio for As-T sand and As-Spfl specimens are slower than T sand and Spfl specimens. Such slow accumulation of excess pore water pressure may be led by interaction between RAP and sandy soil particles.

REFERENCES

- [1] Li, L., Benson, C.H., Edil, T.B., and Hatipoglu, B., Sustainable construction case history: Fly ash stabilization of recycled asphalt pavement material. *Geotechnical and Geological Engineering*. 26, 2008, pp.177–187.
- [2] Wen, H., Warner, J., Edil, T., and Wang, G., Laboratory comparison of crushed aggregate and recycled pavement material with and without high carbon fly ash. *Geotechnical and Geological Engineering*. 28, 2010, pp.405–411.
- [3] Soleimanbeigi, A., Edil, T.B., and Benson, C., Evaluation of fly ash stabilization of recycled asphalt shingles for use in structural fills. *Journal of Materials in Civil Engineering, ACSE*, 25(1), 2013, pp.94–104.
- [4] Soleimanbeigi, A., Edil, T.B., and Benson, C.H., Creep response of recycled asphalt shingles. *Can. Geotech. J.*, 51, 2014, pp.103–114.
- [5] Soleimanbeigi, A., Edil, T.B., and Benson, C., Evaluation of fly ash stabilization of recycled asphalt shingles for use in structural fills. *Journal of Materials in Civil Engineering, ACSE*, 25(1), 2013, pp.94–104.
- [6] Miura, S., Yagi, K., and Asonuma, T., Deformation-strength evaluation of crushable volcanic soils by laboratory and in-situ testing. *Soils and Foundations*. 43(4), 2003, pp.47–57.
- [7] Matsumura, S., Miura, S., Yokohama, S., and Kawamura, S., Cyclic deformation-strength evaluation of compacted volcanic soil subjected to freeze-thaw sequence. *Soils and Foundations*. 55(1), 2015, pp.86–98.
- [8] Lee, K.L., Adhesion bonds in sands at high pressure, *Journal of the Geotechnical Engineering Division, Proceedings of the ASCE*, 103, GT8, 1977, pp.908–913.

QUEZON CITY SOIL PROFILE REFERENCE

Joanel G. Galupino¹ and Jonathan R. Dungca¹

¹Faculty, Civil Engineering Department, De La Salle University, Manila, Philippines

ABSTRACT

The City of Quezon City is one of the highly urbanized cities and one of the fastest growing metropolitan areas in the Philippines, many local and foreign investors are discovering it as a cost-effective business location; many infrastructures were built to serve these growing business hub. Every infrastructure project constructed rests on the ground, without knowing the soil interaction underground, safety is at risk. Thus, this study aims to generate the soil profile of Quezon City using machine learning, specifically, k-Nearest Neighbor (k-NN) algorithm; k-Nearest Neighbor (k-NN) measured the similarity of soil types in terms of distance. The soil profile generated by the model was delineated using computer-aided design (CAD); it was discovered that the underground of the Quezon City is usually dominated by tuff. The generated soil profile will not only serve engineers to decide what type of foundations to be used for a particular site but will also be used for Disaster Risk Reduction (DRR) planning to mitigate ground related disasters; government zoning and policymakers for land use purposes; for real estate industry as their initial reference before investing. The nearest neighbor algorithm model used in the generation of the soil profiles was cross-validated to ensure the predictions are adequate.

Keywords: machine learning, soil profile, nearest neighbor, Philippines, borehole

INTRODUCTION

Every infrastructure project constructed need foundations to stand and these foundations are situated underground. Engineers need to study the soil interaction to economically and adequately design these foundations but without conducting on-site tests, Engineers cannot clearly describe the said interactions underground. In order to reduce the cost of the project, some Engineers rely on previous explorations nearest to project site to approximate the soil properties since these tests are very expensive [1] and some of the soils were stabilized using waste materials [3-10]. Usually, these soils are heterogeneous and it is characterized through a profile by dividing it into horizons based on properties observed in the field [2].

Quezon City being one of the highly urbanized cities of Metro Manila, Philippines, and it is also one of the fastest growing metropolitan areas in the Philippines. Quezon City is a growing enterprise hub, with 58,000 registered business mostly in line with retail trade, restaurants, contractors of goods and services, manufacturers and amusement places. The yearly average of business applicants totaled 11,000 with about 43 establishments registered daily. Many local and foreign investors are discovering Quezon City as a cost-effective business location, shopping malls and a huge Information Technology (IT) parks are being constructed [11], therefore, structures are being constructed to house these developments, and as mentioned, soil explorations are pre-requisite to these projects.

To eliminate the previous information requirement about the interactions among inputs,

parameters, and outputs in soil explorations, different soft computing techniques have effectively been applied. To tackle the limitations of numerical and empirical models, artificial neural network (ANN), fuzzy inference systems (FIS), adaptive-network-based fuzzy inference system (ANFIS), Bayesian network (BN) and genetic programming (GP) are the most common methods being applied. In this study, the k-nearest neighbor (k-NN) algorithm was used because it is mainly employed for measuring the similarity of a set of objects based on some measures of distance and is one the oldest pattern classifier methods with no required pre-processing [12].

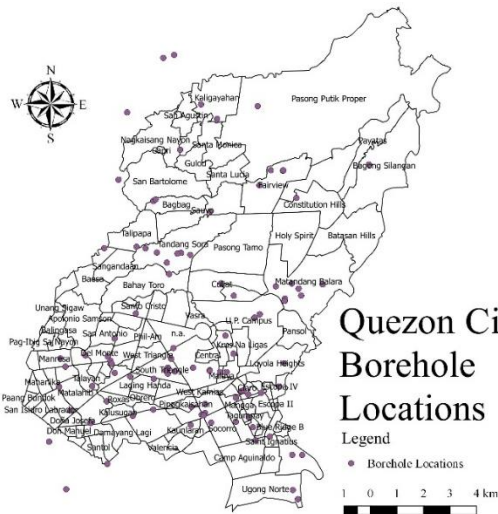
Furthermore, in the dawn of new technology, data are being captured, stored, manipulated, analyzed, managed, and presented. One of the system used is the Geographical Information System (GIS), it is a system that integrates, stores, edits, analyzes, shares, and displays geographic information which can be used in the different technologies, processes, and methods [13]. In the soil profile research, Geographical Information System is a great tool, GIS solves the problematic field delineation of soil horizons.

Thus, this study aims to generate the soil profile of Quezon City using k-NN algorithm that will not only serve as reference for Engineers but will also serve as a guide for policy makers in Quezon City, Philippines.

METHODOLOGY

Soil borehole logs located in Quezon City was

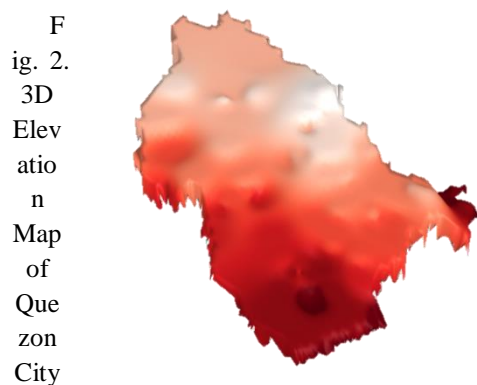
collected and was plotted in a map, shown on Fig. 1. A density of one borehole log per square kilometer was used to describe the soil profile. The distribution



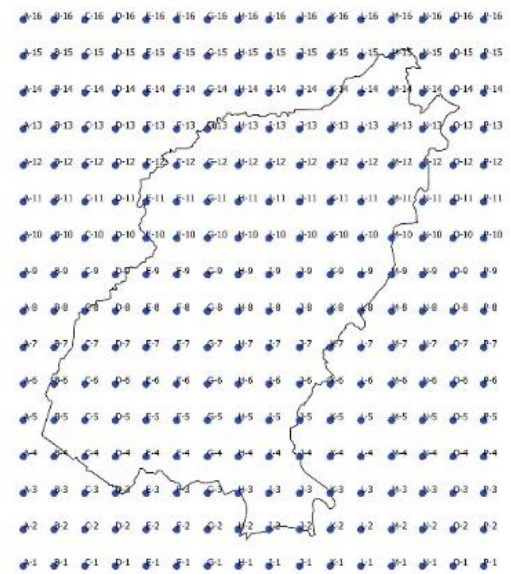
was visually inspected and the areas that needed more data were determined. Borehole logs that seemed erroneous were also removed and disregarded.

Fig. 1. Borehole Locations of Quezon City

The elevations of each boreholes were also plotted because these points are the references for the soil profile characterization, a 3D Elevation Map of Quezon City is shown on Fig. 2. Furthermore, a 16 by 16 grid was used in the study to represent each borehole, shown on Fig. 3.



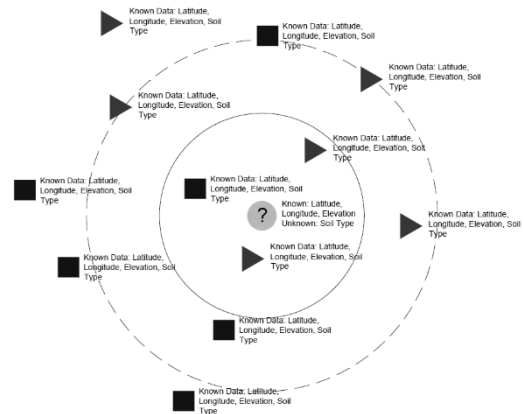
The soils are grouped into classes, which has similar physical properties and general characteristics in terms of behaviors. The grouping system is usually related to its physical properties inherent in the soil and not for a particular use. With only the soil type available it is not sufficient for design purposes but it will give the engineer an



indication of the behavior of a soil when used as a component in construction [14]. The soil types are usually grouped by the following [15], shown on Table 1:

Fig. 3. Grid of Quezon City

A k-Nearest Neighbor (k-NN) algorithm model was used because is one of the simplest classification algorithm and it is one of the most used learning algorithms. It created a model that used the borehole log database in which the data points were separated into several groups to predict the classification of a new sample point. Once the grids have been deployed, the results of the k-NN model will be used in the creation of soil profile using GIS and/or CAD. Each k-NN model consists of a data case having a set of independent variables labeled by a set of dependent outcomes, the research k-NN model classification of is shown on Fig. 4. The shapes signify a particular soil type, shown on Table 1. The independent and dependent variables



can be either continuous or categorical. In the study the dependent and independent variables are shown on Table 2.

Fig. 4. Research k-NN model classification

Table 1. Soil Classification [15]

Soil Type	Description
Sand	Easy to compact and has little effect by moisture. It has the same properties as gravel, the only difference and the division is the No.4 sieve. Rounded to angular, bulky, hard, rock particle, passing No. 4 sieve (4-76 mm) retained on No. 200 sieve (0-74 mm).
Clay	Cohesive soil increases with decrease in moisture. It is usually subjected to expansion and shrinkage with changes in moisture. Its permeability is very low and impossible to drain by regular means. Particles smaller than No. 200 sieve (0-74 mm) ⁽¹⁾ identified by behavior; that is, it can be made to exhibit plastic properties within a certain range of moisture and exhibits considerable strength when air dried.
Silt	Has a tendency to become quick when saturated and is inherently unstable. It is easily erodible and subject to piping and boiling. Particles smaller than No. 200 sieve (0-74 mm) identified by behavior; that is, slightly or non-plastic regardless of moisture and exhibits little or no strength when air dried.
Gravel	Like sand, also easy to compact and has little effect by moisture Gravels are generally more pervious and resistant to erosion and piping compared to sands. Rounded to angular bulky, hard, rock particle, passing 3-in. sieve (76-2 mm) retained on No. 4 sieve, (4-76 mm).
Tuff	Construction material which is generally a limestone precipitated from groundwater. In soil exploration reports, it is a rock mass and its core recovery are usually measured in

Soil Type	Description
	rock-quality designation (RQD). Usually, the foot of foundations rest on tuffs

An estimate of k can be determined using cross-validation. Cross-validation is a well-established technique that can be used to obtain estimates of model parameters that are unknown [16].

Table 2. Dependent and Independent Variables

Independent Variable(s)	Dependent Variable(s)
1. Soil Type	1. Longitude 2. Latitude 3. Elevation

As mentioned, one can make a decision on the class of a sample (query) according to the calculated similarities with the k-NN. Usually, the dependency is computed using Euclidean distance which is defined in Eq. 2 [17]:

$$d(x, y) = \sqrt{\sum_{i=1}^n (x_i - y_i)^2}$$

Where: d(x,y) is the Euclidean distance between the samples x and y, which could have n dimensions in the feature space.

k-NN predictions are based on the intuitive assumption that objects close in distance are potentially similar, it makes good sense to discriminate between the K nearest neighbors when making predictions [16]. By introducing a set of weights W, the closest points among the k nearest neighbors have more influence in affecting the outcome of the query point, shown on Eq. 2:

$$W(x, p_i) = \frac{e^{-D(x, p_i)}}{\sum_{i=1}^K e^{-D(x, p_i)}} \quad (2)$$

Where: D(x,p_i) is the distance between the query point x and the ith case p_i of the example sample.

Once, the k-NN model has been established, the grid points were deployed per elevation, from -23m amsl to 88m amsl, shown on Fig. 5.

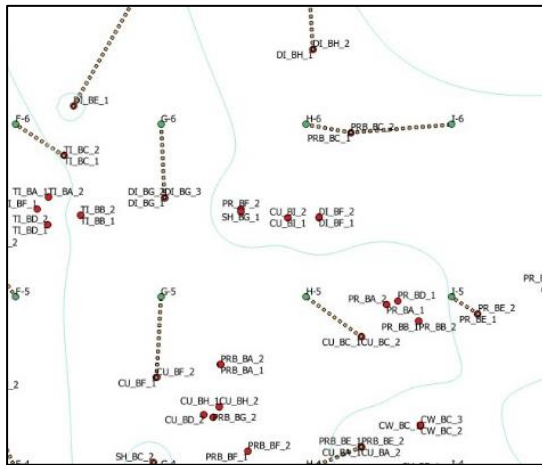


Fig. 5. Deployment of 16x16 grid to the k-NN model

In a particular study [10] which utilized the same machine learning model, it was able to provide a k -nearest neighbor model that served as a reference to predict the compressive strength of concrete while incorporating waste ceramic tiles as a replacement to coarse aggregates while varying the amount of fly ash as a partial substitute to cement.

ANALYSIS AND DISCUSSION

Quezon City is a land locked city bordered by by Caloocan and Valenzuela City to the west and northwest and Manila to the southwest. San Juan and Mandaluyong to the south lie and Marikina and Pasig border the city to the southeast. San Jose del Monte in the province of Bulacan to the north and Rodriguez and San Mateo, both in the province of Rizal to the east.

A relatively high plateau at the northeast of the metropolis situated between the lowlands of Manila to the southwest and the Marikina River Valley to the east, known as Guadalupe Plateau, is where Quezon City lies.

Manila, where Quezon City is located, was submerged at one time in the geologic past. Intermittent volcanic activities followed and after which, volcanic materials were deposited [1]. Volcanic rocks, known as “Adobe”, is the common rock in the underlying layers. It is locally known as the Guadalupe Formation, it is composed of Lower Alat Conglomerate Member and the Upper Diliman Tuff Member. The Diliman Tuff includes the tuff sequence in the Angat-Novaliches region and along Pasig River in the vicinity of Guadalupe, Makati and extending to some areas of Manila and most of Quezon City [1].

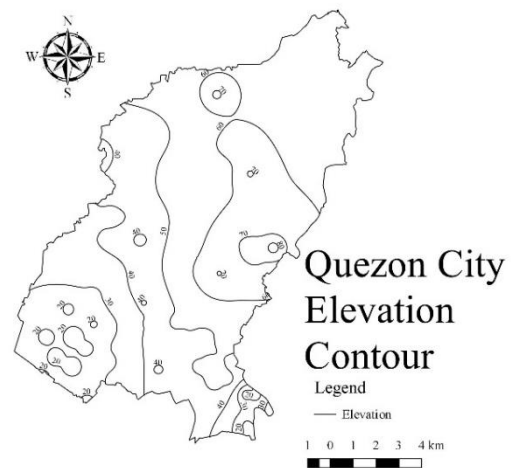


Fig. 6. Elevation Contour of Quezon City

The maximum ground elevation of Quezon City is 88 meters above mean sea level (msl) located at Diliman, Quezon City, and the lowest is 5 meters above mean sea level is at Sta. Mesa border, the Elevation Contour Map is shown on Fig. 6. The minimum level of soil profile elevation was influenced by a particular borehole located near Sta. Mesa which has a ground elevation of 7 meters above msl and its borehole was 30 meters deep, thus, in the study, a minimum of 23 meters (-23m amsl) below msl was used.

Quezon City's soil profile has prevalent tuff layers. Cities with rock formations beneath the surface, such as Quezon City have soils with high bearing capacities at shallow depths. It is recommended to place the foundations on these refusal levels since it is more than capable of carrying loads that are suited for shallow foundations [1].

Longitudinal

The soils are usually grouped into classes as mentioned, groups are based on similar physical properties and general characteristics in terms of behaviors.

Tuff is very prevalent in Quezon City, just several meters below the ground, it would require from Soil Penetration Test (SPT) to Rock Quality Designation (RQD) to accommodate the tuff lying beneath the clay and sand surface, a sample delineation is shown on Fig. 7. There are gravel and clay layers in between the tuff layers, it would not greatly affect the soil bearing capacity of the tuff layer since tuff can handle large amount of load.

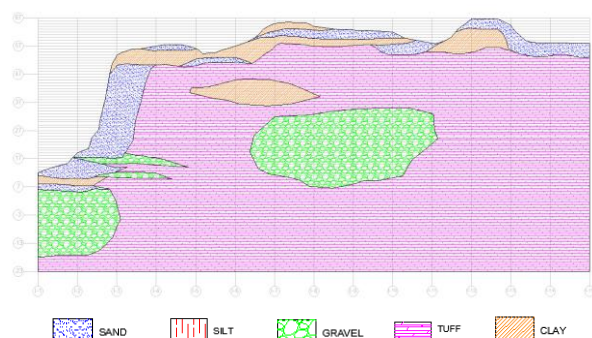


Fig. 7. Soil Profile in the Longitudinal Grid I

Along the longitudinal grid, it was mentioned that there are prevalent tuff layers. Grids C, F, I and L are 78%, 97%, 86% and 29% composing of Tuff, respectively, a chart is shown on Fig. 8. Also in Grids L-O, gravelly layers are prevalent which composes 60% and 84%, respectively. It should be expected that along the Longitudinal Grids, shallow foundations may be recommended. An alternating layer of sand and clay is also prevalent in the shallow layers is due to sediment deposits that are left by the rivers and creeks over time [1].

Traverse

Tuff layer also dominates the underground surface. There are clay, silt and sand layers in the top but several meters below the ground, refusal levels may be expected. Shallow foundations may also be recommended along the Traverse grid. A sample soil profile in the traverse grid is shown on Fig. 9.

Along the traverse grid, a layer of tuff was dominant. Grids 3, 6, 9, 12 and 15 are 89%, 82%, 63%, 47% and 51% Tuff, a chart is shown on Fig. 10. Thus, with the prevalence of Tuff, it should be expected that along the Traverse Grids, shallow foundations may also be recommended. Same with the longitudinal grids, an alternating layer of sand and clay is also prevalent in the shallow layers is due to sediment deposits that are left by the rivers and creeks over time [1].

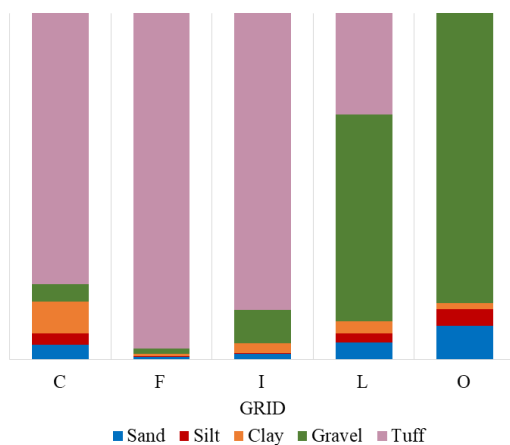


Fig. 8. Soil Types in the Longitudinal Grid

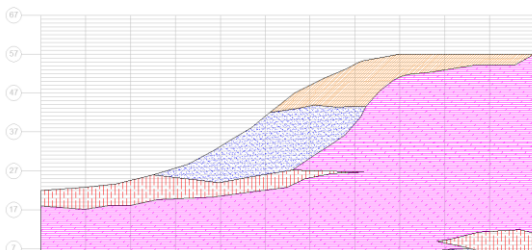


Fig. 9. Soil Profile in the Traverse Grid 6

k-Nearest Neighbor Analysis

k-Nearest Neighbor (k-NN) algorithm is one of the simplest classification algorithm and it is one of the most used learning algorithms. Each k-NN model consists of a data case having a set of independent variables labeled by a set of dependent outcomes. The specifications of the KNN analysis, including the list of variables selected for the analysis and the size of Example, Test, and Overall samples are shown in Table 3.

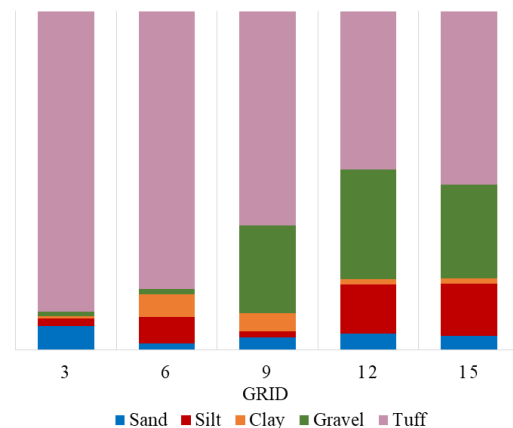


Fig. 10. Soil Types in the Longitudinal Grid

Table 3. Specifications of the k-NN Analysis

Specifications
Dataset Quezon City KNN.sta:
Dependent: Soil Type
Independents: Latitude, Longitude, Elevation
Sample size = 2880 (Examples), 961 (Test), 3841 (Overall)
KNN results:
Number of nearest neighbors =49
Distance measure: Euclidean
Averaging: uniform
Cross-validation accuracy (%) = 75%

The independent variables is standardized to

result in typical case values which fall into the same range. This will prevent independent variables with typically large values from biasing predictions.

With the prevalence of Tuff layers in Quezon City, in the KNN analysis, it is also expected that Tuff will have a higher confidence rate, followed by silt and sand which dominates the top layers of the soil profile. An Elevation vs. Confidence per Soil type is shown on Fig. 11:

Validation

The optimum K has the lowest test error rate. In the k-NN analysis, the model has been forced to fit the test set in the best possible manner. The training set is randomly divided into k groups, or folds, of approximately equal size. The first fold is treated as a validation set, and repeated k times; each time, a different group of observations is treated as a validation set. This process results in k estimates of the test error which are then averaged out, the cross-validation accuracy is shown on Fig. 12.

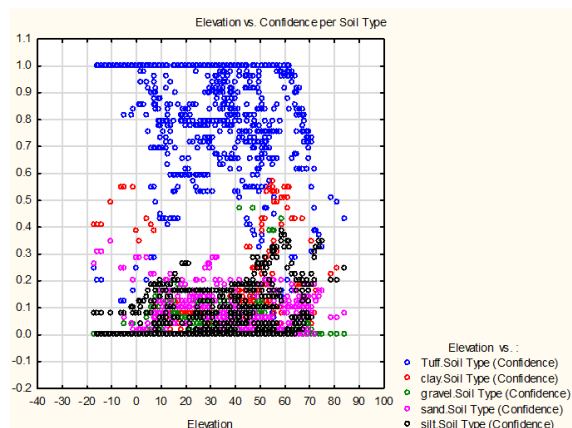


Fig. 11. Elevation vs. Confidence per Soil type

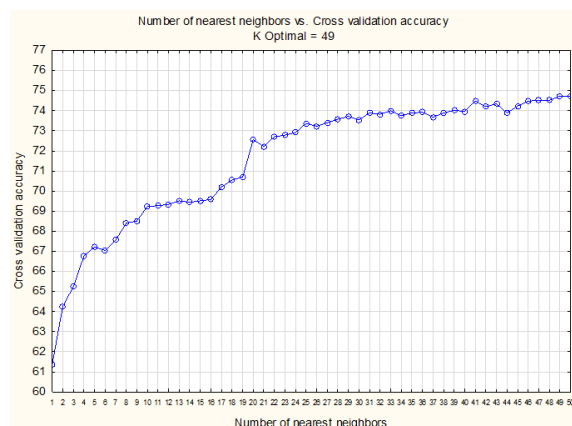


Fig. 12. Cross-Validation Accuracy

A cross validation accuracy of 75% and a k-optimal of 49 was garnered which indicate that there is a strong relationship between the k-Nearest Neighbor (k-NN) model and the observed data.

CONCLUSION

This study was able to generate the soil profile of Quezon City using k-NN algorithm that will not only serve as reference for Engineers but will also serve as a guide for policy makers in Quezon City, Philippines.

The soils are grouped into classes based on similar physical properties and general characteristics in terms of behaviors. Tuff is very prevalent in Quezon City, just several meters below the ground, it would require from Soil Penetration Test (SPT) to Rock Quality Designation (RQD) to accommodate the tuff lying beneath the clay and sand surface. It should be expected that shallow foundations may be recommended.

REFERENCES

- [1] Dungca, J. R., Concepcion, I., Limyuen, M., See, T., & Vicencio, M. (2017). Soil breaing capacity reference for Mtero Manila, Philippines. *International Journal of GEOMATE*, 12(32), 5-11.
- [2] Grauer-Gray, J., & Hartemink, A. (2018). Raster sampling of soil profiles. *Geoderma*, 99-108.
- [3] Dungca, J.R., Jao, J.A.L. (2017). Strength and permeability characteristics of road base materials blended with fly ash and bottom ash. *International Journal of GEOMATE*, 12 (31), pp. 9-15.
- [4] Dungca, J., Galupino, J., Sy, C., Chiu, A.S.F. (2018). Linear optimization of soil mixes in the design of vertical cut-off walls. *International Journal of GEOMATE*, 14 (44), pp. 159-165.
- [5] Dungca, J.R., Galupino, J.G., Alday, J.C., Barretto, M.A.F., Bauzon, M.K.G., Tolentino, A.N. (2018). Hydraulic conductivity characteristics of road base materials blended with fly ash and bottom ash. *International Journal of GEOMATE*, 14 (44), pp. 121-127.
- [6] Dungca, J.R., Galupino, J.G. (2017). Artificial neural network permeability modeling of soil blended with fly ash. *International Journal of GEOMATE*, 12 (31), pp. 76-83.
- [7] Dungca, J.R., Galupino, J.G. (2016). Modelling of permeability characteristics of soil-fly ash-bentonite cut-off wall using response surface method. *International Journal of GEOMATE*, 10 (4), pp. 2018-2024.
- [8] Galupino, J.G., Dungca, J.R. (2015). Permeability characteristics of soil-fly ash mix. *ARPN Journal of Engineering and Applied Sciences*, 10 (15), pp. 6440-6447.

- [9] Dungca, J.R., Codilla, E.E.T., II. (2018). Fly-ash-based geopolymer as stabilizer for silty sand embankment materials. *International Journal of GEOMATE*, 14 (46), pp. 143-149.
- [10] Elevado, K. T., Galupino, J. G., & Gallardo, R. S. (2018). Compressive strength modelling of concrete mixed with fly ash and waste ceramics using K-nearest neighbor algorithm. *International Journal of GEOMATE*, 15(48), 169-174.
- [11] Casanova-Dorotan, F. (2010). *Informal Economy Budget Analysis in Philippines and Quezon City*. Cambridge, MA: Women in Informal Employment: Globalizing and Organizing (WIEGO).
- [12] Nikoo, M., Kerachian, R., & Alizadeh, M. (2017). A fuzzy KNN-based model for significant wave height prediction in large lakes. *Oceanologia*.
- [13] Galupino, J., Garciano, E., Dungca, J., & Paringit, M. (2017). Location based prioritization of surigao municipalities using probabilistic seismic hazard analysis (PSHA) and geographical information systems (GIS). 9th IEEE International Conference Humanoid, Nanotechnology, Information Technology Communication and Control, Environment and Management (HNICEM). Manila: The Institute of Electrical and Electronics Engineers Inc. (IEEE) – Philippine Section.
- [14] Air Field Manuals. (1999, October 27). Materials Testing.
- [15] Wagner, A. (1957). *The Use of the Unified Soil Classification System by the Bureau of Reclamation*. Denver, Colorado: Bureau of Reclamation. Retrieved February 25, 2018, from https://www.issmge.org/uploads/publications/1/41/1957_01_0030.pdf
- [16] Statsoft. (2018, February). k-Nearest Neighbors. Retrieved from Statsoft: <http://www.statsoft.com/Textbook/k-Nearest-Neighbors>
- [17] Ertugrul, O., & Tagluk, M. (2017). A novel version of k nearest neighbor: Dependent nearest neighbor. *Applied Soft Computing*, 480–490.

GEOTECHNICAL PROPERTIES OF SLUDGE BLENDED WITH CRUSHED CONCRETE AND INCINERATION ASH

Muhammad Rashid Iqbal¹, Kento Hashimoto¹, Shinya Tachibana², and Ken Kawamoto¹

¹Graduate School of Science and Engineering, Saitama University, Japan

²Research Center for Urban Safety and Security, Kobe University, Japan

ABSTRACT

To have the effective use of drinking water sludge (DWS) ($< 2\text{mm}$) and DWS blended with crushed concrete ($2-9.5\text{mm}$) and incineration ash ($< 2\text{mm}$) as geotechnical materials, geotechnical properties necessary for examining the suitability of road subgrade and the effective compacting at waste landfill sites were examined in this study. A series of laboratory tests for compaction, California bearing ratio (CBR), and consolidation tests were conducted by changing the mixing proportions of tested materials. The results from compaction tests showed that compaction parameters such as the maximum dry density and optimum water content of DWS were dependent on the mixing proportion of either crushed concrete or incineration ash and they showed unique linear relationships between the compaction parameters and mixing proportions. The results from two set of soaked CBR tests with high energy compaction (1807 kJ/m^3) and low energy compaction (539 kJ/m^3) showed that measured CBR values for DWS blended with crushed concrete with both high and low energy compactations increased with increasing in mixing proportions of crushed concrete. On the other hand, measured CBR values for DWS blended with incineration ash did not increase with increasing in mixing proportions of incineration ash, suggesting that the mixing of incineration ash did not contribute to the improvement of bearing capacity. The blend of crushed concrete reduced significantly compression index (C_c) of DWS as compared to the DWS blended with incineration ash. The reduction of C_c was also observed for the tested samples of DWS blended with both crushed concrete and incineration ash. The blend of crushed concrete increased coefficient of consolidation (C_v) of DWS while the blend of incineration ash did not affect the C_v of DWS.

Keywords: *Drinking Water Sludge, Compaction, California Bearing Ratio (CBR), Compressibility, Crushed Concrete, Incineration Ash*

INTRODUCTION

A large amount of the waste material is produced daily which reduces the virgin material along with the problem of the waste material disposal. With the scarcity of land and increase of the public resistance it is difficult to dispose all the material in the landfill sites.

Recycled solid waste material are normally referred to solid waste material which are collected to curbside; or generated by construction and demolition or commercial or industrial activities [1]. With the increase of population in the urban areas and the development of cities, waste management issues have gained much attention and a lot of money is spent to manage it [2]. Increase of the population demands more drinking water and water treatment plants generate sludge as a by-product due to their operation and treatment process [3]. It is very difficult to avoid the production of sludge from water and waste water treatment plant [4]. It is widely accepted that recycling and subsequent use of the construction and demolition waste will reduce the demand of the virgin material [5]-[6]. Therefore, alternative use along with the landfill sites of the waste material is an essential part to handle the

waste disposal problem.

A lot of research is conducted to utilize the construction and demolition waste e.g. crushed concrete and crushed bricks materials as a road sub-base and base material [1]-[5] as an alternate utilization purpose. Improvement of the sludge properties numerous stabilizer e.g. lime, fly ash, and loess etc. had been utilized as mixer to sludge for its stability and compaction properties [7]. In addition to sludge stability/solidification was also evaluated by mixing the additive such as lime stone, cement and bitumen [3]. Addition of coarser fraction (e.g. crushed bricks, recycled concrete and recycled asphalt pavement) with clay material increases the friction resistance which leads to improve the strength of the mixed material [8].

The objectives of this research are to utilize the drinking water sludge by blending with crushed concrete and incineration ash to use for the road subgrade along with the landfill sites. DWS being a very fine material, does not have good quality and low compaction properties, high compressibility, swelling and low load carrying capacity. It is an economical solution to mixed other waste material instead of adding any admixture or additive for the stability and to improve engineering properties of

DWS material.

MATERIALS AND METHODS

Three types of the waste materials were used as per production proportion of the waste material in Japan. Drinking water sludge (DWS) with particle size less than 2mm, was collected from the intermediate treatment plant Chiba Prefecture, Japan. Crushed concrete with size ranges from 2mm to 9.5mm and incineration ash with particle size less than 2mm were collected from the Intermediate treatment plant Saitama Prefecture, Japan. Crushed concrete and incineration ash were blended with drinking water sludge with different proportions to improve and analyze the effect on DWS engineering properties.

Index properties of waste material were determined by using American Standard for Testing and Material (ASTM) and Japan Industrial Standards (JIS). Particle size distribution (PSD), Atterberg Limits, pH, Electrical Conductivity (EC), compaction properties, California Bearing Ratio (CBR), and one-dimensional consolidation properties were examined.

Standard proctor compaction tests were conducted on individual, 2 mixed and 3 mixed samples with various mixing proportions in a mould having 10cm inner diameter and 12.75cm height, in 3 equal layers with 2.5 kg of rammer and 25 blows per layer at a drop height of 30.5cm [9].

Soaked California Bearing ratio (CBR) test were conducted on two different energy levels. Low energy (539 kJ/m^3) denoted with CBR-A and high energy (design CBR) denoted as CBR-D. Samples were compacted in 3 layers with 20 and 67 blows per layer respectively and soaked for 96 hours. Loading was applied at 1mm/minute up to 12.50mm. Load penetration curve was drawn to determine the CBR values at 2.5mm and 5.0mm penetration and was selected higher value between both.

Consolidation tests were conducted on the modified apparatus of 10cm diameter and 10cm height due to particle size greater than 2mm. Samples were compacted at more than 90% degree of compaction. After fully saturation of the samples at 3.75 kPa to avoid swelling, loading was applied in 8 steps from 7.05 kPa to 905 kPa and prolonged for one day to achieve primary consolidation. Time square root method was used to determine 90% and 100% consolidation [10].

RESULTS AND DISCUSSION:

Physical and Chemical Properties

According to unified soil classification system, DWS was categorized as Fat clay (CH), crushed concrete as a well graded gravel (GW) and

incineration ash as poorly graded sand (SP). According to AASHTO soil classification, DWS was categorized as clay soil (A-7-5), crushed concrete as stone fragment gravel and sand (A-1) and incineration ash as A-1-b. Crushed concrete and incineration ash were considered as good to excellent material while DWS was considered as poor soil. PSD curve of all three materials is shown in Fig.1.

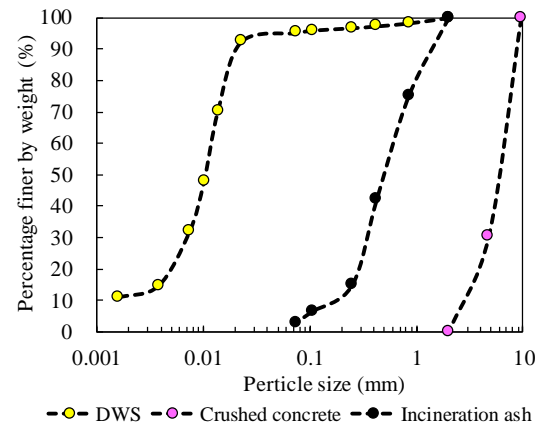


Fig.1 Particle size distribution of tested materials

Table 1 Physical properties of tested materials

Tests	DWS	Crushed Concrete	Incineration Ash
Particle Size (mm)	< 2.00	2 < d < 9.50	< 2.00
LL	260	NM*	NM*
PL	130	NP**	NP**
G _s	2.39	2.59	2.69
pH	6.60	11.0	11.1
LOI (%)	38.2	9.5	1.6
EC (mS/cm)	0.29	0.47	1.99

*NM: Not-measurable, **NP: Non-plastic

Table 1 indicates that DWS was only cohesive material while crushed concrete and incineration ash were cohesionless materials. Based on pH value crushed concrete and incineration ash were basic characteristics in nature while DWS was almost neutral. Atterberg limit of DWS was consistent with the former research LL (%) 262.70 and PL (%) 132.0 of drinking water sludge [7].

Table 2 Chemical analysis of tested materials

Compo nents	DWS (%)	Crushed Concrete (%)	Incineration Ash (%)
Na ₂ O	0.49	1.32	3.24
Al ₂ O ₃	22.7	9.19	10.8
SiO ₂	36.2	39.9	46.0
CaO	1.81	22.5	23.1
Fe ₂ O ₃	5.53	7.52	4.42

SO ₃	0.62	2.27	1.01
K ₂ O	0.96	2.68	1.36

Chemical analysis of the waste composition was conducted with an energy dispersion spectrometry (EDS) to analyze the material components as shown in Table 2. Oxides which carry primary pozzolanic reaction are SiO₂, Al₂O₃, Fe₂O₃, which are major components for binding [11]. These are also abundant in the tested materials.

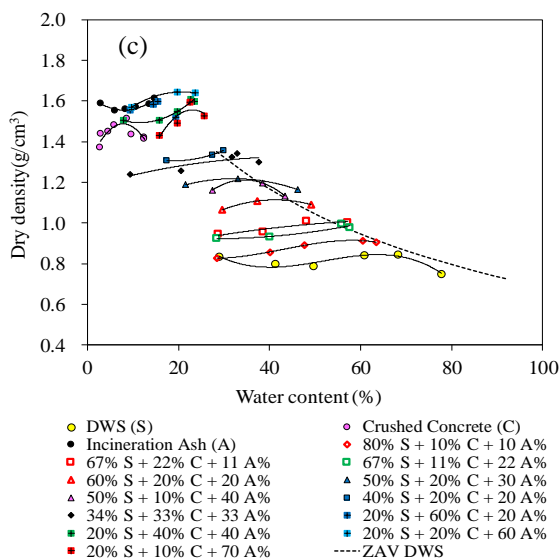
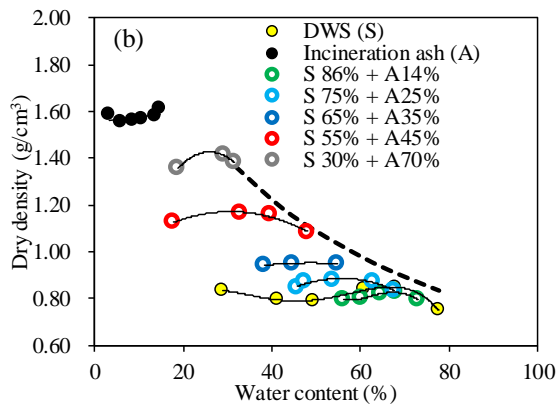
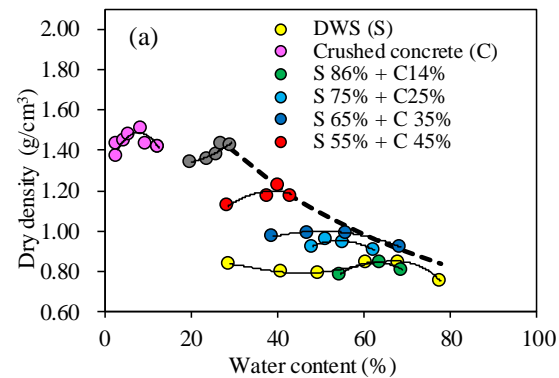
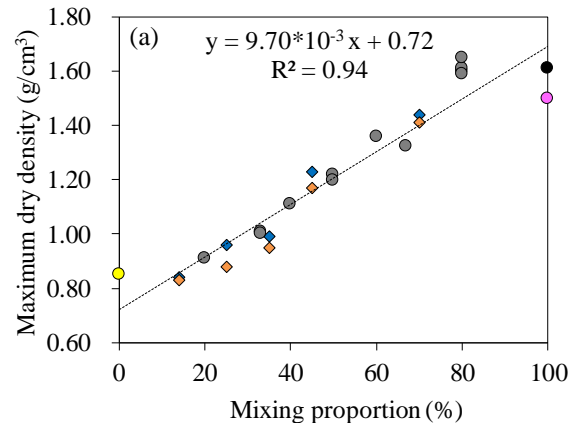


Fig. 2 Compaction curves for (a) DWS blended with crushed concrete, (b) DWS blended with incineration ash, and (c) DWS blended with both crushed concrete and incineration ash.

Compaction Properties

Compaction plays a vital role in improving the packing of the particles of material to reduce the void spaces. Soil can reach to densest condition by optimal wetting and rearranging the particles by water mixing and compaction [11]. Standard proctor test of the DWS showed maximum dry bulk density of 0.85 g/cm³ at optimum water content of 68.20% while previous research revealed that maximum dry bulk density of the MSW was 0.42 g/cm³ and optimum water content of 70% [12]. Maximum dry density of MSW was 1.05 g/cm³ and OWC 42% [7]. Difference of the dry density could be due to the particle size and nature of material. For incineration ash, measured dry densities did not show any peak value and varies from 1.55 to 1.61 g/cm³ with an initial water content of 6% to 14.7%. Crushed concrete is slight dependent on initial moisture contents and shown maximum dry density peak at 8% water contents.



● DWS (S) ● Concrete (C) ● Ash (A)
 ◆ S + C ◆ S + A ● S + C + A

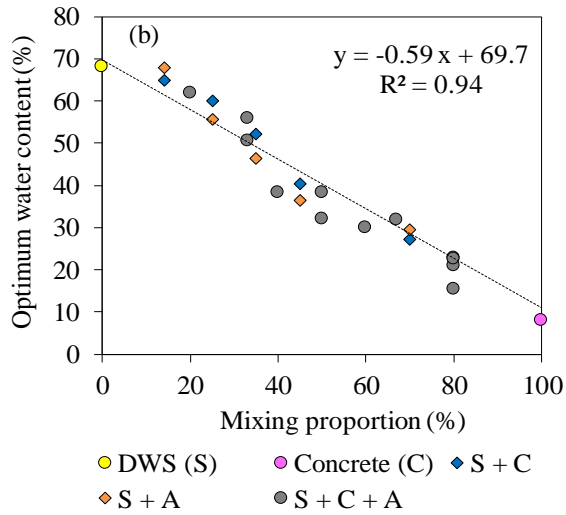


Fig. 3 Relationships between (a) the maximum dry density and mixing proportion, (b) optimum water content and mixing proportion for crushed concrete and/or incineration ash to DWS.

Compaction curve of the different mixtures were examined, mixing of the crushed concrete and incineration ash reduced the over absorption of the DWS and led to improve the interlocking forces amongst the particles on the dry side of the compaction curve which improved the strength of the mixed samples. This trend can be well observed in Figs. 2 (a)-(c). The maximum dry densities and optimum water contents showed a linear relationship with the mixing proportion of crushed concrete and incineration ash addition as shown in Figs. 3(a) and (b).

California Bearing Ratio (CBR)

Soaked CBR tested were conducted at the same initial moisture condition with CBR-D (high energy compaction 1807 kJ/m³) and CBR-A (low energy compaction 539 kJ/m³) on the individuals, concrete and ash mixed waste materials. CBR value increases with the addition of the coarse material. Increase of the CBR value was because of density of the coarse fraction and improvement of frictional resistance [13].

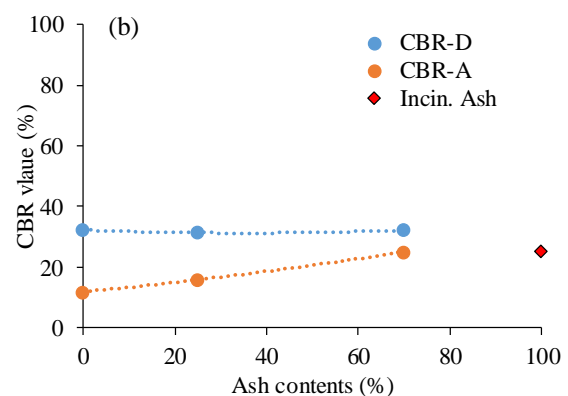
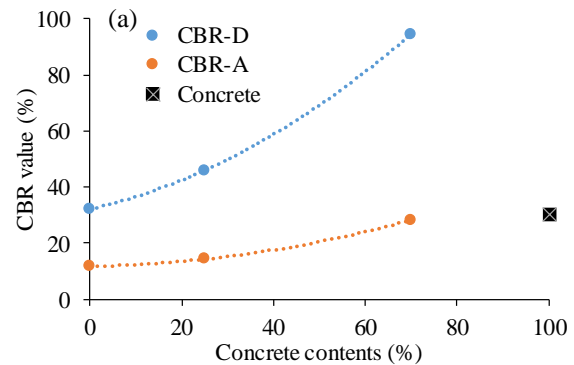
Initial moisture contents and compaction energy play a vital role in the CBR of the material. The blend of granular crushed concrete is the main factor to increase the CBR of the mixed sample as shown in Figs. 4(a)-(c).

CBR-D revealed that addition of concrete proportion with DWS from 25% to 70% enhanced CBR values from 1.44 to 2.97 times as compared to individual materials. This could be due to increase of interlocking and well packing of fine and coarse proportion. Incineration ash did not show any improvement. Addition of concrete and ash to DWS CBR value improved from 1.20 to 1.81 times more than DWS.

Table 3. Measured CBR values at low and high compaction energy

Sample Name	CBR-A (%)	CBR-D (%)
DWS (S)	11.8	32.2
Concrete (C)	22.1	30.4
Incineration ash (A)	13.1	25.2
S75% +C25%	14.3	46.0
S30% +C70%	28.2	94.5
S75% +A 25%	15.8	31.3
S30% +A 70%	25.0	32.2
S80% +C10% +A10%	16.6	37.9
S67% +C11% +A22%	20.1	44.2
S50% +C20% +A30%	24.1	57.8

CBR-A experimental results revealed that the blend of crushed concrete from 25% to 70% increased CBR value from 1.21 to 2.39 times more and in case of same ash mixing to DWS improved CBR value from 1.33 to 2.1 times more. Concrete and ash both mixed with DWS enhanced CBR value from 1.41 to 2.0 times more than that of DWS. Six different doses of cement kiln dust (5%, 10%, 15%, 20%, 25% and 30%) were added to the soil samples. Mixing of up to 20% of cement kiln dust (CKD) to soil improved the CBR value and controlled the swelling ratio as compared to any other dose addition to soil samples[14].



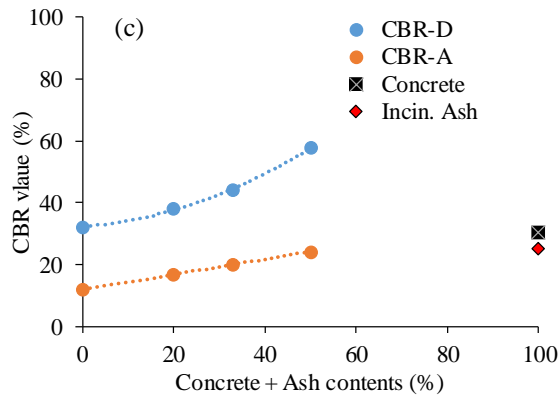


Fig.4 CBR for (a) DWS blended with crushed concrete, (b) CBR for DWS blended with incineration ash, and (c) CBR for DWS blended with both crushed concrete and incineration ash.

Consolidation Properties

Consolidation is expulsion of water under a long-term loading. A series of one dimensional consolidation tests were conducted conforming ASTM standard one dimensional consolidation test [10]. The addition of sand to soil reduces the compressibility significantly as compared to virgin material [15].

DWS is susceptible to more compressibility. Higher mixing proportion of crushed concrete and incineration ash against DWS leads to reduction of compressibility of the blended waste material as shown in Fig. 6.

In Fig. 6, Compression index (C_c) was normalized by 100% DWS and indicated as C_c/C_{c0} . Compressibility of the crushed concrete blended mix reduced significantly more than incineration ash, mixed with DWS. Experimental result showed that C_c of DWS blended with incineration ash reduced from 0.25 to 0.17 which was 1.47 times reduction while crushed concrete blended with DWS reduced from 0.25 to 0.04 which was about 6 times reduction of C_c and same value was obtained in case of three mixed samples S50%+C20%+A30%. Crushed concrete having the rough surface provide more interlocking friction between particle and due to incompressible material leads to improve the C_c value as well.

Coefficient of consolidation (C_v) of DWS blended with crushed concrete improved 10 to 100 times as compared to that of DWS as shown in Fig. 7 (a) but did not improve so much in case of incineration ash mixed with DWS Fig. 7 (b). Different percentage of sand addition to dredged marine soil (DMS) showed similar value of C_v which are well conformed in case of DWS blended with

incineration ash [16]. Addition of the binder provided additional bonding between the particles and C_v values of the binder-sand improved in comparison with the original dredged soil material [16].

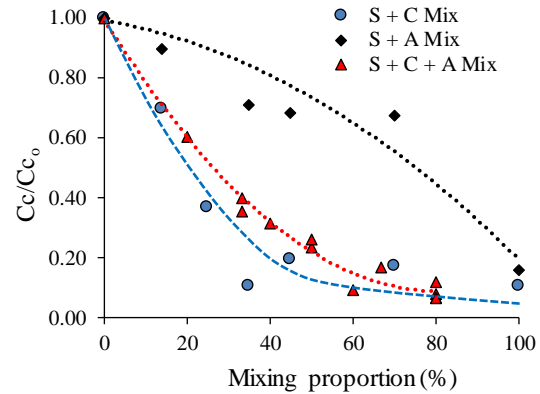


Fig. 6 Variation in C_c/C_{c0} for DWS blended with crushed concrete and incineration ash

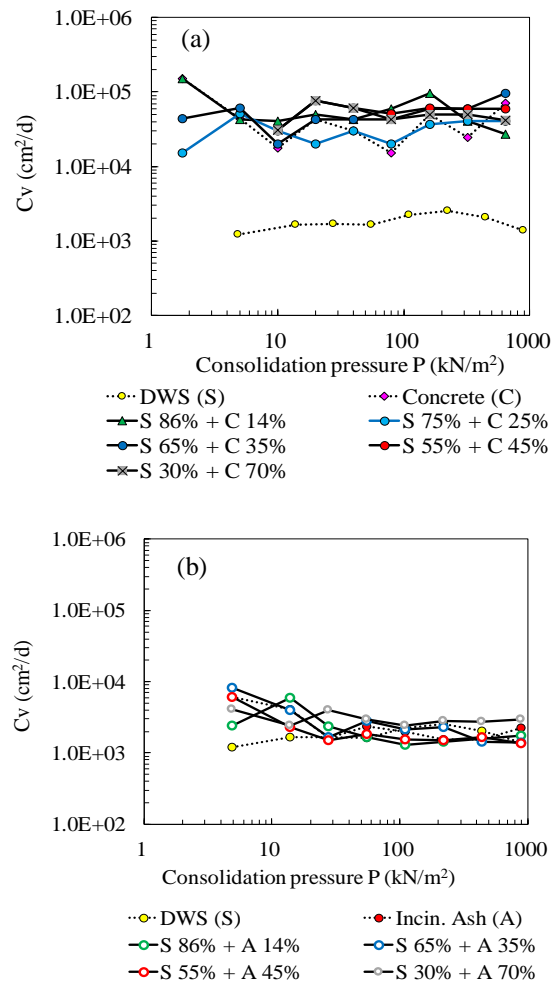


Fig. 7 Coefficient of consolidation C_v for (a) DWS blended with crushed concrete, and (b) DWS blended with incineration ash

blended with incineration ash.

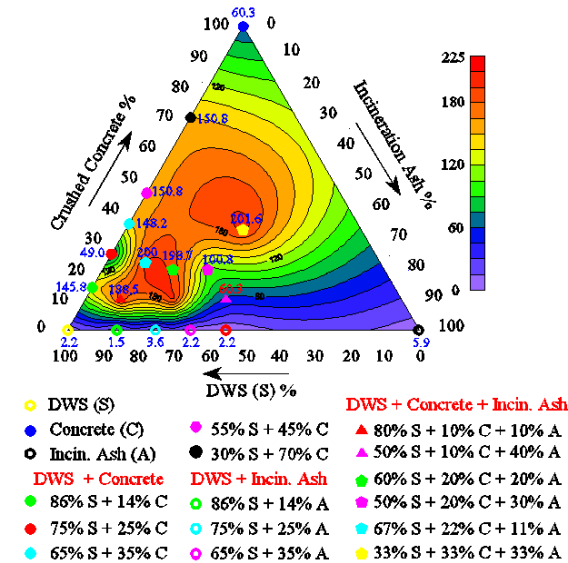


Fig. 8 Contours map of measured C_v values ($\times 10^3$)

Mixing of crushed concrete with DWS enhanced C_v value significantly more as compared to addition of incineration ash to DWS as shown in Fig. 8. It could be because of coarser fraction of crushed concrete particles.

CONCLUSIONS

Based on the above research following conclusions can be drawn:

- (1) Maximum dry densities and OWC showed linear relationship with the addition of mixing proportion of crushed concrete and incineration ash to DWS.
- (2) CBR values increased from 1.44 to 2.97 times and compression index reduced about 6 times with the addition of crushed concrete from 25% to 70% with DWS and enhanced C_v values 10 to 100 times.
- (3) Incineration ash mixed with DWS did not improve of CBR, compression and consolidation properties.
- (4) DWS blended with the crushed concrete can be utilized for the development of road subgrade, along with the landfill site because of load carrying capacity and well compaction properties.

ACKNOWLEDGEMENT

This work is partially supported by SATREPS project of Japan Science and Technology agency (JST) and Japan International Cooperation Agency (JICA).

REFERENCES

- [1] Arulrajah A., Piratheepan J., Aatheesan T., and Bo M. W., Geotechnical and Geoenvironmental

Properties of Recycled Construction and Demolition Materials in Pavement Subbase Applications. *Journal of Materials in Civil Engineering*, Vol. 23, Issue 10, 2011, pp. 1077-1088.

- [2] Shariatmadari N., Machado S. L., Noorzad A., and Karimpour-Fard M., Municipal solid waste Effective Stress Analysis. *Waste Management*, Vol. 29, Issue 12, 2009, pp. 2918-30.
- [3] Lucena L.C.d.F.L., Juca J.F.T., Soares J.B., and Tavares M.F.P.G., Use of Wastewater Sludge for Base and Subbase of Road Pavements. *Transportation Research Part D: Transport and Environment*, Vol. 33, 2014, pp. 210-219.
- [4] Della Z.M., Zerlotti M., Refosco D., Santomaso A.C., and Canu P., Improved Compaction of Dried Tannery Wastewater Sludge. *Waste Management*, Vol. 46, 2015, pp. 472-479.
- [5] Disfani M.M., Arulrajah A., Bo M.W., and Hankour., Recycled Crushed Glass in Road Work Applications. *Waste Management*, Vol.31, 2011, pp. 2341-2351.
- [6] Arulrajah A., Piratheepan J., Aatheesan T., and Bo M. W., Geotechnical Properties of Recycled Crushed Brick in Pavement Applications. *Journal of Materials in Civil Engineering*, Vol. 23, Issue 10, 2011, pp. 1444-1452.
- [7] Lim S., Jeon W., Lee J., Lee K., and Kim N., Engineering Properties Of Water/Wastewater-Treatment Sludge Modified by Hydrated Lime, Fly Ash and Loess. *Water Research*, Vol. 36, 2002, pp. 4177-4184.
- [8] Cabalar A.F., Abdulnaffaa M.D., and Karabash Z., Influence of various construction and demolition materials on the behavior of clay. *Environmental Earth Science*, Vol. 75, Issue 9, 2016 , pp. 841-850
- [9] Standard Test Methods for Laboratory Compaction Characteristics of Soil Using Standard Effort (12 400 ft-lbf/ft³ (600 kN-m/m³)), Vol. 04, 2012.
- [10] ASTM, Standard Test Methods for One-Dimensional Consolidation Properties of Soils Using Incremental Loading 1, Vol. 04, 2004.
- [11] Chen L. and Lin D.F., Stabilization Treatment of Soft Subgrade Soil By Sewage Sludge Ash and Cement. *Journal of Hazard Materials*, Vol. 162, Issue 1, 2009, pp. 321-327.
- [12] Reddy K.R., Hettiarachchi H., Parakalla N.S., Gangathulasi J., and Bongor J.E., Geotechnical Properties of Fresh Municipal Solid Waste at Orchard Hills Landfill, USA. *Waste Manag.*, Vol. 29, Issue 2, 2009, pp. 952-959.
- [13] Kesharwani R.S., Sahu A. K., and Khan N.U., CBR Value of Sandy Subgrade Blended With Coarse Aggregate. *International Journal of*

- GEOMATE, Vol. 10, Issue 2, 2016, pp. 1743-1750.
- [14] Mosa A.M., Taher A.H., and Al-Jaberi L.A., Improvement of Poor Subgrade Soils Using Cement Kiln Dust. *Case Studies in Construction Materials*, Vol.7, 2017, pp. 138-143.
- [15] Shipton B., and Coop M.R., The Compression Behaviour of Reconstituted Soils. *Soils and Foundations*, Vol.52, Issue 4, 2012, pp. 668-681.
- [16] Kalianan S., Chan C.M., 1-D Compressibility Parameters of Lightly Solidified Dredged Marine Soil (DMS) Using Cement, GGBS and Coarse Sand. *International Journal of GEOMATE*, Vol. 12, Issue 33, 2017, pp. 167-171.

NUMERICAL ANALYSIS FOR 3D INFLUENCE OF PILE PULLING-OUT HOLES ON SURROUNDING GROUND

Shuichi Kuwahara¹ and Shinya Inazumi²

¹Marushin Co. Ltd., Japan

²Shibaura Institute of Technology, Japan

ABSTRACT

The demolition of social infrastructures including the civil structures have been increasing because of aging them constructed during in a period of high economic growth and decrease in their utilization with a population decrease, in recent years. As a result, removal works of existing pile in the ground have been increasing. Pulling-out method is adopted for removal of existing a pile foundation in the present circumstances. However, after pulling-out a pipe foundation, decline of mechanical characteristic of surrounding ground is concerned by forming pulling-out holes. There are no regulations yet for filler injected into a pulling hole, and the influence of the strength of the filler on surrounding ground is not considered. This study considers the influence by which a pulling-out hole of a pipe foundation gives it to static characteristics of surrounding ground by using 3D elastic-plastic finite element analysis. The special qualities required for fillers injected into a pulling-out hole are also clarified in this study.

Keywords: Finite element method, Pile foundation, Pulling-out method, Pulling-out hole,

INTRODUCTION

In Japan, many of the city located in the soft ground, there are many structures using a pile foundation. Therefore, to achieve a new land utilization at the place where existed structures are present, it is necessary to remove existed pile supported the structure as well as existed structures for construction of a new structure. Further, existed piles and concrete husk become industrial waste, be left of these industrial waste in the ground is a very difficult problem. In addition, it is seen troubles many as "hidden defect" in the sale of land transactions [1]. Accordingly, it can be said that the removal of existed pile is essential.

The removal method of existed pile, there is a pulling-out method and crushing removal method, and the like. But the crushing removal method are having such as vibration, noise and environmental problems. The pull-out method has been widely used from this thing. However, there are also problems in the pull-out method. The pulling-out hole is formed when pulling out the existed pile. If the pulling-out hole is left, the collapse of the empty drilling part of the earth and sand, and there is a possibility that the subsidence of the ground surface by the gap widening in the ground occurs. Therefore, it is necessary to fill the pulling-out hole by injection of the fillers. About fillers, conventionally, in many cases to construction in mountain sand and recycled sand from construction it is easy and inexpensive. But, by cannot ensure a reliable filling and stable strength, in recent years the flow of processing soil

and cement-bentonite use has increased. However, there are no regulations yet on fillers injected into a pulling-out hole, and the influence by which the strength of the fillers gives it to the surrounding grounds is not also elucidated.

This study considers the influence by which a pulling-out hole of a pile foundation gives it to static characteristics of surrounding grounds by using three-dimensional static finite element analysis. The special qualities required for fillers injected into a pulling-out hole are also clarified in this study.

STUDY SUMMARY ABOUT THE STATIC BEHAVIOR OF THE PULLING-OUT HOLE AND THE ORIGINAL GROUND

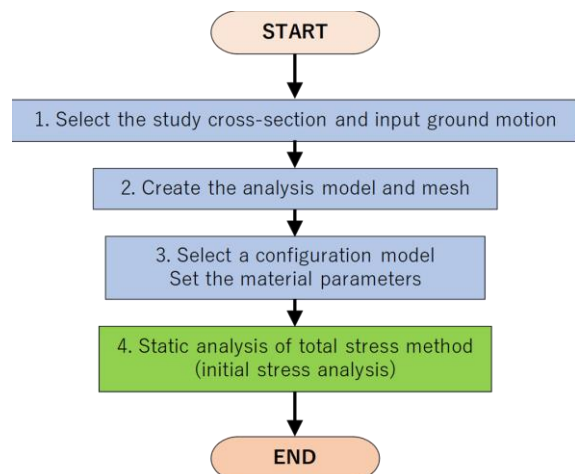
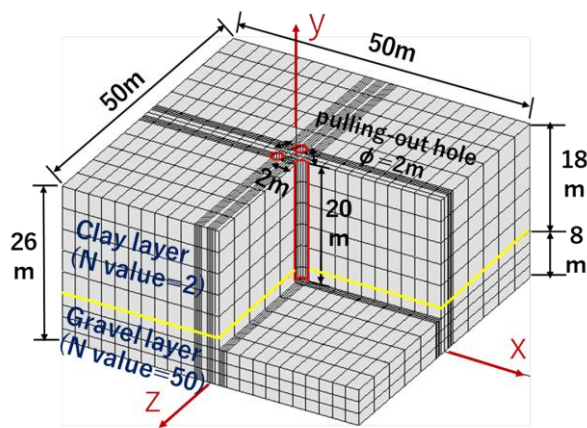
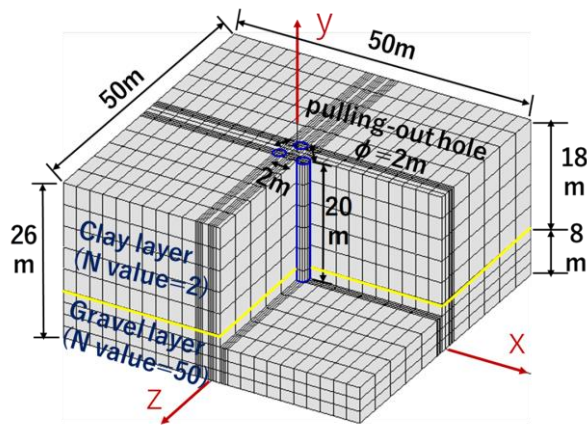


Fig. 1 Analysis procedure



(a) When the pulling-out holes are hollow



(b) When the pulling-out holes are injected the filler

Fig. 2 Sectional view and Analysis model

Describe the content of this study with (1) to (4) (see Fig. 1).

- (1) To select the study cross-section.
- (2) To create the analysis model, based on the selected cross-section in the 1. And the analysis area to mesh division.
- (3) To select an analysis constant. To set the application configuration model and material parameters in the initial stress analysis.
- (4) Perform the initial stress analysis. Analysis technique is a total stress analysis. In this study, elastic-plastic model for the ground material and hollow portion has been applied.

THE STATIC BEHAVIOR OF THE PULLING-OUT HOLE AND THE ORIGINAL GROUND, ANALYSIS MODEL

Analysis Model

Table 1 Element parameters

Material name	Clay layer	Gravel layer	filler
γ_t (kN/m ³)	14	19	15
Constitutive law	Elastic-plastic model		

Table 2 Ground parameters

Material name	Clay layer	Gravel layer
E (kN/m ²)	7900	140000
ν (-)	0.45	0.35
S_u (kN/m ³)	37.8	152.9
ϕ (°)	0	42.3

Table 3 Filler parameters

Filler	q_u (N/mm ²)	E (kN/m ²)	ν (-)	S_u (kN/m ³)	ϕ (°)
1	0.1	1.36×10^5	0.48	38.3	26.0
2	0.5	5.88×10^5	0.48	182.3	39.5
3	1.0	11.5×10^5	0.48	362.2	49.6

In the analysis, the analysis cross-section has a two-layer, upper layer part is clay layer as soft strata, which N value is about 2. And under layer part is gravel layer as strong formations serving as a support layer, which N value is about 50. The front and side width of the analysis cross section is set to 50m, the thickness of the clay layer is 18m, the thickness of the gravel layer is 8m, and the total depth of the cross section is 26m. About pulling-out holes, the number is three, pore diameter is 2m, depth is 20m, and embedment depth into the gravel layer is the 2m. For mesh division, improve the accuracy of analysis by finer mesh spacing near the pulling-out hole. Also, even when filled with pulling-out holes, it is finer mesh in order to examine the behavior of the filling portion of the pulling-out hole. As a boundary condition, the bottom is fixed fulcrum, and the lateral boundary is fixed in the vertical direction.

In the analysis, filler material is fluidization treated soil [2], [3]. The analysis cross-sectional view of the ground, analysis model and axial direction are shown in Fig. 2. In the figure, the portion surrounded by red frame is hollow portion and blue frame is filler portion. And a yellow line indicates a boundary between clay layer and gravel

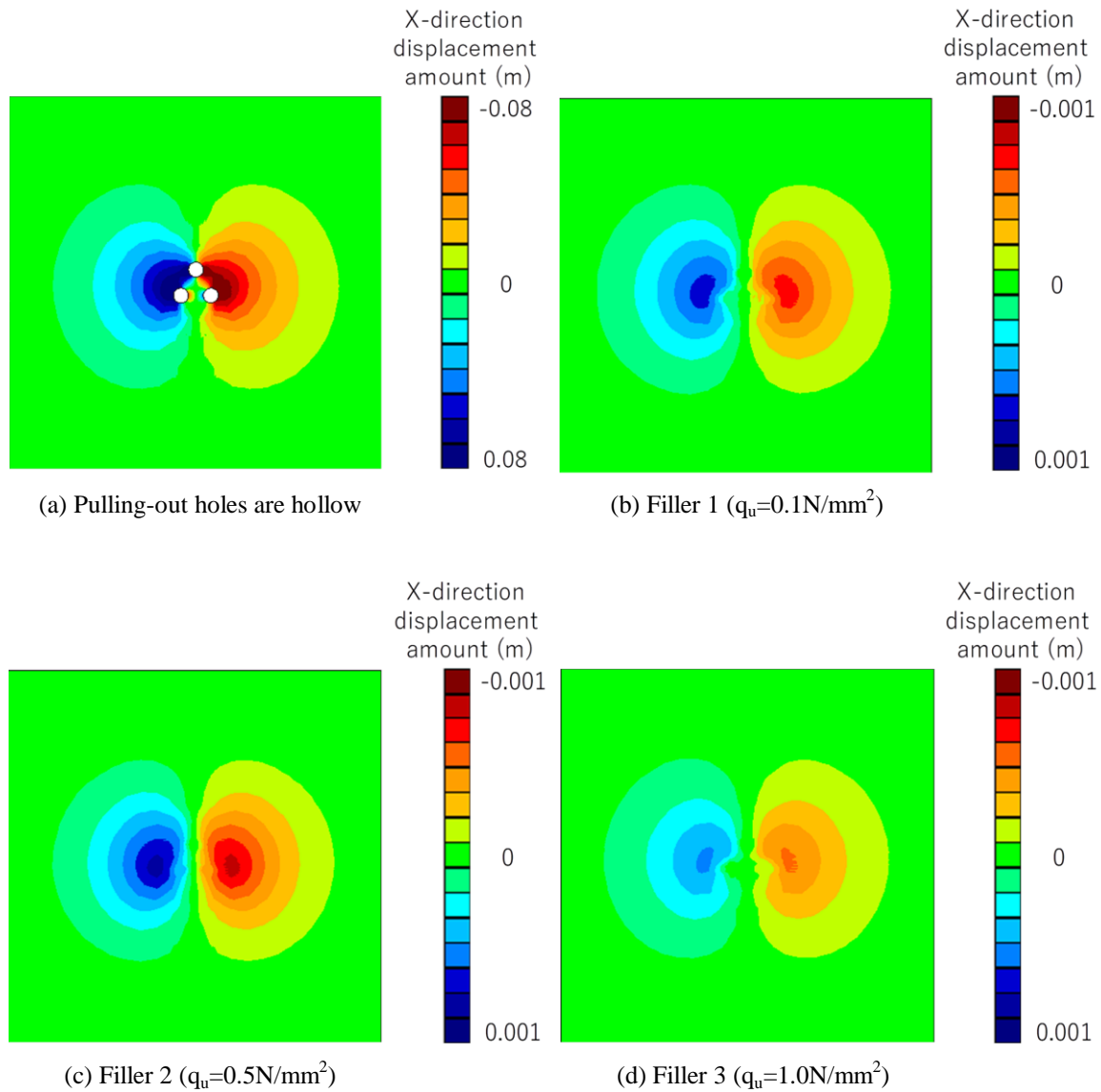


Fig. 3 X-direction displacement amount contour figure at ground surface

layer.

Constitutive Law and Material Parameters

Parameters in the clay layer and gravel layer used for the analysis and soil parameters in the pulling-out hole are shown in Tables 1 and 2. In this analysis, using a fluidizing processing soil that many of the experimental value. In addition, it analyzes in three fillers with different elastic modulus of the fluidizing process soil in order to examine the effect of filler strength has on the ground. From having a small strength, the filler 1, filler 2, filler 3. Parameters used in the analysis is to determine the anamnestic literature reference (see Table 3).

γ_t represents unit volume weight of the soil. E represents elastic coefficient. ν represents Poisson's

ratio. S_u represents shear strength. ϕ represents internal friction angle. q_u represents compressive strength.

ANALYSIS RESULTS AND STUDY ON THE DYNAMIC BEHAVIOR OF THE PULLING-OUT HOLE AND THE ORIGINAL GROUND

In this study, to compare the ground when injecting three types of filler on the ground when the pulling-out holes are hollow, in the static analysis. The results are shown in the following.

Results of the Analysis

Figures 3, 4 and 5 show the results about the

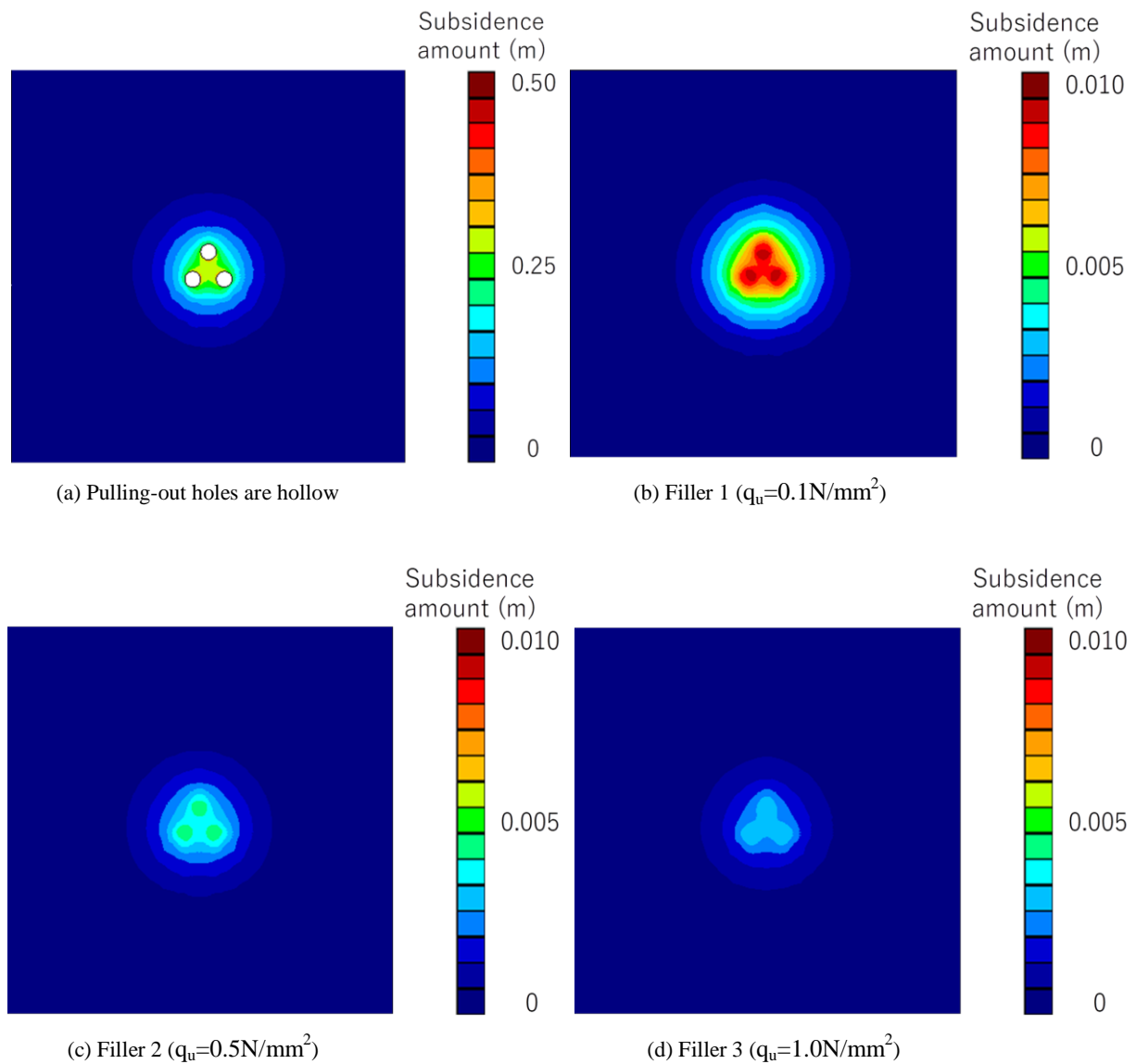


Fig. 4 Settlement amount contour figure at ground surface

effect of the pulling-out holes in the hollow and 3 types of fillers with different strength on the surrounding ground by this study. Figure 4 is the contour figure showing x-direction displacement amount on the ground surface when the pulling-out holes are hollow and when each filler with different strength is fixed. Figure 5 is the contour figure showing settlement amount on the ground surface in the same case as above. Figure 6 is the graph comparing settlement amount on the ground surface in the same case as above. These are premises that the filler is injected uniformly [4].

Study on the Results of the Analysis

From Fig. 3, the maximum x-direction displacement amount is 0.080m when the pulling-

out holes are hollow. In that case, it shows that surrounding ground is deforming to block the pulling-out holes. And the maximum x-direction displacement amount is 0.001m when the pulling-out holes are fixed with filler.

In that case, it shows that surrounding ground on the ground surface is deforming toward the center of the ground surface. It is because of the filler is resistant to deformation due to the filler is injected. So that, it can be said that x-direction displacement is reduced by injecting the filler into the pulling-out holes. And, x-direction displacement reduces as the strength of the filler.

From Figs. 4 and 5 the maximum settlement amount is about 0.30m in the part sandwiched by the pulling-out holes when the pulling-out holes are hollow. It is because that the stress concentrates

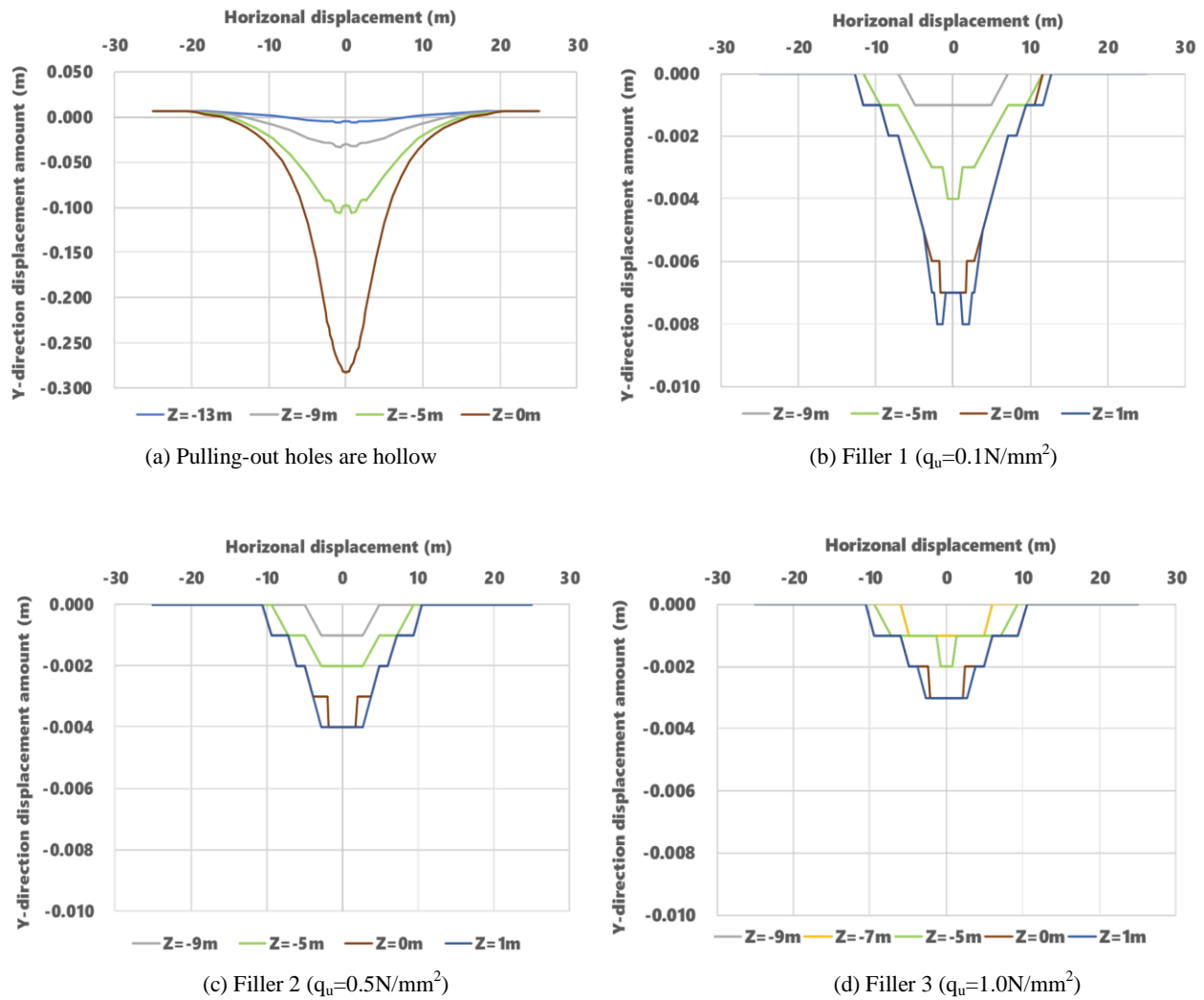


Fig. 5 Settlement amount graph at ground surface

around the pulling-out holes by excavation. The area of influence of settlement in x-direction is -15m to 15m and the ground surface rise in the outside that area. As downward stress acts by initial stress analysis, downward stress is released by excavation and upward stress acts, so it can be said to rise away from the area of influence of settlement. As above, it can be said that ground improvement is necessary because the settlement amount is large.

And the maximum settlement amount is 0.008m when the pulling-out holes are fixed with filler 1 ($q_u=0.1\text{N/mm}^2$). The area of influence of settlement in x-direction is -11m to 11m. And the maximum settlement amount is 0.004m with filler 2 ($q_u=0.5\text{N/mm}^2$). The area of influence of settlement in x-direction is -9.5m to 9.5m. And the maximum settlement amount is 0.003m with filler 3 ($q_u=1.0\text{N/mm}^2$). The area of influence of settlement in x-direction is -9.5m to 9.5m. In the case of injecting filler 1, 2 and 3, no settlement occurs

outside that area. When filler is injected, settlement amount is less than 0.008m, and settlement amount is greatly reduced as compared with when pulling-out holes are hollow. It is because that stress concentration on pulling-out holes can be prevented by injecting the filler. Therefore, it can be said that by filling the pulling-out holes, the settlement of ground is suppressed. And the area becomes smaller as the strength of the filler increases.

From Fig. 4, injecting filler 1 ($q_u=0.1\text{N/mm}^2$), the settlement amount is locally large in the filler part. It is because that the compressive stress acts greatly from the surrounding ground on the filler part due to the small filler strength. Comparing filler 2 ($q_u=0.5\text{N/mm}^2$) and filler 3 ($q_u=1.0\text{N/mm}^2$), the settlement amount has only 0.001m difference, and there is almost no difference in the area of influence of settlement.

The filler of strength 0.5N/mm^2 is defined as the same strength as the ground, which is prescribed in

the “Public building construction standard specification (Building work) [5]”, so it is adopted as standard compound, in recent years. Besides it there is no reason.

However, from the above, in this study’s analysis section, it is desirable to inject the filler of strength 0.5N/mm^2 to the pulling-out holes of existing piles in consideration of economics.

CONCLUSIONS

In this study, the influence of the pulling-out holes on surrounding ground was evaluated by three-dimensional static FEM analysis for development of pulling-out of existing piles.

When the pulling-out holes are hollow, the maximum settlement amount is about 0.30m in the part sandwiched by the pulling-out holes. But, when the pulling-out holes are fixed with filler that strength over 0.1N/mm^2 , the settlement amount is less than or equal to 8mm. And the area of influence of settlement becomes smaller when the filler injects into the pulling-out holes than when the pulling-out holes are hollow. Therefore, it becomes clear that injecting the filler is an effective means to suppress ground settlement.

In this study’s analysis section, the settlement amount is locally large in the filler part when the filler 1 ($q_u=0.1\text{N/mm}^2$) injects. And, it is possible to prevent local settlement when the filler 2 ($q_u=0.5\text{N/mm}^2$) and 3 ($q_u=1.0\text{N/mm}^2$) inject. Comparing filler 2 ($q_u=0.5\text{N/mm}^2$) and filler 3 ($q_u=1.0\text{N/mm}^2$), the settlement amount has almost no difference, and there is almost no difference in

the area of influence of settlement. Therefore, it is desirable to inject the filler of strength 0.5N/mm^2 to the pulling-out holes of existing piles in consideration of economics.

As this study’s future work is that it is necessary to examine the influence of this analysis compared with this analysis result when changing ground parameters, arrangement number of the pulling-out holes, compounding materials for filler. And, identify the strength of filler generally required.

REFERENCES

- [1] Takao M., Leaving the foundation pile, backfilling denied the defects of ground support force of the part, agent of accountability violation was also negative case, RETIO, No.82, pp.166-167, 2011.
- [2] Yasushi F., Futa N., Yasushi U., Keisuke T., Study on the Young's modulus of the fluidized processing soil. Summaries of technical papers of annual meeting Architectural Institute of Japan, pp.591-592, 2014.
- [3] Yasushi F., Deformation properties of the backfill material which has a fluidity and self-hardening, Town Value-up Management report, No.37, pp.41-44, 2011.
- [4] Marushin Co., Ltd., About the pulling out method of the existing pile, Retrieved April 21, 2018, from <http://marushinn.jp/handbook/>
- [5] Ministry of Land, Infrastructure, Transport and Tourism, Public Building Construction Standard Specification (Building Work) 2013 Edition, MLIT, 2016.

POSSIBILITY OF NEUTRAL-BASED SOLIDIFYING MATERIALS FOR PREVENTING ELUTION OF RADIOACTIVE SUBSTANCES FROM RESERVOIRS

Hirpyuki Hashida¹, Shinya Inazumi²
¹ Sumice Kenzai Co. Ltd., Japan
² Shibaura Institute of Technology, Japan

ABSTRACT

The radioactive substances diffused with the occurrence of the 2011 Fukushima I Nuclear Power Plant accident is still deposited in the sediment of the reservoir. In this research, based on the dynamics of radioactive substances in soil by previous research, focusing on solidification of the reservoir sediment, the authors examined the applicability of neutral-based solidifying materials to be used at that time. In particular, the authors compare the difference between cement-based solidifying material and two types of neutral-based solidifying materials and discuss whether it is desirable to use any solidifying material in solidification of the reservoir sediment from the environmental impact after the improvement. In addition, the authors conducted a test on the characteristics required when using neutral-based solidifying materials.

Keywords: Cone index, Neutral-based solidifying materials, pH, Radioactive substances, Reservoir

INTRODUCTION

Radioactive substances released into the atmosphere due to the accident of Tokyo Electric Power Company Fukushima I Nuclear Power Plant generated by Tohoku Pacific Ocean Earthquake in 2011 was deposited on the ground surface over a wide range. Regarding the radioactive substances released by the accident, there are four substances which are the main problems in terms of health and environmental influences, iodine, cesium 134, cesium 137 and strontium. Various other substances have been released, but it is known that both have short half-lives or small radioactivity as compared with these 4 types [1]. For example, although iodine has a short half-life of 8 days, when entering the body 10 to 30% accumulate in the thyroid gland. Then, the thyroid gland receives exposure to beta rays and gamma rays for a while. In case of Fukushima I Nuclear Power Plant accident contamination, there are two types of radioactive cesium, cesium 134 and cesium 137. Cesium 137 has a long half-life of 30 years, and environmental pollution lasts for a long time. Because radioactive cesium is similar in chemical nature to potassium, when entering the body, it is distributed almost entirely like potassium. Because strontium has a long half-life and chemical properties resemble calcium, it accumulates in bone when entering the body. Also, because strontium does not emit gamma rays, it cannot exactly find out where cesium 134 and 137 easily is. In case of an accident of Fukushima I Nuclear Power Plant, it is thought that strontium generated by fission is also present though it is less in quantity than cesium 134 and 137. Plutonium and others derived from the Fukushima I

Nuclear Power Plant accident have also been detected, but quantitatively it is comparable to the measurements observed nationwide before the accident occurred.

In order to evaluate the influence on the environment by released radioactive substances, investigations on accumulation and transfer of radioactive substances in forests and farmlands occupying a large area immediately after the accident have been carried out continuously [2], [3]. At the same time, empirical studies on the actual condition of contamination by radioactive substances and decontamination have been conducted, and many findings have been obtained while being compared with the research at the Chernobyl nuclear accident [4].

The decontamination stipulated in Japan has priority over decontamination of agricultural land, but there is a possibility that agricultural land will be re-contaminated with radioactive substances via agricultural water supplied from reservoir. However, decontamination of reservoir has been postponed. This is because contaminated soil in reservoir was not regarded as a decontamination waste by Pollution Deal Special Measures Law for radioactive substances, and the accepting facility was not decided for a long time. In addition, the concentration of dissolved cesium in the environmental water such as groundwater, river water, reservoir and the like at normal times was almost within the standard, so urgency was not observed in decontamination of reservoir [5]. However, the policy was changed in FY 2014, and the Ministry of the Environment and the Ministry of Agriculture, Forestry and Fisheries announced to implement countermeasure on

radioactive substances at reservoir [6]. The flow of countermeasures against radioactive substances at reservoir are shown in Fig. 1. Regarding reservoir for agriculture, even though it is not a reservoir (see Fig. 2) meeting the criteria of decontamination conducted by the Ministry of the Environment based on Pollution Deal Special Measures Law for radioactive substances, measures must be taken from the viewpoint of resuming farming and reconstruction of agriculture under the technical support of the Ministry of Agriculture, Forestry and Fisheries, prefectural and municipalities were able to take countermeasure projects with the Fukushima Revitalization Acceleration Grant [7].

The decontamination method of reservoir is selected according to the purpose and various conditions by the Technical Measures Manual for radioactive substances at reservoir prescribed by the Ministry of Agriculture, Forestry and Fisheries [8]. Conventionally, many methods of removing sediment contaminated with radioactive substances have been adopted, but there is a limit to carrying out the removed contaminated sediment and storing it in a prescribed storage facility. Therefore, in recent years the necessity to take measures by solidification of the sediment according to reservoir scale and pollution situation is increasing. Therefore, it can be expected that the number of construction projects by solidification of the sediment will increase. In the decontamination method by solidification of the sediment, a ground improvement material is used to harden the sediment contaminated with radioactive substances. Generally, there are many construction examples where cement-based solidifying material is used. Previous studies have shown that it is possible to prevent outflow of radioactive substances by using cement-based solidifying material [9]. However, the sediment improved with cement-based solidifying material shows a strong alkalinity with pH 11-12. For this reason, alkaline components are eluted from the sediment of the surface, and there is a problem that the water quality of reservoir exhibits alkaline properties. It is also demonstrated that radioactive substances tend to be eluted more easily as soil is in the acidic region [10].

This study considers that it is effective to keep the pH concentration of the target soil in the neutral zone when confining the radioactive substances of the reservoir sediment and focuses on the neutral-based solidifying materials which does not change pH of soil. Furthermore, using the neutral-based solidifying materials, the authors verify the possibility of preventing outflow of radioactive substances from reservoir by solidifying reservoir sediment.

CHARACTERISTICS OF NEUTRAL-BASED SOLIDIFYING MATERIALS

Hemihydrate gypsum or magnesium oxide is

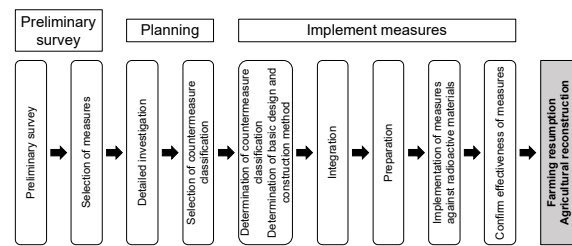


Fig. 1 Flow of radioactive material countermeasure for reservoirs

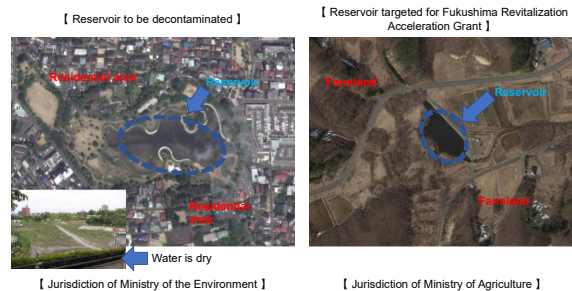


Fig. 2 Classification of jurisdiction over reservoirs

often used as the main ingredient of the material called current neutral-based solidifying materials [11] and solidification is carried out without changing the pH of the target soil. Consequently, the concern of changing the pH of the target soil by the cement-based solidifying material or the lime-based solidifying material to alkaline and adversely affecting the surrounding environment can be solved by using neutral-based solidifying materials. However, the strength characteristics of the treated soil using the neutral-based solidifying materials are inferior to the case of using cement-based or lime-based solidifying material in terms of strength development [12]. Therefore, if neutral-based solidifying materials are required to have a certain strength, it is one of the tasks that additive amount is much larger than cement-based and lime-based types. In addition, it has been shown in the previous study [13] that cement-based solidifying material can prevent elution of radioactive cesium, but the possibility of neutral-based solidifying materials has not been completed yet.

In this research, the authors focus on the characteristics of neutral-based solidifying materials and evaluate the possibility of preventing radioactive substances outflow by solidifying sediment of reservoir contaminated with radioactive substances using neutral-based solidifying materials.

The neutral-based solidifying materials used in this study is a paper sludge based solidifying material

and a gypsum-based solidifying material. The properties of each material are shown below.

Paper sludge-based solidifying material:

- (1) Because no cement is used, there is no worry of hexavalent chromium elution.
- (2) The soils with high water content such as dredging of reservoir can be improved.
- (3) Immediately after mixing, it can be quickly improved by agglomerating without exotherm.
- (4) It is an inorganic powder which can contain odor and harmful substances and shows a neutral zone when the reaction is completed.
- (5) Lead contamination soil can suppress elution by mixing Paper sludge-based solidifying material.
- (6) Improved soil is excellent in permeability and water retention, rich in fusion with existing soil, promotes vegetation.
- (7) Improved soil does not re-elute / resuspend even on returning to the surface of the soil, the ocean floor or the lake bottom.

Gypsum-based solidifying material:

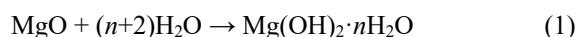
- (1) Because the solidification is fast, the solidification process of the soils with high water content can be continued and the treatment cost can be reduced
- (2) Simultaneous solidification and granulation, moderate to soil suitable for recycling by giving treated soil water permeability and water retention appropriate.
- (3) Because the neutral-based solidifying materials does not change the pH of the soils with high water content by solidification, treated soil is reformed into soil suitable for vegetation without hindering the vegetation held by the soils with high water content.
- (4) Because treated soil has no fish toxicity, it does not harm the ecosystem in water.

Mechanism of Solidification

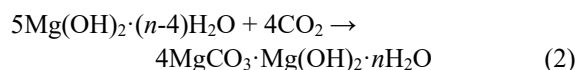
Neutral-based solidifying materials rapidly absorbs moisture and promotes agglomeration when mixed and stirred with high water content sludge and soils with high water content. As a result, it is possible to convert soils with high water content such as construction sludge and dredged sludge into high quality soil which is excellent in water permeability and not soils with high water content, and to give strength to the soil by rolling.

Paper sludge-based solidifying material uses silica powder having a large crystal surface area and high water absorption / adsorption performance as the main raw material. Silica powder refers to powders

from which hazardous substances have been removed by processing paper sludge ash from paper mills. Ettringite (acicular crystals) are formed by reaction with natural minerals in the auxiliary additives, and heavy metals and the like can be confined and insolubilized. In addition, magnesium oxide which is a component of paper sludge-based solidifying material hydrates with water in soil and produces magnesium hydroxide hydrate.

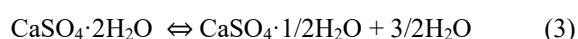


The produced magnesium hydroxide hydrate reacts with phosphoric acid in soil and carbon dioxide gas in the atmosphere to become magnesium phosphate or basic magnesium carbonate, which increases the solidification strength.



Therefore, it is considered that paper sludge-based solidifying material can suppress the change to alkalinity by the buffering action of magnesium.

The gypsum-based solidifying material is a product obtained by pulverizing raw material dihydrate gypsum ($\text{CaSO}_4 \cdot 2\text{H}_2\text{O}$) and calcining it into hemihydrate gypsum ($\text{CaSO}_4 \cdot 1/2\text{H}_2\text{O}$). The calcined hemihydrate gypsum mixes and stirs with water, so that it becomes hydrated gypsum again by hydration reaction within a short time, and the target soil can be solidified by curing at that time.



In addition, gypsum-based solidifying material does not change the influence on the surrounding environment compared to cement-based solidifying material and so on. because the solidification material itself is neutral and the solidification reaction is completed in the neutral state. Also, because the calorific value during reaction is small, there is no fear of ignition or burn due to heat generation.

While gypsum-based solidifying material has such advantages, natural gypsum is hardly produced in Japan, so when producing gypsum-based solidifying material, it is generally preferable to use by-product chemical gypsum (flue gas desulfurization gypsum, phosphate gypsum, hydrofluoric acid gypsum and so on) is used as a raw material. However, major chemical gypsum contains fluorine compounds, so there is concern that treated

soils constructed from solidifying materials made from them will create new Brownfield land. Therefore, the authors must think about countermeasures in the problem of fluoride elution in gypsum-based solidifying material. Fluorine elutes unless fluoride insolubilizer ($\text{CaHPO}_4 \cdot 2\text{H}_2\text{O}$) is added to gypsum containing fluorine. In order to solve this problem, manufacturers of gypsum-based solidifying materials have developed high-performance fluorinated insolubilizers and have taken all possible measures to reduce fluoride elution of gypsum-based solidifying materials. Therefore, it can be safely used against environmental standards for contaminated soils. As shown in Fig. 3, the insolubilizer added as a measure for preventing fluoride elution can be reduced to fluoroapatite by chemical reaction and the elution of fluorine in treated soil can be reduced to less than the reference value. In addition, the insolubilizer to be added is a calcium phosphate salt ($\text{Ca}_{10}(\text{PO}_4)_6\text{F}_2$) whose main component also exists in vivo, it is a safe substance and the mechanism of its insolubilization is clear.

Difference from General Solidifying Materials

The origin of the technical term “solidifying material” is cement-based solidifying material and lime-based solidifying material produced for ground improvement. Therefore, it is not a technical term born from the idea of hardening soil in the neutral zone. Most neutral-based solidifying materials express aggregation effect as solidification. Therefore, it is inferior to cement-based solidifying materials and the like in strength development and economy for ensuring trafficability of soft soil and for building up to the foundation soil, so cases used from special site situations. However, as above mentioned, the neutral-based solidifying materials have superior characteristics with respect to decontamination of reservoir compared to cement-based solidifying material and the like. In addition to these characteristics, in this research, the authors conducted a test to quantitatively understand the solidification properties and pH characteristics of neutral-based solidifying materials.

EXPERIMENTAL EVALUATION OF POSSIBILITY ON NEUTRAL-BASED SOLIDIFYING MATERIALS

The test objects are two types of neutral-based solidifying materials: paper sludge-based solidifying material and gypsum-based solidifying material. The component composition of paper sludge-based solidifying material and gypsum-based solidifying

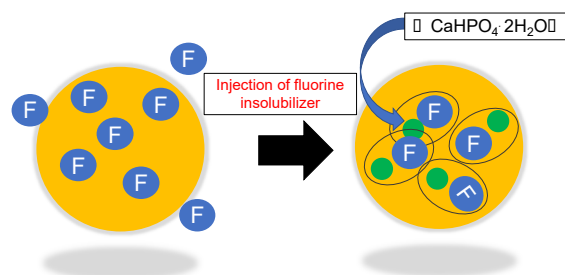


Fig. 3 Measures to prevent dissolution of fluorine

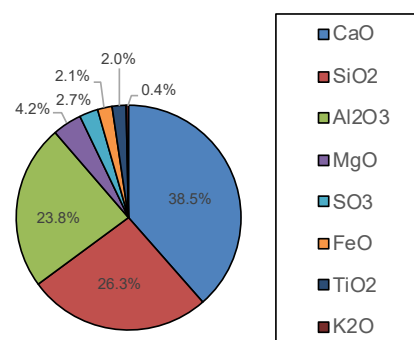


Fig. 4 Composition of paper sludge-based solidifying material

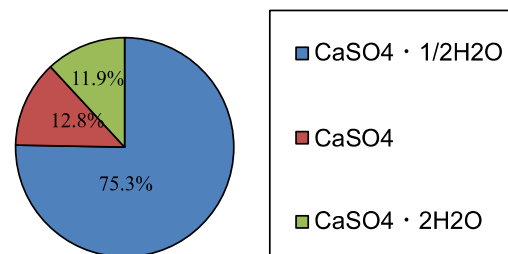


Fig. 5 Composition of gypsum-based solidifying material

Table 1 Properties of target soil

Target soil	Funabashi-silt
Water content (%)	58.2
Wet density (g/cm ³)	1.462
Dry density (g/cm ³)	0.924

material is shown in Figs. 4 and 5. In addition, quicklime and cement-based solidifying material are also used for comparison in the pH test.

For the test, conduct the cone index test of the soil and the pH test of the soil suspension. Each test method is shown below.

Test Methods

Cone index test

The cone index is the penetration resistance when pushing the cone penetrometer into the soil. Under the background of the “Law for the Promotion of the Use of Renewable Resources” which came into effect in October 1990, it is required to classify and use the construction soil according to the particle size and strength characteristics, and cone index is an index for this classification. Table 1 shows the amount of soil used for the cone index test. Same soil was used for the target soil of the specimen used for the pH test. The target soil used for the specimen is a Funabashi-silt having a unit volume weight of 1.6 kN/m^3 and a water content of 58.2%. In the cone index test, a comparison was made to the paper sludge-based solidifying material and gypsum-based solidifying material according to “Cone Index Test Method of Compacted Soil (JIS A 1288)”. Added amount of paper sludge-based solidifying material and gypsum-based solidifying material was 15% of the weight ratio of each specimen. Four specimens with different curing time (1, 3, 24 and 48 hours) were prepared, penetration resistance of each penetration amount (5.0, 7.5 and 10.0 cm) was read from the scale, The average penetration resistance was calculated and divided by the value of the cone bottom area value 3.24 cm^2 to determine the cone index of each.

pH test

Quicklime and cement-based solidifying material were also used. The target soil is Funabashi-silt used at the cone index test. 165 g of the target soil, 7% of the weight ratio of the specimen was added as the neutral-based solidifying materials and 200 kg/m^3 of the quick lime and the cement-based solidifying material were added, respectively. Because the authors assumed reservoir in this study, pH concentration of each specimen was immersed in water with a pH meter at each elapsed time (1, 3, 24, 48 hours).

Results and Discussions

Cone index test

The results of the cone index test are shown in Fig. 6. In the cone index test, the cone index did not change until 24 hours passed since the initial strength was developed, and the strength increased at the lapse of 48 hours. Therefore, although it is a short time until the initial strength is developed, it is necessary to

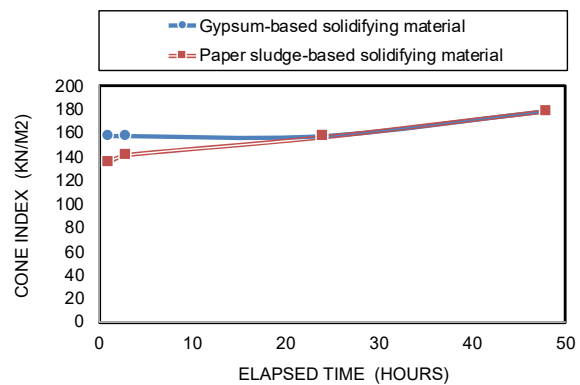


Fig. 6 Results of cone index test

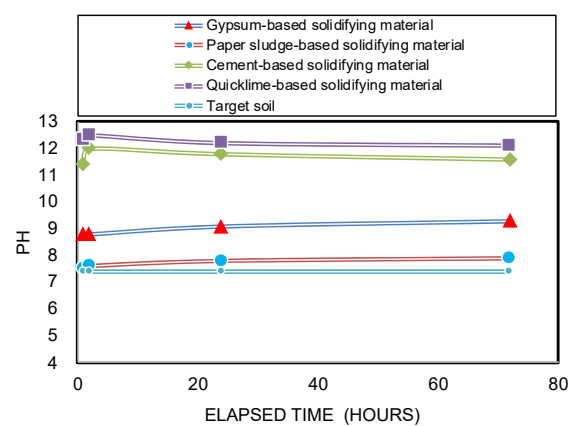


Fig. 7 Results of pH test

have 48 hours or more before the final reaction is completed. Also, in this test result, the authors could not obtain sufficient cone index as improved soil. Furthermore, with the use of neutral-based solidifying materials, it is difficult to carry out with standard specification dump trucks and to secure traffic-ability for heavy machinery to move on after improvement. In order to develop strength only with a neutral-based solidifying material, it is necessary to further increase the amount to be added or to compact after mixing and stirring.

When the target soil is the same, the strength property of the treated soil using any neutral-based solidifying materials are significantly inferior in the ultimate strength development when compared with the case of using the cementitious or lime-based solidifying material. It is clarified in the previous study [14]. Therefore, when neutral-based solidifying materials are required to have a certain strength, the addition amount of neutral-based solidifying materials are considered to be much larger than that of cement and lime type.

In view of this result, the neutral-based solidifying

materials are “a modifying agent with a large cohesive effect to be used when the treated soil itself must be neutral”, and “cement / lime type is a general variety solidification material that takes into account the increase in the ground tolerance of the ground so as to be used in the treatment plant”.

pH test

The results of the pH test are shown in Fig. 7. In the pH test, the pH value did not change substantially even after all of the four types of solidifying material were measured after 1 hour and after 72 hours. In addition, comparing pH of two types of neutral-based solidifying materials, paper sludge-based solidifying material showed higher pH value than gypsum-based solidifying material. This is thought to be the result of alkalization due to the alkaline nature of the silica powder which is the raw material of paper sludge-based solidifying material. In gypsum-based solidifying material, the authors did not change the pH of treated soil after solidification. This can be inferred that the treated soil after the reaction also maintains the neutral region, because the main constituent and the product after the reaction show neutral. In addition, cement-based solidifying material and quicklime made it possible to confirm that the quality of the treated soil and the added water was changed to alkaline (pH 11 to 12).

Here the authors reconsider how soil bases that affect the pH value are present in the soil. In a very fine part of soil, clay mineral and hazardous substances combine to form a clay / humus complex. Usually this state is called soil colloid. As shown in Fig. 8, this soil colloid has a minus (-) charge on its surface and adsorbs cations such as calcium, magnesium, potassium and the like having positive (+) charge. Among the cations adsorbed and retained by this soil colloid and easily replacing other cations, those other than hydrogen ion are called exchangeable bases. Because exchangeable bases are most easily absorbed and used in agricultural crops, it is generally recognized that soil, which contains a large number of exchangeable bases in agriculture, is fertile. The hazardous substances mentioned above are those in which most of the organic substances entering soil as animal and vegetable bodies such as fallen leaves and falling branches are decomposed into water and carbon dioxide by the action of soil microorganisms and are collectively referred to as a part of remaining polymer compounds. Because soil of this study assumes reservoir sediment, it is considered to exist in such soil state. In most soil

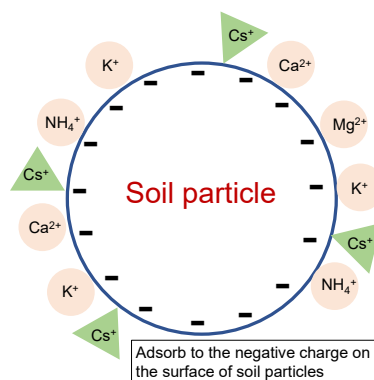


Fig. 8 Cations adsorbed to the soil particles

environments, some of the acidic functional groups contained in the humus manifest negative charges by dissociating hydrogen ions, so humus can be an adsorbent of radioactive cesium.

Next, the relationship between exchangeable base and soil pH will be described. Soil has one showing acidity, one showing neutrality and one showing alkalinity. pH is used to express soil's reaction, that is, the degree of acidity or alkalinity, as a numerical value. The pH is called the hydrogen ion exponent and is defined as $pH = -\log[H^+]$, where $[H^+]$ is the relationship of H^+ concentration in aqueous solution. The pH value in soil is one of important properties, and the chemical form and solubility of the soil component change depending on the pH condition of soil. In Japan with high rainfall, soil showing acidity is widely distributed. The reason why soil is acidic is the exchangeable aluminum ions and exchangeable hydrogen ions adsorbed and retained in acidic substances (nitric acid, sulfuric acid, carbonic acid, acetic acid) and soil colloids dissolved in soil. When the minus charge of soil colloid is saturated with exchangeable base, it is neutral state but base is leached by external factor and hydrogen ion is adsorbed to soil colloid instead of base to become acidic soil. It is known that radioactive substances already adsorbed on soil colloids are likely to be eluted as cations in such acidic soil [15].

In addition, as described above, the radioactive cesium once adsorbed on the sedimentation is mainly caught in the gap between the fine crystal structure of the tributary and the one bonded by the matching by the electrostatic force with the soil. It is thought that there is something missing [16].

The radioactive cesium being attracted to the soil by electrostatic force may release the radioactive cesium instead of attracting the chemical if it is exposed to chemicals with stronger force (ion

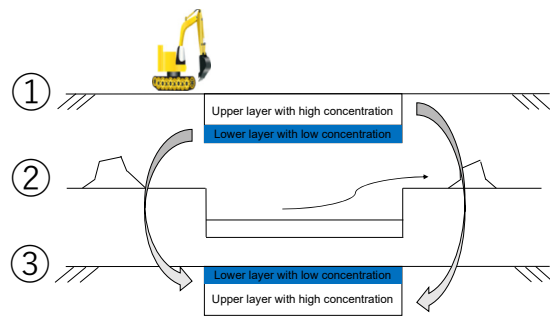


Fig. 9 Image of sediment reversal method

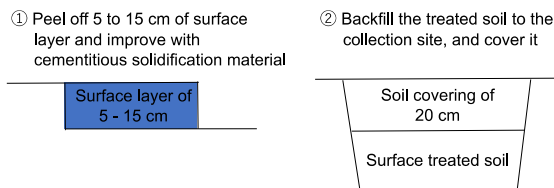


Fig. 10 Image of integrated reversal method

exchange). However, because there are almost no chemicals existing closer to us than cesium (those with a larger ionic radius than cesium), there is a possibility that cesium once adsorbed on the sediment is re-eluted by ion exchange.

CONCLUSIONS

Environmental pollution caused by radioactive cesium is a serious problem, and decontamination in reservoir is also essential. Because radioactive cesium has high water solubility, it releases a wide range of soil pollution through the atmosphere / hydrosphere circulation when released into the environment. For this reason, as a next step of the emergency decontamination which has been carried out until recently, it is an urgent matter to establish a technology that stably confines the radioactive cesium extracted and concentrated from the contaminated topsoil and prevent re-diffusion into the environment. In this research, the authors investigate the possibility of countermeasures against decontamination using neutral-based solidifying materials and summarize the findings of the neutral-based solidifying materials obtained below.

- (1) The two types of neutral-based solidifying materials used in this study could not satisfy cone index 200 kN/m^2 for discharge as construction generated soil. Likewise, no strength development was observed to ensure traffic-ability to withstand construction heavy machinery. In addition,

although two types of neutral-based solidifying materials used in this study can be completed in a short time until the initial strength is developed, it is necessary to have 48 hours or more before the final reaction ends. It could be confirmed. Therefore, in order to develop strength only with neutral-based solidifying materials, it is necessary to further increase the amount added or to consider mixing the cement as a reinforcing material.

- (2) It was confirmed that the gypsum-based solidifying material used in this study maintains the neutral region without changing the pH of the specimen. On the other hand, in paper sludge-based solidifying material, alkaline products are generated during solidification reaction, so pH is weakly alkaline. Further, in the pH test, it was confirmed that the pH value did not substantially change even when measurement was carried out after 72 hours from measurement of all four after 1 hour.

- (3) Because neutral-based solidifying materials expresses the cohesive effect as solidification, it does not necessarily have excellent strength characteristics. That is, neutral-based solidifying materials are a modifying agent having a large cohesive effect to be used when the treated soil itself must be neutral. In addition, the cement / lime system is a solidifying material considering an increase in the ground tolerance of the ground, as it is used in various general processing workers.

Responding to countermeasures on radioactive substances at reservoir, the countermeasure construction method is decided by comprehensively judging construction feasibility, effectiveness, economy and so on according to site conditions. In the actual construction practice, sediment removal is adopted, and there are very few cases where solidification of sediment is selected as a construction method. However, implementing the method shown in Figs. 9 and 10 and taking countermeasures, there is a possibility that countermeasures to contain radiation substances by sediment solidification are also possible. If the authors can prove that the neutral-based solidifying materials satisfy the cone index, it will be possible to pay attention to the water environment of reservoir, so as a development of countermeasures against decontamination of reservoir, the construction method using neutral-based solidifying materials also has size and degree. It is necessary to use properly.

REFERENCES

- [1] Ministry of the Environment,
https://www.env.go.jp/chemi/rhm/kisoshiryo/pdf_h28/2016qa1s01.pdf, refered in June 1, 2018.
- [2] Forestry Agency,
<http://www.rinya.maff.go.jp/j/kaihatu/jittaihaaku/pdf/280325.pdf>, refered in June 1, 2018.
- [3] Ministry of Agriculture, Forestry and Fisheries,
<http://www.maff.go.jp/j/nousin/seko/josen/pdf/tyousa.pdf>, refered in June 1, 2018.
- [4] Imanaka T., <http://www.rri.kyoto-u.ac.jp/NSRG/etc/Kagaku2016-3.pdf>, KAGAKU, Vol.86 No.3, 2016.
- [5] Ministry of Agriculture, Forestry and Fisheries,
http://www.maff.go.jp/j/kanbo/joho/saigai/pdf/ameike_tyousa25.pdf, refered in June 1, 2018.
- [6] Ministry of Agriculture, Forestry and Fisheries,
<http://www.maff.go.jp/j/kanbo/joho/saigai/pdf/tyukan.pdf>, refered in June 1, 2018.
- [7] Fukushima Prefecture,
http://www.maff.go.jp/j/kanbo/joho/saigai/pdf/ameike_tyousa26.pdf, refered in June 1, 2018.
- [8] Ministry of Agriculture, Forestry and Fisheries,
http://www.maff.go.jp/j/nousin/saigai/pdf/tamemanu_zentai_2.pdf, refered in June 1, 2018.
- [9] Kawata N., Shibano K., Endo O, Tsubaki M.,
Runoff control of radioactive material from irrigation pond by solidification of contaminated sediments, *Water, Land and Environmental Enginneerinnng*, Vol.81, No.1, pp.49-52, 2016.
- [10] Gunma Prefecture,
<http://www.pref.gunma.jp/06/f0900088.html>, refered in June 1, 2018.
- [11] Sato K., Oshikata T., Takeshita T.,
https://www.jstage.jst.go.jp/article/jsmcwm/21/0/21_0_98/_pdf/-char/ja, refered in June 1, 2018.
- [12] Okumura M., Nakamura H., Machida M.,
Recent advances of numerical simulation studies for radioactive cesium adsorption on soil materials, *RIST News*, No.55, pp.24-33, 2013.
- [13] Rosen K., Oborn I., Lonsjo H., Migration of radiocaesium in Swedish soil profiles after the Chernobyl accident, 1987-1995, *Journal of Environmental Radioactivity*, Vol.46, Issue 1, pp.45–66, 1999.
- [14] Nishimura T., Migration of radioactive Cs in soil, *Journal of Jpanese Society of Soil Physics*, No.126, pp.37-43, 2014.
- [15] Japanese Geotechnnical Society,
<https://www.env.go.jp/jishin/rmp/conf/15/mat02-2.pdf>, refered in June 1, 2018.
- [16] Koyama H., Hirai K., Ikeda S., Sakurai, N., Nagakawa Y., Okazawa T., Hideo S., Hironari T.,
Radioactive waste sintered with CRT glass, *Bulletin of Tokyo Metropolitan Industrial Technology Research Institute*, No.8, pp.154-155, 2013.

LEAKAGE RISK ASSESSMENT ON SIDE IMPERVIOUS WALLS AT COASTAL LANDFILL SITES

Ken-ichi Shishido¹ and Shinya Inazumi²

¹ Tomec Corporation, Japan;

² Shibaura Institute of Technology, Japan

ABSTRACT

An evaluation method that can express the local leakage of leachate from joint sections in steel pipe sheet pile (SPSP) cutoff walls is discussed, in this study. In particular, the evaluation of environmental feasibility (containment of leachates containing toxic substances) considering a three-dimensional arrangement and hydraulic conductivity distribution of the joint sections in the SPSP cutoff wall is compared with an evaluation that generally uses the equivalent hydraulic conductivity. This equivalent hydraulic conductivity assumes that the joint section and the steel pipe are integrated; therefore, the hydraulic conductivity is substituted with a uniform permeable layer. However, in an evaluation that employs the equivalent hydraulic conductivity, it is difficult to consider the local leakage of leachate containing toxic substances from the joint sections in the SPSP cutoff wall. This paper concluded that evaluations of the environmental feasibilities of the SPSP cutoff walls with joint sections must take into account the local leakage of leachates containing toxic substances from the joint section.

Keywords: Coastal Landfill, Hydraulic conductivity, Impervious wall, Leakage, Toxic substance

INTRODUCTION

Landfill sites are facilities where the final residue is disposed after all possible recycling energy has been recovered from it. Therefore, landfill sites are an important part of civil infrastructure, required for environmental conservation without dumping waste in residential areas. However, in many cases, the construction of landfill sites has been opposed due to concerns of residents living in the vicinity regarding environment safety with regard to situations such as “the leachate from waste may leak out”; hence, the construction of new landfill sites has become more difficult. Moreover, the construction cost of landfill sites has also significantly increased simultaneously due to tighter environmental legislation [1], [2].

In Japan, small-scale inland landfill sites were often constructed in the river-head areas of mountain valleys. With regard to the abovementioned social concerns regarding the landfill sites, the locations of landfills have recently been diversified into coastal areas on a large scale. These sites are developed at urban harbour areas in order to reduce the risk of contaminating the groundwater, which can be caused by the leakage of leachate, and conserve the water resources [3]. In the national statistics of 2003 announced at Ministry of the Environment, the capacity of coastal landfill sites was 23.3% of that of all landfill sites, and particularly in metropolitan areas, it was greater than 80%. These statistics indicate that the role of coastal landfill sites has been increasing steadily. However, the residents living in the vicinity of these sites continue to express the same concerns for environment safety. Therefore, ensuring stable

and systematic operation of the coastal landfill sites in the future and prolonging the life of coastal landfill sites constructed until now are important matters of concern, particularly in metropolitan areas.

A revetment at a coastal landfill site ensures space for waste disposal and harbour maintenance during the disposal of waste, construction sludge, dredged soil etc. A revetment at a coastal landfill site must function as a vertical (side) cutoff barrier that prevents the leakage of leachate containing toxic substances from the landfill waste, into the sea; furthermore revetments must protect the coastal landfill site from various external forces such as earthquakes, ocean waves, high tides and tsunamis [4].

Recently, steel pipe sheet piles (SPSPs), using which the deep-water construction is possible [5], have been widely employed in vertical cutoff barriers at coastal landfill sites due to their workability and economic efficiency. A vertical cutoff barrier employing SPSPs is called a “SPSP cutoff wall” in this study. However, the design and application of SPSP cutoff walls, evaluation of environmental feasibility, construction technology and long-term maintenance are very complicated both experimentally and analytically [6]. This is because of the existence of joint sections in the SPSPs, as shown in Fig. 1.

The appropriately estimation of the hydraulic performance of SPSPs with joint sections (shown in Fig. 1) is an important issue, particularly in the evaluation of environmental feasibility, that is, the containment of leachates containing toxic substances. Figure 2 shows the characterization of the environmental feasibility of vertical and bottom

cutoff barriers as well as the overall landfill site. When evaluating the hydraulic performance of an SPSP cutoff wall, an equivalent hydraulic conductivity is generally obtained [4]. This equivalent hydraulic conductivity assumes that the joint section and the steel pipe are integrated; therefore, the hydraulic conductivity is substituted with a uniform permeable layer (see Fig. 3). However, in an evaluation that employs the equivalent hydraulic conductivity, it is difficult to consider the local leakage of leachate containing toxic substances from the joint sections in the SPSP cutoff wall.

In this study, an evaluation method that can express the local leakage of leachate from the joint sections in the SPSP cutoff walls is discussed. In particular, the evaluation of the environmental feasibility (containment of leachates containing toxic substances) considering a three-dimensional arrangement and hydraulic conductivity distribution of the joint sections in the SPSP cutoff wall is compared with an evaluation that uses the equivalent hydraulic conductivity.

ANALYSIS FOR ENVIRONMENTAL FEASIBILITY

Overview

The development of methods for the detection of the generation points of leachate leakage has been conducted in various different ways at inland and coastal landfill sites in order to determine when the leachate containing toxic substances will leak into the surrounding areas after the land has been reclaimed at the landfill site [7], [8]. However, the present detection methods are insufficient with regard to their durability, and the use of these methods may lead to excess cost and time for repairing the generation points of leachate leakage in the vertical and bottom cutoff barriers at the landfill sites. Therefore, an effective implementation and verification of the seepage and advection/dispersion analysis, considered as a two-dimensional or a three-dimensional problem, of the leaching behavior of leachate containing toxic substances are necessary along with the upgradation of the technique used to repair vertical and bottom cutoff barriers. The structure of vertical and bottom cutoff barriers that can ensure long-term stability as well as the evaluation method for the environmental feasibility of landfill sites must be also discussed.

The leaching behavior of leachates containing toxic substances near the vertical and bottom cutoff barriers at landfill sites must be considered with regard to not only infiltration but also the advection and dispersion phenomena [2]. Therefore, these phenomena must be accurately reproduced in the implementation of the seepage and advection/dispersion analysis. In this study, the

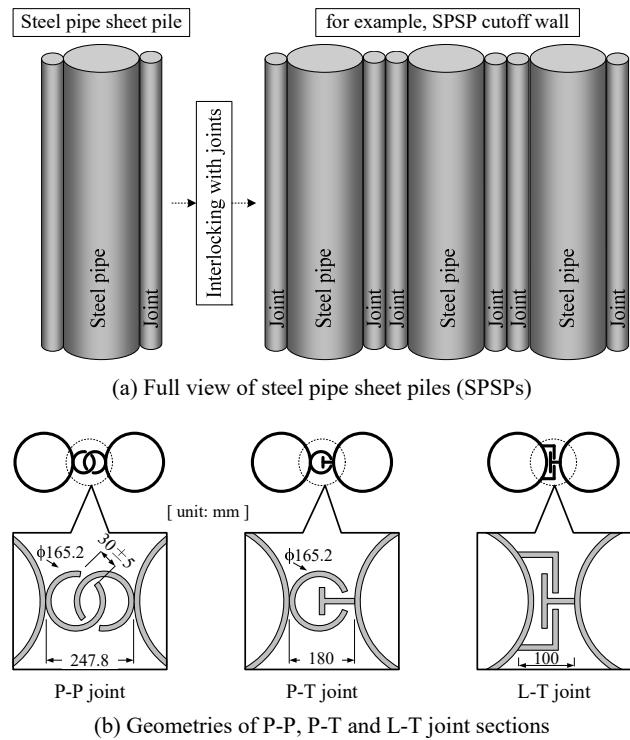


Fig. 1 Schematic diagram of steel pipe sheet piles with joint sections

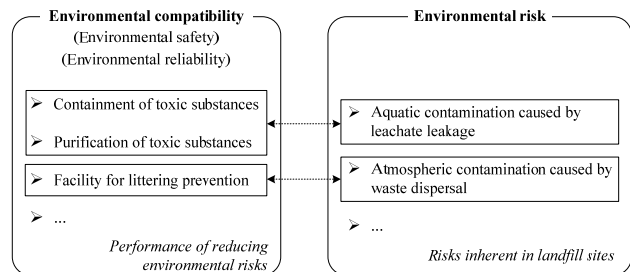


Fig. 2 Characterization of environmental feasibility on vertical and bottom cutoff barriers as well as overall landfill site

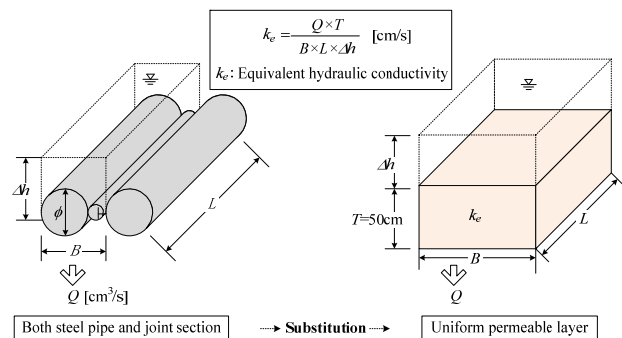


Fig. 3 Concept of equivalent hydraulic conductivity assuming that joint section and steel pipe are integrated

infiltration, advection and dispersion phenomena must be expressed three-dimensionally in order to account for the joint sections in the SPSP cutoff walls. Also, the analysis of coastal landfill sites, unlike that for inland landfill sites, must consider the effect of tides, etc. Furthermore, each vertical and bottom cutoff barrier is a composite structure consisting of synthetic fiber, steel, rubble and the seabed; this composite structure must be reproduced accurately.

The Eulerian-Lagrangian finite-element method is a numerical calculation method that is known to be useful in efficiently reproducing such complicated phenomena. In this study, the seepage and advection/dispersion analysis is performed using Dtransu-3D/EL, which is used as a representative analysis code9).

Objective and Assessment Index

In an SPSP cutoff wall, joint sections are arranged between steel pipes, forming a three-dimensional structure (see Fig. 1). Therefore, it is necessary to accurately reproduce the local leakage of leachates from the joint sections for the evaluation of the environmental feasibility of the SPSP cutoff wall. In this study, the leachate-containment effect of the SPSP cutoff wall is evaluated by using a three-dimensional seepage and advection/dispersion analysis (Dtransu-3D/EL). This analysis reproduces the existence of joint sections more precisely.

Figure 4 shows the three-dimensional cross-section of a landfill site assumed as a basic case in this analysis. The SPSP cutoff wall as well as a part of the composition layer around it in the coastal landfill site is considered for setting the three-dimensional cross-section. At the bottom of the waste layer as well as in the sea bed, a clay deposit layer is assumed to exist, and this layer fulfils the role as a bottom cutoff barrier in the coastal landfill site. The SPSP cutoff wall is penetrated upto a depth of 3 m in the clay deposit layer, and the hydraulic conductivity of the SPSP cutoff wall is varied to provide different examination cases.

In the construction of the SPSP cutoff wall at coastal landfill sites, double SPSP cutoff walls may be used due to ensure mechanical stability and fail-safe concept of landfill sites, as shown in the overview in Fig. 5. Furthermore, the clay deposit layer may be improved by sand compaction pile (SCP) methods in order to enhance the mechanical stability of the SPSP cutoff walls [4]. However, the main objective of this study is the evaluation of the environmental feasibility (containment effect of leachate containing toxic substances) of the SPSP cutoff wall. Therefore, the coastal landfill site is simplified, as shown in Fig. 4, as a three-dimensional cross-section that comprises a single SPSP cutoff wall, waste layer and clay deposit layer. The three-dimensional cross-section assumes the extreme

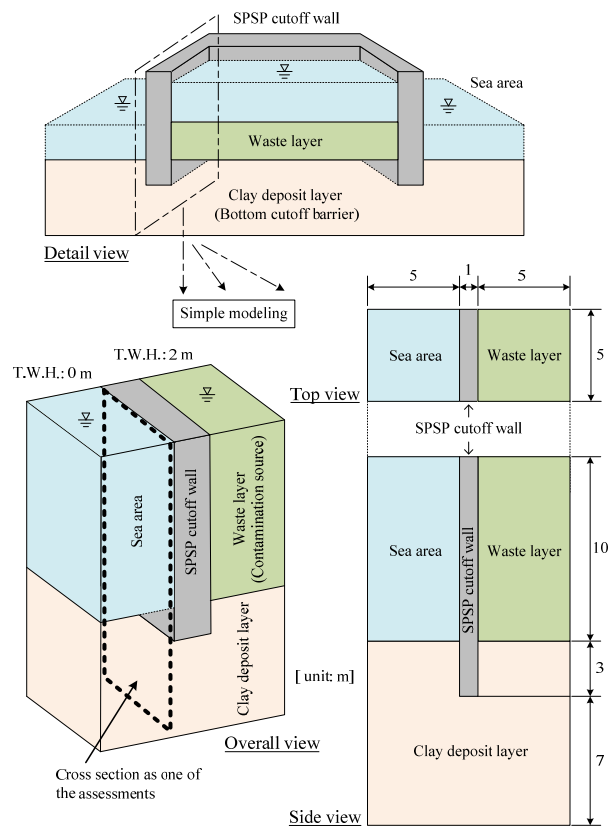


Fig. 4 Three-dimensional cross section of landfill site assumed as a basic case in the analysis

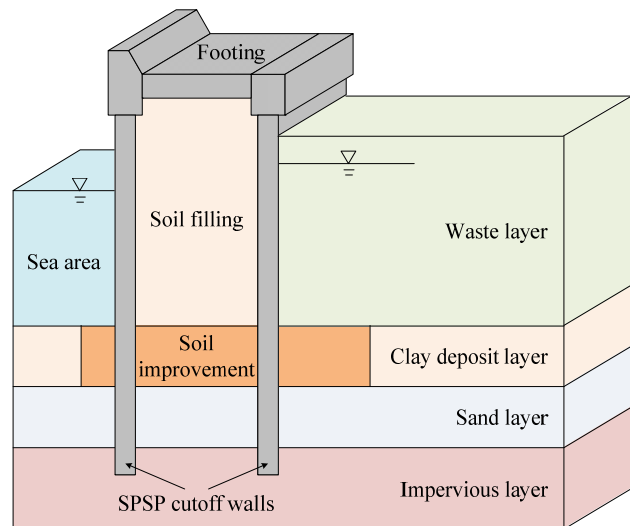


Fig. 5 Overview of vertical and bottom cutoff barriers generally constructing at coastal landfill sites

conditions for the vertical and bottom cutoff barriers that would pose environmental pollution risks to the surroundings affected by coastal landfill sites.

In coastal landfill sites, the difference in the water

Table 1 Seepage, advection and dispersion properties assigned to each composition layer in the analysis

			SPSP cutoff wall			Clay deposit layer	Waste layer	Sea area
			UL-model	SP/JS-model				
				Joint sec.	Steel pipe			
Horizontal hydraulic conductivity	k_H	cm/s	2.0×10 ⁻⁶ ,	2.5×10 ⁻⁶ ,	infinitesimal	7.0×10 ⁻⁷	1.0×10 ⁻⁰	1.0×10 ⁻⁰
			1.0×10 ⁻⁶ ,	1.3×10 ⁻⁶ ,				
			1.0×10 ⁻⁷ ,	1.3×10 ⁻⁷ ,				
			1.0×10 ⁻⁸	1.3×10 ⁻⁸				
Vertical hydraulic conductivity	k_V	cm/s	2.0×10 ⁻⁶ ,	2.5×10 ⁻⁶ ,	infinitesimal	5.0×10 ⁻⁷	1.0×10 ⁻⁰	1.0×10 ⁻⁰
			1.0×10 ⁻⁶ ,	1.3×10 ⁻⁶ ,				
			1.0×10 ⁻⁷ ,	1.3×10 ⁻⁷ ,				
			1.0×10 ⁻⁸	1.3×10 ⁻⁸				
Effective porosity	θ		0.1	0.1	0.1	0.65	1	1
Longitudinal dispersion	α_L	cm	10	10	infinitesimal	10	10	10
Transverse dispersion	α_T	cm	0.1	0.1	infinitesimal	1	1	1
Molecule diffusion coefficient	D_m	cm ² /s	1.0×10 ⁻⁵	1.0×10 ⁻⁵	infinitesimal	1.0×10 ⁻⁵	1.0×10 ⁻⁵	1.0×10 ⁻⁵
Retardation factor	R_d		1	1	1	2	1	1

level between the inside and outside landfill site is controlled on a daily basis so that it may not exceed 2 m [4]. On the other hand, in the three-dimensional cross-section shown in Fig. 4, a controlled water level regulated to 2 m is reproduced by the boundary conditions, that is, a fixed total head of 0 and 2 m are assigned to the upper sides of the sea area and waste layer, respectively. The boundary edges in the three-dimensional cross-section of the coastal landfill site are assumed to be undrained. The seepage, advection and dispersion properties assigned to each composition layer in this analysis are shown at Table 1. These values shown in Table 1 are typical one for heavy metals and composition layers [4], [6].

Presently, in Japan, waste discharge waste is burnt once at a refuse incinerator plant, and the incinerated residue generated from the incinerator plant is mainly used to reclaim land at landfill sites [4]. Therefore, the type of waste dumped in the recently constructed landfill sites has changed from the conventional organic substances to inorganic substances; thus, the heavy metals which may be contained in the incinerated residue are among the major environmental pollutants. If the leachate leakage occurs at a landfill site into the surrounding areas, the heavy metals also may leak out together with the leachate due to the advection-dispersion phenomenon, as heavy metals are soluble in water. Therefore, this study assumes heavy metals as toxic substances that may leak out from coastal landfill sites. This analysis

assumes the waste layer to be a contamination source, and the concentration of toxic substances (heavy metals) at the waste layer is assigned the value of 1 as the initial condition. The initial concentration of toxic substances is initialized to 0 in regions outside the waste layer.

As an environmental conservation standard for coastal landfill sites, the environmental standard values (see Table 2 (b) and (c)) for water quality and bottom sediment of the sea areas near landfill sites equal 0.1 times that of the acceptable standard values (see Table 2(a)) for waste disposed at landfill sites. Therefore, the concentration of toxic substances at the SPSP cutoff wall on the sea side (that is the cross-section delimited by the broken line at Fig. 4) is targeted in this analysis as an important index of the environmental feasibility of SPSP cutoff walls. In this analysis, the elapsed time during which the concentration of toxic substances reaches 0.1 on the sea side of the SPSP cutoff wall is estimated; when this occurs, the SPSP cutoff wall as well as the coastal landfill site is defined as having lost its environmental feasibility.

SP/JS-Model Considering Local Water Leakage

In the evaluation of the environmental feasibility (containment effect of leachate containing toxic substances) of SPSP cutoff walls at coastal landfill sites, the equivalent hydraulic conductivity is

generally used [4]. This method involves calculating the hydraulic conductivity of an SPSP cutoff wall equivalent to a uniform permeable layer of thickness 50 cm (see Fig. 3) by considering the steel pipes and joint sections that constitute the SPSP cutoff wall as a single body. Because the equivalent hydraulic conductivity can be directly verified with the technical standards for vertical and bottom cutoff barriers at landfill sites, it is frequently used in the technical development of the SPSP cutoff wall. However, the value equivalent hydraulic conductivity is the average hydraulic conductivity of the joint sections, which have high permeability, and that of the steel pipe sections, which are impermeable. Therefore, an evaluation using the equivalent hydraulic conductivity cannot easily detect the position or the time of leachate leakage, thus making it difficult to estimate the environmental impact of local leakage from the joint sections of the SPSP cutoff wall. Where, development of these detections will contribute strongly for the optimization of maintenance and management in SPSP cutoff wall.

In this study, an evaluation method that can express the local leakage at the joint sections of SPSP cutoff walls is discussed. The evaluation method using the equivalent hydraulic conductivity is defined as the “UL-model”, and the evaluation method that considers the steel pipe and joint sections, that is, the local leachate leakage, is defined as the “SP-JS-model”. Figure 6 shows a general description of the UL-model and SP/JS-model. In the UL-model (shown in Fig. 6(a)), equivalent hydraulic conductivities of 2.0×10^{-6} , 1.0×10^{-6} , 1.0×10^{-7} and 1.0×10^{-8} cm/s were assigned to the entire SPSP cutoff wall. In the SP/JS-model (see Fig. 6(b)), the joint sections were placed at 0.25-m intervals for steel pipes of diameter 1 m, which represents the standard sizes of the SPSP shown in Fig. 1. Furthermore, hydraulic conductivities were assigned to each steel pipe and joint section in the SP/JS-model such that the entire hydraulic conductivity of the SPSP cutoff wall equals the equivalent hydraulic conductivity assigned in the UL-model, that is, hydraulic conductivities of 2.5×10^{-6} , 1.3×10^{-6} , 1.3×10^{-7} and 1.3×10^{-8} cm/s were assigned to the joint sections, assuming that the hydraulic conductivity of steel pipe is infinitely small. Table 1 shows the seepage, advection and dispersion properties assigned to each composition layer in both the models.

ENVIRONMENTAL FEASIBILITY OF SPSP CUTOFF WALL CONSIDERING LOCAL WATER LEAKAGE

Figure 7 shows the concentration flux (the material quantity passing through a unit area in unit time) of toxic substances leaking from the SPSP cutoff wall on the sea side. The fluxes in the uniform layer of the UL-model and in each steel pipe and joint

Table 2 Environmental conservation standards associated with inland and coastal landfill sites

(a) For industrial waste reclaimed in landfill sites

Type of metals	Allowable limit
Cadmium and its compounds	0.1 mg/L or less
Lead and its compounds	0.1 mg/L or less
Hexavalent chromium compounds	0.5 mg/L or less
Mercury and its compounds	0.005 mg/L or less

(b) For water pollution of groundwater

Type of metals	Allowable limit
Cadmium its compounds	0.01 mg/L or less
Lead and its compounds	0.01 mg/L or less
Hexavalent chromium compounds	0.05 mg/L or less
Mercury and its compounds	0.0005 mg/L or less

(c) For soil contamination

Type of metals	Allowable limit
Cadmium its compounds	0.01 mg/L or less
Lead and its compounds	0.01 mg/L or less
Hexavalent chromium compounds	0.05 mg/L or less
Mercury and its compounds	0.0005 mg/L or less

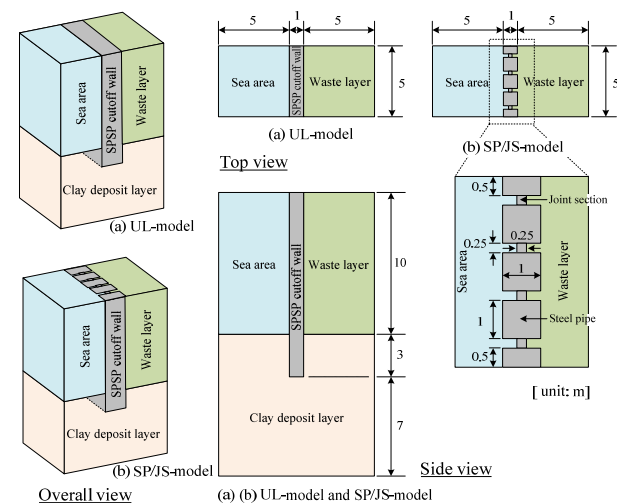


Fig. 6 General description of UL-model and SP/JS-model in the analysis

section of the SP/JS-model are plotted in Fig. 7. The relationship between the elapsed time and the highest concentration of toxic substances leaked from the SPSP cutoff wall on the sea side for both the models is shown in Fig. 8. Figure 9 illustrates the distribution of the concentration of toxic substances leaking out from the waste layer, which is the contaminated source, for both the models. Figure 9 expresses the

distribution of the concentration on the sea side of the SPSP cutoff wall in order to facilitate the comparison of both the models with regard to the leakage of the toxic substance to the surroundings of the coastal landfill site.

In the SP/JS-model, the concentration flux of toxic substances leaked onto the sea side of the SPSP cutoff wall, particularly from the joint sections, is increased as compared to that of the UL-model (see Fig. 7). The SP/JS-model can quantitatively express the concentration of toxic substances at the joint sections of the SPSP cutoff wall, where the hydraulic conductivity is higher than that in the steel pipe. In the UL-model, as shown in Fig. 9, the leachate leaks uniformly from the SPSP cutoff wall onto the sea side, and this leakage tends to uniformly increase with time. In the SP/JS-model, it being different from the UL-model, the leachate leaks locally from the joint sections onto the sea side of the SPSP cutoff wall, and this leakage increases locally with time at the joint sections (see Fig. 9). Consequently, the increase in the concentration of toxic substances leaked from the SPSP cutoff wall onto the sea side is found to occur earlier in the SP/JS-model than in the UL-model, as shown in Fig. 8.

For example, 70 and 110 years, respectively, are required in the SP/JS-model (the hydraulic conductivity of the entire SPSP cutoff wall is 1.0×10^{-8} cm/s) and the UL-model (the hydraulic conductivity of the entire SPSP cutoff wall is 1.0×10^{-8} cm/s) for the concentration of toxic substances in the SPSP cutoff wall on the sea side to reach $C=0.1$, which is assumed as the assessment index. In the other analyzed conditions under which the hydraulic conductivity of the entire SPSP cutoff wall is equivalent in both models, the leakage of leachate is confirmed to occur earlier in the SP/JS-model than in the UL-model due to effect of the local leakage of leachate (see Fig. 10). This tendency becomes more remarkable with increase in the hydraulic conductivity of the entire SPSP cutoff wall (see Fig. 11).

Thus, as mentioned above, the reproduction of the local leakage of leachate generated at the joint sections of SPSP cutoff walls is possible by using the SP/JS-model for the evaluation of the environmental feasibility of SPSP cutoff walls at coastal landfill sites. Furthermore, the SP/JS-model indicates that toxic substances in concentrations exceeding the environmental standard values are leaked out of coastal landfill sites earlier than that estimated using the UL-model (see Fig. 8). Using the UL-model, the local leakage of leachate containing toxic substances from the SPSP cutoff wall cannot be reproduced, although the total quantity of the toxic substances leaked from the SPSP cutoff wall can be estimated. This provides a safer-side estimate of the environmental feasibility from the viewpoint of the time taken for the leakage of toxic substances. In

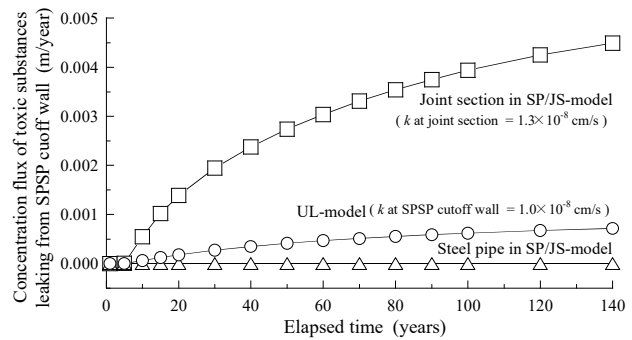


Fig. 7 Concentration flux of toxic substances leaking from SPSP cutoff wall on sea side with elapsed time for both models

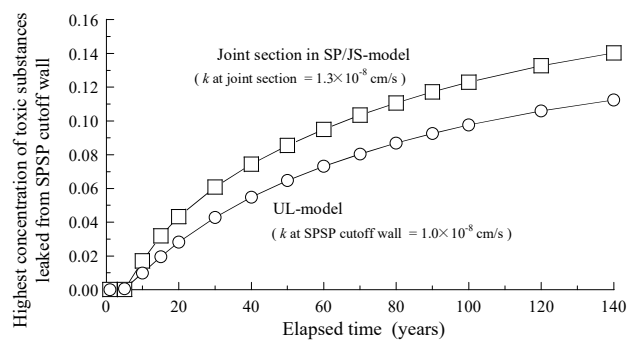


Fig. 8 Relationship between elapsed time and the highest concentration of toxic substances leaked from SPSP cutoff wall on sea side for both models

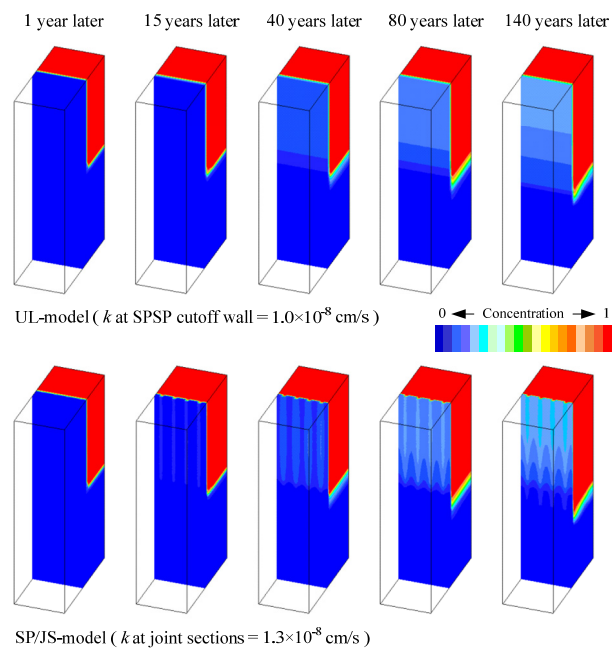


Fig. 9 Distribution of concentration of toxic substances leaking out from waste layer for both models

addition, by using the UL-model, it is difficult to quantitatively detect the generation position in the SPSP cutoff wall where the leachate containing toxic substances are leaked. An appropriate estimation in terms of both position and time at which the loss of environmental feasibility occurs is important in order to control and maintain a long-term SPSP cutoff wall at coastal landfill sites. Based on the abovementioned points, the environmental feasibility of SPSP cutoff walls must be verified by using the SP/JS-model.

CONCLUSIONS

An evaluation method that can express the local leakage of leachate from joint sections in steel pipe sheet pile (SPSP) cutoff walls is discussed, in this study. In particular, the evaluation of environmental feasibility (containment of leachates containing toxic substances) considering a three-dimensional arrangement and hydraulic conductivity distribution of the joint sections in the SPSP cutoff wall is compared with an evaluation that generally uses the equivalent hydraulic conductivity.

Evaluations of the environmental feasibilities of the SPSP cutoff walls with joint sections that have a higher hydraulic conductivity than that of the steel pipe must take into account the local leakage of leachates containing toxic substances from the joint section; this was possible using the SP/JS-model. Due to the local leakage into the surroundings of coastal landfills from joint sections, contamination in excess of the environmental standard values was confirmed to occur earlier than that predicted by the UL-model, which is the current standard evaluation method.

In the current concept employed for the containment of leachates at coastal landfill sites, the hydraulic performance, that is, the containment of toxic substances, at the bottom cutoff barrier must be improved to the same level as that of the SPSP cutoff wall, the vertical cutoff barrier. This is because, as shown in Case-IV, the leakage of leachates tends to occur at lower reaches of the SPSP cutoff wall, occurring via the clay deposit layer, which is one of the bottom cutoff barriers, even if SPSP cutoff wall with greater hydraulic performance are applied. Also, even if the vertical and bottom cutoff barriers achieve perfect hydraulic performance, perfectly preventing leakage of toxic substances, the toxic substances will semipermanently remain at the coastal landfill sites. Thus, the containment of toxic substances at coastal landfill sites requires that the long-term maintenance and management of the vertical and bottom cutoff barriers is performed more strictly. In addition, this will add to the cost and complexity of the redevelopment of coastal landfill sites. Finally, the authors propose that increasing the treatment of landfill waste is required to guarantee the performance of vertical and bottom cutoff barriers as well as to prevent the leakage of landfill waste.

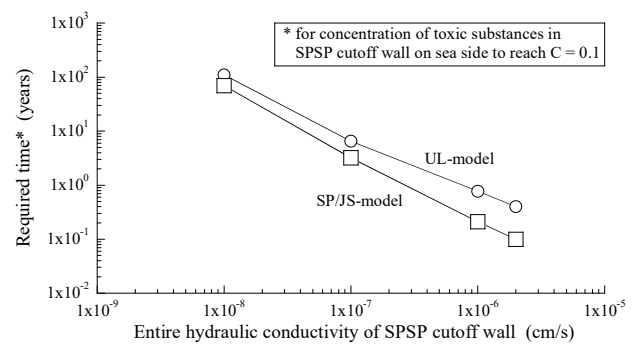


Fig. 10 Required time for concentration of toxic substances in SPSP cutoff wall on sea side to reach $C=0.1$ with entire hydraulic conductivity of SPSP cutoff wall

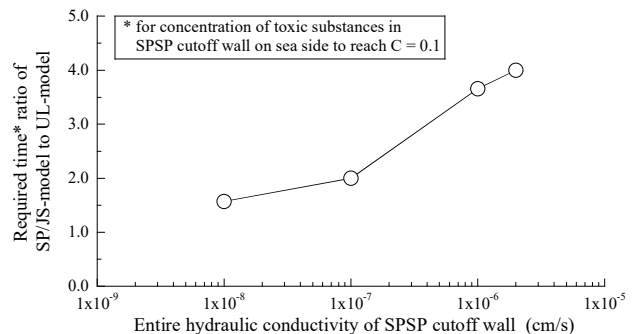


Fig. 11 Required time ratio of both models, for concentration of toxic substances in SPSP cutoff wall on sea side to reach $C=0.1$, with entire hydraulic conductivity of SPSP cutoff wall

REFERENCES

- [1] Shimizu, K. (2003): The latest geotechnical problems in waste landfill (in Japanese), Tsuchi-to-Kiso, Japanese Geotechnical Society, 51/58, 1-4.
- [2] Kamon, M, Inui, T, Katsumi, T. and Torisaki, M. (2007): Risk control in the redevelopment of closed landfill sites from geotechnical viewpoint, Proceedings. of the 7th Japanese-Korean-French Seminar on Geo-Environmental Engineering, 19-24.
- [3] Kamon, M and Inui, T. (2002): Geotechnical problems and solutions of controlled waste disposal sites (in Japanese), JSCE Journal of Geotechnical Engineering 701/III-58, 1-15.
- [4] Waterfront Vitalization and Environment Research Center (2002): Design, Construction and Management Manual for Managed Type Waste Reclamation (in Japanese), Waterfront Vitalization and Environment Research Center.
- [5] Japanese Association for Steel Pipe Piles (1999): Steel Pipe Sheet Pile Foundations -Design and

- Construction- (in Japanese), Japanese Association for Steel Pipe Piles.
- [6] Kamon, M., Katsumi, T., Endo, K., Itoh, K. and Doi, A. (2001): Evaluation of the performance of coastal waste landfill with sheet pile containment system (in Japanese), Proceedings of the 5th Japan National Symposium on Environmental Geotechnology, 279-284.
- [7] Kamon, M. and Jang, Y.S. (2001): Solution scenarios of geo-environmental problems, Proceedings of the 11th Asian Regional Conference on Soil Mechanics and Geotechnical Engineering, 833-852.
- [8] The Landfill System & Technologies Research Association of Japan (2004): Landfills in Japan (Rivised Edition) (in Japanese), The Journal of Waste Management.
- [9] Nishigaki, M. Hishiya, T., Hashimoto, N. and Kohno, I. (1995): The numerical method for saturated-unsaturated fluid density dependent groundwater flow with mass transport (in Japanese), JSCE Journal of Geotechnical Engineering, 501/III-30, 135-144.

DEVELOPMENT OF METAL-INSOLUBILIZING MATERIAL ON SOIL CONTAMINATED WITH HEAVY METALS USING CHEMICAL AND MINERAL ANALYSIS

Shinya Inazumi¹, Ken-ichi Shishido² and Hiroyuki Hashida³

¹ Shibaura Institute of Technology, Japan

² Tomec Corporation, Japan

³ Sumice Kenzai Co. Ltd., Japan

ABSTRACT

Heavy metal ions, one kind of harmful substance, may exist in the soil irrelevant to artificial development, and soil contamination due to soil and rock containing these naturally derived heavy metals has recently become apparent. Thus, in an amendment that came into effect in 2010 of Japan, the scope of countermeasures and regulations for contaminated soil was amended to “contaminated soil derived from artificial development” and “naturally derived contaminated soil”. When naturally derived contaminated soil is encountered during the carrying out of construction work, countermeasures against this type of soil contamination are necessary. In this research, new metal-insolubilizing materials are developed in order to improve the insolubilization treatment which is one method for treating contaminated soil. Specifically, tests are conducted to clarify the insolubilization effect on heavy metals, and the insolubilization mechanism is chemically and mineralogically discussed.

Keywords: Insolubilization treatment, Insolubilization mechanism, Metal-insolubilizing material, Leaching test, Contaminated soil

INTRODUCTION

In recent years, soil contamination caused by naturally occurring heavy metals in the soil has become a problem. One solution is to restore this contaminated soil and put it to practical use. Based on the Soil Contamination Countermeasures Act (Act No. 53 of 2002), Ministry of the Environment, Government of Japan (MOE 2002), the restoration of contaminated soil involves satisfying the environmental quality standards for the amounts leached in soil and content in soil. The most reliable method for restoring contaminated soil is to purify it by soil washing. Purification is a very attractive and highly effective method for dealing with contaminated soil. However, it is not very practical because it is economically inefficient and can be applied only under limited conditions, such as when the clay component of the soil is extremely low (Arao et al. 2010). At present, there are few efficient and economical methods for removing heavy metals, namely, inorganic pollutants, from soil. As with excavation removal, it is common for contaminated soil to be brought to a treatment facility and processed. However, there is a limit to the amount of contaminated soil that can be accepted at existing disposal sites, and establishing new disposal sites is difficult due to the opposition of neighboring residents and the strengthening of regulations. In view of the recent circumstances, it has become

necessary to avoid treatment by landfilling with contaminated soil, to appropriately treat the target soil right at the excavation site, and to create technologies for recycling this soil as earth and sand. Thus, researching new methods for removing harmful substances from soil at a low cost is important.

The focus is now being placed on an insolubilization treatment which can improve contaminated soil while satisfying these conditions. Insolubilization treatment means that when inorganic contaminants, such as heavy metals, are contained in the soil and contaminate it, they are chemically insolubilized by mixing in safe and harmless metal-insolubilizing materials; this eliminates the risks of toxicity. Insolubilization treatment is more economical than other treatments, it does not require the contaminated soil to be transported away from the site, the risk of contamination diffusion at the time of movement is low, and it has advantages such as low energy consumption. In addition, metal-insolubilizing materials which contain an inorganic mineral as the main raw material cause less of an environmental burden than cementitious material. However, with conventional inorganic mineral-based metal-insolubilizing materials, the insolubilization effect is exerted only for certain heavy metals. In some cases, it is not possible to insolubilize plural heavy metals. In addition, considering the environment in which

treated soil is placed, it is important for the pH level to be kept constant over the long term in order to exert the insolubilization of harmful substances over the long term.

In this study, upgrade of metal-insolubilizing materials are proposed that can improve the instability of the insolubilization effect due to the type of heavy metal, which is one of the problems of conventional metal-insolubilizing materials. Specifically, the aims are to conduct leaching tests on the insolubilization effect on heavy metals, to elucidate the insolubilization mechanism from the test results, and to ensure the long-term stability of the insolubilization treatment, as shown in Fig. 1.

EXPERIMENTAL STUDY ON INSOLUBILIZATION EFFECT OF METAL-INSOLUBILIZING MATERIAL

As mentioned earlier, due to the amendment of the Soil Contamination Countermeasures Act in 2010 (MOE 2017; Sakamoto 2011), countermeasures are now required for the development of contaminated soil derived from nature which had not been regulated in the past. Regarding the improvement of contaminated soil derived from nature, the contaminated soil to be improved is widely distributed in many cases, and increases in the environmental load and processing costs are expected in the case of insolubilization treatment with conventional cement-based or lime-based materials. Therefore, it is necessary to carry out mineral stabilization (insolubilization treatment) on construction-generated soil in order to reduce the transportation risk, costs, and environmental load.

In this study, leaching tests by Environment Agency Notification No. 46, announced in 1991, used to determine the insolubilization effect (Shimaoka et al. 2016). The contaminated soil targeted in this study contains naturally derived heavy metals and the like. In order to investigate the insolubilization effect of the metal-insolubilizing material on the contaminated soil, leaching and pH tests were performed. Moreover, in order to verify whether hazardous substances insolubilized by the metal-insolubilizing material could be kept in a stable state for a long time and could withstand the change in pH due to the aging of the soil, acid addition leaching tests were performed based on acid rain precipitation equivalent to 500 years recommended by the Geo-Environmental Protection Center (2008). After insolubilization treatment, it was possible to cast steel pipe piles and to drive concrete, and so on, into the soil via construction work. At this time, the improved soil may be affected by alkali (Malviya & Chaudhary 2006). Therefore, considering the stimulation by alkali, alkali addition tests, recommended by the Geo-Environmental Protection Center (2008) were

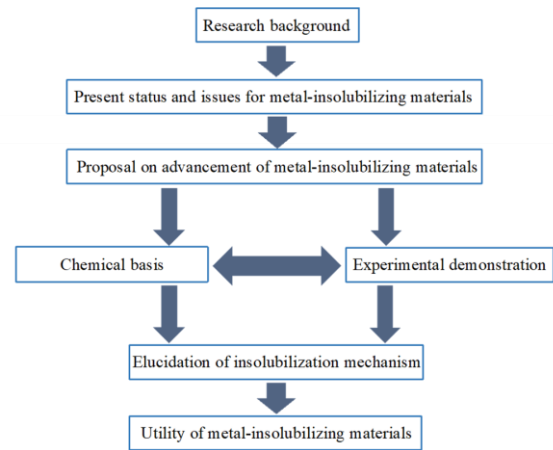


Fig. 1 Purpose and flow of this research

Table 1 Compounding ratio of metal-insolubilizing material A

Main components	Compounding ratio (%)
	Metal-insolubilizing material A
CaO	40
SiO ₂	40
Al ₂ O ₃	20

Table 2 Compounding ratio of metal-insolubilizing material B

Main components	Compounding ratio (%)
	Metal-insolubilizing material B
CaO	10
MgO	60
Al ₂ O ₃	15
SO ₃	15

conducted and the long-term weatherability against alkali was verified.

Characteristics of Metal-insolubilizing Materials

Two kinds of metal-insolubilizing materials, A and B, were used in this study. Metal-insolubilizing material A is composed mainly of calcium, silicon, and aluminum components, as shown in Table 1. Metal-insolubilizing material B newly incorporates a magnesium component into metal-insolubilizing material A, and the magnesium becomes one of the main components instead of the silicon, as shown in Table 2. By adding these materials to contaminated soil, the insolubilization effect brought about by the minerals produced by a chemical reaction can be expected.

Leaching Test

According to the environmental quality standards for the amount leached in soil (Environment Agency Notification No. 18) based on the Soil Contamination Countermeasures Act, the leaching test (specified as Environment Agency Notification No. 46) shall be conducted for lead (Pb), arsenic (As), selenium (Se), and cadmium (Cd) by a measurement method that is compatible with the type of designated hazardous substances (Shimaoka et al. 2016).

The batch typed leaching test method, which is used as the general evaluation method for the leaching test in public works, is employed here, as shown in Fig. 2 (Kanjo 1995; Sakai et al. 1995; Krüger et al. 2012).

pH Test

The pH test (suspension method) is carried out according to the “JGS 0211-2009” standard set by the Japanese Geotechnical Society (JGS 2015). The test method stipulates that the pH be measured as a fluid in a state at which the soil and the water are suspended, and targets particles with a particle size of 10 mm or less.

INSOLUBILIZATION EFFECT ON SOIL CONTAMINATED WITH MULTIPLE TYPES OF HEAVY METALS

In order to evaluate and investigate the insolubilization effect of metal-insolubilizing materials, metal-insolubilizing material A was added to soil contaminated with multiple types of heavy metals and a leaching test and a pH test were conducted, as detailed in Table 3.

The target soil was mudstone contaminated with multiple types of heavy metals, and the soil was acidic (pH = 3.6) before adding the metal-insolubilizing material.

Leaching Test

The results of the leaching test are shown in Table 4 and Fig. 3.

By adding metal-insolubilizing material A, it is clear that the leaching amounts of As, Pb, Se, and Cd are below the environmental quality standards for soil (0.01 mg/L). Regarding Cd, although the leaching amount of the target soil (raw soil) is 0.009 mg/L, less than the environmental quality standard for soil, the leaching amount of Cd was greatly reduced by the addition of metal-insolubilizing material A, and the insolubilization effect is observed. In addition, the leaching amount of Pb in the raw soil is 0.021 mg/L. When 30 kg/m³ of metal-insolubilizing material A is added, the material shows the same value as the environmental quality

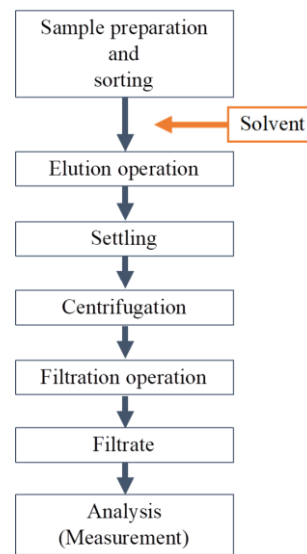


Fig. 2 Flow of leaching test

Table 3 Test method and conditions

Target soil	Mudstone
Metal-insolubilizing material	Metal-insolubilizing material A
Addition amount of metal-insolubilizing material	30, 60 kg/m ³
Leaching test method	Soil Contamination Countermeasures Act
Environmental quality standards for soil (As, Pb, Se, Cd)	0.01 mg/L or less
pH test method	Suspension method
Curing period of sample	3 days

standard for soil; and thus, a sufficient insolubilization effect cannot be obtained. However, when 60 kg/m³ of A is added, the leaching amount of Pb is decreased; and thus, the insolubilization effect is observed for Pb.

pH Test

Regarding the results of the pH test, the pH of the soil after the addition of 30 kg/m³ of metal-insolubilizing material A was 7.5, whereas the pH of the target soil (raw soil) was 3.6. That is, although the raw soil was acidic, the soil was neutral after adding metal-insolubilizing material A. It is thought that the neutralization reaction occurs due to the mixing with the target soil (raw soil), resulting in the increase in pH, since the main component of metal-insolubilizing material A, such as lime, is alkaline.

Issues for Metal-insolubilizing Material A

In order to maintain the insolubilization effect over a long period of time, it is necessary to evaluate and examine the insolubilization effect under external stimulus, such as from acid and alkali. When the contaminated soil is alkaline before the insolubilization treatment, there is concern that the insolubilization effect due to metal-insolubilizing material A cannot be exerted. Therefore, it is necessary to investigate metal-insolubilizing materials that do not cause the soil pH to become extremely acidic or alkaline after the insolubilization treatment.

INSOLUBILIZATION MECHANISM FOR HEAVY METALS

Classification of Insolubilization Mechanism

This study focuses on insolubilization by minerals. Therefore, it is necessary to clarify the mechanism. First, the reaction caused by insolubilization will be summarized. The factors of insolubilization are roughly divided into adsorption and sorption. Adsorption is divided into physisorption and chemisorption depending on the mechanism (Fukushi & Sverjensky 2007(a); 2007(b); Fukushi 2008).

Physisorption:

Physisorption is due to van der Waals' force and Coulomb's force. In particular, adsorption by Coulomb's force (electrostatic force) is called electrostatic adsorption. Such physical adsorption is also called an outer sphere complex formation reaction; it constrains the molecules and ions in the solution by the above-mentioned force and has no chemical bond (Fukushi & Sverjensky 2007(a); 2007(b); Fukushi 2008). Therefore, physisorption is weaker than chemisorption, which will be described later.

Chemisorption:

In chemisorption, electrons are exchanged between adsorbed solutes (molecules and ions) and atoms on a solid surface, resulting in a strong chemical bond. Adsorption with such chemical bonds is also called an inner sphere complex formation reaction (Fukushi & Sverjensky 2007(a); 2007(b); Fukushi 2008).

Sorption:

Sorption is a phenomenon in which adsorption and absorption occur simultaneously. That is, molecules and ions in the solution are adsorbed on the solid surface, and the adsorbates pass through the solid surface layer and enter the inside (Fukushi & Sverjensky 2007(a); 2007(b); Fukushi 2008). In addition, when the adsorbates are incorporated into the solid, it is thought that the crystal structure of the solid changes and a rearrangement occurs. In other words, a new compound is generated, as seen in Fig.

Table 4 Results of leaching test

		Addition amount of metal-insolubilizing material A (kg/m ³)		
		0	30	60
Leaching amount (mg/L)	Cd	0.009	0.001	—
	As	0.011	0.005	—
	Pb	0.021	0.010	0.008
	Se	0.011	0.003	—

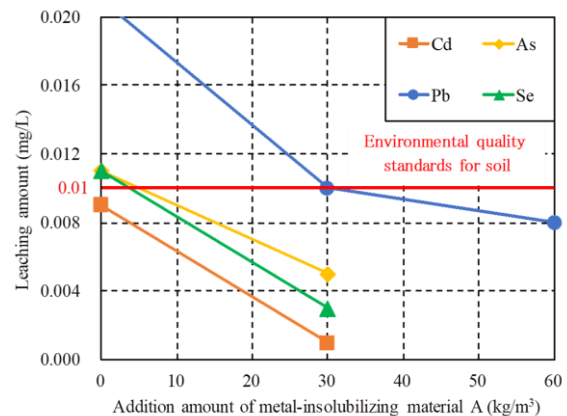


Fig. 3 Results of leaching test

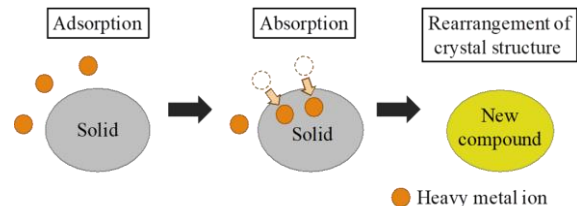


Fig. 4 Image of sorption

4).

Insolubilization by Generated Minerals

Focus is on insolubilization by various kinds of minerals based on the contents described in 6.1. From the above test results, insolubilization by metal-insolubilizing material A is thought to be insolubilization by schwertmannite and apatite. In addition, insolubilization by metal-insolubilizing material B is thought to be insolubilization by hydroxalite together with schwertmannite and apatite, as shown in Figs. 5 and 6. Therefore, the insolubilization mechanism by these minerals, generated after adding the metal-insolubilizing material, is discussed.

Insolubilization by schwertmannite:

After the addition of the metal-insolubilizing material, the iron component, the sulfuric acid

component, and the water in the soil cause a chemical reaction, whereby schwertmannite is generated. Schwertmannite is a metastable phase mineral of goethite, but its solubility decreases due to adsorb anions, such as arsenate ions, and it becomes structurally stable (Inoue & Hatta 2006; Burton et al. 2007).

Regarding the insolubilization mechanism, it is thought that the sulfate ions in the schwertmannite are exchanged for arsenate ($\text{H}_2\text{AsO}_4^{2-}$) ions or the like due to the anion exchange reaction (ligand exchange reaction) and that arsenic is adsorbed, as shown in Fig. 7.

The selectivity of oxy anion species on schwertmannite-holding sulfate ions is “arsenate ion > chromate ion > selenate ion”; arsenate ions are preferentially adsorbed (Takada et al. 2008). In addition, the phase change time from schwertmannite to goethite is also long in the above order, and the retention stability of adsorbed oxy anion species is also high in the above order (Takada et al. 2008).

Therefore, schwertmannite is a long-term stable mineral especially for arsenate ions.

Insolubilization by hydrotalcite:

After the addition of the metal-insolubilizing material, the magnesium component, the aluminium component, and the water in the soil cause a chemical reaction whereby hydrotalcite is generated.

Hydrotalcite has a host layer which is a positively charged octahedral layer formed by substituting Al^{3+} for a part of Mg^{2+} of $\text{Mg}(\text{OH})_2$, and a guest layer which is composed of an anion and interlayer water compensating for this positive charge. Hydrotalcite has a structure in which it is alternately stacked with host layers and guest layers (Kameda et al. 2005).

Regarding the insolubilization mechanism, when the positively charged host layer of hydrotalcite is formed, heavy metal anions, such as water, arsenate ions, selenate ions, and the like, are adsorbed into the guest layer, as shown in Fig. 8.

That is, heavy metal anions are physically (electrically) adsorbed between the hydrotalcite layers; and thereafter, there is a risk of the heavy metal anions re-elution when the heavy metal anions are exchanged for other anions. However, if the heavy metal anions form inner sphere complexes with hydrotalcite surfaces after physisorption, the possibility of re-elution greatly decreases.

Insolubilization by apatite:

After the addition of the metal-insolubilizing material, the calcium component, the phosphoric acid component, and the water in the soil cause a chemical reaction whereby apatite is generated.

For insolubilization by apatite, hydroxyapatite is firstly formed, and then heavy metals are insolubilized by the substitution reaction between the hydroxyapatite and the heavy metal ions.

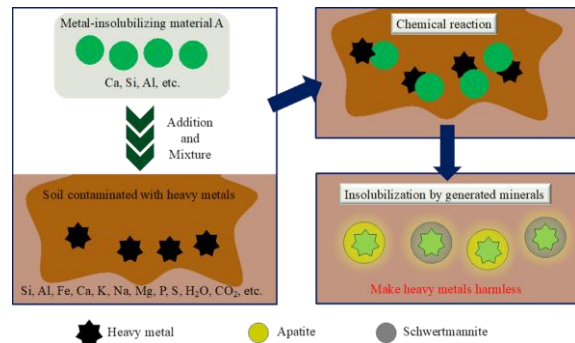


Fig. 5 Insolubilization mechanism by metal-insolubilizing material A

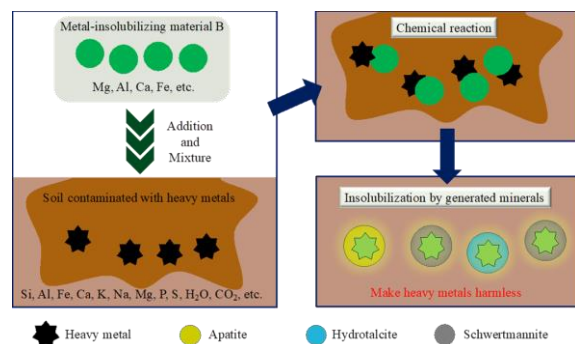


Fig. 6 Insolubilization mechanism by metal-insolubilizing material B

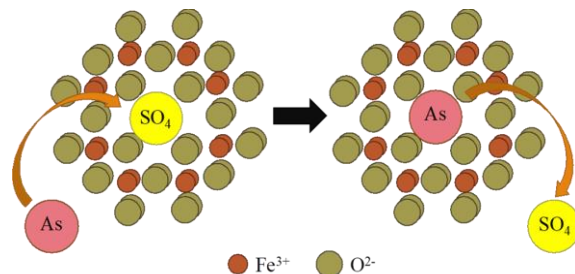


Fig. 7 Insolubilization mechanism by schwertmannite

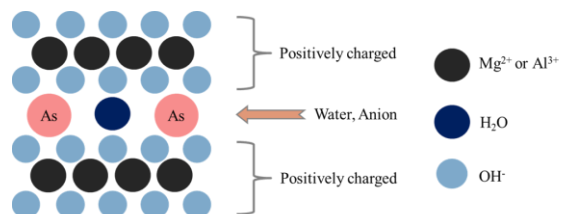


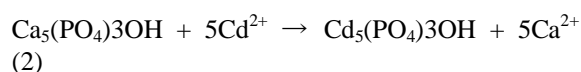
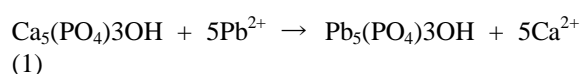
Fig. 8 Insolubilization mechanism by hydrotalcite

Therefore, insolubilization progresses in stages, so it is thought that the above-described sorption occurs. In other words, it is conceivable that heavy metal

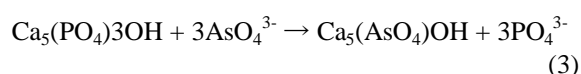
ions are adsorbed on the surface of hydroxyapatite and afterwards incorporated into hydroxyapatite, resulting in the formation of apatite crystals containing heavy metals, as shown in Fig. 4.

Hydroxyapatite is represented by $\text{Ca}_5(\text{PO}_4)_3(\text{OH})$, which can be expected to insolubilize many hazardous substances, such as lead, cadmium and arsenic. The reaction is shown below.

Regarding the insolubilization mechanism for lead and cadmium, lead ions (Pb^{2+}) which are present in an unstable state in the soil are stabilized and insolubilized by substituting them for calcium ions (Ca^{2+}) in hydroxyapatite. In addition, since divalent heavy metal cations show a common behavior, it is thought that cadmium ions (Cd^{2+}) are likewise insolubilized, as seen in Eqs. (1) and (2).



Regarding the insolubilization mechanism for arsenic, the arsenate ions (AsO_4^{3-}) which are present in an unstable state in alkaline soil are stabilized and insolubilized by substituting them for phosphate ions (PO_4^{3-}) in hydroxyapatite, as seen below (Eq. (3)).



CONCLUSIONS

In this study, a leaching test, a pH test, and an acid or alkali addition leaching test were performed on metal-insolubilizing materials A and B with different main components to confirm the insolubilization effect.

When the target soil was acidic and the insolubilization treatment was performed using metal-insolubilizing material A, a sufficient insolubilization effect was obtained for the complex contaminated soil and the treated soil was neutralized. When the target soil was alkaline and the insolubilization treatment was performed using both metal-insolubilizing materials A and B, a sufficient insolubilizing effect on arsenic was obtained for each metal-insolubilizing material, but the pH of the soil after the insolubilization treatment was different. In addition, only metal-insolubilizing material B was able to bring about a long-term insolubilization effect.

In this study, the insolubilization mechanism was clarified from chemical and mineralogical considerations based on the data obtained from the tests. Then, based on phenomena such as adsorption, absorption, and sorption, attention was focused on insolubilization by minerals, such as schwertmannite,

hydroxalite, and apatite.

Moreover, as insolubilization by other minerals and compounds is also conceivable, further consideration is necessary.

REFERENCES

- Arao, T., Ishikawa, S., Murakami, M., Abe, K., Maejima, Y. and Makino, T.: Heavy metal contamination of agricultural soil and countermeasures in Japan, *Paddy Water Environment*, Springer, Vol.8, Issue 3 pp.247-257, 2010.
- Burton, E.D., Bush, R.T. and Sullivan, L.A.: Reductive transformation of iron and sulfur in schwertmannite-rich accumulations associated with acidified coastal lowlands. *Geochimica et Cosmochimica Acta*, Elsevier, Vol.71, Issue 18, pp.4456-4473, 2007.
- Fukushi, K. and Sverjensky, D.A.: A surface complexation model for sulfate and selenate on iron oxides consistent with spectroscopic and theoretical molecular evidence, *Geochimica et Cosmochimica Acta*, Elsevier, Vol.71, Issue 1, pp.1-24, 2007(a).
- Fukushi, K. and Sverjensky, D.A.: A predictive model (ETLM) for arsenate adsorption and surface speciation on oxides consistent with spectroscopic and theoretical molecular evidence, *Geochimica et Cosmochimica Acta*, Elsevier, Vol.71, Issue 5, pp.3717-3745, 2007(b).
- Fukushi, K.: Modeling for ion adsorption on clays (in Japanese), *Journal of the Clay Science Society of Japan*, Vol.47, No.2, pp.93-103, 2008.
- Inoue, A. and Hatta, T.: Co-precipitation synthesis of schwertmannite and its analogues with different anion species, focusing on understanding of the role of anions in the formation of FeOOH mineral (in Japanese), *Journal of the Clay Science Society of Japan*, Vol.45, No.4, pp.250-265, 2006.
- Kanjo, Y.: Leaching test as the screening for the utilization of waste (in Japanese), *Proceedings of the 6th Annual Conference of the Japan Society of the Waste Management Experts*, pp.741-743, 1995.
- Krüger, O., Kalbe, U., Berger, W., Nordhauß, K., Christoph, G. and Walzel, H.P.: Comparison of batch and column tests for the elution of artificial turf system components, *Environmental Science & Technology*, ACS Publications, Vol.46 No.24, pp.13085-13092, 2012.
- Malviya, R. and Chaudhary, R.: Leaching behavior and immobilization of heavy metals in solidified/stabilized products, *Journal of Hazardous Materials*, Elsevier, Vol.137, Issue 1, pp.207-217, 2006.
- Ministry of the Environment (MOE), Government of Japan: <https://www.env.go.jp/council/10dojo/y105-02/ref01.pdf>, 2017.07.
- Ministry of the Environment (MOE), Government of Japan: Soil Contamination Countermeasures Act (Act No. 53 of May 29, 2002), 2002.
- Sakai, S., Mizutani, S., Takatsuki, H. and Kishida, T.: Study about the leaching test for the waste-availability test and pH-dependent test (in Japanese), *Journal of the Japan Society of Waste Management Experts*, Vol.6, No.6, pp.225-234, 1995.
- Sakamoto, D.: The enforcement of the revised soil contamination countermeasures act (in Japanese),

- Japan Technical Association of the Pulp and Paper Industry Journal, Vol.65, No.4, pp.1244-1248, 2011.
- Shimaoka, T., Kuba, T., Nakayama, H., Fujita, T. and Horii, N.: Basic Studies in Environmental Knowledge, Technology, Evaluation, and Strategy: Introduction to East Asia Environmental Studies, Springer, 2016.
- Takada, M., Fukushi, K., Sato, T. and Yoneda, T.: Adsorption of oxyanions and post-adsorption behavior of schwertmannite (in Japanese), Journal of the Clay Science Society of Japan, Vol.47, No.4, pp.255-260, 2008.
- The Japanese Geotechnical Society (JGS): Japanese Geotechnical Society Standards: Laboratory Testing Standards of Geomaterials, The Japanese Geotechnical Society, 2015.

LIQUEFACTION ANALYSIS OF ROAD EMBANKMENT IN PIDIE JAYA DUE TO ACEH EARTHQUAKE IN 2016

M Sofian Asmirza¹, Anissa Maria Hidayati² and Abdul Hakam³, ⁴M Maisaquddus Hape

¹Engineering; Fac., North Sumatra University, Indonesia,

²Engineering Fac., Udayana University, Indonesia,

³Engineering Fac., Andalas University, Indonesia;

⁴ Engineering Fac., Institute Tech. of Bandung, Indonesia

ABSTRACT:

The 6.5 Mw Aceh earthquake has been struck the north-east part of Sumatra Island on 7 December 2016. The strong quake was at a depth of 13 km and categorized as a shallow earthquake. The earthquake has caused many damage on the roads as results of lateral spreading in Pidie Jaya Regency. This study is conducted to analyze the liquefaction phenomena that caused lateral spreading on the Pidie Jaya roads. All of the soil data for the analysis were taken from the field of affected area. First, the soil data are analyzed to examine whether the soil sediment has potential to liquefaction under the earthquake. Then the detail analysis to observe the phenomenon of liquefaction on a particular road embankment is conducted with the use of numerical computer program. This study shows that for a particular soil sediment which has liquefaction potential, the structure stability analyses need to consider liquefaction circumstance in a certain level. Finally, a reasonable geo-construction analysis is suggested for preventive measures of liquefaction.

Keywords: Earthquake, Liquefaction, Road Embankment, Numerical Analysis

1. INTRODUCTION

Sumatra is an island with great earthquake potential. There are at least two big geological conditions that become the main source of seismicity in this island. The first source is coming from the subduction boundaries of Asian continental plates and the Indian Ocean Plate on the western side of the Sumatra island. The second source is the main fault that crosses along the middle of the Sumatra island, named Semangko fault. Both seismic sources have caused major earthquakes that occurred in the beginning of this century.

The first earthquake that inculudes destructive earthquakes on Sumatran island in this century is the Aceh earthquake in 2004. This earthquake resulted in a phenomenal huge tsunami that opened wide the attention all people around the world. Then in 2005 there was the Nias earthquake on the western side of Sumatra which has resulted in liquefaction in some places on that Island [1]. The next is Bengkulu earthquake that happened in 2007 which also caused more than one meter tsunami. The Bengkulu earthquake also resulted in liquefaction in several places in Bengkulu [1]. Then the Padang earthquake in 2009 which resulted in liquefaction in many places in Padang [2]. In 2010, the Mentawai earthquake occurred on the west-central side of the Sumatra island. This earthquake also caused a destructive tsunami in the Mentawai island. Finally the Pidie-Aceh earthquake in the eastern part of the north Sumatra

island.

Pidie earthquake located in the eastern part of the Aceh province in the Sumatra, The Pidie earthquake occurred on December 7, 2016. Pidie earthquake magnitude is 6.5 Mw at a shallow depth of 13 km. This earthquake has caused damages in the access roads in terms of settlement (Fig. 1) and cracks in the road surfaces (Fig. 2). The cracks was caused by liquefaction in the road ground. The cracks mostly extended along the surface of the road, although there are several cross the road. The liquefaction and lateral spreading in some districts of Pidie Jaya is indicated by sand boils at the lower side of the road body (Fig. 3). Liquefactions that caused cracks and settlement of the access roads are also reported to be widespread in Pidie region [3].



Fig.1 Penurunan jalan di Pidie 2016



Fig. 2 Cracks on road in Pidie 2016



Fig. 3 Sand boil due to Aceh earthquake 2016

The studies of liquefaction in general have been done a lot [4], [5], [6]. In this paper, the damage in road embankment due to liquefaction is discussed. The soil and geometric data for that purposes are adopted from field test investigation in Pidie district of the Aceh province.

2. ROAD EMBANKMENT CASE IN PIDIE

The soil data for the purposes of numerical analysis in this study was adopted from the results of the Dutch Cone Penetration test (CPT) data as shown in Table 1 and Fig. 4. Based on that data it can be seen that the soil on the site has a small tip resistance on the near surface to a depth of several meters. The soil type at that location is obtained by analyzing the Friction Ratio (R_f) values of the CPT results. Furthermore, the value of the cones resistances and the friction ratios are plotted together on the soil type chart. The results show that the sandy soil dominates the near surface soil layer (Fig. 5). While the rest is estimated to be a cohesive layer in terms of silt or clay mixtures [7]. The site location is on the edge of the river with relatively shallow ground water level. This situation makes the land in that location will be in water-saturated condition.

In the performed numerical simulations, the soil layer is simply divided into two parts, the top later with the cone average resistance of 25 kg/cm^2 and the bottom one with an average cone resistance of 200 kg/cm^2 . Further, the modulus of soil modulus, E and the shear angle, ϕ and others

parameters for the analysis is calculated based on the total constraint resistance, q_t , the cone resistance, q_c , of the total and effective overburden stress of σ_{vo} and σ'_{vo} with the correlation parameter α_E , using the following equation [7]:

$$E = \alpha_E (q_t - \sigma_{vo}) \quad (1)$$

$$\tan \phi' = \frac{1}{2.68} \left[\log \left(\frac{q_c}{\sigma'_{vo}} \right) + 0.29 \right] \quad (2)$$

Tabel 1. CPT Test results

Dept (m)	CPT-1		CPT-2	
	q_c (kg/cm^2)	R_f (%)	q_c (kg/cm^2)	R_f (%)
0	0	0	0	0
0.2	40	1.25	25	2
0.4	30	1.67	30	1.67
0.6	25	2	25	2
0.8	25	2	25	2
1	25	2	20	2.5
1.2	30	1	15	2
1.4	25	1.2	30	1.67
1.6	25	2	35	1.43
1.8	25	2	40	1.25
2	25	2	45	0.67
2.2	20	2.5	35	0.86
2.4	25	2	180	0.56
2.6	30	3.33	150	0.67
2.8	180	2.22	190	1.05
3	220	1.36	180	1.11
3.2	245	0.2	210	0.71

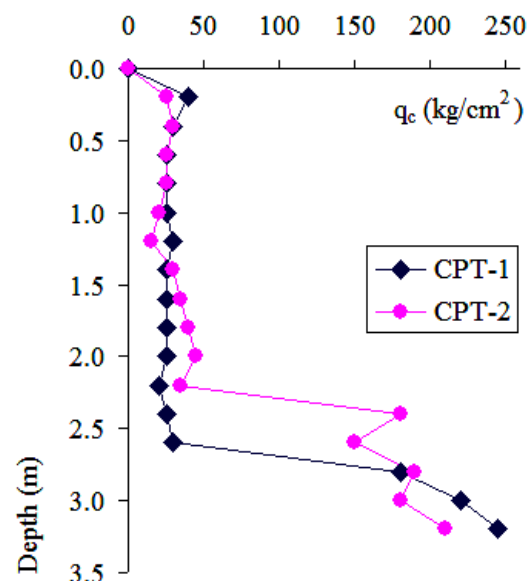


Fig. 4 Cone Penetration Test Data in Pidie

The results of the correlation calculations of

the mechanical parameters for the numerical analysis are shown in Table 2.

Tabel 2. Average values of soil parameters

Parameter	Layer 1	Layer 2
Soil modulus, E (kN/m ²)	22000	29700
Poisson's ratio, μ	0.4	0.3
Friction angle, ϕ (degree)	40	48
Unit weight, γ (kN/m ³)	17.5	18.5

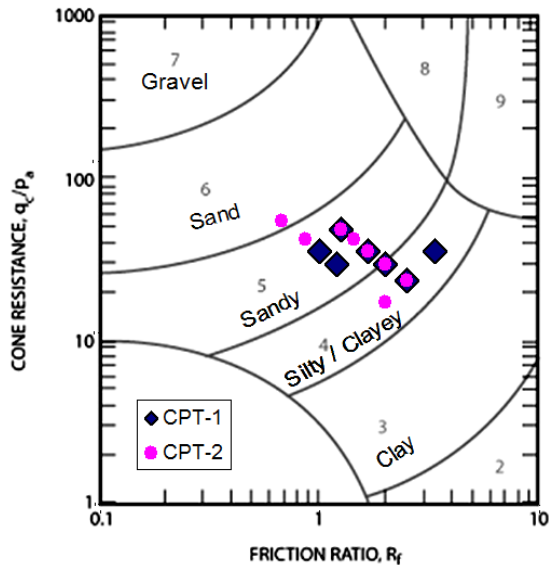


Fig 5. Soil type chart

3. ANALYSES AND RESULTS

In order to investigate the stability of the road embankment against liquefaction, a finite element model of the road embankment on the ground is constructed. The road embankment is made of sandy clay material with a unit weight of 18 kN/m³, the soil cohesion of 1200 kN/m², the internal friction angle of 10° and 29000 kN/m² of soil modulus. The numerical modeling in this study was done by using the plaxis program. Road pile is placed right above ground surface with two types of soil layers. The soil parameters for the model are shown in Table 2. Groundwater table is at the depth of 1m from the ground surface. The geometry of the finite element model is shown in Fig. 6.

The stability of the embankment due to the liquefaction is investigated in two stages. The first stage, the model is executed with its self weight. At this stage the condition of the model is referred as the normal state. The next stage is considering the liquefaction condition in which the increasing pore water pressures happened in the saturated soil mass. In this stage, the pore water pressure due to

liquefaction phenomenon is determined by doubling it from its normal condition. Furthermore, to investigate the stresses in the under the ground, two points are selected that is at a depth of 2m and a depth of 4m from the ground surface.

In the first stage, the displacement pattern due to its self weight is shown in Fig. 7. In this condition the maximum calculated settlement is 0.002m. The value is relatively small and indicates that the embankment is in stable condition with a safety factor of 5.8 which is considered as a good value for the embankment stability.

Furthermore, in the second stage, the pore water pressure on the saturated soil mass is increased by two times from its normal condition. In this condition, the calculated settlement on the embankment is 0.002m. The value is the same as its in the normal condition. The safety factor in this second condition is 4.7 which indicates the stability state is generally safe. The soil mass in this second stage has tensile stresses at the top of embankment surface and plastic conditions have occurred in the ground under the embankment (Figure 8). The possible pattern of collapse of this embankment model is estimated as in Fig. 9.

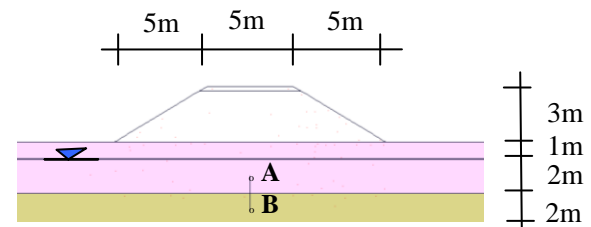


Fig 6. Numerical model

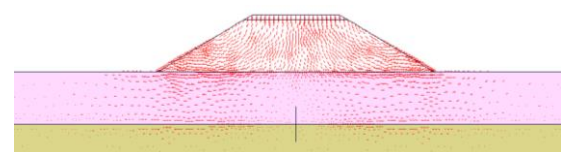


Fig 7. Displacement due to self weight

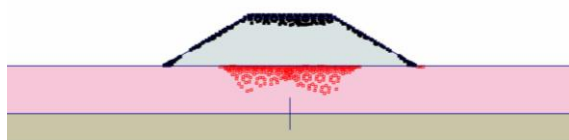


Fig 8. Plastic state due to self weight

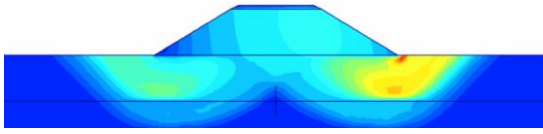


Fig 9. Failure pattern of the embankment

In this analysis it is also given a simulation of increased pore water pressure up to 2.5 times the normal state. At the pore pressure of that value, the ground under the embankment is collapsed. The safety factor under this condition is 0.4 which is indicating the embankment is not in the stable condition anymore.

The numerical simulations also shows that instability condition, the construction suddenly collapse with the increased pore water pressure more than twice in its initial condition (Fig. 10). In the actual circumstances this condition indicates that the liquefaction due to an earthquake will result in a sudden collapse of construction. This is certainly very dangerous since the sudden collapse of construction has given no time for the evacuation action. Although the excess pore water pressures can be monitored with geotechnical equipment, but the collapsed condition remains unexpected in certain circumstance. Therefore, in that such cases, a careful analysis of the construction stability is more necessarily important than the installation of monitoring equipments.

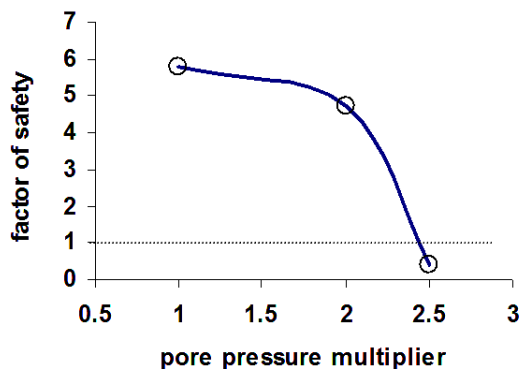


Fig 10. Stability due to incremental pore pressure

Based on these results, it can also be understood that damage and collapse to the embankment of the road can occur suddenly when the pore water increases to a certain incremental value from its normal condition. If this increased pore water pressure has passed away, the embankment will return to its original state.

Therefore, the improvement of the road can be done to restore it to its original condition.

4. CONCLUSIONS

The earthquake that struck Aceh in 2016 has caused damage to a number of road embankment in Pidie Jaya. In order to investigate the effects of that phenomenon on the road embankment stability, the simulation of increase in pore water pressure caused by liquefaction were discussed here. The original ground data was adopted based on cone penetration test results in Pidie - Aceh.

The results of this study indicate that the increase in pore water pressure due to liquefaction, can reduce the stability of road embankment. The increased pore water pressure, at a certain time will result in the loss of stability of the construction suddenly. This indicates that the damage and collapse occurring due to liquefaction and lateral spreading can occur at a short time during the earthquake. Soon after the earthquake passed away, the excess water pressure due to liquefaction returns to its normal state, the embankment construction will also be stable again but in damaged condition. For that then the improvement can be done to restore the road condition to function as normal.

Based on the results in this study it can also be suggested the importance of conducting stability analysis of the construction by considering the liquefaction triggered pore water pressure due to a selected earthquake. Since the sudden collapse phenomenon happens in a very sort time, monitoring equipment installation for early warning for such case purposes seems to be less recommended.

5. ACKNOWLEDGEMENTS

The authors greatly express thank to our colleagues who have helped in the process of finishing this research.

6. REFERENCES

- [1] Aydan, Ö., Imamura F., Suzuki T., Ismail F.A., Hakam A., Masmera, Devi P.R., A Reconnaissance Report On The Bengkulu Earthquake Of September 12, Japan Society of Civil Engineers (JSCE) and Japan Association for Earthquake Engineering (JAEE) With the collaboration of Andalas University, October 2007
- [2] Hakam, A, "Laboratory Liquefaction Test of Sand Based on Grain Size and Relative

- Density", *J. Eng. Technol. Sci.*, Vol. 48, No. 3, 2016, 334-344
- [3] Irsyam M., Hanifa N.R and Djarwadi D, Eds., *Pidie Jaya Earthquake Assessment Acehne Province December 7, 2016 (M6.5)*, (In Indonesian: *Kajian Gempa Pidie Jya Provinsi Aceh Indonesia 7 Desember 2016 (M6.5)*), Mekentrian PUPR, 2017
 - [4] Dellow S., "Liquefaction and lateral spreading, StIRRRD New Zealand": Comparative Study Programme, Christchurch 5-19 June 2015
 - [5] Seed, H. B., and Idriss, I. M. (1971), "Simplified procedure for evaluating soil liquefaction potential." *J. Geotech. Engg. Div. , ASCE*, 97(9) , 1971, pp 1249–1273
 - [6] Hakam, A. and H Darjanto, *Liquefaction Potential in Padang Beach Based on Soil Gradation and Standard Penetration Test* (in Indonesian: *Penelusuran Potensi Likuifaksi Pantai Padang Berdasarkan Gradasi Butiran dan Tahanan Penetrasi Standar*), *Jurnal Teknik Sipil – ITB*, 2012, 33-38
 - [7] P. K. Robertson and K.L. Cabal (Robertson), *Guide To Cone Penetration Testing*, 4th Ed., Gregg Drilling & Testing, Inc., 2010

7. AUTHOR'S BIOGRAPHY

Dr. M Sofian Asmirza is an Associate Professor in the Civil Engineering Department of

North Sumatra University, Indonesia. He was graduated from North Sumatra University, he got Master and Doctor from Universiti Kebangsaan Malaysia. His research interests include general problem in foundation engineering, soil mechanics and soil dynamics. His contact E-mail is asmirza0076@gmail.com.

8. AUTHOR'S CONTRIBUTIONS

Dr. M Sofian Asmirza: Conception, design, acquisition, final approval of the version to be submitted. Dr. Abdul Hakam: Conception, design, final approval of the version and submitte the paper. Dr. Anissa M Hidayati : Critical reviewing, analysis. M Maisaquddus H: Summarizing and Interpretation of data.

9. ETHICS

This article is original and contains unpublished material. The corresponding author confirms that all of the other authors have read and approved the manuscript and no ethical issues involved.

MEASUREMENT OF CEMENT CONTENT IN CEMENT MIXED SOIL BY HYDROCHLORIC ACID HEAT REACTION METHOD

Hiroshi Kubo¹, Toshihiko Miura² and Shinya Inazumi³

¹ Tachibana Material Co. Ltd., Japan

² Obayashi Corporation, Japan

³ Shibaura Institute of Technology, Japan

ABSTRACT

The mixing cement with soft soil to increase their strength has been used in many construction sites and it is important that soil and cement are well mixed. In order to evaluate the mixing level of soil and cement during construction, it may be required to measure the cement content by sampling the cement mixed soil. While there are several methods for measuring cement content, the hydrochloric acid heat reaction method is the easiest and quickest method and the measurement accuracy is relatively high. This method can be easily conducted even in construction sites, therefore it is applied to the quality control of cement mixed soil at the construction sites. The cement content and its reaction heat are proportional. Sampled cement mixed soil and hydrochloric acid are placed in a heat retention container and stirred, and the heat of reaction is evaluated according to the maximum value of the rising temperature (temperature difference with the initial state). The risen temperature reaches the maximum value within 1 minute. A calibration curve of the cement content and the rising temperature is prepared using local soil (soil in the construction sites) and cement. In this paper, the conditions of hydrochloric acid heat reaction method such as hydrochloric acid concentration, amount ratio of sampled cement mixed soil and hydrochloric acid, and influence of elapsed time of cement mixed soil are evaluated. It also discusses the results of applying this method on construction sites.

Keywords: Soil, Cement content, Hydrochloric acid, Temperature

INTRODUCTION

A method of improving the engineering properties of soil by mixing cement with soil is very often adopted in construction works. When cement powder or cement milk is mixed with soft soil, the strength of the soil greatly increases within a short period of time. Its strength increases with the amount of cement added. Prior to construction, the amount of cement added is designed so that target strength can be obtained based on the result of indoor mixing test using local soil. There are various construction machines to add and mix cement into the soil. Broadly speaking, there are a construction method in which cement is added to the local soil and mixed, and a method in which cement is mixed by transferring the local soil to a mixing-plant. In any of the construction methods, the strength of the cement mixed soil increases as the mixing precision of the soil and the cement is good, but becomes lower if it is bad. Ease of mixing of soil and cement varies depending on qualities of soil. For example, consolidated clay requires more energy to mix cement well due to its higher viscosity. Therefore, it is important to determine the conditions suitable for the local soil so that the mixing becomes good while considering economic efficiency, especially in the mixing condition of the mixing machine.

One way to investigate the mixing precision of soil and cement is to collect a large number of samples of cement mixed soil, measure the content of each cement, and statistically process the variation of these values. The cement content test at that time is required to obtain results easily and promptly at the site. The method of chemically analyzing the calcium content which is the main component of cement to determine the cement content requires not only equipment and many reagents but also time. The method of measuring the calcium content and determining the cement content by the fluorescent X-ray apparatus gives results relatively quickly, but the apparatus is expensive. Hydrochloric acid heat reaction method was originally developed as a method to measure cement content for quality control of fresh concrete [1]. The authors considered that this method is a simple and rapid test method and that it is easy to apply to the site, and improved the test method so as to be compatible with the cement mixed soil. In addition, the method was applied to the cement mixed soil [2]. However, there are any questions about the condition of the test method.

This report describes a method of measuring the cement content of cement mixed soil by the hydrochloric acid heat reaction method and its application.

METHODOLOGY

Materials

The soil used is of two types, sandy soil and clay. The clay is mainly composed of kaolin minerals produced in Gifu Prefecture in Japan. The sand was produced in Chiba Prefecture in Japan. Table 1 shows the physical properties of each soil. The particle size distribution curves for the clay and the sand are shown in Fig. 1.

The cement mainly used is blast furnace cement (slag content: 40 to 60%). For comparison, ordinary Portland cement, special cement for ground improvement, quicklime and hydrated lime were also used.

Containers and thermometers

The insulated container and the thermometer used are shown in Fig. 2. The insulated container is glass dewar vessel with a 300 mL. For the temperature sensor, FTNGOPF3 (a resistance bulb thermometer with Pt100Ω) made by Fuji Electric Co., Ltd. was used. As the digital indicator, SD24 made by Shimaden Co., Ltd. was used.

Methods and laboratory procedures

Insulated container, hydrochloric acid, soil, cement and water were used. They were left in the test room for at least one day so as to be at room temperature and equilibrium temperature (T_0 °C.). Collect 100 g of cement or cement mixed soil and place in a heat insulating container. Add 100 mL of hydrochloric acid of a given concentration and mix with a stirring rod connected with a thermometer (a thermometer indicating the maximum temperature). Read the maximum temperature (T_1 °C) and obtain the rising temperature (ΔT °C) by Eq. (1)

$$\Delta T = T_1 - T_0$$

Influence of Hydrochloric Acid Levels on Temperature Rise

The water content of sandy soil was adjusted to 10%, 110 g (100 g as dry soil) was collected as wet soil, 0 to 10 g of blast furnace cement was added, mixed, and put in a heat insulating container. The reason why blast furnace cement was used is that it is adopted most in ground improvement works in Japan. Then, 100 mL each of hydrochloric acid (HCl) having a concentration of 2 to 12 M (mol/L) was added and mixed, and the temperature rise ΔT was measured.

Table 1 Properties of soil samples

	w_n (%)	d_s (g/cm ³)	w_L (%)	w_P (%)	U_c
sand	7	2.71	-	-	2.0
clay	1.3	2.66	41	12	-

Note: w_n ; water content, d_s ; soil particle density, w_L ; liquid limit, w_P ; plastic limit, U_c ; coefficient of uniformity

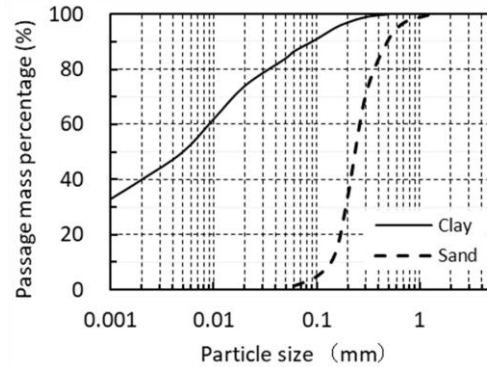


Fig. 1 Particle size distribution of soil samples



Fig. 2 Insulated container and thermometer

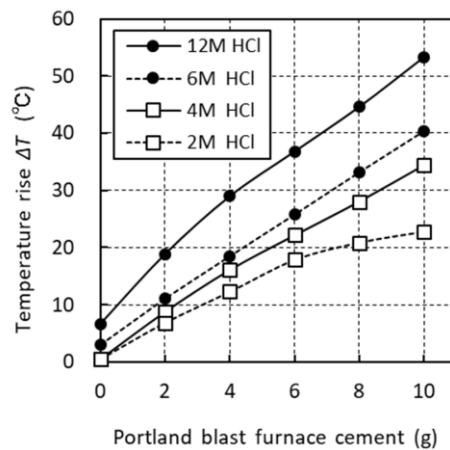


Fig. 3 Relations between cement mass and ΔT with hydrochloric acid levels (Sand; 110g, Water content of the sand; 10%, HCl; 100mL)

Results are shown in Fig. 3. ΔT increased as the amount of cement increased and as the concentration of hydrochloric acid increased.

2M-HCl increased the temperature linearly up to 6 g of cement, but the rise slowed at more than 8 g of cement. This may be due to the shortage of hydrochloric acid in the reaction between cement and hydrochloric acid. Meanwhile, although 12M-HCl caused the maximum temperature rise, the reaction between cement and hydrochloric acid was intense, and there was a tendency of slight deviation from a straight line. Moreover, due to handling, there are many occurrences of hydrogen chloride gas, the risk of burns and so on when it adheres to the skin is large and it cannot be said that safety is high. 6M-HCl and 4M-HCl showed a linear relationship with the amount of cement, the reaction was milder than 12M-HCl, and the risk was greatly reduced. 6M-HCl has an advantage that even when the amount of cement is large, compared with 4M-HCl, hydrochloric acid shortage does not easily occur. Therefore, the concentration of hydrochloric acid reached the conclusion that 6M was optimal. Kanda [1] used concentrated hydrochloric acid (12M) for measuring the amount of cement of ready-mixed concrete, but 6M-HCl was found to be practical in cement mixed soil. The time before reaching the maximum temperature was less than one minute. It was found that cement content in cement mixed soil can be measured if 6M-HCl was used to prepare a calibration curve as shown in Fig. 3.

Temperature Rise of Various Cements and Limes

For cement stabilization work, cement other than blast furnace cement may be used. Therefore, in the same way as in the above blast furnace cement, 0 to 10 g of cement was added to and mixed with 110 g of sandy soil having a water content of 10% for ordinary Portland cement and special cement for soil improvement, and 100 mL of 6M-HCl. The temperature rise due to addition was measured. The results are shown in Fig. 4.

The slope of the temperature rise line was different for the three types of cement. The magnitude of the inclination was ordinal Portland cement > blast furnace cement > special cement. These cements differ in CaO content and so on. It is considered that the difference in chemical composition and mineral composition contributed to the magnitude of heat for hydrochloric acid reaction. It is necessary to prepare a calibration curve for each type of cement to be used.

The authors conducted a test to obtain basic data on temperature rise caused by reaction of lime and cement and hydrochloric acid. Five kinds of quick lime, slaked lime, ordinary portland cement, blast furnace cement and special cement for ground improvement are targeted. The same warmth keeping container was used as before, 100 mL of 6M-HCl was added to 0-6 g of lime or cement and mixed to measure ΔT . However, it was tested with a

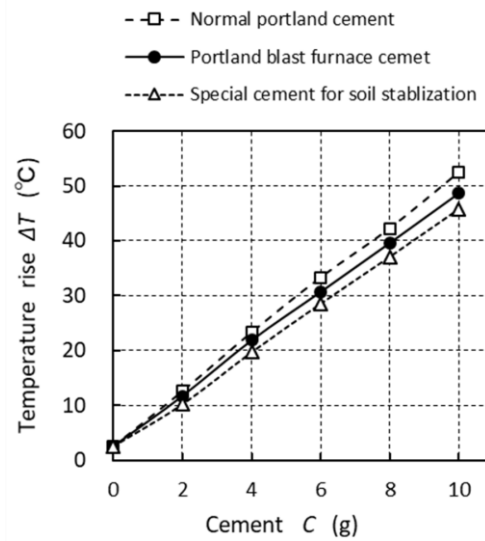


Fig. 4 Relations between three kinds of cements mass and ΔT (Sand;110g, Water content of the sand;10%, HCl;100mL, Concentration of HCl;6M)

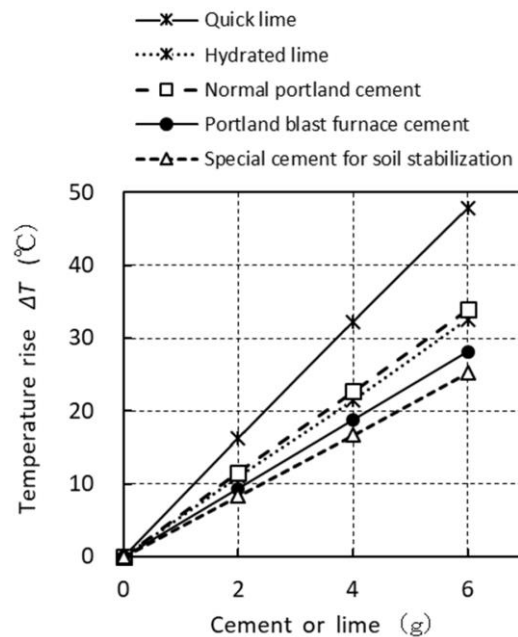


Fig. 5 Relations between cements or limes mass and ΔT (Soils; not included, HCl;100mL, Concentration of HCl;6M)

Table 2 CaO contents and temperature rise per 1g of various lime and cements

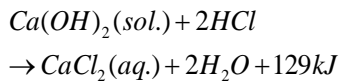
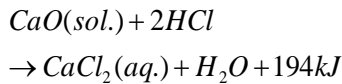
	CaO (%)	H (°C/g)
quick lime	100	8.0
hydrated lime	76	5.4
normal portland cement	64	5.7
portland blast furnace cement	56	4.7
special cement	52	4.2

Note: H; inclinations of the straight lines on Fig.5.

system not containing soil. Results are shown in Fig. 5. The slope H (ΔT °C/g) of each straight line in Fig. 5 is shown in Table 2 together with the CaO content.

The slope of the straight line was in the order of quicklime > ordinary portland cement \geq slaked lime > blast furnace cement > special cement, ordinary portland cement and hydrated lime were excluded, which coincided with CaO content ranking. H in Table 2 is not an accurate value thermochemically because it is not a test with sufficient heat insulation properties. However, because it was tested under unified conditions, it is considered that relative evaluation is possible.

The amount of heat that causes ΔT is the sum of the heat of dissolution of lime and cement [3], the heat of dissolution of a part of soil, the heat of neutralization, and the heat of dilution of hydrochloric acid. In Fig. 4, the increase in temperature with 0 g of cement is due to heat of dissolution, neutralization heat, and dilution heat of a part of the soil. The dissolution reaction of quicklime and hydrated lime with hydrochloric acid is represented by Eqs. (2) and (3).



These are exothermic reactions and contribute most to the temperature rise in Fig. 5. The ratio of quick lime H to slaked lime H in Table 2 is 1.12 when it is equal in molar number. On the other hand, the ratio of the calorific value of Eq. (2) to the calorific value of Eq. (3) is 1.50. This difference is thought to be due to the different rate of exothermic reaction. Cement is a mixture of various minerals and contains many CaO based minerals. Therefore, cement generates ΔT by a dissolution reaction similar to lime.

Influence of Water Content on Temperature Rise

The influence of the water content of sandy soil on temperature rise before cement mixing was tested. Results are shown in Fig. 6.

ΔT showed little difference when compared with the case of 5% water content and 10% case. Then, when the water content was increased to 20%, ΔT decreased by 1 to 3 °C. It is considered that the influence of the water content on ΔT basically follows the heat quantity calculation. When the moisture content of soil falls within $\pm 5\%$, it can be used as a common calibration curve.

Influence of Time after Mixing of Cement and

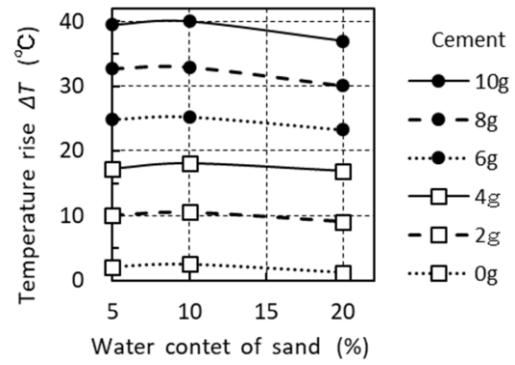


Fig. 6 Relations between water content of sand and ΔT (Sand; 100g as dry mass, HCl; 100mL, Concentration of HCl; 6M)

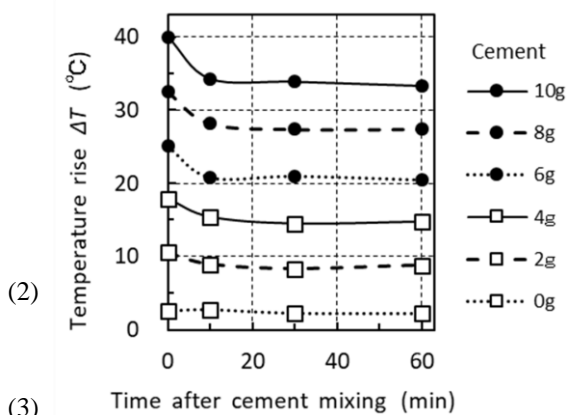


Fig. 7 Relations between time after cement mixing and ΔT (Sand; 100g as dry mass, w=10%, HCl; 100mL, Concentration of HCl; 6M)

Sand on Temperature Rise

The influence of elapsed time from increase of sandy soil and cement to temperature hydrochloric reaction heat test on temperature rise was investigated. The elapsed time was up to 60 minutes. The results are shown in Fig. 7.

ΔT indicates that the elapsed time is 0 minute, that is, it shows the maximum immediately after mixing. In addition, it decreased by 1.6 to 5.7 °C after 5 minutes, almost the same as after 5 minutes after 30 and 60 minutes.

The reason why ΔT decreased after 5 minutes is that the cement hydrates due to moisture in the sandy soil and ΔT decreased by that amount. Also, it is considered that the decrease in ΔT decreased after 5 minutes because it was a test under a relatively small amount of water. Even in the hydrochloric acid heat dissolution test conducted by Kanda [1] on flesh concrete, the decrease in ΔT associated with the elapsed time is greater for the larger amount of water. This suggests that the influence of elapsed time depends on hydration rate of cement. In the case of the result as shown in Fig. 7, it is necessary to carry out the hydrochloric acid heat reaction test avoiding 0 to 5 minutes.

Temperature Rise of Various Cements Mixed with Clay-Sand Slurry

The clay-sand slurry is obtained by adding 8 g of clay per 100 g of sand as a dry mass, and further adding 40 mL of water and mixing well. The amount of slurry was adjusted so that the total amount with cement to this slurry was 100 g, and 0 to 10 g of cement was added and mixed. Hydrochloric acid heat reaction test was carried out for this cement mixed soil. There are three kinds of cement used. The results are shown in Fig. 8.

ΔT increased linearly with any cement. And it showed the same tendency as the result of Fig. 4 which was tested using sand of relatively low water content. And Fig. 8 shows that the slope of the straight line became smaller than in Fig. 4 because the authors used soil with a lot of water. ΔT in 10 g of cement decreased by about 10 °C in Fig. 8 compared with Fig. 4. These are due to an increase in the heat capacity accompanying an increase in the amount of water, and it is considered that estimation of ΔT is possible by calculation of heat quantity.

Influence of Time after Mixing of Cement and Clay-Sand Slurry on Temperature Rise

ΔT was measured by setting blast furnace cement to clay-sand slurry and setting the time to perform hydrochloric acid heat test to 10, 30, 60, 1, 7 and 28 days. Samples were cured at 20 °C with vinyl sealed until testing. The results are shown in Fig. 9.

ΔT has begun to decrease from 10 minutes in any amount of cement. The decrease in ΔT is more prominent as the amount of cement is larger. A decrease in ΔT means that the hydration reaction of the cement has advanced. Under this test condition, the soil contains a sufficient amount of water for hydration of cement, so if the amount of cement is large, the internal temperature rises due to hydration reaction heat and the hydration reaction is assumed to be faster. It is thought that the reaction in which the soil particles adsorb a part of the calcium ions eluted from the cement is also involved. From this, it is important to limit the elapsed time from cement mixing to a certain range and to unify them in preparation of calibration curves and testing of specimens.

In addition, ΔT after 1, 7 and 28 days decreased as compared with ΔT after 10 minutes, but a considerable value remained. This suggests that it is possible to measure the amount of cement for samples of long-term material orders by devising the method of preparing the calibration curve.

RESULTS

In March 2017, construction was carried out to

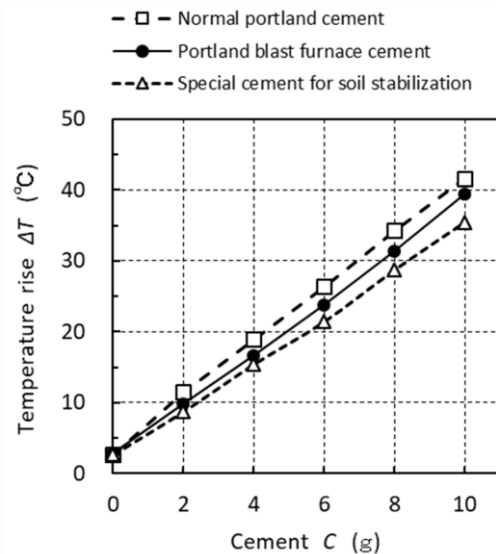


Fig. 8 Relations between cements mass and ΔT (Soils; sand with clay, 100g as dry mass, w=40%, HCl; 100mL, Concentration of HCl; 6M)

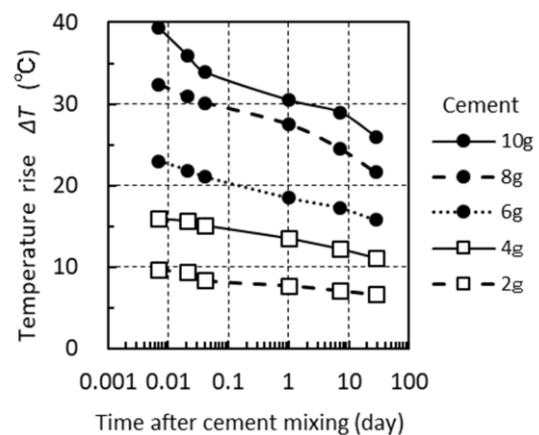


Fig.9 Relations time after cement mixing and ΔT (Soils; clay-sand, 100g as dry mass, w=40%, HCl; 100mL, Concentration of HCl; 6M)

supply cement milk to soft ground and stir and mix in the Tohoku region of Japan. The soil is almost homogeneous clay up to a depth of 10 m and has a natural water content of 74.3 %, a wet density of 1.48 g/cm³, a liquid limit of 77.1 %, a plasticity limit of 44.8%, a 75 μm to 2 mm content of 12%, a <75 μm content of 88%. The improvement depth of the ground was GL.0 m to GL -10 m. In order to improve this ground to the target strength, special cement for ground improvement was mixed with designed addition amount of 80 kg/m³. Cement was supplied in cement milk with a water/cement ratio of 2.28. The stirring and mixing machine is one in which stirring blades are attached to a chain rotating in the vertical direction. Because the soil layer to be improved was a soil that was difficult to mix with a very viscous soft clay, the water ratio of cement milk was set higher.

In this construction, in order to investigate and

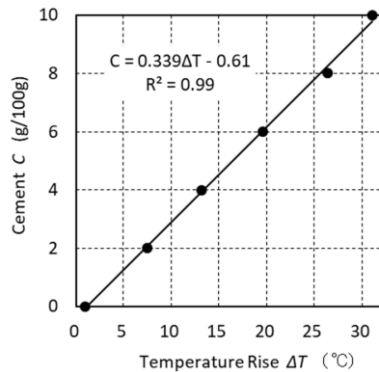


Fig. 10 Example of calibration curve for the site (Soils; 100g as wet mass, w=74%, HCl; 100mL, Concentration of HCl; 6M)

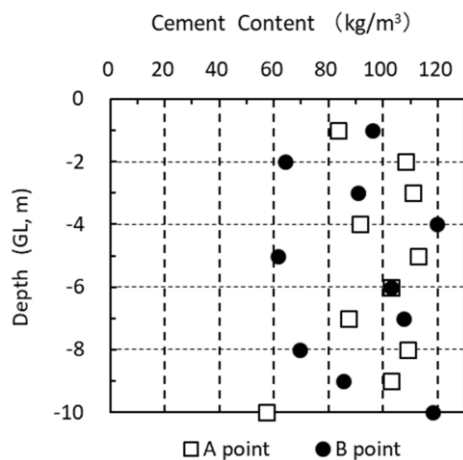


Fig. 11 Example of cement contents for the site

control the mixing precision of cement, the authors brought equipment of hydrochloric acid reaction heat method to the site and measured cement content at the site. A sampling tube was inserted at the site where stirring and mixing of the cement was completed at the site, samples were taken for each depth, and the cement content was measured. An example of the calibration curve is shown in Fig. 10.

A calibration curve was prepared each time the local soil quality changed. For the calibration curve, the horizontal axis represents ΔT and the vertical axis represents the cement content C. An example of the results of the cement content test in the depth direction immediately after cement improvement is shown in Fig. 11.

The points A and B are the points for investigating the construction conditions of horizontal movement (stirring time) of the stirring machine. The mutual distance between the two points is about 3 m. The hydrochloric acid heat reaction method, which was easily made at the site and results quickly contributed to the rationalization of construction.

CONCLUSIONS

In the construction method which increases strength by mixing cement to soft ground, the mixing accuracy of cement affects the quality. Depending on the soil, there are many grounds that cannot be conditions of stirring and mixing, it is necessary to measure the cement content and evaluate the variation at the site.

In this study, hydrochloric acid heat treatment method was tried as a test method which can be easily tested in the field, quick results can be obtained without requiring special mechanical equipment. Detailed test conditions for applying this method to cement mixed soil were investigated.

Take 100 g of the sample in a heat-retentive container, add 100 mL of 6M-HCl, stir with the thermometer inserted, and read the maximum temperature. The initial temperature is measured in advance. If it prepare a calibration curve (relationship between cement amount and rising temperature) using local soil and cement used in construction, the cement content of the sample soil can be determined from the rising temperature of the sample soil. Regarding the influence of water content and elapsed time, there is a practical allowable range, but if it exceeds it, it is necessary to prepare a calibration curve separately.

ACKNOWLEDGEMENTS

The authors got a lot of guidance by Mr. K. Morita and Mr. K. Mochizuki belonging to Obayashi Corporation, Mr. H. Ito and Mr. T. Makino belonging to Kato Construction Co. Ltd., in the field application tests. Also, the authors got kind cooperation from Mr. T. Adachi, Mr. M. Tomita and Mr. Y. Nagao belonging to Tachibana Material Co. Ltd.. The authors would like to express our sincere appreciation to all of them here.

REFERENCES

- [1] M. Kanda: A Measuring method for water cement ratio in fresh concrete, Proceedings of the Japan Society Civil Engineers. Vol.193, pp.115-123 (1971)
- [2] H. Tezuka, T. Yamauchi and A. Kawanishi: Development of quality management for haig pressure injection mixing method, Japanese Geotechnical Jounal. Vol.8, No.2, pp.251-263 (2011)
- [3] Y. Hosokawa et al: Development of a multispecies mass transport model for concrete with account to thermodynamic phase equilibriums. Materials and Structure. Vol.34, pp.1577-1592 (2011)

RELATIONSHIP BETWEEN CONSTRUCTION METHOD OF CRUSHED STONE PILE AND BEARING CAPACITY CHARACTERISTICS

Seiya Yamazaki¹, Naoaki Suemasa¹, Kazuya Ito¹, Makoto Hotta²

¹Tokyo City University Graduate Division, Japan

²Hyspeed Corporation co., Ltd, Japan

ABSTRACT

A crushed stone pile construction method can be cited as one of ground improvement construction methods for detached houses. Since natural crushed stone is used by this construction method as a material, it is less affected by soil modification and the removal is easier than other ground improvement construction methods. On the other hand, it may vary in vertical bearing capacity depending on construction conditions such as crushed stone input amount or compaction degree. Therefore, if the construction conditions are not appropriate, the bearing capacity shortage would be concerned. The purpose of this study is to investigate the influence on the vertical bearing capacity by the difference in the construction conditions. In this report, in order to investigate the bearing capacity characteristics of a crushed stone pile, vertical loading experiments were carried out, where the different compaction loading was applied for same input amount in model experiments. Also, in order to evaluate the effect on the vertical rigidity improved by the crushed stone pile construction, composite grounds were modeled and confirmed the vertical bearing capacity using the experimental value of the load for the same settlement. As a result, it was confirmed that the vertical bearing capacity of crushed stone pile and composite ground increased by increasing the compaction load on the crushed stone piles.

Keywords: Crushed stone pile, Compaction load, Crack, Over compaction

INTRODUCTION

In recent years, construction of houses has been increasing even in unsuitable soft ground for housing in urban areas of Japan due to overcrowding of residential areas. Since collapse of small houses and irregularity subsidence were caused when the Tohoku District Pacific Offshore Earthquake occurred in 2011, the improvement of earthquake resistance of housing foundation has been promoted. A crushed stone pile construction method can be cited as one of ground improvement construction methods for detached houses. In this construction method, crushed stones are compacted in a hole to form a pile figure under house foundation so that the compaction of crushed stones would make the surrounding soil dense by pushing out the hole wall at the time of construction. That is, the mechanism of this method is to support the structure with the composite ground of crushed stone piles and compacted ground. In addition, since crushed stone is natural material, the piles are friendly to the environment and can remove much easier than products in other ground improvement construction methods. On the other hand, the bearing capacity of the pile may vary in response to ground and construction conditions such as crushed stone amount packed or compaction degree of ground. Therefore, if the construction control is not appropriate, the bearing capacity shortage of the pile would be concerned. The purpose of this study is to investigate the influence of pile

construction conditions on the vertical bearing capacity. In this report, a series of vertical loading experiments was carried out where various compaction loads were applied to crushed stone piles installed in model ground.

MODEL GROUND PREPARING

Soil sample for the model ground was prepared by mixing fine clay for pottery and silica sand of No. 7 grain grade at a dry weight ratio of 1: 1, as shown in Figure 1, and adjusted at the optimum water content ratio of 14.2%. Then the sample of 20 kg was spread in a rectangular iron tank with 400 mm width, 1000 mm length and 300 mm height in which each layer is 4 cm in thickness. A model ground was compacted by rolling a small size roller horizontally in the longitudinal direction on the ground surface at a static linear pressure of 8 N / cm in the first step, and 30 N / cm in the following steps. The roller is made of vinyl chloride and its diameter and compaction width are 105 mm and 100 mm, respectively [1]. Figure 2 shows a model ground compacted by the roller in the tank. The vertical load applied to the roller was adjusted by pneumatic pressure using a diaphragm air cylinder. The number of compaction per a layer was set to 8 times (4 round trips) according to the

Table.1 The construction conditions of crushed stone piles

	CASE	Number of compaction (times)	Input amount of crushed stone per layer (g)	Weight of rammer (g)	Fall height (cm)	Total crushed stone amount (g)
Standard	0	0	0	0	0	0
	1	10	30	766	7	90
Energy inputted per layer (Constant)	2	2	6	766	7	96
	3	5	15	766	7	75
	3'	5	15	766	7	95
Potential energy(Constant)	4	10	30	1151	4.7	90
	5	10	30	1501	3.6	95
	6	2	6	1151	4.7	102
	7	2	6	1501	3.6	102

compaction management requirement of the Ministry of Land, Infrastructure and Transport in Japan [2]. Also, height control was carried out based on the Residential Building Regulation Enforcement Order in Japan [3], and the degree of compaction of the ground. Dc was set to be greater than 87%, and checked at every step where each layer was compacted.



Fig.1 Sample used for model ground

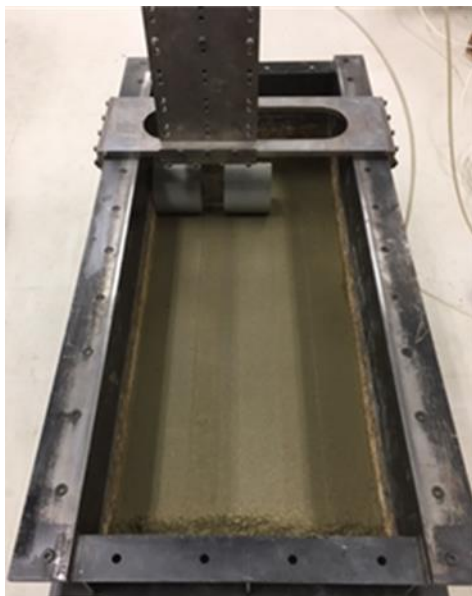


Fig. 2 A model ground compacted by the roller in the tank.

EXECUTION CONTROL OF CRUSHED STONE PILE

There are a lot of unknown points in the installation mechanism of the crushed stone pile. Especially, it is unclear how the performance of crushed stone pile is influenced by the difference in construction conditions such as the number of compaction, the input amount of crushed stone per a layer and the compaction energy per a blow. In this study, therefore, a series of tests was carried out to examine the effects of various construction conditions on the performance. In the model experiments, the crushed stone piles were set at 170 mm length which was determined as the most controllable length for this tank from the results of previous study [4]. The process of constructing a crushed stone pile is as follows. At first, the ground is preliminarily drilled down to a depth of 170 mm using a hand drill with a diameter of 20 mm. Then, a sample mixed with silica sand of No.2 grain grade and No. 6 with a ratio of 1:1 was put into the borehole where coarse sand of No.2 substituted crushed stones and finer sand of No.6 filled the voids in the ground. After that, the sample was compacted by blows with a rammer. Also, in order to confirm the depth of each layer, measurements were made from the top of the borehole to the bottom using a ruler after every compaction of each layer. This process was repeated to complete the construction of crushed stone piles [5]. Table 1 shows the construction conditions of crushed stone pile. Using CASE 1 as the reference case, conditions for other cases were changed in the number of blows, input amount per layer, weight of rammer, etc.

Figure 3 shows the relationship between total weight amount of crushed stones and depth as the results of CASE 1 to CASE 3 where the compaction energy inputted per layer are the same. The difference in depth between before and after the sample compaction represents the compaction amount due to the compaction energy. In addition, it is possible to estimate the pile profile from the graph of total crushed stone amount and depth. As for CASE 2, there was a variation in depth per layer. Therefore, it can be assumed that a part of the specimen was compacted excessively not in the vertical but in the horizontal direction and the outer diameter of the pile consequently became irregular. In CASE 3, since the

initial depth was shallow, it is shown that the soil in the borehole couldn't be sufficiently removed at the time of drilling and the residual soil was left at the bottom of the borehole. It seems possible to create a pile having a uniform outside diameter, since the outline of the graph was substantially linear in CASE 1.

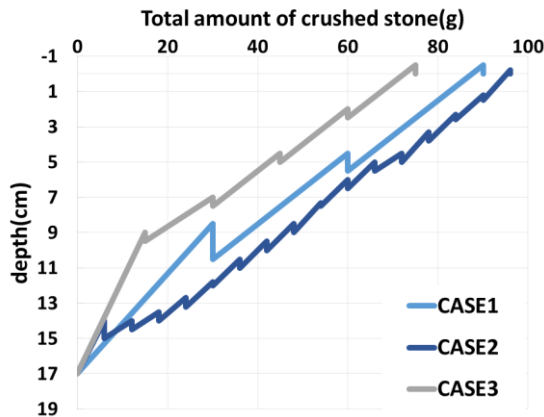


Fig. 3 The relationship between the total weight amount of crushed stones and the depth

VERTICAL LOADING TEST (CRUSHED STONE PILE)

OUTLINE OF EXPERIMENT

From the previous chapter, the profiles of crushed stone piles were confirmed from the outline of the graph of total crushed stone amount and depth. Subsequently, vertical loading tests were conducted to investigate the influence of the difference in compaction load of a crushed stone pile on its bearing capacity. The crushed stone piles for the experiments were constructed in the same way as the mentioned earlier where pre-drilling was performed using a hand drill and then the mixed sample was put into the borehole. Figure 4 shows a loading instrument with bolt mechanism used in the experiments. The instruments were selected corresponding to the depth of boreholes and installed on the top of a crushed stone pile. Thereafter, using a vertical loading device shown in Figure 5, a constant pressure was applied to compact the sample statically [6]. Table 2 shows the construction conditions of crushed stone piles. Using CASE 0' as the reference case which is for an unimproved ground, compaction loads for other cases were changed to investigate the influence on bearing capacity of a pile. In the vertical loading test, a footing with a diameter of 19 mm and a height of 50 mm was installed on the top of a crushed stone pile and then the load was applied until the vertical displacement exceeded 45 mm.



Fig. 4 The loading instrument



Fig. 5 A vertical loading device

EXPERIMENTAL RESULT

Figure 6 shows the relationship between vertical load and vertical displacement. In addition, the test result of CASE 0' for an unimproved ground is also shown as reference. In CASE 8 to 11, where the crushed stone piles were constructed with a constant compaction load, higher initial rigidity and less ground settlement amount showed than those in CASE 0'. In addition, as shown in CASE 10, it was confirmed as well that the large compaction load increased the compaction amount of pile and exerted high bearing capacity. However, in CASE 11 where the compaction load was equivalent to CASE 10, the settlement amount became excessive. Figure 7 shows the surface layer of CASE 11 after reloading. In CASE 11, it is considered that excessive settlement was caused due to cracks in the surface layer. Therefore, it was also found that over-loaded compaction may cause cracks in the surface layer and the desired settlement reduction effect may not be obtained.

Figure 8 shows the relationship between vertical load and vertical displacement describing from the stage of the compaction of third layer to the unloading/reloading. Figure 9 shows the relationship between vertical load and vertical displacement in the cases the compaction loads of 200N, 300N and 400N were

Table.2 The construction conditions of crushed stone piles

CASE	Compaction load of first and second layers (N)	Compaction load of third layer (N)	Input amount of crushed stone per layer (g)	Compaction time (min)	Total crushed stone amount (g)
0'	0	0	0	0	0
8	200	200	30	1	86
9	300	300	30	1	90
10	400	400	30	1	90
11	400	200~400	30	1	90

applied to the third layer stepwise and reloading was carried out after loading and unloading. As the compaction load on the crushed stone pile increased, the compaction amount per layer became larger. It is considered the densities of CASE 8, 9 were not changed so much that the voids of the sample around the crushed stone pile decreased by the compaction load. However, as a sharp increase was seen in the vertical displacement of CASE 10 and 11, it is pointed out that there is the possibility of over compaction when exceeding the compaction load of 380 N. On the other hand, the load-settlement curves of CASE 8 to CASE 10 were substantially similar after reloading. Therefore, it can be said that the load-settlement behavior of the crushed stone pile after construction was attributed to the settlement reduction effect by the compaction load, similarly to the preloading method.

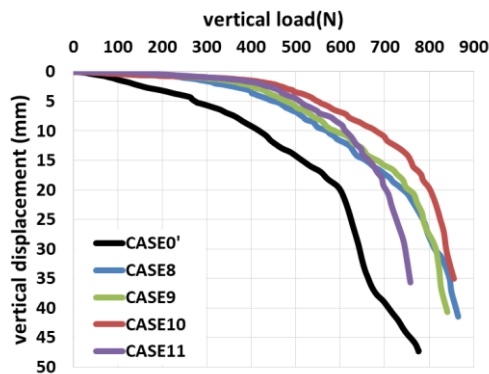


Fig. 6 The relationship between vertical load and vertical displacement.



Fig. 7 The surface layer of CASE 11 after reloading

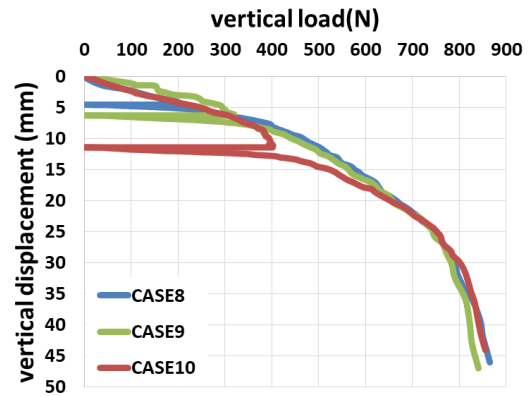


Fig. 8 The relationship between vertical load and vertical displacement.

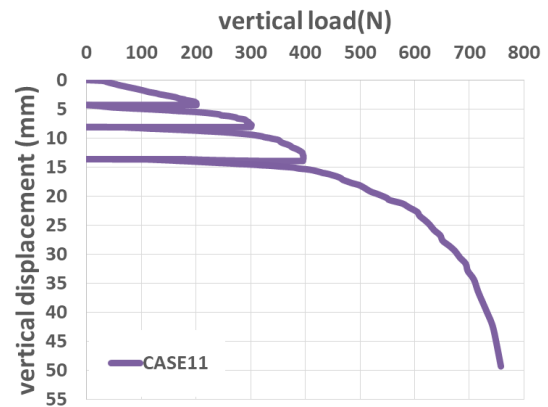


Fig. 9 The relationship between vertical load and vertical displacement.

VERTICAL LOADING TEST (COMPOSITE GROUND)

OUTLINE OF EXPERIMENT

In the previous chapter, the relationship between compaction load of the crushed stone pile and bearing capacity was confirmed. In this chapter, vertical loading tests were conducted on the crushed stone piles constructed under the conditions of CASE 0', CASE 8 and CASE 10 shown in Table 2 for the purpose of confirming the bearing capacity in the composite ground. The pile diameters of CASE 8 and 10 were 23.5 mm and 24.7 mm, respectively. In the vertical loading tests, to load to the composite ground

consisting of a crushed stone pile and the surrounding ground, a five-tooth footing with a length of 100 mm and a width of 100 mm, as shown in Figure 10, was installed on top of the crushed stone pile.

After that, a vertical load up to 2,500 N was applied on the footing.

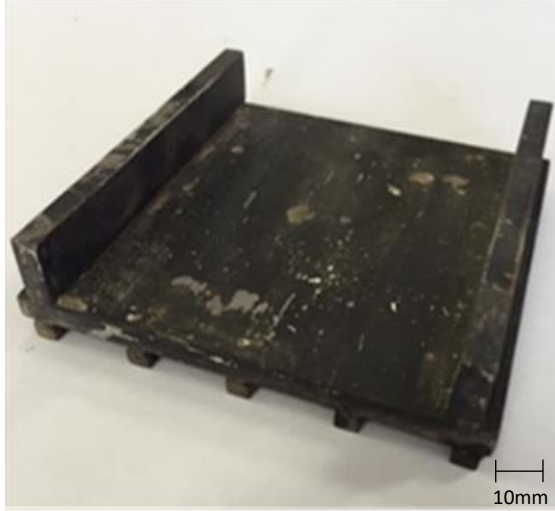


Fig. 10 A five-tooth footing

EXPERIMENTAL RESULTS AND DISCUSSION

Figure 11 shows the relationship between vertical load and vertical displacement. In CASE 10, the composite ground had higher initial rigidity than the other cases. Since the improvement rates of CASE 8 and CASE 10 were almost equal, it is considered that the increase in the compaction load of the crushed stone pile increased the rigidity of the crushed stone pile section in CASE 10. In addition, as the yield points were not observed in CASE 8 and 10, it was confirmed that the bearing capacities were high in both cases compared to CASE 0'. However, the load-settlement curve of CASE 10 matched with that of CASE 8 around 2.0 kN. It seems that their amounts of residual settlement became similar because their total amounts of the crushed stone pile were almost equal.

In order to evaluate the effect on the vertical rigidity improved by the crushed stone pile construction, composite grounds were modeled as shown in Figure 12. At first, the model grounds were prepared assuming that the unimproved ground can be represented by a plurality of independent vertical springs and the crushed stone pile by an independent vertical spring having a different rigidity, respectively. In other words, the improved ground with one crushed stone pile can be represented by replacing one of the springs for unimproved with one stiffer

spring for the crushed stone pile. Based on the load-settlement curves of the spring obtained from the experiment, the vertical bearing capacity can be derived from the following equation using the experimental value of the load for the same settlement.

$$F_c = F_i + \alpha F_p - \beta F_g \quad (1)$$

where F_c is the bearing capacity of the composite ground at a certain settlement (N), F_g is the bearing capacity of the unimproved ground loaded with pile diameter footing (diameter 19 mm) (N), F_i is the bearing capacity of the unimproved ground loaded with a footing of 100 mm length and 100 mm width (N), F_p is the bearing capacity of the ground with crushed stone pile(s) (N), α , β is the interaction coefficients.

The predicted values of the constructed pile were obtained from the Eq. (1). For comparison, the interaction coefficients were defined as $\alpha = 1.0$, $\beta = 1.0$ and $\alpha = 1.2$, $\beta = 1.0$, respectively. Figure 13 shows a comparison of the measured value and the predicted value ($\alpha = 1.0$, $\beta = 1.0$). The experimental value and the predicted value of CASE 10 were approximately same. However, although the similar behaviors were seen up to about 1.7 kN, the settlement largely increased thereafter in CASE 8. As seen in CASE 0', there is a possibility that this deviation was caused by the initial unevenness between ground and footing.

Figure 14 shows a comparison of the measured value and the predicted value ($\alpha = 1.2$, $\beta = 1.0$). Compared to Figure 13, the predicted values were closer to the measured values in both cases. From this fact, it was confirmed that the accuracy of the predicted value can be improved by considering the interaction coefficients which varies depending on the ground conditions.

It was revealed that the improvement effect can be confirmed using a relatively simple formula.

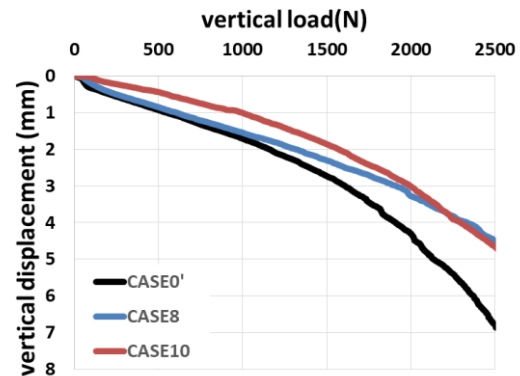


Fig. 11 The relationship between vertical load and vertical displacement.

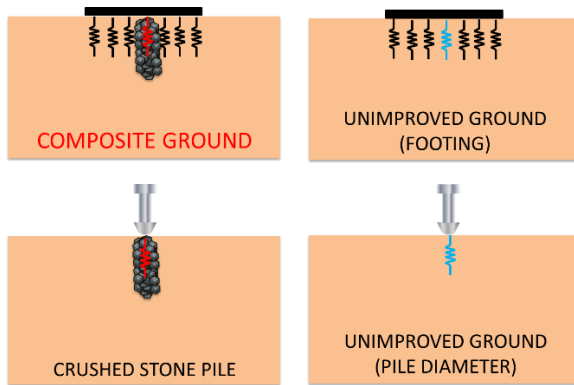


Fig. 12 Modeling of composite ground

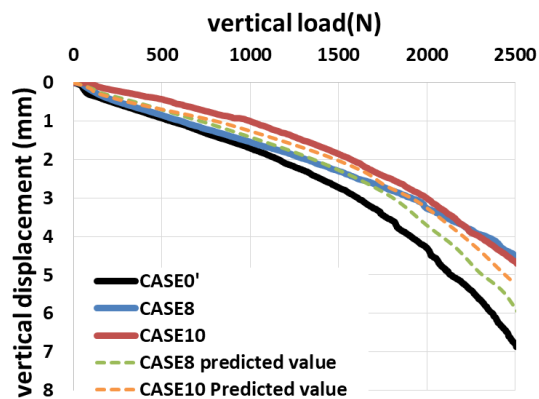


Fig. 13 A comparison of the measured value and the predicted value ($\alpha = 1.0$, $\beta = 1.0$)

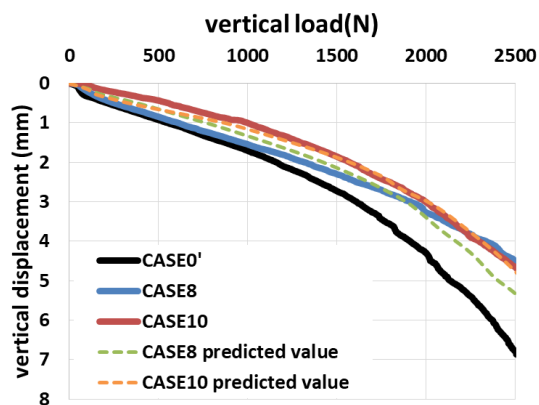


Fig. 14 A comparison of the measured value and the predicted value ($\alpha = 1.2$, $\beta = 1.0$)

CONCLUSIONS

The following findings of the behavior of the crushed stone pile were suggested from the vertical loading tests.

- 1) It was found that the amount of settlement can be reduced due to the compaction load applied to a crushed stone pile.
- 2) On the other hand, expected settlement reduction cannot be obtained when over compaction load is applied to the crushed stone pile during construction.
- 3) The vertical bearing capacity of composite ground can be evaluated by modeling the composite ground as springs with two kinds of stiffness.

REFERENCES

- [1] Kosuke U, Ryotaro M, Naoaki S, Kazuya I, Tsuyoshi T, Makoto H (2016) "Model Test for Combination loading Improved by Crushed Stone Pile" *Kanto Branch of The Japanese Geotechnical Society*, CD-ROM
- [2] Ministry of Land, Infrastructure and Transport (2012) "Infrastructure and Transport, Compaction management of embankment using TS · GNSS"
- [3] Ministry of Land, Infrastructure and Transport "Residential Building Regulation Enforcement Order"
- [4] Ryotaro M, Naoaki S, Makoto H, Hayato K (2014) "Model loading experiment about the crushed stone pile" *Proceedings of the 49th Annual Conference of The Japanese Geotechnical Society*, 817-818
- [5] Seiya Y, Katsuhiro S, Naoaki S, Kazuya I, Tsuyoshi T, Makoto H (2017) "A Fundamental Study on Method of Making Crushed Stone Piles" *Kanto Branch of The Japanese Geotechnical Society*, CD-ROM
- [6] Seiya Y, Katsuhiro S, Naoaki S, Kazuya I, Tsuyoshi T, Makoto H (2018) "Relationship between Construction Method of Crushed Stone Pile and Bearing Capacity Characteristics" *Kanto Branch of the Japan Society of Civil Engineers*, CD-ROM

A STUDY ON INFLUENCE OF PENETRATION DISTANCE ON GEL TIME OF CHEMICAL GROUT

Ryota Nakamura¹, Naoaki Suemasa¹ and Sakamitsu Sasaki² Syunsuke Shimada²

¹ Tokyo City University Graduate Division, Japan

² Kyokado Engineering co.,Ltd, Japan

ABSTRACT

Damage of liquefaction phenomenon caused by earthquakes has become a social problem. A chemical grouting method is one of liquefaction countermeasure methods, which makes it possible to construct even in a narrow place or under existing buildings using oblique boring technology. However, its penetration mechanism is complicated. For examples, since the chemical grout is diluted at time of injection, pH of the chemical grout could change by the reaction with alkali ingredient in soil, which could cause shortage of the gel time. Therefore it is intended to elucidate penetration solidification mechanism in this study. In this report, one-dimensional penetration experiments were conducted using some samples, where the following parameters were measured; pH of the soil and the gel time of chemical grout at different distances from the penetration point in the soil and compared to those before injection. As a result, gel time of injected chemical grout shortened in end part of penetration. Furthermore, it was revealed through the experiments using the sample obtained directly from a site that gel time became considerably shorter when high Ca was contained in the soil.

Keywords: chemical grouting method, penetration distance, gel time, pH

INTRODUCTION

The Tohoku-Pacific Ocean Earthquake occurred on March 11, 2011 and liquefaction caused serious damage in reclaimed land and to the lifeline over a wide range in Japan. As one of the countermeasures to prevent such a liquefaction damage, chemical grouting methods have been used. Fig 1 shows a mechanism of a chemical grouting method. The mechanism of the chemical grouting method is to improve ground by filling injection material in the voids of soil particles without disturbing the deposition state of the ground. However, the problem is that its permeating mechanism is complicated [2] [3] [4]. For examples, since the chemical grout is diluted at time of injection or the pH of chemical grout could change by the reaction with alkali ingredient in soil at the site, the gel time could be shorter than expected. As a result, various phenomena can be caused such as sagging of the grout or a swelling of ground surface [5] [6].

In this report, one-dimensional permeation experiments were conducted using some samples, where the following parameters were measured; the pH and the gel time of the chemical grout extracted from the soil at various distances. The solidification mechanism of the chemical grout in the ground was investigated from the results.

DILUTION EXPERIMENT OF CHEMICAL GROUT

One of the factors to change the gel time is

dilution of chemical grout injected in the ground. Then, a dilution experiment of the gel time was carried out for the purpose of obtaining the basic data. The chemical grout used for the experiment was silica sol having a silica concentration of 9%. Six beakers were prepared, which contained equivalent amounts of the chemical grout with a silica concentration of 9%. Then water was added to them so that their concentrations gradually changed to 6% and the pH and the gel time were measured at the same time. Fig 2 shows the result of the dilution experiment. It also shows the relationship between pH and GT of the chemical grout whose silica concentrations were set at 6, 9 and 12%. As seen from the figure, the gel time became shorter in both cases when the pH approaches neutral at any silica concentrations and when the silica concentration increased at same pH. As a result of the dilution experiment, it was confirmed that the gel time was lengthened but the pH hardly changed by dilution of chemical grout.

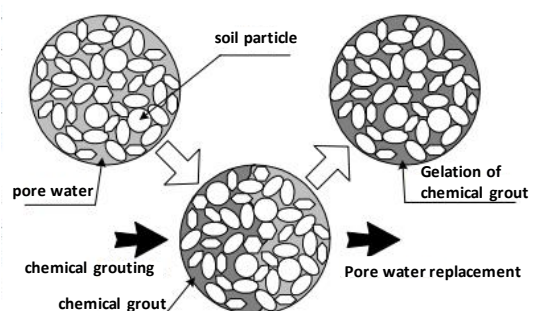


Fig 1 A mechanism of a chemical grouting method [1]

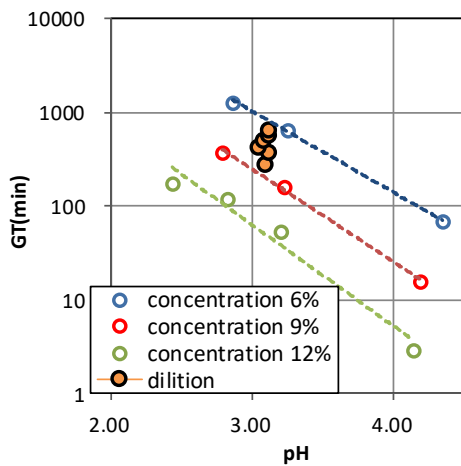


Fig 2 The result of the dilution experiment

CONSTANT SPEED INJECTION EXPERIMENT

EXPPERIMENTAL SETUP

Fig 3 shows the outline of one-dimensional grout injection experiments. The permeation mold is made of acrylic with an inner diameter of = 5cm and a height of = 110cm. Toyoura sand was used as a sample. The specimen was prepared in which the sample in the dry state was compacted by vibration with a hammer every 10cm so that the relative density of the sand specimen inside the mold became 60%, and then saturated with degassed water [7].

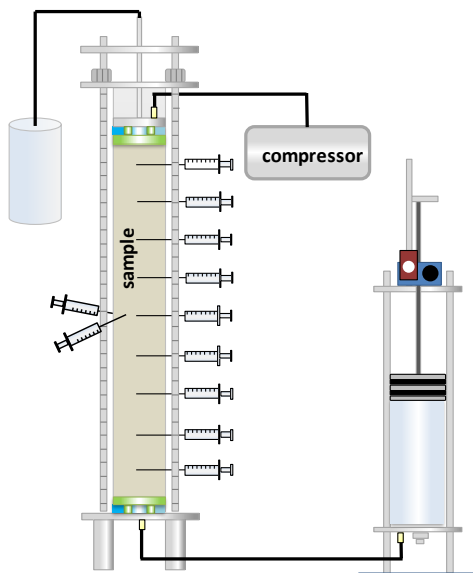


Fig 3 The outline of one-dimensional grout injection experiment

As a chemical grout, active composite silica, called PERMA ROCK ASF-II α , with a silica concentration of 8% was used. In the injected

experiments, the chemical grout was injection from the bottom of the mold to a height of 85cm. At that time, in order to confirm the influence of the difference in the permeation distance on the gel time, the chemical grout was extracted immediately after the completion of the injection using a syringe installed at intervals of 10cm. In order to ascertain the influence of injection rate on gel time, two cases with different injection rates were performed. The injection rates were set at 0.45L/min for Case1 and 0.045L/min for Case2, respectively and the chemical grout was injected up to a height of 85cm of the specimen. The required times were 2 for Case 1 and 16 minutes for Case 2, respectively. Then, the gel time and the pH of the chemical grout were measured, which was injected completely and extracted immediately after the completion. The remained chemical grout, injected in the soil, was also measured the gel time and the pH for comparison. In addition, in Case1, to investigate the influence of the extraction time, two additional syringes were separately installed at a height of 50 cm, and the chemical grout extracted after 30 minutes and 60 minutes were measured in the same way.

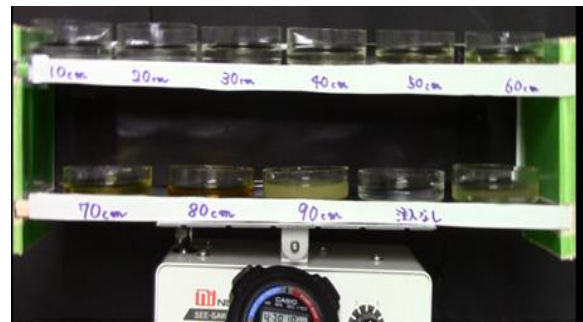


Fig 4 The gel time measure

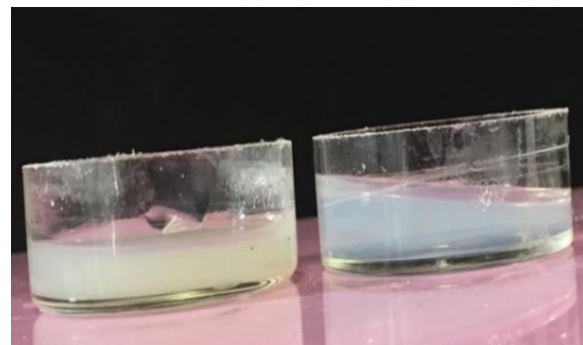


Fig 5 Before and after solidification of the chemical grout.

The measurement process of gel time is as follows. The extracted chemical grout divided according to the permeation distance was placed in glass petri dishes of $\phi=4$ cm and then fixed on a small shaker seesaw. Fig 4 shows the gel time measuring apparatus used in this experiment. Thereafter, this seesaw was shook

regularly on the left and right at an angle of ± 7 degrees from the center, and it was defined as gel time when the liquid level of the chemical grout in the petri dish began to tilt due to solidification. Fig 5 shows a comparison between before and after solidification of the chemical grout.

EXPERIMENTAL RESULT

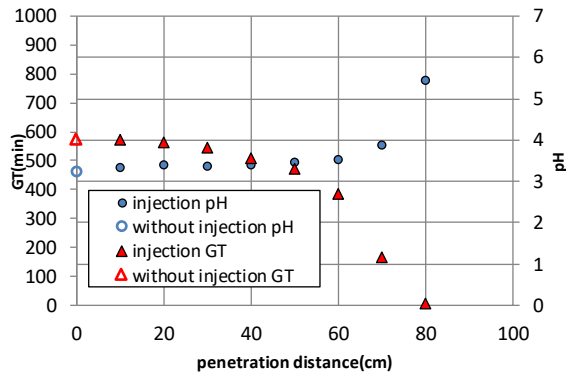


Fig 6 The gel time and the pH corresponding to permeation distance

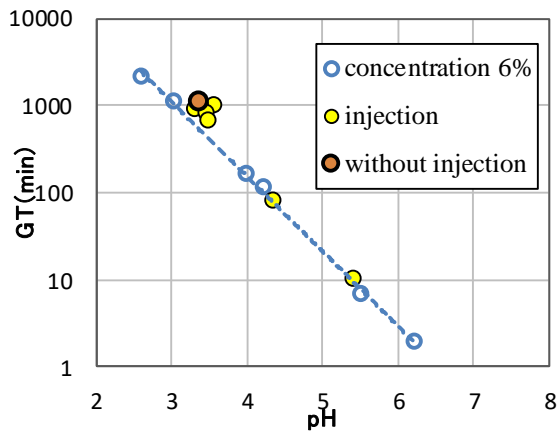


Fig 7 Gel time and pH

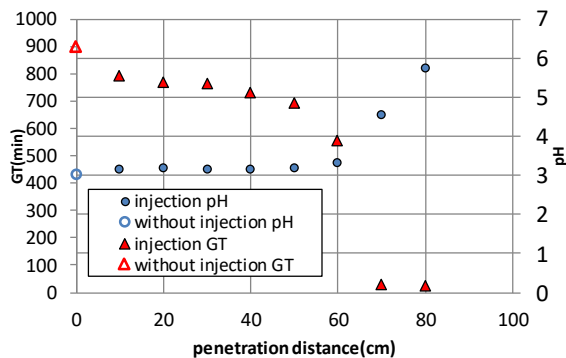


Fig 8 The gel time and the pH corresponding to permeation distance

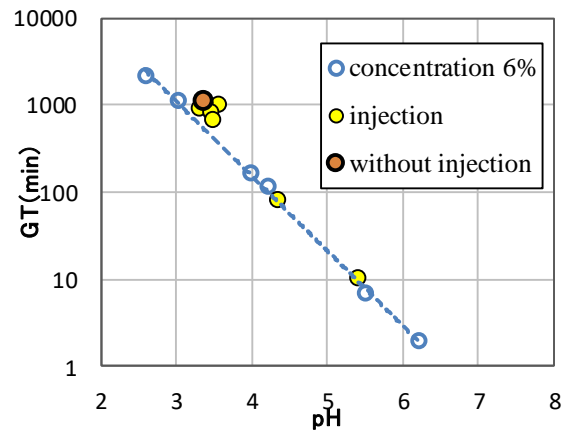


Fig 9 Gel time and pH

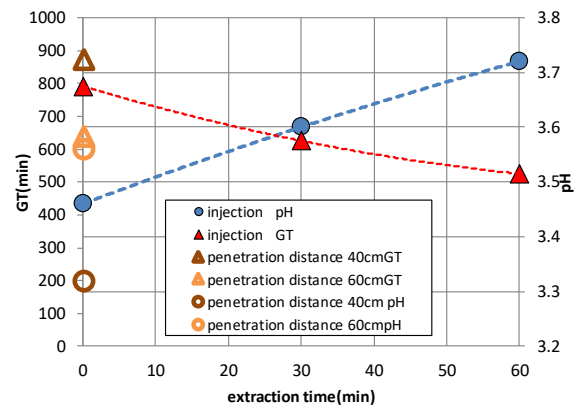


Fig 10 Comparison of extraction times

As the experimental result of Case1, fig 6 shows the gel time and the pH corresponding to permeation distance and fig 7 shows the relationship between gel time and pH. The figure also shows the blending test result of the grout with the concentration of 6% where the gel time is compared as the chemical grout without injection. In the figure, the gel time becomes shorter and the pH tends to become neutral as the permeation distance becomes longer. From the result, it seems that the pH increased because the acid in the chemical grout reacted with the alkali component originally existing in the soil sample and was consumed. Furthermore, the pH increase was remarkable in the preceding chemical grout with a long permeation distance and hardly occurred in the chemical grout subsequently permeated. In other words, a sort of cleaning action or flushing effect might be occurring. Similarly,

The results of Case 2 where the injection rate was set at 0.045L/min are shown in fig 8 and fig 9. Similarly, the longer the permeation distance became, the shorter the gel time became and the tendency that the pH turned to be neutral was observed in this

injection experiment. However, the preceding chemical grout with penetration distance of 70cm and 80cm was solidified earlier than those of Case1. It is considered that this was because the injection rate was lower than that in the previous case and the preceding chemical grout sufficiently reacted with the alkaline component in the sample.

Fig 10 shows the results of the chemical grout which was extracted at 30 minutes and 60 minutes after the injection, respectively. In the figure, the chemical grout extracted at the point of 50cm from the permeation point shows a tendency that the gel time becomes shorter and the pH tends to become neutral as the extraction time becomes longer. Although the change was slightly smaller than that of the preceding chemical solution, it can be seen that the injected chemical grout gradually reacted with the alkali component and the gel time was shorten.

IN SITU SAMPLE EXPERIMENT

SETUP FOR GEL TIME EXPERIMENT IN SOIL

One-dimensional injection experiments using in situ sample were conducted. Fig 11 shows the grain size distribution of the sample and Table1 shows the physical properties of the sample, respectively.

This sample contains 15000mg/kg calcium component and 2.4% fine particle content. As a chemical grout, active composite silica (PERMA ROCK ASF-II α) was used.

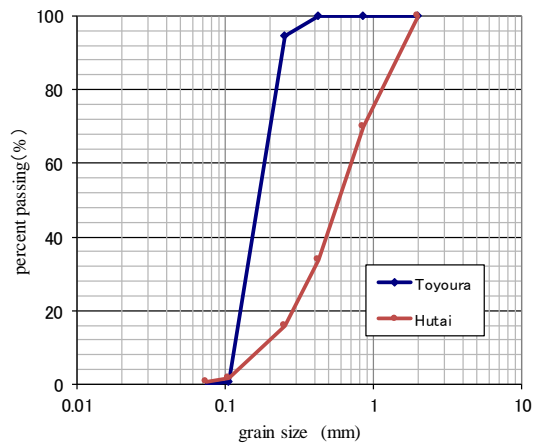


Fig 11 grain size distribution

GEL TIME EXPERIMENT RESULTS IN SOIL

Two different methods were used to measure the gel time of the grout in the soil. One is a measurement of the permeable grouting method, where the soil sample is saturated with distilled water at a ratio volume (or weigh) of 4: 1 and then mixed with

chemical grout at a ratio of 4: 1 [8]. The other is a measurement of the multi-points grouting method, where the sample and chemical grout were mixed with each other at a ratio of 2.5: 1 in drying state [9]. Table 2 shows the gel time of the sample in the soil measured by these methods. As seen from the table, the gel time measured in the multi-points grouting method was shorter than that in the permeable grouting method. The difference between the two is considered to be the effect of the dilution with water. Fig 12 shows the state of gel time measurement in the soil.

Table1 The physical properties of the sample

particle size	hydraulic Conductivity	void
D ₁₀ =0.18 (mm) D ₅₀ =0.43 (mm) D ₉₀ =1.65 (mm)	4.8×10 ⁻² (cm/sec)	e _{max} =0.957 e _{min} =0.558

Table 2 The gel time of the sample in the soil measured

concentration	pH	permeable grouting method GT	multi-points grouting method GT
8%	3.10	19 (min)	2 (min)
	2.47	50 (min)	5 (min)
4%	2.45	—	20 (min)

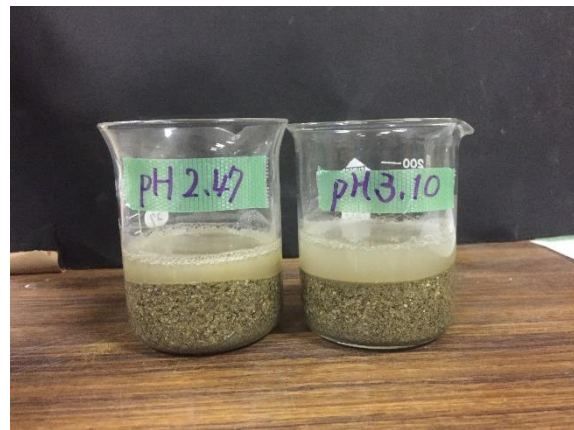


Fig 12 The state of gel time measurement in the soil.

INJECTION EXPERIMENT RESULT

The permeation mold used for the experiment is made of acrylic cylinder with an inner diameter $\phi=5$ cm and height $h=110$ cm. Specimen was prepared by compacting the sample to a relative density of 60% and then saturating it with degassed water.

Injection experiments were conducted using two cases of chemical grout selected from the measurement results of gel time. Table 3 shows the experimental conditions. The injection rate was set at 0.045L/min, the injection distance was 85cm and the injection time was 16 minutes, respectively.

Fig 13 shows the relationship among permeation distance, gel time and pH in Case 4 and Fig 14 shows the change of injection pressure with time. In Case3, although injection of the chemical grout was completed, it was impossible to extract the chemical grout with a syringe. The reason is considered to be due to the gelation in the midst of injection of the chemical grout since the injection pressure started to increase around 100 seconds after injection.

In Case 4, injection was completed without sudden increase in injection pressure and the chemical grout was able to be extracted with a syringe. However, although the gel time became relatively shorter as the penetration distance became longer, it was extremely shorter than that in the air. Also, the pH was neutralized uniformly. Compared to Toyoura sand, this sample contains so much calcium content that it is considered that acid consumption of chemical grout was promoted not only in the preceding drug solution but also all over the chemical grout. Also, both in Cases 3 and Case 4, the effluent discharged from the upper part of the specimen was solidified during the chemical grout injection. It is assumed that this is because obstructions were made in some of voids by the CO₂ produced by the reaction between acid and calcium content or the silica solidified during the injection process [10].

In order to clarify this mechanism, further investigation is necessary in the future through the measurement of the weight or silica content.

Table 3 The experimental conditions

	pH	permeable grouting method GT	multi-points grouting method GT
Case3	2.47	50 (min)	5 (min)
Case4	2.45	—	20 (min)

CONCLUSIONS

In order to investigate the solidification behavior of the chemical grout in the ground, one-dimensional permeation experiments of chemical grout were carried out. As a result, the following results were obtained.

- 1) The gel time of the injected chemical grout became shorter at the preceding part. This is probably because the chemical grout reacts with the alkaline component contained in the soil sample.
- 2) In one dimensional permeation experiments

with in-situ samples, the gel time was considerably shortened due to the high calcium content in the samples.

Further study is needed to clarify the relationship between calcium consumption rate and gelation rate of chemical grout in the future.

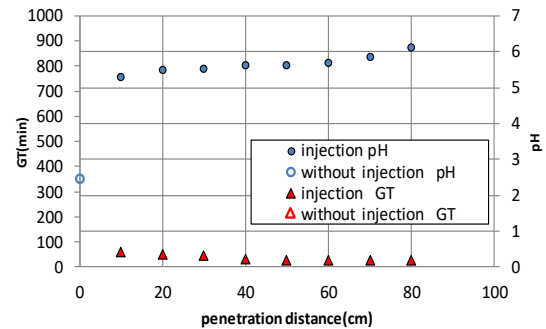


Fig 13 The relationship among permeation distance, gel time and pH

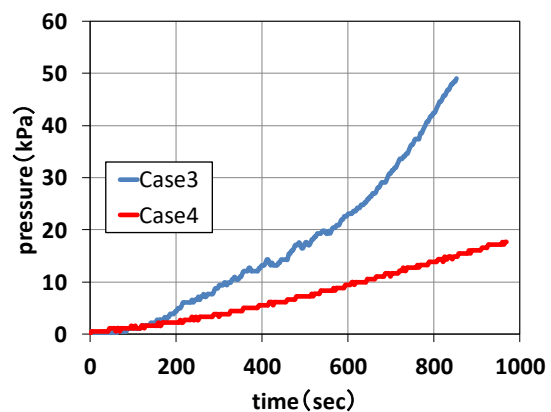


Fig 14 Relationship of injection pressure

ACKNOWLEDGMENTS

In conducting this research, I express my appreciation to Dr. Kenta Mizuno for providing in-situ samples.

REFERENCES

- [1] Goto, K, Tanaka K, Zen K, Kasama K, Kawamura K "Estimation of improved strength by measurement of silica content in solution type chemical grouting method" *Proceedings of the 57th Annual Conference of the Japan Society of Civil Engineers*, pp179-180, 2002
- [2] Takiura S, Suemasa N, Yoshino K, Sasaki T "Grasp on the effect of injection speed and penetration distance on soil improvement by chemical grouting" *Proceedings of the 70th Annual Conference of the Japan Society of Civil Engineers*, pp743-744, 2015

- [3] Yonekura R, Shimada S "Grouting technology for permanent ground improvement" KINDAIKAGAKU, pp106-107
- [4] Hayashi K, Yamazaki H, Zen K " Study on mechanism of strength reduction caused by difference of the grout injection procedures in permeable grouting" *Proceedings of the 70th Annual Conference of the Japan Society of Civil Engineers*, pp.387-394,2014
- [5] The foundation engineering & equipment 2015.Vol.43,No.10, PP31~35
- [6] Sasaki T, Shimada S, Oyama T, Suemasa N "Consideration oh active silica grout ~Factor of ground characteristics causes gel time and unconfined compression strength~" *Proceedings of the 42th Annual Conference of The Japanese Geotechnical Society*, PP889~890, 2007
- [7] Yoshino T " A study on the effect of injection speed and penetration distance on soil improvement by chemical grouting " 2014
- [8] Coastal Development Institute of Technology " Permeable grouting method technical manual " PP56~57, 2003
- [9] Geo-grouting Development Organization " multi-points grouting method technical manual " PP54~55,2011
- [10] Oka F, Kodaka T, Ohno Y " Applicability of permeation grouting method using colloidal silica for coral sand and deformation and strength characteristics of coral sand improved by permeation grouting using colloidal silica" *Proceedings of the National Symposium on Ground Improvement*, PP39-44, 2006

A STUDY ON STRENGTH DEVELOPMENT OF SUSPENDED TYPE INJECTION MATERIAL USING MICROPARTICLES USED FOR LIQUEFACTION COUNTERMEASURE

Takuya MOUE¹, Kentaro UEMURA¹, Koichi NAGAO², Naoki SUEMASA¹, Kazuya ITO¹, Shunsuke SHIMADA³
and Takamitsu SASAKI³

¹ Tokyo City University Graduate Division, Japan

² Sato Kogyo, Japan

³ Kyokado Engineering co.,Ltd, Japan;

ABSTRACT

A liquefaction has been drawn an attention since the Niigata earthquake occurred in 1964 and many technical methods for liquefaction countermeasure have been developed and are practically used at present. Since large equipment is needed for most of the countermeasure methods, permeable grouting methods are widely adopted for the ground under existing buildings. However, compared with large scale land improvement, the cost per unit area for residential areas tends to be so high that the improvement has not been proceeded. For that reason, a material composed of silica and calcium microparticles is proposed as a relatively affordable injection material in this study. The purpose of this paper is to elucidate the strength development by this injection material. Firstly, a series of tests were conducted to determine the most effective blending ratio. Then, the liquefaction strength was verified from undrained cyclic tri-axis experiments. As a result, the strength of the specimen improved with the selected injection material became about 2.2 times as strong as that of the unimproved sand.

Keywords: Liquefaction, The chemical grouting method, Injection material, Microparticles

INTRODUCTION

The liquefaction phenomenon caused by the earthquake will greatly damage infrastructure and detached houses. In recent years, large-scale liquefaction occurred in the 2011 Tohoku Region Pacific Offshore Earthquake, causing serious damage to the structures and became a social problem. Against this backdrop, the necessity of measures for liquefaction, which is inexpensive and has good workability, has increased. As a liquefaction countermeasure method applicable to a narrow land such as an urban area, a chemical liquid injection method can be mentioned. Solution type injection material is commonly used for chemical solution injection methods as a countermeasure against liquefaction [1], but there are cases where sufficient improvement body can't be formed due to factors such as dilution of injected material or sagging phenomenon [2]. In this research, therefore, we focused on fine particles as an injection material. Various types of fine particle injection materials have been developed to date [3]. Floating-type such as cement-based injection materials is expected to be excellent in strength and durability [4] but not suitable for residential areas because the ground strength should be improved to less than 500kN/m² [5] so that the ground can be used for other purposes in future. In this study, a fine particle injected material was investigated, in which silica micro-particles (hereinafter referred to as Si) and calcium

hydroxide micro-particles (CH) are mixed together. When mixing Si and CH together, it is considered that calcium silicate hydrate (C-S-H) is generated resulting from pozzolanic reaction in an alkaline atmosphere and those materials fill the voids of soil skeleton to strengthen the soil in the process of coagulating and solidifying. A series of tests were conducted in this study. Firstly, tests to clarify the optimum combination ratio were conducted by changing the compounding ratio of Si and CH. Secondly, uniaxial compressive strength tests were carried out using the specimens with the effective combination ratios obtained from the first tests. The change in strength with elapse of curing time was confirmed as well. Finally, the liquefaction strength was confirmed by non-draining repetitive triaxial tests.

CONSTITUENT MATERIAL

In this research, a fine particle injection material was used in which amorphous Si and CH are mixed each other. Fig.1 (a) and (b) are Si and CH, respectively observed by scanning electron microscopes (SEM: SU 3500 manufactured by Hitachi High-Technologies Corporation). In general, Si is spherical, while the shape of CH is irregular and has a crystal structure.

Fig.1 (c) shows the result of mixing Si and CH. Slurry of Si and CH was completely dried at low

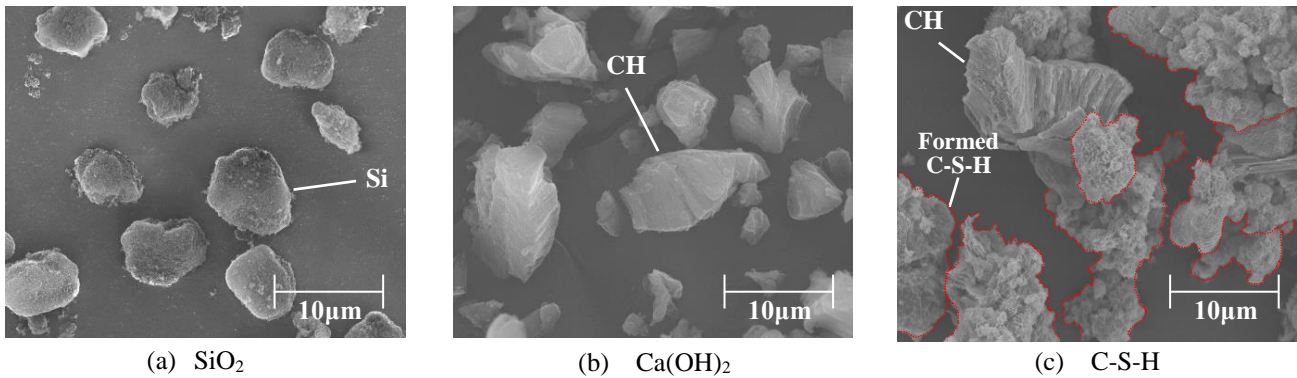
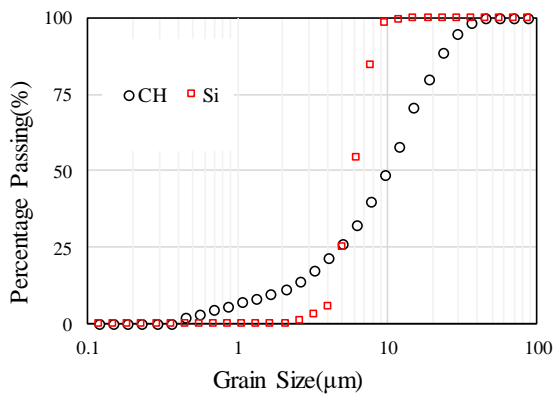


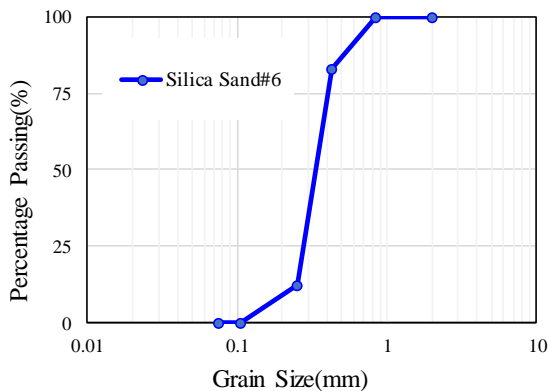
Fig.1 SEM

temperature in a furnace after curing for 3 days. As observed from the photo, consolidated bodies C-S-H are formed as dissolved Si adhered to CH surface.

Fig.2 (a) shows the particle size distribution of microparticles measured by a laser diffraction type particle size distribution measuring apparatus (SALD - 3100 manufactured by Shimadzu Corporation). During the measurement, the particles were dispersed by ultrasonic waves. Fig.2 (b) shows the results of particle size test by sieving silica sand No. 6.



(a) distribution of microparticles



(b) silica sand No. 6

Fig2. results of particle size test

Compounding test

The optimal blend of CH and Si was verified by changing the compounding ratio of CH and Si (hereinafter referred to as CH / Si). Five different ratios were arranged for the tests and the ratio of powder to water: P / W was set at 0.10 all through the tests. The specimens were made by mixing injection material and the silica sand No. 6 in a plastic mold (10 cm in height and 5 cm in diameter) and their relative densities were set at 60%. Uniaxial compression tests were performed using those specimens after curing them for two different periods of time: three and seven days, respectively.

CH/SI RATIO TESTS

Table.1 The conditions of uniaxial compressive strength test (CH/Si ratio)

Case	Injection material		Days
	CH/Si	P/W	
Case1-1	3/7	0.10	3,7
Case1-2	4/6	0.10	3,7
Case1-3	5/5	0.10	3,7
Case1-4	6/4	0.10	3,7
Case1-5	7/3	0.10	3,7

The compounding ratios of specimens were shown in Table 1. Fig.3 shows the results of the maximum compressive strength of the specimens with different CH / Si ratios after three and seven days curing. As can be seen from the Fig.3, the uniaxial compressive strength varies depending on the CH / Si ratios and becomes the highest when CH / Si is 5/5. In addition, since the compressive strength in Case 1-2 and Case 1-3 exceeds 80 kN/m² which is the strength needed for liquefaction countermeasure (80 to 100 kN/m²) [6], it can be said sufficient improvement was developed in both cases. On the other hand, the uniaxial compressive strength tends to

be smaller when the rate of Si is lower than that of CH. The reason is considered that when there is not enough main reaction ingredient: Si, C-S-H is not sufficiently formed which is essential to fill the voids and strengthen the sample. This result corresponds to Nakagawa [3].

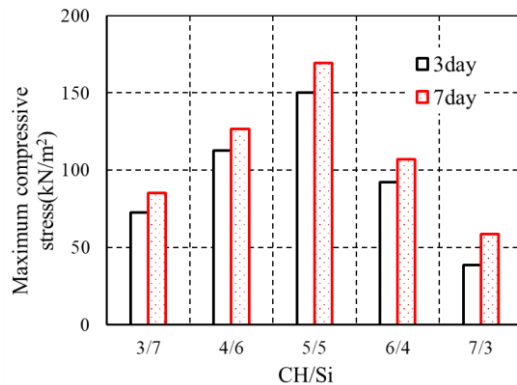


Fig. 3 distribution of maximum compressive strength (CH/Si ratio)

P/W RATIO TESTS

Table.2 The conditions of uniaxial compressive strength test (P/W ratio)

Case	Injection material		Days
	CH/Si	P/W	
Case2-1	4/6	0.08	7
Case2-2	4/6	0.05	7
Case2-3	4/6	0.03	7
Case2-4	5/5	0.08	7
Case2-5	5/5	0.05	7
Case2-6	5/5	0.03	7

Uniaxial compression tests were conducted using the specimens with CH / Si ratio of 5/5 and 4/6 which were verified to be the effective compounding ratios from the previous experiments. Based on the results when P / W was 0.1, concentration P / W were reduced in three steps from 0.08, 0.05 and 0.03 this time. Table 2 shows the conditions of the injection materials.

Fig.4 shows the change of the maximum uniaxial compressive strength depending on various P / W. Case 2-3 is omitted as the sample did not solidify sufficiently. As seen from Fig.4 that the strength uniformly decreases by lowering the P / W and especially when the P / W is changed from 0.08 to 0.05, the strength drops to 1/2 or less. In addition, compared to the case when CH / Si is 4/6, the strength drops significantly with decreasing of P / W when CH / Si is 5/5. The reason is considered that the

amount of Si as the reaction base material is relatively smaller when CH / Si is 5/5 than that when CH / Si is 4/6. It was found that sufficient improvement was developed with P / W of 0.08 as the strength exceeded 80 kN/m² enough for liquefaction countermeasure.

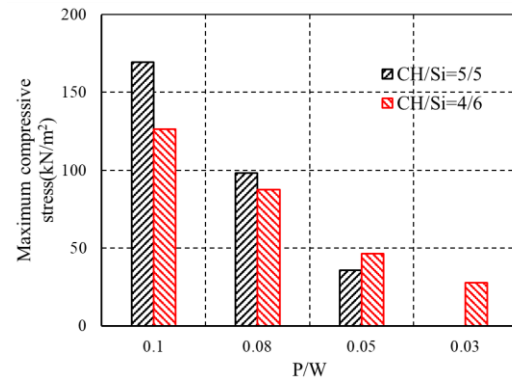


Fig.4 distribution of maximum compressive strength (CH/Si ratio)

Strength Change with Curing Experiment Setup

The change in strength was confirmed depending on the period of curing time. The sample with CH / Si of 4/6 was used for the tests. The specimens were prepared by an injection method where the injection material was injected into the Silica sand No. 6 to be adjusted at a relative density of 60% and injection pressures of 40kPa and 100kPa, respectively.

Uniaxial compression tests were conducted on the specimens which was demolished from the mold after curing for a predetermined period of time and then formed to be 10.0 cm in height.

TEST RESULTS

Fig.5 shows the test results when the injection pressures of 40 kPa and 100 kPa were applied to the specimens. As seen the values in 3 day-curing, when 100 kPa injection pressure was applied to the specimens, the strength increased as much as 80% or more of the strength provided with one month-curing. Thereafter the strength tended to slightly increase over 7 days. Since the reaction between Si and CH would continue on proceeding and more C-S-H would be generated with elapse of time, long-term observation is necessary. In addition, when P / W was 0.10, the maximum compressive stress was higher with the injection pressure of 100 kPa than that of 40 kPa. While, when P / W was 0.05, much difference was not seen in the strength depending on the difference in the injection pressure. The reason is assumed that weak parts were generated in the improved body due to clogging of fine particles when

the injection pressure was low. Fig.6 (a) and 5 (b) show the results when the specimens with P / W of 0.10 were broken. The specimen (a) provided with injection pressure of 40 kPa was weak at its top part, while the specimen (b) with 100 kPa became a barrel shape. Therefore, it was confirmed that clogging can be suppressed by adjusting the injection pressure and the specimens can be strengthened uniformly.

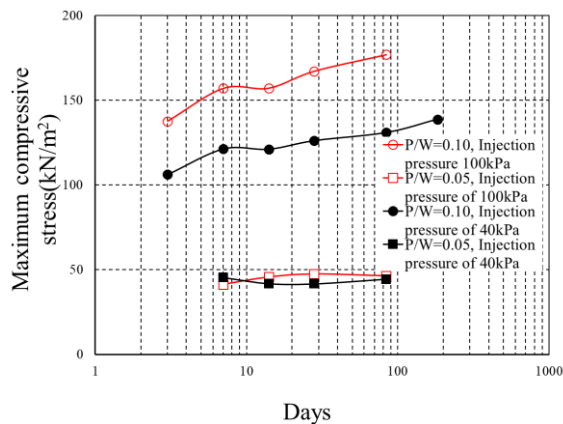


Fig.5 Changing in maximum compressive stress according to days

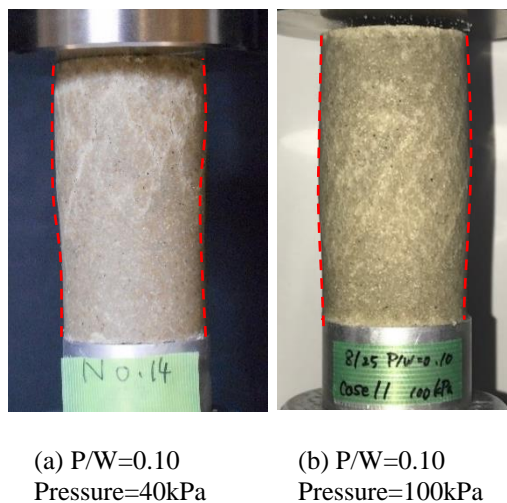


Fig.6 The shape of specimen after loading

LIQUEFACTION TESTS

The test conditions are shown in Table 3. Silica sand No. 6 was used for all specimens. Case 3-a-1 to Case 3-a-5 are unmodified samples with a relative density D_r of 60% prepared using an air pluviation method with setting a membrane in a split mold. While in Case 3-b, specimens were prepared by an injection method with an injection pressure of 100 kPa to uniformly inject with no effect of clogging.

The specimen removed from the mold were cured for 7 days and placed in a triaxial testing machine.

The size of all specimens was 5.0 cm in diameter and 10.0 cm in height. Thereafter all specimens were ventilated with CO_2 and saturated with over 200 ml of deaerated water and the B values were confirmed. The B value is low in Case 3-b-1 to Case 3-b-3 of, but it is considered that bubbles have entered the pore water pressure gauge. BP was set at 100 kPa and σ'_0 was at 100 kPa all through the tests.

Table.3 The conditions of undrained cyclic triaxial experiments

Case	No.	B value	Stress ratio $P/2A_c\sigma'_0$
Case3-a Unmodified	a-1	0.95	0.151
	a-2	0.99	0.154
	a-3	0.96	0.162
	a-4	0.96	0.171
	a-5	0.95	0.177
Case3-b Modified	b-1	0.72	0.450
	b-2	0.80	0.391
	b-3	0.88	0.303
	b-4	0.94	0.396
	b-5	0.92	0.246

Undrained cyclic triaxial experiments

Fig.7 (a) and 8 (b) show the results of undrained cyclic triaxial experiments in Case 3-a-3 and Case 3-b-1 as examples.

Fig. 7 (a) shows the time history of the axial strain. In the unmodified sand Case 3-a-3, the axial strain rapidly increased due to liquefaction occurrence. On the other hand, in the modified sand, Case 3-b-1, the axial strain tended to gradually increase with the increase in the number of cyclic loading. The behavior is similar not to the characteristics of sand during liquefaction but to the characteristics of viscous soil applied with repeated loading.

Fig.7 (b) shows the effective stress path. The average effective stress gradually decreased in the unmodified sand. On the other hand, although the average effective stress in the modified sand decreased at the initial stage of loading, it kept constant values thereafter. In particular, in the result of Case 3-b-1 improved with P/W of 0.08, the average effective stress maintained a positive value. These behaviors are similar to that of the sand improved by a solution type injection material when undrained cyclic shear strain was applied [1].

LIQUEFACTION RESISTANCE STRENGTH

Fig.8 shows the relationship between the repetition number and the stress ratio when the amplitude distortion DA reaches 5%. From the figure, the liquefaction strength R_{L20} of the modified sand is approximately 2.2 times as large as that of the unmodified sand.

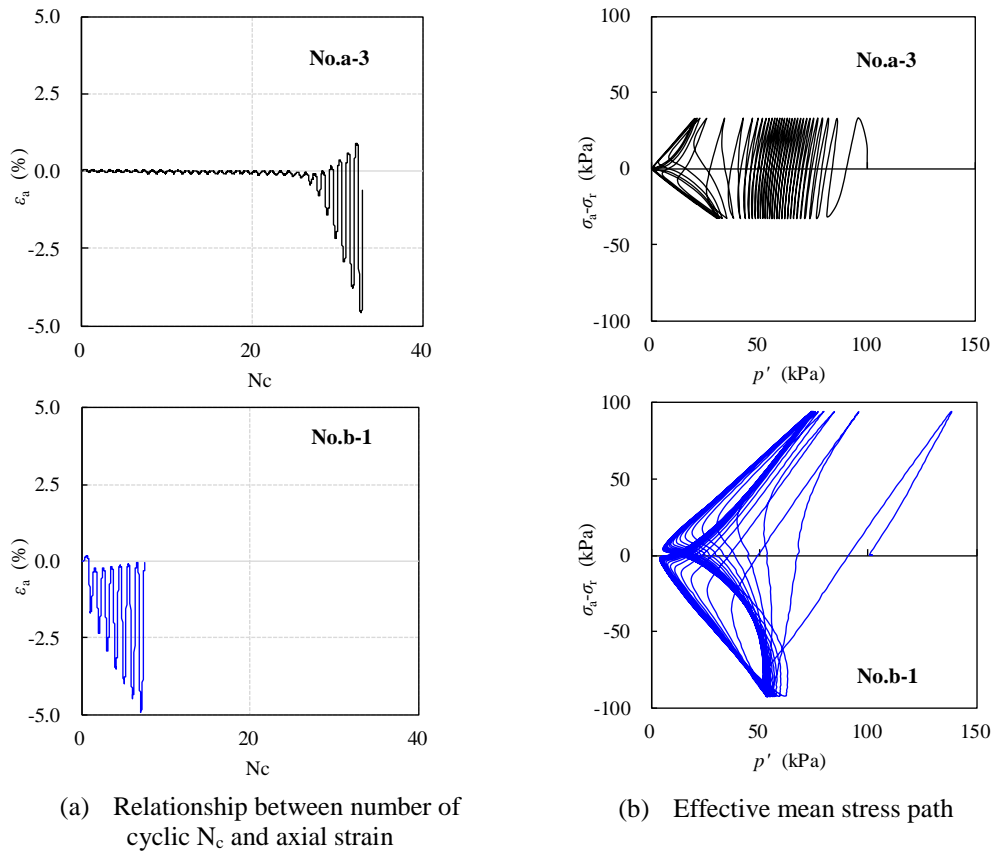


Fig.7 The results of undrained cyclic triaxial experiments as examples

According to the results of uniaxial compression tests, it was predicted that sufficient liquefaction resistance was obtained in the modified case since the uniaxial compressive strength exceeded 80 kN/m². However, it was confirmed that the actually measured R_{L20} was equivalent to the liquefaction strength of the medium density sand [7]. As a result, it was revealed that it is hard to verify the liquefaction resistance only by an uniaxial compression test and it is essential to reconfirm by an undrained cyclic triaxial test.

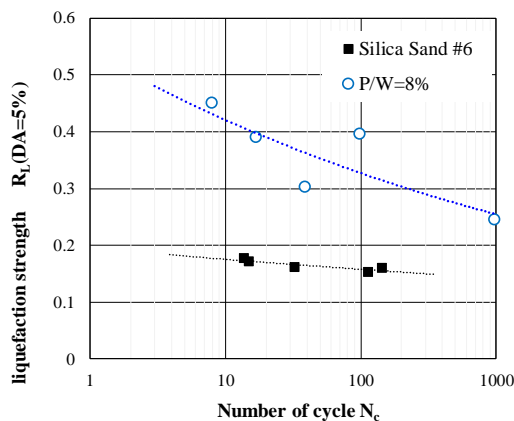


Fig.8 Liquefaction resistance strength

CONCLUSIONS

The following findings are obtained from a series of experiments in this study.

As a result of uniaxial compression tests, the most effective compounding ratio of CH and Si was 4/6 because sufficient uniaxial compressive strength for liquefaction countermeasures was developed and less effected by the decrease of P/W.

As a result of the tests with changing the period of curing time, only 3-day curing can reinforce the strength of improved sand.

As a result of undrained cyclic triaxial tests, the liquefaction strength R_{L20} of improved sand improved with a mixed injection material of CH and Si at P/W of 0.08 was approximately 2.2 as large as that of unimproved sand.

REFERENCES

- [1] Ryoza Yonekura, Shunsuke Shimada : Grouting Technology for Permanent Ground Improvement, Kindaigaku, pp7-25, 2016
- [2] Kentaro HAYASHI, Hiroyuki YAMAZAKI and Kouki ZEN : STUDY ON MECHANISM OF STRENGTH REDUCTION CAUSED BY DIFFERENCE OF THE GROUT INJECTION PROCEDURES IN PERMEABLE

- GROUTING, Journal of Japan Society of Civil Engineers, Ser C, Vol.70, No.4, pp.387-394, 2014
- [3] Yuta NAKAGAWA, Daiki ATARASHI, Akitoshi ARAKI, Etsuto SAKAI : DISPERSION AND REACTION OF ULTRA FINE CALCIUM HYDROXIDE-SPHERICAL SILICA SLURRY, Cement Science and Concrete Technology, No.64, pp.65-70, 2013
- [4] Ichikazu YONEYAMA, Hiroyuki TOSAKA, Tetsuo OKUNO and Takuro NISHI : Fundamental Study on Prediction Method of Penetration Behavior of Cement Grout Material in Rock Crack, Japanese Geotechnical Journal, Vol.10, pp.545-557, 2015
- [5] Makoto NISHIGAKI, Tomohiro KANAZAWA and Larry Pax CHEGBELEH : The examination on Shirasu slope failure prevention measures of cement grouting material by the grouting, Japanese Geotechnical Journal, Vol.6, No.2, pp.213-224, 2011
- [6] Kosuke YAMAZAKI, Koki ZEN and Kensuke KAWAMURA : Study on Applicably of Permeable Grouting Method to Countermeasure against Liquefaction, REPORT OF THE PORT AND AIRPORT RESEACH INSTITUTE, Vol.41, No.2, pp.119-152, 2002
- [7] Hiroshi NAKAZAWA and Kenji HARADAH : REVISION OF RELATIVE DENSITY AND ESTIMATION OF LIQUEFACTION STRENGTH OF SANDY SOIL WITH FINE CONTENT, Journal of Japan Society of Civil Engineers, Vol.68, No.4, pp.282-292, 2012

BIO-INSPIRED STABILIZATION OF EMBANKMENT SOIL MEDIATING *PSYCHROBACILLUS* SP. AND LOW-GRADE CHEMICALS: PRELIMINARY LABORATORY INVESTIGATION

Sivakumar Gowthaman¹, Shumpei Mitsuyama¹, Kazunori Nakashima², Masahiro Komatsu³ and Satoru Kawasaki²

¹Graduate School of Engineering, Hokkaido University, Japan;

²Faculty of Engineering, Hokkaido University, Japan;

³East Nippon Expressway Company Limited, Japan

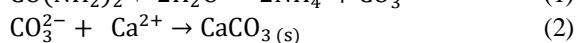
ABSTRACT

Microbial induced carbonate precipitation (MICP) is one of the foremost bio-inspired soil stabilization technique mediated by ureolytic microorganisms through a chain of chemical reactions, which leads to the formation of calcium carbonate bio-cement in soil matrix, and persuades the substantial bonds between the soil particles. This research aims to examine the achievability of embankment soil stabilization by mediating low-grade chemicals via different scales of preliminary laboratory investigations. *Psychrobacillus* sp., indigenous ureolytic bacteria, isolated from the embankment slope of Asari (Hokkaido, Japan), was employed in elementary-scale column and benchtop-scale slope model solidification tests performed at different physio-chemical conditions to optimize the bio-cementing performance. According to the column test results, a better stabilization (UCS of 0.82 MPa) was obtained for the specimen treated mediating low-grade chemicals (urea fertilizer, beer yeast and snow melting reagent), whereas specimen treated mediating pure chemicals resulted only 0.42 MPa. The benchtop-scale test reveals that the highest surface strength of 1.02 MPa was achieved with 0.5 M cementation solution at 30°C. Sets of colorimeter measurements were undertaken on treated slope models to compare precipitation profile at different locations. The results have evidenced the acceptable level of solidifying possibility of surface layer while using low-grade chemicals, which would be adequate to be occupied as crust-layer for the natural embankments.

Keywords: Bio-inspired soil stabilization, Bio-cement, Embankment soil, Ureolytic bacteria, Low-grade chemicals

INTRODUCTION

Many recent investigations have evidenced that the bio-inspired cementation technique can be potentially applied for ground stabilization/reinforcement purposes. The researchers and biotechnologists have used the principle of bio-metabolism to generate sufficient calcium carbonate crystals, thereby enabling bridges between soil particles. Sealing the pore voids with a subsequent change of mechanical properties of soil matrix is found to be an innovative approach in sustainable geotechnics with significant scope for future developments [1], [2]. In detail, the bacteria which produce urease enzyme are used to catalyze the hydrolysis of urea into ammonium and carbonate ions in aquatic medium as presented in Eq. 1.



At the supply of dissolved calcium ions or at the presence of calcium ions in the medium, produced carbonate ions precipitate and form calcium carbonate crystals as given in Eq. 2. Eventually,

desired mechanical strength can be achieved, when the calcium carbonate crystals are precipitated appropriately in pore spaces of soil.

Bio-inspired stabilization method is nondestructive, inexpensive as well as less hazardous over conventional soil improvement methods. The unique advantages of the technique provide a wide range of applicability for the scenarios including liquefaction prevention, settlement reductions, piping prevention of dams and levees, slope stabilizations, erosion control, beach rock formations, land stabling prior to tunneling, immobilization of hazardous contaminants, facilitating impermeable barriers and carbon sequestrations [3], [4]. Up to this moment, feasibility of Microbial induced carbonate precipitation (MICP) for the above applications has been demonstrated mostly in laboratory using elementary-scale column experiments [5] - [7]. The studies have widely investigated and addressed the injection procedures, concentration of reagents and bacterial controls in achieving the desirable behavior of soil matrix. The next step of the MICP technique is to scale up the process using treatment conditions to prove the feasibility of this technique for real applications. Only a very few studies have attempted

the scaling up of MICP as a ground improvement method [1], [8], [9].

In this paper, we aim to upscale the MICP investigation from elementary-scale columns to benchtop-scale slope models. In fact, the benchtop-scale experiments can be considered as an intermediate step between elementary-scale experiments and large-scale/ field *in-situ*. However, the elementary-scale experiments are very essential to experience the feasibility as well as to enable the optimization of treatment before upscaling as stated by DeJong et al. [4]. On the other hand, cost of required substrates (urea, calcium chloride and nutrients for bacterial growth) would be a challenge, when it comes as large-scale investigations/ applications [8]. Thus, paper also focus to investigate the feasibility of using low-grade chemicals in place of laboratory chemicals in MICP as to overcome the economical challenge.

MATERIALS AND METHODS

Ureolytic Bacteria and MICP reagents

The bacteria used in this study is *Psychrobacillus soli*, gram positive strain isolated from Embankment soil of Asari Expressway (Hokkaido, Japan). The detection and isolation methods of the strain are the same as Danjo and Kawasaki [5]. The urease activity of the strain culture was around 0.4 $\mu\text{mol}/\text{min}$ at 30°C. Two types of culture mediums and cementation solutions were used in current experiments, and are described below. CM_{pure} and CS_{pure} were prepared using laboratory pure reagents, whereas low-grade chemicals were used to prepare $CM_{\text{low-grade}}$ and $CS_{\text{low-grade}}$ solutions.

Culture mediums CM

CM_{pure} : 15.7 g/L tris-buffer, 10 g/L ammonium sulfate, 20 g/L yeast extract, distilled water
 $CM_{\text{low-grade}}$: 30 g/L beer yeast, distilled water

Cementation solutions CS (0.5 mol/L)

CS_{pure} : 30 g/L urea, 55.5 g/L CaCl_2 , 3 g/L nutrient broth, distilled water
 $CS_{\text{low-grade}}$: 30 g/L urea fertilizer, 55.5 g/L snow melting agent, 2 g/L beer yeast, distilled water

The natural soil collected from expressway embankment of Asari was used for solidification tests. Natural moisture content and pH are respectively 21.8 ± 1.30 and 7.029.

The purity is the major difference between laboratory chemicals and low-grade chemicals. The urea fertilizer, comprised of 46.0% purity in nitrogen, is widely used in agriculture industry. The snow melting agent (calcium chloride of 74% purity) is applied for melting the ice. Beer yeast is primarily used in food industry to break down sugars.

Column solidification test

The syringes (30 mL in capacity and 25 mm in diameter) were positioned vertically and packed with 45 g by filling with three compacted layers of oven dried (105°C for 48 hours) soil as shown in Fig. 1. All the solutions were injected to the top of the soil columns and allowed to percolate by gravity. Excess solutions were allowed to drain through the bottom of the columns. The movement of the front reaction fluid was permitted under constant flow conditions. Two test conditions were investigated, and are presented in Table 1. In both tests, bacteria culture medium of 10 mL was injected only at the beginning of the experiment. The cementation solution of 6 mL was applied every 24 hours to the column specimens throughout the 10 days of treatment.



Fig. 1 Syringe Columns

Table 1 Conditions of column solidification tests

Test	Bacteria Culture	Cementation solution	Temp. (°C)
1	CM_{pure}	CS_{pure}	30
2	$CM_{\text{low-grade}}$	$CS_{\text{low-grade}}$	30

Slope model solidification test

The size of the slope model used in the experimental study is 10 cm \times 12 cm in bottom and 10 cm in height as shown in Fig.2. In fact, the slope model test is the scaling-up of previous

elementary-scale column tests. At the same time, gradient of 1 : 1.2 was incorporated in the scaled-up slope model in order to represent the standard cut slope of the expressways, which is generally critical in stability compared to that of standard filling/embankment slope (1 : 1.8) [10], [11]. The slope-mould was filled in properly tamped five layers of soil (without oven-dry/sterilization).

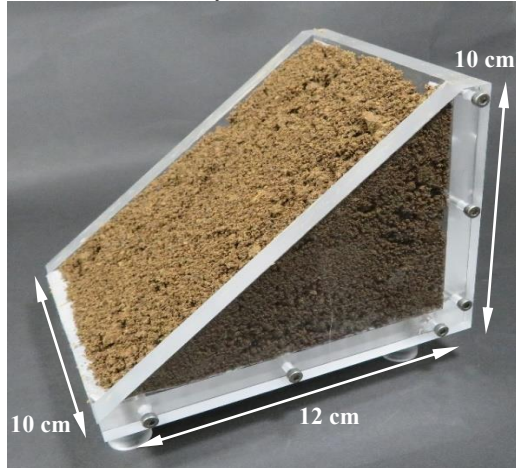


Fig. 2 Slope model

Four test cases were investigated to optimize the slope model solidification, and the test conditions are clearly summarized in Table 2. Based on the observations made at column solidification tests, low-grade chemicals ($CM_{low-grade}$ and $CS_{low-grade}$) were chosen for the slope model solidification tests. All the solutions were continuously and uniformly applied to the slope surface at a slow rate without formation of ponding on the surface.

Table 2 Conditions of slope solidification tests

Test	Bacteria Culture (mL)	Cementation solution (mL)	Temperature (°C)
1	225	135	30
2	100	67	30
3	50	33	30
4	100	67	30

Considering large volume of soil needed to be treated, repeated bacteria culture injection was performed (once in every 5 days during the 10 days treatment period). At the same time, the cementation solution was injected every 24 hours similar to the column tests.

UCS measurements

Similar to the previous studies [5], [7], [12], [13], needle penetrometer (SH-70, Maruto Testing Machine Company, Tokyo, Japan) was used to

estimate the UCS of the treated specimens. Regression relationship given in Eq. 3, which has been developed by analyzing 114 natural rock samples and 50 improved soils with cement, UCS of each treated sample was estimated using the ratio between applied force and settlement of needle.

$$\log (y) = 0.978 \log (x) + 2.621 \quad (3)$$

Where x is the logarithm of “penetration gradient” when the logarithm of y is unconfined compressive strength. Penetration gradient (N/mm) can be determined using penetration and penetration resistance of the needle.

Colorimeter measurements

Color measurements were undertaken using spectro-colorimeter (CM-2600 d, manufactured by Konica Minolta), as to compare the carbonate precipitation on the surface of solidified slope specimen. Color space is defined by the three components: L^* , a^* and b^* (“ a ” from green ($-a$) to red ($+a$), “ b ” from blue ($-b$) to yellow ($+b$) and “ L ” from black ($-L$) to ($+L$)). The precipitation of calcium carbonate significantly affects the lightness measure (L^*) among the three components of the colorimetric system. Thus, the lightness changes (L^*) were measured from six different locations (five readings per each location) of solidified slope surface.

RESULTS AND DISCUSSION

Column solidification

Two number of columns tests were conducted to investigate the feasibility of low grade chemicals in bio-inspired soil stabilization. In order to monitor the internal biogroutting process during treatment, Ca^{2+} ion concentration and pH were measured every day from the percolated solution through syringe column. The concentrations and the pH are presented in Fig. 3. Observations suggest that weak alkali pH (7.0-8.5) conditions were maintained during the treatment process in both test cases. The calcium ion concentration decreased continuously after around 2-3 days of process. The calcium ion reduction coupled with pH increment indicated that the chemical reaction of urea hydrolysis and calcium carbonate precipitation started by the injected ureolytic bacteria.

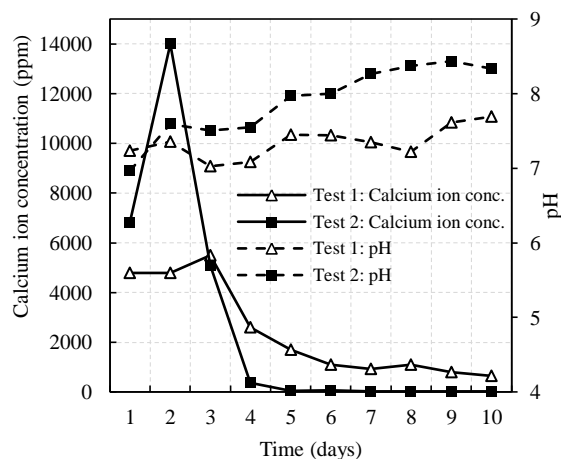


Fig. 3 Calcium ion concentration and pH at treatment

The strength measurements were undertaken on column specimens after ten days of treatment. The values of UCS, obtained using needle penetrometer for the samples treated using pure reagents (Test 1) and low-grade chemicals (Test 2), are compared in Fig. 4. The results show that the specimen strength decreases with the column depth in both cases. At the slow flow rates, the top part of the column was exposed to higher concentration of reactants compared to that of bottom of the column [2], which tends to precipitate relatively high amount of calcium carbonate at top of the column. Thus, the highest strength was obtained at the top, and decreased over the length. At the same time, the low-grade chemicals have exhibited a significant enhancement in solidification. The surface strength of the sample treated under low-grade chemicals is around two times higher than that of sample treated using laboratory chemicals.

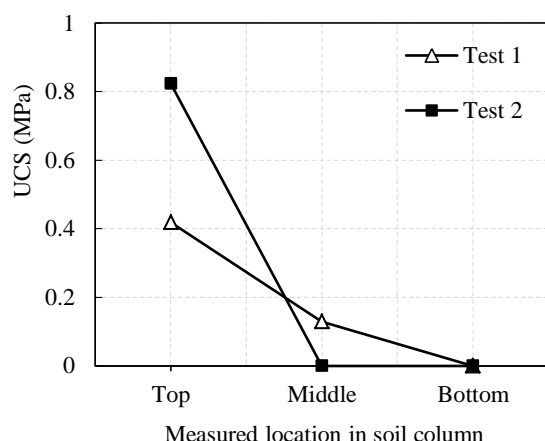


Fig. 4 Strength measures of solidified columns

Slope model solidification

Four cases were undertaken in slope model solidification test. Based on the positive

observations made at column tests, all the slope solidification tests were incorporated with low-grade chemicals. The first three tests (Test 1 - Test 3) were performed to assess the effect of the injection volume of chemicals in cementation. Large quantity of injection was made in Test 1 by assuming that implementation of large number of bacteria would significantly enhances the solidification. In Test 2 and Test 3, the injection volume was respectively set to 1/2 and 1/4 of the volume considered in Test 1. The lightness (L^*) of the slope surface was measured every 24 hours using spectro-colorimeter to experience the formation of calcium carbonate, and the results are given in Fig. 5. The trend of average L^* values of Test 1 slope shows an initial increment, and remains relatively stable thereafter. But, average L^* values of the Test 2 slope increase gradually with the time. At the same time, there was no considerable changes regarding lightness (L^*) obtained in the treated Test 3 slope, which indicates that there was no adequate precipitation of calcium carbonate obtained on the slope surface due to insufficient supply of reactants.

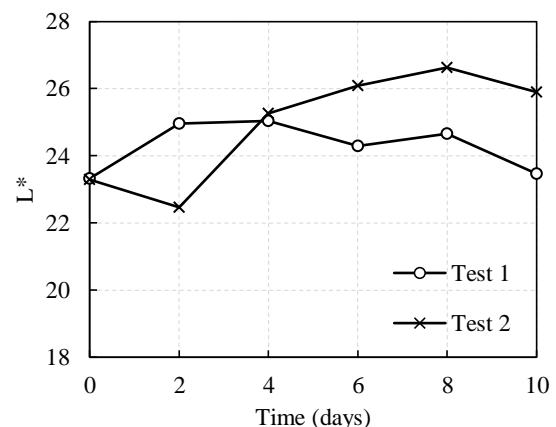


Fig. 5 Lightness (L^*) measure on slope surface using spectro-colorimeter

The surface strength (UCS) distribution of the treated slope specimens of Test 1 and Test 2 are illustrated in Fig. 6. It is well understood that there is a close relationship between color measurement (L^*) and UCS as stated by Amarakoon and Kawasaki [7]. As the solidification occurred only at the certain locations of the slope surface of Test 1 evidenced in Fig. 6 (a), the L^* values failed to exhibit the increasing trend (Fig. 5). In the case of Test 2, the unsolidified surface area reduced (Fig. 6 (b)), thereby resulted the considerable increment in L^* value with the duration. It is well understood that injection volume plays a vital role in solidification process. Injection of the reactants in large quantity might lead to wash out of cells from the soil matrix prior to bacterial immobilization. At the same time, injecting inadequate volume of reactant, would not

be able to contribute significant and uniform cementation.

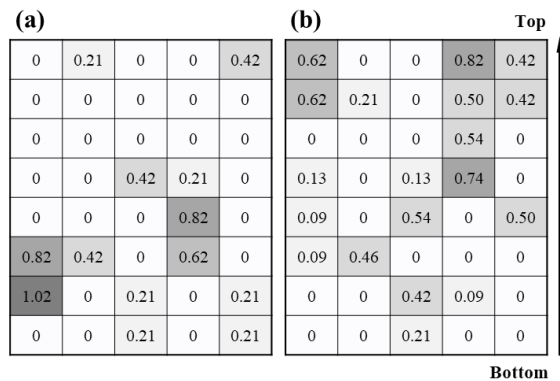


Fig. 6 Obtained UCS values with respect to their locations on the slope surface of the specimen (a) Test 1 and (b) Test 2.

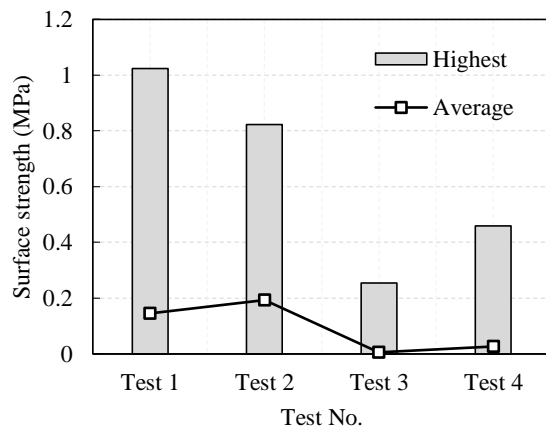


Fig. 7 Surface strength of slope solidified at different test conditions

The highest and average strength of the slopes solidified under all four test conditions are compared in Fig. 7. The average surface strength value comparatively lower in all the cases, whereas the highest value sounds significantly. Among the four test cases, the slope treated under Test 2 reveals relatively a homogeneous surface, although the highest strength is less than that obtained in Test 1. Test 4 was undertaken at the similar injection conditions of Test 2, additionally placing a non-woven fabric on the slope surface. In fact, this was done for two reasons: (i) to keep a higher water content at the surface zone, because Cheng et al [14] have proven that the calcium carbonate precipitation is proportional to the saturation amount of soil, (ii) to prevent the disturbance of slope soil material at the supply of reactant solutions. However, no considerable improvement in solidification was observed at the implementation of non-woven fabric material.

On the whole, continued research must still

address several challenges associated with upscaling the process for *in-situ* treatment and the performance of the induced cementation. Currently, bench-scale laboratory experiments are ongoing to obtain the homogeneous bio-cementation along the slope profile.

CONCLUSION

In elementary and benchtop-scale experiments, it has been explored that the low-grade chemicals can be potentially used instead of laboratory chemicals for the soil stabilization purposes. The elementary-scale column tests reveal that the surface strength obtained from low-grade chemicals is around two times higher compared to that of laboratory chemicals. However, further research should demonstrate what mechanisms are responsible for the observed enhancement of strength. Also, the feasibility of MICP for the slope soil stabilization has been demonstrated by up-scaling the treatment process from column tests to bench-scale slope models. The solidified slopes were analyzed using both non-destructive and destructive methods: spectro-colorimeter measurement and UCS measurements respectively. The slope model tests reveal that volume of the injection reactants plays an important role in microbial stabilization. Injecting either large quantity of reactants or inadequate volume of reactants, would not be able to contribute significant cementation with in soil matrix at the MICP process. Although the solidified slope exhibits higher strength, wide range of heterogeneity in the deposition of calcium carbonate is observed. Further exploration of field implementation strategy and deeper understanding about low-grade chemicals reaction mechanism in MICP are needed to promote this benchtop-scale investigation to the *in-situ* investigation levels.

REFERENCES

- [1] Cheng L. and Cord-Ruwisch R., Upscaling Effects of Soil Improvement by Microbially Induced Calcite Precipitation by Surface Percolation, *Geomicrobiology Journal*, Volume 31, 2014, pp. 396-406.
- [2] Wiffin V.S, van Paassen L.A. and Harkes M.P., Microbial Carbonate Precipitation as a Soil Improvement Technique, *Geomicrobiology Journal*, Volume 24, 2014, pp. 417-423.
- [3] DeJong J.T, Fritzges M.B. and Nusslein K., Microbial Induced Cementation to Control Sand Response to Undrained Shear, *ASCE Journal of Geotechnical and Geoenvironmental Engineering*, Vol 132, Issue 11, 2006, pp. 1381-1392.
- [4] DeJong J.T, Martinez B.C, Mortensen B.M, Nelson D.C, Waller J.T, Weil M.H, Ginn T.R, Weathers T, Barkouki T, Fujita Y, Redden G,

- Hunt C, Major D. and Tanyu B., Upscaling of Bio-Mediated Soil Improvement, Proceedings of 17th International Conference on Soil Mechanics and Geotechnical Engineering, 2009.
- [5] Danjo T. and Kawasaki S., Microbially Induced Sand Cementation Method Using *Pararhodobacter* sp. Strain SO1, Inspired by Beachrock Formation Mechanism, Material Transactions, Vol 57, 2016, pp. 428-437.
- [6] Mahawish A, Bouazza A. and Gates, W.P., Biogrouting Coarse Materials using Soft-lift treatment strategy, Canadian Geotechnical Journal, Vol 53, 2016, pp. 2080-2085.
- [7] Amarakoon G.G.N.N. and Kawasaki S., Factors Affecting Sand Solidification Using MICP with *Pararhodobacter* sp., Material Transactions, Vol 59, 2018, pp. 72-81.
- [8] van Paassen L.A, Ghose R, van der Linden T.J.M, van der Star W.R.L. and van Loosdrecht M.C.M., Quantifying Biomediated Ground Improvement by Ureolysis: Large-Scale Biogrout Experiment, Journal of Geotechnical and Geoenvironmental Engineering, Vol 136, 2010, pp. 1721-1728.
- [9] Martinez B.C, Barkouki T.H, DeJong J.D. and Ginn T.R., Upscaling of microbial induced calcite precipitation in 0.5 m columns: Experimental and Modeling results, Geo-Frontiers, 2011, pp. 4049-4059.
- [10] Road Earthworks - Cutting, Earthquake, Slope Stabilization Guidelines, Japan Road Association, 2009.
- [11] Road Earthworks - Sheng Earth Direction Guidelines, Japan Road Association, 2010.
- [12] Fukue M, Ono S. and Sato Y., Cementation of Sands due to Microbiologically-induced Carbonate Precipitation, Soils and Foundations, Vol 51, Issue 1, 2011, pp. 83-93
- [13] Mitsuyama S, Nakashima K. and Kawasaki S., Evaluation of Porosity in Biogrouted Sand Using Microfocus X-Ray CT, Journal of GEOMATE, Vol 12, 2017, pp. 71-76.
- [14] Cheng L, Cord-Ruwisch R. and Shahin M.A., Cementation of sand soil by microbially induced calcite precipitation at various degrees of saturation, Canadian Geotechnical Journal, Vol 50, 2013, pp. 81-90.

EFFECTS OF THRUST PROTECTING METHOD FOR BURIED PIPE USING GEOGRID GABION OF DIFFERENT SIZES

Hiroyuki Araki¹ and Daiki Hirakawa¹

¹Department of Civil and Environmental Engineering, Chuo University, Japan

ABSTRACT

On the bend of a buried water supply pipeline, the thrust force is applied to the ground. A concrete block is typically installed at the bend section of the pipeline as a thrust protection measure. However, a concern exists that the stability of the concrete block might not be maintained when the ground around the concrete block liquefies during an earthquake. In this study, thrust protection using a gabion composed of a geogrid basket and gravel as a pressure-receiving structure to protect against thrust force is proposed. Further, the effects of this method are evaluated by conducting model experiments. In the model experiments, a constant load simulated thrust force was applied laterally to a buried pipe model in the model ground where the internal effective stress was decreased by increasing hydraulic gradient stepwise. Gabion models of several widths were placed on the ground in the direction of the thrust force. Results revealed that the gabion stabilizes the pipe even when the effective pressure of the surrounding ground decreases significantly, and that the behavior of gabions in the ground is affected by their width. Moreover, the requirements for a gabion to improve a pipe's stability will be discussed herein, based on the results of several test cases.

Keywords: Buried pipe, Thrust force, Gabion, Liquefaction

INTRODUCTION

At the bend of buried pipes in which pressurized water flows, the thrust force caused by the centrifugal force due to the water flow or the imbalance of the water pressure is applied to the ground outside the bend. In design, the stability of the bend is typically judged by considering the passive earth pressure of the ground and the frictional force between the pipe and the ground as the resistance force against the thrust force. If the thrust force exceeds the resistance force, a thrust-protecting method is applied.

A concrete block is typically used as the thrust-protecting method, and is installed at the bend, as shown in Fig. 1a. The concrete block expands the pressure-receiving area of the passive earth pressure and increases the frictional resistance force at the bottom by its weight. However, this protecting method has several problems. The resistance force decreases markedly in the liquefied ground because the frictional force and passive earth pressure are lost. Further, the high inertial force is generated at the bend where the weight is increased by the concrete block. The high inertial force promotes the deformation of the buried pipe. A pipeline damaged in this manner by the inertial force was reported in a past earthquake [1].

A new thrust-protecting method, other than a concrete block, is therefore required to attain the following performances goals: exerting sufficient resistance force against the thrust under normal conditions, retaining the resistance force to prevent significant deformation during an earthquake, and obtaining the resistance force without increasing the weight of the pipe to not grow the inertial force acting on the buried pipe. Kawabata et al. [2] proposed a new thrust-protecting method using a geogrid, in which the geogrid is connected to the

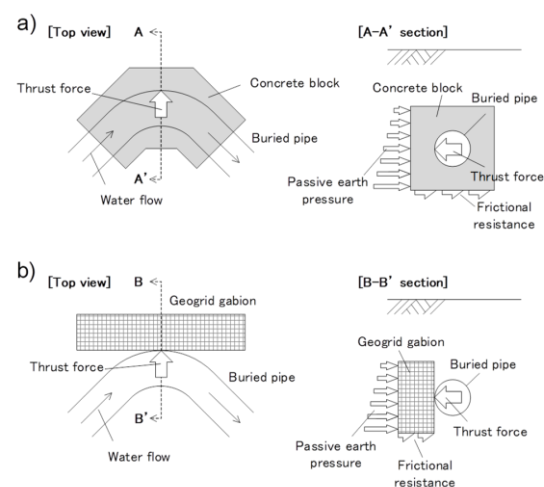


Fig. 1 Schematics of a) a concrete block and b) the proposed method using gabion.

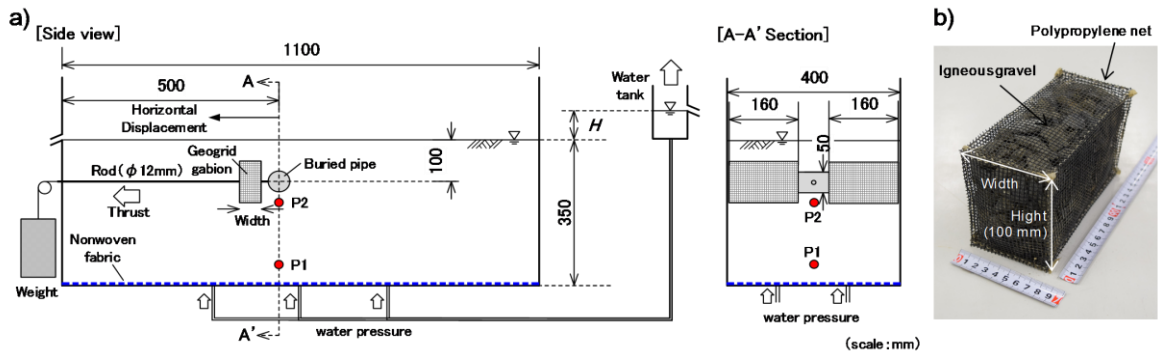


Fig. 2 a) Schematics of the lateral load test and b) photograph of geogrid gabion model (1.5D width).

pipe on the inside of the bend to act as a lateral anchor. They also observed the behavior of a pipe protected by the geogrid in liquefied ground by conducting shaking table tests [3]. It was revealed that the lateral displacement of a pipe protected with the geogrid decreased, compared to that of a pipe protected with a concrete block.

In this study, another type of thrust-protection method is proposed. A geogrid gabion consisting of gravel and a basket constructed from geogrid is installed at the passive area of the buried pipe to receive the thrust force as shown in Fig. 1b. In a previous study [4], it was clarified that the displacement of a pipe was decreased by applying a gabion. In this study, the effects of the gabion size on the thrust protection are clarified by conducting model experiments.

THE PROPOSED THRUST PROTECTING METHOD

If the passive earth pressure is not sufficient to overcome the thrust force from a buried pipe, the ground in the passive area of the buried pipe deforms. Audibert et al. [5] reported that the deformation region was developed from the lateral face of the buried pipe toward the ground surface in the passive area. In the proposed method, the geogrid gabions are installed in the passive area, as shown in Fig. 1b.

The gabion is a basket filled with igneous gravel. The basket is constructed of a polymer geogrid to obtain long-term stability against environmental changes. The gabion is not deformed largely by the thrust force because the gravel material is confined by the geogrid basket. The passive earth pressure indirectly acting on the buried pipe is expected to be increased by a gabion height that is larger than the pipe diameter. Using gravel material of high

permeability as the filling material, the excess pore water pressure around the buried pipe is expected to be dispersed to retain effective stress during an earthquake. These mechanisms might ensure resistance to the thrust force without increasing the weight of the bend.

By conducting the model experiments, it was confirmed that the lateral displacement of a pipe with a gabion decreased compared to that of a pipe without a gabion in the ground where the effective stress decreased [4]. It was concluded that the effects of installing a gabion were due to the increase in the passive earth pressure and the suppression of the local shear deformation of the ground near the buried pipe. However, the effects of the gabion width were not clarified.

OUTLINE OF LATERAL LOAD TEST

Test Conditions

Although the dynamic interaction between a structure and the ground is typically investigated by shaking table tests, the results obtained by such tests are the behaviors in a complicated boundary field where the force acting on the buried pipe changes sequentially. The buried pipe might be affected by not only the thrust force but also the inertial force, which varies hourly.

Herein, the effects of the gabion size on the thrust protection are evaluated by lateral load tests, with reference to Itani et al. [6]. The lateral load tests were conducted in a testing box as shown in Fig. 2a. The pipe model was loaded laterally inside the ground model where the effective stress is controlled by excess pore water pressure.

The ground model was of sandy soil (soil particle density, $\rho_s = 2.680 \text{ g/cm}^3$) with particle size distribution as shown in Fig. 3. The maximum dry

density and the optimum water content of the sandy soil were 1.616 g/cm^3 and 17.2%, respectively. The ground model was created by wet tamping using sandy soil with water content of 17%. The dry density of the ground model was 1.374 g/cm^3 .

In the lateral load test, the three-dimensional interaction between the bend and the ground was simplified to the plane strain problem. Hence, the shape of the pipe model was set as a straight cylindrical shape of 50 mm in diameter and having a length of 390 mm. The pipe model was of solid aluminum to prevent its deformation by loading. The pipe model was subjected to a simulated thrust force laterally-applied via a stainless-steel rod. The simulated thrust force was set as 125 N based on the result of the pre-test in which the pipe model moved significantly.

The gabion model was of igneous gravel ($\rho_s = 2.795 \text{ g/cm}^3$) and polypropylene net as shown in Fig. 2b. The particle size distribution of the gravel is shown in Fig. 3. The dry density of the gabion was set as approximately 1.39 g/cm^3 . The gabions were installed on the front side of thrust force such that the center of gravity position was at the same height as that of the pipe model. Although the gabions should be installed close to the pipe when in actual use, the gabion model was placed with lateral distance to the pipe set as approximately 15 mm to ensure good compaction around the pipe in these tests. In addition, the gabion model was divided into two in the horizontal direction to avoid contacting the loading rod (Fig. 2a).

To prevent the migration of soil into the gabions, a non-woven fabric was laid on only their upper surface. The non-woven fabric was not installed on the side and bottom sections so as to simplify the boundary condition between the gabion and soil in the model test. The ground surface settlement due to the soil migration was not observed in the all-model test in this paper.

Test Cases and Procedure

Four test cases were set as given in Table 1. Case N1 is the test without a countermeasure. In cases A3, B5, and C1, gabions of widths 25 mm, 50 mm, and 75 mm were used, respectively. Using the pipe diameter value of 50 mm, the values of the gabion widths are represented hereafter as 0.5D, 1.0D, and 1.5D respectively. The height of all gabions is 100 mm.

The ground model was saturated with water through the water tank connected to the bottom of

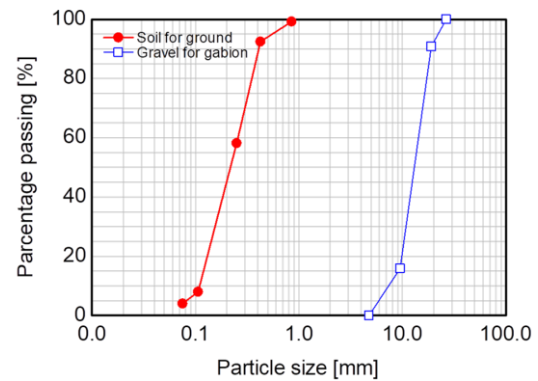


Fig. 3 Particle size distribution of soils used in the model experiments.

Table 1 List of the model experiments.

	Width of gabion	Thrust force [N]	Step No.
Case N1	—	125	1-3
Case A3	0.5D	125	1-7
Case B5	1.0D	125	1-8
Case C1	1.5D	125	1-8

D: a pipe diameter of 50 mm.

Table 2 Conditions at each step.

Step No.	H [mm]	Water condition
1	—	Unsaturated, $w = 17\%$
2	70	Saturated
3	140	Saturated
4	210	Saturated
5	280	Saturated
6	350	Saturated
7	420	Saturated
8	490	Saturated

the testing box. By increasing the water head difference, defined as H , between the ground surface and the water tank stepwise, as shown in Fig. 2, the excess pore water pressure inside the ground model statically increased; subsequently, the effective stress decreased. The values of H and the water condition at each step are listed in Table 2. The value of H was maintained until the pore water pressure in the ground became stable. After the water pressure stabilized, the pipe model was loaded laterally and the displacement of the model pipe, d_p , was measured. The loading was finished when the value of d_p exceeded 25 mm or when a sand boil occurred in the ground.

The deformation of the ground along with the moving pipe was observed at the side of the testing box. The markers were installed on the side of the testing box and moved following the deformation of the ground. The displacement of the markers was measured by image analysis of the photographs obtained during the loading.

TEST RESULTS AND DISCUSSION

Hydraulic Gradient and Pipe Displacement

The pore water pressure in the model ground was measured by water pressure meters P1 and P2 shown in Fig. 2. Assuming that the distribution of the pore water pressure in the ground is linear with the depth, the hydraulic gradient, i_m was obtained based on the values of excess pore water pressure measured by P1 and P2. Meanwhile, the theoretical value of the critical hydraulic gradient, i_{cr} is expressed by following equation:

$$i_{cr} = \frac{\rho_s / \rho_w - 1}{1 + e}$$

where $\rho_s = 2.680 \text{ g/cm}^3$; water density, $\rho_w = 1.000 \text{ g/cm}^3$; and the void ratio, $e = 0.951$ in these test cases. Subsequently, the value of i_{cr} is 0.861. The value of i_m normalized by i_{cr} is equivalent to the ratio of excess pore water pressure to the effective overburden stress in the ground; subsequently, the value of i_m/i_{cr} of 1.0 means that the ground is liquefied.

The relationships between i_m/i_{cr} and H are shown in Fig. 4. The values of i_m/i_{cr} increase linearly as the values of H increase. This indicates that the effective stress in the ground model decrease as the value of H increases. For cases B5 and C1, the values of i_m/i_{cr} were approximately 0.9 at $H = 420 \text{ mm}$ (step 8), indicating that the ground models were almost liquefied.

The relationships between d_p and i_m/i_{cr} are shown in Fig. 5. In all cases, the values of d_p were approximately 4 mm for the unsaturated condition (step 1). The values of d_p hardly increased even when the value of i_m/i_{cr} was 0.0 (step 2). In case N1, however, the pipe moved remarkably at step 3, where the value of i_m/i_{cr} was 0.16. Simultaneously, the values of d_p were approximately 5 mm in cases A3, B5, and C1. In the ground where the value of i_m/i_{cr} was approximately 0.2, the value of the displacements of pipes protected with the gabions having a width of 0.5D to 1.5D were small

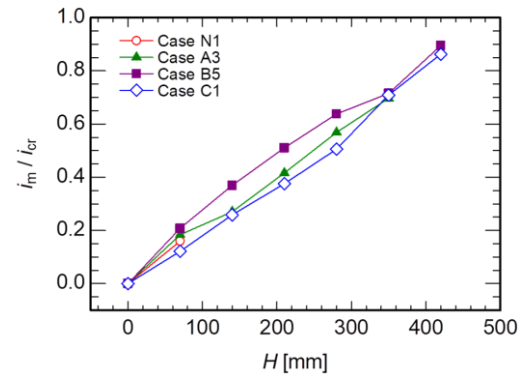


Fig. 4 Relationships between H and i_m/i_{cr} .

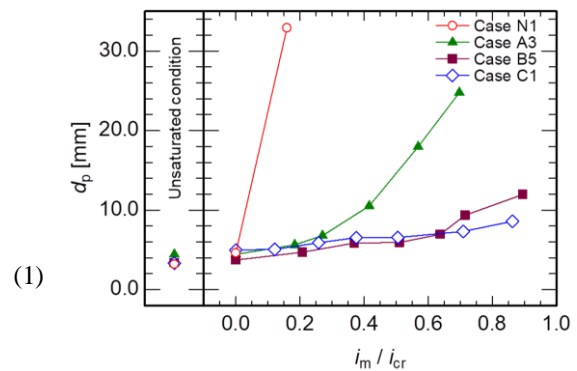


Fig. 5 Relationships between i_m/i_{cr} and d_p .

compared to that without a gabion, and the effect on the displacement resistance of the gabion hardly depended on those widths.

In case A3 using the gabion of 0.5D width, the pipe moved gradually with the increase in i_m/i_{cr} and displaced 23 mm when the value of i_m/i_{cr} was 0.7. Meanwhile, in cases B5 and C1 using the gabion of 1.0D and 1.5D widths, respectively, the values of d_p were approximately 10 mm even when the values of i_m/i_{cr} were approximately 0.9. The effect on the pipe displacement resistance of the gabion of 0.5D width is smaller than that of the 1.0D and 1.5D width gabions.

Behavior of Gabion in the Ground

To evaluate the behavior in the ground and the gabions, the distributions of the maximum shear strain, γ_{max} in the ground were calculated based on the displacement of the markers in the model ground. The strain calculation was performed based on each of the four-node rectangular elements using four markers. The distributions of γ_{max} when d_p is 5 mm to 7 mm, and at the end of each final step are shown in Figs. 6 and 7, respectively. The black squares in

Figs. 6 and 7 indicate the locations of the markers. The ground surface shapes were also shown in Figs.

shaped and was distributed from the front of the buried pipe to the ground surface. The ground

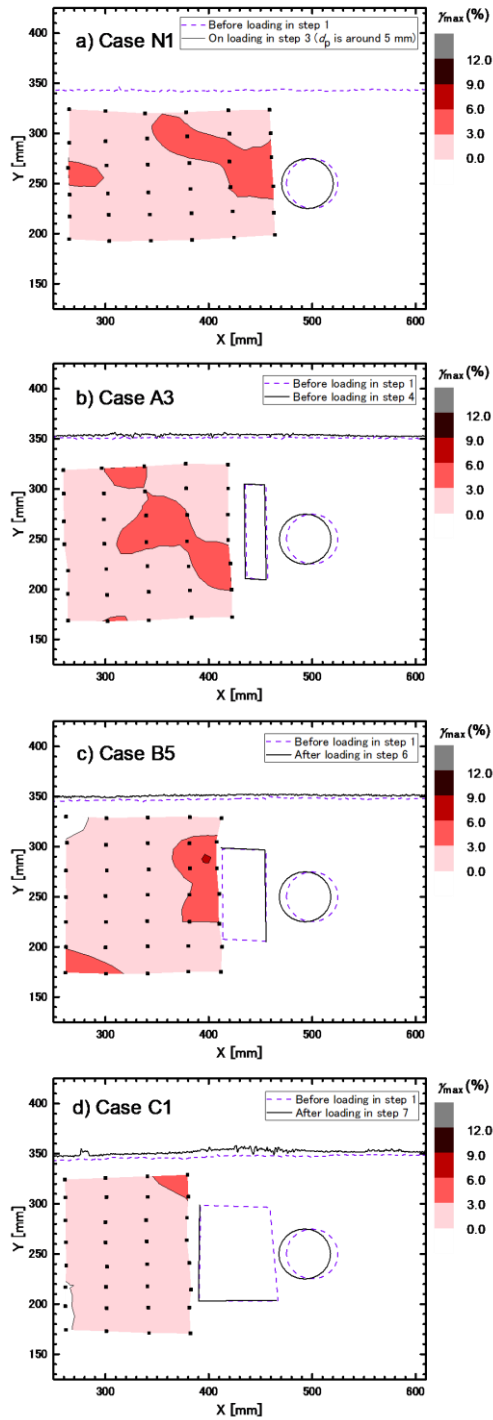


Fig. 6 Distribution of maximum shear strain when d_p is 5 mm to 7 mm.

6 and 7.

The ground deformation and the behavior of the model pipe without a gabion is shown in Figs. 6a and 7a. The region with a high shear strain was strip-

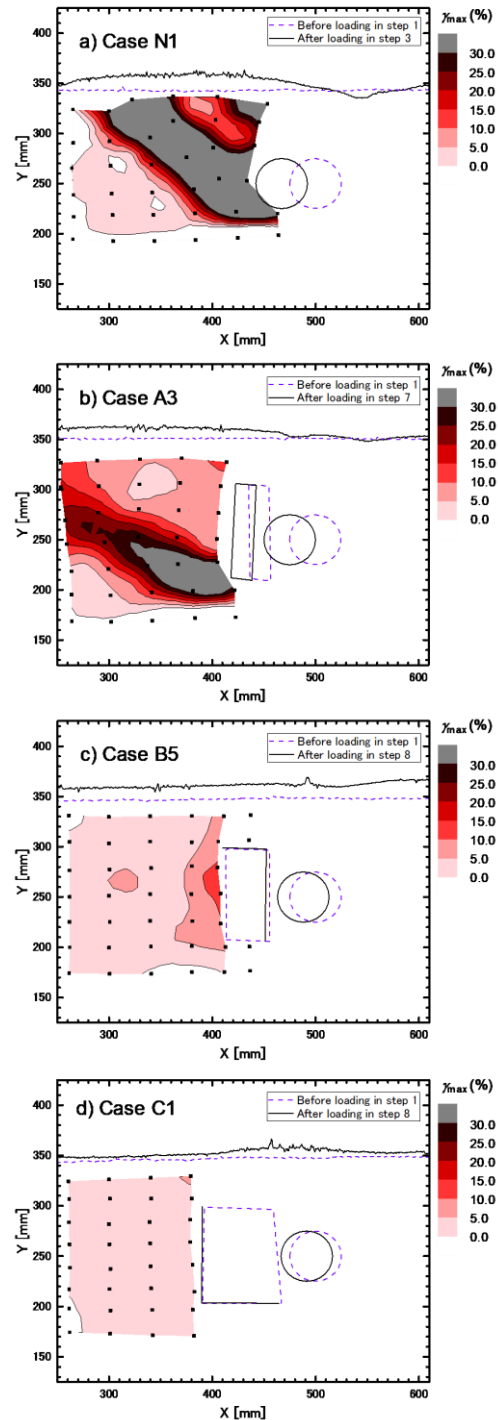


Fig. 7 Distribution of maximum shear strain at the end of each final step

surface of the upper part of the passive area of the pipe was swollen at the end of step 3 (Fig. 7a).

In case A3, the shear deformation spread from the bottom of the 0.5D width gabion to the ground

surface with the increase in the pipe displacement (Figs. 6b and 7b). The location of the gabion shown in Fig. 7b indicates that the gabion was rotating clockwise. In cases B5 and C1, meanwhile, the gabions with a width of 1.0D and 1.5D, respectively, hardly moved, even at the end of step 8 where the values of i_m/i_{cr} were approximately 0.9 (Figs. 7c, d). The high shear strain region from the bottom of the gabion to the ground surface, such as that shown in Fig. 7b, was also not observed in cases B5 and C1.

The phase of the gabion behavior changed significantly between cases A3 and B5. The difference in the test conditions between cases A3 and B5 was the bottom area of the gabion to which the bottom frictional resistance was applied. The bottom frictional resistance is considered to have influenced the rotational behavior of the gabion. The width might be required to be at least 1.0D to obtain a bottom frictional resistance sufficient to prevent the rotational behavior of the gabion under this experimental condition.

The shear strain was also localized at the side of the 1.0D width gabion in case B5, shown in Figs. 6c and 7c, although the location of the gabion hardly changed compared to that of before loading in step 1. The high shear strain at the side of the gabion suggests the bending deformation of the gabion by the thrust force from the pipe. In case C1, meanwhile, the shear strain at the side of the gabion was not localized, and remained under 5.0% throughout, even at the end of step 8. The gabion might be required to have a width of 1.5D to prevent the bending deformation by increasing the bending stiffness of the gabion under this experimental condition.

The relationships between i_m/i_{cr} and d_p shown in Fig. 5 were different for cases A3 and B5; subsequently, the pipe displacement was affected strongly by the rotating behavior of the gabion. Moreover, the effect of the bending deformation on the pipe displacement resistance is likely smaller than that of the rotational movement, causing the relationships between i_m/i_{cr} and d_p to be similar to each other in cases B5 and C1. Therefore, it is important to prevent rotation of the gabion to retain the displacement resistant effect in the ground where the effective stress decreases.

CONCLUSION

Model experiments were conducted on a new thrust protection method using geogrid gabions to

evaluate the effect of the gabion width. The conclusions are summarized as follows:

- 1) In the ground where the value of i_m/i_{cr} was more than 0.2, the values of the displacements of pipes protected with gabions having a width of 0.5D to 1.5D were small compared to that without a gabion.
- 2) For the gabion with 0.5D, the pipe displacement increased gradually, and the gabion moved rotationally as the effective stress decreased in the ground.
- 3) For the gabions with 1.0D and 1.5D widths, the displacements of the pipe were significantly small, and the rotating behavior of the gabion was hardly observed. It is important to prevent the rotating behavior of the gabion to retain the displacement resistant effect.
- 4) By expanding the gabion width, the rotational behavior is suppressed by increasing the frictional resistance of the bottom surface. Furthermore, the bending behavior is also suppressed by the increased bending stiffness of the gabion when its width further expanded.

ACKNOWLEDGEMENTS

This study was supported by JSPS KAKENHI Grant Number JP17K14723.

REFERENCES

- [1] Mohri Y., Yasunaka M. and Tani S., Damage to Buried Pipeline Due to Liquefaction Induced Performance at the Ground by the Hokkaido Nansei-Okai Earthquake in 1993, Proceedings of First International Conference on Earthquake Geotechnical Engineering, IS-Tokyo, 1995, pp. 31–36.
- [2] Kawabata T., Sawada Y., Uchida K., Hirai T. and Saito K., Model Tests on Thrust Protecting Method for Buried Bend with Geogrid, Geosynthetics Engineering Journal, Japan Chapter of International Geosynthetics Society, Vol. 19, 2004, pp. 59–64. (in Japanese)
- [3] Kawabata T., Sawada Y., Mohri Y. and Ling I., Dynamic Behavior of Buried Bend with Thrust Restraint in Liquefying Ground, Journal of Japanese Society of Civil Engineering, Vol. 67, No. 3, 2011, pp. 399–406. (in Japanese)
- [4] Araki H. and Hirakawa D., Model Tests on Thrust Protecting Method for Buried Pipe by Using Geogrid Gabion, Journal of Japanese Society of Civil Engineering, Vol. 74, No. 1, 2018, pp. 106–117. (in Japanese)
- [5] Audibert J. M. E. and Nyman K. J., Soil Restraint Against Horizontal Motion of Pipe,

- Journal of the Geotechnical Engineering Division, Proceedings of the American Society of Civil Engineers, Vol. 103, No. GT10, 1977, pp. 1119–1142.
- [6] Itani Y., Fujita N., Sawada Y., Ariyoshi M., Mohri Y. and Kawabata T., Model Experiment on the Horizontal Resistance Force of Buried Pipe in Liquefied Ground, Irrigation, Drainage and Rural Engineering Journal, Vol. 295, 2015, pp. 77–83. (in Japanese)

EXPERIMENTAL STUDY ON RAINFALL INTENSITY AND SHALLOW LANDSLIDES WITH QUASI-SATURATED STATE

Kota Okazaki¹, Keigo Koizumi¹, Kazuhiro Oda², Katuo Sasahara³ and Keiji Sakuradani⁴

¹Graduate School of Engineering, Osaka University, Japan

²Graduate School of Engineering, Osaka Sangyo University, Japan

³Graduate School of Engineering, Kochi University, Japan

⁴West Nippon Expressway Company Ltd., Japan

ABSTRACT

In recent years, extreme weather has caused rainfall-induced shallow landslides in Japan. To solve this problem, our research group has implemented model slope experiments to obtain predictive information before shear deformation starts. When sprinkling water with a constant intensity on a model slope, the volumetric water content rises and temporarily attains a stable state. Subsequently, the groundwater level is formed on the boundary with the basement layer, the volumetric water content rises again, and shear deformation occurs. Therefore, by defining the state in which the volumetric water content temporarily attains a stable state as quasi-saturated state and by defining the volumetric water content at the point where quasi-saturated state begins as the initial quasi-saturated volumetric water content (IQS), IQS is proposed as an early warning index for rainfall-induced shallow landslides. In this paper, two model slope experiments were conducted – one with a heavy rain intensity and the other with a regular rain intensity – to understand both water infiltration behavior and slope deformation behavior. We confirmed that, when the rainfall intensity is high, the volumetric water content rises again after it exceeds IQS, and shear deformation occurs. On the other hand, when the rainfall intensity is regular, the volumetric water content is constant at IQS, and shear deformation does not occur. These results suggest that shear deformation can be predicted beforehand by monitoring whether the volumetric water content exceeds IQS.

Keywords: Volumetric water content, Rain intensity, Shallow landslide, Model slope, Shear deformation

INTRODUCTION

To solve the problem of rainfall-induced shallow landslides, our research group has implemented model slope experiments to obtain predictive information before shear deformation starts. The relationship between the volumetric water content and shear deformation shown in Fig. 1 was confirmed in a previous study [1] through a water spray experiment using a model slope. In this schematic diagram, when water is sprayed on the model slope with a constant strength, moisture infiltrates into the soil, and the volumetric water content starts to increase. When the volumetric water content approaches the value defined as the initial quasi-saturated volumetric water content (IQS), the rate of increase drastically decreases, and the volumetric water content attains an equilibrium state. Subsequently, the groundwater level is formed from the deep part, the volumetric water content rises again, and a shallow landslide occurs because of shear deformation. Based on this result, we have repeated model experiments under various conditions, focusing on the fact that shear deformation does not occur unless the volumetric water content exceeds IQS, and we verified the reproducibility of the experiment. In this paper, we report a model slope

experiment conducted to compare moisture infiltration behavior and shear deformation behavior between strong and weak rainfall intensities while focusing on the quasi-saturated state.

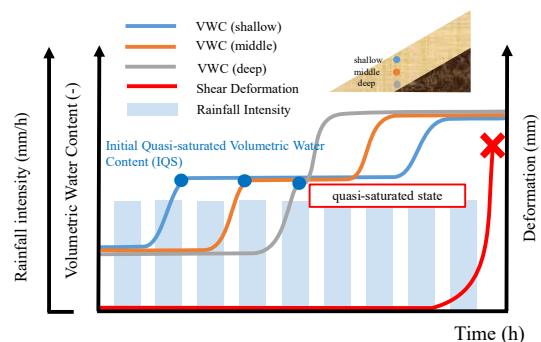


Fig. 1 Volumetric water content and shear deformation on a model slope as functions of time.

EXPERIMENT METHODS

In the experiment, a slope 1200 mm long \times 300 mm wide \times 575 mm high, as shown in Fig. 2, was created. The topsoil layer thickness was 200 mm, and the slope gradient was 30°. An impermeable layer was formed on the base layer with clay to achieve a

non-drainage condition. In addition, to prevent edge erosion with drainage, a net basket and a draining net at the edge of the horizontal layer were set, as shown in Fig. 2. The soil sample is granite soil, and its physical properties are listed in Table 1. In order to confirm the infiltration behaviors in the vertical and the slope directions, a soil moisture meter (EC-5) was installed at nine points, as shown in Fig. 2. In addition, we installed three tensiometers to measure suction in the toe part of the slope, as shown in Fig. 2. To measure the ground surface displacement, image sensing technology [2] was used. Here, a USB 3.0 camera (3376 pixels \times 2704 pixels) was set on the front side of the model slope, and targets for measurement displacement were set at three locations: the toe, middle, and top. The frame rate was set to 2 fps, and the temporal change of the ground surface displacement was measured. Spraying equipment with a misty rain function was used, and the water spraying strength was set to correspond to a rainfall intensity of 100 mm/h (case 1) or 10 mm/h (case 2). In addition, in order to minimize the influence of collapse subsidence of ground surface displacement due to water spraying, the experiment was conducted after a preliminary spraying time of 10 min at a water spraying intensity of 60 mm/h and a drying time of 2 h. The water spraying time was set as 2 h for case 1 and 20 h for case 2. The total precipitation is 200 mm for both cases.

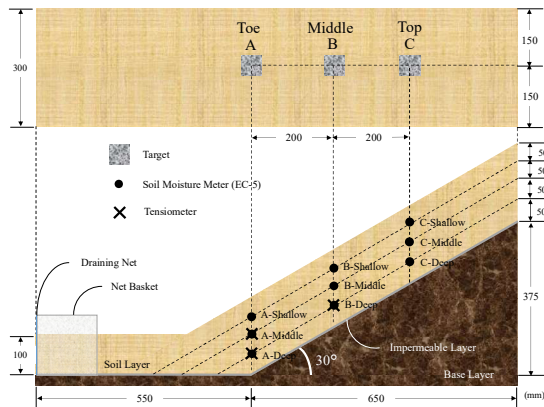


Fig. 2 Summary of the model slope.

Table 1 Physical properties of the soil sample

Sample	Granite Soil
Initial Water Content (w)	5.0 %
Soil Particle Density (ρ_s)	2.607 g/cm ³
Setting Dry Density (ρ_d)	1.629 g/cm ³
Hydraulic Conductivity (k)	1.12×10^{-2} cm/s
Void Ratio (e)	0.6

EXPERIMENTAL RESULTS AND EXAMINATION

Figure 3 shows the temporal change of the volumetric water content and the ground surface displacement in the toe of the slope for case 1. Initially, the volumetric water content increased because of moisture infiltration from the ground surface due to water spraying in the shallow part, followed by the middle part and deep part in order. Subsequently, the rate of change of the volumetric water content decreased, and after reaching the quasi-saturated state, the volumetric water content increased again in the deep part, followed by the middle part and shallow part in order. Because the moisture reaching the impermeable layer gathers in the toe of the slope as seepage flow, the duration of the quasi-saturated state is short in the deep part. In other words, the quasi-saturated state appears in the deep part of the toe of slope soon after the groundwater level is formed. Furthermore, approximately 14 min from the start of sprinkling, displacement occurred, after the volumetric water content exceeded IQS in the toe of the slope. This result is consistent with our previous result, confirming that IQS occurs before displacement.

Figure 4 shows the temporal change of the volumetric water content and suction in the toe of the slope for case 1. The volumetric water content and suction behavior are consistent between the deep and middle parts. In the deep part, since the suction reaches 0 when the volumetric water content is approximately 0.35, it is inferred that field saturation has occurred at this point. In the middle part, it is inferred that field saturation has been reached since the suction value is approximately 0.

Figure 5 shows the temporal change of the volumetric water content and the ground surface displacement in the toe of the slope for case 2. From this figure, it is confirmed that displacement does not occur. After reaching the quasi-saturated state in the shallow part, the second increase of the volumetric water content was not confirmed. On the other hand, the volumetric water content in the deep part of the toe of the slope started to increase immediately after the start of spraying, and the quasi-saturated state was shown for approximately 30 min, following which the volumetric water content increased again; equilibrium was confirmed to occur at a volumetric water content of approximately 0.22. Since the saturated volumetric water content of the soil sample used is 0.375, it can be said that field saturation has not been reached. This result, in addition to infiltration from above in the deep part of the toe of the slope, suggests that unsaturated capillary fringes are formed by the influence of seepage flow on the impermeable layer when the volumetric water content exceeds IQS. Although the volumetric water content exceeded IQS in the deep part of the toe of the slope

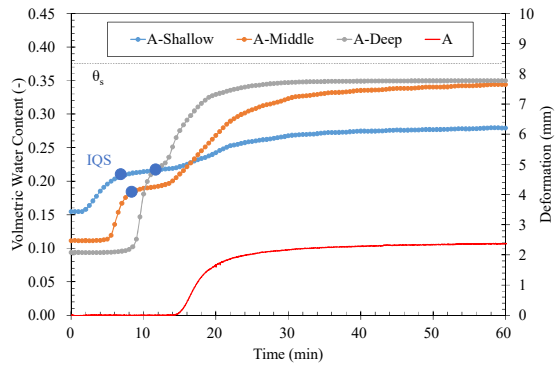


Fig. 3 Volumetric water content and slope deformation as functions of time in the toe of the slope for case 1.

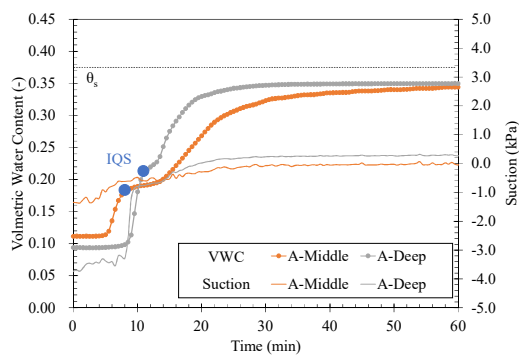


Fig. 4 Volumetric water content and suction as functions of time in the toe of the slope for case 1.

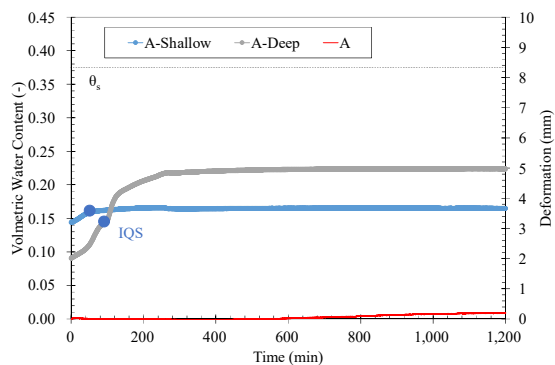


Fig. 5 Volumetric water content and slope deformation as functions of time in the toe of the slope for case 2.

in case 2, the groundwater level was not formed, because of the balance between the inflow and outflow under the unsaturated state, and it is considered that displacement did not occur.

CONCLUSIONS

In this study, we conducted a model slope experiment for two cases – strong and weak rainfall intensity – and analyzed the results based on our previous findings while focusing on the quasi-saturated state. In the case where the rainfall intensity was 100 mm/h, displacement occurred after the volumetric water content exceeded IQS, which is consistent with our previous studies. In the case where the rainfall intensity was 10 mm/h, although the volumetric water content exceeded IQS, the groundwater level was not formed. Consequently, displacement did not occur. This result indicates that the slope maintains the unsaturated state even after sprinkling for a long time, suggesting that displacement does not occur when the rainfall intensity is extremely small compared with the coefficient of permeability of the soil.

ACKNOWLEDGEMENTS

We would like to thank Editage (www.editage.jp) for English language editing.

REFERENCES

- [1] Koizumi K., Sakuradani K., Oda K., Fukuda Y., Takemoto S. and Morishita H., Fundamental Study for Improvement of a Traffic Regulation Standard Based on a Model Slope Experiment, in Proc. Kansai Geo-Symposium, 2015, pp. 187-190.
- [2] Fukuda Y., Koizumi K., Yamamoto T., Kobashi S., Oda K., Sakuradani K. and Maria F., Experimental Study on Slope Deformation Measurement Utilizing a Image Sensing Technology, Proc. Kansai Geo-Symposium, 2016, pp. 243-248.

COLLAPSE MECHANISM OF STEEL PILES BELOW HIGH-RISE BUILDING IN LIQUEFIED SOIL

Moeko Matoba¹ and Yoshihiro Kimura¹

¹Tohoku University, Japan

ABSTRACT

In our previous papers, centrifugal tests for the low- or medium-rise superstructure, the steel pile foundation and the liquefied soil system were conducted, and the dynamic buckling behavior and the buckling strength of the steel pile were elucidated. However, the steel piles below the high-rise building might carry the larger varying axial force generated by the overturning moment than those below the low- or medium-rise building issued from the high height-to-width aspect ratio. In this paper, the collapse behavior and the ultimate strength of steel piles in the liquefied soil below the high-rise building are clarified using centrifugal tests. It is shown that pile's ultimate strength below high-rise buildings can be evaluated by the M-N interaction curves of current Japanese design criteria and the ultimate strength curve, to which the elasto-plastic buckling strength is applied based on the modified slenderness ratio.

Keywords: Steel pile, Dynamic buckling behavior, Liquefaction, Centrifugal tests, high-rise building

INTRODUCTION

In recent years steel piles are applied not only to low-rise buildings but also medium- or high-rise buildings on the soft ground. In general, it is considered that steel piles have large plastic deformation capacity. On the other hand, the ratio of the axial force-to-the yielding strength of the steel pile can be higher than that of the RC pile because of the thin-walled cross-section. In recent real buildings, steel piles are designed to carry the higher compressive axial force generated by taller buildings than those in the past. The steel pile always carries 50% of the yielding strength due to dead load and reaches 70 - 80% of the yielding strength due to the overturning moment of the building during the earthquake.

In Japanese current design criteria [1], the possibility of steel pile's flexural buckling is not taken into account. This is because the damage of pile's flexural buckling has been not found on the past earthquake damage reports [2], and it is assumed that the lateral deformation of piles is well restricted by the ground, no matter how soft is the ground. However, the subgrade lateral stiffness decreases dramatically when the soil liquefaction occurs during a significant earthquake. The slender steel pile beneath the building experiences the axial compression force, which is caused by the overturning moment of the superstructure and the horizontal force generated from the inertia force. Therefore, the pile might lose the vertical bearing capacity due to the dynamic buckling.

In our previous papers, centrifugal tests for the superstructure, the steel pile foundation, and the

liquefied soil system were conducted and the dynamic buckling behavior and the buckling strength of steel piles, which is subjected to the axial compressive force only, were elucidated. Moreover, the collapse behavior and the strength of the steel pile, on which varying axial force and horizontal force act, were clarified. The steel piles below the high-rise building might carry the larger varying axial force generated by the overturning moment than those below the low- or medium-rise building issued from the high height-to-width aspect ratio. Therefore large plastic hinges might occur at the top and the middle part of the steel piles.

In this paper, the centrifugal tests for the high-rise superstructure, steel piles, and the liquefied soil system are conducted. For the flexural buckling of piles in the liquefied soil, the collapse mechanism of the steel piles below the high-rise building is clarified during the significant earthquake, and the ultimate strength of the steel pile is evaluated using the M-N interaction curve according to Japanese design criteria.

OUTLINE OF CENTRIFUGAL TEST

In this chapter, the outline of the centrifugal test using the superstructure, the pile foundation, and the liquefied soil models is described.

Figures 1(a) - 1(d) show the model and instruments. The specimen consists of a superstructure and a pile foundation with mass, bending plates, four piles and a saturated sand layer. The width of the pile foundation and superstructure is 120 mm. The superstructure's height is 90 mm. Four piles are set up as described in Fig. 1(b). Two

piles at the front are “pile A” on the left side and “pile B” on the right side, the others at the back are “pile C” and “pile D”, respectively. The bending plates are “plate X” on the left side and “plate Y” on the right side. As presented in Figs. 1(c) and 1(d), strain gauges are located on the left and right surface, x_i and y_i , of piles and bending plates. In this case, i takes the number between 1–7 for each pile along its height, and 1–3 for each bending plate along its height. Accelerometers are installed on the upper surface of the superstructure and the pile foundation, as well as on the plate at the bottom of the laminar box. Accelerometers and water pressure gauges are located at 80 mm, 140 mm, 200 mm from the ground level as shown in Fig. 1(a). The tests were performed under the centrifugal acceleration of 40G with the centrifugal loading device at the Disaster Prevention Research Institute at Kyoto University.

Table 1 presents the specimen specifications. The pile material is brass C2680, the bending plate material is A5052, and the others are SS400. Figure 2 presents material properties of the brass. In this paper, the elastic proportional limit stress, σ_e , is determined. However, the yielding stress, σ_y , is assumed using 0.2% offset-yield strength because of the material properties with the Round-House type.

Table 2 shows specimen parameters which are the natural period of the superstructure, the height-to-width aspect ratio, and the relative density of the soil. Case 1 is the specimen in [3]. The ratio of the initial axial load to the yielding strength, N_0/N_y , is 0.33, derived from the axial design force of steel piles in real structures.

Figure 3 presents the time history of Coastal Wave as the input wave with maximum input acceleration of 5.0 m/s².

Figure 4 shows the acceleration response spectrum of the input wave. Then the damping ratio is assumed to be 0.02. The equation of the natural period of the superstructure is presented as the following, which consists of the bending rigidity of the superstructure and bending plate.

$$T = 2\pi\sqrt{m_1/nk} \quad (1)$$

$$k = 12EI/h^3 \quad (2)$$

Here, m_1 indicates the superstructure weight, E represents Young's modulus of the bending plate

and I denotes the moment of inertia of area of the bending plate. n and h stand for the number and the length of the bending plate, respectively. In Figs. 4, black triangles indicate the natural period of the superstructure for the specimens calculated by Eqs. (1) and (2). In this paper, the natural period of the superstructure for the specimens of Case 1 and Case 3 is 1.08s, and that of Case 2 and Case 4 is 1.51s for the full-scale model, which is assumed for the medium- and high-rise buildings. Coastal Wave response spectrum has a peak at 0.55 s, and the response acceleration values at 1.08s and at 1.51s are almost the same.

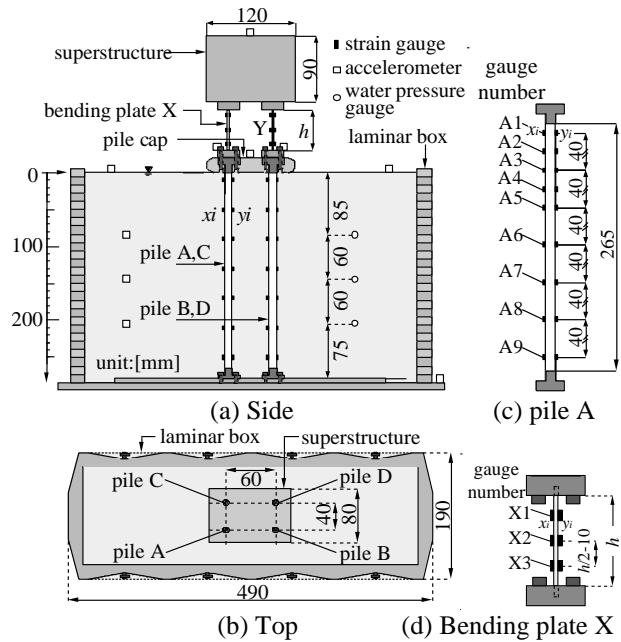


Fig. 1 Specimen and instrumentation

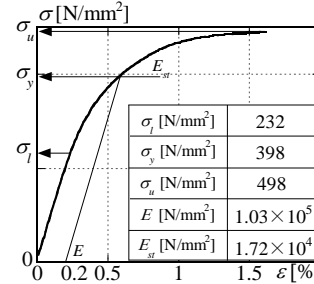


Fig. 2 Pile's material property

Table 1 Details of specimens

	in model's scale	in full scale
superstructure weight: m_1 [N]	66.7	4.27×10^6
bending plate thickness [mm]	2	80
pile cap weight: m_2 [N]	13.0	8.3×10^5
length: l [mm]	265	10600
pile diameter: D [mm]	10	400
thickness: t [mm]	0.2	8

Table 2 Specimen parameters (in full scale)

specimen	boundary condition of pile cap	initial axial force N_0 [kN] (N_0/N_y)	relative density Dr [%]	natural period of the superstructure T_s [s]	length-to-weight ratio	input wave	maximum input wave acceleration [m/s²]	after shaking
Case 1	laterally free	1275 (0.33)	30	1.08	2.8	Coastal Wave	5.0	collapse
Case 2				1.51	3.0			collapse
Case 3			60	1.08	2.8			plasticized
Case 4				1.51	3.0			collapse

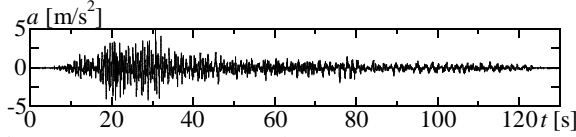


Fig. 3 Input wave (Costal Wave)

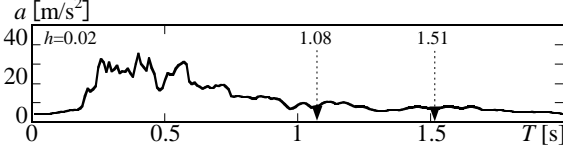


Fig. 4 Response acceleration spectrum of Costal Wave

DYNAMIC BEHAVIOUR OF STEEL PILES IN LIQUEFIED SOIL BY CENTRIGUGAL TEST

Time history

Figures 5 - 8 show response time histories of Case 1 - Case 4. Figures 5(a) - 8(a) show the excess pore water pressure ratio time history. Black and gray lines show the data received from water pressure gauges located on 3.4 m and 5.8 m below the ground surface shown in Fig. 1(a), respectively. Triangles in Figs. 5(a) - 8(a) represent the time of the soil liquefaction. As described in this paper, the liquefaction occurs when the excess pore water pressure ratio reaches almost 1.0.

Figures 5(b) - 8(b) show the response time history of structure's inertial force. Structure's inertial force is calculated from the sum of the shearing force, Q_b , obtained from bending plate's moment distribution and the inertial force of the pile cap, $m_2 a_2$. m_2 and a_2 signify pile cap's weight and horizontal acceleration. Figures 5(c) - 8(c) show the response time history of pile's varying axial force. Pile's varying axial force, ΔN_b , is calculated from the following equations:

$$\Delta N_b = (N_{b,x} - N_{b,y}) / 2 \quad (3a)$$

$$N_{b,(x \text{ or } y)} = \frac{(\varepsilon_{xi} + \varepsilon_{yi})}{2} \times \frac{EA_b}{2} + \frac{m_2 g}{4} \quad (3b)$$

It is assumed that the varying axial forces on the bending plate X and Y are equal and two piles under bending plate X or Y carry identical varying axial force. $N_{b,x}$ and $N_{b,y}$ denote the axial compression force of bending plate X and Y. E_b and A_b indicate Young's modulus and the cross-section area of the bending plate, and ε_{xi} and ε_{yi} represent the bending plate strain. It is confirmed that bending plates for all specimens remain elastic until piles collapse. White triangles in Figs. 5(c) - 8(c) represent the maximum varying axial force before piles collapse. The compressive force is marked as a negative value. The yielding strength of steel piles is 3921 kN.

Figures 5(d) - 8(d) depict pile's bending strain response time histories at the pile top. These values

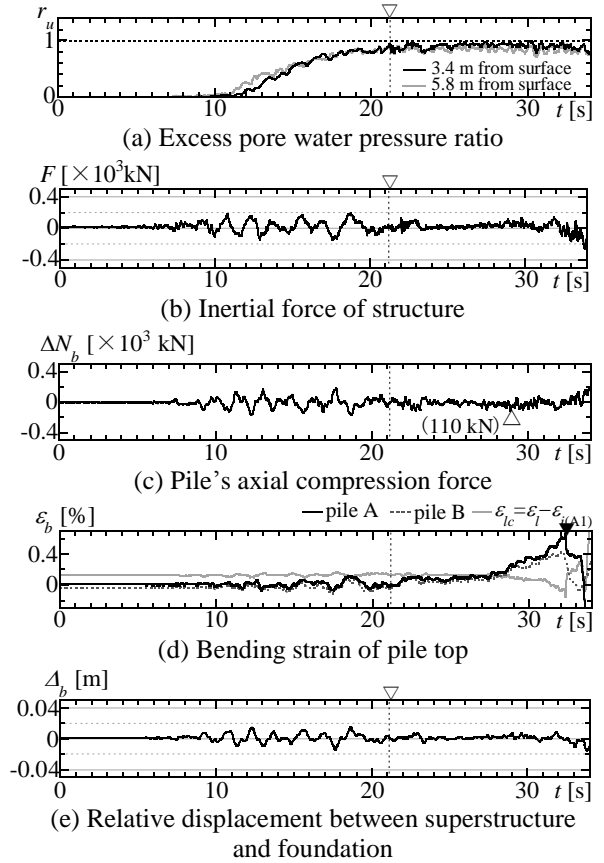


Fig. 5 Response time history of Case 1

are calculated using the following equations with strain gauges as shown in Fig. 1(c).

$$\varepsilon_{bi} = (\varepsilon_{pile,xi} - \varepsilon_{pile,yi}) / 2 \quad (4)$$

$$\varepsilon_{ci} = (\varepsilon_{pile,xi} + \varepsilon_{pile,yi}) / 2 \quad (5)$$

Black triangles indicate the time of the maximum bending strain in Figs. 5(d) - 8(d). The black line represents the response time history of pile top's bending strain, obtained from pile A or B, whichever has the greater maximal bending strain value at the pile's top. ε_{lc} is derived by following equation which deducts pile top's axial strain from the elastic proportional limit strain.

$$\varepsilon_{lc} = \varepsilon_l - \varepsilon_{ci} \quad (6)$$

Figures 5(e) - 8(e) depict the relative displacement between the superstructure and the pile foundation calculated from bending plate's moment.

For all specimens, the whole of the pile-foundation starts to incline while pile's bending strain increases. Finally, the superstructure hits the stopper preventing the collapse of specimens.

The response behavior of specimens with the relative density of 30%, Case 1 and Case 2, are compared. The natural period of the superstructure is 1.08 s for Case 1, and 1.51 s for Case 2. The height-

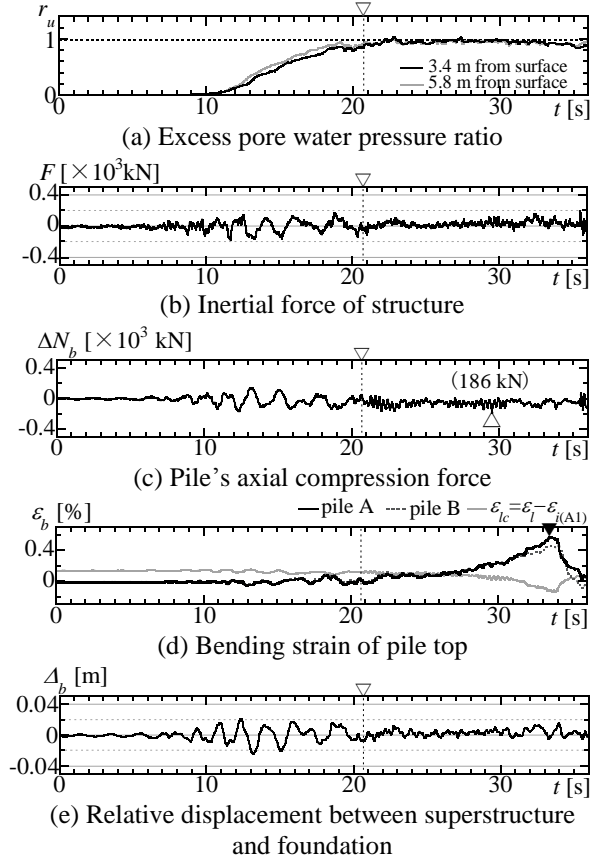


Fig. 6 Response time history of Case 2

to-weight ratio of the superstructure is 2.8 for Case 1 and 3.0 for Case 2.

For Case 1 and Case 2, the excess pore water pressure ratio, r_u , reaches almost 1.0 at about 21 s, and the soil liquefaction occurs as presented in Figs. 5(a) and 6(a). The response of structure's inertia force in Figs. 5(b) and 6(b) and relative displacement in Figs. 5(e) and 6(e) decrease after the soil liquefaction. As shown in Figs. 5(c) and 6(c), the maximum varying axial force after the liquefaction is 110 kN for Case 1 and 186 kN for Case 2. The ratio of the varying axial force to the initial force, $\Delta N_b/N_0$, is 8.6% for Case 1 and 14.6% for Case 2, and the value of Case 2 is larger than that of Case 1 due to height-to-weight ratio being higher. As shown in Figs. 5(d) and 6(d), pile top's bending strain of both specimens gradually increases after the soil liquefaction and reaches the elastic proportional limit strain, ε_{lc} , at about 28 s. After pile top's bending strain attains ε_{lc} , pile top's bending strain drastically increases and becomes the maximum value at 32 s (Case 1) and 33 s (Case 2).

The response behavior of specimens with the relative density of 60%, Case 3 and Case 4, are compared. The natural period of the superstructure is 1.08 s for Case 3, and 1.51 s for Case 4. The height-to-weight ratio of the superstructure is 2.8 for Case 3, and 3.0 for Case 4.

For Case 3 and Case 4, the excess pore water pressure ratio, r_u , reaches almost 1.0 at about 25 s,

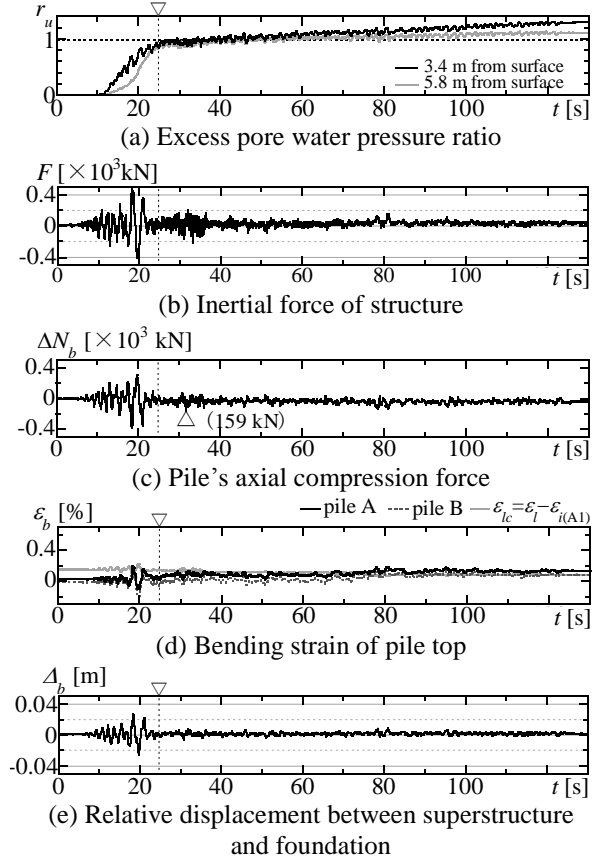


Fig. 7 Response time history of Case 3

and then the soil liquefaction occurs as presented in Figs. 7(a) and 8(a). As shown in Figs. 7(c) and 8(c), the maximum varying axial force after the liquefaction is 159 kN for Case 1 and 270 kN for Case 2. The ratio of the varying axial force to the initial force, $\Delta N_b/N_0$, is 12.5% for Case 3 and 21.2% for Case 4, and the value of Case 4 is larger than that of Case 3. For Case 3, the amplitude of structure's inertia force in Fig. 7(b) and relative displacement in Fig. 7(e) decrease after the soil liquefaction. In Fig. 7(d), the bending strain of the pile top after the liquefaction gets to the elastic proportional strain, ε_{lc} , at about 30 s. However, the bending displacement of the pile foundation scarcely occurs after shaking.

For Case 4, the amplitude of structure's inertia force and relative displacement decreases after the soil liquefaction (Figs. 8(b) and 8(e)). However, the response median gradually moves from about 36 s to the positive side. In Fig. 8(d) the bending strain of the pile top steadily increases during the liquefaction and attains the elastic proportional strain, ε_{lc} . The bending strain continues increasing after the liquefaction until the time of about 30 s, and remains stable between at 30 s and 36 s. From about 36 s, the bending strain increases again and becomes the maximum value at about 48 s, leading to collapse of the pile foundation. For Case 4, it is considered that the bending strain of the pile top increases issued from the additional moment by the $P-\Delta$ effect of the superstructure from about 36 s.

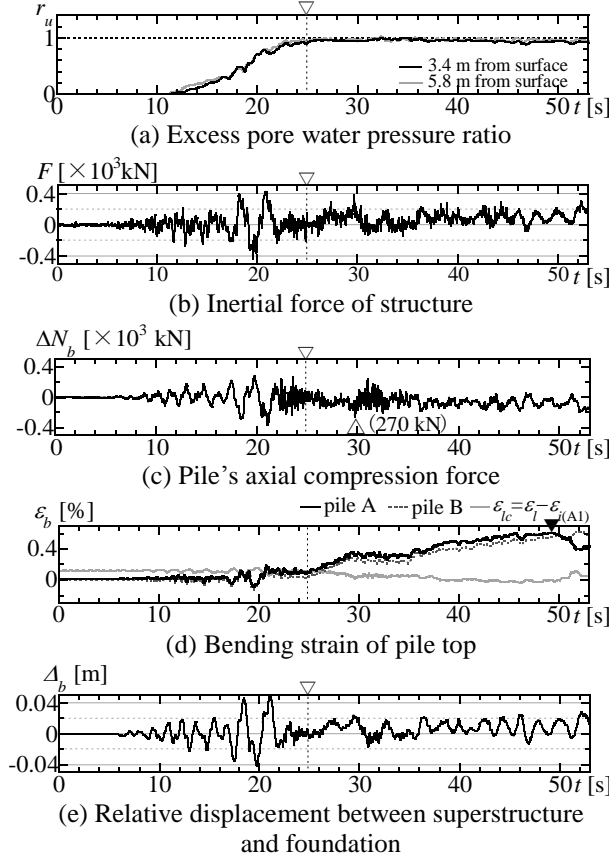


Fig. 8 Response time history of Case 4

Collapse mechanism of steel piles in liquefied soil

In this section, it is shown that the collapse mechanism of steel piles based on the ultimate state.

Figure 9 shows the bending strain distribution of piles at the side where the superstructure leans, until pile's bending strain reaches the maximum value. The vertical axis shows the coordinates of pile's axial direction with the origin located at pile's top, and the horizontal axis represents pile's bending strain. Dashed blue line and solid red line indicate the elastic proportional limit strain, ε_{lc} , and the yielding bending strain, ε_{yc} , reduced by the initial axial force as the following equation.

$$\varepsilon_{(t \text{ or } y)c} = \varepsilon_{(t \text{ or } y)} (1 - N_0 / N_y) \quad (7)$$

Triangles and diamonds show the bending strain

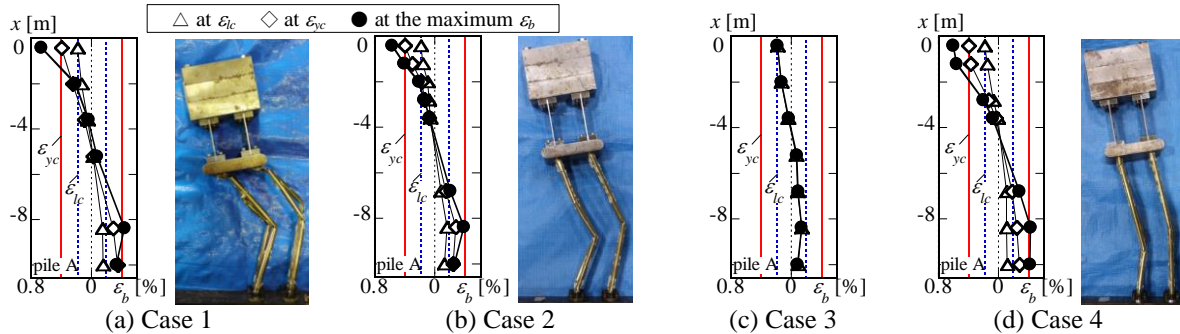


Fig. 9 Piles' bending strain distribution and pile's ultimate state

distribution at ε_{lc} and ε_{yc} of pile top's bending strain, respectively. Black circles symbolize the distribution at the maximum bending strain of the pile top. For Case 1, Case 2 and Case 4 (which collapses during shaking), the piles' bending strain increase, and reach the yielding strain at the pile top and the middle of the pile, and its value gets the yielding strain. Therefore, it is concluded the plastic hinges occur at the pile top and the middle of the pile. Photos in Fig. 9 show the ultimate state of Case 1, Case 2 and Case 4. For Case 1 and Case 2, the local buckling occurs at the pile top and at the one-third distance from the bottom of the pile. For Case 4 with the higher relative density of the soil, the bottom local buckling point of the pile gets lower comparing with Case 1 and Case 2.

EVALUATION OF ULTIMATE STRENGTH OF STEEL PILES IN LIQUEFIED SOIL

In this chapter, the ultimate strength of steel piles which simultaneously experience axial force and bending moment is clarified.

Figure 10 shows the elasto-plastic buckling strength of piles in the liquefied soil and buckling stress curves of Japanese current design criteria. The vertical axis represents the elasto-plastic buckling strength of piles obtained from centrifugal tests and numerical analyses, N_c , divided by the yielding strength, N_y . The horizontal axis shows the modified equivalent slenderness ratio, λ_c , of piles which calculated from the following equation:

$$\lambda_c = \sqrt{N_y / P_{cr}} \quad (8)$$

Here, P_{cr} represents the elastic buckling strength of piles with the lateral restraint provided by the ground. $e\lambda_c$ and $p\lambda_c$ stand for the elastic and plastic critical slenderness ratio, respectively.

The results of centrifugal tests and analyses exceed the curve of Japanese Limit State Design of Steel Structures [4] and are distributed roughly following the curve of Japanese Design Standard for Steel Structures [5]. It is shown that the dynamic buckling strength for steel piles in the liquefied soil can be estimated approximately by the buckling curve according to Japanese Limit State Design of

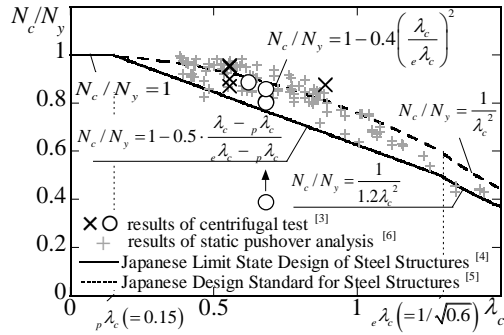


Fig. 10 Estimation of dynamic buckling strength

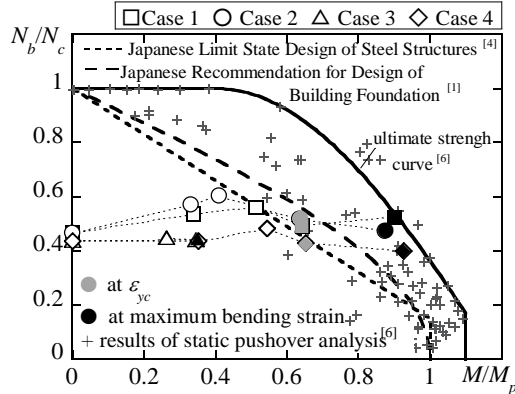


Fig. 11 Evaluation of pile's ultimate strength in the liquefied soil using M-N interaction curves

Steel Structures, to which the modified equivalent slenderness ratio, λ_c , is applied. In this paper, the buckling curve taken from Japanese Limit State Design of Steel Structures [4] is applied to conservatively estimate the piles' elasto-plastic buckling strength.

Figure 11 presents the relation between pile's axial compressive force and bending moment, and the M-N interaction curves of current Japanese design criteria [1] and [4], as well as and the ultimate strength curve [6]. The vertical axis represents the compressive axial force of the pile, N_b , divided by the elasto-plastic buckling strength, N_c . The horizontal axis represents pile's bending moment divided by pile's full plastic moment. The bending moment is calculated from the bending moment-bending strain curve. In Fig. 11, plots show main histories of the axial compressive force and bending moment for all specimens after the soil liquefaction. The gray "plus" symbols show the maximum stress of steel piles obtained from static pushover analyses as described in [6]. The dashed and dotted lines represent the M-N interaction curves from the Japanese Recommendation for Design of Building Foundation [1] and Japanese Limit State Design of Steel Structures [4], while the solid line stands for the ultimate strength curve as presented in [6]. In the same graph, black symbols represent the result when pile's bending strain reaches the maximum value.

For Case 1, Case 2 and Case 4, which collapse during shaking, results at pile's maximum bending

strain are exceeding the M-N interaction curve of Japanese Recommendation for Design of Building Foundation [1], and are distributed roughly following the ultimate strength curve [6]. Thus, it is shown that pile's ultimate strength can be estimated by the M-N interaction curves according to current Japanese design criteria [1], [4] and the ultimate strength curve [6], utilizing the elasto-plastic buckling strength based on the modified slenderness ratio, λ_c , as shown in Eq. (8).

CONCLUSIONS

In this paper, the collapse behavior of steel piles which carry axial force and bending moment are clarified using centrifugal tests of the superstructure, steel piles, and the liquefied soil system. The conclusions are as follows:

- 1) On centrifugal tests, pile's bending strain drastically increases after its magnitude exceeds the elastic proportional limit strain reduced by pile's axial force.
- 2) For the steel pile below the high-rise building, pile's varying axial force is larger than that below the low- or medium-rise building, and pile's bending strain increases due to the $P-\Delta$ effect of the superstructure with the higher relative density of the soil.
- 3) It is shown that pile's ultimate strength below high-rise buildings can be evaluated by the M-N interaction curves of current Japanese design criteria in [1], [4] and the ultimate strength curve in [6], to which the elasto-plastic buckling strength is applied based on the modified slenderness ratio, λ_c , as shown in Eq. (8).

ACKNOWLEDGMENTS

This work was supported by JSPS Grant-in-Aid for Scientific Research (B) Numbers JP 16H04445.

REFERENCES

- [1] Architectural Institute of Japan: Recommendation for Design of Building Foundation. 2001.
- [2] Architectural Institute of Japan: Preliminary Reconnaissance Report of the 2011 Tohoku-Chiho Taiheiyō-Oki Earthquake, Jul. 2011.
- [3] Kimura Y, Matoba M, Goto T and Tamura S: Dynamic Ultimate Strength for Circular Tube Pile Stiffened at Pile Head Based on Centrifuge tests of Superstructure-Pile-Liquefied Soil System, Jour. of Structural and Construction Engineering, Vol.82, No.738, Aug. 2017. pp. 1221-1231. (in Japanese)
- [4] Architectural Institute of Japan: Limit State Design of Steel Structures, 2010.
- [5] Architectural Institute of Japan: Design Standard for Steel Structures, 2005.
- [6] Kimura Y, Tokimatsu K: Ultimate Vertical Strength and Ultimate Flexural Moment of Steel Pile subjected to Vertical and Horizontal Load in Liquefied Soil, Jour. of Structural and Construction Engineering, Vol.77, No.675, May. 2012. pp.775-781. (in Japanese)

MODIFIED NATURAL FIBER ON SOIL STABILIZATION WITH LIME AND ALKALINE ACTIVATION TREATED MARINE CLAY

Fatin Amirah binti Kamaruddin¹, Bujang B.K Huat², Vivi Anggraini³ and Haslinda Nahazanan⁴
^{1,2,4} Faculty of Civil Engineering, University Putra Malaysia, Malaysia; ³ Discipline of Civil Engineering,
Monash University Malaysia, Malaysia.

ABSTRACT

Geotechnical structures and foundations that are constructed on clay soils normally experience serviceability and structural quandaries due to wetting. Traditional and mechanical binder have been widely used for soil stabilization recently in order to improve clay soil. In this study, a comparison was made between lime and alkaline activation treated tropical marine soil reinforced with modified natural fiber. Treatment of soil with lime and alkaline activation show an excessively brittle behavior that influence the stability of the structure. For this purpose, the inclusion of natural biodegradable material which is coir fibre is needed as it enhanced the tensile strength of the soil matrix. The mechanical properties of unconfined compression test were carried out on tropical marine soil stabilized with lime (5%) and alkali activation with class F fly ash as precursor (60%) with and without fiber inclusions at different curing times. Based on the test results, inclusion of modified natural fiber in lime and alkaline activation treated tropical marine clay increased the strength of the soil matrix.

Keywords: Tropical marine soil, Modified natural fiber, Lime, Alkaline activation.

INTRODUCTION

Soft soil is generally recognized as a soil with high water content, high compressibility, low permeability and low shear strength, in which it is mostly found near coastal area. Problems on dealing with this kind of soft soil usually attract researchers to deal with the soil stabilization. There were many studies conducted in the past concerning the strength enhancement of the soil for future development. Enhancement through application of chemical agent and additive was widely been used as soil reinforcement or pavement stabilization mechanisms. The treatment use includes new and old techniques for example using lime, cement, gypsum, fly ash and ground granulated blast furnace. The utilization of this material attracted most researchers to use it as soil reinforcement due to the possibility to increase the strength of the soil.

Treatment of marine soils with chemical stabilizing agents (e.g. cement, gypsum, lime, and other alkaline admixtures) is one of the widely used method for ground improvement [1]-[8]. These stabilizing agents are used to bind the soil particles together through the chemical reactions. Stabilization of clay and lime would increase the optimum moisture content and decrease in the maximum dry density of the soil [9]. By [1], lime is the most effective chemical agents to treating the soil where it is capable of holding large amount of water and the cation exchange capacity (C.E.C). It has great contributions in defining clay minerals especially to facilitate water absorption ability. Apart from that, the marine clay soil is known as

high plasticity and swelling characteristic, the role of lime and soil formed cementation bonds which is able to help in increase and stiffness of the soils [9]-[11].

Furthermore, alkaline activation is one of the treatments that has recently been used. Alkaline activation is also known as “geopolymerisation” which is described as a reaction that chemical integrates minerals that consist of silica and aluminum alternately tetrahedrally interlinked by sharing all the oxygen atoms [12]. [13] stated that, alkaline activation also is a reaction between silica and alumina usually potassium (K) or sodium (Na) or alkali earth ions like calcium (Ca). Other than that, for alkaline activated process, waste materials recently have been used as one of the alternatives mixture for the activated ground improvement such as fly ash, metakaolin, granulate ground blast soil (GGBS), rice husk ash and etc). By [14], usage of waste materials (fly ash) in construction industry is becoming more frequent as it contributes to the reduction in consumption of cement. However, the treated soils exhibit an excessively brittle performance that affects the stability of structures [15]-[16]. This is the main weakness of the treated soil. Therefore, a possible solution has been proposed by some researchers [17]-[19] which is the inclusion of randomly distributed tensile reinforcement elements in soils to effectively increase ductility behavior, reduce the number and width of shrinkage cracks and help to obstruct them [17] and [19].

Therefore, soil reinforcement is one of the preferred alternative methods as it would be able to

help in strengthening the soil, lower the water content and compressibility of the soil. By [20], soil reinforcement is defined as a technique to improve the engineering properties of the soil as it develops the parameters such as compressibility, density, hydraulic conductivity and shear strength. This paper aims to compare the lime and alkaline activation for the modified treated tropical marine clay reinforced with modified natural fiber at the different curing time. A number of untreated and treated soil specimen with lime (5%) and alkaline activation with precursor (60%) were subjected to the unconfined compression strength test. The test was conducted to determine the strength of the soil matrix for different between the treated and untreated soil specimen.

MATERIALS AND METHOD

Materials

Soil Specimen

The tropical clay soil that was used in this study were taken from Klang, Selangor within 2m from the ground surface. The basic engineering property tests of the marine clay soil were conducted such as moisture content, particle size analysis, specific gravity and Atterberg limit. The testing was conducted based on the [21]. Table 1 below shows the basic properties of the marine clay soil that been used in this study. According to the table 1, the soil can be classified as CH which is clays with high plasticity by [22].

Coir Fiber

Coir fiber that was used in this study was taken from a factory in Batu Pahat Johor. The usage of coir fiber as the soil reinforcement where material that is known as environmental friendly, cheap and locally available. [23] highlighted that the coir fibers were used in the study as the materials have the property of elasticity, light, high durability, initial strength and a low light resistance.

Additive

Hydrated lime and fly ash class F are the two additive that been used for the clay soil. The reagent (calcium carbonate) was supplied in pellet by Evergreen Engineering, Selangor. Chemical content of the reagent was up to 99%. The fly ash class F (low calcium) was collected from Lafarge Sdn Bhd, Petaling Jaya Selangor. The fly ash was then mixed with the 10 molar potassium hydroxide (KOH) namely as the precursor of the alkaline activation process. 10 molar KOH concentration was fixed for the alkaline activation according to the previous

findings [24]- [26]. Table 2 shows the chemical and physical properties of the fly ash. Fly ash with low calcium is categorized where the classification of it was based on the total of SiO_2 , Al_2O_3 and Fe_2O_3 must be more than 70% and the CaO must be less than 7%.

Table 1: Basic properties of Marine Clay Soil

Parameter	Values
Moisture Content	72%
Specific Gravity	2.59
Soil Classification	Clays with high plasticity with traces of sand
Particle Size Distribution	Clay- 31% Silt – 67% Sand – 2%
Liquid Limit	57-72%
Plastic Limit	32-40%
Plasticity Index	25-37%
Organic Content	6.88%
pH	7.5
XRD	Monmorillonite-illite, Quartz, Mica, Halloysite, Kaolinite

Table 2: Chemical Composition of Fly Ash

Chemical Composition	(%) by Weight
SiO_2	57.471
Al_2O_3	15.365
Fe_2O_3	4.707
CaO	3.317

Method

Sample Preparation

Two main tests were conducted in this study. First, marine clay soil was dried in the oven for 24 hours at 105°C and was grind into powder until it passes through the sieved of 2 mm. 5% of lime of dry unit weight soil were then mixed together with the soil. [1], [27]-[28], stated the usage of the 5% lime is considering practical experience as lime fixation is for gaining the maximum strength, at which considerable increasing of the workability can be obtained. [34] stated that, the amount of lime related to the montmorillonite- rich clay content normally does not exceed 8%. Next, for alkaline activation process, fly ash was mixed with the 10 molar of KOH. KOH was diluted in 1 liter of distilled water to achieve the concentration of the of 10 molar. As

the mixture were mixed, the reaction of the KOH was extremely strong and the solution needed to cool to ambient temperature before being used [29]. Table 3 shows the mixture proportion of the soil specimen. There are three types of mixtures which based on the soil (S), clay lime fiber (CLF) and clay with alkaline activator fiber (CFAF). The testing of the natural soil sample was included as it was to provide references to the analysis regarding the mixture of CLF and CFAF.

Proctor Test

Standard proctor compaction test was conducted to determine the optimum moisture content and the maximum dry density of the soil specimen. The test was conducted based on [30]. The results were set out as the compaction basis for all of the specimen. The dry soil was initially mixed by hand, with the lime and 1% of treated fiber for lime stabilization and for the alkaline activation, the natural soil was mixed with the fly ash (60%) and the treated fiber. Then, the alkaline solution was added through the soil specimen. Both mixture must be well mixed until a uniform blend is achieved.

Table 3: Mixture Proportion of Various Test Soil specimen.

Croup Series	Test Number	Samples	UCS Test Curing days
C	C	Natural Soil	-
CLF	CL	Clay+ Lime+	7 & 28
	CLF	Clay+ Lime+ Fiber	7 & 28
CFA	CFA	Clay+ FA(60) + 10 KOH	7 & 28
	CFAF	Clay+ FA(60) + 10 KOH + Fiber	7 & 28

Unconfined Compressive Strength Test

The soil specimens were prepared directly right after the determination of the optimum moisture content based on the standard proctor compaction test. A cylindrical mould with the diameter of 50mm and height of 100mm were used to prepare soil specimens. Soil specimens for both lime and alkaline activation were prepared same for this testing. The unconfined compressive strength test (UCS) was conducted according to the [31] in which the test is to gain the strength of the soil specimens. 3 samples were prepared for each test number to make sure the average strength for the specimen is correct. The specimens were then being extruded

and immediately being wrapped with the plastic sheet and aluminum foil. This was done to keep the moisture content and humidity of the specimens for curing date. After the certain curing date, the specimens were tested using the Instron 3366 universal testing machine with the 10 kN load cell. The test was subjected to the loading rate of 1mm/min until it failed and the graph of stress – strain curve was obtained from each test. The testing is applied for both test specimens but for the alkaline activation sample the sample should be submerged in water first for 24 hours before the curing period. [32] highlighted the saturation was made with intention to eliminate the positive effect suction on the specimen and this submerging was exception for the natural soil, where the loss of structural integrity would happen when submerging the soil specimens. Curing time is a parameter that been used to determine the behavior of the soil specimen in for 7 and 28 days curing time. The behavior of the soil specimen in term of the strength of the soil for the untreated soil, treated soil with lime and fiber and treated soil with alkaline activator with fiber were determined. A significant strength behavior between these two curing days were observed. Figure 1 photograph shows UCS test for the soil specimens.



(a)



(b)

Figure 1 (a) & (b): Photograph of UCS Test

Microstructural Analysis

The microstructural analysis was performed based on the changes of the soil specimen before and after the stabilization. Soil specimens were examined in the presence of lime and KOH with and without fiber using Hitachi SU8010 which allows elimination of charging effect with low voltage imaging. Before the analysis was done, the specimens were sputter-coated with platinum using Quorum Q150R S Sputter coater to increase the electrical conductivity of the surface and reduce the charging. Figure 2 shows the photograph of the sputter coater used before the FESEM test was conducted.

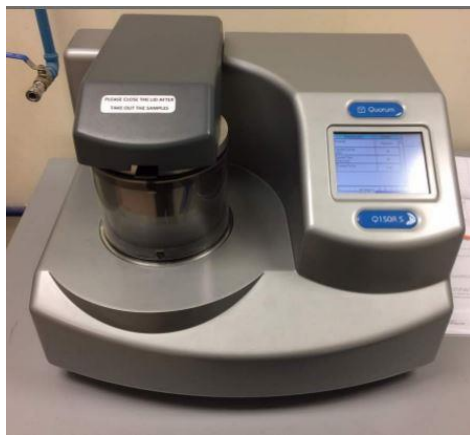


Figure 2: Sputter coater

RESULT & DISCUSSION

Proctor Test

Figure 3 shows the dry density versus moisture content between the natural soil and treated soils for both lime and alkaline activation

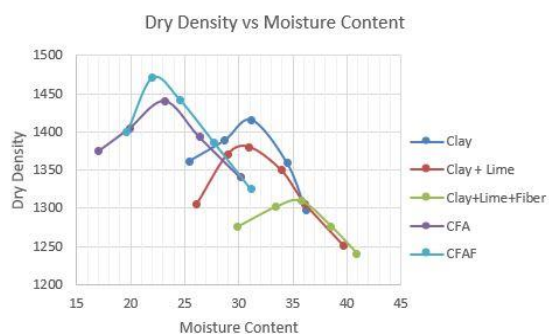


Figure 3: Dry Density versus Moisture Content of

Natural Soil and Treated Soil.

Based on the graph, it can be seen that, the moisture content of lime stabilization with fiber increased as the maximum dry density decrease compared to the natural soil. The increment of the moisture content was from 31% to 36% respectively with the maximum dry density was 1410kg/cm³ to 1310 kg/cm³. This might be due to the applicability of the inclusion of fiber to absorb the water. The statement was supported by [33], [1], where the inclusion of the fiber could improve the water absorption. Other than that, the significant maximum dry density occurred between the lime stabilization and natural soil shows that the inclusion of fiber increases the workability and the strength of the soil. By [34] inclusion of fiber and lime reinforced soil is better than natural soil in term of strength properties.

For alkaline activation, the moisture content show to be decrease as the maximum dry density keep increasing. The trend shows the same with [34] was the optimum moisture content is decreased with the increasing maximum dry density. The decreasing moisture content were about 31% to 23% respectively and the dry density is increasing from 1410 kg/cm³ to 1470kg/cm³. The decreasing of moisture content might be due to the higher percentage of fly ash that has been used in the study that mostly retain to absorb the water. This trend was similar with [35] where the addition of treated POFA would reduce the affinity of the soil for water. [36] also stated that the increasing of maximum dry density attributed to both specific gravity and particle size of the binder and natural soil.

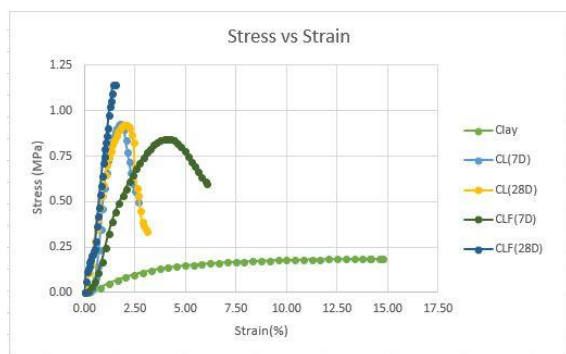
Unconfined Compressive Strength

Figure 4a shows the stress strain behavior of marine clay soil for untreated soil (Clay), treated soil (CL) and soil with the inclusion of fiber (CLF) after curing date of 7 and 28 days. As it can be seen in the graph, clay soil shows obviously low strength of the soil specimens with only 0.19 MPa compared to the CLF after 28 days. The result shows the increased in strength of the soil. The maximum compressive strength of the CLF at 7 and 28 curing days were 0.85 and 1.15 MPa respectively compared to the CL for both 7 and 28 days were only 0.93 MPa. This shows that with the inclusion of the fiber in the lime treated soil increased the strength and stiffness of soil specimens. By [23] inclusion of fiber in lime treated soil would develop the interfacial force and interlocking strength mixtures as it increased in curing age. The fiber content was also found as the main factor that affects the strength of soil specimens [37].

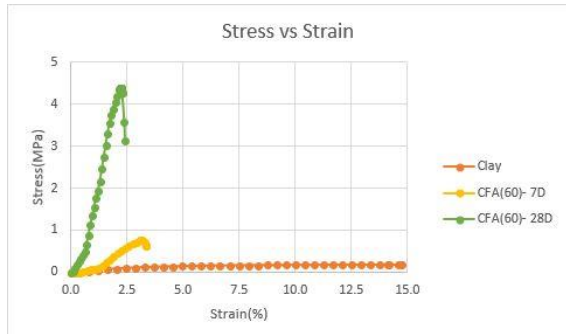
For alkaline activation soil stabilization, Figure 4b the result shows that the compressive strength of CFA for 28 days was higher with 4.40 MPa

compared to the CFA for 7 days with 0.77 MPa. Different increment of soil strength between both 7 and 28 days shows 3.63 MPa. This shows that the higher strength of soil achieved after 28 curing days. The statement was fully supported by [12], longer curing time at ambient temperature is one of economically viable way to further increase the strength level and by [32] the curing time and water content of soil have significant strengthening effect on the treated specimens.

From the figure 4a and b, it can be seen that, the compressive strength test for both treated soil shows that higher increment of strength occurred in alkaline



(a)



(b)

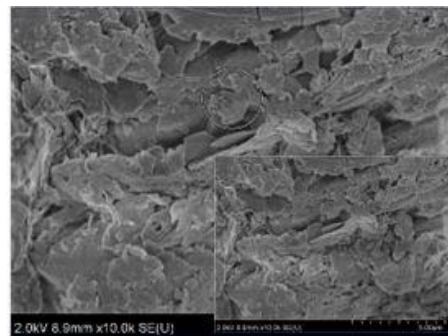
Figure 4: (a) Stress- strain graph for lime treated soil
(b) Stress- strain graph for alkaline activation treated soil

activation compared to lime stabilization. The increase in compressive strength of soil stabilization by using alkaline activator is due to the strong chemical reagent KOH and its high molarity that was used. [38] stated that the increase of compressive strength of the activation samples is related with the high molarity solutions that was used. Supported by [39] high concentration of KOH and NaOH solution increased the speed of chemical dissolution and would develop the higher compressive strength through the early stages of reaction. From the figure it can be concluded that,

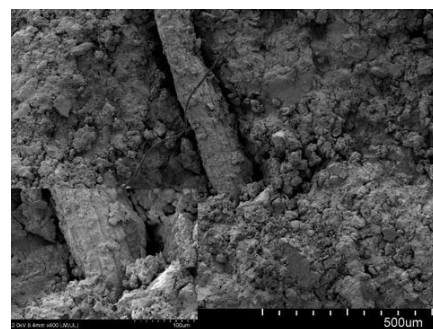
the strength for alkaline activator stabilizer give three times higher compressive strength compared to the lime treated and both with the inclusion of the fiber became beneficial to the soil stabilization.

Microstructural Analysis

Figure 6 shows the changes in morphology in natural soil, CLF and CFAF (60% of fly ash/ KOH 10M). In Figure 10a it can be observed that there is a lot of pores occur in the natural clay soil. After the soil being treated with lime (CLF), the pores in soil been obviously reduced as it can be seen in Figure 10b and it contributes to denser the soil. The soil specimens also show that with the lime and fiber binder together it would reduce pores in the soil and strengthen the soil specimens. By [1] the inclusion of fiber in treated soil would increase the effectiveness of transferring load from the matrix to fibers.



(a)



(b)

Figure 6: FESEM for 28 days (a) Clay, (b) CLF

CONCLUSION

In this study, it can be concluded that the lime-treated and alkaline activation soil stabilization with the inclusion of fiber increased the compressive strength of the soil compared to natural soil. Based

on the compressive strength recorded, the samples of alkaline activation with KOH was about three time higher and stable compared to lime treated for the soil stabilization. It also been supported by the microstructural analysis were the samples treated shows the interaction on treated samples with fiber strengthen the soil modification and improvement towards the properties of soil. This statement was supported by [35], were based on SEM and EDS analyzed the treatment of the matrix was observed because of there was a coexistence of cementitious and pozzolanic reaction between the soil and binder, which it responsible for improving the strength of stabilized clayey soil specimens.

ACKNOWLEDGEMENTS

The author would like to express her gratitude to Universiti Putra Malaysia and Ministry of Science Technology Innovation (MOSTI) for providing the financial support during the research under project no: 06-01-04-SF2387.

REFERENCES

- [1] Anggraini, V. (2015). Reinforcement Effects of Nano-Modified Coir Fibres on Lime-Treated Marine Clay. Universiti Putra Malaysia (UPM): PhD Thesis.
- [2] Anggraini, V., Huat, B.B.K., Asadi, A., & Nahazanan, H. (2015). Effect of Coir Fibers on the Tensile and Flexural Strength of Soft Marine Clay. *Journal of Natural Fibers*, 12 (2), 185-200.
- [3] Balasubramaniam AS, Phienwej N, Lin DG, Karuzzaman AH, Uddin K, Bergado DT. Chemical Stabilisation of Bangkok Clay with Cement, Lime and Fly Ash Additives. In: 13th Southeast Asian Geotechnical Conference, Taipei;1998. P. 253-8.
- [4] Bergado DT, Anderson LR, Miura N, Balasubramaniam AS. *Soft Ground Improvement in Lowland and Other Environments*. USA: ASCE Press; 1996.
- [5] Chen JF, Yu SB. Centrifugal and Numerical Modelling of A Reinforced Lime Stabilized Soil Embankment on Soft Clay with Wick Drains. *Int J Geomech* 2011; 11(3): 167-73.
- [6] Indraratna B. Utilization of Lime, Slag and Fly Ash for Improvement of A Colluvial Soil in New South Wales, Australia. *J Geotech Geol Eng* 1996; 14: 169-91.
- [7] Kamon M, Remediation Techniques by Use of Ground Improvement. In: *Proceeding of conference on soft ground technology*, ASCE Geotechnical Special Publication Number, vol. 112; 2000. p. 374-87.
- [8] Pal S, and Ghosh A. Volume Change Behavior of fly ash- montmorillonite clay mixture. *Int J. Geomech* 2014; 14(1):59-68.
- [9] Bell, F., 1996. Lime Stabilization of Clay Minerals and Soils. *Engineering geology* 42, 223-237.
- [10] Rajasekaran, G., Rao, S.N., 1997b. The Microstructure of Lime-Stabilized Marine Clay. *Ocean Engineering* 24, 867-878.
- [11] Rao, D.K., Raju, G.P., Sowjanya, C., Rao, J.P., 2009. Laboratory Studies on The Properties of Stabilized Marine Clay from Kakinada Sea Coast, India. *International Journal of Engineering Science and Technology* 3, 422-428.
- [12] Pourakbar, S., Asadi, A., Huat, B. B., Cristelo, N., and Fasihnikoutalab, M. H (2015b). "Application of Alkaline- Activate Agro- Waste Reinforced with Wollastonite Fibers in Soil Stabilization." *J. Mater. Civ, Eng.*, 04016206-1-11.
- [13] Cristelo, N., Soares, E., Rosa, I., Miranda, T., Oliveira, D.V., Silva, Rui. A and Chaves, A. (2013). Rheological properties of alkaline activated fly ash used in jet grouting applications. *Construction and Building Material* (48) 925-933
- [14] Kang, X., L. Ge and W. C. Liao (2016). Cement Hydration-Based Micromechanics Modeling 438 of the Time-Dependent Small-Strain Stiffness of Fly Ash-Stabilized Soils. *International 439 Journal of Geomechanics* 0(0): 04015071.
- [15] Sariosseiri F, Muhunthan B. Effect of cement treatment on geotechnical properties of some Washington State soils. *Eng Geol* 2009;104(1–2):119–25.
- [16] Vinod JS, Indraratna B. A conceptual model for lignosulfonate treated soils. In: Khalili N, Oeser M, editors. *13th International Conference of the International Association for Computer Methods and Advances in Geomechanics*. Sydney, Australia:Centre for Infrastructure Engineering and Safety, Sydney, Australia; 2011. p. 296–300.
- [17] Perry, edward B.,. Effect of short polymeric fibers on crack development in clays. *Soils and Foundations*. 1998. 38(1),247-53.
- [18] Estabragh, A.R., Bordbar, A.T., Javadi, A.A.; A study on the mechanical behavior of a fiber-clay composite with natural fiber. *Geotechnical and*

- Geological Engineering. 2013. 31(2), 501-10.
- [19] Fatahi, B. Fatahi, T. M. Le. H, Khabbaz. Small-strain properties of soft clay treated with fibre and cement. *Geosynthetics International*. 2013. 20(4), 286-300.
- [20] Kazemian S, Huat K, Prasad A, Barghchi M. A review of stabilization of soft soils by injection of chemical grouting. *Aust J Basic Appl Sci* 2010; 4:5862-8
- [21] British Standard Institution (1990). *Soils for Civil Engineering Purposes, Part 2: Classification of Tests*. London: BS 1377-2-1990.
- [22] American Society for Testing and Material (1998). *Standard Practice for Classification of Soils for Engineering Purposes (Unified Soil Classification System)*. United States: ASTM D 2487.
- [23] Anggraini, V., Asadi, A., Huat, B.B.K., and Nahazanan, H. "Effects of coir fibers on tensile and compressive strength of lime treated soft soil". *Journal Measurement* 59 (2015) 372-381
- [24] Cristelo N, Glendinning S, Miranda T, Oliveira D, Silva R (2012) Soil stabilisation using alkaline activation of fly ash for self compacting rammed earth construction. *Constr Build Mater* 36:727-735.
- [25] Cristelo N, Glendinning S, Pinto AT (2011) "Deep soft soil improvement by alkaline activation". *Proc ICE-Gr Improv* 164(1):1-10.
- [26] D Bondar, CJ Lynsdale, NB Milestone, N Hassani, AA Ramezaniapour (2011) Effect of type, form, and dosage of activators on strength of alkali-activated natural pozzolans. *Cem Concr Compos* 33(2):251-260.
- [27] Petry, T.M., Little, D.N., 2002. Review of stabilization of clays and expansive soils in pavements and lightly loaded structures—history, practice, and future. *Journal of Materials in Civil Engineering*.
- [28] Dash, S.K., Hussain, M., 2011. Lime stabilization of soils: reappraisal. *Journal of materials in civil engineering* 24, 707-714.
- [29] Phair, J. and Van Deventer, J. 2002. Characterization of fly-ash-based geopolymeric binders activated with sodium aluminate, *Industrial & Engineering chemistry research*, 41, 4242-4251.
- [30] British Standard Institution (1990). *Soils for Civil Engineering Purposes, Part 4: Compaction- related tests*. London: BS 1377-2-1990.
- [31] American Society for Testing and Material (1998). *Standard Test Method for Unconfined Compressive Strength of Cohesive Soil*. United States: ASTM D 2166.
- [32] Pourakbar, S., and Huat, B.B. K (2016). "A review of alternatives traditional cementitious binders for engineering improvement of soils". *International Journal of Geotechnical Engineering*. 1-11.
- [33] Ravishankar, U., Raghavan, S., 2004. Coir stabilised lateritic soil for pavements, *Indian geotech conf*, Ahmedabad, India.
- [34] Ramesh, H., Krishna, K.M., Mamatha, H., 2010. Compaction and strength behavior of lime-coir fiber treated Black Cotton soil. *Geomech Eng* 2, 19-28.
- [35] Pourakbar, S., Asadi, A., Huat, B.B.K., and Fasihnikoutalab, M. H. (2015). "Stabilization of clayey soil using ultrafine palm oil fuel ash (POFA) and cement". *Transportation Geotechnics*, 3(2015) 24-35.
- [36] Degirmenci N, Okucu A, Turabi A. Application of phosphogypsum in soil stabilization. *Build Environ* 2007;42(9):3393-8.
- [37] T. Harianto, S. Hayashi, Y. Du, D. Suetsugu, *Geosynthetics in Civil and Environmental Engineering*, Springer, 2009.
- [38] Alsafi, S., Farzadnia, N., Asadi, A., and Huat, B.B. K. "Collapsibility potential of gypseous soil stabilized with fly ash". *Construction and Building Materials* 137 (2017) 390-409.
- [39] J.G.S. Van Jaarsveld, J.S.J. Van Deventer, Effect of the alkali metal activator on the properties of fly ash-based geopolymers, *Ind. Eng. Chem. Res.* 38 (10) (1999) 3932-3941

Soil Stabilized with Geopolymers for Low Cost and Environmentally Friendly Construction

Wisam Dheyab¹, Afshin Asadi², Bujang B.K. Huat³, Mohd Saleh Jaafar³, and Lokmane Abdeldjouad⁴

¹Dept. of Civil Engineering, Univ. of Putra Malaysia, 43400 UPM, Serdang, Selangor, Malaysia

²Dept. of Civil Engineering, International College of Auckland, Auckland, New Zealand

³Professor, Dept. of Civil Engineering, Univ. of Putra Malaysia, 43400 UPM, Serdang, Selangor, Malaysia.

⁴Dept. of Civil Engineering, Univ. of Putra Malaysia, 43400 UPM, Serdang, Selangor, Malaysia

ABSTRACT

In this paper, a geopolymer synthesized from olivine and an alkaline solution made from sodium hydroxide which incorporate the carbonation process was utilized to stabilize silty clay soil, in order to improve its expediency for different case of construction.

The effect of alkaline molarity, for alkali activation and carbonation processes, on the Unconfined Compression Strength (UCS) of the soil-olivine mixture is important in enhancing the treated soil properties. In this study, use of 4, 6, 8, 10, and 12 molar of NaOH affected the UCS and toughness of the soil mixture. The highest strengths were obtained at 8 and 10 molarities for the carbonated alkali activation process, and 10 and 12 molarities for the alkali activation process only. Micro structural analysis using X-ray diffraction (XRD) and scanning electron microscopy (SEM) tests shows the benefits of carbonation in terms of decreasing the molarity of alkaline agent. This was due to the crystallisation processes which accounts for strength gain after carbonation. This paper highlights a more environmentally friendly procedure of stabilizing soils compared with the traditional binders such as cement and lime.

Keywords: geopolymer, olivine, mineral carbonation, soil stabilization, unconfined compression strength.

INTRODUCTION

Soil firmness is one of the widest range methods used for ground refinement. However, for many cases it is substantial to refine or improve the in-situ soils, with different types of binders, building different kinds of structures on top. Cement, lime and other additives are ordinarily used in construction owing to enhance soil strength, control shrinking and swelling, reduce settlement and reduce permeability. For soil stabilization, cement and lime are the most important and exceedingly used binders (Pourakbar et al., 2015a; Pakbaz and Alipour, 2012; Horpibulsuk et al., 2011). However, cement and lime produce expends fossil fuels which are the main cause in carbon dioxide (CO₂) emissions to the atmosphere. However, cement and lime production has intense environmental influence, consuming large quantities of fossil fuels and being accountable for the emission exceeds than 5% of all the carbon dioxide worldwide (Provis & Deventer, 2014). New researches in ground amelioration have raised the need for utilizing sustainable materials (e.g. zeolite, reactive magnesia

and olivine) or Industrial waste (e.g. ground-granulated blast furnace slag, palm oil fuel ash, cement kiln dust, rice husk ash, recycled glass foam, recycled concrete aggregate and crushed brick, calcium carbide residue and fly ash) for fractional or full surrogate of cement or lime as a result of the considerable environmental influences (Fasihnikoutalab et al., 2017; Fasihnikoutalab et al., 2016; Arulrajah et al., 2015; Cai et al., 2015; Pourakbar et al., 2015; Disfani et al., 2014; Yi et al., 2013a; Du et al., 2011; Jegandan et al., 2010; Basha et al., 2005).

Broadly, alkaline activation is a chemical synthesis in which alumina-silicate materials and alkali or alkali earth materials, which are alkaline ions like potassium or sodium, or alkaline earth ions like calcium are react. It can be substantive as a polycondensation reaction, which contains the process of silica and alumina units connect with each other and engage the oxygen ions. At the molecular

level, substances formed by the interaction between silica and alumina on the one hand and alkaline cations such as sodium or potassium share the characteristics of sharing their stiffness, strength and durability with natural rocks (Davidovits, 1991).

Governments around the world recognize a rising demand for reducing the (CO₂) levels of the atmosphere. CO₂ confinement by utilizing reactive metals has been exceedingly suggested by several researchers (Haug et al., 2011; Andreani et al., 2009; Prigiobbe et al., 2009b ; Chen et al., 2006). Olivine, with chemical composition (Mg,Fe)₂SiO₄, was considered by many researchers as an important candidate in the sequestration of (CO₂) and as a participant in alkali activation (Fasihnikoutalab et. al., 2017; Olajire, 2013; Olsson et al., 2012; Hänchen et al., 2006). All (CO₂) generated by the burning of one liter of fossil fuel can be trapped using less than one liter of olivine; and more accurately 140 g of olivine can trapped more than 176 g of (CO₂) (Schuiling and Praagman, 2011).

For soil refinement implementations, there was a successful attempt to fully replacement of traditional Portland cement with geopolymeric gel formed by alkaline activation of fly ash (Bernal, et al., 2011). Recently researches have been done on utilizing the alkaline activation of olivine to form a geopolymeric gel to increase soil strength (Fasihnikoutalab et. al., 2017). Those researchers utilize the carbonation process in addition to alkali activation process to increase soil strength. The investigation for alternate binders recognizes materials that are would impact the surrounding soil to a minimum range upon treatment and cost-effective.

However, no works have used the alkali reaction method in addition to carbonate for the purpose of soil stabilization using olivine with different molarities of alkaline solutions for use in low cost (e.g. low cost roads in some countries) and fast construction.

Nonetheless, few works have studied the use of geopolymeric binders in soil improvement applications and none as soil stabilization technique for low cost roads (Sara Rios, et al. 2016). In previous work (Rios, et al., 2015), the authors have explored few mixtures and very promising results

were found namely in terms of its stress-strain behaviour by means of triaxial tests. In this work, many mixtures of soil-olivine and sodium hydroxide (NaOH) solution, as an alkaline solution, in different molarities were studied and unconfined compression strength (UCS) tests were have been conducted to assess the possible application of new mixture as a construction material.

Materials and Methodology

Materials

Soil

The soil used in this research contained 60% silt, 30% clay, and 10% sand with a mean particle size (D₅₀) of 11.759 µm and a specific surface area (SSA) of 1.04 m²/g. Table 1 shows the physical, and engineering characteristics of host soil. Table 2 shows chemical characteristics of untreated soil. Depending on the Unified Soil Classification System (USCS), the soil used in this research can be classified as CL.

Olivine

The olivine used in this study was provided by the Maha Chemicals Company of Malaysia. The olivine as-received had a large grain size, which wished for ball milling for 24 h. The speed of ball milling was 60 rpm to decrease the grain size and to give the uniformity to the particle size previously to addition to the soil. The particle size distribution shows that the D₅₀ is around 2.3. The analysis of the specific surface area (after ball milling) shows it is around 6.07 m²/g. Fig. 2 demonstrates the particle size allocation for olivine sample after ball mailing

A laser diffraction particle size analyses (Mastersizer 2000E, ver. 5.52) was used to determine the specific surface area of olivine. The specific surface area and D₅₀ (mean particle size) of the olivine sand were 6.07 m²/g and 2.24 µm, respectively. Table 2 shows the chemical composition of olivine sand according to the supplier in this study.

Table 1 Physical and engineering characteristics of soil

Basic soil property	Standard	Value
Specific gravity (G_s)	BS 1377-2	2.52
Liquid limit (LL) (%)	BS 1377-2	48.7
Plasticity index (PI) (%)	BS 1377-2	34.5
OMC (%)	BS 1377-4	24
MDD (Mg/m^3)	BS 1377-4	1.58
UCS (kPa)	BS 1377-7	380-390

Table 2 Chemical characteristics of host soil

Constituent	Natural soil (%)
Silica (SiO_2)	41.26
Alumina (Al_2O_3)	36.96
Iron oxide (Fe_2O_3)	10.07
Calcium oxide (CaO)	-
Potash (K_2O)	11.71
Magnesia (MgO)	-
Loss on ignition (LOI)	-

Alkali activator

Sodium hydroxide (NaOH) containing Na^+ was selected as activator because of its well-known efficiency (Fasihnikoutalab et. al., 2017). The activator was supplied in pellet form by “R&M Chemical” company and was previously dissolved in distilled water to acquire a

predesigned concentration of 10 Molar. The reaction of the activator (NaOH) with water is strongly exothermic, as well as with all strong Alkalies. Consequently, the alkaline activator was left to cool down to room temperature before use.

Methodology

Mix Composition and Sample Preparation

Table 3 shows the mix compositions of the materials used in this study (soil, olivine, and NaOH). The molarity of NaOH was changed during samples preparation. The first step to prepare the samples was dissolving the alkali activator in distilled water at the desired concentration. The compaction test was done in order to attain the optimum water content (OWC) with maximum dry density (MDD) of the alkaline-activated soil-olivine mixture (British Standards Institution 2002). After drying the host soil for 24 h, the soil was mixed with 30% olivine and alkali activator (NaOH) at different molarities. Control samples of the pure soil were also tested as a reference. Samples were set in cylindrical (50cm diameter and 100cm height) templates onto which suitable modified compaction was done, and extruded. Samples, for alkali activated with and without carbonation, were prepared for UCS at OWC and MDD. After samples extrusion, (CSO_{30-4} , CSO_{30-6} , CSO_{30-8} , CSO_{30-10} and CSO_{30-12}) samples were permeated with CO_2 at 300 kPa pressure and for 7 days curing time (Table 3). Samples without carbonation (ASO_{30-4} , ASO_{30-6} , ASO_{30-8} , ASO_{30-10} and ASO_{30-12}) were wrapped in polythene covers to prevent water loss and cured under ambient temperature in different curing periods prior to UCS testing (Table 3).

Table 3 mix composition of the study samples

Mix	Olivi	O	MD	NaOH	Curing
	ne	W	D	(molar	duration
	(%)	C	(g/c	ity)	

	(%)		m^3		
Host soil (S)	0	24	1.58	0	
Soil+30% olivine (SO ₃₀)	30	18	1.82	0	Without carbonation: 7, 28, and 90 days
ASO ₃₀ -4,6,8,10,12	30	18	1.82	4, 6, 8, 10, and 12	
CSO ₃₀ -4, 6, 8, 10, and 12	30	18	1.82	4, 6, 8, 10, and 12	Carbonated samples : 7days

Carbonation

Instantly after molding, carbonated samples were submitted to carbonation with a confining pressure of 400 kPa, meanwhile CO₂ permeated upward. A triaxial cell was utilized to permeate CO₂ through the carbonated samples CSO₃₀. The pressurized gaseous CO₂ was subjected at 300 kPa through the alkali activated soil-olivine samples for 168 h. The outflow tube was placed under water to detect the samples saturation with gaseous CO₂.

Unconfined Compressive Strength

The UCS test was implemented on carbonated (at 168 h) at different molarities (4, 6, 8, 10 and 12) and uncarbonated (at 7, 14, 28, and 90 days) at different molarities (4, 6, 8, 10 and 12M)

samples instantly after predesigned curing procedure according to BS 1924: Part 7 (British Standards Institution 2003). Instron 3382, with 100 kN capacity, device was used for UCS testing (Seri Kembangan, Malaysia).

Microstructural Analysis

XRD, SEM/EDX and FTIR tests were conducted on samples before and after carbonation at different molarities. Crystalline phases were examined using a Philips (Seri Kembangan, Malaysia) XRD from 20 to 75° 2 θ . For a SEM analysis a JSM 5700 device was used (Seri Kembangan, Malaysia) coupled with an EDX spectrometer. Before SEM/EDX test, samples were sputter covered with gold before test conducting to increase the electrical conductivity of the surface as well as reduce charging. FTIR via a PerkinElmer Paragon 100 spectrometer within a spectra of 4,000–500 cm⁻¹ (Seri Kembangan, Malaysia) was utilized to investigate the composition of samples before and after carbonation.

Results

Unconfined Compressive Strength

Fig. 2 presents the UCS values for natural soil (S), alkali-activated soil-olivine mixture (ASO) at different molarities of NaOH (4, 6, 8, 10 and 12M) at (7days) curing time. Natural soil samples (S) appeared an UCS value of 77.9 kPa. Alkali activation for soil-olivine mixture increased the strength of the mixture to 392.8, 421.4, 583.9, 1082.8 and 904.3 kPa at 7days, and for 2, 4, 6, 8, 10 and 12M respectively. Fig. 3 shows the effect of aging on the UCS values for alkali-activated soil-olivine mixture at 10M of NaOH. Fig. 4 represents the behaviour of carbonated alkali-activated soil-olivine samples at different molarities of NaOH (4, 6, 8, 10 and 12M) at 7days and 300 kPa CO₂ pressure.

The UCS values slightly increased for soil-olivine specimens due to the presence of NaOH. This might be attributed to the role of NaOH in elevate the dissolution of Si, Al and Mg within soil (Fasihnikoutalab et al. 2017). The increase in the strength of ASO was significant with molarity of 10M NaOH. These findings are inconsistent with that

of Cristelo et al. (2011, 2012b). A cumulative increase in UCS values was observed with increasing the curing time from 7 to 90 days. ASO, for 10M, achieved the highest strength within all alkali-activated soil-olivine samples, resulting in 1082, 1728, and 2275 kPa at 7, 28, and 90 days, respectively.

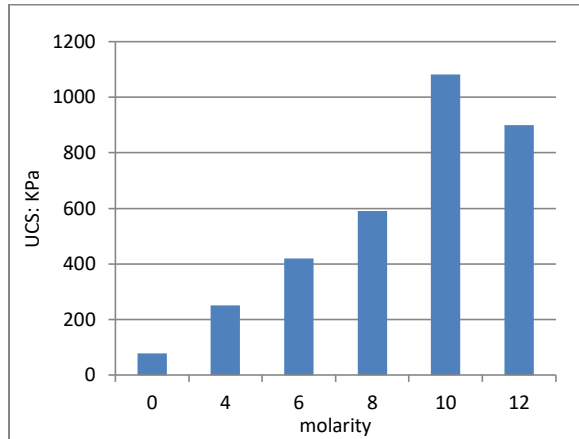


Fig. 2. UCS of alkaline-activated soil-olivine mixture at 7days curing time for different molarities

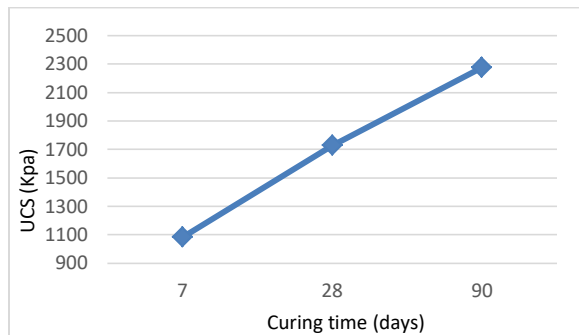


Fig. 3. UCS of alkaline-activated soil-olivine mixture at 7, 28 and 90days curing time for 10M.

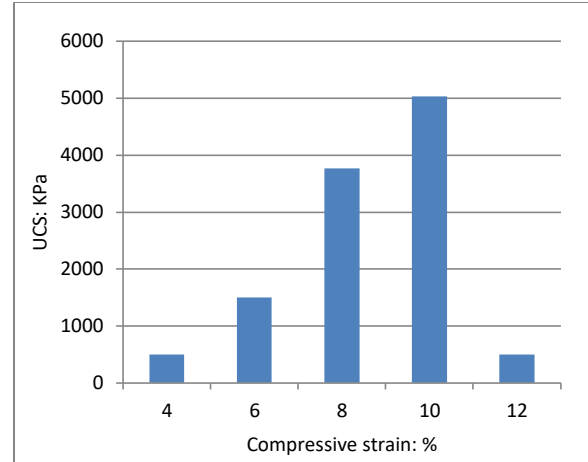


Fig. 4. UCS of carbonated alkaline-activated soil-olivine mixture at 7days curing time for different molarities

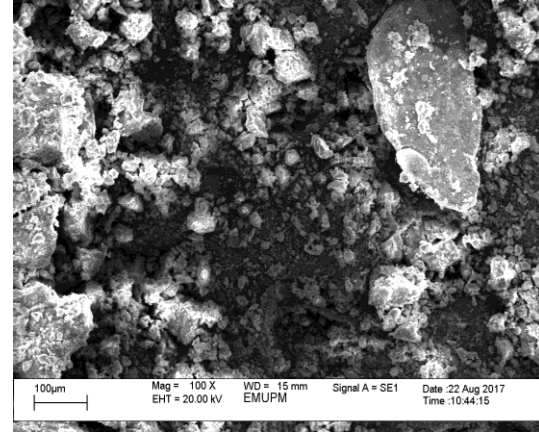
Fig. 4 presents the UCS values of carbonated alkali-activated soil-olivine mixture after 7 days of curing and at 300 kPa CO₂ pressure. The alkali activator molarity was changed from 4 to 12M, and subjected to CO₂ at pressure of 300 kPa for 7days. The increase of alkali activator molarity was accompanied with an increase in the UCS values. A significant increase, in strength, was achieved by increasing the NaOH molar value by 8 and 10 M. While the increase was noticeable by increasing the molarity by values 10 and 12 in uncarbonated alkali-activated soil-olivine samples.

The results show that carbonation technique is a promising technique for soil stabilization and to increase the environmental concerns for alkaline agents. This may be attributed to alkali-activated soil-olivine samples were sufficiently carbonated within a few days to achieve strengths required for ground improvement.

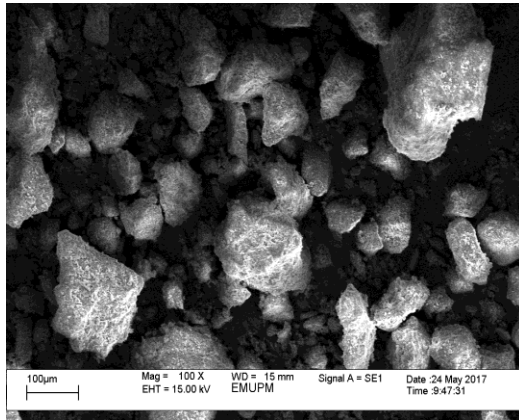
SEM Characterization

The clusters shape particles in Fig. 5(a) actually refer to the soil particles. The microstructure of olivine particles are of irregular shape which can be seen in Fig. 5(b). Fig. 5(c) clarifies the soil-olivine mixture after 7 days of curing. By comparing Figs. 5(a and c) it's clear that the olivine gives a more dense structure for the host soil as a result of its hydration and pozzolanic reaction within the host soil.

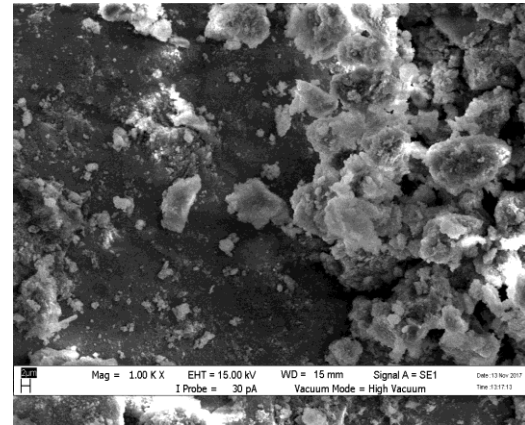
Fig. 5(d) represents the microstructure of host soil mixed with 30% olivine in the existence of 10 M of NaOH after 90 days of curing. SEM images show a dense morphology with less major discontinuities, which is symmetrical with the mechanical characteristics obtained. The raise of a new amorphous phase is obvious in Fig. 5(e), which detect the forming of a gel mass and crystals on the surface of the particles. Fig 5(f) shows the SEM images of carbonated alkali activated samples which subjected to carbonation at a CO₂ pressure of 300 kPa for 7 days. Fig 5(f) reveals a denser and more homogenous microstructure in presence of NaOH.



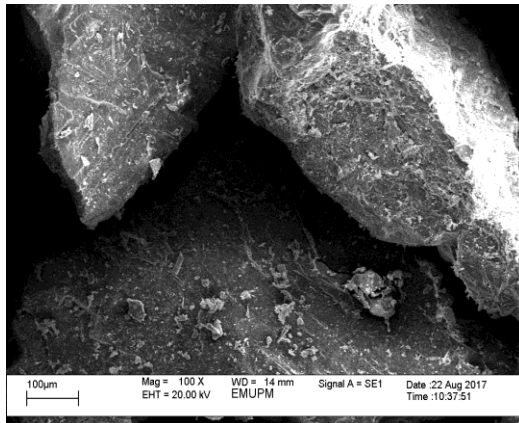
(c)



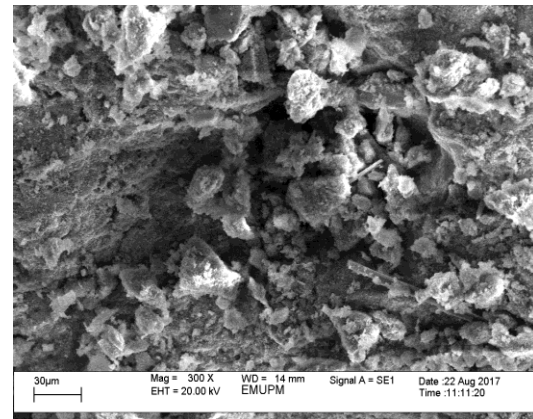
(a)



(e)



(b)

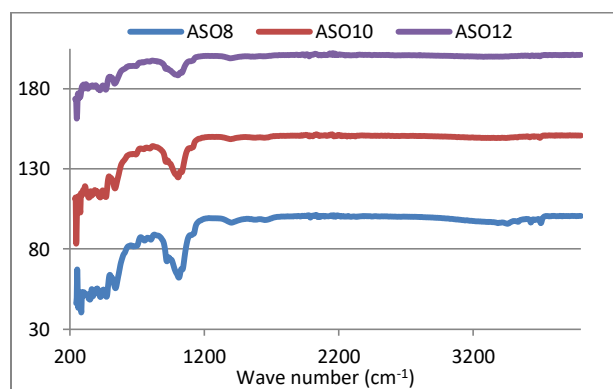


(f)

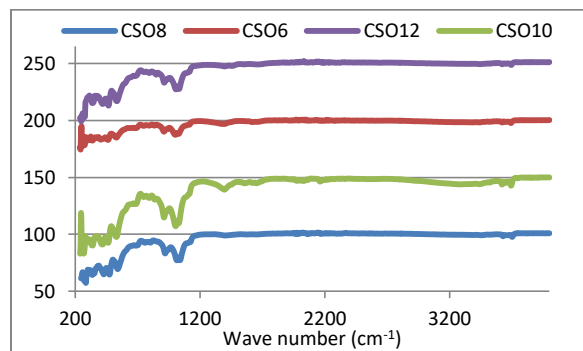
Fig. 5. SEM images of (a) soil; (b) olivine; (c) soil olivine mixture; (d) alkaline-activated soil-olivine mixture; (f) carbonated alkaline-activated soil-olivine mixture.

FTIR Characterization

Fig. 6 (a and b) demonstrates the FTIR of seven samples in the range of 500–4,500 cm^{-1} containing 8, 10, and 12M of NaOH soil-olivine mixture after 90 days for (a) and 6, 8, 10 and 12M of NaOH carbonated alkali activated soil-olivine mixture. From Fig. 6(a), the band at 3,693 cm^{-1} , existing in all samples, is related to O–H stretching which come from brucite. Previous researches showed that the attribute Mg–OH stretch of phyllosilicates near 3,690 cm^{-1} and a low stretch in the Mg–OH zone (Lee and van Deventer 2002b).



(a)



(b)

Fig. 6. FTIR of: (a) alkaline activated soil-olivine mixture for different molarities. (b) carbonated alkaline-activated soil-olivine mixture at 300-kPa pressure for 7 days at different molarities

Bands harmonize to O–H stretching in the domain of 3,394–3,401 cm^{-1} assist H– bonds in all samples, as well as the water will presence even after 90 days of curing. This could clarify that greater strengths could

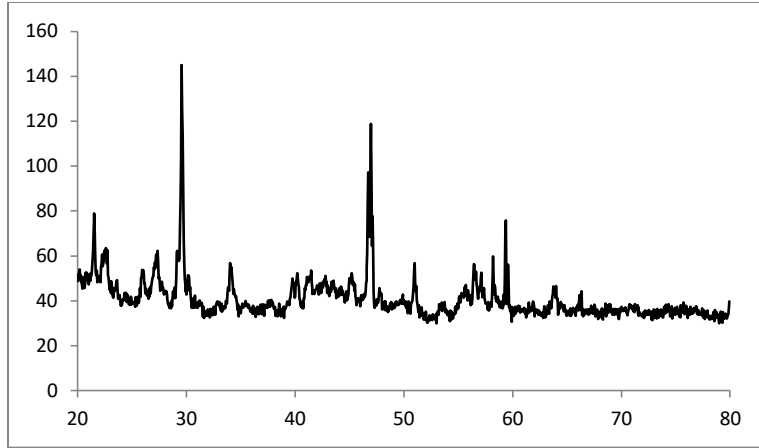
be gain with prolonged curing and high molarity in terms of full reaction. However, very weak reductions near 1,220 cm^{-1} assigned to Si–O stretching may be a sign of silica polymerization which indicates to M–S–H gels formation. These gels, which formed in an amorphous aluminosilicate gel, could be formed due to the dissolution of olivine with higher molarities of NaOH was apparent at 1,080–1,100 cm^{-1} and 980–1,040 cm^{-1} regarding to Si–O bond and asymmetrical stretching vibrations of Si–O/Al–O bonds, respectively (Criado et al. 2005). Bands at 680–650 cm^{-1} , and 914, 790–730 were related to Si–O vibration stretching, and Al–OH, Al–O bond stretching, respectively (Abdul Rahim et al. 2014; Weng and Sagoe-Crentsil 2007). Fig. 6(b) presents the FTIR characterization of carbonated alkali activated soil- olivine mixture after carbonation at a CO_2 pressure of 300 kPa at different molarities of NaOH of 6, 8, 10, and 12M for 7 days curing period. The crests appeared are corresponding to the existence of an aluminosilicate gel in amorphous form. Bands at 950 and 797 cm^{-1} were assigned to the symmetric and asymmetric stretching vibration of Al–O–Si and Si–O–Si bonds, showing that the magnitude of carbonation in these samples. After carbonation there were changes at 1,220 cm^{-1} , and this refer to the chain structure modifications of M–S–H. These modifications may refer to the decomposition of M–S–H during the carbonation process and a higher degree of polymerization, as well as, it may refer to lengthening of silicates within the residual gel. These results establish the results from previous researches on the contribution of carbonation in the slag geopolymerization. So that, the role of Mg^{2+} is possible be as the role of Ca^{2+} since it is present within the geopolymeric gel phase (Lee and van Deventer 2002a, b). The strong peaks present around 1,410 and 1,570 cm^{-1} in Fig. 6(b) are imputed to C–O vibrations from the sequestration of CO_2 and forming of carbonates in solution, that might be in close combination with Na^+ or Mg^{2+} cations (Abdul Rahim et al. 2014). The bands between 1,450 and 1,650 cm^{-1} assigned to the asymmetric stretching of CO_3^{2-} earning strength with increasing NaOH molarity due to the forming of MgCO_3 and NaHCO_3 . This is most noticeable as the molarity of NaOH increased from 6 to 10M, leading to the vanishing of the 3,690 cm^{-1} band originally assigned to brucite.

XRD Characterization

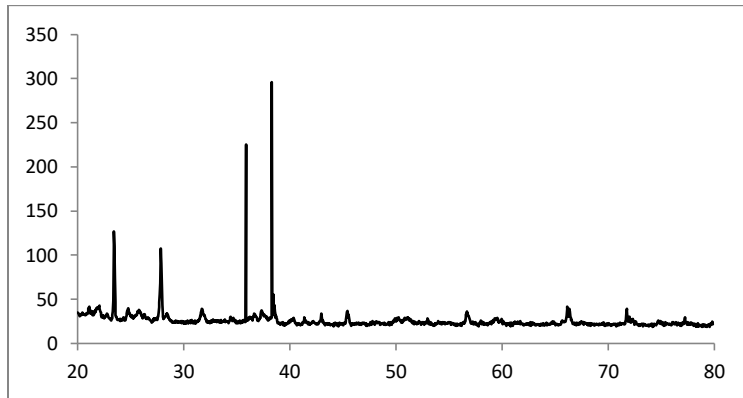
Fig. 7 demonstrates the XRD of alkali activated soil-olivine mixture after 90 days of curing. Brucite, mullite, serpentine, quartz, sodium silicate (Na_2SiO_3), and Mg peaks are revealed due to olivine dissolution through the sodium hydroxide in soil. Peaks of brucite (21° , 36° , and 48°), quartz (SiO_2) (24° , 26° , 28° , 39° , and 45°), and sodium silicate (30° and 35°) were revealed meanwhile the patterns (Komljenović et al. 2010; Yi et al. 2013b). Figs. 8(a–d) present the XRD patterns for carbonated alkali activated soil-olivine mixture for 6, 8, 10 and 12M of NaOH under 200 kPa CO_2 pressure for 7 days curing period.

Discussion

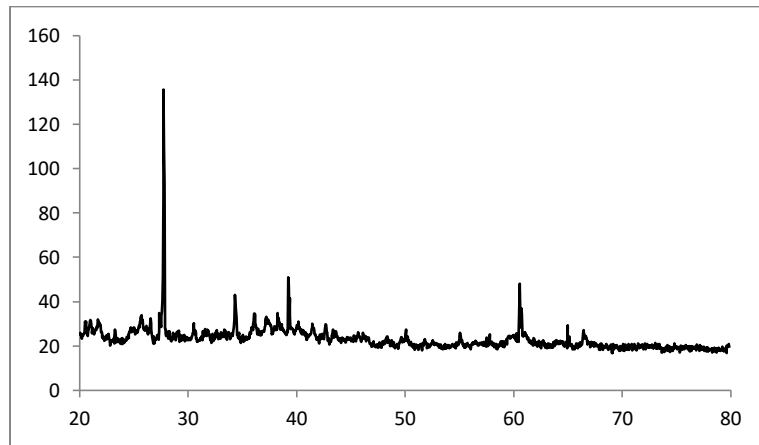
The chemical bonds between olivine compositions will broke down in the presence of NaOH, this will happen when olivine mixes within a soil mass. So that, MgO and SiO_2 will be free and this will lead for leaching the silicon from amorphous phases in olivine particles (Fasihnikoutalab et.al. 2017). So that, $\text{Mg}(\text{OH})_2$ and Na_2SiO_3 are created as approved by FTIR and XRD analyses (Figs. 6 and 7). The Na_2SiO_3 created from the reaction between NaOH and olivine in an aqueous solution. Previous studies show that using of NaOH and/or Na_2SiO_3 as activators to raise phases dissolution and later alkaline activation (Abdul Rahim et al. 2014; Phoon-ngernkham et al. 2015). The appearance of A-S-H gel could be a result of use of NaOH and/or Na_2SiO_3 , which could lead to the leaching of the Si and Al from the amorphous stage of soil. Adding Ca was demonstrated to have a positive impact on the mechanical characteristics of alkali-activated binders (Temuujin et al. 2009; Ryu et al. 2013). The high content of MgO (48%) in olivine makes it a good candidate to release of Mg ions, which may display a comparable behavior to Ca ions convenient to their similar charge. In addition, Al, Si with Mg play an important role in increasing the amount of crystal formed in the new matrix. In the existence of an alkali



(a)



(b)



(c)

Fig. 7. XRD of ASO after 90 days curing time of: (a) 8M, (b) 10M, and (c) 12M

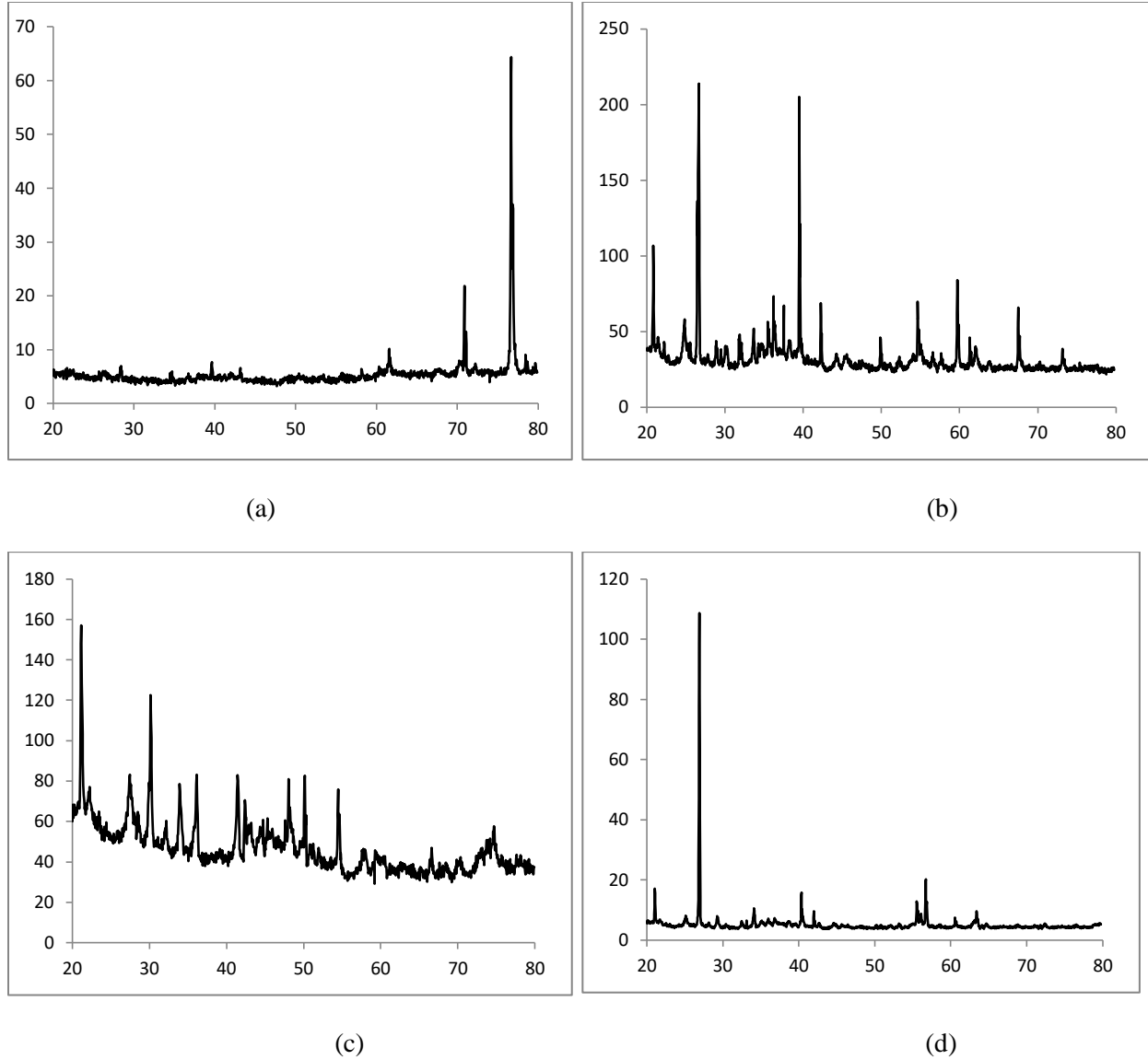


Fig. 8. XRD of carbonated alkali activated soil olivine mixture for (a) 6M; (b) 8M; (c) 10M; (d) 12M NaOH

activator, Mg ions might give more nucleation positions for the deposition of dissolved kinds and give participate to the formation of M–S–H gel (Salih et al. 2014; Yip et al. 2008).

From FTIR and XRD results for carbonated alkali activated samples, reaction between NaOH and olivine leads to creation of Na_2SiO_3 . Thereafter, Na_2SiO_3 reacts with CO_2 dissolved in water, leads to formation of NaHCO_3 and SiO_2 . These reactions will lead to formation of (nesquehonite, dypingite, and hydromagnesite), thereafter, to form well-divergent networks of huge crystals with a high efficiency of binding ability (Yi et al. 2013c). As a result, this led to a denser and more homogenous microstructure for the new matrix of carbonated alkali activated soil-olivine mixture (Fig. 5(f)), converting into increased strength gain. Eitelite $\text{Na}_2\text{Mg}(\text{CO}_3)_2$ has been formed from the reaction between $\text{Mg}(\text{OH})_2$ and Na_2CO_3 at a high pressure of CO_2 , which is another advantage of using olivine in the presence of NaOH. Eitelite includes CO_2 inside its structure in the form of MgCO_3 , that qualifies it to sequester twice the quantity of CO_2 per ton of olivine Mg-rich rock [J. Blencoe and D. Palmer, “Carbonation of metal silicates for long-term CO_2 sequestration,” U.S. Patent No. 8,114,374 (2012)].

The study emphasizes carbonating olivine is potential technique to produce a sustainable binder through the sequestration of CO_2 in the presence of a range of molarities of NaOH. Results demonstrate that olivine can gain high strengths as a result for the sequestration of greater amounts of CO_2 in the presence of NaOH in a wide range of molarities, consequently offers environmental benefits. As well, from economic viewpoint, this technique offers a cost effective candidates (olivine and NaOH), as such candidates have a lower cost in comparable other binders used for soil stabilization such as cement and lime.

Conclusions

This paper presents some results of a silty clay soil stabilized with two techniques: firstly; geopolymer production technique, and secondly; carbonation technique. Both of these techniques were used with a range of molarities of NaOH. The source binder used was olivine. The strength of alkali activated soil-

olivine mixture with 10M of NaOH increased and curing time, achieving a strength gain up to 14 times higher than that of host soil. The carbonated alkali activated soil-olivine mixture at a 300 kPa CO_2 pressure at 7 days curing time, increased the strength of soil up to 65 times higher than the host soil and 4.6 times that of the alkali-activated soil-olivine mixture after 90 days of curing, in the presence of 10M of NaOH. From microstructural analysis, the strength development was assigned to carbonation with the formation of new crystals like nesquehonite, and hydromagnesite and dypingite. The FTIR results confirmed the formation of the final gel.

From the carbonation results, two molarities were selected which showed comparable strength values in contrast with the others, which are 8 and 10M.

From these hopeful results, further tests should be executed in this material, leaching tests and resistance to acidic attack to establish other characteristics of this material that may allow its application in different construction projects.

Acknowledgements

The authors want to express their deep thankful and grateful to the University Putra Malaysia as well as Fundamental Research Grant Scheme (FRGS/1/2015/TK01/UPM/01/2) entitled “Sustainable Soil Stabilization by Olivine and its Mechanisms” funded by the Ministry of Higher Education in Malaysia (Vote Number 5524745) for financial backup of this research.

References

- [1] Abdul Rahim, R. H., Azizli, K. A., Man, Z., Rahmiati, T., and Nuruddin, M. F. (2014). “Effect of sodium hydroxide concentration on the mechanical property of non sodium silicate fly ash based geopolymer.” *J. Appl. Sci.*, 14(23), 3381–3384.
- [2] Andreani M, Luquot L, Gouze P et al. (2009) Experimental study of carbon sequestration reactions controlled by the percolation of CO_2 -rich brine through peridotites. *Environmental Science & Technology* 43(4): 1226–1231.

- [3] Arulrajah A, Disfani MM, Maghoolpilehrood F et al. (2015) "Engineering and environmental properties of foamed recycled glass as a lightweight engineering material." *Journal of Cleaner Production* 94: 369–375.
- [4] Basha EA, Hashim R, Mahmud HB and Muntohar AS (2005) "Stabilization of residual soil with rice husk ash and cement." *Construction and Building Materials* 19(6): 448–453
- [5] Bernal, S., Gutiérrez, R. M., Pedraza, A. L. & Provis, J. L., 2011. Effect of binder content on the performance of alkali-activated slag concretes. *Cement and concrete research*, pp. 41: 1-8.
- [6] British Standards Institution. (2002). "British standard methods of test for soils for civil engineering purposes. Part 4: Compaction-related tests." BS 1377-4:1990, London, 1–53.
- [7] British Standards Institution. (2003). "British standard methods of test for soils for civil engineering purposes. Part 7: Shear strength testsb (total stress)." BS 1377-7:1990, London.
- [8] Cai GH, DU YJ, Liu SY and Singh DN (2015) "Physical properties, electrical resistivity and strength characteristics of carbonated silty soil admixed with reactive magnesia." *Canadian Geotechnical Journal* 52(999): 1–15
- [9] Chen ZY, O'Connor WK and Gerdemann SJ (2006) "Chemistry of aqueous mineral carbonation for carbon sequestration and explanation of experimental results." *Environmental Progress* 25(2): 161–166.
- [10] Criado, M., Palomo, A., and Fernandezjimenez, A. (2005). "Alkali activation of fly ashes. Part 1: Effect of curing conditions on the carbonation of the reaction products." *Fuel*, 84(16), 2048–2054.
- [11] Cristelo, N., Glendinning, S., Miranda, T., Oliveira, D., and Silva, R. (2012b). "Soil stabilisation using alkaline activation of fly ash for self compacting rammed earth construction." *Constr. Build. Mater.*, 36, 727–735.
- [12] Cristelo, N., Glendinning, S., and Pinto, A. T. (2011). "Deep soft soil improvement by alkaline activation." *Proc. ICE–Ground Improv.*, 164(1), 1–10.
- [13] Davidovits, J. (1991). "Geopolymers." *J. Therm. Anal. Calorim.*, 37(8), 1633–1656.
- [14] Disfani MM, Arulrajah A, Haghighi H, Mohammadinia A and Horpibulsuk S (2014) "Flexural beam fatigue strength evaluation of crushed brick as a supplementary material in cement stabilized recycled concrete aggregates." *Construction and Building Materials* 68: 667–676.
- [15] Du YJ, Zhang YY and Liu SY (2011) "Investigation of strength and California bearing ratio properties of natural soils treated by calcium carbide residue." *Geo-Frontiers*: 1237–1244.
- [16] Du YJ, Bo YL, Jin F and Liu CY (2015) Durability of reactive magnesia-activated slag-stabilized low plasticity clay subjected to drying–wetting cycle. *European Journal of Environmental and Civil Engineering* 20(6): 1–16.
- [17] Fasihnikoutalab, M. H., Asadi A., Unluer C., Huat, B. B., Ball R. J., Pourakbar, S. (2017) "Utilization of Alkali-Activated Olivine in Soil Stabilization and the Effect of Carbonation on Unconfined Compressive Strength and Microstructure." *Journal of Materials in Civil Engineering* 29(6) DOI: 10.1061/(ASCE)MT.1943-5533.0001833.
- [18] Fasihnikoutalab, M. H., Asadi A., Huat, B. B., Ball R. J., Pourakbar, S., Singh P. (2016) "Utilisation of carbonating olivine for sustainable soil stabilisation." *Environmental Geotechnics* 4(3): 184-198. doi.org/10.1680/jenge.15.00018.
- [19] Horpibulsuk S, Rachan R and Suddeepong A (2011) "Assessment of strength development in blended cement admixed Bangkok clay." *Construction and Building Materials* 25(4): 1521–1531.
- [20] Haug TA, Munz IA and Kleiv RA (2011) "Importance of dissolution and precipitation kinetics for mineral carbonation." *Energy Procedia* 4: 5029–5036.
- [21] Hänchen M, Prigiobbe V and Storti G (2006) Dissolution kinetics of fosteritic

- olivine at 90–150°C including effects of the presence of CO₂. *Geochimica et Cosmochimica Acta* 70(17): 4403–4416.
- [22] Jegandan S, Liska M, Osman AAM and Al-Tabbaa A (2010) Sustainable binders for soil stabilisation. *Proceedings of the Institution of Civil Engineers – Ground Improvement* 163(1): 53–61, <http://dx.doi.org/10.1680/grim.2010.163.1.53>.
- [23] Komljenović, M., Bascarević, Z., and Bradić, V. (2010). “Mechanical and microstructural properties of alkali-activated fly ash geopolymers.” *J. Hazard. Mater.*, 181(1–3), 35–42.
- [24] Lee, W. K. W., and van Deventer, J. S. J. (2002a). “The effect of ionic contaminants on the early-age properties of alkali-activated fly ash-based cements.” *Cem. Concr. Res.*, 32(4), 577–584.
- [25] Lee, W. K. W., and van Deventer, J. S. J. (2002b). “The effects of inorganic salt contamination on the strength and durability of geopolymers.” *Colloids Surf. A.*, 211(2–3), 115–126.
- [26] Olajire AA (2013) A review of mineral carbonation technology in sequestration of CO₂. *Journal of Petroleum Science and Engineering* 109: 364–392.
- [27] Olsson J, Bovet N, Makovichy E et al. (2012) Olivine reactivity with CO₂ and H₂O on a microscale: implications for carbon sequestration. *Geochimica et Cosmochimica Acta* 77: 86–97.
- [28] Pakbaz MS and Alipour R (2012) “Influence of cement addition on the geotechnical properties of an Iranian clay.” *Applied Clay Science* 67–68: 1–4.
- [29] Provis, J. & Deventer, J. v., (2014). “Alkali Activated Materials: State-of-the-art Report.” RILEM TC 224-AAM.
- [30] Prigiobbe V, Hänchen M, Werner M et al. (2009b) Mineral carbonation process for CO₂ sequestration. *Energy Procedia* 1(1): 4885–4890.
- [31] Pourakbar, S., Asadi, A., Huat, B. B., and Fasihnikoutalab, M. H. (2015a). “Soil stabilization with alkali-activated agro-waste.” *Environ. Geotech.*, 2(6), 359–370.
- [32] Pourakbar S, Asadi A, Huat BBK and Fasihnikoutalab MH (2015) Stabilization of clayey soil using ultrafine palm oil fuel ash (POFA) and cement. *Transportation Geotechnics* 3: 24–35.
- [33] Phoo-ngernkham, T., Maegawa, A., Mishima, N., Hatanaka, S., and Chindaprasirt, P. (2015). “Effects of sodium hydroxide and sodium silicate solutions on compressive and shear bond strengths of FA–GBFS geopolymer.” *Constr. Build. Mater.*, 91, 1–8.
- [34] Ryu, G. S., Lee, Y. B., Koh, K. T., and Chung, Y. S. (2013). “The mechanical properties of fly ash-based geopolymer concrete with alkaline activators.” *Constr. Build. Mater.*, 47, 409–418.
- [35] Rios, S., Cristelo, C., Viana da Fonseca, A. & Ferreira, C., 2015. Structural Performance of Alkali Activated Soil-Ash versus Soil-Cement. *Journal of Materials in Civil Engineering*, pp. DOI: 10.1061/(ASCE)MT.1943-5533.0001398.
- [36] Salih, M. A., Abang Ali, A. A., and Farzadnia, N. (2014). “Characterization of mechanical and microstructural properties of palm oil fuel ash geopolymer cement paste.” *Constr. Build. Mater.*, 65, 592–603.
- [37] Sara Rios, Catarina Ramos, António Viana da Fonseca, Nuno Cruz and Carlos Rodrigues, 2016 “Colombian Soil Stabilized with Geopolymers for Low Cost Roads” *Procedia Engineering*, 143, 1392–1400.
- [38] Schuiling R and Praagman E (2011) “Olivine hills: mineral water against climate change. In *Engineering Earth: The Impacts of Megaengineering Projects* (Brunn S (ed)).” Springer, Dordrecht, the Netherlands, pp. 2201–2206.
- [39] Temuujin, J., Williams, R. P., and van Riessen, A. (2009). “Effect of mechanical activation of fly ash on the properties of geopolymer cured at ambient temperature.” *J. Mater. Proc. Technol.*, 209(12–13), 5276–5280.
- [40] Weng, L., and Sagoe-Crentsil, K. (2007). “Dissolution processes, hydrolysis and condensation reactions during geopolymer synthesis. Part I—Low Si/Al ratio systems.”

- Adv. Geopol. Sci. Technol. J. Mater. Sci., 42(9), 2997–3006.
- [41] Yi Y, Liska M, Unluer C et al. (2013a) Carbonating magnesite for soil stabilization. *Canadian Geotechnical Journal* 50(8): 899–905.
- [42] Yi, Y., Liska, M., Unluer, C., and Al-Tabbaa, A. (2013b). “Carbonating magnesite for soil stabilization.” *Can. Geotech. J.*, 50(8), 899–905.
- [43] Yi, Y., Liska, M., Unluer, C., and Al-Tabbaa, A. (2013c). “Initial investigation into the carbonation of MgO for soil stabilisation.” *Proc., 18th Int. Conf. on Soil Mechanics and Geotechnical Engineering, Paris*, 2641–2644.
- [44] Yip, C. K., Lukey, G. C., Provis, J. L., and van Deventer, J. S. J. (2008). “Effect of calcium silicate sources on geopolymerisation.” *Cem. Concr. Res.*, 38, 554–564.
- [45] Yip, C. K., Lukey, G. C., Provis, J. L., and van Deventer, J. S. J. (2008). “Effect of calcium silicate sources on geopolymerisation.” *Cem. Concr. Res.*, 38, 554–564.

EFFECT OF CURING TEMPERATURE ON THE DEVELOPMENT OF HARD STRUCTURE OF ALKALI-ACTIVATED SOIL

Lokmane Abdeldjouad¹, Afshin Asadi², Bujang B.K.Huat³, Mohd Saleh Jaafar⁴, Wisam Dheyab⁵, and
Ahmed Giuma Elkhebu⁶

^{1,3,4,5}Department of Civil Engineering, Faculty of Engineering, Universiti Putra Malaysia, Serdang, Selangor,
Malaysia

²Department of Civil Engineering, International College of Auckland, Auckland, New Zealand

⁶ Faculty of Civil and Environmental Engineering, Universiti Tun Hussein Onn Malaysia, Batu Pahat, Johor,
Malaysia

ABSTRACT

This study is directed to the feasibility of usage of palm oil fuel ash (POFA) as a precursor of alkaline activation reactions which made by potassium hydroxide in order to stabilize the soil and improve its expediency for different case of construction. The effect of duration and temperature of curing, for alkaline activation process, on the Unconfined Compression Strength (UCS) of the soil-POFA mixture is important in enhancing the treated soil properties. Use of 30, 50, and 100°C of heating affected the UCS of the soil mixture. The highest strengths were obtained at 100°C for the alkali activation process. Microstructural analysis using The Brunauer–Emmett–Teller (BET) and Infrared spectrometric analysis (FTIR) shows the benefits of alkaline activation in terms of decreasing the duration of alkaline process. The pore distribution analysis shown a trend to rise pore size volume with increasing temperature, which affects the mechanical characteristics. This was due to the fastest crystallisation processes which accounts for strength gain after short period of heating. It has been also presented the opportunity of observing the alkaline activation process by FTIR Spectra. This paper highlights a more environmentally friendly procedure of stabilizing soils compared with the traditional binders such as cement and lime.

Keywords: Soil stabilization, Ground improvement, Alkaline activation, Geopolymerisation, Unconfined compression strength

INTRODUCTION

The alkaline activation (in other words, 'geopolymerisation') is described as a polycondensation, this reaction integrates minerals chemically, consisting of aluminum (Al) and silica (SiO₂) alternately tetrahedrally interlinked by sharing all the O₂ (oxygen atoms). This process begins by breaking the covalent bonds Al–O–Si, Si–O–Si, and Al–O–Al from the vitreous phase of the source material due to the high concentration of the hydroxyl in the alkaline medium, which results in transforming the alumina (Al₂O₃) and silica (SiO₂) ions in colloids and releasing them into the solution. At this state, alumino-silicates (Al₂SiO₅) become extremely reactive materials to form a well-structured alumino-silicate polymerised framework [3, 4, 13, 18].

Lately, the mechanism of geopolymerisation (alkaline activation) using a wide variety of alumino-silicate (Al₂SiO₅) source material was further investigated by a growing and large body of literature. And even more, they studied alkaline activators role, which are made by mixing a highly-alkaline solution (as sodium hydroxide (NaOH)) with a silica-rich source (such as sodium silicate),

and the environmental-benefits of the alkaline-activation method [8, 13, 15, 16, 17].

The majority of these studies shows that the proposition; alkali-activated binders have superior performance compared to cementitious binders performance. It consumes lower energy portion; 80% lower than carbon dioxide (CO₂) emissions, has higher strength and obey the principles of sustainable development. Hence, due to all the agreements between governments all around the world about taxing carbon dioxide (CO₂) emissions, the promotion of sustainable and environmentally-friendly materials like alkali-activated binders are encourages, which makes it thought of as the future material [13, 14].

According to this knowledge and advantages, researchers in synthesis of alkali-activated binder field and identification of reaction mechanisms in civil engineering frameworks have intensified their work to reach their goal. However, it is still early to use this technology in ground improvement applications [5, 7, 9, 10, 12, 13].

Some geotechnical scientists have investigated the efficacy of geopolymeric (alkali-activated) high calcium and low calcium fly ash as alumina and silica nebulous source for soil stabilization [5, 6, 7].

Also, a current report by Zhang [19] examined the practicality of utilizing metakaolin as an antacid initiated soil stabilizer at shallow profundity. Such investigations were directed by mixing the alkali-activated binders with weak soils in existence of NaOH (sodium hydroxide) and a sodium silicate (silica-rich source) as based alkaline activator, and their outcomes prescribe the use of the alkali-activated binder as an effective technique of soil stabilization. Likewise, the creators presumed that the geopolymerisation (alkaline activation) technique is a basic procedure and it doesn't include any entanglements or high-cost methods, or even any particular systems.

EXPERIMENTAL METHODS

Depending on the Unified Soil Classification System [1], the chemical composition and physical properties of two type of soils utilized in this research are listed in Tables 1 and 2, respectively.

Table 1 Physical characteristics of soils

Properties	Standard	Soil 1	Soil 2
Liquid limit (LL) (%)	BS 1377-2	48.7	74
Plastic limit (PL) (%)	BS 1377-2	34.5	43
Plasticity index (PI) (%)	BS 1377-2	14.2	31
Specific gravity (GS)	BS 1377-2	2.52	2.34
MDD (Mg/m^3)	BS 1377-4	1.58	1.32
OMC (%)	BS 1377-4	24	30
Sand (%)	USCS	32	-
Silt (%)	USCS	24	78
Clay (%)	USCS	44	22
UCS (kPa) - after compaction test	BS 1377-7	380-390	180-190

The POFA, utilized as a forerunner for the alkaline activation reactions, was gathered from a plant in Johor, in the southern area of Malaysia. As can be seen from the chemical analyses (Table 3), this outstanding farming deposit has a high measure of silica and alumina. In any case, keeping in mind the end goal to accomplish a suitable chemical composition, and in addition a favorable shape and

size, the antecedent was primary exposed to a pretreatment, which involved calcination and grinding, so as to expand the reactivity level of the Al and Si and change the auxiliary coordination between the Al and the oxygen ions.

Table 2 Chemical analysis of soils

Chemical properties	Soil 1	Soil 2
Silica (SiO_2)	41.26	60.6
Alumina (Al_2O_3)	36.96	28.31
Iron oxide (Fe_2O_3)	10.07	5.4
Calcium oxide (CaO)	-	-
Potash (K_2O)	11.71	3.52
Magnesia (MgO)	-	0.6
pH	5.3	3.8

Table 3 Chemical composition of POFA (before and after pre-treatment)

Constituent	Natural POFA	Treated POFA
Physical properties		
Specific gravity (GS)	2.42	2.51
Chemical properties		
Silica (SiO_2)	46.04%	55.78%
Alumina (Al_2O_3)	19.39%	17.29%
Iron oxide (Fe_2O_3)	6.10%	4.17%
Calcium oxide (CaO)	13.87%	11.93%
Potash (K_2O)	8.61%	7.79%
Magnesia (MgO)	-	-
Loss on ignition (LOI)	9.68%	1.5%

Afterward drying the POFA in a stove at 105°C , for 24 hours, the resulting particles were crushed in an 80-cm diameter ball-mill for 24 h and then passed over a 300- μm filter. Different ball sizes were used, in the range of 12–30 mm. The crushing speed of 60 rpm resembled to nearly 65% of the critical speed, which, in turn, was determined by dividing a constant by the square root of the mill diameter. In the subsequent stage, and keeping in mind the end goal to evacuate any unburned carbon, the ground POFA was warmed in an electric stove at 440°C for

around 1 has demonstrated in Figure 3.4. After the pretreatment methodology, X-ray fluorescence (XRF) spectrometry was utilized for essential element investigation. A similar pretreatment has been adopted by different researchers [11, 13], who revealed the technique to be viable in expanding the particular surface and reactivity of the ash.

Potassium hydroxide (KOH), having alkaline cation, was chosen as an activator on account of its outstanding productivity. In spite of the fact that the cost of NaOH is not as much as KOH, the researchers utilized KOH as a soluble base activator in light of the fact that K^+ has a bigger size than the other alkaline metal cation, and in this manner permits more thick and private polycondensation responses, which generously rise the general long-term strength of the alkali-activated soil. As per those analysts' discoveries, networks containing K^+ displayed higher UCS and particular surface region and a lower level of crystallinity in long-term of curing systems. This reagent was provided in pellet form by the organization R&M chemical and was beforehand weakened in refined water to accomplish a predesigned concentration. Note that the response with water of KOH is intensely exothermic, as with every solid base. In this way, the alkaline solution was left to cool to encompassing temperature before utilize.

In this investigation, the UCS tests were directed as per Part 7: Clause 7 of the BS 1377-1990 [2] to assess the effectiveness of source binder and alkaline activators and furthermore to discover the impact of kaolinite content of the original soil that affects the strength behavior of treated soil examples. The UCS tests characterized the corresponding to the peak stress condition. Stress value was estimated at indicated ages in three examples for every mixture and all information focuses veered off under 5% from the normal. For the unconfined compressive strength tests, with a predesigned activator concentration (10M and 12.5M potassium hydroxide) to dry solid amount, a total of two mixtures were prepared by using KOH, with POFA (15 and 20% by dry mass of soil).

To set up the specimens, in the initial step, the alkaline activator was liquefied in the solution at a predetermined absorption. In this progression, refined water was utilized to break down activator pellets to keep away from the impact of obscure contaminants in the mixing water. Since this response was exceedingly exothermic and to avoid from expanding the plasticity of the parent soil, the soluble solutes were cooled and arranged for 24 hours before being utilized as a part of the mixture. In the next step, the required measure of characteristic soils was air dried for 24 hours. In the subsequent stage, the necessary dose of air-dried soil was mixed by including the cooled alkaline solution with the predefined dosages of POFA. Soon after

mixing, samples were placed in a cylindrical mold (50 mm dia. by 100 mm high), applying steady direct compaction in three equivalent layers, and expelled. Since potassium hydroxide is a strong base, compacted specimens within the existence of such activator were not sufficiently solid to be remolded. Subsequently, the chamber tests were expelled with farthest caution. Directly after extrusion, all specimens were putted in oven (Figure 5.1) under different temperature and different time then closely covered in polythene covers to prevent loss of water and cured under different curing regimes (7 and 28 days) prior to testing in a laboratory ambient temperature. After shearing, all specimens were retained for mineralogical analysis.

In order to better understand the effect of temperature on the treated soil mixture, selected specimens were analyzed (after submitted to the respective UCS test) using The Brunauer–Emmett–Teller (BET) method and Infrared spectrometric analysis (FTIR).

RESULTS AND DISCUSSION

Mechanical properties

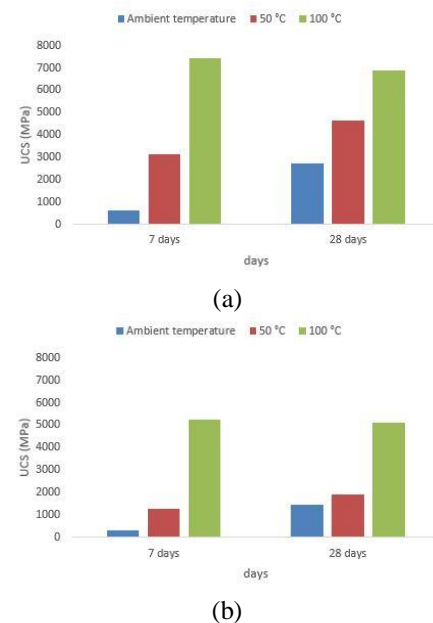


Fig. 1 Development of compressive strength of alkali-activated soils cured at ambient temperature, 50, and 100 °C over time (7 and 28 days). Temperature during curing was carried out for initial 3 h at 50 and 100 °C. (a) Soil 1 (b) Soil 2

Fig. 1 shows the effect of curing temperature on the compressive strengths of 2 alkali-activated soils at the age of 7 and 28 days with 3 hours of heating duration. The reference alkali-activated soils cured at a laboratory ambient temperature achieved the

UCS values of 2.75 and 1.48 MPa for Soil 1 and Soil 2, respectively, at the long-term (28 days). The short-term strengths of geopolymeric (alkali-activated) soils cured at an ambient temperature achieved 0.61 and 0.33 of UCS due to delayed setting of specimens. As estimated, the high temperature quickens the development of tough structure especially in the early age of alkaline activation reaction. The UCS values of both alkali-activated soils cured at 50 or 100°C, respectively, achieved the higher values 7.42 MPa for soil 1 and 5.22 MPa for soil 2 after 7 days and three times surpassed the values noticed for specimens cured at a laboratory ambient temperature. Nevertheless, the quick setting avoids the mixture from the creation of more dense and hard structure; therefore the UCS values in 28 days for soil 1 and soil 2 with 100°C is by 0.54 and 0.12 MPa lower compared to the alkali-activated soils in 7 days, respectively. On the contrary, though the alkali-activated mixtures of soil 1 and soil 2 that were cured at a laboratory ambient temperature exhibit late strengths' improvement, they achieved the values of 2.75 and 1.48 MPa at the age of 28 days. The justification of this performance is similar to the effect of temperature on the strength improvement of metakaolin-based geopolymers [20,21]. At early age, the strengths increase with the temperature since at elevated temperature the alkaline activation degree is higher, and therefore the quantity of reaction produces rises. On the other hand, at longer time, when the strengths is almost similar with those observed after early age for specimens that were treated at 100°C temperature because the loss of water in the system through curing and the resultant shortage of moisture to completely dissolve the glassy component of POFA (first stage of cementitious gel formation) under these conditions [22].

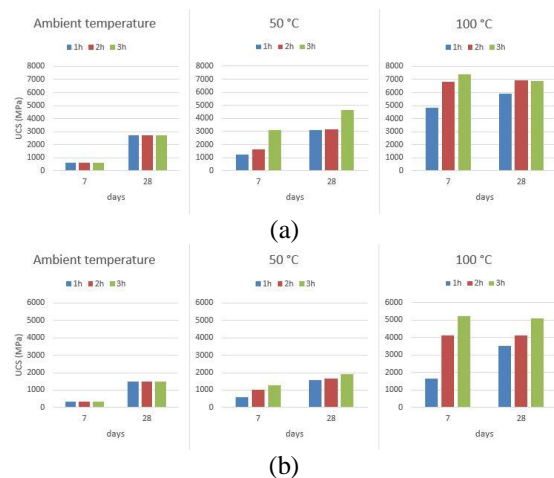


Fig. 2 Influence of curing time on compressive strength of treated soils cured at elevated temperatures (ambient temperature, 50 and 100°C) (a) Soil 1 (b) Soil 2

The study was also concentrated on the effect of curing time at high temperatures. The UCS of treated soils as a function of curing time at identified high temperature is shown in Figure 2. Longer curing of alkali-activated soil mixtures quickens the improvement of strength in the early stage of hardening. In the meantime 7 days compressive strength of alkali-activated soil 1 and soil 2 cured for 1 hour at 50°C was only 1.21 and 0.57 MPa, the strength augmented nearly three times to 3.14 and 1.25 MPa, respectively, when such treating was extended to 3 hours. The highest results of strengths were achieved in 28 days for specimens treated at ambient temperature and 50°C. The effect of curing time on the strength improvement of alkali-activated soils cured at 100°C is very similar. The samples that were treated for two or more hours at 100°C achieved their highest strengths at early age (7 days) with UCS values about 7.42 and 5.22 MPa for soil 1 and soil 2 respectively. On the other hand, when the specimen was exposed to 100°C just for 1 hour, a tendency of the strength improvement is very similar to that detected with 3 hours curing at 50°C. In this case, the short-term UCS values is around 4.85 and 1.63 MPa for soil 1 and soil 2, respectively, but moreover the long term age (28 days) strength is not reduced.

Pore structure analysis

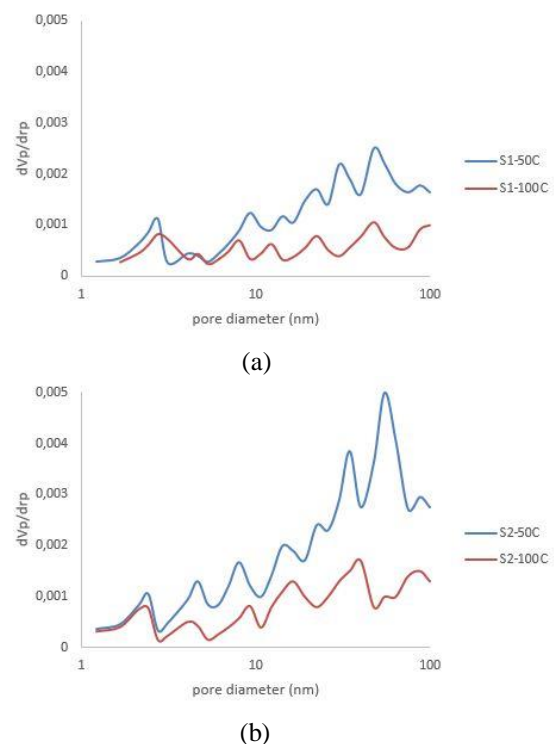


Fig. 3 Comparison of pore distribution of cured at 50 and 100°C at 28 days (curing at 50 and 100°C was carried out for initial 3 h) (a)

Soil 1 (b) Soil 2

The changes in the porosity of specimens were also evaluated by using BET test at 28 days as presented in Figure 3. The higher porosity of samples can quicken cracking of specimens due to exposure to UCS. Figure 3 (a) reveals the differences in BET pattern between the treated soil 1 with elevated temperature 50 and 100°C after 28 days. As can be seen, the higher porosity was recognized in the treated soil 1 cured in 50°C due to the high volume peaks about 0.0021 and 0.0025 with pores diameter around 29.89 and 47.21 nanometer while the peaks of pores volume in the treated soil 1 cured at 100°C were 0.0007 and 0.0009 with the diameters of 54.42 and 86.83 nanometer, respectively. The effects of curing temperature after 28 days on the treated soil 2 samples cured at 50 and 100 °C are illustrated in Figure 3 (b). The same trend was observed for treated soil 1 samples when cured at elevated temperature. It can be observed that treated soil 2 cured at 50°C had higher porosity of 0.0038 and 0.0049 with a diameter about 34.36 and 54.42 nanometer than the recorded results for samples cured at 100°C, porosity of 0.0017 and 0.0015, with diameters about 39.78 and 86.83. As can be seen, the volume and the diameter of the pores decreased with elevation in curing temperature.

Infrared spectrometric analysis

FTIR spectra of treated soils were examined mostly for the asymmetric stretching vibration of Si–O–T linkages that were expected to be signified by the point of maximum absorbance in the main band (section 900–1300 cm^{-1}). Absorption features in the examined area of the spectra are asymmetric and broadened and involve the similarity of more bands. Deconvolution of the main band of hardened treated soils cured at elevated temperature shown the similarity of numerous important bands (Figure 4). The bands related with asymmetric stretching mode at 914 and 1006 cm^{-1} of natural soil 1 with POFA were found in all spectra. Also, the band at 1037 cm^{-1} are related with asymmetric stretching mode of natural soil 2 with POFA and they were observed in all spectra. Noticing this feature even after 28 days implies that an amount of unreacted soil 1 with POFA and soil 2 with POFA still remains in hardened material [23]. The most intensive bands at 1029 and 1113 cm^{-1} characterizes oxygen connections of asymmetric vibration between tetrahedra in geopolymeric structure of treated soil 1 and soil 2, respectively. Weak bands at 1408 and 1410 cm^{-1} is linked with stretching vibrations of band Si–O groups in partially hydrated treated soil 1 and soil 2 [24]. Bands at 752 and 950 cm^{-1} that comes into view in spectrum of original soil 1 and soil 2 with POFA, respectively, and diminishes

through alkaline activation is related with symmetric Al–O–Si stretching vibrations.

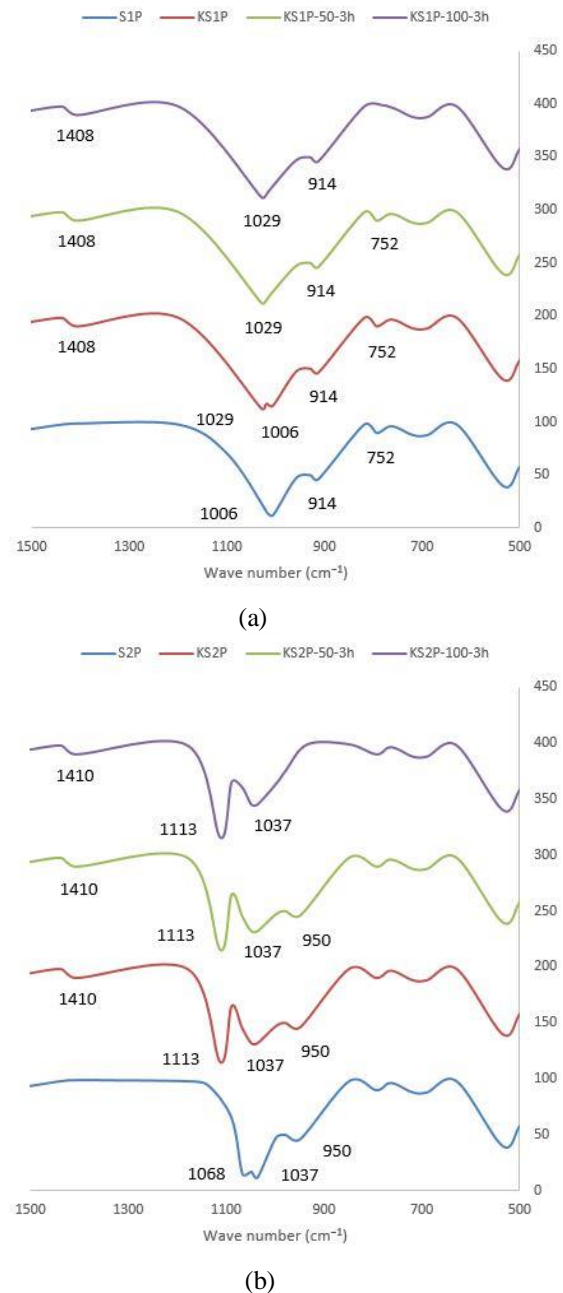


Fig. 4 Deconvolution of the main band related with Si–O–T stretching mode in treated soils cured at elevated temperatures (ambient temperature, 50 and 100°C) (a) Soil 1 (b) Soil 2

Though MAS NMR methods deliver extra comprehensive sight of alkaline activation procedure [20], FTIR spectroscopy is, nevertheless, a potential and unpretentious technique for the checking of alkaline activation procedure and creation of the tough structure. Examination of FTIR spectra in the area of Si–O–T stretching vibrations shown remains

of unreacted soils in hardened treated samples regardless of curing time. It supports a proposition that original materials (soil with POFA) are not completely dissolved through alkaline activation procedure but the reaction occurs in the external layer of the solid elements [20]. The reaction degree is then measured mostly by diffusion of hydroxide and silicate ions during primary gel which is influenced mostly by curing temperature at the short-term of the reaction.

CONCLUSION

In this experiment, the influence of temperature during curing and curing time at high temperatures on the mechanical characteristics of two treated soils was examined by determining compressive strengths' improvement over time. The achieved values were clarified on the base of pore structure investigation executed by utilizing mercury intrusion porosimetry apparatus and the changes of microstructure on molecular level were observed by FTIR spectroscopy. The investigational and analysis led to the subsequent conclusions.

1. Temperature during curing has an important influence on setting and hardening of treated soils. At high and an ambient temperature the matter set practically within 3 hours at the latest. Evaluated mechanical tests showed that 7 and 28 days mechanical characteristics of treated soils are significantly reliant on curing temperature. Elevated temperatures rise the short-term compressive strength, which can even achieve higher values in 7 day. Nevertheless, the long-term (28 days) strengths were obviously fairly lower or similar in comparison with those saw for short-term (7 days) samples that were cured for 2 or 3 hours at 100°C temperature due to the rapid development of the tough structure perhaps does not consequence in such a good quality get product. Furthermore, time of curing affects the effect of temperature during curing. Curing for just 1 hour at a high temperature did not cause significant changes in strengths improvement but longer curing was accountable for a significant quickening of the reaction degree and rise in short-term strengths.
2. Porosimetry analysis presented that the pore size distribution reduced with high temperature, and this was true for both soils. On the other hand, main differences in pore structure came into view between specimens treated at diverse temperatures (50 and 100°C). Elevated temperature of hardening progression led to decrease

larger pores which has a positive consequence on the ending mechanical characteristics of alkali-activated treated soil.

ACKNOWLEDGEMENTS

The authors sincerely thanks Universiti Putra Malaysia (UPM) for providing financial assistance and facilities for this research.

REFERENCES

- [1] ASTM. (2010). "Standard practice for classification of soils for engineering purposes (unified soil classification system)." ASTM D2487, West Conshohocken, PA.
- [2] British Standards Institution. (1990). "Methods of test for soils and civil engineering purposes." BS1377, London.
- [3] Davidovits, J. (1988). "Geopolymer chemistry and properties." Proc., 1st European Conf. on Soft Mineralurgy (Geopolymere '88), J. Davidovits and E. J. Orlinsl, eds., The Geopolymer Institute, Compiègne, France, 25–48.
- [4] Davidovits, J. (1991). "Geopolymers." J. Therm. Anal. Calorim., 37(8), 1633–1656.
- [5] Cristelo, N., Glendinning, S., Fernandes, L., and Pinto, A. T. (2013). "Effects of alkaline-activated fly ash and Portland cement on soft soil stabilisation." Acta Geotech., 8(4), 395–405.
- [6] Cristelo, N., Glendinning, S., Miranda, T., Oliveira, D., and Silva, R. (2012). "Soil stabilisation using alkaline activation of fly ash for self compacting rammed earth construction." Constr. Build. Mater., 36, 727–735.
- [7] Cristelo, N., Glendinning, S., and Pinto, A. T. (2011). "Deep soft soil improvement by alkaline activation." Proc. ICE-Ground Improv., 164(2), 73–82.
- [8] Duxson, P., Provis, J. L., Lukey, G. C., and Van Deventer, J. S. (2007). "The role of inorganic polymer technology in the development of 'green concrete'." Cem. Concr. Res., 37(12), 1590–1597.
- [9] Ariffin, M., Bhutta, M., Hussin, M., Mohd Tahir, M., and Aziah, N. (2013). Sulfuric acid resistance of blended ash geopolymer concrete. Construction and Building Materials, 43, 80–86.
- [10] Habert, G. (2011). d'Espinose de Lacaillerie JB and Roussel N (2011) An environmental evaluation of geopolymer based concrete production: reviewing current research trends. Journal of Cleaner Production, 19(11), 1229–1238.
- [11] Pourakbar, S., Asadi, A., Huat, B. B., and Fasihnikoutalab, M. H., "Stabilization of Clayey Soil Using Ultrafine Palm Oil Fuel Ash (POFA)

- and Cement,” *Transp. Geotech.*, Vol. 3, 2015, pp. 24–35.
- [12] Wallah, S., and Rangan, B. V. (2006). Low-Calcium Fly Ash-Based Geopolymer Concrete: Long-Term Properties. *Res. Report-GC2*. Curtin University, Australia, pp. 76–80.
- [13] Pourakbar, S., Asadi, A., Huat, B. B., and Fasihnikoutalab, M. H., “Soil Stabilization With Alkali-Activated Agro-Waste,” *Environ. Geotech.*, Vol. 2, No. 6, 2015, pp. 359–370.
- [14] Pourakbar, S., Asadi, A., Huat, B. B., Cristelo, N., and Fasihnikoutalab, M. H., “Application of Alkali-Activated Agro-Waste Reinforced With Wollastonite Fibers in Soil Stabilization,” *J. Mater. Civ. Eng.*, 2016, 04016206.
- [15] Khale, D., and Chaudhary, R. (2007). Mechanism of geopolymerization and factors influencing its development: a review. *Journal of Materials Science*, 42(3), 729–746.
- [16] Xu, H., and Van Deventer, J. (2000). The geopolymerisation of aluminosilicate minerals. *International Journal of Mineral Processing*, 59(3), 247–266.
- [17] McLellan, B. C., Williams, R. P., Lay, J., Van Riessen, A., and Corder, G. D. (2011). Costs and carbon emissions for geopolymer pastes in comparison to ordinary portland cement. *Journal of Cleaner Production*, 19(9), 1080–1090.
- [18] Duxson, P., Provis, J. L., Lukey, G. C., Seth, W. M., Waltraud, M. K., Jannie, S. J. V. D. (2005). Understanding the relationship between geopolymer composition, microstructure and mechanical properties. *Colloids and Surfaces A: Physicochemical and Engineering Aspects*, 269(1), 47–58.
- [19] Zhang, M., Guo, H., El-Korchi, T., Zhang, G., and Tao, M. (2013). “Experimental feasibility study of geopolymer as the next-generation soil stabilizer.” *Construction and Building Materials*, 47, 1468–1478.
- [20] Pavel, R., (2010). “Effect of curing temperature on the development of hard structure of metakaolin-based geopolymer.” *Construction and Building Materials*, 24, 1176–1183.
- [21] Mo, B. H., He, Z., Cui, X. M., He, Y., Gong, S. Y., (2014). “Effect of curing temperature on geopolymerization of metakaolin-based geopolymers.” *Construction and Building Materials*, 99, 144–148.
- [22] Kovalchuk, G., Fernandez-Jimenez, A., and Palomo, A., (2007). “Alkali-activated fly ash: Effect of thermal curing conditions on mechanical and microstructural development – Part II.” *Fuel*, 86, 315–322.
- [23] Akolekar, D., Chaffee, A., and Russell, F. H., (1997). The transformation of kaolin to low-silica X zeolite. *Zeolites*, 19(5), 359–365.
- [24] Benesi, H. A., and Jones, A. C., (1959). An infrared study of the water-silica gel system. *J. Phys. Chem.*, 63(2), 179–182.

EFFECTS OF ALKALI-ACTIVATED WASTE BINDER IN SOIL STABILIZATION

Tan Teing Teing¹, Bujang B.K. Huat², Sanjay Kumar Shukla³, Vivi Anggraini⁴ and Haslinda Nahazanan⁵
^{1,2,5}Faculty of Engineering, University of Putra Malaysia; ³Edith Cowan University, Australia; ⁴Monash University, Malaysia

ABSTRACT

Generally, alkali-activated binders have received much attention in recent years due to their energy efficiency, environmentally friendly process, and excellent engineering properties. With respect to this fact, this study aims to investigate the effects of alkaline activation reactions on residual soil by using different percentages of fly ash as a precursor. Precisely, fly ash was incorporated with potassium hydroxide (10M) in order to stabilize the soil and enhance its expediency for various forms of construction. In particular, this experimental study was focused on determining the mechanical performance of stabilized soil. Evidently, the results showed that the different percentages of fly ash (40%, 50%, 60% and 70% by weight) used to stabilize the residual soil affected the unconfined compressive strength of the soil matrix. Also, it was observed that the compressive strength of soil increased progressively with the addition of fly ash. However, the longer the curing period of the stabilized soils, the higher the unconfined compressive strength of the soil. In fact, the microstructural analysis which employed scanning electron microscopy (SEM) revealed the material modifications that can be related to the strength behavior.

Keywords: Alkaline activation, Fly ash, Residual soil, Soil stabilization, Unconfined compressive strength

INTRODUCTION

Basically, stabilized soil is a composite material which is resulted from the combination and optimization of properties in individual constituent materials. Accordingly, well-established techniques of soil stabilization are often employed to obtain geotechnical materials. Subsequently, these materials are further improved through the addition of cementing agents such as Portland cement, lime, asphalt, etc. Currently, soil stabilization with cement and lime is a comprehensively researched treatment technique. Undeniably, these two major components have been widely used to improve the engineering properties of soils, thus allowing them to function as a better subgrade or subbase due to their strength and durability [1-2]. However, these traditional cementitious binders have several shortcomings, especially from the environmental and cost perspective.

Alkali-activated binders are introduced as good replacements for calcium-based binders (i.e., cement and lime) due to their distinctive mechanical properties as well as lower environmental ill effects and processing costs. Essentially, the synthesis of alkali-activated binders is formed by the reaction of any amorphous aluminosilicate materials with alkali (usually Na or K) or alkali-earth (Ca) metals. Typically, this synthesis involves the dissolution of mineral aluminosilicates, followed by the hydrolysis and condensation of the Al and Si components,

resulting in the formation of a three-dimensional amorphous aluminosilicate gel [3-5].

In view of the environmentally friendly process, namely the energy efficiency and excellent engineering properties, alkali-activated binders are fast emerging as materials of choice for high-demand civil engineering applications. Nevertheless, studies regarding the particular application on soil stabilization remain limited. For instance, a few published papers on alkaline activation [6-10] addressed the effectiveness of alkaline activation (AA) on soil stabilization. Based on the microstructural analysis, the researchers discovered that the binding gel (N-A-S-H) evolved inside the soil voids, leading to an improved compressive strength and formation of more compact microstructures.

Inevitably, low calcium fly ash is one of the most abundantly produced waste materials in tropical regions with high content of silica and alumina. Specifically, fly ash is a byproduct produced from burning pulverized coal in electric power generating plants. It consists of inorganic and incombustible matter present in coal which transform into a glassy amorphous structure during combustion. To note, some studies discovered that the appropriate dosage of activated fly ash for soft soil stabilization were 20, 30 and 40% [11]. Despite these positive developments, the state of several issues such as the curing condition, efficacy of high-percentage fly ash, role of parent soil and type of alkaline solute in alkaline activation remain ambiguous. In this context,

the present study explores the possible use of higher percentage of fly ash in stabilizing residual soils under appropriate conditions.

Besides, the present work has aligned the development of an alternative alkali-activated binder for soil stabilization purposes with regards to different percentages of fly ash and concentration of 10M potassium-based activators. Then, the changes in the mechanical behavior of soil for various curing conditions were evaluated based on their unconfined compression strength (UCS). Also, the microstructural changes in soil before and after the treatment were performed to determine the underlying stabilization mechanisms with the aid of scanning electron microscopy (SEM) analyses.

MATERIALS AND METHODS

Materials

Natural soil

The residual soil used in the study was collected from a construction site (1-1.5 m under the natural ground surface) in Selangor, Malaysia. For reference, the physical characteristics of soil are summarized in Table 1 according to the BS (1377-2) [12]. Additionally, the grain size distribution of soil is illustrated in Fig. 1. Based on the Unified Soil Classification System, the investigated soil was classified as high-plasticity clay (CH). In general, this type of soil is often too weak and soft, thus making it unsuitable for earth works or foundation layers. Moreover, X-ray fluorescence analysis (XRF) and X-ray Diffraction (XRD) test were conducted to assess the chemical composition and mineralogy of residual soil, as shown in Table 2 and Fig. 2, respectively.

Table 1 The physical characteristics of natural soil.

Basic soil property	Value
Specific gravity (Gs)	2.6
Liquid limit (%)	61
Plastic limit (%)	30
Optimum water content (%)	23
Maximum dry density (Mg/m ³)	1.62
Organic content (%)	6.04

Fly ash

Particularly, the fly ash of class F (low calcium) used in this study was collected from coal combustion residuals of a thermal power station in Selangor, Malaysia. Then, the X-ray fluorescence (XRF) spectrometry was employed for elemental analysis of Al-Si minerals present in the Fly ash. Evidently, as observed from the chemical analyses of fly ash in Table 2, the residue contains high amount of silica.

Thus, this material can be a potential candidate as a precursor in the alkaline activation.

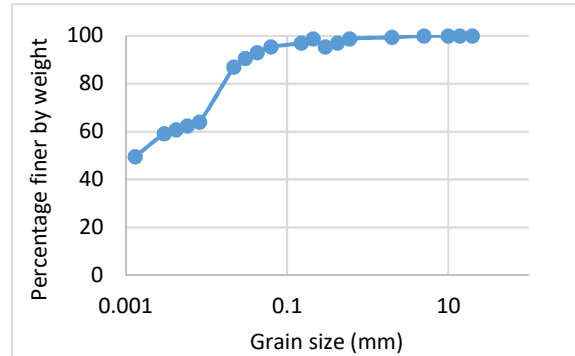


Fig. 1 Grain size distribution curve of soil.

Table 2 Chemical composition of soil and fly ash.

Constituent	Soil	Fly ash
Silica (SiO ₂)	40.62	57.47
Alumina (Al ₂ O ₃)	34.27	15.37
Iron oxide (Fe ₂ O ₃)	10.49	4.71
Calcium oxide (CaO)	0.03	3.32
Potash (K ₂ O)	0.1	0.76
Magnesia (MgO)	0.09	1.23
Loss on ignition	13.37	0.7

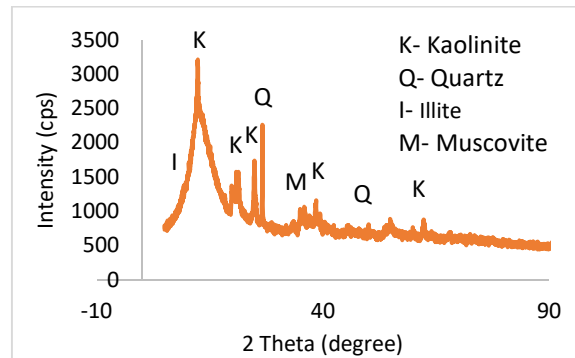


Fig. 2 XRD pattern of the original soil.

Alkaline activator

In this study, potassium hydroxide (KOH), an inorganic compound which contains alkaline cations and anions was selected as an alkali activator due to its suitability for deep mixing and affordability. Specifically, the potassium hydroxide was supplied in the form of pellets from Evergreen Engineering and Resources, Malaysia. Firstly, the activator solution was diluted with distilled water which had a pre-designed concentration of 10 molar. Then, the solution was blended for 10 minutes in order to achieve full dissolution. After 24 hours [13], the solution was used.

Laboratory test

A series of laboratory tests consisting of proctor compaction test and unconfined compression test (UCS) was conducted using different dosages of the fly ash. Besides, microstructural changes of soil before and after the treatment were performed to determine the underlying stabilization mechanisms with the aid of scanning electron microscopy (SEM) analyses.

Precisely, the quantities (or dosages) of selected binders used in this study were 40%, 50%, 60% and 70% by dry mass of the natural soil.

Sample preparation

Table 3 presents the composition of each mixture tested. There are two types of mixtures, based on the stabilization level, i.e., unstabilized soil (S) and activator-soil-binder (KSFA). Testing the original, unstabilized soil was included to provide an adequate reference regarding the analysis of the KSFA mixtures.

Potassium hydroxide (KOH) solutions with 10 molar were used to activate fly ash. The dry soil was initially mixed, by hand, with the fly ash. Then, the alkaline activator solution was then added to the solids and thoroughly mixed until a uniform blend was achieved. During this stage, additional water was added to the mixture to meet the optimum moisture content of the natural soil.

Standard proctor compaction test

For the purpose of conducting standard proctor compaction test, BS 1377–1990: Part 4 [13] was applied to determine the maximum dry density (MDD) and the optimum moisture content (OMC) of the soils. Ultimately, this test was performed to ascertain the moisture-density relationship of the untreated and treated soil. The first series of compaction tests was conducted to identify the compaction properties of the natural soils. This was followed by the second series in order to determine the proctor compaction properties of the soil upon stabilization with varying amounts of fly ash.

For mixing purpose, the natural soil was thoroughly mixed with the fly ash by hand until a uniform color was achieved. Then, water was added to facilitate the mixing and compaction processes.

Unconfined compression test

In this study, the UCS tests were conducted in accordance with Part 7: Clause 7 of the BS1377 standard [14] to evaluate the efficacy of different fly ash percentages on the increase of shear strength with

time after stabilization.

Group series	Test number	Samples	Curing (days)
S	S	Natural soil	7,28
KSFA group	KS40FA	10M KOH + Soil + 40% Fly ash	7,28
	KS50FA	10M KOH + Soil + 50% Fly ash	7,28
	KS60FA	10M KOH + Soil + 60% Fly ash	7,28
	KS70FA	10M KOH + Soil + 70% Fly ash	7,28

Table 3 Mixture proportions of various series of test specimens.

First and foremost, the specimens used for the unconfined compressive tests were air dried for 24 hours to ensure that the soil has zero initial water content. Next, the required dosage rate for stabilizers of each specimen was attained by adding and mixing a calculated weight of additives by dry mass of soil. Subsequently, the specimens then undergo manual compaction in a cylindrical mold which was 50mm in diameter and 100mm in height. Additionally, a 45-mm diameter steel rod was applied as a static load in their similar layers. Importantly, this measure was to eliminate the air pockets and to improve the homogeneity of the specimens. Later, the specimens were extruded and immediately wrapped in plastic sheets and polythene covers to prevent loss of moisture. In this study, the curing occurred at room temperature and humidity, and two different curing periods were considered (7 and 28 days). In order to achieve a state of approximate saturation before the unconfined compression strength test, the samples were unwrapped and submerged in water for the last 24 h of the respective curing period. The intention for this saturation is to remove the positive effects of suction on the specimens' compressive strength. The exception to this saturation procedure were the specimens of natural soil (S) because of the loss of structural integrity when submerged.

Microstructure analysis

The scanning electron microscopy (SEM) and energy dispersive X-ray spectroscopy (EDS) analyses were taken into consideration to analyze the effect of the binder on the original soil. Once the specimens were submitted to the respective UCS tests, the crushed treated soil specimens were mounted on Al-stubs with double-sided carbon tapes and coated with a thin layer of platinum in a sputter coater. In this study, the SEM analysis provides the identification of

pozzolanic reactivity, namely CSH and CAH. Whereas, EDS provides elemental analysis for selected areas of the SEM specimens to examine the occurrence of CSH and CAH gels.

RESULTS AND DISCUSSION

Effect on the compactability

Figure 3 shows the compaction characteristics of soil-fly ash mixture. As depicted by this figure, the addition of 40, 50, 60 and 70% fly ash-soil mixtures exhibited a decrease in both the optimum moisture content (OMC) and maximum dry density (MDD). One probable reason for the reduction in optimum moisture content of the soil is because the addition of fly ash reduced the affinity of the soil for water [15]. Principally, the increase in maximum dry density is an indicator of improvement. Unfortunately, in this study, the addition of fly ash was revealed to reduce the maximum dry density. This unusual occurrence can be explained by the specific gravity and particles size of the soil and stabilizer. The specific gravity of fly ash is lower than that of residual soil. When more amounts of fly ash added to residual soil, the resulting mix will have a lower specific gravity leading to reduce the maximum dry density values. Indeed, the decreasing pattern exhibited by the maximum dry density revealed that a low compactive energy (CE) is required to attain its maximum dry density, thus incurring a lower cost for compaction [16].

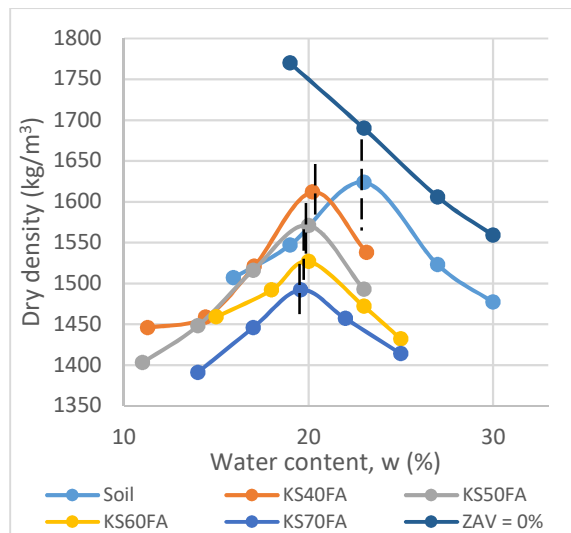


Fig. 3 Compaction curves for Soil-fly ash mixture.

Effect on the unconfined compression strength (UCS)

On top of that, Fig. 4 illustrates the plot between stress-strain behavior of soil and alkaline-activated

soil with different percentages of fly ash (40%, 50%, 60% and 70%) after curing times of 7 and 28 days. Based on the illustration, it can be agreed that the alkaline activation stabilization which utilized potassium hydroxide as the base element of the activator was very effective in enhancing the strength of tested soils.

Initially, the strength of alkaline-activated soil increased until the 60% of fly ash content (KS60FA) but started reducing when fly ash was further added. In particular, this reduction in strength was mainly contributed by the additional quantity of fly ash that became unbound silt particles which have neither an appreciable friction nor cohesion [17].

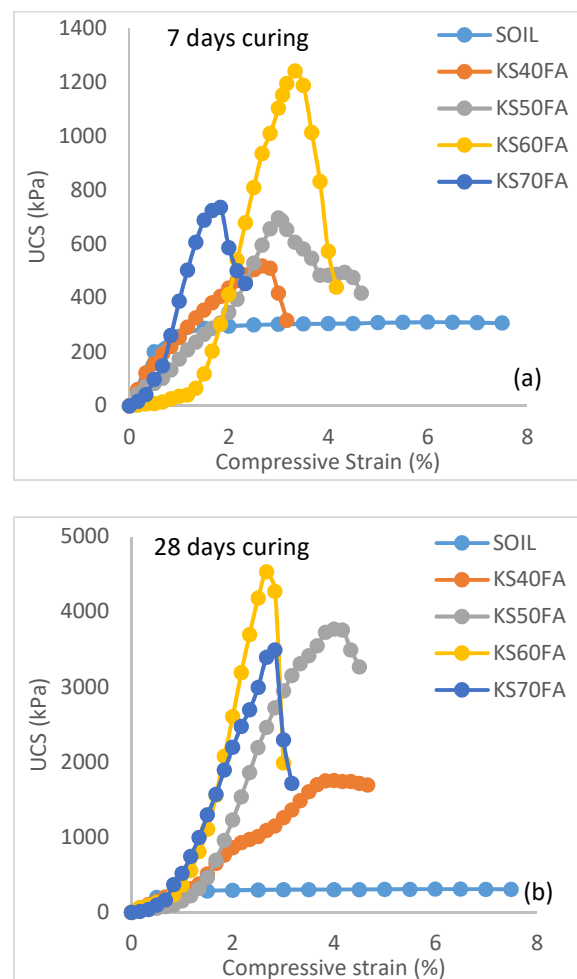


Fig. 4 Stress-strain behavior of treated soil samples after (a) 7 days; (b) 28 days.

Based on Fig. 5, it can be observed that the strength improvement of the treated soil was influenced by the addition of fly ash and the curing time. In this respect, KS60FA achieved the highest strength among all alkali-treated soil samples with readings of 1240 and 4760 kPa at 7 and 28 days, respectively. Undoubtedly, there is a significant

improvement of strength after 28 days. Clearly, this outcome suggests that pozzolanic reactions are time-dependent. With respect to this finding, the bonding of particles with the fly ash progresses with time. Also, since fly ash contains high content of silica, the reaction time will be delayed due to the low reactivity of silica and aluminum. Thus, it can be agreed that a short curing time results in low to moderate strength in the treated specimens.

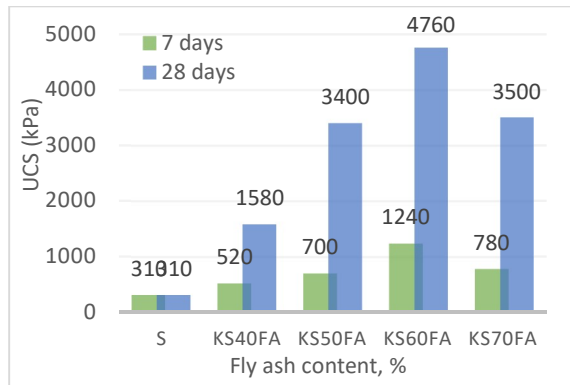


Fig. 5 UCS values of test sample (S, KS40FA, KS50FA, KS60FA and KS70FA) after 7 and 28 days curing.

Effect on microstructures

For a better understanding of the stabilization mechanisms, Fig. 6(a-c) shows the scanning electron microscopy (SEM) of natural residual soil, fly ash and treated soil after curing for 28 days. As a matter of fact, the treated sample (soil specimens treated with fly ash [60% of dry soil]) was subjected to SEM as shown in Fig. 6(c). Clearly, Fig. 6(a) shows the more open texture of the unstabilized soil while Fig. 6(b) shows the heterogeneous and non-uniform particle distribution of the raw fly ash. Based on the observation, the size of particles varied from small to large with smooth spherical shapes and rounded in nature. On the other hand, Fig. 6(c) shows the discrete soil particles appear more closely-bound in the stabilized material with the void seemingly filled.

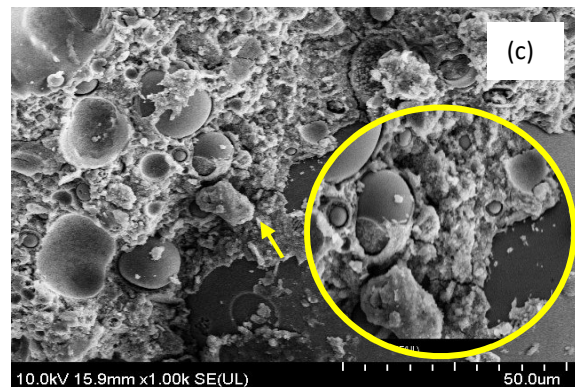
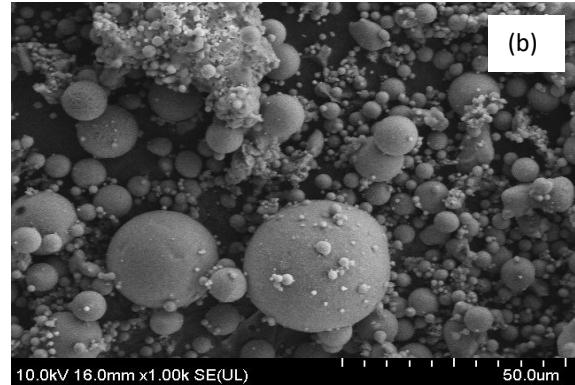
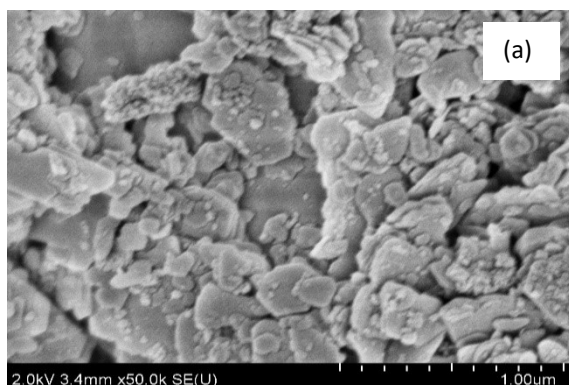


Fig. 6 SEM micrographs of (a) Natural soil; (b) Fly ash; (c) KS60FA.

Concisely, the SEM micrograph of Fig. 6(c) reveals the formation of CSH and ASH gels caused by the hydration and pozzolanic reactions in the pore space, thus reducing the pore space.

Components (%)	K	Al	Si	Ca
Point 1	6.72	11.92	22.00	1.46
Point 2	26.68	7.47	35.03	3.72
Point 3	10.57	6.55	20.76	1.63

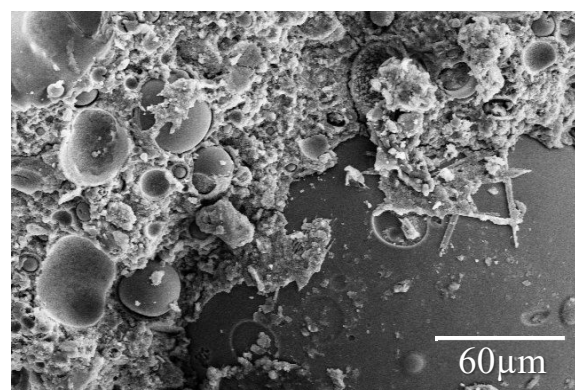


Fig. 7 Micrograph and EDS data of stabilized soil mixture after the curing of 28 days.

CONCLUSIONS

In this study, the use of alkali-activated binders for soil stabilization enabled the researchers to utilize locally available by-products in an efficient way, thus significantly reducing energy consumption while protecting the environment. Primarily, this study investigated the effectiveness of alkaline activation reaction on residual soil with different percentages of fly ash with concentration of 10 molar of potassium hydroxide. Interestingly, it can be deduced from the results that an appropriate quantity of source binder (fly ash) will contribute to higher strength developments. Consequently, the curing time was also affected the strength development of the treated soil. The curing time was depending on the source binders and activator used.

Based on the microstructural analysis, it can be concluded that the simultaneous formation of ASH gel and CSH gel increased the interaction between soil and alkali-activated binders.

ACKNOWLEDGEMENTS

First and foremost, the authors would like to express their gratefulness for the financial assistance provided by the Research Management Center (RMC) of University Putra Malaysia under FRGS. Also, the authors would like to extend their gratitude to Monash University Malaysia for their support during the FE-SEM and EDX analyses.

REFERENCES

- [1] E.A. Basha, R. Hashim, H. B. Mahmud, and A. S. Muntohar, "Stabilization of residual soil with rice husk ash and cement," *Construction and Building Materials*, 19(6), 448-453, 2005.
- [2] J. Prusinski, and S. Bhattacharja, "Effectiveness of Portland cement and lime in stabilizing clay soils," *Transportation Research Record: Journal of the Transportation Research Board*, (1652), 215-227, 1999.
- [3] J. Davidovits, "Geopolymer chemistry and properties." Proc., 1st European Conf. on Soft Mineralurgy (Geopolymere '88), J. Davidovits and E. J. Orlinsl, eds., The Geopolymer Institute, Compiegne, France, 25-48, 1988.
- [4] L. Weng, and K. Sagoe-Crentsil, "Dissolution processes, hydrolysis and condensation reactions during geopolymer synthesis: Part I—Low Si/Al ratio systems." *J. Mater. Sci.*, 42(9), 2997-3006, 2007.
- [5] Z. Yunsheng, S. Wei, L. Zongjin, A. Xiangming, and C. Chungkong, "Impact properties of geopolymer based extrudates incorporated with fly ash and PVA short fiber." *Constr. Build. Mater.*, 22(3), 370-383, 2008.
- [6] S. Pourakbar, B.B.K. Huat, M.H. Fasihnikoutalab, A. Asadi, V, "Impe, Soil stabilisation with alkali-activated agro-wastes," pp. 1-12, 2015.
- [7] N. Cristelo, S. Glendinning, L. Fernandes, A.T. Pinto, "Effect of calcium content on soil stabilisation with alkaline activation," *Constr. Build. Mater*, 29, 167-174, 2012.
- [8] X.Y. Zhuang, L. Chen, S. Komarneni, C.H. Zhou, D. Shen, T. Hui, M. Yang, W.H. Yu, H. Wang, Z. Xy, C.L. Komarneni, Z. Ch, T. Ds, Y. Hm, Y. Wh, H. Wang, "Fly ash based geopolymer: clean production, properties and applications," *J. Clean. Prod.* 125, 253-267, 2016.
- [9] J.S.J. Van Deventer, R.S. Nicolas, I. Ismail, S.A. Bernal, D.G. Brice, J.L. Provis, J.S.J. Van Deventer, R.S. Nicolas, I. Ismail, S.A. Bernal, "Microstructure and durability of alkali-activated materials as key parameters for standardization," vol. 0373, no. November, 2016.
- [10] P. Sargent, P.N. Hughes, M. Rouainia, M.L. White, "The use of alkali activated waste binders in enhancing the mechanical properties and durability of soft alluvial soils," *Eng. Geol.* 152 (1), 96-108, 2013.
- [11] M.C.R. Davies, Editorial, *Proc. ICE – Gr. Improv.* 164 (1) (2011). 1-1.
- [12] G. Cavalieri, "British Standard is licensed to", 2001.
- [13] British Standard Institution, *Methods of test for soils for civil engineering purposes*, BS 1377-1990: Part 2 and 4; 1990
- [14] British Standard Institution, *Methods of test for soils for civil engineering purposes*, BS 1377-1990: Part 7; 1990
- [15] S. Pourakbar, A. Asadi, B. B. Huat, & M.H. Fasihnikoutalab, "Stabilization of clayey soil using ultrafine palm oil fuel ash (POFA) and cement," *Transportation Geotechnics*, 3, 24-35, 2015.
- [16] A. S. Muntohar, G. Hantoro, "Influence of the rice husk ash and lime on engineering properties of clayey subgrade," *Electron J Geotech Eng*, vol. 5 Paper#019, USA: Oklahoma State University; 2000.
- [17] Z. Fusheng, L. Songyu, D. Yanjun, C. Kerui, "Behavior of Expansive Soil Stabilized with FA," *Natural Hazards*, vol 47(3), pp.509-523, 2008.

EVALUATION OF FILLER MATERIAL BEHAVIOR IN PRE-BORED PILE FOUNDATION SYSTEM DUE TO SLOW CYCLIC LATERAL LOADING IN SANDY SOIL

Adhitya Yoga Purnama¹, Noriyuki Yasufuku² and Ahmad Rifa'i³

^{1,2}Faculty of Engineering, Kyushu University, Japan; ³Faculty of Engineering, Universitas Gadjah Mada, Indonesia

ABSTRACT

Pre-bored pile foundation system is typical foundation for integral bridge abutment to supports lateral displacement due to thermal expansion of the girder bridge. Pre-bored pile foundation system can be used to increase the pile flexibility using a pre-bored hole that filled with elastic materials such as bentonite slurry, loose sand or gravel. Some of integral abutment bridges foundation design has proposed, but all have their own limitations and the standard design also different for each country. However, the previous studies only focus on the structural system, the soil characteristic behavior and soil response due to this system are still rarely explained. Therefore, it is necessary to examine the effects of cyclic loads on the filler material inside the pre-bored ring. The soil behavior for ground soil and filler material due to cyclic lateral loading were performed using a macro-scale testing. In this paper, series of two-way lateral cyclic loading tests were performed using different loading frequency to evaluate the effect of slow cyclic lateral loading on the filler material behavior of the pre-bored pile foundation system. The experimental setup was explained in details and the results were presented in the form of normalized bending moment and maximum lateral capacity charts against the number of cycles. Moreover, the densification effect of the filler material inside the pre-bored system due to the cyclic loading were evaluated.

Keywords: Pre-bored pile foundation, Filler material, Cyclic lateral loading, Load frequency

INTRODUCTION

Maintenance of a building in Indonesia is still a main issue. There are so many infrastructures built, but long-term consideration about the maintenance of a building is still neglected. Bridge structure is a building that need to be maintained, especially for the elastomeric bearing. Elastomeric bearing of bridge was made from rubber that combined with steel plate. To maintain this elastomeric bearing, the girder of the bridge needs to be lift upward using heavy equipment that needs a big cost. Integral abutment bridges are becoming popular around the world, but the standard design is different for each country. This causes the different technical approach design to solve the same problem in each country. Conventional bridges are designed with elastomeric bearing and other structural releases that allows the girder to expand or shrink freely due to environmental thermal force.

The integral-abutment bridge is less costly because elastomeric bearings are eliminated in the bridge deck which reduces the initial construction and maintenance costs [1]. However, when the elastomeric bearing and other structural releases are eliminated, thermal forces are followed into the bridge and it needs to be considered in the design approach. More than half of the state highway

agencies have accepted the design of integral abutment bridges, but all have their own limitations on a safe length for such bridges [2]. The American Association of State Highway Officials [3] did not mentioned the integral abutment bridge, but it mentioned that all bridge design should be considered for the thermal movements of the girder. Foundation system of the integral bridge need to be cope with the girder displacement due to thermal expansion that allowed in this system. Pile foundation needs to be more flexible because there is no elastomeric bearing which like provided in a conventional bridge. There is no general standard design to analyze the foundation system of the integral bridge and it is still developed by researchers.

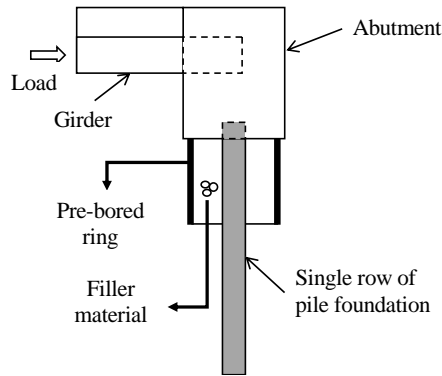


Fig. 1 Typical design of integral abutment bridge with pre-bored hole system.

The integral abutment bridge causes the heads of piles to be fixed. However, it will cause relatively high pile stresses and bending moment due to lateral displacement of the bridge. To reduce the stresses, the connection between abutment and girder can be design as a pinned-head or create a hinge connection. The other method is attaching the piles in pre-bored holes (also called predrilled or pre-excavated) as shown in Fig. 1. Based on [4], it shows that the Iowa Department of Transportation in 2006 proposed the pre-bored hole diameter is as twice the diameter of the pile with 3.05 m of depth. The depth of the holes can be changed for the special condition. The pile is installed on the pre-drilled hole followed by inserted ring in the hole. The area between pile and ring was filled with elastic filler material to maintain the displacement of the pile due to lateral loads. A steel or concrete ring should be placed in the hole to separate the filler material and ground soil. This ring is expected to maintain the filler material properties inside the hole in long term conditions due to cyclic loading.

The thermal loading, equivalent to a change in temperature up to 42 °C, is corresponded to a change in displacement up to 0.023 m (about 6-7% of pile dimension) with pile dimension design of 0.376 m x 0.356 m as shown in [5]. They suggested that a galvanized steel sleeve of 0.6 m in diameter filled with sand is sufficient for accommodating the lateral pressure from the girder bridge due to thermal loading. The holes in empty condition may cause long-term maintenance problems, so the holes should be filled with an elastic material, such as bentonite, loose sand, or pea gravel. The previous researchers only focus on the structural system but the behavior of soil and soil response due to the flexible piling design is still rarely. The characteristic of filler material and standard design of this foundation system is still in development.

In this study, the effectiveness of filler material properties such as soil grain size and density are evaluated to reduce the pile bending moment. The effective dimension of the pre-bored hole also conducted to determine the effective depth of the

system that can reduce the bending moment along the pile. The appropriate filler properties and dimension of this system are expected to reduce the bending moment along the pile due to lateral displacement loading which can solve the problem on the integral abutment bridge foundation. The effective system will be evaluated by considering the soil behavior due to cyclic lateral loading on the pile foundation.

METHODOLOGY

Macro-scale testing of single pile model was performed to determine soil behavior due to cyclic lateral loading and to evaluate the effectiveness of this system.

Properties of Soil and Pile Model

The pile and ring models are manufactured from a closed-end aluminum alloy pipe. The outer diameter (D) of pile model is 15 mm with wall thickness of 1.2 mm and 450 mm of pile length. Three different ring diameters (d) of 45 mm ($3D$), 60 mm ($4D$), and 75 mm ($5D$) with wall thickness of 2 mm and 150 mm of ring length are used in this experiment. The Young's Modulus of the used aluminum alloy pile model is 7×10^{10} kN/m². Equivalence law is used for designing the model pile material, dimensions, and the applied speed and displacement. The scaling formula as shown in Eq. (1), proposed by [6] is used in this research.

$$\frac{E_m I_m}{E_p I_p} = \frac{1}{n^5} \quad (1)$$

Where: E_m is modulus of elasticity of pile model, E_p is modulus of elasticity of prototype pile, I_m is moment of inertia of model pile, I_p is moment of inertia of prototype pile; and n is scale factor for length.

The soil, used in this experimental study, is Toyoura sand, Kumamoto sand of K7 (fine sand) and Mixed soil as a filler material which has uniformity coefficient range from 1.24 to 4.67. The index properties of each soil are given in Table 1. Figure 2 shows the grain size distribution of soil sample used in this study.

Table 1 This is the example for table formatting

Soil properties	Toyourea	K-7	Mix soil
D_{50} (mm)	0.18	0.17	0.29
U_c	1.4	2.96	4.67
Max. dry density	1.6	1.51	1.63

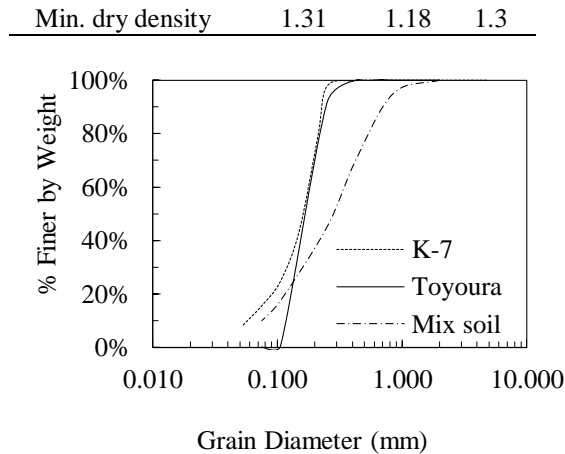


Fig. 2 This is the example for figure formatting.
Experimental Test Setup

Figure 3 shows the laboratory test setup which is used for testing during the experimental course in this study. The testing equipment consists of testing tank that was made from acrylic plate and it is supported by steel frame. The cyclic loading device and measuring device are used to record data and control the number of lateral displacement load applied on the pile head. The laboratory test was performed using a pile model test inserted in sandy soil. On the top area of pile, a ring was placed and filled with filler material that has different soil grain size and uniformity coefficient. Lateral cyclic displacement was applied to the pile head.

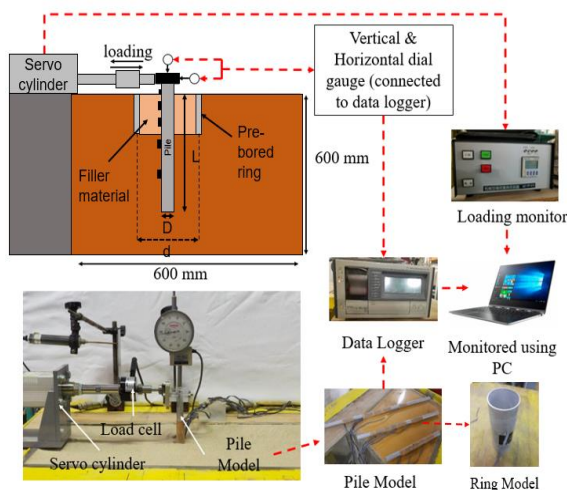


Fig.3 Experimental test setup.

Testing Procedure

Figure 4 illustrates the sinusoidal harmonic lateral displacement applied on the pile head model during experimental testing. Two-way symmetric cyclic lateral loading is horizontally imposed on two opposite sides of a pile head model to provide

horizontal deflection on the pile head. In case of pre-bored pile foundation model test, pile head displacement of 1 mm (about 6% of pile diameter) was applied to evaluate the behavior of soil and pre-bored pile structure impacted by girder displacement due to thermal force. The cyclic lateral load is applied by frequencies in range between 0.0125 Hz to 0.05 Hz. It is applied until 50 times of cycles (N=50) in all experiments, so it can illustrate the impact of the slow cyclic lateral displacement loading of a girder bridge. The bending moment, lateral load capacity, and horizontal displacement were measured and monitored during the test.

Four experimental characteristics were conducted in this experimental study, pre-bored ring filled with different soil density, pre-bored pile filled with different soil type, pre-bored pile with different ring diameter ratio (d/D) and pre-bored pile applied with different loading frequency. All of the cases were tested with two-way symmetric cyclic lateral loading of 1 mm on the pile head until reach 50 times of cyclic loading. The detailed test cases (9 tests) and the associated test conditions are represented in Table 2.

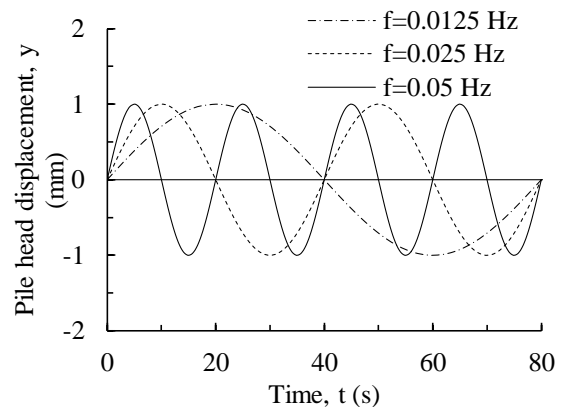


Fig. 4 Typical sinusoidal loading pattern.

Table 2 This is the example for table formatting

Pre-bored system (Ground soil: K7 sand, $D_r=80\%$)				
Test ID	Filler type	D_r (%)	d/D	Load freq. (Hz)
OL01	1-Layered	80	1	0.025
PB01	Toyoura	40	4	0.025
PB02	Toyoura	70	4	0.025
PB03	Toyoura	90	4	0.025
PB04	Toyoura	70	3	0.025
PB05	Toyoura	70	5	0.025
PB06	Toyoura	70	4	0.0125
PB07	Toyoura	70	4	0.05

PB08	K7	70	4	0.025
PB09	Mix soil	70	4	0.025

RESULTS AND DISCUSSIONS

The main focus of this experiment is measurement of the pile bending moment and lateral load capacity which is periodically monitored by using attached strain gauges along the pile. To investigate the effect of filler material to the lateral capacity of pile, the initial modulus of soil subgrade reaction $(K_h)_i$ was generally calculated by using the Eq. (2).

$$(K_h)_i = \frac{\Delta H}{\Delta y \cdot D} \quad (2)$$

Where ΔH is lateral load, Δy is lateral displacement and D is diameter of pile. Initial modulus of soil subgrade reaction $(K_h)_i$ has an essential role in calculating lateral pile capacity [7]. The normalized bending moment, which is the ratio of the measured bending moment to the yielding moment of pile material (M_m/M_y), were estimated. The bending moment is calculated from the bending strain measured at various points along the length of the instrumented model piles using the Eq. (3).

$$M_m = \frac{EI\varepsilon}{r} \quad (3)$$

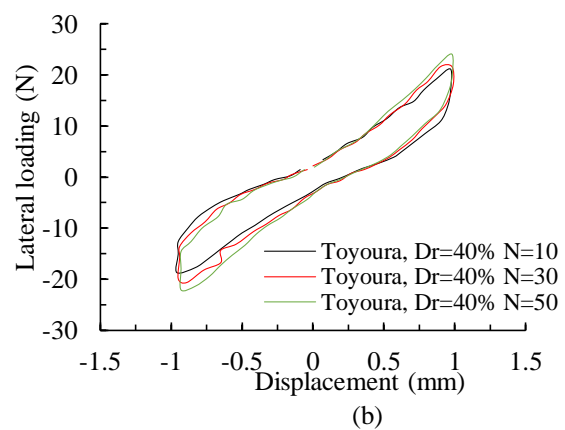
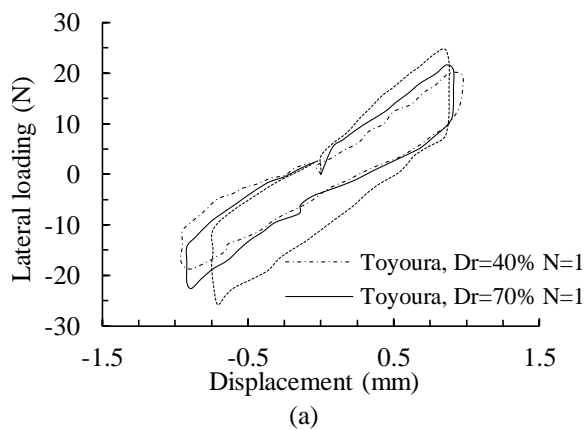
Where, E is Young's modulus of the model pile material, I is moment of inertia of the model pile, ε is measured bending strain and r is horizontal

distance between strain gauge position (outer surface of the pile) and neutral axis. Yielding moment (M_y) of the pile model is calculated by using Eq. (4), with σ_y is yield stress of model pile material.

$$M_y = \frac{\sigma_y I}{r} \quad (4)$$

Lateral Capacity of Pile Due to Cyclic Loading

Results of cyclic lateral load-displacement tests for pre-bored system with different filler material density of 40%, 70% and 90% are shown in Fig. 5. Figure 5 shows the change of maximum lateral pile capacity during the cyclic loading. It was observed that the maximum lateral pile capacity at the first time of cyclic loading reached to 19.68 N, 21.63 N, and 24.79 N for each density of 40%, 70%, and 90%. Based on Fig 5, it can be noticed that the filler material with 40% of density generates a lowest lateral capacity and also lowest value of $(K_h)_i$. However, these values were significantly increase with increasing of loading cycles number (N). For another density the lateral capacity and $(K_h)_i$ were increase, but it is not in a significant different from first cycle until 50 times of cycle. It is indicated that the cyclic loading leads to improve the properties and reduction of void ratio of filler material inside the ring. The soil particle was moving and causing the hardening of soil. Consequently, enhancement of soil properties occurs for loose sand and confining pressure increases during cyclic loading. On the other hand, the 70% and 90% of density provide a stable lateral capacity and $(K_h)_i$ until 50 times of cyclic loading.



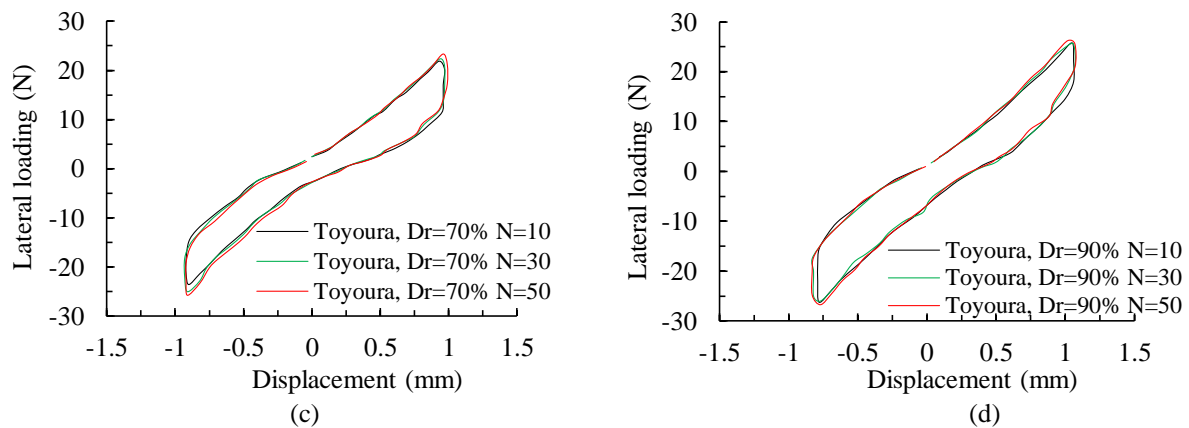


Fig. 5 Hysteretic lateral displacement curves for pre-bored ring system filled with different soil density a) First cyclic for all densities b) $D_r = 40\%$ (PB01) c) $D_r = 70\%$ (PB02) d) $D_r = 90\%$ (PB03).

Figure 6 illustrates the change of maximum measured lateral capacity at different loading frequency. It indicates that the lateral capacity of pile and modulus of soil subgrade reaction (K_h) are increased with increasing of number of cycles (N) and loading time period ($T=1/f$). Based on this condition, the lateral loading frequency applied on the pile head is affected to the soil reaction around the pile.

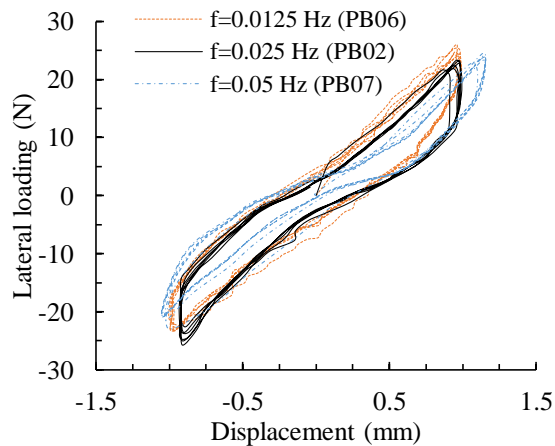


Fig. 6 Hysteretic lateral displacement curves for with different load frequency.

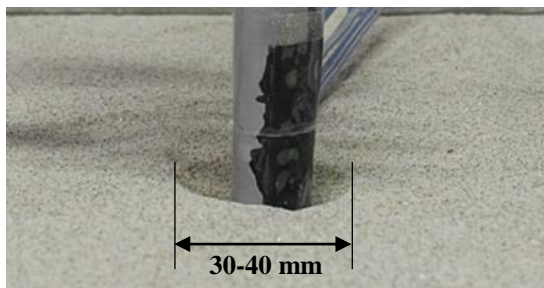


Fig. 7 Conditions after 50 times of loading with pile head displacement of 1 mm.

Effect of Ring Diameter

The plastic deformations of soil which was created on the soil surface due to cyclic lateral loading [8]. It was extended laterally as a shape of ellipse with major and minor axes of $6D$ and $4D$ after applying 50 two-way lateral cyclic loading with 3 mm of pile head displacement. Based on the test results of one-layered test with 1 mm pile head displacement (OL01), the plastic deformation width of soil is about 30-40 mm, or 2 to 3 times of pile diameter as shown in Fig. 7.

Three type of ring diameter were used in this experimental study. The ring diameter ratio, the ratio between ring diameter (d) and pile diameter (D), of $3D$, $4D$, and $5D$ were used to determine the effect of ring diameter on filler material behavior due to cyclic lateral loading. Figure 8 shows the effect of ring diameter on the bending moment of pile during the cyclic loading. Based on Fig. 8, the bigger diameter of ring provides a smaller bending moment of pile during the cyclic loading. The ring diameter ratio lower than 4 provides a similar result of bending moment during the cyclic loading. It indicates that the bending moment of pile can be affected by attachment of pre-bored ring. However, the ring diameter inside the plastic deformation area of soil is not recommended because it can inflict the movement of pre-bored ring.

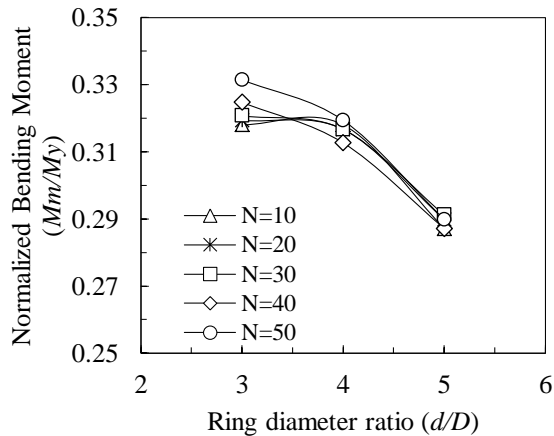


Fig. 8 Effect of ring diameter due to cyclic loading.

Effect of Soil Type as a Filler Material

The effect of soil type also evaluated to determine the effect of filler material properties that can maintain the pile bending moment during the lateral cyclic loading. Three types of soil with uniformity coefficient in range of 1.40 to 4.67 were used as filler material. Toyoura sand with the lowest and Mix soil with the highest uniformity coefficient. The result was shown in Fig. 9. Based on Fig. 9, the K7 soil provides the lowest and Mix soil provide the highest bending moment at the first time of loading (static load).

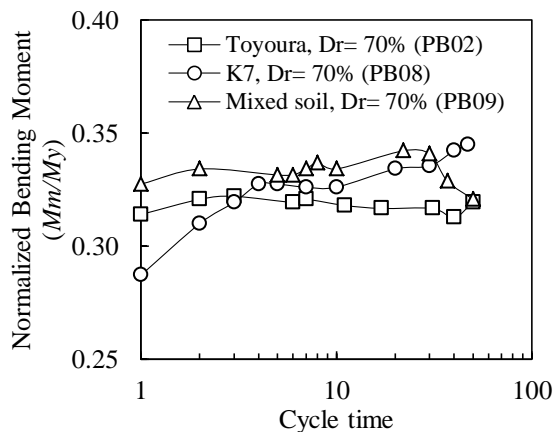


Fig. 9 Effect of soil properties on pre-bored pile system.

However, the value of bending moment on K7 soil is increase significantly during the cyclic loading. This occurred due to the K7 sand consists of some fine particles that is filled the particle void during the cyclic loading and increase the stiffness of soil. The mix soil which has a well graded particle distribution provide the highest bending moment. However, after 20 times of cyclic loading, the values of bending moment are reduced until the end of loading. This happened due to the plastic

deformation occurred on the soil, as shown in Fig. 10, that reduced the soil-pile interaction.

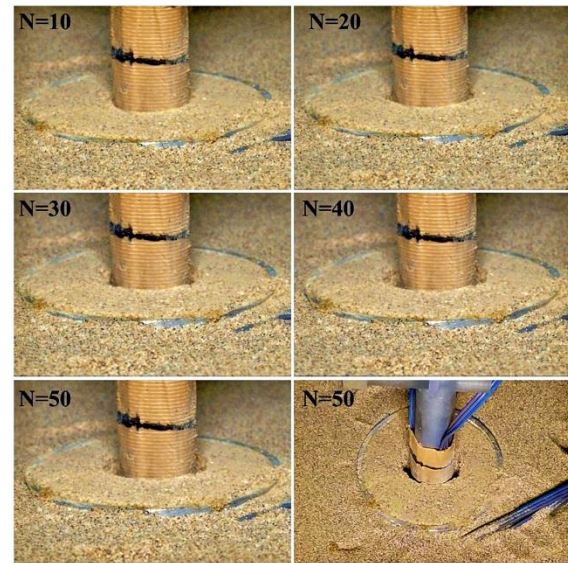


Fig. 10 This is the example for figure formatting.

Based on Fig. 10, it shows that the plastic deformation occurred after cyclic loading number (N) of 20 and it increases until 50 times of cyclic loading. This plastic deformation effect on the soil-pile interaction that reduce the soil resistance on pile during the lateral cyclic loading.

CONCLUSION

Determination of filler material properties inside the ring and dimension of pre-bored ring is important to effectively reduce the pile bending moment with the same displacement load. The filler material with low uniformity (uniform soil) provide a stable bending moment value during the cyclic loading. On the other hand, the utilization of filler material using non-uniform soil cannot maintain the filler properties because the soil hardening was occurred during the cyclic loading. This soil hardening inflicts a plastic deformation on the top area of pile and it effect on the soil-pile interaction that reduce the soil resistance on pile during the lateral cyclic loading. Loose density of filler material provides the lowest values of lateral capacity and modulus subgrade. However, it cannot maintain the properties because the density could be changed during the cyclic loading.

Furthermore, determination of the effective diameter of ring is important to separate the filler material inside the ring and ground soil. The effective diameter of ring is recommended more than the plastic deformation area of the filler material due to cyclic lateral loading. The large diameter will provide a lower pile bending moment, but it need a larger area and larger amount of filler

material.

REFERENCES

- [1] Girton, D. D., Hawkinson, T. R., and Greimann, L. F., Validation of Design Recommendations for Integral-Abutment Piles. *Journal of Structural Engineering*, Vol 117 (7), 1991, pp.2117-2134.
- [2] Greimann, L. F., Abendroth, R. E., Jonshon, D, E., and Ebner, P. B., Pile Design and Tests for Integral Abutment Bridges. Final Rep. Iowa DOT Project HR-273, ERI Project 1780, Iowa State Univ., 1987, pp.3-6.
- [3] The American Association of State Highway Officials, Standard Specifications of Highway and Bridges. The Association of General Offices, Ed. 11, 1973, pp.108.
- [4] Dunker, Kenneth F., and Liu, Dajin., Foundations for Integral Abutments. *Pract. Period. Struct. Des. Constr.*, Vol 12 (1), 2007, pp.22-30.
- [5] Khodair, Yasser A and Hassiotis, Sophia., Analysis of Soil-pile Interaction in Integral Abutment. *Computers and Geotechnics*, Vol 32, 2005, pp.201-209.
- [6] Wood, D., Crewe, A. and Taylor, C., Shaking Table Testing of Geotechnical Models. *International Journal of Phys Model Geotech*, Vol 1, 2002, pp.1-13.
- [7] Awad-Allah, M.F., Yasufuku, N., and Abdel-Rahman, A.H., Factors Controlling the Behavior of Piled Foundations Due to Cyclic Lateral Loading. In *Proc. The 6th Japan-Taiwan Joint Workshop on Geotechnical Hazards from Large Earthquakes and Heavy Rainfalls*, 2014, pp.555-568.
- [8] Awad-Allah, M.F., Yasufuku, N., and Mandandhar, S., Three-dimensional (3D) Failure Pattern of Flexible Pile Due to Lateral Cyclic Loading in Sand. *Lowland Technology International*, Vol 19 (1), 2017, pp.1-12.

DENSITY DISTRIBUTIONS WITHIN CERAMIC MATERIALS SATURATED FOR USE IN SUCTION MEASUREMENT

Katsuyuki KAWAI¹, Shinya KIKUI², Naoki YOSHIKAWA³ and Takayuki FUMOTO¹

¹Dept. of Civil and Environmental Engineering, Kindai University, Japan; ² Osaka Prefectural Government, Japan; ³ Kinki Regional Development Bureau, Ministry of Land, Infrastructure, Transport and Tourism, Japan

ABSTRACT

Unsaturated soil contains air and water within the voids of the skeleton formed by soil particles. To investigate the complicated behavior of these materials through unsaturated soil testing, pore air and water pressure must be measured and controlled independently. For this purpose, a microporous ceramic material is used. The ceramic, which is installed in tensiometers and other experimental apparatus used for testing unsaturated soil, must be saturated using degassed water. The degree of saturation of the ceramic influences the accuracy of measuring and controlling suction. However, microporous ceramic is difficult to saturate. Currently, ceramic material is saturated using empirical methods, the applicability of which have not been confirmed up until now. In this study, the effects of ceramic saturation methods were investigated. Three kinds of saturation methods, the vacuum method, the pressurization method and the Berthelot method, were utilized. In each method, saturation time and the number of saturation cycles was varied. The saturated ceramic was also exposed to air drying to check the saturation effect, and X-ray computed tomography was used to visualize the degree of saturation of the ceramic. These efforts determined that trends in the distribution of saturation within the ceramic are dependent on saturation method.

Keywords: Tensiometer, Ceramic, X-ray computed tomography

INTRODUCTION

Recently, landslide disasters due to rainfall occur frequently. Natural slopes remain stable under unsaturated conditions, while the decrease in suction due to rainfall infiltration leads to a loss of slope stability. Therefore, the suction-dependent behavior of unsaturated soil is investigated through lab-tests and in-situ monitoring. Suction is the pressure difference between pore air and water, as demonstrated by the following equation;

$$s = p_a - p_w \quad (1)$$

Here, s is suction; p_a is pore air pressure; and p_w is pore water pressure. Pore water pressure must be measured or controlled independently of pore air pressure. For this unsaturated soil testing, a microporous ceramic is used to isolate pore water pressure from pore air pressure. Figure 1 shows the principle of pore water pressure measurement using the ceramic material. Pore water pressure within unsaturated soil is smaller than pore air pressure. In most cases, since pore air pressure corresponds to atmospheric pressure, pore water pressure indicates a negative value for gauge pressure. If the pressure measurement is directly applied to unsaturated soil, the measurable pressure is pore air pressure. For this,

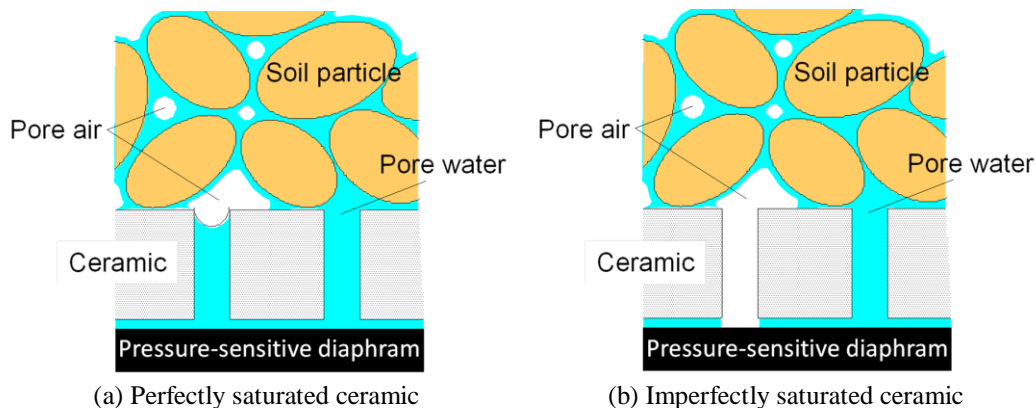


Figure 1 Measuring pore water pressure using ceramic material



(a) Exterior (b) Interior
Figure 2 X-ray CT scanner system

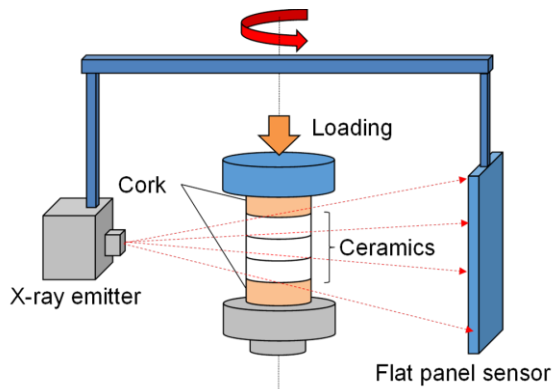
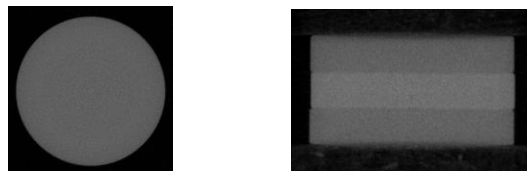


Figure 3 X-ray CT scan



(a) X-Y coordinate (b) X-Z coordinate
Figure 4 Example of a CT image

Table 1 Average density obtained from the supplier's catalog

Ceramic (A.E.V)	Perfectly dried (g/cm^3)	Perfectly saturated (g/cm^3)
1bar	1.92	2.46
3bar	1.74	2.27
5bar	1.73	2.14

saturated ceramic material is used. Ceramic is a microporous material. Once this microporous structure is saturated with water, air cannot pass through due to the resistance induced by water surface tension (as Fig.1 (a)). Under these conditions, continuous water can pass through the ceramic, and a pressure-sensitive diaphragm can measure pore water pressure within the unsaturated soil. However, when the ceramic is imperfectly saturated, as in Fig. 1 (b), the pressure-sensitive diaphragm measures pore air pressure. The degree of saturation of the ceramic strongly influences the accuracy of the

suction measurement. When suction is controlled in lab tests, air pressure is applied to the specimen under drained condition. In this circumstance, water pressure can be regarded as zero, and suction corresponds to applied air pressure, according to equation (1). When applied air pressure exceeds a certain value, or when pore water pressure falls below a certain negative value that corresponds to the surface tension induced by the water within ceramic micropores, then air can pass through ceramic micropores and make the ceramic become unsaturated. This value is called the air entry value (A.E.V), and commercial ceramics each have their own A.E.V. This introduces difficulty into the process measuring and controlling relatively high suctions and long-term testing on unsaturated soil. Though the degree of saturation for a ceramic material is very important, a robust ceramic saturation method has not been established up to this point. In this study, the effects of the ceramic saturation method are investigated.

EXPERIMENTAL PROCEDURE

In this study, three kinds of ceramic plates (41mm diameter and 7mm thickness), having 1, 3 and 5 bar A.E.V., were employed. The average specifications of these commercial ceramic plates were available from the supplier's catalog. Table 1 summarizes each ceramic plate's completely dried and completely saturated density, as calculated from the weight, volume and porosity specifications in the catalog. The ceramic plates were first oven-dried at 110°C for 24 hours and then saturated by either the vacuum method, the pressurization method or the Berthelot method. The saturated ceramic was then air dried. The degree of saturation of the ceramic was estimated using an X-ray computed tomography (CT) scanner. The X-ray CT scan is a non-destructive monitoring instrument used for visualizing inner density distributions. When ceramic micropores are saturated by water, they exhibit a higher density on a CT image. Figure 2 shows the X-ray CT scanner system used for this study. This system was developed by Fumoto [1]. In this system, loading is possible by turning both the X-ray emitter and the flat panel sensor (seen in Figure 3). Figure 4 shows an example of a CT image. A saturated ceramic plate was sandwiched between unsaturated ceramic plates on an X-ray scanner to clarify the outline of the target ceramic (seen in Figure 4 (b)). The sandwiched, saturated ceramic showed a whiter image than the unsaturated outer ceramics. This whiter color indicates a greater density. X-ray CT scans were conducted four times, at 15min, 30min, 1hour and 2 hours after saturation of the air-dried ceramic.

Vacuum method

The vacuum method, standardized by the Japanese Geotechnical Society [2], is generally used for saturating ceramic materials. Figure 5 shows the vacuum method procedure. Two desiccators are utilized, into which dried ceramic material and degassed water are placed, respectively. A vacuum of -98kPa is applied for 24 hours (Figure 5(a)). Next, the water from one desiccator is poured into the desiccator that contains the ceramic material under vacuum and left to soak under vacuum for 24 hours (Figure 5(b)). Figure 6 shows the relationship between the CT number obtained from the X-ray CT scan of the ceramic material dried and saturated by the vacuum method and its density as provided in Table 1. The broken line in the figure represents the following equation.

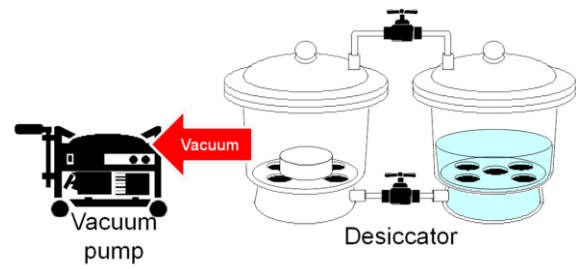
$$\rho = 1.0 + \frac{CT}{1000} \quad (2)$$

Here, ρ is density and CT is the CT number obtained from an X-ray CT scan. CT number is generally considered dependent on density, as well as other factors. However, we assume that the other factors are negligible under the conditions in this study and use equation (2) in the following section. Equation (2) is based on the concept that the CT number is a comparative value between -1000, seen in air density, and 0, seen in water density. All data are plotted on the line expressed by equation (2). This infers that the qualities of the commercial ceramic, such as porosity, density and so on, are consistent to some degree and that we can use equation (2) to estimate density from CT number.

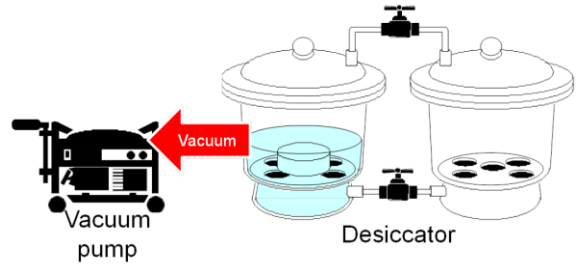
In this study, three different soaking vacuum periods, 3, 12 and 24 hours, were used to investigate the effect of vacuum period on the degree of saturation of the ceramic.

Pressurization method

Ridley and Burland [3] indicated that careful saturation of ceramic by degassed water under vacuum and subsequent pressurization at a pressure higher than A.E.V. could provide a satisfactory suction measurement. In this study, the saturation effect of the pressurization method was investigated. The dried ceramic was set, together with degassed water, in a box made of duralumin, to which 0.8MPa pressure was applied (seen in Figure 7). Three pressurization periods, 3, 12 and 24 hours, were investigated. An X-ray CT scan of the ceramic saturated by this method was conducted after pressurization.



(a) Preliminary vacuum



(b) Soaking vacuum

Figure 5 Vacuum method

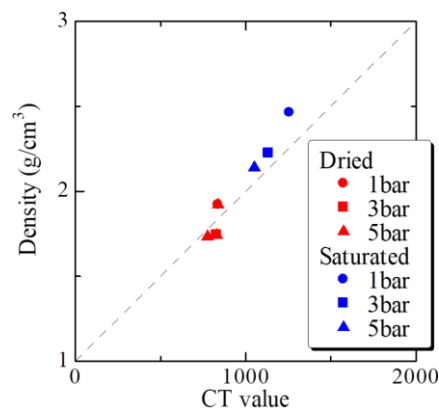


Figure 6 CT value of dried and saturated ceramic material

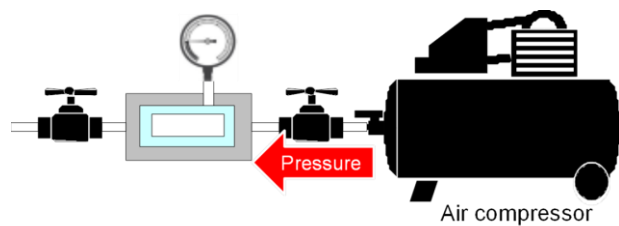


Figure 7 Pressurization method

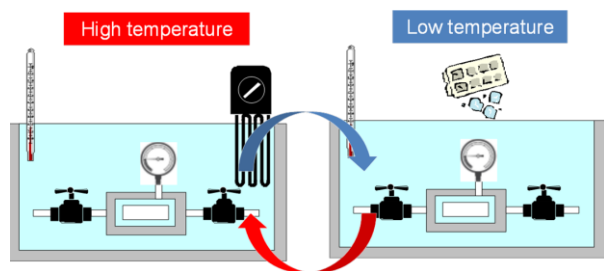


Figure 8 Berthelot method

Berthelot method

The cavitation of water that typically occurs at high negative gauge pressures has been generally explained by the inability of water to sustain tensile stress. Liquids under negative pressures are thermodynamically metastable and easily make the transition to a stable state after cavitation occurs. Berthelot [4] proposed a method to create high negative liquid pressures without cavitation. In this method, application of a high and low temperature cycle to a sealed metal case containing liquid can change liquid pressures at a constant volume due to the difference in thermal expansion rate between the metal and the liquid. Moreover, Hiro et al. [5] determined that the main factor preventing liquid from achieving high negative pressures is the bubbles in micro crevasses on the surface of the solid contact with the liquid. These bubbles do not originate from the liquid. The Berthelot method can decrease these bubbles and diminish the occurrence of cavitation. Tarantino and Mongiovi [6] indicated that the repeated application of pre-pressurization to ceramic is effective in saturating the material. This effect can be considered equivalent to the Berthelot method. In this study, the Berthelot method was used for saturating the ceramic. A duralumin box that contained dried ceramic material and degassed water was soaked in high temperature water of 80°C and low temperature water of 10°C, repeatedly. The number of temperature cycles was set to 20n, 30 and 40.

EXPERIMENTAL RESULTS AND DISCUSSION

To investigate the distribution of density within the ceramic, CT numbers obtained from X-ray CT scans were divided into 6mm layers by thickness. Figure 9 shows an example of a CT number distribution obtained from a scanned image of one layer. Trends in density distribution can be compared by statistical coefficients, such as mode, median, average, and standard deviation, as illustrated in Figure 9.

Figure 10 shows the difference in density distributions among different A.E.V. ceramics saturated by the vacuum method for 12 hours. Densities were obtained by substituting the mode of the CT number distribution in equation (2). A period of 24 hours is generally considered necessary to saturate the ceramic by the vacuum method. Density decreases with elapsed time in all figures. This means that the ceramic kept drying with exposure to air. The drying tendency was more obvious in ceramic with a higher A.E.V.. As ceramic material with a higher A.E.V. has a smaller microporous structure, it can be more difficult to saturate. Because of this, 12 hours was not enough time to

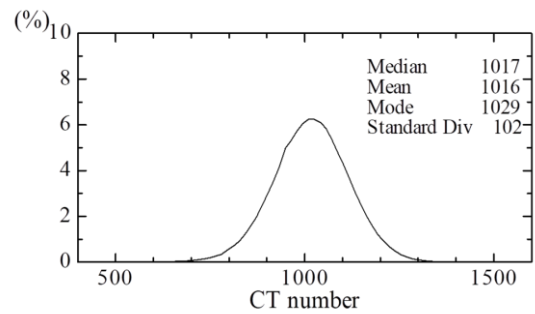
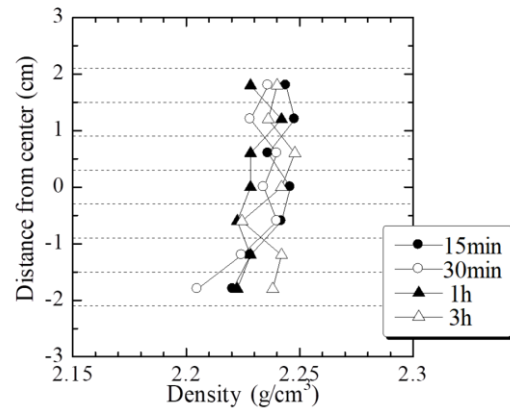
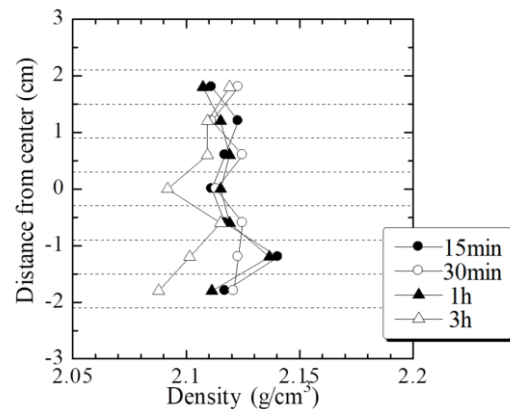


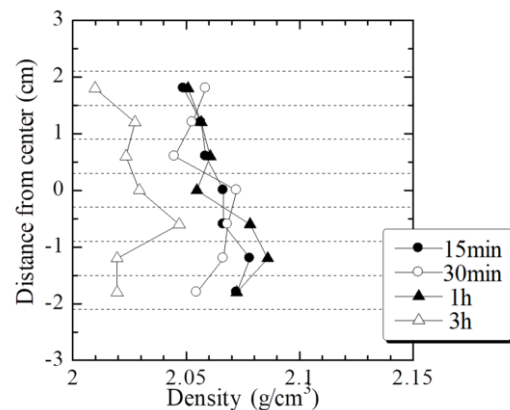
Figure 9 Example of CT number distribution



(a) 1bar ceramic



(b) 3bar ceramic



(c) 5bar ceramic

Figure 10 Density distributions of ceramic saturated by the vacuum method (12hours)

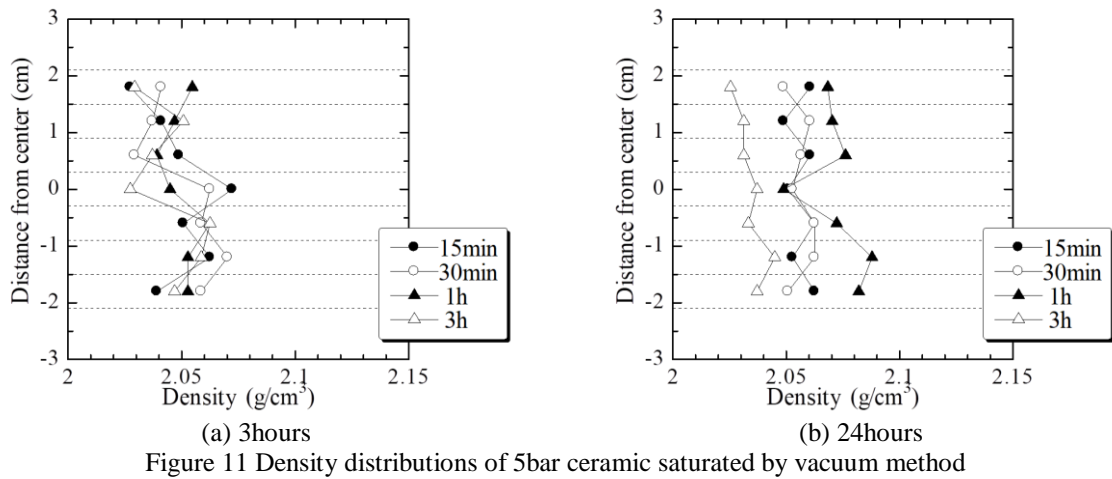


Figure 11 Density distributions of 5bar ceramic saturated by vacuum method

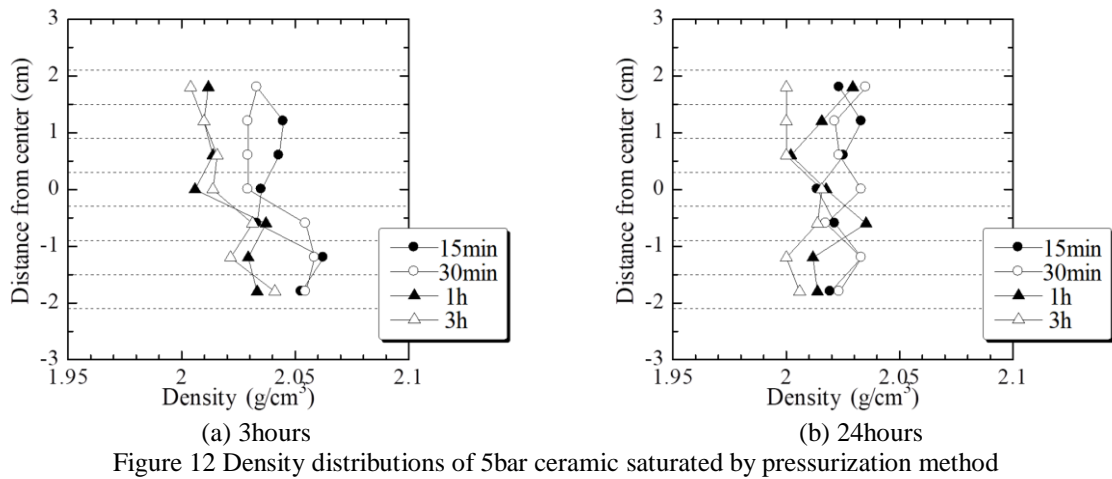


Figure 12 Density distributions of 5bar ceramic saturated by pressurization method

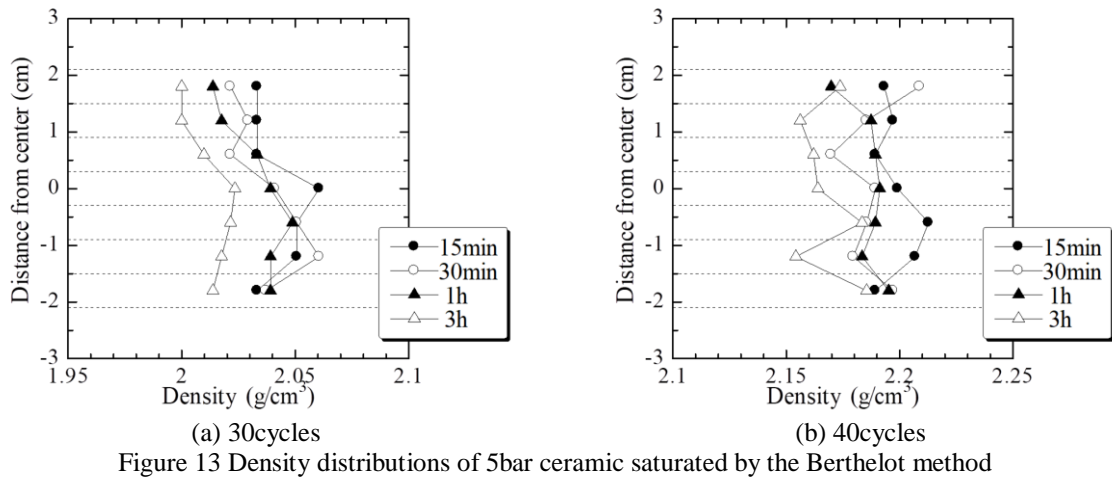


Figure 13 Density distributions of 5bar ceramic saturated by the Berthelot method

saturate the higher A.E.V. ceramic perfectly. The effects of vacuum period were investigated in Figure 11. Here, the density distributions for the 5bar ceramic showed saturation at a different vacuum period length than in Figure 10(c). With a longer vacuum period, the density distribution immediately following saturation (15min) was higher and the drying tendency was smaller.

Figure 12 investigates the effects of pressurization periods, illustrating the density distributions in the 5bar ceramic saturated by the pressurization method. Comparing Figure 12 with Figure 11 indicates that the vacuum method is more effective than the pressurization method. In the pressurization method, the ceramic was oven dried prior to pressurization. In this condition, inner air within the ceramic tended

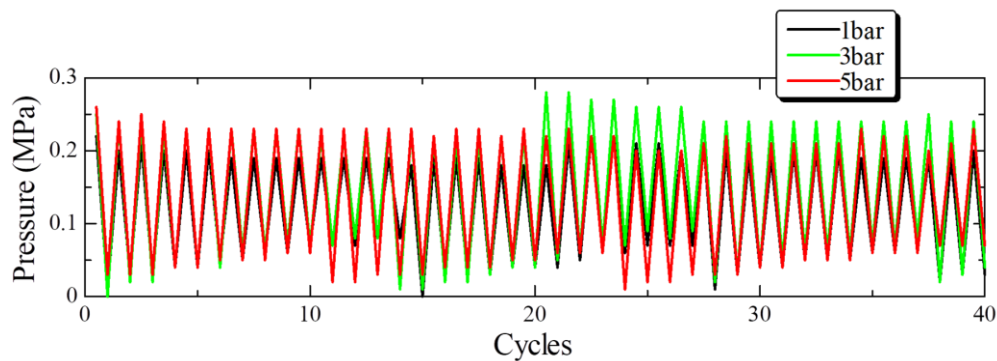


Figure 14 Water pressure fluctuation observed during temperature cycles in the Berthelot method

to become entrapped by infiltrated water due to pressurization. The objective of the pressurization method is to dissolve this entrapped air into high pressure water. From this experiment, the pressurization period does not appear to be sufficient. Likely, pressurization can be effective as a supplement to the vacuum method, as employed by Ridley and Burland (1995).

Figure 13 shows the density distributions of the 5bar ceramic saturated by the Berthelot method. The density distribution is higher with a greater number of temperature cycles. From these data, the Berthelot method appears effective for saturating the ceramic, especially in Figure 12(b). However, the density decrease was not small, considering the initial density. Figure 14 shows fluctuations of water pressure during temperature cycles. The observed pressures were not so high, making it difficult to regard the effects of the Berthelot method as that of cyclic pressurization. Likely, these results derive from, not only saturation, but also other factors. First, water viscosity is also dependent on temperature and it can facilitate water infiltration into ceramic micropores. Second, density distributions in the ceramic also changed due to damage to the ceramic as it was exposed to pressure changes and/or temperature cycles. Further investigation and an accumulation of experimental data is needed to fully assess the effects of the Berthelot method.

CONCLUSIONS

In this study, the method to saturate the ceramic material used for unsaturated soil testing was investigated. The ceramics saturated by each method were scanned by X-ray, and the degree of saturation of the interior structure was determined from the density distributions. From this, the following findings were obtained.

- (1) An X-ray CT scan is applicable for detecting the effects of method on ceramic saturation.

- (2) Saturation method effects are dependent on a ceramic's A.E.V. A longer saturation period is needed with a higher A.E.V. ceramic because of its smaller micropores.
- (3) The pressurization method is not so effective for saturating ceramic material, and it is only applicable as a supplement to the vacuum method.
- (4) The effect of the Berthelot method is not due to cyclic pressurization, and the saturation effect of this method is not confirmed.

REFERENCES

- [1] Fumoto, T., Development of a new industrial X-ray CT system and its application to compression test of polymer concrete, *Journal of JSCE E2*, Vol.69, No.2, 2013, pp.182-191 (in Japanese).
- [2] JGS0527 Method for Triaxial Compression Test on Unsaturated Soils, Japanese Geotechnical Society Standards Laboratory Testing of Geomaterial, Vol.2. 2009.
- [3] Ridley, A. M. and Burland, J. B., Measurement of suction in materials which swell. *Applied Mechanics Reviews*, Vol.48, No.9, 1995, pp.727-732.
- [4] Berthelot, M., Sur quelques phénomènes de dilatation forcée des liquides. *Annales de Chimie et de Physique*, Vol.30, 1860, pp.232-239.
- [5] Hiro, K., Ohde, Y. and Tanzawa, Y., Stagnations of increasing trends in negative pressure with repeated cavitation in water/metal Berthelot tubes as a result of mechanical sealing. *Journal of Physics D: Applied Physics*, Vol.36, No.5, 2003, pp.592-597.
- [6] Tarantino, A. and Mongiovi, L., Experimental procedures and cavitation mechanics in tensiometer measurements. *Geological and Geotechnical Engineering*, Vol.19, No.3, 2001, pp.189-210.

PREDICTION METHOD FOR LONG-TERM SETTLEMENT OF HIGHLY ORGANIC SOIL USING NATURAL STRAIN

Shoji KAMAO

Department of Civil Engineering, Nihon University, Japan

ABSTRACT

One of the prediction method of the long-term settlement of soft clay is to predict it by defining the linear slope of the latter half of the $s \sim \log t$ curve, as the rate of secondary consolidation. This method has some disadvantages, because the slope of the straight line is depending on how to set the origin of elapsed logarithmic time, and how to determine the initial thickness of soil layer, and so on.

The author carried out a series of laboratory experiments using oedometer apparatus against some kinds of highly organic soil and one silty clay sampled in Japan [1],[2],[3]. From the experimental results, the author proposed a prediction method for long-term settlement of highly organic soil based on the isotache theory using natural strain which can be used conveniently by eliminating previous problems.

To confirm the applicability of the proposed prediction method, some field measurement data were used, constructed in Japan. They were good correlations, and the applicability of proposed method was proved in this study.

Keywords: Highly organic soil, long-term settlement, Isotache method, Natural strain

INTRODUCTION

Highly organic soil is known for its high compressibility, high water-contents and low unconfined compression strength. For geotechnical engineers, highly organic soil is treated as a problematic soil for design and construction of buildings. Especially, large settlement occurs not only during construction but also after construction period.

Research was conducted by Ohira [4], Matsuo [5] and Kogure [6] regarding long-term settlement prediction methods, which is the subject of the present paper; the hyperbolic method, \sqrt{t} hyperbolic method, $s\text{-}\log t$ method, etc. have been proposed and are currently used in design practice. In Hokkaido, a long-term settlement prediction method based on the in-situ measurement data of local peaty ground was proposed and is used in practice.

Research on the applicability of the isotache model to highly organic soil has been conducted. The isotache model is a time-dependent compression model in which the time and settlement curves trace the same curve regardless of clay layer thickness and hysteresis of consolidation pressure in the case of soil of the same nature; it has previously been reported on by Imai [7], Matsuo[8] and Den Haan [9].

Imai [7] conducted a step loading test with separate-type-oedometer, experimentally explained the isotache model in clayey soil, and discovered the uniqueness of the relationship between the state index and natural strain rate.

Matsuo [8] conducted laboratory experiments on highly organic soil and explained the isotache model in normally consolidated highly organic soil. It was reported that when focusing on the relationship between the unique void ratio of highly organic soil and consolidation pressure and applying the isotache model to highly organic soil, it is desirable to apply the isotache model by paying attention to the linearity of the relationship between the specific volume and consolidation pressure rather than the relationship between the void ratio and consolidation pressure.

Den Haan [9] proposed an a-b-c model that predicts the long-term settlement of highly organic soil by using natural strain to focus on the state curved surface constructed by natural strain, consolidation pressure, and natural strain rate.

Tanaka [10] investigated the dependency of the isotache model in the peaty ground widely distributed in Hokkaido area using a laboratory test and reported that peat has higher strain rate dependency than clayey soil.

Long-term settlement occurring over a long period in highly organic soil is a major problem, but one of the long-term settlement prediction methods is a method of calculation by utilizing the rate of secondary consolidation defined by the gradient of the latter half of the linear part of the $s\text{-}\log t$ curve, on which the consolidation time is displayed on the logarithmic scale, and this method is widely used in practice.

However, the conventional method has a disadvantage regarding the fact that depending on where the consolidation time reference point (origin

of time) is selected when plotting the settlement amount on a semi-logarithmic scale, the gradient of the latter half of the linear part of the s-log t curve differs. When calculating the settlement amount by defining the gradient of the latter half of the linear part of the s-log t curve with rate of secondary consolidation, it is necessary to always clarify where the reference point of time was selected. It is indicated by Imai [7] that attention should be paid to the method of selection of the reference point of consolidation time.

The author has conducted experimental research based on the isotache concept regarding the fact that the relationship between consolidation pressure and strain is uniquely determined by the value of strain rate as a method of establishing the settlement prediction method, which can eliminate this problem and uniformly express settlement behaviors. The author proposed a long settlement prediction method using natural strain and natural strain rate, verified it using in situ measurement data, and demonstrated the utility of the proposed prediction method.

The present paper is a summary of these research results.

In this study, natural strain (ϵ^H) is adopted as a representation method of strain occurring under a consolidation pressure. The strain rate is also expressed by the natural strain rate (ϵ^H).

THE PREDICTION METHOD OF LONG-TERM SETTLEMENT USING NATURAL STRAIN

The strains dealt with in this paper are linear strain (ϵ^C) and natural strain (ϵ^H), which are defined as Eq. (1) and Eq. (2), respectively. Fig. 1 shows a symbolic description of linear strain (ϵ^C) and natural strain (ϵ^H). From this figure, the linear strain ϵ^C is obtained by dividing the strain amount Δl by the initial sample height l_0 (soil layer thickness), and is defined by the Eq. (1).

$$\epsilon^C = \frac{l_0 - l}{l_0} = \frac{\Delta l}{l_0} \quad (1)$$

$$\epsilon^H = -\int_{l_0}^l \frac{dl}{l} = -\ln \frac{l}{l_0} = -\ln(1 - \epsilon^C) \quad (2)$$

Fig. 2 (a) and (b) shows the ϵ^C and the ϵ^H values with respect to the settlement of the simulated specimen.

Fig.3(a) shows settlement of a specimen in a simulated manner assuming initial specimen height (L) is 100 mm. Fig.3(b) shows a value of linear strain and natural strain at this time, respectively.

From these figures, the maximum ϵ^C was calculated less than 1.0, but calculated ϵ^H exceed 1.0, and reach

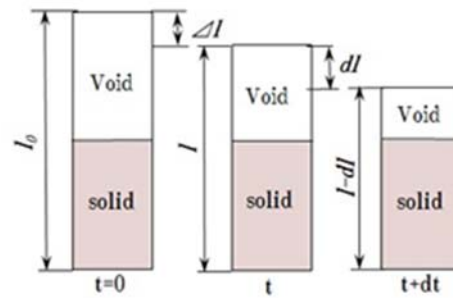


Fig. 1 A symbolic description of linear strain (ϵ^C) and natural strain (ϵ^H)

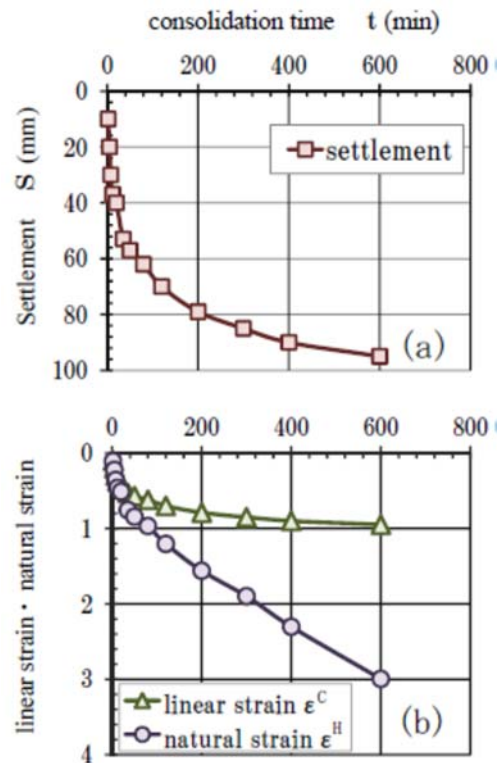


Fig. 2 Relationship between settlement, linear strain and natural strain

2 or even 3, because it is calculated by using the specimen height as a reference which may change from moment to moment.

For highly organic soil, it is more advantageous to use natural strain, which the values of natural strain become larger than the linear strain closing to 1 as the settlement increases. This paper summarizes the prediction method of highly organic soil using natural strain and natural strain rate.

There are few studies about the prediction method of long-term settlement of highly organic soil using natural strain and its rate. Therefore, the author would like to propose a new long-term settlement prediction approach by conducting the conventional oedometer

test apparatus with constant incremental loading tests standardized by JIS A 1217 and a long-term consolidation test as well as interpreting test results.

USED SOILS AND TEST PROGRAMS

Table 1 shows the typical properties of used five soils. The soil A, B, C and D are highly organic soil sampled in Hokkaido, Japan. The soil E is silty clay sampled in Tokyo.

All specimens are used as remolded conditions under re-consolidation pressure of 20 kPa. They are prepared as follows; the water content of the disturbed sample is first adjusted to be twice as liquid limit (L.L.) and then consolidated under the re-consolidation pressure of 20kPa for about two weeks. Re-consolidation apparatus is shown in Fig. 3.

A series of laboratory test using conventional standard oedometer test apparatus standardized by JIS A 1214 were done against four Japanese highly organic soils and one Japanese marine silty clay.

EXPERIMENTAL RESULTS

Oedometer tests were done against 5 soil (4 highly organic soil and 1 silty clay). While the linear gradient of the curve's latter part is what is conventionally called as the rate of secondary consolidation, we call it as the rate of long-term settlement for distinguishing from those and obtained each value by defining formulas (3) to (6) since results are interpreted here by using natural strain.

The rate of long-term settlement (C^{Ht}) in formula (3) is expressed by displaying $\log t$ on the horizontal axis and natural strain on the vertical axis, depicting natural strain - $\log t$ curve, and showing linear gradient of the curve's latter part. The rate of long-term settlement ($C^{HH'}$) in formula (4) is expressed by displaying natural strain on the horizontal axis and natural strain rate ($\dot{\epsilon}^H$) on the vertical axis, depicting natural strain - natural strain rate curve, and showing a gradient of the curve's latter linear part.

$$C^{Ht} = \Delta \epsilon^H / \Delta \log t \quad (3)$$

$$C^{HH'} = \Delta \epsilon^H / \Delta \log \dot{\epsilon}^H \quad (4)$$

$$C^{Ct} = \Delta \epsilon^C / \Delta \log t \quad (5)$$

$$C^{CC'} = \Delta \epsilon^C / \Delta \log \dot{\epsilon}^C \quad (6)$$

The rate of long-term settlement (C^{Ct}) in Eq. (5) is expressed by conventional linear strain, depicting linear strain - $\log t$ curve, and showing a linear gradient of the curve's latter part in order to compare with those in Eqs. (4) and (5) based on natural strain. Similar to Eq. (6), the rate of long-term settlement ($C^{CC'}$) is also expressed by depicting linear strain - linear strain rate curve and showing a linear gradient of the curve's latter part.

Fig. 4 shows the relationship between natural strain and consolidation time of soil A and B, respectively. Natural strain was chosen, instead of linear strain. Fig. 5 shows relationship between natural strain and natural strain rate ($C^{HH'}$).

From Fig. 4, it can be seen that an inverted S-shaped curves are drawn for A soil, and the curve in the latter half linearly advances with respect to elapsed consolidation time. It can be seen that the linear gradient of this part has almost the same slope during the normally consolidated region.

Fig. 5 shows the natural strain rate ($\dot{\epsilon}^H$) on the horizontal axis instead of consolidation time in Fig. 4. The similar trend can be seen from Fig. 5. (inverted S-shaped curves and same gradient during normally consolidated region) The values of the rate of secondary consolidation and the rate of long-term settlement for other soils, are almost same tendency as soil A, even silty clay also. The linear gradients in the latter half of Figs. 4 to 7 were calculated for each loading step and are summarized in Table 2.

Table 1 Typical soil properties

parameter	symbol	unit	A	B	C	D	E
Soil particle density	ρ_s	g/cm ³	1.77	1.82	1.56	2.28	2.71
Initial water content [※]	w_0	%	621	471	522	237	71
Liquid limit	w_L	%	551	435	367	186	71
Plastic limit	I_p	—	208	189	221	85	33
Ignition loss	L_{ig}	%	82	73	50	30	7
Void ratio [※]	e_0	—	8.22	8.37	8.01	5.40	1.88

※after re-consolidation pressure of 20 kPa

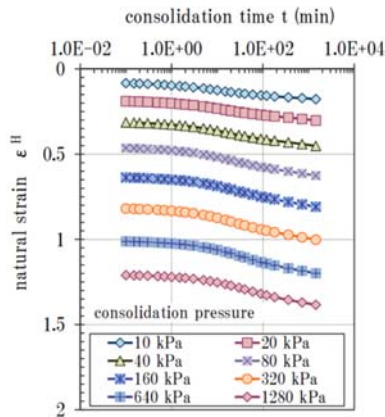


Fig. 3 Relationship between natural strain and consolidation time. (Soil A)

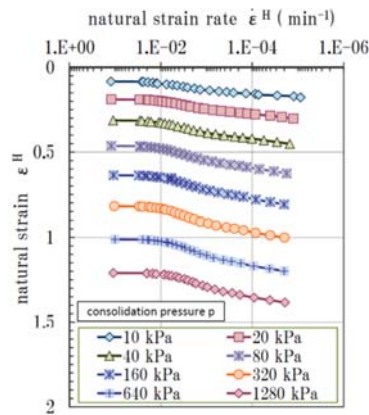


Fig. 4 Relationship between natural strain and its rate. (Soil A)

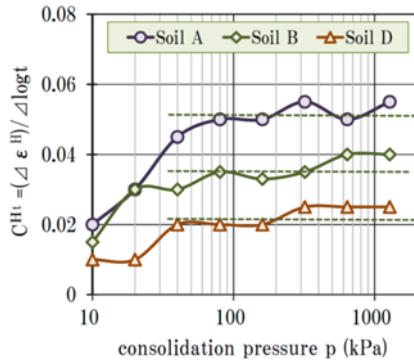


Fig. 5 Relationship between C^{Ht} and p

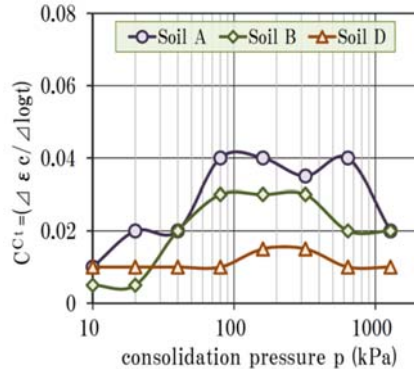


Fig. 6 Relationship between C^{Ct} and p

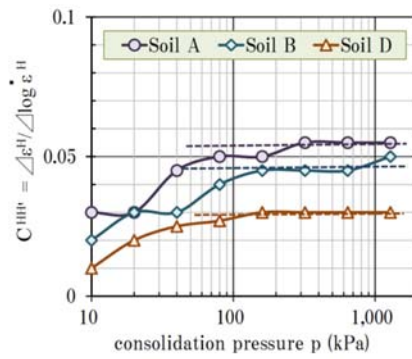


Fig. 7 Relationship between $C^{HH'}$ and p

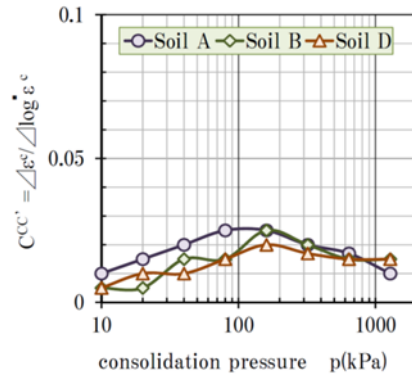


Fig. 8 Relationship between $C^{CC'}$ and p

Fig. 5 shows the relationship between C^{Ht} and p for soils A, B, and D. The value of C^{Ht} is given as a substantially constant value during normally consolidated region ($p > 40$ kPa). On the other hand, the value of C^{Ct} has peak values around 3 to 6 times the pre-consolidation pressure. This is the same trend as Yasukawa's report [12].

Fig. 7 shows the tendency for the value of $C^{HH'}$ to be constant with normally consolidated region when using the natural strain rate. It was found that the values of C^{Ct} for each loading step in Fig. 8, are curved shape that is convex upward.

Fig. 9 shows the relationship between $C^{HH'}$ and C^{Ht} . Both parameters tend to be almost the same values from this figure.

When the elapsed time is displayed using a logarithmic scale, the gradient of the straight line changes depending on the method of setting the origin of the time. Therefore, in the present paper, the author proposes to use natural strain rate rather than logarithmic time.

In the laboratory experiment, it was found that the rate of long-term settlement (linear gradient) obtained from logarithmic time and the linear gradient obtained from the natural strain rate showed approximately the same values.

That is, it is the authors' opinion that when predicting field measurement data from a laboratory

Table 2 The numbers of calculated C^{Ht} , $C^{HH'}$, C^{Ct} and $C^{CC'}$.

Soil parameter p (kPa)	Soil A ($w_0=621\%$)				Soil B ($w_0=471\%$)				Soil D ($w_0=237\%$)			
	C^{Ht}	$C^{HH'}$	C^{Ct}	$C^{CC'}$	C^{Ht}	$C^{HH'}$	C^{Ct}	$C^{CC'}$	C^{Ht}	$C^{HH'}$	C^{Ct}	$C^{CC'}$
	$\frac{\Delta \varepsilon^H}{\Delta \log t}$	$\frac{\Delta \varepsilon^H}{\Delta \log t^H}$	$\frac{\Delta \varepsilon^C}{\Delta \log t}$	$\frac{\Delta \varepsilon^C}{\Delta \log t^C}$	$\frac{\Delta \varepsilon^H}{\Delta \log t}$	$\frac{\Delta \varepsilon^H}{\Delta \log t^H}$	$\frac{\Delta \varepsilon^C}{\Delta \log t}$	$\frac{\Delta \varepsilon^C}{\Delta \log t^C}$	$\frac{\Delta \varepsilon^H}{\Delta \log t}$	$\frac{\Delta \varepsilon^H}{\Delta \log t^H}$	$\frac{\Delta \varepsilon^C}{\Delta \log t}$	$\frac{\Delta \varepsilon^C}{\Delta \log t^C}$
10	0.02	0.03	0.01	0.02	0.005	0.02	0.005	0.005	0.01	0.01	0.01	0.005
20	0.02	0.03	0.02	0.02	0.005	0.03	0.005	0.005	0.01	0.01	0.01	0.01
40	0.03	0.04	0.02	0.02	0.02	0.03	0.02	0.015	0.015	0.015	0.01	0.03
80	0.04	0.04	0.04	0.025	0.03	0.04	0.03	0.015	0.015	0.025	0.01	0.02
160	0.05	0.05	0.02	0.025	0.07	0.045	0.02	0.025	0.02	0.025	0.015	0.02
320	0.06	0.05	0.02	0.015	0.07	0.05	0.03	0.02	0.025	0.03	0.015	0.015
640	0.05	0.06	0.02	0.02	0.1	0.05	0.02	0.02	0.035	0.035	0.015	0.02
1280	0.06	0.06	0.02	0.01	0.09	0.05	0.02	0.015	0.03	0.03	0.015	0.02

experiment, accurate prediction can be made by using natural strain rate instead of logarithmic time.

Fig. 9 shows the rate of long-term settlement ($C^{HH'}$) and water content.

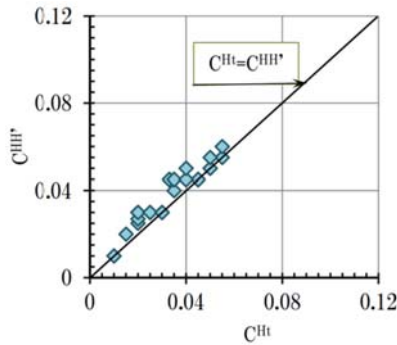


Fig. 9 Relationship between C^{Ht} and $C^{HH'}$

It was shown that according to the quantity of water content, the rate of long-term settlement also became linearly larger, and it can be approximated by Eq. (7).

$$C^{HH'} = 0.1 \times w / 100 \quad (7)$$

where w: initial water content (%)

That is, in order to predict the rate of long-term settlement at the site, it is possible to predict the water content of the soil (Fig. 10).

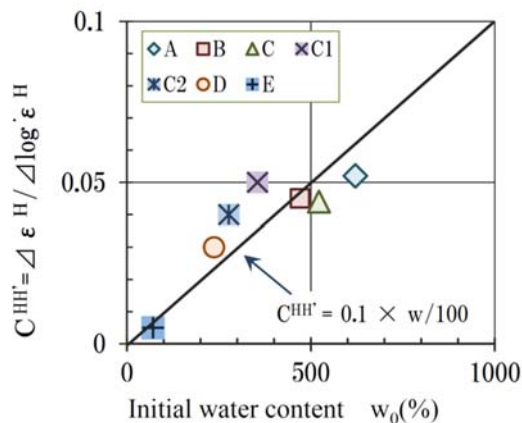


Fig. 10 Relationship between $C^{HH'}$ and w

COMPARISON BETWEEN PREDICTION AND FIELD MEASUREMENT DATA

In this chapter, the author shall compare the laboratory experiments and field measurement data. Following example is the previous field measurement data of highway embankment construction in Japan. This example [13] is the measurement data of Tomei Highway at Aiko area. The thickness of highly organic soil deposit is about 5.3 m and water contents are 350~700 %. The construction details and soil profiles are shown in Fig. 11 and Table 3, respectively.

Fig. 12 shows a plot of the natural strain and elapsed time. Because the origin of time is set as the embankment start time, it can be seen that the long-term speed of the indoor experiment and field measurement data do not match in the figure. That is, this signifies that the gradient of the straight line differs.

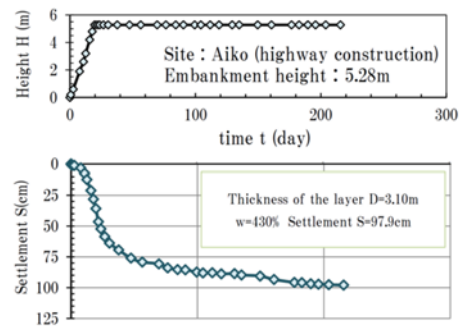


Fig. 11 Field measurement data

Table 3 Details of construction and soil profiles

Name of Site			Aiko
Embankment height	H	m	5.28
Embankment loading	p	kPa	85
Duration	t	day	216
Total settlement	S	cm	97.9
Soil profile	Thickness of layer	D	cm
	Wet density	ρ_t	g/cm ³
	Water content	w_n	%
	Liquid limit	I_p	—
	Ignition loss	L_{ig}	%

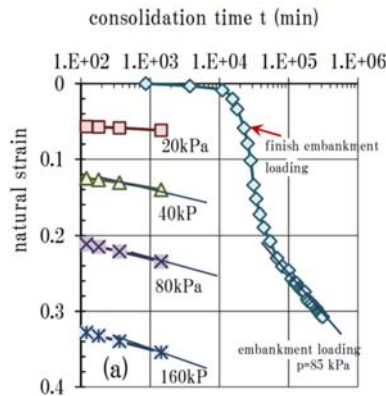


Fig. 12 Comparison between laboratory experiment and field measurement data (ϵ^H -log t)

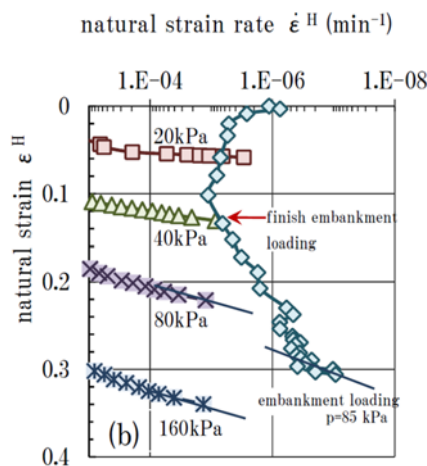


Fig. 13 Comparison between laboratory experiment and field measurement data (ϵ^H - $\dot{\epsilon}^H$)

However, rather than a logarithmic scale of time, the natural strain rate is shown in Fig. 13; from this figure, it was shown that the laboratory experiment and rate of long-term settlement of field measurement data were mostly consistent.

CONCLUSION

- (1) The rate of long-term settlement (C^{Ht}) is given as a substantially constant value during normally consolidated region of highly organic soil.
- (2) When the elapsed time is displayed using a logarithmic scale in ϵ^H -log t curves, the gradient of the straight line changes depending on the origin of the time.
- (3) The rate of long-term settlement ($C^{HH'}$) can be predicted also in the method using the natural strain rate instead of log t. The value of $C^{HH'}$ can be predicted using the properties of soil (water content, etc.).
- (4) The value of $C^{HH'}$ was found to be useful also in the comparison between laboratory test and field measurement data.

ACKNOWLEDGEMENT

Several helpful discussion and suggestion with Dr. E. Fukazawa of Central Giken co., LTD. are gratefully acknowledged.

REFERENCES

- [1] S. Kamao, T. Wakisaka and K. Yamada : Long-term settlement of highly organic soil using natural strain, 48th Symposium on Geotechnical engineering of JGS, pp77-82, 2003.
- [2] S. Kamao, T. Saito : Long-term settlement of over-consolidated highly organic soil using natural strain, 50th Symposium on Geotechnical engineering of JGS, p.237-244, 2005. (in Japanese)
- [3] Den Haan & Kamao : Obtaining isotache parameters from a C.R.S. K0-Oedometer, Soils and Foundations, vol.43, No.4, pp203-214, 2003.
- [4] Y. Ohira, K. Kogure, Y. Yamaguchi and H. Ono : Consolidation behavior of peat, Annual meeting of JGS , pp.205-208 , 1982. (in Japanese)
- [5] K. Matsuo, H. Yamaguchi and Y. Ohira : Coefficient of secondary consolidation of peats, oils and Foundations, Vol.NO.1, pp.139-150 , 1986. (in Japanese)
- [6] K. Kogure : Geotechnics of highly organic soil, Toyo Shoten, 1995, (in Japanese)
- [7] G. Imai : Consolidation theory based on isotache rule and its application method, Work shop on new idea and method of consolidation settlement, Japanese Geotechnical Society, pp79-102, 2002. (in Japanese)
- [8] K. Matsuo : Consolidation behavior of normally consolidated of peat, Soils and foundations, Vol.43, No.2, pp143-150, 2003
- [9] E. J. den Haan & T. B. Edil : Secondary and tertiary compression of peat, Advances in understanding and modeling the mechanical behavior of peat, pp49-60, 1994.
- [10] H. Tanaka, H. Hayashi: Applicability of Isotache model to peaty ground, Japanese Geotechnical Journal, vol.9, No.2, pp.275-286, 2015. (in Japanese)
- [11] S. Kamao, K. Yamada : Characteristics of long-term settlement after removal of pre-load (1~4) , Annual meeting of JGS, 1990-1993. (in Japanese)
- [12] I. Yasukawa, M. Kamon : Effect of loading condition on secondary consolidation of cohesive soils, Soils and Foundation, Vol.27, No.2, pp 93-106, 1987. (in Japanese)
- [13] Japan Highway Public Corporation : Report on Tomei highway road Aiko test embankment construction, 1966. (in Japanese)

DIAPHRAGM WALL SUPPORTED BY GROUND ANCHORS AND INCLINED STRUTS: A CASE STUDY

Adnan Anwar Malik¹, Gorkem Dora², Ramy Derar³ and Majid Naeem⁴

¹Science & Engineering, Saitama University, Japan; ^{2,4}Ammico Contracting Company, Qatar; ³Qatar Industrial Manufacturing Company, Qatar

ABSTRACT

Diaphragm wall is one of the option to support deep excavation for the construction of basements in an urban area having constraints of space due to nearby structures. The type of diaphragm wall such as cantilever or propped is decided with respect to subsurface conditions and surrounding existing structures. Here is a case study on a diaphragm wall for Qatar Industrial Manufacturing Company Building that comprises of 4 basements, ground floor, mezzanine, podium and 38 floors. The excavation depth that needed to be retained was 15.95m. The subsurface ground was consisted of made ground/fill material, caprock, Simsima Limestone, Midra Shale and Rus formation. Plaxis 2D software was used to analyzed the diaphragm wall. The analysis results showed that ground anchors were required to limit the deflection of wall within the allowable deflection. Moreover, due to unavailability of foundation details for neighbor building, the ground anchor option was dropped and inclined steel struts were considered, only at that section. As the inclined steel struts were supported by pile foundation, therefore lateral load analysis was performed through LPile software. Staad Pro software was also used to analysis the waler beams. The deflection of diaphragm wall was monitored through survey points.

Keywords: Deep excavation, Diaphragm wall, Ground anchors, Inclined Struts, Plaxis 2D analysis

INTRODUCTION

Any excavation whose depth is more than 6 m is considered as a deep excavation [1, 2]. However, with the advancement in construction technology, and the use of computer programming makes it possible to analysis and design excavation support system for all depths, following the same theories. Therefore, the division of shallow and deep excavation is not meaningful anymore [3]. The selection of excavation support system mainly depends upon the subsurface conditions, excavation depth, adjacent structures, space within the site for machinery, access to the site for the machinery and economics. Diaphragm wall is one of the options if the planned excavation is deep and surrounding by existing structures. It was used first time in the 1950s in Italy, after that it's use increased throughout the world [3].

Wall displacement is the important criteria for the safety of the support system and surrounding structures. The horizontal movement of the wall up to 2 % of the ultimate depth of excavation is the common range in underground construction [4, 5, 6]. However, this horizontal displacement range is not suitable for the situation where shoring is adjacent to neighbor building/structure. Based on the case histories, Clough and O'Rourke [7] found that the maximum lateral wall movement was approximately 0.2 % of excavation depth. The effect of excavation depth by using finite element method (FEM) on

wall-soil deformation was studied by Bose and Som [8]. The numerical study on ground displacement due the excavation was conducted and a method was proposed to predict the ground displacement [9]. Zhang et al., [10] presented a semi-empirical model for estimating the maximum wall deflection for braced excavations in clays. A case study on the surface settlement and the lateral deformation of the diaphragm at Ahwaz Metro Station was conducted by Pakbaz et al. [11]. Another case study on the performance of diaphragm wall with tie-back anchors was conducted and indicated the advantage of numerical simulation for an efficient design in Noida, India [12].

As the subsurface conditions, adjacent structures, foundation details of adjacent structures and excavation depth varies from location to location; therefore, case studies always provide a guide to designers to enhance their designing approach for future works. In this regard, the current paper comprises a case study of deep excavation supported by diaphragm wall in Doha, Qatar. Ground anchors and inclined struts were used to restrict the horizontal movement of the diaphragm wall. The preference for the selection of ground anchors and inclined struts at the diaphragm wall was based on the available information of the adjacent building's foundation details. Advance computing software's such as Plaxis 2D, Staad Pro and LPile were used for analyzing various components of the diaphragm wall. The movement of the diaphragm wall was monitored

through survey target points.

DESCRIPTION OF SITE

The proposed site is located at the West Bay, Doha – State of Qatar as shown in Fig. 1. The proposed commercial building consisted of four (04) basements, a ground floor, mezzanine, podium and thirty eight (38) upper floors. The building is owned by Qatar Industrial Manufacturing Company (QIMC). The site is surrounded by two existing building and roads. The adjacent building at North-East side of the site consisted of one (01) basement, ground floor and two (02) upper floors, and the building at North-West side of the site consisted of one (01) basement, ground floor and six (06) upper floors. The remaining sides of the site consisted of roads.



Fig. 1 Location of the QIMC Tower

SUBSURFACE CONDITION

The geotechnical investigation report was provided by the client. Based on the report, the subsurface stratigraphy of the site consisted of made ground (silty, very gravely sand) followed by caprock, Simsima Limestone, Midra Shale and Rus Formation. The engineering parameters of each strata is based on the recommendation of the geotechnical investigation report and local experience of nearby projects. The engineering parameters along the depth are presented in Fig. 2.

+2.50 m QNHD	Unit Weight = 18 kN/m ³	Friction Angle = 30°	Modulus = 20 MPa	Cohesion = 0 kPa	Made Ground
-1.50 m QNHD	Unit Weight = 20 kN/m ³	Friction Angle = 30°	Modulus = 70 MPa	Cohesion = 60 kPa	Caprock
-3.50 m QNHD	Unit Weight = 21 kN/m ³	Friction Angle = 30°	Modulus = 300 MPa	Cohesion = 60 kPa	Simsima Limestone
▼ -7.10 m QNHD Water Level					
-18.50 m QNHD	Unit Weight = 20 kN/m ³	Friction Angle = 30°	Modulus = 250 MPa	Cohesion = 60 kPa	Midra Shale & Rus Formation
End of Borehole					

Fig. 2 Subsurface condition of the site

The water table was encountered at a depth of 9.6 m below the existing ground level i.e. at elevation of -7.10 m QNHD (Qatar National Height Data). However, water level of -1.0 m QNHD was considered in the design of shoring system based on the historical ground water level at this area and project specifications.

DESIGN METHODOLOGY

The maximum excavation depth of 15.95 m, requirement of water-tight shoring system and adjacent existing structures suggested to consider Diaphragm wall as a best solution for this site. The existing ground level of the site was considered at +2.50m QNHD based on the site topography and provided construction drawings of the QIMC tower. The shoring system of the whole site was divided into three main sections based on the existing nearby structures and their foundation details as shown in Fig. 3.



Fig. 3 Division of shoring system along the perimeter

Initially, ground anchors were considered in the analysis of the shoring system at all sections, but later on, changed to inclined struts at section 3 due to the unavailability of the pile foundations precise location under existing building. Rigorous finite element analysis (by using Plaxis 2D) was conducted on all the sections to finalize the diaphragm wall dimensions and associated supporting element. The final shoring details at each section is presented in Table 1.

Table 1 Finale diaphragm details

Section	Width (m)	Depth (m)	Support
Sec 1	0.64	21.5	Anchors

Sec 2	0.64	22.0	Anchors
Sec 3	0.80	19~22	Struts

The following sections contains the results of the design approach and analysis that was adopted at section 2 and section 3 of diaphragm wall.

RESULTS AND DISCUSSION

Design Approach and Analysis at Section 2

The location of foundation piles under the existing building at section 2 forced us to divided this section into three sub-sections i.e. 2A, 2B, and 2C as shown in Fig. 4. Three rows of ground anchors were considered in the finite element analysis software (Plaxis 2D) to limit the diaphragm wall horizontal movement within the acceptable level. The spacing and inclination of ground anchors and diaphragm wall layout were adjusted to avoid the clashing of anchors with the existing foundation piles.

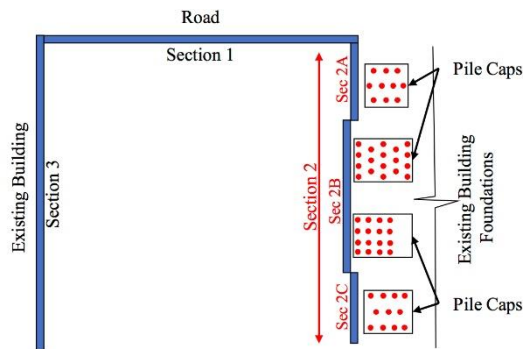


Fig. 4 Foundation details at section 2

Plaxis 2D analysis at section 2

Finite element software Plaxis (2D) was used to analysis the shoring system. The diaphragm wall was modelled as a plate element. The soil/rock-wall interface reduction factor of 0.67 was considered in the analysis. As per the available information of the existing building adjacent to section 2, In Plaxis, surcharge load was simulated through foundation piles with pile caps at the top. The foundation piles were modelled with embedded beam element and pile caps were modelled as volume element with linear elastic concrete material properties. The ground anchors were provided at three levels i.e. -1.5m QNHD, -4.0m QNHD and -10.0m QNHD. The anchor spacing at top two levels will be variable during the construction stage to avoid any interference with the existing building foundation piles. However, in the analysis the spacing was considered at unity. The exact load of the anchor was estimated by multiplying with exact spacing of the anchors. The top two anchors were modelled as a fixed end anchor in the Plaxis software. The free

length of the third level anchor was estimated by considering potential wedge zone that will be 35° from the toe of the wall along with 3.0 m of buffer zone as per British code [13]. In Plaxis, the free length was modelled with node to node element. The grout portion of the anchor was modelled with embedded pile element available in Plaxis. In the analysis, all the logical construction stages were considered that reflect the actual excavation activity. Moreover, the de-stressing of anchors during the construction of raft and basement slabs were also considered in the analysis. The raft/basement slabs were modelled as a fixed end anchor element in the software. The final excavation stage of the model is presented in Fig. 5.

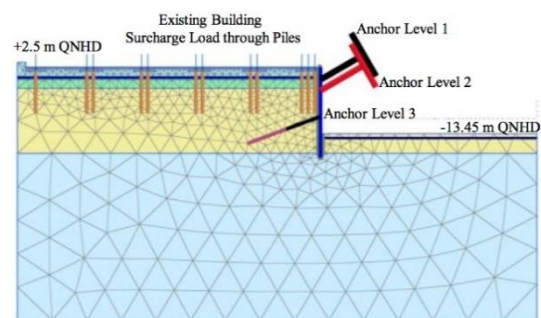
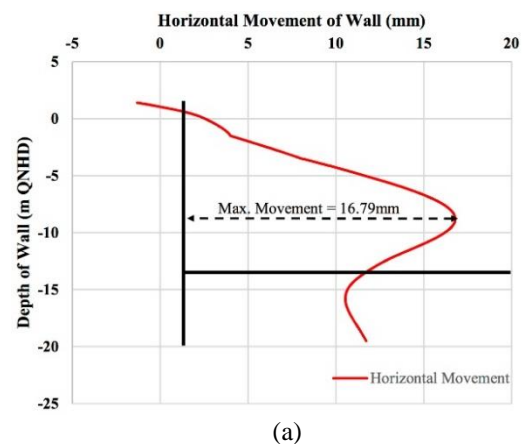


Fig. 5 Model construction stage at final excavation

The horizontal movement, bending moment and shear force at the final stage (including destressing stage of all anchors) of section 2 is presented in Fig. 6. The max. deflection at final excavation stage was 13.2 mm.



(a)

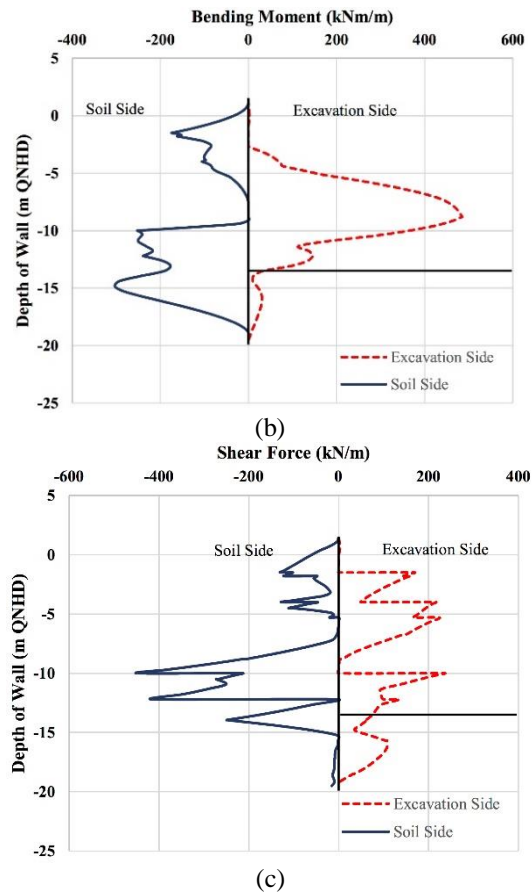


Fig. 6 (a) Horizontal movement of wall at final stage of analysis
(b) Bending moments at excavation and soil side of the wall, at final stage of analysis
(c) Shear forces at the excavation and soil side of the wall, at final stage of analysis

The above bending moments and shear forces were used to design the reinforcement details of the diaphragm wall through British code [14], and also verified from ACECOM software. The forces obtained at each level of ground anchors are shown in Table 2. These forces were used to define the bond length and number of strands.

Table 2 Forces on ground anchors

Anchor Level (m QNHD)	Lock-off Load "Plaxis Input" (kN/m)	Design Load "Plaxis Output" (kN/m)
-1.5	250	321.69
-4.0	250	287.12
-10.0	550	511.11

It was not possible to install the 1st layer of ground anchors at regular spacing for section 2B

(refer Fig. 4) due to the presence of foundation piles of existing building. Thus, anchors of 1st layer was designed with waler beam to achieve uniform distribution of anchor loads at diaphragm wall panels. To determine the anchor force for section 2B, anchors and waler beam were modelled in the structural software (Staad Pro) with exact anchor spacing. The unit anchor force determined from Plaxis was used to analysis the model in Staad Pro. Anchors were modelled as a spring element with appropriate stiffness based on number of strands, free length, inclination, area of strands and strands material modulus. The analysis provided exact anchor force at each anchor location and forces in the waler beam i.e. bending moment and shear forces. Figure 7 shows the Staad Pro model for anchors and waler beam at section 2B with bending moment and shear forces.

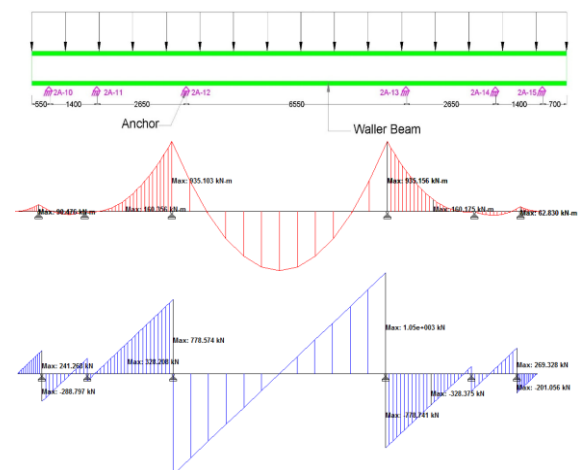


Fig. 7 Output of Staad Pro model

Design Approach and Analysis at Section 3

The section 3 was divided into two sub-sections namely, 3-1 and 3-2 based on the distance of adjacent building from the diaphragm wall. The layout of the section is shown in Fig. 8. The top level of diaphragm wall at section 3-1 was +2.5 m QNHD whereas the top level of diaphragm wall at section 3-2 was -0.50 m QNHD. Inclined steel struts were used to limit the horizontal movement of the diaphragm wall.

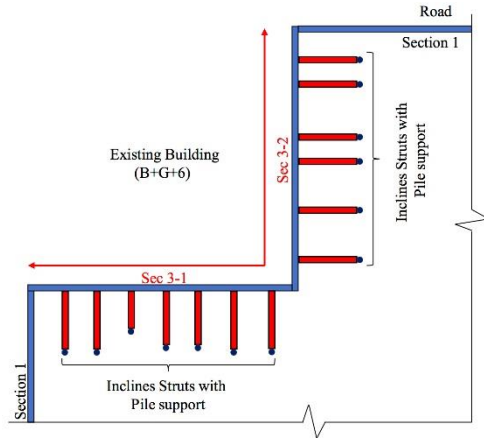


Fig. 8 Layout of section 3

Plaxis 2D analysis at section 3

Finite element software Plaxis (2D) was used to analysis the section. The diaphragm wall was modelled as a plate element. The soil/rock-wall interface reduction factor of 0.67 was considered in the analysis. Surcharge load of 130 kPa at 5 m away from the diaphragm wall was considered at section 3-1. Whereas, surcharge load of 130 kPa right behind the diaphragm wall was considered at section 3-2. Inclined strut was modelled as a fixed-end anchor and was installed at a level of -4.0 m QNHD. The inclination of the strut was 45 degrees. The spacing between the struts was 7.5m. In the analysis, all the logical construction stages were considered that reflect the actual excavation activity. Moreover, the removal of struts during the construction of raft and basement slabs were also considered in the analysis. The raft/basement slabs were modelled as a fixed end anchor element in the software. The final excavation stage of the model at section 3-1 is presented in Fig. 9.

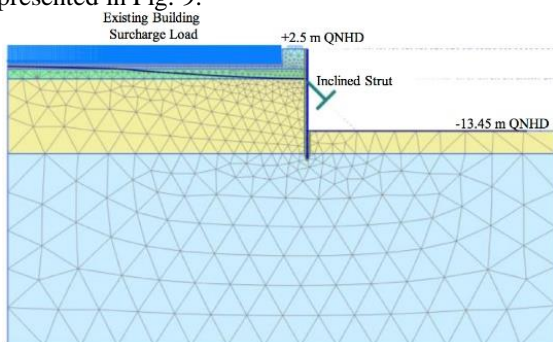
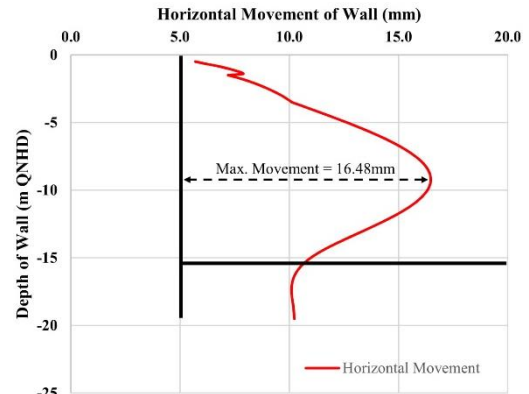
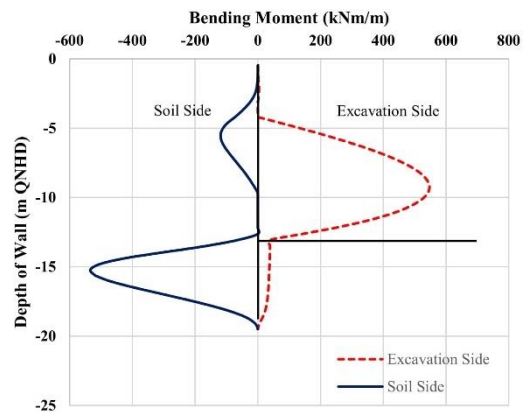


Fig. 9 Model construction stage at final excavation

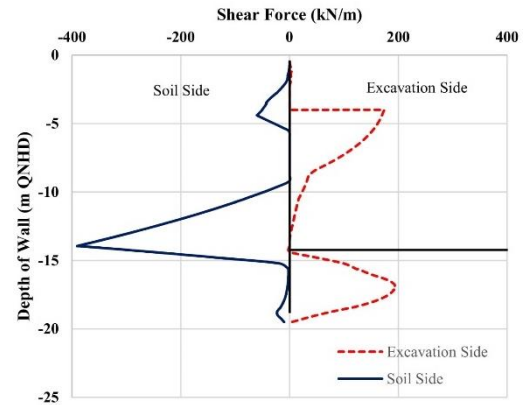
The horizontal movement, bending moment and shear force at the final stage (including removal of strut stage) of section 3-2 is presented in Fig. 10.



(a)



(b)



(c)

Fig. 10 (a) Horizontal movement of wall at final stage of analysis
(b) Bending moments at excavation and soil side of the wall, at final stage of analysis
(c) Shear forces at the excavation and soil side of the wall, at final stage of analysis

The above bending moments and shear forces were used to design the reinforcement details of the diaphragm wall through British code [14], and also verified from ACECOM software. The forces obtained from the fixed-end element (strut) was 452.39 kN/m at section 3-1 and 288.44 kN/m at section 3-2. These forces were applied on the waler

beam with exact spacing of the struts in Staad Pro structural software, to get the bending moments and shear force in the waler beam along with the exact load on the struts. The determined load on the strut was then used in LPILE software to define the strut supporting pile. The details of the supporting pile are give in the Table 3.

Table 3 Strut supporting pile details

Section	Vert. / Hori. Load (kN)	Pile Dia. (mm)	Pile Length (m)
Sec 3-1	2760.90	1200	8.0
Sec 3-2	1942.42	1200	6.0

The bending moments and shear forces obtained from LPILE (supporting pile) and Staad Pro (waler beam) were used to define the reinforcement details through British code [14]. These reinforcement details were also verified by using ACECOM software.

MODEL VERIFICATION THROUGH FIELD MEASURED WALL DEFLECTIONS

After the approval of design and construction drawings from the Consultants, the diaphragm wall was constructed with state of the art equipment. Upon the completion of diaphragm wall, the site was excavated up to the final excavation level as shown in Fig. 11.



Fig. 11 Final excavation level at site

The diaphragm wall horizontal movements were recorded during the excavation stage at various control points along the perimeter of the wall through survey target points. Table 4 shows the comparison of max. horizontal movement of the diaphragm wall at specific sections measured through survey target points at the top of wall with the results of Plaxis analysis at final excavation stage.

Table 4 Wall deflection comparison (Top of wall)

Sections	Target Location	Analysis Plaxis (mm)	Measured At Site (mm)
Sec 2B	Center	1.3	8.0
Sec 3-2	Center	5.7	12.0

The difference between analyzed and measured diaphragm wall deflection was the impact of the installation of foundation piles. The drilling of boreholes close to the shoring were causing an unexpected impact to the shoring wall as the foundation pile boreholes were drilled without temporary casing. However, the max. measured wall deflection was 0.075% of the excavation depth which was under the max. limit as per previous studies [8].

CONCLUSION

This paper focuses on the design methodology of diaphragm wall used to retain the excavation depth of 15.95 m. It also showed the importance of knowing the foundation details of surrounding buildings so that adequate supporting system can be designed.

This study provides a guidance to engineers for effectively designing of inclined struts and ground anchors supported shoring system with a combination of software. The difference between the analyzed and measured wall deflection was due to the impact of foundation pile installation close to the shoring wall. However, the maximum measured wall deflection was 0.075% of the excavation depth which is within the maximum limit suggested in the previous studies.

REFERENCES

- [1] Terzaghi A., and Peck R.B., Soil Mechanics in Engineering Practice, John Wiley & Sons, New York, 1967.
- [2] Peck R.B., Hanson, W.E., and Thornburn, T.H., Foundation Engineering, John Wiley & Sons, New York, 1977.
- [3] Ou C.Y., Deep Excavation: Theory and Practice, Taylor and Francis, London, 2006.
- [4] Moormann C., Analysis of wall and ground movements due to deep excavations in soft soil based on a new worldwide database. Soils and Foundations, col. 44, Issue 1, 2004, pp. 87-98.
- [5] Long M., Database for retaining wall and ground movements due to deep excavations. Journal of Geotechnical and Geoenvironmental Engineering, Vol. 127, Issue 3, 2001, pp. 203-224.
- [6] Ou C.Y., Hsieh P.G., and Chiou D.C.,

- Characteristics of ground surface settlement during excavation. *Canadian Geotechnical Journal*, Vol. 30, Issue 5, 1993, pp. 758-767.
- [7] Clough G.W., and O'Rourke T.D., Construction induced movements of in situ walls. *Proceeding of ASCE Conference on Des. And Perf. of Earth Retaining Structure*, Geotech. Spec. Publ. No. 25, ASCE, New York, 1990, pp. 439-470.
- [8] Bose S.K., and Som N.N., Parametric study of braced cut by finite element method. *Computer Geotechnics*, Vol. 22, Issue 2, 1998, pp. 91-107.
- [9] Yoo C., and Lee D., Deep excavation-induced ground surface movement characteristics – a numerical investigation. *Computer and Geotechnics*, Vol. 35, Issue 2, 2008, pp. 231-252.
- [10] Zhang W., Goh A.T.C., and Xuan F., A simple prediction model for wall deflection caused by braced excavation in clays. *Computer Geotechnics*, Vol. 63, 2015, pp. 67-72/
- [11] Pakbaz M.S., Imanzadeh S., and Bagherinia K.H., Characteristics of diaphragm wall lateral deformations and ground surface settlements: Case study in Iran-Ahwaz metro. *Tunnelling and Underground Space Technology*, Vol. 35, 2013, pp. 109-121.
- [12] Nisha J.J., and Muttharam M., Deep excavation supported by diaphragm wall: A case study. *Indian Geotechnical Journal*, Vol. 47, Issue 3, 2017, pp. 373-383.
- [13] BS 8081, British standard code of practice for ground anchorage. 1989.
- [14] BS 8110, Structural use of concrete. Code of practice for design and construction. 1997.

AN ANALYSIS OF VERIFICATION ON THE INFLUENCE OF LIQUEFACTION ON UNDERGROUND STRUCTURE

Keita Sugito¹, Tetsuya Okano² and Ryoichi Fukagawa³

^{1, 2}Graduate School of Science and Engineering, Ritsumeikan University, Japan; ³Department of Science and Engineering, Ritsumeikan University, Japan

ABSTRACT

It is widely recognized that the Kansai area will be attacked by a plate boundary type huge earthquake within these 30 years. When the earthquake happens, the ground with underground structure, like a tunnel, would be struck by severe liquefaction disasters. Therefore, we tried to analyze the ground behavior using LIQCA, which is well used for liquefaction analysis in Japan. The input earthquake motion is the seismic standard spectrum I which is commonly used in Japan. The calculation time continued until excess pore water pressure dissipated. The ground has the underground structure, so we investigated not only the liquefaction phenomenon of the ground itself but also the behavior of the underground structure. Furthermore, we focused on the boundary condition between the tunnel and the adjacent ground. Three patterns are prepared for this boundary condition. First, the boundary condition between the tunnel and the ground is free in the vertical direction and fixed in the horizontal direction. Second, this boundary condition is fixed in the vertical direction and the horizontal direction is fixed. Third the joint elements are installed between the tunnel and the ground. Under each condition, we examine the effect of liquefaction on tunnel. Also, we compare the three patterns and verified realistic damage.

Keywords: Liquefaction, Numerical simulation, Tunnel, Float up

INTRODUCTION

There is a high probability of a large, plate boundary-type earthquake occurring within 30 years in the Kansai area, Japan. The western part of the country will be severely damaged by this earthquake. In particular, the Osaka Gulf coast is predicted to suffer from a severe liquefaction disaster [1]. Therefore, a liquefaction simulation was applied to a typical site on the Osaka Gulf coast. The simulation is based on the LIQCA [2] program, which is widely used as a liquefaction simulation tool in Japan. The target ground has an underground tunnel; it is known that liquefaction affects tunnels, but concrete indications of it have not been found. So, we investigated not only the liquefaction phenomenon of the ground itself, but also the behavior of the underground structure. During the simulation, by changing the boundary condition between the tunnel and the adjacent ground, the difference in the amount of the tunnel floating when liquefaction occurs should be noted.

OUTLINE OF ANALYSIS

Ground to be analyzed

The analysis target is some area on the Osaka Gulf coast, which is characterized by alluvium deposits. Figure. 1 shows the cross section of this target; the cross section has a length of 100 m in the horizontal

direction and a depth of 40 m. The tunnel is located near the surface in the center of the ground. The soil layers that may liquefy are the As1, As2 and Tsg1 layers. Other layers are composed of clayey soil and hard sandy soil, and thus, their liquefaction is not considered to be a significant risk.

The groundwater level is set at GL-2.3 m. The Oc layer is the basal surface in this cross section. The B layer, the layer above the groundwater level, is considered hard to liquefy, so the Ramberg-Osgood model is applied to this layer. The layer below the groundwater level is modeled by the cyclic elastoplastic constitutive model. Table 1 lists the material parameters used in the analysis. The liquefaction layers and non-liquefaction layers are fitted based on the respective standards. The liquefaction layers have liquefaction strength curves based on the Design Standards for Railway Structures and Commentary [3]. The shear modulus and shear strain relationship ($G/G_{\max} \sim \gamma$), historical attenuation and shear strain relationship ($h \sim \gamma$) were referenced using element simulations. These were used to determine the nonlinear properties of the non-liquefaction layers. Since $G/G_{\max} \sim \gamma$ and $h \sim \gamma$ relationship are different for each soil, and these relationships are highly dependent on the constraining pressure, it is preferable to calculate these variables by an indoor test, such as a repeated triaxial test of the sampled specimen. The non-liquefaction layers are fitted to the Yasuda-Yamaguchi model [4].

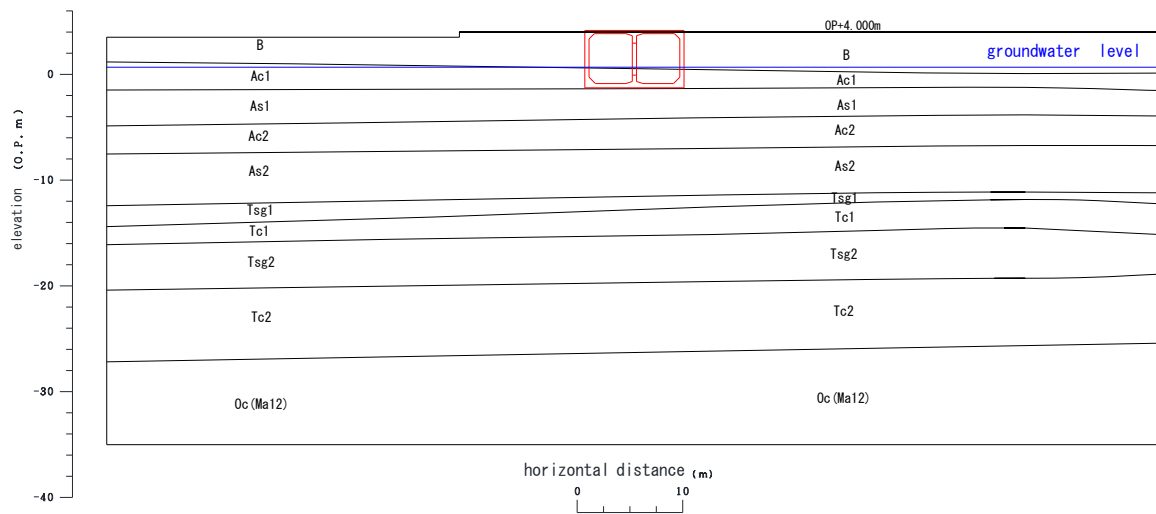


Figure. 1 Cross section of the target area

Table 1 List of material parameters

	①		②	③		④	⑤	⑥	⑦	⑧	⑨
	B		As1	Ac1, Ac2		As2	Tsg1	Tc1	Tsg2	Tc2	Oc
type	Y	X	X	Y	X	X	X	Y	Y	Y	Y
γ (kN/m ³)	18.0	18.0	18.0	16.0	18.0	16.0	18.0	16.0	16.0	16.0	18.0
ρ (g/cm ³)	1.8	1.8	1.8	1.6	1.8	1.6	1.8	1.6	1.6	1.6	1.8
k (m/s)	1.47	1.47	1.47	9.00	5.17	2.60	1.20	1.00	7.50	1.12	1.12
e_0	0.658	0.658	0.990	1.038	0.505	0.724	0.777	1.098	1.799	0.673	0.673
Vs (m/s)	120	140	120	120	240	200	260	208	208	170	170
λ		0.002	0.002		0.001						0.1
κ		0.025	0.02		0.001						0.02
OCR*		1.3	1.0		1.6						1
G_0/σ'_{m0}		935.5	445.3		1104						646.1
M^*_m		0.909	0.909		0.909						0.909
M^*_f		1.012	0.966		1.215						0.958
B^*_0		3500	2500		10000						5000
B^*_1		80	50		20						100
C_f		0	0		0						0
γ^{Pr}_r		0.02	0.002		0.005						0.02
γ^{Er}_r		0.001	0.3		0.001						0.3
D^*_0		1.0	1.5		4.0						4
n		7.0	2.0		8.0						6
C_d		2000	2000		2000						2000
v	0.496			0.496		0.494	0.488	0.492	0.492		
c (kPa)	0			33		198	0	149	149		
ϕ (deg)	30.9			0		0	34	0	0		
a	6977			2241		4939	8530	4533	4165		
b	0.5			0.5		0.5	0.5	0.5	0.5		
α	1.89			16.7		2.3	2	1.4	1.5		
r	1.92			1.78		2.1	3	1.7	1.6		

Notations: X: cyclic elastoplastic constitutive model, Y: R-O model, γ : unit weight, ρ : density, k : coefficient of permeability, e_0 : initial void ratio, V_s : shear wave velocity, λ : compression index, κ : expansion index, M_f : stress ratio parameter corresponding to failure angle, OCR^* : factoid overconsolidation ratio, G_0/σ'_{m0} : non-dimensional initial shear modulus, M_m : stress ratio parameter corresponding to phase transformation angle, B^*_0 , B^*_1 , and C_r : plastic modulus parameters, γ_r^{P*} : plastic strain, and γ_r^{E*} : elastic strain, D^*_0 , n : dilatancy coefficient, C_d : anisotropy elimination parameter, ν : Poisson's ratio, c : cohesion, ϕ : internal friction angle, and a , b , α , and r : R-O parameters

Tunnel model

Figure. 2 shows model of the tunnel within the ground. The yellow lines indicate the structure of the tunnel. The tunnel consists of an upper and lower base plate, a sidewall, and a center pillar. The structure of this tunnel is represented by a beam element. Table 2 lists the tunnel parameters used in the analysis. B is the horizontal length of the element, and H is the vertical length of the element. The tunnel is comprised of four kinds of boards.

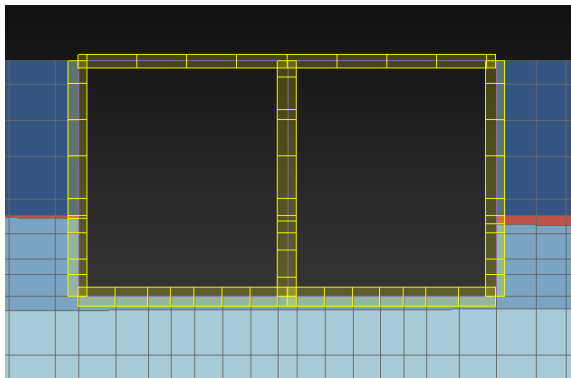


Figure.2 Tunnel model

Table 2 Tunnel parameters

	upper	lower	side	center
B (m)	1	1	1	2.3
H (m)	0.3	0.4	0.4	0.4
Pitch (m)	1	1	1	4
γ (kN/m ³)	25	25	25	25
A (m ²)	0.3	0.4	0.4	0.92
I (E-03m ⁴)	1.13	2.67	2.67	6.00
G (kN/m)	7.5	10	10	5.75

Notations: γ : Unit volume weight, A: Sectional area, I: Sectional Secondary moment, G: Unit length Weight

Boundary conditions

Soil skeleton

In the analysis model, the bottom of the boundary is an elastic base (viscous boundary). The elastic base is placed as a dashpot on the bottom of the model. The input earthquake motion is a 2E wave. In LIQCA, only the horizontal lower boundary can be set for the viscous boundary. When a consolidation analysis is conducted, the dashpot is automatically replaced with a rigid spring. The side boundary is a method of connecting a wide free ground part, which is not easily influenced by the FEM region, to the side surface when the soil layer configuration of the side boundary is different.

Tunnel

Three patterns are prepared for this boundary condition. First, the boundary condition between the tunnel and the ground is free in the vertical direction and fixed in the horizontal direction; the boundary condition between the tunnel and adjacent ground is free from friction in the vertical direction, and the tunnel and its adjacent ground behave similarly in the horizontal direction. The second boundary condition is fixed in both the vertical and horizontal directions. The friction between the tunnel and the ground is set not to be lost in both the horizontal direction and the vertical direction. In the third pattern, joint elements are installed between the tunnel and the ground. A joint element is a model that can install a virtual spring, which takes sliding and peeling between the structure and the ground into account. Parameters are set as shear direction spring constant $k_s = 5.0 \times 10^5$ (kN/m²) and vertical direction spring constant $k_n = 5.0 \times 10^5$ (kN/m²). We refer to method of making these magnitudes about 10 times larger than the spring constant of the adjacent ground [5].

Input earthquake motion

The input earthquake motion is the seismic standard spectrum I, which is commonly used in Japan. The waveform is shown in Figure. 3. The increment of the calculation time is 0.005 s. The Newmark method coefficients are $\beta = 0.3025$ and $\gamma = 0.6$. These values are common in LIQCA simulations. The constant of the Rayleigh attenuation (α_1) is equal to 0.001–0.003. After seismic motion, consolidation analysis is carried out until the vertical settlement converges.

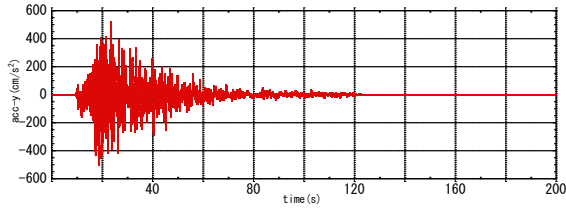


Figure.3 Waveform of seismic standard spectrum I

Initial stress analysis

The initial values of the soil skeleton displacement and excess pore water pressure are all 0. The soil skeleton displacement and excess pore water pressure in LIQCA are the increments from the initial state, that is, the incremental values at the time of the earthquake. Under these initial conditions, it is necessary to set the initial effective stress of the ground. Therefore, it is important to estimate the initial stress state in the ground, which was completed by a self-weight analysis. The self-weight analysis calculates the initial stress by applying self-weight to the model used for the liquefaction analysis in the zero-gravity state. It considers the increase in ground rigidity and nonlinearity caused by adding weight to the model.

ANALYSIS RESULT

The analysis results are shown below. After the earthquake motion, a consolidation analysis was carried out until the convergence of the vertical displacement was confirmed. The effective stress decreasing ratio (ESDR) is used as an index for determining liquefaction. It is shown in the following equation:

$$ESDR = 1 - \frac{\sigma'_m}{\sigma'_{m0}} \quad (1)$$

σ'_m : average effective stress corresponding to some elapsed time (kN/m²)

σ'_{m0} : average effective stress in the initial stress state (kN/m²)

When this value reaches 1, liquefaction occurs in the ground. The results can be divided into three patterns according to the boundary condition between the tunnel and the adjacent ground, as previously mentioned. The analysis results are summarized according to these three patterns.

Free boundary condition

Figure. 4 shows the ESDR values of the ground layers As1, As2, and Tsg1. These results indicate that these soil layers become liquefied during a large earthquake. The effective stress reduction ratio

decreases after 10⁸ s (approximately 3 years). This indicates that the excess pore water pressure that occurs by liquefaction is dissipated, and that the consolidation settlement converges. Figure. 5 shows the vertical displacement of the tunnel during the earthquake. After the consolidation of the soil, the tunnel has risen by 0.9 m.

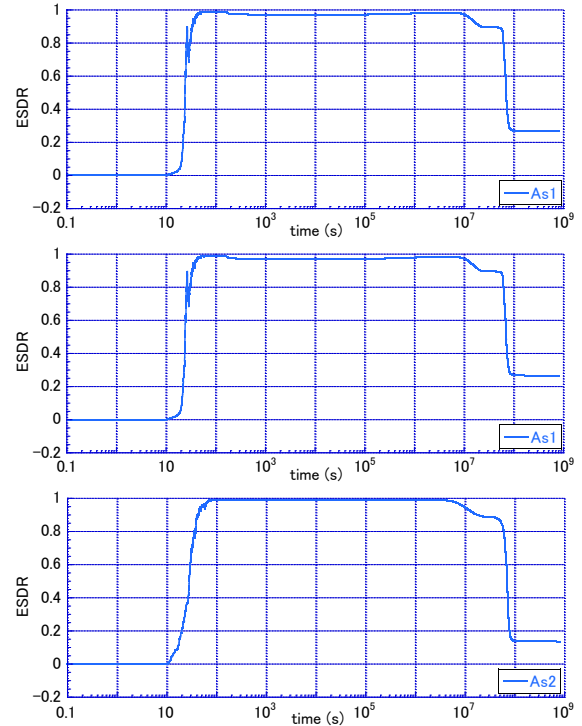


Figure. 4 Effective stress decreasing ratio of As1, As2, and Tsg1

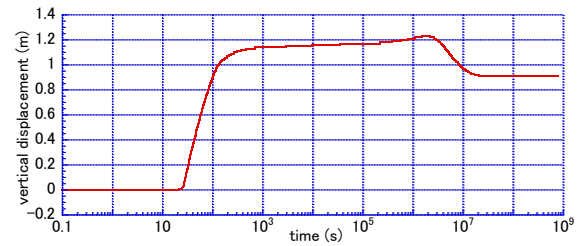


Figure. 5 Vertical displacement of the tunnel under the free boundary conditions

Fixed boundary condition

Figure. 6 shows the ESDR value of As1, As2, and Tsg1 under the fixed boundary condition. Under these conditions, the results indicate that these layers do become liquefied. This indicates that the excess pore water pressure that occurs by liquefaction is dissipated, and that the layers consolidate. Figure. 7 show the vertical displacement. After the consolidation of the layers, the tunnel settles by 0.2 m.

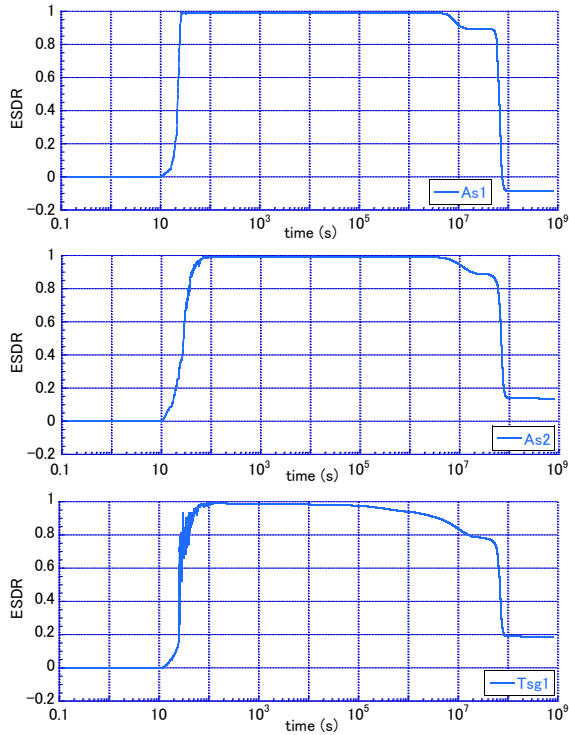


Figure. 6 Effective stress decreasing ratio of As1, As2, and Tsg1

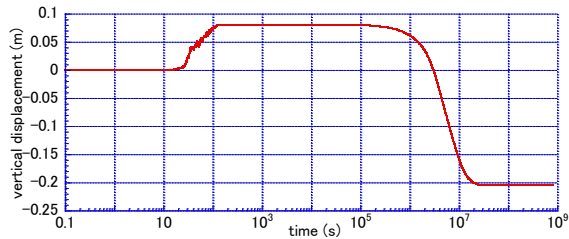


Figure. 7 Vertical displacement of the tunnel under the fixed boundary conditions

Joint element

Figure. 8 shows the ESDR of the soil layers As1, As2, and Tsg1 under the addition of the joint element. As with the previous models, the results show that the layers do become liquified under strong ground motion. This indicates that the excess pore water pressure dissipates, and the soil layers undergo consolidation. Figure.9 shows vertical displacement, after consolidation, the tunnel rises by 0.8 m. It is considered that the parameter of the joint element affects the uplifting of the tunnel seen at liquefaction occurrence.

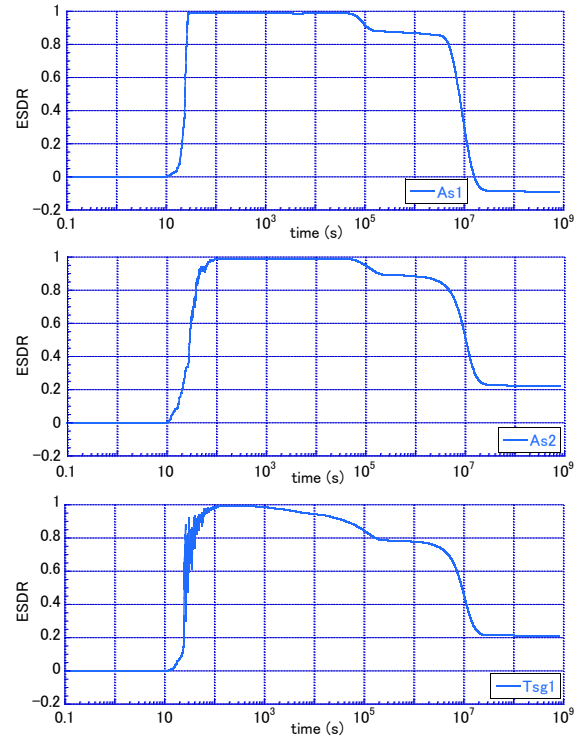


Figure. 8 Effective stress decreasing ratio of As1, As2, and Tsg1

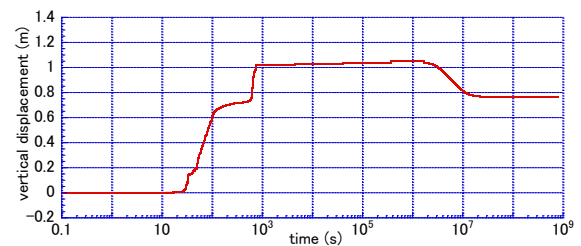


Figure. 9 Vertical displacement of the tunnel in the joint element condition

Displacement of the ground surface

Figure. 10 shows the vertical displacement for each time history. The data corresponds to the state of the initial coordinate and vertical coordinate of three patterns after consolidation of the ground surface coordinates. The tunnel is located between 45 and 55 m along the X axis. In the rest of the cross section, both the free and joint element models show almost the same amount of settlement. The tunnel was uplifted most under the free boundary conditions but settled under fixed boundaries. The phenomenon observed under the free boundary condition is caused by the lack of vertical friction between the side surface of the tunnel and the surrounding ground. Therefore, a rise of 0.9 m is thought to be the maximum floating amount. The fixed boundary condition is not thought to be realistic because it is supposed that the friction between the tunnel and the

adjacent ground is not lost when liquefaction occurs. The joint element model takes into consideration the reduction in shear strength due to the rise of excess pore water pressure, which is observed when liquefaction occurs. Even assuming actual phenomena, peeling and slipping may occur at the boundary between the tunnel and the ground, and so the use of joint elements is appropriate.

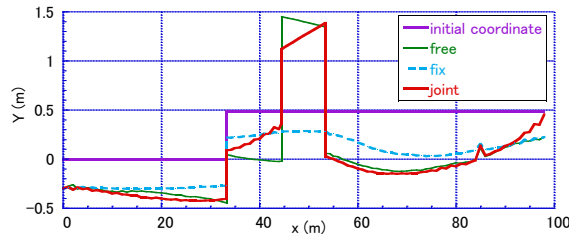


Figure. 10 Vertical displacement for each time history

CONCLUSION

When an earthquake, corresponding to seismic standard spectrum I, occurs at the target ground of the Osaka Gulf coast, the results of a liquefaction simulation based on LIQCA indicate that the ground becomes liquefied and the tunnel at the surface of the target ground rises by between 0.8 m and 0.9 m. This phenomenon is caused by the boundary condition between the tunnel and the surrounding ground.

Although the boundary between the tunnel and the adjacent ground can be modelled to some extent using the joint elements model, it is still necessary to make this phenomenon more realistic. The buoyancy problem may be difficult to reconcile, and therefore, this paper will further investigate the boundary condition between the sidewall of the tunnel and the adjacent ground to conduct more realistic simulations.

REFERENCES

- [1] Matsuoka S, Wakamatsu K, and Hashimoto K., "Estimation method of liquefaction risk based on topography: Ground classification 250 m mesh map", in Proc. of the Japan Earthquake Engineering Association, 2011, pp. 35–36.
- [2] LIQCA Liquefaction Geo-Research Institute., LIQCA 2 D 15 · LIQCA 3 D 15 material, 2015.
- [3] Railway Technical Research Institute., Design Standards for Railway Structures and Commentary, 2012.
- [4] Yasuda S, and Yamaguchi I., "Dynamic deformation characteristics of various undisturbed soils", of the 20th Soil Engineering Research Presentation, 1985, pp. 539–542.
- [5] Civil Engineering Association Partial, Dynamic Analysis Method, Dynamic Analysis and Seismic Design Vol. 2, Gihodo Shuppan Publishing, 1989, pp.123–125.

CALCULATION FORMULA FOR PULLOUT RESISTANCE EXERTED BY OPEN-WING-TYPE GROUND ANCHOR

Kota Kono¹, Akihisa Nakahashi², and Ryoichi Fukagawa³

¹ Graduate School of Science and Engineering, Ritsumeikan University, Japan; ² NIPPON KOEI CO.,LTD Japan; ³ Ritsumeikan University, Japan

ABSTRACT

Ground anchor systems (also known as earth anchor systems) are installed to stabilize structures or slopes by connecting a structure or a slope to the anchorage zone using the frictional force between grouting material and surrounding ground. However, the pullout resistance of anchors decreases over long periods of time, causing the anchor to finally pulled out from the ground owing to the decreasing friction between grouting material and surrounding ground. An open-wing type (OW) anchor has been developed by our research group as a new type of earth anchor system to address the issues associated with the currently existing methods. The method uses open wings to exert the pullout resistance. Our research group conducts experiments to examine the effects of number of wings, root depth, and type of ground on the pullout resistance exerted by OW anchors. The experimental results shows the reduction rate of maximum pullout resistance exerted by OW anchor compared to that exerted by disk does not change with the values of relative density and root depth under similar ground conditions. In this study, a formula to calculate the pullout resistance exerted by OW anchor is proposed. The developed formula is based on the formula used for calculating the maximum pullout resistance exerted by a disk as an earth anchor model. The proposed formula relies on the results of experiments to evaluate the pullout resistance exerted by OW anchor.

Keywords: Slope collapse suppression method, Ground anchor method, Open-Wing-type anchor, Formula of computation of extreme pullout resistance exerted by OW anchor

INTRODUCTION

In recent years, large-scale sediment-related disasters have occurred in Japan causing human injuries. Anchoring methods are used as effective measures to prevent and control landslides. The method involves connecting a land retaining structure or a slope to the anchorage zone using the frictional force between anchor grouting material and surrounding ground. A variety of anchoring systems are used, including ground anchor, earth anchor, and ground reinforcing methods. They are installed in many construction sites to maintain slope stability, prevent overturning of retaining structures, stabilize earth-retaining walls, etc.

The pullout resistance of anchors relies on the anchor function component and grouting material, which is made of mortar. The grouting material acts as an adhesive to connect the anchor via friction to its surrounding ground. However, it has been known that friction decreases over time, reducing the anchorage bond with surrounding ground as the anchor is pulled out from its anchorage zone. The open-wing-type (OW) anchor is a new earth anchor technique that has been developed to address the issues associated with the currently existing methods using open wings to increase pullout resistance [1].

The unique design criterion of OW anchors must be incorporated in the original criteria of anchoring

systems to ensure the practical application of OW anchors. Thus, developing a formula to calculate the pullout resistance exerted by OW anchor is absolutely imperative. This study presents a formula for the computation of pullout resistance exerted by OW anchors. Experiments were conducted to examine the effects of number of wings, root depth, and type of ground on the pullout resistance exerted by OW anchors and proposed a calculating formula to express these conditions.

LITERATURE REVIEW

Formula to Calculate Pullout Resistance Exerted by Disk-shaped Earth Anchor

A formula must be derived to calculate the pullout resistance exerted by OW anchor in order to determine the unique design criteria of OW anchors. Hence, the equation to calculate the pullout resistance exerted by disk-shaped earth anchor was used as a reference in this study. Many researchers proposed equations to calculate pullout resistance exerted by disk-shaped earth anchors using earth cone method [2], earth pressure method [3], shearing method [4], and another method proposed by Balla [5], in which the experiment results were based on the assumptions that the sliding surface is determined by $\lambda \equiv D/2B$ ($2B$: diameter of disk, D : root depth of anchor),

sliding surface is expressed by a circular arc determined only by the internal friction angle. Katsumi and Nishihara used the sliding surface proposed by Balla as reference because it is close to the actually measured sliding surface and involves simple calculation procedures compared to other calculation formulas [6]. In their proposed calculation formula, the pullout resistance is calculated based on the vertical component of force perpendicular to the sliding surface that was not considered by Balla.

Calculation Formula Proposed by Katsumi and Nishihara [6]

Equation (1) was proposed by Katsumi and Nishihara to calculate the pullout resistance exerted by disk-shaped earth anchor.

$$Q = G_1 + T_v + G_2 \quad (1)$$

where G_1 is the weight of soil mass, T_v is the sum of the perpendicular components of shear resistance force and perpendicular components of force exerted on a slide plane and G_2 is the self-weight of anchor.

G_1 can be obtained by Eq. (2) using the symbols shown in Fig. 1. B is the radius of the disc and D is the root depth.

$$G_1 = \pi B^2 D \gamma F_1(\phi, \lambda) \quad (2)$$

Katsumi and Nishihara proposed Eq. (3) to easily set up $F_1(\phi, \lambda)$. Fig.2 can be used to set up $f_{11}(\phi)$, $f_{12}(\phi)$ in Eq. (3).

$$F_1(\phi, \lambda) = 1 + \lambda f_{11}(\phi) + \lambda^2 f_{12}(\phi) \quad (3)$$

Equation (4) is used to calculate T_v .

$$T_v = \pi B^2 D \gamma \left[\frac{c}{D \gamma} F_2(\phi, \lambda) + F_3(\phi, \lambda) \right] \quad (4)$$

Eqs (5) and (6) were proposed by Katsumi and Nishihara to easily set up $F_2(\phi, \lambda)$ and $F_3(\phi, \lambda)$. Figs 3 and 4 are used to set up f_{21} and f_{22} in Eq. (5) and f_{31} and f_{32} in Eq. (6), respectively.

$$F_2(\phi, \lambda) = \lambda f_{21}(\phi) + \lambda^2 f_{22}(\phi) \quad (5)$$

$$F_3(\phi, \lambda) = \lambda f_{31}(\phi) + \lambda^2 f_{32}(\phi) \quad (6)$$

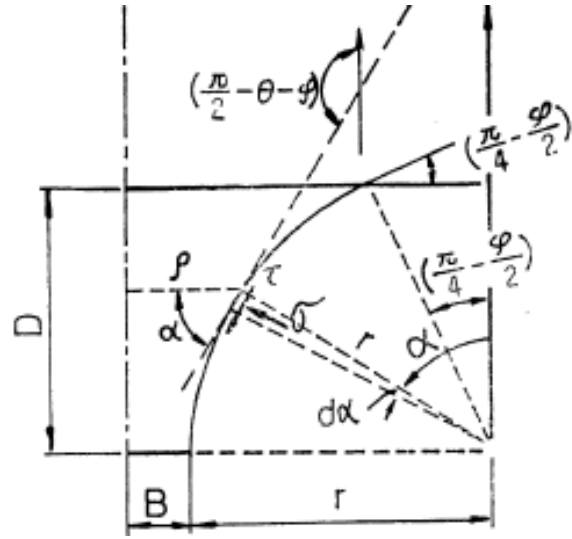


Fig. 1 Stresses acting on slip line. [6]

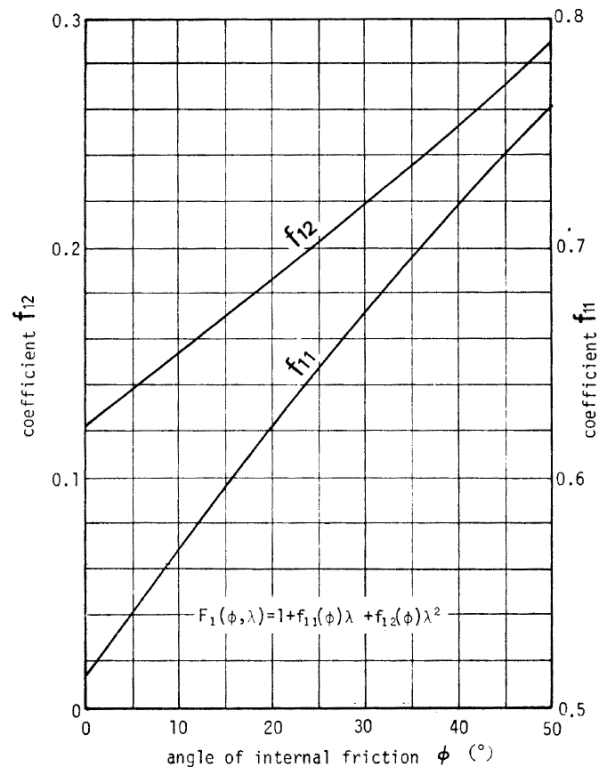
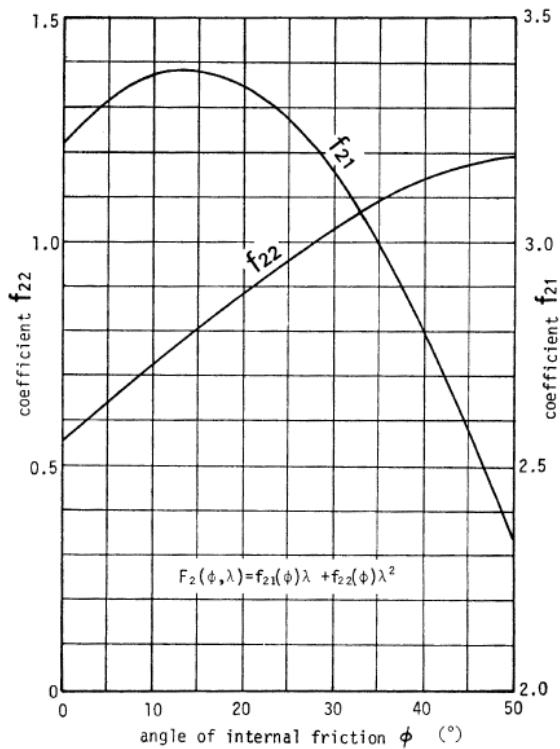
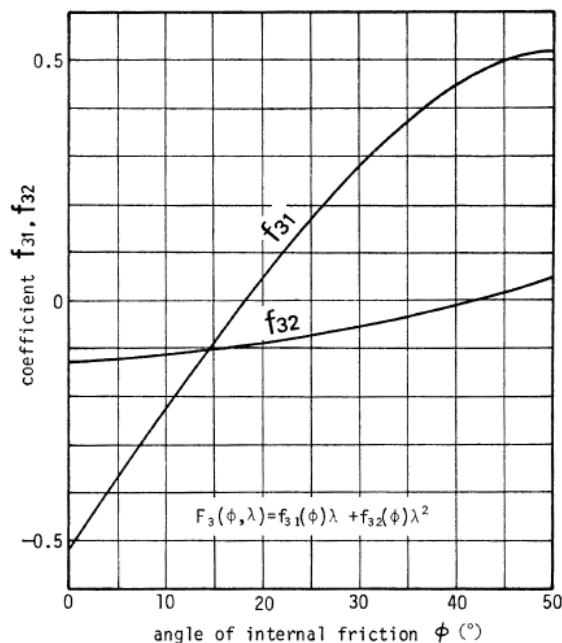


Fig.3 Pullout capacity factor $F_1(\phi, \lambda)$. [6]

Fig.3 Pullout capacity factor $F_2(\phi, \lambda)$. [6]Fig.4 Pullout capacity factor $F_3(\phi, \lambda)$. [6]

EXPERIMENTS TO ESTIMATE PULLOUT RESISTANCE OF OW ANCHOR

Experimental Method

The influence of number of OW anchor wings was examined to evaluate the pullout resistance exerted by OW anchor. Five OW anchors with different numbers of wings (two, three, four, six, and eight wings) and a disk were used in this experiment. Three experimental conditions are listed in Table 1.

Table 1 Specifications of three experimental conditions

Experimental conditions	Condition 1	Condition 2	Condition 3
Type of soil	Decomposed granite soil	Toyoura sand	Toyoura sand
The maximum particle size (mm)	2	0.25	0.25
Relative density (%)	100	80	35
Root depth (mm)	200	200	400
Moisture content (%)	10	0	0

When the experiment was conducted using decomposed granite soil, widespread shearing of soil was detected reaching the top of soil. Thus, a large soil tank was used to prevent shear planes from reaching the wall surface of earth tank. A cylindrical soil tank with bore diameter of 800 mm and height of 600 mm was used in the experiment conducted using decomposed granite soil, as shown in Photo 1. Model ground with bore diameter of 800 mm and height of 200 mm was formed in this soil. When the experiment was conducted using Toyoura sand, a smaller acrylic soil tank was used compared to that used in the decomposed granite soil experiment because the influence and size of shear bands developed in Toyoura sand are less than those developed in decomposed granite soil. An acrylic soil tank with width of 600 mm, depth of 400 mm, and height of 400 mm was used, as shown in Photo 2.



Photo 1 Soil tank.

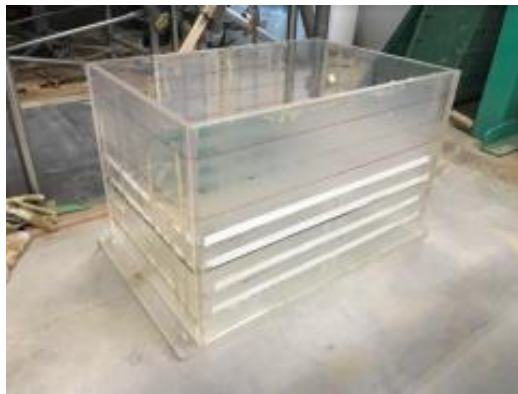


Photo 2 Acrylic soil tank.

Experimental Results

The experimental results are shown in Figs. 5-7. Fig. 5 shows the results by the experiments conducted using decomposed granite soil (with 100% relative density and 200 mm root depth). Fig. 6 shows results obtained using Toyoura sand (with 35% relative density and 400 mm root depth). Fig. 7 shows the results obtained using Toyoura sand (with 80% relative density and 200 mm root depth). The maximum pullout resistance was determined for each experimental condition. It found that the highest pullout resistance was achieved when the experiment was conducted using disk in all experiments and the second highest pullout resistance was obtained using OW anchor with eight wings. In addition, the maximum pullout resistance decreases as the number of wings of OW anchor decreases.

The experimental results were compared to determine the relationship between of the maximum

pullout resistance and number of wings. Fig. 8 shows the reduction rate of maximum pullout resistance exerted by OW anchor compared to that exerted by disk when the experiments were conducted using decomposed granite soil (with 100% relative density and 200 mm root depth), Toyoura sand (with 35% relative density and 400 mm root depth), and Toyoura sand (with 80% relative density and 200 mm root depth). Different values of pullout resistance were obtained when Toyoura sand was used owing to the different values of relative density and root depth. However, regardless of the sand physical properties, the reduction rate of maximum pullout resistance determined by the number of wings was comparable with that obtained by disk. Accordingly, the reduction rate does not change with the values of relative density and root depth under similar ground conditions. Furthermore, lower reduction rate was obtained in decomposed granite soil than in Toyoura sand. This can be attributed to the difference in the values of cohesion and inter frictional angle. Thus, the reduction rate of maximum pullout resistance is dependent on the number of wings when OW anchors are used, while it depends on the ground condition and ground strength parameters when using disks.

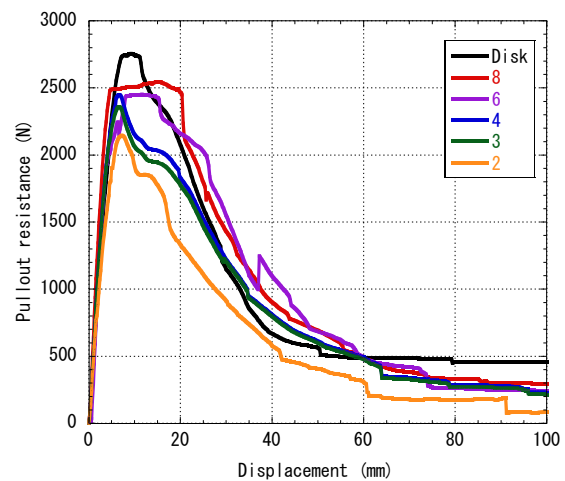


Fig. 5 Condition 1 results.

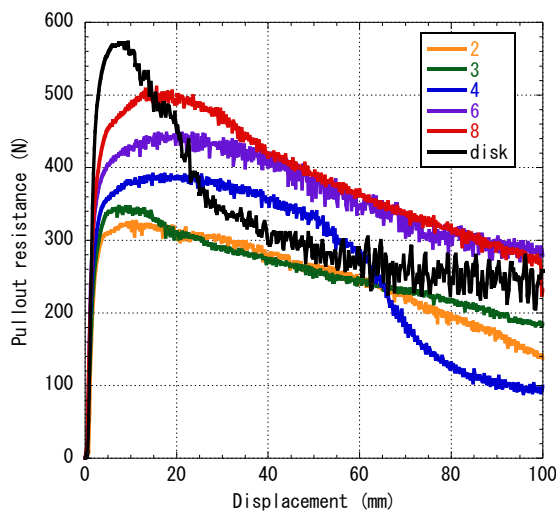


Fig. 6 Condition 2 results.

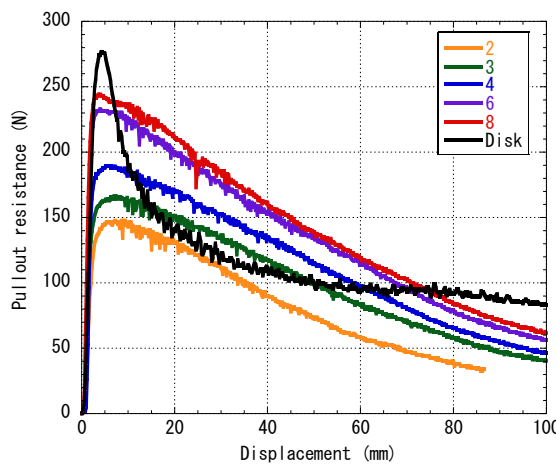


Fig. 7 Condition 3 results.

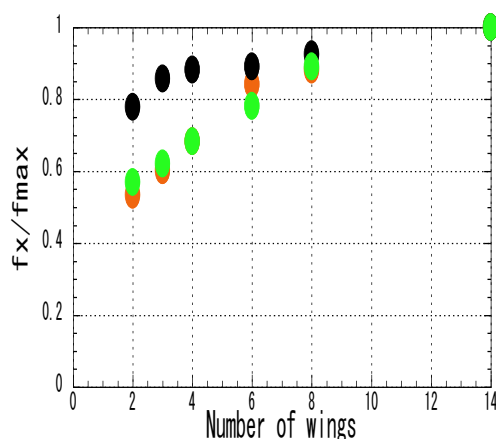


Fig. 8 Reduction rate of maximum pullout resistance.

FORMULA TO CALCULATE MAXIMUM PULLOUT RESISTANCE EXERTED BY OW ANCHOR

A formula to calculate the maximum pullout resistance exerted by OW anchor was derived using the results obtained from soil tank experiments and based on the formula proposed by Katsumi and Nishihara to calculate the pullout resistance exerted by disk-shaped earth anchor. As discussed above, the reduction rate of maximum pullout resistance exerted by OW anchor is comparable with that obtained by disk anchors, which depend on the value of cohesion and inter frictional angle. Hence, the formula proposed by Katsumi and Nishihara can be updated to derive an original formula to calculate the maximum pullout resistance of OW anchor by incorporating the number of wings, cohesion, and inter frictional angle into the formula developed by Katsumi and Nishihara. When OW anchors with large number of wings (6 wings, 8 wings, etc.) are used, the soil mass surrounding the OW anchor is approximately equal to the case of disk anchors with less pullout resistance exerted by OW anchor compared to the case of disk because of the reduced amount of soil released through the wing gaps. However, this concept cannot be applied if OW anchors with fewer number of wings (2 wings, 3 wings, etc.) are used. For example, that the apparent sliding surface in case of OW anchor with two wings differs from that shaped by disk as the amount of soil in the apparent contact area surrounding the OW anchor depends on the number of wings. Thus, the reduction rate of maximum pullout resistance exerted by OW anchor cannot be unconditionally expressed using the number of wings. Hence, a formula to calculate the maximum pullout resistance exerted by OW anchor is derived by multiplying the coefficient that depends on the type of ground and number of wings by the formula f developed by Katsumi and Nishihara to calculate the maximum extreme pullout resistance exerted by disk anchors.

The maximum pullout resistance exerted by OW anchor can be calculated by Eq. (7).

$$Q = a_n(G_1 + T_v + G_2) \quad (7)$$

where G_1 is the weight of soil mass. T_v is the sum of perpendicular components of shear resistance force exerted on a slide plane and the perpendicular components of force perpendicularly exerted on a slide plane. G_2 is the self-weight of the anchor. a_n is coefficient depend on the number of wings of OW anchor. a_n is the corresponding reduction rate of maximum pullout resistance determined by number of wing when compared to disk for a specific type of ground. Fig. 8 can be used to determine a_n .

CONCLUSION

Our research group conducts experiments to evaluate the pullout resistance exerted by OW anchor. Five OW anchors with different numbers of wings and a disk were used in this experiment and three experimental conditions are used. The experimental results shows the reduction rate of maximum pullout resistance exerted by OW anchor compared to that exerted by disk does not change with the values of relative density and root depth under similar ground conditions.

In this study, a formula to calculate the pullout resistance exerted by OW anchor is proposed. The developed formula is based on the formula used for calculating the maximum pullout resistance exerted by a disk as an earth anchor model proposed by Katsumi and Nishihara. The proposed formula relies on the number of wings of OW anchor.

FUTURE RESEARCH

As mentioned in the previous section, the formula developed to calculate the maximum pullout resistance exerted by OW anchor is achieved by multiplying the formula proposed by Katsumi and Nishihara by a coefficient. However, incorporating the relationship between the number of wings, cohesion, and inter-frictional angle into the developed formula can potentially result in more flexible calculation procedures of the maximum pullout resistance without relying on the ground condition and number of wings. Hence, our future research will

focus on investigating the relationship between the number of wings, cohesion, and inter-frictional angle using experiments or computer simulations.

REFERENCES

- [1] Danjo T., Teramoto T., Miyajima Y., Fukushima N., Fujimoto M., and Fukagawa R., A series of model experiments for development of Unfolding ground anchor, Proceedings of the 7th Symposium on Sediment-Related Disasters, 2014, pp. 241-246.
- [2] Mors H., Das Verhalten von Mastgründungen bei Zugbeanspruchung, Die Bautechnik, Issue 10, 1959, pp. 367-378.
- [3] Mors H., Methods of Dimensioning for Uplift Foundations of Transmission Line Towers, Conference Internationale des Grands Reseaux Electriques a Haute Tension, Session 1964, 210, pp. 1-14.
- [4] Paterson G. and Urie R.L., Uplift Resistance Tests on Full Size Transmission Tower Foundations, Conference Internationale des Grands Reseaux Electriques a Haute Tension, Session 1964, 203, 1964, pp. 1-22.
- [5] Balla A., The Resistance to Breaking out of Mushroom Foundation for Pylons, Proc. 5th. Int. Conf. Soil Mech. and Found. Eng., Vol. 1, 1961, pp. 569-576, .
- [6] Katsumi T. and Nishihara A., Fundamental studies on pullout resistance of earth anchors, J. Jpn. Soc. Civil Eng., Issue. 276, 1978, pp. 65-76.

INVESTIGATION OF CYLINDRICAL SPECIMEN COLLAPSE BEHAVIOR USING 3D SMOOTHED-PARTICLE HYDRODYNAMIC ANALYSIS

Tetsuya Okano¹, Yukiko Sumi², Tsutomu Matsuo³, and Ryoichi Fukagawa⁴
^{1,3,4} Ritsumeikan University, Japan; ² Taisei Corporation, Japan

ABSTRACT

Smoothed-particle hydrodynamics (SPH) is a computational method used to simulate the dynamics of continuum media, such as solid mechanics and fluid flows. Much research has been conducted using this method to simulate the collapse behavior of soils; however, most of this research has focused on two-dimensional SPH analysis. There is currently little research into modelling the collapse behavior of soil using three-dimensional SPH analysis. Therefore, this paper presents the results of a collapse behavior study of cylindrical sand specimens, comparing experimental results with a three-dimensional SPH analysis. The experiments were conducted by pulling a cylindrical container from a column of sand and measuring the dimensions of the resulting diffusion cone. The frictional properties of the table surface and the rate of pulling were varied to determine their effects and compare analysis results. The diffusion cone geometries determined by SPH analysis showed good consistency with the observed experimental results, suggesting promising application of three-dimensional SPH analysis to the modelling of soil collapse behavior.

Keywords: SPH analysis, Cylindrical specimen, Collapse behavior, Decomposed granite

INTRODUCTION

Traditionally, finite element method (FEM) analysis has been widely used as a representative stress-deformation analysis method for in-situ soils. The FEM analysis method consists of a series of small elements, each of which is defined by a linear function, collectively describing the properties of an object by combining the discrete behavior of these many small regions. However, while FEM analysis is widely used in many different applications, other analysis methods are typically used to model large deformation problems. Among these methods, smoothed-particle hydrodynamics (SPH), a continuum analysis method, is a type of analysis used to express large deformations, including in geotechnical engineering applications. Several dissertations have relied upon two-dimensional SPH analysis for geotechnical engineering applications [1], [2].

In this study, sand column specimen collapse behavior is both experimentally evaluated and numerically analyzed using three-dimensional SPH analysis, and the shapes of the resulting diffusion cones are compared to validate the use of SPH analysis.

EXPERIMENTAL CONDITIONS

Outline of Experiment

Fig. 1 illustrates an outline of the experiment.

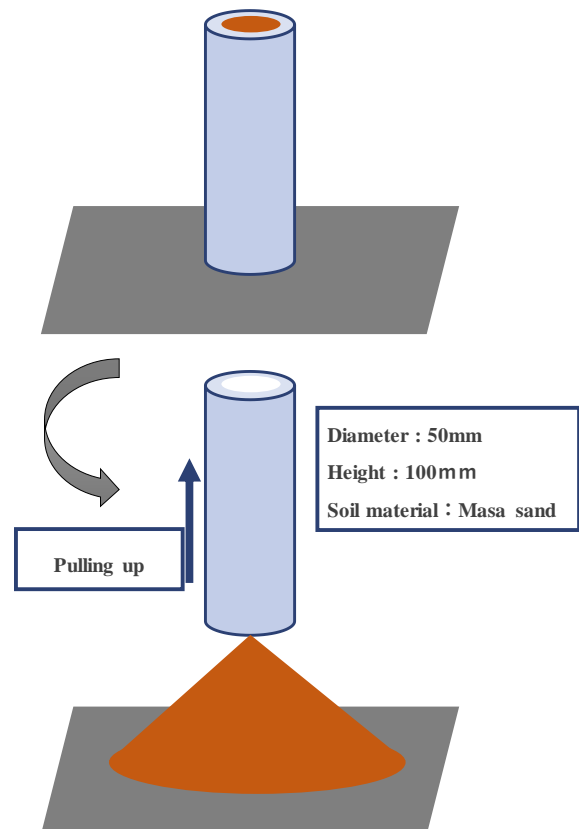


Fig.1 Outline drawing of experiment of pulling up cylindrical sands

The material used was a Masa soil, that is decomposed granite soil obtained from Shigaraki, packed in a cylindrical container with an inner diameter of 5 cm and a height of 10 cm. This cylindrical container was connected to a threaded rod that was used to pull the cylinder up vertically. Fig. 2 shows a photograph of the equipment during the experiment.

Because the cylinder was pulled up manually, the velocity of pulling varied. To capture the pulling velocity during the experiment, the pulling time was measured by a 40-fps video camera, and the mean pulling velocity was calculated by dividing the displacement by the time it took to raise the cylinder.

If the velocity at which the container is pulled is too fast, the friction between the cylindrical specimen and the container becomes a dominant cause of dynamic deformation. In this study, the friction between the specimen and the container was minimized to the extent possible by applying an electrostatic discharge spray to the inside of the container. Based on the parameters of the spray, the ideal pulling velocity was targeted at 50 cm/s to minimize the remaining friction between the sand and the cylinder. Target pulling velocities of 50, 40, 30, 20, and 10 cm/s were then experimentally applied, and each experiment was conducted four times for each different pulling velocity.

To account for the influence of friction between the table surface and the specimen as it diffused, two different table surface materials were used for each set of test parameters: ultra-high molecular weight polyethylene (UHMWPE), widely used for sliding surfaces in biomaterials such as artificial joints and industrial materials because of its superior wear and

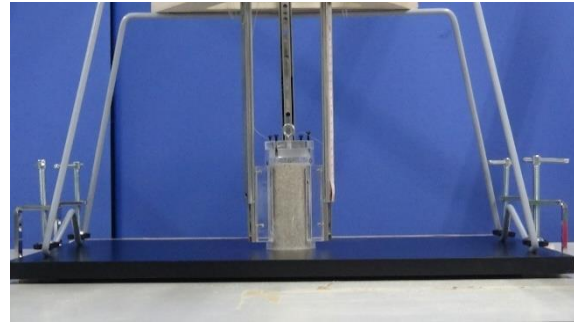


Fig.2 Experimental equipment

corrosion resistance, and a decorative board with a general surface coating.

The resulting diffusion cones of the collapsed specimens were quantified using two dimensions: the maximum diffusion diameter and the maximum height. The maximum diffusion diameter is defined as the diameter of the base of the diffusion cone and is shown in Fig. 3. The maximum height is the height of the diffusion cone and is shown in Fig. 4. The analytical and experimental results were then compared using these two dimensions for the two types of table surfaces, and the effect of friction was determined with respect to the applied pulling velocity. The experimental procedure employed was as follows:

1. The experimental instruments were placed on the table surface.
2. The electrostatic diffusion spray was applied to the table surface and the inner wall of the cylindrical container.
3. The sand was prepared in the cylindrical container.
4. The container was pulled upward manually as



Fig. 3 Maximum diffusion diameter

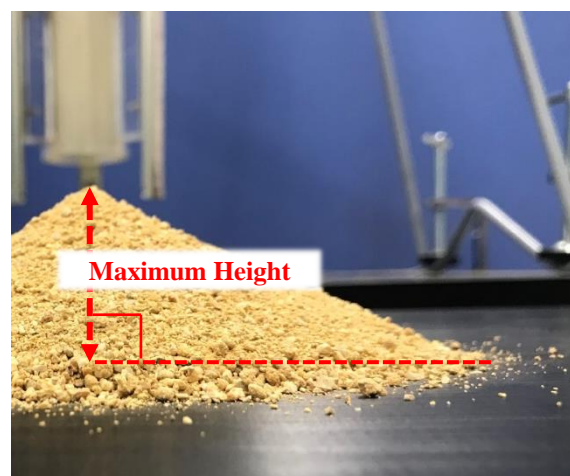


Fig.4 Maximum height and the boundary for Maximum diffusion diameter

constantly as possible at the target rate.

5. The maximum diffusion diameter and maximum height of the diffusion cone were then measured.

Material Parameters

Table 1 provides the material parameters of the Shigaraki decomposed granite. The internal friction angle ϕ and Young's modulus E were determined from triaxial compression test results transferred as per Moriyoshi [3] from the stress-strain curve. As the specimens used in this study were air-dried, the cohesion $c = 0 \text{ kN/m}^2$.

Table 1 Material parameters of Shigaraki decomposed granite

Parameters	Variables	Units	Values
Unit weight	γ	kN/m^3	14.7
Young's modulus	E	MN/m^2	2.309
Poisson's ratio	ν	—	0.33
Cohesion	c	kN/m^2	0.0
Internal friction angle	ϕ	deg	32
Dilatancy angle	ψ	deg	0.0

NUMERICAL ANALYSIS

Analysis Conditions

The experimental arrangement was numerically analyzed in three dimensions using an SPH analysis program created by Bui [1]. The state at which the displacement converged after the specimen was loaded with its own weight was taken as the initial state. Table 2 provides the SPH method parameters used for the analysis.

Table 2 Parameters of the SPH simulation

Parameters	Variables	Values
Initial Particle diameter	dx	2.5 mm
Smoothing length	h	3.0 mm
Initial smoothing length	kh	6.0 mm
Parameter for boundary condition	β	1.75
Number of particle	n	3160

The model used in the analysis is shown in Fig. 5. The bottom of the specimen was set as $Z = 0 \text{ cm}$, at which location the bottom layer of real particles was used for the first step of the analysis inside a circle

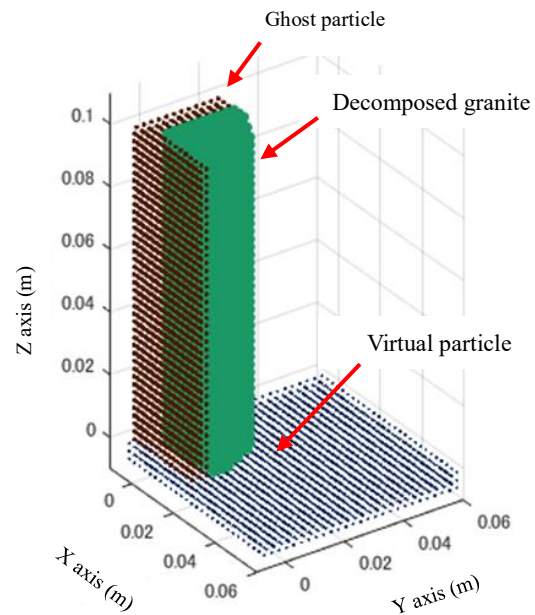


Fig.5. Outline of simulation case

with a radius of 2.5 cm in the XY plane. Considering the axial symmetry of the cylinder, a cross section consisting of one quarter of the section of the whole cylinder was analyzed to reduce the computational complexity.

Real particles were stacked from the bottom to a height of 10 cm. Three layers of boundary particles were distributed on the bottom surface to support the real particles, and three layers of ghost particles were arranged at the boundary between the quarter-cylinder specimen and the XZ and YZ planes.

The maximum value β_{max} of the coefficient β_0 , related to the relative velocity between the real particles and the boundary particles, was set to 1.75 to prevent particles from getting too close to the boundary. Bui et al. [1] recommend that β_{max} be set between 1.5 and 2. It was confirmed by preliminary testing prior to conducting the SPH simulation that the value of β_{max} influences the analysis result, so this constant value was selected by more detailed examination.

The boundary conditions selected to simulate the pulling of the cylindrical container were determined to reflect the pulling velocity using ghost particles. The ghost particles were initially placed around the specimen circumference and the lifting of the container was then simulated by sequentially removing these ghost particles from the bottom upward. In this process, the distance from the bottom surface to the lower edge of the circumferential ghost particles was defined as TR .

By increasing TR by ΔTR each step, the raising rate of the experimental container could be expressed.

RESULTS AND DISCUSSION

Confirmation of Analytical Symmetry

In this section, the results of the three-dimensional SPH analysis are evaluated to ensure appropriate symmetry in the circumferential direction. Fig. 6 depicts the horizontal diffusion of the simulated specimen particles when the container is instantaneously removed, thus the rate at which TR was increased was infinite. The color map depicts the degree of displacement of each particle.

Fig. 7 and 8 depict the cross-sectional diffusion of the simulated specimen particles, in which the angle indicates the degree of rotation from the model y axis towards the x axis.

Fig. 9 depicts a superposition of the cross-sectional diffusion at 45 and 60 degrees shown in Figs 7 and 8, respectively, for the instantaneous cylinder removal case, generated by ImageJ [4], an image processing software package used at the National Institute of Health. Fig. 7 is processed into a red fluorescent image and Fig. 8 is processed into a blue fluorescent image, and these are superimposed. Thus, overlapping points are displayed in purple. It can be seen that the results in different directions are in good agreement, demonstrating that there is almost no difference in particle diffusion with circumferential location.

Effects of Different Pulling Velocities

In this section, the distribution predicted by the SPH analysis is compared with that observed in the experiments. Fig. 10 is a typical example of the resulting three-dimensional particle diffusion after removing the cylinder, as determined by analysis. Table 3 provides a comparison between the maximum diffusion diameter, maximum height, and pulling velocity of the experimental (A) and analytical (B) results, in which it can be seen that the models and the experiments show generally good agreement.

Fig. 11 depicts relationship between the pulling velocity and the resulting experimental and analytical maximum diffusion diameters. Regression curves have been added to approximate the correlation between pulling velocity and maximum diffusion diameter and aid comparison. Clearly, the maximum diffusion diameter and pulling velocity are positively correlated in both the experimental

and analytical results. Additionally, it can be observed that the total variation in diffusion

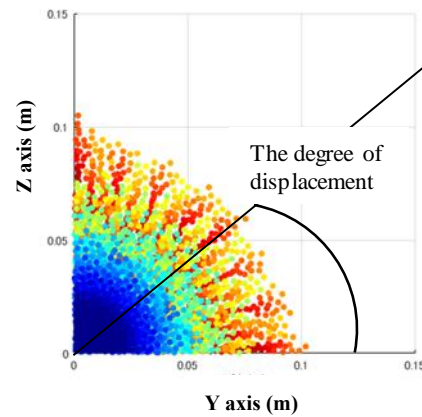


Fig.6 Displacement when the experiment container is instantaneously removed

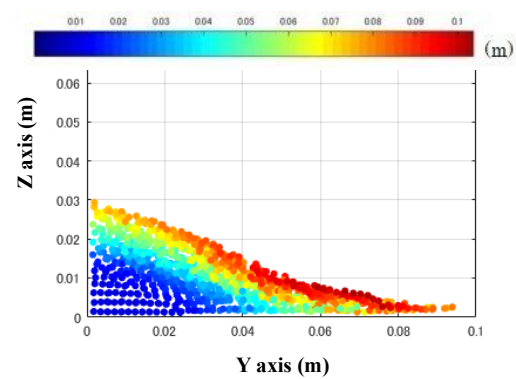


Fig.7 Displacement of 45°

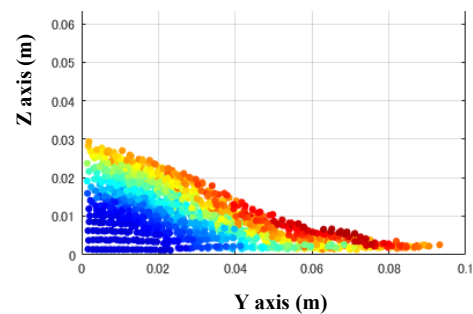


Fig.8 Displacement of 60°

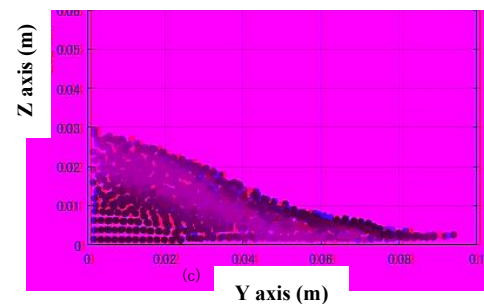


Fig.9 Superposition of the displacement diagram

diameter with pulling velocity is particularly large for the UHMWPE board, yet the shape of the regression curves for the UHMWPE and decorative boards are similar. For both table surface materials, the diffusion diameter increases with the pulling rate. Finally, note that the regression curves for the experimental data and the regression curve for the analytical data are quite similar.

Fig. 12 depicts the relationship between the pulling velocity and the resulting experimental and analytical maximum height of the diffusion cone. At a pulling velocity greater than 10 cm/s, the maximum height is nearly constant regardless of the table surface material, but when comparing the regression curves, it is clear that the use of the UHMWPE plate (which has a smaller coefficient of friction) generally results in a smaller maximum height. Though the analysis results also indicate a nearly constant maximum height at pulling velocities greater than 10 cm/s, the maximum height predicted is smaller than the experimentally determined values. It is inferred from this result that because the table surface friction is neglected in the analysis, the smaller the table surface friction, the smaller the maximum height of the diffused cone.

Clearly, though quantitatively small differences in diffusion cone geometry were obtained, qualitatively speaking, when comparing the shapes of the regression curves, the SPH analysis very nearly reproduced the observed experimental behavior.

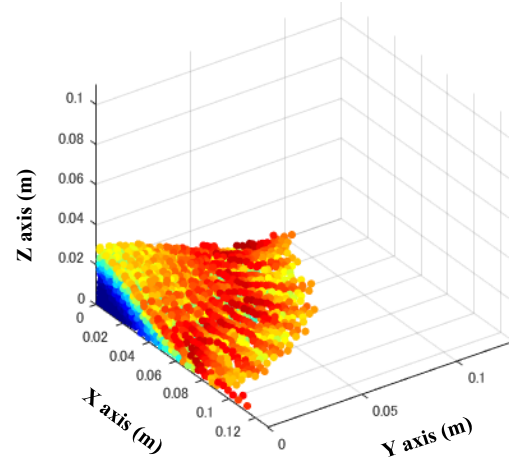


Fig.10. An example of analysis result

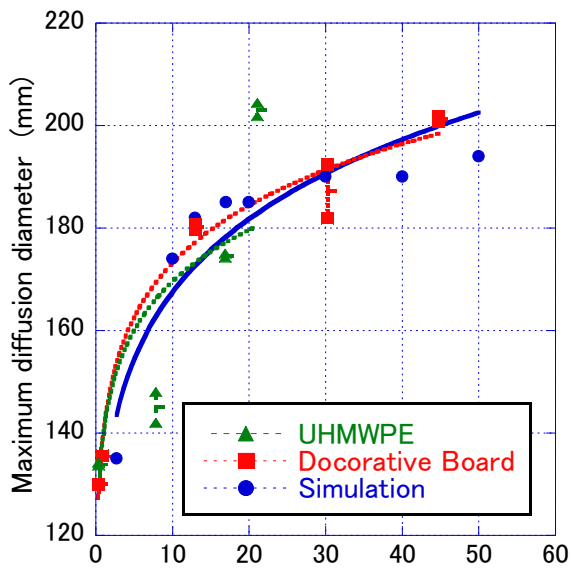


Fig.11 Relationship between pulling velocity and maximum diffusion diameter

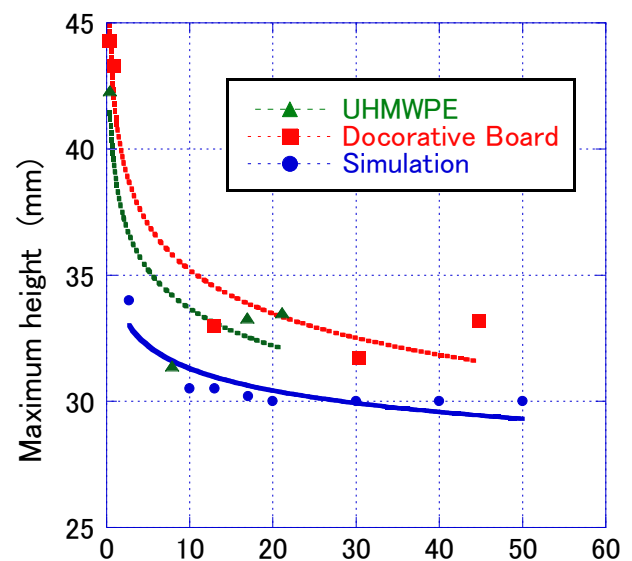


Fig.12. Relationship between pulling velocity and maximum height

Table 3 Comparison of analytical and experimental results

Exp. no.	Max. diffusion diameter (mm)			Max. height (mm)	Pulling velocity (cm/s)
	X axis	Y axis	Ave.		
A-1	—	—	194*	30.0	50.0
B-9	202	201	201	33.2	44.8
A-2	—	—	190*	30.0	40.0
B-4	182	193	187	31.7	30.3
A-3			190*	30.0	30.0
B-1	195	186	191	39.3	24.5
B-7	204	202	203	33.5	21.1
A-4	—	—	185*	30.0	20.0
A-5	—	—	185*	30.2	17.0
B-8	175	175	174	33.3	16.9
A-6	—	—	182*	30.5	13.0
B-10	181	180	180	33.0	13.0
B-2	148	142	145	31.4	7.9
A-7	—	—	174*	30.5	10.0
A-8	—	—	135*	30.4	2.7
B-5	136	136	136	43.3	0.9
B-3	134	134	134	42.3	0.4
B-6	130	130	130	44.3	0.3

Note: A: Analytical case; B: Experimental case

CONCLUSIONS

In this study, the collapse behavior of a simple cylindrical specimen was reproduced and analyzed using an SPH analysis accounting for the physical properties of the experimental samples. A parametric study was then conducted by changing the pulling velocity of the cylindrical container. By comparing the results of the experiment and analysis, the accuracy of the three-dimensional SPH analysis method was verified. The following conclusions were obtained:

- 1) It was confirmed that the diffusion cone shape of a cylindrical specimen after collapse differs depending on the table surface material and the container pulling velocity.

- 2) It was confirmed that the three-dimensional SPH analysis of a cylindrical specimen provides consistent and circumferentially symmetric results, yielding particle displacements that were nearly the same value in different angular directions.
- 3) It was confirmed that the change in pulling rate could be accurately expressed by the three-dimensional SPH analysis in terms of changes in the diffusion cone geometry.
- 4) The results of the three-dimensional SPH analysis and the experiments provided roughly the same maximum diffusion diameters for different pulling velocities, indicating that the accuracy of the three-dimensional SPH analysis is high.
- 5) When the pulling velocity was relatively slow, the same values for maximum height were obtained from both the three-dimensional SPH analysis and the experimental results, and when the velocity was high, the maximum height predicted by the SPH analysis was smaller, but qualitatively similar in trend to that determined by experiment.

In future work, the authors will investigate the effects of a wider variety of table surfaces and cylinder friction conditions, conduct further verification of the SPH method, and attempt to apply it to the analysis of slopes and tunnels.

REFERENCES

- [1] Bui H.H. Ryoichi Fukagawa, Kazunari Sako and Shintaro Ohno: Lagrangian meshfree particles method (SPH) for large deformation and failure flows of geomaterial using elastic-plastic soil constitutive model. International Journal for Numerical and Analytical Methods in Geomechanics, 32, pp.1537-1570, 2008.
- [2] Tsutomu Matsuo, Kunio Mori, Nobutaka, Hiraoka, Mengxia Son and Ryoichi Fukagawa, A basic study of applicability for the SPH simulation on tunnel face collapse behavior around tunnel portal zone, Japanese Geotechnical Journal, Vol.10, No.4, pp.569-582, 2015.
- [3] Moriyoshi Y., Improvement of slope earthquake resistance by surface reinforcement installed on slope including slack area, Undergraduate Thesis, Ritsumeikan University, Shiga Prefecture, Japan, 2015. (In Japanese)
- [4] Schneider C.A., Rasband W.S., Eliceiri K.W., NIH Image to ImageJ: 25 years of image analysis, Nature Methods, Vol.9, No.7, 2012, pp.671-675.

CALIBRATION OF EARTH PRESSURE CELL FOR A SPECIFIED LABORATORY APPLICATION

Mohammad Zahidul Islam Bhuiyan¹, Shanyong Wang¹, Scott William Sloan¹, Daichao Sheng¹ and Harry Michel¹

¹ARC Centre of Excellence for Geotechnical Science and Engineering, Faculty of Engineering and Built Environment, The University of Newcastle, Australia

ABSTRACT

Nowadays soil pressure transducers are widely used to measure the soil stress states in laboratory and field experiments. The soil pressure transducers, investigated here, are traditional diaphragm-type earth pressure cells (DEPC) based on strain gauge principle. It is found that the output of these sensors varies with the soil conditions as well as the position of a sensor. Therefore, it is highly recommended to calibrate the pressure sensors based on the similar conditions of their intended applications. The factory calibration coefficients of the EPCs are not reliable to use since it is normally calibrated by applying fluid (a special type of oil) pressure only over load sensing zone, which does not represent the actual field conditions. Thus, the calibration of these sensors is utmost important and it plays a pivotal role for assessing earth pressures precisely. In the present study, a special type of TML soil pressure sensor is used to compare its sensitivity under different calibration systems, for example, fluid and soil calibration using a simple test arrangement. The results report that the sensor provides higher sensitivity under fluid calibration compared to soil calibration. In addition, the calibration apparatus system used in this study could be a basic or simple guideline for the engineers and researchers for the future calibration of the earth pressure transducer.

Keywords: Soil pressure transducer, Sensitivity, Calibration, Earth pressure

INTRODUCTION

An earth pressure cell (EPC) is a pressure transducer that is frequently applied in laboratory and field studies to monitor the soil stress. They are traditionally diaphragm-type earth pressure cells (DEPC) based on strain gauge principle. The behaviour of these sensors are quite irregular and controversial, and the output of these sensors varies with the soil conditions i.e., soil type, moisture content and density as well as the position of sensor – embedded (installed inside soil mass or filled up by soil) or boundary (installed at soil-structure interface) as reported by Selig [1] and Weiler and Kulhawy [2]. In addition, Selig [1] also reported the sensor response is also affected by its configuration, for example, stiffness, thickness, sensing area and total area. Therefore, it is highly recommended to calibrate the pressure sensors based on the similar conditions of their intended applications. However, normally earth pressure cells are calibrated under uniform loading condition, which is called fluid calibration where special type of arrangement is used to apply oil pressure over only the sensing area of a cell, and this type of calibration is practiced by the cells' manufacturers. In addition, Gade and Dasaka [3] reported that sensor performs better under fluid calibration method than that of dead weight calibration (DWC) due to uniform

distribution of normal pressure on it.

Since, the main purpose of the EPC is to measure the soil stress in a soil mass but the distribution of normal contact stress at the EPC-soil interface may not be uniform like as fluid pressure. The insertion of rigid diaphragm type sensor in a soil mass may results in inclusion and arching effects. In situ stress distribution of soil is changed due to the presence of soil sensor, which acts as a stress attractor and the cell tends to overestimate the measured soil stress. On the other hand, arching phenomenon may develop due to the diaphragm deflection, which might cause the under-registration of the measured value and this could be occurred for the development of resistive shear along the mobilized soil mass [4]. Conversely, arching effect is dominant in dense sand whereas inclusion effect is prevailing in loose sand.

The main objective of this calibration work is to demonstrate the behaviours of these controversial transducers and to compare their sensitivity (sensor output per applied physical load) under different boundary conditions. In this study, a detailed fluid and soil calibration has been conducted by using two simple calibration systems for the earth pressure sensor with a flush of 1 mm made by TML, Japan. The calibration study reports that the sensitivity values of fluid calibration are almost same as that supplied by the manufacturer. Sensitivity of

embedded sensor in soil is slightly lower than (9.0%) that of fluid calibration for a specified soil dry density of 1.57 g/cc. Another important finding is that embedded sensor with sensing face upside down against the normal loading shows higher sensitivity (approximately 18.0%) compared to fluid sensitivity.

EARTH PRESSURE CELL

The soil pressure transducer used for calibration purpose is small in size strain gauge type pressure gauge (whetstone bridge principle) and it has a dual diaphragm structure that minimizes the displacement of pressure sensing face. Typically, it is widely applied to monitor soil stress in physical model experiments. In addition, it can measure dynamic earth pressure as well [5]. Fig.1 demonstrates the detailed dimensions of the cell. The soil pressure transducer has a rigid outer/inactive rim around the sensing face/area of 46 mm in diameter, which is formed by the part of steel casing as illustrated in Fig. 1(b) and it also has special flushing face of 34 mm in diameter within the total sensing area. The total outside diameter along the sensing zone is 50 mm and hence the thickness to diameter ratio is 0.226 and the sensing area to total surface area is 0.92, which are higher than recommended values 0.2 and 0.25-0.45 respectively as reported by Peattie and Sparrow [6] and Weiler and Kulhawy [2]. As a result, this type of sensor might experience stress concentration due to inclusion effect and Theroux et al. [4] reviewed that the cell error, the ratio of the difference between measured cell stress and exiting soil stress to the soil stress, increases gradually with the increment aspect ratio (cell thickness to diameter ratio). In addition, they also outlined that cell error is independent of the elastic moduli of the cell (M_c) and soil (M_s); the error is less than 10% when the ratio of elastic moduli (M_c/M_s) is greater than 10. The stress concentration (cell error) can be minimized by increasing the outer rim diameter and decreasing the cell thickness compared to the cell diameter [7], [8].

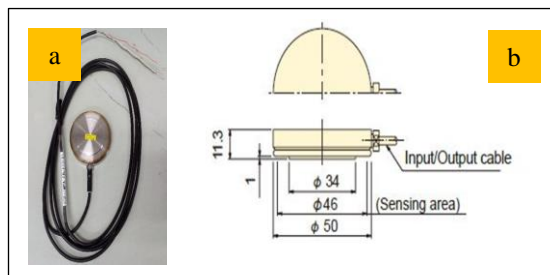


Fig. 1 (a) the EPC; (b) the detailed dimensions in mm [4].

FLUID CALIBRATION

For fluid calibration of the earth pressure sensor, firstly it was placed inside a sealed steel cylinder of 90 mm in diameter and 147 mm in height, which is filled up with de-aired water. A GDS controller was used to control the applied pressure inside the chamber and Fig.2 illustrates the simple fluid calibration system. Pressure in GDS controller is regulated from 0.0 to 1000 kPa with the increment of 100 kPa and the corresponding output from the soil pressure transducer (SPT) is recorded by a DataTaker. For the case of bridge type sensor, the data logger provides the output reading in ppm (parts per million), which is equivalent to micro volt per volt ($\mu V/V$). Fig.2 shows the comparison of the output data recorded by the SPT for different applied pressures under fluid calibration. Sensitivity is defined as the response (output) of a cell against the applied physical load, e.g., pressure [9]. The higher value of sensitivity coefficient of a cell in a specific type of media indicates its greater response for that type of media. From the sensitivity plot as illustrated in Fig.3(a), it is seen the cell does not any show hysteresis behaviour for hydrostatic loading condition; therefore, loading and unloading cycle coincides each other. Fig.3(b) demonstrates the actual calibration equation of the cell under fluid calibration condition.

The actual calibration coefficient (1.5651 kPa/ppm) found from the calibration plot is slightly lower (-1.09%) than that (1.5823 kPa/ppm) supplied by manufacturer. The results found from the hydrostatic loading system show in good agreement with the uniaxial fluid loading system used by the cell manufacturer [7]. In addition, the diameter (1.8 times of cell dia.) of the calibration chamber used in this study does not have any significant effects on the fluid calibration although a concern was initially raised by Gade and Dasaka [3].

Hence, it could be said that for checking the functionality of the EPC, whether it is working properly or not, it is not necessary to use a special calibration system (uniaxial fluid loading system) for applying vertical pressure just over only the sensing area, which could normally be used by the manufacturers [10].

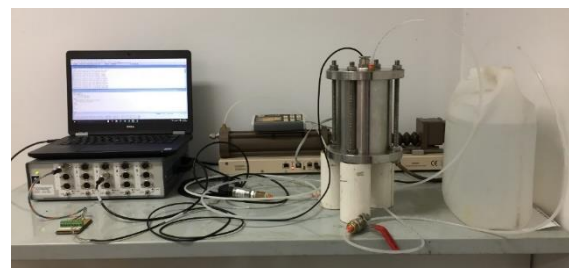
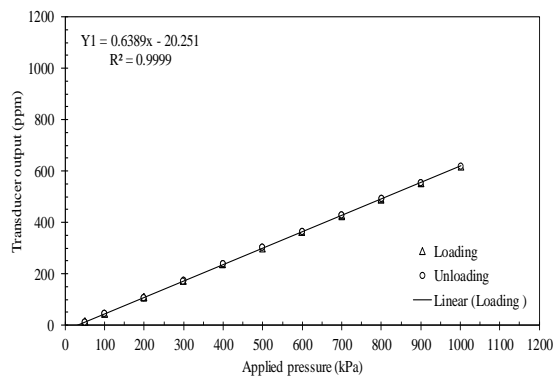
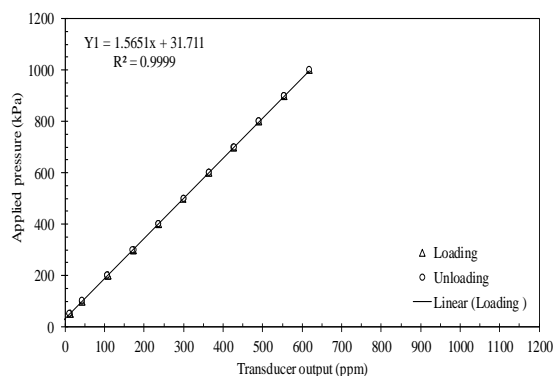


Fig. 2 Fluid calibration system showing calibration chamber



(a)



(b)

Fig. 3 Fluid calibration graphs of EPC: (a) sensitivity plot and (b) calibration coefficient plot.

IN-SOIL CALIBRATION

In the case of fluid calibration, a uniform pressure was applied on the earth pressure cell, although the normal pressure acting on the cell within a soil mass is not uniform. Consequently, the factory calibration (fluid calibration) is not sufficient to represent actual field application of the cell as well as unable to provide correct measurement of soil stress. In this regard, soil calibration is essential to get an accurate estimation of normal stress from a cell [11].

In-soil calibration were conducted based on the application of the EPC in a physical model study. Fig.4 outlines the positions of the six EPCs (rectangular in shape) along with other sensors used for laboratory scale model study of the fracture grouted soil-nail system. From the Fig.4, it is seen that all the cells are in embedded condition and except the locations of SL1 to SL2 and all the remaining cells are placed by facing the sensing area upside down to monitor the injection pressure of

grouting for a specified applied overburden pressure.

Since, the physical model experiments will be conducted under different moisture contents (3-6%) to find out the suction effect over the pullout capacity for the innovated soil-nail (named as x-Nail), the cells need to be calibrated for that condition as well along with dry soil calibration. For the brevity of the presentation, the calibration results of a single EPC are demonstrated and compared for different conditions as mentioned earlier.

For in-soil calibration, a bigger calibration chamber is required to minimize the boundary and the side friction effect of the chamber over the cell sensitivity in soil; Selig [1] recommended that the calibration chamber diameter should be 3 to 5 times of the cell diameter. By considering the issues, a modified calibration system was developed and applied for the soil calibration. The calibration chamber used in this study is a steel cylinder with a diameter of 190 mm and height of 300 mm - the diameter is 3.8 times of the cell diameter (D). Since the chamber is small in diameter, it is likely to have the side friction effects over the applied pressure at the cell position. Therefore, a thin sheet of polyethylene with lubricating oil was attached on the inside walls of the chamber in order to minimize the side friction, for example, Lazzarin [8] and Talesnick [12]. In addition, a special pure gum rubber sheet of 3 mm thickness was mounted under the top cover plate of the chamber to form a rubber bag for applying normal pressure using a GDS controller on the compacted sand through a plastic loading platen of 12 mm thickness. Fig.5 demonstrates the details of modified in-soil calibration system.

As a soil, uniformly graded fine sand is used for the cell calibration and this type of soil actually is applied for the model experiments. The index properties of the sand has already been reported by Bhuiyan [13]. Furthermore, Talesnick [12] found that the stress cell was more sensitive in fine sand compared to in coarse sand. The sand was compacted in three layers to achieve an estimated relative compaction (C_R) of 88% of the maximum dry density and to maintain the soil dry bulk density of 1.50 g/cc. However, in case of sensor calibration in dry sand, the bulk dry density of the soil was achieved to 1.57 g/cc by free falling (sand-raining) the dry sand into the chamber since it was quite hard to maintain the dry density of 1.50 g/cc for the completely dry sample. By considering the loading platen effect over the non-uniform vertical stress distribution depth (2/3 times of loading platen diameter) and the critical arching height (2 to 3 D), beyond this height there is no arching effect, the stress cell was embedded at the middle height of the chamber -150 mm from the top cover plate [4], [14].

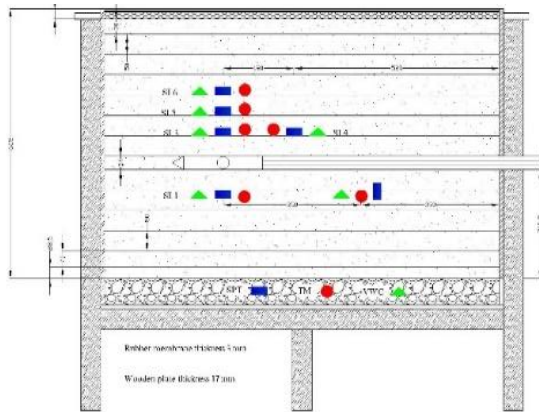


Fig. 4 Schematic of physical model showing sensors positions

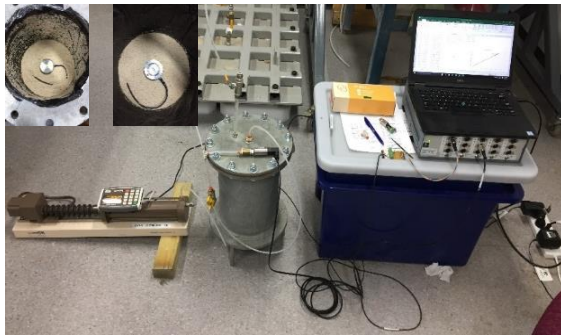
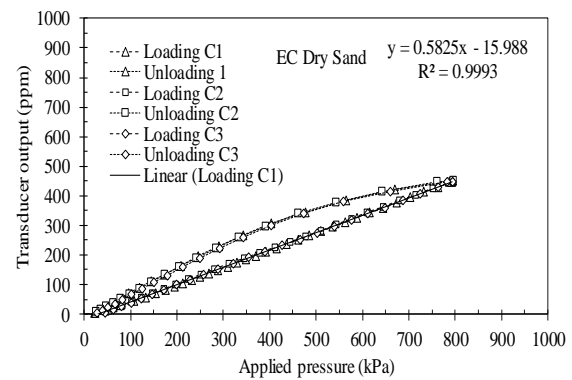


Fig. 5 Photograph of In-soil calibration system showing GDS controller, calibration chamber, pressure transducer, and embedded EPC with sensing area facing up and down (inset).

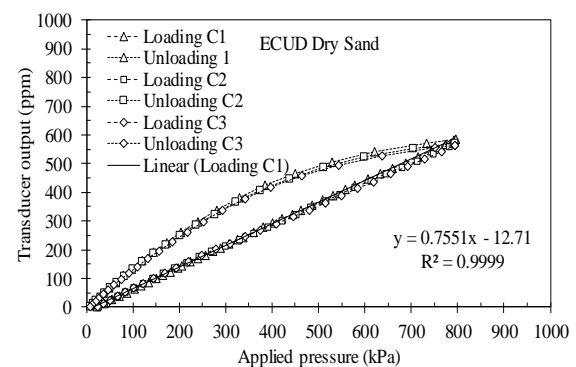
Fig.6 demonstrates the sensitivity behaviour of the embedded stress cell in dry sand for three cycles of loading and unloading under different orientations of the sensing face. The sensitivity of the cell is determined from the slope of the first loading cycle (virgin loading) and it is expressed in ppm per kPa. From the Figure it is seen that the cycle 2 and 3 almost coincides with the virgin cycle (cycle 1) for the both cases of the sensor's orientations. Unlike fluid calibration, the cell shows nonlinear and hysteresis behaviour during unloading, which could be resulted from frictional interlocking among the sand particles – where the compacted sand grains interlock each other and momentarily sustain a portion of the applied load. The effect of hysteresis disappears ultimately after complete unloading. This type of behaviour was also observed in the previous investigations conducted for In-soil calibration of diaphragm type of stress cell [7], [14], [15].

By comparing the Figs.6a and 6b, two interesting

findings can be observed that the sensitivity of the embedded cell with sensing area facing upside down is higher (0.7551 ppm/kPa) compared to that of facing up condition (0.5825 ppm/kPa). In addition, the hysteresis, the measured gap between the loading and unloading curves, is greater for the embedded cell with facing down compared to the normal orientation condition (Fig.6b). This might be happened due to having more uniform pressure distribution on the sensing area for the case facing down installation. Garnier et al. [16] reported that the face-up and face-down installation does not affect significantly the cell registration for the hydraulic cell. Nevertheless, in the case of diaphragm cell, the registration ratios, ratio of soil sensitivity (S_s) to actual fluid sensitivity (S_f), are 0.91 and 1.18 for normal and face down installation respectively. In other words, the embedded cell in soil with facing down yields a higher output for a specified applied pressure, which indicates the cell is over-registered, since the sensitivity of the faced-down cell is 18.0% greater than fluid sensitivity (0.6389 ppm/kPa). On the other hand, the cell embedded normally in soil experiences under-registration due to its lower sensitivity (-9.0%) compared to the fluid sensitivity, and this observation can be supported by the findings of Labuz and Theroux [7] in which a special diaphragm cell (Kulite cell) experiences soil sensitivity of about 20 % lower than fluid sensitivity.



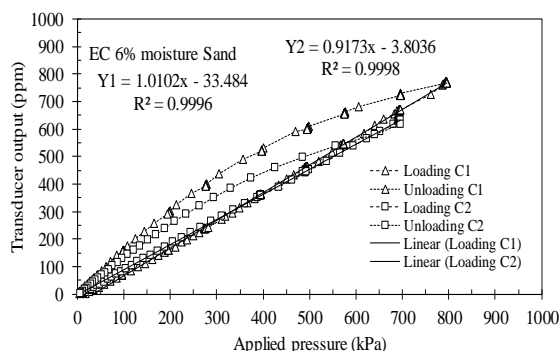
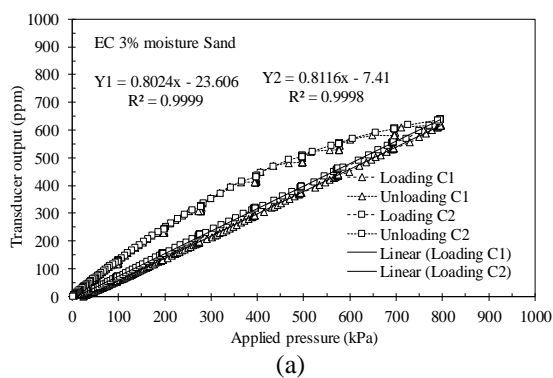
(a)



(b)

Fig. 6 Sensitivity plots of the embedded cell in dry sand for: (a) sensing area facing up and (b) sensing area facing upside down.

Fig.7 demonstrates that the sensitivity increases with the moisture content and hysteresis behaviour is higher in moist sand compared to dry sand. The higher hysteresis might be resulted from the frictional interlocking along with inter-particle surface tension (cohesion) in moist sand of low water contents. Fig.7a shows that the registration ratio for the virgin loading-unloading cycle (cycle 1) is 1.26 which is approximately equal to that (1.27) for cycle 2. In addition, by comparing the sensitivity of the moist sand (3% water content by weight) against the dry sand, it is found that the normally embedded stress cell over-registers approximately 38% higher compared with the dry soil calibration. For the case of 6% moist sand (Fig.7b), the soil sensitivity of cycle 1 is higher than that of cycle 2 and this behaviour is in good agreement with the findings reported by Talesnick [12] for dry soil calibration in which the diaphragm cell showed more sensitivity for first load-unload cycle in comparison with second cycle. The registration ratio for 6% moist sand is about 1.58 and 1.44 for cycle 1 and 2 respectively. However, the moist soil calibration indicates that the stress cell experiences over-registration of about 73% higher against the dry soil calibration. Overall, the results reveal that the cell sensitivity in soil is significantly affected by the moisture content as mentioned by Selig [1].



(b)

Fig. 7 Sensitivity graphs of the embedded cell in moist sand: (a) 3% and (b) 6% moisture content.

CONCLUSION

In this study, a series of cell calibration tests was executed in different medium and the sensitivities of the stress cell were compared against different boundary conditions. The following major conclusions can be outlined from this comprehensive study:

- Fluid sensitivity measured using the exiting simple fluid calibration system is very close to the manufacturer's provided one and hence, the hydrostatic pressure system can easily be applied for checking functionality of the EPC.
- Normally embedded cell (sensing area facing up) in soil experiences lower sensitivity of about 9.0% against the fluid sensitivity.
- Embedded cell in soil with the sensing area facing upside down registers higher sensitivity, which is almost 18% in comparison with the fluid sensitivity.
- Registration ratios for the embedded cell in moist sand are 1.26 and 1.58 for 3 and 6% moisture content (by weight) respectively. In addition, soil sensitivity of the stress cell embedded in moist sand increases with the increment of the moisture content.

Overall, it could be concluded that soil calibration is more appropriate for the stress cell calibration against fluid calibration. The application of fluid sensitivity in the cell could lead to under- or over-registration of earth pressure.

REFERENCES

- [1] Selig E., Soil Stress Gage Calibration, Geotechnical Testing Journal, Vol. 3, Issue 4, 1980, pp. 153-158.
- [2] Weiler W. A. and Kulhawy F. H., Factors affecting stress cell measurements in soil, Journal of the Geotechnical Engineering Division, Vol. 108, Issue 12, 1982, pp. 1529-1548.
- [3] Gade V. K. and Dasaka S. M., Calibration of Earth Pressure Sensors, Indian Geotechnical Journal, Vol. 48, Issue 1, 2017, pp. 142-152.
- [4] Theroux B., Labuz J. F. and Drescher A., Calibration of an earth pressure cell, University of Minnesota, USA, 2000, pp. 1-

- 120.
- [5] TML, Soil Pressure Gauge KDE-PA/KDF-PA, *In: TML, J. (ed.)*, 2018, Tokyo Sokki Kenkyujo Co. Ltd, Japan.
 - [6] Peattie K. R. and Sparrow R. W., The Fundamental Action of Earth Pressure Cells. *Journal of the Mechanics and Physics of Solids*, Vol. 2, Issue 3, 1954, pp. 141-155.
 - [7] Labuz J. F. and Theroux B., Laboratory Calibration of Earth Pressure Cells. *Geotechnical Testing Journal*, Vol. 28, Issue 2, 2005, pp. 188-196.
 - [8] Lazzarin F., Measurement of Soil Stresses In Small Scale Laboratory Model Tests on Granular Soils, B.Sc Thesis, 2015, University of Padova, Italy, pp. 1-77.
 - [9] Dunnicliff J., *Geotechnical Instrumentation for Monitoring Field Performance*, John Wiley & Sons, 1993.
 - [10] Gobrial, T., RE: Soil Pressure Transducer Type to Bhuiyan M. Z. I., 2017.
 - [11] Wachman G. S. and Labuz J. F., Soil-Structure Interaction of An Earth Pressure Cell, *Journal of Geotechnical and Geoenvironmental Engineering*, Vol. 137, Issue 9, pp. 843-845.
 - [12] Talesnick M., Measuring Soil Contact Pressure on a Solid Boundary and Quantifying Soil Arching, *Geotechnical Testing Journal*, Vol. 28, Issue 2, 2005, pp. 171-179.
 - [13] Bhuiyan M. Z. I., Experimental and Numerical Study of Fracture Grouted Soil-Nail. PhD Confirmation Report, The University of Newcastle. Australia, pp. 1-149.
 - [14] Zhu B., Jardine R. J. and Foray P., The Use of Miniature Soil Stress Measuring Cells In Laboratory Applications Involving Stress Reversals, *Soils and Foundations*, Vol. 49, Issue 5, 2009, pp. 675-688.
 - [15] Talesnick M., Measuring Soil Pressure Within A Soil Mass, *Canadian Geotechnical Journal*, Vol. 50, Issue 7, pp. 716-722.
 - [16] Garnier J., Ternet O., Cottineau L.M. and Brown C., Placement of Embedded Pressure Cells, *Géotechnique*, Vol. 49, Issue 3, pp. 415-421.

SLOPE STABILITY ANALYSIS OF FRICTIONAL FILL MATERIALS PLACED ON PURELY COHESIVE CLAY

Kongkit Yingchaloenkitkhajorn

Department of Civil Engineering, College of Industrial Technology and Management,
Rajamangala University of Technology Srivijaya, Nakhon Si Thammarat, Thailand

ABSTRACT

This paper presented slope stability analysis by considering the problem of slope stability with special effects that it was filled with frictional materials and placed on purely cohesive clay. The finite element limit analysis of two-dimensional plane strain was employed to analyze the stability of this problem. The slope height (H), the depth factors (d/H) and the slope angle (β) for the finite element limit analysis of frictional fill materials was modeled as a volume element with the properties of Mohr-Coulomb material in drained condition. And the clay was modeled as a volume element with the properties of Tresca material in undrained condition where the parameters were soil unit weight (γ), undrained shear strength (s_u) and friction angle (ϕ'). Parametric studies consisted of three dimensionless variables including depth factors (d/H), friction angle (ϕ') and slope angle (β). Results were summarized in the form of the dimensionless stability number ($s_u/\gamma H(FS)$) as a function of those input variables and the failure mechanisms associated with dimensionless variables were also proposed in this paper.

Keywords: Slope stability, Soil fill, Finite element limit analysis, Stability number

INTRODUCTION

Slope stability is a common problem that is found in various civil engineering projects. Today, the predicting of the slope stability is an important role for geotechnical engineers. In general, there are several effects on the slope stability, such as slope's physical properties, strength parameters, and slope geometry and the construction process is also affected to the slope. Moreover, slope can be categorized into natural slope or construction processed slope and most of the fill slopes are often found in ramp construction. [1], [2]

There are many researchers that are interested in analyzing slope stability by using limit analysis such as in [3]–[6]. On the other hand, some researchers have studied in order to find solutions to the case of layered soil slope and cohesive-frictional slope such as in [7], [8]. However, there are not many researches on the solution which is obtained from the slope analysis of frictional fill materials placed on purely cohesive clay by using finite element limit analysis. Therefore, the research in this topic is still important and should be placed for the further research in this topic.

This paper proposed the slope stability analysis by considering the problem of slope stability with special effects that it was filled with frictional materials and placed on purely cohesive clay by using finite element limit analysis both upper and lower bound on plane strain. (2D Plane strain)

MEHOD OF ANALYSIS

This research used finite element limit analysis program (OptumG2) [9] to simulate and analyze upper bound (Upper Bound, UB) and lower bound (Lower Bound, LB) solutions. This was an analytical method based on the principle of plastic limit theorem, which provided accurate analysis results and could be applied to common parameters in geotechnical engineer. Finding the answer with plastic bound theorems by using those principles was that if the answer could be limited to a certain period of time and the computational system was improved until the whole range of answers was closest to each other. Therefore, the solution will be closed to the most exact solution. The plastic bound theorems were divided into two theorems: lower bound theorem and upper bound theorem.

In this study, the unit weight of frictional fill material was equal to the unit weight of purely cohesive clay. The Eq. (1) had been discovered and was highlighted as a major discovery in the study in [10]. However, the friction angle (ϕ') value was not included in Eq. (1), which could be illustrated by numerical solutions in the form of stability graph by considering the difference in ϕ' value. In addition, failure mechanisms, which were found, had the appearance of rotational failure (Base slide) and this kind of failure mechanisms would occur in the soft

clay layer that was placed on the stiff clay layer. Therefore, it was shown that the clay layer was related to failure mechanism of fill slope.

In this study, the results will be presented by using the dimensionless stability number, as shown in Eq. (1)

$$N_{sc} = \frac{s_u}{\gamma H (FS)} \quad (1)$$

Slope height (H), depth factors (d/H) and slope angle (β) for finite element limit analysis of frictional fill materials were modeled as a volume element with the properties of Mohr-Coulomb material in drained condition. And the purely cohesive clay was modeled as a volume element with the properties of Tresca material in undrained condition. The parameters were soil unit weight (γ), undrained shear strength (s_u) and friction angle (ϕ') as shown in Fig. 1.

At the boundary condition of this model, the lower bound was neither horizontal nor vertical ($u_x = u_y = 0$). The left and right bound could not move in a horizontal plane ($u_x = 0$). The ground surface of this model was a free model, without any axial anchorage, as shown in Fig. 2.

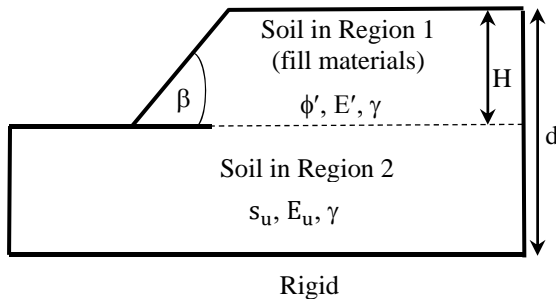


Fig. 1 The problem of slope with frictional fill materials placed on purely cohesive clay and the parameters used in the analysis.

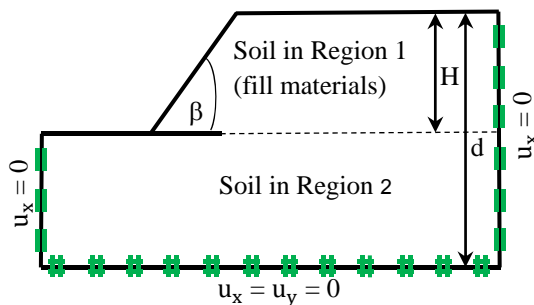


Fig. 2 Boundary condition and model geometry.

The model was a plane strain which the soil element of the finite element mesh of lower bound

was a triangular element with three points of nodal unknown stresses. And the upper bound had a triangular element with six points of nodal unknown displacement node, as shown in Fig. 3.

The researcher had considered for using OptumG2 program which this program used finite element limit analysis. Moreover, there was a special function, which the model could add more elements or adaptive mesh itself and it could make the solution of the problems closer to the exact solution. The model was designed for five adaptive iterations per the solution analysis of one problem. This function would increase the number of elements in areas with high stress and strain changes, also known as effective area, such as the position that occurred the slip-line field. Five adaptive steps were selected to obtain an accurate solution, where an initial mesh with the number of 5,000 elements was automatically adapted an increased to a final mesh with the number of 30,000 elements

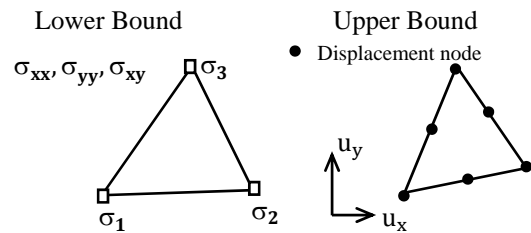


Fig. 3 Triangular elements for lower and upper bound analysis

The slope angles (β) were 15° , 22.5° , 30° and 40° and were considered to use for analyzing and the friction angles (ϕ') 25° , 30° , 35° and 45° and set the value of $\psi = \phi'$. It was necessary to analyze slope stability of frictional fill materials placed on purely cohesive clay which was a rigid-perfectly plastic with associated flow rule and undrained Young's modulus ($E_u/s_u = 300$). For the case of drained young's modulus ($E' = 2,800N$), the undrained poisson's ratio (ν_u) was 0.495 and the drained poisson's ratio of frictional fill materials (ν') was 0.35, including the value of depth factors (d/H) which was between 1.5, 2, 3, 4 and 5. When considering the depth factors of $d/H = 1$, it was equal to the homogeneous slope which the solution of the stability number in this case corresponded to the solution given by [11]. The solution from the finite element limit analysis was summed in the form of the dimensionless stability number, $s_u/\gamma H(FS)$, as shown in Eq. (1).

RESULTS AND DISCUSSION

Figure 4 shows the results of the last adaptive

mesh of slope with frictional fill materials placed on purely cohesive clay and on two-dimensional plane strain for the case of $\beta = 15^\circ$, $\phi' = 25^\circ$, $d/H = 3$ which compared to the solution of the lower and upper bound. After the 5th adaptive mesh, the number of elements of the model was increased in the effective area or in the shifted section of high shear stress. During the transition period of high shear stress, it could be seen as a curve through the entire base slide which the position and appearance of the shear stresses were occurred when the soft soil horizon was placed on hard soil horizon.

Figure 5 shows the location of the incremental shear strain dissipation of slope with frictional fill materials placed on purely cohesive clay for the case of $\beta = 15^\circ$, $\phi' = 25^\circ$, $d/H = 3$ which compared to the solution of the lower and upper bound. And when compared to the same mesh, it could be seen that the displacement as well as the shear strain were in the same position as Fig. 4.

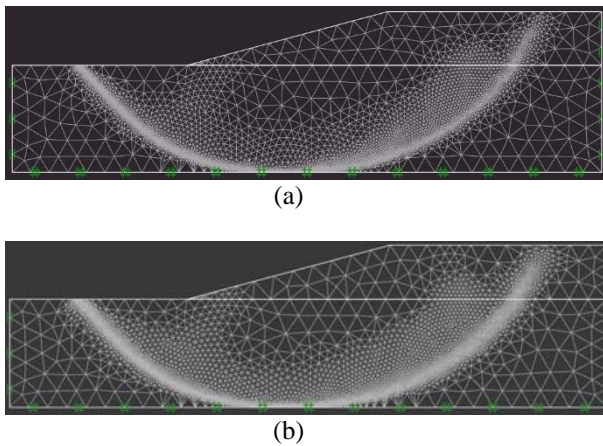


Fig. 4 Final adaptive mesh for $\beta = 15^\circ$, $\phi' = 25^\circ$, $d/H = 3$, (a) LB, (b) UB

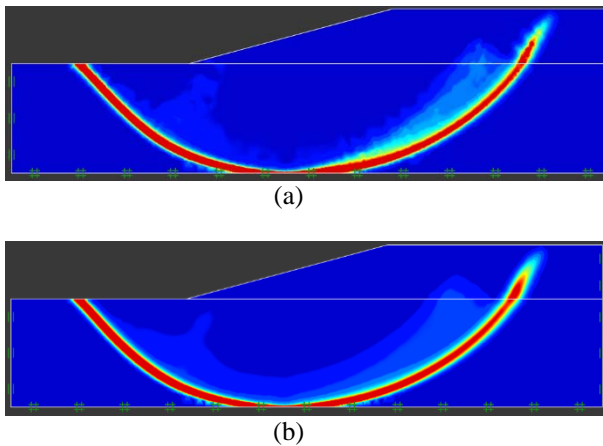


Fig. 5 Incremental shear strain dissipation for $\beta = 15^\circ$, $\phi' = 25^\circ$, $d/H = 3$, (a) LB, (b) UB

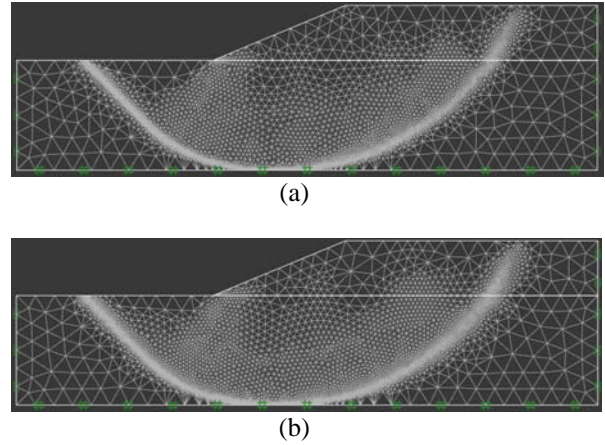


Fig. 6 Final adaptive mesh for $\beta = 22.5^\circ$, $\phi' = 30^\circ$, $d/H = 2$, (a) LB, (b) UB

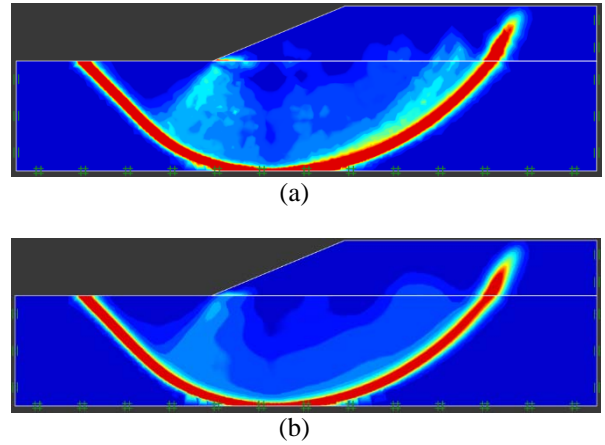


Fig. 7 Incremental shear strain dissipation for $\beta = 22.5^\circ$, $\phi' = 30^\circ$, $d/H = 2$, (a) LB, (b) UB

Figure 6, 7 show the result of adaptive mesh and the incremental shear strain dissipation of slope with frictional fill materials placed on purely cohesive clay for the case of $\beta = 22.5^\circ$, $\phi' = 30^\circ$, $d/H = 2$, which could be seen as a curve through the entire base slide. The position and appearance of the shear stresses occurred when the soft soil horizon was placed on hard soil horizon as shown in Fig. 4 and 5.

Figure 8, 9 illustrate the solution from finite element limit analysis by using the OptumG2 program. The solution was the relationship between dimensionless variables of the stability number, $s_u/\gamma H(FS)$ and depth factors, d/H from 1.5 to 5, which had the slope angle, $\beta = 15^\circ$ and 22.5° . Thus, the graph in this figure was divided into two types: the solution of the lower bound was a dashed line, while the solution of upper bound was a solid line. From the figure, it could be seen that the solution had non-linear relationship which the lower bound and the upper bound were nearly the same, almost the same line, indicating that the solution had a close value with the exact solution. The lines in Fig. 8 and Fig. 9

show different friction angle values (ϕ'). The value of the top line was $\phi' = 25^\circ$ and the value of the bottom line was $\phi' = 45^\circ$ which the bottom line in this case had the maximum value of friction angle that was caused the slope to remain stable. However, for the case of slope angle value, $\beta = 30^\circ$ and 40° which had the high slope, there was friction angle value that could maintain the stability of the slope ($FS > 1$) which the value was between $\phi' = 35 - 45^\circ$ for the case $\beta = 30^\circ$ and $\beta = 40^\circ$ as shown in Fig. 10 and 11, respectively.

Figure 10 and 11 illustrate the solution from finite element limit analysis by using the OptumG2 program. The solution was the relationship between dimensionless variables of the stability number ($s_u/\gamma H(FS)$) and depth factors (d/H) from 1.5 to 5 which had the slope angle (β) 30° and 40° . Thus, the graph in this figure was divided into two types: the solution of the lower bound was a dashed line, while the solution of upper bound was a solid line. From the figure, it could be seen that the solution had non-linear relationship which the lower bound and the upper bound were nearly the same, almost the same line, indicating that the solution had a close value with the exact solution. The lines in Fig. 10 and 11 had different friction angle values (ϕ'). The value of the top line was $\phi' = 35^\circ$ and the value of the bottom line was $\phi' = 45^\circ$ which the bottom line in this case had the maximum value of friction angle that could be caused the slope to remain stable.

Figure 12 and 13 show the relationship between dimensionless variables of the stability number ($s_u/\gamma H(FS)$) and depth factors (d/H) as well but the lines in this figures showed the different value of slope angle (β). The value of the bottom line was $\beta = 15^\circ$ and the value of the top line was $\beta = 22.5^\circ$ which the bottom line in this case had the low value of friction angle that could have caused the slope to remain very stable. On the other hand, when the value of slope angle was increased, the slope stability would also decrease which all the solution in these figures were $\phi' = 25^\circ$ and $\phi' = 30^\circ$ respectively.

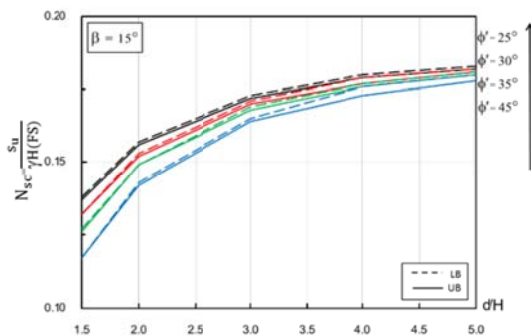


Fig. 8 Stability number for $\beta=15^\circ$ for various friction angle

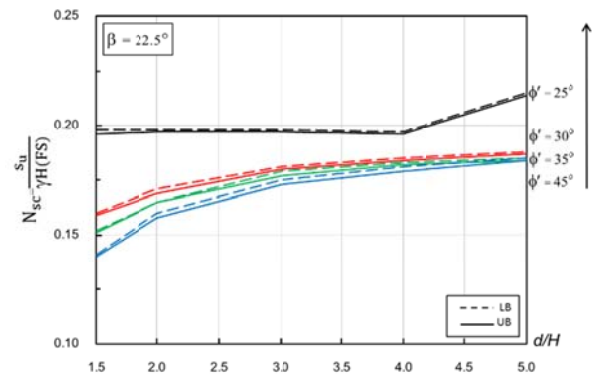


Fig. 9 Stability number for $\beta=22.5^\circ$ for various friction angle

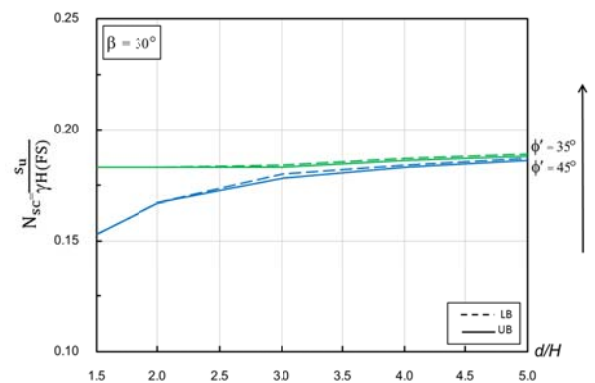


Fig. 10 Stability number for $\beta=30^\circ$ for various friction angle

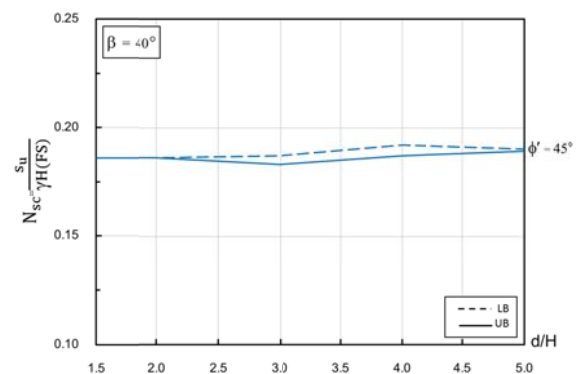


Fig. 11 Stability number for $\beta=40^\circ$ for various friction angle

Figure 14 shows the relationship between dimensionless variables of the stability number ($s_u/\gamma H(FS)$) and depth factors (d/H) as shown in Fig. 13 but the lines in this figures showed the different value of slope angle (β), which were as follows $\beta = 15^\circ$, 22.5° and 30° . The solution was very close to the same line and the stability of the

slope would decrease from the bottom line to the top line which every solution in this figure was $\phi' = 35^\circ$.

Figure 15 shows the relationship between dimensionless variables of the stability number ($s_u/\gamma H(FS)$) and depth factors (d/H) as shown in Fig. 13 but the lines in this figures showed the different value of slope angle (β), which were as follows $\beta = 15^\circ, 22.5^\circ, 30^\circ$ and 40° . The solution was very close to the same line and the stability of the slope would decreased from the bottom line to the top line which every solution in this figure was $\phi' = 45^\circ$ and it could be seen that the stability number would start with a constant value when the depth factors was $d/H \geq 3$.

From that relationship, Fig. 8 to Fig. 15, it could be concluded that most of the solutions of stability, $s_u/\gamma H(FS)$ and when considering the slope angle (β) between 15° to 40° and depth factors (d/H) between 1.5 to 3, it showed a decrease in dimensionless stability number ($s_u/\gamma H(FS)$). This meant that when the slope was filled with frictional materials to increase the height of the original soil layer, it would reduce the stability of the slope. In addition, when considering the depth factors (d/H) which the value is between 4 to 5, it was found that the dimensionless stability number ($s_u/\gamma H(FS)$) was slightly changed and the slope was still stable ($FS > 1$). Moreover, it was shown that when it was filled with frictional materials for the construction of the slope, the depth factors would not affect the slope stability.

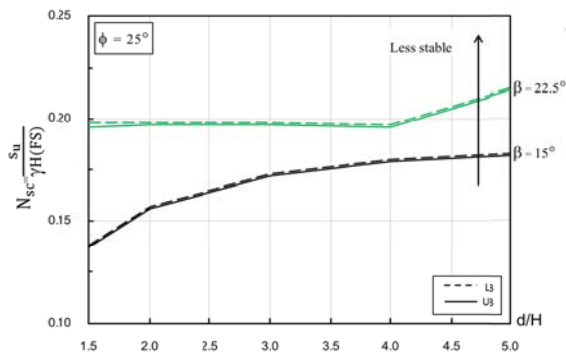


Fig. 12 Stability number for $\phi' = 25^\circ$ for various slope angle

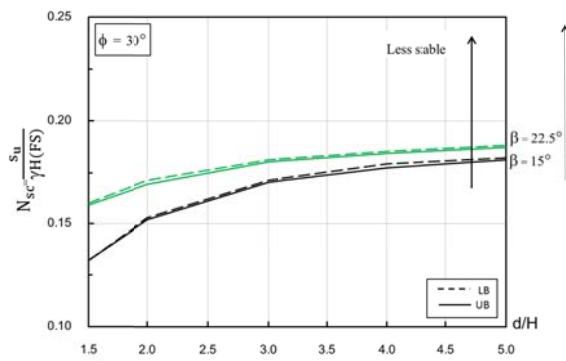


Fig. 13 Stability number for $\phi' = 30^\circ$ for various slope angle

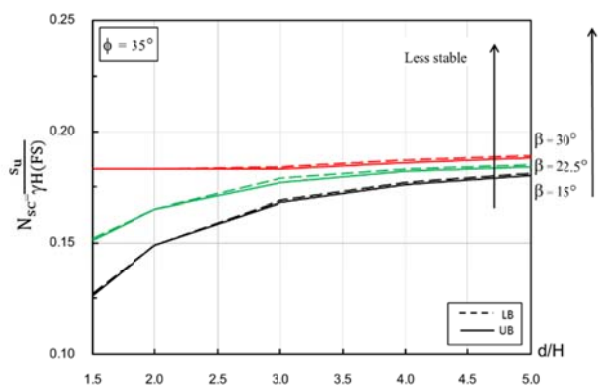


Fig. 14 Stability number for $\phi' = 35^\circ$ for various slope angle

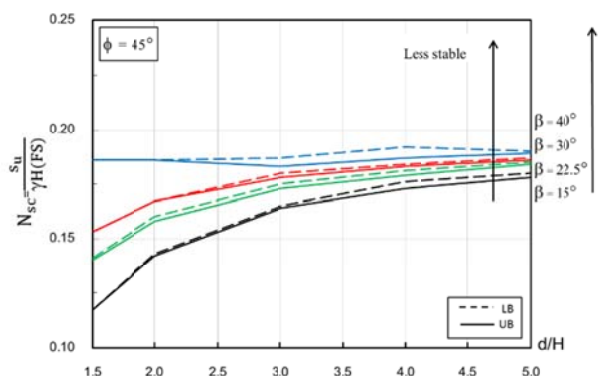


Fig. 15 Stability number for $\phi' = 45^\circ$ for various slope angle

CONCLUSIONS

This paper presented slope stability analysis by considering the problem of slope stability with special effects that it was filled with frictional materials and placed on purely cohesive clay. The finite element limit analysis of two-dimensional plane strain was employed to analyze the stability of

this problem. Parametric studies consisted of three dimensionless variables including depth factors (d/H), friction angle (ϕ') and slope angle (β). Results were summarized in the form of the dimensionless stability number ($s_u/\gamma H(FS)$) as a function of those input variables.

The solution presented in the form of failure mechanism which consisted of the adaptive mesh and incremental shear strain dissipation. From the analysis result, it was found that the number of elements increased significantly at high shear strain dissipation and it can be seen as a curve through the entire base slide which the nature of the position was consistent with the research by Lim et al., (2015) [8]. That meant the curvature of failure occurred when the soft soil layer was placed on the hard soil layer. And when the depth factors was $d/H = 1.5 - 3$, it was shown that the dimensionless stability number ($s_u/\gamma H(FS)$) tendency decreased ($FS < 1$). This meant that when the slope was filled with frictional materials to increase the height of the original soil layer, it would reduce the stability of the slope. In addition, when considering the depth factors (d/H) which the value was between $d/H = 4 - 5$, it was found that the dimensionless stability number ($s_u/\gamma H(FS)$) was slightly changed and the slope was still stable ($FS > 1$). Therefore, when it was filled with the frictional fill materials, such as sand and gravel for the slope construction with the depth factors was $d/H \geq 4$, it would not affect to the slope stability.

The solution was shown in the graph of the relationship between the dimensionless stability number ($s_u/\gamma H(FS)$) and the depth factors (d/H). From the comparison, the dimensionless stability number ($s_u/\gamma H(FS)$) was significantly reduced when the depth factors (d/H) was between 1.5 to 3 and friction angle (ϕ') was increased and slope angle (β) was reduced. Moreover, when the depth factors (d/H) was between 4 to 5, it was found that the dimensionless stability number ($s_u/\gamma H(FS)$) was slightly changed and the slope was more stable compared to the range of the depth factors (d/H) was between 1.5 to 3.

REFERENCES

- [1] Indraratna B., Balasubramaniam A., and Balachandran S., Performance of Test Embankment Constructed to Failure on Soft Marine Clay, *Journal Geotechnical Engineering*, Vol. 118, Issue 1, 1992, pp. 12–33.
- [2] Al-Homoud A. S., Tal A. B., and Taqieddin S. A., A Comparative Study of Slope Stability Methods and Mitigative Design of a Highway Embankment Landslide with a Potential for Deep Seated Sliding, *Engineering Geology*, Vol. 47, Issue 1-2, 1997, pp. 157–173.
- [3] Michalowski R. L., Slope Stability Analysis: A Kinematical Approach, *Géotechnique*, Vol. 45, Issue 2, 1995, pp. 283-293.
- [4] Donald I. B., and Chen Z., Slope Stability Analysis by The Upper Bound Approach: Fundamentals and Methods, *Canadian Geotechnical Journal*, Vol. 34, Issue 6, 1997, pp. 853-862.
- [5] Chen J., Yin J. H., and Lee C. F., Upper bound limit analysis of slope stability using rigid finite elements and nonlinear programming, *Canadian Geotechnical Journal*, Vol. 40, Issue 4, 2003, pp. 742-752.
- [6] Chen J., Yin J. H., and Lee C. F., Rigid Finite Element Method for Upper Bound Limit Analysis of Soil Slopes Subjected to Pore Water Pressure, *Journal of Engineering Mechanics (ASCE)*, Vol. 130, Issue 8, 2004, pp. 886-893.
- [7] Kumar J., and Samui P., Stability Determination for Layered Soil Slopes Using the Upper Bound Limit Analysis, *Geotechnical and Geological Engineering*, Vol. 24, Issue 6, 2006, pp. 1803-1819.
- [8] Lim K., Lyamin A. V., Cassidy M. J., and Li A. J., Three-Dimensional Slope Stability Charts for Frictional Fill Materials Placed on Purely Cohesive Clay, *International Journal for Geomechanics*, Vol. 16, Issue 2, 2015, pp. 1-7.
- [9] Krabbenhoft K., Lyamin A. V., and Krabbenhoft J., Optum Computational Engineering (OptumG2), OptumG2 Company, 2017.
- [10] Li A. J., Cassidy M. J., Wang Y., Merifield R. S., and Lyamin A. V., (2012). Parametric Monte Carlo Studies of Rock Slopes Based on the Hoek–Brown Failure Criterion, *Computers and Geotechnics*, Vol. 45(Sep), 2012, pp. 11–18.
- [11] Taylor D. W., Stability of Earth Slopes, *Journal of the Boston Society of Civil Engineers*, Vol. 24, Issue 3, 1937, pp. 197–246.

WEST SUMATRA COASTLINE CHANGE DUE TO ABRASION PROTECTION STRUCTURES: PADANG BEACH

Abdul Hakam¹, Junaidi¹, Bayu M Adji¹, Shafira Rahmadilla Hape²

¹Engineering Fac., Andalas University, Indonesia; ² Engineering Fac., Gadjah Mada University, Indonesia

ABSTRACT

The abrasion disaster that has resulted in remarkable coastline changes is one of the national disasters that concern the Indonesian government. The West Sumatra Government which has a significant long beach has made many abrasion prevention structures to stop losing of hundreds of meters of land due to abrasion. In fact the abrasion prevention structures not only protect the beach but on the other hand they also change the shape of the beach. A field study has been conducted and found that beaches that have been protected with abrasion prevention structures are susceptible to changes in shape. On the one side, the change provides benefits but on the other hand it causes a new problem. This paper explains the relationship between the dimensions of the coastal abrasion prevention structure and the properties of adjacent beach sediment related to the shoreline changes occurring in West Sumatra. This study is very important to provide prediction of shoreline changes due to the prevention of abrasion related to the beach soil properties. The result can be used to determine the precise abrasion prevention structures in accordance with the conditions of sediment on the beach for future expected change.

Keywords: West Sumatra Coastline, Abrasion protection structure, Field Survey

1. INTRODUCTION

West Sumatra has been experiencing beach abrasion since hundred years ago. The history of abrasion especially has been recorded since 1890 in Padang. The abrasion is generally due to the Indian ocean waves and currents. In Padang, the abrasion has been cause damaged to public facilities and the beautiful environment such as sandy beach (Fig.1).

Abrasion is known as part of the natural phenomenon in terms of erosion and sedimentation cycles along the coastline. But for developed area, the abrasion may result many disadvantages such as cutting the accesses, destruction of houses and even the loss of beautiful public play ground. With so many losses due to abrasion, the Indonesian government has included this natural phenomenon into one of disaster that needs to be managed [1].

In order to minimize the negative effects of abrasion to the coastline, engineered beach protections such as groin construction can be used [2]. Even though building such wave protector to prevent abrasion could not restore back the lost of beautiful sandy beaches. In Padang beach, the breakwater construction has been built since the last century. (Fig.2).

Damage of beaches due to erosion or abrasion become a matter of concern to researchers since decades. Researches on coastal abrasion become excessive by linking up to the issue of global warming. A number of reports from the 19th to the 20th centuries on relationship of sea levels and

coastal damage have summarized by Zhang et al in 2004 [3]. They found that the damage to the beaches has been twice over with the rate of actually sea level rise. This study also notified that with the global warming scenario, the coastal abrasion problems that already look severe in the last century will be worse in the this century. The other studies concerned the changes in the coastal environment due to land use and global warming [4].



Fig.1 Padang Beach in 1890 [5]



Fig.2 Groins in Padang Beach

Even the abrasion protection using hard structures can eliminate the natural and may not be beautiful [6], but the natural protections as an alternative may need several time before the work. The hard structure can be designed and built in months. Then the West Sumatra Government has made many abrasion prevention structures to stop loosing of hundreds of meters of land due to abrasion.

The Priority areas in the construction of coastal structure in West Sumatra are the areas that have a historical record of abrasion. One of them is in the Padang city, where the historical record of abrasion has been begun since more than 100 years ago. The abrasion in the Padang city has resulted in lost of shoreline more than 50m.

This paper will discuss the influence of abrasion prevention structures located in Padang beach, especially those located in downstream of Banjir Kanal River (Flood Control Canal). This area is quite interesting because beside it was influenced by the sea, abrasion and accretion in this area is influenced also by the existence of Banjir Kanal River.

2. GROINS DI PADANG

Padang is a Capital City of West Sumatra which originally developed by Dutch colonists in the early of 1800s, when its abrasion record was begun. The cause of abrasion in Padang Beach is expected due to the Littoral Barrier in the form of Padang Mountain which stops the sediment transport from the south- part to the north-part of it. In addition, the development of Banjir Kanal River since 1926 which divided the volume of water Batang Arau River causing disruption of coastal equilibrium around Padang Mountain to Banjir Kanal River. Banjir Kanal River reduces the sediment supply from Batang Arau River, resulting in abrasion in Padang Beach (Fig.3). Meanwhile, the causes of abrasion in the form of waves and currents from the Indian Ocean is ignored and has not been observed yet.



Fig.3 Birdseye of Padang Beach

The development aimed for dealing with abrasion using groins in Padang Beach was carried out since 1969 [7]. At that time in Padang Beach there was a special building called Wisma Pancasila where the adjacent beach has been eroded so. It was predicted that if it just let it goes, the foundation of the building would be eroded. For that reason, the first 40m groins were constructed in the perpendicular direction to the coastline. Later in the year of 1970 to 1980 the Government made additional groins along the coast of Padang from Gunung Padang to the Banjir Kanal River (Fig.4).

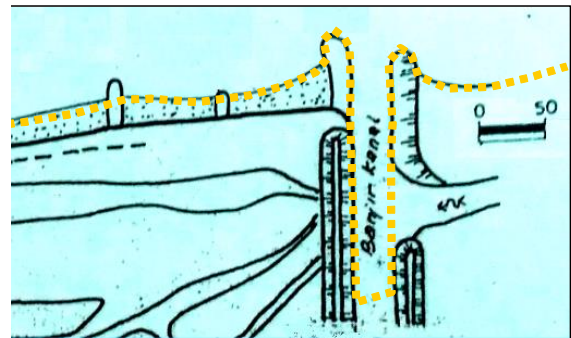


Fig.4 Padang Beach's Groins in 1980s

In this study a review of the effects offshore construction around the area. There two point will be discuss, the coastline change and physical of sediment around the Banjir Kanal. The existing abrasion prevention constructions in this Padang Beach area are groins with main shape towards to the sea. This groin constructions were built in 1980 and then were enlarged in 2008. The main material used for this constructions are cobbles and boulders. The design plan of the main jetty and groin structures are shown in Fig.5. The jetty is designed to trap sediment behind it, mean while the groin is to protect the right-beach from Banjir Kanal current.

While the shoreline changes in the last 10 years, may occur due to the addition of long of the groin and jetty constructions at the mouth of Banjar Kanal river. This form of change is still appropriate with the theoretically prediction, even the sediments in the eastern part of the jetty exceeds the predicted amount.

Estimated sediments trapped by this jetty have been predicted in the design phase. The trapped sediments behind the jetty are used by the Padang Government as a public playground. However, the amount of sediments trapped is not calculated properly due to the lack of marine data. The condition of trapped sediment actually consistent with one of the conclusions of the past study on coastline changes due to the groin effect. That study also concluded the amount of accretion and erosion does not show a balanced amount [10].

4. SEDIMENT GRAIN SIZE

This study also attempts to investigate the changes that occur in the nature of the sediment on the coastline. For that reason, the sediment samples have been taken from Padang Beach at the location adjacent to the mouth of Banjar Kanal. Furthermore, sieve analysis of sediment sand is conducted. The laboratory test results are plotted on the graph in Fig.9.

In the Figure also plotted the results of the sieve analysis of the sand beach sample in the same location 35 years ago. From the picture it is seen that there is no significant change in sand gradation at that point. It is possible that the newly beach sand is originally come from the same area as in the previous year. The source of new sand sediments is likely to originally come from the mouth of the Banjar Kanal where in front of the jetty before it is built. Meanwhile, after the construction of the jetty and groin structures in the mouth of the Banjar Kanal, this sediment was pushed by the sea water and moved to the beach side. This phenomenon is also marked by the loss of breaking wave in the mouth of Banjar Kanal that existed before the construction. Breaking waves can occur when the seabed undergoes a siltation in this case is sand sedimentation, and it is moved after the jetty construction.

This result differs from previous studies in which there was a change in the physical properties of sediment in the same place [11]. The study reported that surface sediment on the eastern part of the dock became coarser while on the west

part became finer during the 4-year period. The increase and alteration of physical properties in the sediment may be caused by the wind regime as well as the presence of offshore structure.

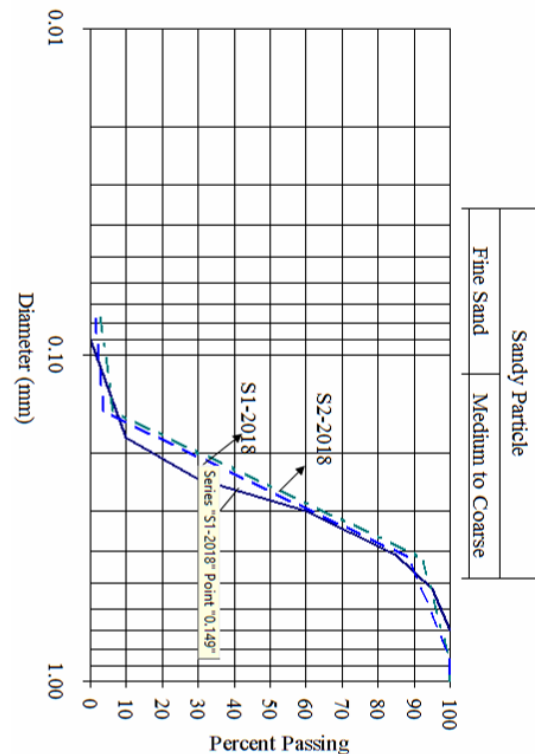


Fig.9 Grain distribution of Padang Beach sands

5. CONCLUSIONS

Abrasion is one of Indonesian national disasters that has resulted in disadvantage as well as advantage coastline changes. The impact of abrasion that has wiped out the mainland can be reduced by constructing hard structures such as jetties or groins. Even this unnatural ways have less beautiful, but for Padang city the structures have significant way to draw back the beach sediment that has been wiped away in the past.

This study has been conducted by comparing at present condition and the one in the past. The change that occurred in the Padang Beach is observed by comparing the laboratory test and secondary data from the past with the recent condition.

This study found that there is change in coastline of Padang due to the existence of abrasion protection structure. The coastline change in Padang Beach as observed in this study is found almost agree with the expected one.

This study has also found that the sediment in the area of study are just moving closed by. It was shown by the similar grain distributions of the sand sediment event it has 35 years of time different.

6. ACKNOWLEDGEMENTS

This research is funded by Andalas University under Professor Research Grant in 2018. Special thanks to our colleagues who have helped in the process of finishing this research.

7. REFERENCES

BNPB, The Regulation of the Head of National Disaster Management Agency No. 07/2012: Guidelines for Data Management and Disaster Information in Indonesia (in Bahasa: Peraturan Kepala Badan Nasional Penanggulangan Bencana Nomor 07 Tahun 2012 Tentang Pedoman Pengelolaan Data dan Informasi Bencana Indonesia), Jakarta 2012

Empung, Hiron N. and Chobir A., Oscillating Water Column (OWE) Building Performance Analysis As Beach Abrasion Reducing, IIOABJ Vol. 7, Suppl. 1, pp. 515–520, 2016

Zhang, K., Douglas, B.C. & Leatherman, S.P., Global Warming and Coastal Erosion, Climatic Change, 64: 41, May 2004

Soedarto, Y.W., Hanum, L., Lestari, M.S., Analysis and Identification of Landuse on the Coastal Environment of South Sumatra using GIS, International Journal on Advanced Science, Engineering and Information Technology, Vol. 7 (2017) No. 3, pages: 785-791, 20 July 2017

Ohgituto, Minangkabau Tempo Doeloe #1 - Padang, <http://ohgituto.blogspot.co.id>, 27 Nov. 2012

Jenifer E. Dugan, David M. Hubbard, Ivan F. Rodil, David L. Revell and Stephen Schroeter, Ecological effects of coastal armoring on sandy beaches, Marine Ecology 29, Suppl. 1, pp. 160–170, 2008

Soeuhinto Sadikin, Observation and Research of Effect of Crib to Sedimentation Padang Beach Project: Final Report (in Bahasa: Finalt Repot Pekerjaan Pengamatan dan Penelitian Krib terhadap (Pengaruh) Endapan Pantai Padang), CV. Tri Udaya Sakti, Mei 1983

West Sumatra Public Service, Design Note: Jetty Design of Downstream Flood Canal in Padang (In Bahasa: Note disain: Pekerjaan Perencanaan Bangunan Jetty Muara Banjir Kananl Kota Padang), Dinas PSDA, November 2007

Anonymous, <http://koleksitempodoeloe.blogspot.com/2010/03/peta-kuno-kota-padang-sumatera-barat.html>

Badiei P, J. William Kamphuis, J.W. and Hamilton D.G., Physical Experiments on the Effects of Groins on Shore Morphology, Cpt. 128 in Coastal Engineering, ASCE, 1994, pp. 1782-1796

Barnes P.W. and Minkier P.W., Sedimentation in the vicinity of a causeway groin - Beaufort Sea, Alaska, U.S. Geological Survey Menlo Park, California, Open File Report 82-615

8. REFERENCES

[1] BNPB, The Regulation of the Head of National Disaster Management Agency No. 07/2012: Guidelines for Data Management and Disaster Information in Indonesia (in Bahasa: Peraturan Kepala Badan Nasional Penanggulangan Bencana Nomor 07 Tahun 2012 Tentang Pedoman Pengelolaan Data dan Informasi Bencana Indonesia), Jakarta 2012

[2] Empung, Hiron N. and Chobir A., Oscillating Water Column (OWE) Building Performance Analysis As Beach Abrasion Reducing, IIOABJ Vol. 7, Suppl. 1, pp. 515–520, 2016

[3] Zhang, K., Douglas, B.C. & Leatherman, S.P., Global Warming and Coastal Erosion, Climatic Change, 64: 41, May 2004

[4] Soedarto, Y.W., Hanum, L., Lestari, M.S., Analysis and Identification of Landuse on the Coastal Environment of South Sumatra using GIS, International Journal on Advanced Science, Engineering and Information Technology, Vol. 7 (2017) No. 3, pages: 785-791, 20 July 2017

[5] Ohgituto, Minangkabau Tempo Doeloe #1 - Padang, <http://ohgituto.blogspot.co.id>, 27 Nov. 2012

[6] Jenifer E. Dugan, David M. Hubbard, Ivan F. Rodil, David L. Revell and Stephen Schroeter, Ecological effects of coastal armoring on sandy beaches, Marine Ecology 29, Suppl. 1, pp. 160–170, 2008

[7] Soeuhinto Sadikin, Observation and Research of Effect of Crib to Sedimentation Padang Beach Project: Final Report (in Bahasa: Finalt Repot Pekerjaan Pengamatan dan Penelitian Krib terhadap (Pengaruh) Endapan Pantai Padang), CV. Tri Udaya Sakti, Mei 1983

[8] West Sumatra Public Service, Design Note: Jetty Design of Downstream Flood Canal in Padang (In Bahasa: Note disain: Pekerjaan Perencanaan Bangunan Jetty Muara Banjir Kananl Kota Padang), Dinas PSDA, November 2007

- [9] Anonymous, [http: // koleksitempodoele.blogspot.com/2010/03/peta-kuno-kota-padang-sumatera-barat.html](http://koleksitempodoele.blogspot.com/2010/03/peta-kuno-kota-padang-sumatera-barat.html)
- [10] Badiei P, J. William Kamphuis, J.W. and Hamilton D.G., Physical Experiments on the Effects of Groins on Shore Morphology, Cpt. 128 in Coastal Engineering, ASCE, 1994, pp. 1782-1796
- [11] Barnes P.W. and Minkier P.W., Sedimentation in the vicinity of a causeway groin - Beaufort Sea, Alaska, U.S. Geological Survey Menlo Park, California, 1982, Open File Report 82-615

9. AUTHOR'S BIOGRAPHY

Dr. Abdul Hakam is a Professor in the Civil Engineering Department of Andalas University, Indonesia. He was graduated from Andalas University, his Master from Institute Technology of Bandung, both in Indonesia and got Doctor from New South Wales University, Australia. His research interests include general problem in foundation engineering, soil mechanics and soil

dynamics as well as disaster risk reduction subjects. His contact E-mail is ahakam@ft.unand.ac.id and abdulhakam2008@gmail.com.

10. AUTHOR'S CONTRIBUTIONS

Dr. Abdul Hakam: Conception, design, acquisition, final approval of the version to be submitted. Dr. Junaidi: Conception, critical reviewing, analysis and interpretation of data and drafting the article. Dr. Bayu M Adji: Conception, critical reviewing the article. Shafira R Hape, ST: Summarizing data and reviewing the article.

11. ETHICS

This article is original and contains unpublished material. The corresponding author confirms that all of the other authors have read and approved the manuscript and no ethical issues involved.

EFFECT OF TUNNEL SIZE AND LINING THICKNESS ON TUNNEL DEFORMATION DUE TO ADJACENT PILE UNDER LOADING

Prateep Lueprasert¹, Pornkasem Jongpradist², Kodchamon Ruangvirrojanakul³ and Suchatvee Suwansawat¹

¹Faculty of Engineering, King Mongkut's Institute of Technology Ladkrabang, Bangkok, Thailand

²Faculty of Engineering, King Mongkut's University of Technology Thonburi, Bangkok, Thailand

³Sansiri Public Company Limited, Bangkok, Thailand

ABSTRACT

With rapid urbanization, large number of tunnels with various dimensions have been constructed for transportation and utility systems in the many big cities. At the same time, the constructions of infrastructures using a pile foundation system are also necessary in urban area. With limited space, the existing tunnels can be inevitably impacted by the newly constructed pile-supported structures. With various design criteria of tunnel lining, the size and thickness are varied from project to project. With an adjacent pile under loading, different degrees of impact on these tunnels are expected. This study numerically investigates the effect of tunnel diameter and lining thickness on tunnel deformation due to adjacent pile under loading. The MRTA and WMA tunnels in Bangkok subsoil are chosen as the reference cases for investigation. From a series of parametric study, a relationship between the tunnel deformation and dimensionless parameter, which include the size and thickness of lining, can be successfully established.

Keywords: Existing tunnel, Tunnel size, Lining thickness, Out-of-roundness, Pile under loading, Numerical analysis

INTRODUCTION

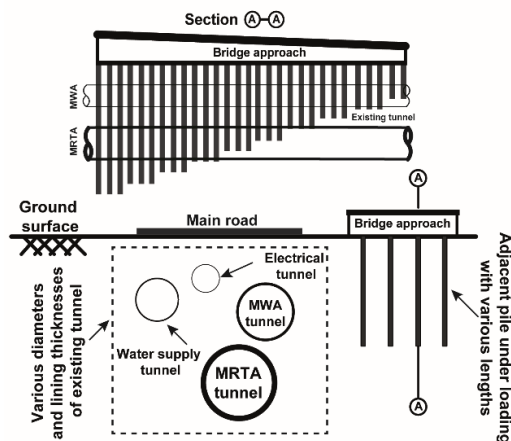


Fig. 1 newly structures constructed to adjacent existing tunnels.

To deal with the problem of limited space in major cities, large number of tunnels, e.g. transportation tunnels, electricity tunnels and water supply tunnels, have been constructed for transportation and utility systems. At the same time, more new infrastructures are also constructed in these urban areas, e.g. flyovers and tall buildings, all of which require pile foundation system. The piles of these new structures are inevitably close to existing tunnels as shown in

state and deformation of surrounding soils, resulting to an impact on the existing tunnels. An assessment on the stability and integrity of the tunnels due to the impact of piles under loading is essential. Although different assessment methods in terms of tunnel deformation were considered in the previous researches [1]-[5], a specific tunnel diameter and thickness were considered in each study. In engineering practice, with various purposes of the tunnel utilization, the tunnel diameter (D) and lining thickness (t) are varied. Bakker and Blom [6] investigated the parameters to get the most economic tunnel design by using analytical method. The study indicates that the ratio between lining thickness and tunnel diameter (t/D) is the key design parameter and strongly influence on tunnel deformation.

Therefore, the effect of tunnel size and lining thickness on tunnel deformation due to adjacent pile under loading are investigated by finite element method (FEM) in this study. The Mass Rapid Transit Authority (MRTA) Blue Line extension project and Metropolitan Waterworks Authority (MWA) tunnels in Bangkok subsoil are chosen as the reference cases for investigation. From a series of parametric study, a simple relationship between the tunnel deformation and dimensionless parameter, which include the size and thickness of lining, can be established as a guideline for tunnel assessment due to adjacent loaded pile.

CHARACTERISTICS OF CASE STUDIES

The characteristics of the MRTA and MWA

Fig. 1.

Many previous studies [1]-[5] reveal that the piles under loading can induce the change of stress

tunnel projects in Bangkok subsoil with piezometric drawdown are considered to preliminarily investigate the effect of tunnel size and lining thickness on tunnel deformation due to loaded pile as depicted in Fig. 2. The MRTA and MWA tunnels having outer diameters of 6.30 m and 4.07 m, lining thicknesses of 0.30 m and 0.15 respectively, are located at the depth, L_T , of 20 m below the ground surface. The Bangkok subsoil based on the actual tunnel alignment of those projects where the tunnel located in stiff clay is considered in this study. Besides, a tunnel in the soft clay referred to as the tunnel transition section, is also modelled. The pile tip positions (indicating the different pile lengths and their clearances) compared to the outer tunnel diameter (D_T) varied in this study are also shown in Fig. 2 .

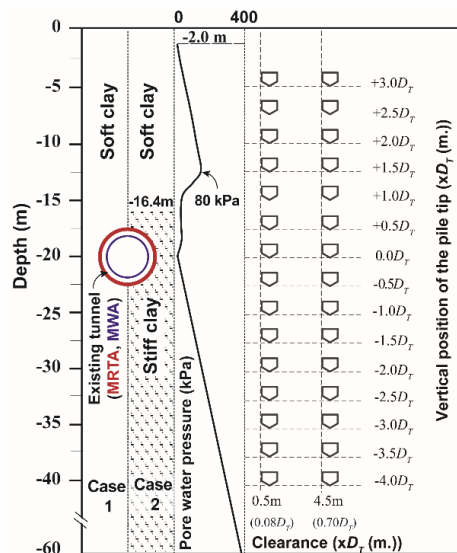


Fig. 2 Illustration of pile tip positions and soil profiles considered in this study.

ANALYSIS METHOD

The FE analysis consists of two parts. The primary investigation of the size and thickness effects of tunnel lining based on MRTA and MWA projects due to loaded pile on tunnel deformation are firstly examined. The parametric analysis, where various sizes and thicknesses of lining are considered, is conducted to establish a relationship between the tunnel deformation and dimensionless parameter in terms of a simple equation. The details of simulation method, meshing, analysis conditions, material properties are described below.

Finite element model

Mesh

To simulate a tunnelling problem in three-dimensional model, the FE model is sufficiently

extended to avoid the boundary effect. From previous study [7], a distance of $4.0D_T$ in lateral and longitudinal directions from the centre of FE model are sufficient. Thus, the meshed domain had an extent of 60 m ($\approx 9.5 D_T$) in the vertical and longitudinal directions and 80m ($\approx 12.5 D_T$) in the transverse direction as shown in Fig. 3.

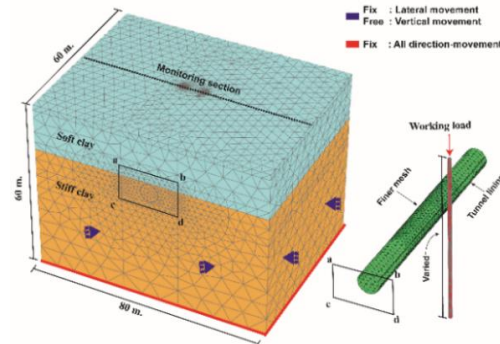


Fig. 3 Example of finite element mesh for the tunnel constructed in stiff clay.

The monitoring section was at the centre of longitudinal direction. The soil stratum and bored pile were discretized into the 10-node tetrahedral elements. The 6-node triangular plate elements were used to simulate the tunnel lining. The finer discretization mesh with suitable aspect ratio was used to accommodate the accuracy of the solutions, especially in the zone between pile and tunnel. The PLAXIS version 2013 software was implemented for mesh generation and analysis [8].

Analysis condition

For initial stress state, the vertical and horizontal effective stresses were determined by given unit weight of soil and coefficient of static earth pressure, K_0 , for all strata. The pore water pressure was also generated by giving piezometric drawdown condition. The undrained analysis was considered.

In order to control the displacement boundary condition, the lateral boundaries of the mesh were horizontally fixed (allowed for vertical movements) and the bottom boundary is fixed (no vertical and horizontal movements).

Material properties

Table 1 Material properties of the bore pile and tunnel lining [9].

EPB Elements	Young modulus [E] (kN/m ²)	Poisson's ratio [ν]	Unit weight [γ] (kN/m ³)
Tunnel and Bored pile	31 x 10 ⁶	0.20	24

The tunnel and bored pile were assumed to be a linear elastic material as depicted in Table 1.

All analyses have been performed using the material parameters with Hardening Soil (HS) model presented in Table 2. The HS model parameters adopted from Rukdee Chuai [10] were mainly calibrated from laboratory testing results of soil samples together with the field measurement conducted by Prust [11]. The parameters have been used to analyse the tunnel work in Bangkok [5], [9].

Table 2 Soil model parameters [5], [9], [10]

Soil layer	Soft clay	Stiff clay
Material model	Hardening Soils (HS model)	
E_{oed}^{ref} (kPa)	5,000	63,158
E_{50}^{ref} (kPa)	5,000	63,158
E_{ur}^{ref} (kPa)	15,000	189,474
γ_{sat} (kN/m ³)	16	18
ν_{ur} (-)	0.2	0.2
ϕ' (°)	22	22
c' (kPa)	5	18
m (-)	1	1
p_{ref} (kPa)	100	100

Analysis process

The simulation process, which is carried out by 3D FEA, is divided into two stages. The tunnelling process with the Earth Pressure Balance (EPB) shield method is simulated by following the method proposed by Lueprasert [12]. The tunnelling process was verified by comparing, measured surface settlement of MRTA and the structural forces of previous researches [13], [14]. The second stage is to assess the tunnel deformation due to the application of the axial load to the single pile modelled wished-in-place. The applied load is the predetermined working load based on the alpha method [15]. The tunnel deformation is assessed by using the method proposed by Lueprasert [5] as shown in Fig. 4.

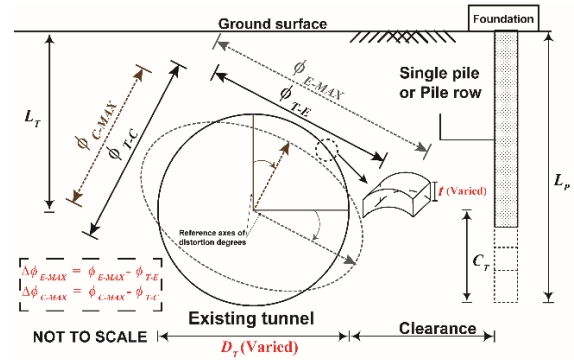


Fig. 4 The schematic of the assessment method in terms of the maximum changes in tunnel diameter.

The figure shows the assessment method used to trace the maximum tunnel deformation due to a loaded pile located on one side of the existing tunnel. The $\Delta\phi_{E-MAX}$ and $\Delta\phi_{C-MAX}$ denote the difference between the largest widening and shortening tunnel diameters, respectively, due to loaded pile after tunnel excavation complete. Note that only the deformation due to an adjacent pile under loading is considered; that due to the excavation process is not included.

To investigate the effect of tunnel diameter and lining thickness, they are varied in the analyses to assess $\Delta\phi_{E-MAX}$ or $\Delta\phi_{C-MAX}$ for the first part analysis.

The second part is to establish a relationship between the tunnel deformation and dimensionless parameters from a series of parametric study conducted by 2D FEA. The impact of row pile on the existing tunnel, which can be more serious than that of single pile in engineering practice, is modelled. Various tunnel diameters and lining thicknesses, which are considered by ratio of tunnel diameter to lining thickness, are simulated. Generally, with conservative design of tunnel lining, the ratio of tunnel diameter to lining thickness can be classified into a thick shell structure. However, from the previous study [16], the results indicate that whether thin or thick shell elements can give a reasonably accurate distortion of cylindrical tubes. Thus, the thin shell structure formulated in PLAXIS code, is adopted to simulate the tunnel lining in this study.

RESULTS

The results are divided into two parts: the first one is the investigation of the effects of adjacent pile under loading on the maximum change in tunnel diameter, $\Delta\phi_{E-MAX}$ or $\Delta\phi_{C-MAX}$, of different tunnel sizes based on MRTA and MWA projects. For the second part, the relationship between the out-of-roundness and dimensionless parameters is carried out to establish the relevant equation and the chart indicating the effects of loaded pile on allowable

tunnel deformations referred from Land and Transport Audibility (LTA) code [17].

The investigation of the effect of tunnel diameter and lining thickness on the maximum change in tunnel diameter

Different tunnel diameters

The lining thickness of 0.30 based on MRTA tunnel are fixed while the tunnel diameters of 4.07 and 6.30 m are modelled to investigate the impact of the adjacent bored pile under loading.

Because the previous research [5] reveals that both the trend and magnitude of $\Delta\phi_{E-MAX}$ and $\Delta\phi_{C-MAX}$ are almost identical to each other, so only the results for $\Delta\phi_{E-MAX}$ are shown herein. $\Delta\phi_{E-MAX}$ for the tunnel located in soft clay and stiff clay against various normalized pile tip level to tunnel depth (L_p/L_T) and clearance of 0.5 and 4.5 m are illustrated in Figs. 5a and b, respectively. The normalized distance from tunnel spring line to tunnel diameter, C_T/D_T , are also provided on the right side of the y-axis.

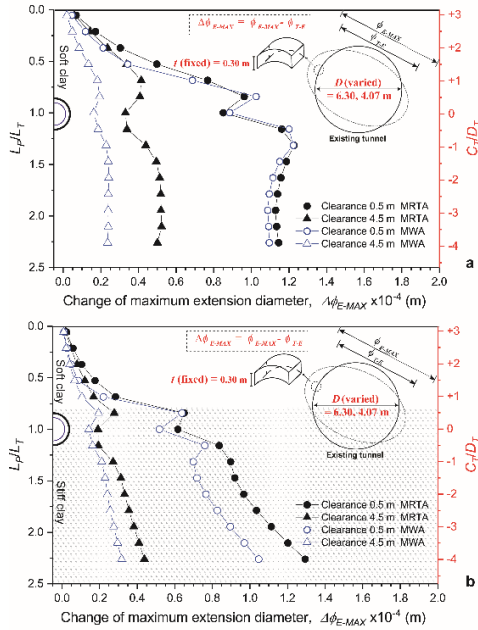


Fig. 5 The maximum extension changes of tunnel diameter due to pile under loading for different tunnel diameters. (a) for a tunnel located in soft clay, (b) for a tunnel located in stiff clay

For tunnel located in soft clay (Fig. 5a), $\Delta\phi_{E-MAX}$ of 6.3 m tunnel is slightly larger than that of 4.07 m tunnel, especially the loaded pile located at clearance of 0.5 m. $\Delta\phi_{E-MAX}$ increases with increasing L_p when the pile tip is located above the tunnel crown ($C_T/D_T \geq 0.5$) and becomes decreasing before increasing again. When the pile tip is located below the tunnel invert, $-0.5D_T$, $\Delta\phi_{E-MAX}$ slightly increases and reaches the maximum value at the pile tip located approximately $-1.0D_T$. When pile tip is

located in the range of $-2.0D_T$ to $-4.0D_T$, $\Delta\phi_{E-MAX}$ remains almost constant.

For the case of the tunnel located in stiff clay as shown in Fig 5b, the larger $\Delta\phi_{E-MAX}$ of 6.3.m tunnel can clearly observed, especially in the range of pile tip located below tunnel invert. The $\Delta\phi_{E-MAX}$ are generally smaller than those of tunnel located in soft clay, especially when the pile tip located in soft clay. When the pile tip is extended into stiff clay ($+0.5D_T$), the $\Delta\phi_{E-MAX}$ drastically increases because of a larger working load on bored pile.

By considering the constant lining thickness of 0.30 m, the result described above indicates that the tunnel diameter has influence on the tunnel deformation due to nearby loaded pile.

Different lining thicknesses

The distribution patterns of $\Delta\phi_{E-MAX}$ for both cases are similar to those of $\Delta\phi_{E-MAX}$ from the previous section (different tunnel diameters) for the same case as shown in Fig. 6. The $\Delta\phi_{E-MAX}$ of tunnel with the lining thickness of 0.15 m is clearly larger than that with the lining thickness of 0.30 m. This indicates that the lining thickness has an influence on the tunnel deformation due to pile under loading.

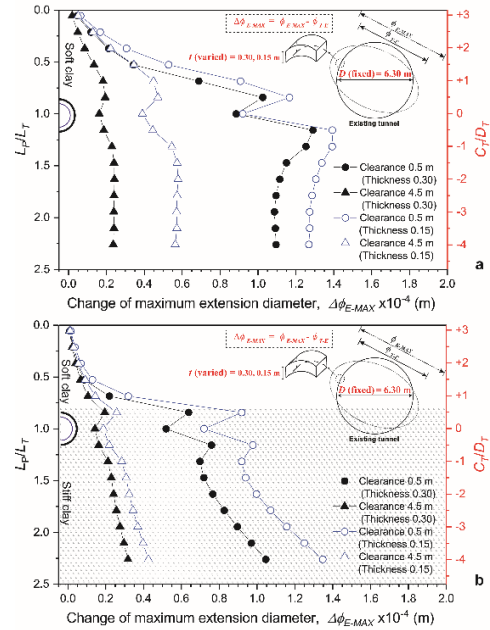


Fig. 6 The maximum extension changes of tunnel diameter due to a pile under loading for different lining thicknesses. (a) for a tunnel located in soft clay, (b) for a tunnel located in stiff clay

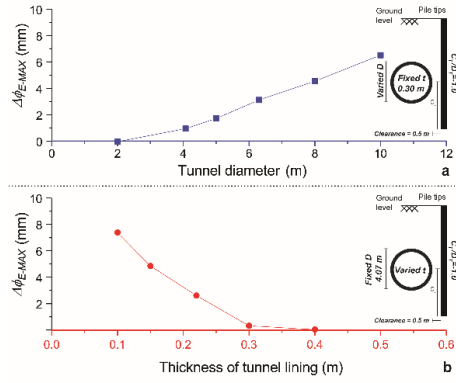


Fig. 7 The effects of different tunnel diameters and lining thicknesses on the maximum extension changes of tunnel diameter.

Fig.7 shows the maximum extension change in tunnel diameter, $\Delta\phi_{E-MAX}$, on y-axis against the varied tunnel diameter and lining thickness as shown in Figs.7a and b, respectively, on x-axis. The maximum effect of the loaded pile located at $-1.0 D_T$ and clearance of 0.5 m on $\Delta\phi_{E-MAX}$ obtained from the previous section is considered with different tunnel diameters and lining thicknesses.

For different tunnel diameters (lining thickness of 0.30 m is fixed) as depicted in Fig7a, $\Delta\phi_{E-MAX}$ increases with increasing tunnel diameter. By considering different tunnel thicknesses (tunnel diameter of 4.07 m is fixed) as depicted in Fig7b, the decreasing of $\Delta\phi_{E-MAX}$ with increasing lining thickness can be seen. This can evidently confirm that the tunnel diameter and lining thickness parameters have strongly influence on the effects of loaded pile on the tunnel deformation.

Application of tunnel deformation in preliminary assessment of tunnels with various diameters and lining thicknesses

In order to assess the tunnel deformation in this section, inferring from assessment method of bending strain in surface lining [18] and the principal of circularity shell structures (e.g., pipelines, tanks, and steel lining), the unsymmetrically distortional shapes can be assessed by the percentage of out-of-roundness defined in terms of parameters including the minimum, maximum, and nominal diameters of a distorted structure as shown in Eq. (1) [19].

$$\text{Out-of-roundness (\%)} = \frac{D_{\max} - D_{\min}}{D} \times 100 \quad (1)$$

Where D_{\max} and D_{\min} denote for the maximum and minimum tunnel diameters after distortion. The dimensionless parameter, which relatively involves with the lining thickness (t) and the tunnel diameter

(D), is established from the moment of inertia of tunnel lining and the length of bored pile (L_p). The L_p implies the magnitude of applied axial load of bored pile. The moment of inertia of 1 m wide tunnel lining is $t^3/12$, whereas $\pi D^2/4$ represents the tunnel size. Based on the preliminary investigation, it reveals that the tunnel deformation increases as tunnel size and pile length increase and the thickness decreases. Therefore, the dimensionless parameter is postulated as ratio of lining thickness to tunnel diameter and length of bored pile as $t^3/D^2 L_p$.

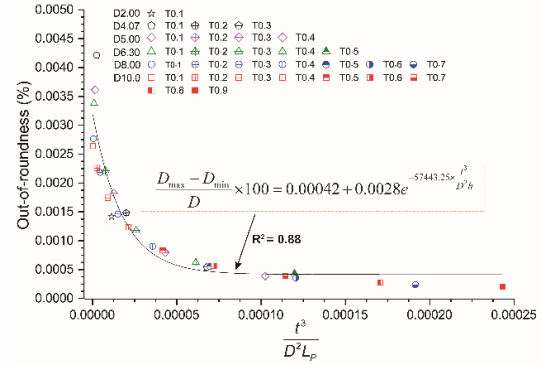


Fig. 8 The relationship between out-of-roundness and influencing factors on the tunnel deformation.

Series of parametric study regarding relative influencing factors on the tunnel deformation due to adjacent bored pile as mentioned above, is conducted using the 2D-FE to synthetically establish the simple equation in this section. The tunnel located in soft clay and pile tip located at $-1.0 D_T$ and clearance of 0.5 m resulting to the maximum value of tunnel deformation are chosen. The tunnel diameter and lining thickness are varied between 2.0 to 10.0 m and 0.10 to 0.90 respectively, in the analyses.

Fig. 8 shows the plotted between out-of-roundness and the dimensionless parameters of $t^3/D^2 L_p$. An equation can be generated by the curve fitting method with R^2 of 0.88 as shown in Eq. 2.

$$\frac{D_{\max} - D_{\min}}{D} \times 100 = 0.00042 + 0.0028e^{-57443.25 \times \frac{t^3}{D^2 L_p}} \quad (2)$$

According to the allowable deformation of 15 mm for 6.40 m tunnel regulated by LTA [17], it is postulated herein that the allowable deformation of tunnels with other sizes can be considered so as to keep the ratio of allowable deformation-to-tunnel-diameter constant. By using the Eq.2, tunnel deformation in terms of $D_{\max} - D_{\min}$ for various tunnel diameters and lining thicknesses can be calculated. Together with the allowable deformation, the chart for estimating the percentage of tunnel deformation can be established as shown in Fig 9.

The chart provides the preliminary assessment of the impact for adjacent loaded pile.

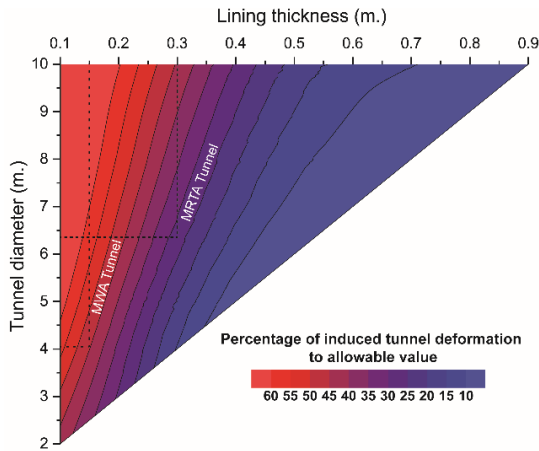


Fig. 9 The assessment chart for tunnels with various tunnel diameters and lining thicknesses.

The interpretation from the chart using the geometries of MRTA and MWA tunnels reveals that the percentage between maximum possible deformation to allowable value of MRTA tunnel is smaller than that of the MWA tunnel. This is because the serviceability regarding train operation governs the design concept of MRTA. In other words, the MRTA tunnel is safer than the MWA tunnel.

CONCLUSION

The effect of tunnel size and lining thickness on tunnel deformation due to adjacent pile under loading is numerically investigated by choosing the MRTA and WMA tunnels in Bangkok subsoil as the reference cases. Series of parametric study regarding relative influencing factors on the tunnel deformation due to adjacent loaded pile, e.g. tunnel diameter, lining thickness, pile length, is conducted. The results can conclude as follows:

1. The tunnel diameter and lining thickness have strongly influence on the effects of tunnel deformation due to loaded pile.
2. The proposed parameters, t^3/D^2L_p , can appropriately estimate the tunnel deformation in terms of out-of-roundness due to adjacent loaded pile.
3. With a certain criterion, it is possible to establish a chart that can be used to assess the degree of tunnel deformation due to pile under loading for tunnels with various diameters and lining thicknesses.

ACKNOWLEDGEMENT

The authors would like to acknowledge the financial support from King Mongkut's Institute of

Technology Ladkrabang through Grant KREF035001.

REFERENCES

- [1] Schroeder F.C., Potts D.M. and Addenbrooke T.I., The influence of pile group loading on existing tunnels. *Géotechnique* 54 (6), 2004, pp.351–362.
- [2] Yao J., Taylor R.N. and McNamara A.M., The Effects of Loaded Bored Piles on Existing Tunnels. *Geotechnical Aspects of Underground Construction in Soft Ground - 6th International Symposium (IS-Shanghai)*, 2008, pp. 735–41.
- [3] Heama N., Jongpradist P., Lueprasert P. and Suwansawat S., Investigation on tunnel responses due to adjacent loaded pile by 3D finite element analysis. *International Journal of GEOMATE*, Vol.12, Issue 31, 2017, pp. 63–70.
- [4] Lueprasert P., Jongpradist P., Charoenpak K., Chaipanna P. and Suwansawat S., Three-dimensional finite element analysis for preliminary establishment of tunnel influence zone subject to pile loading. *Maejo International Journal of Science and Technology*, Vol. 9, 2015, pp. 209-223.
- [5] Lueprasert P., Jongpradist P., Jongpradist P. and Suwansawat S., 2017. Numerical Investigation of Tunnel Deformation Due to Adjacent Loaded Pile and Pile-Soil-Tunnel Interaction. *Tunnelling and Underground Space Technology*, Vol. 70, 2018, pp. 166–81.
- [6] Bakker K.J. and Blom C.B.M., Ultimate Limit State Design for Linings of Bored Tunnels. *Geomechanics and Tunnelling*, Vol.2(4), 2009, pp. 345–58.
- [7] Mroueh H., and Shahrour I., A Simplified 3D Model for Tunnel Construction Using Tunnel Boring Machines. *Tunnelling and Underground Space Technology*, Vol.23(1), 2008, pp.38–45.
- [8] Brinkgreve R., Engin E. and Swolfs W., PLAXIS Version 2013 manual, 2013.
- [9] Jongpradist P., Kaewsri T., Sawatpanich A., Suwansawat S., Youwai S., Kongkitkul W. and Sunitsakul J., Development of tunneling influence zones for adjacent pile foundations by numerical analyses. *Tunnelling and Underground Space Technology*, Vol. 34, 2013, pp. 96–109.
- [10] Rukdee Chuai T., Jongpradist P., Wonglert A. and Kaewsri T., Influence of soil models on numerical simulation of geotechnical works in Bangkok subsoil. *EIT Research and Development Journal*, Vol. 20, 2009, pp.17-28.
- [11] Prust R.E., Davies J., and Hu S., Pressure meter Investigation for Mass Rapid Transit in Bangkok Thailand. *Journal of the Transportation Research Board* 1928, 2005, pp. 207–217.

- [12] Lueprasert P., Jongpradist P. and Suwansawat S., 3D-FEM of EPB shield tunnel excavation using shell element and grouting layer, *International Journal of GEOMATE*, Vol.12, Issue 31, 2017, pp. 51–57.
- [13] Working Group No. 2 ITA., *Guidelines for the Design of Shield Tunnel Lining*. Elsevier Science Ltd Published, 2000.
- [14] Moller S., *Tunnel induced settlements and structural forces in linings*. Doctoral Thesis, University of Stuttgart, Germany, 2006.
- [15] Skempton A. W., *Cast In-Situ Bored Piles in London Clay*. *Géotechnique*, Vol. 9(4), 1959, pp. 153–73
- [16] Sadowski Adam J., and Michael Rotter J., *Solid or Shell Finite Elements to Model Thick Cylindrical Tubes and Shells under Global Bending*. *International Journal of Mechanical Sciences*, Vol. 74, 2013, pp. 143–53.
- [17] Land Transport Authority (LTA), *Code of Practice for Railway Protection*, October 2004 ed. Development and Building Control Department, Singapore, 2004.
- [18] Mohamad H., Kenichi S., Adam P., and Peter J. B., *Performance Monitoring of a Secant-Piled Wall Using Distributed Fiber Optic Strain Sensing*. *Journal of Geotechnical and Geoenvironmental Engineering*, Vol. 137(12), 2011, pp. 1236–43.
- [19] European Committee for Standardization (CEN), *Design of steel structures, Part 1–6 general rules: Supplementary rules for shell structures*. Eurocode 3. Brussels, Belgium, 1999.

DISCRETE PARTICLE SIMULATION MODEL FOR SLAKING OF GEOMATERIALS INCLUDING SWELLING CLAY MINERALS

Yutaka Fukumoto¹ and Satoru Ohtsuka¹

¹ Department of Civil and Environmental Engineering, Nagaoka University of Technology, Japan

ABSTRACT

The slaking of geomaterials often causes some unexpected geohazards, such as slope failures, debris flows, rockfalls, and so on. In particular, the process of slaking is highly enhanced when the geomaterials include swelling clay minerals such as montmorillonite and saponite. In order to investigate the mechanisms of the slaking phenomenon from a microscopic point of view, this study presents a particle simulation model based on the discrete element method (DEM) that can reproduce the slaking process of geomaterials that include swelling clay minerals. The properties of swelling and shrinking are modeled by changing the diameter of the DEM particles which are assumed to comprise the swelling clay minerals and several sand particles. A series of simulations of the deformation of mudstone under a wet-dry cyclic condition is performed in both two and three dimensions. As a result of the analyses, the applicability of the proposed model to the slaking phenomenon is confirmed.

Keywords: Slaking, Swelling clay mineral, Mudstone, Discrete element model, Granular materials

INTRODUCTION

The slaking phenomenon is described as the process in which compacted soils or rocks gradually disintegrate into fine fractions under a wet-dry cyclic condition. The slaking of geomaterials often contributes to the risk of some geohazards, such as slope failures, debris flows, rockfalls, and so on [1]. In particular, when the geomaterials include swelling clay minerals, such as montmorillonite and saponite, which are classified in the smectite group, the slaking phenomenon is highly enhanced and the potential for geohazards increases considerably. Previous researches have revealed that many factors can trigger the slaking phenomenon [2], [3], but each factor has not yet been systematically defined.

In order to investigate the mechanisms of the slaking phenomenon from a microscopic point of view, this study presents a particle simulation model based on the discrete element method (DEM) that can reproduce the process of the slaking of geomaterials that include swelling clay minerals. In the model, the characteristics of swelling and shrinking are modeled by changing the diameter of the DEM particles which are assumed to comprise the clay minerals and several sand particles. In addition to this model, a model of cohesion is introduced to the contact logic between the DEM particles so that cohesive materials, such as compacted soils and rocks, can be reproduced in the framework of the DEM.

A series of simulations of the deformation of mudstone, subjected to cycles of wetting and drying, is performed in both two and three dimensions. As a result of the analyses, the applicability of the proposed model to the slaking phenomenon is

confirmed.

The present paper is organized as follows. At the beginning of the paper, the numerical methods are firstly described. Details of the results of the numerical simulations and discussions are then given in the following sections. A summary and the limitations of the proposed numerical model are presented in the final section.

MODEL OF SWELLING AND SHRINKING

A numerical model which can simulate the characteristics of the swelling and shrinking of clay minerals is developed on the basis of the conventional DEM [4]. In the proposed model, the DEM particles are assumed to represent the area where several sand particles and clay minerals exist, as shown in Fig. 1, where the dotted circles indicate the DEM particles. When the soil contains water, the clay minerals swell and are pushed inside the pores of the sand particles; and thus, they enlarge the size of the DEM particles. When the soil is exposed to a dry condition, on the other hand, the clay minerals shrink; and thus, the size of the DEM particles also shrinks. Such a model, which deals with the changing size of DEM particles, is found in some literature [5], [6], where the patterns of the surface cracks of the clay soils are studied.

The initial diameter of DEM particles is defined as D_{ini} (m). In the following sentences, the direction of swelling is negative and that of shrinking is positive. The upper limit of the amount of swelling is defined as $-\alpha_{sw}D_{ini}$ (m), while the upper limit of the amount of shrinking is defined as $\alpha_{sh}D_{ini}$ (m), as shown in Fig. 2. It should be noted here that swelling coefficient α_{sw} is a negative value and that shrinking

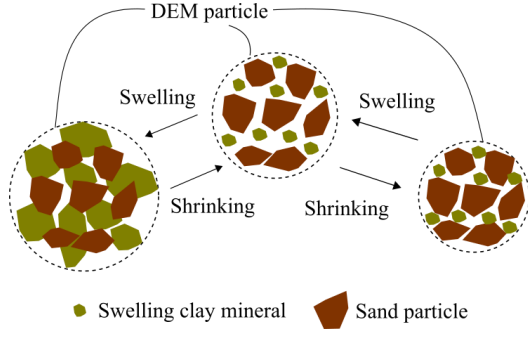


Fig. 1 Model of swelling and shrinking in the framework of DEM

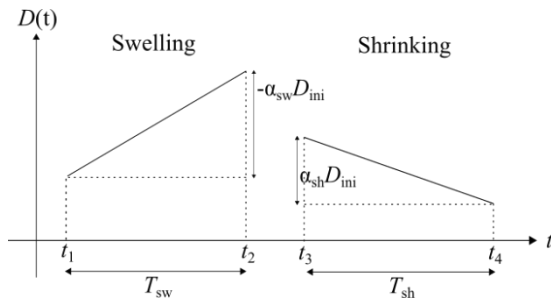


Fig. 2 Parameters for model of swelling and shrinking

coefficient α_{sh} is a positive value. The values for α_{sw} and α_{sh} are non-dimensional. The variation in the diameter of each DEM particle against time is assumed to be linear for simplicity.

The times required to reach the limit value of the swelling and the shrinking are T_{sw} (s) and T_{sh} (s), respectively. When t_1 (s) is the starting time of the swelling, t_2 (s) is the ending time of the swelling, t_3 (s) is the starting time of the shrinking, and t_4 (s) is the ending time of the shrinking, the diameter of the DEM particles at t (s) is obtained as follows:

$$D(t) = D(t_1) - \frac{\alpha_{sw} D_{ini}}{T_{sw}} (t - t_1), t_1 < t < t_2, \quad (1)$$

$$D(t) = D(t_2) - \frac{\alpha_{sh} D_{ini}}{T_{sh}} (t - t_3), t_3 < t < t_4, \quad (2)$$

where t (s) is the time. The velocity of the swelling is $-\alpha_{sw} D_{ini} / T_{sw}$ (m/s) from Eq. (1) and the velocity of the shrinking is $-\alpha_{sh} D_{ini} / T_{sh}$ (m/s) from Eq. (2). From the viewpoint of computational costs, the values for T_{sw} (s) and T_{sh} (s) in the numerical simulations are set to be smaller than the actual scale of time.

In this model, the shape of $D(t)$ is linear and it is independent of the water content of the soils. A non-linear model for $D(t)$, which can consider the water content or the chemical reactions, is a topic for future study because the slaking phenomenon includes not

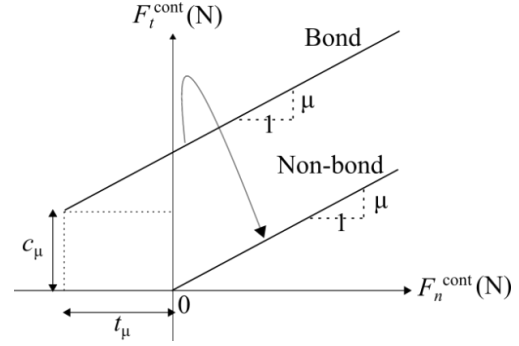


Fig. 3 Model of linear contact bond

only a mechanical process, but also a hydraulic process and a chemical process.

MODEL OF COHESION

Contact logic

In addition to the model of the swelling and shrinking, a model of the cohesion is introduced to the contact logic in order to express the compacted soils or rocks. The model of the cohesion is composed of two models, namely, the linear contact bond model and the rolling friction model. The total of the three input parameters is attached to the model of the cohesion.

The DEM permits the neighboring particles to be bonded together by springs which can transmit both attractive and repulsive forces. Among these bond models, the linear contact bond model [7], [8] requires only two micromechanical parameters for a transformation from the unbonded case to the bonded case. This bond model is characterized by the adaptation of the Mohr-Coulomb failure criterion into the $F_n^{\text{cont}} - F_t^{\text{cont}}$ plane, as shown in Fig. 3, where F_n^{cont} (N) is the normal contact force and F_t^{cont} (N) is the tangential contact force. The values for the slope of the lines in Fig. 3 indicate the coefficient of sliding friction μ . The two kinds of input parameters are the contact bond force in the tangential direction, c_μ (N), and the contact bond force in the normal direction, t_μ (N).

Furthermore, in order to consider the effect of the inter-particle cohesion on the torque of the DEM particles, a rolling friction model [9] is also introduced. The rolling friction model employed in this study is the same as that employed in our previous research [9]. The moment of rolling resistance, resulting from the rolling friction, is defined as a function of the normal contact force, F_n^{cont} (N), and a length parameter to represent the contact area, b . Length parameter b is a ratio of the width of the virtual contact area to the diameter of the DEM particles, and it is the input parameter for the rolling friction model.

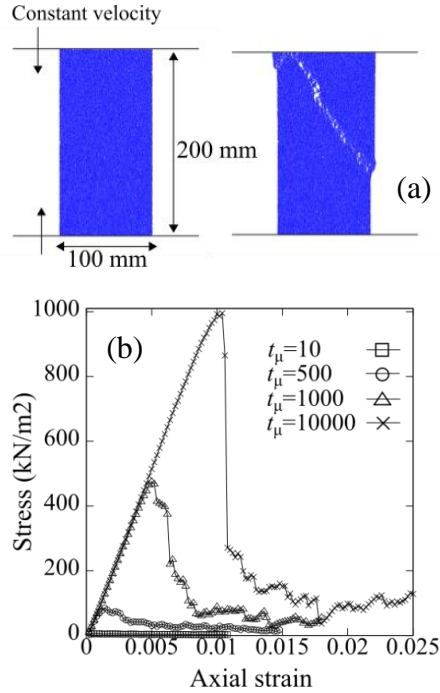


Fig. 4 Simulation of uniaxial compression test

Uniaxial compression test

Two-dimensional simulations of the uniaxial compression test are performed, as illustrated in Fig. 4 (a), so that the correlations between the micromechanical parameter and the uniaxial compressive strength can be obtained. In the simulation, the upper wall and the lower wall are controlled with the same constant velocity in the direction of compression.

The specimen is 100 (mm) in width and 200 (mm) in height. The specimen consists of 23,397 DEM particles whose average diameter is 1 mm. The density of the circular DEM particles is 2600 (kg/m³). The contact springs, for both the particle-particle contacts and the particle-wall contacts, are assumed to be linear. The value for $k_n/k_t = 4$ (k_n (N/m) = 1.0×10^8 and k_t (N/m) = 2.5×10^7), where k_n and k_t are the normal and the tangential spring constants, respectively. In addition, viscous damping is introduced so that the equilibrium state can be achieved. The damping was constrained to be small enough so as not to have any effect on the results presented in this study. The value for the coefficient of the sliding friction is 0.5. The value for the rolling friction parameter is 0.1. The values for the contact bond force in the normal direction, t_μ (N), are set to be in the range of 10 to 10,000, while those for the contact bond force in the tangential direction, c_μ (N), are set to be 0.

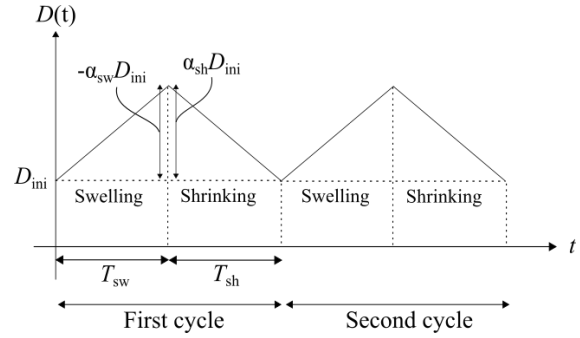


Fig. 5 Parameters for simulation of wet-dry cyclic condition

Figure 4 (b) plots the stress – strain curves obtained from the uniaxial compression test. The results of t_μ (N) = 10, 500, 1000, and 10000 are presented here. The maximum values for the compressive stress indicate the uniaxial compressive stress. It can be seen from the figure that the values for the obtained strength depend on the contact bond force and vary in the range of 0 to 1000 (kN/m²). The model of the cohesion is appropriate for the purposes of the present research because the typical value for the uniaxial compressive stress of mudstone often varies in the range of 100 to 10000 (kN/m²). It should be noted here that further investigations, such as a uniaxial tension test and a diametral compression test, in addition to the uniaxial compression test, are necessary for determining more detailed relationships between the micromechanical parameters and the micromechanical strength.

2D SIMULATION OF SLAKING PHENOMENON

The numerical simulation of the slaking of mudstone under a wet-dry cyclic condition in two dimensions is performed in order to confirm the applicability of the proposed model. The initial size of the specimen at t (s) = 0 is 100 mm in width and 100 mm in height. The number of DEM particles which comprise the specimen is 12,998, and the average diameter of each DEM particle is 1 mm. The time step is 5.0×10^{-7} (s). The values for the normal and the tangential spring constants are 1.0×10^8 (N/m) and 2.5×10^7 (N/m), respectively. The values for μ and b are 0.5 and 0.1, respectively. The above numerical conditions are almost the same as those used in the uniaxial compression test.

In terms of the model of the swelling and shrinking, the input parameters are set as described in Fig. 5: $\alpha_{sw} = -0.1$, T_{sw} (s) = 2.0, $\alpha_{sh} = 0.1$, and T_{sh} (s) = 2.0. The cycle of swelling and shrinking is repeated two times, i.e., the total time of the simulation is 8.0 s. In the first cycle, the shrinking process is started

immediately after the end of the swelling process. At the beginning of the second cycle, the swelling process is started immediately after the end of the shrinking process.

Figure 6 shows the snapshots of the cases of contact bond force, t_μ (N) = 10, 50, and 100, in which three different patterns of slaking are obtained. When the value for t_μ (N) is larger than 100, the specimen shows little change from the initial state. Neither deformations nor small cracks can be observed inside the specimens in such cases.

At first, Fig. 6 (a) shows the case of t_μ (N) = 10 where the contact bond is very small. From the illustrations, it can be seen that the specimen already begins to collapse at t (s) = 2.0 and largely collapses at t (s) = 8.0. With this pattern of the slaking phenomenon, the magnitude of the collapse is very large and the soil specimen cannot retain the original shape at the end of the second cycle.

Next, the case of t_μ (N) = 50 is presented in Fig. 6 (b). Based on the snapshots, there are neither cracks nor deformations inside the specimen at the end of the first cycle. However, at the end of the second cycle, it can be seen that the specimen has changed a little in shape. From the enlarged drawing at t (s) = 8.0, which is illustrated in Fig. 7 (a), there are some voids inside the specimen, i.e., cracks are generated. In the second pattern of the slaking phenomenon, the soil specimen deforms to a small extent and a lot of cracks appear at the final state.

Finally, Fig. 6 (c) shows the case of t_μ (N) = 100. In this case, the shape of the specimen remains square at the end of the second cycle. From Fig. 7 (b), it can also be observed that there are no cracks or deformations. When the value for t_μ (N) is larger than 100, the specimen shows the same trends as the case of t_μ (N) = 100. In the third pattern of the slaking phenomenon, the soil specimen retains the original shape, even though it is subjected to two cycles of wetting and drying.

In order to discuss these changes in the mudstone in detail, the evolution of the number of bonded contacts between the DEM particles is presented in Fig. 8 (a). For all cases, in the first cycle of the wet-dry condition, a lot of the bonded contacts are broken in the swelling process in comparison to the shrinking process. In particular, in the cases of t_μ (N) = 10, the same trends are also obtained in the second cycle. However, in the cases of t_μ (N) = 50 and 100, the variation in bonded contacts has a different tendency from that in the first cycle. From Fig. 8 (b), which is the extended view of Fig. 8 (a) in the second cycle, the decrease in bonded contacts in the shrinking process is larger than that in the swelling process. It is believed that the microscopic mechanisms of slaking at a particle resolution may also be different

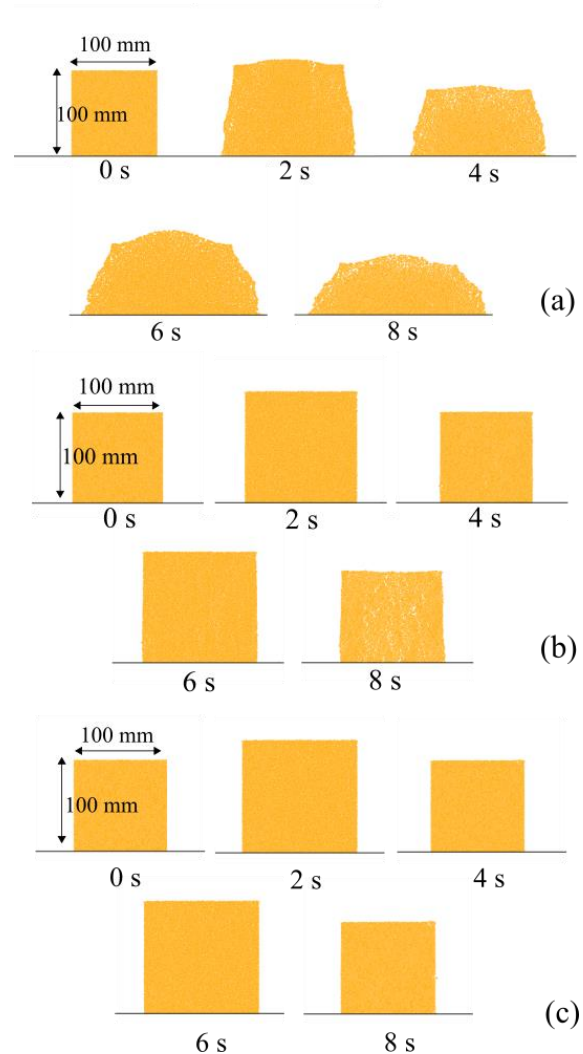


Fig. 6 Snapshots of simulation: (a) t_μ (N) = 10. (b) t_μ (N) = 50. (c) t_μ (N) = 100

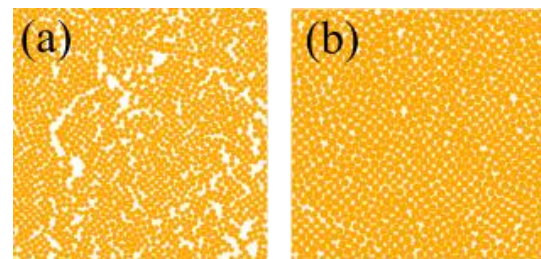


Fig. 7 Enlarged illustrations at t (s) = 8.0: (a) t_μ (N) = 50 (b) t_μ (N) = 100. Magnification ratio of the figure is about 20

from the patterns of the macroscopic deformations.

As stated in the above discussions, the presented simple numerical model can obtain three types of slaking behavior of the mudstone that depend on the parameters of the contact bond. However, the numerical conditions of t_μ (N) = 10, 50, and 100 do

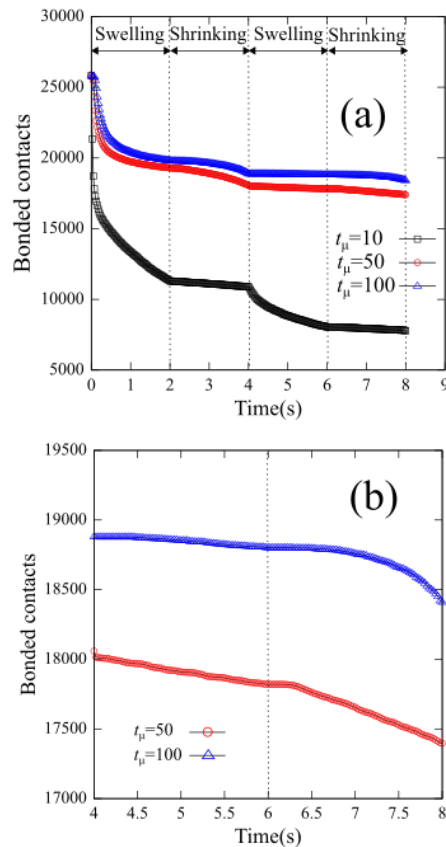


Fig. 8 (a) Time evolution of bonded contacts (b) Extended view of time evolution of bonded contacts in second cycle

not correspond to the actual uniaxial compression strength of mudstone, as discussed in the previous section. To solve this problem, a model of the cohesion which varies according to the water content is needed in the future.

3D SIMULATION OF SLAKING PHENOMENON

In addition to the investigation in two dimensions, the results of the three-dimensional simulation are discussed briefly in order to validate the applicability of the proposed model in the 3-D condition. The simulation demonstrates the deformation of a cylindrical sample of mudstone taken by a boring exploration in a core box, as shown in Fig. 9. The mudstone sample includes swelling clay minerals and is subjected to wetting and drying in the same manner as the investigation in the 2-D condition.

At the initial state, the diameter of the specimen is 50 (mm) and the length of it is 320 (mm). The interior of the core box has the same length. The number of DEM particles which comprises the specimen is about one hundred thousand, and the average diameter of each DEM particle is 2 (mm).

The time step is 2.0×10^{-7} (s). The values for the normal and the tangential spring constants are 1.0×10^7 (N/m) and 2.5×10^6 (N/m), respectively. The values for μ , b , t_μ (N), and c_μ (N) are set to be 0.5, 0.1, 100, and 50, respectively.

The parameters for the model of the swelling and shrinking are listed below: $\alpha_{sw} = -0.1$, T_{sw} (s) = 1.0, $\alpha_{sh} = 0.1$, and T_{sh} (s) = 1.0. The cycle of swelling and shrinking is repeated only one time. The total time of the simulation is 2.0 (s). The shrinking process is started immediately after the end of the swelling process. This calculation is performed on a graphic processing unit. The parallelized algorithm for the DEM [10] is incorporated into our in-house code.

Figure 9 shows snapshots of the results of the numerical simulation. In the figure, the specimen positioned in the back shows the initial state at t (s) = 0 and that in the front shows the final state at t (s) = 2.0. It can be found that the left part of the specimen largely deforms. This is because shear stress acts on the specimen due to the restriction of the fixed side boundaries in the swelling process. In fact, such a deformation pattern can be observed in the actual soil sample taken by a boring exploration. On the other hand, a linear crack is generated on the surface of the lateral side of the cylinder. Several layered cracks are also observed in the actual soil sample, but this investigation cannot reproduce them.

SUMMARY

This paper has presented a simple discrete particle simulation model for the slaking phenomenon of geomaterials that include swelling clay minerals. In the investigation in two dimensions, three types of slaking behaviors of mudstone, that depend on the parameters of the contact bond, were successfully obtained. In the investigation in three dimensions, it was demonstrated that there are future prospects in the application of the model to 3-D problems. In a future study, it will be necessary for both the model of the swelling and shrinking and the model of cohesion to consider the effect of the water content and the chemical reaction. It will also be important to develop a detailed method to determine the input parameters from the results of laboratory experiments.

ACKNOWLEDGEMENTS

This work was supported by research funding from the Niigata Construction Technology Center.

REFERENCES

- [1] Kiyota, T., Sattar, A., Konagai, K., Kazmi, Z. A., Okuno, D., and Ikeda, T., Breaching failure of a huge landslide dam formed by the 2005 Kashmir earthquake. *Soils and Foundations*, Vol. 51, Issue



Fig. 9 Simulation of deformation of cylindrical sample of mudstone taken by boring exploration in core box. Magnification ratio of the figure is 1.0

- 6, 2011, pp. 1179-1190.
- [2] Kikumoto, M., Putra, A. D., and Fukuda, T., Slaking and deformation behaviour. *Géotechnique*, Vol. 66, Issue 9, 2016, pp. 771-785.
- [3] Chigira, M., and Oyama, T., Mechanism and effect of chemical weathering of sedimentary rocks. *Engineering Geology*, Vol. 55, Issue 1-2, 2000, pp. 3-14.
- [4] Cundall, P.A. and Strack, O.D.L., A discrete numerical model for granular assemblies. *Géotechnique*, Vol. 29, Issue 1, 1979, pp. 47-65.
- [5] Péron, H., Delenne, J. Y., Laloui, L., and El Youssofi, M. S., Discrete element modelling of drying shrinkage and cracking of soils. *Computers and Geotechnics*, Vol. 36, Issue 1-2, 2009, pp. 61-69.
- [6] El Youssofi, M. S., Delenne, J. Y., and Radjai, F., Self-stresses and crack formation by particle swelling in cohesive granular media. *Physical Review E*, Vol. 71, Issue 5, 2005, 051307.
- [7] Utili, S., and Nova, R., DEM analysis of bonded granular geomaterials. *International Journal for Numerical and Analytical Methods in Geomechanics*, Vol. 32, Issue 17, 2008, pp. 1997-2031.
- [8] Fukumoto, Y., Particle Based Multiphysics Simulation for Applications to Design of Soil Structures and Micromechanics of Granular Geomaterials, Ph. D thesis of Kyoto Univ., 2015.
- [9] Fukumoto, Y., Sakaguchi, H., and Murakami, A., The role of rolling friction in granular packing. *Granular Matter*, Vol. 15, Issue 2, 2013, pp. 175-182.
- [10] Nishiura, D., and Sakaguchi, H., Parallel-vector algorithms for particle simulations on shared-memory multiprocessors. *Journal of Computational Physics*, Vol. 230, Issue 5, 2011, pp. 1923-1938.

EVALUATION OF BEARING CAPACITY ON SOIL-CEMENT MIXING WALL USING PERMANET PILE

Koji Watanabe¹ and Minoru Mizumoto²

¹Technical Research Institute, Obayashi Corporation, Japan; ² Obayashi Corporation, Japan

ABSTRACT

Soil-cement mixing wall is constructed by mixing the in-situ soil with cement milk in column shapes and inserting core members, such as H-section steel, into the columns. Soil-cement mixing wall is commonly utilized as earth retaining wall and impervious wall during excavation process. If soil-cement mixing wall were also utilized as permanent pile and its bearing capacity and lateral resistance were considered, the design and the construction period of foundation structure could be rationalized. The vertical bearing capacity of the soil-cement mixing wall where the embedded portion is used as a permanent pile was examined by hypothesizing two types of failure modes: failure of the ground and sliding failure between the soil-cement and the H-shaped steel surface. This study aimed for the use of the embedded portion of soil-cement mixing wall as a permanent pile, and evaluated the magnitude of the shaft friction and the magnitude of the bearing capacity in a full-scale load test. This paper firstly describes the background and the previous study, secondly indicates the load test, then presents the results of full-scale load test, and finally discusses the evaluation of pile resistance on soil-cement mixing pile.

Keywords: Soil-Cement Mixing Wall, Full Scale Load Test, Bearing Capacity

INTRODUCTION

An examination was performed on the use of soil-cement mixing walls, which have been treated previously as temporary structures left buried in the ground, as permanent piles in order to rationalize foundation structures and to reduce environmental burdens (Fig. 1). The core materials of such walls, which are used as the foundation pile and whose embedded portions act as a permanent pile, comprise the stress-transmitting member in the soil-cement column. The construction machinery used to build temporary structures using such walls was used to construct the soil-cement mixing wall in this study, and the range for the strength of the soil-cement was assumed to be in the commonly adopted range (0.5 to 2.0N/mm²). The vertical bearing capacity of the soil-cement mixing wall where the embedded portion is used as a permanent pile was examined by hypothesizing two types of failure modes: failure of the ground and sliding failure between the soil-cement and the H-shaped steel surface.

There are some previous researches on the use of soil-cement mixing wall as a permanent pile. Watanabe et al. [1] carried out in-situ full scale load test to confirm the bearing capacity of soil-cement mixing pile. They reported that the bearing capacity of soil-cement mixing pile is equivalent to the bearing capacity of a cast-in-place concrete pile. Moreover, it is important to obtain the bearing properties of pile body because the failure of pile

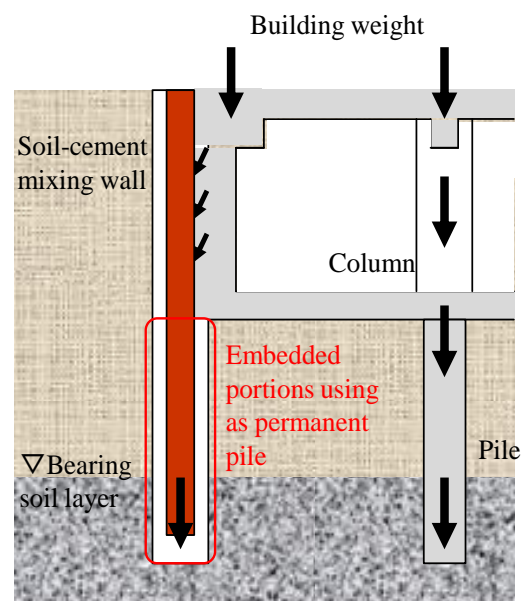


Fig. 1 Schematic View of Soil-cement Mixing Wall Using Permanent Pile.

body is considered such as bond failure between soil-cement and surface of H-shaped pile, and compression failure at pile tip between H-shaped pile and soil-cement. Mizumoto et al. [2] were carried out the model load test to confirm the load transfer mechanism of pile body on soil-cement mixing pile. They examined the stud effect and the effect of confining pressure acting to the pile body.

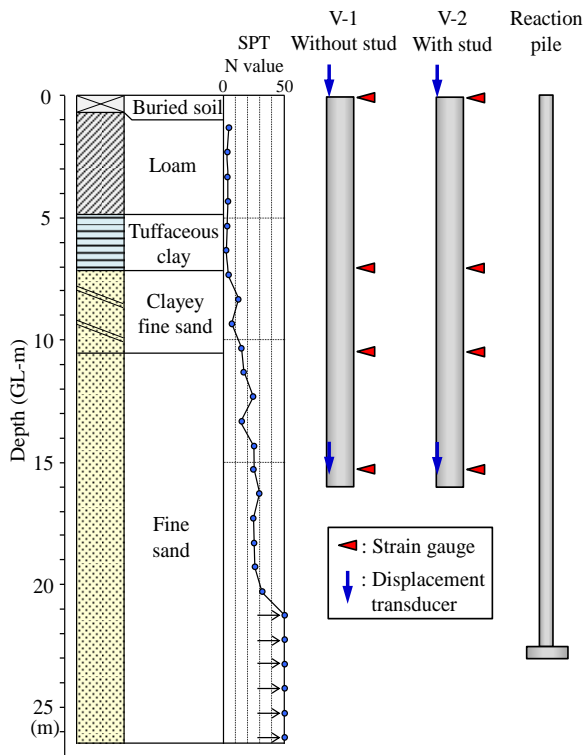


Fig. 2 Soil condition and test piles.

Table 1 Test conditions.

Test pile	Length of soil-cement column (m)	Length of H-shaped steel (m)	Diameter of soil-cement column (mm)	Design strength of soil-cement (N/mm^2)	With or without of stud
V-1	16.0	15.0	600	0.5	Without
V-2					With

The bond strength between soil-cement and surface of H-shaped pile was reported by Watanabe et al. [3]. They concluded that the peak bond strength is estimated by 11~21% of unconfined compressive strength and the residual bond strength is estimated by 3% of unconfined compressive strength. From these study, the load transfer mechanism from the H-shaped steel, which acted as the stress-transmitting member, to the soil cement had to be examined.

This study aimed for the use of the embedded portion of such a structure as a permanent pile, and evaluated the magnitude of the shaft friction and the magnitude of the bearing capacity in a full-scale load test. This paper firstly describes the background and the previous study, secondly indicates the load test, then presents the results of full-scale load test, and finally discusses the evaluation of pile resistance on soil-cement mixing pile.

SUMMARY OF LOAD TEST

The ground conditions and test piles are described in Fig. 2. The test ground was comprised of loam soil and tuffaceous clay down to

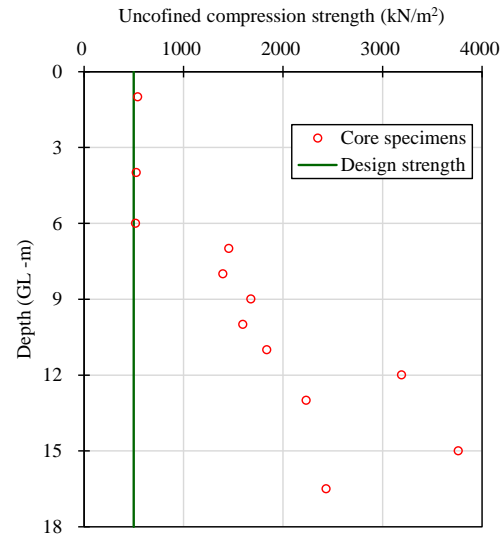


Fig. 3 Results of unconfined compression test.

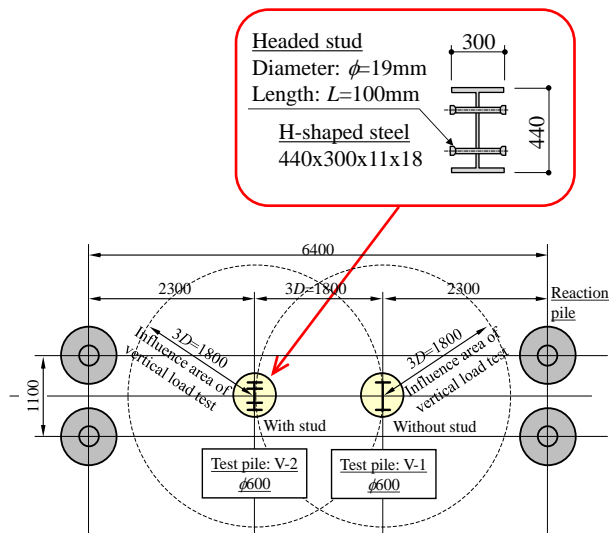


Fig. 4 Arrangement of test piles and reaction piles

approximately GL -5.0m, then comprised primarily with medium-grain and fine-grain sand at depths of GL -5.0m and deeper. There were two static load test piles, a parameter of which was whether studs were present. The specifications for the test piles are listed in Table 1. The test piles were embedded in the ground with the pile tip driven into the ground to an N value of approximately 20. Furthermore, a diameter of 600mm was adopted for both V-1 and V-2 of the soil-cement improving body diameter (pile diameter) of the test piles, while dimensions of H-400×200×8×13 were adopted for the H-shaped steel.

The results of unconfined compression tests for core specimens are shown in Fig. 3. The design strength of the soil-cement improving body was $0.5 N/mm^2$. The strength of the soil-cement improving body was confirmed to satisfy the design strength of $0.5 N/mm^2$, based on the results from an

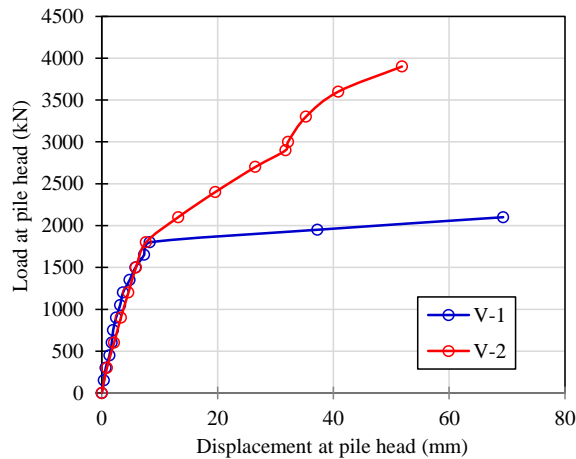


Fig. 5 Relationships between load and displacement at pile head.

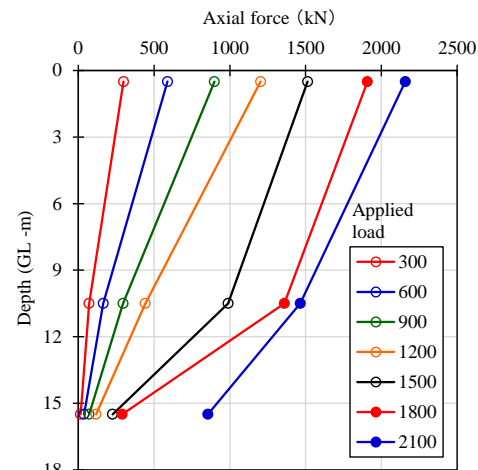
unconfined compression test performed after the load test had been completed, on specimens with their cores extracted.

The arrangements of test piles and reaction piles are shown in Fig. 4. Test piles were arranged between for reaction piles, out of consideration for their influence range. The load test was performed in compliance with the standard of the Japanese Geotechnical Society entitled Method for Vertical Load Test [4]. Stepwise loading and the multiple-cycle method were adopted as loading methods. The duration of the new loading step was set to 30min, while the duration of the historical loading step was set to 2min and the duration of the zero-loading step was set to 15min. The measurement items consisted of the load and displacement of the pile top as well as the strain of the H-shaped steel. The measurements of the displacements at pile tip were taken using the double-pipe method.

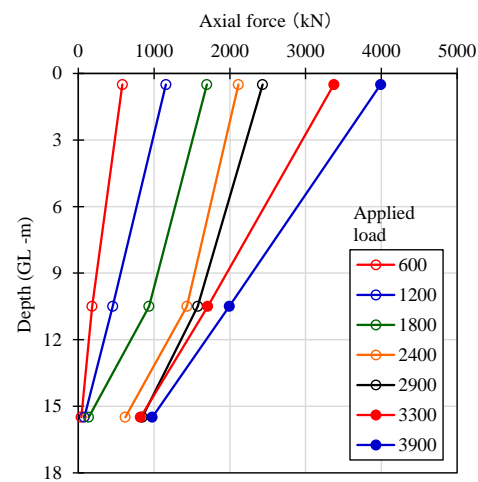
RESULTS OF LOAD TEST

The relationship between the load and displacement for the pile heads of V-1 and V-2 is shown in Fig. 5. The curve rose from the initial stage of loading with both types of test piles and reached the maximum load. A comparison of the initial stiffness of the respective types of piles shows no significant difference based on whether or not studs were present. However, the load bearing on V-2, which had studs, was greater for the same displacement as the displacement progressed, which is believed to have shown the effectiveness of the studs. The maximum loads of the respective types of piles were recorded as 2,100kN for V-1 and 3,900kN for V-2.

The depth distributions of the axial forces of the respective piles are shown in Figs. 6 (a) and (b). The calculation of the axial force was performed by multiplying the measured strain of the H-shaped



(a) V-1 (Without stud).

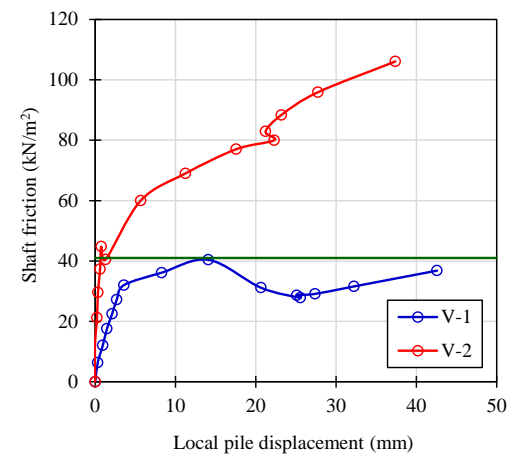


(b) V-2 (With stud).

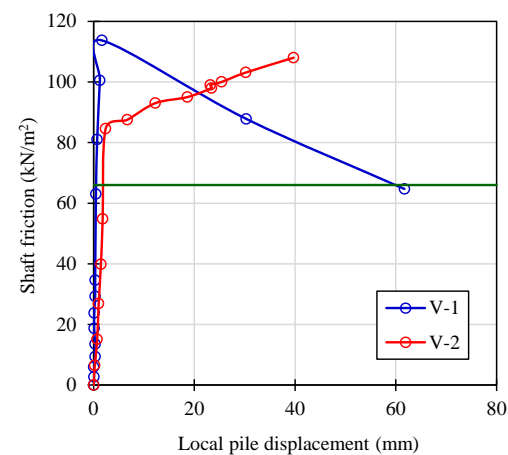
Fig. 6 Axial force distributions.

steel by the elastic modulus of the steel material and the cross-sectional area of the H-shaped steel. Figs. 6 (a) and (b) reveals that the gradient of each segment increased with increasing the applied load. Thereafter, as the applied load was further increased, the gradient decreased in the cohesive soil segment of the upper region but the gradient of the axial force difference became greater in the sandy layer segment of the lower region.

The relationships between the magnitude of the shaft friction and the local pile displacement in respective segments are shown in Figs. 7 (a) and (b). The magnitude of the shaft friction in this instance was calculated by subtracting the peripheral surface area from the axial force difference in the respective segment. The soil cement improvement body diameter was used to calculate the peripheral surface area. The maximum magnitude of the shaft friction was found to be 40-100kN/m² in the cohesive soil layer of the upper region, according to Fig. 7(a), with this tendency reaching an ultimate state and then remaining in a residual state with V-1. In



(a) GL-0~10.5m.



(b) GL-10.5~15m.

Fig. 7 Relationships between shaft friction and local pile displacement.

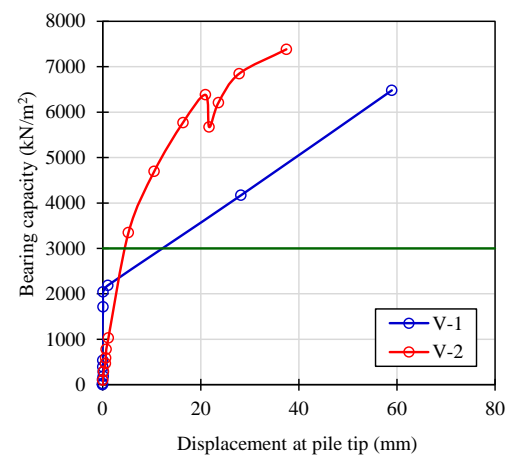


Fig. 8 Relationships between bearing capacity and displacement at pile tip.

contrast, the ultimate state was never reached with V-2, which showed a gradually increasing trend. The manifested magnitude of the shaft friction is believed to have exceeded the undrained shear strength of the ground, as shown in Fig. 7(a), based

on a comparison with the average value of 41 kN/m^2 for the unconfined compression strength for the ground in the corresponding segment. Furthermore, the magnitude of the shaft friction for the sandy soil layer in the lower region as shown in Fig. 6(b) was found to have been about 110 kN/m^2 . Thus, it was determined that it reached an ultimate state with V-1. A comparison between the magnitude of the shaft friction for this segment and the magnitude of the shaft friction of $3.3N$ (66 kN/m^2) for the cast-in-place piles indicated in Recommendations for Design of Building Foundations [5] for revealed that a sufficient magnitude of shaft friction was manifested.

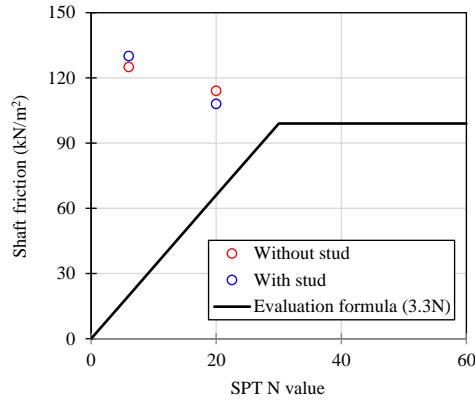
The relationship between the magnitude of the bearing capacity, calculated by subtracting the enveloped area of the H-shaped steel from the axial force reached by the tip of the pile, and the displacement at pile tip is shown in Fig. 8. The value derived by using the magnitude of the bearing capacity evaluation formula for cast-in-site concrete piles, described in Recommendations for Design of Building Foundations [5], is also shown in Fig. 8. Figure 8 reveals that sufficient displacements occurred with the piles of V-1, and the magnitude of the bearing capacity reached an ultimate state. The trend was that of a gradual increase with V-2, which had studs. However, it is surmised that it did not reach an ultimate state. A comparison of the value calculated using the magnitude of the bearing capacity evaluation formula, described in Recommendations for Design of Building Foundations [5], revealed that the magnitude of the bearing capacity for each pile exceeded the value derived by the evaluation formula. This is particularly the case with the piles of V-2, which had studs, with the magnitude of the bearing capacity found to be about twice as large. This is believed to have been due to the behaviors of the H-shaped steel and soil cement, which occurred simultaneously in association with the progression of the displacement because of the presence of the studs.

Another load test have been carried out on soil-cement mixing pile [1], in addition to the load tests presented in this paper. In these load tests, axial force measurements were carried out thoroughly in order to estimate the shaft friction and bearing capacity. It may be useful to establish the evaluation formula for design estimation of the shaft friction and bearing capacity based on these load test results.

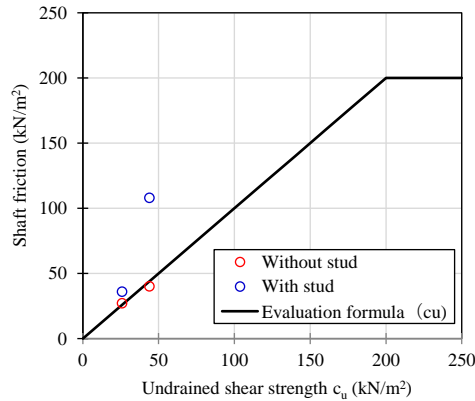
Equations (1) and (2) are the proposed evaluation formula for estimation of shaft friction τ for sandy and clayey soils, respectively. Moreover, the proposed evaluation formula for bearing capacity p_b is also shown in equation (3).

$$\text{Sandy soil: } \tau = 3.3N \quad (1)$$

$$\text{Clayey soil: } \tau = c_u \quad (2)$$



(a) Sandy soil layer.



(b) Clayey soil layer.

Fig. 9 Relationships between shaft friction and SPT N value and/or undrained shear.

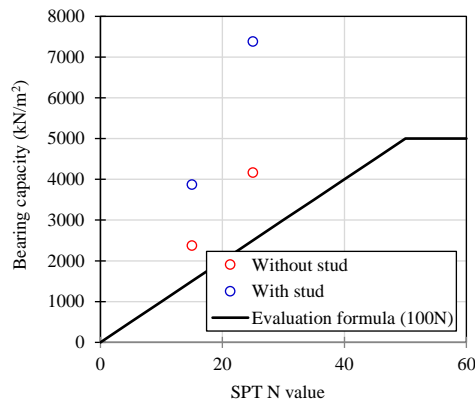


Fig. 10 Relationships between bearing capacity and SPT N value.

Where, N : SPT N value corresponding segment,
 c_u : Undrained shear strength corresponding segment
 Sandy soil: $p_b = 100N_b$ (3)

Where, N_b : Average SPT N value at pile tip

Figure 9 shows the relationships between shaft friction and SPT N value or undrained shear strength. These equations on shaft friction as shown in equations (1) and (2) are the lower value which was obtained from the load tests of soil-cement mixing pile. The relationships between bearing capacity and SPT N value are shown in Fig. 10. The experimental value as shown in Fig. 10 is satisfied the evaluation

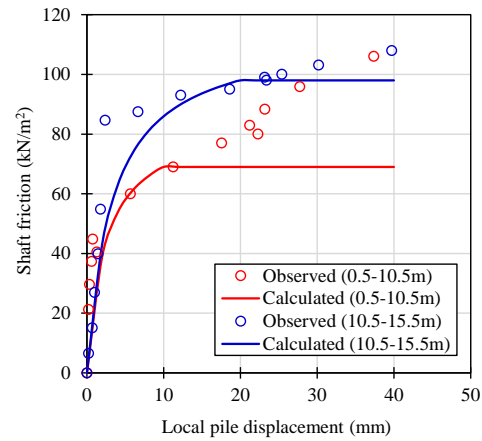


Fig. 11 Evaluation of shaft friction and displacement relationship.

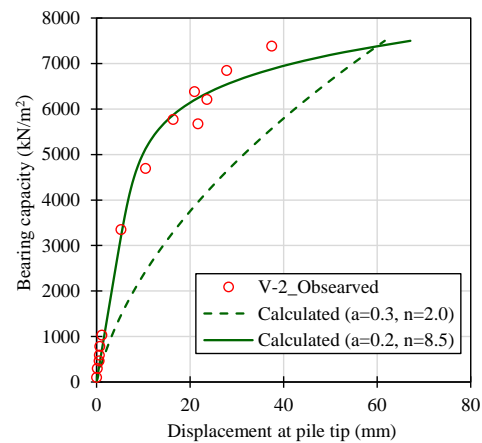


Fig. 12 Evaluation of bearing capacity at pile tip and displacement relationship.

formula on bearing capacity as inserted in equation (3). It can be seen that the proposed evaluation formula give a lower bound of the observed value, indicating that the proposed evaluation formula can be used for design purpose.

EVALUATION OF PILE RESISTANCE

The modelling of pile resistance in the case of V-2 which indicated the ground failure was carried out. The evaluation of pile resistance is both the shaft friction and the bearing capacity at pile tip.

Isemoto et al. [6] proposed the hyperbolic curve to evaluate the relationship between shaft friction and displacement for cast-in-place concrete piles as shown in Eq. (4).

$$\frac{\tau}{\tau_{\max}} = \frac{0.1\delta}{a + b\delta} \quad (4)$$

Where, τ : Shaft friction (kN/m^2), τ_{\max} : Maximum shaft friction (kN/m^2), δ : Displacement (mm), a and b : Coefficient based on statistical analysis of load test data

The coefficient a and b are used in cast-in-place concrete piles as shown below;

Clayey soil: $a=0.19$, $b=0.081$

Sandy soil: $a=0.28$, $b=0.086$

Figure 11 shows the relationships between shaft friction and displacement for both the observed value and calculated curve. According to Fig. 11, the calculated shaft friction at the segment of 0.5-10.5m indicates the small value compared to the observed value. However, the calculated curve agreed with the observed value at the segment of 10.5-15.5m. Thus, it may be said that the shaft friction can be calculated by using Eq. (4).

The evaluation of bearing capacity and displacement at pile tip for cast-in-place concrete piles was proposed by Yamagata et al. [7] as shown in Eq. (5).

$$\frac{s_p/d_p}{0.1} = a \frac{R_p/A_p}{(R_p/A_p)_u} + (1-a) \left\{ \frac{R_p/A_p}{(R_p/A_p)_u} \right\}^n \quad (5)$$

Where, s_p : Displacement at pile tip (mm), d_p : Pile diameter (m), R_p : Axial force at pile tip (kN), A_p : Pile tip area (m²), a and n : Coefficient based on statistical analysis of load test data

Figure 12 indicates the relationships between bearing capacity and displacement at pile tip for both the observed value and the calculated curve. Figure 9 has two types of curves. One is used the proposed value ($a=0.3$ and $n=2.0$) for cast-in-place concrete piles to estimate the curves, the other is used the value ($a=0.2$ and $n=8.5$) to obtain the most fitted curve compared to the observed value. From Fig. 12, the observed bearing capacity has the large stiffness and the large bearing capacity compared to the calculated curve by using the value for cast-in-place concrete pile. Therefore, it can be said that the recommended coefficient is $a=0.2$ and $n=8.5$ when the relationship between bearing capacity at pile tip and displacement for the soil-cement mixing wall is estimated.

CONCLUSION

An evaluation of the vertical bearing capacity was conducted by performing a full-scale load test, with the objective of using soil cement mixing walls as permanent piles. The following findings were obtained from this study.

1) From the results of full scale load tests, it was examined the shaft friction and bearing capacity

on the soil-cement mixing pile. The evaluations revealed that the findings for our test piles were of the same or higher levels than those of the cast-in-place piles, irrespective of whether or not studs were present.

2) The evaluation formulas for design estimation of the shaft friction and bearing capacity were proposed in this paper. It is found that the experimental value is satisfied the evaluation formula on the shaft friction and bearing capacity.

3) The evaluation of shaft friction-displacement relationship and bearing capacity-displacement relationship was carried out by the proposed model. It is found that the evaluated values agree almost with the observed values. Therefore, it is said that the proposed model for cast-in-concrete piles can be applied to evaluate the pile resistance.

REFERENCES

- [1] Watanabe K., Ishii Y., Mizumoto M. and Sato M., In-situ Full Scale Load Test of Soil-Cement Mixing Wall (Part 1 and 2), Proceedings of Annual Conference of Architecture Institute of Japan, 2013, pp.487-490. (in Japanese)
- [2] Mizumoto M., Watanabe K., Arakawa M. and Enomoto H., Model Load Test of Soil-cement Mixing Wall on Load Transfer Mechanism, Proceedings of Annual Conference of Architecture Institute of Japan, 2013, pp.491-492. (in Japanese)
- [3] Watanabe K., Ishii Y., Mizumoto M. and Sato M., A Study on Bond Behavior of Soil Cement Mixing Wall Using Permanent Piles, Proceedings of Annual Conference of Architecture Institute of Japan, 2014, pp.495-496. (in Japanese)
- [4] The Japanese Geotechnical Society, JGS Standard "Method for Vertical Load Test", 2002, (in Japanese)
- [5] Architecture Institute of Japan, Recommendation for Building Foundation, 2001. (in Japanese)
- [6] Iseimoto N., Katsura Y. and Yamada T., Bearing Capacity of Cast-in-place Concrete Pile (Part 2), Proceedings of Annual Conference of Architecture Institute of Japan, 2000, pp.727-728. (in Japanese)
- [7] Yamagata K., Ito A., Yamada T. and Tanaka T., Statistical Study on Ultimate Point Load and Point Load-Settlement Characteristics of Cast-in-place Concrete Piles, Journal of Struct. Constr. Engng., Architecture Institute of Japan, No. 423, 1991, pp.137-146. (in Japanese)

FUNDAMENTAL STUDY OF THE EFFECT OF WATER LEVEL LOWERING IN THE GROUNDWATER DRAINAGE WORK UTILIZING SIPHON

Takeshi YAMAMOTO¹, Yuki MINAMIGUCHI², Keigo KOIZUMI³, Mitsuru KOMATSU⁴,
Kazuhiro ODA⁵, and Adrin THOHARI⁶
^{1,2,3} Osaka University, Japan; ⁴ Okayama University, Japan; ⁵ Osaka Sangyo University, Japan;
⁶ LIPI, Indonesia

ABSTRACT

In recent years, rainfall-induced landslides due to rising groundwater have occurred all over the world causing human and economic losses. A simple and low-cost countermeasure against landslides is to lower the groundwater level with a drainage system utilizing a siphon (the siphon method). In the siphon method, a pipe is installed in a borehole, and groundwater flows from A to B when the total head of A is higher than total head of B. Though it has been successfully deployed in field demonstrations, at this time a design method for the application of the siphon method has yet to be established. Therefore, the purpose of this study is to work toward a design method for slope stability by conducting an investigation of the effects of the siphon method. First, to clarify the quantitative relationship between drainage volume and water level, the validity of a relationship proposed in a previous study was verified through slope model experiments. Second, to investigate the relationship between the siphon spacing and water level considering slope stability, a two-dimensional seepage flow analysis and stability analysis were conducted. Although this research was only conducted at the model level, it demonstrated that the siphon spacing and the target water level in the siphon hole required to ensure slope stability can be determined.

Keywords: siphon, landslide, groundwater, slope stability, slope model experiment

INTRODUCTION

Landslides, caused by an increase in groundwater level due to rainfall, are occurring more frequently in Southeast Asia due to an increase in abnormal weather. Thus the lowering of the groundwater level is an important measure for preventing landslides. The horizontal drilling and drainage well methods are typically used to provide groundwater drainage, and are capable of draining groundwater from its deepest reaches. However, the maintenance of these methods is difficult because the long drainage pipe is buried deep in the ground. Additionally, the cost of these methods is high when the slope length is long, so it remains necessary to develop an easy and inexpensive method for groundwater drainage.

With this background, studies on groundwater

drainage work using siphons (the siphon method) have been conducted. In the siphon method, a pipe is installed in a borehole, and groundwater flows through the pipe from A to B when the total head at A is higher than total head at B (Fig. 1). Mrvik and others have conducted experiments demonstrating the siphon method in the field, successfully lowering the groundwater level and stabilizing the target slope [1]-[3]. However, a design method of the siphon method has yet to be developed because the quantitative relationship between drainage volume and water level, and the relationships among the safety factor, installation spacing of pipes, and water level remain unknown. Therefore, the objective of this research is to determine these relationships. First, to clarify the quantitative relationship between the drainage volume and water level, the validity of a relational expression proposed in a previous study is verified through slope model experiments. Second, to investigate the relationship between siphon spacing and water level and its effects on slope stability, a two-dimensional seepage flow analysis and stability analysis are conducted.

RELATIONSHIP BETWEEN DRAINAGE VOLUME AND WATER LEVEL

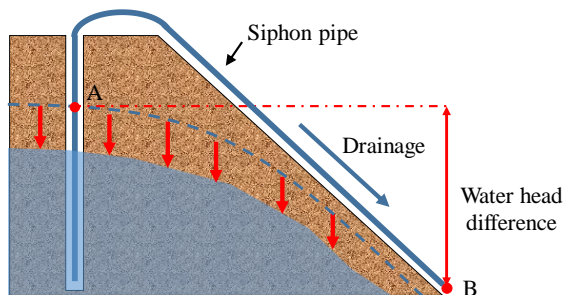


Fig. 1 Schematic diagram of siphon method

Slope model experiment

Description of slope model

Figure 2 shows a schematic diagram of the slope model used in this experiment. It was 500-mm wide, 1650-mm long, and 800-mm high. This slope model was surrounded by the soil tank whose framework, bottom, and back of the tank were made of 5-mm thick steel plate and sides of the tank were made of 10-mm thick acrylic plate. A steel plate with a large number of 5-mm diameter slits was installed 210 mm from the left wall of the soil tank, to the left of which was a gravel layer and to the right of which was the sand slope. The gradient of the slope was 35°. Table 1 provides the physical properties of the sand. Four polyvinyl chloride pipes simulating boreholes were installed at 300-mm intervals in the direction of the downward slope, beginning 150 mm from the left end of the sand layer. These holes are indicated as Holes ①, ②, ③, and ④ ordered from the top to the toe of the slope. A number of holes were opened in the pipes to secure the passage of water, and the pipes were protected by a net to prevent a decrease in drainage function due to the inflow of finesand.

Water was introduced into the model by two hoses with an inner diameter of 38.1 mm feeding from the water tank. The water level was measured using manometers installed at the bottom of the model at intervals of 100 mm, and water level gauges (Oneset, U20-001-04) were installed in each hole. The water level in the model was controlled by elevating the water tank. One siphon pipe, consisting of a polyurethane tube with an inner diameter of 5 mm and a length of 3100 mm, was installed in Hole ①.

Description of experiment

The experimental method was as follows. Initially, the tank was raised to a set height and water was allowed to flow into the slope model. After confirming with the manometer that the water level had reached a constant level, drainage was started using the siphon pipe. After confirming the presence of a steady state, drainage volume and water level were measured. The experiment was conducted for three tank height cases: 45, 55, and 65 cm.

Experimental Results

Figure 3 provides the water level in the initial and steady states for each tank height case. Clearly, the closer to the siphon hole, the lower the water level, except for the location within the gravel layer. the drainage volume in Case 45, Case 55 and Case 65 were 4.13, 4.60 and 8.33 cm³/s. In Case 65, collapse occurred from the middle to the toe of the slope before completely draining, but the experiment was continued.

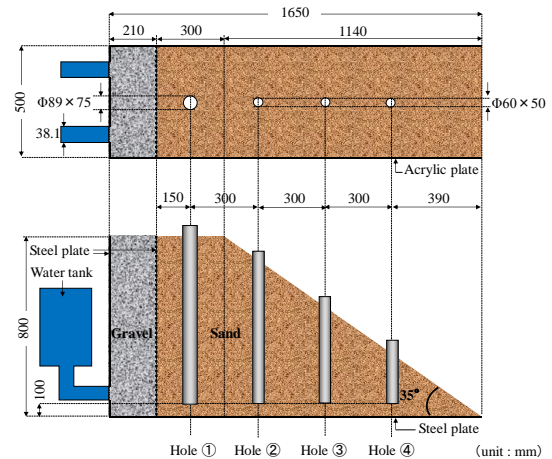


Fig. 2 Schematic diagram of slope model

Table 1 Physical properties of the sand

Density of soli particles [g/cm ³]	2.63
Dry density [g/cm ³]	1.62
Void ratio [-]	0.60
Vertical permeability [cm/s]	4.17×10^{-3}
Horizontal permeability [cm/s]	1.88×10^{-2}

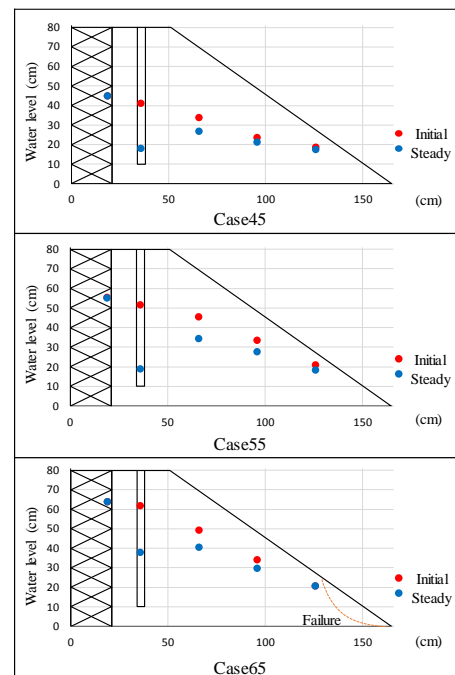


Fig. 3 Water level in initial and steady state

Determination of relationship between drainage volume and water level

Relationship between drainage volume and water level

As illustrated in Fig. 4, the relationship between drainage volume and water level for a well, assuming inflow from one direction, has been proposed by J.C. Gress as Eq. (1) [4].

$$Q = \frac{h_0^2 - h_1^2}{\frac{h_0 + h_1}{ap_0k} + \frac{1}{\pi k} \ln\left(\frac{a}{2\pi r_w}\right)} \quad (1)$$

where Q is the drainage volume from the pipe [cm^3/s]; h_0 and h_1 are the water level before and after drainage, respectively [cm]; a is the siphon spacing [cm]; p_0 is the gradient of the water surface before draining [unitless]; k is the permeability coefficient [cm/s]; and r_w is the well radius [cm]. Using Eq. (1), the experimental results were evaluated. Table 3 shows the parameters used to calculate the drainage volume in each case: a was set to 50 cm because only one pipe was installed at the center of the 50-cm wide segment; k was set to the horizontal permeability coefficient; and r_w was set to the radius of the polyvinyl chloride pipe. Because no method for determining p_0 has been previously established, in this study, the drainage was calculated from two gradients: the gradient describing the linear approximation of the initial water level across the entire slope (p_a), and the

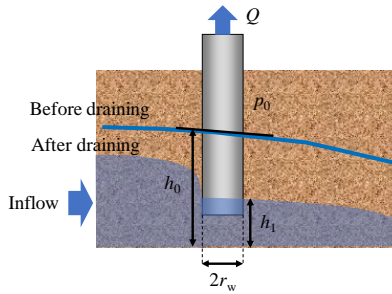


Fig. 4 Schematic diagram of vertical drainage

Table 3 Parameters used to calculate drainage volume

	Case 45	Case 55	Case 65
h_0 [cm]	41.0	51.7	61.7
h_1 [cm]	17.9	18.9	37.9
a [cm]	50	50	50
k [cm/s]	1.88×10^{-2}	1.88×10^{-2}	1.88×10^{-2}
r_w [cm]	4.5	4.5	4.5
p_a [-]	0.26	0.33	0.43
p_b [-]	0.25	0.21	0.41

Table 4 Calculated and measured drainage volumes

		Case 45	Case 55	Case 65
Q [cm^3/s]	p_a	5.43	9.76	9.26
	p_b	5.22	6.30	8.84
	Measurement	4.13	4.60	8.33

gradient between the initial water level at Hole ① and that at Hole ② (p_b). The drainage volumes calculated using the two gradients were compared with the measured values.

Calculated drainage volume

Table 4 compares the calculated and measured drainage volumes. When p_0 was set to p_a , the calculated value was close to the measured value in Cases 45 and 65, but the calculated value was more than twice the measured value in Case 55. When p_0 was set to p_b , the error decreased in each case to less than 2 cm^3/s . Thus, it is possible to accurately determine the relationship between the drainage volume and the water level by setting the gradient to its value at the position where the water level directly decreases due to drainage.

RELATIONSHIP BETWEEN SIPHON SPACING AND WATER LEVEL CONSIDERING SLOPE STABILITY

Reproduction of siphon experiment by seepage flow analysis

Outline of analysis

In this study, 2D-Flow, a two-dimensional saturated-unsaturated seepage flow analysis software package based on the finite element method, was used for analysis. The governing equation for seepage flow is given in Eq. (2).

$$\frac{\partial}{\partial x} \left(k_x \frac{\partial \psi}{\partial x} \right) + \frac{\partial}{\partial z} \left(k_z \frac{\partial \psi}{\partial z} + k_z \right) = (C + \alpha S_s) \frac{\partial \psi}{\partial t} \quad (2)$$

where k_x and k_z are the unsaturated permeability coefficients in the x and z directions, respectively [cm/s]; ψ is the pressure head [cm]; C is the specific water capacity [$1/\text{cm}$]; α is a parameter that is set to 1 in a saturated region and to 0 in an unsaturated region; and S_s is the specific storage coefficient [$1/\text{cm}$]. For the unsaturated permeation characteristic model, Van-Genuchten's Equation (Eq. (3)) [5] and Mualem's Equation (Eq. (4)) [6] were used.

$$S_e = \frac{\theta - \theta_r}{\theta_s - \theta_r} = \left[\frac{1}{1 + (\alpha \psi)^n} \right]^{1 - \frac{1}{n}} \quad (3)$$

$$k_r = \frac{k}{k_s} = S_e^{\frac{1}{2}} \left[1 - \left(1 - S_e^{\frac{1}{m}} \right)^m \right]^2 \quad m = 1 - \frac{1}{n} \quad (4)$$

where S_e is the effective saturation degree [unitless]; θ , θ_r , and θ_s are the volumetric, residual volumetric, and saturated volumetric water content, respectively [unitless]; α [$1/\text{cm}$] and n [unitless] are parameters describing the shape of the soil-water characteristic curve; and k , k_r , and k_s are the unsaturated, relative, and saturated permeability coefficients, respectively [cm/s].

Setting boundary conditions

In order to accurately reproduce the siphon experiments using two-dimensional seepage flow analysis, it was necessary to consider the differences in the shape of the water level in each cross section. At the transverse (slope crest to toe) section where the siphon tube was installed, the water level severely decreased near the hole, and once rose in the direction of the descending slope (Fig. 5). This is because the water level decreased near the pipe in the longitudinal section where the siphon pipe was installed (Fig. 6), and as the surrounding water flowed down in the direction of the slope, it gathered in the central cross section. On the other hand, near the side face of the model, the water level consistently decrease in the direction of the descending slope. In a two-dimensional analysis, because the water level decreased in the direction of the slope from the point of the water head boundary, it is impossible to reproduce the longitudinal variation in water level at the section in which the siphon tube was installed. Therefore, the location with the highest water level in the longitudinal section at the siphon pipe was made the focus, and the method for obtaining this water level was investigated.

In this study, the water level at the model side was roughly calculated using Eq. (5) from the water level in the hole and the drainage volume by approximating the relationship as a gravity well (Fig. 7) [7].

$$Q = \pi k \frac{h_2^2 - h_1^2}{\ln(\frac{r_2}{r_1})} \quad (5)$$

where r_1 and r_2 are two distances from the well [cm]; and h_1 and h_2 are the water levels at r_1 and r_2 , respectively. Equation (5) can be rearranged into Eq. (6) to obtain the water level at the model side.

$$h_2 = \sqrt{h_1^2 + \frac{Q}{\pi k} \ln(\frac{r_2}{r_1})} \quad (6)$$

in which k was set to the horizontal permeability coefficient; r_1 was set to the tube radius; and r_2 was set to half the width of the slope. Table 5 shows the parameters used to evaluate each case and the subsequently obtained water level at the model sides. From this table, h_2 can be seen to be about 7 cm higher than h_1 .

Based on the above calculations, the analysis model and the boundary conditions for numerically reproducing the experiment are shown in Fig. 8. The number of divisions in the vertical direction was 23, which is the maximum division number in the analysis, and the number of divisions in the horizontal direction was set to 5 divisions on the left side of the soil-gravel interface and to 23 divisions on the right side. The left end was provided with the water head dictated by the level of water in the gravel layer, and the position 15 cm from the left end was provided with the water head dictated by the water level at the model side, h_2 . The

far end was assigned a non-seepage boundary and the right end, the face of the slope, was assigned a seepage boundary. The parameters used for the analysis were as referenced in [8] and [9]: the porosity of the soil θ_s was 0.375; θ_r was 0.045; S_s was 1.7×10^{-6} 1/cm; α was 0.145 1/cm; and n was 2.68.

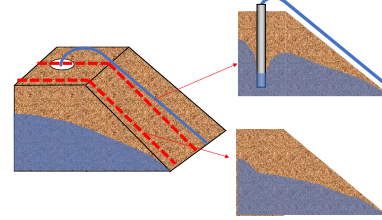


Fig. 5 Water level in the transverse section

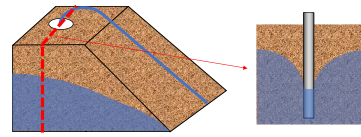


Fig. 6 Water level in the longitudinal section

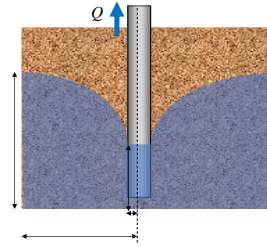


Fig. 7 Schematic diagram of gravity well

Table 5 Parameters used to obtain h_2

	Case 45	Case 55	Case 65
h_1 [cm]	17.9	18.9	37.9
Q [cm ³ /s]	4.13	4.60	8.33
k [cm]	1.88×10^{-2}	1.88×10^{-2}	1.88×10^{-2}
r_2 [cm]	25	25	25
r_1 [cm]	0.25	0.25	0.25
h_2 [cm]	25.3	26.8	45.7

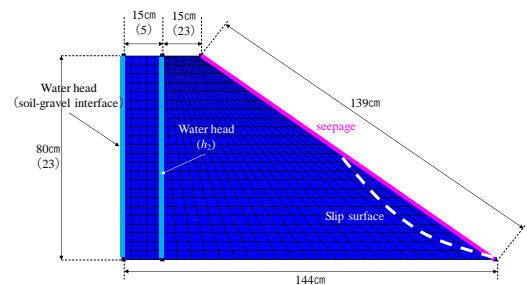


Fig. 8 Analysis model and the boundary conditions

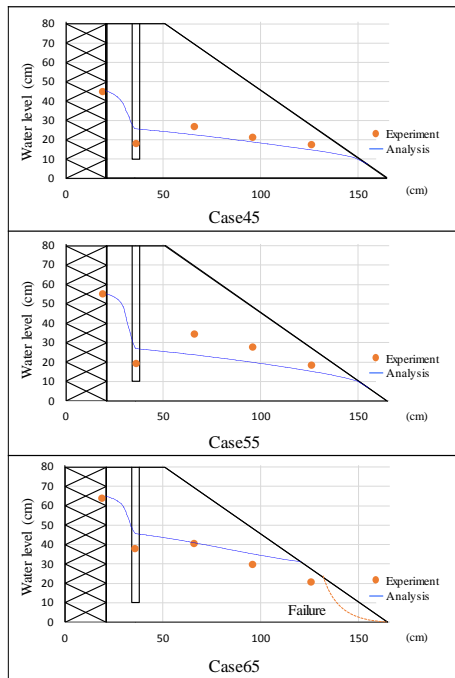


Fig. 9 Analytical results and experimental results of the water level at the side

Analytical and experimental results

Figure 9 compares the analytical and experimental results of the water level at the model side. In Case 45 and Case 55, although the analytical results were lower than the experimental results, the overall trend was the same. In Case 65, the results were nearly the same near the siphon hole, but the experimental results greatly decreased relative to the analytical results near the toe of the slope because the toe of the slope collapsed. Clearly, the water level in the siphon can be closely reproduced by a 2-D seepage flow analysis.

Determination of relationship between siphon spacing and water level considering slope stability

To determine the relationship between siphon spacing and water level considering slope stability, Case 65, in which collapse occurred before drainage in the slope experiment, is made the focus of investigation. Figure 10 depicts the flow chart of the evaluation. To provide a point of reference, the water level at an arbitrary point in the longitudinal section in which the siphon pipe was installed is referred to as the "water level at the siphon position."

First, in order to determine the water level at which the slope stabilizes, the relationship between the water level and the safety factor was determined by stability analysis (Step ① in Fig. 10). To conduct this stability analysis, the circular slip calculation function installed in the 2D-Flow software was used. At this time, the model shown in Fig. 8 was used. The safety factor was 1.2, which is used for general embankment design. The value of the internal friction angle was set 36.6

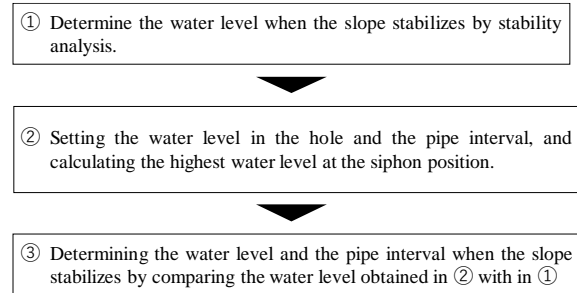


Fig. 10 Flow chart for determining slope stability parameters

Table 8 Relationship between water level and safety factor

Water level [cm]	48.0 . . . 47.4	47.3 . . . 47.0
Safety factor [-]	1.19 . . . 1.19	1.20 . . . 1.20

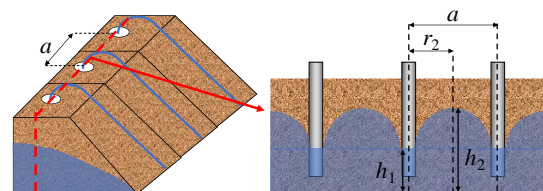


Fig. 11 Schematic diagram of the transverse section with siphon tube

degree and the cohesion was set to 0.26 kN/m². In this case, the slip surface with the lowest safety factor was taken from the set of slip surfaces that reproduced the experimentally observed collapse, which occurred from the middle to the toe of the slope (Fig. 8). The water level at the soil-gravel interface was set to 65 cm. Multiple water levels at the siphon position were set as the boundary conditions, and the relationship between the safety factor and water level was then investigated with the results reported in Table 8. When the water level was 47.3 cm or less, the safety factor was 1.20 or greater, indicating a stable slope. This water level is referred to as the "critical water level". As shown in Fig. 11, the shape of the water level at the siphon position greatly differs. When the highest water level (h_2 in Fig. 11) in this longitudinal section falls below the critical water level, a landslide will not occur. Therefore, the highest possible water level was investigated.

Assuming that the slopes models were arranged side by side as shown in Fig. 12, the siphon spacing and the water level in the hole before and after drainage (h_0 and h_1) were set, and the drainage volume Q was calculated using Eq. (1). The highest water level at the siphon position h_2 was then used to obtain Q by Eq. (6) (Step ② in Fig. 11). Here, h_0 was set to 61.7 cm from the experimental results. It was assumed that

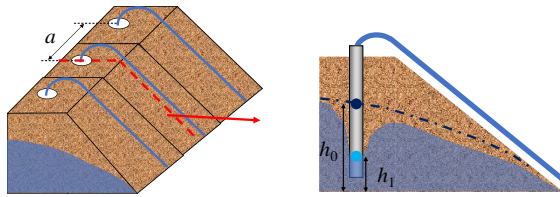


Fig. 12 Schematic diagram of the cross section with siphon tube

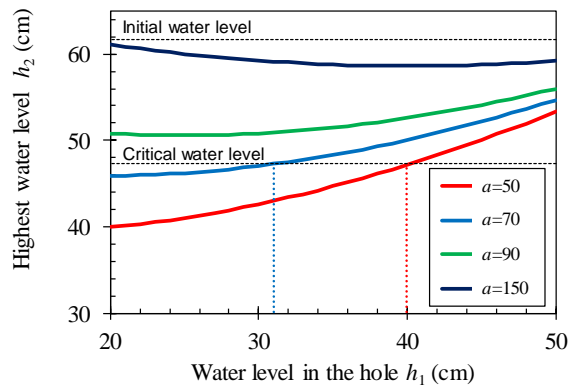


Fig. 13 Relationship between h_1 and h_2

the highest water level would be halfway between siphons, so r_2 was set to half of a . The other parameter setting methods were the same as described in the previous section. Figure 13 depicts the relationship between h_1 and h_2 when a was set to 50 cm, 70 cm, 90 cm, and 150 cm.

The values of a and h_1 were determined for the condition of slope stability by comparing the critical water level determined in Step ① (47.3 cm) with the value of h_2 shown in Fig. 13 (Step ③ in Fig. 10). From this figure, it was determined that the slope stabilizes when h_1 is 40 cm or less at a siphon spacing of 50 cm, and when h_1 is 31 cm or less at a siphon spacing of 70 cm because h_2 is less than the critical water level by siphon method. However, at siphon spacings of 90 cm and 150 cm, h_2 is over 47.3 cm in any case. Additionally, h_2 shows little decrease at a siphon spacing of 150 cm. It indicates that h_2 is larger as a siphon spacing increases, and the siphon no longer functions. Thus, it is possible to estimate the range of influence of a single siphon tube by increasing the spacing between the siphon tubes until h_2 no longer varies.

As a result of the above examination, it is confirmed that the procedure shown in Fig. 10 is an effective method for determining the appropriate siphon spacing and water level for slope stabilization using the siphon method.

CONCLUSIONS

In this study, an investigation into methods for the design of the siphon method to ensure slope stability

was conducted using a model slope experiment and numerical analysis. The major findings are:

- (1) The quantitative relationship between drainage volume and water level can be determined using the water level gradient near the siphon pipe.
- (2) The water level at the model side in the siphon experiment can be reproduced using a 2-D seepage flow analysis.
- (3) Although this research was only conducted on the model level, the ideal siphon spacing and target water level in the siphon hole to ensure slope stability was able to be accurately determined.

ACKNOWLEDGEMENTS

This research was partly supported by JSPS Bilateral Joint Research Projects and Grant-in-Aid for Scientific Research (17K00615). We express our gratitude.

REFERENCES

- [1] Mrvik O. and Bomont S., Experience with Treatment of Road Structures Landslides by Innovative Methods of Deep Draining, Proceedings of the 3rd International Conference on Debris Flow, Milano, 2010, pp.113-124.
- [2] Mrvík O., Bomont S., and Vrábek B., Experience with Drainage and Ground Stabilization by Siphon Drains in Slovakia, Czech geotechnical magazine "Geotechnics", 2012, pp.60-65.
- [3] Mrvik O. and Glück, M., Stabilisierung Hangrutsch-gefährdeter Gebiete durch Siphon-Drainagen, BHM, Vol.161, No.12, 2016, pp. 600-604.
- [4] Gress J.C., New Formulae to Assess Soil Permeability Through Laboratory Identification and Flow Coming Out of Vertical Drains, 10th International Symposium on Landslides and Engineered Slopes, 2008, pp.361-364.
- [5] Van Genuchten M. T., A Closed-form Equation for Predicting the Hydraulic Conductivity of Unsaturated Soils, Soil Sci. Soc. Am. J., Vol.44, No.5, 1980, pp.892-898.
- [6] Mualem Y., A New Model for Predicting the Hydraulic Conductivity of Unsaturated Porous Media, Water Resources Research, Vol.12, No.3, 1976, pp.513-522.
- [7] Hall H. P., A Historical Review of Investigation of Seepage Toward Wells, J. Boston Soc. C. E., Vol.41, 1954, pp.251-311.
- [8] Carsel R. F. and Parrish R. S., Developing Joint Probability Distribution of Soil Water Retention Characteristics, Water Resour. Res., Vol.24, No.5, 1988, pp.755-769.
- [9] Domenico P. A. and Schwartz F. W., Physical Guide to Hydrogeology, John Wiley & Sons, New York, 1990, p.727.

METHODS TO MEASURE THE INITIAL QUASI-SATURATED VOLUMETRIC WATER CONTENT OF SOIL

Miki Nishimura¹, Hiroshi Kita², Mitsuru Komatsu³, Keigo Koizumi⁴, Kazuhiro Oda⁵ and Keiji Sakuradani⁶
^{1,4}Graduate School of Engineering, Osaka University, Japan; ²Tokyu Co. Ltd., Japan; ³Graduate School of
Environmental and Life Science, Okayama University, Japan; ⁵Faculty of Engineering, Osaka Sangyo
University, Japan; ⁶West Nippon Expressway Co. Ltd., Japan

ABSTRACT

Rainfall-induced shallow landslides have recently become more frequent in Japan owing to the occurrence of extreme weather. To address this problem, local governments and Japanese expressway companies have begun providing residents or customers, respectively, with rainfall prediction data-based early warning information on rainfall-induced disasters. However, sometimes it is difficult to judge whether a shallow landslide will occur, because the rainfall prediction data do not directly reflect the soil moisture contents of the slope. Moreover, sufficient lead time is necessary to announce evacuations and road closures. To overcome these problems, the initial quasi-saturated (IQS) volumetric water content has been proposed as an early warning index for rainfall-induced shallow landslides. Our past research indicated that no surface displacement occurs unless the soil moisture content exceeds IQS. However, in order to apply IQS to a real slope, it is necessary to understand the relationship between IQS and rainfall intensity. Thus, in this study, on-site and laboratory-based measurement methods were developed to estimate the relationship between IQS and rainfall intensity. The results demonstrate agreement between the data obtained via on-site and laboratory measurement methods, and confirm the usefulness of the proposed measurement methods.

Keywords: Volumetric water content, Rainfall infiltration, Shallow landslide, Quasi-saturated phenomenon, Field measurement

INTRODUCTION

Rainfall-induced shallow landslides have recently become more frequent in Japan as a result of extreme weather. Consequently, rainfall data-based slope failure predictions have been deemed a better solution to this problem. However, although this method seems easy and convenient, it is actually less accurate because rainfall data do not directly reflect the soil moisture contents of the slope [1]–[3].

Thus, our research group proposes using the initial quasi-saturated volumetric water content as an early warning index for rainfall-induced shallow landslides—denoted as the IQS in this paper. As the constant rainwater penetrates into a slope, the volumetric water content rises and reaches a temporary equilibrium state. This state indicates that the inflow and outflow of water are in equilibrium. The inflow indicates rainfall intensity and the outflow, controlled by the unsaturated hydraulic conductivity of the soil, balances the rainfall intensity.

We define the temporary equilibrium state as the quasi-saturated phenomenon. Furthermore, we define the state in which the volumetric water content reaches an equilibrium state as IQS [4]. Figure 1 illustrates the concept of slope-failure

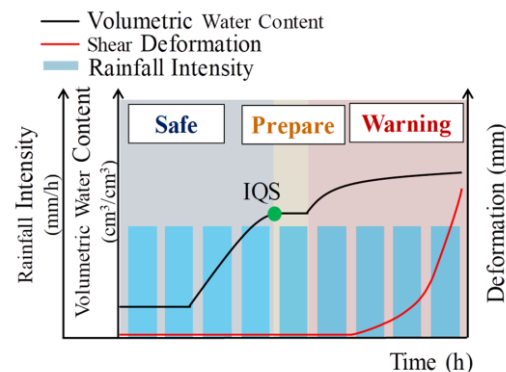


Fig. 1 Concept of slope-failure prediction, which entails the application of IQS as an early warning index for rainfall-induced shallow landslides.

prediction, which applies IQS as an early warning index. No slope deformation occurs unless the volumetric water content exceeds the value of IQS. Therefore, the period with the yellow band in Figure 1 can be used as the lead time for announcement of evacuations and road closures.

However, it is necessary to clarify the relationship between rainfall intensity and IQS, because IQS changes according to the rainfall

Table 1 Physical properties of the soil samples at a depth of 100 cm

Samples	Decomposed granite soil
Initial water content (%)	15.1
Soil particle density (g/cm^3)	2.625
Dry density (g/cm^3)	1.514
Void ratio	0.734
Hydraulic conductivity (cm/s)	2.05×10^{-3}

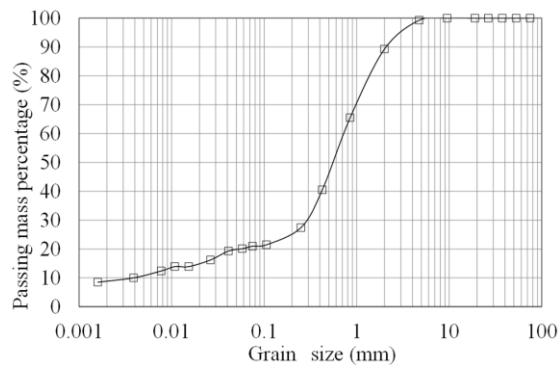


Fig. 2 Grain size accumulation curve.

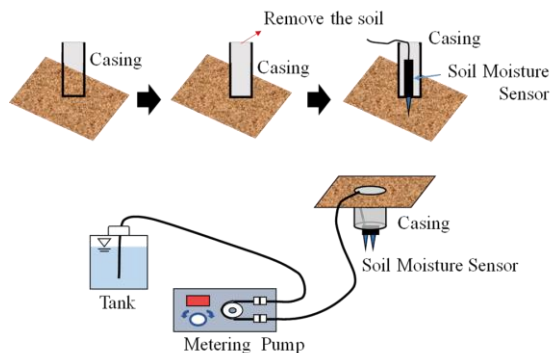


Fig. 3 Schematic of on-site measurement method

Table 2 Physical properties of soil sample used in metering-pump laboratory experiment

Samples	Decomposed granite soil	
Case	1	2
Initial water content (%)	14.1	15.8
Soil particle density (g/cm^3)	2.625	
Dry density (g/cm^3)	1.514	
Void ratio	0.734	
Hydraulic conductivity (cm/s)	2.05×10^{-3}	

real slope has not been presented. Therefore, this study was conducted with the aim of clarifying the relationship between rainfall intensity and IQS, and developing IQS measurement methods.

IQS MEASUREMENT METHODS

We developed on-site and laboratory-based measurement methods to measure IQS; the soil samples obtained from the on-site slope were used in the laboratory experiment. The results were used to verify the relationship between rainfall intensity and IQS, and to validate the proposed measurement methods.

Method 1: On-Site Measurement

In this study, the target site for slope measurements was a recently constructed site along an expressway in the Kinki region in Japan. It is an embankment slope that has filled a small valley located between man-made slopes with granite soil. Table 1 details the physical properties of the soil samples retrieved at a depth of 100 cm, and Figure 2 shows the grain size distribution. The slope composition is homogeneous decomposed granite soil.

Figure 3 provides a basic illustration of the implemented on-site measurement method. First, a casing ($\Phi 56 \times 150$ mm) was hammered vertically downward into the slope. Then, the soil in the casing was removed. To measure the volumetric water content, a soil moisture sensor, EC-5 (measurement accuracy: $\pm 3.0\%$), was installed as shown in Figure 3, with the measurement interval set to 10 seconds. A metering pump (peristaltic pump) was used to ensure that the operator was able to change the volume of water pouring onto the slope. In other words, the operator can change the intensity at which the water is poured. Two rainfall intensities were calculated from the relationship between the volume of pouring water and the area of the casing base: 20 mm/h and 50 mm/h. To clarify the relationship between rainfall intensity and IQS, IQS values were measured using the soil moisture sensor. The measurement was concluded when equilibrium was achieved via vertical penetration, as illustrated in Figure 1.

Method 2: Metering-Pump Laboratory Experiment

This laboratory experiment was performed under conditions comprising rainfall intensities of 20, 40, 50, 60, 70, and 90 mm/h. Table 2 shows the physical properties of the soil sample for this laboratory experiment, and Figure 4 depicts the experimental setup. As shown in the figure, a cylindrical acrylic column ($\Phi 56 \times 400$ mm) was used, with boundary

intensity. In addition, a method to measure IQS in a

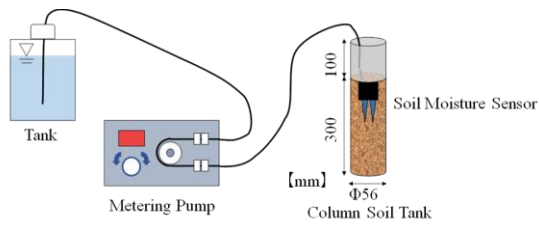


Fig. 4 Experimental setup for metering-pump laboratory experiment.

Table 3 Physical properties of soil sample used in sprinkler-system laboratory experiment

Samples	Decomposed granite soil
Initial water content (%)	13.7
Soil particle density (g/cm^3)	2.625
Dry density (g/cm^3)	1.514
Void ratio	0.734
Hydraulic conductivity (cm/s)	2.05×10^{-3}

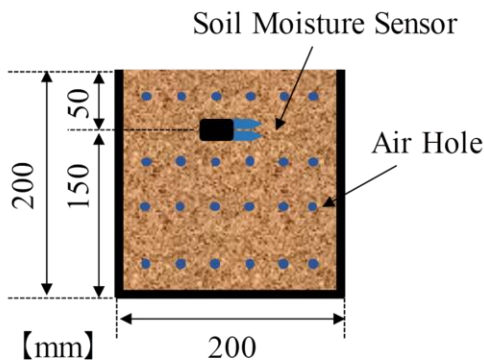


Fig. 5 Experimental setup for sprinkler-system laboratory experiment.

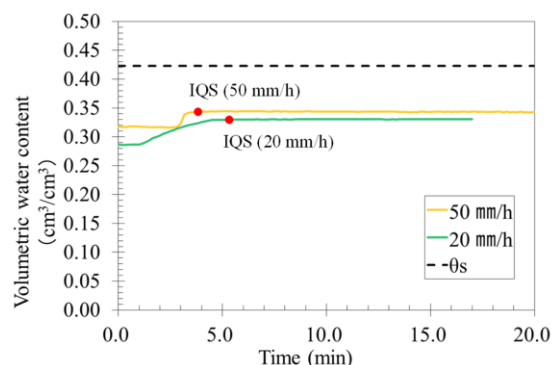


Fig. 6 Volumetric water content as a function of time

conditions as follows: open top, impermeable sides

with 48 air holes at 2-mm in-diameter for air removal, and an impermeable base. The soil moisture sensor and metering pump used to perform the laboratory measurements were identical to those used to perform the on-site measurements. The sensor was vertically installed, and measurements were taken in 10-s intervals. The rainfall intensity was calculated by dividing the volume of water poured onto the sample by the cross-sectional area of the column. As with the on-site measurements, the volume of pouring water was determined by measuring the weight of the tank after the experiment. Further, the measurement process was concluded when equilibrium was achieved via vertical infiltration.

Method 3: Sprinkler-System Laboratory Experiment

Table 3 shows the physical properties of the soil sample, and Figure 5 depicts the experimental setup used in this experiment. The soil sample was identical to that used in the metering-pump laboratory experiment. As shown in the figure, a cylindrical acrylic column ($\Phi 200 \times 200$ mm) was used, with boundary conditions as follows: open top, impermeable sides with 32 air holes at 2-mm in-diameter for air removal, and an impermeable base. The soil moisture sensor was installed at a depth of 50 mm, and was horizontally installed into the ground to prevent its cable from playing the role of the water path. The measurement interval was one minute. The experiments were carried out under the conditions of 10- and 50-mm/h rainfall intensities, and constant sprinkling water intensity. Further, the measurement process was concluded when equilibrium was achieved via vertical infiltration.

RESULTS

Result 1: On-Site Measurement

Figure 6 shows how the volumetric water content changed over time for 20-mm/h and 50-mm/h rainfall intensities. As previously mentioned, at the start of the pouring water, the volumetric water content began increasing. An equilibrium state was observed when the volumetric water content reached values of approximately 0.330 and 0.344 for rainfall intensities of 20 mm/h and 50 mm/h, respectively. Thus, the IQS values were approximately 0.330 and 0.344 for rainfall intensities of 20 mm/h and 50 mm/h, respectively. In both cases, the equilibrium state indicated the existence of quasi-saturated phenomena.

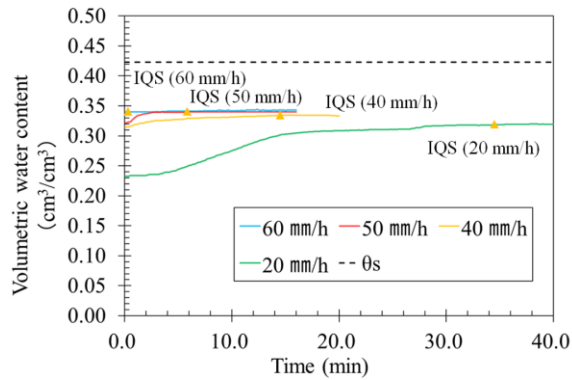


Fig. 7 Volumetric water content as a function of time for the metering-pump laboratory experiment in the cases of rainfall intensities of 20, 40, 50, and 60 mm/h.

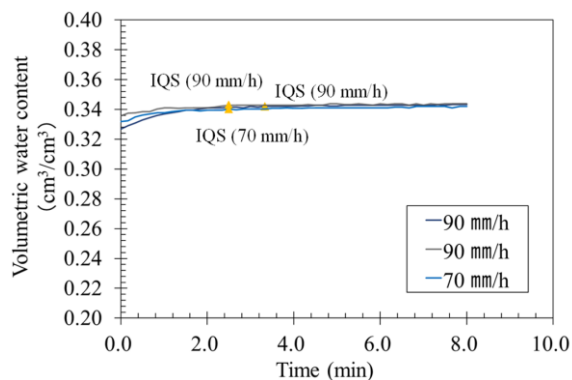


Fig. 8 Volumetric water content as a function of time for the metering-pump laboratory experiment in the cases of rainfall intensities of 70 and 90 mm/h.

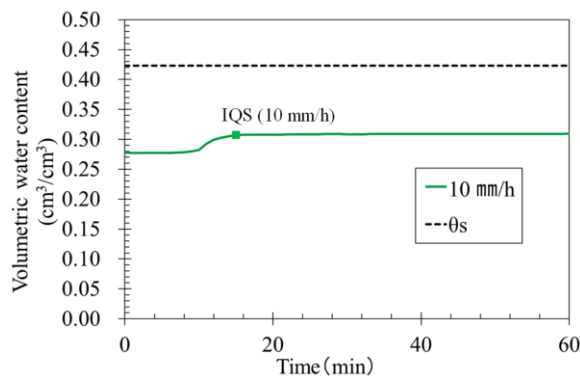


Fig. 9 Volumetric water content as a function of time in the case of 10-mm/h rainfall intensity.

Result 2: Metering-Pump Laboratory Experiment

Figure 7 illustrates how the volumetric water content changed over time under the respective conditions of rainfall intensities of 20, 40, 50, and 60 mm/h. The increase in volumetric water content in response to the added water was found to reach an equilibrium state when the volumetric water content was approximately 0.319, 0.334, and 0.340 for rainfall intensities of 20, 40, and 50 mm/h, respectively. Thus, the IQS values were approximately 0.319, 0.334, and 0.340 for rainfall intensities of 20, 40, and 50 mm/h, respectively. As previously mentioned, in all cases, an equilibrium state denotes a quasi-saturated phenomenon. In the case of 60-mm/h rainfall intensity, the volumetric water content did not increase, and an equilibrium state was observed at a volumetric water content value of approximately 0.340. Therefore, the IQS value was approximately 0.340 for rainfall intensities of 60-mm/h.

Figure 8 shows the volumetric water content as a function of time for rainfall intensities of 90 and 70 mm/h. The volumetric water content began increasing in response to the added water, and an equilibrium state was observed when the volumetric water content value reached approximately 0.342, 0.343, and 0.340 in response to rainfall intensities of 90, 90, and 70 mm/h. Thus, the IQS values were approximately 0.342, 0.343, and 0.340 in response to rainfall intensities of 90, 90, and 70 mm/h. Additionally, Figure 8 illustrates that, when the rainfall intensity exceeded 50 mm/h, the peak volumetric water content values associated with equilibrium were similar. As is the case for all measurements, this equilibrium state indicates the existence of the quasi-saturated phenomenon at the measurement point.

Result 3: Sprinkler-System Laboratory Experiment

Figures 9 and 10 illustrate volumetric water content as a function of time under the conditions of 10- and 50-mm/h rainfall intensities, respectively. After the water sprinkler system was turned on, the volumetric water content increased, and an equilibrium state was found to correspond to volumetric water content values of approximately 0.307 and 0.332 for rainfall intensities of 10 mm/h and 50 mm/h, respectively. Thus, the IQS values were approximately 0.307 and 0.332 for rainfall intensities of 10 mm/h and 50 mm/h, respectively.

DISCUSSION

This section compares the results of the on-site measurement and the two laboratory experiments. The results of each type of measurement were used to derive the relationship between the rainfall intensity and IQS, which is shown in Figure 11.

According to Figure 11, a positive correlation exists between rainfall intensity and IQS when the rainfall intensity is below 50 mm/h. Moreover, although there is a slight margin of error, similar results were obtained from the on-site measurement and the two laboratory experiments. In addition, under the condition of a high coefficient of determination, the results were confirmed to be consistent.

The metering-pump laboratory experiment results confirmed minimal variation of IQS for rainfall intensities exceeding 50 mm/h. This suggests that the value of the volumetric water content in this

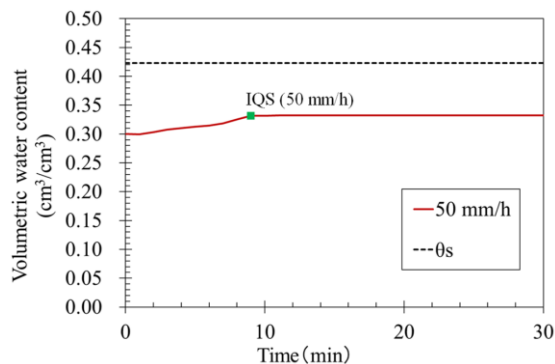


Fig. 10 Volumetric water content as a function of time in the case of 50-mm/h rainfall intensity.

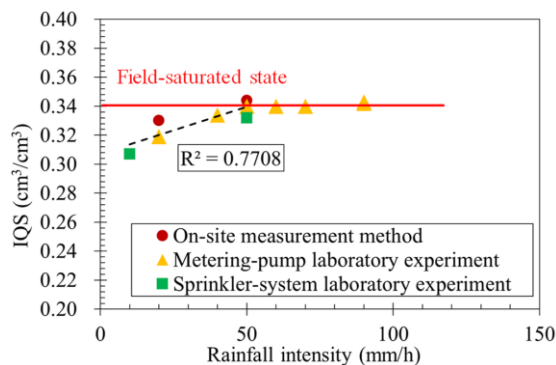


Fig. 11 Relationship between the rainfall intensity and IQS for each of the three experiments.

soil sample denotes the field-saturated state. In general, the field-saturated state shows the maximum level of saturation under the saturated state with entrapped air in a real slope, because rainwater infiltration cannot fully saturate the soil [5]. In this soil sample, the maximum rain intensity balanced with the coefficient of water permeability of the soil was approximately 50 mm/h. As a result, IQS peaked at 0.34 under the experimental condition.

CONCLUSION

In this paper, we discussed how to measure IQS and surveyed the relationship between IQS and rainfall intensity. Our research findings are as follows.

First, we developed three IQS measurement methods—an on-site method, and two laboratory methods—using either a metering pump or sprinkler system. A comparison of the results of all three measurement methods demonstrated that they were consistent. In addition, a positive correlation was observed between the rainfall intensity and IQS. Furthermore, the results of each method presented here demonstrate that it is necessary to consider the field-saturated state when implementing IQS as an early warning index for rainfall-induced shallow landslides.

ACKNOWLEDGEMENTS

This research was partly supported by a Grant-in-Aid for Scientific Research (17K00615), for which we express our gratitude.

REFERENCES

- [1] Okada K., Relationship between Rain and Land-disasters by Soil Water Index, Proceedings of Symposium on sediment disaster, 2006, pp. 105–110.
- [2] Sato W., Slope Failure Forecasting Methods, Journal of JGS, Vol. 61, No. 9, 2013, pp. 10-13.
- [3] Tachihara S., Start of Sediment Disaster Warning, Tenki, Vol. 53, 2006, pp. 11–15.
- [4] Koizumi K., Sakuradani K., Oda K., Ito S., Fukuda Y., Feng M.Q., and Takemoto M., Fundamental Research on Advancement of Regulation Standard for Expressway Management against Rainfall-induced Surface Failure, Journal of JSCE Ser. C (Geo-engineering), Vol. 73, No. 1, 2017, pp. 93–105.
- [5] Takeshita Y. and Morii T., Field Measurement of Field Saturated and Unsaturated Hydraulic Conductivity Using Soil Moisture Profile, Journal of JSCE Ser. C, Vol. 62, No. 4, 2010, pp. 250–263.

DESIGN CONCEPT FOR AN ANCHORED DIAPHRAGM WALL IN PROJECT ADP ASTANA, KAZAKHSTAN

Askar Zhussupbekov¹, Abdulla Omarov¹, Gulzhanat Tanyrbergenova¹ and Karlygash Borgekova¹
¹Department of Civil Engineering, L.N. Gumilyov Eurasian National University, Astana, Kazakhstan

ABSTRACT

Abu Dhabi Plaza (Further ADP) is an under construction in Astana, Kazakhstan, consisting of offices, residential and shopping spaces also hotels. The completed project will be has five towers with different heights, the tallest construction will be 310 m with 75 floors and it will be the tallest building in Central Asia. The design of project provides a four-level basement and tower buildings, which intend to use for offices and residential buildings. The structure includes 5 towers: 14 storey Hotels (Tower 1), 75 storey Residential (Tower 2) and 30 storey Offices (Tower 3); and a 17 storey Residential (Tower 4), 31 storey Office (Tower 5). The internal dimensions of the sub-structure itself are approximately 220m x 195m on plan and they are typically 17.4m deep. Shoring system consists of one section and the maximum design excavation level is - 19.30 m. Shoring system is planned as 1000 mm thick diaphragm wall, which is supported with 4 layers of pre - stressed anchorages. The shoring system has been designed by PLAXIS, industry standard finite element software, which can assess in very detail the deformations and settlements in soil. The basement slab is to be a pile-supported raft, which is a made up of discrete sections to accommodate thermal and lateral movements.

These numerical methods were carried out in Kazakhstan first time within the investigation of the interaction of anchored diaphragm wall of high-rise buildings with soils in the problematic ground conditions of Astana.

Keywords: CPT, diaphragm wall, Plaxis 2D, anchor

INTRODUCTION

High-rise buildings (buildings with a height of more than 75 m) pose new challenges for engineers, especially in the field of calculations and design of above-ground structures, bases and foundations. Therefore, designers of both above-ground and underground parts of the building are forced to resort to more complex methods of calculation and design. Especially this applies to geotechnical engineers, who are involved in the design of foundations for high-rise buildings.

By complexity, problematic design, erection, operation, impact on the environment and people, high-rises can be attributed to the structures of increased danger and complexity. Buildings above 75 m require completely different approaches to design.

Kazakhstan has its own modern experience in designing and erecting high-rise buildings above 75 m of unique structures, including the Emerald Quarter building (210 m), Northern Lights 1 building (180 m) in Astana, Railways Towers (174/156 m), Transportation Tower (the building of the Ministry of Transport and Communications) (155 m), Khan-Shatyr shopping mall (150 m) [1].

After the construction, ADP will become the tallest building in Kazakhstan and Central Asia, the height of one of the blocks of the complex will be 320 m.

The architectural concept is a shown in Figure 1,

which represents the construction site - in the center of which a skyscraper should rise.

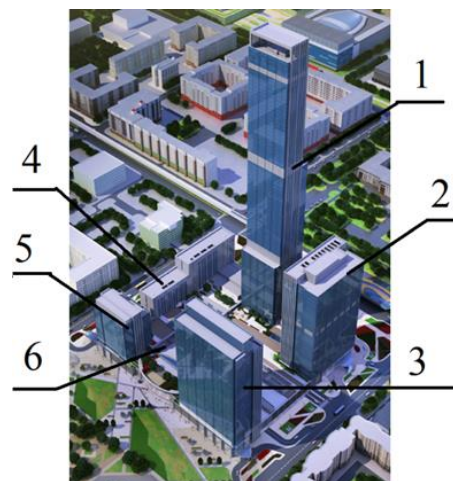


Fig. 1 Project of Abu Dhabi Plaza in Astana.

Before you start laying the foundation, you need to decide on its technology and depth. It depends on the expected load on it and the features of the natural conditions, namely the type of soil and the depth of the groundwater. Abu-Dhabi Plaza residential skyscraper consists of 5 main towers (see Figure 1):

- 1) Block R- offices and living quarters (75-Storey Mixed Use 450 Apartments 69,000 m² Office 37,000 m²);
- 2) Block O- office building (30-storey Office

69,000 m²);

3) Block Y- offices of class «A» (31-Storey Office 65,000 m²);

4) Block H- hotel and furnished rooms (14-Storey Hotel 190 Guest Rooms 100 Serviced Apartments 32,000 m²);

5) Block Z-residential apartments (17-Storey Residential 20,000 m²);

6) Block P (2-Storey Podium Retail 50,000 m²).

The Features of high-rise buildings present high requirements to the results of the EGS (engineering and geotechnical survey) and should solve the following main tasks in their implementation:

- study of the geological structure of the soil massif with large volume (up to 60 m in depth and at least 2 foundation widths beyond its contour)

- reliable assessment of the hydrogeological and hydro chemical conditions of both the compressible soil massif, and in the excavation zone and adjacent territory with the establishment of their corrosive aggressiveness, in time;

- Determination of deformation and strength properties of dispersed and rocky soils at large ranges of voltage changes;

- Instrumental observation and monitoring of deformations of the soil massif of the basement foundation and the adjacent territory under static effects.

DESCRIPTION OF CONSTRUCTION SITE CONDITIONS

It is well known that the central Kazakhstan was dominated by “schist’s, slates, mafic igneous rocks, and granites”, since interpreted to reflect the dominance of large former subduction accretion complexes. The monotony of their basalt/ chert/ turbidite-dominated lithology’s and the nearly chaotic aspect of their penetrative internal structure make it extremely difficult to find markers in large subduction-accretion complexes by which to outline their large-scale structures. The oldest rock in this area are Precambrian granites and gneisses overlain by Neoproterozoic to Cambrian carbonates and carbonate-rich slate, which in turn are unconformable covered by Ordovician volcanic and sedimentary rocks. These rocks were deformed and intruded by granite at the end of the Ordovician. After the early Devonian, south east Kazakhstan continued to be the area of active volcanism with some interruptions, until the Late Permian and locally Early Triassic. Continental sedimentary deposits of Jurassic and younger age overlie the Paleozoic volcanic with a major angular unconformity. In our study area Early Carboniferous volcanic rocks rest with a weak angular unconformity on Devonian rocks and with a major unconformity on older complexes.

Based on the field description of the soils

confirmed by the results of static sounding and laboratory tests, a division of the soils composing the site of prospecting for engineering-geological elements in the stratigraphic sequence of their occurrence was a carried out [2]-[4].

All experiments were a performed with CPT surface (see Figure 2). Soil test at each point of penetration came to the ends under the limit forces on the probe in accordance to GOST 19912-2001 (2001).

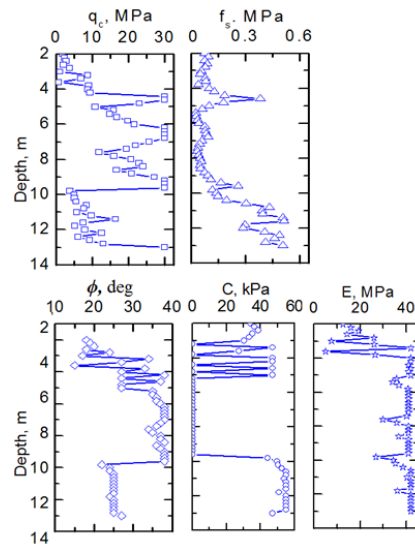


Fig. 2 Results of CPT-1 in construction site ADP, Astana, Kazakhstan.

Seismic risk distribution map of Kazakhstan is a given in Figure 3. According to below map, Astana is located in the region, which has very low risk in terms of seismic hazard. According to seismic risk distribution map, peak ground acceleration a_{max} should be taken a value between 0 m/s² to 0.2 m/s² which is equal to 0.02 g therefore could be ignored in structural design [5].

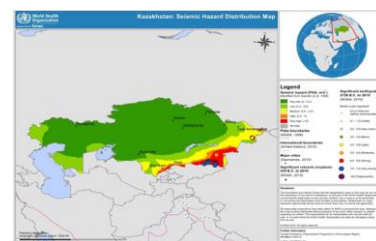


Fig. 3 Seismic Risk Distribution Map [5].

DESIGN PARAMETERS THE DIAPHRAGM WALL

The design of anchored retaining structures providing lateral support for deep temporary excavations in urban areas was traditionally based on simple numerical models.

Joining for the diaphragm wall panel –

Diaphragm wall cannot be constructed continually for a very long section due to limitation and size of the mechanical plant. The wall is usually constructed in alternative section. Two stop end tubes will be placed at the ends of the excavated trench before concreting. The tubes are withdrawn at the same time of concreting so that a semi-circular end section is formed. Wall sections are a formed alternatively leaving an intermediate section in between. The in-between sections are built similarly afterward but without the end tube. At the end a continual diaphragm wall is constructed with the panel sections tightly joined by the semi-circular groove. Soil profile at southern section related to new diaphragm wall location is adopted from actual site observations during diaphragm wall construction at the south side for Phase - 1 works. Elevations of soil layers are taken from average levels recorded in as built elevation drawings related to south side of phase - 1 works[6].

The ground water level is taken at a depth approximately 4.0 m to below the ground level. Recommended soil parameters given in the Interpretive Report (Waterman, May 2010) were an inspected and geotechnical parameters relevant to the calculations used for the design of the shoring system are a summarized in the table 1.

Table 1 Geotechnical Parameters for Shoring Design

E G E	Depth (m)	γ , kN/m ³	ϕ' , deg	c' , kN/ m ²	E, MPa
1	4.0	18.5	25	1	15
2	4.5	19	35	1	25
3	5.5	18.5	26	30	30
4	1.5	20.5	35	1	50
5	2.0	23.5	38	40	65
6	Below	24.0	38	50	100

Note: EGE-1 Clay /Loam, EGE-2 Sand & Gravel, EGE-3 Loam & Clay, EGE-4 Rock Debris, EGE-5 Sandstone, EGE-6 Hard Sandstone.

ANCHOR CALCULATIONS

Pre - stressing loads (tension: T forces) of ground anchors are shown on the shoring section drawing as determined 'Pre - tensioning forces' in Plaxis inputs dividing to the tension forces by spacing (distance) between adjacent anchors on the same level for the anchored section (see Figure 4). After these pre - stressing stages, the tension forces on the ground anchors generally increase up to the capacity of the anchor tendons with a safety factor.

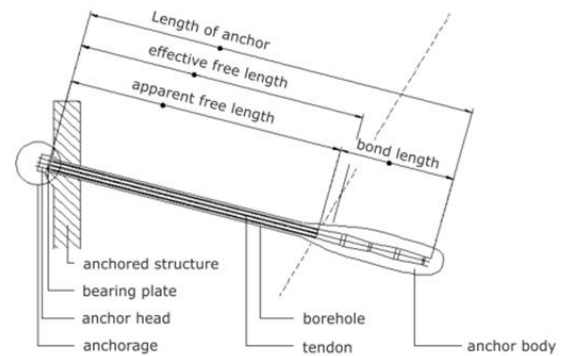


Fig. 4 Typical section of anchored diaphragm wall.

The finite element method is a based on a model in which the behavior of soil and structure is integrated. The properties of soil are an introduced by means of stress-deformation relations. With this method, fundamental calculations of stresses and deformations of soil and structural members can be made. The method can be used to calculate sectional forces of the structural members, verify the global stability of the structure and to calculate and verify deformations (see Figure 5).

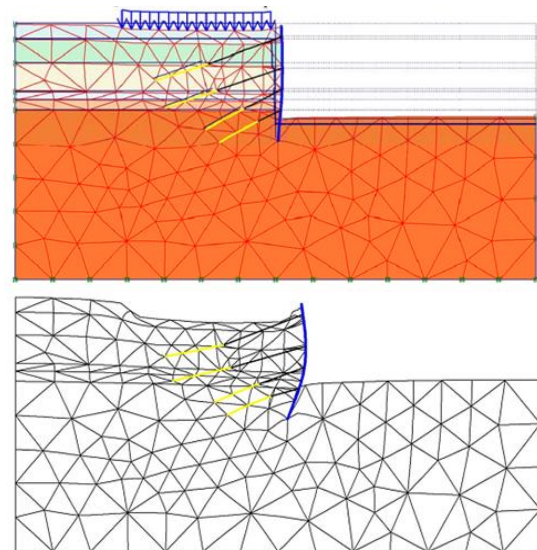


Fig. 5 Deformed mesh in Plaxis 2D, Section 1.

When a load is an applied to soil, the water in the pores as well as the solid grains carries it. The increase in pressure within the pore water causes drainage (flow out of the soil), and the load is transferred to the solid grains. The rate of drainage depends on the permeability of the soil. The strength and compressibility of the soil depend on the stresses within the solid grains called effective stresses (see Figure 6). The effective stresses are a measure for the forces in the contact points of the grains. Thus, the total stress is a summation of the effective stress and the pore water pressure [7].

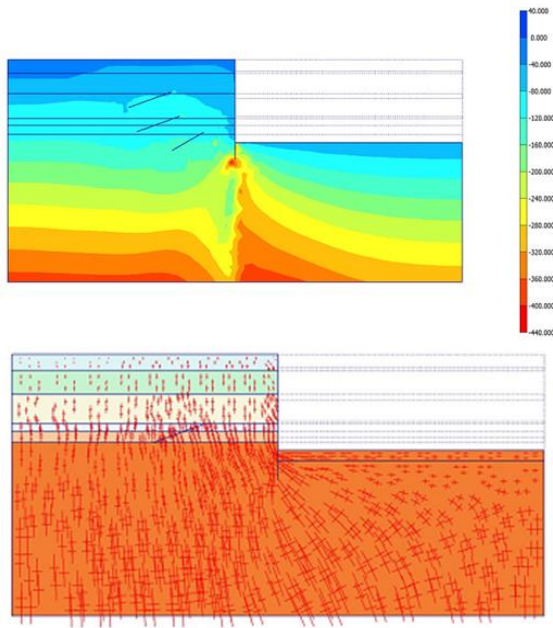


Fig. 6 Effective stresses.

After these pre - stressing stages, the tension forces on the ground anchors generally increase up to the capacity of the anchor tendons with a safety factor (see Table 2 and Figure 7).

Table 2 Results Plaxis 8 for Section 1

Anchorage Summary Table	Number anchors			
	1	2	3	4
Level (-)	3.0	9.0	13.0	17.0
Spacing, m	2.20	1.65	1.65	1.65
Free Length, m	15	13	8	5
Grout Length, m	10	10	8	8
Angle, degree	20	20	30	30
Total Length, m	25	23	16	13
Prestressing Load, kN	460	530	570	640
Calculated Anchorage Load, kN (:Cal=Tw)	607	672	670	675
Test Load, kN (=Cal*1.25) (=Tw*1.25)	759	840	838	844
Locking Load, kN (=Cal*1.10) (=Tw*1.10)	668	739	737	743

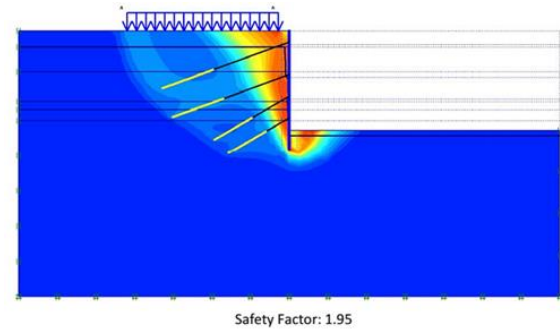


Fig. 7 Safety Factor Section1.

DIAPHRAGM WALL CONSTRUCTION TECHNOLOGY, CONSTRUCTION SITE ADP, ASTANA

This method need to construct a R.C. retaining wall along the area of work. Because the wall is a designed to reach very great depth, mechanical excavating method is an employed. Typical sequence of work includes:

1) Construct a guide wall; 2) Excavation for the diaphragm wall; 3) Excavation support using betonies slurry; 4) Inert reinforcement and concreting.

Guide wall – guide wall is two parallel concrete beams constructed along the side of the wall as a guide to the clamshell, which is a used for the excavation of the diaphragm wall, trenches (see Figure 8).



Fig. 8 Construction of guide wall in site ADP.

Excavation for the diaphragm wall – In normal soil conditions excavation is done using a clamshell or grab suspended by cables to a crane. The grab can easily chisel boulder in soil due to its weight (see Figure 9).



Fig. 9 Excavation for the diaphragm wall in ADP.

Excavation support – excavation for the diaphragm wall produces a vertical strip in soil which can collapse easily. Betonies slurry is used to protect the sides of soil. Betonies is a naturally occurring clay which, when added to water, forms an impervious cake-like slurry with very large viscosity. The slurry will produce a great lateral pressure sufficient enough to retain the vertical soil. **Reinforcement** – reinforcement is inserted in form of a steel cage, but may require to lap and extend to the required length. **Concreting** – concreting is done using termite. As Concrete being poured down, betonies will be displaced due to its density is lower than concrete. Betony is then collected and reuse. Usually compaction for concrete is not required for the weight of the betonies will drive most of the air voids in concrete.

MONITORING OF DIAPHRAGM WALL, CONSTRUCTION SITE ADP, ASTANA

One of the most important challenges at this stage is to review the work, which has been done by the previous contractor. The inspection of the existing construction helps the engineers to decide whether to carry on or to modify it [9].

The objective was the structural inspection of the diaphragm wall in comparison to theoretical position. In this case, the level of tolerance of the deviation from the theoretical position must be minimal since the design involves the construction of the inner wall (or parking wall) along the diaphragm wall, within a distance of 15 cm. More specifically, the distance between the inner sides of the diaphragm wall to the outer side of the parking wall must be 15cm,

according to the design [9].

The high level of detail, which is required, made it necessary to utilize a method, which allows us to get the as-built situation as it is and to analyze into an advanced CAD system [9].

Recent advances in generating 3D environments using laser-scanning technologies, and acquiring quality information about built environments using embedded and other advanced sensors provide the capability to the frequently gather an integrated and accurate three-dimensional and material quality related as-built data. This information is a combined with the design model with an objective to create an integrated model, which is a dynamically updated during the construction period [9].

The resulting model constitutes a color-based deviation model, as is indicated in Figure 10.

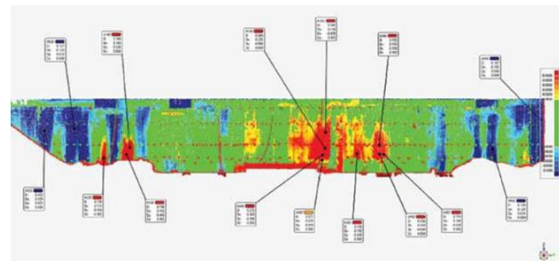


Fig. 10 Color based deviation model of the west section of the wall [9].

The site scanning, with the usage of the laser scanner technology, was the completed in four days with 400 scans in total. Advanced computer software gives us the ability to generate vertical and horizontal cross sections, along the diaphragm wall, allowing the user to define the interval between the consecutive cross sections. The decision was the based on the length of the panels, which constitute the diaphragm wall. Therefore, an interval of five meters between two consecutive cross sections allows us to check the as-built condition of every panel [9].

CONCLUSION

There is need to consider the anticipated responses of the adjacent buildings during construction. This will require the design professional to survey the condition of the adjacent properties to understand their present condition and fragility, establish acceptable limits, conduct soil-structure analyses of various support systems and develop limits on their respective movements, and develop a monitoring strategy.

The color is an assigned according to the value of the deviation between the as-built measured data and the design model. In Figure 11, the areas, which are colored red, represent the highest deviation with values, which exceed 150 mm, in contrast to the

green colored areas, which present the lowest deviation with the values, which fluctuate between 0 mm and 150 mm. The positive pattern of deviation is an illustrated in red while the negative deviation is in blue. The red colored areas indicate the areas where the wall penetrates the parking wall and therefore must be a trimmed. The green areas indicate the parts of the wall where the deviation fluctuates within acceptable limits while the blue color indicates the areas where the wall deviates into the opposite direction.

REFERENCES

- [1] Zhussupbekov, A., Omarov, A., Zhukanova, G., Tanyrbergenova, G. (2017). Pile Foundations of Mega Projects: New Railway Station and LRT in Problematical Soil Ground of Astana. *Procedia Engineering*, Vol. 189, Pages 511-518.
- [2] Zhussupbekov A.Zh., Lukpanov R.E., Omarov A.R. (2016). Experience in Applying Pile Static Testing Methods at the Expo 2017 Construction Site. *Journal of Soil Mechanics and Foundation Engineering*. Volume 53, Issue 4, Pages 251-256.
- [3] Zhussupbekov A., Omarov A. (2016). Modern Advances in the Field Geotechnical Testing Investigations of Pile Foundations. *Procedia Engineering*, Vol. 165, Pages 88-95.
- [4] Zhussupbekov A., Lukpanov R., Omarov A. (2016) The Results of Dynamic (Pile Driving Analysis) and Traditional Static Piling Tests in Capital of Kazakhstan. 13th Baltic Sea Region Geotechnical Conference. Vilnius, LITHUANIA. SEP 22-24, Pages 201-205.
- [5] Zhussupbekov A.Zh., Syrlybaev M.K., Lukpanov R.E., Omarov A.R.. (2015). The applications of dynamic and static piling tests of Astana. 15th Asian Regional Conference on Soil Mechanics and Geotechnical Engineering, ARC 2015: New Innovations and Sustainability, 2015, Pages 2726-2729.
- [6] Omarov, A.R., Zhussupbekov, A.Z., Tulegulov, A.D., Zhukanova, G.A., Tanyrbergenova, G.K. (2016). The analysis of the piling tests on construction site "The future of the free country". *Proceedings of the 8th Asian Young Geotechnical Engineers Conference*, 8th AYGEC. Astana, Kazakhstan. Pages 127-130.
- [7] Zhussupbekov A.Zh., Omarov A.R. (2016). Geotechnical and construction considerations of pile foundations in problematical soils. *Proceedings of the 8th Asian Young Geotechnical Engineers Conference*, 8th AYGEC. Astana, Kazakhstan. Pages 27-32.
- [8] Zhussupbekov, A.Z., Lukpanov, R.E., Omarov, A.R. (2016). Bi-directional Static Load testing. *Fourth Geo-China International Conference (Geotechnical Special Publication)*. Shandong, China. Pages 35-42.
- [9] Uakhitov A.B., Igilmanov Zh.A. ANALYSING DEFORMATIONS USING LASER SCANNING IN ASTANA. *Proceedings of the IX International Scientific Conference for students and young scholars «Science and education - 2014»*

EVALUATION OF THE CALIBRATION ACCURACY OF SOIL MOISTURE USING A NEW MICROCHIP SENSOR

Mitsuru Komatsu¹, Masato Futagawa² and Yasushi Fuwa³

¹ Graduate School of Environmental and Life Science, Okayama University, Japan;

² Department of Electrical and Electronic Engineering, Shizuoka University, Japan;

³ Integrated Intelligence Center, Shinshu University, Japan;

ABSTRACT

This study aims to estimate soil moisture using microchip sensors. This method could be employed in the in situ monitoring of slope disasters due to heavy rain. A new sensor chip sized 5 mm × 5 mm was fabricated using Large-scale integrated circuit of the silicon substrate (Si-LSI) technology, based on a multimodal sensor chip. The measured values of impedance, phase, and temperature were converted to a digital signal, and transferred to a cloud server automatically through a wireless transmitter. In this paper, the calibration accuracy of the new microchip sensor and commercially available capacitance sensors were discussed to summarize the applicability for measuring the volumetric moisture content of various soil materials. The results of this study show the possibility of estimating volumetric moisture content with a rainfall infiltrating behavior, with an accuracy of approximately ±15%. The microchip sensor must thus be improved before it can be used to estimate the rainfall behavior at natural slopes.

Keywords: soil moisture sensor, volumetric moisture content, Si-LSI microchip, capacitance

INTRODUCTION

Slope failures and debris flow induced heavy-rainfall occurs worldwide. On August 20, 2014, a series of slope failures and debris flow occurred in Hiroshima, Japan [1]. Wired, tilt sensor, and GPS sensors [2], which can detect the commencement of soil sliding, are useful for facilitating the announcement of an evacuation signal immediately before slope failure occurs. When the risk of a slope failure can be detected before its occurrence, evacuees are afforded sufficient time to evacuate. Researchers have investigated methods to monitor soil moisture content [3]-[5]. When the water content in soil is increased, the soil frictional force is decreased, and the soil weight is increased. The water content measurement is thus capable of detecting dangerous levels of the natural slope.

Several types of measurement methods can be employed in a soil moisture sensor: tensiometers [6], which measure suction force; electrical impedance sensors, which are primarily capacitance-measurement-type sensors [7]-[8]; TDR-type sensors [9]; ADR-type sensors [10]; TDT-type sensors [11]; and electrical-conductivity-type sensors [12]-[13]. Soil measurements using electrical impedance exhibit the advantages of long-term determination, and the measurements do not require any periodic maintenance. Our group studied the miniaturized impedance sensor fabricated using Si-LSI technology [14], for the measurement of soil

moisture content. This sensor, which is inexpensive and compact, is advantageous because it is easier to install into the soil compared to other sensors [15]. In this study, the calibration accuracy of this microchip sensor and commercially available capacitance sensors were discussed to summarize the applicability for measuring the volumetric moisture content of various soil materials.

FABRICATION OF PROPOSED MICROCHIP SENSOR

The proposed microchip sensor [16] is a multimodal type integrated with an impedance sensor using a Pt electrode, a temperature sensor using a p-n junction diode, and a pH sensor using an ion-sensitive FET. In this study, a new sensor chip, as shown in Fig. 1, was fabricated using Si-LSI technology based on a multimodal sensor chip. The sizes of the chip, Pt electrode, and poly-Si shield structure were 5 mm × 5 mm, 3.9 mm × 0.9 mm, and 3.94 mm × 9.3 mm, respectively. The shielding structure was located under the Pt electrode. The SiO_x insulation layer was sandwiched between the Pt electrode and the shielding structure to provide isolation. In the measurement of the soil moisture content, it is necessary to detect small magnitudes of current and perform measurements at a high frequency. An operational amplifier suitable for this condition will ideally have a high bandwidth. However, an excessively high bandwidth might

induce oscillations; therefore, in the proposed circuit, an operational amplifier, LT 1055 with a bandwidth of 5 MHz was used. Furthermore, sufficient amplification was obtained using a two-stage amplification circuit.

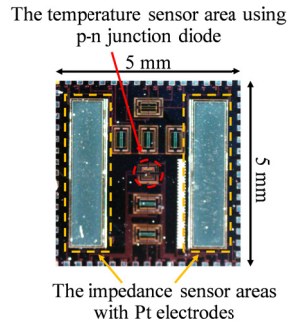


Fig. 1 Photograph of the proposed microchip sensor.

The photograph of the sensor used for measurement is shown in Fig. 2. The traffic light from a sensor can be conveyed to the connector of the above-ground part through a board. The board used is designed in a shape that allows it to be inserted into the soil; it has a length of 240 mm, a width of 8 mm, and a thickness of 2 mm. Fig. 3 shows the conceptual diagram of two measurement systems for the proposed microchip sensor. This method is to allow for the measurement of the average value between the sensors by a tomography method using two probes, as well as a typical single probe.

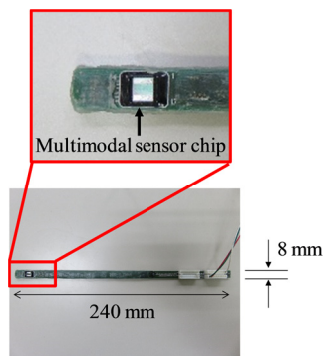


Fig. 2 Photograph of the soil insertion probe.

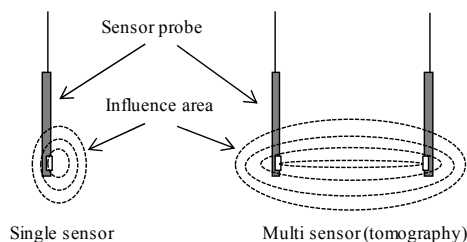


Fig. 3 Conceptual diagrams of two measurement systems.

METHOD

The calibration measurement was performed using the proposed microchip sensor and two commercial sensors for four types of soil. The commercial sensor is one of the EC-5 sensors (Decagon Devices, Inc.) used in the capacitance-/frequency domain technology, the other is the SM300 (Delta-T Devices Ltd.), which is a frequency-domain reflectometry probe [15].

Four soil materials were used for the calibration measurement. Granite soil and silica sand (#7) were obtained from the Okayama prefecture and Gifu prefecture, respectively. Organic soil was obtained at the monitoring slope in the Nagano prefecture, as shown in Fig. 4 (a); colluvial soil consisting of mudstones was obtained in the Shizuoka prefecture is shown in Fig. 4 (b). The soil particle density (ρ_s) of each sample is listed in Table 1.



Fig. 4 Photograph of the field measuring situation in the (a) Nagano site, (b) Shizuoka site.

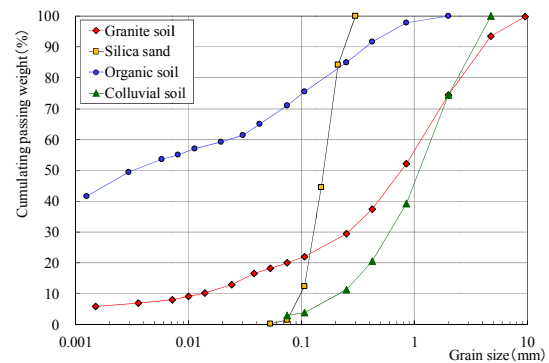


Fig. 5 Grain size distribution

Table 1 Physical properties of soil samples

	Granite soil	Silica sand	Organic soil	Colluvial soil
ρ_s (g/cm ³)	2.630	2.560	2.572	2.692
ρ_d (g/cm ³)	1.600	0.700	0.619	1.020
n	0.392	0.727	0.759	0.621

An acrylic container of diameter 150 mm was used for the calibration measurement, as shown in Fig. 6. Table 1 also lists the physical properties of the soil sample. The test specimen for measurement-type A was compacted with a rammer at a specified

dry density and volume moisture content in a 300 mm high container. This method could not produce test specimens of uniform moisture condition when approximately 50% of the saturation degree has been exceeded. Further, the test specimen was applied a different method. Measurement-type B consists of a 100 mm high column, the height of soil column are 550 mm (silica sand), 650 mm (granite soil) and 850mm (organic soil and colluvial soil), respectively. The test specimen became nearly saturated with carbon dioxide, and de-aired water was injected from the bottom of the test specimen.

For the measurement, a sensor probe was installed such that the top and bottom were 150 mm or beyond the soil to consider the influence range of the sensor, as shown in Fig. 7. In measurement-type A, a sensor probe was inserted at a predetermined depth beforehand in compaction, and a probe was inserted sequentially, while the upper columns were individually dismantled in measurement-type B. The EC-5 and SM300 sensors were inserted from the surface of the test specimen.

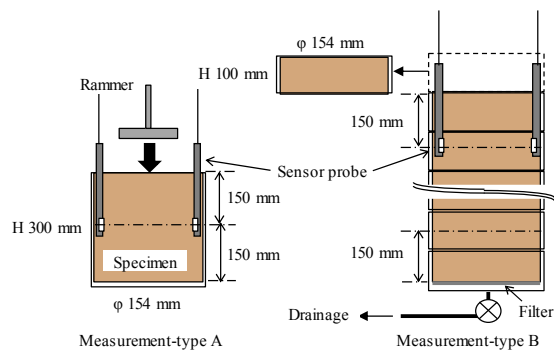


Fig. 6 Method of the calibration measurement.

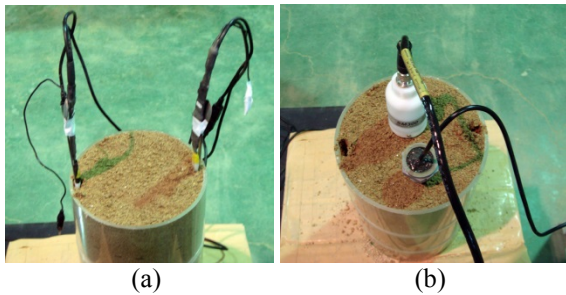


Fig. 7 Measurement of (a) microchip sensor and (b) commercial sensors (EC-5 / SM300).

RESULTS AND DISCUSSIONS

The relations between the height of the soil column and volumetric moisture content (cm^3/cm^3) or degree of saturation (%) in measurement B are shown in Fig. 8. The averages of the height, center height of the column, volumetric moisture content, and degree of saturation were plotted for each column. Each test specimen showed a saturation

degree of approximately 90% in the bottom column. As for the organic soil, the specimens show a saturation degree higher than approximately 60%, whereas for the others, it was higher than approximately 50%. The relations between the saturation degree and porosity of all specimens are shown in Fig. 9. It is understood that the specimens are measured in all degrees of saturation, although some unevenness occurred in the porosity. In addition, in measurement A, the data of 100% saturation degree are the test specimens that were provided by de-airing a test specimen in water.

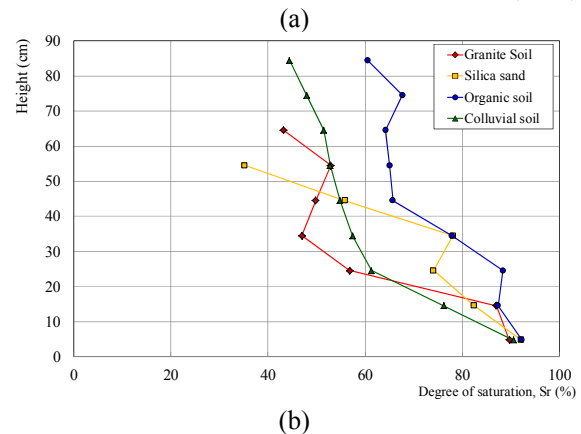
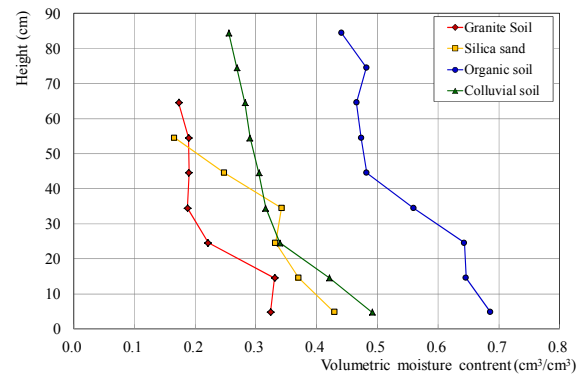


Fig. 8 Relationships between height of soil column and volumetric moisture content or degree of saturation for measuring-type B.

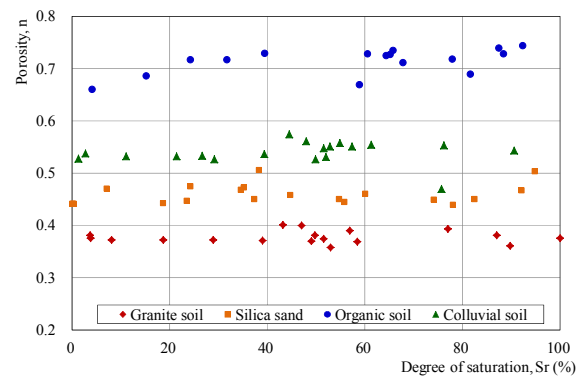
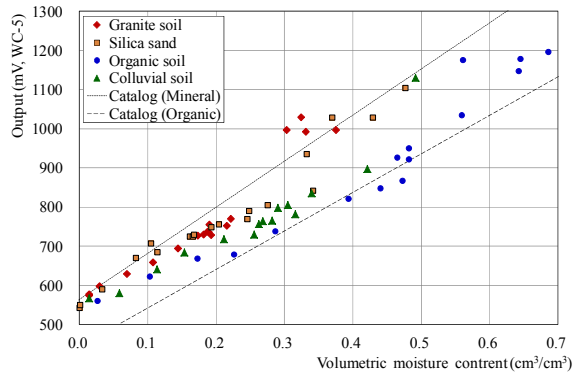
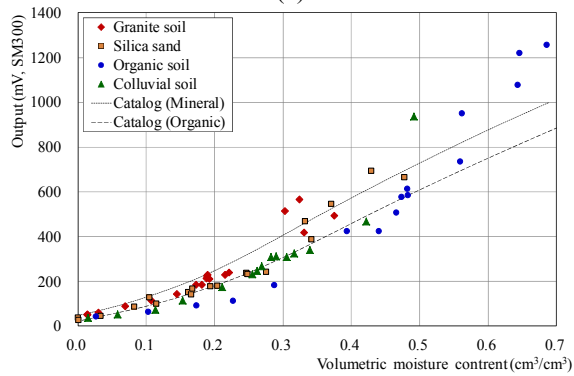


Fig. 9 Relationships between porosity and saturation degree for all specimens.

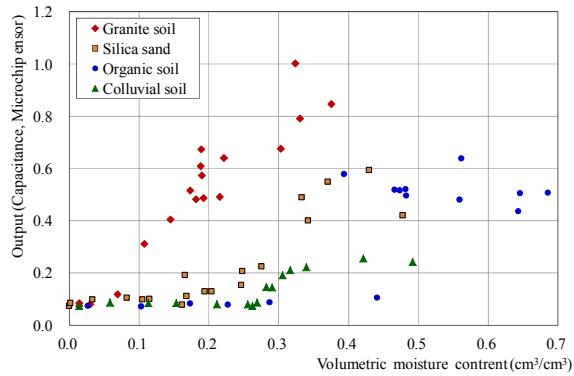


(a)

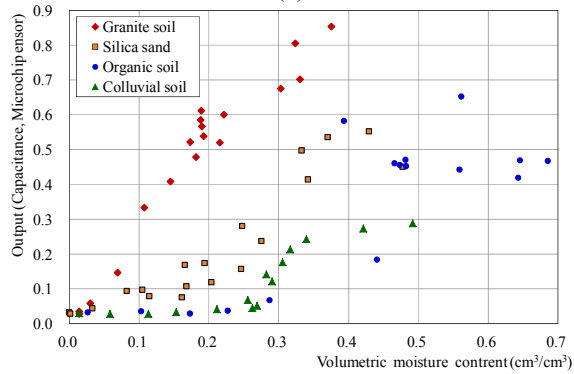


(b)

Fig. 10 Relationships between volumetric moisture content and output (mV) of (a) EC-5, (b) SM300

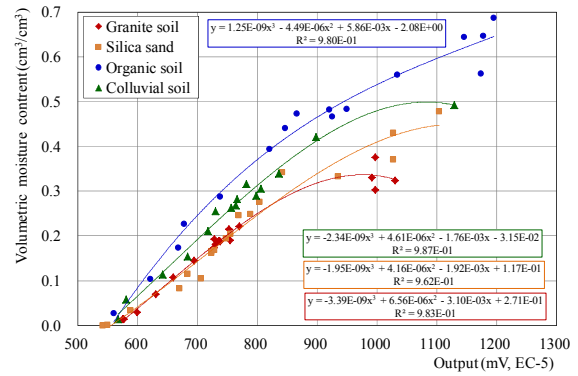


(a)

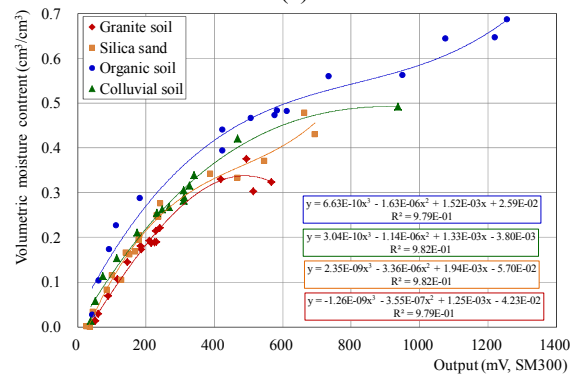


(b)

Fig. 11 Relationships between volumetric moisture content and output (capacitance) of (a) single type, (b) multi type (scanning)

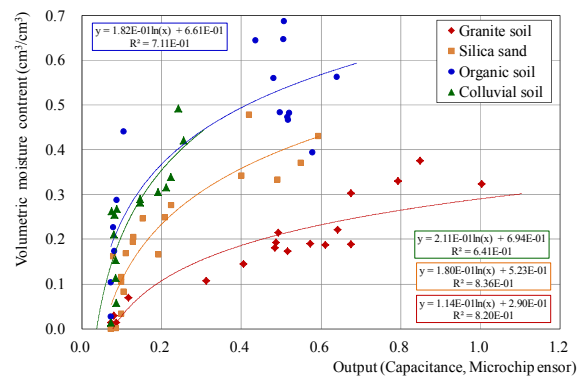


(a)

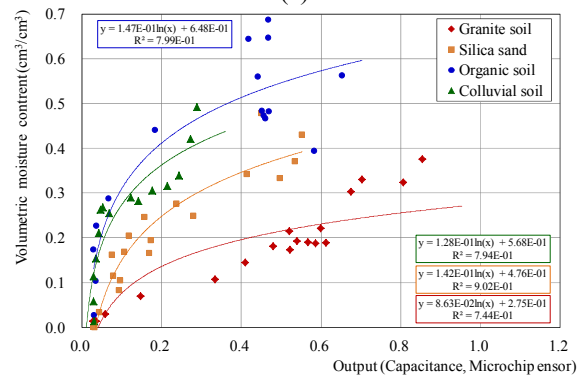


(b)

Fig. 12 Calibration curve of (a) EC-5, (b) SM300



(a)



(b)

Fig. 13 Calibration curve of (a) single type, (b) multi type (scanning)

Fig. 10(a) and (b) show the relationships between the volumetric moisture content and output (mV) for

the measurements by the EC-5 and SM300, respectively. The calibration curves of the mineral soil and organic soil in the catalog were plotted on the graphs. The measurement results for all soils are plotted between these two lines except the high moisture areas of SM300. Fig. 11 shows the relationships between the volumetric moisture content and the output (capacitance), respectively, of a single and multi-type (scanning) microchip sensor. The effective change in the output level is not seen in the area of low volumetric moisture content, except for granite soil. This depends on the output lower-limit level of the sensor.

Based on Fig. 10 and 11, the results that produced the calibration curves are shown in Fig. 13 and Fig. 14, respectively. In Fig. 13, the calibration curves are shown as the third multinomial expression. In Fig. 14, a logarithmic expression was applied to it because the measurements of the microchip sensor exhibited a slight change in the low volumetric moisture content.

The accuracies of the calibration curve are shown in Fig. 13 and Fig. 14, respectively. EC-5 and SM300 show errors of less than $\pm 5\%$, but the microchip sensor error is approximately $\pm 15\%$. It is necessary to improve the structure and increase the contact area because these err is related to the sensor tip contact to the soil.

CONCLUSION

In this study, the calibration accuracy of a new microchip sensor and commercially available capacitance sensors were discussed to summarize the applicability for measuring the volumetric moisture content of four soil materials. The results of this study show that EC-5 and SM300 had good potential in estimating the volumetric moisture content within $\pm 5\%$ accuracy. Meanwhile, the precision of the microchip sensor is inferior to the EC-5 and SM300. The single-type and multi-type microchip sensors show an error of approximately $\pm 15\%$. The microchip sensor must be improved before it can be used to estimate the rainfall behavior at the natural slopes.

ACKNOWLEDGEMENT

A part of this study was performed through the support of the Communications R&D Promotion Program (SCOPE) of the Ministry of Internal Affairs and Communications, specifically, the "Research and Development of a Communications Infrastructure System in a Sensor Network for Flexibly Responding to Disasters for Collecting Disaster Information in Remote Locations (142304006)" (2014 to 2016).

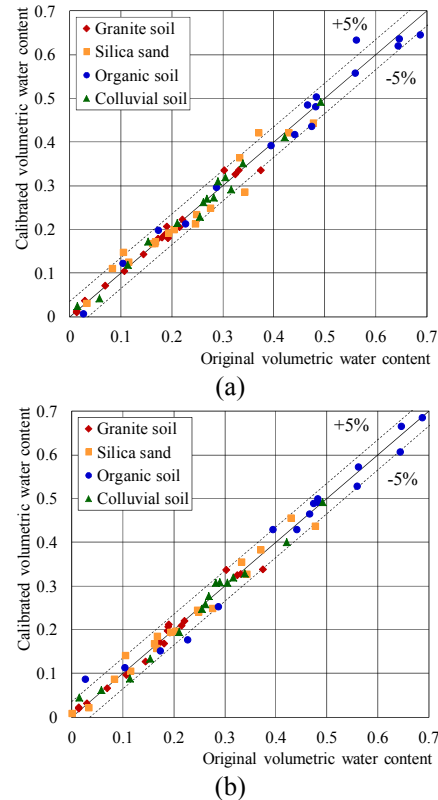


Fig. 14 Accuracy of calibration results of (a) EC-5, (b) SM300

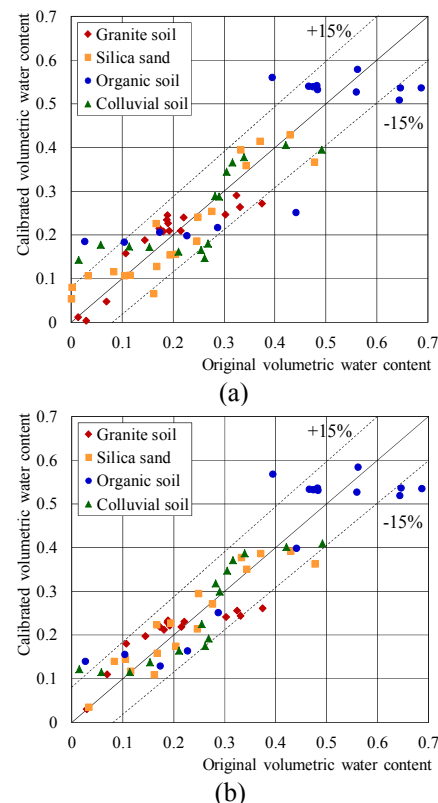


Fig. 15 Accuracy of calibration results of (a) single type, (b) multi type (scanning)

REFERENCES

- [1] Tsuchida T., T. Moriwaki, N. Kumamoto, K. Ichii, S. Kano and S. Nakai, Investigation of debris flow and damaged areas of 2014 Hiroshima landslide disaster, *Japanese Geotechnical Journal*, Vol. 11, Issue 1, 2016, pp.33-52.
- [2] Uchimura T., I. Towhata, T. T. L. Anh, J. Fukuda, C. J. B. Bautista, L. Wand, I. Seko, T. Uchida, A. Matsuoka, Y. Ito, Y. Onda, S. Iwagami, M. Kim and N. Sakai, Simple Monitoring Method for precaution of Landslides Watching Tilting and Water Contents on Slopes Surface, *Landslides*, Vol. 7, 2010, pp. 351-357.
- [3] A. Tohari, M. Nishigaki, M. Komatsu, Laboratory Rainfall-Induced Slope Failure with Moisture Content Measurement, *Journal of Geotechnical and Geoenvironmental Engineering*, Vol. 133, No. 5, 2007, pp.575-587.
- [4] Iida T., M. Fujimoto, N. Kumakura, D. Takasaki, N. Hiraoka and R. Fukagawa, A method to judge slope failures using soil moisture characteristics, *International Journal of GEOMATE* Vol. 10, Issue 22, 2016, pp.2094-2100.
- [5] Koizumi K., K. Sakuradani, K. Oda, S. Ito, Y. Fukuda, M. Q. Feng, M. Takemoto, Fundamental research on advancement of regulation standard for expressway management against rainfall-induced surface failure”, *J. of Japan Society of Civil Engineers, Ser. C (Geo-engineering)*, Vol.73, No. 1, 2017, pp. 93-105. (in Japanese with English abstract)
- [6] Richards L. A., Soil Moisture Tensiometer Materials and Construction, *Soil Science*, Vol. 53, Issue 4, 1942, pp. 241-248.
- [7] Eller H. and A. Denoth, A Capacitive Soil Moisture Sensor, *Journal of Hydrology*, Vol. 185, Issues 1-4, 1996, pp. 137-146.
- [8] Robinson D. A., T. J. Kelleners, J. D. Cooper, C. M. K. Gardner, P. Wilson, I. Lebron, and S. Logsdon, Evaluation of Capacitance Probe Frequency Response Model Accounting for Bulk Electrical Conductivity, *Vadose Zone Journal*, vol. 4, no. 4, 2005, pp. 992-1003.
- [9] Topp G. C., J. L. Davis and A. P. Annan, Electromagnetic Determination of Soil Water Content: Measurements in Coaxial Transmission Lines, *Water Resources Research*, Vol.16, No.3, 1980, pp.574-582.
- [10] Gaskin G. J. and J. D. Millker, Measurement of soil water content using a simplified impedance measuring technique, *Journal of Agricultural Engineering Research*, No.63, 1996, pp.153-160.
- [11] Miyamoto H. M. Uemura and Y. Hirashima, Digital TDT sensor for coupled measurement of soil moisture and electrical conductivity, *Journal of Groundwater Hydrology*, Vol.59, No.1, 2017, pp.11-19. (in Japanese with English abstract)
- [12] Yurui S., P. S. Lammers, M. Daokun, L. Jianhui, and Z. Qingmeng, Determining soil physical properties by multi-sensor technique, *Sensors and Actuators A*, Vol. 147, 2008, pp. 352-357.
- [13] Saito T., H. Fujimaki, and M. Inoue, Calibration and Simultaneous Monitoring of Soil Water Content and Salinity with Capacitance and Four-electrode Probes, *American Journal of Environmental Sciences*, Vol. 4, Issue. 6, 2008, pp. 683-692.
- [14] Futagawa M., M. Komatsu, H. Suzuki, Y. Takeshita, Y. Fuwa, K. Sawada, Fabrication of a Slope Failure Prediction Sensor using Miniaturized EC Sensor, *IEEJ Transaction on Sensors and Micromachines*, Vol. 133, No. 9, 2013, pp. 278-283. (in Japanese with English abstract)
- [15] Steven R. Evett, Judy A. Tolk and Terry A. Howell, Soil Profile Water Content Determination, *Vadose Zone Journal*, Vol. 5 No. 3, 2006, pp. 894-907.
- [16] Futagawa M., S. Ogasahara, T. Ito, M. Komatsu, Y. Fuwa, H. Hirano, I. Akita, K. Kusano, M. Watanabe, Fabrication of a low leakage current type impedance sensor with shielding structures to detect a low water content of soil for slope failure prognostics, *Sensors and Actuators A: Physical*, Vol.271, 2018, pp.383-388.
- [17] Kodešová R., V. Kodeš and A. Mráz, Comparison of Two Sensors ECH2O EC-5 and SM200 for Measuring Soil Water Content, *Soil and Water Research*, Vol.6, No.2, 2011, pp.102-110.

SLOPE STABILITY ANALYSIS OF INTEGRATED MUNICIPAL DISPOSAL SITE BASED ON ORGANIC CONTENT CHANGE TO OPTIMIZE EMBANKMENT CAPACITY

Ahmad Rifa'i¹, I Wayan Ariyana Basoka² and Fikri Faris³

^{1,2,3}Department of Civil and Environmental Engineering, Universitas Gadjah Mada, Indonesia

ABSTRACT

Municipal Solid Waste Embankment has become a common problem in urban areas. Increasing the amount of waste will cause landfill capacity to be more critical, resulting in a slope failure disaster and environmental disaster if not handled properly. Acquiring locations to expand landfills is difficult, several efforts are needed to maintain the stability of waste embankments in order to optimize the landfill capacity. The research is located in Integrated Municipal Disposal Site Piyungan Yogyakarta. The objective is to obtain the geotechnical properties of waste embankment due to the decomposition process for slope stability analysis to optimize embankment capacity and as reference for design and infrastructure development. Samples were taken from different waste's age. The field density, organic content, shear strength parameters, permeability and suction measurement were conducted. The rainfall data is taken from 4 rainfall stations. Numerical simulation was carried out for analyzing rainfall behavior and slope stability modeling. The longer the age of waste, shear strength is increased due to the decrease of organic content and the increase of density. The existing waste embankment is in stable condition with the safety factor of 1.906 and decreases to 1.779 with very heavy rain conditions of 5 hours. The embankment capacity can be upgraded to a height of 10 meter with a 30 degrees slope angle with a reinforcement and gave the safety factor of 1.866.

Keywords: Solid waste embankment, Organic content, Rainfall, Landfill capacity, Slope stability

INTRODUCTION

Consumptive behavior of human from time to time increasing, the increase in this behavior increases the amount of waste. Waste is a residual activity of human being and natural process. The waste produced will be recycled and sorted out which garbage can still be utilized, the remaining waste that can not be processed will then be disposed to disposal site. Reference number [1], waste in Yogyakarta City is transported to Integrated Municipal Disposal Site Piyungan in 2012 of 722 m³/day. Municipal Solid Waste Embankment has become a common problem in urban areas. Increasing the amount of waste will cause landfill capacity to be more critical, resulting in a slope failure disaster and environmental disaster if not handled properly. Acquiring locations to expand landfills is difficult, several efforts are needed to maintain the stability of waste embankments in order to optimize the landfill capacity

Reference number [2] research on waste is also on the influence of composition and weathering on shear strength parameters (cohesion and friction angle). The waste taken from 2 different samples is then included in the reactor anaerobic laboratory to obtain different degradation compositions. It is

expected from this research to obtain the characteristics of waste in Disposal Site Piyungan and the stability of the existing and final waste embankment from Disposal Site Piyungan with the influence of rain.

LITERATURE REVIEW

Landslide

Indonesia is a country located in the ring of fire, causing Indonesia to have hilly contours, there are many valleys with the potential to slide. Landslide is a mass movement of soil or rock in a potential landslide field. Mass movement is the movement of a large mass of land along its critical landslide. This soil mass movement is a downward slides movement of slope-forming materials, which may be soil, rocks, soil embankments or mixtures of other materials. When the mass movement of the soil is very excessive, it is called landslide (landslide) reference number [3]. Reference number [4] summarized some of the occurrences of waste avalanches that have occurred in Table 1.

Table 1 Waste embankment failure as in [4]

Location	Year	Victims
Leuwigajah, Bandung, Indonesia	2005	147
Bantargebang, Bekasi, West Java, Indonesia	2006	28
Bogor, West Java, Indonesia	2010	4
Cianjur, West Java, Indonesia	2013	1
Tuban, East Java, Indonesia	2012	1
Bantargebang, Bekasi, West Java, Indonesia	2012	1

Waste

According to reference number [5], waste is the rest of the daily activities of humans and/or processes in the solid form. With the growing population growing annually it will inevitably increase the consumption of society, which creates an increase in waste from year to year, which is not balanced with proper processing.

Shear Strength

Shear strength of waste is important in analyzing the stability of the landfill embankment during service period or after completion of service period. The shear strength parameters illustrated by Mohr-Coulumb failure criteria (c = cohesion, ϕ = internal friction angle) are often used to calculate shear strength parameters of waste. These shear strength parameters can be measured directly through laboratory testing, field scale testing, and back calculate of either existing or failing slopes as in [2].

Hydraulic Conductivity

According reference number [6] the Hydraulic Conductivity of the waste ranges from $1 \times 10^{-3} m/s$ to $1 \times 10^{-9} m/s$, although typically used range 10^{-5} to $10^{-6} m/s$. Preparation of hydraulic conductivity range on waste is not very helpful because of the very large range of possibilities, partly due to the composition of waste and the density that affects the hydraulic conductivity in understanding or possibly up to the way of predicting.

Soil Water Characteristic Curve (SWCC)

Suction (ψ) increasing with decreasing moisture content, moisture moves to smaller pores. At certain moisture levels, suction will depend on the nature of

porous media including matrix structures, cavities between particles, and particle size, shape and texture. The relationship between suction and water content is conventionally expressed by water retention curve (WRC), WRC also known as soil water characteristic curve (SWCC). In Fig. 1 can be seen comparison of SWCC curve from various waste samples.

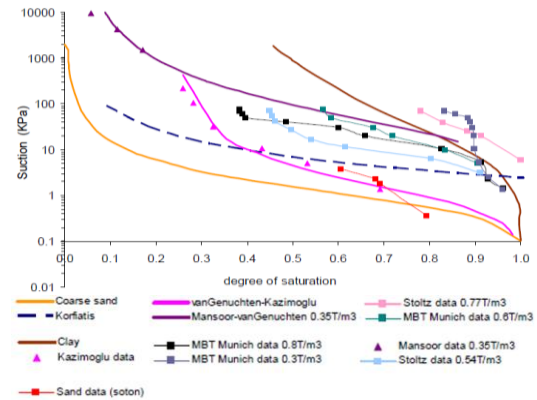


Fig. 1 Comparison of SWCC curves from various waste samples as in [7]

Rainfall Modelling

According reference [8] rainfall modeling is done by looking at rain patterns for 10 years. Then the rain data per day is processed using frequency analysis. Frequency analysis aims to find the relationship between the magnitude of extreme events against the frequency of events by using probability distribution.

RESEARCH METHOD

Research Location

The location of this research is Integrated Waste Disposal Site Piyungan, Ngablak, Sitimulyo, Piyungan Subdistrict, Bantul Regency of Yogyakarta province can be seen in Fig. 2.



Fig. 2 Disposal Site Piyungan.

Sampling

Samples were taken in disturbed condition considering the difficulty of undisturbed sampling on waste. Sampling was taken 3 points by pit test with depth of 1 - 1.5 m.

Rainfall Data Processing

The modeling of rain infiltration into the waste is modeled by using SEEP/W to obtain water infiltrating to the waste material. SEEP/W itself is a finite element method that is able to model the fluid flow in the soil (seepage), this waste material will be approached to the soil material with parameters obtained in laboratory testing.

Calculation of Slope Stability

Slope stability at Disposal Site Piyungan is modeled using the SLOPE/W program based on the limit equilibrium method where stability calculations are based on the forces that occur in each pieces of the slice. In SLOPE/W, slopes modeling also included rain effect which had previously running in SEEP/W program.

RESULT AND DISCUSSION

Properties of Waste

Based on the field and laboratory tests obtained the following results:

Table 2 Results of laboratory test.

Sample	S1	S2	S3
Organic Content (%)	72.41	69.86	43.68
Specific Gravity	1.82	1.93	2.05
γ_d (kg/cm^3)	0.43	0,60	0,89
ϕ (°)			
Reduction 25%	35.02	36.10	41.98
$k(cm/s)$	4.32×10^{-5}	4.43×10^{-5}	3.27×10^{-5}

In Table 3 there are differences in parameters due to the duration of accumulation of waste, the results of this test will be input for the next analysis.

Soil Water Characteristic Curve (SWCC) Result

One important parameter for modeling a pourous medium with unsaturated conditions is the Soil Water Characteristic Curve (SWCC). Based on the result of suction test using tensiometer and water

content using decagon devices. The result of SWCC graph in this research are plotted to the previous research. In Fig. 3 it can be seen that the result of the fitting using the Soil Vision program produces a graph that is in the range of the typical SWCC curve.

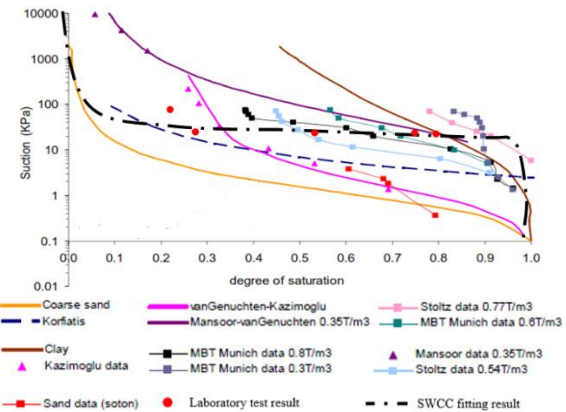


Fig. 3 Comparison of soil water characteristic curve

Rainfall

This research used data from 4 rainfall station which closest to research location that is Siluk station, Karang Ploso, Bedukan, and Terong station from 2006 until 2015. The maximum daily rainfall is processed into the form of statistical distribution to find the re-time value from rain occurred at the study site. Table 4 is the result of processing the statistical distribution of the rainfall occurring in the research area, from the four distributions, it is tested the suitability of the distribution and produce the Log-Pearson III distribution that best represents the conditions in the field.

Table 3 Rainfall distribution

Probability	Return Period	Frequency Distribution
		Log-Pearson III
0.9	1.1	57.44
0.5	2	82.60
0.2	5	110.48
0.1	10	130.93
0.05	20	152.11
0.02	50	182.02
0.01	100	206.50
0.001	1000	302.72

Rainfall modeling is chosen with return period of 1.1 (57.44mm) and 20 years (152.11 mm) which represents normal and very heavy rain. From rainfall data available for 10 years, data processing is done to obtain the average duration of rain and hourly rain distribution in the research area. From the existing rain data obtained 317 rain events with rainfall above 50 mm, the average rainfall in the study area

of 5 hours. After obtaining the duration of rain in the research area, then searched the rain distribution of the clocks by making the curve of the relationship between the percentage of rain depth and the rain duration of all the rain data so that the observed rainfall distribution curve obtained in Fig. 4.

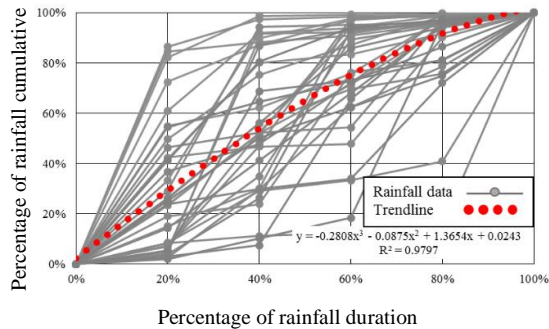


Fig. 4 Rainfall distribution curve

From Fig. 4 there are equation from regression analyzes $y = -0.2808x^3 - 0.0875x^2 + 1.3654x + 0.0243$ representing the rain distribution in the research area, so that the 5 hour rain distribution in the research area can be seen in Table 5. In addition to extreme duration rainfall modeling (field events) and extreme intensity rain for 5 days in Fig. 5 and Fig. 6.

Table 4 distribution of hourly rain with a 5 hour rain

Rain Distribution (5 hours)					
Percent Cumulative Hours	20	40	60	80	100
Percent Cumulative	29.16	53.85	75.14	91.69	100
Percent Hourly	29.16	24.69	21.29	16.55	10.45

Table 5 Model Analyzed

Model	Name			
	Scenario 0 (initial condition)	Scenario 1	Scenario 2	Scenario 3
without reinforcement	Height of Embankment is 36 m, slope angle 26°	Height of Embankment is increased up to 10 m from initial conditions, slope angle 26°	Height of Embankment is increased up to 10 m from initial conditions, slope angle 30°	Height of Embankment is increased up to 10 m from initial conditions, slope angle 34°
with reinforcement	-	Height of Embankment is increased up to 10 m from initial conditions, slope angle 26°, with bench geometry and reinforcement	Height of Embankment is increased up to 10 m from initial conditions, slope angle 30°, with bench geometry and reinforcement	Height of Embankment is increased up to 10 m from initial conditions, slope angle 34°, with bench geometry and reinforcement

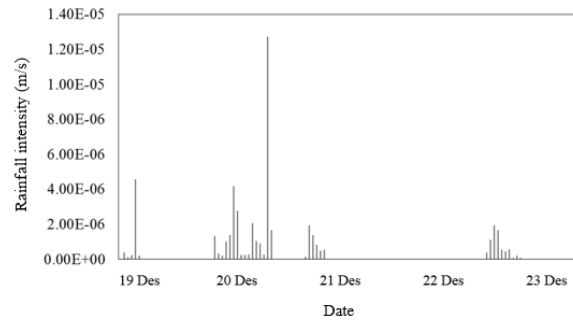


Fig. 5 Rainfall with extreme duration

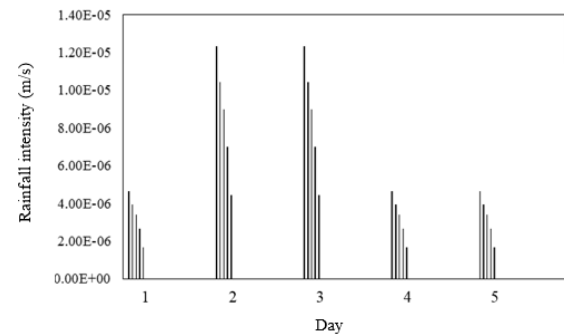


Fig. 6 Rainfall with 5 day duration

Slope Stability Analysis

In stability analysis of pile slope in Disposal Site Piyungan conducted some analysis that is slope condition without influence of water, and with influence of water. The slopes of waste piles are reviewed without changes in the geometry of the benches and slopes with the geometry of the bench. The model analyzed can be seen in Table 5.

Result Comparison of Safety Factor for Each Scenario

After analyzing each condition, then proceed by analyzing the safe number against the existing

standard. The analysis of safety factor against existing regulations according to reference number [9], [10], and [11] can be seen in Table 6.

Table 6 Control the model safety factor with reinforcement

Control the model safety factor without reinforcement								
Scenario	Safety Factor					Safety factor control		
	1	2	3	4	5	Bowles(1984) >1.25	Standard national of Indonesia >1.40	Indonesia public works ministry >1.50
Scenario 0	1.906	1.790	1.779	-	-	√	√	√
Scenario 1	1.779	1.760	1.709	-	-	√	√	√
Scenario 2	1.621	1.578	1.554	-	-	√	√	√
Scenario 3	1.416	1.386	1.386	-	-	√	-	-
Control the model safety factor with reinforcement								
Scenario 1	1.901	1.826	1.821	-	-	√	√	√
Scenario 2	1.866	1.796	1.793	1.769	1.758	√	√	√
Scenario 3	1.527	1.479	1.474	-	-	√	√	-

1 = without rain, 2 = with normal rainfall, 3 = with heavy rainfall,

4 = rain with extreme duration, 5 = 5 days rain

√ = Fullfied - = Unfullfied

CONCLUSION

Based on the analysis that has been done then it can be concluded as follows. The organic content decreased from 72.41% to 43.68%, the specific gravity increased from 1.82 to 2.05, the dry density in the field also increased from 0.43 kg/cm³ to 0.89 kg/cm³. The value of waste permeability decreased but not very significant. For shear strength parameters increased over time, where the friction angle value changed from 35.02° to 41.98° and the obtained cohesion value was 0 kPa, reduced organic level and waste density changes affecting the increase in shear strength parameters. Hydraulic conductivity gained 3.27×10^{-5} cm/s up to 4.32×10^{-5} cm/s. All test results are in accordance with the range in the existing literature.

Based on the analysis that has been done can be seen that the rain gives an effect on the stability of the slope where the rain that occurs decrease the value of the safety factor on the slope of the waste embankment. The effect of rain on the stability of waste embankment in scenario 2 of normal rainfall conditions and very heavy rain reduces the safety factor rate by 3.75% for normal rain and 3.91% for very heavy rains from conditions without rain effect, in extreme duration rain conditions can decrease the Safety factor up to 5.20%, in the event of successive rainy conditions for 5 days can reduce the safety

factor up to 5.79%.

From the analysis of the higher and steeper the embankment of waste will be reduced stability, seen from the decrease in the safety factor of each scenario, the rain proved to have an effect on the stability of the slope of waste embankment by minimizing the safety factor at the time of the rain. From the analysis it can be seen that scenario 2 is the most optimum scenario with the addition of height up to 10 m with the slope slope of 30°, the safety is still included in the existing regulation standard whether it is not rain or rain. From the analysis it can be seen that scenario 2 is the most optimum scenario with the addition of height up to 10 m with the slope slope of 30° with geometry change and gabions reinforcement, the safe number is 1.866 in the condition without rain and 1.758 in the rain condition which lasted for 5 days is still included in the existing regulatory standards either when conditions are not rain or rain. So scenario 2 is the most optimum scenario that can increase the capacity of Disposal Site Piyungan. The addition of gabions in scenario 2 does not play a direct role in maintaining the stability of the waste embankment but is needed in the implementation because it plays a role in holding waste deposits from erosion (waste material moving due to rain).

ACKNOWLEDGEMENTS

The authors express their gratitude to Universitas Gadjah Mada for financial supporting by Research Grant of Department Civil and Environmental Engineering Universitas Gadjah Mada with contract no. 597/H.1.17/TKS/PL/2017, dated April 3, 2017. The authors also would like to thanks to colleagues of Department of Civil and Environmental Engineering, UGM and government of Yogyakarta province (Balai PISAMP Dinas PUP-ESDM Pemda DIY) for their helpful.

REFERENCES

- [1] BPS-Statistic of D.I. Yogyakarta Province. (2012). *Environmental Statistics of D.I. Yogyakarta*, BPS-Statistic of D.I. Yogyakarta Province, Yogyakarta.
- [2] Bareither, Cristopher A. Benson, Craig H., edil Tuncer B., (2012), Effects of Waste Composition and Decomposition on the Shear Strength of Municipal Solid Waste. *Journal of Geotechnical and geoeviromental engineering*. ASCE. 138(10).
- [3] Hardiyatmo, H.C., (2012), *Tanah Longsor dan Erosi - Kejadian dan Penanganan*, Gadjah Mada University Press, Yogyakarta.
- [4] Lavigne, F., Wassmer, P., Gomez, C., Davies, T. A., Hadmoko, D. S., Iskandarsyah, T Yan W M, Gaillard, JC., Fort, M., Texier, P., Heng, M.B., Pratomo, I. (2014). the 21 February 2005, catastrophic waste avalanche at Leuwigajah dumsite, Bandung, Indonesia. *Geoenvironmental Disasters a SpringerOpen Journal*. 1:10.
- [5] Republic of Indonesia, (2008). *Undang-Undang No.18 tahun 2008 tentang Pengelolaan Sampah*. State Secretariat, Jakarta.
- [6] Zekkos, Dimitrios, (2008), Geotechnical Characterization. Field Measurement, and Laboratory Testing of Municipal Solid Waste, *Proceedings of the 2008 International Symposium on Waste Mechanics*, New Orleans, March 13 2008.
- [7] Zardava, K., Powrie, W. and White, J.K. (2009). "The determination of the moisture retention characteristics of waste materials using vertical drainage experiments."In: *Proceedings Sardinia 2009, 12th International Waste Management and Landfill Symposium*, S.Margherita Dipula, Cagliari, Italy. 5-10 October 2009.
- [8] Triatmodjo, Bambang. (2009). *Hidrologi Terapan*. Beta Offset. Yogyakarta
- [9] Bowles, J.E. (1984). *Physical and Geotechnical Properties of Soils, 2nd edition*. McGraw-Hill Inc, New York.
- [10] National Standardization Agency of Indonesia, (1990), *Tata Cara Perencanaan Penanggulangan Longsor*. National Standardization Agency of Indonesia. Jakarta.
- [11] Minister of Public Works of Indonesia, (2013). *Peraturan Menteri Pekerjaan Umum Republik Indonesia Nomor 03/Prt/M/2013 Tentang Penyelenggaraan Prasarana dan Sarana Persampahan Dalam Penanganan Sampah Rumah Tangga Dan Sampah Sejenis Sampah Rumah Tangga*. Ministry of Public Works of Indonesia, Jakarta.

STABILITY PERFORMANCE OF LOADING TEST FOR SHORT PILED RAFT FOUNDATION SYSTEM ON PEAT

Sajiharjo Marto Suro¹, Adnan Zainorabidin², Agus Sulaeman³ and Ismail Bakar²
¹STT-PLN, Indonesia; ²UTHM, Malaysia; ³ST-INTEN, Indonesia

ABSTRACT

A foundation system should be known its stability performance related to adequate bearing capacity and immediate settlement. Therefore a loading test is needed to ensure the stability performance of the foundation system, no exception for Short Piled Raft foundation system as well. The loading test was conducted according to ASTM Standard D 1143 - 81: Standard Test Method for Piles under Static Axial Compressive Load. This test method covers procedures for testing vertical or batter piles individually or groups of vertical piles to determine the response of a pile or pile group to a static compressive load applied axially to the pile or piles within the group, regardless of their method of installation. Based on this standard, when the foundation has no failed up to 160% of design load, the time needed for monitoring and reading the vertical movement is 62 hours nonstop. It is caused by monitoring and reading of movement at each load increment up to 1 hour with 5 – 10 minutes time interval. Whereas based on the data of loading test, the difference movement at the beginning and at the end of reading was not significant, in the range of 3% up to 15%. It was because peat has high permeability, so water could spread rapidly and made it enable skeletons became denser in the short time. Hence, there is possibility to shorten the time for monitoring and reading vertical movement at each step of load increment.

Keywords: Stability performance, Loading test, Short piled raft, Vertical movement.

INTRODUCTION

In the last few decades, many construction projects have penetrated into the problematic soil area, with some of the problems faced. Completion of construction by using a conventional foundation system such as pile foundation system is still considered to be quite expensive [1]. To overcome these problems, several foundation systems have been developed, among others, is a piled raft foundation, which the concept of this system has received considerable attention in recent years [2] and even proves to be more effective on such conditions, increasingly recognized as a foundation more economical and effective on problematic soil [3].

Moreover, especially at the peat area, the construction method on peat is different for the different depth of peat [4]. For peat with depth less than 3 m, the removal and replacement method are usually used. For the depth 3 m to 10 m, engineers normally used sand drain, lightweight fills and stone column. While for the depth more than 10 m, the suitable method is deep stabilization techniques such as pile and dynamic compaction. This condition motivates to develop a foundation that can be directly applied on peat with the depth 3 m to 10 m, neither using removal and replacement method nor soil stabilization.

In this study, a Short Piled Raft foundation system was introduced, built on peat which is known

as problematic soil. Short Piled Raft foundation system is a modified piled raft foundation system, which is a combination between pile foundation and raft foundation, with the pile length relatively shorter, and considered as a reinforced concrete slab resting on a number of piles.

Piles in piled raft foundation can be used for two reasons: To reduce total settlement in rigid raft and to reduce total and differential settlement in flexible raft [5].

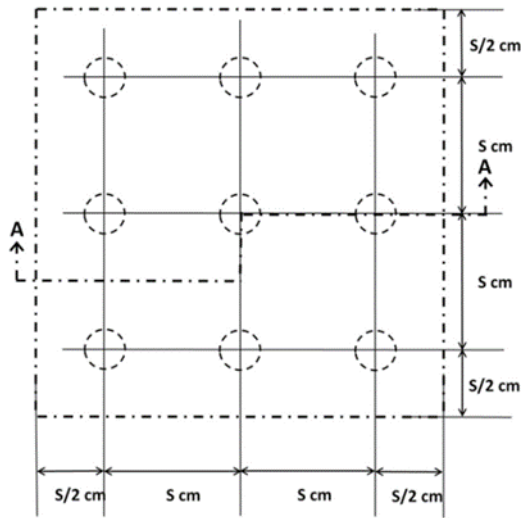
SCOPE, LIMITATION AND OBJECTIVE

The scope of this study was to observe the stability performance of a large scale model of Short Piled Raft foundation system on peat during loading test, especially related to immediate settlement. The static load acted on the center of the concrete slab.

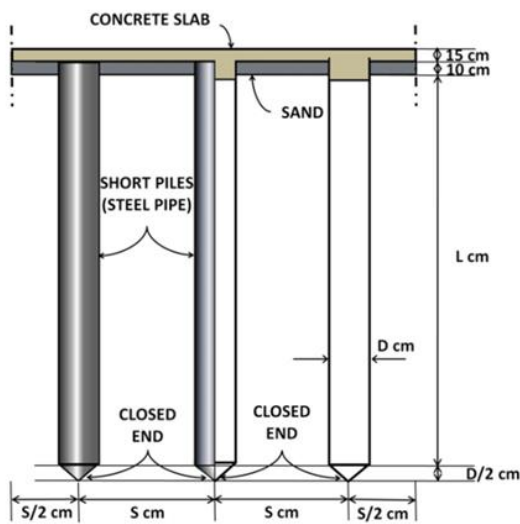
The limitation of this study was that the size of the model to be 3.0 m x 3.0 m, with 0.15 m thickness of concrete slab, piled by 9 short piles of 3.0 m length, outer diameter was 0.32 m and thickness of wall was 0.003 m. The pile was closed end galvanized steel pipe. Figure 1 shows plan and section of large scale model of Short Piled Raft foundation system with the pile spacing of 1.00 m, as optimum spacing [6] and constructed on peat with the layer thickness of 3.5 m.

While the objective of the study was to evaluate the immediate settlement and possibility to shorten the time for monitoring and reading vertical

movement at each step of load increment or decrement during loading test.



(a)



(b)

Fig. 1 Short Piled Raft Foundation System; (a) general plan; (b) cross section A-A

METHODOLOGY

Loading test was conducted according to ASTM Standard D 1143 - 81: Standard Test Method for Piles under Static Axial Compressive Load. This test method covers procedures for testing vertical or batter piles individually or groups of vertical piles to determine response of pile or pile group to a static compressive load applied axially to the pile or piles within the group, regardless of their method of installation. There are three methods of applying load, nevertheless considering that peat is very soft soil, therefore the most suitable method is the Load Applied to Pile or Pile Group by Hydraulic Jack

Acting against a Weighted Box or Platform, although still needed to be modified as shown in Fig. 2.

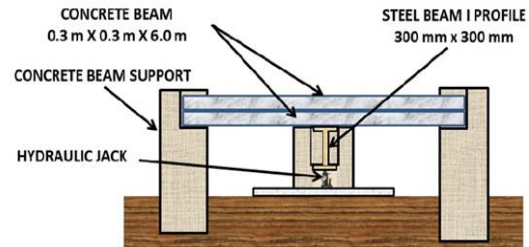


Fig. 2 Modified method of applying load for Loading Test

For conducting loading test, 16 concrete beams of 0.40 m x 0.40 m x 6.0 m were provided and laid on an I profile steel beam. Loading was carried out by jacking the steel beam at the center point of concrete slab. Location of point load and points observed shown in Fig. 3.

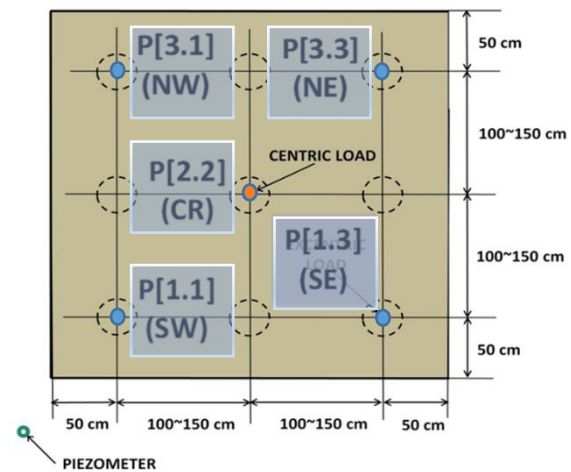


Fig. 3 Location of Point Load and Point Observed

Loading Procedure

Unless failure occurs first, loading the pile up to at least 160% of the design load, or until the settlement equals to 16% of the pile diameter. Due to the magnitude of the decline could not be precisely predicted, therefor constant time interval loading was suitable procedure to be applied. Thus, applying load increments of 20% of the design load with 1 hour between load increments and unload with 1 hour between load decrements.

Procedure of Measuring Movements

For measuring movements, a leveling instrument

(Sprinter) was used to measure some staff gauges that installed at several certain observed points, as shown in Fig. 4.

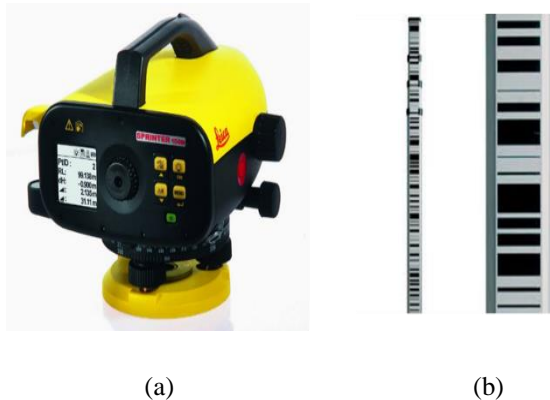


Fig. 4 Leveling instrument, (a) Sprinter and (b) staff gauge.

Before testing, no-load reading should be taken for all instruments, including staff gauge, and ground water level meter. Taking the reading of time, load and movement, and record them before and after the application of each load increment or the removal of each load decrement. Applying the load by jacking the steel beam as shown in Fig. 5.



Fig. 5 Hydraulic jack in operation during loading test

During loading, as far as the test pile group has not failed, additional readings should be taken and recorded them at intervals 5 minutes during the first ½ hour for each load increment. After the total load has been applied, as far as the test pile group has not failed, readings and record should be taken at the interval of 20 minutes during the first 2 hours and 1 hour for the next 10 hours, and 2 hours for the next 12 hours. If pile failure occurred, the readings should be taken immediately before removing the first load decrement. During unloading, readings and record should be taken at intervals of 20 minutes. A final rebound reading has been taken 12 hours after all load has been removed.

Due to the sequence of loading test should be conducted continuously, therefor conducting at the night could not be avoided, as shown in Fig. 6.



Fig. 6 Conducting loading test at the night

RESULTS AND DISCUSSIONS

Loading test was conducted by the load reached 160 kN or equal to 160% of design load (100 kN) and the foundation had no failed. It took the time of 62 hours nonstop.

The results of maximum immediate settlement was 7.60 mm under the load of 100 kN and 29.70 mm under the load of 160 kN, occurred at the center of concrete slab, less than 50 mm and still tolerable [7]. The pattern of settlement at every point observed under the load up to 100 kN at each stage of loading, as shown in Fig. 7, while for reloading under the load up to 160 kN as shown in Fig. 8.

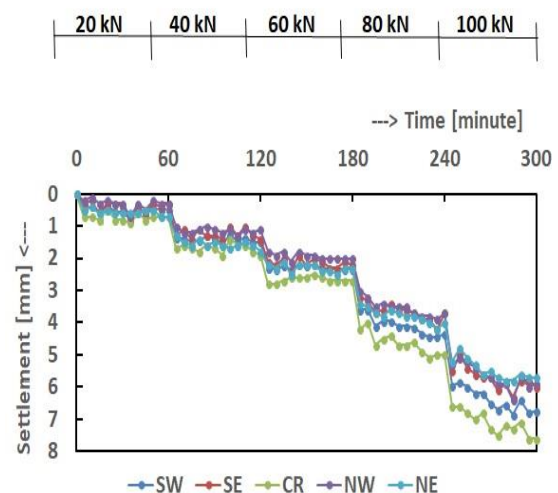


Fig. 7 Relationship between load and settlement at every phase of loading up to 100 kN.

It can be seen that the patterns of relationship between loading up to 100 kN and settlement were similar at every point, although with the different

magnitude. At the beginning of every loading, produced significant settlement then followed by small increment.

While for reloading up to 160 kN, the patterns from the beginning were also the same, but after the load of 120 kN, the patterns became steeper.

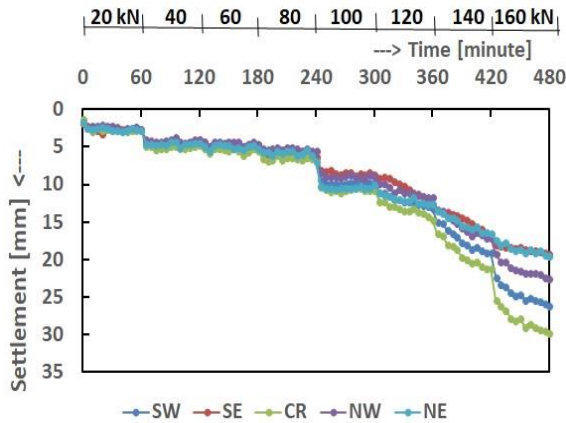


Fig. 8 Relationship between load and settlement at every phase of reloading up to 160 kN.

Relating to unloading phases, the results at every point observed under the load from 80 kN decreased to 0 kN at each stage of unloading, as shown in Fig. 9, while for unloading from 140 kN decreased to 0 kN as shown in Fig. 10.

Furthermore for unloading from 80 kN, the patterns at the beginning were relatively gentle and after the load of 20 kN were little bit steeper.

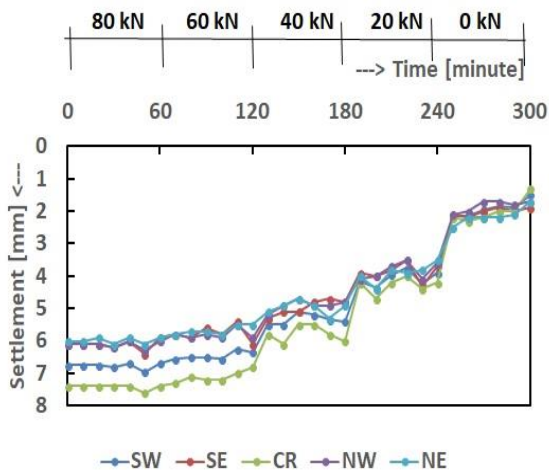


Fig. 9 Relationship between load and settlement at every phase of unloading from 80 kN.

As well as for unloading from 140 kN, it seemed that at the beginning, the patterns were very gentle up to 80 kN, after that the patterns became relatively steeper.

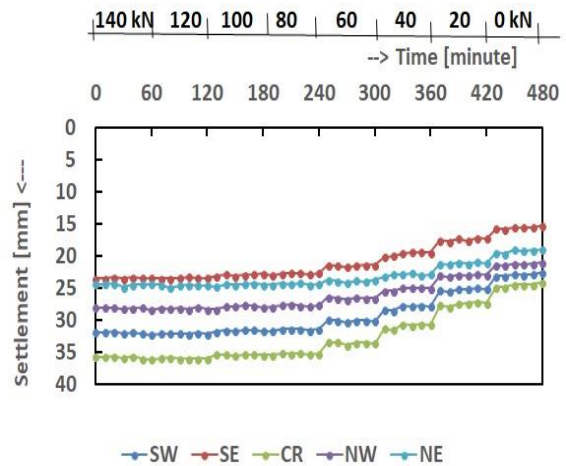


Fig. 10 Relationship between load and settlement at every phase of unloading from 140 kN.

Besides that, the movement of each point at every step of reading along its duration was very gentle, except at the beginning of changing the load. It was because peat had high permeability, so the water could spread rapidly and made it enable skeletons became denser in the short time [8].

In order to get a better understanding, point at the center (CR) was selected, arguing that point at the center was exactly under the load and faced the largest settlement. Afterward the reading time was reduced to be 50% of the original duration and the result was tabulated in Table 1. The settlements recorded were not changing significantly, with the range of 3% to 15%. Figure 11 shows that the pattern of settlement recorded by 50% duration reading time has a good agreement with the pattern of settlement recorded by 100% or original based on ASTM D 1143 – 81 [9] duration reading time. Therefore, shortening the duration of reading time is possible, as far as related to vertical movement monitoring only.

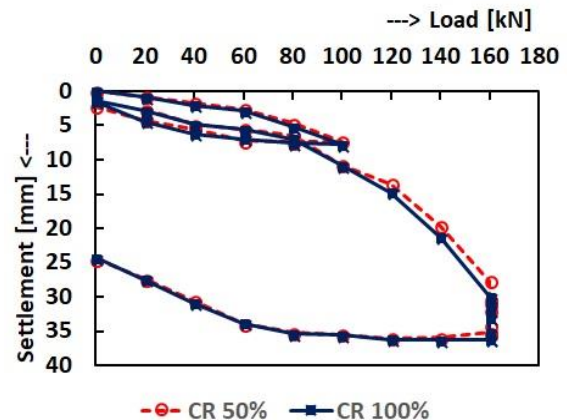


Fig. 11 Relationship between load and settlement at point CR with different duration of reading.

Table 1. Relationship between load and settlement at point CR based on original and shortened reading time

Phase	Duration [minute]	Load [kN]																	
		0		20		40		60		80		100		120		140		160	
		Settlement [mm] and difference reading [%]																	
Loading	30	-	-	0.70	14.29	1.70	10.53	2.60	3.70	4.70	6.00	7.30	3.95	-	-	-	-	-	-
	60	-	-	0.80		1.90		2.70		5.00		7.60		-	-	-	-	-	-
Unloading	30	2.30	15.00	4.20	0.00	5.50	8.33	7.20	5.88	7.40	0.00	-	-	-	-	-	-	-	-
	60	2.00		4.20		6.60		6.80		7.40		-	-	-	-	-	-	-	-
Reloading	30	-	-	2.70	0.00	4.00	4.26	5.50	1.85	6.40	5.88	10.80	0.93	13.50	7.53	19.70	6.64	27.70	6.73
	60	-	-	2.70		4.70		5.40		6.80		10.70		14.00		21.10		29.70	
Unloading	30	24.50	1.66	27.40	0.37	30.60	0.33	33.90	0.89	35.20	0.00	35.50	0.28	36.00	0.00	35.90	0.55	-	-
	60	24.10		27.30		30.70		33.60		35.20		35.40		36.00		36.10		-	-

CONCLUSION

The objective of the study was to evaluate the immediate settlement and possibility to shorten the reading time for loading test of Short Piled Raft foundation system.

Based on the discussion, it can be concluded as follows.

1. The loading test of Short Piled Raft foundation system reached the load up to 160 kN or 160% of design load, shown that maximum immediate settlement was 7.60 mm under the load of 100 kN and 29.70 mm under the load of 160 kN, occurred at the center of concrete slab, less than 50 mm and still tolerable.
2. Shortening the duration of reading at every step of loading during loading test of Short Piled Raft foundation system on peat will not affect significantly to the reading of settlement produced. Therefore, shortening the duration of reading time is possible, as far as related to vertical movement monitoring only.

ACKNOWLEDGEMENTS

The research work reported in this paper was funded by Contract Research Grant U260 ORICC, Universiti Tun Hussein Onn Malaysia (UTHM).

The authors wish to express their gratitude to RECESS - UTHM and Geomatic Engineering Laboratory, FKAAS - UTHM in providing the equipments during carrying out this research.

REFERENCES

- [1] Effendi, S., Cakar Ayam Soft Foundation System Revisited. Soft Soil Engineering

International Conference 2013, Kuching, Sarawak, Malaysia, 2013.

- [2] Prakoso, W. A. and Kulway, F. H., Contribution To Piled Raft Foundation Design. Journal of Geotechnical and Geoenvironmental Engineering, 2001, pp.17-24.
- [3] Srilakshmi, G. and Moudgalya, D., Analysis of Piled Raft Foundation Using Finite Element Method. International Journal of Engineering Research and Science & Technology, Vol. 2, No. 3, 2013, pp.89-96.
- [4] Bakar, I., Challenges in Peat Soil Research - Malaysian Experiences. South East Asia Conference on Soft Soils Engineering and Ground Improvement, Bandung, 2014.
- [5] Patil, J. D., Vasanvala, S. A., Solanki, C. H., A Study on Piled Raft Foundation: State of Art, International Journal of Engineering Research & Technology (IJERT), 2013, pp.1464-1470.
- [6] Suro, S. M., Bakar, I. and Sulaeman, A., Pile Spacing Optimization of Short Piled Raft Foundation System for Obtaining Minimum Settlement on Peat, IOP Conference Series: Materials Science and Engineering, Volume 136, Conference 1, 2016.
- [7] Das, B. M., Principles of Foundation Engineering, Seventh Edition, Cengage Learning, 2011

- [8] Huat, B. B. K., Prasad, A., Asadi, A. and Kazemian, S., *Geotechnics of Organic Soils and Peat*. CRC Press/Balkema, 2014, pp. 10-11.
- [9] ASTM, Standard Test Method for Piles Under Static Axial Compressive LOAD, Designation D 1143 – 81 (Reapproved 1994).

ASSESSING THE ULTIMATE BEARING CAPACITY OF FOOTING IN A TWO-LAYERED CLAYEY SOIL SYSTEM USING THE RIGID PLASTIC FINITE ELEMENT METHOD

Kazuhiro KANEDA¹, Masamichi AOKI¹ and Satoru OHTSUKA²

¹Researcher, Takenaka Corporation, Japan; ²Professor, Department of Civil and Environmental Engineering
Nagaoka University of Technology, Japan

ABSTRACT

Ultimate bearing capacity formulae for foundations are specified in the guideline published by the Architectural Institute of Japan for design of building foundations. The rigid plastic finite element method was developed by Tamura and Ohtsuka to estimate the ultimate bearing capacity of footing. Unlike deformation analysis, this method employs limited soil constants; it uses only the strength parameters of cohesion c and friction angle ϕ as it considers the limit state directly and disregards the deformation of the building and ground. A series of rigid plastic finite element analyses was conducted to compare the ultimate vertical and inclined bearing capacities of spread foundations between the simulation results and the theoretical formula for a two-layered clayey soil system. The change in failure mode of the ground was discussed using the geometrical ratio between the width of the footing and the height of the surface layer. The strength ratio of the surface and second ground layer was clearly shown to affect the formation of failure mode. The applicability of the rigid plastic finite element method for the assessment of the ultimate bearing capacity of a two-layered clayey soil system was successfully demonstrated.

Keywords: Two-layered clayey soil, Ultimate bearing capacity, Rigid plastic finite element method, Vertical and inclined load

INTRODUCTION

The calculation of the ultimate bearing capacity of soil is important when designing a building (Terzaghi et al., 1967). The ultimate bearing capacity formulae for building foundations are specified in the guideline published by the Architectural Institute of Japan (AIJ, 2001). These formulae were based on experiments as well as theoretical considerations with regard to risk avoidance. However, the vertical bearing capacity of two-layered clayey soil has not been adequately investigated. In this research, the vertical bearing capacity of two-layered clayey soil was analyzed using numerical simulations. The bearing capacity under squeeze breakdown of clayey soils was last discussed at GEOMATE2017 (Kaneda et.al, 2017). In this case, while the soil was assumed to be two-layered, the lower clay layer was very stiff compared to its upper counterpart. Thus, shear failure occurs in the upper clay layer. In this research, it is assumed that the strengths of the upper and lower clay layers are relatively similar. Shear failure in both the upper and lower clay layers was considered. Moreover, the inclined bearing capacity was investigated in specific cases. First, the bearing capacity of the two-layered clayey soil was simulated (Kaneda et al., 2013, 2018), and subsequently, the associated inclined bearing capacity was discussed. The

analysis uses the rigid plastic finite element method (RPFEM), which was developed separately by Tamura and Ohtsuka (Tamura et al., 1984; Asaoka and Ohtsuka, 1986). This method was employed to estimate the ultimate bearing capacity of footing. The Drucker–Prager yield function was adopted as the soil constitutive equation, and associate and non-associate flow rules were introduced to establish the configuration relationship of the ultimate state. Hoshina et. al.(2012)(Nguyen, Du L.. et.al., 2015, 2016) applied higher order soil constitutive equation. Using this method, the structural safety assessment or calculation of soil bearing capacity was evaluated. A characteristic of this method is that, in contrast with deformation analysis, it applies limited soil constants; it uses only strength parameters such as cohesion and friction angle, because it addresses the limit state directly by disregarding the deformation of the building and ground. Since the RPFEM uses the upper bound theorem of plastic theory, the end result is slightly larger than the true value.

SIMULATIONS OF VERTICAL BEARING CAPACITY OF TWO-LAYERED CLAYEY SOIL

**Review of the bearing capacity of two-layered
clayey soil**

This research considers two key parameters. The first is B/H , where B is the foundation width and H is the height of the upper clayey soil. The other is c_{u2}/c_{u1} , where c_{u1} and c_{u2} are the shear strength of the upper and lower clayey soil, respectively. The vertical bearing capacity of two-layered clayey soil was reported by Vesic (1975) as follows.

1. $c_{u1} > c_{u2}$: Calculate the vertical bearing capacity by applying the distributed fracture mode.
2. $c_{u1} \ll c_{u2}$: Calculate the vertical bearing capacity by squeeze breakdown of clayey soils.
3. $c_{u1} < c_{u2}$: Calculate the vertical bearing capacity by interpolation between the results from the above two methods.

In the case of $c_{u1} < c_{u2} < \infty$, the vertical bearing capacity is calculated as follows.

$$q_f = c_{u1}N_m + \gamma_t D \quad (1)$$

q_f (kPa) is the vertical bearing capacity, γ_t (kN/m^3) is the unit weight, and N_m is as seen in figure 1. D (m) is the penetration depth.

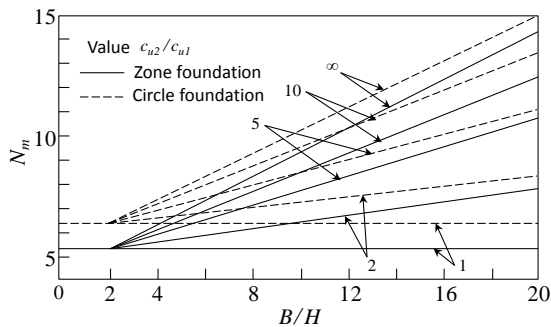


Fig. 1 Bearing capacity of two-layered clayey soils (after Yamaguchi, 1982)

Numerical conditions

Figure 2 shows the numerical meshes for a plain strain condition. Figure 2(a) shows that the mesh is 200 m wide, and the depth of the upper layer is 15 m while that of its lower layer is 35 m. The foundation width was set to 30 m ($B/H = 2$). Figure 2(b) shows that the mesh is 390 m wide, and the depths of the upper and lower layers are 5 m and 95 m, respectively. The foundation widths were thus set to 18, 30, 42, 50, 78, and 102 m ($B/H = 3.6-20.4$). In the RPFEM, the numerical mesh only needs to be set within the failure mode. The required conditions for the numerical meshes are satisfied with Figure 2. The strength of the upper clay layer was set to $c_{u1} = 10$ kPa, while that of the lower clay layer was set to $c_{u2} = 12, 15, 20, 30, 50, 75$, and 100 kPa. The strength of the foundation was set to $c = 100,000$ (kPa), assuming a rigid foundation.

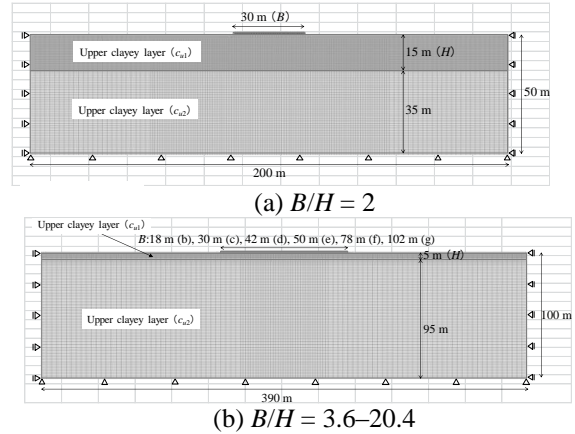


Fig. 2 Numerical meshes

Numerical results

Numerical simulations were conducted for $c_{u1} < c_{u2} < \infty$. Table 1 shows the results of c_{u2}/c_{u1} for different values of B/H . Figure 3 shows the relationship between N_m and B/H as per figure 1. In figure 1, N_m increases as B/H increases. Moreover, the larger the value of c_{u2}/c_{u1} , the larger the slope of B/H with respect to N_m . Figure 3 shows that as B/H increases, N_m also increases. However, for small values of c_{u2}/c_{u1} , the increase in N_m is not observed, and N_m approaches a constant value. This tendency becomes increasingly prominent as c_{u2}/c_{u1} decreases.

Table 1 Variation in N_m as per c_{u2}/c_{u1} and B/H

B/H	c_{u2}/c_{u1}						
	1.2	1.5	2.0	3.0	5.0	7.5	10.0
2.00	5.55	5.48	5.40	5.39	5.39	5.39	5.39
3.60	5.94	6.49	6.45	6.35	6.34	6.34	6.34
6.00	6.12	7.09	8.05	7.81	7.74	7.74	7.74
8.40	6.28	7.36	8.84	9.50	9.27	9.20	9.20
10.00	6.25	7.46	9.25	10.88	10.23	10.20	10.19
15.60	6.33	7.69	9.74	12.94	14.12	13.86	13.83
20.40	6.27	7.66	9.84	13.55	18.15	17.06	16.87

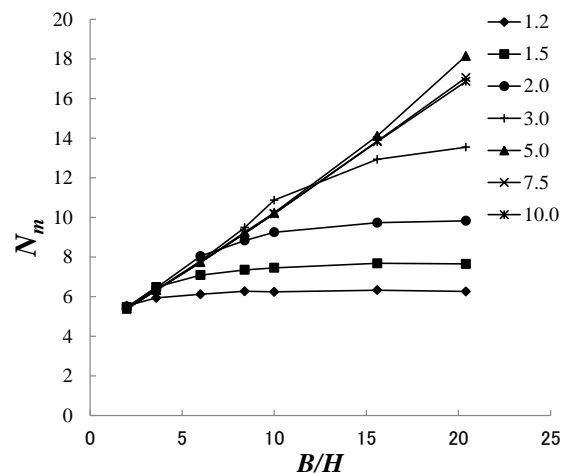


Fig. 3 Relationship between N_m and B/H

Figure 4 shows the shear strain contours at failure for $B/H = 3.6$ and 15.6, and $c_{u2}/c_{u1} = 3$. The red line marks the boundary between the upper and lower clayey soil layer. When $B/H = 3.6$, the

squeeze breakdown mode of clayey soils was observed. On the other hand, when $B/H = 15.6$, the whole failure mode, including the lower clayey layer, was observed. When B/H is relatively small, the squeeze breakdown of clayey soils occurs because the strength of the lower clayey layer is higher than that of the upper layer. On the other hand, when B/H is larger, whole failure occurs. In the case of squeeze breakdown of clayey soils as B/H increases, N_m increases linearly, as shown in figure 1. Conversely, it is clear that when whole failure occurs, even if B/H increases, the increase in N_m will cease.

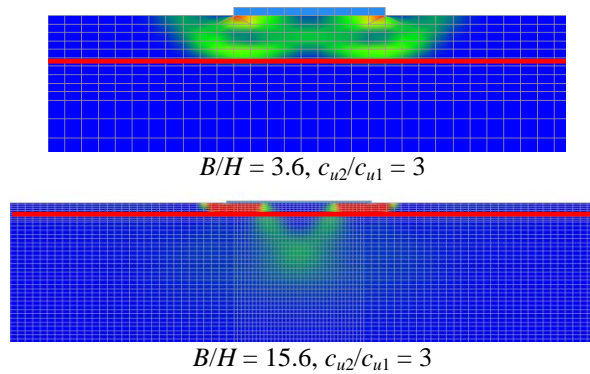


Fig. 4 Shear strain contours

Figure 5 shows the shear strain contours at failure for $B/H = 10.0$ and 15.6 , and $c_{u2}/c_{u1} = 7.5$ and 10.0 . All failure modes show squeeze breakdown of clayey soils, and the vertical bearing capacity was calculated using the following equation (Meyerhof and Chapin, 1953).

$$q_f = 4.14c_u + \frac{c_u B}{2H} \quad (2)$$

where q_f , c_u , B , and H are the ultimate bearing capacity of squeeze breakdown (kN/m^2), undrained strength (kN/m^2), foundation width (m), and height of the clay layer (m), respectively. The bearing capacity during squeeze breakdown of clayey soils is a function of c_u (c_{u1} : strength of the upper clayey layer) and B/H , as seen in equation (2). When the strength of the clay was constant, the bearing capacity of squeeze breakdown in clayey soils follows a linear relationship with B/H .

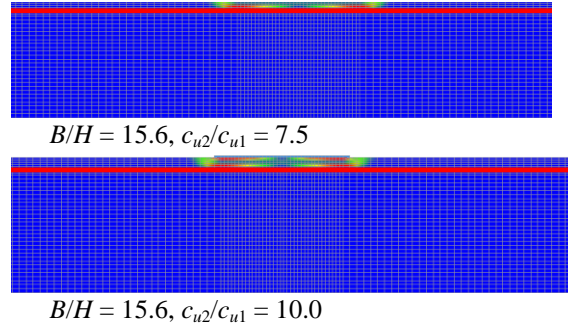
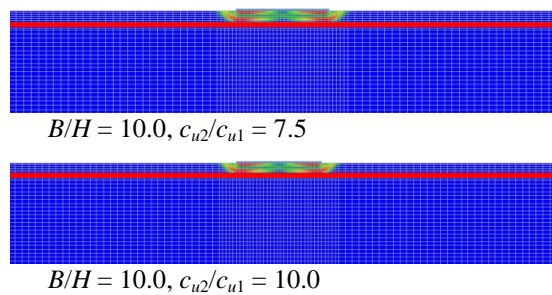


Fig. 5 Shear strain contours

Remarks

Vesic (1975) concluded the following. When the strength of the lower clayey soil reaches ∞ , squeeze breakdown occurs, and the vertical bearing capacity increases linearly in relation to B/H . When the ratio between the upper and lower clayey soil strength (c_{u2}/c_{u1}) exceeds 10.0, whole failure (including the lower clayey layer) takes place. However, using the RPFEM, the threshold for the squeeze breakdown of clayey soils and whole failure, including that of the lower clayey layer, is 3 ($c_{u2}/c_{u1} > 3.0$). Comparing figures 1 and 3 with regard to the slope between N_m and B/H , the formula proposed by Vesic provides a different result, that is, lower than the numerical results of this study. This can be attributed to the factor of safety in design. However, when $c_{u2}/c_{u1} > 3.0$, the vertical bearing capacity corresponds to the upper limit for B/H , and thus, it is clear that the method proposed by Vesic for bearing capacity calculations may result in a dangerous design.

SIMULATIONS OF THE VERTICAL BEARING CAPACITY OF TWO-LAYERED CLAYEY SOIL WITH AN INCLINED LOAD

The simulations for bearing capacity were also performed with an inclined load. They were conducted for three inclined angles (10° , 20° , and 30°) at $B/H = 2.0$ and 20.0 , and $c_{u2}/c_{u1} = 1.2$ and 10.0 . The numerical mesh and conditions are the same as those in figure 2.

Numerical results

Figure 6 shows the relationship between the inclined angle and N_m at $B/H = 2.0$ and $c_{u2}/c_{u1} = 1.2$ and 10.0 . The theoretical bearing capacity (Th) was calculated following equation (3), as proposed by AIJ (2001) for $c_u = 1.0$ (upper clayey layer strength) and 1.2 (lower clayey layer strength).

$$q_f = c \times i_c \times \alpha \times N_c \quad (3)$$

where q_f , i_c , α , and N_c are the ultimate bearing capacity (kN/m^2), correction factor of the inclined load ($i_c = (1 - \theta/90)^2$), (θ : inclined angle ($^\circ$)), shape coefficient ($= 1.0$), and coefficient of bearing capacity ($= 5.1$ at $\phi = 30^\circ$), respectively.

Figure 7 shows the shear strain contours at failure for $B/H = 2.0$, $c_{u2}/c_{u1} = 1.2$ and 10.0 , and angle = 0° and 30° . At $c_{u2}/c_{u1} = 1.2$ and inclined angle = 0° , the simulation provides values for N_m between those for $c_u = 1.0$ (Th) and $c_u = 1.2$ (Th). As the inclined angle increases, the simulated value of N_m approaches the theoretical value of N_m at $c_u = 1.0$ (Th). At $c_{u2}/c_{u1} = 10.0$ and inclined angle = 0° , the effect of c_{u2}/c_{u1} is not evident as B/H is small. Therefore, shear failure of the upper clayey soil layer occurs (shown fig.7(a, c)). However as the inclined angle increases, the failure mode changes from total wedge failure to slip failure for the upper clayey soil layer (shown fig.7(b, d)). Therefore, for larger inclined loads, the simulated bearing capacity approaches the bearing capacity calculated using the strength of the upper clayey layer of soil.

Figure 8 shows the relationship between the inclined angle and N_m at $B/H = 20.0$ and $c_{u2}/c_{u1} = 1.2$ and 10.0 . Figure 9 shows the shear strain contours at failure for $B/H = 20.0$, $c_{u2}/c_{u1} = 1.2$ and 10.0 , and inclined angle = 0° and 30° . At $c_{u2}/c_{u1} = 1.2$ and inclined angle = 0° , the simulated value of N_m lies between the N_m at $c_u = 1.2$ (Th). The failure mode in figure 9(a) indicates that the strength of the lower clayey layer plays a dominant role in bearing capacity. As the inclined load increases, the simulated values of N_m approach the theoretical values of N_m at $c_u = 1.0$ (Th) because of the slip failure mode of the upper clayey soil layer (shown in fig.9(b)). At $c_{u2}/c_{u1} = 10.0$ and inclined angle = 0° , the simulated value of N_m is 16.9. From equation (2), the vertical bearing capacity during squeeze breakdown is 14.1, and thus, the numerical result is slightly larger than theoretical value. As the inclined load increases, simulated value of N_m approaches the theoretical value of N_m at $c_u = 1.0$ (Th). This is due to the slip failure of the upper clayey soil layer, in a manner similar to that described above (shown in fig.9(d)).

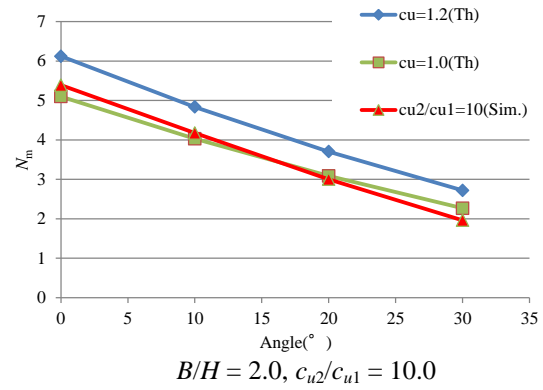
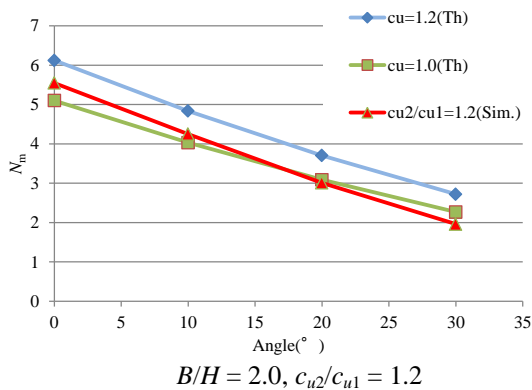


Fig. 6 Relationship between inclined angle and N_m

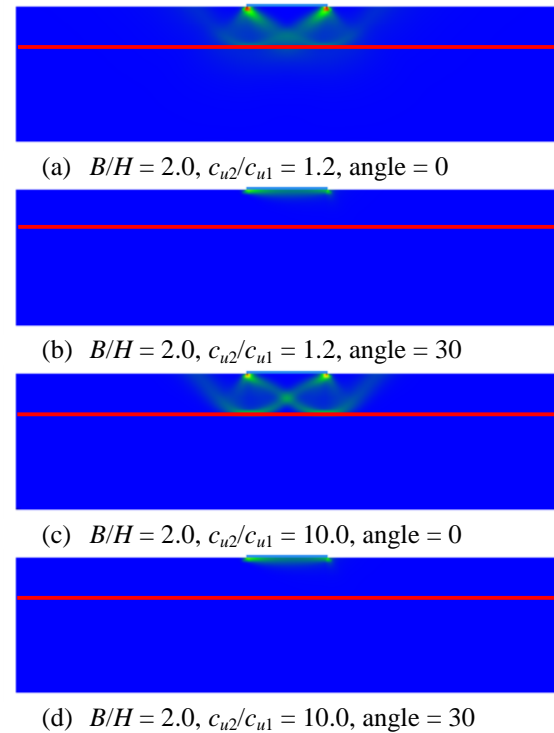
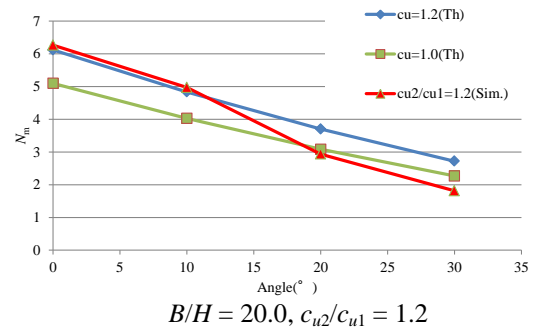


Fig 7. Shear strain contours



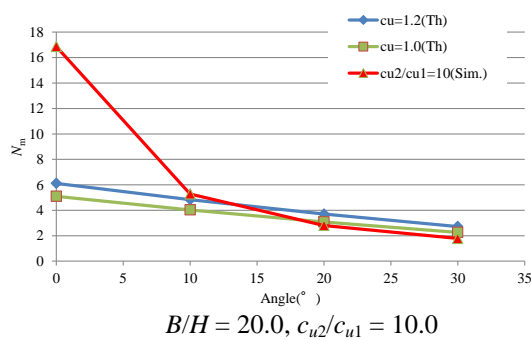
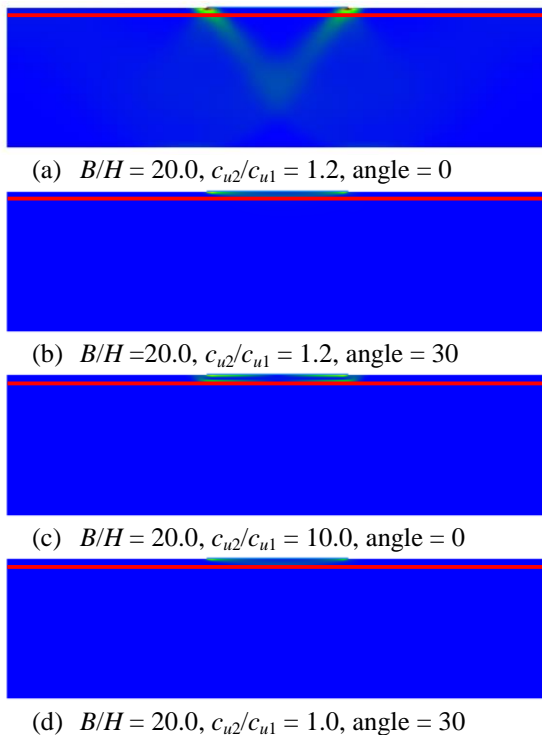
Fig. 8 Relationship between inclined angle and N_m 

Fig. 9. Shear strain contours

CONCLUSION

Numerical simulations of the vertical bearing capacity of a footing in a two-layered clayey soil system were conducted using the RPFEM. When c_{u1} (strength of the lower clayey layer) $< c_{u2}$ (strength of the upper clayey layer) $< \infty$, failure occurs across both soil layers. The greater the values of B/H (B : foundation width, H : height of the upper clayey soil) and c_{u2}/c_{u1} , the greater the bearing capacity. When squeeze breakdown failure occurs, the bearing capacity increases linearly with respect to B/H . On the other hand, when c_{u2}/c_{u1} is small, the increase in bearing capacity levels off, reaching a constant value despite the increase in B/H . The result shows that this tendency is more prominent as c_{u2}/c_{u1} becomes smaller, and the bearing capacity becomes constant with a smaller B/H . In the case of $c_{u2}/c_{u1} > 3.0$, the whole failure mode with upper and lower clayey soil

layer occurred from the squeeze breakdown failure mode. Thus, the findings proved that the bearing capacity calculation method proposed by Vesic (1975) is inadequate and can result in an unsafe design. In the case of inclined loads, when the inclined load was larger, the simulated bearing capacity approached the value of the bearing capacity calculated for the upper layer of clayey soil; for large inclined angles, the slip failure mode occurs in the upper layer of the clayey soil. Thus, the applicability of the RPFEM for the assessment of the ultimate bearing capacity of a two-layered clayey soil system is successfully demonstrated.

REFERENCES

- [1] Asaoka, A. and Ohtsuka, S.: "The analysis of failure of a normally consolidated clay foundation under embankment loading", Soils and Foundations, Vol.26, No.2, pp.47-59, 1986.
- [2] Architectural Institute of Japan, AIJ (1988, 2001), Recommendations for design of building foundation, pp.105-111, 2001. (in Japanese)
- [3] Hoshina, T., Ohtsuka, S. and Isobe, K., Ultimate bearing capacity analysis of ground by rigid plastic finite element method taking account of stress dependent non-linear strength property, Journal of JSCE, Ser.A2 (Applied Mechanics), Vol.68, No.2 I_327-I_336, 2012. (in Japanese)
- [4] Kaneda, K., Tanikawa, T., Hamada, J., Ohtsuka, S., and Aoki, M.: "Analysis of ultimate bearing capacity of footing of two layered clayey soil system by rigid plastic finite element method", AIJ Journal of Technology and Design, Vol.19, No.43, pp. 881-885, 2013. (in Japanese)
- [5] Kaneda, K., Aoki, M., Tanikawa, T., and Ohtsuka, S.: Ultimate vertical bearing capacity of clayey footing under squeeze breakdown using rigid-plastic finite element method, Seventh International Conference on Geotechnique, Construction Materials and Environment, Mie, Japan, Nov. 21-24, 2017, ISBN: 978-4-9905958-8-3 C3051.
- [6] Kaneda, K., Aoki, M., and Ohtsuka, S.: Ultimate vertical bearing capacity of spread foundation on sandy soils using rigid plastic finite element method, Numerical Analysis in Geotechnics – NAG2018, Ho Chi Minh City, Vietnam, 22nd March 2018.
- [7] Nguyen, Du L., Ohtsuka, S., Hoshina, T. and Isobe, K., Discussion on size effect of footing in ultimate bearing capacity of sandy soil using rigid plastic finite element method. Soils and Foundations. 56 (1), 93-103, 2016.
- [8] Nguyen Du L., Ohtsuka S., and Kaneda K.: Ultimate bearing capacity of footing on sandy soil against combined load of vertical horizontal and moment loads. GEOMATE2015, 2015.

- [9] Tamura, T., Kobayashi, S., and Sumi, T.: "Limit analysis of soil structure by rigid plastic finite element method", *Soils and Foundations*, Vol.24, No.1, pp.34-42. 1984.
- [10] Terzaghi, K. and Peck, R.B.: *Soil Mechanics in Engineering Practice*, John Wiley & Sons, pp. 472-569. 1967.
- [11] Yamaguchi, H.: Theory and applications of bearing capacity and deformation of shallow foundation, *Soil Japanese Society of Soil Mechanics and Foundation Engineering*, No.2, pp.85-91, 1982. (in Japanese)
- [12] Meyerhof, G.G. and Chaplin, T.K.: "The compression and bearing capacity of cohesive layers", *British Journal of Applied Physics*, Vol.4, No.1, 1953.
- [13] Vesic, A.S., : *Bearing Capacity of Shallow Foundation*, *Found. Engineering* ed. by Winterkorn & Fung, van Nostrand Reinhold, 1975.

SETTLEMENT BEHAVIOUR OF PARIT NIPAH PEAT UNDER STATIC EMBANKMENT

Adnan Zainorabidin¹, Mohamad Niizar Abdurahman², Azman Kassim³, Mohd Firdaus Md DanAzlan⁴ and
Siti Nooraiin Razali⁵

^{1,4} Faculty of Civil and Environmental Engineering / Research Center for Soft Soil (RECESS),
Universiti Tun Hussein Onn Malaysia, Malaysia;

² Public Works Department, Malaysia

³ Faculty of Civil Engineering, Universiti Teknologi Malaysia, Malaysia;

⁵ Center for Diploma Studies, Universiti Tun Hussein Onn Malaysia, Malaysia

ABSTRACT

Peat is considered as a very challenging soil when constructing any structure. It's known with high compressibility, high moisture content, low shear strength and long term settlement when subjected to load. These characteristics always posed constant problem for sustainable construction on peat. This study aims to investigate the settlement behaviour of peat fortified with concrete slab under embankment loading through full scale testing at Parit Nipah, Johor, Malaysia. The peat is categorized as hemic with moisture content greater than 500%. A concrete raft sized 3.6 m x 3.6 m with thickness of 150 mm was built on the site. The 3.6 m x 3.6 m slab was subjected to non-uniform loading. Results indicated that the installation of slab on peat able to reduce the settlement of peat under embankment loading. The study shows potential to mitigate or reduce long term post construction settlement on peaty ground.

Keywords - Peat, Concrete slab, Embankment, Settlement

INTRODUCTION

Geotechnical properties of foundation soil such as shear strength and compressibility of the soil are significant for construction of stable civil engineering structures [1]. Peat is defined as partially decaying vegetation remains amassed under saturated surroundings and in the absence of oxygen [2]. Approximately 143,974 ha of land in Johor is covered with peat [3]. High compressibility of peat due to high void ratio, results in higher values of compression index, C_c and secondary compression, C_{α} compared to other types of soil [5]. According to Ibrahim [10], the void ratio, e_0 for peat reported up to 25 and compression index, C_c value for tropical peat can be up to 10 compared to clay which is only between 0.2 to 0.8. Such attributes of peat pose undesirable challenges to the engineers in the field of construction [1].

Various construction methods and innovative approaches have been developed to mitigate settlement of structures on peat [1]-[2]. According to Ibrahim [10], the construction methods on peat can be categorized into two aspects – (1) construction by removal of peat and (2) construction by peat left in place. Construction by peat left in place is carried out by modifying the ground using different techniques to increase the soil strength and thus making it sustainable to support the intended construction [10]. Five construction techniques under the peat left in

place method are accelerating consolidation, ground improvement, stabilization, load modification and piling [10] & [13].

The concrete raft foundation is categorized under load modification techniques. It is also considered as a floating foundation [10]. Munro [13] stated that, concrete rafts have been used successfully in Ireland and Scotland from the 1920's through to the 1950's. Concrete rafts can perform effectively by reducing the total and differential settlement of a foundation by decreasing the net applied load by excavation [14]. Table 1 lists the advantages of concrete raft construction. Concrete rafts are still in service over a deep blanket of bog deposits in Northern Scotland providing a stable load bearing platform for modern traffic [13].

Table 1 Advantages of concrete raft techniques [13]

Technique	Advantage
Concrete Raft	<ul style="list-style-type: none">• Limited site disturbance.• Provides long term stiff foundation for the embankment.• Aids stability.• Reduce differential settlements and lateral stress on the peat land surface.• Minimizes need for embankment fill material.



Fig. 1 Concrete raft used as a floating housing road in the Netherlands [13]

MATERIAL AND EXPERIMENTAL METHOD

The study was carried out at Parit Nipah, Johor, Malaysia. The thickness of peat at the study location is about 4 m and the ground water table is found at less than 1m from the ground surface. Underlying this layer is silty clay. Peat samples collected from the site and tested in the laboratory to determine the index properties of Parit Nipah peat (PNpt). As shown in Table 2, the index properties test results of PNpt are within the range as reported by [6]-[9]. The PNpt is categorized as Hemic peat according to fiber content percentage and Von Post scale.

Table 2 Index properties of Parit Nipah peat

Parameter	Parit Nipah Peat	Range [6]-[9]
Moisture Content, %	635	236-784
Liquid Limit, %	252	220-417
Specific Gravity, G_s	1.34	1.27-1.56
Bulk Density, kN/m^3	10.45	7.95-11.5
Organic Content, %	95.5	78.77-95.44
Fiber Content, %	37.8	40.97-63.77
Von Post Scale	H6	H5-H6

Field Test and Monitoring

Figure 2 shows concrete raft built on site sized 3.6 m x 3.6 m x 0.15 m subjected to non-uniform load.



Fig. 2 Setting up of raft for non-uniform loading

Embankment construction was done using sand in stages as shown in Table 3. The final loading applied on the raft was 10 kPa [4], [12] & [16]. The sand was packed in heavy-duty plastic bags with fixed weight of 20 kg.

Table 3 Multi-stage loading for non-uniform embankment

Stage	Mass, kg	Stress, kPa
Concrete Slab	4665.6	3.53
1 st Layer Sand	2880.0	2.18
2 nd Layer Sand	2640.0	2.00
3 rd Layer Sand	2400.0	1.82
4 th Layer Sand	2160.0	1.64
5 th Layer Sand	1920.0	1.45
6 th Layer Sand	1212.0	0.92

Instrumentation

The vertical settlement (displacement) of soil was monitored using geodetic surveying method. TOPCON AT-B4 auto level equipment was used to measure the settlement value with accuracy up to 0.001 m. Special settlement gauge staffs which are light and can withstand any weather conditions were developed and used in this study. Nine settlement gauge staffs were installed on the concrete raft and eight settlement gauge staffs installed on the ground surrounding the raft. Figure 3 illustrates the layout of instrumentations installed on site. The reading of the settlement and pore water pressure after application of load monitored and recorded every two hours during daylight (from 8 am till 6 pm) every day. The next layer of embankment load only added to the previous layer when the settlement readings were stable for more than 24 hours. Stable reading is considered achieved when the settlement reading is constant for at least 24 hours. This process repeated until the final layer of embankment load was completed.

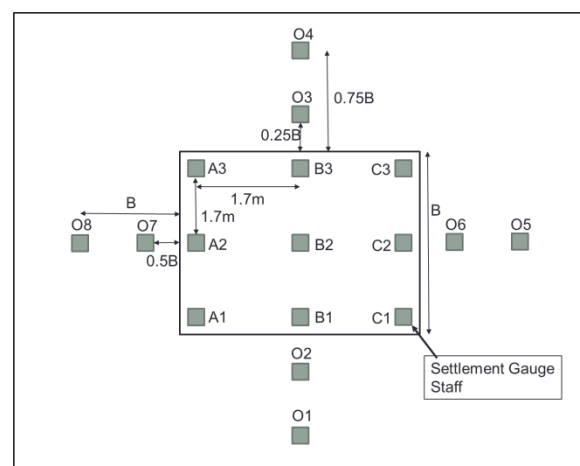


Fig. 3 Layout of instrumentation at site

RESULT ANALYSIS AND DISCUSSIONS

The average total settlement of the concrete raft measured for the duration of 75 days reaches 83.5 mm. As indicated in figure 4, the highest settlement rate was detected at point A3 measuring 104 mm, whereas the lowest settlement reading recorded at point C1 gauging 63 mm. After the end of embankment construction at 1468 hours, average settlement post construction recorder until 1786 hour was 9 mm. This is in line with the behavior of peat where it is susceptible to long term post construction settlement [17].

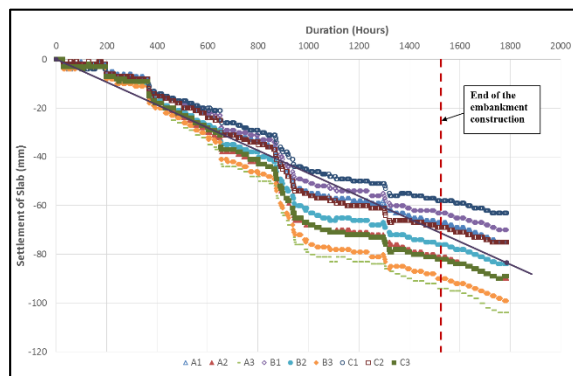


Fig. 4 Measured total settlements on the concrete raft

The settlement value of the concrete raft according to the load imposed is shown in Table 4. Due to the embankment loading, the raft is found to be tilting in the direction of point A3. Albeit tilting towards point A3, it is observed that the raft experience settlement at all points.

Table 4 Settlement value of concrete raft

Point	Load (kPa)					
	2.18	4.18	6.00	7.64	9.09	10.0
Settlement (mm)						
A1	2	8	25	36	58	75
A2	3	10	32	45	72	90
A3	3	11	37	52	84	104
B1	3	8	23	34	55	70
B2	3	10	29	42	67	83
B3	4	11	34	49	80	97
C1	4	8	21	31	51	63
C2	2	8	25	37	61	75
C3	3	9	31	45	73	89

Figure 5 exhibits the settlement of raft under various loads imposed on it. Higher settlement values were recorded for load 6.00 kPa and 9.09 kPa compared to other load groups. The higher settlement reading is due to the duration that was

taken for the reading to be stable under the concerning loads. The duration taken for the loads 6.00 kPa and 9.09 kPa were 12 days and 18 days respectively. Whilst for the other loads, the duration of the loading were between 7 to 9 days. Other factor that influence compressibility characteristics of peat is soil particle arrangements [18]. The crushing of peat fibers under 6.00 kPa and 9.09 kPa loads particularly might have caused increment in volume change of the soil due to the decrement of void ratio as a result of rearrangement of peat fibers and drainage of excess pore water pressure. Therefore longer duration taken for the settlement reading to be stable thus producing higher settlement values compared to other loads.

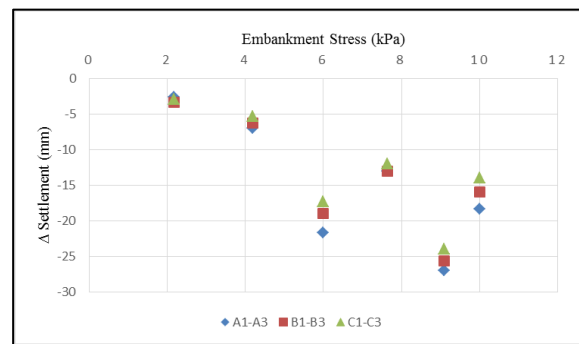


Fig. 5 Settlement of concrete raft under various embankment loadings

Figure 6 indicates that the soil surrounding the concrete raft experience deformation due to the embankment loading. Settlement gauge staffs placed at the distance of 0.25B and 0.5B have settled between 3 mm to 19 mm. Whereas reading of settlement gauge staffs located at 0.75B and 1B indicates occurrence of soil heaving between 1 mm to 9 mm. The results also show that the increment of ground water table due to heavy rain causes the soil to swell and thus reducing the settlement or increasing the heaving. Nevertheless, the average settlement and heaving of the surrounding soil were 9 mm and 4 mm respectively. These values are still small if compared to the average settlement of raft, 83.5 mm.

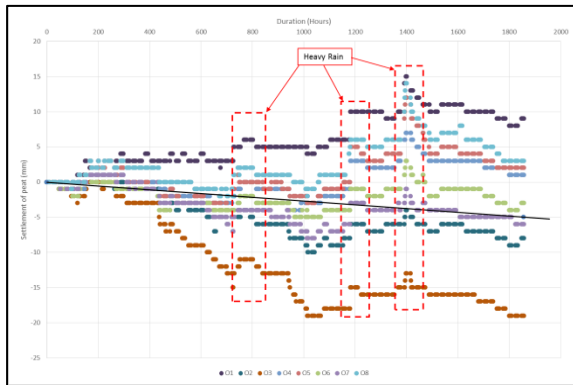


Fig. 6 Deformation of soil surrounding the concrete raft

CONCLUSION

Based on the review of the experimental results, the following concluding remarks were reached:

1. Stage loading method alleviates the immediate settlement of peat thus avoid unwarranted structural failure.
2. Usage of concrete raft foundation generates uniform settlement of peat under the embankment.
3. Fluctuation of ground water table effects the deformation of peat due to its shrinkage and swelling properties.
4. The settlement pattern of the concrete raft foundation is similar to that of punching shear.

ACKNOWLEDGEMENTS

The technical support provided by RECESS laboratory is duly acknowledged. Financial support for this study was provided by Research Grant TIER 1 Phase 1/2017, Office for Research, Innovation, Commercialization and Consultancy Management (ORICC), Universiti Tun Hussein Onn Malaysia. Scholarship funding by Jabatan Kerja Raya Malaysia is also very much appreciated.

REFERENCES

- [1] Wijeyesekera D. C., Numbikannu L., Ismail T. N. H. T., and Bakar I., Mitigating Settlement of Structures Founded on Peat. Soft Soil Engineering Conference, 2015.
- [2] Zainorabidin A., Static and Dynamic Characteristics of Peat with Macro and Micro Structure Perspective, University of East London, 2010, Ph.D Thesis.
- [3] Wetlands International, A Quick Scan of Peatlands in Malaysia, Wetlands International Malaysia, 2010.
- [4] Construction Research Institute of Malaysia (CREAM), Guideline for Construction on Peat and Organic Soils in Malaysia, 2015.
- [5] Sa'don N. M., Abdul Karim A. R., Ahamad Z., and Mariappan A., Sarawak Hemic Peat Consolidation Settlement and Shear Strength Behaviour, 15th International Peat Congress, 2016.
- [6] Zainorabidin A., and Mohamad H. M., Engineering Properties of Integrated Tropical Peat Soil in Malaysia, Electronic Journal of Geotechnical Engineering, Vol. 22, Bund. 02, 2017, pp. 457-466.
- [7] Zainorabidin A., Saedon N., and Mohd Seth N. F., An Investigation of Soil Volume Changes at Four Dimensional Points of Peat Soil in Parit Nipah and Pontian, International Integrated Engineering Summit, 2014.
- [8] Zainorabidin A., Zolkefle S. N. A., Lim A. J. M. S., Mohamad H. M., and Mohd Razali S. N., Comparison Study of the Dynamic Loading Characteristics between Peat and Sand on its Physical Properties, Applied Mechanics and Materials, 2015, pp. 1460-1465.
- [9] Zainorabidin A., and Bakar I., Engineering Properties of In-Situ and Modified Hemic Peat Soil in Western Johor, In Proceedings of 2nd International Conference on Advances in Soft Soil Engineering and Technology, 2003, pp. 173-182.
- [10] Ibrahim A., Huat B. B. K., Asadi A., and Nahazanan H., Foundation and Embankment Construction in Peat: An Overview, Electronic Journal of Geotechnical Engineering, Vol. 19, Bund. Z₂, 2014, pp. 10079-10094.
- [11] Waruwu A., Hardiyatmo H. C., and Rifa'i A., Compressive Behavior of Bagansiapiapi-Riau Peat in Indonesia, Electronic Journal of Geotechnical Engineering, Vol. 21, Bund. 16, 2016, pp. 5217-5227.
- [12] Sasaki Y., Characterisation of Expended Polymer Resin and Expansive Soil Composites, University of Newcastle, 2008, Ph.D Thesis.
- [13] Munro R., Dealing with Bearing Capacity Problems on Low Volume Roads Constructed on Peat, The Highland Council, Transport, Environmental & Community Service, HQ, Glenurquhart Road, Inverness IV3 5NX Scotland, 2004.
- [14] Mohsenian S., Eslami A., and Kasaei A., Geotechnical Aspects for Design and Performance of Floating Foundations, ASCE Geo-Frontiers, 2011, pp. 56-65.
- [15] Suro S. M., Bakar I., and Sulaeman A., Pile Space Optimization of Short Piled Raft Foundation System for Obtaining Minimum Settlement on Peat, Material Science and Engineering, 2016, pp. 1-7.
- [16] Tuan Ismail T. N. H., A Critical Performance Study of Innovative Lightweight Fill to Mitigate

- Settlement of Embankment Constructed on Peat Soil, Universiti Tun Hussein Onn Malaysia, 2017, Ph.D Thesis.
- [17] Mohd Razali S. N., Bakar I., and Zainorabidin A., Behavior of Peat Soil in Instrumented Physical Model Studies, *Procedia Engineering* 53, 2013, pp. 145-155.
- [18] Kazemian S., Huat B.K.K., Prasad A., and Barghchi M., A State of Art Review of Peat: Geotechnical Engineering Perspective, *International Journal of the Physical Sciences* Vol. 6(8), 2011, pp. 1974-1981.

LAND SUBSIDENCE IN SUMATERA PEATLAND FOREST

Nurhamidah Nurhamidah, Bujang Rusman, Bambang Istijono, Abdul Hakam,
Ahmad Junaidi, Taufika Ophiyandri
University of Andalas, Padang, Indonesia

ABSTRACT

A large area of peat swamp forests has disappeared due to either legally or illegally logging, drainage, agricultural conversion, fire, deforestation or large-scale developments for residential centers and industries. In Indonesia, less than 3% of the remaining forest is protected; the rest is available for logging and conversion to other land uses. Over 93% of the remaining swamp forests in Sumatera had been heavily degraded. Change the land use to agriculture dramatically changes the characteristics of the peat substrate. Once drained, peat is highly flammable and the fires can burn for month difficult to extinguish. The peat forest change to agriculture practices and other land use supposed to create a short or long term consequences. One of the consequences is surface degradation due to oxidation process.

A set of field measurements has been conducted using Hobo loggers. The measurement aimed at collecting data about the groundwater level and the soil temperature. The data was gathered within one and half year. The measurements were carried out on two conditions: during dry and wet periods.

The difference of the model to other approaches into the measurement of land subsidence rate, this model adapts to the characteristics of the soil, the different temperature and the groundwater level over time as three additional factors that strongly affect to the rate of subsidence. Using the Stephen Equation, the rate of subsidence in Sumatera varies from 2 until 13 cm per year due to the oxidation processes.

Keywords: peat soils, ropical forest, Hobo logger, land subsidence.

INTRODUCTION

Tropical peat land forests represent approximately 60% of peat in Asia land areas, of which 80% is situated in Indonesia [1] [2]. Southeast Asian peat land forests are among the last vast tracks of rainforest in the region. They are home for many rare animal species and critical for world carbon storage. Peat lands in the coastal areas, such as on the east coast of Sumatera, act as freshwater buffers against saltwater intrusion and they protect valuable agricultural areas between the peat and the sea.

Peat lands are essential for water regulation. A volume of peat soil consists of 90% of water (Warburton, Holden et al. 2004). Peat soils are generally meters deep and they store and maintain large quantities of water. Therefore, the peat land forests play important role as a retention area for adsorbing floodwater for preventing or mitigating floods in downstream areas.

A large area of peat swamp forests has disappeared due to either legally or illegally logging, drainage, agricultural conversion, fire, deforestation or large-scale developments for residential centers and industries. By 2006, close to 45% of the remaining forests had been severely affected [3]. In Indonesia, less than 3% of the remaining forest is protected, the rest is available for logging and conversion to other land uses [4]. The original area of peat swamp forest in Sumatera was 7 million ha (FAO, 1982). By 1988, over 93% of the remaining swamp forests in

Sumatera had been heavily degraded [5] [4]. Vast areas of the forests in Indonesian have been cleared for transmigration programs. Large-scale plantation companies are now finding the swampy areas increasingly attractive for various reasons [6]. Indonesia is the largest producer of palm oil; oil palm plantation has been the core of plantation in Sumatera since the late 1990s and rapidly expanded because of their vast forests and climate conditions that are suitable for the oil palm [7] [8].

Change the land use to agriculture dramatically changes the characteristics of the peat substrate. Once drained, peat is highly flammable and the fires can burn for month difficult to extinguish. Swamp forest fires of Kalimantan and Sumatera have been known since 1988. In 1997, due to the peat land fires in both islands 240 people were killed, 3 million were affected and the damage cost 8 billion US dollar [9] [10] [11]. The fires can clear layers of peat causing an additional land subsidence, which follows immediately by increasing the depth of flood water, generating of floods in the river basin, and leading to an increase of downstream flood.

There appears to be no capacity to deal with this huge problem of degradation of the tropical peat land forests in Sumatera (specifically) and in Indonesia [12]. Consequently, the undisturbed tropical forest areas have become extremely rare, even in the protected areas. It is argued then, in order to cope with the current conditions of the forests, the need of an integrated assessment of all

indirect and direct factors that contribute to the potential impacts become apparent.

RESEARCH METHODOLOGY

Description of study area

The data of the present study was gathered from the middle of the Sumatera delta, i.e. on $100^{\circ}28' - 102^{\circ}12'$ East longitudes and $0^{\circ}20' - 1^{\circ}16'$ North latitude. The area was covered by tropical rainforests and approximately 40% of these rainforests grew up at lowland forests. These forests are mostly located on the eastern coast of Sumatera. 56.6% of the areas are layered with peat soils. 30 % of these layers have more than 4 m depth. In natural conditions, the swamp areas of the eastern cost of Sumatera function as a retention area by absorbing floodwater.

Thereby, they prevent or mitigate flood in downstream area. The areas along the rivers in the area of interest serve as overflow areas during flood periods in the wet season, while in the dry season the stored water is slowly released.

Figure 1 and 2 present that peat soils are functioned around the eastern coast of Sumatera for crop production and forestry, as well as wildlife and recreation. The organic material can be harvested for horticultural potting soil and for heating and electricity. If the soils are used for crop production, extensive drainage is required. As a rule of thumb, the subsidence should have occurred at a rate of 1 inch of soil per year. However, the drainage leads to a more rapid subsidence due to the oxidation biochemical process and the drained Peat soils are vulnerable to fires.

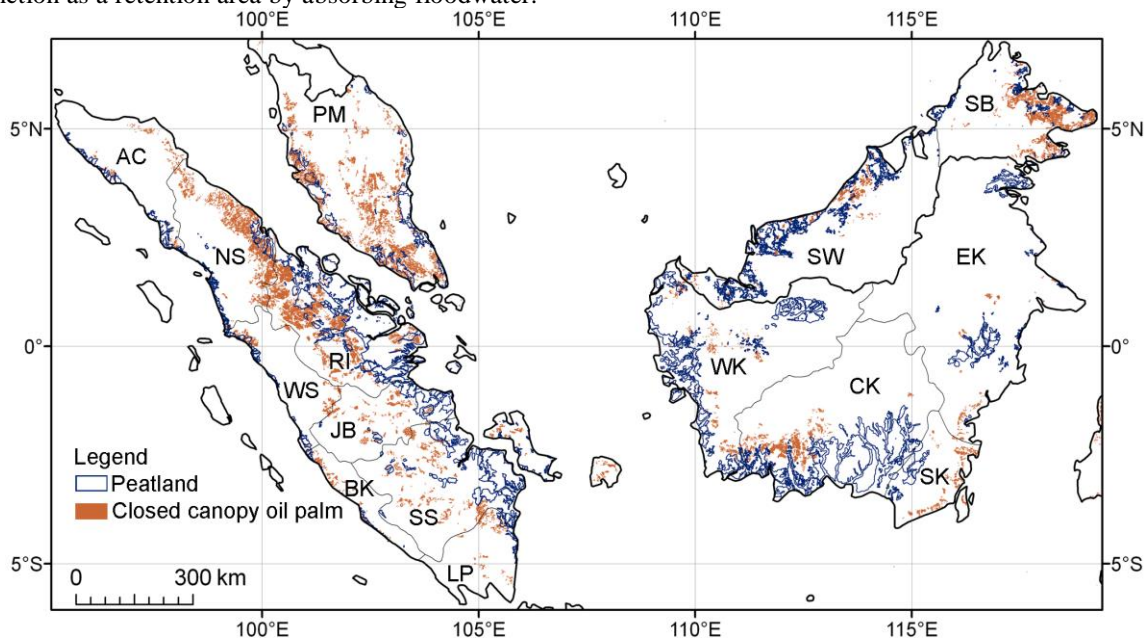


Fig. 1 Peat land distribution on Sumatera and Borneo island

Data acquisition

We conducted a set of field measurements using Hobo loggers. The measurement aimed at collecting data about the groundwater level and the soil temperature. The data was gathered within one and half year. The measurements were carried out on two conditions: during dry and wet periods. According to Figure 3, based on the results of monitoring in the field, soil temperature varies inversely with groundwater level. The soil temperature increase at the time of level the groundwater level down, and increasing groundwater level have the potential to the soil temperature declined. The process of the rise and down of soil temperature and groundwater level led to a decline of land surface. The rate of declining depends on the characteristics of peat soil. We also

took into account three different peat soil characteristics. These characteristics were based on the three of the peat soil characteristics in doses.

Adaptive land subsidence measurement

The previous overview from literatures shows that oxidation is the major cause of peat soil subsidence in many countries in the world. The overview also shows that other factors beside extreme rainfall, such as the latitude of the area, the soil temperature rate and the groundwater level, affect greatly on the long-term subsidence rates from one climatic region to the other. However, we found that the current approaches into the measurement of land subsidence rates do not take into account these factors. Here, we aim to develop a model of land subsidence that adapts to the type of peat soils, the soil temperature and the changes of groundwater level.

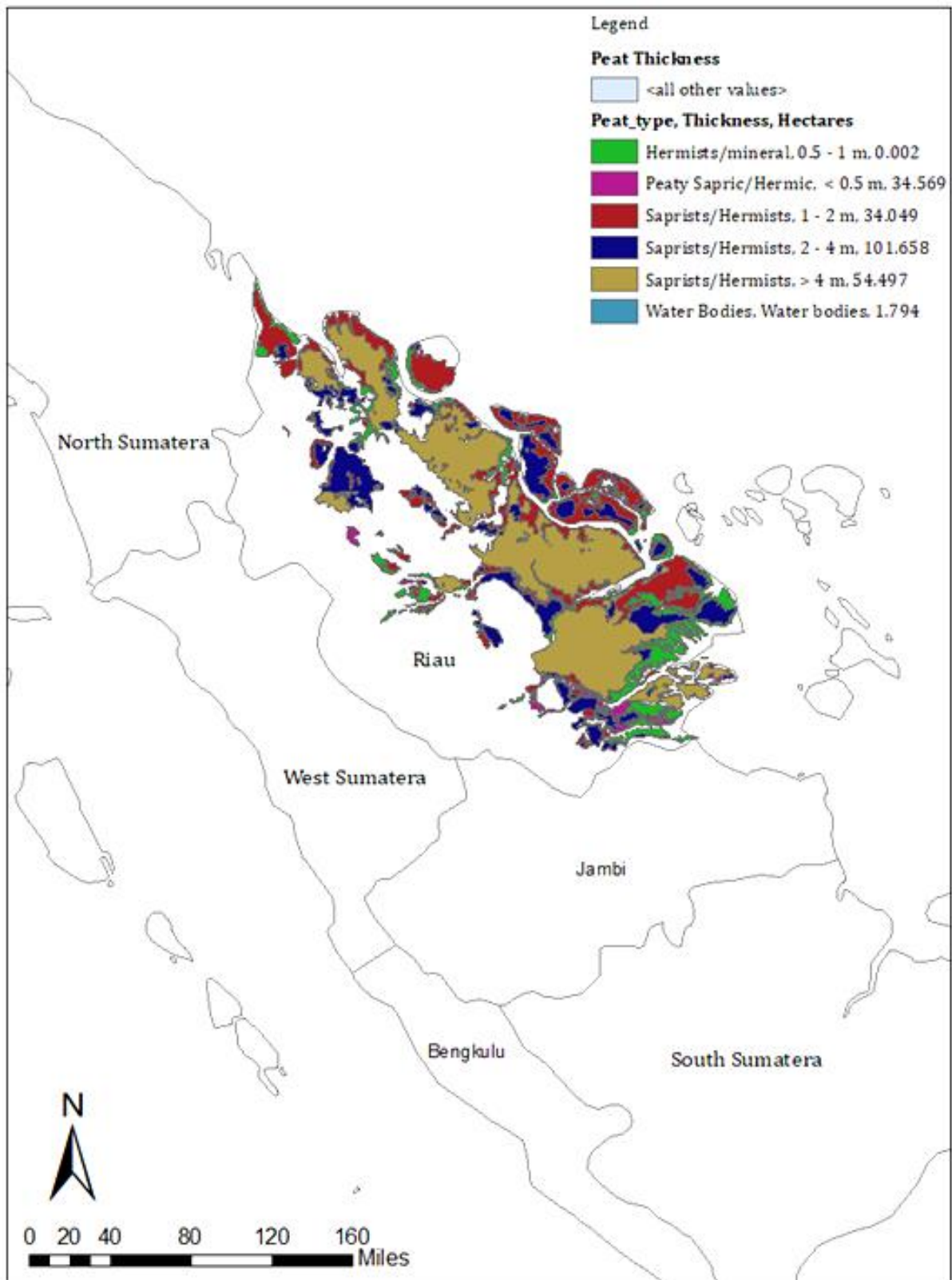


Fig. 2 Peat land distribution and peat thickness on Riau province



Fig. 3 Field Measurement using Hobo Logger

The linear reservoir concept is used to design the proposed model. We consider the concept mainly because it takes into account parameters used in the Arrhenius law, linear regression and the Stephen equation. To develop the model we followed the following procedures. Firstly, we designed the adaptive land subsidence model based on the linear reservoir concept. This step results a formula to measure the land subsidence, which takes into account the characteristics of the soils, the different of the temperature soils, and the change of the groundwater level. Here, we also identified necessary parameters that were needed to be collected from the field.

Secondly, we used the satellite imaginary maps for selecting locations where the monitoring devices were placed.

Thirdly, we conducted a set of field measurements on the selected locations within a year following the two seasons that occurred in the area. This activity measured the identified necessary parameters, i.e. the temperature soils and the groundwater level. During this field measurement, we also monitored the land subsidence from the selected locations within a year. These data were used to compare the results of the measurement using the adaptive land subsidence model with the actual data.

Finally, we simulated the land subsidence in the selected location by plotting the parameters into the adaptive land subsidence model. Then, we compared the simulation with the results for the field monitoring. Based on this comparison, we presented the validation and the analysis of the proposed model.

RESULT AND DISCUSSION

LAND SUBSIDENCE MODELING

Arrhenius equation

According to Arrhenius law, oxidation and densification are a consequence of draining peat soils. Alternatively when the density of peat soils is increased, this results in compaction, desiccation, and loss of groundwater buoyant force. Arrhenius also provides that subsidence can be realized in the short and long term. Densification leads to subsidence within a short duration. Subsidence is realized after a long duration, due to biochemical oxidation. This is especially the case in warm climatic conditions. Arrhenius law uses the Q_{10} concept where most of these reactions have a Q_{10} value that ranges between 1.5 and 2.5 and averages approximately 2.0. It has been applied to calculate organic soil subsidence in Everglades and it was recognized that as the ground water level lowered it resulted in the continuation of subsidence on peat soils.

Beside the ground water level, temperature is also a key factor in determining whether there will be a continuation of subsidence on peat soils. The higher the temperature: the higher the chemical reaction by the peat soils. This change in reaction is as a consequence of increased or reduced temperature and is expressed by the term Q_{10} . With every temperature change of 10 C there is a subsequent chemical reaction, according to the Arrhenius law.

$$S_2 = S_1(Q_{10})^x$$

S_1 = The known oxidative subsidence rate at known soil temperature T_1

S_2 = Corresponding oxidative subsidence rate at soil temperature T_2

Q_{10} , represents the change on reaction rate for each 10°C temperature change

$$x = \frac{T_2 - T_1}{10} = \frac{\Delta T}{10}$$

From the evidence explained that we have assumed that the biochemical reactions responsible for the decomposition of peat have a Q_{10} value of 2.0, and that the base temperature at which decomposition becomes significant is $+5^\circ\text{C}$

[13] suggested that although equation (1) can be used to evaluate the soil temperature effects on the rate of organic soil decomposition, however algebraic equations for evaluation is probably much better to use.

Linear regression

Long-term effect of land subsidence for limited data was developed by Wosten as the following formula:

$$\text{Subsidence rate (cm/year)} = 0.04 \times \text{groundwater level (cm)}$$

According to [14, 15], increasing of subsidence rate at initial phase was 0.9 cm per year and experienced a decrease to 0.4 cm per year. The formula was admitted as the best prediction for long-term effect of groundwater level changes as consequences of land use change in Malaysia peninsular. To prove it, the formula compared with the empirical model which has developed by Stephens and Stewart (1976). The result of the application has been using for Florida and peninsular Malaysia.

Stephen equation

Stephen and Stewart determined the Arrhenius law to evaluate the biochemical subsidence rate for low moor organic soil at each location using the annual average soil temperature at the 10 cm depth.

The basic subsidence equation is:

$$S_T = (a + bD)Q_{10}^{(T-T_o)/10} \dots\dots\dots(1)$$

S_T = biochemical subsidence rate at temperature, T . D = depth of water table. T = annual average soil temperature at the 10 cm depth. T_o = base soil temperature, by assuming as 5°C . a and b are constants.

Q_{10} refers to equation (1), represents the change on reaction rate for each 10°C temperature change assumed as 2, therefore equation (1) is written as:

$$S_T = (a + bD)(2)^{(Tx-5)/10} \dots\dots\dots(2)$$

This equation has been used to estimate the annual subsidence rate at the Lullymore Experimental Station in the Irish Republic for the arable low moor soils, where the average annual soil temperature is 8.5°C and the water table depth is held at 90 cm. Therefore the equation to represent this region is:

$$S_L = (-0.1035 + 0.0169 \times 90)(2)^{(8.5-5)/10} \dots\dots(3)$$

Steven and Stewart argued, for similar type of peat soil in tropical countries which have degree temperatures around 30°C , the equation can be adjusted as :

$$S_x = (-0.1035 + 0.0169 \times 90)(2)^{(30-5)/10} \dots\dots(4)$$

Therefore, formula of land subsidence which used at Florida can be derived as following:

$$S_x = (0.0169D - 0.1035)x2^{(T-5)/10} \dots\dots\dots(5)$$

Meanwhile, subsidence formula that applied for Malaysia, as shown as following [14, 15]:

$$S_x = (0.093 + 0.00524 \times GL)x2^{(T-5)/10} \dots\dots(6)$$

From those formulas which have been applied in different latitude, it appears that there are similarities to the assumptions for the value of base soil temperature (T_o) i.e. at 5°C and the value of Q_{10} equal to 2, even though located at difference climate and consisted of difference type of peat soils.

Long term effect of climate on organic soil subsidence (3)

Data from field measurements are used in order to determine the value a and b . Field measurement was taken for a year and carried out on soil temperature and the ground water level. The reaction of land surface caused a decrease due to changes in temperature and soil water table depth.

Equation (6) can be used to estimate the biochemical subsidence rate for organic soils at Sumateradelta where the data of soil temperature at the 10-cm depth is as shown as figure 4.

In natural conditions, swamp areas function as a retention area by adsorbing floodwater, thereby preventing or mitigation flood in downstream areas. Swamp areas along the river serve as

overflow areas during flood periods, while in the dry season the stored water is slowly released.

In Sumatra, the study of land subsidence was conducting by installing Hobo logger. Measurements are taken for one and half year form 2012-2013 for every ten minutes as shown as figure 4. It gives information about groundwater and soil temperature measurements. Measurements have been formulated on two conditions; during dry and wet period. At first installation, data is recorded every ten minutes each 3 months during wet and dry season. Based on these measurements, land subsidence due to peat oxidation are analyzed by develop algebraic Stephen equation nr. 6 .

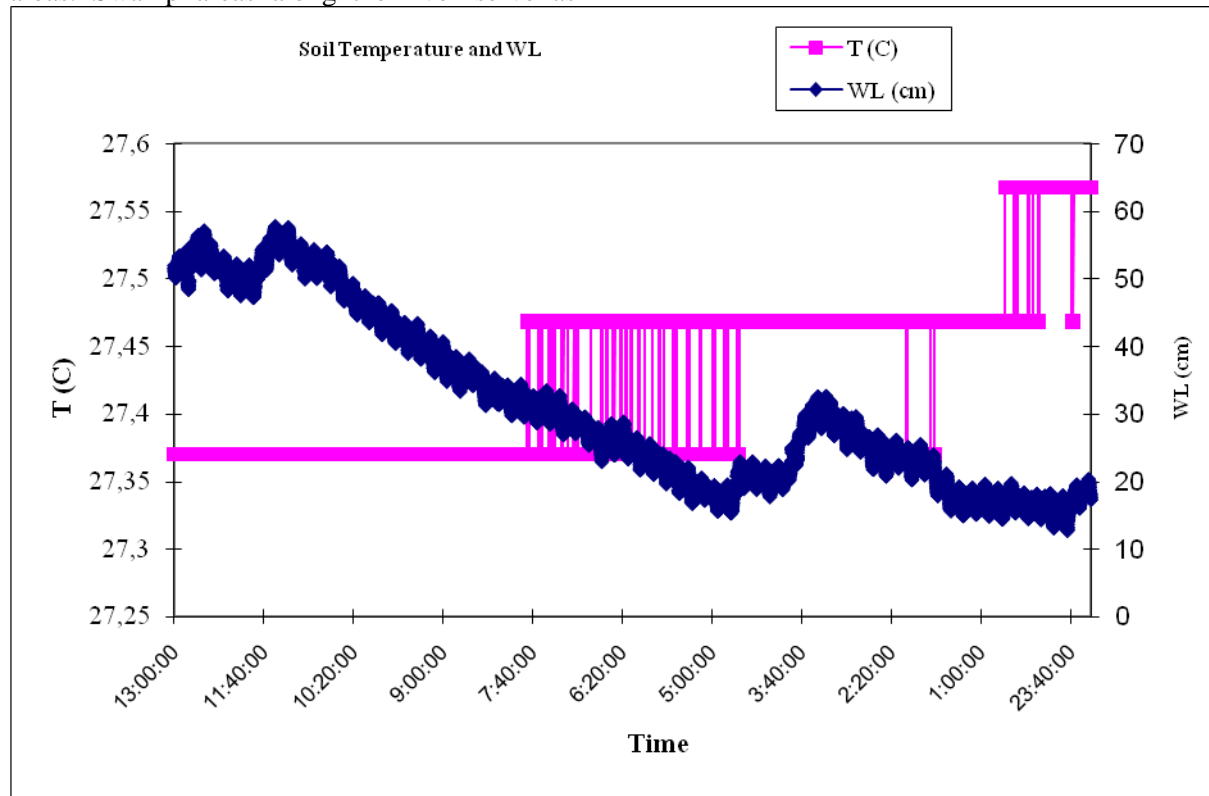


Fig. 4. Soil temperture and groundwater level measurement during dry and wet season

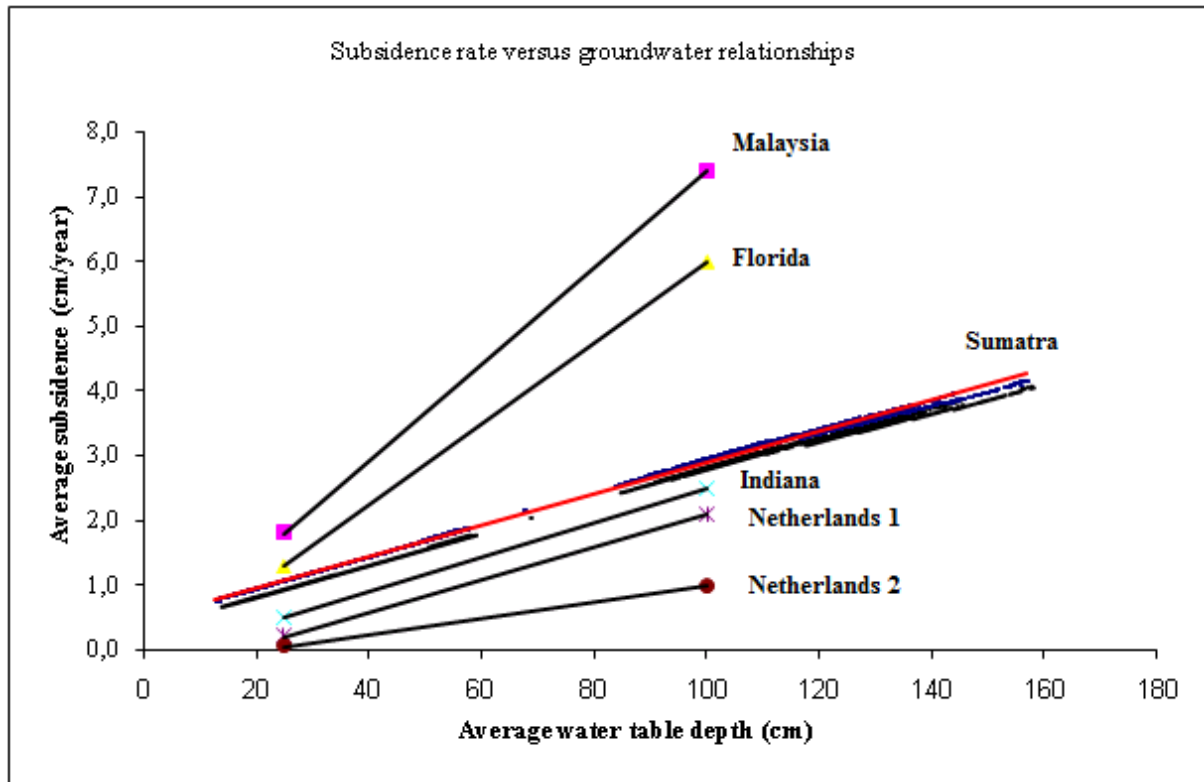


Fig. 5. Land subsidence Sumatera and around the world using stephen equation

Histosols is used for crop production and forestry, as well as wildlife and recreation. The organic material can also be harvested for horticultural potting soil and for heating and electricity. They can be production crop soils, however extensive drainage is required.

Unfortunately, drainage trigger to subsidence. Subsidence is the loss of soil depth. Subsidence happens when water is drained from the profile. The organic materials “float” in saturated conditions and become more compact when drained. Once drained, the soil begins to oxidize and microbes consume the organic matter and slowly turn it into carbon dioxide with time. Subsidence, as a rule of thumb, occurs at a rate of 1 inch of soil per year. This creates problems for drainage ditch maintenance and long-term uses of agricultural soils. Histosols, when drained, are also vulnerable to fires.

CONCLUSIONS

The state-of-the-art in land-subsidence analysis progresses unevenly because the degree of understanding of various subsidence mechanisms varies. Most study has been

directed to subsidence related to man’s engineering activities. This is facilitated by availability of data on quantities of subsurface material removed (or injected), on rates and duration of extraction operations, and on changes in ground-water levels. Natural processes are not as easily quantified.

A case of land subsidence is necessarily the integrated surface expression of whatever processes may be active at that site, whether natural or manmade, or both. A working hypothesis as to the mechanism or combination of mechanisms operative at the specific site is requisite for designing control measures. The complexity of subsidence mechanisms and their interaction requires cooperative effort among different disciplines, both in collecting physical evidence and in developing the rationale for the processes involved. The hydrologic sciences have been, and will continue to be, significant contributors to land subsidence investigations.

ACKNOWLEDGEMENTS

I would like to express my deep gratitude to University of Andalas for the Research Grant No. 43/UN.16.17/PP.RGB/LPPM/2018 dated 23 April 2018.

REFERENCES

1. Page, S., et al., Restoration ecology of lowland tropical peatlands in Southeast Asia: current knowledge and future research directions. *Ecosystems*, 2009. **12**(6): p. 888-905.
2. Page, S.E., et al., Review of peat surface greenhouse gas emissions from oil palm plantations in Southeast Asia. White Paper, 2011(15): p. 76.
3. Hooijer, A., et al., Current and future CO₂ emissions from drained peatlands in Southeast Asia. *Biogeosciences*, 2010. **7**(5): p. 1505-1514.
4. MacDicken, K. Cash for tropical peat: land use change and forestry projects for climate change mitigation. in *Peatlands for people: natural resource functions and sustainable management: proceedings of the International Symposium on Tropical Peatlands*, held in Jakarta, Indonesia on 22-23 August 2001. 2002: Agency for the Assessment and Application of Technology (BPPT) and Indonesian Peat Association (IPA), Jakarta, Indonesia.
5. Silvius, M.J. and W. Giesen. Integration of Conservation and Land-Use Development of Swamp Forest of East Sumatra. in *Proceedings of the Workshop on Sumatra, Environment and Development: its past, present and future*. Bogor. 1992.
6. Sundari, R., Conservation and sustainable use of peat swamp forests by local communities in South East Asia. *Suo*, 2005. **56**(1): p. 27-38.
7. McCarthy, J.F., Processes of inclusion and adverse incorporation: oil palm and agrarian change in Sumatra, Indonesia. *The Journal of peasant studies*, 2010. **37**(4): p. 821-850.
8. Thorburn, C.C. and C.A. Kull, Peatlands and plantations in Sumatra, Indonesia: Complex realities for resource governance, rural development and climate change mitigation. *Asia Pacific Viewpoint*, 2015. **56**(1): p. 153-168.
9. Occasional, C., Fires in Indonesia. 2003.
10. Meijaard, E., Indonesia's Fires in the 21st Century: Causes, Culprits, Impacts, Perceptions, and Solutions. *Pollution Across Borders: Transboundary Fire, Smoke And Haze In Southeast Asia*, 2018: p. 103.
11. Margono, B.A., et al., Mapping and monitoring deforestation and forest degradation in Sumatera (Indonesia) using Landsat time series data sets from 1990 to 2010. *Environmental Research Letters*, 2012. **7**(3): p. 034010.
12. Margono, B.A., et al., Primary forest cover loss in Indonesia over 2000â€“2012. *Nature Climate Change*, 2014. **4**(8): p. 730.
13. Stephens, J.C. and E.H. Stewart, EFFECT OF CLIMATE ON ORGANIC SOIL SUBSIDENCE.
14. Wosten, J.H.M., A.B. Ismail, and A.L.M. vanWijk, Peat subsidence and its practical implications: A case study in Malaysia. *Geoderma*, 1997. **78**(1-2): p. 25-36.
15. Wosten, J.H.M., et al., Peat-water interrelationships in a tropical peatland ecosystem in Southeast Asia. *Catena*, 2008. **73**(2): p. 212-224.
16. Nurhamidah and A. Junaidi, Linear reservoir-based adaptive land subsidence model: Case of Sumatera peat lowland forests. *Lowland technology international: the official journal of the International Association of Lowland Technology*, 2016. **18**(3): p. 173-182.
17. Ho, Y.S. and G. McKay, The kinetics of sorption of divalent metal ions onto sphagnum moss peat. *Water Research*, 2000. **34**(3): p. 735-742.

COMPARISON OF BEARING CAPACITY IMPROVEMENT FOR SOFT CLAY USING SOIL-LIME AND SOIL-CEMENT COLUMNS

Satyajit Patel¹, Amruta Joshi² and Shravan Sukumaran³

¹Assistant Professor; ² Research Scholar; ³Former Post Graduate Student, Applied Mechanics Department, Sardar Vallabhbhai National Institute of Technology, Surat, Gujarat, India

ABSTRACT

Challenge of construction in highly compressible and weak soils can be addressed by choice of suitable deep foundation or ground improvement of available strata. Stone column technique is one amongst the best suited method for ground improvement in case of compressible soils. But stone columns constructed in very soft soils can lose backfill material due to low confinement provided by surrounding material. Hence, soil-lime and soil-cement column can represent better alternative for stone columns.

This paper presents study of soft soil improved with soil- lime and soil-cement columns. Stone columns and soil columns with dosages of 3, 6 and 9% of lime and cement were casted and testes in circular mould in laboratory. The performance of soil- lime and soil-cement columns are compared with that of stone columns using results of experimental work and finite element analysis.

From the experimental studies, Soil lime and soil cement columns were found to perform better than stone columns. Results obtained were validated with finite element software Plaxis 3D. A finite element analysis was done on the group of soil- lime and soil cement columns. A case of group of column in triangular and square pattern of installation was modeled and analyzed by Plaxis 3D. Bearing capacities of soil improved by the group of columns were compared with soil without column inclusion. From experimental and FEM studies, performance of soil lime mix was found to be better in comparison with soil cement mix in the range of 6-9% binder addition.

Keywords: Stone column, Soil-lime column, Soil-cement column, Ground improvement

INTRODUCTION

Rapid urbanization causes the unavailability of land and a hike in its price. As a result land area which is having good geotechnical property is scarcely available and it forces the engineers to think about making structures in weak soils which otherwise would have been avoided. In order to construct structures on such type of soils either we have to choose deep foundations such as pile foundation or we have to go for ground improvement. If the structure is having less no of stories and also can tolerate settlement up to a limit (structures like liquid storage tank) then the suitable solution is ground improvement and stone column is one among the best suited method of ground improvement. The main aim this work is with the same concept of stone column but instead of granular backfill, two types of mixtures are used, i.e. soil lime mix and soil cement mix. The installation and basic assumptions in modeling are the same as stone columns.

The technique of soil – lime and soil cement column was considered as an alternative to rigid inclusion and stone column. Actually the stone column was generally assumed to be too soft in terms of stiffness and bearing capacity and the rigid inclusions are too stiff, the soil- lime/ cement columns represents the intermediate case which provides better homogenous

distribution of load on the subgrade layer and provides almost uniform settlement profile.

Use of prefabricated vertical drains (PVD) is another technique for soft soil stabilization. But Stone columns are adventitious over PVDs in terms of strength as well as cost effectiveness.

The presented work is the study of improved soft soil by soil – lime and soil cement column application. Here lime/cement is mixed with soft clay in definite proportion and that mixture is used for the construction of soil- lime and soil cement column. The soil- lime and soil cement column which is having more stiffness as compared with the surrounding clay and ultimately it act as reinforcement for the weak soil.

Scope of the presented work was as follows;

- 1) To investigate the load settlement behaviour of the soft ground improved by the application of soil – lime and soil-cement column into the soft soil.
- 2) Comparison of the result obtained with the improvement made by stone column, both in terms of efficiency in improvement as well as cost.
- 3) To determine the optimum column length up to which the soil lime column is effective in the improvement of the soft ground.
- 4) Comparison of the laboratory model and finite element model with the help of finite element software Plaxis 3D.

5) Study of group effect of soil – lime and soil cement columns using Plaxis 3D.

MATERIALS USED

The black cotton soil was used in soil lime/cement columns as well as in backfill surrounding the columns. The properties of this soil are as shown in table 1. The lime used in study was hydrates lime. Cement used in this work is ordinary Portland cement of grade 53. Crushed aggregates of size ranging from 1 mm to 4.75mm were used in stone columns.

Table 1 Properties of soil used in study

Sieve analysis	Black cotton soil
Gravel %	0
Sand %	14.5
Silt %	40
Clay %	45.5
Specific gravity	2.58
Liquid limit (%)	58
Plastic limit (%)	28
Plasticity index	30
OMC (%)	19
MDD (g/cm ³)	1.78

METHODOLOGY

The stress strain curves obtained from the results of UCS tests with different water content of 35 %, 40% and 45% respectively had shown that 45% the soil loses its shear strength to a large extent. Hence, density of 1.4 gm/cc and water content of 45% was considered for compaction.

Mould with a height of 175mm and 150 mm diameter is used for the study, and a steel rod of 225 mm length is used for construction of column, as the steel rod is kept in the centre of the mould during the time of preparation of surrounding clay bed. The installation method opted is replacement method, by which the column position is marked on the soil bed and then inserting a pipe of required diameter gently without causing much disturbance to the soil bed and then using an auger, scoop the soil out carefully.

The parameters used for the study were lime/cement content in column and their optimum percentage and varying lengths of the columns. A term ' L_r ' (length ratio) which is the ratio of the total length of column to the depth of mould is used for representing effect of variation in length of columns. For a full length, half length and $3/4^{\text{th}}$ length column, length ratio L_r is 1, 0.5 and 0.75 respectively.

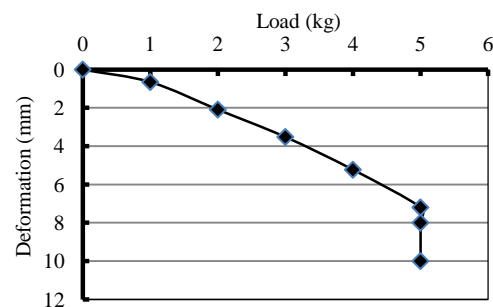
The results for soil-lime and soil-cement columns were compared with each other and with only soil. Finally stone column were prepared with the above mentioned column lengths and study was done on the effectiveness on settlement reduction of black cotton soil by soil lime and soil cement columns comparing to the stone column. Total 4 series of tests were conducted. First series consisted of tests with soil only, and then next series with soil lime column with three lime contents like 3%, 6%, 9% and also with varying the column depth like full length, half-length and $3/4$ length of column. The third series has the same particulars as the former one with cement replaced with lime in column. In the fourth test series stone columns are employed in the place of soil lime and soil cement columns.

To obtain load-settlement behaviour of soil, soil-lime, soil-cement and stone columns, loading plate with 50 mm height and 30mm diameter was used and the load was applied at the rate of 1.2mm/minute.

RESULTS AND DISCUSSIONS

Load settlement behaviour of only soil

The load settlement behaviour of only soil was studied initially. The specimen is prepared in the mould with only soil and loaded. The study of the unimproved soil has to be considered in the later stage for ascertaining the degree of improvement achieved for the soil which is improved using soil



lime and soil cement and also with the stone column.

Fig. 1 load Settlement behaviour of only soil

Study on effect of Variation of lime content and Length of column in soil - lime column

As the lime content increases, the load carrying capacity of the columns has been increased. As compared to the only soil, the load carrying capacity of 3% lime content is significant, but while comparing with 6% and 9% columns strength it is much less. The increase in terms of strength is very high when it comes from 3 to 6%. But comparing

the strength characteristics of 6% and 9% lime content the increase in strength is very minute. So the optimum lime content should be within 6 to 9 percentage. Further increase in lime content is of no use. Various studies on optimum lime content has point out that increase in lime content beyond an optimum value will not increase its strength, on contrary it will decrease the strength and performance of improved soil. The decrease in strength may be due to that, excess lime which remains unused in the soil and act as a weakening agent, as all useful quantity of lime has been utilized already for strengthening the soil.

Table 2 Maximum load taken by columns of various length ratio and lime dosages at 10 mm settlement

Lime Content in column	Maximum load carried at 10 mm settlement (kg)		
	Lr = 0.5	Lr = 0.75	Lr = 1
3%	33	35	28
6%	53	57	37
9%	57	60	39

From table 2, it is clear that the optimum column length lies between 75% of total length to 100%.

Study on effect of Variation of lime content and Length of column in soil - lime column

As the cement content in column increases, the load carrying capacity of the column also increases. The rate of increase of load carrying capacity was very high as the dosage of both lime and cement changes from 3% to 6%, but it was not evident when the dosage changes from 6% to 9%.

Table 3 Maximum load taken by columns of various length ratio and cement dosages at 10 mm settlement

Cement Content in column	Maximum load carried at 10 mm settlement (kg)		
	Lr = 0.5	Lr = 0.75	Lr = 1
3%	31	33	36
6%	39	48	51
9%	41	52	56

From table 3, it is clear that there is a considerable difference in strength of a column with length ratio (L_r) 0.5 and 0.75. In the same time the difference in strength between column with length ratio 0.75 and 1 was found to be less. This shows that increasing column length after a particular length will not have any remarkable effect on load carrying capacity of column.

Comparison of performance of soil lime, soil cement and stone columns

Figure 2 shows that load taken by different types of columns with a change in length ratio, and from that figure it become clear that when the length ratio is less that is when it is equal to 0.5 (half-length column) the load carrying capacity of each columns lies in the range of 30 to 40 kg. The only exception was the stone column. As the length ratio has increased from 0.5 to 0.75, the load carried by columns with binder content of 6% and 9% was increased considerably, represented by the increase in slope of the curve in between the portion 0.5 and 0.75. Further increase in length ratio, i.e. from 0.75 to 1 the curve become flatter for all cases of binder content. This points that the effect of critical length.

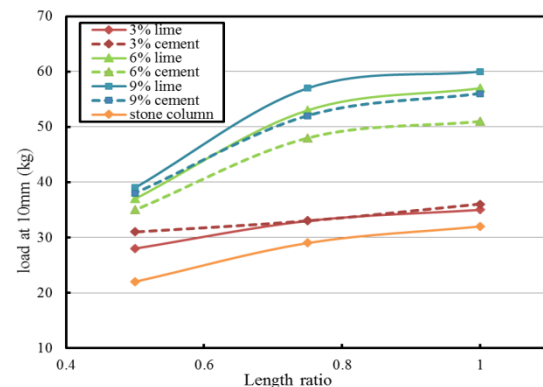


Fig 2 Performance of various types of columns with change in length ratio

So, if the column length is increased further beyond a particular length there is no considerable increase in load carrying capacity of columns, whether it is soil- lime or soil – cement or stone columns.

Validation of experimental models

For the validation purpose full length soil lime columns of 6 and 9% lime contents were considered. For validation purpose, the modulus of elasticity values of the soil lime and soil cement columns are required. These values were obtained from stress strain curves obtained from UCS test results. As the stress strain curve changes at various points, three modulus of elasticity are considered for the analysis. During the first calculation phase where the curve is linear, considered the maximum E value and form the next phase the E value decreases as the slope of the curve become flatter. So three best fitting lines were drawn on each curve and which is represented as E_1 , E_2 and E_3 in each plots respectively. The Mohr column model was chosen for the analysis purpose of both the surrounding soil and soil lime and soil cement columns. The validations were done for end bearing columns of both soil lime and soil cement columns. The figure below shows the experimental and FEM analysis curves.

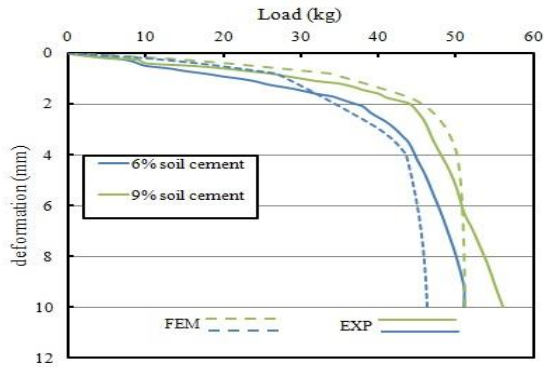


Fig 3 Finite element validation of 6% and 9% soil lime columns

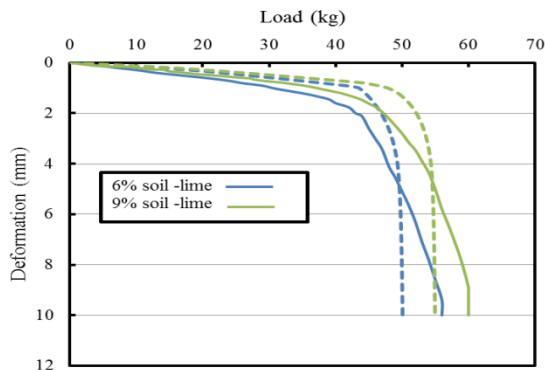


Fig 4 Finite element validation of 6% and 9% soil cement columns

Analysis of a group of end bearing columns

For the analysis of end bearing columns, the bottom of the column has to be fixed in all direction. In the first case square pattern of installation was studied and the diameter adopted was 1m. The spacing given was conforming to IS 15284- 2003, according to which the effective diameter around a column in case of a square pattern is 1.13times the spacing adopted and the spacing adopted was 2 m, which is equal to two times the diameter of the column.

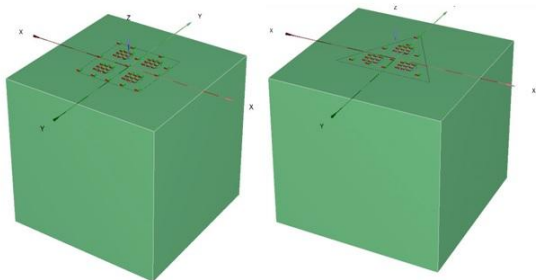


Fig 5 Model created for square pattern and triangular pattern in Plaxis 3D

A group of soil lime columns, soil cement columns and stone columns were done. For the comparison purpose the triangular pattern was also analyzed. In such cases the effective diameter of the column equal to 1.05 times the spacing between the

columns. In order to compare the bearing capacity in both pattern of installation, the spacing and diameter were kept same. Figure 5 and 6 show the model created in Plaxis 3D 2013.

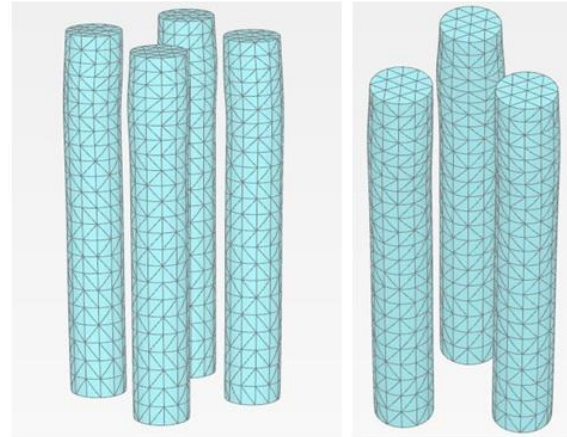
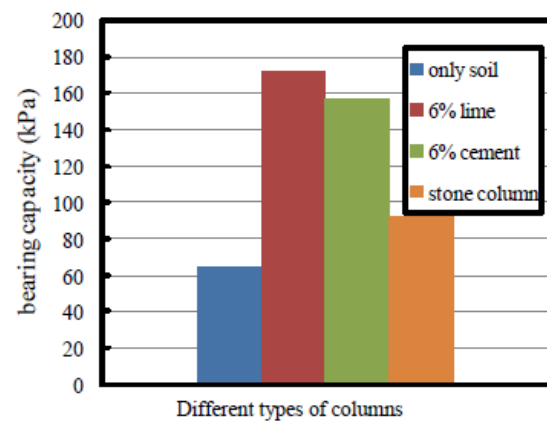
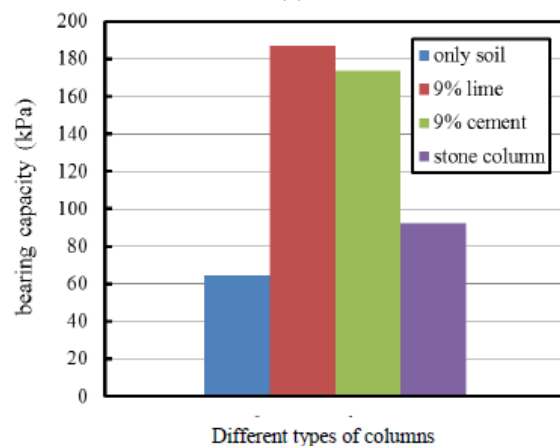


Fig 6 bulging of columns: Square pattern and Triangular pattern



(a)



(b)

Fig 7 Bearing capacity of group of column installed in square pattern for 80 mm settlement (a) 6% binder content (b) 9% binder content

From fig 7 and fig 8, it can be clearly seen that, the performance of soil-lime and soil-cement column in

both square and triangular pattern is superior to soil without columns and stone columns.

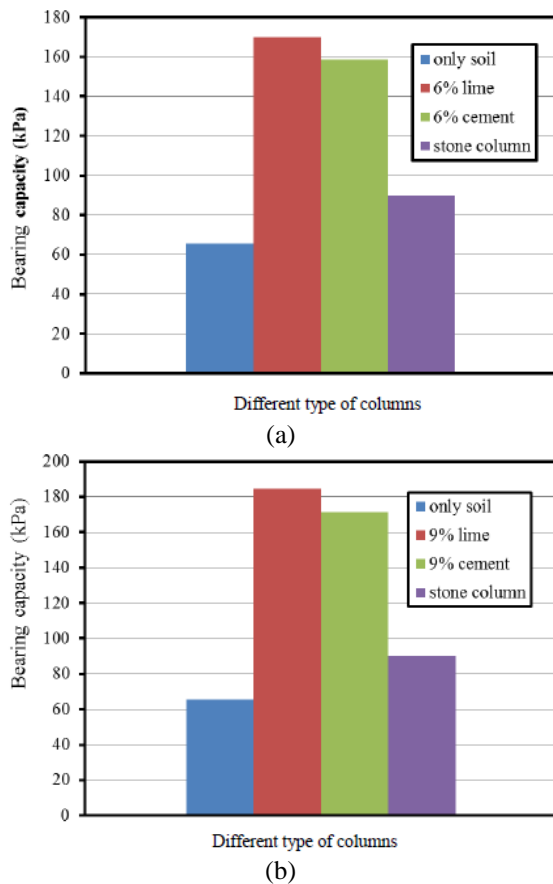


Fig 8 Bearing capacity of group of column installed in triangular pattern for 80 mm settlement (a) 6% binder content (b) 9% binder content

The bearing capacity found out for both square and triangular pattern was almost same. The percentage increase in bearing capacity in case of soil lime, soil cement and stone column for both 40mm and 80mm settlements are shown in the table given below.

Table 4 Bearing capacity at 40 mm and 80 mm for end bearing columns in Square pattern

Type of column	Bearing capacity@ 40 mm (kPa)	% Increase in bearing capacity	Bearing capacity@ 80 mm (kPa)	% Increase in bearing capacity
Only soil	54.62	--	64.66	--
6% lime	128.07	134 %	172.06	166 %
6% cement	101.1	85 %	157.32	143 %
9% lime	145.88	167 %	187.12	189 %
9% cement	120.88	121 %	173.73	168 %
Stone column	77.08	41 %	92.12	42 %

Table 5 Bearing capacity at 40 mm and 80 mm for end bearing columns in triangular pattern

Type of column	Bearing capacity@ 40 mm (kPa)	% Increase in bearing capacity	Bearing capacity@ 80mm (kPa)	% Increase in bearing capacity
Only soil	55.52	--	65.3	--
6% lime	130.45	135 %	169.66	160 %
6% cement	103.4	86 %	158.65	143 %
9% lime	148.05	167%	184.5	182 %
9% cement	123.372	122%	171.4	62 %
Stone column	75.38	36%	90.1	38 %

Bearing capacity improvement is maximum in case of 9% of lime content and even at 6% of lime content it has improved the bearing capacity of the soft soil higher than 9% cement content which matches well with the experimental study. The performance of stone column found to be bad compared to the performance of soil lime and soil cement columns, as the increase in bearing capacity were only 1.38 times and there is no significant increase after a settlement of 40 mm. At 40 mm the increase in bearing capacity was found to be 1.36 times that of an unreinforced soil.

CONCLUSIONS

Following are the conclusions from my studies on soil lime and soil cement columns for improving black cotton soil.

- 1) Inclusion of soil lime and soil cement mixture in to black cotton soil, will improve its strength remarkably. Strength of unreinforced soil (only soil) was very poor, i.e.; between 5 to 6 kg.
- 2) The soil lime and soil cement column was compacted to the same density as the surrounding soil i.e. 1.4g/cm³. But the strength increase was nearly 30-35 kg for 3% dosage of lime and cement. The strength increases up to 50 to 55 kg for 6% of dosage of both lime and cement. And it crosses 60 kg in the case of 9 % dosage of lime.
- 3) For lower values of dosages like 3% and up to 6%, lime has shown better performance than cement. When the binder content increases from 6 to 9% the soil cement column shows strength near to the soil lime columns.
- 4) Critical length of column lies between 75% and 100% of total depth of mould. When the length ratio of column equal to 0.75, the column has shown the strength nearer to the strength of full length column.
- 5) Half-length column performance was not good especially at lower binder content of 3% as it is having soil behaviour predominant.
- 6) From the model test, a relationship between critical column length and the diameter of the

column can be established, critical column length lies between $4d$ to $5d$, where ' d ' is the diameter of column.

7) From the load – displacement plots of various dosages and different lengths it is evident that the load carrying capacities of the columns are maximum up to a deformation of 2- 3mm.

8) The maximum load carrying capacity of columns lies approximately up to a deformation of 0.1d, where ' d ' is the diameter of the column. From 3mm to 10mm the rate of load increment eventually decreases and in the case of half-length column it remains almost constant.

9) Tests conducted on stone columns shows that, the load taken by stone columns are very less compared to the soil lime column. Even 3% soil lime and soil cement columns were performed better than stone columns.

10) From the test results, it can be concluded that, the effective percentage of lime for the field application is in the range of 6 to 9%. And for black cotton soil used for current study, the lime has performed better than cement at both 6 and 9%, so lime can be used as a binder material in field.

12) A brief study of performance of group columns of both 6% and 9% soil cement, soil lime columns and stone columns, each group containing four number of end bearing columns were conducted using the finite element software Plaxis 3D 2013.

13) The result obtained from FEM analysis shows that, group of columns containing soil lime columns performed better. And stone column group has performed poorly as compared to the other.

REFERENCES

- [1] Ahmed Farouk, Marawan, M. Shahien (2013), "Ground Improvement using Soil – Cement columns: Experimental Investigation", Alexandria Engineering Journal 52, 733-740.
- [2] Ambily, A. P. And Gandhi, S. R. (2007) "Behaviour of Stone Columns Based on Experimental and FEM analysis." Journal of Geotechnical and Geo Environmental Engineering (2007) ASCE, Vol 133 :405-415.
- [3] David L.D (2003) "Guidelines for Design and Installation of Soil Cement stabilization", Grouting and ground treatment Grouting 2003, ASCE.
- [4] Ilan Juran and Oraccio Riccobono (1991) "Reinforcing Soft soil with Artificially Cemented Compacted Sand Columns", Journal of Geotechnical Engineering, Vol. 117, No. 7, ASCE, 1042-1060.
- [5] Indian Standard design and construction for ground improvement — guidelines part 1 stone columns (IS 15284 (Part 1) :2003).
- [6] J. Han, J. Huang, and A. Porbaha (2005) "2D Numerical Modelling of A Constructed Geosynthetic-Reinforced Embankment over Deep Mixed Columns" Contemporary Issues in Foundation Engineering. ASCE, 1-11.
- [7] Kasali Gyimah and Osamu Taki (2004) "Design and Construction aspects of Soil Cement columns as Foundation elements", Grouting and ground treatment Grouting 2003, ASCE.
- [8] Kumar Rakesh and Jain P.K (2013), "Soft Ground Improvement With Fiber Reinforced Granular Pile", International Journal of Advanced Engineering Research and Studies Vol II, Issue III., 42-45.
- [9] Malarvizhi S.N., K. Ilamparuthi, (2004) "Load versus Settlement of Clay bed stabilized with Stone & Reinforced Stone Columns", Proceedings of the 3rd Asian Regional Conference on Geosynthetics, GEOASIA, Seoul, Korea (2004), pp. 322-329.
- [10] Melvin I. Esrig, P.E., and Peter E. MacKenna (2001) "Lime Cement Column Ground Stabilization For I -15 in Salt Lake City" Practice Periodical on Structural Design and Construction, ASCE, Vol. 6, No. 3, 104-115
- [11] Muntohar, S. A., Halaman. (2010), "A Laboratory Test on The Strength and Load Settlement Characteristic of Improved Soft Soil Using Lime Column", Dinamika Teknik SIPL Vol. 10, No 3, 202-207.
- [12] Muzamir bin Hasan, Aminaton binti Marto and Masayuki Hyodo (2011), "The strength of soft clay Reinforced with Singular and Group Bottom Ash Columns" EJGE Vol.16..
- [13] Ney Augusto Nascimento, José Luiz G. Brandi and Rogério F. Kuster Puppi (2012) "Measured Settlement of Mat foundation on Soft Clay with and without Reinforcement from Sand column", Full scale Testing and Foundation Design ASCE
- [14] Nicholson, P.J., "An Abstract on Cement Soil Mixing in Soft Ground", University of Houston, Texas, USA, 1998.
- [15] Ogundipe, Moses, O (2013) "An Investigation Into The Use Of Lime-Stabilized Clay As Subgrade Material", International Journal of Scientific & Technology Research Volume 2, Issue 10, October 2013, 82- 86.
- [16] Pivarc, J (2011) "stone columns- determination of the soil improvement factor", Slovak Journal of Civil Engineering Vol. XIX, 2011, No. 3, 17 – 21.
- [17] Shahu, J. T and Reddy, Y.R (2011) "Clayey Soil Reinforced with Stone Column Group: Model Tests and Analyses" Journal of Geotechnical and Geo Environmental Engineering (2011) ASCE, Vol 137:1265-1274.
- [18] Tan, S.A, Ng, K.S. and Jie Sun (2014), "Column Group Analysis for Stone Column Reinforced Foundation", From Soil Behaviour Fundamentals to Innovations in Geotechnical Engineering: pp. 597-608, ASCE.

THE EFFECT OF L-SHAPED SHEAR WALL ON STUDENT DORMITORY BUILDING OF ANDALAS UNIVERSITY, PADANG, INDONESIA

Fauzan¹, F A Ismail¹, M W Rizki¹, I Fikri¹, and Z A Jauhari²

¹Department of Civil Engineering, Andalas University, Padang, Indonesia

²Department of Civil Engineering, Bengkalis State Polytechnic, Bengkalis, Indonesia

ABSTRACT

Student dormitory building of Andalas University is one of the buildings for new students who come from outside of Padang City. The University of Andalas received aid from the Ministry of Public Works of Indonesia to build a dormitory building. The building was designed by a design consultant using reinforced concrete (RC) structure with a straight shape (I-shaped) shear wall. Based on the review result of the design from Technical Engineer of Andalas University, it was found that the designed building is not strong enough to resist the working loads, especially due to earthquake load. Therefore, a strengthening of the building should be done. In this study, the strengthening method used is by substituting the type of shear wall from “I”-shaped to be “L”-shaped shear wall, which is installed at the corners of the building. The effect of the L-shaped shear wall on the student dormitory building of Andalas University is discussed in this paper.

Keywords: Shear wall, Strengthening, RC structure, Student dormitory building, Seismic load

INTRODUCTION

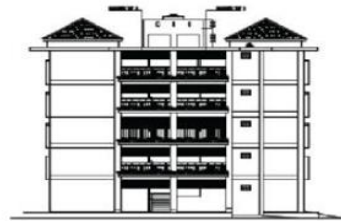
The structure of multi-story buildings is vulnerable to lateral force, especially due to the earthquake [1]. Earthquake risk has resulted in damage to the buildings, so the building should have a strong structure to resist the force caused by the earthquake. One way to strengthen the building is by using the shear wall [2]. Shear wall is a wall that serves as a stiffener which proceeds to the foundation. With the rigid shear walls in the building, most of the earthquake loads in multi-story buildings will be absorbed by the wall [3]. Student dormitory building of Andalas University is one of the buildings for new students who come from outside of Padang City. The building is made of reinforced concrete (RC) structure, which is designed using the I-shaped shear wall. Based on review results from Technical Engineer of Andalas University, it was found that the building has not enough capacity to resist the working loads. Therefore, strengthening the building by modifying the shear wall from I-shaped to be L-shaped has been conducted. This paper discussed the effect of the L-shaped shear wall on the dormitory building.

ANALYSIS OF STRUCTURES

Modelling and analyzing structures of the dormitory building are conducted by using 3D structural modelling with ETABS v9.7.1 software [4]. Figs. 1 and 2 show the view and plan of the dormitory building.



(a) The front view of the building



(b) The side view of the building

Fig. 1 The front and side views of the dormitory building.

Modeling

To perform the analysis of the building structure, the following technical data of the building from design consultant was used:

- Location: Andalas University, Limau Manis, Padang City.
- Type of structures: RC Structure.
- Concrete compressive strength, $f'_c = 34.34$ MPa.
- Yield stress of steel, $f_y = 390$ MPa.
- The number of floors: 5.

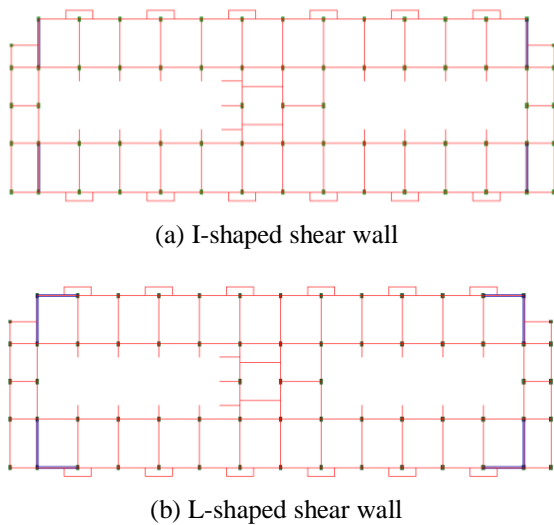
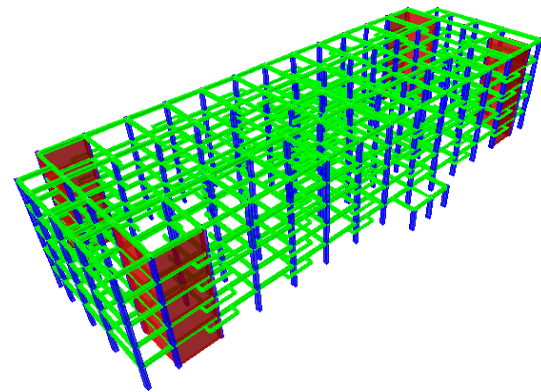
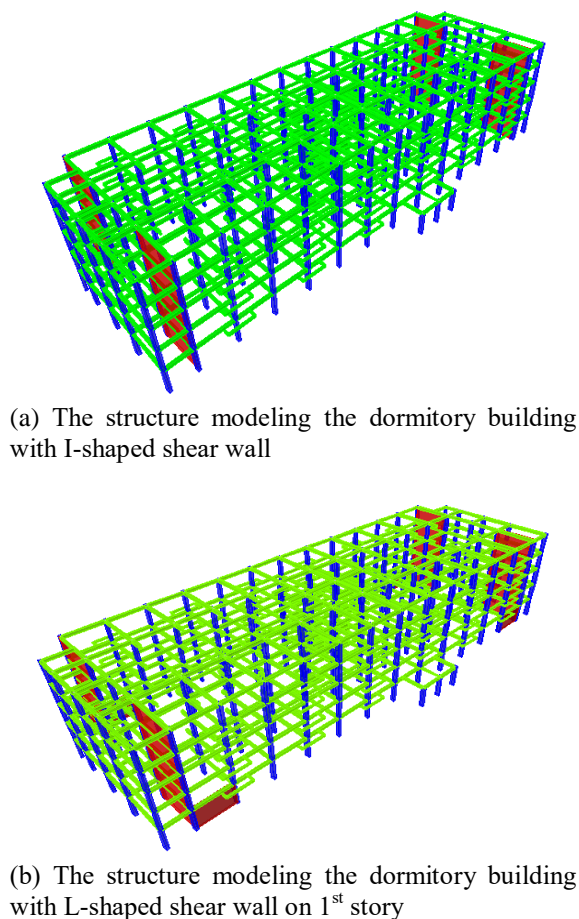


Fig. 2 The plan of the dormitory building with I-shaped and L-shaped shear walls.

Columns and beams in the building were modeled as frame elements, while slabs, stairs, and shear walls were modeled as the wall element, as shown in Fig. 3 [5]. In this study, L-shaped shear walls were installed on the corners of the building on the first story only (Fig. 3 (b)) and on all stories (Fig. 3(c)).



(c) The structure modeling the dormitory building with L-shaped shear wall on all stories.

Fig. 3 The structure modeling of the dormitory building with different types of the shear wall.

The Design of Load

The calculation of the dead load is taken by its own weight building materials and components of the building. Live load is modelled based on SNI 1727:2013, which are taken based on criteria for the use of floor in the dormitory building, for the residential area: 250 kg/m^2 and for torn water area: 2000 kg/m^2 [6].

Spectrum Response Analysis

The seismic load based on SNI 1726:2012 [7] obtained from the website http://puskim.pu.go.id/Aplikasi/desain_spektra_indonesia_2011 was used. According to the soil test result, the soil on the building was classified as soft soil. Fig. 4 shows the spectrum response design on soft soil type of Padang city.

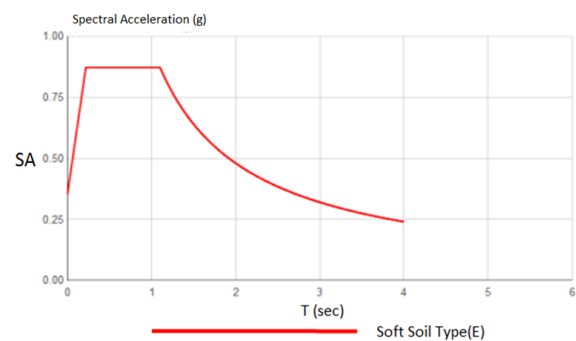


Fig. 4 Spectrum response design for the earthquake load in Padang city based on SNI 1726:2012.

The location point of columns and beams to compare the structural response is shown in Fig. 5. The positions are taken from one interior beam, and one interior column in the centre of each floor.

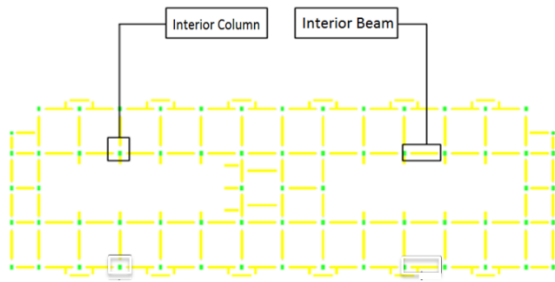


Fig. 5 The location point of the structural element to compare the analysis results.

RESULT OF STRUCTURAL ANALYSIS

In this study, the results of structural analysis such as internal forces and displacement of the buildings with L-shaped shear walls were compared with the I-shaped one.

Internal force in columns

Fig. 6 shows the comparison of internal forces in the interior column between the buildings using the I-shaped shear wall and L-shaped shear wall at 1st floor.

From Fig. 6, it is seen that the axial force in interior column on the building with the L-shaped shear wall was almost similar with the L-shaped shear wall installed on the 1st floor, while the shear force and bending moments of the column decreased significantly in the first floor of the building. The decrease in the shear force and bending moment in the first floor is about 90 % and 84 %, respectively.

Similar results were also found out in the building with the L-shaped shear wall installed on all stories. As seen in Fig. 7, the axial force of the building is almost similar with one with the I-shaped shear wall. However, the significant decrease of shear force and bending moment of this building were found out on all stories. This indicated that the presence of L-shape shear wall on all stories of the building increases the capacity of the structure, in which the shear wall reduces the shear force and bending moment of the column on all stories significantly.

Internal Forces In Beams

Fig. 8 shows the comparison of internal force in the interior beam between the building using the I-shaped shear wall and the building using the L-shaped shear wall on the 1st floor.

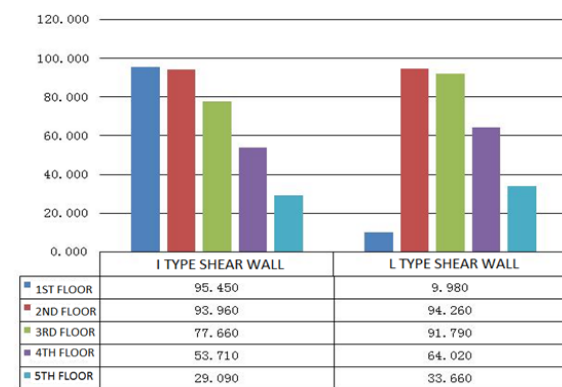
As can be seen in the Fig. 8, the present of the L-shaped shear wall on the 1st floor of the building affected the internal forces on the beam, especially on the first floor of the building. The shear force and

bending moment of the building decrease in the first floor, about 23 % and 35%, respectively.

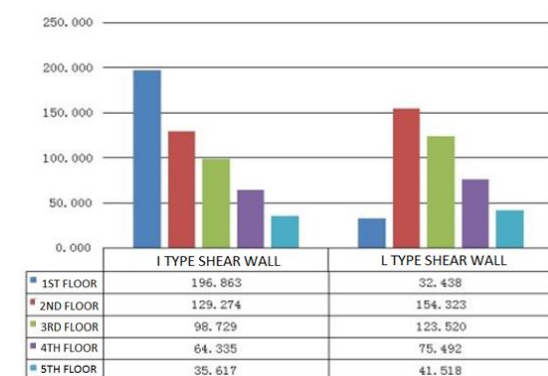
The presence of L-shaped shear wall on all stories of the building reduced the internal forces of the beam on all stories, as shown in Fig. 9. As seen in this figure, the shear force and bending moment decrease about 25 - 40% and 39 - 60%, respectively.



(a) Axial force

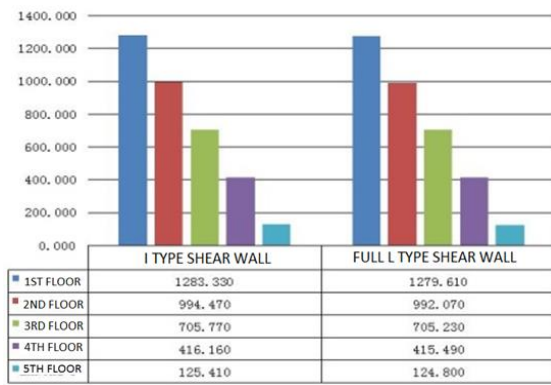


(b) Shear force



(c) Bending moment

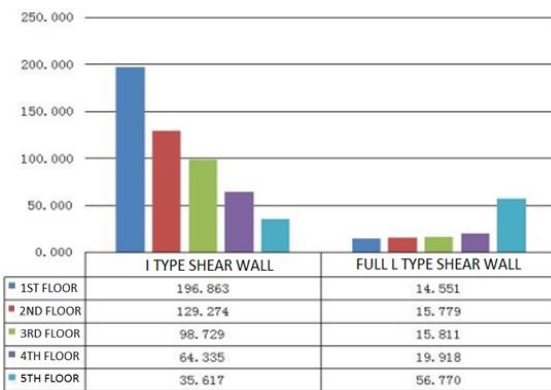
Fig. 6 The comparisons of internal forces in the interior column between the buildings using the I-shaped and the L-shaped shear walls.



(a) Axial force



(b) Shear force



(c) Bending moment

Fig. 7 The comparisons of internal forces in the interior column between the buildings using the I-shaped and the L-shaped shear walls.

Displacement

Fig. 10 shows the comparison of displacement between the buildings using I-shaped shear wall and L-shaped shear wall at the 1st floor. Displacement of the building structure is taken from the largest value of displacement in each floor. As seen in the figure, the presence of the L-shaped shear wall on the first floor of the building reduces displacement of the building in X-direction about 60% on the top floor,

while slightly decrease was found out in Y-direction displacement.

The similar trend was also found in the building with L-shaped shear wall installed on all stories. As seen in Fig. 11, the presence of L-shaped shear wall on all stories reduced the displacement significantly in X-directions and slightly reduced in Y-direction. The maximum reduction of displacement in X-direction is about 77% on the top floor of the building.

Inter-story Drift

The values of inter-story drift of the building with the L-shaped on the 1st floor and the L-shaped on all stories in X and Y-directions can be seen in Tables 1 and 2, respectively.

As seen in the tables, the inter-story drift of the buildings with L-shaped shear wall meets the requirement based on Indonesian standard code SNI 1726-2012. From the tables, it is also seen that the presence of L-shaped shear wall on all stories of the building reduced the inter-story drift, especially in X-direction.

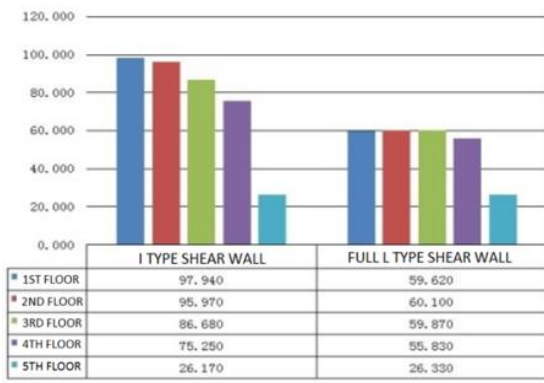


(a) Shear force

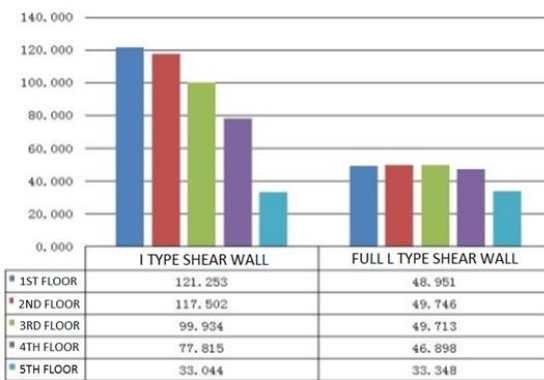


(b) Bending moment

Fig. 8 The comparisons of internal forces in the interior beam between the buildings using the I-shaped and the L-shaped shear walls.



(a) Shear force



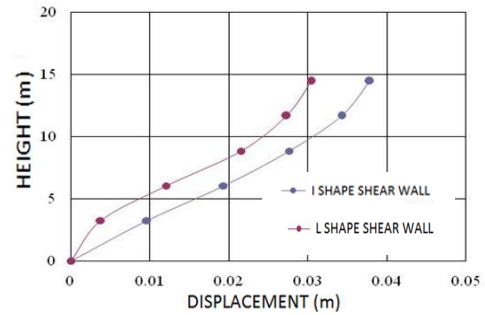
(b) Bending moment

Fig. 9 The comparisons of internal forces in the interior beam between the buildings using I-shaped shear wall and L-shaped shear wall until the 5th floor.

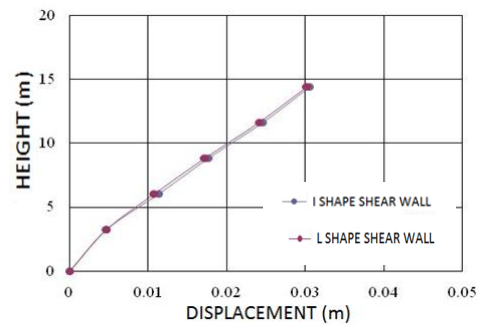
Table 1 Inter-story drift in X and Y-directions of the building using the L-shaped shear wall on the 1st floor.

Story	H (mm)	Δa^a (mm)	UX (mm)	Drift X (mm)	Δs^b X (mm)	Δs X $\leq \Delta a$
Base	0	0	0	0	0	OK
1	3250	62.5	3.84	3.84	21.12	OK
2	2800	53.85	12.06	8.22	45.21	OK
3	2800	53.85	21.51	9.45	51.98	OK
4	2800	53.85	27.32	5.81	31.96	OK
5	2800	53.85	30.41	3.09	16.99	OK

Story	H (mm)	Δa^a (mm)	UY (mm)	Drift Y (mm)	Δs^b Y (mm)	Δs Y $\leq \Delta a$
Base	0	0	0	0	0	OK
1	3250	62.5	4.68	25.74	25.74	OK
2	2800	53.85	10.83	33.83	33.83	OK
3	2800	53.85	17.27	35.42	35.42	OK
4	2800	53.85	24.10	37.57	37.57	OK
5	2800	53.85	30.24	33.77	33.77	OK

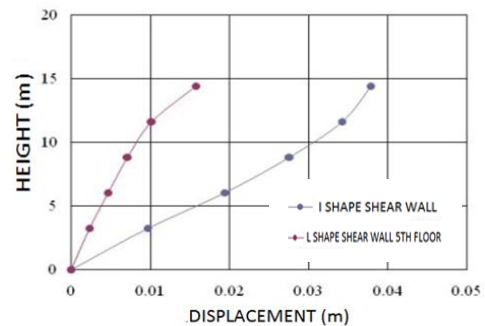


(a) X direction

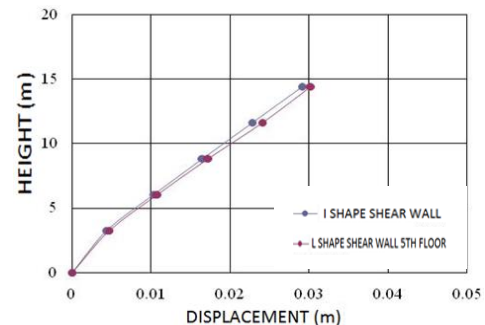


(b) Y direction

Fig. 10 The comparison of displacement in the structures between the buildings with I-shaped shear wall and L-shaped shear wall on the 1st floor.



(a) X-direction



(b) Y-direction

Fig. 11 The comparison of displacement in the structure between the buildings with I-shaped shear wall and L-shaped shear wall until the 5th floor.

Table 2 Inter-story drift in X and Y-directions of the building using the L-shaped shear wall until the 5th floor.

Story	H (mm)	Δa^a (mm)	UX (mm)	Drift X (mm)	Δs^b X (mm)	Δs X $\leq \Delta a$
Base	0	0	0	0	0	OK
1	3250	62.5	2.28	2.28	12.54	OK
2	2800	53.85	4.66	2.38	13.09	OK
3	2800	53.85	7.15	2.49	13.69	OK
4	2800	53.85	10.19	3.04	16.72	OK
5	2800	53.85	15.72	5.53	30.41	OK

Story	H (mm)	Δa^a (mm)	UY (mm)	Drift Y (mm)	Δs^b Y (mm)	Δs Y $\leq \Delta a$
Base	0	0	0	0	0	OK
1	3250	62.5	4.39	4.39	24.15	OK
2	2800	53.85	10.34	5.95	32.73	OK
3	2800	53.85	16.59	6.25	34.38	OK
4	2800	53.85	22.83	6.24	34.32	OK
5	2800	53.85	29.17	6.34	34.87	OK

Note: $\Delta a = 0.015 \times H / \rho$.

$\Delta s = \delta \times C_d / I_e$.

CONCLUSION

1. The presence of L-shaped shear wall in the first floor only of the dormitory building reduced the shear force and bending moment on the first floor about 90% and 84%, respectively and not much effect on the other floors, while the addition of the L-shaped shear wall until the 5th floor decreased shear force and bending moment on columns in all floors.
2. The addition of L-shaped shear wall on the 1st floor at the dormitory building reduced the shear force and bending moment of the building about 23 % and 35%, respectively, while the presence of L-shaped shear wall on all stories reduced the internal forces of the beam on all stories.

3. The presence of the L-shaped shear wall reduced displacement of the building, especially in X-direction. The reduction of the displacement in X-direction reached 77% for building with L-shaped shear wall installed on all stories.
4. The inter-story drift of the building with L-shaped shear wall meets the requirement based on standard code SNI 1726:2012. The reduction of inter-story drift of the building was more decreased by installment of the L-shaped shear wall on all stories, especially in X-direction.

ACKNOWLEDGEMENTS

The authors would like to acknowledge the funding support provided by the University of Andalas, Padang, Indonesia.

REFERENCES

- [1] Purwono R., The Design of Earthquake-Resistant Structures, Jakarta, ITS Press, 2010.
- [2] Fintel M., Shearwall an Answer for Seismic Resistance, ACI Structural Journal, vol 13 (7), 1991, pp. 48-53.
- [3] Ismail M., Analysis of Structural Performance on Seven Floors Building with Dimension and Location Variations of Shear Wall, Journal of Civil and Environmental Engineering, vol 2 (1), 2014.
- [4] CSI ETABS, 2013, ETABS Version 9.7.1, USA.
- [5] Andalas University, Construction Report of Dormitory Building of Andalas University, Padang, 2014.
- [6] National Standardization Agency of Indonesia, Minimum load for the design of buildings and other structures, SNI 1727:2013, Jakarta, Indonesia, 2013.
- [7] National Standardization Agency of Indonesia, Design Method of Earthquake Resistance for Buildings and Other Structures, SNI 1726:2012, Jakarta, Indonesia, 2012.

STRUCTURAL EVALUATION OF NURUL HAQ SHELTER BUILDING CONSTRUCTED ON LIQUEFACTION PRONE AREA IN PADANG CITY-INDONESIA

Rina Yuliet¹, Fauzan², Abdul Hakam³, Helza Riani⁴
^{1,2,3,4}Engineering Faculty, Andalas University, Indonesia

ABSTRACT

West Sumatra Province, especially Padang City, is an area prone to earthquake and tsunami disaster. In order to face the disaster, the Padang city government planned to build as many as shelters as a vertical evacuation building. One of them is Nurul Haq shelter located in a coastal area that has liquefaction potential. A structural evaluation of the shelter was conducted to check the capacity of the existing shelter structure in resisting the working loads. From the result of the soil evaluation, it was found that the soil in the shelter location has high liquefaction potential. Therefore, the shelter structure is analyzed using specific response spectrum of the earthquake loads considering soil liquefaction, which is 1.5 higher than those on the non-soil liquefaction. The tsunami loads were calculated used based on FEMA P-646. The analysis result shows that the shelter building is not capable of resisting the working loading, in which the elements of the beams and foundations don't have enough capacity to resist the working loads, especially earthquake and tsunami loads. Furthermore, the shelter building should be retrofitted before being used as a vertical evacuation building.

Keywords: Earthquake, Tsunami, Shelter, Soil Liquefaction, Structural Evaluation

INTRODUCTION

The city of Padang has experienced major earthquakes, as happened on September 30, 2009, which caused much damage to the buildings and infrastructure of Padang city. The city of Padang, located on the West Coast of Sumatra, which borders on the open sea (Indian Ocean) and the active two-plate collision zone, the Indian and Asian Plates, makes Padang City one of the most earthquake-prone and tsunami-wasting cities. Therefore, after the earthquake, the government began to take action by establishing a vertical evacuation building called a shelter. By using the shelter, people in Padang City can reach a safe place from a tsunami puddle in a shorter period of time when horizontal evacuation cannot run properly. One of the shelters is Nurul Haq Shelter, located in Parupuk Tabing sub district, Padang City, Indonesia.

Shelters are usually built in residential areas close to the coast because shelters can be used by people around the settlement to take shelter when the earthquake and tsunami occur. However, this becomes dangerous because the shelter is likely to be built in areas where the soil has the potential to liquefy. This makes the shelter collapse before it can be used as a shelter after the earthquake. Therefore, it is necessary to study/evaluate the structure of the Nurul Haq shelter building, whether this shelter has taken into account the potential aspects of liquefaction, earthquake, and tsunami-resistant building standards in its planning design.

EVALUATION OF LIQUEFACTION POTENTIAL

During earthquakes, major destruction of various types of structures occurs due to the creation of fissures, abnormal and or unequal movement and loss of strength or stiffness of the ground. The loss of strength or stiffness of the ground results in the settlement of buildings, failure of earth dams, landslides and another hazards. The process by which loss of strength occurs in soil is called soil liquefaction.

Another way of evaluating the soil liquefaction potential is to prepare correlation charts with the Standard Penetration Resistance, as shown in Fig. 1. This figure can be used for determination of the liquefaction potential in the field. The corrected N-SPT value (N') can be obtained using the Equation 1:

$$N' = C_N N \quad (1)$$

Where :

N = Field standard penetration test value

C_N = Correction factor to convert to a effective overburden pressure (σ'_v) of 100 kPa

The correction factor can be expressed as in Equation 2) [1].

$$C_N = 9.78 \sqrt{\frac{1}{\sigma_v'}} \quad (2)$$

Where σ_v' is in kPa

From Fig. 1, it can be seen that if N' is more than 30, the liquefaction is unlikely to occur [1].

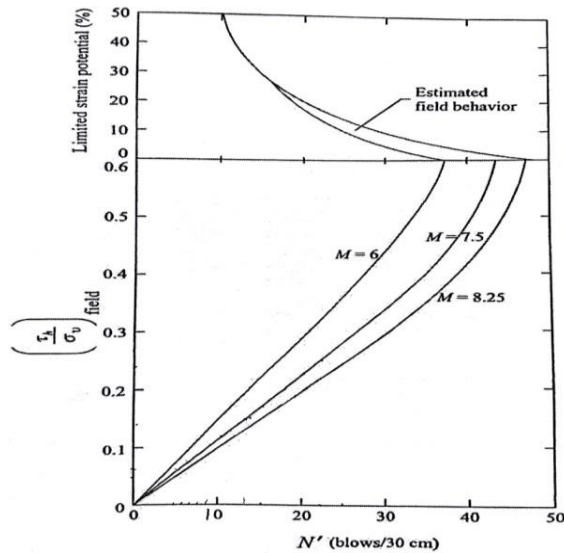


Fig. 1 Variation of $(\tau_h/\sigma_v)_{\text{field}}$ with N' and M [1]

According to Seed and Idris, the maximum shear stress determine from the shear stress-time history during the earthquake can be converted into an equivalent number of significant stress cycle [1], using equation 3:

$$\tau_{av} = 0.65 C_D \left[\left(\frac{\gamma h}{g} \right) a_{\max} \right] \quad (3)$$

Where C_D is a stress reduction factor. The range of C_D for different soil profiles is shown in Fig. 2, along with the average value up to a depth of 12 m.

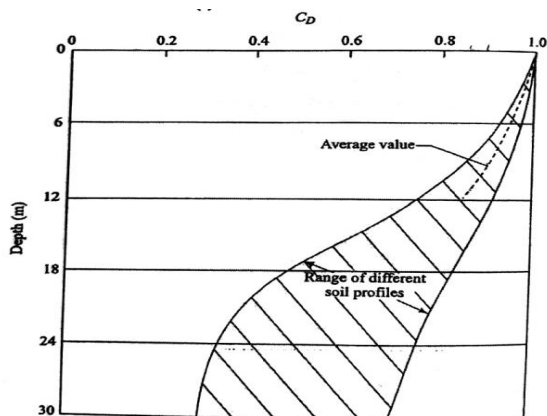


Fig. 2 Range of the shear stress reduction factor C_D for the deformable nature of soil [1]

A geotechnical investigation carried out in a deposit of soil provided the field SPT-N at Nurul Haq Shelter as given in Table 1.

Table 1 Field SPT-N Value

Range of depth (m)	Depth (m)	SPT-N (blows/30 cm)	SPT-N average (blows/30 cm)
0 - 6	1.55	34	46.7
	3.55	54	
	5.55	52	
6 - 11	7.55	48	49
	9.55	50	
11 - 18	11.55	38	22
	13.55	18	
	17.55	10	
18 - 22	19.55	8	8
	21.55	8	
22 - 25	23.55	12	12
	25.55	10	
	27.55	24	
25 - 30	29.55	28	20.7
	31.55	19	
	33.55	14	
30 - 40	35.55	40	29.4
	37.55	44	
	39.55	30	

Table 2 shows an empirical relationship between N' value and relative density (D_r), the angel of lateral friction (ϕ) and unit weight of granular soils (γ). The SPT-N average on Table 1 can be used to approximate moist unit weight, γ , w and saturated unit weight, γ_{sat} of granular soils in Table 2.

Correlations of cohesive soil physical properties with N values are crude and therefore, correction of N values in cohesive soils is not necessary [2]. From Table 1, it can be seen that depths of soil between 30 m and 40 m is silt soil with SPT-N average of 29.4 (correction not necessary).

Table 2 Empirical values for ϕ , D_r and unit weight of granular soils based on SPT-N in the field [2]

Description	Very loose	Loose	Medium	Dense	Very Dense
Relative density, D_r	0-0.15	0.15-0.35	0.35-0.65	0.65-0.85	0.85-1
SPT- N value	0-4	4-10	10-30	30-50	≥ 50
Approximate angel of internal friction, ϕ (°)	25-30	27-30	30-35	35-40	38-43
Range of approximate unit weight, γ (kN/m ³)	11-15.7	14.1-18.1	17.3-20.4	17.3-22	20.4-23.6

Soil profile at the Nurul Haq shelter is shown in Fig. 3. The groundwater table is encountered at a depth of 1.5 m measured from the ground surface. The maximum peak ground acceleration at the site $a_{\max} = 0.6$ g, with an earthquake magnitude of 7.6.

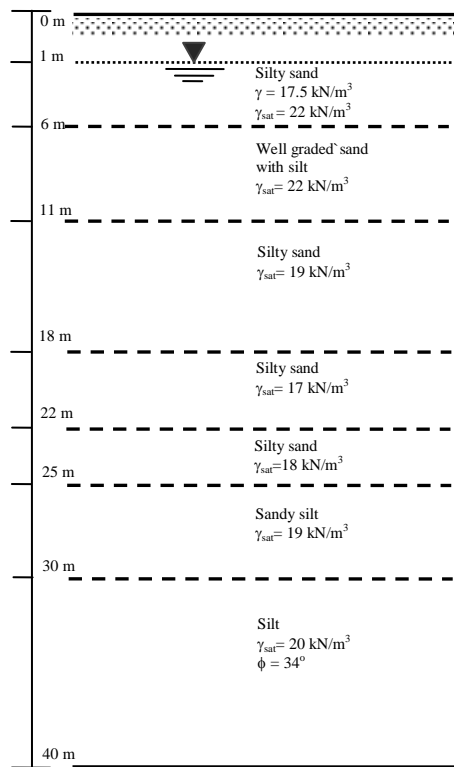


Fig. 3 Soil Profile at Nurul Haq Shelter

Calculating the shear resistance available and calculating the shear stress induced in the sand deposit at different depths can be done using the following steps:

Step 1. Table 3 can be used to calculate the shear resistance available in the sand deposit at different depths

Table 3 Calculating the available shear resistance

Depth (m)	N _E (blows/30 cm)	Vertical eff. stress (kPa)	C _N [Eq. (2)]	N' (blows/30 cm)	(t _h /s _h) _{icu} [Fig. 1]	t _b (kPa)
1.55	34	24.2	1.99	67.6	*	*
3.55	54	48.58	1.40	75.8	*	*
5.55	52	72.96	1.14	59.5	*	*
7.55	48	97.32	0.99	47.6	*	*
9.55	50	121.7	0.89	44.3	*	*
11.55	38	144.45	0.81	30.9	0.34	49.1
13.55	18	162.83	0.77	13.8	0.15	24.4
17.55	10	199.59	0.69	6.9	0.075	15.0
19.55	8	247.5	0.62	5.0	0.051	12.6
21.55	8	261.9	0.60	4.8	0.05	13.1
23.55	12	277.7	0.59	7.0	0.075	20.8
25.55	10	294.6	0.57	5.7	0.06	17.7
27.55	24	312.98	0.55	13.3	0.15	46.9
29.55	28	331.36	0.54	15.0	0.16	53.0
31.55	19	351.3	*	*	*	*
33.55	14	371.68	*	*	*	*
35.55	40	392.06	*	*	*	*
37.55	44	412.44	*	*	*	*
39.55	30	432.82	*	*	*	*

From Table 3, it can be seen that SPT-N' is greater than 30 at the depths of soil between 1.55 m and 9.55 m. According to Seed, Idriss and Arango (1983) and Seed and Idriss (1982), if N' is more than 30, liquefaction is unlikely to occur [1].

Step 2. Table 4 can be used to calculate the shear stress induced in the soil deposit at different depths

Table 4 Calculating the induced shear resistance

Depth (m)	Total vertical stress (kN/m ²)	a _{ms} /g	C _D Fig. 2	t _w kPa, [Eq. (3)]	Liquefaction Potential
1.55	29.6	0.6	*	*	Not liquefaction
3.55	73.6	0.6	*	*	Not liquefaction
5.55	117.6	0.6	*	*	Not liquefaction
7.55	161.96	0.6	*	*	Not liquefaction
9.55	205.96	0.6	*	*	Not liquefaction
11.55	248	0.6	0.87	84.1	Liquefaction
13.55	286	0.6	0.68	75.8	Liquefaction
17.55	362	0.6	0.50	70.6	Liquefaction
19.55	396.9	0.6	0.43	66.6	Liquefaction
21.55	431	0.6	0.40	67.2	Liquefaction
23.55	466.5	0.6	0.35	63.7	Liquefaction
25.55	503.5	0.6	0.32	62.8	Liquefaction
27.55	541.6	0.6	0.30	63.4	Liquefaction
29.55	579.6	0.6	0.30	67.8	Liquefaction
31.55	619.15	0.6	*	*	Not liquefaction
33.55	659.15	0.6	*	*	Not liquefaction
35.55	699.15	0.6	*	*	Not liquefaction
37.55	739.15	0.6	*	*	Not liquefaction
39.55	779.15	0.6	*	*	Not liquefaction

From Fig. 2, it can be seen that C_D value at the depths > 30 m is not available so that the shear stress induced (τ_{av}) cannot be determined, so liquefaction is unlikely to occur in this depths.

Step 3. Check to see if τ_{av} ≥ τ_h at any depth in the soil deposit. From Tables 3 and 4 above, it can be seen that τ_{av} is greater than τ_h at the depths of soil between 11.55 m and 29.55 m, so **liquefaction occurs** between this depths.

Based on the evaluation of the soil liquefaction, it is found that the location of the shelter building has a high liquefaction potential.

EVALUATION OF BUILDING STRUCTURE

Location of Existing Shelter

Nurul Haq Shelter is located close to the coastline, with a distance of 0.37 km towards the coastline of Padang. The pattern of land use around the location is a residential area.

Tsunami Vulnerability Level

Based on the tsunami hazard map of Padang city

issued by the Regional Development Planning Board of Padang City, the depth of tsunami inundation in the location of the plan is 4-5 m. The estimated depth of tsunami inundation is based on the contours of the Padang City area and the prediction of tsunami waves in Padang City.

Data of Building Structure

- a. Structural Type : Reinforced concrete
- b. Concrete strength, f_c' : 30 Mpa
- c. Steel yield strength, f_y : 400 MPa
- d. Number of Floors : 7 (Seven) Floor
- e. Building Height : 23,12 m
- f. Building Area : 36 m x 18 m
- g. Thickness of Slab : 15 cm

Modeling of Existing Structure

Fig. 4 shows the 3D modeling of the shelter structure using ETABS commercial software. The columns and beams of the building structure are modeled as frames while the floor plates are modeled as slab elements.

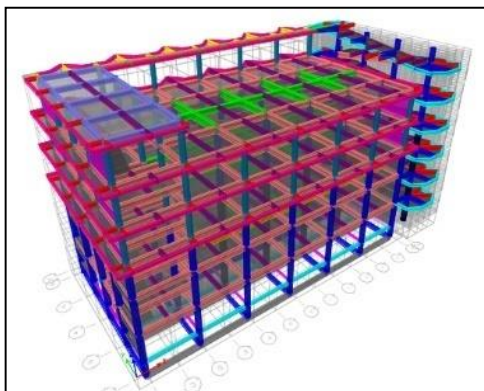


Fig. 4 Modeling of Existing Structure

Loading

The dead and live load refers to Minimum loads for Building Design and Other Structures of SNI 1727-2013 [3]. The analysis of earthquake load using dynamic analysis (earthquake response spectrum) for Padang City based on SNI 03-1726-2012 [4] and the earthquake hazard map 2017 by making its own design of response spectrum. Refugee Live Load refers to FEMA P-646 [5], which was 250 kg/m².

From the N-SPT soil data, soil condition of shelter location is the middle ground (SD), which can be seen from the N-SPT value of 22.35. According to SNI 03-1726-2012 and SNI 8460-2017, the value of N-SPT of medium soil ranges from 15

to 50 [7-8].

However, the soil at that location has the potential for liquefaction to be categorized as special soil (SF) according to SNI 03-1726-2012 or SNI 8460-2017. Therefore, the design response spectrum should be multiplied by 1.5. The comparison of the response spectrums between the SD and SF soil conditions can be seen in Fig. 5.

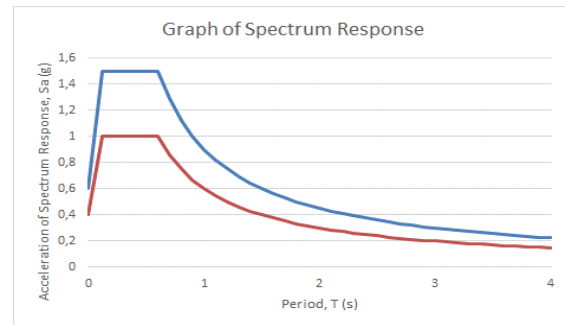


Fig. 5 Comparison of Response Spectrum between SD and SF soil Conditions at the Nurul Haq shelter building

Tsunami loads are calculated according to the FEMA P-646 standard [5]. The magnitude of each load value based on the predicted wave height of the tsunami, the ground elevation of the shelter area, the distance from the shore and other assumptions used, which can be seen in Fig. 6.

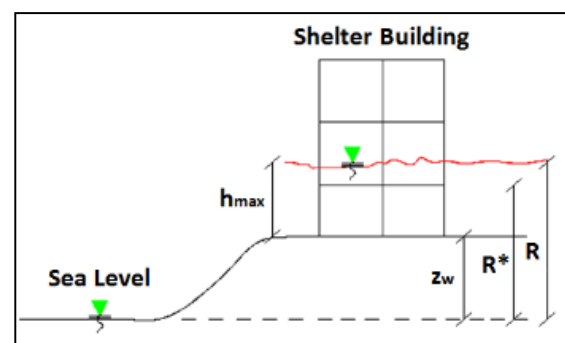


Fig. 6 Inundation Plan of the Tsunami [5]

The tsunami loads were calculated based on FEMA P-646 [5], as follows:

1. Hydrostatic Force
This load is given centered on the column as high as 1/3 the maximum height of water in a tsunami-immersed area in the direction of the tsunami.
2. Buoyant Force
Buoyant force loads are evenly distributed on the tsunami's upper floors.
3. Hydrodynamic Force
Hydrodynamic force loads are concentrated at the column as high as 1/2 of tsunami water puddle

in all the affected columns of tsunami flows in the direction of the tsunami.

4. Impulsive Force

The impulse force load is evenly distributed on the structural wall as high as a tsunami puddle in the direction of the tsunami.

5. Impact Force

The force of the impact of the debris is evenly distributed on the first part of the structure of the affected part of the stream.

6. Debris Force

The force due to debris is given evenly on structural elements with a minimum width of 40 ft (12 m).

7. Extra Gravity Load

The added gravity load is evenly distributed on the top floor affected by the tsunami.

8. Uplift Hydrodynamic Force

The hydrodynamic lift force is evenly distributed on the top floor affected by the tsunami.

The calculation results of applied tsunami loads on the analysis of the Nurul Haq Shelter are shown in Table 5.

Table 5 Recapitulation of Tsunami Load

No.	Tsunami Load	Force
1	Hydrostatic load	28,541.7 kg
2	Buoyant Force	5,830 kg
3	Hydrodynamic Force	7,595.78 kg
4	Impulsive Force	11,393.7 kg
5	Impact Force	63,593.2 kg
6	Debris Force	151,916.0 kg
7	Extra Gravity Load	6,116 kg/m ²
8	Uplift Hydrodynamic Force	6.54938 kg/m ²

Capacity of Structure

Column Capacity

P-M interaction diagram is a diagram illustrating the ability or capacity of the column based on the relationship between the moment and axial load of the column. Figs. 7-10 show P-M interaction diagrams of columns obtained from the results of the structural analysis.

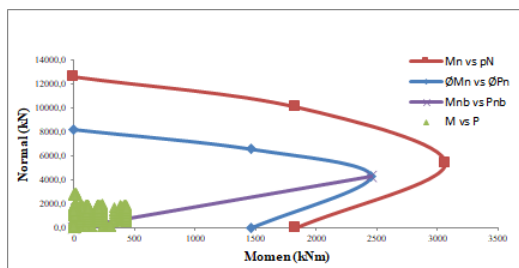


Fig. 7 P-M Interaction Diagram of Column K1 (Ø 70 cm) on 1st Floor

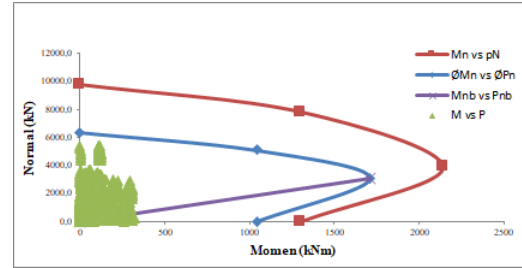


Fig. 8 P-M Interaction Diagram of Column K2 (Ø 60 cm) on 1st Floor

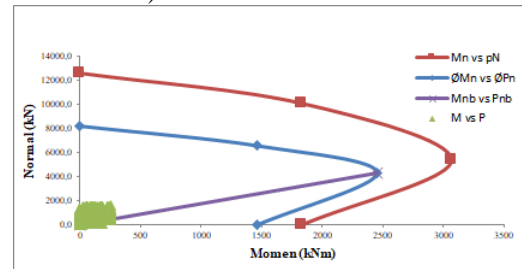


Fig. 9 P-M Interaction Diagram of Column K1 (Ø 70 cm) on Mezzanine Floor

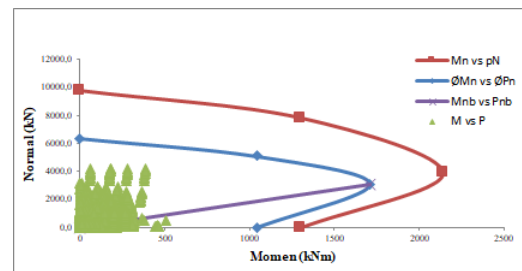


Fig. 10 P-M Interaction Diagram of Column K2 (Ø 60 cm) on Mezzanine Floor

Based on these P-M diagrams, it can be seen that the flexural capacity of the 1st and mezzanine floor columns can withstand the working loads including earthquake and tsunami loads because all axial and bending moment data are within the P-M column interaction diagram. For columns on the 2nd, 3rd, 4th and roof floor also have enough capacity of resisting the working loads.

The shear capacity of the columns has been calculated with the results shows that the shear capacity of the columns is able to resist the loads acting on the shelter structure.

Beam Capacity

Tables 6 show the flexural capacity of the beam elements. From Table 6, it can be seen that beam elements on the 1st floor, the mezzanine floor, and the 2nd floor are unable to withstand the working loads. Meanwhile, the beams in other floors are able to resist the loads.

Table 6 Beam Flexural Capacities of the Shelter

Recapitulation of Beam Flexural Capacity						
Floor	Type of Beam	Num. of steel Bar		ØMn	Mu	Note
		Tens.	Comp.			
First	B1	6 D 22	3 D 22	399	279	OK
	30 x 60	3 D 22	6 D 22	203	232	NOT OK
	B1	6 D 22	3 D 22	399	489	NOT OK
	30 x 60	3 D 22	6 D 22	203	483	NOT OK
	B2	8 D 22	4 D 22	677	1381	NOT OK
	35 x 75	4 D 22	8 D 22	343	1320	NOT OK
	BA	3 D 19	3 D 19	97	162	NOT OK
	25 x 40	3 D 19	3 D 19	97	212	NOT OK
Mezza-nine	B1	6 D 22	3 D 22	399	261	OK
	30 x 60	3 D 22	6 D 22	203	235	NOT OK
	B1	6 D 22	3 D 22	399	462	NOT OK
	30 x 60	3 D 22	6 D 22	203	475	NOT OK
	BA	3 D 19	3 D 19	97	137	NOT OK
	25 x 40	3 D 19	3 D 19	97	212	NOT OK
Second	B1	6 D 22	3 D 22	399	238	OK
	30 x 60	3 D 22	6 D 22	203	209	NOT OK
	B1	6 D 22	3 D 22	399	281	OK
	30 x 60	3 D 22	6 D 22	203	234	NOT OK
	B2	8 D 22	4 D 22	677	289	OK
	35 x 75	4 D 22	8 D 22	343	225	OK
	BA	3 D 19	3 D 19	97	30	OK
	25 x 40	3 D 19	3 D 19	97	17	OK

Tables 7 show the shear capacity of the beam elements. As seen in the table, the beams don't have enough shear capacity, especially on the 1st floor and the mezzanine floor.

This indicates that the beams should be strengthened to improve its flexural and shear capacities before using the building as a shelter for the earthquake and tsunami disasters.

Table 7 Beam Shear Capacities the Shelter Building

Recapitulation of Beam Shear Capacity					
Floor	Beam	Num. of Bar	Vr	Vu	Note
First	B1	D13 - 150	420	203	OK
	30 x 60	D13 - 175	377	218	OK
	B1	D13 - 150	420	487	NOT OK
	30 x 60	D13 - 175	377	488	NOT OK
	B2	D13 - 100	747	872	NOT OK
	35 x 75	D13 - 150	554	873	NOT OK
	BA	D13 - 150	262	151	OK
	25 x 40	D13 - 200	212	151	OK
Mezza-nine	B1	D13 - 150	420	218	OK
	30 x 60	D13 - 175	377	211	OK
	B1	D13 - 150	420	487	NOT OK
	30 x 60	D13 - 175	377	513	NOT OK
	BA	D13 - 150	262	158	OK
	25 x 40	D13 - 200	212	152	OK

EVALUATION OF FOUNDATION

The foundation analysis is carried out on the foundation bearing capacity. According to SNI 8460-2017 of article 12.2.4.3, stated that for the pile foundation, the shaft resistance at the soil layer with

liquefaction potential should be ignored or not taken into account the axial or uplift capacity [6].

Fig. 11 shows the foundation plan of the shelter. The Foundation and Soil Data are as follows:

- Types of Foundation: Pile
- Depth: 30 m
- Foundation Size: Ø350
- Concrete Comp. Strenght, f_c' : 55 Mpa

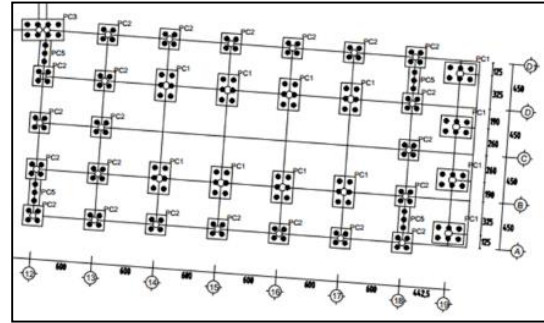


Fig. 11 Foundation Plan of the Nurul Haq Shelter [8]

Determination of Ultimate Bearing Capacity for Pile

The ultimate bearing capacity of the pile (Q_u) is taken using Equations 4 or 5:

$$Q_u = R_s + R_t \quad (4)$$

or

$$Q_u = f_s A_s + q_t A_t = f_s C_d \Delta d + q_t A_t \quad (5)$$

The allowable bearing capacity of the pile (Q_a) is taken using Equation 6:

$$Q_a = \frac{Q_u}{FS} = \frac{R_s}{FS_1} + \frac{R_t}{FS_2} \quad (6)$$

R_s = The shaft resistance

R_t = The toe resistance

f_s = The unit shaft resistance

q_t = The unit toe resistance

Meyerhof (1976) recommended that the unit toe resistance, q_t , in kPa for pile driven into sands and gravels is approximated by [1] (Equation 7):

$$f_s = 2N' \leq 100 \text{ kPa} \quad (7)$$

Static capacity calculation in silt soil can also be performed using an effective stress based method, where the effective soil friction angel, ϕ' , should be used in parameter selection [1]. The unit toe resistance, q_t , in kPa is calculated using Equation 8:

$$q_t = N_t p_t \quad (8)$$

N_t = Toe bearing capacity coefficient
 P_t = Effective overburden pressure at the pile toe in kPa

The Interpreted soil profile from Nurul Haq Shelter [8] can be seen Fig. 12.

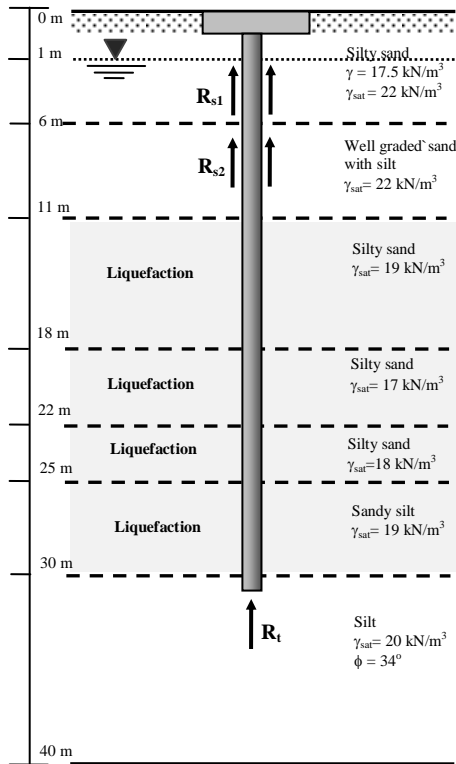


Fig. 12 Interpreted Soil Profile from Nurul Haq Shelter .

Table 8 Summary of Pile Foundation Capacity

Group pile	Calculated ultimate capacity of single pile (Q_u)			Ultimate capacity of pile group, Q_{ug} (kN)	Calculated allowable capacity of pile group, Q_{ag} (kN), (FS = 3)	Load
	R_u (kN)	R_s (kN)	Q_{tu} (kN)			
PC 1 (6 pile)	1,165.5	1,361.8	2,527.3	15,163.8	5,054.6	5526
PC 2 (4 pile)	1,165.5	1,361.8	2,527.3	10,109.2	3,369.6	2859

The ultimate pile group capacity at the Nurul Haq Shelter is be taken as the sum of the ultimate capacities of the individual piles in the group. From calculation results (Table 8), it is found that the allowable pile group capacity on the PC 1 is 5,054.6 kN, which is less than that of the required allowable pile group capacity of 5526 kN. This means that the PC 1 foundations don't have enough capacity to resist the shelter building. The strengthening of this foundation should be done if the building will be used as a shelter.

For PC2 Pile foundations, On the other hand, the allowable pile group capacity based on the design recommendations 2 is 3,369.6 kN, which is higher than that of the required allowable pile group capacity of 2,859 kN.

CONCLUSION

1. The Soil condition at the Nurul Haq Shelter between the depths of 11.55 m and 29.55m has a high potential of liquefaction.
2. The result of the structural analysis showed that flexural and shear capacities of columns are able to loads applied on the shelter structure, but the flexural and shear capacities of beams on floor 1, mezzanine and second floor have not strong enough capacities to resist the working loads.
3. The allowable pile group capacity on the PC 1 is less than that of the required allowable pile group capacity, which means that this foundation does not strong enough capacity to resist the weight of the shelter building, especially when the earthquake and liquefaction occur.
4. The shelter building should be retrofitted before being used as a vertical evacuation building for the earthquake and tsunami.

ACKNOWLEDGEMENTS

The authors would like to acknowledge the funding support provided by Andalas University, Padang, Indonesia.

REFERENCES

- [1] Das B.M., Ramana G.V. (2011), Principles of Soil Dynamics, Cengage learning, pp. 433 – 443.
- [2] FHWA, (2006), Design Construction of Driven Pile Foundations, Reference Manual Volume I, Publication No. FHWA NIII-05-042, pp.4-29.
- [3] National Standardization Agency. Minimum Loads for Building Design and Other Structures. SNI 1727-2013, Jakarta, Indonesia
- [4] National Standardization Agency. Earthquake Resilience Planning Procedure for Building and Non-Building, SNI 1726-2012, Jakarta, Indonesia
- [5] FEMA P646-2012. Guidelines for Design of Structure for Vertical Evacuation from Tsunami. Federal Emergency Management Agency. Washington D.C, USA
- [6] National Standardization Agency. Geotechnical Design Requirements. SNI 8460-2017. Jakarta, Indonesia.

TESTING OF FOAM CONCRETE FOR DEFINITION OF LAYER INTERACTING WITH SUBSOIL IN GEOTECHNICAL APPLICATIONS

Marian Drusa¹, Jozef Vlcek¹, Walter Scherfel² and Bronislav Sedlar³

¹Faculty of Civil Engineering, University of Zilina, Slovakia; ²iwtech Ltd., Trencin, Slovakia;

³CEMEX Czech Republic Ltd., Prague, Czech Republic

ABSTRACT

Today's production of foam concrete (FC) has become more suitable for various types of applications due to the usage of new additives and improved technology. One typical application of foam concrete in Europe is creation of a sub-base layer of floor of multi-storey buildings, where thermal and noise insulation functions are required. The main advantage of foam concrete production is its unlimited variety of desired properties, which must be properly balanced for a specific application and its interacting structure. Produced FC can have unit weight from 300 to 900 kg.m⁻³, compression strength from 0.4 to 12 MPa, elasticity modulus from 1200 to 2500 MPa and coefficient of thermal conductivity from 0.15 to 0.30 W.m⁻¹K⁻¹. Thanks to these properties, FC can be used for construction of foundation slabs of passive houses, as a sub-base layer of industrial floors and as a filling material of narrow excavated shafts. As for concrete, reinforcement can improve tensile properties, but due to corrosion, iron bars or nets must be replaced by special material bars, nets, geogrids or geotextiles. For the mentioned type of structures and loading of FC layers, importance of laboratory and in-situ testing is crucial. This article presents laboratory tests of one of the selected parameters, which is flexural strength of FC in various unit weights, and demonstrates a significant improvement of strength when non-woven geotextile and mesh type reinforcement was used. Use of geotextile at the bottom part of samples increased flexural strength from 30 to 60%, mesh reinforcement can have doubled basic flexural strength. Crack propagation with respect to time was also observed during tests in order to compare results of reinforced FC with no reinforced layer.

Keywords: Flexural strength, Foam concrete, Geotextile, Reinforcement

INTRODUCTION

The successful cooperation between academic and private sectors brings new possibilities for the use of progressive and multifunctional materials, which foam concrete (FC) is without any doubt.

The aim was to verify the usage of FC of various bulk densities as a subbase layer for industrial floors, foundation structures or pavements, thereby providing the investor with benefits in terms of cost savings, improved subbase homogeneity and increasing durability with favorable thermal properties.

Utilization of the FC is dependent on the relevant investigation of material properties. For the design of the above mentioned structures, estimation of some mechanical characteristics is important, especially the compressive and flexural strength or modulus of elasticity.

Considering the load mechanism of such a layer in the horizontally situated and vertically loaded structure, the flexural strength can be the limiting factor.

This paper presents the bend testing using 4-point flexural test and possible ways to improve this important parameter.

FOAM CONCRETE

Foam concrete (FC), as a mixture of cement, water, additives and technical foam, has been in principle well known for more than 30 years. It is a building material with good mechanical properties, low thermal conductivity, suitable for simple or even technological treatments. Foam concrete contains closed void pores that allow to achieve a low bulk density with a low material requirement of raw materials. Thanks to its properties, it is usable as a replacement of conventional subbase layers of the floors, the pavements or as a part of the foundation structures of passive buildings [1]-[4].

Mixture composition of foam concrete can be prepared for production of various bulk densities. Our special mixing machines can produce FC of dry bulk density of 300, 400, 500, 600 and 700 kg.m⁻³. For each density of foam concrete, simple names are used FC300, FC400, FC500, FC600 and FC700. For the application in the industrial floors, foam concrete layer is equipped with non-woven geotextile (GTX-N) at the bottom. Nowadays the foam concrete with densities 300 – 400 kg.m⁻³ is most often used as a floor levelling layer of administrative and residential

buildings. Realized research shows that its utilization in various densities can be much wider, [5]. The conventional subbase layer of aggregate can be replaced with the layer of the foam concrete FC with the corresponding density.

Mechanical Characteristics

Mechanical characteristics are necessary inputs of the structural analysis. In order to provide required parameters, a series of material tests has to be performed. Measured parameters of the foam concrete are listed below.

Compressive strength

In contrast to the fill materials for the subbase layers, the foam concrete is capable of bearing the compressive load. Compressive strength of the foam concrete depends on the formula based upon required bulk density. Time-dependent propagation of the compressive strength for bulk densities 500, 600 a 700 kg.m^{-3} is plotted in Fig. 1.

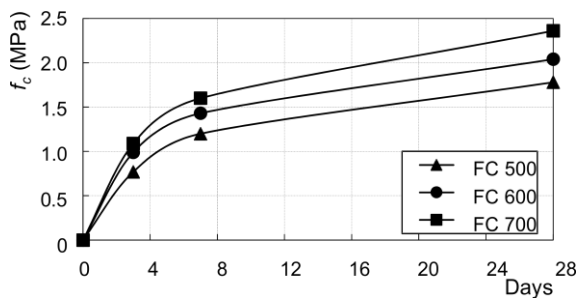


Fig. 1. Time dependence of compressive strength of the foam concrete.

For all bulk densities, 3-day's compressive strength reaches a minimum of 50% of the 28-day's compressive strength.

Flexural strength

Significantly higher tensile strength of the foam concrete is an advantage in comparison to the granular materials used for the subbase layers. A 4-point flexural test is usually performed to measure the flexural strength of the hardened concrete and this method is also suitable for the simple foam concrete. Preliminary tests show that 3-day's tensile strength reaches a minimum of 50% of the 28-day's flexural strength similar to compressive strength.

Flexural strength of the plain foam concrete can further be improved by the geotextile (GTX-N) at the bottom face of the layer. Geotextile is a regular part of the final subbase layer design. To achieve a further increase of the flexural strength, additional reinforcement can be added. The influence of the reinforcement will be presented in this paper.

Elasticity Modulus and Poisson's ratio

Elasticity modulus is a crucial parameter for the design of the floor or foundation slabs and their interaction analysis, [5, 6]. In practical design, a multi-layered subbase compound usually requires the substitution of the particular materials with the homogenous and isotropic half-space, which is described by the modulus of subgrade reaction or the modulus of elasticity. Dependency of the modulus of elasticity and the bulk density is plotted in Fig. 2.

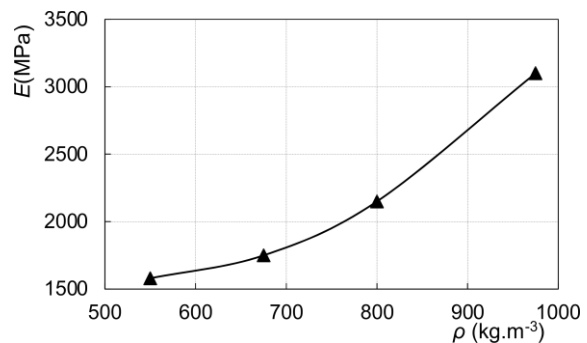


Fig. 2. Modulus of elasticity vs. bulk density of foam concrete.

Poisson's ratio is determined during compressive stress at a defined stress level up to 68% of the final compressive strength. Typical values of Poisson's ratio of the foam concrete FC 500 are presented in table 1.

Table 1. Poisson's ratio of foam concrete FC 500

Compressive stress [kPa]	472	708	944	1180
Poisson's ratio [-]	0.11	0.20	0.24	0.33

REINFORCEMENT OF FOAM CONCRETE

The principle of reinforcement of FC layer is similar to conventional concrete. Reinforcing elements are bars, meshes or fibers or their combinations. Contribution of the reinforcing elements in the foam concrete is most noticeable at the tensile loading of the layer, when brittle materials like foam concrete or regular concrete bear only a limited amount of tensile forces. In practical design, tensile forces are usually borne by the reinforcing members. The tests of the flexural strength presented in this article were aimed at the contribution of the reinforcement to the mechanical properties of the foam concrete. The first step represents the geotextile at the bottom of the foam concrete as a permanent part of the design. Despite its low tensile strength and high ductility, geotextile

structure together with the fresh foam concrete creates a reinforced layer at the bottom and causes a larger flexural strength. In opposite to the classic concrete or crushed gravel layer, liquid foam concrete leaks into a geotextile structure between fibers and creates a high interaction mechanism.

Use of additional reinforcement elements brings another increase of the flexural strength and overall roughness, which is a phenomenon observed at the concrete reinforced with the dispersed fibers. When tensile failure occurs, the resistance of the specimen still increases as the activation of the reinforcement takes place. Because our main goal was to utilize the FC in the subbase layer, reinforcement by meshes was considered. Preliminary flexural tests aimed at the foam concrete formula improvement show a significant increase of the flexural strength using basalt meshes. Standard steel meshes have to be installed with some covering layer of the concrete to restrict the negative impacts of environment and concrete itself. Basalt meshes are non-corrosive and dielectric and no covering layer is required. Mesh can be placed right on the geotextile without distance elements. Liquid FC leaks through the mesh openings right to the geotextile and creates a composite structure "FC-GTX-mesh".

Reinforcement Types

Preliminary flexural testing was aimed at the selection of the appropriate reinforcing elements. Main criterion was the highest possible peak flexural strength achieved with particular reinforcement type.

Geotextiles

After first tests, it was obvious that even non-woven separation geotextile (GTX-N) can cause an increase of the flexural strength. But overall contribution of the stiffer geotextiles does not correspond to the higher stiffness and cost. Exclusion of the woven geotextiles was the next step, when only regular non-woven geotextile of separation and filtration function was used, with area weights from 200 to 500 g.m⁻². Further tests show that geotextile with the weight of 200 g.m⁻² is almost comparable with heavier geotextiles in terms of flexural strength contribution, beside the lower costs, so it was selected as geotextile layer for the flexural tests presented in this paper.

Basalt mesh reinforcement

Foam concrete is similar to the conventional concrete in some ways and its reinforcement by basalt mesh (rods of basalt fibers arranged in net) is one of the suitable for them. Application of FC is aimed rather on the subbase layers and extensive reinforcement is not required. Plate load tests

performed on the 22 cm layer of the FC at the in-situ testing field of the University of Zilina show about 20% increase of the measured modulus of elasticity, when basalt reinforcing mesh was used. Following those findings, several specimens for the flexural testing were prepared with this type of reinforcement. Except the meshes, reinforcing bars can be used but their application in the foam concrete is not suitable at the moment because of the loading mechanism of the subbase layer made from the foam concrete. Mesh structure creates a uniformly reinforced structure during the "leak in" process with a higher flexural strength and roughness in opposite to the distinct bars with a significantly higher stiffness when interaction mechanism between reinforcement and softer surrounding foam concrete needs to be verified.

Combined reinforcement

Combigrid as a combination of the biaxial bonded geogrid and non-woven geotextile was also tested. Surprisingly, the flexural strength was lower than with the geotextile alone. Reason for this phenomenon is the flat shape of the geogrid with relatively smooth surface of the ribs. This imperfection disturbs the "composite effect" of the FC and the geotextile. Usability of the combined reinforcement thus depends on the ability of the composite system "foam concrete-combined reinforcement" to provide a sufficient interaction level between particular elements of the system.

FLEXURAL TEST OF FOAM CONCRETE

Flexural test provides values of the modulus of elasticity of bending or flexural strength. Usually, a 3-point or 4-point flexural test can be used. Preparation of the specimen and the test procedure itself are simple but the results can be affected by the specimen irregularities, loading geometry or strain rate. This mechanism of loading takes place in two-dimensional horizontal structures such as slabs or layers in the floor, foundation or pavement structures [4]. Tensile or flexural strength becomes a crucial parameter of the particular material in the design. Hardened foam concrete is very similar to the conventional hardened concrete, so flexural test simulating real load conditions can be adopted to determine the flexural strength of the test specimen [7]. A 4-point flexural test was performed with the FC beams of the selected bulk density.

Test Geometry and Specimens

Test specimens were prepared in accordance with the standards for the flexural testing of the conventional concrete, [8]. Nominal dimensions of the beam were $d_1 = d_2 = d = 100$ mm and $L = 400$

mm. Span of the supports was $l = 300$ mm. Distance of the loading pins was $d = 100$ mm (Fig. 3).

Force is distributed from the hydraulic cylinder through spreader to the loading pins. Load cell is situated at the connection of the cylinder and the spreader.

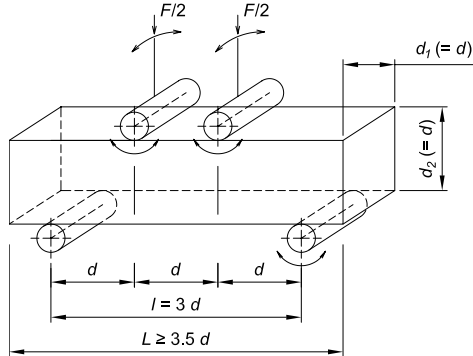


Fig. 3. Geometry of the flexural test.

Flexural strength f_{cf} for the 4-point bending test is calculated as follows:

$$f_{cf} = \frac{F \cdot l}{d_1 \cdot d_2^2} \quad (1)$$

Each specimen was created in the form with the open upper surface. When the foam concrete was poured out to the form, the upper surface was levelled after a few hours. The beam was then removed from the form after 3 days and it was covered by a foil to avoid the extensive evaporation that can cause a deprivation of the strength. The foil was removed right before the test which took place 28 days after the specimen creation. Geotextile was placed on the bottom of the form before the foam concrete. When basalt mesh was used, it was placed directly on the geotextile (Fig. 4).



Fig. 4. Basalt mesh on geotextile in the form.

Foam Concrete Parameters

A total of four mixtures of foam concrete were prepared for the testing. Each mixture is represented

by the nominal bulk density which is given by the corresponding formula. Nominal bulk density is the density of the dry specimen while normal density during the test is the density of the specimen with some moisture content. Nominal and average normal bulk densities during the test calculated from 3 measurements on the 28-day's beams are displayed in table 2.

Table 2. Bulk densities of the foam concrete

Name	FC 300	FC 400	FC 500	FC 600
Average density (kg.m ⁻³)	397	522	584	735

Reinforcement Parameters

Non-woven separation geotextile Geofiltex 63/20 was used in the first step of reinforcing. Parameters of the geotextile are shown in table 3.

Table 3. Parameters of geotextile Geofiltex 63/20

Parameter	Value
weight (g.m ⁻²)	200
tensile strength (kN.m ⁻¹)	
- longitudinal direction	12.0
- transversal direction	7.5
ductility (%)	
- longitudinal direction	75
- transversal direction	115
dynamic puncture resistance (mm)	14
static puncture resistance (N)	1 400
material type	PP

Basalt reinforcement was represented by the composite mesh ORLITECH MESH® [9] made from rods located in mutually perpendicular directions connected in node by a special mass. Rods are crafted from basalt fibers with the resin binder (Fig. 4). Parameters of the basalt mesh are shown in table 4.

Table 4. Parameters of the basalt mesh

Parameter	Value
weight (g.m ⁻²)	360
rod distance (mm)	100 × 100
rod diameter (mm)	3
tensile strength (MPa)	1 300
modulus of elasticity (GPa)	47
ductility at maximum force (%)	2.5

Test procedure

Specimen was placed in the test apparatus

according to the scheme in Fig. 3. After initial “zero” loading involving the weight of the spreader, the loading began with the rate of 5 to 8 kg.s^{-1} . Test ends when maximum loading force is achieved at the total failure of the specimen. In case of the reinforced foam concrete, the force may still increase as the full activation of the reinforcement takes place.

RESULTS AND DISCUSSION

Three specimens of each combination of bulk density and reinforcement were tested. Typical propagation of the test for one specimen is plotted in the Fig. 5.

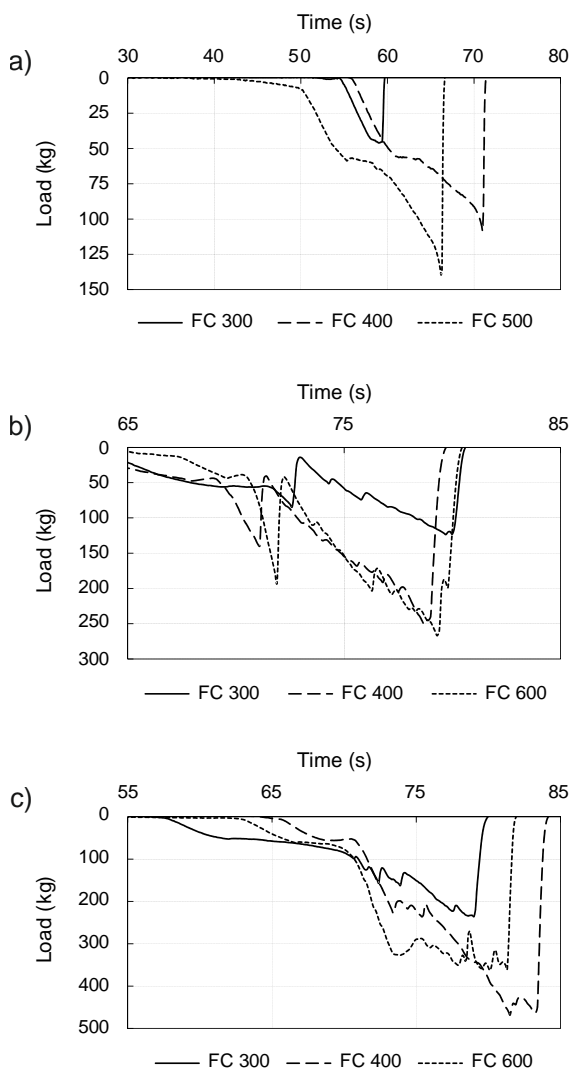


Fig. 5. Propagation of the time/load dependency for selected flexural tests,
a) plain foam concrete
b) foam concrete with geotextile
c) foam concrete with geotextile and mesh.

Increase of the bulk density is proportional to the increase of the flexural strength. Behavior of the

specimens is similar across the bulk densities. Average flexural strength for the particular bulk density and the reinforcement is plotted in Fig. 6.

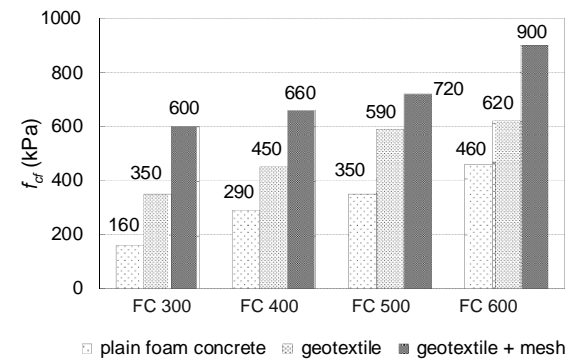


Fig. 6. Flexural strength of the tested FC mixtures.

Fig. 7 shows a direct comparison of the time/load dependency for the reinforced and non-reinforced specimen of FC 400. When peak loading was achieved, the tensile stress rapidly dropped to “zero” values in case of the plain foam concrete. On the contrary, tensile strength raised again after some drop, when cracks occurred in case of the reinforced foam concrete. Drop after first cracks is more evident at the specimen with geotextile only, while after-crack increase of tensile stress is much larger at the specimen with both geotextile and mesh.

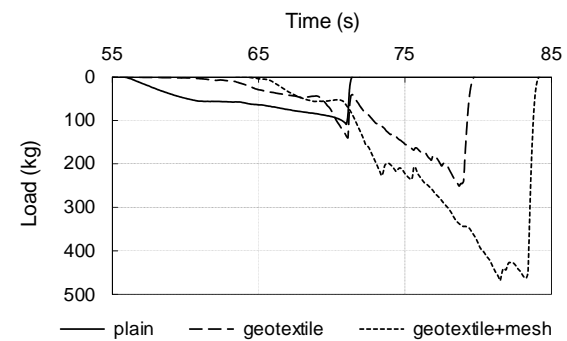


Fig. 7. Propagation of the time/load dependency for the foam concrete FC400 with various reinforcements.

Confirmation of plotted behavior can be seen at the investigation of specimens after testing. In the case of plain FC, a simple vertical crack occurs approximately in the middle of the specimen (Fig. 8a). Cracks appear very quickly and the damage of the specimen is almost instant. In case of the geotextile, multiple cracks take place in lines intersecting the positions of loading pins (Fig. 8b). After the initial break, geotextile activates and the specimen behaves as a viscoelastic element. Extended tensile load at the bottom is accompanied by the compressive load at the top of the specimen.

Total break takes place when breakage of the compressed part occurs together with the loss of connection between the geotextile and the foam concrete. Added basalt mesh induced another set of cracks related to the mesh ribs (Fig. 8c). These cracks are inclined from the center of loading zone and end at the edge at points where transversal mesh ribs are located. Overall behavior till the total breakage of the specimen is similar to the geotextile reinforcement.

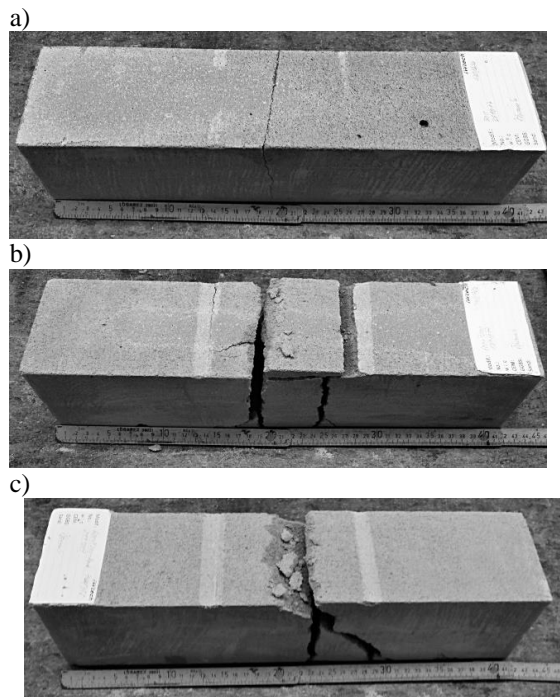


Fig. 8. Failure mechanisms of the FC specimens,
a) plain foam concrete,
b) foam concrete with geotextile,
c) foam concrete with geotextile and mesh.

Use of reinforcement elements with a good level of mutual interaction significantly increases the available flexural strength and some level of flexural roughness can be achieved. This allows to utilize the post-crack part of the flexural strength similar to the conventional concrete with dispersed fibers.

CONCLUSION

Presented tests were aimed at the flexural strength testing as a crucial parameter for the design of the subbase layer of the several structures. Results show that normal flexural strength of the foam concrete can be further increased by the reinforcing elements such as geotextile alone or combination of the geotextile and the basalt reinforcing mesh. Addition of the geotextile contributes 30% to 60% increase of the first-crack flexural strength in comparison to the plain foam concrete. Additional

mesh could rise basic flexural strength twice time.

An increase of roughness is observed at the reinforced specimens. This means that final flexural strength at total breakage can be higher than first-crack flexural strength. Post-crack part of the flexural strength is then available similarly to the conventional concrete reinforced with the dispersed fibers. That opens up the opportunity for further research using experimental and new computational approaches. Based on these laboratory experiments, characteristics of the FC layer can be established, and material model can be formulated, which describes stress strain behavior of FC interacted with subsoil.

ACKNOWLEDGEMENTS

This work was supported by the Scientific Grant Agency of the Ministry of Education of the Slovak Republic, grant VEGA No. 1/0926/16 and grant KEGA No. 051ZU-4/2018.

REFERENCES

- [1] Decky M., Drusa M., Zgutova K., Blasko M., Hajek M. and Scherfel W., Foam Concrete as New Material in Road Constructions. *Procedia Engineering*, Vol. 161, 2016.
- [2] Vlcek J., Drusa M., Scherfel W., Sedlar B., Experimental Investigation of Properties of Foam Concrete for Industrial Floors in Testing Field, WMES 2017, in IOP EES, Vol. 95, 2017, 022049, doi: 10.1088/1755-1315/95/2/022049
- [3] Kadela M., Kozlowski M., Foamed Concrete Layer as Sub-Structure of Industrial Concrete Floor. *Procedia Engineering*, WMCAUS 2016, Vol. 161, 2016, pp. 468-476.
- [4] Kadela M., Model of Multiple-layer Pavement Structure-Subsoil System. *Bulletin of the Polish Academia of Sciences, Technical Sciences*, Vol. 64 (4), 2016, pp. 751-762.
- [5] Drusa M., Knoppik-Wróbel A., Rudišin R. Scherfel W.: Potential of composite foam concrete as an alternative layer for load transfer platform, in XXI RSP Seminar: Arkhangelsk, 3.07-6.07.2012, Warszawa: ISBN 978-83-7814-021-4. pp. 523-530
- [6] Kozlowski M., Kadela M. and Gwozdz-Lason M., Numerical Fracture Analysis of Foamed Concrete Beam Using XFEM Method. *App. Mech. and Mat.*, Vol. 837, 2016, pp. 183-186.
- [7] Kozlowski M., Kadela M. and Kukielka A., Fracture Energy of Foamed Concrete Based on Three-Point Bending Test on Notched Beams. *Procedia Engineering*, MATBUD 2015, Vol. 108, 2015, pp. 349-354.
- [8] EN ISO 12390-5 Testing Hardened Concrete. Flexural Strength of Test Specimens, 2009.
- [9] <http://www.orlimex.cz/kompozity/> on-line 04/18.

SEDIMENT FLOW CHARACTERISTICS ON SEABED SUBJECTED TO STATIONARY WAVES WITH DIAGONAL INCIDENT WAVE LOADING NEAR LINE STRUCTURES

Anh Quang TRAN¹, Kinya MIURA², Tatsuya MATSUDA³ and Takahito YOSHINO⁴

^{1,4}Graduate School of Architecture and Civil Engineering, Toyohashi University of Technology, Japan

^{2,3}Department of Architecture and Civil Engineering, Toyohashi University of Technology, Japan

ABSTRACT

Typical stationary waves are caused by overlapped the incident and reflected wave, when the plane wave vertically meets a line structure. In this case characteristic sediment flow behavior is observed and seabed is suffered from configuration change such as erosion and deposition. In more general situations where plane wave meets line structures in diagonal direction, however, overlapped waves would behave in three-dimensional manner. The stability of structures subjected to stormy ocean waves or tsunami depends on the integrity of seabed foundation ground, as well as the wave pressure acting directly on the structures. Thus reliable analysis method for evaluating the sediment flow on seabed and associated erosion-deposition is needed. The present study aims to clarify the sediment flow characteristics induced by the diagonal incident and reflected waves which meet line structure and broken line structure, with seabed effective stress response to sea wave loading into account. Erosion-deposition behavior was quantitatively examined based on the calculated results.

Keywords: Erosion-deposition Behavior, Effective Stress Response, Linear wave theory, Traction flow

INTRODUCTION

Because the stability of structure subjected to ocean waves depends on not only wave force, but also on seabed which support it, reasonable analysis method of the deformation of seabed induced by sediment flow is needed.

The scour phenomenon is evaluated in the forms of the sheet flow, the suspended load transport, and the bedload transport, etc. caused as a function of the flow velocity at the seabed. On the other hand, the stability of the structures is sometimes affected by the effective stress change in seabed [1]. From the geotechnical point of view, seabed is modeled as a continuum, and the effective stress response to the pressure variation is calculated [2,3].

In the present study, we propose an analysis method for evaluating sediment flow regarding the response of effective stress to wave loading. Miura, Morimasa, Otsuka, Yamazaki and Konami [4] qualitatively examined the characteristic sediment flow under traveling wave, stationary wave, and irregular wave. In this study, we quantitatively examine the sediment flow behavior near line structures including broken line structure with right angle corner.

ANALYSIS METHOD

The analysis method used consists of a wave analysis with linear wave theory, an effective stress analysis with a poro-elastic model, and an empirical

evaluation of sediment flow quantity by traction force.

Wave Analysis

Velocity potential was derived within the frame of the linear wave theory, and an incident wave and associated reflected waves were superimposed. In the analysis the seabed was assumed to be uniform, infinite in depth, and impermeable.

When wave travels along x -axis, the water surface and the velocity potential are presented by Eq. (1a, b) for the plane wave with wave height of H , wavelength of L , and period of T . The velocity potential function was modified for the traveling wave in an arbitrary direction by Eq. (2). The velocity components and water pressure can be calculated as the derivatives of the velocity potential function.

$$\eta(x, y, t) = \frac{H}{2} e^{i(\lambda x - \omega t)} \quad \because \lambda = \frac{2\pi}{L}, \quad \omega = \frac{2\pi}{T} \quad (1a)$$

$$\phi(x, y, z, t) = i \frac{gH}{2\omega} \frac{\cosh \lambda(h+z)}{\cosh \lambda h} e^{i(\lambda x - \omega t)} \quad (1b)$$

$$\phi = i \frac{gH}{2\omega} \frac{\cosh \lambda(h+z)}{\cosh \lambda h} e^{i(\lambda x \cos \alpha + \lambda y \sin \alpha - \omega t)}$$

$$\because x \rightarrow x \cos \alpha + y \sin \alpha$$

$$(2)$$

$$v_i = -\dot{\phi}_i, \quad p = \rho_w(\dot{\phi} - gz) \quad (3)$$

Reflection at line structure

When the plane wave meets a line structure at an angle of $\alpha_i = \alpha$, the traveling direction angle of the reflected wave becomes $\alpha_r = 180^\circ - \alpha$ as shown in Fig. 1(a). Thus the overlapping wave is expressed as Eq. (4) from the boundary condition ($v_x = 0$ at $x = 0$). The wave height of the overlapping wave becomes $2H$. Both of the characteristics of stationary wave and traveling wave are recognized in x -direction and y -direction, respectively, where wavelengths along coordinate axes are expressed by Eq. (5).

$$\phi = \phi_i + \phi_r = i \frac{gH}{\omega} \frac{\cosh \lambda(h+z)}{\cosh \lambda h} \times \cos(\lambda x \cos \alpha) e^{i(\lambda y \sin \alpha - \omega t)} \quad (4)$$

$$L_x = L / \cos \alpha, \quad L_y = L / \sin \alpha \quad (5)$$

Reflection at broken line structure

As shown in Fig. 1(b, c), we considered a plane wave which meets broken line structure. The part of the incident wave in right hand side of coordinate origin is first reflected on y -axis (reflected wave r_y)

and then on x -axis (reflected wave r_{yx}). The other part of the incident wave in left hand side is reflected first on x -axis (reflected wave r_x) and then on y -axis (reflected wave r_{xy}). From the boundary condition ($v_x = 0$ at $x = 0$; $v_y = 0$ at $y = 0$), the traveling direction angle of this reflected wave and the velocity potential of the overlapping wave can be expressed as follows.

$$\alpha_i = \alpha, \quad \alpha_{ry} = 180^\circ - \alpha, \quad \alpha_{rx} = -\alpha, \quad (6)$$

$$\alpha_{ryx} = \alpha_{rxy} = 180^\circ + \alpha$$

$$\phi = \phi_i + \phi_{ry} + \phi_{rx} + \phi_{ryx} = i \frac{2gH}{\omega} \frac{\cosh \lambda(h+z)}{\cosh \lambda h} \times \cos(\lambda x \cos \alpha) \cos(\lambda y \sin \alpha) e^{-i\omega t} \quad (7)$$

The reflected wave r_{yx} and the reflected wave r_{xy} are opposite to the incident wave. The characteristics of the stationary wave can be recognized both in x - and y -directions. The node appears on the rectangular grid, but the loop appears at the center of the grid including the coordinate origin. Wavelengths are the same as those in Eq. (5).

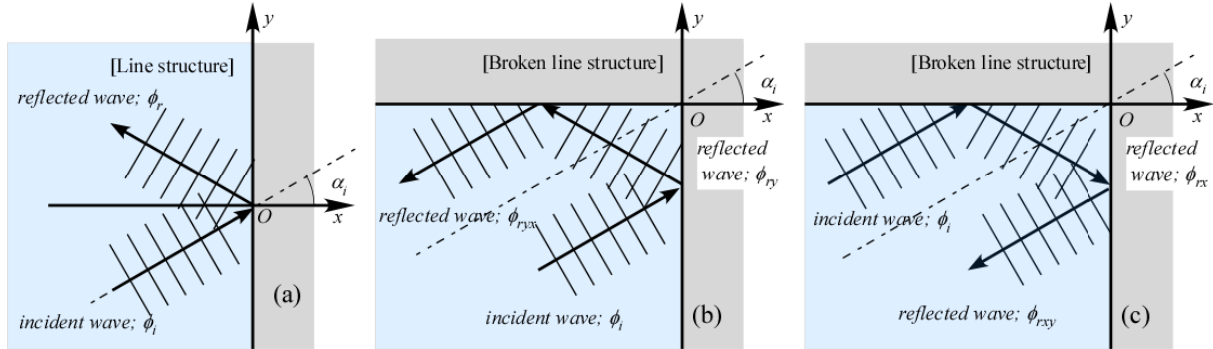


Fig. 1 Reflection of diagonal incident waves. (a) line structure; (b), (c) broken line structure: (b) y - x reflection, (c) x - y reflection

Effective Stress Response Analysis of the Seabed

The effective stress response in seabed to wave loading was analyzed by using poro-linear-elastic model [2]. The simultaneous differential equations which are derived for porous solid phase formed with soil particles and fluid phase including averaged pore water and pore air, are formulated in the model. Miura, et al [5] examined the applicability of formulation under the wide conditions, according to which we employed the u-p formulation under quasi-dynamic, one-dimensional condition. For the homogeneous seabed, when the boundary condition is taken in infinite depth, the component of variation of the pore water pressure and the effective stress is computable by Eq. (8). E_u , B_f are the modulus of rigidity of the solid phase, the

liquid phase, respectively, and complex parameter ζ is related with coefficient of hydraulic consolidation h_v (s/m²) in Eq. (9) [5].

$$\Delta p(z, t) = \Delta p_o \frac{1}{B_f + E_u} (B_f + E_u e^{-\zeta z}) e^{-i\omega t}$$

$$\Delta \sigma_z(z, t) = \Delta p_o \frac{E_u}{B_f + E_u} (1 - e^{-\zeta z}) e^{-i\omega t} \quad (8)$$

$$\therefore \Delta p_o e^{-i\omega t} = \rho_w \dot{\phi} \quad \text{at } z = -h \text{ (on seabed surface)}$$

$$\zeta = \sqrt{i\omega h_v} \quad (9)$$

Calculation of Sediment Flow and Storage

Based on the idea of the Shields number, we

evaluated the amount of sediment flow. First, the shear stress acting on the seabed was evaluated as a function of seawater flow velocity. Next, the thickness of sediment shear flow layer was decided from frictional resistance related to the effective stress in seabed ground. Then triangular flow velocity was assumed within the shear flow layer. Storage was calculated from the balance of inflow and out flow of infinitesimal area.

Sediment flow amount

The shear stress, traction force per specific seabed surface area, was assumed to be proportional to the seawater flow velocity squared. We employed the Eq. (10), where dimensionless coefficient C_b was assumed to be 1/40.

$$\tau_b = C_b \rho_w v_b^2 \text{ (N/m}^2\text{)} \quad (10)$$

It was assumed that the sediment fluidization is mobilized within the layer of d_f in thickness where

shear stress τ_b exceeds shear resistance τ_f which is calculated as a function of effective stress σ_z and internal friction angle ϕ as shown in Eq. (11). Finally we could determine the fluidization depth d_f (m).

$$\tau_f = \sigma_z(z) \tan \phi \text{ (kN/m}^2\text{)} \quad (11)$$

$$\tau_b = \tau_f \Rightarrow z = d_f \text{ (m)} \quad (12)$$

It was assumed that the distribution of sediment flow velocity v_f in the fluidization layer is triangular along depth as shown in Fig. 2. Thus the amount of sediment flow per unit width q was calculated by Eq. (13). The dimensionless coefficient C_q was introduced for the difference between seawater velocity v_b and sediment flow velocity v_f ; the value of C_q was assumed to be 1/2.5.

$$q = \frac{1}{2} d_f v_f = \frac{1}{2} d_f C_q v_b \text{ (m}^2\text{/s)} \quad (13)$$

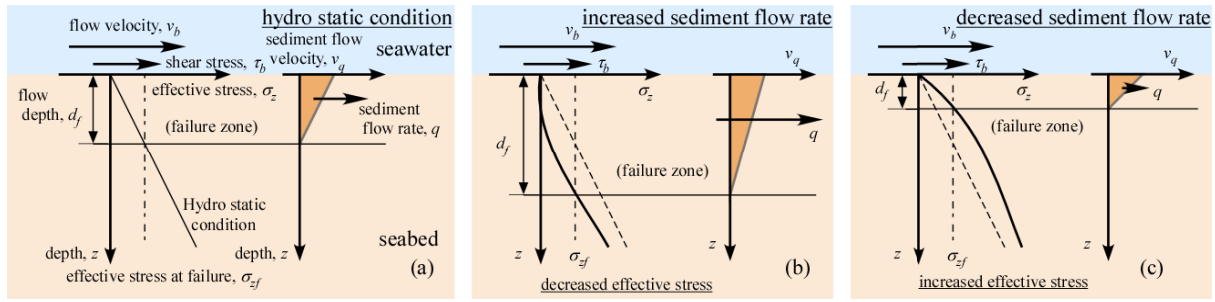


Fig. 2 Sediment flow behavior: (a) hydrostatic pressure condition, (b) effective stress decrease condition, (c) effective stress increase condition

Sediment storage rate: erosion and deposition

As shown in Fig. 3, the rate of sediment storage designated as Q can be calculated from the total balance of inflow and out flow in both x - and y -directions of an infinitesimal rectangular area. The storage rate Q is a function of coordinates as well as time in Eq. (14); Q is a summation of the derivatives of q in x - and y -directions.

$$\begin{aligned} Q &= -\frac{q_x(x+\Delta x/2, y) - q_x(x-\Delta x/2, y)}{\Delta x} \\ &\quad -\frac{q_y(x, y+\Delta y/2) - q_y(x, y-\Delta y/2)}{\Delta y} \\ &\rightarrow -\left(\frac{\partial q_x}{\partial x} + \frac{\partial q_y}{\partial y}\right) \quad (\Delta x \rightarrow 0, \Delta y \rightarrow 0) \text{ (m/s)} \end{aligned} \quad (14)$$

The positive and negative values of sediment storage rate Q correspond to deposition and erosion, respectively. The sediment flow velocity q and

storage rate Q both can be integrated during a sea wave period T for evaluating the total behavior of sediment flow; the integration values were defined as q_T (m²) and Q_T (m), respectively.

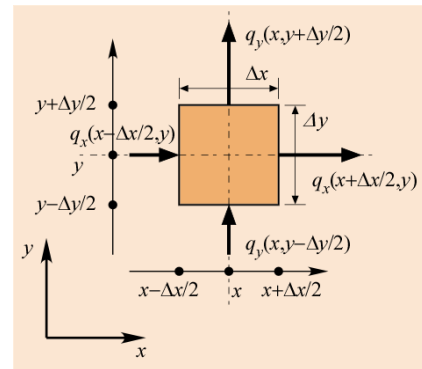


Fig. 3 Calculation of the sediment storage from the balance of inflow and out flow

WAVE CONDITION AND GROUND

MATERIAL PROPERTIES

Seawater with uniform depth of $h = 20\text{m}$ is assumed. The period of incident wave is $T = 13\text{s}$ (wavelength $L = 167.5\text{m}$), and wave height is $H = 10\text{m}$; H was parametrically changed. The Japanese Coastal Engineering Committee in Japan Society of Civil Engineers organized the intensive study with several researchers on the effective stress response in seabed ground to sea wave loading [6]. In the present study we selected physical and mechanical properties of seabed material as well as sea wave condition according to the committee report. The properties determined for typical loose sand was employed (as shown in Table 1), because the loose sand shows the notable effective stress response compared with other types of soils, such as gravel, silt, and clay [6].

Table 1 Mechanical properties of loose sand

E_u : Stiffness of solid phase (kN/m^2)	1.40×10^5
B_f : Stiffness of pore fluid phase (kN/m^2)	0.93×10^5
h_v : Coefficient of hydraulic consolidation (s/m^2)	1.75×10^{-3}

EXAMINATION OF CALCULATED BEHAVIOR AND DISCUSSION

Line Structure with Perpendicular Incident Wave

First, the case where the plane wave travels onto a line structure is examined. Figure 4 shows the sediment flow behavior per a period over a wavelength; the wave height H is changed from 10m to 2m parametrically. The short dashed line is for sediment flow amount q_{Tx} and the solid line for sediment storage Q_T per period. The variation of sediment flow q_{Tx} is skew-symmetrical with respect to two nodes ($x/L = -6/8, -2/8$); this behavior suggests that sediment flow into the nodes in both left and right hand directions. As a result the storage Q becomes positive at the nodes. On the other hand, Q becomes negative at loops ($x/L = -8/8, -4/8, 0/8$). This behavior suggests that sediment is deposited at the nodes, while seabed is eroded at the loops including the line structure side. As the wave height H becomes lower, the characteristic sediment flow behavior becomes not clear, and sediment tends to deposit at points a little distant from the nodes.

Figure 5 shows the form of the entire stationary wave, and the relation between water pressure and flow velocity on the seabed surface at the mid-points ($x/L = -1/8, -3/8$) between the node and loop.

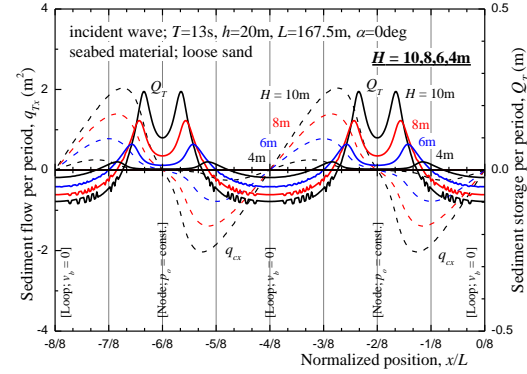


Fig. 4 Sediment flow behavior when wave meets perpendicularly to line structure

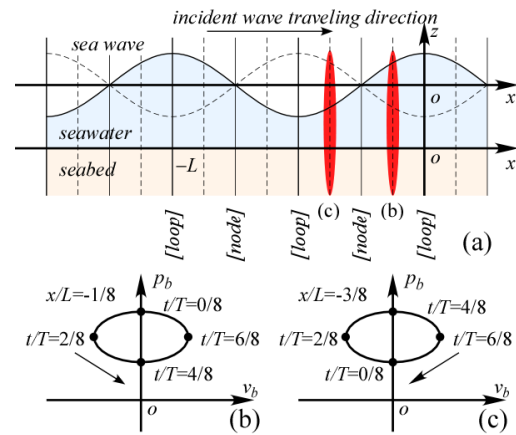


Fig. 5 Schematic explanation of the stationary wave perpendicular to line structure: (a) formation of wave; relation of water pressure vs. flow velocity on seabed (b) $x/L = -1/8$, (c) $x/L = -3/8$

In addition, Figs. 6, 7 show schematically the behavior of the sediment flow at the mid-points. In the cycle of sea wave period, a decrease in water pressure p on seabed surface causes effective stress to decrease and become less than the hydrostatic state. As a result the fluidization depth d_f becomes deeper during the decrease of p . As shown in Fig. 6, at the mid-point on right hand side of the node ($x/L = -1/8$) the sediment flow in negative direction is accelerated ($t/T = 2/8$). On the other hand, at the mid-point on left hand side of the node ($x/L = -3/8$) the sediment flow in positive direction is accelerated ($t/T = 6/8$) as shown in Fig. 7. Finally under the influence of effective stress response, sediment moves toward to the node from both sides. This behavior is clearly shown by the variation in the storage per period Q_T ; at the nodes Q_T becomes positive meaning cumulative deposition, and at the loops it becomes negative meaning cumulative erosion.

Line Structure with Diagonal Incident Wave

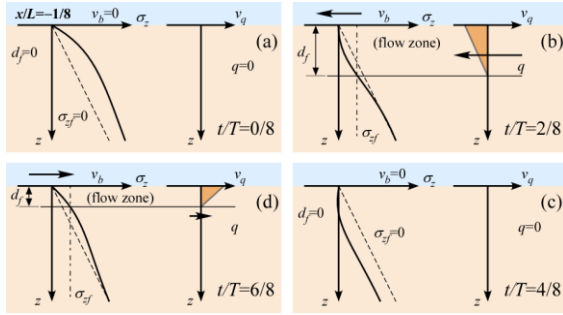


Fig. 6 Negative sediment flow at mid-point between node and loop ($x/L = -1/8$): (a-d) $t/T = 0/8, 2/8, 4/8, 6/8$

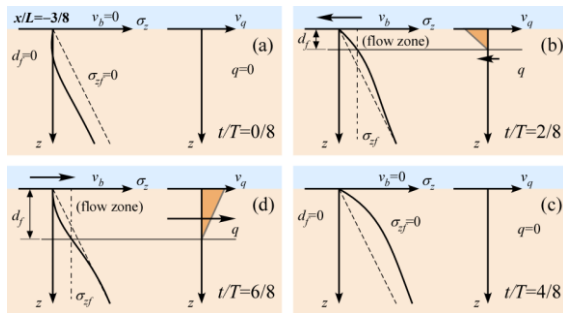


Fig. 7 Positive sediment flow at mid-point between node and loop ($x/L = -3/8$): (a-d) $t/T = 0/8, 2/8, 4/8, 6/8$

In the case where a plane wave ($H = 10\text{m}$) meets line structure with $\alpha = 30^\circ$, the sea surface level at $t/T = 0$ is indicated with contour lines and color gradation, and the horizontal velocity by vectors in Fig. 8. Along the node lines sea surface does not fluctuate vertically, but horizontally. One can recognize the characteristics of stationary wave in x -axis direction, and those of traveling wave in y -axis direction as in Eq.(4), (5).

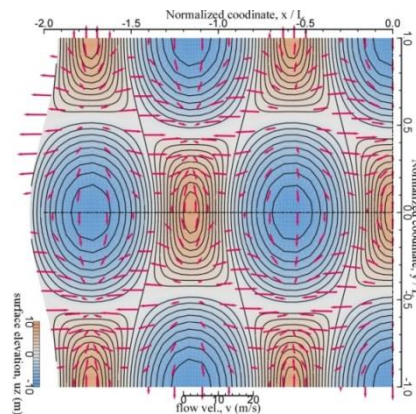


Fig. 8 Water level and flow velocity on sea surface near line structure

Figure 9 shows the sediment flow per period q_T by vectors, and the storage by contour lines and

color gradation. In this condition, because the characteristics of the stationary wave appear only in x -axis direction, the node lines and loop lines are parallel to the y -axis. The erosion and deposition of sediment occur within narrow bands parallel to y -axis. In the y -axis direction, the vectors q_T are heading to the opposite direction of wave traveling.

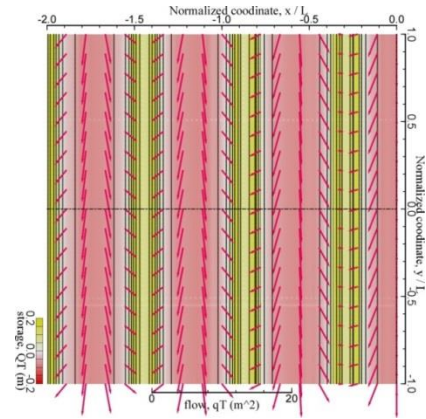


Fig. 9 Sediment flow, erosion-deposition behavior per period near line structure

Broken Line Structure with Diagonal Incident Wave

In the case where a plane wave ($H = 5\text{m}$) meets broken line structure with $\alpha = 30^\circ$, the behavior of the sea surface at $t/T = 0$ is shown in Fig. 10; the elevation of sea surface is indicated by contour lines and color gradation, and horizontal velocity by vectors. The characteristics of stationary wave are recognized in both x - and y -directions as shown in Eq. (5), (7). Node appears along the grid lines, and loops at the center of the rectangular grid cells. As shown in Figs. 8, 9, in the case of the line structure, nodes do not appear along structure independently of incident wave angle; however, in the case of the broken line structures, loops and nodes both appear periodically along the structures.

Figure 11 shows the sediment flow per period q_T by vectors, and the sediment storage per period Q_T by contour lines and color gradation. The sediment is eroded near the loop points, and deposited on the node lines. It is notable that at the corner of the line structure, seabed sediment is eroded, and sediment is deposited and eroded periodically along the side of the structures.

Influence of Incident Wave Direction on Sediment Erosion-deposition Behavior

For both the line structure and the broken line structure, the erosion (negative storage per period) at the node (including coordinate origin) and the deposition (positive storage per period) are plotted against the incident angle in Fig. 12. The deposition

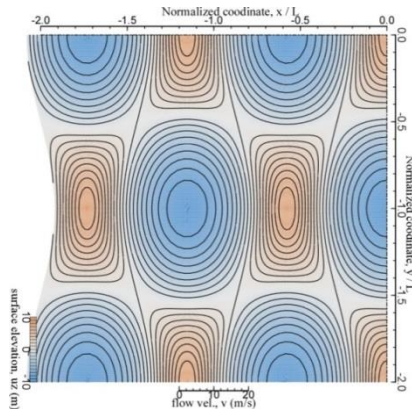


Fig. 10 Water level and flow velocity on sea surface near broken line structure

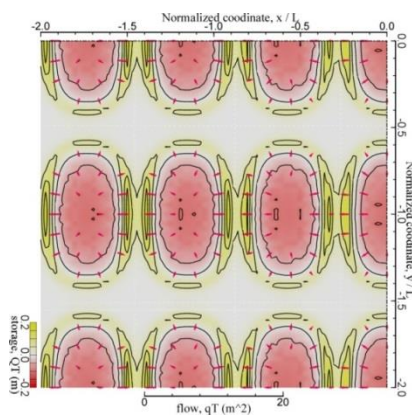


Fig. 11 Sediment flow, erosion-deposition behavior per period near broken line structure

at node monotonously decreases with the incident angle α . It is notable that the difference of amount of deposition between the line structure and broken line structure is not recognized. It is clear that in the line structure, the amount of erosion at loop gradually decreases, as α increases. In the broken line structure, however, the erosion amount at the loop is constant independently of α .

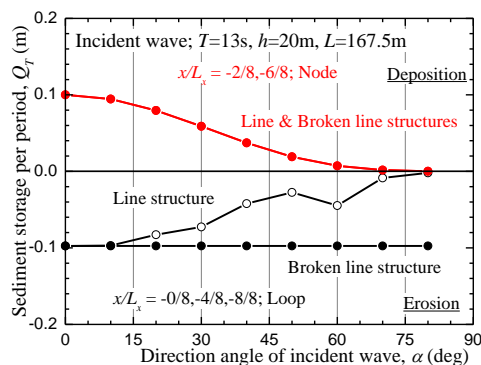


Fig. 12 Influence of angle of incidence of wave on erosion-deposition of sediment

CONCLUSIONS

We explained the analysis method for the traction sediment flow induced by traveling wave and stationary waves that meet line structures. We can summarize findings in the quantitative examination of the calculation results.

Under the traveling wave sediment flow occurs in opposite direction to wave traveling direction, and erosion nor deposition occurs. The characteristics of stationary wave appeared only in perpendicular direction in the case of line structures, but in both perpendicular directions in the case of broken line structures. Under the stationary waves, sediment is eroded near loops, and deposited near nodes.

ACKNOWLEDGEMENTS

The authors are grateful to the Japan Society for the Promotion of Science for its financial support with Grant-in-Aid for Research Activity Start-up 26889035 and Grants-in-Aid for Scientific Research (C)17K06553.

REFERENCES

- [1] Oka F., Yashima A., Miura K., Ohmaki S. and Kamata A., Settlement of Breakwater on Submarine Soil Due to Wave-induced Liquefaction, 5th ISOPE, Vol.2, 1995, pp.237-242.
- [2] Yamamoto T., H. S. L. Koning and E. Van Hijum, On the Response of a Pore-elastic Bed to Water Waves, J. of Fluid Mechanics, Vol. 87, Part 1, 1978, pp.193-206.
- [3] Zen, K. and Yamazaki, H. : Mechanism of wave-induced liquefaction and densification in seabed, Soils and Foundations, Vol.30, No.4, pp.90-104, 1990.
- [4] Miura K., Morimasa S., Otsuka N., Yamazaki H. and Konami T., Combined Effect of Flow Velocity and Water Change on Wave-induced Seabed Destabilization, J. of Japan Society of Civil Engineers, Ser. B2 (Coastal Engineering), Vol. 66, Issue 1, 2010, pp.851-855 (in Japanese).
- [5] Miura K., Asahara S., Otsuka N. and Ueno K., Formulation of The Ground for Coupled Analysis of The Seabed Response to The Wave, Proceedings of Symposium on Geotechnical Engineering, Vol. 49, 2004, pp.233-240 (in Japanese).
- [6] Coastal Engineering Committee, Coastal Wave, Japan Society of Civil Engineers, 1994, pp.430-503 (in Japanese).

THE SIMPLE METHOD OF SHEAR WAVE VELOCITY PROFILE FROM EXPLOSION SOURCE IN SURIN, THAILAND

Pithan Pairojn¹

¹ Faculty of Science, Chandrakasem Rajabhat University, Thailand

ABSTRACT

This study aimed to propose a correlation of shear wave velocity (V_s) derived from explosives using the Simple Method (SM). The SM is a technique for surveying shear wave velocity, and is used to analyze vibration records at the surface through an established dispersion curve. The seismic wave was generated below ground surface. The shear wave emanates from the source is detected by a geophone at ground surface and measure travelling time of shear wave for calculated shear wave velocity to estimate soil layer. The tested site was in Surin Province, northern Thailand (large-scale underground petroleum seismic survey area). In the present study, the SM technique was adopted to evaluate the shear wave velocity profile from underground explosives. The results showed that the SM agreed with those obtained from the Downhole Seismic Test (DH). The DH is geophysical surveys for determine shear wave velocity. Required parameters were then obtained through calibration with the results from the DH test. Subsequently, the shear wave velocity profiles from SM using explosives in the test area were then obtained. The SM has been used for vibration and shear wave velocity analysis of soil.

Keywords: Simple method; Shear wave velocity; Explosives; Vibration

INTRODUCTION

Shear wave velocity (V_s) is an important factor in measuring the dynamic and cyclic responses of subsoil layers. Advanced laboratory procedures have been developed over decades to determine the shear wave velocity in a soil sample; i.e. the resonant column test, cyclic torsional and triaxial tests, bending element test, etc. The results of these advanced laboratory tests have played a crucial role in establishing various important correlations between shear wave velocity, states of stresses, density, etc. At the same time, shear wave velocity field measurements have also been vastly improved; i.e. down hole and cross hole seismic tests, seismic cone penetration test, etc. Although, field measurement has grown in popularity, the attempt to apply well established laboratory correlations to field measurement has not been successful [1]-[7].

METHODOLOGY

General Site Information

Figure 1 shows the general subsoil profile in the study area (Latitude 15°21'32.8''N, Longitude 103°23'55.6''E). There are 4 main soil types at the site as follows: First, Silty sand layer (SM): the layer extends from the surface to a depth of about 4.5 m. It mostly contains silt mixed with very fine sand. The relative density measured using split spoon ranged from medium to dense. Second, Fine to coarse sand

layer (SP, SP-SM): this layer of medium to dense coarse sand is found beneath the top silty sand layer. It extends to a depth of about 15 m from the surface. Third, Silt-coarse sand layer (SM, SP-SM): this silty sand is found between 15 m to 25 m from the surface. The relative density ranged from medium to very dense. Fourth, Cemented coarse sand layer: this very dense cemented coarse sand lies beneath the site to a depth of 32 m (end of boring).

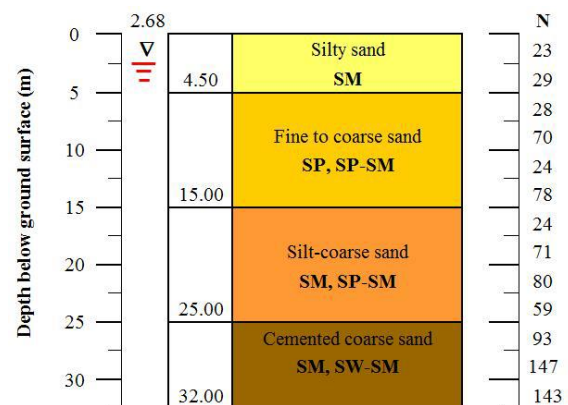


Fig. 1 Soil profile in Surin province.

Field Measurement

In the present study, the Simple Method (SM) was adopted to analyze the surface waves generated from underground explosives. The tested site in

Surin province was under a large scale underground petroleum seismic survey. The explosives used were single hole shot point at approximately 13 m depth. The explosive was 4 kg of ammonium nitrate emulsion Emulex 700 (Figs. 2 and 3). A series of sixteen well calibrated 4.5-Hz vertical-component geophones were placed on the surface at various distances from selected explosives to record the ground surface motions. The maximum investigation depth of the project was around 30 m. The nearest offset to first geophone (X_1) was 10 m with an interval of 20 m (d), 300 m (D), and total spread (Table 1 and Figs. 4-5). The maximum investigation depth is normally half of the longest wavelength. Figures 6 and 7 show the field blasting and path of the wave, which is used to determine shear wave velocity.

Table 1 Geophone array in Surin province

Geophone, X_1 (m)	Explosive (kg)	d (m)
10	4	20

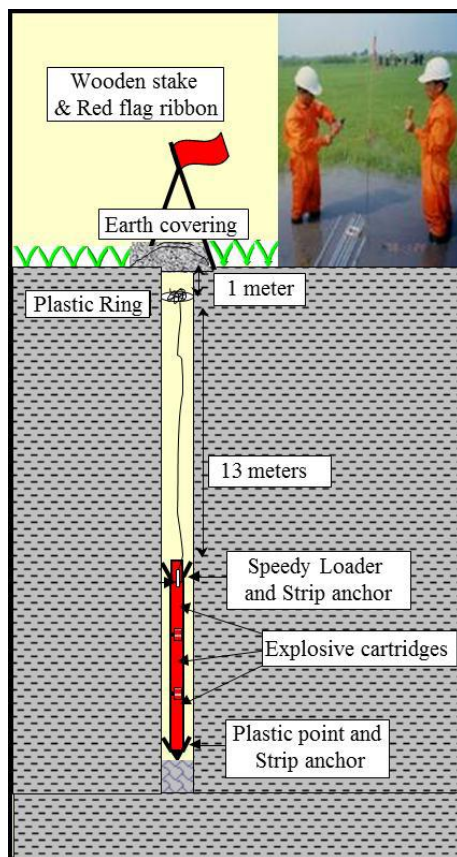


Fig. 2 Emulex-700 Ammonia Nitrate Emulsion.



Fig. 3 Explosive installation.

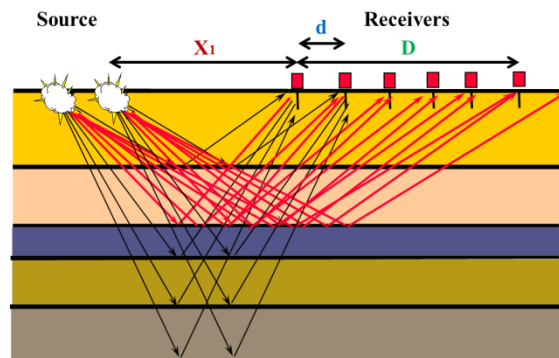


Fig. 4 Geophone array.



Fig. 5 Geophone installation.



Fig. 6 Blasting shot point.

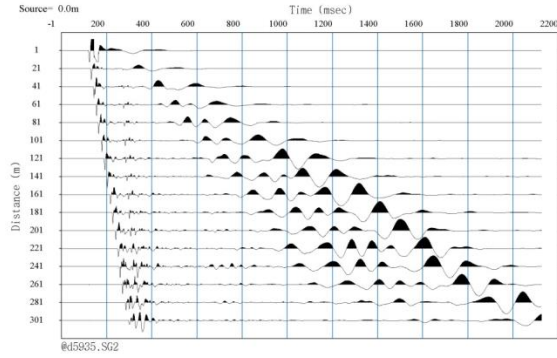


Fig. 7 The typical record of wave arrival.

Simple Method (SM)

Simple Method are a new approach to analyzing the characteristics of primary wave (S_1) and surface wave (S_2 to S_6). First, shot data is gathered and converted to period by Eq. (1) as shown in Fig. 8 and converted to dispersion curve technique ($v-f$) by Eqs. (2)-(3) as shown in Fig. 9. Shear wave velocity can be derived by Eq. (4) and inverting the the depth of the soil layer by Eqs. (5)-(6).

$$T_i = S_i \quad (i = 2-6) \quad (1)$$

$$f = 1/T_i \quad (2)$$

$$v = \Delta x / \Delta t \quad (3)$$

$$V_s \approx 1.1v \quad (4)$$

$$\lambda = v / f \quad (5)$$

$$Z \approx \lambda / 2 \quad (6)$$

Where S_i is time (s); T_i is period (s); f is frequency (s^{-1}); x is geophone array (m); v is phase velocity (m/s); λ is wavelength (m); V_s is shear wave velocity (m/s) and Z is depth (m)

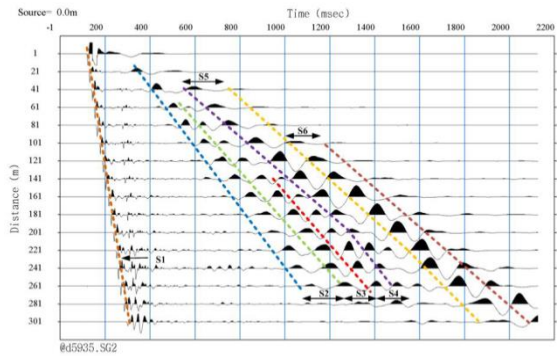
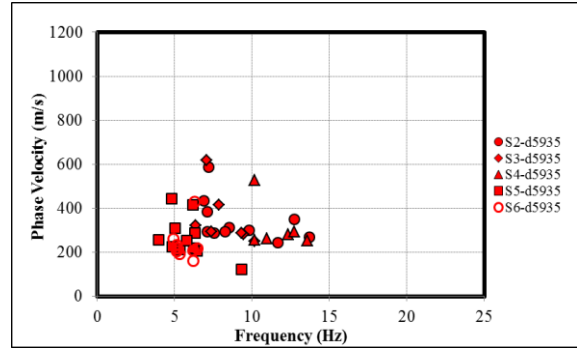


Fig. 8 Interpretation of SM.


 Fig. 9 The dispersion curve technique ($v-f$).

Downhole Seismic Test (DH)

A Downhole Seismic Test is performed by installing a movable seismic receiver in the borehole and measuring excitation at the surface (Fig. 10) [8]-[10]. The recorded waves arriving at different depths are then analyzed to compute the shear wave velocity of the corresponding soil in Eqs. (7) - (8). A typical record of wave arrival in the DH test is shown in Fig. 11.

$$t_c = \frac{D \cdot t}{R} = \frac{D \cdot t}{\sqrt{D^2 + H^2}} \quad (7)$$

$$V_s = \Delta D / \Delta t_c \quad (8)$$

Where t is measured travel time (s); D is the testing depth from the surface (m); H is the distance between the source and receiver in the horizontal path (m); R is the distance between the source and receiver in the inclined path (m); t_c is corrected travel time (s) and V_s is shear wave velocity (m/s) (Fig. 12)

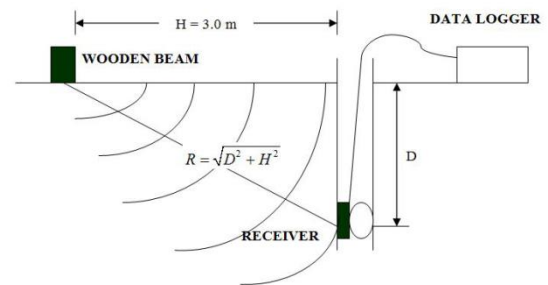


Fig. 10 Field measurement of DH.

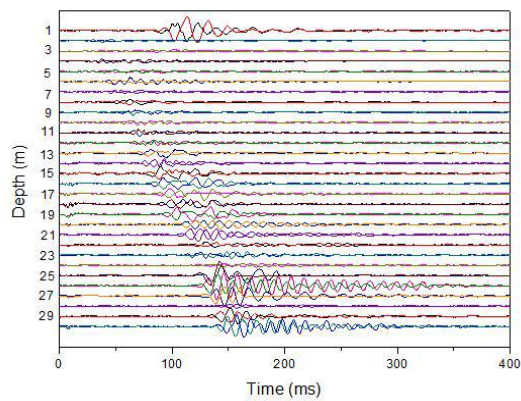


Fig. 11 Typical record of wave arrival in the DH.

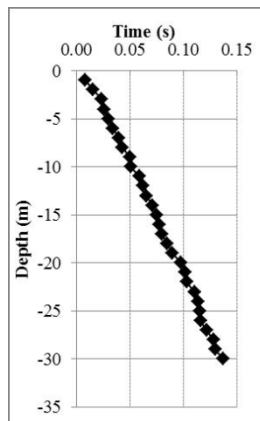


Fig. 12 Interpretation of DH.

RESULTS AND DISCUSSION

Figure 13 shows that analysis of the data using the Simple Method established the relationship between the phase velocity and frequency (Dispersion curve), with inversion to determine the shear wave velocity at the depth of the soil layer. The results established an empirical correlation between shear wave velocity and depth as shown in Eq. (9).

$$V_s = 10.32Z + 79.66 \quad (9)$$

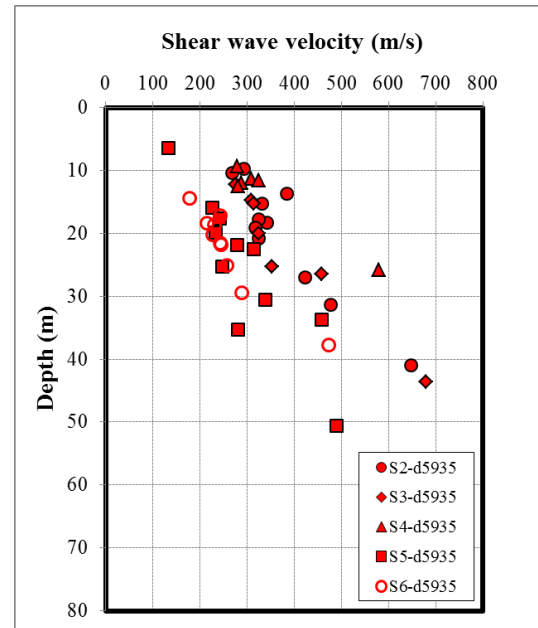


Fig. 13 Shear wave velocity profile by SM.

Figure 14 shows the result of analysis of the Downhole Seismic Test data in Eqs. (7) and (8). The V_s can be calculated by the traveling time (Fig. 12). The calculation must be done sequentially from the top to the bottom of the borehole.

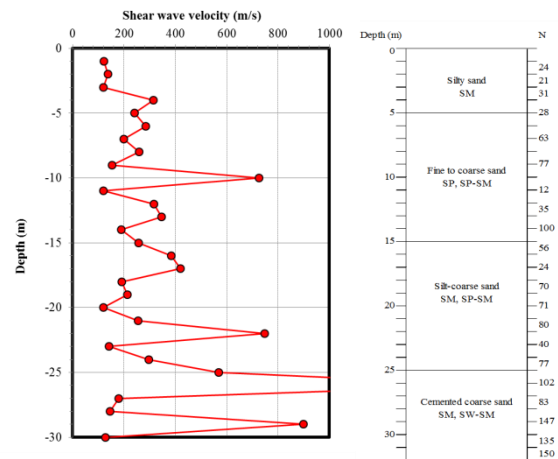


Fig. 14 Shear wave velocity profile by DH.

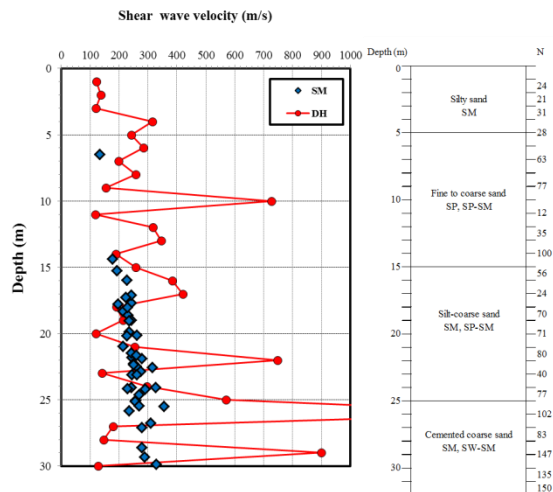


Fig. 15 A comparison of shear wave velocity.

Based on V_s profile from the Surin test sites, the average shear wave velocity at 30 m (V_{s30}) with the Simple Method (SM) was calculated by Eq. (9) and compared with the velocity with the Downhole Seismic Test (DH) as shown in Fig. 15. The Shear wave velocity from the explosives was about 10% higher with the SM than that from DH as shown in Table 2.

Table 2 Comparison of V_{s30} between SM and DH

Site area	V_{s30} (m/s)		Different of SM and DH (%)
	SM	DH	
Surin	389.35	354.49	9.83

CONCLUSION

This research compared the relationship between shear wave velocity and depth obtained from the SM with underground explosives and DH. Since there is an abundance of ground motion records from seismic surveys; i.e. the petroleum source survey, the shear wave velocity profile can be easily obtained as a byproduct from such projects. The Simple Method (SM) has been used for vibration and shear wave velocity analysis of soil.

ACKNOWLEDGEMENTS

This research received no specific grant from any funding agency in the public, commercial, or not-for-profit sectors.

REFERENCES

- [1] Hardin B.O., and Drnevich V.P., Shear Modulus and Damping in Soils: Measurement and Parameter Effect. *Journal of Soil Mechanics and Foundations Engineering ASCE*, Vol. 98, Issue 6, 1972, pp. 603–624.
- [2] Iwasaki T., Tatsuoka F., and Takagi Y., Shear Moduli of Sands under Cyclic Torsional Shear Loading. *Soils and Foundations*, Vol. 18, Issue 1, 1978, pp. 39–56.
- [3] Roesler S.K., Anisotropic Shear Modulus due to Stress Anisotropy. *Journal of the Geotechnical Engineering ASCE*, Vol. 105, Issue 7, 1979, pp. 871–880.
- [4] Yu P., and Richart F.E., Stress Ratio Effects on Shear Modulus of Dry Sands. *Journal of Geotechnical Engineering ASCE*, Vol. 110, Issue 3, 1984, pp. 331–345.
- [5] Teachavorasinskun S., Thongchim P., and Lukkunaprasit P., Shear Modulus and Damping of Soft Bangkok Clays. *Canadian Geotechnical Journal*, Vol. 39, Issue 5, 2002a, pp. 1201–1208.
- [6] Teachavorasinskun S., and Amornwithayalax T., Elastic Shear Modulus of Bangkok Clay during Undrained Triaxial Compression. *Geotechnique*, Vol. 52, Issue 7, 2002, pp. 537–540.
- [7] Teachavorasinskun S., and Lukkunaprasit P., Stress Induced and Inherent Anisotropy on Elastic Stiffness of Soft Clays. *Soils and Foundations*, Vol. 48, Issue 1, 2008, pp. 127–132.
- [8] Teachavorasinskun S., and Lukkunaprasit P., A Simple Correlation for Shear Wave Velocity of Soft Bangkok Clays. *Geotechnique*, Vol. 54, 2004, pp.1–4.
- [9] Kim D.S., Bang E.S., and Kim W.C., Evaluation of Various Downhole Data Reduction Methods for Obtaining Reliable v_s Profiles. *Geotechnical Testing Journal*, Vol. 27, 2008, pp. 1–13.
- [10] Pairojn P., and Teachavorasinskun S., An Identification of Shear Wave Velocity Profile in Northeastern Thailand by Downhole Test. *International Journal of Applied Engineering Research*, Vol. 9, Issue 22, 2014, pp. 13503–13510.
- [11] Briaud J.L., *Geotechnical Engineering: Unsaturated and Saturated Soils*, John Wiley & Sons, 2013, pp.1–998.

LOADED SWELL TESTS TO ESTIMATE THE HEAVE OF THE EXPANSIVE SOIL IN INSTRUMENTED SOIL COLUMN

Udukumburage RS¹, Gallage C² and Dawes L³

^{1,2,3}Science and Engineering Faculty, Queensland University of Technology, Australia

ABSTRACT

Expansive soils are naturally occurring, moisture sensitive, relatively high plastic clays which swell and shrink in significant amounts due to moisture variations in the soil. The swell behaviour of such soils can be predicted using the oedometer based loaded swell tests. Apart from the empirical models that can be used to predict the mechanical behaviour of expansive soils, the oedometer based estimations provide more accurate and less costly approach for geotechnical decision making. In this study, a series of loaded swell tests have been conducted to predict the heave under different loading and initial water content conditions. The swell predictions from the swell tests were used to validate the surface and subsoil movements of a large instrumented soil column under a wetting cycle. The results obtained from the soil column depict a close agreement ($R^2 = 0.98$) with the loaded swell tests results, proving the applicability of the loaded swell tests in prediction of the expansive behaviour of the Vertosol under different dry densities and initial water contents.

Keywords: Loaded swell tests, Expansive soils, Soil column, Heave prediction

INTRODUCTION

The expansive soils consist of smectite clay minerals that cause shrink-swell behaviour under soil moisture variations. These reactive soils are well recognized for the problematic behaviour that causes serious damages to the residential buildings and other light weight structures founded on and in them [1] -[7]. During the wet seasons after an extended dry periods, the expansive soils absorb the moisture and swell in greater proportion which induce high stresses on the structures founded on such soils. The swell strain of expansive clays can be determined by simple empirical models [8] - [15]; however, these might create excessive over/under estimations due to the variability of the soil type.

The laboratory triaxial and suction controlled oedometer apparatus can be used to investigate the expansive behaviour of clay soils [16] - [27]. The requirements of specialized technical knowledge to operate such sophisticated apparatus, time-consuming test procedure and expensiveness hinders the applicability of triaxial/suction controlled Oedometer for routine engineering decision making.

The conventional oedometer test can provide soil-specific swell strains under different surcharge pressures which might slightly overestimate the swell potential of the expansive soil considered. This will prevent structural damages that may cause by the underestimation of the swell potential of such soils. There have been many oedometer based research conducted for the past 3 decades [23] - [30]; however, extremely limited studies had been carried out for the Vertosol with valid verification from the laboratory simulated ground conditions.

In this study, an actual ground has been simulated by an instrumented expansive soil column to determine the subsurface movements under fully saturated conditions. The subsoil displacement was monitored at five different levels using the settlement plates attached to linear vertical displacement transducer (LVDT) units up to the total ground height of 1.0 m. The saturation of the expansive soil under constant head wetting was monitored by embedding MP406 moisture sensors at selected depths.

A series of conventional loaded swell tests was carried out for the same compacted expansive soils to determine the swell strain under fully saturated conditions. The results obtained from the loaded swell tests series comprise of a good agreement with the simulated actual ground movements measured in the soil column and thereby, proving the practical applicability of conventional loaded swell tests for the accurate estimation of the fully saturated soil heave for routine geotechnical engineering decision making of the structures founded on or in reactive soils.

TEST MATERIAL

The expansive soil (Brown Vertosol) for the laboratory simulated ground and loaded swell tests series was extracted from 0.5 m below the ground surface in South-east Queensland (27°31'47.942"S 152°59'10.568"E). Table 1 summarises the laboratory tests conducted to determine the index properties of the soil according to Australian standards. This characterises the type of soil as CH (inorganic clays of high plasticity) on Casagrande's

plasticity chart. Further, the results from the X-ray diffraction (XRD) analysis was carried out to verify the composition of the smectite and kaolinite. According to the interpretation of the mineralogical analysis, the sample displays the attributes predominantly of smectite group minerals.

Table 1 Soil property table

Classification Test	Results
Grain size distribution	% finer than 75 μ m > 77% Fraction of clay = 39.0 %
Atterberg Limits	LL = 67.0 % PI = 37.2 %
Linear Shrinkage	LS = 13.39 %
X-ray diffraction (XRD)	Smectite Group
Specific Gravity	G _s = 2.67

METHODOLOGY

A series of oedometer based conventional loaded swell tests and laboratory simulated actual ground displacements were monitored and compared to investigate the practicality and the applicability of the swell tests to predict the actual ground movements.

Laboratory Instrumented Soil Column

A large instrumented soil column of 0.39 m in diameter and 1.0 m in height was built by compacting 50 mm lifts of grounded expansive soil material. The initial gravimetric water content and the dry density of the compacted soil was 15% and 1.2 g/cm³, respectively. Figure 1 shows the schematic diagram of the instrumented soil column and the sensor embedded depths.

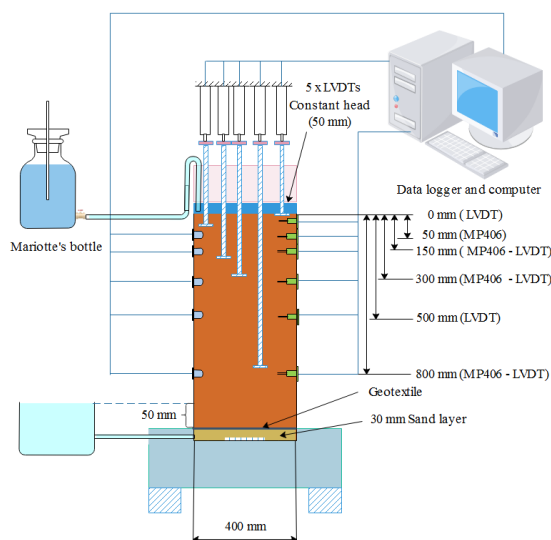


Fig. 1 Schematic diagram of the instrumented soil column

The instrumented soil column was subjected to a constant head wetting cycle by employing a Mariotte bottle and the corresponding sensor responses were monitored and recorded for a period of 4 months until the total soil column get fully saturated. The sensor responses from the MP406 moisture sensors and the corresponding sub-soil movements were analysed to determine a valid relationship between the soil displacements under saturated conditions.

The sub-soil movements were captured by the displacement of the adjacent settlement plates. For the ease of the computations, sub-soil were layered according to the placement of the settlement plates and thereby correlates with the swell strain of the expansive soil under saturated condition. The saturated condition of the expansive soil layers were verified using the MP406 moisture sensor responses.

Loaded Swell Tests

In this study, a series of oedometer based swell tests were conducted for the samples having same initial gravimetric water content (ω) and dry density (ρ_d) under different surcharges. The samples were cured for 4 days prior to the swell tests. The soil samples were prepared for known gravimetric moisture content (15%) and the target density of 1.2 g/cm³ was achieved by static compaction of the test specimens. Subsequently, a representative sample was cut into a consolidation ring, followed by the placement of filter papers and porous disks, at the top and the bottom of the sample.

The samples were subjected to different surcharges to cover up the vertical stress variation within the soil column under fully saturated condition. The selected surcharges for the loaded swell test series were 1 kPa, 5 kPa, 10 kPa and 15 kPa.

The water was introduced from the top of the compacted soil sample (fig. 2) until the sample was inundated. Subsequently, the samples were allowed to swell for 48 hours to reach the maximum swell strain under the test conditions. The test run time of 48 hours was selected from the past experience with the expansive soil and the increment of the swell thereafter occurs at a negligible rate for this particular soil type. After the samples had swelled, the water was removed from around the samples. After, the top porous disk was removed, the sample mass with the ring was weighed and a representative portion of the sample was oven-dried to ascertain the final moisture content.

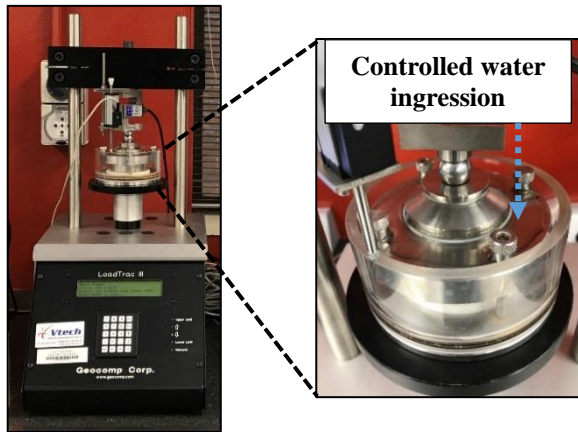


Fig. 2 Constant load Oedometer apparatus

RESULTS & DISCUSSION

Soil Column Based Test Results

The subsoil layers were considered as fully saturated, once the sensor responses reach a plateau as depicted in fig. 3. Since, the swell behaviour of the subsoil was conspicuous from fig. 4, the ground heave monitoring was continued until the swelling rate of all the soil layers were below 1.0 mm/month. In this study, the maximum positive swell strain of 15.4% was observed at the top most 150 mm soil layer. The minimum positive swell strain of 1.8% was identified at 300 mm to 500 mm marked soil layer.

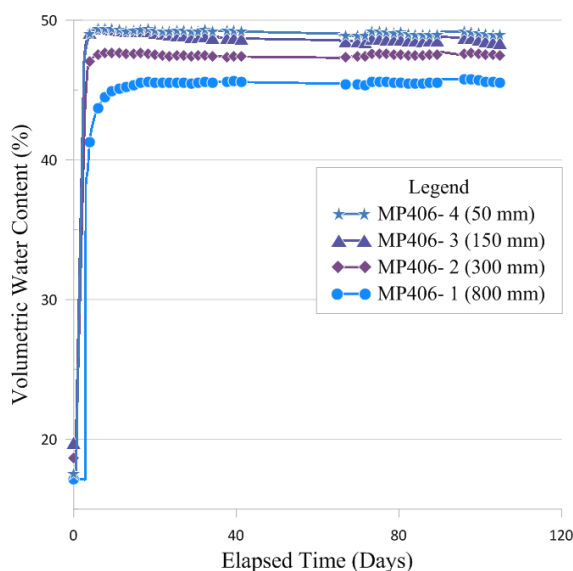


Fig. 3 MP406 moisture sensor responses vs time

Figure 5 depicts the swell strain occurred for the selected layers under fully saturated condition. The swell strain variation from the ground surface to the

bottom of the soil column indicated a distinctive drop due to the overburden pressure acting on the underlying soil layers. To be specific, a shrinkage of the soil layers was observed after the 500 mm depth mark. Figure 6 shows the variation of the soil swell observed under different surcharges in the instrumented soil column.

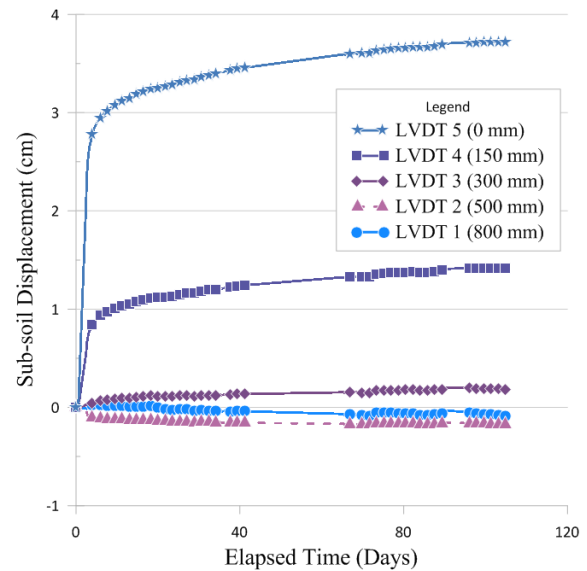


Fig. 4 LVDT sensor responses over time

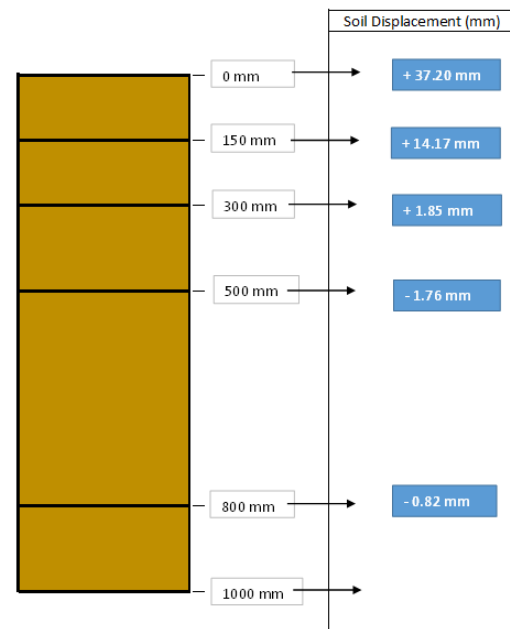


Fig. 5 Soil column based swell analysis

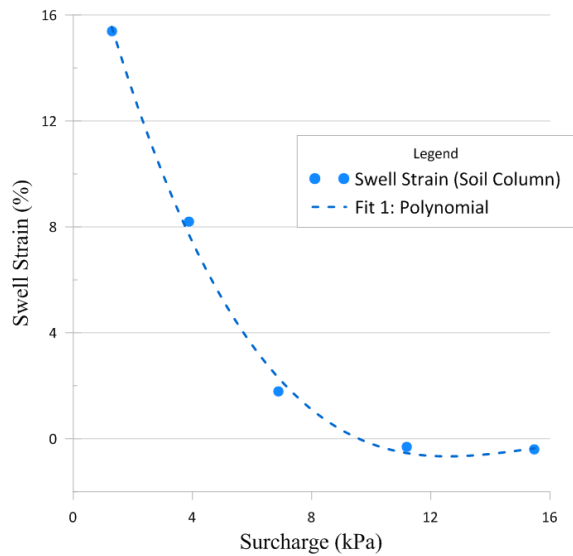


Fig. 6 Swell strain variation in the soil column over the surcharge

Oedometer Based Test Results

Figure 7 shows the swell strain variations under different surcharges for both oedometer based (1-D) and soil column based test results. The comparison of the results at lower surcharges provided a higher agreement whereas the higher surcharge values depicted a clear difference between the vertical heave of the column and oedometer results. The main reason for that could be the oedometer tests provide 1 dimensional heave under higher lateral confinement due to smaller sample sizes. On the contrary, the large soil column has an insignificant lateral confinement (compared to the oedometer samples) which allows lateral expansion of a representative elemental volume (REV). To

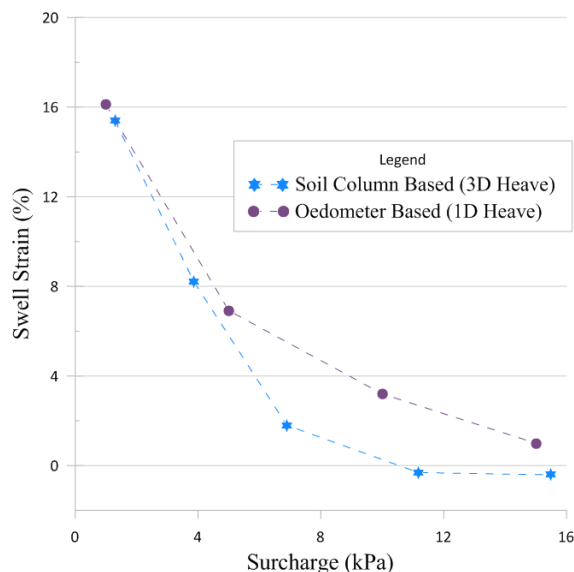


Fig. 7 Comparison of swell strain variation with the surcharge in soil column and oedometer samples

compensate the over-measurement of vertical swell from oedometer based test results, a correction factor based on the confinement was introduced to simulate the ground results.

The obtained relationship (Eq. (1) & Eq. (2)) of swell strain variations in between the laboratory simulated actual ground (ϵ_{act}) and the oedometer based (ϵ_{oed}) variations under different surcharges, provided a very good agreement ($R^2 = 0.98$) as depicted in fig.8. The soil specific constants (α, β) can be correlated with the applied surcharge and lateral restraint factor. To determine a blatant relationship between these constants would require more time and testing to be conducted in future.

$$\epsilon_{act} = 1.1786 * \epsilon_{oed} - 3.1281 \quad (1)$$

$$\epsilon_{act} = \alpha * \epsilon_{oed} + \beta \quad (2)$$

Whereas;

ϵ_{act} = Actual ground swell strain (%)

ϵ_{oed} = Oedometer based swell strain (%)

α = Soil specific constant 1

β = Soil specific constant 2

α, β = f {Surcharge, Lateral Restaint}

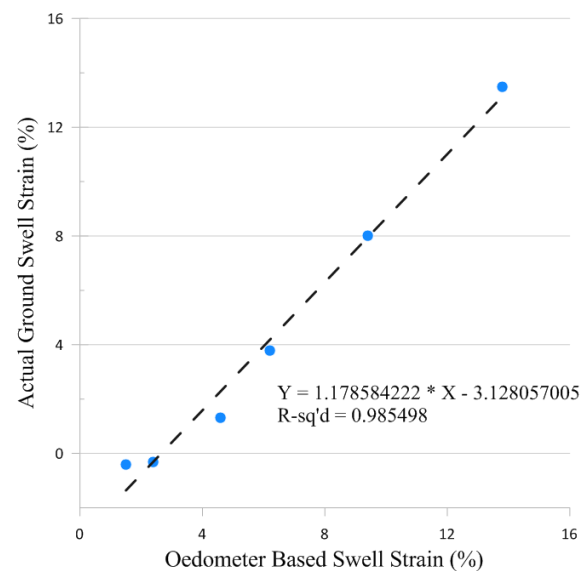


Fig. 8 Relationship between the oedometer and column based swell strains

CONCLUSION

The instrumented soil column based test results provided the simulated actual ground behaviour of expansive soil under fully saturated conditions. However, the saturation period of the 1m high soil column took 4 months of constant head wetting and

the applicability of such an expensive, time-consuming and complex method is not practical for routine decision making of geotechnical engineers. Therefore, the conventional oedometer based swell tests can be used for the same purpose in much economical manner. The loaded swell tests conducted for the same soil and conditions provided a good agreement ($R^2 = 0.98$) with the laboratory simulated actual ground heaving under fully saturated conditions, proving the practical and economical applicability for prediction of the expansive soil heave.

ACKNOWLEDGEMENT

Authors gratefully acknowledge the technical staff at Queensland University of Technology (QUT) for providing the on-campus & off-campus (Banyo Pilot Plant) laboratory facilities to conduct the test series. Further, the gratitude should be extended to Steve Hackworth from 'The SoilTesters' for providing the in-kind support for the project. The first author acknowledges the scholarship for doctoral degree received from QUT, Australia.

REFERENCES

- [1] Bose, B. (2012). Geo-engineering properties of expansive soil stabilized with fly ash. *Electronic Journal of Geotechnical Engineering*, 17, 1339-1353.
- [2] Liu, J., Shi, B., Jiang, H., Bae, S., & Huang, H. (2009). Improvement of water-stability of clay aggregates admixed with aqueous polymer soil stabilizers. *CATENA*, 77(3), 175-179.
- [3] Petry, T. M., & Little, D. N. (2002). Review of stabilization of clays and expansive soils in pavements and lightly loaded structures-history, practice, and future. *Journal of Materials in Civil Engineering*, 14(6), 447-460.
- [4] Puppala, A. J., & Pedarla, A. (2017). Innovative ground improvement techniques for expansive soils. *Innovative Infrastructure Solutions*, 2(1), 24.
- [5] Seco, A., Ramírez, F., Miqueleiz, L., & García, B. (2011). Stabilization of expansive soils for use in construction. *Applied Clay Science*, 51(3), 348-352.
- [6] Weston, D. (1980). Expansive roadbed treatment for Southern Africa. In *Proceedings of the Conference on Expansive Soils ASCE, Denver, Colo., June 16-18, 1980*. (pp. 339-360).
- [7] Yong, R. N., & Ouhadi, V. R. (2007). Experimental study on instability of bases on natural and lime/cement-stabilized clayey soils. *Applied Clay Science*, 35(3-4), 238-249.
- [8] McKeen, R. G. (1992). A model for predicting expansive soil behavior. In *Proc., 7th Int. Conf. on Expansive Soils* (Vol. 1, pp. 1-6): ASCE Reston, VA.
- [9] Nelson, J. D., Chao, K. C., Overton, D. D., & Schaut, R. W. (2012). Calculation of heave of deep pier foundations. [Article]. *Geotechnical Engineering*, 43(1), 12-25. Retrieved from Scopus.
- [10] Overton, D. D., Chao, K.-C., & Nelson, J. D. (2006). Time rate of heave prediction for expansive soils. In *Proceedings of the ASCE Conference GeoCongress* (Vol. 187, pp. 162-168).
- [11] Smith, R. (1993). Estimating soil movements in new areas. In *australian geomechanics society seminar: extending the code beyond residential slabs and footings, Victoria Branch, Melbourne, Australia* (pp. 1-6).
- [12] Van der Merwe, D. (1964). *The prediction of heave from the plasticity index and the percentage clay fraction* (Vol. 6): South African Council for Scientific and Industrial Research.
- [13] Vanapalli, S., & Lu, L. (2012). A state-of-the art review of 1-D heave prediction methods for expansive soils. *International Journal of Geotechnical Engineering*, 6(1), 15-41.
- [14] Vijayvergiya, V., & Ghazzaly, O. (1973). Prediction of swelling potential for natural clays. In *Proceedings of the Third International Conference on Expansive Clay Soils* (Vol. 1, pp. 227-234).
- [15] Walsh, P., Fityus, S., & Kleeman, P. (1998). A Note on the Depth of Design Suction Change for Clays in South Western Australia and South Eastern Queensland. *Australian Geomechanics*, 33(Part 3), 37-40.
- [16] Gallage, C., Udukumburage, R., Uchimura, T., & Abeykoon, T. (2017). Comparison of direct and indirect measured soil-water characteristic curves for a silty sand. *International Journal of GEOMATE*, 13(39), 9-16.
- [17] Gallage, C. P., Kodikara, J., Chan, D., & Davis, P. (2008). A comparison of the results of the numerical analysis and the physical behavior of a pipe buried in reactive clay. In *Proc., 12th Int. Conf. of Int. Association for Computer Methods and Advances in Geomechanics (IACMAG)*.
- [18] Gallage, C. P. K., & Uchimura, T. (2010). Effects of dry density and grain size distribution

- on soil-water characteristic curves of sandy soils. *Soils and Foundations*, 50(1), 161-172.
- [19] Briaud, J.-L., Zhang, X., & Moon, S. (2003). Shrink test–water content method for shrink and swell predictions. *Journal of geotechnical and geoenvironmental engineering*, 129(7), 590-600.
- [20] Day, R. W. (1994). Swell-shrink behavior of compacted clay. *Journal of geotechnical engineering*, 120(3), 618-623.
- [21] Fityus, S. G., Cameron, D. A., & Walsh, P. F. (2005). The shrink swell test.
- [22] Gao, Y., Sun, D., & Wu, Y. (2017). Volume change behaviour of unsaturated compacted weakly expansive soils. [Article in Press]. *Bulletin of Engineering Geology and the Environment*, 1-12. Retrieved from Scopus.
- [23] Ito, M., & Azam, S. (2010). Determination of swelling and shrinkage properties of undisturbed expansive soils. [Article]. *Geotechnical and Geological Engineering*, 28(4), 413-422. Retrieved from Scopus.
- [24] Mishra, A. K., Dhawan, S., & Rao, S. M. (2008). Analysis of Swelling and Shrinkage Behavior of Compacted Clays. [journal article]. *Geotechnical and Geological Engineering*, 26(3), 289-298.
- [25] Nelson, J., & Chao, K. (2014). Relationship between swelling pressures determined by constant volume and consolidation-swell oedometer tests. In *Proceedings of the UNSAT2014 Conference on Unsaturated Soils*.
- [26] Nelson, J. D. (2015). Time dependence of swelling in oedometer tests on expansive soil. In *15th Asian Regional Conference on Soil Mechanics and Geotechnical Engineering, ARC 2015: New Innovations and Sustainability* (pp. 490-493).
- [27] Nelson, J. D., Reichler, D. K., & Cumbers, J. M. (2006). Parameters for heave prediction by oedometer tests. In *Geotechnical Special Publication* (pp. 951-961).
- [28] Pino, A., Pedarla, A., Puppala, A., & Hoyos, L. R. (2016). Evaluation of swell behaviour of expansive clays from specific moisture capacity. In *E3S Web of Conferences* (Vol. 9).
- [29] Rao, A. S., Phanikumar, B. R., & Sharma, R. S. (2004). Prediction of swelling characteristics of remoulded and compacted expansive soils using free swell index. [Article]. *Quarterly Journal of Engineering Geology and Hydrogeology*, 37(3), 217-226. Retrieved from Scopus.
- [30] Sridharan, A., Rao, A. S., & Sivapullaiah, P. V. (1986). Swelling pressure of clays. *Geotechnical Testing Journal*, 9(1), 24-33.

MULTI-CHANNEL FIBRE BRAGG GRATING SENSORS (MC-FBGs) FOR UNIAXIAL COMPRESSIVE TEST ON LIMESTONE ELASTICITY BEHAVIOUR

Isah B. W.¹, Mohamad H.² and Ahmad N. R.³

^{1,2,3}Faculty of Engineering, Universiti Teknologi PETRONAS (UTP), Malaysia

ABSTRACT

In rock mechanics, measurement of small strain response is the most basic and significant means of assessing rock mechanical and elasticity behavior. To overcome the difficulties of mounting, handling many cables, dependency of the strain responds measured to the properties of the sensor components, this paper intends to explore the applicability of a novel multi-channel Fiber Bragg Grating sensors (MC-FBGs) for determining small strain response of cylindrical rock specimen under uniaxial compression test for assessing deformability properties. The concept, design and embedment technique of MC-FBGs employed in the experiment are illustrated concisely. To analyze the stress-strain respond of a cylindrical limestone specimen, two axial FBGs placed diametrically opposite to each other along the longitudinal axis of the specimen and two radial FBGs embedded opposite to each other circumferentially within the central one-third portion of the specimen were adopted for axial and radial strain response measurement. In addition, two electrical resistance-based strain gauges (SG), one mounted axially and the other attached radially along the circumference, are used for comparative measurements with the FBGs. The values of unconfined compressive strength, young's modulus, crack initiation and crack damage stress obtained from MC-FBGs and SG are in good agreement. It could be deduced that MC-FBGs can measure small strain response of limestone, stiffness anisotropy as well as measure the vital stages of rock failure mechanisms proficiently. MC-FBGs could serve as an alternative approach for determining reliable, accurate and precise compressive strain response of a limestone.

Keywords: Multichannel FBG sensor, Uniaxial compression test, Strain Response, Limestone

INTRODUCTION

The study of mechanical behaviour of rocks under the influence of external loading is very vital as it set a platform for understanding various natural geophysical processes that occurred in earth's crust, also to provide engineering solutions associated with the wide range of human activities especially with the evolvement of large geotechnical engineering structures such as deep tunnels, boreholes for oil and gas and tunnel for storage of radioactive waste. Strain response plays an important role in analyzing the mechanical behavior of rocks either in small-scale specimen or large-scale geotechnical structures especially for structural health assessment. Most rocks are very stiff, therefore their strain response to loading is very small (micro strain) [1]. This require a very accurate and high precision device to obtain a realistic stress-strain relationship of the rocks.

In the laboratory, uniaxial compression test (UCT) is one of the basic and vital test routinely performed on rock specimens[2]. It is imperative to highlight that UCT is methodized by both International Society for Rock Mechanics (ISRM) and American Society for Testing and Materials (ASTM). Varieties of instruments and devices are coopted during the UCT test to characterize the small

strain response of rocks with reasonable accuracy. Over the years, various devices were implemented to measure strain in UCT of rocks; Linear variable differential transducers (LVDT) [3], strain gauges (SG) [4], acoustic emission (AE) [5], digital image correlation (DIC) [6], extensometer [7], and digital terrestrial photogrammetry [8]. Despite the fact that the existing strain monitoring techniques are comparatively considered precise and reliable throughout the measuring period, the inherent limitations or deficiencies of non-immune to electrical short-circuiting, effect of lightning, electromagnetic interference (EMI), difficulties in mounting, signal loss over long range experience by some of the techniques, use of many cables and post experimental calculations steal continued to exist [9]. Moreover, the measured strain from the conventional strain devises is heavily dependent on the properties of the device components, defective component leads to uncertainty in results. Which is why many other new techniques have continued to evolve.

MC-FBGs have continued to gain more attraction due to its diversity in measurement of quantities (e.g.; strain, temperature, pressure, force, displacement, vibration etc) [10]. The versatility of MC-FBGs is due to magnificent advantages of being; light in weight, small in size, single and multi-points sensing,

resistance to harsh laboratory environmental condition, multifunctioning, linear output, resistance to corrosion, immune to electrical short circuiting, effect of lightning and EMI [11]. FBGs have demonstrated wide range of application in , security, pipelines, wells, seismic, and for smart structures in civil engineering [12]–[17].

Nevertheless, it is useful to mention some of the disadvantages of using FBGs; limited suppliers and lack of standards. FBGs provide point or quasi-distributed sensing measurements. Where distributed measurement is required, distributed fibre optics sensors based on Brillouin Optical Time Domain Analysis (BOTDA) or Brillouin Optical Time Domain Reflectometry (BOTDR) are most suitable [18], [19].

Over the year, FBG sensor have gain acceptance for use in determining the mechanical behaviour of rocks[11], [20]–[22].

In this paper, a new method of measuring strain response on limestone specimen using multi-channel FBGs is initiated and implemented on brittle rock (limestone) to capture the axial and radial strain response of a cylindrical core specimen. By equating the measured values obtained from FBGs with that of the SG, the practicability and efficiency of the FBGs arrangement is asserted.

WORKING PRINCIPLE OF MULTICHANNEL FBG SENSOR

FBGs is a distributed Bragg reflector embossed within a small section of a single mode optical fibre SMOF which can reflect a specific wavelength of light and transmits all the other wavelengths. FBGs are formed by engraving an unseen permanent periodic refractive index change in SMOF core. The components of SMOF are cladding and core, the refractive index of the core (inner part) is greater than that of the cladding (surrounding) which ensure total internal reflection. Schematic diagram of FBGs working principle is shown in Fig. 1. External factors such as heat and pressure will cause a shift in the wavelength of the reflected light; this variation can then be translated in to physical engineering units such as amplitude, strain, and temperature with the help of interrogator. Interrogators like Micron optics Si 155 can detect a shift in the Bragg wavelength of as small as 1pico meter (10^{-12} m).

From Fig. 1, the reflected light's wavelength can be obtained using Eg. (1) [23].

$$\lambda_B = 2n_{eff}\Lambda \quad (1)$$

Where; n_{eff} is the refraction index of the fiber core and Λ is the grating period of index modulation. Shift in the wavelength ($\Delta\lambda_B$) during experiment can be determined using Eg. (2) [24].

$$\Delta\lambda_B = \lambda_B(1 - p_e)\Delta\epsilon + (\alpha + \xi)\Delta T \quad (2)$$

Where; p_e is effective photo-elastic constant of the fiber core material, $\Delta\epsilon$ is change in the strain, ξ and α are temperature coefficients, and ΔT is change in temperature.

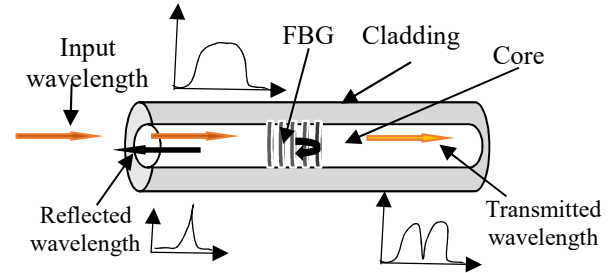


Fig.1 Schematic diagram of FBG working principle

When temperature is constant, Eq. (2) can be written as Eq. (3):

$$\Delta\lambda_B = \lambda_B k \epsilon \quad (3)$$

Where k is a strain constant $\cong 0.78$ for an ordinary bare SMOF. The entire compression test experiment was conducted in a relatively short period of time, therefore thermal variation within the vicinity of the gratings is neglected.

Design of Multichannel FBGs

The whole experiment was conducted using standard SMOF (SMF-28e) to eradicate attenuations resulting from transmission medium or bending. Two MC-FBGs having two gratings inscribed in one SMOF were formed. Each grating is assigned a different Bragg wavelength (λ_B) which enable the interrogator to record readings from various gratings at the same time using wavelength division multiplexing (WDM) program. Various wavelengths assigned are within the range of 1528 nm-1560 nm making sure that each sensor works within a distinctive spectral range. Table 1 depicted the specifications of the FBG sensors deployed.

With the aid of epoxy resin adhesive, FBGs are embedded into the limestone. Limestone surface was furnished using sand paper, FBGs are bonded and the bonding cured for 24 hours.

Table 1 Detail specifications of the FBG sensors Utilized

Component	V1	V2	L1	L2
λ_B (nm)	1560.1	1545.5	1535.1	1538.5
L (mm)	30	30	30	30
FWHM	0.3	0.3	0.3	0.3
± 0.1 (nm)				
BW@3dB (nm)	0.168	0.157	0.138	0.151
SLSR (dB)	16	16	17	20
Reflectivity (%)	90	90	90	90

L: Length of the gratings

λ_B : Central wavelength (CW) corresponding to each grating

SLSR (Side Lobe Suppression Ratio): Highest secondary peak bigger than 3 dB amplitude within ± 3 nm from CW. For Standard FBGs SLSR >15 dB

FWHM (Full Width at Half Maximum): FBGs width at 50% (-3 dB) from FBGs maximum Reflectivity, measured from Reflection Spectra

Reflectivity R% = $1-10(T(\text{dB})/10)$: Measured from transmission spectra

EXPERIMENTAL SET UP

Specimen Preparation

A 50mm diameter limestone rock core obtained from tunneling site in Ipoh, Perak, Peninsular Malaysia was used in the study. The rock core was cut into the laboratory testing specimen's size using aspect ratio (ratio of length to diameter) of 2.0 at thin section laboratory, located at block 15, UTP. The two faces are trimmed making sure that a perfect right circular cylinder is obtained in accordance with ISRM standard. Prior to the testing, the specimen is oven dried for 24 hours to ensure testing on dry state. Table 2 depicted the properties of the specimen.

Table 2 Properties of the test specimen

Sample	Height (mm)	Dia. (mm)	Weight (g)	Vol. (mm ³)	Density (g/cm ³)
Limestone	99.95	49.92	570.1	195,649.23	2913.89

Apparatus

The test is conducted using RT-1000 testing machine manufactured by IPC global rock tester with axial loading capacity of 1000 kN. A single desktop computer with the software of the machine installed is fully dedicate to the machine. The software provides the user with several options including the type of the test (dynamic or static) and the loading condition (axial force-controlled, or displacement-controlled mode). Limestone core (instrumented with strain SG and FBGs positioned along axial and radial

direction to record axial (ϵ_a) and radial (ϵ_r) strain respectively) is placed on the lower plate of the machine (Fig. 2). For better comparison of the recorded data, the SG and the FBGs are positioned adjacent to each other respectively (Fig. 3). The test was carried out using displacement-controlled rate of 0.5 mm/s.

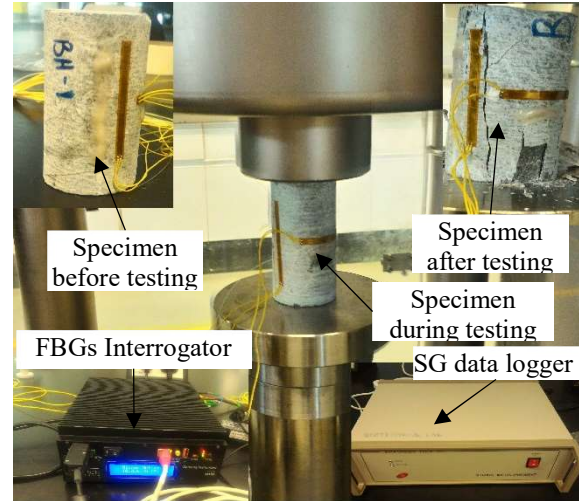


Fig. 2 Pictorial view of experimental apparatus and testing procedure

RESULTS AND DISCUSSION

This section introduces the outcome of the compression test conducted on limestone core in IPC global rock tester machine using MC-FBGs and SG. The entire experiment was performed at relatively room temperature to prevent the effect of temperature variations on FBGs. the axial force recorded during the test is divided by the initial cross-sectional area of the specimen to obtain the axial stress. The stress plotted against the axial and radial strain responses recorded by FBGs and SG, is presented in Fig. 4 with each response indicated with a distinct color. The strain response portrait by FBGs (ϵ_a - FBG and ϵ_r -FBG) signifies the average strain accorded by the two axial (V1 and V2) and two radial (L1 and L2) FBGs respectively. ϵ_r -SG and ϵ_a -SG represent the radial and axial strain by SG while ϵ_v -FBG and ϵ_v -SG denotes the volumetric strain by FBGs and SG respectively. The results of the compression test indicated that the strain response recorded by FBGs and SG are in good agreement. The strain measured by the FBGs and SG are almost similar. During the study, limestone surface was furnished, and adhesive was applied on top of the FBGs. Perhaps if methanol is used to clean the surface of the limestone after furnishing and epoxy adhesive is applied before and after embedding the FBGs, a better performance could be noticed.

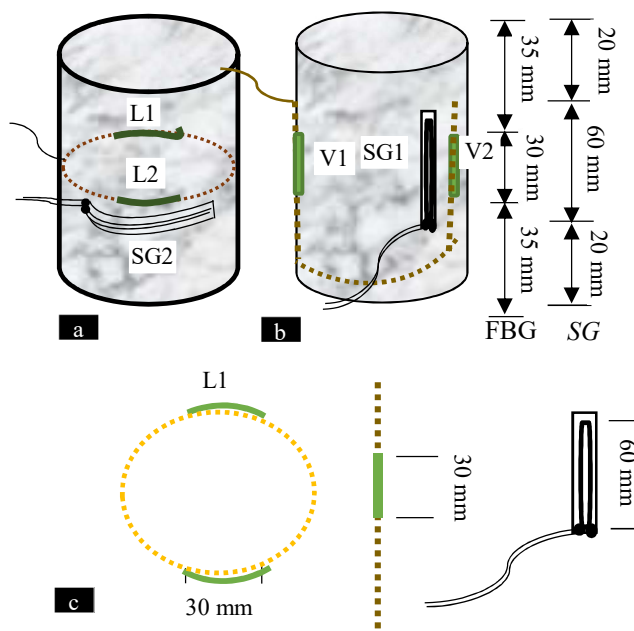


Fig. 3 Schematic view of sensors layout and embedment on limestone: (a) Radial layout of FBGs and SG (b) Axial layout of FBGs and SG (c) Dimension and radial positioning of the sensors

The failure pattern of the limestone core tested is vertical splitting[25]. Figure 4 explain the existing crack closure scenario in the specimen. Subsequently, FBGs was able to locate widely accepted four- stage model of rock failure mechanism: crack closure (σ_{cc}), crack initiation stress (σ_{ci}), crack damage stress (σ_{cd}) and uniaxial strength (UCS) which are very important parameters in the analysis of limestone behavior. Also, elastic parameters (young's modulus and poison's ratio) which provides essential information needed for design of excavation, borehole stability and defining parameters needed for constitutive models (Table 3) are determined.

Comparatively, values obtained by FBGs and SG are in close agreement (Table 3). Even though both sensors provide reliable information, FBGs have shown promising performance. Therefore FBG can reliably measure the strain response and potential crack grows of a limestone core specimen effectively. Moreover, reliable ,accurate and high precision data of rock deformation are extremely useful and valuable to provide raw data and theoretical mechanism needful for further experimental analysis , numerical simulation and field applications. While FBGs can be most suitable for use in certain difficult areas, huge gap exist in the field especially with the evolvement of large underground tunnel construction, particularly around Ipoh area where it is

predominantly underlaid by limestone. FBGs application in the laboratory UCT is fundamental for more complex test and field monitoring application.

Table 3. Estimated parameters from the test

Variables	FBGs	SG
σ_{cd} (Mpa)	54	53
σ_{ci} (Mpa)	39	40
E (Gpa)	37.812	40.7
Poison's Ratio	0.236	0.26
UCT (Mpa)	58	58

CONCLUSION

Smart way of measuring strain response of limestone rock significantly with high precision using a new MC-FBGs, under uniaxial compression for on-specimen measurement is presented. The advantages offered by FBG sensing techniques couple with the need for an alternate simple and accurate technique to breach the shortcomings of the existing are the stimuli for this study.

MC-FBG is shown to be effective in monitoring the strain responses of limestone core specimen subjected to UCT with ease high resolution and accuracy. It was found out that the results recorded by FBGs resemble those obtained by SG.

The experiment reported is an effort and try-out on the use of FBGs to measure the strain responses of limestone core specimen under UCT not considering the influence of temperature. Further investigation may incorporate the influence of temperature on FBG and more complex laboratory experiments on sedimentary rock cores.

ACKNOWLEDGEMENTS

The authors are grateful to Universiti Teknologi PETRONAS (UTP) for the financial support given through the graduate assistantship (GA) scheme.

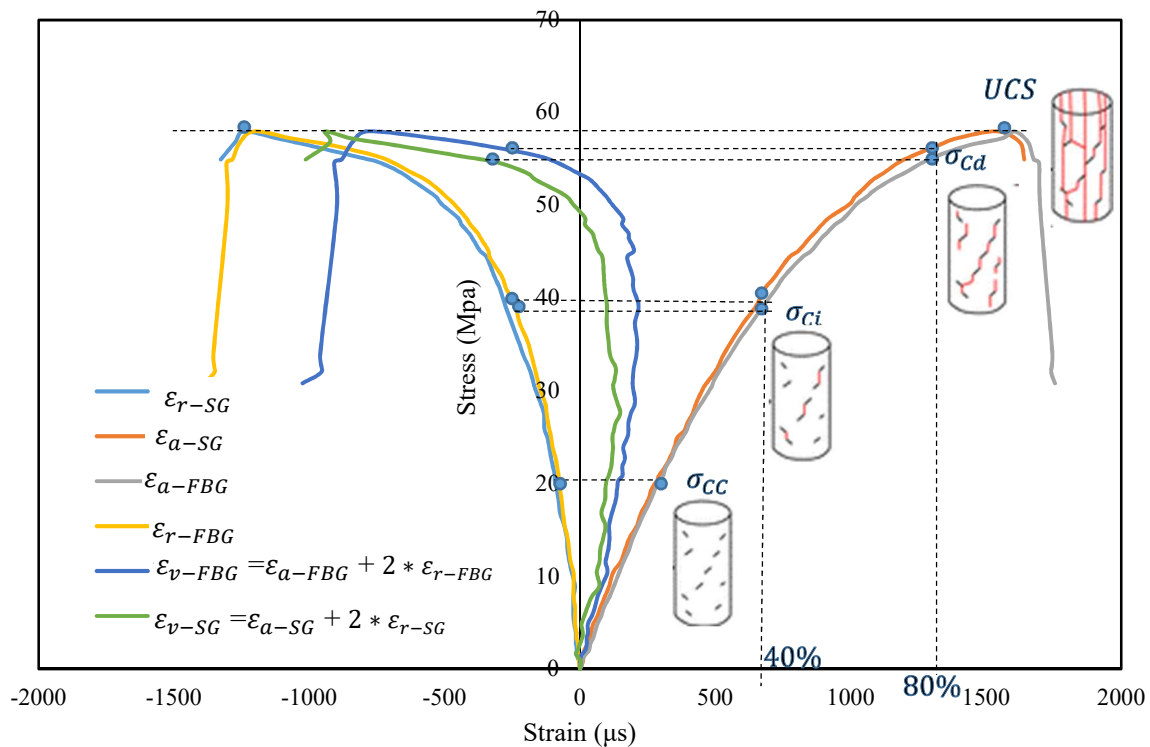


Fig 4. Stress-strain curve of limestone specimen under uniaxial compression test

REFERENCES

- [1] P. Hamdi, "Characterization of Brittle Damage in Rock from the Micro to Macro Scale," p. 230, 2008.
- [2] H. Roshan, H. Masoumi, and P. Hagan, "On size-dependent uniaxial compressive strength of sedimentary rocks in reservoir geomechanics," in *50th US Rock Mechanics/Geomechanics Symposium, ARMA*, 2016, vol. 3, p. pp: 2322 – 2327.
- [3] K. Bartmann and M. Alber, "Experimental Determination of Crack Initiation and Crack Damage of Two Granites," *Procedia Engineering*, vol. 191, pp. 119–126, 2017.
- [4] H. Roshan, H. Masoumi, and K. Regenauer-Lieb, "Frictional behaviour of sandstone: A sample-size dependent triaxial investigation," *J. Struct. Geol.*, vol. 94, pp. 154–165, 2017.
- [5] E. Hoek and C. D. Martin, "Fracture initiation and propagation in intact rock—a review," *J. Rock Mech. Geotech. Eng.*, vol. 6, no. 4, pp. 287–300, 2014.
- [6] H. Munoz, A. Taheri, and E. K. Chanda, "Pre-Peak and Post-Peak Rock Strain Characteristics During Uniaxial Compression by 3D Digital Image Correlation," *Rock Mech. Rock Eng.*, vol. 49, no. 7, pp. 2541–2554, 2016.
- [7] H. Munoz and A. Taheri, "Specimen aspect ratio and progressive field strain development of sandstone under uniaxial compression by three-dimensional digital image correlation," *J. Rock Mech. Geotech. Eng.*, vol. 9, no. 4, pp. 599–610, 2017.
- [8] G. Firpo, R. Salvini, M. Francioni, and P. G. Ranjith, "Use of Digital Terrestrial Photogrammetry in rocky slope stability analysis by Distinct Elements Numerical Methods," *Int. J. Rock Mech. Min. Sci.*, vol. 48, no. 7, pp. 1045–1054, 2011.
- [9] B. W. Isah, H. Mohamad, and I. S. H. Harahap, "International Journal of Advanced and Applied Sciences Measurement of small-strain stiffness of soil in a triaxial setup: Review of local instrumentation," vol. 5, no. 7, pp. 15–26, 2018.
- [10] Y. Sun, Q. Li, and C. Fan, "Laboratory core flooding experiments in reservoir sandstone under different sequestration pressures using multichannel fiber Bragg grating sensor arrays," *Int. J. Greenh. Gas Control*, vol. 60, pp. 186–198, 2017.
- [11] J. Park, Y. S. Kwon, M. O. Ko, and M. Y. Jeon, "Dynamic fiber Bragg grating strain sensor interrogation with real-time measurement," *Opt. Fiber Technol.*, vol. 38, pp. 147–153, 2017.
- [12] C. Y. Hong, Y. F. Zhang, M. X. Zhang, L. M. G. Leung, and L. Q. Liu, "Application of FBG sensors for geotechnical health monitoring, a review of sensor design, implementation methods and packaging

- techniques,” *Sensors Actuators, A Phys.*, vol. 244, pp. 184–197, 2016.
- [13] A. Bin Huang, C. C. Wang, J. T. Lee, and Y. Te Ho, “Applications of FBG-based sensors to ground stability monitoring,” *J. Rock Mech. Geotech. Eng.*, vol. 8, no. 4, pp. 513–520, 2016.
- [14] G. C. Kahandawa, J. Epaarachchi, H. Wang, and K. T. Lau, “Use of FBG sensors for SHM in aerospace structures,” *Photonic Sensors*, vol. 2, no. 3, pp. 203–214, 2012.
- [15] S. Koyama, A. Sakaguchi, H. Ishizawa, and K. Yasue, “Vital Sign Measurement Using Covered FBG Sensor Embedded into Knitted Fabric for Smart Textile,” *J. Fiber Sci. Technol.*, vol. 73, no. 11, pp. 300–308, 2017.
- [16] C. C. Lee, K. Hung, W.-M. Chan, Y. K. Wu, S.-O. Choy, and P. Kwok, “FBG sensor for physiologic monitoring in M-health application,” in *SPIES-OSA-IEEE*, 2011, vol. 8311, p. 83111S.
- [17] J.-Y. Wang, T.-Y. Liu, C. Wang, X.-H. Liu, D.-H. Huo, and J. Chang, “A micro-seismic fiber Bragg grating (FBG) sensor system based on a distributed feedback laser,” *Meas. Sci. Technol.*, vol. 21, no. 9, p. 094012, 2010.
- [18] H. Mohamad, P. J. Bennett, K. Soga, A. Klar, and A. Pellow, “Distributed Optical Fiber Strain Sensing in a Secant Piled Wall,” *7th FMGM 2007*, no. Fmgm, pp. 1–12, 2007.
- [19] H. Mohamad, K. Soga, and P. Bennett, “Monitoring twin tunnel interaction using distributed optical fiber strain measurements,” *J. Geotech. Geoenvironmental Eng.*, vol. 138, no. August, pp. 957–967, 2011.
- [20] A. Castro-Caicedo, M. J. Nieto-Callejas, and P. Torres, “Fiber Bragg grating strain sensor for hard rocks,” no. September, p. 963449, 2015.
- [21] C. Schmidt-Hattenberger, M. Naumann, and G. Borm, “Fiber Bragg grating strain measurements in comparison with additional techniques for rock mechanical testing,” *IEEE Sens. J.*, vol. 3, no. 1, pp. 50–55, 2003.
- [22] Y. Zhao, N. Zhang, and G. Si, “A fiber bragg grating-based monitoring system for roof safety control in underground coal mining,” *Sensors (Switzerland)*, vol. 16, no. 10, 2016.
- [23] W. Morey, G. Meltz, H. Glenn, and W. Glenn, “Fiber optic Bragg grating sensors,” *Proc. SPIE Fiber Opt. Laser Sensors VII*, vol. 1169, pp. 98–107, 1989.
- [24] K. O. Hill and G. Meltz, “Fiber Bragg Grating Technology Fundamentals and Overview,” *IEEE J. Light. Technol.*, vol. 15, no. 8, pp. 1263–1276, 1997.
- [25] J. F. Hazzard, R. P. Young, and S. C. Maxwell, “Micromechanical modeling of cracking and failure in brittle rocks,” *J. Geophys. Res. Solid Earth*, vol. 105, no. B7, pp. 16683–16697, 2000.

VOLUME LOSS CAUSED BY TUNNELLING IN KENNY HILL FORMATION

C.M. Khoo¹, T. Gopalan², N.A. Abdul Rahman² and H. Mohamad¹

¹Faculty of Engineering, Universiti Teknologi PETRONAS, Malaysia;

²Mass Rapid Transit Corporation, Malaysia

ABSTRACT

The Klang Valley MRT Sungai Buloh – Kajang (SBK) Line, Malaysia's first mass rapid transit line involved the construction of 9.5km twin bored tunnels in the densely populated urban area of Kuala Lumpur city. The underlying geological conditions can be distinctly demarcated to two main formations namely Kuala Lumpur Limestone and Kenny Hill Formation, of which 5.262km of bored tunnelling was carried out in the Kenny Hill Formation. The bored tunnel construction in the Kenny Hill Formation was undertaken with the use of Earth Pressure Balance (EPB) Tunnel Boring Machine (TBM). The ground settlement due to tunnelling is largely dependent on the volume loss induced by the tunnel excavation. At present, little information has been published on actual volume loss encountered during tunnel construction in the various soil types in Malaysia. Surface settlement markers among other instruments that were placed at selected intervals along the SBK Line tunnelling route as an instrumentation and control measure offer an opportunity to evaluate and back analyze the ground response due to tunnelling works. This paper presents and discusses the volume loss caused by EPB TBM tunnelling in the Kenny Hill Formation. Back analysis on trough width parameter from the available data has also been carried out. The findings of this study could be useful as a reference for future tunnelling projects in similar ground conditions.

Keywords: Volume loss, Ground settlement, Trough width parameter, TBM tunnelling, Kenny Hill formation

INTRODUCTION

Malaysia's first mass rapid transit (MRT) line, the 51km-long Klang Valley MRT Sungai Buloh – Kajang (SBK) Line features a central 9.5km underground section within the densely populated urban area of Kuala Lumpur city. It comprises of seven underground stations with twin bored tunnels running through two distinctive geological formations, namely the Kuala Lumpur Limestone and Kenny Hill Formation, and is connected to the adjacent elevated sections via the north and south portal. The twin bored tunnels have an internal diameter of 5.8m. The lining is 275mm thick precast steel fibre reinforced concrete comprising of 7 segments plus one key. The bored tunnelling works commenced in June 2013 and was successfully completed in April 2015 and subsequently followed by the SBK Line opening for passenger service on 17 July 2017.

Based on the published geological map of Kuala Lumpur and corroborated with a total 496 number of boreholes carried out during tender and detailed design stage of the project, it was established that the tunnel alignment from Ch. 1+048 to Ch. 6+310 (approximately 5.262km) is within the Kenny Hill Formation and the remaining Ch. 6+310 to Ch. 10+307 (approximately 3.997km) is in the Kuala Lumpur Limestone Formation. The Kenny Hill

Formation consists of layers of highly weathered metamorphic rock of sedimentary origin with typically more than 15% silt and some quartzite and phyllite.

In the Kenny Hill Formation, the soil is expected to be slightly cohesive which had resulted in the selection of Earth Pressure Balance (EPB) Tunnel Boring Machine (TBM) for the tunnelling works. The EPB TBM utilizes the excavated soils to exert support pressure to the tunnel face where a mixture of foam and water was used as conditioning agent in the cutting face and excavation chamber. The TBM drive, with excavated diameter 6.684m, was done in closed mode operation with an operational pressure of about 135kPa to 275kPa maintained at the face. High penetration of more than 20mm/rev and average production rate of 9.8m advance per day with maximum production of 19.6m/day were reported by Chin *et al.* [1]. The overburden above the tunnel crown generally ranges from 9m to 26m. The lateral distance between the centre line of the twin tunnels varies from 12.7m to 17.5m. For most parts, the tunnels were at a parallel configuration and located at the same elevation except where it approaches the stacked Bukit Bintang Station.

In this paper, the data from the instrumentation measurements collected during the construction of tunnels have been used to study the volume loss caused by tunnelling in the Kenny Hill Formation.

The volume loss is obtained by best fitting the Gaussian curve to the measured settlements along the traverse sections of the tunnels. Back analysis of the trough width parameter has also been carried out. The findings of this study could be useful as reference for future tunnelling projects in similar ground conditions. Efforts to continually build up the field database to further refine the deduced volume loss is in progress over the course of construction for subsequent Klang Valley MRT tunnels.

THE KENNY HILL FORMATION

Kenny Hill Formation is a sequence of clastic sedimentary rocks consisting of interbedded shales, mudstones, siltstones and sandstones of the Upper Palaeozoic period. Typically characterized by undulating terrain of low hills and shallow and broad valleys in its outcrop as observed in the Klang Valley of Peninsular Malaysia, in particular Kuala Lumpur Business District and its surroundings. Figure 1 shows the geology of the Kuala Lumpur area with indication of SBK Line tunnel alignment.

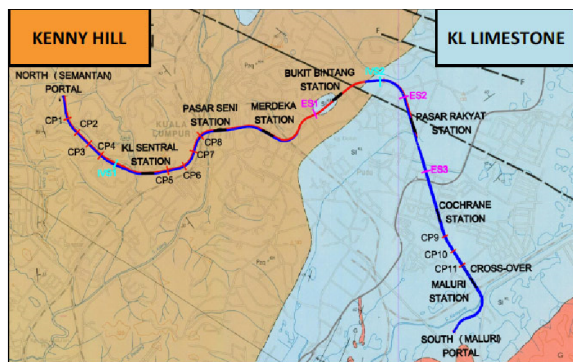


Fig. 1 Geology of Kuala Lumpur superimposed with tunnel alignment.

The subsurface investigation confirmed that the Kenny Hill Formation along the alignment to be a sequence of interbedded sandstone, siltstones and shales/ mudstones overlain by stiff over-consolidated soils predominately of sandy silty Clay and silty Sand. At certain stretches, the formation has undergone metamorphic event resulting in changes of sandstone/ siltstones to quartzite and schist/ phyllite respectively.

Its Engineering Properties

In the Kenny Hill Formation it is typical that beyond a depth of about 10m below existing ground level, the formation becomes very hard with SPT greater than $N = 50$ [2]. Toh *et al.* [3] and Wong & Singh [4] discussed some engineering properties of Kenny Hill Formation in Kuala Lumpur.

From site-specific data, the measured bulk unit weights typically ranged from 15.8 kN/m^3 to 21.9 kN/m^3 for residual soils; and increases up to

24.0 kN/m^3 for highly weathered rock (Grade IV). The fines composition of the residual soils are generally made of SILT and CLAY with low to high plasticity as shown in Figure 2.

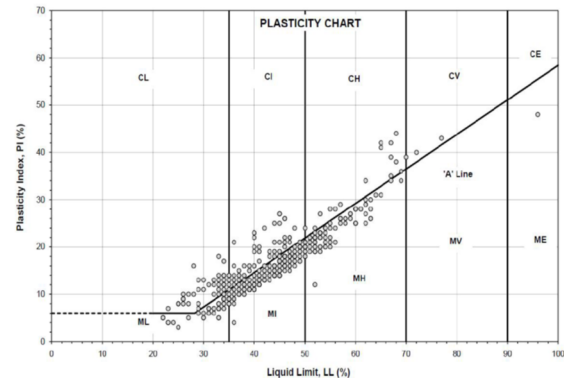


Fig. 2 Plasticity chart for residual soils

The effective shear strength parameters interpreted from CIU and direct shear tests are $c' = 5 \text{ kN/m}^2 - 10 \text{ kN/m}^2$ and $\phi' = 28^\circ$ for residual soils with $\text{SPT} \leq 100$; $c' = 15 \text{ kN/m}^2$ and $\phi' = 29^\circ$ with SPT greater than 100. These values are generally within the range of effective shear strength parameters suggested by Wong & Singh [4]. For highly weathered rock (Grade IV), the equivalent Mohr-Coulomb strength parameters are $c' = 30 \text{ kN/m}^2$ and $\phi' = 34^\circ$ assessed using method proposed by Hoek and Brown [5].

In general, the permeability of residual soils ranges from $7.1 \times 10^{-7} \text{ m/s}$ to $1.6 \times 10^{-5} \text{ m/s}$ based on the variable-head field permeability tests.

APPLICATION OF THEORY TO SETTLEMENT ANALYSIS

The empirical formulation commonly used in engineering practice for estimation of tunnelling-induced ground settlements had been developed by Schmidt [6] and Peck [7]. Peck [7] assumed that the transverse ground settlement trough can be reasonably represented by a Gaussian distribution curve - an idealisation which has considerable mathematical advantages. Two parameters, namely the ground loss V_l (sometimes referred to as volume loss) and the point of inflection i of the curve, are needed to fit the surface settlement. Cording and Hansmire [8] defined the ground loss as the volume of soil that is displaced across the perimeter of a tunnel. Whatever the soil type, it is convenient to express the volume loss in terms of the volume of the surface settlement trough V_s expressed as a percentage fraction of the excavated area of the tunnel per unit length of tunnel constructed, i.e. for a circular tunnel. The percentage volume loss V_l is defined as follows,

$$V_t = \frac{V_s}{V_t} \cdot 100\% \quad (1)$$

where V_s = settlement trough volume
 V_t = tunnel opening volume ($\pi.D^2/4$)
 D = diameter of the tunnel

Based on the shape of the normal distribution curve, Peck [7] showed that the maximum settlement occurring above the tunnel axis, S_{max} can be given by,

$$S_{max} = \frac{0.314.V_t.D^2}{i} \quad (2)$$

where i = the horizontal distance from the tunnel centre line to the point of inflection of the settlement trough

The settlement at various points of the trough, $S_v(x)$ is then given by,

$$S_v(x) = S_{max} \cdot \exp\left(\frac{-x^2}{2i^2}\right) \quad (3)$$

where x = the horizontal distance from the tunnel centre line

The definition is illustrated in Figure 3.

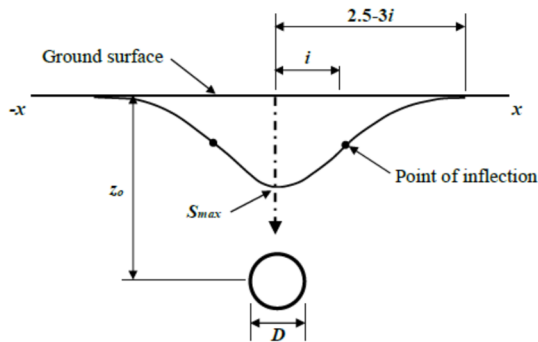


Fig. 3 Definition of settlement trough of Gaussian form

O'Reilly and New [9] showed that the trough width i is an approximately linear function of the depth z_o in relation to a trough width parameter K and broadly independent of tunnel construction method and tunnel diameter (except for very shallow tunnels where the cover to diameter ratio is less than one). The validity of the proposed simple approximate relationship of

$$i = K \cdot z_o \quad (4)$$

where K = trough width parameter
 z_o = depth to tunnel centre line

was generally confirmed by Rankin [10] for a wide variety of tunnels and for most soil types from around

the world. Generally, for tunnels in clay strata, the full width of the transverse settlement trough is about three times the depth of the tunnel [11]. The choice of an appropriate value of K may require some judgement, since it depends on whether ground is primarily cohesive or frictional. Numerically, the parametric study conducted by Khoo *et al.* [12] revealed that for majority of cases, $K \geq 0.5$ would be applicable for the typical soil types encountered in the Klang Valley of Malaysia and hence confirms the conclusion of O'Reilly and New [9] that $K = 0.5$ is appropriate for practical purposes.

It should be noted that Gaussian function is normally applied to the immediate surface settlements associated with tunnel construction. The immediate settlement mainly results from the ground loss at the tunnel face, the overcut effects of the shield passing and tail void closure. Additional post-construction settlement due to consolidation tends to cause wider settlement troughs and this complicates the interpretation of the settlement data. Softer clays are more susceptible to appreciable consolidation settlement, which could develop rapidly and can be difficult to separate from the immediate construction settlement; this may partly explain the observation by Peck [7] that wider settlement troughs are observed above tunnels in soft clays than in stiff clays.

In addition to the settlement volume V_s one has to consider the ground loss V_l which is the volume of the ground that has deformed into the tunnel after the tunnel has been constructed. For tunnelling in undrained soil (constant volume), the settlement volume is more or less equal to the ground loss, but the settlement volume tends to be somewhat smaller for water-drained excavations. The dilation and swelling due to the unloading may result in soil expansion, such that $V_s < V_l$. However, differences tend to remain small and it can be assumed that $V_s = V_l$. Nevertheless, it should be noted that the trough width parameter is independent with volume loss [13].

GROUND SURFACE SETTLEMENT MONITORING

Arrays consisting of several settlement markers are generally needed to deduce information about the shape and width of the surface settlement profiles. The concept hinges on the assumption that the shape of transverse settlement profiles developed during tunnel construction can be characterized by a Gaussian distribution.

Considering factors such as site constraints, surface topography and ground condition, a total of 18 representative monitoring arrays along the tunnel alignment in Kenny Hill Formation were selected and analysed in this study. The arrays consisted of 5 to 9 numbers of settlement markers to monitor the ground settlements prior to, during and after the excavation

of tunnels. All the instruments were aligned along the transverse direction of the tunnel drive. A sectional view showing the general arrangement of the instruments is depicted in Figure 4.

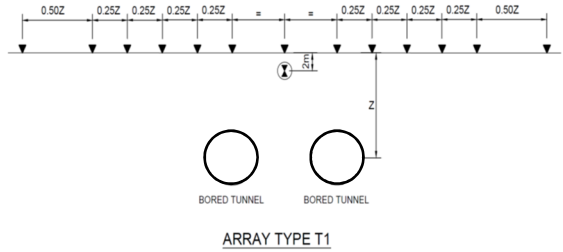


Fig. 4 Typical array of surface settlement monitoring

General Ground Condition at Monitoring Array

From the SPT values, the ground conditions at the monitored arrays appears to be fairly homogeneous with two distinct sub-divisions at N value 50. The overlying fill and residual soils generally extends down to a depth of 4.5m to 12m below the ground surface. Below this layer, the hard-weathered materials ($N \geq 50$) of Kenny Hill Formation is encountered where the tunnels are located. Groundwater tables were measured at about 2m to 3m below ground level. The corresponding ground information and tunnel alignment data at the selected monitoring arrays are presented in the Figure 5.

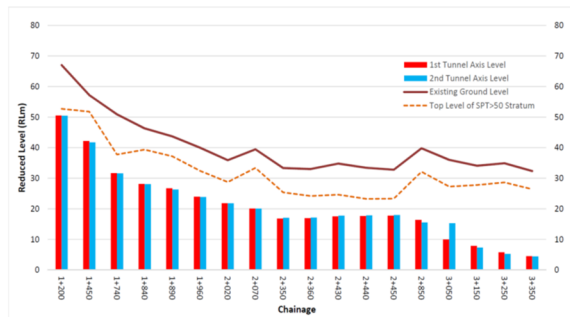


Fig. 5 Anticipated ground conditions and tunnel depth at selected monitoring arrays

Settlement Data and Considerations

Figure 6 shows the settlement trend plotted against time for the respective settlement markers located within the array. The magnitude of settlement induced by TBM passages of both tunnels bound was obtained from reading the surface settlement at the relevant dates when the TBMs crossed the monitoring array. Negative displacements indicate settlement whilst positive displacements indicate ground heave. Based on the settlement trend, it is observed that the settlements are mostly immediate settlements that

happened upon the TBM passage and within a short period thereafter. The short-term settlements are usually found to be almost complete when the TBMs are at a distance about approximately 20m to 30m beyond the monitoring array, i.e. about 3-5 times the tunnel diameter.

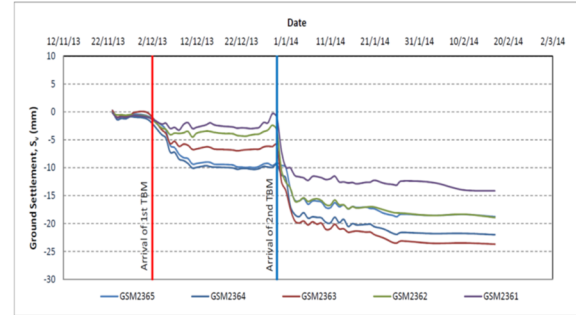


Fig. 6 Typical surface settlement trends when TBM passed through

In the interpretation of the data, influences such as TBM operating parameters, construction timing and cutter-head intervention, long term settlements due to consolidation are not considered in the study.

BACK ANALYSIS OF VOLUME LOSS AND TROUGH WIDTH PARAMETER

Study of Volume Loss

Theoretically, the volume of a measured settlement trough per unit length, V_s can be obtained by integrating Eq. (2)

$$V_s = \sqrt{2\pi} \cdot i \cdot S_{max} \quad (4)$$

By assuming the volume loss is equal to the volume of settlement trough, the loss V_l can be written as in Eq. (1) as

$$V_l = \frac{4V_s}{\pi D^2} \cdot 100\% \quad (5)$$

The above methodology requires reasonable assumption of appropriate trough width parameter to rationalise the Gaussian curve. For the purpose of this study, the actual volume loss is also obtained by adjusting the volume loss and trough width parameter input to match the measured settlement trough. The process is repeated for the second tunnel to match the combined settlement trough plotted from monitoring data to obtain the second set of parameters. Figure 7 shows an attempt to approximate measurement results by a Gaussian settlement trough.

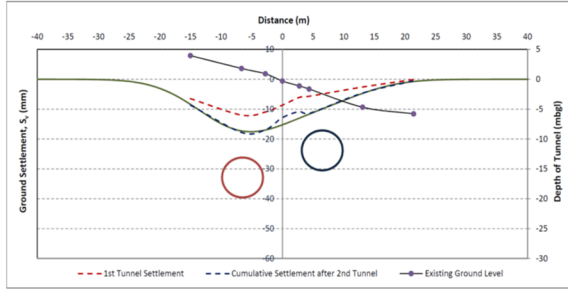


Fig. 7 Indicative cross section settlement trough

Based on the curve matching technique adopted to derive the actual volume loss, the 18 array sections were analysed. Figure 8 shows the volume loss derived. The volume loss ranges from as minimum as 0.10% to maximum of 1.35%. Statistically, 95% of the data points show the magnitude of volume loss is well below 1%.

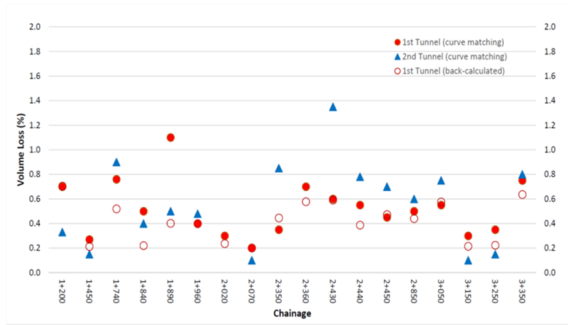


Fig. 8 Back-analysed volume loss in Kenny Hill Formation by EPB TBM

The back-calculated magnitudes of volume loss based on the maximum settlement of the field measurements (with assumption of $K = 0.5$) for the 1st tunnel are also included in Figure 8.

Study of Trough Width Parameter

Determination of the settlement trough width parameter K based on the approach described by Mair *et al.* [13] requires the maximum settlement S_{max} as an input value for each settlement profile. In the absence of data, the maximum settlement can be estimated by fitting a theoretical settlement profile to the measured data.

According to Eq. (4), the parameter i/z_0 is required to determine the trough width parameter K and this can be obtained by plotting $\log_e(S/S_{max})$ versus $(x/z_0)^2$. Substituting K into Eq. (3) and rearranging gives

$$\log_e\left(\frac{S}{S_{max}}\right) = -\frac{1}{2K^2} \cdot \left(\frac{x}{z_0}\right)^2 \quad (6)$$

Once the $\log_e(S/S_{max})$ versus $(x/z_0)^2$ is plotted for each monitoring array, K can be calculated from the slope of the best fit linear line as

$$K = \sqrt{\frac{1}{2[\text{slope of } \log_e(\frac{S}{S_{max}}) \text{ versus } (\frac{x}{z_0})^2]}} \quad (7)$$

Again, the basis of this expression is derived assuming that the shapes of the settlement profiles are characterized by a Gaussian distribution.

The values of the apparent trough width parameter K as defined in Eq. 7 determined based on the slope of the best fit lines for the 1st tunnel data set are given in Figure 9. From the back-calculation plot, the K value is computed to be 0.61.

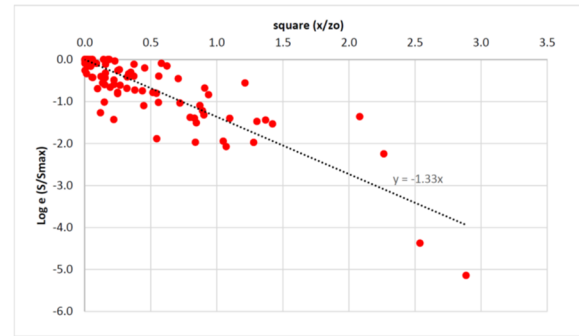


Fig. 9 Back-calculated trough width parameter

Apart from the back-calculated K via above equation, the trough width parameter is also obtained by fitting a theoretical settlement profile to the measured data as discussed earlier. It can be seen from Figure 10 the curve-matched K values exhibit some scatter ranging from 0.4 to more than 0.8 but with the majority being within 0.5 and 0.7. This shows that the settlement profile calculated based on K defined by Eq. (7), in general, yielded similar results.

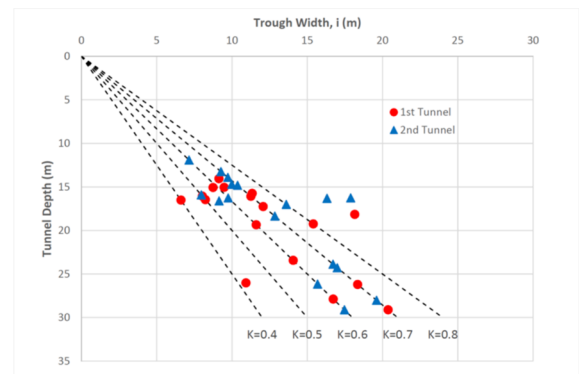


Fig. 10 Values of trough width parameter obtained from curve matching

In summary, K value of 0.5 as had been adopted for the residual soil of Kenny Hill Formation in the original design is reasonable for practical purposes. However, this study has shown that the K value is slightly higher between 0.5 to 0.7 with an average value of 0.6 based on the measured data set. It shall also be noted that the linear expression developed for Kenny Hill Formation may not be a unique expression for all soil layers but could differ due to differing overburden depth, soil stiffness, tunnelling method, face pressure and various other factors. A more comprehensive study of the surface settlement profiles together with the geological conditions and TBM operating parameters is however essential to further confirm the results and this is currently in the progress.

CONCLUSION

This paper had presented and discussed the volume loss caused by tunnelling in Kenny Hill Formation by EPB tunnel boring machine. Back analysis of trough width parameter had also been carried out. Tunnelling in Kenny Hill Formation has achieved a volume loss ranging from 0.10% to 1.35%. However, the majority of the volume loss is below 1.0%. Trough width parameter, K of between 0.5 and 0.7 was obtained with an average value of 0.6. The results provide valuable knowledge on ground responses to tunnelling in Kenny Hill Formation.

However, a generalization of the volume loss magnitude for use is cautioned against, owing to the specific nature of this project where the tunnel horizons were mostly at depths where the SPT values are above 50 and where typically an overburden of 2D above the tunnels crown was evident which can be viewed as favorable for tunnelling.

With more tunnelling projects on-going and coming up in Malaysia, more monitoring data will become available. Further work is needed to expand the current database of monitoring results to confirm and refine these findings.

ACKNOWLEDGEMENTS

The authors are grateful to the management of Mass Rapid Transit Corporation Sdn Bhd for their permission to publish this paper and their positive support in the success of this paper. Special gratitude is also dedicated to Ms. Nur Amanina Mazlan for her untiring efforts in data collection and analysis.

REFERENCES

[1] Chin R. M., Salehudin M. S. and Abdullah Husairi N., Performance of EPB Tunnelling in Kenny Hill Formation. Proc. of International Conference and Exhibition on Tunnelling and Underground

Space, Kuala Lumpur, 2015, pp. 298-301.
 [2] Ooi T. A., Design and Construction Problems of Foundation for Highrise Structures in the Kuala Lumpur Areas. Proc. of IEM-ISSMFE Joint Symposium on Geotechnical Problem, Kuala Lumpur, 1986, pp. 112-122.
 [3] Toh C. T., Ooi T. A., Chiu H. K., Chee S. K. and Ting W. H., Design Parameters for Bored Piles in a Weathered Sedimentary Formation. Proc. of 12th International Conference on Soil Mechanics and Foundation Engineering, Rio de Janeiro, 1989, Vol. 2, pp. 1073-1078.
 [4] Wong J. and Sing M., Some Engineering Properties of Kenny Hill Formation in Kuala Lumpur. Proc. of 12th South-East Asian Geotechnical Conference, Kuala Lumpur, 1996, pp. 179-187.
 [5] Hoek E. and Brown E. T., Practical Estimates of Rock Mass Strength. International Journal of Rock Mechanics and Mining Sciences, Vol. 34, No. 8, 1997, pp. 1165-1186.
 [6] Schmidt B., Settlements and Ground Movements Associated with Tunnelling in Soil. PhD Thesis, University of Illinois, 1969.
 [7] Peck, R. B., Deep Excavation and Tunnelling in Soft Ground – State-of-the-Art Report. Proc. of 7th International Conference on Soil Mechanics and Foundation Engineering, Mexico, 1969, pp. 225-290.
 [8] Cording E. J., Hansmire W. H., Displacements Around Soft Ground Tunnels. General Report, 5th Pan-American Conference on Soil Mechanics and Foundation Engineering, Buenos Aires, 1975, pp. 571-632.
 [9] O'Reilly M. P. and New B. M., Settlement above Tunnels in the United Kingdom – Their Magnitude and Prediction. Tunnelling 82, IMM, London, 1982, pp. 173-181.
 [10] Rankin W. J., Ground Movements Resulting from Urban Tunnelling. Proc. of Conf. Eng. Geol., Underground Movement, London Geological Society, Nottingham, 1988, pp. 79-92.
 [11] Mair R. J., Taylor R. N. and Burland J. B., Prediction of Ground Movements and Assessment of Risk of Building Damage due to Bored Tunnelling. Geotechnical Aspects of Underground Construction in Soft Ground, Mair & Taylor (eds), Balkema, Rotterdam, 1996, pp. 713-718.
 [12] Khoo C. M., Idris N. I. S. I., Mohamad H. and Abdul Rashid A. S., Numerical Evaluation of Settlement Trough Width Parameter, Proc. of International Conference on Civil, Offshore and Environmental Engineering, Kuala Lumpur, 2018.
 [13] Mair R. J., Taylor R. N. and Bracegirdle A., Subsurface Settlement Profiles above Tunnels in Clay. Geotechnique 43, Vol. 2, 1993, pp. 315-320.

THE NECESSITY OF EMPLOYING THREE DIMENSIONAL CONCEPTS IN SLOPE STABILITY ANALYSIS

Roohollah Kalatehjari¹, Ahmad Safuan Abdul Rashid², and Mostafa Babaeian Jelodar³

^{1,3} Built Environment Engineering Department, School of Engineering, Computer and Mathematical
Sciences, Auckland University of Technology, Auckland 1010, New Zealand;

² Faculty of Civil Engineering, Universiti Teknologi Malaysia, 81310, Johor Bahru, Malaysia

ABSTRACT

Analysis of slope stability is an unavoidable task in construction associated with mountainous areas and nearby man-made earth modifications. This analysis has been in continuous development and improvement since the introduction of equation of safety factor. Several methods made it available to determine safety factor of slopes through two-dimensional (2D) and three-dimensional (3D) analyzes. Among them, the 2D limit equilibrium methods are the most common practices because of their clarity of equations and reliability of solving processes. However, the complexities in the slope surface geometry and the variation of the soil strata increasingly reduce the reliability of the traditional methods when facing real 3D conditions. In addition, meaningful number of roadside landslides especially in developing countries highlights the importance of seeking more reliable approaches. Therefore, 3D analyzes are gaining more attention due to considering less assumptions and more variables in conjunction with rigorous solutions. Some of the new concepts introduced along with these methods are the directional factor of safety, the unique direction of sliding, and the 3D failure surfaces of various shapes, from simple weak planes to non-uniform rational base spline (NURBS). Although the integration of each concept with the traditional approaches can improve the reliability of the slope stability analysis, only a rigorous system of equations that includes all the three notions can provide the most reliable result when true 3D analysis is required. This article presents a detailed study on the need to contract the 3D aspects in slope stability analysis and demonstrates the drawbacks of ignoring them in practice.

Keywords: Slope Stability, Three-dimensional analysis, Critical failure surface, NURBS, Landslide

INTRODUCTION

The most common approach of slope stability analysis, limit equilibrium method, was founded based on the behavior of slope material at the verge of failure. This method does not engage with the stress-strain relationship nor the deformation within the soil body. As a result, it requires to take assumptions regarding the shape of potential failure surface to develop its moment and force equilibriums. Factor of safety (FOS) at the verge of failure is then defined as the ratio of the available shear strength of the soil to the prominent shear stress along the assumed failure surface. The failure surface is usually assumed planar or cylindrical if the slope geometry and geotechnical properties of the soil are simple enough to be modelled by plain strain condition. However, the complexity of the slope condition may enforce more complicate surfaces to the analysis. The required shearing resistance for maintaining the static equilibrium is estimated by considering the plastic behavior and utilizing Mohr-Coulomb failure criterion along the slip surface. This leads to calculation of the FOS in an iterative process.

The above mentioned process is usually conducted by two-dimensional (2D) approaches due to the limitations that are discussed in this paper. However, the comparisons made during past decades on the results of slope stability analysis methods have demonstrated that three-dimensional (3D) analysis is the better option - if not the necessity - when facing complicated slope stability problems [1]–[23].

In this paper, a 2D model including a soil slope with six alternative conditions was extended to the third dimension by assigning different lengths for the slip surface. Simplified and rigorous 3D methods were used to calculate the FOS and the effect of the third dimension on the value of FOS was investigated by comparing the results of 2D and 3D methods. The necessity of employing 3D concepts was demonstrated through comparisons and discussions.

2D ANALYSIS OF SLOPE STABILITY

In order to simplify the problem, evaluation of slope stability is usually performed by 2D methods. These methods simplify the geometry of the slope

by transforming the problem into 2D framework. Some internal and external forces are inevitably simplified or ignore in this process. This simplification is believed to be the main reason of the differences between the results of 2D and 3D methods. Various 2D approaches have been developed in the past decades based on the limit equilibrium method. These methods are generally classified into the circular methods (e.g. Swedish circle and friction circle methods), non-circular methods (e.g. log-spiral method), and methods of slices (e.g. Fellenius [24], Bishop [25], Janbu [26]–[27], Morgenstern and Price [28], and Spencer [29] methods). This diversity comes from different assumptions and simplifications engaged with the analysis as well as using different equilibriums to develop equation of FOS.

Method of slices is the most commonly applied 2D method due to its ability to consider different soil and water conditions, complex 2D geometries, and external forces [30]. This method divides the soil body into vertical slices, with external and internal forces applied on each. Static equilibriums are then developed base on the applied forces and are satisfied using the equations, assumptions, and simplifications. Finally, the FOS is calculated by comparing the strength and stress available along the failure surface. Mohr-Coulomb failure criterion is commonly employed to establish the equation of FOS.

In order to analysis the stability of a slope by using the method of slices, the slope has to be considered unconstructed in length. Therefore, the static equilibrium of the soil mass is developed for a number of vertical slices with unit thickness. This problem is statically indeterminate, because the static elements of the problem together with the failure criterion of the soil mass are not enough to overcome all the existence unknowns. Consequently, additional assumptions or simplifications are needed to make the problem statically determinate.

The Simplified Bishop method is the most common method of slices [25]. It assumes a circular rotational slip surface, with all the interslice shear forces neglected. Point of application of each base normal force is assumed at the center of slide base. The summation of forces in vertical direction is used to calculate normal forces. Then the equation of FOS is established by taking the moment over the center of rotation of the slip surface. The accuracy of this method is reasonably in agreement with the results of rigorous 2D methods, although it does not satisfy all the conditions of equilibriums [29]–[30].

3D ANALYSIS OF SLOPE STABILITY

The soil volume beneath the ground surface and above the failure surface is called the sliding mass. In the 3D method of slices, the sliding mass is divided into a series of columns, hence the corresponding method is called the method of columns. The columns inside the boundaries of sliding mass are called active columns and are labeled by their relative position in x- and y-directions, as i and j, respectively. The equation of FOS can be established based on the static equilibriums and Mohr-Coulomb failure criterion. Fig.1 illustrates the internal and external forces acting on a typical soil column.

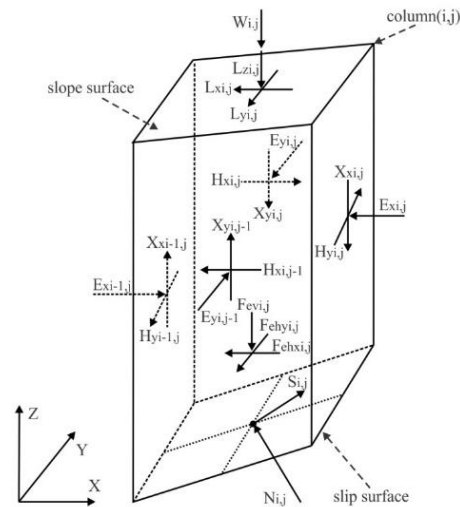


Fig. 1 Applied forces on a typical soil column.

Where; W = weight of soil column;
 L_z, L_x, L_y = external load on column;
 F_{ev}, F_{ehx}, F_{ehy} = earthquake forces on column;
 $E_x, E_y, X_x, X_y, H_x, H_y$ = intercolumn forces;
 S = mobilized shear strength at the base of column;
 N = total normal force at the base of column

The first 3D method used in this paper was developed by Huang and Tsai [31] as an extension of Simplified Bishop method [25]. This 3D Simplified Bishop method can handle semi spherical as well as composite slip surfaces. All horizontal intercolumn forces are ignored and the axis of rotation is assumed parallel with y-axis. The second method was developed by the authors as an extension of Huang et al. method [32]. This method works with ellipsoid, spherical and composite slip surfaces. There is no need for an axis of rotation and intercolumn forces are included in this method.

STABILITY ANALYSIS OF A SOIL SLOPE

Fredlund and Krahn [30] compared the performance of different 2D methods by analyzing a

benchmark soil slope. The problem includes both circular and composite slip surfaces, a weak layer, and different water conditions, which totally creates six different conditions for the slope. The authors have extended all the six cases in to the third dimension by gradually increasing lengths of slip surfaces. In the first case, the circular slip surface was extended to an ellipsoid with a circular central section. In the second case, a weakness plane was added to the slope and it was assumed that the failure surface cannot penetrate it. So, a composite slip surface was created. The third and the forth cases were designed by adding a pore water pressure coefficient (r_u) into the first and the second (Table 1). In the final two cases, the coefficient of pore water was replaced by a piezometric line. Both the mentioned 3D methods were employed to calculate the values of FOS.

Table 1 Properties of the slope materials [30].

Layer	c' (kN/m ²)	ϕ' (degree)	γ (kN/m ³)	r_u
Soil	29	20	18.80	0.25
Weak	0	10	18.80	0.25

The Geometry and Material of the Slope

The 2D sections were used as the central sections of the 3D cases. The range of extended lengths and volumes of sliding mass are shown in Table 2. The problem involved a symmetrical slope of 18.3m height and V:H gradient of 2:1. The center point of the failure surface was located at the central section. Equal semi-radiuses of 24.4m were used in y- and z-directions, while the semi-radius in x-direction has gradually increased during the analysis.

Table 2 Properties of sliding mass in the six cases.

Case	Length of slip surface (m)	Volume of sliding mass (m ³)
1	10-67	1613.4-11808.0
2	10-105	1478.7-17075.0
3	10-130	1613.4-23020.0
4	10-160	1501.1-26067.0
5	10-100	1613.4-17690.0
6	10-107	1478.7-17406.0

RESULTS AND DISCUSSION

Variations of FOS for the six cases are shown in Table 3, while the properties of the produced models for different cases are shown in Table 4. Different lengths of the failure surface (R_x) were used to evaluate the end effect. The range of R_x was selected from a minimum applicable to a maximum efficient length. Fig.2 illustrates case 6 as a geometrically complicated case modeled by the authors' code.

Table 3 Variations of FOS for different cases

Case	Length (m)	Range of 3D FOS	
		Simplified Bishop	Rigorous
1	10-67	2.44-2.09	2.71-2.34
2	10-105	1.98-1.59	2.14-1.76
3	10-130	2.17-1.82	2.41-2.05
4	10-160	1.80-1.35	1.97-1.52
5	10-100	2.29-1.91	2.56-2.19
6	10-107	1.87-1.45	2.05-1.66

Fig.3 shows the 3D FOS versus the length of the slip surface. A decreasing trend is observed for all six cases by increasing the length of the failure surface, which eventually tends to horizon. The condition of a uniform 3D problem becomes more similar to the plain strain assumption applied to the 2D methods. The shorter the length of the slip surface is, the greater end effect is expected from 3D analysis. The calculated 3D FOS for all cases were compared with the results of Fredlund and Krahn's 2D analysis [29] as shown in Table 5. The results show that the 3D FOS is always greater than the results of 2D methods. The difference is more significant when comparing the results of rigorous methods. The minimum and maximum difference ratios between the FOS of the simplified methods belong to cases 1 and 4 with the values of 0.24% and 37.45%, respectively. These ratios belong to cases 1 and 4 in rigorous methods, with the values of 16.73% and 43.25%, respectively.

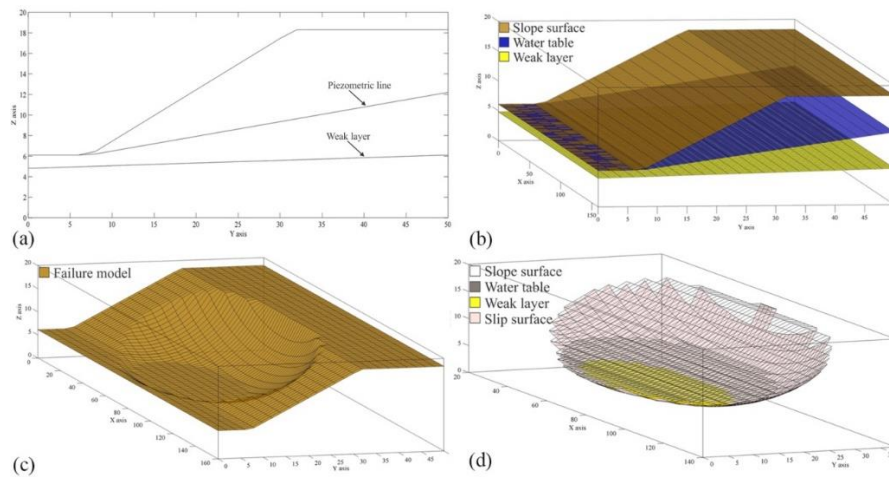


Fig.2 Generated models for case 6 including (a) section, (b) slope model, (c) failure mode, and (d) sliding mass.

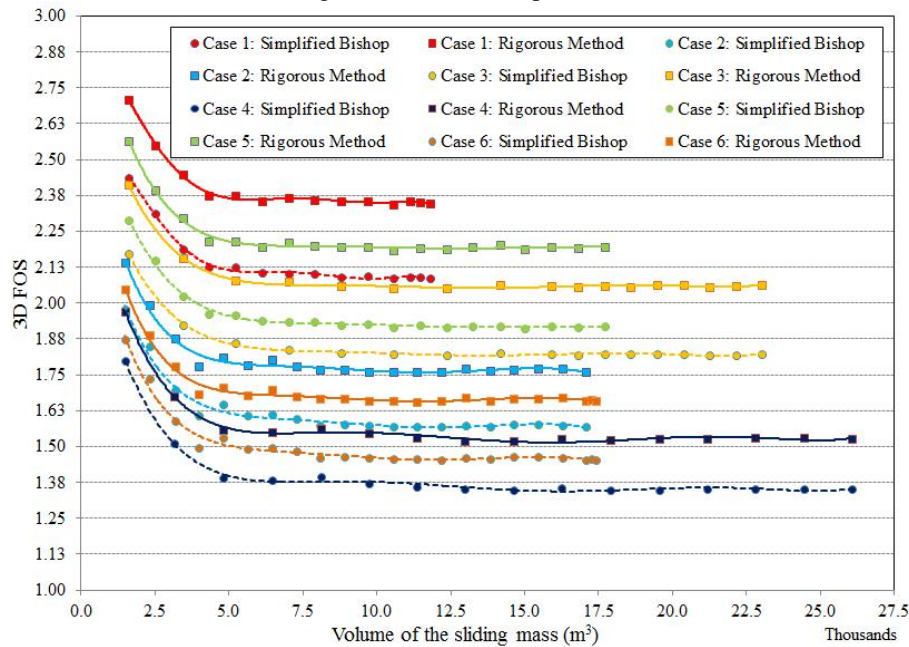


Fig.3 Trends of the 3D FOS versus length of the failure surface for all six cases.

Case 1 is the simplest with the minimum complexity, while case 4 is the most complicated cases. This shows that the complexity of the slope condition may cause larger difference between the results of 2D and 3D methods. In addition, considering the fact that the maximum differences for both simplified and rigorous methods occurred for the shortest length of the slip surface suggests that applying 2D methods for analyzing slopes with short lengths may introduce larger inaccuracy to the results.

CONCLUSION

Simplified and rigorous 3D methods were applied to a benchmark soil slope to calculate the

FOS for six different cases. In order to evaluate the effect of the third dimension on the value of FOS, failure surfaces with different lengths were assigned to each case. The modeling and calculation were done by a computer code, developed by the authors in Matlab.

The calculated values of 3D FOS were compared with the results of different 2D methods from the literature. It was found that the 3D FOS is always greater than the 2D FOS for all the cases. The minimum and maximum difference between the results of 2D and 3D methods were observed in the simplest and the most complicated cases. In addition, a decreasing trend of 3D FOS was detected by increasing the length of the failure surface.

It is concluded that for each of the cases, the difference between the FOS of the rigorous methods is always greater than that of the simplified methods. The results also indicated that the maximum differences between the results of 2D and 3D methods occurs with the shortest length of the failure surface.

Despite the proven advantages of 3D analysis over the past decades, majority of the commercially available 3D software are unable to consider the shear resistance at the side of the columns [33]. Consequently, the calculated 3D factor of safety is underestimated, while the back-calculated shear strengths can be overestimated [34].

In overall, all the achieved results agree on the significance of 3D analysis in terms of calculated

FOS, especially when the failure surface is confined.

A summary of the cons and pros of employing 3D slope stability analysis is presented in Table 6, based on the results of this paper. From here, it is the geotechnical engineer's job to decide on the best method of analysis for each slope. Investment in purchasing a 3D software with higher price than traditional packages may seem to be one of the main drawbacks of 3D methods. This is based on the fact that researchers can produce their own software, but practitioners usually have to go to the marketplace to buy a package that suits their needs.

The authors believe that this paper together with the significant amount of studies carried out in this field during the past decades highlight the necessity of employing the 3D concepts more often in practice.

Table 4. Properties of the produced models in different cases.

Case	Slope length (m)	Slip surface coordinate (m)						Weak layer	Water condition
		Xc	Yc	Zc	Rx	Ry	Rz		
1	100	50	13.4	27.4	10-67	24.4	24.4	-	-
2	160	80	13.4	27.4	10-105	24.4	24.4	Yes	-
3	200	100	13.4	27.4	10-130	24.4	24.4	-	r_u
4	250	125	13.4	27.4	10-160	24.4	24.4	Yes	r_u
5	160	80	13.4	27.4	10-100	24.4	24.4	-	ps
6	160	80	13.4	27.4	10-107	24.4	24.4	Yes	ps

Note: P_s = piezometric surface, r_u = coefficient of pore water pressure for both materials

Table 5. Properties of produced models in different tests.

Method of Analysis		Value of FOS					
		Case 1	Case 2	Case 3	Case 4	Case 5	Case 6
2D Simplified Bishop*		2.080	1.377	1.766	1.124	1.834	1.248
3D Simplified Bishop**	Max	2.438	1.979	2.172	1.797	2.288	1.873
	Min	2.085	1.568	1.817	1.348	1.913	1.454
Difference ratio (%)	Max	14.68	30.42	18.69	37.45	19.84	33.37
	Min	0.24	13.87	2.89	19.93	4.31	16.51
2D Spencer*		2.073	1.373	1.761	1.118	1.803	1.245
2D Rigorous Janbu*		2.008	1.432	1.708	1.162	1.776	1.298
2D Morgenstern-Price*		2.076	1.378	1.765	1.124	1.833	1.250
3D rigorous Method**	Max	2.707	2.142	2.412	1.970	2.563	2.047
	Min	2.344	1.758	2.050	1.518	2.186	1.656
Difference ratio (%)	Max	25.82	35.90	29.19	43.25	30.71	39.18
	Min	16.73	28.04	20.02	35.78	23.09	33.01

Note: *Results of Fredlund and Krahn [30], **Results of the present study

Table 6. Cons and pros of employing 3D slope stability analysis.

Cons of 3D	Pros of 3D
<ul style="list-style-type: none"> Higher initial investment for software More complexity in slope design Practitioners to learn new soft skills More detailed site investigation needed 	<ul style="list-style-type: none"> Lower slope modification costs Possibility to extract 2D section of a 3D model Less judgement involved with analysis Basic geotechnical properties of soil needed

REFERENCES

- [1] Anagnosti, P. (1969). Three-dimensional stability of fill dams. Proceeding of 7th. International Conference on Soil Mechanics and Foundation Engineering. Mexico: NRCan Library. 275-280
- [2] Baligh, M. M., & Azzouz, A. S. (1975). End effects on stability of cohesive slopes. Journal of Geotechnical and Geoenvironmental Engineering, 101(ASCE# 11705 Proceeding).
- [3] Hovland, H. (1977). Three-dimensional Slope Stability Analysis Method. Journal of Geotechnical Engineering Division, 103(9): 971-986.
- [4] Azzouz, A., and Baligh, M. (1978). Three-dimensional Stability of Slopes. Alexandria, VA, USA: National Technical Information Service.
- [5] Chen, R., and Chameau, J. (1983). Three-dimensional Limit Equilibrium Analysis of slopes. Geotechnique, 32(1): 31-40.
- [6] Azzouz, A., and Baligh, M. (1983). Loaded Areas on Cohesive Slopes. Journal of Geotechnical Engineering Division, 109(5): 724-729.
- [7] Hungr, O. (1987). An Extension of Bishop's Simplified Method of Slope Stability Analysis to Three Dimensions. Geotechnique, 37(1): 113-117.
- [8] Ugai, K. (1988). Three-dimensional Slope Stability Analysis by Slice Methods. Proceeding of the International Conference on Numerical Methods in Geomechanics. Innsbruck, Austria, 1369-1374.
- [9] Xing, Z. (1988). Three-Dimensional Stability Analysis of Concave Slopes in Plan View. Journal of Geotechnical Engineering, 114(6): 658-671.
- [10] Gens, A., Hutchinson, J., and Cavounidis, S. (1988). Three-dimensional Analysis of Slides in Cohesive Soils. Geotechnique, 38(1): 1-23.
- [11] Hungr, O., Salgado, F., and Byrne, P. (1989). Evaluation of a Three-Dimensional Method of Slope Stability Analysis. Canadian Geotechnical Journal, 26: 679-686.
- [12] Cavounidis, S., and Kalogeropoulos, H. (1992). End Effects on the Stability of Cuts in Normally Consolidated Clays. Rivista Italiana Gi Geotecnica, 2: 85-93.
- [13] Leshchinsky, D., and Huang, C. C. (1992). Generalized Three-Dimensional Slope Stability Analysis. Journal of Geotechnical Engineering, 118(11): 1748-1764.
- [14] Lam, L., and Fredlund, D. (1993). A General Limit Equilibrium Model for Three-Dimensional Slope Stability Analysis. Canadian Geotechnical Journal, 30: 905-919.
- [15] Yamagami, T., and Jiang, J. C. (1996). Determination of the sliding direction in three-dimensional slope stability analysis. Proceedings of the 2nd International Conference on Soft Soil Engineering. Part 1. Nanjing: Hohai University Press, 567-572.
- [16] Yamagami, T., and Jiang, J. C. (1997). A Search for the Critical Slip Surface in Three-dimensional Slope Stability analysis. Soils and Foundations, 37(3): 1-16.
- [17] Chen, Z., Mi, H., Zhang, F., and Wang, X. (2003). A Simplified Method for 3D Slope Stability Analysis. Canadian Geotechnical Journal, 40: 675-683.
- [18] Jiang, J. C., and Yamagami, T. (2004). Three-Dimensional Slope Stability Analysis Using an Extended Spencer Method. Journal of the Japanese Geotechnical Society of Soils and Foundations, 44(4): 127-135.
- [19] Cheng, Y., and Yip, C. (2007). Three-Dimensional Asymmetrical Slope Stability Analysis Extension of Bishop's, Janbu's, and Morgenstern-Price's Techniques. Journal of Geotechnical and Geoenvironmental Engineering, 133(12): 1544-1555.
- [20] Zheng, H. (2009). Eigenvalue problem from the stability analysis of slopes. Journal of geotechnical and geoenvironmental engineering, 135(5), 647-656.
- [21] Sun, G., Zheng, H., and Jiang, W. (2011). A global Procedure for Evaluating Stability of Three-Dimensional Slopes. Natural Hazards, 61(3): 1083-1098.
- [22] Kalatehjari, R., Rashid, A. S. A., Hajihassani, M., Kholghifard, M., & Ali, N. (2014). Determining the unique direction of sliding in three-dimensional slope stability analysis. Engineering Geology, 182, 97-108.
- [23] Kalatehjari, R., Arefnia, A., A Rashid, A. S., Ali, N., & Hajihassani, M. (2015). Determination of three-dimensional shape of failure in soil slopes. Canadian Geotechnical Journal, 52(9), 1283-1301.
- [24] Fellenius, W. (1936). Calculation of the Stability of Earth Dams. Proceeding of the 2nd Congress on Large Dams, Washington, DC, 445-463.
- [25] Bishop, A. W. (1955). The Use of the Slip Circle in the Stability Analysis of Earth Slope. Geotechnique, 5(1): 7-17.
- [26] Janbu, N., Bjerrum, L., and Kjarnsli, B. (1956).

- Stabilitetsberegning for Fyllinger Skjaeringer og Naturlige Skraninger. Oslo, Norway: Norwegian Geotechnical Publication.
- [27] Janbu, N. (1957). Earth Pressure and Bearing Capacity Calculations by Generalized Procedure of Slices. The Proceeding of the fourth International Conference on Soil Mechanics and Foundation Engineering, London, 207-212.
- [28] Morgenstern, N., and Price, V. (1965). The Analysis of the Stability of General Slip Surfaces. *Geotechnique*, 15(1): 79-93.
- [29] Spencer, E. (1967). A Method of Analysis of the Stability of Embankments Assuming Parallel Inter-Slice Forces. *Geotechnique*, 17(1): 11-26.
- [30] Fredlund, D. G., and Krahn, J. (1977). Comparison of slope stability methods of analysis. *Canadian Geotechnical Journal*, 16: 121-139.
- [31] Huang, C. C., & Tsai, C. C. (2000). New method for 3D and asymmetrical slope stability analysis. *Journal of Geotechnical and Geoenvironmental Engineering*, 126(10), 917-927.
- [32] Huang, C. C., Tsai, C. C., and Chen, Y. H. (2002). Generalized Method for Three-Dimensional Slope Stability Analysis. *Journal of Geotechnical and Geoenvironmental Engineering*, 128(10): 836-848.
- [33] Stark, T. D., & Eid, H. T. (1998). Performance of 3D slope stability methods in practice. *Journal of Geotechnical and Geoenvironmental engineering*, 124(11), 1049-1060.
- [34] Arellano, D., & Stark, T. D. (2000). Importance of three-dimensional slope stability analyses in practice. In *Slope Stability 2000* (pp. 18-32)

SEISMIC MICROZONATION OF SEMARANG, INDONESIA, BASED ON PROBABILISTIC AND DETERMINISTIC COMBINATION ANALYSIS

W. Partono¹, M. Irsyam², M. Asrurifak², I.W. Sengara², A. Mulia², M. Ridwan³ and L. Faizal³

¹Engineering Faculty, Diponegoro University, Indonesia; ²Faculty of Civil and Environmental Engineering , Bandung Institute of Technology, Indonesia; ³Ministry of Public Works and Human Settlements, Indonesia

ABSTRACT

Research and development of new Indonesian seismic hazard maps were already finished on 2017. One of the most important information obtained from this research related with new seismic source which is crossed the city of Semarang, Indonesia. Based on the new Indonesian Seismic Hazard Maps 2017, Semarang fault is to be categorized as the new dangerous seismic source and shall be taken into account for seismic mitigation of this city. This paper describes the result of seismic microzonation of Semarang by conducting a combination of probabilistic and deterministic hazard analysis. The objective of this research is for developing risk maps for Semarang by conducting one percent probability of building collapse in 50 years. The analysis was performed by conducting the same method used for developing risk targeted Maximum Considered Earthquake (MCE_R) maps 2012 by improving beta (logarithmic standard deviation) value equal 0.65 and direction factor 1.1 and 1.3 for short and long period 84th percentile deterministic spectral accelerations respectively. Due to the existing of Lasem fault the maximum 2012 MCE_R spectral acceleration results were identified on the eastern part of the city. However due to the new identified Semarang fault source the maximum MCE_R spectral accelerations were measured on the northwestern part of the study area. The differences of those two MCE_R distribution results caused by the location of Lasem fault and Semarang fault seismic sources. Lasem fault is located on the eastern part however Semarang fault is located on the northwestern part of the city.

Keywords: Seismic microzonation, shallow crustal fault, probabilistic, deterministic, MCE_R

INTRODUCTION

The new Indonesian seismic hazard maps were already developed on 2017 by National Center for Earthquake Studies [1] by conducting probability seismic hazard analysis (PSHA). Eight different maps with different probability of exceedance, from 20% probability of exceedance in 10 years (50 years of return periods) through 1% probability of exceedance in 100 years (10000 years of return periods), were implemented during 2017. Major improvements on historical earthquakes data, earthquakes faults assessments and seismotectonic maps data and minor improvements on ground motion prediction equations were implemented for developing those eight seismic hazard maps [2]. One of the most important seismic hazard maps used for developing Indonesian Seismic Code for Building Resistance is 2500 years of return periods (2% probability of exceedance in 50 years). Development of new seismic hazard maps for building design is still ongoing and following the same procedures implemented for developing 2012 Indonesian seismic code for building and other structures design [3]. The new MCE_R maps will be developed using a combination of probabilistic (2% probability of exceedance in 50 years) and deterministic hazard

analysis and conducting risk targeted ground motion (RTGM) analysis of probabilistic seismic hazard analysis for producing 1% probability of building collapse in 50 years [3], [4]. The new RTGM analysis will be performed by conducting modified beta (β), logarithmic standard deviation, value and modified direction factor for 0.2 second and 1 second spectral acceleration. The RTGM analysis will be developed for the whole area of the country from 94° to 142° east longitude and from 8° north to 12° south latitude and conducting 0.1 degrees grid spacing on both longitude and latitude directions.

A combination of probabilistic and deterministic seismic hazard analysis was then implemented for developing maximum considered earthquake (MCE) for the whole area of the country. Three risked targeted maximum considered earthquake ground motion (MCE_R), i.e. peak ground acceleration (PGA), short period (0.2 second) and long period (1 second) maps will be developed for the whole area of Indonesian country.

This paper describes the development of seismic microzonation of Semarang, Indonesia, by conducting a combination of probabilistic and deterministic seismic hazard analysis for developing three MCE_R maps (MCE_S for 0.2 second period, MCE_1 for 1 second period and MCE_G for peak

ground acceleration). The development of seismic microzonation of the city was implemented at 288 boring locations by conducting weighting interpolation of four closest points of national MCES, MCES1 and MCEG result calculations. All boring investigations were performed from 2009 until 2017 with minimum 30 meters depth. Average shear wave velocity (V_{s30}) were already calculated using standard penetration test data (N-SPT) and conducting three empirical formulas proposed by [5], [6] and [7]. Fig. 1 shows V_{s30} maps of Semarang, boring locations and two fault traces. A comparative study was implemented in this study to evaluate all MCES and MCES1 values calculated at 288 boring locations based on 2018 and 2012 data.

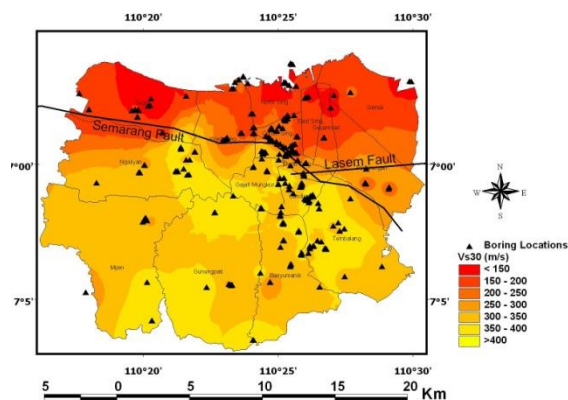


Fig. 1 V_{s30} map and boring positions.

SEISMIC HAZARD ANALYSIS

Seismotectonic Data for Seismic Hazard Analysis

Major improvement of seismotectonic data of Semarang were conducted for seismic hazard analysis. Seismotectonic data for 2010 seismic hazard analysis were dominated by 5 (five) shallow crustal fault sources (Cimandiri, Lembang, Yogya, Lasem and Opak) and 1 (one) subduction source (Java Megathrust). However for 2017 seismic hazard analysis 8 (eight) shallow crustal fault data (Cimandiri, Lembang, Baribis-Kendeng, Ciremai, Ajibarang, Opak, Merapi-Merbabu and Pati) have been clearly identified and located within a radius of 500 km from the city of Semarang. All crustal fault data are divided into 26 (twenty-six) fault segments. Table 1 shows the seismotectonic data of 26 fault segments used for seismic hazard analysis. Seismic parameters SR, SM, D, L, M, RS and SS on this table stands for slip rate (mm/year), seismic mechanism, dip (degree), long (km), maximum magnitude (Mw), reverse-slip and strike-slip respectively.

For 2017 seismic hazard analysis 1 (one) subduction source (Java Megathrust) was clearly identified and located on the southern part of Java

island. For seismic hazard analysis Java subduction megathrust source is divided into two, i.e. West and Central-East Java segments. Table 2 shows all parameter data used for Java subduction megathrust source, L, W, SR and M stands for Long (km), Width (km), Slip Rate (cm/year) and Maximum Magnitude (Mw) respectively. Fig. 2 shows seismotectonic of Java Island used for developing seismic hazard map. Fault number on Fig. 2 related with segment fault number on Table 1.

Seismic hazard analysis was performed by conducting earthquake databases from 1901 until 2014 [2]. All earthquake data were collected from Meteorological Climatological and Geophysical Agency (BMKG), focal mechanism from International Seismological Commission (ISC) databases, EHB catalog and Preliminary Determination of Epicenters (PDE) [2]. All hypocenter earthquake data have been relocated to the correct positions [2].

Table 1 Shallow crustal fault parameter data [1]

No	Fault Segments	SR	SM	D	L	M
1	Cimandiri	0.55	RS	45	23	6.7
2	Cibeber	0.40	RS	45	30	6.5
3	Rajamandala	0.1	SS	90	45	6.6
4	Lembang	2.0	SS	90	29.5	6.8
5	Subang	0.1	RS	45	33	6.5
6	Cirebon-1	0.1	RS	45	15	6.5
7	Cirebon-2	0.1	RS	45	18	6.5
8	Karang Malang	0.1	RS	45	22	6.5
9	Brebes	0.1	RS	45	22	6.5
10	Tegal	0.1	RS	45	15	6.5
11	Pekalongan	0.1	RS	45	16	6.5
12	Weleri	0.1	RS	45	17	6.5
13	Semarang	0.1	RS	45	34	6.5
14	Rawapening	0.1	RS	45	18	6.5
15	Demak	0.1	RS	45	31	6.5
16	Purwodadi	0.1	RS	45	38	6.5
17	Cepu	0.1	RS	45	100	6.5
18	Waru	0.05	RS	45	64	6.5
19	Surabaya	0.05	RS	45	25	6.5
20	Blumbang	0.05	RS	45	31	6.6
21	Ciremai	0.1	SS	90	20	6.5
22	Ajibarang	0.1	SS	90	20	6.5
23	Opak	0.75	SS	60	45	6.6
24	Merapi-Merbabu	0.1	SS	90	28	6.6
25	Pati	0.1	SS	90	69	6.5
26	Lasem	0.5	SS	90	114.9	6.5

Table 2 Subduction parameter data [1]

No	Segment	L	W	SR	M
1	West	320	200	4.0	8.8
2	Central-East	400	200	4.0	8.9

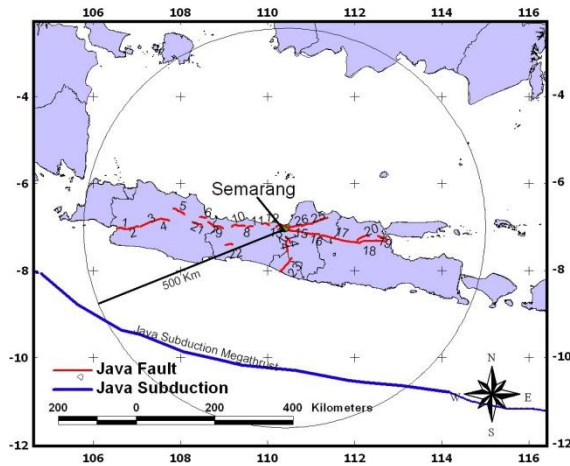


Fig. 2 Seismotectonic map of Java Island.

Ground Motion Prediction Equations

Selection of ground motion prediction equation (attenuation function) is important for calculating or predicting spectral acceleration at specific site. Following the same method implemented for Indonesian 2010 seismic hazard maps all attenuation function used for 2017 seismic hazard maps are divided into four different seismic source mechanism, i.e. shallow crustal fault, shallow background, subduction megathrust (Interface) and deep background (Benioff). Compare to 2010 seismic hazard maps a minor improvement of attenuation function was conducted for 2017 seismic hazard maps. BCHydro [8] attenuation function was conducted for subduction interface to replace Young's 1997 attenuation function [9]. Table 3 shows all attenuation functions used for developing Indonesian 2017 seismic hazard maps.

Table 3 Attenuation functions used for developing 2017 seismic hazard maps

Seismic Mechanism	Attenuation Functions
Shallow Crustal Fault and Shallow Background	[10], [11], [12]
Interface Megathrust	[8], [13], [14]
Benioff Subduction Intraslab	[9], [14]

Probabilistic and Deterministic Hazard Analysis

Two seismic hazard, probabilistic (PSHA) and deterministic (DSHA), analysis were performed for

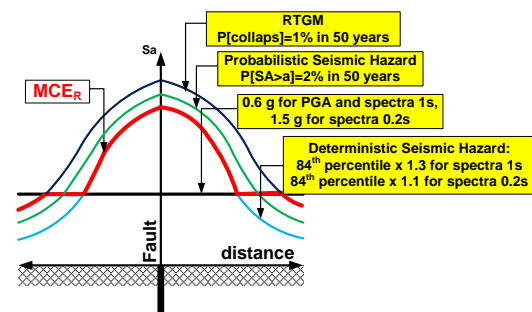
obtaining spectral acceleration at bedrock elevation. PSHA was implemented using total probability theorem [15]. Equation 1 shows the basic formula for obtaining the total average rate of exceedance of earthquake (λa^*) with acceleration greater than specific acceleration value a^* . $P_m(m)$ and $P_r(r)$ on this equation represents probability distribution function of magnitude (m) and distance (r) respectively and v represents mean rate of exceedance. DSHA was implemented using 84th percentile or equal to 150% of median spectral acceleration.

$$\lambda a^* = v \int \int (P_a > a^* | m, r) P_m(m) P_r(r) dr dm \quad (1)$$

Following the same steps conducted for developing 2010 national seismic hazard maps and 2012 national seismic code [3], integrating of PSHA and DSHA was implemented for developing new MCE_R 2018 maps for the whole area of the country. MCE_R values was calculated by combining risk targeted ground motion analysis (RTGM) with 1% probability of collapse in 50 years and 84th percentile deterministic seismic hazard analysis and adjusting direction factor 1.1 for 0.2 second period and 1.3 for 1 second period spectral acceleration and conducting β (logarithmic standard deviation) equal to 0.65. The 2012 Indonesian seismic code used β value equal to 0.7, direction factor 1.05 and 1.15 for short and long period spectral acceleration respectively. Equation 2 and equation 3 shows a log-normal distribution function of building collapse capacity for developing RTGM maps with 'c' represents spectral acceleration and $c_{10\%}$ is 10th percentile collapse capacity [3], [4]. Fig. 3 shows illustrated procedure for developing new MCE_R 2018 maps by combining RTGM and 84th percentile deterministic seismic hazard [3], [16] and [17].

$$f_F(c) = \frac{1}{c\beta\sqrt{2\pi}} \exp \left[-\frac{\ln c - (\ln c_{10\%} + 1.28\beta)^2}{2\beta^2} \right] \quad (2)$$

$$P[\text{collaps}] = \int_0^{\infty} f_F(c) P[S > c] dc \quad (3)$$

Fig. 3 New MCE_R 2018 design procedure.

REUSLTS AND DISCUSSIONS

Seismic microzonation of Semarang was developed based on national MCE_R analysis results by combining risk targeted ground motion analysis (RTGM) with 1% probability of collapse in 50 years and 84th percentile deterministic seismic hazard analysis and adjusting direction factor 1.1 for 0.2 second period and 1.3 for 1 second period spectral acceleration. Fig. 4, Fig 5 and Fig 6 show 2018 MCEG, MCES and MCES1 maps respectively. As it can be seen on Fig. 4 and Fig. 5 maximum MCEG and MCES spectral acceleration were identified on the western part of the city with maximum MCEG is 0.45g and maximum MCES is 0.95g. As it can be seen on Fig. 6 MCES1 values in between 0.35g to 0.4g are identified for the whole part of the city.

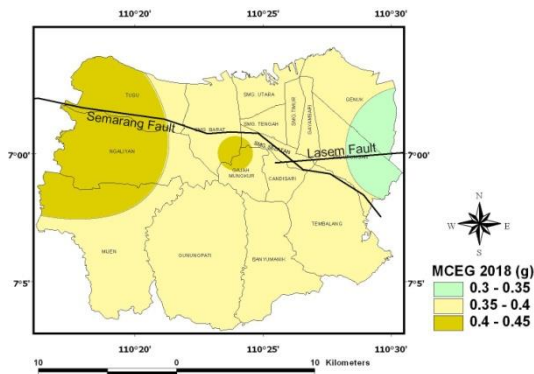


Fig. 4 MCEG 2018 map for Semarang.

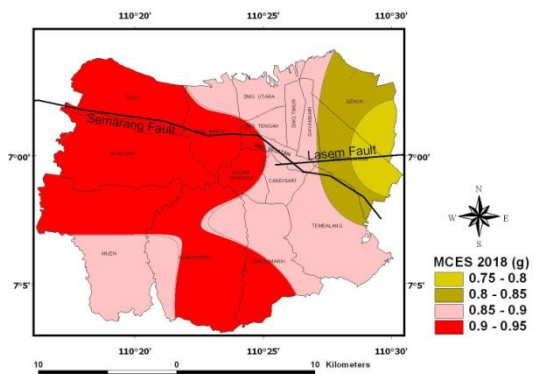


Fig. 5 MCES 2018 map for Semarang.

MCE_R calculation for evaluating the MCEG, MCES and MCES1 distributions in terms of V_{s30} was conducting at 288 boring locations. The purpose of the analysis is to obtain the correlation between V_{s30} and MCEG, MCES and MCES1 values. The V_{s30} value was implemented in this study due to the important correlation between V_{s30} and site class for developing surface spectral accelerations [17].

The analysis for 288 boring positions was performed by conducting weighting interpolation for each boring position with four closest data of national MCE_R analysis results. The MCE_R (MCEG, MCES and MCRS1) values at each boring position were interpolated by using equation 4 and equation 5 where M_b is MCE_R value at each boring position. M_i is MCE_R value at point 'i' where $i = 1$ to 4, ' d_i ' is minimum distance of each boring position to point 'i' and ' w_i ' is weight factor of boring position number 'i'. Fig. 7 shows a scatter MCE_R distribution chart calculated at 288 boring positions in terms of V_{s30} value. It can clearly identified that the value of MCEG, MCES and MCES1 tends to slightly increase due to increasing of V_{s30} value from 120 m/s to 420 m/s.

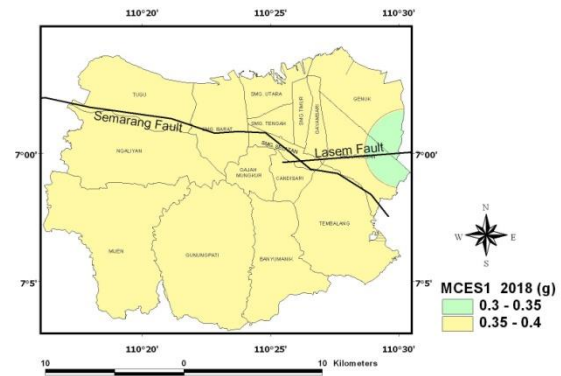


Fig. 6 MCES1 2018 map for Semarang.

$$w_i = \frac{1/d_i}{\sum_{i=1}^4 1/d_i} \quad (4)$$

$$M_b = \sum_{i=1}^4 (w_i * M_i) \quad (5)$$

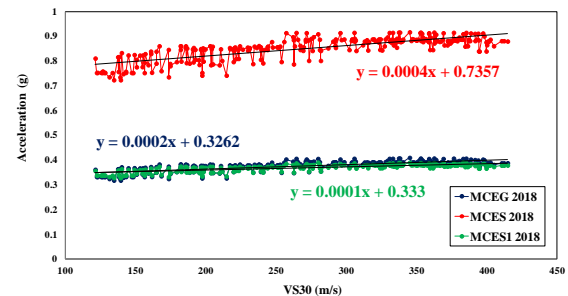


Fig. 7 MCEG, MCES and MCES1 (2018) distribution in terms of V_{s30} .

Comparative analysis of 2018 and 2012 MCES and MCES1 values was implemented at 288 boring locations. The purpose of the analysis is to obtain

the difference between 2018 and 2012 MCES and MCES1 distribution for Semarang. Fig. 8 shows the distribution of 2012 MCES values and Fig. 9 shows the distribution of 2012 MCES1 values. As it can be seen on Fig. 8 the maximum 2012 MCES values were identified on the eastern part of the city with maximum 1.4 g. Maximum 2012 MCES1 values were identified on the small eastern part of the study area with maximum 0.5 g.

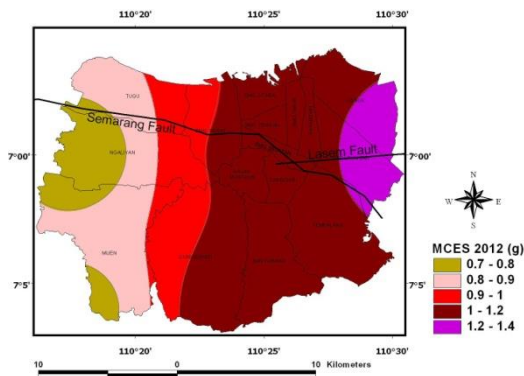


Fig. 8 MCES 2012 map for Semarang.

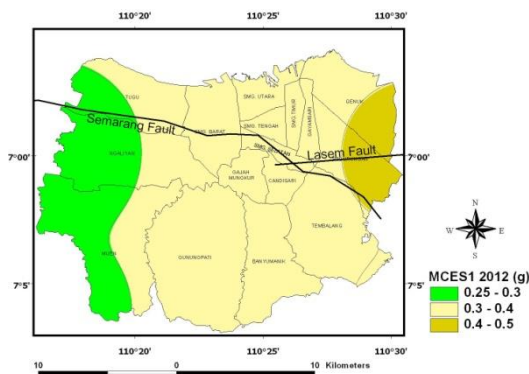


Fig. 9 MCES1 2012 map for Semarang.

The difference between 2018 and 2012 MCES and MCES1 distribution values in terms of V_{S30} can be seen on Fig. 10 and Fig. 11. Fig. 10 shows the difference between 2018 and 2012 MCES values. As it can be seen on this figure the 2012 MCES values in average are relatively greater than 2018 MCES values. Fig. 11 shows the difference between 2018 and 2012 MCES1 values. As it can be seen in this figure the 2012 MCES1 values are relatively smaller than the 2018 MCES1 values. Although the maximum 2018 MCES1 value as it can be seen on Fig. 6 is less than the maximum 2012 MCES1 value on Fig. 9, the maximum 2012 MCES1 values are distributed on the small area on the eastern part of the city. Based on Fig 7, Fig 10 and Fig 11 all 2012 and 2018 MCES and MCES1 values tend to be linearly scattered. The 2018 MCES and MCES1

distributions are slightly better (well distributed) compare to 2012 MCES and MCES1 distributions.

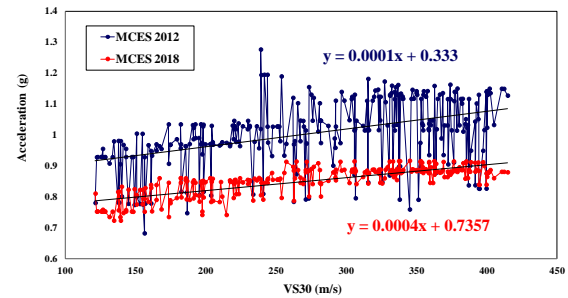


Fig. 10 MCES distributions (2018 and 2012).

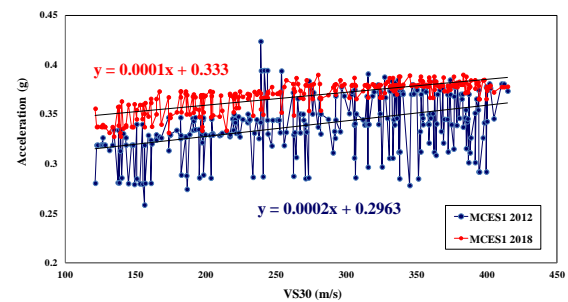


Fig. 11 MCES1 distributions (2018 and 2012).

CONCLUSION

Seismic microzonation of Semarang, Indonesia, was already implemented based on the combination analysis of probabilistic seismic hazard and deterministic seismic hazard analysis. Risk targeted ground motion (RTGM) analysis by conducting β value 0.65 and directivity factor 1.1 for 0.2 second spectral acceleration and 1.3 for 1 second spectral acceleration was implemented in this study. The purpose of this study is to evaluate the distribution of maximum considered earthquake (MCE_R) values of Semarang based on the new 2017 seismic hazard maps. Comparative study to 2012 MCE_R values (used for 2012 Indonesian seismic code) was also implemented in this study.

The maximum 2018 MCE_R (MCE_G , $MCES$ and $MCES1$) values for Semarang are distributed on the western part of the city. The maximum 0.45 g for MCE_G , 0.95 g for $MCES$ and 0.4 g for $MCES1$ values were identified on 2018 MCE_R maps. The opposite condition was identified on 2012 MCE_R distribution values. The maximum 2012 $MCES$ and $MCES1$ are identified on the eastern part of the city.

Comparative analysis was implemented in this study by comparing 2018 and 2012 MCE_R values. The analysis was performed for $MCES$ and $MCES1$ values at 288 boring locations. Graphical analysis was implemented for comparing both values. On average the 2018 $MCES$ values are smaller than

2012 MCES values. However the 2018 MCES1 values on average are greater than the 2012 MCES1 values.

ACKNOWLEDGEMENTS

The authors appreciate to the Ministry of Public Works and Human Settlements Indonesia and National Center for Earthquake Studies for providing data and technical supports on the development of this study.

REFERENCES

- [1] Pusat Studi Gempa Nasional, Peta Sumber Dan Bahaya Gempa Indonesia Tahun 2017, Pusat Litbang Perumahan dan Pemukiman, Kementerian Pekerjaan Umum dan Perumahan Rakyat (National Center for Earthquake Studies, Indonesian Seismic Sources and Seismic Hazard Maps 2017, Centre for Research and Development of Housing and Resettlement, Ministry of Public Works and Human Settlements), ISBN 978-602-5489-01-3, 2017, pp. 1-377.
- [2] Irsyam M., Hendriyawan, Natawijaya D.H., Daryono M.R., Widiyantoro S., Asrurifak M., Meilano I., Triyoso W., Hidayati S., Rudiyanto A., Sabarudin A. and Faisal L., Development of new seismic hazard maps of Indonesia, Proceedings of the 19th International Conference on Soil Mechanics and Geotechnical Engineering, Seoul, 2017, pp. 1525-1528.
- [3] Sengara I.W., Irsyam M., Sidi I.D., Mulia A., Asrurifak M. and Hutabarat D., Development of Earthquake Risk-Targeted Ground Motions for Indonesian Earthquake Resistance Building Code SNI 1726-2012, Proceedings of the 12th International Conference on Applications of Statistics and Probability in Civil Engineering, ICASP12, Vancouver Canada, July 12-15, 2015, ISBN 978-0-88865-245-4.
- [4] Luco N., Ellingwood B.R., Hamburger R.O., Hooper J.D., Kimbal J.K. and Kircher C.A., Risk-Targeted versus current seismic design maps for the conterminous United States, Structural Engineers Association of California 2007 Proceedings, 2007, pp. 163-175
- [5] Ohsaki Y. and Iwasaki R., On dynamic shear moduli and Poisson's ratio of soil deposits, Soils and Foundations, Vol. 13 (4), 1973, pp. 59-73.
- [6] Ohta Y. and Goto N., Empirical Shear Wave Velocity Equations in terms of characteristic soil indexes, Earthquake Engineering and Structural Dynamics, Vol. 6, 1978, pp. 167-187.
- [7] Imai T. and Tonouchi K., Correlation of N-Value with S-Wave velocity and Shear Modulus, Proceedings of Second European Symposium on Penetration Testing, Amsterdam, The Netherlands, 1982, pp. 67-72.
- [8] Abrahamson N.A., Gregor N. and Addo K., BC Hydro ground motion prediction equations for subduction earthquakes, Earthquake Spectra, Vol. 32(1), 2016, pp. 23-44
- [9] Youngs, R.R., Chiou, S.J., Silva, W.J. and Humphrey, J.R., Strong ground motion attenuation relationships for subduction zone earthquakes, Seismological Research Letters, Vol. 68(1), 1997, pp.58-73.
- [10] Boore D.M. and Atkinson G.M., Ground-Motion Prediction Equations for the Average Horizontal Component of PGA, PGV, and 5%-Damped PSA at Spectral Periods between 0.01 s and 10.0 s, Earthquake Spectra, Earthquake Engineering Research Institute, Vol. 24, No. 1, 2008, pp. 99-138.
- [11] Campbell K.W. and Bozorgnia Y., NGA Ground Motion Model for the Geometric Mean Horizontal Component of PGA, PGV, PGD and 5% Damped Linear Elastic Response Spectra for Periods Ranging from 0.01 to 10 s, Earthquake Spectra, Earthquake Engineering Research Institute, Vol. 24, No. 1, 2008, pp. 139-171.
- [12] Chiou B. S. J. and Youngs R. R., NGA Model for Average Horizontal Component of Peak Ground Motion and Response Spectra, PEER 2008/09, Pacific Engineering Research Center, College of Engineering, University of California, Berkeley, 2008, pp. 1-94.
- [13] Zhao J.X., Irikura K., Zhang J., Fukushima Y., Somerville P.G., Asano A., Ohno Y., Oouchi T., Takahashi T. and Ogawa H., An empirical site-classification method for strong-motion stations in Japan using H/V response spectral ratio, Bulletin of the Seismological Society of America, Vol. 96(3), 2006, pp.914-925.
- [14] Atkinson G.M. and Boore D.M., Empirical ground-motion relations for subduction-zone earthquakes and their application to Cascadia and other regions, Bulletin of the Seismological Society of America, Vol. 93(4), 2003, pp.1703-1729.
- [15] McGuire R.K., Probabilistic Seismic Hazard Analysis and Design Earthquakes, Closing the Loop, Bulletin of The Seismological Society of America, Vol. 85, 5, 1995, pp.1275-1284.
- [16] Leyendecker E.V., Hunt E.J., Frankel A.D. and Rukstales K.S., Development of Maximum Considered Earthquake Ground Motion Maps, Earthquake Spectra, Vol. 16, No.1, 2000, pp 21-40.
- [17] ASCE/SEI 7-10, Minimum Design Loads for Buildings and Other Structures, American Society of Civil Engineers, Virginia, 2010, pp 1 – 608.

UNDRAINED RESPONSE OF SILTY SAND UNDER STATIC AND CYCLIC LOADING

Akhila M¹, Dr. K Rangaswamy² and Dr. N Sankar³

¹Research Scholar, ²Asst. Professor, ³Professor, Dept. of Civil Engineering, NIT Calicut, India

ABSTRACT

Silty soils are widespread in many countries, particularly in the United States, China, and India; hence it is essential to get an idea of the response of such soils under different forms of loading. In this paper, the results based on undrained triaxial tests, under static as well as cyclic loading, which were carried out on the silty sands (fine sand mixed with non-plastic fines at different percentages) are presented. The samples were prepared at the required unit weight ($D_r = 50\%$), saturated by using back pressure and cell pressure increments and consolidated isotropically. Each consolidated sample is then subjected to static/cyclic loading. The results of the static triaxial testing showed that the non-plastic fines have a significant influence on the behaviour of fine sand. The dilation tendency decreases with the addition of fines. In the case of cyclic triaxial testing, as the fines content increases, the rate of generation of excess pore water pressure and axial strain on cycles of loading was found to increase and hence the liquefaction susceptibility.

Keywords: Liquefaction, Silty sands, Triaxial test, Undrained response

INTRODUCTION

The liquefaction may occur in fully saturated sands, silts and low plastic clays. When the saturated soil mass is subjected to seismic or dynamic loads, there is a sudden build-up of pore water within a short duration, and it could not dissipate which leads to reducing the effective shear strength of soil mass. In this state, the soil mass behaves like a liquid and causes to large deformations, settlements, flow failures, etc. This phenomenon is called soil liquefaction. As a result, the ability of soil deposit to support the foundations of buildings, bridges, dams, etc. are reduced.

Since the 1964 Niigata and Great Alaska earthquakes, numerous research studies have been performed on liquefaction of sand. It was believed that only “clean sand soils” with few amounts of fines could liquefy, and cohesive soils were considered to be resistant to cyclic loading due to cohesion component of shear strength. The researchers have not realised about the liquefaction susceptibility of clay soils until the 1994 Northridge, 1999 Adapazari and Chi-Chi earthquake events. In series of 1999 Chi-Chi earthquake, a lot of evidence on liquefaction failures in cohesive soils were observed, indicating that the soils with fines may liquefy. Hence recent research works are mainly focused on liquefaction susceptibility of silt and clay soils.

Many researchers have studied the effect of fines on liquefaction potential of soils. An increase of

liquefaction potential with the increase in fine content was observed by Kuerbis et al. (1988) and Amini and Qi (2000). An inverse relation was suggested by Xenaki (2003), Papadoulou (2008) and Cubrinovski et al. (2010). But Thevanayagam (2000) and Polito and Martin (2001) put forward an inverse proportion at low fines content and direct proportion at high fines content. (Note: All the fines were non-plastic, except for the studies by Amini and Qi). Even though these studies indicate the cyclic loading mechanism, the mechanism under static and cyclic loading are strongly related.

Significant findings from the recent literature papers are proven that the fine-grained soils (soils with considerable amount particles less than 75 microns) are more susceptible to liquefy, but the state criteria on liquefaction of cohesive soils are not yet conclusive, and a lot of contradictory results are reported. Therefore, more research efforts are needed for a good understanding of the liquefaction behaviour of fine-grained soils. Hence, the current research study is mainly focused on the undrained response of fine-grained soils contains the non – plastic fines content up to 40%.

METHODOLOGY

It contains sequential stages of materials collection, processing the soil combinations, testing for index properties and carry out the triaxial tests to analyze the effect of fines content on the undrained response of fine sands under both static and cyclic loading. The soil materials, fine sand and crushed stone

powder, are collected from various locations of Kerala state. Totally five soil combinations were prepared after mixing the non-plastic silty fines in different amounts into the fine sand. All the basic properties tests were performed on the soil combinations, and the properties are listed in table 1. A combined dry sieve and hydrometer analysis were performed to obtain the particle size distribution of various soil combinations. The gradation curves of all the soil combinations are shown in fig.1.

Table 1 Basic properties of various soil combinations

Notation	FS	SS10	SS20	SS30	SS40
Sand, %	100	90	80	70	60
Silt, %	0	10	20	30	40
G	2.62	2.66	2.71	2.72	2.69
D_{50} , mm	0.28	0.26	0.23	0.2	0.15
C_u	2.36	4.00	4.67	6.25	7.33
C_c	0.87	1.28	1.17	0.72	0.74
ρ_{max} , g/cc	1.66	1.71	1.81	1.86	1.79
ρ_{min} , g/cc	1.41	1.44	1.48	1.52	1.42

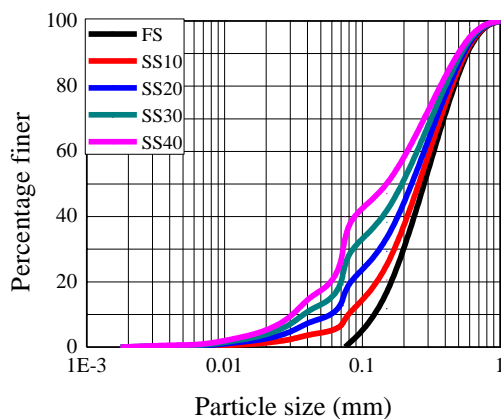


Fig. 1 Particle size distribution curves

A series of undrained static and cyclic triaxial tests were performed using a servo-controlled computerised cyclic triaxial testing device (Make: HEICO Pvt. Ltd, New Delhi, India), which is fully automated and controlled by a data acquisition system and test software (see fig. 2). The testing was conducted in sequential stages of triaxial sample preparation; assemble into the triaxial chamber, saturation of soil, consolidation, and application static/cyclic loading in the undrained state of the soil sample. For the present study, the cylindrical soil samples with 50 mm in diameter and 100 mm in height are prepared at 50% relative density to constitute a medium dense state of field soil. The

cylindrical samples were moulded in the split spoon sampler by using moist tamping method with the under-compaction procedure, as suggested by Ladd (1978). A schematic of the triaxial cell with the sample is shown in fig. 3 and a photograph is given as fig. 4.



Fig. 2 Photographic overall view of the cyclic triaxial system at CED, NIT Calicut

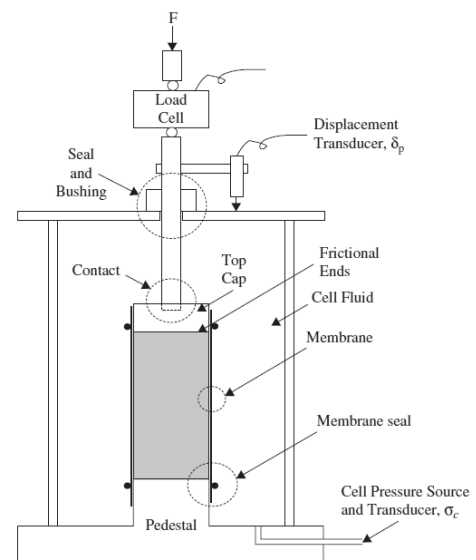


Fig. 3 Test schematic representation



Fig. 4 Soil sample in the triaxial cell

Saturation of the samples was accomplished in two stages: initial saturation and back pressure saturation. After completion of the saturation stage, all the samples were isotropically consolidated to the

desired effective consolidation pressure. The sample was allowed to consolidate in drained condition until there is no further significant volume change occurred. The undrained stress controlled cyclic triaxial tests were performed on the consolidated samples as per ASTM d 5311-92 testing procedures. More detailed description of each stage is given in Akhila et al. (2017). In the case of static testing, tests were conducted on each soil combinations according to standard procedures adopted by Bishop and Henkel (1969). The strain rate of 0.625 mm/min was maintained throughout the test.

RESULTS AND DISCUSSIONS

Results of tests on fine sand

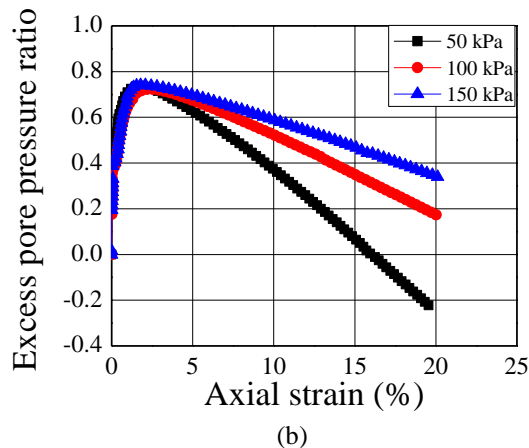
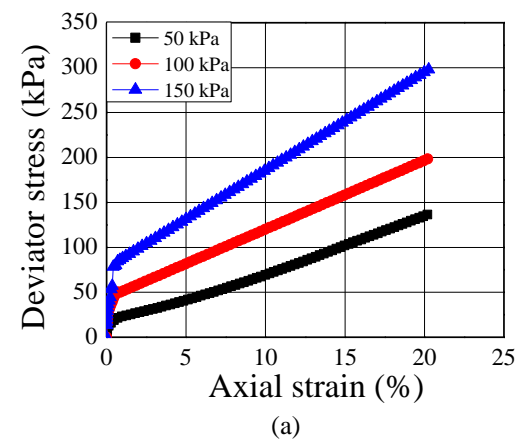


Fig. 5 Undrained response of fine sand under static loading at different consolidation pressures

To study the effect of consolidation pressure on the undrained response of fine sand, static triaxial tests were performed on fine sand samples consolidated at different pressures (50, 100 and 150 kPa). The relative density is fixed at 50%, i.e., the medium dense state. Fig. 5 shows the undrained response in the medium dense fine sand at different consolidation pressures. Fig. 5(a) shows the stress-

strain characteristics of silty sand consolidated at different pressures. The response curves are illustrating that the dilation tendency decreases with increase in consolidation pressures. The fine sand consolidated at low consolidation pressures behave as dilative and vice versa. At a particular density of fine sand, while increasing the consolidation pressures, the state of soil changes from dilative to contraction nature.

The result of the undrained cyclic triaxial test, in terms of axial strain propagation, pore pressure build-up and hysteresis loops performed on the fine sand sample at $CSR = 0.178$ ($D_{ro} = 50\%$ and $\sigma'_c = 100$ kPa) is shown in Fig. 6. Initial liquefaction occurred at 28 cycles.

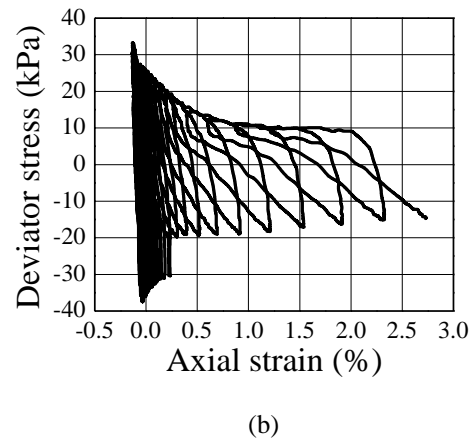
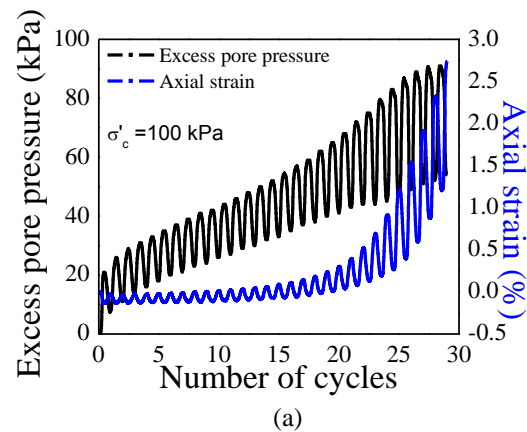


Fig. 6 Undrained response of fine sand under cyclic loading at 100 kPa consolidation pressure

Figure 6(a) shows the insignificant development of axial strain up to 20 numbers of load cycles and further the strain is propagating rapidly towards the initial liquefaction state. The strain was progressed in compression side only and it may be due to the medium dense state of the soil. After triggering the liquefaction state, there is a sudden flow failure with large deformations. The sudden increase of such

deformation is due to loss of effective strength of the soil at liquefaction state. Stress-strain hysteresis in the form of loops, as shown in Fig. 6(b), demonstrates that the loops of cycles are close to each other and formed in a thicker band with an insignificant deformation less than 0.5%. Further, the loops are widened with the rapid increase of strain levels in compression side towards the liquefaction state.

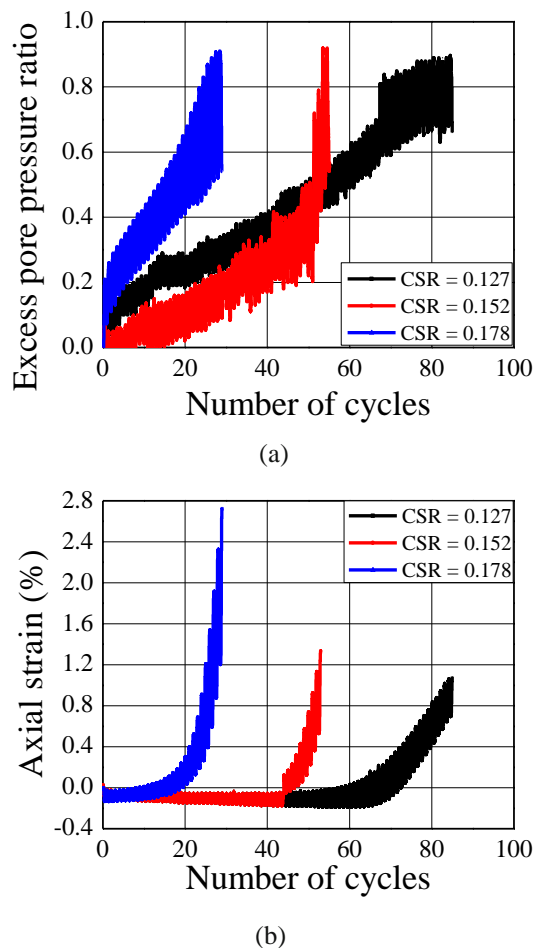


Fig. 7: Effect of CSR on (a) pore pressure ratio buildup and (b) axial strain propagation in fine sands with load cycles

The effect of applied cyclic stress amplitude, the, i.e. cyclic stress ratio (CSR) on the undrained response of fine sand ($D_{r0}=50\%$, $\sigma'_c=100$ kPa) is presented in fig. 7. It can be observed from fig. 7 that the pore pressure ratio and axial strains are accumulated gradually under cyclic loading with low CSR levels whereas they develop at a faster rate under cyclic loading with high CSR amplitudes. The large amplitude of strains occurs in the sand subjected the high CSR values and reaches the liquefaction state faster. The pore pressure build-up showed in Fig. 7(a) indicates that the sand sample subjected to high cyclic stress amplitude of 0.178 was liquefied at about 28 cycles of loading, whereas

at small CSR of 0.127 the sample liquefied at about 78 load cycles. At 28 cycles of loading, the pore pressure build-up in the sand subjected to CSR of 0.127 is less than 40% only. It can be concluded that the number of cycles is causing liquefaction increases with a decrease in the cyclic stress amplitudes.

Effect of fines under static loading

To study the effect of fines on the undrained response of fine sand under static loading, static triaxial tests were conducted on the silty sand samples at consolidation of 100 kPa. The results are shown in Fig 8. The non-plastic fines have a major influence on the behaviour of fine sand. From Fig. 8, it is clear that the fine sand is more dilative compared to the sand-silt mixtures. The dilation tendency decreases with the addition of fines. These results are in good agreement with the published literature.

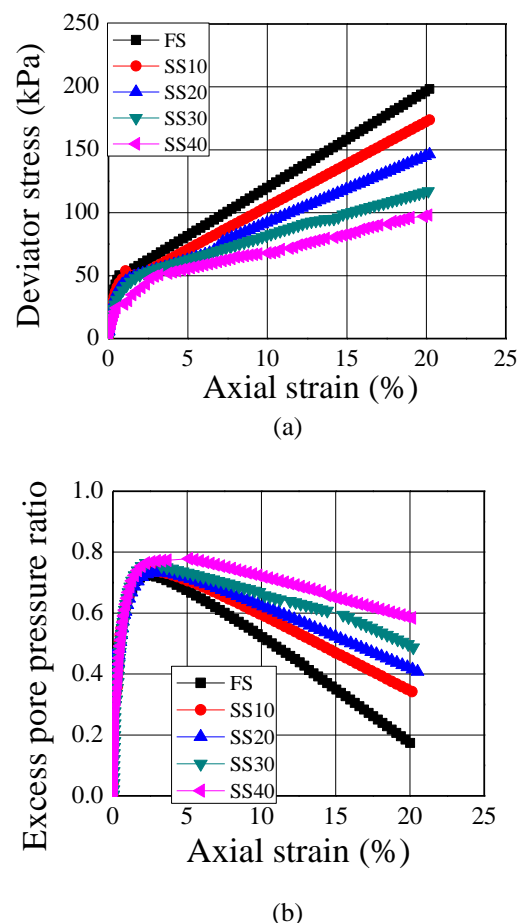


Fig. 8 Effect of fines on the undrained response of fine sand under static loading

The effect on non-plastic fines on the pore pressure generation at various consolidation pressures is shown in fig. 8 (b). Initially, there are an increase in the pore pressure ratio due to initial

contraction; but afterwards the pore pressure ratio decreases. The decrease is rapid in the case of fine sand when compared to the silty – sand combinations. The slower reduction indicates the contractive nature, and it results in the decrease in undrained strength.

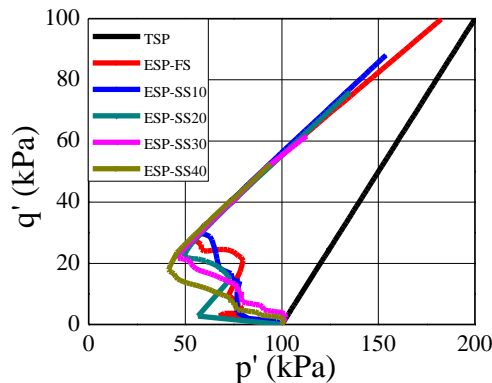
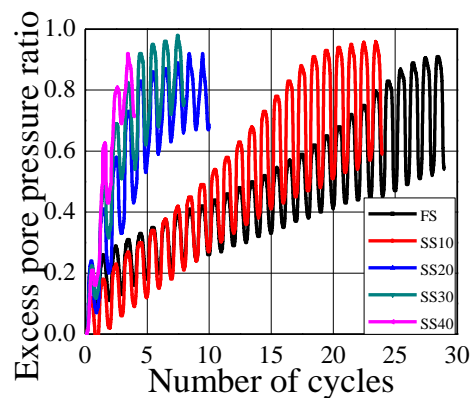
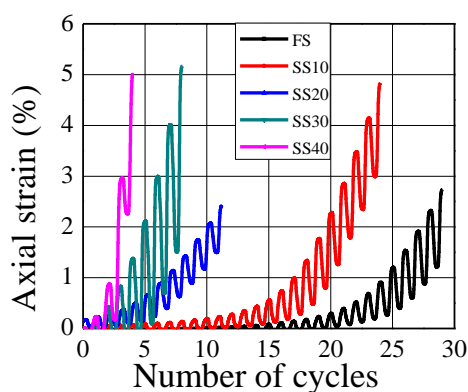


Fig. 9 p' - q' plot



(a)



(b)

Fig. 10 Effect of silt fines on (a) pore pressure ratio buildup and (b) axial strain propagation during load cycles (CSR=0.178)

The p' - q' plot of all soil combinations is given in fig. 9. The black line indicates the total stress path of the fine sand sample. The stress paths of other

samples are coinciding with this. From the effective stress paths, it is clear that the samples experience an initial contraction and then becomes dilative. The contraction tendency increases with the addition of fines into the sand sample.

Effect of fines under cyclic loading

To study the effect of fines on the undrained response of fine sand under cyclic loading, cyclic triaxial tests were conducted on the silty sand soil sample combinations at CSR = 0.178. The results are shown in fig 10. It indicates that the number of load cycles causing liquefaction at particular cyclic stress level decreases with the addition of silt fraction into the fine sand. It is demonstrated that the silty sands are susceptible to severe liquefaction than the fine sands and causing large deformation at the liquefaction state. Similar results have been reported by Boominathan et al. 2010 and Rangaswamy et al. (2010).

CONCLUSION

Undrained static, as well as cyclic triaxial tests, have been performed on fine sand samples with 0, 10, 20, 30 and 40% fines ($D_r = 50\%$ and effective confining pressure = 100 kPa). The following conclusion can be drawn:

Tests on fine sand: From the static triaxial testing conducted on fine sand, it can be concluded that the fine sand consolidated at low consolidation pressures behave as dilative and vice versa. The results of cyclic triaxial testing on fine sand indicate that the pore pressure ratio and axial strains are accumulated gradually under cyclic loading with low CSR levels whereas they develop at a faster rate under cyclic loading with high CSR amplitudes.

Effect of fines under static loading: The non-plastic fines have a major influence on the behaviour of fine sand. The fine sand is more dilative compared to the sand-silt mixtures. The dilation tendency decreases with the addition of fines. The pore pressure response of silty sands also indicates a contractive nature.

Effect of fines under cyclic loading: The pore pressure builds up is rapid in last few cycles of the loading. The axial strain development is negligible in initial cycles of loading, and large strains are developed just after the failure. As the fines content increases, the rate of generation of excess pore water pressure on cycles of loading was found to increase. Therefore, it can be concluded that the liquefaction resistance of fine sand decreases with increase in silt content.

REFERENCES

- [1] Akhila, M., Rangaswamy, K. and Sankar, N., Effect of Non-Plastic Fines on Liquefaction Susceptibility of Fine Sand. Proceeding of DFI India, 2017.
- [2] Amini, F. and Qi, G. Z., Liquefaction Testing of Stratified Silty Sands. Journal Of Geotechnical And Geoenvironmental Engineering, Vol. 126, No. 3, 2000, pp. 208-217.
- [3] Bishop, A.W. and Henkel, D.J., The Measurement of Soil Properties in the Triaxial Test, William Clowes And Sons Ltd., London, 1969.
- [4] Boominathan, A., Rangaswamy, K. and Rajagopal, K., (2010) Effect of Non-plastic fines on Liquefaction Resistance of poorly graded Gujarat sand. International Journal of Geotechnical Engineering, Vol 4, 2010, pp. 241-253
- [5] Cubrinovski, M., Rees, S., and Bowman, E., Chapter 6: Effects of Non-Plastic Fines on Liquefaction Resistance of Sandy Soils. Earthquake Engineering in Europe, Springer, 2010, pp. 125-144.
- [6] Kuerbis, R., Nequeeeey, D. and Vaid, Y. P., 1988. Effect Gradation and Fines Content on the Undrained Response of Sand. Geotechnical Special Publication, No. 21, 1988, pp. 330-345.
- [7] Ladd, R.S., Preparing Test Specimens using Undercompaction. Geotechnical Testing Journal, Vol. 1, No.1, 1978, pp. 16-23.
- [8] Papadopoulou, A. and Tika, T., The Effect of Fines on Critical State And Liquefaction Resistance Characteristics of Non-Plastic Silty Sands. Soils And Foundations, Vol. 48, No. 5, 2008, pp. 713-725.
- [9] Polito, C. P. and Martin, J. R., Effects of Nonplastic Fines on the Liquefaction Resistance of Sands. Journal Of Geotechnical And Geoenvironmental Engineering, Vol. 127, No. 5, 2001, Pp.408-415.
- [10] Rangaswamy, K., Bhoominathan, A., and Rajagopal, K., Undrained response and liquefaction behaviour of non-plastic silty sands under cyclic loading. Proceedings of 5th International Conference on recent advances in geotechnical earthquake engineering and soil dynamics, California, 2010, Paper no. 4.21a.
- [11] Thevanayagam, S., Liquefaction Potential and Undrained Fragility of Silty Soils. Proceedings of the 12th World Conference on Earthquake Engineering, Auckland, New Zealand, Paper 2383, 2000.
- [12] Xenaki, V. C. and Athanasopoulos, G. A., Liquefaction Resistance of Sand-Silt Mixtures: An Experimental Investigation of The Effects of Fines. Soil Dynamic Earthquake Engineering, Vol. 23, 2003, pp. 183-194.

CONSTRUCTION OF EARTH FILL STRUCTURE FOR SMALL FARM POND BY USING BHUTANESE TRADITIONAL WALL MAKING METHOD

UENO Kazuhiro¹, NATSUKA Isamu², SATO Shushi³, ONJO Norio⁴, Karma Tshethar⁵ and
Kelzang Tenzin⁵

¹ Faculty of Life and Environmental Science, Shimane University, JAPAN,

² Emeritus Professor in Shimane University, Shimane University, JAPAN,

³ Natural Science Cluster, Kochi University, JAPAN,

⁴ Agricultural Development Consultants Association, JAPAN,

⁵ Department of Agriculture, Ministry of Agriculture and Forests, The Kingdom of Bhutan,

ABSTRACT

The Kingdom of Bhutan has mountains as high as 7,000 meters height at the east end of Himalayas and semitropical region at an altitude of 100 meters in its south area. Because of its precipitous terrain, stable supply of water for irrigation is difficult without efficient water supply system such as reservoirs, pipelines and so on. Based on the results of preliminary field investigations, existing reservoirs in the Kingdom of Bhutan often have structural problems in its body and foundation. To contribute to an increase in agricultural production in the Kingdom of Bhutan through a development of construction techniques for reservoirs, an earth fill structure for small farm pond was suggested and constructed in 2015. In this construction, Rammed earth method, which is well known as Bhutanese traditional wall making method, was applied as a compaction technique of soil. Authors conducted a follow-up of the earth fill structure in September 2017 to confirm performance of the wall making method as a construction technique for reservoirs. Based on the results of the portable dynamic cone penetration tests, it is supposed that this rammed earth method couldn't achieve sufficient compaction energy for construction of earth fill structures for reservoirs because observed *N* values were comparatively small compared with that obtained from embankments constructed by modern compaction techniques. Therefore, in the construction of earth fill structures for farm pond by utilizing the rammed earth method, improvement in compaction technique should be considered.

Keywords: The Kingdom on Bhutan, Wall making method, Earth fill structure, Small-scale reservoir, The portable dynamic cone penetration test

INTRODUCTION

Although agriculture is a key industry in the Kingdom of Bhutan (hereafter call KB) (agriculture constitutes 30 – 40 % of GDP), it has problems in an improvement of agricultural productivity. KB has mountains as high as 7,000 meters height at the east end of Himalayas and semitropical region at an altitude of 100 meters in its south area. Because of its precipitous terrain, stable supply of water for irrigation is difficult without a proper management of water resource and reservoirs for storing irrigation water. Based on the results of preliminary field investigations, existing reservoirs in KB often have structural problems in its body and foundation. A water management system and construction techniques for reservoirs which can be applied to KB should be developed.

To contribute to an increase in agricultural production in KB through a development of construction techniques for reservoirs, an earth fill structure for small farm pond was constructed by

Bhutanese people with advices from one of co-author in 2015. In this construction, Bhutanese traditional wall making method was applied as a compaction technique of soil to enable the sustainable construction and maintenance of reservoirs in KB. The wall making method is a traditional technique to make walls by compacting cohesive soil in formwork and is used in construction of houses in KB. Authors conducted a follow-up of the earth fill structure in September 2017 to confirm performance of the wall making method as a construction technique for reservoirs.

In this paper, a concept and a construction procedure of the earth fill structure for small farm pond constructed in KB are described. Then, results of follow-up of the earth fill structure are also reported.

EARTH FILL STRUCTURE FOR SMALL FARM POND CONSTRUCTED IN THE KINGDOM OF BHUTAN

Recently, large-scale reservoirs for electric power generation have been constructed in KB. However, construction techniques for dam bodies of KB are not sufficient yet because most of those reservoirs were constructed with technical supports from foreign engineers. In the preliminary field investigation conducted in 2014 and 2015, existing reservoirs constructed by KB own techniques often have structural problems in its body and foundation. Typical problem observed in the investigations was leakage of storage of water through foundation, abutment and boundary between dam body and foundation. Especially, poor treatment of the boundary seemed a main cause of leakage of storage of water because, for those reservoirs, sealing work have not been applied to boundary between dam body and foundation. Improvement in design and construction techniques for reservoirs is required to ensure a stable supply of water and to increase agricultural production.

Concept of the Small-Scale Reservoir

In the northern and central parts of KB, agricultural lands are mostly in the form of stepped terrain because of precipitous terrain in those regions. To enable a stable supply of water to such agricultural lands, small-scale reservoirs to be constructed by farmers themselves would be one of effective solutions against water shortage. If farmers have construction techniques even for small-scale reservoirs, development of water resource for irrigation according to their water demand become possible by farmers own effort. Moreover, even if reservoirs is damaged due to natural disaster and their function is degraded with age, farmers can repair and maintain reservoirs by themselves. For this concept, construction of a reservoir with techniques which can be handled easily by farmers was planned. In this plan, application of Bhutanese traditional techniques for making stone wall and soil wall was attempted.

As mentioned above, a majority of agricultural lands in KB have a form of stepped terrain. When Bhutanese people develop agricultural lands on precipitous terrain, stone masonry is made for stabilizing walls existing between each stepped agricultural land. So, the stone masonry work have been familiar to Bhutanese people as a technique for stabilization of wall and slope. On the other hand, Bhutanese people build their houses by using the wall making method (Fig.1). The wall making method is a traditional technique for making walls by compacting cohesive soil in formworks. Most important things required to reservoirs, which body is made from earth materials, for continuing storage of water are stability as well as impermeability of earth fill structure. To ensure those functions of earth fill structures, in the construction of reservoirs

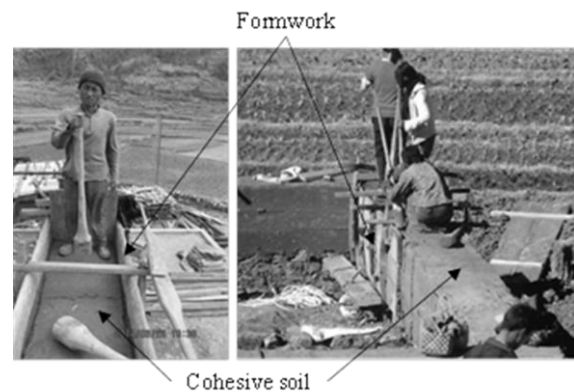


Fig. 1 The wall making method

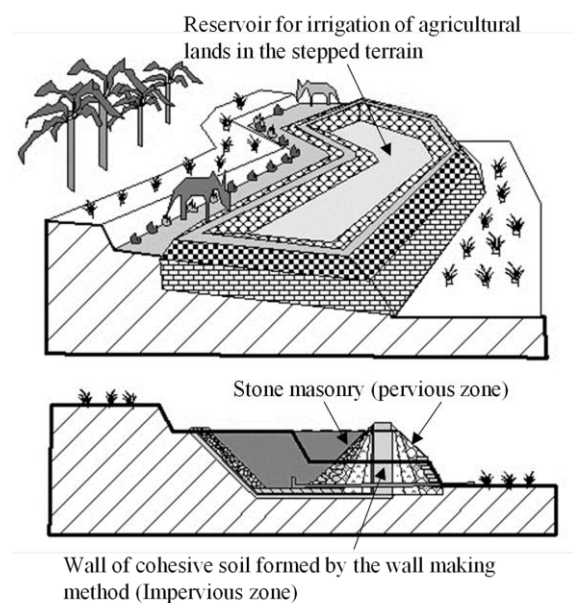


Fig. 2 Schematic diagram of the small-scale reservoir with the concept in which Bhutanese traditional techniques is actively utilized

with modern design concept, bodies of reservoir have often been designed with a couple of zones of earth materials which have high strength (for pervious zone) or low permeability (for impervious zone). In the construction of such zoned bodies of reservoir, the stone masonry work seemed applicable to construction of pervious zone because stone masonry have a stable structure. On the other hand, permeability of the wall of cohesive soil formed by the wall making method would be small, so this technique may be applied to construction of impervious zone. The design and construction techniques for small-scale reservoirs in which Bhutanese traditional techniques is actively utilized should be developed for sustainable agricultural production in KB. Fig. 2 shows schematic diagram of the reservoir for irrigation of agricultural lands in the stepped terrain with the concept mentioned above.



Fig. 3 Location of Gebekha village

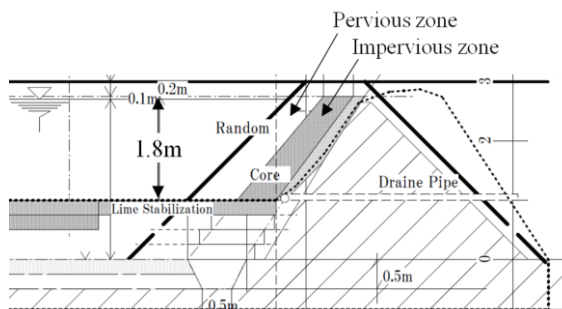


Fig.4 Cross section of the small farm pond originally planned

Construction Procedure of the Earth Fill Structure for Small Farm Pond

Construction of the earth fill structure for small farm pond was started with support of Japanese NGO in Gebekha village (Fig. 3) in 2015. Cross section of the small farm pond in original plan is shown in Fig.4. Originally, cross section of the small farm pond was planned as a sloping core type dam. A time line of the construction is outlined below.

- 1) The construction was started at October 26 and it continued until October 30 with advices from co-authors.
- 2) After October 30, the construction was suspended until mid-November because farmers had to harvest agricultural product.
- 3) After harvest, farmers restarted the construction by themselves. Although co-authors left advices about construction techniques and procedure, farmers didn't obey those advices. As a result, as described latter, the small farm pond completed quite differ from that originally planned. Unfortunately, we don't know how the earth fill structure was constructed after the restart until completion.
- 4) Ceremony for the completion of the small farm pond was held on December 19.
- 5) Follow-up of the small farm pond was conducted in 2017. Result of this follow-up will be described in next section.



Fig.5 Stabilization treatment of foundation by cement-mixed soil

On October 26, construction of the earth fill structure for small farm pond was started with farmers in Gebekha village and co-authors. Detailed construction procedures is described below.

1) Stabilization treatment of foundation

Firstly, stabilization treatment of foundation was conducted. Machinery excavation of original ground up to 1.5m depth was initially planned to obtain more stable foundation. However, this plan was changed to manual excavation up to 25 – 50 cm depth because excavation machine couldn't be prepared. After removing unsuitable things for foundation of reservoirs such as plant fragments from excavated soil, foundation was reconstructed by tamping cement-mixed soil which was obtained by mixing the excavated soil and cement because enough bearing capacity of foundation couldn't be achieved by only tamping the excavated soil. Mixing ratio of cement was around 6 %. Fig.5 shows stabilization treatment of foundation by cement-mixed soil.

2) Construction of impervious zone

Earth material used for impervious zone was gathered from abandoned paddies and fields near from construction site. After removing large size gravel, water content of earth material was adjusted by sprinkling water from mountain stream. Although natural and optimum water contents couldn't be measured, water content of earth material suitable for compaction was decided according to its texture. In the compaction of impervious zone, the wall making method was utilized (Fig. 6). Thickness of each layer of earth material was controlled so as to be about 8 cm after compaction. Every completion of compaction of three layers, permeability of compacted layer was measured by in-situ permeability test.



Fig. 6 Compaction of impervious zone by the wall making method

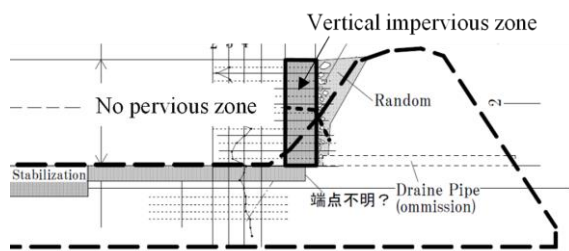


Fig. 7 Cross section of the small farm pond completed

After confirming hydraulic conductivity of compacted layer was lower than 1×10^{-5} cm/sec, compaction of upper layers were started. Dry density of compacted layers were not measured.

3) Completion of the earth fill structure for small farm pond

After harvest of agricultural products, farmers restarted the construction of the earth fill structure for small farm pond by themselves. Co-authors left advices about construction techniques and procedure according to original plan. However, farmers didn't completely obey those advices. They changed cross section of the small farm pond. Cross section of the small farm pond completed is shown in Fig. 7. The small farm pond completed quite differ from that originally planned. Firstly, although cross section of the small farm pond was planned as a sloping core type dam as shown in Fig.4, that was changed to a vertical core type dam. Secondly, there was no pervious zone which should exist in front of impervious zone. Pervious zone is very important to increase the resistance of body of reservoir against external forces and to protect the impervious zone from erosion. However, impervious zone of the small farm pond completed have been exposed to impounded water and rain. Reasons why farmers changed cross section of the small farm pond were that they didn't want to reduce

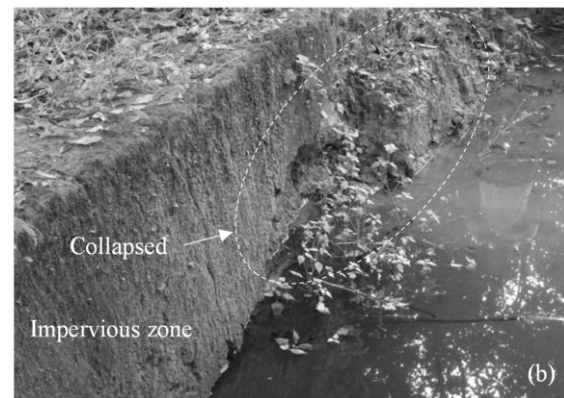


Fig. 8 Condition of the earth fill structure at the follow-up

a reservoir capacity and that they couldn't understand importance of pervious zone. For developing water resource steadily by farmers themselves, it is crucial to obtain a better understanding of farmers about design concepts of reservoirs.

FOLLOW-UP OF THE EARTH FILL STRUCTURE FOR SMALL FARM POND

Authors conducted a follow-up of the earth fill structure for small farm pond in September 2017 to confirm the current condition of the small farm pond and to evaluate performance of the wall making method as a construction technique for reservoirs. External observation and the portable dynamic cone penetration tests were performed. Fig. 8 (a) and (b) shows condition of the small farm pond at the time of the investigation. Water was stored up to half of a full capacity. Impervious zone had been collapsed partly because it was formed into shape of vertical wall and was not protected from impounded water and rain by pervious zone (Fig.8 (b)).

The portable dynamic cone penetration tests (JGS 1433) were conducted at impervious zone of the small farm pond which was constructed by utilizing Bhutanese traditional wall making method in 2015 (Fig. 6). This tests were performed at three

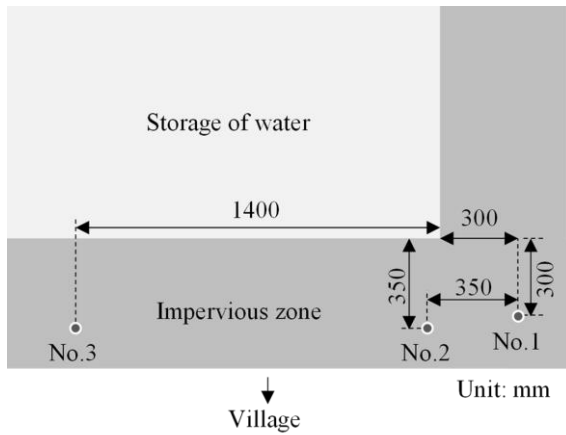


Fig. 9 Testing points of the portable dynamic cone penetration test

points. The testing points are shown in Fig. 9. In this tests, a cone with a diameter of 25 mm was driven into impervious zone in steps of 100mm by blows from a slide hammer with a mass of 5 kg falling through a distance of 500 mm. The numbers of blows required for this penetration were recorded as the penetration resistance N_d . Test results N_d were converted into N value which obtained by the standard penetration test (SPT), by employing following equations^[1].

$$\begin{aligned}
 &N_d > 4 \\
 &\quad N = 0.7 + 0.34 N_d \text{ (Coarse-grained material)} \\
 &\quad N = 1.1 + 0.30 N_d \text{ (Sand)} \\
 &\quad N = 1.7 + 0.34 N_d \text{ (Cohesive soil)} \\
 &N_d \leq 4 \\
 &\quad N = 0.50 N_d \text{ (Coarse-grained material)} \\
 &\quad N = 0.66 N_d \text{ (Sand)} \\
 &\quad N = 0.75 N_d \text{ (Cohesive soil)}
 \end{aligned}$$

where N_d is the number of blows required for the penetration of 100mm and N is N value obtained by SPT. In this investigation, the equations for cohesive

soil were employed.

Relationships between N value and depth are shown in Fig. 10. With an increase in depth, N values increase gradually. Variation of N values between each testing point was comparatively large for No.1, while it was not so large for No.2 and No.3. Difference in variation of N value might have been resulted by difference in compaction conditions because No.1 was on a corner of impervious zone. In the corner of impervious zone, around No.1, compaction energy might have been biased due to a restriction of working space. Almost N values are plotted in a range of 3 to 5. Based on the results of the portable dynamic cone penetration tests, it is supposed that the wall making method couldn't achieve sufficient compaction energy for compaction of bodies of reservoir because observed N values were comparatively small compared with that obtained from embankments constructed by modern compaction techniques. Therefore, in the construction of bodies of reservoir by utilizing Bhutanese traditional wall making method, improvement in compaction technique should be considered according to conditions of bodies of reservoir to be constructed and its foundations.

Possible measures for improving compaction technique utilizing Bhutanese traditional wall making method are listed below:

- 1) Increase in compaction energy

According to the test standard of JIS A 1210, compaction energy is calculated by following equation.

$$E_c = \frac{W_R \cdot H_R \cdot N_B \cdot N_L}{V} = \frac{W_R \cdot H_R \cdot N_B}{H_L}$$

where, E_c is compaction energy, W_R is weight of rammer, H_R is fall height of rammer, N_B is the number of blows by rammer, N_L is the number of layer of earth material, V is volume of a mold and H_L is height of layer of earth

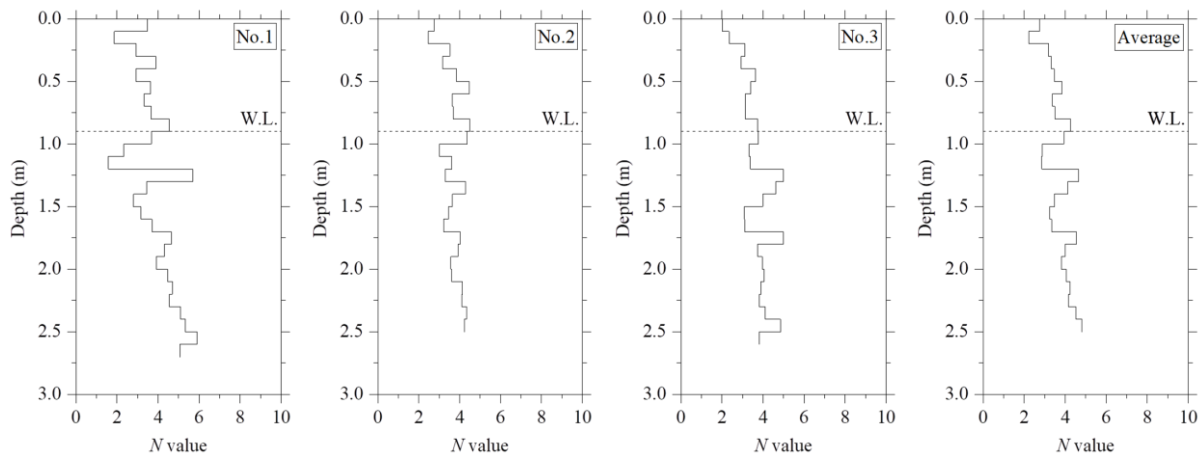


Fig. 10 Relationships between N value and depth

material. Increase in W_R , H_R and N_B and decrease in H_L is effective to increase in compaction energy and to stabilize reservoirs to be constructed. Compaction energy which can be achieved by Bhutanese traditional wall making method and its effect on improvement in properties of compacted soil should be revealed.

2) Use of proper material

It is well known that dry density of soil compacted under prescribed compaction energy is strongly affected by water content of soil. It is important to determine the compaction curve of earth material to be used in construction of reservoirs and to adjust water content of the earth material to around optimum water content.

3) Zoning of body of reservoir

In modern design concept, bodies of reservoir have often been designed with a couple of zones of earth materials which have high strength (for pervious zone) or low permeability (for impervious zone). Pervious zone is effective to compensate for low strength of impervious zone constructed by Bhutanese traditional wall making method. The stone masonry work which is one of Bhutanese traditional techniques seem applicable to construction of pervious zone because stone masonry have a stable structure. Design concept for reservoirs in which Bhutanese traditional techniques is actively utilized should be developed.

CONCLUSION

Development of construction techniques for reservoirs which can be handled by farmers themselves as well as development of large-scale

reservoirs with modern construction techniques would be an effective solutions to contribute to an increase in agricultural production in KB. For this concept, an earth fill structure for small farm pond was constructed by farmers by utilizing Bhutanese traditional wall making method in 2015. However, the small farm pond completed quite differ from that of originally planned by co-authors because farmers couldn't understand the importance of design concepts for reservoirs. In the follow-up of the small farm pond conducted in 2017, it was confirmed that impervious zone which was formed into shape of vertical wall and was not protected from impounded water and rain by pervious zone had been collapsed partly. Moreover, Based on the result of the portable dynamic cone penetration tests, it is supposed that the wall making method couldn't achieve sufficient compaction energy for compaction of bodies of reservoir. Improvements in construction techniques utilizing Bhutanese traditional techniques and transfer of design concepts and construction techniques for reservoirs are needed to contribute to an increase in agricultural production through a stable supply of water for irrigation in KB.

ACKNOWLEDGEMENTS

This work was supported by JSPS KAKENHI Grant Number 17H04632.

REFERENCES

- [1] Okada K., Sugiyama T., Noguchi T., and Muraishi H., A Correlation of Soil Strength between Different Sounding Tests on Embankment Surface. Soil Mechanics and Foundation Engineering, (40)4, 1992, pp.11-16 (In Japanese).

QUANTITATIVE ANALYSIS OF MOISTURE INDUCED ALTERATIONS ON THE DIMENSIONS OF GRAVITY FLOW EXTRACTION ELLIPSOID OF COARSE GRAINED PARTICLES IN A GLASS-BOX MODEL

Uziell Boringot¹ and Juan Fidel Calaywan²

¹Department of Mining, Metallurgical and Materials Engineering,
²University of the Philippines Diliman

Quezon City, Philippines

ABSTRACT

Caving methods in underground mining operations heavily rely on the principles of gravity flow of broken materials. Models and in-situ studies have confirmed that gravity flow of broken material approximates the shape of an ellipsoid. The eccentricity of this ellipsoid is influenced by different parameters such as draw height, extraction opening width, and particle size. This paper aims to present the effects of moisture and fine-grain constituents to the width of the extraction ellipsoid, since underground mines are inevitably exposed to ground water. The experiment was done in a 5x40x60cm glass box using 6.4-12.7mm coarse grained particles mixed with 0.1-mm fine-grained particles at 0%, 10%, and 20% (w/w) percentages. Water was added at 0%, 2.5%, 5%, 7.5% and 10% (w/w) percentages. Material extraction has been done using the aggregate of broken materials at different water content and fine-grain settings. The mass of the extracted material was used to calculate the volume of the ellipsoid generated and the corresponding width of the extraction ellipsoid. It was observed that ellipsoidal width generally decreases as the moisture content increases. The same is observed with increasing fine-grain particles. Interactions of moisture and the 10% and 20% fine-grain particle mix produced a 4th degree polynomial graph having their minima at 2.5% and 7.5% moisture settings respectively. This sudden increase in ellipsoidal width was explained by the presence of pore water pressure inducing smoother material flow. Ultimately, the graphs of 0%, 10%, and 20% fine-grained mixture converge to a single point at 10% moisture setting. Hence, it was concluded that ellipsoidal width decreases with the presence of moisture and increasing fine-grain constituents and the trend of the changes in ellipsoidal widths approximates a single point.

Keywords: Extraction ellipsoid, Gravity Flow, Moisture, Caving methods

INTRODUCTION

Caving methods in underground mining operations provide advantages such as high productivity, high efficiency, low cost, operational safety and breadth of geologic application [1]. Thorough understanding of gravity flow principles is prerequisite in efficiently designing draw chutes maximizing ore recovery in mine caving operations. The geometry and behavior of gravity flow ellipsoids are governed mainly by the size of the particle, dimensions of the chute opening, and height of extraction. However, water seeping underground tends to interact with the broken material inside the stope and alter the dimension of the gravity flow ellipsoid. This is common in underground mines situated below the water table. Furthermore, this phenomenon results in lower ore recoveries due to hang-ups and stack-ups. This study was conducted to observe and quantitatively analyze if there is a significant change to the width of the gravity flow ellipsoid due to the presence of moisture in a fine grain and coarse grain broken material mix using a

glass box model. If this study happens to prove that a remarkable change occurs to the ellipsoidal width due to the presence of moisture, the knowledge from this research would further refine the calculations of ellipsoidal widths and chute spacings. This would result to a significant increase in ore recoveries by minimizing passive zones and ore stack-ups.

This study limits the analysis on the effects of the differences only within the particle sizes, size distribution range, particle angularity, specific gravity, moisture content, and model dimensions used. Other factors such as the mechanical compaction of the broken ore due to material weight and blasting/caving impact, prolonged exposures to different wet and dry conditions of broken materials, cementation of fine-grained particles between coarse-grained particles due to the presence of water, and significantly long non-extractive periods during the mine operation cycle were not taken into consideration since the study focuses on only on the two parameters (moisture content and fine-grain percentages).

REVIEW OF RELATED LITERATURES

Principles of Gravity Flow, Extraction Ellipsoid and Chute Spacing

The shape of the gravity flow ellipsoid as observed by R. Kvapil approximates an ellipsoidal shape. He characterized the ellipsoid formed by the extracted material as *extraction ellipsoid* where the volume of the extracted material is approximately equal to the volume of the extraction ellipsoid [2]. To maximize ore recovery and minimize ore hang-ups, draw chute spacing should be less than the width of the extraction ellipsoid which results in an overlap of the adjacent ellipsoids as in Fig 1. Non-overlapping extraction ellipsoids may create passive zones where the ores are irrecoverable.

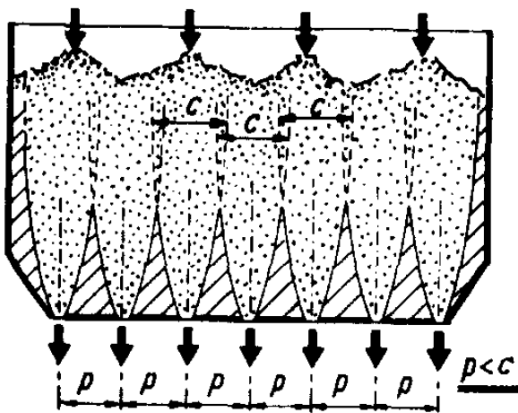


Fig. 1 Overlap of the chute intervals (p) and the width of the extraction ellipsoid (c) [2].

The width of the extraction ellipsoid was approximated as a function of extraction height using the following formula:

$$W_T = W' + a - 1.8 \quad (1)$$

Where W' is the theoretical extraction width corresponding to the extraction height graphically derived using Fig. 2.

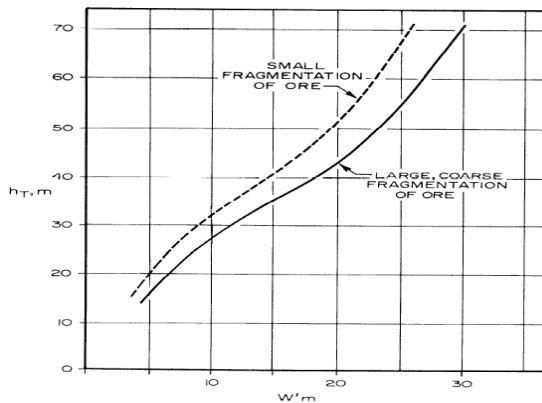
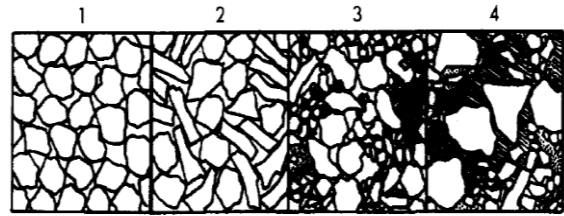


Fig. 2 Theoretical width of extraction, W' , as a function of extraction height [2].

Particle Mobility

Particles undergoing gravity flow exhibits primary and secondary motions [3]. Primary motion is along the direction of gravity while secondary



motion is the tilting and rotational movement experienced by the particle. The particle's unhindered execution of these two motions influences the ease of gravity flow and the extraction ellipsoid. Moist, non-loose materials (earthy-clayey particles incorporated within coarse grained matrix) [4] have the greatest difficulty in executing particle movement as in Fig 3. Fig. 3 Types of coarse-grain and fine-grain mixtures [4].

Arching, Pressure Transmission, and Pore Water Pressure

Particles stored in hoppers or bins experience stress and compaction due to the overlying weight. These particles are in contact with each other in many different ways (point-like, along the edge, or flat) [3]. Pressure is developed and transmitted in these points of contact. Material arching develops near the chute opening where friction between the particles is greatly increased. However, the presence of sufficient moisture in these systems develop pore water pressure [5] which may counteract interparticle pressure transmission and provide smoother gravity flow.

METHODOLOGY

The experiment is conducted to observe how the moisture affects the width of the extraction ellipsoid and observe the effects of the interactions of different fine-coarse grain mixture ratios. The experiment was conducted in a 5x40x70cm glass box model using 6.35-12.7mm coarse grain particles and <0.11mm fine grain particles at 0 – 20% (w/w) fine grain contents at 10% intervals each setting. Water is mixed in the setup at 0 – 10% (w/w) at 2.5% intervals. The sample aggregates were loaded in the glass-box model and extraction was initiated through the opening at the bottom. Distinctly colored stones (3-5 pcs) were placed at the top of the aggregates. Appearance of these colored stones at the extraction orifice marks the end of the extraction. The mass of

the extracted material is used to calculate the volume of the ellipsoid generated and consequently the width of the ellipsoid. A minimum of thirty (30) trial runs for each of the thirteen (13) settings were conducted to satisfy the minimum population number for statistical analysis.

Sample Preparation

The samples were crushed and grind using jaw crusher and roller crusher. The crushed samples were sieved using a 1/4" and 1/2" sieves to attain desired size range using standard procedures. Each setting was prepared using the exact combinations of moisture and fine-grain constituents based on their weights. The bulk density of the samples used in each setting is obtained.

Data Analysis

Ellipsoidal width calculation

The width of the extraction ellipsoid is calculated using the mass of the extracted material each trial run using Eq. 2.

$$w_{EE} = \frac{\frac{M_E}{\pi h_{EE} \rho_B} + \sqrt{\left(\frac{M_E}{\pi h_{EE} \rho_B}\right)^2 + \frac{4}{3}x^4}}{x} \quad (2)$$

Where M_E is the mass of the extracted material, d_B is the bulk density and x is the ellipsoidal cap distance. The ellipsoidal cap distance used in this experiment is 2.5cm. This formula was derived using the volume of a truncated ellipsoid that fits the shape of the model.

Statistical Analysis

The data obtained in the experiments were analyzed using one-way ANOVA to check if there is a significant difference between the ellipsoidal widths obtained in each setting. Tukey-Kramer HSD method was used as a post-hoc test to check which settings are insignificantly different.

Nomenclature

For the ease of discussion, the following naming for each setting shall be used:

$$xF - yM$$

where x is the fine percentage and y is moisture content.

RESULTS AND DISCUSSION

Using one-way ANOVA, the p-value obtained was 6.0×10^{-223} , hence the null hypothesis that the

means of each of the settings is statistically equal is rejected. This statistical analysis states that at least one pair of all the settings used in this experiment is statistically different. To further check which settings are statistically different, Tukey-Kramer method was used to find the honest significant difference (HSD) of each setting. Majority of the points yielded statistically significant difference between each other.

The average ellipsoidal widths for each setting was summarized in Table 1 and graphed in Fig 2.

Table 1 Width of extraction ellipsoids at different settings (in cm)

	0F	10F	20F
0M	20.243	19.399	17.410
2.5M	N/A	14.678	14.103
5M	16.746	15.080	13.050
7.5M	N/A	15.593	10.658
10M	16.023	15.789	15.404

Note: The 0F – 2.5M and 0F – 7.5M settings were not conducted since the 0% Fine settings showed a continuous decreasing trend with no inversion of the trend slope as in Fig 3.

Figure 4 shows that as the fine grain contents increases, the width of the extraction ellipsoid decreases. The presence of fine-grained particles in the mixture poses difficulty in executing secondary motion of the particles. This is represented by a Type 4 mixture in Fig 3. As the execution of the secondary motion is hindered, the mobility of the particles is hampered and the width of the ellipsoid decreases. It was also observed that the settings with 5% moisture has a steeper negative slope than those with 10% moisture content. This shows that the presence of moisture counteracts the hampering effect of the fine-grain constituents to a certain extent.

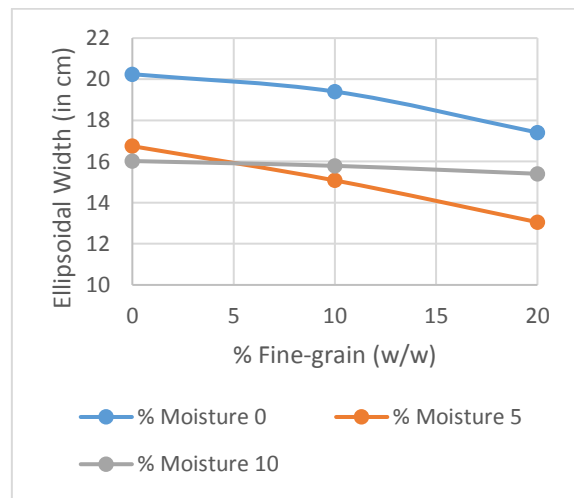


Fig. 4 Ellipsoidal width at varying fine-grain contents

Similarly, as the moisture content increases, the width of the extraction ellipsoid generally decreases within the 0 – 10% moisture content range. However, a deflection of the trend slope was observed in the 10% and 20% fine grained settings. The apparent minima of the 10% fine trend was observed within settings in combination with 2.5% moisture. The minima of the 20% fine trend was observed at 7.5% moisture content. As shown in Fig 5, minimal amounts of moisture decrease particle mobility. This is especially true in the settings where no fine-grained constituents are present. The sudden change in the trend slopes of the 10F – yM and 20F – yM settings are brought about by the increased moisture content. Significant amounts of moisture introduce pore water pressure to the system which counteracts interparticle friction, overburden pressure, arching, and the compaction of the particles. This effect is minimal in the 0F – yM settings since moisture isn't held in the system. However, fine-grained particles have the ability to hold moisture and give pore water pressure an avenue to relieve interparticle pressure. In contrast, small amounts of moisture in the system causes particles to stick to each other especially in the cases where fine-grained particles are present. Small amounts of moisture cause fine-grained particles to adhere to the surfaces of larger particles further inhibiting the particles' primary and secondary movement and decreasing ellipsoidal widths.

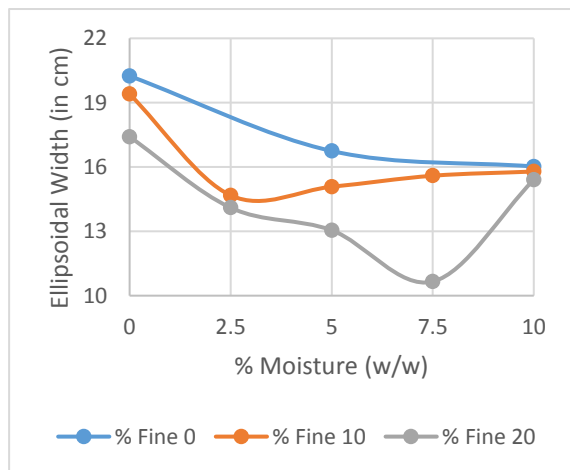


Fig. 5 Ellipsoidal width at varying moisture contents

Finally, all three trendlines of the 0%, 10% and 20% fine-grain settings at different moisture contents appear to converge to a single point at 10% moisture content settings.

CONCLUSION

The experiment confirmed that there is a statistically significant change to the width of

extraction ellipsoid due to the varying amounts of moisture in the system. Even though moisture at certain amounts can actually induce failure and increase particle mobility, the ellipsoidal widths are still less than the dry samples (xF – 0M settings). This shows that the presence of moisture in the system decreases the width of the extraction ellipsoid.

Also, at the 10% moisture settings, the widths of extraction ellipsoid of each setting seem to converge to a single point without any statistical difference. This point can be used as the basis for design since all the trends approach this point provided that presence of moisture is at least 10%.

The sudden increasing trend caused by pore water pressure seems to be a promising subject for future research. The scope of this experiment is only within 0% - 10% moisture range, yet it showed an increasing trend. Hence, it may be beneficial to check the behavior of ellipsoidal widths beyond 10% moisture where the system approaches saturation and the properties governing it is similar to mudflow.

ACKNOWLEDGEMENTS

The authors would like to acknowledge Philsaga Mining Corporation for their technical inputs that greatly inspired the inception of this research. The parameters of the model used in this experiment is patterned to their mining method. This research was made possible by the unrelenting support of our families. All glory to God.

REFERENCES

- [1] G. Chen, "Stochastic Modeling of Rock Fragment Flow Under Gravity," *International Journal of Rock Mechanics*, vol. 34, no. 2, pp. 323-331, 1997.
- [2] R. Kvapil, "Suvlevel Caving," in *SME Mining Engineering Handbook*, Littleton, Colorado, Society for Mining, Metallurgy, and Exploration, Inc., 1992, pp. 1789-1814.
- [3] R. Kvapil, "Gravity Flow of Granular Materials in Hopper and Bins - I," *International Journal of Rock Mechanics*, pp. 35-41, 1965.
- [4] R. Kvapil, "Gravity Flow of Granular Materials in Hoppers and Bins in Mines - II," *International Journal of Rock Mechanics*, pp. 277-304, 1965.
- [5] R. E. Goodman, *Introduction to Rock Mechanics*, Canada, 1989.

INFLUENCE OF INITIAL CONDITIONS ON UNSATURATED GROUNDWATER FLOW MODELS

Aizat Mohd Taib¹, Mohd Raihan Taha² and Dayang Zulaika Abang Hasbollah³

^{1,2}Faculty of Engineering and Built Environment, Universiti Kebangsaan Malaysia; ³Faculty of Civil Engineering, Universiti Teknologi Malaysia.

ABSTRACT

Slope failure in unsaturated soils is common in tropical countries due to the seasonal pattern of abundant rainfall preceding a period of prolonged drying. Much research has been undertaken to understand the behaviour of unsaturated slopes and reduce the number of catastrophic failures. The initial conditions are important factors in numerical modelling of the groundwater flow yet rarely considered in detail in the literature. This paper presents a parametric study of the initial conditions at a slope in Bukit Timah, Singapore. The intensity and duration of rainfall are varied to assess the effect on the pore-water pressure in the slope. The generated pore-water pressure profile is compared with field measurements and previous numerical studies. It is discovered that a low rainfall, with an intensity of 1×10^{-7} m/s over a period of 62 days, results in initial pore-water pressure which is consistent with data recorded at the field. Unlike the duration, changes in the rainfall intensity are shown to have a significant effect on the pore-water pressure in the slope. This study, therefore, demonstrates the importance of determining appropriate initial conditions in unsaturated groundwater flow analysis.

Keywords: Unsaturated soils, rainfall, groundwater flow.

INTRODUCTION

Rainfall has been recognized as the dominant triggering event for landslides in Singapore [2]. These natural disasters cause loss of life and economic losses [3] and have drawn the attention of many researchers to investigate slope behaviour in unsaturated soils by undertaking physical and numerical studies. Several research works were conducted in physical modelling, but many were modelled numerically due to cost and time constraints such as the research work by Oh et al. [4] and Zhang et al. [5]. Nevertheless, there are also many challenges in numerical modelling for example to determine appropriate initial conditions. Many numerical studies have been conducted using assumed or common values for the input parameters due to the lack of field data. By executing these options, the calculation may reduce the accuracy in predicting realistic soil behaviour.

In numerical modelling, the initial condition is an important phase as it generates the initial pore-water pressure of the slope profile. There is limited information in the literature about the procedures to develop the initial conditions. The method is crucial for certain geotechnical software packages that do not provide pre-setting conditions (i.e. initial pore-water pressure) and rely on generating the pore-water pressure manually. One recognised method which is normally used is to apply a small amount of rainfall. In addition, the major factors that can be taken into

account in generating the pore water pressure are the intensity and duration of rainfall.

To model the infiltration of rainfall corresponding to soil behaviour, the interaction of soil and water has to be carefully determined. In unsaturated soil mechanics, the soil hydraulic properties can be measured as the volumetric water content and the coefficient of permeability with respect to matric suction, using the soil-water characteristic curve (SWCC) and permeability function respectively. The SWCC is a relationship between the water content and suction in the soil while the permeability function is the relationship between the coefficient of permeability and soil suction [6]. Many equations of these curves have been introduced over the decades and the most implemented ones are those by Van Genuchten [7] and Fredlund et al. [8].

This paper aims to model the groundwater flow in unsaturated slopes with the effect of rainfall using the SWCC and permeability function by Fredlund et al. [8] and Fredlund et al. [9] respectively. The hydraulic properties are calibrated and the mechanical properties are gathered from the literature as input data for the groundwater flow analysis. Parametric studies of the initial groundwater conditions are undertaken by applying small amount of rainfall to the slopes. Two major factors are considered: rainfall intensity and duration. Validation of the pore-water pressure generated is performed by comparing the results of a slope failure case study in Bukit Timah, Singapore performed by Rahardjo et al. [10].

UNSATURATED GROUNDWATER FLOW

The investigation of unsaturated groundwater flow is important to understand the behaviour of the unsaturated soils with the effects of rainfall. Over the decades, the behaviour of partially saturated soils has been widely modelled using the SWCC and the permeability function. As there are many equations available in the literature, it is important to select a suitable equation in order to predict realistic soil behaviour. The governing equation applied in modelling the groundwater flow is presented below. In general, the fundamental theory of flow by Darcy's Law is widely adopted in many groundwater flow analyses. Many other theories were later developed for more complex soil profiles. Hence, the two theories of SWCC and permeability functions are essential in capturing the groundwater flow in partially saturated soils.

Unsaturated Soil

Unsaturated soil is formed above the phreatic level due to the cyclic weathering process of prolonged drying and abundant rainfall. The SWCC is used to describe the water extraction for drying and the permeability function for the rate of water seepage. The curve as proposed by Fredlund et al. [8] consists of the water content at specific suction, θ_w , and at saturation, θ_s , degree of saturation, S , suction given as the difference of pore-air pressure and pore-water pressure, $(u_a - u_w)$, e as a natural number with value of 2.71828, $C(\psi)$ as the correction factor and the three shape-parameters; a , n and m that refers to the air-entry value (AEV), pore size distribution and the slope of the SWCC respectively. The SWCC is given as:

$$\theta_w = C(\psi) \frac{\theta_s}{\{ \ln[e + (u_a - u_w/a)^n] \}^m} \quad (1)$$

They further suggested an additional parameter which is the residual water content, θ_r , as it will plot a sigmoidal curve. Leong et al. [11] concluded that sigmoidal curve is more versatile and perform better fit of the SWCC.

Fredlund et al. [8] also discovered that when $C(\psi)$ is taken as 1.0, the equation can be used with less complexity. Therefore, the equation is given by Equation (2) and it is used in this study.

$$\theta_w = \theta_r \frac{\theta_s - \theta_r}{\{ \ln[e + (\psi/a)^n] \}^m} \quad (2)$$

Moreover, the permeability equation defines the coefficient of permeability with respect to water, k_w , as a function of both the void ratio and water content [12]. By using k_w which can be derived from the SWCC corresponding at any value of the water content, Childs et al. [13] suggested the

transformation of the SWCC, $\theta_w(\psi)$ into $\theta_w(r)$ where r is the pore radius. The transformation requires tedious work thus Marshall [14] improved the permeability function and recommended the application of identical water content intervals leading to the following equation:

$$k_w(\theta_w) = \frac{T_s^2}{2\rho_w g \mu} \frac{n^2}{m^2} \sum_{i=1}^l \frac{2(l-i)-1}{\psi_i^2} \quad (3)$$

Where T_s is the surface tension of water, ρ_w is the density of water, μ the dynamic viscosity of water, n the porosity of soil, m as the total number of intervals given by $= (\frac{\theta_s}{\Delta\theta_w})$, l as the number of intervals corresponding to θ_w given by $= (\frac{\theta_w}{\Delta\theta_w})$, ψ_i as the matric suction corresponding to the midpoint of the i th interval of the SWCC. This permeability function has been adopted to calculate the saturated coefficient of permeability.

Groundwater Flow

The groundwater flow analysis can be performed using finite element codes program with an initial phase of steady state and a series of transient seepage phases. Commonly, groundwater flow is governed by the fundamental Darcy's law and the continuity equations. In three dimensions the flow equation can be written as in Equation (4) [15].

$$\underline{q} = \frac{\underline{k}}{\rho_w g} (\underline{\nabla} p_w + \rho_w \underline{g}) \quad (4)$$

$$\text{Where } \underline{\nabla} = \begin{bmatrix} \delta/\delta x \\ \delta/\delta y \\ \delta/\delta z \end{bmatrix} \text{ and } \underline{g} = \begin{bmatrix} 0 \\ -g \\ 0 \end{bmatrix}$$

The terms q , k , g and ρ_w are the specific discharge (fluid velocity), permeability tensor, acceleration vector due to the gravity and the density of water, respectively. The groundwater flow is the resultant of the pore-water pressure gradient presented as $\underline{\nabla} p_w$. However, when hydrostatic conditions are assumed, the term $\rho_w g$ will be used because the flow is no longer affected by the gradient of pore-water pressure in vertical direction. In unsaturated soil mechanics, the coefficient of permeability, \underline{k} is related to soil saturation by:

$$\underline{k} = k_{rel} \times \underline{k}^{sat} \quad (5)$$

$$\text{Where } \underline{k}^{sat} = \begin{bmatrix} k_x^{sat} & 0 & 0 \\ 0 & k_y^{sat} & 0 \\ 0 & 0 & k_z^{sat} \end{bmatrix}$$

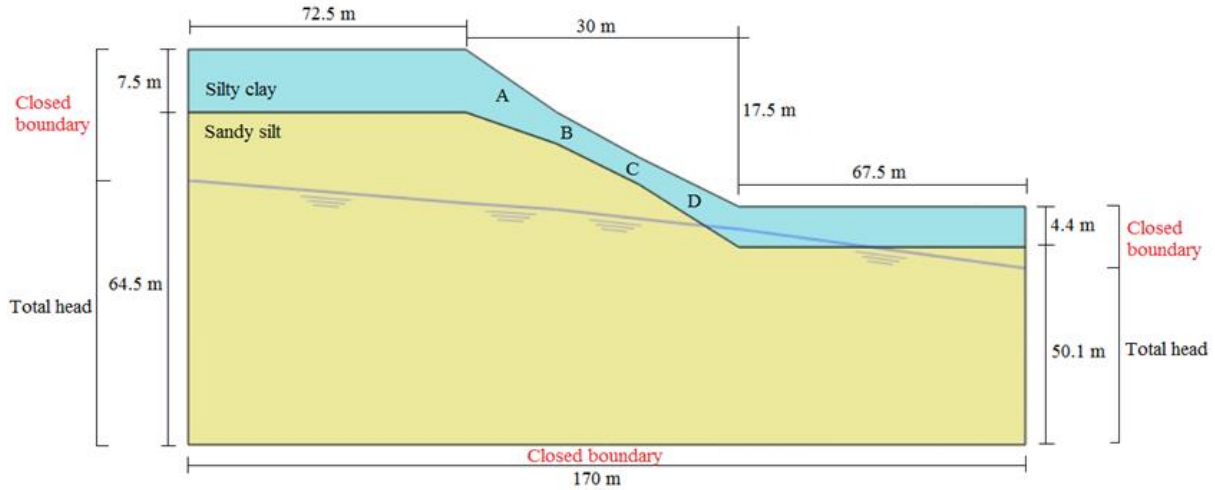


Figure 1 Slope geometry and boundary conditions [1]

The k_{rel} is the ratio of permeability at a specific saturation of the permeability in saturated state, k_{sat} . For the continuity equations, the simplified transient groundwater flow by neglecting the displacement is given as:

$$\nabla^T \cdot \left[\frac{k_{rel}}{\rho_w g} k_{sat} (\nabla p_w + \rho_w g) \right] - n \left(\frac{s}{K_w} - \frac{\partial s}{\partial p_w} \right) \frac{\partial p_w}{\partial t} = 0 \quad (6)$$

In steady-state conditions, where $\frac{\partial p_w}{\partial t} = 0$, the formula is given as in Equation (7). The parameters n and S are the porosity and the degree of saturation respectively.

$$\nabla^T \cdot \left[\frac{k_{rel}}{\rho_w g} k_{sat} (\nabla p_w + \rho_w g) \right] = 0 \quad (7)$$

The saturation and permeability with respect to pressure head determine the unsaturated groundwater flow in the Plaxis2D software [16], as explained in Plaxis [17].

NUMERICAL MODELLING

A parametric study is undertaken to investigate the effect of rainfall intensity and duration on the initial pore-water pressure. The geometry of the slope and the flux boundary conditions applied are shown in Figure 1. The lateral boundaries are assigned with impermeable layers above the groundwater table and total head below the phreatic level. Furthermore, the slope surface is modelled with precipitation while the bottom boundary is assumed impermeable. There are two different soil layers with different soil parameters as shown in Table 1 for mechanical and hydraulic properties of the soil.

The calibrated SWCC and permeability function are shown in Figure 2 and the typical rainfall intensity used in the simulation is plotted in Figure 3. The filed

data of the pore-water pressure are recorded by the tensiometers placed at locations indicated in Figure 1 at the crest, mid-slope and toe of the slope as A, B, C and D. All locations are calculated at same depth of 2.08 m.

Table 1 Mechanical soil properties used in the simulations [10]

Description	Silty sand	Sandy silt
<i>Mechanical properties</i>		
Effective cohesion, c' (kPa)	9	0
Effective angle of friction, ϕ' (°)	34	33
Total density, ρ_t (Mg/m ³)	2.03	1.88
Specific gravity, G_s	2.66	2.58
Void ratio, e	0.8	0.86
<i>Hydrological properties</i>		
Saturated coefficient of permeability, k_s (m/s)	6×10^{-6}	3.3×10^{-5}
Saturated volumetric water content, θ_s	0.6	0.5306
Fitting parameter, a (kPa)	1.1	7
Fitting parameter, n	0.55	5
Fitting parameter, m	1.33	0.7
Air-entry value, (AEV)	15	5
Residual volumetric water content, θ_r	0.15	0.15
Residual suction ψ_r (kPa)	6000	22

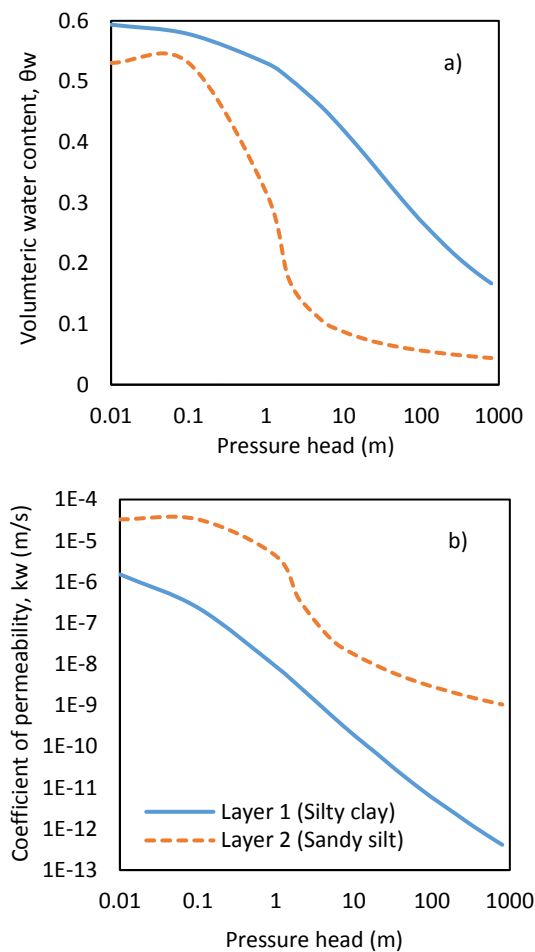


Figure 2 (a) SWCC (b) permeability function

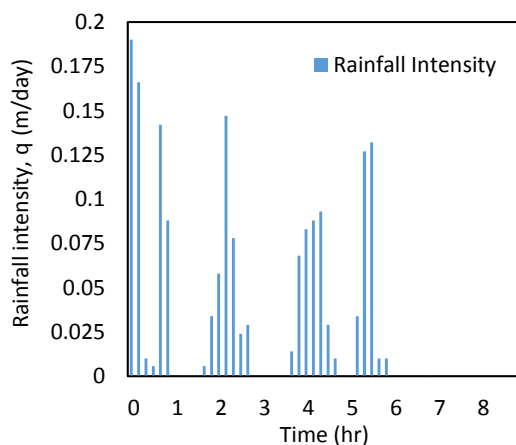


Figure 3 Typical rainfall in Singapore

RESULT AND DISCUSSION

Effect of Rainfall Intensity

The pore-water pressure calculated using groundwater flow analysis in Plaxis was compared with the results obtained using Seep/W[18]. The results of pore-water pressure are calculated at

locations A, B, C and D (see Figure 1) are presented in this paper. Five different intensities have been applied to the slope model with one control value. Based on the report from the MET Office [17], Singapore has two major periods of abundant rainfall which is in the mid-year in between June to August and another at the end of the year in between November and January. The heaviest rainfall is recorded at 200 mm per month on average. Hence, the control value is selected based on the heavy rainfall with an amount of 8.64 mm/day. In this study, the rainfall intensity is converted to 1×10^{-7} m/s for a period of 62 days. From the results shown in Figure 4, the pore-water pressure has changed more at the toe, represented at location D. At the toe, a lower negative pore-water pressure was captured at the earlier duration compared to other locations but suction was eliminated when larger rainfall intensity (i.e. 5.5×10^{-7} m/s) was used. It can be said that slow infiltration occurred at the toe due to higher saturation at the surface which causing ponding to occur. When a lower rainfall intensity of 5.5×10^{-8} m/s was applied, it can be observed in Figure 4 that the negative pore-water pressure reduced very minimal compared to other rainfall intensities. Zhang, Fredlund [5] stated that when the water flux is less than the saturated coefficient of permeability, the matric suction can decrease but not disappear entirely which explains the low reduction of suction in this case.

When a higher rainfall intensity had been applied, the negative pore-water pressure continues to reduce but at a faster rate. The largest rainfall intensity applied in the parametric study shows that the negative pore-water pressure reduced at the highest rate and it remains constant over the period of rainfall. This can be explained by the large amount of rain water infiltrated into the soil and once the soil has reached saturation, the negative pore-water pressure becomes steady. Thus, a wetting front is identified. The formation of the wetting front however only occurs for larger amount of rainfall intensity which is in this case, $q = 5.5 \times 10^{-7}$ m/s. Other intensities applied did not show any formation of the wetting front. The second largest amount is indicating a formation of wetting front in progress. With longer duration, the wetting front might fully form unless saturation is reached.

Effect of Rainfall Duration

The duration applied for the small rainfall is also an important variable in order to determine the most suitable initial pore-water pressure. Five durations were used to investigate the behaviour of the slope with short and prolonged rainfall selected at 14 days and 31, 62, 93 and 186 days respectively. This is conducted to evaluate the infiltration rate and amount of the rainwater allowed to percolate into the soil.

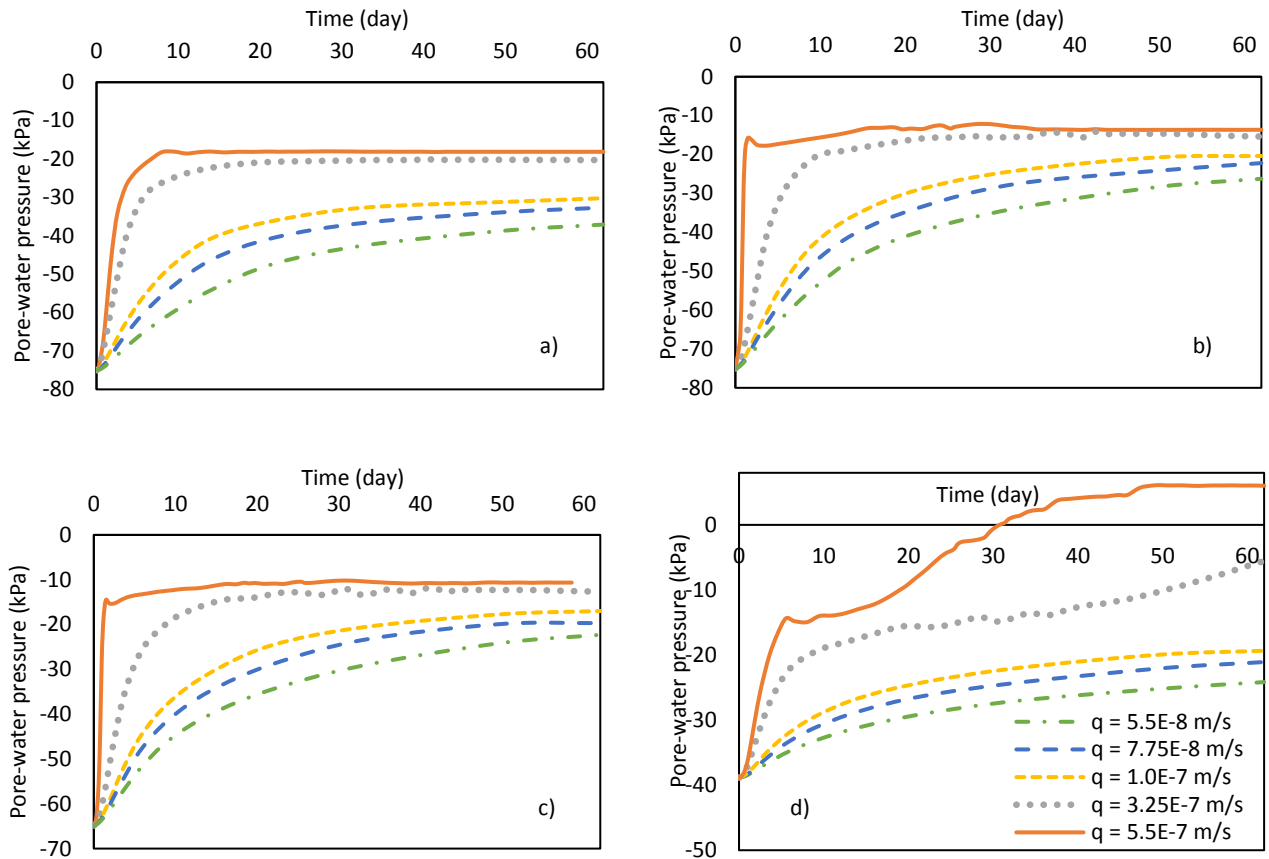


Figure 4. Initial PWP for different rainfall intensity at depth of 2.08 m for location: (a) A, (b) B, (c) C and (d) D [1]

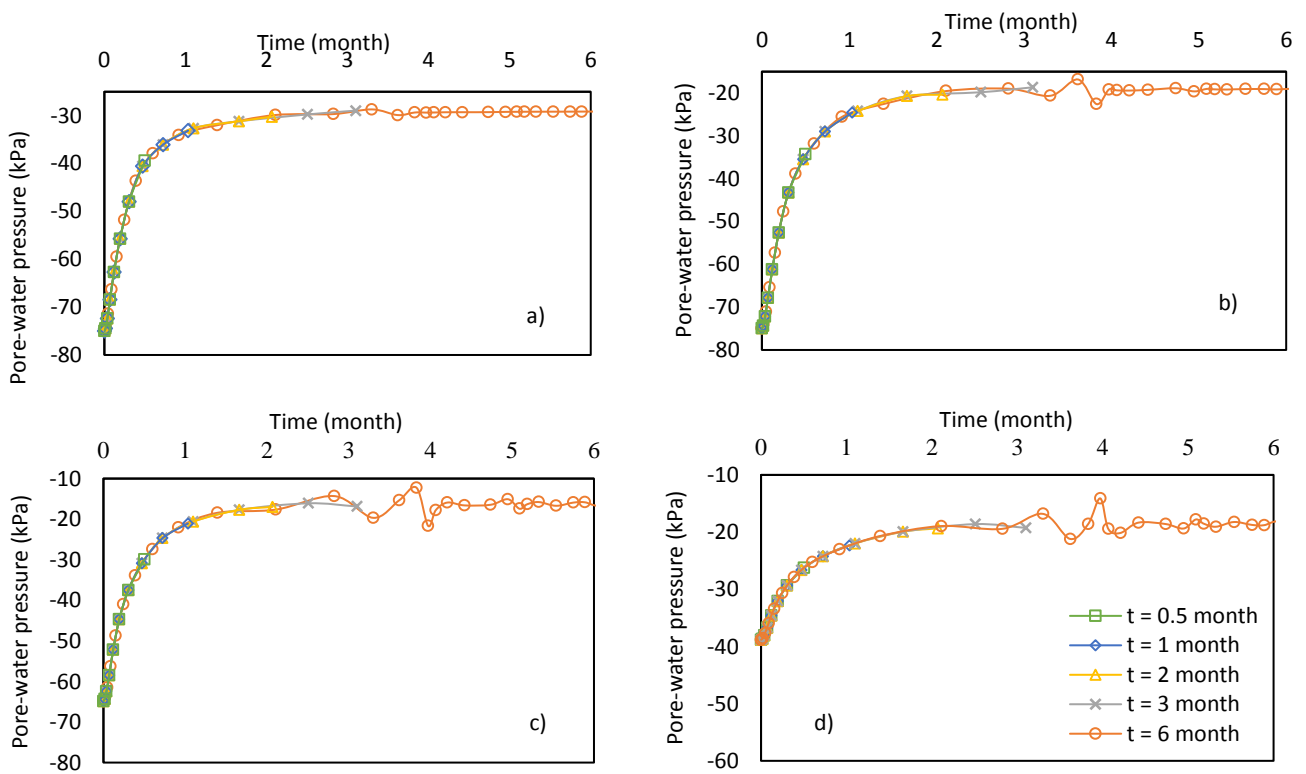


Figure 5. Initial PWP for different durations at depth of 2.08 m for location (a) A, (b) B, (c) C and (d) D [1]

From the results shown in Figure 5, although the pore-water pressure recorded at Location D is lower at the beginning of the duration, the pore-water pressure increases and reaches saturation at a similar rate for the first two months. Due to the fact that the difference is not large, it can be said that the duration does not affect the generation of initial pore-water pressure significantly when a constant and low rainfall intensity is used (i.e. 1×10^{-7} m/s) for shorter durations.

However, based on Figure 5, upon reaching the third months, the pore-water pressure show fluctuation values at a lower depth from the depth of 1.31 m (Location B) and onwards. One of the factors that can be related to this changing pressure could be the effect of the groundwater table as the depth increases. Also, Ng et al. [19] mentioned that a long duration of rainfall influences greater changes in deeper groundwater. In this scenario, the depth does not change because all locations of the pore-water pressure were calculated at similar depth of 2.08 m. Nevertheless, the location which indicated by the crest, mid-slope and toe differentiates the generation of the pore-water pressure. It can be said the fluctuations of the pore-water pressure are caused by the different locations with different height of the slope. Higher locations are less affected from the water accumulated from the rainfall unlike the toe which faces larger amount of water for infiltration. Therefore, the duration of the initial pore-water pressure is only affected after a period of two months depending on the intensity as well as the locations of the pore-water pressure calculated.

CONCLUSION

The effect of the initial condition in modelling unsaturated groundwater flow were investigated. The initial pore-water pressure generated due to the rainfall applied was modelled using seepage analysis. Initially, small amount rainfall was applied to generate the initial pore-water pressure where the intensity and duration of rainfall were varied. A case study was used to validate the unsaturated flow model with the field and numerical results by Rahardjo et al. [10]. From the parametric study, it can be concluded that the intensity affects the initial pore-water pressure. The duration, however, does not have a major impact depending on the rainfall intensity and location or depth of the calculated pressure. Moreover, saturation also showed an influence on the pore-water pressure when small rainfall intensity was used. Further improvement can be achieved to develop extensive model by modifying the magnitude of permeability, adjusting the infiltration boundary and taking into account the different depth of the calculated pressure.

ACKNOWLEDGEMENTS

The author would like to thank the people involved in the research project: Dr Mohamed Rouainia, Reader in the School of Engineering, Faculty of Science, Agriculture and Engineering, Newcastle University, UK, Professor Harianto Rahardjo and Dr Alfredo Satyanaga Nio, Academic and Research staff in the Faculty of Civil and Environmental Engineering, Nanyang Technological University, Singapore.

REFERENCES

- [1] Aizat, M.T., *Numerical modelling of unsaturated tropical slopes*, in *School of Engineering*. 2018, Newcastle University: Newcastle upon Tyne, UK.
- [2] Toll, D.G., 2001. *Rainfall-induced landslides in Singapore*. *Geotechnical Engineering*, 149(4): p. 211-216.
- [3] Tsaparas, I., H. Rahardjo, D.G. Toll, and E.C. Leong, 2002. *Controlling parameters for rainfall-induced landslides*. *Computers and Geotechnics*, 29(1): p. 1-27.
- [4] Oh, S. and N. Lu, 2015. *Slope stability analysis under unsaturated conditions: Case studies of rainfall-induced failure of cut slopes*. *Engineering Geology*, 184: p. 96-103.
- [5] Zhang, L.L., D.G. Fredlund, M.D. Fredlund, and G.W. Wilson, 2014. *Modeling the unsaturated soil zone in slope stability analysis*. *Canadian Geotechnical Journal*, 51(12): p. 1384-1398.
- [6] Zhang, L.L., D.G. Fredlund, L.M. Zhang, and W.H. Tang, 2004. *Numerical study of soil conditions under which matric suction can be maintained*. *Canadian Geotechnical Journal*, 41(4): p. 569-582.
- [7] Van Genuchten, M.T., 1980. *A closed-form equation for predicting the hydraulic conductivity of unsaturated soils*. *Soil Science Society of America Journal*, 44(5): p. 892-898.
- [8] Fredlund, D.G. and A. Xing, 1994. *Equations for the soil-water characteristic curve*. *Canadian Geotechnical Journal*, 31(3): p. 521-532.
- [9] Fredlund, D.G., A. Xing, and S. Huang, 1994. *Predicting the permeability function for unsaturated soils using the soil-water characteristic curve*. *Canadian Geotechnical Journal*, 31(4): p. 533-546.
- [10] Rahardjo, H., V.A. Santoso, E.C. Leong, Y.S. Ng, and C.J. Hua, 2011. *Numerical analyses and monitoring performance of residual soil slopes*. *Soils and foundations*, 51(3): p. 471-482.
- [11] Leong, E.C. and H. Rahardjo, 1997. *Review of soil-water characteristic curve equations*.

- Journal of geotechnical and geoenvironmental engineering, 123(12): p. 1106-1117.
- [12] Leong, E.C. and H. Rahardjo, 1997. *Permeability Functions for Unsaturated Soils*. Journal of Geotechnical and Geoenvironmental Engineering, 123(12): p. 1118-1126.
- [13] Childs, E.C. and N. Collis-George, 1950. *The Permeability of Porous Materials*. Proceedings of the Royal Society of London. Series A, Mathematical and Physical Sciences, 201(1066): p. 392-405.
- [14] Marshall, T.J., 1958. *A relation between permeability and size distribution of pores*. Journal of Soil Science, 9(1): p. 1-8.
- [15] Galavi, V., *Groundwater flow, fully coupled flow deformation and undrained analyses in PLAXIS 2D and 3D*. 2010, Plaxis BV.
- [16] Plaxis, *Scientific manual*. 2012.
- [17] Plaxis, *Material models manual*. 2012.
- [18] GeoSlope, I.L., *SEEP/W User's Guide for Finite Element Seepage Analysis*. 2004, GEO-SLOPE International Ltd, Calgary, Alta.
- [19] Ng, C.W., B. Wang, and Y.K. Tung, 2001. *Three-dimensional numerical investigations of groundwater responses in an unsaturated slope subjected to various rainfall patterns*. Canadian Geotechnical Journal, 38(5): p. 1049-1062.

Construction Materials

MECHANICAL PROPERTIES OF CONCRETE WITH RECYCLED COMPOSITE AND PLASTIC AGGREGATES

Dan Li¹ and Sakdirat Kaewunruen²

¹Department of Civil Engineering, School of Engineering, The University of Birmingham, U.K,

²Birmingham Centre for Railway Research and Education, The University of Birmingham, U.K

ABSTRACT

This project is aimed at studying the influence of incorporating recycled plastic and composite aggregate on the workability, mechanical property, water absorption, and electrical resistance of silica fume concrete. Secondly, the paper will evaluate the possibility to use recycled plastic concrete (RPC) in railway track application (i.e. traditional ballasted track and ballastless track). Two replacements (10% and 20%) of natural coarse aggregate by 3.35mm, 5.6mm and mixed size recycled plastic aggregate are introduced. The experimental results confirm that the workability is improved with an increase in the plastic aggregate replacement. In addition, it is found that mechanical strength and durability in terms of water permeability are reduced, whilst electrical resistance is improved. The result also reveals that application of this environment friendly recycled plastic concrete in railway tracks sustainably can improve ability to absorb vibration energy of railway system.

Keywords: Mechanical properties, recycled composite, plastic aggregates, concrete.

INTRODUCTION

Rapid industrialization and urban development globally have led to many waste handling and disposal problems. The rapid growth affects the uses of raw materials, which are available only in limited quantities. The pressure on finite resources and burdensome wastes results in both economic and societal constraints. The problem of remaining wastes is of major concern around the globe. However, plastic waste is one of materials that have potential for recycling. The management and recycling of plastic waste is rapidly growing. The utilization of recycled plastics in concrete is a partial solution to resolve environment and ecological problem. In this study, the research mainly focuses on the application of concrete to railway tracks and evaluates the feasibility to utilize recycle plastic aggregate concrete. Two type of railway track systems will be analysis and compared including traditional ballasted tracks (sleeper) and ballastless track (Slab Track). A number of experiments will be carried out to evaluate the physical and mechanical properties of the plastic aggregate concrete. The concrete has included Mixed Engineering Polymer (MEP) aggregate as partial replacement of conventional coarse aggregate to create plastic aggregate concrete.

Over the past 50 years, railway systems have been revolutionizing rapidly. The train speed and axle load have come to commuters' primary concern nowadays. Because of these challenges, slab track has been a breakthrough technology to replace conventional ballasted track system. Slab track technology offers a proven higher performance in

services and a longer life span than traditional ballasted tracks. It is a modern form of track construction, which has been used successfully throughout the world for heavy rail, high speed lines, light rail as well as tram systems. Slab track technology offers proven higher performance in service and a longer life compare to traditional ballasted track. Table 1 shows how successful that slab track is constructed around the world.

Table 1 Slab track projects in the world

Project	Country	Track fom
Shinkansen	Japan	Shinkansen
Dueme	The Netherlands	Em bedded Rail
Best	The Netherlands	Em bedded Rail
Cnew e-Kidsgrove	UK	BBEST Em bedded Rail
High Speed Line HSL Zuid	The Netherlands	Rheda 2000
Cologne-Frankfurt High Speed Line	Germany	Rheda Züblin
Hibel & Prestbury Tunnels	UK	Rheda 2000
Nuremberg-Ingolstadt High Speed Line	Germany	Rheda 2000FF-Bögl
Taipei and Kaohsiung High Speed Rail	Taiwan	Rheda 2000
Eje Atlántico	Spain	Rheda 2000
Peñagón-Figueroas	Spain	Rheda 2000
Guadarrama Tunnel	Spain	Rheda 2000
Beijing-Tianjin Intercity Railway	China	Rheda 2000
TGV Méditerranée	France	Sateba booted sleeper
Channel Tunnel	UK/France	Sonneville block
Channel Tunnel Rail Link Phase II	UK	Booted sleeper
Gothard Tunnel	Switzerland	Booted sleeper
St. Pancras	UK	Resilient baseplate
Docklands Light Railway	UK	Resilient baseplate
Athens Attiko Metro	Greece	Booted sleeper
Hong Kong MTR	Hong Kong	Resilient baseplate Floating track slab
Kuala Lumpur Star LRT	Malaysia	Resilient baseplate
London Underground	UK	Resilient baseplate
Tamway de Grenoble	France	Booted sleeper
Nottingham Express Transit	UK	Em bedded Rail
Sheffield Supertram	UK	Em bedded Rail

The design life for traditional ballasted tracks is typically around 50 years. But concrete track slabs (see Fig. 1) offer longer design life up to at least 60 years. In addition, track slab do not require frequent inspections and maintenance. Comparing to ballasted tracks, slab track system is fixed in

position therefore it is not necessary to carry out regular realignment of the rails. By considering the aspect in maintenance and design life, track slab is a sustainable option over a 60 year and 120 year lifecycle.



Fig. 1 A typical slab track

DESIGN PARAMETERS FOR SLAB TRACKS

For the slab track construction (see Fig. 2), a stabilized subbase are required to provide a more uniform distribution of wheel load stresses which reduces the subgrade stresses and provides a degree of frost protection. Stable subgrade is also an important aspect to consider. The subgrade need to be uniform, well prepared, with adequate strength and well drained. Poor subgrade may lead to pier settlement and cause rail deformation. Slab track will exhibit failure such as cracking, faulting and pumping due to poor subgrade condition. The failure modes are similar to concrete pavement. Weak subgrade soil and soils are susceptible to frost heave and should be removed and replaced with compacted granular soil. The adjustments to track geometry after construction are very limited. Hence, special preparation of subsoil before construction is essential.

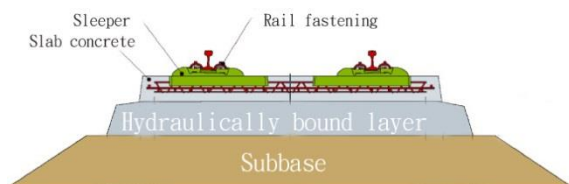


Fig. 2 Typical cross section of a slab track

Concrete used for slab track construction is similar to highway pavement construction. Therefore, material specification developed by the local jurisdiction (state or provincial railway

agencies) can be directly adopted [1]. The followings are the minimum requirements:

- Minimum 28 days compressive strength - 27 MPa
- Minimum 28-day flexural strength - 4.1 MPa
- Cement meeting requirement of ASTM C150
- Aggregate meeting requirement of ASTM C33 A. 25 to 38 mm maximum aggregate size may be used. Special attention should be paid to susceptibility to freezing, thawing and alkali-aggregate reactivity.
- Air entrainment based on exposure condition. Typically 4 to 7% total air content is specified for mild to severe exposure conditions.

RECYCLED PLASTICS

As the world population increasingly growing, much more wastes are being generated. Plastic waste is one of the major issues affecting the globe environment. In the past 50 years, world consumption and production of plastics have continued to go up. 260 million tons of plastic was generated worldwide in 2008, plastic consumption is to reach 297.5 million tons by the end of 2015 [2]. As its nature, plastics belong to a chemical family of high polymers, they are essentially made up of a long chain of molecules containing repeated units of carbon atoms. Because of this inherent molecular stability (high molecular weight), plastics do not easily breakdown into simpler components [3-4]. Therefore, it is very essential to find a sustainable way to solve this issue. It is extremely difficult that the recycled plastic is usable. That's because plastic waste contains many different types of plastic that have to be treated in different ways for recycling. Now, a new method designed to create expanded construction nodules from mixed plastic waste may replace the expanded clay traditionally used in light concrete that is not used for structural part of a building and often contains air bubbles [5-9].



Fig. 3 Mixed plastic waste

Under a project supported by the EU's eco-innovation programme, plastic waste has been successfully converted into a high-performance aggregate for use in making lightweight concrete and mortar, as shown in Fig. 3. However, many researchers have demonstrated that use of recycled plastic in concrete partial replacement of aggregate significantly reduces its mechanical properties dependent on the replacement level [9-17]. Therefore, the recycled plastic concrete still requires further development.

CONCRETE MIX DESIGN

For the concrete mix design used in this research, the proportion of content was calculated by the method documented in the "Design of normal concrete mixes" published by the building research Establishment. Prestressed concrete sleeper (or railroad ties) are usually designed using high strength concrete (around 50-80). Therefore, the control mixes were designed aiming to achieve a target mean strength of 63 MPa (also known as C 50/60) at 28 day. A water-cement ratio of 0.44 was designed on the basis of the target mean strength, the cement strength class and as well as the type of the aggregate. The amount of free water content used to achieve the designed w/c ratio was based on the desired slump, the maximum size and the type of aggregate. Cement content was calculated by the values of w/c ratio and the amount of free water. Mixed engineering polymers (MEP) sizes of 5.6mm and 3.35mm were used to replace 10% and 20% of coarse aggregate using direct volume replacement method. In addition, MEP without sieve was also used to replace 10% of coarse aggregate. Silica fume was also added to replace 10% of cement by volume in all MEP concrete. Due to lack of time, 20% MEP without sieve concrete haven't conduct in the reports. Seven concrete mixtures are prepared (as tabulated in Table 2) for this research program to study the

effect of MEP sizes and their distribution: RFC, SFC, SFRC-5.6-10, SFRC-5.6-10, SFRC-3.35-10, SFRC 3.35-20 and SFRC mix-10.

Cement:

The cement used for the present investigation was Ordinary Portland type 1 with characteristic strength of 52.5MPa according BS EN 197-1.

Aggregate:

Fine aggregate with a maximum particle size of 5mm. Coarse aggregate with a maximum size of 10mm

Silica Fume:

Elkem Silica fume, grade 940 was replace 10% of cement by volume in all recycled plastic concrete to enhancing the machanical properties.

Recycled plastic aggregate:

In this study, recycled plastic aggregates also called Mixed Engineering Polymers (MEP) were used to replace the coarse aggregate to study the property of plastic aggregate concrete. The MEP were kindly supplied by Axion Polymers. This type of MEP is a mixture of clean, wasted granular chips rich in PP with regular particle size. MEP sizes of 6.7mm, 5.6mm, 4.75mm and 3.35 mm were classified from the sieving vibrator. Two different sizes of MEP are used in this study: 5.6 mm and 3.35 mm.

WORKABILITY

Slump tests are carried out to determine the workability of the fresh concrete. The procedure of slump tests complies with BS EN 12350-2. Fresh concrete is filled to the cone in three stages. In each stage, the layer is compacted 25 times with a rod or stick. At the end of the third stage, the protruding concrete on the top of the mould is struck off flush with a trowel. The mould is then lifted vertically upward. Finally, the slump is then measured.

Table 2 Mix design

No	Kg/m ³						
	Mixes	Cement	Water	Gravel	Sand	Silica fume	MEP
1	RFC	530	233	986	630	0	0
2	SFC	477	233	986	630	53	0
3	SFC-5.6-10%	477	233	887.4	630	53	98.6
4	SFC-5.6-20%	477	233	788.8	630	53	197.2
5	SFC-3.35-10%	477	233	887.4	630	53	98.6
6	SFC-3.35-20%	477	233	788.8	630	53	197.2
7	SFC mix-10%	477	233	887.4	630	53	98.6

Workability of concrete is measured in terms of ease and homogeneity with which a freshly mixed concrete or mortar can be mixed, transported to construction site, placed in forms and compacted. The higher the slump, the easily the concrete to mixed, transported, placed and compacted. From the result obtained from the Slump test, replace 10% cement by silica fume to significantly reduce the workability about 50%. The workability can improve by low replacement rate of silica fume around 2-3% by mass of cement, but can reduce workability when added at higher replacement rates. Fig. 4 clearly shows that adding plastic can enhance the workability.

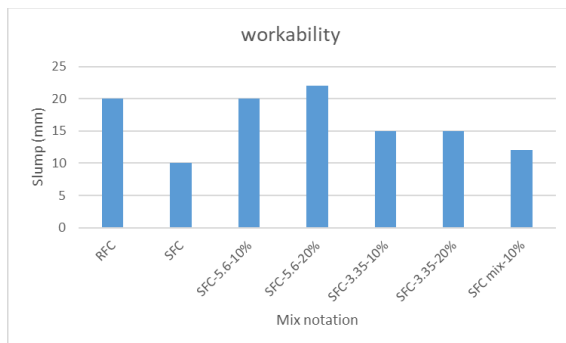


Fig. 3 Slump of concrete

COMPRESSIVE STRENGTH

Six 100mm x 100mm x 100mm cube test were casted per concrete mixture. Three cubes were tested at 7 days and the other three cubes were tested at 28 days. The compressive strength tests were carried out on those cubes. The compressive strength test was conducted according to BS EN 12390-3.

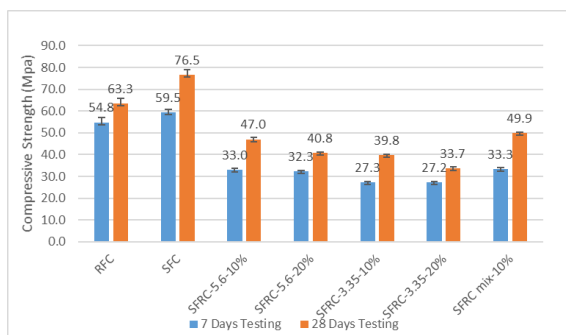


Fig. 4 Compressive strength of concrete

As earlier mentioned, this type of concrete are designed to apply for railway applications either concrete sleeper or slab track. The control concrete (RFC) was designed to have the target mean strength of 62 MPa at 28day in order the meet the minimum requirement of concrete sleeper which is 55 MPa. Each mechanical property value presented in Fig. 4

is the average value obtained from tests performed on three specimens. It can be seen that a reduction in the mechanical strength according to increase in percentage of MEP in the silica fume concrete.

TENSILE STRENGTH

Cylinder splitting test was conducted according to BS EN 12390-6. Three sample of 100mm diameter x 200mm long concrete cylinder per mixture were used. The splitting tensile strength of concrete specimen in MPa was calculated by using the below formula according to BS EN 12390-6

$$f_t = \frac{2P}{\pi DL}$$

where:

f_t is the splitting tensile strength of concrete specimen (MPa)

P is the applied failure load obtained from the testing machine

D is the cross-sectional diameter of cylinder(mm)

L is the cylinder length(mm)

The effect of EMP content on the splitting tensile strength of silica fume concrete show in Fig. 5. At 28-day testing result showed that the splitting tensile strength of all concrete mixes have a similar trend to compressive strength. The SFC still was the highest tensile strength of 3.85MPa which is approximately 22.9% increase compare to RFC.

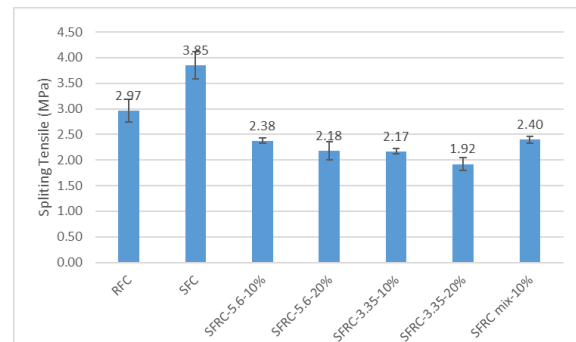


Fig. 5 Tensile strength of concrete

CONCLUSION

This research focused on the study and evaluation of the environment-friendly concrete containing with recycled plastic aggregate (5.56, 3.35 and mixed size) to utilize for railway concrete sleepers and ballastless tracks. Seven concrete mix tests were conducted to investigate the possibility of using those concrete in the railway industry. The test aimed to study the effects on workability and mechanical properties due to the presence of plastic

inside the concrete. The experiment result have showed that the utilization of the plastic material in making concrete can provide an alternative solution to minimize the environmental impact due to unscientific disposal of waste plastic.

The following conclusions are drawn from this study:

- Plastic can enhance workability of concrete which facilitate mix, transport, place and compact process.
- Presence Plastic aggregate will leading to significant reduction in mechanical strength e.g. Compressive and tensile strengths, however adding 10wt % silica fume can slightly compensate the loss of the strength. SFCA – 5.6-10% and SFCA-mix-10% obtain the highest strength compare to other plastic.
- All of the EMP concrete failed to meet the concrete sleeper minimum compressive strength requirement of 55MPa. However all the MEP concrete can be use in ballastless track since all the concrete compressive strength excess 27 MPa
- SFCA -5.6-20% and SFCA-3.35-10% can be used in light weigh concrete such as back-filling trench, pavement, or in nonstructural element which not required high strength.

ACKNOWLEDGEMENTS

The second author wishes to gratefully acknowledge the Japan Society for Promotion of Science (JSPS) for his JSPS Invitation Research Fellowship (Long-term), Grant No L15701, at Track Dy-namics Laboratory, Railway Technical Research Institute and at Concrete Laboratory, the Universi-ty of Tokyo, Tokyo, Japan. The JSPS financially supports this work as part of the research project, entitled “Smart and reliable railway infrastructure”. Special thanks to European Commission for H2020-MSCA-RISE Project No. 691135 “RISEN: Rail Infrastructure Systems Engineering Net-work” (www.risen2rail.eu). In addition, the sponsorships and assistance from CEMEX, Network Rail, RSSB (Rail Safety and Standard Board, UK) are highly appreciated. Financial support from BRIDGE Grant (Collaboration between University of Birmingham and University of Illinois at Urbana Champaign) is also grate-fully acknowledged.

REFERENCES

- [1] Meesit, R. and Kaewunruen, S. (2017) "Vibration Characteristics of Micro-Engineered Crumb Rubber Concrete for Railway Sleeper Applications", *Journal of Advanced Concrete Technology*, 15(2), pp. 55-66. doi: 10.3151/jact.15.55.
- [2] Hossain, M., Bhowmik, P. and Shaad, K. (2016) "Use of waste plastic aggregation in concrete as a constituent material", *Progressive Agriculture*, 27(3), p. 383. doi: 10.3329/pa.v27i3.30835.
- [3] Liu, F., Yan, Y., Li, L., Lan, C. and Chen, G. (2015) "Performance of Recycled Plastic-Based Concrete", *Journal of Materials in Civil Engineering*, 27(2), p. A4014004. doi: 10.1061/(asce)mt.1943-5533.0000989.
- [4] Kaewunruen, S., Remennikov, A. and Murray, M. (2014). Introducing a New Limit States Design Concept to Railway Concrete Sleepers: An Australian Experience.
- [5] Michas, G. (2012). Georgios michas slab track system, pp. 86-89.
- [6] Hellemans, A. (2012) Using mixed plastic waste as a component of light concrete, Youris.com. Available at: http://www.youris.com/Environment/Recycling/Plastic_Waste_Set_In_Concrete.kl (Accessed: 12 August 2017).
- [7] Tayabji, S. and Bilow, D. (2001). Concrete Slab Track State of the Practice. Transportation Research Record: Journal of the Transportation Research Board, 1742, pp.25-26.
- [8] Constructionclimatechallenge (2017) waste plastic recycled into high-performance aggregate for construction. Available at: <http://constructionclimatechallenge.com/2014/07/28/waste-plastic-recycled-into-high-performance-aggregate-for-construction/> (Accessed: 12 August 2017).
- [9] Ozturan T. (1993) A re-evaluation of IV international conference on the use of fly ash, silica fume, slag and natural pozzolans in concrete. Proceeding of symposium on the use of industrial solid waste in construction sector. Turkey pp 57-58
- [10] Aköz, F., Türker, F., Koral, S. and Yüzer, N. (1999) "Effects of raised temperature of sulfate solutions on the sulfate resistance of mortars with and without silica fume", *Cement and Concrete Research*, 29(4), pp. 537-544. doi: 10.1016/s0008-8846(98)00251-8
- [11] Kumaran, M.Nidhi, Bini P.R. (2015) "Evaluation of strength and Durability of waste plastic Mix concrete" *International Journal of Research in Advent Technology* pp 37.
- [12] Kaewunruen, S.; Meesit, R. Sensitivity of crumb rubber particle sizes on electrical resistance of rubberised concrete. *Cogent Engineering*. 2016, 3 (1), 1126937.
- [13] Kaewunruen, S.; Meesit, R.; Mondal, P. Early-age dynamic moduli of crumbed rubber concrete for compliant railway structures. *J. Sust. Cement-based Mat.* 2017, 6(5), 281-292.
- [14] Akono, A.-T.; Chen, J.; Kaewunruen, S. Friction and fracture characteristics of

- engineered crumb-rubber concrete at microscopic lengthscale. *Constr. Build. Mater.* **2018**, 175, 735-745.
- [15] Kaewunruen, S.; Wu, L.; Goto, K.; Najih, Y.M. Vulnerability of Structural Concrete to Extreme Climate Variances. *Climate* **2018**, 6, 40.
- [16] Siddique R, Khatib J, Kaur I, "Use of recycled plastic in concrete: a review", Waste management, 2008, in press.
- [17] Ismail, ZZ., Al-Hashmi, E.A., "Use of waste plastic in concrete mixture as aggregate replacement", Waste management, 2008, in press.

ASSESSMENT OF QUALITY OF DIFFERENT AGGREGATES FOR ROAD CONSTRUCTION IN THE CENTRAL DIVISION OF FIJI

Atinesh Vijay Prasad, Darga N Kumar
Fiji National University. Suva, Fiji

ABSTRACT

Fiji is one of the developing countries in the Pacific region and road upgrading has been one of its major focus in the recent years to ensure access to both, rural and urban areas to achieve its development goals. A huge amount of the national budget is specially allocated every year towards maintenance and upgradation of roads in Fiji. One of the challenges facing contractors is sourcing sufficient quantities of good quality aggregates for road construction. Thus, this paper presents the study of the quality of aggregates available for road construction and check if these materials were conforming to the specifications set out in the standards. The test results of different aggregate samples used for base and sub base courses in road construction in the Central Division of Fiji were obtained from one of the road contractors. Also, analysis has been made towards understanding their behavior on the ground as road material. From the assessments carried out through the results obtained, the characterization of aggregates with respect to their suitability to the road works is discussed and presented. This work enables the road engineer to identify a suitable aggregate which can give better life span for different environmental and traffic conditions of Fiji roads.

Keywords: Urban roads, quarry sites, aggregate characteristics, road stabilisation.

INTRODUCTION

Fiji is in the Melanesia, Oceania and covers a total area about 194,000 square kilometres of which around 10% is land. Fiji is the hub of the South West Pacific, midway between Vanuatu and Tonga. Fiji consists of 332 islands in the southwest Pacific Ocean about 1,960 miles (3,152 km) from Sydney, Australia. About 110 of these islands are inhabited. The two largest islands are Viti Levu (10,642 sq km) and Vanua Levu (5,807 sq. km). The population of Fiji was estimated to be 884887 people as of January 2017 census.

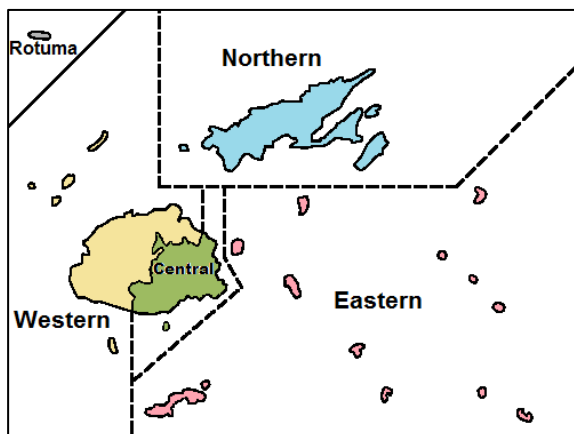


Fig. 1 Map of Fiji – Central Division, Fiji

Majority of Fiji's islands were formed through volcanic activity starting around 150 million years ago. The two larger islands are mountainous with peaks rising to 1300m. This results in a wet

windward southeastern side and a dry-season leeward western side thus central division of Fiji is usually subjected to huge amount of rainfall annually.

Through the various test pits conducted over the central division it is visible that most of the existing pavement is sub-standard with very high moisture content and plasticity index. This is because, the most common type of soil found in the subgrade layer of most roads in the Central parts of Fiji is black/grey soapstone and clay which is notably moist and semi firm. Even the Sub-base course contains a mixture of crushed and uncrushed brown mixed with black river gravel and the base course contains a combination of crushed mixed with uncrushed pink and black rocks.

To make it worse, continuous rainfall throughout the year contributes further towards the massive damages done to the roads. This is caused through the raise in water table and water logs which starts breaking the existing weak sub-base and base course over time due to vehicular loadings causing the layers to split allowing the clay from subgrade layer along with water to seep up to the top seal causing pot holes. Furthermore, the overloading of trucks has been a contributing factor for the rapid failures of roads in Fiji.

Sometimes recycled aggregates play a vital role to solve the construction related issues. The recycled materials market, comprised of reclaimed asphalt pavements, lightweight aggregates, fly ash, and quarry by-products. The recycling efforts are

extremely crucial to identify potential recycled/secondary materials and investigate their promising applications towards achieving sustainability especially in the road projects. [4] highlighted the importance of recycling in the transportation industry. Also reported that the sustainability aspects of ground improvement projects for pavement construction face difficult questions related to the engineering, socioeconomic and environmental aspects of the construction projects. [5]-[7] highlighted the need for performance-based specifications of the recycled materials for sustainable pavement design procedures. [6] presented a study of the case-specific geotechnical properties of quarry fines when used as embankment material in a limestone quarry. [8] reported that depending upon the gradation, larger sizes can be used in concrete mixtures as fine aggregate (sand) to occupy a large volume and in lateritic soil to improve its properties. [9] studied different recycled materials including RAP and ground granulated blast furnace slag (ggbfs) as pavement bases in full-scale accelerated pavement testing sections and reported that the ground ggbfs stabilised with blended calcium sulfate provided a cost-effective alternative to conventional pavement base materials.

The performance of a construction material can be considered as being influenced by a combination of internal factors, such as engineering characteristics, and external factors such as climate, construction methods and maintenance. Selection of materials cannot, therefore, be based solely on material character[1]. Some of the road environment factors impacting on road construction materials include; Climate – wet climate: seasonal and diurnal variations, rainfall intensity, evapotranspiration; dry climate: rainfall occurrences temperature variation; Hydrology – surface water run-off and drainage patterns, seasonal groundwater changes; Topography – high relative relief and steep terrain patterns relative to route alignment, low relative relief and flat terrain patterns relative to route alignment; Excavation and Processing – excavation and transport methods, crushing and sizing operations, stockpiling; Engineering Context – road section in embankment, road section in cut, road section in mixed cut and embankment; Construction Method – compaction plant and procedures, haul road and temporary works layouts, quality control procedures; Construction Method – compaction plant and procedures, haul road and temporary works layouts, quality control procedures; Road Maintenance Programme – good maintenance guaranteed likely to continue through design life of road, effective maintenance unlikely[1].

Through the governments initiatives to upgrade

these roads, the contractors are ensuring that the roads are build back better and to do this they need to use the right quality of aggregates replacing the sub-standard existing pavement layers. However, due to limited source/quarries available in the Central Division, these contractors face a lot of challenges in terms of aggregate quantity and quality.

Nevertheless, for any contractor awarded the contract, they must ensure quality assurance checks are done at every stage. Thus, this paper will discuss on the different quality checks done on the aggregates from different suppliers to ensure it meets the specifications before being used.

METHODOLOGY ADOPTED

Testing of materials is central to cost-effective road design, construction and performance and as such will be integral to any road project. To be effective, materials testing programmes should be considered not only to the selection of appropriate tests but also such factors such the capacity of the laboratory and staff to undertake the tests and quality manage the data produced. Any laboratory can produce numbers; it is the mark of good laboratory to translate these data into believable and useful project information.

The Fiji Roads Authority requires all its contractors to ensure that any aggregates used for the repair/remake of roads in Fiji meets the specifications as outlined in Transit New Zealand M/4:2006 and Public Works Department (Fiji) standards.

All sampling and testing needs to be performed by an IANZ Accredited laboratory. There are many approaches that can be taken to repair/remake road sections. Upon the test pit assessment, it is decided if the existing road materials are good enough to be reused and if so, they can be modified through the latest techniques (Cement Stabilisation, KOBM Stabilisation, Foam Bitumen Stabilisation) to improve its quality. But, in cases where the existing materials are found to have badly deteriorated over time, they could be replaced with a standard AP 65(All Passing 65mm sieve) crushed aggregate for basecourse and AP 40 (All Passing 40 mm sieve) crushed aggregate for sub-basecourse. Thus, this paper will focus on the scenarios where the construction requires complete replacement of the existing base and sub-base course aggregates. Fig. 2 presents the flow chart of aggregate testing. The Public Works Department (Fiji) standard clearly states that the aggregate source with Sedimentary rocks shall not be used for production of crushed rock base. Igneous or Metamorphic rocks shall be used provided its test results are within the

acceptable figures. The aggregates shall be broken or crushed from either: waterworn gravel; quarried rock or from other sources. Source material shall consist of hard, sound material of uniform quality, free from soft or disintegrated stone or other deleterious material. Source properties shall be sampled and tested at a rate of at least one sample for every 10,000 m³ of source material.

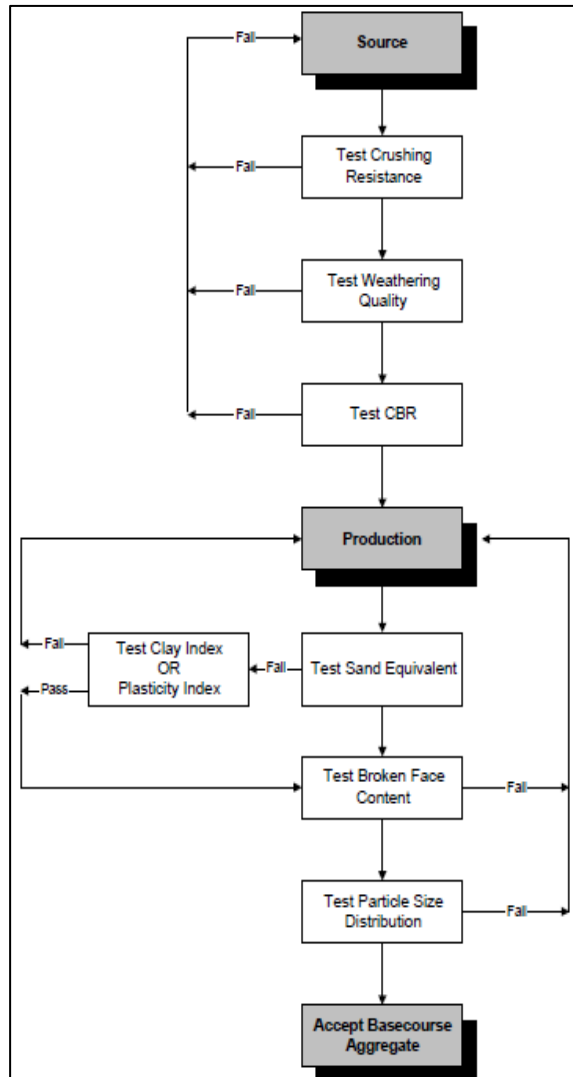


Fig. 2 Flowchart for Aggregate Tests [2].

As per the main contractor responsible for the repair/remake of the roads in the Central Division of Fiji, there are limited quarry sites available within the division which supplies good aggregates for road construction. Thus, two quarry sites were selected to study the aggregate quality for this paper.

The various test results were obtained for these sites to make a comparison and check if it meets the specifications of the Transit New Zealand M/4:2006 and Public Works Department (Fiji) standards [2]-[3]. The following test results were studied; Los

Angeles Abrasion Loss, Liquid Limit, Plasticity Index, Sand Equivalent, Californian Bearing Ratio, Flakiness Index, Grading and Maximum Dry Density.

RESULTS

The Table 1 and 2 presents the soil and aggregate results for both the quarry sites as per the AP40 (All Passing Through 40 mm Sieve) and AP65 (All Passing Through 65 mm Sieve). The particle size distribution curves are presented in Figs. 5 to 7 as per the AP65 and AP40 for both the sites. From the results, the aggregate is mixed with certain portion of soil, but it is non-swelling nature.

Table 1 Test Results for the two Quarry Sites

Tests	Accepted	Site 1	Site 2
Abrasion	AP 40: max 30	16.1	18
Loss	AP 65: max 35	25	-
Liquid Limit	AP 40: max 30	25	21
	AP 65: max 40	28	-
Plasticity	AP 40: 2-6	7	6
Index	AP 65: 2-12	np	-
Sand	AP 40: min 50	60	37
Equivalent	AP 65: min 50	35	-
Californian	AP 40: min 80	66	82
Bearing	AP 65: min 30	65	-
Ratio	AP 40: max 35	23	11
Flakiness	AP 65: max 35	20	-
Index	AP 40: Lab	2.003	2.200
Maximum	MDD		
Dry Density	AP 65: Lab	2.004	-
	MDD		

Table 2 Particle Size Distribution for two Quarries

Sieve Size (mm)	Percentage Passing			
	Site 1 AP 65	AP 40	Site 1 AP 40	Site 2 AP 40
63.0	100			
37.5	64	100	100	100
19.0	37	66-81	68	72
9.5	19	43-57	45	50
4.75	12	28-43	33	35
2.36	8	19-33	28	27
1.18	6	12-25	22	20
0.600	4	7-19	18	15
0.300	3	3-14	15	11
0.150	1	0-10	12	8
0.075	0	0-7	9	6

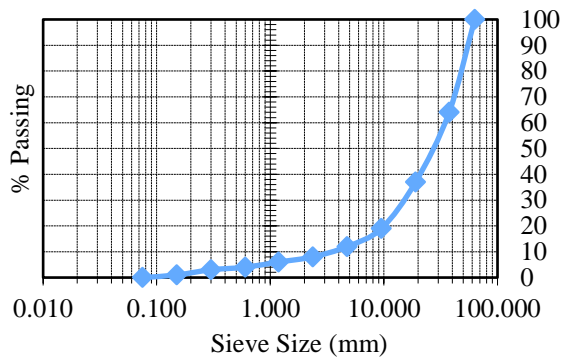


Fig. 3 Site 1 AP 65 - PSD Curve

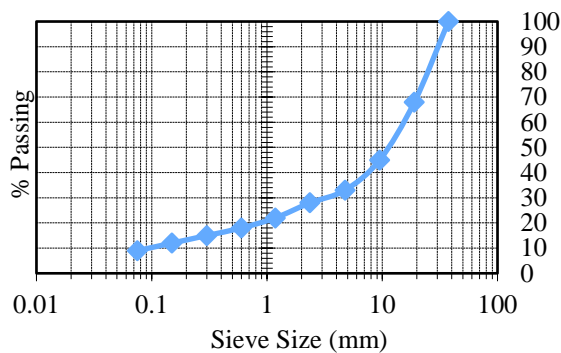


Fig. 4 Site 1 AP 40 - PSD Curve

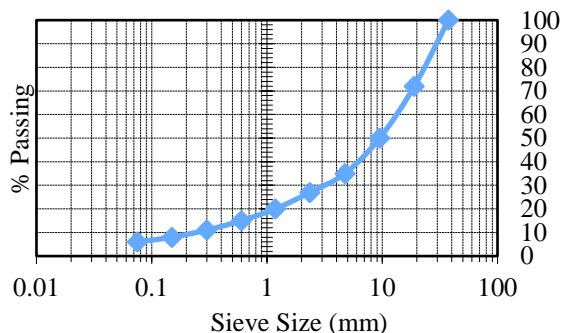


Fig. 5 Site 2 AP 40 - PSD Curve

DISCUSSIONS

Pavements are typically constructed in distinct layers, with each layer serving a purpose in the overall pavement structure. While focusing on the assessment of different quality of aggregates this section shall also discuss the following: existing pavement layers, types of pavement failures and its causes and fixing sub-standard base course – pavement modification and stabilisation.

Existing Pavement Layers

Through the several test pits in central division over the years, it can be said that one of the major

causes of pavement failures is because the pavement material has degraded over time.

Common Existing Base (Fig. 6): It consists of 40-65 mm brown mixed with black crushed river gravel with high contents of fine particles and inadequate broken faces. Some cases also show 40 mm crushed pink stones which is no longer recommended on Fiji roads due to low crushing resistance property compared to the black aggregates.



Fig. 6 Existing Base Material

Common Existing Subbase (Fig. 7): It consists of 65 mm crushed black/pink basalt mixed with crushed brown rocks. In most cases the sub base contains a lot of fines and is mixed with some uncrushed material. Some sections also show yellow coral – nominal size of 100 mm which has proven to be firm when compared to the pink/brown crushed aggregates. Common Existing Subgrade (Fig. 8): Almost all the roads in the central division have either grey/black/brown soap stone as its subgrade. The black/grey soapstone has proven to be more firm compared to the brown ones.



Fig. 7 Existing Subbase Material



Fig. 8 Existing Subgrade Material

Types of Pavement Failures on Existing Roads and its Causes

The primary failure mode for most of the road sections is varying proportions of poor historic maintenance, surfacing failure and moisture sensitive basecourse. The very poor condition of the road surfaces suggests that the basecourse materials are highly moisture sensitive and have degraded due to poor surfacing integrity/maintenance. The basecourse may not be providing sufficient stiffness to avoid overstressing the surfacing which is extremely fatigued due to one or all: lack of reseal in a timely manner, oxidization of the bitumen, inadequate shear strength of the basecourse. The fatigued surfacing combined with the moisture sensitive basecourse aggregate and poor surface shape results in rapid deterioration once the surface integrity is compromised.

There may be some subgrade strain type failure where the pavement has inadequate cover to subgrade. The existing pavements has insufficient aggregate thickness to limit subgrade strains and provide confidence that the design traffic can be accommodated for all load cases. The numerous patches and subsequent patches within patches, cracked surfacing and this combined with the flat cross fall and poor drainage path to both kerb and channel and side swales/shoulder drainage is contributing to the poor performance of most roads.

Fixing Sub-standard Base Course – Pavement Modification and Stabilisation

The recommended rehabilitation involves addressing the area of inadequate pavement depth, correcting geometrics/drainage path, overlaying and rejuvenating insitu basecourse materials, constructing a robust waterproof surfacing and implementing an appropriate surfacing maintenance through the design life to ensure seal integrity. In some cases, it becomes necessary to do a full depth construction whereby the existing deteriorated materials and removed and replaced with new good quality aggregates which is mostly the base course layer. In other cases, the existing base course might not be of the required depth. So, the additional depth of aggregates is overlaid on the existing layer and constructed.

Quality of Aggregates Through Test Results from Selected Quarries

As shown in Table 1, there are no test results for AP 65 from Site 2. The respective test results as stated in Table 1 and Figures 3, 4 & 5 shall be

discussed below.

Los Angeles Abrasion

The abrasion loss indicates the aggregates toughness and abrasion characteristics that helps to determine how the aggregate will perform with traffic loads if it is used as a base or subbase in road constructions. It is evident that the materials from both the quarries are achieving a percentage abrasion loss that is within the acceptable limits.

Atterberg Limits (Liquid Limit and Plasticity Index)

While the liquid limit values are all within the acceptable range, the plasticity index is out of range for both, AP 40 and AP 65 at Site 1. These tests are very important for any materials used in road construction as it gives an idea as to how the aggregates will perform with the variation in water content.

Sand Equivalent

While sand needs to be present in the road aggregates to aid in underground water drainage, silt/clay is avoided as it promotes water logs within the pavement layers causing failures. Thus, sand equivalent is another important test to be done on aggregates before they are used in road construction. The test results as shown in Table 1 are not too favourable except for the AP 40 at Site 1.

Californian Bearing Ratio

When roads are designed, it is designed to a certain traffic loading and during the construction, it needs to be ensured that the right type of aggregates are used for the base and subbase so that it withstands the vehicular loadings. The Californian bearing ratio test is used to verify this and as per Table 1, the CBR value for AP 40 from Site 1 is not within the acceptable limits.

Flakiness Index

This again serves as one of the key tests for base and subbase materials because the aggregates need to be of the right shape so that it can interlock with each other to provide a strong bond that can sustain vehicular loadings without collapsing/breaking. The test results from both the sites as shown in Table 1 are evidently within the acceptable limits.

Particle Size Distribution

As shown in Table 2, the AP 40 from both the quarries are falling within the acceptable percentage passing range except for a slight off limit in the finer

sieve sizes for Site 1. This is clearly shown in Fig 4. The AP 65 from Site 1 is also showing off the limits on the larger sieve sizes which is evident in Fig 3 as well.

SUMMARY

Based on the test results for a small sample from the two selected quarry sites, it has been noted that the aggregates produced are almost meeting the specifications to be given an endorsement to be used as road construction materials in the base and subbase pavement layers but with minor alterations subject to the designs. Adding on, there is not many quarry sites available within the central division that would give a variety of options to choose the best grade of aggregates.

To make it worse, these quarries are not located in the hub of the division which makes it difficult as there are massive cartage costs in getting the materials on sites. Adding on, huge truck loads carrying aggregates for about 90-130 km from the quarries to the sites impact the existing road network due to excessive vehicular loadings. This also consumes a lot of time in carting the aggregates to site and/or stockpiling it close to the site so that there are no delays during the actual construction phase.

As discussed earlier, the existing pavement layers are generally having inferior quality of materials due to its degradation over time and if there is a bad base, it will require good materials to upgrade the roads. Thus, it is a challenge for the road contractors to find enough good quality aggregates. Shortage of sufficient quantity of good aggregates is probably one of the reason why the country has opted the latest pavement treatment techniques whereby these existing materials which is not fully meeting the specifications are modified to get the end strength of the pavement layers as per the designs.

A good quality aggregate will lead to a good base of a pavement and a good base will give the pavement a good life span. Using quality/standard materials for pavement repair/reconstruction increases the strength of pavement allowing it to hold the vehicular loads that it is designed for a good number of years. It also reduces the risk of early failures which means no maintenance will be required thus, reducing the costs. Therefore, it becomes the responsibility of the road contractors to ensure proper quality checks are done on any newly produced aggregates before it is used in the construction.

CONCLUSION

However, in the central division of Fiji or in the entire country, neither the existing pavements are good due to overtime degradation nor there are enough good aggregates available. So, the following methods are used to modify/repair the existing pavement sections so that it can last for the next few decades with a massive increase in the number of vehicles in the country; Cement Stabilisation, KOBM Stabilisation and Foam Bitumen Stabilisation. Also, recyclable material technology which can provide sustainable road construction can be established in Fiji Islands.

ACKNOWLEDGEMENT

Sponsor - Ba Provincial Holding Company Limited

REFERENCES

- [1] Transport Research Laboratory, Infrastructure and Urban Development Division (IUDD), Department for International Development (DFID), Guidelines on the selection and use of road construction materials, pp. 5-1.
- [2] Transit New Zealand, Specification for Basecourse Aggregate, pp. 1-15.
- [3] Public Works Department, Section 301 – Materials for Pavement Construction, pp. 1-4.
- [4] Ellis SJ (2003). Recycling in transportation. In Transportation Geotechnics (Frost MW, Jefferson I, Faragher E, Roff TEJ and Fleming PR (eds)). Thomas Telford, London, pp. 177–188.
- [5] Fleming PR, Rogers CDF, Thom NH and Frost MW (2003). A performance specification for pavement foundations. In Transportation Geotechnics (Frost MW, Jefferson I, Faragher E, Roff TEJ and Fleming PR (eds)). Thomas Telford, London, pp. 161–176.
- [6] Fraser J and McBride RA (2002). The utility of aggregate processing fines in the rehabilitation of dolomite quarries. Land Degradation and Development 11: 1–17.
- [7] Lambert P, Fleming PR and Frost MW (2006). Material testing for sustainable pavement foundation design. Proceedings of the Institution of Civil Engineers, Construction Materials 159(4): 139–146.
- [8] Soosan TG, Jose BT and Abraham BM (2001). Use of quarry dust in embankment and highway construction. In Proceedings of Indian Geo-Technical Conference, Indore. New Phoenix, New Delhi, India, pp. 274–277.
- [9] Tao M, Zhang Z and Wu Z (2008). Simple procedure to assess performance and cost benefits of using recycled materials in pavement construction. Journal of Materials in Civil Engineering, ASCE 20(11): 718–725.

DEVELOPMENT OF CARBON FIBER REINFORCED THERMOPLASTIC STRAND ROD

Y Mochida¹, Y Imoto¹

¹Graduate School of Science and Engineering, Ritsumeikan University, Japan

ABSTRACT

The purpose of the main research is to develop a more linear shape structural member using Carbon Fiber Reinforced Thermoplastic composite material. This paper will discuss the production stage begin with the instrumentation and machinery used in manufacturing, material selection for manufacturing the three layer basic structure, and some improvement especially in material strength such as the tensile strength. In the process, fiber content and cavity ratio test, tensile strength test, alkali resistance test, temperature dependency test, weather resistance test, etc. is performed. Products that satisfy the expected performance were applied to actual construction project. However, Carbon fiber composite materials are not included in designated building materials in the Japanese building standard. Therefore, it is difficult to apply the carbon fiber composite material in building construction in the present. An example case on real project, carbon fiber composite materials used in structural member into the earthquake (horizontal) force resistant members.

Keywords: CF RTP, thermoplastic, structural performance, seismic reinforcement

INTRODUCTION

Carbon fiber reinforced thermoplastic resin (CF RTP) strand rod is known as a lightweight and sturdy material and when it is used as construction material, it will give benefits such as in cost and construction period reduction because of it does not need heavy equipment in the installation process. However, there are also disadvantages such as high material cost of carbon fiber and low fire resistance. It is also not been recognized yet by Japanese Standards as a construction material, therefore its utilization in construction practices is limited.

Measurement tests on basic performance of materials in the development process are conducted in this research, with purpose to understand the structural performance required for CF RTP. The observed structural performance is used in actual project, using CF RTP as material for seismic reinforcement. Carbon fiber (CF RTP) material used in this research is carbon fiber composite material Torayca® T700SC shown by Figure 1.

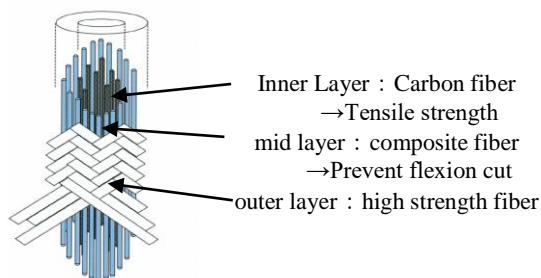


Fig. 1 Structure of Carbon Fiber

VERIFICATION OF MATERIAL PERFORMANCE

Fiber Volume Content (VF)

Volume content (V_f) is measured by performing combustion process shown by Figure 2. Tests were conducted based on the fiber content and cavity ratio test method of carbon fiber reinforced plastic as recommended by JIS K 7075. The volume content can be calculated by:

$$V_f = W_f \cdot \frac{\rho_c}{\rho_f} \quad (1a)$$



Fig. 2 Volume content measurement

$$V_f = W_f \times \rho_c / \rho_f = 82.62 \times 1.33 / 1.8 = 61.1 (\%)$$

Specimen density $\rho_c = 1.33$ (g) Carbon fiber density $\rho_f = 1.8$ (g)

Volume content of carbon fiber in the CF RTP used in this study was 61.1%, therefore, the ratio of the resin contained in CF RTP was 38.9%.

Tensile Strength Test

Tensile strength test was performed to understand the performance of CF RTP based on its tensile

strength, standard deviation, and rigidity. Specimen used in the test listed in Table 1 and the test results for each specimen shown by Figure. 3 to Figure. 6 (each Figure shows maximum load on top left, histogram of rigidity on top right, and stress-strain relation on bottom).

a) Experiment Result of Specimen No. 1

The average of the maximum load P_{max} is 62.19 kN, with standard deviation σ_p of 3.74, and the average of the stiffness k is 75.1 kN / mm, with standard deviation σ_k of 11.9. The number of carbon fibers is 4.8×10^5 pieces, and the cross-sectional area of the carbon fiber is 18.33 mm².

Standard deviation obtained from this specimen is the largest compared to others and it probably caused by shape of CFRTP. Bundled carbon fiber material was manually cut and introduced into resin, and the tip was processed into tea whisker shape.

b) Experiment Result of Specimen No. 2

The average of the maximum load P_{max} is 40.39 kN, with standard deviation σ_p of 3.28, and the average of the stiffness k is 5.93 kN / mm, with standard deviation σ_k of 0.22. The number of carbon fibers is 2.4×10^5 pieces, and the cross-sectional area of the carbon fiber is 9.17 mm².

Standard deviation for both of the maximum load and the rigidity resulted is smaller than that resulted in the specimen No. 1. This is may be caused by the manufacturing process of specimen no. 2. Unlike specimen no. 1, specimen no. 2 was manufactured using machinery.

c) Experiment Result of Specimen No. 3

The average of the maximum load P_{max} is 56.33 kN, with standard deviation σ_p of 1.71, and the average of the stiffness k is 4.20 kN / mm, with standard deviation σ_k of 0.16. The number of carbon fibers is 2.4×10^5 pieces, and the cross-sectional area of the carbon fiber is 9.17 mm².

Standard deviation resulted was the smallest among specimens no. 1, no. 2 and no. 3 (all of three specimens are straight shaped carbon fibers). Small standard deviation resulted in this specimen might be caused by improvement of accuracy in manufacturing process. Outer layer of carbon fibers were made from PET fiber to glass fiber.

d) Experiment Result of Specimen No. 4

The average of the maximum load P_{max} is 87.22

Table 1. Specimen used in tensile strength test and results

No.	Production	Configuration	Outer layer	Edge	Amount for test	Ply/twist
1	Manual	20 pieces of 24K	PET	No	52	No
2	Manufactured	1 pieces of 24K $\times 10$	PET	Yes	57	No
3	Manufactured	1 pieces of 24K $\times 10$	Glass	Yes	100	No
4	Manufactured	3 pieces of 24K $\times 7$	Glass	Yes	400	Yes

Carbon fiber: Torayca®T700SC Jig: Twist cutting steel pipe

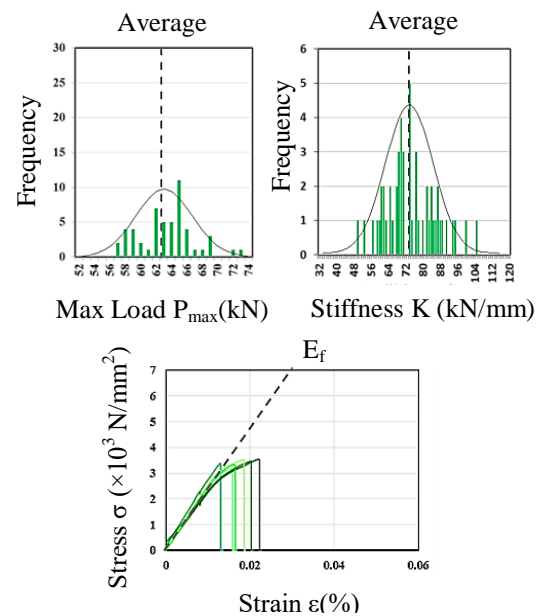


Fig. 3 Tensile test result of specimen No. 1

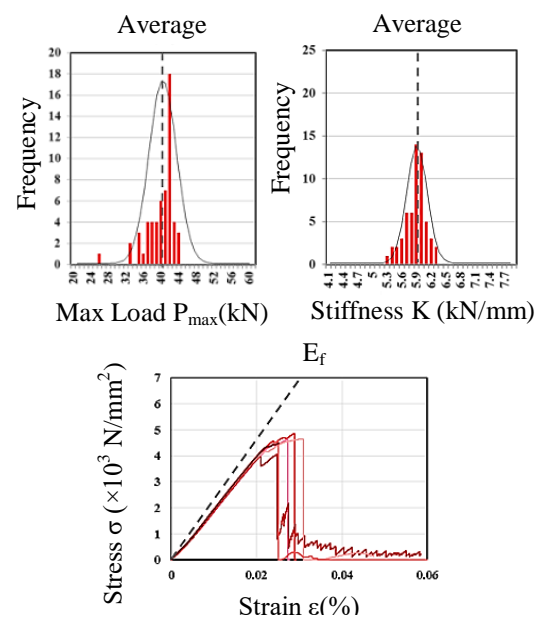


Fig. 4 Tensile test result of specimen No. 2

kN, with standard deviation σ_p of 4.25, and the average of the stiffness k is 8.81 kN / mm, with standard deviation σ_k of 0.82. The number of carbon fibers is 5.04×10^5 pieces, and the cross-sectional area of the carbon fiber is 19.25 mm².

Standard deviation resulted was bigger than that resulted in specimen no.3. This might be caused by the variation due to the shape of the specimen, which was manufactured in the twisted shape.

e) The evaluation value σ_{cu} of the reinforcing material tensile strength was calculated from the following formula (1 b)

$$\sigma_{cu} = V_f \sigma_f \left(1 + \frac{1 - V_f}{V_f} \cdot \frac{E_m}{E_f}\right) \quad (1b)$$

Fiber Volume Content $V_f = 0.611$

Fiber Tensile Strength $\sigma_{fu} = 4900$ N / mm²

Matrix elastic modulus $E_m = 2770$ N / mm²

Fiber elastic modulus $E_f = 23500$ N / mm²

f) The average tensile strength $av\sigma_{cu}$ of only the fibers was calculated from the following formula (1c)

$$A_e = \frac{t_c}{d_c} \cdot n \quad (1c)$$

Fineness $t_c = 1650$ g / 1000 m

Density $d_c = 1.8$ g / cm³

n = Number of fibers

g) Design standard strength $d\sigma_{cu}$ was calculated from the following equation (1 d)

$$d\sigma_{cu} = (av\sigma_{cu} \cdot \alpha \cdot \sigma) \cdot \gamma_b \quad (1d)$$

$av\sigma_{cu}$ = The calculated average tensile strength

α (coefficient of reduction) = 3.1

σ_p = Standard deviation

γ_b (safety factor) = 0.9

Comparison of the tensile strength test result between CFRTP specimens and steel material is shown in Table 2. Maximum tensile force of specimen no. 4 (7 bundles of 24k 3 pieces) is appeared to be the same for maximum tensile force resulted from tensile strength test of PC steel. The effective strength of the carbon fiber of specimen 1 is $3,393 / 4900 = 0.69$ and this strength arises due to the addition of strength from glass fiber.

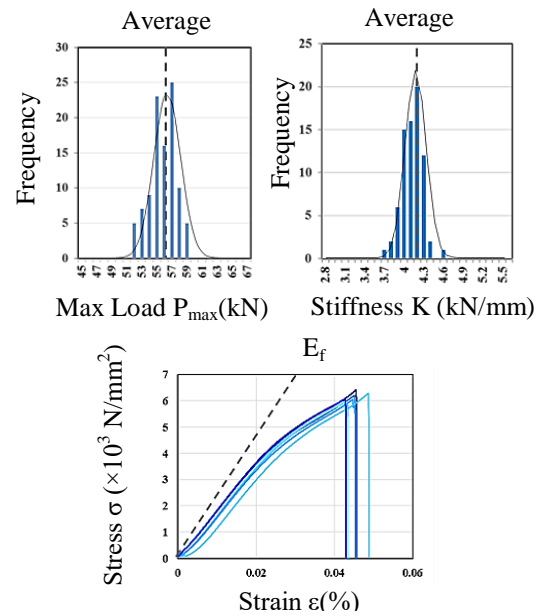


Fig. 5 Tensile test result of specimen No. 3

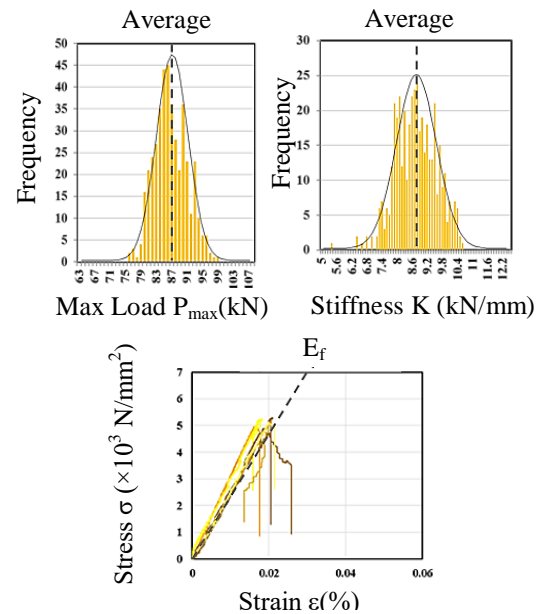


Fig. 6 Tensile test result of specimen No. 4

Table 2. Comparison with steel material

Name	Diameter mm	Area (Carbon fiber) mm ²	Max Load kN	Tensile strength N/mm ²	Design strength N/mm ²
No. 1	6.9	18.33	62.19	3,393	3,302
No. 2	9.4	9.17	40.39	4,405	3,987
No. 3	9.4	9.17	56.33	6,143	5,508
No. 4	9	19.25	87.22	4,531	4,048
Seven pieces twisted PC steel wire "	9.3	51.6	88.8	1,720	1,548

Thermal Expansion Coefficient

Observation of strength and thermal characteristics of CFRTP was conducted in this study using specimens listed in Table 3. Prior to the test, specimens were kept for 24 hours or more at a temperature of 20 ± 2 °C. and a relative humidity of $65 \pm 5\%$ according to Standard temperature state class 2 and standard humidity state class 2 (JIS K 7100), then stored for another 48 hours at the measurement maximum temperature. Measurement conditions for measurement of thermal expansion coefficient are in accordance with Test method of thermal expansion coefficient by thermo mechanical analysis of continuous fiber reinforcement (draft) (JSCE-E 536-1995). From the result of the measurement of the thermal expansion coefficient, contraction starts when temperature exceeding 50 °C. This is considered to be caused by dehydration caused by dehydration and desolvation. Heat treatment is necessary as a pretreatment from this occurrence. Based on the relationship between thermal expansion coefficient measurement and pretreatment time, the specimens pretreated at 70 °C were stable at 1.64 to 1.98×10^{-6} / °C. The processing time is considered to be sufficient for 12 hours. The thermal expansion coefficient of the carbon fiber strand rod is less than 2×10^{-6} / °C. The thermal stability of CFRTP is higher than that of steel materials and concrete as shown by Table 4.

Alkali Resistance Test

Alkali resistance test of CFRTP was performed measurement of changes in appearance and maximum tensile load of the specimen after dipping in an aqueous alkaline solution. Alkaline concentration should be pH13 or higher and immersed at 60°C for 28 days. Test conditions conform to Alkali resistance test method for continuous fiber reinforcement (draft) (JSCE-E 538-1995). The test was performed using 5 specimens listed in Table 5. Table 6 shows the results of tensile strength test, and Figure. 7 shows comparison of strength development. It was confirmed that the tensile strength after immersing in an alkaline solution at a pH of 13 or more was retained to be proof stress of more than 70%. Since the glass fiber used for the outer layer of No. 5 is a general-purpose type, it is very likely that about 30% reduction in strength was observed. Therefore, alkali-resistant glass is considered to be superior in concrete composite materials.

Temperature Dependence Test

Temperature dependency of tensile strength is confirmed by measuring tensile strength based on the condition of the specimens. Specimens used in

Table 3. Thermal expansion test and test specimen

Carbon fiber	Carbon fiber 24K, 20 pieces (T700SC-24000)
Outer layer	PET1000d×2 pieces×12 strokes
Impregnation resin	Thermoplastic epoxy resin

Table 4. Thermal expansion coefficient of each material

Material	Thermal expansion coefficient ($\times 10^{-6}/^{\circ}\text{C}$)
Epoxy	55~60
Steel	12
Concrete	7~13

Table 5. Alkali resistance test and test specimen

No.	Outer layer of fiber
1	PET fiber 1100dtex 1×1×8 strike
2	Aramid fiber 1670dtex 1×1×8 strike
3	Aramid fiber 1670dtex 1×1×8 strike
4	PET fiber 1100dtex 1×1×8 strike
5	Vynylon fiber 1100dtex 1×1×8 strike
6	Glass fiber75 1/3 3.8S 1×1×16 strike
	Basalt fiber 4000dtex 1×1×8 strike
	Carbon fiber structure: 24K 1 pieces ×10 pieces with 300mm length
	End/tip part (outer layer): exist, fixing resin: UM890-T80
	Steel pipe nipple: diameter 14mm/20mm, with length of 120m

Table 6. Alkali resistance test: tensile strength test result

No	Average value of maximum load	
	Before impregnated	After impregnated
1	34.39	30.45 (88.5%)
2	53	52.72 (99.5%)
3	47.88	45.06 (94.1%)
4	44.16	42.69 (96.7%)
5	56.42	40.34 (71.5%)
6	57.55	42.8 (74.4%)

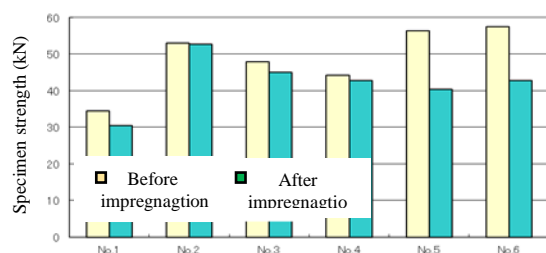


Fig. 7 Comparison of strength development

the test are listed in Table 7. The test conditions are based on ASTM D 3090, where the test temperature shall be at -20 °C, 23 °C, 50 °C, or 82 °C. The results of the tensile strength test are shown in Table 8 and the displacement of the maximum load by the ambient temperature is shown in Figure. 8. The maximum load decreases as the ambient temperature rises. It is considered that it might be caused by the effect of temperature to the thermoplastic resin in the CFRTP.

Weather Resistance Test

Weather resistance performance test is conducted by performing tensile strength test after accelerated exposure test using specimens listed in Table 9. The test conditions are in accordance with Promotional exposure test method for plastic building materials (JIS A 1415), and perform accelerated exposure test using sunshine weather meter and metering weather meter. Tensile strength test results of the specimens using the sunshine weather meter and metering weather meter are shown by Table 10 and Table 11 respectively. The sunshine weather meter 2000 hours (equivalent to 10 years), Metering ring weather meter 500 hours (equivalent to 50 years). There was almost no decrease in strength in the tensile strength test after exposure.

CONSTRUCTION CASE

Case Study

CFRTP of No. 4 listed in Table 1 is used is actual seismic retrofit project of a building, which was a three-story office building built in 1968. Figure. 9 and Figure. 10 show the exterior reinforcement and interior seismic reinforcement respectively. The building geometrically regular (no eccentricity) and the structure is a rigid frame structure, with general information as follow.

Project name: Seismic retrofit/ repair work of the K

head office building

Total floor area 2777 m²

Building area 959 m²

Floor configuration: 0 Basement 3 Floors above ground

Structure type: Reinforced concrete Construction

period: From February 12 to November 10, 2015

Seismic Retrofit

This building was designed in compliance with earthquake resistance standard at the time of construction, however it was judged to be questionable on seismic resistance on the first and second floors in the X direction and the whole Y

Table 7. Temperature dependent test and test specimen

Structure of carbon fiber	24K 1 pieces ×10 pieces
Outer layer	Glass fiber
Specimen number	3
Fixation resin	UM890-T90
	Curing time: 23°C 1h+100°C 1h
Fixation jig	Steel pipe nipple

Table 8. Temperature dependent test and tensile strength test

Temperature	Failure mechanism	Average value of max. load
-20°C in the atmosphere	Base material failure	56.64
23°C in the atmosphere	Base material failure	55.86
50°C in the atmosphere	Base material failure	52.83
82°C in the atmosphere	Base material failure	35.88

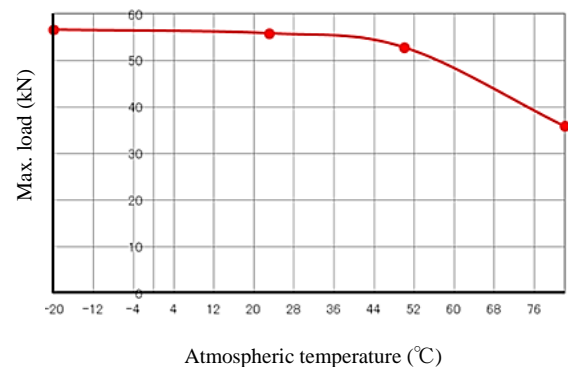


Fig. 8 Atmospheric temperature and maximum load

Table 9. Temperature dependent test and test specimen

No.	Outer layer of fiber
1	PET fiber 1100dtex 1×1×8 strike
2	Aramid fiber 1670dtex 1×1×8 strike
3	Aramid fiber 1670dtex 1×1×8 strike
4	PET fiber 1100dtex 1×1×8 strike
5	Vinylon fiber 1100dtex 1×1×8 strike
	Glass fiber 75 1/3 3.8S 1×1×16 strike
Carbon fiber structure: 24K 1 pieces ×10 pieces	
Fixing resin: UM890-T90	
(Curing condition: 23°C 1h+100°C 1h)	
Steel pipe: Threaded steel pipe	
(φ: 14mm/20mm, length 120mm)	

direction after various examination on appearance observation, drawing collation, concrete strength, and the concrete neutralization. Therefore, seismic retrofitting is necessary for the first and second floors in the X direction and all floors in the Y direction.

Since CFRTP is a very high-strength material, it has a performance that can be used in seismic retrofit of the entire building. Initially, it was considered to retrofit to building entirely using CFRTP, however, due to authorization limitation, CFRTP is used as an addition to conventional retrofitting to such as structural walls and slit dampers.

SUMMARY

In this research, CFRTP with more linear shape has been developed and used as a construction material. Starting with the development of materials manufacturing machinery, it was possible to produce materials with the required performance, focusing on the tensile strength development of the CFRTP material in the three-layer structure. However, the application of CFRTP material is still a challenge because it is yet to be used as construction material due to limitation by Japanese Building Standard. This research is expected will be useful as a pioneering effort to make high-strength fiber composite materials widely used in the future and future research in material improvement such as fire resistance is recommended.

ACKNOWLEDGEMENTS

This research is the development of a manufacturing apparatus for CFRTP rods, the project to promote the location of innovation in 2012 (example of development of facilities such as demonstration and evaluation of enterprises): Ministry of Economy, Trade and Industry 2012/07 - 2014 / 03

REFERENCES

- [1] Maeda Yutaka: cutting edge technology of carbon fiber "Diffusion Edition", CMC Publishing, April, 2013
- [2] Yuzuka Yoshio: Carbon Fiber - Challenge to Complex Era -, Fiber Company, March, 2012
- [3] Design and Construction Guidelines for Concrete Structures Using Continuous Fiber Reinforcement (draft), Civil Engineering Society, September, 1996
- [4] Continuous fiber reinforced concrete structural design and construction guidelines, Japan Architectural Institute, April, 2002

Table 10. Sunshine weather meter results

No	Outer layer of fiber	Average value of max load	
		Initial condition	2000 hours
1	PET	34.39	37.42(109%)
2	Aramid	53.17	53.17 (100%)
3	Aramid/PET	46.92	46.92 (100%)
4	Vynylon	44.22	43.12 (97.5%)
5	Glass	56.42	51.68 (91.6%)

Table 11. Metaling weather meter results

	Average value of max. load	Failure mechanism
Initial condition	56.42 (100%)	Base material failure
100 hours	53.59 (95%)	Base material failure
500 hours	55.86 (99%)	Base material failure
Carbon fiber structure: 24K 1 pieces ×10 pieces outer layer: glass		



Fig. 9 Exterior Reinforcement

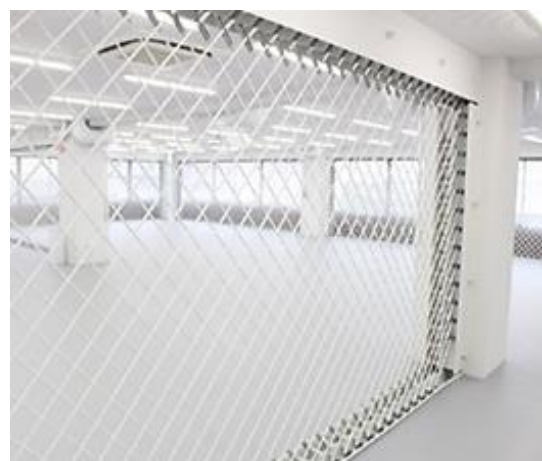


Fig. 10 Interior Reinforcement

QUICK ASSESSMENT PROCEDURES FOR TWO STORIES BUILDING BASED ON NUMERICAL SIMULATION RESULTS

Febrin Anas Ismail¹, Abdul Hakam¹, M Maisaquddus Hape², M Sofian Asmirza³

¹Engineering Fac., Andalas University, Indonesia; ² Civil and Environmental Engineering Fac.,
Institut Teknologi of Bandung, Indonesia, ³Engineering Fac., North Sumatra University, Indonesia

ABSTRACT

Quick assessment is one of an important step in emergency respond following an earthquake. This step is mainly purposed to estimate the financial lost based on the building damage criteria. The result of quick assessment is also needed to determine whether the damaged building can be repaired and reused or not. There are three damage level which is classified based on the building conditions after the earthquake. Based on the experience, there is a time constraint in the conducting the building assessment. Then a quick-correct method is very important to accomplish the task in the limited time. Base on the series of numerical simulation, the quick assessment procedure is proposed in this study. The structural elements that need to be checked in quick assessment are including column, beam, plate and foundation. The numerical result was conducted for number of two stories buildings with minimum reinforcement on those structural members. The minimum reinforcement requirements are base on Indonesia code SNI-1736-2012. The critical point of every structural components to be checked, especially columns, are discussed here.

Keywords: earthquake, quick assessment, non-engineered two story building, Indonesian code

1. INTRODUCTION

West Sumatra is a very earthquake prone province in Indonesia where great earthquakes has been experienced during last years in this century. In this province there are two big geological conditions that become the main source of seismicity. The first source is coming from the subduction boundary in the west part of the province. The subduction boundary takes place at convergent boundaries of tectonic plates of Asian continental and the Indian Ocean Plate on the western side of the West Sumatra province. The second source is the great fault of Sumatra that crosses along the middle of the Sumatra island. This fault called Semangko fault that takes place in the eastern part of the Province. Both seismic sources have caused big earthquakes that resulted damages in the West Sumatra province.

The first big earthquake that caused many construction damages in the West Sumatran island in this century is Singkarak earthquake that happened in 2005. This earthquake happened on the Semangko fault at Singkarak segment. The second big earthquake that includes destructive earthquakes in the West Sumatran island in this century is Bengkulu earthquake that happened in 2007. This earthquake also triggered one meter tsunami along the south part of West Sumatra province. The Bengkulu earthquake also resulted in liquefaction in several places [1]. Then the Padang earthquake in 2009 which resulted in liquefaction in many places in Padang [2]. In 2010, the Mentawai earthquake occurred on the west-

central side of the Sumatra island. This earthquake also caused a destructive tsunami in the Pagai island, the western part of West Sumatra province. The focus of last three earthquake is at the subduction zone. Those earthquake become the reason for the revising the Indonesian earthquake code [3].

All of big earthquakes in West Sumatra have resulted in the damage of many civil constructions including two storey structure buildings. During Padang earthquake in 2009, hundreds of two storey buildings have been damaged. The soil characteristics and the structure design is the main reasons why so many two storey buildings suffer from the earthquake. In this paper, the results of numerical simulation with take intention on soil characteristics and structural strength are discussed. The purpose of this study is for developing quick assessment procedures which is one of an important step in emergency respond following a big earthquake. This step is mainly purposed to estimate the financial lost based on the building damage criteria.

The other purpose of quick assessment is also determining the damaged building for reparation and re-occupation. There are three damage level generally introduced in Indonesia for classifying the building conditions after the earthquake. Based on the experience in conducting quick assessment, there is very important to accomplish the task in the limited time. Even the beam and the plate may be damaged by earthquake, but the column of the two storey building generally destroyed. Then in this discussion, the column capacity during the

design earthquake in Padang become the main point.

The study on the building assessment in terms of the vulnerability of reinforced concrete buildings against earthquake loads has been done by some researchers [4, 5]. This works indicate the importance of the building assessment related to the earthquake, especially in seismic prone areas.



Fig.1 Damaged building due to 2009 earthquake

2. NUMERICAL SIMULATIONS

It is very necessary to analyze the structure responses together with the soil in the same calculation named soil-structure interaction. This analysis has main advantage of having near real behavior of the structure related to the groin type. The modeling of soil structure interaction is done by some researcher [6, 4].

The soil characteristics in Indonesia earthquake code are categories in six sites. However, for general building purposes, there are only three categories are adopted, that are hard soil, medium and soft sites. Those three categories are differed based on the average of soil strength in terms either Standard penetration value, N_{spt} , Shear wave velocity, V_s , or, Soil strength, S_u . Those tree value are rewritten in Table 1.

Based on those values, the numerical simulation then are conducted with take the advances of soil-structure interaction methods. The data for the purposes of numerical analysis in this study was adopted from those values. The soil modulus parameters for the numerical analysis are calculated based on the following equation:

$$E = G \cdot 2(1+\mu) \quad (1)$$

$$G = \rho \cdot V_s^2 \quad (2)$$

Where G is the shear modulus of soil, ρ is the density and μ is the Poisson.s ratio.

Table 1. Site type based on soil characteristic [3]

Site type:	Hard	Medium	Soft
N_{spt} (blows)	> 50	15 - 50	< 15
V_s (m/s ²)	> 350	175 - 350	<175
S_u (kN/m ²)	>100	50-100	< 50

The results of the correlation calculations of the soil mechanic parameters for the numerical analysis are shown in Table 2.

Table 2. Average values of soil parameters

Parameter	Hard	Medium	Soft
Modulus, E (kN/m ²)	563500	265300	90000
Poisson's ratio, μ	0.4	0.3	0.25
q_u (kN/m ²)	200	150	80
Density, γ (kN/m ³)	18	16	14

The structural elements of building are design as reinforced concrete with the minimum reinforcement. This design then give the minimum capacity required for two storey building and will be discussed in the results section. The typical soil-structure interaction model for numerical simulation are shown in Fig. 2

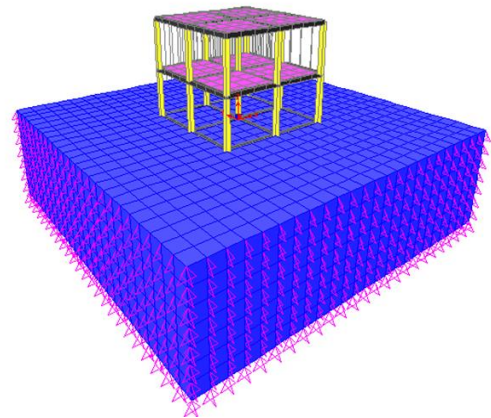


Fig. 2 Typical soil-structure model for analysis

3. ANALYSES AND RESULTS

In order to investigate the strength of the building against earthquake, finite element models of two storey structures the three types of ground types are constructed. The geometry of the finite element model shown in Fig. 2 has height of 3.5 m every level and 4.0m between columns.

The applied load on the models are the self weight load, life load and earthquake load. The earthquake load is adopted from the calculation results by Ministry of Public Service of Indonesia

as shown in Fig. 3.

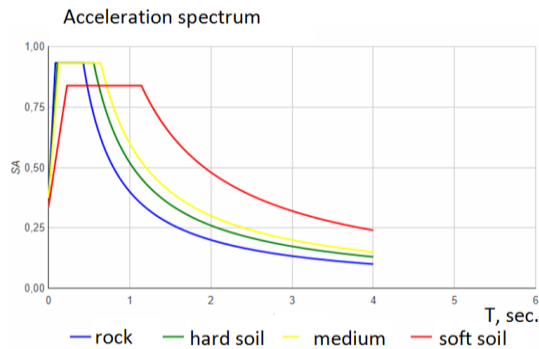


Fig. 3 Earthquake load for analysis

The displacement pattern due to the earthquake load is shown in Fig. 4. Meanwhile the typical internal moment is shown in Fig. 5. The value of displacement and internal forces due to the applied load are given in Table 3.

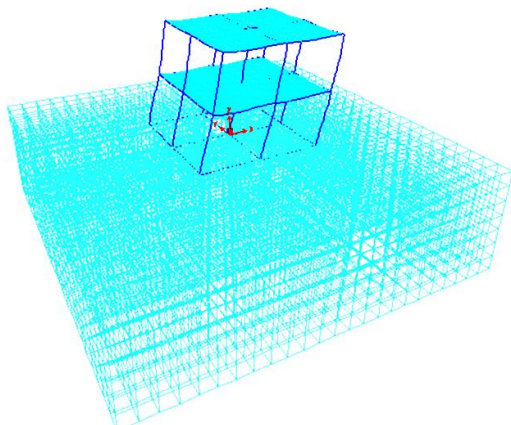


Fig. 4 Typical displacement of the models due to applied earthquake load.

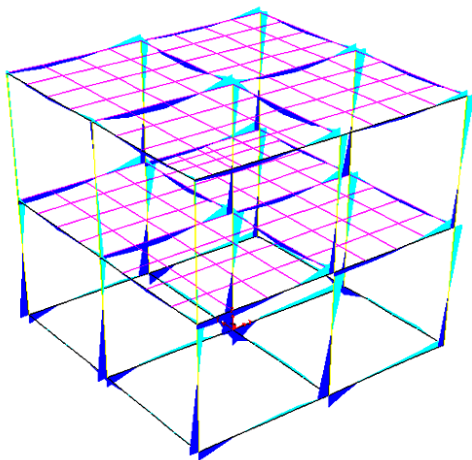


Fig. 5 Typical internal moment due to loads.

Table 3. Internal force values in column

Hard soil site			
Column position	Axial	Shear	Moment
Edge 2nd storey	-3497	306	-1068
Edge 1st storey	-5704	2876	5879
Side 2nd storey	-10455	-345	-977
Side 1st storey	-18904	2744	5800
Middle 2nd storey	-28915	2778	-5281
Middle 1st storey	-56483	4559	8236
Medium soil site			
Column position	Axial	Shear	Moment
Edge 2nd storey	-3661	208	-918
Edge 1st storey	-5973	2937	5918
Side 2nd storey	-10474	-490	-1261
Side 1st storey	-18821	2913	6132
Middle 2nd storey	-28095	2777	-5305
Middle 1st storey	-54976	4708	8429
Soft soil site			
Column position	Axial	Shear	Moment
Edge 2nd storey	-3990	-36	-569
Edge 1st storey	-6739	2720	5505
Side 2nd storey	-10625	-805	-1776
Side 1st storey	-19247	2761	5920
Middle 2nd storey	-27204	2506	-4807
Middle 1st storey	-53316	4359	7744

From the numerical results it can be seen that even though the applied earthquake loads for medium soil site and hard soil site are the same, but the response of the structure give different values. The medium site gives larger internal forces in general. Furthermore, the earthquake load applied to the structure in the soft soil is 10% less than the others. But the responses in terms of internal forces give bigger in some points.

The numerical simulations then will be compared to the strength of the structural element to give the idea for built the quick assessment procedure. This work is still under the investigation and will be report soon after it ready to be presented. However this preliminary results have given the idea to see the soil characteristic in the location of building during the investigating the building assessment, especially soon after the earthquake.

4. CONCLUSIONS

Padang is the capital city of the West Sumatra is a very earthquake prone city in Indonesia. The city has experienced from many big during last years in this century. There are two main sources of earthquake in Padang, first is coming from the subduction boundary in the west part and the second source is the great fault of Sumatra the eastern part. Many big earthquakes have resulted damages in the West Sumatra province from that sources.

In purpose of build quick assessment tool, it is very important to accomplish numerical simulations of typical building structures in the different soil type sites. two storey building generally destroyed by the earthquake, in this paper the earthquake loaded building in Padang become the main point.

The numerical results shows that for the medium soil site and hard soil site with the same load, give different responses of the structure. Furthermore, for the soft soil with 10% less earthquake load, the responses in terms of internal forces give bigger in some points. Even though this work is still under the further investigation but results have given the idea to see the differences in soil characteristic during the conducting the building assessment due to the earthquake.

5. ACKNOWLEDGEMENTS

The authors greatly express thank to our colleagues who have helped in the process of finishing this research.

6. REFERENCES

- [1] Aydan, Ö., Imamura F., Suzuki T., Ismail F.A., Hakam A., Masmera, Devi P.R., A Reconnaissance Report On The Bengkulu Earthquake Of September 12, Japan Society of Civil Engineers (JSCE) and Japan Association for Earthquake Engineering (JAEE) With the collaboration of Andalas University, October 2007
- [2] Hakam, A, "Laboratory Liquefaction Test of Sand Based on Grain Size and Relatife Density", J. Eng. Technol. Sci., Vol. 48, No. 3, 2016, 334-344
- [3] SNI-1736-2012, Indonesian Earthquake code, Indonesian Public Service Ministry, 2012
- [4] Wahyuni E., Vulnerability Assessment of Reinforced Concrete Building Post-Earthquake, Procedia Earth and Planetary Science, Volume 14, 2015, Pages 76-82
- [5] Sarmah T., Earthquake Vulnerability Assessment for RCC Buildings of Guwahati City using Rapid Visual Screening, Procedia Engineering Volume 212, 2018, Pages 214-221
- [6] Tumeo R., Soil-Structure Interaction Effects on the Seismic Performances of Reinforced Concrete Moment Resisting Frames Procedia Engineering Volume 199, 2017, Pages 230-235
- [7] Menglin L., Structure-Soil-Structure Interaction: Literature Review, Soil Dynamics and Earthquake Engineering Volume 31, Issue 12, December 2011, Pages 1724-1731

7. AUTHOR'S BIOGRAPHY

Dr. Febrin Anas Ismail is an Associate Professor in the Civil Engineering Department of Andalas University, Indonesia. He was graduated and got Master from Institute Technology of Bandung. His Doctor is from Yokohama University, Japan. His research interests include general problem in structural engineering and dynamics of structure. His contact E-mail is febrin@eng.unand.ac.id.

8. AUTHOR'S CONTRIBUTIONS

Dr. Febrin Anas Ismail: Conception, design, acquisition, final approval of the version to be submitted. Dr. Abdul Hakam: Conception, design, final approval of the version and submit the paper. Dr. M Sofian Asmirza: Critical reviewing, analysis. M Maisaquddus H: Summarizing and Interpretation of data as well as conducting numerical model.

9. ETHICS

This article is original and contains unpublished material. The corresponding author confirms that all of the other authors have read and approved the manuscript and no ethical issues involved.

COMPRESSED EARTH BLOCKS WITH POWDERED GREEN MUSSEL SHELL AS PARTIAL BINDER AND PIG HAIR AS FIBER REINFORCEMENT

Bernardo A. Lejano¹, Ram Julian Gabaldon², Patrick Jason Go², Carlos Gabriel Juan², and Michael Wong²

¹Faculty, Gokongwei College of Engineering, De La Salle University, Philippines;

²Student, Gokongwei College of Engineering, De La Salle University, Philippines

ABSTRACT

Compressed Earth Blocks (CEB) made from soil and compacted using a mechanical molder can be stabilized using cement. Moreover, CEB can perform as well as concrete hollow blocks (CHB) when properly strengthened with ordinary Portland cement. Due to the low tensile strength of CEB, pig hair fibers (PHF) which is a waste material, can be utilized as fiber reinforcement to improve the performance of CEB against cracking. Due to the high cost of cement, green mussel shells (GMS), which is another waste material, can be used as partial cement substitute in compressed earth blocks. In this study, CEBs with PHF and GMS were subjected to compressive, flexural, and drip erosion tests. By using 4 variations of fiber content of PHF (0, 0.5%, 0.75%, and 1%) and 3 variations of percentages of cement replacement with GMS (0, 5%, and 10%) resulted to 12 PHF-GMS mix combinations. The compressive strength at 7, 14 and 28 days were evaluated for each mix combination. A total of 276 specimens were prepared in this study. Statistical analysis using the software Stata was conducted to filter the test results. ANOVA and T-Test were also used to determine the significance of the increase in strength with reference to the control specimen. Using the validated test results, the best performing mix was determined. The results showed that CEB with 0.75% PHF and 10%GMS is the best mix among those tested. It yielded 67% increase in compressive strength and 626% increase in flexural strength. Lastly, the same specimens, 0.75%PHF-10% GMS, also performed well in the drip erosion test.

Keywords: Earth Blocks, Fiber Reinforcement, Cement Replacement, Pig Hair, Green Mussel Shells

INTRODUCTION

Compressed earth blocks (CEB) are construction materials made from soil that is compacted using a molder, turning it into a block. CEB is considered to be a good alternative material because it is relatively cheap compared to other materials and is readily available, it requires low technical skills to work efficiently, and it has good natural thermal and sound-proofing capability.

However, it also has weaknesses that are not present in other construction materials. Some of these weaknesses include low strength, low resistance to water penetration which results to crumbling failure, low abrasion resistance which results to the need for more maintenance requirement, etc. Thus, the stabilization of CEBs is needed. The addition of cement will help strengthen the blocks, resulting to a more stabilized compressed earth blocks. The amount of cement affects the strength of the CEB. The more cement added, the stronger the CEB [1].

Some studies have researched on incorporating fibers as reinforcement for earth blocks which improves the performance of the blocks [2]-[4]. Originally, fibers had been used in concrete as fiber reinforcement. It has been widely used in the

construction industry due to its ability to improve the concrete's strength and other parameters [5].

In this study, pig hair which is a waste product from slaughterhouses, is utilized as fiber reinforcement. Pig hairs are non-biodegradable waste materials which usually end up in landfills. It is a cheaper alternative to other fiber reinforcement like glass fibers, steel fibers, synthetic fibers, and plant-based fibrous materials.

Another alternative material that is used in this study is powdered green mussel shells. Green mussel shells or commonly known as "tahong" in the Philippines are grown and harvested in bays to be used as food. However, their shells are non-biodegradable and are considered wastes [6]. Based on chemical and microstructure analysis, green mussel shells were found to be mostly made of calcium carbonate (CaCO₃) and other impurities in small amounts [7]. When green mussel shells are exposed to heat, it turns brittle and can be turned into powder by grinding. By turning green mussel shells into powder, it is possible to use green mussel shells as cement replacement.

A previous study had already shown the possibility of use of both pig hair fibers and green mussel shells in enhancing concrete [8]. The combination yielded positive results which mean

that the combination could be further explored for use in other construction materials, such as CEB.

The main objective of this study is to determine the effects of incorporating pig hair fibers and powdered green mussel shells to compressed earth blocks. The following are the specific objectives: a) to investigate the effects of different percentage of pig hair fibers (PHF) to the strength of CEB, b) to investigate the effects of different amounts of powdered green mussel shell (GMS) as partial substitute to cement, and c) to investigate the effects of fiber reinforcement and cement substitution in the durability of CEB through drip erosion test.

METHODOLOGY

The study investigated the combination of GMS and PHF at varying amounts in the mixture of conventional CEB. However, the following parameters were made constant: amount of cement/binder which is set at 5% by weight of the mixture; the length of the pig hair was maintained from 20mm to 40mm, and the GMS powdered particles have a diameter of less than 1mm.

The study incorporated 3 independent variables in the mixture of CEB. These are the following; 1) the percent of GMS powder as partial cement substitute, 2) the percent of PHF as fiber reinforcement, and 3) the specimen curing age. The amount of GMS powder was varied from 0%, 5%, and 10% by weight of the amount of cement. Meanwhile, the percentages of PHF fiber reinforcement were 0%, 0.5%, 0.75%, and 1% of the total weight of the mix. This resulted to 12 mix combinations. To identify the specimens, the mix code used was based on the percentage GMS and percentage PHF. For example, 10%GMS-7.5%PHF means 10% GMS cement replacement and 0.75% pig hair fiber reinforcement.

Materials Used

To make CEBs suitable building material, the soil properties have to be determined. The strength of CEB depends on the character of soil it uses. The soil used in the research is the typical soil found in Quezon City, Metro Manila. The soil was first sieved using a #10 sieve to ensure that large particles of soil will not be included in the mixture. Soil properties that were determined in the laboratory were; a) grading, b) specific gravity, c) optimum moisture content (OMC), and d) Atterberg limits.

The cement used was a Type I Portland Cement. According to New Mexico Earth Block Building Code of the New Mexico Adobe Code (NMAC) [9], which complies with ASTM D1633 [10], blocks must contain a minimum of 6 percent Portland cement by weight. The amount of cement adopted in this study was 5%. It was made a little bit lower on

the idea that the additional alternative materials may help in improving the strength of the CEB.

Shown in the Fig. 1 are the pictures of the GMS and PHF for reference.



Fig. 1 Photo of GMS (top) and PHF (bottom)

The shells were obtained from a tahong chip factory in Bacoor, Cavite. The shells were heated until they were brittle enough to be crushed into powder so that particle size would be less than 1mm. The specific gravity of GMS was found to be 2.62.

The pig hair fibers were obtained from two different slaughterhouses. One was from Dasmarinas, Cavite and the other from Quezon City, Metro Manila. However, investigation showed that the properties of the pig hair from the two sources are the same. The pig hair fibers were found to have a density of 1300 kg/m³.

Production of CEB

The materials used for the CEB were weighed according to their proportion. The powdered GMS were mixed first with cement. Then the soil, cement and PHF were dry-mixed for 10 to 15 minutes until uniform distributed. Water was gradually added for the mixture to reach the OMC of the soil. After which, the mixture was placed in the mechanical molder which compacted the specimen to a block size of 30cm x 15cm x 10cm as shown in Fig. 2.

The CEBs were cured in a dry place and keeping them covered with plastic sheets so that water in the CEB would not evaporate. This condition has been maintained until the testing of the specimens.

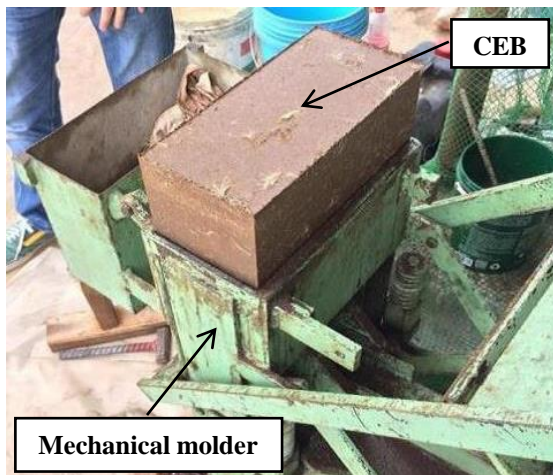


Fig. 2 Photograph of the production of CEB using a mechanical molder.

Experimental tests

The experimental tests were the compressive strength test, flexural strength test and drip erosion test. The compressive strength tests were done for 3 different curing ages: 7, 14, and 28 days. The flexural strength was obtained by measuring the modulus of rupture of the CEB using center-point loading with the supports placed 50mm from each end of the CEB. Flexural strength was evaluated for 28-day curing age. Five specimens were prepared for each strength test. For the drip erosion test, three specimens were prepared for each mix combination and tested at 28-day. This resulted to a total of 276 specimens, 240 specimens for the strength tests and 36 specimens for the drip erosion test.

Strength tests were conducted in a universal testing machine. These tests were performed in accordance with NMAC [9]. The load was applied at a rate of 500 psi/ min or 0.0575 MPa/s.

The drip erosion test or also known as Swinburne accelerated erosion test was developed by the University of Technology of Swinburne, Australia to determine the quality of the block after a simulated rainfall. Drip Erosion tests were done to test the water resistivity of CEBs. This testing method is done by subjecting a specimen to a constant water fall for a certain amount of time [11]. Three specimens for each mix combination were tested. The specimens were qualitatively evaluated by subjecting the specimens with drip test using 2250 mL water bottle that lasts for about 30 minutes.

RESULTS AND DISCUSSION

The properties of soil were evaluated because they affect the quality of CEB that will be produced. The properties of the soil used in this study are tabulated in Table 1.

Table 1 Properties of soil used in making CEB

Property	Value	Property	Value
OMC	11.7 %	% Gravel	0%
MDD	17.25 kN/m ³	% Sand	92%
Liquid limit	60	% Fines	8%
Plastic limit	32	SG	2.66

Note: OMC = optimum moisture content, MDD = maximum dry density, SG = specific gravity

The USCS classification for the soil used in this study was found to be Poorly Graded Clayey Sand (SP-SC). This is a good soil to be used to be able to produce CEB with compressive strength of about 2 MPa which is the recommended minimum compressive strength based on NMAC [9]. This strength is also the usual minimum strength requirement for concrete hollow blocks used in housing construction.

Statistical analysis of the strength test results

The data from the strength tests were filtered using Stata. The strength test data were processed using a 95% confidence interval to determine if a data in a group is considered as an outlier so that it can be removed. However, very few data were considered as outlier.

To verify whether the difference in strength between mixes is significant, the statistical software ANOVA was used. It was found out that mixes had significant difference between them. Furthermore, the T-Test: 2 Variables Assuming Unequal Variance was used to verify whether the increase or decrease in the strength is significant or not. In this test, the control specimen was set as the independent variable while the other specimens were set as dependent variables. This verified the hypothesis that the incorporation of GMS and PHF significantly affected the strength of the specimen.

Compressive strength of CEB

The average compressive strength of statistically validated specimens for each mix combination and for the different curing ages is tabulated in Table 2.

It can be observed that some specimens did not reach the target strength of 2 MPa, even at the 28-day. However, it can also be noted that when the amount of GMS and PHF were increased, it tends to increase the strength of the specimens, except when the amount of PHF exceed 0.75%. This shows that certain mix combination yields positive results. The results indicate that the optimal amount of GMS is 10%, except when no PHF is incorporated. In addition, the strongest CEB was produced at 10% GMS and 0.75% PHF. At 28 days, the strength of

this mix is 4.16 MPa. Compared to the control, which had 2.36MPa compressive strength at 28 days, the increase is 67%.

Table 2 Averaged compressive strengths of CEB

Mix Code of Specimen	Comp. Strength (MPa)		
	7day	14day	28day
Control	1.76	1.88	2.36
0%GMS-0.5%PHF	1.39	1.40	1.74
0%GMS-0.75%PHF	2.25	2.27	2.34
0%GMS-1%PHF	1.93	1.98	1.90
5%GMS-0%PHF	1.53	1.55	1.80
5%GMS-0.5%PHF	1.94	2.13	1.84
5%GMS-0.75%PHF	1.94	1.95	2.06
5%GMS-1%PHF	2.82	2.60	2.66
10%GMS-0%PHF	0.61	1.30	1.92
10%GMS-0.5%PHF	3.17	2.51	2.71
10%GMS-0.75%PHF	4.44	4.01	4.16
10%GMS-1%PHF	2.60	2.69	3.49

Note: Control specimens are those with mixture of 0% GMS and 0% PHF

To have a better assessment of effect of GMS and PHF, the ratio of the compressive strength with respect to the target strength of 2 MPa were calculated and tabulated in Table 3. Values less than 1 indicate that the target strength was not reached while values greater than 1 indicate that it exceeded the target strength.

Table 3 Ratio of the averaged compressive strengths with respect to the target strength of 2 MPa

Mix Code of Specimen	Ratio		
	7day	14day	28day
0%GMS-0%PHF	0.88	0.94	1.18
0%GMS-0.5%PHF	0.69	0.70	0.87
0%GMS-0.75%PHF	1.12	1.13	1.17
0%GMS-1%PHF	0.97	0.99	0.95
5%GMS-0%PHF	0.76	0.77	0.90
5%GMS-0.5%PHF	0.97	1.06	0.92
5%GMS-0.75%PHF	0.97	0.98	1.03
5%GMS-1%PHF	1.41	1.30	1.33
10%GMS-0%PHF	0.30	0.65	0.96
10%GMS-0.5%PHF	1.59	1.25	1.36
10%GMS-0.75%PHF	2.22	2.01	2.08
10%GMS-1%PHF	1.30	1.35	1.74

The increasing value of ratio of the control specimen shows that it had a significant amount of strength development compared to the other specimens. Table 3 also shows that GMS as a partial binder alone (those shaded in grey) helped establish a good strength development but did not help much

in surpassing the target strength. All others showed almost constant strength from 7 days to 28 days, indicating that the full strength was already attained at an early age of 7 days. This means that the incorporation of PHF together with GMS may have helped in attaining an early strength. Moreover, specimens with 10% GMS will achieve the optimum strength when PHF is incorporated. Lastly, the combination that has the greatest strength increase is 10% GMS and 0.75% PHF specimens. More than double the target strength was attained at this mix proportion.

Graphical representation of the effect of GMS and PHF to the compressive strength of CEB is shown in Fig. 3. Only the plot for the 28-day curing age is shown because the same trend will also be seen if plots for the 7-day and 14-day are included.

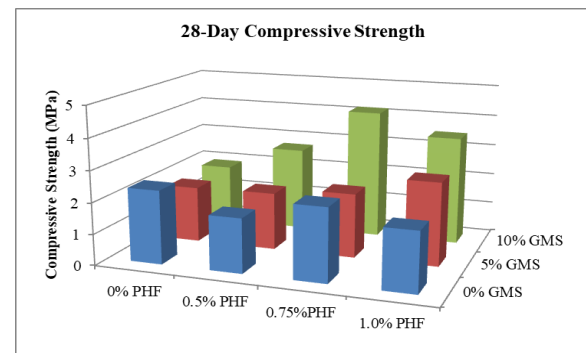


Fig. 3 Graphical plot of the 28-day compressive strength as affected by GMS and PHF

By looking at the graph, the effects of GMS in CEBs can be analyzed. It can be easily seen in the 3D graphs, that the highest strength obtained is at 10% GMS and 0.75% PHF. Higher compressive strengths can be seen in the specimens with 10% GMS with any amount of PHF. In the 10% GMS combination, the 0.75% PHF has the highest strength, followed by the 0.5% and 1% PHF respectively. The specimen with 5%GMS-1%PHF also performed well because its strength is near the other specimens with 10% GMS. The 5%GMS-0.75%PHF and 5%GMS-0.5%PHF did not perform well compared to the specimens with 10% GMS. The 10% GMS specimens with no PHF is even weaker compared to specimens with 5% GMS with any amount of PHF. This shows that the effectiveness of GMS in CEB is influenced by two things; the amount of GMS incorporated should be 10% and should be combined with PHF.

Flexural strength of CEB

The results of the flexural strength tests are tabulated in Table 4. The minimum strength requirement is 0.345 MPa according to NMAC. The increase or decrease in flexural strength with respect

to the control specimens was calculated and also tabulated in Table 4.

Table 4 Averaged flexural strengths of CEB

Mix Code of Specimen	Strength (MPa)	Increase(+)/Decrease(-)
0%GMS-0%PHF	0.106	0%
0%GMS-0.5%PHF	0.238	125%
0%GMS-0.75%PHF	0.357	237%
0%GMS-1%PHF	0.210	99%
5%GMS-0%PHF	0.082	-22%
5%GMS-0.5%PHF	0.025	-76%
5%GMS-0.75%PHF	0.143	35%
5%GMS-1%PHF	1.053	896%
10%GMS-0%PHF	0.206	95%
10%GMS-0.5%PHF	0.156	47%
10%GMS-0.75%PHF	0.768	626%
10%GMS-1%PHF	0.706	568%

Note: 0%GMS-0%PHF is the mix code for the control specimens

It can be seen in Table 4 that some of the specimens, especially the control specimen, did not pass the standard flexural strength of 0.375 MPa set by the NMAC. However, it can be observed that some combinations improved the flexural strength; the highest by as much as 896%. This means that the incorporation of certain combinations of PHF and GMS helps in the improvement of CEBs against flexural loads.

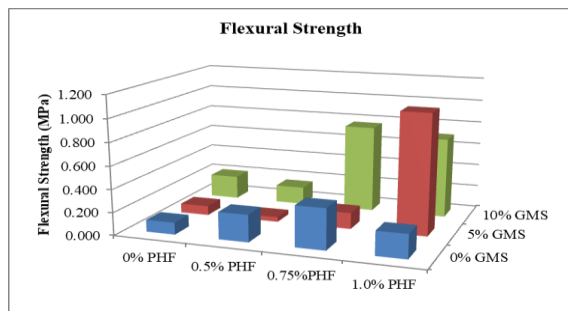


Fig. 5 Graphical plot of the flexural strength as affected by GMS and PHF

In Figure 5, a 3D plot of the flexural strengths as affected by GMS and PHF is shown. The specimens with 10% GMS performed better compared to the other percentages of GMS. As for PHF, the best amount of PHF for 0% and 10% GMS is 0.75% while the best amount of PHF for 5% GMS is 1% PHF. The best combination for flexural strength is 10%GMS-1%PHF. This is followed by the mix 10%GMS-0.75%PHF. Although it comes second, it is given more emphasis because it corresponds to the highest compressive strength. For this mix, the

flexural strength increased by 626% with respect to the control specimen, and 2.05 times compared to the minimum required strength of 0.375 MPa.

Results of drip erosion tests

Table 5 presents the rubric that was developed to evaluate the specimens subjected to the drip test. The rubric consists of 8 damage criteria. Criteria 1-5 are artificial damages, while 6-8 are natural damages. Artificial damages are damages occurring during the handling of the block after the test, while natural damages occur during the drip test itself. With these criteria, the score of the block, which is initially 200 points at the start, will be decreased for each damage criterion that will happen. The point deduction assigned for each criterion depends on the quality of the block as described by the criteria.

Table 5 Rubric for quality checklist of CEB subjected to drip test

Criteria	Description	Point deduction
1	Breaks when lifted	-50
2	Easily dented	-10
3	Corners break off	-15
4	Edges break off	-15
5	Scratched	-10
6	Fractured to pieces	-50
7	Cracks appeared	-25
8	Erosion occurred	-25

Table 6 Drip erosion test results

Mix Code of Specimen	Criteria								Score
	1	2	3	4	5	6	7	8	
0%GMS-0%PHF			x	x	x				160
0%GMS-0.5%PHF	x	x	x	x				x	85
0%GMS-0.75%PHF		x	x	x	x				150
0%GMS-1%PHF	x				x				140
5%GMS-0%PHF	x	x	x	x	x	x	x	x	0
5%GMS-0.5%PHF	x		x	x		x	x		45
5%GMS-0.75%PHF	x	x	x	x	x			x	75
5%GMS-1%PHF	x		x		x				125
10%GMS-0%PHF	x	x	x	x	x		x	x	50
10%GMS-0.5%PHF			x	x					170
10%GMS-0.75%PHF			x						185
10%GMS-1%PHF			x	x					170

Note: x indicate that damage criterion occurred

Shown in Table 6 is the tabulation of the results of the drip erosion test. By this scheme, the drip erosion performance of the specimens can be compared to each other. The higher the score means better performance. As observed in the drip test, the

control specimen performed fairly well with a score of 160 points. The worst performance is that of 5%GMS-0%PHF wherein all damage criteria were observed. In terms of GMS, the best performing specimens are those with 10%GMS. It can also be observed that specimens with 0% GMS had better scores than the 5% GMS. In general, it seems higher amount of PHF tends to improve the drip erosion performance of the specimens. Lastly, among those tested, the best performing specimen is 10%GMS-0.75%PHF, with a score of 185.

CONCLUSION

Based on the experiments results, the following conclusions were arrived at:

GMS and PHF have the capacity to improve the performance of CEB. It was observed that GMS and PHF combination helped in attaining early full strength development. However, only certain mix combinations of GMS and PHF improved the performance of CEB. There were mix combinations that even exhibited poorer performance than the control specimen.

The combination of GMS and PHF proved to be an effective combination. Specimens with either PHF only in their mix or GMS only in their mix had lower compressive and flexural strength compared to specimens with both GMS and PHF in their mix.

In terms of compressive strength, the best mix among those tested is 10%GMS-0.75%PHF. With this mix, the compressive strength was increased by 67% with respect to the control specimens, and more than doubled as compared to the target compressive strength of 2MPa.

In terms of flexural strength, the highest strength was obtained in 5%GMS-1%PHF followed next by 10%GMS-0.75%PHF. For the 10%GMS-0.75%PHF, the increase was 626% with respect to the control specimen.

In terms of the drip erosion test, the specimen 10%GMS-0.75%PHF exhibited the best performance. This shows that the GMS-PHF combination is effective in making CEBs durable against water exposure.

In general, it may be said that among those tested the best mix proportion to recommend is 10%GMS-0.75%PHF.

ACKNOWLEDGEMENTS

The authors express their gratitude to the faculty and staff of the CE Department of DLSU for all their help. Special appreciation is also due to the parents of the students who undertook this research. The authors also acknowledge the support of the DLSU Science Foundation and the office of VCA, DLSU.

REFERENCES

- [1] Morel J.C., Pkila A., & Walker P., Compressive Strength Testing of Compressed Earth Blocks. *Construction and Building Materials*, Vol.21, Issue 2, 2007, pp. 303- 309.
- [2] Lejano B.A, and Pineda K.S., Investigation of the Effects of Different Natural Fibers on the Strength of Compressed Stabilized Earth Blocks (CSEB). *International Journal of GEOMATE*, Vol. 14, Issue 42, 2018, pp.37-43.
- [3] Danso H., Martinson D.B., Ali M. & Williams J.B., Physical, Mechanical and Durability Properties of Soil Building Blocks Reinforced with Natural Fibres, *Construction and Building Materials*, Vol 101, No.1, 2015, pp. 797-809.
- [4] Donkor P, & Obonyo E, "Earthen construction materials: Assessing the feasibility of improving strength and deformability of compressed earth blocks using polypropylene fibers", *Materials & Design*, Vol. 83, 2015, pp. 813-819.
- [5] American Concrete Institute (ACI), "State-of-the-art Report on Fiber Reinforced Concrete", ACI Committee, Detroit Michigan, USA, 1996.
- [6] Talagtag, R.E, Sarao, E.F., Ngo, K.S., & Lejano, B.A., Utilization of Perna Viridis as Partial Substitute to Cement in Concrete Mix, 7th ASEAN Environmental Eng'g Conference (7th AEEC), 2014, Paper No. GI07.
- [7] Yoon G.L., Kim B.T., Kim B.O., Han S.H., Chemical-Mechanical Characteristics of Crushed Oyster-shell, Elsevier: *Waste Manag.*, Vol. 23, Issue 9, 2003, pp. 825–834.
- [8] Gagan J.L. & Lejano B.A., Optimization of Compressive Strength of Concrete with Pig-Hair Fibers as Fiber Reinforcement and Green Mussel Shells as Partial Cement Substitute", *International Journal of GEOMATE*, Vol. 12, Issue 31, 2017, pp. 37-44.
- [9] New Mexico Adobe Code (NMAC), "Chapter 7 Building Codes General: Part 4 New Mexico Earthen Building Materials Code", Housing and Construction, 2009.
- [10] ASTM D1633-17, Standard Test Methods for Compressive Strength of Molded Soil-Cement Cylinders, ASTM International, West Conshohocken, PA, 2017, www.astm.org.
- [11] Cid-Falceto J., Mazarrón F. R., & Cañas I., Assessment of Compressed Earth Blocks Made in Spain: International Durability Tests, *Construction and Building Materials*, Vol. 37, 2012, pp. 738-745.

INVESTIGATION OF THE FLEXURAL STRENGTH OF COLD-FORMED STEEL C-SECTIONS USING COMPUTATIONAL AND EXPERIMENTAL METHOD

Bernardo A. Lejano¹ and Eyen James D. Ledesma²

¹Faculty, Gokongwei College of Engineering, De La Salle University, Philippines

²Graduate Student, Gokongwei College of Engineering, De La Salle University, Philippines

ABSTRACT

The use of cold-formed steel (CFS) as structural materials has gained popularity because of its high strength-to-weight ratio. In the Philippines, the demand to use it as structural member has increased recently. However, verification of its actual strength is not extensively studied in the country. To conform to the design standards of the local code, the National Structural Code of the Philippines (NSCP), CFS as a structural member are required to be ductile. However, it was discovered in the study that CFS with higher strength but with brittle behavior is also being commercially distributed in the country. The objective of this study is to investigate the flexural strength of CFS made of these steel materials with the use of computational and experimental method. The computational method covers the calculation of the theoretical flexural strength based on the NSCP provisions while the experimental method covers the actual flexural strength based from the four-point bend test. A total of 24 specimens of back-to-back C-sections of different thicknesses and lengths were tested. Additional finite element method (FEM) calculation was also conducted using ANSYS. The main failure modes were distortional (DB) and lateral-torsional buckling (LTB). For the ductile CFS, DB and LTB were observed in 86.1% and 13.9% of the specimen population, respectively. While for the brittle CFS, DB and LTB were observed in 75.0% and 25.0%, respectively. Moreover, it was also found that the computational strengths were lower than the experimental strengths. The FEM analysis results were close to the experimental results thus validating the experimental results.

Keywords: Cold-formed Steel, C-section, Four-Point Bend Test, ANSYS, NSCP

INTRODUCTION

There are two types of steel mostly used in the construction industry: hot-rolled steel and cold-formed steel (CFS). CFS is composed of flat sheets and strips of metal shaped by either rolling or pressing. It can be produced economically by the cold-forming process, and favorable strength-to-weight ratios can be obtained [1]. Figure 1 shows the typical configuration of a CFS C-section.

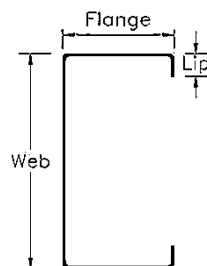


Fig. 1 Typical configuration of CFS C-section

In the Philippines, CFS are locally produced and manufactured. But foreign standards have been adopted ever since its use and application in the

country. CFS is not extensively studied in the country and its design is based on foreign standards, mostly based on the American Institute of Steel Construction (AISC), as specified in the National Structural Code of the Philippines (NSCP) [2]. It is a practice that if the code is simply followed then the design work is acceptable. To conform to the design provisions and standards, CFS as a structural member are required to be typically ductile. However, it was discovered in the study that CFS with higher strength but with brittle behavior is also being commercially distributed in the country. Whether ductile or brittle, the actual performance of locally distributed CFS needs to be investigated if their actual strength is consistent with the theoretical strength based on the NSCP. Previous studies, have already reported inconsistencies in the computation of the concentric compressive strength of C-section and Z-section based on NSCP as compared to experimental values [3], [4]. In line with this, the aim of this study is to investigate the actual flexural strength of CFS C-sections made of both ductile and brittle steel materials and compare this with the values obtained from computational (based on NSCP) and numerical method (based on finite element analysis).

METHODOLOGY

This study covers both computational and experimental method. The computational method covers the calculation of the theoretical flexural strength based on the NSCP provisions for CFS while the experimental method covers the actual flexural strength based from the four-point bend test conducted for each steel material. Additional analysis and comparison were also done using the finite element analysis software, ANSYS. This helped in further analyzing the accuracy of the results of the two methods for both types of steel.

CFS C-section specimens

The C-section used in the study is defined as a singly-symmetric section. The section size of the specimens used conforms to the dimensional limits specified in NSCP Section 553.3. A 50 mm (flange) x 100 mm (web) C-section with lip stiffeners was used in the study since this is the most commonly used section in the industry. The section used has lips which act as edge stiffener to the flanges but has no intermediate stiffeners along the web of the member. Three lengths and two thicknesses were used for both ductile (DS) and brittle steel (BS). Three trials were considered for the ductile CFS, while only one trial for the brittle CFS, for a total of 24 back-to-back CFS C-section (48 individual CFS) tested in this study; 18 DS and 6 BS.

The lengths used for the specimens were limited due to the space that can be accommodated in the testing lab. The thicknesses were based on the commercial availability of the members. A digital Vernier caliper was used to measure the actual dimensions of the specimens to assure accurate calculations. Table 1 shows the specimen codes used in the study.

Table 1 Specimen codes used

Code	Steel Type	Length (mm)	Thickness (mm)
A1	DS	1000	2.0
A2	DS	2000	2.0
A3	DS	3000	2.0
B1	DS	1000	1.2
B2	DS	2000	1.2
B3	DS	3000	1.2
C1	BS	1000	2.0
C2	BS	2000	2.0
C3	BS	3000	2.0
D1	BS	1000	1.2
D2	BS	2000	1.2
D3	BS	3000	1.2

For example, code A1 refers to C-section CFS with ductile steel material with 1000 mm length and 2 mm thickness.

Material properties were determined following the procedure from ASTM E8 (Standard Test Methods for Tension Testing of Metallic Materials) [5]. Metal strips conforming to the standard of ASTM E8 were cut and tested in tension to determine the actual yield strength and modulus of elasticity of both steel materials. The load-strain curves were also plotted so that the behavior of the CFS can be visualized. These properties, along with the actual dimensions of the specimens, were used in computing for the theoretical flexural strength of the members based on NSCP.

Experimental setup of four-point bend test

Figure 2 and 3 show the schematic drawing and actual setup of the four-point bend test used in the study, respectively. The end supports for the test were simply supported, with the applied loads passing through the centroid of the back-to-back channels. The load was applied using a hydraulic jack and monitored using a load cell. The adopted experimental setup for the study was mostly based on the experimental setup used by Wang and Young [6], which also cover CFS sections subjected to bending.

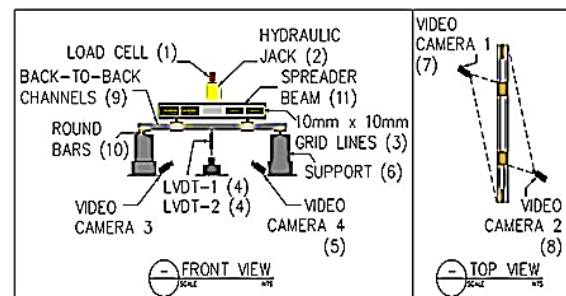


Fig. 2 Schematic drawing of four-point bend test



Fig. 3 Actual setup of four-point bend test

Based on the experimental setup, two channels

bolted back-to-back were tested at the same time to avoid out-of-plane bending of the member. These channels were bolted to T-shaped wooden blocks. They are placed at the end supports and at the loading points to act as stiffeners to the web of the member in order to prevent crippling and sudden failure at those points.

Two displacement transducers (LVDT 1 and 2) were placed at the middle of the moment span under each specimen in order to record its vertical displacement. The entire experimental test was captured and recorded using four high speed video cameras to precisely evaluate the buckling failure modes manifested by each member. Gridlines, 10 mm x 10 mm, were placed along the length of the member to help in scaling the movement of its elements.

In addition, round high-tempered steel bars were used to act as roller supports in the test setup. For the spacing of the back-to-back channels, the clear distance between webs was established as twice the distance of shear center from the web of one channel. In theory, setting this spacing makes the line of action of the applied load pass not only to the centroid and shear center of the back-to-back channel, but also to the shear center of one channel. This avoided the complication of the application of torsion in the section.

Failure modes

The main modes of failure for CFS members in flexure are yielding, distortional buckling (DB) and lateral-torsional buckling (LTB). However, only DB and LTB were manifested by the specimens in the experiment. Most of the time local buckling triggers the movement of the failure modes. It is not listed as a mode of failure in the NSCP but was considered as a factor to the strength calculation of the member by using its effective area. Figure 4 shows the different modes of failure that can be exhibited by a member loaded in flexure. Movement of the elements shown can vary and show a more complex configuration. It is important to note that multiple modes of failure can be manifested by a member simultaneously.

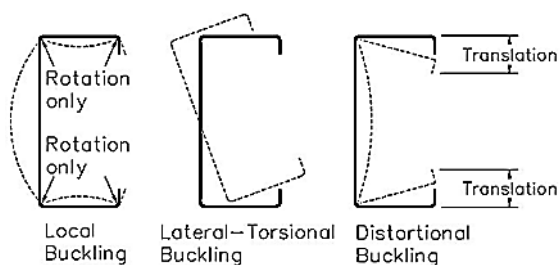


Fig. 4 Failure modes for C-section CFS flexural members

RESULTS AND DISCUSSION

Two steel materials, namely ductile and brittle steel, were investigated in the study for the CFS members. The tensile test results attained for the material properties of the members were based on ASTM E8 [5]. For the ductile and brittle CFS, the average yield strength obtained using ASTM E8 was 265.27 MPa and 561.82 MPa, respectively, while the average modulus of elasticity was 39.09 GPa and 58.49 GPa, respectively.

It was observed from the tension testing that the ductile CFS clearly exhibited yielding plateau after the elastic stage was exceeded. On the other hand, the brittle CFS exhibited sudden drop in strength after reaching the yielding stress.

Experimental flexural strength

Since back-to-back channels were tested simultaneously in the four-point bend test, the actual flexural strength for each specimen was taken as the maximum load recorded from the load cell divided by two. This is termed as the experimental strength. It was used instead of the flexural moment for easier comparison with the calculation results. In addition, the self-weight of the member, weights of the T-shaped wooden blocks, round bars at the loading points, hydraulic jack and spreader beam were all accounted for in computing the experimental strength for each member. Table 2 shows the average experimental strength for all trials of the specimen.

Table 2 Experimental strengths (kN)

Code	1	2	3
A	38.69	17.53	10.59
B	19.70	9.69	6.93
C	44.45	28.47	12.71
D	26.43	12.96	7.17

Based on the experimental strengths shown in Table 2, it can be observed that the strength of the member is affected by both its length and thickness. Shorter length members attained larger strengths than the longer ones. The length mostly influenced the type of failure mode for the member in terms of its global buckling while the thickness influenced the local buckling response of the members.

Relating the difference of the corresponding results for the ductile and brittle CFS, it is also observed that the strengths attained for the longer lengths by the ductile CFS were marginally lower than the brittle CFS. However for the shorter lengths, it is comparatively higher. Hence, the substantial difference between both steel materials' yield strength only had a minimal effect on their

experimental strengths for the longer lengths, but for the shorter lengths it had a sizeable difference.

DB and LTB were the main failure modes manifested in the experiment. Figure 5 and 6 shows example for both DB and LTB failure observed in the experiment.



Fig. 5 Distortional buckling failure



Fig. 6 Lateral-torsional buckling failure

Computational flexural strength

The computational strengths of the specimens were computed using the design provisions of the NSCP for CFS, which can be found in Section 552 and 553 of the code. Yielding, DB and LTB are the main failure modes specified in the NSCP for CFS flexural members. The governing strength was taken as the lowest moment computed amongst the three. Table 3 summarizes the average computational strengths for all trials.

Table 3 Computational strengths (kN)

Code	1	2	3
A	22.90	12.40	7.77
B	11.37	5.27	3.73
C	49.49	18.56	12.85
D	20.46	10.12	4.30

The same observation as that of the experimental results can be said for the computational results shown in Table 3, though it can be observed that the strengths attained by the ductile CFS were comparatively lower than the brittle CFS for all lengths and thicknesses. In addition, only DB was calculated as the governing failure mode for all the computational strengths.

FEM flexural strength

The FEM strengths were determined by generating the model for each specimen and simulating it using ANSYS. The gathered results were used to further compare and analyze the results from the computational and experimental method.

Models for each specimen were generated by using their actual dimensions and properties. Measured densities of 7786 kg/m^3 and 7185 kg/m^3 were used for the ductile and brittle CFS, respectively. Boundary conditions were also set to simulate the actual supports used in the experiment. Table 4 shows the average FEM strengths for all trials generated by the software.

Table 4 FEM strengths (kN)

Code	1	2	3
A	35.17	26.83	17.23
B	15.76	6.84	5.32
C	50.90	31.81	21.44
D	23.77	9.83	4.47

A unit load for the two loading points was used as the initial load for the FEM. Dummy plates were modeled to transfer the unit load to the shear center. Eigenvalue buckling analysis in ANSYS was used to simulate the buckling modes [7]. Figure 7 illustrates the failure mode for specimen B1. The strength is equal to the load multiplier multiplied by two (due to two loading points), with the units in Newton.

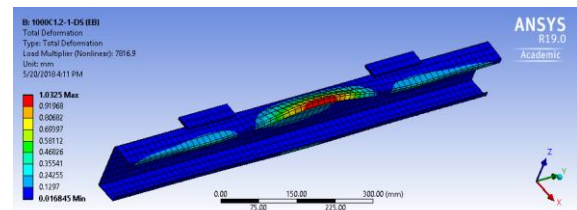


Fig. 7 Buckling-failure of specimen B1 in ANSYS

Evaluation of flexural strength results

Determining the failure mode is important in the evaluation of the strength of CFS. The results indicate that majority of specimen population has similar failure mode observed in the experiment and obtained in computation. For the ductile CFS, 86.1% of the computed failure modes agreed with the experiment results, while for the brittle CFS, a value of 75.0% was obtained.

A summary and comparison of the strengths and failure modes are shown in Table 5. In the computational method, only DB failure was attained. This may be because the section is an open section making it prone to distortional deformation. However, in the experimental tests, although most exhibited DB failure, LTB failure was observed when the length of the specimen became longer. This resulted to 86.1% that failed in DB and 13.9% in LTB for ductile CFS. In the case of brittle CFS, 75.0% failed in DB while 25.0% in LTB.

Table 5 Failure modes and strengths summary

Code	Comp Fail.	Expt Fail.	Expt (kN)	Expt / Comp	Expt / FEM
A1	DB	DB	38.69	1.70	1.11
A2	DB	DB	17.53	1.43	0.66
A3	DB	LTB	10.59	1.37	0.62
B1	DB	DB	19.70	1.74	1.26
B2	DB	DB	9.69	1.85	1.47
B3	DB	LTB	6.93	1.86	1.31
C1	DB	DB	44.45	0.90	0.89
C2	DB	DB	28.47	1.55	0.91
C3	DB	LTB	12.71	0.99	0.59
D1	DB	DB	26.43	1.29	1.11
D2	DB	DB	12.96	1.30	1.39
D3	DB	DB	7.17	1.71	1.66

To have a better comparison between the experimental strength and the computational strength, the ratio between the two (Expt/Comp) is calculated and tabulated in Table 5. The ratio of experimental strength with respect to FEM strength (Expt/FEM) is also tabulated. Ratios greater than 1.0 mean conservative predictions. It can be seen that generally the computed values, as well as FEM values, are conservative. For ductile CFS, the average Expt/Comp ratio is 1.66, while the average Expt/FEM ratio is 1.07. It means that experimental values are closer to the FEM than the computational. On the other hand, for the brittle CFS, the difference between the average ratio of FEM and the average ratio of computational to the experimental (1.09 and 1.29, respectively) was lower compared to the ductile CFS.

Figure 8 and 9 show the comparison of the strengths, by plotting the experiment values against the computed or FEM strength values.

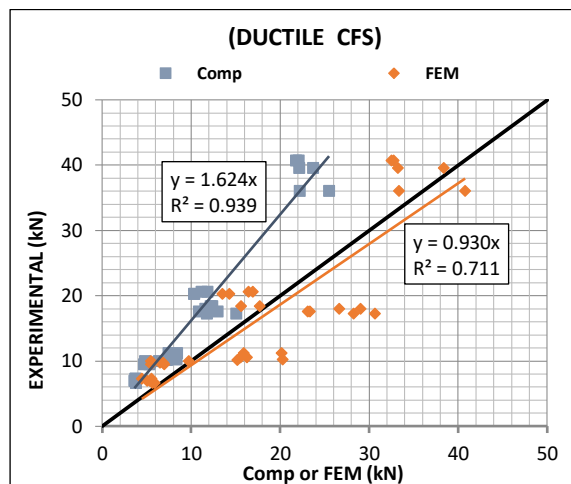


Fig. 8 Strengths comparison (Ductile CFS)

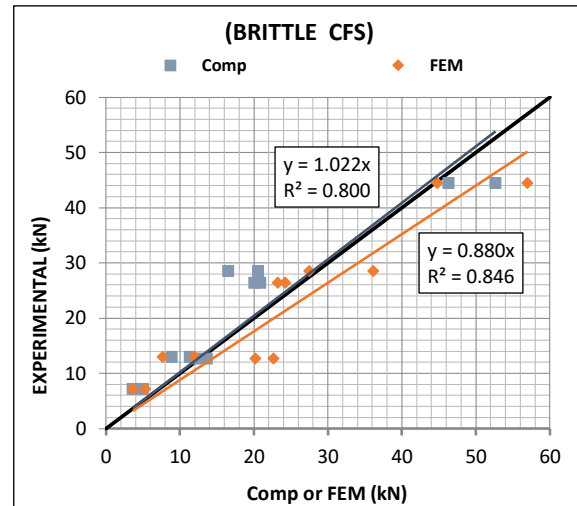


Fig. 9 Strengths comparison (Brittle CFS)

The diagonal line in the graphs is the equality line. It represents points in which the computational equal to the actual (experimental). The diagonal line also represents points in which the FEM equal to the experimental. The graph shows the regression line along with its corresponding correlation coefficient (R^2) for both steel types. It can be seen that the values R^2 are close to 1.0 indicating good fit of the data to the regression line. Based on the graphs, the R^2 of ductile CFS for computational strength (0.939) shows a better fit than FEM (0.711). On the other hand, for the brittle CFS, its R^2 values for the computation and FEM results (0.800 and 0.846, respectively) only show small difference.

For the ductile CFS, the regression line of the computational data points fall above the equality line, which indicate that it is conservative (see Fig. 8). On the other hand, for the brittle CFS, the regression line of the computational data points is almost coinciding with equality line (see Fig. 9). Hence, the ductile CFS is more conservative than the brittle CFS. It may be said that the ductile CFS has a factor of safety of 1.624 based on the slope of the regression line.

The regression lines of the FEM data points of both ductile and brittle CFS are below but very close to the equality line. Thus, the FEM seems to overestimate the strength (hence non conservative), but only by small amount. The brittle CFS is more non conservative than the ductile CFS.

Based on the foregoing statements, the computational strength of the ductile CFS may be applied with a modification factor to bring it close to the experimental (actual) strength. However, the other thought is that the ductile CFS is already conservative, and modifying it may pose danger. So the other alternative is to bring the brittle CFS to a conservative estimate similar to the ductile CFS. This is more appealing to safeguard against abrupt failure of a brittle material. To do this, the

computational strengths of the brittle CFS will be applied with a modification factor instead. The computational strength of the brittle CFS may be adjusted by multiplying it with 0.60. This value was obtained by considering that the average Expt/Comp is 1.66 for ductile CFS. Since, the regression line of the computational strength of the brittle CFS almost coincide with the equality line, the modification factor can be obtained by simply taking the reciprocal of 1.66 which is equal to 0.60. After applying the modification factor, the resulting regression line is shown in Fig. 10.

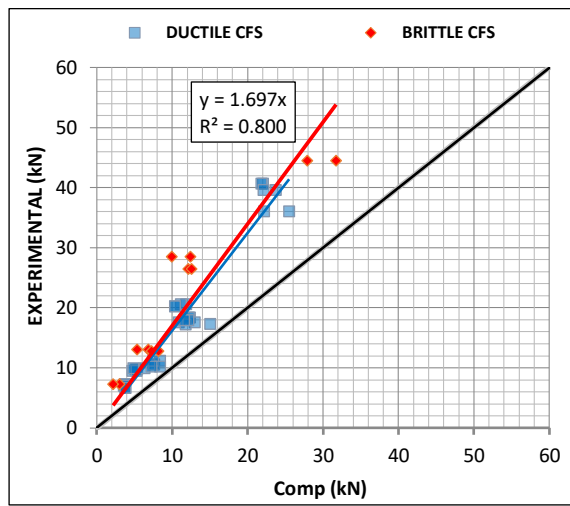


Fig. 10 Modified strengths for brittle CFS

Figure 10 illustrates the modified strengths for the brittle CFS. The red data points and line represent the adjusted strengths. Now, it is almost coinciding with the ductile CFS, hence, it has almost the same factor of safety as that of the ductile CFS.

CONCLUSION

Experimental, computational, and numerical evaluation of the flexural strength of C-section CFS were conducted. Based on the results, the following may be concluded.

In terms of failure mode, majority of the experimental failure modes agreed with computational failure modes. For the ductile CFS, 86.11% of its failure mode in the computation agrees with the experiment, while 75.0% for the brittle CFS. The computation based on NSCP resulted only to distortional buckling. However, when the specimen becomes longer, LTB was observed in the experimental test, especially when the length becomes longer.

FEM analysis was also done to compare further the results attained in the experiment and computations. The FEM and experimental strengths showed good agreement, such that it may be said that the FEM verified the experimental results.

Furthermore, the average ratio between the experimental and computational results was 1.66 for ductile CFS and 1.29 for brittle CFS. Based on these results, it may be concluded that the computed flexural strength based on NSCP is conservative.

Lastly, a modification factor of 0.60 is recommended to be applied to the computation of strength of brittle CFS. With this, the brittle CFS will have almost the same factor of safety that the ductile CFS has.

ACKNOWLEDGEMENTS

The authors would like to acknowledge De La Salle University – Manila for providing the testing lab and equipment used for the study. Most of all, this research would not have been possible without the help of our family, mentors, and colleagues. They are truly appreciated for their guidance and help for the completion of the study.

REFERENCES

- [1] Yu W.W., Cold-Formed Steel Design, John Wiley & Sons, Inc., 3rd ed., 2000, pp. 2-3.
- [2] Association of Structural Engineers of the Philippines, Inc. (ASEP), National Structural Code of the Philippines, 7th ed., Vol. 1, 2015, pp. 228-279.
- [3] Yu A. and Lejano B.A., Investigation on the Strength of Cold-Formed Steel C-Section in Compression, International Conference on Advances on Civil, Structural, Environmental and Bio-Technology CSEB 2014, Kuala Lumpur, Malaysia, 2014.
- [4] De Jesus J.M. and Lejano B.A., An Investigation on the Strength of Axially Loaded Cold-Formed Steel Z-Sections, International Journal of GEOMATE, Vol. 14, Issue 42, 2018, pp. 30-36.
- [5] American Society for Testing and Materials (ASTM), ASTM E8: Standard Test Methods for Tension Testing of Metallic Materials, 2010.
- [6] Wang, L., & Young, B., Design of cold-formed steel channels with stiffened webs subjected to bending, Thin-Walled Structures, December 2014, pp. 81-92.
- [7] ANSYS® Academic Research Mechanical, Release 19.0, Help System, Coupled Field Analysis Guide, ANSYS, Inc., 2018.

STUDY ON STRENGTH ESTIMATION OF SOIL CEMENT USED IN THE EMBEDDED PILE METHOD BY ELECTRICAL RESISTIVITY MEASUREMENT

Y Mochida¹, M Matsuura²

¹ Ritsumeikan University, Japan

² Graduate School of Science and Engineering, Ritsumeikan University, Japan

ABSTRACT

Problems caused by poor quality control and quality assurance of the pre-boring embedded pile construction, such as on domestic apartment house are still occurring nowadays. An adequate consideration for invisible risks inside or below the ground is important in pile foundation construction therefore the demand for advanced and reliable quality assurance is increase in the future. In this research, to understand the quality of the construction at early stage, the compressive strength of cement-soil mixture of pile construction after 28 days is estimated using electrical resistivity value of the mixture. More accurate measurement for electrical resistivity value is conducted by inserting the electrodes without using potassium chloride solution as a catalyst. The result showed that there is a certain tendency in the electric resistivity value at the early age regarding to the type of soil (sand, clay) mixed in. The most accurate estimation was achieved from the electric resistivity value at the first day and several days onwards, and from the compressive strength after 3 days.

Keywords: Soil cement, Embedded pile, Electrical resistivity, Quality control

INTRODUCTION

The purpose of this research is to study the utilization of electrical resistivity measurement to predict compressive strength and to perform quality control of cement slurry used in bored precast pile construction technique [1][2][4][5]. This paper consists report and recommendation for electrical resistivity measurement technique [3], quantification and estimation technique of electrical resistivity, compressive strength estimation formula based on electrical resistivity value and quality control method using strength prediction of cement slurry through indoor/laboratory and field examination [3][4][5].

LABORATORY EXPERIMENT OF SOIL CEMENT MIXTURE

The electrical resistivity measurement methods were decided prior to laboratory examination. The following three patterns of electrical resistivity measurement methods were performed at the same time and suitable method is studied.

1. At 28 days from pouring without removing cell and no pore water.
2. Only measure bleeding water at early stage by making hole with diameter same as cell in specimens. After that stage, 0.1% KCl solution is used as pore water.
3. Using KCl solution with the same electrical resistivity value as specimen right after poured into cell. After that stage, the same procedure as number 2.

Considering actual soil configuration, cement

slurry only, cement with sand, cement with clay and cement with sand and clay, three variants of mixture is used for laboratory examination. Electrical conductivity meter and schematic view of measurement are shown in Figure 1.

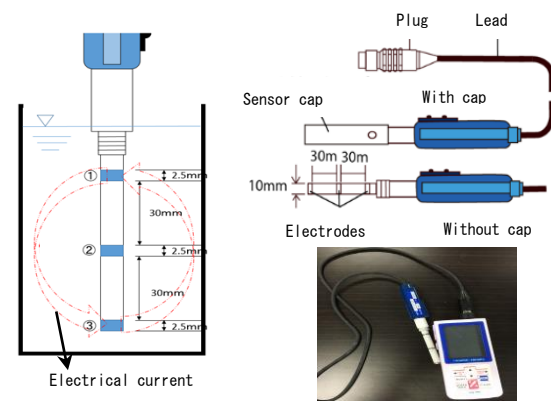


Fig.1 Electrical conductivity meter and measurement

Laboratory examination mixture using cement slurry

Electrical resistivity value change with time shown by Figure 2 gives information that electrical resistivity value is tends to be the same regardless of mixture and cement amount. For mixture curing age of one day, electrical resistivity value is greatly affected by pore water for method number 1 and number 2, therefore, method number 1 is recommended for electrical resistivity measurement. In addition, temperature change also influences electrical resistivity value.

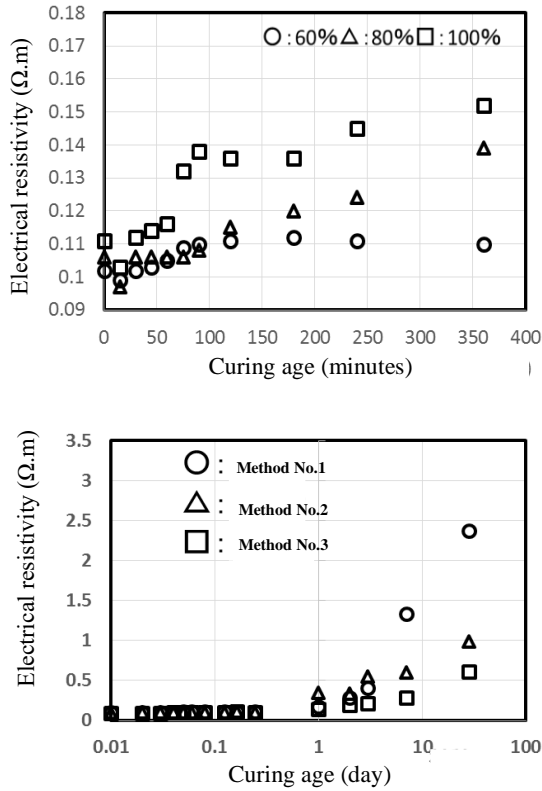


Fig. 2 Electrical resistivity value change with time

Relationship between compression strength and electrical resistivity value measured by method number 1 as shown by figure 3 resulted to conclusion that relation between qu_{28}/ρ_{28} and qu_3/ρ_3 was more correlative than $\Delta qu/\Delta \rho$ and qu_3/ρ_3 . In other hand, measurement methods number 2 and 3 also had similar result, therefore, compression strength estimation formula using relationship between qu_{28}/ρ_{28} and qu_3/ρ_3 is recommended. Here, qu is compressive strength, ρ is electrical resistivity and subscript number indicates specimen curing age in day(s) unit.

Method 1 :

$$qu_{28} = \{0.1058.(qu_3/\rho_3) + 8.8964\} \rho_{28} \quad (1)$$

Method 2 :

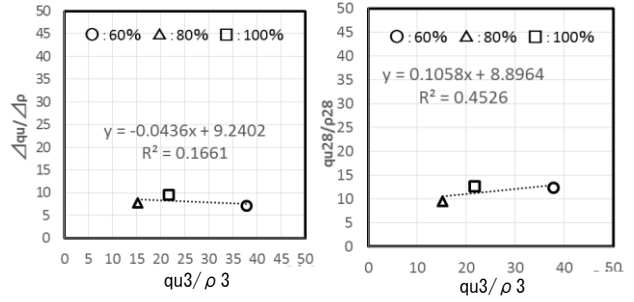
$$qu_{28} = \{3.3823.(qu_3/\rho_3) - 63.551\} \rho_{28} \quad (2)$$

Method 3 :

$$qu_{28} = \{0.5807.(qu_3/\rho_3) + 9.3560\} \rho_{28} \quad (3)$$

Since electrical resistivity value tends to change regarding to time (curing age), compressive strength can be estimated using ρ value from early curing age until reached final curing age (28 days). Electrical resistivity changes due curing age is observed to decide the suitable time for estimating the compressive strength as shown by figure 4. Relationship between ρ_3 and ρ_{28} recommends

equation 4, equation 5 and equation 6 for estimating ρ value. In addition, considering ρ value at early age and onwards due to pore water existence, relationship between ρ_0 and ρ_3 is used for measurement method 1 and ρ_1 vs ρ_3 for method 2 and 3 recommends equation 7 ~ equation 9 for estimating ρ value. Therefore, equation 4 ~ equation 9 is used for estimating electrical resistivity value (ρ).



Method 1 :

$$\rho_{28} = 7.8687 \cdot \rho_{31.5779} \quad (4)$$

Method 2 :

$$\rho_{28} = 0.8950 \cdot \rho_{30.153} \quad (5)$$

Method 3 :

$$\rho_{28} = 3.5787 \cdot \rho_{31.1367} \quad (6)$$

Method 1 :

$$\rho_3 = 0.0015 \cdot \rho_{0-2.483} \quad (7)$$

Method 2 :

$$\rho_3 = 1.8722 \cdot \rho_{11.1642} \quad (8)$$

Method 3 :

$$\rho_3 = 4.0211 \cdot \rho_{11.5936} \quad (9)$$

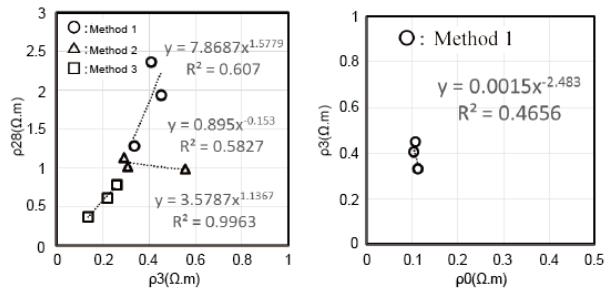


Fig. 4 Relationship between ρ_3 and ρ_{28} and ρ_0 and ρ_3

Subsequently, estimation formulation for compressive strength prediction was also attempted. Equation 10 is formulation recommended by Japan Society of Civil Engineering (JSCE) [6], is used and applied for laboratory examination in this research. Where α and β is material constants and t is specimen's curing age. Calculation of performed by linear interpolation of $qu_{28}/qu(t)$ vs t recommended by JSCE (Figure 5) and listed in Table 1.

Table 1 Laboratory experiment mixture condition

Sample condition (W/C)	α	β
60%	0.84	4.86
80%	0.68	9.53
100%	0.79	6.08
Average	0.77	6.6233

$$qu(t) = qu(28) \times \frac{t}{\alpha \times t + \beta} \quad (10)$$

Estimation of compressive strength using equation 1 to equation 9 and laboratory compressive strength test are attempted and the result is compared as shown by figure 6. Estimated value and measured value are nearly consistent for measurement method 1. Estimated value is larger than measured value for method 2 while Measured value is larger than estimated value for method 3. Hence, method 1 is possible and recommended for estimating electrical resistivity value.

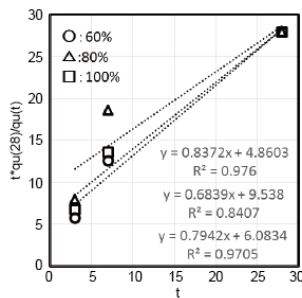


Fig. 5 Relationship of t and $t \cdot qu_{28}/qu_t$

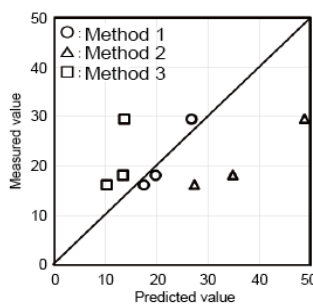


Fig. 6 Comparison of measured vs predicted value of compressive strength (right)

Laboratory examination mixture using sandy soil and clayey soil

Laboratory examination for sandy and clayey soil assumption are performed and the procedures are shown by figure 7 and mixture condition listed in table 2. Electrical resistivity value changes by material age (time) for sandy soil is different from cement only and cement with clay soil due to

precipitation influence. For clay soil, specimen is expanding and cracks occurs during curing process causing variation in electrical resistivity value. Furthermore, for clay soil, the viscosity of the soil cement slurry was very high therefore the compressive strength test could not performed as shown by figure 8.

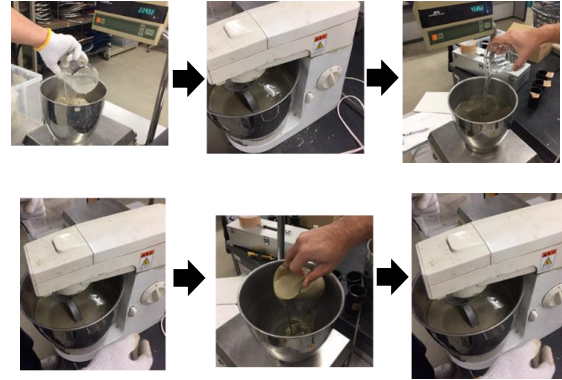


Fig. 7 Soil cement mixing procedure

Table 2 Sandy soil assumed mixture condition

W/C ratio (%)	Mud water ratio	Cement milk : mud water	Replacement soil percentage (%)
60	1.5	1:3	A
60	1.5	1:5	B
60	1.5	1:10	C
100	1.5	1:2	D
100	1.5	1:2.5	E
100	1.5	1:2	F

Compressive strength estimation for sandy soil specimen are also conducted using the same procedure as cement slurry only specimen and recommended formulation, equation 11 ~ equation 19 and equation 10, and comparison between measured and estimated value is shown by figure 9.

As a result, for every measurement method, compressive strength prediction is possible even when sand is mixed. There was specimen with large error of compressive strength value, however, bleeding water effect during curing process might cause this phenomenon.

Method 1 :

$$qu_{28} = \{0.2514 \cdot (qu_3/\rho_3) + 0.6748\} \cdot \rho_{28} \quad (11)$$

Method 2 :

$$qu_{28} = \{0.451 \cdot (qu_3/\rho_3) + 0.5002\} \cdot \rho_{28} \quad (12)$$

Method 3 :

$$qu_{28} = \{0.9578 \cdot (qu_3/\rho_3) + 2.9513\} \cdot \rho_{28} \quad (13)$$

Method 1 :

$$\rho_{28} = 0.2807 \cdot \rho_3^{-2.071} \quad (14)$$

Method 2 :

$$\rho_{28} = 0.7269 \cdot \rho_3^{-0.2769} \quad (15)$$

$$\text{Method 3 :} \\ \rho_{28} = 0.9634 \cdot \rho_3^{0.572} \quad (16)$$

$$\text{Method 1 :} \\ \rho_3 = 0.5048 \cdot \rho_0^{0.2804} \quad (17)$$

$$\text{Method 2 :} \\ \rho_3 = 0.0946 \cdot \rho_1^{-0.599} \quad (18)$$

$$\text{Method 3 :} \\ \rho_3 = 0.7643 \cdot \rho_1^{0.7377} \quad (19)$$



Fig. 8 Experiment on clay soil

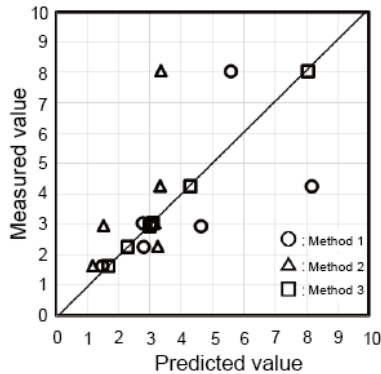


Fig. 9 Predicted vs measured value

Laboratory mix examination assuming actual ground

Laboratory mixing experiment assuming actual soil condition was performed using sand and clay mixed together with mixing conditions listed in table 3. The experiment results lead to inconsistent change of electrical resistivity value with time along with large variation. Similar method to predict compressive strength of the specimen using relationship between qu_{28}/ρ_{28} and qu_3/ρ_3 also applied in this procedure and came to results that equations 20~28 are recommended for compressive strength prediction. Comparison between predicted value and measured value shown by figure 10.

$$\text{Method 1 :} \\ qu_{28} = \{0.2662(qu_3/\rho_3) + 1.9764\} \rho_{28} \quad (25)$$

$$\text{Method 2 :} \\ qu_{28} = \{4.1042(qu_3/\rho_3) - 81.007\} \rho_{28} \quad (26)$$

$$\text{Method 3 :} \\ qu_{28} = \{2.8788(qu_3/\rho_3) - 51.029\} \rho_{28} \quad (27)$$

$$\text{Method 1 :} \\ \rho_{28} = 3.2724 \rho_3^{0.6215} \quad (28)$$

$$\text{Method 2 :} \\ \rho_{28} = 66.139 \rho_3^{3.2056} \quad (29)$$

$$\text{Method 3 :} \\ \rho_{28} = 278.01 \rho_3^{4.227} \quad (30)$$

$$\text{Method 1 :} \\ \rho_3 = 0.5048 \rho_0^{0.2804} \quad (31)$$

$$\text{Method 2 :} \\ \rho_3 = 0.7679 \rho_1^{0.7792} \quad (32)$$

$$\text{Method 3 :} \\ \rho_3 = 0.4656 \rho_1^{0.4635} \quad (33)$$

Table 3 Sand with clay soil assumed mixture condition

W/C ratio (%)	Mud water amount ratio	Cement milk : mud water	Sand : clay	Replacement soil percentage (%)
60	1.6	1:1	G	3:7
60	1.6	1:1	H	6:4
60	1.6	1:1	I	8:2

Measurement method 1 and 2 gives prediction with high accuracy, however not with method 3. It is understood that the mixture of sand and clay has moderate density and reduce bleeding process, therefore increase accuracy in measuring electrical resistivity and improves accuracy of prediction formulation.

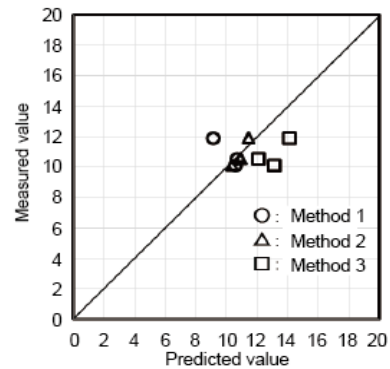


Fig. 10 Predicted vs measured value for sand with clay soil assumed specimen

OUTDOOR EXPERIMENT

Figures or Tables should be sized the whole width of a column, as shown in Table 1 or Fig.1 in the present example, or the whole width over two columns. Do not place any text besides the figures or tables nor place them altogether at the end of the manuscript.

Examination of pile hole at the construction site

Bored pile construction site in Arahama, Kashiwa city of Niigata prefecture is selected for outdoor experiment. The specifications were bored

pile hole with diameter of 530mm, depth of 20m and with W/C ratio of 60%. Collection of unsolidified sample was carried out from overflow and mortar plant and the universal water sampler shown in figure 11 and was conducted from depth of 2.5m, 5.0m, 10m, and the specific resistance value on the ground are Measured. Soil until depth of 15m was sandy soil. At the same time, electrical resistivity value near depth of 5.0 m was also measured using custom made electrical conductivity meter with cord length of 30 m.



Fig. 11 Tools and sample collection

Changes of electrical resistivity value was rapid as shown by figure 12. It is believed that summer season condition caused the acceleration of specimen curing process. Figure 12 also shows that the temperature rise is extremely low inside the hole, the influence of the outside air is small at the depth of 5.0m and the influence on the quality by the temperature is not significant.

The result of compressive strength value using prediction equation is shown as listed in table 4. An Accurate strength prediction performed by sample collected from inside the bored hole. In addition, it is possible to predict the compressive strength with an error of about 1.0 N / mm² for safety consideration. However, for sample collected from the plant gives more variation as effect of temperature change is believed to cause this large margin of error.

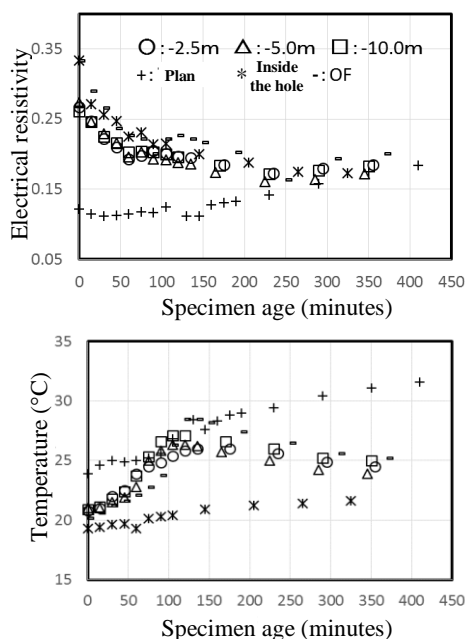


Fig. 12 Electrical resistivity value and temperature change

Table 4 Compressive strength of specimen at each collection location

	Plant	Depth = 0m	Depth = 2.5m	Depth = 5.0m	Depth = 10.0m	Inside the hole
qu_{28} (pr)	11.1	3.036	4.43	4.24	4.64	3.04
qu_2 (me)	29.52	4.282	4.28	4.28	4.28	4.28
ρ_0 (me)	0.122	0.333	0.273	0.273	0.261	0.333
Eq.	1.2.7. A	10.13 .16.A	10.13 .16.A	10.13 .16.A	10.13. 16.A	10.13. 16.A

Laboratory mixing experiment using site soil

Soil sample also collected from the same construction site in Arahama, Kashiwazaki-shi, Niigata prefecture. Sample was taken using from the bored hole depth of 21.0m (sandy soil) and 51.0m (gravel ground) and cement milk with water cement ratio 60%. Similar mixture experiment was conducted and the condition is listed in table 5. Electrical resistivity value is shown in figure 13 and mixture P and Q has different initial electrical resistivity value compare other mixture. The influence of variation in gravel size of site soil is believed as a factor and temperature also has significant effect.

Table 5 Compressive strength of specimen at each collection location

W/C ratio (%)	Soil class	Mud water	Cement milk : mud water		Replacement soil percentage (%)
60	Sand	1.6	1:1	J	100
60	Sand	1.6	1:1.5	K	150
60	Sand	1.6	1:2	L	200
60	Gravel	1.7	1:1	P	100
60	Gravel	1.7	1:1.5	Q	150
60	Gravel	1.7	1:2	R	200

Compressive strength was also calculated using prediction formulation (equation 25 to equation 31) and obtained the same results for every mixture sample. This is believed caused by large error of predicted value when assumed ρ_0 was larger than soil electrical resistivity value. Based on this result, it is necessary to collect more data on the electric resistivity value estimation formula and modify it to an estimation formula incorporated to actual soil

conditions.

ELECTRICAL RESISTIVITY MEASUREMENT BASED OF STRENGTH PREDICTION RECOMMENDATION

Based on performed laboratory experiment in this research, prediction formulation for compressive strength of bored pile construction using electrical resistivity measurement procedure is recommended by following diagram shown by Figure 14.

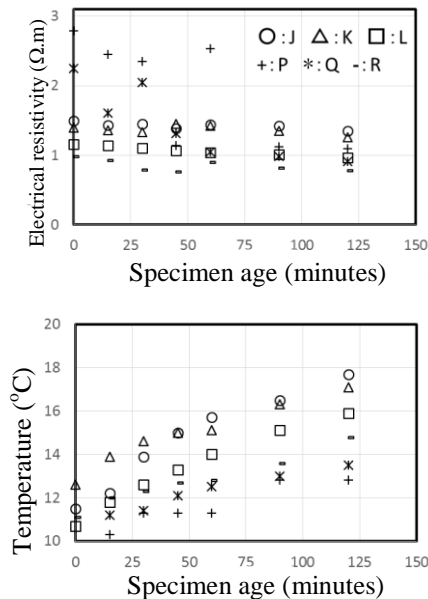


Fig. 13 Electrical resistivity value and temperature change with time

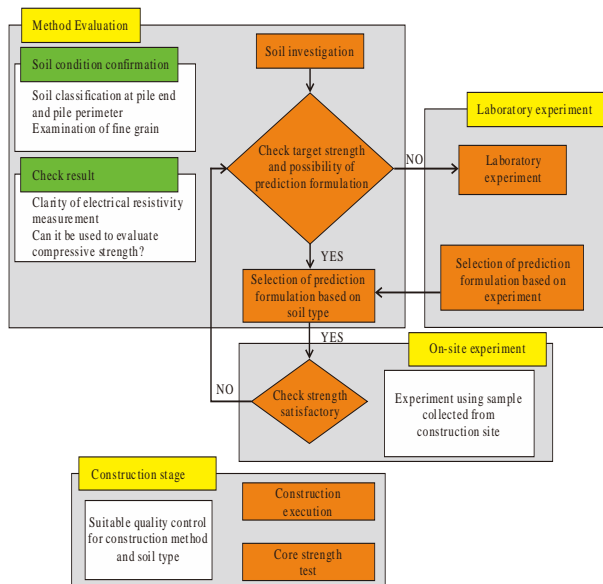


Fig. 14 Recommendation procedure for compressive strength prediction soil cement mixture

CONCLUSION

1. Electrical resistivity measurement method 1 was the most suitable method to predict compressive strength of cement milk or cement soil mixture
2. Electrical resistivity value of specimen at early age tends to be consistent regardless to mixture configuration and cement amount if the particle size of soil is uniform to some extent
3. The temperature change of the specimen is greater than Atmospheric temperature has more influence to temperature change of the specimens rather than the heat emission due to the hydration reaction.
4. The relationship between qu_{28}/ρ_{28} and qu_3/ρ_3 is better than $\Delta qu/\Delta \rho$ and qu_3/ρ_3
5. It is possible to use measurement method 2 and 3 for laboratory experiment, however correction process is necessary.
6. Based on outdoor experiment, temperature change does not have significant effect to compressive strength.
7. It is necessary to perform another experiment to understand the influence of soil classification and particle size of soil to electrical resistivity value.
8. Equation 1 to equation 33 may be applied to predict compressive strength of actual condition, however accurate electrical resistivity measurement and measurement data accumulation is necessary.

REFERENCES

- [1] Tsuchiya T, Kuwabara F, 2012, Study on the Method of Constructing the Root-Hardened Part of the embedded Pile and its Strength Development (Japan: Japan Architectural Institute Technical Report Vol. 18)
- [2] Tsuciya T, 2014, Relationship Between the Strength of the Unsolidified Sample of the Root-Hardened Part and The Ground in the High Supportive Pile, (Japan: The Architectural Institute of Japan Summary of Academic Papers Summary)
- [3] Komatsu G, Fujii M, 1998, Quality Evaluation of Pile Tip Root-Hardened Part of Buried Pile Using Electric Resistivity, (Japan: Summary of the Architectural Institute of Japan, page 621-622)
- [4] Kato Y et al., 2000, Basic Study on Strength of Pile Fixed Portion of Embedded Pile, (Japan: Summary of the Architectural Institute of Japan, page 755-756)
- [5] Tomita K et al., 2001, Quality Evaluation of Solidified Body of Pile Fixing Solution, (Japan: Summary of the Architectural Institute of Japan, page 693-694)

- [6] Society of Civil Engineers: Concrete Standard Formulation Established in 1996 [Construction Edition]

CENTRIFUGE TEST OF SUPERSTRUCTURE-SC PILE-LIQUEFIED SOIL SYSTEM AND SC PILES' DYNAMIC BUCKLING BEHAVIOR

Hiroki Goto¹, Moeko Matoba¹ and Yoshihiro Kimura¹

¹Tohoku University, Japan

ABSTRACT

It is assumed that steel piles do not buckle because of the soil restraining the lateral deformation of the piles. The subgrade lateral stiffness decreases drastically when liquefaction occurs during a significant earthquake. When the steel piles experience high compressive axial forces caused by the overturning moment, the flexural buckling occurs. In our previous papers, the centrifuge tests of the superstructure with the pile foundation system in liquefied soil were conducted on the model with the piles' cap being laterally free and rotationally fixed. Based upon this assumption the steel piles' dynamic buckling behavior was clarified. Dynamic buckling of SC piles, as well as steel piles, may occur when piles experience significant axial compressive forces in liquefied soil. An SC pile is a composite pile in which the concrete is attached to the steel pipe by application of the centrifugal force. Even though the axial compressive force's ratio of the SC pile is equal to that of the steel pile, the compressive force which the steel pipe carries is higher than that of the concrete in the SC piles. Therefore the steel pipe in SC piles yields and collapses earlier than steel piles. In this paper, the centrifuge tests of the superstructure with the SC pile foundation system in liquefied soil are conducted as SC piles' cap is assumed to be laterally free and rotationally fixed as in previous research. The SC piles' dynamic buckling behavior is clarified and, by using the M-N interaction curves, the ultimate strength is estimated.

Keywords: SC pile, Dynamic Buckling, Centrifuge test, Liquefied soil

INTRODUCTION

When the ground liquefies during an earthquake, its lateral stiffness drastically reduces. The slender steel piles experience the axial compression force issued from the overturning moment of a building, which generated by the inertia force, it is assumed that the flexural buckling of steel piles occurs. In our previous papers in [1] and [2], the centrifuge tests of the superstructure, the steel pile foundation and the liquefied soil system were conducted, and the dynamic buckling behavior of steel piles was clarified.

On the other hand, it is assumed that the SC pile with higher strength than the steel pile is used at the pile top where the large bending moment occurs in a real structure. SC piles consist of the composite elements of steel tube and concrete which with higher compressive strength of about 80 N/mm² is placed to the inside of the steel pipe using the centrifugal force. In previous papers about SC piles' mechanical behavior [3], ultimate strength of SC piles is still not evaluated even though the bending tests in the full-scale model were conducted. On the other hand, in Japanese current design code, the possibility of SC piles' flexural buckling is not taken into account. As with the steel pile, the SC pile might dynamically buckle when the pile experiences the significant axial force in the liquefied soil.

In this paper, the centrifuge tests of the

superstructure, the SC pile foundation, and the liquefied soil system are conducted on the small-scale model, and SC piles' dynamic buckling behavior is clarified. Moreover, the ultimate strength of the SC pile is evaluated by the M-N interaction curves in current Japanese design code [4] and [5].

BENDING MOMENT CALCULATION PROCEDURE

In this section, the bending moment calculation procedure for SC piles is suggested. Figure 1 represents procedure to calculate the bending moment of the SC pile before yielding. In this paper, it is assumed that the cross-section of the SC pile yields when the stress at the edge of the steel pipe's section or that of the concrete section reaches yielding stress, σ_y or compressive strength, σ_b . Also, the axial and bending stress distribution in the pile's section is assumed as follows.

- 1) The axial force acts over the entire section, and the axial forces of the steel and concrete parts are carried in proportion to axial rigidities.
- 2) Navier hypothesis is applied to the strain distribution at material elasticity.
- 3) The concrete part cannot carry the tensile stress.

Figures 2(a) - 2(c) display the strain distribution of the SC pile's cross-section before the steel part reaches yielding stress. Figures 2(a) and 2(b) portray the distribution of the axial strain and the bending

strain, respectively, and Fig. 2(c) depicts the sum of the axial and bending strain distribution. Figures 3(a) and 3(b) represent the stress distribution of SC pile's cross-section obtained by the strain distribution in Fig. 2(c). Figures 3(a) and 3(b) describe the stress distribution of the concrete and the steel parts, respectively. Here, C_c denotes the compressive force acting on the concrete part, which is calculated from the compressive stress multiplied by cross-section of the concrete part. C_s and T_s signify the compressive and the tensile forces acting on the steel part. C_s and T_s are estimated to multiply the compressive stress or the tensile stress by the cross-section of the steel part, respectively. The balance equation of the axial forces, N_0 is shown as the following.

$$N_0 = C_c + C_s - T_s \quad (1)$$

The bending moment of the SC pile is obtained by integration of the stress and cross-section over the entire section under the condition of Eq.(1). If Eq. (1) is not satisfied, the calculation procedures 2) - 9) in Fig. 1 is carried out again. The yielding moment, M_y is estimated with the above calculation procedure as described in Fig. 1.

Next, the procedures to calculate the bending moment is shown as the following, after SC pile's cross-section yields. In this paper, the stress-strain model of the material is assumed to apply perfect elasto-plasticity. Figures 4(a) and 4(b) show the stress distributions in elasto-plasticity and full plasticity, respectively. Where σ_y represents the steel yielding strength, and σ_B stands for the concrete compressive strength. $c\sigma(y)$ and $s\sigma(y)$ display the stress of the concrete and the steel part at y . The position of the neutral axis is decided as Eq. (1) is satisfied. The stress in the yielded section increases in the elastic part after yielding. The bending moment after yielding can be calculated to add the stress increment in the yielded section on the yielding moment, M_y . The full plastic moment of the SC pile $_{sc}M_p$ can be calculated from the stress distribution in full plasticity as shown in Fig. 4(b).

Moreover, the relation between bending moment-bending strain of the SC pile is modeled as follows in order to estimate SC pile's ultimate strength. Figure 5 shows the material property of the brass C2680, which is substituted for the steel in the centrifugal test. The broken line is the result of the tensile test. As shown in Fig. 5, σ_u , σ_y and σ_l denote the tensile strength, the 0.2% offset yielding strength and the elastic proportional limit stress, respectively. Also E_s and E_{st} represent Young's modulus, and the strain hardening gradient. The black and the gray lines depict the bilinear and the trilinear models in Fig. 5. For the bilinear model, the elastic limit stress is defined as σ_y , and the second gradient is modeled

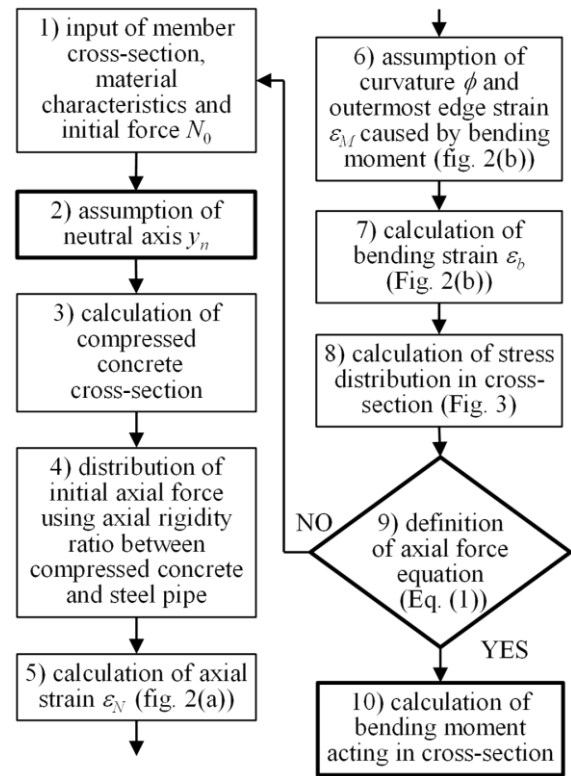


Fig. 1. Bending moment calculation procedure

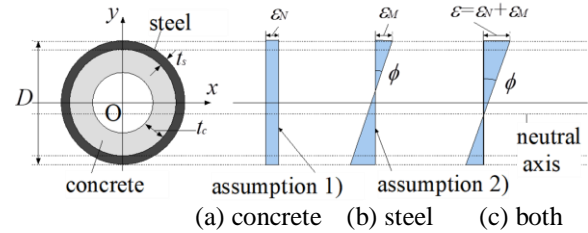


Fig. 2. Strain distribution

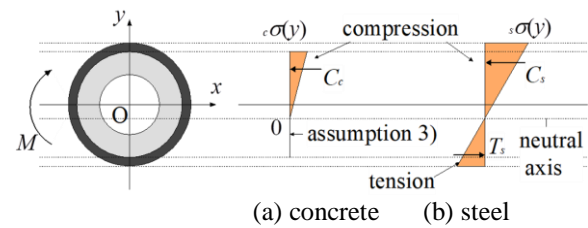


Fig. 3. Stress distribution (before yielding)

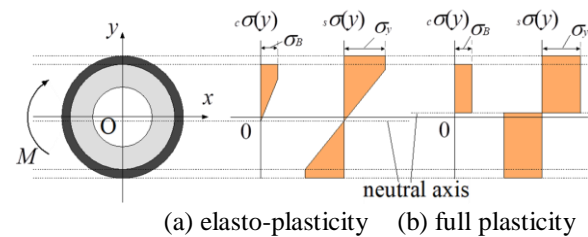


Fig. 4. Stress distribution (after yielding)

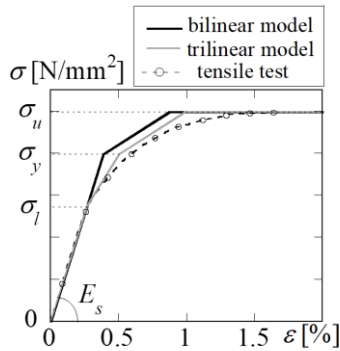


Fig. 5. Stress-strain relation

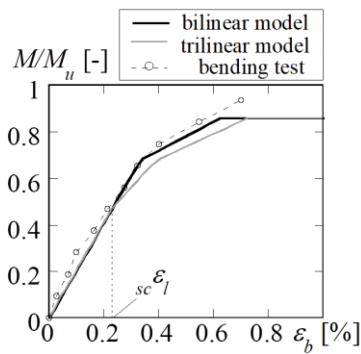


Fig. 6. Relation between bending moment and bending strain

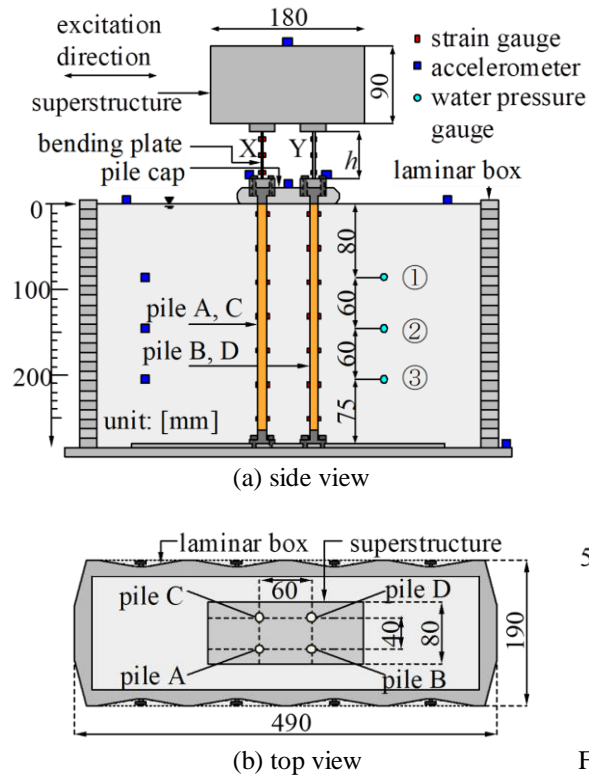


Fig. 7. Specimen and instrumentation

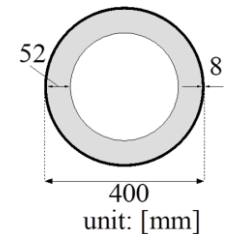


Fig. 8. SC pile's cross-section

as $E_s / 5$ after the stress reaches σ_y . For the trilinear model, the elastic limit stress and the second gradient are determined as σ_l and $E_s / 2$. Moreover, after the stress reached σ_y , the third gradient is defined as $E_s / 5$. After the stress reached σ_u , the stress is the constant value of σ_u in both models. The bilinear model is simplified modeling, on the other hand, the trilinear model agrees with the result of the tensile test. Figure 6 shows the relation between bending moment-bending strain of the SC pile. The broken line portrays the result of SC pile's bending test with the small-scaled model. The black and gray lines represent the value applied by the bilinear and trilinear stress-strain models, respectively. The relation between the bending moment-bending strain calculated from the bilinear modeling is almost the same as the result of the bending test, and that calculated from the trilinear modeling is lower than the others. In section 4, the bending moment of the SC pile specimen for the centrifuge tests is evaluated with the bilinear or trilinear bending moment-strain model.

CENTRIFUGE TESTS ON SUPERSTRUCTURE - SC PILES - LIQUEFIED SOIL SYSTEM

Outline of Centrifuge Tests

Figures 7(a) - 7(c) show the specimen and the instrument. Figures 7(a) and 7(b) depict the side and the top view of the instrument. Fig. 7(c) is the enlarged view of pile A. The instrument consists of the superstructure, the SC piles and the liquefied soil. Two piles at the front of the instrument are pile A on the left side and pile B on the right side. The others at the back are pile C and pile D. The bending plates are plate X on the left side and plate Y on the right side. Pile's strain gauges on the left and the right surface of piles are determined as x_i and y_i as presented in Fig. 7(c). Here, i denotes the strain gauge numbers 1 to 7. Accelerometers are placed at the top surface of the superstructure, the pile cap, and at the bottom of the laminar box. Besides, accelerometers and water pressure gauges are located at 80 mm, 140 mm, 200 mm from the ground level as shown in Fig. 7(a). The horizontal displacement of the superstructure is measured by a laser displacement meter. The following is represented in a full-scale.

Table 1 and 2 display the specimens' properties and their parameters. Figure 8 shows SC pile's cross-section of the specimen for Case 2-1. Case 1 series is the specimens with steel piles, and Case 2 series is with the SC piles. The initial axial force ratio is determined at 0.30 and 0.33 for Case 1 by reference to the axial design force of steel piles for a real structure. For Case 2 series, the initial axial

Table 1 Specification of specimens

			model scale	full scale
superstructure	weight:	Case 1	66.7	4.27×10^6
	m_1 [N]	Case 2	100.05	6.40×10^6
bending plate	thickness: t_b [mm]		2	80
	length: h [mm]		55	2200
pile cap	weight: m_2 [N]		13.0	8.3×10^5
	length: l [mm]		265	10600
pile	thickness of steel: t_s [mm]		0.2	8
	thickness of cement: t_c (mm)		1.3	52

Table 2 Specimen parameters

specimen		diameter D [mm]	initial axial force ratio N_0/N_y	relative density Dr [%]	input wave	maximum input wave [m/s^2]
Case1-1	steel	400	0.33	30	coastal wave	5.0
Case1-2	pile	440	0.30			
Case2-1	SC	400	0.34			7.5
Case2-2	pile	440	0.30			

Table 3 Material properties of piles (unit: $[\text{N/mm}^2]$)

cement	E_c	12000
paste	σ_B	41

force ratio is set to 0.30 and 0.34. For the yielding strength of the SC piles, its value is the sum of the yielding strength of the steel pipe and the compressive strength of the filled concrete. The compressive design strength of the cement paste is 27 N/mm^2 . In Case 2 specimens, the weight of the superstructure is 1.5 times of Case 1. The SC piles materials are brass of C2680 as shown in Fig. 3 and the cement paste, the bending plate material is aluminum of A5052, and the others are steel of SS400. Table 3 shows the material properties of the cement paste. Here, E_c and σ_B signify Young's modulus and compressive strength of the cement paste obtained by the compressive test.

Result of Centrifuge Tests

Figure 9 presents the time history of the coastal wave acceleration as the input wave. The maximum value of the coastal wave is set to 5.0 m/s^2 in Case 1 series and 7.5 m/s^2 in Case 2 series. Figures 10 and 11 display the response time histories of Case 1-1 and Case 2-1 specimens. Figures 10(a) and 11(a) show the response time history of the superstructure acceleration. Figures 10(b) and 11(b) represent the excess pore water pressure ratio, Figs. 10(c) and 11(c) indicate pile's axial compressive force time history. Figures 10(d), 10(e), 11(d) and 11(e) stand for the bending strain of $i=1, 2$ around the pile top. In Figs. 10(b) and 11(b), the triangle symbol indicates

the time of the liquefaction. In this paper, it is assumed that the soil liquefaction occurs when the excess pore water pressure ratio reaches 1.0. In Figs. 10(c) and 11(c), the triangle symbols stand for the maximum compressive axial force between the soil liquefaction and the superstructure collapse. In Figs. 10(d), 10(e), 11(d) and 11(e), the black triangle symbols represent the maximum value of the bending strain in pile A or B. The bending strain is calculated from the following equations.

$$\varepsilon_b = (\varepsilon_{xi} - \varepsilon_{yi}) / 2 \quad (2)$$

For Case 1-1 specimen, the result obtained by strain gauge D1 is substituted for gauge B1 because gauge B1 was disconnected during the experiment.

For Case 1-1 specimen, the excess pore water pressure ratio r_u reaches 1.0 at about 19 sec, and the soil liquefaction occurs in Fig. 10(b). In Fig. 10(c), the maximum axial compressive force of the pile is 259kN at about 29 sec, which is equivalent to the initial axial force of 20 %. In Fig. 10(d), the bending strain of the pile top suddenly increases from about 27 sec. The maximum bending strain of A1 arrives at 0.66 % at about 32 sec. The bending strain of D1 attains the maximum value of 0.43% at the almost same time as that of A1 in Fig 10(e).

For Case 2-1, which is the specimen of the SC pile model, the excess pore water pressure ratio r_u reaches 1.0 at about 17 sec, and the soil liquefaction occurs in Fig. 11(b). In Fig. 11(c), the maximum axial compressive force of the SC pile is 318kN at about 19 sec, which is equivalent to the initial axial force of 18 %. The bending strain of A1 reaches the maximum value of 0.66 % at about 32 sec in Fig

11(d). This value is about 70 % of the value at A1 of Case 1-1. In Fig 11(e), the bending strain of B1 gets to 0.24 % when the bending strain of A1 reaches the maximum value. After that, the bending strain of B2 suddenly increases in the negative side. Its minimum value becomes -0.44% at about 27 sec. The acceleration response of the superstructure for Case 2-1 increases after the maximum bending strain of B2 as shown in Fig. 11(a).

Figures 12(a) and 12(b) show the bending strain distribution at the maximum bending strain in pile A and B for Case 1-1 and Case 2-1. Also, Figs. 1(a) and 1(b) display the final states of Case 1-1 and Case2-1. Here, ε_{yc} signifies the yielding bending strain reduced by the initial compressive axial force in Figs. 12(a) and (b). For Case1-1 specimen in Fig. 12(a), the bending strains at the top and the bottom of pile A and B exceed ε_{yc} , and the plastic-hinges

occur. For Case2-1 specimen in Fig. 12(b), the bending strain at A1 and B2 around the pile top, and the middle of pile B almost reach ε_{yc} . It is presumed that after the stress of the piles is redistributed with the plastic-hinge at the top of pile A, and the superstructure collapses issued from the plastic-hinges at the top and the middle of pile B.

EVALUATION OF SC PILE'S ULTIMATE STRENGTH IN THE LIQUEFIED SOIL

Figure 14 presents the relation between pile's axial compressive force and bending moment of the result on the centrifugal tests. The vertical axis represents the value of pile's compressive axial force N_b for all specimens divided by the elasto-plastic buckling strength N_c . The elasto-plastic buckling strength N_c is obtained by the buckling stress curve of the Japanese limit state design of steel structures [5] applied with the modified equivalent slenderness ratio λ_c in [2]. λ_c is gained from the ratio of the yielding strength to pile's elastic buckling load in the liquefied soil P_{cr} as the following Eq. (3).

$$\lambda_c = \sqrt{N_y / P_{cr}} \quad (3)$$

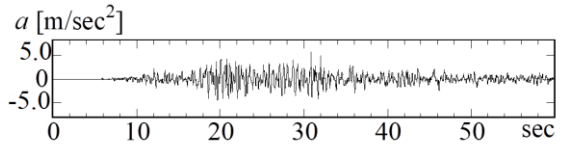
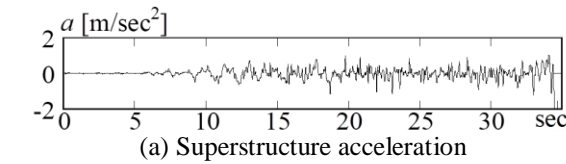
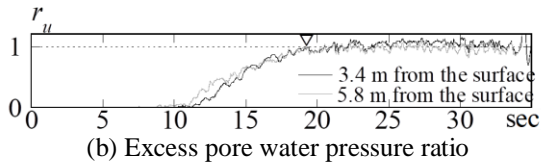


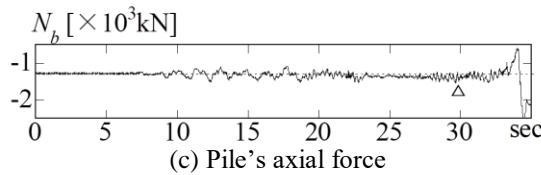
Fig. 9. Input wave (the coastal wave)



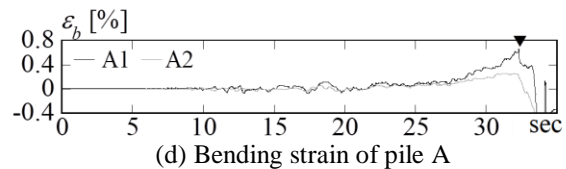
(a) Superstructure acceleration



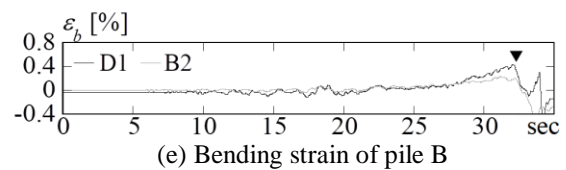
(b) Excess pore water pressure ratio



(c) Pile's axial force

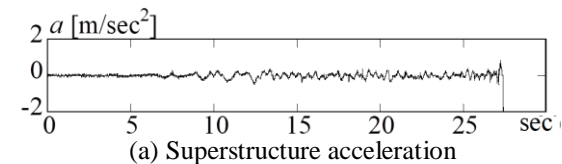


(d) Bending strain of pile A

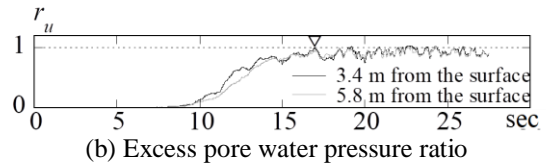


(e) Bending strain of pile B

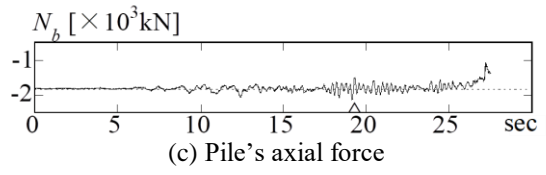
Fig. 10. Response time history of Case 1-1



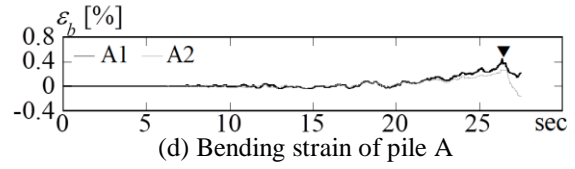
(a) Superstructure acceleration



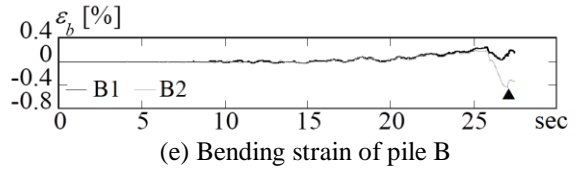
(b) Excess pore water pressure ratio



(c) Pile's axial force



(d) Bending strain of pile A



(e) Bending strain of pile B

Fig. 11. Response time history of Case 2-1

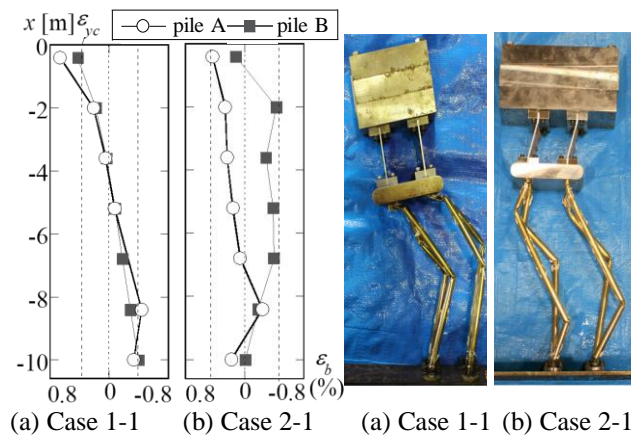


Fig. 12. Pile's bending strain distribution

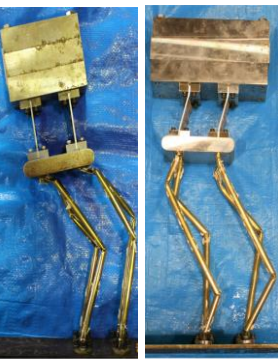


Fig. 13. Pile's bending deformation

For the SC pile specimens, the flexural rigidity EI_{sc} can be calculated by using the procedure as described in Fig. 2 of section 2. The horizontal axis in Fig. 14 represents the maximum bending moment of the piles divided by the full plastic moment of the steel pile M_p for Case 1 series. In Case 2 series, the full plastic moment of the SC pile M_u is applied as described in Fig. 4(b) in chapter 2. On the other hand, SC pile's bending moment on the centrifugal tests is calculated by using the bending moment-bending strain curve in Fig. 6. In Fig. 14, the black and gray plots for Case2 series show the bending moment which is calculated with the bilinear and trilinear models illustrated in Fig. 6, as the representative values in the histories. The broken and dotted lines respectively represent the M-N interaction curves of the Japanese recommendation for design of building foundation in [4], and the Japanese design standard for steel structures in [5]. The solid line describes the ultimate strength curve in [6]. The results at the pile's maximum bending strain exceed the M-N interaction curve of the Japanese design standard for steel structures [5] and are distributed as the upper-bound for the ultimate strength curve [6].

It is shown that the ultimate strength of the SC pile can be evaluated by using the M-N interaction curve of Japanese current design criteria in [5] and the ultimate strength curve in [6], to which the elasto-plastic buckling strength is applied with the modified equivalent slenderness ratio.

CONCLUSION

The conclusions of this research are shown as follows:

- 1) The Centrifuge tests of the SC pile which is subjected to the varying axial force and horizontal force in the liquefied soil are conducted, and the collapsing behavior of the SC pile is clarified.
- 2) It is shown that the ultimate strength of the SC

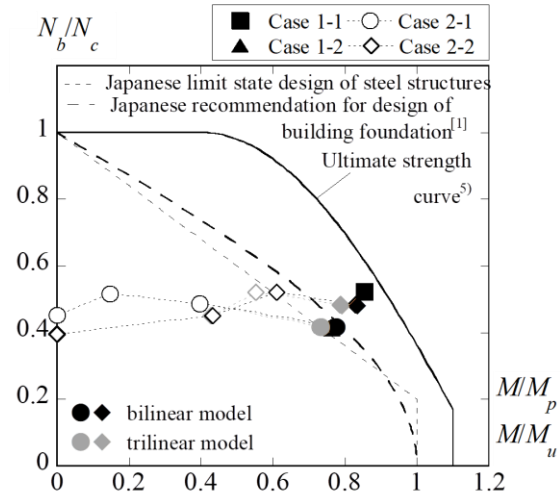


Fig. 14 Estimation axial force and bending moment of piles using M-N interaction curves and ultimate strength curve

pile in the liquefied soil can be evaluated by the M-N interaction curves applied the elasto-plastic buckling strength of the Japanese limit state design of steel structures.

REFERENCES

- [1] Kimura Y, Kishino Y, Tamura S: Dynamic Flexural Buckling for Circular Tube Piles Based on Centrifuge Tests of Superstructure Pile Liquefied Soil System, Jour. of Structural and Construction Engineering, Vol.80, No.717, Nov. 2015. pp.1707-1716. (in Japanese)
- [2] Kimura Y, Matoba M, Goto T, Tamura S: Dynamic Collapse Mechanism and Ultimate Strength for Circular Tube Pile Based on Centrifuge Tests of Superstructure-Pile-Liquefied Soil System, Jour. of Structural and Construction Engineering, Vol.81, No.730, Dec. 2016. pp.2079-2089. (in Japanese)
- [3] Tanaka Y, Sekiguchi T, Nakai S, Nakai S: A Study on Effects of Fill in Hollow Part of SC Piles Based on Sample Beam Bending Test, Jour. Of Structural and Construction Engineering, Vol.82, No.736, Jun. 2017. pp.823-829. (in Japanese)
- [4] Architectural Institute of Japan: Recommendation for Design of Building Foundation. 2001. (in Japanese)
- [5] Architectural Institute of Japan: Limit State Design of Steel Structures, 1998. (in Japanese)
- [6] Kimura Y, Tokimatsu K: Ultimate Vertical Strength and Ultimate Flexural Moment of Steel Pile subjected to Vertical and Horizontal Load in Liquefied Soil, Jour. of Structural and Construction Engineering, Vol.77, No.675, May. 2012. pp.775-781. (in Japanese)

VOLUME CHANGE BEHAVIOR OF SEA WATER EXPOSED COAL ASH USING HYPERBOLIC MODEL

Erica Elice S. Uy¹, Jonathan R. Dungca¹ and Mary Ann Q. Adajar¹

¹Graduate Student, De La Salle Univeristy, Philippines

ABSTRACT

The Philippines greatly relies on coal-fired power plants as a source of electricity. These power plants produce a by-product or waste material called coal ash. In recent years, the country has been experiencing continuous urbanization. As a result, there is an increase in the demand for electricity consumption. This can also result in an increase of production of coal ash. There are several studies that suggest the potential of coal ash as a construction material. In this study, the coal ash was exposed to sea water. In order to investigate the potential of coal ash as a construction material to structures that will be exposed to the sea. Consolidated drained triaxial test was performed considering the following level of exposure namely, no exposure, immediate exposure, and prolonged exposure. A hyperbolic model was used to model the stress-dependent volume change behavior of the material towards sea water. In the model, the Poisson's ratio parameters were determined. The tangent value of Poisson's ratio and its relationship with the applied stressed was evaluated.

Keywords: Bottom Ash, Volume Change, Poisson's Ratio, Hyperbolic Model

INTRODUCTION

Coal-fired power plants remain to be a dominant producer of energy in the Philippines. According to BMI research, the share of coal in energy production is continuously increasing. The predicted increase in 2017 was only up to 50 percent. However in 2018, the predicted increase will be more than 50 percent and this trend is expected to occur until the year 2027 [1]. About 75% of the coal supply is imported from Indonesia and Australia [1]. The importation will be lessened since there is an increase in production from a power plant at Visayas and a newly operated power plant at Mindanao. Semirara Mining and Power Corporation is one of the leading coal producer in Visayas aims to increase its production. A target production of 16 million metric tons in two or three years is the goal of the company in order to meet the demand of the consumers [2]. The continuous increase in demand can result to more production of waste materials. These waste materials or by-product are called coal ash. These are stored in ash ponds. The increase in demand can cause a shortage in storage facilities. This might lead to the improper way of disposal due to the lack of available ash ponds. To avoid this, several researches were conducted to determine the potential of coal ash as a construction material. There are many types of coal ash by-products or coal combustion by-products (CCB). The most frequently studied in researches are fly ash and bottom ash [3]-[8]. These waste materials were utilized as a road base construction material as a partial substitute to

conventional materials [3]-[6]. The performance of these by-products to improve the hydraulic conductivity characteristics of road base was explored. Blending the by-products had an effect towards the hydraulic conductivity of soils. A percentage substitute ranging from 40% to 60% of bottom ash resulted to the highest vertical hydraulic conductivity [3]. The use of bottom ash in highway embankments, subgrades and subbases were also investigated. Based on the results, the by-product was able to satisfy the material specification for a subgrade and subbase [4]. In another study, the performance of coal ash as a construction material for land reclamation near the sea was evaluated. Coal ash was exposed to sea water to simulate the actual conditions of the reclamation site. Modified Cam Clay model was incorporated in the study. The model resulted to determining the maximum deviator stress and maximum mean normal effective stress of coal ash at its elastic state. The maximum deviator stress has a value of 600 kPa while the maximum mean normal effective stress is 500 kPa. Based on their findings, bottom ash has the potential to be used as a construction material for a reclamation project [7]. The potential of coal ash as a road embankment exposed to sea water was also investigated. A Hyperbolic model was used in the study to establish the parameters and understand the material's stress-strain response. The prediction showed an increase in the ultimate deviator stress the by-product can accommodate [8]. Although several studies showed the potential of coal ash as a construction material, its volume change behavior

with regards to sea water exposure needs to be further understood. This behavior needs to be understood due to the growing population in major cities such as Manila and Cebu City. Most of these cities experiences congestion which resulted to constructing additional infrastructures at bodies of water. It is therefore the objective of this study to understand the volume change behavior of coal ash exposed to sea water. A hyperbolic model was used to model and predict the volume change behavior of coal ash towards the sea water. Furthermore, hyperbolic parameters with respect to the Poisson's ratio and bulk modulus were also obtained. Sea water exposure was performed in three levels of exposure namely, no exposure (S1), immediate exposure (S2) and prolonged exposure (S3). Consolidated drained triaxial test was performed.

INDEX PROPERTIES OF BOTTOM ASH

The bottom ash used in the study was obtained from a power plant in central Philippines. The index properties of bottom ash are tabulated in Table 1. These were established based on the procedures specified by the American Society for Testing Materials. Based on the results, the by-product was classified as silty sand (SM) with no plasticity. It also contains sufficient amount of sand particles with fines content. The result of specific gravity was compared to other studies. A range of 1.899 to 1.903 was established [9]. It can be seen that the specific gravity determined had a larger value. It is rather close to the typical values for silty sand which is 2.6 to 2.9 [10]. The location where the tested coal ash was different from the coal ash tested from the other study. This could have contributed to the difference in result of the tested coal ash.

EXPERIMENTAL PROGRAM

Sea water Preparation and Exposure Levels

The Standard Practice for the Preparation of Substitute Ocean Water (ASTM D 1141 – 98) was used to artificially prepare the sea water. Actual sea water was not used due environmental concerns. The chemical compositions used for the mixing of artificial sea water are tabulated in Table 2. Sea water exposure level was divided into three namely, no exposure (S1), immediate exposure (S2) and prolonged exposure (S3). In a no exposure level, distilled water was used in the sample preparation and in the experiment. The immediate exposure on the other hand had sea water exposure during the experiment. Lastly, the prolonged exposure level is where sea water was used in the sample preparation and in the experiment.

Table 1. Index properties

Index Property	
Specific gravity(Gs)	2.25
Liquid limit(LL)	0.00%
Plastic limit (PL)	0.00%
Maximum void ratio (e_{max})	0.94
Minimum void ratio (e_{min})	0.85
Maximum dry unit weight(γ_{dmax})	13.94 kN/m ³
Optimum water content (ω_{opt})	15.85%
USCS	SM
%Gravel	0.86
%Sand	50.44
%Fines	48.70

Table 2 Chemical composition of sea water

Compound	Concentration,g/L
NaCl	24.53
MgCl	5.2
NaSO	4.09
CaCl	1.16
KCl	0.695
NaHCO	0.201
KBr	0.101
HBO	0.027
SrCl	0.025
NaF	0.003
Ba(NO	9.94E-05
Mn(NO	3.40E-05
Cu(NO	3.08E-05
Zn(NO	9.60E-06
Pb(NO	6.60E-06
AgNO	4.90E-07

Sample Preparation

Coal ash was prepared by moist tamping. The relative compaction was used as the parameter to reach the initial target condition. This parameter was used in order to simulate actual site conditions. The maximum dry density was used as the reference to reach the desired relative compaction. A 95% relative compaction was the initial target condition and this value was also the desired in-situ condition. For the sample preparation of S1 and S2, the amount of distilled water mixed with coal ash was referenced with the optimum moisture content. Similarly for the sample preparation of S3, the value of optimum moisture content served as the reference parameter in order to determine the amount of sea water to be mixed with coal ash. The samples for all levels were soaked for 16 hours as stipulated in the ASTM provisions.

Consolidated Drained Test

British Standard (BS) 1377-8: 1990 was the standard applied in performing the Consolidated

Drained Test. Based on the standard, there are three stages in the experiment namely, saturation, consolidation and shear. The saturation stage is where additional water is added to the sample. In the study especially in S3, salt water was added in this stage. In order to ensure that a fully saturated condition was achieved a B-value or the ratio of the change in pore water pressure and confining pressure was checked. This parameter must have a value greater than 0.95. In the consolidation stage, the confining pressures (σ_3) used are 50 kPa, 100 kPa, and 200 kPa. In S2 and S3 the sea water was used to confine the sample during the consolidation and shearing stage. For the shearing stage, the rate of loading of 0.05 mm/min was implemented. This rate was used in order to facilitate the proper dissipation of pore water pressure. The shearing stage lasted for a minimum of 4 hours to a maximum of 7 hours due to the slow rate. A total of 18 samples were tested for this study.

HYPERBOLIC MODEL

The Hyperbolic model is based on the hyperbolic stress-strain relationship [11]. It is an incremental stress-dependent model which is based on the incrementally nonlinear elastic behavior. The model can represent the nonlinear behavior of the volume change through hyperbolas. Poisson's ratio can be determined from the model through the analysis of the volume changes in a triaxial test. This parameter is computed through determining the radial strains as shown [12]:

$$\varepsilon_r = \frac{1}{2}(\varepsilon_v - \varepsilon_a) \quad (1)$$

where ε_v = volumetric strain; ε_a = axial strain.

The variation of ε_a with ε_r is when plotted can result to the following hyperbolic equation [12]:

$$\varepsilon_a = \frac{-\varepsilon_r}{v_i - d\varepsilon_r} \quad (2)$$

When ε_r is normalized with ε_a , the equation can be rewritten as shown in Eq.2. Typical results are shown in Fig.1. This equation can determine the value of the Poisson's ratio or initial Poisson's ratio [12].

$$-\frac{\varepsilon_r}{\varepsilon_a} = v_i - d\varepsilon_r \quad (3)$$

where v_i = initial Poisson's ratio (at zero strain) or the y-intercept of the plot; d = parameter representing the change in the value of Poisson's ratio with radial strain or the slope of the plot.

The equation of each plot in Fig. 1 are expressed as:

$$-\frac{\varepsilon_r}{\varepsilon_a} = 0.4811 - 1.0316\varepsilon_r \quad (5)$$

$$-\frac{\varepsilon_r}{\varepsilon_a} = 0.4406 - 0.5477\varepsilon_r \quad (6)$$

$$-\frac{\varepsilon_r}{\varepsilon_a} = 0.4980 - 2.0892\varepsilon_r \quad (7)$$

where Eqn 5 is the plot for 50kPa cell pressure; Eqn 6 is the plot for 100kPa cell pressure; Eqn 7 is the plot for 200kPa cell pressure.

Poisson's ratio was found to be affected by the change in confining pressure. The volume change behavior therefore can be represented through varying Poisson's ratio with confining pressure as shown in Eqn. 8 [12].

$$v_i = G - F \log_{10} \left(\frac{\sigma_3}{P_a} \right) \quad (8)$$

where G = the value of v_i at a confining pressure of one atmosphere; F = the reduction in v_i for a ten-fold increase in confining pressure.

The parameters presented in Eqn. 8 can be determined by plotting v_i against the ratio of the confining pressure and atmospheric pressure. Typical results are shown in Fig. 2.

The instantaneous slope, tangent value of Poisson's ratio (v_t), of the variation of ε_a with ε_r can also be related to the changes in stress of the sample. It can be defined by the following expression [12]:

$$v_t = \frac{G - F \log \left(\frac{\sigma_3}{P_a} \right)}{\left[1 - \frac{d(\sigma_1 - \sigma_3)}{K P_a \left(\frac{\sigma_3}{P_a} \right)^n \left[1 - \frac{R_f(\sigma_1 - \sigma_3)(1 - \sin \varphi)}{2 C \cos \varphi + 2 \sigma_3 \sin \varphi} \right]} \right]^2} \quad (9)$$

where K = primary loading modulus; n = exponent number; C = cohesion; R_f = failure ratio; φ = angle of internal friction; P_a = atmospheric pressure ($P_a = 101.325$ kPa).

Bulk modulus was replaced by Poisson's ratio in analyzing the volume change behavior of the soil [13]. This parameter is independent of changes in deviator stress. However, it still varies with confining pressure. Bulk modulus therefore can provide approximations that are reasonable to the behavior of changes in volume. Moreover, assuming that the bulk modulus is independent of the changes in deviator stress can appropriately characterize the response of the soil with respect to the variations in the mean stresses. Based on the theory of elasticity, bulk modulus can be defined by the following expression:

$$B = \frac{\Delta \sigma_1 + \Delta \sigma_2 + \Delta \sigma_3}{3 \varepsilon_v} \quad (10)$$

where B = bulk modulus; $\Delta \sigma_1$, $\Delta \sigma_2$ and $\Delta \sigma_3$ = changes in the values of the principal stresses; $\Delta \varepsilon_v$ =

change in volumetric strain.

In a conventional triaxial test, Eqn.10 can be re-written to Eqn.11 since the confining pressure is maintained as a constant value while the deviator stress is being increased.

$$B = \frac{\sigma_1 - \sigma_3}{3\varepsilon_v} \quad (11)$$

The bulk modulus can be computed with respect to the variation of confining pressure in relation to the hyperbolic model. As the confining pressure increases the bulk modulus also increases [13]. The bulk modulus therefore can be approximated by this equation:

$$B = K_b P_a \left(\frac{\sigma_3}{P_a} \right)^m \quad (12)$$

where K_b = bulk modulus number; m = bulk modulus exponent.

The parameters K_b and m are determined by plotting the normalized bulk modulus against confining pressure in a logarithmic scale. Typical results are shown in Fig. 3. Parameter m is the slope of the plot while parameter K_b is the y-intercept.

VOLUME CHANGE BEHAVIOR OF COAL ASH

The hyperbolic parameters with respect to the volume change behavior of the coal ash exposed to sea water were determined. The results related to Poisson's ratio are tabulated in Tables 3-5.

Table 3 Hyperbolic Parameters for S1

σ_3 kPa	d	ν	G	F	ν_t
50	1.0316	0.4811			0.1379
100	0.5477	0.4406	0.4524	0.0181	0.0032
200	2.0892	0.4980			0.1320

Table 4 Hyperbolic Parameters for S2

σ_3 kPa	d	ν	G	F	ν_t
50	1.1094	0.5217			0.0085
100	0.1292	0.5018	0.5187	0.0072	1.5407
200	0.6955	0.5078			0.2294

Table 5 Hyperbolic Parameters for S3

σ_3 kPa	d	ν	G	F	ν_t
50	0.2857	0.5045			0.7956
100	0.1582	0.5018	0.4960	0.0085	0.6776

200	2.2760	0.5136	0.0096
-----	--------	--------	--------

The results from different level of sea water exposure were compared. Based on the results, it was observed that at 100 kPa all the parameters are smaller than the results from 50 and 200 kPa except the trend for the tangent value of Poisson's ratio. The tangent value of Poisson's ratio has no distinct trend. The results were greatly affected by K , n , R_f , C , and the angle of internal friction. The parameters K , n and R_f used are tabulated in Table 7. It can be observed that K and n for S1 and S2 are the same while a smaller value was observed for S3. The angle of internal friction for S1, S2 and S3 are 33.77° , 27.03° and 33.91° , respectively [8]. The cohesion for S1, S2 and S3 are 28.56 kPa, 49.91 kPa and 15.43 kPa, respectively [8]. The angle of internal friction for S2 exposure was smaller compared to the other samples. On the other hand, its cohesion is larger. These parameters affected the results of the tangent value of Poisson's ratio.

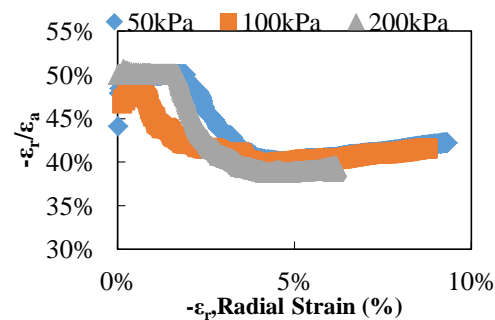


Fig.1 Hyperbolic axial strain-radial strain curve.

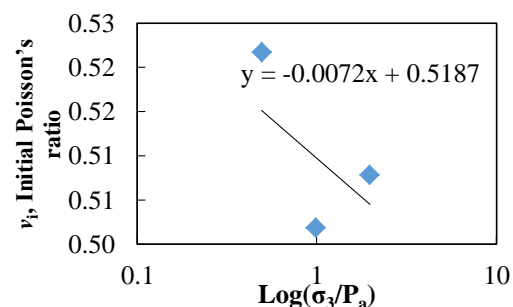


Fig.2 Variation of ν_i with σ_3 .

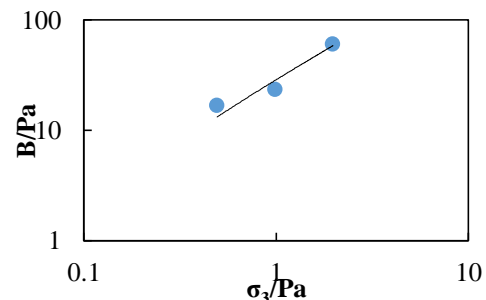


Fig. 3 Variation of bulk modulus with σ_3 .

The hyperbolic parameters with respect to the bulk modulus were also obtained. Results are

tabulated in Table 6. The bulk modulus was determined with respect to a constant m and K_b and increasing confining pressure. It can be seen that as the confining pressure was increased the bulk modulus also increases. The bulk modulus can better approximate the volumetric response of the soil. Therefore, it was used to predict the volume change of each sea water exposure levels. The typical results of S1 and S2 are shown in Figs.4-6 and Figs7-9, respectively. The typical results for S3 are similar to S2. The predicted results for S1 at 50 kPa coincided with the experimental results but this was towards the end of the plot. For 100 kPa, only a part in the plot coincided with the predicted results. For 200 kPa, the predicted results only followed the trend of the experimental results. As a whole the predicted results for S1 was larger than the experimental results. For the results of S2, the predicted results for 50 kPa and 200 kPa had a similar trend. The predicted results coincided towards the end of the plot. The 100 kPa predicted results on the other hand was larger than the experimental data.

Table 6 Hyperbolic Parameters with respect to B

	m	K_b	σ_3 , kPa	B , kPa
S1	0.9303	29.2216	50	1,534.8211
			100	2,924.8450
			200	5,573.7558
S2	0.7295	48.5097	50	2,936.0899
			100	4,868.2738
			200	8,071.9906
S3	1.3238	226.22973	50	8,999.2595
			100	22,526.7661
			200	56,388.5495

Table 7 Hyperbolic stress-strain parameters [8].

	K	N	σ_3 , kPa	R_f
S1	5.9900	1.34	50	0.9998
			100	0.9324
			200	0.5335
S2	5.9900	1.34	50	0.9051
			100	0.9282
			200	0.8309
S3	4.6600	0.22	50	0.9946
			100	0.9192
			200	0.8207

Based on the results, the hyperbolic model was not able to fully predict the volume change behavior of the coal ash. The parameters established were affected by the behavior of volume change data of each sea water level exposure. For all samples tested it was observed that the volume change behavior did

not reach a stable value. Especially for the samples exposed to sea water. The pore water pressure was not able to properly dissipate.

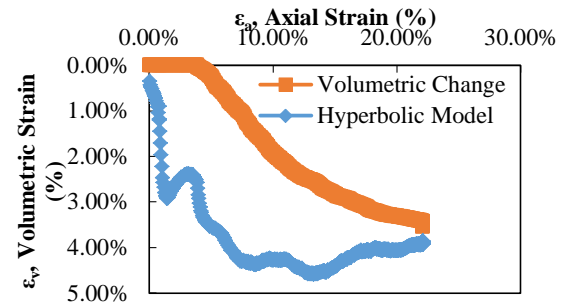


Fig.4 Results for S1 at 50kPa.

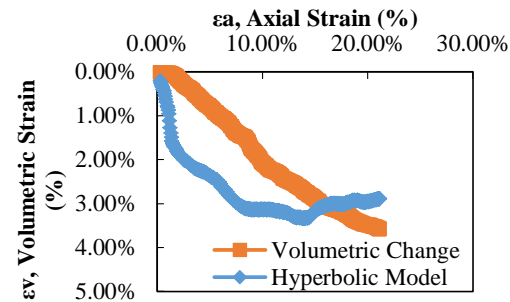


Fig.5 Results for S1 at 100kPa.

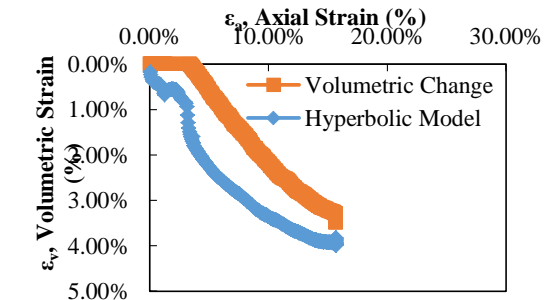


Fig.6 Results for S1 at 200kPa.

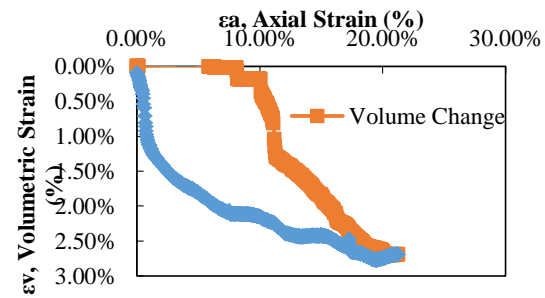


Fig.7 Results for S2 at 50kPa.

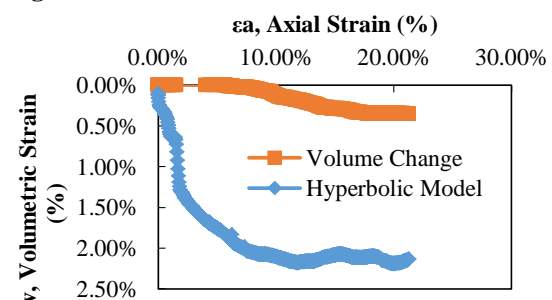


Fig.8 Results for S2 at 100kPa.

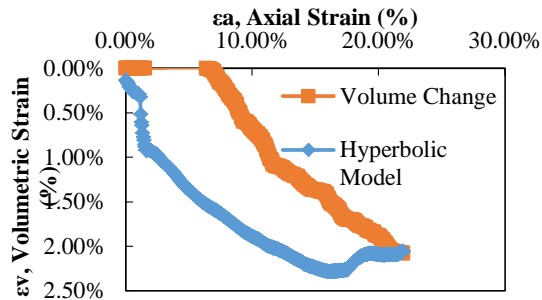


Fig.9 Results for S2 at 200kPa.

Sea water greatly affected the drainage condition during the experiment. For the results of S2 and S3, they were affected by the consistency of the relative compaction. The mixture of sea water with respect to the coal ash was the main factor that affected the relative compaction. The established hyperbolic parameters were observed to be highly affected by the drainage conditions and the reaction of sea water when mixed to the bottom ash.

CONCLUSION

The hyperbolic model was implemented to investigate on the volume change behavior of the coal ash exposed to sea water. Based on the results, the parameter representing the change in the value of Poisson's ratio with radial strain (d), the value of v_i at a confining pressure of one atmosphere (G) and the reduction in v_i for a ten-fold increase in confining pressure (F) are affected by the amount of confining pressure. The tangent value of Poisson's ratio on the other hand is affected by the primary loading modulus (K), exponent number (n), failure ratio (R_f), cohesion (C) and the angle of internal friction. For the prediction of the volume change behavior of the hyperbolic model, it was observed that the model was not able to fully predict the volume change behavior of the coal ash. The parameters obtained were observed to be affected by the drainage conditions and the reaction of sea water when mixed to the bottom ash. It is recommended to perform more experiments having a wider range of confining pressure. A different loading rate should also be considered. This is to improve the parameter determination with respect to the hyperbolic model.

ACKNOWLEDGEMENTS

The researcher would like to express her deep gratitude towards Dr. Mary Ann Adajar, Dr. Jonathan Dungca and De La Salle University for their support.

REFERENCES

[1] The Inquirer. "Coal Remain Dominant In Philippine Energy Mix",

<http://business.inquirer.net/243956/coal-remain-dominant-ph-energy-mix>, 2018.

- [2] Department of Energy. "Coal Top 55 Philippine Power Mix 2027", <https://www.doe.gov.ph/energist/coal-top-55-ph-power-mix-2027>, 2018
- [3] Yoon, S., Ph, D., Balunaini, U., Yildirim, I. Z., Prezzi, M., and Siddiki, N. Z., "Construction of An Embankment with A Fly And Bottom Ash Mixture : Field Performance Study", *Journal of Materials in Civil Engineering*, Vol.21, 2009, pp.271-278
- [4] Dungca, J. R. and Jao, J. A. L., "Strength and Permeability Characteristics of Road Base Materials Blended With Fly Ash and Bottom Ash", *International Journal of GEOMATE*, Vol.12, Issue 31, 2017, pp. 9-15.
- [5] Dungca, J. R., Galupino, J.G., Alday, J.C., Baretto, M.A.F., Bauzon, K. G. and Tolentino, A. N., "Hydraulic Conductivity Characteristics of Road Base Materials Blended with Fly Ash And Bottom Ash", *International Journal of GEOMATE*, Vol.14, Issue 44, 2018, pp.121-127.
- [6] Huang, W. H., "The Use of Bottom Ash in Highway Embankments, Subgrades and Subbases", Retrieved from docs.lib.purdue.edu/cgi/viewcontent.cgi?article=1782&context=jtrp. 1990.
- [7] Uy, E. E. S. and Dungca, J. R., "Constitutive Modeling of Coal Ash using Modified Cam Clay Model. *International Journal of GEOMATE*, Vol. 12, Issue 31, 2017, pp.88-94.
- [8] Uy, E. E. S. and Dungca, J. R., "Hyperbolic Model Parameters of Philippine Coal Ash", *International Journal of GEOMATE*, Vol. 15, Issue 47, 2018, pp.95-102.
- [9] Antonio, O. V. M., and Zarco, M. A. H., "Engineering Properties of Calaca Batangas Bottom Ash", Vol. 28, Issue 1, 2007, pp.37-56.
- [10] Das, B. & Sobhan, K., "Principles of Geotechnical Engineering", Sixth Edition, United States: Chris Carson, 2014
- [11] Stark, T. D., Ebeling, R. M. & Vettel, J. J., "Hyperbolic stress-strain parameters for silts. *Journal of Geotechnical Engineering*", Vol.120, Issue 2, 1992, pp.420-441.
- [12] Duncan, J. and Wong, K., "Hyperbolic Stress-Strain Parameters for Nonlinear Finite Element Analyses of Stress and Movements in Soil Masses", Report No TE-74-3, University of California, Berkeley, California, 1974.
- [13] Duncan, J. and Wong, K., "Strength, Stress-strain and Bulk Modulus Parameters for Finite Element Analysis of Stresses and Movements in Soil Masses", Report No. UCB/GT/80-01, University of California, Berkeley, California, 1980.

FINITE DIFFERENCE METHOD FOR SOLVING HEAT CONDUCTION EQUATION OF THE GRANITE

Dalal Adnan Maturi¹

¹Departement of Mathematics, Faculty of Science, king Abdulaziz University, Saudi Arabia

ABSTRACT

In this paper, the finite difference method has been presented to solve the heat conduction equation of the Granite. This method solves the heat conduction equation of the Granite with the help of Matlab. Also, five numerical examples are illustrated by this method. The results reveal that this method is very effective and prove the Granite is a material resistant to various high temperatures.

Keywords: Finite Difference Method, Heat Conduction Equation, Granite, Matlab.

INTRODUCTION

Finite differencing methods describe functions as discrete values across a grid, and approximate their derivatives as differences between points on the grid. Knowing a little about how difference methods are formulated and in what regimes they are stable can help save a lot of time, both in the design of finite differencing algorithms, and in the time that they take to run, the finite difference approximations for derivatives are one of the simplest and of the oldest methods to solve differential equations.

We need a fast, realistic and reliable method to solve the heat conduction equation of the Granite. It is one of the types of igneous rocks that form in the ground under the influence of high thermal pressure, usually consists of the main minerals in the form of alcohols and aluminum alkali silks. In addition, plagioclase, these three metals give the granite stone colors are characterized by crimson or light gray. According to biologists, it is formed by crystallization of magma by the slow cooling that came on the fringes of the fusion of buried rocks at a depth of 25-40 km below the surface Land, and because of this common rock-proliferation must recognize the advantages and disadvantages of granite close.

Advantages and disadvantages of granite, it is lighter than the rest of the surrounding rocks in the ground, the sizes of granite granules vary between medium and large size, Silica contains silica in abundance among its components, the most common types of rock, it is very beautifully unique due to its color overlap, and It is also characterized as a dielectric material, so the mica sheets are extracted from it and used in the production of insulation purposes.

FINITE DIFFERENCE METHOD FOR HEAT CONDUCTION EQUATION

The linear second order partial differential equation

$$Au_{xx} + 2Bu_{xy} + Cu_{yy} + Du_x + Eu_y + Fu + G = 0$$

as a parabolic equation if $B^2 - AC = 0$. A parabolic equation holds in an open domain or in a semi-open domain.

Consider a thin homogeneous, insulated bar or a wire of length l . Let the bar be located on the x - axis on the interval $[0, l]$. See the rod have a source of heat. For example, the rod may be heated at one end or at the middle point or has some source of heat. Give $u(x, t)$ denote the temperature in the rod at any instant of time t . The problem is to study the flow of heat in the rod. The partial differential equation governing the flow of heat in the rod is given by the

parabolic equation

$$u_t = c^2 u_{xx}, \quad 0 \leq x \leq l, \quad t > 0.$$

Where c^2 is a constant and depends on the material properties of the rod.

The heat conduction equation of the Granite

$$\begin{aligned} u_t &= (0.011)u_{xx} \\ u(0, t) &= u(1, t) = 0, \forall t \in (0, t_F) \\ u(x, 0) &= u_0(x), \quad \forall x \in [0, 1], \end{aligned}$$

Where t_F Denotes the terminal time for the model. Here without loss of generality, we assume that the spatial domain is $[0, 1]$.

At first divide the physical domain $(0, t_F) \times (0, 1)$ by $N \times J$ uniform grid points

$$\begin{aligned} t_n &= n\Delta t, \Delta t = \frac{t_F}{N}, n = 0, 1, \dots, N, \\ x_j &= j\Delta x, \Delta x = \frac{1}{J}, j = 0, 1, \dots, J. \end{aligned}$$

Then, we denote the approximate solution $u_j^n \approx u(x_j, t_n)$. At an arbitrary point (x_j, t_n) . To obtain

a finite difference scheme, we need to approximate the derivatives in (1) by some finite differences. (Explicit scheme)

Substituting

$$u_t(x_j, t_n) \approx (u_j^n - u_j^{n-1})/\Delta t,$$

$$u_{xx}(x_j, t_n) \approx (u_{j+1}^n - 2u_j^n + u_{j-1}^n)/(\Delta x)^2,$$

Into (1), another difference scheme for (1) can be constructed as:

$$\frac{u_j^n - u_j^{n-1}}{\Delta t} = \frac{u_{j+1}^n - 2u_j^n + u_{j-1}^n}{(\Delta x)^2}, \quad 1 \leq j \leq J-1, 1 \leq n \leq N.$$

SEVERALS EXAMPLES

(i) Example1. Find the solution of the heat conduction equation of the Granite

$$u_t = (0.011)u_{xx} \quad 0 < x < 1, \quad t > 0;$$

$$u(0, t) = u(1, t) = 0, \quad t > 0;$$

$$u(x, 0) = \sin \pi x, \quad 0 \leq x \leq 1.$$

Applying the finite difference method using Matlab, then the result show as follows.

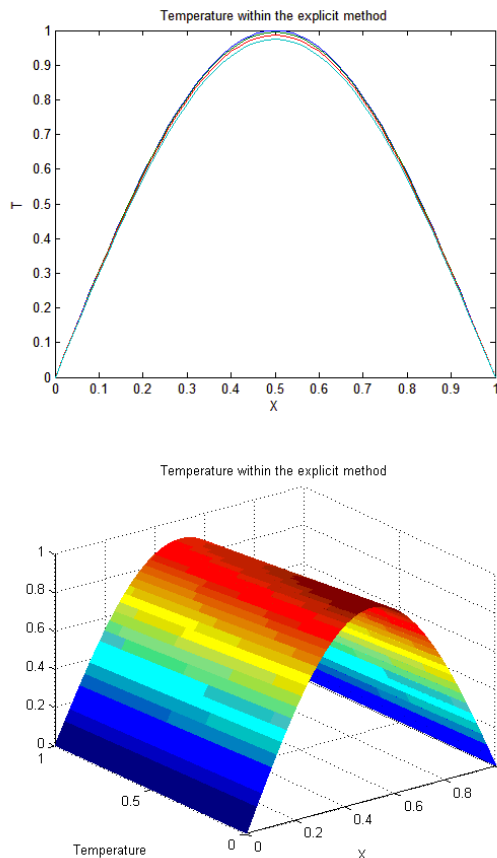


Fig.1 Temperature distributions at several times for the heat conduction of the Granite for example 1.

(ii) Example2. Find the solution of the heat conduction equation of the Granite

$$u_t = (0.011)u_{xx} \quad 0 < x < 1, \quad t > 0;$$

$$u(0, t) = u(1, t) = 0, \quad t > 0;$$

$$u(x, 0) = \sin 2\pi x - \sin 5\pi x, \quad 0 \leq x \leq 1.$$

Applying the finite difference method using Matlab, then the result show as follows.

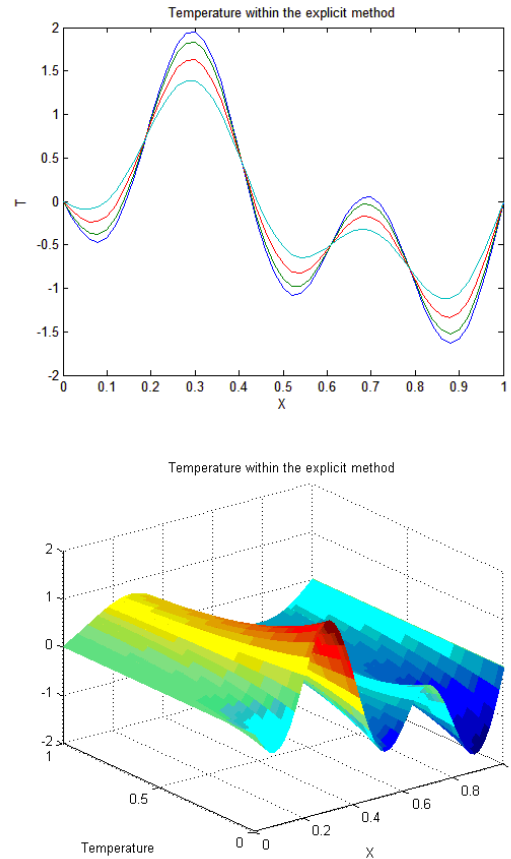


Fig.2 Temperature distributions at several times for the heat conduction of the Granite for example 2.

(iii) Example3. Find the solution of the heat conduction equation of the Granite

$$u_t = (0.011)u_{xx} \quad 0 < x < 1, \quad t > 0;$$

$$u(0, t) = u(1, t) = 0, \quad t > 0;$$

$$u(x, 0) = 2 \sin(\pi x/2) - \sin \pi x + 4 \sin 2\pi x, \quad 0 \leq x \leq 1.$$

Applying the finite difference method using Matlab, then the result show as follows.

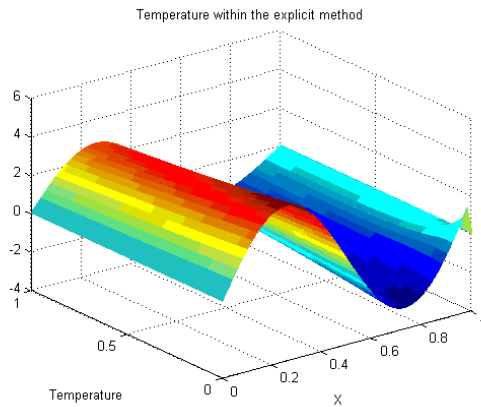
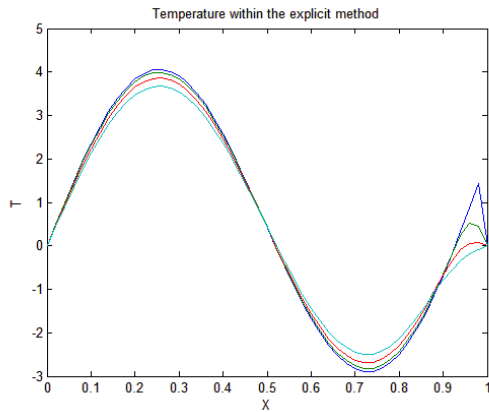


Fig.3 Temperature distributions at several times for the heat conduction of the Granite for example 3.

(iv) Example4. Find the solution of the heat conduction equation of the Granite

$$\begin{aligned} u_t &= (0.011)u_{xx} \quad 0 < x < 1, \quad t > 0; \\ u(0, t) &= u(1, t) = 0, \quad t > 0; \\ u(x, 0) &= x(1 - x), \quad 0 \leq x \leq 1. \end{aligned}$$

Applying the finite difference method using Matlab, then the result show as follows.

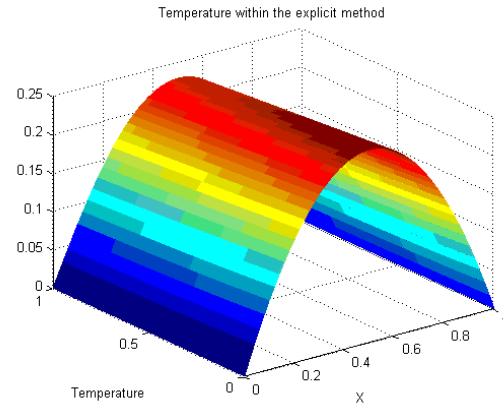
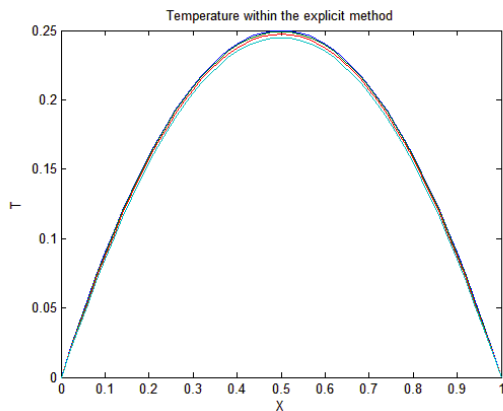


Fig.4 Temperature distributions at several times for the heat conduction of the Granite for example 4.

(v) Example5. Find the solution of the heat conduction equation of the Granite

$$\begin{aligned} u_t &= (0.011)u_{xx} \quad 0 < x < 1, \quad t > 0; \\ u(0, t) &= u(1, t) = 0, \quad t > 0; \\ u(x, 0) &= \sin(x) - 3 \cos 4x, \quad 0 \leq x \leq 1. \end{aligned}$$

Applying the finite difference method using Matlab, then the result show as follows.

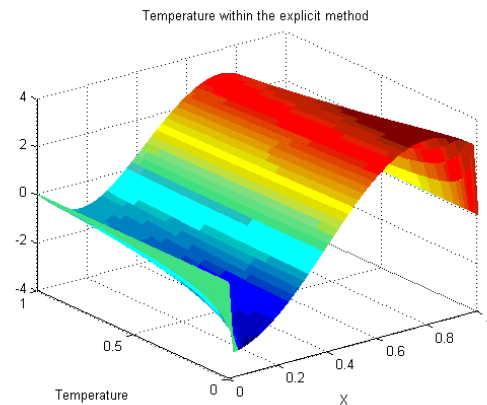
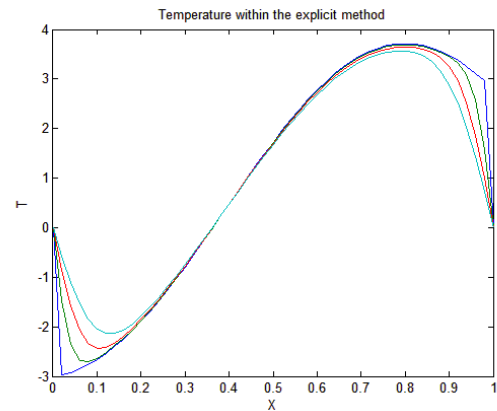


Fig.5 Temperature distributions at several times for the heat conduction of the Granite for example5.

CONCLUSION

In this paper, the Finite difference method for solving heat conduction equation of the Granite .

All the examples show that the finite difference method is a powerful mathematical tool for solving heat conduction equation of the Granite. Graphical figures we presented to determine the higher accuracy and simplicity of the proposed method.

Moreover , it should be mentioned that the propounded method can be easily generalized for more heat conduction for another materiels different.

This work is focused on rocks especially Granite because it is very high hardness.It can be relied upon in various construction works, due to its high resistance to weathering factors; therefore it is used in the construction of temples, palaces and museums.

ACKNOWLEDGEMENTS

This paper was supported by the Deanship of Scientific Research (DSR), King Abdulaziz University, Jeddah.

REFERENCES

- [1] William. F. A., Numerical Methods for Partial Differential Equations. Academic Press, New York, NY, 3rd edition, 1992.
- [2] Jim. D., and H.H. R., On the numerical solution of heat conduction problems in two and three space variables. Trans. Amer. Math.Soc., 82:421–439, 1956.
- [3] A.R. Mitchell and D.F. Griffiths. The Finite Difference Method in Partial Differential Equations. John Wiley & Sons, Chichester, 1980.
- [4] A.R. Mitchell and D.F. Griffiths. The Finite Difference Method in Partial Differential Equations. John Wiley & Sons, Chichester, 1980.
- [5] Dalal A.M, Amani..Z.B.I, Badreeh..M. G., Numerical Solution of Volterra Integral Equation of Second Kind Using Implicit Trapezoidal, Journal of Advances In Mathematics, Vol8,No.2,pp.1540-1553,2014.
- [6] Dalal .A. M., Adomian Decomposition Method of Fredholm Integral Equation of the Second Kind Using Maple, Journal of Advances In Mathematics, Vol9,No.1,pp.1868-1875,2014.
- [7] Dalal. A.M., Application of Adomian Decomposition Method for Solving of Fredholm Integral Equation of the Second Kind, European Journal of Science and Engineering, Vol9,No.2,pp.1-9,2014.
- [8] Dalal .A.M., Adomian Decomposition Method for Solving of Fredholm Integral Equation of the Second Kind Using Matlab, International Journal of GEOMATE, Dec., 2016, Vol. 11, Issue 28, pp.2830-2833.Special Issue on Science, Engineering and Environment, ISSN: 2186-2990, Japan.
- [9] Dalal A.M. and Honida M.M., Numerical Solution of System of Three Nonlinear Volterra Integral Equation Using Implicit Trapezoidal, Journal of Mathematics Research, Vol.10, No. 1, February 2018,ISSN 1916-9795 E-ISSN 1916-9809.

REGRESSION MODELING OF BREAKOUT STRENGTH OF AN EXPANSION ANCHOR BOLT AS INFLUENCED BY CONCRETE AGGREGATES

Gilford B. Estores¹, Wyndell A. Almenor² and Charity Hope A. Gayatin³
^{1,2,3}Faculty, Mapua University, Philippines

ABSTRACT

The frictional resistance of an expansion anchor bolt depends directly on the normal forces generated by the anchor expansion mechanism around the anchorage zone of the concrete base material. However, only the concrete aggregates around the anchorage zone have the direct shear contact with the anchor. This study aims to develop a regression model that predicts the breakout strength of an expansion anchor in plain concrete as influenced by the coarse aggregate size, coarse aggregate content, and fine aggregate content. Crushed coarse aggregates of sizes 10mm, 12.5mm, 19mm, and 25mm were used. The coarse aggregate content for each coarse aggregate size was 0.3452, 0.4046, 0.4462, and 0.4750, respectively. The fine aggregate content for each coarse aggregate size was 0.4243, 0.3771, 0.3514, and 0.3341, respectively. A heavy duty type of an expansion anchor bolt was used. There were five samples of base material specimens considered for each size of coarse aggregate. Each specimen was tested first for its compressive strength to ensure that it will meet the designed compressive strength and it will vary only at an acceptable deviation before the installation of the expansion anchors. The installed anchor bolts were then tested for pull-out. Tests results showed that among the parameters considered, coarse aggregate size is the most significant factor that could influence the breakout strength of an expansion anchor and it is optimum at 19mm size. A polynomial regression model is recommended to predict the concrete breakout strength of an expansion anchor bolt as influenced by the coarse aggregate size.

Keywords: Concrete Breakout Strength, Coarse Aggregate Size, Expansion Anchor Bolt, Regression Modeling, Coarse Aggregate Content

INTRODUCTION

Anchor bolts are widely used in composite construction such as for steel-to-concrete connections. The selection of anchor bolt is based on structural considerations typically designed and detailed by a structural engineer because they are relevant to life safety and failure could pose a threat to life or could bring about significant economic loss. Due to his involvement in the design criteria, the structural engineer should be able to consider not only the properties of anchor bolts, but also the properties of the concrete base material, which could influence its pull-out resistance. This is essential, for when anchors are subjected to extreme tensile load, they become prone to breakout failure - concrete block breaking out from the bulk concrete. Thus, such failure evidently impend the safety and reliability of structures built with over loaded anchor connections. A number of researches have attempted to investigate the influence of base material on anchor properties. One research about possible effects of masonry aggregate in the highly stressed anchorage area of an anchor was investigated. Masonry aggregate concrete was introduced because in theory, with mixed recycled aggregates, it is most probable that only concrete aggregates will be

located around the anchorage zone [1]. Another researchers did an extensive study on pull-out strength of fasteners under static load. As stated in their research, concrete breakout failure load is influenced by the concrete mechanical properties E_c (Modulus of Elasticity) and G_f (Fracture Energy). Moreover, given that these properties are related to the compressive strength of concrete, it is assumed that the compressive strength of concrete and the effective embedment length of the anchor bolt, that the failure load is proportional to the square root of compressive strength [2]. However, it should be noted that for the same compressive strength, E_c and G_f may also be influenced by the concrete mix, in particular, the type and the maximum size of aggregate. On the other hand, another study concluded that a nominal maximum aggregate size has an influence on the concrete compressive strength [3]. From these researches, it is thought that the size of coarse aggregates will have an effect on the anchor bolt pull-out performance.

In this study, the pull-out load capacity of an expansion anchor bolt at concrete breakout failure or simply breakout strength of an expansion anchor bolt was investigated as influenced by the concrete aggregates. Expansion anchors are post-installed anchors that transfer tension load to the concrete

principally by friction. The frictional resistance of the anchor depends directly on the normal forces generated by the anchor expansion mechanism during installation and throughout the life of the anchorage. It is assumed that concrete aggregates located around the anchorage zone have sole direct shear contact with the anchor. These are fine aggregates and coarse aggregates. The influence of these aggregates in concrete breakout strength relative to its size and content was done by the demonstration of the pull-out test which measures the pull-out load capacity of the anchor bolts embedded in the concrete. Specifically, the factors considered in the investigation to influence the breakout strength of an expansion anchor bolt were coarse aggregate size, coarse aggregate content and fine aggregate content. The size of the coarse aggregate was selected since it covers more direct shear contact around the anchorage zone as compared to fine aggregates. This research was conducted to give significant information needed by a structural engineer on the design of expansion anchor bolts connection to structural concrete members relative to its concrete aggregate size and content. Specifically, this research will lead the construction industry to take a new approach involving the safe design of expansion anchor bolts connection for new construction or in some cases where there is a need for connecting a new structural member to an existing structural concrete member.

This research attempted also to identify factors of concrete aggregates that will optimize the breakout strength of an expansion anchor bolt in concrete. Lastly, this study aims to develop a regression model that could predict the breakout strength of an expansion anchor bolt as influenced by the concrete aggregates used relative to its size and content.

METHODOLOGY

Materials

The components of the pull-out specimens used in this research were the expansion anchor bolt and the concrete base material. In this research, a heavy-duty torque controlled mechanical expansion anchor bolt was used, with a diameter of 8mm, with a total length of 98mm and with a nominal tensile strength of 800MPa. The technical data of the anchor bolt is presented in Table 1 (i.e. required torque (T), effective embedment depth (h_{ef}), drilling depth (h_d), drilled hole diameter (D), and base thickness (H).

Table 1 Technical data of expansion anchor bolt

Type	T	h_{ef}	h_d	D	H
	(Nm)	(mm)	(mm)	(mm)	(mm)



25 70 80 12 125

The concrete base material was composed of cement (C), water (W), fine aggregates (FA), and coarse aggregates (CA). Portland cement from Norzagaray, Bulacan Cement Plant that meets the American Society for Testing and Materials (ASTM) standard specification C150 was used in the design mix [4]. The water used was clean and of good quality. Crushed coarse aggregates with four sizes were considered - 10mm, 12.5mm, 19mm, and 25mm having a mass density of 1651kg/m³ and 1.00% absorption were used as shown in Fig. 1. These coarse aggregates came from a single crusher located in Montalban, Rizal. For fine aggregates, sand with 2.6 fineness modulus and 0.80% water absorption was used.



Fig. 1 Crushed coarse aggregates sizes (25mm, 19mm, 12.5mm and 10mm)

Specimens

Different concrete mixture proportions were used for different concrete specimens. The specimens varied according to their coarse aggregate size (S), coarse aggregate content (CAC), and fine aggregate content (FAC). The coarse aggregate content for each coarse aggregate size was 0.3452, 0.4046, 0.4462, and 0.4750, respectively. The fine aggregate content for each coarse aggregate size was 0.4243, 0.3771, 0.3514, and 0.3341, respectively. Although the mixture proportions varied, a uniform compressive strength of 21MPa at 28days curing period had been considered in the design mixture. This is to ensure that the compressive strength of the concrete specimens would not interfere with the pull-out performance of the expansion anchor bolts. The mixture proportions of the different concrete base specimens are presented in Table 2.

Table 2 Mix proportions of the specimens

S	W	C	CA	FA
(mm)	(kg/m ³)	(kg/m ³)	(kg/m ³)	(kg/m ³)

10	222.84	304.66	790.13	970.98
----	--------	--------	--------	--------

Table 2 Mix proportions of the specimens (cont.)

S (mm)	W (kg/m ³)	C (kg/m ³)	CA (kg/m ³)	FA (kg/m ³)
12.5	214.67	291.61	938.28	874.36
19	203.62	274.20	1053.51	829.82
25	195.33	261.14	1135.82	799.04

Five samples were used for each type of coarse aggregate size, this is in accordance with ASTM E 488-96 [5]. The rectangular solid base material specimens measuring 350mm x 350mm x 125mm were made and cured for 28days. Then, the expansion anchors were installed in these base materials following the setting instructions recommended by the manufacturer as shown in Fig. 2. Simultaneously, 150mm concrete cube specimens for compressive strength test were prepared for each type of concrete base specimen. Two samples were used for each type of coarse aggregate size in accordance with ASTM C 39-05 [6]. After pouring, all the specimens were cured for 28days to attain the design compressive strength of 21MPa. During curing, the specimens were placed in an area where the rays of the sun could not reach; this is to ensure that the air temperature within the area was controlled.



Fig. 2 Installed expansion anchor bolts in concrete bases

Testing

The compressive strength of each specimen was tested according to ASTM C39-05 after 28days of curing period. Before the pull-out test of the expansion anchor bolts in concrete base material specimens takes place, actual compressive strength (f_c) test result should meet the designed compressive

strength (f_c) and should vary only within the acceptable deviation as per ASTM C39-05 [6]. The results from the compressive tests were first analyzed to check if all the concrete specimens have met the consistency requirement for compressive strength as specified by ASTM C 39-05 [6]. The consistency were also tested statistically using a one sample mean t-test at a level of significance of $\alpha = 0.01$. Specifically, the null hypothesis (H_0) was tested, i.e., if there is a significant difference between the actual compressive strength of the concrete specimens and the design compressive strength. The one sample mean t-test equation given by Scheaffer et al., is

$$t\text{-stat} = (\bar{x} - \mu) (\sqrt{n}/s) \quad (1);$$

where \bar{x} = sample mean, μ = population mean, n = sample size, and s = standard deviation of the samples [7]. The setup for the pull-out test and the concrete base specimen's failure mode are illustrated in Fig. 3.

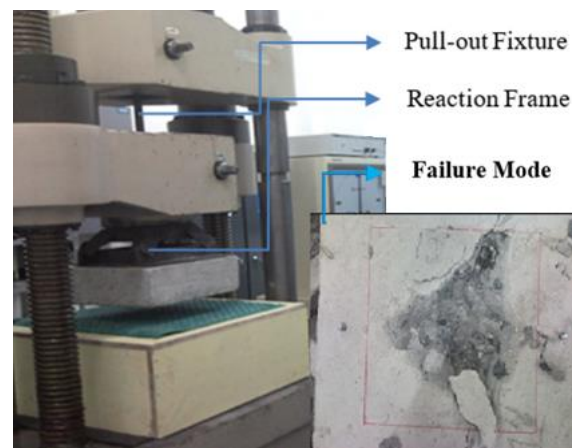


Fig. 3 Pull-out test setup and concrete breakout failure mode

The loading device is positioned in such a way that it is centered over the anchor bolt that is to be tested. A reaction frame with four legs and with a side dimension greater than the diameter of cone failure was placed on the concrete base specimen to provide a uniform contact between the surface of the structural member and the support frame. This is done in such a way that a concrete breakout failure was free for pull-out. Then, a pulling fixture was inserted at the anchor's head to pull it up vertically from the structural specimen as the load was applied slowly by Universal Testing Machine (UTM) to the pulling fixture. The pulling fixture shown in Fig. 3 was of sufficient size to ensure that it would not fail when pulling the expansion anchor bolt from the

concrete specimen. The concrete breakout failure, as also shown in Fig. 3, occurred after the point of maximum pull-out load.

Regression Modeling

The next step was to model the pull-out test results by linear and polynomial regression. These regression models display the effect on one variable when the response of the other variable is either a linear or curvilinear. General principles of multiple regressions also apply here. In this study, the influence of coarse aggregate size, coarse aggregate content and fine aggregate content to influence the concrete breakout strength of an expansion anchor bolt were checked. The linear and polynomial regression model as given by Montgomery and Runger are generally defined as

$$\hat{y} = \hat{\beta}_0 + \sum_{i=1}^k \hat{\beta}_i x_i \quad (2)$$

$$\hat{y} = \hat{\beta}_0 + \sum_{i=1}^k \hat{\beta}_i x_i + \sum_{i=1}^k \hat{\beta}_{ii} x_i^2 + \sum_{i < j} \hat{\beta}_{ij} x_i x_j \quad (3);$$

where \hat{y} is the concrete breakout strength, x_i, x_j

are the factors of concrete aggregates, and $\hat{\beta}$ is the least squares estimate of model coefficients [8]. The significance and adequacy of these models were checked using F-test at $\alpha = 0.01$. This is to ensure that the recommended model will give a satisfactory estimate of the true system. Then, adjusted coefficient of multiple determination, R^2_{adj} and error metric were defined for each regression model and were compared. The adjusted coefficient of multiple determination or R^2_{adj} is a good measure for multiple predictor variables that estimate Pearson's correlation ratio with value from 0 to 1 and is defined as:

$$R^2_{adj} = 1 - [SS_E / (n - p)] / [SS_T / (n - 1)]$$

(4);

where SS_E is the sum of squares of the residuals, SS_T is the total sum of squares, n is the total samples used and $p = k + 1$ degrees of freedom at their corresponding regressor (k). While, the metric of error used was the mean square of error or MSE. The MSE as defined by Montgomery and Runger is [8],

$$MSE = SS_E / (n - p) \quad (5).$$

Finally, the regression model with highest R_{adj} and with least MSE was selected and its optimum result was compared to ETAG 001 (Guideline for

European Technical Approval of Metal Anchors for Use in Concrete), and NSCP 2015 (National Structural Code of the Philippines 2015) equations for verification.

ETAG 001 equation for concrete breakout of a single anchor in non-cracked plain concrete is given by [9],

$$N = 10.1 \sqrt{f_{c_{cube}}} h_{ef}^{1.5} \quad (6)$$

The compressive strength using cylinder specimen was computed using the equation of Kumavat, HR and Patel, VJ [10],

$$f_c = 0.95 f_{c_{cube}} \quad (7)$$

While, the NSCP 2015 equation for concrete breakout of a single post-installed anchor in non-cracked plain concrete is given by [11],

$$N = 9.8 \sqrt{f'_c} h_{ef}^{1.5} \quad (8)$$

RESULTS AND DISCUSSION

Compressive Strength

The concrete cube specimens with dimension 150mm x 150mm x 150mm were tested for compressive strength, followed by the pull-out test of the expansion anchor bolt. The actual compressive strength (f_c) of the concrete cube specimens as compared to the design compressive strength (f'_c) was statistically tested to check their significant difference. The result of compressive strength test and test of significant difference is presented in Table 3 and Table 4, respectively.

Table 3 Compressive strength at 28 days result

CAS (mm)	Load, P (KN)	Stress, f_c (MPa)	Mean f_c (MPa)
10	410.3	18.24	
10	468.7	20.83	19.53
12.5	455.4	20.24	
12.5	426.3	18.95	19.59
19	449.7	19.99	
19	463.6	20.60	20.30
25	446.6	19.85	
25	454.9	20.22	20.03

Note: Mean f_c Average = 19.86 MPa

Coefficient of Variance (CV) = 1.83%

Acceptable CV = 3.20%

It can be observed in Table 3 that all the compressive stress values show no difference with the required compressive stress. The actual coefficient of variance, CV of the mean f_c for all cases is 1.83%, which is less than the acceptable CV of 3.20% as set by ASTM C 39-05. This only shows that the test result for compressive strength as a whole is consistent. The consistency of the f_c results were tested further for their significance difference using t-test as indicated in Table 4.

Table 4 t-test result

Parameters	Remarks
H_0	$f_c = f'_c$
H_1	$f_c \neq f'_c$
n	8
t-statistics	-2.6306
t-critical	3.5
α , df	0.01, 7

Table 4 indicates that the t-statistics is numerically less than the t-critical. This results in the acceptance of the null hypothesis (H_0) and the rejection of the alternative hypothesis (H_1) at 0.01 level of significance (α) and at degrees of freedom (df) equals 7. This leads to a decision that there is no significant difference between f_c and f'_c of the concrete specimens. This means that f_c of all concrete specimens are the same with those of f'_c . This result allowed the pull-out test to proceed.

Concrete Breakout Strength

After passing the consistency requirements for f_c , all the expansion anchor bolts were installed in their respective concrete base materials and then tested for pull-out. The results of the pull-out test at concrete breakout failure are shown in Fig. 4, Fig. 5 and Fig. 6 relative to the coarse aggregate size, coarse aggregate content, and fine aggregate content, respectively. From these scatter plots, the response of breakout strength to each concrete aggregate regressor is obviously curvilinear rather than linear.

Among the concrete aggregate factors, the coarse aggregate size gives the best polynomial fit to the response as shown in Fig. 4. The increased in breakout strength occurred only from 10mm up to 19mm size and then decreased at 25mm. The breakout strength measures 20.14KN initially at 10mm and increased to 23.10KN by 14.70% and increased again to 26.32KN at 19mm by 14.00% and then decreased to 25.76KN at 25mm by 2.20%. It only implies that the breakout strength is optimum at 19mm coarse aggregates size.

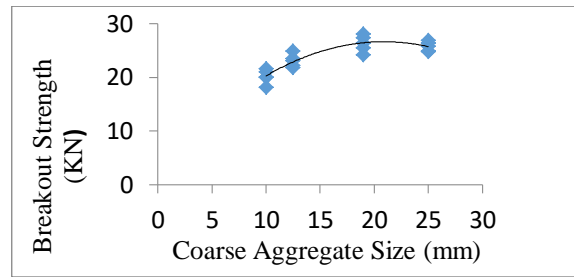


Fig. 4 Scatter plot of breakout strength against coarse aggregate size

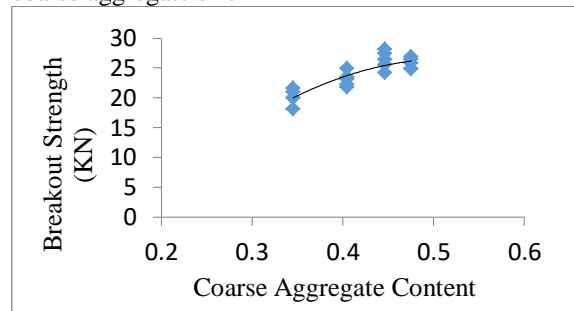


Fig. 5 Scatter plot of breakout strength against coarse aggregate content

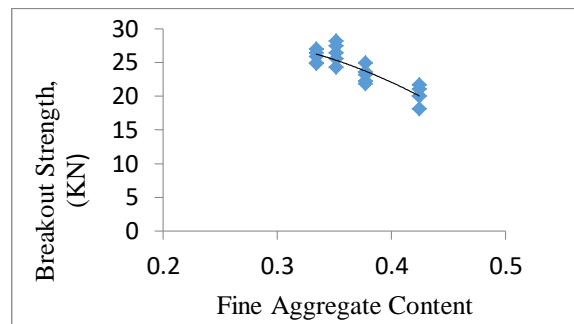


Fig. 6 Scatter plot of breakout strength against fine aggregate content

Table 5 shows the best performance of linear and polynomial regression model to predict the breakout strength of an expansion anchor bolt in concrete. Each regression was tested for the adequacy using the R_{adj} , MSE, and F-test at $\alpha = 0.01$. It is noticeable that breakout strength is best predicted using the polynomial regression model with coarse aggregate size as the sole predictor with R_{adj} of 0.894 and MSE of 1.55.

The optimum result of this model at 19mm coarse aggregate size and using cube compressive strength of 19.86MPa and $h_{ef} = 70$ mm was verified to Eq. (6) and Eq. (8) as shown in Table 6. Note that

the cylinder compressive strength was computed using Eq. (7).

Table 5 Comparison of regression models

Model	R_{adj}	MSE	F	$F_{\alpha,k,n-p}$
Poly(S, S^2)	0.894	1.55	38.74	6.11
Lin (S , CAC, FAC)	0.889	1.62	24.83	5.29

Note: S = Coarse Aggregate Size
CAC = Coarse Aggregate Content
FAC = Fine Aggregate Content

Table 6 Verification of polynomial regression model with other models

Model	Breakout Strength (KN)
Polynomial	26.455
NSCP 2015	24.930
ETAG 001	26.361

It can be observed that breakout strength result using the polynomial regression model is equally comparable to the results calculated from NSCP 2015 and ETAG 001 equations. This only implies that polynomial regression model can be used to estimate the breakout strength of an expansion anchor bolt in concrete with coarse aggregate size as its predictor. The polynomial regression model is given by

$$N = -0.0539S^2 + 2.2493S + 3.1762 \quad (9);$$

where N is the breakout strength of an expansion anchor bolt at $h_{ef} = 70\text{mm}$, and S is the coarse aggregate size. This model applies only to crushed coarse aggregate size ranging from 10mm to 25mm and to concrete base material with compressive strength ranging from 19MPa to 21MPa.

CONCLUSION

Among the concrete aggregate predictors considered, coarse aggregate size turned out as the most significant variable to influence the breakout strength of an expansion anchor bolt embedded in concrete using polynomial regression model.

Test results also show that breakout strength is optimum at 19mm coarse aggregate size.

ACKNOWLEDGMENTS

The following are acknowledged for their contribution in the completion of this research. Hilti for the HSL-3 M8/20 expansion anchor bolt used and Mapua University for its unceasing and vital support.

REFERENCES

- [1] Hordijk D. and Pluijm R., Pullout Capacity of Spatial Anchors, *Journal of Engineering Computations*, Vol. 2, 2001, pp. 805-824.
- [2] Eligenhausen R., Mallee R., and Silva J., *Anchorage in Concrete Construction*, Ernst & Sohn, Berlin, Germany, 2006.
- [3] Yousif A.A., Specimen and Aggregate Size on Compressive Strength, *Journal of Cement, Concrete and Aggregates*, Vol. 22 (2), 2000.
- [4] ASTM C 150, Specification for Portland Cement, *ASTM Standards in Building Codes*, Vol. 1 (43), 2006.
- [5] ASTM E 488-96, Standard Test Methods for Strength of Anchors in Concrete and Masonry Elements, *ASTM Standards in Building Codes*, Vol. 4 (43), 2006.
- [6] ASTM C 39-05, Standard Test Method for Compressive Strength of Cylindrical Concrete Specimens, *ASTM Standards in Building Codes*, Vol. 1 (43), 2006.
- [7] Schaeffer R.L., MuleKar M.S. and McClave J.T., *Probability and Statistics for Engineering Students. Inference for Regression Parameters. Other Regression Models*. Cengage Learning Asia Pte. Ltd., Philippines. SEC Co. Ltd., Wonheon-Dong, Suwon, South Korea, 2011, pp. 539-544.
- [8] Montgomery D.C. and Runger G.C., *Applied Statistics and Probability for Engineers* 5th ed. SI. Version, John Wiley and Sons, Inc., Printed in Asia, 2011, pp. 619-636.
- [9] ETAG 001, Guideline for European Technical Approval of Metal Anchors for Use in Concrete, Annex C: Design Method for Anchorages, Brussels, Belgium, 1997, pp. 16-19.
- [10] Kumavat H.R. and Patel V.J., Factors Influencing the Strength Relationship of Concrete Cube and Standard Cylinder, *International Journal of Innovative Technology and Exploring Engineering*, Vol. 3 (8), 2014, pp. 76-79.
- [11] NSCP, National Structural Code of the Philippines, 7th edition. Volume 1 Buildings, Towers, and other Vertical Structures. Chapter 4 Structural Concrete. Section 417, Anchorage to Concrete, 2015.

CORROSION CURRENT DENSITY OF MACROCELL OF HORIZONTAL STEEL BARS IN REINFORCED CONCRETE COLUMN SPECIMEN

Nevy Sandra^{1,2}, Keiyu Kawaai¹ and Isao Ujike¹

¹Graduate School of Science and Engineering, Ehime University, Matsuyama, 790-8577, Japan;

²Department of Civil Engineering, Universitas Negeri Padang, Indonesia

ABSTRACT

Chloride-induced corrosion of steel bar in concrete is one of the main problems affecting the durability of reinforced concrete (RC) structures. Expansive products are formed due to corrosion at the interface between concrete and steel bar. In this study, the differences in the magnitude of the macrocell corrosion current density in RC column specimens cast using copper slag fine aggregate and fly ash replacement were examined. This study aimed at investigating corrosion formation with respect to macrocell corrosion current density. The experimental study was carried out through dry and wet (NaCl 10%) cycles for specimens with different cover depths, which was investigated by electrochemical measurements. The result shows that the largest macrocell corrosion current density was measured in the steel bars located at the upper part of reinforced column specimens for each case of the specimens with a cover depth of 30 mm. This could be partly attributed to the loss of the integrity of the steel and concrete interface which is examined based on the oxygen permeability in the upper and lower sides of segmented steel bars. The variation of oxygen permeability contributes to the macrocell corrosion formation especially in the steel bars affected by bleeding water. Besides the integrity between steel bars and concrete cover, the quality of concrete cover and variations in chloride ion concentrations are significant factors contributing to the macrocell corrosion formation.

Keywords: Chloride-induced corrosion, Macrocell corrosion current density, Oxygen permeability, Horizontal steel bar, Copper slag fine aggregate

INTRODUCTION

Chloride-induced corrosion is a concern for RC structures that are attacked by chlorides from seawater especially in the tidal, splash and spray water zones. The mechanisms of chloride-induced corrosion of steel in concrete structures are complex. Some research on the corrosion process and the influencing parameters have been carried out. Measurement of macrocell corrosion current flow is one of electrochemical technique investigating the mechanisms and the influencing factors of chloride-induced corrosion of steel in concrete. Locally separated anodes and cathodes in concrete specimens have been measured by electrical current [1].

Steel bars in good quality concrete do not corrode even if sufficient oxygen and moisture are available. This is due to the spontaneous formation of a thin passive film on the steel surface in highly alkaline (pH 12.5-13.5) of the pore solution of the concrete. This passive film can be destroyed by carbonation of concrete or by the presence of chloride ions, and the steel bar is then depassivated. Once the passive layer breaks down then areas of rust will start appearing on the steel surface in the presence of water and oxygen. The corrosion of steel

in concrete is an electrochemical process, where at the anode iron is oxidized to iron ions that pass into solution and at the cathode oxygen is reduced and together with electrons and water are converted into hydroxyl ions. Anode and cathode form a short-circuited corrosion cell, with the flow of electrons in the steel and of ions in the pore solution of the concrete [2, 3].

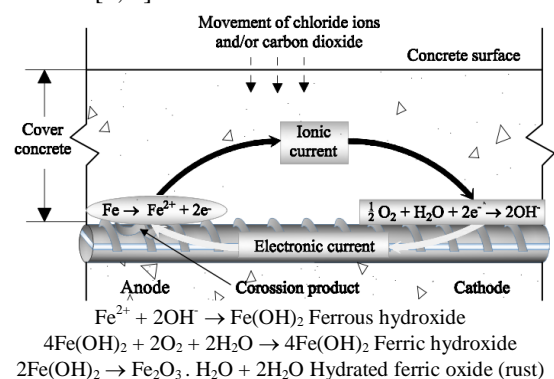


Fig. 1 The anodic, cathodic and oxidation and hydration reactions for corroding steel [3].

According to the different spatial location of anode and cathode, corrosion of steel in concrete can occur as microcells leading to uniform iron removal

and macrocells causing local iron removal or pitting corrosion:

- (a) Microcell corrosion, consisting of pairs of immediately adjacent anodes and cathodes, leading to uniform iron dissolution over the whole surface. Uniform corrosion is generally caused by carbonation of the concrete over a wide area or uniformly very high chloride contents in the vicinity of the steel.
- (b) Macrocell corrosion, consisting of spatially isolated anodes and cathodes, normally where the critical chloride content has been reached, and large cathodes being next to the anodes or sometimes also quite far away from the anodes up to a distance of a few meters. Macrocells occur mainly in the case of chloride-induced corrosion (pitting). Generally, the anode is small respect to the total (passive) rebar surface. A typical coplanar or face to face situations of anode and cathode can be distinguished by macrocell corrosion [1-5].

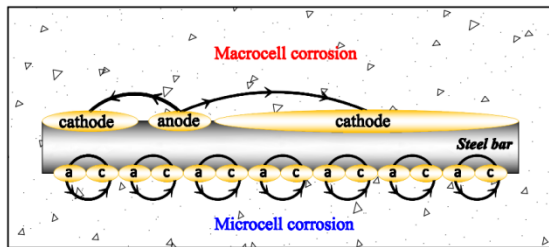


Fig.2 Microcell and macrocell corrosion.

Macrocell corrosion is of great concern because the local dissolution rate (reduction in cross-section of the rebar) may greatly be accelerated due to the existence of large active steel bar areas in electrical contact with passive areas [1, 2, 5]. The values of local corrosion rates up to 1 mm/year will lead rapid corrosion attack to the structure if not detected early [2]. Chloride content, concrete quality, concrete cover and environmental conditions are parameters influencing the corrosion rate of macrocell in a concrete structure. Additionally specific resistance of anodic, cathodic and the electrolyte (concrete), and geometry of the corrosion cell also influence the macrocell corrosion rate directly. It affects the prediction of the macrocell current becomes quite difficult [1].

In this study, bleeding is unavoidable when column specimens are cast from the height of 1.5 m. Bleeding in the form of segregation is one of the factors affects the quality of concrete. Bleeding significantly influenced the macrocell and microcell corrosion rates in the steel bars. As a result of bleeding, water pockets trapped under the coarse aggregates and underneath the steel bars caused the formation of gaps between the steel and concrete. This vulnerable zone affects the integrity of reinforced concrete, allowing corrosion cells to develop on the horizontal bar. Also, the presence of

gaps/vulnerable zone at the steel-concrete interface causes the complete loss of passivity with the presence of chloride. A part of concrete affected by bleeding exhibited weaker strength, higher permeability, lower concrete resistance, and higher oxygen permeability [6, 7].

It was reported that the rate of oxygen permeability is an influencing factor greatly affecting the corrosion of steel bars in concrete in which oxygen is consumed on the surface of the steel bars [8-10]. The concentration of oxygen in corrosion process was shown in the behavior of the cathodic polarization curve. The reduction in oxygen content shifts the cathodic curve to lower current densities over a wide range of potentials. This curve indicates the improvement of corrosion performance when used fly ash as a material replacement which attributes to the reduction of available oxygen by densifying the pore structure by the pozzolanic reaction around steel bars [9, 10]. Thus the cathodic reaction is controlling the overall reaction in the macrocell in the case of chloride-induced corrosion [11]. Also, the electrical resistivity of concrete depth is a significant factor contributing to the corrosion processes when macrocell formation occurs, and corrosion rate increased with a decrease in cover depth [12].

In this study, common acceleration technique by wet and dry cycles was used. Copper slag (CUS) and fly ash (FA) as replacement for fine aggregate and cement were used. This paper examines the corrosion formation respect to the differences in the magnitude of the macrocell corrosion current density of reinforced concrete column specimens. Both oxygen permeability and macrocell corrosion current density within the concrete cover are considered in the electrochemical analysis.

METHODOLOGY

Specimen Overview

Concrete column specimens of the cross-section 300 x 300 mm and the height of 1500 mm were cast with water to binder ratio (W/B) of 47% for FA mixtures and 55% for CUS and OPC mixtures in this study (Figure 1). After casting, the specimens were cured for 28 days in room conditions. Segmented steel bars comprising D32 deformed steel bars were embedded at the height of 250, 750, and 1250 mm from the bottom surface. The smaller specimens (300 x 100 x 132) mm were subsequently cut out from the column with the cover depths of 30 and 40 mm and then chloride-induced corrosion tests were carried out. Table 1 shows the mix proportions of concrete mixtures in this experiment. The fine aggregate was crushed sand obtained from sandstone (S1), and limestone (S2) with a specific gravity, water absorption capacity and F.M. of S1 (2.61

g/cm³, 1.06 %, and 2.88), S2 (3.55 g/cm³, 0.04 %, and 2.29). The coarse aggregate was crushed sandstone (G1) with a specific gravity and water

absorption are 2.62 g/cm³ and 0.64 %. The slump and air content were specified as 8.0 cm and 4.0% respectively.

Table 1 Mix proportions of concrete specimens

Mixtures	W/B (%)	Unit weight (kg/m ³)					(g/m ³)		
		W	C	FA	Fine aggregate		Coarse aggregate	Chemical admixtures	
					S1	S2		AEAWRA	AEA
FACUS 30	47	165	281	70	587	342	912	5265	35.1
CUS30	55	175	318	-	596	347	925	3818	-
OPC	55	175	318	-	857	-	932	4772	15.9

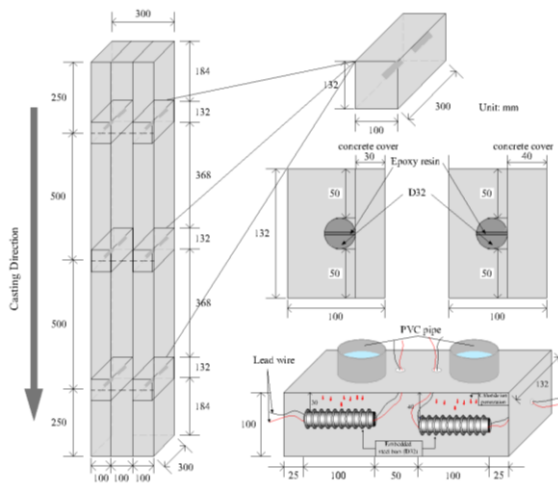


Fig. 3 Reinforced concrete column specimen.

Interfacial Transition Zone

The strength of a bond between concrete and steel bars is of considerable importance concerning structural behavior. In the case of deformed bars, bond arises primarily from friction and adhesion between concrete and steel, and from mechanical interlocking. The bond strength involves not only the properties of the concrete but also the geometry of the reinforcement and the structure such as the thickness of cover to the reinforcement [13].

The interfacial transition zone is a layer (usually several tens of micrometers thick) of hydrated cement paste in contact with aggregates. It is the strength limiting phase in concrete. The transition zone becomes the weakest link in concrete mass on account of the dissimilar material, lack of bond, higher w/c ratio, and bleeding water. Under load and the increasing of stress level, microcracks propagate and spreads throughout the mass further starting from largest microcracks. The micro cracks in the transition zone at the interface with steel bars becomes more permeable than the corresponding hydrated cement paste or mortar and admits air and water to promote corrosion of steel reinforcement. The volume of voids and microcracks present of the

interfacial transition zone has a great influence on the stiffness of concrete [10, 16]. Also, bleeding which some of the water in the mix tends to rise to the surface gets intercepted by aggregates then gets accumulated at the interface between paste and aggregates.

Macrocell (Corrosion Rate)

The macrocell corrosion current density in the steel bar was measured using an ammeter. The equipment is permanently set up and can be used to monitor the total charge passing with time between steel elements in segmented steel bars connected with epoxy resin. The macrocell current flowing can be calculated based on Eq. (1), the readings obtained from the ammeter and dividing them with the surface area of the steel [7].

$$I_{macro} = \frac{I_i}{S_i}$$

where I_{macro} : macrocell corrosion current density (A/cm²); I_i : current flowing of steel element (A); and S_i : surface area of steel element i (cm²)

Oxygen Permeability (Cathodic Polarization)

The electrochemical measurement set up for the cathodic polarization consisted of a counter electrode (steel plate), a working electrode (steel bar with lead wire attached to it) and a reference electrode (Ag/AgCl). For this measurement technique, the half-cell potential of the steel bar was gradually shifted to -1V, and the current density was measured. The rate of oxygen permeability was calculated based on Eq. (2) when the potential difference was assumed to reach the limiting current density (-860 mV) [7].

$$\frac{dQ}{dt} = -\frac{i_{lim}}{nF}$$

where dQ/dt : the rate of oxygen permeability (mol/cm²/sec); i_{lim} : limiting current density (A/cm²); F : Faraday's constant (96,500 coulombs/mol); and n : the number of electron exchanged equal to 4.

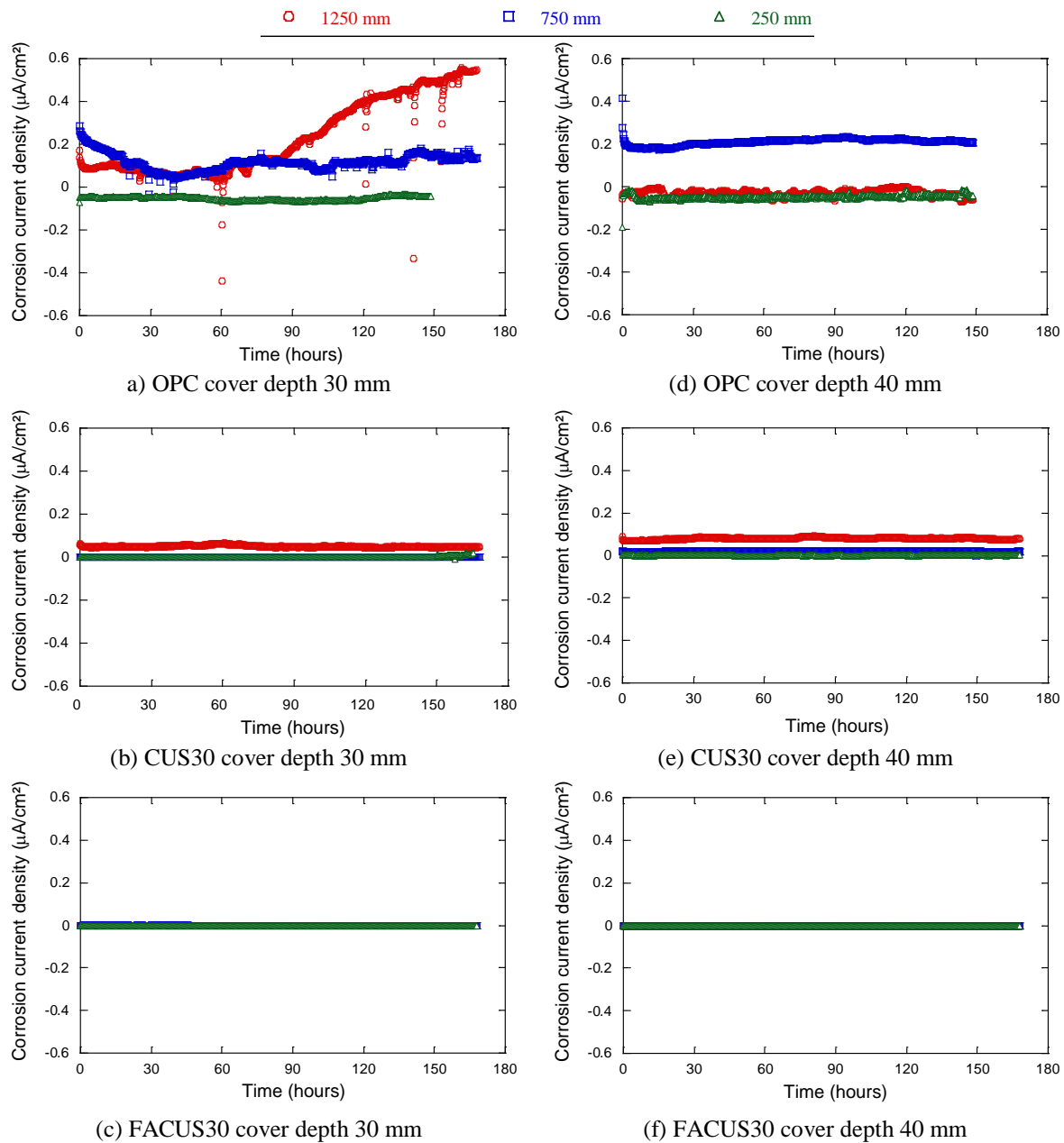


Fig. 4 Macrocell corrosion current density

RESULTS AND DISCUSSION

Macrocell (Corrosion Rate)

The macrocell corrosion current density measured at the ages of 420 days at a cover depth 30 mm and 40 mm are shown in Fig. 4 for the different type of specimens. The largest macrocell current density was measured in the steel bars located in upper part (1250 mm from the bottom surface) for each case of the specimens with 30 mm cover depth. OPC specimens showed the higher value of the macrocell corrosion current density. This could be partly attributed to the loss of the integrity of the steel and concrete interface which is examined based

on the oxygen permeability in the upper and lower sides of segmented steel bars.

The smaller macrocell corrosion current density was shown from the specimens of 40 mm cover depth. This could be explained by the fact that concrete cover depth influences the ingress of chlorides and oxygen into the concrete. The smaller the cover depth reduces the time interval of the oxygen and the chloride ions to reach embedded steel bar, and vice versa. Also, the quality of the concrete cover, especially with respect to its permeability, determines the ease of ingress of the chloride ions, and it is a significant factor contributing to the macrocell corrosion formation. On the other hand, FA specimens with the cover

depth of 30 mm and 40 mm showed the lowest values of macrocell corrosion current density. Based on the results obtained, it assumed that more uniform pore structure in the FA specimens. The pozzolanic reaction of FA could densify the pore structure around steel bars and protected the steel bars from the ingress of chloride ions and lead to a lower rate of oxygen permeability.

Oxygen Permeability

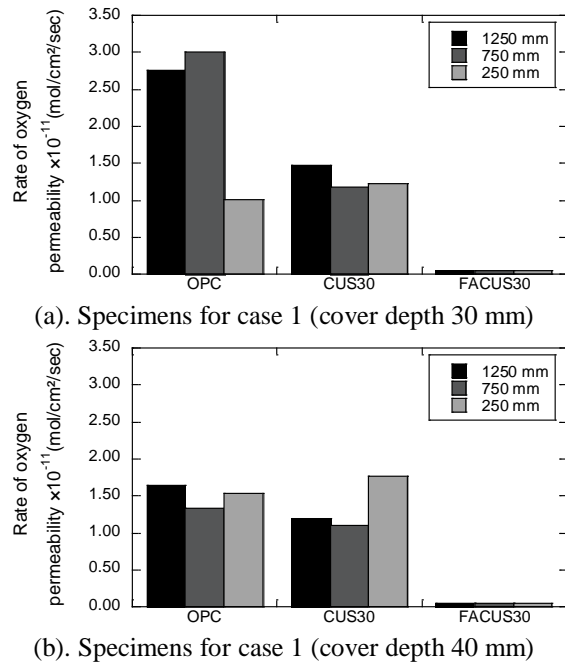
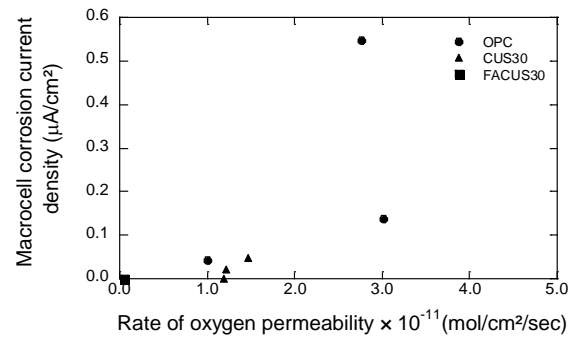
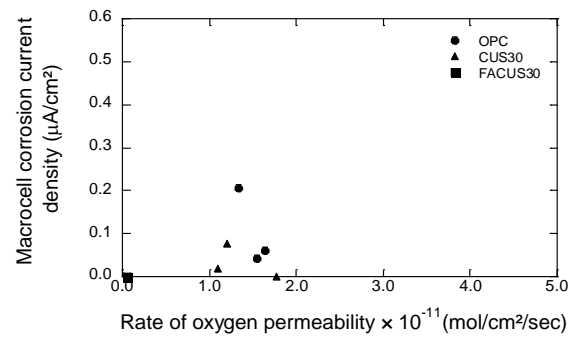


Fig 5. The rate of oxygen permeability

Figure 5 shows the rate of oxygen permeability was obtained by cathodic polarization curve at the age of 420 days. As expected, higher oxygen permeability ensued due to the poor quality of concrete in the upper layer which was 64% higher compared to the rate of oxygen permeability in the bottom layer in the case of OPC specimen with the cover depth of 30 mm. But for OPC specimens with cover depth 40 mm, CUS30 with the cover depth of 30 mm and 40 mm, the rate of oxygen permeability was comparable among all parts of the column specimens. The rate of oxygen permeability of FA mixtures is very low compared to the OPC and the CUS30 mixtures. This could be explained by the fact that pozzolanic reactions of FA mixture reduce the influence of material segregation due to bleeding. Based on the results, a more permeable condition in the upper part of the concrete column specimen affected more prone to corrosion. This condition may be due to the adverse effect of bleeding on the concrete cover and lack of integrity cover concrete and horizontal steel bars in the vulnerable zone.



(a). Specimens for case 1 (cover depth 30 mm)



(b). Specimens for case 1 (cover depth 40 mm)

Fig 6. Microcell corrosion current density and the rate of oxygen permeability

Figure 6 shows the relationship between the macrocell corrosion current density and the rate of oxygen permeability. The macrocell corrosion current density was increased with the higher rate of oxygen permeability regardless of the mixtures and concrete cover. The CUS30 specimens showed lower macrocell corrosion current density compared to OPC. The results displayed that the partial replacement of CUS30 and FACUS30 in fine aggregate could enhance the resistance against chloride ingress. Also, increasing of cover depth decreased the corrosion current density.

CONCLUSION

This study aimed at examining corrosion formation respect to macrocell corrosion current density. The variation of oxygen permeability contributes to the macrocell corrosion formation which was affected by the integrity of steel and the concrete interface. The result shows that the largest macrocell corrosion current density was measured in the steel bars located at the upper part of reinforced column specimens for each case of the specimens with 30 mm cover depth. This could be partly attributed to the loss of the integrity of the steel and concrete interface which is examined based on the oxygen permeability in the upper and lower sides of segmented steel bars. Besides the integrity between

steel bars and concrete cover, the quality of concrete cover is significant factors contributing to the macrocell corrosion formation. The more uniform pore structure in the FA specimens could be formed which led to higher corrosion resistance. The pozzolanic reactions of fly ash specimens exhibited the ability to reduce oxygen availability which leads to enhancement in corrosion performance. Also, CUS30 shows lower macrocell corrosion current density compared to OPC. This could be advantageous for the partial replacement of CUS in fine aggregate in improving corrosion-resistance.

ACKNOWLEDGEMENTS

This research is fully supported by Department of Civil and Environmental Engineering, Ehime University; Indonesian Endowment Fund for Education (LPDP), Ministry of Finance; and the Directorate General of Higher Education (DIKTI), Ministry of Research, Technology and Higher Education, Republic of Indonesia. This study is financially supported by Grant-in-Aid for Young Scientists (B) 15K18100.

REFERENCES

- [1] Raupach M., Chloride-induced Macrocell Corrosion of Steel in Concrete – Theoretical Background and Practical Consequences, Construction and Building Materials, Vol. 10, No. 5, 1996, pp. 329-338.
- [2] Elsener B., Macrocell Corrosion of Steel in Concrete – Implications for Corrosion Monitoring, Cement & Concrete Composites, Vol. 24, 2002, pp. 65-72.
- [3] Broomfield J. P., Corrosion of Steel in Concrete, Edition, Taylor & Francis Group, 2007, pp. 6-15.
- [4] Cao C., Cheung M. and Chan B., Modelling of Interaction between Corrosion-induced Concrete Cover Crack and Steel Corrosion Rate, Corrosion Science, Vo. 69, 2013, pp. 97-109.
- [5] Andrade C., Maribona I. R., Feliu S., Gonzales J. A. and Feliu J_R S., The Effect of Macrocells between Active and Passive Areas of Steel Reinforcements, Corrosion Science, Vol. 33, No. 2, 1992, pp. 237-249.
- [6] Mohammed T.U., Otsuki N., Hamada H. and Yamaji T., Chloride-Induced Corrosion of Steel Bars in Concrete with Presence of Gap at Steel-Concrete Interface, ACI Materials Journal, Vol. 99, 2002, pp. 149-156.
- [7] Baccay, M. A., Nishida, T., Otsuki, N. and Chin, K., Influence of Bleeding on Minute Properties and Steel Corrosion in Concrete, Journal of Advanced Concrete Technology, Vol. 2, No. 2, 2004, pp. 187-199.
- [8] Bertolini L., Elsener B., Pedeferri P. and Polder, R. P., Corrosion of Steel in Concrete, 2nd Edition, WILEY-VCH Verlag GmbH & Co. KGaA, 2004, pp. 129-139.
- [9] Madlangbayan M., Otsuki N., Nishida T. and Baccay M., Corrosion Behavior of Steel Bar in Chloride Contaminated Mortars with Fly Ash, Philippine Engineering Journal, Vol. 26, No. 2, 2005, pp. 13-24.
- [10] Sandra N., Kawaai K., Ujike I., Nakai I. and Nsama W., Effects of Bleeding on Corrosion of Horizontal Steel Bars in Reinforced Concrete Column Specimen, Jurnal Teknologi, 2018 (in press).
- [11] Raupach M. and Gulikers J., Investigations on Cathodic Control of Chloride Induced Reinforcement Corrosion, Proceedings of EUROCORR, 1999.
- [12] Otieno M., Beushausen H. and Alexander M., Chloride-induced Corrosion of Steel in Cracked Concrete-Part I: Experimental Studies under Accelerated and Natural Marine Environments, Cement and Concrete Research, Vo. 79, 2016, pp. 373-385.
- [13] Neville, A. M., Properties of Concrete, 5th Edition, Pearson, 2011, pp. 313.

SIMULATING LUNAR HIGH LAND ROCKS USING JAPANESE IGNEOUS ROCKS

Hiroyuki Ii¹ and Hiroshi Kanamori²

¹Faculty of Systems Engineering, Wakayama University, Japan;

²Japan Aerospace Exploration Agency, Japan

ABSTRACT

Before performing various experiments and activities on the moon, the simulation of lunar soil is critical to examine the feasibility of artificial systems which theoretically should function properly on the moon, as well as to investigate the possibility of In-Situ Resource Utilization. Previously, a simulant of the regolith of moon mare had been made however a simulant of “high land” on the moon had not. Therefore, a simulant for “high land” rocks on the moon was designed using Japanese igneous rocks. From mineralogy and chemistry, the use of plagioclase phenocrysts found in Miyakejima and Fugoppe, enabled simulation of ferroan anorthosites (anorthite content over 90%). Both plagioclase phenocrysts had high anorthite content, 94 to 98 % and 92 to 95 % whereas the plagioclase found in gabbro or anorthosite on earth does not have high anorthite content, 70 to 90 %. Both plagioclase phenocrysts were easy to separate from rocks because plagioclase phenocrysts occurred as a volcanic bomb in Miyakejima and as soft tuff in Fugoppe. Similarly, using gabbro and dunite in Horoman and basalt in Miyakejima enabled the simulation of Mg-rich rocks and KREEP rocks respectively. “high land” rocks on the moon are composed mainly of ferroan anorthosites, less of component Mg-rich rocks and KREEP rocks. Therefore the mineralogy and chemical mixing of these rocks enabled the simulation of “high land” rocks in the moon.

Keywords: Ferroan anorthosite, Mg-rich rock, KREEP rock, Plagioclase phenocryst

INTRODUCTION

The surface of the moon is covered by basaltic sand called regolith of which the majority of particle size lies below 10 [mm] [1]. Experimental studies of the interaction of basaltic regolith with the environment have been almost exclusively based on simulants (JSC-1, MLS-1 [2], [3], [4]), which only reproduce some aspects of the genuine regolith. In Japan, Shimizu Corporation collaborated with NASDA (currently JAXA) and succeeded in manufacturing a regolith simulant named FJS-1 [5], whose characteristics, such as particle size distribution and chemical composition were similar to the samples returned by the Apollo 11, 12 and 14 missions. Chemical and mineralogical properties (including moisture and ice content), surface roughness, effective surface contact area or effective packing fraction, might all exert large effects on the results of dust impact, dusty plasma, or In-Situ Resource Utilization related experiments. Therefore, simulating lunar soil is critical in examining the feasibility of artificial systems which need to function properly on the moon, and to investigate the possibility of In-Situ Resource Utilization [1], [2], [3], [4], [5].

Basaltic regolith was mainly sampled at the “mare” on the moon whose color is dark, while the moon’s white color area, known as “high land,”

consists of anorthosite containing the white color mineral, plagioclase [1]. Therefore, simulants, JSC-1, MLS-1, and FJS-1, which had not been previously simulated, were basaltic regolith and high land anorthosite. The purpose of this study was to research how to make a new simulant for high land on the moon using Japanese rocks because demand for such a simulant may occur in the future if a large scale experiment such as rover test on the simulated lunar were performed.

METHOD

Most petrologists distinguish three major classes of pristine igneous lunar highland rocks as ferroan anorthosites, Mg-rich rocks, and KREEP rocks [1], [5] estimated from the Apollo 15, 16 and 17 missions and Lunar missions. The ferroan anorthosites and Mg-rich rocks are rarely found as plutonic (coarsely crystalline) rocks, though most occur as monomict breccia. Volumetrically, KREEP rocks are far less important than ferroan anorthosites and Mg-rich rocks. The precise compositional range of the Mg-rich rock group is not well defined. Rocks in this group range from olivine-rich rocks (dunite) to rocks composed of pyroxene and Na-rich plagioclase. Therefore, in order to make a simulated

lunar highland rock, the best method is to prepare each simulated rock, the ferroan anorthosites, Mg-rich rocks, and KREEP rocks and then mix them. The mixing ratios change according to simulated place or condition. The simulated rock was determined by mineralogy and main chemical composition. The mineralogy and main chemical composition of ferroan anorthosites, Mg-rich rocks, and KREEP rocks are compared with those of Japanese igneous rocks. The possibility of digging the candidate rocks was confirmed in the field as for amount of volume.



Fig.1 Sampling points for simulant rocks

RESULTS

Ferroan anorthosite

From the modal mineral composition of the ferroan anorthosite [1], [2], [3], [4], [5], plagioclase content varies 34 to 99 % and is over 90 % for the most of rocks. The residual modal olivine and pyroxene contents of the ferroan anorthosites are very low, 0 to several %. Anorthite ($\text{CaAl}_2\text{Si}_2\text{O}_8$) content of plagioclase in the ferroan anorthosites is very high and 96 to 98 % [1], [2], [3], [4], [5]. Plagioclase is in complete solid solution between anorthite and albite ($\text{NaAlSi}_3\text{O}_8$).

First candidate rock is thought to be a Japanese anorthosite. Anorthosite mainly consists of feldspar is very rare in Japan and was found only in Mt. Tsukuba. Granite, gabbro and anorthosite were distributed at Mt. Tsukuba. Anorthosite was found only around the east peak of Mt. Tsukuba, Nyotaizan. Gabbro and anorthosite at Tsukuba area contains hornblende. Generally moon rocks are lack of

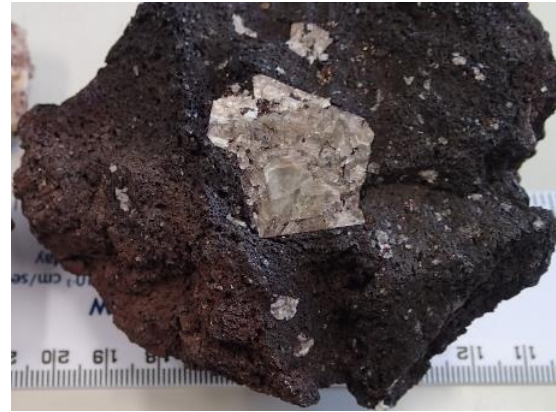


Fig.2 Plagioclase phenocrysts in basalt at Miyakejima



Fig.3 Plagioclase phenocrysts at Miyakejima



Fig.4 Volcanic sediments with plagioclase phenocrysts at Hyoutanyama in Miyakejima

hydrous minerals therefore hornblende was not found on the moon. Anorthite content of plagioclase in the anorthosite of Tsukuba is quite low, 70 to 90 %. Therefore, anorthosite of Tsukuba was not suitable for material of simulant of high land rocks because of the occurrence of hornblende and low anorthite content [6], [7]. In, America, Stillwater complex contained anorthosite however Anorthite

content of plagioclase is not high, 77% [8], [9].

Next, use of plagioclase crystal is thought to be candidate as the simulated rock for the ferroan anorthosite and then olivine and pyroxene crystal can be added as spice arranging final mineralogy and chemistry. Anorthite content of plagioclase in most Japanese gabbro is not high as well as anorthosite of Tsukuba [6], [7].

Japanese basalt and andesite rocks contain sometimes big (several cm in size) and high Ca feldspar (anorthite content is over 90 %) crystals as phenocrysts as shown in Fig.2. Generally, plagioclase phenocrysts in basalt or andesite are surrounded with groundmass and it is very difficult to distinguish phenocrysts from groundmass.



Fig.5 Plagioclase phenocrysts at Fugoppe



Fig.6 Plagioclase phenocrysts in tuff at Fugoppe

Plagioclase crystals in Miyakejima and Fugoppe are isolated from surrounding rock as shown in Fig.1. Plagioclase phenocrysts in Miyakejima basalt are volcanic bombs and reach over 3 cm in size as shown in Fig.3. It is covered with thin basaltic lava and includes olivine crystals. Anorthite content of plagioclase phenocrysts in Miyakejima is 94 to 98 %

[10], [11], [12] as shown in Table 1 and their chemical composition were between the minimum and maximum values of ferroan anorthosites on the moon as shown in Table 2 excluding low SiO_2 . On the other hand, chemistry of plagioclase phenocrysts with lava and olivine inclusion in Miyakejima was between between the minimum and maximum values of ferroan anorthosites on the moon as shown in Table 2 excluding high Al_2O_3 .

Table 1 Chemical composition (%) of plagioclase phenocryst in Miyakejima

	No.1	No.2	No.3	No.4
SiO_2	44.03	44.49	43.13	42.98
TiO_2	n.d.	n.d.	n.d.	n.d.
Al_2O_3	36.80	36.00	35.87	35.31
Fe_2O_3	n.d.	0.08	0.45	0.96
FeO	n.d.		0.29	0.57
MnO	n.d.	n.d.	n.d.	tr.
MgO	0.20	0.04	0.08	0.35
CaO	19.29	19.49	19.27	19.46
Na_2O	0.23	0.59	0.65	0.35
K_2O	n.d.	0.03	0.05	0.04
An	An	An	An	An
Content	98	95	94	97

Plagioclase phenocryst in Miyakejima basalt is isolated as a volcanic bomb from Hyoutanyama volcanic cone at the east of Miyakejima Island and precipitated with scoria, tuff and lava around the Hyotanyama volcanic cone as shown in Fig.4. It is easy to pick up plagioclase phenocryst from sediments around the volcanic cone and to keep several kg is possible as shown in Fig.4.

Plagioclase phenocrysts in Fugoppe are included in andesite tuff and reach over 2 cm in size as shown in Fig.5. It is possible to separate crystals from tuff because of the softness of tuff as shown in Fig.6. Plagioclase phenocrysts are accompanied with pyroxene crystals. Anorthite content of plagioclase phenocrysts in Fugoppe is 92 to 95 % [13], [14] and their chemical composition were between the minimum and maximum values of ferroan anorthosites on the moon as shown in Table 1 excluding high Al_2O_3 .

Plagioclase phenocrysts in Fugoppe are taken from cliffs located in the forest and digging tuff is necessary for picking up them however plagioclase phenocryst concentration of the tuff layer is not high as shown in Fig.6.

Table 2 Chemical composition (%) of Ferroan anorthosites on the moon and plagioclase phenocryst in Miyakejima and Fugoppe (Detection limit is 0.01%)

	plagioclase phenocryst average values			ferroan anorthositic rocks	
	Miyakejima		Fugo ppe	Minu mum value	Maxi mum value
	With lava, olivine	No lava			
SiO ₂	41.25	43.66	43.41	41.90	48.00
TiO ₂	0.03	n.d.	0.12	0.01	1.36
Al ₂ O ₃	33.20	36.00	36.17	11.10	35.60
Fe ₂ O ₃	2.83	0.70	0.56		
FeO	0.72	0.43	n.d.	0.15	15.70
MnO	0.04	n.d.	0.01	0.00	0.24
MgO	3.59	0.17	0.09	0.14	10.10
CaO	18.34	19.38	19.27	13.00	20.40
Na ₂ O	0.48	0.46	0.50	0.18	0.57
K ₂ O	0.01	0.04	0.03	0.01	0.11
P ₂ O ₅	0.00	n.d.	0.00	0.01	0.05

Chemically plagioclase phenocrysts in both Miyakejima and Fugoppe are good agreements with the ferroan anorthosites on the moon excluding high Al₂O₃. On the other hand, plagioclase phenocrysts with olivine inclusion and lava cover in Miyakejima also coincided with the ferroan anorthosites excluding low SiO₂.

Therefore, mixing rocks of plagioclase phenocrysts with olivine inclusion and lava cover in Miyakejima and plagioclase phenocrysts accompanied in Fugoppe are thought to be best candidate rocks for the ferroan anorthosites.



Fig.7 Gabbro (left) and dunite (right) in Horoman

Mg-rich rock

Mg-rich rocks are all coarse grained high land rocks which are various, olivine rich, pyroxene and Na-rich plagioclase rocks and various ultrabasic rocks excluding ferroan anorthosite. Then, in this study, peridotite and gabbro were selected for simulated as Mg-rich rocks.

The Horoman area in the south of Hokkaido, Japan is a famous for peridotite, in particular, various kinds of peridotite and gabbroic rocks and then rocks in Horoman area were thought to cover with most kinds of Mg-rich rocks. Table 3 shows chemistry of representative gabbroic rocks and peridotite [14]. Both rocks were sampled at the lower stream of Horoman River. Gabbro is composed of mainly plagioclase and pyroxene as shown in Fig.7. Plagioclase and pyroxene grains are coarse and the plagioclase and pyroxene content is widely changeable. Then, the chemistry for gabbro in Horoman is separately analyzed. Table 3 shows chemistry of plagioclase and pyroxene in gabbro at Horoman and both values were between the maximum and minimum values of Mg-rich rocks.

Table 3 Chemistry of representative gabbroic rocks and peridotite and Mg-rich rocks in Highland

	Horoman in Hokkaido			Mg-rich rocks in highland	
	Gabbro		Dunite	Minimum	Maximum
	plagioclase	pyroxene			
SiO ₂	46.27	41.31	41.20	37.50	52.00
TiO ₂	0.11	0.03	n.d.	0.03	1.03
Al ₂ O ₃	27.83	14.69	1.31	1.30	28.70
Fe ₂ O ₃	2.63	10.38	0.86		
FeO	0.99	6.20	4.13	2.25	17.10
MnO	0.05	0.16	0.38	0.03	0.20
MgO	4.73	22.30	48.81	6.90	45.40
CaO	13.77	6.62	1.96	1.10	15.90
Na ₂ O	2.69	1.11	n.d.	0.02	0.91
K ₂ O	0.16	0.08	n.d.	0.00	0.23
P ₂ O ₅	0.01	0.00	n.d.	0.03	0.11
Cr ₂ O ₃	0.06	0.04	0.46	0.02	0.38

(Detection limit is 0.01%)

Dunite, olivine rich rock in Horoman was between the maximum and minimum values of Mg-

rich rocks excluding MgO. Actual high land rocks on the moon were changeable and to adjust mixing ratio of the prepared three rocks enable to coincide with chemistry for each Mg-rich rocks. Therefore, gabbro and dunite in Horoman are thought to be suitable simulated rocks for the Mg-rich rocks.

KREEP rock

The KREEP rocks are named for their high content of incompatible elements, especially K, rare earth elements (REE), and P. Comparing with Japanese basalt, K and P contents are not too high from Table 4. As plagioclase phenocryst in Miyakejima is a candidate for the simulated ferroan anorthosites, effectiveness of basalt in Miyakejima is also checked. Basalt chemistry at some places, Ako, Benkenemisaki and Imasaki in Miyakejima are between the minimum and maximum values of KREEP basalt as shown in Table 4 excluding high Na_2O and low P_2O_5 .

Basalt in Miyakejima widely contains olivine and pyroxenes however, the olivine in KREEP basalt is rare but pyroxene is common and shows a characteristically wide range in composition. Precise simulation for the KREEP is difficult for both element and mineral compositions. However volumetrically, KREEP rocks are far less important than ferroan anorthosites and Mg-rich rocks. Then basalt in Miyakejima is selected with effectiveness of wide distribution as shown in Fig.8.

Table 4 Chemical composition of basalt in Miyakejima and KREEP rocks (Detection limit is 0.01%)

	Basalt in Miyakejima			KREEP rocks	
	Ako	Benkenemisaki	Imasaki	Minimum	Maximum
SiO_2	49.90	50.76	51.80	48.00	52.80
TiO_2	1.14	1.23	1.42	1.03	2.23
Al_2O_3	15.63	15.55	14.51	13.30	16.40
Fe_2O_3	2.97	2.59	3.40		
FeO	10.76	10.19	10.64	9.20	15.50
MnO	0.27	0.25	0.25	0.14	0.23
MgO	5.26	5.43	4.42	6.80	10.50
CaO	11.27	10.73	10.09	7.10	11.10
Na_2O	2.04	2.16	2.42	0.29	0.89
K_2O	0.24	0.38	0.42	0.25	0.67
P_2O_5	0.07	0.16	0.20	0.46	0.70



Fig.8 Basalt lava flow widely distributed in Miyakejima

CONCLUSION

The purpose of the study was to design a simulant for high land rocks on the moon from Japanese ingenious rocks. A simulant of regolith for mare and high land on the moon is necessary to develop because many kinds of experiments and activities need such a simulant of lunar soil. Simulant for the regolith of mare of moon had been made in the past however a simulant for high land on the moon had not been made. A simulant for high land rocks on the moon was designed. High land rocks on the moon are composed of the main ferroan anorthosites (anorthite content over 90%), and to a lesser degree of Mg-rich rocks and KREEP rocks. Therefore in order to make a simulated lunar high land rock, the best method is to prepare each simulated rock, the ferroan anorthosites, Mg-rich rocks, and KREEP rocks and then mix them. From mineralogy and chemistry, using plagioclase phenocrysts from Miyakejima and Fugoppe enabled the simulation of ferroan anorthosites. Both plagioclase phenocrysts were high in anorthite content, 94 to 98 % and 92 to 95 % whereas the plagioclase in gabbro or anorthosite on the earth is low in anorthite content, 70 to 90 %. Both plagioclase phenocrysts are easy to separate from rocks because plagioclase phenocrysts occurred as a volcanic bomb in Miyakejima and plagioclase phenocrysts occurred in soft tuff in Fugoppe. Similarly, using gabbro and dunite in Horoman and basalt in Miyakejima enabled the simulation of Mg-rich rocks and KREEP rocks respectively. As a result, mineralogy and chemistry mixing of these rocks enabled the simulation of high land rocks in the moon.

REFERENCES

- [1] Grant H. H, David T. V, and Bevan M. F. LUNAR sourcebook, Cambridge: Cambridge

- University Press, 1991, pp.212–231.
- [2] Bradley L. J, Mark A. W, Charles K. S, and Clive R. N. New Views of the Moon, Mineralogical Society of America, Vol.60, 2006, pp.1–721.
 - [3] Papike J.J. Chapter 5 Lunar Samples, Planetary Materials, Mineralogical Society of America, Vol.36, 2000, pp.5-001-5-234.
 - [4] Jolliff, B. L., Gaddis, L. R, Ryder, G., Neal, C. R., Shearer, C. K., Elphic, R. C., Jonson, J. R., Keller, L. P., Korotev, R. L., Lawrence, D. J., Lucey, P. G., Papike, J. J., Pieters, C. M, Spudis, P. D., and Taylor, L. A., New views of the Moon: Improved understanding through data integration. *Eos*, Vol.81, No.31, 2000, pp. 354-355.
 - [5] Arai T., Recent lunar image from meteorite of moon, *The Japanese Society for Planetary Sciences*, Vol.20, No.1, 2011, pp. 28-35.
 - [6] Takahasi Y. Miyazaki K. and Nisioka Y., Plutonic rocks and metamorphic rocks in the Tsukuba Mountains, *Journal of Geological Society of Japan*. Vo.117. 2011. Pp.21-31.
 - [7] Tagiri M. Yano T. and Koiske W., Layered Structure and Intrusive Form of Tsukuba Gabbroic Body, *Bull.Ibaraki Nat. Mus.* Vol.16, 2013. Pp.1-8.
 - [8] Czamanske G.K. and Bohlwn S.R., The Stillwater Complex and its anorthosites: An accident of magmatic underplating?, *American Mineralogist*. Vol.75, 1990, pp.37-45.
 - [9] Salpas P.A. and Haskin L.A., Stillwater Anorthosites; A Lunar Analog?, *Proceedings of the Fourteenth Lunar and Planetary Science Conference, Journal of Geophysical Research*, Vol.88, 1983, pp.B27-B39.
 - [10] Kimata M. Nishida N. and Murakami H., Plagioclase Megacrysts Including Native Copper and Hydrocarbons, *Journal of the Mineralogical Society of Japan*, Vol.23, No.2, 1994, pp45-58.
 - [11] Arakawa Y. Murakami H. abd Kimata M., Strontium isotope compositions of anorthite and olivine phenocrysts in basaltic lavas and scorias of Miyakejima volcano, Japan, *Journal of Mineralogy petrology economic Geology*, Vol.87. 1992, pp.226-239.
 - [12] Isshiki N., Miyake-jima (Geological map of Japan 1:50,000), *Geological Survey of Japan*, 1960, pp.61–62.
 - [13] Nakata E, and Watanabe M., Dissolution and precipitation between pH 3.8-, CO₂ dissolved solution and anorthite rich tuffaceous sandstone by using high temperature flow-through reactor, *Journal of Mineralogical and Petrological Sciences*, Vol.38, 2009, pp.161–174.
 - [14] Funabashi M., and Igi S., Horoizumi (Geological map of Japan 1:50,000), *Geological Survey of Japan*, 1956, pp.43–44.

RELIABILITY ASSESSMENT OF WOODEN TRUSSES OF A HISTORICAL SCHOOL

Alvin Quizon¹ and Lessandro Estelito Garciano²

¹PHDCE Student, De La Salle University, Philippines; ²Associate Professor,
De La Salle University, Philippines

ABSTRACT

Records show that the National Structural Code of the Philippines (NSCP 2015) wind load requirements changes (increase) over time as extreme data becomes available. Increase wind velocity arises from stronger typhoon events translating to additional wind pressure. These changes pose a threat to existing structure, especially historical structures. Historical structures such as Gabaldon schools which were designed and constructed more than hundred years ago are not spared especially if the roof is still made of timber. The Department of Education (DepEd), recognizing its significant role in the history of Philippine education, continues its efforts in its conservation. Reliability assessment is necessary to check if there is a need to retrofit to maintain its function as well as to preserve its significance in the country's history.

In the analysis of the roof trusses which is directly affected by wind load, all loads are considered as constant except for the uniformly distributed wind load which is random in nature. These constant loads serve as the baseline information of initial stresses acting within the truss members. Uniformly distributed wind load are then transferred to purlins then to truss members which eventually produces additional stress on top of the initial stress. Any changes in the amount of uniformly distributed wind load constitute proportionally to changes in stresses of truss members. Using a commercially available software, it is easy to replicate by applying different amount of wind load that will give corresponding stresses. Using a spreadsheet, the results from the software can generate a simple graphical model and equation expressing the relationship between wind velocity against axial force, shear force and bending moment. Mechanical properties of wood establish the limits of its strength which eventually can be converted and calculated to wind velocity using the graph and equation obtained. Failure of truss can be projected in terms of wind velocity which even ordinary people can easily perceived and understood.

Keywords: Retrofitting, Proportional changes, Simple graphical model, Mechanical properties

1. INTRODUCTION

The Philippines is located along a typhoon belt and the so-called Ring of Fire, a vast Pacific Ocean region where many of Earth's typhoon, earthquakes, and volcanic eruptions occur.

According to state weather bureau Philippine Atmospheric, Geophysical and Astronomical Services Administration (PAGASA), the Philippines is visited by at least 20 tropical cyclones every year with 5 having the potential to be destructive ones as shown in Figure 1.

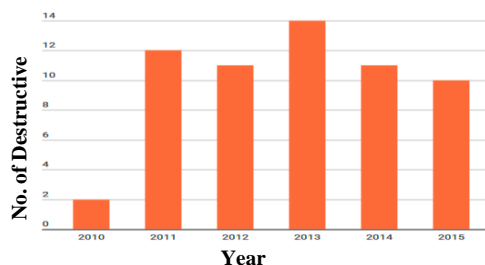


Figure 1 - Number of destructive tropical cyclones that entered the Philippines (2010 – 2015). Source: NDRRMC

According to the 3rd edition of National Structural Code of the Philippines (NSCP) that was released on 2001, the basic wind speed requirement was 200km/h for Zone 2 whereas the current 7th edition of NSCP that was released on 2015, the basic wind speed requirement is 260km/h for the same location. This only proves that wind load requirement for a given building increases from time to time.

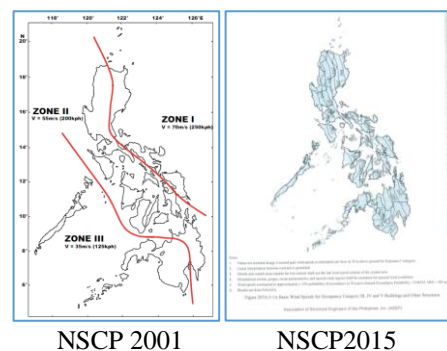


Figure 2 – Wind requirement difference between NSCP 2001 and NSCP 2015

This increase in basic wind speed pose hazard to existing structures. Historic structures such as

Gabaldon schools are not exempted from this hazard for they were built during the American Regime. The Department of Education (DepEd), recognizing its significant part in the history of Philippine education, continues its efforts in the conservation of the Gabaldon and heritage school buildings.

According to PAGASA, there is already a storm categorized as signal#5 with very strong winds of more than 220 kph.

Super typhoon Yolanda (Haiyan) hit land with sustained winds of 196mph and even stronger gusts which ripped off roofs, collapsed buildings, shattered windows and inundated coastal regions with an incredible storm surge that left the majority of homes either completely destroyed or uninhabitable.

Typhoon Lawin tears through the Philippines leaving homes damaged, roofs ripped off school buildings and trees uprooted. Lawin, a category 5 entered the Philippines with winds gusting up to 315kph but weakened to category 4 just before making landfall.

This study is an initial effort to address deficiencies and inefficiencies such as additional loadings which are not included in the original design and in past construction practices of structural engineering concepts through a comprehensive design evaluation approach that draws on existing and innovative engineering technologies in a practical manner.

The desired effect to continuously improve the value of historical structure of Gabaldon School in San Rafael, Bulacan in terms of economy and structural performance can be started through the reliability assessment of wooden truss which is directly affected by wind.

But why Gabaldon school when such structure is a symbol of oppression, subjugation, and injustice? Fr. Ted Milan Torralba's paper "Making Cultural Heritage Alive in Contemporary Philippine Culture" pointed out that principle of identity that constitutes an extension of who we are and that every heritage is a knowledge resource.

Numerous studies are being done to know and address the effects of wind load on structures. Numerical Assessment of Roof Panel Uplift Capacity under Wind Load written by Weixian He (2010, October), highlights the impact of construction error in terms of missing nail effects. Analysis indicates that missing a single nail could reduce the mean of the panel uplift capacity by 10%, and missing two nails could reduce the mean of R by as much as about 23%.

Gavansk et al (2014) in their paper entitled "Reliability Analysis of Roof Sheathing Panels on Wood-Frame Houses Under Wind Loads in Canadian Cities" found that relatively small

differences in fastener size result in large differences in roof sheathing performance.

Kyung Ho Lee and David V. Rosowsky. (2004, December) in their paper "Fragility Assessment For Roof Sheathing Failure In High Wind Regions" developed complementary fragilities in the form lognormal cumulative distribution. A study in "In Situ Nail Withdrawal Strengths in Wood Roof" by Prevatt, David O., et al. (2014, May) indicates that premature failure of wood roof sheathing under wind loading has been primarily blamed on poor nail installation resulting in reduced nail withdrawal strengths.

Garciano et al., (2013) in their study developed a vulnerability assessment of low-cost housing in Malate, Metro Manila. The results obtained show that pullout failure is the main mode of failure attaining a maximum of 27.2% for a 150-year wind return period (200 km/h wind speed).

Finally, the study follows the same objective of the study "The reliability assessment of wooden roof trusses of historical churches in Laguna" written by Dr. Garciano (2017) which generally studied the reliability of historical churches that lead to a conclusion of considering a restoration and retrofitting of the church structures in the future.

2. STUDY DETAILS

Gabaldon schools are under the supervision of DepEd and National Historical Commission of the Philippines.

Presently, part of Gabaldon school in San Rafael, Bulacan, functions as classrooms for students and part functions as activity hall for general assembly.

Roof trusses of the school are typically designed. It consists of 19 trusses having same specifications and dimensions as shown in Figure 3. The original timber truss is made of Yakal wood and the reinforcement is made of Apitong wood having the mechanical properties shown in Table 1.

Table 1. Graded Wood Characteristic of Yakal and Apitong

80% Stress Grade	Strength	
	Yakal	Apitong
Bending/ Tension Parallel to Grain, MPa	24.5	16.5
Modulus of Elasticity in Bending, MPa	9.78x10 ³	7.31x10 ³
Compression Parallel to Grain, MPa	15.8	9.56
Compression Perp. to Grain, MPa	6.27	2.20
Shear Parallel to Grain, MPa	2.49	1.73

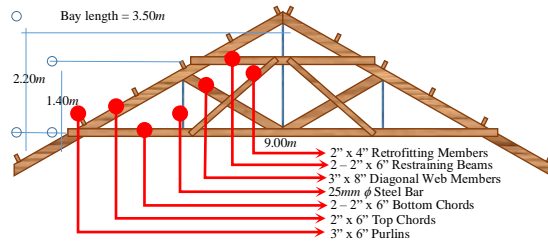


Figure 3. Typical Detail of Truss

The roof panel is made up of Ga. 20 Corrugated GI sheet. GI plates equally spaced at 0.25m on center are riveted to the roof panel which are then anchored by 2 screws on the purlins.

Data from the nearest Agromet station were incomplete which lead to the use of estimated wind requirement of 255kph based from NSCP2015 as shown in Figure 4.

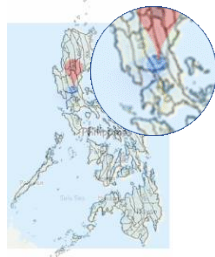


Figure 4. Superimposed map on NSCP 2015 basic wind speed requirement

3. MATHEMATICAL FORMULATION

3.1 Maximum Allowable Strength

Three equations will be used to determine the allowable strength of the truss members.

Simple stress formula will determine the maximum capacity in terms of compressive and tensile strength of truss members and is defined as

$$P = SA \quad (1)$$

where S denotes the maximum stress capacity of the truss members found in Table 1. and A is the cross section of the truss members.

Shear stress in rectangular beam will be used to determine the allowable shear and is represented by

$$S_s = \frac{3V}{2A}; \quad V = \frac{2AS_s}{3} \quad (2)$$

where S_s denotes the maximum stress capacity of truss members found in Table 1. and A is the cross section of the truss members.

Flexure formula will used to determine the bending moment capacity defined as

$$f_b = \frac{MC}{I} = \frac{6M}{bd^2}; \quad M = \frac{bd^2 f_b}{6} \quad (3)$$

where f_b denotes the maximum stress capacity by the truss members found in Table 1, b is the width of the beam and d is the height of the beam.

The calculation for the uplift load on purlins, wind pressure on the components and cladding and total uplift pressure will be taken from NSCP2010/2015 as seen in the following equations below.

$$q_h = 47.3 \times 10^{-6} K_z K_{zt} K_d V^2 I_w \quad (4)$$

$$p = 0.80 q_h (GC_p - GC_{pi}) \quad (5)$$

$$S_p = T_A (DL + q_h) \quad (6)$$

The pull-over and pull-out resistance of the rivet and roof panel R_p represented by the formula below.

$$R_p = 1.5 d_w F_u t \quad (7)$$

$$R_w = w \times p \quad (8)$$

where F_u is the tensile strength of the member in contact with rivet head, t is the thickness of material and d_w is the diameter of the rivet head.

The methodology consists of six components:

1. Actual inspection of the truss to determine the wooden properties of truss members.
2. Analysis of truss members stresses using SAP2000 having zero wind load as the baseline information and different amount of wind load as samples both for transverse and longitudinal directions.
3. The results of the most critical element in each of the seven typical members were selected: purlins, top chord, bottom chord, vertical web members, retrofitting members, straining beam and vertical web members.
4. Generation of simple graphical model (SGM) and equation using Microsoft Excel, expressing the relationship between wind velocity against axial force, shear stress and bending moment.
5. Determination of allowable axial force, shear and moment using Eq. (1), Eq. (2) and Eq. (3) then substitute to the generated graphical model to determine the projected wind velocity that will cause damage or failure.
6. Determination of uplift load per purlin, S_p , pull-over resistance of the roof panel, R_p , and pull-out resistance of Rivet, R_w .

3.2 Simple Graphical Model

A simple graphical model is to be constructed by plotting the axial force, stress or moment on the y-axis versus the wind velocity on x-axis as shown in Figure 5.

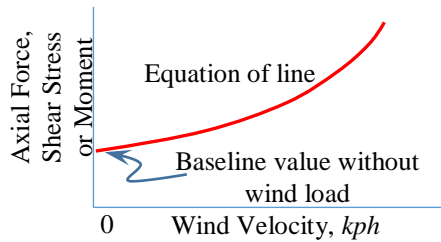


Figure 5. Simple graphical model of wind velocity versus axial force, shear stress or bending moment.

The study requires graphical models for the three (3) mode of failure of truss members, namely: axial force, shear stress and bending moment.

4. DATA AND RESULTS

In this study, timber used in trusses were identified and proper mechanical properties were applied (see Table 1.)

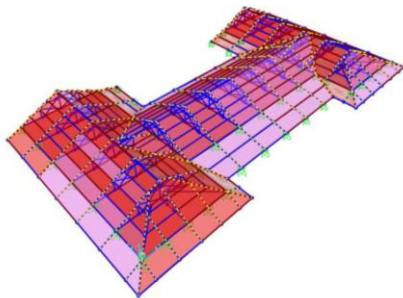


Figure 6. 3D Model of Truss Frame Using SAP2000

Using SAP2000 for 3D modeling as shown in Figure 6 and selecting only the most critical element from the result for the seven subdivided members, relationship with wind velocity against force, shear or moment is obtained. Due to the huge data, only the most critical in three modes of failure among the seven typical member is shown in Table 2.

Table 2. Selected Critical Value from SAP2000 Analysis

Wind Velocity kph	Max. Force KN	Max. Shear KPa	Max. Moment KN.m
0	84.538	18.260	4.0649
50	84.538	18.313	4.0649
100	85.104	18.472	4.0678
150	86.490	18.738	4.1189

200.6465	88.429	19.111	4.1903
255 (NSCP)	93.880	19.643	4.3542
300	98.817	20.686	4.5581
500	134.369		5.8640

Figure 7 shows the curve line that represents the relationship between axial force and wind velocity. Equations of the lines were generated by Excel software.

Using Eq. (1), the maximum allowable P obtained is 177.75KN which will then be substituted to the equation of the curve line on Figure 7 to get the projected wind velocity to cause damage or failure. The obtained value of wind velocity is 614.1529kph denoting it safe and adequate.

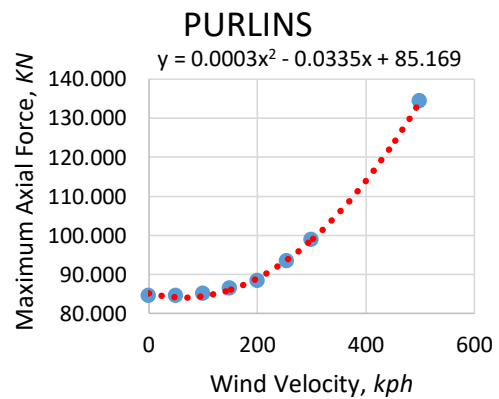


Figure 7. Simple graph representing maximum axial force vs wind velocity from Table 2

Using Eq. (2), the maximum allowable V obtained is 1.722KN which will then be substituted to the equation of the curve line on Figure 8 to get the projected wind velocity to cause damage or failure. The obtained value of wind velocity is 514.3937kph denoting it safe and adequate.

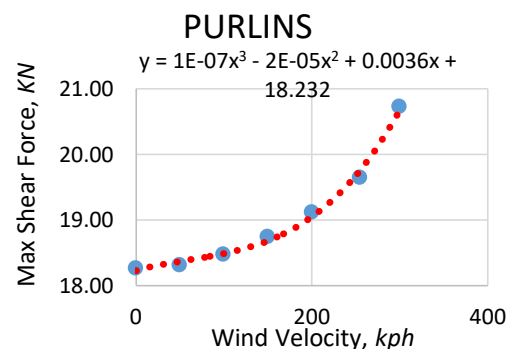


Figure 8. Graph representing maximum Shear Force vs wind velocity from Table 2

Using Eq. (3), the maximum moment M obtained. is 12.25KN.m. The value will then be used to the equation of the curve line on Figure 9

to get the projected wind velocity to cause damage or failure. The obtained value is 975.9581kph denoting it safe and adequate.

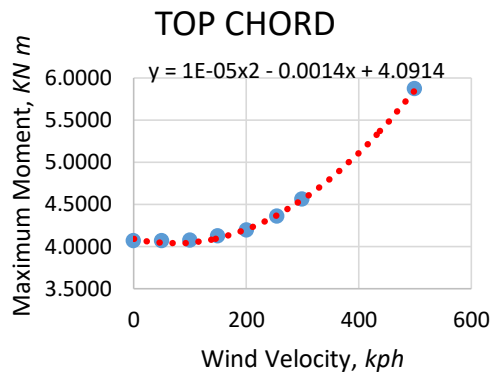


Figure 9. Graph representing maximum moment vs wind velocity from Table 2

Due to limited and unavailability of sample, roof panel was assumed to have tensile strength of 311MPa for schedule 40 which are considered the weakest among the available roof panel in the market for safety purposes. Using Eq. (6), the value obtained for the uplift load on purlins is 15.8016KN which is less than 53703.293KN for pull-over resistance of roof panel obtained using Eq. (7). This indicates that it is still safe and adequate even for the worst case scenario. Another unavailable sample is the rivets which were assumed to be made of aluminum with strength of 320lb. Assumption was done through the exposed head diameter and selecting the weakest material among available rivet in the market. Using Eq. (8), the total pull-out capacity of 14 rivets is 19.9766KN which is greater than the uplift force of 15.8016KN indicating safe and adequate.

5. CONCLUSION

Reliability assessment was done and indicates that the overall performance of the roof structure is still good and safe. The most critical of all elements is the purlins but still considered safe and adequate by having 259.3937kph wind velocity allowance before reaching failure. Previous NSCP wind speed requirements show that it would take decades for the wind velocity to increase by 100kph. With the result of failure of truss in term of wind velocity, even ordinary people can now perceive and understand the limitation of structure because here in the Philippines typhoons are categorized based on their wind speed. Due to unavailability of data and sample, some were assumed for the worst case scenario but still analysis indicates that truss members are still considered safe and adequate. A more detailed analysis including seismic analysis of the whole

structure is encouraged in the future. It is also necessary for the immediate review of other existing structure.

6. ACKNOWLEDGEMENTS

The authors would like to acknowledge the assistance of CHED, Mr. Albert Ulac, Ms. Mercedes Fernando of NSWRDC, Dr. Rene R. Escalante of NHCP, Engr. Marc Gerald Sarabia and Engr. Annabelle R. Pangan of DepEd and faculty & staff of Gabaldon Elementary School.

7. REFERENCES

- [1] Torralba, Ted Milan. Making Cultural Heritage Alive in Contemporary Philippine Culture. Retrieved December 9, 2017 from www.cilam.ucr.edu/diagonal/issues/2008/Torralba2.pdf
- [2] Weixian He. (2010, October). Numerical Assessment of Roof Panel Uplift Capacity under Wind Load. Retrieved December 7, 2017 from r.lib.uwo.ca/cgi/viewcontent.cgi?article=1088&context=etd.
- [3] Gavanski, Kopp and Han Ping Hong. (2014). Reliability Analysis of Roof Sheathing Panels on Wood-Frame Houses Under Wind Loads in Canadian Cities. Canadian Journal of Civil Engineering, 2014, Vol. 41, No. 8 : pp. 717-727.
- [4] Kyung Ho Lee, David V. Rosowsky. (2004, December). Fragility Assessment For Roof Sheathing Failure In High Wind Regions. Retrieved December 7, 2017 from <https://www.cs.rice.edu/~Roof%20safety%20in%20high%20wind%20regions.pdf>.
- [5] Prevatt, David O., et al. (2014, May) In Situ Nail Withdrawal Strengths in Wood Roof structures. Journal of Structural Engineering/Volume 140 Issue 5. Retrieved December 8, 2017 from [https://ascelibrary.org/doi/full/10.1061/\(ASCE\)ST.1943-541X.0000990?src=recsys&](https://ascelibrary.org/doi/full/10.1061/(ASCE)ST.1943-541X.0000990?src=recsys&)
- [6] Garciano, Alvarez, Colobong, Decal and Tan. (2013). Mapping the vulnerability of Low-Cost House Roofs in Malate, Metro Manila Due to Extreme Wind Speeds. Retrieved December 9, 2017 from <https://eprints.lib.hokudai.ac.jp/dspace/handle/2115/54217>
- [7] Garciano, Lessandro Estelito O. (2017). The Reliability Assessment of Wooden Roof Trusses of Historical Churches In Laguna.
- [8] Aban, Abinales, Aguel, Alfiler, Anonical, Aquino, . . . Zarco. (2010). National Structural Code of the Philippines, Volume 1.
- [9] American Wood Council.(2015). National Design for Wood Construction, 2015 edition.

- Retrieved from <http://awc.org/pdf/codes-standards/publications/nds/AWC-NDS2015-ViewOnly-1411.pdf>
- [10] Philippines News Agency. (2015). House Approves Proposed Conservation of Gabaldon and Other Heritage School Buildings. Retrieved November 30, 2017 from www.canadianinquirer.net/2015/06/21/house-approves-proposed-conservation-of-gabaldon-and-other-heritage-school-buildings/
- [11] Ang, Jeremy Sebastian S. et al. (2017). Reliability Assessment of Wooden Supported Roofs of Selected Historical Churches in Laguna.
- [12] Ellingwood, Ellingwood and Jun Hee Kim. Fragility Assessment of Light-Frame Wood Construction Subjected to Wind and Earthquake Hazards. *Journal of Structural Engineering*, Vol. 130, No. 12, December 1, 2004. ©ASCE, ISSN 0733-9445/ 2004/12-1921-1930/\$18.00. Retrieved December 9, 2017 from pdfs.semanticscholar.org/7d39/6e5137bce11a16b1bac60e285d15e6611d9d.pdf.
- [13] Ignacio, Jose F. Challenges In Preserving the Heritage Houses of Batanes, Philippines. Retrieved December 9, 2017 from rizal.lib.admu.edu.ph/conf2005/conf/ARCH.%20JOSE%20IGNACIO%20PAPER%20FOR%20ATENEO.
- [14] Mara Cepeda. (2017, April). House bill seeks to conserve Gabaldon school buildings. Retrieved December 9, 2017 from www.rappler.com/nation/167054-house-bill- conserve-gabaldon-school-buildings.
- [15] Providing For The Protection And Conservation Of The National Cultural Heritage, Strengthening the National Commission for Culture and The Arts (NCCA) and Its Affiliated Cultural Agencies, and For Other Purposes Act of 2010, Fourteenth Congress of the Third Regular Session 2010.
- [16] Stedman, Derek A. (2014, April). Full-Scale Tests of a Wood-Frame Structure under Extreme Wind Loads . Retrieved December 7, 2017 from ir.lib.uwo.ca/cgi/viewcontent.cgi?article=3484&context=etd
- [17] Valerio, Ma. Luisa M. (2012), Presentation, National Historical Commission of the Philippines. Retrieved December 9, 2017 from www.kyotoheritage.jp/PDF/UNESCO_summer_school_2012.
- [18] Villalon, Augusto F. (2015). In Focus: Getting Our Heritage to Survive the Ages. Retrieved December 9, 2017 from <http://ncca.gov.ph/about-culture-and-arts/in-focus/getting-our-heritage-to-survive-the-ages/>

EXPERIMENTAL STUDY ON CHEMICAL GROUTING INTO CALCIUM-CONTAINING SAND

Hidetake Matsui¹, Yusuke Tadano¹ and Hiroyasu Ishii¹

¹Taisei Corporation, Japan

ABSTRACT

Chemical grouting which injects a low viscosity solution into the pore space in soil is often used as a countermeasure against soil liquefaction. In contrast to in-situ ground improvement methods such as cement-soil mixing, jet grouting and dynamic soil densification, the method does not disturb soil structures during execution; therefore, the method provides good applicability around existing structures. On the other hand, the quality and the accuracy of grouting is significantly affected by properties of both target soil and chemical grout. According to recent studies, injection procedure with appropriate gel time allows to ensure “ball-shaped” solidification as planned. However, it has been known that the gel time is shortened by calcium compound contained in soil e.g. provided by fragmented shells. Although this may cause reduction of improvement quality, the effect of calcium containment has not been investigated enough to take the effect into grouting practice. This paper reports a series of experimental injection tests using model grounds containing fragmented shells. The test results show 1) during injection process, injection rate was oscillated, it may have been caused by carbon dioxide gas generated by a chemical reaction between calcium compound and acid in chemical grout; 2) although the shape became irregular not like “ball-shaped”, solidified soil had been created; 3) a reduction in unconfined compressive strength occurred in comparison with the case not contained fragmented shells. These findings may be important knowledge for grouting practice, which lead to a major step forward to optimize chemical grouting procedure in calcium-containing soil.

Keywords: Chemical grouting, Calcium-containing sand, ground improvement, soil liquefaction

INTRODUCTION

In reaction to the occurrence of the 2011 Great East Japan Earthquake and the possibility of a large-scale earthquake that may occur along the Nankai Trough and under the Tokyo metropolitan area, Basic Act for National Resilience, which was promulgated and enforced in December 2013 [1], showed basic policy to minimize the influence of large-scale natural disasters on the lives of the citizenry and the national economy. The Fundamental Plan for National Resilience, which was approved in a Cabinet meeting in June 2014 [1], provides for promotion policies for seismic reinforcement work of important infra-structures such as major road, port and airport. In this circumstance, applying liquefaction countermeasures for these infrastructures is an urgent issue, not only in new construction projects but also for existing structures in Japan.

Chemical grouting which injects a low viscosity solution into the pore space in soil is often used as a countermeasure against soil liquefaction. In contrast to in-situ ground improvement methods such as cement-soil mixing, jet grouting and dynamic soil densification, chemical grouting does not disturb soil structures during execution; therefore, it provides good applicability around existing structures.

On the other hand, the quality and the accuracy of grouting is significantly affected by properties of both target soil and chemical grout.

According to recent studies, appropriate gel time in ground has been considered as a main influence factor [2], [3]. Gel time in ground is defined as a period between starting injection and gelling. To ensure good injection state, gel time in ground should be long as low viscosity is required to be permeated into the pore space in soil. On the other hand, it has been pointed out that overlong and/or too short gel time in ground lead to irregular shape of solidified area and strength reduction as a result of gravity settling and spreading of grout [3].

Gel time of grout can be adjusted by changing its pH [4]. However, gel time in ground could be shortened by calcium compound contained in soil e.g. provided by fragmented shells [5]. Although a certain improvement quality in calcium-containing ground has been reported [6], [7], the effect of calcium containment on injection process has not been investigated enough to take the effect into practice.

In order to obtain useful knowledge for appropriate execution of chemical grouting in calcium containing ground, a series of injection tests using model grounds containing fragmented shells has been carried out. This paper shows test results such

as injection flow rate, injection pressure, shape and strength of solidified soil.

METHODOLOGIES

Preparation of model ground

Figure 1 shows schematic cross-section of model ground. The container was made of a steel drum and the model ground is 500 mm in diameter and height. Model ground was made by following preparation procedure cited from reference [3];

- 1) Bottom lid of a steel drum is removed and the drum is placed upside down in order to use an oil filler hole on the top lid as a bottom inlet. Then bonded textile is pasted on inner surface of the drum.
- 2) A layer of gravel is placed on the bottom of the drum with the thickness of 50 mm.
- 3) Four drainage pipes are placed on inner surface of the bonded textile.
- 4) To achieve the target relative density 80 %, model ground material is placed in the drum and compacted by compaction rod in four layers.
- 5) A layer of gravel is placed upper the ground material with the thickness of 50 mm.
- 6) 700 liter carbon dioxide gas, that is 5 times as large as a volume of the drum, is injected from the bottom of the drum. Then, tap water is injected from the bottom of the drum and the model ground is saturated.
- 7) To avoid disturbance of model ground during the test, mortar is placed on the top of the upper gravel layer as a lid.

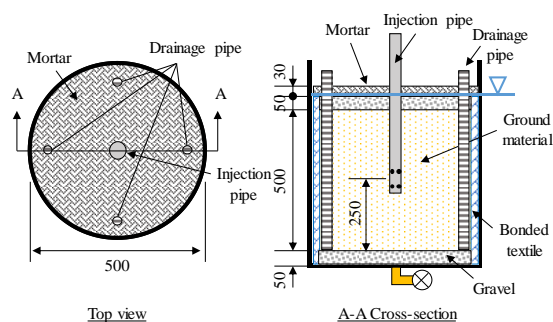


Fig. 1 Schematic cross-section of model ground.

Test conditions

Injection tests were carried out 3 days after mortar was placed. To make “ball-shaped” solidified soil which is 300 mm in diameter, 6 liter non-alkaline chemical grout is injected through an injection pipe at 0.2 L/min injection rate. In this plan, 30 minutes are required to inject above mentioned volume of grout.

Table 1 shows test conditions. In No.s 1-3 that were carried out as comparison cases, only silica sand was used for model ground material and three

different length of gel time in ground were planned to confirm the effect of gel time on injection process and the quality of solidified soil. In No.s 4-6 that were carried out as calcium-containing cases, commercially available fragmented shell and silica sand were blended and used for model ground material. The contents of fragmented shell were 3 %, 6% and 9% in weight ratio. In these cases, gel time in ground was set to within 30 minutes after finishing injection as an appropriate condition to achieve “ball-shaped” solidified soil derived from prior study using silica sand [3].

Table 1 Test conditions (planned and actual)

No.	Ground material	Planned		Actual		Difference between actual gel time and actual injection period (min)
		Injection period (min)	Gel time in ground (min)	Injection period (min)	Gel time in ground (min)	
1	Silica sand	30	30	17*	40	23
2	Silica sand	30	60	30	85	55
3	Silica sand	30	90	30	147	117
4	Silica sand + 3% shells	30	30-60	30	26	-4
5	Silica sand + 6% shells	30	30-60	30	54	24
6	Silica sand + 9% shells	30	30-60	30	21	-9

* Stopped in the middle of injection because of unexpected increment of pressure.

TEST RESULTS

Gel time control

Measured actual gel time in ground is also shown in Table 1 in contrast to planned value. Actual injection period was equal to planned value except No. 1 which was stopped in the middle of injection because of unexpected increment of injection pressure. Although there was a gap between measured and planned gel time in ground, three different length of gel time in ground were ensured in No.s 1-3 and gel time of No.s 4-6 were approximately equal to injection period or within 30 minutes after finishing injection.

Injection state

Figure 2 shows measured injection flow rate and injection pressure against injection period. In No. 1, test was stopped in the middle of injection with an increase of injection pressure. In contrast to No. 1, No. 2 and 3 achieved stable injection flow rate according to longer gel time in ground.

Calcium-containing cases, No.s 4-6, averagely achieved planned injection flow rate but it oscillated; it might be caused by carbon dioxide gas generated by a chemical reaction between calcium compound and acid in chemical grout. In contrast to No.s 1-3, injection pressure of these cases was stable.

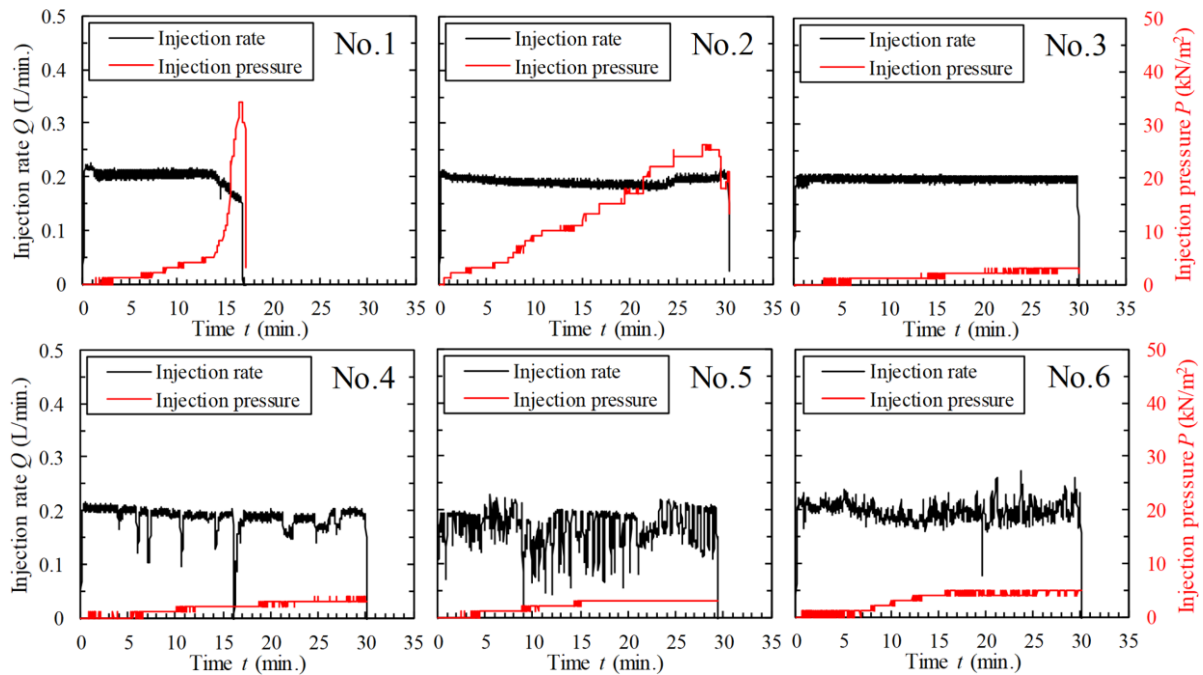


Fig. 2 Measured injection flow rate and injection pressure against injection period.

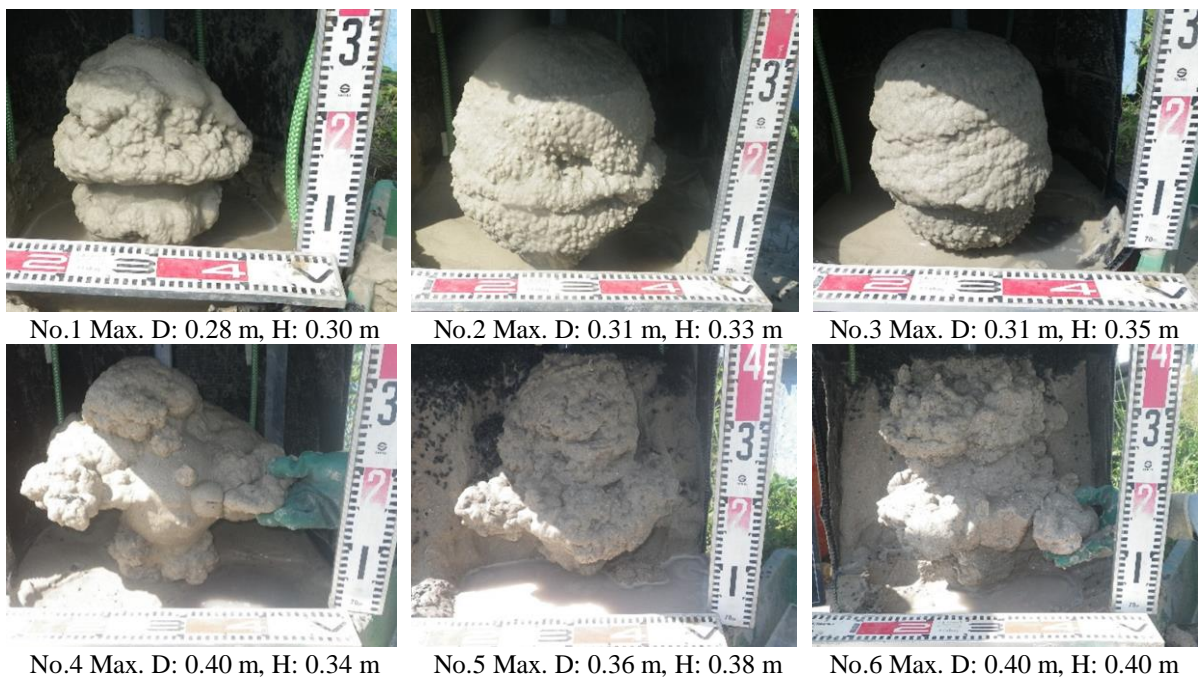


Fig. 3 Actual shapes of solidified soil.

Shape of solidified soil

Actual shapes of solidified soil were observed two weeks after injection tests. Figure 3 shows photos of actual shapes of solidified soil. As shown, No.s 1-3 achieved “ball-shaped” solidification. Solidified volume of No. 1 was smaller than planned volume due to the short injection period. In addition, surface of No. 1 was a little bumpy in comparison

with those of No. 2 and 3. It seems to be caused by movement of grout like magma which called “magma action [8]”; injected grout was turned into a gel due to short gel time in ground and solidified surrounding soil and then following grout tended to mount those solidified area. To compare No.2 and No. 3, solidified soil of No. 3 was a little vertically longer than No. 2 due to longer gel time in ground which might cause gravity settling and spreading of grout.

Calcium-containing cases, No.s 4-6, did not achieve “ball-shaped” solidification. In these cases, magma action might be occurred and solidified area was developed irregularly probably because the gelling was caused by chemical reaction between randomly distributed calcium compound and acid in chemical grout so solidified area was made at random. On the other hand, magma action was also occurred in No. 1 but the solidified area was developed like a ball because the gelling was caused by shorter gel time so solidified area developed concentrically.

Strength of solidified soil

Needle penetration resistance

To investigate a distribution of strength inside solidified soil, needle penetration resistance was measured using sampled solidified soil according to JGS 3431-2012 [9]. Measurement was carried out for four cases, No. 1, 2, 4 and 6, two weeks after injection tests, i.e. immediately after the above observation. For each case, needle penetration resistance was measured on vertical and horizontal axes through the injection point.

Figure 4 shows distribution of needle penetration resistance on the horizontal axis. The result of No. 2, which achieved stable injection, shows the highest resistance followed by No. 1, 4, 6. In all cases, the resistance increases as distance from the injection point and reduction of strength is observed after peak value. Including No. 4 and 6, not achieved “ball-shaped” solidification, needle penetration resistance is distributed symmetrically.

Figure 5 shows distribution of needle penetration resistance on the vertical axis. Also in this figure, No. 2 shows the highest resistance. However, the distribution of the resistance is not symmetric and specific tendency is not found.

Unconfined compressive strength

To investigate strength of solidified soil directly, unconfined compressive strength was measured using a cut out specimen which is 50 mm in diameter and 100 mm in height according to JIS A 1216:2009 [10]. In each case, three specimens were used for the test; one specimen was cut out from each of three layers: upper, middle and bottom of solidified soil.

Figure 6 shows the result of the test. No.s 1-3 show 150 kN/m² strength on average except upper specimen of No. 1 which has small strength for some reasons. No. 3 shows smaller strength than No. 1 and 2. It might be caused by gravity settling and spreading of grout due to longer gel time in ground. No.s 4-6 show 80 kN/m² strength on average which is smaller than average of those of No.s 1-3. Prior

studies show that carbon dioxide gas, generated by a chemical reaction between calcium compound and acid in chemical grout, remains in solidified soil and reduces strength [4], [6]. On the other hand, prior studies show carbon dioxide gas is not likely to remain in solidified soil under confined pressure [4], [6]. As significant reduction of density was not observed in No.s 4-6, remaining carbon dioxide might be limited in these cases due to the sufficient confined pressure provided by the mortar placement. These test results indicate that reduction of strength might be caused by any reason other than remaining of carbon dioxide. Chemical reaction between calcium and acid also generates a calcium salt and water that may remain in the pore space in soil and reduce the strength of solidified soil.

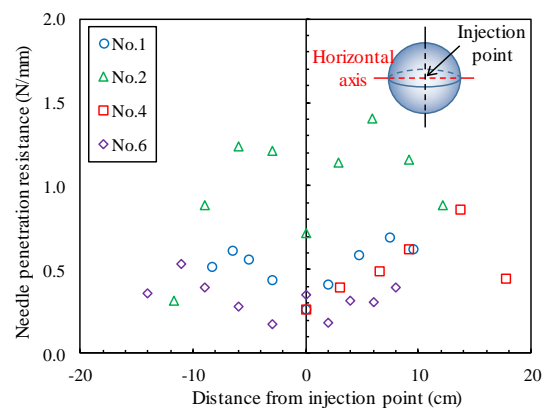


Fig. 4 Distribution of needle penetration resistance on the horizontal axis.

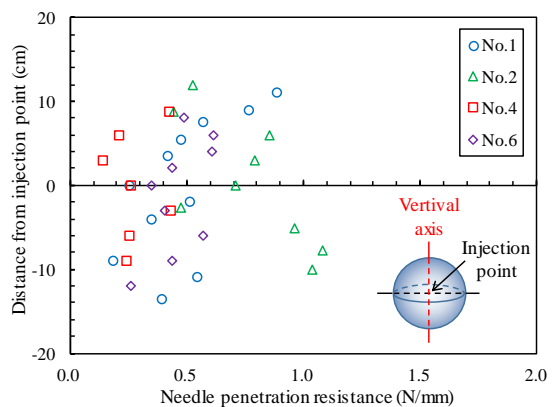


Fig. 5 Distribution of needle penetration resistance on the vertical axis.

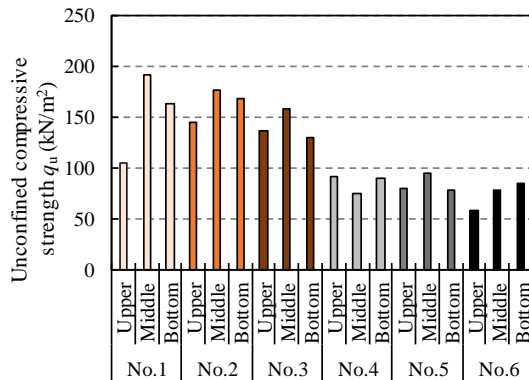


Fig. 6 Unconfined compressive strength of solidified soil.

CONCLUSION

The test results of calcium-containing cases show as follows:

- 1) during injection process, injection rate was oscillated; it may have been caused by carbon dioxide gas generated by a chemical reaction between calcium compound and acid in chemical grout.
- 2) although the shape became irregular not like “ball-shaped”, solidified soil had been created.
- 3) a reduction in unconfined compressive strength occurred in comparison with the case not contained fragmented shells.

These findings may be important knowledge for grouting practice, which lead to a major step forward to optimize chemical grouting procedure in calcium-containing soil.

REFERENCES

- [1] Website of the Japanese Cabinet Secretariat, https://www.cas.go.jp/jp/seisaku/kokudo_kyoujinka/index_en.html (accessed June 10, 2018)
- [2] Sasaki T., Koyama T., Shimada S. and Suemasa N., Influence of gelling time on permeability and strength of ground improved by chemical

grouting method, proceedings of the 47th annual conference of Japanese Geotechnical Society, 2012, pp. 787-788. (in Japanese)

- [3] Hayashi K., Yamazaki H. and Zen K., Study on mechanism of strength reduction caused by difference of the grout injection procedures in permeable grouting, Journal of Japan Society of Civil Engineers, Vol. 70, No. 4, 2014, pp. 387-394. (in Japanese)
- [4] Sasaki T., Koyama T., Shimada S. and Suemasa N., Influence of acid reactant type on gelling time and strength of ground improved by chemical grouting method, proceedings of the 48th annual conference of Japanese Geotechnical Society, 2013, pp. 751-752. (in Japanese)
- [5] Coastal Development Institute of Technology, Technical manual of permeation grouting method, 2010. (in Japanese)
- [6] Oka F., Kodaka T. and Ohno Y., Applicability of permeation grouting method using colloidal silica for coral sand, Journal of Japan Society of Civil Engineers, Vol. 64, No. 3, 2008, pp. 571-584. (in Japanese)
- [7] Okada K., Mizuno K., Gobou M. and Okamura I., Permeation grouting method for liquefaction measure in shell binding sand (part 1) - Confirmation on construction summary and effect of improvement-, proceedings of the 47th annual conference of Japanese Geotechnical Society, 2012, pp. 783-784. (in Japanese)
- [8] Towhata I., Shimada S., Yonekura R. and Shamoto Y., Soil liquefaction and earthquake, Index Press, 2010. (in Japanese)
- [9] Japanese Geotechnical Society, Japanese geotechnical Society standards -Geotechnical and geo-environmental investigation methods-, Maruzen Publishing Co., Ltd., Vol. 3, 2018.
- [10] Japanese Geotechnical Society, Japanese geotechnical Society standards -Laboratory Testing Standards of Geomaterials-, Maruzen Publishing Co., Ltd., Vol. 1, 2015.

EXPERIMENTAL STUDY ON THE EFFECT OF REBAR CORROSION ON THE MEASUREMENTS OF VARIOUS NONDESTRUCTIVE TESTS

Kohei Mishima¹, Kenichi Kondo², Isao Ujike¹, Chun Pang-jo¹ and Keiyu Kawaai¹

¹Department of Civil and Environmental Engineering, Ehime University, Japan

²Construction Materials Development Laboratory

ABSTRACT

For bridges, tunnels, etc., visual observation should be closely conducted according to standards set by the government. However, the visual inspection is usually conducted empirically and qualitatively, thus there are problems that the evaluation result may vary depending on the technical knowledge and experiences of inspectors. In addition, it is very difficult to detect internal damages which do not appear on the surface such as corrosion of reinforcing bars in concrete structures. Based on the above background, this study aimed at clarifying whether the internal damages present inside concrete structures can be detected at an early stage based on the measurements by several nondestructive tests. An air permeability test (Double chamber method), an electrical resistivity measurement test (Wenner method), a surface roughness measurement test (Two dimensional laser displacement meter), an ultrasonic pulse velocity test, compressive strength test (Estimated by concrete tester) are carried out simultaneously with visual inspection. After reinforced concrete specimens with $120 \times 120 \times 540$ mm are corroded by electrolytic corrosion, those nondestructive tests are carried out. The results suggest that the internal damages could be detected at an early stage based on the result of the air permeability coefficient and electrical resistivity. Also, there is no clear change in the arithmetic average roughness, the ultrasonic pulse velocity and the compressive strength during the testing periods.

Keywords: Corrosion, air permeability, electrical resistivity, surface shape, ultrasonic wave, concrete tester

INTRODUCTION

In recent years, deterioration and damage of reinforced concrete structures built during the period of high economic growth are becoming obvious, and maintenance and performance evaluation methods are urgently required. For bridges, tunnels, etc., visual observation should be closely conducted according to standards set by the government. However, the visual inspection is usually conducted empirically and qualitatively, thus there are problems that the evaluation result may vary depending on the technical knowledge and experiences of inspectors. In addition, it is very difficult to detect internal damages which do not appear on the surface such as corrosion of reinforcing bars in concrete structures. Based on the above background, this study aimed at clarifying whether the internal damages present inside concrete structures can be detected at an early stage based on the measurements by several nondestructive tests. An air permeability test (Double chamber method), an electrical resistivity measurement test (Wenner method), a surface roughness measurement test (Two dimensional laser displacement meter), an ultrasonic pulse velocity test, compressive strength test (Estimated by concrete tester) are carried out simultaneously with visual inspection.

OUTLINE OF EXPERIMENT

Outline of specimen

In this study, a rectangular column specimen of $120 \times 120 \times 540$ (mm) was prepared and one reinforcing bar of D16 was buried. A schematic diagram of the specimen is shown in Fig.1. The fog was 20 and 40 mm. Also, to confirm the position of the fog visually, 20 mm both ends of the reinforcing bar are exposed from the concrete. Incidentally, 90 mm both ends of the reinforcing bar is coated with epoxy resin. Table.1 shows the composition table of concrete, and Table 2 shows the test results of compressive strength of each water cement ratio. The physical properties of the aggregate are shown in Table.3. In the following discussion, each specimen is referred to as FC36, FC49, FC56, and FC61 based on the result of compressive strength.

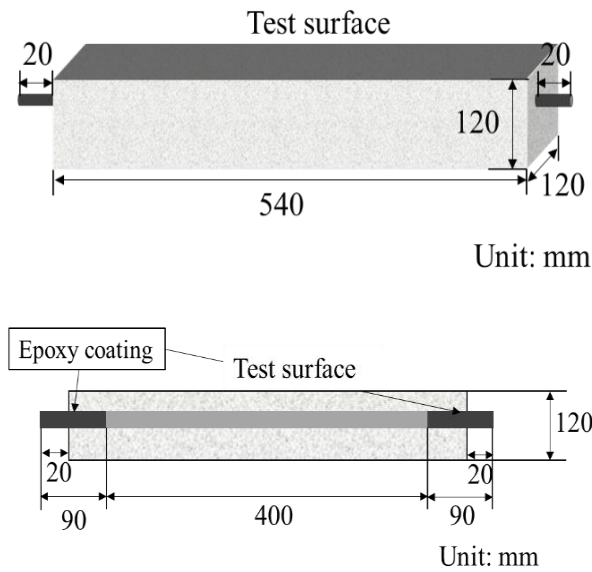


Fig.1 Specimen overview

Table.1 Recipe

Water cement ratio(%)	Compressive strength(N/mm ²)	Unit amount (kg/m ³)							
		W	C	S1	S2	S3	G1	G2	AD
40	FC61	180	449	482	234	108	464	476	4.50
50	FC49	177	346	560	270	122	450	460	2.78
60	FC56	178	296	606	294	132	428	440	2.38
70	FC36	179	259	636	308	140	420	430	2.08

Table.2 Results of compressive strength test of each water cement ratio

Water cement ratio W/C(%)	Compressive strength(N/m ²)
40	FC61
50	FC49
60	FC56
70	FC36

Table.3 Physical properties of aggregate

Fine aggregate	S1	Lime crushed sand from the Niitatsu mine founded in Tsukumi City Oita prefecture
	S2	Grinding sand produced by Yamanouchi, Tokyu-shi, Ehime Prefecture
	S3	Sumitomo Metal Mining Co., Ltd. Copper slag from Toyo factory
Coarse aggregate	G1	Crushed stone from Yamanouchi, Tokyu-shi, Ehime Prefecture
	G2	Crushed stone from Tanaki Tanbaru-machi, Saijo city, Ehime prefecture
Admixture	AD	Fluoric RV 10 which is the AE water reducing agent delay type (type I)

Test overview

In this test, we aimed to promote corrosion of reinforced concrete and to induce internal cracks. As shown in Photo.1, two test tanks with different fogging were divided into two test tanks, and two tanks of 900×200×2750 mm were prepared. The experimental procedure is shown below. In each tank, tap water was filled at a height of 20 mm and 40 mm from the bottom, a stainless steel plate was placed on the bottom of the tank, and the test specimens were placed side by side with the test surface facing downward. In order to electrically connect the specimens, crimp terminals at the end of the lead wires attached to the rebar were attached with bolts. Next, a DC stabilized power source was connected to the reinforcing bar (anode) and the stainless steel plate (cathode), and a direct current of 0.2A was applied to corrode the rebar. Figure.2 shows a schematic diagram of the corrosion test. After two days of energization, the experiment was carried out by taking out the specimen from the water tank and drying it in an indoor environment of 20°C. for 5 days as one cycle. In addition, various nondestructive tests were conducted in a constant temperature room at 20°C.

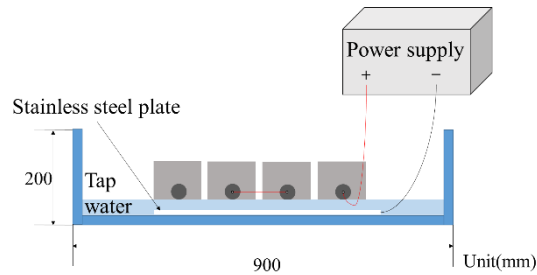


Figure.2 Electrographic test outline drawing



Picture.1 Test status

Measurement test overview

The non-destructive test carried out in this experiment was carried out by air permeation test (Torrent method [1]), electrical resistivity measurement test (Wenner method), surface shape measurement test (two dimensional laser displacement meter), ultrasonic test, compressive strength test (concrete tester). Are the five test methods. Table 4 summarizes the evaluations obtained by various non-destructive tests. In the air permeability test, the density of concrete can be evaluated by sucking up the air inside the concrete, and the air permeability coefficient can be calculated by sucking air by a chamber having a double structure. In the case of internal damage, the air gap in the concrete becomes depopulated and the amount of air sucked increases, so the air permeability coefficient increases. The electrical resistivity measurement test is a test that can calculate the electrical resistivity by applying voltage and current inside the concrete. In the case of internal damage, the air gap in the concrete becomes depopulated and the electric current hardly flows, so the electric resistivity increases. The surface shape measurement test is a test that can detect a fine deformation appearing on the concrete surface due to internal expansion caused by rusting of the reinforcing bars inside the concrete. When internal expansion occurs and fine concavity is present on the concrete surface,

the concavoconvexity increases, so the arithmetic mean roughness (JIS B 0601) for evaluating the fine deformation of the concrete surface increases. The ultrasonic test is a test that can arithmetically calculate the propagation time between the transmitting side that oscillates the P wave and the receiving side that receives it. In the case of internal damage, the propagation time is prolonged by the depopulation of the voids inside the concrete, so that the ultrasonic wave propagation velocity decreases. The compressive strength test using a concrete tester is a test that can indicate the strength and soundness by hitting the concrete surface with a hammer. In the case of internal damage, the compression strength decreases due to depopulation of the voids inside the concrete. Based on the above, the evaluation of this study is to evaluate whether the permeability coefficient, the electric resistivity and the arithmetic average roughness are continuously increasing, those in which the propagation speed and the compressive strength continuously decrease, It was evaluated as damaged and suggested that it can be detected early in various nondestructive tests.

Table.4 Evaluation obtained by various nondestructive testing

Various non destructive test	Evaluation obtained
Air permeability test	Material penetration resistance of concrete
Electrical resistance measurement test	Denseness and moisture condition of covering concrete
Surface shape measurement test	Fine deformation appearing on the surface as the concrete deteriorates
Ultra sonic test	Presence of damage and defect inside the concrete
Compressive strength test	

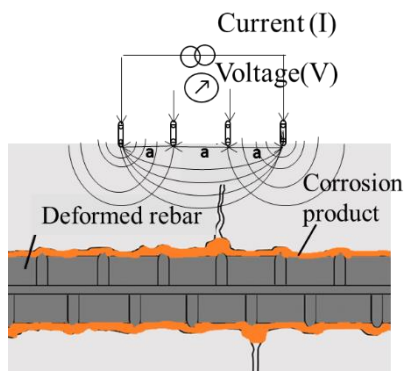


Fig.3 Schematic diagram of current flow

EXPERIMENTAL RESULTS AND DISCUSSION

In the air permeability test, the electrical resistivity test, and the surface profile measurement test, assuming that the internal damage causes the permeability coefficient, the electrical resistivity, and the arithmetic average roughness (JIS B 0601) to increase, I will consider whether it is possible. Figure 4 shows the time course of the change rate obtained by dividing the result of the air permeability coefficient measured after each elapsed days by the initial value. From the Figure 3, the rate of change of the air permeability coefficient of each specimen of 20 mm shows an increasing trend after 20 days in FC56 and 18 days in FC36. It is recognized that the rate of change of the air permeability coefficient of each specimen of 40 mm shows an increasing trend from FC36 after 18 days. In addition, the large decrease in the air permeability coefficient change rate from the 0th day to the 2nd day is largely affected by the water absorption of the concrete by the dry / wet repeated test. Next, Fig.5 shows the change with time of the rate of change obtained by dividing the measurement result of the electrical resistivity by the initial value. The rate of change in the electric resistivity of each specimen of 20 mm from the figure shows an increasing trend after 14 days in FC61, after 14 days in FC56, after 24 days in FC49 and 22 days in FC36. In addition, it is recognized that the rate of change of the air permeability coefficient of each specimen of 40 mm shows an increasing trend after 16 days in FC61, after 14 days in FC56, 36, and after 10 days in FC49. The large decrease in the air permeability coefficient change rate from the 0th day to the 2nd day is largely affected by the water absorption of the concrete by the dry / wet repeated test. Next, time-dependent changes in the arithmetic average roughness calculated using the surface shape measurement result are shown in Fig.6. The arithmetic average roughness of each specimen for both 20 and 40 mm shows that although there is data variation at each compressive strength, it hardly

changes. From the above results, it is suggested that damage may be detected at an early stage based on the results of the air permeability coefficient and the electric resistivity although the elapsed days for which results suggesting the existence of internal damage are different in each test result. Next, in the ultrasonic test and the compressive strength estimation test using the concrete tester, it is examined whether damage detection is possible on the assumption that ultrasonic propagation speed and compressive strength decrease as accumulation of internal damage of concrete accumulates. Fig.7 shows the change with time of the change rate obtained by dividing the measurement result of the ultrasonic wave propagation speed by the initial value. In addition, Fig.8 shows the change with time of the rate of change obtained by dividing the estimation result of compressive strength by the initial value. No clear change suggesting the existence of internal injury is observed from either result. This is thought to be because the number of elapsed days after the galvanic corrosion was as short as 30 days and the damage did not proceed to such an extent that the damage would noticeably affect each non-destructive test. The results of each non-destructive test divided for each fog are summarized in Table.5.

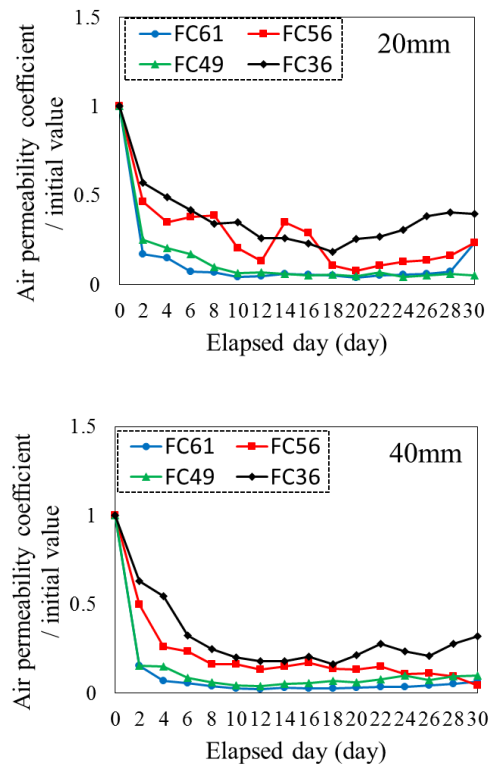


Fig.4 Changes over time of the rate of change of the air permeability coefficient (upper 20 mm, lower 40 mm)

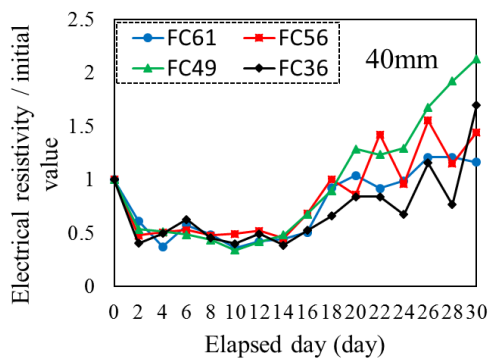
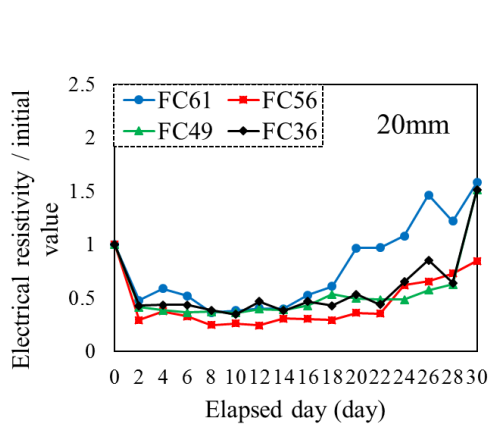


Fig.5 Changes over time of change rate of electric resistance
(upper 20 mm, lower 40 mm)

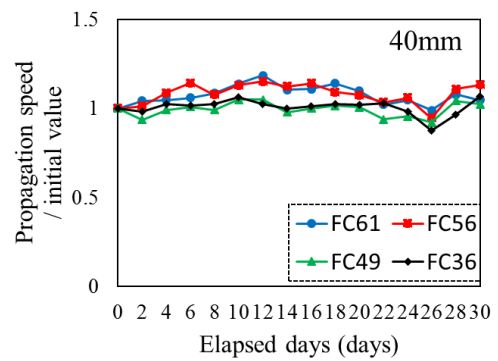
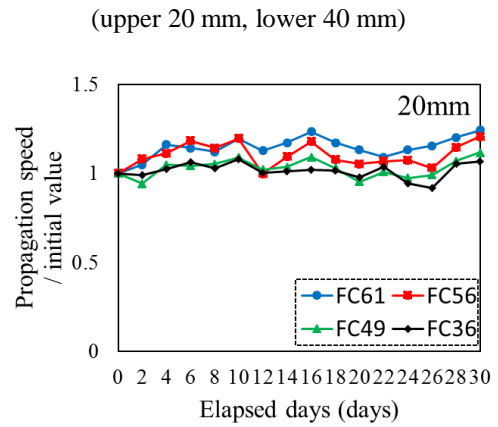


Fig.7 Change with time of the rate of change of the propagation speed
(upper 20 mm, lower 40 mm)

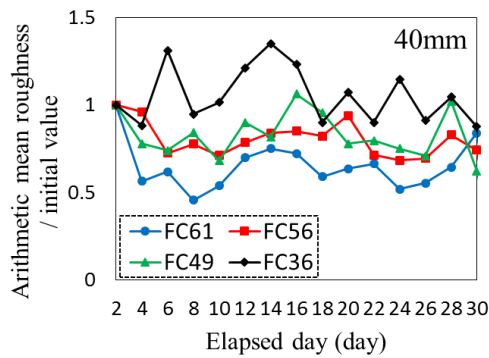
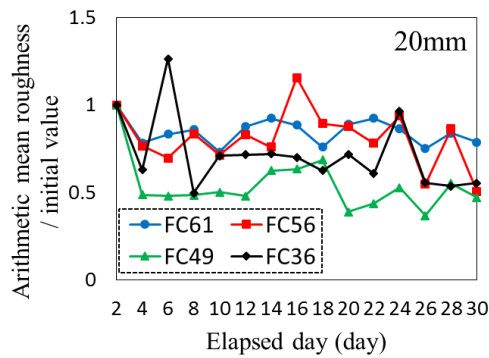


Fig.6 Changes with time of the rate of change of the arithmetic average roughness

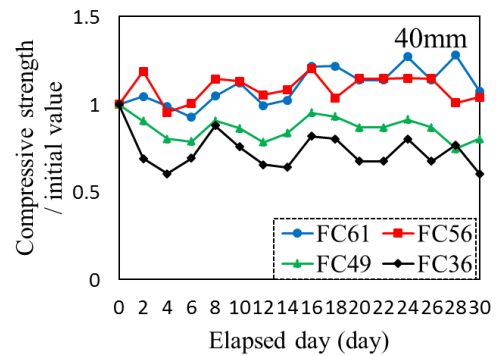
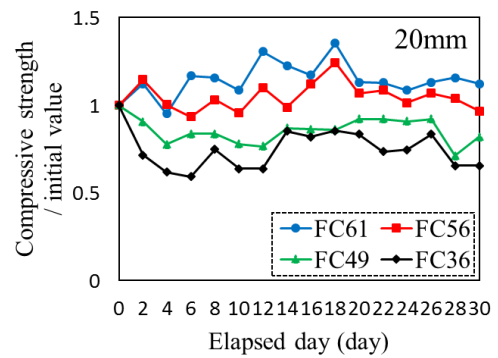


Fig.8 Changes with time of the rate of change in compressive strength

(upper 20 mm, lower 40 mm)

Table.5 Various non destructive test results
(upper 20 mm, lower 40 mm)

Compressive strength (N/mm ²)	Cover age (mm)	Air permeability test	Electrical resistance measurement test	Surface shape measurement test	Ultrasonic test	Compressive strength test
FC61	20	×	○	×	×	×
FC56	20	○	○	×	×	×
FC49	20	×	○	×	×	×
FC36	20	○	○	×	×	×

Compressive strength (N/mm ²)	Cover age (mm)	Air permeability test	Electrical resistance measurement test	Surface shape measurement test	Ultrasonic test	Compressive strength test
FC61	40	×	○	×	×	×
FC56	40	×	○	×	×	×
FC49	40	×	○	×	×	×
FC36	40	○	○	×	×	×

SUMMARY

Table.6 shows a summary of the number of elapsed days when damage was detected for each specimen showing the possibility of detecting damage due to corrosion of the reinforcement by each fog. From the table, the possibility of damage detection is suggested in the result of the electric resistivity measurement test of each compressive strength. It is thought that this is because it affects the corrosive organisms of rebar and its accompanying electrical resistance. In addition, in the case of FC 56 and FC 36 with a fog of 20 mm, it can be considered that the presence or absence of damage inside the concrete can be evaluated from the increase trend of the measured value accompanying internal damage also in the test result of the air permeability test. On the other hand, with respect to arithmetic average roughness, ultrasonic test and compressive strength test (concrete tester), since it is considered that the damage has not progressed to such an extent that it

affects the measurement result, by continuing the acceleration days and measuring, It is planned to further investigate whether damage inside the concrete can be detected from the decrease trend of measured values. In this study, we believe that the results obtained in indoor experiments and the actual structure can obtain the same result. However, it is a future task to confirm whether a similar result can be obtained by carrying out a nondestructive test even for a real structure.

Table.6 Results of damage detection by various non destructive testing

Compressive strength (N/mm ²)	Cover age (mm)	Air permeability test	Degradation start date	Electrical resistance measurement test	Degradation start date
FC61	20	-	/	○	14~
	40	-	/	○	16~
FC56	20	○	20~	○	22~
	40	-	/	○	14~
FC49	20	-	/	○	24~
	40	-	/	○	10~
FC36	20	○	18~	○	22~
	40	-	/	○	14~

REFERENCES

- [1] R.J Torrent: A two-chamber vacuum cell for measuring the coefficient of permeability to air of the concrete cover on site, *Materials and Structures*, Vol. 25, 1992, pp.358-365.

Basic Study of Cement Solidification Technology for Solidification of Cesium Adsorbed Zeolite Evaluation of Microscopic Structure of Cement Solidification

Taisei SAKAI¹ and Kazuhito NIWASE¹

¹National Institute of Technology, Hachinohe College (Tamonoki Hachinohe 039-1192, JAPAN)

ABSTRACT

On March 11, 2011, an accident occurred in Fukushima's first nuclear power plant and caused highly concentrated radioactive contaminated water, produced by the groundwater, which flowed into the nuclear reactor and core cooling. This radioactive contaminated water was removed by cesium adsorption, which is a main nuclide of zeolite. For a required matter: restraining the leakage of radioactivity, production of characteristics to the disposal material in the high radiation environment, and substantial experiment costs. In this study, I evaluate the properties of matter of the cement solidification body whereby I mixed zeolite as the fundamental research for possible examination of the cement solidification technology of the cesium adsorption zeolite. As the real cesium adsorption zeolite is exothermic, it is important that I also examine the influence on internal structure with heat. Based on it, I changed a condition of the curing temperature and measured the effective diffusion coefficient by electrophoresis, pore size distribution by the mercury penetration method and calcium hydroxide quantity by TG-DTA. As a result, in the high temperature environment, I think that enough nuclide enclosure performance may be provided with a promotion in pozzolanic reaction; by mixing fly ash. In addition, the possibility of that a pozzolanic reaction occurring to the zeolite was suggested.

Keywords: Cesium adsorbed zeolite, Cement solidification, Disposal of low level radioactive waste, Effective diffusion coefficient

INTRODUCTION

The Tohoku district Pacific offshore earthquake that occurred in March 2011 caused a nuclear accident involving the release of radioactive substances such as meltdown etc. to the Fukushima Daiichi Nuclear Power Station. At present, disposal of radioactive waste is a problem towards the decommissioning furnace of Fukushima Daiichi Nuclear Power Station. Radioactive contaminated water generated by the accident has been treated by adsorbing cesium, which is regarded as the principal nuclide, with zeolite having the property of physically adsorbing. The cesium adsorbed zeolite which is generated in large amount as secondary waste of this radioactive contaminated water treatment is a highly exothermic radioactive waste with a high dose but the disposal method has not been established and the vessel is kept in concrete box culvert. It is the current situation that it is temporarily stored in [1]. For final disposal of cesium adsorbed zeolite, it is necessary to prevent transportation improvement and leakage of radioactive materials by solidifying. As items required for solidification, it is necessary to consider not only leakage of radioactivity but also

manufacturability under high radiation environments and economy based on the large amount of generation thereof. Cement solidification technology is one of the options as a processing method that can satisfy the above-mentioned requirements from the results of disposal of low-level radioactive materials buried.

In this research, we believe that it is necessary to grasp the basic physical properties of solidified bodies in order to investigate feasibility of cement solidification technology. Based on the material

Table.1 Material used

material	mark	notes
Ordinary Portland cement	O	density: 3.16g/cm ³ , specific surface area: 3340cm ² /g
High early strength Portland cement	H	density: 3.14g/cm ³ , specific surface area: 4490cm ² /g
Fly ash	FA	density: 2.19g/cm ³ , specific surface area: 3610cm ² /g
Fine aggregate	S	Absolute dry density: 2.65g/cm ³ , Limestone crushed sand
Natural zeolite	Z	Absolute dry density: 0.727g/cm ³ , mordenite type, Particle size <0.5mm

Table.2 Mix proportion

Name	W/B	S/C	Unit content (kg/m ³)					Zeolite water absorption W' (kg/m ³)
			W	B		S	Z	
				C	FA			
Mortar	0.5	2.0	318	637	-	1273	-	
O	0.5	-	318	637	-	-	349	
H	0.5	-	318	635	-	-	349	
O-FA15	0.5	-	311	529	93	-	349	
O-FA30	0.5	-	305	427	183	-	349	
H-FA30	0.5	-	304	426	183	-	349	

+

-
188
188
188
188
188

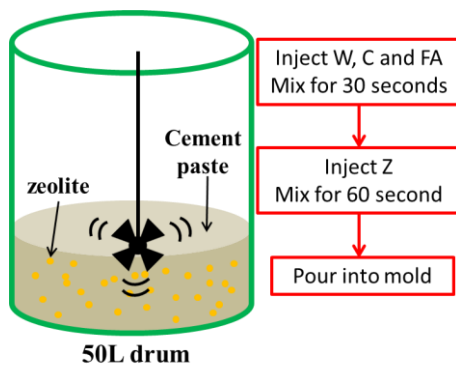


Fig.1 Fabrication of specimen

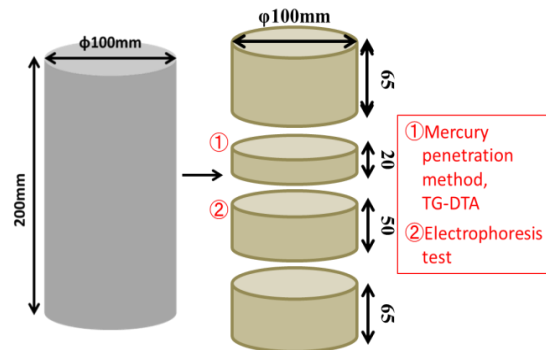


Fig.2 Sampling position

permeability and the void characteristics of cement solidified material (hereinafter referred to as Z solidified material) mixed with zeolite. Focusing on the relationship of curing temperature, physical property values were evaluated. In the tests conducted, the effective diffusion coefficient of chloride ion by electrophoresis test, the measurement of pore size distribution by mercury intrusion test, the amount of calcium hydroxide (hereinafter referred to as CH) by thermogravimetric differential thermal analysis (TG-DTA).

(1) Material used, Compounding condition

Table.1 shows the materials used in this study. The formulation of solidified bodies is shown in Table.2. Compounding of solidified bodies is roughly classified into two types, commonly mortar (Mortar) and Z solidified body, and W / B is unified at 50%. The description of the blending name of the Z solidified body is as follows. The first letter indicates cement type (O: ordinary portland cement, H: High early strength portland cement), FA indicates that fly ash is mixed in, FA number is the replacement rate of fly ash (internal division: 15% 30%). Five cases were chosen according to the difference of binder (cement type, fly ash) for Z solidified formulation.

In addition to Ordinary Portland cement, High early-strength Portland cement is adopted as a binder because the hydration may be required to be fast in

actual solidification of cesium adsorbed zeolite. Cesium adsorbed zeolite has exothermicity and radioactivity. Therefore, at the time of solidification, due to dissipation of water due to heat generation and radiation decomposition, water necessary for hydration may decrease with time. For the above reasons, early-strength portland cement with an early reaction rate was added to the compounding conditions. Moreover, the use of fly ash is expected to be effective for densification.

Normally mortar was compared, and Z solidified body was mixed with zeolite which was co-integral with fine aggregate of mortar. The zeolite used this time has a particle diameter of 0.1 mm or less and was used in an absolutely dry state. Since zeolite is porous and highly absorbent material, when used in an absolutely dry condition, it absorbs water from the cement paste and remarkably impairs the fresh properties. Apart from the unit water amount, water having a water absorption of zeolite (water absorption rate: 53.9%) was added at the time of kneading separately from the unit water amount to secure the fresh performance. It is confirmed through preliminary experiments that water in cement milk is absorbed instantaneously when contacting zeolite and cement milk [2]. In addition, s / c was set to 2.0 from the viewpoint of workability after confirming that Mortar's s / c exceeded 3, flowability deteriorated and uniform specimen could not be produced.

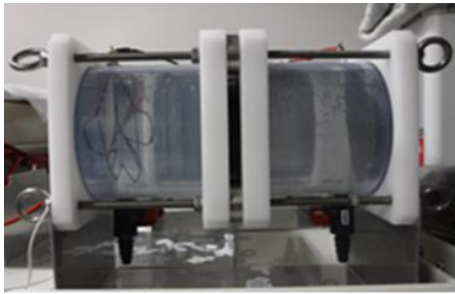


Fig.3 Diffusion cell

(3) Procedure for preparing specimen

In this research, in order to simulate the solidified body production by the in-drum method, a manufacturing method was adopted in which mixing was carried out with a 50 L drum can and a hand mixer. The manufacturing method is shown in Fig.1. 1- Inserting water (including external split) and binding material into the drum, 2- Kneading in a hand mixer for 30 seconds, then 3- Adding zeolite (fine aggregate in case of Mortar) and kneading for 60 seconds, 4- Driven into a formwork ($\phi 100 \times 200$ mm), 5- After standard curing for 24 hours, it was demolished. At the time of actual waste preparation, it is assumed that water is required for hydration due to radiative decomposition and heat generation of water during the hardening period of the cement solidified body. Therefore, after demoulding, epoxy resin was coated on the specimen surface to block water from the outside. After coating, curing was started under each condition. After the prescribed curing period elapsed, the specimen was cut or crushed into a shape corresponding to each test to prepare a sample. The sampling position of each test sample from the specimen is shown in Fig.2.

(4) Curing condition and method

In this study, high-temperature curing was carried out to simulate the heat effect due to heat generation of zeolite. It is assumed that the thermal influence becomes a temperature exceeding 100°C depending on the concentration, but as practical concentration adjustment is carried out after a certain half-life, the curing temperature is 20°C , 50°C and 80°C . The curing period was one month. Cylindrical specimens were covered with epoxy resin and placed in a high temperature constant temperature curing tank and curing was carried out.

(5) Electrophoretic method

In this study, effective diffusion coefficient of chloride ion by electrophoresis test was measured as an alternative index of substance permeation resistance of cesium in solidified body. The test method was conducted in accordance with the



Fig.4 Specimen for electrophoretic method

Society of Civil Engineers' Procedure "TEST METHOD FOR EFFECTIVE DIFFUSION COEFFICIENT OF CHLORIDE ION CONCRETE BY MIGRATION" (JSCE-G 571-2003)[3]. As the specimen, a column specimen cut into a size of $\phi 100 \times h 50$ mm was used.

The diffusion cell used in this test is shown in Fig.3. This diffusion cell is taken into consideration so that the side of the specimen is made into the state shown in Fig.4 with the epoxy resin and the heat shrinkable rubber, and the cells on the NaCl solution side and the NaOH solution side are crowded thereon. As a result, chloride ion moves only in the specimen, and movement from the joint surface at the side of the specimen is blocked. Even when solution leakage occurs from a fine gap, there is no contact of the solution outside the specimen, so it has an advantage that is not reflected in the data.

(6) Mercury porosimetry method

In this study, measurement of pore size distribution using mercury intrusion porosimeter was performed. The cut cylindrical specimen was crushed to a particle size of 2.5 to 5.0 mm, dipped in acetone for 24 hours and subjected to furnace drying treatment to stop hydration as a sample.

In the mercury porosimetry method, the void structure is evaluated by calculating the void diameter from the injection pressure and the amount of mercury injected when mercury intrudes into the void. The relationship between the pressure at the time of injecting mercury and the gap diameter d is expressed by the following Washburn equation (1) from the measured pressure p , the surface tension γ of mercury, and the contact angle θ of mercury and the wall surface of the gap[4].

$$d = -\frac{4\gamma}{p} \cos\theta \quad (1)$$

(7) TG-DTA

H is generated by hydration reaction of cement. Since CH forms a region (hereinafter referred to as "transition zone") having a large void volume at the aggregate interface, it is known that it adversely affects material permeation resistance, strength, and

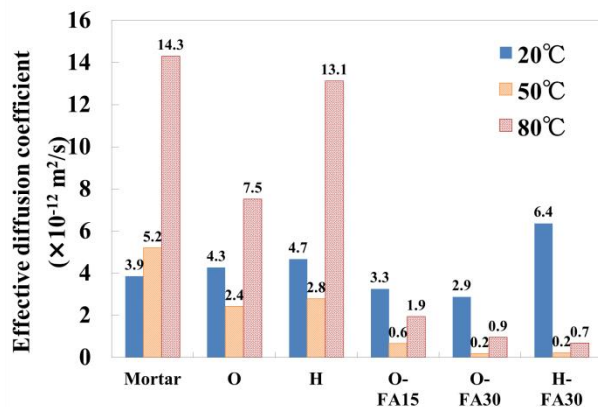


Fig.5 Result of electrophoresis

the like. On the other hand, when fly ash is mixed, the transition zone decreases and the substance permeation resistance improves as the main component silica (SiO_2) and alumina (Al_2O_3) generate pozzolanic reaction with CH.

In this study, CH content was measured by TG-DTA (compliant standard) in order to confirm the degree of progression of pozzolanic reaction in solidified bodies. The rate of temperature rise was set to $20^\circ\text{C}/\text{min}$, and the rate of weight loss at the endothermic peak around 400 to 450°C was calculated [5]. The amount of CH is sorted out by dividing the weight loss rate by the unit cement amount. This is because the difference in the amount of unit cement depending on compounding conditions is thought to affect the amount of generated CH.

RESULT AND CONSIDERATION

(1) Electrophoretic method

Figure.5 shows the effective diffusion coefficient measured by the electrophoretic test. Focusing on changes due to differences in cement types, H was higher in O and H, earlier strong portland cement was coarser than in ordinary Portland cement compared to ordinary Portland cement. However, it was confirmed that the influence of FA addition was dominant at high temperature curing, and the difference between O and H was not large.

Subsequently, focusing on changes due to curing temperature, at the curing temperature of 20°C ., the effective diffusion coefficient was of the order of $1 \times 10^{-12} \text{ m}^2/\text{s}$ under all compounding conditions. Since zeolite is a porous material, it was predicted that the effective diffusion coefficient of the solidified material will be large, but the result was comparable to Mortar. From this, it is considered that diffusion of chloride ions in the zeolite is limited. In Mortar, the effective diffusion coefficient increased as the curing temperature increased. The reason for this may be that the hydration reaction was excessively

promoted at high temperature curing and the concrete structure became coarse.

On the other hand, in the formulations of O series and H series, the effective diffusion coefficient was lower than 20°C . at 50°C ., but it showed a tendency to become higher at 80°C . As a reason for showing a tendency different from that of Mortar, there is a possibility that the pozzolanic reaction is occurring in the zeolite in the solidified body. Since the main component of zeolite is also silica or alumina, it can be considered sufficiently due to pozzolanic reaction, densification of internal structure, improvement of water tightness and reduction of transition zone. It is known that the pozzolanic reaction is accelerated as the curing temperature increases. At 50°C ., the pozzolanic reaction was promoted and it is considered that the effective diffusion coefficient became small. It was considered that the effective diffusion coefficient became large at 80°C because the effect of becoming a coarse structure due to promotion of excessive hydration reaction was greater than the influence of pozzolanic reaction.

On the other hand, paying attention to the amount of FA addition, at the curing temperature of 50°C and 80°C ., the effective diffusion coefficient decreases as the added amount of FA increases, especially O-FA30 and H-FA30 are $1 \times 10^{-13} \text{ m}^2/\text{s}$. It showed very small values with orders. This is probably because the pozzolanic reaction was caused by zeolite and fly ash.

(2) Mercury porosimetry method

Figures.6 to 11 show the results of the pore size distribution obtained by mercury intrusion test.

When comparing Mortar and O, the void volume of O is larger than that of Mortar at all curing temperatures of 20°C , 50°C and 80°C . In particular, the void volume of 40 nm or less increases. The amount of void around $1 \mu\text{m}$ is also slightly increased. This is considered to reflect the internal voids of the porous zeolite. In natural zeolite, the void volume around 100 nm is large. In O, since the pore diameter which is supposed to reflect the voids in the zeolite is 40 nm or less, it is confirmed that the position of the peak differs between natural zeolite and O. The reason for this is that the densification of the natural zeolite occurs and the possibility that the voids around 100 nm has decreased is considered. Since the main component of zeolite is silica or alumina similar to fly ash, pozzolanic reaction occurs and there is a possibility that it is densified.

O, O-FA15 and O-FA 30, there is no significant difference in the pore size distribution between O and O-FA15 when comparing O and O-FA15 at the curing temperature of 20°C and 50°C . At the curing temperature of 80°C ., the total amount of voids was slightly smaller in O-FA15 than in O. On the other hand, in the O-FA30, there was a tendency that the

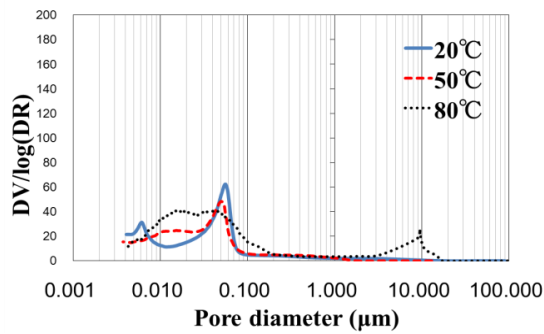


Fig.6 Mortar of pore size distribution

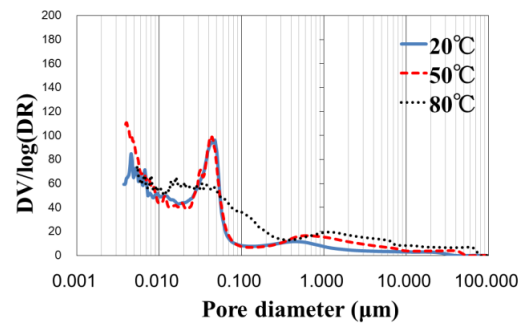


Fig.7 O of pore size distribution

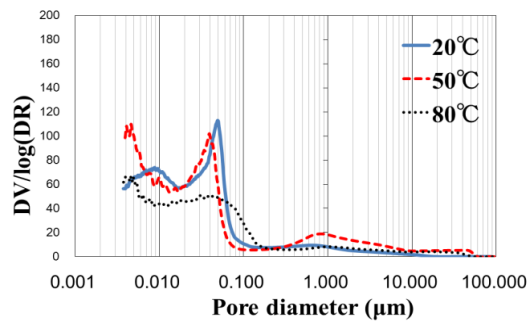


Fig.8 O-FA15 of pore size distribution

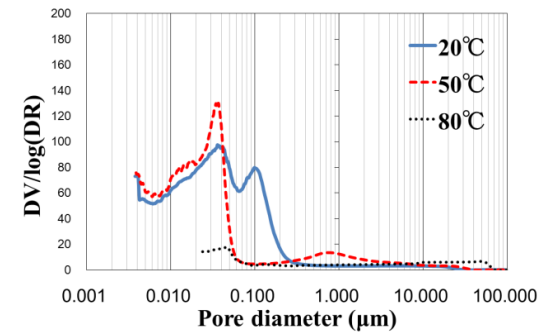


Fig.9 O-FA30 of pore size distribution

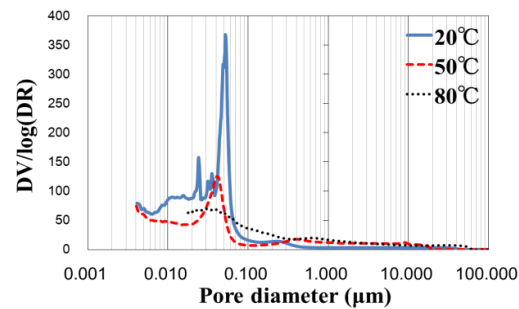


Fig.10 H of pore size distribution

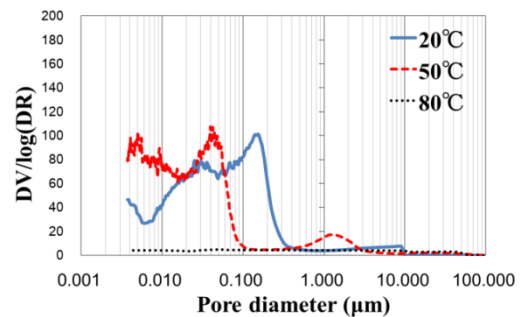


Fig.11 H-FA30 of pore size distribution

densification advanced in comparison with O and O-FA15. At the curing temperature of 20°C, the first peak is present in the vicinity of 40 nm and the second peak is in the vicinity of 100 nm. When the curing temperature reaches 50°C, the peak near this several hundred nm disappears and the peak around 40 nm increases. This is considered to be the effect of densification due to pozzolanic reaction promoted by high temperature curing. In the pore diameter distribution at the curing temperature of 80°C, the graph is discontinued at several tens of nm. The re-measurement was carried out twice, but similar results were obtained. This may be due to the fact that the sample was destroyed during the measurement. In the mercury porosimetry method, the smaller the pore diameter to be measured, the higher the pressure at the time of mercury intrusion. Therefore, there is a possibility that the solidified body tissue was destroyed due to pressure at the time of press-fitting and it was impossible to measure. In addition, there is a possibility that hydrated products

of solidified bodies may differ at high temperature curing at 80 ° C. Regarding this point, it is necessary to study in the future. Comparison of O, H, O-FA 30 and H - FA 30 shows that when comparing O and H at a curing temperature of 20°C., the peak of O is around 40 nm whereas the peak of H is around 50 nm, it is huge. Even in comparison between the O-FA30 and the H-FA30, the air gap size at the peak of the H-FA30 is larger than that of the O-FA30. As described in the results of the electrophoresis test, early intense Portland cement was coarser than the ordinary portland cement, as a result of initial electrophoretic test. At the curing temperature of 50°C, the peak pore volume of H was higher, but peaks existed around 40 nm in both formulations, resulting in a pore size distribution showing a similar tendency. Likewise, at the curing temperature of 80°C, the pore size distribution showed a similar trend. In the H-FA30 at the curing temperature of 20°C, there is a gap peak at around 100 nm. This is the same pore diameter as the

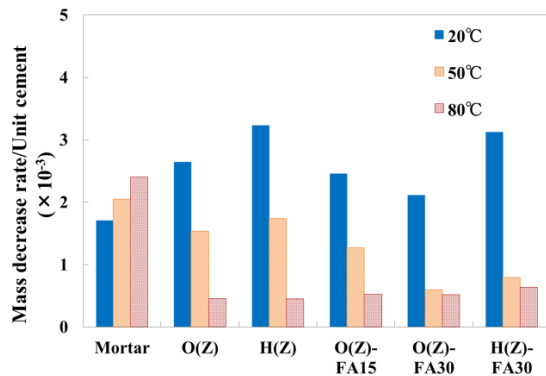


Fig.12 CH amount per unit cement

second peak in the aforementioned N-FA30. This is considered to be due to the fact that the hydrated reaction rate of early-strength Portland cement is so fast that the solidified body structure is rough. When the curing temperature reaches 50°C, the gap peak of the H-FA30 also shifts to a smaller diameter from 100 nm. It is thought that pozzolanic reaction was promoted by high temperature curing and densification occurred. In addition, it can be seen that the H-FA30 has a remarkably large number of voids of 10 nm or less. At the curing temperature of 80°C, the void volume of the O-FA30 and H-FA30 was extremely small as a whole. It is thought that this is due to promotion of pozzolanic reaction by high temperature curing, but it is necessary to confirm the pore size distribution at 80°C curing including the experimental system in the future.

(3) TG-DTA

Figure.12 shows the results of TG-DTA. The larger the weight loss rate means, the larger the amount of CH generated in the solidified body is. In Mortar, the amount of CH increases as the curing temperature increases. This is probably because hydration reaction was promoted by high temperature curing and calcium hydroxide was produced in large amount. On the other hand, in the Z solidified body, the CH content tends to decrease as the curing temperature increases. This is considered to be due to pozzolanic reaction caused by zeolite. As the curing temperature increases, it is considered that the pozzolanic reaction is promoted and CH is consumed. In the change from 20°C, to 50°C, the difference between O-FA30 and H-FA30 is large. It is thought that this was influenced by consumption of CH by pozzolanic reaction by fly ash in addition to zeolite.

At 20°C, the amount of CH in compounding conditions using early-strength Portland cement is high. Since Ordinary Portland cement, High early-strength Portland cement contains a lot of alite, it can be confirmed that there are many CHs generated correspondingly.

From the above results, it is considered that transition zones occurring at the zeolite interface decreased in the Z solidified body, and the substance permeation resistance in the solidified body improved.

CONCLUSION

- (1) The effective diffusion coefficient of the solidified body was reduced to the same degree at 20°C as compared with mortar, and decreased at 50°C and 80°C. Therefore, by using FA even at high temperature, high nuclear confinement performance can be expected. Also, diffusion of chloride ions in zeolite is considered to be limited.
- (2) In the solidified body, the distribution of zeolite itself has many voids of several tens of nm. At a curing temperature of 50°C, there was a tendency that densification occurred as a whole. On the other hand, it is necessary to study pore size distribution at 80°C in future.
- (3) In mortar, the amount of CH increased as the curing temperature increased, but decreased in the Z solidified matter. The reason for this is considered to be that CH was consumed by pozzolanic reaction of zeolite.

ACKNOWLEDGEMENTS

Part of this present research work was funded by the Japan Society for the Promotion of Science (JSPS KAKENHI Grant Number JP17K07015).

REFERENCES

- (1) Tokyo Electric Power Company Holdings, Inc.: Status of consideration for treatment of secondary waste water treatment 10th February, 2017 (in Japanese)
- (2) H. Mawatari, K. Niwase and M. Satou, Evaluation of Physical Properties of Fast Ash Cement and Fly Ash Combination Type Filler in Cement Solidification Technique of Cesium Adsorbing Zeolite, Cement and Concrete Collected Papers, Vol.71, Mar. 2018 (in Japanese)
- (3) JSCE STANDARD "TEST METHOD FOR EFFECTIVE DIFFUSION COEFFICIENT OF CHLORIDE ION CONCRETE BY MIGRATION" (JSCE-G 571-2003)
- (4) Washburn E.V. : Dynamics of Capillary Flow, Physical Review, Vol. 17, pp.273-283 (1921).
- (5) S. Shirakawa, Y. Shimazoe, M. Aso and S. Nagamatsu, Influence of hydration on carbonation mechanism in hardened cement paste, Japan Concrete Institute, vol.24, No.1, 2002(in Japanese).

Effect of Chemical Admixture on Cement Solidification of Cesium Adsorbed Zeolite

Sora SUTO¹ and Kazuhito NIWASE¹

¹National Institute of Technology, Hachinohe College (Tamonoki Hachinohe 039-1192, Japan)

ABSTRACT

On March 11, 2011, atomic energy accident occurred by the pacific coast of Tohoku earthquake in Fukushima first nuclear power plant. After the accident, a large quantity of contaminated water with cesium occurred in the Fukushima first nuclear power plant. As temporary disposal of contaminated water, cesium is adsorbed by a mineral called the zeolite cesium adsorption zeolite, continues increasing as second waste, so processing is necessary. In this study, I studied the influence of the chemical admixture to zeolite as fundamental researches for the solidification body manufacture including the zeolite. I used a hardening accelerator and two kinds of super plasticizer. Using those, I made initial mix proportion. Using decided mix proportion, I did slump flow test and mortar flow test, V funnel test, and compression strength test. From the results, soon after having finished mixing it, all mix proportions became high fluidity. But the fluidity falls with the progress of time. The mix proportion using only super plasticizer maintains its fluidity. The mix proportion which have super plasticizer called Master Ease added to the continued high fluidity for two hours. When I added Master Ease and hardening accelerator to mix proportion, the strength became high.

From all test results, Master Ease showed most suitable reaction to zeolite. Master Ease is the important material to increase quantity of the disposal of zeolite. There is a possibility that the mixing ratio of zeolite can be increased by reducing the strength by adjusting the addition amount of the chemical admixture.

Keywords: Cesium adsorbed zeolite, Cement solidification, Disposal of low level radioactive waste, Chemical admixture

1. INTRODUCTION

Treatment of radioactive contaminated water accompanying accidents at Fukushima first nuclear power plant is now a problem. Radioactive contaminated water contains a large amount of cesium 134 and 137. Treatment of contaminated water removes cesium by adsorbing it on zeolite. The half-life of cesium is about 2 years for Cs 134 and about 30 years for Cs 137. Therefore a treatment and disposal method considering long-term safety is required, and various studies have been made. Among the processing methods currently considered, cement solidification technology has already been proved in disposal of low level radioactive waste, and it is a technology that is relatively feasible.

In this study, the ultimate objective was to propose cement solidification technology from the viewpoint of reliability and economy as a treatment method of cesium adsorbed zeolite. In this study, we investigated cementitious solidification material and examined the manufacturability of waste, and obtained basic data on possibility of solidification of cement.

The feature of this research is to confirm the influence of chemical admixture on zeolite. Since research on cementitious materials mixed with zeolite is not enough at present, fundamental research was conducted in this research. When

considering the mix proportion, we adjusted the mix proportion with the aim of enabling solidification of many zeolites with minimum cement solidified material.

The chemical admixtures used in this study were all three types, and two types of super plasticizer (hereinafter referred to as SP) and one kind of hardening accelerator were used. As a measure for adjusting the amount of addition, we carried out with considering the manufacturability, to be a mix proportion with high flow and appropriate viscosity.

Since it is a work in the place of high radiation at the time of processing, it is important to make the unmanned as much as possible. Furthermore, it is necessary to consider the influence of heat generation of cesium for cementitious solidification material.

2. EXPERIMENT OUTLINE

In this study, the mix proportion was decided in consideration of fluidity and strength. The fluidity was examined by the mortar flow test, the slump flow test and the V funnel test (JIS A 1150). The slump flow aimed at 65 ± 10 cm. As for the strength, uniaxial compressive strength necessary for treatment and disposal by a compression test was confirmed.

2. 1 SETTING OF MIX PROPORTION

Table-1 shows the preliminary study mix proportion and Table-2 shows Use materials.

In the preliminary study mix proportion, three types of ordinary portland cement (OPC), low heat portland cement (LPC), high early strength portland cement (HPC), were used to confirm the effect of cement type and fluidity. Combined with various chemical admixtures, a total of 15 mix proportion were made. W/B was determined to be 50%, and the mixing ratio of zeolite was decided to 50%. In this study, the mixing ratio of zeolite is the ratio of the volume of zeolite to the volume of cement paste. Master Glenium SP8SV (MG) and Master Ease 3030 (ME) were used for SP. The main component of MG is a polycarboxylic acid ether compound. The main component of ME is a PAE compound.

Master X-Seed 120 JP (MXS) was used as the curing accelerator. It's based on nanoparticles of calcium silicate hydrate and promotes hydration.

The amount of use of the three chemical admixtures

Table-1 Preliminary study mix proportion

	Unit volume weight(kg/m ³)					
	W	C	FA	ZP	SP	MXS
OPC-FA(Z)	391	547	235	242	-	-
OPC-FA(Z),MG	386	547	235	242	4.92	-
OPC-FA(Z),MG,MXS	370	547	235	242	4.92	16.41
OPC-FA(Z),ME	386	547	235	242	4.92	-
OPC-FA(Z),ME,MXS	370	547	235	242	4.92	16.41
LPC-FA(Z)	393	550	236	242	-	-
LPC-FA(Z),MG	388	550	236	242	4.95	-
LPC-FA(Z),MG,MXS	372	550	236	242	4.95	16.50
LPC-FA(Z),ME	388	550	236	242	4.95	-
LPC-FA(Z),ME,MXS	372	550	236	242	4.95	16.50
HPC-FA(Z)	390	546	234	242	-	-
HPC-FA(Z),MG	385	546	234	242	4.92	-
HPC-FA(Z),MG,MXS	369	546	234	242	4.92	16.39
HPC-FA(Z),ME	385	546	234	242	4.92	-
HPC-FA(Z),ME,MXS	369	546	234	242	4.92	16.39

Table-2 Use materials

Material	Abbreviation	Overview
CEMENT	OPC	Ordinary Portland Cement
		Density=3.160g/cm ³
		Specific surface area=3340cm ² /g
	LPC	Low Heat Portland Cement
		Density=3.220g/cm ³
		Specific surface area=3530cm ² /g
	HPC	High Early Strength Portland Cement
		Density=3.140g/cm ³
		Specific surface area=4490cm ² /g
FLY ASH	FA	Density=2.190g/cm ³
		Specific surface area=3610cm ² /g
Zeolite	ZP	Absolute dry density=0.727g/cm ³ Mordenite type, Particle size<0.5mm
Super plasticizer	SP	MG
		Master Glenium SP8SV PCE, Amount to use=Cx0.5-3.0%
	ME	Master Ease 3030 PAE, Amount to use=Cx0.5-3.0%
Hardening accelerator	MXS	Master X-Seed 120 JP Amount to use=Cx0.5-6.0%

is the ratio to the amount of cement.

2.2 EVALUATION OF FLUIDITY

After mixing the preliminary study mix proportion by a mortar mixer, a mortar flow test was carried out. The mix proportion used in this study had high fluidity and it was difficult to measure with mortar flow table. Therefore, the mortar flow test was carried out using mortar flow cone and flat plate of slump flow.

Photographs and results of the mortar flow test are shown in Figure-1 and Figure-2, respectively. The flow became homogeneous in all mix proportions, and no separation of water was observed at the edge(Figure-1).

As shown in Figure-2, the mix proportion to which SP was added was about 100 mm larger than that of the mix proportion without addition of SP. On the other hand, the mix proportion using both the SP and the curing accelerator increased the ME by about 10mm and the MG by about 35mm than the mix proportion containing only SP.

In the mix proportion with MG added, the result was OPC the largest value, whereas HPC and LPC

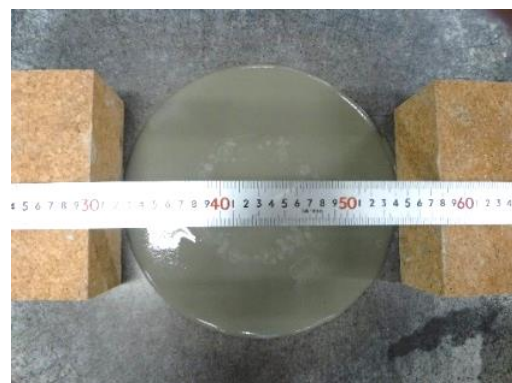


Figure-1 Mortar flow

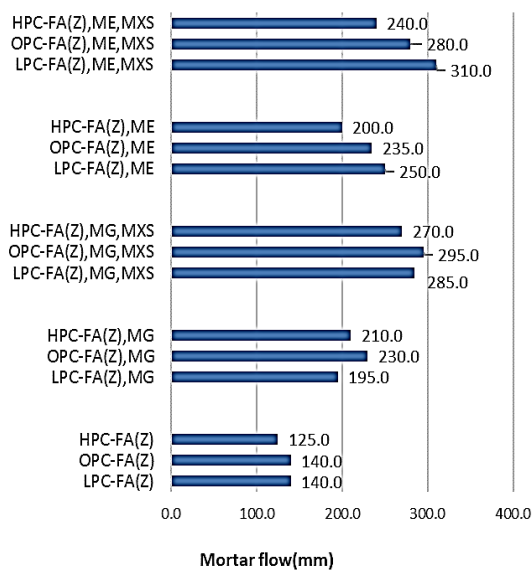


Figure-2 Mortar flow test result

were low values. In the mix proportion with ME added, the result was the largest value for LPC, and it became low in the order of OPC and HPC. When comparing in each cement type, there was a difference, but it was judged that there was no big influence. Since the range of the SP addition rate is 0.5 to 3.0 %, 0.9% of this mix proportion has margin, we considered that by increasing the SP addition rate, even if the mixing ratio of zeolite is increased, the fluidity can be secured.

2.3 ADJUSTMENT OF MIX PROPORTION

The composition after adjustment is shown in Table-3. Changes from the preliminary study mix proportion are cement type, mixing ratio of zeolite, addition rate of SP. Low heat portland cement, which has the largest difference in specific gravity with respect to zeolite, was used for cement type to confirm the separation. The mixing ratio of zeolite was 100% which is twice the preliminary study mix proportion. The zeolite mixing ratio was set to 100%.

The SP addition rate was $C \times 0.9\%$ of the standard usage amount, 3 cases of $C \times 3.0\%$ of the maximum usage amount and $C \times 2.0\%$ of the average usage amount. Mortar flow test was carried out again.

The results of the mortar flow test with a zeolite mixing ratio of 100% are shown in Figure-3. SP addition rate was 0.9% was lower than the value

Table-3 Mix proportion (ZP100%)

	Unit volume weight(kg/m ³)				
	W	C	FA	ZP	SP
LPC-FA(Z),MG(0.9%)	291	413	177	364	3.7
LPC-FA(Z),MG(2.0%)	287	413	177	364	8.3
LPC-FA(Z),MG(3.0%)	283	413	177	364	12.4
LPC-FA(Z),ME(0.9%)	291	413	177	364	3.7
LPC-FA(Z),ME(2.0%)	287	413	177	364	8.3
LPC-FA(Z),ME(3.0%)	283	413	177	364	12.4

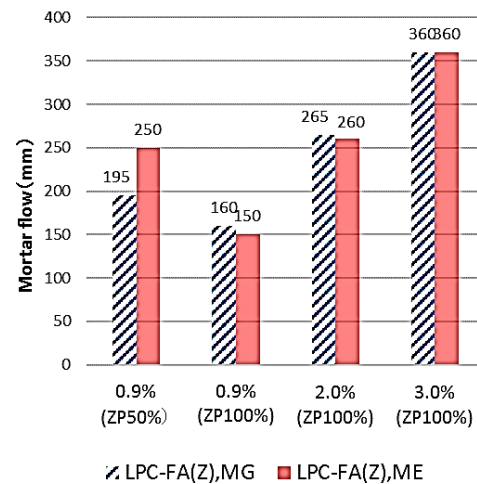


Figure-3 Mortar test results for each addition rate

when the zeolite mixing ratio was 50%. There was a difference of 35mm for MG addition and 100mm for ME addition. On the other hand, at the SP addition rate of 2.0%, MG was about 70mm and ME was about 10mm higher than at 50% mixing. With 3.0% maximum SP addition rate, both MG and ME increased about 100mm more than at 2.0%. Although it was anticipated that the value of mortar flow will be decreased by increasing the mixing ratio of zeolite, it was newly confirmed that the degree of influence varies depending on the type of SP.

From the results of the mortar flow test of all mix proportions, it was revealed that even when zeolite was used, the fluidity was improved by the increase in the SP addition rate.

The fresh properties were homogeneous in all mix proportions as well as at 50%, and no separation of water was observed.

From the above results, the SP addition rate was set to 3.0%, which is the highest fluidity.

2.4 DETERMINATION OF MIX PROPORTION

From the results so far, the ratio was determined to be 100% zeolite mixing ratio, W/B=50%, SP addition rate 3.0%. The determination mix proportion is shown in Table-4. In the preliminary examination of fresh properties, LPC was considered to be the most likely to cause segregation of cement type, but in the decision mix proportion, the strength was expressed as standard OPC.

Mixing of the determined formulation was made by simulating the in-drum method using a drum can and a hand mixer, assuming actual waste production. The mixing procedure is as follows. Figure-4 shows Drums and hand mixers.

- 1) Add water, cement, fly ash to the drum.
- 2) Mix for 30 seconds using a hand mixer.

Table-4 Determination mix proportion

	Unit volume weight(kg/m ³)					
	W	C	FA	ZP	SP	MXS
OPC-FA(Z)	293	411	176	364	—	—
OPC-FA(Z),MG	281	411	176	364	12.3	—
OPC-FA(Z),MG,MXS	268	411	176	364	12.3	12.3
OPC-FA(Z),ME	281	411	176	364	12.3	—
OPC-FA(Z),ME,MXS	268	411	176	364	12.3	12.3



Figure-4 Drums and hand mixers

- 3) Add zeolite in three times. Mix 15 seconds for each addition.
- 4) Finally mix for 30 seconds.

A slump flow test and a V funnel test were carried out according to the determined mix proportion. The results are shown in Figure-5 and Figure-6. In addition, OPC-FA (Z) is excluded because it does not become high flow.

From Figure-5, it can be seen that the formulation to which only SP was added has a high flow. On the other hand, in the two mix proportions in which SP and curing accelerator were used in combination, MG was about 200mm and ME was about 100mm lower.

Furthermore, as we looked at each elapsed time, it was confirmed that the blending of only SP keeps the state of the flow for 120 min although there is a decrease in fluidity. It can be seen that the two mix proportions using the curing accelerator failed to maintain fluidity for 120 min.

Next, in the result of Figure-6, the flowing time of the V funnel immediately after kneading was equivalent to that of 4 mix proportions. Mix proportions of only SP was possible to maintain fluidity for 120 min, but with the addition of the curing accelerator, the fluidity can not be maintained for 120 min as time elapses as in the result in Figure-5.

From this result, it was judged that the mix proportion with the zeolite mixing ratio of 100% and

the SP addition rate of 3.0% was a mix proportion with good manufacturability. Particularly, since the fluidity of the ME is relatively long, ME can be manufactured with a margin in time. On the other hand, in the mix proportion with MXS added, the ME did not flow down in 30 minutes and the MG did not flow down in 60 minutes, so it was desired to use it only when it can be manufactured in short time from the kneading. In the case of a mixing method using an in-drum, since it is unnecessary to maintain fluidity for a long time, it is also possible to use a formulation using a curing accelerator.

3. PREPARATION OF SPECIMEN

Specimens were prepared in the determination mix proportion (Table 4). The specimen was a cylinder specimen of $\phi 100 \times 200$ mm, and three curing periods were prepared per condition at 1 month and 6 months. A total of 30 bodies were made in total. Curing was carried out after releasing one day after implantation, and it was treated as standard curing.

4. EVALUATION OF STRENGTH

The results of the compressive strength test for one month of curing period are shown in Figure-7. From the results, the compressive strength of the mix proportion using only SP and the mix proportion not using SP were close values. Meanwhile, in the two mix proportions containing MXS, the ME was about 26 N/mm^2 and the MG was about 7 N/mm^2 higher than the mix proportion of only SP. Different conditions in these two mix proportions were only the SP type, but a difference of about 5 N/mm^2 occurred. The maximum stress when ME and MXS were used in combination was a particularly large value when compared with the other 4 mix proportions.

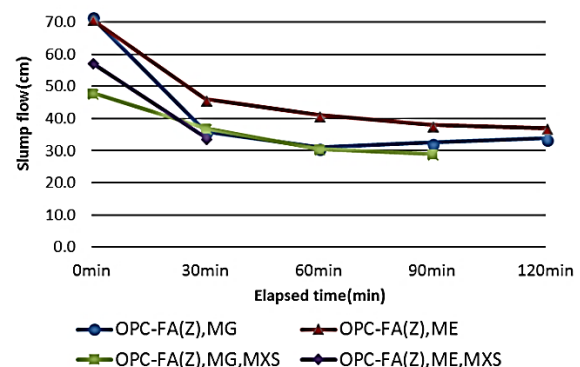


Figure-5 Slump flow test result

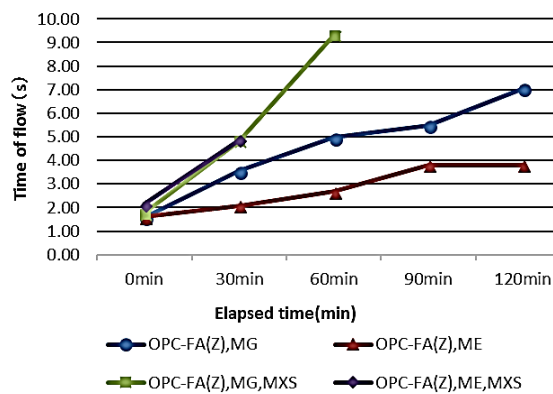


Figure-6 V funnel test result

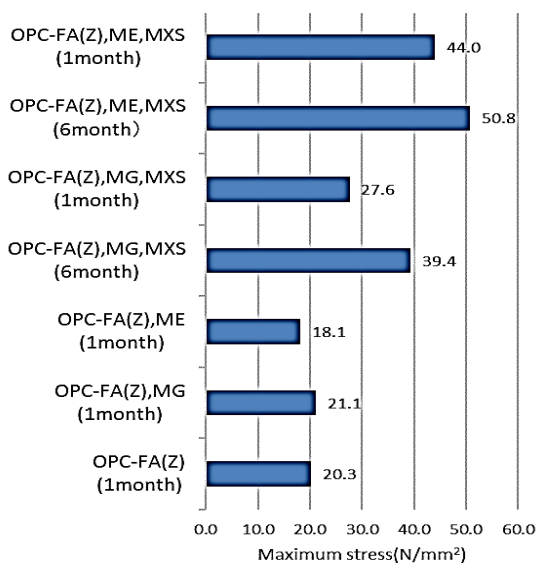


Figure-7 Compressive Strength Test Result

Considering the time required for the pozzolanic reaction, compression testing of the 6 months curing specimen was also conducted. The mix proportion was two mix proportions in which SP and curing accelerator were used in combination. First, compared to the one month curing data, the strength was increased by about 7 N/mm^2 when ME was used, and the strength was increased by about 12 N/mm^2 when MG was used. There was no noticeable difference in strength growth and it did not become a big change, but it seems that it is a reasonable result because strength was strongly developed at the time of curing for one month.

Next, when comparing the results of ME and MG, it was confirmed that high strength is still maintained when ME and MXS are used again for both 1 month and 6 months.

5 Compressive strength values differed, but it was confirmed that it exceeds 1.5 N/mm^2 which is necessary for treatment and disposal in all mix proportions. In fact, in construction at the site of Fukushima first Nuclear Power Plant, by confirming the confinement performance and adding an improvement taking into consideration the balance

between strength and throughput, we can increase the throughput per process conceivable.

5. CONCLUSION

- From the present study, In the final mixing ratio, the addition ratio of SP and MXS was set to 3.0% under the condition of 100% zeolite mixing ratio and W/B is 50%. If importance is attached to fluidity and viscosity at the time of solidification, it is desirable to add only SP without adding MXS. Especially for zeolite ME was more suitable than MG.
- Regarding strength, since it is confirmed the strength that necessary for treatment and disposal in all mix proportions, it is possible to select each mix proportion according to the situation at the time of solidification. In the compressive strength test, the compressive strength was maximized when ME and MXS were added. It is necessary to clarify the cause of the difference in compressive strength with other mix proportions.
- It was confirmed that in all mix proportions, the required strength was greatly exceeded. Therefore, it is necessary to consider the mix proportion which decreases the strength and increases the solidification amount.

6. FUTURE TASKS

Working under high radiation environments is assumed at actual site, so it is necessary to consider the mixing method etc. in an unmanned state based on the situation at the time of this test specimen preparation.

It is possible to treat and dispose of many cesium adsorbed zeolites at once by increasing the mixing ratio of zeolite. Therefore, it is necessary to increase the mixing ratio of zeolite as much as possible. However, when increasing the mixing ratio of zeolite, the addition rate of SP must also be increased. Then, with the mixing ratio of zeolite being 100%, the maximum addition ratio was already required. And it is difficult to increase the mixing ratio. Therefore, it is necessary to study the influence due to the difference of the components of the two kinds of SP used in this study.

As for the reason why the compressive strength greatly differs depending on the type of SP, it is necessary to continue discussion focusing on the reaction of SP and the components contained in the curing accelerator. Depending on the results, it can be said that there is a possibility that not only the treatment and disposal of cesium adsorbed zeolite but also other fields can be used for features of high flow and high strength.

ACKNOWLEDGEMENTS

Part of this present research work was funded by

the Japan Society for the Promotion of Science (JSPS KAKENHI Grant Number JP17K07015).

REFERENCES

- 1) Tokyo Electric Power Company Holdings, Inc.: Study status for treatment of secondary waste of water treatment, 5th Specific Nuclear Facilities Radioactive Waste Regulation Committee (2017) (in Japanese)
- 2) H.Mawatari, K.Niwase and M.Satou: Evaluation of Physical Properties of Fast Ash Cement and Fly Ash Combination Type Filler in Cement Solidification Technique of Cesium Adsorbing Zeolite, Cement and Concrete Collected Papers, Vol.71, Mar. 2018 (in Japanese)
- 3) Isao Yamagishi et al.: Characterization and storage of radioactive zeolite waste, Journal of Nuclear Science and Technology, Volume 51, Nos.7-8, July-August 2014
- 4) Promotion of nuclear energy development · Cash management center: Technical standards required for waste of low-level radioactive waste, promotion of nuclear energy environment · Cash management center HP (<http://www.rwmc.or.jp/library/pocket/low-level/>)(in Japanese)

A FUNDAMENTAL EXPERIMENT ON PNEUMATIC TOMOGRAPHY OF UNSATURATED SOIL GROUND USING A HORIZONTAL ONE-DIMENSIONAL COLUMN

Naoya Nishihara¹ and Mitsuru Komatsu²

^{1,2} Graduate School of Environmental and Life Science, Okayama University, Japan

ABSTRACT

In a communication test using pneumatic pressure at a river levee, a method is required for evaluating continuous weak parts, which could be water paths, from the response behavior obtained at the receiving hole. Therefore, in this study, a horizontal one-dimensional elemental test was conducted in the laboratory and it was examined as a method to estimate the relative density from the response ratio based on a set injection pressure. As a result, it was concluded that the relative density of the target region could be estimated from the obtained response ratio when the water content is known.

Keywords: River Levee, Water Path, One-dimensional Column, Communication Test, Air Permeability Test

INTRODUCTION

In recent years, the development of countermeasures against seepage failure of river levee has acquired importance, and in order to make a risk assessment of further detailed investigation in the location of the weak parts, it is necessary to determine the continuity of the permeable layer. If the ground to be investigated is located below the groundwater level, it can be ascertained by the propagation behavior of the hydraulic pressure [1], but in most cases, it is located above the groundwater level, except during the flood season. Therefore, it is necessary to develop a method to investigate the continuity of the permeable layer and the water path in the unsaturated soil ground in advance. This study focused on the investigation technique by pneumatic tomography, which was used to evaluate the storage amount and heterogeneity of fractured rock [2]. The pneumatic tomography was carried out as a crosshole test, and the air permeability and filling degree were evaluated. In addition, a three-dimensional numerical inverse analysis method for interpretation of the test results was established [3]. However, there are no previous studies on porous media. Therefore, in this study, as a fundamental research, an elemental experiment, comparable to the communication test using pneumatic pressure, was conducted using a horizontal one-dimensional column 1 m in length [4]-[5]. The process of pressure propagation and response behavior obtained from the experiment were summarized. Furthermore, based on the results, assuming that the water content at the site was known, a method of estimating the relative density using the response ratio, expressed as the ratio of the set injection pressure to the pressure detected at the receiving hole, was determined.

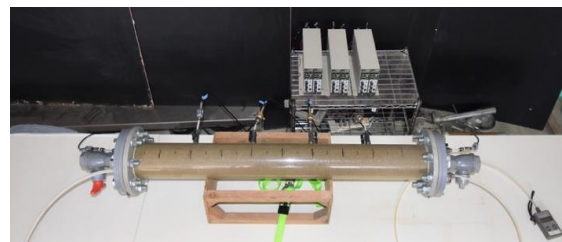


Fig. 1 Photograph of 1 m long one-dimensional column.

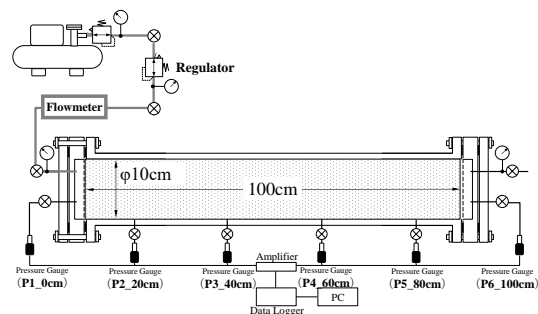


Fig. 2 Schematic of experimental apparatus.

Experimental Apparatus and Method of Manufacture of Specimen

The elemental experiment using the horizontal one-dimensional column used in this research is illustrated in Fig. 1, and the schematic drawing is shown in Fig. 2. The specimen container was a PVC column with a diameter of 10 cm and a length of 1 m with flanges at both ends, and two lids having porous plates with stainless-steel meshes adhered to them were attached, one at each end, to the supply side and

Table 1 Physical properties of sample

Sample		River Sand
Soil Particle Density	$\rho_s(\text{g/cm}^3)$	2.682
Maximum Dry Density	$\rho_{d\max}(\text{g/cm}^3)$	1.759
Minimum Dry Density	$\rho_{d\min}(\text{g/cm}^3)$	1.449
Maximum Void Ratio	e_{\max}	0.851
Minimum Void Ratio	e_{\min}	0.525

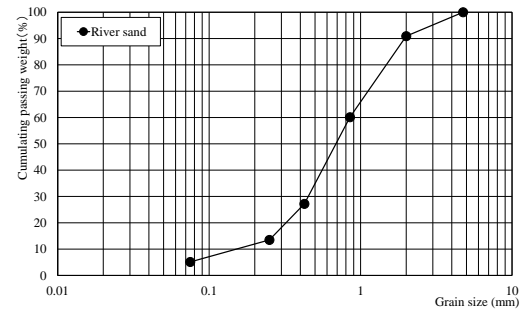


Fig. 3 Grain size accumulation curve

Table 2 Case list of pressure test and air permeability test

Case	Set Value		Experimental Value				
	Relative Density	Volumetric Air Content	Relative Density	Volumetric Air Content	Degree of Saturation	Water Content	Dry Density
	$D_{r\text{set}} (\%)$	$\theta_{\text{aset}} (-)$	$D_r (\%)$	$\theta_a (-)$	$S_r (\%)$	$w (\%)$	$\rho_d (\text{g/cm}^3)$
1-1	80	0.300	79.7	0.293	21.2	4.7	1.686
1-2		0.275	78.4	0.270	27.5	6.1	1.681
1-3		0.250	79.4	0.264	29.1	6.4	1.685
1-4		0.225	80.6	0.213	42.6	9.3	1.689
1-5		0.200	81.7	0.206	44.1	9.6	1.693
2-1	90	0.300	89.2	0.299	16.7	3.5	1.719
2-2		0.275	90.8	0.275	22.9	4.7	1.725
2-3		0.250	90.6	0.247	30.8	6.4	1.724
2-4		0.225	87.7	0.231	36.0	7.6	1.714
2-5		0.200	90.5	0.195	45.4	9.4	1.724
3-1	100	0.300	99.4	0.301	12.9	2.5	1.757
3-2		0.275	98.4	0.277	20.1	4.0	1.753
3-3		0.250	99.7	0.252	26.8	5.2	1.758
3-4		0.225	98.8	0.229	33.8	6.7	1.754
3-5		0.200	99.7	0.203	41.1	8.1	1.758

the exhaust side. For measuring the air pressure, a diaphragm type pressure sensor connected to a Teflon tube via a valve was used, and together with the lids at both ends, a total of six valves were installed at a distance of every 20 cm. The data was logged in at intervals of 0.1 s.

For the preparation of the specimen, after tilting the column with the chain block, the periphery of the column was tapped with a hammer and compacted with a compaction bar to obtain a predetermined water content and dry density. In addition, in order to prepare the specimens as even sets of dry density, the compaction was a 5 cm pitch per layer.

Method of the Experiment

The following two tests were carried out in succession:

(1) Pressure test

Assuming a field situation in which there is no permeable end such as a pile in the target area, the terminal valve was exposed to atmospheric pressure and an air pressure of 10 kPa was applied for 60 s through the regulator from the compressor. As soon as the valve was opened, fine particles migrated and there was a risk of clogging and collapsing of the soil particle skeleton. Therefore, with the start end valve closed, the exhaust valve was slowly opened manually after application of each 0.5 kPa until the pressure reached atmospheric pressure.

(2) Air permeability test

An air flow meter was installed between the regulator and the starting valve. The regulator was adjusted so that the flow rate was in 5 steps of 2 L/min, 4 L/min, 6 L/min, 8 L/min, and 10 L/min, and after checking that the pressure was in a steady state, the air flow rate and value of pressure at that time was recorded.

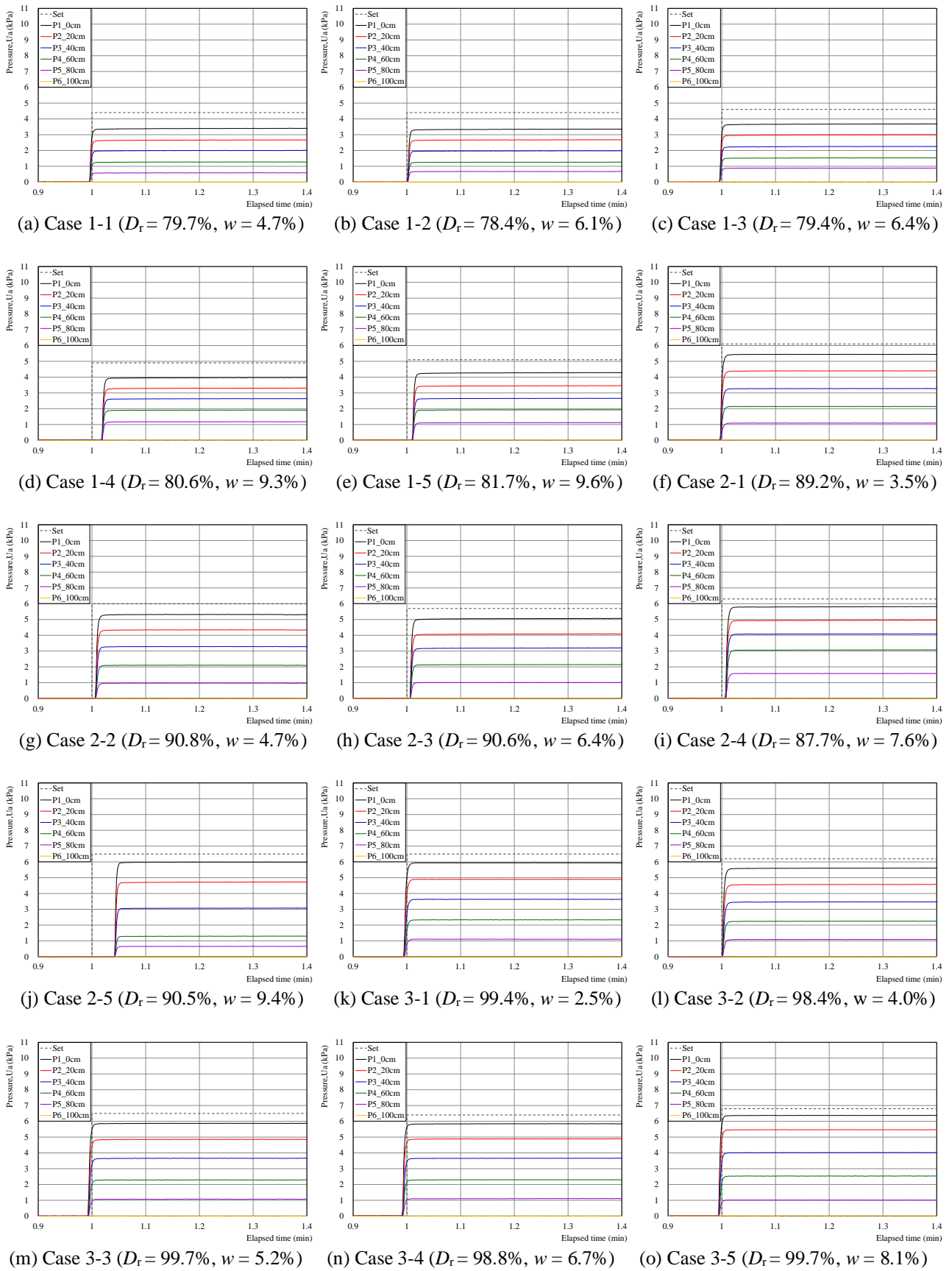


Fig. 4 Response behavior of air pressure to each case of relative density and water content.

Physical Properties of Sample and Different Cases

Table 1 presents the results of the physical property test of river sand, which was used as the sample, and Fig. 3 shows the grain size accumulation curve. Table 2 lists the values of various parameters in different experimental cases. Case 1 was set at a relative density of 80%, Case 2 at 90%, and Case 3 at a relative density of 100%; specimens were prepared according to the difference in the volumetric air content which is the difference between porosity and volumetric water content and a parameter representing the air volume present in the specimen. This parameter was used to determine the change in permeability coefficient due to the amount of air. The dry density in Table 2 is based on the actual weight. The degree of saturation and relative density are based on the value of dry density and determined by using the values of the soil particle density, maximum dry density and minimum dry density given in Table 1.

EXPERIMENTAL RESULTS

Pressure Test

The response behavior of air pressure in all the cases viz. Cases 1 to 3 are shown in Fig. 4 as time-dependent changes in air pressure when the terminal end valve was opened. When the water content was low, since the pressure loss increased, the measured pressure decreased. In contrast, as the water content increased, the pressure loss decreased; therefore, the measured pressure increased. It was also confirmed that the measured pressure increased with increase in the relative density.

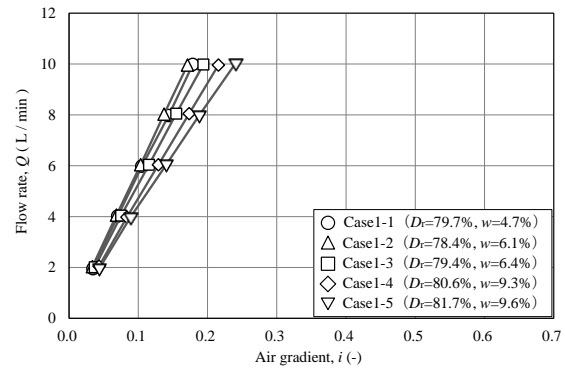
Air Permeability Test

The relationship between air gradient and flow rate at each set relative density, which is summarized from the results of the air permeability test at the set flow rates of 2, 4, 6, 8, and 10 L/min in 5 steps is shown in Fig. 5. The choice of using Darcy's law for calculating the air permeability coefficient or an equation that treats air as a compressible fluid is based on the graph of the air flow rate vs the air gradient. Since the results obtained in this test showed a linear relationship in every case, it was decided to calculate the air permeability coefficient by using Darcy's law. An approximation was also made by Yoshimi et al.'s equation [6].

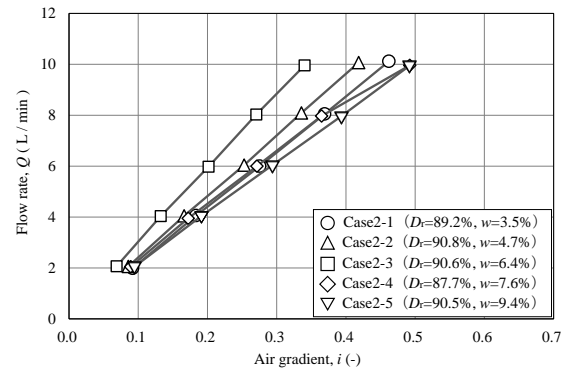
$$\log k_a = a + b \log \{e (1 - S_r / 100)\} \quad (1)$$

where the variables a and b in Eq. (1) are constants determined from the state of the soil.

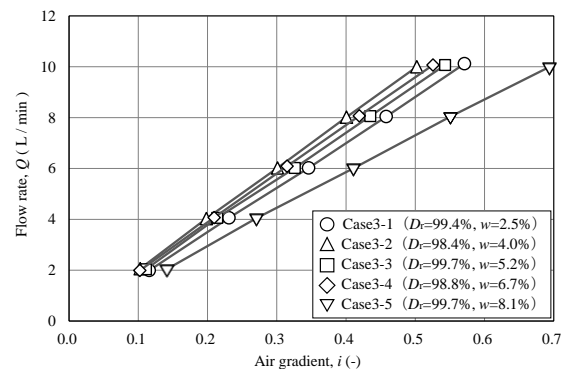
The relationship between the air permeability



(a) Case 1, $D_{rset} = 80\%$



(b) Case 2, $D_{rset} = 90\%$



(c) Case 3, $D_{rset} = 100\%$

Fig. 5 Relationship between flow rate and air gradient

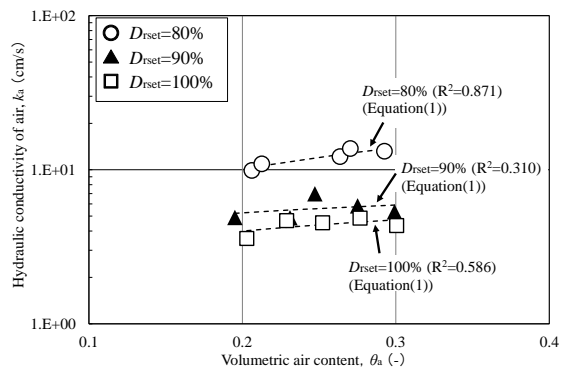


Fig. 6 Relationship between air permeability and volumetric air content.

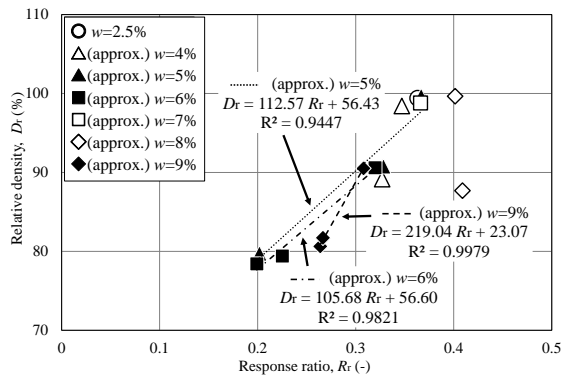


Fig. 7 Relationship between relative density and response ratio

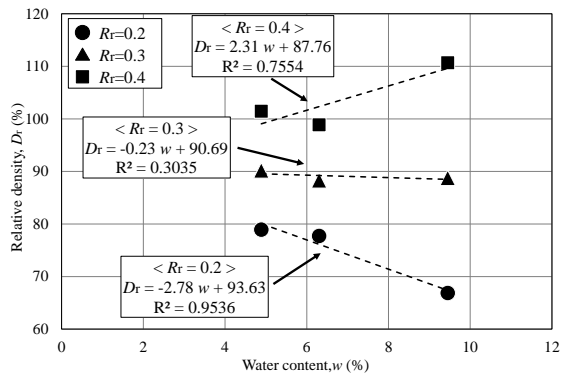


Fig. 8 Relationship between relative density and water content

coefficient and volumetric air content is shown in Fig. 6. With the same volumetric air content, air of the same volume exists in the specimen, and it is considered that even if the relative density changes, the air permeability coefficient does not change. However, in practice, it was found that the air permeability coefficient tended to increase as the relative density decreased even with the same volumetric air content. In Case 1, the values of the variables a and b in Eq. (1) are 1.395 and 0.785, respectively. In Case 2, a and b are 0.865 and 0.286, and in Case 3, they are 0.815 and 0.414, respectively.

DISCUSSION

Relationship between Response Ratio and Relative Density

The response ratio is the result at measurement point P3 (40 cm) as P3 is farthest from the start end (0 cm), which is the injection hole of air pressure, and it is also far from the endpoint (100 cm) where the pressure is the atmospheric pressure. The results of measurement at other points from P1 to P6 were used to ascertain the air gradient in order to calculate the air permeability.

Fig. 7 shows the relationship between the relative density and response ratio plotted for each value of water content, and Fig. 8 shows the relation between

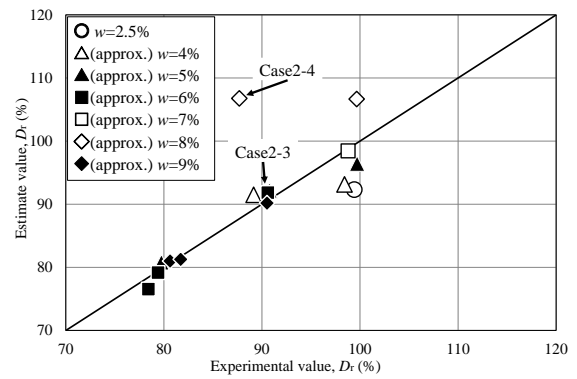


Fig. 9 Relationship between estimated value and experimental value of relative density

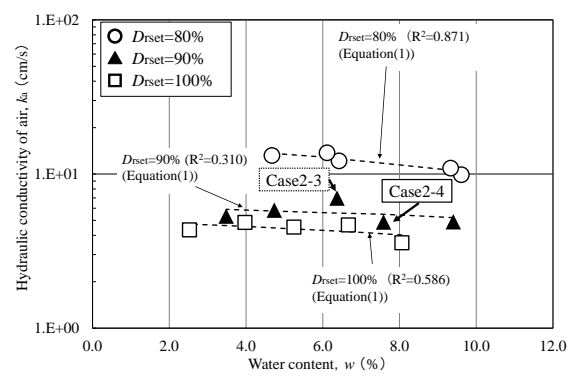


Fig. 10 Relationship between air permeability and water content.

relative density and water content plotted for each response ratio. The response rate generally increased as the water content increased. Further, it could be confirmed that a higher relative density corresponded to a higher response rate.

Estimation of Relative Density

Assuming that the water content was known, the relative density of the target region was estimated using the response ratio.

The relationship between the relative density and water content was summarized at an arbitrary response ratio, and is shown in Eq. (2). The variables a and b in the equation represent the slope and intercept, respectively. The relationship between each variable and the response ratio is shown in Eqs. (3) and (4).

$$D_r = a' * w + b' \quad (2)$$

$$a' = 25.46 R_r - 7.87 \quad (3)$$

$$b' = -29.36 R_r + 99.50 \quad (4)$$

The relative density was estimated by substituting the obtained response ratios in Eqs. (3) and (4), and the values of a and b thus obtained from each equation and the water content in Eq. (2). The relationship between the estimated and experimental (measured) values of the relative density is shown in Fig. 9. The

estimated value generally agreed with the measured value, and when the water content was known, it was suggested that the relative density of the target region could be estimated from the obtained response ratio.

It was seen that the estimated value deviated from the measured value in Case 2-4, and a variation was also noted at the relative density of 100%.

Evaluation of Estimation of Relative Density with reference to Air Permeability Coefficient

The cause of the large deviation between the estimated and measured values of the relative density was attributed to the possible formation of an air path due to the variation in the density of the specimen. In order to verify this, the measured value of the relative density was compared with the estimated value with reference to the results of the air permeability test. Fig. 10 shows the relationship between the air permeability coefficient and water content. Case 2-3 showed a result deviating from the relationship between water content and air permeability coefficient estimated from Yoshimi et al.'s equation, but it can be seen that there is almost no discrepancy between the estimated and measured values of relative density in this case as seen in Fig. 9. Moreover, in Fig. 9, Case 2-4 shows that the estimated and measured values of relative density greatly deviate from each other, and in Fig. 10, the result of Case 2-4 is not separated from the approximate relationship as in Case 2-3. This was thought to be due to the line representing the water content of 9% in Fig. 7 being extended and having an intersection in the vicinity of the relative density of 90%. In contrast, as the water content rose, the air permeability coefficient tended to decrease; hence, the formation of an air path due to variation in density cannot be considered as a possibility. Therefore, it is inferred that the measured and estimated values of relative density greatly differed due to an error in the measurement of the response ratio used for the estimation.

CONCLUSIONS

In this study, a method was determined to ascertain the physical properties of the target area from the response behavior obtained from the laboratory elemental test corresponding to the pneumatic communication test to investigate the continuity of weak parts in the foundation of the river levee.

Based on the elemental test results in a horizontal one-dimensional column 1 m in length, the relative density was estimated from the response ratio representing the degree of air pressure propagation and compared with the actual measured values.

The contents of this study are summarized below:

- (1) It was confirmed that there was an increase in the propagated pressure along with the rise in water content. Moreover, the same tendency was shown even when the relative density was changed.
- (2) The response ratio, as well as the relative density, generally showed a tendency to increase with an increase in the water content.
- (3) If the water content was already known, it was possible to estimate the relative density from the response ratio.

ACKNOWLEDGMENTS

This work was partly supported by Japan Society for the Promotion of Science (JSPS) KAKENHI [grant number 16H02577]. We express our gratitude.

REFERENCES

- [1] Yeh, T. J. Yeh, Mao D., Zha Y., Hsu K.-C., Lee C.-H., Wen J.-C., Lu W., and Yang J., Why Hydraulic Tomography Works?, *Groundwater*, Vol.52, No.2, 2014, pp.168-172.
- [2] Illman, W. A., Thompson D. L., Vesselinov V. V., Chen G., and Neuman S. P., Single-and cross-hole pneumatic injection tests in unsaturated fractured tuffs at the apache leap research site near superior, Arizona, phenomenology, spatial variability, connectivity, and scale, NUREG/CR-5559, U.S. Nucl. Regul. Comm., Washington, D.C., 1998, 186p..
- [3] Velimir, V. V., Neuman S. P., and Illman W. A., Three-dimensional numerical inversion of pneumatic cross-hole tests in unsaturated fractured tuff 1. Methodology and borehole effects, *Water Resources Research*, Vol.37, No.12, 2001, pp.3001-3017.
- [4] Komatsu M., Nishihara N., Niimura T., Tatekawa I., Nishigaki M., A Basic Experiment on Field communication Test to Investigate Weak Zone on Unsaturated Ground Using a Horizontal One-dimensional Column, *Ground Engineering, Journal of Chugoku Branch of Japanese Geotechnical Society*, Vol.35, No.1, 2017, pp.101-108. (in Japanese)
- [5] Niimura T., Nishigaki M., Komatsu M., Tatekawa I., Application of communication test using pneumatic pressure to river levee, *The 52nd Japan National Conference on Geotechnical Engineering*, 0477, 2017, pp.951-952. (in Japanese)
- [6] Yoshimi Y. and Osterberg J. O., Compression of partially saturated cohesive soils, *Journal of the Soil Mechanics and Foundations Division, Proceedings of the American Society of Civil Engineers*, Vol.89, Issue 4, 1963, pp.1-24.

PARAMETRIC STUDY OF CES COMPOSITE COLUMNS WITH FRC USING FINITE ELEMENT ANALYSIS

Fauzan¹, Ruddy Kurniawan², Zev Al Jauhari³, and Nabila Felicia⁴

^{1,2,4} Civil Engineering Department, Andalas University, Indonesia; ³ Bengkalis State Polytechnic, Indonesia

ABSTRACT

To simplify and reduce the cost in construction works for SRC structures, the new composite structural systems consisting of only steel and concrete, the concrete encased steel (CES) structures, have been developed in Japan. An experimental study on CES column using fiber reinforced concrete (FRC) panel has been carried out by one of the authors to investigate the seismic performance of the column. In this paper, a detailed three-dimensional (3D) nonlinear finite element (FE) model is developed to study the response and predict the seismic performance of CES using FRC panel composite columns subjected to constant axial and lateral cyclic loads. The column model was modeled using solid elements and analyzed by using ANSYS APDL v.14. The model was validated with previous test results and was used as a reference for the parametric study. The parameters considered in the study was the tensile strength of FRC. The analytical results obtained from the finite element analysis is able to accurately simulate the behavior of the CES columns on the experimental study. The CES column using full FRC is also modeled in order to know the influence of the full FRC on the CES composite column. Numerical results show that CES using FRC panel and CES using full FRC have an excellent seismic performance with a stable pinching and spindle shape hysteresis characteristic, respectively. Moreover, the results of the parametric study show that the tensile strength of FRC has great influence on the seismic behavior of the CES column, with the increment of flexural capacity of 5% to 17% by rising of FRC tensile strength from 8 to 16 MPa.

Keywords: *Fiber Reinforce Concrete, Concrete Encased Steel, Finite Element Analysis, Composite Column*

INTRODUCTION

Composite steel section and reinforced concrete structure which called SRC structure have been widely used for buildings with more than seven stories in Japan since these structures provide an excellent seismic performance with high capacities and deformability. However, some disadvantages of SRC structures are found due to the complexity of construction works, especially in constructing the steel section and reinforced concrete. In order to solve this problem and reduce the cost of construction works for SRC structures, concrete encased steel structures consisting of only steel section and concrete, hereafter called to as CES structures, have been developed by Kuramoto in Japan [1]. Figure 1 shows the schematic view and cross section of CES column.

Some experimental studies have been conducted to examine the structural performance of CES columns [1,2,3]. The results show that the hysteretic characteristics of the CES columns are almost similar to those of SRC columns. In the feasibility study to examine the structural performance of CES columns, it was confirmed that damages of the columns with an increase of lateral deformation such as cracking and crushing in concrete can be reduced by using fiber reinforced concrete (FRC) instead of normal concrete [2]. The experimental studies on

CES columns using FRC panel as a column cover have been conducted by one of the authors in Japan.

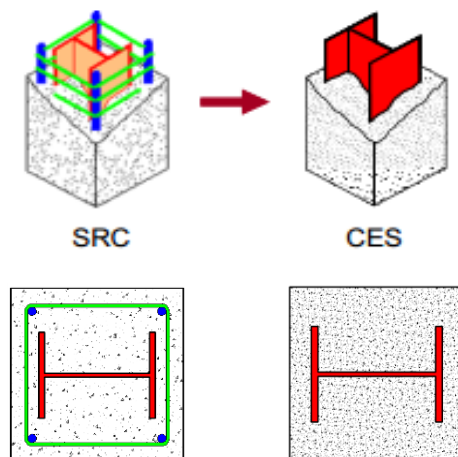


Fig. 1 The 3D view and cross section of SRC and CES columns.

In order to validate the experimental results of the column, the three-dimensional finite element (FE) model is developed by using a finite element program, ANSYS APDL v.14. This paper presents the numerical study on the behavior of CES composite column, which compared to the experimental data. Furthermore, a parametric study

is performed with parameters of the tensile strength of FRC panel. The CES column using full FRC is also built in order to know the influence of the full FRC on the CES composite column.

MATERIAL AND METHODS

The Geometry of 3D Finite Element Model

Details of the experimental program in terms of the geometry of steel section, concrete, and FRC panel are described in Figure 2. The specimen had 1600 mm height and 400 mm² section area. The specimen is covered by an FRC panel with a 45 mm thickness, while the core section is concrete encased steel. Steel encased in the column had a cross shape H-section of 300 x 220 x 10 x 15 mm. The dimensions and geometrical configuration of the test specimen are used to construct the FE model.

Concrete, steel, and FRC are modeled as the block and solid cube with an equivalent length representing the total area of the specimen. The mesh density is chosen so that the element aspect ratio is nearly equal to one [5]. This provides adequate accuracy and fair computational time in modeling the CES column. The total numbers of element used are 5095 elements.

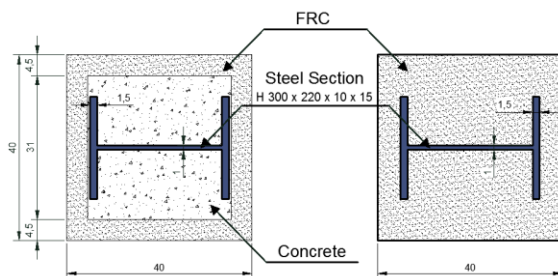


Fig. 2 The dimension and detail of specimens.

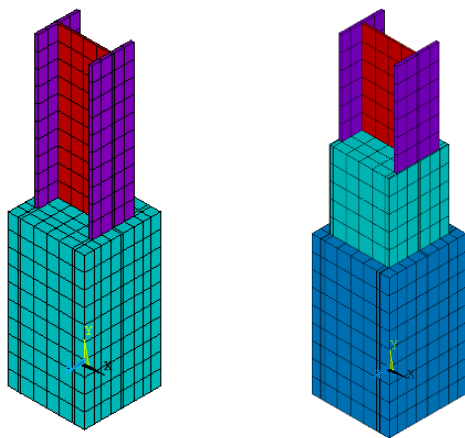


Fig. 3 The construction of 3D FE models.

Mesh size average of 20 mm was employed for the entire element of the steel encased, concrete, and FRC panel to balance between the accuracy of the numerical results and computational time. The connections between concrete and steel elements were assumed to be a perfect bond connection [11].

Two types of elements are used in the modeling of steel H-section, concrete, and FRC panel. ANSYS solid element, SOLID185 is used to model the steel section, while SOLID65 is used to model the concrete and FRC of the columns. The SOLID185 and SOLID65 elements are a 3D hexahedral elements using 8-node brick elements with three translation degree of freedom at each node defined by eight nodes, as shown in Figure 3 [12].

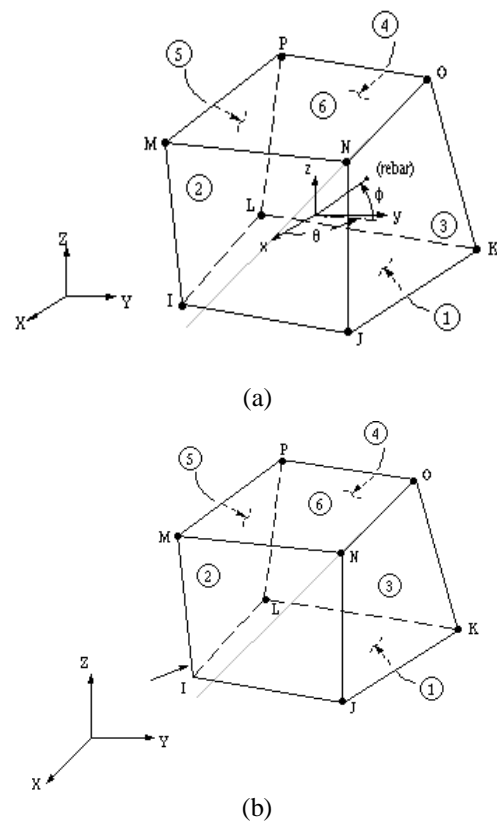


Fig. 4 (a) Solid65 and (b) Solid185 ANSYS elements.

Properties and Model Constitutive of Material

Concrete

The compressive strength of normal concrete used the model is 35 MPa. A peak concrete strain of 0.0025 is used in the analysis. Figure 5 presents the tensile stress-strain curve for the concrete. The stress-strain relationship is designed on the model developed by Saenz [7], which is built into the program. The tensile relaxation (softening) is presented by a sudden reduction of the tensile strength to $0.6 \times f_t$ reach the tensile cracking strain

ϵ_{cr} . After this point, the tensile response decreases linearly to zero stress at a strain of $6 \times \epsilon_{cr}$, as shown in Figure 6. The Al-mahaidi [8] model was used as the shear transfer model after cracks occurred in the concrete element, with a value of 0.75 and 0.9 for β_t and β_c , respectively. The fracture criterion of concrete is applied by the adoption of the five parameter model of William-Warke [9].

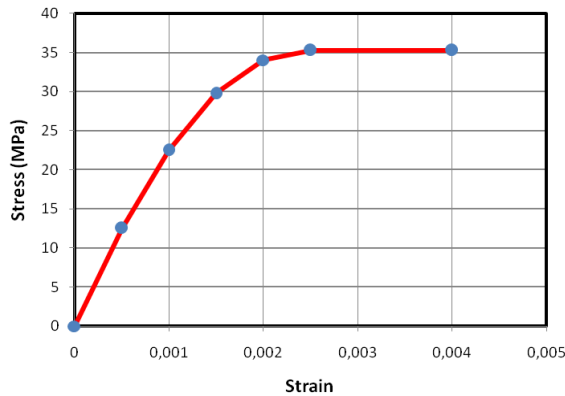


Fig. 5 Idealized of compressive stress–strain curve for concrete.

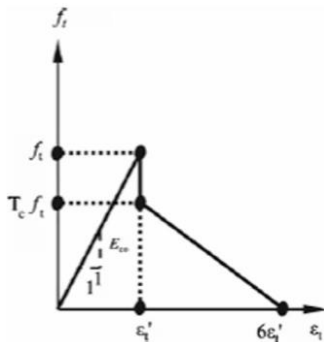


Fig. 6 Idealized of tensile stress–strain curve for concrete.

Steel Encased

The yield strength of the encased steel used in the FE model is 293.6 and 313.3 MPa for flange and web, respectively. To describe the stress-strain behavior of steel encased, the perfectly elastic-plastic criterion material was used. The stress-strain curve for flange and web was input into the ANSYS package, as shown in Figure 7.

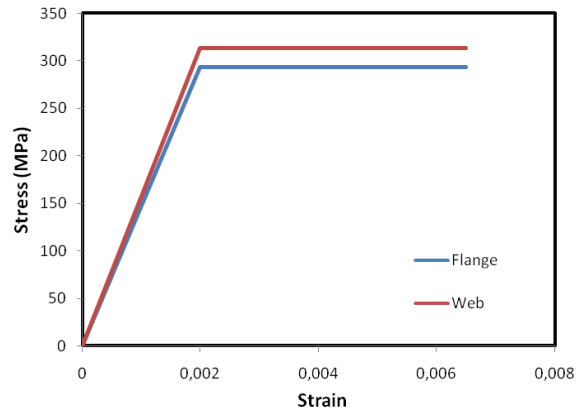


Fig. 7 Stress–strain curve for the encased steel.

At first, this curve is elastic, then it is assumed to be perfectly plastic (bilinear isotropic model). This curve is suitable for representing stress-strain characteristics of normal and high-quality steel section. Von Mises yield criterion is applied in a constitutive model of the steel.

Fiber Reinforced Concrete

Mechanical properties of FRC obtained from materials test at the age of 28 days are respectively 39.6 MPa and 7.97 MPa for compressive and tensile strengths. For Specimen CES column using FRC panel, Poly-vinyl Alcohol fibre (PVA fibre: REC100L) with 0.66 mm diameter and 30 mm length is used. The volume content ratio of the fiber is 1.5%. The features and related data of other structural elements in numerical simulations of FRC remain constant and similar to normal concrete.

Boundary Conditions and Loads

The boundary conditions are made to consider the test setup, as seen in Figure 8. An anchor plate/ stub (700.700.400 mm) is used in the model at the top and bottom of the column. The final boundary conditions of the FE model is shown in Figure 9 [13]. Loading was applied in a displacement control mode at the top of a CES column to simulate the lateral cyclic loading condition. The ends of the CES column were fixed against all degree of freedom except for the vertical displacement at the top end. The finite element model is shown in Fig. 4 [12].

The loads in this study are applied in the FE model as follows:

- The constant axial load is applied to the top stub of column approximately 1031 kN. This is represented in the FE model by applying a point pressure of 1.4 kN on the stub elements with a total nodal of 717.
- The lateral cyclic load is represented in the FE model by applying the displacement at the top

edge of the stub column. The increment of lateral loading cycles is controlled by story drift, R , defined as the ratio of lateral displacement to the column height, δ/h . The lateral load consists of one cycle to each R of 0.5, 1, 1.5, 2, 3, 4% and followed by half cycle to R of 5%, as shown in Figure 10.

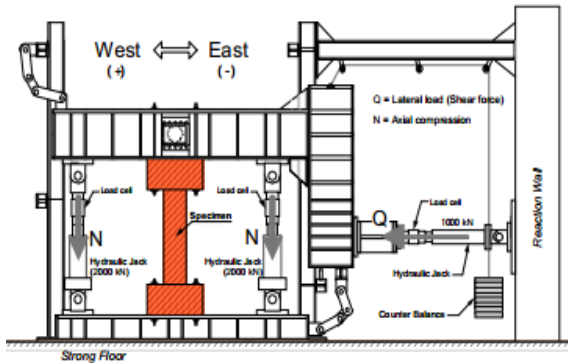


Fig. 8 Schematic view and photo of test setup.

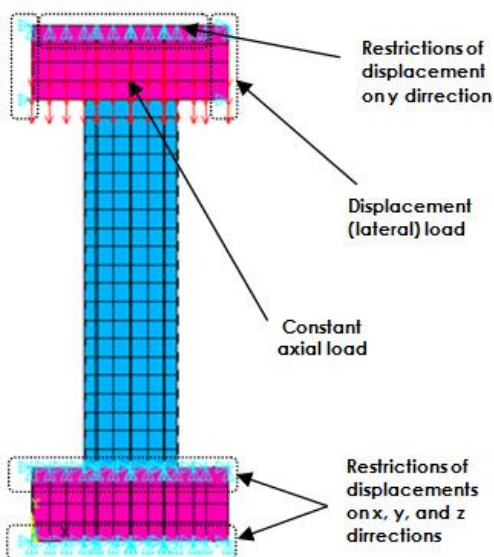


Fig. 9 Boundary conditions.

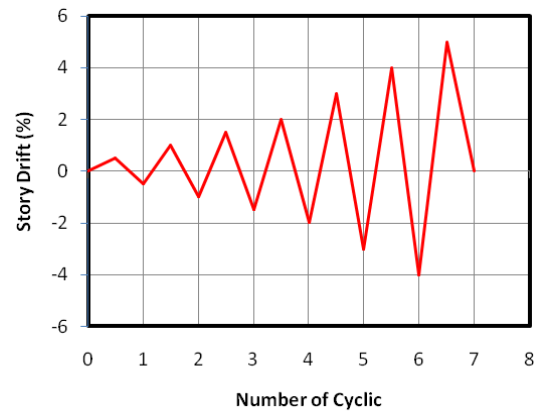


Fig. 10 Lateral cyclic load applied in FE models.

Nonlinear Convergence

The applied cyclic displacements are divided into a series of increments called load steps and load substeps. The automatic time stepping option is enabled in this analysis to predict and control the load step size increments. Newton–Raphson equilibrium iterations are updated the model stiffness in ANSYS. In this study, the convergence criteria for the elements are based on displacement. ANSYS convergence tolerance default values of 5% for displacement checking are initially selected. It is found that convergence is difficult to achieve using the default values due to the associated large deflections and the highly nonlinear behavior of the concrete elements. Thus, in order to obtain convergence of the equilibrium iterations, the convergence tolerance limits are increased to 10% for the displacement checking criterion [9].

VALIDATION OF PROPOSED FE MODEL

Hysteresis Characteristics

The experimental hysteresis loop (shear force vs story drift) for the CES composite column is compared to those obtained from the numerical analysis, as shown in Figure 11. The maximum shear force for the FE model is 836 kN obtained at R 5%. This is approximately 2.2% higher than the results obtained from the experimental (817 kN at R 3%). The FE model behaved higher dissipated energy in the last stages of loading cycles than the experimental data. The average of the different percentage of lateral shear force in each stage of loading cycles between the FE analysis and the experimental results is around 12%.

In the FE model, the peak load in each cyclic always increase, while in the test result, the peak load after R 3% decreased slightly. The difference between the FE and experimental results at different stages of loading can be attributed to mesh refinement, idealized boundary conditions in the FE

model, material nonlinearity, and the specified coefficient of friction between contact surfaces at the material interface of the columns.

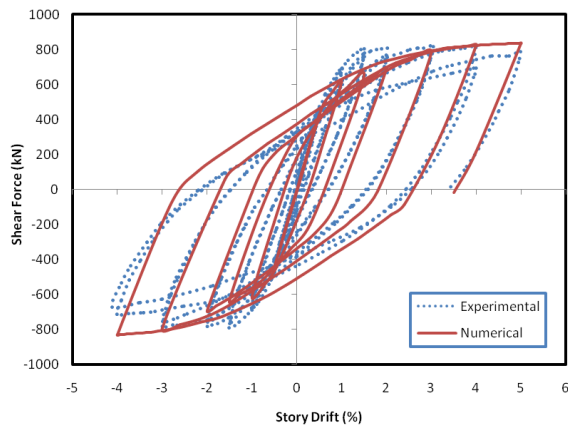


Fig. 11 Comparison of the hysteresis loop of CES column between FEA and experimental results.

Failure Patterns and Principal Stress Distribution

Evaluation of the failure modes is as important as determining the seismic behavior of column. The modes of failure are mainly of yielding, first crack and crush both concrete core and FRC panel, and buckling [12]. The stress in the each of material is also analyzed to validate the FE model. A principal strain of 0.002 has been reached in the encased steel of the CES model at story drift 0.6%, as indicated that the steel has the first yield in red in Figure 13. The elastic modulus of the steel is 156700 MPa, with a corresponding stress equal to the yield stress 325 MPa. On the other hand, the first yield in the corner region both of the top and bottom of the steel during experimental is at R 1%.

In the model, the first crack in the concrete occurs at R 0.4% in the strut zone of FE model, indicated by maximum principal stresses (tensile) is greater than the tensile strength of concrete (1.8 MPa), as shown inside the oval shape in Figure 14. The cracks occur spread on the strut area and propagate along the horizontal direction. These results indicate that the FE model satisfactory portray the behavior of the composite columns.

In the model, the shear crack occurred first at R about 0.3% at both the top and bottom of the column, as shown in Figure 15. With an increase of story drift, the shear cracks propagate and disperse all over the column. These results indicated that the FE model satisfactory portrays the behavior of the column.

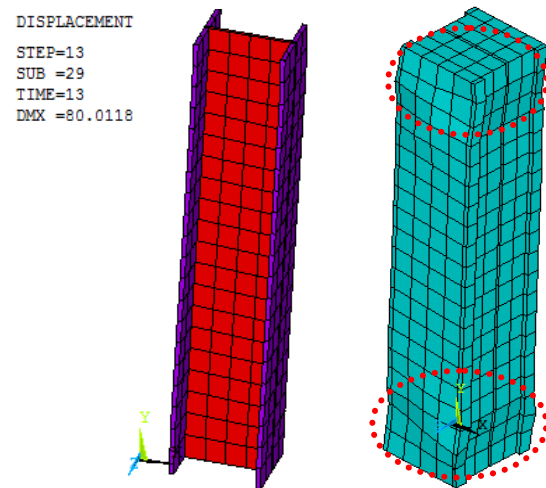


Fig. 12 Steel and concrete failure patterns of CES composite column in the numerical result.

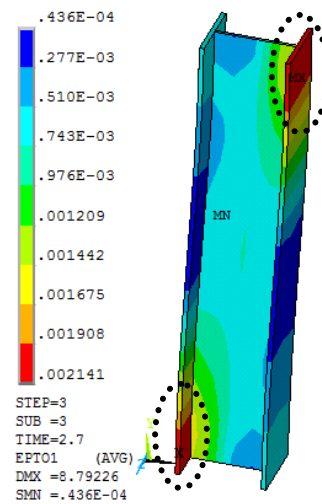


Fig. 13 First yield in the encased steel of FE model.

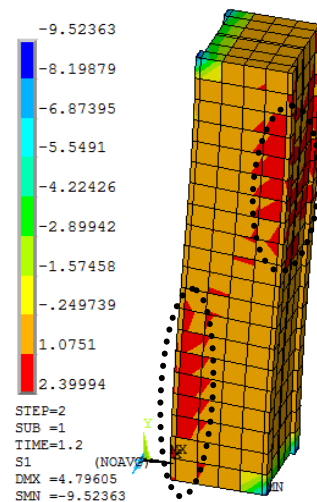


Fig. 14 First crack in the concrete core of FE model.

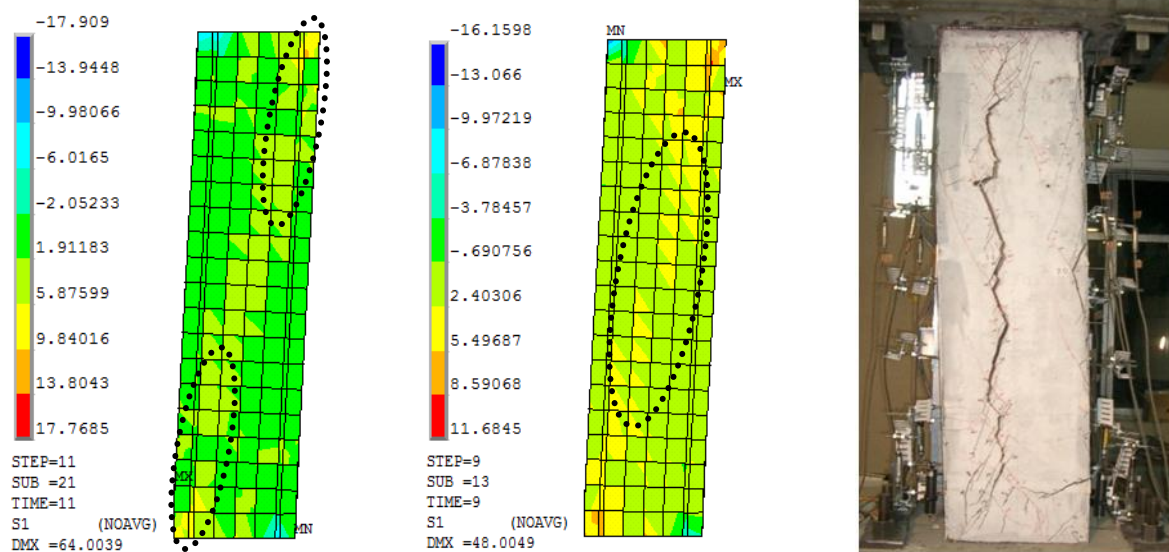


Fig. 15 Comparison of FRC panel failure patterns in the CES column between experimental and numerical results.

PARAMETRIC STUDY

From the above numerical analysis of CES composite column, the FE model can provide an accurate prediction for its seismic behavior, which has been compared to the experimental program. A parametric study is performed to deeply understand the CES column behavior and identify a proportion of FRC that has a greater influence on the column. The parameters studied are tensile strength of FRC and concrete compressive strength. This parameter is chosen because of the importance of the material in structural resistance and it can improve seismic behavior without changing the column dimensions. There are three different values used in each parameter, as shown in Table 1. The numerical model, which is validated with the test results, is called the reference model in the parametric study [12].

Table 1 Parameters value selected for parametric study

Parameter	Value
Tensile strength in FRC panel	8, 12, and 16 MPa
Tensile strength in full FRC	8, 12, and 16 MPa

Effect of Tensile Strength in FRC Panel

FRC panel is a column component that provides the core confinement and resistance to bending moment, shear force and column buckling. The tensile strength of the FRC panel is varied to evaluate the influence of this parameter on the

column behavior. The tensile strength used in the parametric analysis are determined by commonly fiber used of the FRC panel ranges from 1-3%. The material properties of other material, such as the compressive strength, elastic modulus, and other coefficients, are the same as those in the reference model. Figure 16 presents the shear force versus story drift (hysteresis loop) of CES column with having variation the tensile strength of FRC panel. This curve illustrates the differences between the stiffness, strength, and energy dissipation of each model, as listed in Table 2.

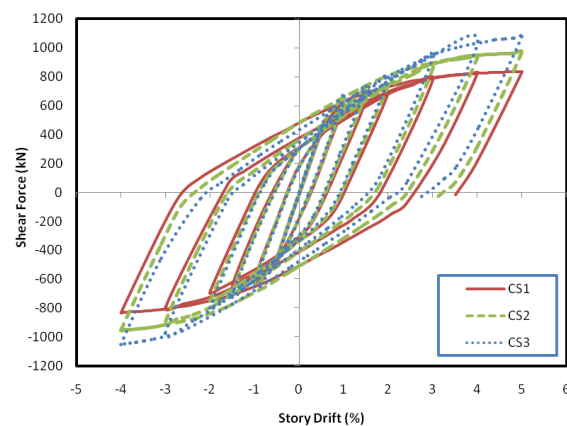


Fig. 16 Comparison of the hysteresis loop of CES column varying the tensile strength of FRC panel.

The model with FRC panel tensile strength of 12 MPa (Model CS2) displays a stiffness of 13% greater than the reference model (Model CS1), whereas the model with FRC panel tensile strength

of 12 MPa (Model CS3) displays a 14% higher than Model CS1. The increase of tensile strength of FRC panel can increase the flexural capacity by around 15%. The absorbed energy calculated from areas under force - deflection curve [12].

A higher tensile strength of FRC panel leads to a higher energy dissipation of around 6-10%. The results of simulations indicate that the tensile strength of FRC panel has a significant influence on the seismic behavior of the column.

Table 2 Comparison of CES column seismic criteria with varying the tensile strength of FRC panel

Model	Max. Strength (kN)	Stiffness (kN/mm)	Energy Diss. (kJ)
CS1 (8 MPa)	836.1	11.56	218.2
CS2 (12 MPa)	966.7	13.32	225.6
CS3 (16 MPa)	1074.2	14.76	231.7

Effect of Tensile Strength in Full FRC

The proportion of FRC used in this parametric study is based on the comparison of the seismic behavior of CES columns between those using only as panel and full in concrete with varying the tensile strength of FRC. The features of other structural elements in numerical simulations of parametric analysis remain constant. The related data for parametric analysis are similar to reference model analysis. Figure 18 and Table 3 show the comparison of hysteresis loops and seismic criteria of CES column with respectively having variation in the tensile strength of FRC.

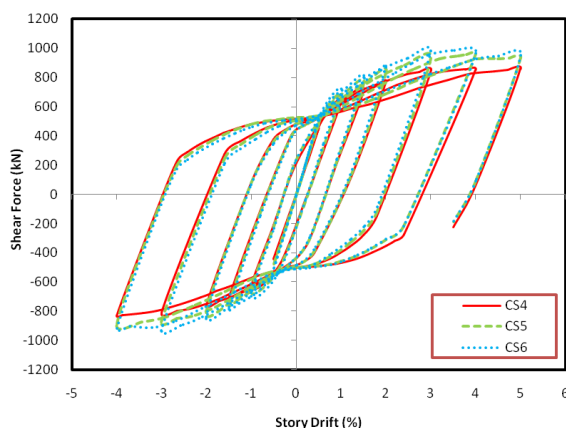


Fig. 17 Comparison of the hysteresis loop of CES column varying the tensile strength of FRC.

Table 3 Comparison of CES column seismic criteria with varying the tensile strength of FRC

Model	Max. Strength (kN)	Stiffness (kN/mm)	Energy Diss. (kJ)
CS4 (8 MPa)	859.1	11.73	255.1
CS5 (12 MPa)	960.4	12.65	262.6
CS6 (16 MPa)	984.8	12.99	269.3

The model with FRC tensile strength of 16 MPa (Model CS6) displays a stiffness of 9% greater than the reference model (Model CS4), whereas the model with FRC tensile strength of 12 MPa (Model CS5) display a 2.71% greater than Model CS4. A higher tensile strength of concrete lead to a higher energy dissipation by around 8-12%. Model CS6 display a 3.4% increase in maximum flexural capacity, while Model CS5 display a 3.7% increase in maximum flexural capacity to resist the lateral load. These results indicate that the increase of FRC tensile strength influence on the maximum flexural capacity of the CES column with full FRC.

CONCLUSION

In general, the hysteresis loop and failure mode of the FE model of CES column satisfactory portray the behavior of the test column both in elastic and plastic ranges. The FE model has a stable spindle-shape hysteresis characteristic by having little damage on the column even at a final story drift. A good correlation exists in all stages of cyclic loading. Specifically, the FE results for the peak loads are higher than the test results (within 4-15%) in each stage of cyclic loading. The results of this parametric analysis demonstrate that the tensile strength of FRC panel has great influence on the seismic behavior of CES column, in which the rising of the tensile strength of FRC from 8 to 16 MPa increase the flexural capacity around 17%.

REFERENCES

- [1] Kuramoto H., Adachi T., and Kawasaki K. Behavior of Concrete Encased Steel Composite Columns using FRC, Proceedings of Workshop on Smart Structural Systems Organized for US-Japan Cooperative Research Programs on Smart Structural Systems (Auto-Adaptive Media) and Urban Earthquake Disaster Mitigation, Tsukuba, Japan, 2002, pp.13-26.
- [2] Adachi T., Kuramoto H., Kawasaki K., and Shibayama Y. Study on Structural Performance of Composite CES Columns Using FRC Subjected to High Axial Compression, Proceedings of Japan Concrete Institute, Vol. 25, No. 2, 2003, pp. 289-294.

- [3] Taguchi T., Nagata S., Matsui T., and Kuramoto H. Structural Performance of CES Columns using Single H-shaped Steel, Proceedings of Japan Concrete Institute, Vol. 28, No.2, 2006, pp.1273-1278.
- [4] ANSYS Version 14. User's and Theory Reference Manual, 2010.
- [5] Ithikkat V. V. and Dipu V. S., Analytical Studies on Concrete Filled Steel Tubes, International Journal of Civil Engineering and Technology (IJCIET), Vol. 5, Issue 12, 2014, pp. 99-106.
- [6] John A. and Usha S. Analytical Study on Stress-strain Behavior of Reinforced Concrete Column. International Journal of Civil Engineering and Technology (IJCIET), Vol. 5, Issue 12, 2014, pp. 45-55.
- [7] Saenz L. P., Discussion of Equation for The Stress-Strain Curve of Concrete, Journal American Concrete Institute, 61(9), 1964, pp. 1229 –1235.
- [8] Al-Mahaidi, R. S. H. Nonlinear Finite Element Analysis of Reinforced Concrete Deep Members, Rep. No. 79 (1), Dept. of Structural Engineering, Cornell Univ., Ithaca, NY, 1979.
- [9] William K. L. and Warnke E. P. Constitutive Model for the Triaxial Behavior of Concrete, Int. Association for Bridge and Structural Engineering Proc., Vol. 19, 1975, IABSE, Zurich, Switzerland.
- [10] Hawileh R. A., Rahman A., and Tabatabai, H. Nonlinear Finite Element Analysis and Modeling of A Precast Hybrid Beam-Column Connection Subjected to Cyclic Loads, Journal Applied Mathematical Modelling, Vol. 34, 2010, pp. 2562-2583.
- [11] Warakorn T. C. H., Piyapong W., and Taweep C., Flexural Reinforced Concrete Members With Minimum Reinforcement Under Low-Velocity Impact Load, International Journal of GEOMATE, Vol.14, Issue 46, 2018, pp.129-136.
- [12] Chinnapat B., Chayanon H., and Nutchanon U., Analysis of Square Concrete-Filled Cold-Formed Steel Tubular Columns Under Axial Cyclic Loading, International Journal of GEOMATE, Vol.15, Issue 47, 2018, pp.74-80.
- [13] Fauzan, Ruddy K., and Zev A. J., Finite Element Analysis of EWECS Columns with Varying Shear Span Ratio, International Journal of GEOMATE, Vol.14, Issue 43, 2018, pp.1-7.

ASSESSMENT TECHNIQUES FOR ALKALI SILICA REACTION DIAGNOSIS IN MASS CONCRETE STRUCTURE

Suvimol Sujjavanich¹, Thanawat Meesak², Krit Won-in³ and Viggo Jensen⁴

¹Department of Civil Engineering Kasetsart University, Thailand; ^{2,3} Kasetsart University, Thailand

⁴Norwegian Concrete and Aggregate Laboratory LTD, Norway

ABSTRACT

This paper reported the results of several techniques used to diagnose Alkali-Silica Reaction (ASR) distress in concrete. Two screening tests looked for the appearance of fluoresced gel of uranyl acetate treated samples and the changed color areas of the chemical staining treated samples. The results agreed well with expansion of the cored samples in warm water and in NaOH solution and also supported the previous measured expansion in field. The petrographic analysis found many microcracks with ASR gel filling in cement paste, interface zone (ITZ) between aggregates and paste, and internal cracks in aggregates. Microstructural analysis revealed the characteristics of slow reactive aggregates and two forms of products; amorphous gel with shrinkage cracks in cement paste cracks and in the ITZ, and cryptocrystalline reaction products consisting of plate formed crystals, rosettes and globular found mostly in internal cracks of aggregates and air voids. The SEM/EDS analysis differentiate reactive from non-reactive aggregates. Lining ettringite were also observed in air voids and some cracks but there was no evidence linking it to the cause of continued expansion. Fine grain black quartzite within the aggregates and sericite were identified as the cause of ASR. The combination of different techniques effectively identified ASR as the primary cause of deterioration and the continued expansion of the investigated structure.

Keywords: ASR, Screening, Petrographic, Accelerated, Microstructural Analysis

INTRODUCTION

Alkali-silica reaction (ASR) has been globally recognized since 1940. Since then numerous research have been conducted on the mechanisms, assessment and mitigation [1]-[3]. Because the problem is naturally complicated and some symptoms look alike to those of other problems, to identify the cause and severity is important but difficult and need expertise, time and expenses [4].

Several qualitative and quantitative methods have been proposed for ASR assessment. Some are widely accepted as standard methods. However, because of the strength and weakness of individual method, none is accepted as one sole methods that is capable of definitive identification of the problem [5], [6].

The first ASR related-problem in Thailand in mass foundation of a large infrastructure project was reported in 2009[7], [8]. During the first 10 years of service visual inspection reported extensive cracks of about 20 % of the surveyed footings and the continued expansion in the mass foundations. The typical grid pattern cracks of about 0.50 m apart, accompanied by randomly finer cracks [7]. Several causes of distress were eliminated and finally the two suspicious causes; ASR and DEF or Delayed Ettringite Formation, were focused and led to the detail investigation to confirm the root cause of

problem.

The expansion and cracking are characteristics of both ASR and DEF but the causes are different. ASR originated from unstable silica forms in aggregates react with alkali, in particular hydroxyl ion in pore solution, which directly related to sodium and potassium in cement. The product: alkali silica gel is capable of imbibing water from the surrounding, expand and cause cracking or other deficiencies as reported worldwide [9]. On the other hand, DEF is an internal sulfate attack caused from the later ettringite formation in hardened concrete. Several factors were found to relate to DEF occurrences such as sulfate in clinker, high temperature, alkali and water [10],[11]. Both ASR and DEF caused expansion, cracks and are often found in the same structure. The causes, timeline of occurrence and the possible correlation of these two processes are still being researched.

Due to these complications, six techniques were employed to identify the main deterioration cause of this case. These are: two screening tests, expansion test, microstructural and petrographic analysis and SEM/EDS. This paper presents the experimental detail and the results to provide the accurate diagnosis of the premature deterioration.

STUDY PROGRAM

Thirty-three concrete samples of 75 mm in diameter and 500 mm in length were randomly cored from 12 footings, in vertical and horizontal direction. After coring, all samples were carefully wrapped with paper, plastic wrap and kept in the air-tight plastic bag for later investigation process. After visual inspection in laboratory, samples were cut into 75 mm in diameter and 150 mm in length for compression test, to determine the concrete strength after ten years of service. Some were used for screening test and other investigation to investigate the main cause as the following.

Screening Test

Two simple qualitative methods using uranyl acetate solution and geochemical methods were applied on the new fresh cut surfaces of concrete discs to detect the evidence of alkali silica gel. The first, aimed to observe fluoresced greenish-yellow rim of the adsorbed uranyl ion exchanged with negative charge ion in gel, under ultraviolet light [12]. However, the fluorescence may also be found from ettringite as well as in carbonated concrete. The second, two substances of sodium cobalinitrite and rhodamine based were used to stain and detect K-rich Na-K-Ca-Si gels and alkali poor Ca-Si gels [13].

Accelerated Expansion Test

The cored samples of 150 mm in length, from different location were submerged in 38°C water for 24 hours first, reference lengths were then measured. The specimens were then put in two accelerating conditions. These were warm water of 38°C, and the 1M NaOH at 80°C, until the time of measurement, until 64 days.

Microstructural Analysis, Petrographic Analysis And SEM/EDS

In the first part, the thin slabs of about 10 mm thickness were cut parallel to the longitudinal axis of the core samples, impregnated with fluorescence dye and investigated visually and by stereo microscope under both ordinary polarizing and fluorescence light. To prepare specimens for the second part, the concrete samples were cut at the depth about 0.5-1cm below the surface, to avoid the carbonated part of concrete. Polished thin sections (TS) were carefully prepared to the thickness of 20 microns, coated with carbon and carefully examined under polarizing microscope mounted with UV- filters. The prepared polished thin sections were also examined with SEM/EDS technique, using Scanning Electron Microscope LEO 1450 VP mounted with a

Oxford Instrument model 7366 EDS.

RESULTS AND DISCUSSIONS

Screening Test

From uranyl acetate test, the 8 of 10 concrete samples showed the greenish- yellow rims under UV light, around some coarse aggregates, in some internal cracks and often, extended to cement paste as showed in Fig 1a. The different amount of the observed gel and their observed characteristics indicated the different severity level. The accumulated fluoresced glow found in some specific areas, as in (b), may indicate the potential collection of gel in the vicinity of the aggregates and the severe local reactivity. The evidences from this test were confirmed with the geochemical test in (c).

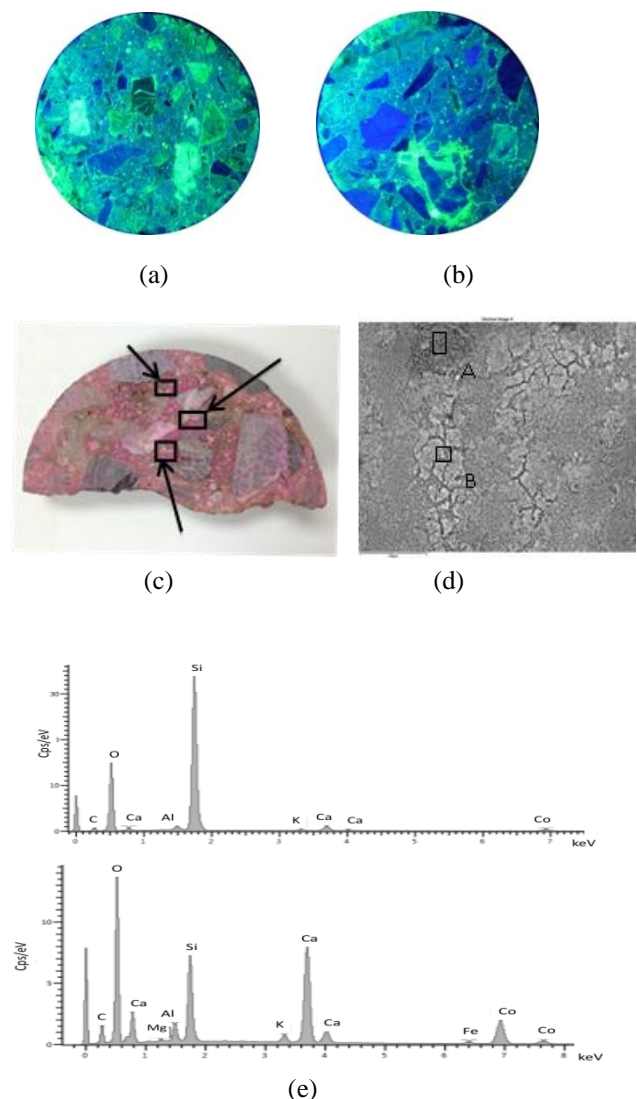


Fig. 1 samples under UV light in in uranyl acetate test, (a) high severity (b) very high severity, and (c) different stained color from geochemical test and (d) pecified area for SEM/EDX in (e), (e) analysis of stain on interface in area A and B

The example areas "A" and "B" of the observed stain, in (d) corresponding to geochemical test in (c) was investigated by SEM micrographs. The performed EDX analysis (e) showed high amount of Ca, Si, and O in pink area, particular high Si in "A" and high Ca in "B".

Expansion Test

The expansion under both accelerated conditions agreed well with the screening test result, particular from the uranyl acetate test. The calculated reactive aggregates area of the companion samples from the same core in Table 1, agreed well with the expansion in Fig.2 [14].

Table 1 Percentage of calculated area of reactive aggregates

C-ID	React.agg.		Non react.agg.	
	Area, cm ²	%	Area, cm ²	%
A	6.9	47.3	7.7	52.7
C	1.0	8.1	11.3	91.9
D	10.5	65.9	5.4	34.1

Note: C-ID= core ID

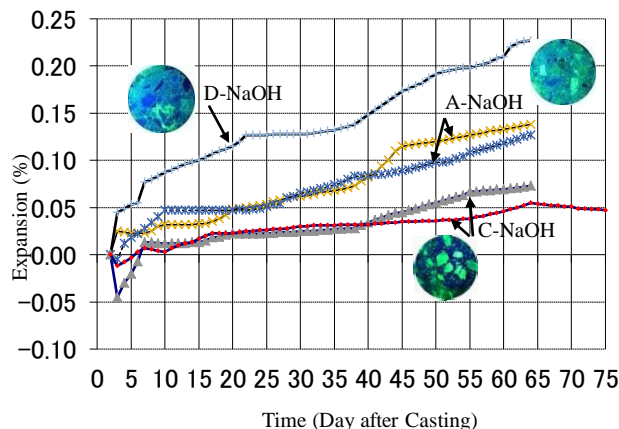


Fig. 2 Expansion of core samples in different accelerated conditions [7]

Both high temperature and alkali environment accelerated ASR reactivity of aggregates but not DEF. Large expansion of samples D and A in NaOH 80°C confirmed ASR occurrence. The results supported the observed-continued expansion in the field. The much smaller expansion of sample C in similar condition and even observed shrinking in warm water confirmed the small effect of ASR. Warm water promoted both ASR and DEF, but the alkali leaching effect may retard ASR while accelerate DEF [14].

Microstructural Analysis

Analysis of the thin slab showed cracks in paste, in Interfacial Transition Zone (ITZ) around reactive aggregates and inside aggregates. Several microcracks in reacted coarse aggregates sometimes continued into cement paste and connected between aggregates as shown by circle in Fig.3(a), suggesting the detrimental ASR in an advanced stage. The high intensity of microcracks in paste was observed. This confirmed the findings from screening test of most ASR- affected samples. Two special features similar to those of widely reported in slow reactive aggregates were observed [15]. As shown in TS sample under the fluorescence light in (b), a lot of fine cracks were observed near the edge of aggregate and the forming of outer dense zone (show by the arrow). Under the polarized light in (c), the crack inside reacted aggregate connected to the paste and brownish reaction products (arrows) was observed. Cryptocrystalline reaction products were observed in some reacted aggregates but insignificant amount of amorphous gel was found except in the contact zone near cement paste. Ettringite in cracks in cement paste (arrows) were also observed.

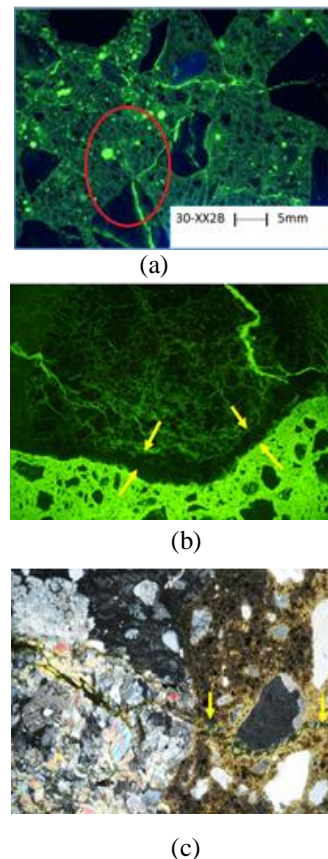


Fig. 3 (a) cracks in paste, around ITZ and inside aggregates (b) the dense zone in reactive aggregate and internal microcracks (c) continued aggregate's crack into paste

Petrographic Analysis

The investigated polished thin sections (TS) showed that the majority of the coarse aggregates were granitic rocks, quartz with mica traces and sericite contained feldspar, quartz and muscovite. Black quartzite with pyrite was also observed in samples. Typical microcracks in paste of 10-25 micron wide and filled with ASR gel were observed as well as cracks in ITZ as shown by arrows in Fig.4 (a). Delayed ettringite formation (DEF) was also found in both air voids (mostly spherical, less than 1 mm) as in (b) and lining in some ITZ cracks with some ASR extrusion products. The evidence of gel extrusion from reactive aggregates, particular sericite cut into the cracks around ITZ originally filled with DEF as previously reported [16] as also shown in Fig.3 (c). These showed that the results obtained from these techniques provided both useful information and possible clues as to the cause and timeline of the deterioration.

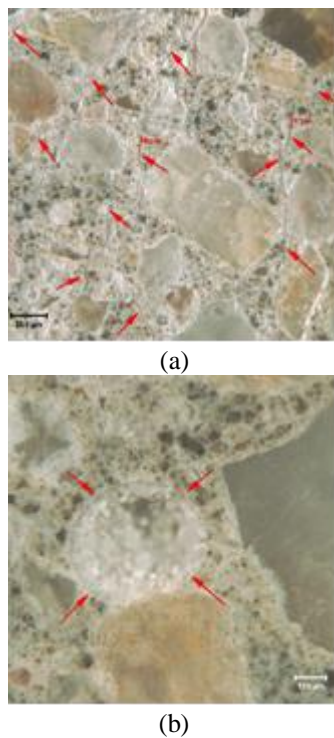


Fig. 4 (a) microcracks in paste filled with ASR gel (b) air void filled with ettringite

SEM/EDX

The morphological study of products identified two types of gel as shown in Fig.5. Most amorphous gels, often with shrinkage cracks, were found in cement paste cracks and ITZ as in (a) (under Back-scattered Electrons, BSE). Cryptocrystalline gels were normally found in internal cracks of sericite or also in some granitic aggregates without cataclastic

texture. Developed cryptocrystalline gel surrounded by gel in the reacted sericite rock are shown in (b).

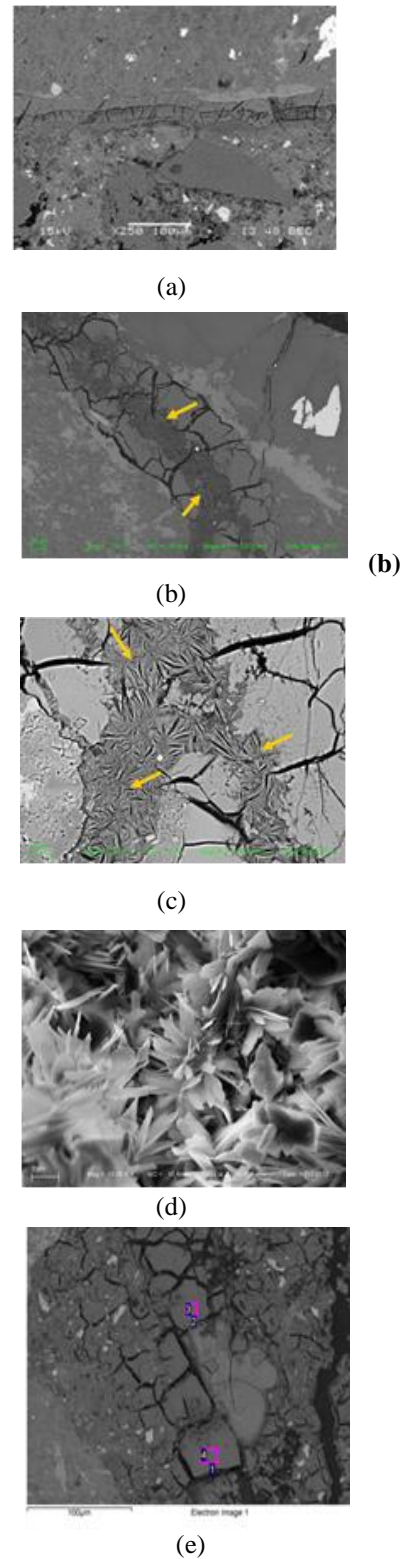


Fig. 5 (a) internal microcrack in paste, filled with ASR gel (b) cryptocrystalline gel in crack (c) the closed detail of gel in (b) (d) the rosette form of gel in sericite rock (e) close-up of gel in cement paste

The enlarged area (c) shows cryptocrystalline globular reaction products (arrows) among the surrounding gel. These secondary crystalline products internally occur in the crack are believed to be crystallised from the precursor gel. The plate formed crystals in rosette formed agglomerates from a fragment of sericite rock were also observed as in (d). The example of detail analysis of gel in crack in (e) is shown in Table 2

Table 2 Detail analysis of gel in each location in cement paste in (e)

Processing option: Oxygen by Stoichiometry (Normalised)

Spectrum	In stats.	Mg	Al	Si	Ca	Total
1	No	1.21	1.81	92.1	4.89	100.0
2	No		2.10	92.4	5.50	100.0
3	No		3.39	92.1	4.47	100.0
4	No	1.25	3.12	01.1	4.49	100.0
Max.		0.00	0.00	0.00	0.00	
Min.		0.00	0.00	0.00	0.00	

Note: all results in compounds %

In general, gel products in cement paste's crack were composed of silica, aluminium and calcium, but the slight different compositions were found in different observed areas. Gels in reacted aggregates-cracks contained higher potassium and sodium compared to those in paste and ITZ. Alkali ions in gel found in cement paste were probably "reduced" by reaction by the cement paste as reported in the literature [17]

CONCLUSIONS

1. Several techniques can be combined and effectively used to identify ASR, as the primary cause of deterioration and the continued expansion of the investigated structures.

2. Both simple qualitative screening tests agreed well with the results of other tests, particularly the expansion test, but other techniques must be used for further confirmation.

3. The expansion test in different environments can identify the behaviors under the acceleration conditions which led to the suggested cause of problem. The detail studies from microstructure analysis, petrographic analysis and SEM/EDS confirmed the cause of the problem, identifying materials and significant features, in both qualitative and quantitative aspects.

4. Two forms of ASR gel were observed; amorphous gel found in cracks in cement paste, ITZ and some air voids, and cryptocrystalline gel found mostly in aggregates cracks. DEF was also found in cracks and air void, but there was no correlation to

the continued expansion.

ACKNOWLEDGEMENTS

The authors acknowledge funding supports from the Faculty of Engineering, Kasetsart University and Kasetsart University Research and Development Institute (KURDI).

REFERENCES

- [1] Stanton T.E., Influence of cement and aggregate on concrete expansion, Eng News-Rec. 123(5), 1940, pp. 59-61.
- [2] Stanton T.E., Expansion of concrete through reaction between cement and aggregate, T Am Soc Civ Eng. 107(1), 1942, pp.54-84.
- [3] Thomas M., Dunster A., Nixon P. and Blackwell B., Effect of fly ash on the expansion of concrete due to alkali-silica reaction-exposure site studies, Cem. Concr Compos. 33, 2011, pp. 359-367.
- [4] RILEM Working Group (TC 191), Guide to diagnosis and appraisal of AAR damage to concrete in structures: Part 1 Diagnosis (AAR 6.1), in: B. Godart, M.de Rooji, and J.G.M. Wood (Eds.), RILEM State-of-the Art-Reports vol. 12, 2013.
- [5] ASTM, Standard Test Method for Potential Alkali Reactivity of Aggregates (Mortar-Bar Method): ASTM C 1260, 2003.
- [6] Du-You L., Fournier B., and Grattan-Bellew P.E., Evaluation of the Chinese Accelerated Test for alkali-carbonate reaction, J. ASTM Int. 3, 2006, pp.1-10.
- [7] Sujjavanich S., Suwanvitaya P., and Rothstein D., Investigation of ASR in mass concrete structures: A case study, in: S.O. Cheung, S. Yazdani, N. Ghafoori and A. Singh (Eds.), Modern Methods and Advances in Structural Engineering and Construction, 2011.
- [8] Sujjavanich, S., Won-In, K., Meesak, T., Wongkamjan, W., & Jensen, V. Investigation of Potential Alkali-Silica Reactivity of Aggregates Sources in Thailand, International Journal of GEOMATE, Vol.13, Issue 35, 2017. pp. 108-113.
- [9] Swamy R.N., The Alkali-Silica Reaction in Concrete. Taylor & Francis e-Library, 2003.
- [10] Grantham M.G., Gray M.J., and Eden M.A., Delayed ettringite formation in foundation bases, A case study, Structural Faults + Repair-99., 1999.
- [11] Famy C., Scrivener K.L., Atkinson A., and Brough A.R., Influence of the storage conditions on the dimensional changes of heat-cured mortars, Cem.Conc. Res. 31, 2001, pp. 795-803.
- [12] ASTM, Standard Practice for Petrographic Examination of Hardened Concrete, in Annual

- Book of ASTM Standards Vol 04.02 Concrete and Aggregates ASTM C 856 – 04, 2004.
- [13] Guthrie J.G.D., and Carey J.W., A simple environmentally friendly , and chemically specific method for the identification and evaluation of the alkali -silica reaction, Cem.Conc. Res. 21, 1997, pp.1407-1417.
- [14] ACI Committee 221, State-of-the-Art Report on Alkali-Aggregate Reactivity: ACI 221.1R-98, American Concrete Institute, 1998.
- [15] Jensen V., Alkali aggregate reaction in Southern Norway, Doctoral, University of Trondheim (NTH), Trondheim, 1993.
- [16] Jensen V. and Sujjavanich S., ASR and DEF in concrete foundation in Thailand, in Pro. of the 15th Int. Conf. on Alkali-Aggregate Reaction: Alkali -Aggregate Reactions in Concrete, Brazil, 2016.
- [17] S. Diamond, R.S.Jr. Barneyback, and L.J. Struble, Physics and chemistry of alkali-silica reactions, in Proc. of the 5th Int. Conf. on Alkali-Aggregate Reaction: Alkali -Aggregate Reactions in Concrete, South Africa, 1981.

BACK PROPAGATION ARTIFICIAL NEURAL NETWORK MODELING OF FLEXURAL AND COMPRESSIVE STRENGTH OF CONCRETE REINFORCED WITH POLYPROPYLENE FIBERS

Stephen John C. Clemente¹, Edward Caesar D.C. Alimorong² and Nolan C. Concha³
^{1,2,3}Civil Engineering department, FEU Institute of Technology, Manila, Philippines

ABSTRACT

The production of fiber reinforced concrete involves a complex reaction system. This imposes an immense challenge in deriving appropriate material proportions of concrete to achieve desirable mechanical properties. In order to facilitate selection of design matrix for fiber reinforced concrete, a novel artificial Neural Network models for compressive and flexural strengths using back propagation feed forward algorithm were proposed in this research. A wide range of varied concrete design mixes of cylindrical and beam samples were respectively tested for compressive and flexural tests. A polypropylene type of fiber reinforcement was used in the preparation of samples that were cured for 28 days in a water saturated lime. Results showed that the compressive and flexural strength models provided predictions in good agreement with experimental results as described by high correlation values of 99.46% and 98.57% respectively. Mean squared errors of 0.0024 and 0.44 were obtained respectively in selecting the best fit model for compressive and flexural strengths. In the parametric analysis conducted, the proposed models were able to describe analytically the constitutive relationships of the material components and capture the dominant characteristics of concrete samples.

Keywords: Concrete, Fiber reinforcement, Flexural strength, Compressive strength, Artificial neural network

INTRODUCTION

Fiber reinforced polymer remains a highlight in the development of concrete technology to deliver better performance and sustainability of concrete structures. This short discrete fibrous material that is introduced in the concrete mix enhances both the mechanical and serviceability performance of concrete. The efficiency of fiber reinforced concrete is dependent on the proportions of material components. The fiber material type such as Polypropylene, Nylon, and steel fibers offer individual distinct benefits. In some cases blending is necessary to integrate the desirable properties [1-4]. In the study of Hsie et al. [5] the hybridization of two different forms of polypropylene fibers offered 24.6% increase in the flexural strength of beams tested using third point loading. Combined steel and polymer fibers improved resistance of the concrete in the development of cracks [6]. Shape, dosage, distribution, and orientation in particular are also key factors in developing high performance concrete [7] – [9]. Various studies were conducted to develop guidelines for engineers to properly design fiber reinforced concrete [10] – [14].

In the interest of providing prediction models on the mechanical performance of concrete with fiber reinforcement, adaptation of system simplifications in parallel with destructive testing of concrete is necessary. In understanding the micromechanical

properties and geometry of concrete samples with arbitrarily dispersed fibers, an explicit analytical model in predicting the flexural resistance of concrete was developed [15]. The model utilized the concrete components and sample geometry and provided estimated results in good agreement with values obtained from the experiment. The effect of fibers on the flexural strength of concrete as well as the interactions of the concrete components is complex in nature. The use of Artificial Neural Network (ANN) can work on such system to capture the complex nonlinear relationships between the variables [16] – [19]. Neural network is a powerful algorithm that process information based on the biology of human nervous system. The algorithm is allowed to learn from an existing training data of input-output observations forming a network of interconnected neurons that can estimate values from a large number of inputs. ANN was used to develop shear capacity model of concrete beams and compared with different existing models available in the literature [20]. The derived equation provided high accuracy in forecasting shear strengths in comparison with results from laboratory tests.

The mechanism of the interaction of material components in the mixture defines the overall resistance of hardened concrete. It is hardly possible to obtain a suitable design concrete mix without understanding the contribution of every material component in the flexural performance of concrete.

There are simplified assumptions considered in developing empirical, numerical, and analytical models that are inconsistent with actual concrete mixture conditions. This in turn provides significant deviations of the predicted values against experimental results. In the presence of highly complicated interactions involve in the system, neural network is found to be useful to develop the models [21]. This method is proven to be effective and convenient means of analyzing complex relationships from nonlinear data. Thus a novel prediction model using artificial neural network for flexural strength of fiber reinforced concrete is proposed in this study. The equation will be able to identify the actual properties of the concrete matrix eliminating ideal assumptions and thereby expected to provide realistic prediction results in a simple and rapid approach.

METHODOLOGY

Reinforcing Fiber

The reinforcing fiber used in this study was polypropylene with a tensile strength of 570 to 660 MPa. The length of the fiber varies from 38mm to 54mm with a specific gravity of 0.91 that conforms to the standard of ASTM C1116 (Standard Specification for Fiber-Reinforced Concrete). The fiber used was a blend of two fibers, the first one is the standard fibrillated polypropylene fiber that can control temperature cracks and the other one is monofilament fiber made from synthetic copolymer that has significant contribution to post crack performance.

Mixture Composition

Forty mixtures with different amounts of cement, sand, gravel, water and fiber reinforcement were produced and used as input data for the models. The mixtures in 6''x6''x21'' beam mold and 6'' diameter x 12'' height cylindrical mold were tested for compressive and flexural strengths, respectively. Center point loading was used for the testing of flexural strength and compressive strength test for the cylinders. The samples were cured in water for 27 days, air dried for a day and tested at the 28th day. The maximum and minimum amount of each parameter was reflected in Table I.

Table 1 Mixture composition

	w/c	cement kg/m ³	water kg/m ³	sand kg/m ³	gravel kg/m ³	fiber kg/m ³
max	0.5	460	153	950	1050	1.80
min	0.3	300	138	820	920	1.00

ANN Modeling

The researchers utilized ANN toolbox from Matlab 2015b for the creation of models to forecast the flexural resistance and compressive strength of fiber reinforced concrete. Eighty five percent of the data were used as training and validation of the models. The remaining 15% were utilized as testing for the accuracy of the models. The researchers applied feed forward back propagation algorithm for modeling. The best models were selected based on the least value of Mean Squared Error (MSE) [22-23]. Fig.1 shows an example of an ANN structure that will be derived from the results of training. Biases and weights are the key components being optimized to yield better prediction of the models.

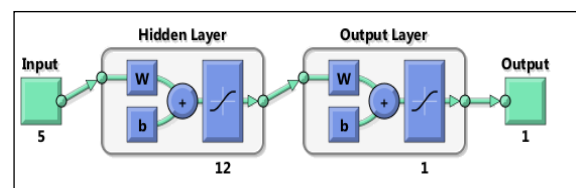


Fig. 1 Artificial neural network structure.

RESULTS AND DISCUSSION

Mechanical Tests

Table II shows the minimum and maximum flexural and compressive strengths of all samples. These results were used as output data for the ANN modeling and accuracy test of the derived models.

Table 2 Mechanical test result

	flexural test MPa	28 th day compressive test MPa
max	6.07	38.00
min	1.90	20.67

Table III show results of Pearson Coefficient (P) and Regression (R), cement (0.92 and 0.89) and water (0.72 and 0.81) are the two factors significantly contributing to the strength of the concrete mixture. Although not significant (0.19 and 0.15), polypropylene fiber reinforcement imparts additional strength to both flexural and compressive. The main purpose of the fiber in concrete is to minimize the micro cracks that will yield to long term deflection and durability. In general, both concrete strength demonstrates positive linear association with cement and negative for water as described by their respective correlation coefficients.

Table 3 Statistical analysis

material	statistic	fb	fc'
cement	R	0.921095	0.888967
	P	3.76E-17	1.86E-14
water	R	-0.71762	0.814452
	P	1.87E-07	1.62E-10
sand	R	0.159918	0.154527
	P	0.32428	0.341067
gravel	R	0.071629	0.048801
	P	0.660499	0.764911
fiber	R	0.192133	0.153558
	P	0.23494	0.344139

Artificial Neural Network Modeling

The set of data were split for the three phases of modeling which are training, validation, and testing as shown in Fig. 2 and Fig. 3. Training data composed of 70% of the total data and 15% for the validation data were used in the derivation of the models. Validation data was simultaneously simulated on the derived model which was created based on the training data. The validation was used as a tool to minimized the over-fitting which is the typical problem for ANN modeling. The mean squared errors for validation of flexural strength and compressive strengths models was 0.0024 and 0.44 respectively.

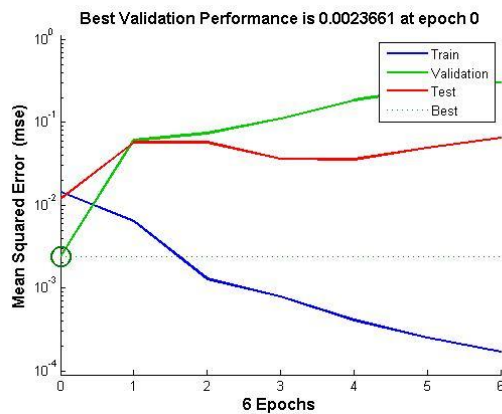


Fig. 2 Validation performance for flexural model.

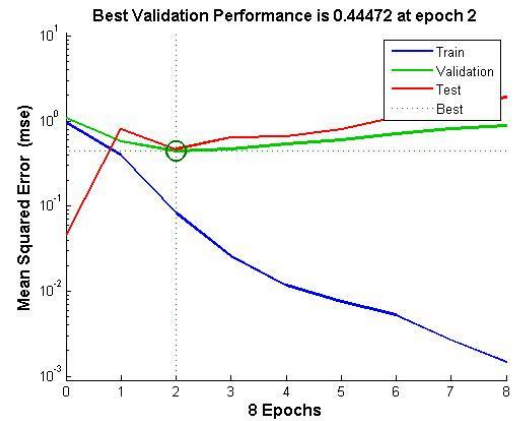


Fig. 3 Validation performance for flexural model.

Simulations

Remaining 15% of the data was independently used to test the accuracy of the models. The recorded R values of 0.995 and 0.986 for flexural and compressive strength models respectively represents a highly correlated results as shown in fig. 4 and fig. 5. These values provided accurate model prediction in excellent agreement with experimental results.

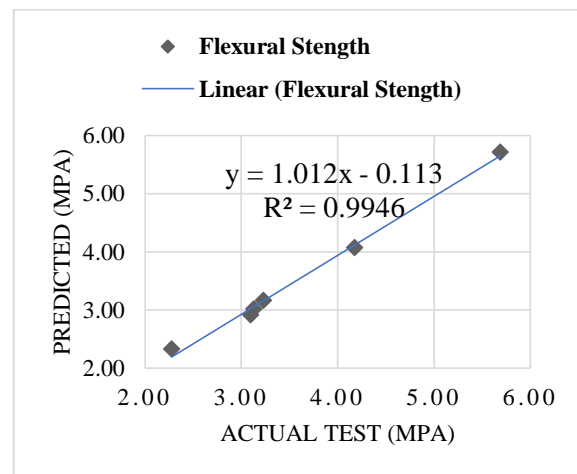


Fig. 4 Accuracy test - flexural.

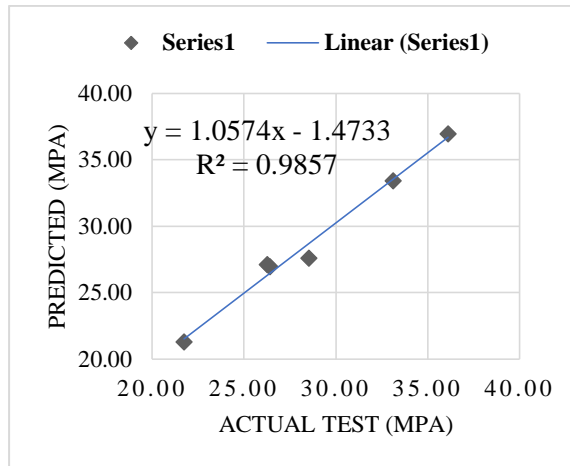


Fig. 5 Accuracy test - compressive.

Parametric Study

Parametric study for the fiber content was conducted to show the impact to the strength of concrete. Five increment of fiber content were used. Mixture with the term “high” and “low” was based on the mixture that yields the maximum and minimum flexural and compressive strength from the actual test. An increase of 29.79% for high and 51.43% for low of flexural strength were obtained when the dosage of fiber was increased from 1 kg/m³ to 1.8 kg/m³. Compared to flexural strength, fibers contributed minimal enhancement for compressive strength, 14.18% and 17.88% for high and low respectively as shown in Fig. 6 and Fig. 7. It was evident that there is no significant increase in the compressive strength of concrete from 1.6 kg/m³ [24]

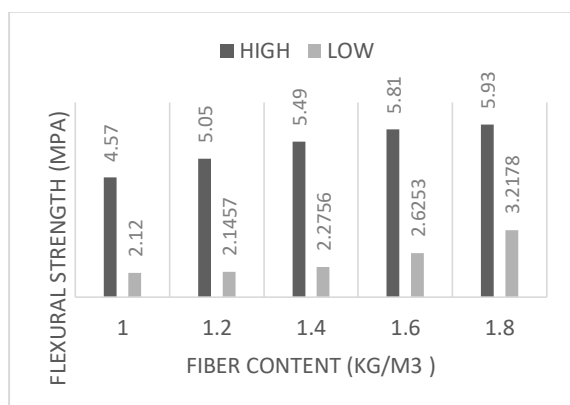


Fig. 6 Parametric study - flexural.

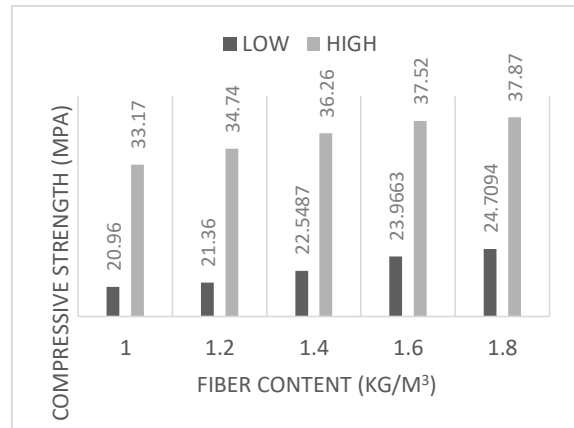


Fig. 7 Parametric study - compressive.

CONCLUSION

The models derived using Neural Network showed satisfactory predicting ability for both flexural and compressive strength of concrete as described by highly correlated R values above 0.98. The models were able to provide prediction results in good agreement with experimental values. Compressive strength and flexural resistance are at the highest when the fiber content is at 1.8kg per cubic meter of mix.

An increase of 29.79% and 51.43% were recorded for low and high flexural strengths corresponding to an addition of 1 kg/m³ to 1.8 kg/m³ of fiber reinforcement.

An increase of 14.18% and 17.88% were recorded for high and low compressive strengths corresponding to an addition of 1 kg/m³ to 1.8 kg/m³ of fiber reinforcement. The added compressive and flexural strength of fiber in concrete may vary in its distribution throughout the mixture. It is necessary to use mixer in the preparation of the mixtures [25].

ACKNOWLEDGEMENT

The researchers would like to give credit to the Far Eastern University Institute of Technology for the unending support to the study, furthermore, to the Civil Engineering Department for their cognitive ideas that are helpful to the research. Lastly, to our director, Engr. Orlando P. Lopez for his initiatives to pursue the study.

REFERENCE

- [1] P. Rossi, G. Chanvillard G (eds), "Fibre Reinforced Concretes. In: RILEM Proceedings of the 5th RILEM Symposium (BEFIB 2000) ", PRO15. RILEM Publications S.A.R.L., Bagneux, France, 2000.
- [2] P. Song, S. Hwang and B. Sheu, "Strength properties of nylon- and polypropylene-fiber-reinforced concretes", *Cement and Concrete Research*, vol. 35, no. 8, pp. 1546-1550, 2005.

- [3] H. Reinhardt, A. Naaman, "High Performance Fibre Reinforced Cement Composites (HPFRCC5) ", Rilem Publication S.A.R.L., PRO5, 2005.
- [4] R. Gettu, "Fibre Reinforced Concrete: design and applications", Bagnaux, France, RILEM Publications S.A.R.L., PRO60, 2008.
- [5] M. Hsie, C. Tu and P. Song, "Mechanical properties of polypropylene hybrid fiber-reinforced concrete", *Materials Science and Engineering: A*, 494(1), 153-157, 2008.
- [6] N. Banthia and N. Nandakumar, "Crack growth resistance of hybrid fiber reinforced cement composites", *Cement and Concrete Composites*, 25(1), 3-9, 2003.
- [7] R. Zollo, "Fiber-reinforced concrete: an overview after 30 years of development", *Cement and Concrete Composites*, 19(2), 107-122, 1997.
- [8] S. Barnett, J. Lataste, T. Parry, S. Millard and M. Soutsos, "Assessment of fibre orientation in ultra high performance fibre reinforced concrete and its effect on flexural strength", *Materials and Structures*, 43(7), 1009-1023, 2010.
- [9] N. Banthia and R. Gupta, "Influence of polypropylene fiber geometry on plastic shrinkage cracking in concrete", *Cement and Concrete Research*, 36(7), 1263-1267, 2006.
- [10] M. Di Prisco, G. Plizzari and L. Vandewalle, "Fibre reinforced concrete: new design perspectives", *Materials and Structures*, 42(9), 1261-1281, 2009.
- [11] ACI Committee 318, "Building code and commentary, Report ACI 318-08/318R-08", American Concrete Institute, Farmington Hills, 2008.
- [12] L. Vandewalle, "Recommendation of Rilem TC162-TDF: test and design methods for steel fibre reinforced concrete: design of steel fibre reinforced concrete using the r-w method: principles and applications", *Mater Struct* 35:262-278, 2002.
- [13] A. Deutscher, "Guidelines for steel fiber reinforced concrete"—23th Draft—richtlinie Stahlfaserbeton—DIN 1045 Annex parts 1-4, August 2007.
- [14] CNR-DT 204, "Guidelines for design, construction and production control of fiber reinforced concrete structures", National Research Council of Italy, Italy, 2006.
- [15] L. Vandewalle, "Recommendation of Rilem TC162-TDF: test and design methods for steel fibre reinforced concrete: design of steel fibre reinforced concrete using the r-w method: principles and applications", *Mater Struct* 35:262-278, 2002.
- [16] F. Yan and Z. Lin, "New strategy for anchorage reliability assessment of GFRP bars to concrete using hybrid artificial neural network with genetic algorithm", *Composites Part B: Engineering*, 92, 420-433, 2016.
- [17] M. Mashrei, R. Seracino and M. Rahman, "Application of artificial neural networks to predict the bond strength of FRP-to-concrete joints", *Construction and Building Materials*, 40, 812-821, 2013.
- [18] N. Concha, "Rheological Optimization of Self Compacting Concrete with Sodium Lignosulfate Based Accelerant Using Hybrid Neural Network-Genetic Algorithm." *Materials Science Forum*. Vol. 866. Trans Tech Publications, 2016.
- [19] N. Concha and , E. Dadios. "Optimization of the rheological properties of self compacting concrete using neural network and genetic algorithm." *Humanoid, Nanotechnology, Information Technology, Communication and Control, Environment and Management (HNICEM), 2015 International Conference on*. IEEE, 2015.
- [20] R. Perera, M. Barchín, A. Arteaga and A. De Diego, "Prediction of the ultimate strength of reinforced concrete beams FRP-strengthened in shear using neural networks" *Composites Part B: Engineering*, 41(4), 287-298, 2010.
- [21] Clemente, S.J.C. & Oreta, A.W.C. (2015). Artificial neural network modeling og rheological parameters and compressive strength of self-compacting concrete with zeolite mineral as partial replacement for cement. Manuscript, De La Salle University, Manila.
- [22] Ongpeng, J., Soberano, M., Oreta, A., & Hirose, S. (2017). Artificial neural network model using ultrasonic test results to predict compressive stress in concrete. *Compt,Concr*, 19, 59-68.
- [23] Roxas, C.L.C., & Ongpeng, J.M.C. (2014, March). An artificial neural network approach to structural cost estimation of building projects in the Philippines. In *Proc. DLSU Research Congress*.
- [24] Song, P. S., & Hwang, S. (2004). Mechanical properties of high-strength steel fiber-reinforced concrete. *Construction and Building Materials*, 18(9), 669-673.
- [25] Song, P. S., & Hwang, S. (2004). Mechanical properties of high-strength steel fiber-reinforced concrete. *Construction and Building Materials*, 18(9), 669-673.

EFFECT OF MANUFACTURED DOLOMITIC LIMESTONE SAND AS ALTERNATIVE FINE AGGREGATES FOR SHOTCRETE WET-MIX APPLICATION

Benedicto, Patrizia S.¹, Calaywan, Juan Fidel B.¹, Ebueng, Rio Jocelle A.¹, and Matba, Ylam Shalev dT.¹

¹Department of Mining, Metallurgical, and Materials Engineering, University of the Philippines – Diliman,
Quezon City, Philippines

ABSTRACT

One solution to meet the demand for depleting natural sand sources is by using manufactured aggregates. The production of manufactured aggregates unavoidably produce particles finer than 5mm dolomitic limestone sand (S1) as by-products. This study evaluated concrete with S1 sand as fine aggregates for its uniaxial compressive strength (ASTM-C31/C31M), flexural strength by third point loading (ASTM-C78/C78M), slumping (ASTM-C143/C143M), and rebound percentage (JSCE-F563-2005) in three levels with each having three replicates. After 28 days of dry curing, compressive strength results showed a significant difference ($\alpha=5\%$) with 100% river sand (RS) having higher average than 100%S1 at 28.22MPa and 13.66MPa, respectively. The rebound rate and flexural strength results confirmed no significant difference for 100%S1 (21.98% and 3.54MPa) and 100%RS (35.13% and 4.77MPa) averages, respectively. Data curves were generated to show that slump tests having S1 admixtures required higher water content (1.39:1) for the same slump height in 100%RS (1.89:1).

Keywords: Manufactured fine aggregates; Wet-mix shotcrete; Dolomitic limestone; Rebound rate

INTRODUCTION

Manufactured dolomitic limestone sand (in this study, will be referred to as S1 sand) are produced as end by-products of the aggregates manufacturing process, and its unavoidable production has led to the accumulation of large stockpiles that have now taken up a huge amount of space in the Republic Aggregates Bulacan (RAB) plant. S1 sand particles are smaller than 5mm, which are produced from a series of screening and comminution operations. Natural sand is usually used in concrete mixes because it is readily available and can be mixed easily with other materials. But sand mining can have several impacts on the river environment, it changes the channel form and disturbs the river's ecosystem [1]. Laws like Executive Order No. 224 are implemented in the Philippines, it states that local taxes, fees and charges will be collected from legitimate sand and gravel operators or permit holders which is why sand mining can be very expensive. There is therefore a significant need to find alternative sources of fine aggregates to replace the use of natural sand.

Manufactured sand differs from natural river sand (RS) in terms of shape, grading and content of stone powder (micro fines), therefore the properties (workability, water demand, mechanical properties) and durability of manufactured sand concrete also differs from RS concrete [2]. The particles of

manufactured sand have and angular shape while RS has a rounded shape and a smoother surface [3]. The shape of the particles can affect the compressive and flexural strength of the shotcrete [4].

This study focused on using S1 sand as alternative fine aggregate for shotcrete wet-mix. Shotcrete is one of the commonly used stabilization system for secondary rock support and has been used for ground support applications for more than 50 years [5]. According to ACI 506.2-95 (Specification for Shotcrete), shotcrete is a mortar or concrete that is pneumatically projected onto a surface at high velocity. Mortar is a mixture of fine aggregates, cement and water while concrete is a composite material that is composed of coarse and fine aggregates, cement and water. There are two types of shotcrete application: dry-mix and wet-mix. Compared with the dry-mix process, the wet-mix shotcrete process produces less wasteful rebound, dust, and facilitate placement of larger mixture volumes in a shorter time period [6]. In application to mining, shotcrete is used for stabilization inside underground tunnels or final pit slope in surface mines. The wet mix shotcrete process also enables mixing of all the ingredients with any type of admixtures and required additives. It also commonly uses natural aggregates from river, land, and sea sand because of their abundance [7].

FUNDAMENTALS OF WET-MIX SHOTCRETE

Manufactured fine aggregates are process-controlled, crushed aggregate produced from quarried stone by crushing or grinding, and the subsequent screening to obtain a controlled gradation product which pass through sieves with sizes like 9.5 mm. The “dust-of fracture” or microfine particles are produced as a result of the deliberate fracturing of the rock for aggregate production. This dust typically passes through the No. 200 sieve (75 μm). Because of this dust, manufactured fine aggregates contain finer particles than natural river sand (RS) [8].

Crushed aggregates generally contain more angular particles with flatter faces and rougher surface textures than natural sands, which are more rounded as a result of weathering over time [8]. Because it has more angular particles, more voids are also present [9].

The amount of water, cement, and both fine and coarse aggregates are crucial to the optimization of the concrete, and therefore of shotcrete as well. Shotcrete differs from concrete not only by the method of application but also by their mixture proportions. Unlike concrete, shotcrete contains a bigger percentage of fine aggregates compared to the coarse aggregates in the mixture. Fine aggregates have greater surface areas, therefore there is more water demand for shotcrete as compared to concrete because it contains more fine aggregates [8].

The water demand is also greater when manufactured fine aggregates are used since its particles are more angular. In a study conducted by Nichols (1982), the water demand increases for concrete with a given slump as the angularity increases and it contains more microfine particles. Therefore, mixtures containing manufactured sand require more water to obtain the same slump with those made with natural sand [9].

Rebound comes with the placement of both wet-mix and dry-mix shotcrete. However, there is less rebound in the wet-mix application. It signifies the shootability of wet-mix shotcrete. It generates losses and, in turn, the cost increases, therefore it must be minimized. However, it is complementary to the pumpability, indicated by the slump test, of the mixture [7]. Therefore, it is important to find the balance between the two factors.

Compressive strength has little direct correlation with the durability of concrete in general. However, it is the most commonly specified material parameter for the acceptance of concrete as it is the capacity of the material to withstand loads, and is therefore essential to concrete and shotcrete studies. In a study made by Ahmed and El-Kourid (1989) about the behavior of concrete made with different amounts of microfine aggregates, it was observed that with a constant slump, the water demand increases [10]. It

would then result to a lower compressive strength. The decrease in compressive strength was also attributed to the higher angularity of the manufactured fine aggregates, which increased the void content of the concrete mixture [8]. According to a study conducted by Rhesi (1983) and another one by Borhan (2016), the increase of MgO content also resulted to a decrease in the compressive strength of the concrete especially at later ages [11]-[12].

Since shotcrete is used as structure support and stabilization, it is important that the flexural strength be determined. In a study conducted by Celik and Marar (1996) [8] as the microfine aggregates increased, the 28-day flexural strength decreased 10 percent as compared to the control concrete mixture with no dust, with the mixtures having different water contents to achieve the same slump. Like the compressive strength, the water content had the most significant influence on the flexural strength of the concrete.

LABORATORY SAMPLING OF FINE AGGREGATE SAMPLES

Materials

Aggregates

Crushed basalt with a maximum size of 9.5mm was used. For the control sample design mix, natural river sand was employed as fine aggregates. S1 sand, characterized as crushed dolomitic limestone particles smaller than 5mm, were used for replacement in different set levels. The S1 sand has a specific gravity of 2.709.

Cement

A PNS 63-2006 accredited 49.8 grade commercial ordinary Portland cement (OPC) was used as the primary binder for the slump test, compressive strength test, and third-point loading flexural strength test. Table 1 shows the physical and chemical properties of the aforementioned cement binder.

Mixture Proportions

Tests carried out in this paper followed a design mix based on American Concrete Institute guidelines and other related literature which based calculations from practical experiments. The mixture proportions listed in Table 2 were accustomed to slump tests (ASTM C143/C143M - Standard Test Method for Slump of Hydraulic-Cement Concrete) with values that range nearest to 3.00 inches [13]. Failed slump tests were still noted down and included in graphing to show the behavior of the mixtures at varying

cement-water ratios. The final mixture proportions which qualified the range were redone thrice for consistency of data, and the cement-water ratios for each level was made final throughout the experiment.

Experimental Methods

Preparation of test specimens

Uniaxial compressive strength molds with dimensions 4 in diameter by 8 in length were casted 28 days prior to testing. The same number of concrete beams with dimensions 6 in x 6 in x 21 in were also casted 28 days prior to flexural testing in the laboratory. Both concrete mold preparation procedures were dry cured and carried out with accordance to ASTM C192/C192M (Standard practice for making and curing concrete test specimens in the laboratory) [14].

Physical and chemical properties of fine aggregates

The fineness modulus defines the proportions between fine and coarse aggregates in the mixture. The S1 sand's fineness modulus value of 3.18 failed the standard for fine aggregate mixtures of 2.3 to 3.1 according to the ASTM C33/C33M (Standard Specification for Concrete Aggregates) [15]. Materials finer than #200 sieve was 20.97% by weight based on ASTM C136/C136M (Standard Test Method for Sieve Analysis of Fine and Coarse Aggregates) [16]. To validate this specification, sieve analysis was conducted with a mechanical sieve shaker.

The S1 sand chemical properties were reported to have a CaO content of 30-40% and an MgO content of 10-12%, with the rest composed mostly of silica. RS sand, on the other hand, mostly contained SiO₂. S1 and RS samples were crushed manually using a mortar and pestle and were analyzed using X-Ray Diffraction (XRD) to confirm their mineral composition.

Measurement of hardened properties

Both compressive and flexural strength properties of the wet-mix shotcrete samples were measured using a Riehle Universal Testing Machine. The uniaxial compressive strength and third-point loading flexural strength tests were conducted in accordance with the ASTM C39/C39M (Standard Test Method for Compressive Strength of Cylindrical Concrete Specimens) and ASTM C78/C78M-18 (Standard Test Method for Flexural Strength of Concrete Using Simple Beam with Third-Point Loading), respectively [17]-[18].

Measurement of rebound rate

The process for measuring the rebound rate employed the use of an improvised shotcrete machine due to financial constraints in acquiring a commercially used machinery. The mixed fresh wet-mixture was conveyed through a 50-mm diameter hose with a length of only 12 inches excluding the nozzle. The nozzle had a diameter of only 38 mm, which is smaller than the hose to increase the velocity of the shotcrete pumping. The equipment included a water pump with a power of 3 HP. A 200 CFM air compressor was used at the nozzle tip during the pumping process.

In this study, rebound rate was evaluated in accordance with the slope stabilization requirements as specified in JSCE-F 563-2005 (Test Method of Rebound Percentage of Sprayed Concrete) by applying fresh wet-mix shotcrete into a 200 x 200 x 300 mm panel propped up 50 cm from the ground, angled at 70° (Figure 3.9). This was done after the panel was weighed. 25 kg of freshly mixed sample (using PPC instead of OPC) was sprayed onto the panel. The rebound rate was also evaluated based on calculations from JSCE-F 563-2005 [19]

$$W_s = W_1 + W_p \quad (1)$$

$$W_r = \frac{W_2 \times 100}{W_s + W_2} \quad (2)$$

where

W_s : Mass that has bonded on the form (kg)

W_p : Mass of the panel form (kg)

W_1 : Mass of the panel form and concrete bonded on it (kg)

W_r : Rebound ratio (%), and

W_2 : Mass of concrete rebound on the sheet (kg).

LABORATORY TESTING OF SHOTCRETE SAMPLES

Characteristics of the Fine Aggregates

Particle size analysis (Physical characteristics)

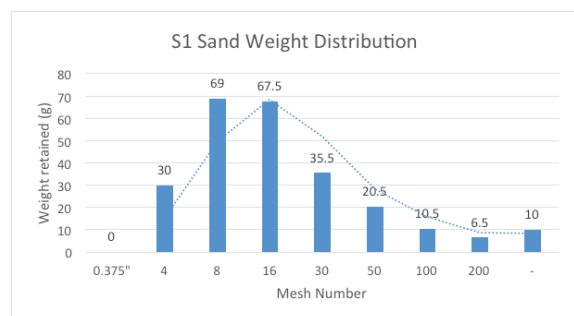


Fig 4.1. Weight distribution for the S1 sand.

Table 1. Physical & Chemical properties of Portland Cement Type 1P (Republic Portland Plus).

Fineness					Setting Time (Vicat Test)			Compressive Strength		
% Residue on 325 - M		(Blaine) Specific Surface, m²/kg, minimum			Time of Setting, Not less than	Time of Setting, Not more than		3 Days	7 Days	28 Days
7.1		382			217	376		15.8	21.1	30.1
CHEMICAL COMPONENTS										
SiO₂	Al₂O₃	Fe₂O₃	CaO	MgO	Loss of Ignition	Insoluble Residue		Sulfur Trioxide		Free Lime
25.7	7.2	5.2	49.8	3	4.2	--		2.8		0.96

Table 2. The layout of levels of concrete mixtures used in the experiment.

Set-up	Cement-water ratio (cm/w)	Weight Percentage in the Mixture (%)				Number of Replications
		Fine Aggregates	Coarse Aggregates	Cement	Water	
0% S1, 100% RS	1.86:1	45.48	24.38	19.73	10.61	3
50% S1, 50% RS	1.59:1	44.48	23.95	19.38	12.19	3
100% S1, 0% RS	1.39:1	43.71	23.54	19.05	13.70	3

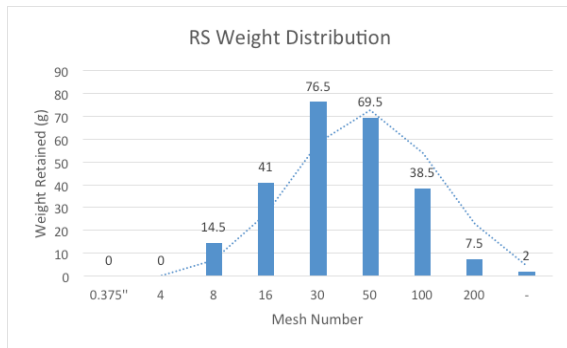


Fig. 4.2. Weight distribution for the RS sand.

Particle size analysis confirmed the particle size distribution of S1 sand from the quality control laboratory archive of RAB. This means that the S1 sand contained sand particle sizes as minute as 74 μm (#200 mesh), and as large as 4.76 mm (#4 mesh). This also showed the difference in particle weight distribution with RS. It can be observed by comparing Figures 4.1 and 4.2 that S1 sand had unusually more microfines than that of RS suggesting a higher total surface area for S1 sand and thus higher water content needed for the same value of slumping.

X-Ray Diffraction (Chemical characteristics)

The X-ray diffraction results were analyzed using the software Match!-Phase Identification from Powder Diffraction by Dr. Holger Putz. As shown in Figure 4.3 and Table 6, the obtained peaks for RS were indexed and matched and the main phase found was quartz (SiO₂). RS was mostly composed of quartz since it is the most frequent constituent of sand in inland continental settings. Quartz is also one of the most common mineral because almost every rock type contains quartz and it is also the most usual mineral resistant to weathering.

The obtained peaks for the S1 sand were also indexed and matched and the main phases were found to be dolomite (CaMg(CO₃)₂) and periclase or magnesium oxide (MgO). Both the dolomite and periclase are great sources of Mg. It is then confirmed that the S1 sand, which is crushed dolomitic limestone with an MgO percentage of 22.4%, exceeded the maximum amount of 6% for Portland Cement and blended hydraulic cement [20, 21].

Water content and slump

The slump of the fresh mixture was considered to

be the pumping performance factor in the study. This means that the mixtures of different levels would have the same consistency and workability in the shotcrete equipment if the cement-water ratio (cm/w) used in one level gives approximately the same slump for the other levels. The cm/w was supposed to be kept constant for all of the levels in the study. However, at the same cm/w, the slump of mixtures with 100% RS and 100% S1 were different, which indicated that there was a significant difference in their compositions and water absorptions.

For each level, test mixtures with varying cm/w were made to find the optimal ratio. The cm/w used for each level is the value that gave the slump that lies in the range of 3-3.5 inches (Figure 4.5). For 0% S1, the cm/w used was 1.86:1. On the other hand, 50% S1 used 1.59:1, and then 100% S1 used 1.39:1. These ratios were kept constant for each level and were used throughout the strength and rebound rate tests.

After the cm/w ratios were determined, the slump tests were each repeated three times for consistency of results. As shown in Table 8, the average slump values still fit in the range of 3-3.5 inches. With this, the consistencies and workabilities of the mixtures used throughout the study were kept constant. It shows, however, that concrete mixtures with S1 as its fine aggregates need more water to be optimum for shotcrete pumping as compared to mixtures with RS.

Effect of S1 on the Strength of the Wet-mix Shotcrete

Figure 4.6 shows the effect of the S1 sand to the compressive strength of the concrete samples after it was dry-cured for 28 days. From the figure, it can be observed that as the ratio of S1 sand was increased, the compressive strength decreased. The sample with 0% S1 had an average strength of 28.22 MPa, the sample with 50% S1 had an average strength of 19.55 MPa, and the one with 100% S1 had an average strength of 13.66 MPa.

From the PSA results in this study, S1 sand has more fine particles than river sand. The decrease in the compressive strength can be explained using the study made by Ahmed and El-Kourid in 1989, where it was concluded that the decrease in compressive strength is due to the increase of water content [10]

S1 sand has angular shaped particles compared to RS, which have rounded particles. This is because it was deliberately crushed and fractured, as compared to the RS, which was weathered over time. As supported by a study Nichols (1982), as the angularity of particle increased the amount of voids also increased which was another factor that caused the water requirement to increase as well. The voids formed in the cylinder sample made the samples with

more S1 sand weaker in terms of compressive strength [9].

The S1 sand contains 22.4% MgO according to the results of the X-Ray Diffraction. The decreasing compressive strengths of the samples made with increasing amounts of S1 sand suggests that the MgO in the S1 sand particles that passed through the No. 200 sieve reacted with water to form $Mg(OH)_2$. This led to inner stresses in the hardened samples, decreasing their compressive strengths.

The compressive strength of the samples made with S1 sand was significantly lower than that made of RS. It was shown in the statistical analysis by one-way ANOVA that at a confidence interval of 95%, the mean strengths (in MPa) are significantly different. It suggests that concrete made with S1 sand as fine aggregates was not competent in terms of compressive strength.

Figure 4.7 shows the effect of the S1 sand to the flexural strength of the concrete samples after it was dry-cured for 28 days. From figure 4.9, as the ratio of S1 sand was increased, the flexural strength decreased. The average flexural strength from 4.77 MPa at 0% S1 decreased to 3.54 MPa at 100% S1. The decrease in flexural strength suggests the same reason with the observation in the compressive strength: the increase of water in the mixture lowered the flexural strength. It also suggests that the high MgO content of the S1 sand had the same lowering effect of the flexural strength with that of the compressive strength because of the formation of $Mg(OH)_2$ and the addition of inner stresses in the hardened samples.

However, statistical analysis by one-way ANOVA showed that at 95% confidence interval, there is sufficient evidence to say that there are no significant differences in the mean strength (in MPa) of the three levels. Therefore, it can be concluded that the S1 sand can be used as fine aggregates in concrete in terms of flexural strength.

Effect of S1 on Rebound Rate

Rebound rate determines the shootability of the wet-mix shotcrete, the lower is its rebound rate the better is its shootability. Due to the limitations of the improvised shotcrete machine, PPC was used in the fresh wet-mix shotcrete mixtures instead of OPC. The mixtures made using OPC as the cement hardened quickly and the machine did not have the capacity to pump it out on time.

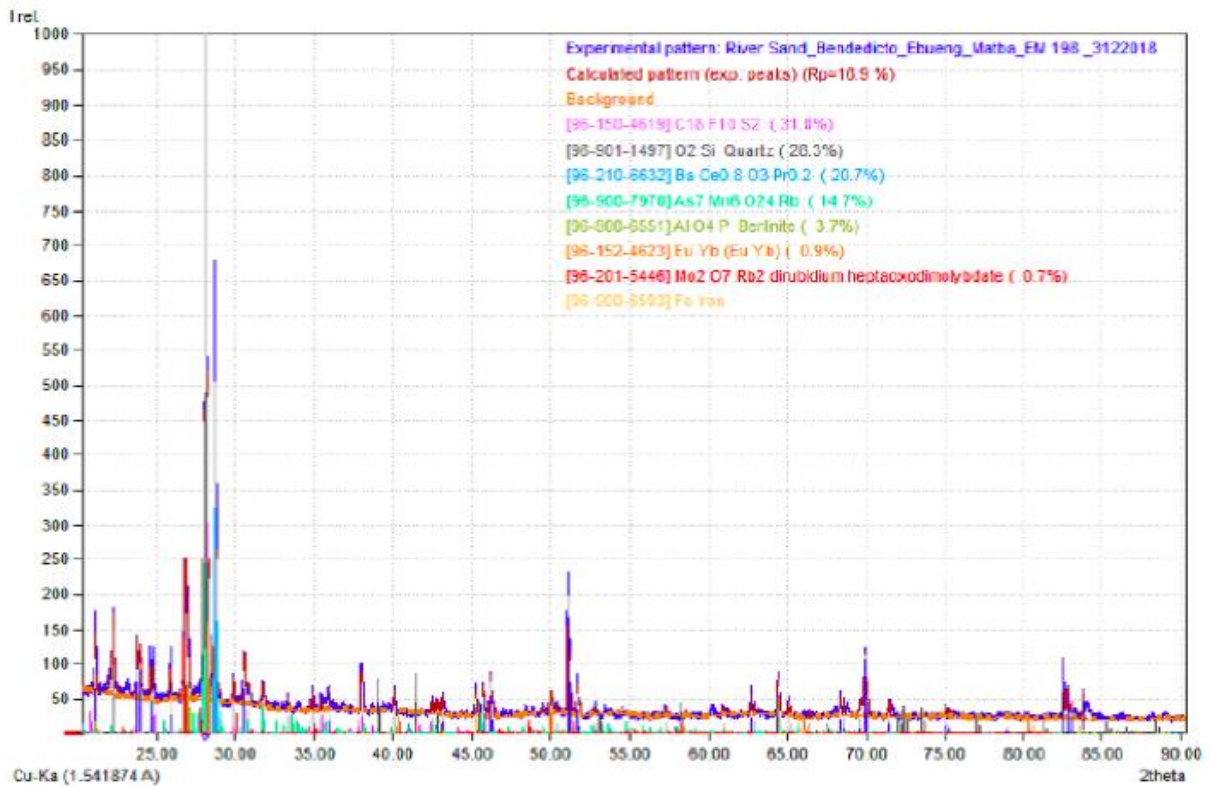


Fig. 4.3. XRD result for RS.

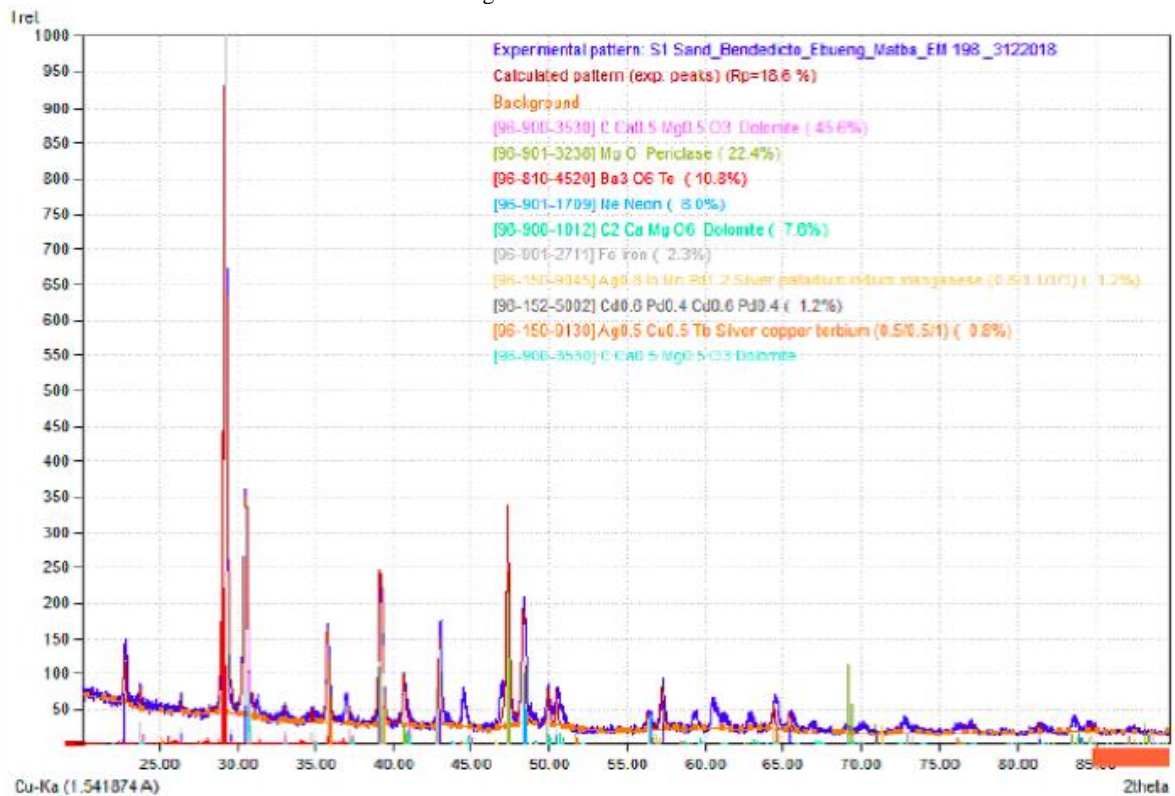


Fig. 4.4. XRD result for S1 sand

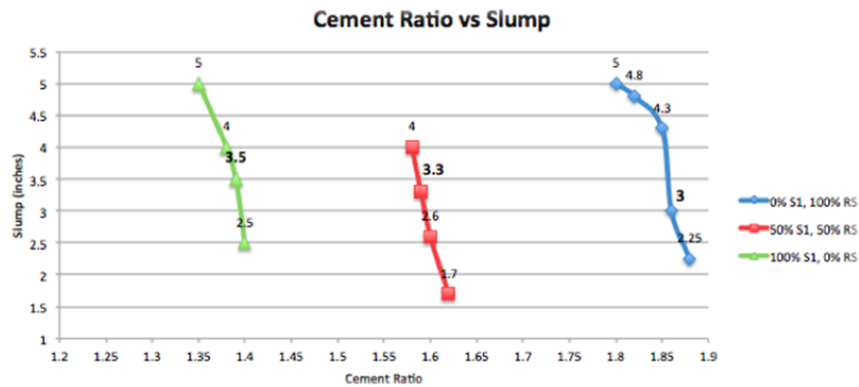


Fig. 4.5. The slump (inches) for the three levels at different cement ratios.

Table 8. The slump values for 3 repetitions of slump tests for the fixed cm/w ratios.

Water Ratio	Cement Ratio	% S1	Slump (in)			Average
			Trial 1	Trial 2	Trial 3	
1	1.86	0	3	2.8	3.2	3.00
	1.59	50	3.3	3.5	3.4	3.40
	1.39	100	3.5	3.5	3.4	3.47

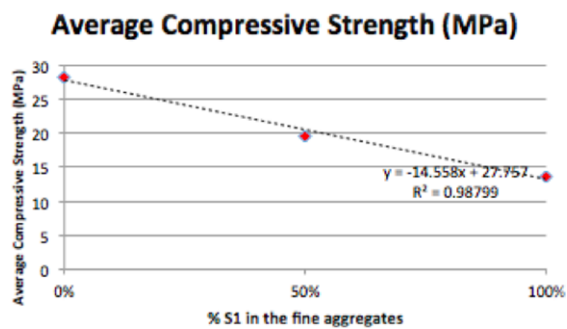


Fig. 4.6. Average compressive strength (MPa) readings for each level.

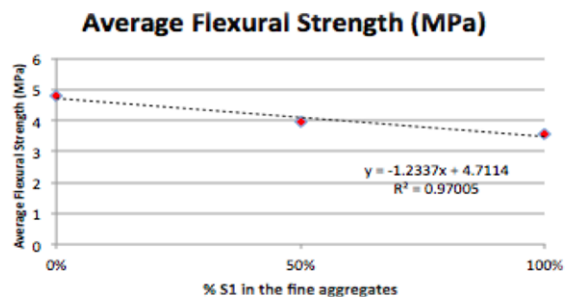


Fig. 4.7. Third-point flexural strength (MPa) readings of each sample grouped by trial.

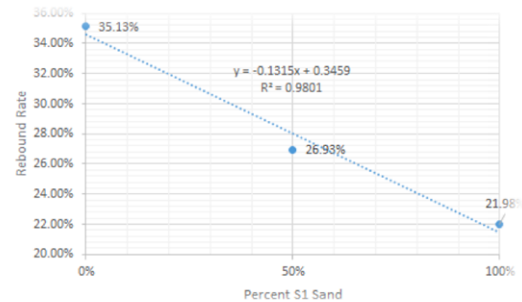


Fig. 4.8. Average rebound rate of each level.

According to Fig. 4.8, the average rebound rate of 0% S1 is 35.13% which decreased to 21.98% at 100% S1 sand. The rebound rate decreased almost linearly as the replacement of RS with S1 sand in the mixture increased. S1 sand is made up of dolomitic limestone, which contains a high percentage of MgO and a low percentage of CaO. With that, the dolomitic limestone failed to meet the required CaO and MgO percentages for making cement. Despite that, since S1 sand is crushed dolomitic limestone, it still possesses pozzolanic or cementitious properties. The lower rebound rate of the mixtures with more S1 sand suggests that it is more effective in sticking to the area where it is applied compared to mixtures made with RS.

In the statistical analysis of the rebound rate test, assumption of normality was satisfied but the homogeneity of variances assumption was not. This means that the rebound rate values in each level had

significantly different discrepancies. With that, the Welch F-test was used. It was concluded that at 95% confidence interval, there is sufficient evidence to say that there are no significant differences in the mean rebound rate of the three levels. This implies that the wet-mix shotcrete made with S1 sand as fine aggregates is competent with that made with RS.

CONCLUSION

This research was successful in producing wet-mix shotcrete using S1 sand as the fine aggregates. It was also able to perform the slump test, unconfined compressive strength test, and flexural test on the produced wet-mix shotcrete in three different levels: 0% S1 & 100% RS, 50% S1 & 50% RS and 100% S1 & 0% RS.

During the slump test, the researchers observed that as the percentage of S1 sand increased, the water content needed for optimum shotcrete pumping also increased. From the results of the compressive strength test and flexural strength test, the researchers found out that as the percentage of S1 sand increases, the compressive strength and flexural strength of the shotcrete wet-mix decreases.

One-way ANOVA was used to analyze the data from the compressive strength test and flexural strength test. At 95% confidence interval, the mean compressive strengths are significantly different which means that the S1 sand is not competent in terms of its compressive strength compared to RS. Also at 95% confidence interval, there are no significant difference in the mean flexural strength of the three levels which means that using S1 sand as fine aggregates in shotcrete is comparable to using RS in terms of its flexural strength.

The researchers encountered a problem for the rebound rate test. Due to the limitations of the improvised shotcrete machine, it was not possible to conduct a rebound rate test for the wet-mix shotcrete made with OPC since the mixture hardened too quickly. The researchers used a different type of cement (PPC) in order to perform the rebound rate test. The rebound rate test of the shotcrete wet-mix that used PPC was successful and the researchers learned that, as the percentage of S1 sand increases, the rebound rate decreases.

The Welch F-test was used to analyze the data from the rebound rate test. It was found out that at 95% confidence interval, there is no significant difference in the mean rebound rate of the three levels.

For the overall conclusion of the study, it is concluded that wet-mix shotcrete containing S1 sand produces comparable flexural strength with that made of RS. On another note, the research concludes that wet-mix shotcrete using S1 as fine aggregates is not comparable with that using RS due to its lower compressive strength and higher amount of water required.

ACKNOWLEDGEMENTS

This work was supported by Republic Cement and Building Materials, Inc. of the Philippines and Davao Techno Craft (Grainmaster) of Nabunturan, Compostela Valley, Philippines. Majority of the laboratory experiments were conducted in the Institute of Civil Engineering and Department of Mining, Metallurgical, and Materials Engineering, both in the University of the Philippines - Diliman.

REFERENCES

- [1] Pitchaiah, P. S. (2017). Impacts of Sand Mining on Environment – A Review. SSRG International Journal of Geo Informatics and Geological Science (SSRG-IJGGS), 4(1), 1–6.
- [2] Shen, Weiguo, et al. "Characterization of manufactured sand: particle shape, surface texture, and behavior in concrete." *Construction and Building Materials*, 2016: 595-601.
- [3] Hasdemir, S., Tug̃rul, A., & Yılmaz, M. (2016). The effect of natural sand composition on concrete strength. *Construction and Building Materials*, 940-948.
- [4] Yamei, H., & Lihuab, W. (2017). Effect of Particle Shape of Limestone Manufactured Sand and. *Procedia Engineering*, 87-92.
- [5] Moffat, R., Jadue, C., Beltran, J. F., & Herrera, R. (2017). Experimental evaluation of geosynthetics as reinforcement for shotcrete. *Geotextiles and Geomembranes*, 45(3), 161–168. <https://doi.org/10.1016/j.geotexmem.2017.01.007>
- [6] Armengaud, J., Casaux-ginestet, G., Cyr, M., Husson, B., & Jolin, M. (2017). Characterization of fresh dry-mix shotcrete and correlation to rebound. *Construction and Building Materials*, 135, 225–232. <https://doi.org/10.1016/j.conbuildmat.2016.12.220>
- [7] Choi, P., Yun, K. K., & Yeon, J. H. (2017). Effects of mineral admixtures and steel fiber on rheology, strength, and chloride ion penetration resistance characteristics of wet-mix shotcrete mixtures containing crushed aggregates. *Construction and Building Materials*, 142, 376–384. <https://doi.org/10.1016/j.conbuildmat.2017.03.093>
- [8] Ahn, N., & Fowler, D. (2001). An experimental study on the guidelines for using higher contents of aggregate microfines in portland cement concrete . University of Texas, International Center for Aggregate Research. Virginia: Aggregates Foundation for Technology, Research, and Education.
- [9] Nichols, Jr., F. P. (1982). *Manufactured Sand and Crushed Stone in Portland Cement Concrete*.

- Concrete International, 4(8), 56-63.
- [10] Ahmed, A.E., and El-Kour, A.A., (1989). Properties of Concrete Incorporating Natural and Crushed Stone Very Fine Sand. *Materials Journal*, 86(4), 417-424.
- [11] Rhesi, S. (1983, December). Magnesium Oxide in Portland Cement. *Advances in Cement Technology*.
- [12] Borhan, T. M. (2016). Combined Effect of MgO and SO₃ Contents in Cement on Compressive Strength of Concrete. *Al-Qadisiyah Journal for Engineering Sciences*, 9 (4).
- [13] ASTM C143/C143M. (2015). Standard Test Method for Slump of Hydraulic-Cement Concrete. *Astm C143*, (1), 1-4. <https://doi.org/10.1520/C0143>
- [14] ASTM C192/C192M. (2016). Standard Practice for Making and Curing Concrete Test Specimens in the Laboratory. *American Society for Testing and Materials*, 1-8. <https://doi.org/10.1520/C0192>
- [15] ASTM C33/C33M. (2018). Standard Specification for Concrete Aggregates. *ASTM International*, 1-12. www.astm.org
- [16] ASTM C136. (2014). Standard Test Method for Sieve Analysis of Fine and Coarse Aggregates. *Annual Book of ASTM Standards*, 1-5. <https://doi.org/10.1520/C0136>
- [17] ASTM C39/C39M (2014). Standard Test Method for Compressive Strength of Cylindrical Concrete Specimens. *ASTM International*, 1-7. www.astm.org
- [18] ASTM C78 /C78M (2018). Standard Test Method for Flexural Strength of Concrete (Using Simple Beam with (Third-Point Loading). *ASTM International*, 1-5. www.astm.org
- [19] JSCE. (2005). JSCE-F 561-2005: Method of Making Specimens for Compressive Strength Tests of Sprayed Concrete (Mortar) (Draft).
- [20] ASTM C150-07 (2007). Standard Specification for Portland Cement. https://kupdf.com/download/astm-c150_59ce2cb208bbc53442686f47_pdf
- [21] ASTM C-595-03 (2003). Standard Specification for Blended Hydraulic Cements. <http://www.c-s-h.ir/wp-content/uploads/2014/12/C-595.pdf>

STRENGTH AND FLOWABILITY OF HIGH WATER CONTENT STABILIZED SOIL AT EARLY CURING TIME

Vincentius Harry¹, Luky Handoko¹, Sumiyati Gunawan¹, John Tri Hatmoko¹ and Jim Shiau²

¹Faculty of Engineering, Universitas Atma Jaya Yogyakarta, Indonesia

² School of Civil Engineering and Surveying, University of Southern Queensland, Australia

ABSTRACT

Pipe mixing method is commonly used as filled material by mixing soil with cement at high water content. Both strength and flowability of the material at early curing time are two key elements to be studied in order ensure the success of this method. In this study, a series of strength and flowability tests are conducted with specimen less than 3 days. Strength of the specimen is determined using uniaxial compression test whilst flowability of the specimen determined using L-shape box. The specimen were prepared under two different soil water contents (w_c), i.e. at the liquid limit (w_L) and twice of the (w_L). Cement content (c_c) were varied between 2%-10% to set the amount of cement (C) between 20kg/m³ and 70 kg/m³. For the same water content, the results show that the higher the strength improvement of cement treated clay, the higher the cement content. Lower cement content has higher flowability at the same curing time. Flowability of cement treated soil decreases as the curing time increases.

Keywords: strength, flowability, cement-treated soil, high water content soil

INTRODUCTION

High water content soil is abundant and normally categorized as waste if not properly used [1-3]. This type of soils may be obtained from contaminated river bed dredging activities [4], harbor maintenance activities [1, 5] and industrial byproduct [6, 7]. In order to be used in geotechnical application, soil stabilization method by adding cementing agent such as lime and cement to the high water content soil is not uncommon [8-10]. Improvement of soil properties of cement treated soil has been investigated by many researchers by focusing on strength [10, 11], stiffness [12, 13], compressibility [11] and permeability [14, 15]. Pipe mixing method is commonly used to mix high water content soil with cement and to transport the mixture to the construction site which is not easy to reach [16]. The success of this method is very depending on the strength and flowability of soil-cement mixture especially at early curing time.

This research discusses the laboratory test results on strength and flowability cement treated high water content soil at early curing time. Clay soil from Sidoarjo district which originally come from mud eruption is used. Specimen were prepared by varying water content (w_c), cement content (c_c) at different curing time.

MATERIALS AND SPECIMEN PREPARATION

Sidoarjo mud volcano normally has very high content of water and was chosen in this study. Basic

properties of this soil are presented in Reference [17]. Specimen were prepared at designed w_c and c_c as shown in Table 1. Associated amount of cement (C) in weight per total volume of mixture also shown in Table 1. Specimen were prepared at two different w_c which are equal to soil liquid limit, w_L ($w_c=w_L=60\%$) and twice of w_L ($w_c=120\%$). Specific code were given to each specimen which shows its w_c and c_c . For example, S60-2 refers to a specimen with $w_c=60\%$ and $c_c=2\%$.

Wet soil were checked for their water content. Water were added or removed from the soil to reach designed water content. After reaching the designed w_c , cement were added to wet soil and then mixed by using electronic mixer for 10 minutes. The amount of cement added to soil is calculated based on percentage from soils dry weight. Strength of soil specimen were evaluated based on uniaxial compression test based on ASTM 2166. Specimen for uniaxial compression test is cylinder with 5 cm in diameter and 10 cm in height. The ability of mixture to flow were evaluated using L-shape box following BS EN 12350-10. The flow ratio is used

Table 1 Specimen preparation

Code	w_c (%)	c_c (%)	C (kg/m ³)
S60-2	60	2	20.1
S60-4	60	4	39.9
S60-6	60	6	59.4
S120-8	120	8	49.5
S120-10	120	10	61.6

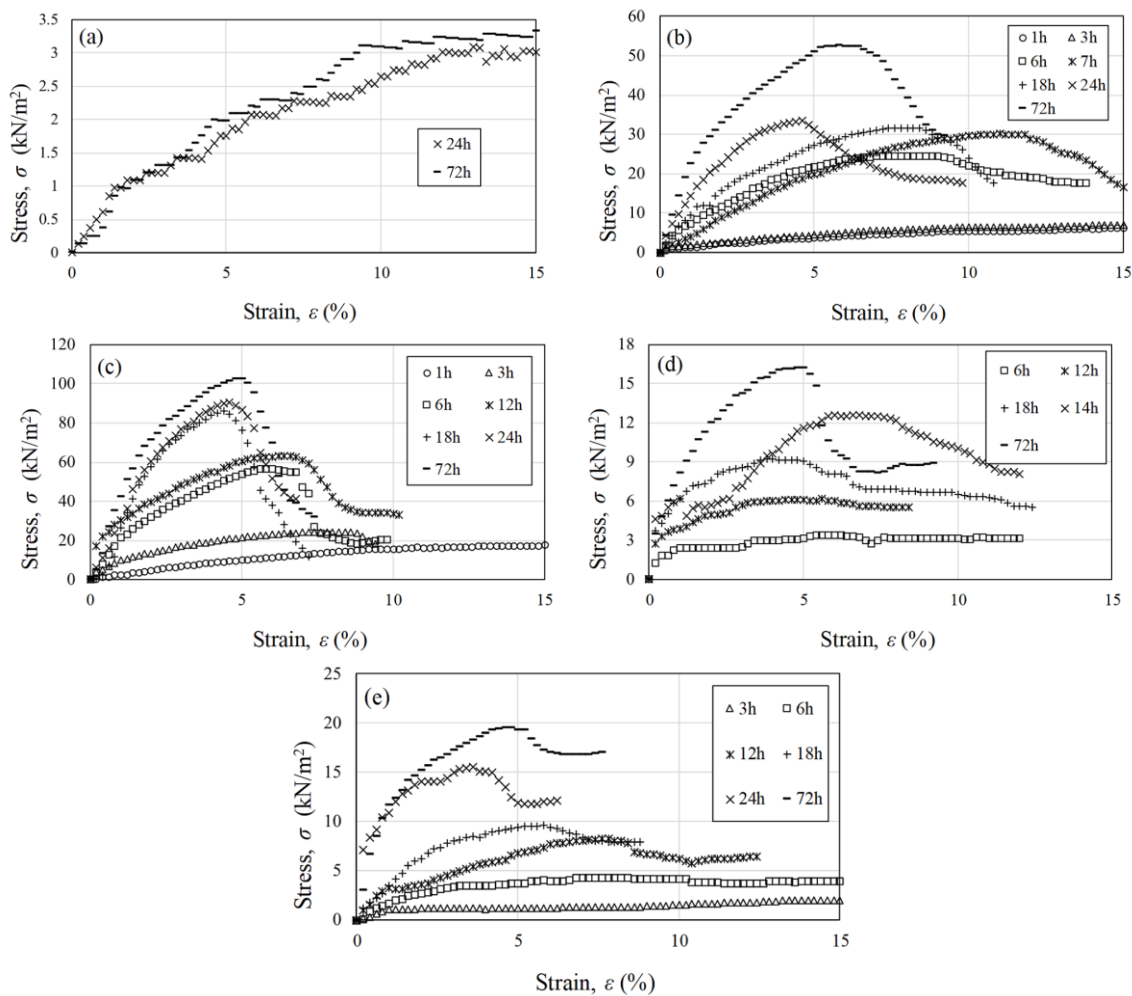


Fig. 1 Uniaxial compression test result for all specimen with curing time variation: (a) S60-2; (b) S60-4; (c) S60-6; (d) S120-8 and S120-10

as indicator of material ability to flow. It is the ratio between the height of material at the end of flow and the height of material at the source of flow.

RESULT AND DISCUSSION

Strength of cement treated soil

Strength improvement of specimen were obtained from hydration reaction within the specimen. Time is required for hydration reaction to occur. The stress-strain relationship of specimen at the same w_c and c_c at different curing time are shown in Fig. 1. This result indicates that as the curing time increases, the specimen obtain higher strength as shown by the increase of peak stress. The stiffness of the specimen are also increases as the stress-strain curve is steeper for the specimen with longer curing time.

Reference [10] conducted test on cement treated high water content soil at early curing time. The test results indicate that the increase of strength can be

divided into two stage. Each stage has linear correlation between q_u and curing time plotted in log scale. The boundary between first stage and second stage is at 3 days curing time. Similar result is obtained by this paper as shown in Fig. 2. At curing time less than 1 day, the correlation between q_u and curing time can be represented by single linear curve, while at curing time more than 1 day, it can be represented by other linear curve.

The amount of hydration reaction product is dependent on the amount of cement added. Fig. 3 shows the strength of specimen against c_c at the varies curing time and at certain w_c . At low cement content, the q_u does not change much as the increase of curing time. However, at higher cement content, the change of q_u is clearly observed. This may be caused by the hydration product of specimen with higher c_c is more than the lower c_c . The relation between q_u and c_c can be represented by linier curve when the w_c and curing time are constant.

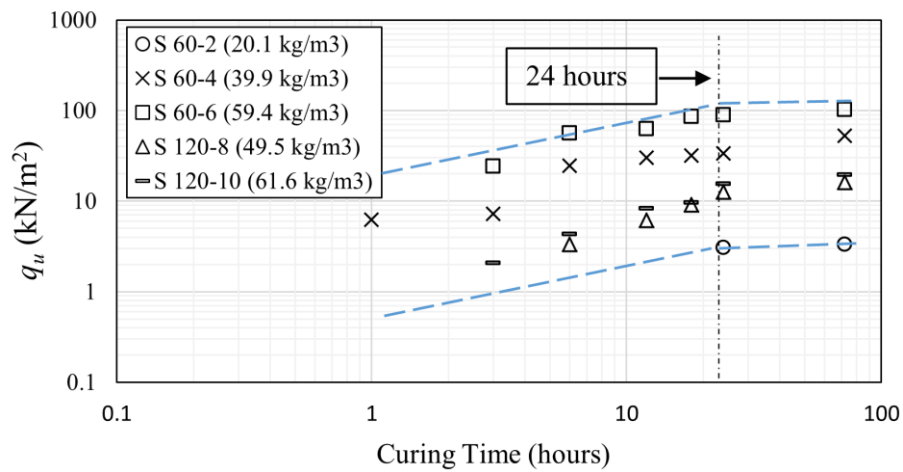


Fig. 2 Relationship between q_u and curing time

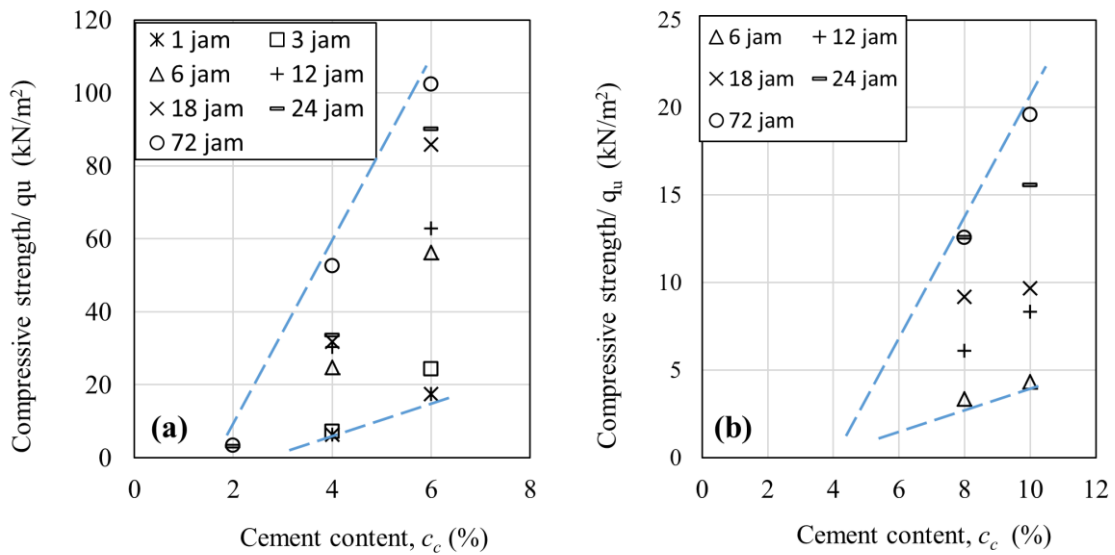


Fig. 3 Relationship between q_u and c_c at (a) $w_c=60\%$ and (b) $w_c=120\%$

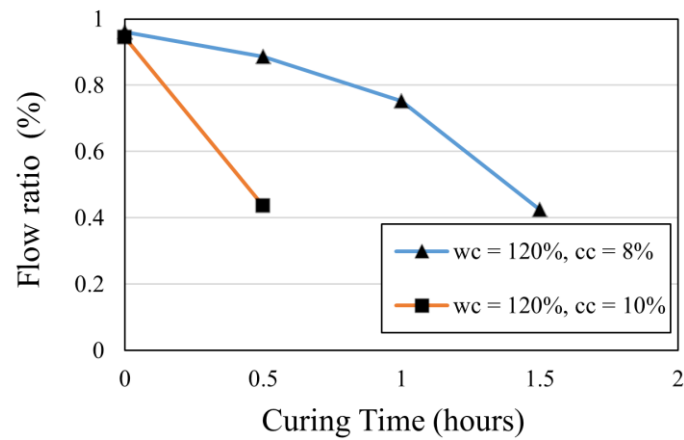


Fig. 4 Relationship between q_u and curing time

Flowability of cement treated soil

Flowability test result are shown in Fig. 4. Based on the result, all the mixture material with $w_c = 60\%$ does not have the capability to flow. The mixture material never reach the end of the flow of the L-shape box. This may be caused by the hydration reaction requires water to start. It makes the total water contained in the mixture reduce and causes no flow. On the other hand, the mixture material with $w_c = 120\%$ have capability to flow as shown in Fig. 4. The result shows that at the same curing time, material that contain higher c_c has lower capability to flow than lower c_c . It may be caused by hydration product of material with higher c_c is more than the lower c_c at same curing time. This results agree with the result of q_u . Another result obtained is that the longer curing time makes lower flowability. For S120-8, the material has no capability to flow after 0.5 hour of curing time, while for S120-10 the material has no capability to flow after 1.5 hour.

CONCLUSION

The strength and flowability of cement treated high water content soil has been evaluated at its early curing time. The following conclusions are drawn based on the test results:

1. As the curing time increases, the specimen gain more strength and stiffness.
2. The evolution q_u against curing time can be divided into 2 stages which are less than 1 day and more than 1 day. Each stage has linier correlation between q_u and curing time when plotted with logarithmic scale.
3. Correlation of q_u against c_c can be represented with linier line for constant curing time and constant water content
4. Higher c_c produces less flowability than lower c_c at the same w_c . Longer curing time also reduces the flowability of the specimen.

ACKNOWLEDGEMENTS

The authors express their gratitude to Institute of Research and Community Service of Universitas Atma Jaya Yogyakarta for the financial support under internal funding scheme No. 079/HB-PEN/LPPM/III/2018.

REFERENCES

- [1] Bennert, T.A., et al., *Use of Dredged Sediments from Newark Harbor for Geotechnical Applications*, in *Geotechnics of High Water Content Materials*, T.B. Edil and P.J. Fox, Editors. 2000, American Society for Testing and Materials: West Conshohocken.
- [2] Berilgen, M.M., I.K. Ozaydin, and T.B. Edil, *A Case History: Dredging and Disposal of Golden Horn Sediments*, in *Geotechnics of High Water Content Materials*, T.B. Edil and P.J. Fox, Editors. 2000, American Society for Testing and Materials: West Conshohocken.
- [3] Douglas, W.S., A. Maher, and F. Jafari, *Analysis of environmental effects of the use of stabilized dredged material from New York/New Jersey Harbor, USA, for construction of roadway embankments*. Integr Environ Assess Manag, 2005. 1(4): p. 355-64.
- [4] Kamon, M., T. Katsumi, and K. Watanabe, *Heavy-Metal Leaching from Cement Stabilized Waste Sludge*, in *Geotechnics of High Water Content Materials*, T.B. Edil and P.J. Fox, Editors. 2000, American Society for Testing and Materials: West Conshohocken.
- [5] Maher, A., et al., *Geotechnical Properties of Stabilized Dredged Material from New York-New Jersey Harbor*. Transportation Research Record: Journal of the Transportation Research Board, 2004. 1874: p. 86-96.
- [6] Klein, A. and R.W. Sarby, *Problems in Defining the Geotechnical Behavior of Wastewater Sludges*, in *Geotechnics of High Water Content Materials*, T.B. Edil and P.J. Fox, Editors. 2000, American Society for Testing and Materials: West Conshohocken.
- [7] Benson, C.H. and X. Wang, *Hydraulic Conductivity Assessment of Hydraulic Barriers Constructed with Paper Sludge*, in *Geotechnics of High Water Content Materials*, T.B. Edil and P.J. Fox, Editors. 2000, American Society for Testing and Materials: West Conshohocken.
- [8] Watabe, Y., et al., *Mechanical characteristics of a cement treated dredged soil utilized for waste reclamation landfill*, in *International Symposium Yokohama*, T. Tsuchida, et al., Editors. 2003, Taylor Francis: Yokohama. p. 739-744.
- [9] Tang, Y.X., Y. Miyazaki, and T. Tsuchida, *Practices of reused dredgings by cement treatment*. Soils and Foundations, 2001. 41(5): p. 129-143.
- [10] Kang, G., T. Tsuchida, and A.M.R.G. Athapaththu, *Strength mobilization of cement-treated dredged clay during the early stages of curing*. Soils and Foundations, 2015. 55(2): p. 375-392.
- [11] Miura, N., S. Horpibulsuk, and T.S. Nagaraj, *Engineering behavior of cement stabilized clay at high water content*. Soils and Foundations, 2001. 41(5): p. 33-45.
- [12] Kang, G.-o., T. Tsuchida, and Y.-s. Kim, *Strength and stiffness of cement-treated marine dredged clay at various curing stages*.

- Construction and Building Materials, 2017. 132: p. 71-84.
- [13] Yang, L. and R.D. Woods, *Shear stiffness modeling of cemented clay*. Canadian Geotechnical Journal, 2015. 52(2): p. 156-166.
- [14] Quang, N.D. and J.C. Chai, *Permeability of lime- and cement-treated clayey soils*. Canadian Geotechnical Journal, 2015. 52(9): p. 1221-1227.
- [15] Yu, Y., et al., *A study on the permeability of soil-cement mixture*. Soils and Foundations, 1999. 39(5): p. 145-149.
- [16] Kitazume, M. and T. Satoh, *Development of a pneumatic flow mixing method and its application to Central Japan International Airport construction*. Proceedings of the Institution of Civil Engineers - Ground Improvement, 2003. 7(3): p. 139-148.
- [17] Handoko, L., N. Yasufuku, and A. Rifa'i, *Comparison of consolidation curves for remolded mud volcano of Sidoarjo, Indonesia*. Journal of Geotechnique, Construction Materials and Environment, 2016. 10(22): p. 1978-1982.

Environment

TOPOGRAPHIC CONTROL ON GROUNDWATER FLOW IN CENTRAL OF HARD WATER AREA, WEST PROGO HILLS, INDONESIA

T. Listyani R.A.¹, Nana Sulaksana², Boy Yoseph CSSSA³ and Adjat Sudradjat⁴

¹Geological Engineering, Padjajaran University; Sekolah Tinggi Teknologi Nasional, Yogyakarta, Indonesia;

²⁻⁴ Geological Engineering, Padjajaran University, Indonesia

ABSTRACT

West Progo Hills is one of some hard water area in Indonesia. The area may be regarded as “non-groundwater basin” because there is difficult to get groundwater. Groundwater can only be found in some places with random point. Dug wells usually found in narrow area, as well as springs. By geological as well as hydrogeological approaches, this research wants to know about the relation between groundwater table to the topography of West Progo Hills. The groundwater mapping has been done at Girimulyo-Kaligesing and surrounding area, to get some geologic data, water table measurement and geomorphological data. The isotopic data is used to complete the analysis. Result of the research shows that groundwater table usually adjust the local topography. Groundwater table ranges 0.9 – 8 m below surface, which means shallow groundwater. Dug wells only locally found, as well as springs. Some springs often found at break of slope, it means that they're controlled by topography. Based on groundwater table from dug wells data, groundwater is conformable to topographic condition. The relationship between elevation and groundwater table give correlation coefficient (r) as much as 99.99%. It means that reliefs are followed by groundwater level. It can be concluded that relief has strong correlation with shallow groundwater in research area, although the isotopic data doesn't support the altitude effect of it. Groundwater flows from high to low land, such as upper slope of hills to valleys.

Keywords: Groundwater, topography, spring, dug well, isotope

INTRODUCTION

This research has been carried out in a central part of West Progo Hills, it includes Kaligesing, Central Java Province and Girimulyo, West Progo, Yogyakarta Province, Indonesia (Fig. 1). The central of West Progo Hills is a hard water area. There is difficult to find groundwater resources. However, some dug wells and spring still can be found in random places, narrow area although in small numbers.

West Progo Hills belongs to West Progo Dome physiography [1]. This area even includes in “non groundwater basin” [2]. This area is not potential for groundwater. However, at this research area, it can be found some springs and dug wells. The springs and dug wells spread in random area, sometimes many of them gathered in narrow area, but it may be not found at other areas.

Groundwater resource in the research area has been studied by several researchers. The potential of groundwater in relation with the lineament also analyzed to understand the influence of lineament's characteristics [3]. There is strong correlation between the distance of lineament – spring to the numbers of spring. The springs are usually acted as discharge of groundwater flow in local area.

Groundwater resource of study area can be

examined by looking at numbers of spring as well as dug well. This potential of groundwater can also be discussed in its relationship to the topography.

The study area is hilly morphology with mainly steep slope and high dissected morphology [3]. The coarse relief is usually shown by narrow valley, steep slope and blunt peak hills. There are some break of slope feature in several location in which the spring may be appear.

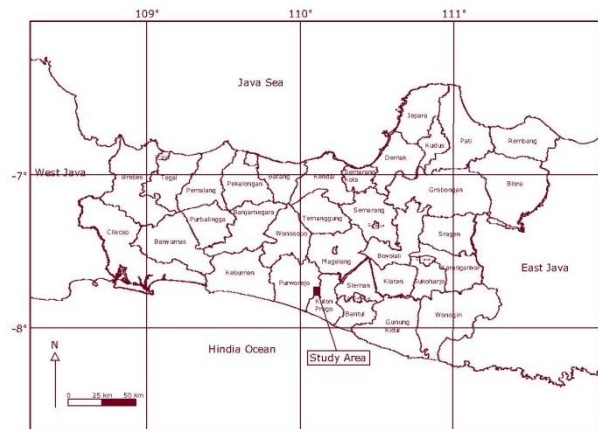


Fig 1. The research area include in central part of West Progo Dome [1].

METHODS

The research has been done by hydrogeological and geomorphological mapping in the central of West Progo Hills. The data collected includes hydrogeological variables (groundwater table and spring type) and also geomorphological variables (slope, elevation, relief). Stable isotopic data of ^{18}O and d have been taken to complete the analysis.

Geological equipment used includes GPS, hammer, compass and loupe. Slope is calculated from topographic map and also directly measured in the field.

REGIONAL HYDROGEOLOGY

West Progo Hills is a dome physiography which has built mainly by three big ancient volcanoes i.e. Gadjah, Ijo and Menoreh [1]. These volcanoes has produced andesitic rocks such as andesite breccia and andesite lava. These volcanic products include in Old Andesite Formation. Beside this formation, West Progo Hills is also built by a series of Tertiary sedimentary Formation such as Nanggulan, Sentolo and Jonggrangan formation. The research area in central part of the dome is mainly built by Jonggrangan and Old Andesite Formations. Jonggrangan Formation is consists of coral, bedded limestone, tuffaceous marl, conglomerate and calcareous sandstone [4].

The aquifer system in the study area was constructed by andesitic volcanic rocks with a thickness of more than 300 m. These rocks have locally undergone quite intensive weathering, and form a thick soil (5-10 m). Based on the characteristic layers of massive, densely fractured rock, and groundwater occupies the cracks, the aquifer system in the study area can be classified as a cracked volcanic aquifer [5]. Groundwater in this cracked aquifer system flows as a complex flow and creates seepages. On a local scale the groundwater level is not related in one place to another.

The existence of the basement rock of the Old Andesite Formation aquifer in stratigraphy cannot be detected because this formation is a body of intrusion and thick lava. The aquifer system in this area is interpreted as aquifers that are completely composed by volcanic rocks reach the basement. Because these volcanic rocks are exposed widely on the surface and are directly related to the atmosphere, the aquifer system can be classified as an unconfined aquifer [5].

Jonggrangan Formation mainly consists of bedded tuffaceous limestone which built an aquifer by its intergranular porosity. This formation is also densely cracked therefore secondary porosity is also well developed. This aquifer is supported by cracks and solution porosity, especially in coral, reef limestone.

RESULT AND DISCUSSION

Morphology of Research Area

The study area occupies in central West Progo Hills or core of dome physiography. It has variable morphology, mainly composed of high dissected, steep slope morphology. This area has elevation of 187.5 to 850 m asl, with slope developed from 5% (undulating) until more than 100% (very steep) [3].

Fig 2 shows some lineaments of escarpments of research area. This morphology can also be looked in 3D block diagram as shown in Fig. 3 below.



Fig. 2. Morphology of research area as seen from Jatimulyo Village, Girimulyo (top); and from Tlogoguwo Village, Kaligesing (bottom).

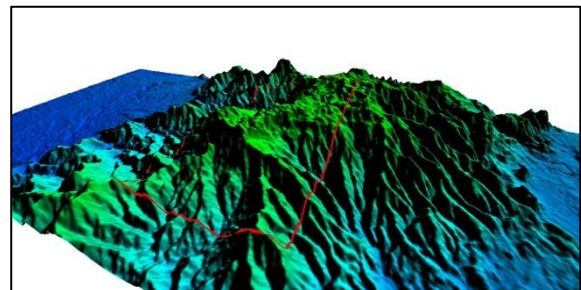


Fig. 3. Landscape of research area in 3D diagram seen from east direction.

The research wants to know about relationship between groundwater flow and topographic aspects, therefore the observation locations has been chosen in dug wells and surroundings area (Table 1; Fig. 4). This table shows morphometric variables include elevation and slope of landform.

Table 1. Location of dug well as observation spot area.

Well	UTM coordinate		Elevation (m)	Slope (%)	Gw. table (m)
	Northing	Easting			
W1	402803	9146709	717	15	715.5
W2	403055	9146716	741	17	736.4
W3	402914	9146504	716	18	711.44
W4	402972	9146491	716	15	710.6
W5	403071	9146491	427	17	424.8
W6	403323	9144843	734	14	730.2
W7	403644	9144597	743	20	738.83
W8	403578	9144480	754	21	747.9
W9	399443	9143192	298	25	296.1
W10	399483	9143149	294	28	292.1
W11	401554	9142896	600	28	598.8
W12	401440	9142800	600	24	598.6
W13	403058	9143528	687	12	682
W14	403056	9143501	687	14	681.5
W15	402955	9143421	687	13	680.5
W16	402868	9143319	687	15	681
W17	402905	9143289	687	15	680.5
W18	403033	9143066	725	17	719.2
W19	403033	9143019	725	20	719
W20	402912	9142833	750	21	744.3
W21	403302	9143013	717.46	25	716.56
W22	402746	9139995	669.4	30	667.4
W23	402877	9139999	643.6	31	635.6
W24	403430	9138812	520.88	30	519.6
W25	403527	9138406	482.67	33	481.45
W26	403071	9138006	324.3	32	321.3
W27	399665	9138373	462.68	15	461.6
W28	399723	9138318	465.8	18	464.8
W29	399015	9137910	391.8	45	390.6
W30	399333	9137742	476.8	47	474.8
W31	399284	9137727	476.6	46	475.1
W32	400808	9143186	502	25	499.9
W33	400865	9143223	512	15	511
W34	400002	9138458	444	35	441.1
W35	399839	9138247	437	30	434.2

Similar with Fig. 3, the morphology of research area can be noticed from southern side [3]. The study area is a hard rock terrain built by hard, compacted rocks and made coarse relief.

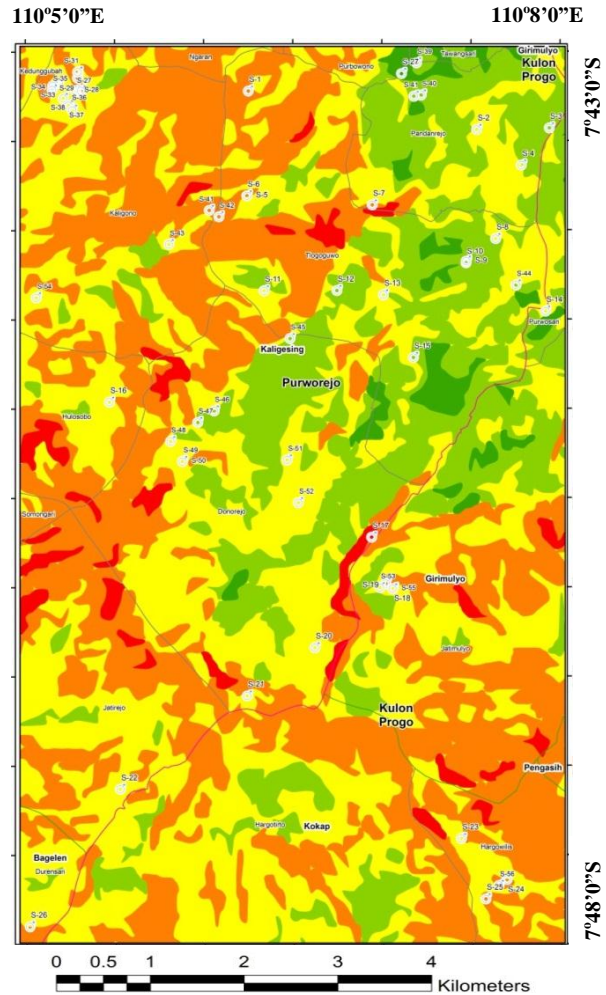
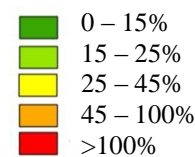


Fig 4. Map of slope of landform in study area.

Legend:



From the slope map on Fig. 4 it appears that the research area is dominated by a landform with fairly steep slopes. The valley between the hills usually has relatively gentle slope and generally found locally in a relatively narrow area.

The landscape of research area is similar with Samigaluh area which is located on the east of it, which has coarse relief, strong dissected hilly morphology [6]. This area is usually affected by vertical erosion that is balanced in intensity with horizontal erosion. However, there are poor correlation between elevation and the other morphometric variable responses of stream.

Groundwater Flow

Groundwater flow can be interpreted based on the local groundwater table (Fig. 5). Unfortunately, dug wells are only found locally in several locations, even many areas do not have dug wells. It means that the availability of dug wells at research area relatively small and the distribution is uneven.

Due to the availability of dug wells and local distribution, the groundwater contour pattern cannot be generated throughout the study area. This pattern of groundwater contours can only be made around dug wells areas, so that the groundwater flow pattern cannot be interpreted in relation to other areas.

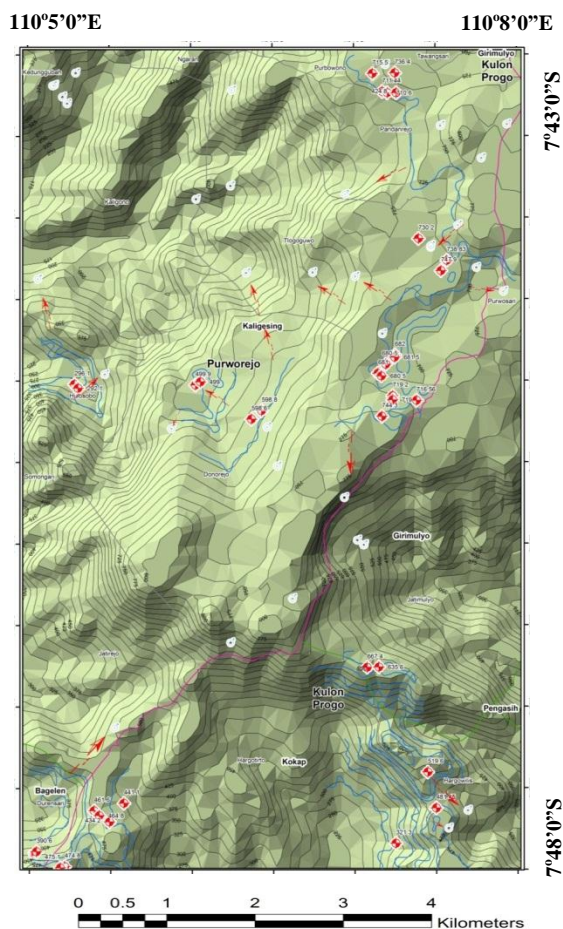


Fig. 5. Groundwater flow of shallow aquifer.

Legend:

- Spring
- ★ Dug well
- Groundwater table contour
- Groundwater flow

Groundwater flow develops as local flow system in the area. This system usually develops along with local relief [7]. In the local flow condition, the topography usually influence groundwater table. The

water table is coincident with the ground surface in the valley, sometimes produced spring, and forms a weak replica of the topography on the hills (Fig. 6). The flow lines deliver groundwater from recharge areas to discharge areas.

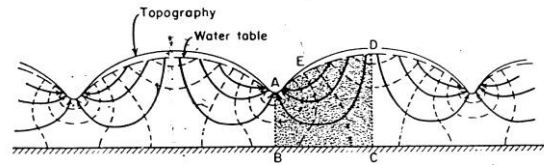


Fig. 6. Groundwater flow net in a two dimensional vertical cross section (after Hubert, 1940 in [7]).

Discharge of groundwater occurs in nature when water emerges from underground [7]. Most natural discharge occurs as flow into surface water bodies, flow to the surface appears as a spring. This fact let the appearance of depression spring type. The depression spring is formed where the ground surface cuts the water table.

There are some depression springs found in the research area (Table 2 and Fig.7). These springs mainly found at steep morphology of Old Andesite Formation, and sometimes can be met at Jonggrangan Formation rocks with single or combination type. For example, Mudal spring (S17) develops as depression, fracture, tubular spring. The tubular porosities even grow to be cavity ones.

The depression spring prove that there are groundwater table lines cross steep cliffs or slope of morphology. It means that actually morphology or topography also control groundwater flow. In this term, spring will be a discharge of groundwater flow. Therefore, some groundwater flow lines usually lead toward spring as discharge of it.

Topographic Control on Groundwater Flow

There are at least two parameters of topography that can be analyzed to see their influence to groundwater flow, i.e. elevation and slope. Groundwater tends to flow from higher hydrostatic head (groundwater table) to the lower ones. The groundwater flow is represented as groundwater table. These relationships can be seen at Fig. 8 - 9.

Relation between elevation and groundwater table gives coefficient correlation value of 99.99% (Fig. 8). It means that groundwater table always follows relief of topography. There may any variations in groundwater table depth in peak of hill if it is compared in the valley. Sometimes, groundwater table is found deeper in the hilltop. But in general, the groundwater flow line in vertical cross section will be similar with topography (see Fig. 6).

Table 2. Some depression type springs in research area.

Spring code	Location	Coordinate		Spring Type
		Northing	Easting	
S1	Pandanrejo	401223	9146528	Depression
S2	Tlogoguwo	403580	9146131	Depression
S5	Tuk Songo	401210	9145447	Depression
S6	Tuk Songo	401208	9145447	Depression
S8	Tlogoguwo	403774	9145005	Depression
S9	Tlogoguwo	403471	9144773	Depression
S10	Tlogoguwo	403468	9144755	Depression
S11	Pagertengah	401387	9144466	Depression
S12	Tlogoguwo	402137	9144468	Depression
S15	Kalilo	402925	9143777	Depression
S16	Hulosobo	399792	9143316	Depression
S17	Mudal	402496	9141923	Depression, fracture, cavity
S24	Clapar 1	403892	9138389	Depression
S27	Kaligono	399464	9146723	Depression
S28	Kaligono	399223	9146585	Depression
S29	Kaligono	399205	9146580	Depression
S30	Kaligono	399314	9146451	Depression
S31	Kaligono	399368	9146377	Depression

Meanwhile, the relationship between slope and groundwater table show worse value (Fig. 9). This relation is indicated by the r^2 value of 0.2933 or coefficient correlation (r) of 54.16% (medium).

Although the relationship between slope and groundwater flow only shows medium correlation, there are many discharge of groundwater flow controlled by break of slope of landforms. It means that landforms actually control groundwater flow because the flow usually goes toward spring as discharge point.

Many steep slope landscapes made break of slope in the research area. This condition triggers the occurrence of springs. Then, those springs can change the direction of groundwater flow. The groundwater flows principally from recharge to discharge area.

The addition of dug wells will also cause the groundwater flow to change direction. Therefore, in urban area, groundwater flow may vary locally from time to time and can be change depending abstraction. Nevertheless, the study area is not an urban area so there is rarely the addition of dug wells.

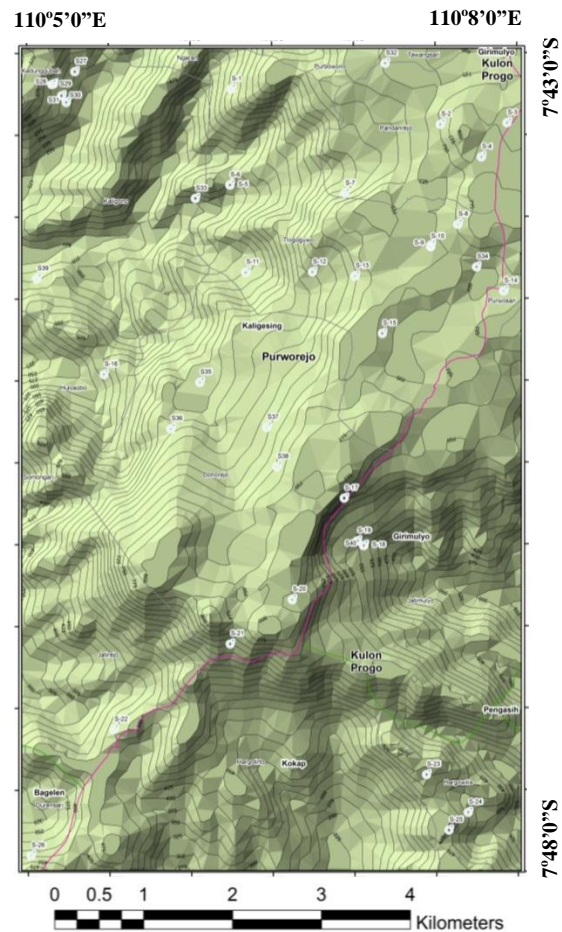


Fig. 7. Location of springs in research area.

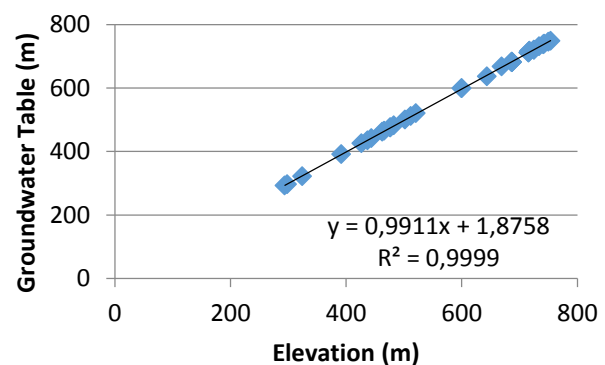


Fig. 8. Relationship between the elevation of area and groundwater table.

In any certain area regionally, there is altitude effect can be determined from isotopic data of springs from some different elevations. This phenomena yield a distinct correlations exists between the ^{18}O and D values and elevation [9]. Unfortunately, this altitude effect in the research area is invisible (Fig. 10).

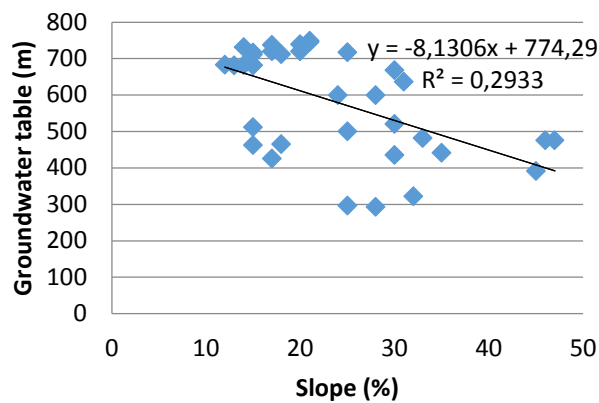


Fig. 9. The relationship between slope and groundwater table.

Fig. 10 explains that there is very weak correlation between elevation and groundwater. This correlation only has r^2 very small. Nevertheless, the isotopic value usually more lighter with the increasing of altitude.

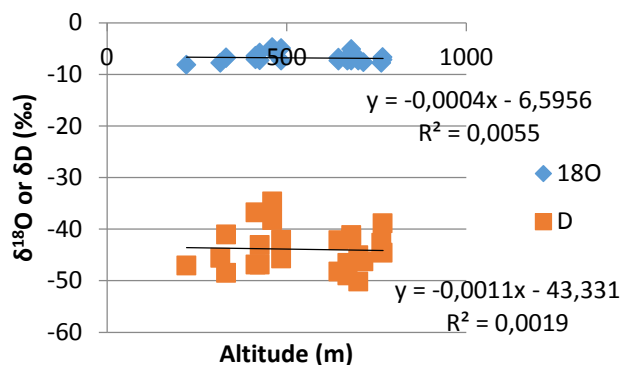


Fig. 10. Poor relationship between ^{18}O and D values and elevation in the research area.

Actually, there is narrow range of altitude in study area. Moreover, there is coarse relief result an unclear difference in isotopic values. It can also be interpreted that groundwater flows in local system, in short time, where evolution process hasn't been occurred to make any change of isotopic value or enrichment. The recharge may be in near area with no significant difference of altitude, it seems no obvious isotope enrichment.

CONCLUSION

The topographic parameters that affect groundwater flow are elevation and slope of landscape with medium - very strong correlation. The relationship between elevation and groundwater

gives r value of 99.99%, while slope make r value of 54.16%. Unfortunately, the isotopic value doesn't support the phenomena, but this isotopic data prove a variable value of local groundwater flow that is not controlled by altitude effect.

ACKNOWLEDGEMENTS

The authors would like to express gratitude to STTNAS and Ministry of Research, Technology and Higher Education for funding from DIPA-042.06.1.401516/2018, December 5th, 2017. The award is also dedicated to UNPAD for the encouragement of this research.

REFERENCES

- [1] Van Bemmelen, R.W., The Geology of Indonesia. Vol. 1A, Martinus Nijhoff, The Hague, Netherland, 1949, pp. 546, 594 – 602.
- [2] Geological Agency, Atlas of Groundwater Basin Indonesia, Department of Energy and Mineral Resources, Bandung, ISSN 987-602-9105-09-4, 2011, pp. 14.
- [3] Listyani, T., Sulaksana, N., Alam, B.Y.C.S.S.S.A., Sudradjat, A. and Haryanto, A.D., Lineament Control on Spring Characteristics at Central West Progo Hills, Indonesia, International Journal of GEOMATE, Vol.14, Issue 46, 2018, pp.177-184.
- [4] Rahardjo, W., Sukandarrumidi, and Rosidi, H.M.D., Geological Map of Yogyakarta, Scale 1 : 100.000, Center for Geological Research and Development, Bandung, 1995.
- [5] Kusumayudha, S.B., Model Konseptual Hidrogeologi Kubah Kulonprogo berdasarkan Pemetaan dan Analisis Geometri Fraktal, Proceedings of the 39th IAGI Annual Convention and Exhibition, Lombok, 2010.
- [6] Listyani, T., Sulaksana, N., Alam, B.Y.C.S.S.S., and Sudradjat, A., Quantitative Geomorphology of Landform at Samigaluh and Surrounding Area, West Progo, Central Java, Indonesia, Proceedings of The 2nd Join Conference of Utsunomiya University and Universitas Padjajaran, Japan, 2017, pp. 242 – 247, <http://hdl.handle.net/10241/10929>.
- [7] Freeze, R.A. and Cherry, J.A., Groundwater, Prentice-Hall, Inc., Englewood Cliffs, New Jersey, 1979, pp.193 – 196.
- [8] Todd, D.K., Groundwater Hydrology, 2nd Ed. John Wiley & Sons Inc, New York, 1980, pp. 13 – 17, 47 - 50.
- [9] Lee, K.-S., Wenner, D.B., Lee, I., Using H-and O-isotopic Data for Estimating The Relative Contributions of Rainy and Dry Season Precipitation to Groundwater: Example from Cheju Island, Korea, Journal of Hydrology, Elsevier, Vol. 222, 1999, pp. 65 – 74.

COMMUNITY EMPOWERMENT IN PLANTING VEGETATION TO REDUCE COASTAL ABRASION IN WEST SUMATRA

Taufika Ophiyandri¹, Bambang Istijono¹ and Abdul Hakam¹
¹Disaster Studies Center, Andalas University, Padang, Indonesia

ABSTRACT

The length of the West Sumatra Province coastline is 420 km. The coastal area has many settlements and as a source of natural attraction for tourism industry. However, in recent years there has been considerable damage due to abrasion occurring at approximately 180 km of coastal length. This paper aims to identify the relationship between the types of vegetation that grow along the coast with the abrasion rate and to identify the role of the community for conservation of vegetation. The aim is achieved through literature review, observation, and interviews with government official and communities who live on the beach. Data processing is done by analyzing the relationship between abrasion rate and vegetation type, and by conducting content analysis on interview data. It was found that certain types of plants have the ability to cope with and reduce abrasion rates. Plant breeding and planting is recommended to be a part of non-structural mitigation efforts. Community empowerment in planting and maintaining vegetation provides excellent results for sustainability.

Keywords : community empowerment, disaster, abrasion, coast, vegetation

INTRODUCTION

Indonesia is one of the largest archipelagic countries in the world and has a long coastline. The Geospatial Information Agency of Indonesia (BIG) [1] states that the total length of the Indonesian coastline is 99,093 kilometers. The coastal area of Indonesia has a huge natural resource, both its term of resources and its beauty that can attracts tourists. However, the condition of coastal areas in Indonesia is very worrying due to the occurrence of abrasion [2]. Diposaptono [2] states that around 100 locations in 17 Provinces with a coastline of approximately 400 km have experienced a severe coastal erosion. Hakam et al [3] adds that some areas that are at high risk for abrasion are South Aceh and Banda Aceh City in Aceh Province, Medan City, North Jakarta Municipality, Rembang Regency in Central Java, Bali, Sikka Regency in East Nusa Tenggara, Selayar Regency in South Sulawesi, and including some areas in West Sumatra Province.

A study conducted by BWSS V [4] has identified 14 critical beaches in West Sumatra Province, namely Air Bangis Beach, Sasak Beach (Pasaman Barat Regency); Tiku Beach (Agam Regency); Pasir Baru Beach, Pariaman Beach, Ketaping Beach (Padang Pariaman Regency); Pasir Jambak Beach, Padang Beach, Bungus Beach (Padang City); and Carocok Painan Beach, Luhung Beach, Surantih Beach, Kambang Beach, Air Haji Beach (Pesisir Selatan Regency). Furthermore BWSS V [4] noted that from 420 km of total coastline of West Sumatera, 45% (approximately 180 km) of which are severely damaged by abrasion. The abrasion has negative impacts, such as the damage to houses on the beach, the destruction of roads, and the

destruction of several beaches used as tourist attractions. As a result, the community's economy becomes disrupted. Therefore, it is necessary to mitigate abrasion disaster in West Sumatera Province.

Abrasion mitigation efforts can be carried out in several ways. One of them is by constructing coastal protection buildings, such as groin, jetty, and seawall. However, this method is very expensive, thus due to budget limitations not all beaches can get this kind of protection. A cheaper way is to plant / conserve plants that can reduce abrasion rates, such as mangrove trees, waru trees, coastal pines, and ketapang trees. This type of conservation has begun to be encouraged in West Sumatra, especially since 2010. Planting can be carried out by the government themselves or in cooperation with local community.

Based on above, the objective of the paper is to identify the correlation between vegetation that grows along the coast and the abrasion rate, and to explore the role of community in beach conservation.

LITERATURE STUDY

The coast is the border between land and sea which is affected by the highest tide and the lowest tide. Yuwono [5] explains that the coast is influenced by two factors: the influence of land and the influence of the oceans. Coastlines may change due to: the dynamic of wave characteristic, abrasion, sedimentation, and beach construction [3].

According to BNPB [6], abrasion is a process of coastal erosion by destructive sea power and ocean currents. Abrasion is often referred to coastal erosion. Coastal damage due to abrasion is triggered by the disruption of the natural balance of the coastal

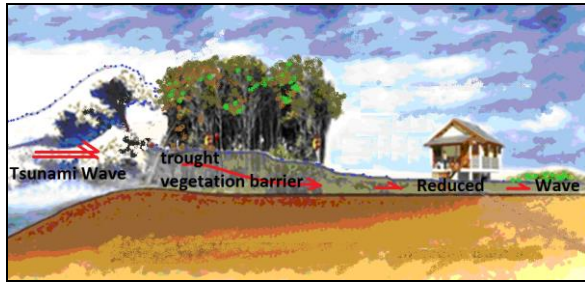


Fig. 2. Coastal vegetation can also inhibit the rate of tsunami waves.

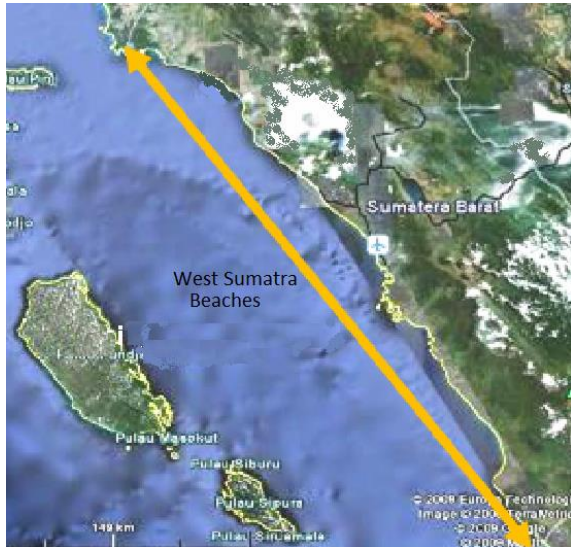


Fig. 3. The location of the coast of West Sumatra Province is the location of the case study

The first step of the study was to conduct a literature study related to coastal abrasion that occurred in West Sumatra. Journals, books, and project reports related to coastal safety are the key materials to be studied. This is done to get an overview of the abrasion conditions and what efforts have been made to mitigate abrasion disasters.

Further, interviews were conducted, both with government and community. The questions asked are related to abrasion, mitigation efforts, the results obtained from the mitigation that has been done, and how the model of community empowerment has been implemented. The number of government respondents is 4, consisting of 2 persons in the Office of Marine and Fisheries (DKP), 1 person from the Department of Tourism, and 1 person from the Department of Forestry. Interviews were conducted at the offices of each respondent. While for the community, interviews is carried out directly at the observation area. The people interviewed are individuals and some are in groups. The question posed is how severe the effects of abrasion after planting the coastal vegetation, and what their role and involvement in vegetation planting.

Along with community interviews, field observations were also conducted to see the impact

of vegetation in reducing abrasion rate. The observation areas are several beaches in Pesisir Selatan, Padang, Padang Pariaman, and Agam.

After the data were collected, an analysis of the correlation between vegetation and abrasion rate was done, as well as discussion on community participation and conservation of vegetation.

RESULTS AND DISCUSSION

In West Sumatra, the type of vegetation that commonly planted for abrasion mitigation is the cultivation of coastal pine. Planting mangroves is very rare because mangrove requires a very special treatments and some prerequisites to grow well, such as the land has to be muddy, relative flat slope, steady ocean waves, specific tides of sea water. Such conditions are very rare on the west coast of West Sumatera. Respondents from the Office of Marine and Fisheries and Department of Forestry are also stressing above condition.

On the other hand, the cultivation of pine crops does not necessarily require special conditions. These plants can be grown easily on sandy beaches. Data from the Directorate of Coastal and Marine Department [8] shows that total land that has been planted with coastal vegetation is 52.54 ha consisting of 56,926 sea pines and 1,451 breadfruit stems. The spacing of the pine is 3 x 3 meters. Detail of planting location as seen in Table 1.

Fig. 4 shows the cultivation of sea pine at Tiku beach, Agam Regency. On the right it can be seen young pines are still protected with fence.

If it has grown up, the sea pine looks very beautiful and can make the shore area becomes shady. In some areas, beaches that have been successfully planted sea pine have turned into a tourist attraction as shown in Fig. 5.



Fig. 4. Planting pine on the beach of Tiku

Field observations shows that sea pine plantation can reduce abrasion rate (Fig. 6 and Fig. 7). The investigation on the effects of the sea pine to the coastal abrasion also has been observed [9]. The one of advantage the tree for coastal protection is the shoreline change can be limited. It is better than the use of hard structures which can create accretion and erosion [10] in the shoreline. Fig. 6 shows the height

difference between the shoreline due to the roots of the pine trees that still hold the sand. While Fig. 7 shows the ability of pine culls to retain coastal erosion.

Table 1. Location of pine cultivation in West Sumatera Province

No.	Regency	County	Total Area (m ²)
1	Pasaman Barat Regency	Nagari Sasak	12,292.0
2	Pasaman Barat Regency	Nagari Katiagan	10,850.0
3	Agam Regency	Nagari Tiku V	44,883.0
4	Agam Regency	Nagari Tiku V	41,496.0
5	Padang Pariaman Regency	Nagari Sungai Limau	48,258.0
6	Padang Pariaman Regency	Nagari Kataping	49,914.0
7	Pariaman City	Nagari Manggung	37,970.7
8	Pariaman City	Nagari Pasir Sunut	46,370.0
9	Padang City	Kel. Pasio Batigo	18,342.1
10	Padang City	Kel. Pasio Batigo	9,684.7
11	Pesisir Selatan Regency	Nagari Surantih	31,380.0
12	Pesisir Selatan Regency	Nagari Sungai Tunu Barat	33,959.0
13	Pesisir Selatan Regency	Nagari Punggasan Utara	42,377.0
TOTAL			525,426

In addition to the above field observations, the results of interviews with communities living in coastal areas also show that pine cultivation has been able to reduce the rate of abrasion. According to the community, the rate of abrasion is faster in areas not cultivated sea pine compared with areas planted by sea pine. Another positive impact that is not less important is to be a source of income for the local community. With more beautiful and shady beaches planted by sea pine, more tourists come the location. People can sell food and rent tents to tourists who come.

The success of pine cultivation is not easily obtained. According to one respondent, there was initially a refusal from the community to participate in the planting. The public doubts the success of this program. However, over time, by looking at the results that have been obtained by society, now community is asking their beach to be also planted

by sea pine.



Fig. 5. Adult sea pines make the beach area become shady and become a tourist destination



Fig. 6. Beach line height difference



Fig. 7. Sea pine roots are able to reduce the rate of abrasion

The success of this program lies in the empowerment of local communities. In the early stages, government conducted a socialization of the program. After that, formed a community group that will be responsible for planting and maintaining the plant. The formation of community groups is carried out by taking into account the economic and social conditions of the local community. Community groups can be established through the lowest administrative government unit in the village, called *lorong*, or can also be carried out by youth community.



Fig. 8. Fence for young sea pine

Treatment to sea pine is only needed when the plants are still young. In this case, communities are responsible for watering and making fences (Fig. 8).

The fences are made so that the cattle of the community such as goats or cows do not eat young new leaves. Because fencing and maintenance cost money, the government gives some money to the community to make the fence as well as to maintain it. Because the local community has been given the responsibility, then of course people will maintain the plants very well. This shows the sense of belonging of the community because it is

empowered by the government to participate in this conservation program.

According to community information, sea pine plants can grow rapidly. At the age of 1.5 - 2 years, the height of the tree can reach 3 meters.

CONCLUSION

The conclusions that can be drawn from this research is the planting of coastal vegetation, in this case the sea pine, can reduce the abrasion rate. After the plants become mature, the cultivated coastal area is transformed into a tourist destination that can increase the income of the community. Local community empowerment for planting and maintenance is an important element in coastal conservation success.

ACKNOWLEDGMENTS

This research is funded by Andalas University under Research Grant "KLAster RISET-PUBLIKASI GURU BESAR" in 2018. Thanks for our colleagues who has been budgeting such as research grant in our university.

REFERENCES

- [1] Geospatial Information Agency (BIG), 2013, available: <http://www.bakosurtanal.go.id/berita-surta/show/pentingnya-informasi-geospasial-untuk-menata-laut-indonesia>, accessed on 30 April 2017
- [2] Diposaptono, S., 2011, Disaster Mitigation and Climate Change Adaptation, Ministry of Marine Affairs and Fisheries, Directorate of Marine and Coastal and Small Islands. Jakarta.
- [3] Hakam, A., Istijono, B., Ismail, FA., Zaidir, Fauzan, Dalrino, and Revalin, 2013, Coastal Abrasion Handling in Indonesia, Proceedings of the National Seminar on Disaster Research, Mataram, 8-10 October 2013
- [4] Sumatra River Basin (BWSS) V, 2009, Identification of Critical Coast in West Sumatra Province, Project Report.
- [5] Yuwono, N., 2000, in the Inaugural Speech of UGM Professor.
- [6] BNPB, 2017, Defenition and Disaster Type, available at: <https://www.bnpb.go.id/home/definition>, accessed on April 30, 2017
- [7] Opa, ET., 2011, Coastal Line Changes Bentenan Village Pusomaen Sub-district, Minahasa Tenggara, Journal of Fisheries and Tropical Marine, Vol II-3, December 2011.
- [8] Directorate of Coastal and Marine Affairs, 2013, Coordination Meeting on Greenbelt Monitoring Result in West Sumatera, Exposure Material.

- [9] Istijono B., Hakam A. and Ophiyandri T., Investigation of The Effects of Plant Variety and Soil Sediment to The Coastal Abrasion in West Sumatra, International Journal of GEOMATE, April 2018, Vol.14, Issue 44, pp.52-57
- [10] Soedarto, Y.W., Hanum, L., Lestari, M.S., Analysis and Identification of Landuse on the Coastal Environment of South Sumatra using GIS, International Journal on Advanced Science, Engineering and Information Technology, Vol. 7 (2017) No. 3, pages: 785-791, 20 July 2017

THE EFFECT OF FLOOD TO QUALITY INDEX OF SOIL PHYSICAL PROPERTIES AT THE DOWNSTREAM OF KURANJI RIVER WATERSHED, PADANG CITY

Aprisal, Bambang Istijono, Taufika Ophiyandri and Nurhamidah
Andalas University, Padang, Indonesia

ABSTRACT

The downstream of the Kuranji watershed of Padang City is vulnerable to flood due to the changes of land use into settlements area. Land use changes have changed the soil physical properties and its infiltration. The inundation has changed soil physical properties, such as layers, textures, volume weight, pores, permeability, and soil organic matters. The objective of this research is to analyze the quality index of soil physical properties due to flood at the watershed of the downstream area of Kuranji River of Padang City. Research methodology adopted is by conducting a field survey. Location of the soil sample is selected by purposive random sampling and was analyzed at the Department of Soil Science Andalas University. Soil physical properties data was arranged as minimum data sets (MDS) to be analyzed with principal component analysis to identify the main factors most affected by the flood. The results show that the main soil physical properties influenced by the flood are texture and soil organic matter. Based on the calculation of selected values from the MDS data, the quality of the downstream Kuranji watershed is moderate to good.

Keywords: flood, watershed, soil quality index, soil physical properties.

INTRODUCTION

Floods can be inferred as a relatively high flow that transcends natural or artificial embankments in the river, varying magnitude by season, month to month, year to year [1]. Flooding can also be inferred as the flow of river water flow that is relatively larger than usual as a result of rain down in the upstream or in a specific place continuously so that can not be accommodated by the existing river flow, the water overflows out and inundates the area surrounding [2]. Flood is an ordinary natural event, then becomes a problem when it interferes with human life and livelihood.



Fig. 1 Area Flooded at Dadok Tunggul Hitam, Downstream of Kuranji Watershed.

Flood happens in Padang frequently, especially in the downstream of watersheds such as Kuranji watersheds (Fig. 1). The flood itself is a natural occurrence that occurs not suddenly but always

preceded by symptoms. These symptoms can, among others, arise due to the improper natural management of humans. Floods frequently occur in areas that have low elevation. According to Aprisal et al [3] floods generally are influenced by three main factors, namely (1) meteorological factors, (2) watershed factors, and (3) human factors. Critical meteorological factors are precipitation or rain.

The amount of rainfall in the upper watershed area of Kuranji river is quite high with an annual average of about 3,000-5,000 mm, and the erosion (rain damage to soil 5,603.11) is also high. Therefore, when viewed from the aspect of conservation, some of the land conditions in Kuranji watershed are critical because the surface flow and erosion of this land are quite high. This can be seen every time the incidence of heavy rain then visible fluctuations of river flow Kuranji river is very high with the color of dark brown (dirty water). This condition is an indicator that such rapid fluctuations are due to the high surface flow of rainfall due to low soil absorption. Correspondingly, high soil erosion causes the water to become cloudy. Whereas, the upstream watershed is expected to produce water that can flow into the middle of the city and as a source of life for the people of Padang. Frequent flooding in some areas downstream Kuranji watershed this floods occur due to high surface runoff and soil recharge that decreases due to damage to soil physical properties. According to the Public Works Department [4] floods are overflowing of water in river bodies due to silting by high

sedimentation, urban drainage channels and punishment whose capacity is smaller than the peak discharge of surface runoff due to more rain. This flood will inundate the lower regions.

RESEARCH METHODOLOGY

Time and Place

This research was conducted from March to May 2018 at the downstream Kuranji watershed in Padang city, West Sumatera province (Fig. 2). The name of specific locations are also shown in Fig. 2 that are:

- 1 Aie pacah 1
- 2 Aie Pacah 2
- 3 Gunung Sarek
- 4 Kurao Pagang
- 5 Gunung Pangilun
- 6 Ampang
- 7 Korong Gadang
- 8 Dadok Tgl. Hitam

Tools and Materials

The tool used in this research was a set of computer with ArcView / ArcGIS program, Microsoft Excel, measuring cylinder, bucket, Global Positioning System (GPS), infiltrometer, roller meter, ring sample, plastic, rubber, and book munsel.

Materials used in this study are Digital Elevation Model (DEM) data in the form of Triangulated Irregular Network (TIN), Kuranji watershed administrative map, land use map, soil type map, monthly rainfall data and water flow of Kuranji river.

Research Methodology

The research method conducted in the field was a survey method consisting of several stages: (1) preparation, including secondary data collection; (2) preliminary survey; (3) main survey; (4) analysis of soil in the laboratory; and (5) data processing and report preparation.

Preparation (collection and secondary data review)

a. Topographic maps

The basic maps used are 1: 200,000 scale topographic maps and SRTM data. This topographic map is used as the basis for drawing the boundary of the study site and the basis for the slope grade determination.

b. Slope class map

The slope map is derived from a 1: 200,000 topographic map interpretation and DEM data as well as the contours of SRTM processed using

ArcGIS 10.2 software. From the slope map is obtained classification of the slope class.

c. Land use map

Land use map is the result of interpretation of land cover map Indonesia year 2012 sheet 0814 Padang which then digitized using ArcGIS software 10.2.1.

d. Land map

The land map was obtained from the Land Sheet and Land Unit Map of Padang by the Soil and Agro-climate Research Center, Bogor in 1990 with a scale of 1: 250,000. Based on the map of land unit Padang sheet will be obtained land units in the river area Kuranji Padang.

e. Field unit map

Map of land was obtained by overlapping slope maps, land use maps and land maps. From overlay of slope map, land use map and land type map.

f. Rainfall data

Rainfall data used was the result of rainfall recordings from the rainfall precipitation station in Kuranji watershed area.

Preliminary Survey

The preliminary survey was to review secondary data, such as rainfall data, flood data or inundation in Kuranji watershed, especially in downstream areas. Then also to know the real state of the field and prepare and facilitate the primary survey. In the preliminary survey, checks on each unit of land. Inspections were conducted on land slope, land use and soil type, to determine the sampling points of the soil.

Main survey

At this stage, soil sampling was conducted for the analysis of soil physical characteristic determined by Purposive Random Sampling on units of land that have been identified as flood-prone areas. In addition, the measurement of infiltration rate of soil using double ring infiltrometry in each set of land has been determined. To establish a position at the point of sampling of the land that has been determined in the preliminary survey used Global Positioning System (GPS).

Laboratory analysis

Laboratory analysis was performed to assess the soil quality, analyzing the bulk density, total pore space by using the gravimetric method, the organic

material percentage by Walkley and Black method, soil permeability using Constant Head Permeability method, and soil surface texture by pipette and sieve method, while soil structure observed in the field. Analysis of rainfall data and its relation to Kuranji river debit of each rainfall by using the rainfall-runoff method.

Data processing

Data analyzing was done in two ways, first was the measurement data analysis using Microsoft Office Excel. Data analysis using Microsoft Office Excel is done by using the necessary equations and then entering the data into the equations. Second, used Minitab 17 software, for correlation analysis of soil physics and principal component analysis (PCA).

Soil quality can not be measured directly, but the indicator of soil quality is measurable. Each of these indicators is assigned a value and weight which will then be used as the basis for calculating the Soil Quality Index. The soil quality indicator is the nature, characteristic, or process of physics, chemistry, and biology that can describe soil conditions [5]. According to Partoyo [6], soil quality can be measured based on indicators of soil quality, the measurement of soil quality indicator will produce soil quality index. The soil quality index is an index calculated based on the value and weight of each indicator of soil quality. These soil quality indicators are selected from the characteristics that indicate the capacity and function of the soil.

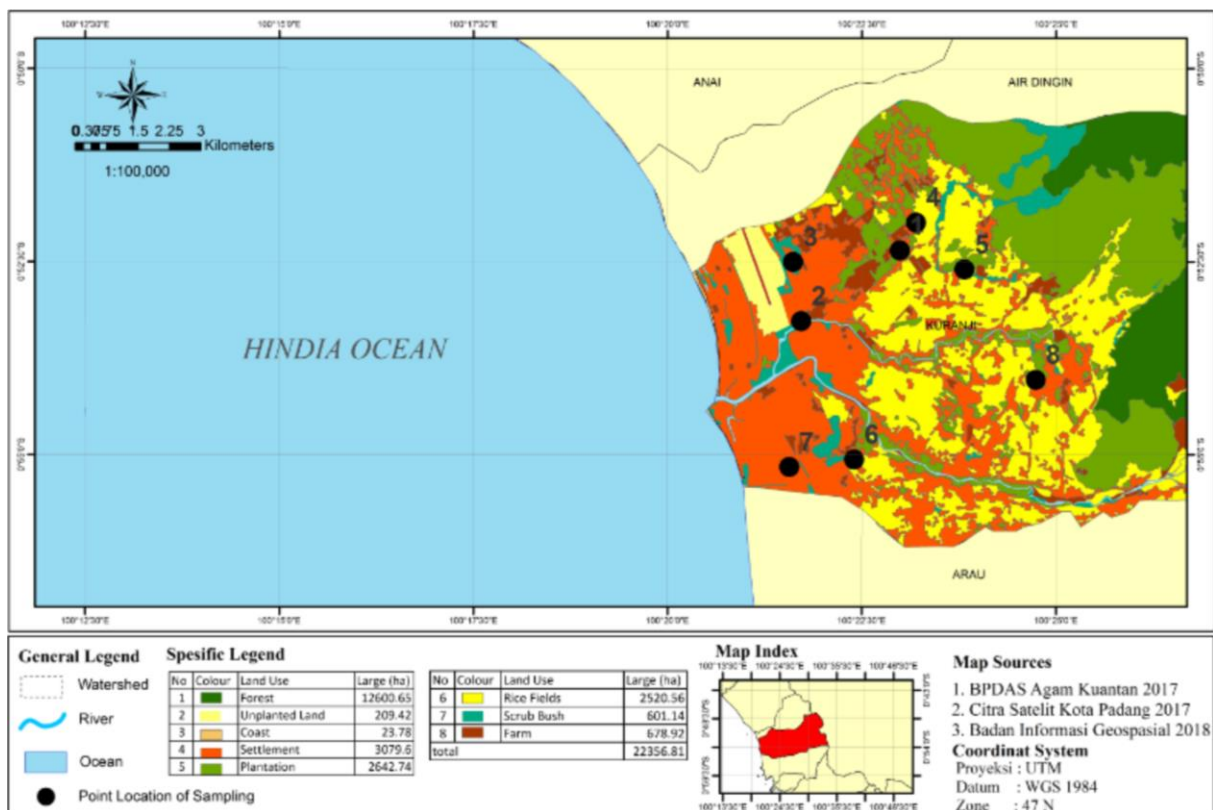


Fig. 2 Map of Kuranji Watershed Padang, plan of research location.

The sum of the indicator scores into an index of soil quality is carried out using the formula disclosed by Andrews et al. [7]: Soil quality calculation is done by multiplying the weight of MDS and scores of soil analysis results then summing the scores obtained on each land use. The data analysis score is 1-5. Systematically, soil quality rating can be calculated using Soil Quality Index (SQi) formula as follows;

$$SQ_i = \sum_{i=1}^n (W_i \times S_i) \quad (1)$$

Annotation :

SQ_i = Soil quality index

W_i = Weighting factor in PC

S_i = Score index

PC = Primary component of soil quality

If the index value has been obtained and to facilitate the quality of the soil in the lower Kuranji watershed, it can be done as described in Table 1. The result of Soil Quality Index (SQI) has a range between 0-1. The closer the SQI to 1, the better the value.

Table 1 Soil Quality Index

No	Value	Soil Quality Criteria
1	0.80-1.00	Very Good
2	0.6 - 0.79	Good
3	0.4 – 0.59	Fair
4	0.20 – 0.39	Bad
5	0.00 – 0.19	Very Bad
Source		Partoyo, 2005

Table 2 Soil Quality Indicator Score Criteria

No.	Indicator	Score					Sources
		1	2	3	4	5	
1	Depth of rooting (cm)	<10	10-15	15-20	20-25	>25	
2	Infiltration cm/hour	<5	5-10	10-15	15-20	>20	Arsyad, 2000 [8]
3	Soil content C–Org (%)	<1	1-2	2-3	3-5	>5	Balittanah, 2005
4	BV (g/cm ³)	>1,52	1,14-1,51	0,86-1,13	0,67-0,85	<0,66	Modification of LPT Bogor, 1979
5	Porosity (%)	<57	58-64	>88	75-88	65-74	Modification of LPT Bogor, 1979
6	Texture	S, Si	LS	SL, L, SiL	SiC, SC, SCL	SiCL, SC, C	Balittanah, 2005
7	Aggregate stability (%)	<40	41-104	105-200	201-328	<328	Modification of Balittanah, 2005
8	Permeability (cm/hour)	<0,5	0,6-10,4	10,5-25,4	25,5-45,3	>45,4	Modification of Arsyad, 2000 [7]

Remarks :

S	: Sandy	S _c	: Silty Clay
S _i	: Silty	CL	: Clay Loam
LS	: Loamy Sand	SCL	: Sandy Clay Loam
SL	: Sandy Loam	S _i CL	: Silty Clay Loam
L	: Loam	SC	: Sandy Clay
S _i L	: Silty Loam	C	: Clay

RESULT AND DISCUSSION

Principal Component Analysis

Based on the results of principal component analysis and correlation analysis (Table 1 and 2) shows that soil physical properties of porosity, permeability, volume weight, organic matter, infiltration, sand, dust, clay and soil depth are correlated. All physical factors are then analyzed using principal component analysis (PCA). In the research used as an MDS indicator based on principal component analysis are a sand fraction, volume weight, effective soil depth, and dust fraction (Table 3). The soil quality index is calculated only on the basis of the selected variables from the PCA analysis [9]. From the results of the major component analysis, there are some main factors that influence the quality of Kuranji watershed section based on the analysis of soil syphilis properties.

Correlation Between Soil Physics Characteristics in the Lower Kuranji Watershed

Soil porosity characteristics indicate the quality of soil because the porosity of soil determines the movement of water into the soil. The weight of the soil volume also indicates whether the soil conditions are solid or loose. The volume weight corresponds to the porosity of the soil; if the weight of the soil volume is high, then this indicates the soil is dense enough to be penetrated by the roots so that the plant can not develop properly.

Purkait [10] also states that soil physical characteristics are often determined by soil texture, since soil texture greatly affects other physical properties, such as bulk density, groundwater movement, specific surface area and soil density.

Soil Quality Index (SQI) in downstream Kuranji watershed will be analyzed using correlation analysis with sampling point taken to see the

correlation between sampling site characteristics with Kuranji River Basin Downstream SQI from soil physical characteristics aspect. The physical properties of the soil are greatly influenced by the processes occurring in the soil. According to Arsyad [7], the mechanisms in the binding of primary grains such as sand, dust, and clay to aggregate work in the soil, namely (1) The physical binding of primary grains by fungal mycelia and actinomycetes. The formation of this structure can occur the existence of clay fraction; (2) chemical bonding of the primary grains by bonding between the positive part of the clay grains with the negative cluster of long-chain organic compounds; (3) chemical bonding of clay grains by bonding between the negative part of the clay and the negative group in long-chain organic compounds with the base linkage (Ca, Mg, Fe) and hydrogen bonds; 4) chemical bonding of clay grains through the negative bonds with the positive cluster (amine, amide, amino) groups in organic compounds in the form of polymer chains; (5) chemical bonding of negatively charged clay beam through cation linkage and in this event dipole water molecules play an essential role at the initial stage; (6) chemical bonding of clay grains through the positive part of a grain with another part of the negative grain.

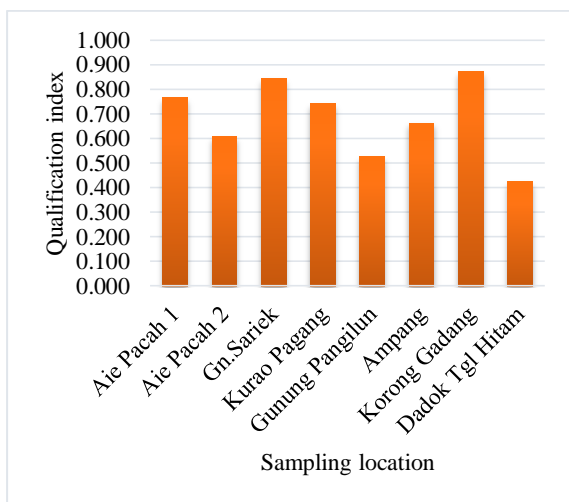


Fig. 3 Quality Index at the Sampling Location in Kuranji Padang Downstream.

Quality Index of Kuranji Downstream Watershed

Quality index of Kuranji downstream watershed from the soil physical characteristic aspect is shown in the Table. The quality range of the lower Kuranji watershed was 0.424 to 0.873.

Based on the analysis of the soil quality indicator characteristic of the physical aspects of the watershed, the value of the soil quality index (Table 3) was obtained. The result of calculation of soil quality index found that soil physical properties factors that affect the quality index are texture properties, bulk density, and effective depth of soil. The excellent soil quality index value is found in Aie Pacah 1, Aie Pacah 2, Gunung Sariak, Kurao Pagang, Ampang, and Korong Gadang. The excellent quality of soil in this area is caused by the soil is still overgrown by vegetation that can improve the soil properties due to the influence of the crops. Supriyadi et al. [8] and [11] it also shows that tree crops such as agroforestry can improve soil physical characteristics due to a significant amount of cellulose content and litter produced. This material will be composed to improve soil characteristics.

Bad condition was found in the area of Gunung Pangilun and Dadok Tunggul Hitam (Figure 3). The occurrence of soil quality index decline in some locations in downstream Kuranji watershed, caused by the damage to physical properties such as soil texture due to the enrichment of materials inundation and sedimentation ponds. This also leads to soil compaction due to soil pores that are softened by fine fractions such as sand, dust and clay from sedimentary materials. This causes the difficulty of water flow to the deeper layer of soil and easily caused puddle in case of more rain. Soil damage will also increase if water puddles occur for a long period of time. Usually, this kind of effective soil depth is also swallowed. For example Dadok Tunggul Hitam area and Gunung Pangilun, the groundwater is only about 20 cm. So in these areas often occur inundation if more rain happened. Harjowigeno [12]. In addition, the soil in the downstream river basin is strongly influenced by the nature of texture, organic matter and soil porosity as well as ground material. This soil is generally an alluvial soil which is the soil of sediment from the runoff of the flood. These soil characteristics greatly affect the quality of the soil in the watershed. The degradation of soil quality will be due to the ecological function of the soil in the watershed. According to Seybold et al. [13]: (1) maintain the activity, diversity, and biological productivity of soil, (2) regulate the availability of water and solutes, (3) as filters and buffers, suppress immobilization and detoxification (1998) organic and inorganic materials including industrial and municipal wastes, (4) storing and recycling organic and inorganic elements in the earth's biosphere; (5) providing socio-economic structural support and protecting archaeological remains related to human habitation.

Table 3 Correlation of Soil Characteristic Variables in Lower Kuranji Watershed, Padang

	KI	BV	TRP	C ogk	Perme	Sand	Dust	Clay
BV	-0.186 0.631							
TRP	0.186 0.631	-1.000 *						
C ogk	-0.351 0.355	0.116 0.765	-0.116 0.765					
Perme	0.819 0.007	-0.386 0.305	0.386 0.305	-0.004 0.991				
Sand	0.572 0.107	-0.774 0.014	0.774 0.014	-0.358 0.344	0.709 0.033			
Dust	-0.635 0.066	0.521 0.150	-0.521 0.150	0.135 0.729	-0.723 0.028	<u>-0.861</u> 0.003		
Clay	-0.404 0.281	0.822 0.007	-0.822 0.007	0.467 0.205	-0.553 0.123	-0.910 0.001	0.572 0.107	
Depth	0.640 0.063	-0.062 0.874	0.062 0.874	-0.672 0.047	0.322 0.399	0.451 0.223	-0.539 0.134	-0.287 0.454

Cell Contents: Pearson correlation, P-Value

Table 4 Result of MDS (Minimum Data Set) Analysis Using Principal Component Analysis

Eigenvalue	5.1358	1.8711	1.2268	0.4349	0.2283	0.0831	0.0201	0.0000	0.0000
Proportion	0.571	0.208	0.136	0.048	0.025	0.009	0.002	0.000	0.000
Cumulative	0.571	0.779	0.915	0.963	0.989	0.998	1.000	1.000	1.000
Variable	PC1	PC2	PC3	PC4	PC5	PC6	PC7	PC8	PC9
KI	0.303	0.411	-0.280	0.352	-0.435	0.437	-0.396	-0.000	0.000
BV	-0.341	0.428	-0.132	0.067	0.395	-0.041	-0.144	0.499	-0.501
TRP	0.341	-0.428	0.132	-0.067	-0.395	0.041	0.144	0.499	-0.501
C ogk	-0.177	-0.355	-0.673	-0.261	-0.144	-0.315	-0.448	0.000	0.000
Perme	0.333	0.122	-0.509	0.381	0.085	-0.386	0.560	0.000	-0.000
Sand	0.431	-0.061	0.007	-0.094	0.381	0.022	-0.216	-0.553	-0.551
Dust	-0.371	-0.095	0.268	0.587	-0.320	-0.398	-0.139	-0.280	-0.279
Clay	-0.392	0.176	-0.230	-0.327	-0.352	0.289	0.461	-0.343	-0.342
Depth	0.234	0.529	0.221	-0.441	-0.314	-0.561	-0.093	0.000	0.000

CONCLUSIONS

Table 5 Quality Index Value of Physical Aspects of Downstream Kuranji Watershed, Padang

1	Aie pacah 1	0.766	Good
2	Aie Pacah 2	0.608	Good
3	Gunung Sariiek	0.843	Very Good
4	Kurao Pagang	0.741	Good
5	Gunung Pangilun	0.527	Fair
6	Ampang	0.663	Good
7	Korong Gadang	0.873	Very Good
8	Dadok Tgl. Hitam	0.424	Fair

Based on the research in downstream Kuranji watershed in Padang, it can be concluded:

1. The result of correlation analysis of soil physics showed that each soil physics characteristics has a strong correlation.
2. PCA analysis results show that the main factors in influencing soil quality in downstream Kuranji watershed are soil texture characteristics, bulk density, and soil depth.
3. Based on the soil physical characteristics calculation, the quality index on the downstream Kuranji watershed includes the criteria of moderate to excellent. Dadok Tunggul Hitam area is a concern because it is somewhat more prone to flood.

ACKNOWLEDGMENTS

This research is funded by Andalas University under Research Grant No 43/UN.16.17/ PP.RGB /LPPM/ 2018 dated April 23, 2018.

REFERENCES

- [1] ChowVenTe, Maidment, Mays Larry W.,1988, Applied Hydrology, McGraw-Hill International Edition.
- [2] Agriculture Dictionary. 1997. Published PT. Penebar Swadaya, Jakarta.
- [3] Aprisal, Bujang Rusman and Darmawan. 2017. The optimization of land use in the Batang Masang watershed to reduce the rate of surface flow, erosion, and sediment. (Case studies, Batang Masang watershed in Agam district, West Sumatra). Proceeding National Conference, University of Riau.
- [4] Flood and Sediment Control of Kuranji river, Padang City, Public Works Departement. 2015 (in Indonesia: Upaya Pengendalian Banjir dan Sedimen Batang Kuranji di Kota Padang). <http://pu.go.id/berita/10072/Upaya-Pengendalian-Banjir-dan-Sedimen-Batang-Kuranji-Di-Kota-Padang>, accessed Januari, 2, 2017.
- [5] Guidelines for Soil Quality Assessment in Conservation Planning. 2001. Natural Resources Conservation Services. Soil Quality Institute USDA.
- [6] Partoyo. 2005. Analysis of Soil Quality Index for Agriculture in Samas Beaches (in Indonesia: Analisis Indeks Kualitas Tanah Pertanian di Lahan Pasir Pantai Samas) Yogyakarta. Journal of Ilmu Pertanian Vol 12 (2) : 140 – 151.
- [7] Andrew SS, JP Mitchell, R Mancinelli, DL Karlen, TK Hartz, WR Howarth, GS Pettygrove, KM Scow, and DS Munk. 2002. On-farm Assessment of soil quality in California's Central Valley. Agron. J.94: 12-23.
- [8] Arsyad, S. 2010. Soil and Water Conservation (in Indonesia: Konservasi Tanah dan Air) IPB Press. Dargama, Bogor.
- [9] Supriyadi, Sumarno, Sri Hartati, Cristiningsih. Assessment the Sustainability of Watershed with Soil Quality Based on Soil Physical Properties of Various Type Agroforestry. Proceedings of the National Seminar on Land of Suboptimal, Palembang 26-27 September 2014 ISBN : 979-587-529-9.
- [10] Purkait, B. 2010. The Use of Grain Size Distribution Patterns to Elucidate Aeolian Processes on a Transverse Dune of Thar Desert, India. Earth Surface Processes Landforms. 35 : 525-530.
- [11] Istijono.B. 2006. Watershed Conservation and Economic Analysis (in Indonesia: Konservasi Daerah Aliran Sungai dan Pendapatan Petani : Studi Tentang Integrasi Pengelolaan Daerah Aliran Sungai (Case study: Sumani River Basin, Solok District/Solok City, West Sumatera). Dissertation of PPs. Andalas University.
- [12] Hardjowigeno. 2007. Soil Sciences (in Indonesia: Ilmu Tanah). PT. Mediatama Sarana Perkasa. Jakarta.
- [13] Seybold, C.A., Mausbach, M.J., Karlen, D.L., and Rogers, H.H. 1998. Quantification of Soil Quality. p. 387 – 404. In : R. Lal, J. M Kimble, R.F. Follett, and B.A. Stewart (eds.) Soil Processes and The Carbon Cycle. CRC Press, Boca Raton.

ENVIRONMENTAL PARAMETERS CONTROLLING THE HABITAT OF THE BRACKISH WATER CLAM *CORBICULA JAPONICA* IDENTIFIED BY PREDICTIVE MODELLING

Yukari Sugiyama¹, Mikio Nakamura¹, Suguru Senda² and Michiko Masuda²

¹Japan Corbicula Research Institute Inc., Japan; ² Faculty of Engineering, Nagoya Institute of Technology,
Japan

ABSTRACT

The *C. japonica* is an ecologically important species in estuaries and brackish waters, as well as a very important fishery resource. However, the relationship between its habitation conditions and environmental factors remains unclear. We therefore made a habitat prediction model using GLM to define the environment of the *C. japonica* habitat of Lake Shinji, incorporating data acquired from 1982 through 1983 which measured population density, location, silt/clay content, ignition of physical environmental data, pH, dissolved O₂ density, chloride ion concentration, and COD of the quality of the water. Our analysis showed that the standardization parameter ignition loss, measuring organic matter and carbonate content in the sediment, was the main effect in the predictive model (estimate -2.22), and had the greatest absolute value. Thus the *C. japonica*'s distribution is dependent on ignition loss, in the predictive model. As for interaction terms modifying distribution, the dissolved O₂ and silt/clay content ratio had the largest absolute value at -2.12. In addition, it was revealed that the environmental factors which limit population levels of the *C. japonica* every season are different. These results, while derived from *C. japonica*, also suggest that our GLM model is effective to more fully understand the habitation area of immobile benthoses in general.

Keywords: *C. japonica*, GLM, Habitat suitability, Environment factor

INTRODUCTION

The *Corbicula japonica* is a representative species of estuaries and brackish waters. In Japan, it is widely distributed in brackish water lakes and rivers extending from Hokkaido to Kyushu, and has been considered to be an important resource for the brackish water ecosystem as well as playing a major role in the fresh water fisheries.

Brackish water ecosystems are inhabited with a relatively fewer number of species compared to fresh water or saltwater ecosystems [1]. Here, the species must adjust their bodies to the changes in salt concentration by regulating osmotic pressure. On the other hand, the species inhabiting both fresh water and seawater do not have the ability for such adaptation to survive a change in salinity. It is this limitation in physiological function which is thought to constrain the inhabitability of brackish water to adequately adapted species.

The *C. japonica* has a wide salt tolerance, and can survive at all salt concentrations between 0 and 22 ppt [2]. However, although it can survive in both freshwater and seawater, reproduction is severely inhibited. Instead, it requires 5 ppt for reproduction, and 1.5 to 22.5 for long-term survival. Because the *C. japonica* can adapt to salt concentration changes, it has become the overwhelming dominant species of estuaries and brackish water lakes in Japan. In

addition, the *C. japonica* plays an important role in nitrogen cycle of brackish water area [3]. Therefore it is thought that it is related to maintaining the quality of the water of brackish water area.

Lake Shinji of Shimane Prefecture is a brackish water lake with a large population of *C. japonica*. Present day Lake Shinji is derived from the Old Lake Shinji Gulf, formed when the sea level rose after a global thaw approximately 7,000 years ago. Over time, Old Lake Shinji Gulf and its derivatives have experienced numerous changes in salinity. 5000 years ago, due to an influx of sand and soil supplied by the Hiikawa River, Old Lake Shinji Gulf was separated from the Sea of Japan on the westside, but was still connected to the Sea of Japan through the Nakaumi Sea on its east side. As the sea level once again rose 1,200 years ago, seawater returned once more and Lake Shinji became higher in salinity, even more than at the present.

300 years ago, "Tatara iron-making" technology in the mountains near Lake Shinji developed rapidly, causing an increase in sediment runoff which eventually discharged into local streams and the Hiikawa River. As a result of this sediment discharged into Lake Shinji, the bottom of the lake on the east side rose, thus blocking the its outflow to the Nakaumi Sea, transforming Lake Shinji into a freshwater lake. Lake Shinji remained a freshwater lake for hundreds of years until the Ohashi River

was dredged, starting in 1924 and continuously thereafter. At this point, seawater flowing into Lake Shinji increased and it became the current brackish water lake.

As the Lake Shinji has had good salinity conditions for *C. japonica* in particular, and they were allowed to thrive more than other species, an industry tailored toward harvesting them at Lake Shinji was developed. The catch of the *C. japonica* in Japan was approximately 60,000 tons in the 1970s, although it has drastically decreased since then, with a catch of approximately 7,800 tons in 2012. Lake Shinji in Shimane Prefecture is the main production center of *C. japonica*, with the largest fish harvests in the country. Approximately 20,000 tons were harvested in 1973, but likewise decreased continually thereafter, and the yield of the *C. japonica* in Lake Shinji became approximately 3,400 tons in 2014. Initially, fishermen thought the lower catch was due to a decrease in the natural population of *C. japonica* and set catch limits, however the decrease in catch amounts did not stop.

Several factors may have influenced the drop in the *C. japonica* population. Rapid economic growth from the 1960s through the 1970s led to increased water pollution in Lake Shinji. Construction of the Ohara dam on the Hiikawa River was completed in the 1980s. Furthermore, the construction of Hiikawa River and the Hiikawa flood control channel to provide linkage with the Kando River began in the 1990s. Thus the environment of the watershed surrounding Lake Shinji has greatly changed artificially. The ecosystem may also be greatly influenced by conventional maintenance such as river repair [4]. It is therefore necessary to examine the relationship between the river environment and the change of the quantity/quality of the natural resources used by *C. japonica*.

Importantly, the ecology of the *C. japonica* has many factors which have not been elucidated, and it has been difficult to identify the factors that has led to the reduction in its population. We therefore made a habitat prediction model using GLM (generalized linear model) to further define the environment of the *C. japonica* habitat. In a protection plan of the animal, analysis using GLM is carried out for relation about habitation density and environmental factors [5].

In this analysis, we considered the habitation restriction factors of the *C. japonica* in Lake Shinji.

MATERIAL AND METHODS

Study site

The place of investigation was Lake Shinji, located in northeast Shimane Prefecture, Japan (Figure1). Lake Shinji is approximately 17 km east-to-west and 6 km north-to-south, with a

circumference of 47 km and an area of 79.25 km². Its mean water depth is 4.5 m, and maximum depth of the water is 6.4m. Lake Shinji is the seventh largest lake in Japan by area. The average temperature is 14.4°C and receives 1800 mm of precipitation per year. Especially, it is much precipitation in summer and winter. The inflow rivers to Lake Shinji flows in from the north, the west, and the south, with the Hiikawa River being the greatest. Lake Shinji outflows to the Sea of Japan through the Nakaumi Sea and subsequently the Sakaisuido Channel via the Ohashikawa River, from where mingling seawater and freshwater produce the brackish lake water.

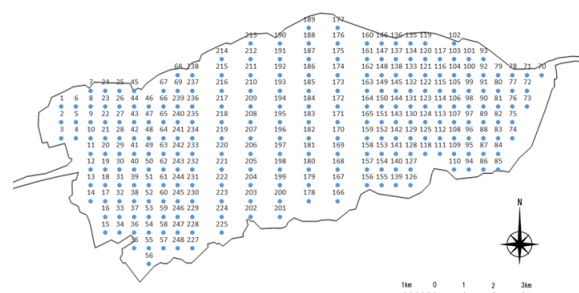


Fig. 1 Lake Shinji and the dots indicate the sampling spots.

Sampling methods

The samplings were carried out on 248 plots in summer (18th Jul. to 11th Aug in 1982), on 60 plots in spring (25th to 30th Apr. in 1983) and in autumn (25th to 30th Oct. in 1983). The eight environmental parameters, water depth, water temperature, pH, dissolved oxygen density, chloride ion concentration, chemical oxygen demand (*COD*), loss on ignition, clay sediment granulometry (<75 μ m, 75 μ m - 2 mm, >2 mm), and silt content, were measured in each season. The sampling method of bottom water was done by Kitahara-type B sampler within 10cm from the bottom. The sampling of bottom mud was done by Ekman-Birge grab. The water pH was measured pH meter (TOYO TD21R), Dissolved oxygen density was measured sodium azide variant method, chloride ion concentration was measured Mole method, chemical oxygen demand was Alkaline permanganate acid method. Dried cores were burned in the muffle furnace (800°C 4days) to measure loss on ignition. Clay/silt ratio was measured 0.075mm mesh sieve.

To counting the number of *C. japonica*, we used Smith McIntire grab (0.05 square meters) 1 to 3 times at each plot. The sampling mud was washed by a 0.05 mm mesh sieve and remained matter was fixed with 10% formalin. Over 4 mm size of *C.*

japonica were counted in each plot.

Statistical analysis

We performed analysis using GLM (using quick-R: correspondence analysis program) to elucidate habitation density of the *C. japonica* and its relationship to environmental factors. The environmental parameters used in this study assumes eight kinds of measurement data. The population of *C. japonica* at each plot was converted to individual counts per square meter.

In this study, the response is the population density of the *C. japonica*. Thus, we supposed that the probability distribution of the response obeyed negative binominal distribution. In the case of zero data (plots where 0 individuals were recovered), these were excluded from the response model.

To explain the distribution of density, our model assumes a main effect term (when a factor acts alone) and an interaction term (when two factors interact). In the case of interaction terms, we performed centration for 2 variables beforehand and incorporated it as an explanation variable. In total the model assumes 28 variables of interaction between 2 factors as explanation variables, in addition to the main effect variable(8 variables).

As a standard to evaluate the good model, we used by Akaike information criterion (AIC).

RESULTS

Field census

The population density of the *C. japonica* varied according to the season. The result of each season is compiled in Table 1. The summer season had the highest density as compared to spring and fall (Table 1, Figure 2).

Figure 3 shows the environmental descriptors of water and bottom sediment in summer. The water depth of Lake Shinji was 0-6 m, and it is deepest at the center of the lake. The maximum water depth was 5.6 m. Seasonal change in water depth was not observed.

The water temperature (Temp) was uniform in the summer. But a part of the north lake shore and south lake shore exceeded 28 °C. The summer term was 8°C warmer than the other seasons. pH measurements ranged from 7-8 within the whole lake. Dissolved oxygen (DO) was less than 3 ppm at the center of lake in the summer. In other seasons, the same values as described were seen except for dissolved oxygen, which was lower in summer.

Chloride ion density (Cl⁻) was also higher in the center of lake than other plots in summer.

The values of COD (chemical oxygen demand) and ignition loss (IL) showed distributions at the center of lake at levels detrimental for habitation. The distribution of the clay silt ratio (S) showed a value of 80-90% in the center of the lake, 4 times higher than other areas throughout the season.

Table 1 The density of *C. japonica* (number/m²) in each plot. Number of plots was indicated in parenthesis.

Season(No.)	Mean±SD	Max	Min (No.)
Summer(248)	329±1,134	5,030	0(125)
Summer(60)	463±857	3,890	0(26)
Spring(60)	229±410	1,620	0(26)
Fall(60)	256±407	2,140	0(27)

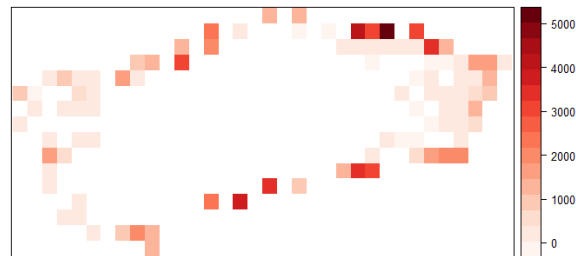


Fig. 2 The population density of the *C. japonica* in summer. The unit of range is number/m².

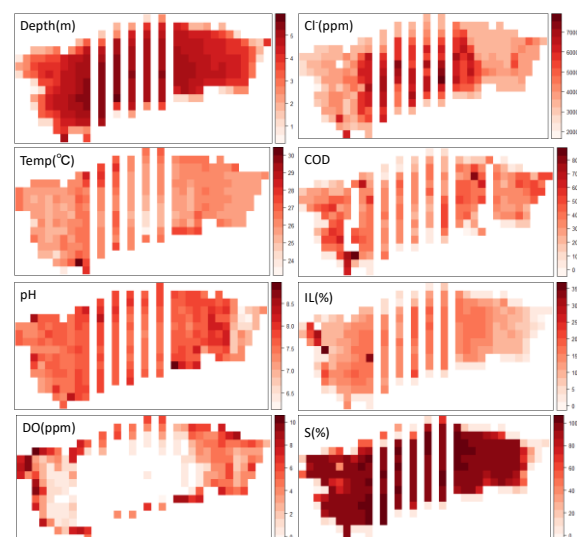


Fig. 3 Environmental parameters as indicated of each plot in the summer census of Lake Shinji.

C. japonica habitation model

A newly created *C. japonica* habitation model of the summer season found the main relationship effect variable on population density to be the

standardization parameter ignition loss (IL), with a value of -2.22. This was the biggest value by absolute value of all effects calculated. The Wald statistic value was -5.644 indicating significance. As for interactions, the value of the standardization parameter dissolved oxygen (DO) and the clay silt ratio (S) was calculated to be -2.22, which was the largest absolute value of all interaction terms. Furthermore, the clay silt ratio (S) influences many parameters, and it is thought that it is an important parameter.

In the model of the spring season, statistical significance was confirmed in all parameters. As for interactions, the value of the standardization parameter of COD and the clay silt ratio (S) by was calculated to be 25.06, which is the largest absolute value. Secondly, the parameter of COD and the clay silt ratio (S) was 23.98.

In the fall, significance was confirmed in all parameters. As for interactions, the value of the standardization parameter water depth (D) and COD was calculated to be -166.49 and is the biggest by absolute value. Secondly, ignition loss (IL) and the clay silt ratio (S) was -111.79.

Suitable habitation model

Figure 4 shows the habitation model for each season from the GLM. Large parts of the calculated habitation model agree with the observed distribution data.

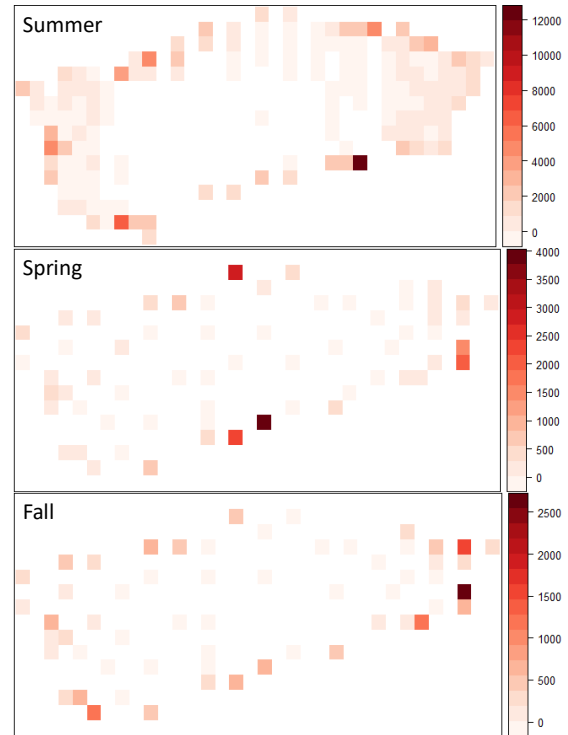


Fig. 4 Suitable habitation model of *C. japonica* predicted density. The unit of range is number/m².

From the data of the census and the expectation model, Figure 5 shows there was a relationship between expected density and the observed density. The model of the fall season is most consistent with observed data.

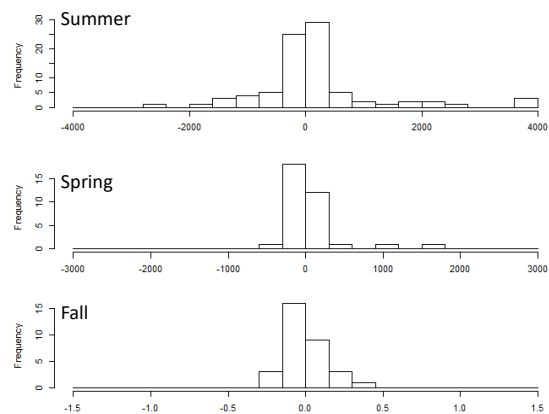


Fig. 5 The histogram is the differences of population between predicted value and the observation value of each season.

DISCUSSION

In this study, we performed analysis based on a supposition that an error structure of response y obeyed negative binominal distribution. However, the response had many 0 data, and a state of the overdispersion was confirmed. When a response has a significant amount of 0 data, statistics processing

becomes difficult. This is because bias is given to the distribution model [6], [7]. It has been suggested that GLM is not a good model for analysis of distribution as they had used all data points. In this paper, we used GLM analysis excluding only the 0 data, which greatly reduced the numbers of samples analyzed. However, our model was able to be predictive due to the high number of samples. The precision of the predictive model using GLM was low when there were many 0 data in the study of Silveira and others [8]. After performing analysis with the data from three seasons in this model, it was shown that environmental factors affecting the habitation of the *C. japonica* by season were different. In other words, it was revealed that it is applicable to GLM by considering the data between seasons when there were many 0 data. Specifically, as the benthos in particular has low mobility and is easy to receive environmental action [9], it is thought that the construction of the habitation model using GLM is effective. In the analysis of GLM for animals having high mobility, importance of the seasonal variation is suggested [10].

Lake Shinji is a main production district of the *C. japonica* and harvesting of the *C. japonica* is carried out through the year. The fisherman of Lake Shinji have been limiting fish catches and the fishery size for fisheries resource conservation. Only large individuals are removed from Lake Shinji by fishing. On the other hand, small individuals are not affected by the fishery. Thus, in the area where the fishery is prosperous, it is important to investigate the habitation conditions of the small individuals and their environment. Despite this, it is thought that there is a large natural decrease in population prior to maturation. After having shifted to bottom dwelling after the floating larva period, increased damage to the population of the next generation of natural resources will occur if there are few individuals which are able to mature. Therefore the construction of a habitation model of the *C. japonica* that focuses on the habitat environment of the small individual is in demand.

Recently maintenance of a river and the wetlands by flood measures has been an important issue. At the same time, such a maintenance is demanded from the consideration to environment. Some models for the purpose of the environmental grasp are thought about [11]. While such efforts are necessary for the maintenance of the environment, there are many uncertain points. As a result of this analysis, we have shown it is possible to apply a

model by GLM about *C. japonica* and various environmental factors. However, it is necessary for the survey data to be considered seasonally. By the assessment of the maintenance of rivers and wetlands, it is thought that a habitat environment prediction of the *C. japonica* is possible from the result of the four seasons investigation.

CONCLUSION

The following conclusions are drawn from the study.

- 1) The GLM model is effective to more fully understand the habitation area of *C. japonica*, immobile benthos in general.
- 2) However, it is necessary to take the data every season because there is a seasonal change in the habitation situation.
- 3) From a predictive model, we were able to predict a condition necessary for the environmental maintenance of the future lake.

ACKNOWLEDGEMENTS

We send thanks to Dr. Timothy F. Day which cooperated with the correction of this study. We also thank Dr. Kano and Diversity promotion center in Nagoya Institute of Technology.

REFERENCES

- [1] Remane A., Schlieper C., Schweizerbart'sche Verlagsbuchhandlung, Stuttgart. Die Biologie des Brackwassers, 1958, pp.348
- [2] Nakamura M., Shinagawa A., Toda A., and Nakao S., Environmental Tolerance of four kinds bivalves From Lake Shinji and Nakaumi sea. Aquaculture Science, Vol. 45, 1997, pp. 179-185.
- [3] Nakamura M., Yamamuro M., Ishikawa M., Nishimura H., Role of the bivalve *Corbicula japonica* in the nitrogen cycle in a mesohaline lagoon. Marine Biology, Vol. 99, Issue 3, 1988, pp.369-374
- [4] Masuda M., Sakakibara R., Sugimura N., and Nishimura F., Impact of Flood Disturbance Evaluation on the Structures of Ground-Beetle Assemblage at Biotopes. International Journal of GEOMATE, Vol. 5, Issue 9, 2013, pp.628-633.
- [5] Christophe J., and Antoine G., Modelling the distribution of bats in relation to landscape structure in a temperate mountain environment. Journal of Applied Ecology, Vol. 38, Issue 6, 2001, pp.1169-1181
- [6] Minami N., Cleridy E. L., The Analysis of Data with Much Zero: Excessive Estimate of The Tendency by The Negative Clause 2 Regression

- Model. Proceedings of the Institute of Statistical Mathematics, Vol. 61, Issue 2, 2013, pp.271-287.
- [7] Zeileis A., Kleiber C., Jackman S., Regression Models for Count Data in R. Journal of Statistical Software, Vol. 27, Issue 8, 2008.
- [8] T. C. L. Silveira, A. M. S. Gama, T. P. Alves and N. F. Fontoura, Modeling habitat suitability of the invasive clam *Corbicula fluminea* in a Neotropical shallow lagoon, southern Brazil. Braz. J. Biol., Vol. 76, No. 3, 2016, pp. 718-725.
- [9] Michael B., For Part1 in ECOLOGY, 4th ed., Wiley-Blackwell, 2005, pp.3-29.
- [10] Yokohata Y., Kitamura E., Suzuki M., Analyses of Relationships between the Abundance of Two Morphs of an Abomasal Nematode Species, *Spiculopteragia houdemeri*, in Sika Deer (*Cervus nippon*) from Hokkaido, Japan, and Some Relevant Factors using a Generalized Linear Model. Japanese Journal of Zoo and Wildlife Medicine. Vol.18, Issue3, 2013, pp.99-105
- [11] Irena N., Noorul H. Z., Sharif M. S., Nur 'A. R., Zulkifli Y., Mohd Ridza Bin Mohd H., Ranking of Skudai river sub-watersheds from sustainability indices-Application of promethee method. International Journal of GEOMATE. Vol.12, Issue29, 2017, pp.124-131

THE MANAGEMENT OF RIVERBANK MAINTAINS THE DUNE PLANT POPULATION, ESPECIALLY AN ENDANGERED SPECIES, *FIMBRISTYLIS SERICEA*

Michiko Masuda¹, Sota Yotsuya² and Fumitake Nishimura³

¹Department of Civil and Environmental Engineering, Nagoya Institute of Technology, Japan, ²Taisei Corporation, Japan, ³Department of Environmental Engineering, Kyoto University, Japan

ABSTRACT

The habitat of riverbank dune nurses several endangered species. Why did this area maintained endangered species despite of invasion of alien species? Then growth of an endangered species (*Fimbristylis sericea*) and an alien species (*Diodia teres*) was studied in a greenhouse experiment in which the species were grown alone or together and the resultant effects of shoot and root competition were assessed. In the alone growth experiment, the survival rates of the both species were same. In the shoot competition experiment, the *D. teres* reduced growth rate of *F. sericea*. In the root competition experiment, the *F. sericea* reduced growth rate of *D. teres*. In the total competition, *F. sericea* were superior to *D. teres*. From the experiments, *F. sericea* was more competitive than *D. teres* under the waterless same habitat. *D. teres* was more competitive than *F. sericea* under the waterrich condition. The habitat of riverbank dune is always affected strong wind, than the disturbance of sand moving. When *D. teres* is grown up, the sand moving prevented growth of *D. teres*. In the long term, the vegetation succession will reduce the disturbance frequency and will be occurred the extinction of endangered species.

Keywords: Endangered species, Alien plants, Riverbed dune, Water condition, Organic matter

INTRODUCTION

In Japan, dune vegetation and its endemic species are now in danger of extinction. Not more than a hundred years ago, it was not difficult to find extensive sandy beaches with huge dunes along the seashore. Like many other natural ecosystems, however, the area and number of extensive sandy beaches covered by typical dune vegetation had considerably decreased with the advance of modernization [1]. Especially the riverbank dunes are almost disappeared except Kiso river. There were mainly 3 riverbank dunes in Japan from some papers that reported about riverbank dune [2]-[4]. The dunes of Tone River and Kitakami River have been covered with vegetation, we cannot see the dune anymore except for Sobue dune in Kiso River.

Sobue dune allocated 25km from the mouth of Kiso River. Sobue dune have been maintained by the strong wind from the mountains and sand from the river stream. Furthermore, artificial disturbances are very important at Sobue dune. Athletics, a forest and a water sports place are maintained in the site, and such as the Bon dance is held, Sobue dune bustles with many people through a year. Especially disturbance by bulldozers has been done for the sand festival from 1990. The sand dune environment is maintained, there are many kinds of endangered species *Chenopodium virgatum*, *Fimbristylis sericea*, *Artemisia capillaris* and so on. These plants have

drying stress tolerant and regenerative power from the sand buried [5]. Therefore, sand dune vegetation peculiar to a sand dune is formed [1]. Further hard wind condition humus derives from organic matter at a sand dune. But it's little and scarce in the natural provision of the fertilizer components [5]. There are almost no cases that a plant specialized in adaptation to such sand dune environment goes into the environment besides the sand dune.

Recently some alien plants have invaded into the sand dunes [6]. Alien plants affected the growth of native plant and prevent the reproduction [7]-[9]. Alien species can easily invade in riverbed dune because Sobue sand dune is located near the city, and the disturbance frequency of Sobue dune is so high that invasion is easily petmitted.

F. sericea is endangered species in Japan. Their distribution is mainly on a coast in western Japan. The habitat of the species is only dune, so the area of the habitat will be smaller and smaller because of the human construction. The Sobue dune is rare habitat of the *F. sericea*, It's important to know what kind of influence of maintenance mechanism in a sand dune is having on an endangered plant species.

It's necessary to do a measure of maintenance of the sand dune area, prevention of planting trees and an extermination of alien species in preservation of the sand dune environment. In this study, we focused on the relationships between the ecology of *F. sericea* and sand dune condition. The methods of

endangered species conservation are proposed from the angle of river management on it. The purpose of our study is to find what kind of river management is useful for conservation of endangered species.

We have three hypothesis, 1)The dune condition is very dry and cannot maintain water, 2)the dry condition is very convenient of *F. sericea* because they have dry stress tolerant, 3)the light condition is very important for the species. It was paid attention to the three points and analyzed.

MATERIALS AND METHODS

The Study Site

The study was carried out on the riverside of Kiso River at Aichi Pref. (North 35°15'48", East 136° 42'19"), the middle of Japan. The area has been managed as wild nature plaza that called "Sario Park Sobue". In the Park there are some ecotone along the sand dune, river bed forest, low grassland and bare land. The area was divided 4 plots along with the vegetation types. Plot A was vegetation cover percentage was under 10%, plot B was from 10 to 50%, plot C was from 50 to 80% and plot D was over 80% (Fig. 1).

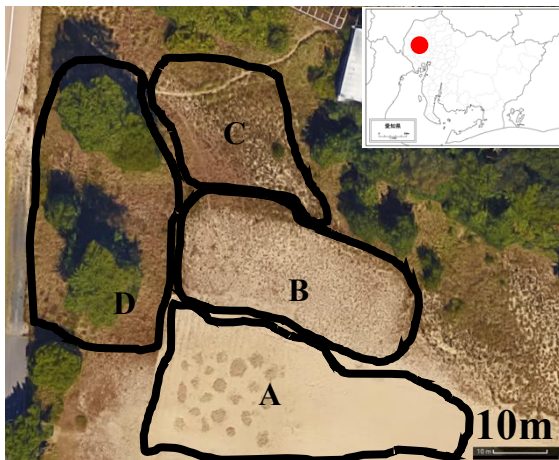


Fig. 1 The vegetation cover of each plots.

The Study Plant

Fimbristylis sericea (CYPERACEAE) is a perennial grass in sand habitat along the coast (Fig. 2-A). The species distributes from East Asia to South of Australia. The habitat of *F. sericea* is dry open sand condition, that is very rare habitat in Japan for the reason of dams and harbor construction and so on. Regardless rich number of individual, only four populations of the species observed in Aichi Pref., so the species was endangered species rank Vulnerable (VU) in Aichi Pref.

Diodia teres (RUBIACEAE) is annual plant introduced from North America in 1920's (Fig.2-B). The species is ruderal and strong competitor at the

river bed and sea shore. It has long stems, and lean and covered with other species. Recently many river and coast endangered species are affected by the species.

Environmental Condition Measurement

To measure the capacity of retained water in each plot, the soil samplings were done on 28th April (rainfall over 10mm), 29th (no rainfall) and 30th (no rainfall), 2016. Core sampling size was 60 mm in diameter and 45 mm in high. 10 cores were collected in each plot on every three days. The weight of fresh core samples were measured immediately. After drying in the drying machine (100°C 24hr), dried core samples were measured. The water content of core samples was calculated as (fresh weight – dry weight)/dry weight. Furthermore, dried cores were burned in the muffle furnace (1000°C 24hr) to measure loss on ignition. The loss on ignition was calculated (dry weight -burn weight)/burn weight. To detect the difference among plots, Shapiro-Wilk test for the distribution check and Wilcoxon rank sum test were used on non-normal distribution, and t-test were done on normal distribution.

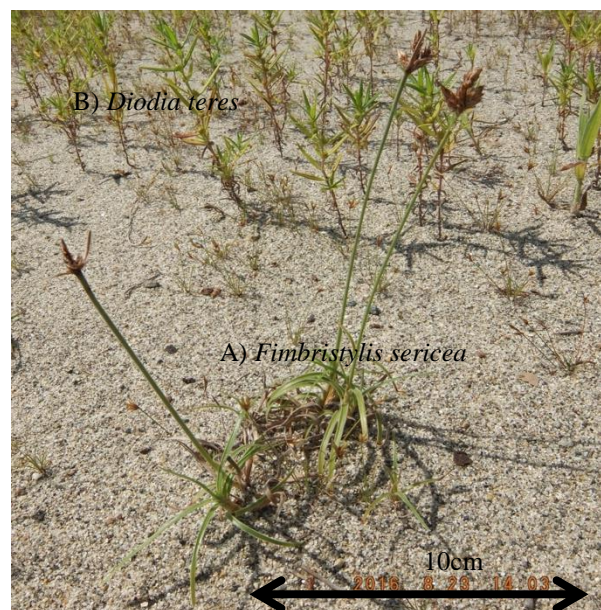


Fig. 2 Photograph of *F.sericea* and *D. teres*.

Competition Experiment

Four conditions were prepared to measure the competition between *F. sericea* and *D. teres*. First condition was single cultivate, second was competition between roots, third was upper side, forth was total competition (Fig 3). Each pot (9cm diameter 12cm high) was filled with 50ml volcano ash soil and 200ml sand as the habitat of *F. sericea* with low nutrient and water. This experiment done from 19th June to 27th July in 2016 in open area. Watering was performed every 2 days to prevent dry

up. Every week the survival rate was counted, and measured leaf number (LN) and leaf length (LL)(mm) on *F. sericea*, diameter of stem (DS)(mm) and height (DH) (cm) on *D. teres* to measure the growth four times.

Comparison of Growth

Fifteen *F. sericea* and 26 *D. teres* were collected to measure the expect dry weight (DW) of plants. It was measured about collected plants that leaf number and leaf length at *F. sericea*, diameter of stem and height at *D. teres*. Then each plants were dried (100°C 24hr). From the data, the regression was lead out, expected weight of plants was calculated.

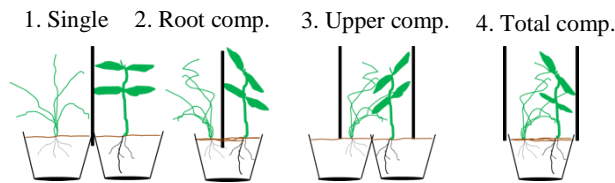


Fig. 3 Condition of four competition.

RESULTS

Water Condition

About the water contents on rainy day, there was no differences among the plots. But the decrease curve of the water condition was different among the plots. The distributions of each plot on 30th were normal distributions. Then the pairwise tests were done between two plots, there was a significant difference between plot A and plot B. Fig. 4 shows the water condition curve in each plot. Plot D had the high ability of water maintenance.

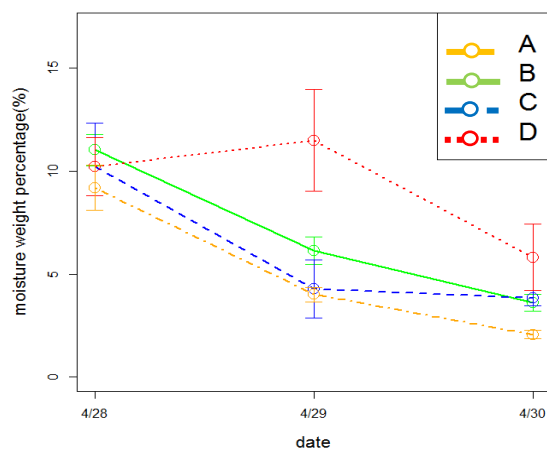


Fig. 4 The water loss curve of each plots after rainfall.

The loss on ignition at each plot were shown in Fig. 5. The loss on ignition was related to the vegetation cover rate. That of D was the highest in all plots. The nutrient of plot A was low for the shortage of organic substance. Though the distributions of plot A, B, D were normal, that of plot C is non normal. Then nonparametric test (Wilcoxon rank sum test) was done at plot C. There were significant differences between plot C and other plots ($P < 0.001$). Welch t-test was done at other plots. There were significant differences between plots ($P < 0.001$).

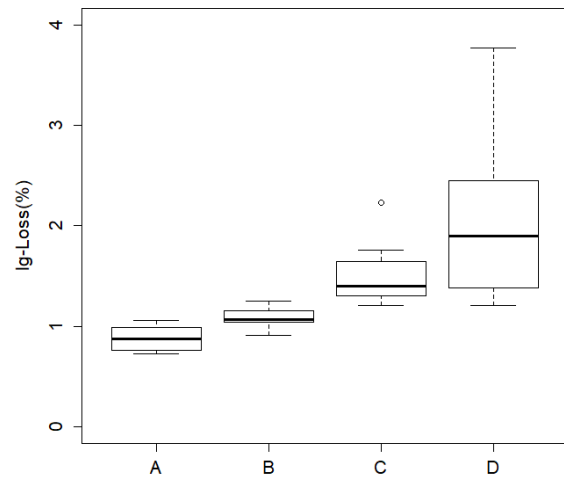


Fig. 5 The loss on ignition in each plot.

Competition Experiment

Fig. 6 showed the survival ratio in each competition. At the value of the single competition there was no difference between two species. But *D. teres* was superior to the *F. sericea* at upper part competition. At root competition and whole competition *F. sericea* was superior to *D. teres*.

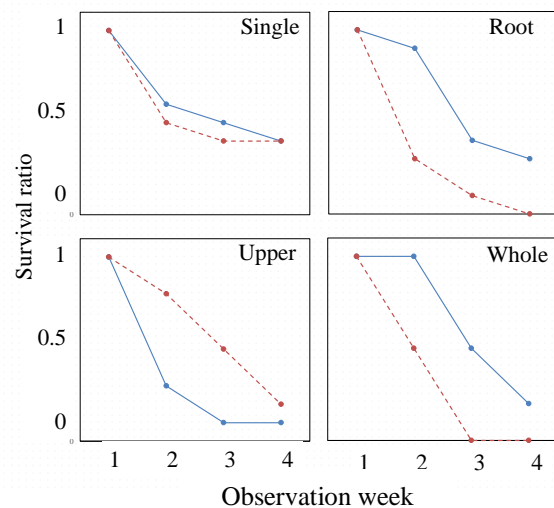


Fig. 6 The survival ratio at each competition (solid

line was *F. sericea*, dotted line was *D. teres*). Single: no competition, Root: upper part was separated, root was same pot, Upper: upper part competition with each pot, Whole: growth in same pot and no separation upper part.

The model of the dry weight at each measurement were Eq. (1) at *F. sericea* and Eq. (2) at *D. teres*.

$$\text{DW(mg)} = 0.0003 \times \text{LN} \times \text{LL} - 0.0061 \quad (1)$$

$$\text{DW(mg)} = 0.0009 \times \text{DS} \times \text{DH} + 0.0045 \quad (2)$$

Fig. 7 showed the growth ratio at each competition using Eq.(1) and Eq(2). There was differences between two species at each competition. At the no competition and upper competition, the growth ratio of *D. teres* was higher than that of *F. sericea*. On the other hand, at the root competition and total competition, the growth ratio of *F. sericea* was superior to alien species.

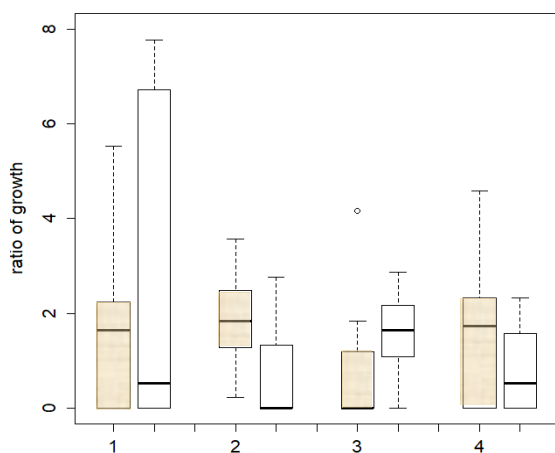


Fig. 7 The growth ratio of two species (hatched distribution: *F. sericea*, white distribution: *D. teres*) at each competition (1: single growth, 2: root competition, 3: upper competition, 4: total competition).

DISCUSSIONS

Form our research, it was revealed that the ecology of the *F. sericea* was adapted dry and oligotrophic condition. The physiology of the species was the character of dune plants [10]-[12]. For sufficient temperature and precipitation, the vegetation succession was occurred in all over Japan. Especially river environment has been stable for the dam and soil erosion control work construction [13][14]. The condition of the dune was destroyed the vegetation succession. When the succession promotes, the water condition was changed and the

nutrient supply occurred. The habitat of the *F. sericea* has been reduced from the river control.

Now the invasion of alien plants is serious problem in the river system [8][9]. But *D. teres* cannot invade the dune condition where the water and nutrient supply was not sufficient as other species, *Miscanthus sinensis* and *Imperata cylindrica* [15][16]. The native species *F. sericea* was superior to the strict condition. If the succession began, the light condition would be worse and the reduction of the distribution occurred. The light condition is another problem of sand area plant species. The artificial disturbance of the Sobue dune is very important for the endangered species.

The manager of Sobue dune is faced the financial crisis to maintain the dune. The cost of bulldozer to maintain the dune is almost two million yen per year. The manager wants to cut off the cost. And some nature conservation groups call for the halt to the disturbance by bulldozer for other animals.

For the biodiversity, it will be very good condition that many kinds of vegetation are maintained in the Park. Around Sobue dune, there are many kinds of biomes, like river bed dune, low grassland, dune, wetland, and so on. For other animals there are many places prepared. The succession is proceeded, it becomes all same vegetation, the unification advances. It is necessary to maintain the dune for the biodiversity.

The biodiversity has been reduced by the construction, the cost should be needed to maintain the biodiversity for the mitigation. And our research confirms the merit of the endangered species about the disturbance. The invasion of alien plants will be prevented by the disturbance. The manager of the Sobue dune has contributed to the maintenance of the biodiversity.

CONCLUSION

The following conclusions are drawn based on the study:

1) river dune condition is very strict for plants, because there are few water and nutrient for the sand as seashore dune, 2) *F. sericea* is stress tolerant about water stress and lack of nutrient, beside light condition, 3) light condition is very important for the species because *F. sericea* lost at the competition to the other taller plants, 4) *D. teres* (alien plant) cannot invade into the dune condition.

Based on the conclusion, two proposals about the management method of the disturbance, 1) the disturbance should be done before winter in order to release the nutrient matter from the sand, 2) the disturbance should be done in the area where the alien plants invaded, 2) the cost of the disturbance

must be needed for the construction to maintain the biodiversity for the mitigation.

ACKNOWLEDGEMENTS

We wish to thank the member of the Kiso river Office at Ministry of Land, Infrastructure, Transport and Tourism. We also thank the members of our laboratory for their assistance in the field works with statistical works.

REFERENCES

- [1] Yura H., Crisis and its factors of coastal dune vegetation, Japanese Journal of Landscape Ecology, Vol. 19, Issue 2, 2014, pp. 5-14.
- [2] Tada F., Sand dunes along the middle course of Tone River, Geographical Review of Japan, series A, Vol. 21, Issue 1, 1947, pp. 1-5.
- [3] Kagose Y., The Riverbed dune of Kitakami River, Geography of Japan, Vol. 10, Issue 1, 1965, pp.1-6.
- [4] Naruse T., Coastal sand dune in Japan, Geographical Review of Japan, series A, Vol. 62, Issue 2, 1989, pp. 129-144.
- [5] Sato, I., Sand Dune, nature and utilization, Seibunsha, 1986, pp. 36-37.
- [6] Yura, H. and Kaihatsu, N., The white paper of Seashore vegetation, Foundation of Japan nature conservation cooperation, Tokyo, 2008, pp.14.
- [7] Andersen, U. V., Comparison of dispersal strategies of alien and native species in the Danish flora, in Plant Invasion Pysek P. et al ed. Academic Publishing , Amsterdam, 1995, pp. 61-70.
- [8] Masuda, M., Ito, Y. and Nishimura, F., Process of invading the alien plant species into the river ecosystem, International Journal of GEOMATE, Vol. 1, Issue 7, 2011, pp. 437-442.
- [9] Masuda, M. and Nishimura, F., Seasonal variation of the alien plants invasion into river ecosystem, International Journal of GEOMATE, Vol. 8, Issue 11, 2015, pp. 1263-1270.
- [10] Marshall, J. K., *Corynephorus canescens* (L.) P. Beauv as a model for the *Ammophila* problem. Journal of Ecology, Vol. 53, Issue 2, 1965, pp. 447-463.
- [11] Van der Valk A. G., Environmental factors controlling the distribution of forbs on coastal foredunes in Cape Hatteras National Seashore. Canadian Journal of Botany, Vol. 52, Issue 5, 1974 pp 1057-1073.
- [12] Moreno-Casasola, P., Sand movement as a factor in the distribution of plant communities in a coastal dune system. Vegetatio, Vol. 65, Issue 2, 1986, pp67-76.
- [13] Koike K., Friendship of seashore, Iwanami Press, Tokyo, 1997, pp.131.
- [14] Sakio K., The history of tree in wetland, the University of Tokyo Press, 2017, pp.189-234.
- [15] Kachi N., and Hirose T., Multivariate approaches to the plant communities related with edaphic factors in the dune system at Azigaura, Ibaraki Pref. I. Association-analysis. Japanese Journal of Ecology, Vol. 29, Issue 1, 1979, pp 17-27.
- [16] Ishikawa S., Furukawa A. and Oikawa T., Zonal plant distribution and edaphic and micrometeorological conditions on a coastal sand dune. Ecological Research, Vol. 10. Issue 3, 1995, pp 259-266.

APPROACH TO ASSESSMENT OF SOIL AND WATER CONTAMINATION BY MINING ACTIVITIES IN MANDALAY REGION, MYANMAR

Than Htike Oo¹, Toshiro Hata¹

¹Graduate School of Engineering, Toyama Prefectural University, Japan

ABSTRACT

In Myanmar, the mining sector is playing an important role in contributing to the country's income. Thus, environmentally and economically sustainable mining activities are essential for the long-term development of the sector. In Myanmar, there were a few research for the contamination of surface soil and groundwater of harmful effects caused by improper mining activities. Most of the research interests are geologically mapping for potential area and chemical refining effect, not including the point of view about the environmental issue in mining areas. The environmental investigation is required in the near future to determine the detailed situation for surface and groundwater quality and human health. According to the previous study, arsenic concentration of groundwater has been found in some places of Sagaing, Mandalay, and Magway regions are higher than the WHO drinking water guideline value of 10 µg/L. Gold and copper mineralization is distributed with sulfide minerals in Mandalay region, Myanmar. Arsenic and heavy metal can be distributed into the environment naturally from the weathering, oxidation, and erosion of sulfide minerals. In this paper, authors presented the overview of drinking water standards from four Asian countries such as Indonesia, Japan, Myanmar and Sri Lanka. As a preliminary study, arsenic and some other heavy metal concentration in soil and rock (ore) samples will study from Gold and Copper mining site in Mandalay Region, Myanmar by different methods. The analytical method is also very important to approach the assessment of environmental contamination because Myanmar is launching the practice of environmental assessment.

Keywords: Mandalay region, Arsenic, Drinking water standards, Analytical methods

INTRODUCTION

At the present time, the crisis of decreasing water resources, rare of safe drinking water and impact of natural environment were facing in a lot of country in the world but the rate of population in the world is gradually increased day by day [1], [2]. Water is not only an essential material for the daily life of all living organism but also a crucial requirement to access the safe water for human health. Therefore, water quality guidelines and drinking water standards are also very important to assessment by waterborne pathogens and chemical to prevent the health of humans [2]-[4]. The means of safe drinking water is "does not represent any significant risk to health over the lifetime of consumption, including different sensitivities that may occur between life stages" which is defined in the WHO Guidelines [4]. In this paper, authors presented the overview of drinking water standards from four Asian countries such as Indonesia, Japan, Myanmar and Sri Lanka.

Such as industry and agriculture are the main ways for heavy metals to enter the environment by the human activities. Heavy metals produced during mining process have become one of the primary sources of soil pollution in the mining area. The

presence of heavy metals in contaminated soils is of great concern as they are not biodegradable and thus pose a risk for humans and the environment [5], [6]. Among them, arsenic (As) is one of the most common metals in contaminated sites because of its widespread accumulation in air, rock, soils and water by naturally and industrially [7]. In Myanmar, the mining sector is playing an important role in contributing to the country's income as a country endowed with rich mineral resources and long history of mining. In some gold mine, they use cyanide and amalgam so it affected the nearest stream or river water [8], [9]. Thus, environmentally and economically sustainable mining activities are essential for the long-term development of the sector. In Myanmar, there were a few research for the contamination of and surface and groundwater of harmful effects caused by improper mining activities. Most of the research interests are geologically mapping and chemical refining effect, not including the point of view about the environmental issue in mining areas. The environmental investigation is required in the near future to determine the detailed situation surface and groundwater quality and human health. Gold and copper mineralization is abundant distributed and associated with sulfide minerals in Mandalay

region, Myanmar [10]. Arsenic and heavy metal can be distributed into the environment naturally from the weathering, oxidation, and erosion of sulfide minerals [6], [11]. The main objective of this paper is heavy metal concentration in soil and rock (ore) samples will study from near area of gold mining site and Copper mining site in Mandalay Region, Myanmar by different methods in this paper as a preliminary study. The analytical method is also very important to approach the assessment of environmental contamination because Myanmar is launching the practice of environmental assessment. Because mining activities may be detrimental to the environment, any negative effects caused by mining activities should be mitigated.

THE COMPARISON OF ENVIRONMENTAL STANDARD

There are different indices in each country standards but toxicological index and radioactive index will be expressed in this paper, because those index were closely related to mining sector. Although some of the limitations of standard values from each country are same, some are different not only the item (parameters) number but also the standard values when compared (**Table 1**) and it may depend on the situation or technical limitation of the countries [12]-[15]. According to 2014 Environmental Performance Index Rating, Japan is standing in rank 26 out of 178 countries but it is the first rank of accessibility for drinking water.

Myanmar is standing at rank 164 and access to drinking water rank is 125. Ranking 112 and 124 of access to drinking water for Indonesia and Ranking 69 and 95 of access to drinking water for Sri Lanka were respectively standing [16]. Water pollution is basically linked with an inadequacy of environmental sanitation [17]. Water contamination in Myanmar, especially in risk is becoming alarming and must be taken into consideration. The potential pollution contributed by runoff water originating from communities, cattle-farming, mining and agricultural drainage system is not under-estimated or ignored. The growth of industrialized development, using the more fertilizers and pesticides to boost efficiency of farmers and mining with intensive use of the chemical in association with sprawling mine sites the introduction of losing technical systems in the country are all going to significantly contribute to the generation of contamination loads [18]. Hence, such structures should be considered in water pollution control programs. Water Resources Utilization Department (WRUD) and the Department of Development Affairs firstly reported the concentration of arsenic for the national-scale survey supported by some international NGOs. According to that previous survey data, arsenic concentration of groundwater has been found in some places of Sagaing, Mandalay, and Magway regions are higher than the WHO drinking water guideline value of 10 µg/L [19].

Table 1. Comparison of Drinking Water Quality Standards from four countries

Toxicological Indices						
No.	Parameters	Units	Myanmar	Japan	Srilanka	Indonesia
1	Antimony	mg/L	0.02	-	-	0.02
2	Arsenic	mg/L	0.05	0.01	0.01	0.01
3	Barium	mg/L	0.7	-	-	0.7
4	Boron	mg/L	2.4	1.0	-	0.5
5	Cadmium	mg/L	0.003	0.003	0.003	0.003
6	Chromium	mg/L	0.05	0.05	0.05	0.05
7	Copper	mg/L	2	1.0	1	2
8	Cyanide	mg/L	0.07	0.01	0.05	0.07
9	Fluoride	mg/L	1.5	0.8	1	1.5
10	Lead	mg/L	0.01	0.01	0.01	0.01
11	Manganese	mg/L	0.4	0.05	0.1	0.4
12	Mercury (Total)	mg/L	0.001	0.0005	0.001	0.001
13	Nickel	mg/L	0.07	-	0.02	0.07
14	Nitrate	mg/L	50	10	50	50
15	Nitrite	mg/L	3	0.04	3	3
16	Selenium	mg/L	0.04	0.01	0.01	0.01
17	Uranium	mg/L	0.03	-	-	0.015
Radioactive indices						
No.	Parameters	Units	Myanmar	Japan	Srilanka	Indonesia
1	Gross Alpha	Bq/L	0.5	-	-	0.1
2	Gross Beta	Bq/L	1	-	-	1

Save the Children Fund, (UK) conducted as a preliminary study in March-May 2000. In that study, 35% of 145 shallow tube wells in 63 communities those situated in Ayeyarwaddy region that result showed the arsenic concentration is also exceeded the proposed national standard 0.05 mg/L in Myanmar. The further study of UNICEF survey to 1912 wells in Ayeyarwaddy Region analyzing by Atomic Absorption Spectrometry (AAS) found 21% of test wells with concentration of arsenic is above 0.05 mg/L and retested in subsequent survey by AAS and field test kit result in some well too. This concentration is also exceeding the WHO standard and proposed national standard [20]. The concentration of arsenic, manganese, fluoride, iron and uranium in well water from around Myingyan Township in Mandalay Region, Myanmar are also exceed the public health concern levels [21]. In some river sediments are contaminated by mercury. Mercury concentration in muddy sediment is higher than 10 µg/g and total mercury level in hair of miner is 0.6 to 6.9 µg/g. Buffer of Tabaitgine and Sintku in the north of Mandalay Region is the main focus area in that study because there is a major artisanal and small-scale gold mining areas in Myanmar [8].

MATERIAL AND METHODS

Study Area

Soil samples were collected from near area of Mo Di-Mo Mi gold mine which is located in Yamethin Township, Mandalay Region and, Rock (ore) samples were collected from Zabutalu copper mine which is located in Sabe Taung area, Kyaukse Township, Mandalay Region. **Figure 1.** shows the location map of sampling sites, Mandalay Region, in Myanmar.

Sample Preparation

Soil samples were air dried for Japan, Ministry of Environment (MoE) Announcement 46 and 19 and dried in oven at 105° C until 2 hours but it may depend on moisture of sample for acid digestion method. And soil samples were separated grain sizes and grind the soil mass and agglomerates except for small and medium gravels. After grinding, samples were sieved through a non-metallic 2 mm eye sieve. Preparation for analysis involved crushing is made approximately 20 g of samples. Rock (ore) samples were dried in an oven at 105° C for 24 hours. After drying the samples were made the powder by manually grind and using the 200 mesh sieve for all methods.

Japan, Ministry of Environment (MoE) Announcement 46

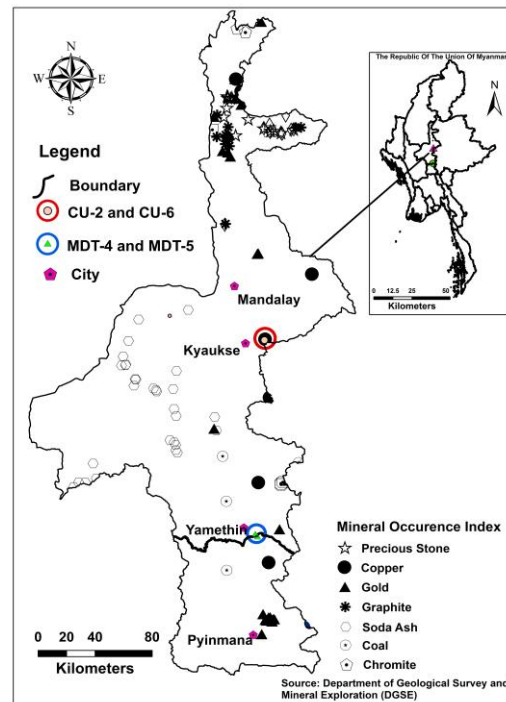


Figure 1. Map of sampling locations

A sample (unit g) and a solvent (hydrochloric acid is added to pure water so that the hydrogen ion concentration index is (5.8 to 6.3 or less) are mixed at a weight ratio of 10%. Make sure that the mixture is 500 ml or more. The prepared sample solution was shaken at room temperature (roughly 20 ° C) at atmospheric pressure (roughly 1 atm), (the shaking frequency was adjusted to about 200 times per minute and the shaking width was adjusted to 4 - 5 cm) and continuously shake for 6 hours. The sample solution obtained by carrying out the procedures was allowed to stand for about 10 to 30 minutes. After that, centrifuged at about 3,000 rpm for 20 minutes and the supernatant was filtered with membrane filter with a pore size of 0.45 µm, weigh the amount necessary for quantification accurately and use it as a test solution. Only 3 g sample powder was used and followed by procedure in this experiment because sample amount which is expressed in announcement is much. These sample were dilute with 1% HNO₃ prepared for analyzing because the sample solution will be reliable with standard solution.

Japan, Ministry of Environment (MoE) Announcement 19

Weigh 6 g or more of the sample and mix the solvent (hydrochloric acid added to pure water so that the concentration of hydrochloric acid is 1 mol/l) (unit ml) at a ratio by weight of 3%). The prepared solution was shaken at room temperature (roughly 25° C) at atmospheric pressure (roughly 1

atm), (the shaking frequency was adjusted to about 200 times per minute and the shaking width was adjusted to 4 – 5 cm) and shake for 2 hours. A shaker container is a polyethylene container or a container which does not adsorb or dissolve substances to be measured and has a volume of 1.5 times or more the solvent. Leave the sample solution obtained by shaking for about 10 to 30 minutes. Centrifuge the sample solution if necessary and filter the supernatant with membrane filter with a pore size of 0.45µm and weigh the amount necessary for quantification accurately and use it as a test solution. 1 g sample powder was used followed by procedure in this experiment although expressed to use 6 g or more sample to use in announcement procedure because sample amount which is expressed in announcement is much. These sample were dilute with 1% HNO₃ prepared for analyzing because the sample solution will be reliable with standard solution.

Acid Digestion Method (Department of Geological Survey and Mineral Exploration, Ministry of Natural Resources and Environmental Conservation, Myanmar)

Dry sample powder 1 g were weight and separately placed in 60 ml Pyrex beakers and then slowly add 10 ml of HCl and digest to nearly dryness on a hotplate at over 150 ° C. After nearly dryness, cool down that and add 10 ml of HNO₃ and digest to nearly dryness on a hotplate at over 150 ° C again. After that, 10 ml of HNO₃ and 5 ml de-ionized water were added into these beakers and boil for 10 minutes on the hot plate and covered with watch glass for every step. The digested samples were settle down and filtered into 100 ml volumetric flask using Millipore Millex-GP 0.22 µm and the volume made up to the marks with de-ionized water.

RESULT AND DISCUSSION

In order to determine the concentration of B, As, Se, Cd and Pb in soil and rock, three methods were used: Japan, Ministry of Environment Announcement No. 46, 19 and acid digestion method which is using in Department of Geological Survey and Mineral Exploration, Ministry of Natural Resources and Environmental Conservation, Myanmar. Inductively coupled plasma/mass spectrometer (ICP-MS) were used to analyze element concentration. Results were expressed as the means of three replicates ± standard deviation (SD). The obtained results mean value in samples of B, As, Se, Cd and Pb with standard deviation for each method are shown in **Table 2**. These results are pointed to methodological differences between the three different methods as shown in **Table 3**.

Two types of acids such as HNO₃ and HCl were used and heating on hot plate and it take about 7 hours in acid digestion method. Only HCl were used and it takes about 2 hours only in Japan, Ministry of Environment (MoE) Announcement 19 method. B, As, Se, and Pb concentrated as the most abundant of heavy metal in the sample CU-2 and CU-6. Those are mining rock (ore) from the copper mining site. Lead-zinc and barite veins associated with copper in carbonates were distributed in that area by geologically [10]. Copper-bearing minerals are chalcopyrite, tetrahedrite, bornite, chalcocite, pyrite, malachite and azurite and often associated with minor gold [10]. Oxidation of sulphide minerals such as pyrite, arsenopyrite, galena, chalcopyrite and sphalerite can release the arsenic and heavy metals [22]. That's why, the result show the high concentration of B, As, Se, and Pb. Pb were only rich in sample MDT-4 and MDT-5. Those sample are soil sample from near area of gold mining site. According to the result, that area can be assumed that the other 4 elements did not leach that area although near the mining site. Cd concentration can only be seen in sample CU-6 but in sample MDT-4, MDT-5 and CU-2 was undetected with three methods. This might be due to the fact that Cd is present in small amount in these samples. This study investigates in mining area and presents analytical data on heavy metal distribution may be the first time because it is not include for B, As, Se, Cd and Pb although Kyi Tun (2014) [9] and T. Osawa and Y. Hatsukawa(2015) [8] investigated the valuable data on the state of mining in Myanmar. And, most of other researchers are also mainly focus on the wells in public area for arsenic in groundwater contamination not for mining area.

CONCLUSION

Japan, Ministry of Environment (MoE) Announcement 19 method was the most efficient method in terms of the recovery of As, Se, and Pb than other and did not take long time. But Acid digestion method is more recoverable for B than other two methods except in sample CU-6. Cd is also more recoverable for sample CU-6 in acid digestion method. In summary, Japan, Ministry of Environment (MoE) Announcement 19 method is recommended as a method for the analysis of As, Se, and Pb. Acid digestion method is recommended as a method for the analysis of B and Cd. Japan, Ministry of Environment Announcement No. 46 method is not recommended for the analysis of the metal concentration because of the its low recovery and it take a long time. It should be used for the human risk evaluation from drinking groundwater which located that the downstream basin residential area from the mining site. Even though the data

obtained in this study may not represent all the mining activities, the results from this research evidence that the environment of mining area could be contaminated with arsenic and some other heavy metals. Further detail investigation of environmental contamination in mining areas, Myanmar are necessary because of the lack of previous data. Moreover, Environmental remediation plans should also be considered for recover the contamination of surface soil and groundwater of harmful effects caused by mining activities. Authors collected the specific plant that is the hyperaccumulation of the arsenic and will start the cultivation test with this sample such as *Pteris vittata* from Myanmar.

ACKNOWLEDGEMENTS

The authors wish to their gratitude to U Kyaw Zaw Tun from Department of Mines who help to collecting samples, Daw Myat Kay Thi Department of Geological Survey and Mineral Exploration, Ministry of Natural Resources and Environmental Conservation, Myanmar who explained for the digestion/analytical method and all people who was supported for this studied. This study was financially supported by MEXT, Japanese Government.

Table 2. Concentration of different metals ($\mu\text{g/g}$) in samples using different methods

Sample	Methods	B	As	Elements Se	Cd	Pb
MDT - 4	(MoE) anno- uncement 46	0.25 \pm 0.09	0.03 \pm 0.04	0.01 \pm 0.00	0.00 \pm 0.00	0.08 \pm 0.04
	(MoE) Anno- uncement 19	0.33 \pm 0.19	2.47 \pm 0.39	0.43 \pm 0.15	0.00 \pm 0.00	13.57 \pm 2.17
	Acid Diges- tion Method	2.27 \pm 0.58	0.71 \pm 0.30	0.55 \pm 0.21	0.00 \pm 0.00	12.07 \pm 2.28
MDT - 5	(MoE) anno- uncement 46	0.18 \pm 0.02	0.00 \pm 0.00	0.01 \pm 0.00	0.00 \pm 0.00	0.08 \pm 0.03
	(MoE) Anno- uncement 19	0.00 \pm 0.00	1.89 \pm 0.25	0.45 \pm 0.15	0.00 \pm 0.00	24.36 \pm 1.38
	Acid Diges- tion Method	3.43 \pm 1.40	0.65 \pm 0.17	0.86 \pm 0.23	0.00 \pm 0.00	15.56 \pm 3.21
CU - 2	(MoE) anno- uncement 46	0.34 \pm 0.04	0.17 \pm 0.03	0.01 \pm 0.00	0.00 \pm 0.00	0.05 \pm 0.02
	(MoE) Anno- uncement 19	0.00 \pm 0.00	0.87 \pm 0.19	21.99 \pm 7.57	0.00 \pm 0.00	22.55 \pm 1.86
	Acid Diges- tion Method	2.49 \pm 0.60	2.33 \pm 0.93	1.72 \pm 0.59	0.00 \pm 0.00	1.97 \pm 0.11
CU - 6	(MoE) anno- uncement 46	0.71 \pm 0.00	0.14 \pm 0.04	0.01 \pm 0.01	0.00 \pm 0.00	0.02 \pm 0.01
	(MoE) Anno- uncement 19	5.67 \pm 3.27	483.39 \pm 30.47	6.88 \pm 6.42	2.64 \pm 0.24	17.63 \pm 5.57
	Acid Diges- tion Method	3.80 \pm 2.48	13.83 \pm 5.79	1.31 \pm 0.43	43.66 \pm 9.89	21.16 \pm 5.77

Table 3. Comparison table of three chemical methods in this research

Requirements	(MoE) Announcement No. 46	(MoE) Announcement NO. 19	Acid Digestion Method
Sample amount	3 g	1 g	1 g
Reagents	Deionized Water (pH 5.8 – 6.3)	HCl	HCl, HNO ₃ and Deionized Water
Reaction	Shaking (200 times per minute)	Shaking (200 times per minute)	Heating on Hot Plate
Total Reaction Time	6 hours	2 hours	About 7 hours

REFERENCES

- [1] World Health Organization, "Drinking water quality in the South-East Asia Region," *Print. India*, 2010.
- [2] KHin Sein Kyi, "Water Quality monitoring program and activities in Myanmar," [http://www.unescokyotosympo2015.org/abstracts/Kyi - Water Quality monitoring program and activities in Myanmar.pdf](http://www.unescokyotosympo2015.org/abstracts/Kyi-Water%20Quality%20monitoring%20program%20and%20activities%20in%20Myanmar.pdf).
- [3] H. Utsumi and Y. Tsuchiya, "Water Quality and Standards," vol. I.
- [4] F. Edition and W. H. O. (Who), "Guidelines for Drinking-water Quality," *World Health*, vol. 1, no. 3, 2011, pp. 104–8.
- [5] A. Boularbah, C. Schwartz, G. Bitton, W. Abouddrar, A. Ouhammou, and J. L. Morel, "Heavy metal contamination from mining sites in South Morocco: 2. Assessment of metal accumulation and toxicity in plants," *Chemosphere*, vol. 63, no. 5, 2006, pp. 811–817.
- [6] F. Html, "Heavy Metals in Contaminated Soils: A Review of Sources, Chemistry, Risks and Best Available Strategies for Remediation," 2017, pp. 1–17.
- [7] U. States and I. Agency, "What is the role of arsenic in the mining industry?," *Fraser Inst.*, no. April, 2012.
- [8] T. Osawa and Y. Hatsukawa, "Artisanal and small-scale gold mining in Myanmar: Preliminary research for environmental mercury contamination," no. 25, 2015, pp. 221–230.
- [9] K. Htun, "Sustainable Mining in Myanmar," vol. 36, no. 1, 2014, pp. 25–35.
- [10] K. Zaw, Y. M. Swe, T. A. Myint, and J. Knight, "Copper deposits of Myanmar," 2017, pp. 573–588.
- [11] B. Keshavarzi, F. Moore, F. Rastmanesh, and M. Kermani, "Arsenic in the Muteh gold mining district, Isfahan, Iran," *Environ. Earth Sci.*, vol. 67, no. 4, 2012, pp. 959–970.
- [12] M. of Health, "Proposed National Drinking Water Quality Standards of Myanmar." 2014.
- [13] H. Wakayama, "Revision of Drinking Water Quality Standards in Japan," 2015, pp. 74–88.
- [14] SLS, "DRINKING WATER STANDARD - First Revision (Sri Lanka Standards for potable water – SLS 614: 2013)," 2013, pp. 1–2.
- [15] Peraturan Menteri Kesehatan No. 492/MENKES/Per/IV/2010, "Peraturan Menteri Kesehatan Republik Indonesia NOMOR 492/MENKES/PER/IV/2010," *Peraturan Menteri Kesehatan Republik Indonesia*. p. MENKES, 2010.
- [16] A. Hsu *et al.*, "The 2014 Environmental Performance Index. Full Report and Analysis," *Yale Univ.*, vol. 1, no. 203, 2014, pp. 1–172.
- [17] International Institute for Environment and Development, "Environment, Water and Sanitation," *Irish Aid Keysheet No.11*, 2008, p. 12.
- [18] J. H. Kim, "Surface Water Pollution in Myanmar (Burma)," in *TU Delft Weblog*, 2016, pp. 1–5.
- [19] R. Paul Pavelic, Sonali Senaratna Sellamuttu, S. Johnston, Matthew McCartney, Touleelor Sotoukee, G. L. Balasubramanya, Diana Suhardiman, A. Somphasith Douangsavanh, Olivier Joffre, Khin Latt, C. C. and Y. Kyaw Zan, Kyaw Thein, Aye Myint, and T. Htut, *Integrated Assessment of Groundwater Use for Improving Livelihoods in the Dry Zone of Myanmar (IWMI Research Report 164)*. 2015.
- [20] T. N. Tun, "Arsenic contamination of water sources in rural Myanmar," 2003, pp. 219–221.
- [21] T. Bacquart *et al.*, "Multiple inorganic toxic substances contaminating the groundwater of Myingyan Township, Myanmar: Arsenic, manganese, fluoride, iron, and uranium," *Sci. Total Environ.*, vol. 517, 2015, pp. 232–245.
- [22] M. Lim, G. C. Han, J. W. Ahn, K. S. You, and H. S. Kim, "Leachability of arsenic and heavy metals from mine tailings of abandoned metal mines," *Int. J. Environ. Res. Public Health*, vol. 6, no. 11, 2009, pp. 2865–2879.

DEVELOPMENT OF THE MODIFIED EICP FOCUSED ON THE HIGH STRENGTH UNDER LOW CALCITE PRECIPITATION RATE

Yusui Murata¹, Toshiro Hata¹

¹ Graduate School of Engineering, Toyama Prefecture University, Japan

ABSTRACT

Treatment with a solidifying material were used such as cement and lime in the most of construction sites. However, most of the this types of artificial materials currently used are cement, and cement-based solidified ones, and the use of these existing materials accompanies with many environmental burdens such as greenhouse gas emissions. Therefore, authors proposed the newly solidification method which is expected to have less carbon dioxide emissions than the conventional one. In this study, focusing on the EICP (Enzyme Induced Carbonate Precipitation) treatment method that increases the strength under low calcite precipitation rate into the soil pore. Moreover, some types of laboratory test done and evaluation of the effectiveness of this technique by using natural materials expected to produce high strength in a short time curing for conversion one. The results of unconfined compression strength tests, acid decomposition test for evaluating the calcite precipitation rate, SEM images of after treatment sand particle surface explained. The primary outcomes of this research are 1) Modified EICP can increase the UCS less than conventional EICP method. 2) A thin film covered with the sand particle surface after treated with the proposed method.

Keywords: Unconfined compression strength, Carbonate precipitation, Urease activity, SEM

INTRODUCTION

As a method for improving the ground composed of loose sand etc., treatment with a solidifying material is often used. For example, cement and cement-based solidification materials are applying for many of ground improvement sites. However, the use of these conventional materials is accompanied by many environmental burdens such as emission of green-house gases. In Japan, carbon dioxide emissions 10 % is emitted from the construction engineering field and 30 % of them are discharged when cement is generated. Therefore, it is required to reduce carbon dioxide emissions even in the construction engineering field. [1]

BACKGROUND

In this study, proposed the newly solidification method expected to have less carbon dioxide emissions than conventional ground improvement using cement and cementitious materials. Enzyme Induced Carbonate Precipitation (EICP) method was focused this techniques, which uses calcite precipitation based on the enzymatic activity to increase the strength of the ground by precipitating calcium carbonate in the sand gap as one of the environmentally conscious soil improvement technology construction method [2], [3]. The effectiveness of proposed method which focused on the low calcite contents and short-term curing method combined EICP with natural materials.

MATERIALS AND METHODS

(1) First Tests (Organic effects)

First tests are expected to dissolve natural materials (organic substance) and dry them, so that sand particles are bonded to each other and solidified. Thus, these tests are conducted to evaluate the addition amount of natural materials and the influence of curing temperature. In addition, chemical compositions of each case are shown in **Table 1**. The specimens were made from 140 g of Toyoura sand added with 20 mL or 14 mL of each cases solution. The amount of solution added was determined from the optimum moisture content of Toyoura sand [4]. In addition, to confirm the influence on strengths exerted by curing temperature, specimens were prepared at 4, 20, and 105 °C.

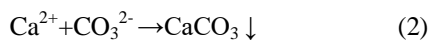
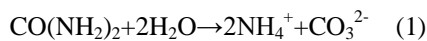
Table 1. List of test cases (First tests)

CASE	1	2	3	4
CO(NH ₂) ₂ (mol/L)	0.25			
Urease (g/L)	0.2			
Natural Material (g/L)	28	37		
Pure water (mL)	20	14		
Curing Temperature (°C)	20		4	105

Four test cases (CASE 1 to 4) prepared. In CASE 1, the addition amount of natural materials is small as compared with other cases. In CASE 2 to 4, the same amount of natural material added and the curing temperature is changed. In CASE 2 to 4, since the specimen could not be compacted, pure water was reduced to 42 mL.

(2) Second Tests (Organic with inorganic effect)

From first tests result, these were confirmed that the adhesive effect using the natural material was effective. Therefore, second tests were conducted to complement the strength by combining this natural material with the EICP method. Since natural materials are used as an aid to the EICP method, the amount of natural materials added in second tests are reduced compared to first tests. EICP method is solidify by precipitating calcium carbonate generated from carbonate ions generated by hydrolysis of urea in the sand gap using an enzyme preparation. Formulas (1) and (2) describe chemical reaction formulas of calcite precipitation.



Six test cases (CASE 5 to 10) with different amounts of urea, calcium chloride and natural materials added were made in second tests. In addition, chemical composition of each cases are shown in **Table 2**. For the procedure, Solution A and Solution B were separately prepared and stirred for about 5 minutes, then 30 mL each was added to a

total of 60 mL to Toyoura sand 420 g. The chemical composition and the amount of Toyoura sand were used per 3 test specimens. Thereafter, this mixed solution and sand were mixed by hand mixing after wearing a plastic glove, and the mixture was used.

The concentration of CaCl_2 shown in solution A was 0.67 mol/L in test CASE 5 and 6, 1.00 mol/L in CASE 7 and 8, and 1.36 mol/L in CASE 9 and 10. The concentrations of $\text{CO}(\text{NH}_2)_2$ were 1.00 mol/L in Test CASE 5 and 6, 1.49 mol/L in CASE 7 and 8, and 2.03 mol/L in CASE 9 and 10. The prepared sand was divided into three layers and tamped so as to have $\text{Dr} = 80\%$ to prepare specimens of $\phi = 35$ mm and $H = 88$ mm. When specimens were made in order to facilitate demolding, a film was wound on the side of the mold and grease was applied between the film and the mold was used. The experimental flow is shown in **Figure 1**. From the first test result, the curing temperature of the second test was determined to be 105°C . When drying the specimen in the furnace drying, lay saran wrap on the magnetic dish so that the specimen will not stick to the magnetic dish. In the tests, the unconfined compression test of soil (JIS A 1216: 2009) was carried out in six cases with different concentrations of urea, calcium chloride and natural materials, and the effectiveness of strength enhancement effect by UCS strength was investigated. In the unconfined compression test of soil, three test specimens were prepared in each case, and the strength enhancement effect was evaluated based on the average value of the UCS strength of the three pieces. In addition, observation of the surface of sand particles with an electron microscope (SEM) was conducted for cases

Table 2. List of test cases (Second test)

CASE		5	6	7	8	9	10
Solution A	CO(NH ₂) ₂ (mol/L)	1.00		1.49		2.03	
	CaCl ₂ (mol/L)	0.67		1.00		1.36	
Solution B	Urease (g/L)	3.0					
	Natural material (g/L)	<div></div>	4.0	<div></div>	4.0	<div></div>	4.0
Sand class		Toyoura sand					
Pure water (mL)		60					
Test Specimen height (mm)		88					
Test specimen diameter (mm)		35					

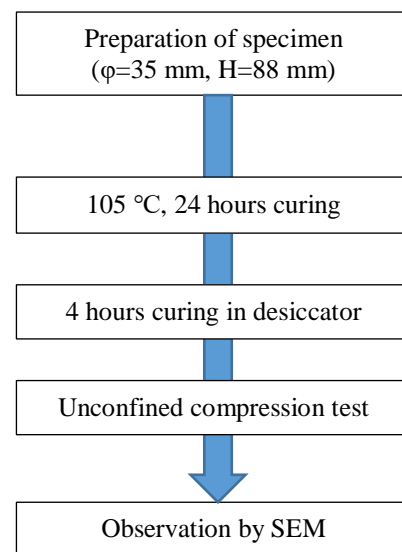


Figure 1. Test flow (Second test)

with and without natural materials. SEM imaging was conducted for CASE 5 and 6.

RESULT AND DISCUSSIONS

(1) Result of First Tests (UCS Strength)

The purpose of first tests was to prepare specimens with different concentrations of natural materials or different curing temperatures and to evaluate the influence on the strength given by these specimens. The unconfined compression test results of specimens prepared with the cases in **Table 1** are shown in the **Figure 2**. It is clear from the figure that higher concentrations of natural materials can be expected to enhance strength. In addition, it was confirmed that when the curing temperature was 105 °C, the strength was highest. From these results, in second tests, curing temperature was determined to be 105 °C. In addition, CaCl₂ was added to prepare specimens with a smaller addition amount of natural materials than the first test, and the effect of adding natural materials to the EICP method was evaluated.

(2) Results of Second Tests (UCS Strength)

The results of UCS tests in each case are shown in **Figure 3**, and the test summarized results in **Table 3**, respectively. Second tests result of UCS strength are showed the average value of three specimens prepared for each case. From the figure, in the test case excluding CASE 10, UCS strength variations of about 450 kN/m² at maximum and about 1100 kN/m² in CASE 10 were confirmed. Focusing on CASE 5 and 6, CASE 6 using a natural material combined case shows the UCS strength higher by about 200 kN/m² than CASE 5 which is not combined natural material. On the other hand, when comparing CASE 8 which is used in combination with CASE 7 with no natural material, CASE 8 has UCS strength higher than CASE 7 by about 260 kN/m². Likewise, in CASE 9 and 10, the UCS strength was about 750 kN/m² higher. **Figure 4** shows the relationship between the UCS strength and the calcium carbonate precipitation rate against the sand weight shown in **Figure 3**. The precipitation rate was calculated as the calculated maximum value from the amount of CaCl₂ added. It is clear from the **Figure 4** that the number of samples are little small. However, the UCS strength increases as the calcium precipitation rate increases. From the figure, it can be considered that it is possible to calculate the necessary strength from the precipitation rate of calcium carbonate.

(3) The Surface Observation of the Sand Particle with SEM (KEYENCEVE-8800)

Figure 5-8 shows the photographing results of the sand particle surfaces of CASE 5 and 6. From **Figure 5** and 6, when the observations magnify

cation of the CASE 5 is 300 times and 1000 times, crystals of large and small calcium carbonate such as 3.3 to 16.5 μm

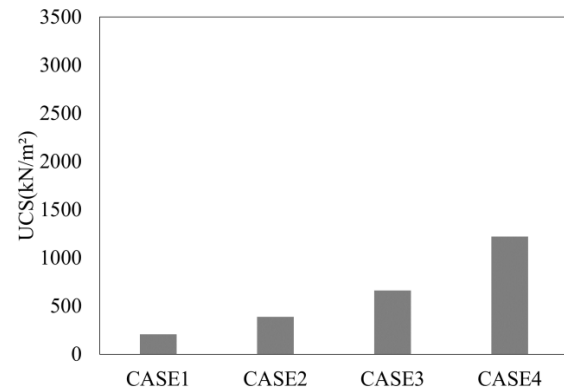


Figure 2. UCS strength (First test)

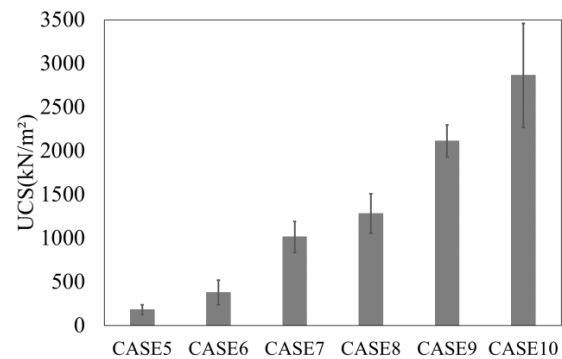


Figure 3. UCS strength (Second test)

Table 3. Test conditions for UCS

CASE	CaCl ₂ (mol/L)	Natural material	UCS (kN/m ²)
5	0.67	×	181
6		○	379
7	1.00	×	1014
8		○	1281
9	1.36	×	2112
10		○	2863

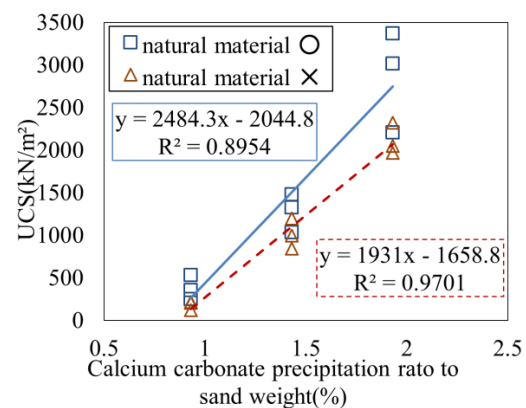


Figure 4. Relationship between calcium carbonate precipitation rate and UCS

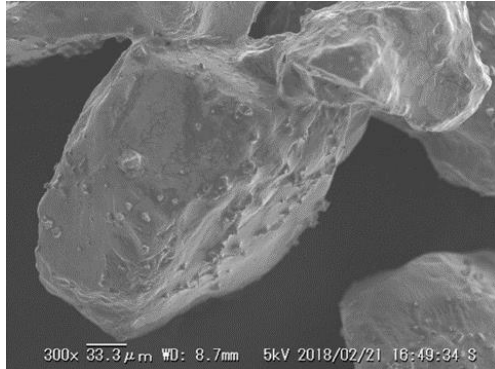


Figure 5. CASE 5 300 times



Figure 6. CASE 5 1000 times

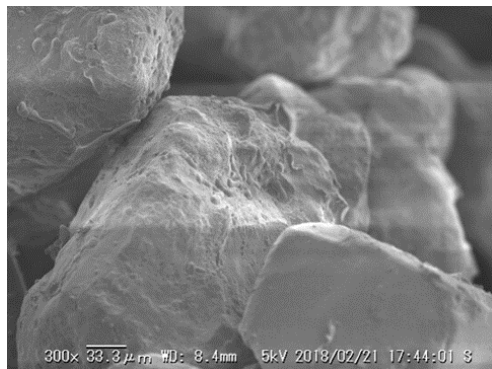


Figure 7. CASE 6 300 times

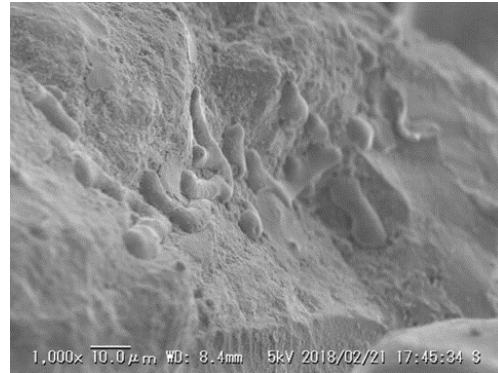


Figure 8. CASE 6 1000 times

(Blue circle of figure 6) are confirmed on the surface of the sand particles. On the other hand, paying attention to the observation magnification of the CASE 6 in **Figure 7** and **8**, 300 times and 1000 times, it was confirmed that a film-like substance was formed on the calcium carbonate deposited on the surface layer. The reason for the increase in strength is that the film was formed on calcium carbonate on the surface of the sand particles, which suggests that the bonding strength between the sand particles increased by filling the gap more.

CONCLUSIONS

From the results of first tests, it was confirmed that the most UCS can be expected when the addition amount of the natural material is increased or the curing temperature is set at 105 °C. From the results of second tests, it was confirmed that all the test cases showed an increase in the strength of the specimen with a combination of natural materials. In the case of adding a high concentration solution, the UCS was the largest increase in each case, but in the case of the increase rate, it showed a high increase rate in the low concentration case. In addition, as a result of electron microscope photographing, it was confirmed that film was formed on calcium carbonate in the case of using natural materials in combination, and the film filled the gaps between the sand particles to increase the strength. The future task is to clarify the influence on strength by adding a lower concentration solution.

ACKNOWLEDGEMENTS

This work was partially supported by JSPS KAKENHI Grant Number JP15H02634.

REFERENCES

- [1] Oso Y., Tachino N., Sakai M., Hata T., and Inagaki Y., An Experimental Study on a New Present Ground Improvement Technique Using Microbial Function, Civil Engineering Society, 2010, V II -38.(In Japanese)

- [2] Edward K., Nasser H., Enzyme Induced Carbonate Precipitation (EICP) Columns for Ground Improvement, Geotechnical Special Publication, 2015.
- [3] Tebakari C., Hata T., Hatakeyama M. and Abe H., Experimental Study on the Improvement of Liquefaction Strength Based on the Various Types of Urease Production Bacterium, Japanese Geotechnical Journal, Vol.11, No.1, 2016, pp.1-9.(In Japanese)
- [4] Yasuda S., kishino H., Yoshisaki K. and Hayakawa S., Experiment and analysis on fault countermeasure of buried pipe using lightweight soil. The 27th JSCE Earthquake Engineering Symposium, Vol.27, 2003, pp.31. (In Japanese)

WATER RETENTION, GAS TRANSPORT PARAMETERS, AND THERMAL PROPERTIES FOR ROADBED MATERIALS UTILIZING CONSTRUCTION DEMOLITION WASTE AND INDUSTRIAL BYPRODUCTS

Mohd Redzuan MOHD SAUFI¹, Takeshi SAITO¹, Taro UCHIMURA^{1,2}, and Ken KAWAMOTO^{1,2}

¹Graduate School of Science and Engineering, Saitama University, Japan

²International Institute of Resilient Society, Saitama University, Japan

ABSTRACT

Permeable pavement system (PPS) has been widely used as urban stormwater management system and can be expected to reduce urban heat island effect. However, measurements of mass transport parameters for unsaturated road subbase materials are very limited. In this study, water retention properties, gas transport parameters, and thermal properties for graded road subbase materials using recycled materials from construction and demolition waste (CDW) and industrial byproducts mixed with fine grains under variable saturated conditions were measured. Graded recycled concrete and steel slag (< 30mm) were used as graded aggregate base materials while granulated municipal solid waste (MSW) slag and autoclaved lightweight concrete (ALC) were used as fine grains (0.106- 2mm). Water retention properties were conducted on single and mixed samples to evaluate the effect of fine grains under different matric potential. Recycled concrete showed higher water retention characteristics compared to steel slag and both materials showed enhancement in water retention properties with additional ALC mixture. As for gas transport parameters and thermal transport properties, gas diffusion coefficient (D_p), air permeability (k_a), and thermal diffusivity (K_T) with their dependency on air-filled porosity (ε) and volumetric water content (θ) were examined. Samples with MSW slag mixture resulted in improved D_p and k_a caused by less tortuous pore-network. On the other hand, only slight improvement of K_T were observed with the mixture of ALC fines compared to MSW slag as θ shows more significant effect towards K_T for all tested materials.

Keywords: Construction and demolition waste, Mass Transport, Water retention, Recycled Materials, Industrial Byproducts, Roadbed materials

INTRODUCTION

Solid waste can be categorized into several classifications such as residential, commercial, institutional, municipal, construction demolition, industrial and agricultural waste. Among the solid waste, construction and demolition waste (CDW) is originated from wastage from construction sites, demolition of roads, demolition of buildings and excavated waste [1]. The recycled waste can be derived from CDW, industrial byproducts, or even municipal solid waste (MSW).

Million tons of waste are produced annually worldwide and a typical recycling method is to apply recycled materials for the road pavement systems. Among road pavement systems, in especial the permeable pavement system (PPS), is capable of reducing water runoff volume and reducing water outflow rate [2] can be expected to prevent flood disaster and reduce urban heat island effect [3].

Numerous studies have been done to characterize hydraulic and mechanical properties for road subbase materials in PPS [4][5][6], however, measurements of mass transport parameters for unsaturated road subbase materials are very limited. In this study, we measured mass transport parameters such as gas diffusion, air permeability, and thermal diffusion, and water retention properties for graded road subbase materials (recycled concrete and steel slag) mixed with fine grains (granulated MSW slag and ALC) under variable saturated conditions.

MATERIALS & METHODOLOGY

Graded recycled concrete and steel slag, granulated MSW Slag and ALC were used in this study (Fig. 1). The particle size distributions (PSD) for recycled concrete and steel were prepared based on the technical standards for road subbase prescribed in Japan Road Association and Japan Industrial

Standards (JIS) [8][9]. MSW slag and ALC were sieved and prepared with their PSD ranging between 0.106 mm to 2.0 mm (Fig. 2). The samples were packed in a cylindrical stainless core (inner diameter 15 cm, height 12 cm, and volume 2120 cm³) using Modified Proctor D method under variable saturated condition. Duplicate samples were prepared for all single and mixed material samples for all conducted tests.

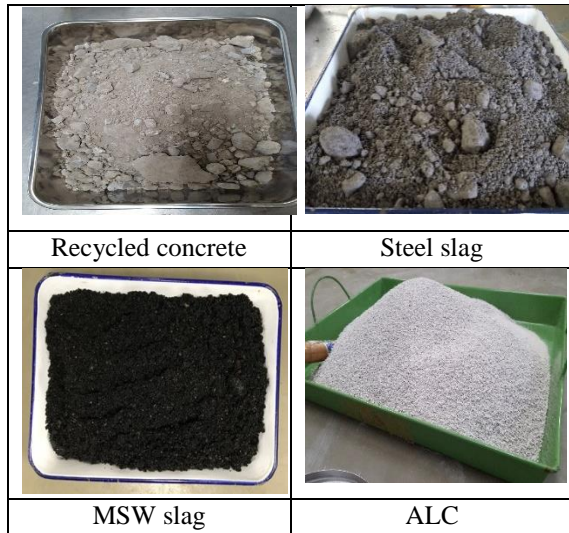


Fig. 1: Researched materials in this study

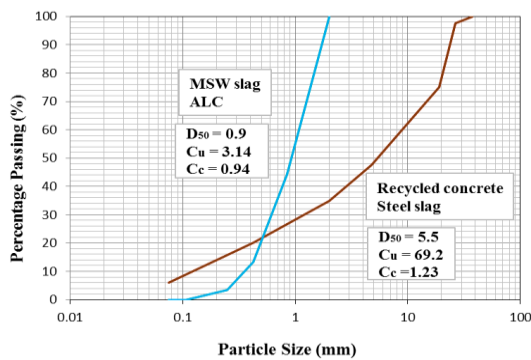


Fig. 2: Particle size distribution for tested materials.

D_{50} : 50 % of particle diameter
 C_u : Coefficient of uniformity
 C_c : Coefficient of curvature

Table 1 shows the basic physical and chemical properties of used materials in this study. Recycled concrete and ALC show the highest air-dried water content of 3.5% and 3.3%. ALC has the highest water absorption properties of 57.1% that might be beneficial to water retention properties.

Table 1: Basic physical and chemical properties of used materials

Tested Material	PSD		Water Absorption (%)		pH		EC		LOI
	mm	%	>4.75mm	<4.75mm	1MKCL	mS/cm	%		
Concrete	0-31.5	3.5	2.59	6.5	10.7	11.6	1.8	9.5	
Steel Slag	0-31.5	0.60	3.18	3.8	12.4	12.6	6.9	6.2	
MSW Slag	0.106-2	0.20	2.82	0.8	9.4	7.9	0.048	0.0	
ALC	0.106-2	3.3	2.49	57.1	10.0	8.3	2.0	8.4	

Water retention properties

Water retention properties test was done on compacted samples based on each material's optimum water content value. Measurements were conducted under air-dried condition and between matric potential, ψ of 10 (-cm H₂O) to 10⁴ (-cm H₂O). Both recycled concrete and steel slag were used for single sample water retention test, while only 8:2 ratio (recycled concrete/ steel slag: MSW slag/ ALC) of mixed samples were investigated in this test.

Hanging water column and sandbox method was used for the measurements of 10 (-cm H₂O), 10^{1.5} (-cm H₂O), and 10² (-cm H₂O) while for higher matric potential, ψ value of 10³ (-cm H₂O), 10^{3.5} (-cm H₂O), and 10⁴ (-cm H₂O) measurements, pressure chamber method was used. Finally, potentiometer was used for measuring matric potential, ψ of all samples under air-dried condition.

Gas Transport Parameters

Gas diffusivity

A conventional gas diffusion chamber method was used to measure gas diffusion coefficient, D_p (cm² s⁻¹) [11] in a temperature controlled room at 20 °C as shown in Fig. 3. For the D_p measurement, O₂ gas was used as a tracer gas. The D_p was referred to Fick's second law in Eq. (1). Measured D_p was normalized by the O₂ diffusion coefficient in free air, D_o (= 0.205x10⁻⁴ m²/s), and represented as D_p/D_o .

$$\frac{\partial c}{\partial t} = D_p \frac{\partial^2 c}{\partial x^2} \quad (1)$$

C: gas concentration (diffusion chamber) (g/m³)

D_p : gas diffusion coefficient (m²/s)

x: diffusive length of sample (m)

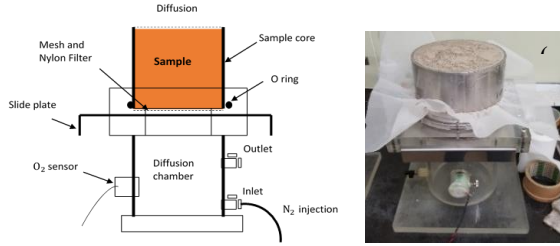


Fig. 3: Schematic diagram and experimental setup for measuring D_p

Air Permeability

Air permeability coefficient, k_a (μm^2), was measured by flowing air through the sample using an air compressor and monitored flow rate and pressure difference between inlet and outlet of the sample shown in Fig. 4. Darcy's law in Eq. (2) was used to calculate k_a .

$$q = \frac{Q}{A} = \frac{k_a}{\eta} \frac{dP}{dx} \quad (2)$$

q : advective gas flux (m/s)

Q : flow rate (m^3/s)

A : sample cross sectional area (m^2)

k_a : air permeability (m^2/s)

η : dynamic air viscosity ($=1.86 \times 10^{-5} \text{ Pa}$)

dP/dx : air pressure gradient (Pa/m)

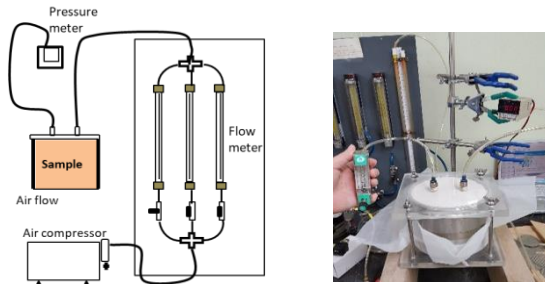


Fig. 4: Schematic diagram and experimental setup for k_a measurement

Thermal properties

Thermal diffusivity, K_T ($\text{cm}^2 \text{ s}^{-1}$) were measured using a portable thermal properties analyzer with a dual-needle probe (KD2-Pro and SH-1, Decagon Devices, USA) in a temperature controlled room at 20°C as shown in Fig. 5. For each sample, at least three readings at different points were taken to determine the Thermal diffusivity, K_T (m^2/s). The K_T was referred to Heat Flow equation in Eq. (3) and can be represented by using thermal conductivity, λ , and volumetric heat capacity, σ , as shown in Eq. (4).

$$\frac{\partial T}{\partial t} = K_T \frac{\partial^2 T}{\partial z^2} \quad (3)$$

$$K_T = \frac{\lambda}{\sigma} \quad (4)$$

K_T : Thermal diffusivity (m^2/s)

λ : Thermal conductivity ($\text{W}/\text{m}/\text{K}$)

σ : Volumetric heat capacity ($\text{MJ}/\text{m}^3/\text{K}$)

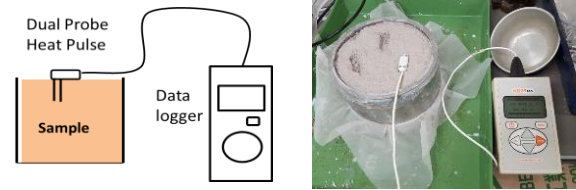


Fig. 5: Schematic diagram and experimental setup for thermal properties measurement

RESULTS AND DISCUSSIONS

Water retention properties

Figure 6 shows measured water retention curves for tested materials. For single materials, recycled concrete showed a slightly better water retention ability compared to steel slag which affected by higher water absorption value of recycled concrete than steel slag. Based on the figure, mixed samples between Recycled concrete and ALC showed quite significant increase in water retention properties compared to MSW slag mixture. This shows that the high micropores structures within ALC material generates beneficial effects towards water retention ability. In contrast, MSW slag with glass-like surface leads to lower water capillary force causing water retention properties to be lower when mixed. The same result was also displayed for steel slag mixed samples.

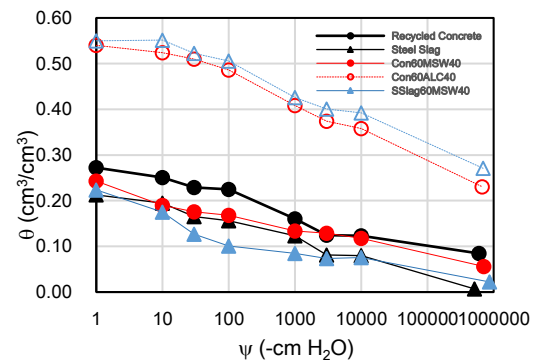


Fig. 6: Water retention curves for all tested samples

Gas transport parameters

Gas diffusivity

Figure 7 indicates measured D_p/D_o for tested single samples and the effect of ϵ and θ . All samples showed the same trend where D_p/D_o increases with increasing ϵ and showed reverse pattern with increasing θ where water blockage effect took place.

While Fig. 8 shows the effect of adding fine grains of MSW slag and ALC with recycled concrete and steel slag. The results for both recycled concrete and steel slag mixed samples show the increased D_p/D_o with higher proportion of fine grains verifying the improvement D_p/D_o of with higher fine grains mixture. The MSW slag mixture show the increased of D_p/D_o value under almost the same air-filled porosity, ϵ value. On the other hand, ALC mixture increases ϵ in order for D_p/D_o value to increase.

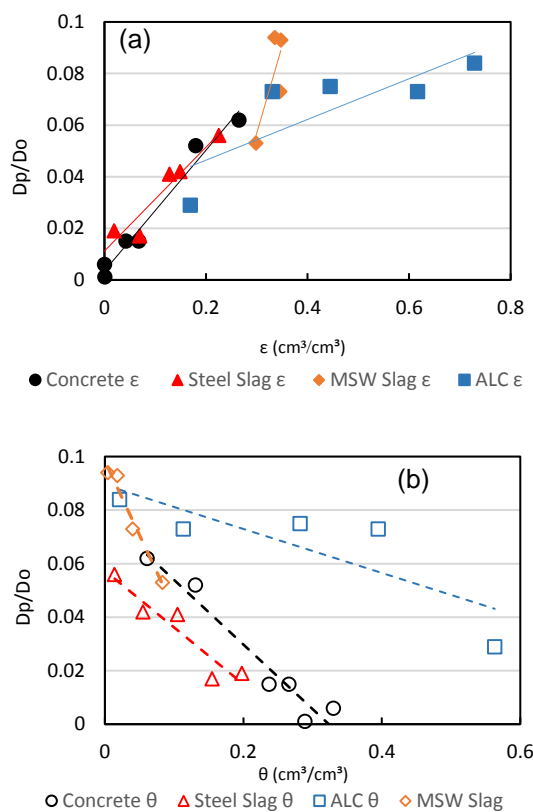


Fig. 7: Measured D_p/D_o as function of a) air-filled porosity (ϵ) and b) volumetric water content (θ) for all single samples

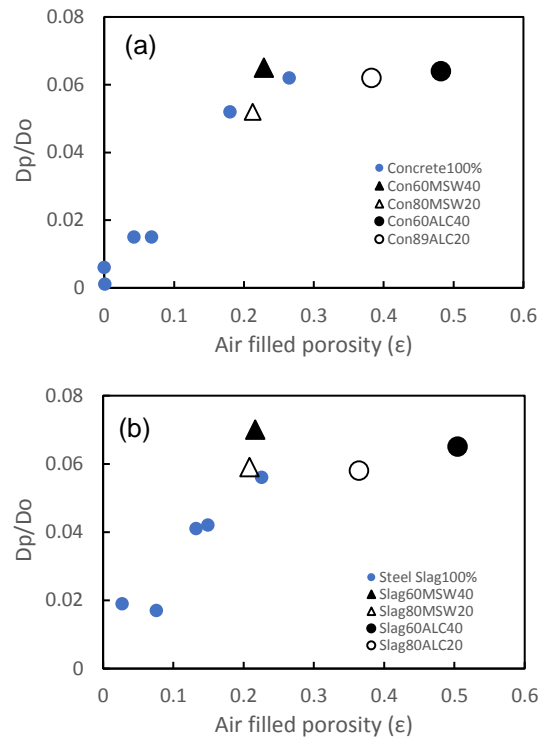


Fig. 8: Measured D_p/D_o as function of air-filled porosity (ϵ) for a) mixed recycled concrete and b) mixed steel slag

Air permeability

Figure 9 indicates measured k_a for tested single samples and the effect of ϵ and θ . Except for ALC, k_a values increased with increasing in ϵ and decreased with increasing in θ .

Fig. 10 indicates the effect of adding MSW slag and ALC to recycled concrete and steel slag samples where higher ratio of both fine grains increases k_a value. Adding ALC increases the ϵ and slightly improved k_a , however with MSW slag mixture, ϵ doesn't increased but it increases the k_a value.

The k_a value didn't show expected value for ALC and little unstable for unsaturated condition of recycled concrete and steel slag. This might occur because of the disconnected pores inside samples as air permeability is highly affected by continuous connectivity of larger pore networks. A further pore distribution analysis using mercury intrusion pore network analyzer is needed to confirm the results.

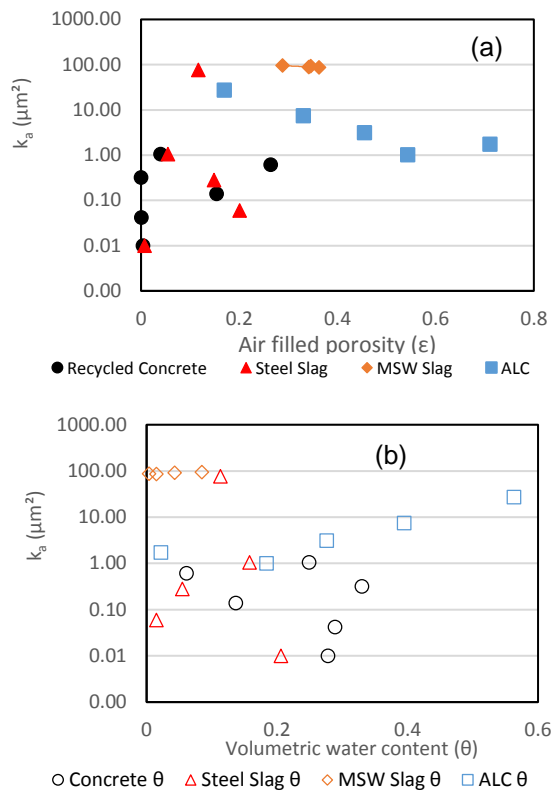


Fig. 9: Measured k_a as function of a) air-filled porosity (ϵ) and b) volumetric water content (θ) for all single samples

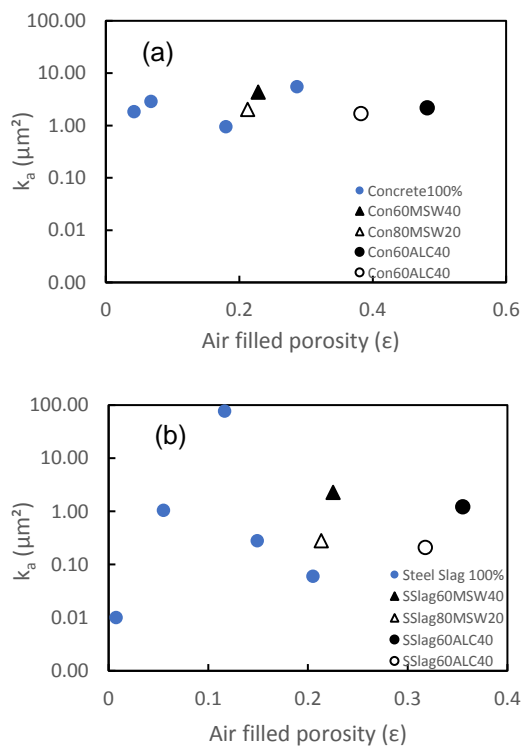


Fig. 10: Measured k_a as function of air-filled porosity (ϵ) for a) mixed recycled concrete, and b) mixed steel slag

Thermal properties

Figure 11 shows the effect of water content on measured K_T values. All materials showed increasing value as θ increases, however compared to the others, recycled concrete and steel slag indicated steeper K_T increment. There were no significant differences among concrete and steel slag samples, and their mixed samples with MSW slag at air-dried condition in Fig. 12 but a slight improved K_T with ALC mixture was monitored. The measure values for all tested samples ranged $1.70 \times 10^{-3} \text{ cm}^2 \text{ s}^{-1}$ and $6.78 \times 10^{-3} \text{ cm}^2 \text{ s}^{-1}$.

This shows, apart from the material itself in transferring heat through the samples, water content, θ in samples plays a significant effect in heat transportation. Thus, materials with higher water retention capacity might be able to improve thermal diffusivity value inside subbase leading to Urban Heat Island (UHI) reduction.

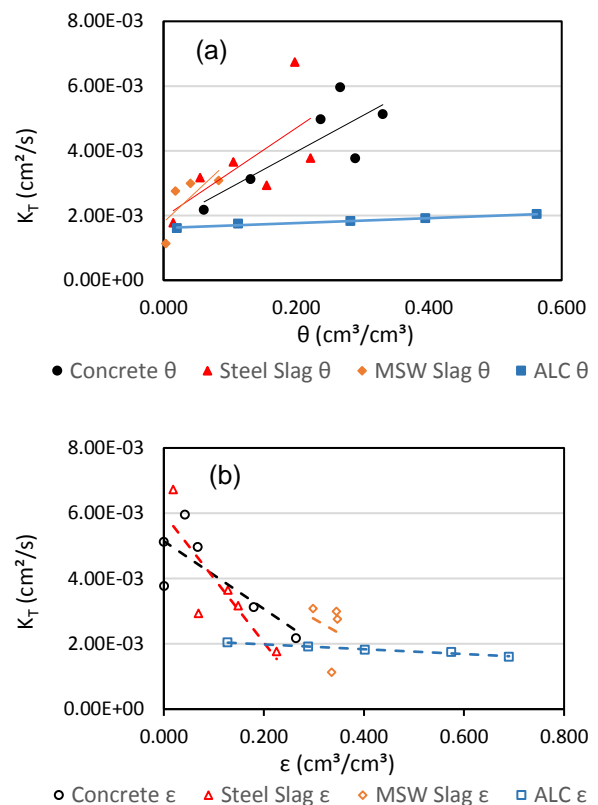


Fig. 11: K_T measurement as function of a) volumetric water content (θ) and b) air-filled porosity (ϵ) for all single samples

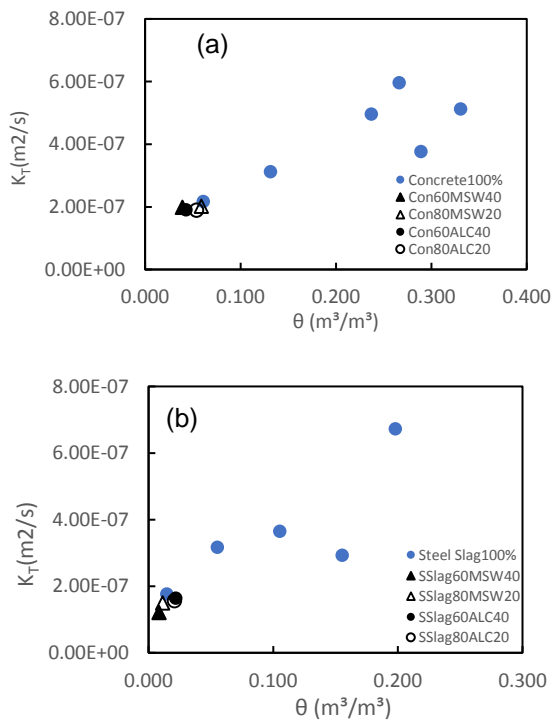


Fig. 12: K_T measurement as function of volumetric water content, θ for a) recycled concrete mixture and b) steel slag mixture

CONCLUSION

The ALC mixture with recycled concrete and steel slag showed advantageous result in increasing thermal diffusivity through subbase and increase water retention properties compared to MSW Slag. However, it was found that the mixing of MSW slag was effective to increase gas diffusion and air permeability for the concrete and steel slag samples. On the other hand, the mixing of ALC grains did not contribute to the increase in gas diffusion and air permeability. Based on the measured water retention properties, gas and thermal transport parameters data obtained, the results can be utilized in studies of vapour, heat transport in unsaturated roadbed materials and simultaneous analysis of water that is necessary to further examine flood control and UHI reduction effect in PPS.

ACKNOWLEDGEMENTS

We acknowledge to Saitama City East Environmental Center, Masuo Recycling Co. Ltd, Nippon Steel & Sumitomo Metal Corporation, and Asahi Kasei Construction Materials Corporation for providing us experimental materials. This work was supported by

the research grant from Steel Foundation for Environmental Protection Technology and by the research grant from the JST/JICA Science and Technology Research Partnership for Sustainable Development (“SATREPS”).

REFERENCES

- [1] European Commission (2016) - EU Construction & Demolition Waste Management Protocol.
- [2] Andersen, C.T., I. D. L. Foster, C. J. Pratt (1999). The role of urban surfaces (permeable pavements) in regulating drainage and evaporation: development of a laboratory simulation experiment.
- [3] Branea Ana-Maria, Danciu Mihai Ionut, Keller Alexandra Iasmina (2016). Urban Heat Island: State of the art review.
- [4] Tong T. Kien (2013) – Utilisation of construction demolition waste as stabilized materials for road base applications
- [5] Md. Aminur Rahman, Monzur Imteaz, Arul Arulrajah, Jegatheesan Piratheepan, Mahdi Miri Disfani (2014) – Recycled construction and demolition materials in permeable pavement: geotechnical and hydraulic characteristics
- [6] Arul Arulrajah, Suksun Horpibulsuk, and Farshid Maghool (2016) – Recycled construction and demolition materials in pavement and footpath bases
- [7] Arul Arulrajah, Suksun Horpibulsuk, and Farshid Maghool (2016) – Recycled construction and demolition materials in pavement and footpath bases
- [8] Japan Road Association (2010). Handbook on Pavement Reclamation.
- [9] JIS A 5015 (2013). Iron and steel slag for road construction.
- [10] JGS 0711 (2009). Test method for soil compaction using a rammer.
- [11] Rolston, D. E. and Moldrup, P. (2002). Chapter 4.3. Gas Diffusivity. In: Methods of Soil Analysis, Part 4, SSSA Book, Ser. 5. J. H. Dane and G. C. Topp (eds.). ASA and SSSA, Madison, WI, pp. 1113-1139.
- [12] Iversen, B. V., Schjønning, P., Poulsen, T. G., and Moldrup, P. (2001). In situ, on-site and laboratory measurements of soil air permeability: Boundary conditions and measurement scale. Soil Science 166, 97-106.

WATER QUALITY AND SEDIMENTATION MODELING IN SINGKARAK LAKE, WESTERN SUMATRA, INDONESIA

Harman Ajiwibowo¹, R.H.B. Ash-Shiddiq¹, Munawir B. Pratama¹

¹ Faculty of Civil and Environmental Engineering, Institut Teknologi Bandung, Indonesia

ABSTRACT

Numerical modeling of the spatial distribution of water quality in Singkarak Lake, Western Sumatra, Indonesia is conducted. Field measurement data are collected, including bathymetry, water level, current velocity, and water quality data. The measured parameters in the water quality survey are the total suspended sediment (TSS), chemical oxygen demand (COD), biochemical oxygen demand (BOD), dissolved oxygen (DO) and phosphate (P). The finite element model is implemented using a surface-water modeling system (SMS). The model includes flow, constituent, and sedimentation models. Validation of the flow model is achieved by matching the current and the water elevation between the model and the field data. The validation shows good agreement. The model is aimed at observing yearly water quality and sedimentation change at the lake. The results from the constituent model show that the Sumpur and Sumani Rivers are having the greatest effect on the water quality of the lake in its northern and southern regions, respectively. A bed change of around 30–40 cm per year is found at the inlets of both of these rivers. Overall, the model shows that the lake water is only suitable for irrigation or fishing hatchery, and not for drinking water, according to the criteria for water quality standards in the Indonesian government's Regulation 82 of 2001.

Keywords: Numerical modeling, Water quality, Singkarak Lake

INTRODUCTION

Water pollution has been one of the most important issues concerning the environment. Not only in large oceans but also in rivers and lakes which are closely related to daily life. Few studies on lake-water pollution have been taken in countries such as Egypt, Iran, and the USA. The study in Egypt was carried out by Farhat and Aly (2018) [1]. They found that the sedimentation pattern in Lake Nasser is affected by the semi-enclosed embayment and the metal pollutions are brought by floods. Mardi et al. (2018) studied aerosol pollution in Lake Urmia, Iran [2], whereas Sherchan et al. (2017) particularly assess fecal pollution in Lake Pontchartrain, Louisiana [3].

In this study, hydrodynamic numerical modeling on Singkarak Lake, Western Sumatra, Indonesia is performed. The model is provided to predict the material distribution in the water [4]–[6]. Surface-water modeling system (SMS) tools such as RMA2, RMA4, and SED2D are used. Besides SMS, Deflt3D [7], MIKE [8], EFDC [9], and CE-QUAL-W2 [10] are widely used to model the ecosystems of lakes or other bodies of water.

The studied material is COD, BOD, DO, and phosphate, which highly influences the lake water quality [11]–[13]. High land use for agriculture and fish farming can lead to high phosphorus pollution. This study also includes field measurements and numerical model resulting in a spatial variations of

parameters after a year. The resulted contaminant distribution will be compared with the local authority regulation [14] which classify lakes into 4 classes based on the contaminants content.

Overview of Singkarak Lake Condition

The province of Western Sumatra is 42,297.3 km². There are five lakes in the province. They are Maninjau Lake, Singkarak Lake, Dibawah Lake, Diatas Lake, and Talang Lake, as seen in Fig. 1, and indicated by numbers 1 to 5, respectively. Singkarak Lake is the largest in Province of Western Sumatra and the second largest in Sumatra Island with an area of around 109,082 km² [14].

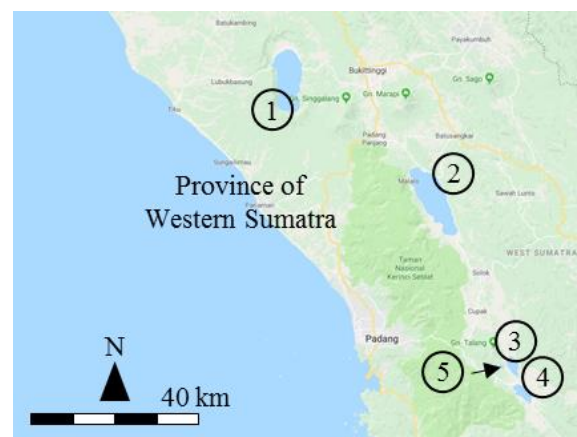


Fig. 1 Lakes in Western Sumatra, Indonesia.

Singkarak Lake has an indispensable role in West Sumatran development. Until now, Singkarak Lake has been a water reservoir to supply the needs of daily activity, farm irrigation, and a hydropower plant. Recreational, transportation, and fish farming activities also take place in Singkarak Lake. At the same time, Singkarak Lake also becomes a basin for containing waste from sources such as housing and markets, agriculture, and from recreational and transportation activities.

The wastes converging in Singkarak Lake are identified as the main cause of lake quality degradation. In the Bali Agreement of 2009, Singkarak Lake is one among 14 lakes in Indonesia to be prioritized under an integrated management [14], as well as Maninjau Lake.

Study Location

The study takes place in Singkarak Lake located in Province of Western Sumatra (see Fig. 1). There are nine rivers flowing into Singkarak Lake: Sumani, Sumpur, Anak Cangking, Ambius, Paninggahan, Sibaladi, Batu Panjang, Pingai, and Malalo Rivers. They are denoted by R1 to R9 (see Fig. 2), respectively. There is one river flowing out from Singkarak River, namely Ombilin River.

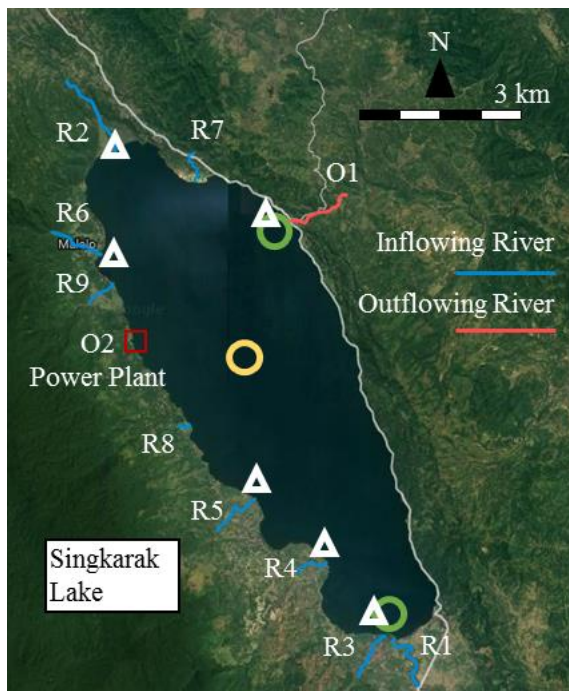


Fig. 2 The overview of Singkarak Lake including locations of rivers, power plant, and survey points.

Jeanse (2015) in his thesis shows the detail of the most significant rivers around Singkarak watershed. Among the 10 rivers in Fig. 2, the Sumani, Sumpur,

and Ombilin Rivers are found to have a great sub-basin area. The Sumani and Sumpur Rivers flowing into Singkarak Lake have sub-basin areas of 482.5 and 164.1 km² with major river lengths of 52.6 and 4.16 km, respectively [15].

The lake water also supplies water to the Singkarak hydropower plant since 1998 [16]. The power plant uses around 35 m³/s of water from the lake in a given month and the amount remains constant for the year. The Singkarak power plant is shown in Fig. 3 and the location is given in Fig. 2 as a red box placed between Malalo and Pingai River.



Fig. 3 Singkarak Hydro-based Power Plant.

METHODOLOGY

Field data measurements includes bathymetric, water level, current velocity, and water quality measurements.

Bathymetric Field Data

The bathymetric data are needed for the model domain base map. The lake-bed depth data are measured using a transducer and a single-beam echo-sounder attached to a boat moving in the lake. Fig. 4 shows the lake-bed depth field data acquisition. The covered survey area is around 10,800 hectares. The lake-bed elevation data are taken along lines parallel with the lake width in every 200 meters.



Fig. 4 Documentation of bathymetric field data acquisition.

Water Level Field Data

One of the model validation methods is using water level at the lake. The hourly water level data are manually taken for two weeks by installing a staff gauge in the lake nearshore. The location of water level data acquisition is given in Fig. 2 as the yellow circle. The survey result as the black line are given in Fig. 9 in the figure of water level validation result. Different with the water level survey at an open water bodies (such as estuary, strait, or open sea), the taken data is not having the phase of tidal. The lake water elevation is dominantly affected by the volume of rivers discharge.

Current Velocity Field Data

The flow velocity resulted from the model is also validated using field current velocity. The survey uses current meter which record the current magnitude in a specify time. There are two current data acquisition points as indicated by green circles in Fig. 2. The points are located at the river-mouth of the Sumani and Ombilin Rivers. The velocity data are taken four times in one day throughout the day. They are at 7 am, 11 am, 14 pm and 18 pm. Fig. 5 shows the documentation of the data acquisition. The white buoy floating in the lake show the current meter deployment point.



Fig. 5 Documentation of current velocity survey.

Water Quality Field Data

The water quality data acquisition is required to determine the boundary conditions of the model. The field data acquisition is conducted by taking water samples using Nansen bottle and then stored in a sample bottle, as documented in Fig. 6. The water samples are tested by researcher in the local government certified water laboratory to get the values of total suspended sediment (TSS), chemical oxygen demand (COD), biochemical oxygen demand (BOD), dissolved oxygen (DO), and



Fig. 6 Documentation of water quality field data acquisition.

phosphate. These parameter values recorded by the lab test will become the boundary conditions and initial conditions of the water quality model.

The water samplings are carried out at five points (see white triangles in Fig. 2). They are located at the mouth of the Sumpur, Malalo, Paninggahan, Sumani, and Ombilin Rivers.

River Discharge Analysis

Besides the values of TSS, COD, BOD, DO, and phosphate, the boundary conditions of inflowing and outflowing river discharges are also calculated. The river discharge is analyzed using a mock analysis method by considering the watershed area of each river and using the rainfall data from Sialaing Bawah, Saniang Baka, Sumani, and Linta Buo rainfall stations. The monthly river discharges are given in Fig. 7.

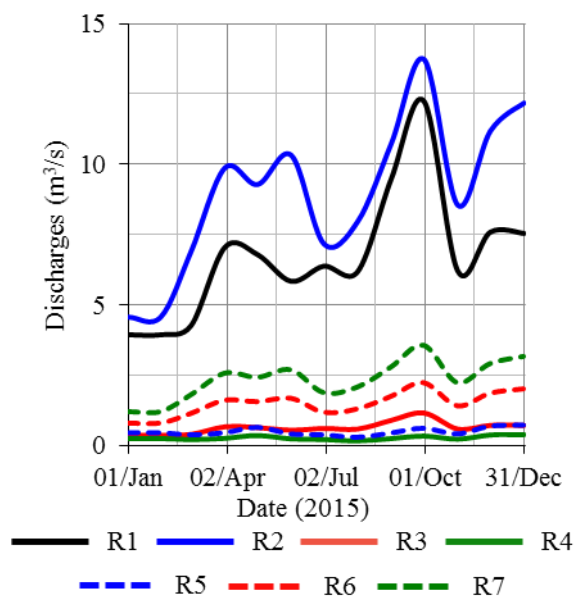


Fig. 7 Monthly river discharges.

From the graph in Fig. 7, the Sumani (R1, black

line) and Sumpur (R2, blue line) Rivers are rivers with the highest discharge. The peak discharges are around 12 and 14 m³/s for Sumani and Sumpur Rivers, respectively, which occurs in September. For the outflowing water, the Ombilin River and Singkarak Power Plant discharges are set to be constant at 11.5 and 35 m³/s, respectively.

HYDRODYNAMIC MODEL

Governing Equations

The basic flow model is constructed using RMA2 of the Surface-water Modeling System version 8.1 (SMS). It is developed by the US Army Corps of Engineering Waterways Experiment Station or USACE-WES. The model uses a two-dimensional finite element method to simulate the flow condition forced by the tide or sources/sinks. The governing equations are given below. Equation 1 is the continuity equation. Equations 2 and 3 are the x-direction, and y-direction momentum equations, respectively [17].

$$\frac{\partial h}{\partial t} + h \left(\frac{\partial u}{\partial x} + \frac{\partial v}{\partial y} \right) + u \frac{\partial h}{\partial x} + v \frac{\partial h}{\partial y} = 0 \quad (1)$$

$$h \frac{\partial u}{\partial t} + hu \frac{\partial u}{\partial x} + hv \frac{\partial u}{\partial y} - \frac{h}{\rho} \left[E_{xx} \frac{\partial^2 u}{\partial x^2} + E_{xy} \frac{\partial^2 u}{\partial y^2} \right] + gh \left[\frac{\partial a}{\partial x} + \frac{\partial h}{\partial x} \right] + \frac{g n^2}{\left(1.486 h^{1/6} \right)^2} \left(u^2 + v^2 \right)^{1/2} - \zeta V_a^2 \cos \psi - 2 h v \omega \sin \Phi = 0 \quad (2)$$

$$h \frac{\partial v}{\partial t} + hu \frac{\partial v}{\partial x} + hv \frac{\partial v}{\partial y} - \frac{h}{\rho} \left[E_{yx} \frac{\partial^2 v}{\partial x^2} + E_{yy} \frac{\partial^2 v}{\partial y^2} \right] + gh \left[\frac{\partial a}{\partial y} + \frac{\partial h}{\partial y} \right] + \frac{g v n^2}{\left(1.486 h^{1/6} \right)^2} \left(u^2 + v^2 \right)^{1/2} - \zeta V_a^2 \sin \psi + 2 h u \omega \sin \Phi = 0 \quad (3)$$

The term definitions are given; h is the water depth, x and y are the Cartesian coordinates, t is the time, u and v are the velocities in Cartesian coordinates, ρ is the fluid density, E is the eddy viscosity coefficient, g is the acceleration due to gravity, a is the elevation of the bottom, n is the Manning's roughness n -value, 1.486 provides the conversion from SI to non-SI units, ζ is the empirical wind shear coefficient, V_a is the wind speed, ψ is the wind direction, ω is the rate of angular rotation of the Earth, and Φ is the local latitude. Beside RMA2 for basic flow model, the RMA4 and SED2D modules are used for the water

quality and sedimentation model.

Model Construction

The lake water flow model grid is generated. The model domain and mesh are given in Fig. 8. The locations of the mentioned river inlets are presented as R1 to R7 and O1. The power plant is indicated by the red box. Tidal effects in the model are assumed to be small and the only applied forcing is from the discharges and intakes of the rivers and power plant. The parameters used for the modeling are given in Table 1.

Table 1 The parameter properties used for numerical modeling

A. RMA2 Parameter Properties	
Turbulence parameter	Isotropic values
	Peclet number method
	Exx ratio 1.0
	Peclet number 20.0
	Min velocity 0.5 m/s
Roughness	0.02
Fluid temperature	28°C
Fluid density	1000 kg/m ³
Initial water surface	362.5 m
Simulation type	Dynamic
Iterations	4
Time step	1.0 hour
Number of time step	8760
B. RMA4 Parameter Properties	
Diffusion coefficient	-1.0
C. SED2D Parameter Properties	
Bed type	Sand
Diffusion coefficient	100.0
Settling velocity	0.01 m/sec
Gravitation	9.806650 m ² /s
Hydraulic bed shear stress	Manning equation
Specific gravity	2.65
Layer thickness	1.0 m
Grain size	0.81 mm

The locations of water level and current velocity survey points are given as yellow and green circles in Fig. 2, respectively. The model is run in the same time frame as the field data collection; thus the model results can be compared with the field data. For the flow model, the main results are the water level and current velocity parameters. The comparison will show the level of validity of the model.

After the flow model is validated, the hydrodynamic model is then expanded to incorporate the water quality and sedimentation models. For the water quality model, the

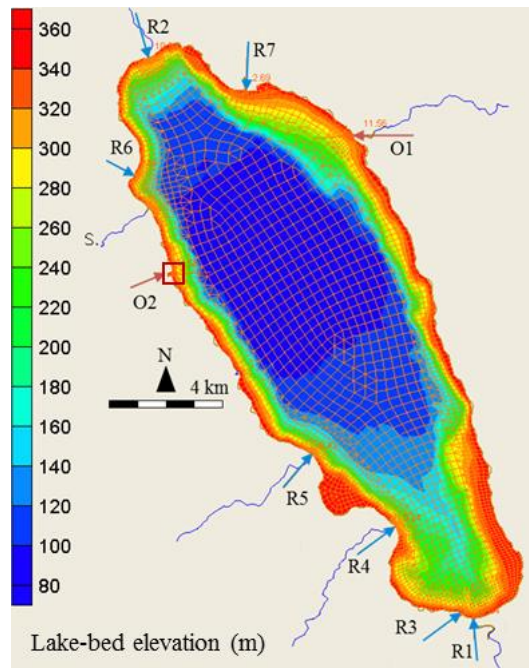


Fig. 8 The domain and mesh of numerical model.

concentration of the investigated parameters must be included in the model. The input for TSS, COD, BOD, DO, and phosphate values are given in Table 2.

Table 2 The parameter concentrations in (mg/l) at the initial and rivers boundary conditions

	TSS	COD	BOD	DO	Phosphate
Initial	33	15.59	3.305	5.62	0.202
R1	51	21.33	5.460	5.16	0.280
R2	260	13.33	2.190	6.25	0.275
R3	51	21.33	5.460	5.16	0.280
R4	35	5.53	1.070	5.95	0.056
R5	42	21.33	4.460	6.01	0.268
R6	20	16.00	3.450	5.10	0.048
R7	25	16.00	3.200	5.25	0.286

Model Validation

The water levels and current velocities resulting from the model are validated using field data. Fig. 9 shows the water level validation. The black and dotted green lines are the field and model data, respectively. Both lines show similar trends in amplitude and phase. Fig. 10 shows the current velocities validation. The x- and y-axes present the current velocity of field data and model data, respectively. The current data are in good agreement with the model results with errors around 0–2 cm/s.

RESULTS AND DISCUSSION

Sedimentation

The final TSS value after the one-year simulation

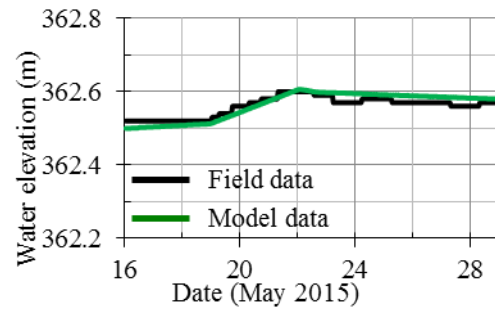


Fig. 9 Water elevation validation.

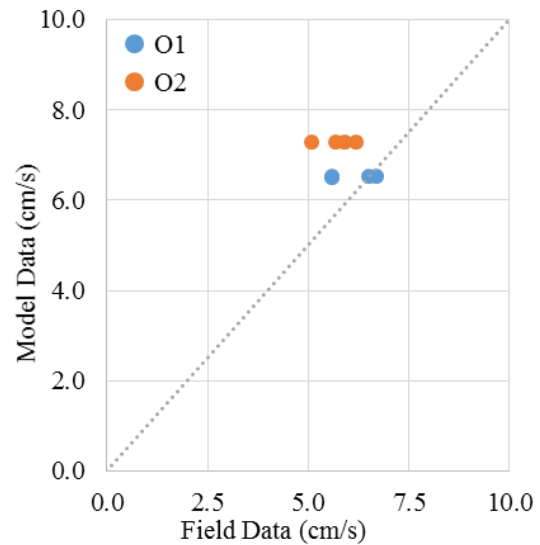


Fig. 10 Current velocity validation.

is given in Fig. 11a. The highest final value is situated at Sumani River with an increase of 30 mg/L. The spatial bed change for lake area is given in Fig. 11b. It is found that rivers with large river discharge result in a high bed change, as seen with the Sumani and Sumpur Rivers. The change after a year is around 40 cm for both locations.

Water Quality

The resulting spatial concentrations after one year of simulation time are given. The COD, BOD, DO, and phosphate concentrations are given in Figs. 12a to 12d, respectively. The final concentration of the investigated parameters after one year of simulation is summarized in Table 3.

Table 3 The resultant concentrations (mg/l) in the inlet of rivers for a simulation of one year

	COD	BOD	DO	Phosphate
Initial	15.59	3.31	5.620	0.202
R1	16.00	3.50	5.600	0.210
R2	15.50	3.25	5.650	0.210
R3	15.80	3.42	5.600	0.205
R4	15.70	3.37	5.615	0.204

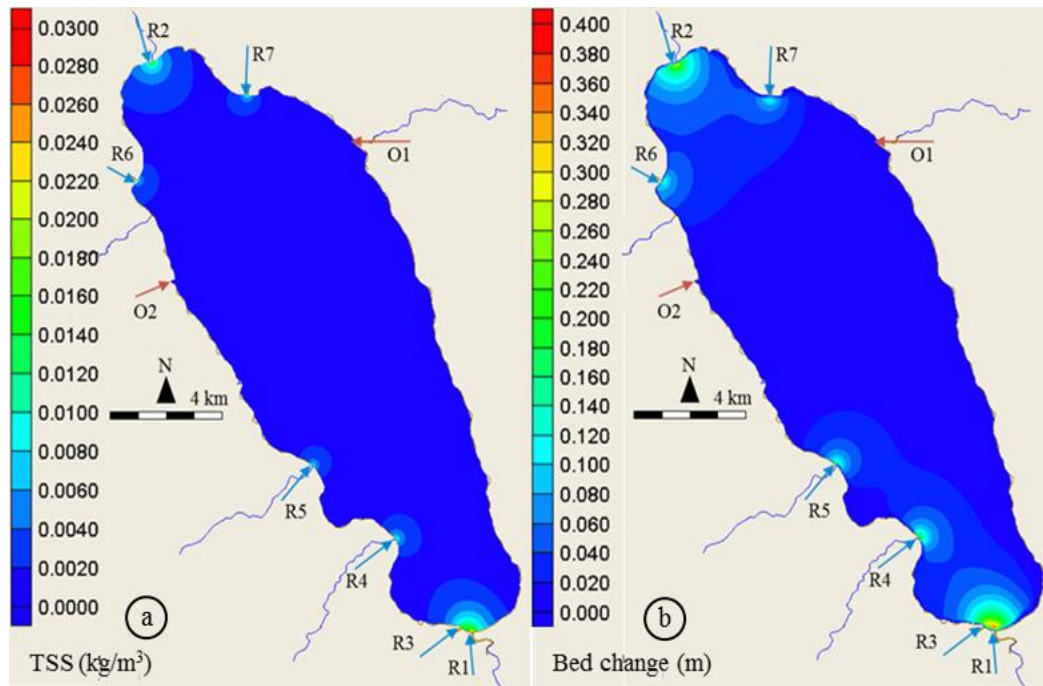


Fig. 11 The spatial distributions of TSS and bed change resulted from the numerical model.

R5	15.65	3.35	5.615	0.204
R6	15.65	3.35	5.600	0.200
R7	15.65	3.35	5.600	0.210
O1	15.65	3.35	5.615	0.204

The initial condition of COD for the lake is 15.587 mg/L. As presented in Fig. 12a, high concentrations are found at the Sumani, Cangking, and Ambius Rivers. (R1, R3, and R4) which exceeded 15.7 mg/L. The only concentration below 15.5 mg/L is obtained at Sumpur River, R2. For BOD parameters, the dispersal is given in Fig. 12b. The trend is quite similar with COD dispersal where the highest and lowest concentrations are located at Sumani and Sumpur River with values of 3.50 and 3.25 mg/L, respectively. The initial value is 3.31 mg/L.

The Sumani and Sumpur Rivers are also dominant in the analysis of phosphate and DO models. The Sumani and Sumpur Rivers contain high phosphate concentrations. The Sumpur River has the highest DO concentration, while the Sumani River has a low concentration that is shared by three other rivers. The Ombilin River consistently has parameter concentrations at a medium value.

Lake Status

The government document on the preservation of Singkarak lakes (called *Gerakan Penyelamatan Danau or Germadan*) includes field surveys conducted in 2012. The comparison of *Germadan* data, field data, and model results are given in Table 4. The nitrate content from the *Germadan* Survey had doubled in 2015. However, a nitrate model is not provided in this study.

For the phosphate content, the concentration value in the *Germadan* Survey covers the total value of phosphorus. Based on work by Haryadi et al. (1991), the total phosphorus consists of polyphosphate, phosphate, and orthophosphate [18]. In the field survey and resultant model data, the investigated content is only the phosphate. However, the phosphate content in the Ombilin Lake is still greater than the total phosphate in the *Germadan* Survey. It indicates that there is an increase of phosphate content inside the lake.

According to regulations for water quality

Table 4 The comparison of *Germadan*, field, and model data

Concentrations in mg/L	2012, <i>Germadan</i> Survey			2015, Field Data			2016, Model Results		
	Sumani River	Center of the Lake	Ombilin River	Sumani River	Center of the Lake	Ombilin River	Sumani River	Center of the Lake	Ombilin River
Phosphate	0.479	0.172	0.276	0.280	-	0.286	0.2100	0.2035	0.2035
Nitrate	0.806	0.513	0.487	1.740	-	1.960	-	-	-

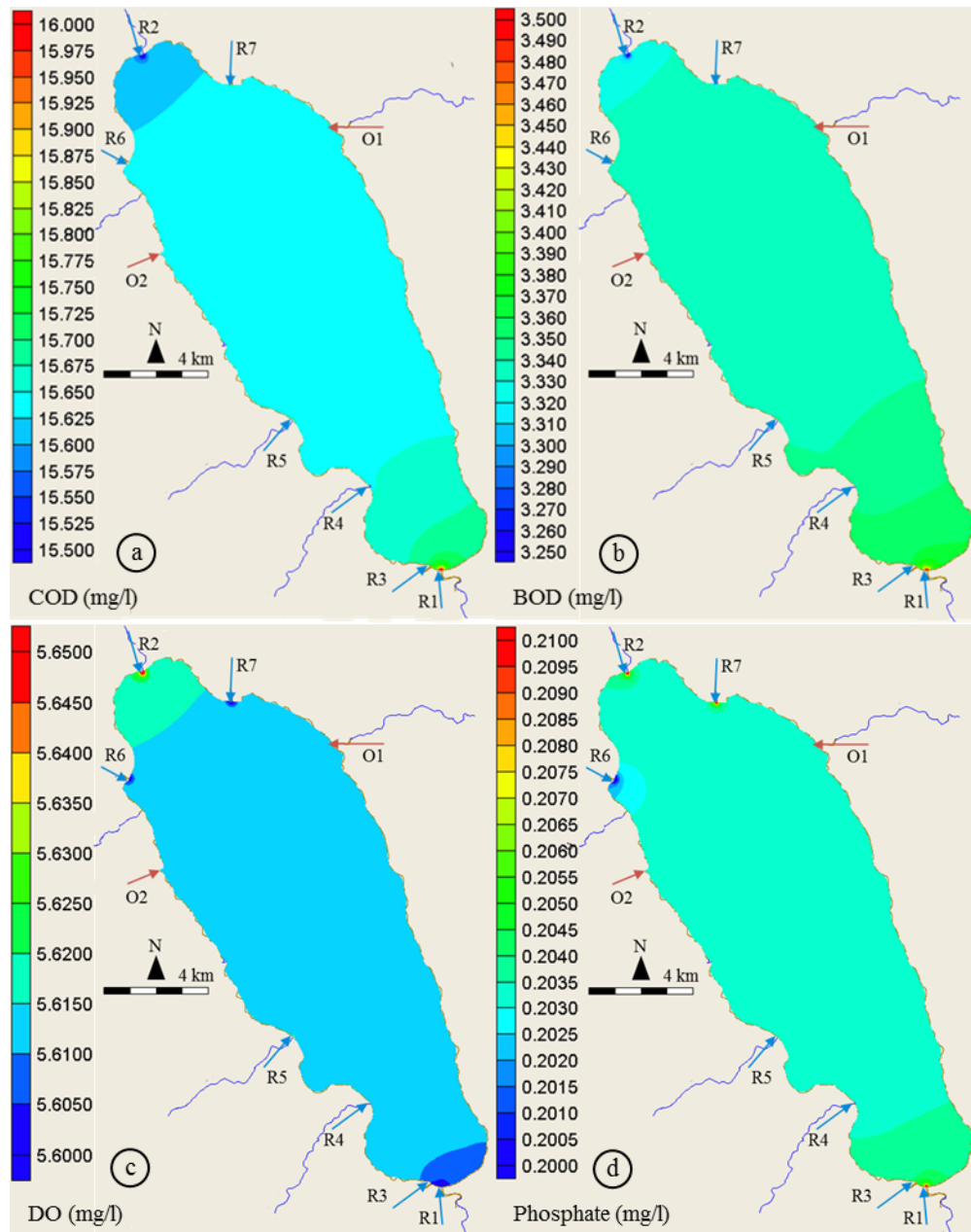


Fig. 12 The spatial variations of water quality model resulted from numerical model.

management and water pollution control in Indonesia, written as Government Regulation No. 82/2001, the lake class can be divided into four classes based on parameter values given in Table 5 [19]. Class I is the standard for raw water for drinking. Classes II, III, and IV are water for irrigation, fisheries, and so on.

Table 5 The standard parameters based on lake classification

Parameters (mg/L)	Class			
	I	II	III	IV
TSS (max)	50	50	400	400
COD (max)	10	25	50	100
BOD (max)	2	3	6	12

DO (min)	6	4	3	0
Total Phosphorus (max)	0.2	0.2	1	5

The TSS value for Singkarak Lake is in the first class with the maximum value below 50 mg/L, which is 30 mg/L. The COD and DO values are in the second class with values of 16 and 5.6 mg/L, respectively. The BOD and phosphate values are in the third class. With this class distribution, the Singkarak Lake overall is suitable for the third class, appropriate only for fish farming and farm irrigation.

CONCLUSION

The COD, BOD, and phosphate in Sumani and Sumpur Rivers are consistently high. The bed

change is also relatively high, the maximum values are between 30–40 cm a year. The Sumani and Sumpur Rivers play important roles in the condition of Singkarak Lake.

One suggested mitigation action is a collaboration between local residents and authorities to maintain lake sustainability by controlling wastes, such as detergent waste, and waste from agriculture and fish farming. These wastes mainly originate from these two rivers. It is also shown that the lake is only appropriate for irrigation or fishing hatcheries, not for drinking water as according to criteria for water quality standards set by the Indonesian government. Another mitigation regarding sedimentation is maintenance of rivermouth of each river coming into the Singkarak Lake by conducting dredging every two years when the bed change already reaches around 1 meter.

ACKNOWLEDGMENTS

The authors would like to thank the Indonesian Ministry of Public Work and Housing for funding this research and also the Indonesian Ministry of Environment and Forests for providing the open access document of *Germadan* of Singkarak Lake.

REFERENCES

- [1] Aly W., and Farhat H. I., Effect of Site in Sedimentological Characteristic and Metal Pollution in Two Semi-enclosed Embayments of Great Freshwater Reservoir: Lake Nasse, Egypt. *J. Afr. Earth Sci.*, Vol. 141, 2018, pp. 194-206.
- [2] Mardi A. H., Khaghani A., MacDonald A. B., Nguyen P., Karimi N., Heidary N., Saemian P., Sehatkashani S., Tajrissy M., and Sorooshian A., The Lake Urmia Environmental Disaster in Iran: A Look at Aerosol Pollution. *Sci. Total Environ.*, Vol. 633, 2018, pp. 42-49.
- [3] Sherchan S., Xue J., Lin S., Lamar F. G., and Lamori J. G., Assessment of Fecal Pollution in Lake Pontchartrain, Louisiana. *Mar. Pollut. Bull.*, In Press Corrected Proof, 2017.
- [4] Song W., Pang Y., Wang J., Pang M., Zhang P., Shao Y., Li L., and Xu Q., Research Into the Eutrophication of an Artificial Playground Lake Near the Yangtze River. *Sustainability*, Vol. 10, Issue 3, 2018, pp. 867-884.
- [5] Zhao X., Shen Z. Y., Xiong M., and Qi J., Key Uncertainty Sources Analysis of Water Quality Model Using the First Order Error Method. *Int. J. Environ. Sci. Technol.*, Vol. 8, 2011, pp. 137-148.
- [6] Sagehashi M., Sakoda A., and Suzuki M., A Mathematical Model of a Shallow and Eutrophic Lake (The Keszthely Basin, Lake Balaton) and Simulation of Restorative Manipulations. *Water Res.*, Vol. 35, 2001, pp. 1675-1686.
- [7] Fang H., Huang L., He G., Jiang H., and Wang C., Effects of Internal Loading on Phosphorus Distribution in the Taihu Lake Driven by Wind Waves and Lake Currents. *Environ. Pollut.*, Vol. 219, 2016, pp. 760-773.
- [8] Doulgeris C., Georgiou P., Papadimos D., and Papamichail D., Ecosystem Approach to Water Resources Management using the MIKE 11 Modeling System in the Strymonas River and Lake Kerkini. *J. Environ. Manage.*, Vol. 94, Issue 1, 2012, pp. 132-143.
- [9] Arifin R. R., James S. C., Pitts D. A., Hamlet A. F., Sharma A., Fernando H. J. S., Simulating the Thermal Behavior in Lake Ontario using EFDC. *J. Great Lakes Res.*, Vol. 42, Issue 3, 2016, pp. 511-523.
- [10] Sadeghain A., Chapra S. C., Hudson J., and Wheeler H., Lindenschmidt K. E., Improving In-Lake Water Quality Modeling using Variable Chlorophyll A/Algal Biomass Ratios. *Environ. Model. Softw.*, Vol. 101, 2018, pp. 73-85.
- [11] Luo Y., Yang K., Yu Z., Yang Y., Zhao L., and Zhou X., Spatial and Temporal Variations in the Relationship Between Lake Water Surface Temperatures and Water Quality – A Case Study of Dianchi Lake. *Sci. Total Environ.*, Vol. 624, 2018, pp. 859-871.
- [12] Lin C., Hu W., Xu J., and Ma R., Development of a Visualization Platform Oriented to Lake Water Quality Targets Management – A Case Study of Lake Taihu. *Ecol. Inform.*, Vol. 41, 2017, pp. 40-53.
- [13] Paytan A., Roberts K., Watson S., Peek S., Chuang P. C., Defforey D., and Kendall C., Internal Loading of Phosphate in Lake Erie Central Basin. *Sci. Total Environ.*, Vol. 579, 2017, pp. 1356-1365.
- [14] Syandri H., Nasaruddin, Manurung H., Harahap T.N., Retnowati I., Rachmiati S., Rustadi WC, Azrita, *Gerakan Penyelamatan Danau (Germadan) Singkarak*, Indonesian Ministry of Environment, 2014, pp. 1-61.
- [15] Jeanes K., Forest Loss Impact on River Flow Regimes of the Singkarak – Ombilin River Basin, West Sumatra, Indonesia, Australian National University, 2015, pp. 1-366.
- [16] Peranginangin N., Sakthivadivel R., Scott N. R., Kendy E., and Steenhuis T. S., Water Accounting for Conjunctive Groundwater/Surface Water Management: Case of the Singkarak – Ombilin River Basin, Indonesia. *J. Hydrol.*, Vol. 292, 2004, pp. 1-22.
- [17] User Guide to RMA2 WES Version 4.5. USA: US Army Engineer Research and Development Center, Waterways Experiment Station, Coastal and Hydraulics Laboratory, 2005, ch. 2, pp. 4-6.
- [18] Haryadi S., Suryadiputra., and Bambang W., *Limnologi: Metode Analisis Kualitas Air*,

Fakultas Perikanan dan Ilmu Kelautan IPB, 1991.
[19] Indonesian Government, Lampiran Peraturan
Pemerintah nomor 82 Tahun 2001 tentang

Pengelolaan Kualitas Air dan Pengendalian
Pencemaran Air, 2001, pp. 1-3.

INTEGRATED LAND USE – FLOOD MANAGEMENT APPROACH IN URBAN SPRAWL OF LAFIA, NASARAWA STATE OF NIGERIA

Danjuma Inarigu¹, Zakiah Ponrahono¹, Mohammad Firuz Ramli¹ and ZulfaHanan Ashaari¹

¹Faculty of Environmental Studies, Universiti Putra Malaysia

ABSTRACT

This study investigates the land cover change for the period 1997 and 2016 using satellite remote sensing data. The investigation was necessitated to determine the changes over time and how these changes influence urban flooding in Lafia, Nasarawa State Nigeria. Landsat imageries used include LANDSAT ETM of 1997 and NIGERSAT -1 of 2016. The classes of land use adopted are; cultivated area, bare surface, built-up area, natural vegetation and water bodies. The results showed that bare surface accounted for 0.72% in 1997 and increased to 1.91% in 2016, built up area occupy land cover of 2.63% in 1986 and increased to 3.55% in 2005, the cultivated area covers 27.88% in 1997 and increased 56.57% in 2016. Natural vegetation of forested area and grass land decreased 25.43% in 2016. Meanwhile, the water bodies covered of 9.43% in 1997 increased to 12.53% in 2016. To ascertain the cause of the flood, the rainfall data for 30 years (1980-2010) was analyzed. Results show that Lafia has a magnitude rainfall ($P < 0.05$ (alpha level)), an indication that the upward trends could be random and consequently, the possibility of flooding.

Keywords: Urban flood, Urban centers, Urbanization, Land use change, Landsat

INTRODUCTION

Flooding is a common phenomenon occurring in various part of the world caused by various factors such as land use change. The frequency of major floods in many places around the world seems to be increasing [1], [2] flash floods occurred throughout Europe in June 2016; the Elbe and Danube flooded in June 2013, just 10 years after the 2002 “millennium” flood; in the UK severe winter flooding in both 2013/2014 and 2015/2016; and many more examples from all around the world. Land use change resulting from both natural and made-made activities contributes immensely in flood occurrences. Large areas have been deforested or drained, thus either increasing or decreasing the nature of soil moisture and triggering erosion. Hill slopes were modified for agricultural production, thus changing flow paths, flow velocities, and water storage, and consequently flow connectivity and concentration times [3]. The impact of land-use changes on storm runoff generation, which has been confirmed by several studies showed that land-use changes are most susceptible to convective storms with high

precipitation intensities and rapid flood runoff production [4]–[8].

Land-use changes have a remarkable influence on flood peak magnitude and runoff volume[9]. In another study [8], applies the hydrological Soil and Water Assessment Tool (SWAT) model to assess the impact of land use changes on the annual water balance and temporal runoff dynamics in a mesoscale catchment [10]. Simulation of the land-use changes effects on floods in the Meuse River with the Distributed Water Balance Flood Simulation Model (LISFLOOD) also successful in modeling the flood events [11].

Study Area

Lafia (Figure 1) is both the capital of Nasarawa State and headquarters of Lafia Local Government Area. With a land area of 2, 797.5sq.km and a population of 330, 712 people [12]. Lafia is located between latitudes 80 20'N and 80 38'N and between longitudes 80 20' E and 80 40'E. Lafia town is found on the edge of a low plateau extending eastward and northward. With a steep slopes of about 80-150 in the

south western part dipping northward in the northern part. [13].

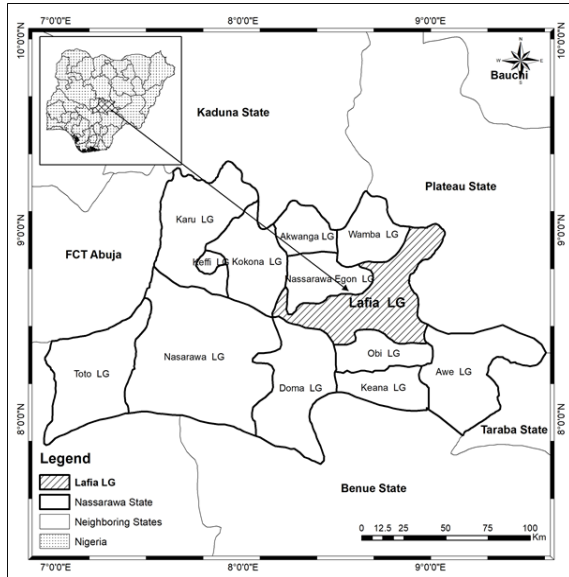


Figure 1: Study Area

Urban land use changes on flood events in Lafia.

Flooding became a serious environmental menace when Nasarawa State was built in 1996 and Lafia was established as state capital. Lafia witnessed the influx of people to the town which has led to the indiscriminate building of structures in places within the natural courses of the municipality. Lafia lies in the low land area of the Benue which makes it more prone and vulnerable to flooding. Lafia suffers from perennial problem of flooding during the rainy season as a result of improper drainage designs and poor maintenance systems. [14] The objectives of this paper include examining changes in urban growth in the Lafia using remotely sensed data and GIS techniques by identifying and mapping out the various land use change over time between 1997 and 2016.

Materials and Method

The data used for this study include LANDSAT ETM of 15th November 1997 with a ground sampling distance of 30 m, and NIGERSAT -1 of 17 October 2016 with a ground sampling distance of 32 m, with sensors in 3 spectral bands (0.52-0.62 μm), red (0.63-0.69 μm) and near infrared (0.76-0.9 μm). These satellite imageries were obtained from the National

Space Research and Development Agency (NASRDA) and the National Centre for Remote Sensing Jos, Nigeria respectively. ArcGIS technique was employed to analyze the images. A supervised classification (Maximum likelihood algorithm) was performed on false color composite (bands 4, 3 and 2) into the following land use and land cover classes; Built-up area, bare surface, cultivated area, Natural vegetation and water bodies. Change Detection method was used to compare the various Landsat imageries collected over the same area at different times and to highlight features that have changed, area calculation in km^2 for each class was examined.

Daily rainfall data was acquired from the archive of the Nigerian Meteorological Agency in Lafia for the period of 1980 to 2010.

Analysis of Rainfall data

The frequency of urban floods in Lafia was analyzed using the procedure developed [15] is in four parts:

- i. The observed rainfall values are ranked in descending order;
- ii. The recurrence interval of each observation is computed using the formula:

$$T = \frac{n+1}{m}$$

Where T = recurrence interval in years

n = number of observations in the series

m = rank of a particular observation

- iii. The observed rainfall values are plotted against their computed recurrence intervals.
- iv. A continuous line is fitted to the scatter of points by eye.

Results and Discussion

The analysis on Land use and land cover data of the study area, gave birth to five classes of relative distribution of land cover in the study area and they include: Bare surface, Built-up area, cultivated area, Natural vegetation and water bodies

Magnitude and rate of changes in Land use and cover between 1997 and 2016

The magnitude of change (C) for 1997 and 2016 is calculated by subtracting the area of each land use and land cover type for 1997 (Table 1 and Figure 2).

(A) From 2016 (B) that is (B- A). The percentage of change (E) is calculated by dividing the magnitude of change (C) of each land use/ land cover class by the value of the base year (1997), then multiplying the result by one hundred.

Bare surface: Bare surface, which include rock outcrop, wasted land and sand deposit, accounted for 0.72% in 1997 and increased to 1.91% in 2016. Table 1. The magnitude of change in bare surface area between 1997 and 2016 was 2.02km² with an annual change rate of 0.11 km² and percentage change of 165.57%. This magnitude of change indicates an increase in bare surface from 1997 to 2016. Built up area occupy land cover of 2.63% in 1997 and by 2016, it increased to 3.55% the magnitude of change in built up area between 1997 and 2016, shows an increase in land area from 4.45km² to 6.01km² with an annual change rate of 0.08km² and a percentage change of 35.06%.

Cultivated area: Cultivated area covers 27.88% in 1997 and in 2016 it increased to 56.57% (Table 1). Between the periods of 1997 to 2016, the magnitude of change had increased to 48.54km² with an increased annual change rate of 2.56km² and the percentage change of 102.88%.

Natural vegetation: Natural vegetation, which includes all forested area and grass land in 1997 decreased in 2016 to 25.43% (Table 1). The magnitude change of natural vegetation between the periods of 1997 to 2016 was -67.37 km² with an annual change rate of -4.20 km² and a percentage change of 67.10%.

Water bodies: water bodies, which include all the surface water found in the study area such as ponds, streams, rivers, marshes and lakes covered 9.43% in 1997 as a result of climate change, domestic and industrial water uses while in 2016, it increased to 12.53% owing to climate change and water collected in big gullies as a result of erosion. The magnitude of change between the periods of 1997 to 2016, the magnitude of change of water bodies was 6.19 km².

With an annual change rate of 0.31 km² and percentage

Change of 41.21%. this implies that between 1997 to 2016, water bodies experienced increase, this could be as a result of the fact that population has really increased and human activities on the land, which causes erosion to pave way for additional water bodies (collected water in big gullies) and drainages found in homes to channel water out of buildings, flood and water logs had become the order of the day owing to unplanned residential area.

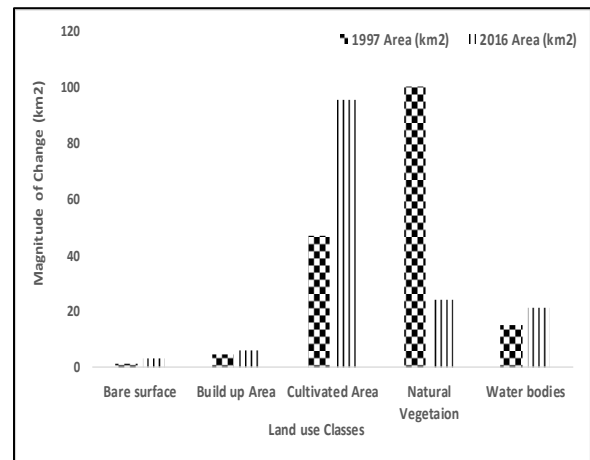


Figure 2: Land use land cover change

Rainfall Data analysis

The data given on table 2 is a daily rainfall data acquired from the archive of the Nigerian Meteorological Agency in Lafia for the period of 1980 to 2010.

Table 1: showing Total Rainfall (mm) Trend from 1980-1990

YEAR	MEAN ANNUAL RAINFALL	SAI
1980	37.4±28.69	3.4
1981	33.3±31.1	3.3
1982	27.55±30.5	2.5
1983	25.8±29.1	2.6
1984	36.7±35.6	3.2
1985	40.2±37.3	-2.8
1986	37.9±36.3	2.1
1987	29.9±28.5	3.6
1988	27.4±25.8	3.5
1989	31.9±31.9	-2.1
1990	94.1±107.7	3.5

The annual rainfall trend was studied using regression analysis [16]. The result (Table 3, 4 and 5)

of the upward trends of Lafia is statistically significant since the $P \leq 0.05$, an indication that the upward trend could be random disagreeing with the findings of [17] which revealed no established trend in the rainfall of West Africa.

Table 2: showing Total Rainfall (mm) Trend from 1980-1990

YEAR	MEAN ANNUAL RAINFALL	SAI
1991	994.6±82.9	3.7
1992	828.8±69.1	2.7
1993	1540.2±128.4	3.1
1994	1430.7±119.2	-0.1
1995	1357.7±113.1	3.5
1996	1381.2±115.1	3.5
1997	1206.2±100.5	2.1
1998	915.3±76.3	3.3
1999	934.6±77.9	4.9
2000	946.9±78.9	3.8

The Rainfall trend was analyzed using Simple Linear Regression and the trend values using Time Series Analysis. The result is given below:

Table 3: Showing the Correlation Coefficients and the coefficient of Determination of Lafia Station

Predictor	Coef.	StDev.	T	P
Constant	341.75	94.25	3.63	0.001
Year	38.38	5.142	7.45	0.000

Correlation of Year and Rainfall (mm) = 0.810. The regression equation is Rainfall (mm) = 342 + 38.3 Year

Table 4: Analysis of Variance

Source	DF	SS	MS	F	P
Regression	1	3638921	3638921	55.50	0.000
Error	29	1901532	65570		
Total	30	5540454			

Table 5: showing Total Rainfall (mm) Trend from 2001-2010

YEAR	MEAN ANNUAL RAINFALL	SAI
2001	1274±106.2	-2.6
2002	1286.7±107.2	2.9
2003	1172±97.7	3.7
2004	1296.7±108.1	2.3
2005	1129.4±94.1	2.1
2006	1347.3±112.3	-1.2
2007	1387.2±115.6	4.5
2008	1137.6±94.8	4.5
2009	1455.7±121.3	2.8
2010	1503.9±125.3	2.5

Anomaly Index for determining Rainfall Variability

The Rainfall variability was calculated using the Standardized Anomaly Index (SAI). The mean and

the standard deviation for the annual rainfall were computed and the result is presented on Figure 5.

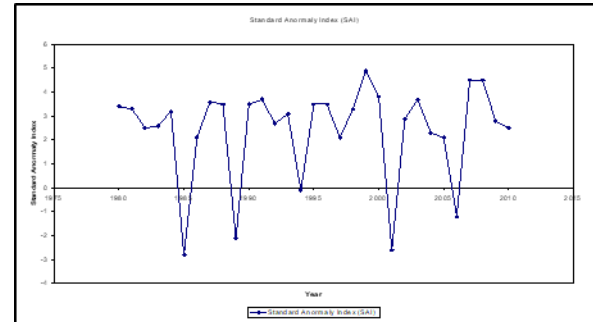


Figure 3: Graph showing the Standardized Anomaly Index Chart

Lafia has a positive correlation which indicates upward annual rainfall trends and consequently, (Figure 3) the possibility of flooding. The present study is in conformity with the works of [13] which revealed an apparent trend in rainfall over the whole of Nigeria, hence.

Flood Magnitude and Frequency Analysis

The Flood Frequency Analysis was analyzed using Histogram graph, and the Flood Magnitude with Gumbel Probability (Figure 4). The result is given below:

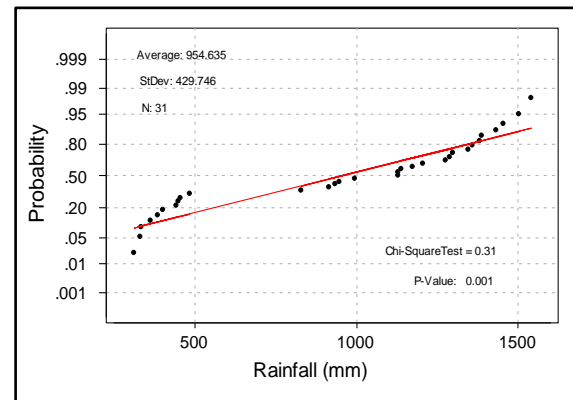


Figure 4: Magnitude of Flood in Lafia

Frequency of heavy rainfall equal or greater than 25.00mm is very high between the months of May to October. There were other months with a high frequency of heavy rainfall in which no flood occurred. This is in conformity with the work of [18] who stresses the needs to analyze heavy rainfall equal

or greater than 25.00mm in any environment for an understanding of flood generating mechanism.

Frequency analysis is performed [15] in order to determine flood magnitude of different return period; the fitness of the data series with the frequency distribution methods i.e. Gumbel distribution methods.

Figure 5 shows the fitness of the annual maximum flow of Lafia Station data with Gumbel distribution performed in order to calculate the extreme flood magnitude with its recurrence period, based on the Chi-Square Test goodness of fit test. The Gumbel distribution (Chi-square value = 0.31), which shows that the data set is at best fit.

The analysis was based on the monthly rainfall (July to October) occurring in the year 1980-2010 in Lafia. Data was based on the month of July to October, on the ground that in most cases, the maximum monthly rainfall in the year in Lafia are recorded from July to October. Data from Table 6 shows that the months of July to September (81%) could be regarded as Flood season in Lafia.

The identification of the most important environmental parameters (that is hazard and vulnerability indices) influencing flood risk is employed the parameters are: depth of flooding (metres), duration of flood (hours/weeks), perceived frequency of flood occurrence, perceived extent of damage arising from flood, percentage deviation of seasonal rainfall (mm) from the mean, area or location/relief, proximity to hazard source (e.g. to source of river), land use or dominant economic activity and adequacy of flood alleviation measures.

Table 6: Flood Risk Classes for Land Use Planning

S/N	FLOOD RISK INDICES	FLOOD RISK CLASS	REMARKS
1.	< 100	I	Low flood risk
2.	100 – 600	II	Moderate flood risk
3.	> 600	III	High flood risk

The parameters were selected based on previous scholars [19] findings on strong positive bearing on flood generating and vulnerability components of

flood hazard. Additionally, the additive method of computing indices which assumed the different parameters add together without interference[9].

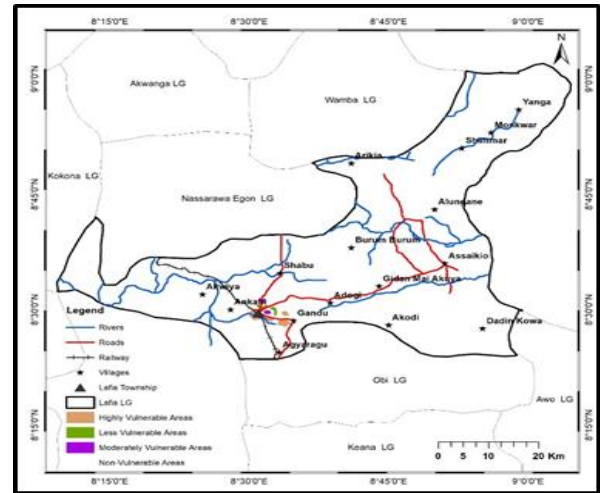


Figure 5 Risk Assessment map

Implication of the changes on the environment

The results of the changes between 1997 and 2016 in Lafia have some adverse effects on the environment. Increase in cultivated area at an annual rate of 2.55 km² between 1997 and 2016 is an indication of an increase in population. The study also revealed that heavy rainfall of long durations and river overflow are the major causes of flooding in Lafia. The depth of flooding, duration of flood, perceived frequency of flood occurrence, perceived extent of damage arising from flooding, percentage deviation of seasonal rainfall from the mean, area or location/relief, proximity to hazard source, land use or dominant economic activity as well as adequacy of flood alleviation measures are the main factors influencing the incidence of flooding phenomenon in Lafia.

Conclusion

The outcome of this study provides an important illustration of the cause-effect relationship between urban areas changes and flood event. Firstly, urban areas changes cause large population concentration in the floodplain areas thereby increasing the risk of the flooding. Secondly, increased development of urban areas changes the environmental natural conditions. Land use changes (deforestation, destruction of wetlands) are prone for the change in rainfall-runoff processes and the increasing peak-flows. It generates

more frequent and severe flood disasters. The relationship between flood event and amount of rainfall indicates that flooding occurs at a time when the amount of rainfall is at its peak and surface runoff is also at its optimum so the land-use changes directly affect surface runoff which eventually leads to flooding. Land-use planning in urban flood management, especially in reducing the flood exposure of cities is vital to overcome the issue.

REFERENCES

- [1] H. F. Lins and J. R. Slack, "Streamflow trends in the United States," *Geophys. Res. Lett.*, vol. 26, no. 2, pp. 227–230, 1999.
- [2] J. Hall *et al.*, "Understanding flood regime changes in Europe: A state-of-the-art assessment," *Hydrol. Earth Syst. Sci.*, vol. 18, no. 7, pp. 2735–2772, 2014.
- [3] M. Rogger *et al.*, "Land use change impacts on floods at the catchment scale: Challenges and opportunities for future research," *J. N. Quint. J. L. Salinas J. Szolgay J. J. H. van den Akker*, vol. 18, no. 21.
- [4] A. Brath, A. Montanari, and E. Toth, "Neural networks and non-parametric methods for improving real-time flood forecasting through conceptual hydrological models," *Hydrol. Earth Syst. Sci.*, vol. 6, no. 4, pp. 627–640, 2002.
- [5] F. Naef, S. Scherrer, and M. Weiler, "A process based assessment of the potential to reduce flood runoff by land use change," *J. Hydrol.*, vol. 267, no. 1–2, pp. 74–79, 2002.
- [6] D. Niehoff, U. Fritsch, and A. Bronstert, "Land-use impacts on storm-runoff generation: Scenarios of land-use change and simulation of hydrological response in a meso-scale catchment in SW-Germany," *J. Hydrol.*, vol. 267, no. 1–2, pp. 80–93, 2002.
- [7] B. Saghaian, H. Farazjoo, B. Bozorgy, and F. Yazdandoost, "Flood intensification due to changes in land use," *Water Resour. Manag.*, vol. 22, no. 8, pp. 1051–1067, 2008.
- [8] N. Fohrer, S. Haverkamp, K. Eckhardt, and H.-G. Frede, "Hydrologic Response to Land Use Changes on the Catchment Scale," *Pergamon Phys. Chem. Earth (B)*, vol. 26, no. 7, pp. 577–582, 2001.
- [9] D. M. Brooks, L. Pando-Vasquez, and A. Ocmin-Petit, "The relationship between environmental stability and avian population changes in Amazonia," *Ornitol. Neotrop.*, vol. 16, no. 3, pp. 289–296, 2005.
- [10] A. P. J. de Roo, C. G. Wesseling, and W. P. A. van Deursen, "Physically based river basin modelling within a GIS: the LISFLOOD model," *Hydrol. Process.*, vol. 14, no. 11–12, pp. 1981–1992, 2000.
- [11] S. Miller and D. Semmens, "GIS-based hydrologic modeling: the automated geospatial watershed assessment tool," *Proceeding Second Fed. Interag. Hydrol. Model. Conf.*, pp. 1–12, 2002.
- [12] NPC, "Nigeria's Population now 182 million," *National Population Commission*, 2015. [Online]. Available: <http://population.gov.ng/nigerias-population-now-182-million-npc/>.
- [13] N. L. Binbol and N D Marcus, "Geography of Nasarawa: A study of Flora and Fauna." .
- [14] F. A. Yusufu, "An Analysis of the Perception of Floodplain Resident ' s to the Risk of Flooding in Lafia Local Government Area ," vol. 3, no. 1, pp. 9–12, 2016.
- [15] D. Keast and J. Ellison, "Magnitude frequency analysis of small floods using the annual and partial series," *Water (Switzerland)*, vol. 5, no. 4, pp. 1816–1829, 2013.
- [16] I. O. Adelekan, "Spatio-temporal variations in thunderstorm rainfall over Nigeria," *Int. J. Climatol.*, vol. 18, no. 11, pp. 1273–1284, 1998.
- [17] J. V Sutcliffe, "Historical variations in African water resources," no. 168, pp. 463–476, 1987.
- [18] O. J. Olaniran, "Flood generating mechanisms at Ilorin, Nigeria," *GeoJournal*, vol. 7, no. 3, pp. 271–277, 1983.
- [19] C. H. Li, N. Li, L. C. Wu, and A. J. Hu, "A relative vulnerability estimation of flood disaster using data envelopment analysis in the Dongting Lake region of Hunan," *Nat. Hazards Earth Syst. Sci.*, vol. 13, no. 7, pp. 1723–1734, 2013.

GEOCHEMISTRY ANALYSES OF SEA FLOOR SEDIMENTS FROM THE COASTS OF SHIKINE ISLAND IN JAPAN INDICATE AN INFLUENCE OF CO₂ SEEPS TO COASTAL ENVIRONMENTS

Hirosuke Hirano¹, Koetsu Kon², Masa-aki Yoshida³, Ben Harvey², Davin H. E. Setiamarga^{4,5,6}

¹ Department of Civil Engineering, National Institute of Technology, Wakayama College, Japan,

² Shimoda Marine Research Center, University of Tsukuba, Japan

³ Oki Marine Biological Station, Shimane University, Japan,

⁴ Department of Applied Chemistry and Biochemistry, National Institute of Technology, Wakayama College,
Japan

⁵ Department of Ecosystem Engineering, Faculty of Advance Engineering, National Institute of Technology,
Wakayama College, Japan

⁶ The University Museum, The University of Tokyo, Japan

ABSTRACT

Recently, two shallow CO₂ seeps were described in Mikama Bay and Ashitsuki (Shikine Island, Japan). These sites were deemed to have potentials for studying the impacts of ocean acidification. Here, we report geochemistry analyses of seawater and sea floor sediments collected from the shallow coasts on and around the two CO₂ seeps. Seawater analyses indicated that shallow waters in the area share similar acidic characteristics (e.g. Avg. pH = ca. 7.1), supporting the result of a previous study. Next, the sediments from all sampling loci also share similar properties (Avg. Fe:Si = 0.043; Avg. organic content = 1.26%; Avg. relative Si content = 75.25%). However, sediments from Matsugashitamiyabi hot spring, which is located near the Ashitsuki seep, showed high Fe:Si ratio (1.250) when compared to other loci. This is most likely a local phenomenon, where iron accumulates in the sediment by the precipitation of rust produced through the mixing of FeS from the hot spring and carbonated seawater of the nearby CO₂ seep. We also compared seawater (e.g. Avg. pH = 8.3) and sediments (Avg. Fe:Si = 0.126; Avg. organic content = 2.06%; Avg. Si = 69.06%) of the Hidaka Port in Wakayama (as a standard sample of coastal surface water environment), to the Shikine Island samples excluding the Matsugashitamiyabi hot spring samples. The differences in characteristics (i.e. lower seawater pH and lower Avg. Fe:Si ratio of the latter) were probably caused by CO₂ seep influence, and indicate that the influence of the hot spring water to the sediment of both CO₂ seeps was minimal, or probably none. Accordingly, these seep sites are useful for future studies on the effects of ocean acidification on sea floor sediment composition, and its implication to biodiversity and the ecosystem.

Keywords: Geochemistry, Sediment, CO₂ Seep, Ocean Acidification, Shikine Island

1. INTRODUCTION

Ocean acidification is defined as the decrease of the global ocean's pH caused by dissolved CO₂ in the seawater [1]. In Earth's geological past, various events such as volcanism have caused drastic increases of atmospheric CO₂, which eventually had caused ocean acidification events. For example, ocean acidification and the anoxic surface sea caused by dissolved CO₂ emitted by volcanism was thought to be one of possible causes of the Permian/Triassic Extinction (PTE), where more than 92% of multicellular organisms went extinct [2]. Recently, a new geological epoch called the Anthropocene has been proposed. This epoch, which thought to start right after the Holocene, was characterized by significant climate change caused

by humans' combined activities [3]. While humans have radiated to every corners of the planet Earth, their activities have left strong carbon footprints, especially after the industrial revolution leading to present modern society [4]. This unprecedented increase of atmospheric CO₂ has brought many ecological and environmental implications, including ocean acidification.

Past geological extinctions such as the PTE have suggested that living organisms, in most cases, react adversely to the drastic pH drop. Therefore, present anthropogenic ocean acidification may have significant ecological impacts. However, since the actual direct effects differ from organism to organism, an overall assessment of the effect at the ecosystem level is difficult to conduct [5] [6] [7]. Previous reports suggested that studies on

ecosystems located at naturally occurring CO₂-seeps (submarine CO₂ vents) could remedy this problem [8]. Therefore, shallow underwater CO₂ vent discoveries, and their geochemical characterizations, are important for future ecological studies of the effect of CO₂-caused ocean acidification.

Recently, Agostini et al [8] and Wada and Agostini [9] reported the discoveries and geochemical characterizations of two naturally occurring CO₂ seeps at the shallow continental floor of the Shikine Island in Japan. They suggested that these CO₂ seep sites are practical and useful for

further studies of the effect of ocean acidification on organisms and ecosystems.

Taking off from their paper, in this study, we report the result of our geochemical analyses of the bottom sediments collected from the two CO₂ seeps, as well as the nearby surrounding area. We also conducted analyses of the seawater taken from the corresponding loci of our bottom sediment samples, which also includes samples taken from similar locations of the previous paper. Our geochemistry characterizations indicate that both the seawater and bottom sediments of the locations along the southern coastline of Shikine Island, where the two CO₂ seeps are located, are chemically affected by the CO₂ seeps. Our results presented here thus strongly corroborate the results of the previous studies by Agostini et al [8] and Wada and Agostini [9]. Moreover, the information we provide in this study will also be useful for further geochemistry, ecology, and biology at the CO₂ seeps in Shikine Island, as well as studies on other shallow marine CO₂ seeps.

Table 1: Sample collection location coordinates in Shikine island

Samples No.	Coordinate of collections
1	34° 19' 18" N., 139° 13' 11" E.
2	Same coordinate as No. 1 Or within 10 meters radius
3	Same coordinate as No. 1 Or within 10 meters radius
4	Same coordinate as No. 1 Or within 10 meters radius
5	Same coordinate as No. 1 Or within 10 meters radius
6	34° 19' 15" N., 139° 13' 6" E.
7	34° 19' 15" N., 139° 12' 10" E.
8	Coordinate within 50 meters radius, from No. 7
9	Coordinate within 50 meters radius, from No. 7
10	Same coordinate as No. 6

2. MATERIALS AND METHODS

2.1 Sampling

The "Ashitsuki" CO₂ seep is in close proximity to the Kamanoshita Coast, as our coordinates shown. Therefore, the name of the sampling locations of samples collected from the Kamanoshita Coast CO₂ seep will be called "Ashitsuki", to maintain nomenclature coherency with Agostini et al [9].

Sediment samples (ca. 20 gram) from the area around Ashitsuki (samples 1–5) and Mikama Bay (samples 7–9) CO₂ seeps were collected in May 2016. Sediment samples from Matsugashitamiyabi hotspring (samples 6, 10) in Shikine Island were

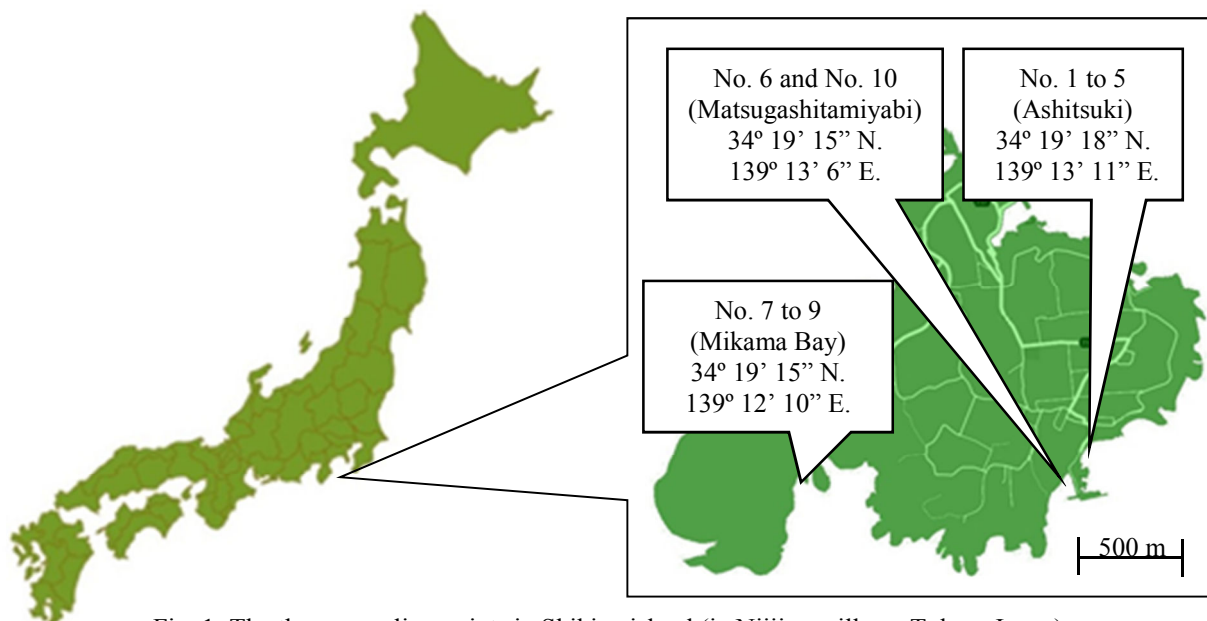


Fig. 1: The three sampling points in Shikine island (in Niiijima village, Tokyo, Japan)

collected twice in May 2016 and in December 2017.

Shallow bottom seawater samples from Ashitsuki CO₂ seep and Matsugashitamiyabi hot spring were collected twice, in May 2016 and in December 2017. In May 2016, only less than 1 mL of seawater was collected from each location, along with the sediment samples. Meanwhile in December 2017, ca. 30 mL of the bottom seawater was collected. Also, seawater samples from the Mikama Bay CO₂ seep were collected only once in May 2016, because weather and terrain conditions did not allow us to collect samples in December 2017.

The coordinates of sampling loci are given in Table 1 and Fig. 1.

2.2 Analysis of sediment samples

We conducted Thermo-Gravimetric (TG) analyses on the oven-dried (at 100°C) sediment samples in order to obtain the information of the organic content. We conducted TG analyses in three conditions: (1) the original dried sediment samples, (2) dried-up samples further burnt at 100°C in order to obtain information about both inorganic and organic contents, and (3) dried samples burnt twice, first at 100°C and later at 600°C, to get rid of the organic matter completely. Therefore, the mass lost after burning can be considered as the total mass of organic content. We then inferred the inorganic content of samples by calculating the mass left after burning at 100°C and 600°C, considering sample (1) (the solid/dried soil sample) as the standard.

Next, we measured silicon (Si), aluminum (Al), iron (Fe), sulfur (S), potassium (K), magnesium (Mg) and calcium (Ca) in surface of sediments by energy dispersive X-ray spectrometry (EDX; Miniscope TM-3000; Hitachi Ltd.) using the scanning electron microscope with EDX capability (SEM-EDX). Sample preparation was as follows: First, wet sludge samples were dried in an oven at 100°C for 10–15 minutes. Dried sample clumps were then crushed in order to turn them into coarse powder. We then mounted the powder onto a carbon

Table 2: Accuracy of pH litmus test paper

Samples	pH paper	pH meter
pH standard solutions (4.01)	4.0	4.0
pH standard solutions (6.86)	7.0	6.9
Ion-exchanged water (6.3)	6.0	6.3
Dec. 2016	8.0	8.2
Sea water in Hidaka port		
Feb. 2017	7.0	8.1
May 2017	9.0	8.3
Aug. 2017	8.0	8.0
Dec. 2017	8.0	7.6
Average	8.0	8.1

stage using carbon tapes. Mounted samples were then analyzed using the SEM-EDX. From the analysis, it was possible to obtain percentage values showing proportions of the seven elements analyzed relative to one another. These values were then used to calculate the proportions in the total inorganic content. For each set of samples, three mounted powder samples were prepared and analyzed in order to avoid sampling bias.

2.3 Analysis of seawater samples

We measured the pH of all seawater samples collected in both May 2016 and December 2017. The pH values of samples from May 2016 were measured using litmus test paper (TRITEST; Macherey-Nagel GmbH & Co.), because of the meager amount of seawater samples. We compared the obtained color with the provided standard using image-analyzing software to obtain approximate pH values. We also confirmed the accuracy of the pH measurement using litmus paper strips by conducting the same measurement method on standard solutions and ion-exchanged water, where we obtained the same values as when measured using a portable pH meter (Table 2). Meanwhile, for samples from December 2017, portable pH meter (Pen Type pH Meter-pH-009 (I)A), as we could obtain the necessary quantity of water samples.

For comparison with seawater collected from a

Table 3: Sample availabilities used in present analyses, based on the time of their collections

Samples No.	Sediments collecting time	Seawater samples collecting time
1	May 2016	May 2016 Dec. 2017 (for pH)
2	May 2016	May 2016 Dec. 2017 (for pH)
3	May 2016	May 2016 Dec. 2017 (for pH)
4	May 2016	May 2016 Dec. 2017 (for pH)
5	May 2016	May 2016 Dec. 2017 (for pH)
6	May 2016	May 2016 Dec. 2017 (for pH)
7	May 2016	May 2016
8	May 2016	May 2016
9	May 2016	May 2016
10	Dec. 2017	Dec. 2017

"standard" ocean environment without any CO₂ seep, seawater from Hidaka Port in central Wakayama was collected multiple times in December 2016, February 2017, May 2017, August 2017 and December 2017), with the pH being measured using both paper strips and a portable pH meter.

We measured the concentration of potassium (K⁺), calcium (Ca²⁺), and magnesium (Mg²⁺) ions in the seawater only on samples collected in May 2016 using ion chromatography (Table 3).

3. RESULTS

3.1 Seafloor sediment geochemical characteristics

Measurement results of the organic content of the sediments are shown in Tables 4. The average value of organic content of samples from the Ashitsuki CO₂ seep site was 1.42%, while that of the Mikama Bay was 1.00%. On the other hand, the average organic content in Matsugashitamiyabi was 7.64%, and thus higher than the sediments sampled from around both CO₂ seeps.

The average value of Si content of the sediments collected from the Ashitsuki site was 69.84%, and 73.10% for the Mikama Bay site. The high average Si contents (ca. 70%) of the sample from both CO₂ seeps are close to that of the sand. The inorganic mineral contents of the samples are shown in Table 5. The average Fe content of Ashitsuki was 2.21%, while that of Mikama Bay was 0.37%. The average Al ion concentration of Ashitsuki was 11.82%, while that of Mikama Bay was 11.94%. Meanwhile, the average Si content of the Matsugashitamiyabi

sediment samples was ca. 29.26%, Fe was ca. 57.16%, and Al was ca. 1.07%. Metal ion concentrations for the sediments from the Hidaka Port were as follow: Si = 62.23%; Fe = 9.04%; Al = 19.43%.

3.2 Seawater chemical characteristics

The average value of the pH of the seawater

Table 4: Organic contents in sediment samples

Samples No.	Organic contents [%]
1	0.75
2	1.00
3	0.98
4	4.11
5	0.23
6	6.79
7	0.56
8	1.06
9	1.39
10	8.48
Average of Ashitsuki	1.42
Average of Mikama Bay	1.00
Average of Matsugashitamiyabi	7.64

Table 5: Rate of inorganic contents in sediment samples

Samples No.	Si [%]	Al [%]	Fe [%]	S [%]	K [%]	Mg [%]	Ca [%]
1	65.51	13.41	1.44	4.72	3.52	9.00	2.40
2	77.13	7.60	3.78	3.39	3.93	1.78	2.39
3	73.65	14.14	1.08	2.08	4.51	1.75	2.78
4	74.51	11.73	2.11	2.64	4.81	2.92	1.28
5	74.70	12.23	2.65	1.74	3.23	1.51	3.94
6	33.70	0.82	51.01	1.87	1.51	8.82	2.28
7	60.41	10.33	0.75	11.01	3.59	9.07	4.83
8	72.30	12.24	0.22	1.62	4.24	2.90	6.48
9	76.82	13.25	0.13	1.77	5.56	1.86	0.61
10	24.82	1.33	63.31	0.62	0.85	7.37	1.71
Average of Ashitsuki	73.10	11.82	2.21	2.92	4.00	3.39	2.56
Average of Mikama Bay	69.84	11.94	0.37	4.80	4.46	4.61	3.97
Average of Matsugashitamiyabi	29.26	1.07	57.16	1.24	1.18	8.10	1.99

collected from the Ashitsuki site was ca. 7.4, and the Mikama Bay site was ca. 6.7. Meanwhile, the average pH of the Matsugashitamiyabi seawater samples was ca. 6.5. The average pH of samples from the Hidaka Port was ca. 8.0. Seawater samples pH values are shown in Table 6.

Ion concentrations as measured by ion chromatography are shown in Table 7. The average value of potassium ion concentration in the seawater samples from all sites in Shikine Island were approximately three times higher than that of the Hidaka Port. For calcium ion concentrations, samples from Shikine Island showed values approximately four times higher than that of Hidaka Port. Meanwhile, the average magnesium ion concentration of the samples from Shikine Island was about twice bigger than that of the Hidaka Port. The anomalously high metal ion concentrations in samples from Shikine Island might be explicable by the presence of CO₂ seep sites in the area (and hot spring in Matsugashitamiyabi), causing the reduced pH, which might eventually had caused metal to dissolve in the seawater.

Table 6: pH of seawater

Samples	Paper	Equipment
	Average of May 2016	Average of Dec. 2017
Ashitsuki	7.4	7.3
Mikama Bay	6.7	-
Matsugashitamiyabi	6.0	7.0

Table 7: Metal ions in seawater

Samples No.	Measured values [mg/L]		
	K ⁺	Ca ²⁺	Mg ²⁺
1	873.2	1385.0	2533.0
2	1525.9	2618.2	2676.8
3	2102.0	2338.3	2198.9
4	1262.1	3703.6	1.1
5	1318.8	2212.3	113.4
6	1037.2	1311.9	1701.7
7	1158.1	3486.7	1787.8
8	1329.9	3912.5	2023.1
9	1239.9	1264.0	3625.0
10	1806.6	2779.6	2618.8
Average of Ashitsuki	1416.4	2451.3	1504.2
Average of Mikama Bay	1242.6	2887.7	2478.7
Average of Matsugashitamiyabi	1421.9	2045.7	2160.3

4. DISCUSSION

4.1 Geochemical values of the sediment and seawater samples from Hidaka Port

In our previous studies, we analyzed the chemical characteristics of sedimentary sludge samples collected by dredging from the Hidaka Port in Wakayama (afterward: Hidaka-1), and samples collected manually from the shallow seas of the Funabashi Port in Chiba [10]. We found that samples from the Hidaka Port has a low average organic content (ca. 7.27%) compared to that of the Funabashi Port (ca. 23.61%).

Meanwhile, we also analyzed the dynamics of organic content [11] and inorganic content [12] of samples collected manually from the shallower part of the Hidaka Port (afterward: Hidaka-2). As a comparative data, we used some data from these previous publications of Hidaka-2, while adding some more new data. The average organic content of Hidaka-2 is 2.84% in average.

When compared with the organic content of sediments taken from Hidaka Port as the standard coastal area with no CO₂ seep, it is clear that the organic contents of both samples from the CO₂ seep sites were very low.

4.2 Geochemical characteristics of the seawater and sediment samples

The difference of seawater pH between Ashitsuki and Hidaka port was ca. 0.6–0.8, while Mikama Bay and Hidaka port was ca. 1.3, and Matsugashitamiyabi and Hidaka port was ca. 1.1–2.0. This indicates that the seawater pH from all sites in Shikine Island are lower than those of Hidaka Port. Moreover, our ion concentration measurements also indicate that metal ion concentrations in the Shikine Island sites are several times higher than those of Hidaka Port.

When we look also at the result of sediment analyses, we found that in general, the two CO₂ seep sites in Shikine Island had only half of the organic content of the samples from Hidaka Port (Hidaka-2). However, the Matsugashitamiyabi samples showed about twice the value of Hidaka-2, which is ca. the same as Hidaka-1. Although this is an interesting phenomenon, at present, we are unable to confidently pinpoint a possible cause for this difference. A previous study has shown that low pH does not affect the decomposition of organic matter in sediments [13]. Previously, Okamoto et al showed that seeping oxygen microbubbles into sedimentary sea sludge caused organic matter decomposition [14]. However, since the CO₂-enriched seawater is likely to have low DO or hypoxic conditions, then this could not be the explanation for the low organic content. Meanwhile, Hirano et al showed that, even

in a hypoxic environment, organic matter decomposed rapidly, probably because of the presence of anaerobic bacteria [15]. Also, we cannot rule out the possibility of the presence of a strong underwater current, which might have prevented organic matter deposition and settlement at the seafloor [16]. The possibility of a sampling location bias and rapid degradation of reactive organic matter deposited in these sediments also cannot be ruled out [17]. Therefore, while it is possible that the low organic content in Ashitsuki and Mikama Bay sediments may have been probably caused by the

low pH caused by the presence of CO₂ seeps, further studies to pinpoint the actual cause is still needed.

Metal ion values in both the sediment and seawater samples from the CO₂ seeps allow us to infer that metals such as Ca and Al were probably dissolved in the low pH seawater caused by either the CO₂ seeps or the sulfuric hot spring. This could bring implications to living organisms with external calcified structures such as mollusks (e.g. gastropods and cephalopods) and radiolarians [18]. Further studies will be needed to confirm this.

To conclude, we could probably say that the geochemical characteristics of the Mikama Bay and Ashitsuki are: (1) reduced seawater pH; (2) low organic content and metal ion content in the sediments; and (3) high dissolved metal ion content in the seawater. Such characteristics could be explained by the presence of shallow CO₂ seeps in the area.

Also, the geographical coverage of our present study was not extensive. For example, this study did not include non-CO₂ seep locations and riverine inputs. In order to confirm that the geochemical characteristics observed here are localized to the area around a CO₂ seep, and not the characteristics of the whole coastal waters of Shikine Island, further studies must include such locations. Such study could include explorations to the coastal area facing Honshu Island, which is on the opposite side of the two CO₂ seep locations previously reported by Agostini et al [9].

4.3 The possibly special condition of the Matsugashitamiyabi hot spring

Interestingly, sediments from Matsugashitamiyabi hot spring, which is located near the Ashitsuki seep, showed high Fe:Si ratio (1.250) when compared to other loci. This is most likely a local phenomenon, where iron accumulates in the sediment by the precipitation of rust produced through the mixing of FeS from the hot spring and carbonated seawater of the nearby CO₂ seep. Meanwhile, the presence of sulfur-rich hot spring in Matsugashitamiyabi might explain for the acidic environment of the area, besides the possible effect of the nearby Ashitsuki CO₂ seep [19].

The stark differences of organic and mineral contents of the two CO₂ seep sites and Matsugashitamiyabi, despite their proximities, suggest that the water environment around the Matsugashitamiyabi hot spring was probably different from those around the CO₂ seeps.

Ashituki is located near the Matsugashitamiyabi hot spring, which is known to gush out water with iron sulfide (FeS). Therefore, it is possible that Fe in the hot spring may flow to CO₂ seep in Ashitsuki and affect the water's pH. However, based on our result, we can safely say that the environmental effects

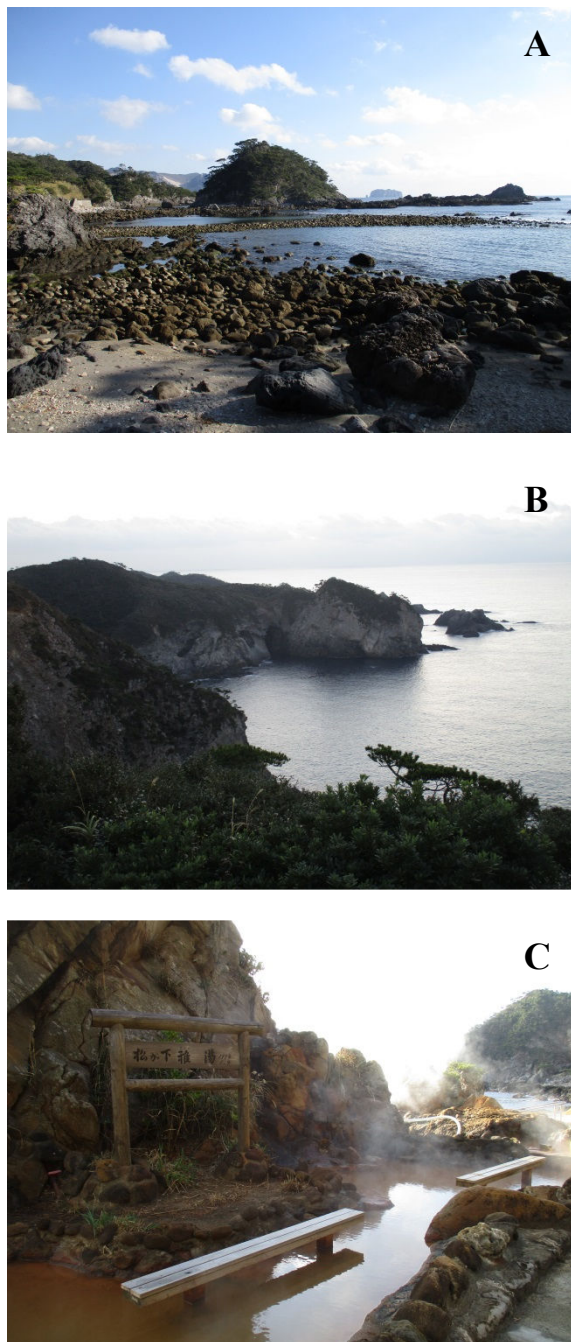


Fig. 2: (A) Ashitsuki; (B) Mikama Bay; (C) Matsugashitamiyabi hot spring

from the Matsugashitamiyabi hot spring to Ashitsuki water is minimal, if not none. This is indicated by the fact that Ashitsuki's Fe concentration is very small (2.21%), which is only less than 5% of that of Matsugashitamiyabi (57.16%).

4.4 Concluding Remarks

In this study, we showed that the geochemistry of the two CO₂ seep sites in Shikine Island are acidified by the CO₂-enrichment. Future studies addressing some questions, such as the geochemistry of locations around Shikine Island, and studies on microbial fauna and biomineralizing organisms are still needed. However, our result suggests that these seep sites accessibilities are definitely useful for future studies on the effects of ocean acidification on sea floor sediment composition, and its implication to biodiversity and the ecosystem.

ACKNOWLEDGEMENTS

HH would like to thank Takeshi Toyama (Nihon University) for his assistance during SEM-EDX analyses. All authors are grateful to Sylvain Agostini (University of Tsukuba) for his invaluable comments on the manuscript. This study was partially supported by the Internal Grant for Research and Education, National Institute of Technology, Wakayama College 2016 (DHES, HH, each separately), and The Asahi Glass Foundation Research Grant 2016 (DHES).

REFERENCES

- [1] Doney S. C., Fabry V. J., Feely, R. A., and Kleypas J. A., Ocean acidification: the other CO₂ problem. *Annual Review of Marine Science*, 1, 2009, pp. 169–192.
- [2] Clarkson M. O., Kasemann S. A., Wood R. A., Lenton T. M., Daines S. J., Richoz S., Ohnemüller F., Meixner A., Poulton S. W., and Tipper E. T., Ocean acidification and the Permo-Triassic mass extinction. *Science*, Vol 348, Issue 6231, 2015, pp. 229–232.
- [3] Jan Z., Mark W., Alan H., and Michael E., The Anthropocene: a new epoch of geological time?. *Philosophical Transactions of The Royal Society A*, 369, 2011, pp.835–841.
- [4] Takahashi T., Sutherland S. C., Wanninkhof R., Sweeney C., Feely R. A., Chipman D. W., Hales B., Friedrich G., Chavez F., Sabine C., Watson A., Bakker D. C. E., Schuster U., Metzl N., Yoshikawa-Inoue H., Ishii M., Midorikawa T., Nojiri Y., Körtzinger A., Steinhoff T., Hoppema M., Olafsson J., Arnarson T. S., Tilbrook B., Johannessen T., Olsen A., Bellerby R., Wong C. S., Delille B., Bates N. R., and de Baar H. J. W., Climatological mean and decadal change in surface ocean pCO₂ and net sea-air CO₂ flux over the global oceans. *Deep-Sea Research II*, 56, 2009, pp.554–577.
- [5] Ferrari M. C. O., McCormick M. L., Munday P. L., Meekan M. G., Dixon D. L., Lonnstedt Ö., and Chivers D. P., Putting prey and predator into the CO₂ equation: Qualitative and quantitative effects of ocean acidification on predator-prey interactions. *Ecology Letters*, 14, 2011, pp. 1143–1148.
- [6] Doropoulos C., Ward S., Diaz-Pulido G., Hoegh-Guldberg O., and Mumby P. J., Ocean acidification reduces coral recruitment by disrupting intimate larval-algal settlement interactions. *Ecology Letters*, 15, 2012, pp. 338–346.
- [7] Sunday J. M., Crim R. N., Harley C. D. G., and Hart M. W., Quantifying rates of evolutionary adaptation in response to ocean acidification. *PLoS ONE*, 6, 2011, e22881.
- [8] Wada S., and Agostini S., Effect of ocean acidification on primary producer in coastal environment: Change of ecosystems in CO₂ seeps. *Chikyukagaku (Geochemistry)*, Vol. 51, 2017, pp. 195-205 [IN JAPANESE].
- [9] Agostini S., Wada S., Kon K., Omori A., Kohtsuka H., Fujimura H., Tsuchiya Y., Sato T., Shinagawa H., Yamada Y., and Inada K., Geochemistry of two shallow CO₂ seeps in Shikine Island (Japan) and their potential for ocean acidification research. *Regional Studies in Marine Science*, Vol. 2, 2015, pp. 45–53.
- [10] Hirano H., Toyama T., Nishimiya N., Setiamarga D.H.E., Morita S., Uragaki Y., and Okamoto K., Artificial Sludge Based on Compositional Information of a Natural Sea Sludge. *International Journal of GEOMATE*, Vol. 12, Issue 31, 2017, pp. 95–99.
- [11] Okamoto K., Toyama T., and Komoriya T., Ocean Decontamination: High Ability Removal Method to Radioactive Cesium from Ocean Sludge by Using Micro Bubbles and Activating Microorganisms. *International Journal of GEOMATE* Vol. 12, Issue 32, 2017, pp.57–62.
- [12] Hirano H., Toyama T., and Setiamarga D.H.E., Changes-over-time of inorganic and organic contents observed in sea sludge samples collected monthly from Hidaka Port in Wakayama, southwest Japan, for a period of 16 months, 3rd EMBRIO INTERNATIONAL SYMPOSIUM, 2017
- [13] Kelly C.A., Rudd J.W.M., Furutani A., and Schindler D.W., Effects of lake acidification on rates of organic matter decomposition in sediments. *Limnology and Oceanography*, Vol. 29, Issue 4, 1984, pp. 687–694
- [14] Hirano H., Nishimiya N., Kojima Y., Toyama T., Umegaki T., and Okamoto K., Investigation of radioactive cesium decontamination from sea sludge using microbial activity. *The International Symposium on Inorganic and Environmental Materials 2013*, 2013, pp. 117–120

- [15] Hirano H., Semura D., Sakamoto K., Toyama T., and Setiamarga D. H. E., A Dynamic changes of organic content over time in the sea sludge collected from the Gobo/Hidaka coastal area in Wakayama, southwest Japan. IOP Conference Series: Earth and Environmental Science, (**Accepted**).
- [16] Burone L., Muniz P., Pires-Vanin A. N. S., and Rodrigues M., Spatial Distribution of Organic Matter in The Surface Sediments of Ubatuba Bay (Southeastern – Brazil). Annals of the Brazilian Academy of Sciences, Vol. 75, Issue 1, 2003, pp. 77–90.
- [17] Burdige D. J., Preservation of Organic Matter in Marine Sediments: Controls, Mechanisms, and an Imbalance in Sediment Organic Carbon Budgets? Chemical Reviews Vol. 107, 2007, pp. 467–485.
- [18] Duquette A., McClintock J. B., Amsler C. D., Pérez-Huerta A., Milazzo M., and Hall-Spencer J. M., Effects of Ocean Acidification on The Shells of Four Mediterranean Gastropod Species Near a CO₂ Seep. Marine Pollution Bulletin Vol. 124, Issue 2, 2017, pp. 917–928.
- [19] Igarashi T., and Oyama T., Acidification of Reservoir and Leaching of Aluminum by Oxidation-reduction Reactions of Pyrite. Journal of The Japanese Society of Engineering Geology, Vol. 38, Issue 5, 1997, pp. 244–251 [IN JAPANESE].

AN ALTERNATIVE INTEGRATED OCCUPATIONAL HEALTH, SAFETY AND ENVIRONMENTAL MANAGEMENT SYSTEM FOR SMALL AND MEDIUM-SIZED ENTERPRISES (SMEs) IN THAILAND

Thepporn Jaroenroy¹, Chutarat Chompunth²

¹School of Environmental Development Administration, National Institute of Development Administration,
Thailand; ²School of Environmental Development Administration, National Institute of Development
Administration, Thailand

ABSTRACT

Small and medium-sized enterprises (SMEs) are drivers of Thailand's economy and represent the largest number of all firms in Thailand. SMEs in Thailand always face safety and environmental issues, while worldwide safety and environmental management systems are difficult to implement within limited resources. This research aimed to develop a conceptual framework for an alternative integrated occupational health, safety, and environmental management system (OHS&EMS) that fits the characteristics of small and medium sized steel manufacturer. This research is qualitative, and a literature review on the safety and environmental management system literature, and interviews with experts as well as focus group discussions, were conducted. The results were analyzed using content analysis. It was determined that the Plan-Do-Check-Act (PDCA) is the cycle that must be maintained for an alternative integrated management system with key requirements, including organization and stakeholder assessment, hazard identification and risk assessment, environmental aspects, actions plans for risk and impact mitigation, internal audit, and corrective action and management review. For the success of alternative management system implementation, communication processes that will convince SMEs to accept and realize the benefits of an integrated OHS&EMS must be carried out prior to its implementation. Less documentation must be considered in order to avoid the difficulty of management system implementation. Furthermore, it is suggested that SMEs need support from external parties in terms of finances and consultation, as well as surveillance audits in order to ensure the continual improvement of their safety and environmental performance.

Keywords: Safety management system, Environmental management system, Alternative management system, Integrated management system, Small and medium-sized enterprises (SMEs)

INTRODUCTION

SMEs represent 99.72% of all firms in Thailand and account for 80.44% of employment as well as contribute 41.1% to the total GDP in Thailand [1]. A large number of SME firms and a large amount of employment from SMEs influence the high injury and illness rate in Thailand. There is clear evidence that occupational accidents in SMEs are greater than those in large enterprises [2]. In environment terms, SMEs generate approximately 70% of the global pollution [3]. Currently, Thailand is still facing air quality problems and increasing hazardous waste from industries, and a large number of SMEs in Thailand are realizing that SMEs are significant sources of pollution [4].

Many scholars have indicated that SMEs have difficulty managing occupational health, safety, and environment issues in their firms. With the limitations of SMEs in terms of economic, human, and technology resources, specific methods are necessary for SMEs to promote occupational health and safety (OHS) awareness and management within their organization [5]. Moreover, SMEs need alternative environmental management systems that better suit the characteristics of SMEs [6]. In

order to ensure good results in terms of profit and reliability, many companies have implemented quality, environmental, and occupational health and safety management systems [7]; however, in order to obtain more benefits from the adoption of various management systems, many organizations are selecting the implementation of integrated management systems instead each management system being implemented separately [8]. Thus, the safety and environmental problems in SMEs in Thailand require a specific integrated OHS&EMS in order to fit the characteristics of SMEs successfully so that their safety, occupational, and environmental performance can be elevated.

SIGNIFICANCE OF THE STUDY

Steel manufacturers in Thailand are upstream in terms of the production chain; however, steel manufacturers generated the highest injury and illness rate per 1,000 employees in 2014 and 2015, with 34.09 cases and 29.04 cases respectively [9]. Further, the iron and steel industries have had a significant impact on the global environment by generating a huge amount of pollutants, solid by-products and residue, and wastewater sludge [10]. In order

to reduce the accident rate and environmental problems from the operation of the steel manufacturers' business, effective occupational health, safety, and environmental practices are needed. However, it has been proven that the models developed for large enterprises are ineffective and difficult to implement in relation to SMEs—many aspects are different between large enterprises and SMEs, especially in terms of financial resources and organization structure [11]. The limitations of resources in SMEs might be the reason why an environmental management systems (EMS) has been implemented by larger companies and its use has decreased with smaller companies [6]. For one thing, a formal safety management system is difficult to maintain in SMEs because of an informal culture [12]. Thus, SMEs need a specific integrated OHS&EMS. This study aims to create a new integrated OHS&EMS for steel manufacturer SMEs in Thailand so that they can manage the environmental aspects of their operations, prevent injuries and illness, as well as manage their business risks with fewer resources. Moreover, this study identifies the motivators and barriers to implementing an integrated management system, how to implement such an integrated management system in SME organizations, and what the resources are that the government should support in order to implement an integrated OHS&EMS effectively. Steel manufacturer SMEs are the target business of this study especially, in Eastern Economic Corridor (EEC) of Thailand (Chonburi, Rayong, and Chachoengsao province) to support economic growth in this area.

METHODOLOGY

In this study, a qualitative approach was applied to establish an alternative integrated OHS&EMS for the small and medium-sized enterprises of steel manufacturers in Thailand. Expert interviews and document reviews were conducted to collect data for creating a conceptual framework for an alternative integrated OHS&EMS and then focus group discussion with experts was employed to review the conceptual framework in order to ensure that it would fit the characteristics of steel manufacturer SMEs in Thailand. The occupational health, safety and environmental management system consists of ISO 14001:2015, ISO 45001:2018, and OHSAS 18001:2007, which have been reviewed so that they could be integrated together; additionally, research on the management of safety, occupational health, and the environment of SMEs has been reviewed in order to understand how SMEs manage their risks and environmental aspects. In this study, the key informants were experts that had specific knowledge and experience about safety, occupational health, and environmental management systems, and that were familiar with the work of SMEs. Expert semi-structured interviews were conducted with 14 experts in order to meet theoretical saturation that is a point where no new information is obtained from further data [13] in order to

create a framework for an alternative integrated OHS&EMS from the point of view of professionals regarding safety, occupational health, and the environment.

Finally, focus group discussion with 10 experts was employed to discuss the constructed alternative integrated OHS&EMS for SMEs in Thailand in order to ensure it would be simple and effortless to implement and also fit the characteristics of steel manufacturer SMEs.

RESULTS AND DISCUSSION

A Conceptual Framework For An Alternative Integrated OHS&EMS For SMEs In Thailand

The integrated OHS&EMS of an organization is a systematic process of identifying its risks and environmental aspects and how to manage those risks and environmental aspects, including embedding this system into the organization. The data from a literature review and expert interviews as well as focus group discussion were analyzed using content analysis and a conceptual framework was constructed, as shown in figure 1.

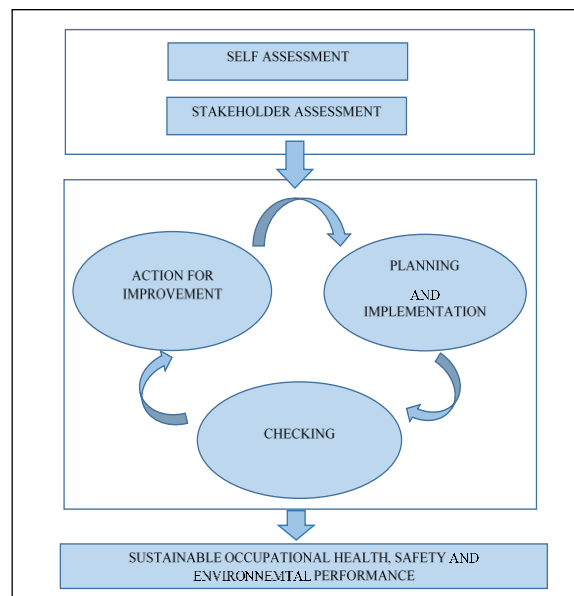


Fig.1 Conceptual framework for an alternative integrated OHS&EMS for SMEs in Thailand.

The PDCA cycle is a mandatory concept for the construction of the conceptual framework according to the agreement of all experts with the following requirements.

1. Organization assessment consists of 2 requirements: 1.1) self-assessment is an important part for identifying the organization's processes, strengths, and weaknesses for better understanding of their business and for eliminating all business threats for sustainable growth; and 1.2) stakeholder assessment must be carried out in order to define the

demands of all stakeholders. The data for the self-assessment and stakeholder assessment were used to establish occupational health, safety and environmental policy.

2. The planning and implementation stage consists of 6 requirements: 2.1) Occupational health, safety, and environmental policy: Policy must be identified by top management in order to direct the organization's commitment regarding occupational health, safety, and the environment. 2.2) Identification and assessment of safety and environment problems: Hazard identification and risk assessment must be conducted for all activities of the organization, including the assessment of significant risks. Environmental aspects of the organization's activities, products, and services must also be identified with criteria for significant aspect consideration. 2.3) Action plan for risks and impact mitigation: Occupation health, safety, and environmental targets shall be determined in order to ensure that policy will be fulfilled and that these targets will be implemented at the operation level of the organization to ensure that all risks and impacts are under the control of the organization. The risks from self-assessment and stakeholder assessment must be addressed with the action plan in order to improve business performance. The action plan for each target must be employed by a responsible person, within the specified time frame and using essential resources to achieve the target and finally all action plans must be followed up periodically by the organization. 2.4) Legal and other requirements: The organization shall identify the legal and other requirements regarding occupational health, safety, and the environment, as well as other requirements that are applicable, and this information shall be kept up to date. Further, the process of compliance evaluation must be carried out periodically. 2.5) Training: The organization shall provide occupational health, safety, and environmental training in order to ensure that related employees are aware of hazards and environmental aspects, and they also should know how to manage related risks and how to control and mitigate the impact on the environment. The following topics are a minimum for training courses related to the education of employees: 1) Occupational health, safety, and environmental policy; 2) Hazards and environmental aspects related to their work and how to manage those risks and environmental aspects; 3) Roles and responsibilities related to legal and other requirements. The organization shall identify the processes for evaluating training results. 2.6) Documented information: The organization shall identify the processes of document control in order to be certain that all documents in the management

system are updated and used appropriately with the intention of each document. The organization shall control the documents using the following processes:

1) Approve the documents for adequacy prior to use; 2) Ensure that the changes and current version status of the documents are identified; 3) Documents must be reviewed appropriately; 4) Define the retention time of the records in the management system.

3. Checking: The effectiveness of an alternative integrated OHS&EMS needs to be monitored periodically. The checking phase consists 2 requirements: 3.1) Internal audit: The organization shall conduct an internal audit at planned intervals to determine the conformity of the alternative integrated OHS&EMS for SMEs. Audit programs shall be planned. The determination of the audit method, audit criteria, the responsibilities of the auditors, and audit reporting shall be defined. 3.2) Accident investigation: The organization shall provide reports and investigate accidents if they have taken place. Investigations shall be conducted in order to determine the root causes of occupational health and safety deficiencies and other factors, and corrective action will be employed in order to identify and eliminate the root causes. The results of the investigation shall be communicated with related employees so that they are aware of the issues and can prevent the recurrence of accidents.

4. Action for improvement: Action for improvement is the last phase to ensure the continual improvement of an alternative integrated OHS&EMS for SMEs. Action for improvement consists of 2 requirements: 4.1) Corrective action: The organization shall correct the nonconformity that has been found within the organization. A nonconformity investigation shall be conducted in order to determine its cause so that the recurrence of such nonconformity can be prevented, A record of corrective action shall be retained within the organization. 4.2) Management review: Top management shall review the organization's OHS&EMS at least once a year in order to ensure its continual adequacy and effectiveness. Input to management reviews shall include: 1) Follow-up actions from previous management reviews; 2) Safety, occupational health, and environmental policy; 3) Needs and expectations from stakeholders; 4) Significant hazards and environmental aspects; 5) Business risks; 6) Achievement of action plan for risks and impact mitigation; 7) Safety, occupational health, and environmental performance of the organization; 8) Adequacy of resources; 9) Recommendations for improvement. The output from the management review shall be provided with the decisions of top management and the actions for improving the performance of the management system shall be

identified. Records of the management review shall be retained.

Importantly, in order to encourage the SMEs to implement an integrated OHS&EMS easily, a manual for implementation should be provided with all details of the implementation steps, including all forms and templates. Especially, the methods for the identification and assessment of safety and environment problems should be simple and easy to understand, and a list of hazards and environmental aspects should be provided for steel manufacturers, in addition to a list of the methods for managing risks and environmental aspects. The methods for self-assessment and stakeholder assessment shall be identified in the implementation manual in order to provide ideas for SMEs regarding business risk assessment. An internal audit process for monitoring the effectiveness of the management system shall be conducted at least annually. Instructions for accident investigation must be provided in an easy form that can encourage an accident reporting system. Finally, a management review shall be conducted at least annually to guarantee the continual improvement of the integrated management system.

OHS&EMS Implementation within SMEs Organizations

The points of view of all 24 experts on how to implement an integrated OHS&EMS successfully in SMEs have been summarized. The motivators and barriers that need to be considered for SMEs to design an alternative integrated OHS&EMS that fits SMEs are defined as follows.

Motivators

1) A flat and simple hierarchy of the organization is the strength of SMEs for implementing a management system. 2) The internal communication of SMEs can be done quickly due to the small number of employees within the organization. 3) Decision-making can be made by the owner-manager, so that actions for eliminating all risks can be managed quickly. 4) A good relationship between the owner-manager and employees can encourage the participation of employees for implementing an occupational health, safety and environmental management system. 5) There is no need formal control and formal documentation for the implementation of an integrated OHS&EMS.

Barriers

1) Lack of internal experts to implement an integrated OHS&EMS within the organization. 2) Most of the SMEs focus on the day-to-day operations of their business to

ensure that their business will survive and maximize benefits. SMEs consider that OHS&EMS are the management of constraints and not their main business [14]. 3) Lack of information concerning an integrated OHS&EMS. Although the Thai government is making an attempt to share information, many SMEs still do not have information on OHS&EMS, including the information on how to implement a management system within the organization. 4) Lack of time for OHS&EMS. Most of SMEs are faced with time to implement OHS&EMS because the owner-manager is the person that is responsible for most of the administration tasks, including safety and health management [15]. 5) Lack of a specific OHS&EMS for SMEs. 6) Existing international OHS&EMS, i.e. ISO 14001:2015[16], ISO 45001:2018[17], and OHSAS 18001:2007[18] require many documents in order to comply with the management system while SMEs need a management system with fewer documents. 7) A complex OHS&EMS is a barrier for SMEs because SMEs lack safety and environmental experts in the organization, so a simple management system is needed for SMEs.

How To Implement An Integrated OHS&EMS In SMEs?

In order ensure the success of integrating an integrated OHS&EMS in SMEs, the strategy of implementation shall be prepared with the understanding of the nature of SMEs. The results from the experts can be categorized into 4 groups: resources, method, engagement, and awareness and monitoring.

1) Resources: Top management needs to provide the essential resources for the implementation of an integrated OHS&EMS; especially, top management must assign one staff member to implement the management system. The implementation time for the OHS&EMS in SMEs should take time more than for large enterprises due to the limitation of resources. 2) Method: An integrated OHS&EMS for SMEs must be constructed using the PDCA cycle in order to ensure the continual improvement of the management system and to reduce the documents that are generated for compliance with the requirements. In addition, self-assessment must be carried out in order to understand the current status of the occupational health, safety, and environmental performance of the organization before beginning to implement the management system. 3) Engagement and Awareness: The owner-manager of SMEs shall be educated and urged to understand the benefits of an OHS&EMS implementation and how occupational health, safety, and the environment can improve their business. Furthermore, all employees must participate in the OHS&EMS. Especially regarding safety management system implementation, the main motivators are the positive attitude of management and workers towards health and

safety [19]. 4) Monitoring: In order to maintain an OHS&EMS in SMEs, an annual surveillance audit program from a third party beyond the internal audit process with support from the government shall be provided.

Which Resources Should The Government Use To Support SMEs So That They Can Implement an Integrated OHS&EMS?

The government should provide assistance to SMEs in order to encourage them to implement an integrated OHS&EMS within their organization. The assistance for SMEs can be defined as follows. 1) A consultant should be provided to assist SMEs in implementing the integrated OHS&EMS, and the consultant should be a person that has experience in how to implement an integrated OHS&EMS in SMEs. 2) Financial support for integrated OHS&EMS implementation should be provided, including training, consultant fees, surveillance audit fees, and a budget for unsafe condition improvements. 3) The owner-manager should be educated to understand how to manage hazards and environmental impacts as well as business risk mitigation. 4) The government should cooperate with large enterprises to add occupational health, safety, and the environment as criteria for selecting SMEs for the procurement process, which would be a significant driver for all SMEs to adopt an integrated OHS&EMS into their organization. 5) The government should provide special benefits: a tax reduction rate and financial support for workplace improvement to reward SMEs that have implemented management system SMEs, and all rewards should be demonstrated to SMEs that occupational health, safety, and environment implementation can provide benefits to the organization. 6) The government should provide an auditor for management system surveillance audits in order to urge SMEs to improve their integrated OHS&EMS as a concept of continual improvement by conducting a surveillance audit at least once a year. 7) The government should provide a list of SMEs that have implemented OHS&EMS so that their contribution to occupational health, safety, and the environment is recognized. Moreover, the list of SMEs that have demonstrated good performance in terms of safety and the environment can be used by large enterprises for their partner selection.

SMEs need a great deal of support from the Thai government in order to improve their performance in terms of occupational health, safety, and the environment because SMEs have limitations in terms of human and financial resources [20].

CONCLUSION

Simpler and fewer documents, and a specific integrated OHS&EMS are needed for the steel manufacturer SMEs in Thailand. With the integration of ISO 45001:2018, ISO 14001:2015, and OHSAS 18001:2007, the PDCA cycle is necessary for management system construction in order to ensure continual improvement of the management system. The requirements of an integrated OHS&EMS should contain only the key requirements in order to reduce the time of implementation and to involve fewer staff members, and to create as few documents in the management system as possible. Integrated OHS&EMS implementation should begin with organization assessment, which consists of self-assessment and stakeholder assessment, in order to understand business strengths and weaknesses. The planning and implementation step, focusing on occupational health, safety, and environmental policy, will be generated from the organization assessment. The identification and assessment of safety and environment problems, and how to manage and eliminate hazards and significant environmental aspects, as well as how to manage the business risks that have been identified by the organization's assessment, are an important part of this management system so that safety, occupational health, and environmental performance can be improved. In order to fulfill compliance with local legal and other requirements, the organization should identify related occupational health, safety, and environmental laws and other requirements, and implement and conduct compliance audits. Training also needs to be provided in order to be certain that employees can work properly without harm and without an impact on the environment. Documents in the management system should be updated and provided in order to demonstrate evidence of system implementation. Checking steps will focus on the internal audit process and accident investigation in order to identify nonconformity and the lack of control measures in the management system. Action for improvement steps consists of corrective action and management reviews in order to ensure that all nonconformities are solved, and actions to improve the management system must be considered and generated annually for continual improvement.

For the successful implementation of an integrated OHS&EMS in SMEs in Thailand, especially in the steel industry, a manual of implementation should be provided with specific instructions. However, SMEs must be communicated with concerning the benefits of an integrated OHS&EMS to convince and motivate them to adopt it within their organization voluntarily.

Although a simple and well-integrated OHS&EMS can be constructed for steel manufacturer SMEs, Thai steel manufacturer SMEs still need

support from external parties in terms financial resources and consultants, as well as auditors for surveillance audits in order to strengthen the effectiveness of the management system adoption within their organization.

REFERENCES

- [1] The Office of Small and Medium Enterprises Promotion (2015), Chapter 4, SMEs Annual Report, pp. 4-3-4-8
- [2] Sørensen, O. H., Hasle, P., & Bach, E. (2007). Working in small enterprises—is there a special risk?. *Safety Science*, 45(10), pp. 1044-1059.
- [3] Jamian, R., Ab Rahman, M. N., Deros, B. M., & Ismail, N. Z. N. (2012). a conceptual model towards sustainable management system based upon 5s practice for manufacturing SMEs. *Asia pacific journal of operations management*, 1(1), pp. 19-31.
- [4] Pollution control department (2016). Thailand state of pollution report 2016, pp. 5-9.
- [5] Pingqing, L., Fang, L., & Chunjing, G. (2006). Occupational Health and Safety (OHS) in Small and Medium Size Enterprises (SMEs): A Primary Review1/SANTE ET SECURITE PROFESSIONNELLES (OHS) DANS LES PETITES ET MOYENNES ENTREPRISES (PME): UNE REVUE PRIMAIRE. *Canadian Social Science*, 2(3), pp. 7.
- [6] Granly, B. M., & Welo, T. (2014). EMS and sustainability: experiences with ISO 14001 and Eco-Lighthouse in Norwegian metal processing SMEs.
- [7] Sanz-Calcedo, J. G., González, A. G., López, O., Salgado, D. R., Cambero, I., & Herrera, J. M. (2015). Analysis on integrated management of the quality, environment and safety on the industrial projects. *Procedia Engineering*, 132, pp. 140-145.
- [8] Raisiene, A. G. (2011). Advantages and limitations of integrated management system: the theoretical viewpoint. *Socialines Technologijos*, 1(1).
- [9] The social security office of Thailand (2015). Injury and illness report 2015, pp. 16
- [10] South East Asia Iron and Steel Institute (2008). Dealing with Environmental Pollution in the Iron and Steel Industry : The China Case Study.
- [11] Surienty, L. (2012). Management practices and OSH implementation in SMEs in Malaysia. School of Management, USM Minden, Pulau Pinang.
- [12] Bragatto, P. A., Ansaldi, S. M., & Agnello, P. (2015). Small enterprises and major hazards: how to develop an appropriate safety management system. *Journal of Loss Prevention in the Process Industries*, 33, pp. 232-244.
- [13] Suchart Prasithrathsin (2011), The new era of qualitative Research Methodologies, pp. 248-251
- [14] Duijm, N. J., Fiévez, C., Gerbec, M., Hauptmanns, U., & Konstandinidou, M. (2008). Management of health, safety and environment in process industry. *Safety Science*, 46(6), pp. 908-920.
- [15] Mudavanhu, N., Zhou, T., & Dzomba, P. (2013). An assessment of small and medium enterprise owners' occupational safety and health efforts: the case of Southerton, Harare, Zimbabwe. *Journal of Scientific Research & Reports*, 4(3), 407-418.
- [16] International Organization for Standardization (ISO) (2015) ISO 14001 : Environmental management systems – Requirements with guidance for use. 3rd Edition, ISO Copyright Office, Geneva.
- [17] International Organization for Standardization (ISO) (2018) ISO 45001 : Occupational health and safety management systems – Requirements with guidance for use. 1st Edition, ISO Copyright Office, Geneva.
- [18] British Standards Institution (BSI) (2007) BS OHSAS 18001: Occupational Health and Safety Management Systems – Requirements. 2nd Edition, BSI Limited, London.
- [19] Masi, D., Cagno, E., & Micheli, G. J. (2014). Developing, implementing and evaluating OSH interventions in SMEs: a pilot, exploratory study. *International Journal of Occupational Safety and Ergonomics*, 20(3), pp. 385-405.
- [20] European Commission (2003). Commission recommendation of 6 May 2003 concerning the definitions of micro, small and medium-sized enterprises. Official Journal of the European Union.

SOME INSIGHT INTO DIRECT OBSERVATION OF HYDROLOGICAL PARAMETERS IN PEATLAND AREA OF THE SOUTH SUMATERA

Muhammad Irfan^{1,2}, Wijaya Mardiansyah¹, M. Yusup Nur Khakim¹, Menik Ariani¹, Albert Sulaiman³ and Iskhaq Iskandar^{1,2}

¹Department of Physics, Faculty of Mathematics and Natural Sciences, Sriwijaya University, Indonesia;

²Graduate School of Sciences, Faculty of Mathematics and Natural Sciences, Sriwijaya University, Indonesia; ³Agency for Assessment and Application Technology, Jakarta, Indonesia

ABSTRACT

An integrated observation system so-called SEnsory data transmission Service Assisted by Midori Engineering laboratory (SESAME) has been deployed in the peatland area of the South Sumatera Province, Indonesia since June 2017. The system directly measures and records the ground water level, soil moisture, skin temperature and rainfall in the peatland area. In this study, we used data recorded at four locations, two sensors located at the Peatland Hydrological Unit (PHU) of the Saleh River and the other two are located at the PHU of the Lumpur River. Data for a period of 17 June 2017 to 31 March 2018 were used to evaluate the characteristics of hydrology and climatology of the peatland in the South Sumatera. It was found that a high rainfall is associated with low skin temperature, high soil moisture, and shallow ground water level. Furthermore, it was found that the observed ground water level is significantly correlated with the observed rainfall. Interestingly, the adjusted ground water level from TRMM rainfall show significant correlation with the number of hotspot during dry-season (July-October). Therefore, we may use the observed rainfall for peat fire early morning.

Keywords: Ground Water Level, Hotspot, Peatland, Rainfall, SESAME

INTRODUCTION

One of the important ecosystem types found in Indonesia is peatland. Peatland is a wetland ecosystem characterized by high accumulation of organic materials with low decomposition rate. Tropical peatlands cover an area of approximately 40 million ha, of which about 50% are located in Indonesia. It means that about 10.8% of the land area in Indonesia is peatland. Indonesia's peatlands are spread over several islands, including Sumatra, Kalimantan, Sulawesi and Papua. 35% of the total peatland in Indonesia are found on the Sumatera Island. The main distributions of peatlands on the Sumatera Island are in Riau, Jambi and South Sumatra [1-3].

The peatland is vulnerable to the fire. In 2015, the El Niño event co-occurred with a positive Indian Ocean Dipole (IOD) event. It has been known that the El Niño and positive IOD events caused deficit rainfall over the Indonesian region [4-5]. This causes the extreme climate events in Indonesia triggering many environmental issues. For example, the forest fire over 2000 – 2002 had caused a huge area of forest loss in Indonesia [6]. In addition, previous study has also reveal that the fires on the forested peatland and vegetation in Indonesia during 1997 El Niño event released about 0.81 and 2.57 Gt of carbon to the atmosphere [7].

In order to better predict the occurrence of forest

fire, in particular the peat fire, since June 2017 the Indonesian government through the Peatland Restoration Agency has initiated a direct observation system of hydrological parameters on peatland area so-called a SEnsory data transmission Service Assisted by Midori Engineering laboratory (SESAME). The parameters measured are Rainfall (RF), Skin Temperature (T), Soil Moisture (SM), and Ground Water Level (GWL).

In this study, the SESAME data combined with the data from satellite remote sensing were used to evaluate the hydrological characteristics of the peatland area in the South Sumatera for a possible application on the mitigation of extreme climate events. In particular, this study is intended to address the following questions:

1. What is the pattern of RF, T, SM, and GWL on the Peatland Hydrological Unit of Lumpur River and Saleh River in the South Sumatra based on the SESAME data?
2. Is there any relation between the GWL and RF?
3. Can we use the RF data to predict the peat fires?

DATA

SEnsory Data Transmission Service Assisted by Midori Engineering Laboratory (SESAME)

SESAME is a comprehensive system that can collect data using sensors, record them on the spot, transmit them to remote sensors via mobile communications networks, process and transmit data, deliver output in an analytical format, and transmit output to a user's computer [8].

Application of the SESAME system is primarily used for data purposes related to climate variations. The number of measurement points ranges from 14,000 points categorized for measurements related to control of Ground Water Level (GWL) on peatlands, estimated amount of carbon dioxide in peatland, early warning of floods and natural disasters, and weather observation [8].

In Indonesia, in total there are 17 locations where the SESAME was installed. In particular, in the South Sumatra there are 8 SESAME. This study will be conducted at two Peatland Hydrological Unit (PHU) in South Sumatra, namely PHU Lumpur River and PHU Saleh River. On each PHU, 2 SESAME system were installed (Figure 1). Detailed location of the SESAME system used in this study is presented in Table 1.



Fig 1. Map of SESAME location in the South Sumatera.

Table 1. Name and location of the SESAME used in this study.

No.	Name	Coordinate of the Location
1.	Lumpur River 1	-3.143, 105.184
2.	Lumpur River 2	-3.458, 104.921
3.	Saleh River 1	-2.911, 105.082
4.	Saleh River 2	-2.677, 105.143

Tropical Rainfall Measuring Mission (TRMM)

TRMM was developed by National Aeronautics and Space Administration (NASA) and Japan Aerospace Exploration Agency (JAXA), which

produces precipitation data obtained from TRMM meteorological satellites. The TRMM satellite began operations in 1997 [9]. The satellite brings 5 channels of PR (Precipitation Radar), TMI (TRMM Microwave Channel), VIRS (Visible and Infrared Channel), CERES (Clouds and the Earth's Radiant Energy System), and LIS (Lightning Imaging Sensor). In particular the PR and TMI channels have missions in rainfall estimates. Both channels are able to observe rain structures and play an important role in knowing the mechanisms of global climate change and monitoring of environmental variations.

Comprehensive data on rainfall on TRMM has been available since 1998 [9-10]. Rainfall data generated by TRMM has a fairly diverse type and shape that starts from level 1 to level 3 [10]. Level 1 is data that is still in raw form and has been calibrated and corrected geometrically. Level 2 is a data that already has a picture of the rain geophysical parameters at the same spatial resolution, but still in the original condition of the rain when the satellite passes through the recorded area. Level 3 is data that already has rain values, especially the monthly rainfall condition which is a combination of rain conditions from level 2. In this study, we used the TRMM data level 3, with a spatial resolution of $0.25^\circ \times 0.25^\circ$ and temporal resolution of 3 hours. Data over a period of January 2000 to September 2017 will be used in this study.

Moderate Resolution Imaging Spectroradiometer (MODIS)

This study used hotspots data obtained by the MODIS satellite. The MODIS satellite is one of the main instruments brought by the Earth Observing System (EOS) Terra and Aqua satellites, part of the US Aerospace program, National Aeronautics and Space Administration (NASA) [12]. The MODIS detects an object on the earth surface that has a relatively higher temperature compare to the surrounding temperature. If the temperature detected is greater or equal to 320 K (noon) and 315 K (night), then it is called as a hotspot. This study used daily hotspots data over a period of January 2000 to September 2017.

METHODOLOGY

In order to address the above research questions, we first evaluate the hydrological parameters observed by the SESAME system. Note that the final goal of this study is to evaluate the SESAME data for a possible application on the mitigation of extreme climate events, in particular the peat fires in the South Sumatera. Note that previous study has shown that the peat fire is strongly correlated with

the ground water level [13]. Therefore, we first evaluate the relation between the SESAME rainfall data and the SESAME ground water level data. This relation is, then, used to create a long-term adjusted ground water level. The final data is correlated with the hotspot data to obtain a possible mechanism of the peat fires.

The correlation coefficient (r) is determined by [14-15]:

$$r_{xy} = \frac{1}{N-1} \frac{\sum_{i=1}^N (x_i - \bar{x})(y_i - \bar{y})}{S_x S_y} \quad (1)$$

where S_x and S_y are the standard deviation of each time-series.

RESULTS

Patterns of Observed Hydrological Parameters

Figure 2 shows the daily variations of observed temperature, rainfall, soil moisture and ground water level at PHU Lumpur River-1 (*see* Table 1). Note that due to limited space, only data at one location just for a period of 1 – 29 July 2017 is presented. As expected, it can be seen that a high rainfall is associated with a low skin temperature, high soil moisture and shallow ground water level. This relation is also applied to other SESAME locations at the PHU Lumpur River and PHU Saleh River.

The statistical analysis of hydrological parameters observed at 4 SESAME stations is presented in Table 2. It appears that the maximum values of skin temperature are very high and could reach 50°C. It is argued that a high observed skin temperature is due to the position of the temperature sensors. The sensor is stored in a closed-box to avoid vandalism. Thus, it may cause the observed temperature is higher than the actual temperature (outside of the box).

Table 2. Statistics of the SESAME data

Lo	T (°C)		RF (mm)		SM (%)		GWL (cm)	
	Mn	Mx	Mn	Mx	Mn	Mx	Mn	Mx
L1	18	48	0	40	79	167	-43	43
L2	17	50	0	44	49	135	-14	89
S1	19	44	0	85	99	136	-.1	37
S2	22	46	0	27	79	114	-22	27

Note: Mn = minimum, Mx = maximum

L1 = Lumpur River-1, L2 = Lumpur River-2

S1 = Saleh River-1, S2 = Saleh River-2

In addition, it also appears that the maximum values of observed soil moisture are above 100%. It is suggested that this high value is caused by the estimation of the soil moisture on the SESAME system, which is based on the comparison between water mass and soil mass. Note that, the peatland water mass may be greater than soil mass. Therefore,

the estimated soil moisture can be larger than 100%.

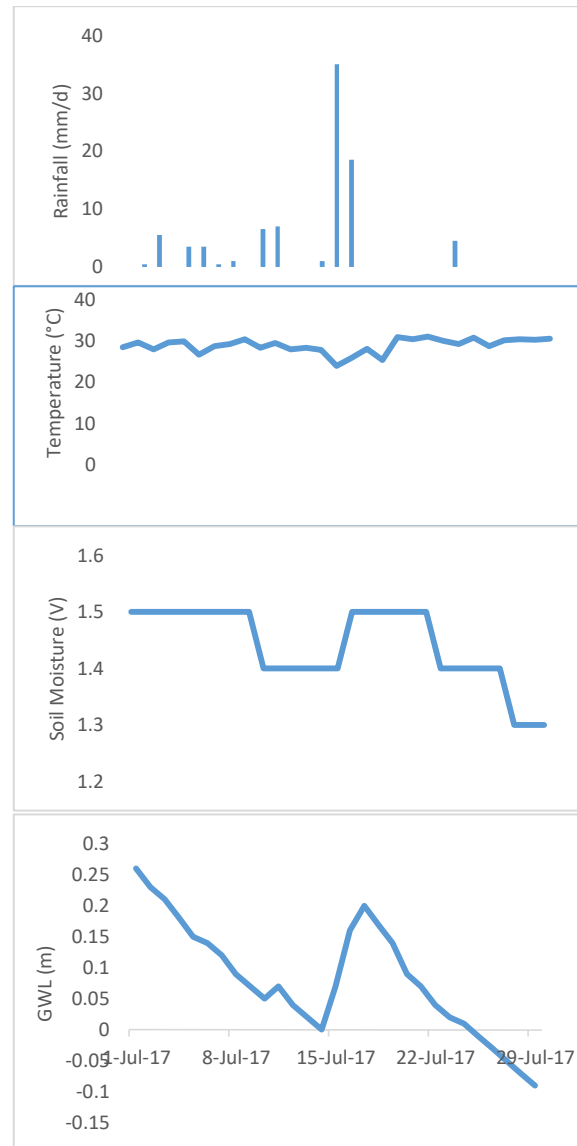


Fig 2. Time series of the observed skin temperature, rainfall, soil moisture and ground water level at the PHU Lumpur River 1 for a period of 1 – 29 July 2017.

Correlations among Observed Hydrological Parameters

First, the correlation between observed rainfall from the SESAME data and the TRMM data was calculated. Figure 3 shows the scatter plot of daily rainfall correlation between the SESAME data at the Lumpur River 1 and the TRMM data for a period 2 July to 29 August 2017. The analysis shows that the TRMM data are significantly correlated with the SESAME data with correlation coefficient of $r = 0.88$. Similar analysis has also performed on the other SESAME stations and it show similar results, in which the TRMM data are significantly correlated

with the SESAME data. The correlation coefficient for the Lumpur River 2, Saleh River 1 and Saleh River 2 are 0.94, 0.87 and 0.91, respectively. Thus, it is suggested that the TRMM data can be used to represent the rainfall variability at both PHU. Hereafter, the analysis is focused on the Lumpur River 1 data, which is considered to represent three other locations.

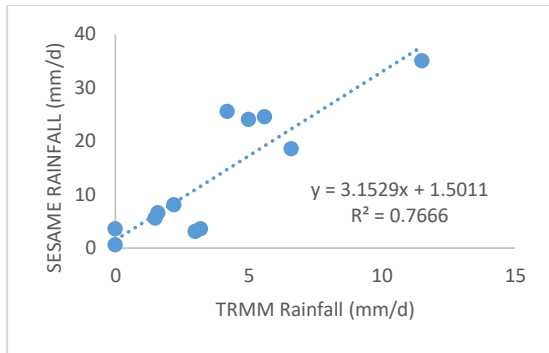


Fig 3. Scatter plot of rainfall correlation between the SESAME data and TRMM data at the PHU Lumpur River-1

Then calculate the correlation of the ground water level and rainfall observed by the SESAME system. Daily data for a period of 2 July to 12 August 2017 are used for the calculation. Figure 4 shows the scatter plot of the correlation between the observed daily ground water level and rainfall. The result shows that the observed ground water level is significantly correlated with the observed rainfall with correlation coefficient of $r = 0.93$.

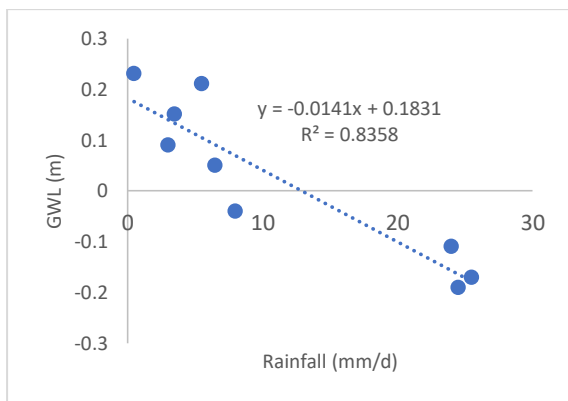


Fig 4. Same as Fig. 3 except of the observed ground water level and rainfall at the PHU Lumpur River 1.

It has been found that SESAME rainfall data and the TRMM data have strong correlation. It has also been found that the SESAME ground water level and the SESAME rainfall also have strong correlations. Therefore, the GWL could be estimated from the TRMM rainfall using linear

equation shown in Figure 4. Hereafter, the result of the calculation is called as the adjusted GWL.

Correlation Between the Adjusted GWL and the Number of Hotspots

In order to evaluate the relation between GWL and hotspots in the study area, the seasonal average of the adjusted GWL and the number of hotspot was first calculated. The analysis is focused on the dry-season (July-October). The results are presented in Table 3.

Table 3. Seasonal averaged (2002-2017) of the adjusted GWL and the number of hotspots during dry season (July – October) at the PHU Lumpur River-1

Year	Adjusted GWL (m)	Number of Hotspots
2002	0.1	70
2003	0.40	6
2004	1.40	30
2005	0.63	14
2006	0.19	55
2007	0.56	6
2008	0.27	5
2009	1.18	29
2010	0.23	3
2011	0.48	33
2012	1.36	14
2013	0.06	8
2014	0.58	44
2015	3.59	125
2016	0.10	1

It is shown that the adjusted GWL does not show robust coherency with the number of hotspots. However, the correlation analysis shows that the adjusted GWL has high correlation with number of hotspots with correlation coefficient of $r = 0.78$.

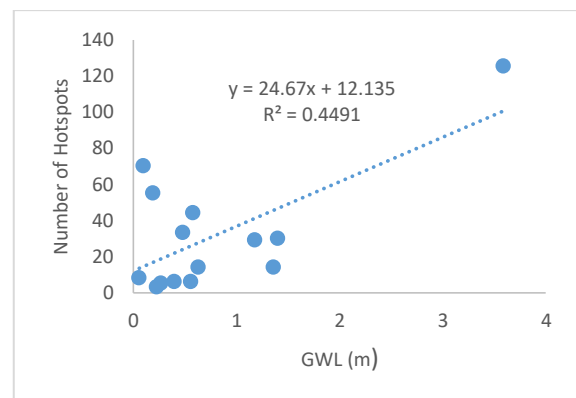


Fig 5. Same as Fig.3 except for the adjusted GWL and the number of hotspot during dry-season (July – October) at the PHU Lumpur River-1

CONCLUSION

Hydrological characteristics of two PHU in the South Sumatera, namely the PHU Lumpur River and the PHU Saleh River were evaluated using data recorded by the SESAME system. It is shown that the SESAME system provides valuable hydrological data for monitoring peat fires. However, it should be noted that the SESAME system might overestimate the observed skin temperature as the temperature sensor is installed within a closed-box to avoid vandalism.

The analysis shows that the observed ground water level from the SESAME is significantly correlated with the observed rainfall. Therefore, we used the regression relation between the observed ground water level and the observed rainfall to estimate a long-term ground water level. We called this estimated ground water level as the adjusted GWL. Seasonally averaged of the adjusted GWL during the dry-season (July-October) shows significant correlation with the number of hotspot. However, we still need a high temporal resolution of the ground water level for a better prediction of the peat fire.

ACKNOWLEDGEMENTS

We thank the Peatland Restoration Agency for providing us the SESAME data. This study is supported by the University of Sriwijaya through the *Hibah Unggulan Profesi* 2018 for the last author (Number: 0006/UN9/SK.LP2M.PT/2018) and *Hibah Unggulan Kompetitif* for the first author.

REFERENCES

- [1] Osaki M., and Tsuji N., Tropical Peatland Ecosystem, Springer Japan, 2016.
- [2] Sulaiman A., Sari ENN., and Saad A., Panduan Teknis Pemantauan Tinggi Muka Air Lahan Gambut System Telemetry, Badan Restorasi Gambut Repulik Indonesia, 2017.
- [3] Hamada Y., Tsuji N., Kojima Y., Qirom M.A., Sulaiman A., Sari E.N.N., Firmanto, Jagau Y., Irawan D., and Naito, Guidebook for estimating carbon emission from tropical peatland in Indonesia, IJJREED+ Project, 2016.
- [4] Iskandar, I., Utari, P.A., Lestari, D.O., Sari, Q.W., Setiabudidaya, D., Khakim, M.Y.N., Yustian, I., Dahlan, Z. Evolution of 2015/2016 El Niño and its impact on Indonesia, AIP Conference Proceedings, Vol. 1857, 2017, Article number 4987095.
- [5] Lestari, D.O., Sutriyono, Sabaruddin, Iskandar, I., Severe Drought Event in Indonesia Following 2015/16 El Niño/positive Indian Dipole Events, Journal of Physics: Conference Series, Vol. 1011, Issue 1, 2018, Article number 012040.
- [6] Margono, B A., Potapov P.V., Turubanova S., Stolle F., Hansen M. C. "Primary forest cover loss in Indonesia over 2000–2012." Nature Climate Change. Supplementary Information, 2014. DOI: 10.1038/NCLIMATE2277.
- [7] Page S.E., Siegert F., Rieley J.O., Boehm H.D., Jaya A., and Limin S. The amount of carbon released from peat and forest fires in Indonesia during 1997, Nature, 2002, Vol. 420 (6911):61-5.
- [8] Shigenaga Y., Takahashi H., Teguh R., Kencana W., Yokoyama S., and Jaya A., Field Data Transmission System, SESAME-SATREPS, by using Cell-phones Digital telecommunications network.
- [9] Kummerow, C., et al., The status of the Tropical Rainfall Measuring Mission (TRMM) after two years in orbit. J. Appl. Meteorol., 2000, Vol. 39, pp. 1965–1982.
- [10] Cao Y., Zhang W., and Wang W., Evaluation of TRMM 3B43 Data over The Yangtze River Delta of China, Scientific Reports 8, article number 5290, 2018.
- [11] Hidayat H., Teuling A.J., Vermeulen B., Taufik M., Kastner K., and Gersema T.J., Hidrologi of Inland Tropical Lowlands: The Kapuas and Mahakam Wetlands, Hidrol. Earth. Sci. Discuss, 2016, pp. 388.
- [12] Miller S.D., Hawkins J.D., Lee T.F., Turk F.J., Richardson K., and Kuciauskas A.P., MODIS Provides a Satellite Focus on Operation Iraqi Freedom, International Journal of Remote Sensing, Vol. 27, Issue 7, 2006, pp. 1285-1296.
- [13] Susilo, G. E., Yamamoto, K., and Imai, T. Modeling groundwater level fluctuation in the tropical peatland areas under the effect of El Nino, Procedia Environmental Sciences. 2013, Vol. 17, pp. 119 – 128
- [14] Emery W.J., and Thomson R.E., Data Analysis Method in Physical Oceanography, 2nd Edition, Elsevier B. V., Amsterdam, The Netherlands, 2004, pp. 638.
- [15] Iskandar I., Irfan M., Syamsuddin F., Johan A. and Poerwono P., Trend in Precipitation over Sumatra under the Warming Earth, Int. Jour. of Remote Sensing and Earth Sci., Vol. 8, 2012, pp. 19-24.

SHEAR BEHAVIOUR OF CONNECTION BETWEEN STEEL AND REINFORCED CONCRETE MEMBERS ADOPTING A NEW COLUMN BASE SYSTEM ALLOWING THE STEEL MOMENT-RESISTING FRAME TO PERFORM BEAM YIELDING MECHANISM

Sachi Furukawa¹, Yoshihiro Kimura², Katsunori Kaneda³ and Akira Wada⁴

¹Assistant Prof., Tohoku Univ., Japan; ²Prof., Tohoku Univ., Japan; ³Structural Design PLUS ONE Co. Ltd., Japan; ⁴Emeritus Prof., Tokyo Institute of Technology

ABSTRACT

To avoid formation of plastic hinges in the first-story columns of moment-resisting steel frame during earthquakes, the authors have previously proposed the application of a pin connection system between the upper steel column and bottom reinforced concrete column extending from the base beam. A single anchor bolt is adopted as a connection devise to reduce its rotational stiffness, which is accompanied by cross-shaped steel plates with a round plate on top. To minimize damage of the connection to ensure the superstructure maintains stable seismic behavior, series of horizontal loading tests of the RC column the connection was conducted to examine their shear behaviour. Shear transmission mechanism between an connection device and the RC column is clarified, and shear strength of the connection was evaluated based on observation about its shear force bearing mechanism.

Keywords: Steel structure, Column base, Composite action, Shear strength

INTRODUCTION

Steel moment-resisting frames with conventional column bases, such as exposed- and embedded-type column bases, are likely to develop plastic hinges in first-story columns because of different support conditions at the top and bottom ends of the column. The formation of plastic hinges in first-story columns may give rise to a soft-storey mechanism during significant earthquakes [1]. To achieve a beam-yielding mechanism for steel moment-resisting frames, the authors have previously proposed the application of a pin connection system to midpoints of first-story columns in order to control their moment distributions, i.e., moment demands at their top and bottom ends [2]. With the proposed pin connection system, the upper steel column and the bottom reinforced concrete (RC) column extending from the base beam are connected by a single anchor bolt located along the centre axis of the column to sufficiently reduce rotational stiffness. Cross-shaped steel plates (i.e., shear plates) with a round plate (i.e., a cover plate) on the top are welded to an anchor bolt to facilitate shear and compression force transmission to the lower RC column. The configuration of the proposed connection system results in combined mechanical characteristics of two conventional steel column base system; an exposed-type column base where a steel column is connected to an RC base beam via a

group of anchor bolts, and a concrete-encased column base where they are connected by embedding a steel column into an RC column.

Seismic behaviour of the proposed system has been examined in cyclic loading tests of a partial frame consisting of the first-storey column with a proposed pin connection system, accompanied by a pair of second-floor beams [3]. The results showed that the connection performance classifies it as a pin, and that the yielding of the columns was prevented. Practical application of this system has also been promoted; eight steel moment frames were built so far using the proposed pin connection (Photo 1).



Photo 1 Practical application of proposed connection

The proposed pin connection has to reliably

sustain stresses transmitted from the upper steel moment-resisting frame until it reaches the ultimate horizontal strength, i.e., the corresponding base shear ratio of 0.4 in current Japanese design practice. This paper examines shear mechanical behaviour of the reinforced concrete columns with the proposed connection. Cyclic loading tests of the connection are conducted to observe the shear fracture mechanism of the connection, to examine the shear transmission mechanism between the anchor bolt with welded plates and the reinforced concrete columns. In addition, the ultimate shear capacity of the connection is evaluated.

CYCLIC HORIZONTAL LOADING TEST OF CONNECTION

Test program

Figs. 1 and 2 show the cyclic loading system of horizontal force and specimen details: (a) ties and rebars arrangement and (b) the proposed connection device, hereinafter named as an anchor bolt set. The specimen was an RC column with a section $400 \text{ mm} \times 400 \text{ mm}$ and a height of 800 mm , as highlighted in Fig. 1. The specimen's overall setting followed that adopted in the previous partial frame test [3]. The RC column was supposed to sustain 400 kN as a dead load of the steel moment-resisting superstructure; consequently, corresponding ultimate horizontal strength became 160 kN . The test parameter was ties arrangement (Fig. 2(a)). The anchor bolt set with a depth of 300 mm was embedded at the top of the RC column. A group of anchorage rebars was welded on the bottom of four shear plates, respectively (Fig. 2(b)). Other specimen settings can be found in Fig. 2. Table 1 lists material properties.

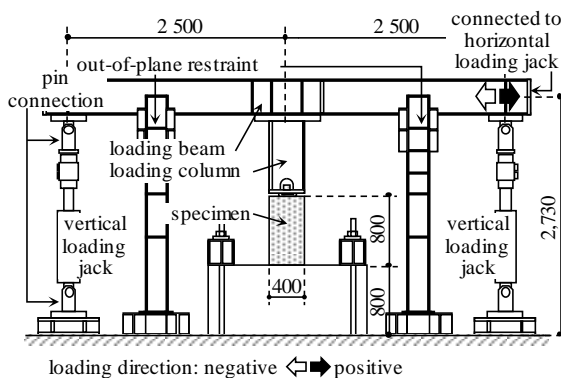


Fig. 1 Loading system and specimen

Horizontal force acted on the anchor bolt extended from the top of the RC column, which was

inserted into the centre hole of the base plate of the loading column (Fig. 1). The sum of vertical forces in the pair of jacks on the both side of the specimen was controlled to maintain the zero value not to restrain the pull-out action of the connection.

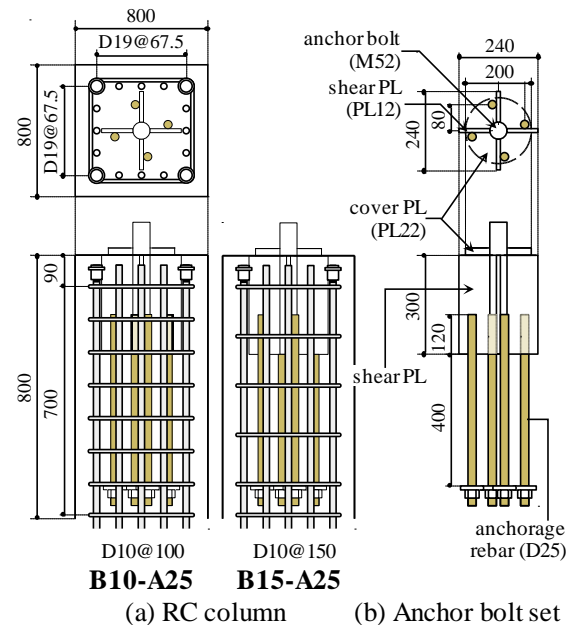


Fig. 2 Specimen detail

Table 1 Material properties [MPa]

		yielding	ultimate
steel		σ_y	σ_u
a. bolt	M52	379	546
cover PL	PL-22	385	531
shear PL	PL-12	393	565
anch. rebar	D25	394	590
rebar	D19	408	572
tie	D10	344	515
		split tens.	comp.
concrete		σ_{st}	σ_c
normal concrete		2.8	28.8

Global shear-resisting behaviour of the connection

Fig. 3 shows the first quadrant of the hysteresis loops of horizontal force P and element drift ratio θ . The element drift ratio θ is defined as a fraction of the relative horizontal displacement of the cover PL (Fig. 2) to the base beam and the vertical distance between two measure points. The figure presents as well yielding points of ties, rebars and anchorage rebars. From Fig. 3, it can be seen that two specimens had similar global hysteresis behaviour: the horizontal stiffness apparently started to degrade

after exceeding $P = 160$ kN. After ties and anchorage rebars yielded, it reached the maximum strength P_{max} . Therefore, both specimens sufficiently sustained horizontal force till the corresponding superstructure reached to the ultimate horizontal strength and had only 5% difference in P_{max} .

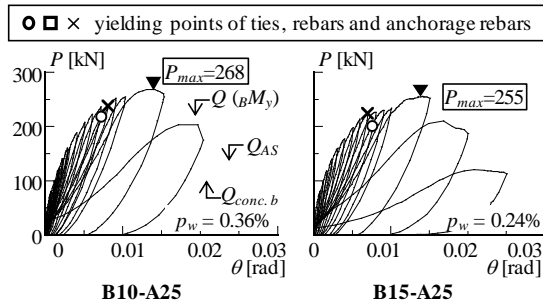


Fig. 3 Hysteresis loop (first quadrant only)

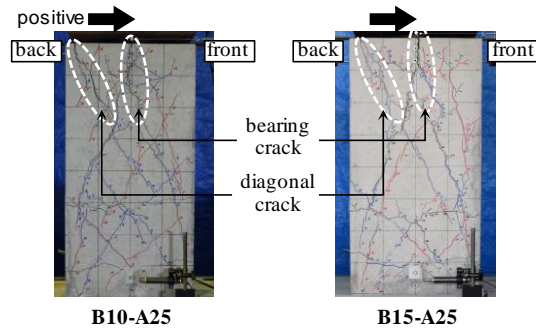


Photo 2 Specimen at $\theta = 0.020$ rad

Photo 2 shows crack condition at element drift ratio θ of 0.02 rad. A bearing crack due to shear PL perpendicular to the loading axis started to propagate downward from the top center at $P = 100$ to 120 kN (Photo 2). After reaching $P = 200$ kN, diagonal cracks also started to propagate from the backward side of the top end. Diagonal cracks mean that horizontal force transmitted from the anchor bolt set to the front-ward side of the RC column was sufficiently transferred to the backward side via ties arranged at the top of the RC column. The observed fracture mechanism was similar to that of the concrete encased-type column.

Global shear-resisting behaviour of the c o n n e c t i o n

Fig. 4 shows strain gage arrangement of the anchor bolt, shear plates and anchorage rebars. In this figure, the x - y - z axes of the specimen are also defined.

Fig. 5 shows vertical (z -axis) strain distribution of (a) shear PLs ($z = -30, -110, -190, -270$ mm) and (b) anchorage rebars ($z = -330$ mm). In the figure, a diameter of anchor bolt ($-36.7 \text{ mm} \leq x \leq 36.7 \text{ mm}$)

and that of anchorage rebars were highlighted. From Fig. 5(a), it can be said that the two specimens exhibited similar strain distribution with the following common characteristics: (1) the significant flexural strain sustained by the top part of the anchor bolt ($z = -30$ mm) was neutralized at the depth of $z = -110$ mm, and the stress distribution shifted to a linear distribution along the cross section of the anchor bolt set; (2) The notable vertical strain sustained by shear PLs ($z = -30$ mm) indicated that a significant amount of vertical reaction force acted on the bottom side of the cover PL bearing on the top of the reinforced concrete column. (3) The vertical strains were significantly reduced at the depth of $z = -270$ mm, which means that almost no stress was transferred via the bottom ends of the shear PLs.

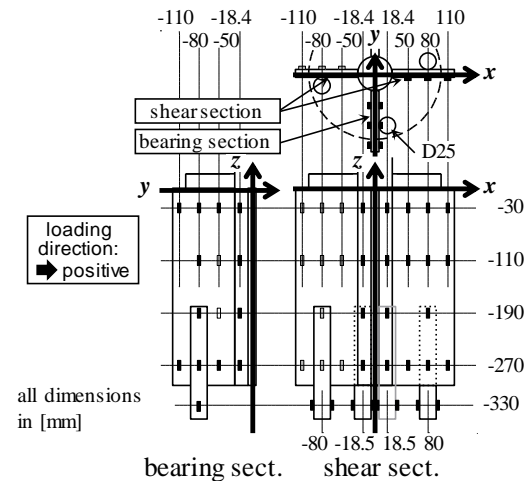


Fig. 4 Arrangement of strain gages on anchor bolt

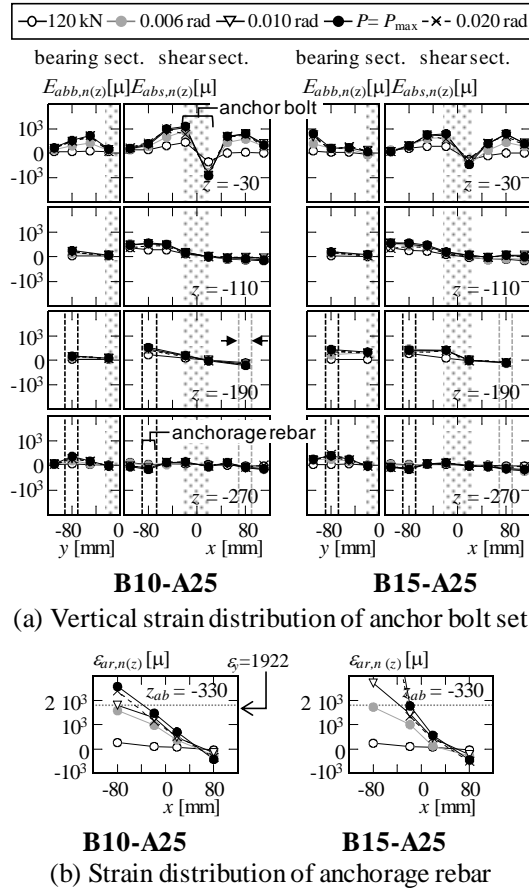


Fig. 5 Strain distribution of anchor bolt set

From Fig. 5(b), it can be seen that strain distribution of a group of four anchorage rebars maintained a linear distribution; sustaining moment and axial force in a group.

MODELING OF THE HORIZONTAL FORCE TRANSMISSION MECHANISM AND THE SHEAR BEARING MEACHNISM OF THE CONNECTION

Modeling of transmission mechanism

Fig. 6(a) shows images of force distribution acting on the anchor bolt set, modeled based on outcomes from Fig. 5. As shown in Fig. 6, the loading force P and a pair of reaction forces on the upper and lower surfaces of the bearing sections (F_u and F_{lv}) are considered as major horizontal acting forces. One of horizontal reaction forces is a lever reaction forces F_{lv} so that acting direction becomes the same as the loading force P . Similarly, axial forces of a group of anchorage rebars N_a and the vertical reaction force on the bottom of the cover PL V_{cp} can be considered as major vertical acting forces, where friction force and bonding stress between plates and surrounding concrete are neglected. The rotational reaction of the system is given by a pair

of horizontal reaction forces F_u and F_{lv} , moment of anchorage rebar M_a , and moment sustained by couple forces of N_a and V_{cp} , whose moment is defined as M_{cp} . Moment of anchorage rebar M_a is a summation moment given by multiplying axial force of an anchorage rebar and its x -axis coordinate (bottom of Fig. 4), respectively.

Fig. 6(b) shows moment distributions of an anchor bolt set, consisting moment related to a group of anchorage rebars M_a , M_{cp} , moment of anchor bolt M_{ab} and moment of shear PLs M_{sp} .

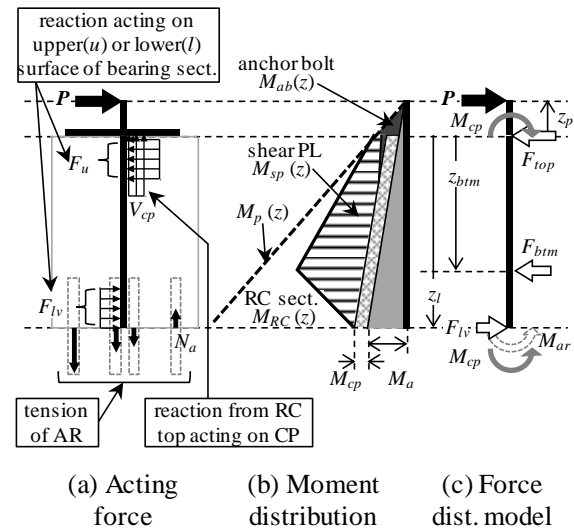


Fig. 6 Stress transmission mechanism.

Fig. 7 shows moment distribution of the anchor bolt set at $P=120$ and P_{\max} , calculated from vertical strain distribution shown in Fig. 5. In Fig. 7, moments are generalized by moment at the bottom of the anchor bolt set ($z = -300$ mm) produced by loading force P , or M_p . The plotting format follows Fig. 6(b). Therefore, each moment of M_a , M_{cp} , M_{ab} , M_{sp} are given by a difference between two adjacent lines.

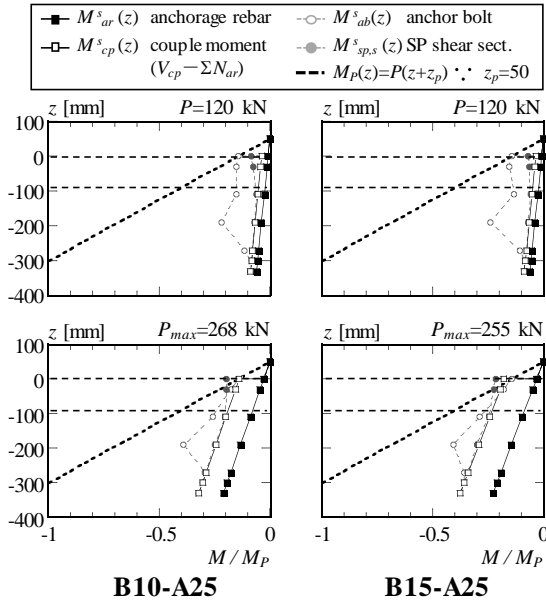


Fig. 7 Estimated moment distribution of connection

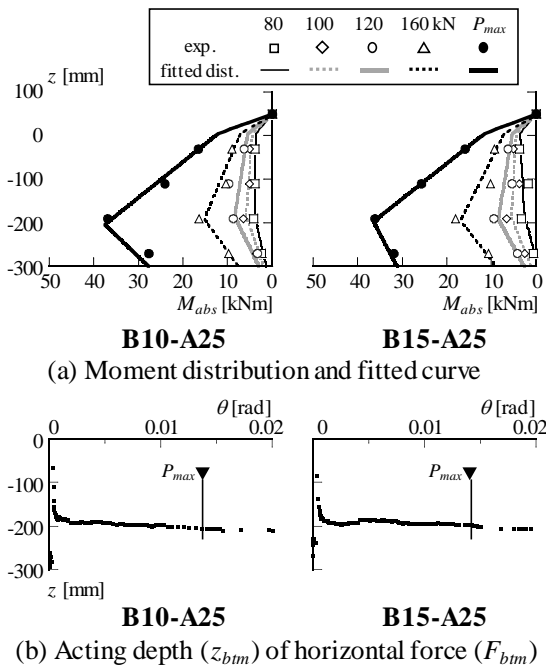


Fig. 8 Strain distribution of anchor bolt set

The outer plots of estimated moment distribution, i.e., moment distribution of the anchor bolt set, are plotted in Fig. 8(a) for particular loading force P . Change of slope angles in moment distribution means that an external force is acting on the corresponding depth, and the plots of Fig. 8(a) apparently indicates additional horizontal force F_{btm} acting on the anchor bolt set at the depth of around $z = -200$ mm, in addition to horizontal force F_{top} acting on the RC top ($z = 0$ mm). A lever action force F_{lv} also acts on the bottom of the anchor bolt set. The updated model of acting force

distribution on the anchor bolt set are shown in Fig. 6(c). The equivalent equations of horizontal force and moment with respect to $z = 0$ mm are expressed as follows:

$$P - F_{top} - F_{btm} + F_{lv} = 0 \quad (1)$$

$$Pz_p + F_{btm}z_{btm} - F_{lv}z_l - M_a - M_{cp} = 0 \quad (2)$$

Fitted theoretical moment distribution calculated based on Fig. 6(c), whose variables fulfill Eqs. (1) and (2), are added by lines in Fig. 8(a). Fig. 8(b) shows estimated acting depth of F_{btm} , z_{btm} , with respect to the element drift ratio θ . Fig. 8(b) shows z_{btm} drops by approximately 200 mm, regardless of difference in the tie arrangement.

The estimation distribution of forces acting on the anchor bolt set

Fig. 9 shows a backbone hysteresis curve of the loading force P shown in Fig. 3, estimated acting force on the anchor bolt set F_{top} , F_{btm} , and F_{lv} . In addition, the summation of positive horizontal force (F_{top} and F_{btm}), which is amplified by F_{lv} , are shown as $F_u (=P + F_{lv})$. From Fig. 9, it is notable that loading force P was sustained dominantly only by F_{top} for the loading force P of lower than 120 kN, upon when a bearing crack started to propagate (Photo 2). After the loading force P reaching 120 kN, F_{btm} and F_{lv} started to increase. In the meanwhile, F_{top} became almost constant.

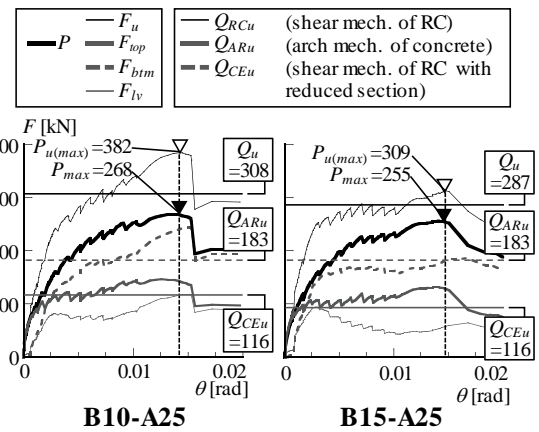


Fig. 9 Estimated horizontal forces acting on anchor bolt set

Modeling of the shear bearing mechanism

An embedded anchor bolt set amplified the load P acting on the RC column by a lever action F_{lv} . Fig. 10 describes the shear bearing mechanism model. In Fig. 10(a), the RC column is divided into three parts: domain I, II and III. Domain I is where RC section with an anchor bolt set sustains amplified horizontal

force F_u . Domain II, located lower than an anchor bolt set, which consists of the RC section only, but sustains F_u because amplified horizontal force being not fully canceled by a lever action F_{lv} acting on the bottom of the anchor bolt set. The remaining domain III is the bottom segment, where P is sustained. In this case, domain III never controls shear strength of the RC column.

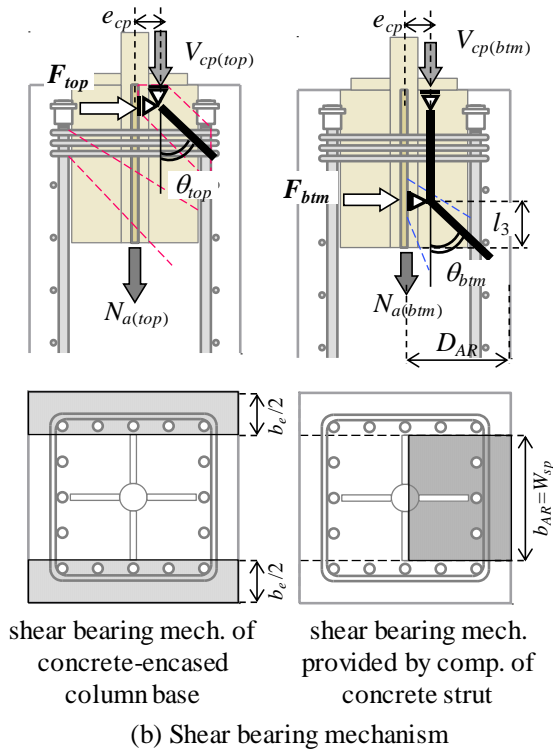
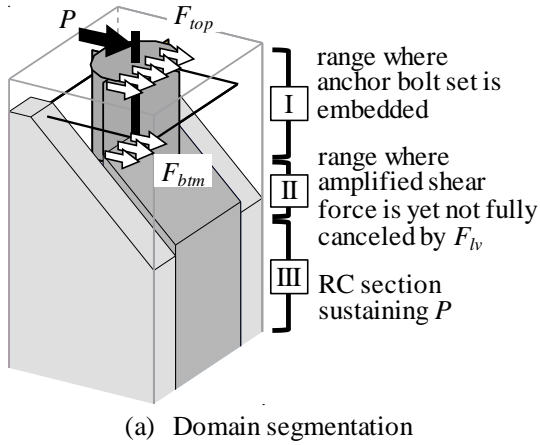


Fig. 10 Shear bearing mechanism model

In domain II, transmitted forces F_{top} and F_{btm} are considered to be borne by respective shear bearing mechanism, as shown in Fig.10(b). F_{top} is considered to be sustained by shear bearing mechanism similar to that of concrete-encased column base. In this mechanism, shear is sustained by a reduced RC section with effective width of b_e (Fig.10(b), left), and the corresponding shear strength is defined as

Q_{CEu} . Because of this bearing action controlling fracture mechanism of the top of the RC column, diagonal crack propagated from the top of the RC column in the test (Photo 2). F_{btm} is considered to be sustained by compression strut formed at the front half of the remaining concrete section ($D_{AR} \times b_{AR}$) (Fig.10(b), right). In this mechanism, shear is sustained only by concrete section, and corresponding shear strength is defined as Q_{ARu} . The vertical component of concrete compression field in both mechanism is provided by the reaction from the bottom side of the cover PL V_{cp} , or tension force of anchorage rebars N_a . Therefore, shear strength of both shear mechanisms is limited by yielding strength of anchorage rebars.

In the domain III, the summation of F_{top} and F_{btm} (or $P + F_{lv}$) is sustained by the full section of the RC column, whose shear strength is evaluated by the ultimate shear strength of the RC section, Q_{RCu} .

Evaluation of estimated shear strength of the connection

Shear strengths (Q_{CEu} , Q_{ARu} , Q_{RCu}) are added to Fig. 9, which are estimated by following the Japanese current design practice [4]-[6], as shown in Fig. 10. Because anchorage rebars did not reach their yielding axial force (Fig. 5(b)), no limitation applied to the estimated shear strength by properties of anchorage rebars. As can be seen, Shear strengths of Q_{CEu} , Q_{ARu} and Q_{RCu} are suitably evaluate the corresponding shear force of F_{top} , F_{btm} and F_u .

CONCLUSION

Shear transmission mechanism and shear bearing mechanism of the proposed column base system for a steel moment-resisting frame were examined by conducting a cyclic horizontal loading test of the RC column with the proposed connection. Major findings are as follows:

- (1) Shear force transmitted from the anchor bolt set to the RC column, which are amplified by a lever action, divided into two parts: One was a force acting on the top of the column and the other was a force acting on the depth of about 200 mm.
- (2) Respective shear bearing mechanism are considered to be formed for the divided forces: one is that similar to a concrete-encased column base where shear was borne by a reduced section of the RC column, while the other is that provided by an compression strut of concrete formed by the remaining section.
- (3) In addition, amplified shear force by a lever action also has to be sustained by the RC section right below the anchor bolt set, where shear sustained by the RC section is not fully canceled by

a lever action force.

(5) Shear strength of (3)(4) sufficiently evaluate the test results.

REFERENCES

- [1] Journals: Suita, K., Matsuoka, Y., Yamada, S., Shimada Y., Akazawa, M., Tada, M., Ohsaki, M., and Kasai, K. (2008). "Outline of full-scale 4-story building collapse test (E-Defense Experimental Projects for Steel Buildings –Part 21-24)", International Journal of Engineering Science, ID:22417-22320.
- [2] Kaneda, K., Kimura, Y., Hamasaki, S., and Wada, A. (2010). "Proposal of new column support system for multi-story steel moment resisting structures to perform beam yielding mechanism," Journal of Structure and Construction Engineering, Architectural Institute of Japan, Vol. 75, No. 654, pp.1537-1546.
- [3] Sachi Furukawa, Yoshihiro Kimura, Katsunori Kaneda and Akira Wada, "Cyclic loading test of substructure frame with new column support system for steel moment resisting structures to perform beam yielding mechanism," STESSA, Shanghai, China, July 1-4, 2015.
- [4] Recommendation for Design of Connections in Steel Structures, 3rd ed. Vol. 2, Architectural Institute of Japan, pp.326-328.
- [5] Design Guideline for Earthquake Resistant Reinforced Concrete Buildings Based on Ultimate Strength Concept, 1st ed., Vol.3, Architectural Institute of Japan, pp.106.
- [6] AIJ Standard for Structural Calculation of Reinforced Concrete Structures –Based on Allowable Stress Concept- revised 2010, 8th ed., Vol.3, Architectural Institute of Japan, pp.157-160.

DEVELOPING REHEATED MOTORCYCLE EXHAUST FOR PM_{2.5} EMISSION

Wardoyo, Arinto Y.P. Dharmawan, Hari A.
Laboratory of Air Quality and Astro Imaging
Physics Department Brawijaya University
Jl. Veteran, Malang Indonesia

ABSTRACT

Motor engine has been identified to produce particulate emission in different size distribution and has serious impacts on health and influence of air quality. Especially, PM_{2.5} which are known as particulate matters with the diameter less than 2.5 μm , induce a major health problem due to the reactive characteristic and the high exposure level in the human. In order to reduce the concentration of PM_{2.5} in the ambient, we have developed a new exhaust used to maximize the released combustion energy for reducing PM_{2.5} concentration. The exhaust was accomplished with a heating chamber and a copper net tube in the dimension of 25 cm in diameter and the varied length of 4 cm, 5 cm, and 6 cm. The tube was wired by copper with the diameter of 0.5 cm. The exhaust was characterized by measuring temperature and the capability in reducing PM_{2.5} concentration. The result showed that the exhaust worked well in reducing PM_{2.5} concentration with the efficiency reaching up to 24 % depending on the dimension of the net tube.

Keywords: Design, Motorcycle exhaust, PM_{2.5}, Thermal Radiation, Efficiency.

INTRODUCTION

Particulate matters or particles mostly are from natural sources such as fire forest or dust storm [1]. Moreover, industrial process [2] and vehicles usage [3] have contributed significantly in addition to particles in the air. Industrial particle emissions affect directly into the human health especially for people living in the range of the exposure area (Eeftens et al. 2015; Smargiassi et al. 2014). Meanwhile, vehicle particles widely have an impact on the people living close to road and motor users [6].

The motorcycle is one type of motor vehicles commonly used in developing countries. The number of motorcycles has increased extensively in the last decade (Marquet & Miralles-guasch 2016; Mishima 2004; DayalSharma et al. 2011). Motorcycle particles have been reported increasingly in the ambient air [10]. In the previous research, there was shown a relation between the motor vehicle usage and the particle concentration [11]. This result brought bad news for the human by the fact that the particles are very dangerous especially for the health [12]. Motorcycle particles are produced by the incomplete burning process of the fuel [13], [14]. The particles are in different size distribution and chemical substances (Tsai et al. 2014; Morawska et al. 2008). The particles have the ability to move freely in the air, increase the health risk [16], [17], and penetrate in cellular level [18] and into a human through the skin via intracellular

process [19]. Even though, the particles were found to have an ability to infiltrate into human cardiovascular via respiratory system [20]–[22]. A variety of health problems due to vehicle particle emission has been reported in the previous studies [23]–[26].

Reducing motorcycle particles has been attempted in the past decade. Various methods have been developed and tested in order to reduce the concentration. Planting of trees in the roadside is the common method to reduce ambient particles (Gromke & Blocken 2015; Nowak et al. 2013). Another method was conducted by improving the engine capability to burn the fuel more efficient [30]–[32]. The exhaust filtering system has been developed for gas emissions [33]–[35]. Exhaust filtering system has limited to particle emissions because of high particle concentration leading to the filter saturation that increases a risk of the filter or even the engine damage [36].

A particulate filter using coconut fiber for motorcycle emission was developed before. In the research, the filter was depended on the number of the filter layer [37]. In the other research, a particulate filter was build by using capacitive concept with low DC current to generated electric field to trapping the charge particulate emission. The efficiency of the filter was found depend on the number of the gap to traps the particulate matter [38]. In this study, we develop an exhaust accomplished by an particulate removal system to optimize the released heat for reducing PM_{2.5}.

METHODS

We designed a heating compartment in the motorcycle exhaust to optimize the waste engine thermal energy capture. The compartment was constructed in the tube form with the dimension of 10 cm in the height and 9 cm in the diameter. A cooper wired aluminum net was positioned in the compartment in order to capture the released heat in the chamber. The net was arranged as a tube with the diameter of 2.5 cm and the length that was varied of 4 cm, 5 cm, and 6 cm labeled as F1, F2, and F3 respectively. The cooper wire with diameter 0.2-mm was applied spirally in the tube with the distance for each winding of 0.5-cm. The geometry detail of the designed compartment and the net position is shown in the Fig.1.

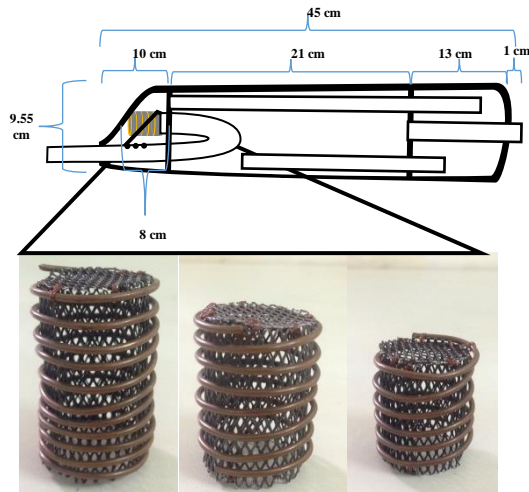


Fig. 1 The exhaust design and cooper wired aluminum net.

Three motorcycles with same engine capacity and fuel type were used to test the exhaust. The brand of motorcycles was hidden to avoid any a conflict of interest. The motorcycle was labeled as M1, M2, and M3 respectively. The observation was conducted for four configurations consist of without exhaust system (C0), the designed exhaust without system (Cf0), with F1 (Cf1), F2 (Cf2), and F3 (Cf3) every motorcycle. The exhaust test was carry out for the motorcycle was operating in the idle condition to avoid a driving style, vehicles load, and roadsfactor for 30-minutes.

Kanomax Digital Dust monitor model 3443 was used to measure the $PM_{2.5}$ concentration. The measurement was processed in the semi-isolated room with the temperature 27° and humidity under

50%. The measurement was done by quantify the concentration of $PM_{2.5}$ in the distance of 30-cm from the exhaust. At least 10 data was recorded in every 5-minute for 30-second engine run. The route was repeated for the C_{F1} , C_{F2} , and C_{F3} in cold engine start procedure. The temperature in the exhaust compatement was measured by using thermocouple and stated as T_0 , Tf_0 , Tf_1 , Tf_2 , and Tf_3 . The efficiency of the system was calculated by comparing the concentration of the $PM_{2.5}$ from the engine before entering the exhaust and after passing out the exhaust using equation 1.

$$Eff\% = (C_0 - C_F) / C_0 \times 100\% \quad (1)$$

With C_f is the concentration of the $PM_{2.5}$ with the designed exhaust and system applied (F1, F2, and F3). C_0 is the concentration of the $PM_{2.5}$ without exhaust. A smoke flow rate was measured by using Kanomax *anemomaster flowrate* A310 series in the exhaust output. An analyst was conducted to find the relationship of the thermal energy increase that effected the $PM_{2.5}$ reduction.

RESULT

Smoke Flow Rate

Applying the exhaust system resulted in the reduction of the smoke flow rate as presented in the table.1. The flow rate of the emission from the engine was measured of 3.2 m/s in average for M1 and M2. For the M3, the average flow rate was measured of 4.4 m/s. After the designed exhaust was applied, the flow rate reduced to 20% for M1 and M2, but 30% for M3. The flow rate reduction was found the same for F1, F2, and F3.

Table 1 The smoke flow rate of the emission for M1, M2, and M3

Minute	Net	Flow rate (m/s)					
		5	10	15	20	25	30
M1	Ex0	3.4	3.2	3.1	3.1	3.8	3.3
	F1	2.5	2.2	2.6	2.5	2.2	2.5
	F2	2.9	2.9	3.0	2.9	2.9	2.9
	F3	2.5	2.5	2.4	2.5	2.4	2.5
M2	Ex0	3.3	3.4	3.0	3.4	3.3	3.1
	F1	2.6	2.4	2.3	2.4	2.5	2.5
	F2	2.8	3.0	2.8	2.7	2.6	2.5
	F3	2.3	2.3	2.4	2.5	2.6	2.4
M3	Ex0	4.4	4.3	4.5	4.4	4.5	4.4
	F1	3.1	3.0	3.0	3.0	3.1	3.0
	F2	3.4	3.2	3.0	3.3	3.2	3.2
	F3	3.0	3.3	3.0	3.1	3.1	3.3

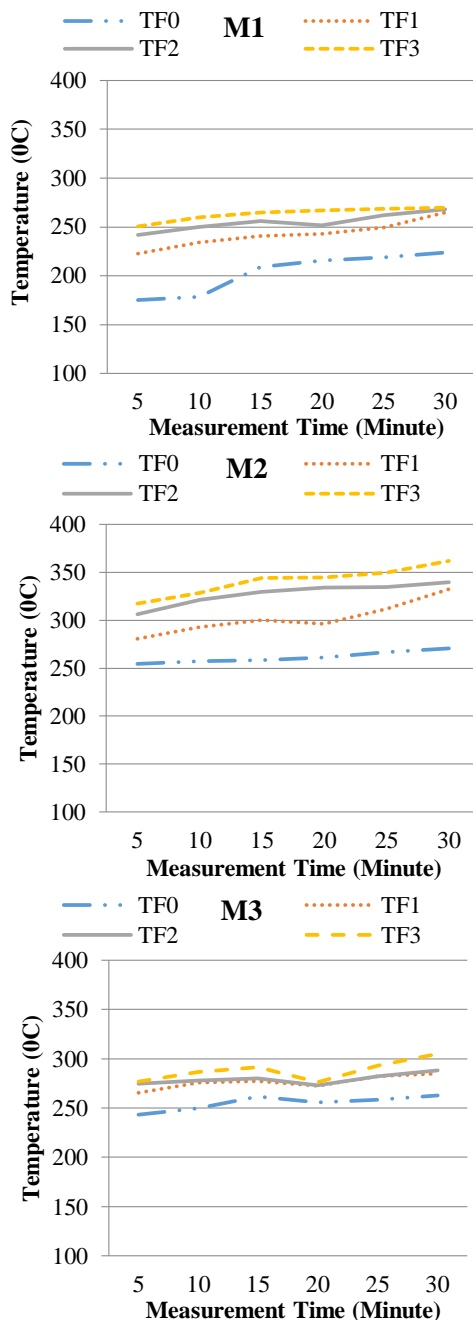
Exhaust Temperature

Fig. 2 The exhaust temperature for the system with F3 was measured for M1, M2, and M3. Longer engine run was observed to increase the temperature.

The increase of the compartment temperature is caused by the released heat emission and by the effects of the cooper wired aluminum net. By operating the motor engine results in a released heat emission. The heat emission was observed increase by the longer engine activation. In the minute five of engine runs, we observed the temperature TF0 of 175°C. In the minute 10, the temperature became to

179°C. In the minute 15, 20, 25, the temperature was recorded of 209°C, 216°C, and 219°C respectively. In the minute 30, the temperature reached to 224°C. For the sample motorcycle M3, we found the temperature increase in the different trend. The temperature was in a saw tooth pattern. The temperature was of 243°C, 250°C, and 261°C in the minute 5, 10, and 15. In the minute 20, the temperature reduced to 256°C and gradually increases into 258°C and 263°C in the minute 25 and 30. The temperature trend was obtained similarly by applying the filter of F1, F2, and F3.

The effect of applying the cooper wired aluminum net in the exhaust, the temperature increases was found larger rather than without applying the net. The temperature increase was 46°C for applying F1, 67°C for F2, and 75°C for F3. This shows that the dimension of the filter influencing the heat energy increase in the exhaust. The increasing temperature as the effect of applying the F1, F2, and F3 for all sample motor are present in the Fig.2. In the Fig.2, the double dot dash line presents the temperature of the system before the net applied. The dot, line, and dash line show the system with F1, F2, and F3.

PM_{2.5} Concentration

The PM_{2.5} concentration became lower for the longer engine run and the longer net. For the engine is operated for a long period of time, the temperature become higher and reduce particulate concentration due to the perfect combustion [39]. In this study, we found the PM_{2.5} concentration for longer period of the engine operating. For the M1 and M2, we observed the PM_{2.5} concentration to reduce gradually from $35.8 \times 10^{-3} \text{ mg/cm}^3$ and $33.2 \times 10^{-3} \text{ mg/cm}^3$ in the minute 5 into $27.8 \times 10^{-3} \text{ mg/cm}^3$ and $27.0 \times 10^{-3} \text{ mg/cm}^3$ in the minute 30. Meanwhile in the sample motorcycle M3, we found the highest PM_{2.5} concentration in the minute 20, then the concentration reduced in the minute 5, 10, and 15 minutes which was of $31.2 \times 10^{-3} \text{ mg/cm}^3$, $30.8 \times 10^{-3} \text{ mg/cm}^3$. We assumed that the motorcycle characteristic was responsible for this.

The effect of applying the net in the exhaust, we found the relationship between the PM_{2.5} concentration reduction and the temperature increase. The correlation was found consistently when the system was applied for the different motor samples. The measured concentration of PM_{2.5} for the motor samples with and without applying the filtering system is shown in Table 2.

Table.2 The measured PM_{2.5} concentration

Time (Minute)	PM _{2.5} in C x 10 ⁻³ mg/cm ³				
	C0	Fc0	Fc 1	Fc 2	Fc 3
M1					
5	35.8	34.2	32.6	29.6	28.6
10	34.4	32.6	30.4	29.2	26.2
15	31.6	29.2	28.2	26	24
20	29.6	28	27.2	26.2	24.8
25	29.4	27.6	25.8	25.4	23.6
30	27.8	24	23.8	23.4	21.4
M2					
5	33.2	31.8	28.8	28.8	27.8
10	32	30.6	28.2	28	25.6
15	32	29.2	27	26	24.2
20	31	29.4	26.2	26.6	24
25	29.7	27.2	25.2	25.2	22.2
30	27	25	23.8	23.6	20.4
M3					
5	31.2	30	27.2	26.8	25.2
10	29.4	28.2	26.6	25.6	23.4
15	26.8	25.6	24	21.8	20.2
20	30.8	29.8	26	25.2	24.8
25	26.2	25.2	23	22.8	21.4
30	25	23	22	20.8	19.8

Filter Efficiency

Fig.3 shows the efficiency of the PM_{2.5} removal system. The length of the applied net in the exhaust influences the ability of reducing PM_{2.5} concentration. The efficiency varies for different period of the engine operating. The efficiency change is in the range of 8%-16% for Fc1, 12%-19% for Fc2, and 16%-25% for Fc3. The average efficiency of the system is 12%, 15%, and 21% for Fc1, Fc2, and Fc3 respectively.

DISCUSSION

Particulate matter with the diameter less than 2.5 µm or PM_{2.5} can be formed in the several ways. In this study, PM_{2.5} are formed by the fuel combustion in the engine chamber [40]. In the engine, the fuel is injected into the combustion chamber together with the air before igniting in a high compression level [41]. The result is a very high kinetic energy that is used to push the piston and to move the vehicle [42]. The combustion process results in emissions (gas and particles) and thermal energy as the products. In

the other word, the thermal energy leaves the engine through a convection process. The exhaust system such as a muffler or a silencer that is made of metal is used to absorb the thermal energy. Consequently, the emission eventually loses their temperature and become a cooling down [43]. This process leads to develop the secondary particles.

focused on the filter regeneration to increase the system life span [46]. The self-regeneration filter was pursued in order to build a longer filter usage [47], [48]. However, self-regeneration filter was resulted in the increase of operational cost.

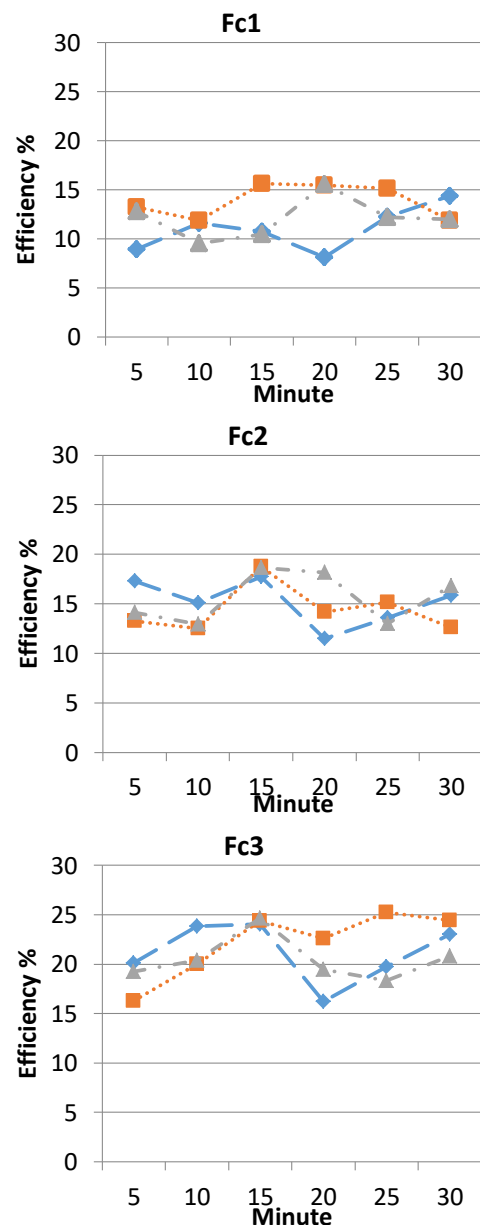


Fig. 3 The exhaust efficiency with applying a net with different length

A commercial filter is used porosity based system that works by capturing the designed

particulate only [44]. In the longer usage periods, the particulate was found to block filter porous and lead into the engine damage [45]. Another study was

In this study, we applied the metal net as a filter that increases the temperature through radiation process when it is passed by the convective thermal energy released by the motor engine. The thermal radiation energy is shown by increasing the temperature of the system. The metal net enlarges the radiation area and raises the surrounding temperature [49]. The radiation thermal energy may reduce a particle nuclei radius [50]. In our design, we do not try to filter but deform the particulate emission. The method would have some benefit in the system life span and risk of particle blockades the system as soot [51].

The flow rate reduction was found in the same level for M1, M2, and M3 that indicates the net effect in the flow rate reduction is insignificant. The flow rate of the system was found constant after the engine run for 30 minutes. This result indicates that the blocking effect of the system is low. For example, the flow rate of the emission in the minute 5, 15, 10, 50, 25, and 30 was measured reduces of 0.2 for M1 with F1. The F2, and F3 for M1, M2, and M3 were found in similar manner. By taking into account this result, the system regeneration may unneeded.

The $PM_{2.5}$ concentration reduces after applying the net in the exhaust. We found the temperature increases was up to $362^{\circ}C$ while the reduction of the concentration was up to 25%. The $PM_{2.5}$ concentration reduction is found inversely with the temperature with the $R^2 = 1$, This shows that the strong correlation between the temperature increase and particulate concentration [52]. The dimension of the metal net influences to the exhaust efficiency in reducing the $PM_{2.5}$ concentration.

In the filtering system based on the porosity, the risk of the system blocking the emission flow is high when the efficiency of the system is high [51], [53]. The result would be fatal in the engine. However, in this research, we found the efficiency of the system in reducing particulate matter that was relatively constant of 12 %, 15%, and 1 % for Fc1, Fc2, and Fc3 respectively. The system is unblocked of the particulate emission due to the heat radiation in removing $PM_{2.5}$.

CONCLUSION

The motorcycle exhaust that was developed based on thermal radiation had an ability in reducing

the $PM_{2.5}$ emission depending on the dimension of the applying metal net. Longer metal net resulted in higher thermal radiation having the consequent in reducing the $PM_{2.5}$ concentration.

ACKNOWLEDGEMENTS

All the authors are grateful to Directorate General of Higher Education, for providing funding for this research project. The kind hands of Eko Teguh, Arif Budianto, Mia Anggun, Fikri Assufi, Arsyah Mahardika Ikta Fiana, Rizal Bagus A involving in this study are gratefully acknowledged.

REFERENCES

- [1] Borgie, M.; Ledoux, F.; Dagher, Z.; Verdin, A.; Cazier, F.; Courcot, L.; Shirali, P.; Greigerges, H.; Courcot, D. Chemical Characteristics of $PM_{2.5-0.3}$ and $PM_{0.3}$ and Consequence of a Dust Storm episode at an Urban Site in Lebanon. *Atmos. Res.* 2016, *180*, 274–286.
- [2] Irfan, M.; Riaz, M.; Saleem, M.; Muhammad, S.; Saleem, F.; Berg, L. Van Den. Estimation and Characterization of Gaseous Pollutant Emissions from Agricultural Crop Residue Combustion in Industrial and Household Sectors of Pakistan. *Atmos. Environ.* 2014, *84*, 189–197.
- [3] Lang, J.; Zhou, Y.; Cheng, S.; Zhang, Y.; Dong, M.; Li, S.; Wang, G.; Zhang, Y. Science of the Total Environment Unregulated Pollutant Emissions from on-Road Vehicles in. *Sci. Total Environ.* 2016, *573*, 974–984.
- [4] Eeftens, M.; Phuleria, H. C.; Meier, R.; Aguilera, I.; Corradi, E.; Davey, M.; Ducretstich, R.; Fierz, M.; Gehrig, R.; Ineichen, A.; et al. Spatial and Temporal Variability of Ultra Fine Particles, NO_2 , $PM_{2.5}$, PM_{10} and PM_{Coarse} in Swiss Study Areas. *Atmos. Environ.* 2015, *111* [2], 60–70.
- [5] Smargiassi, A.; Goldberg, M. S.; Wheeler, A. J.; Plante, C.; Valois, M.; Mallach, G.; Marie, L.; Shutt, R.; Bartlett, S.; Raphoz, M.; et al. Associations between Personal Exposure to Air Pollutants and Lung Function Tests and Cardiovascular Indices among Children with Asthma Living near an Industrial Complex and Petroleum Refineries. *Environ. Res.* 2014, *132*, 38–45.
- [6] Morawska, L.; Ristovski, Z.; Jayaratne, E. R.; Keogh, D. U.; Ling, X. Ambient Nano and Ultrafine Particles from Motor Vehicle Emissions: Characteristics, Ambient Processing and Implications on Human

- Exposure. *Atmos. Environ.* 2008, 42 [35], 8113–8138.
- [7] Marquet, O.; Miralles-guasch, C. City of Motorcycles . On How Objective and Subjective Factors Are behind the Rise of Two-Wheeled Mobility in Barcelona. *Transp. Policy* 2016, 52, 37–45.
- [8] Mishima, K. Motorcycle Industry in Vietnam , Thailand and Indonesia. 2004, 1–3.
- [9] DayalSharma, R.; Jain, S.; Singh, K. Growth Rate of Motor Vehicles in India - Impact of Demographic and Economic Development. *J. Econ. Soc. Stud.* 2011, 1 [2], 137–154.
- [10] Chen, Y.; Chen, L.; Jeng, F.; Chen, Y.; Chen, L. Analysis of Motorcycle Exhaust Regular Testing Data — A Case Study of Taipei City. *J. Air Waste Manage. Assoc.* 2009, 59 [November], 757–762.
- [11] Tung, H. D.; Tong, H. Y.; Hung, W. T.; Anh, N. T. N. Science of the Total Environment Development of Emission Factors and Emission Inventories for Motorcycles and Light Duty Vehicles in the Urban Region in Vietnam. *Sci. Total Environ.* 2011, 409 [14], 2761–2767.
- [12] Thi, N.; Oanh, K.; Thi, M.; Phuong, T.; Permadi, D. A. Analysis of Motorcycle Fl Eet in Hanoi for Estimation of Air Pollution Emission and Climate Mitigation Co-Bene Fi T of Technology Implementation. *Atmos. Environ.* 2012, 59, 438–448.
- [13] Macedo, C.; Daemme, L. C.; Penteado, R.; Heloísa, N.; Corr, S. M. BTEX Emissions from Fl Ex Fuel Motorcycles. *Atmos. Pollut. Res. J.* 2017, 1–10.
- [14] Li, L.; Ge, Y.; Wang, M.; Li, J.; Peng, Z.; Song, Y. Effect of Gasoline / Methanol Blends on Motorcycle Emissions: Exhaust and Evaporative Emissions. *Atmos. Environ.* 2015, 102, 79–85.
- [15] Tsai, J.; Huang, P.; Chiang, H. Characteristics of Volatile Organic Compounds from Motorcycle Exhaust Emission during Real-World Driving. *Atmos. Environ.* 2014, 99, 215–226.
- [16] Yu, Q.; Lu, Y.; Xiao, S.; Shen, J.; Li, X.; Ma, W.; Chen, L. Commuters ' Exposure to PM 1 by Common Travel Modes in Shanghai. *Atmos. Environ.* 2012, 59, 39–46.
- [17] Yan, C.; Zheng, M.; Yang, Q.; Zhang, Q.; Qiu, X.; Zhang, Y.; Fu, H.; Li, X.; Zhu, T.; Zhu, Y. Commuter Exposure to Particulate Matter and Particle-Bound PAHs in Three Transportation Modes in Beijing , China. *Environ. Pollut.* 2015, 204, 199–206.
- [18] Lu, S.; Zhang, W.; Zhang, R.; Liu, P.; Wang, Q.; Shang, Y.; Wu, M.; Donaldson, K.; Wang, Q. Comparison of Cellular Toxicity Caused by Ambient Ultrafine Particles and Engineered Metal Oxide Nanoparticles. *Part. Fibre Toxicol.* 2015, 1–12.
- [19] Eun, K.; Cho, D.; Jeong, H. Air Pollution and Skin Diseases: Adverse Effects of Airborne Particulate Matter on Various Skin Diseases. *Life Sci.* 2016, 152, 126–134.
- [20] Iversen, N. K.; Frische, S.; Thomsen, K.; Laustsen, C.; Pedersen, M.; Hansen, P. B. L.; Bie, P.; Fresnais, J.; Berret, J. F.; Baatrup, E.; et al. Superparamagnetic Iron Oxide Polyacrylic Acid Coated γ -Fe₂O₃ Nanoparticles Do Not Affect Kidney Function but Cause Acute Effect on the Cardiovascular Function in Healthy Mice. *Toxicol. Appl. Pharmacol.* 2013, 266 [2], 276–288.
- [21] Nemmar, A.; Al-Maskari, S.; Ali, B. H.; Al-Amri, I. S. Cardiovascular and Lung Inflammatory Effects Induced by Systemically Administered Diesel Exhaust Particles in Rats. *Am. J. Physiol. Lung Cell. Mol. Physiol.* 2007, 292 [3], L664–L670.
- [22] Mühlfeld, C.; Rothen-Rutishauser, B.; Blank, F.; Vanhecke, D.; Ochs, M.; Gehr, P. Interactions of Nanoparticles with Pulmonary Structures and Cellular Responses. *Am. J. Physiol. Lung Cell. Mol. Physiol.* 2008, 294 [5], L817–L829.
- [23] Sierra-Vargas, M. P.; Guzman-Grenfell, A. M.; Blanco-Jimenez, S.; Sepulveda-Sanchez, J. D.; Bernabe-Cabanillas, R. M.; Cardenas-Gonzalez, B.; Ceballos, G.; Hicks, J. J. Airborne Particulate Matter PM_{2.5} from Mexico City Affects the Generation of Reactive Oxygen Species by Blood Neutrophils from Asthmatics: An in Vitro Approach. *J. Occup. Med. Toxicol.* 2009, 4, 17.
- [24] Kumar, P.; Morawska, L.; Birmili, W.; Paasonen, P.; Hu, M.; Kulmala, M.; Harrison, R. M.; Norford, L.; Britter, R. Ultrafine Particles in Cities. *Environ. Int.* 2014, 66, 1–10.
- [25] Feng, C.; Li, J.; Sun, W.; Zhang, Y.; Wang, Q. Impact of Ambient Fine Particulate Matter [PM_{2.5}] Exposure on the Risk of Influenza-like-Illness: A Time-Series Analysis in Beijing , China. *Environ. Heal.* 2016, 1–12.
- [26] Zhang, F.; Liu, X.; Zhou, L.; Yu, Y.; Wang, L.; Lu, J.; Wang, W.; Krafft, T. Spatiotemporal Patterns of Particulate Matter [PM] and Associations between PM and Mortality in Shenzhen , China. *BMC Public Health* 2016, 1–11.
- [27] Gromke, C.; Blocken, B. Influence of Avenue-Trees on Air Quality at the Urban Neighborhood Scale . Part II: Traf Fi c Pollutant Concentrations at Pedestrian Level. *Environ. Pollut.* 2015, 196, 176–184.
- [28] Wardoyo, A. Y. P.; Morawska, L.; Ristovski, Z. D.; Marsh, J. Quantification of Particle Number and Mass Emission Factors from

- Combustion of Queensland Trees. *Environ. Sci. Technol.* 2006, 40 [18], 5696–5703.
- [29] Nowak, D. J.; Hirabayashi, S.; Bodine, A.; Hoehn, R. Modeled PM_{2.5} Removal by Trees in Ten U.S. Cities and Associated Health Effects. *Environ. Pollut.* 2013, 178, 395–402.
- [30] An, P.; Sun, W.; Li, G.; Tan, M.; Lai, C.; Chen, S. Characteristics of Particle Size Distributions about Emissions in a Common-Rail Diesel Engine with Biodiesel Blends. *Procedia Environ. Sci.* 2011, 11 [PART C], 1371–1378.
- [31] Tang, S.; Laduke, G.; Chien, W.; Frank, B. P. Impacts of Biodiesel Blends on PM_{2.5}, Particle Number and Size Distribution, and Elemental / Organic Carbon from Nonroad Diesel Generators. *FUEL* 2016, 172, 11–19.
- [32] Geng, P.; Zhang, H.; Yang, S. Experimental Investigation on the Combustion and Particulate Matter [PM] Emissions from a Port-Fuel Injection [PFI] Gasoline Engine Fueled with Methanol – Ultralow Sulfur Gasoline Blends. *FUEL* 2015, 145, 221–227.
- [33] Zhang, R.; Liu, C.; Hsu, P.; Zhang, C.; Liu, N.; Zhang, J. Nano Fiber Air Filters with High-Temperature Stability for Efficient PM_{2.5} Removal from the Pollution Sources. *NANO Lett. Am. Chem. Soc.* 2016, 16 [6], 3642–3649.
- [34] Ardkapan, S. R.; Johnson, M. S.; Yazdi, S.; Afshari, A.; Bergsøe, N. C. Filtration Efficiency of an Electrostatic Fibrous Filter: Studying Filtration Dependency on Ultrafine Particle Exposure and Composition. *J. Aerosol Sci.* 2014, 72, 14–20.
- [35] Giechaskiel, B.; Maricq, M.; Ntziachristos, L.; Dardiotis, C.; Wang, X.; Axmann, H.; Bergmann, A.; Schindler, W. Review of Motor Vehicle Particulate Emissions Sampling and Measurement: From Smoke and Filter Mass to Particle Number. *J. Aerosol Sci.* 2014, 67, 48–86.
- [36] Taylor, P.; Presser, C.; Conny, J. M.; Nazarian, A.; Presser, C.; Conny, J. M.; Nazarian, A. Effects on Particle Absorption Optical Properties Filter Material Effects on Particle Absorption Optical Properties. 2014, No. November, 37–41.
- [37] Wardoyo, A.; P. Juswono, U.; Riyanto, S. Developing Particulate Thin Filter Using Coconut Fiber for Motor Vehicle Emission. In *AIP Conference Proceedings*; 2016; Vol. 1719, p 30043.
- [38] Wardoyo, A. Y. P.; Budianto, A.; Abdurrouf. Filtration of Submicron Particles from Motorcycle Emission Using a DC Low Electrostatic Filter. *Int. J. Appl. Eng. Res.* 2017, 12 [8], 1725–1728.
- [39] Wardoyo, A.; Budianto, A. A DC Low Electrostatic Filtering System for PM_{2.5} Motorcycle Emission. In *Conference: 2017 International Seminar on Sensors, Instrumentation, Measurement and Metrology [ISSIMM]*; 2017; pp 51–54.
- [40] Verma, G.; Prasad, R. K.; Agarwal, R. A.; Jain, S.; Agarwal, A. K. Experimental Investigations of Combustion, Performance and Emission Characteristics of a Hydrogen Enriched Natural Gas Fuelled Prototype Spark Ignition Engine. *FUEL* 2016, 178, 209–217.
- [41] Yu, F. Chemiions and Nanoparticle Formation in Diesel Engine Exhaust. *Geophys. Res. Lett.* 2001, 28 [22], 4191–4194.
- [42] Olcay, K.; Hikmet, T. Combustion Efficiency Analysis and Key Emission Parameters of a Turboprop Engine at Various Loads. *J. Energy Inst.* 2015, 88, 490–499.
- [43] Haiyang, H.; Qiang, W. Calculation of Wall Temperature for Aircraft Exhaust System with Considering Gas Radiation Heat Transfer. *Chinese J. Aeronaut.* 2009, 22 [6], 590–598.
- [44] Choi, S.; Oh, K.; Lee, C. The Effects of Filter Porosity and Flow Conditions on Soot Deposition / Oxidation and Pressure Drop in Particulate Filters. *Energy* 2014, 77, 327–337.
- [45] Hua, X.; Herrin, D. W.; Wu, T. W.; Elnady, T. Simulation of Diesel Particulate Filters in Large Exhaust Systems. 2013, v, 1326–1332.
- [46] Dwyer, H.; Ayala, A.; Zhang, S.; Collins, J.; Huai, T.; Herner, J.; Chau, W. Emissions from a Diesel Car during Regeneration of an Active Diesel Particulate Filter. *J. Aerosol Sci.* 2010, 41 [6], 541–552.
- [47] Tang, T.; Zhang, J.; Cao, D.; Shuai, S.; Zhao, Y. Experimental Study on Filtration and Continuous Regeneration of a Particulate Filter System for Heavy-Duty Diesel Engines. *JES* 2014, 26 [12], 2434–2439.
- [48] Zhang, B.; Jiaqiang, E.; Gong, J.; Yuan, W.; Zhao, X.; Hu, W. Influence of Structural and Operating Factors on Performance Degradation of the Diesel Particulate Filter Based on Composite Regeneration. *Appl. Therm. Eng.* 2017, 121, 838–852.
- [49] Zhang, B.; Qi, H.; Sun, S.; Ruan, L.; Tan, H. Solving Inverse Problems of Radiative Heat Transfer and Phase Change in Semitransparent Medium by Using Improved Quantum Particle Swarm Optimization. *Int. J. Heat Mass Transf.* 2015, 85, 300–310.
- [50] Taylor, P.; Cozzi, C.; Cadorin, D. Growth and Coagulation of Solid Particles in Flames. *Combust. Sci. Technol. Nucleation*, 2007, No. January 2015, 37–41.
- [51] Fang, J.; Meng, Z.; Li, J.; Pu, Y.; Du, Y.; Li, J.; Jin, Z.; Chen, C.; G. Chase, G. The Influence of Ash on Soot Deposition and Regeneration Processes in Diesel Particulate Filter. *Appl. Therm. Eng.* 2017, 124, 633–640.

- [52] Eeftens, M.; Meier, R.; Schindler, C.; Aguilera, I.; Phuleria, H.; Ineichen, A.; Davey, M.; Ducret-stich, R.; Keidel, D.; Probst-hensch, N.; et al. Development of Land Use Regression Models for Nitrogen Dioxide , Ultrafine Particles , Lung Deposited Surface Area , and Four Other Markers of Particulate Matter Pollution in the Swiss SAPALDIA Regions. *Environ. Heal.* 2016, 1–14.
- [53] Fino, D.; Bensaid, S.; Piumetti, M.; Russo, N. Applied Catalysis A : General A Review on the Catalytic Combustion of Soot in Diesel Particulate Filters for Automotive Applications: From Powder Catalysts to Structured Reactors. *Appl. Catal. A Gen.* 2016, 509, 75–96.

THE INFILTRATION CAPACITY OF THREE-DIAMOND PAVER TYPE IN LOW RAINFALL INTENSITY

Jeanelly Rangkang¹, Lawalenna Samang¹, Sakti Adji Adisasmita¹ and Muralia Hustim¹
¹ Civil Engineering Faculty, Hasanuddin University, Indonesia

ABSTRACT

The implementation of the paving block as permeable pavement surface layer in Indonesia is still not popular. So far it only considers the aesthetic side, while the hydraulic benefits are neglected. Actually, the hydrological benefits of this material can solve the problems of stormwater runoff in urban areas. As a surface layer, paving blocks allow water to infiltrate through gaps between pavers to the underlying layer. The infiltration process will reduce rainwater runoff and bring positive implication in controlling peak discharge. This research is carried out in the laboratory with some boundaries, namely: paving block used is Three-Diamond pavers type of 80 mm thick, gaps between pavers is 5 mm wide, the slopes of the test field are 0%, 2%, and 4%, rainfall intensities are 50.84 mm/hour and 75.58 mm/hour, developed box model for infiltration capacity test is 1 m² which are equipped with a modified rainfall simulator, and the bedding layer thickness is 100 mm. The main conclusions of this study are: (a) No surface runoff of two intensities scenarios, (b) Requires more than 0.047 m³/minute volume of water to generate surface runoff, (c) At low rainfall intensity, the infiltration capacity of the concrete block increases along with the increase in slopes, (d) The equilibrium time range investigated in this study is in range of 20 minutes to 30 minutes from commencement inflow.

Keywords: Infiltration, Runoff, Three-diamond paver, Permeable pavement.

INTRODUCTION

Increased paved areas in urban areas are closely related to land use changes, that are known as urbanization of catchments. This is caused by the shifting function of the water catchment areas into residential areas and/or other commercial areas. The above phenomenon causes an increase in the volume and the ability of stormwater runoff to transport pollutant substances from the catchment surface to the downstream area. As a consequence, there is an increase in the volume of rainfall runoff that must be handled by the urban drainage system.

The conventional approach to deal with stormwater runoff is to drain water as quickly as possible through urban drainage system to water bodies, such as beaches, lakes and rivers or creeks. If the rainwater runoff is discharged unprocessed, then it may affect water quality in water bodies that are known as the sensitive ecological zone. In fact, the public demand that rainwater runoff that is discharged into water bodies should not cause a degradation of water quality [1].

The impact of stormwater runoff brings a significant problem in urban areas since urban areas typically have a much wider proportion of paved area than that of unpaved. US EPA [2] publishes that approximately 10% of rainwater that is falling on the natural ground cover will become runoff, while in the impervious cover is 55%. It means that urbanized area produces more than 5 times more

runoff than that of wooded area. Therefore, a strategy is needed to control peak discharge by reducing rainwater runoff through implementation of Three-Diamond paver type as a permeable pavement surface layer. This kind of pavement is still not popular in Indonesia. Implementation of the paving block so far is still used from the aesthetic side only, while the hydraulic benefits are neglected. Actually, the hydrological benefits of this material can solve the problems of stormwater runoff in urban areas.

The objective of the study is to analyse the infiltration capacity of permeable surface of Three-Diamond paver type concrete blocks in different scenarios of slopes and rainfall intensity.

RESEARCH METHODOLOGY

The Cantabrian Fixed Infiltrometer (CFI) developed in the Universidad de Cantabria (UC) is a laboratory device that is created to measure the infiltration capacity of permeable surfaces [3]. Several studies have been conducted by some researchers by using the CFI, such as Sañudo-Fontaneda L. A., Castro-Fresno D., Rodriguez-Hernandez J. and Borinaga-Treviño R., [3] and others [4-7]. The CFI allows testing pervious pavement with any kind of surface layer. The CFI test piece area is 0,25 m², rainfall intensities range is 10-150 mm/h and surface slope test is between 0% to 10% [4]. Zhang J., Jayasuriya N. and Setunge S. [8] constructed a steel box test model with

infiltration holes set up on the bottom plate. The laboratory device that was developed in UC [3] and that was constructed by Zhang J., Jayasuriya N. and Setunge S. [8] have become the basis of the development of the steel box test model used in this study.

Infiltration Test Apparatus

The sketch of the apparatus that is developed in this study is shown in Fig. 1. This equipment was designed to test the infiltration capacity of paving area 1 m long and 1 m wide. It only allows measuring the direct infiltration capacity for vertical rain falling, where the rain intensities could be independently adjusted to the target intensity. The equipment consists of three main parts, namely: test frame, grid, and modified rainfall simulator.

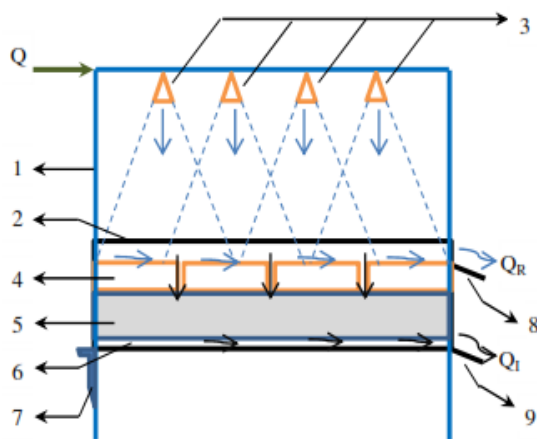


Fig. 1 The sketch of the developed apparatus.

The numbers and letters in Fig. 1 depict the parts of the apparatus, they are:

- 1 tests frame;
 - 2 is grid;
 - 3 is the sprinklers that produce raindrops;
 - 4 is pavers;
 - 5 is bedding layer;
 - 6 is geotextile filter cloth;
 - 7 is long threaded screws to adjust grid's slope;
 - 8 is a roof sheeting to collect runoff water (Q_R);
 - 9 is the subsuperficial flow water funnel for collecting infiltrated water (Q_I), and;
- Q is selected inflow rate, wich can be calculated from the following formula:

$$Q = Q_I + Q_R \quad (1)$$

where Q_I is runoff outflow rate, Q_R is infiltrated outflow rate.

Frame and grid

The frame that supports the grid on which the

pavements are placed, has four legs. The frame and grid are both made of steel. The slope is adjusted via two long threaded screws that are placed on one side of the frame. It is possible to adjust the grid's slope for varying slopes test. The slopes in this study are 0%, 2%, and 4%.

Moreover, the grid is equipped with a subsuperficial flow water funnel to collect infiltrated water and a roof sheeting 50 mm wide to collect runoff water. Both the subsuperficial flow water funnel and the roof sheeting are placed on the opposite side of the slope adjusted screws position. Assumed that infiltrated water will infiltrate through the bedding layer to the bottom of it, and then flow to the subsuperficial flow water funnel that is placed right below the roof sheeting.

Modified Rainfall Simulator

The important part of the developed apparatus is rainfall simulator. It is placed to a separte upper frame, right above the pavement.

The modified rainfall simulator is designed to produce raindrops through simple pipelines with sprinklers, that are positioned directly over the pavement area. This rain source is connected to a valve to adjust flow rate in order to get a specific intensity. The intensities taken for this study are 50,84 mm/h and 75,58 mm/h.

Pavement Samples

The permeable pavement samples analysed consist of a geotextile filter cloth, bedding layer and three-diamond concrete blocks respectively, that are marked with number 6, 5 dan 4 in Fig. 1.

Geotextile and bedding layer

Based on literature studies, geotextile has an important role in the pavement structure. Pratt [9] explains the six principles application of geosynthetics in civil engineering, as follows:

- erosion protection;
- filtration/sediment trapping;
- separation layer;
- deflection resistance;
- void forming; and
- pollutant trapping/supporting bio-remediation.

The geotextile is placed at the base of the grid. The selected geotextile in this study was polypropylene filter cloth whose technical specifications are the weight of 350 g/m² and permeability of 117.9 L/m²s. Unfortunately, the presence of geotextile in this study is not taken into calculation. The utilization of geotextile is only as a filter in order to protect the bedding layer material so as not to be carried by water.

The bedding material is placed on top of geotextile. The bedding was 100 mm deep, compacted and levelled manually. The gradation of the bedding material was chosen based on ASTM C 33[10]. This material was taken from a quarry located in North Sulawesi Indonesia. Figure 2 shows the bedding layer gradation according to ASTM C 33. As can be seen from Fig. 2, the blue line with square red dots was the gradation curve of the selected material for this study. While the two black lines with black round dots are both gradation envelope of ASTM C 33 specification.

Three-diamond concrete blocks

The three-diamond paver is Indonesian name for trihex paver shape. The trihex is a commercial term of the pavers, which stands for three hexagonal. This type of paving is commonly used in Indonesia. The blocks tested were produced by Super Star Enterprise in North Sulawesi Indonesia. Furthermore, blocks tested were made of Portland Composite Cement (PCC) that is widely used in Indonesia. PCC has a high compressive strength [11].

The pavers are formed by three united regular hexagons with vertex configuration. The length of

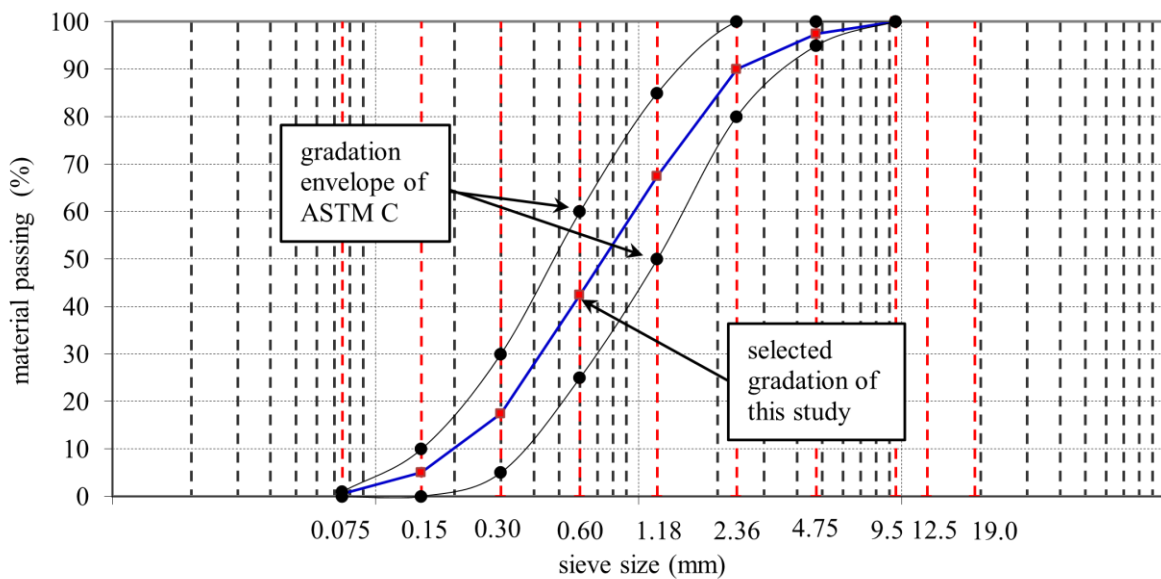


Fig. 2 Grading curve of bedding material.

Bedding materials are also used to fill the gap between paving block as jointing sand. The primary functions of jointing sand in the segmental concrete pavement are to create interlocking between paving blocks and to help seal the pavement [10]. Table 1 lists the bedding material properties that are obtained through laboratory investigation.

Table 1 Bedding material properties

Properties of material bedding		value
Max. Dry density, γ_d	(gr/cm^3)	1.47
Specific gravity, G_s		2.655
The density of water, γ_w	(gr/cm^3)	1.00
Void ratio, e		0.806
Porosity, n	(%)	44.6
Hydraulic conductivity, k	(mm/s)	4.325×10^{-1}

each the hexagon side is 60 mm and 80 mm in height, while the surface area (A) of the upper side of the paving block is $280,59 \text{ cm}^2$ and the circumference surface area (S) of the paving block is 576 cm^2 . The tested pavers' shape is shown in Fig. 3. The pavers were placed on top of bedding layer, whose gaps between pavers are 5 mm. The gaps filled with graded sand used as bedding layer material.

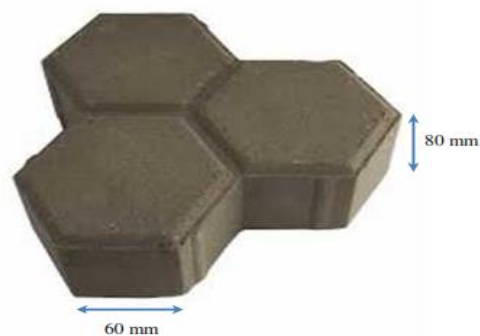


Fig. 3 The shape of paver tested.

The reason for this treatment is a result of a laboratory study on pavement using fine and coarse joint sand. The study concluded that the performance of the pavement will be better when having a coarser gradation of joint sand. However, the jointing sand maximum size should be less than the joint width [12].

The other factor of paver tested that should be concerned is its permeability. Reported by some researchers that the permeability of concrete block is very low, and the capillary porosity of concrete determines the degree of concrete block permeability. In their study, the permeability of concrete was taken as a constant value of 1×10^{-4} m/sec. The result of the study was that permeability of concrete block has no considerable effect on pavement surface permeability [13]. In this study, the permeability of concrete block is not considered.

RESULTS AND DISCUSSION

The results presented were obtained in the series of a laboratory test. There are two scenarios of rainfall intensity with 3 gradients of slopes that were developed to analyse the infiltration capacity behavior of three-diamond pavers. Some treatments applied to the study are:

- Newly built surface, so no clogging scenario applied.
- The water infiltrates not through pavers, through the gaps of the paver.
- Two different direct rainfall storms of uniform intensity were simulated.
- No runoff simulator.
- Five minutes is the time interval to collect water flow until the flow rate was almost constant.

To obtain the characteristics of infiltration through the whole pavement structure of each rainfall intensity, the water flow through the pavement was collected based on specified time intervals. Figure 4 and 5 depict the output rates subjected to pavement surface slopes at rainfall intensities of 50.84 mm/h and 75.87 mm/h, respectively.

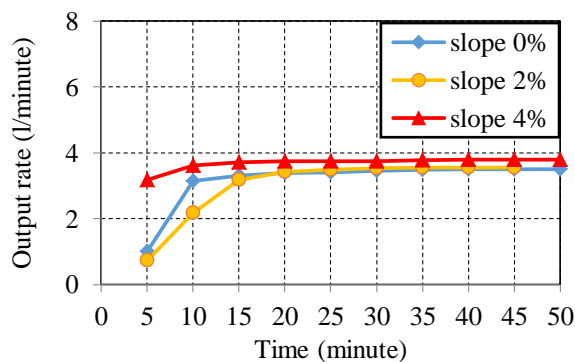


Fig. 4 Experimental output rate subjected to slopes, at the intensity of 50.84 mm/h.

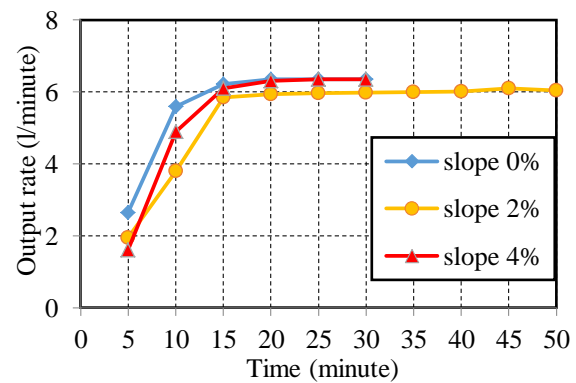


Fig. 5 Experimental output rate subjected to slopes, at the intensity of 75.87 mm/h.

Laboratory storm simulation shows that there is no surface runoff of two intensity scenarios. This can be due to the following reasons [8]:

- The permeability of bedding material was very high
- There was no sub-base or subgrade layer beneath the bedding layer, where in field practice the water infiltration in the permeable pavement structure highly depended on the subgrade layer (bottom soil) and the drainage on the pavement structure.

The first reason mentioned above have a close relation to bedding material properties as shown in Table 1. The values of void ratio, porosity, and hydraulic conductivity are considered to be high. Moreover, hydraulic characteristic of infiltrated water first fills the voids in the whole pavement, then flows to the bottom of the bedding layer. The phenomenon has a tight relationship with the volume storage of whole pavement. Tabel 2 shows the calculation result of volume storage of whole pavement.

Table 2 Total volume of pavement storage

Pavement details		Value
Surface pavement area		1.00 m ²
Bedding layer thickness		0.1 m
Three diamonds paver thickness		0.08 m
Gaps between pavers		0.005 m
Porositas		44.6%
Volume storage	bedding layer	0.0446 m ³
	Gaps	0.002 m ³
	Total	0.047 m ³

Table 2 depicts that if the whole pavement has storage volume up to 0.047 m³, then it requires more than 0.047 m³ volume of water to generate surface runoff.

Furthermore, the collected water increases at any given time interval, until the flow through the pavement becomes uniform and is under equilibrium conditions. Theoretically, in the equilibrium condition, the input flow rate is equal to the output flow rate. The calculation on that matter is presented in Table 3.

Table 3 Relationship of input flow rate, output flow rate and equilibrium time.

Test No.	Slope %	Inflow rate l/min	Outflow rate at equilibrium l/min	Inflow to outflow at equilibrium %	Time to equilibrium min
1	0		0.7	82.64	30-40
2	2	0.847	0.71	83.83	30-40
3	4		0.76	89.73	20-30
4	0		1.27	100	20-30
5	2	1.27	1.21	95.28	20-30
6	4		1.27	100	15-20

As can be seen from Table 3, the required time to achieve the equilibrium conditions in each simulation varied, however, the equilibrium condition was achieved in the time range from 20 minutes to 30 minutes. These values are also illustrated in Fig. 4 and Fig. 5. The equilibrium time range investigated in this study is equal to the result of study obtained by other researchers [14]. Furthermore, Table 3 also clarifies the input flow rate and output flow rate that are almost equal in all tests, even on tests no. 4 and 6 at an inflow rate of 1.27 l/minute that is a hundred percent equal. So it can be said that when the rainfall intensity increases, the pervious pavement output rate increases as well.

In relation to infiltration capacity subjected to slopes, Fig. 6 and Fig. 7 show the relationship between those parameters.

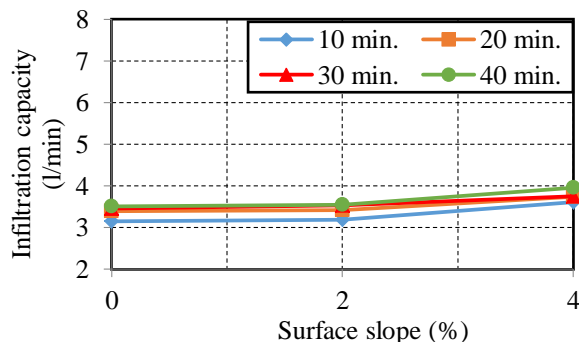


Fig. 6 Infiltration capacity subjected to slopes, at the intensity of 50.84 mm/h.

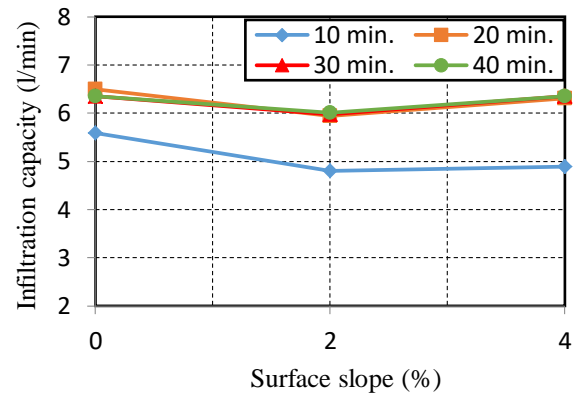


Fig. 7 Infiltration capacity subjected to slopes, at the intensity of 75.87 mm/h.

On one hand, at low rainfall intensity, the infiltration capacity of the concrete block increases along with the increase in slope (Fig. 6), which is the contradiction phenomenon. On the other hand, Fig. 7 shows that the infiltration capacity of concrete blocks slightly decreases with the increase of the slope at high rainfall intensity.

CONCLUSION

Referring to the implemented research boundaries, the conclusion points of this study, are:

- No surface runoff of two intensity scenarios
- Requires more than 0.047 m³/minute volume of water to generate surface runoff.
- At low rainfall intensity, the infiltration capacity of the concrete block increases along with the increase in slopes.
- The equilibrium time range investigated in this study is between 20 minutes to 30 minutes from commencement inflow.

This study also refers to aspects in designing pervious pavement because the physical properties of the aggregates are the important factors to be concerned. Therefore, the initial tests carried out on the aggregate physical properties should be properly investigated.

On the next level, an analytical calculation should be developed, in order to validate the results obtained in the laboratory. Also, further study will be done on other shapes and dimensions of paving blocks, by applying the same laboratory methodology. The study should be conducted to characterize the permeable pavement infiltration behavior, in order to obtain the influence of the paving block shapes on the infiltration rate.

ACKNOWLEDGEMENTS

This work is part of Jeanelly Rangkang's final project for the Ph.D. at Civil Engineering Faculty of Hasanuddin University and is part of the research

project entitled Implementation of Eco-concrete Paving Block As a Pavement Surface Layer For Flooding Mitigation, financed by The Ministries Of Research, Technology, And the Higher Education Republic Of Indonesia.

REFERENCES

- [1] Shackel B., Ball J., and Mearing M. Using Permeable Eco-paving to Achieve Improved Water Quality for Urban Pavement. Proceedings of 7th International Conference on Concrete Block Paving, 12th -15th Oct 2003 Sun City.
- [2] U.S. EPA. Fact Sheet: Clean Water Is Everybody's Business. 2003, EPA 841-F-03003.
- [3] Sañudo-Fontaneda L. A., Castro-Fresno D., Rodriguez-Hernandez J. and Borinaga-Treviño R., Comparison of The Infiltration Capacity of Permeable Surfaces for Rainwater Energy Valorization. 12st International Conference on Urban Drainage, Porto Alegre/Brazil, p 11-16 September 2011
- [4] Sañudo-Fontaneda L. A., Rodriguez-Hernandez J., Vega-Zamanillo A. and Castro-Fresno D., Laboratory Analysis of The Infiltration Capacity of Interlocking Concrete Block Pavements in Car Parks. Water Science & Technology 67.3 ©IWA Publishing 2013.
- [5] Castro D., González-Angullo N., Rodríguez J. and Calzada M. A., The Influence of Paving-block Shape on The Infiltration Capacity of Permeable Paving. Land Contamination & Reclamation, 15 (3), 2007. EPP Publications Ltd.
- [6] Rodriguez-Hernandez J., Castro-Fresno D., Fernández-Barrera A. H. and Vega-Zamanillo Á., Characterization of Infiltration Capacity of Permeable Pavements with Porous Asphalt Surface Using Cantabrian Fixed Infiltrometer. Journal of Hydrologic Engineering © ASCE / May 2012 p. 597-603.
- [7] González-Angullo N., Castro-Fresno D., Rodriguez J. and Davies J. W., Runoff Infiltration to Permeable Paving in Clogged Conditions. Urban Water Journal 5 (2), 2008 p. 117-124.
- [8] Zhang J., Jayasuriya N. and Setunge S., Application of Pervious Pavements – A Laboratory Scale Study. 7th Urban Drainage Modelling and the 4th Water Sensitive Urban Design, Melbourne, Australia, 2nd -7th April 2006, pp 227-234
- [9] Pratt, C. J., Application of Geosynthetics in Sustainable Drainage Systems. 1st International Geosynthetics Society, UK Chapter 'Geosynthetics: Protecting the Environment', Loughborough, 17 June 2003. Thomas Telford.
- [10] Interlocking Concrete Pavement Institute. ICPI Tech Spec No. 17. Revised January 2015.
- [11] Tjaronge M. W., Irmawaty R., Sakti Adji Adisasmita, Arwin Amiruddin and Hartini, Compressive Strength and Hydration Process of Self Compacting Concrete (SCC) Mixed with Sea Water, Marine Sand, and Portland Composite Cement. Advanced Materials Research Vol. 935 (2014) pp 242-246. Online available since 2014/May/07 at www.scientific.net © (2014) Trans Tech Publications, Switzerland.
- [12] Panda and Ghosh, Structural Behavior of Concrete Block Paving. I: Sand in Bed and Joints. Journal of Transportation Engineering, March 2002. 128: 123-129.
- [13] Abolfazl Hassani and S. Mohammad, Seepage Analysis of Interlocking Concrete Block Pavements. Road Material and Pavement Design. Vol. 9 – No. 2/2008, p 311-321.
- [14] Zhang Jie, A Laboratory Scale Study of Infiltration from Pervious Pavements. A master thesis. School of Civil, Environmental and Chemical Engineering Science, Engineering and Technology Portfolio RMIT University. 2006. p. 62.

HYDROLOGICAL CHARACTERISTICS AND WATER MANAGEMENT IN THE AIR SUGIHAN SUB-RIVER BASIN, SOUTH SUMATERA, INDONESIA

Wijaya Mardiansyah^{1,2}, M. Yusup Nur Khakim¹, Dedi Setiabudidaya¹, Satria J. Priatna³ and Iskhaq Iskandar¹

¹Faculty of Mathematics and Natural Sciences, Sriwijaya University, Indonesia;

²Graduate School of Sciences, Faculty of Mathematics and Natural Sciences, Sriwijaya University, Indonesia; ³Faculty of Agriculture, Sriwijaya University, Indonesia

ABSTRACT

Characteristics of suboptimal land, which is usually located in a river basin area, is strongly influenced by soil conditions, hydrology and climate, in which its management requires an integrated data assessment and utilization. In order to examine the climatic and hydrological conditions as well as the tidal effect in the Air Sugihan sub-river basin, a water balance analysis was conducted on the combined climatic data obtained from satellite remote sensing and in-situ monthly tidal data for a period of 2001-2013. The climatic data includes a monthly precipitation data, surface winds, surface temperature, surface and subsurface runoff. The water balance analysis shows that the average total annual runoff occurring in the study area was about 87.7 mm/month or equal to 102.67 m³/s. In addition, the water balance in the study area indicates an annual variation, in which the water deficit conditions are occurring in April to September with a peak during a dry season in August, while the surplus peak are occurring in November-December. However, the area is still experiencing a net annual surplus of about 302,468.81 m³/month. Furthermore, the water balance conditions in the Air Sugihan sub-river basin are significantly correlated with the tidal fluctuations indicated by a coefficient correlation of $r = 0.88$.

Keywords: Air Sugihan Sub-River Basin, Hydrology, Precipitation, Tidal Effect, Water Balance

INTRODUCTION

The hydrological cycle describes water cycle on the earth surface. Solar radiation and other climate factors cause evaporation on the Earth surface (land, ocean and other water bodies) and vegetation. The most air will be lifted and become cool, then it will be transported by the wind which depends on the atmosphere condition. Some of the water vapor condenses to form clouds and returns to the Earth surface as precipitation. As the water from precipitation reach the Earth surface, some parts will penetrate the Earth surface and become groundwater, and others will be accommodated temporarily in the surface basins (surface detention) then flow to the ocean through the river before it evaporate back into atmosphere [1]. The hydrological cycle forms a water balance on the Earth system. Therefore, sustainable exploitation of natural resources is a key role in managing the hydrological cycle. Forest vegetation is an important factor for regulating evapotranspiration, soil humidity, infiltration, and increasing surface runoff. Note that the surface runoff significantly influences the debit flow [2].

Management of the suboptimal land requires a good management on the water balance, so that it may become a productive land for cultivation. In Indonesia, most of suboptimal land are

agroecosystem lands, which are sour-dry land, dry land in the tropical area, tidal swamp land and swamp land. The sour-dry land less of nutrient, sour and dry, while the dry land in the tropical area usually does not have enough water for cultivation and it is usually rocky land with thin topsoil layer. The tidal-swamp land has several problems, such as it is difficult to set the water management, it has pyrite layer and thick peat layer, and it experiences seawater intrusion. On the other hand, in the swamp land, it is difficult to predict and set the water level and soil sour [3]. In addition, previous study has shown that the productivity of the tidal land or suboptimal land is very diverse. This productivity diversity is influenced by soil types, water supply and climate [4].

In order to manage suboptimal land, an agricultural conservation is required [5]. The planning of agricultural conservation system involves three following inventory steps:

1. Inventory of biophysical resource. This inventory is designed to evaluate the land capability/suitability class for a specific commodity, required agro-technology and conservation techniques, as well as the level of land damage.
2. Inventory of farmer socio-economic conditions, and

3. Inventory of external influences, such as trading of agricultural commodities products, condition and distance to the trading places, education/training tools, rural financial institution and farmer community organizations.

This study is designed to analyze possible impacts of climate condition and tidal on the hydrological cycle in the Air Sugihan sub-river basin. The analysis is based on the water balance calculation that utilize several data, including precipitation, surface winds, temperature, surface and subsurface runoff and the tidal data in the study area.

DATA AND METHODS

Study Area

Study area covers the Air Sugihan sub-river basin having a total area of $\pm 303,402,358$ ha (Fig 1). It is located between 2 (two) regencies, namely the Banyuasin and the Ogan Komering Ilir regencies. The majority of Air Sugihan sub-river basin is a lowland with a slope of about 0 to 2%. Note that the estuary of the Sugihan River is located in the open sea, therefore it gets an influence of tidal variability from the Bangka Strait.



Fig. 1. The study area in the Air Sugihan Sub-River Basin bounded by yellow line with total area of $\pm 303,402,358$ ha.

Data

This study used precipitation data recorded by rain gauge at Kenten station managed by the National Agency of Meteorologi, Climatology and

Geophysics (BMKG). In addition, the Tropical Precipitation Measurement Mission (TRMM) data were also used in this study [6]. We also used precipitation data observed by rain gauge located at the Sultan Mahmud Badaruddin II Airport Palembang. In order to evaluate the tidal effect, we also utilized the hourly tidal data recorded by a tide gauges located at the Tanjung Buyut station, Musi River for a period of 1 October – 1 November 2016, and at the Sugihan River a period of 2 - 22 October 2016.

In addition, the assimilation data with resolution of $0.25^\circ \times 0.25^\circ$ was used in this study, covering the area of the Air Sugihan sub-river basin for a period of January 2001 to December 2013. The data was derived from the Global Land Data Assimilation System (GLDAS) provided by the National Aeronautics and Space Administration (NASA). The data were based on an assimilation of the satellite- and ground-based observational data products, using advanced land surface modeling and data assimilation techniques [7]. This study used monthly products, which were generated by temporal averaging of the 3-hourly products. List of the GLDAS data used in this study are presented in Table 1.

Table 1 List of parameter from GLDAS products used in the present study

No	Parameter	Unit
1	Surface net radiation	W m^{-2}
2	Shortwave radiation	W m^{-2}
3	Longwave radiation	W m^{-2}
4	Heat flux	W m^{-2}
5	Soil heat flux	W m^{-2}
6	Atmospheric pressure	Pa
7	Wind speed	m s^{-1}
8	Surface temperature	K
9	Air temperature	K
10	Surface albedo	%

Methods

The satellite TRMM precipitation data were first evaluated by calculating the correlation between the TRMM precipitation data and the rain gauge data. Following [8], we calculate the correlation coefficient as follow,

$$r = \frac{1}{N-1} \sum_{i=1}^N \frac{(x-\bar{x})(y-\bar{y})}{s_x s_y}, \quad (1)$$

where S_x and S_y are the standard deviation of each variables.

The evapotranspiration in the study area is calculated by [9]:

$$ETP = \frac{R_n - G - H}{\lambda}, \quad (2)$$

where ETP is the evapotranspiration (mm/day), R_n is surface net radiation (W/m^2), G indicates the soil heat flux (W/m^2), H represents the heat flux (W/m^2), and λ is the evaporation of latent heat at the $20^\circ C$ ($2.45 MJ kg^{-1}$).

The surface net radiation is calculated as follow [9]:

$$R_n = (1 - \alpha)RS_{in} + RL_{in} - RL_{out}. \quad (3)$$

Note that the RS_{in} indicates the incoming shortwave radiation (W/m^2), RL_{in} and RL_{out} are the incoming and the outgoing longwave radition (W/m^2), respectively.

Meanwhile, the heat flux is calculated as follow:

$$H = \gamma \frac{900}{T_a + 273} \Phi U_2 (T_s - T_a), \quad (4)$$

where γ is psychrometric constants ($kPa/^\circ C$), U_2 is the wind speed at 2 m above ground (m/s), T_s is the surface temperature ($^\circ C$) and T_a is the air temperature ($^\circ C$). Note that the constant Φ is defined as $0.665 \times 10^{-3} * P$, where P is the atmospheric pressure (kPa).

RESULTS AND DISCUSSION

Hydrological Characteristics

In order to evaluate the precipitation over the Air Sugihan sub-river basin, we first compared monthly precipitation data recorded by rain gauge at Kenten station managed by the BMKG Indonesia with those obtained from the TRMM data for the period of January 2001 – December 2013.

Figure 2 shows scatter plot for comparison of precipitation data obtained from the rain gauge and those from the TRMM. It is shown that the TRMM data are significantly correlated with the rain gauge data with correlation coefficient of $r = 0.82$ (above 95% confidence level). This indicates that the TRMM data is suitable for analysis of the precipitation over the Air Sugihan sub-river basin.

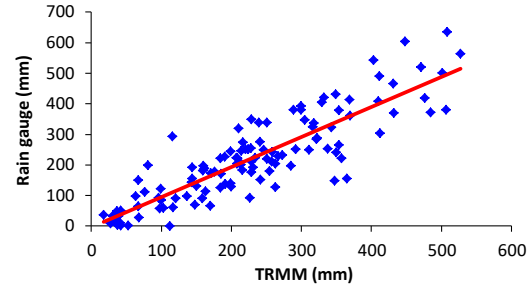


Fig. 2. Scatter plot of correlation between the rain gauge data and the TRMM data for a period of January 2001 – December 2013.

Monthly climatology of the precipitation over the Air Sugihan sub-river basin is presented in Fig 3. It is clearly shown that the monthly climatology of the precipitation has two peaks in March - April and November – December, and one trough in July – August. This result differs from that suggested in previous study in which the precipitation type in this area only has one peak and one trough [10]. This discrepancy could be related to the data period used in their study, which was from January 1961 – December 1993.

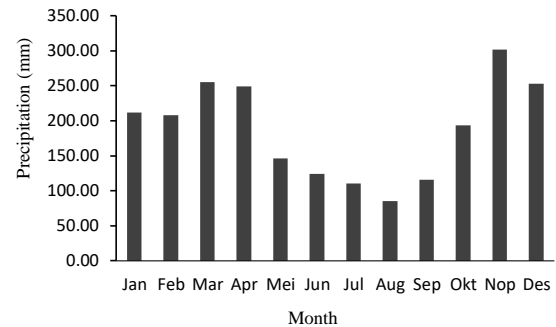


Fig. 3. Monthly climatology of the precipitation over the Air Sugihan sub-rive basin obtained from the TRMM data for a period of January 2001 – December 2013.

Analysis on the tidal data recorded at the Tanjung Buyut station, Musi River and the Sugihan River reveals that the tidal type observed at both stations is the mixed-predominantly diurnal tide with Forzal number of 2.99 and 2.03, respectively (Fig 4). The tides are dominated by three tidal constituents, namely K_1 , O_1 and P_1 with periods of 23.93, 25.82, and 24.07 hour, respectively. Note that the tidal constituent of K_1 defines the soli-lunar constituent, O_1 is the main lunar constituent, and K_1 represents the main solar constituent.

The magnitudes of tidal constituents at the Tanjung Buyut station are $K_1 = 1.46$ m, $O_1 = 0.52$ m, and $P_1 = 0.64$ m. Meanwhile, the magnitudes of tidal constituents at the Sugihan River are $K_1 = 0.18$ m, $O_1 = 0.21$ m and $P_1 = 0.07$ m.

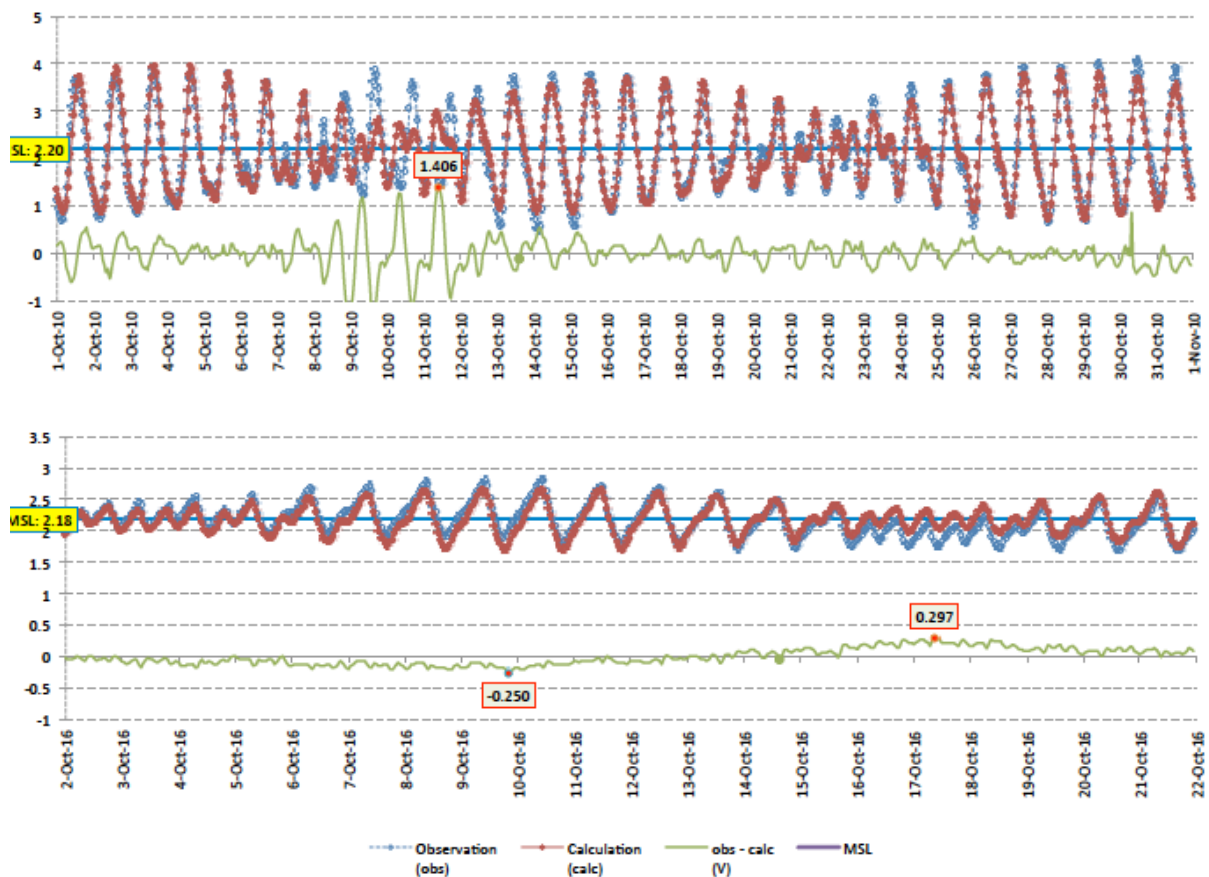


Fig. 4. Time series of water level at (a) Tanjung Buyut (b) Sugihan River stations

Water Balance

Table 1 shows the data for water balance calculation in the Air Sugihan sub-river basin. The calculation indicates that study area experiences an

annual net surplus of about 0.1 mm/month or equal to 302,468.81 m³/month. The average total runoff is 87.7 mm/month or equal to 102.67 m³/s.

Table 1. Data for the water balance analysis in the Air Sugihan sub-river basin

Parameter	Jan	Feb	Mar	Apr	May	Jun	Jul	Aug	Sep	Oct	Nov	Dec	Ave.
Precipitation (mm)	211.6	208.0	255.6	249.4	145.9	124.2	110.5	85.3	116.1	193.8	301.9	252.8	187.9
Surface Temperature (°C)	26.0	26.3	26.6	26.9	27.2	26.8	26.3	26.6	26.9	27.3	26.9	26.2	26.7
Evapotranspiration (mm)	93.1	101.3	108.3	109.5	104.5	100.7	97.9	102.9	97.9	95.9	97.1	92.3	100.1
Wind magnitude (m/s)	1.7	1.7	1.3	1.1	1.4	1.5	1.7	1.9	1.9	1.5	1.1	1.4	1.5
Surface Runoff (mm)	7.4	6.2	6.8	6.2	2.2	2.8	1.6	1.2	2.2	4.6	17.2	7.9	5.5
Sub Surface Runoff (mm)	113.6	100.1	131.6	137.8	83.7	46.7	27.9	23.3	25.5	46.5	101.9	147.9	82.2
Total Runoff (mm)	120.8	106.3	138.4	143.9	85.9	49.5	29.5	24.5	27.7	51.1	119.0	155.9	87.7

Based on the field survey, it is found that the water debit in the estuary of the Sugihan River is about 200 – 300 m³/s. Meanwhile, based on the water balance analysis, it is obtained that the water debit in the upper stream of the Sugihan River is

about 102.67 m³/s. Therefore, we may suggest that the Sugihan River receives additional water flush from the Musi River. In other words, it may conclude that the water level in the Musi River is higher than that in the Sugihan River.

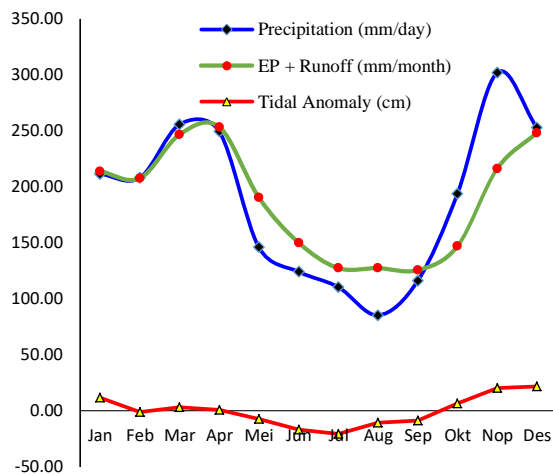


Fig. 5. Monthly water balance at the Air Sugihan sub-river basin together with tidal anomaly at Tanjung Buyut station, Musi River.

Figure 5 shows the monthly water balance in the Air Sugihan sub-river basin, together with the monthly tidal anomaly observed in the Tanjung Buyut station, Musi River. It is shown that the dry season (*low precipitation*) occurs in August, while wet season occurs twice a year; March – April and November – December. By combining the precipitation data and the evapotranspiration as well as the total runoff data, we found that the deficit period is started in April until September.

Based on the water balance analysis, it is found that monthly water storage in the Air Sugihan sub-river basin is about 0.1 mm/month. It means that most the precipitation becomes surface runoff and only about 0.05% of the daily precipitation is storing in the area. Main factor affecting this runoff is land use. Fig 1 shows that most the area in the Air Sugihan sub-river basin are rice fields, shrubs and swamp, which are covered by less vegetation.

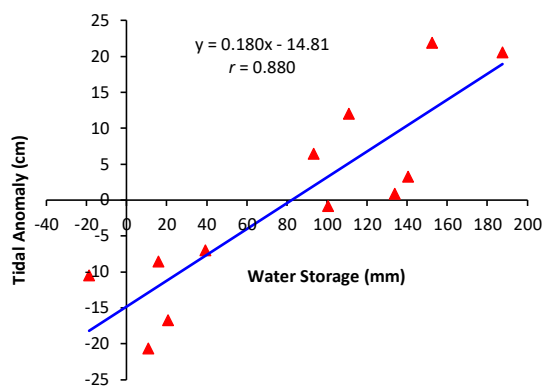


Fig. 6. Scatter plot of correlation between the water storage in the Air Sugihan sub-river basin and tidal data recorded at the Tanjung Buyut station.

In addition, the Air Sugihan sub-river basin is located in the tidal peat swap and near the coast. Therefore, tidal effects may also modulate the water balance in the area. Fig 6 reveals that the water storage in the Air Sugihan sub-river basin is highly correlated with the tidal with correlation coefficient of $r = 0.88$ (without subsurface runoff calculation) and $r=0.70$ if subsurface runoff calculated.

CONCLUSION

Hydrological characteristic and water balance in the Air Sugihan sub-river basin is analyzed by using combined direct observation data, satellite remote sensing data and reanalysis data.

The analysis shows that the Air Sugihan sub river-basin experiences rainy season twice a year in March - April and November – December, and one dry season in July – August. Meanwhile, the tidal analysis reveals that the Air Sugihan sub-river basin is dominated by the mixed-predominantly diurnal tide with Forzal number of 2.03. The magnitudes of tidal constituents at the Sugihan River are $K_1 = 0.18$ m, $O_1 = 0.21$ m and $P_1 = 0.07$ m.

The water balance analysis in the Air Sugihan sub-river basin shows that the area experiences an annual net surplus of about 0.1 mm/month or equal to 302,468.81 m³/month. The average total runoff is 87.7 mm/month or equal to 102.67 m³/s. In addition, the area has monthly water storage is about 0.1 mm/month. Most of the precipitation becomes surface runoff and only about 0.05% of the daily precipitation is storing in the area.

ACKNOWLEDGEMENTS

This study is supported by the University of Sriwijaya through the *Hibah Unggulan Profesi* 2018 for the last author (Number: 0006/UN9/SK.LP2M.PT/2018). Part of this study is supported by the PT. OKI Pulp and Paper Mills.

REFERENCES

- [1] Asdak, C., Hidrologi dan Pengelolaan Daerah Aliran Sungai. 2007, Gadjah Mada University Press, Yogyakarta
- [2] Muchtar A. and Abdullah N., Analisis Faktor-Faktor yang Mempengaruhi Debit Sungai Mamasa, Jurnal Hutan dan Masyarakat, Vol. 2(1), 2008, pp. 174-187.
- [3] Benyamin Lakitan and Nuni Gofar, Kebijakan Inovasi Teknologi untuk Pengelolaan Lahan Suboptimal Berkelanjutan, Prosiding Seminar Nasional Lahan Suboptimal “Intensifikasi Pengelolaan Lahan Suboptimal dalam Rangka Mendukung Kemandirian Pangan Nasional, 2013, ISBN 979-587-501-9
- [4] Armanto, M.E., S.M. Bernas and R.H. Susanto.

- 2010, Land Evaluation as a Basic for Directing of Landuse to Support an Increase of Cropping Index in Reclaimed Tidal Land Area. The First Year of 2010, Final Research Report of Competitive National Strategy Research Grant. DIKTI, National Education Ministry of Indonesia, Jakarta, 2010.
- [5] Naik Sinukaban, Potensi dan Strategi Pemanfaatan Lahan Kering dan Kering Masam untuk Pembangunan Pertanian Berkelanjutan, Kebijakan Inovasi Teknologi untuk Pengelolaan Lahan Suboptimal Berkelanjutan, Prosiding Seminar Nasional Lahan Suboptimal “Intensifikasi Pengelolaan Lahan Suboptimal dalam Rangka Mendukung Kemandirian Pangan Nasional. ISBN 979-587-501-9, 2013.
- [6] Xianwu Xue, Yang Hong, Ashutosh S. Limaye, Jonathan J. Gourley, George J. Huffman, Sadiq Ibrahim Khan, Chhimi Dorji, Sheng Chen, Statistical and hydrological evaluation of TRMM-based Multi-satellite Precipitation Analysis over the Wangchu Basin of Bhutan: Are the latest satellite precipitation products 3B42V7 ready for use in ungauged basins?. *Journal of Hydrology*. 2013, 499 (2013) 91–99.
- [7] Rodell, M., et al., The Global Land Data Assimilation System, *Bull. Am. Meteorol. Soc.*, 85, 381–394.
- [8] Emery, W. J. and Thomson, R. E.: *Data Analysis Methods in Physical Oceanography*. Second Edi. New York: Elsevier B.V, 2004.
- [9] Narasimhan, B., R. Srinivasan, J.G. Arnold, and M. Di Luzio, Estimation of Long-Term Soil Moisture Using a Distributed Parameter Hydrologic Model and Verification Using Remotely Sensed Data. *Transactions of Agricultural Engineers*, 2005, 48(3):1101-1113.
- [10] Aldrian, E. and R. D. Susanto, Identification of Three Dominant Rainfall Regions within Indonesia and Their Relationship to Sea Surface Temperature, *J. Int. Climatology*, 2013, 23, 1435 – 1452.

CONCENTRATIONS OF METAL(LOID)S IN OUTDOOR AND INDOOR DUST FROM RUSSIAN CITY

T.G. Krupnova¹, I.V. Mashkova¹, S.V. Gavrilkina², E.D. Scalev¹ and N.O. Egorov¹

¹Chemistry Department, South Ural State University, Russia

²Ilmen State Reserve UrB RAS, Miass, Russia

ABSTRACT

The metal(loid)s content in the environment is one of the important issues in the environmental management. The metal(loid)s may be present in the both from natural like natural components of the Earth's crust and anthropogenic sources as human activity affects. Some metal(loid)s are toxic and dangerous for environment. We have chosen for researching typical industrial Russian city, Chelyabinsk. Road dust and household dust were collected to investigate the contamination of metal(loid)s (Cr, Ni, Cu, Zn, As and Pb) in outdoor and indoor urban. A total 32 road dust and 17 household dust samples were collected in the urban area during August 2017. The concentrations of metal(loid)s in the dust samples were determined using Analyst 400 (Perkin-Elmer) atomic absorption spectrometer with a flame atomization mode. The average content of Zn was the highest in road dust. The average contents of As and Ni were the highest in household dust. Cu, Pb, Zn and Cr contamination were significantly elevated in outdoor and indoor dust.

Keywords: Metal(loid)s, Road dust, Household dust, Urban Area

INTRODUCTION

Dust is a common urban air pollutant. It plays an important role on human health. One of the most dangerous components of urban dust is heavy metals and metal(loid)s. There are a lot of research dealing with contents of metal(loid)s in the street and household floor dusts [1]-[5].

The exposure to inhalable airborne particulate matter in the size range $<10\ \mu\text{m}$ (PM_{10}) and $<2\ \mu\text{m}$ ($\text{PM}_{2.5}$) emissions from roads is implicated as detrimental to human health [1], [6], [7]. Especially household dust is dangerous and associated with increased risk of respiratory illnesses [8] because It is reported that people have more than 70% of the day time stay at indoor environment [9], [10].

Road dust is generated by many different sources and activities such as public transportation emission [11]-[13], industrial emission [13], [14], surface particles erosion of buildings and roads [14] and other human activities [14], [15]. It is known that the large number of PM_{10} is mechanically generated by studded tyres and traction material during cold winter in regions as Russia, Nordic countries, northern part of USA, Canada [16].

Also metal(loid)s can transfer from the outdoor to the indoor by the soil or dust that stick to footwear [17] and by outdoor air drift in house [18]. The concentrations of metal(loid)s in house dust depends on the chemical composition of the soil and outdoor

dust [17], the height of the building, the frequency and time of windows opened [19], the number of residents and pets in house, smoking, sweeping frequency, the use of air conditioning and rubber carpet products, paint and cooking frequency [19], [20].

There is no study of metal(loid)s content in indoor dust and limited studies [21] of outdoors urban dust in Russia during recent years.

The aim of this work was to investigate contamination and distribution of metal(loid)s in outdoor and indoor dust collected from the Chelyabinsk urban area.

METHODS

Study area

Chelyabinsk is industrial Russian city. It is located at the geographic coordinates of 55°N and 61°E (Fig. 1). The main sources of pollution in Chelyabinsk are equally industry and transport [22]. The population of Chelyabinsk is 1 199 thousand people [23] with more than 390 thousand registered motor vehicles [24].

Sampling was carried out in August 2017. A total of 17 indoor dust samples were collected from urban area (12 residential and 5 office). Also we collected 32 outdoor dust samples.

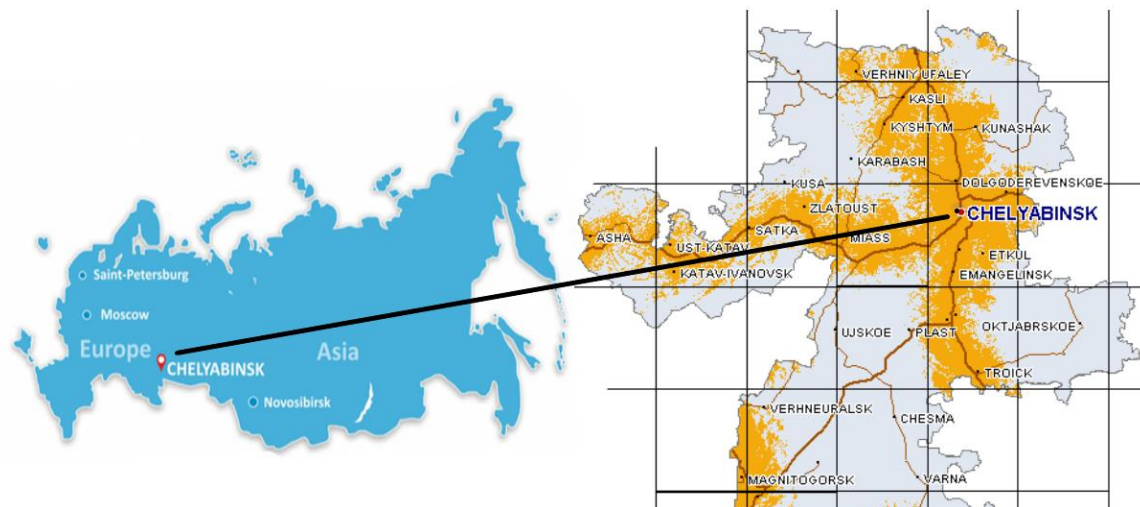


Fig. 1 Study area.

Figure 2 shows the location of sampling sites in the study area.

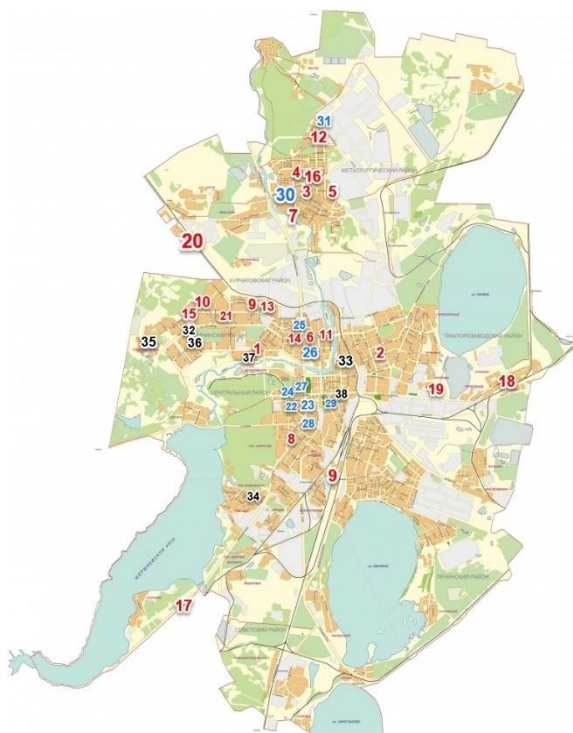


Fig. 2 The locations of sampling sites. Red, blue and black numbers are sampling sites of indoor dust, both indoor and outdoor dust, and outdoor dust, respectively.

Sampling

At the sampling sites, about 500 g of road dust sample was collected by sweeping using soft touch brush and plastic dust pan. A minimum of three

samples were collected from each sites in August 2017. The road dust samples were stored in self sealed polyethylene bags and carefully labeled. The samples were carefully air-dried in the laboratory for fo1 week and sieved through a 250 μm mesh nylon sieve to remove debris. The samples were then ground using a pulveriser and sieved through 100 μm nylon mesh sieve.

Indoor dust samples were obtained from vacuum cleaner bags in regular use of participating students-volunteers for the purpose of cleaning homes or offices. The volunteers were asked to answer some questions about the general condition of the sampling location. The data covered the following information: age of building, floor cover, smoking, number of occupants, floor level, cleaning frequency, air conditioning, walls, roof and floor cover, the time for last paint, cooking fuel, cooking frequency, and pet.

For the whole residential/office area and to facilitate, we used indoor dust sampling method described by Kurt-Karakus [19]. We collected the vacuum cleaner bag dust containments of the respective homes/office. The bags from the homes/offices of volunteers dismantled, placed in a resealable bag, labeled and returned to the laboratory. In case of use of bagless vacuum cleaners, the content of the dust compartment of the vacuum cleaner was emptied into a plastic bag, sealed, labeled and returned to the laboratory. The dust samples were placed in a desiccator for 24 h, sieved through a 100-mesh polystyrene sieve and then oven dried at 105 $^{\circ}\text{C}$ for 24 h.

All outdoor and indoor dust samples were taken to the laboratories of the South-Ural Common Use Center of the Ilmen State Reserve UrB RAS for elemental analysis. Consequently, all concentrations reported in the current study are on a dry weight (dw) basis.

Table 1 The concentrations of metal(loid)s in outdoor (n=32) and indoor (n=17) dust from Chelyabinsk urban area ($\text{mg}\cdot\text{kg}^{-1}$ dw). Different letters indicate significant differences among the species according to Mann–Whitney test ($p<0.05$)

Metal(loid)	As		Ni		Cu		Pb		Zn		Cr	
Outdoor (Out)/ Indoor (In)	Out	In	Out	In	Out	In	Out	In	Out	In	Out	In
Mean	2.5a	7.1b	26a	34b	32a	29a	86a	129a	888a	956a	53a	44a
S (Dis)	1.6	3.2	11	11	8	10	51	137	608	529	22	15
Min	0.9	3.9	15.0	21.0	23.0	15.0	30	27	200	330	25	28
Max	5.6	15.9	65.0	57.0	45.0	45.0	250	520	2200	2240	89	71

Table 2 Mean national standard, natural geochemical background concentrations and global concentrations of metal(loid)s in soil, indoor and outdoor dust ($\text{mg}\cdot\text{kg}^{-1}$ dw). n.a.: didn't report

Location	Type of dust/soil	As	Ni	Cu	Pb	Zn	Cr	Ref.
Russian National Standard	soil	2	4	3	32	23	6(III)/0.05(VI)	[25]
Chelyabinsk region	soil	n.a.	34.2	21.6	12.88	78.9	n.a.	[26]
Chengdu, China	indoor dust	n.a.	52.6	161	123	675	82.7	[20]
Istanbul, Turkey	indoor	n.a.	282	200	30	984	89	[19]
Guangzhou, China	outdoor	20	41	192	387	1777	176	[27]
Jeddah, Saudi Arabia	outdoor	21.55	51.29	139.11	140.73	487.5	65.43	[28]

Sample analysis

Dust samples were microwave digested with 65% HNO_3 acid. After digestion, extracts were filtered through a 0.45- μm Millipore filter and diluted to a volume of 25 ml with Mili-Q water. The filtered supernatant was analysed for metal(loid)s determination (Cr, Ni, Cu, Zn, As and Pb) using Atomic Absorption Spectrophotometer (Perkin Elmer AAS Analyst 400).

QA/QC

All of the samples were tested in triplicate. Analytical blank and reference materials were included in every sequence. Certified reference material GSO 10413-2014 CO of structure (agrochemical indicators) of the soil of cespitose and podsolic srednesuglinisty (SADPP-10) was obtained from I BEND Rosselkhozakademiya's VNIIA (Russia) The recoveries for metal(loid)s ranged from 90% to 110% (Cr, Ni, Cu, Zn, As and Pb).

The limits of quantification (LOQs) were calculated from the lowest concentration of the calibration curve. The LOQ of metal(loid)s analyzed in samples was $0.1 \text{ mg}\cdot\text{kg}^{-1}$

Statistical analysis

Microsoft Excel 2013 and SPSS 24.0 software

were used to organize and analyze the data. The Kolmogorov–Smirnov test was used to test data normality. Non-normal distributions of concentration ($\text{mg}\cdot\text{kg}^{-1}$ dw) data were assumed for all heavy metals in both sampling environment.

In the case of presence of only two groups, the procedure reduces to the Mann–Whitney test, the nonparametric analog of the two-sample t-test to compare the means of two groups.

The relationship between the data was determined using the Spearman rank-order correlation coefficient.

RESULTS AND DISCUSSION

Metal(loid)s in outdoor and indoor dust

The concentrations ($\text{mg}\cdot\text{kg}^{-1}$ dw) of metal(loid)s (Cr, Ni, Cu, Zn, As and Pb) on a dry weight basis in outdoor and indoor dusts from Chelyabinsk were showed in Table 1. Zn showed the highest concentration ($888\pm 608 \text{ mg}\cdot\text{kg}^{-1}$) and ($956\pm 529 \text{ mg}\cdot\text{kg}^{-1}$) in outdoor and indoor dust, respectively. The concentrations of As were the lowest ($2.5\pm 1.6 \text{ mg}\cdot\text{kg}^{-1}$) and ($7.1\pm 3.2 \text{ mg}\cdot\text{kg}^{-1}$) in outdoor and indoor dust, respectively.

The concentrations of metal(loid)s in outdoor dust may be arranged in the following order: $\text{As} < \text{Ni} < \text{Cu} < \text{Cr} < \text{Pb} < \text{Zn}$. While in indoor dust the ratio between the elements was $\text{As} < \text{Cu} < \text{Ni} < \text{Cr} < \text{Pb} < \text{Zn}$.

Table 3 Correlation coefficients for outdoor dust samples

	As	Ni	Cu	Pb	Zn	Cr
As	1	0.42*	0.42**	0.51**	0.35*	0.10
Ni		1	0.39*	0.47**	0.32	0.16
Cu			1	0.67**	0.62**	0.27
Pb				1	0.50**	0.27
Zn					1	0.03
Cr						1

** Correlation is significant at the 0.01 level (2-tailed).

* Correlation is significant at the 0.05 level (2-tailed).

Table 4 Correlation coefficients for indoor dust samples

	As	Ni	Cu	Pb	Zn	Cr
As	1	-0.189	0.717**	-0.079	-0.198	0.462*
Ni		1	0.112	-0.024	0.027	-0.020
Cu			1	-0.09	-0.106	0.564**
Pb				1	-0.098	-0.061
Zn					1	-0.063
Cr						1

** Correlation is significant at the 0.01 level (2-tailed).

* Correlation is significant at the 0.05 level (2-tailed).

The average contents of As and Ni were the higher in household dust than in street dust. Mann–Whitney test showed that Cu, Pb, Zn and Cr contamination were significantly elevated in outdoor and indoor dust.

Concentrations of metal(loid)s in dust were much higher than the maximum allowable levels according national standard for soil and natural geochemical background concentrations (Tables 1 and 2).

For overall data set, concentrations of metal(loid)s in analyzed samples were within the mean values reported in literature (Tables 1 and 2) or they showed concentrations lower mean values compared to values reported in literature (Tables 1 and 2).

We observed high correlation between As and Cu, Pb, Ni; Zn and As, Cu, Pb; Pb and Cu, Ni in road dust (Table 3) and Zn, As and Pb in household dust (Table 4). The reason of these facts can be the common source of elements, particularly those metals coming from brake and tire wears [29]. Zn is a common element in motor vehicles, including tires, vehicle brake linings, metallic parts. Cu and Pb also are a part of tire [29]. Ni alloys in cars and yellow paint on roads [30]. The dust is mechanically generated by studded tyres and traction material during cold winter in Russia [16].

The relations between metal(loid)s concentrations and household factors

The information gathered on household factors based on questionnaires showed that 80.95% and 19.05 of the houses were located in the urban and rural areas, respectively (Fig. 3a). And 76.19% and 23.81% of the studied apartments were home and office, respectively (Fig. 3a). Age of buildings was

less than 10, 20, 30, 40, 50 and 60 years in 9.51%, 19.05%, 19.05%, 9.52%, 28.57% and 14.29% of cases, respectively.

And 85.71% of the houses had smokers and 23.81% of the houses had pet (Fig. 3a). Previous studies reported that cooking and smoking may be other contributors to heavy metals in urban household environment [25], [28]. The percentage of fuel types used for cooking was 61.9% and 14.29% for natural gas and electricity, respectively (Fig. 3a). Moreover, people were cooking one, two and three times during the day in 4.76%, 28.57% and 38.10% of cases, respectively, and people were not cooking in 28.57% of the houses (Fig. 3b). 23.81% of the households were facing to a busy traffic street, 33.33% of the homes had conditioner (Fig. 3a), cleaning frequency was 1, 2, 3 and 7 times in a week for 42.86%, 14.29%, 19.05% and 23.81% of the houses (Fig. 3b).

The survey results also showed 4.76%, 38.1%, 33.33%, 14.29% and 9.52% of the houses had parquet, laminate, linoleum, wood and moquette, respectively. 52.38% of houses had wallpaper and those ones were water-emulsion paint, 9.52% of the house walls had MDF panels, and the time for last paint of 9.52% houses was less than 1 year (Fig. 3b). Roof cover was white lime painted, latex painted and suspended ceiling in 47.62%, 23.81% and 28.57% of houses, respectively (Fig. 3b).

The results showed that the smoking was the important factor of heavy metals enriched in household dust, especially for Pb, Zn and AS, and the Spearman's correlation coefficient for smoking - Pb, smoking - Zn and smoking - As was 0.607 ($p < 0.01$), 0.449 ($p < 0.05$) and 0.584 ($p < 0.01$), respectively (Table 4).

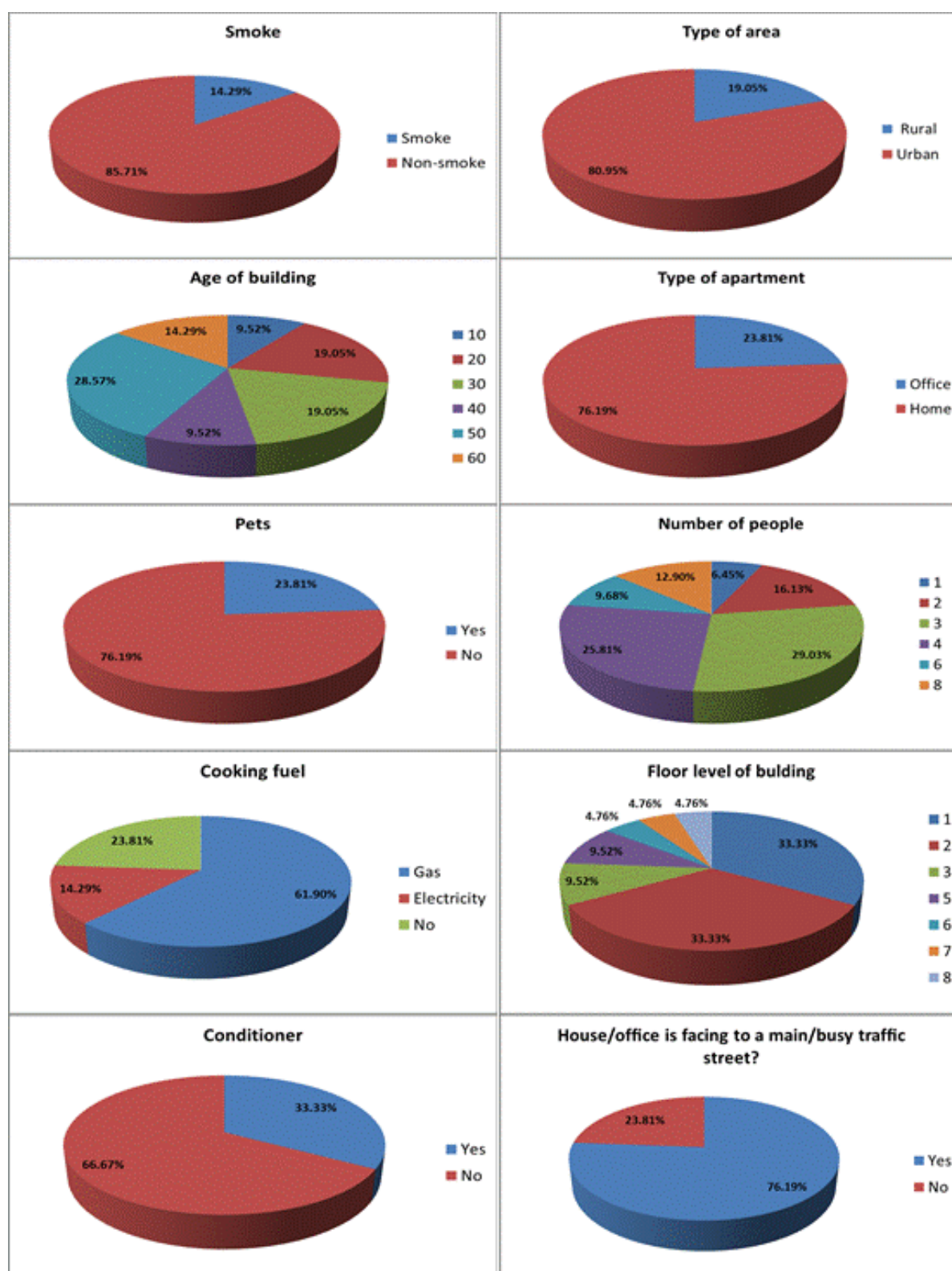


Fig. 3a House factors based on questionnaire results in Chelyabinsk households.

Those results could be explained by the amount of metal(loid)s in cigarette. This result is similar with the previous study [20].

Also, the wall, floor and roof covers had the

important effects on the concentrations of metals in the household dust (Table 5), and the Spearman's correlation analysis showed that As-wall cover, Pb - wall cover and Zn-roof cover were significant

correlation ($p < 0.05$), also As-floor cover, Zn-floor cover, Cu-wall cover and Pb-roof cover were significant correlation ($p < 0.01$) (Table 5). There are some Zn^{2+} and Cu^{2+} in the antibacterial fungicide of different building materials, as well as As and Pb can be part of the paints [3], [19], [20].

Furthermore, the Spearman's correlation coefficient for Zn-the time for last paint and As-age of building were -0.562 ($p < 0.05$) and 0.441 ($p < 0.01$), respectively (Table 5), which could be due to the flaking of paint off the wall. The previous researchers have received similar results [20], [31].

There was significant correlations between As and the cooking fuel ($p < 0.05$). Also Cr-cooking frequency was significant correlation ($p < 0.01$). The previous study showed that the household cooking was one of indoor pollution sources [3].

CONCLUSION

The present study investigated the concentrations of metal(loid)s (Cr, Ni, Cu, Zn, As and Pb) in outdoor and indoor dust from Chelyabinsk, Russia.

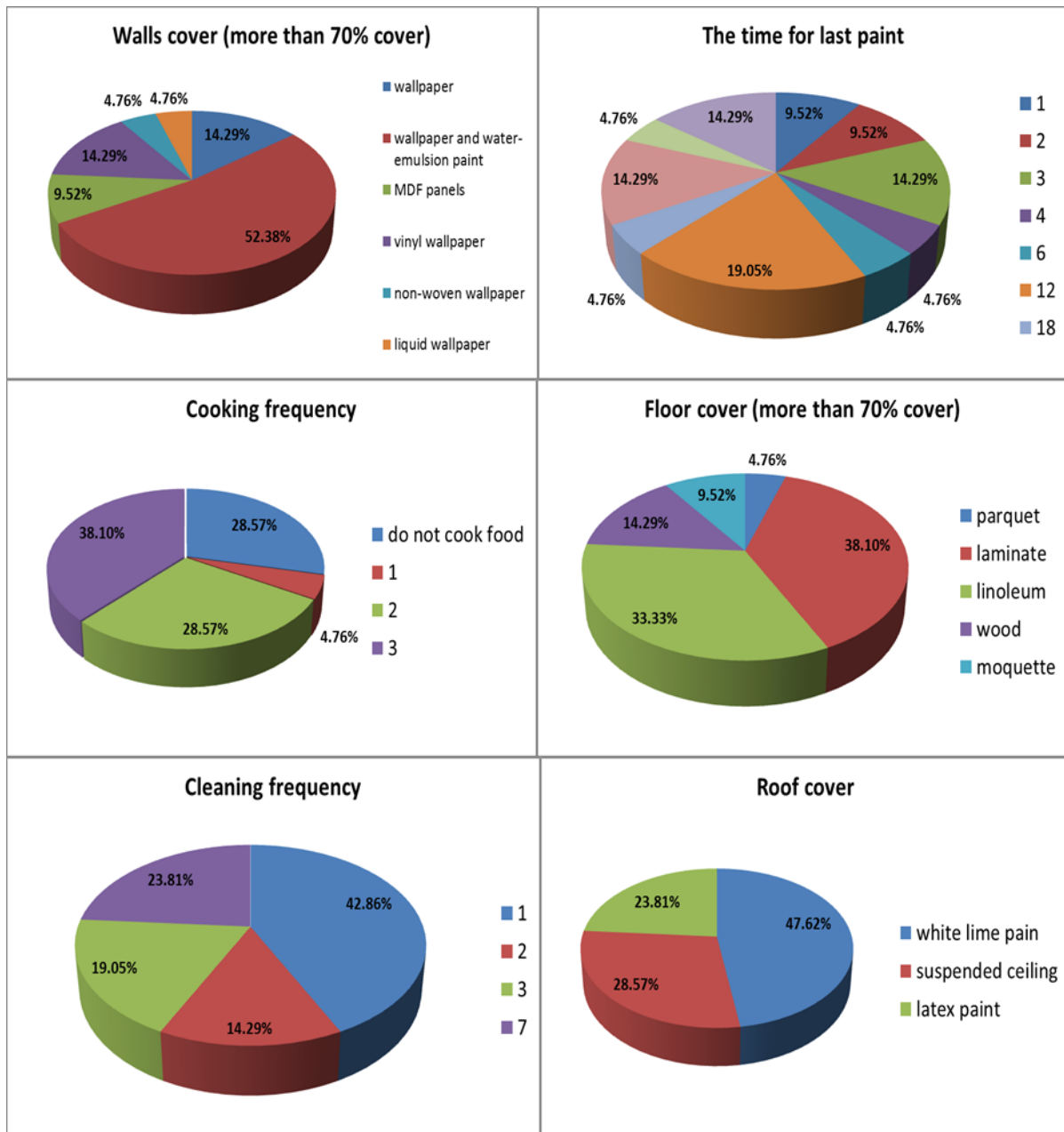


Fig. 3b House factors based on questionnaire results in Chelyabinsk households.

Table 5 The bivariate correlation analysis of metal(loid)s in household dust and the household factors

	As	Ni	Pb	Cr	Cu	Zn
Smoking	0.584**	0.102	0.607**	0.35	-0.35	0.449*
Age of building	0.441*	0.012	0.429	-0.156	0.075	0.29
Number of people	-0.141	0.112	-0.283	-0.023	0.278	-0.278
Pet	-0.452	0.056	-0.258	-0.074	-0.176	-0.48
Cooking fuel	0.463*	-0.084	0.336	-0.087	0.148	0.042
Floor	-0.099	0.3	-0.036	-0.063	0.296	-0.119
House/office is facing to a main/busy traffic street?	-0.055	0.083	0.018	-0.306	0.12	-0.203
Cooking frequency	-0.57	-0.048	-0.431	0.447*	0.272	-0.264
Cleaning frequency	0.361	-0.04	0.126	-0.248	0.134	0.057
Time for last paint	0.066	0.144	-0.191	0.206	-0.235	-0.562**
Conditioner	-0.359	0.126	-0.284	0.017	-0.025	0.002
Wall cover	0.540*	-0.014	0.488*	0.312	-0.164	0.176
Floor cover	0.558**	-0.039	0.393	-0.049	-0.273	0.569**
Roof cover	0.376	-0.026	0.592**	-0.062	0.059	0.476*

** Correlation is significant at the 0.01 level (2-tailed).

* Correlation is significant at the 0.05 level (2-tailed).

The average content of Zn was the highest in road dust. The average contents of As and Ni were the highest in household dust. Cu, Pb, Zn and Cr contamination were significantly elevated in outdoor and indoor dust. Smoking, buildings' age, cooking fuel and frequency, the wall, floor and roof covers were the significant factors leading differences in concentrations of metal(loid)s.

ACKNOWLEDGEMENTS

The work was supported by Act 211 Government of the Russian Federation, contract № 02.A03.21.0011.

REFERENCES

- [1] Huang M., Wanga W., Chan C.Y., Cheunga K.C., Mana Y.B., Wang X. and Wong M.H., Contamination and risk assessment (based on bioaccessibility via ingestion and inhalation) of metal(loid)s in outdoor and indoor particles from urban centers of Guangzhou, China, *Science of the Total Environment*, Vol. 479–480, 2014, pp. 117-124.
- [2] Al-Khashman O., Heavy metal distribution in dust, street dust and soils from the work place in Karak Industrial Estate, Jordan. *Atmos. Environ.*, Vol. 38, 2004, pp. 6803-6812.
- [3] Chattopadhyay G., Lin K.C.P. and Feitz A.J., Household dust metal levels in the Sydney metropolitan area. *Environ. Res.*, Vol. 93, 2003, pp. 301-307.
- [4] Hassan S., Metal concentrations and distribution in the household, stairs and entrywaydust of some Egyptian homes, *Atmos. Environ.*, Vol. 54, 2012, pp. 207-215.
- [5] Atiemo M.S., Ofosu G. F., Kuranchie-Mensah H., Tutu A.O., Palm N.D.M.L. and Blankson S.A., Contamination Assessment of Heavy Metals in Road Dust from Selected Roads in Accra, Ghana, *Research Journal of Environmental and Earth Sciences*, Vol. 3, Issue 5, 2011, pp. 473-480.
- [6] Phetrawech T and Thepanondh S., Evaluation of resuspension of road dust in a cement industrial complex area, *International Journal of GEOMATE*, Vol.12, Issue 33, 2017, pp. 96-103.
- [7] Apeagyei E., Bank M.S. and Spengler J.D., Distribution of heavy metals in road dust along an urban-rural gradient in Massachusetts, *Atmospheric Environment*, Vol. 45, 2011, pp. 2310-2323.
- [8] Butte W. and Heinzow B., Pollutants in house dust as indicators of indoor contamination. *Rev. Environ. Contam. Toxicol.*, Vol. 172-175, 2001, pp. 1-46.
- [9] Maertens R.M., Bailey J., White P.A., The mutagenic hazards of settled house dust: a review. *Mutat. Res. Rev. Mutat. Res.*, Vol. 567, 2004, pp. 401-425.
- [10] US EPA, Exposure factors handbook. National Center for Environmental Assessment. Office of Research and Development, Washington, D.C., 1997.
- [11] Amato F., Alastuey A., de la Rosa J., Gonzalez Castanedo Y., Sánchez de la Campa A.M.,

- Pandolfi M., Lozano A., Contreras González J., and Querol X., Trends of road dust emissions contributions on ambient air particulate levels at rural, urban and industrial sites in southern Spain, *Atmos. Chem. Phys.*, Vol. 14, 2014, pp. 3533-3544.
- [12] Denier van der Gon H., Gerlofs-Nijland, M E., Gehrig R., Gustafsson M., Janssen N., Harrison R.M., Hulskott J., Johansson C., Jozwicka M., Keuken M., Krijgsheld K., Ntziachristos L., Riediker M., and Cassee F.R., The Policy Relevance of Wear Emissions from Road Transport, Now and in the Future, An International Workshop Report and Consensus Statement, *J. Air. Waste Manage.*, Vol. 63, 2013, pp. 136-149.
- [13] Zibret G., Van Tonder D. and Zibret L., Metal content in street dust as a reflection of atmospheric dust emissions from coal power plants, metal smelters, and traffic, *Environ. Sci. Pollut. Res. Int.*, Vol. 20, Issue 7, 2013, pp. 4455-4468.
- [14] Kuang C.I., Neumann T., Norra S. and Stüben D., Land use-related chemical composition of street sediments in Beijing, *Environ. Sci. Pollut. Res. Int.*, Vol. 11, Issue 2, 2004, pp. 73-83.
- [15] Morton-Bermea O., Hernández-Álvarez E., González-Hernández G. and Romero F., Assessment of heavy metal pollution in urban topsoils from the metropolitan area of Mexico City, *J. Geochem. Explor.*, Vol. 101, 2008, pp. 218-224.
- [16] Gustafsson M., Blomqvist G., Gudmundsson A., Dahl A., Swietlicki E., Bohgard M., Lindbom J. and Ljungman A., Properties and toxicological effects of particles from the interaction between tyres, road pavement and winter traction material, *Sci. Total Environ.*, Vol. 393, 2008, pp. 226-240.
- [17] Hunt A., Johnson D.L. and Griffith D.A., Mass transfer of soil indoors by track-in on footwear. *Sci. Total Environ.* Vol. 370, 2006, pp. 360-371.
- [18] Thatcher T.L., Layton D.W. and Deposition, resuspension, and penetration of particles with in a residence. *Atmos. Environ.* Vol. 29, 1997, pp. 1487-1497.
- [19] Kurt-Karakus P.B., Determination of heavy metals in indoor dust from Istanbul, Turkey: estimation of the health risk, *Environ. Int.* Vol. 50, 2012, pp. 47-55.
- [20] Cheng Z., Chen L.-J., Li H.-H., Lin Z.-B., Yang Y.-X., Xu X.-X., Xian J.-R., Shao J.-R. and Zhu X.-M., Characteristics and health risk assessment of heavy metals exposure via household dust from urban area in Chengdu, China, *Sci. Total Environ.*, Vol. 619-620, 2018, pp. 621-629.
- [21] Kaygorodov R.V., Tiunova M.I. and Druzshinina A.A., Polluting substances in a dust of travellers of parts and in wood vegetation of roadside strips of a city zone, *Bulletin of Perm. University*, 2009, Vol 10, Issue 36, pp. 141-146. (Rus).
- [22] Bityukova V.R. and Kasimov N.S., Atmospheric pollution of Russia's cities: Assessment of emissions and immissions based on statistical data *GEOFIZIKA*, Vol. 29, Issue 1, 2012, pp. 53-67.
- [23] Russian State Statistics Service of Chelyabinsk region, The report, the population of the Chelyabinsk region in General, and cities with a permanent population of 100 thousand or more by sex and age on 1 January 2017, 2017. (Rus).
- [24] Russian State Statistics Service of Chelyabinsk region, Report Transport and communications in Chelyabinsk region, 2017. (Rus).
- [25] GN 2.1.7.2041-06, National Standard Russian Federation. Maximum Permissible Concentration of Chemicals in the Soil. 2006. (Rus)
- [26] Zybalov V.S. and Yudina E.P. Influence of Heavy Metals on Agricultural Soils of Chelyabinsk Region. *Bulletin of the South Ural State University. Ser. Chemistry.* Vol. 8, no. 3, pp. 13-18 (Rus)
- [27] Huang M., Wang W., Chan C.Y., Cheung K.C., Man Y.B., Wang X. and Wong M.H., Contamination and risk assessment (based on bioaccessibility via ingestion and inhalation) of metal(loid)s in outdoor and indoor particles from urban centers of Guangzhou, China. *Sci. Total Environ.*, Vol. 479-480, 2014, pp. 117-124.
- [28] Shabbaj I.I., Alghamdi M.A., Shamy M., Hassan S.K., Alsharif M.M. and Khoder M.I. Risk assessment and implication of human exposure to road dust heavy metals in Jeddah, Saudi Arabia. *Int. J. Environ. Res. Public Health*, Vol. 15, Issue 1, 2018.
- [29] Apeagyei E., Bank M.S. and Spengler J.D., Distribution of heavy metals in road dust along an urban-rural gradient in Massachusetts. *Atmos. Environ.* Vol. 45, Issue 13, 2011, pp. 2310-2323.
- [30] Madany I.M., Akhter M.S. and Jowder O.A.A., The correlations between heavy metals in residential indoor dust and outdoor street dust in Bahrain. *Environ. Int.* Vol. 20, Issue 4, 1994, pp. 483-492.
- [31] Rasmussen P. E., Levesque C., Chénier M., Gardner H.D., Jones-Otazo H. and Petrovic S., Canadian House Dust Study: Population-based concentrations, loads and loading rates of arsenic, cadmium, chromium, copper, nickel, lead, and zinc inside urban homes, *Sci. Total Environ.*, Vol. 443, 2013, pp. 520-529.
- [32] Khan M.N., Nurs C.Z.B., Islam M.M., Islam M.R. and Rahman M.M., Household air pollution from cooking and risk of adverse health and birth outcomes in Bangladesh: a nationwide population-based study, *Environmental Health*, Vol. 16, Issue 1, 2017, p.1.

EFFICIENT REPAIR SCHEDULING STRATEGY OF A MULTIPLE-SOURCE LIFELINE NETWORK USING CONSTRAINED SPANNING FOREST (CSF)

Lessandro Estelito Garciano¹, Agnes Garciano², Mark Tolentino³ and Abraham Matthew Carandang⁴
¹Associate Professor, De la Salle University, Philippines; ²Associate Professor, Ateneo de Manila University, Philippines; ³Assistant Professor, Ateneo de Manila University; ⁴Graduate student, De La Salle University

ABSTRACT

Pre-disaster programs, especially for seismic hazards, are necessary to quickly recover the services of a lifeline network. In the case of a multi-source (or multi-root) water lifeline network, an efficient repair schedule must be implemented immediately after an earthquake to assist in post-disaster activities as well as to minimize the subsequent health problems caused by the lack of potable water supply. As such water lifeline operators must establish restoration strategies especially if the supply of water comes from different sources and spatially distributed. For single-source water network, Horn's algorithm can be used to determine an optimal restoration strategy. However a variation of this algorithm is necessary in order to allow simultaneous repairs at any given time for a multiple-source lifeline water network. In this research, the authors employ a constrained spanning forest (CSF) algorithm to decompose the network into trees rooted at each source. After the decomposition, Horn's algorithm is used to determine the optimal restoration strategy for each tree in the network with the objective of minimizing a penalty value. Restoration of each node in the spanning forest is carried in sequence according to availability of the crew and allows simultaneous jobs to be done on consecutive arcs in the sequence.

Keywords: water lifeline, Horn's Algorithm, CSF

1. INTRODUCTION

Water distribution networks (WDNs) are vulnerable during strong ground motion events such as those experienced during the earthquakes in Kumamoto Japan [1], Christchurch, New Zealand [2] and Surigao Philippines [3]. Since modern society is very much dependent on this important lifeline, quick recovery is essential specifically for health and sanitation reasons and for post-seismic activities. It is also worth noting that a continuing inability to supply water to the affected area leads to the reduction of its habitability.

The estimation or modeling of the risk or damage of WDNs due to natural hazards has been studied extensively [4] – [6]. However literature regarding optimal sequencing of the repair of a WDN after a seismic event [7], [8] are few. In these papers, Horn's algorithm was employed to determine an optimal restoration strategy for a single-source water network. However, if the WDN has multiple-sources a variation of this algorithm is necessary in order to allow simultaneous repairs at any given time.

The aim of this paper is to formulate and solve the problem of managing the repair of a network damaged due to a natural hazard such as an earthquake. The network in consideration is a water pipeline system in a particular region in the Philippines. Here, we use a constrained spanning

forest (CSF) algorithm to decompose the network into trees each of which contains exactly one water source. Assuming simultaneous repair jobs can take place at any given time, the problem of determining which node to be prioritized by the repair teams is solved using Horn's algorithm, which gives the optimal repair sequence.

The notion of a minimal CSF was used in order to extend the Christofides heuristic to a k -depot version of the Travelling Saleman Problem [9]. In their study of a resource allocation algorithm for multi-vehicle (i.e. unmanned aerial vehicles) systems, Rathinam et al. proved that the problem of finding a minimal CSF can be converted into a minimal spanning tree problem by introducing zero-weight edges between vertices that represent the vehicles / depots [10]. After the network has been decomposed into trees, the authors use Horn's algorithm [12] to determine an optimal repair sequencing of the damaged pipeline network.

2. MATHEMATICAL FRAMEWORK

In this study, the formulation requires that the network in consideration be represented as a weighted and connected graph. A graph is a $G = (V, E)$ consists of a set V of vertices or nodes and a set E of edges uv where $u, v \in V$. We say that u and v are *adjacent vertices* in G if $uv \in E$. A graph G is connected if for any two vertices u and v , there is a sequence of consecutively

adjacent vertices from u to v . A weighted graph is one where each edge is assigned a value, called its weight. A graph is called a *tree* if it contains no cycles, and is called a *forest* if it is a union of trees. A rooted tree is a tree where one vertex is designated as a root. The reader is referred to [11] for a more exposition on these terminologies.

In the pipeline network being considered, five water sources were identified. The repair work necessarily involves restoring the links from these sources in order initiate the delivery of water to other nodes. However, a major consideration is that each node x has a specific demand value $V(x)$ and pipes linking two nodes have a given length. An efficient way to determine which community to service first is of utmost importance.

The initial task involves finding a minimal constrained spanning forest (CSF) of the network with roots at the five identified water sources. The following algorithm for determining the minimal CSF is based on an algorithm in [10]. For this study, we assume that the sources are not adjacent; that is, there is no direct edge between any two source vertices.

Algorithm 1 (Prim's Algorithm for Minimal CSF).

1. Introduce a zero-weight edge between any pair of source vertices and denote by G' the resulting graph.
2. Apply Prim's algorithm to find the minimal spanning tree of G' : that is:
 - (a) Initialize a tree with a single vertex, chosen arbitrarily from the graph
 - (b) Grow the tree by one edge; of the edges that connect the tree to vertices not yet in the tree, find the minimum-weight edge, and transfer it to the tree
 - (c) Repeat step (b) until all vertices are in the tree
3. Remove the zero-weight edges from the constructed MST; the outcome is the minimal CSF.

The next task is to determine an optimal repair sequence per tree in the minimal CSF. We also assume that there is a repair crew for tree. Furthermore due to logistical constraints, a repair crew is designated to exactly one tree only. Finally, we assume that water flow from a source and from each node is uni-directional, hence we can assume a precedence relation among the nodes. This means that if x and y are nodes of a tree, then x precedes y (written as xPy) if there is a directed path from x to y .

Algorithm 2 (Horn's Algorithm)

In [12], Horn provided an algorithm which gives an optimal job sequence in a tree-like structure with precedence relations. Given a vertex x in a rooted forest N , let $V(x)$ and $T(x)$ correspond to the value of the restoration job at vertex x and the time to complete the job at node x respectively.

Let $\mathcal{T}[x]$ denote the set of all trees rooted in a vertex x . For $S \in \mathcal{T}[x]$ let

$$V(S) = \sum_{u \in S} V(u) \text{ and } T(S) = \sum_{u \in S} T(u).$$

For any tree rooted in a vertex x , The best ratio at x , denoted by $r(x)$, is defined as

$$r(x) = \max \left\{ \frac{V(S)}{T(S)} : S \in \mathcal{T}[x] \right\} \quad (1)$$

A maximal family tree of x , denoted by F_x is an element of $\mathcal{T}[x]$ for which the best ratio is achieved.

A repair sequence of the forest N is a bijection $\sigma: V \rightarrow \{1, 2, 3, \dots, n\}$ assigning to each vertex $x \in V$, its position number $\sigma(x)$ in the repair sequence. An optimal repair sequence is one in which the value

$$f(\sigma) = \sum_{x \in X} V(x) \left(\sum \{T(y) : \sigma(x) \leq \sigma(y)\} \right)$$

is minimum. This function is called a linear delay penalty function.

Horn asserts that an optimal repair sequence is achieved by a two-step process:

- (i) For each node x , calculate the best ratio $r(x)$ and the maximal family tree F_x .
- (ii) By comparing the best ratios, an optimal repair sequence of the network is determined.

3. WDN MODEL

The WDN network considered in this paper is managed and operated by SMWD or Surigao Metropolitan Water District. The network consists of transmission lines with a total length of 62 kilometers and 150 kilometers of distribution pipelines. At present, it serves 23 out of 33 mainland barangays of Surigao City (Figure 1). According to SMWD, as of August 2017, they supply water to more than 86% of Surigao City's population of 158,865 people. Unfortunately, in February 10, 2017, the city was hit by a 6.7 magnitude earthquake with epicenter located off the coast of Surigao Del Norte. This event compromised the water delivery services to the residents.





Fig.1 WDN model

To assess the vulnerability of the WDN to seismic hazard, the authors employed a probabilistic seismic hazard analysis (PSHA) within the WDN area. Figure 2 shows the results of the PSHA with the corresponding peak ground acceleration contours. The analysis reveals that the main city can experience a peak ground acceleration (pga) from 0.6g to 0.8g.

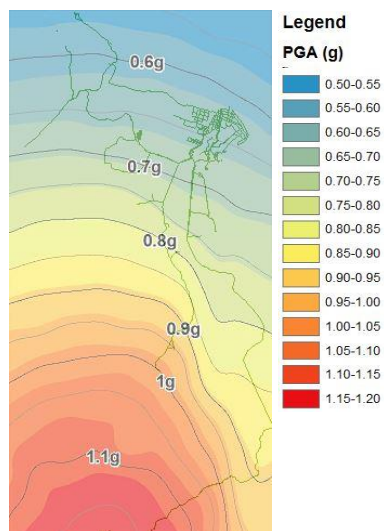


Fig. 2 PSHA pga map of the WDN

Since the range of the pga in the area is relatively high, the WDN is vulnerable to damage during a major seismic event. Thorough analysis of the network show that the pipeline network consists of 416 nodes (junctions) and 415 links (pipes). Table 1 below shows sample nodes i and j with corresponding lengths. The weight of each edge is assumed to be the length of the edge.

Table 1. Link / Length of each pipe

Link	Node i	Node j	Length (m)
448	352	354	1432

564	354	355	425
562	348	347	1531
444	348	349	581

4. DATA AND RESULTS

In the WDN, the nodes represent the water demand in a specific area and the links represent the supply pipes. Each node x has a value $V(x)$ corresponding to the base demand in liters per second. Furthermore we define $T(x)$ to be the time (proportional to the length of the pipe in meters) to supply water to node x . Sample data are given in Table 2.

Table 2. Sample nodes with corresponding values of $V(x)$ and $T(x)$

Node (x)	$V(x)$ (in lps)	$T(x)$ (proportional to length in m)
393	0	5691
360	0.89	313
358	0.081	95

Using Prim's algorithm, a minimal spanning forest for the entire network is obtained with root at junctions 206, 207, 376, 174, and 160. The entire spanning forest consists of 416 nodes and 415 links, removing 127 links from a total of 542 pipes as shown in Figure 3. The minimal spanning forest consists of 5 minimal spanning trees, each corresponding to roots (water supply sources) at junctions 206, 207, 376, 174, and 160, respectively. Due to the huge data, only the schematic overview of the minimal spanning forest and portions of the 5 minimum-weight spanning trees are shown in Figure 4.

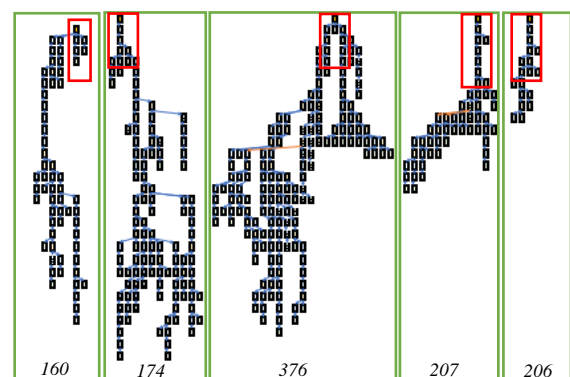


Fig.3 Overview of the minimum spanning forest

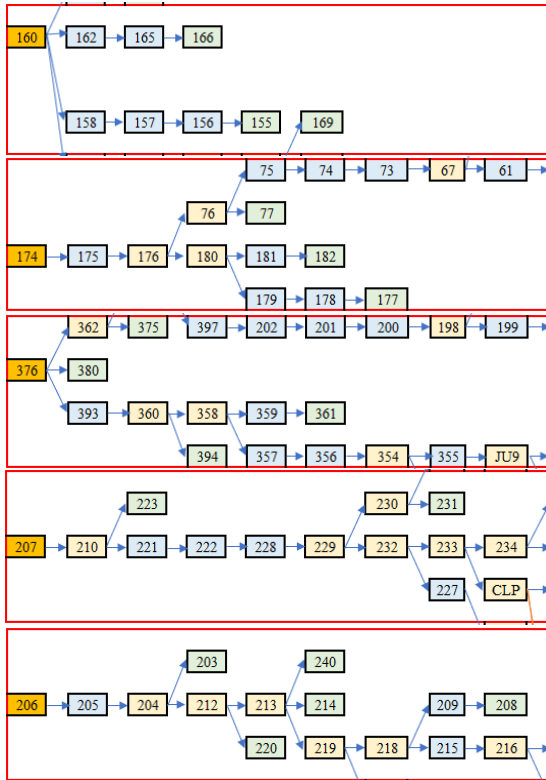


Fig 4. Portions of the minimum weight spanning trees (rooted at nodes 160, 174, 376, 207, and 206)

The spanning trees rooted at 206, 207, 376, 174, and 160 have 18 nodes and 17 links, 53 nodes and 52 links, 167 nodes and 166 links, 116 nodes and 115 links, and 62 nodes and 61 links, respectively.

Applying Horn's algorithm to the rooted trees obtained above yield an optimal repair sequence for the network. The sequencing of repairs of the first 10 nodes of each tree in the network is shown in Table 3. The value of the least penalty functions $[f(\sigma)]$ for the network rooted at 206, 207, 376, 174, and 160 are 5888.94, 33676.48, 2839893.03, 393536.46, and 104829.95, respectively.

Table 3. First 10 restoration jobs in an optimal sequencing for the 5 minimum spanning trees

Root 160			
order $\sigma(x)$	node x	order $\sigma(x)$	node x
1	158	6	162
2	157	7	164
3	156	8	161
4	159	9	163
5	154	10	155
Root 174			
order $\sigma(x)$	node x	order $\sigma(x)$	node x
1	175	6	77
2	176	7	178
3	76	8	177
4	180	9	75

5	179	10	74
Root 376			
order $\sigma(x)$	node x	order $\sigma(x)$	node x
1	393	6	356
2	360	7	354
3	358	8	352
4	359	9	353
5	357	10	348
Root 207			
order $\sigma(x)$	node x	order $\sigma(x)$	node x
1	210	6	232
2	221	7	233
3	222	8	234
4	228	9	235
5	229	10	241
Root 206			
order $\sigma(x)$	node x	order $\sigma(x)$	node x
1	205	6	203
2	204	7	219
3	212	8	218
4	213	9	215
5	214	10	216

Restoration curves

Figures 5 to 9 show the restoration process of the water pipeline of SMWD. These restoration curves are non-decreasing functions [7] and show the repair on a node-to-node basis until the entire network is in full operation.

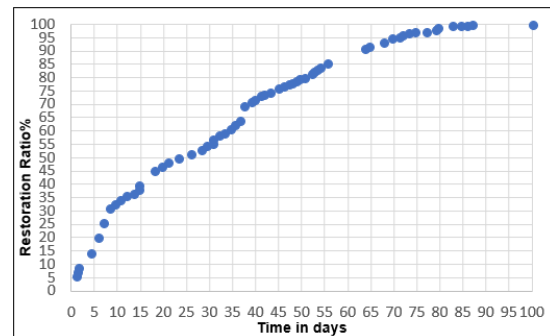


Fig. 5. Restoration Curve (rooted at 160)

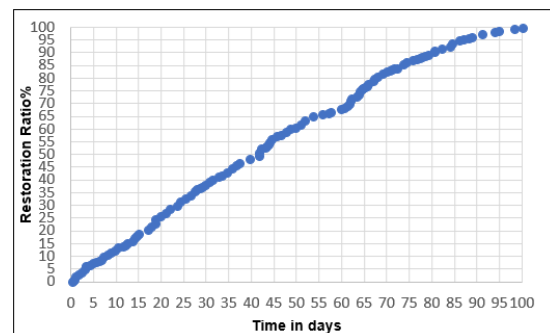


Fig. 6. Restoration Curve (rooted at 174)

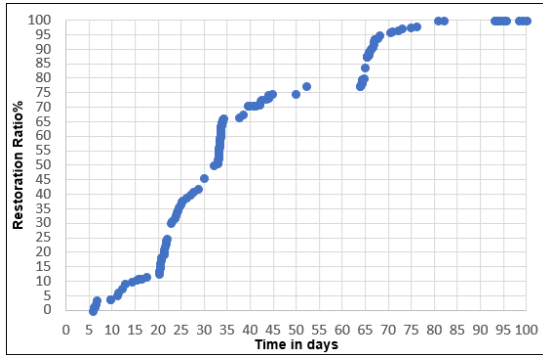


Fig. 7. Restoration Curve (rooted at 376)

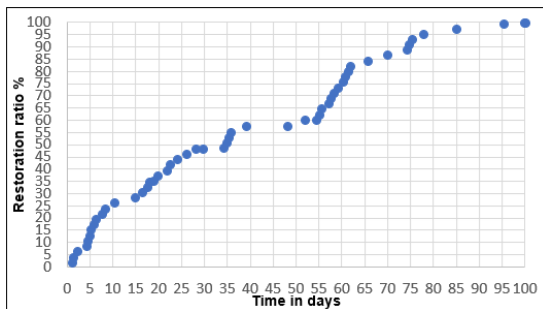


Fig. 8. Restoration Curve (rooted at 207)

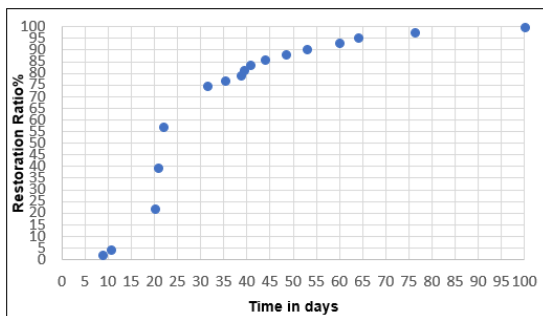


Fig. 9. Restoration Curve (rooted at 206)

6. CONCLUSION

In this paper, the authors employed a variation of Horn's algorithm to allow simultaneous repairs at any given time for a multiple-source lifeline water network. The use of a minimal spanning forest from a network with multiple roots (supply sources) is essential in order to remove redundancy of pipelines and minimize total repair time.

A constrained spanning forest (CSF) algorithm was used to decompose the WDN into trees rooted at each water supply source. After the decomposition, Horn's algorithm is used to determine the optimal restoration strategy for each tree in the network with the objective of minimizing a penalty value. Restoration of each node in the spanning forest is carried in sequence according to availability of the crew and allows simultaneous jobs to be done on consecutive arcs in the sequence.

For future work, the direction of study is to find a framework whereby a repair crew may be assigned to an incomplete restoration job to further reduce repair time and corresponding penalties.

5. ACKNOWLEDGEMENTS

The authors would like to acknowledge the assistance of Metro Surigao Water District (MWSD).

6. REFERENCES

- [1] Nojima, N., and Maruyama, Yoshihisa (2016), Comparison of functional damage and restoration processes of utility lifelines in the 2016 Kumamoto Earthquake, Japan with two great earthquake disasters in 1995 and 2011. *JSCE Journal of Disaster FactSheets*, FS2016-L-0005.
- [2] Milashuk, S. and Crane, W. (2012), Pipeline damage caused by transient ground deformation: Case study of 2010 Darfield and 2011 Christchurch earthquakes. *Soil Dynamics and Earthquake Engineering*, 41, pp. 84-88.
- [3] Jarde, S. L., Garciano, L. E., and Sison (2017), Infrastructure damage during the Feb. 10, 2017 Surigao, Philippines Earthquake. *JSCE Journal of Disaster FactSheets*, FS2017-E-0001.
- [4] Bagriacik, A., Davidson, R., Hughes, M., and Bradley B. (2018), Comparison of statistical and machine learning approaches to modeling earthquake damage to water pipelines, *Soil Dynamics and Earthquake Engineering*, 112, pp. 76-88.
- [5] Porter, K. (2016), Damage and Restoration of Water Supply Systems in an Earthquake Sequence. *ESM 13-01*, Structural Engineering and Structural Mechanics Program, Department of Civil Environmental and Architectural Engineering, University of Colorado Boulder.
- [6] Eskandari, M., Omidvar, B., Modiri, M., Nekooie M. A., and Alesheikh, A. A. (2017), Geospatial analysis of earthquake damage probability of water pipelines due to multi-hazard failure, *ISPRS Int. J. of Geo-Information*, 6(6), 169.
- [7] Nojima N. and Kameda H. (1992), Optimal strategy by use of tree structure for post-earthquake restoration of lifeline network system. Conference proceedings, in Proc. 10th World Conference on Earthquake Engineering, 1992, Balkema, Rotterdam, pp. 5541 - 5546.
- [8] Garciano, A., Garciano, L. E., Tanhueco, R. M., and Abubo, T. J. (2018), Optimal Restoration Strategy of a Water Pipeline Network in Surigao City, Philippines. *International Journal of GEOMATE*, Vol. 14, Issue 42, pp. 25 - 29.

- [9] Xu, Z., Xu, L., Rodrigues, B. (2011). An analysis of the extended Christofides heuristic for the k-depot TSP. *Operations Research Letters*, 39, 218-223.
- [10] S. Rathinam, R. Sengupta, S. Darbha (2007), A resource allocation algorithm for multi-vehicle systems with Nonholonomic constraints, *IEEE Transactions on Automation Science and Engineering* 4 (1) 98 - 104.
- [11] West, D. (2001), *Introduction to Graph Theory*, 2nd Ed., Pearson Education, Inc.
- [12] Horn, W. A. (1972), Single-machine job sequencing with treelike precedence ordering and linear delay penalties, *SIAM, Journal of Applied Mathematics*, 23(2), pp. 189 - 202.

PHYSIO-ECOLOGICAL ACTIVITY OF PHRAGMITES JAPONICA AS A GREEN INFRASTRUCTURE PLANT

Taizo Uchida¹, Teruo Arase², Yohei Sato³ and Daisuke Hayasaka⁴

¹Faculty of Architecture and Civil Engineering, Kyushu Sangyo University, Japan; ²Faculty of Agriculture, Shinshu University, Japan; ³Professor Emeritus, Tokyo University, Japan; ⁴Faculty of Agriculture, Kindai University, Japan

ABSTRACT

Little research has been conducted into physio-ecological characteristics of *Phragmites japonica* Steud., which is often used in green infrastructure along waterfronts, perhaps due to its narrow distribution in the Far East. Thus, the objective of this study is to obtain the information on *P. japonica* for its use in green infrastructure. In this study, allelopathic effects of aqueous extracts (5.0 g L⁻¹) from leaves or stems of six hygrophytes, *Typha latifolia* L., *Phragmites australis* (Cav.) Trin., *Lythrum salicaria* L., *Phalaris arundinacea* L., *Phragmites japonica* Steud. and *Scripus tabernaemontani* Gmel., on the activities of *P. japonica* seed and epigeal stolon were assayed under laboratory conditions, and growth after transplanting was also evaluated. All aqueous extracts from six hygrophytes produced no inhibition on seed germination. The radicle length of the seedlings, however, was inhibited by treatment with aqueous extracts from leaves of *P. australis*, *L. salicaria* and *P. arundinacea* (35.5-57.2% of untreated control). Further, these inhibitory effects on the radicle length of the seedling are likely caused by some kind of allelochemicals, based on the lack of effect with preparations of the aqueous extracts on polymeric absorbent (Amberlite XAD-4 resin). For epigeal stolon activity, no negative effects were observed for aqueous extracts of any of the hygrophytes. Dry weights of the above- and below-ground organs formed from epigeal stolon also reached 7.3 times of those of seedlings after the transplanting.

Keywords: Allelopathy, Aqueous extract, Green infrastructure, Hygrophyte, Polymeric absorbent

INTRODUCTION

Safety and security, convenience, comfort, and aesthetic beauty in cities have been ensured. Over about the last decade, “biodiversity” in cities has been also achieved through management of natural and manmade features, such as ponds, parks, wetlands, rivers, gardens, groves, and masonry revetments [1], [5], [6], [9], [13], [18], [20], [24], [26], [32], [34]. Further, a new keyword, green infrastructure, frequently appears when considering urban design and planning as the “strategic utilization, maintenance, connection and/or creation of natural and semi-natural areas, such as groves, parks, farmlands, ponds and rivers in urban areas as infrastructure features equivalent to roads, bridges and ports that function to mitigate the heat island effect, deterioration in biodiversity and damage due to weather events, such as severe rainstorms” [2], [16], [17], [25].

Many kinds of plant species have been used in green infrastructure projects. Among them, especially *Phragmites australis* (Cav.) Trin. is particularly suitable in green infrastructure projects along waterfronts because it exhibits a wide range of functions, such as filtering nutrients and sediments of water (purification), binding soils (erosion control), and offering habitats for wild animal communities,

fish, birds, and mammals [8], [10], [11], [19], [21], [30].

Phragmites (Poaceae) includes several species including the aforementioned *P. australis*. In Japan, *Phragmites japonica* Steud. along with *P. australis*, is a frequently used plant material in green infrastructure projects along waterfronts. Compared to *P. australis*, which is used along relatively stable waterfronts, *P. japonica* has been used in more unstable areas such as along rivers owing to its high tolerance to flood (disturbance); it can regrow rapidly after disturbance by elongating the epigeal stolons, which are also known as runners (Photo 1) and which attain lengths of 3-4 m or more and form clonal shoots at each node, by which its territory is expanded [22].

Although *P. australis* is a cosmopolitan species with a long and extensive body of research into its ecological, morphological and cytogenetical properties [3], [4], [7], [8], [10], [11], [19], [21], [23], [30], little research has been conducted on *P. japonica*, likely due to its restricted distribution in Japan, Korea, China and Ussuri [12].

In this study, the objective is to collect physio-ecological information on *P. japonica* relevant to its use in green infrastructure. Here, the allelopathic effects of aqueous extracts from leaves or stems of six hygrophytes on the activities of *P. japonica* seed and epigeal stolons in laboratory studies, and their growth

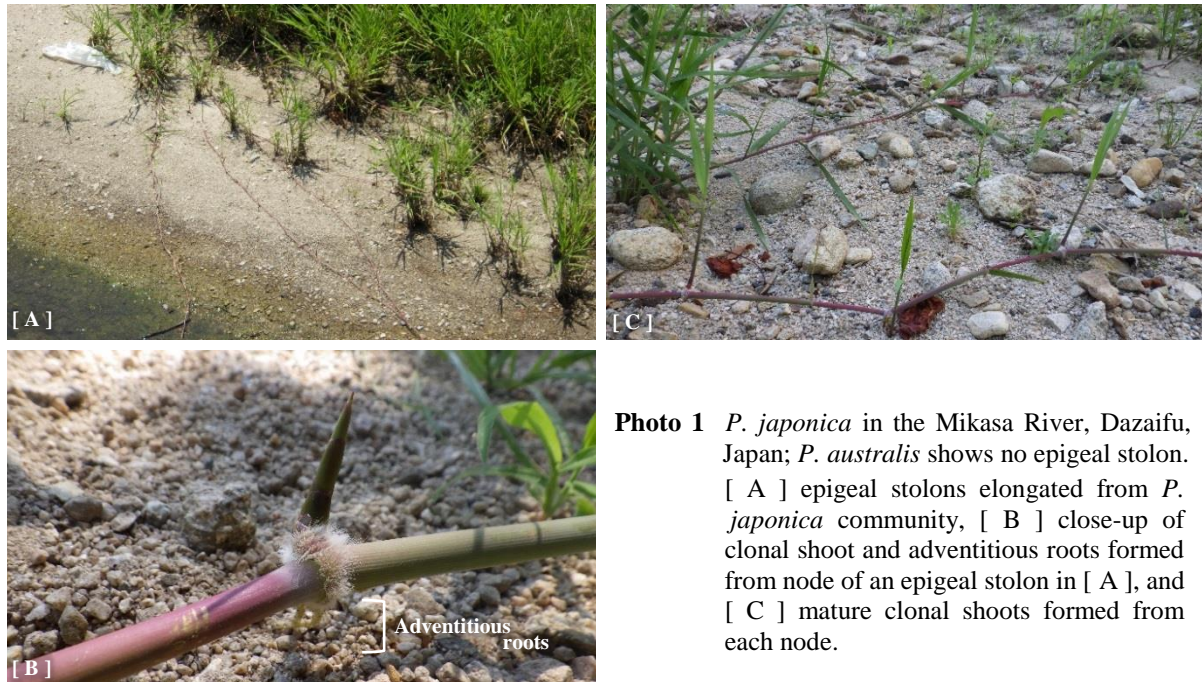


Photo 1 *P. japonica* in the Mikasa River, Dazaifu, Japan; *P. australis* shows no epigeal stolon. [A] epigeal stolons elongated from *P. japonica* community, [B] close-up of clonal shoot and adventitious roots formed from node of an epigeal stolon in [A], and [C] mature clonal shoots formed from each node.

after transplanting were examined.

MATERIALS AND METHODS

Allelopathic Effects of Aqueous Extracts

Aqueous extract preparations

Leaves of five species of perennial hygrophytes, *Typha latifolia* L., *P. australis*, *Lythrum salicaria* L., *Phalaris arundinacea* L. and *P. japonica*, and stems of one species of perennial hygrophyte, *Scripus tabernaemontani* Gmel., which shows no leaf, were used as test materials. The leaves and stems of these hygrophytes were collected during early summer (May to June) in Hokkaido, Japan, rinsed with distilled water and air dried at room temperature (18–20 °C). They were then cut into lengths of 2–4 cm and ground up into fine powder using a MC210-YE grinder (Sanyei Corporation, Tokyo, Japan). To prepare solutions for testing effects on *P. japonica*, 0.5 g of each hygrophyte powder was weighed and suspended in 100 mL of distilled water. After 24 h at room temperature, the aqueous extracts (5.0 g L⁻¹) were strained through two layers of cheesecloth and then through two layers of Whatman No. 2 filter paper (Whatman International Ltd., Maidstone, England) to remove solid materials. These aqueous extracts were further strained through 0.2 µm membrane filters (Nalge Nunc International Corporation, Rochester, USA) to remove bacteria prior to use in bioassays.

The extracts had a pH in the range of 5.1 to 6.0 and EC of 12.56 to 94.21 mS m⁻¹ at room temperature.

Bioassay-I

(1) Seeds

Phragmites japonica seeds were obtained from Snow Brand Seed Co. Ltd, Sapporo, Japan. For each hygrophyte, 5 mL of aqueous extract (or distilled water as a control) was added to eight Petri dishes (90 mm diameter) each lined with three layers of Whatman No. 2 filter paper and containing 36 *P. japonica* seeds. The Petri dishes were sealed with film paraffin (American National Can Company, Chicago, USA) to prevent loss of moisture and incubated at 25 °C under daylight at the greenhouse of the Center for Regional Collaboration in Research and Education, Obihiro University, Japan for 7 days. Seed germination was recorded. Radicles were fixed in FAA (ethanol:formalin:acetic acid:distilled water = 10:1:1:8), and the radicle length was measured and expressed as a percentage of the control.

(2) Epigeal stolons

Epigeal stolons of *P. japonica* were obtained from natural communities growing along the Satsunai River, Obihiro, Japan. The epigeal stolons were cut into several segments, 15 cm in length with one node for bioassay use; a clonal shoot and adventitious root could be formed from the node under appropriate moisture conditions (Photo 1). Twenty epigeal stolon segments were placed in a plastic dish (10.0 × 32.5 × 3.5 cm height), and 300 mL of aqueous extract (or distilled water as a control) was added to the plastic dish. Five replicates were used for each hygrophyte or control. The total aqueous extract or distilled water

volume in the plastic dish was maintained throughout the experimental period by adding distilled water daily. The epigeal stolon segments were incubated at 25 °C under daylight at the greenhouse mentioned above for 21 days. At the end of the incubation period, the number of nodes that formed clonal shoots was counted. The epigeal stolon segments were fixed in FAA, and the length of the formed adventitious root was measured. The number of nodes forming clonal shoots was expressed as a percentage, shoot formation rate (%), using the following equation (1), while adventitious root length was expressed as a percentage of the control.

$$\text{Shoot formation rate (\%)} = \text{NNFC} / \text{TNN} \times 100 \quad (1)$$

Where NNFC is the number of nodes that formed clonal shoots per plastic dish, and TNN is 20 for this study, or the total number of nodes (epigeal stolon segments) per plastic dish.

Bioassay-II

In this study, aqueous extracts were passed through Amberlite XAD-4 resin (hereafter, XAD-4 resin; Rohm & Haas, Philadelphia, USA), a polystyrene-based absorbent with a high surface area that removes various allelochemicals [14], [27], [28], [29]- the aqueous extracts were strained twice through an 88 mL volumetric column (150 mm diameter × 500 mm height) filled with 50 mL of XAD-4 resin at a flow rate of 3 mL min⁻¹ using a PST-100N peristaltic pump (Asahi Techno Glass Corporation, Tokyo, Japan). The resulting solutions (hereafter, XAD-4 preparations) had a pH in the range of 5.1 to 6.6 and EC of 12.14 to 92.11 mS m⁻¹ at room temperature.

The same bioassays described in bioassay-I were performed but with XAD-4 preparations and distilled water as a control with five replicates for only those hygrophytes that showed inhibitory effects on the radicle length of seedlings in bioassay-I.

Growth after Transplantation

Seeds and epigeal stolons, which were cut into 5, 10 and 15 cm segments with one node each, were incubated at 18 °C in the light in distilled water in a MIR-553 incubator (SANYO Electric Co., Ltd., Osaka, Japan). Eight seedlings and epigeal stolon segments that formed clonal shoots from the node were then immediately transplanted to individual 1/5000a Wager pots (Fujiwara Scientific Company, Tokyo, Japan) filled with soil (volcanic ash soil:alluvial soil:vermiculite = 6:3:1) and further incubated at 25 °C under daylight with regular watering at the greenhouse mentioned above. No fertilization was used for cultivation. Dry weights of stems, leaves, radicles (or adventitious roots for

clonal shoots) and rhizomes in seedlings and clonal shoots were measured at 120 days after transplanting.

Data Analysis

Differences among the means were analyzed by one-way analysis of variance (ANOVA). Probabilities less than 0.05 were considered significant. Differences between means were determined using Bonferroni's multiple comparison test.

RESULTS

Allelopathic Effects of Aqueous Extracts

Compared to the control (Table 1), no aqueous extracts from the six tested hygrophytes inhibited seed germination ($p=0.072$). The radicle length of the seedlings, however, was inhibited by treatment with aqueous extracts from *P. australis*, *L. salicaria* and *P. arundinacea* ($p<0.001$) compared to the control. Incidentally, the radicle length of *P. japonica* seedlings was not inhibited by treatment with an aqueous extract from its own leaves compared to the control.

For all aqueous extracts, no inhibitory effects were observed for shoot formation rate from epigeal stolon segments ($p=0.220$). There were significant differences in the length of adventitious roots formed from clonal shoots between when treated with aqueous extracts of *S. tabernaemontani* and when treated with those of *P. japonica* ($p=0.025$), but none of the aqueous extracts from the six hygrophytes inhibited adventitious root length of the clonal shoot compared to the control.

Allelopathic Effects of XAD-4 Preparations

The bioassay with *P. japonica* seeds was repeated using XAD-4 preparations from the three hygrophytes, *P. australis*, *L. salicaria* and *P. arundinacea* that produced inhibition of the radicle length in seedlings (Tables 1 and 2). The aqueous extract from *P. australis* had no effect on seed germination, and there was also no effect of XAD-4 preparations on seed germination ($p=0.209$) compared to the control. The aqueous extract from *P. australis* inhibited the radicle length of the seedlings, and the XAD-4 preparation also inhibited the radicle length of seedlings ($p<0.001$) compared to the control.

Similarly, no allelopathic effect was observed for the aqueous extract from *L. salicaria* or for its XAD-4 preparation on seed germination ($p=0.475$). The aqueous extract from *L. salicaria* inhibited the radicle length of seedlings ($p<0.001$), but no inhibition was observed for the XAD-4 preparation compared to the control. Similar results were also observed for *P. arundinacea*. That is, the allelopathic effects of the

Table 1 Allelopathic effects of aqueous extracts on seed germination, radicle length of seedling, shoot formation rate from epigeal stolon, and adventitious root length of clonal shoot in *P. japonica*.

Test plant	Seed		Epigeal stolon	
	<i>n</i> =8		<i>n</i> =5	
	Germination (%)	Radicle length (% of control) ^{††}	Shoot formation rate (%)	Adventitious root length (% of control) ^{††}
Control [†]	89.9 ± 6.8 A	100.0 ± 17.8 B	76.0 ± 4.3 A	100.0 ± 12.2 AB
<i>T. latifolia</i>	89.6 ± 3.9 A	110.1 ± 13.9 B	80.2 ± 4.1 A	99.1 ± 8.7 AB
<i>P. australis</i>	86.5 ± 6.7 A	57.2 ± 18.5 A	76.9 ± 4.8 A	98.8 ± 8.2 AB
<i>L. salicaria</i>	87.8 ± 4.9 A	35.5 ± 6.5 A	80.1 ± 7.2 A	106.5 ± 11.9 AB
<i>P. arundinacea</i>	87.2 ± 4.4 A	38.1 ± 17.1 A	81.8 ± 2.5 A	91.2 ± 18.0 AB
<i>S. tabernaemontani</i>	88.9 ± 4.5 A	101.7 ± 10.0 B	75.9 ± 6.0 A	86.2 ± 9.7 A
<i>P. japonica</i>	94.4 ± 4.2 A	84.7 ± 7.7 B	81.7 ± 3.1 A	110.3 ± 11.2 B
<i>p</i> -value	<i>p</i> =0.072	<i>p</i> <0.001	<i>p</i> =0.220	<i>p</i> =0.025

[†], Distilled water. ^{††}, Values are expressed as a percentage of length of the control.

Mean ± S.D. The levels of significance are also shown.

Within any column, values followed by the different letters are significantly different using Bonferroni's multiple comparison test.

Table 2 Allelopathic effects of XAD-4 preparations from the three hygrophytes on seed germination and radicle length of seedling in *P. japonica*.

Test plant	Solution	Germination (%)	Radicle length (% of control) ^{††}
<i>P. australis</i>	Control [†]	91.1 ± 6.6 A	100.0 ± 21.5 B
	Aqueous extract	86.1 ± 8.8 A	53.7 ± 14.1 A
	XAD-4 preparations	93.9 ± 3.0 A	47.2 ± 16.4 A
<i>p</i> -value		<i>p</i> =0.209	<i>p</i> <0.001
<i>L. salicaria</i>	Control [†]	91.1 ± 6.6 A	100.0 ± 21.5 B
	Aqueous extract	89.4 ± 5.0 A	41.2 ± 4.3 A
	XAD-4 preparations	86.1 ± 7.3 A	69.0 ± 8.7 AB
<i>p</i> -value		<i>p</i> =0.475	<i>p</i> <0.001
<i>P. arundinacea</i>	Control [†]	91.1 ± 6.6 A	100.0 ± 21.5 B
	Aqueous extract	87.8 ± 2.5 A	35.2 ± 16.6 A
	XAD-4 preparations	92.8 ± 4.6 A	96.2 ± 12.2 B
<i>p</i> -value		<i>p</i> =0.295	<i>p</i> <0.001

[†], Distilled water. ^{††}, Values are expressed as a percentage of length of the control.

Values are the means of five replications with S.D. The levels of significance are also shown.

Values followed by the different letters are significantly different using Bonferroni's multiple comparison test.

aqueous extract from *P. arundinacea* and the XAD-4 preparation showed no effect on seed germination (*p*=0.295), while the aqueous extract from *P. arundinacea* inhibited the radicle length of the seedlings (*p*<0.001) compared to the control, but the XAD-4 preparation did not.

Growth of Seedlings and Epigeal Stolon Segments

The segment length of epigeal stolon had no effect on the timing of the initiation of clonal shoot formation and dry weight after transplanting (Table 3).

Although the timing of the beginning of seed germination was significantly earlier (*p*<0.001), the 120 day dry weights of seedlings were remarkably

Table 3 Growth of *P. japonica* seedlings and clonal shoots from epigeal stolon segments of different lengths at 120 days after transplanting.

Item	Seed	Length of epigeal stolon segment (cm)			p-value
		5	10	15	
Weeks for seed germination or clonal shoot formation	0.59 ± 0.10 A	1.73 ± 0.54 B	1.74 ± 0.51 B	1.86 ± 0.57 B	p < 0.001
Stems (g-DW / individual)	0.16 ± 0.05 A	1.78 ± 0.24 B	1.63 ± 0.31 B	1.75 ± 0.28 B	p < 0.001
Leaves (g-DW / individual)	0.18 ± 0.05 A	1.71 ± 0.31 B	1.71 ± 0.21 B	1.66 ± 0.24 B	p < 0.001
Radicles (g-DW / individual)	0.35 ± 0.08 A	1.95 ± 0.24 B	2.11 ± 0.29 B	2.01 ± 0.19 B	p < 0.001
Rhizomes (g-DW / individual)	0.20 ± 0.03 A	1.08 ± 0.16 B	0.99 ± 0.14 B	1.17 ± 0.27 B	p < 0.001

Values are the means of eight replications with S.D. The levels of significance are also shown.

Within any row, values followed by the different letters are significantly different using Bonferroni's multiple comparison test.

lower in all organs ($p < 0.001$) compared to those of clonal shoots from the epigeal stolon. Further, dry weights of above- and below-ground organs of clonal shoots were 7.3 times of those of the seedlings.

DISCUSSION

P. japonica is one of the crucial plant materials in green infrastructure, especially along water edges. However, perhaps due to their restricted distributions in the Far East [12], there have been few physiological studies on *P. japonica*. As allelopathy is one of the mechanisms to explain the propagation strategies of plant species, the allelopathic effects of aqueous extracts from different hygrophytes on the activities of *P. japonica* seeds and epigeal stolons were assayed here, along with growth after transplanting.

Our results show that the epigeal stolon is more tolerant to allelopathic inhibitory effects of aqueous extracts from various hygrophytes than the seed (Table 1). Further, the dry weight of the above- and below-ground organs of clonal shoots from the epigeal stolon reached 7.3 times of those of the seedlings after transplanting (Table 3). These data suggest that the invasion success of *P. japonica* is mainly attributable to epigeal stolons, which can grow vigorously regardless of segment length (Table 3), a finding that is supported by the observation that *P. japonica* seedlings are seldom observed in natural settings.

On the other hand, allelopathic inhibitory effects on the radicle length of seedlings were not observed in tests with XAD-4 preparations (Table 2), unlike in the case of aqueous extracts (Table 1). That is, some compounds that are absorbed by Amberlite XAD-4 resin, e.g. 3-hydroxyhydrocinnamic acid, vitexin, isovitexin, C-glucosyl flavonoid and benzyl isothiocyanate [14], [15], [27], [28], [29], apparently contribute to the inhibitory effects on the radicle length of seedlings as allelochemicals. Interestingly, self-inhibition among *P. japonica* is unlikely because

adverse impacts were not observed in the treatment with an aqueous extract from its own leaves both in seeds and in epigeal stolons (Table 1).

ACKNOWLEDGEMENTS

This work was supported by JSPS KAKENHI Grant Number JP02J07477, and an outline of this study including preliminary results was presented at CIGR and the EAFES Congress [31], [33].

REFERENCES

- [1] Barrico L. Castro H., Coutinho A.P., Gonçalves M.T., Freitas H. and Castro P., 2018. Plant and microbial biodiversity in urban forests and public gardens: Insights for cities' sustainable development. *Urban Forestry & Urban Greening* 29, 19-27.
- [2] Chenoweth J., Anderson A.R., Kumar P., Hunt W.F., Chimbandira S.J. and Moore T.L.C., 2018. The interrelationship of green infrastructure and natural capital. *Land Use Policy* 75, 137-144.
- [3] Clevering O.A. and Lissner J., 1999. Taxonomy, chromosome number, clonal diversity and population dynamics of *Phragmites australis*. *Aquatic Botany* 64, 185-208.
- [4] Engloner A.I., 2009. Structure, growth dynamics and biomass of reed (*Phragmites australis*)- A review. *Flora* 204, 331-346.
- [5] Francis, R.A. and Hoggart S.P.G., 2008. Waste not, want not: The need to utilize existing artificial structures for habitat improvement along urban rivers. *Restoration Ecology* 16, 373-381.
- [6] Furuno M., Uchida T., Xue J.H., Hayasaka D. and Arase T., 2014. Multifunctional roles of street trees: Plant biodiversity in urban areas. *Proceedings of the 4th International Conference of Urban Biodiversity and Design*. p.344.
- [7] Gries C., Kappen L. and Lösch R., 1990. Mechanism of flood tolerance in reed, *Phragmites australis* (Cav.) Trin. ex Steudel. *New Phytologist*

- 114, 589-593.
- [8] Harald Küshl H. and Kohl J.-G., 1992. Nitrogen accumulation, productivity and stability of reed stands (*Phragmites australis* (Cav.) Trin. ex Steudel) at different lakes and sites of the lake districts of Uckermark and Mark Brandenburg (Germany). *Hydrobiology* 77, 85-107.
- [9] Jaganmohan M., Vailshery L.S., Mundoli S. and Nagendra H., 2018. Biodiversity in sacred urban spaces of Bengaluru, India. *Urban Forestry & Urban Greening* 32, 64-70.
- [10] Kato T., Xu K., Chiba N., Kashiuchi T., Hosomi M. and Sudo R., 1988. Evaluation for the creation of reed fields with seedlings on dredged sediments. *Trans. JSIDRE* 594, 1-10. *In Japanese*
- [11] Kiviat E., 2013. Ecosystem services of *Phragmites* in North America with emphasis on habitat functions. *AoB PLANTS* 5, <https://doi.org/10.1093/aobpla/plt008>
- [12] Koyama T. 1987. Grasses of Japan and its neighboring regions: an Identification manual. Kodansha. 582pp.
- [13] Lepczyk C.A., Aronson M.F.J., Evans K.L., Goddard M.A., Lerman S.B. and MacIvor J.S., 2017. Biodiversity in the city: Fundamental questions for understanding the ecology of urban green spaces for biodiversity conservation. *BioScience* 67, 799-807.
- [14] Li A., Zhang Q., Zhang G., Chen J., Fei Z. and Liu F., 2002. Adsorption of phenolic compounds from aqueous solutions by a water-compatible hypercrosslinked polymeric absorbent. *Chemosphere* 47, 981-989.
- [15] Lin S.H. and Juang R.S., 2009. Adsorption of phenol and its derivatives from water using synthetic resins and low-cost natural adsorbents: A review. *Journal of Environmental Management* 90, 1336-1349.
- [16] Lique C., Kleeschulte S., Dige G., Maes J., Grizzetti B., Olah B. and Zulian G., 2015. Mapping green infrastructure based on ecosystem services and ecological networks: A Pan-European case study. *Environmental Science & Policy* 54, 268-280.
- [17] Meerow S. and Newell J.P., 2017. Spatial planning for multifunctional green infrastructure: Growing resilience in Detroit. *Landscape and Urban Planning* 159, 62-75.
- [18] Müller N., Werner P. and Kelcey J.G., 2010. Urban biodiversity and design. Blackwell Publishing. 626 pp.
- [19] Nevel B.E., Hanganu J. and Griffin C.R., 1997. Reed harvesting in the Danube Delta, Romania: Is it sustainable? *Wildlife Soc. Bulletin* 25, 117-124.
- [20] Niemelä J., 2011. Urban ecology, Oxford University Press. 374 pp.
- [21] Onisi M., 1995. Lake shore Renaissance of Otsu. *Environ. Syst. Res.* 23, 627-631. *In Japanese*
- Osada T. 1989. Illustrated gasses of Japan. Heibonsha. 759pp. *In Japanese*
- [23] Packer J.G., Meyerson L.A., Skálová H., Pyšek P. and Kueffer C., Biological flora of the British isles: *Phragmites australis*. *Journal of Ecology* 105, 1123-1162.
- [24] Puppim de Oliveira J.A., Balaban O., Doll C.N.H., Moreno-Peñaranda R., Gasparatos A., Iossifova D. and Suwa A., 2011. Cities and biodiversity: Perspectives and governance challenges for implementing the convention on biological diversity (CBD) at the city level. *Biological Conservation* 144, 1302-1313.
- [25] Saaroni H., Amorim J.H., Hiemstra J.A. and Pearlmutter D., 2018. Urban Green Infrastructure as a tool for urban heat mitigation: Survey of research methodologies and findings across different climatic regions. *Urban Climate* 24, 94-110.
- [26] Sirakaya A., Cliquet A. and Harris J., 2018. Ecosystem services in cities: Towards the international legal protection of ecosystem services in urban environments. *Ecosystem Services* 29, 205-212.
- [27] Stevens Jr. G. A. and Tang C.S., 1985. Inhibition of seedling growth of crop species by recirculating root exudates of *Bidens pilosa* L. *Journal of Chemical Ecology* 11, 1411-1425.
- [28] Tang C.S. and Takenaka T., 1983. Quantitation of a bioactive metabolite in undisturbed rhizosphere-benzyl isothiocyanate from *Carica papaya* L. *Journal of Chemical Ecology* 9, 1247-1253.
- [29] Tang C.S. and Young C.C., 1982. Collection and identification of allelopathic compounds from the undisturbed root system of Bigalta Limpograss (*Hemarthria altissima*). *Plant Physiol.* 69, 155-160.
- [30] Uchida T. and Tazaki F., 2005. New methods and allelopathic considerations of riparian buffer zones using *Phragmites australis* (Cav.) Trin. *Ecological Engineering* 24, 559-569.
- [31] Uchida T., Arase T. and Sato Y., 2004. Propagations and control strategies of strong weed, *Phragmites japonica* Steudel. Collection of extent abstracts, 2004 CIGR International Conference (Volume 2: V), p.168.
- [32] Uchida T., Furuno M., Minami T., Yamashita S., Uchiyama T., Arase T. and Hayasaka D., 2015. Ecological significance of masonry revetments in plant biodiversity. *Int. J. of GEOMATE* 9, 1353-1359.
- [33] Uchida T., Sakamoto N. and Saruhashi A., 2004. Allelopathic effects of hydrophyte extracts on *Phragmites japonica*. *Proceedings of the First EAFES International Congress.* 209-210.
- [34] Uchida T., Xue J.H., Hayasaka D., Arase T., Haller W.T. and Gettys L.A., 2014. The relation between road crack vegetation and plant biodiversity in urban landscape. *Int. J. of GEOMATE* 6, 885-891.

SOIL QUALITY INDEX ANALYSIS UNDER HORTICULTURAL FARMING IN SUMANI UPPER WATERSHED

¹Aprisal, ²Bambang Istijono, ³Juniarti and ⁴Mimin Harianti

^{1,3,4}Faculty of Agriculture, Andalas University, Padang, Indonesia ²Faculty of Engineering,
Andalas University, Padang, Indonesia

ABSTRACT

The intensive use of land for farming and horticulture results in soil degradation. The loss of nutrient elements contributes to the decline in soil quality index. This study aimed to investigate the major factors that contribute to soil degradation in the upper section of the Sumani Basin. Soil quality index is obtained as an indicator of soil functions. Thus, this study used this parameter to investigate the factors that contribute to the decrease in soil fertility. A purposeful random sampling method was used to obtain samples from different sample points. The biophysical properties of the soil samples were analyzed in the laboratory at the Department of soil science. The Principal Component Analysis (PCA) of the samples were carried out by using a data processing application software (mini tap 17.0). These results were used to determine the Minimum Data Set (MDS) for each soil sample. This research study showed that the two types of soil obtained from the various sample points were inceptisol and andisol. The major factors that influence soil quality include bulk density, soil CEC, root depth, and soil texture. The soil sample obtained from the third farmland group (Group C) had the best soil quality.

Key word: horticulture, quality index, watershed upstream.

INTRODUCTION.

Horticultural or vegetable farming in the upper watershed of Sumani, Solok is the main source of livelihood for people who live in the surrounding area. This area lies on the slopes of Mount Talang; it has fertile soils formed in volcanic ash. Based on soil classification [1], the soil around the foot of the mountain is classified as andisol. This type of soil is black and has a high fertility. Thus, it supports various farming activities, especially the cultivation of vegetable crops (horticulture) which provide a decent source of livelihood to farmers.

However, if the fertile soil is not managed by good soil and water conservation principles, the fertility or quality level of the soil will decrease drastically. This will result in a decrease in productivity of the land and low acceptance of the peasant community. This turn of events may result in huge losses to farmers. Therefore, it is necessary to evaluate the soil fertility level in this area as well as the major factors that contribute to the decrease in soil fertility in the upper section of the Sumani Basin. The study conducted by [2] documented that quality evaluation is critical to the determination of the soil's ability to function as a growing medium that provides water and nutrients in the root zone of plants. Thus, this can be considered to be a solution in land management. The quality of land must be improved and maintained to ensure that vegetable farming in the area becomes sustainable.

Soil quality can also be defined as the ability of soils to function within ecosystems by supporting

crop and animal productivity, maintaining/improving water and air quality, and promoting human and environmental health [3], [4] [5]. Some experts have stated that the quality of the soil determines the amount of crops produced in each season. In addition, soil quality greatly affects crop yield because it determines the quality of nutrients absorbed by plant roots.

The soil acts as a store that provides nutrients and water to the root of plants. Thus, there is a need to investigate the physical, chemical and biological properties of the soil in order to determine the extent to which its condition supports current crop growth. The soil properties analyzed are the minimal properties that influence its quality or Minimum Data Set (MDS). Soil properties include soil texture, bulk density, total pore space, permeability, pH, Cation Exchange Capacity (CEC), and organic matter

MATERIALS AND RESEARCH METHODOLOGY

Time and Location

This study was conducted during the periods of February, 2018 to June, 2018 at multiple sample points in the upstream watershed of the Sumani horticultural land, Solok regency of West Sumatra (Figure 1). Soil Quality Indicator Analysis was carried out at the Laboratory of Soil Department, Faculty of Agriculture, University of Andalas.

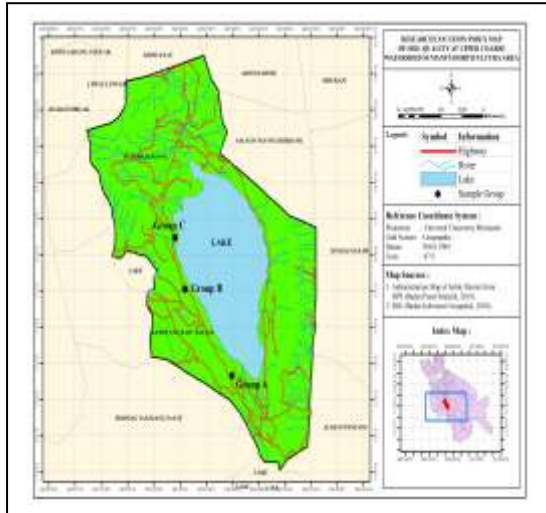


Figure 1. Map of the Sumani Basin of Upper Section

Research Materials and Tools

The materials used in this study include chemical reagents used to analyze the physical, chemical and biological properties of the. The tools used to determine the soil quality for horticultural production include the Global Positioning System (GPS), loops, maps, sample

rings, knives, plastics, and label paper. The tools used for laboratory analysis of soil samples include the desiccator, oven, Erlenmeyer flasks, scales, analytical scales, goblets, spectrophotometers, Whatman filter papers, funnel, Kjeldhal tube, burette, distillation flask, and stative/ measuring pipette.

Research Methodology

A field survey was conducted to obtain both secondary and primary data. Secondary data was obtained from rainfall data, interview with the farmers and related officials in agricultural institutions. Primary data was obtained from the land samples collected at several points in the study location. Soil samples were collected using a purposeful random sampling technique. The samples were taken to the laboratory and analyzed for physical, chemical and biological properties. Soil samples were collected at a depth of 20 cm.

Table 1. Minimum Data Set (MDS) parameters for the analysis of soil quality at horticulture production centers, Sumani.

Observation Variables	Variables	Methods
Soil Physical Characteristic	Texture	Pipette
	Permeability	Darcy's Law
	Infiltration	Horton
	Aggregate stability	Vilansky
	The effective depth of the roots	Bor belgi
Soil Chemical Characteristic	Bulk density	Volumetric
	H ₂ O pH	PH meter
Soil Biological Characteristic	CEC	Washing with Ammonium
	Soil organic material	Wakey and black

The location point of soil sampling was three groups of the horticultural farming around the lake, below and on the upper section of the Sumani Basin. (2) Secondary data about some aspects of horticultural farming and current condition of the area were obtained via the collection of data from several related agencies and the conduction of interviews with the farmers. The findings obtained from these interviews were scored and used as supporting information on horticultural produc-

tivity in the area. (3) The MSD parameters used in the determination of soil quality are listed in Table 1. These parameters were determined by using minitab 17.0.

The Principal Component Analysis (PCA) method was used to select the most appropriate indicator that would produce the data referred to as Principal Components (PC). The soil quality assessment was performed by using a soil quality index that was scored on selected variables of the

PCA and the Minimum Data Set (MDS). The PC used as MDS had an Eigen value that is more than 1; the weightiest factor was selected as a principal component.

The value of the selected indicator on each PC was multiplied by its scores to determine the soil quality index at each sample point. The score interval was 1 to 5 with a value of 0.1; 0.25; 0.5; 0.75; and 1. The higher the score of a variable, the higher the quality of the soil. The calculation of soil quality was done by multiplying the score of the variable by the weighted index [6].

According to [7], the assessment of soil quality can be calculated by using the formula for Soil Quality Index (SQI) or IKT;

$$SQI = \sum_{i=1}^n W_i \times S_i$$

Annotation:

SQI = Soil Quality Index

W_i = Weighting Factor

S_i = Score Index

If the index value has been obtained, the soil quality can be determined using Table 2.

Table 2. Classes of Soil Quality

Soil Quality	Scale	Class
Very Good	0.8 – 1	1
Good	0.6 – 0.79	2
Fair	0.35 – 0.59	3
Bad	0.20 – 0.34	4
Very Bad	0 – 0.19	5

RESULTS AND DISCUSSION

Biophysical properties

The research location for this study was three farmland groups denoted as group A, B, and C. The type or order of the soil in each group were inceptisol, and andisol (Table 3). The commodities grown in each farmland group were potatoes, red chilis, red onions, and carrots (Table 3).

The description of the biophysical conditions of the soil in study area is shown in Table 4. The soil sample from group A had a sandy clay texture, Group B had a clay loam texture and Group C had a loamy texture. The bulk density was very low in

all three groups, this places them in the fair criteria for soils. Based on the biophysical properties of the soil, they were considered as fertile. This is due to the origin of the soil's parent material.

Table 3. Farmer groups, types of soil, and cultivated crops.

Location	Soil Classification USDA	Number of Sampling Points	Plant Type
Farmer Group A	<u>Inceptisol</u>	Three points	Potato Red Chili Carrot
Farmer Group B	<u>Andisol</u>	Three points	Red onion Red Chili Carrot
Farmer Group C	<u>Inceptisol</u>	Three points	Red onion Red Chili Carrot

Farming systems are cultivated continuously without any fallow or rest. This will have an impact on soil quality if farm management is poor. Based on the results of the study [8] stated that the causes of the decline in soil fertility include the washing away of nutrients and low soil organic matter. Furthermore, [8] suggested the conduction of integrated soil management (which utilizes organic fertilizer) to maintain the balance of nutrients in the soil. The results [9] show that changes in land use from secondary forests to fields cause land degradation due to the low content of soil organic matter and rapid decomposition.

PCA Analysis

The main components that greatly affect soil quality is shown in Table 5. Factors that act as a determinant of soil quality index had an Eigen value that is more than 1. The result of the PCA analysis revealed four component factors, namely PC1, PC2, PC3, and PC4.

Table 4. Biophysical characteristics of the soil on three farmland groups, upstream Sumani section

Famer group	Bulk density g/cm ³	Total of pore space %	Organic matter %	depth (cm)	sand %	dust %	clay %	Hydrology conductivity cm/jam	CEC (cmol/kg)	PH H2O
A	0.5	80	1.3	15.7	46.9	24.8	28.3	35.0	17.1	6.4
B	0.8	70	0.5	29.3	13.7	55.6	30.7	30.2	10.0	6.1
C	0.8	70	0.4	16.3	44.4	32.8	22.9	20.3	9.3	6.7

Table 5. Principal component analysis result

Eigenvalue	2.9210	2.6160	2.2153	1.5912
Proportion	0.266	0.238	0.201	0.145
Cumulative	0.266	0.503	0.705	0.849
Variable				
Variable	PC1	PC2	PC3	PC4
Infiltration capacity	0.409	0.217	-0.039	-0.236
Bulk density	0.527	-0.027	-0.106	0.282
Total of pore space	-0.527	0.027	0.106	-0.282
Organic matter	0.014	0.317	0.482	0.143
Soil depth	0.028	0.112	0.614	-0.009
Sand	-0.019	0.477	-0.093	-0.483
Dust	0.384	-0.294	0.218	-0.106
Clay	-0.352	-0.121	-0.130	0.509
Permeability	-0.057	-0.375	0.217	-0.370
CEC	-0.034	0.425	0.300	0.353
H2O pH	0.011	0.436	-0.396	-0.014

Soil Quality Index

The Soil Quality Index (SQI) in each farmland group was determined the multiplication of the value of the selected soil properties score (Si) with the weighted index (Wi). The weighted index is the highest value in each selected PC column. Based on the results of major component analysis (PCA), the soil properties used in the determination of soil quality index were bulk density (BV), pH, rooting zone depth, and clay fraction.

Bulk density is an important principal component which determines root development in the plant root zone. The root zone is another important component because the depth of the soil determines the roots' ability to absorb nutrients. According to [10], the root zone (a.k.a. rhizosphere) is heavily influenced by root exudates. The high activity of micro-organisms in the area makes the soil fertile

The pH and texture of the soil determines the availability of nutrients for plants.

The soil pH and clay fraction strongly determine its cation exchange capacity (CEC). CEC is an important soil property that indicates whether the land is fertile or not. A high soil CEC indicates that the soil will be effective in providing nutrients to plants, especially nutrients from fertilization.

Macro and micro elements will not be available to plants if cation exchange capacity is low, and vice versa. This is because CEC holds and prevent the nutrient elements from being washed away. The presence of organic matter greatly influence the cation exchange capacity of soils. This is because organic materials have a high CEC. Thus, they can increase the cation exchange capacity by three folds compared to mineral soil. In addition, cation exchange capacity is influenced by the type and content of clay in the soil [11]. Thus, these four variables are referred to as the minimum data set.

The results of the calculations of soil quality (Table 7) indices in group A ranged from medium to very good (Table 7). There were also variations in the soil quality index between different sampling points. This was due to the cultivation of different types of vegetable crops in each sample point (i.e. potatoes, red pepper and carrots).

Table 6. Calculated value of soil quality index in each farmland group based on PC factors.

Location	SQI	S1 BV	W1 BV	S2 sand	W2 sand	S3 d soil	W3 d soil	S4 CEC	W4 CEC
			0.527		0.477		0.614		0.353
Group A	0.79	0.25		0.5		0.25		0.75	
	0.71	0.1		0.5		0.25		0.75	
	0.44	0.25		0.25		0.25		0.1	
Group B	0.88	0.25		0.75		0.5		0.25	
	0.84	0.1		0.5		0.75		0.25	
	0.83	0.5		0.5		0.25		0.5	
Group C	0.66	0.25		0.1		0.5		0.5	
	0.85	0.25		0.5		0.5		0.5	
	0.68	0.25		0.75		0.25		0.1	

Annotation; SQI (Soil quality Index), BV (soil bulk density), d (soil depth), CEC (Cation Exchange Capacity), S (score factor of value), W (weighting factor index).

Table 7. Calculated values of Soil Quality Index in each location

Location	Soil Quality Index	Criteria
Group		
A1	0,85	Very Good
A2	0,71	Good
A3	0,43	Fair
B1	0,88	Very Good
B2	0,96	Very Good
B3	0,83	Very Good
C1	0,66	Good
C2	0,67	Good
C3	0,67	Good

The three groups of farmland had a relatively high soil quality index and met the good criteria for soils. This shows that there is a good land management input from farmers. The types of plants cultivated include red chili, onions, and carrot (Table 3). The soil quality index in farmland group B (Table 5) was very good. The commodities planted on the land include red chili, carrots, and onions. According to [12], the high variability of soil characteristic is due to the different agricultural management of the soils (organic or traditional; arable, scrublands or woodland), cultivation of different crops (barley, corn, green manure, meadow, sugar beet, tomato, wheat and alfalfa) and fertilization (traditional or sewage sludge).

The land quality index of the three horticultural farming groups were different (Table 7). This indicates that there are differences in land location, soil type, plant type, and soil maintenance

management, especially the application of principal soil conservation.

The soil characteristics of each farmland group influenced the morphology of the plants grown in each sample point. Potato, carrot and onion plants need good soil conditions (such as aeration, good organic matter, presence of micro- and macro-nutrients) for optimum growth. On the other hand, red chili plants have roots that penetrate deeply into the soil to absorb nutrients. A study conducted by [13], showed that the presence of low soil pH and high clay fraction in utisol affected the growth of peanuts, corn, and soybean plants. It resulted in the poor development of the plants' roots. Contrastingly, plants cultivated on soil treated with compost and manure had well-developed roots and higher crop yield.

Poorly treated soils do not have the essential nutrients required for plant growth. It also has a higher tendency to lose its nutrients during water erosion, thereby resulting in the low saturation of the base. [14]. The percentage of basic saturation required for optimal soil productivity is $\geq 80\%$. Soils with a basic saturation below 40% results in the poor growth of plants [15]. Conservation efforts toward the prevention of soil erosion on horticultural farmland involve the application of soil conservation methods on slopes (e.g. the cultivation of crops according to the contour and the creation of a gulud terrace). Some research studies have documented that the cultivation of seasonal crops using contours and royal grass strips can reduce soil erosion by 45 percent in community farms around the Singkarak Water Capture Area [16].

CONCLUSION

This research study showed that the two types of soil obtained from the various sample points were Inceptisol and Andisol. The major factors that influence soil quality include bulk density, soil CEC, root depth, and soil texture. The soil sample obtained from the third farmland group (Group C) had the best soil quality.

REFERENCE

- [1] USDA, 2014. Key to Soil Taxonomy. Soil Survey Staff, USDA, Ames. USA.
- [2] Larson, W. E. and Pierce, F. J. 1991. Conservation and Enhancement of Soil Quality. In Dumanski, J, E. Pushparajah, M. Latham and R. Myers, (ed). Evaluation for Sustainable Land Management in the Developing World. *Publ. International Board for Soil Research and Management, Bangkok, Thailand*. Vol. 2:175-204.
- [3] Wander Michelle M, Gerald L Walter, Todd M Nissen, German A Bollero, Susan S. Andrews, Deborah A Cavanaugh-Grant 2002. Soil quality: science and process. *Agronomy Journal* 94.
- [4] Karlen, D.L., M.J. Mausbach, J.W. Doran, R.G. Cline, R.F. Harris, and G.E. Schuman. 1997. Soil quality: A concept, definition, and framework for evaluation. *Soil Sci. Soc. Am. J.* 61:4 10.
- [5] Weil, R.R. and F. Magdoff. 2004. Soil Organic Matter in Sustainable Agriculture: Significance of Soil Organic Matter to Soil Quality and Health. CRC Press. Florida.
- [6] Pratono, S. A. C., Supriyadi, and Purwanto. 2011. Zoning of Rice Field Quality in Industrial Area of Bengawan Solo Watershed Area of Karanganyar Regency. *Journal of Soil Science and Agroklimatologi* 8 (1) : 1-12
- [7] SQI, 2001. *Guidelines for Soil Quality Assessment in Conservation Planning*. Soil Quality Institute. Natural Resources Conservation Services. USDA.
- [8] A.Kasno, J.S. Adiningsih, Djokosantoso and Earn Nursyamsi. Integrated nutrient management for improving and maintaining productivity of dry land to sour. Pros. No. 14. Land Research 1998. ISSN. 0854-5588

ACKNOWLEDGEMENT

My deepest gratitude goes to the University of Andalas for giving me the rare opportunity to attend an international seminar. I also appreciate all the students who helped in the collection of soil samples from the study location..

- [9] Alda 2018. Determination of Soil Quality Index Based on Soil Physical Characteristic on Various Land Use in Sub-watershed of Batang Arau Hulu "so that further can be known the appropriate management to maintain and improve upstream function of Batang Arau watershed. Bachelor's Thesis Agriculture Faculty of Agriculture Universitas Andalas.
- [10] Soemarno. 2010. Systems Approach and Modeling. Post Graduate Program Universitas Brawijaya. Malang.
- [11] Tan, Kim h. 1998. The basics of soil chemistry. Yogyakarta: Gadjah Mada University Press.
- [12]. Aspetti G.P., Boccelli Raffaella, Ampollini Danio, Del Re Attilio A.M., Capri Ettore . 2010. Assessment of soil-quality index based on microarthropods in corn cultivation in Northern Italy *Jounal Ecological Indicators* 10 (2010) 129–135
- [13] Aprisal. 2000. The study of the reclamation of imperata marginal land and integrated farming system modesl for sustainable agriculture development in transmigration area Pandan Wangi Peranap Riau. Disertation of PhD at griculture of University Bogor.
- [14] A & L Canada Laboratories Inc. in 2002. Understanding cation exchange capacity and% base saturation. Fact sheet No. 54. London.
- [15] Arsyad.S. 2010. Konservasi Tanah dan Air. IPB Press
- [16] Aprisal, Bujang Rusman, Refdinal. 2013. Land Management in building Conservation farming for the integration of food security in the rural catchment Singkarak. Pros. No.1. National seminar on Soil and Water Conservation Society. Palembang 6-8 November 2013. ISBN: 978-602-70116-0-1

THE EFFECT OF REBAR IN A SHORT HEIGHT CONCRETE WALL FOR THE ULTIMATE LATERAL STRENGTH

Tetsuya Ohmura¹, Dong Hesong¹, Kyouhei Iwasaki¹ and Mamoru Kawasaki²

¹Faculty of Architecture, Tokyo City University, Japan;

² Taisei Corporation, Japan

ABSTRACT

A concrete wall has the vertical and horizontal rebar, and is effective earthquake resisting element for lateral force in concrete buildings. So lateral force concentrate on concrete walls because they are much stiffer than columns, concrete walls would influence lateral strength of a building. Therefore, a seismic evaluation for walls is consequence, especially for a building with small amount of concrete walls. Generally, the vertical and horizontal rebar are effective to evaluate the flexural moment strength and lateral strength, respectively. However, for a short height concrete wall, the vertical and horizontal rebar might not be necessarily effective to flexural moment strength and shear strength respectively. In some past studies, the effect of rebar in a concrete wall was tend to be limited for the strength for short height concrete walls, however, the relationship between the height and the strength has been not obvious yet. In this paper, some short height (short shear span) concrete walls were modeled and FE analyses were performed. The result of the test and analysis was verified first, the concrete compressive strut and rebar stress distribution were examined. In our analysis results, the horizontal rebar effect was reduced, following decrease of the shear span. In addition, the vertical rebar is generally effective to moment strength, however, they were not necessary effective to moment strength in concrete walls with short shear span but for shear strength. Finally, we suggested to modify the Japanese standard formula for the shear strength.

Keywords: Concrete wall, Shear span, Horizontal and vertical wall rebar, FE analysis, Shear strength

INTRODUCTION

When a building would be designed, the key things must be the seismic assessment for the lateral strength of the building in the region with earthquakes often occurred. The lateral strength of a building would depend on the strength of concrete walls, because they are effective to resist earthquakes. In addition, the lateral load would tend to be concentrated to concrete walls, because concrete walls are definitely stiffer than columns. Therefore, the accuracy of the strength and the stiffness evaluation for a concrete wall is consequence.

Shear span ratio a/D (the wall height “a” divided by the wall depth “D”) of a multi-story concrete wall often located in a condominium tends to be 1.0 or more. However, a/D of a one or two-story concrete wall often located in an office or a school building tends to be 1.0 or less, because the diversity of the floor planning was needed.

The shear strength is given in the Japanese standard^[1] by

$$Q_{su} = \left\{ \frac{0.068 p_{te}^{0.23} (F_c + 18)}{\sqrt{a/D + 0.12}} + 0.85 \sqrt{\sigma_{wh} \cdot p_{wh}} + 0.1 \sigma_0 \right\} \cdot t_e \cdot j_e \quad \dots\dots\dots (1)$$

where

p_{te} = volumetric ratio of equivalent tensile longitudinal rebar, %

$F_c (=fc')$ = compressive strength of concrete, N/mm²

σ_{wh} = yield strength of the horizontal rebar

p_{wh} = volumetric ratio of horizontal rebar

σ_0 = axial load stress ratio to fc'

t_e = equivalent wall thickness, mm

j_e = distance between tension and compression resultants

Equation (1) is based on the experimental database, however, a/D of the most of the specimen in the database were 1.0 or more. In addition, when a/D would be 1.0 or less, 1.0 should be substituted for a/D according to the note^[1] of equation (1).

On the other hands, some past studies were reported that shear strength of a concrete wall with a/D of 1.0 or less might be increased. The reports indicated that shear strength of a concrete wall with a/D of 1.0 or less has much safety allowance.

A building with concrete walls must have superior seismic safety, because equation (1) would evaluate shear strength with much safety allowance as mentioned above. In other words, old buildings having concrete walls with a/D of 1.0 or less might

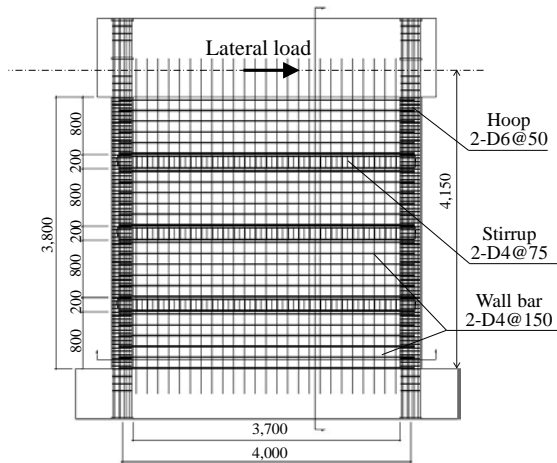


Fig. 1 Bar arrangement and the geometry (mm)

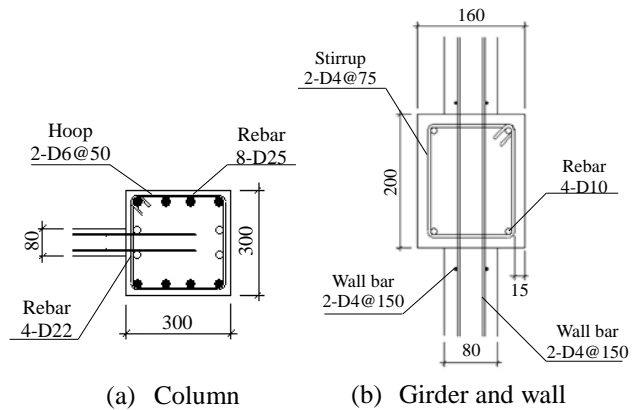


Fig. 2 Section of the column and girder (mm)

Table1 Concrete properties

Story	Young modulus (kN/mm ²)	Concrete strength (N/mm ²)	Tensile strength (N/mm ²)
1, 2	21.5	29.4	2.59
3, 4	23.2	26.6	2.36

have enough seismic safety, although they would be reported to lack of seismic safety in the seismic assessments for old buildings.

An old building assessed lack of seismic safety might be unnecessarily strengthened, though it might be safe. The key in a seismic assessment is the accuracy of the strength evaluation. Much of the safety allowance might be not necessarily valuable.

In this paper, a short height concrete wall with a/D of 1.0 or less was focused, an effect of rebar in a concrete wall was examined to evaluate shear strength of a concrete wall.

ANALYSIS

Our analysis must be verified at first, the analyses results would be examined next. The test specimen [2] was analyzed as shown Fig. 1 to 3.

The specimen was one-third scale, and had columns, girders and walls with rebar. The total height was 3,800mm (12.5 ft.) and the length between the center of the columns was 4,000mm (13.1 ft.). The section was 300mm (11.8 in.) square for the column, and the wall thickness was 80mm (3.2 in.).

The concrete strength was 29.4 N/mm² (4.3 ksi.) for the first and the second story, and 26.6 N/mm² (3.9 ksi.) for the third and the fourth story.

Table 1 to 3 show the material property of the re-

Table2 Rebar properties

Size (grade)	Location	Young modulus (kN/mm ²)	Yield strength (N/mm ²)	Tensile strength (N/mm ²)
D4(SD295A)	Wall	172	351	518
	Stirrup	163	323	490
D6(SD295A)	Hoop	190	366	491
D10(SD345)	Girder	185	385	594
D22(SD345)	Column	185	563	738
D25(SD345)	Column	185	535	722

Table3 Diameter and area of rebar

Imperial Bar Size	Soft Metric Size	JIS Size	Area (mm ²)
N/A	N/A	D4	14
N/A	N/A	D6	32
#3	#10	D10	71
#4	#13	D13	127
#5	#16	D16	199
#6	#19	D19	287
#7	#22	D22	387
#8	#25	D25	507

bar. The rebar was made based on the Japanese Industry Standard (JIS). The yield strength of D4 to D10 (#1 to #3) were 323 to 385 N/mm² (47 to 56 ksi.) as mild steel. D22 and D25 (#7 and #8) were quenched and the yield strength were 563 and 535 N/mm² (82 and 78 ksi.) respectively.

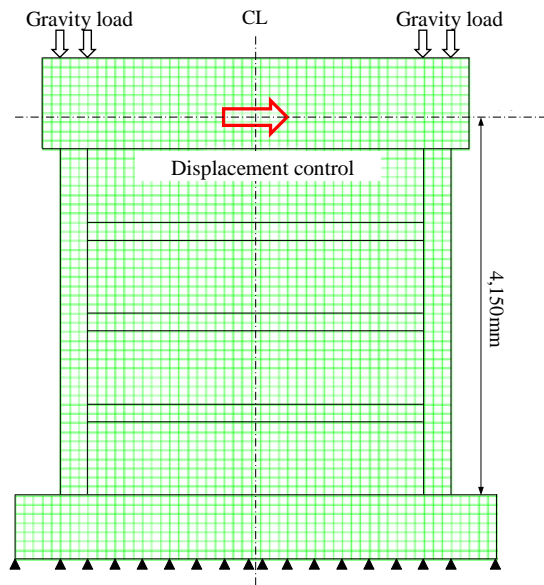


Fig. 3 Meshed model

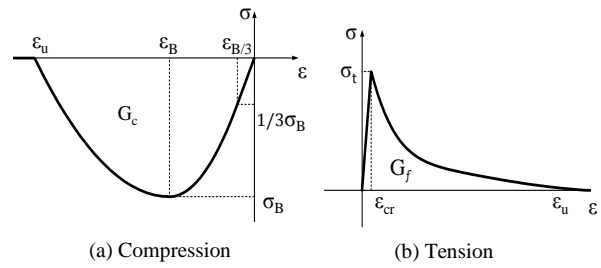


Fig. 4 Concrete model

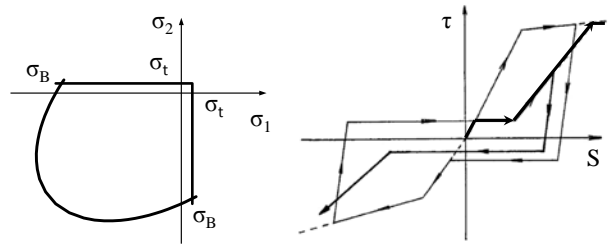


Fig. 5 Criterion

Fig. 6 Bond slip

Model

The specimen was modeled for the FE analysis as shown as Fig. 4 to 6. Four nodes and quadrate iso-parametric plan stress element is applied for concrete and each elements are 100mm square. Embedded element is applied for rebar. Bond slip is considered for longitudinal bar, and other bar is assumed to be perfectly bonded. The base stub is fixed, the gravity load and lateral displacement are forced at the top of the wall as shown Fig. 3.

All of four models has the same section and the same flexural moment strength, and only a/D is varied.

Material property

The parabola model of Feenstra^[3] is applied for the relationship between concrete stress and strain. 0.2% strain of maximum compressive stress is assumed. The fracture energy of 9.5N/mm for column and girder, and 7.2N/mm for wall are considered based on Nakamura, et al.^[4] Hordijk^[5] model with 0.1N/mm) of fracture energy is applied for the relationship between tensile stress and strain. The fracture criterion of concrete under biaxial stress is based on Von Mises yield criterion.

Rebar is modeled as bi-linear without strain hardening. Bond slip model is based on Morita, Kaku, and et al.^[6] as shown Fig 6.

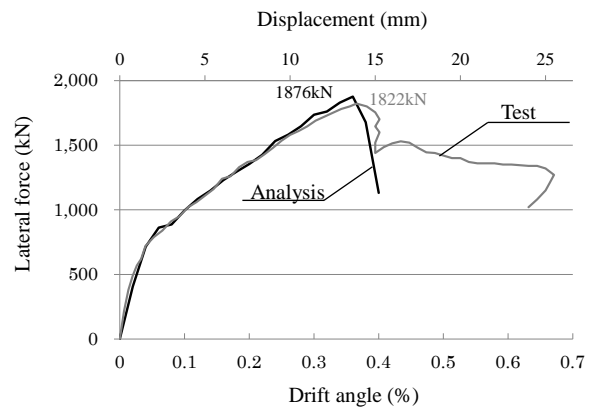


Fig. 7 Lateral force versus drift angle

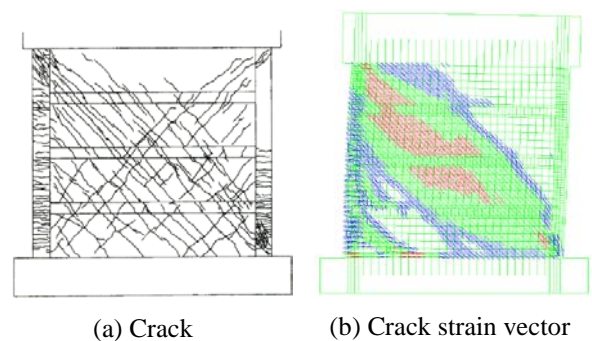


Fig. 8 Crack and Crack strain vector at the peak

VERIFICATION

Our analysis must be verified before the examination as mentioned. The analysis result of the hysteresis curve and the crack strain vector would be compared with the test result.

Hysteresis curve

Fig. 7 shows the lateral force versus drift angle. The maximum lateral force are 1,822kN at 0.37% drift angle in the test and 1,876kN at 0.36% in our analysis. Our analysis result is suited to the test result up to at around the peak, because the lateral strength in our analysis is 103% of one in the test.

Cracking

Fig. 8 shows the cracking in the test^[2] and crack strain vector in our analysis at 0.4% drift angle. The failure mode was concrete compressive failure at the bottom of the wall in both results. The diagonal crack was observed overall the wall in the test. The crack strain vector was shown overall the wall in our analysis. Good agreement was shown in the test and our analysis results up to at around the peak of about 0.4% drift angle.

RESULT

Our analysis was verified in the above section, because our analysis result was approximately suited to the test results. In this section, the additional three models were analyzed and the results were examined.

Table 4 shows the analysis models. Each model has a/D varied to 0.27, 0.50, 0.73 and 0.97. All of the four models had the same section of column, girder and wall.

The shear strength was given by the equation (1) as mentioned above.

The moment strength was given^[7] by

$${}_wM_u = a_t \cdot \sigma_{sy} \cdot l_w + 0.5 \Sigma(a_{wv} \cdot \sigma_{wy}) \cdot l_w + 0.5N \cdot l_w \quad (2)$$

where

a_t = longitudinal rebar area of the tensile side column, mm²

σ_{sy} = yield strength of the longitudinal rebar of the tensile side column, N/mm²

l_w = length between the both center of the column, mm

a_{wv} = vertical wall rebar area, N/mm²

σ_{wy} = yield strength of the vertical wall rebar, N/mm²

N = axial load, N

And the shear force at the flexural moment strength is

given by

$$Q_{mu} = {}_wM_u / a/D \quad (3)$$

Hysteresis curve

Fig. 9 shows the lateral load versus drift angle.

The stiffness was decreased following increase of the drift angle, and the lateral load reached to the maximum strength at the drift angle of 0.36% to 0.44%.

The drift angle 0.4% of at the maximum strength was indicated in the standard^[7], and the approximately same one was shown in the analysis results.

The maximum strength was decreased following increase of a/D , because the flexural moment is increased by a/D .

Table 4 Design strength

No.	a/D	Q_{mu} (kN)	Q_{su} (kN)	$\frac{Q_{su}}{Q_{mu}}$
1	0.97	3,553	1,556	0.44
2	0.73	4,681	1,556	0.37
3	0.50	6,858	1,631	0.30
4	0.27	12,821	1,631	0.20

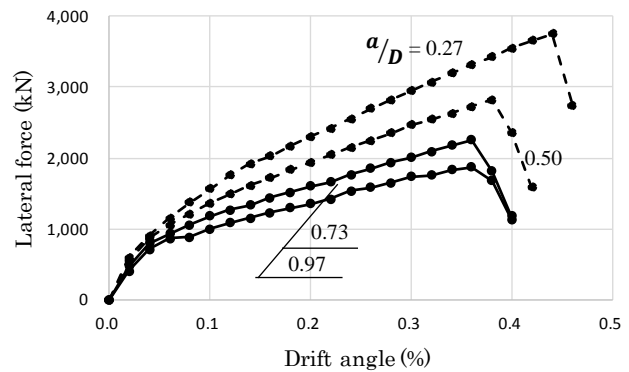


Fig. 9 lateral force versus drift angle

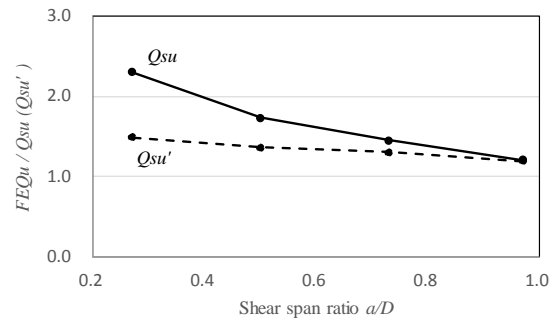


Fig.10 Comparison with analysis result versus Q_{su} and Q_{su}'

Comparison with design shear strength

Fig. 10 shows the strength ratio defined as ratio of the maximum lateral force in the analysis result to the design shear strength.

a/D of 1.0 or less as well as the models in this paper is out of the applicability in equation (1), because equation (1) was regressed in test data with a/D of 1.0 or more. In addition, few of tests with a/D of 1.0 or less were performed in past studies.

Equation (1) was applied to the analysis models, while they were out of the applicability in equation (1).

The solid line in Fig. 10 shows the strength ratio for Q_{su} by equation (1). The strength ratio for Q_{su} was at most 2.3. It indicated equation (1) overestimated to these models.

Q_{su} that the a/D even if it's 1.0 or less was substituted against the note ^[1] that 1.0 should be substituted when it's 1.0 or less was defined as Q_{su}' . The dash line in Fig.10 shows one for Q_{su}' . The strength ratio for Q_{su}' was better than one for Q_{su} .

It indicated a/D influenced to Q_{su} , even if the a/D was 1.0 or less.

Concrete compressive strut

Fig.11 shows concrete compressive strain distribution at the peak.

The strain at the left top and right bottom were the largest, moreover, the concrete compressive strut was formed from left top to the right bottom.

White lined area with black indicate the strain of 0.2% or more. Compressive strut width was increased from 300 to 2,700mm following decrease of a/D .

In addition, the strain of 0.2% or more was observed overall of the wall for the model with a/D of 0.27 as shown Fig.11(d).

Concrete compressive strut behavior was definitely changed when a/D was 1.0 or less.

Vertical rebar stress distribution

Fig.12 shows stress distribution of the longitudinal rebar and vertical wall rebar. The dash lined area indicated their yield stress.

Generally, vertical rebar was effective to flexural moment, and the flexural moment strength depend on the amount of the vertical rebar as shown

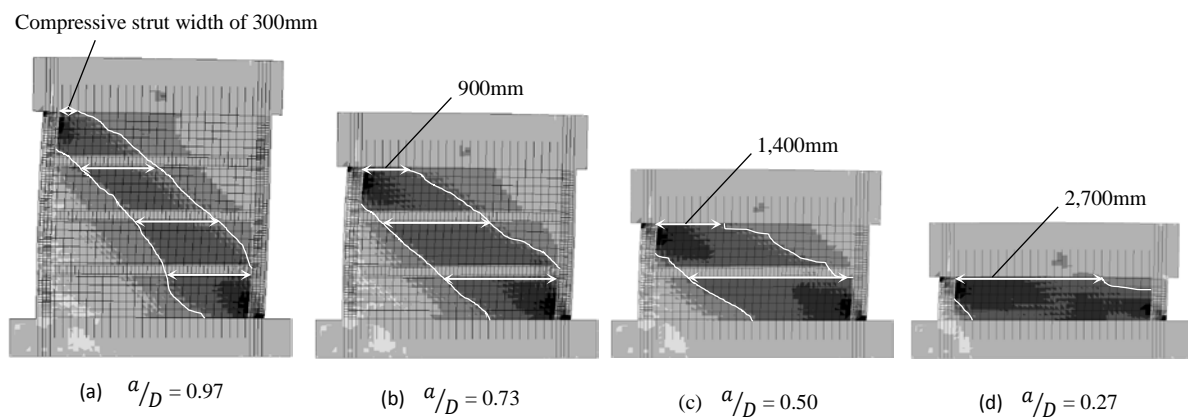


Fig. 11 Concrete strain distribution

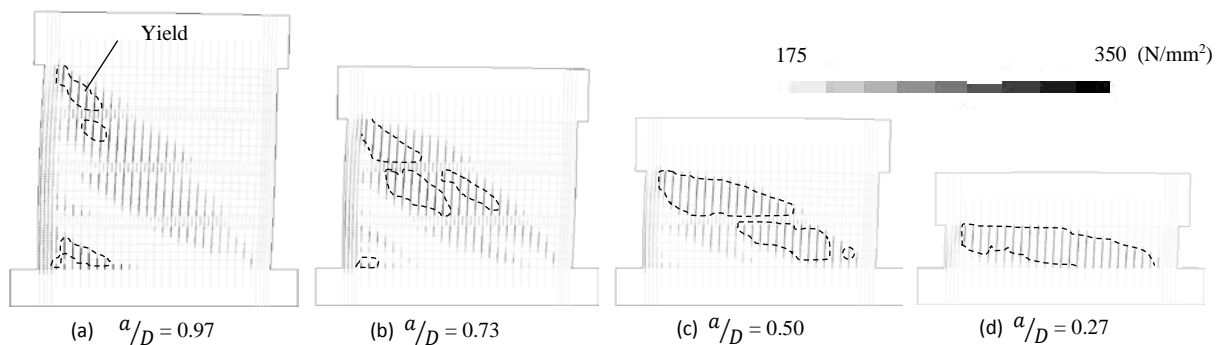


Fig. 12 Stress distribution of the longitudinal rebar and vertical wall rebar

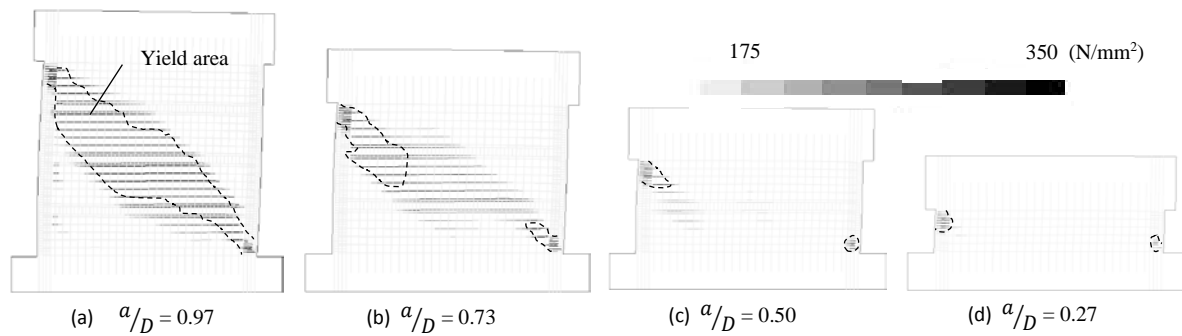


Fig. 13 Hoop and horizontal wall rebar stress

equation (2). In other words, the shear strength does not almost depend on the amount of the vertical rebar.

The tendency was observed in the model with a/D of 0.97 as shown in Fig.12 (a). However, their yield stress of the vertical rebar were observed the models with a/D of 0.73 or less as shown Fig.12 (b) to (d).

Namely, the vertical rebar was effective to increase the shear strength of the concrete wall with a/D of 0.73 or less.

Horizontal rebar stress distribution

Fig.13 shows stress distribution of the horizontal wall rebar. The dash-lined area indicated their yield stress.

Generally, horizontal rebar would be effective to shear force, and the shear strength would depend on the amount of the horizontal rebar in past studies.

The same tendency was observed in the model with a/D of 0.97 as shown in Fig.13 (a). However, their yield stress area of the horizontal rebar were decreased in the models with a/D of 0.73 or less as shown Fig.13 (b) to (d).

Namely, the horizontal rebar was not necessarily effective to increase the shear strength of the concrete wall with a/D of 0.73 or less.

Effective ratio to shear strength

Fig.14 shows effective ratio to design shear strength by equation (1).

Equation (1) is composed of three terms, concrete, horizontal wall rebar and axial load.

The effective ratio of concrete was slightly increased following decrease of a/D , although the compressive concrete strut width were definitely increased as shown Fig.11.

The effective ratio of horizontal wall rebar was

slightly decreased following decrease of a/D , although the yield area of the horizontal wall rebar were definitely decreased.

CONCLUSIONS

Four short height (short shear span) concrete walls were modeled and FE analyses were performed.

The result of the test and analysis was verified first, the concrete compressive strut and rebar stress distribution were examined.

Concrete compressive strut behavior was definitely changed when a/D was 1.0 or less, while the effective ratio of concrete was slightly increased following decrease of a/D .

Q_{su} that the a/D even if it's 1.0 or less was substituted against the note [1] that 1.0 should be substituted when it's 1.0 or less was defined as Q_{su}' . The strength ratio for Q_{su}' was better than one for Q_{su} .

The horizontal rebar effect was reduced, following decrease of the shear span, while the amount of the horizontal wall rebar was not depend on the shear span in equation (1).

Out of applicability for equation (1) to the concrete wall with a/D of 0.97 or less and the necessary to modify it were indicated.

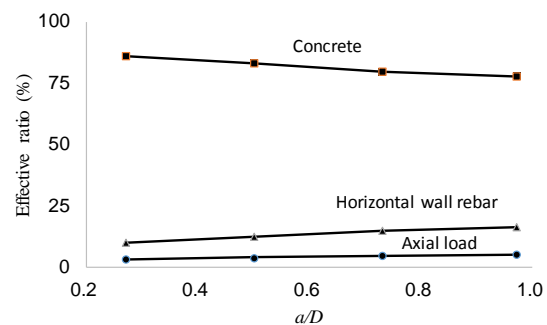


Fig.14 Effective ratio to design shear strength

ACKNOWLEDGEMENTS

The analyses results reported herein are based on M.S. thesis of Mamoru Kawasaki and Ryota Ishii at Tokyo City University. The authors also wish to express their gratitude to students in our laboratory.

REFERENCES

- [1] Structural engineering standard and guideline 2015 edition, Building Center of Japan (In Japanese)
- [2] Hiroki TAUCHI, Masaomi TESHIGAWARA, Yo HIBINO, Toshikatsu ICHINOSE, Hiroshi FUKUYAMA, EFFECT OF INNER BEAMS OF MULTI-STORY SHEAR WALL ON ITS SHEAR STRENGTH, Journal of structural engineering, Vol.56 B, pp61-66, 2010, March (In Japanese)
- [3] Feenstra, P.H., Computational Aspects of Biaxial stress in Plain and Reinforced Concrete, PhD Thesis, Delft University of Technology, 1993
- [4] H.Nakamura, T.Higai, Compressive Fracture Energy and Fracture Zone Length of Concrete, Seminar on Post-peak Behavior of RC Structures subjected to Seismic Loads, JCI-C51E, Vol.2, pp256-272, 1999
- [5] Cornelissen, H.A.W., Hordijk, D.A., and Reinhardt, H.W. Experimental Determination of Crack Softening Characteristics of Normal Weight and Light Weight Concrete, Heron 31, 2, 1986
- [6] Shirou Morita, Kaku Tetsuzou : Bond property between rebar and concrete under cyclic load, Journal of Structure and Construction Engineering, Architectural Institute of Japan, No.229, pp15-24, 1975, (In Japanese)
- [7] Japan Building Disaster Prevention Association (2017), Seismic Evaluation Standard and Commentary for Existing Concrete buildings (In Japanese)

FORECAST OF PRODUCTIVE AND BIOLOGICAL EFFECTS OF METAL NANOPARTICLES ACCORDING TO TOLERANCE INDEX

Elena Sizova^{1,2}, Sergey Miroshnikov¹, Nikolai Balakirev³

¹ Federal Research Centre of Biological Systems and Agro-technologies of the Russian Academy of Sciences, 29, 9 Yanvarya St, Orenburg 460000, Russia

² Orenburg State University, Pobedy pr. 13, Orenburg, 460018, Russia,

³ Moscow State Academy of Veterinary Medicine and Biotechnology named after K.I. Scriabin, 23, Academician Scriabin Street, Moscow, 109472, Russia

ABSTRACT

Nanoparticles (NPs) of metals find wide application in feed additives as sources of microelements. However, NPs of the same name, which differ in their production technology and basic characteristics, demonstrate various biological effects. This circumstance does not allow applying them in practice without preliminary studies and continuous safety control. In this connection, the research objective was a comparative study of biological effects of metal NPs in the inhibition test of bacterial bioluminescence using the genetic engineering luminescent strain *Echerichia coli* K12 TGI and the model of broiler chickens (*Gallus gallus*) in order to develop a method for predicting the effect of NPs used as a mineral fodder additive.

In the experiment, different-sized NPs of the same elements are compared: iron nanoparticles sized 50.0 ± 15 nm (Fe_aNPs) and iron nanoparticles sized 80.0 ± 5 nm (Fe_bNPs); copper nanoparticles sized 55.0 ± 15 nm (Cu_aNPs) and copper nanoparticles sized 103.0 ± 2 nm (Cu_bNPs). Studies have shown that metal NPs with different physicochemical characteristics show different activity against *E. coli* K12 TGI and have different productive effects on broiler chickens. The experimentally established constants of NP concentrations that determine the "quenching" of bioluminescence are closely related to the presence of biological action of metals on chicken model. A new criterion for predicting the productive effect of NPs is proposed - the tolerance index (TI). The balance of the toxic dose of metal-microelement (EC_{50} for *E. coli*) and the biological level of microelement consumption determines the biological meaning of TI for broiler chickens ($\text{mmol/kg W}^{0.75} \times 24$ hours). As follows from calculations for metal nanoparticles having $\text{TI} < 1$, the absence of a productive effect is characteristic, for metal nanoparticles having $\text{TI} > 1$, on the contrary, the growth-stimulating effect on the model of broiler chicken is characteristic. Signs of the presence of oxidative stress and cell cytolysis, revealed by the activity of ALAT, ACAT, LDG, GGT, CT, T-SOD, MDA were registered with the introduction of small-sized copper and iron nanoparticles with $\text{TI} < 1$.

Keywords: Bioluminescence, Iron and Copper nanoparticles, *E. coli* K12TGI, *Gallus gallus*, Tolerance index.

INTRODUCTION

By various estimates, the total world market of nanotechnologies will be from 3 [1] to 3.4 trillion USD by 2020 [2]. Nanotechnologies can significantly affect the agro-industrial complex and make this industry more efficient and environmentally friendly [3]. Obviously, nanomaterials (NPs) will find wide application in crop production due to growth promoters [4], fertilizers, pesticides and herbicides [5]. In veterinary medicine, NPs will be widely used as antibiotics [6], in the production and use of vaccines [7], for the diagnosis of diseases [8].

It is expected to use wide range of NPs for the creation of feed additives. The prospects of using NPs as sources of microelements [9], OVO additives [10], optimizers of the microbioma of animals, enhancers of immunity [11, 12] and reproduction [13], growth promoters [14], for correction of weight

gain composition and improvement of feed efficiency [15] have been shown.

Once in the digestive tract of broilers, nanoparticles give ions during digestion and they are further involved in metabolism. The main organs of biotransformation of nanoparticles are liver, spleen and kidneys. These organs, in general, are not used in human food. In the muscle tissue (meat) that a human consumes, nanoparticles do not accumulate. Thus, there is no reason to consider these nanoparticles environmentally hazardous.

Meanwhile, NPs of the same essential element, depending on the production technology, size, surface characteristics and other causes, exhibit different biological effects [16], [17], which does not allow using them in practice without preliminary studies and continuous monitoring of production.

Studies on farm animals require a lot of time and considerable resources. In this regard, research using simple biological models including *E.coli* are promising. These bacteria are a widespread model in

modern toxicology [18]. Especially, recombinant luminescent *E. coli* strains are popular, which provide detailed information on the biological activity of test compounds in real time [19]. Previously inducible luminescent bacteria of *E. coli* strains were widely used to assess the toxicity of a wide range NPs [20] - [23].

In this regard, the study was aimed at a comparative study of the biological effects of metal nanoparticles in the inhibition test of bacterial bioluminescence (*E. coli*) and on model of broiler chickens in order to develop a method for predicting the productive effect of nanoscale preparations.

MATERIAL AND METHODS

Production and Certification of NPs

NPs of iron and copper, produced by various technologies were used in the study. NPs were purchased from Advanced Powder Technologies (Russia) and the Institute of Energy Problems of Chemical Physics of RAS, (Russia). Material certification (Table 1) (particle size, polydispersity, volume, quantitative content of fractions, surface area) of the studied samples of metal nanoparticles included: electron scanning, transmission, atomic force microscopy using LEX T OLS4100, JSM-7401F, JEM-2000FX (JEOL, Japan). Size distribution of particles was studied on a Brookhaven 90Plus/BIMAS Zeta PALS and Photocor Compact (Fotokor, Russia) nanoparticles analyzer in lyzoles obtained by dispersing on an ultrasonic disperser UZDN-2T (Russia) under conditions f-35 kHz, N-300 W, A-10 μ A, for 30 minutes.

Table 1 – Physical and chemical characteristics of tested metal nanoparticles

NPs	Size, nm	Chemical and phase composition	Z-potential, mV	Specific surface $S_{sp}, m^2/g$
Cu _a	55 ±15	Cu ⁰ 99.7±2.5%	31±0,1	9±0,8
Cu _b	103 ±2	Cu ⁰ 96±4% CuO 4,0±0.4%	25±0,5	8±0,5
Fe _a	50 ±15	Fe ⁰ 99.8±0.2%	13±0,5	7,7±0,7
Fe _b	80±5	Fe ₃ O ₄ , α -Fe ₂ O ₃	15±0,2	32±2,3

Studies on *E. coli*

Estimation of toxic effects of the studied samples of metal nanoparticles was carried out in a wide range of equimolar concentrations (4 M - 6×10^{-6} M). The genetically engineered luminescent strain *E. coli* K12 TG1, constitutively expressing the luxCDABE genes of the natural marine microorganism

Photobacterium leiognathi 54D10, produced by Immunotekh NV (Russia, Moscow) in a lyophilized state was used as a bioengineering object under the commercial name «Ecolum».

The bacterial luminescence inhibition test was performed using a microplate spectrophotometer Infinite PROF200 (TECAN, Austria) dynamically recording the intensity of glow of the resulting mixtures within 180 minutes with intervals of 5 minutes. The results of the influence of nanomaterials on the intensity of bacterial bioluminescence (1) were estimated using formula:

$$I = \frac{I_{c0min} \times I_{tn min}}{I_{cnmin} \times I_{t0min}}, \quad (1)$$

where I_c and I_t are luminescence intensity of the control and the tested samples at the 0th and nth minutes of measurement.

Studies on *Gallus gallus*

Studies were carried out on broiler chickens "Smena-8" in the conditions of vivarium. Feeding of poultry was carried out with complete feed fodders, compiled taking into account the recommendations [24]. For the experiment, 200 broiler chickens aged 1 day were selected (selection condition is a good development, differences in live weight not more than 5%). At selection chickens were divided by sex. Based on data of individual daily weighing of chickens and accounting of feed costs by the method of pair analogues at 14 days of age, five groups (n = 40) were formed: one control (I) and four experimental (II, III, IV, V). Within the first 14 days, birds consumed the same diet, in the following (28 days) the chickens were transferred to an experimental diet. The diet of the control group was balanced by the estimated elements through additional sulfate administration, at a rate of 8 mg / kg iron and 1.7 mg/kg copper. In the diet of chickens of II and III groups, ferrous sulfate was replaced by Fea and Feb NPs, in the diet of IV and V groups copper sulfate was replaced by Cua and Cub in equivalent dosages. Lysozoles of nanoparticles were prepared by an ultrasonic treatment of aqueous suspensions of NPs. Then, lysozoles were introduced to the mixed fodder by stepwise mixing.

Blood samples were taken from birds in the morning, on an empty stomach, before slaughter at 21, 28, 35 and 42 days old from the axillary vein. Biochemical blood analysis was performed on an automatic biochemical analyzer CS-T240 (Dirui Industrial Co., Ltd, China) using commercial biochemical sets for veterinary DiAVetTest (Russia) and commercial biochemical kits Randox Laboratories Limited (UK).

In the course of studies, the size of the pool of 24 chemical elements in the body of chickens was estimated. The slaughter was carried out at the end

of the experiment - at the age of 42 days. The method of euthanasia was used: decapitation under nembutal anesthesia. Individually, for each animal, feather, skin, flesh of carcass, internal organs, gastrointestinal tract, internal fat, blood, etc. was weighed. Then, the elemental composition of tissue homogenate was determined. The size of pool of chemical elements in the body was established by summing the weight of elements in separate organs and tissues.

Elemental Analysis

The content of elements in the resulting ash was estimated using an Elan 9000 mass spectrometer (Perkin Elmer, USA) and an Optima 2000 V atomic emission spectrometer (Perkin Elmer, USA). The size of pool of chemical elements in body was established by summing the weight of elements in separate organs and tissues.

Statistical Analysis

Performing the research, we proposed a new evaluation criterion for metal NPs - potential preparations – micronutrients as a tolerance index (TI):

$$TI = \frac{EC_{50}}{c} \quad (2)$$

being: - EC_{50} – concentrations of preparation that cause a 50% quenching of biosensor luminescence (*E. coli* K12 TG1 with cloned luxCDABE-genes of *P. leiongnathi* 54D10) compared to control, M;
- C-biotic level of consumption, mmol/kg W0,75 × day; for copper it was 0.0048 mole/kg, for iron it was 0.052 mol/kg.

The statistical analysis of results was carried out using Statistika-10 computer software package. Statistical comparison of the results was carried out using The Mann-Whitney U-test and Student's t-test. The parameter $P < 0.05$ was taken as the limit of significance.

RESULTS AND DISCUSSION

Assessment of biotoxicity of nanoparticles using bacterial luminescence inhibition test

The activity degree of NPs upon contact with *E. coli* K12 TG1 with cloned luxCDABE genes *P. leiongnathi* 54D10 is shown in Table 2.

Table 2 - Toxicity degree* of different concentrations of NPs after 60 min of contact with *E. coli* K12 TG1 with cloned lux CDABE-genes *P. leiongnathi* 54D10.

Concentration, M	NPs			
	Cu _a	Cu _b	Fe _a	Fe _b
0,25	Tox	Tox	EC ₇₀	EC ₃₀
0.1	Tox	Tox	EC ₅₀	NOEC
0.05	Tox	Tox	EC ₂₀	NOEC
0.025	Tox	Tox	EC ₃₀	NOEC
0.0125	Tox	EC ₇₀	NOEC	NOEC
0.00625	EC ₇₀	EC ₅₀	NOEC	NOEC
0.003	EC ₅₀	EC ₂₀	NOEC	NOEC
0.0015	EC ₂₀	NOEC	NOEC	NOEC

*Tox – concentrations causing 100 % luminescence quenching of biosensor; EC₇₀, EC₅₀, EC₃₀, EC₂₀ – concentrations causing 70, 50, 30, 20 % luminescence quenching comparison with control; NOEC – concentrations with no effect [25].

The obtained results allowed to calculate the EC₅₀ value - the molar concentration causing 50% inhibition of bacterial bioluminescence in comparison with the control after different exposure (Table 3).

Table 3 - EC₅₀ (M) values after contact of *E. coli* K12 TG1 test organism and cloned luxCDABE-genes *P. leiongnathi* 54D10 and the studied ultrafine particles

NPs	Duration, min		
	60	120	180
Cu _a	3×10^{-3} ±0.004	3×10^{-3} ±0.002	3×10^{-3} ±0.0001
Cu _b	6.25×10^{-3} ±0.003	6.25×10^{-3} ±0.001	6.25×10^{-3} ±0.0002
Fe _a	5×10^{-2} ±0.00031	5×10^{-2} ±0.00031	5×10^{-2} ±0.00031
Fe _b	> 0.25	> 0.25	> 0.25

The peculiarities of the synthesis technology determined the same effect of 50 % bioluminescence inhibition at 60th min of contact for Cu_aNPs 0.003 M and Cu_bNPs 0.00625 M in nanoform.

Table 4 - EC₅₀ (M) values after contact of *E. coli* K12 TG1 cloned luxCDABE-genes *P. leiongnathi* 54D10 with test preparation

Substance	Duration of contact, min		
	60	120	180
CuSO ₄ ×5H ₂ O	$4 \times 10^{-5} \pm$ 0.000072	$2 \times 10^{-5} \pm$ 0.000043	$6 \times 10^{-6} \pm$ 0.000001
FeSO ₄ ×7H ₂ O	$1 \times 10^{-5} \pm$ 0.00008	$1 \times 10^{-5} \pm$ 0.000014	$5 \times 10^{-6} \pm$ 0.0000011

Biological evaluation of mineral salts used as control showed luminescence inhibition at all time stages of contact (60-180 min) (Table 4).

Growth intensity of broiler chicken

The productive effect of the compared preparation of iron and copper NPs, estimated by live weight increase of chickens, was different (Table 5).

Feeding with Fe_aNPs was accompanied by a decrease in live weight gain of broiler chickens during the experimental period by 8.4% ($P \leq 0.01$), Cu_aNPs by 12.4% ($P \leq 0.01$) in comparison with the control.

Table 5 - Dynamics of live weight of broiler chickens, g

Index	Control	NPs administered with feed			
		Fe _a	Fe _b	Cu _a	Cu _b
Live weight, g	2470.0 ±32.6	2285.3 ±24.9*	2590.0 ±29.9*	2194.7 ±23.4*	2573.0 ±35.8*
Live weight gain, g	2238.9 ±21.23	2051.8 ±19.31	2353.9 ±18.23	1961.4 ±17.54	2334.9 ±20.21
Weight gain difference compared, %	0	- 8.4	5.1	- 12.4	4.3

Note: * - a significant difference of the experimental groups with the control group ($P \leq 0.05$)

At the same time feeding with Fe_bNPs was accompanied by an increase in live weight gain by 5.1% ($P \leq 0.05$), the use of Cu_bNPs resulted in weight gain increase by 4.3% ($P \leq 0.05$) relative to the control.

Biochemical parameters of blood serum of broiler chickens

Data on bioindication on the model of *E. coli* have been confirmed in studies on poultry (Fig. 1).

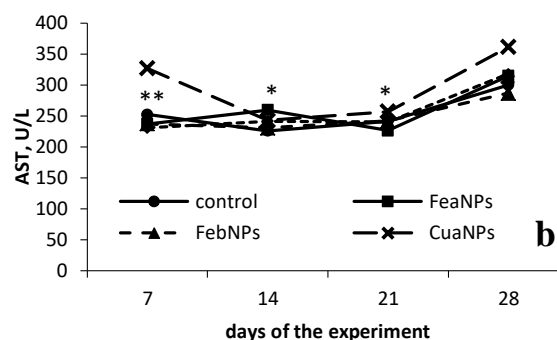
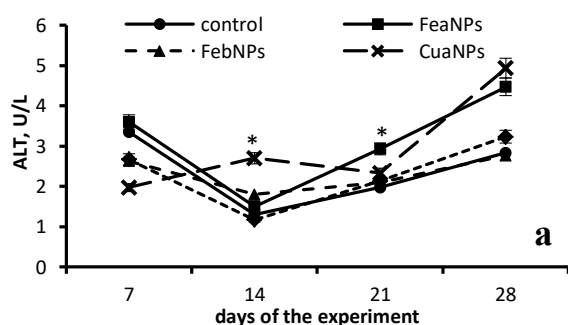


Figure 1. Selected ALT (a) and AST (b) of broiler chickens ($n = 10$); * - a significant difference of the experimental groups with the control group $P \leq 0.05$, ** - $P \leq 0.01$

The catalytic activity of aminotransferases as a consequence of metabolic shifts against the background of the introduction of NPs into the body of broiler chickens, is different from the control values. Thus, the use of Fe and Cu_aNPs in feeding in contrast to their analogues was accompanied by a more significant increase in the activity of alanine aminotransferase (ALT), and aspartate aminotransferase (AST) in blood serum.

We found no significant increase in activity of serum gamma-glutamyl transferase (GGT) and lactic dehydrogenase (LDH). LDH activity largely more than the control, was recorded on the 21st and 28th days of the experiment against the background of feeding with small-sized Fe_aNPs and Cu_aNPs (Fig. 2 a, b).

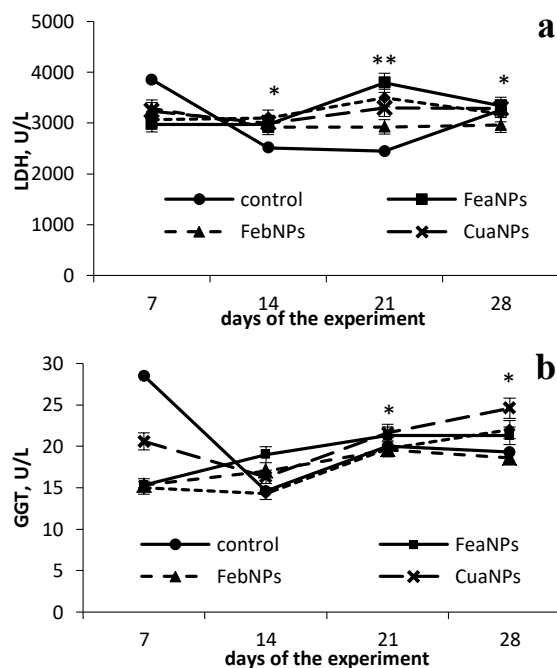


Figure 2. Selected LDG (a) and GGT (b) of broiler chickens ($n=10$); *-a significant difference of the experimental groups with the control group $P \leq 0.05$.

Such dynamics of GGT and LDH activity may indicate the destruction of membranes of a small population of cells and weak induction of microsomal oxidation under the influence of metal NPs of variable valence [26]. At the same time, increasing exposure duration up to 28 days, the activity of GGT against the background of feeding with Cu_aNPs increased by 27% ($P < 0.05$), while feeding with Fe_aNPs - by 10.3% ($P < 0.05$), which can be estimated as a sign of oxidative stress, induced by small-sized NPs [27].

Prooxidant and Antioxidant Activity of blood broiler chickens

The dynamics of the activity of CT and SOD indicated the manifestation of oxidative stress during feeding with Fe_aNPs and Cu_aNPs (Table 6, 7).

Table 6. Prooxidant and antioxidant activity of blood broiler chickens crosses Smena 8 ($n = 10$).

Days	Control	NPs	
		Fe _a	Fe _b
CT, μm H ₂ O ₂ /l×min			
7	9160.3	9193.2	8011.2
	±89.48	±278.45	±68.07
14	7516.1	11688.5	6480.3
	±98.06	±233.16***	±66.35
21	8162.7	15726.1	4566.4
	±54.39	±323.75**	±67.33
28	5431.4	15792.6	4234.4
	±95.90	±154.01**	±72.39
SOD, activity unit/Hb mg			
7	641.6	724.4	740.4
	±22.59	±42.89	±19.51
14	323.3	654.9	656.0
	±17.43	±23.93	±39.65
21	1291.3	883.4	944.9
	±46.59	±45.57	±26.24
28	869.4	409.0	646.0
	±43.35	±29.28**	±3320
MDA, μm/l			
7	0.11±0.068	0.15±0.026*	0.12±0.039
14	0.11±0.006	0.14±0.036	0.12±0.011
21	0.11±0.003	0.17±0.007**	0.13±0.006
28	0.12±0.011	0.12±0.011	0.12±0.011

Note:* - a significant difference of the experimental groups with the control group $P \leq 0.05$, ** - $P \leq 0.01$, *** - $P \leq 0.001$

Peaks of CT indices were recorded after feeding with Fe_aNPs (14th, 21st and 28th days, with difference with the control by 1.5 ($P < 0.001$), 1.9 ($P < 0.01$), 2.9 times ($P < 0.01$). The difference in CT activity when feeding with large NPs (Fe_b, Cu_b) was less pronounced, and at some points below control values.

Table 7. Prooxidant and antioxidant activity of blood broiler chickens crosses Smena 8 ($n = 10$).

Days	Control	NPs	
		Cu _a	Cu _b
CT, μm H ₂ O ₂ /l×min			
7	9160.3	8897.7	10473.7
	±89.48	±75.94	±142.77
14	7516.1	17923.4	12423.4
	±98.06	±156.65**	±179.18*
21	8162.7	3951.9	4581.4
	±54.39	±57.14	±90.45
28	5431.4	6336.7	5483.1
	±95.90	±67.30	±98.98
SOD, activity unit/Hb mg			
7	641.6	582.7	684.2
	±22.59	±3388	±20.26
14	323.3	763.2	742.2
	±17.43	±29.43*	±58.09
21	1291.3	2671.3	1194.6
	±46.59	±120.79**	±99.10
28	869.4	252.8	508.0
	±43.35	±14.14**	±27.36*
MDA, μm/l			
7	0.11±0.068	0.18±0.040	0,10±0.034
14	0.11±0.006	0.14±0.029	0,14±0.019
21	0.11±0.003	0.14±0.013	0,16±0.028
28	0.12±0.011	0.13±0.011	0.11±0.013

Note:* - a significant difference of the experimental groups with the control group $P \leq 0.05$, ** - $P \leq 0.01$

The administration of Cu_aNPs caused a surge in CT activity on the 14th day of the experiment (difference with the control by 2.4 times), by 21 and 28 days the activity of CT was below the control values. Apparently, in response to increased lipid peroxidation and accumulation of hydrogen peroxide and other products of oxidative stress, CT is activated, which metabolizes them and prevents their accumulation in cells.

Elemental Status of Broiler Chickens

The use of metal NPs as microelement preparations did not equally affect the exchange of some optimized elements. An increase of iron in chickens after feeding with Fe_bNPs was 37.2% ($P \leq 0.05$), while using Fe_aNPs was only 2.3%. Feeding with Cu_aNPs was accompanied by an increase in the content of copper in the body by 51.4% ($P \leq 0.05$), Cu_bNPs by 65.5% ($P \leq 0.01$).

The use of the similar nanoparticles was accompanied by various changes in elemental status of chickens. Thus, feeding with Fe_b NPs leads to an increase in the deposition of iron in body by 34% ($P \leq 0.01$) compared with the level achieved by feeding with Fe_aNPs.

The similar copper NPs show the same trend. Thus, the deposition of copper during the consumption of Cu_bNPs is higher by 9.3% ($P \leq 0.05$) in comparison with Cu_aNPs.

The preparation of nanoforms is considered as one way to increase the bioavailability of food components [28], including trace elements [29], [30]. This determines the interest in creating new food and feed additives with nano-sized components [31].

Meanwhile, the unique prospects for using NPs are largely related to their extraordinary biological properties. The small size, ability to penetrate into tissues and organs, high surface area [32] form previously unknown biological effects, including toxicity. Therefore, as new technologies of nanoparticle synthesis are developed, and because of high variability of properties of the same substances [33], [17], the need to create effective methods for predicting biological effects of NP by simple and accessible methods becomes evident. It includes maximal replacement of tests with animals used [34].

Therefore, methods using various test organisms are increasingly used [35].

One of the promising are tests of bacterial bioluminescence inhibition [36], it is confirmed by toxicity tests for a wide range of chemicals [37], [38] and environmental samples, including wastewater, waste, soil, etc. [39], [40].

Assessment of the experimental material accumulated in the course of our work has made it possible to establish various effects of NP preparations of the same metal. This was expressed both in changes of biological activity in microorganism strain, and in various productive effects on the model of chickens. In particular, Cu_aNPs with a size of 55 nm caused a 100% quenching in the dilution series to a concentration of 0.0125 M, 50% and 20% at concentrations of 0.003 and 0.002 M, while Cu_bNPs with a 103 nm had a smaller toxicity, providing 100% inhibition of bioluminescence in the concentration range from 4 to 0.025 M. The dilutions that did not have a significant effect on bacterial luminescence, were characterized as biotic doses, and began at 0.00078 M and below.

It should be pointed out that Fe_bNPs and Fe_aNPs have differences in biological activity already observed at the 60th minute of contact, with a similar trend after prolongation of contact up to 120 and 180 min.

The *E. coli* K12TG1 test proved to be promising for predicting the productive effect of trace element preparations on the model of broiler chickens. In particular, using iron nanoparticles we showed that Fe_aNPs demonstrated EC₅₀ at a dose of 0.05 M on the model of *E. coli*. At the same time, on the model of broiler chickens, Fe_aNPs had no increase in bird growth rate, etc. At the same time, Fe_bNPs, demonstrating EC₅₀ at a dose of 0.25 M on the

model *E. coli*, in contrast, had a growth-stimulating effect on *Gallus gallus*.

It should be noted that our data are consistent with earlier studies [41] with more than four dozen chemicals used as samples, and it was demonstrated that EC₅₀ for *P. Phosphoreum* inhibition of bioluminescence correlates ($p = 0.20-0.79$) with acute toxicity data for daphnia, fish, animals and human cell lines, rodents, dogs and humans. Thus, an increase in the activity of ALT and AST in blood of experimental animals receiving NPs indicates the presence of cytolysis processes. The increase of MDA is registered against the background of the consumption of Fe_aNPs. It can be caused either by an increase in the formation of peroxides and a decrease in the activity of antioxidant defense enzymes, in response to the chronic effects of low-frequency metals [42]. The use of Fe_aNPs and Cu_aNPs was accompanied by an increase in the content of essential and conditionally essential microelements in the poultry organism to 1.96 and 2.14 $\mu\text{mol} / \text{g}$, which exceeded these values in groups receiving Fe_b and Cu_b by 17.7% ($P \leq 0.05$) and 45.9% ($P \leq 0.01$), respectively. A similar difference in the content of macronutrients in the body was 17.9% ($P \leq 0.05$) and 40.4% ($P \leq 0.05$), respectively. At the same time, feeding Fe_aNPs and Cu_aNPs was accompanied by a decrease in the content of toxic elements in the body to 0.0396 and 0.0577 $\mu\text{mol/g}$, or 32.1% ($P \leq 0.05$) and 8.7%, respectively.

Analysis of the experimental material let us propose a new criterion for predicting the productive effect of NPs - the tolerance index (TI). The biological significance of TI is determined by the proportionality of toxic dose of the metal-trace element (EC₅₀ for *E. coli*) and the biological level of consumption by broiler chickens. As follows from our calculations of metal NPs with a value of $TI < 1$, there is no productive effect on the model of broiler chickens, which is probably determined by toxicity. At the same time, on the contrary, growth-stimulating effect is characteristic of metal NPs with $TI > 1$. In particular, TI of Fe_aNPs was 0.96, while TI Fe_bNPs was greater than one (4.8). A similar dynamics of TI was demonstrated by copper NPs. Thus, TI of Cu_aNPs = 0.63, TI of Cu_bNPs = 1.3.

The tolerance index can be used to predict the productive effect of metal NPs. In fact, expressing the productive effect (Δm) after the use of NP preparation (the difference in live weight gain of the control and experimental groups) through the tolerance index can be expressed in two equations of linear dependence.

$$(\text{FeNPs}) \Delta m = 3.52 \text{ TI} - 11.8$$

$$(\text{CuNPs}) \Delta m = 25.7 \text{ TI} - 29.1$$

Obviously, the coefficients 3.52 and 25.7 correspond to the tangent of the slope of the direct dependence of Δm from TI to the abscissa axis. The

biological significance of these values is the "speed" of the increase of NP effects after feeding to animals. It can be assumed that the difference in the rate of increase of the effect from the use of CuNPs and FeNPs is 7.3 times. This is similar to the difference in the value of biogenic standards of consumption of these two metals (each copper atom in the bird's diet, prepared according to the modern standards, should contain 7 to 8 iron atoms).

CONCLUSION

The productive effect of metal nanoparticle preparations produced by various technologies can be predicted by calculating the tolerance index - EC₅₀ inhibition ratio of *E. coli* bioluminescence and the biological level of micronutrient consumption by broiler chickens.

ACKNOWLEDGEMENTS

The research was performed with financial support of the Russian Science Foundation, project No. 14-16-00060 P

REFERENCES

- [1] Roco M.M., The long view of nanotechnology development: the National Nanotechnology Initiative at 10 years. *J Nanopart Res.*, No.13, 2011, pp.427-445.
- [2] Hooley G. and Piercy N.F., Nicoulaud B Prentice Hall/Financial Times; London: Marketing Strategy and Competitive Positioning. (ISBN 9780273740933), 2012.
- [3] Sabourin V. and Ayande A., Commercial opportunities and market demand for nanotechnologies in agribusiness sector. *J Technol Manag Innov*, No.10, 2015, pp. 40-51.
- [4] Mishra S., Keswani C., Abhilash P.C., Fraceto L.F. and Singh H.B., Integrated Approach of Agri-nanotechnology: Challenges and Future Trends *Front Plant Sci.*, No.8, 2017, pp. 471.
- [5] Sekhon B.S., Nanotechnology in agri-food production: an overview. *Nanotechnol Sci Appl.*, No.7, 2014, pp. 31-53.
- [6] Wang L., Hu C. and Shao L., The antimicrobial activity of nanoparticles: present situation and prospects for the future. *Int J Nanomedicine*, Vol. 14, Issue 12, 2017, pp. 1227-1249.
- [7] Cheng J., Wen S., Wang S., Hao P., Cheng Z., Liu Y., Zhao P. and Liu J., gp85 protein vaccine adjuvanted with silica nanoparticles against ALV-J in chickens. *Vaccine Jan.*, Vol.5, No.35(2), 2017, pp 293-298.
- [8] Emami T., Madani R., Rezayat S.M., Golchinfar F. and Sarkar S., Applying of gold nanoparticle to avoid diffusion of the conserved peptide of avian influenza nonstructural protein from membrane in Western blot. *J Appl Poult Res.*, Vol. 21. No.3, 2012, pp. 563-566.
- [9] Zhang J. and Spallholz J., Toxicity of selenium compounds and nano- selenium particles. In: Casciano D, Sahu SC, editors. *Handbook of Systems Toxicology*. West Sussex, UK: John Wiley and Sons, 2011.
- [10] Bakyaraj S., Bhanja S.K., Majumdar S. and Dash B., Modulation of post-hatch growth and immunity through in ovo supplemented nutrients in broiler chickens. *J Sci Food Agric.*, No.92, 2012, pp. 313-320.
- [11] Fondevila M., Herrer R., Casallas M.C., Abecia L. and Duchá J.J., Silver nanoparticles as a potential antimicrobial additive for weaned pigs. *Animal Feed Science and Technology Vol. 150*, No.3-4, 2009, pp. 259-269.
- [12] Pineda L., Sawosz E., Lauridsen C., Ricarda M.E., Jan E., Hotowy A., Sawosz F. and Chwalibog A. Influence of in ovo injection and subsequent provision of silver nanoparticles on growth performance, microbial profile, and immune status of broiler chickens. *Open Access Anim Physiol.*, No.4, 2012, pp.1-8.
- [13] Safa S., Moghaddam G., Jozani R.J., Daghigh Kia H. and Janmohammadi H., Effect of vitamin E and selenium nanoparticles on post-thaw variables and oxidative status of rooster semen. *Anim Reprod Sci.*, No.174, 2016, pp.100-106.
- [14] Yausheva E., Miroshnikov S., Sizova E., Miroshnikova E. and Levahin V.I., Comparative assessment of effect of cooper nano and microparticles in chicken. *Oriental Journal of Chemistry*, Vol. 31, No. 4, 2015, pp. 2327-2336.
- [15] Wang M.Q., Wang C., Li H., Du Y.J., Tao W.J., Ye S.S. and He Y.D., Effects of chromium-loaded chitosan nanoparticles on growth, blood metabolites, immune traits and tissue chromium in finishing pigs. *Biol Trace Elem Res.*, No.149, 2012, pp.197-203.
- [16] Arsenyeva I.P., Zotova E.S., Folmanis G.E., Glushchenko N.N., Baytukalov T.A., Olkhovskaya I.P., Bogoslovskaya O.A., Baldokhin Yu.V., Dzidziguri E.L. and Sidorova E.N., Certification of metal nanoparticles used as biologically active preparations. *Nanotechnics*, No.10, 2007, pp. 72-77.
- [17] Yang L., Kuang H., Zhang W., Aguilar Z.P., Xiong Y., Lai W., Xu H. and Wei H., Size dependent biodistribution and toxicokinetics of iron oxide magnetic nanoparticles in mice. *Nanoscale*, Vol. 14, No.7(2), 2015, pp. 625-636.
- [18] Girotti S., Ferri E.N., Fumo M.G. and Maiolini E., Monitoring of environmental pollutants by bioluminescent bacteria. *Analytica Chimica Acta*, No.608(1), 2008, pp. 2-29.
- [19] Ivask A., Bondarenko O., Jephthina N. and Kahru A., Profiling of the reactive oxygen species-related ecotoxicity of CuO, ZnO, TiO₂, silver and fullerene nanoparticles using a set of recombinant luminescent *Escherichia coli* strains: differentiating the impact of particles and solubilised

metals. *Analytical and Bioanalytical Chemistry*, No.398(2), 2010, pp. 701-716.

[20] Deryabin D.G., Aleshina E.S. and Efremova L.V., Application of the inhibition of bacterial bioluminescence test for assessment of toxicity of carbon-based nanomaterials. *Microbiology*, No.81(4), 2012, pp. 492-497.

[21] Jia K., Marks R.S. and Ionescu R.E., Influence of carbon-based nanomaterials on lux-bioreporter *Escherichia coli*. *Talanta*, No.126, 2014, pp. 208-213.

[22] Efremova L.V., Vasilchenko A.S., Rakov E.G. and Deryabin D.G., Toxicity of Graphene Shells, Graphene Oxide, and Graphene Oxide Paper Evaluated with *Escherichia coli* Biotests. *Biomed Res Int* 869361, 2015.

[23] Deryabin D.G., Efremova L.V., Karimov I.F., Manukhov I.V., Gnuchikh E.Y. and Miroshnikov S.A., Comparative Sensitivity of the Luminescent Photobacterium phosphoreum, *Escherichia coli*, and *Bacillus subtilis* Strains to Toxic Effects of Carbon-Based Nanomaterials and Metal Nanoparticles. *Mikrobiologiya*, No.85(2), 2016, 177-186.

[24] Fisinin V.I., Egorov I.A., Lenkova T.N., Okolelova T.M., Ignatova G.V. and Shevyakov A.N., Methodical instructions on optimization of recipes for mixed fodders for agricultural poultry. VNITIP. M., 2009. 80.

[25] Jackson P., Jacobsen N.R., Baun A., Birkedal R., Kühnel D., Jensen K.A., Vogel U. and Wallin H., Bioaccumulation and ecotoxicity of carbon nanotubes. *ChemCent J*, Vol 13, No.7(1), 2013, p. 154.

[26] Karlsson H.L., Cronholm P., Gustafsson J. and Möller L., Copper oxide nanoparticles are highly toxic: a comparison between metal oxide nanoparticles and carbon nanotubes. *Chem Res Toxicol*, No.21(9), 2008, pp.1726-1732.

[27] Hussain S.M., Hess K.L., Gearhart J.M., Geiss K.T. and Schlager J.J., In vitro toxicity of nanoparticles in BRL 3A rat liver cells. *Toxicol In Vitro*, No.19(7), 2005, pp. 975-983.

[28] Maarit J.R., Renouf M., Cruz-Hernandez C., Actis-Goretta L., Thakkar S.K. and Pinto M. da S., Bioavailability of bioactive food compounds: a challenging journey to bioefficacy. *Br J Clin Pharmacol*, No.75(3), 2013, pp.588-602.

[29] Raspopov R.V., Trushina É.N., Gmshinskiĭ I.V. and Khotimchenko S.A., Bioavailability of nanoparticles of ferric oxide when used in nutrition. Experimental results in rats. *Vopr Pitan*, No.80(3), 2011, pp. 25-30.

[30] Kowalczyk M., Banach M. and Rysz J., Ferumoxytol: a new era of iron deficiency anemia treatment for patients with chronic kidney disease. *J Nephrol*, No.24(6), 2011, pp. 717-722.

[31] Bhupinder S.S., Nanotechnology in agri-food production: an overview. *Nanotechnol Sci Appl*, No.7, 2014, pp. 31-53.

[32] Barbu E., Molnar E., Tsibouklis J. and Gorecki D.C., The potential for nanoparticle-based drug delivery to the brain: overcoming the blood-brain barrier. *Expert Opin Drug Deliv*, No.6(6), 2009, pp. 553-565.

[33] Yu S.S., Scherer R.L., Ortega R.A., Bell C.S., O'Neil C.P., Hubbell J.A. and Giorgio T.D., Enzymatic- and temperature-sensitive controlled release of ultrasmall superparamagnetic iron oxides (USPIOs). *J Nanobiotechnology*, Vol.27, No.9(7), 2011.

[34] Carere A., Stamatii A. and Zucco F., *In vitro* toxicology methods: Impact on regulation from technical and scientific advancements. *Toxicol Lett*, No.127, 2002, pp. 153-160.

[35] Lopes I., Ribeiro R., Antunes F.E., Rocha-Santos T.A., Rasteiro M.G., Soares A.M., Gonçalves F. and Pereira R., Toxicity and genotoxicity of organic and inorganic nanoparticles to the bacteria *Vibrio fischeri* and *Salmonella typhimurium*. *Ecotoxicology*, No.21(3), 2012, pp. 637-648.

[36] Deryabin D.G. and Aleshina E.S., Effect of salts on luminescence of natural and recombinant luminescent bacterial biosensors. *Appl Biochem Microbiol*, No.44, 2008, pp. 292-296.

[47] Loibner A.P., Szolar O.H.J., Braun R. and Hirmann D., Toxicity testing of 16 priority polycyclic aromatic hydrocarbons using Lumistox. *Environ Toxicol Chem.*, No.23, 2004, pp. 557-564.

[38] Mortimer M., Kasemets K., Kurvet I., Heinlaan M. and Kahru A., Kinetic *Vibrio fischeri* bioluminescence inhibition assay for study of toxic effects of nanoparticles and colored/turbid samples. *Toxicol. In Vitro*, No.22, 2008, pp. 1412-1417.

[39] Wang C., Yediler A., Lienert D., Wang Z. and Kettrup A., Toxicity evaluation of reactive dyestuff, auxiliaries and selected effluents in textile finishing industry to luminescent bacteria *Vibrio fischeri*. *Chemosphere*, No.46, 2002, pp. 339-344.

[40] Manusadzianas L., Balkelyte L., Sadauskas K., Blinova I., Pöllumaa L. and Kahru A., Ecotoxicological study of Lithuanian and Estonian wastewaters: Selection of the biotests and correspondence between toxicity and chemical-based indices. *Aquat. Toxicol*, No.63, 2003, pp. 27-41.

[41] Kahru A., Ecotoxicological tests in non-ecotoxicological research: Contribution to the three Rs. Use of luminescent photobacteria for evaluating the toxicity of 47 MEIC reference chemicals. *ALTEX*, No.23, 2006, pp. 302-308.

[42] Ates M., Arslan Z., Demir V., Daniels J. and Farah I.O., Accumulation and toxicity of CuO and ZnO nanoparticles through waterborne and dietary exposure of goldfish (*Carassius auratus*). *Environ Toxicol*, No.30(1), 2015, pp. 119-128.

3D MODEL-BASED IMAGE REGISTRATION FOR CHANGE DETECTION IN HISTORICAL STRUCTURES VIA UNMANNED AERIAL VEHICLE

Apichat Buatik¹ and Krisada Chaiyasarn²

^{1,2} Department of Civil Engineering, Thammasat University, Pathumthani, Thailand

ABSTRACT

Visual inspection is a common technique to detect and examine the state of health of structural system. Periodic inspection is carried out to determine if anomalies, such as cracks and surface paint, found in previous visits have changed in appearance over time. The image-based change detection techniques require accurate geometrical and photometrical corrections in pre-processing steps to minimize errors. Although several techniques have been proposed to remove geometrical errors, they still fail to align image correctly, which often results in inaccuracy in a change detection system. In this paper, a change detection system is proposed to tackle this problem. The system acquired images via an unmanned aerial vehicle. Then, the acquired images were manually processed to identify damages, such as cracks, which were used to guide a drone to obtain more images of damages areas for monitoring purpose. The images were then used to obtain a 3D surface model and camera calibration through Structure from Motion (SfM), which were used in the image synthesis technique to obtain an image with identical camera parameters as a queried image for accurate geometrical adjustment. The synthesized images were used to compare with the queried image to see if there were changes between them. In this research project, we showed that the drone can be used to monitor problematic areas and the image synthetic technique via 3D modelling can be used in geometrical registration to improve a change detection system.

Keywords: Visual inspection, Change detection, UAVs, Structure from Motion, Historical buildings.

INTRODUCTION

Visual inspection is a common procedure to examine and assess the current state of historical buildings. However, this procedure is laborious and time-consuming as it normally involved inspectors travelling to interested sites to assess the structures' conditions based on their visual appearance. Hence, the process cannot be conducted frequently due to high labour cost, prone to human-error, site accessibility. Failure to detect problems can lead to disastrous effects.

Many temples in Ayutthaya province, Thailand, contain damages, such as plants growing on the structures and cracks. These structures may require frequent monitoring and inspection to assess if the structures need repair. The change in damages in these structures require closed monitoring to determine if the damages require intervention. This research project aims at improving techniques in change detection to determine if the structures and damages have changed in appearance over time. This project explored the use of an unmanned aerial vehicle for data collection, which is also used to acquire images of problematic areas for monitoring. The acquired images are used in the proposed change detection system, which exploits the technique called Structure from Motion to help removing geometrical errors, a common problem in change detection systems.

Figure 1 shows example pictures of cracks in a stupa from Wat Chai Wattanaram obtained from a DSLR camera. This temple has been deteriorating due to natural disasters, in which the Fine Arts department began a renovation program in 1969 and the city was declared a UNESCO World Heritage Site in 1991. Yet, this site still has areas where damages are present; therefore, frequent inspection and monitoring is required. In this paper, we propose techniques to improve a change detection system. We first obtained images via an Unmanned Aerial Vehicle (UAV) to build a reference 3D model from images via the Structure from Motion technique. Then, the obtained images were manually identified for interested areas from the re-constructed 3D model, in which the locations of the areas were used to guide the drone to obtain more images of such areas. The 3D model was then used to create synthetic images, which were used to compare with the real images to create change masks. This process is called geometrical registration, which is essential in removing unwanted noise due to viewpoint difference in a change detection process. The contribution of this paper is, firstly, we show that the 3D model from SfM can be used to guide the drone to monitor problem areas, and secondly, we propose a new technique in geometrical registration to improve change detection systems.

The rest of the paper is organized as follows, Section 2 is Literature Review, which summarizes

previous work in visual inspection and 3D modelling, and change detection systems. The methodology is explained in Section 3, and Section 4 presents experiments, results and discussion. The paper ends with conclusion in Section 5.



Fig. 1 Example image of cracks on the surface of stupas visible in many locations around Wat Chai Wattanaram, a temple located in the historic province of Ayutthaya, Thailand.

RELATED WORK

Historical inspection based on image-based 3D modelling

Three-dimensional digital technologies, such as 3D laser scanners, have been utilised in the conservation works of historical sites, such as in surveying, in archiving and in damage inspection. The technologies offer a number of advantages including speed, convenience, cost-saving and accuracy. For inspection and damage assessment, Armesto [10] applied Terrestrial Laser Scanner (TLS) in a masonry bridge to estimate the bridge deformation based on an arch symmetry. Fregonese [12] applied Terrestrial Laser Scanner to monitor out-of-plane displacement of an ancient building by registering two sets of laser scan data to several georeferenced control points, and monitor from difference in displacements. Pieraccini [13] measured the tilt angle of the “Torre del Mangia” (Mangia’s tower) in Siena (Italy) using 3D information from TLS. Costanzo [1] presented a methodology that combined Terrestrial Laser Scanner and infrared thermal image for inspection of St. Augustine Monumental in Calabria (South Italy). Achille [7] demonstrated the applicability of photogrammetry using Unmanned Aerial Vehicle (UAV) to survey the historical structure “Santa Barbara” bell tower in Mantua (Italy). Pesci [3] applied TLS with digital images to detect the trace of restoration in the ancient part of Palazzo d’Accursio in Bologna, Italy. Kouimtzoğlu [17] applied image data from DSLR camera to create a structural plan to restore the Plaka Bridge, an ancient structural heritage in Greece.

The use of digital images in visual inspection is important in providing information about the current state of structural systems. However, its limitations due to inaccessible areas, in which abnormalities may be present, makes the inspection problem hard. This

problem may be overcome by the use of an Unmanned Aerial Vehicle (UAV). Achille [7] applied photogrammetry using Unmanned Aerial Vehicle (UAV) to survey the Santa Barbara, which is historical structure in Mantua (Italy). Bhakapong [4] used a 3D model created from the SfM technique to estimate the tilt angle of Wat Yai Chai Monkol in Ayutthaya Thailand, in which the images were obtained using a drone. It can be seen that UAVs have been applied in the inspection work of historical sites to aid with the data collection process, which can be cumbersome.

Change Detection

Change detection is a technique that can be used to detect changes in anomalies such as cracks on structures’ surface. A change detection system normally consists of pre-processing steps (i.e. geometrical and photometric adjustments) and a change detection step. The pre-processing steps remove unwanted noise, which is not a real change, from images before the change detection step is applied. Lim [11] propose a system for monitoring the changes in cracks from multi-temporal images. The system is based on a 2D projective transformation that can accurately extract the size of the cracks, which are then monitored in the images as cracks propagate. Delaunoy [8] applies an SFM system to synthesize new views by using geometric adjustment for change detection in coral reef. In this work, it is concluded that an SFM system provides an accurate method for synthesizing new views for change detection. Guo [9] proposed the detection of change (i.e. change detection) is the main component in image interpretation for pipe inspection. Guo [9] presented algorithms for crack detection generally involve a pre-processing step and a crack identification step. The preprocessing step applies image processing techniques to extract potential crack features, such as edges. Chen and Hutchinson, [6] propose a framework for concrete surface crack monitoring and quantification. The method is based on optical flow, which is used to track the movement of cracks. The regions, where the cracks become larger, are labelled as having changed. Chaiyasarn, [5] proposed a system for multi-view change detection using images to detect changes of crack on a concrete beam with the use of the SfM for geometrical adjustment. Saur and Krüger [15] present a change detection system using images obtained from a UAV to detect changes between image pairs from video frames. It can be seen that pre-processing steps are important for change detection systems, in

which this project is aimed to tackle.

METHODOLOGY

Figure 2 shows the outline of the method proposed in this paper. The system starts with image acquisition (explained in section 3.1), where two sets of images are collected, the first set S_1 taken at time t_1 is used for creating a reference 3D model, and the second set S_2 is taken at time t_2 is images of interested areas for monitoring purpose. The images from S_1 is input into Image-based 3D modelling module (explained in Section 3.2) to build a 3D model. The images from S_2 are then registered into the 3D model in the Camera registration module. In the Image synthesis step, a 3D model is rendered using the camera parameters from a queried image I_q , which is a real image from either the set S_1 or S_2 to create a synthesized image I_s (explained Section in 3.3). This process is called geometrical adjustment, which is an essential pre-processing process in change detection to remove noise due the effect from different camera viewpoint. In the Change detection module, a change mask is created from I_s and I_q to see if there are changes between images (explained in Section 3.4).

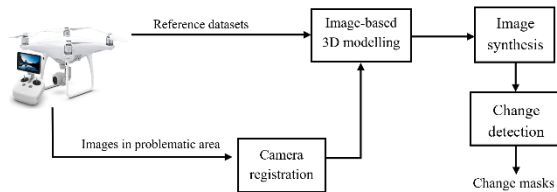


Fig. 2 The outline of the proposed system.

Image acquisition

Firstly, images are collected to create a reference set S_1 for creating a 3D model. We collected images by a UAV using the Point of Interest (POI) flight strategy to ensure a full coverage of the stupa and to obtain a highly-detailed 3D model. Figure 3(a) show the POI strategy, in which the drone flies around an interested object in a circular motion. The flight strategy can be pre-programmed for a radius from an interested object and height. The UAV's camera was programmed to fixate its viewing angle to a stupa. The UAV was programmed to collect images every 2-3 seconds as it moved around the stupa and the images were collected from 3 different heights, i.e. high, mid and ground levels. The ground level was collected manually as the POI cannot be applied as it was too low and the UAV will hit obstruction on the ground level. Example images obtained from the UAV are shown in Figure 3(b). In this work, the UAV flight paths were pre-programmed in an iOS application and a DJI Phantom 4 was used. Note that

the GPS of each image were also recorded such that the positions images can be registered and estimated in a 3D model.

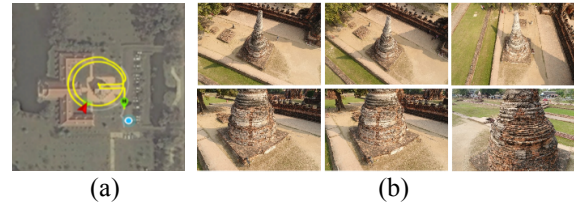


Fig. 3 (a) An image showing the Point of Interest flight path for a UAV to collect images around a stupa, (b) Example images of a stupa from Wat Chai Wattanaram.

Image-based 3D modelling

The images from Section 3.1 are used to create a 3D model of a stupa in Wat Chai Wattanaram using the Agisoft Photoscan software package, which is based on Structure from Motion and interested readers can refer to Snavely [14] for more detail of the theory and technology. Figure 4(a) shows a sparse point cloud model of a stupa and Figure 4(b) shows a dense point cloud model with camera calibrations for all images. As shown Figure 4(b), each camera also has latitude and longitude information, which helps with creating the 3D model. To obtain a watertight model, a mesh can be created to provide a more realistic 3D model as shown in Figure 5(a). The mesh is composed of a collection of triangular mesh, in which texture from 2D images is projected onto. The textured model is shown in Figure 5(b).

Camera registration

Images from the reference set S_1 are then identified for interested areas either manually or automatically from the 2D images. An example of an interested area is where cracks appear, in which cracks can be detected automatically from 2D images, but automatic crack detection is beyond the scope of this study. In this work, we manually identified interested areas manually and the latitude and longitude of the images of the interested areas were used to collect more images from the site as shown in Figure 6. The new set of images or S_2 are registered onto S_1 by matching similarity between images and by using the GPS information in Agisoft. The 3D model was then re-optimized to update the camera parameters. As shown in Figure 6, we obtained more images at the interested locations by using the drone to collect more close-up images of the areas.

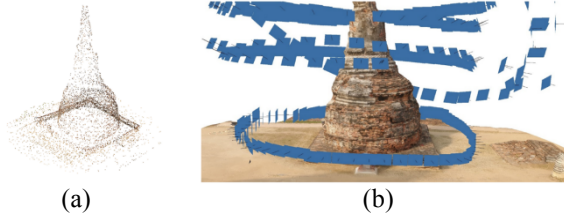


Fig. 4 (a) a sparse 3D point cloud of a stupa (b) a dense point cloud model with camera calibration.

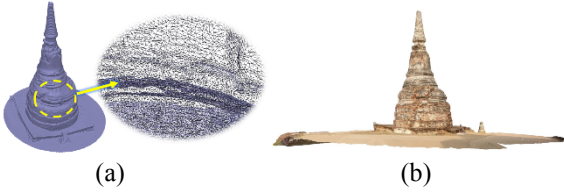


Fig. 5 (a) 3D mesh model of a stupa, (b) a textured model of a stupa.

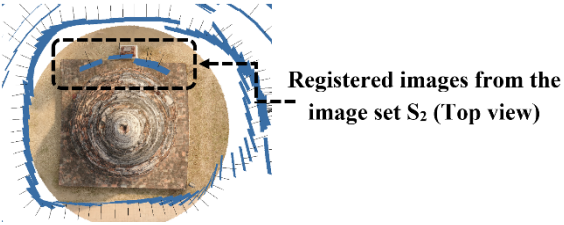


Fig. 6 A new set of images is registered onto the reference 3D model, viewed from the top.

Image synthesis

A textured 3D model and camera parameters from Section 3.2 are used to synthesize an image from an interested area. This is a geometrical adjustment process, where a real image is compared with a synthesized image as if they are viewed from an identical viewpoint and location. A queried image is a real image, which can be from either S_1 or S_2 will be called I_q with the camera parameters as a rotation matrix R_q and a translation vector t_q and an intrinsic matrix K_q with a set of reference 3D surface as P_r , a synthesized image I_s can be created using the following equation,

$$I_s = K_q [R_q t_q] P_r \quad (1)$$

Figure 7(a) shows an example of a real queried image I_q and synthesized image I_s , the two images must also be adjusted photometrically. We correct images photometrically by the histogram matching technique. Also, we applied a mask to blackout the background on I_q such that the two images are as similar as possible. Figure 7(b) shows a queried

image with lighting adjusted and the background is removed. As shown in the Figure 7(b) and (c), I_q and I_s appear to have identical viewpoints and similar lighting.

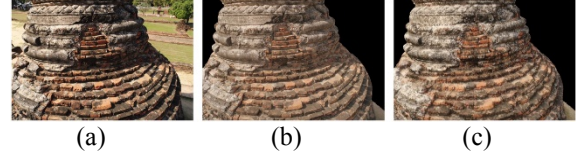


Fig. 7 (a) original queried image I_q , (b) a queried image I_q with photometrical adjustment and mask applied, and (c) a synthesized image I_s .

Change detection

Similarity measure

We applied similarity measure to compare similarity between images. The Mean Squared Error (MSE) method is applied, this metric indicates difference between two images, 0 means perfect similarity and 255 means the two images are dissimilar. MSE can be described as

$$MSE = \frac{1}{mn} \sum_{i=0}^{m-1} \sum_{j=0}^{n-1} [I(i, j) - K(i, j)]^2 \quad (2)$$

where $I(i, j)$ is a pixel value at i, j of image 1 and $K(i, j)$ is a pixel value of image 2.

Change mask

To create a change mask, we compared pixel values between I_s and I_q by subtracting gray scale values between the two images using the following equation,

$$D(x) = |I_s(x) - I_q(x)| \quad (3)$$

Then the change mask $B(x)$ is generated according to the following decision rules using the following equation.

$$B(x) = \begin{cases} 1 & \text{if } |D(x)| > \tau \\ 0 & \text{otherwise} \end{cases} \quad (4)$$

Where τ is a specified threshold. The threshold is usually chosen empirically in order to produce different change masks.

EXPERIMENTS AND RESULTS

Image-based 3D modelling

In our experiment, we collected images for a reference set S_1 using a UAV and applied the Circular POI flight paths at the 30, 35 and 40 meters. We also collected images manually on the ground level to ensure the full coverage. The UAV was pre-programmed to take pictures every 2-3 seconds to ensure that an overlap between consecutive images is at least 50%. We collect 520 images of size 5472 x 3642 from a stupa in Wat Chai Wattanaram. Also, we collected 5 images for the set S_2 , and this set contains closed-up views of images of an interested area.

The reference 3D model of a stupa has 6,658 points for a sparse model, 5,195,908 points for a dense model, and 10,848,033 mesh for a mesh model. Figure 4 and 5 show the results of our work, the sparse model, the dense model and the textured model. As can be seen from the figure, the dense and textured model provide good 3D visualization for the temple.

For camera registration, Agisoft can register images using GPS and without using GPS. Table 1 shows the results of registration errors when GPS was applied. As can be seen from the table, the errors from all images from S_2 is large and the values are more than 10. This large error is not acceptable. The errors occurs due to that fact that when we collected the dataset S_2 , our starting positions was not in a similar location as the starting position when we collected the S_1 data. This results in the errors in the GPS information. Therefore, in our experiment, we did not use GPS in our registration process. The registration process without GPS works by image matching based on automatically detected keypoints, such as Scale Invariant Feature Transform (SIFT) keypoints (see Snavely [14]) and camera locations are estimated by Triangulation methods. Nevertheless, using the GPS information will provide better estimate for camera parameters in the real world coordinates.

Table 1 The results of accuracy in image registration using GPS.

Example of dataset	Picture name	Accuracy (m)	Error (m)
S_1	DJI_0576	10	1.519775
S_1	DJI_0577	10	1.477171
S_2	DJI_0646	10	27.562193
S_2	DJI_0662	10	27.063962
S_2	DJI_0697	10	26.596530







Change detection

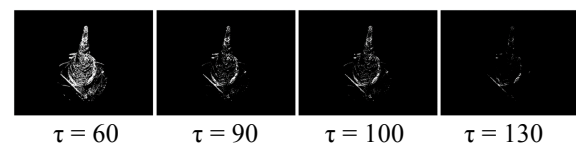
In this experiment, we applied the change detection technique for queried and synthetic images in 3 different distance from the stupa, far, medium and close. It is worth noting that there are no changes

occurred between the datasets S_1 and S_2 as the time difference between the two timeline is not large enough for any change to occur. The change in structures is a slow process, and to observe a change can be difficult. Therefore, in our experiment, we expect to see no change in our sets of pictures. Table 2 shows the summary results from example images. It can be seen from the table that the far images have the smallest MSE, while the close-up images have the largest MSE. This means that the far images are the most similar. This is due to the fact that the texture of our 3D model is not fine enough to provide sufficient detail in the synthetic images. Our 3D model is created from images that are taken from far distance, therefore the detail of the 3D model we obtained can only be as fine as the far images can provide. To obtain a more detailed 3D model, more close-up images of the stupa may be required.

Figure 8 shows the results of change masks between image pairs in different threshold. The changed pixels are in white and the non-change pixels in black. As mentioned, we expect no change between image pairs. As can be observed from the results, higher threshold is more accurate as seen in small number of changed pixels in all image pairs. We can also observe that changed pixels are still present irrespective of threshold set, and these changed pixels are from noise due to the 3D model that does not provide sufficient details for synthetic images. Nevertheless, we can see that for our result to work, we need to set higher threshold.

Table 2 A summary table of Mean Square Errors between queried and synthetic images

Distance from Stupa	Query image	Synthesis image	MSE (pixel ²)
Far (from S_1)			117.54
Medium (from S_1)			250.06
Close-up (from S_2)			2,053.73



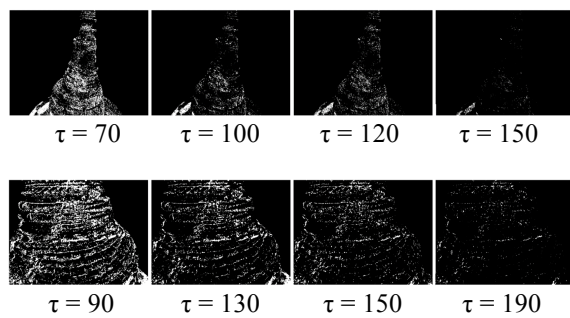


Fig. 8 Change masks from sample images in various thresholds, (Top) far distance image pair, (middle) medium distance, and (bottom) close distance.

Discussion

This paper proposed techniques to guide a drone to monitor problem areas and a new technique in geometrical registration for a change detection system. It can be seen that the UAV can be used to monitor problematic areas periodically and obtain flight paths to acquire more images in these areas. The images acquired later can be used to update the 3D model such that the model will be more detailed and allow synthetic images to be more realistic. The system can be combined with damage detection system so that problematic areas can be identified automatically, although this is beyond the scope of this paper. In order to get more accurate 3D models, the models should be created using GPS, therefore the UAV must be taken off in similar locations when collecting data at different times. Nevertheless, this research project has demonstrated that we can use a drone to monitor problematic areas.

This research project demonstrates the method to create synthetic images from a 3D model to remove geometrical errors in change detection systems. To improve our results, we require a better 3D model. The current watertight 3D model used in our work may not be sufficient to provide a more realistic synthetic image. Since the watertight model available is created from mesh, in which the texture in each mesh has been smoothened, therefore there will be loss in the details of a synthetic image due to the smoothing process. To improve the 3D model, more closed up images may be required. The propose change detection algorithm is simple, it may not be suitable for a complex surface, like historical structures. Nevertheless, our method may work well with simpler surface, such as concrete surface.

Since changes can be slow process and to verify a change detection system with real datasets can be cumbersome. A laboratory work is required to verify our method, which we aim to publish in the future.

CONCLUSION

The pipeline of a change detection system for historical structures via a guided UAV is presented in this study. The system acquires images via a UAV, in which the acquired images are manually processed to find damages and a 3D model. The UAV can be guided to acquire more image from the problematic areas for periodical inspection and monitoring.

The research proposed method for accurate geometrical adjustment in a change detection system. The adjustment method was achieved by creating a synthetic image from a 3D model. The results of our synthetic image provide a result which can help to remove geometrical errors, although further improvement is required to make a 3D model better to allow a more detail synthetic image for a change detection system to work.

ACKNOWLEDGEMENT

The authors would like to thank the Research Division, Faculty of Engineering, Thammasat University, Thailand Research Fund and the Fine Art Department in Thailand for providing funding and support for the research project.

REFERENCE

- [1] Costanzo, A., Minasi, M., Casula, G., Musacchio, M. and Buongiorno, M., "Combined Use of Terrestrial Laser Scanning and IR Thermography Applied to a Historical Building", *Sensors*, 15(1), 2014, 194-213.
- [2] Agisoft LLC., Agisoft PhotoScan User Manual : Professional Edition, Version 1.2 downloads: http://www.agisoft.com/pdf/photoscan-pro_1_2_en.pdf, 2016.
- [3] Pesci, A., Bonali, E., Galli, C. and Boschi, E., "Laser scanning and digital imaging for the investigation of an ancient building: Palazzo d'Accursio study case (Bologna, Italy)", *Journal of Cultural Heritage*, 13(2), 2012, 215 – 220.
- [4] Bhadrakom, B. and Chaikasarn, K., "As-built 3D modelling based on structure from motion from deformation assessment of historical buildings", *International Journal of GEOMATE*, 11(24), 2016, 2378 – 2384.
- [5] Chaikasarn, K., *Damage Detection and Monitoring for Tunnel Inspection based on Computer Vision*, University of Cambridge, 2014.
- [6] Chen, Z. and Hutchinson, T., "Image-based framework for concrete surface crack monitoring and quantification." *Advances in Civil Engineering*, 2010.
- [7] Achille, C., Adami, A., Chiarini, S., Cremonesi, S., Fassi, F., Fregonese, L. and Taffurelli, L., "UAV-Based Photogrammetry and Integrated

- Technologies for Architectural Applications Methodological Strategies for the After-Quake Survey of Vertical Structures in Mantua (Italy)”, *Sensors*, 15(7), 2015, 15520-15539.
- [8] Delaunoy, O., Gracias, N., and Garcia, R., “Towards detecting changes in underwater image sequences.” *OCEANS 2008-MTS/IEEE Kobe Techno-Ocean*, 2008, 1–8.
- [9] Guo, W., Soibelman, L., and Garrett, J., “Automated defect detection for sewer pipeline inspection and condition assessment.” *Automation in Construction*, 18(5), 2009, 587–596.
- [10] Julia Armesto-González, Belén Riveiro-Rodríguez, Diego González-Aguilera, and M. Teresa RivasBrea., Terrestrial laser scanning intensity data applied to damage detection for historical buildings. *Journal of Archaeological Science*, 2010, 37(12):3037–3047.
- [11] Lim, Y., Kim, G., Yun, K., and Sohn, H., “Monitoring crack changes in concrete structures.” *Computer-Aided Civil and Infrastructure Engineering*, 20, 2005, 52–61.
- [12] Luigi Fregonese, Gaia Barbieri, Luigi Biolzi, Massimiliano Bocciarelli, Aronne Frigeri, and Laura Taffurelli. Surveying and monitoring for vulnerability assessment of an ancient building. *Sensors*, 13(8):9747– 9773, July 2013.
- [13] Pieraccini, M., Dei, D., Betti, M., Bartoli, G., Tucci, G. and Guardini, N., “Dynamic identification of historic masonry towers through an expeditious and no-contact approach: Application to the Torre del Mangia in Siena (Italy)”, *Journal of Cultural HerCombined Use of Terrestrial Laser Scanning and {IR} Thermography Applied to a Historical Buildingitage*, 15(3), 2014, 275-282.
- [14] Snavely, N., Seitz, S., and Szeliski, R., “Photo tourism: exploring photo collections in 3d.” *ACM Transactions on Graphics*, 25(3), 2006, 835–846.
- [15] Saur, G. and Kruger, W., “Change detection in UAV video mosaics combining a feature based approach and extended image differencing”. *The International Archives of the Photogrammetry, Remote Sensing and Spatial Information Sciences*, 2016, Volume XLI-B7.
- [16] Szeliski, R., *Computer vision : algorithms and applications* . Springer- Verlag New York, Inc, 2010.
- [17] Kouimtoglou, T., Stathopoulou, E. K., Agraftotis, P. and Georgopoulos, A., Image-based 3D reconstruction data as an analysis and documentation tool for architects: the case for the Plaka bridge in Greece, *The International Archives of the Photogrammetry, Remote Sensing and Spatial Information Sciences*, Volume XLII-2/W3, 2017, 1–3 March 2017, Nafplio, Greece.

DEFECT-DRIVEN DEVELOPMENT: A NEW SOFTWARE DEVELOPMENT MODEL FOR BEGINNERS

Wacharapong Nachiangmai, Sakgasit Ramingwong and Kenneth Cosh
Department of Computer Engineering, Faculty of Engineering,
Graduate School, Chiang Mai University, Thailand.

ABSTRACT

It is normal for software developers to find some problems with their software design, especially during their beginner days. Defect-driven development (DDD) is a concept proposed to tackle such problems. DDD utilizes benefits of software defect knowledge base by collecting defects data from experienced programmers and teach beginners to avoid these problems. This method can help beginners to produce more high quality software. This research implemented the DDD concept for undergraduate students and compared their performance with the generic personal software process.

Keywords: Defect-driven development, Software development model, Quality software development, Personal software process, Personal process improvement.

INTRODUCTION

In academic, during the beginning of general software development programs, students take courses to increase their comprehension of how software works in real-world situations [1]. Gradually, they keep on practicing to gain more understanding of the discipline. As their experience grows, they learn how to prioritize tasks, complete their job and, simultaneously, learn how to avoid causing software defects.

The software quality process focuses on controlling product quality and aims to produce non-defective or less-defective products. In real situations, defects can be created at every stage of software process [2]. For example, the defects could be originated by stakeholders, the product owner, or the software development team since the requirement engineering phase. Moreover, different environments could be the cause of errors, e.g., hardware specification, platform and the social environment, including culture and tradition, etc.

The general software process consists of 5 steps as follows: requirement analysis, design, construction, test, and delivery and maintenance. Research in 1992 [2] reported that the defects can occur in every phase of the software process. Those software defects could be avoided with increasing the experience of software developers. With a sufficient level of cautiousness and experience,

engineers are more likely to develop their code without repeating their old mistakes.

As mentioned earlier, inexperienced software developers tend to create more simple defects than experienced ones. In addition, such defects may be caused by the changes of development environment. The defect format normally occurs in the repetitious and similar format [2]. So, this research focuses on whether the beginner software developers can use the defect knowledge from experienced software developers to decrease defects in their projects.

This research attempts to introduce a new approach which facilitates the software process for software developers, especially the beginners. Its objective is to decrease potential errors of the products produced by novice developers. Several tools such as software defect pattern is used in this concept.

The concept of Defect-driven Development (DDD)

The concept of “Defect-driven Development (DDD)” that uses the knowledge of software defects to preventively drive the software process. The knowledge base of software defects is collected from every step of the software process by experienced software developers. Then it is normalized to a standard format and rearranged as the software defects pattern for beginners.

The principle of the Defect-driven Development (DDD) focuses on proactive activities to check the design and types of error that it might lead to and how to avoid them before coding. This is done by referencing software defect knowledge that was previously collected from experienced software developers. Software developers can use defect information in the design phase to decide either to deal with those defects or redesign that software to avoid problems. DDD's objective is similar to those of Test-driven Development (TDD) hoping that developers foresee the potential problems before coding stage. The difference is TDD involves a design of unit tests before coding which may not be a natural process for beginners; while DDD more subtly adds a defect checklist during the design. This arguably makes a slight but important change in the process and is likely to be more comfortable for beginners. Yet, both concepts can be implemented simultaneously.

This idea proposes the benefits of using the software defect knowledge from the expertise for producing a framework for beginner software developers. Moreover, this can provide some basic suggestions on how to solve common problems and beginners could learn how to develop software together with the software defect management. These would entail the quality software developers in the future.

Each symbol in detail-design is mapped to the category of software defect in the knowledge of software defect. Then, the system would show defect information that are related with the function in the designed format for example in a checklist or table, etc.

RELATED WORK

Test-driven Development

"Test-driven development (TDD)" [3] or "Test-first development" is one of the techniques that is proposed in "Extreme Programming Model" [4]. It has different steps from general software processes. Developers who implement TDD will create unit tests before the program coding stage. This method will drive programmers to be conscious about software defects first. So, this concept proposes to decrease the error of the products.

The research from IBM Corporation and North Carolina State University reported that projects which applied TDD can reduce defects by 40% when compared with others that use the general process [5]. Research claimed that TDD decreases the quantity of defect and it also influences a proper design of software. In addition, TDD improves communication among the development team and business as well [6].

Another research reports that TDD is less efficient in terms of defect detection compared to

code inspection technique. TDD is chosen for the reason of budget because it can save costs compared with code inspection [7]. Lastly, a study reported that TDD is not different from traditional software development in 3 indexes including (i) programming speed, (ii) program reliability, and (iii) program understanding measured as proper reuse of existing methods [8].

Software defect taxonomy

Controlling defects is one of the most important aspects of software quality management. There are many researchers that study on the nature of the software defects, particularly in defect classification. One group of researchers [2] present their idea for classifying software defect by using cause-effect analysis. They collect feedbacks on defects from the software developers. This includes the phase of defects injection, the cause of the defect and the effect of those defects.

The result of this study demonstrates 7 classes of defect including, Function, Interface, Checking, Assignment, Timing/Serialization, Documentation and Algorithm [2]. They are distributed in all of the stages of a software process. It is defined as "Orthogonal Defect Classification (ODC)"

ODC was used to implement in many studies of software engineering areas, i.e., to classify software defect in a specific phase of software process or using for software defects prediction, etc. [2]. The example of studies that use ODC to implement in their research is the research in 2010 [9], which illustrates the new concept of defect classification for black-box testing. In addition, it demonstrates that the ODC is not applicable to black-box defects which resulted in accumulating the defects from the step of black-box testing. It is the appropriate process for their work. In the result, they represent this concept as "Orthogonal Defect Classification for Black-box Defect (ODC-BD)" [9].

Software defect pattern

Software defect pattern collects of software defects from the real work with an aim to reduce repetitive defects. Defects are recorded and categorized by the cause of that error, the phase of injection, the effect of that defects and how to remove it. Another important information from the pattern is the knowledge that can guide developers on how to prevent defects.

A study in 2009 investigated an implementation of software defect pattern in the software process. The purpose of that research was to increase the reliability of software design [10].

This research implements this set of defect classification in the Knowledge of Software Defect (KSD). It could identify the defect information in the right stage of software process. The detail of KSD in

this experiment is reported in the research design section.

Personal Software Process

Personal Software Process (PSP) is a tool for investigating and improving the personal performance in software development [11],[12]. PSP collects and shows the statistics that are calculated from the data that engineers record. These results can be used to analyze the strength and weakness of an individual. Thus, engineers can continually improve themselves.

PSP can be applied in various areas of software engineering. There is no limitation of computer language or software process model. It can be implemented in pair programming [13] and M-V-C frameworks [14]. Researchers reported that PSP can improve the personal performance of students in both of solo and team programming styles.

A research in 2015 presented an experiment of MVC-PSP to increase the reliability of defect logging [15]. Two activities including Defect Detection Capability Test (DDCT) and Defect Standard Table (DST). DDCT is a test for calculating the engineers defect detection capability. DST is a review of the team to generate and update the standard of defect detection. Based on the results, it is concluded that the defect standard table has a higher reliability. As a result, this research proposes that the defect standard table can be effective for defect logging.

RESEARCH DESIGNS

Participants

This research was implemented in 3 batches during 3 undergraduate courses on Mobile Application Development. There were 18, 21 and 38

students who studied in the department of software engineering, department of information technology, department of computer engineering and department of business computer. These students have different programming experiences.

In each batch of experiment, students were organized into 2 groups based on the result of the Defect Detection Capability Test. The better performance group of the student was assigned to group A as the control group and the lower group was assigned to group B. The DDD's methods were implemented in only group B.

Duration

Each batch of experiments took 6 weeks to complete. It involved 6 programming exercises. Detail of the exercises is described in the following section. This research took 4 months to complete all experiments.

The experiments were designed to provide feedback to each other. The result of the first experiment had been used as input data for the second one and later. The result of the second experiment was also input data for the third experiment.

Exercises in experiment

There are 6 exercises in this experiment shown in Table 2. The structure of these exercises follow official PSP training scheme. The first exercise is easy so that the participants adjust their working process to get used to PSP framework. Only working process, time spent on each step, errors occurred in the working process are recorded. The second exercise develops an Android application which calculates geometric shapes. It introduces resource estimation in PSP framework.

The third to fifth exercise is related to general calculations with the addition of decision process. Full PSP process, including reviewing of design and code, are included in these exercises. The last

Table 2. Workshop Exercises

Ex.#	Android Application	PSP Level.	Data Collection	Difficulty Level/Expected Development Time (min.)	Skill Needed
1	Simple Calculator	0	1, 2	1/115	• Simple Calculation
2	Areas of Geometric Shapes Calculator	1.0	1, 2, 3, 4, 5, 6	1/135	• Simple Calculation • Class and Object
3	Body mass index (BMI) Calculator	2.0	1, 2, 3, 4, 5, 6, 7, 8	2/175	• Complex Calculation • Class and Object • Defensive Programming
4	Mini Horoscope	2.1	1, 2, 3, 4, 5, 6, 7, 8	2/110	• Complex Calculation • Class and Object • Defensive Programming • Logic and Decision
5	Taekwondo point calculator	2.1	1, 2, 3, 4, 5, 6, 7, 8	2/130	• Complex Calculation • Class and Object • Defensive Programming • Logic and Decision
6	To Do Listing	2.1	1, 2, 3, 4, 5, 6, 7, 8	3/220	• Class and Object • Defensive Programming • Logic and Decision • Database Programming

Note: • 1: Time, 2: Defect, 3: Time Estimation, 4: Size Estimation, 5: Actual Time, 6: Actual Size, 7: Design Review, 8: Code Review

exercise is the only exercise of this research study that must be connected to a database.

METHODOLOGY

Workshop Iteration

Each batch of the workshop involved 6 exercises. Control Group students were instructed to build projects based on their normal procedures. At the same time, DDD Group who displayed less capability of error detection during the test, implemented DDD's activities. These activities help students to detect defects that should be occurs in their projects according to their design prior to the step of coding. KSD has displayed the information about those defects, how to prevent or debug that error. Finally, they could choose to implement the project with this problem or re-designing procedure.

When students of DDD group found defects during their coding, they can search the KSD for debugging guidelines. They can continuously add new information of software defect solving to KSD too. Fig.1 displayed the experiment processes.

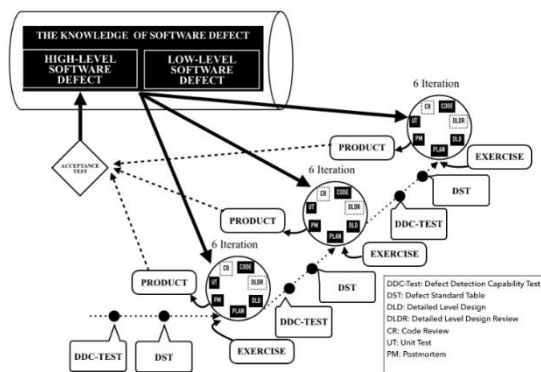


Fig. 1. The research processes.

RESEARCH RESULTS

After the students finished all 3 batches, their development data were compared. There are 4 indexes for investigating as follows: (i) Defect Density, (ii) Yield%, (iii) Time used and (iv) Productivity. All of those indexes can project the efficiency of DDD in this experiment. Other indexes also contribute supplement information to conclude this research.

The Defect density illustrates the intensity of defect in software building processes. It is calculated by the number of defects by the total line of code written in the project. The lower value of defect density represents the less defects in software. The average value of defect density of DDD group students is expected to be less than Control group.

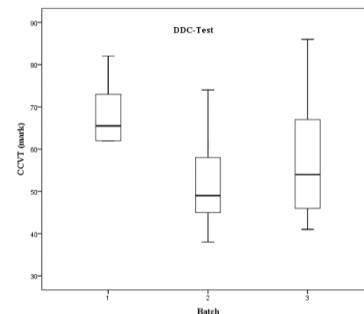
Yield% shows the capability of defect detection before the compile phase. The higher value of yield% means the developer detected more errors. That value of DDD group is expected to be greater than Control group.

The DDD group may take more time to complete than those of Control group as they must complete more activities. Nevertheless, it is expected that the time spent by DDD group should not be significantly different than control group as it would affect projects with limited time frames.

Lastly, productivity is the value showing the overall efficiency of personal process, calculated by code size and the total time spent in completing all work. The DDD students are hypothetically expect to yield less productivity than the control group due to more activities.

The defect capability test result

Fig 2 shows the defect capability test result of all 3 batches. The defect capability test result projected the Java programming skill of all students. Students of the second batch scored 52.05 in average. It showed that they have the least skill in error detection in Java. The first batch' students had the highest skill with the score of 68.19 in average. This is not surprisingly since they were third-year software engineering students. The last batch had the most variety of programming skills because they



consist of students from 3 study program who had different experience in computer programming. So, the standard deviation value of this group is the highest and their average score was 57.55.

Fig. 2. The defect capability test result

Exercise result

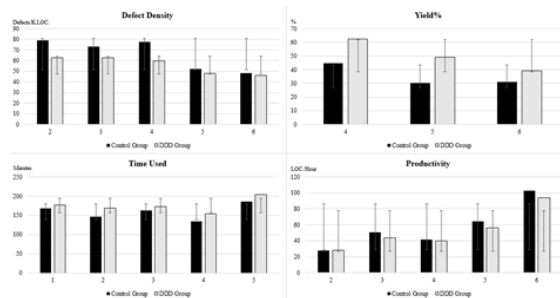
The results from the study are displayed in Table 3. The software' size is not different because all batches used the same set of exercises. However, the time used is different. As mentioned above, the second batch' students had the least programming skill in Java, so they used the longest time to finish the exercises more than others.

Table 3. Exercise result

Ex.	Average size (SD)						Average time used (SD)						Average defects (SD)					
	Batch 1		Batch 2		Batch 3		Batch 1		Batch 2		Batch 3		Batch 1		Batch 2		Batch 3	
	A	B	A	B	A	B	A	B	A	B	A	B	A	B	A	B	A	B
1	-	-	-	-	-	-	113.57 (5.26)	134.82 (5.95)	145.40 (2.33)	148.36 (3.11)	94.79 (1.32)	114.11 (2.73)	4.29 (1.39)	6.82 (1.53)	6.40 (1.28)	6.55 (1.62)	7.05 (1.76)	6.00 (1.38)
2	93.43 (1.40)	110.64 (7.04)	111.10 (1.37)	111.09 (1.88)	112.00 (1.65)	112.26 (1.65)	152.14 (2.36)	158.64 (3.31)	204.30 (1.55)	207.09 (1.56)	146.32 (1.69)	166.79 (2.40)	6.00 (1.07)	5.36 (1.82)	6.40 (1.36)	5.27 (1.66)	5.42 (1.31)	4.89 (1.02)
3	112.86 (4.58)	118.91 (3.53)	120.40 (1.28)	120.45 (1.88)	119.26 (0.91)	119.05 (0.89)	129.86 (1.64)	138.18 (3.95)	195.20 (1.17)	212.91 (1.88)	115.68 (3.01)	155.16 (4.26)	6.57 (1.05)	6.45 (1.62)	5.90 (1.97)	5.55 (2.39)	6.95 (2.76)	5.00 (1.59)
4	97.14 (2.70)	105.09 (4.21)	107.80 (2.96)	107.91 (3.26)	110.47 (1.43)	108.58 (1.31)	115.29 (4.37)	123.36 (4.60)	226.20 (1.25)	236.09 (1.16)	146.63 (2.18)	161.32 (3.37)	5.29 (1.48)	4.91 (1.44)	5.80 (2.40)	4.82 (0.83)	6.58 (1.43)	4.26 (1.02)
5	137.71 (1.67)	136.73 (1.35)	140.50 (0.81)	140.27 (1.21)	140.32 (1.30)	139.68 (1.08)	107.43 (2.06)	122.82 (6.45)	163.29 (1.45)	190.09 (5.37)	130.89 (2.27)	147.26 (1.94)	5.43 (1.29)	5.18 (1.19)	6.14 (1.42)	5.55 (1.29)	5.74 (1.41)	5.05 (1.05)
6	310.00 (6.57)	312.64 (4.07)	316.20 (1.72)	315.73 (2.38)	321.89 (2.34)	321.11 (1.74)	167.14 (3.83)	174.36 (3.47)	204.60 (6.20)	227.45 (2.78)	185.05 (2.86)	211.21 (4.16)	12.00 (3.30)	12.73 (2.53)	16.00 (1.41)	15.00 (0.74)	13.37 (3.01)	11.74 (2.51)

The average value of defects amount is not different. But the sixth exercise was different, because it is the biggest size of the code. The function of this project had to connect to the database engine with the Android platform. The student had to spend part of the time to manage the database structure. This exercise is not only the most time consuming but also led to the most defects.

All batch's result



Note: * Defect density can be calculated from the 2nd exercise.
* Productivity can be calculated from the 2nd exercise.
* Yield% can be calculated from the 4th exercise.

Fig. 3. Result of all batch's experiment

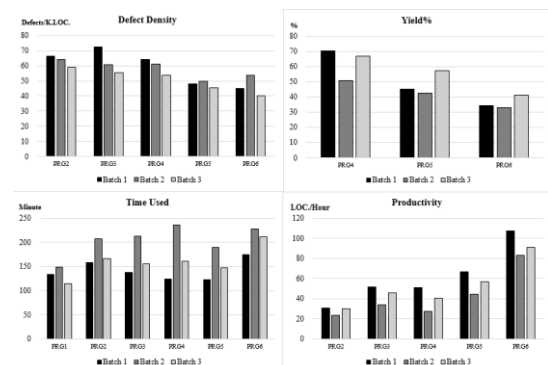
The experiment result of all batches is shown in Fig 3. The average value of defect density of students in DDD group is significantly less than the Control group in every exercise. The average value of yield% of DDD group is significantly greater than the Control group in every project too. It is noted that the yield% value is calculated from the 4th exercise since the essential data was not previously collected because the earlier exercises used the lower level of PSP that appropriates with the easy projects.

For the time used to complete workshops, the students of DDD group spent the additional time for DDD's activities. So, they used more time than the Control group members with the same size of

program code. Then, the productivity of Control group is higher than DDD group in every exercise excluding the first one as expected.

The result comparison of students in DDD's group

Fig 4 shows the result that compares DDD group students with the other three batches. It illustrates the evolution of DDD model and the KSD. This result shows that students who implemented DDD model in software projects, tended to reduce their defects. It is referenced from the downward trend of



defect density value. While the yield% tenor is increased similarly with the value of time used.

Fig.4. The result comparison of students in DDD's group

CONCLUSION

DDD model is the concept of software development process to use the benefit of the Knowledge of Software Defect (KSD) which collected defect data from experienced software developers. KSD provides information of software defects for novices in the early phase of software process. They can use this information to handle problems in their project.

From the result of the experiment as reported above, it shows that students who implemented the Defect-driven development's concept produced software with less defects than others who applied the general personal software processes. It is claimed in two indicators including, I) the value of defect density and II) the value of yield%. However, DDD's members use more time on additional activities. Then, the productivity value of them is less than the general processes.

REFERENCES

- [1] P. Letouze, J. I. M. de Souza, and V. M. Da Silva, "Generating Software Engineers by Developing Web Systems: A Project-Based Learning Case Study," 2016 IEEE 29th Int. Conf. Softw. Eng. Educ. Train., pp. 194–203, 2016. <http://doi.org/10.1109/CSEET.2016.11>
- [2] R. Chillarege et al., "Orthogonal Defect Classification-A Concept for In-Process Measurements," IEEE Trans. Softw. Eng., vol. 18, no. 11, pp. 1245–1254, 1992. <http://doi.org/10.1109/32.177364>
- [3] K. Beck, Test Driven Development: By Example, 1st ed. Addison-Wesley Professional, 2002.
- [4] K. Beck, Extreme Programming Explained: Embrace Change. Addison-Wesley Professional, 2004.
- [5] L. Williams, E. M. Maximilien, and M. Vouk, "Test-driven development as a defect-reduction practice," 14th Int. Symp. Softw. Reliab. Eng. 2003. ISSRE 2003., pp. 1–12, 2003. <http://doi.org/10.1109/ISSRE.2003.1251029>
- [6] L. Crispin, "Driving software quality: How test-driven development impacts software quality," IEEE Softw., vol. 23, no. 6, pp. 70–71, 2006. <http://doi.org/10.1109/MS.2006.157>
- [7] J. W. Wilkerson, J. F. Nunamaker, and R. Mercer, "Comparing the defect reduction benefits of code inspection and test-driven development," IEEE Trans. Softw. Eng., vol. 38, no. 3, pp. 547–560, 2012. <http://doi.org/10.1109/TSE.2011.46>
- [8] M. M. Müller and O. Hagner, "Experiment about test-first programming," IEE Proc. - Softw., vol. 149, no. 5, p. 131, 2002. <http://doi.org/10.1049/ip-sen:20020540>
- [9] N. Li, Z. Li, and X. Sun, "Classification of software defect detected by black-box testing: An empirical study," Proc. - 2010 2nd WRI World Congr. Softw. Eng. WCSE 2010, vol. 2, pp. 234–240, 2010. <http://doi.org/10.1109/WCSE.2010.28>
- [10] F. Zeng, A. Chen, and X. Tao, "Study on software reliability design criteria based on defect patterns," Reliab. Maintainab. Safety, 2009. ICRMS 2009. 8th Int. Conf., pp. 723–727, 2009. <http://doi.org/10.1109/ICRMS.2009.5270095>
- [11] W. S. Humphrey, PSP(sm): A Self-Improvement Process for Software Engineers, 1st ed. Addison-Wesley Professional, 2005.
- [12] W. S. Humphrey, "The personal process in software engineering," in Proceedings of the Third International Conference on the Software Process. Applying the Software Process, 1994, no. c, pp. 69–77. <http://doi.org/10.1109/SPCON.1994.344422>
- [13] G. Rong, H. Zhang, M. Xie, and D. Shao, "Improving PSP education by pairing: An empirical study," Proc. - Int. Conf. Softw. Eng., pp. 1245–1254, 2012. <http://doi.org/10.1109/ICSE.2012.6227018>
- [14] W. Nachengmai and S. Ramingwong, "Implementing Personal Software Process in Undergraduate Course to Improve Model-View-Controller Software Construction," in Lecture Notes in Electrical Engineering, vol. 339, 2015, pp. 949–956. http://doi.org/10.1007/978-3-662-46578-3_113
- [15] W. Nachengmai and S. Ramingwong, "Improving Reliability of Defects Logging in MVC-PSP," in 2015 2nd International Conference on Information Science and Security (ICISS), 2015, pp. 1–4. <http://doi.org/10.1109/ICISSEC.2015.7371007>
- [16] S. Thisuk and S. Ramingwong, "WBPS: A new web based tool for Personal Software Process," in 2014 11th International Conference on Electrical Engineering/Electronics, Computer, Telecommunications and Information Technology (ECTI-CON), 2014, pp. 1–6. <http://doi.org/10.1109/ECTICon.2014.6839821>
- [17] C. Larman and V. R. Basili, "Iterative and incremental developments. a brief history," Computer (Long. Beach. Calif.), vol. 36, no. 6, pp. 47–56, Jun. 2003. <http://doi.org/10.1109/MC.2003.1204375>
- [18] D. Liu, S. Xu, and W. Du, "Case study on incremental software development," Proc. - 2011 9th Int. Conf. Softw. Eng. Res. Manag. Appl. SERA 2011, pp. 227–234, 2011. <http://doi.org/10.1109/SERA.2011.43>
- [19] K. Schwaber and M. Beedle, Agile Software

- Development with Scrum, 1st ed. Pearson, 2001.
- [20] Y. Zhang and S. Patel, "Agile model-driven development in practice," *IEEE Softw.*, vol. 28, no. 2, pp. 84–91, 2011. <http://doi.org/10.1109/MS.2010.85>

DEVELOPMENT OF ASSESSMENT FOR POTENTIALLY TOXIC ELEMENT CONTAMINATION INDICATOR IN CLOSED LANDFILLS AND PROSPECTIVE GEOSTATISTICAL ANALYSIS

Azizi Abu Bakar^{1,2}, Minoru Yoneda¹, Nguyen Thi Thuong¹ and Noor Zalina Mahmood²

¹Laboratory of Environmental Risk Analysis, Department of Environmental Engineering, Graduate School of Engineering, Kyoto University, Cluster C, Kyoto daigaku-Katsura, Nishikyo-ku, Kyoto 615-8540, Japan

²Institute of Biological Sciences, Faculty of Science, University of Malaya,
50603 Kuala Lumpur, Malaysia

ABSTRACT

Landfills' post-closure management in Malaysia is not including assessment of contaminant level in abiotic and biotic that inhabits on the aged surface topsoil of closed landfills. Considering the bioaccumulation effect in ecosystem, post-closure classification with status of contaminant concentration below the permitted level does not promise safety closure to ecosystem as time passing by. Thus, substantial and constant qualitative analysis on contaminant concentration needs to be developed for sustainable management of landfill post-closure. In this work, heavy metals in common constituents (abiotic and biotic factor) of a closed landfill were selected i.e. soil, stagnant water and common community of plant species in both closed sanitary and non-sanitary landfills in Selangor were studied. Analysis result demonstrated that concentration of Cd was not detected in soil of both landfills but present the highest concentration in the leaves of *A. conyzoides* compared to other plant species at both study sites. Parallel situation for Cd concentration in water stagnant at Ampar Tenang landfill was not detected but contained in the leaves of *A. conyzoides*. Sensitivity and affinity of *A. conyzoides* for accumulating heavy metals in this study revealed particularly for Cd. Hence, this study suggesting *A. conyzoides* as promising trace metals contamination indicator for closed urban landfills. Additionally, Guess-Field Kriging is believed to be a useful geostatistical tool to interpolate potential contamination area by utilising the abiotic and biotic factors as assistant variable to the target variable i.e. soil.

Keywords: *Ageratum conyzoides*; Environmental Risk; Landfill Aftercare; Solid Waste Management; Trace Metal

INTRODUCTION

Municipal solid waste management in a developing country with upper middle-income economy such as Malaysia has now improving its path towards proper waste management. Recent mandated requirement for solid waste segregation at source is now imposed at several states albeit there are certain flaws existing. As projected by Lau [1] municipal solid waste in Malaysia is estimated to increase from 292 kg/capita in 2000 to 511 kg/capita in 2025. This increment is possible to occur due to the status of developing country with rapid development of economic activities will produce more waste in future. Among thirteen states and three federal territories in the country, Selangor state is the most developed state in Malaysia located at the west coast of Peninsular Malaysia with 7,930 km² surface area and 6.38 million people population estimated in mid-year of 2017 [2]. The state encircling the federal territories of Kuala Lumpur and Putrajaya (capital city and the federal administrative centre of Malaysia respectively), both of which were formerly part of Selangor. Following

the statistics, growing number of landfill in urban area to feed in growing urban population and waste generation result in increasing number of closed landfill.

Unfortunately, there is lack information regarding heavy metal content and monitoring in closed landfill although heavy metal pollution has become a severe problem in many parts of the world particularly in soil and its surrounding ecosystem [3]. Despite it is known that heavy metal enrichment in environment results from natural processes and it is also believed as consequence of widespread historical pollution, soils (topsoil) in urban areas are considered to be regional sinks of chemical emissions depending on the economic activities and definitely resource consumption are frequently rich in heavy metals [4]. Importantly, heavy metals enrichment or excessive accumulation of heavy metal in soil can be transferred to other ecological resources, such as plants or water bodies (underground and surface) and affects the environmental quality.

Thus, the objective of the study is to assess the heavy metal contamination (inorganic

micropollutant) in the closed landfill area by developing an effective and applicable methodology. This work also to identify possible heavy metal contamination indicator in closed landfill as well as predicting by possible estimation assessment for the potential of environmental risk that may occur in the future.

MATERIALS AND METHODS

Closed Landfills (Sanitary and Non-Sanitary)

Closed urban landfills (sanitary and non-sanitary) studied were both situated in the state of Selangor. i.e. Air Hitam landfill (sanitary landfill) located at Puchong and Ampar Tenang landfill (non-sanitary landfill) located at Sepang. Both landfills were fed with non-segregated waste from the capital city and cities around centre and southern part of Selangor (the capital city and the federal territory were inclusive).

Air Hitam Landfill (AH) was first engineered sanitary landfill in Malaysia, operated for 11 years since 1995 till 2006 (more than 10 years closure) and located approximately 25 km southwest of Kuala Lumpur city centre. The landfill zone is near to the Air Hitam Forest Reserved in Puchong, Selangor and surrounded by developed residential area. A total of 6.2 million tons of non-segregated waste (municipal solid waste) was properly cap in the landfill. After five years of landfill closure maintenance plan, the landfill turns to park and officially open to public since 2011. The landfill is operating leachate treatment and renewable energy plant with recreational facilities around the landfill area.

Ampar Tenang Landfill (AT) site is located near Kota Warisan, Sepang area, approximately 49 km south of Kuala Lumpur city centre. The landfill zone is bordered primarily by oil palm plantation and housing projects are being developed at adjacent areas. The landfill site (a closed open tipping and then upgraded to a controlled waste disposal site but with no proper liner system) started operation in year 2000 and ended in 2010 (less than 10 years closure) and has received about 100 tons domestic waste per day [5]. Both landfills were first operated by local authorities and then privatised with concession period to manage operation or closure of the site.

Sample Preparation and Laboratory Analysis

Surface topsoil samples (0-30 cm) were collected randomly from the selected closed urban landfills in triplicate during northeast monsoon season (November – March) under tropical climate. The

soil samples at each site were assembled together and collection were using stainless steel shovel. A stagnant water and leaves/grass sample also taken in the two sites with similar species or family of leaves and grass. All types of the samples were located at close proximity to justify heavy metal content in the abiotic and biotic factor. Water samples were acidified with conc. HNO_3 to pH <2. All samples were then sealed in an airtight, clear glass bottles separately and then transported to laboratory for pretreatment.

The soil, stagnant water and leaves/grass samples were sterilised with autoclave 121°C for 15 minutes. Once sterilised, the soil and leaves/grass samples were air dried at room temperature. The air-dried soil and leaves/grass samples were then further dried in microwave at 60°C and 65°C respectively until constant dry, before being powdered and homogenised within an agate mortar. Larger particles (2 mm) in the soil samples were then removed by sieving. For microwave-assisted acid digestion procedure, approximately 0.5 g of dry homogenized soil and 0.1 g of dried leaves samples were weighed into a vessel and successively digested with 10 mL of conc. HNO_3 in a microwave digestion system (MARS 6, CEM, USA). After cooling, the digest was transferred into conical centrifuge tubes and adjusted to a volume of 50 mL with Milli-Q water. The sample was then finally filtered through a membrane filter (cellulose acetate with a $0.45\ \mu\text{m}$ pore size; Advantec, Japan).

Heavy metal concentrations in stagnant water, acid digested soil and leaves/grass samples were determined by using a Thermo Scientific iCAP Q mass spectrometry with inductively coupled plasma (ICP-MS). Standard operating procedures, calibration with standards, analysis of reagent blanks, and replicates were practiced to ensure the precision of analytical data. All samples were carried out in triplicate to obtain mean as final data.

Quantification of C/p for Heavy Metals in Soil

Contamination/pollution index (C/p) and its significance interval was analysed by adaptation from Lacatusu [6] as followed:

$$C/p = \frac{C_{\text{soil}}}{C_{\text{reference soil}}} \quad (1)$$

where: C_{soil} – concentration of an examined metal in soil, $C_{\text{reference soil}}$ – concentration of the reference metal in soil from Malaysian Natural Occurring Range, DOE (2009). The following terminology may be used for the C/p value as specified by

Lacatusu [6]: $C/p < 0.1$ = very slightly contamination; $0.10 - 0.25$ = slight contamination; $0.26 - 0.50$ = moderate contamination; $0.51 - 0.75$ = severe contamination; $0.76 - 1.00$ = very severe contamination; $1.1 - 2.0$ = slight pollution; $2.1 - 4.0$ = moderate pollution; $4.1 - 8.0$ = severe pollution; $8.1 - 16.0$ = very severe pollution; $C/p > 16.0$ = excessive pollution.

Quantification of RI for Heavy Metals in Water

Potential ecological risk index (RI) was utilised as a diagnostic tool for water pollution control purposes. The RI was adapted from Hakanson [7] as followed:

$$RI = \sum_{i=1}^m Er^i = \sum_{i=1}^m Tr^i \cdot C_f^i \quad (2)$$

where: m – number of studied metal, Er^i – the potential ecological risk factor for studied metal (i), Tr^i – the toxicity response factor for studied metal [7], C_f^i – the contamination factor. The following terminology may be used for the RI value as specified by Hakanson [7]: $RI < 150$ = low ecological risk; $150 \leq RI < 300$ = moderately ecological risk; $300 \leq RI < 600$ = considerable ecological risk; $RI \geq 600$ = very high ecological risk.

Quantification of EF for Heavy Metals in Plant

Enrichment factor (EF) was analysed to measure the origin of metals that compares relative concentration of the metals in plant to soil. The EF was adapted from Klos, Rajfur and Wacławek [8] as followed:

$$EF = \frac{(C_x/C_{Fe})_{plant}}{(C_x/C_{Fe})_{soil}} \quad (3)$$

where: C_x – concentration of an examined metal in plant or soil, C_{Fe} – concentration of the reference element i.e. Iron (Fe) in plant or soil. The enrichment factor close to unity ($EF = 1$) indicates the element considered originally from the soil.

Statistical Analysis

The descriptive statistical analysis was conducted by applying SPSS 24.0 (IBM, Chicago, Illinois, USA). Regression analysis was done to understand the relationship between heavy metals in soil and water samples in both landfills. The differences of heavy metals in soil and stagnant water sample at each landfill were tested using a parametric test; One Sample t Test whilst heavy metals in plants' foliar organ (leaves) at both landfills were tested by analysis of variance; One-Way ANOVA. Differences were considered

significant when $P < 0.05$.

RESULTS AND DISCUSSION

Heavy Metals in Soil

The concentration of heavy metals in soil for Air Hitam (AH) landfill followed the decreasing order of $Mn > Pb > Cr > Cu > Fe > Cd$ and Ampar Tenang (AT) landfill; $Fe > Mn > Cr > Pb > Cu > Cd$. Concentration of Cd for both landfills soils were not detected due to below detection limit. Result shown that all of the mean content of heavy metals from both landfills' surface topsoils was lower compared to other limits except for Mn in Ampar Tenang (AT) landfill which maximum content is slightly higher than natural occurring content range. Despite of the below permissible limits, C/p index of all heavy metals tested shown in Table 1 described that both landfill soils were very slightly contaminated.

Table 1 C/p index of heavy metals in soils of Air Hitam and Ampar Tenang landfills

HM	^a AH	^b AT	Symbol
Cr	8.252×10^{-3}	0.124×10^{-3}	v.s.l.
Mn	0.381×10^{-3}	0.873×10^{-3}	v.s.l.
Fe	1.152×10^{-8}	6.254×10^{-7}	v.s.l.
Cu	3.874×10^{-5}	3.412×10^{-5}	v.s.l.
Cd	ND	ND	-
Pb	4.682×10^{-5}	3.930×10^{-5}	v.s.l.

Note: HM: heavy metal; ^aAH: Air Hitam landfill; ^bAT: Ampar Tenang landfill; v.s.l.: very slightly contamination.

Both of the studied landfills were closed less than 20 years and contamination of heavy metals with exceeding of acceptable limits occurs on a closing period of more than that. It is reported a non-sanitary landfill in Beijing, China closed for almost 30 years resulted with contamination of Zn, Cd, Ni and Hg whereas As, Cu, Cr and Pb were met the regulatory limits [9]. In addition to that, a long term artisanal gold mining activities operated for more than 30 years in Shanxi, China has resulted a serious contamination of heavy metals in soil i.e. Hg and Cd due to the tailings produced as mining waste were dumped untreated [10]. Moreover, increased accumulation of Cd, Cu, Pb and Zn were detected in Planty Park's surface soil surrounding the Historic Centre of Krakow, Poland [4].

High content of Mn and Fe in surface topsoil of Ampar Tenang landfill could be originated from the previous land use of the site as palm oil plantation. Moreover palm oil plantation is still actively operating at surrounding area of the closed landfill. This is parallel to Olafisoye, Oguntibeju and Osibote [11] on the findings of high content of Mn and Fe but below the permissible limits in palm oil

plantation soils under tropical climate in Nigeria. The very slightly contamination of Cr, Cu and Pb in both closed landfills reflects the content of heavy metals in sediment or pedogenic factor at the topsoils layer of the landfills which are generally present in trace concentrations and result in low toxicity [12]. Possible anthropogenic source of Cr in the closed landfills could be from abundance of chrome plating or stainless steel apparatus disposed in the landfills e.g. cutlery, saucepan and other rust-resistance of alloy-based tools. Hence, this mixed type of waste weathered in the landfills could be the main source of the metals availability. Furthermore, the vehicles carrying waste and soil e.g. waste and soil compactor or roll-off/dump truck during the landfills operation contributes to the availability of the metals. As reported by Smichowski, Gomez, Frazzoli and Caroli [13] brake wear and loss of lead wheel balance weights promoted the enrichment of soil Pb. Similar to Cu releases to environment from corrosion of metal components due to oxidation of lubricants at high temperature [14].

Heavy Metals in Water

Heavy metals in stagnant water samples resulted heavy metals concentration in Air Hitam (AH) landfill followed decreasing order of $Mn > Fe > Pb > Cd > Cu > Cr$ and Ampar Tenang (AT) landfill followed decreasing order of $Fe > Cr > Mn > Cu > Pb > Cd$. Concentration of Cd in stagnant water sample from Ampar Tenang landfill was not detected due to below detection limit. The concentrations of Cr in water samples at both landfills were higher compared to the landfills soils. Conversely to Fe content in water samples were lower compared to both landfills soils. Manganese, Cu and Pb content in water samples at Air Hitam landfill showed similar trend of comparison which were higher compared to its landfill soil. Contrariwise to Mn, Cu and Pb content in water samples at Ampar Tenang landfill were lower compared to its landfill soil. Cadmium only exists in water sample at Air Hitam landfill although it is not present in its landfill soil. A linear regression was calculated to predict relationship of heavy metals based on concentration in soil and water samples analysis. A close relationship obtained with $R^2 = 0.871$ for heavy metals in soil and water samples at Ampar Tenang landfill. It is inferred that the source of heavy metals in the water samples at Ampar Tenang landfill was originally from the soil landfill. Researchers have considered the effect of dissolved oxygen concentration on potential metal releasing and accumulation, and found that the increasing of dissolved oxygen concentration could enhance the mobility of heavy metals [15]. Furthermore, the mobility of heavy metals in aerobic water-soil

interface condition is intensifying under tropical climate due to high temperature.

The potential ecological risk factor (Er^i) and potential ecological risk index (RI) for both closed landfills were adapted to evaluate potential risk of heavy metal content in the stagnant water at both landfills. It is indicated that both landfills are belong to low ecological risk level and suggest that no threatening effects to the environment.

Heavy Metals in Plants

Figure 1 depicted comparisons of heavy metals content according to plant species collected from both landfills. The highest uptake of Cr in both landfills showed in *Cynodon dactylon* (6.063×10^{-3} ppm; 16.65% in the plant) at Air Hitam landfill, Mn in *Imperata cylindrica* (14.24×10^{-3} ppm; 42.18% in the plant) at Air Hitam landfill, Fe in *Ageratum conyzoides* (28.84×10^{-3} ppm; 63.97% in the plant) at Air Hitam landfill, Cu in *Leucaena leucocephala* (7.827×10^{-3} ppm; 34.92% in the plant) at Air Hitam landfill, Cd in *A. conyzoides* (0.934×10^{-3} ppm; 3.20% in the plant) at Ampar Tenang landfill and Pb in *I. cylindrical* (6.707×10^{-3} ppm; 24.15% in the plant) at Air Hitam landfill. It can be hypothesised here that most species were highest in metal accumulation in longer period of a landfill closure since Air Hitam landfill was closed for more than 10 years whilst Ampar Tenang less than 10 years. It is essential to note that, *A. conyzoides* showed the sensitivity by percentage of accumulating all selected heavy metals compared to other common plant species from both landfills. This is evident from the percentage content of Cd in *A. conyzoides* compared to other plant species. Percentage of content for each plant species based in concentration (mg/kg) as shown in Fig. 1, Cd accumulated in the leaves of *A. conyzoides* were 3.20% and 2.38% for Ampar Tenang landfill and Air Hitam landfill respectively irregular to other plant species at both landfills with percentage below 0.5%.

Ageratum conyzoides L., or commonly known as billy goat weed is a tropical plant found in some regions of Africa, Asia and South America [16] and occupation of *A. conyzoides* is easily succeeded because of its wide adaptability in the environment and its superior reproductive potential [17].

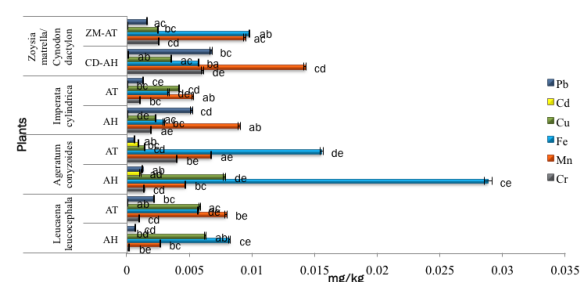


Fig. 1 Comparison of heavy metal content (mg/kg) among selected plants in closed non-sanitary Ampar Tenang landfill (AT) and closed sanitary Air Hitam landfill (AH), Selangor. Values are mean and standard error (mean \pm S.E.M.; $n = 3$) followed by different letters is statistically different. (One-Way ANOVA, $P < 0.05$).

Apart from that, it is widely used in traditional medicine in several countries around the world as a purgative, febrifuge, anti-inflammatory, analgesic, anesthetic and in treatment of ulcers [18]. Although there is vast information about the chemical property, biochemical activity as well as anatomical description of *A. conyzoides*, there are few studies on the heavy metal uptake in relation to heavy metal sensitivity of the species particularly in closed landfill area. Hence, this study proposing the species as biotic indicator for potentially toxic metal contaminated land such as closed landfills.

Source of the studied metals is inspected by Enrichment factor (EF). All of the heavy metals resulted EF below 1.0 for plant species in Air Hitam landfill whereas only Pb in *A. conyzoides* showed EF below 1.0 for plant species in Ampar Tenang landfill. The results can be postulated that most of the heavy metals in the plant species at Air Hitam landfill were formerly from contaminated surface topsoil of the closed landfill. In case of Ampar Tenang landfill, other than non-segregated municipal waste disposed, possible anthropogenic source of the heavy metals in the foliar organ (leaves) could be from deposition of heavy metal-rich vehicle exhaust transferring from neighboring proximity where residence area was actively under construction. It is discovered that the heavy metals can be transported further mainly by wind beyond the source-activities vicinity [19]. This is contradicting to the ambience of Air Hitam closed landfill that is functionally opened as urban recreational park adjacent to the city reserved forest with restriction of vehicle entrance.

Potential Geostatistical Analysis

It is anticipated to estimate the possibility of environmental risk by means of spatial interpolation that may occur in the future by applying Guess-Field Kriging. The estimation is by regression relation between target variable and assistant variable as shown in Eq. 4.

$$Z_1(X) = g[Z_2(X)] + \varepsilon(X) \quad (4)$$

where: $g[Z_2(X)]$ – arbitrary regression equation, $\varepsilon(X)$ – error term of average 0 (independent each other).

In this work, the target variable is the content of heavy metals in the surface topsoil of the closed

landfills. Whereas the assistant variable are the heavy metals content in water and plants collected at the similar area of the soil sampled. In this interpolation calculation, it is also possible to measure the possibility of the contamination in surface topsoil by utilising an accurate method of measurement i.e. instrumental analysis, coarse sampling grid, etc. and simple method measurement i.e. portable measurement, narrow sampling grid, etc. at the same time resulting more efficient of field investigation.

The Guess-Field Kriging is preferable compared to other geostatistical methods due to comparison of hotspots of the measured contaminants and the deduced area resulted from the geostatistical analysis. This ensued certain hotspots where are not thought to be contaminated. Although there are uncertainties, the resulted contourlines can be useful as a guide for sampling strategy. Consequently, sampling can be intensified in locations with large kriging errors [20]. Therefore, contamination assessment in the tested area is close to accuracy.

CONCLUSION

This study perceived that potentially toxic elements' contamination is considerably based on its resident time in the close landfills' abiotic and biotic factors. Both landfills showed that the soils are very slightly contaminated, low ecological risk for the stagnant water on the landfills' surface topsoils and identification of metals-sensitive plant i.e. *Ageratum conyzoides* as potential indicator for heavy metals contamination in closed urban landfills. It is known the plant beneficial latent qualities in traditional medicine or agricultural use in tropical climate region and yet precaution is needed when it comes from contaminated area due to its affinity to accumulate micropollutant particularly in its foliar organ i.e. leaves. Hence, the results of heavy metal contamination from the soil, stagnant water and plants in the closed landfills can be developed as indicator to comprehend level and source of contamination as well as selection of potential indicator from abiotic and biotic factor for future constant assessment. This study proposing an assessment plan i.e. assessing contaminants' indicator and geostatistical analysis for heavy metal contamination in closed landfills that can be a useful tool in avoiding costly environmental risk assessments for the countries with limited financial endowment. Nevertheless caution must be restored in the evaluation of single index for abiotic and biotic factors selected to estimate contamination as such value could obscure metals contamination.

ACKNOWLEDGEMENTS

The authors are thankful to Japan Society for the

Promotion of Science (JSPS), Tokyo, Japan under the program of RONPAKU (FY2016) for the financial support and Kyoto University under the Department of Environmental Engineering, Graduate School of Engineering for the laboratory facilities. We are also thankful to Institute of Research Management and Services (IPPP), University of Malaya for the ROGS grant (BR005-2016) providing as research seed fund for this project. Special thanks to Nagaya Taiki and Setouchi Daiki from Environmental Risk Analysis Laboratory, Kyoto University for facilitating laboratory analysis as well as to Benjamin Ong and Dr. Sugumaran Manickam (botanists) from Institute of Biological Sciences (ISB), University of Malaya for identification of plant species.

REFERENCES

- [1] Lau, V.L., 2004. Case Study on the Management of Waste Materials in Malaysia. *Forum Geookol.* Vol. 15, Issue 2.
- [2] Department of Statistics Malaysia (Official Portal), 2017. Current Population Estimates Malaysia 2017. <https://www.dosm.gov.my> (accessed 21 July 2017).
- [3] Pan, L.B., Ma Jin, Wang, X.L., Hou Hong, 2016. Heavy metals in soils from a typical county in Shanxi Province, China: Levels, sources and spatial distribution. *Chemosphere* Vol. 148, pp. 248-254.
- [4] Gasiorek, M., Kowalska, J., Mazurek, R., Pajak, M., 2017. Comprehensive assessment of heavy metal pollution in topsoil of historical urban park on an example of the Planty Park in Krakow (Poland). *Chemosphere* Vol. 179, pp. 148-158.
- [5] Taha, M.R., Yaacob, W.Z.W., Samsudin, A.R., Jasni Yaakob, 2011. Groundwater quality at two landfill sites in Selangor, Malaysia. *Bulletin of the Geological Society of Malaysia* Vol. 57, pp. 13-18.
- [6] Lacatusu, R., 1998. Appraising levels of soil contamination and pollution with heavy metals, in: Heinike, H.J., Eckselman, W., Thomasson, A.J., Jones, R.J.A., Montanarella, L., Buckeley, B. Ed. *Land information systems for planning the sustainable use of land resources*. European Soil Bureau Research Report No. 4. Office of Official Publication of the European Communities, Luxembourg, pp. 393 – 402.
- [7] Hakanson, L, 1980. An ecological risk index for aquatic pollution control. A sedimentological approach. *Water Res.* Vol. 14, pp. 975-1001.
- [8] Klos, A., Rajfur, M., Waclawek, M., 2011. Application of enrichment factor (EF) to the interpretation of results from the biomonitoring studies. *Ecol. Chem. and Eng., S* Vol. 18, Issue 2, pp. 171-183.
- [9] Rong, L., Zhang, C., Jin, D., Dai, Z., 2017. Assessment of the potential utilization of municipal solid waste from a closed irregular landfill. *J. Clean Prod.* Vol. 142, pp. 413-419.
- [10] Xiao, R., Wang, S., Li, R., Wang, J.J., Zhang, Z., 2017. Soil heavy metal contamination and health risks associated with artisanal gold mining in Tongguan, Shaanxi, China. *Ecotoxicol. Environ. Saf.* Vol. 141, pp. 17-24.
- [11] Olafisoye, B.O., Oguntibeju, O.O., Osibote, O.A., 2016. An assessment of the bioavailability of metals in soils on oil palm plantations in Nigeria. *Pol. J. Environ. Stud.* Vol. 25, No. 3, pp. 1125-1140.
- [12] Chen, T., Chang, Q., Liu, J., Clevers, J.G.P.W., Kooistra, L., 2016. Identification of soil heavy metal sources and improvement in spatial mapping based on soil spectral information: A case study in northwest China. *Sci. Total Environ.* Vol. 565, pp. 155-164.
- [13] Smichowski, P., Gomez, D., Frazzoli, C., Caroli, S., 2007. Traffic-related elements in airborne particulate matter. *Appl. Spectrosc. Rev.* Vol. 43, pp. 23-49.
- [14] Leeners, H., Okx, J.P., Burrough, P.A., 1990. Comparison of spatial prediction methods for mapping floodplain soil pollution. *Catena* Vol. 17, pp. 535-550.
- [15] Song, Z., Shan, B., Tang, W., Zhang, C., 2017. Will heavy metals in the soils of newly submerged areas threaten the water quality of Danjiangkou Reservoir, China? *Ecotoxicol. Environ. Saf.* Vol. 114, pp. 380-386.
- [16] Rafaela, F.S., Barbara, M.N., Rafaela, D.S., Luiz, A.L.S., Karina, P.R., 2016. Morpho-anatomical study of *Ageratum conyzoides*. *Rev. bras. farmacogn.* Vol. 26, pp. 679-687.
- [17] Kong, C., Liang, W., Hu, F., Xu, X., Wang, P., Jiang, Y., Xing, B., 2004. Allelochemicals and their transformations in the *Ageratum conyzoides* intercropped citrus orchard soils. *Plant Soil* Vol. 264, pp. 49-157.
- [18] Leita, F., Leita, S.G., Fonseca-Kruel, V.S., Silva, I.M., Martins, K., 2014. Medicinal plants traded in the open-air markets in the State of Rio de Janeiro, Brazil: an overview on their botanical diversity and toxicological potential. *Rev. Bras. Farmacogn.* Vol. 24, pp. 225-247.
- [19] Mehr, M.R., Keshavarzi, B., Moore, F., Sharifi, R., Lahijanzadeh A., Kermani, M., 2017. Distribution, source identification and health risk assessment of soil heavy metals in urban areas of Isfahan province, Iran. *J. Afr. Earth Sci.* Vol. 132, pp. 16-26.
- [20] Arendt, F., Annokkée, G.J., Bosman, R., van den Brink, W.J. Contaminated Soil'93, in *Proc. 4th International KfK/TNO Conference on Contaminated Soil*, 1993, p. 594.

EVALUATING POSSIBLE AVENUES FOR SOIL IMPROVEMENT BY BIOCEMENTATION IN SRI LANKA: A PRELIMINARY INVESTIGATION

P.G.N. Nayanthara¹, A.B.N. Dassanayake², Kazunori Nakashima³ and Satoru Kawasaki³

¹Graduate School of Engineering, Hokkaido University, Japan; ²Faculty of Engineering, University of Moratuwa, Sri Lanka; ³Faculty of Engineering, Hokkaido University, Japan

ABSTRACT

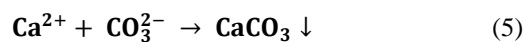
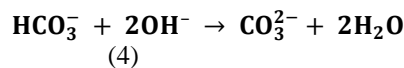
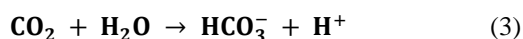
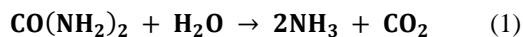
Bioengineering has paved way into multidiscipline as a more sustainable and eco-friendly solution to numerous problems. Among them, microbial geotechnology deals with utilizing microbial activities to improve engineering properties of soils in which biocementation is one of the promising approaches. Biocementation is based on the principle of strengthening soil matrix by Microbially Induced Carbonate Precipitation (MICP) by urea hydrolysis. The success of the biocementation process depends on various physical and biological factors whereas the selection of the most appropriate bacteria is prominent among them. Therefore, the current research study was conducted with the intention of finding appropriate local ureolytic bacteria from Sri Lankan soils and evaluating their feasibility for MICP. To shed light on the above aspects, bacterial colonies were isolated from soil samples and tested for urease activity. A strain of *Sporosarcina* sp. was selected among them and proceeded with further analysis. Experiments conducted on bacterial growth and urease activity on the selected isolate confirmed satisfactory cell growth and urease producing capability whereas MICP test results showed ample avenues for biocementation by the isolated bacteria species. However, detailed analysis on biocementation by the selected isolate is recommended prior to any large scale applications.

Keywords: Biocementation, Microbially induced carbonate precipitation, *Sporosarcina* sp., Urea hydrolysis, Urease activity

INTRODUCTION

Bio-mediated soil improvement is one of the research areas that have drawn much attention in recent years in the field of geotechnical engineering for its sustainability. Among them, biocementation by Microbially Induced Carbonate Precipitation (MICP) is considered the most common approach which has proved its viability for reducing the liquefaction potential of soil, enhancing soil stability, improving the soil strength and stiffness and high potential for self-healing [1] – [4].

Biocementation is achieved by hydrolysis of urea by microbial urease which causes calcium carbonate to precipitate in the presence of a calcium source. Loose sand grains are then bound together by the resulting calcium carbonate crystals thereby improving engineering properties of the soil. The secretion and execution of urease enzyme that degrades urea controls the whole mechanism. The overall process can be explained by the following equations [5].



There are extensive literatures on various microorganisms capable of producing urease enzyme and showing the ability to be utilized for MICP applications [6]. However, the bacteria must produce urease constitutively or inducibly and should be non-pathogenic to be used for MICP successfully [7].

Sporosarcina sp. (formerly known as *Bacillus*) is identified as an ideal bacteria to catalyze hydrolysis of urea because of its high biosafety level and high urease activity [8] and [9]. As per literature, members of *Sporosarcina* genus have been isolated from wide variety of sources ranging from different types of soils, water, and ocean to human blood samples and soy sauce [10].

The high dependency of MICP on the microbial growth makes it necessary to optimize the process to provide most suitable conditions for the bacteria in action, because each bacterium has unique conditions at which urease activity will be maximum; physical parameters such as temperature and pH greatly influence the bacterial growth [7]. On the other hand using local bacteria for

biocementation applications in real field can provide more suitable environment for the process while minimizing adverse effects associated with introducing foreign bacteria to the soil in concern.

During a study focused on finding urease producing bacteria capable of MICP process, a strain belonging to *Sporosarcina* genus was isolated from a soil sample collected from the tropical climate in Sri Lanka. The main aim of the research study presented by this paper was to evaluate the feasibility for biomediated soil improvement using the strain isolated to be applied in soil improvement applications in Sri Lanka. As a preliminary investigation, the aforementioned objective was achieved by conducting a series of simple calcium carbonate precipitation tests. Therefore, main aims of this research study can be stated as (1) isolation of a ureolytic bacteria from soil samples from Sri Lanka (2) identification of the isolated strain (3) quantifying the microbial growth and urease activity and (4) evaluating their role in MICP using calcium carbonate precipitation tests and Scanning Electron Microscope (SEM).

MATERIALS AND METHODS

Soil Sampling and Isolation of Ureolytic Bacteria

About 50 g of soil was collected from a public park in Sri Lanka (06° 54' 43.2" N, 79° 51' 36.3" E) to a sterile test tube, imported to Japan and stored at 4°C. Soil sample was then serially diluted (10^1 - 10^6 times) and plated on NH_4 -YE agar medium (1.575 g Tris buffer, 1 g NH_4SO_4 , 2 g agar, 2 g yeast extract). After incubating at 30°C for 2 days, colonies were identified from a plate with 30-200 colonies. Different types of colonies were selected and separately cultivated on the plates prepared in the same manner described above.

A simple urease activity test was then conducted for qualitative assessment of urease producing bacteria. Each colony was mixed with 20 mL of cresol red solution containing urea and incubated at 45°C for two hours. Colonies that changed the initial yellow colour to pink (Cresol red changes from yellow to pink when pH changes to 7.2-8.8 which is accomplished during urea hydrolysis) were identified as urease producing bacteria. Among four ureolytic bacteria, the one showing the highest pH increase was selected for further analysis.

Identification of Bacteria

16S rDNA Gene Amplification and sequencing was carried out for the isolate. The analysis of the DNA sequences was performed by using the DB-BA 12.0 (TechnoSuruga Laboratory) and International Nucleotide Sequence Database (DDBJ / ENA (EMBL) / GenBank) by TechnoSuruga Laboratory,

Japan.

Measurement of Microbial Growth and Urease Activity

NH_4 -YE medium (1.575 g Tris buffer, 1 g NH_4SO_4 , 2 g yeast extract prepared with distilled water) was used for culturing the bacteria. The cells were precultured in 5 mL medium at 30°C and 160 rpm for 24 hours. Temperature of 30°C was selected for preliminary investigations, so that it complies with the tropical climate prevailing in Sri Lanka. One mL of the preculture was inoculated with 100 mL of the fresh medium and incubated under the same conditions. Microbial cell concentration was determined in terms of optical density at a wave length of 600 nm (OD_{600}) using a UV-VIS spectrophotometer (V-730, JASCO Corporation, Tokyo, Japan) at regular intervals of 24 hours. Several tests were conducted by changing the pH of the main culture to determine the pH dependency of the strain.

Urease activity of the bacterial cells was evaluated by cells suspended in a solution containing urea. 1 mL from microbial cell culture was transferred to 100 mL of the substrate solution of 0.1 mol/L (M) sodium phosphate buffer (pH adjusted to 7.01) containing 0.1 M urea. The reaction mixture was continuously stirred and kept at the desired temperature using a water bath. Ten mL of the reaction mixture was sampled at 5 minutes interval, added alkaline hypochlorite reagent to terminate the reaction followed by addition of phenol reagent. The solution was incubated at 60°C for 10 minutes for blue colour generation by the reaction between ammonium ions and phenol in the presence of hypochlorite. The intensity of the colour was measured using UV-VIS spectrophotometer at 630 nm wavelength which is proportional to the NH_4^+ ion concentration. The urease activity was expressed in terms of the amount of enzyme required to hydrolyze one micromole of urea per minute (U) per milliliter. The same procedure was repeated at regular intervals of 24 hours.

Microbially Induced Calcium Carbonate Precipitation

Microbially Induced Calcium Carbonate Precipitation tests were conducted in 10 mL tubes under varying experimental conditions to evaluate feasibility of using isolated bacteria strain for biomediated soil improvement. Calcium chloride reagent was used as the calcium source and three different concentrations of CaCl_2 and urea were used.

In order to distinguish the precipitation capacity of the bacteria strain when cell culture is directly used against when supernatant and cell pellets are used separately, 3 different cases (Case 1, Case 2 and Case 3) were implemented as shown in Table 1.

Table 1 Experimental conditions for the MICP tests.

Case No	CaCl ₂ (M)	Urea (M)	Bacteria	OD ₆₀₀
1	0.5	0.5	Cell pellet	0.2
2	0.5	0.5	Supernatant	negligible
3	0.5	0.5	Cell culture	0.2
4	0.5	0.5	Cell culture	0.1
5	0.3	0.3	Cell culture	0.1
6	0.1	0.1	Cell culture	0.1

For this, cell pellets were obtained by centrifugation of the bacterial culture at 10°C and 8000 rpm for 5 min. The schematic diagram for the process of obtaining cell pellets and supernatant is given below (Fig. 1) The cell pellets were washed and once again dispersed to original OD₆₀₀ value using distilled water. Aforementioned cases were duplicated for better results.

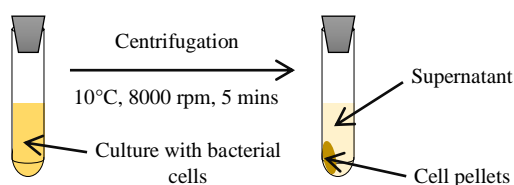


Fig. 1 The schematic diagram for the process of separating cell pellets and supernatant.

Total volume of all the samples were adjusted to 10 mL and kept in a shaking incubator at 30°C and 160 rpm for 48 hours. Supernatant was then filtered through a filter paper and filter papers and tubes with the precipitates were oven dried at 105°C for 24 hours to measure the dry weights of the precipitates. Precipitated specimens were analyzed using the SEM to evaluate the morphology of the resulting calcium carbonate crystals.

RESULTS

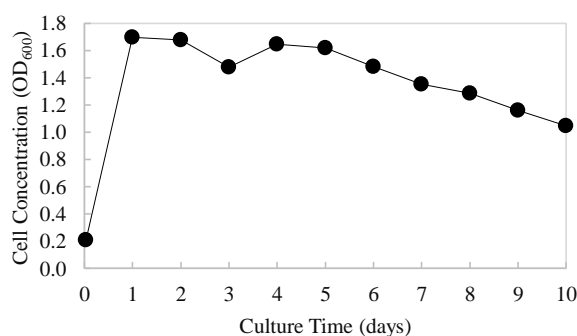
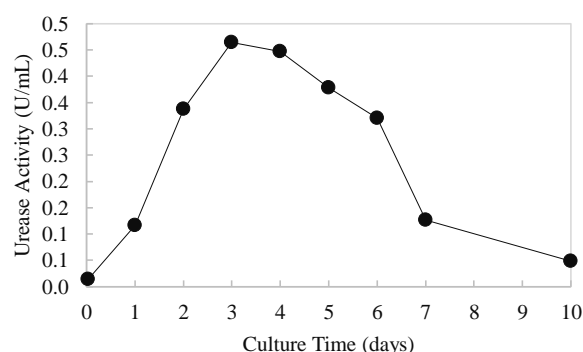
Isolation and Identification of Bacteria

The isolate was identified as a strain of *Sporosarcina* sp. with 99.7% sequence similarity.

Microbial Growth and Urease Activity

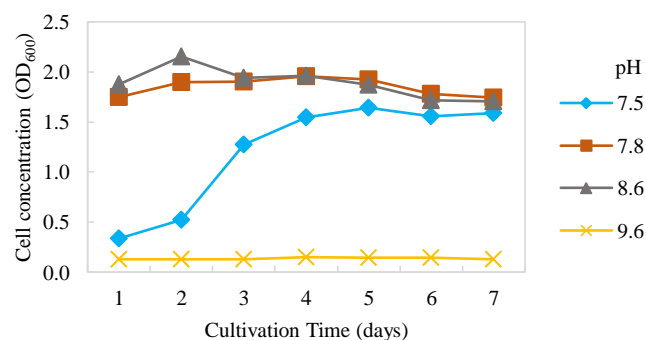
The microbial cell concentration of the strain for a period of 7 days is shown in Fig. 2. According to the results, cell growth rises when transferred to the fresh medium up to a maximum within 24 hours. It remains almost constant for next 24 hours and shows a sudden drop during third day after cultivation. However, cell concentration gradually decreases with time afterwards.

Figure 3 depicts how urease activity of the strain varies over the same time period. Activity increases proportional to increase in cell growth and achieves the maximum activity during 3rd and 4th days after cultivation irrespective of the lower cell growth during 3rd day. Further, it maintains a considerable level of activity for about 6 days which is required if the strain is to be used for biocementation applications in the future.

Fig. 2 Cell growth of *Sporosarcina* sp. isolated from Sri Lankan soil (pH = 8.3).Fig. 3 Urease activity *Sporosarcina* sp. isolated from Sri Lankan soil.

pH Tolerance of the Isolated Bacteria

The pH dependency of the strain was analysed with the intention of finding optimum growth conditions for the bacteria. The change in OD₆₀₀ corresponding to change in pH is shown in Fig. 4.

Fig. 4 pH tolerance of *Sporosarcina* sp. isolated

from Sri Lankan soil.

The bacteria strain showed a favourable stable growth at pH of 7.8 and 8.6. For the culture prepared for pH 7.5, there was sharp increment over the time course. Results indicate that highly alkaline conditions like pH = 9.6 in not favourable for the bacterial growth.

Calcium Carbonate Precipitation by *Sporosarcina* sp.

Precipitation tests were done for 6 different cases (Refer Table 1 for the 6 cases studied). The weight of the precipitate formed for each case is shown in Fig. 5 below. The amount of CaCO_3 precipitate formed when cell pellets were used was much higher than when bacterial culture was used for the same OD_{600} value. For Case 2, where supernatant was used, although absolute precipitation weight is low, it can be considered significant when compared with Case 4 - Case 6. This is an indication of the fact that *Sporosarcina* sp. used in this study has the ability to secrete the enzyme into the extracellular environment resulting higher activity in the supernatant as well.

The comparison between Case 3 and Case 4 elaborate the fact that higher cell growth leads to better precipitation, which means better biocementation when used for soil improvement applications. Case 5 to Case 6 shows varying degrees of precipitation for the same OD_{600} value depending on the concentrations of CaCl_2 and urea.

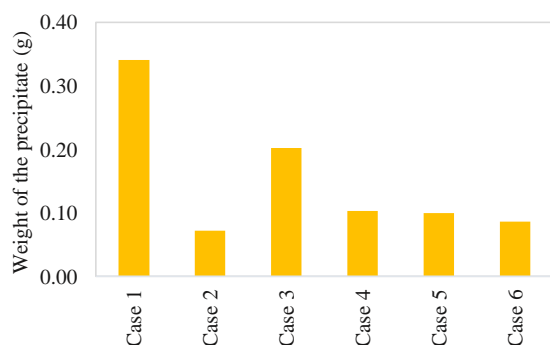


Fig. 5 Comparison of CaCO_3 precipitation under varying experimental conditions

Morphology of CaCO_3 Crystals

When morphology of the CaCO_3 crystals formed was observed using the SEM, few variations were identified. For the case where only cell pellets were used (Case 1), well developed rhombohedral crystals were dominant. Further, agglomerations of spherical crystals were also observed as in Fig. 6.

The CaCO_3 crystals obtained when only the supernatant was used primarily consisted almost perfectly shaped hemispherical crystals slightly

covered with irregular agglomerations (Fig. 7).

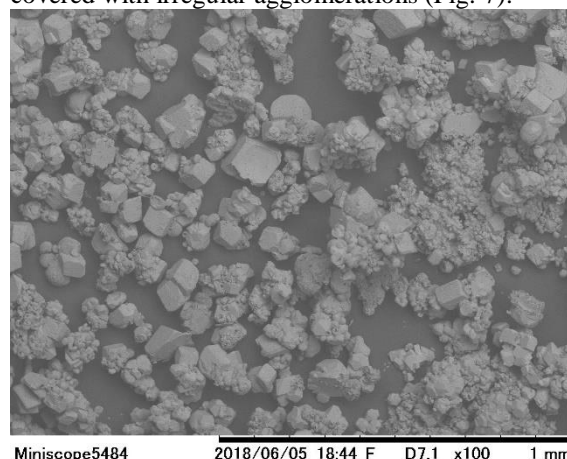


Fig. 6 SEM images of CaCO_3 crystals formed when only cell pellets were used (Case 1).

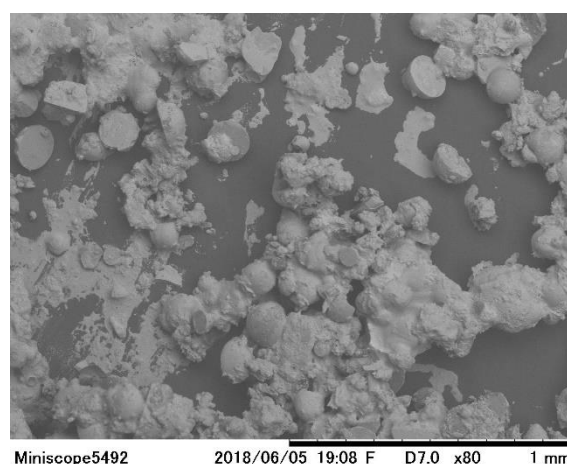


Fig. 7 SEM images of CaCO_3 crystals formed when only supernatant was used (Case 2).

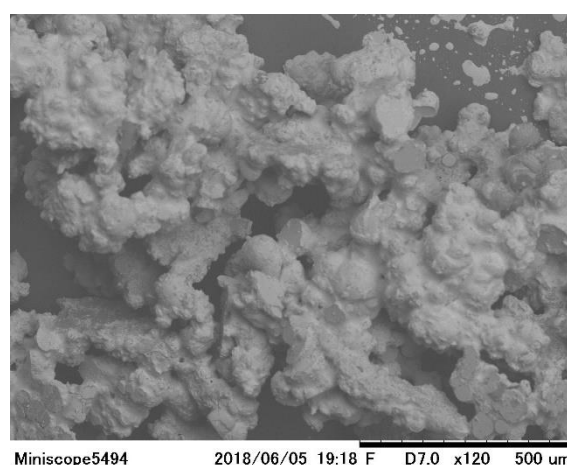


Fig. 8 SEM images of CaCO_3 crystals formed when culture medium with bacterial cells was used (Case 3 – Case 6).

In all other scenarios, CaCO_3 precipitation was exercised with culture medium containing cells and obtained morphologies similar to Case 2 in which only supernatant was used. However, the hemispherical crystals are covered by higher proportions of irregular agglomerations as indicated by Fig. 8.

DISCUSSION

The present research was aimed at evaluating the feasibility of using biocementation in Sri Lanka as a novel soil improvement technique. The urea hydrolysis capability of the bacteria under specific conditions is a key factor in the process. According to the literature available, members of *Sporosarcina* genus are ideal candidates for biocementation applications and have proven its efficiency in many laboratory investigations [8] and [9].

The *Sporosarcina* sp. strain isolated from Sri Lankan soil showed satisfactory cell growth and urease activity to be used for MICP applications. Furthermore, its activity decreases to a considerably lower value only after 6 days from initial cultivation. The current experimental results showed that the growth will be optimum at an approximate pH range of 7.8-8.6. Extreme pH levels above or beyond those limits seem to be not favourable.

Microbially Induced Calcium Carbonate Precipitation tests confirmed that considerable amounts of precipitates are formed in each case either cell pellets and supernatant are used separately or culture medium with overall cells are used in combine. This testifies to the fact that the strain is capable of secreting the enzyme into the extracellular substrate present.

For Case 4 and Case 5, the weights of precipitates observed are almost same for varying CaCl_2 and urea concentrations. This reflects that, although CaCl_2 and urea concentrations are increased there is a maximum limit up to which bacteria will be effective in hydrolyzing urea. Therefore, it is necessary to find the optimum concentrations of feeding solution based on the bacterial density in order to optimize the costs and benefits in real field scenarios.

For each case aforementioned, varying CaCO_3 morphologies were observed. Cell pellets in reaction solution gave rise to rhombohedral crystals whereas supernatant and culture medium with cells resulted in hemispherical crystals predominantly. The reason for change in morphology of the crystals has not yet been fully understood. However, the change can be briefly attributed to the effects from amino acids/organic acids etc. in the culture medium or extracellular polymeric substances provided to the substrate by cells.

Finally, it is important to optimize the

mechanism by providing the optimum concentrations for feeding solutions, pH, bacteria cell concentration and other governing factors prior to any large scale experiments.

CONCLUSIONS

This study addresses the current knowledge gaps related to the possibility of implementing MICP by local bacteria as a soil improvement technique in Sri Lanka. However, this study is only a preliminary investigation on finding a urease producing bacteria which can be used for the Microbially Induced Carbonate Precipitation (MICP) process and evaluating its growth conditions and urease producing capability. From the results gathered during the study, following conclusions can be made.

The *Sporosarcina* sp. strain isolated from the Sri Lankan soil samples has shown high feasibility for MICP applications in the past. The tests confirmed a satisfactory level of urease activity for about 6 days after cultivation which corresponds with the cell concentration. Bacteria showed favourable growth conditions for pH around 7.8-8.6. The results from the precipitation tests confirmed that significant amounts of CaCO_3 precipitate was obtained for all the experimental conditions. The precipitates from cell pellets and supernatant confirmed that urease enzyme is distributed in/on the cell as well as in the supernatant. However, use of cell pellet is recommended for future work which is more likely to produce highest biocement. Temperature used for the current study was 30°C with the intention of mimicking the temperature of the original climate and subsequently showed the ability for biocementation under natural climatic conditions. Furthermore, a drastic change in the morphology of crystals from well-developed rhombohedral to hemispherical shape was exhibited when separated bacterial cell pellets and intact culture medium with bacterial cells were used respectively.

As a conclusion, it can be confirmed that, *Sporosarcina* sp. isolated from Sri Lankan soil shows high possibility to be used for biocementation as a remediation technique for loose weak soils. However, extensive studies are mandatory prior to implementing the biocementation technique using the isolated bacteria for large scale applications.

ACKNOWLEDGEMENTS

This work was partially supported by JSPS KAKENHI, Grant number JP16H04404, Japan. The authors gratefully acknowledge the support.

REFERENCES

- [1] Ivanov V. and Chu J., Applications of microorganisms to geotechnical engineering for bioclogging and biocementation of soil in situ, *Rev. Environ Sci Biotechnol*, Vol. 7, 2008, pp. 139-153.
- [2] Montoya B.M., DeJong J.T. and Boulanger R.W., Dynamic response of liquefiable sand improved by microbial-induced calcite precipitation, *Geotechnique*, Vol. 63, Issue 4, 2013, pp.302-312.
- [3] van Paassen L.A., Ghose R., van der Linden T.J.M, van der Star W.R.L. and van Loosdrecht M.C.M., Quantifying biomediated ground improvement by ureolysis: large-scale biogROUT experiment, *Journal of Geotechnical and Geoenvironmental. Engineering*, Vol. 136, Issue 12, 2010, pp.1721-1728.
- [4] Whiffin V.S., van Paassen L.A. and Harkes M.P., Microbial carbonate precipitation as a soil improvement technique. *Geomicrobiology Journal*, Vol. 24, Issue 5, 2007, pp. 417–423.
- [5] Charpe A.U., Latkar M.V. and Chakrabarti T., Microbially assisted cementation – A biotechnological approach to improve mechanical properties of cement. *Construction and Building Materials*, Vol. 135, 2017, pp. 472–476.
- [6] Sarayu K., Iyer N.R. and Murthy, A.R., Exploration on the biotechnological aspect of the ureolytic bacteria for the production of the cementitious materials—a review, *Appl. Biochem. Biotechnol*, Vol. 172, Issue 5, 2014, pp. 2308–2323.
- [7] Omoregie A.I, Khoshdelnezamiha G., Senian N., Ong D.E.L. and Nissom P.M., Experimental optimisation of various cultural conditions on urease activity for isolated *Sporosarcina* sp. strains and evaluation of the biocement potentials, *Ecological Engineering*, Vol. 109, 2017, pp.65-75.
- [8] Canakci H., Sidik W. and Kilic I.H., Effect of bacterial calcium carbonate precipitation on compressibility and shear strength of organic soil, *Soils and Foundations*, Vol. 55, Issue 5, 2015, pp.1211-1221.
- [9] Cheng L., Shahin M. A. and Cord-Ruwisch R., Bio-cementation of sandy soil using microbially induced carbonate precipitation for marine environments. *Geotechnique*, Vol. 64, Issue 12, 2014, pp.1010–1013.
- [10] Sun Y., Zhao Q., Zhi D., Zining W., Wang Y., Xie Q., Wu Z., Wang X., Li Y., Yu L., Zhou J. and Li H., *Sporosarcina terrae* sp. nov., isolated from orchard soil, *International Journal of Systematic and Evolutionary Microbiology*, Vol. 67, 2017, pp.2104-2108.

BUILDING MASS RAIL TRANSIT IN KUALA LUMPUR: IS IT GOOD TRANSPORT ECONOMICS?

Hamid AHA¹, Tabassi AA² and Samsurijan MS³

^{1,2}School of Housing, Building & Planning, USM, Malaysia; ³School of Social Sciences, USM, Malaysia

ABSTRACT

Kuala Lumpur city is hoping to join the public transport club of elite capital cities. Most successful capital cities in the world has good even outstanding public transport system in particular rail based systems such as LRT or MRT. The cost of MRT system is high and sometimes takes a toll on the finances of a city even a country. This paper discusses the merits and drawbacks of building MRT system for Kuala Lumpur. The paper traces the beginnings, present and future outlook of rail-based public transport system in the Klang Valley in general and in Kuala Lumpur in particular. The economics of building MRT as opposed to improving and adding new bus lines are compared. The paper concludes that not all mass public transport systems are necessarily economical if less expensive alternatives have not been matured. A case study was used to demonstrate the parameters of transport system that can be evolved and matured. These parameters included system capacity, scheduling, coverage area, and accessibility among others.

Keywords: Rail, LRT, MRT, Public Transport, Transport Economics, Kuala Lumpur

INTRODUCTION

Transport infrastructure facilities in urban areas in Malaysia, which are becoming increasingly sophisticated, modernised, systematic and user-friendly, have enhanced the accessibility level of urban inhabitants.

The evaluation of distance reflects the inhabitant's level of accessibility in a particular setting and their well-being. An environment or setting that has a high accessibility often becomes the choice of most of the daily activities. The ability to carry out daily activities without any hindrances is part of a prosperous life that is wished upon by the population [1]. According to [2,3], people accessibility to places of work and daily activities such as government offices, supermarkets or service counters have varying values of interest. The evaluation also influences the form and type of transportation that needs to be used, such as private or public transportation [3]. Thus, among the factors that influence the inhabitant's evaluation of the distance of accessibility are the rapid urban development, the town's surrounding area, the access time and the road infrastructure facilities in the town [4,5].

Public transport especially of the rail-based system provide mass transportation for urban dwellers in a city. Most major cities in the world have good LRT or MRT systems in place for their citizens. Kuala Lumpur also wish to join these group of successful cities. In 2010 the federal government of Malaysia declared that the MRT line 1 and 2 will

be built to increase public transport use in Kuala Lumpur. In July 2017, the MRT line 1 was completed[6]. This paper discusses the question whether the MRT system is, after all, a good investment economically from the transportation point of view.

THE KL MRT SYSTEM

The KL MRT (line 1) system is 51 km long starting from Sungai Buloh in the north to Kajang in the south. The system was planned to carry 150000 passengers per day[6]. The tickets are priced from RM1.10 to RM 6.40 for the whole length of the line.

Area of Service

The alignment of the MRT line 1 takes a traveller across Kuala Lumpur city in the north-south direction. The proposed MRT line 2 is suppose to connect Sungai Buloh to Putrajaya, the administrative capital of the country. The MRT line 3 has now been postponed as part of the austerity drive by the new Malaysian government.

Traffic in the Area

Urban transportation infrastructure has made the physical structural elements around the city, which it makes the city looks modern, sophisticated and contemporary. Transportation service facilities such as the monorail, commuter trains, buses and taxis are often evaluated as a basic urban development feature

[4,7]. Central Kuala Lumpur has a population of about 1.7 million while the Greater Kuala Lumpur area has some 7 million people living in it. The number of private cars in the whole of the Kuala Lumpur area stands around 3.9 million resulting in some 16,000 numbers of cars per km² requiring parking spaces[8]. Clearly, for a city where land value is high, the land use is better utilised for economic activities rather than for parking purposes.

EXISTING RAIL, BUS AND TAXIS SERVICES

KL already have LRT and monorail lines serving a fair section of the metropolitan area. The Kelana Jaya Line, Sri Petaling Line and Ampang Line are all operated by Rapid Rail. All three lines carry a combined total of 300,000 commuters per day[6]. These lines are supplemented by the KL Rapid bus and city cab and taxi services. Metered taxis are available throughout the city but maybe difficult to get during rush hours. GRAB car e-hailing service now provides a good alternative to taxis and other transport modes.

Cost of Buses & Operations

In general, a large size bus carrying some 60 passengers cost RM500k each. A medium size bus with a capacity of 35-40 will cost RM300k each. A mini bus whose capacity is about 20 (including standing passengers) can cost upto RM100k.

Buses use existing roads and each bus type caters for the limitations of the road configurations. Smaller buses are used for narrow winding roads with limited roadside space. The bigger buses are used for wide straight roads with dedicated bus-stops facilities and terminal locations.

Figure 1 shows the carrying capacity of buses as compared to MRT for the same amount of investment i.e. the money spent building the MRT infrastructure or the money spent buying buses. Clearly, buses can carry a larger number of passengers if we compare Ringgit to Ringgit spent.

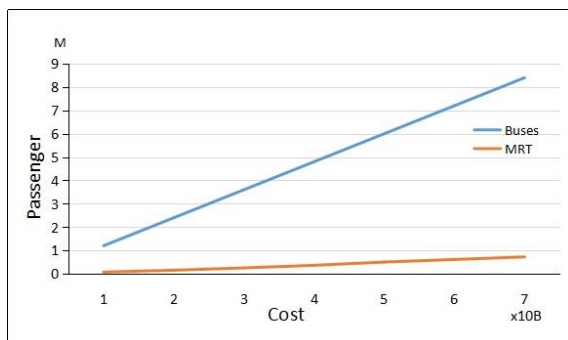


Fig. 1 No. of passengers versus investment cost

If we take the case of the MRT line 1 which cost RM 21 Billion to be built, that same amount

could buy 40,000 buses at a cost of RM500k each. If one bus can carry 60 passengers, then 40,000 buses will be able to carry 2.4 M passengers. This number is 16 times more than number of passengers that could ride the MRT line 1 which is 150,000 passengers in a day[9,10].

Number of Cars Removed

Another criteria used to justify the construction of the MRT system is the number of cars removed from the roadways because of mode shift[10]. Assuming all cars are single occupant vehicles (SOV) then if 150,000 people opted for the MRT then it is argued that the same number of cars will be removed from the city roadways. Using the same argument, for buses this would mean some 2.4M cars would be removed from the roads if people opted for the 40,000 buses provided. Figure 2 shows the relationship between number of cars removed against investment for both buses and MRT.

TRANSPORT ECONOMICS AND USER MODE CHOICE

As indicated earlier, travel mode choice in Kuala Lumpur is quite varied[11]. Besides the private transport such as cars and motorcycles, travellers can choose taxis, buses and rail based systems. The overall modal split in Kuala Lumpur presently stands at 25% public transport, still a long way from the targeted 40% by 2030 declared by the government [6].

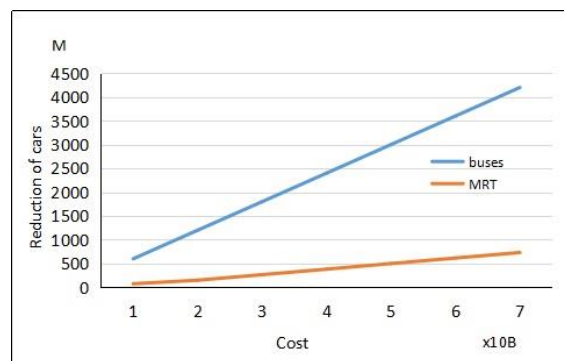


Fig. 1 Reduction of cars versus investment cost

Increasing the reach of bus services

While the bus service in Kuala Lumpur is as old as the city, its status as popular mode of travel has been a roller coaster. In the late 1970-80s buses were quite popular especially with the presence of mini-buses which were cheap and convenient. System modernisation via regularisation of service providers saw the many bus operators being replaced by the KL Bus Rapid service. The implementation of the

Monorail and LRT lines within the KL city center however somewhat diminished the utilisation of buses primarily because bus network generally remained unchanged, catering for existing and historical routes. Many newly developed areas with large number of residents were not privy to bus services.

COMPARING MRT WITH BUSES

It has been also argued that since KL's integrated urban transit system covers a limited number of routes, it cannot be fully effective without feeder buses. Since KL has a tropical climate, many of the residents may not comfortable to walk more than 600 m under conditions of almost high temperature and high relative humidity. Therefore, people who use public transportation either living very close to the railway stations or travel by car to the station. Inappropriately, the limited parking spaces at stations restricts the available carpark and the demand always outstrips the supply. As a consequence, good feeder bus services are required to increase the catchment areas and improve accessibility to and from the stations [12]

The end objective of a transport system is to move people across a city to their desired destinations. In transport economics, the issue of return on investment cannot be ignored. Table 1 shows the comparison of several items linked to construction/provision cost for the MRT and bus services.

Clearly, buses provides more value for the amount of money spent compared to the MRT system. The contention of course is that buses have been around for a long time and yet it has not managed to garner enough interest of the public (16% in 2005)[10]. Hence, there are reservations to invest in more buses as the newer LRT/MRT systems seemed to draw better patronage.

Table 1 Comparison of bus and MRT operations

System	Capacity/ day	Fare/ km (sen)	Capacity/ Construction cost
MRT	150000	12.5	7.1×10^{-6}
Buses	2.4M	8.0	1.2×10^{-4}

Note: Inflation rate not accounted for - construction cost as at completion. Comparison is for the same amount of investment.

The bare facts are that the utilisation of rail-based public transport has been on the down trend since 2014[13]. Figure 3 shows this pattern quite clearly. Besides the availability of e-hailing systems such as Uber (formerly) and GRABcar giving residents alternative travel options, the issue of the

first and last mile dis-connectivity and/or inaccessibility also can make rail-based system less attractive.

The MRT management has provided feeder buses and parking facilities to support patronage of their system. While the feeder services are limited, with only 300 buses for the entire line 1, parking places are not free. Commuters have complained that it cost them more to ride the MRT system as compared to driving on their own.



Figure 3. Daily Ridership Q1 2014 - Q2 2017 [13]

CONCLUSION

The sophisticated and effective transportation infrastructure in cities contributes towards the overall quality of life of urban populations. A good transportation infrastructure is capable of enhancing their accessibility, in which the inhabitants have the opportunity to choose a suitable and comfortable form of transportation. A high level of accessibility affords the urban village populations the ability to adapt with the city surroundings that are ever changing. The transportation infrastructure around a city is essential in assuring the quality of life and well-being of urban village inhabitants.

According to [12] the last decade has witnessed rapid development of rail-based public transportation systems in KL. Future development will concentrate on expanding the network, adding stations and facilities, improving standards, and improving feeder access. There are many challenges in integrating the diversity of services into a system that satisfies passengers' requirements for efficient, seamless, flexible and inexpensive public transport [12]

The MRT system while proven elsewhere to be fundamentally useful for reducing private vehicles in cities, has not been able to do the same for Kuala Lumpur[13]. The most dominant drawback of the KL MRT is the ROI per passengers carried. It is shown that the conventional bus system could provide similar carrying capacity at a much lesser cost. Buses can also penetrate a much wider area merely by accessing existing road networks[14].

However, while the MRT system suffers from the first and last mile connectivity issues, bus usage needs to be promoted for it to gain patronage[15]. It is not difficult to envisage that once the bus system has matured and is able to deliver commuters to their destinations, rail-based system such as MRT can then do the heavy haulage of readily available commuters much like the expressway does to carry heavy traffic.

LIMITATIONS AND FUTURE RESEARCH

This study only focused on comparing the cost implications of building a MRT system against providing buses as an alternative travel mode. Future work should also look at the alignment of the MRT system and its station locations with respect to population and economic hotspots. Such studies will help us to better understand the respective needs and constraints of mass urban travel in cities like Kuala Lumpur.

ACKNOWLEDGEMENTS

This research was supported by the HBP-Infratech Research Unit, School of Housing, Building & Planning, Universiti Sains Malaysia, Penang.

REFERENCES

- [1] Abou-Zeid, M. & Ben-Akiva, M. (2011) "The effect of social comparisons on commute well-being", *Transportations Research Part A: Policy Practice*, 45(4), pp. 345–361.
- [2] Anable, J., & Gatersleben, B. (2005) "All work and no play? The role of instrumental and affective factors in work and leisure journeys by different travel modes", *Transportations Research Part A: Policy Practice*, 39(2-3), pp. 163–181.
- [3] Beirao, G., & Cabral, J.A.S. (2007) "Understanding attitudes towards public transport and private car: a qualitative study", *Transportations Policy*, 14 (6), pp. 478–489.
- [4] Stradling, S., Carreno, M., Rye, T. & Noble, A. (2007) "Passenger perceptions and the ideal urban bus journey experience", *Transportations Policy*, 14 (4), pp. 283–292.
- [5] Tyrinopoulos, Y., Aifadopoulou, G. (2008) "A complete methodology for the quality control of passenger services in the public transport business", *European Transportations*, 38, pp. 1-16.
- [6] Afiq A, Malaysians warm up to public transport - slowly, but surely, [https:// themalaysianreserve.com/2018/03/20/malaysians-warm-up-to-public-transport-slowly-but-surely/](https://themalaysianreserve.com/2018/03/20/malaysians-warm-up-to-public-transport-slowly-but-surely/)
- [7] Yanliu Lin & Bruno De Meulder (2012) "A conceptual framework for the strategic urban project approach for the sustainable redevelopment of "villages in the city" in Guangzhou", *Habitat International*, 36, pp. 380-387
- [8] Phooi W.H, Ghadiri, S.M., and Rajagopal P., Future Parking Demand at Rail Stations in Klang Valley, MATEC Web of Conferences 103, 09001 (2017), ISCEE 2016
- [9] Jonathan J.T., KL folk spend 250 million hours a year stuck in jams, metro-level transport planning needed - World Bank, <https://paultan.org/2015/06/17/world-bank-malaysia-economic-monitor-transforming-urban-transport/>
- [10] MRT-SBK Line breaks 140,000 daily ridership, <https://www.thestar.com.my/news/nation/2017/07/23/>
- [11] Onn Chiu Chuen, Mohamed Rehan Karim, and Sumiani Yusoff , Mode Choice between Private and Public Transport in Klang Valley, Malaysia, *Scientific World Journal* Volume 2014, Article ID 394587
- [12] Hilmi Mohamad. (2003). Rail Transportation in Kuala Lumpur. *Japan Railway and Transport Review* 35: 21-27
- [13] Ong K.M, Public transport ridership falling, despite the billions spent, <https://www.malaysiakini.com/news/397308>, 2017
- [14] Norizan A.M, New bus fare starts today, http://www1.utusan.com.my/utusan/info.asp?y=2000&dt=0701&pub=utusan_malaysia&sec=Muka_Hadapan&pg=fp_03.htm
- [15] Yahaya, N.Z., Kholitiza, S.N., Ishak, F, Towards Sustainable Transportation System: Malaysian Experience, ESCAP

UNDERSTANDING OF FIRE DISTRIBUTION IN THE SOUTH SUMATRA PEAT AREA DURING THE LAST TWO DECADES

Raden Putra¹, Edy Sutriyono², Sabaruddin³ and Iskhaq Iskandar⁴

¹Graduate School of Environmental Science, University of Sriwijaya, Indonesia; ²Faculty of Engineering, University of Sriwijaya, Indonesia; ³Faculty of Agriculture, University of Sriwijaya, Indonesia; ⁴Faculty of Mathematics and Natural Sciences, University of Sriwijaya, Indonesia.

ABSTRACT

Peat fire is an annual catastrophic event in Indonesia, particularly in South Sumatra region during the dry season. Several previous studies have suggested that anthropogenic force in land cover is contributing to peat fires. Understanding the distribution of hotspots in land cover on peatlands is needed to address future peat fires. This study is aimed to evaluate the distribution of hotspots on the land cover type of the South Sumatra peat area during the last two decades (1997-2016). Remote sensing technique with visual image interpretation method using multitemporal satellite images is used to identify the variations of land cover in the study area. The results show that the peat area of South Sumatra in 2013 is dominated by ferns/ shrub (58%) and only about 10% is covered by peat swamp forest (PSF). The largest distribution of hotspot during the last two decades was in land cover types of Ferns/ shrub (34.808 hotspots) and Industrial Plantation (7.223 hotspots). Note that the densest hotspot is located on an industrial plantation with an average of 37 hotspots every 100 km² areas per year. While during the two decades of observation, only a small percentage of the hotspots located in PSF and hotspots appeared consistently in the last five years. Based on results, the South Sumatra peatland is very vulnerable to burn during the dry season in the future. The government as policymakers must be able to protect the existence of peat swamp forests and keep the ferns/ shrub from the fires and subsequent land cover changes (Industrial plantation or small holder area).

Keywords: Peatland, Peat Fire, Hotspots, Land Cover

INTRODUCTION

Peat fire is an annual catastrophic event in Indonesia, particularly in South Sumatra region during the dry season. Several previous studies have suggested that anthropogenic force in land cover is contributing to peat fires [1]–[3]. Fire is widely used in the land clearing and preparation of agriculture and plantations on a small and large scale [4], [5]. Using fire as a tool in land preparation can improve the efficiency of production costs but in practice, peat fires cause serious environmental and human problems [6].

The health issues are a major problem faced when the peat fires occur during the dry season. There are at least 19 deaths and half a million of cases of acute respiratory infections in the catastrophic fires event during 2015 [7], [8]. In addition, peat fires also contribute to global warming due to carbon emissions into the atmosphere when fires occur. Approximately 11.3 Tg CO₂ per day emitted into the atmosphere during Sept-Oct 2015, this rate is the worst since 1997 [9]. In that event, South Sumatra peatland became the region with the worst impact of fire compared to other regions based on the data of the Indonesian Ministry of Environment, 2016.

Over the past two decades under current management practices, peatlands in Indonesia face a very serious threat of degradation. The threat comes from fire, deforestation and anthropogenic drainage in peat areas [10], [11]. This study will identify land cover of South Sumatra peat areas and evaluate the distribution of hotspots on the land cover type of the South Sumatra peat area during the last two decades (1997-2016). It's important to understand the characteristics of the hotspot distribution on different types of land cover so that future fires events can be predicted and addressed properly.

DATA AND METHODS

Study Area

The research area is peatlands of South Sumatra with an area of 1.48 million ha which has varying levels of depth and peat maturity [12]. The distribution of peatland in South Sumatra is mostly scattered in the northern part of South Sumatra areas (Fig.1). The condition of the peatlands in the study area has been degraded from the PSF land cover type to unmanaged type (ferns/ shrub) and ends up as a managed land cover type (agriculture or plantation) [13]–[15].

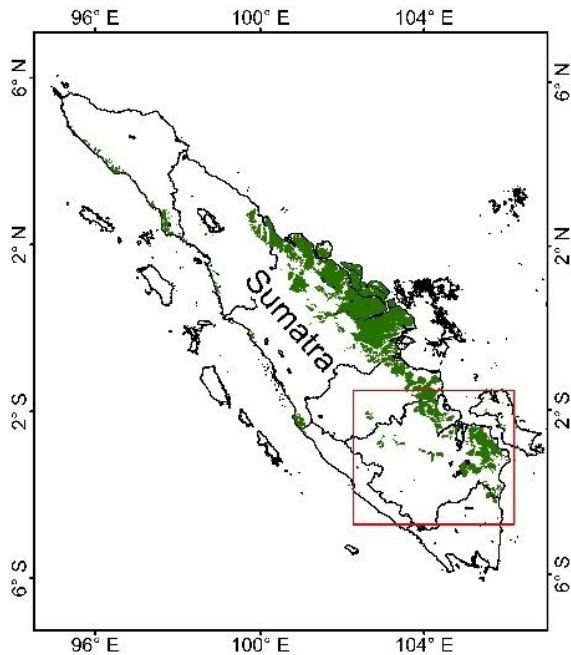


Fig. 1 Study area (red line present South Sumatra region and green shading indicate a peatland area)

Satellite Data

To identify the land cover types of South Sumatra peat areas, this research uses Landsat 7 and 8 satellite imagery were recorded in April-August 2013. This satellite image has a spatial resolution of 30 meters with an area coverage of 185 x 185 km. While the validation of classified data using high-resolution satellite images of Spot 5 and 6 was recorded in 2013 (data derived from The Indonesian National Institute of Aeronautics and Space / LAPAN Indonesia). This high-resolution image data has a spatial resolution of 5 meters with a coverage area of 60 x 60 km.

Classification of Land Cover

The land cover classification in this study is based on literature review [16] and regulations of the Indonesian Ministry of Environment and Forests of 2015 on land cover monitoring guidelines. The

classification scheme classifies land cover into 8 types of land cover (Built-up area, Cleared area, Ferns/ Shrub, Industrial plantation, Primary Peat Swamp Forest/ PSF, Secondary PSF, Small holder area, and Water). The classification method used is visual images interpretation method, where the classification is done gradually until the resulting 8 types of land cover.

Hotspot Data

The data of the hotspot distribution used in this study sourced by Along Track Scanning Radiometer World Fire Atlas (ATSR-WFA Algorithm 2) for observation during 1997-2002. The ATSR-WFA Algorithm 2 data has a spatial resolution of 1 km and the hotspot is identified when the surface temperature reaches ≥ 308 Kelvin [17]. While for observation during 2003-2016, this research uses Moderate Resolution Imaging Spectroradiometer (MODIS) and data of Visible Infrared Imaging Radiometer Suite (VIIRS) from Fire Information For Resource Management System (FIRMS) website. VIIRS data has a better resolution of 375 m compared to MODIS data which has a resolution of 1 km [18], [19].

RESULTS AND DISCUSSION

Of all the land cover identification mapped on peatlands in South Sumatra region, more than half (58%) were occupied by ferns/shrubs (Fig.3). Meanwhile, only 10% or approximately 1500 km² of the peatland is covered by Peat Swamp Forest (PSF) and largely under the management of protected forests in the northern part of South Sumatra (Fig.2). Furthermore, at least 21% of The South Sumatra peatland is occupied by the managed land cover (Industrial plantation and Small Holder area). The results show the variation of land cover that is relatively comparable with some previous research [13], [20]. Furthermore, the hotspot distribution for two decades of observation will be spatially analyzed overlay using the land cover classification that has been produced.

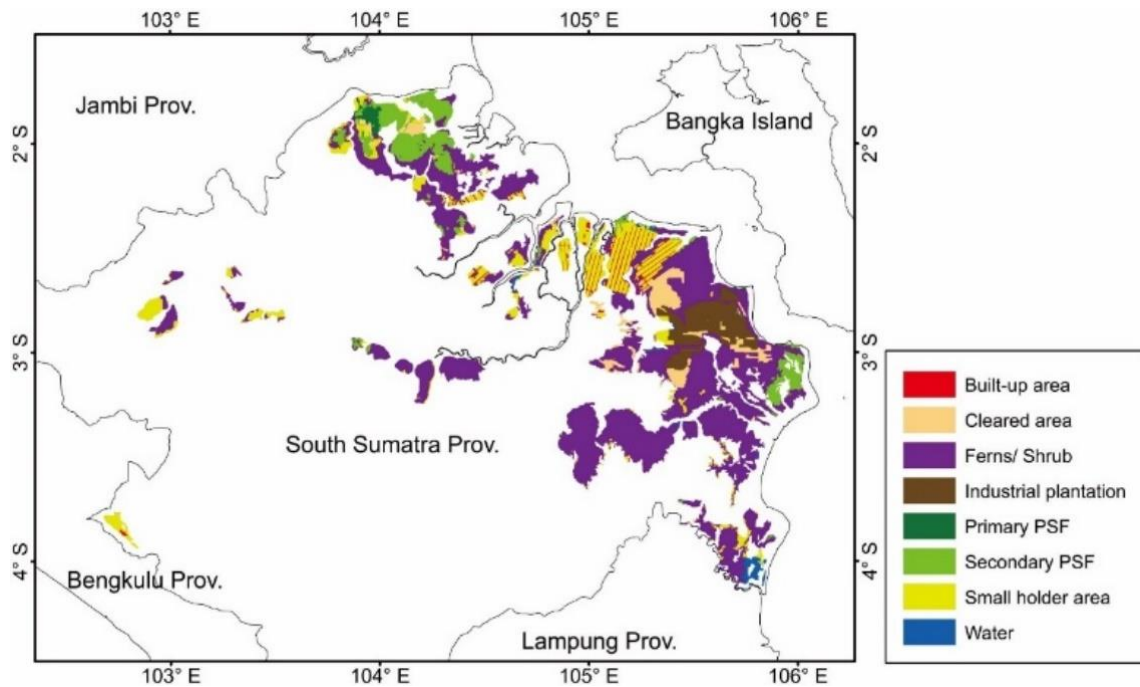


Fig. 2 Land cover classification map of South Sumatra peat area

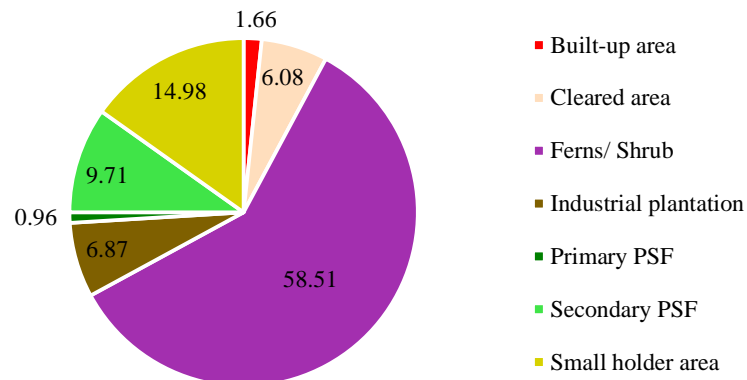


Fig. 3 Percentage of land cover on the South Sumatra peat area

In the last two decades, there have been three great peat fires events in South Sumatra (1997, 2006, and 2015). The events coincided with the phenomenon of El Niño – Southern Oscillation (ENSO) and the Indian Ocean Dipole (IOD) which resulted in extreme deficit rainfall in Indonesia particularly in the South Sumatra region [21], [22]. At least more than 37000 hotspots detected in the research area during those three events, with a density of 2 hotspots / km². While during 1998 and 2000-2001 Hotspot is almost undetectable in the South Sumatra peatland. Based on observations, 2015 is the largest fire event in the research area,

where the hotspots are detected across the land cover types (Table 1).

The largest spread of hotspot during the last two decades was in land cover types of Ferns/ shrub (34.808 hotspots) and Industrial Plantation (7.223 hotspots). While the land cover types of built-up area and primary PSF were the land cover that has the least hotspot. The land cover type of industrial plantation has the highest density of hotspots in the last two decades. In 2015, the densest hotspot was in the primary PSF (5 hotspot / km²), which is interesting because in previous years the hotspot was in the land cover type of industrial plantation.

Table 1. Distribution and density of hotspots on several variations of land cover, note that the density of hotspots is presented per 100 km (BUA: built-up area, CA: cleared area, F/S: ferns/ shrub, IP: industrial plantation, P-PSF: primary peat swamp forest, S-PSF: secondary peat swamp forest, and SHA: small holder area)

Year	BUA		CA		F/S		IP		P-PSF		S-PSF		SHA		Total Hotspot
	hs	dens	hs	dens	hs	dens	hs	dens	hs	dens	hs	dens	hs	dens	
1997	2	1	529	62	2707	33	874	90	8	6	94	7	327	15	4761
1998	0	0	0	0	1	0	0	0	0	0	0	0	7	0	8
1999	0	0	1	0	1	0	117	12	0	0	0	0	10	0	142
2000	0	0	0	0	0	0	0	0	0	0	0	0	0	0	0
2001	1	0	0	0	2	0	2	0	0	0	0	0	1	0	7
2002	0	0	93	11	53	1	149	15	0	0	0	0	12	1	334
2003	13	6	13	2	198	2	25	3	1	1	7	1	200	9	488
2004	20	9	206	24	1918	23	384	40	7	5	96	7	318	15	3094
2005	5	2	6	1	70	1	1	0	2	1	4	0	77	4	175
2006	33	14	1373	160	4930	60	1667	172	1	1	192	14	830	39	9519
2007	3	1	11	1	282	3	6	1	1	1	7	1	57	3	383
2008	3	1	20	2	239	3	34	4	0	0	5	0	58	3	379
2009	21	9	78	9	2144	26	47	5	3	2	109	8	194	9	2675
2010	0	0	14	2	32	0	0	0	0	0	3	0	17	1	69
2011	6	3	83	10	2528	31	154	16	12	9	387	28	166	8	3461
2012	13	6	105	12	2771	34	22	2	53	39	625	46	274	13	4030
2013	2	1	4	0	94	1	9	1	6	4	16	1	28	1	172
2014	7	3	547	64	4529	55	627	65	128	95	150	11	310	15	6624
2015	16	7	1865	218	12281	149	3098	320	709	526	2807	205	842	40	23112
2016	0	0	15	2	28	0	7	1	0	0	11	1	4	0	69
Total	145	3	4963	29	34808	21	7223	37	931	35	4513	17	3732	9	59502

The percentage of hotspot distribution in Fig. 4 Indicates hotspots consistently appear on the ferns/ shrub, small holder area, and industrial plantation during the last two decades. While forest cover (primary and secondary PSF) becomes the land cover type that has the least hotspot. But in the last five years (2011-2016) hotspots always appear on forest cover types.

The consistency of hotspots in ferns/shrubs is caused by the dry conditions on the peatlands and vegetation above which are highly vulnerable to burn during the dry season. In addition, the area of ferns/ shrubs that dominate more than half of the

South Sumatra peat area is also the cause of hotspots that consistently appear on this type of land cover. As for the hotspots that appear on the type of managed peatland (small holder area, and industrial plantation) indicates that water management in managed peatlands has not proceeded properly during the dry season. In the last five years, hotspots have also consistently appeared in peat swamp forests, where most of the peat swamp forests are under the management of protected forests (conservation). The existence of hotspots in conservation areas can be assumed that illegal logging takes place in this land cover.

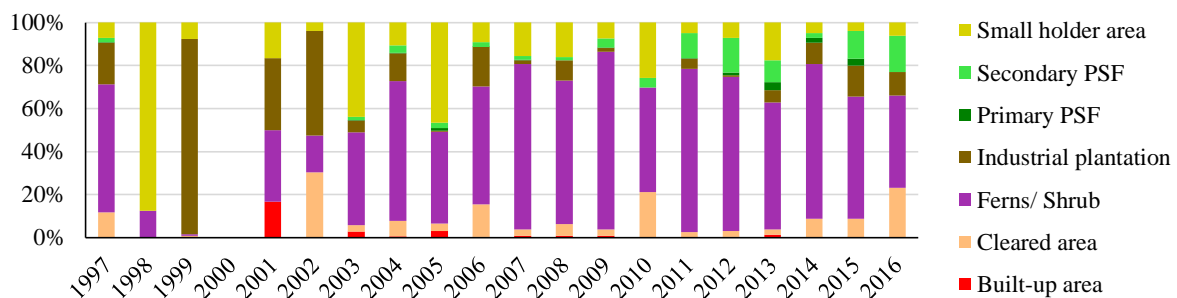


Fig. 4 Percentage of hotspots distribution on several variations of land cover for two decades of observation (1997-2016)

CONCLUSION

The land cover classification results indicate that the South Sumatra peatland was in the dangerous condition because the land cover was dominated by ferns/ shrub which is vulnerable to burn. Moreover, in another study [23] represents that the land cover of ferns/ shrub is the stage of intermediate change to the managed land type (Industrial Plantation or Smallholder Area). The largest hotspot distribution during the last two decades was in the land cover type of ferns/shrubs because the South Sumatra peatland was dominated by those land cover type. The highest hotspot density on the land cover type of industrial plantation indicates that the changed in the peat hydrological system result in dry condition and vulnerable peatlands to burn during the dry season.

The forest cover (primary and secondary PSF) is the land cover type that has the least hotspot distribution in the last two decades, although the hotspots appeared consistently in the last five years. The governments as policymakers should be able to protect the existence of peat swamp forests and keep the ferns/ shrub from the fires and subsequent land cover changes (Industrial plantation or small holder area). This is important to avoid the catastrophic haze disaster caused by peat fires in the future.

ACKNOWLEDGEMENTS

The first author was supported by the *Pendidikan Magister Menuju Doktor Untuk Sarjana Unggul* (PMDSU) scholarship program from the Ministry of Research, Technology and Higher Education of Indonesia.

REFERENCES

- [1] Langner A., Miettinen J., and Siegert F., Land Cover Change 2002-2005 in Borneo and The Role of Fire Derived From MODIS Imagery, *Global Change Biology*, Vol. 13, Issue 11, 2007, pp.2329-2340.
- [2] Cattau M.E., Harrison M.E., Shinyo I., Tungau S., Uriarte M., and DeFries R., Sources of Anthropogenic Fire Ignitions on The Peat-Swamp Landscape in Kalimantan, Indonesia, *Global Environmental Change*, Vol. 39, 2016, pp.205-219.
- [3] Dohong A., Aziz A.A., and Dargusch P., A Review of The Drivers of Tropical Peatland Degradation in South-East Asia, *Land Use Policy*, Vol. 69, Issue May, 2017, pp. 349-360.
- [4] Qadri S.T., Fire, Smoke, and Haze: The ASEAN Response Strategy, *Asian Development Bank*, Vol. 10, Issue 5, 2001, pp. 278.
- [5] Dennis R.A., Mayer J., Applegate G., Chokkalingam U., Colfer C.J.P., Kurniawan I., Lachowski H., Maus P., Permana R.P., Ruchiat Y., Stolle F., Suyanto and Tomich T.P., Fire, People and Pixels: Linking Social Science and Remote Sensing to Understand Underlying Causes and Impacts of Fires in Indonesia, *Human Ecology*, Vol. 33, Issue 4, 2005, pp. 465-504.
- [6] Sloan S., Locatelli B., Wooster M.J., and Gaveau D.L.A., Fire Activity in Borneo Driven by Industrial Land Conversion and Drought During El Niño Periods, 1982-2010, *Global Environmental Change*, Vol. 47, Issue September, 2017, pp. 95-109.
- [7] Glauber A.J., and Gunawan I., The Cost of Fire. An Economic Analysis of Indonesia's 2015 Fire Crisis, *World Bank*, Vol. 17, Issue 5, 2015, pp. 403-408.
- [8] Koplitiz S.N., Mickley L.J., Marlier M.E., Buonocore J.J., Kim P.S., Liu T., Sulprizio M.P., DeFries R.S., Jacob D.J., Schwartz J., Pongsiri M., and Myers S.S., Public Health Impacts of The Severe Haze in Equatorial Asia in September-October 2015: Demonstration of a New Framework for Informing Fire Management Strategies to Reduce Downwind Smoke Exposure, *Environmental Research Letter*, Vol. 11, Issue 9, 2016.
- [9] Huijnen V., Wooster M.J., Kaiser J.W., Gaveau D.L.A., Flemming J., Parrington M., Inness A., Murdiyarso D., Main B., and Van Weele M., Fire Carbon Emissions Over Maritime Southeast Asia in 2015 Largest Since 1997, *Scientific Reports*, Vol. 6, Issue May, 2016, pp. 1-8.
- [10] Miettinen J., Shi C., and Liew S.C., Land Cover Distribution in The Peatlands of Peninsular Malaysia, Sumatra and Borneo in 2015 With Changes Since 1990, *Global Ecology and Conservation*, Vol. 6, 2016, pp. 67-78.
- [11] Page S.E., and Hooijer A., In The Line of Fire: The Peatlands of Southeast Asia, *Philos. Trans. R. Soc. B: Biol. Sci.*, Vol. 371, Issue 1696, 2016, pp. 20150176.
- [12] Wahyunto S., Ritung, Suparto, and H. Subagjo, Map of Peatland Distribution Area and Carbon Content in Kalimantan, 2000-2002, Bogor, Indonesia: Wetlands International—Indonesia, Programme & Wildlife Habitat Canada (WHC), 2004.
- [13] Miettinen J., and Liew S.C., Status of Peatland Degradation and Development in Sumatra and Kalimantan, *Ambio*, Vol. 39, Issue 6, 2010, pp. 394-401.

- [14] Miettinen J., Shi C., and Liew S.C., Deforestation Rates in Insular Southeast Asia Between 2000 and 2010, *Glob. Chang. Biol.*, Vol. 17, Issue 7, 2011, pp. 2261–2270.
- [15] Miettinen J., Shi C., and Liew S.C., Two Decades of Destruction in Southeast Asia's Peat Swamp Forests, *Front. in Ecol. and the Environ.*, Vol. 10, Issue 3, 2012, pp. 124–128.
- [16] Page S.E., Rieley J.O., and Banks C.J., Global and Regional Importance of The Tropical Peatland Carbon Pool, *Global Change Biology*, Vol. 17, Issue 2, 2011, pp. 798–818.
- [17] Arino O., and Casadio S., ATSR World Fire Atlas : Can We Find a Trend in The Longest Global Fire Distribution Series ? The European Space Agency World Fire Atlas project 3, *WFA Products : a Global View*, 2008.
- [18] Schroeder W., Oliva P., Giglio L., and Csiszar I.A., The New VIIRS 375m Active Fire Detection Data Product: Algorithm Description and Initial Assessment, *Remote Sens. Environment*, Vol. 143, 2014, pp. 85–96.
- [19] Giglio L., Schroeder W., and Justice C.O., The Collection 6 MODIS Active Fire Detection Algorithm and Fire Products, *Remote Sens. Environment*, Vol. 178, 2016, pp. 31–41.
- [20] Miettinen J., Shi C., Tan W.J., and Liew S.C., 2010 Land Cover Map of Insular Southeast Asia in 250-m Spatial Resolution, *Remote Sensing Letter*, Vol. 3, Issue 1, 2012, pp. 11–20.
- [21] Iskandar I., The Role of Equatorial Oceanic Waves in the Activation of the 2006 Indian Ocean Dipole. Vol. 44, Issue 2, 2012, 113–128.
- [22] Iskandar I., Utari P.A., Lestari D.O., Sari Q.W., Khakim M.Y.N., Yustian I., and Dahlan Z., Evolution of 2015 / 2016 El Niño and its Impact on Indonesia Evolution of 2015/ 2016 El Niño and Its Impact on Indonesia, *AIP Conference Proceedings* 1857, Vol. 080001, 2017, doi: 10.1063/1.4987095.
- [23] Miettinen J., Hooijer A., Wang J., Shi C., and Liew S.C., Peatland Degradation and Conversion Sequences and Interrelations In Sumatra, *Reg. Environ. Chang.*, Vol. 12, Issue 4, 2012, pp. 729–737.

PADDY FIELD MAPPING USING UAV MULTI-SPECTRAL IMAGERY

Rokhmatuloh¹, Supriatna¹, Tjong Giok Pin¹, Ronni Ardianto², Oka Setiawan², Iqbal Putut Ash Shidiq¹,
Adi Wibowo¹ and Riza Putera¹

¹Department of Geography, Faculty of Mathematics and Natural Sciences, University of Indonesia, Indonesia; ² PT. Pangripta Geomatika Indonesia, Indonesia

ABSTRACT

Paddy is the most famous crop in Indonesia, which dominantly planted in every region primarily the west and central part of Indonesia. Rice paddy field is the main food source for most of the Indonesian and Indonesian government are very considered about the stability of their food security program. Therefore, monitoring and evaluation of its sustainability and availability become a national priority. One of the solution to agricultural monitoring and management program is mapping through remote sensing system. In this study, we used high-resolution multi-spectral imagery collected from unmanned aerial vehicles (UAV) to map paddy field and differentiate them based on their spectral characteristics. An Object-Based Image Analysis method is applied to the image for classifying the stage rice paddy field based on their spectral signature. The result of this study are: (i) a high-resolution map of paddy field and its classifications (ii) a comparison table showing different spectral response for different type of crop such as banana and tea. We hope that this study can support government program on food security with valuable baseline information vegetation on the paddy field.

Keywords: Paddy field mapping, UAV, spatial analysis, OBIA, NDVI

INTRODUCTION

Today we have been faced by the growing need of spatial data. It is not just about the accuracy, proper planning, evaluation and monitoring process are also depending on the temporal coverage of the data [1]. An example of spatial database is vegetation data, which is highly needed by many parties such as government and agricultural sector [2], especially in Indonesia.

Agriculture is one of the critical sector in Indonesia. One of the main source of food in Indonesia is rice which produced from this sector. The nation's total land area is around 190 million hectares. From the total, 55 million hectares are agricultural area and 129 million hectares are covered by forest. From the agricultural area, 24 million hectares are arable land and 20 million hectares are planted with permanent crops [3].

In this sector, agricultural areal mapping has been important to provide database for management, improvement and food security purposes. Regarding the methods in data collection, remote sensing technology has big advantage over conventional terrestrial survey. This technology allows rapid data collection for relatively larger mapping area. UAV system presents as an alternative to the more-conventional airborne or satellite remote sensing system [1]. The objectives of this study are to test the capability of UAV-based multispectral system to map rice paddy field; to generate vegetation index from UAV; and to use the value of vegetation index for classifying different types of crop.

METHODS

Study Area

This study was conducted in Parakansalak, Sukabumi, West Java. The area comprised 70 hectares, covered with various kinds of land-use such as paddy field, tea plantation, mixed garden and settlement area (Figure 1).

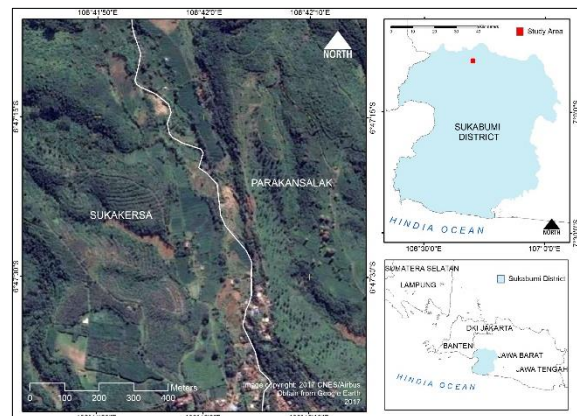


Fig. 1 Study area.

Image Acquisition

This study used Parrot Sequoia, a lightweight four bands multi-spectral sensor (72 gram). The sensor has four bands (green, red, red edge and near-infrared), each equipped in 1.2 megapixels global

shutter camera. This device is coupled with a Sunshine sensor contained similar bands and GPS. The multi-spectral sensor was mounted on DJI Phantom 4, a four-rotor UAV controlled by ground operator.

There are several things need to be considered in mapping activity using UAV, such as altitude, overlapping, flying time and flight plane. The altitude is related with the image resolution. Overlapping determines the quality of the image especially when creating digital elevation model (DEM). Flight time is very much related with battery capacity. Flight plan determines the mapping area. Flight plan are designed using Pix4d software (Figure 2). Criteria used in this study are served in Table 1. Workflow for data acquisition is shown by Figure 3.

Table 1 Flying criteria in this study.

Criteria	This study
Flight time	10-15 minutes
Flight plan	± 300 x 400 meter
Overlap	80 %
Altitude	100 meter above ground

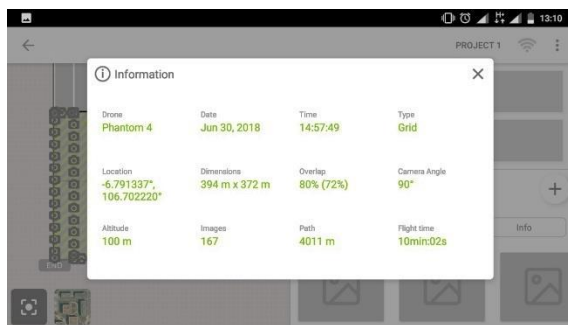


Fig. 2 Flight plan design using Pix4d software.

Vegetation index were generated using different bands from the sensor. This study used NDVI as a tool to differentiate different types of crop. NDVI has been widely used in many application and one of them is for identifying plant characteristics in the ground [4,5,6]. NDVI are calculated with the following formula [7]:

$$NDVI = \frac{\rho_{NIR} - \rho_{red}}{\rho_{NIR} + \rho_{red}} \quad (1)$$

where ρ_{red} and ρ_{NIR} are reflectance value of red and near infrared bands.

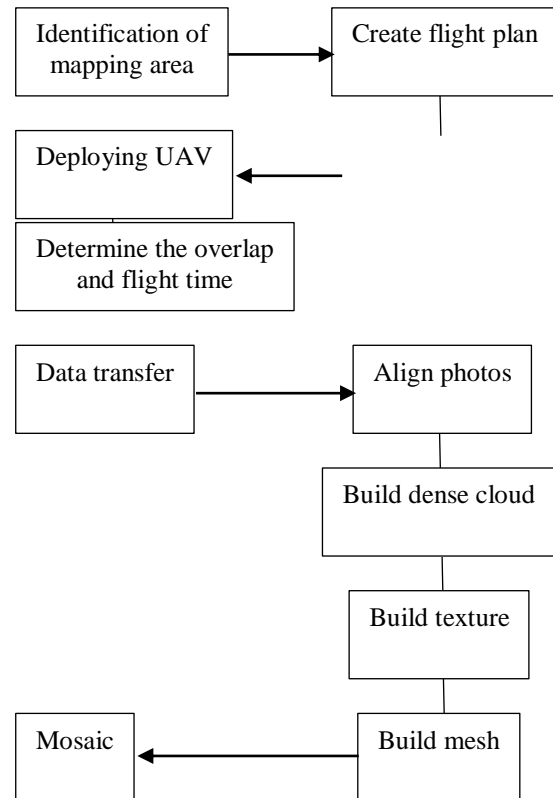


Fig. 3 Workflow of image generation from UAV.

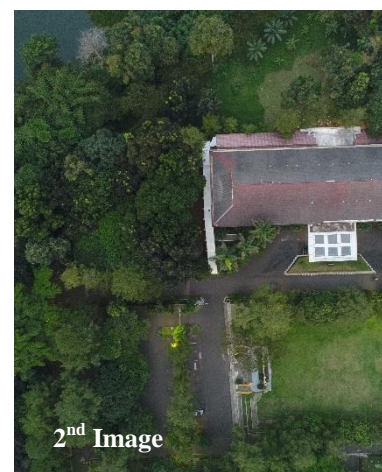
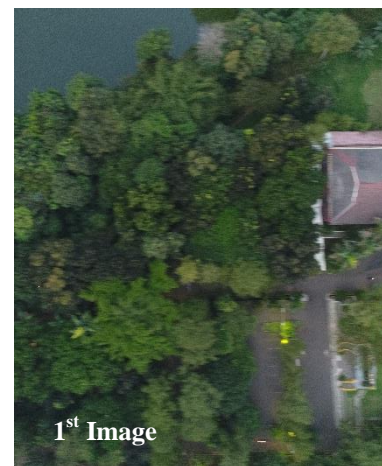


Fig. 4 Sample of image from the UAV with 80% overlap.

Field Data Collection

Field survey was conducted in June 2017. 34 sample points were collected during field survey. Field survey was conducted for collecting ground data such as types of crops, growth stages of paddy and ground control points for image rectification. Sample distribution is shown by Figure 5. There are three types of crop founded in the area, such as paddy, banana and tea.

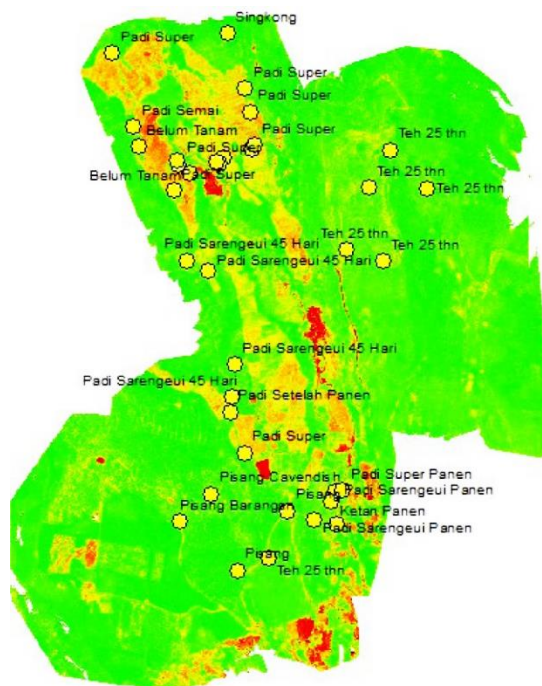
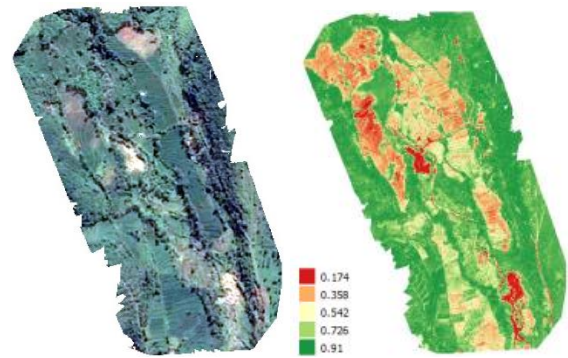


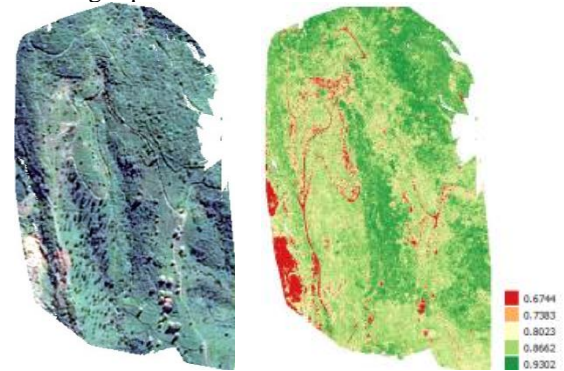
Fig. 5 Ground samples distribution in study area.

RESULTS

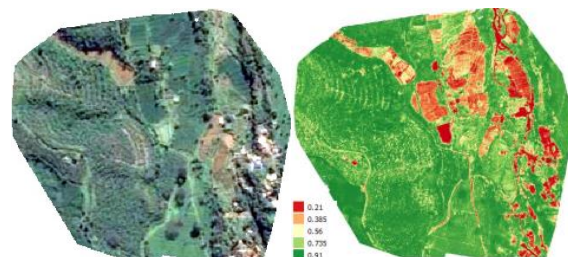
There are four flight plans used in this study. All of them are covering around 70 hectares of agricultural area planted with different types of crop such as paddy, banana, cassava and tea. Each flight plan covers different area. Area covered by each flight plan and the resulted NDVI are present in Figure 6(a-d).



6a – Flight plan 1



6b – Flight plan 2



6c – Flight plan 3





Fig. 6 Sample of image from the UAV with 80% overlap.

The NDVI value are varied on each flight plan area. The value is ranged from 0.16 to 0.93. Based on the sample points, the NDVI value is ranged from 0.21 (paddy) to 0.90 (banana). The range of NDVI values for each crop are presented in Table 2.

Table 2 Range of NDVI values for each crop.

	Min	Max	Mean	Stdev
Paddy	0.21	0.85	0.61	0.25
Banana	0.56	0.90	0.78	0.14
Tea	0.71	0.86	0.69	0.30

Source: data processing, 2018

Based on the result, the NDVI values for paddy ranges from 0.21 (Sarengui paddy) to 0.84 (Sarengui paddy to be harvested). The range of NDVI values for paddy are presented in Table 3.

Table 3 Range of NDVI values for paddy.

	Min	Max	Mean	Stdev
Sarengui Paddy	0.21	0.80	0.58	0.27
Sarengui Paddy (45 days)	0.79	0.84	0.82	0.02
Sarengui Paddy (to be harvested)	0.38	0.85	0.66	0.25
Super Paddy	0.31	0.83	0.64	0.19

Source: data processing, 2018

The NDVI value can be used to distinguish different types of crop. This study utilized mean and standard deviation values to differentiate crop types. Figure 7 is a boxplot showing a clear separation between paddy and banana. Unfortunately, the separation is rather unclear for tea, because it can be

misinterpreted.

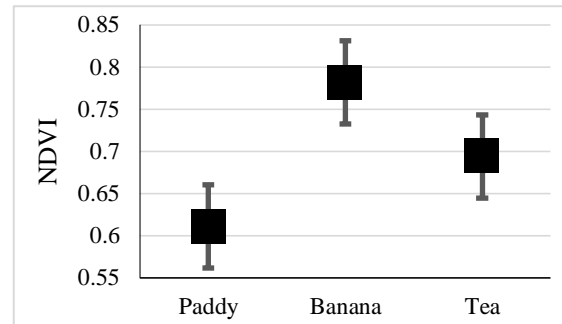


Fig. 7 Separation plot of paddy, banana and tea based on NDVI value.

The NDVI value also can be used to distinguish different types/period of paddy field. Figure 8 shows that NDVI can be utilized to highlight 45 days Sarengui Paddy. From the value we can separate 45 days Sarengui Paddy from other types/periods of paddy. Unfortunately, the separation is rather unclear for other types/periods of paddy.

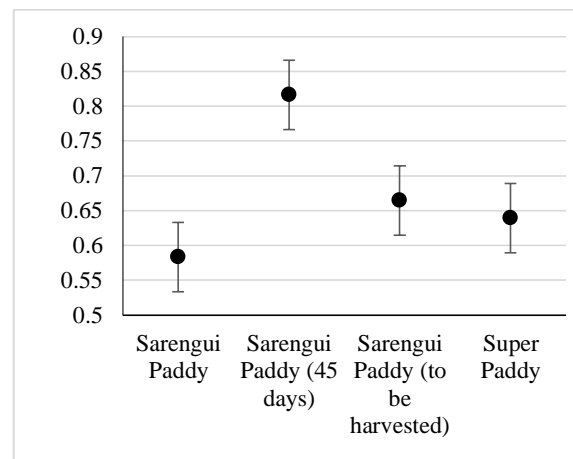


Fig. 8 Separation plot of different types/period of paddy based on NDVI value.

CONCLUSION

The multispectral sensor mounted on UAV platform has been successfully used to generate NDVI. The NDVI has been helpful in image separation process. The NDVI value is useful in discriminating different types of crop such as paddy and banana. Moreover, NDVI also can be used to differentiate types and period of paddy field. However, the NDVI values are still vary. Same types of crop might have different NDVI values. Therefore, future works is needed, especially to measure spectral value of different vegetation using spectroradiometer and use it to verify the result from NDVI.

ACKNOWLEDGEMENTS

This study is supported and funded by the Ministry of Research and Higher Education, under the Penelitian Dasar Unggulan Perguruan Tinggi (PDUPT) or the Basic Primary Research for Higher Education grant no: 378/UN2.R3.1/HKP.05.00/2018.

REFERENCES

- [1] Foody G, Fritz S, Fonte C C, Bastin L, Olteanu-Raimond A-M, Mooney P, See L, Antoniou V, Liu H-Y, Minghini M and Vatseva R 2017 *Mapping and the Citizen Sensor*, ed G Foody *et al* (London: Ubiquity Press) p 1471.
- [2] Shidiq, I. P. A., Wibowo, A., Kusratmoko, E., Indratmoko, S., Ardianto, R., & Nugroho, B. P. (2017a). Urban forest topographical mapping using UAV LIDAR. In *IOP Conference Series: Earth and Environmental Science* (Vol. 98, No. 1, p. 012034). IOP Publishing.
- [3] Quincieu, E. (2015). Summary of Indonesia's Agriculture, Natural Resources, and Environment Sector Assessment, Asian Development Bank.
- [4] Kou, W., Xiao, X., Dong, J., Gan, S., Zhai, D., Zhang, G., Qin, Y. & Li, L. 2015. Mapping deciduous rubber plantation areas and stand ages with PALSAR and Landsat images. *Remote Sensing* 7: 1048-1073.
- [5] Chen, B., Li, X., Xiao, X., Zhao, B., Dong, J., Kou, W., Qin, Y., Yang, C., Wu, Z., Sun, R., Lan, G. & Xie, G. 2016. Mapping tropical forests and deciduous rubber plantations in Hainan Island, China by integrating PALSAR 25-m and multi-temporal Landsat images. *International Journal of Applied Earth Observation and Geoinformation* 50: 117-130.
- [6] Shidiq, I. P. A., Ismail, M. H., Ramli, M. F., & Kamarudin, N. (2017b). Combination of ALOS PALSAR and Landsat 5 imagery for rubber tree mapping. *The Malaysian Forester*, 80(1), 55-72.
- [7] Rouse Jr, J., Haas, R. H., Schell, J. A. & Deering, D. W. 1974. Monitoring vegetation systems in the Great Plains with ERTS. *NASA Special Publication* 351: 309.

SUITABILITY ANALYSIS OF SEAWEED (*Eucheuma cottonii*) BASED ON ENSO VARIABILITY IN AMAL COAST, TARAKAN ISLAND, INDONESIA

Dewi Susiloningtyas¹, Tuty Handayani¹ and Della Ayu Lestari¹

¹ Geography Department, Faculty of Mathematics and Natural Science, Universitas Indonesia, Margonda
Raya, Depok, 16424, Indonesia;

ABSTRACT

Seaweed is one of the important ecosystem for people living at coastal areas such as at Amal Coast, Tarakan Island. *Eucheuma cottonii* is one type of seaweed that has high economic value. This research aimed to analyze suitability of *Eucheuma cottonii* against ENSO variability. The suitability level required from calculation sea surface temperature, chlorophyll-a and salinity in the Amal Coast. Remote sensing oceanography of Landsat 8 OLI and has been applied to study environmental changes of those variables. The results showed the spatial and temporal condition of the Amal Coast conditions strongly influenced by the ENSO variability and it became barrier factor on the suitability of *Eucheuma cottonii* cultivation. In the La Nina period the potential area for seaweed cultivation was wider than El Nino period. Based on the results of data processing, at the El Nino period and La Nina period, the coastal part of Amal Coast has the highest recommendation or appropriate for the development of seaweed cultivation.

Keywords: *Eucheuma cottonii*, *el nino*, *la nina*, *suitability area*

INTRODUCTION

Indonesia is known as a country that has a natural wealth very abundant, one of its natural wealth is in coastal areas. The coastal area is unique because it is an area between land and sea, where the land area has the characteristics of its land and marine areas also have the characteristics of the oceans and have an impact which is significant to the characteristics of the region itself becomes more typical [16]. This is not surprising because 70% of Indonesian territory is sea with coastline more than 81,000 km and consists of 13,677 islands. From a wide range of potentials, one of the potentials that can be developed is seaweed [1].

Seaweeds that has economic value and high benefits is a type of *Eucheuma cottonii*. One of the areas in Indonesia that has seaweed ecosystem *Eucheuma cottonii* species are found in Amal Coast, Tarakan Waters, North Kalimantan. Seaweed cultivation in Amal Coast has been going on for a long time, especially for the type of *Eucheuma cottonii*. At first it was only an alternative income for local fisherman when they were unable to go out to sea. But apparently seaweed cultivation business is very promising so that seaweed cultivation business in Amal Coast is growing very rapidly and has a pretty good prospect, because it already has a market and an attractive price. With the rapid advancement of remote sensing oceanography, can used to know the characteristics of seaweed cultivation *Eucheuma cottonii* which has high economic value and is currently a prima donna seaweed farmers community in Amal Coast. Remote

sensing of oceanography can be use to determine the rapid changes in seawater conditions due to the seasons and climate and how changes in parameters of aquatic environments such as temperature, salinity, currents, and so on affect the conditions of seaweed growth in on the Amal Coast accurately [3].

However, at present, the provincial government of Tarakan City does not yet have sufficient spatial (space) or temporal (time) oceanographic data and information [3]. Therefore, this research is conducted by utilizing satellite oceanographic technology to simplify the monitoring of Amal Coast environmental condition caused by ENSO change and how its effect on the development of seaweed cultivation type of *Eucheuma cottonii*. This study is expected to provide general information on the variability of oceanographic conditions with parameters of Sea Surface Temperature, Chlorophyll-a and salinity of Amal Coast which is influenced by ENSO changes through satellite oceanographic studies in particular by using Landsat 8 OLI. From this research, it is expected to know the area of development of seaweed cultivation of *Eucheuma cottonii* which is optimal in Pantai Amal by paying attention changes in aquatic environments.

METHODS

The territorial waters of the Amal Coast are quite extensive and has enormous potential for the cultivation of various commodities, especially for seaweed cultivation [3]. Seaweed cultivation that has been running has not achieved optimal results,

because the unsuitable between the seaweed biota with the cultivation area or unsuitable cultivation patterns based on the optimal development season for seaweed. Based on these conditions, one of the efforts made to improve the optimization of seaweed cultivation production is to conduct a good study on the suitability of the land as well as the suitability of spatial and temporal sea cultivation vegetation (based on ENSO variability) using remote sensing approach.

Data processing for variables such as sea surface temperature, chlorophyll-a and salinity can be known by remote sensing data using image data, in this study the image used by Landsat 8 OLI. Image data and Landsat 8 OLI obtained by downloading through the website <https://earthexplorer.usgs.gov/>. From this suitable analysis, the potential location of the seaweed cultivation development of *Eucheuma cottonii* in Amal Coast is based on the variability of ENSO (El Nino/La Nina). This image data processing using image processing software. The initial processing of this image that must be done is the process of preprocessing with calibration and image correction.

Sea surface temperature data obtained from the extraction of radians value spectral imagery, then searched the temperature value of each pixel of radians calculated based on the spectral radiance value by using the following equation [8] :

$$TR = K2 / \ln (K1 / L\lambda + 1) \quad (1)$$

Where :

TR = Radian temperature (K)

K2 = Calibration Constants 2 (1321, 08 K)

K1 = Calibration Constants 1 (774.89 K)

Lλ = Spectral Radiance

Chlorophyll-a can be detected by the image because it is able to absorb and reflect the spectrum of sunlight. Channel 3 and 4 of Landsat satellite imagery can be used to detect a-chlorophyll concentration in waters[17]. The algorithm used in this research is the result of the development of algorithm conducted:

$$C = 0.2818 \times ((B4 + B5) / B3) \quad (2)$$

Where

C = Chlorophyll-a concentration (mg / m3)

B3 = The reflectance values of Landsat channel 3

B4 = The reflectance values of Landsat channel 4

B5 = The reflectance values of Landsat channel 5

The algorithm equation in determining salinity value of aquatic uses algorithm obtained from research of estuary zonation boundary determination [13].with equation of algorithm as follows:

$$\text{Salinity} = 29,983 + 165,047 (B2) - 260,227 (B3)$$

$$+ 2,609 (B4) \quad (3)$$

Where:

B2 = blue channel

B3 = green channel

B4 = red channel

In this study descriptive analysis and comparative analysis were conducted to see the spread and potential of *Eucheuma cottonii* seaweed area based on ENSO. Descriptive analysis is used to describe the data that has been collected descriptively so as to create a general conclusion, and comparative analysis by comparing the general value or data in each variable. To get the area of suitability, matrix and weighting method were used (Table 1)

Table 1 The Matrix and Weight of Suitability

Parameters	Class / Class	Score	Weight
Temperature (° C)	25-30	3	4
	30-37	2	
	<25 or> 37	1	
Chlorophyll-a (mg / L)	3.5-10	3	3
	0.2-3.5	2	
	<0.2	1	
Salinity (‰)	30-34	3	3
	25-29 or 33-37	2	
	<25 or > 37	1	

Weighting is based on the importance of each parameter sequentially, from the most important to the least important. other than that each parameter will be divided into several classes that are scored and weighted based on the level of conformity value. Each parameter, weighting, and class score are determined by literature study, and justification from competent experts in the field fisheries, both in writing and orally. The total value of the multiplication of the weighted value of the parameter with the score then used to determine the suitability class of seaweed cultivation area based on water quality characteristics with the following calculation:

$$Y = \sum a_i \cdot X_n \quad (4)$$

Where:

Y = Final Value

ai = Weight factor

Xn = Value of land suitability

The land suitability class is obtained based on the Equal Interval method [11] to divide the range of values attribute into sub-ranges of the same size. Calculation are as follows:

$$I = ((\sum a_i \cdot X_n) - (\sum a_i \cdot X_n) \min) / k \quad (5)$$

Where:

I = Interval of land suitability class

k = Number of land suitability classes used

a_i = Score parameter to i ; $i = 1, 2, 3 \dots$ etc

X_n = weight to n

DISCUSSION

Analysis of spatial (space) and temporal (time) distribution of oceanographic parameters of sea surface temperature (SST), chlorophyll-a, and the salinity in the waters of the Amal Coast due to regional climate change ENSO (El Nino Southern Oscillation) specially at the period of El Nino and La Nina conducted using remote sensing of oceanography (Landsat 8 OLI) in order to know the best condition / in accordance with the growth of seaweed.

ENSO (El Nino / La Nina Southern Oscillation) is an anomaly that occurs in extreme climatic changes that occur beyond its normal frequency over the long term. El Nino occurs because the East Pacific Ocean is under low pressure and the West Pacific Ocean is under intense pressure, causing the winds to weaken, even reversing the direction that causes eastern Australia to have rainfall under normal conditions [6]. This resulted in some areas in Indonesia being dry, due to the decrease in rainfall under normal conditions. On the other hand, La Nina occurs because the temperature of the sea surface in the East and Central Pacific Oceans is so low that the winds blow very hard and bring a moist air mass, resulting in the rainfall in eastern Australia to exceed its normal condition [4]. This resulted in some regions in Indonesia will experience an increase in rainfall above normal conditions. ENSO variability reviewed on period of El Nino were represented by the data on 28 August 2018 and La Nina are represented by the data on 15 september 2016.

Sea Surface Temperature

Temperature is one of the most important factors in regulating the life processes and spread of organisms [7], [9]. Based on previous research, several researchers reported a significant effect of temperature changes on seaweed growth, among others, affecting metabolism, nutrient uptake, and seaweed survival [18]. In addition, the temperature also affects the process of photosynthesis [5]. The ability of seaweed to adapt to the temperature of the environment is different, so that required temperature suitable for seaweed growth. The appropriate temperature for seaweed cultivation is in the range of 25° - 30° C. Analysis of variability of sea surface temperature during El Nino is shown in the Fig.1(above). Sea surface temperatures that were unsuitable with the suitability of seaweed (20° - 25° C) only slightly that was near the coast of Amal Coast. Sea surface temperature that were moderately suitable dominate mainly in the north

and west waters of the Amal Coast with the temperature of 30° - 37° C. Sea surface temperatures in suitable class is at the coast of Amal Coast and south of the waters of the Amal Coast with the temperature 25° - 30° C.

Whereas the analysis of variability of sea surface temperature during the La Nina is shown on the Fig.1 (below). Sea surface temperatures were unsuitable with the suitability of seaweed are scattered in the north and south waters of Amal Coast with temperature 20° - 25° C. Sea surface temperatures that were moderately suitable class was dominated same as El Nino period specially in the north and south waters of Amal Coast. For the suitable class of sea surface temperatures (25° - 30° C) were spread over the north and south waters of the Amal Coast. Overall, sea surface temperatures that suitable for seaweed cultivation were found greater in La Nina than El Nino. The suitable class of sea surface temperature region of La Nina is spread by 37% while in El Nino it spreads 31% of the total water area. However, the moderately suitable class were found more in El Nino which is 49% of the total area while at La Nina by 40% of the total area.

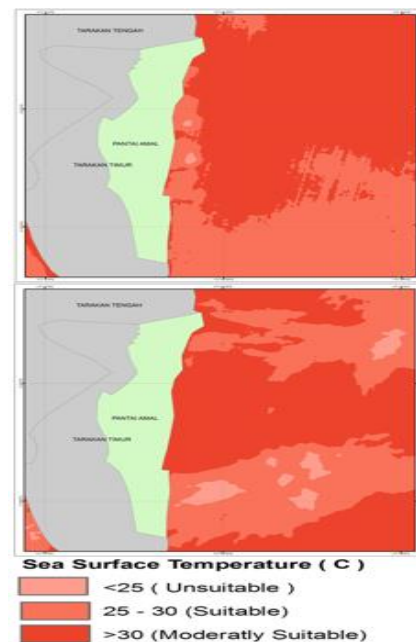


Fig.1 Sea surface temperature in El Nino period (above) and sea surface temperature in La Nina period (below)

Chlorophyll-a

Chlorophyll is a pigment contained in phytoplankton consists of three types of chlorophyll-a, b and c. These three types of chlorophyll are very important in the process of photosynthesis of plants to produce organic compounds [18]. The most

dominant content possessed by phytoplankton is chlorophyll-a. Chlorophyll is one of the parameters that determine primary productivity in the waters. Chlorophyll-a is the necessary green pigment of phytoplankton for photosynthesis. Distribution and high chlorophyll content are closely related to the oceanic condition of a waters. The feasibility of aquatic for fisheries activities can be known by looking at the composition of phytoplankton and chlorophyll content [12].

Analysis of variability of chlorophyll-a concentration during El Nino is shown in the Fig.2 (above). Chlorophyll-a concentrations that were unsuitable with the suitability of seaweed (<0.2 mg / L) were only slightly at the south of the waters in Amal Coast. Chlorophyll-a concentrations that were in moderately suitable ($0.2 - 3.5$ mg / L) was dominated almost all parts of the waters in Amal Coast. The suitable area of chlorophyll-a concentration to suitability of seaweed ($3.5 - 10$ mg / L) were spreads on the coast of Amal Beach.

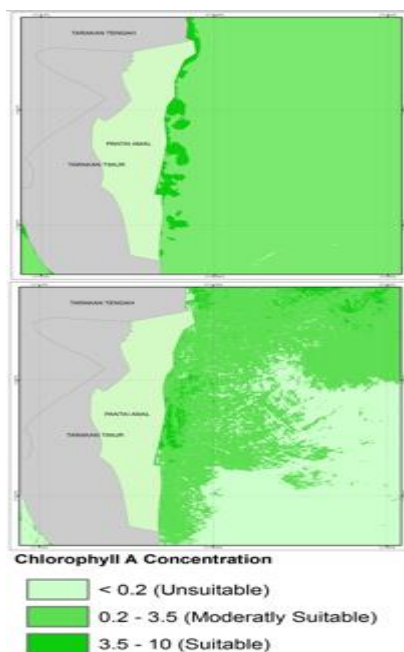


Fig.2 Chlorophyll-a concentration in El Nino period (above) and chlorophyll-a concentration in La Nina period (below)

While the analysis of variability of chlorophyll-a concentrations during La Nina is shown on the Fig.2 (below). Chlorophyll-a concentrations that were unsuitable with the suitability of seaweed (<0.2 mg / L) on the southern territorial waters of the Amal Coast. Chlorophyll-a concentrations that were in moderately suitable ($0.2 - 3.5$ mg / L) was dominated same as in El Nino period but its spread in the central and northern of the waters in Amal Coast. For the suitable class ($3.5 - 10$ mg / L) were scattered in the north and west waters of the Amal

Coast. Overall, chlorophyll-a concentration that suitable for seaweed cultivation were found greater in El Nino than La Nina. The suitable class of chlorophyll-a concentration region of in El Nino is spread by 21% while in La Nina it is 14% of the total water area. The area of chlorophyll-a concentration with moderately suitable class were also found in El Nino, which is 85% of the total area, while La Nina is 57% of the total area.

Salinity

Salinity is one factor that is very influential on the process of osmoregulation in seaweed plants [2]. Each type of seaweed is tolerant to different salinity changes, the salinity conditions suitable for seaweed growth are about 15-43 ppt [10]. The salinity range for growth of *Kappaphycus alvarezii* between 29-34 ppt [15]. The salinity that is good for the growth of seaweed *Eucheuma cottonii* ranges from 32-34 ppt [14]. From some of the above opinions it can be concluded that good salinity for seaweed growth ranges from 30 to 34 ppt with a maximum value of 34 ppt.

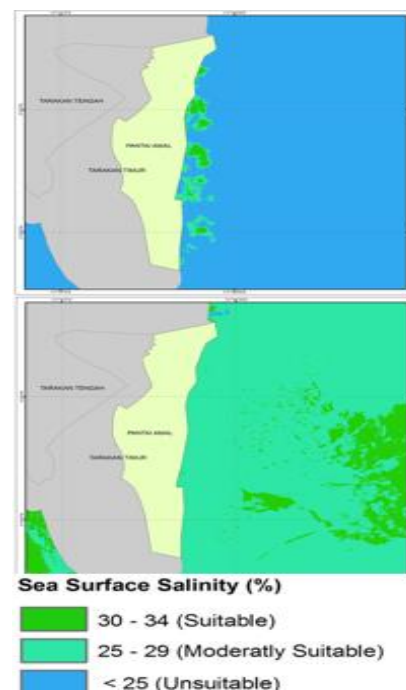


Fig.3 Salinity value in El Nino period (above) and salinity value in La Nina period (below)

Analysis of salinity variability during El Nino is shown in the Fig.3 (above). The value of salinity that were in unsuitable area (<25 ppt) were dominated almost at all the waters of the Amal Coast. The salinity value that were in moderately suitable (25-29 ppt) were at the coast of Amal Beach. The salinity value that were suitable for seaweed (30-34 ppt) were at the coast of the Amal Beach that close

to the moderately suitable area.

While the analysis of salinity variability during La Nina is shown in the Fig.3 (below). The salinity value for unsuitable area (<25ppt) were few and scattered on the waters of the northwest region of Amal Beach. For the moderately suitable area (25-29 ppt) were dominated and spread almost all parts of the waters of the Amal Coast. Then, for suitable area of salinity value (30-34 ppt) were spreads over the eastern waters of the Amal Coast. Overall, salinity value that suitable for seaweed cultivation were found greater in La Nina than El Nino. The region with an appropriate salinity value in La Nina is spread by 29% of the total area while in El Nino it is 14% of the total water area. The area of salinity value with moderately suitable class is also found in La Nina by 69% of the total area, while in El Nino only 16% of the total area

The Potential Area of Seaweed During EL Nino and La Nina

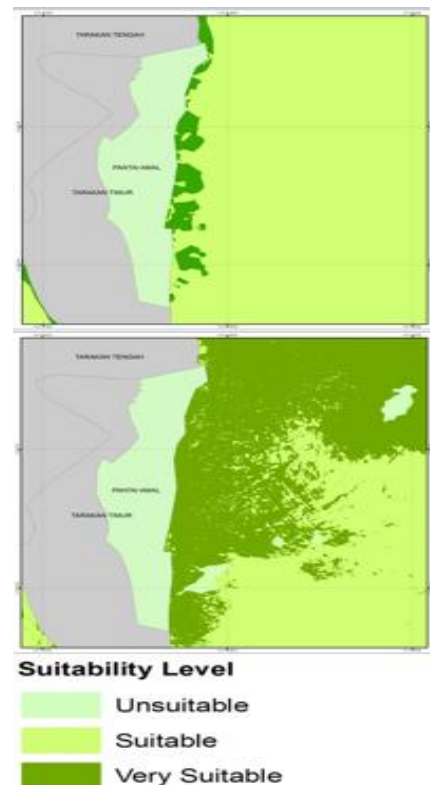
Based on the physical condition and distribution of seaweed that has been discussed, it can be determined the potential area of development of seaweed cultivation type *Eucheuma cottonii*. This potential area is a potential area for seaweed cultivation development which can be analyzed by the condition of coastal physical condition by looking at sea surface temperature, chlorophyll-a and salinity as previously discussed.

Model Builder used with enter a formula consisting of a matrix calculation suitability of parameters having weights and scoring. Model Builder is an application that is inside the ArcGIS software useful for creating, modifying and organizing models, ie deep layers raster shapes that can be connected to each other by using geoprocessing device. Matrix analysis of conformity for marine aquaculture activities begins with the preparation of suitability matrix. The computation matrix of suitability was performed for the grading of the rating scale as shown at Table 2.

Table 2. Suitability scores area of *Eucheuma cottonii*

No.	Total Score	Suitability level	Evaluation
1	67.336 - 76	S1	Very suitable
2	58.668 – 67.335	S2	Suitable
3	0 – 58.667	N	Unsuitable

S1 (Suitable), if the land has no significant restrictions to maintain the level of applied management. S2 (moderately suitable), if the land



has a rather significant barrier to maintain the level of management should be applied. N (unsuitable) has a low feasibility where the waters have a strong limiting factor for seaweed cultivation, so it is very influential on the quality of the waters. This condition is not possible for the development of seaweed cultivation.

Fig.4 The potential area in El Nino period (above) and the potential area in La Nina period (below)

Fig.4 (above) is a map of the suitability of *Eucheuma cottonii* seaweed in the waters of the Amal Coast in El Nino period. At the time of El Nino there are only two suitability classes that are appropriate and highly appropriate classes. In El Nino period, At there were only two suitability classes, very suitable class and suitable class. The suitable class were dominated almost the entire territorial waters with an 87% of the total area whereas the very suitable class was located in the coastal area with 23% of the total area. A very different pattern was found on the map of the suitability of *Eucheuma cottonii* seaweed in the waters of the Amal Coast at La Nina period. In La Nina period there are three classes, very suitable, suitable and unsuitable. The class of very suitable were dominated which is spread in coastal area and

the northern waters of Amal Coast with 61% of the total area. The suitable class were spreads over the eastern and southern waters of the Amal Coast with 32% of the total area whereas the unsuitable class were scattered in the northeast and southwest with 7% of the total area. Overall, at the La Nina period the potential area for seaweed cultivation was wider than El Nino period.

CONCLUSION

Eucheuma cottonii is one type of seaweed that has high economic value. One of the areas that have potential in the development of seaweed *Eucheuma cottonii* this is the City of Tarakan, especially on the waters of the Amal Coast. However, at present, the provincial government of Tarakan City does not have adequate spatial and spatial oceanographic data and information so that this study identifies spatial variability based on ENSO at the time of El Nino and La Nina.

The remote sensing of oceanographic (Landsat 8 OLI) shows the spatial and temporal condition of the Amal Ocean coastal conditions strongly influenced by the ENSO variability and became barrier factor on the suitability of seaweed cultivation of *Eucheuma cottonii*. In the El Nino period, the coast of Amal Beach shows the most potential areas for seaweed cultivation while in the period of La Nina the most potential area is along the coast and north waters of the Amal Coast. Overall, in the La Nina period the potential area for seaweed cultivation was wider than El Nino period. Based on the results of data processing, at the El Nino period and La Nina period, the coastal part of Amal Beach has the highest recommendation or appropriate for the development of seaweed cultivation.

REFERENCES

- [1] Anggraini, O. Restropective Study of Community Economic Empowerment Program. Journal of Public Policy and Administration. Vol.10, No.1, 2015
- [2] Aslan, M. L. Seaweed Cultivation. Kanisius Publisher Yogyakarta. 1991, pp.105
- [3] Aviati, Evie. Utilization of Satellite Technology Suitability of Seaweed Cultivation *Eucheuma cottonii* in Tarakan Waters. Segara Journal. Vol.11, No.1 August 2015, pp. 13-24
- [4] Doan-Nhu, Hai., Nguyen-Ngoc, Lam & Chi-Thoi Nguyen. ENSO Impacts on Phytoplankton Diversity in Tropical Coastal Waters. Journal of Progress in Oceanography. Elsevier, Vol, 140, 2016, pp.1-13
- [5] Eki, N. Y., Sahami, F & Hamzah, S. N. Seagrass Density and Diversity in Ponelo Village, Ponelo Sub-District, North Gorontalo District. Scientific Journal of Fisheries and Marine. Volume 1, No. 2, 2014, pp.65-70.
- [6] Hamada, J.-I., M. D. Yamanaka, J. Matsumoto, S. Fukao, P. A. Winarso, and T. Sribimawati. Spatial and Temporal Variations of the Rainy Season Over Indonesia and Their Link to ENSO, J. Meteorol. Jurnal Soc. Japan, Vol.2, 2002, pp.285- 310.
- [7] Ji, Chenxu., Zhang, Yuanzhi., Cheng, Qiuming., Tsou, JinYeu & X. San Liang. Evaluating Impact of SST on Spatial Distribution of Chlorophyll-a Concentration in East China Sea. Journal of Int J Appl Earth Obs Geoinformation. Elsevier, Vol. 68, 2018, pp.252-261
- [8] Qin, Z., Karnieli, A., & Berliner, P. A Mono-window Algorithm For Retrieving Land Surface Temperature from Landsat TM Data to the Israel-Egypt Border Region. International Journal Remote Sensing, Vol. 22, No.18, 2001, pp.3719-3746.
- [9] Sarangi, R.K & K. Nanthini Devi. Space-based Observation of Chlorophyll, Sea Surface Temperature, Nitrate, and Sea Surface Height Anomaly Over the Bay of Bengal and Arabian Sea. Journal of Marine Ecosystem Division. Elsevier, Vol.59, Issue,
- [10] Segovia, Isabel Fernandez., Garcia, Maria Jesus Lerma., Fuentes, Ana & Jose M Barat. Characterization of Spanish Powdered Seaweeds. Journal of Food Research International. Elsevier, Vol.111, 2018, pp.212-219
- [11] Septian, I, Suherman, H., Harahap, S.A. Mapping of Aquatic Suitability for Seaweed Cultivation in Anambas Islands of Kepulauan Riau Province. Journal of Fisheries of Strength, Vol.5, No.2, 2014, pp.240-247
- [12] Sukal M, Indra J. Z, Jabang N. Composition and Content of Chlorophyll-a Phytoplankton In East and West Season at Peniti River Estuary, West Kalimantan. Proceeding Semirata FMIPA University of Lampung, 2013
- [13] Supriatna, L., Supriatna, J., & Koetsoer, R. Algorithm model for the determination of Cimandiri Estuarine boundary using remote. AIP Conference Proceedings. 2016.
- [14] Syaputra, Y. Growth and Caraginan Cultivation of Seaweed Cultivation *Eucheuma cottonii* on Different Environmental Conditions and Treatment of Planting Distance in Lhok Bay, Seudu. Thesis IPB, 2005, pp.34
- [15] Trono, G.C. and Fortes. Philippina Seaweed. National Book store, Inc Metro. Manila. 1980, pp.330
- [16] Wahyudin, Yudi. Coastal and Marine Resource Characteristics of Palabuhanratu Bay Area, Sukabumi Regency. Bogor: PKSPL-IPB. 2011.

- [17] Wibowo, A., Sumartono, B., Setyantini, W. H., & Populus, J. The Application of Satellite Data Improvement Site Selection and Monitoring Shrimp Pond. Remote Sensing and Geographic Information System, 1994, pp. 16-17
- [18] Zhang, Yuchao., Ma, Ronghua., Duan, Hungtao & Jindou Xu. A Novel MODIS Algorithm to Estimate Chlorophyll-a Concentration Ineutrophic Turbid Lakes. Journal of Ecological Indicators. Elsavier, Vol. 191, 2016, pp.878-886

SEISMIC RELIABILITY ANALYSIS OF LIFELINE: A CASE STUDY ON THE WATER NETWORK SYSTEM OF BIÑAN CITY, LAGUNA

Rainier Lawrence A. Valdez¹, Lessandro Estelito O. Garciano² and Takeshi Koike³

¹De La Salle University-Manila, Philippines; ²Faculty, De La Salle University; ³Kyoto University, Japan

ABSTRACT

Lifelines are essential networks and it is vital for these network systems to remain properly functional during or after destructive earthquakes. In the Philippine geographical context, West Valley Fault which traverses Metro Manila, is a seismic threat capable of producing a maximum magnitude of 7.2. In this study, the reliability of Laguna Water network system was assessed under earthquake loads due to West Valley Fault. Probabilistic seismic hazard analysis (PSHA) was utilized to estimate the seismic hazard of the network area. Recorded earthquake history from the Philippine Institute of Volcanology and Seismology was used as part of the seismic analysis. The analysis estimated the ground motion values by using a similar Ground Motion Prediction Equation (GMPE) used in the latest Philippine Earthquake Model (PEM). Seismic hazard analysis shows that the earthquake hazards for the site are peak ground accelerations of 0.52g and 0.62g for return periods of 500 and 2500 years respectively. Using the ground motion intensity, ground strain value was attained ranging from 0.02% to 0.16% at scales of 0.1g to 1.0g. Monte Carlo simulation was used to determine the probability of damage. Using the unscaled peak ground acceleration, the probability of minor damage ranges from 15% to 19%. Given a 2500-year return period, seismic hazard analysis resulted to a peak ground acceleration of 0.62g which has a 20% probability for pipes to experience minor damage. Subsequently, the entire network system has a 1% probability of minor damage given the same return period of seismic hazard.

Keywords: Water pipelines, PSHA, Reliability, Monte Carlo simulation

INTRODUCTION

Earthquake is a natural hazard which is one of the most destructive occurrences. Numerous destructive magnitudes of this hazard happened in different countries which resulted to damages in structures most especially on built environments. As such, earthquake indirectly causes death toll through collapse of buildings and secondary hazards such as water scarcity and fire. In the 1995 Kobe earthquake in Japan, fire occurred in an area of about 1 square kilometer due to natural gas release and electricity sparks [1]. As such, earthquake leads to damage not just on structures but also in buried lifelines. Other than lifeline central facilities, transmission components such as pipelines should also be assessed since the system spatially extends over a wide area of distances and could be subjected to different seismic loading despite being under the same earthquake hazard [2]. The risk analysis of lifelines involves seismic hazard estimation as input data and damage, reliability, restoration and mitigation as output data [3]. Previous studies analyzed the probability of damage of water network subjected to seismic loading under different sources of earthquake [4]-[5].

Philippines is located at the Ring of Fire where numerous occurrences of earthquake happened. In the past five years, there were two major earthquakes that hit the country. In 2013, a M7.2 earthquake hit the

areas of Bohol and Cebu City which resulted to a death toll and injuries of 227 and 996 individuals, respectively [6]. Meanwhile, a M6.7 earthquake in 2017 affected 11 towns in Surigao which resulted to water scarcity due to busted pipelines [7]. As such, one of the seismic events being prepared is due to the West Valley Fault which traverses Metro Manila and neighboring provinces. The said fault can produce a magnitude of 6.0 with a peak up to 7.2 [8].

Given the risk imposed by West Valley Fault, the purpose of this paper is to assess the system reliability of water network of Laguna Water. This process involves Probabilistic Seismic Hazard Analysis (PSHA) to determine the ground motion in terms of peak ground acceleration (PGA) [9]. The PGA values are related to pipe strain values for the load parameter [10]. Then, the probability of damage of each component are obtained using Monte Carlo simulation. Subsequently, the probability of damage of each component are used to calculate the system reliability [11].

SITE INFORMATION

Biñan City is a municipality in the province of Laguna located in the Southern Luzon of Philippines. The city is 34 kilometers south of Manila, the capital of the country, and it is a first-class city in terms of income classification. The city has a population of

approximately 334,000 having a density of 1,000 individuals per square kilometer [12]. In addition, situated in the city are two world-class industrial parks. Geographically, Biñan City is being traversed by West Valley Fault in three (3) of its barangays. In the Philippine Earthquake Model (PEM) released by Philippine Institute of Volcanology and Seismology (PHIVOLCS), the city falls within the PGA of 0.4g and 0.5g for a return period of 500 years as shown in Fig. 1 [13].



Fig. 1 PGA map for 500-year return period

Water Network of Biñan City

Laguna Water is the provider of water services in Biñan City together with other two municipalities nearby. Figure 2 shows the map of the water network provided by Laguna Water. The water network data includes coordinates, length, sizes and material of the pipes. The network is composed of steel pipes with arc-welded joints with 9 different diameter sizes ranging from 50 to 500 millimeters. These sizes are classified as main and distribution lines. In this study, the assessment focuses on main pipes which were assumed to have a diameter of at least 150 millimeters.

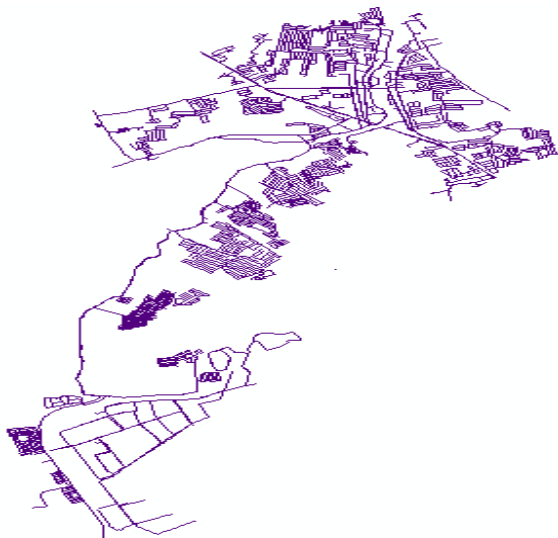


Fig. 2 Biñan City water network system

PROBABILISTIC SEISMIC HAZARD ANALYSIS (PSHA)

Seismic hazard analysis is used to estimate the PGA at the site with West Valley Fault as the seismic source. The stochastic approach considers uncertainties particularly distance, magnitude and ground motion probabilities [9]. The outputs in this analysis are Uniform Hazard Response Spectra (UHRS) which shows the acceleration values at different periods. As such, the PGA values are used to generate a spectral map.

Distance Probability

The seismic source considered in the research is only West Valley Fault. Since the fault is not linear and extends for about 95 kilometers, it is linearized into three segments. Table 1 shows the length of each segment and the number of 500-meter strips for source-to-site distances. Meanwhile, the site is the area covered by the water network system. As such, it is represented as grid point spaced at 500 meters. Assuming that earthquake could occur anywhere within the fault line, there are 190 source-to-site distances for each grid points.

Table 1 Fault segment details

Segment	Connecting Points	Distance (km)	No. of Strips
1	1 and 2	26.5	53
2	2 and 3	27.5	55
3	3 and 4	41	82
		95	190

Figure 2 shows the distance probability distribution, clustered into 10-kilometer groups, out of the 190 strips of the West Valley Fault. It is evident that the probability of an earthquake occurring within 20-kilometer radius is 42%. Moreover, the likelihood decreases at larger distances wherein 90 kilometers is the largest distance possible.

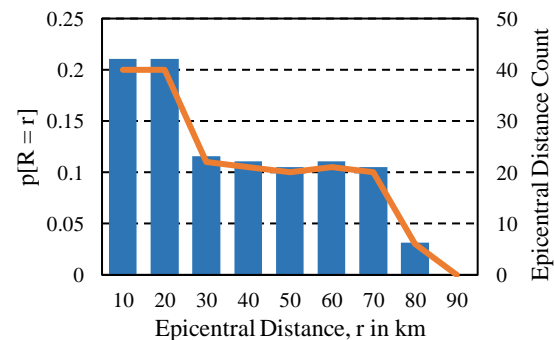


Fig. 3 Distance probability distribution

Magnitude Probability

The seismic data used are based on the historical earthquake data from PHIVOLCS recorded from 1900 to 2015 [14]. The analysis used moment magnitudes of engineering interest only having a value of M5.2 and above [13], [15]. Seismic data was also filtered based on coordinates which are located within 50 kilometers from the fault line as shown in Table 2. The relationship between the seismic events and magnitudes was established through bounded Gutenberg-Richter Recurrence Law as represented by Eq. (1).

Table 2 West Valley Fault seismic data

Lat.	Long.	Depth, (km)	Mw			Mw
			MI	Mb	Ms	
14.50	121.50	33	0	0	7.5	7.47
14.20	120.60	60	0	0	6.8	6.77
14.00	121.00	50	0	0	5.7	5.89
13.96	120.87	49	0	5	0	5.24
13.98	120.74	4	0	5.1	0	5.30
14.70	121.20	22	0	4.9	0	5.18
13.94	120.67	21	0	5.3	0	5.44
14.00	120.70	33	0	4.9	0	5.18
14.02	120.65	5	4.7	5.7	5.1	5.81

$$\log \lambda_m = a - bm \quad (1)$$

where λ_m is the mean annual rate of exceeding magnitude m , and a and b are constants from recurrence function.

The probability of distribution of a magnitude, $P[M]$ in a given interval is expresses as,

$$P[m_l < m < m_u] = [f_M(m)](m_u - m_l) \quad (2)$$

where m_l and m_u are lower and upper limits of magnitude respectively, and $f_M(m)$ is the magnitude probability density function.

Figure 4 shows the magnitude distribution function magnitudes M5.30 up to M7.36.

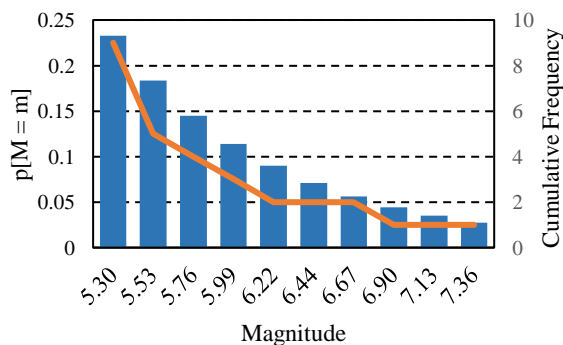


Fig. 4 Magnitude Probability Distribution

Ground Motion Probability and Mean Annual Rate of Exceedance

In this process, the ground motion values are estimated and compared to obtain the rate of exceeding target ground motions from 0.1g to 1.0g. The values of rate of exceedance are used to calculate the PGA at return periods of 500 and 2500 years.

Ground motion prediction equation (GMPE)

The GMPE used to estimate the motion values is based on the similar model used by PHIVOLCS in the generation of PEM. The attenuation model by Youngs, Chiou, Silva and Humphrey [16] predicts the PGA, $\ln y$ generated by subduction zone earthquakes and represented by the expression,

$$\ln y = -0.6687 + 1.438M_w + C_1 + C_2(10 - M_w)^3 + C_3 \ln[r + 1.097e^{0.617M_w}] + 0.00648H + 0.3643Z_T \quad (3)$$

where M_w is the moment magnitude, r is the source-to-site distance, H is the focal depth, $Z_T = 0$ for interface earthquake = 1 for interslab earthquake, and C are constants from Table 3.

Table 3 Constants for attenuation model

Period	C1	C2	C3	C4	C5
0	0.00	0.00	-2.329	1.45	-0.1
0.075	2.4	-0.0019	-2.697	1.45	-0.1
0.1	2.516	-0.0019	-2.697	1.45	-0.1
0.2	1.549	-0.0019	-2.464	1.45	-0.1
0.3	0.793	-0.0020	-2.327	1.45	-0.1
0.4	0.144	-0.0020	-2.230	1.45	-0.1
0.5	-0.438	-0.0035	-2.140	1.45	-0.1
0.75	-1.704	-0.0048	-1.952	1.45	-0.1
1.0	-2.870	-0.0066	-1.785	1.45	-0.1
1.5	-5.101	-0.0114	-1.470	1.5	-0.1
2.0	-6.433	-0.0164	-1.290	1.55	-0.1
3.0	-6.672	-0.0221	-1.347	1.65	-0.1
4.0	-7.618	-0.0235	-1.272	1.65	-0.1

Mean annual rate of exceedance

This process involves the combination of the three calculated probabilities wherein seismic hazard curves are generated. The annual rate of exceedance of a ground motion, λ_{y^*} is expressed as,

$$\lambda_{y^*} = \sum_{i=1}^{N_S} \sum_{j=1}^{N_M} \sum_{k=1}^{N_R} \lambda_m P[Y > y^*] P[M = m_j] P[R = r_k] \quad (4)$$

where $P[Y > y^*]$ is the ground motion probability, $P[M = m_j]$ is the magnitude probability, and $P[R = r_k]$ is the distance probability.

Uniform Hazard Response Spectrum (UHRS)

The UHRS was generated by evaluating the corresponding PGA of a certain return period. As such, 2% and 10% exceedance in 50 years are used which are also equivalent to 2500 and 500 years respectively. Figure 5 presents the calculated PGA at both return periods from 0 to 4.0 seconds. The PGA values of 0.62g and 0.52g occurs at 0.1 seconds for 2% and 10% exceedance, respectively.

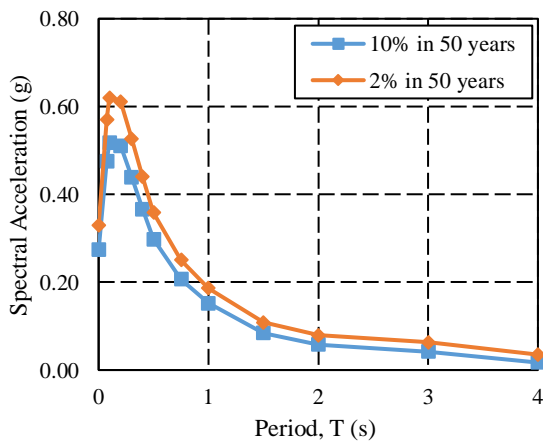


Fig. 5 Uniform hazard response spectrum

Spectral Map

By taking the PGA at 2500 years of all grid points of the water network area, seismic map of Biñan City was generated. As shown in Fig. 6, PGA values ranges from 0.56g to 0.62g depending on the location. Areas closer to the West Valley Fault produced higher ground motion values.

PIPE STRAIN ESTIMATION

Shinozuka and Koike [10] established a model on the relationship between seismic ground motion, particularly spectral velocity, and pipe strain given the site condition and details of the pipe. As such, the computed PGA values are converted to velocity using the model for Level 2 ground motion in Japan as shown in Eq. (5) [17]. This level of ground motion is similar to an event with return period of 2500 years.

$$S_v = \frac{S_a}{0.2} S'_v \quad (5)$$

where S_v is the spectral velocity, S_a is the spectral acceleration, and S'_v is the response spectral velocity for Level 2 ground motion.

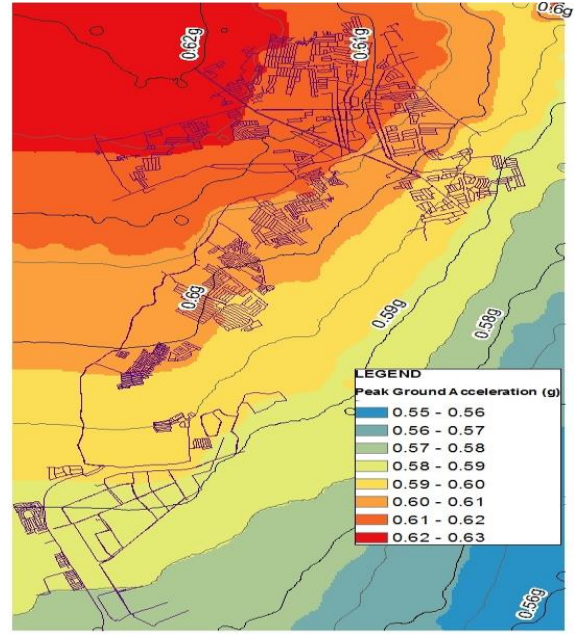


Fig. 6 Spectral map at 2500-year return period

The spectral velocity is related to ground response displacement $U_h(x)$ and ground strain ε_G which are both dependent on site conditions. These site conditions are patterned on the constants used in the PEM [13]. The expressions are represented as,

$$U_h(x) = \frac{2}{\pi^2} S_v T_G K_{h1} \cos\left(\frac{\pi x}{2H}\right) \quad (6)$$

$$\varepsilon_G = \frac{\pi U_h(x)}{L} \quad (7)$$

where T_G is the typical period of ground surface, K_{h1} is the seismic intensity for underground structures, x is the pipe depth, H is the ground layer thickness, and L is the wavelength.

The ground strain is then translated to pipe strain ε_p by multiplying to a conversion factor α_1 which is based on the material properties of the pipe. It can be expressed as,

$$\varepsilon_p = \alpha_1 \varepsilon_G \quad (8)$$

$$\alpha_1 = \frac{1}{1 + \left(\frac{2\pi}{\lambda_1 \times L'}\right)^2} \quad (9)$$

$$\lambda_1 = \sqrt{\frac{K_{g1}}{EA}} \quad (10)$$

where L' is the apparent wavelength, K_{g1} is the axial stiffness between surrounding soil and pipe, E is the elasticity modulus of pipe, and A is the cross-sectional area of pipe.

RELIABILITY ANALYSIS OF PIPELINE

Monte Carlo Simulation

The simulation generated 10,000 random samples given the mean and standard deviation from PGA. The capacity of the pipe is based on theoretical values for the critical strain of steel pipes with arc-welded joints upon reaching buckling strain [18]. The performance function is expressed as,

$$P(\text{damage}) = [\varepsilon_{cr} - \varepsilon_p < 0] \quad (11)$$

where $P(\text{damage})$ is the probability of damage and ε_{cr} is the critical strain of pipe.

Figure 7 shows the plot of the Monte Carlo simulation. It shows that some samples passed the critical strain for minor damage which indicates that the joints are vulnerable to leaking. Moreover, no sample exceeded the moderate critical strain.

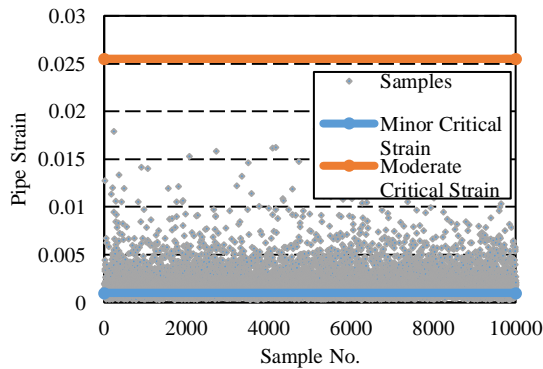


Fig. 7 Monte Carlo simulation

Component Reliability

Based on the PGA for 2500-year return period, the damage probability for each pipe diameter from 150 to 500 millimeters is established as shown in Fig. 8.

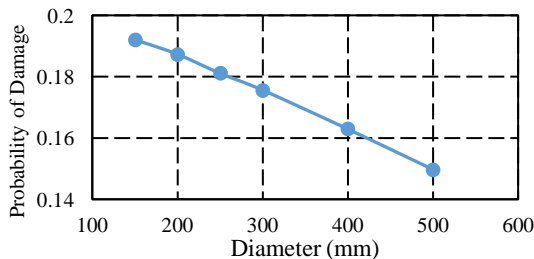


Fig. 8 Damage probability of pipe diameters

Figure 8 shows that pipes of larger diameter produced a lower probability of damage compared to smaller pipe diameter. However, the difference between the maximum and minimum diameters is only 5%.

The probability of damage of a single pipe depending on the scale of PGA from 0.1g to 1.0g is shown in Fig. 9. It is evident that a PGA of 0.62g for a return period of 2500 years will produce a 20% probability for a pipe to experience minor damage. In addition, by evaluating the graph function, a 100% chance of damage will occur at a PGA of 2.33g.

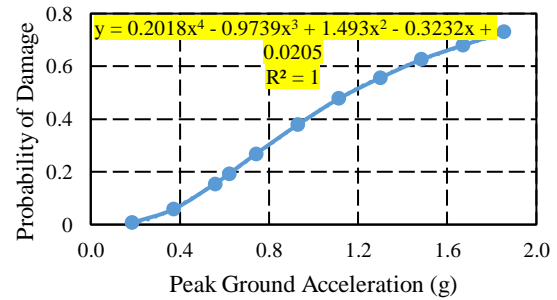


Fig. 9 Fragility curve for minor damage state

System Reliability

The expression used to calculate the system reliability of the entire water network considers the component reliability of each pipe [11]. It is the union of the probabilities of tie-sets. A tie-set is a series of pipes from source node to distribution node. The probability of damage of each tie-set is permitted by taking the product of probabilities of each component. The equation is expressed as,

$$P[C(\text{damage})] = P\left[\bigcup_{i=1}^{NT} T_k(\text{damage})\right] \quad (12)$$

$$P[T_k(\text{damage})] = \prod_{i=1}^{TL_k} P(\text{damage}) \quad (13)$$

where $P[C(\text{damage})]$ is the probability of damage of the system, $P[T_k(\text{damage})]$ is the probability of damage of a tie-set, NT is the number of tie-sets, and TL_k is the number of links in a tie-set.

Since system probability of damage was taken as product of component probabilities, tie-sets with less number of links resulted to a higher probability value. The plot of the fragility curve for system reliability is shown in Fig. 10. Based on the PGA of 0.62g from PSHA, the system has 1% probability of damage. As such, through the graph function, the system has a 100% chance of damage given a PGA of 2.58g which is close to 2.33g value from component reliability.

CONCLUSION

Based on the PSHA conducted in the area covered by the water network, seismic activity has a 42% probability of occurring within 0 to 20 kilometers from anywhere within the West Valley Fault to the

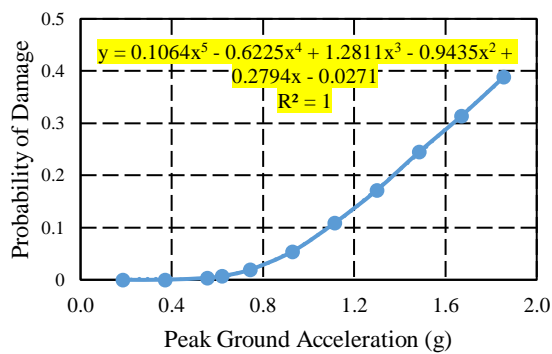


Fig. 10 System fragility curve

site. In addition, UHRS was generated for return periods of 500 and 2500 years wherein it is concluded that the earthquake hazards for the site are PGAs of 0.52g and 0.62g respectively. Subsequently, spectral map was established for the site area.

In the Monte Carlo simulation, all samples did not exceed the moderate damage state limit. Therefore, the water network system will only experience minor damage state at the event of seismic activity. Using the unscaled PGA, the probability of minor damage ranges from 15% to 20% at increasing diameter of pipe. As such, the chance of a pipeline to be surely damaged will occur at a PGA of 2.33g. As a system, the governing probability of damage came from tie-sets of least number of links and smallest diameters. Therefore, there is 1% that the entire water network system would experience minor damage.

ACKNOWLEDGMENTS

The authors would like to acknowledge the Engineering Research and Development for Technology (ERDT) of the Department of Science and Technology (DOST) of the Philippines for funding the dissemination of this research. Similarly, the authors would like to thank Laguna Water and PHIVOLCS for their kind participation and valuable assistance in the completion of this research.

REFERENCES

[1] Aydinoglu M., and Erdik M., Hyogo-Ken Nanbu (Kobe) Earthquake Reconnaissance and Assessment Report. Bogazici University Kandilli Observatory and Earthquake Research Institute, Istanbul, 1995.

[2] Selcuk A., and Yucemen M., Reliability of Lifeline Networks Under Seismic Hazard. Reliability Engineering and System Safety, Issue 65, 1988, pp. 213-227.

[3] Javanbarg M., and Takada S., State of the Art in Seismic Risk Assessment and Mitigation of Water

Supply Systems. American International Group, 2013.

[4] Panoussis G., Seismic Reliability of Lifeline Networks. SSDA, Civil Eng, Cambridge, 1974.

[5] Better S.I., and Garciano, L.E., Vulnerability Assessment of Surigao Metro Water District Under Seismic Hazard. International Journal of GEOMATE, Vol. 14, Issue 43, 2018, pp. 77-82.

[6] NDRRMC (National Disaster Risk Reduction and Management Council)., Final Report re Effects of Magnitude 7.2 Sagbayan, Bohol Earthquake, 2013.

[7] Inquirer., Water filtration systems sent to quake-hit Surigao, 2017.

[8] Mirabueno H., Nelson A., Personius, S., Rasdas A., Rimando R., and Punongbayan R., Multiple Large Earthquakes in The Past 1500 Years on A Fault in Metropolitan Manila, The Philippines, Bulletin of the Seismological Society of America, Vol. 90, 2000, pp. 84.

[9] Reiter L., Earthquake Hazard Analysis - Issues and Insights, Columbia University Press, 1990.

[10] Shinzuka M., and Koike T., Estimation of Structural Strains in Underground Lifeline Pipes. Proceedings of the Lifeline Earthquake Engineering Symposium at the 3rd National Congress on Pressure Vessels and Piping, 1979, pp. 31-48.

[11] Koike T., Damage Prediction on Buried Pipeline Under Seismic Risk. Proceedings of Ninth World Conference on Earthquake Engineering, 1988.

[12] NSO (National Statistics Office). City of Binan. Retrieved from Department of Interior and Local Government, 2016.

[13] Philippine Institute of Volcanology and Seismology. Philippine Earthquake Model, 2017.

[14] Seismicity Map and Catalogue of Surigao Del Norte Earthquakes Magnitude 2.0 and above. 1900-2015.

[15] Thenhaus P., Hanso S., Algermissen S., Bautista B., Bautista M., Punongbayan B., and Punongbayan R., Estimates of The Regional Ground Motion Hazard of The Philippines. Natural Disaster Mitigation in the Philippines, 1994, pp. 45-60.

[16] Youngs R.R., Chiou S.J., Silva W.J., and Humphrey J.R., Strong Ground Motion Attenuation Relationships for Subduction Zone Earthquakes, Seismological Research Letters, Vol. 68, Issue 1, 1997, pp. 58-73.

[17] Koike T., Seismic Risk Assessment of a Water Supply Lifeline System in Baku. Reliability Engineering Conference. Azerbaijan, 2009.

[18] Koike T., and Imai T., Seismic Performance of Arc-Welded Steel Pipes for Water Lifelines. 15th World Conference on Earthquake Engineering, 2012.

PASSENGER BEHAVIORAL MAPPING AND STATION FACILITIES DESIGN AT COMMUTER LINE TRAIN STATION (CASE: TANGERANG STATION, INDONESIA)

Ahmad Zubair¹, Lita Sari Barus¹ and Jachrizal Soemabrata²

¹School of Strategic and Global Studies, Universitas Indonesia, Indonesia; ² Faculty of Engineering,
Universitas Indonesia, Indonesia

ABSTRACT

Commuter Line became the best public transportation in Jakarta and surrounding cities. But unfortunately, there were still many Commuter Line passengers who did not aware in using the station facilities. This led to a "dilemma" for station managers to design station facilities that meet the needs of passengers. Therefore, the research was focused on the behavior of Commuter Line passengers based on the deviation that occurred. A behavior mapping approach was conducted to understand passenger behavior and its influence to the design of train station facility. The research was instrumental case study, mean study of the case for external reasons was not merely an intention to know it's origin, but the case was only an instrument to explained and proved the existing theory. By mapping the passenger behavior, station managers at least got an overview of the passenger's pathway, favorite places to wait for trains, crowded places during peak time, platform capacity, railway crossing capacity, the availability and lack of primary, secondary and tertiary facilities. The research results told us many stories. The results showed some explanation about passenger movement behavior based on three components of station zone: arrival zone, main facility zone and platform zone. The conclusion of the research explained that in designing a station facility, the station managers has not fully understood the passenger behavior. In other way, they should pay attention to that vital aspect.

Keywords: Passenger behaviour, Passenger behavioural mapping, Station facilities, Public transportation, Commuter line

INTRODUCTION

Commuter Line has become the best public transportation in Jakarta, Bogor, Depok, Tangerang and Bekasi [1] - [3]. If anybody asks "What kind of inexpensive, fast, safe and convenient transportation?" Then most of the people living in Jakarta and surrounding cities will answer the Commuter Line. Currently, Commuter Line is managed by PT. KCI (Commuter Train Indonesia)

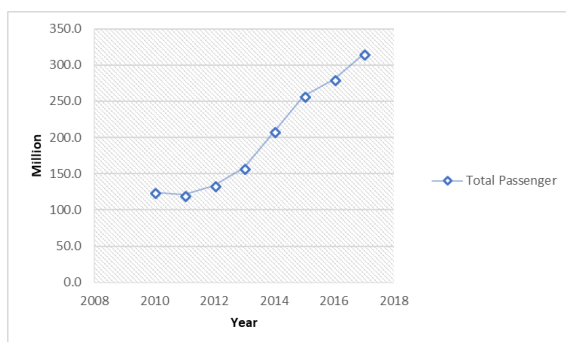


Fig. 1 Total commuter line passengers

Figure 1 shows the number of Commuter Line passengers each year. Increased number of passengers occurred since 2010. In 2017, PT. KCI has achieved the highest passenger volume record in history with 1,045,823 passengers a day and total of

315 million passengers a year.

Under these conditions, if the company / government is unable to provide facilities and infrastructure associated with increasing demand, it will lead to various transportation problems [4]. Woodson [5] argued that transport space should pay more attention to the diverse characteristics of passenger's attitude and behavior.

Understanding the attitudes and behavior of passengers is important to anticipate operational and service issues [5]. Arrangement of station space that is not in accordance with the passenger's need will result an inconvenience and security of passengers. Such discrepancies can be reflected from how the passengers' attitude in responding to the space provided. Sears [6] suggests that there are three components for viewing attitudinal forms, among which are the cognitive, affective and behavioral components themselves. Therefore, behavioral mapping is urgently needed to study passenger's behavior in station.

Researchers have used behavioral mapping to study people's activities in neighborhood open space, children's museums, schools and zoos [7], senior residences [8], grocery stores [9] and hospitals [10]. In this study, the main focus area is in Tangerang Station which become major station in Jakarta's surrounding cities, especially Tangerang City. The purpose of this study is also to provide an overview of the passenger's behavior at Tangerang Station.

METHODOLOGY

This research is a mixed method research with instrumental case study. The study of the case for external reasons is not merely an intention to know the nature of the case, but the case only serves as an instrument to understand something other than the case to prove an existing theory. A behavior mapping approach is used to understand passenger behavior patterns. Data were collected by observation, video counting and in-depth interviews to station manager. The data is processed through the mapping and design concept of station facilities by using GIS (Geographical Information System).

Behavior Mapping Approach

Observation using Behavior Mapping method. Behavioral or Behavior Mapping is a survey technique developed by Ittelson [11]. According to Ittelson [11], there are five basic components of behavior mapping: basic sketch of area or setting to be observed; Clear definitions of behavioral forms to be observed, quantified, described and dichotomized; Inform a clear time plan at which the observations will be made; A clear systematic procedure shall be followed during the observation and; An efficient coding / tagging system to further streamline the observation work. The method is divided into two types. These two methods are named respectively place-centered and individual-centered mapping [12]

Person Centered Mapping

Person Centered Mapping technique emphasizes the movement of passengers over a period of time. Thus, the technique will relate not only to one place or location but to multiple places or locations. The goal of these maps is to uncover whether a location is

used or not, at what time, by which type of people, and what activities are performed in different areas of the studied location [12]. The technique delivers a passenger mapping and describes the pattern of passenger behavior and activity.

Place-Centered Mapping

Place centered map method to see how humans organize themselves in a particular location [12]. The technique aims to find out how passengers, use or accommodate their behavior in a particular time at station. Thus, sketching a place or setting is required, including a physical element that is expected to affect the passenger's space. In other word, basic map is needed (Fig. 2).

Behavior Settings

Behavior settings can be considered the units of analysis in place-centered maps. The choice of the time when observations take place is fundamental because the same place can be used very differently depending on the time of the day.

Table 1 List of behavior settings

Settings	Weekdays		Weekend	
	Peak	Off peak	Peak	Off Peak
Arrival Zone	128	58	106	45
Main Facility Zone	36	27	33	30
Platform Zone	103	68	38	37

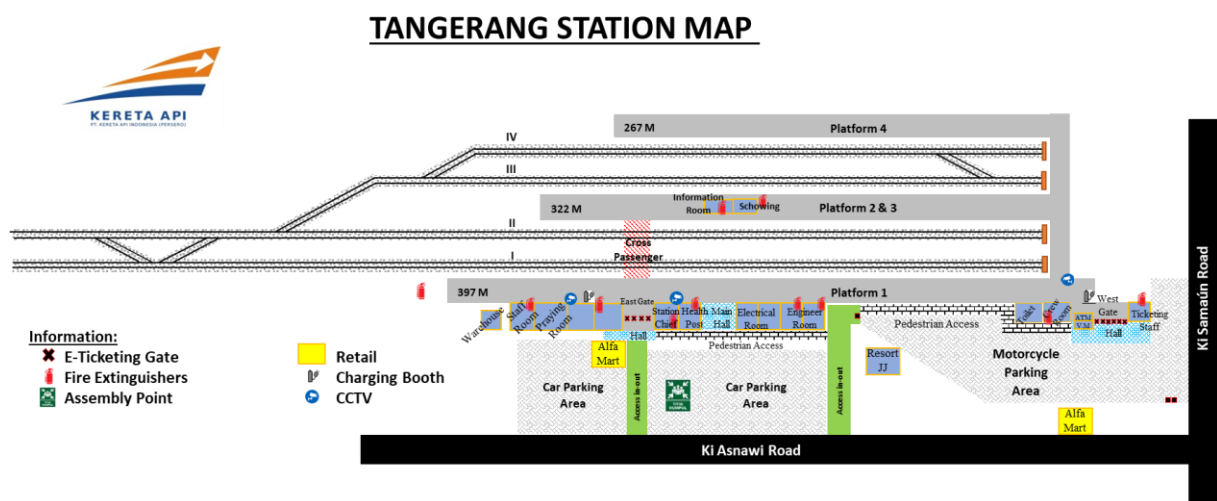


Fig. 2 Tangerang station basic map

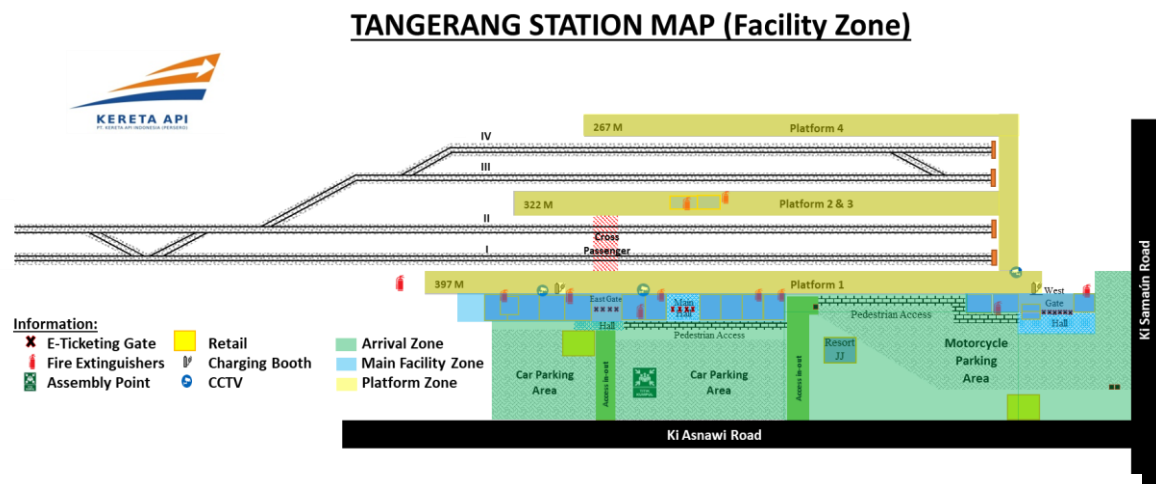


Fig. 3 Tangerang station with facility zone by Luis Vidal concept

The station settings were conducted by Vidal [13]. He divided station facility zone into three components: arrival zone, main facility zone and platform zone. Each zone has the characteristics of facilities and different forms of passenger behavior. Therefore, each zone is observed at different times (weekdays and weekend) and at different hours as well (peak hours and off-peak hours).

The analysis can be centered on a specific setting or focus on the movements of passenger at each zone due to station facilities. The movements of passenger can be counted and tracked by video analytics or using Closed Circuit Television [14]. It was also conducted by Larson [9] have used time-lapse photography, video recording, or radio frequency identification systems to collect behavioral data. Then consider and compare the data and check the interpretation meaning of field findings, use related cases and discard the non-steady relationship [15].

RESULT

Behavior Mapping

The majority of total passenger observations were distributed across three types of passenger behavior: light, moderate and slow movement (Table 2). On weekdays, the majority (10%) of average passenger behavior at peak time (06-08 AM) was observed in three types of movement: light (81.50%), moderate (14.50%), slow (4%).

At different time, 153 passengers were observed at off-peak time (10-12 AM) on weekdays. The result showed that passenger behavior with light movement (56.00%) still dominant. The pattern was same but the total of average passengers was different, light movement in the 1st position, moderate in 2nd (38.00%) and slow in 3rd (6.00%).

On weekend, the pattern was changed. It was because the characteristic of passenger and their activity. At peak time (06-08 AM), 177 passengers were observed resulting dominant behavior by light movement (51.60 %), moderate (21.00%) and slow (27.40%). Table 2 showed that slow movement passenger was higher than moderate movement. At off peak time, the pattern was changed again. 112 passengers were observed resulting dominant behavior by moderate movement (44.70 %), slow (31.30 %) and light (24.00 %).

DISCUSSIONS

Differences in passenger movement created by different types of behavior setting and by different forms of the same type of behavior setting (arrival zone, main facility zone and platform zone). It was also created by the characteristics of the passenger. For workers on weekdays, it was clear that they had a light movement, indicating that they were not too concerned about the facilities in each zone. It was different for family at weekend, they were more having moderate and slow movement in each zone.

Table 2 Passenger movement by different time

	Time	Average Passengers	No. Observations	Light (%)	Moderate (%)	Slow (%)	Total
Weekdays	Peak (06-08 AM)	2670	267	81.50	14.50	4.00	100%
	Off-Peak (10-12 AM)	1530	153	56.00	38.00	6.00	100%
Weekend	Peak (06-08 AM)	1774	177	51.60	21.00	27.40	100%
	Off-Peak (10-12 AM)	1121	112	24.00	44.70	31.30	100%

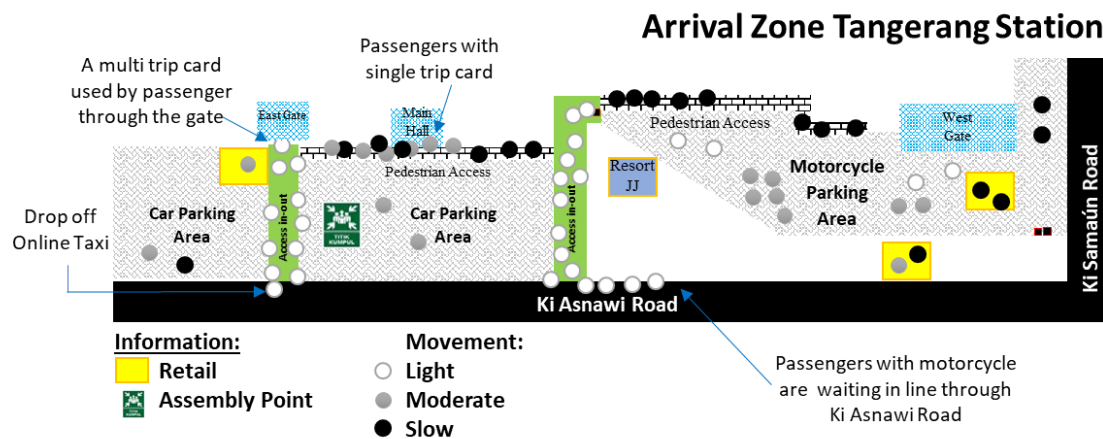


Fig. 4 Passenger behavior at arrival zone

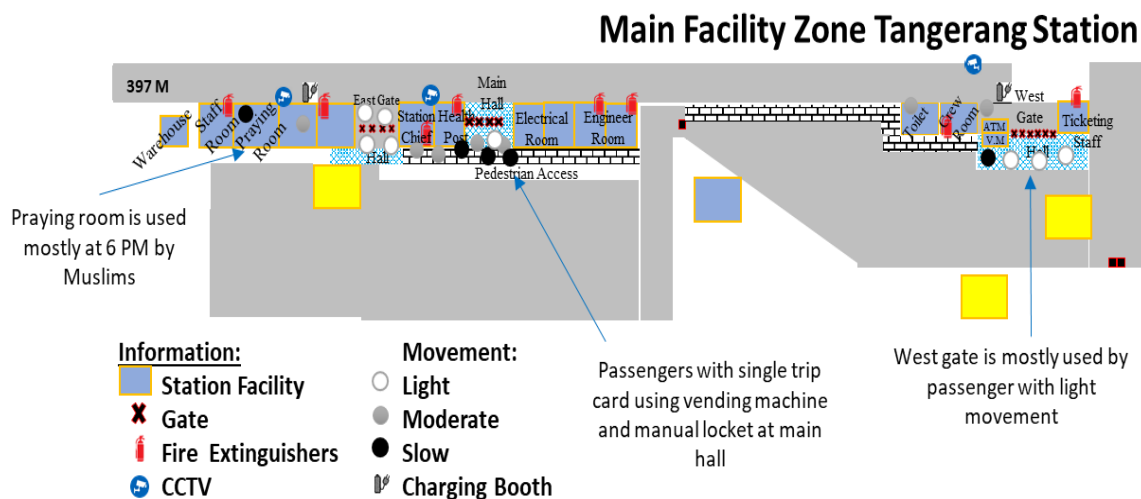


Fig. 5 Passenger behavior at main facility zone

Arrival Zone

This area is the largest zone of the station. Thousands of passengers come down and meet to enter the station. Differences in passenger behavior is

Table 4. Passenger characteristic at arrival zone

Settings	Weekdays	Weekend
Arrival Zone	Mostly workers with light movement and used multi trip card, most of them used motorcycle, car and online taxi	Mostly family with children with moderate and slow movement and used single trip card, almost used motorcycle

observed at two main access to the station (Fig 4). This zone is connected to three gates (west gate, east gate and main hall). These three gates show significant differences in passenger behavior. East gate is mostly used by passenger with the multi trip card (Table 4). It means most of them have light movement and use less facilities (e.g. ATM, vending machine, toilet). West gate is mostly used by passenger with motorcycle with light movement. These types of passenger usually commute from Tangerang to Jakarta daily.

Passengers with single trip card usually have moderate and slow movement in this zone. They use vending machine, buying drink and food at retail area and most of them use pedestrian access. These passengers are commonly a family with children on weekend (Table 4). As described above, the behavior setting at this zone has a significant role by providing appropriate facilities to passenger.

For the future station design, this zone will be developed a vertical parking area for motorcycle. It means the capacity of this zone can be doubled up.

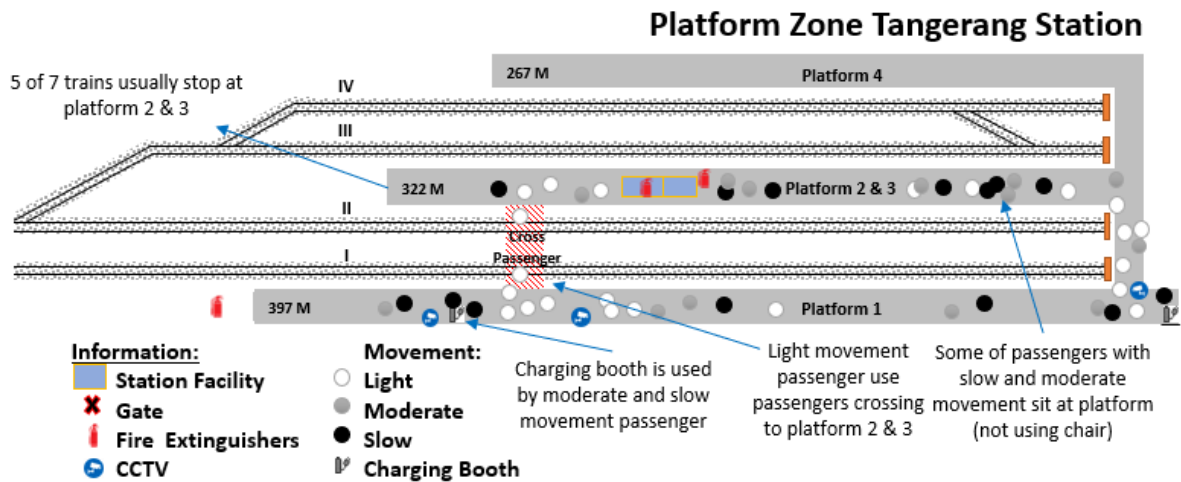


Fig. 6 Passenger behavior at platform zone

Main Facility Zone

This area is the smallest zone in the station. It can make a problem because the station's main facilities are in this zone (Vending machine, manual lock, charging booth, toilet, praying room, information room). It means the facilities need more larger area to ease passenger's need.

Table 5 Passenger characteristic at facility zone

Settings	Weekdays	Weekend
Main Facility Zone	Mostly workers with light movement and use multi trip card and walk direct to platform zone	Mostly family with children with moderate and slow movement and use single trip card, most of them use vending machine to top up

The most used facility is the vending machine for single trip card. Mostly passenger have to queue to buy tickets at the main hall. On weekend, passenger queue line could be stretched until the pedestrian access, even the main road (Fig 5). It is very common phenomenon in Tangerang Station and can make serious impact for the traffic in the arrival zone. The problem was not the gate, but the lack of vending machine and manual lock. It should be considered that station manager has to pay attention due to further facilities, especially the policies of multi and single trip card. We can identify the problem and do the next step by designing the station facilities. We can conclude that the main facility zone should be larger and wider. Thus, the movement of passengers can be more efficient and effective.

Platform Zone

Vidal [13] concept argued this zone basically used by passenger only for boarding. The facilities in platform zone are only for boarding too (Information board, platform line, cross passenger). Based on the survey, this concept is no longer used by the station manager. There is dualism bias concept whether this zone is used by passenger for only boarding or for waiting the train too.

Table 6 Passenger characteristic at platform zone

Settings	Weekdays	Weekend
Main Facility Zone	Workers stand near the platform line, passenger with light movement usually run for the train	Mostly family with children with moderate and slow movement, most of them sit in the platform (not using waiting chair)

In Tangerang Station, there are several facilities in the platform zone (Charging booth, information board, cross passenger, chair, trash can, platform line) (Fig 6). These facilities influence the passenger behavior. The passengers can charge the phone while the train is not coming yet and sitting in the platform (not using waiting chair) (Table 6). Unfortunately, the station manager didn't see it as a problem. For them, it is more important that all the passengers in platform zone are transported.

For the next plan, the station manager will build 2 additional platforms (platform 5 and 6). Therefore, the frequency of train departures and arrivals can be improved. In designing such facilities, it is necessary considered that the plan have to build waiting room for the passengers separately.

CONCLUSION

Behavior mapping can be used to measure relationships between Commuter Line passenger behavior and station facilities. The method can be used to accurately link behavioral components and affordances of behavior settings to passenger movement. Such evidence may be used to develop policies and standards for adoption by station manager to help guide the station design and investment in station facilities. The station manager should more aware to identify specific passenger behavior components associated with increased passenger movement activity. Research results may provide guidance for facility design interventions that could help create efficient and effective Commuter Line Station. Further research can focus on station manager training by increasing awareness about how the passenger behavior and its components influence the policies due to station facility design.

ACKNOWLEDGEMENTS

This article is part of Grant of International Publications for Students Final Project of Universitas Indonesia: Analysis and Evaluation of Urban Community Behavior on Urban Transport Facilities and Policies.

REFERENCES

- [1] Basyarah Z., Affordances and Passengers Adaptation on Commuter Line, Universitas Indonesia, 2014, pp.1-57.
- [2] Kusumaningtyas B.M., Impelentation of Railway Management Policy (Facilities and Infrastructure Study of Commuter Line Duri-Tangerang), Universitas Indonesia, 2014, pp. 1-114.
- [3] Hendro, A.P., Quality Service of Women's Special Train at Jakarta-Bogor Route, Universitas Indonesia, 2012, pp.1-94.
- [4] Adhi, P. R., Preference for Mode Selection in the Movement of Passengers Corridor Bogor-Jakarta Associated with the Selection of Residence (Case Study: AC Bus and Express KRL), Journal of Regional and City Planning, Vol. 23, No.1, 2012, pp.67-84.
- [5] Woodson, W., Human Factors Design Handbook: Information and Guidlines for the Design of systems, Facilities, Equipment and Products for Human Use, New York McGraw-Hill, 1981.
- [6] Sears, D. O., Freedman, J. L., & Peplau, L. A., Social Psychology 5th Edition, Jakarta Erlangga, 1992.
- [7] Cosco, Nilda G., Robin C. Moore, and Mohammed Z. Islam., Behavior mapping: A Method for Linking Preschool Physical Activity and Outdoor Design, Medicine & Science in Sports & Exercise 42, No. 3, 2010, pp.513-519.
- [8] Milke, Doris, Charles Beck, Stefani Danes, and James Leask., Behavioral Mapping of Residents' Activity in Five Residential Style Care Centers for Elderly Persons Diagnosed with Sementia: Small Differences in Sites can Affect Behaviors, Journal of Housing for the Elderly Vol. 23, No. 4, 2009, pp.335-367.
- [9] Larson, Jeffrey S., Eric T. Bradlow, and Peter S. Fader., An Exploratory Look at Supermarket Shopping Paths, International Journal of Research in Marketing Vol. 22, 2005, pp. 395-414.
- [10] Bernhardt, Julie, Helen Dewey, Amanda Thrift, and Geoffrey Donnan., Inactive and Alone: Physical Activity Within the First 14 Days of Acute Stroke Unit Care, Stroke Vol.35, 2004, pp. 1005-1009.
- [11] Ittelson, William H., Leanne G. Rivlin, and Harold M. Proshansky., The Use of Behavioral Maps in Environmental Psychology., Environmental Psychology: Man and His Physical Setting, ed. Harold M. Proshansky, William H. Ittelson, and Leanne G. Rivlin, New York Holt, Rinehart and Winston, 1976, pp. 340-351.
- [12] Sommer, Robert, and Barbara B. Sommer., A Practical Guide to Behavioral Research, New York, Oxford University Press, 2001.
- [13] Vidal, Luis., Urban Rail Transit Design Manual. Hong Kong Design Media Publishing Limited, 2013.
- [14] SITA., Passenger Counting and Tracking Technology: Comparison Fact Sheet, New York. PBD/ASL, 2016, pp. 1-12.
- [15] Miles, M.B and Huberman, A.M., Qualitative Data Analysis: A Source Book of New Methods, California, Sage Publication, 1984.

PHYSICAL ANALYSIS CONDITIONS AROUND MRT STATION TO BE A TRANSIT ORIENTED DEVELOPMENT AREA BY SOME INDICATORS (CASE STUDY: LEBAK BULUS MRT STATION, SOUTH JAKARTA, INDONESIA)

Doddy Apriansyah¹, Lita Sari Barus¹, Ahmad Zubair¹, H. Andi Simarmata¹, Jachrizal Sumabrata²

¹ School of Strategic and Global Studies, University of Indonesia, Indonesia; ² Faculty of Engineering,
University of Indonesia, Indonesia

ABSTRACT

Transit-oriented development (TOD) is one of the concept of sustainable urban development in tackling congestion, environmental degradation and energy efficiency. In an effort to realize transit-oriented development, the government issued a transit-oriented development policy at every MRT station in DKI Jakarta, one of which is Lebak Bulus MRT Station. In the concept of transit-oriented development there are several criteria such as land use, mobility and infrastructure that support the function of the MRT station thus reducing dependence on private vehicles. The criteria are broken down into several indicators that are analyzed based on the characteristics of the existing area conditions. This study aims to determine the extent to which the area around Lebak Bulus MRT station can support the development policy of TOD area. The research method used is quantitative method in the form of descriptive analysis by using Geographic Information System (GIS). The result of the research is explanation and the concept of transit-oriented development concept in DKI Jakarta. The research conclusions and recommendations will focus on establishing transit-oriented development areas around Lebak Bulus MRT Station in accordance with government policies and TOD indicators.

Keywords: transit-oriented development, TOD indicator, Lebak Bulus MRT Station.

INTRODUCTION

Transit Oriented Development (TOD) is one of the concept of sustainable urban development in overcome congestion, environmental damage and energy efficiency. This concept aims to overcome urban sprawl and divert dependence on the use of private vehicles [1]. Transit Oriented Development (TOD) is also a relatively new model of environmental development that has been conceptualized as urban development with a combination of nodes such as transit stations and places such as environments [2]. Through the provision of a good and balanced transportation between mass transport and private vehicles can improve the efficiency of urban economy [3].

As an effort to make it happen the government makes transit-oriented development policy at every MRT station in Jakarta Capital City. Transit-oriented development concept in Indonesia began to be developed in big cities. Transit-oriented development provisions in Indonesia shall be regulated in the Regulation of the Minister of Agriculture and Spatial-BPN [4]. Meanwhile, transit-oriented development in Jakarta Capital City is regulated in Jakarta Governor Regulation No. 44/2017.

In both policies, transit-oriented development has 3 area typologies namely the area of development of TOD Regions, TOD City Area and Environmental TOD Area.

TOD development policy in the capital city of Jakarta there are several stages, the current TOD development plan that was developed one of them is the TOD area of Lebak Bulus MRT Station in South Jakarta which is currently still in the preparation of the Urban Design Guide. Based on Jakarta Governor Regulation, TOD Lebak Bulus area is directed as TOD Territory with regional service function.

However, this policy needs to be supported by the physical condition in the designated area. Although the preparation of the Lebak Bulus City Design Guideline is currently underway, it is necessary to conduct a study of the potential of the area around MRT Lebak Bulus Station, whether the physical characteristics of the area currently available, the area has the potential to be developed as a region-scale TOD based on the criteria transit-oriented development and can support government policy in the implementation

of TOD area development around Lebak Bulus MRT Station.

LITERATURE REVIEW

Transit Oriented Development (TOD) is a community with mixed use in an average distance of 2,000 feet or approximately 600 meters from transit stop and commercial center. The TOD region when applied on a regional scale can provide a mixed network of environments that can help balance urban development with the suburbs by creating solid and centralized growth set around the regional transit system (Calthrope, 1993). Criteria of TOD area based on Calthrope, consist of Location and TOD type criteria, where TOD location is within 2,000 feet or approximately 600 meters with two types of TOD, urban TOD and Environmental TOD.

Land Use criteria where each TOD type must have a core commercial area with mixed use be equipped a public area (open space or plaza), a core area area of at least 10% of the total area of TOD. Housing density at Urban TOD approximately 15 units / acre or 15 units or 4,046 square meters, while the housing density at Environmental TOD is approximately 10 units / acre or 10 units / 4,046 square meters.

Criteria for *Road and Circulation Network Systems*, designed to maximize pedestrian safety. The vehicle path is designed to narrow the vehicle speed. Traffic speed is not more than 15 mph or 24 km / h with width of 8 - 10 feet or 2.4 meters - 3 meters.

Criteria for *Pedestrian and Bicycle Paths*, must be located along a road network connected to commercial areas and transit stations equipped with comfort, safety and security features in walking and cycling. The pedestrian track in the residential area has a width of 5 feet or 1.5 meters, and the commercial area has a pedestrian foot width of 10 feet or 3 meters.

Then the criteria of the *transit system* must be in accordance with the location characteristics, density and growth potential of the area, so that the transit system must be able to accommodate the maximum area limit of TOD area development. Transit stop is centrally located and adjacent to the core commercial area, then the transit station is equipped with easy accessibility and convenient for transit passengers, and accommodates year-round weather conditions.

Parking requirement criteria, parking capacity in the TOD area should be reduced to encourage a pedestrian friendly environment. Parking location should not be adjacent to transit station, then park

and ride location and drop-off bus should not isolate pedestrian path from access to station transit station. Then the cumulative parking is put into place in commercial, retail, office and entertainment areas.

Florida TOD Guide Book, has several criteria for TOD areas such as where the concentration of TOD area development is within ¼ mile (400 m) radius called transit core with an area of about 125 Ha, then the radius distance up to ½ mile (800 m) from a transit station is marked by a reduction in intensity and density of land use is called a "*transit neighborhood*" with an area of 375 Ha, so on until a radius of 1 mile (1,600 m) is a "*transit supportive area*".

Transit cores and *transit neighborhoods* reflect a comfortable and safe walking area within 5 to 10 minutes of walking distance, then a transit supportive area marked by cycling activity [5]. The Florida TOD *framework* establishes 3 (TOD) types of Regional Centers, Community Centers and Neighborhood Centers. The division of TOD type aims to regulate the development and pattern of urban mobility in Florida, by differentiating each type of TOD based on the density and intensity of buildings, mixed usage, road network patterns, transportation mode services and parking lots.

In TOD Standard v3.0, the TOD development area has an area of ¼ mile - ½ mile or 400 m - 800 m in walking distance, with the central node area being a transit station. Some criteria based on TOD Standard, among others [6]:

Walk, building an environment that supports walking activities. *Cycle*, giving priority to non-motorized transportation network with the target network of cycling infrastructure is complete and safe. *Connect*, creates a congested network of roads and pedestrian paths with short route targets for walking and cycling, direct and varied.

Transit, puts development near a high quality public transport network. With high-quality public transport targets accessible on foot as a TOD requirement, the furthest distance to public transport stations as far as 1,000 m or less for fast transit (MRT, LRT and BRT) and 500 m or less for direct service (bus local).

Mix use, plan development with land use, mixed income and demographics (use for settlements and non-settlements within the same block). *Densify*, optimize the space density and adjust the capacity of public transport.

Compact, build areas with short travel distance requirements. *Shift*, increasing mobility through parking arrangements and road usage policies with a reduction target of the infrastructure used for motor vehicles.

Development of TOD area in Indonesia, regulated in Regulation of the Minister of Agrarian Affairs and Spatial-BPN No. 16/2017

with several criteria, namely *Delineation of region*, where TOD is within 400 m - 800 m from transit station which is limited by physical boundaries such as road, river and so on which shows a unity of characteristics.

Mixed land use, Comparison of mixed space utilization and diversity in TOD area between housing: non-residential ie 20% -60%: 40% -80% for TOD Service Center City, 30% -60%: 40% -70% for TOD Sub City Center and 60% -80%: 20% -40% for TOD Environmental scale. *Density area*, of TOD area based on occupancy, for TOD Kota Kota with high density 20 - 75 units / 1000 square meters, for TOD Sub City Center with medium to high densities 12-38 units / 1.000 m2 and Environment TOD with medium density 15-20 units / 1,000 square meters.

Road pattern system, has a block dimension of 70 - 130 m for City Center TOD, 70 - 200 m for TOD Sub Center and 70 - 270 m for Environmental TOD.

Parking restrictions, parking space at TOD Town Center, 1 parking / unit for housing, 1 parking / 100 square meters for non housing, 10% from kaveling area on ground floor with shared park. While parking is available at TOD Sub City Center for 1.5 parking / unit housing, 2 parking / 100 square meters for non housing, 15% from kaveling area on ground floor of building with shared parking pattern. Then at the TOD Environment, parking 2 housing parking / unit, 3 parking / 100 m2 for non residential, 20% from the width of the ground floor of the building with the use of shared parking.

Transit system, Transit system development at City Center TOD and Sub City TOD have the

same transit system development that is heavy rail transit, light rail transit, Bus Rapid Transit (BRT), Local Bus and ferry is possible. While the transit system on the Environmental TOD ie light rail transit, Bus Rapid Transit (BRT), Local Bus, Bus feeder and commuter line can serve the Environmental TOD.

STUDY AREA

Lebak Bulus TOD area is partly located in Kelurahan Pondok Pinang Kebayoran Lama Subdistrict and some others are located in Lebak Bulus Village, Cilandak Subdistrict, South Jakarta. The study area is located at a radius of 400 meters from the current Lebak Bulus MRT station which is currently not operationalized. Lebak Bulus MRT Station is the center (nodes) while 400 meter radius is the development of TOD (places) which is the core area of TOD.

Land use in the area of radius of 400 meters from the MRT station is dominated by the functions of housing, offices and trade and services. As for the transportation area is served by the primary arterial road network system (RA Kartini road, Pasar Jumat road and Ciputat Raya road), then access to enter the inner-city toll road connected by the RA. Kartini road.

Then there is a Transjakarta bus shalter located opposite the MRT Station and Inter-City Inter- Provincial bus terminal (AKAP) located on Pasar Jumat road, so the radius of 400 meters from Lebak Bulus MRT Station is served by rail transportation mode (MRT), TransJakarta bus rapid transit (BRT), and Inter-City Inter-Provincial Bus (AKAP).

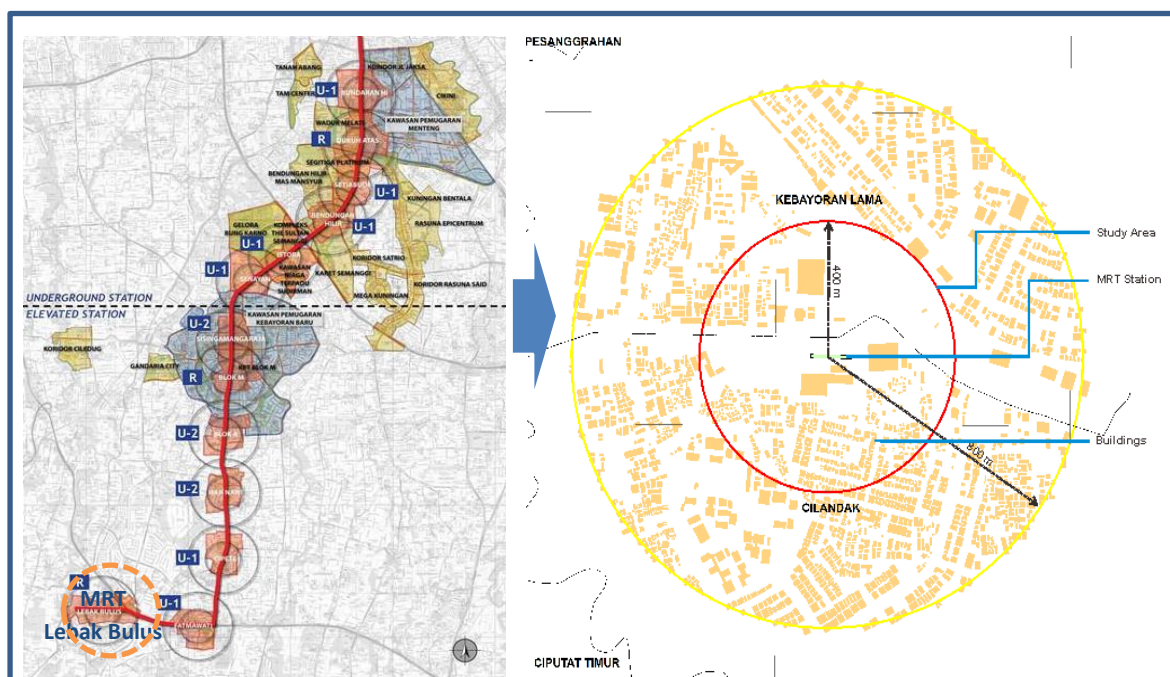


Fig. 1 Location of Study Area

METHODOLOGY

In this study, researchers used visual observation methods at the study site by observing the characteristics of the area, the function of land use, the condition of the road network and the availability of transportation facilities and infrastructure. Every observation made, the researcher refers to the criteria and indicators of TOD area development based on the literature study and the prevailing laws and regulations in Indonesia.

Then to strengthen the result of visual observation, the researcher perform spatial analysis by using Geography Information System (GIS) program. The use of this program aims to determine the level of density and density of buildings. As for calculating the density of the building the researchers used the ratio of the number of building units in each 1.000 square meters with the formula:

$$\text{Density building} = \frac{\text{Building Units} \times 1.000}{\text{Area wide (m}^2\text{)}}$$

DISCUSSION

Physical descriptive analysis of the study area focuses on the analysis of land use in the area of 400 m from Lebak Bulus MRT station, which revealed that there are several TOD criteria and indicators that have been met and which have not been met according to the TOD area.

Land Use

In the land use criteria, among others, the use of mixed land, where there are several functions of commercial activities, offices, housing, and shopping centers. For the analysis of mixed use the author only identified between the use of residential and non-residential land, where in the radius of 400 m from Lebak Bulus MRT station the use of mixture is still dominated by housing activities. While the density of buildings in this area, based on the results of spatial analysis using GIS only has a density of 1.7 units / 1000 square meters, where the density of TOD region scale should have a density of 20 - 75 units / 1000 square meters. For the intensity of the building, this area has a maximum height of the building based on the Aviation Safety Operation Area (KKOP) according to the Letter of Command of the TNI AU 1 No.B / 1700-09 / 21/05 / Halim dated December 16, 2011 altitude lebak bulus 110 meters or around 27 floors.



Fig. 2. (1) Mixed land use and (2) Building density

Mobility

On mobility criteria in the area of 400 m from Lebak Bulus MRT station, there are many connected access in this area, that is Pasar Jumat road, RA. Kartini road connected with Ir. H. Juanda road and Metro road as primary arterial road and secondary artery.

Then in this area there are busway transit shelters (bus rapid transit) corridor 8 which serves the trip Lebak Bulus - Harmoni. There is also an inter-city bus terminal between provinces that supports trips outside Jakarta. It is more impressed that the construction of the Lebak Bulus MRT Station has been operated to support the movement in Jakarta.

Infrastructure

The availability of TOD's supporting infrastructure is largely available, but the quality and quantity is inadequate. For pedestrian paths are available, but the width of the line is only 1 meter, while the TOD standard for the pedestrian path is 1.5 meters. Based on visual observation, the availability of pedestrian is not available along the road, only on some roads and lack of supporting facilities of pedestrian facilities. While the availability of bicycle cycles in the area of 400 m from Lebak Bulus MRT station, is still not available. See table 1.

CONCLUSION AND RECOMMENDATIONS

This paper has evaluated the physical characteristics of a radius of 400 meters from Lebak Bulus MRT Station against TOD area criteria and indicators based on several literatures. It is generally found that the physical area of Lebak Bulus MRT Station has the criteria that can be developed as TOD area, there are only some unfulfilled indicators such as building density, building height, bicycle path availability, pedestrian facilities and connectivity between MRT Station, BRT Shalter busway) and Inter-city Bus Terminal. While the indicators of mixed land use, building intensity and service mode now has the potential as a TOD area.

Based on the results of the analysis that has been done, to make the radius area of 400 meters from Lebak Bulus MRT Station as TOD area service area there are some recommendations that are:

1. Building density indicator, can be increased with vertical development pattern, increasing the intensity of building through local government policy, so that land parcels can be reduced and the number of building units in each block can be more and more compact.
2. Increasing the intensity of buildings can be optimized according to the provisions of the Area of Flight Operations Safety (KKOP) up to 110 meters or 27 floors. This can be used as an incentive and disincentive from the Local Government of the region to encourage the creation of TOD area.
3. Pedestrian and bicycle path system can be made through urban design guide line by increasing the widening of pedestrian, greening, seat on certain spot and other equipments supporting safety and comfort for pedestrians. As for the bike path can take advantage of some of the road used by the vehicle (lane division), so the road capacity for the vehicle is reduced to reduce the speed of the vehicle.

Table 1. Analysis of Physical Area Character

Criteria	Indicators	TOD Lebak Bulus Area Radius (400 m) from MRT Station	Explanation
Land Use	Density	Building density at 400 m radius of 1.7 units / 1,000 m ²	Can be developed more intensively for commercial areas such as shopping centers, restaurants, entertainment centers and so on with the concept of vertical buildings in order to create a dense area or meeting.
	Building Intesitas	The height of the building is limited by KKOP (Aviation Safety Operation Area) according to the Letter of Command of the TNI AU 1 No.B / 1700-09 / 21/05 / Halim dated December 16, 2011 altitude 110 meters	The vertical development pattern has the potential to be developed up to 27 floors as there are stipulations on building height limits based on the Aviation Safety Operation Area
	Mixed Use	Area of radius of 400 m is dominated by residential, office, trade and services functions	Potential to develop mixed use function
Mobility	Radius from MRT Station	Within a radius of 400 m from MRT Station	as the core area of TOD
	Accessibility	There are many accesses connected to St. MRT is Jl. Market Friday, Jl. RA. Kartini, Jl. Ir. H. Juanda, Jl. Metro Pondok Indah There is St. MRT, Bus Terminal and Bus Way Corridor 8 (lebak bulus - Harmoni)	There needs to be a separation path for bicycle users.
	Service Mode	Terdapat St. MRT, Terminal Bus, dan Bus Way koridor 8 (lebak bulus – Harmoni)	A connectivity system between the MRT station, the bus terminal and the BRT (bus rapid transit) shalter should be made.
Infrastructure	Road Network	Arterial road networks and collectors are dominated by motorcycle	Motor vehicle restrictions are required, to prioritize walking activities in the TOD area
	Pedestrian and Bicycle Paths	Pedestrian path already exist only non-continuous and not connected to building blocks No bicycle lane in particular / separate	Pedestrian construction is required along the road in this area, as well as adequate pedestrian width and the addition of comfort features on foot, such as greening, chairs, lamps and other instruments
	Parking	The parking system is not integrated and is still scattered on each building (not yet centralized)	It requires the construction of centralized parking with limited capacity to encourage walking activity and use of public transport.

4. To support the function of shifting modes in this area, it is necessary to connect facilities between MRT Station, Shalter Busway (BRT) and inter-city bus terminal, so that the connectivity of movement in TOD area around MRT Lebak Bulus.

ACKNOWLEDGEMENT

This article is part of an international publication grant for a university student final project. Analysis and evaluation of urban community behavior on urban transport facilities and policies.

REFERENCES

- [1]Calthorpe, Peter (1993).*The New American Metropolis*. New York, NY: Princeton Architectural Press.
- [2]Kamruzzaman, Baker,Washington, Turrell, (2013). *Advance transit oriented development typology: case study in Brisbane, Australia*. Journal of Transport Geography. Published by Elsevier Ltd.
- [3]Carlton, Ian. (2007). *Histories of Tranist-Oriented Development: Perspectives on the Development of the TOD concept*. University of California, Berkeley.
- [4] Ministry of agrarian and spatial planning BPN (2017). *transit-oriented development guidelines*. Regulation of the Minister of Agriculture and Spatial BPN, Republic of Indonesia No.16 / 2017,
- [5]Busha, Michael ., et., (2012). *Florida TOD Guidebook*, Florida Departement of Transportastion.
- [6]Institute for Transportation and Development Policy (2017). *TOD Standard*,.3rd ed. New York.

IMPACT OF 2016 WEAK LA NIÑA MODOKI EVENT OVER THE INDONESIAN REGION

Deni Okta Lestari¹, Edy Sutriyono², Sabaruddin³, and Iskhaq Iskandar⁴

¹Graduate School of Environmental Science, University of Sriwijaya, Indonesia; ²Faculty of Engineering, University of Sriwijaya, Indonesia; ³Faculty of Agriculture, University of Sriwijaya, Indonesia; ⁴Faculty of Mathematics and Natural Sciences, University of Sriwijaya, Indonesia

Corresponding author: iskhaq@mipa.unsri.ac.id

ABSTRACT

After an extreme 2015/16 El Niño phenomenon, the Pacific Ocean witnessed a La Niña Modoki event, while a strong negative IOD simultaneously took place in the Indian Ocean. The event was weaker in intensity and shorter in time, compared to the similar case in 1998/99. Using the combined monthly sea surface temperature (SST) derived from the Optimum Interpolation Sea Surface Temperature (OISST) version 2, the atmospheric reanalysis data from the National Center for Environmental Prediction and the National Center for Atmospheric Research (NCEP/NCAR) and the precipitation data from the Tropical Rainfall Measuring Mission (TRMM), the dynamics and possible impact of this event were investigated. The 2016 La Niña Modoki initially developed in boreal summer, subsequently matured in autumn, and abruptly terminated in winter. This short-live La Niña Modoki was associated with a unique SST anomaly (SSTA) pattern in the Indo-Pacific region. Strengthened easterly wind in the central tropical Pacific Ocean was associated with a warming SST over the western Pacific Ocean and triggered convergence in the lower atmosphere causing upward motion and enhanced convective process over the Indonesian region. As a consequent, most of the Indonesian region experienced excess precipitation during boreal summer, except in the northern part of the Sumatra Island.

Keywords: Atmosphere Circulation, Indonesian Region, La Niña Modoki, Precipitation

INTRODUCTION

El Niño-Southern Oscillation (ENSO) Modoki is one type of the interannual climate variability that has intensively discussed in the recent years [1]–[3]. ENSO Modoki is associated with typical warming sea surface temperature (SST) anomaly in the central tropical Pacific Ocean (TPO) with cooling SST anomaly (SSTA) both side in the western and eastern TPO [1].

After a super El Niño in 2015/16 [4], [5], TPO witnessed a unique cooling SSTA. This pronounced phenomenon was similar to that occurred after an extreme 1997/98 El Niño. We expected that the phenomenon was also associated with a new flavour of coupled ocean-atmosphere interaction, so-called La Niña Modoki, which is referred to the cooling phase of ENSO Modoki. Previous study has founded that La Niña Modoki has affected climate variability in some region [6]. It caused excess rainfall extending from the northwestern Australia to the northern Murray-Darling Basin, as consequence of shifting convection process more westward in the TPO. La Niña Modoki was also increased above normal precipitation anomalies leading severe flooding in the Southeast Asia region [7].

Considering the geographic position of the Indonesia, climate variability in this area has

strongly influenced by the climate modes took place in the TPO [8]. Therefore, this study is designed to investigate the 2016 La Niña Modoki event and evaluate its possible impact on precipitation over the Indonesian region. Although several La Niña Modoki events have occurred several times, this study focused only on the 2016 La Niña Modoki event by comparing with a strongest La Niña event occurring during the three decades, namely 1998/99 La Niña Modoki events.

The rest of this paper is organized as follows. Section 2 describes the data and method used in this study. Section 3 illustrates the tropical ocean-atmosphere response and evolution of the event as well as discusses its possible impact on the Indonesian climate. Final section gives a conclusion.

DATA AND METHODS

The monthly SST data used in this study are obtained from National Oceanographic and Atmospheric Administration (NOAA) Optimum Interpolation Sea Surface Temperature (OISST) Version 2 with horizontal resolution $0.25^\circ \times 0.25^\circ$. This data available from September 1981 to February 2018.

The low-level wind data at 850 mb are from the National Center for Atmospheric Environmental

Prediction-National Center for Atmospheric Research (NCEP-NCAR) Reanalysis [9]. The data covers a period of January 1948 to June 2018 with horizontal resolution of $2.5^\circ \times 2.5^\circ$.

The monthly precipitation data are from the Tropical Rainfall Measurement Mission (TRMM), in which only data over land are used in this study. The data have horizontal resolution of 0.25° in both longitude and latitude, and cover a period of January 1999 to April 2018.

To evaluate the evolution and possible impact of the climate mode on Indonesian region, we first calculate the anomalies of each data. Anomalies of all variables are defined by subtracting the monthly climatology from the monthly data. Note that the monthly climatologies for SST and precipitation were calculated based on the period of January 2001–December 2015, while for the low-level wind was calculated based on period of January 1948–December 2013. In order to analyze the seasonal variation, we calculate the seasonal mean by running 3-month-average data; March to May (MAM) season, June to August (JJA) season, September to November (SON) season, and December to February (DJF) season, respectively for all data.

Furthermore, to identify the La Niña Modoki event, El Niño Modoki Index (EMI) was used in this study. The EMI was defined as average SST anomaly over the central TPO (165°E to 140°W , 10°S to 10°N) minus SST anomaly in the eastern (110°W to 70°W , 15°S to 15°N), and western (125°E to 145°E , 10°S to 20°N) TPO regions [1]. Following Ashok et al. (2007), the negative index below one standard deviation for at least three consecutive seasons (from summer to winter season) is categorized as La Niña Modoki event.

RESULTS

Evolution of the 2016 La Niña Modoki event

Figure 1 shows the time series of the EMI from January to December 1998-99 (red solid line) and 2016-17 (blue dashed line). Based on the EMI, it can be seen that the 2016 La Niña Modoki event had shorter-live time and weaker intensity compared to 1998/99 La Niña Modoki. The EMI revealed that evolution of 1998/99 La Niña Modoki event started in boreal spring (April 1998), reached its peak in boreal summer and autumn (August and October 1998) with maximum intensity about -1.6°C and terminated in boreal spring (April 1999). Meanwhile, 2016 La Niña Modoki event started to develop with a relatively weak intensity in early boreal summer (June 2016). Then, it reached its peak in the end of autumn (November 2017) with maximum intensity of about -0.9°C . After reaching its peak, the intensity of the 2016 La Niña Modoki

was weakened and abruptly terminated in the early winter season (December 2016). Considering the intensity during the evolution and peak of the EMI, 2016 La Niña Modoki can be categorized as a weak La Niña Modoki event.

The seasonal evolution of SSTA and low-level wind anomalies of the 2016 La Niña Modoki are illustrated in Fig. 2e-h. The initial development of this event can be identified by the gradual cooling of SSTA firstly observed in the eastern to the central TPO (80°W to 165°W) just after the termination of the 2015/16 super El Niño event (Fig. 2f). During boreal summer 2016, the easterly wind anomalies were also developed in western TPO. As a result, the cooling intensity of SSTA was strengthened and extended more westward near the date line during boreal autumn. Meanwhile, in the western TPO and the Indonesian waters covered by positive SSTA.

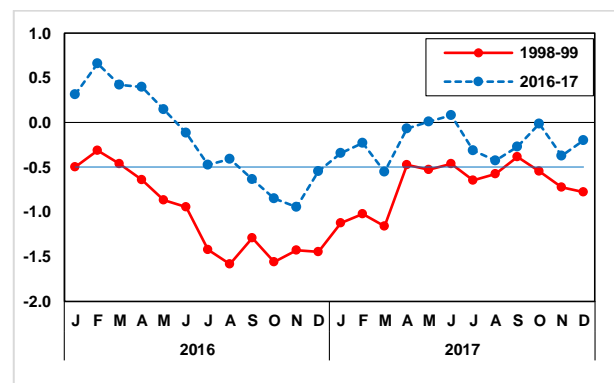


Fig 1. Times series of EMI for 1998/99 (red) and 2016 (blue) La Niña Modoki events.

It was shown that the cold SSTA was centred at 150°W to 170°W with maximum intensity of about -2.5°C . At the same time, strong easterly wind anomalies over the eastern TPO, which are the peculiar features during La Niña Modoki event, can be observed during mature phase of the 2016 La Niña Modoki. The easterly wind anomalies were observed along the eastern half of the equatorial Pacific Ocean, while the westerly wind anomalies were found in the western TPO and northwesterly wind anomalies were blowing along the southeastern coast of the TPO. As a consequence, a warmer than normal SSTA was observed in the vicinity of the Indonesian region and in the southeastern TPO, while colder than normal SSTA only observed in the eastern half of the equatorial region of the Pacific Ocean. Furthermore, the cold SSTA pattern was abruptly decayed in boreal winter, leaving just a little part of cold SSTA near the date line with very weak intensity.

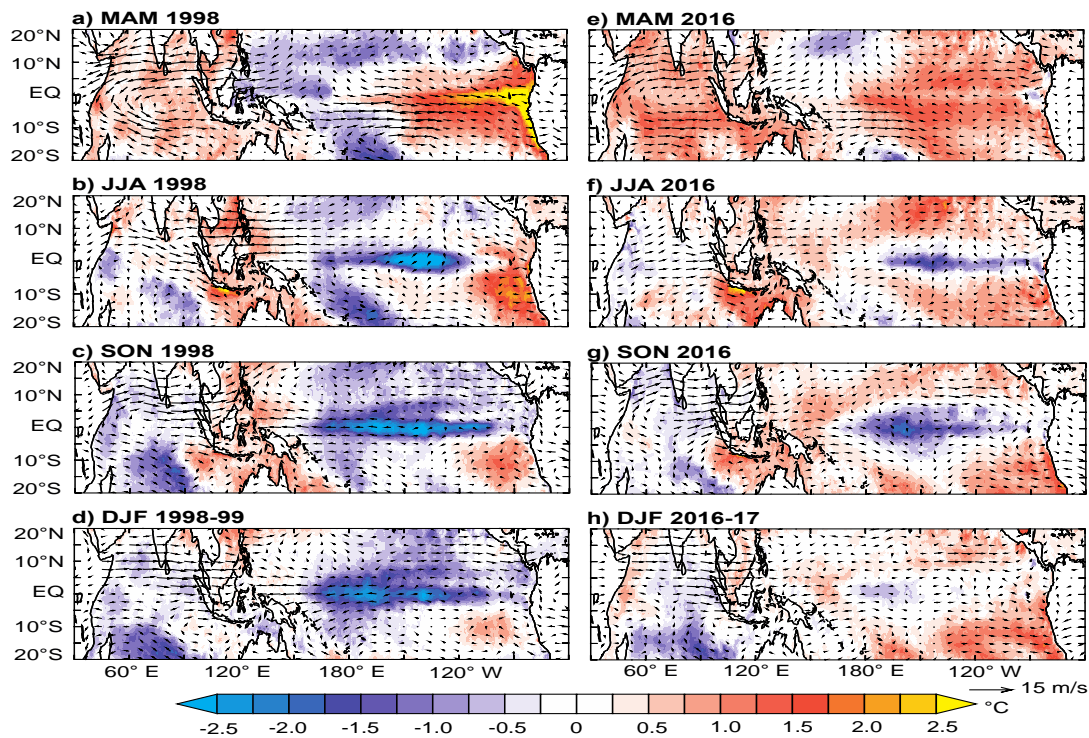


Fig 2. Seasonally averaged of SST anomaly ($^{\circ}\text{C}$) during 1998-99 (left) and 2016-17 (right) in (a,e) boreal spring (MAM), (b,f) boreal summer (JJA), (c,g) boreal autumn (SON), and (d,h) boreal winter (DJF), respectively.

Comparison with 1998/99 La Niña Modoki event

During 2015/16, the TPO witnessed a super El Niño [4], [10], which terminated at the end of boreal spring 2016 [10], [11]. Following the termination of super El Niño, however, the TPO did not experienced a strong La Niña Modoki event as it did in 1998 just after an extreme El Niño in 1997.

Figure 2 presents the distinct SSTA patterns during 1998/99 and 2016/17. The spatial distribution of SSTA in 2016/17 revealed a weak La Niña Modoki event. The colder SST anomalies observed in the central TPO, although with weak intensity and shorter live time.

Meanwhile, a strong La Niña Modoki event existed in the TPO during 1998/99. The strong 1998/99 La Niña Modoki event reveals contrast wind anomaly and SSTA patterns with those observed during the 2016 La Niña Modoki event.

Stronger than normal easterly wind anomaly were observed from the eastern to the western equatorial Pacific Ocean during the peak phase of the event. As a result, cold tongue (cold SSTA) was extended to the west in contrast to that observed in 2016 La Niña Modoki event. Furthermore, narrower warm SSTA compared to that of 2016 event covered the Indonesian region and far western TPO region. These distinct wind anomaly and SSTA patterns result in different response of the precipitation over the Indonesian region. We will discuss the mechanism in the following sub-section.

It also can be seen that tropical Indian Ocean (TIO) also witnessed strong negative Indian Ocean Dipole (IOD), both in 1998 and 2016 [12]. A strong negative IOD triggered strong convective process over the Indonesian region causing heavy rainfall in this region.

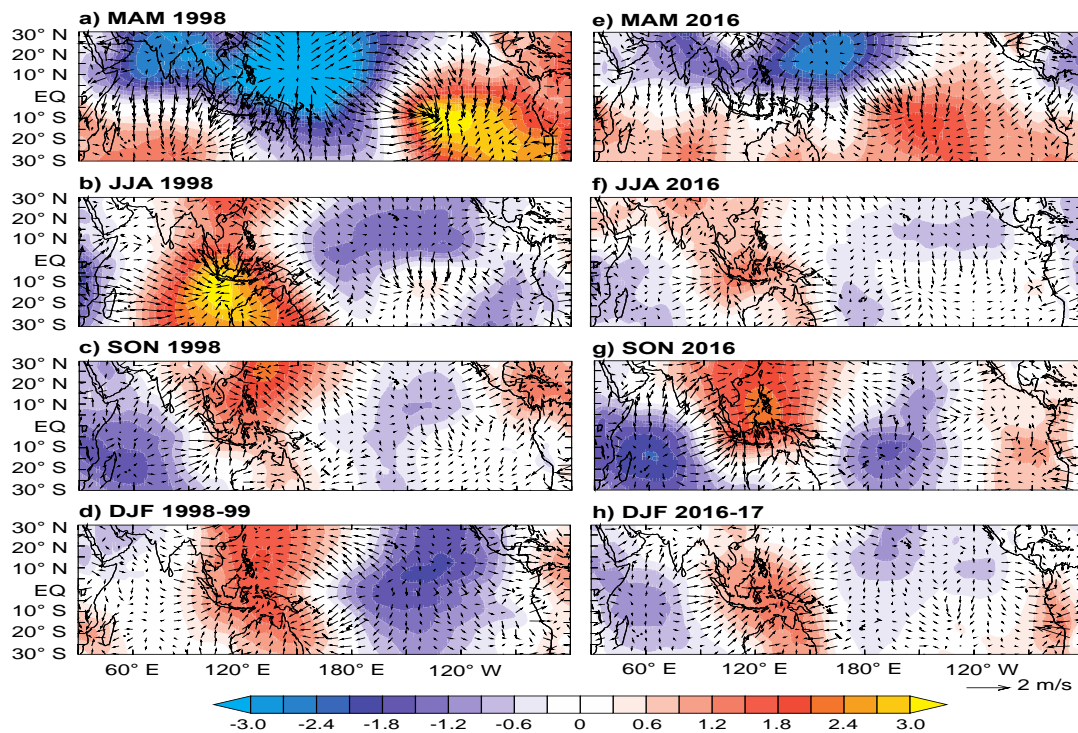


Fig 3. Same as Fig. 2, but for velocity potential anomalies (shaded; $10^5 \text{ m}^2 \text{ s}^{-1}$) and convergent/divergent winds anomalies (vector; m/s) at 850 mb.

During boreal summer 1998, strong northwesterly wind anomalies blowing from northwestern TIO to Indonesian region. The colder SST anomalies in the central TPO also triggered strong westerly wind anomalies blowing to Indonesian region. Associated with this condition, there were a convergent zone over the Indonesian region and divergent zone over the western TIO and central-western TPO at the low-level atmosphere (Fig. 3b). The vertical motion anomalies in Fig. 4b confirmed this response. There were two-cell of Walker circulation that have developed. Strong descending motion dominated over central to western TPO ($165^\circ\text{W} - 135^\circ\text{E}$) with stronger ascending motion in the eastern TIO ($90^\circ\text{E} - 120^\circ\text{E}$) and weaker ascending motion in the eastern to central TPO ($90^\circ\text{W} - 150^\circ\text{W}$) consistent with SST anomaly pattern. The different response is shown during boreal summer 2016, the convergence zone covered narrow area and moved more westward to central part of Indonesian region compared to those occurring during 1998 event. As a result, the intensity of Walker circulation anomalies is also

weaker. However, convergence zone over the Indonesian region triggered ascending atmospheric motion and increased convective activities causing excess precipitation in this area.

Impact of the 2016 La Niña Modoki on the Indonesian Climate

In general, the Indonesian region experienced excess precipitation during 2016 La Niña Modoki as shown in Fig. 5. During boreal summer, the above normal precipitation observed almost all of Indonesian region, except northern part of Sumatra Island. The maximum precipitation with intensity above 100 mm/month covered the area of central Java and the southern Papua Island. In autumn season, the coverage area of the 2016 La Niña Modoki impact shifted to the central-eastern Indonesian region. The northern-eastern part of Kalimantan Island also experienced more surplus precipitation compared to that during boreal summer.

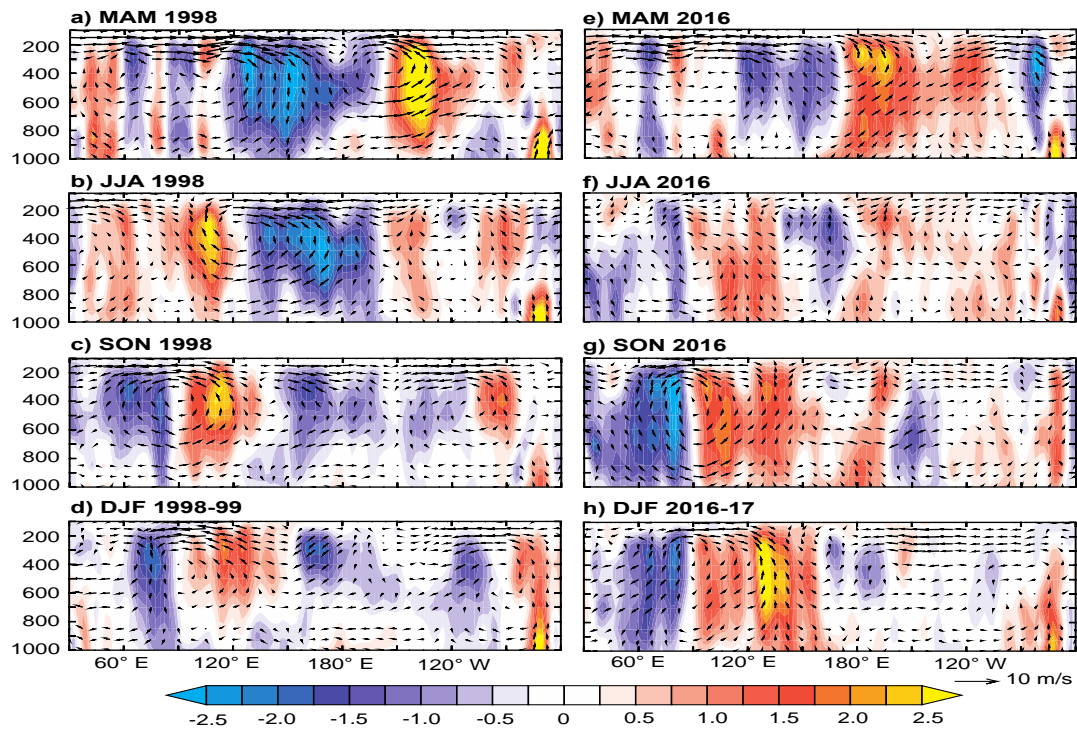


Fig 4. Same as Fig. 2, but for seasonally Walker circulation (m/s) in tropical Indian-Pacific Ocean.

Interestingly, it also shown that deficit precipitation existed over the central to the northern part of Sumatra and over the northeastern part of Kalimantan. Note that these areas were surrounded by cold SSTA indicating a strong couple ocean-

atmosphere interaction. Finally, the impact of 2016 La Niña Modoki was terminated during winter season, with small areas of the Indonesian region still have above normal precipitation.

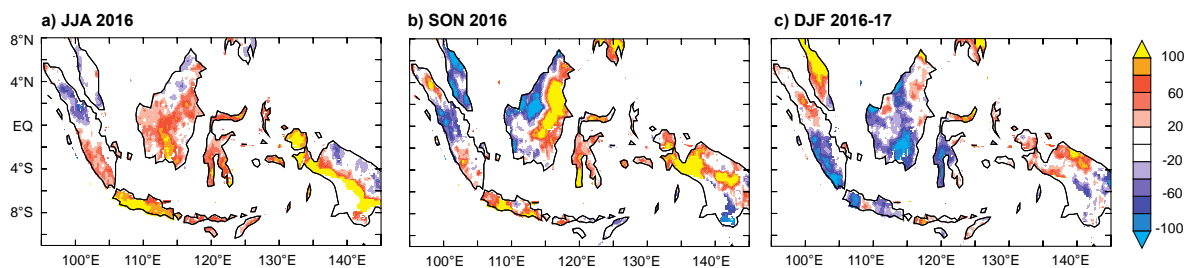


Fig 5. Seasonally averaged of precipitation anomaly (mm/month) during boreal summer until boreal winter.

CONCLUSION

Based on the spatial distribution of sea surface temperature anomaly, the evolution of unique cooling pattern in the central tropical Pacific Ocean during 2016/17 can be identified as a weak La Niña Modoki. It also was confirmed by El Niño Modoki index, which reveals negative values below one standard deviation for three consecutive seasons (from summer 2016 to winter 2016). The event initially developed in early boreal summer (June 2016). Then, it matured at the end of autumn season

(November 2016) and abruptly terminated in the early winter season (December 2017).

The onset of 2016 La Niña Modoki was linked to strong easterly wind anomalies observed in the western tropical Pacific Ocean and stronger than normal northwesterly wind anomalies found in the southeastern tropical Pacific Ocean. As a result, there was cooling SSTA in the eastern to central tropical Pacific Ocean. During the peak of this event, the cooling sea surface temperature anomaly was extended more westward near the date line, with maximum sea surface temperature anomaly centred

around 150°W to 170°W. Meanwhile, in the southeastern tropical Pacific Ocean and western part of the tropical Pacific Ocean warm sea surface temperature anomaly was observed. This cooling (warming) sea surface temperature triggered divergence (convergence) zone and descending (ascending) atmospheric motion, and suppressed (enhanced) convective process in the central tropical Pacific Ocean (Indonesian) region. As a consequence, the Indonesian region experienced excess precipitation, except northern part of Sumatra and north-western Kalimantan Islands. The maximum precipitation above 100 mm/month observed over central Java, north eastern Kalimantan, and northern Papua Island.

This study suggests that it is important to fully understanding the dynamic and the possible impact of this event on Indonesian region. Accordingly, the next step toward evaluating of this phenomenon by using long-term data are under way.

ACKNOWLEDGEMENTS

This research is supported by the Minsitry of Research, Technology and Higher Education of the Republic of Indonesia through the PMDSU Scholarship for the first author. The last author was supported by a grant of the *Penelitian Berbasis Kompetensi 2018*.

REFERENCES

- [1] Ashok K., Behera S. K., Rao S. A., and Weng H., El Niño Modoki and its possible teleconnection, *J. Geophys. Res.*, Vol. 112, C11007, 2007, pp. 1–27.
- [2] Kao H. Y., and Yu J. Y., Contrasting Eastern-Pacific and Central-Pacific types of ENSO, *J. Clim.* Vol. 22, 2009, pp. 615–632.
- [3] Yeh S., Kug J., Dewitte B., Kwon M., Kirtman B. P., and Jin F., El Niño in A Changing Climate, *Nature*, Vol. 461, 2009, pp. 511–674.
- [4] Ren H. L., Wang R., Zhai P., Ding Y. and Lu. B., Upper-ocean dynamical features and prediction of the super El Niño in 2015/16: A comparison with the cases in 1982/83 and 1997/98, *J. Meteorol. Res.*, Vol. 31, 2017, pp. 278–294.
- [5] Iskandar I., Lestari D. O., Utari P. A., and Sari Q. W., How strong was the 2015 / 2016 El Niño event ? *AIP Conf. Proc.*, Vol. 1011, 2018, pp.1-5.
- [6] Cai W., and Cowan T., La Niña Modoki impacts Australia autumn rainfall variability, *Geophys. Res. Lett.*, Vol. 36, L12805, 2009, pp. 1-4.
- [7] Feng J., and Wang X., Impact of two types of La Niña on boreal autumn rainfall around Southeast Asia and Australia Impact of two types of La Niña on boreal autumn rainfall around Southeast Asia, *Atmos. Ocean. Sci. Lett.*, Vol. 11, 2018, pp. 1–6.
- [8] Hendon H. H., Indonesian Rainfall Variability: Impacts of ENSO and Local Air-Sea Interaction, *J. Clim.*, Vol. 16, 2003, pp. 1775–1790.
- [9] Kalnay E., Kanamitsu M., Kistler R., Collins W., Deaven D., Gandin L., Iredell M., Saha S., White G., Woollen J., Zhu Y., Chelliah M., Ebisuzaki W., Higgins W., Janowiak J., Mo K. C., Ropelewski C., Wang J., Leetmaa A., Reynolds R., Jenne R. and Joseph D., The NCEP/NCAR 40-year Reanalysis Project Bull. *Am. Meteorol. Soc.*, Vol. 77, Issue 3, 1996, pp. 437–471.
- [10] Iskandar I., Utari P. A., Lestari D. O., Sari Q. W., Setiabudidaya D., Khakim M. Y. N., Yustian I. and Dahlan Z., Evolution of 2015/2016 El Niño and its impact on Indonesia, *AIP Conference Proceedings*, Vol. 1857, 2017, pp. 080001-1-08001-5.
- [11] Lestari D. O., Sutriyono E., Sabaruddin and Iskandar I., Severe Drought Event in Indonesia Following 2015 / 16 El Niño / positive Indian Dipole Events, *J. Phys. Conf. Ser.*, Vol. 1011, 2018, pp. 1-5.
- [12] Iskandar I., Lestari D. O., Utari P. A., Supardi., Rozirwan., Khakim M. Y. N., Poerwono P. and Setiabudidaya D., Evolution and impact of the 2016 negative Indian Ocean Dipole, *J. Phys. Conf. Ser.*, Vol. 985, 2018, pp. 1-5.

DEVELOPMENT OF RISK EVALUATION METHOD CONSIDERING AFTERSHOCKS

Sei'ichiro Fukushima¹, Hiroyuki Watabe² and Harumi Yashiro³

¹RKK Consulting Co., Ltd, Japan; ²Tokio Marine & Nichido Risk Consulting Co., Ltd, Japan;

³ National Defense Academy, Japan

ABSTRACT

As shown in 2016 Kumamoto earthquake, it has become an issue that the damage or loss by aftershocks is greater than those by main shock. This situation is caused by the following two facts; the ground motion intensity by aftershocks are larger than that by main shock depending on the locations of aftershocks, and capacity of buildings is reduced by main shock. This paper proposes the methodology to probabilistically evaluate risks, such as loss or damage rate, considering the aftershocks. The methodology employed is the multi-event approach in which numerous events are generated with their location, shape, magnitude and occurrence probability so that the risk of not only a single building, but portfolio of buildings can be evaluated. This paper adds two features on the method; one is generating the conditional aftershock events, and the other is reducing the capacity of buildings reflecting damage status by main shock event. Model buildings located in the area where the effects of aftershocks cannot be ignored is used for application simulation with three conditions; no aftershocks, followed by aftershocks without capacity degradation, and followed by aftershocks with capacity degradation. The deference in the risks are evaluated by the risk curves. Through the simulation it is concluded that the proposed method can evaluate the risks considering aftershocks adequately.

Keywords: Aftershock, Risk evaluation, Seismic risk, Multi-event model, Risk curve

INTRODUCTION

Recently, it has become an issue that the damage or loss by aftershocks is greater than those by main shock. So, it is important for central and local government to evaluate risks not only by main shocks but also by aftershocks for adequate response against earthquakes. The above situation is caused by the following two facts; the ground motion intensity by aftershocks are larger than that by main shock depending on the locations of aftershocks, and capacity of buildings is reduced by main shock.

The methodology employed is the multi-event approach in which numerous events are generated with their location, shape, magnitude and occurrence frequency so that the risk of not only a single building, but portfolio of buildings can be evaluated. This paper adds two features on the method; one is generating the conditional aftershock events, and the other is reducing the capacity of buildings reflecting damage status by main shock event.

SEISMIC HAZARD ANALYSIS

Generally, aftershocks are removed in the evaluation of seismic activity for the following reasons; aftershocks are dependent event of main shock and ground motions by aftershocks are assumed smaller than one by main shock. These reasons are adequate if aftershocks occur in the

vicinity of main shock. However as observed in some past earthquakes, the ground motion by aftershocks can be greater than one by main shock due to the location of site and seismic source.

Seismic Hazard Analysis

Seismic hazard is evaluated by combining the seismic hazard by main shock and one by aftershocks. The concept of seismic hazard analysis for a given main shock is introduced in order to facilitate explanation. It is noted that ground motion measure employed is the peak ground velocity (hereinafter referred as PGV) unless otherwise noted.

Seismic hazard by a given main shock

Let v_m , \bar{x}_m and ζ_m be annual occurrence frequency, median of PGV and log normal standard deviation of PGV, respectively. The annual frequency $v(x_m > y)$ that PGV by main shock x_m exceeds the given threshold y is obtained by Eq. (1).

$$v(x_m > y) = v_m \cdot \left[1 - \Phi \left(\frac{\ln(y/\bar{x}_m)}{\zeta_m} \right) \right] \quad (1)$$

The annual probability $p(x_m > y)$ that PGV by main shock exceeds the given threshold is obtained by Eq. (2).

$$p(x_m > y) = 1 - \exp[-v(x_m > y)] \quad (2)$$

Seismic hazard by aftershocks

Aftershocks are modeled as background earthquakes, whose activity is given by Gutenberg-Richter's (hereinafter G-R's) formula. Let j and $v_{j|m}$ be the index of j^{th} aftershock and conditional frequency, respectively. The conditional frequency $v_c(x_j > y)$ that PGV by j^{th} aftershock x_j exceeds the given threshold y is obtained by Eq. (3).

$$v_c(x_j > y) = v_{j|m} \cdot \left[1 - \Phi \left(\frac{\ln(y/\bar{x}_j)}{\zeta_j} \right) \right] \quad (3)$$

Therefore, the conditional frequency $v_c(x_a > y)$ that PGV by aftershocks exceeds the given threshold is obtained by Eq. (4).

$$v_c(x_a > y) = \sum_{j=1}^n \left[v_{j|m} \cdot \left[1 - \Phi \left(\frac{\ln(y/\bar{x}_j)}{\zeta_j} \right) \right] \right] \quad (4)$$

The conditional probability $p_c(x_a > y)$ that PGV by aftershocks exceeds the given threshold is obtained by Eq. (5).

$$p_c(x_a > y) = 1 - \exp[-v_c(x_a > y)] \quad (5)$$

Finally, unconditional probability $p(x_a > y)$ that PGV by aftershocks exceeds the given threshold is obtained by multiplying the occurrence probability of main shock as shown by Eq. (6).

$$p(x_a > y) = [1 - \exp(-v_m)] \cdot p_c(x_a > y) \quad (6)$$

Integration of seismic hazards by main shock and aftershocks

Since aftershocks are dependent event of main shock, Eq. (7) is employed to integrate the hazards by main shock and aftershocks.

$$p(x > y) = \max[p(x_m > y), p(x_a > y)] \quad (7)$$

Modeling of Aftershocks

As mentioned above, aftershocks are modeled as background earthquakes. Condition setting is based on Choi et al. (2013) [1].

Location of aftershocks

Aftershocks are assumed to occur uniformly in the region whose area A_a is given by Eq. (8) with the magnitude of main shock M_m .

$$A_a = 10^{0.778M_m - 1.60} \quad (8)$$

Maximum magnitude of aftershocks

The maximum magnitude of aftershocks is given by Eq. (9) with the magnitude of main shock M_m .

$$M_a = M_m - 1.0 \quad (9)$$

Seismic activity of aftershocks

Let M_m and T_1 be the magnitude of main shock and elapsed time in day, respectively. The number of aftershocks is given by Eq. (10).

$$N(T_1, M_m) = 10^{0.88M_m - 4.51} \frac{(T_1 + c)^{1-p} - c^{1-p}}{(90 + c)^{1-p} - c^{1-p}} \quad (10)$$

Parameters p and c are constants in modified Omori formula [2]. This paper employs 1.05 for p and 0.1 for c . b -value in G-R's formula is set 0.83.

Application

The model site is shown in Fig. 1. The site is considered to be affected by large earthquakes with high potential of generating aftershocks.

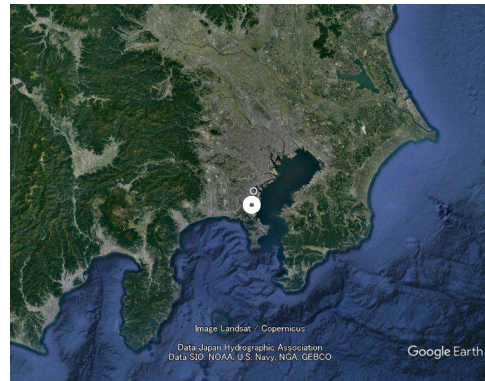


Fig. 1 Location of model site

Seismic source model

For the purpose of accountability, seismic sources were modeled based on the database used in "Japan Seismic Hazard Information Station", in which Poisson's process was employed. Aftershocks were modeled in accordance with the policy.

Ground motion prediction model

Attenuation formula used in the "Technical Note of the National Research Institute for Earth Science and Disaster Resilience, No. 336" was employed in the analysis. Equation (11) shows the attenuation formula for PGV.

$$\log PGV = \begin{cases} a_1 M_w + b_1 X - \log(X + d_1 \cdot 10^{0.5 M_w}) - c_1 & (11) \\ a_2 M_w + b_2 X - \log(X) - c_2 \end{cases}$$

PGV : peak ground velocity
 M_w : moment magnitude
 X : shortest distance
 D : focal depth
 a_1, b_1, c_1, d_1 : coefficients ($D \leq 30$)
 a_2, b_2, c_2 : coefficients ($D > 30$)

Correction factor for ground motion by surface layer was also calculated by Eq. (12).

$$G = p \log(AVS30) + q \quad (12)$$

G : correction factor
 p, q : coefficients
 $AVS30$: mean shear wave velocity of surface soil to a depth of 20 m

Results

The probabilistic hazard curves at model site is shown in Fig. 2, from which it can be seen that the contribution of aftershocks appears in the range of low exceedance probability since the aftershocks are dependent events of huge earthquakes with small occurrence probability. On the contrary, the contribution in the range of high exceedance probability is negligible. It is also observed that the PGV by aftershocks is greater than that by main shock in the range of extremely low exceedance probability.

Figure 3 shows the hazard curves by each aftershock with that by main shock, from which it can be seen that the seismic hazard by aftershocks shown in Fig. 2 is dominated by three aftershocks occurred in Nankai Trough.

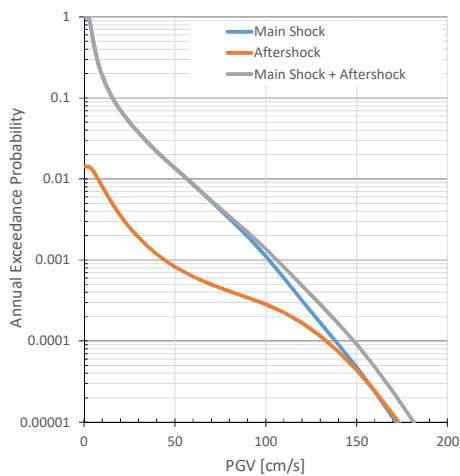


Fig. 2 Seismic hazard curve at model site

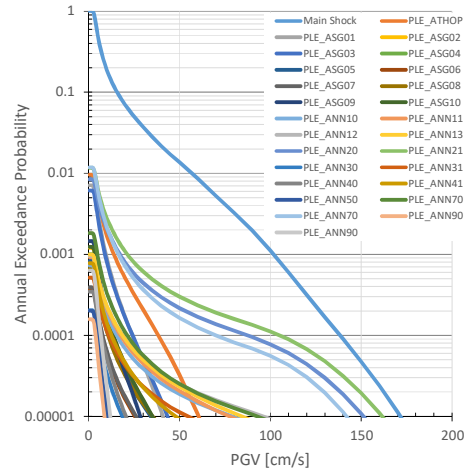


Fig. 3 Seismic hazard curve by aftershocks

SEISMIC FRAGILITY ANALYSIS

In risk evaluation considering aftershocks it is necessary to take the damage by main shock into account. For that purpose, this paper proposes the modification of damage function (hereinafter called DF) that is the relationship between ground motion intensity and damage ratio according to the damage by main shock.

Basic Idea of Modification of DF

Let x and $R_m(x)$ be PGV and DF for main shock, respectively. Two ways to modify DF can be considered; one is to adjust PGV, and the other is to adjust damage ratio. This paper employs the former way because of the following reasons; the damage ratio possesses the upper and lower limits so that multiplying a constant may bring the inadequate damage ratio, and change of DF is caused by the reduction in median capacity velocities of fragility curves by damage.

Let $R_a(x)$ be DF for aftershocks. This paper assumes that $R_a(x)$ can be calculated by Eq. (13).

$$R_a(x) = R_m(k_D(r) \cdot x) \quad (13)$$

$k_D(r)$ is the factor to adjust PGV according to the damage ratio r by main shock. It is noted that $k_D(r)$ equal to or greater than unity. In this paper $k_D(r)$ is referred to as DF modification factor. One advantage to employ the DF modification factor is that the DF for main shock can be used for aftershocks with no modification.

Evaluation of DF Modification Factor

DF modification factor was evaluated statistically

using the results of numerical calculations, in which eight model buildings (two structural types times four types of stories) converted into SDOF system were employed.

Seismic capacity of buildings

Seismic capacity of each building was expressed by the tri-linear skeleton curve of equivalent SDOF model, whose characteristics were summarized in Tables 1 and 2.

Table 1 Parameter for skeleton curves (before main shock)

Parameters	Setting policy
Initial Stiffness	$k_0 = m \left(\frac{2\pi}{T} \right)^2$
Stiffness after cracking	$k_1 = \frac{k_0}{3}$
Stiffness after yielding	$k_2 = 0$
Cracking strength	$s_1 = \frac{s_2}{3}$
Yielding strength	$s_2 = 1.2 \times s_d$
m : mass	
T : natural period	
s_d : design capacity	

Table 2 Parameter for skeleton curves (after main shock)

Parameters	Setting policy
Initial Stiffness	k'_0 : secant stiffness corresponding to damage
Stiffness after cracking	$k'_1 = k_1$, if $d'_c \leq d'_y$ $k'_1 = 0$, if $d'_c > d'_y$
Stiffness after yielding	$k'_2 = 0$
Cracking strength	$s'_1 = \alpha \cdot s_1$
Yielding strength	$s'_2 = \alpha \cdot s_2$
d'_c : cracking displacement	
d'_y : yielding displacement	
α : strength reduction factor	

Table 3 summarizes the drift angle to estimate displacement and strength reduction factor for each damage level. Drift angles for given damage states were given based on the existing research and strength reduction factors were estimated based on the Japanese guideline for seismic diagnosis [3].

Equivalent building height to calculate the displacement of SDOF system H_r was calculated by Eq. (14), where H is the building height.

$$H_r = \frac{2n+1}{3n} H \quad (14)$$

Table 3 Reference drift angle and strength reduction factor

Damage	Drift angle		Strength reduction factor
	RC	S	
No Damage	-	-	1.00
Slight	1/240	1/160	1.00
Moderate	1/120	1/80	0.95
Severe	1/60	1/40	0.90
Collapse	1/30	1/20	0.80

Examples of skeleton curves of SDOF systems that correspond to RC-8 story building and S-8 story are shown in Fig. 4, in which legend shows the damage by main shock. It is noted that the strength is given by response acceleration instead of story shear force. From the figure it can be seen that capacity of buildings will be largely reduced if buildings reach to the severe damage by main shock.

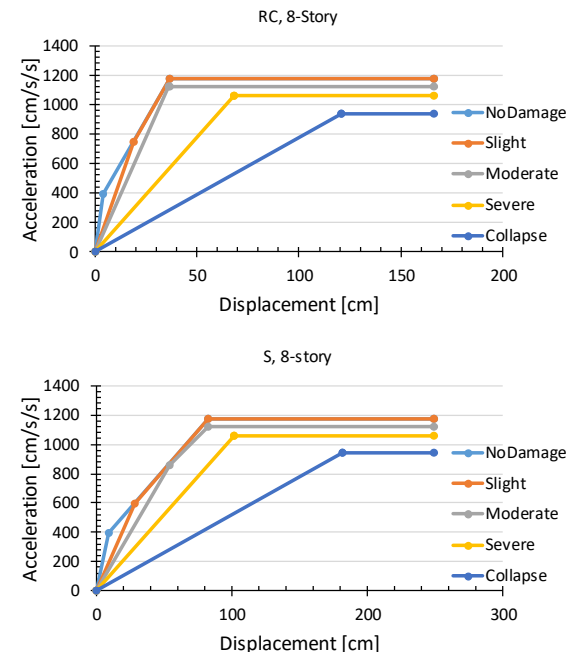


Fig. 4 Examples of skeleton curves

Change of capacity velocity after main shock

In this paper, response of SDOF system was obtained as the intersection of capacity spectra whose samples are shown in Fig.4 and demand spectra shown in Fig. 5. This demand spectrum was selected as standard soil, whose magnitude is dependent of ductility factor of SDOF system.

Since capacity spectrum method cannot evaluate velocity that bring the buildings to given damage state, this paper assumed that the reduction of demand spectrum that cause the buildings damage is proportional to the reduction of capacity velocity.

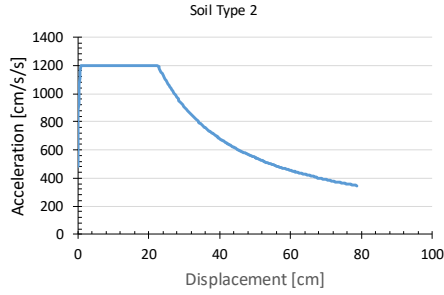


Fig. 5 Demand spectrum

Examples of reduction of demand spectrum for two sample buildings are shown in Fig. 6, in which the reduction is given by the ratio of the magnitude of demand spectrum. It is noted that the damage ratios for “slight”, “moderate”, “severe” and “collapse” were set 0.025, 0.075, 0.2 and 0.65, respectively.

Regression of reduction ratio

In addition to the reduction ratios shown in Fig. 6, other ratios for buildings of three, five and twelve stories were calculated for regression analysis in parameter r , which is the damage ratio by main shock.

Figure 7 shows the average relationship between damage ratio and reduction ratio of demand spectrum, in which it can be seen there is little difference about structural type. Therefore, regression analysis was done regardless of structural type.

Let r and y be damage ratio and reduction ratio of demand spectrum, respectively. Considering the shape of curve in Fig. 7, the following equation was obtained by the regression analysis.

$$y = \min[-0.114 \ln(r) + 0.6007, 1.0] \quad (15)$$

The DF modification factor $k_D(r)$ is given as a reciprocal of Eq. (15) as follows.

$$k_D(r) = \max\left[\frac{1}{0.6007 - 0.114 \ln(r)}, 1.0\right] \quad (16)$$

RISK ANALYSIS

As risk analysis, this paper evaluates event risk curve which is the relationship between the damage and its annual exceedance probability. It is noted that the risk of concern is the 90th percentile value of damage ratio derived from probabilistic distribution function of damage ratio of each event. The concrete procedures are illustrated in Fukushima et al. (2002) [4].

Probability Function of Damage Ratio

Probability distribution function of damage ratio is evaluated by Monte Carlo simulation. Followings

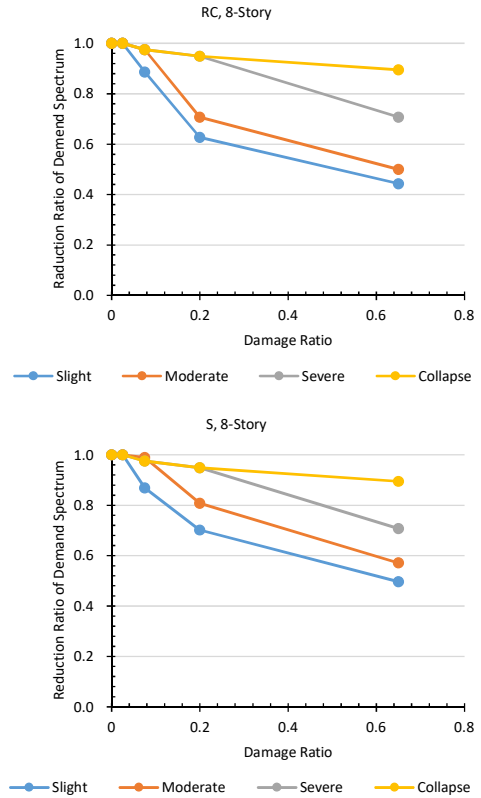


Fig. 6 Example of reduction of demand spectrum

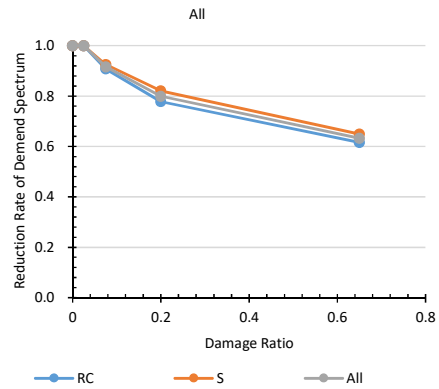


Fig. 7 Reduction of demand spectrum

are explanations of evaluation of damage ratio for a given Monte Carlo trial.

Let x_i and $R_i(x_i)$ be PGV at site and damage ratio by i^{th} main shock, respectively. Then, let x_j be PGV at site by j^{th} aftershock that is dependent event of main shock. The damage ratio by j^{th} aftershock is given by $R_j(k_D(r) \cdot x_j)$, where $k_D(r)$ is the DF modification factor mentioned before.

Let n_i and v_j be the number of aftershocks and the conditional occurrence frequency, respectively. And, let R_i and R_j be damage ratios by main shock and j^{th} aftershock for simplicity. The composite

damage ratio \hat{R}_i is calculated by Eq. (17). In case when no aftershock occurs or damage ratio by aftershocks are negligible, \hat{R}_i and R_i are identical.

$$\hat{R}_i = 1 - (1 - R_i) \cdot \prod_{j=1}^{n_i} (1 - R_j)^{v_j} \quad (17)$$

Condition Setting for Risk Analysis

Four DFs shown in Fig.8 were employed to investigate the effect of the difference in DFs on the event risk curves. Also, three analysis cases were introduced as follows.

- Case-1: No aftershocks occur.
- Case-2: Aftershocks occur.
Building's capacity is decreased.
- Case-3: Aftershocks occur.
Building's capacity is not decreased.

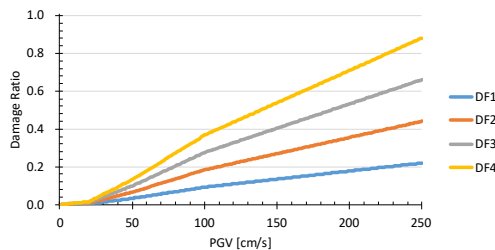


Fig. 8 DFs for risk evaluation

Comparison of Risk Curves

Event risk curves are shown in Fig. 9. Since aftershocks are dependent event of main shock, their effect on the risk curve does not appear in the range of high occurrence probability. And, even though in the low occurrence probability range, DF1 and DF2 do not bring the effect of aftershocks, since damage ratios by main shock are negligible. On the contrary, DF3 and DF4 bring the effect of aftershocks due to the reduction of building's capacity by main shock.

It is noted that DF3 and DF4 bring the effect of aftershocks in Case-2 though no capacity reduction exists. This may be caused by the increment of PGV by aftershocks.

CONCLUSION

This paper adds two features on the risk evaluation method; one is generating the conditional aftershock events, and the other is reducing the capacity of buildings reflecting damage status by main shock event. Through the simulation it is found that the less of building capacity is, the greater the effect of aftershocks on risk is, and is also concluded that the proposed method can evaluate the risks

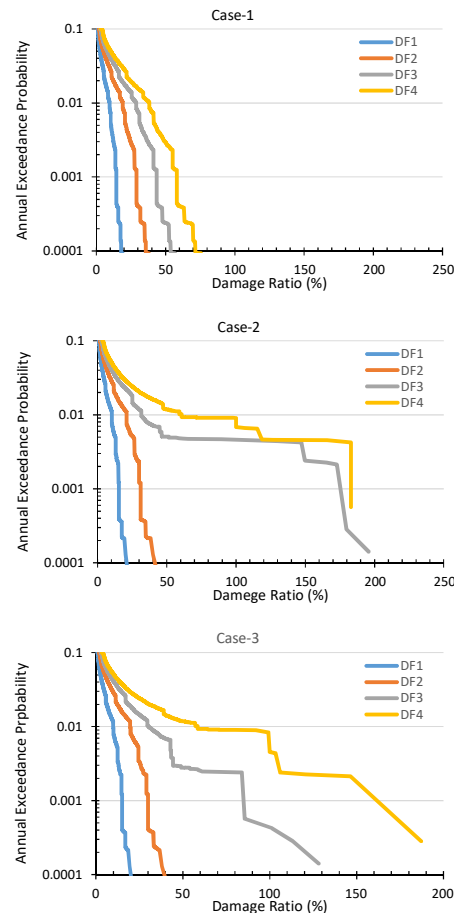


Fig. 9 Event risk curves

considering aftershocks adequately. This method is useful to evaluate risk for regions where large earthquakes with their aftershocks can occur. This method will be applied to the large active faults as next step.

REFERENCES

- [1] Choi B., Itoi T., Takada T., Probabilistic aftershock occurrence model and hazard assessment for post-earthquake restoration activity plan, J. Struct. Constr. Eng., AIJ, Vol.78 No.690, 2013, pp.1377-1383, (in Japanese)
- [2] The Headquarters for Earthquake Research Promotion, On probabilistic evaluation method, "http://www.jishin.go.jp/main/yoshin2/yoshin2.htm", (in Japanese)
- [3] Japan Building Disaster Prevention Association, Standard for seismic evaluation of existing reinforced concrete buildings, 2001, (in Japanese)
- [4] Fukushima S., Yashiro H., Seismic risk analysis on portfolio of buildings J. Archit. Plann. Environ. Eng., AIJ, No.552, 2002, pp.169-176, (in Japanese)

THE EFFECTS OF TRANSLUTHRIN AS THE ACTIVE SUBSTANCE OF ONE PUSH AEROSOL REPELLENT ON ORGANS DAMAGE OF MICE (*MUS MUSCULUS*) (CASE STUDY OF LUNG, LIVER, BLOODS, AND KIDNEY)

Unggul P. Juswono¹, Arinto Y. P. Wardoyo¹, Chomsin S. Widodo¹, and Johan A. E. Noor¹
¹Faculty of Mathematics and Natural Sciences, Brawijaya University, Indonesia

ABSTRACT

One push aerosol repellent used by the public contains an active substance called transluthrin. Transluthrin is mostly pyrethroid synthetic which has functions as neurotoxin substance. It may act as free radicals in the body due to the compounds which have one free electron that makes it reactive. The purpose of this study was to investigate the effects of transluthrin on mice organs. In this study, the experimental animals (Wistar mice) were put in an exposure chamber and exposed by one push aerosol repellent contains around 20-25% of transluthrin one time a day for 15 days. The damage of mice organs was identified by the microscopic picture (400x of magnification). The results showed that the expose of repellent contains about 20-25% of transluthrin on mice increase the damage of lung, liver, blood, and kidney cells from 13% to 24%, 12% to 27%, 9% to 69% and 22% to 55%, respectively.

Keywords: Transluthrin; Lung cells; Liver cells; Blood cells; Kidney cells

NOMENCLATURE: ATN (Acute Tubular Necrosis); ATP (Adenosine Triphosphate); DNA (Deoxyribonucleic Acid); DSA (Alveolar Septal Destruction); ROS (Reactive Oxygen Species)

INTRODUCTION

Air as one of the natural resources which are the main need for a living thing and non-renewable. Air pollution has negative effects on human health. Substances that are often used in daily life and potentially as air pollutants (pollutants) are cigarette smoke [1], air freshener aerosol, and insecticide aerosol [2]. Increased concentrations of air pollutants are related to various diseases such as lung cancers, Parkinson, and many others [3–5].

Pollutants, both gaseous and particulates are very harmful to the health of the human body. Pollutants can pass through the body through respiration and oral processes. The presence of pollutants in the body will be able to disrupt the function of organs, including the kidney as the main organ in the excretory system [6,7], the lungs as respiratory organs [8], the liver that plays an important role in the process of detoxification, and blood as the most fluid in the body [9,10].

The degree of an organ damage caused by particulate matters of pollutants is strongly influenced by particle size [11,12]. The size of the particulate matter varies greatly. Based on its size, the particles can be classified into three kinds, i.e. coarse particles, fine particles, and ultrafine particles. Ultrafine-sized particles give a greater effect than larger particles. The results showed that the fraction of ultrafine particles was the most damaging particulate matter [13].

One of the substances that are often used in daily life and potentially as a pollutant is one push aerosol mosquito repellent. Indonesia is one country that has a tropical climate, where the tropical climate is very suitable for the breeding process of insects, especially mosquitoes. Mosquitoes themselves can cause various diseases. The effort to overcome the increasing number of diseases caused by mosquitoes is to use some chemicals insecticide-containing mosquito repellent.

For each type of a mosquito repellent contains different ingredients depending on the brand and their types. One of the most popular mosquito repellents in the market is the one-push aerosol which has a variety of content one of which is transluthrin chemicals. Transluthrin is one of the pyrethroid insecticides that produces a rapid reaction with low persistence. Pyrethroid insecticide has a very specific effect on insect nerve cells, so it needs a little amount to have the required effect [14].

One push aerosol mosquito repellent is mostly used in a closed room. The scent of mosquito repellent is an indication that the harmful compound of mosquito repellent is still spreading in the room as well as an indication of the residue in the room. This can disrupt the respiratory tract. If the particles enter the lung, it will flow in the blood so it will give certain effects such as inflammation of the sensitive organs [3,15]. The transluthrin active ingredients contained in one push aerosol can decrease the erythrocytes.

The pulmonary lung is the organ that first contacts directly with particles. Particles that enter the lungs will be carried by the blood and circulated throughout the body. The blood then goes to the kidney for a filtering. The filtered residues will be detoxified by the liver. So that the potential organs affected by the active ingredients of the mosquito repellent are lung, blood, kidney, and liver.

Based on the description of the dangers of mosquito repellent and the potential impact on the organs, it is necessary to conduct a research to investigate the impact of mosquito repellent on organs. However, there are limited studies on the impacts of the indoor aerosol one push mosquito repellent, and no available data on the effect of transfluthrin on organ damage. Hence, this study was aimed to investigate the damage level of the kidney, liver, lung and blood organ in mice exposed by the indoor aerosol one push mosquito repellent. This study will contribute to a better understanding of the pollutant impact on the anatomy, structure, and work function of the organ.

MATERIALS AND METHODS

Experimental Animals and Treatments

We used 2-3-month-old male mice (Wistar) as the experimental animals that were divided into three groups: a control group, a treatment group A and a treatment group B. The control group was unexposed mice. The treatment group was sprayed with the different mosquito repellent. The group A and B were exposed by the transfluthrin content of 21.3% and 25% respectively. The exposure dose was given for five spray pushes. After the mice were sprayed, they were placed in the exposure chamber with the dimension of 20 cm x 20 cm x 30 cm for 20 minutes (Fig. 1). Then the chamber was opened to the mice breathed free air. After spraying for 15 days, the mice were dissected to take the organ: lungs, blood, kidneys, and livers.

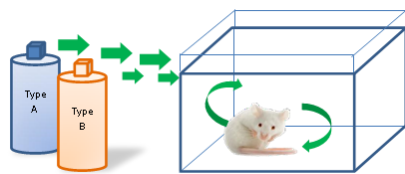


Fig. 1 Chamber of exposure to mice with mosquito repellent.

Preparation and Histological Examination

Kidneys, Livers, and Lungs

The mice from the control group and the treatment groups were sacrificed by a cervical dislocation. The kidneys, livers, and lungs were

cleaned using NaCl (0.9%). They were fixed in a buffered formalin (10%) for a week and dehydrated in upgraded ethanol series. After being processed to the paraffinization, they were cut using a microtome and were colored using HE (hematoxylin and eosin) [6].

Blood

The blood smears were placed onto the object glasses. They were fixed with 70% methanol solution and then covered with the cover glasses. When they came dried (± 5 minutes), they were stained using a Giemsa and buffer pro-Giemsa solution [10].

Histological Examination

The cells deformation was observed using a microscope (400x of magnification). The damage level of the observed organ was calculated using Eq. (1) [6]:

$$\text{Damage (\%)} = \frac{\Sigma \text{deformed cells}}{\Sigma \text{observed cells}} \times 100\% \quad (1)$$

RESULTS

Lung Damage

The microscopic picture of the lung treatment group mice is shown in Fig. 2.

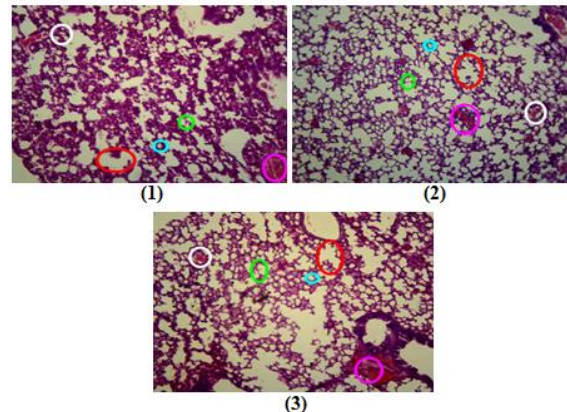


Fig. 2 Microscopic pictures of lungs of mice (1) control (without treatment), (2) type-A and (3) Type-B. The red, green, and grey circles show the emphysema, DSA, and edema, respectively. The pink circles indicate the bleeding.

Lung emphysema is a disease whose primary symptom is an airway obstruction because the air sacs in the lungs are excessively bulging and suffered extensive damage. Edema is characterized by the presence of fluid-filled alveoli and an increased laxity of the alveolar septum. Alveolar

septal destructions (DSAs) are characterized by the thinning of the alveolar septum, atrophy, and in some parts a total damage of the alveolar septum that spherical formed and may also be accompanied by enlargement of the ducts and alveolar sacs. For normal alveolar cells characterized by an almost spherical (poly) cell shape with a size of 4-5 μ m [8]. The lung damage is calculated by counting the normal cells and the damaged cells in five random fields to determine the cell deformation [16]. The percentage of the cell deformation is presented in Fig. 3.

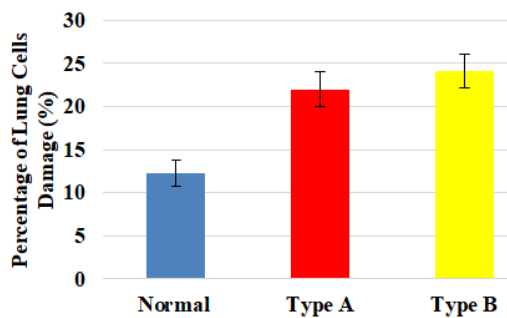


Fig. 3 Damage percentages of the mice lungs.

Red Blood Cells Damage

The microscopic picture and percentage of blood cells damage of red blood cells can be seen in Fig. 4.

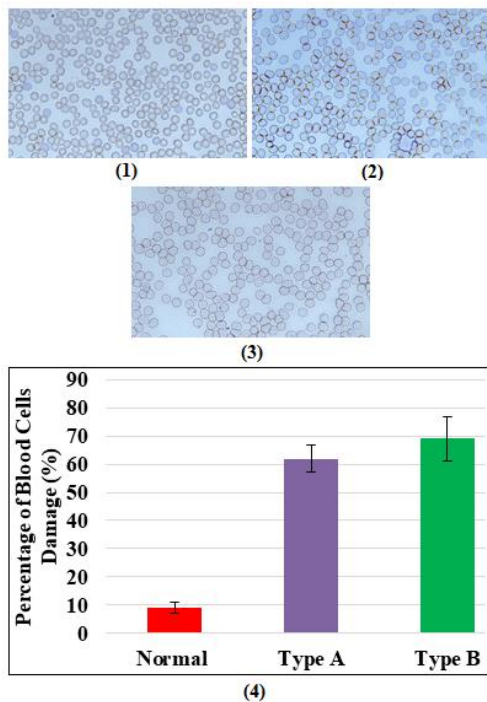


Fig. 4 Microscopic pictures of red blood cells of mice (1) control (without treatment), (2) type-A and (3) Type-B. The percentage of red blood cells damage (4).

The physical changes were determined by the comparison between the size and shape of normal cells and the abnormal cells [10]. The abnormal blood cells are classified into 9 types of cellular damage, i.e., cell target, teardrop, crystal, roll cell, polychromasia, sickle cell, stomatocyte, and basophilic [17,18]. Cell targets are the blood cells that have erythrocytes that look like shoots or Mexican hats. Teardrop is a pear-shaped blood cell or like water droplets. Krista is a blood cell that has a straight or crooked or slightly square shape. Roll cell is a blood cell that holds each other. Sickle cell is a damage that has erythrocytes shaped crescents, stiff, and chronic hemolytic anemia. Stomatocyte is a type of blood cell that has erythrocytes in the form of a central pallor such as the mouth. Basophilic is a blood cell damage that has a slim/ rounded granule. Keratocyte is a blood cell damage that has a barrier shape.

Kidney Damage

The observation of the kidney cell damage was demonstrated by the microscopic images of the glomerular cells and tubules (Fig. 5) [6]. The results of the glomerular observation (green arrows) and kidney tubular mice showed that the pollutant exposure can cause the damage of the kidney structure that is known as the glomerulus and tubular damage. Glomerular damage is characterized by the widening of Bowman space [19,20]. Tubular damage is characterized by narrowing of the tubular lumen (orange circles). The increasing of the glomerular and tubular damage will cause necrosis or cell death called Acute Tubular Necrosis (ATN). ATN is caused by lack of oxygen (ischemic ATN) and the influence of toxic substances in cells (nephrotoxic ATN). Microscopically, there is a pigment of hemoglobin pigment scattered in the tubules. The percentage of the kidney cells damage is presented in Fig. 6.

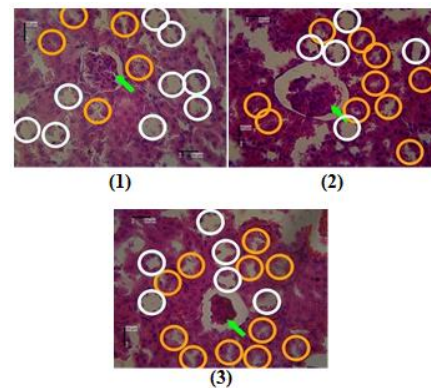


Fig. 5 Microscopic pictures of kidneys of mice (1) control (without treatment), (2) type-A and (3) Type-B. White circles show normal tubules.

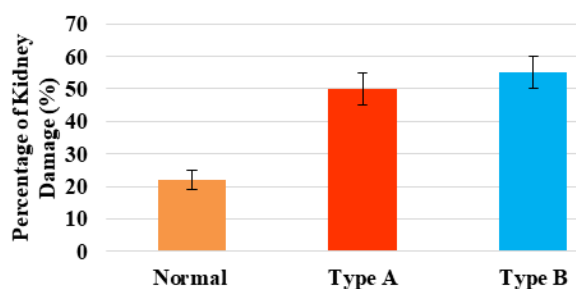


Fig. 6 Damage percentages of the mice kidneys.

Liver Damage

The changes in the mice liver include the central vein, hepatocyte cell form, and sinusoid blood vessel (Fig. 7) [9]. The centralist vein shape that is originally a spherical shape and unbroken. After receiving treatment, the vein began to break. Similarly, hepatocyte cells also had to change the shape. Meanwhile, the sinusoidal blood vessels became wider. The observation of liver cells showed that spraying of pollutant material in mice had the adverse effects on the liver organ of mice where the administration of these pollutants affected the shape and structure of mice liver cells. Dosage type B-type mosquito spray for high intensity can cause blood cells to get worse. At a spray dosage of 5 times obtained damage of liver cells reached 27.49%.

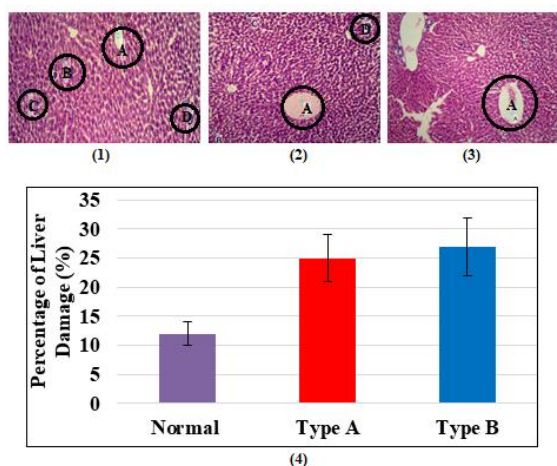


Fig. 7 Microscopic pictures of livers of mice (1) control (without treatment), (2) type-A and (3) Type-B. Captions: A = Vein Centralist, B = Normal Cell, C = Binucleus, D = Parenchymal Degeneration. The percentage of liver cells damage.

DISCUSSION

Insecticide one push aerosol is considered the most powerful in killing or eradicating mosquitoes. There are 5 ways insecticide work on the insect body

that affects the nervous system, inhibits energy production, affects the endocrine system, inhibits cuticle production and inhibits water balance. Transfluthrin contained in both types of mosquito repellents is a pyrethroid class II obtained from the synthesis of pyrethrin. Based on their toxicity and structure, pyrethroid is classified as type I and type II. Type I is a pyrethroid group that has no α -cyano group and type II has an α -cyano group.

The interaction between blood and transfluthrin occurs when the blood passes through the lungs. Blood contains hemoglobin which acts as an oxygen binder. With the transfluthrin entering the lungs, the hemoglobin will tend to bind transfluthrin rather than oxygen gas to be circulated throughout the body. The blood containing transfluthrin can affect other substances needed by the body such as nutrients, hormones, fats, sugars, and proteins. Pyrethroid is able to increase activation and prevent deactivation. The impact of the event resulted in the ion channel open longer. At the cellular level, pyrethroid interferes with nerve activity, membrane depolarization, and synaptic disorders [21]. The membrane of a protein affected by pyrethroid causes the change of the action potential of the cells.

Enzymes that hydrolyze ATP have been found to be sensitive to pyrethroid reactions. ATPase neural membrane is a target for pyrethroid in invertebrate insects, whereas in rats it is synaptosome. Pyrethroid joins the lipid bilayer layer to interfere with phospholipid conditions and cause instability in the membrane. The mechanism of neurotoxicity begins with an interruption in the activity of Ion Na^+ , K^+ and ATP ions and membrane instability.

Several types of pyrethroid are known to produce poisoning symptoms similar to poisoning due to cyanide and aldehyde. Pyrethroid is thought to be capable of generating free radicals and causing stress on cells. Pyrethroid manifold cypermethrin and fenvalarete have been known to produce oxidative stress and changes in antioxidant enzymes [22]. Oxidative stress is a condition where there is a disturbance of balance between the production of free radicals with antioxidants that cause tissue damage. Oxidative stress can be caused by a reduction in natural antioxidant levels in the body and increased free radical production [12]. Oxidative stress occurs due to the presence of reactive oxygen species (ROS) in cells more than the natural oxidant compounds in cells. Free radicals are substances, molecules, compounds that have highly cellular reactive properties. If radicals are not inactivated, their reactive characteristic can damage all types of cellular macromolecules such as carbohydrates, proteins, lipids, and DNA. Free radicals generally stand on their own, with very fast reactions with other atoms filling in the vacancy of an unpaired orbital. Transfluthrin is a free radical of the C atoms in the structure of benzene.

The kidneys function to produce urine from the body's metabolic processes. The kidney is the main path of toxic substances (toxins). The release of the substance is carried out by three processes: filtration by the glomerulus, reabsorption by tubules, and secretion by tubules. The kidneys also concentrate toxically on the filtrate and carry the toxic via tubular cells. Glomerular damage will lead to disruption of the filtration process in the glomerulus so that the ability to filter blood is reduced, the proteins and blood cells will accumulate in the tubules.

Tubules serve as a place of reabsorption and secretion in the process of formation of urine. Damage to the kidney tubules is characterized by the presence of tubular cells that swell due to fluid shift from outside the cell into the cell. This shift occurs because the toxic substances contained in ultrafine particles from pollutants cause changes in the surface charge of the tubule epithelial cells, the active transport of ions and organic acids, and the ability to concentrate from the kidneys that eventually lead to damaged tubules, impaired urinary flow, increased via tubular pressure. This cell swelling causes the tubular lumen to become narrowed until closure. If the tubule cell is damaged, it will interfere with the system of urine formation in the kidney, then the substance that is not needed by the body cannot be removed from the body, so it will be toxic that can damage the kidney organ [23,24].

CONCLUSION

The results of the research have shown that there is damage to organ cells in mice due to the pollutant exposure. The transfluthrin active substances contained in one push aerosol affect the mice organ with the different damage degrees. The blood is the worst damage with the percentage of 69%. Meanwhile, the lung is the least damage of 24%. The damage depends on the transfluthrin content. A more dose of transfluthrin caused more damage.

REFERENCES

- [1] Wardoyo A. Y. P., Santjojo D. J. D. H., Rahayu T., and Subagyo S., Influence of smoking rate on ultrafine particle emission of cigarette smoke. *J. Biol. Res.*, Vol. 23, 2018, pp.90–94.
- [2] Lü D., Zhang X., Wu W., and Jiang W., Measurement and statistic analysis of combustion heat of two kinds of household spray aerosols in China. *Procedia Eng.*, Vol. 45, 2012, pp.638–642.
- [3] Buonanno G., Giovenco G., Morawska L., and Stabile I., Lung cancer risk of airborne particles for Italian population. *Environ. Res.*, Vol. 142, 2015, pp.443–451.
- [4] Allen J. L., Liu X., Weston D., Conrad K., Oberdörster G., and Cory-Slechta D. A., Consequences of developmental exposure to concentrated ambient ultrafine particle air pollution combined with the adult paraquat and maneb model of the Parkinson's disease phenotype in male mice. *Neurotoxicology*, Vol. 41, 2014, pp.80–88.
- [5] Sioutas C., Delfino R. J., and Singh M., Exposure assessment for atmospheric ultrafine particles (UFPs) and implications in epidemiologic research. *Environ. Health Perspect.*, Vol. 113, 2005, pp.947–956.
- [6] Wardoyo A. Y. P., Juswono U. P., and Noor J. A. E., Varied dose exposures to ultrafine particles in the motorcycle smoke cause kidney cell damages in male mice. *Toxicol. Reports.*, Vol. 5, 2018, pp.383–389.
- [7] Passagne I., Morille M., Rousset M., Pujalté I., and L'Azou B., Implication of oxidative stress in size-dependent toxicity of silica nanoparticles in kidney cells. *Toxicology*, Vol. 299, 2012, pp.112–124.
- [8] Wardoyo A. Y. P., Juswono U. P., and Noor J. A. E., Comparison of lung damages due to petrol and diesel car smoke exposures: histological study. *Int. J. GEOMATE*, Vol. 15, 2018, pp.124–129.
- [9] Wardoyo A. Y. P., Juswono U. P., and Noor J. A. E., An observation of histological evidence on internal organ damages in mice caused by repeated exposures to motorcycle emissions, in *Proc. AIP Conf. Proc.*, 2017, pp.020007-1-020007-11.
- [10] Wardoyo A. Y. P., Juswono U. P., and Noor J. A. E., A study of the correlation between ultrafine particle emissions in motorcycle smoke and mice erythrocyte damages. *Exp. Toxicol. Pathol.*, Vol. 69, 2017, pp.649–655.
- [11] Yang H., Chang S., and Lu R., The effect of particulate matter size on cardiovascular health in Taipei Basin, Taiwan. *Comput. Methods Programs Biomed.*, Vol. 137, 2016, pp.261–268.
- [12] Upadhyay S., Ganguly K., and Stoeger T., Inhaled ambient particulate matter and lung health burden. *Eur. Med. J. Respir.*, Vol. 2, 2014, pp.88–95.
- [13] Oberdörster G., Maynard A., Donaldson K., Castranova V., Fitzpatrick J., Ausman K., Carter J., Karn B., Kreyling W., Lai D., and Olin S., Principles for characterizing the potential human health effects from exposure to nanomaterials: elements of a screening strategy. *Part. Fibre Toxicol.*, Vol. 35, 2005, pp.1–35.
- [14] Miao J., Wang D., Yan J., Wang Y., Teng M., Zhou Z., and Zhu W., Comparison of subacute

- effects of two types of pyrethroid insecticides using metabolomics methods. *Pestic. Biochem. Physiol.*, Vol. 143, 2017, pp.161–167.
- [15] Buonanno G., Stabile L., and Morawska L., Personal exposure to ultrafine particles: The influence of time-activity patterns. *Sci. Total Environ.*, Vol. 468–469, 2014, pp.903–907.
- [16] Wang T., Miao M., Bai M., Li Y., Li M., Li C., and Xu Y., Effect of *Sophora japonica* total flavonoids on pancreas, kidney tissue morphology of streptozotocin-induced diabetic mice model. *Saudi J. Biol. Sci.*, Vol. 24, 2017, pp.741–747.
- [17] Almeida L. E. F., Wang L., Kamimura S., Wong E. C. C., Nouraie M., Maric I., Albani S., Finkel J., and Quezado Z. M. N., Rapamycin increases fetal hemoglobin and ameliorates the nociception phenotype in sickle cell mice. *Blood Cells, Mol. Dis.*, Vol. 55, 2015, pp.363–372.
- [18] Pretorius E., Mbotwe S., and Bester J., Erythrocytes and their role as health indicator: Using structure in a patient-orientated precision medicine approach. *Blood Rev.*, Vol. 30, 2016, pp.263–274.
- [19] Sarkar A., Das J., Manna P., and Sil P. C., Nano-copper induces oxidative stress and apoptosis in kidney via both extrinsic and intrinsic pathways. *Toxicology*, Vol. 290, 2011, pp.209–218.
- [20] Momeni H. R., Professor A., and Eskandari N., Effect of curcumin on kidney histopathological changes, lipid peroxidation and total antioxidant capacity of serum in sodium arsenite-treated mice. *Exp. Toxicol. Pathol.*, Vol. 69, 2017, pp.93–97.
- [21] Soderlund D. M., Molecular mechanisms of pyrethroid insecticide neurotoxicity. *Arch. Toxicol.*, Vol. 86, 2013, pp.165–181.
- [22] Akbar S. M. D., Sharma H. C., Jayalakshmi S. K., and Sreeramulu K., Effect of pyrethroids, permethrin and fenvalerate, on the oxidative stress of *Helicoverpa armigera*. *World J. Sci. Technol.* Vol. 2, 2012, pp.1–5.
- [23] Grigoryev D. N., Liu M., Hassoun H. T., Cheadle C., Barnes K. C., and Rabb H., The local and systemic inflammatory transcriptome after acute kidney injury. *J. Am. Soc. Nephrol.*, Vol. 19, 2008, pp.547–558.
- [24] Xu D., Chen M., Ren X., Ren X., and Wu Y., Leonurine ameliorates LPS-induced acute kidney injury via suppressing ROS-mediated NF- κ B signaling pathway. *Fitoterapia*, Vol. 97, 2014, pp.148–155.

INTEGRATION OF SPATIAL CHARACTERISTIC TO HEALTH SERVICES: A CASE STUDY OF CHILDREN HEALTH IMPROVEMENT COMPARE TO THE ENVIRONMENTAL MANAGEMENT AT DEPOK CITY SCALE- INDONESIA

Irene Sondang Fitrinitia¹, Esty Suyanti¹, Purnawan Junadi¹, Hardya Gustada²

¹School of Strategic and Global Studies, Universitas Indonesia, Indonesia

²Faculty of Medicine, Universitas Indonesia, Indonesia

ABSTRACT

Health issues are always related with environment condition. Regarding urban context, city has a double burden diseases in addition to infectious diseases as well as for degenerative diseases because life's pattern in city increasingly aggravating. Environmental risk factors are related to the type of diseases, evidently. Hence, in realization these several kind of diseases is not comparable and proportional to the number and coverage of health services. In particular children health, their growth is very sensitive to environment exposures. So environment factors could be the important aspects that consider with the children activities. At least, it happened in Depok City, one of middle city where close to the capital city of Indonesia. Through this research we would like to see the relevance of urban spatial elements especially the environmental aspects with the health risk factors of children compared to the number of health services and their coverage. In addition, we will also conduct spatial mapping of Depok City against the risk factors of children's health on the urban environment. The methodology that we used was a mix method between qualitative through FGD and quantitative including GIS. Based on the findings, it is known that the health risk including children due to the decrease of environmental character in Depok is divided into three classes that are dominated in high risk class. However, health facilities such as hospitals, Puskesmas (small hospitals), treatment services are low in coverage. This suggests that there is less integration between the spatial characteristics of the region and urban planning specifically related to health issues.

Keywords: Water sensitive city, Water supply, Middle city, Peri-urban

INTRODUCTION

As a city demanded to be dynamic, transformations that occurred are often caused by changing demands and conditions of city inhabitants [1] [2]. The changing could be the positive or the negative ones. The easiest identification to support that statement is the development of infrastructure, which indirectly has an effect on the health status of its citizens, whether good or bad. The health status of a person or even a community is the result of the interaction of various factors, both internal and external factors from human itself [3]. This internal factor composed physically and socially elements. External factors consist of various factors such as social, cultural society, environment, politics, economics, education and so on. Interactive relationships between humans and their behavior deal with potentially hazardous environmental components, also known as the process of disease incidence. Meanwhile, the process of disease incidence with each other has its own characteristics. In this case, environmental factors play a very important role. Human interaction with the environment has caused contact between germs and humans. Oftenly, the germs that live in the host body then migrate to humans because humans are not able

to keep the environment clean. This is reflected in the high incidence of environment-based diseases that are still the biggest health problem of Indonesian society. To reduce the health problems caused by environmental diseases is to plan and implement a region-based disease management [4].

Most of discussions in this paper are about of urban health then deciding factor to be considered is the environmental health of the city. The impact of industrialization in the form of exposure to pollution, misuse of innovation and technology up to environmental threats adds health risks to city dwellers.

Lack of public awareness due to the dynamic and high pressure of city life causes the disease is also known at the stage that is already acute. Generally, because the character of urban society is dynamic and has a lot of harmony to the action of health is curative rather than preventive.

Urban environment studies plays an important role in minimize public health risks including on child health. It leads many research to cope with many problems in tropical cities like Indonesia that consist a mixture of vectors, climatic conditions and the connection of local environment and human behavior which triggers for the rapid spread of epidemics of infectious diseases. Children become the media most

at risk of exposure to diseases caused by environmental factors such as poor sanitation, poor water quality to air pollution. With the city conditions in such a way can be a threat to the health of children ranging from diarrhea, respiratory infection, skin diseases and other infectious diseases.

Therefore through this paper, we want to contribute the spatial pattern of health status in middle city like Depok. It means to convey the characteristics of space that are risk to the child's special health. We chose Depok city to study more deeply as a case study. Depok city as a medium-sized city that became the satellite city of Jakarta experienced massive growth and rapidly. The location directly adjacent to Jakarta makes the city of Depok as a dormitory for workers in Jakarta. Therefore this city is growing based on high demand for housing but inadequate planning. Another indication of this massive development is the side effects on degraded environments and ultimately harmful to the health of their citizens. Also, we would like to see the relevance of urban spatial elements especially the environmental aspects with the health risk factors of children compared to the number of health services and their coverage. In addition, we will also conduct spatial mapping of Depok City against the risk factors of children's health on the urban environment.

METHODOLOGY

In this research we use several approaches to underpin the assumption of the findings. Based on the concept we had, we used to as fond to collect and analyzed the data. The approaches consist of qualitative and quantitative techniques. It makes information from data collecting could be wide and depth as well.

By using GIS Depok City divided unto district (kecamatan) area. Furthermore, the data collecting and analyzing are using "district" as mapping unit. In Indonesia district means "kecamatan", the third layer administrative boundaries after province, city/municipalities then after that district.

In Depok case, there are 11 districts consist of : beji, Bojong Sari, Cilodong, Cimanggis, Cinere, Cipayung, Limo, Pancoran Mas, Sawangan, Sukmajaya, Tapos. These eleven districts will be peeled with several spatial topics related with health issues like potential disease or health services at city scales.

GIS helps to analyze data within region, shows the distribution of regions that have the same data group or data characteristic in particular health issues. The objectives of GIS are the information system management with analysis tools (statistical and spatial modeling) and can be displayed of spatial information and made meaningful results [5]. We also use the overlay techniques to present the

comparison between the health risks condition and the needs of Depok City due to health facilities.

We collected the tabular and spatial data to enrich the article with visualization. Each data in this research are secondary source, based on the report literature or previous research in Depok. We did not use the primary data since it costly and long duration achievement.

Actually, this research was conducted while we had community development research regarding the use of self-diagnose mobile application to children health in Depok. We need to attach the spatial map and region characteristic to the apps. Therefore we should have data to give the big picture of Depok city.

ENVIRONMENTAL RISK TO HEALTH STATUS

Health status in one city is very affected from the physical environment. The better is the environment condition so the healthier people who lived on it. It is based on the empirical studies on the connection between the health status and the condition of environment. The connection are shown by the measurement of human function from physically, mentally, emotionally and socially [6]. It been indicated from life expectancy, physical disability, mental disability, social behaviors, self-reported feelings about one's health, presence of disease, lab test values, and assessed emotions

Furthermore we can check to Blum's classic model due to elements that determine health status consist of health as physical (somatic), mental (psychic), and social well-being. The environmental risk occurs when physical and sociocultural conditions affect the human lives. Many environmental elements affect health, such as sanitation, violence, sunlight, employment opportunities, population density, and air pollution. According to Blum the environment has the most powerful effect on health, indicated by environment having the thickest (strongest) arrow in the exhibit. Not only the natural physical environment but also the man made built environment like park, private and public building. The quality of building materials and equipment varies greatly that gives healthy living environment potentially harmful. Staying in such living environment lurking high levels of dangerous environmental factors for a long time become an issue particularly children's health problems that need attention [7]. The environmental elements are the ultimate factors that define children's health. Critical situations due to access to drinkable water, sewage disposal and housing conditions are the factors remarkable morbidity and mortality of children in developing countries [8].

The report of UNICEF Indonesia 2012 stated that child mortality becomes a trend in Megapolitan Jabodetabek. According to the report, rapid

urbanization has an effect on excessive population density, poor sanitation conditions for the urban poor, poor service quality in urban areas. Ultimately this big city became endemic to diarrhea and claimed to account for 31 percent of child deaths between the ages of 1 month to 1 year, and 25 percent of child deaths between the ages of one to four. Therefore, the study that has been done by many stakeholders is to convey that there is a valid relationship between the quality of the environment with the main health status of children. The worse the environmental conditions make the child's health is also to be worse [9].

The approach of Environmental Risk Health Assessment was the best choices to shown the environment status that can be risked to ruin one's health condition. The assessment had been conducted in several countries as a background of decision maker to decisive to policy actions in several countries [10]. In Indonesia especially Depok city they assessed according with Depok characteristics.

Factors that use to be as the indicator of Environmental Risk Health Assessment in Depok such as waste disposal management, clean water existences, sanitation condition, settlement drainage until hygiene behavior of Depok's residents. This assessment also insert on indicator which is the occurrence of diarrhea disease in child. These factors made a comprehensive approach in terms of environment profile.

DEVELOPMENTS IN DEPOK AND ITS IMPACT TO HEALTH CONDITION

Massive developments that happened in middle cities in Indonesia trigger nation growth. Depok is one of middle city that includes in Jakarta Megacities. The role as satellite city made Depok certainly under pressure from Jakarta and has a significant impact such as an increase in population. The population growth doubled increase because of the existence of UI campus that trigger mix used area to be developed.

Then, Depok City for 16 years since it was declared has 2,106,102 of population or increased by 75% in 2015 with the density of population reaching 10,255 people per km² [11]. The composition of the population based on the general structure of the population <5 year is the second largest, reaching 202,831 people.

Since Depok was an area that included of Jakarta Megacities, so Depok had an impact of Jakarta development automatically. Hence, the developments are being run from the Jakarta and local development from Depok itself. At north of Depok where the neighborhood with Jakarta are consist of dense area/district. However the densest one is in the middle of Depok. While the east, west or even the south still undeveloped yet as much as center part.

The rapid changes can be shown from the composition of land uses that been developed in

Depok. The built up area are dominated at the land use map since the last 2 decades. Over exploitation because of development decreased the quality of environment These situations cause a negative impact to health risk. Moreover, contagious disease could harm peoples includes in Depok City.

Toddler age is quite susceptible to the type of disease either contagious or not contagious. Based on outpatient data in hospitals at Depok City in 2015, for age <1 year URI (Upper Respiratory Tract Infectionsuffered) suffered by 32%, followed by flu (19%) and dermatitis (12%). Most of the illnesses suffered by children 1-4 years was URI as much as 51%, diarrhea (13%) and febris (9%). Data from Puskesmas (Health Public Center) showed that most of the disease suffered by children <1year was URI of 28%, nasopharyngitis (27%) and cough (11%). Most of the illnesses suffered by children aged 1-4 years were URI as much as 30%, nasopharyngitis (23%) and cough (14%). [12].

In Depok, infants and toddlers are also susceptible to other infectious diseases, some potentially infectious diseases to infants and toddlers are dengue fever, filariasis, diarrhea, leprosy, pneumonia, diphtheria, tetanus, measles, hepatitis, pertussis, and poliomyelitis. [13].

The contagious with uncontagious were sometimes lead infants to dead attack. The infant mortality rate in Depok City quite high [14].

Table 1 Infant Mortality Index by District

No	District	Infrants	Mortality Index
1	Beji	13	Low
2	Bojongsari	3	High
3	Cilodong	5	High
4	Cimanggis	14	Moderate
5	Cinere	6	High
6	Cipayung	3	High
7	Limo	0	High
	Pancoran		
8	Mas	14	Very High
9	Sawangan	5	High
10	Sukmajaya	12	Very High
11	Tapos	6	Low

Based on this report we knew that Pancoran Mas and Cimanggis were the severe district regarding the average of mortality.

This result also strengthens the finding from the environmental health risk assessment map. It concludes the center area of Depok which are Pancoran Mas and Sukmajaya were in the class of high risk district exposed by the environment degradation.

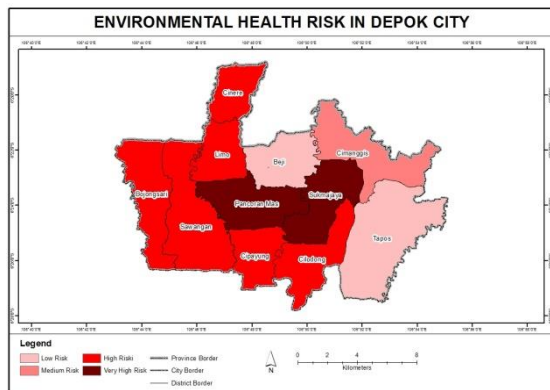


Fig. 1 Environmental health risk map

Due to the densest district in Depok, Pancoran Mas and Sukmajaya have the largest of slum area. The data from Settlement and Housing Agency Depok stated that almost 6 percent of Pancoran Mas is slum and squatter. Even though the percentage is small but it is the highest number among the whole districts in Depok. The characteristics of slum area contribute the high risk of environmental health. Although it not automatically related to health issues, daily practices tendentious to have un-hygiene behavior. So, it affect to the exposure having the disease.

Depok Health Data in 2015 states that the coverage of healthy homes in Depok has reached 85.93%. Community access to clean water is filled from ground water and Water Supply Company. Residents who have access to clean water use health standards as much as 74%. Fulfillment of sanitation (latrines) healthy in depok declared feasible as much as 73.5%. In addition to the environmental factors of society behavior also affect the health status of society. The coverage of clean and healthy households in Depok city by 2015 is 77.5%.

HEALTH INFRASTRUCTURES SERVICES IN DEPOK

The population of Depok City is 2,106,100 peoples with growth of 3.57 percent in 2015. This number is huge enough for the middle city like Depok. Consequently, sufficient public facilities needed to be fulfilling for daily life. This also includes health facilities and infrastructures. However, the fact is not as proper as the planning. Number and distributions of health facilities were enough for existing condition, but still did not meet for the ideal condition. It exacerbated for disease impacts exposure. The symptom already occurred when environmental risk is high and it should treat as soon as possible by the health services. This role should be taken by the government or private sector to provide hospital, clinic and health center. Furthermore, children as the most vulnerable exposed

by this risk need special treatment deal with the environment degradation.

In Indonesia beside clinic and hospital, we have public health center called Puskesmas. Based on the regulation the existence of Puskesmas minimal must be 1 unit at 1 sub district (Kelurahan). Below is the number of hospital and Puskesmas in Depok:

Table 2. Health Care Service by District

No	District	A	B	C	D	E
1	Beji	3	2	2	5	9,8
2	Bojongsari	2	0	0	2	3,92
3	Cilodong	3	0	2	5	9,8
4	Cimanggis	6	1	4	10	19,61
5	Cinere	1	0	1	2	3,92
6	Cipayung	2	1	0	2	3,92
7	Limo	1	0	0	1	1,96
8	Pancoran Mas	3	0	4	7	13,73
9	Sawangan	4	1	2	6	11,76
10	Sukmajaya	4	0	2	6	11,76
11	Tapos	5	1	0	5	9,8

Note: A (puskesmas), B (2nd class Puskesmas), C (Hospital), D (Total), E (% /Percentage of Settlement)

Based from the table above describes that Cimanggis has the biggest number of health infrastructures. Not only in a matter of quantities, have Cimanggis also had the complete range of services from Puskesmas, hospital until 2nd class Puskesmas. Hospital as the first grade health services centralized in Cimanggis and Pancoran Mas as seen in the distribution map (Fig 2). From the map below we can see the distribution either disperse or centralized at some certain places

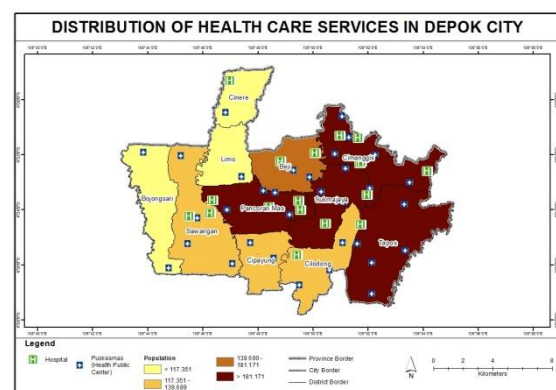


Fig. 2 Health care service distribution

HEALTH RISKS STATUS OF DEPOK

Discussing in terms of health status, we must have a comparison analysis between the “problems” and “potential solutions”. In this context, “problems” will be the environment risk that affect to health and

the other side “potential solution” will be the health services facilities.

Moreover by using the overlay techniques in GIS, we can compare two models of data which are tabular and spatial map. We have two result pictures and one table recapitulation to describe the finding.

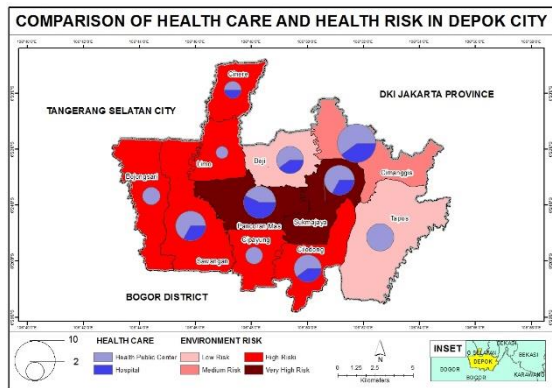


Fig. 3 Health care and health risk comparison

Despite the health infrastructure already developed for the Depok population, it still did not meet with the environmental risk that potentially harms the Depok's residents.

Sukmajaya that has significant level of harmful risk but have a moderate number of health services. Tapos is under services but it is logic since the environment not too risky. Meanwhile Limo and Bojong sari are the worst case, the environment quite risky but the health services still in moderate level. So it is inadequate to fulfill the services.

Completing the comprehensive analysis due to comparison, we also insert the overlay map between environmental risk and health workers in Depok city (Fig 4)

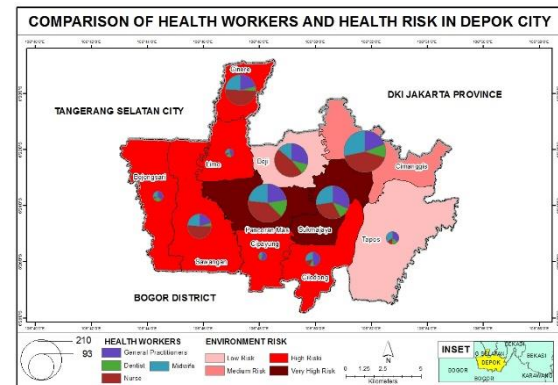


Fig. 4 Health workers and health risk comparison

Table 3. Recapitulation Results Among 11 Districts

District	Settlement (%)	Slum (%)	Environment Index	Infant Mortality	Health Cares (%)	Health Workers (%)	Distribution of Health Cares
Sawangan	49.18	1.20	High Risk	Medium	11.76	8.22	Disperse
Bojongsari	32.99	-	High Risk	Low	3.92	1.86	Rare
Pancoran Mas	43.20	-	Very High Risk	High	13.73	18.55	Centralized
Cipayung	50.92	0.40	High Risk	Low	3.92	1.24	Disperse
Sukmajaya	56.74	2.73	Very High Risk	High	11.76	14.40	Disperse
Cilodong	42.84	4.82	High Risk	Medium	9.80	3.36	Disperse
Cimanggis	38.92	-	Medium Risk	High	19.61	21.20	Sentralized
Tapos	49.21	5.82	Low	Medium	9.80	2.74	Disperse
Beji	29.32	3.87	Low	Medium	9.80	14.75	Disperse
Limo	53.78	2.94	High	None	1.96	1.24	Rare
Cinere	33.22	-	High	Medium	3.92	12.46	Rare

The figure 3 showed the comparison of the size (quantity and quality) health care and environment risk. Even though Pancoran Mas is the worst at environment risk, but at this scale it already has the sufficient of health facilities. Slightly different with

Based from the picture above the highest number of health worker and practitioner were in Cimmangis and Pancoran Mas. Both of these districts have a similarity which dominated with settlement area. Although, the difference between them are associate to environmental risk exposures. Pancoran

Mas has a high rank of health harmful, meanwhile Cimanggis slightly below for the risks. The best one is Beji, with the low risk of environment harmful but it has moderate number of health worker and practitioners.

To sum up the findings, we establish recapitulation table that compare on indicator to others. According the recapitulation we can classify into three class regarding the health and environment status among 11 districts in Depok. The three classes in districts will be:

1. Manageable But Risky, consist of Sawangan, Cipayung, Sukmajaya, Cilodong, Cimanggis
2. Manageable, consist of Beji, Tapos
3. Unmanageable and Risky consist of Bojongsari, Pancoran Mas, Limo, Cinere

The manageable but risky means, the districts has already enough modal to manage the health issues even though the harmful possibilities from the environmental degradation still wide open. Depok has 5 districts in this category.

The unmanageable and risky will be the worst case. Double burden issues like less health services combine with the high risk environmental degradation. Depok has 4 districts in this category

The last should be the best one is the manageable. It means number of health services are sufficient enough compare to the low risk of health issues. In Depok case, there are only 2 districts in this categorize.

CONCLUSION

Based on the findings, it is known that the health risk including children due to the decrease of environmental character in Depok is divided into three classes which are district with manageable but risky status, district with manageable status and district with the unmanageable and risky status. This suggests that there is less integration between the spatial characteristics of the region and urban planning specifically related to health issues.

ACKNOWLEDGEMENTS

This article is part of Superior Research of Universities (Ministry of Research, Technology and Higher Education) that conducted by Prof Purnawan Junadi.

REFERENCES

- [1] Wilson, D. (2007). City transformation and the global trope: Indianapolis and Cleveland. *Globalizations*, 4(1), 29-44.
- [2] Malone, P. (2013). *City, capital and water*: Routledge.
- [3] Blum, Henrik L. (1983): "Health Planning: Lessons for the Future." (390-391).
- [4] Profil Kesehatan Indonesia (2015) Kementrian Kesehatan Republik Indonesia
- [5] Kandwal, Rashmi P.K. Garg, R.D. Garg (2009) Health GIS and HIV/AIDS studies: Perspective and retrospective. *Journal of Biomedical Informatics* Vol 42 page 748-755
- [6] Fos P.J, D. Fine, (2005) *Managerial epidemiology for health care organizations* (2nd ed), Jossey-Bass, San Francisco
- [7] Wei, Shanshan, Yang Lv, Baiin Fu, Hiroshi Yoshino (2016) The correlation study on the living environment and children's health problem in Dalian. *Procedia Engineering*, Volume 146, Pages 158-165
- [8] Mello-da-Silva, Carlos Augusto, Ligia Fruchtengarten (2005) Environmental chemical hazards and child health. *Jornal de Pediatria*
- [9] Laporan Tahunan UNICEF Indonesia. 2012
- [10] Tal A (1997). Assessing the environmental movement's attitudes towards risk assessment. *Environmental Science and Technology*, 31 (10):470A-476A.
- [11] Ali, Firdaus, et al (2018) Initiative Urban Water Studies At Depok, Peri-Urban City - Toward The Implementation Of Water Sensitive City Concept. *International Journal of Geomate*
- [12] [13] [14] Profil Kesehatan Kota Depok 2016

EVALUATION OF DRAINAGE PROCESS IN POROUS MEDIA BY INVADDED PERCOLATION PROBABILITY

Junichiro Takeuchi¹ and Masayuki Fujihara¹
¹Graduate School of Agriculture, Kyoto University, Japan

ABSTRACT

Invasion processes, such as the imbibition and drainage processes, through porous media could be modeled by the invasion percolation model in a pore-network that is extracted from actual or virtual packed grains. It is well known that water retention properties depend on the pore structures such as pore shape, pore-size distribution, and pore-connectivity. But in our previous works, it is confirmed that there is a spatial structure even in a porous medium packed with single-size grains, and that if the spatial structure of pores is not disturbed, different water retention curves obtained from different pore-size distributions for imbibition process can be unified into a single curve by using the invaded percolation probability, which is the proposed index based on the percolation probability. In this study, the drainage process is evaluated by the water retention curves and the invaded percolation probability through numerical experiments. The results show that the different water retention curves were unified into a certain curve based on the percolation probability, but relatively large variation were seen in the rising point in the curves that corresponds to the air-entry point, which was not seen in the imbibition process.

Keywords: Water Retention Property, Pore-network, Invasion Percolation, Percolation Probability

INTRODUCTION

Displacement of immiscible fluids such as air and water in porous media, which is represented by drainage and imbibition processes, is quite important in many disciplines as well as industrial and agricultural fields. To pursue an underlying principle of it could lead to better understanding of the mechanism and more effective usage of porous materials.

It is well-known that the water retention property of soils is variable depending on soil type, and that the variability is caused by pore properties such as size distribution, geometry, wettability of grain surface, and connectivity to other pores [1]. But apparently different water retention curves could be unified into a single curve or several curves if those are re-evaluated from a viewpoint of the percolation theory [2]. It was presented that the imbibition process of porous media with various pore-size distributions, which show different water retention curves definitely, can be unified into a single curve if it is evaluated by a method called an invaded percolation probability (IPP), while the drainage process shows a certain level of variability [3], [4]. The invaded percolation is based on the percolation probability, which is used for evaluating the degree of connectivity of a network. It was also presented that the pores of single-size spherical grains randomly packed has a positive spatial autocorrelation of about 0.19 score in the global

Moran, and that the pores of virtual porous media randomly generated following a certain probability density distribution has no spatial autocorrelation [5]. Furthermore, it was revealed that the imbibition process is strongly effected by the spatial autocorrelation [4]. In this study, dependency of spatial autocorrelation and the cause of variability in the invaded percolation probability in the drainage process are investigated through numerical experiments.

METHOD

Pore-network Model

From a virtual porous media made by packing single-size spherical grains randomly with the discrete element method, a pore-network model is extracted with the modified Delaunay tessellation method proposed by Al-Raoush et al. (2003) [6]. A pore-network model consists pore bodies (PBs) which are relatively large pores formed by four or more grains and pore throats (PTs) which are relatively small pores connecting two PBs [7]. Through the extraction process, the coordinate, size, and connectedness to surrounding pores of each pore are obtained. PBs are represented as a sphere and the size equals to the maximum inscribed sphere in each gap formed grains. PTs are represented as a tube, and the length is the one between the two PBs that the PT connects and the size is the maximum inscribed circle in a gap formed by grains.

If PBs and PTs are regarded as sites and bonds, respectively, which are the terms in the percolation theory, the extracted pore-network model can be presumed to be a network literally. Each element (site or bond) has a state of 'open' or 'close'. When an element is 'open', the element can convey something (the objective depends on a target system) to the neighbor elements. Then a network can convey it holistically if the network has enough open elements. Thus connectivity of a network is a quite important index.

Distributions of the coordinate number and the percolation probability are analyzed to know connectivity of the pore-network as a network. The coordinate number is the number of sites/bonds that a site/bond connects, and the percolation probability is the one with which a site/bond belongs to the infinite 'open' cluster in a case of an infinite network when a certain probability for 'open' is given to a network. In a case of a finite network (the presented case is also finite one), the percolation probability is calculated as the proportion of the size of the maximum 'open' cluster to the size of the network.

In this pore-network, each pore has a set of two components for a state. One is about invadability of the objective pore, and the other is about occupied fluid in the pore. The former takes one state from {invadable, uninvadable}, and the latter takes one state from {invaded, not-invaded}. In a case of the drainage process, the invadability index I is defined from the capillary pressure p_C and the local air-entry pressure p_{AE} as follows,

$$I = p_C - p_{AE} \quad (1)$$

with

$$p_C = p_{air} - p_{water}, \quad p_{AE} = P\sigma \cos \theta / A \quad (2)$$

$$p_{water} = p_{btm} - \square z \quad (3)$$

where p_{air} and p_{water} are the air- and water-pressures in the vicinity of an air-water interface, respectively, and p_{air} is constant here. A and P are the cross-sectional area and circumference of the inscribed circle in a pore, respectively, σ and θ are the surface tension of water and the receding contact angle, respectively, and p_{btm} is the water pressure imposed on the pore-network bottom, and $\square z$ is the difference in height between the bottom and the objective pore. If $I > 0$, the pore is invadable, and if $I \leq 0$ the pore is uninvadable.

When a certain pressure condition for air and water is given, the former state of all pores is determined, assuming that each pore is facing an air-water interface that satisfies the continuity rule as described below. If the proportion of the invadable pores is large enough, invading fluid begins invading continuously in the invasion percolation manner. The threshold of the proportion, which is referred to the critical percolation threshold, is quite

important for soil science, and it corresponds to the air and water entry pressures in the drainage and imbibition processes, respectively. From the critical percolation threshold, we can know how much pores need to be invadable to begin imbibition or drainage.

Invasion percolation

A displacement process of immiscible fluids in a pore-network is modeled by the invasion percolation [8]. The invasion percolation is a temporally and spatially discretized model of a progressive process whereby one fluid invades into invadable pores occupied by the other fluid. The following settings for a drainage process are given to a pore-network. Top and bottom faces of the pore-network are connected to outside air and water reservoirs, respectively, and air and water can inflow and outflow freely. But air and water cannot pass through the four side faces.

The procedure of the invasion percolation for a drainage process is described below [9],[10].

1. As an initial state, all or a part of pores are occupied by water, and a certain pressure is imposed on the pore-network bottom.
2. All water-filled pores that are facing air-filled pores, satisfying the continuity rule, are sorted in descending order of invadability.
3. The top N^{IP} pores are invaded by air (i.e., water in the pore is drained) simultaneously, where N^{IP} is the number of pores invaded in one time step.
4. Processes 2 and 3 are iterated until no pores change their stat, and the saturation and IPP are calculated.
5. The pressure imposed on the bottom is changed, and the process returns to 1 or 2.

To move an air-water interface, the continuity rule need to be satisfied. Namely, both of air and water need to connect to their outside reservoir through pores filled with the same kind fluid.

Invaded Percolation Probability (IPP)

After reaching the steady state in each pressure condition, IPP as well as saturation is calculated. While water retention curve (WRC) is a relation between pressure head (matric potential) and saturation (water content), IPP is a relation between the proportion of potentially invadable pores and that of actually invaded pores.

In a case of a normal network, percolation probability is calculated based on sites or bonds (PTs or PBs in a pore-network). As described above, both PBs and PTs plays an important role in the invasion percolation in a pore-network. Hence, in addition to PB-basis and PT-basis (invaded) percolation probabilities, PB-PT-basis ones are proposed in this study.

NUMERICAL EXPERIMENTS

In this study, mainly three matters are investigated through numerical experiments using a pore-network extracted from randomly packed grains. Firstly, which invaded percolation probability is suit for evaluating a drainage process among PT-basis, PB-basis, and PB-PT-basis ones. Secondly, how much influence is given to water retention property and invaded percolation probability when pore-size distribution is changed without disturbing arrangement of pores. To investigate this, the average of pore-size distribution is shifted without changing the distribution shape (average-shift) or the variance is changed without changing its average (variance-change). Thirdly, the effect of spatial autocorrelation is investigated. The original pore-network has spatial correlation although the degree is low, but it is clearly distinguished from random pore-arrangement [5]. Then, pore-arrangement is randomly shuffled without changing a network topology to make a

pore-network that has no spatial autocorrelation. Moreover, to investigate the effect of overlap in PB- and PT-size distributions, uniform distributions with various overlap each other are given.

RESULTS AND DISSCUSSION

Pore-network

About 5800 spherical grains whose size is 0.2 mm in diameter are randomly packed in a 32.8 mm³ cubic container with the discrete element method (Fig. 1 (a)), and a pore-network is extracted from the virtual porous media (Fig. 1 (b)). The pore-network consists of 13,804 PBs and 35,233 PTs, and the distributions of the pore-size and coordinate number are shown in Fig. 2. The pore-network size is sufficiently large compared with the standard proposed by Reeves and Celia (1996) [11] and actually almost same pore-size and coordinate number distributions were obtained from different grain-packing in the cubic container [4].

The three types of percolation probability, those are PB-basis, PT-basis, and PB-PT-basis ones, are shown in Fig. 3. In each percolation probability, pore-size-basis one is shown in addition to the

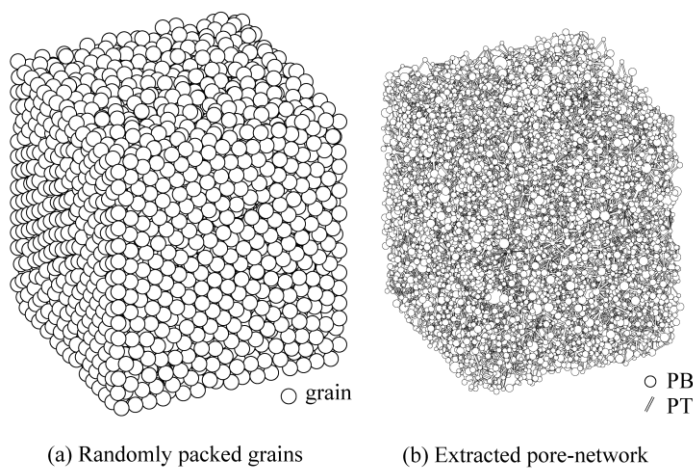


Fig. 1 Virtual porous medium

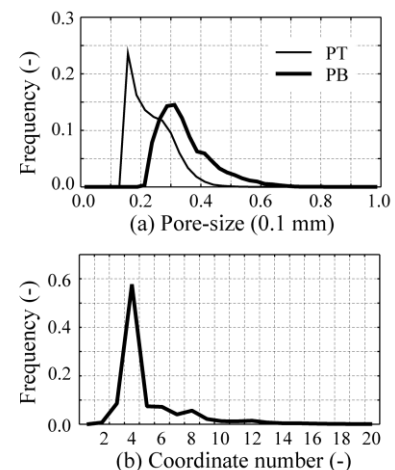


Fig. 2 Pore-size and coordinate number

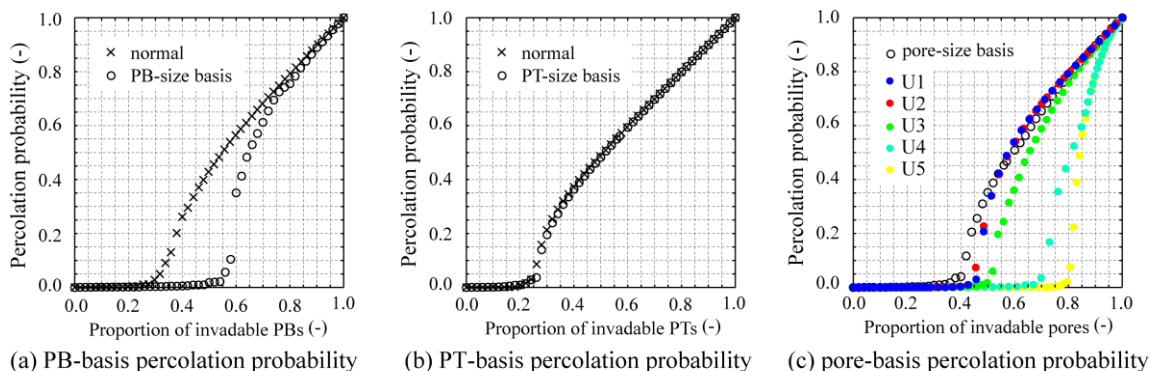


Fig. 3 Percolation probability of pore-network

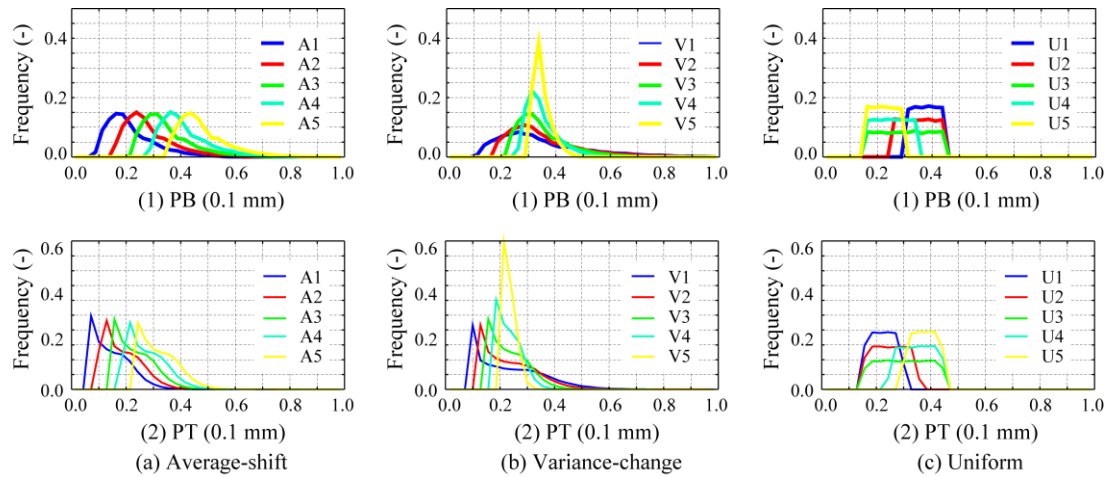


Fig. 4 Pore-size distributions for numerical experiments

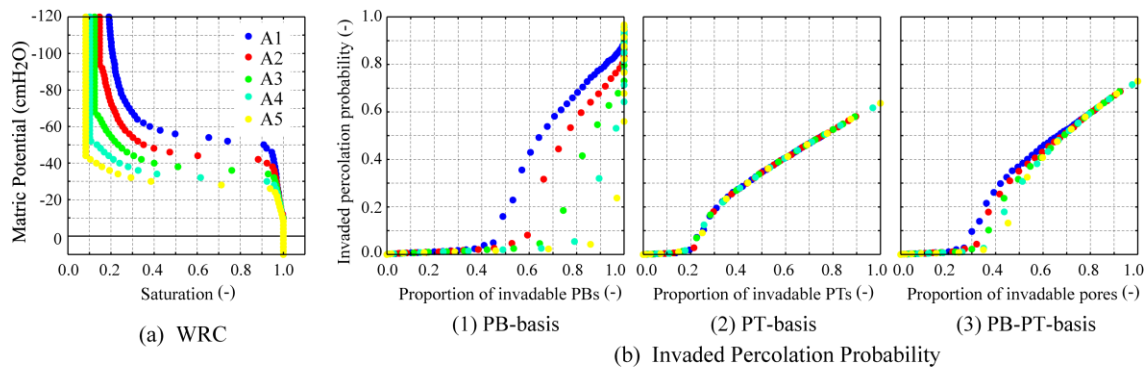


Fig. 5 WRC and IPP of Average-shift Distributions with Spatial Autocorrelation

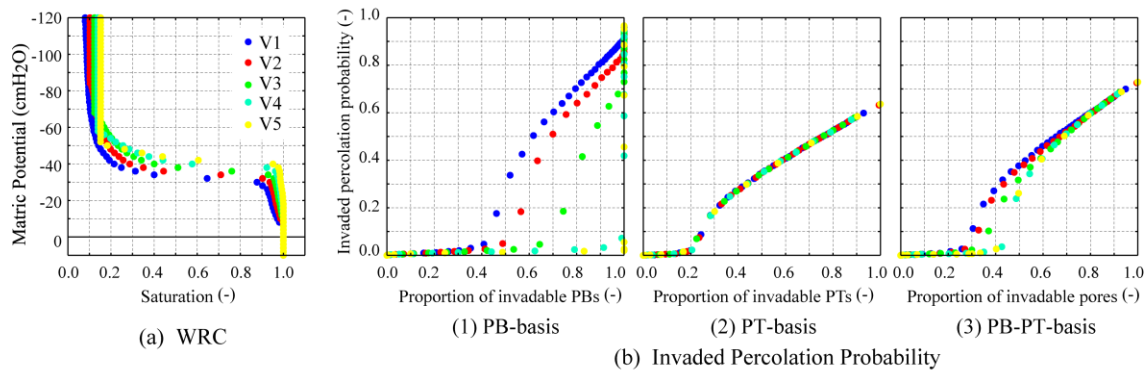


Fig. 6 WRC and IPP of Variance-change Distributions with Spatial Autocorrelation

normal one, which is obtained by giving sites and/or bonds random number to evaluate connectivity as a network. For the uniform distribution, the distribution shown in Fig. 4 (c-1) and (c-2) is applied instead of normal one to check the effect of overlap in PB- and PT-size. The pore-size-basis percolation probability corresponds to the actual pore-network that has spatial autocorrelation in pore-arrangement, and the normal one to a simple pore-network without spatial autocorrelation. Figure 3 (a) implies that PBs have somewhat spatial unevenness in arrangement because to surpass the

critical percolation threshold more invadable PBs are needed compared with the normal percolation probability. Figure 3 (b) implies that PTs has no spatial autocorrelation because the normal and pore-size-basis ones almost identical. Figure 3 (c) shows the percolation probability varies depending on the size relation of PBs and PTs. In a case of drainage in normal (hydrophilic) soil, U1 type is held, that is, PBs are larger than PTs to which the PB connects.

WRC and IPP

From the conducted numerical experiments with various pore-size distribution, WRC and IPP are calculated. The used pore-size distributions are shown in Fig. 4.

the critical percolation threshold varies. PB-basis one is considered to be less useful to evaluate a drainage process.

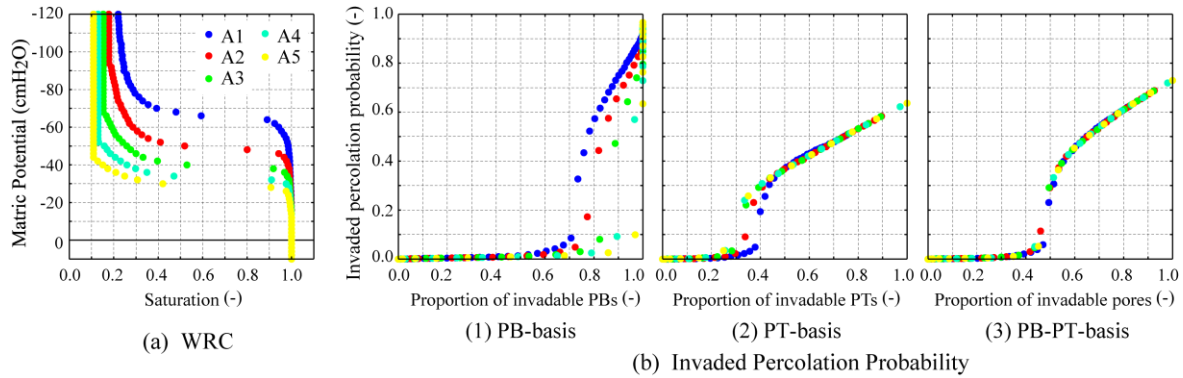


Fig. 7 WRC and IPP of Average-shift Distributions without Spatial Autocorrelation

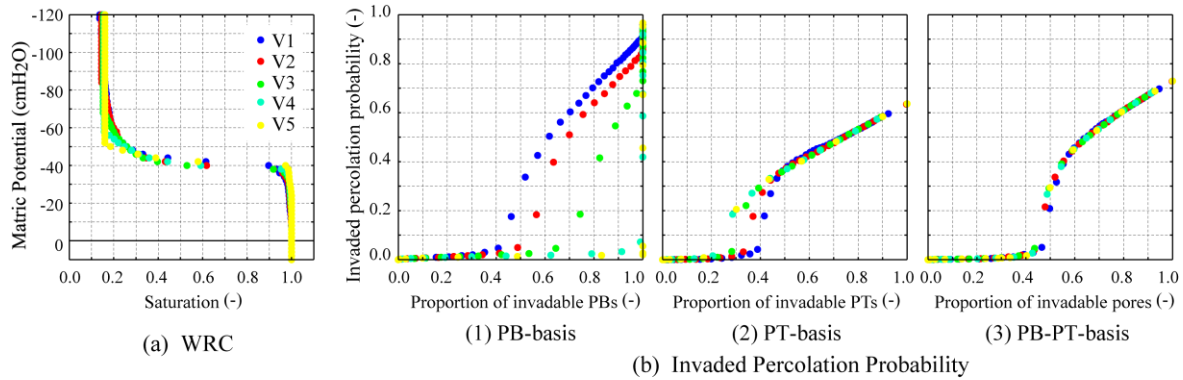


Fig. 8 WRC and IPP of Variance-change Distributions without Spatial Autocorrelation

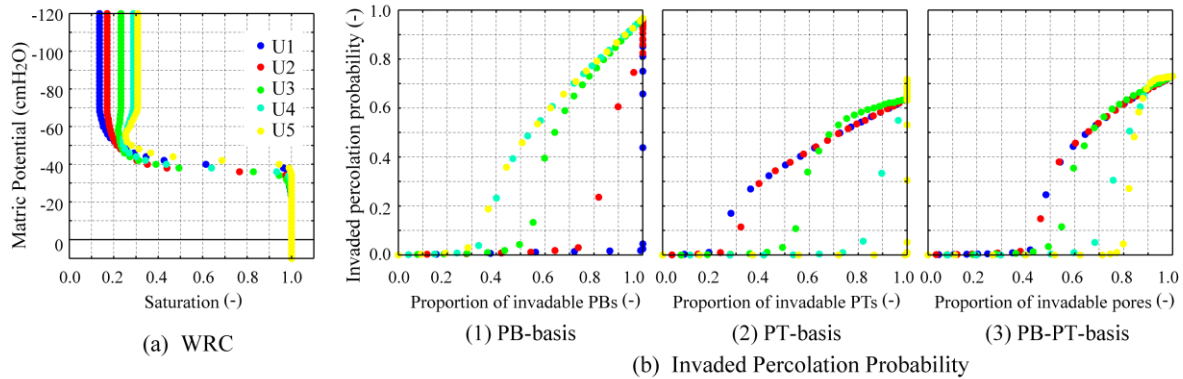


Fig. 9 WRC and IPP of Uniform Distributions without Spatial Autocorrelation

Pore-network with spatial autocorrelation

The obtained results of a drainage process in the pore-network with spatial autocorrelation, that is, it has original pore-arrangement, are shown in Figs. 5 and 6. Figures 5 (a) and 6 (a) shows that different WRCs are obtained from different pore-size distributions. But among the three types of IPP, PT-basis one shows unified curve (Figs. 5 (b-2) and 6 (b-2)). PB-PT-basis IPP shows relatively good coincidence compared with PB-basis one although

Pore-network without spatial autocorrelation

The obtained results of WRC and IPP of pore-network without spatial autocorrelation in pore-arrangement are shown in Figs. 7 through 9. Similarly, various WRCs are obtained depending on pore-size distributions (Figs. 7 (a), 8 (a), and 9 (a)). In a case of a pore-network without spatial autocorrelation, PT-basis IPP shows variation in the critical percolation threshold, and PB-PT-basis IPP become unified curve (Figs. 7 (b), 8 (b), and 9(b)).

From these results, it is found that only PT-basis IPP is applicable to evaluate a drainage process only when used soil satisfies the following condition that PBs are larger than PTs to which an objective PB connects.

CONCLUSION

In this study, usefulness of the invaded percolation probability, which is an evaluating method based on the percolation probability in the percolation theory, was investigated through numerical experiments with a pore-network. In the numerical experiments, drainage process is modeled by the invasion percolation. Various pore-size distributions are given to the pore-network, and water retention curves and the invaded percolation probability were calculated. The obtained results show that the water retention curves vary depending on pore-size distribution. Unlike a imbibition process, only PT-basis IPP can be unified into a single curve only when PBs are larger than PTs to which an objective PT connects. But normal (hydrophilic) soil satisfies this condition, and hence IPP is considered to be useful.

ACKNOWLEDGEMENTS

This study was supported by JSPS KAKENHI Grant Number 16K07971.

REFERENCES

- [1] van Genuchten MT, "A closed form equation for predicting the hydraulic conductivity of unsaturated soils", *Soil Sci. Soc. Am. J.*, Vol. 44, 1980, pp. 892–898.
- [2] Hunt A and Ewing R, "Percolation theory for flow in porous media", Springer, Heidelberg, 2009, p. 319.
- [3] Takeuchi J, Tsuji H, and Fujihara M, "The effect of capillary radius distribution on the hydraulic properties of porous media", *Precision Farming and Resource Management*, Excel India Publishers, New Delhi, 2016, pp. 292–304.
- [4] Takeuchi J and Fujihara M, "Evaluation of Imbibition Process in Porous Media by Invaded Percolation Probability", *Int. J. GEOMATE*, Vol. 14, 2018, pp.1–7.
- [5] . Takeuchi J, Fujihara M, "Spatial Statistical Analysis of Pores in Single-size Grains Packing", *Proceedings of JRCSEA 2017 Annual Congress*, 2017, pp.18–21 (in Japanese).
- [6] Al-Raoush R, Thompson K, and Willson CS, "Comparison of network generation technique for unconsolidated porous media", *Soil Sci. Soc. Am. J.*, Vol. 67, 2003, pp. 1687–1700.
- [7] Fatt I, "The network model of porous media", *Trans. AIME*, Vol. 207, 1956, pp. 144–181.
- [8] Wilkinson D and Willemsen JF, "Invasion percolation: a new form of percolation", *J. Phys. A: Math. Gen.*, Vol. 16, 1983, pp. 3365–3376.
- [9] Takeuchi J, Sumii W, and Fujihara M, "Modeling of fluid intrusion into porous media with mixed wettabilities using pore-network", *Int. J. GEOMATE*, Vol. 10, 2016, pp. 1971–1977.
- [10] Takeuchi J, Tsuji H, and Fujihara M, "Modeling of permeability of porous media with mixed wettabilities based on noncircular capillaries", *Int. J. GEOMATE*, Vol. 12, 2017, pp. 1–7.
- [11] Reeves PC and Celia MA, "A functional relationship between capillary pressure, saturation and interfacial area as revealed by a pore-scale network model", *Water Resour. Res.*, Vol. 32, 1996, pp. 2345–2358.

DAMAGE DETECTION AND LOCALIZATION IN MASONRY STRUCTURE USING FASTER REGION CONVOLUTIONAL NETWORKS

Luqman Ali¹, Wasif Khan¹ and Krisada Chaiyasam²

¹ Department of Computer and Electrical Engineering, Thammasat University Thailand; ² Department of Civil Engineering, Thammasat University Thailand

ABSTRACT

Manual on-site inspection can be assisted by automatic inspection, which is cost-effective, efficient and not subjective. In previous work, various image-based techniques have been applied to detect damages in heritage structures based on hand-designed feature extraction and classifiers. A heritage structure is composed of masonry walls, which are the components that are typically subjected to severe damages. This paper proposed a damage detection algorithm for a masonry structure based on Faster Region Convolutional Neural Networks (FR-CNN). A labelled dataset for training the damage detection system in heritage masonry structure is created in this study. Then, second contribution is the creation of a state of the art object detection system based on FR-CNN to detect and localize damages in masonry structures is proposed. The results show that the proposed system performs well and can be used to detect damage in masonry structures with promising computational speed.

Keywords: Object Detection, Faster Region Convolutional Networks, Masonry Structure, Automatic Inspection

INTRODUCTION

Thailand is rich in cultural heritage and many historic structures. These historic structures are vital to Thailand tourist industry. The preservation of culture heritage is of the utmost importance as it maintains nation's history and transfers valuable knowledge and skills of their ancestors. Many historical structures in Thailand have been deteriorating due to ageing, man-made activities and natural activities. Figure 1 shows Wat Chai Wattanaram, a temple dated back to 16th century, located in a historic province of Ayutthaya, Thailand. Various damages can be found in this temple which is caused by aging, natural causes or manmade activities. The country requires expertise and research to establish a methodology for historical structures maintenance.

Visual inspection technique is a commonly used technique to examine the present condition of historic structures. This method is usually carried out by trained inspectors to detect various defects in historical structures. Visual inspection cannot be carried out regularly as it is laborious, costly and prone to human error. Most of the sites are inaccessible to humans especially the top of stupa. These structure requires regular inspection as failure to detect defect on time can lead to failure of the structure. In order to overcome this problem this paper proposed to use a state of the art object detection system based on Faster Region Convolutional Neural Network F-RCNN for the detection and localization of damages in masonry

structures. Figure 2 shows example images of various defects found around the temple walls.

Current defect detection algorithm depends on handcrafted features which are not comprehensive. This method is complex and dependent on researcher's experience. As the texture become complex, it is very hard to distinguish between the targets and background regions. Defect detection systems using handcrafted feature consists of two major steps. The first step is to extract relevant features by using various feature extraction algorithms such as gray level co-occurrence matrix (GLCM) [1], edges [2], multifeatures [3], principal component analysis [4], and histograms etc. In the second step, classification is done by classifiers such as Support Vector Machines (SVM) [8], Neural Networks [5]. To avoid handcrafted feature extraction, CNN is then used for automatic feature extraction.



Figure 1: Wat Chai Wattanaram, a temple located in the historic province of Ayutthaya.

In this paper Faster R-CNN is used for automatic defect detection in masonry structure in real time. The data has been collected by using unmanned aerial vehicles (UAVs) from heritage masonry structures in Thailand. The rest of the paper is organized as follows. In section 2 related work is discussed. In section 3 overview of the proposed method is discussed. In section 4 database generation and implementation of the algorithm is explained. In section 5 experimental results are discussed. The proposed paper ends with conclusion, future work and references in last sections.

RELATED WORK

Literature review reveals that majority of damage detection system are based on handcrafted features. Kabir (2010) [6] used gray level co-occurrence matrix (GLCM) features and artificial neural network (ANN) classifier for detection of alkali-aggregate reaction (AAR) damage. Abdul- Qader (2003) [7] worked on crack identification in bridges using edge detection techniques. The limitation of edge detection algorithms is noise. Nishikawa (2012) [9] used multiple sequential image filtering for crack detection in concrete structures. German (2012) [10] implemented a machine vision system for the detection and properties measurement of concrete spalling for post-earthquake safety assessment. Yuen (2015) [11] proposed a vision-based automated crack detection system for the inspection of bridges. Cha (2016) [12] proposed a vision-based system for the detection of loosened bolts using Hough transform features and Support Vector Machine classifier. Zalama (2014) [13] used visual features extracted by Gabor filters for the detection of road pavement. Wu (2016) [14], Liao (2016) [15], Chen (2012) [16], Mirzaei (2016) [17] have worked to improve the accuracy of image processing techniques for crack detection but these methods still require post processing and preprocessing algorithms which can be computationally expensive.

Automatic feature extraction based on learning techniques such as deep learning can perform efficiently when compared to the techniques based on handcrafted features. Cha (2017) [18] proposed CNN based crack detection system for the detection of cracks in concrete structures. Zhang (2016) [19] proposed a deep convolutional neural network for road crack detection using images collected by a low cost smart phone. The CNN has capability to classify multiple classes. For damage localization, a sliding window technique can be applied. However, finding the optimal size of window is difficult as the size of the images varies. To address the problem, Girshick (2014) [20] proposed R-CNN in which object proposals and images are given as an input to the system. R-CNN use CNN for automatic feature extraction and SVM classifier for localization and

classification. R-CNN can increase the accuracy of recognition and detection tasks but it was computationally slow, costly and hard to use. To overcome these issues, He (2014) [21] proposed a spatial pyramid pooling network (SPP-net). The speed of the proposed network was greater than R-CNN but the implementation and training process of the network is hard as R-CNN. To address the issues associated with both SPP-net and R-CNN Girshick 2015 [22] proposed Fast R-CNN. The proposed Fast R-CNN has better performance and speed than SPP-net and R-CNN but still its speed is slow due to generation of object proposal from method such as selective search. To address the issue Ren (2016) [23] proposed a faster R-CNN by combining Fast R-CNN with region proposal network. Faster R-CNN has low computational cost and high accuracy in addition to real time object detection. In the proposed work, Faster R-CNN is used to provide automatic vision-based damage detection in masonry structures. The proposed architecture is used to provide quasi real-time damage detection in masonry structures. In this study only one type of damage is considered however the other defect types can also be added to the same architecture.

PROPOSED METHOD

The overall outline of the damage detection and localization system is shown in Figure 2 below. The proposed system consists of three main modules as explained in detail below.

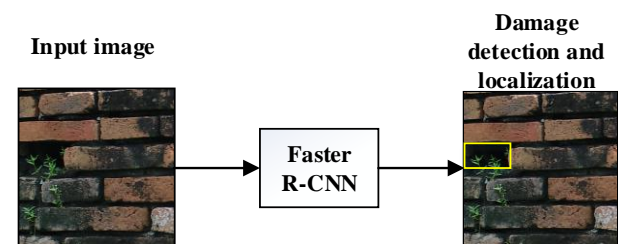


Figure 2: Outline of the proposed method

Image Acquisition

The application of UAVs for civil inspection tasks is an increasing trend recently and has potential to replace conventional inspection methods since they are cheaper, faster and simpler. In the proposed research work DSLR camera and a drone DJI phantom 4 was used for data acquisition. The full coverage of the structure is obtained by flying drone in preplanned flight path strategy known as Point of interest (POI) strategy. In the proposed strategy drone flew around the object of interest at the pre-determined radius and picture were taken around 2-3

seconds to ensure 50% overlap between consecutive images as shown in Figure 3. The drone flight is preprogrammed using Auto Flight Logic application, which requires input parameters, radius, velocity, including altitude and camera viewing angles. The drone flight has planned carefully in order to ensure that it can performed the task in the specified battery time. At the ground level some close-up images were collected by researchers similar to drone motion around the building as shown in Figure 9. The close-up images were collected so that the features are more prevalent in images.



Figure 3: Sample images of the structure taken by drone.

Faster R-CNN

The architecture of a Faster R-CNN is shown in Figure 4. In Faster R-CNN, the feature extraction computation of CNN is shared between the region proposal network (RPN) and Fast R-CNN. The main advantage of Faster R-CNN is that selective search used in Fast R-CNN is replaced by RPN which makes Faster R-CNN faster and second the convolutional maps are shared between RPN and detection network which makes the RPN almost cost free.

Convolutional Neural Network

Damage detection system using Faster R-CNN is divided into main networks, Fast R-CNN and RPN. Both networks perform damage detection by sharing the same CNN architecture. Convolutional neural network is a type of multilayer feed forward artificial neural network which has shown significance in solving real world problems. In the proposed work ZF-net is used for training and testing purposes as it is fast and has proven efficient in many real time detection problems (Li 2016 [24]; Ren 2016 [23]). ZF-net architecture is composed of 13 layers, Convolution layer, max pooling layer, and softmax layer.

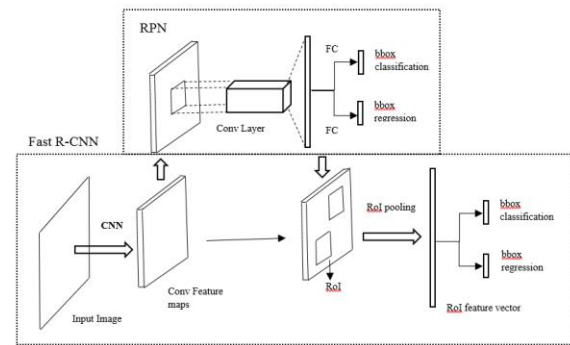


Figure 4: The architecture of Faster R-CNN

In the proposed Faster R-CNN damage detection system, the architecture of ZF-net is modified for both Fast R-CNN and RPN. In case of RPN 2 layers are modified, one is the last max pooling layer and FC layer. These layers are replaced by sliding CONV and FC layer which has feature vector with depth of 256. Secondly, the softmax layer is modified with softmax and regressors. In the case of ZF-net Fast R-CNN architecture modification, the last max-pooling layer is modified by RoI pooling layer. Drop out layers having threshold of 0.5 are sandwiched between the first and second FC layers in order to prevent over fitting problem during the training process and similarly the drop out layers are inserted between the second and third FC layer of ZF-net. The softmax layer is modified to softmax and regressors. The details modified specification of both the RPN and Fast R-CNN layer is shown in Table 1 and 2 below.

Region Proposal Network

As shown in Figure 5, a regional proposal network is a fully convolutional network (FCN) that outputs a set of object proposals as rectangular bounding boxes (bbox) from input images [25]. Firstly, in RPN the features maps are obtained by using CNN. After obtaining the feature maps a CONV layer followed by ReLU activation function is slid on each pixel to obtain feature maps. Each sliding window features are mapped onto a vector and are given to a softmax layer and a regressor, which gives the coordinated prediction of rectangular bounding boxes and the probability of object in each box. These rectangular boxes are known as anchors. The anchors are usually nine in number and are found in the combination of various aspect ratios such as 1:1, 2:1, 1:2. The three recommended dimensions of anchors are 128×128, 256×256 and 512×512. The obtained region proposal described by the prediction of rectangular bounding boxes and probability of object in each box is given to Fast R-CNN for further refinement in order to improve the process of classification. The detail of RPN layer are shown in Table 1 below.

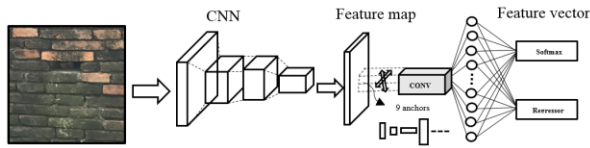


Figure 5: The schematic architecture of Region proposal network RPN.

Table 1 RPN layer specifications

Layer	Name	Filter size	Depth	stride
1	Conv+ReLU	7×7	96	2
2	LRN	--	--	--
3	Max Pooling	3×3	96	2
4	Conv+ReLU	5×5	256	2
5	LRN	--	--	--
6	Max Pooling	3×3	256	2
7	Conv+ReLU	3×3	384	1
8	Conv+ReLU	3×3	384	1
9	Conv+ReLU	3×3	256	1
10	Sliding Conv+ReLU	3×3	256	1
11	FC	--	256	--
12	Softmax & Regressor	--	--	--

Fast R-CNN

The Fast R-CNN takes object proposal obtained from RPN as a input and similarly to RPN, it extracts feature maps by using CNN from input images. The obtained proposal region from RPN is overlaid on the obtained feature map. Object proposal bounded features are known as a region of interest (RoI). In RoI pooling RoIs are given and max pooling operation is applied in order to obtain feature vectors with a fixed size from each RoI. The vector obtained is given to FC layers. The FC layers are followed by Softmax layer and then a regressor. Softmax layer calculate the probability of damages in the image while the regression layer show the location and size of the anchors.

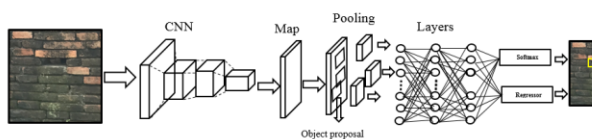


Figure 6: The schematic architecture of Faster R-CNN

Table 2 Fast R-CNN layers specifications

Layer	Name	Filter size	Depth	stride
1	Conv+ReLU	7×7	96	2
2	LRN	--	--	--
3	Max Pooling	3×3	96	2
4	Conv+ReLU	5×5	256	2
5	LRN	--	--	--
6	Max Pooling	3×3	256	2
7	Conv+ReLU	3×3	384	1
8	Conv+ReLU	3×3	384	1
9	Conv+ReLU	3×3	256	1
10	RoI Pooling	--	256	--
11	FC+ReLU	--	4096	--
12	Dropout	--	--	--
13	FC+ReLU	--	4096	--
14	Dropout	--	--	--
15	FC+ReLU	--	6	--
16	Softmax & Regressor	--	--	--

Network Training

The training process of the damage detection system for masonry structures is composed of four main steps. In each step, various parameters related to the networks are tuned. The process of training starts with RPN. The RPN is trained with pre-trained CNN initialized weights and object proposals are generated for fast R-CNN. The second step in training is initialization of fast R-CNN with the pre trained weight obtained from the object proposal generation step. In step 3 RPN is again trained with the weights obtained from previous step, the object proposal are generated again and in step 4 fast R-CNN takes the generated object proposal and is trained with the initial parameters obtained from step 3.

EXPERIMENTS AND RESULTS

Database creation

For the creation of training and testing dataset, 466 images were taken. In these images 163 images with the dimensions of 4864×3468 are taken by using DJI phantom 4 drone as shown in Figure 1. The remaining 303 with the dimension of 3024×4032 are taken by an iPhone 7 camera. These images contain structural damages. The images are converted into patches of 500×500 dimension. Out of the total patches only 1000 patches are selected which

contains damages as shown in Figure 7 below.



Figure 7: Sample images of patches created for training, testing and validation.

Implementation details

The experiment in the proposed work are implemented by using an open source library of Faster R-CNN [23], python tensor flow, CUDA 8.0, CUDNN 5.1 using a core i7-7820X computer @ 3.6 GHz CPU, 64 GB DDR4 memory, and an 4GB NVIDIA GeForce GTX 1070 GPU. The RPN and Fast R-CNN learning rate is taken 0.001 while the momentum is taken 0.9. For 80,000 and 40,000 iterations the weight decay is taken 0.0005. An Average precision is used as an evaluation criterion for the damage detection system.

Experimental Results

The network is trained by using the four step procedure explained above. In the training process GPU mode takes approximately, 4 hours while CPU modes takes almost 1.5 days. The evaluation time for 500×500-dimension image in GPU mode is 0.040 sec while in case of CPU mode its almost 1 sec. For testing new images, the trained model with mean average precision of 96.50% is selected and a new set of test images is given to the damage detection system for testing. The test result shows a few errors which is due to different lighting conditions in patches. However, the overall performance of the proposed damage detection is promising and can be used in real time for damage detection in masonry structures. The results of the test data are shown in Figure 8. The training loss of the proposed system is shown in Figure 9.

DISCUSSIONS AND CONCLUSION

From the experiments, it can be concluded that the emerging class of technologies known as Faster R-CNN offers the possibility of automatic defect detection for masonry structures. In this work Faster R-CNN is implemented to automatically detect and localize the defects in images of masonry structures. The proposed system can be used for inspection in real time. The accuracy of the proposed system can be further improved by using a larger training dataset.

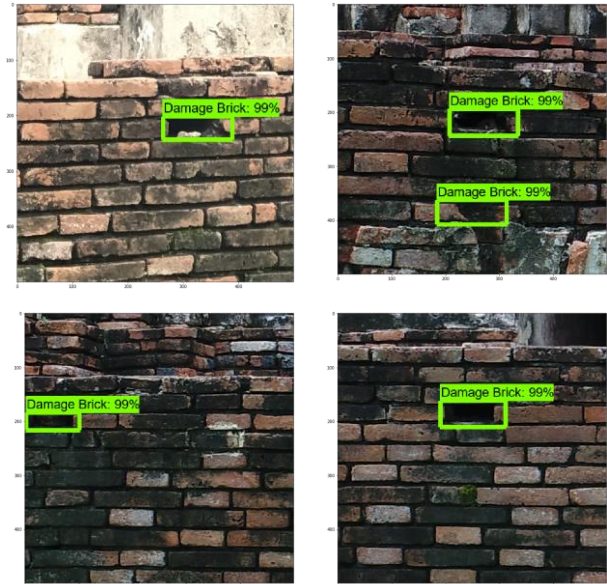


Figure 8: The Test Results of the proposed system

It can also be concluded that defect detection on masonry structures are difficult as masonry texture is complex. Therefore, it is difficult to create a good dataset. Human may not be able to identify damages in masonry structures as surface is complex and confusing. Nevertheless, good datasets are still required. The system is evaluated on the dataset and it can be concluded that deep learning algorithm like Faster R-CNN can be trained with sufficient amount of training data and the system can easily learn how to detect the damage automatically.

FUTURE WORK

In the proposed research work only one case of structural damages is studied, in the future the focus is to implement damage detection system for multiple types of defects in masonry structures. Also the research team is working on the modification of architecture of Faster RCNN to achieve an accelerated object detection system for civil inspection.

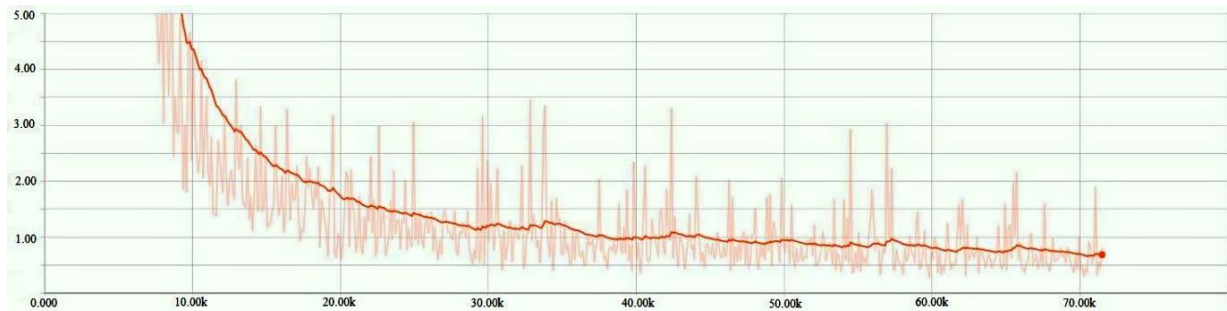


Figure 9: Training loss of the proposed system

ACKNOWLEDGEMENTS

The authors would like to thank the grant from the Research Division, Department of Engineering, Thammasat University to allow this research to be successfully completed.

REFERENCES

- [1] Hu, Y., Zhao, C. X., & Wang, H. N. (2010). Automatic pavement crack detection using texture and shape descriptors. *IETE Technical Review*, 27(5), 398-405.
- [2] Abdel-Qader, I., Abudayyeh, O., & Kelly, M. E. (2003). Analysis of edge-detection techniques for crack identification in bridges. *Journal of Computing in Civil Engineering*, 17(4), 255-263.
- [3] Prasanna, P., Dana, K. J., Gucunski, N., Basily, B. B., La, H. M., Lim, R. S., & Parvardeh, H. (2016). Automated crack detection on concrete bridges. *IEEE Transactions on automation science and engineering*, 13(2), 591-599.
- [4] Abdel-Qader, I., Pashaie-Rad, S., Abudayyeh, O., & Yehia, S. (2006). PCA-based algorithm for unsupervised bridge crack detection. *Advances in Engineering Software*, 37(12), 771-778.
- [5] Kaseko, M. S., & Ritchie, S. G. (1993). A neural network-based methodology for pavement crack detection and classification. *Transportation Research Part C: Emerging Technologies*, 1(4), 275-291.
- [6] Kabir, S., Rivard, P., & Ballivy, G. (2006). Detection of AAR deterioration patterns in concrete using wavelets for multiscale texture analysis. *Special Publication*, 234, 127-146.
- [7] Abdel-Qader, I., Abudayyeh, O., & Kelly, M. E. (2003). Analysis of edge-detection techniques for crack identification in bridges. *Journal of Computing in Civil Engineering*, 17(4), 255-263.
- [8] Suykens, J. A., & Vandewalle, J. (1999). Least squares support vector machine classifiers. *Neural processing letters*, 9(3), 293-300.
- [9] Nishikawa, T., Yoshida, J., Sugiyama, T., & Fujino, Y. (2012). Concrete crack detection by multiple sequential image filtering. *Computer-Aided Civil and Infrastructure Engineering*, 27(1), 29-47.
- [10] German, S., Brilakis, I., & DesRoches, R. (2012). Rapid entropy-based detection and properties measurement of concrete spalling with machine vision for post-earthquake safety assessments. *Advanced Engineering Informatics*, 26(4), 846-858.
- [11] Yeum, C. M., & Dyke, S. J. (2015). Vision-based automated crack detection for bridge inspection. *Computer-Aided Civil and Infrastructure Engineering*, 30(10), 759-770.
- [12] Cha, Y.-J., You, K. & Choi, W. (2016). Vision-based detection of loosened bolts using the Hough transform and support vector machines. *Automation in Construction*, 71(2), 181- 88.
- [13] Zalama, E., Gómez-García-Bermejo, J., Medina, R., & Llamas, J. (2014). Road crack detection using visual features extracted by Gabor filters. *Computer-Aided Civil and Infrastructure Engineering*, 29(5), 342-358.
- [14] Wu, L., Mokhtari, S., Nazef, A., Nam, B., & Yun, H. B. (2014). Improvement of crack-detection accuracy using a novel crack defragmentation technique in image-based road assessment. *Journal of Computing in Civil Engineering*, 30(1), 04014118.
- [15] Liao, K. W., & Lee, Y. T. (2016). Detection of rust defects on steel bridge coatings via digital image recognition. *Automation in Construction*, 71, 294-306.
- [16] Chen, P. H., Shen, H. K., Lei, C. Y., & Chang, L. M. (2012). Support-vector-machine-based method for automated steel bridge rust assessment. *Automation in Construction*, 23, 9-19.
- [17] Mirzaei, G., Adeli, A., & Adeli, H. (2016). Imaging and machine learning techniques for diagnosis of Alzheimer's disease. *Reviews in the Neurosciences*, 27(8), 857-870.

- [18] Cha, Y. J., Choi, W., & Büyüköztürk, O. (2017). Deep Learning-Based Crack Damage Detection Using Convolutional Neural Networks. *Computer-Aided Civil and Infrastructure Engineering*, 32(5), 361-378.
- [19] Zhang, L., Yang, F., Zhang, Y. D., & Zhu, Y. J. (2016, September). Road crack detection using deep convolutional neural network. In *Image Processing (ICIP), 2016 IEEE International Conference on* (pp. 3708-3712). IEEE.
- [20] Girshick, R., Donahue, J., Darrell, T., & Malik, J. (2014). Rich feature hierarchies for accurate object detection and semantic segmentation. In *Proceedings of the IEEE conference on computer vision and pattern recognition* (pp. 580-587).
- [21] He, K., Zhang, X., Ren, S., & Sun, J. (2014, September). Spatial pyramid pooling in deep convolutional networks for visual recognition. In *European conference on computer vision* (pp. 346-361). Springer, Cham.
- [22] Girshick, R. (2015), Fast R-CNN, in *Proceedings of the IEEE International Conference on Computer Vision*, Santiago, Chile, 07–13 December 2015, 1440–48.
- [23] Ren, S., He, K., Girshick, R., & Sun, J. (2017). Faster R-CNN: towards real-time object detection with region proposal networks. *IEEE transactions on pattern analysis and machine intelligence*, 39(6), 1137-1149.
- [24] Li, C., Kang, Q., Ge, G., Song, Q., Lu, H. & Cheng, J. (2016), Deep: learning deep binary encoding for multilabel classification, in *Proceedings of 2016 IEEE Conference on Computer Vision and Pattern Recognition Workshops (CVPRW)*, Las Vegas, NV, 26 June–1 July 2016, 744–51.
- [25] Suh, G., & Cha, Y. J. (2018, March). Deep faster R-CNN-based automated detection and localization of multiple types of damage. In *Sensors and Smart Structures Technologies for Civil, Mechanical, and Aerospace Systems 2018* (Vol. 10598, p. 105980T). International Society for Optics and Photonics.

TEMPORAL CHANGES OF SESIMIC LOADS USING PROBABILISTIC SEISMIC HAZARD ANALYSIS WITH A RENEWAL PROCESS

Takayuki Hayashi¹ and Harumi Yashiro²

¹ Tokio Marine & Nichido Risk Consulting Co. Ltd., Japan; ² National Defense Academy, Japan

ABSTRACT

Probabilistic seismic hazard analysis (PSHA) is carried out during the seismic design of structures, and a seismic load corresponding to a certain return period is calculated. In PSHA, there are cases where a renewal process is adopted for some large specific earthquakes. When the probability of the occurrence of an earthquake increases within a certain period, the seismic load based on PSHA also increases. Here, we study the temporal change of the seismic hazard and the influence of the epistemic uncertainty on the occurrence probability of a large earthquake around Japan. When calculating the occurrence probability of earthquakes around the Nankai Trough and the Sagami Trough, the occurrence history is not clearly known, hence, a large epistemic uncertainty arises about the parameters of the Brownian Passage time (BPT) distribution, such as the average recurrence interval, and the aperiodicity parameter alpha. In order to consider such an uncertainty, we employ the Monte Carlo method with a large number of input parameters to grasp the temporal change of the occurrence probability. In addition, the calculated occurrence probability is incorporated into the seismic hazard analysis. Here, we conduct a risk assessment for sample sites and discuss the notion that the influence of the epistemic uncertainty on seismic loads varies greatly from one region to another.

Keywords: Probabilistic Seismic Hazard Analysis, Temporal Change, Renewal Process, Epistemic Uncertainty

INTRODUCTION

Seismic ground motions, calculated with a certain probability from the seismic hazard curve, are usually adopted as the seismic load in the seismic design of structures based on the probabilistic seismic hazard analysis (PSHA). In Japan, the Headquarters for Earthquake Research Promotion (hereinafter called HERP), established by the government, conduct PSHA with a spatial resolution of 250m mesh all over Japan and have released a Japanese national seismic hazard map (hereinafter called the Japanese NSHM). In this Japanese NSHM, the probability of earthquake occurrences in the next 30 or 50 years from a reference date and their seismic intensity or peak ground velocity with respect to a certain probability value are made open to the public through a website on the Internet. This period of 30 or 50 years is considered long enough to account for earthquake risks, the service life of structures, and the lifetime of humans. The Japanese NSHM is updated every year with new information about the probabilities of earthquakes. Unless a large earthquake occurs in a certain year, the hazard at the same site in the next year increases each year. Therefore, the building load guidelines by the Architectural Institute of Japan [2] suggest that the seismic load for structures is calculated on the basis of the time-dependent seismic hazard curve according to the Japanese NSHM. However, it is not practical from the seismic design point of view that the load value changes

depending on the reference date and the period to be considered.

Meanwhile, the US seismic hazard map that was published by the United States Geological Survey shows long-term and short-term models. The long-term model is characterized by the earthquake occurrence probability being given by the Poisson process and considering the epistemic uncertainty for some parameters and equations. Since the Poisson process is adopted, the seismic load value does not change at any time in the long-term model. The short-term model takes into account one-year seismic activities such as cascading earthquakes. Therefore, structural designers can set the seismic load considering the structural performance while comparing the loads of the long and short-term models. When using the two models in this way in Japan, the occurrence period of a large earthquake is estimated as a few hundreds of years, which is relatively small, so it is important to capture the time change of the seismic load by PSHA.

In this report, we adopt a renewal process using the Brownian passage time (BPT) distribution and evaluate the temporal change of the time-dependent hazard curve by analyzing a sample site. In this study, the epistemic uncertainty of the parameters of the BPT distribution seems to have a large influence on the result. Therefore, we derived the time-dependent occurrence probability of earthquakes at the sample sites from their occurrence year using the Monte Carlo method with many input parameters for

the BPT distribution, and incorporated it into the seismic hazard analysis. We then analyzed the seismic hazard of the sample sites and discussed the temporal change of the seismic load. Furthermore, the results are compared to the seismic load calculated using the time-independent hazard curve with the Poisson process.

CALCULATION OF THE EARTHQUAKE OCCURRENCE PROBABILITY WITH A RENEWAL PROCESS

In this paper, we conduct PSHA using the seismic source model of the Japanese NSHM. The seismic hazard curves are calculated for some sample sites in the regions of Kanto, Tokai, and Kinki, as described in the next section. Earthquakes in the Nankai Trough and Sagami Trough (class M8), for which the renewal process in this seismic source model is adopted, are major earthquakes around Japan and have a significant effect on the results of these regions.

According to the long-term evaluation of the Sagami Trough earthquake reported by HERP [5], the earthquake occurrence sequence was generated using the Monte Carlo method, with the average occurrence interval and the variation value as the sample value, assuming that the earthquake occurrence interval follows the BPT distribution. The data series satisfying the past earthquake occurrence histories were selected, and the time-dependent occurrence probability was calculated from this data. We adopted a similar procedure in this study. When calculating the probability according to the unique probability distribution and the parameter pair consisting of the average occurrence interval and the variation value, the result may be dominated by the shape of the distribution in the region with an extremely low probability.

Our proposed method aims to address this issue by considering the epistemic uncertainty and using several parameters. The probabilities for all other earthquakes in the seismic source model are calculated using the same method as the Japanese NSHM.

Nankai Trough Earthquake

The parameters for calculating the occurrence probability of Nankai Trough earthquakes are determined on the basis of the reference report detailing the past earthquake occurrence history [6]. First, referring to the past earthquake occurrence

history from [6], pairs of these two parameters are generated as uniform random numbers with an average recurrence interval of 50-300 years and an aperiodicity parameter of 0.1-0.5. Using these parameter pairs, we then generate the earthquake occurrence year series with the Monte Carlo method dating back to the latest earthquake occurrence year. We then select 3,000 pairs of the parameters where the year sequence satisfies the past historical earthquake sequence. Since the 1605 Keicho earthquake was a tsunami earthquake, it is not clear whether it was an earthquake around the Nankai Trough. Therefore, as shown in Table 1, we consider two cases: Case 1 (C1), where the 1605 Keicho earthquake is considered, and Case 2 (C2), where it is not. When calculating the hazard curves to be described later, these cases are considered with equal weights in the logic tree. Parameters are selected out of the 3,000 pairs for each case. The latest earthquake occurrence year was 1944.9 on average for the Showa Tonankai and the Showa Nankai earthquakes. When selecting a parameter pair for the BPT distribution satisfying the earthquake history sequence, it is difficult to generate samples with the year that completely matches the time history. Therefore, the data where the earthquake samples occurred in the five years before or after the past earthquake occurrence year is judged to satisfy the condition. This is because the confidence interval of the sample occurrence is about 5%. Next, using the BPT distribution of the pair of selected parameters, 1,000 samples of occurrence years of the next future earthquake are generated for each case using the Monte Carlo method. As a result, we obtained 3,000,000 samples of the years of the next earthquakes.

Table 2 shows the results of parameter generation. In Case 1, the average occurrence interval is about 125 years, whereas in Case 2, the Keicho earthquake was not considered, and hence the average occurrence interval was about 151 years, which is about 20% larger than in Case 1. In addition, α tends to be slightly larger in Case 2. The average of the coefficient of variation is about 0.14 and 0.15 for each case, respectively. Figure 1 shows the sampling results of the occurrence year of the next future earthquake, generated using the Monte Carlo method with these parameters. The probability of the earthquake occurrence in each year as of January 1, 2018, is shown in Table 3. The probability of earthquake occurrence is 0.65% in 2018, but it greatly rises over time and becomes

Table 1 Historical Nankai Trough earthquakes

No.	Date	Name	Case 1	Case 2
1	Jun., 1361	Shohei	*	*
2	Jul., 1498	Meiou	*	*
3	Jan., 1605	Keicho	*	-
4	Aug., 1707	Houei	*	*
5	Dec., 1854	Ansei	*	*
6	Aug., 1944	Showa	*	*

*: included, -: excluded

Table 2 Samples Obtained for the BPT distribution parameters: the Nankai Trough earthquake

Samples	Case 1		Case 2	
	t	α	t	α
Average	125	0.32	151	0.33
Standard deviation	17	0.05	22	0.05
Max.	194	0.46	251	0.50
Min.	75	0.16	92	0.16

t: recurrence interval year

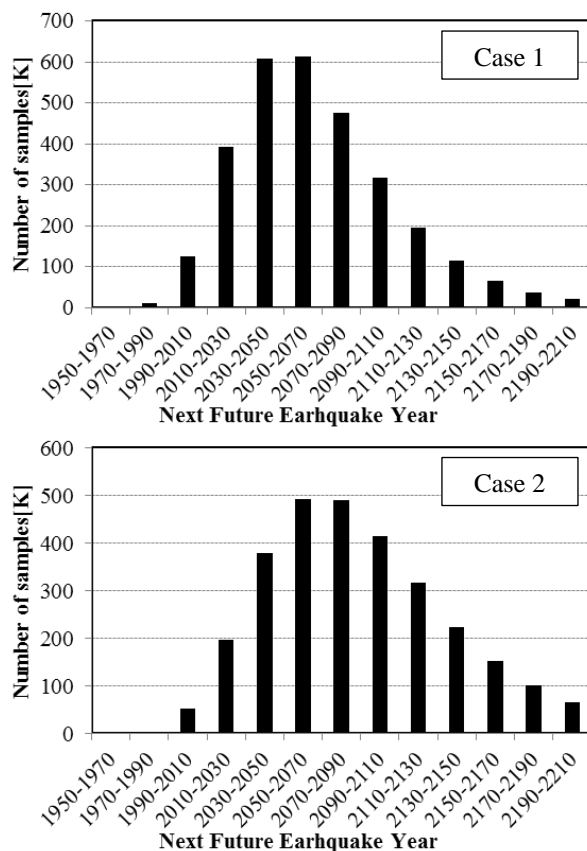
 α : aperiodicity parameter

Fig. 1 Samples of the occurrence year of the next earthquake for the Nankai Trough earthquake

Table 3 Earthquake probability in each occurrence year as of January 1, 2018: the Nankai Trough earthquake

Year	Occurrence Probability	
	Case 1	Case 2
2018	0.65%	0.29%
2023	0.79%	0.38%
2028	0.90%	0.46%
2033	1.02%	0.55%
2038	1.09%	0.63%
2043	1.14%	0.69%
2048	1.17%	0.75%

about 1.17% after 30 years. Case 2 also has an occurrence probability more than twice as much as 30 years later.

Sagami Trough Earthquake

The occurrence probability of the Sagami Trough earthquake is calculated using the parameters provided in the report by HERP [5]. First, referring to the result of the Monte Carlo simulation in [5], parameter pairs are generated using uniform random numbers similar to the Nankai Trough earthquake case that was presented in the previous section. The range of the average recurrence interval is from 50 to 300 years, and α range from 0.1 to 0.8. The history of the Sagami Trough earthquake, which is used for selecting the samples, is shown in Table 4. The latest Sagami Trough earthquake occurred in August 1923. We generated next earthquake year samples of 1,000 after selecting 3,000 pairs for the BPT distribution parameter. Furthermore, the earthquake history is the same as the condition reported in [5], and the 1703 Genroku Kanto earthquake is excluded from the time series.

Table 5 shows the result of the parameter generation. The average of the recurrence interval of all data is about 356 years, and the average of the coefficient of variation α is 0.35, resulting in a large uncertainty. The latest interval is 220 years between the Genroku Kanto earthquake in 1703 and the Taisho Kanto earthquake in 1923. Since this was excluded from the condition, the result is larger than the generally known recurrence interval. There is room for further discussion on adding the Genroku Kanto earthquake to the time series, but since the elapsed time from the latest earthquake occurrence is still short and the probability is small during the

period of several decades from the present time, we think that this result is sufficient for subsequent studies.

Figure 2 and Table 6 show the calculation results for the occurrence of the next earthquake, which is most likely to occur around 2250 AD. As of January 1, 2018, the probability of the earthquake occurrence in the next 30 years is 0.53%. HERP's report says that the occurrence probability of the Sagami Trough earthquake of magnitude 8 is approximately 0–5% in the next 30 years, which is consistent with our result. Although the probability in 2018 is 0.008%, it rises with time, and after 30 years, it will be quadrupled to 0.030%. We think that these probabilities have no significant effect on the seismic loads in PSHA for extremely low probabilities.

PROBABILISTIC SEISMIC HAZARD ANALYSIS

Application to PSHA

PSHA is carried out according to the studies reported in [7, 8]. We calculated the peak ground acceleration (PGA) at the engineering bedrock defined as shear wave velocity, $V_s = 292\text{m/s}$, by the GMPE of Kanno et al. (2006)[9], and did not consider the amplification of the ground motion by the soil surface. The seismic source model is also in accordance with [8]. However, we used the occurrence probabilities as established in the previous section for major earthquakes around the Nankai Trough and the Sagami Trough. The time-dependent earthquake probabilities are calculated as of January 1, 2018. The target sites are the locations of the prefectural governmental office in Tokyo, Kanagawa, Shizuoka, Aichi, and Osaka. From the viewpoint of the relation between the evaluation site and the epicenter location, Shizuoka, Aichi, and Osaka are affected by the Nankai Trough, whereas Tokyo and Kanagawa are in the areas where the Sagami Trough has a great influence.

The result of the seismic hazard curve considering the time change is shown in Fig. 3. The dotted curves are time-dependent, adopting the average probability of Case 1 and Case 2, and the solid curve is time-independent, using the Poisson process. The obtained hazard curves show that the hazard risk increases with the passage of time, depending on the imminent earthquake at every site. The probability of the Nankai Trough earthquake rises within the estimated period. Therefore, the hazard risk rises, especially in Aichi and Shizuoka that are close to the source area of the Nankai Trough earthquake. In Shizuoka, Aichi, and Osaka, the time-dependent curve exceeds the non-time-dependent curve within the considered period. The

Table 4 Historical Sagami Trough earthquakes

No.	earthquakes occurrence history
1	5400-5300 BP
2	5000-4800 BP
3	4800-4250 BP
4	4250-3950 BP
5	3800-3600 BP
6	3300-3100 BP
7	3050-2850 BP
8	2750-2700 BP
9	2500-2400 BP

Table 5 Samples Obtained for the BPT distribution parameters: the Sagami trough earthquake

(N = 6,000)		
Samples	t	α
Average	366	0.36
Standard deviation	36	0.10
Max.	510	0.73
Min.	249	0.11

t: recurrence interval year

α : aperiodicity parameter

Table 6 Earthquake occurrence Probability in each year as of January 1, 2018: the Sagami trough earthquake

Year	Occurrence probability
2018	0.008%
2023	0.011%
2028	0.015%
2033	0.017%
2038	0.021%
2043	0.027%
2048	0.032%

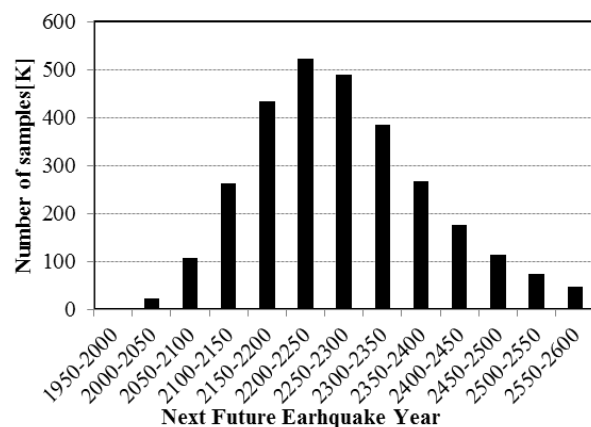


Fig.2 Samples of the occurrence year of the next earthquake for the Sagami Trough earthquake

temporal change of the PGA with a 10% annual exceedance probability in the next 50 years is shown in Table 7. Shizuoka has the largest PGA, followed by Kanagawa and Tokyo. Shizuoka also has the highest rise in the hazard risk within this period, and the PGA increases by about 32% for Shizuoka and about 24% for Aichi. In Tokyo and Kanagawa, the probability of the Sagami Trough earthquake does not rise so much, so the increase in the PGA after 30 years is relatively small.

Discussion

From the above results, we discussed the method of setting the seismic load on the basis of the stochastic approach. The time dependence of the hazard curve is strongly related to on the imminent earthquake and the distance from its source area. As time passes and the occurrence probability of a major earthquake rises, an earthquake will constitute a greater hazard risk. the earthquake will dominate the hazard risk greatly. Therefore, when setting seismic load, it is necessary not only to examine seismic loads only from the hazard curve, but also to disaggregate the hazard curve and grasp the contribution of each earthquake and its characteristics such as the magnitude, epicenter distance and occurrence probability. Then, it is important to comprehensively consider both the deterministic and the probabilistic approaches.

Table 7 PGA at 10% of the annual exceedance Probability in the next 50 years (cm/sec^2)

Site	Year				POI
	2018	2028	2038	2048	
Tokyo	789	797	805	813	970
Kanagawa	969	977	986	995	1164
Shizuoka	1197	1394	1520	1581	1431
Aichi	620	696	748	773	710
Osaka	588	609	624	632	613

POI: Poisson process (time-independent)

CONCLUSION

In this paper, we studied the temporal change of the earthquake hazard around Japan and the epistemic uncertainty about the earthquake occurrence probability for major earthquakes. We also conducted a seismic hazard analysis for some sample sites, and quantitatively showed that the seismic hazard greatly changes with time.

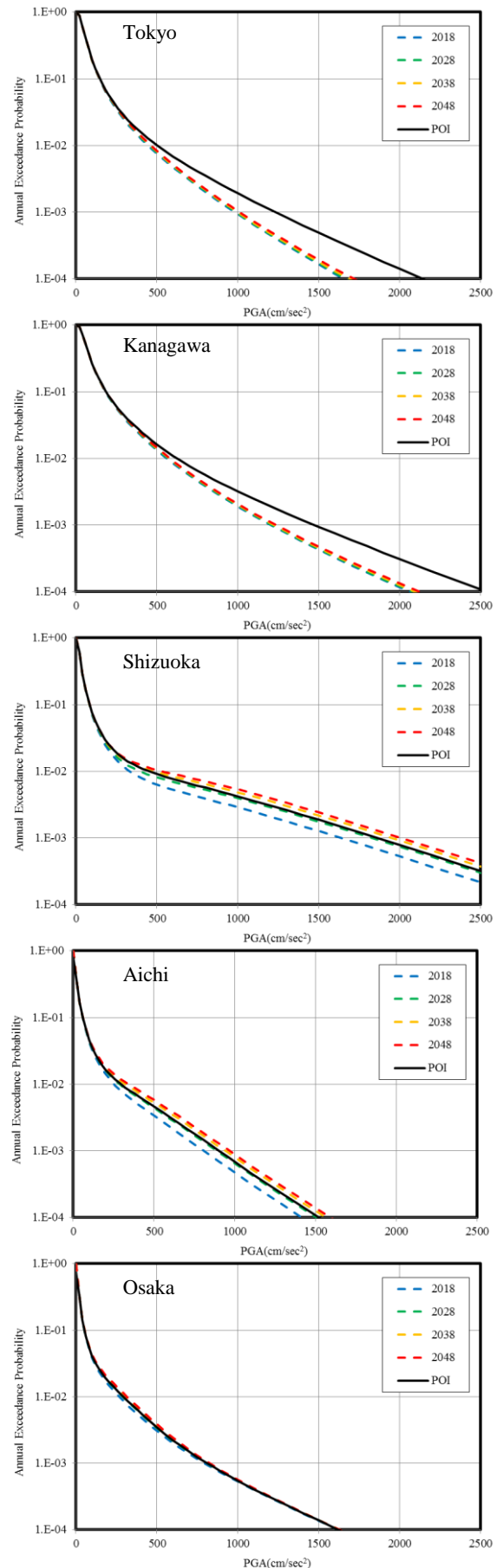


Fig.3 Hazard curves of each site

REFERENCES

- [1] Headquarters for Earthquake Research Promotion, National seismic hazard Maps for Japan (2017 Edition), 2017.
- [2] Architectural Institute of Japan, AIJ Recommendations for Loads on Buildings (2015 Edition), 2015.
- [3] Petersen, M.D., Moschetti, M.P., Powers, P.M., Mueller, C.S., Haller, K.M., Frankel, A.D., Zeng, Yuehua, Rezaeian, Sanaz, Harmsen, S.C., Boyd, O.S., Field, Ned, Chen, Rui, Rukstales, K.S., Luco, Nico, Wheeler, R.L., Williams, R.A., and Olsen, A.H., 2014, Documentation for the 2014 update of the United States national seismic hazard maps: U.S. Geological Survey Open-File Report 2014–1091, 243 p.
- [4] Petersen, M. et al., 2018 One-Year Seismic Hazard Forecast for the Central and Eastern United States from Induced and Natural Earthquakes - Seis. Res. Lett., doi.org/10.1785/0220180005.
- [5] Headquarters for Earthquake Research Promotion, Long term evaluation for the earthquakes around Sagami Trough (2nd Edition) , 2014.
- [6] Headquarters for Earthquake Research Promotion, Long term evaluation for the earthquakes around Nankai trough (2nd Edition), 2013.
- [7] Hiroyuki F., Shunichi K., Shin A., Nobuyuki M., et. al., A study on National Seismic Hazard Maps for Japan, Technical Note of the National Research Institute for Earth Science and Disaster Prevention, No.336, 2009.
- [8] National Research Institute for Earth Science and Disaster Resilience, Japan Seismic Hazard Information Station, <http://www.j-shis.go.jp>, 2017 (online)
- [9] Kanno T, Narita A, Morikawa, N, Fujiwara H and Fukushima Y, A new attenuation relation for strong ground motion in Japan based on recorded data, Bulletin of the Seismological Society of America, Vol. 96, No.3, 2006, pp. 879-897.

THE ASSOCIATION AND DISSOCIATION OF ENVIRONMENTALLY SIGNIFICANT MINERALS ON STRENGTH PROPERTIES OF SEDIMENTS IN OCEAN ENVIRONMENT

J. Rajaraman¹, PhD, S. Narasimha Rao², PhD

¹Professor, AMET University, India; ²Director, Dredging Corporation of India (Govt. of India), India

ABSTRACT

Ocean environment in its natural state maintains the normal geotechnical properties of the marine soils. Change in environment will modify the geotechnical properties. In this paper the precipitation effects in relation to pH and its impact on geotechnical properties are emphasized along with discussion on sodium carbonate and calcium carbonate. It is important that care should be taken to maintain ocean pH in the higher side of alkaline state to maintain natural properties of marine soils. Calcium chloride, one of the important constituents which controls the strength properties of marine soils, optimizes the situation to maintain normal strength. It is the selective precipitation which plays an important role in maintaining enormous clay varieties in the ocean in relatively low strength. The optimal production of calcium chloride maintains normal geotechnical properties of marine soils. In marine environment the calcium carbonate's association, dissociation tendencies modify the strength properties.

Keywords: Mineral, Shear Strength of soil, Turbidity Current, CCD, Carbonate Compensation Depth

INTRODUCTION

Geotechnical conditions of marine formations or any other formation are only the results based on experimental facts. But causes are more important than results. Causes are intimately related to geomorphological processes. Alteration of conditions or alternate remedies are possible only after understanding the geomorphologic processes. These processes are time dependents. Broadly the processes could be classified as long and short time. Processes identified as geological should be grouped under long time. In short time processes pollution and local environmental changes dominate. However, the actual impacts by way of dangers are independent whether duration is longer or shorter. In this paper strength of Soil Includes shear strength also.

IMPORTANCE OF CALCIUM CHLORIDE

In nature the formation of calcium chloride is restricted by many factors, such as (1) weathering, (2) pH activity in ocean, (3) solute and solution, (4) pH and pollution, (5) selective precipitation, (6) transportation, (7) basic rock forming minerals and (8) deposition of minerals. The above factors are identified to establish the fact how in formation calcium chloride is restricted under marine environment and how the factors are associated with the strength properties of marine soils. Though plenty of calcium is available in nature along with aluminium, it is not available as calcium

chloride. Only carbonates and silicates dominate in calcium combinations.

WEATHERING AND CALCIUM CHLORIDE

Primary and secondary rocks weather and produce clay rich marine soils. Marine soils have relatively low strength, natural conditions prevailing prevents formation of high strength clays. Calcium chloride is one of the strength producing agents. But in the products of weathering calcium chloride is only a trace. Even in the formation of chlorides, sodium chloride alone is produced in abundance.

PH AND PRODUCTION OF CALCIUM CHLORIDE

pH of ocean environment is slightly alkaline (8.1). For pH above 8 calcium chloride production increases. As the strength of marine soil is controlled by calcium chloride content the amount of it gains importance. But the pH around 8.1 in marine environment prevents production of calcium chloride. This favors production of marine soils of low strength. Calcium Chloride remains in solution.

Calcium carbonate + magnesium chloride
(insoluble) (soluble)

= Magnesium carbonate + calcium chloride
(insoluble) (soluble)

This is fundamental reactions for calcite and dolomite formations. It is seen that calcium chloride, is more soluble and so remains in solution and only carbonates are formed. So calcium chloride in soil is prevented. It is retained in the solution itself. This

favours low strength soil formations under marine conditions.

COASTAL POLLUTION EFFECT

Partially isolated water masses in coastal areas such as lagoon etc., Industrial wastes and other pollution effects tend to reduce pH to acidic conditions. In this way Calcium chloride precipitation is eliminated. Calcium chloride is conspicuously absent in lower pH conditions.

SELECTIVE PRECIPITATION EFFECTS

Even adverse pH condition for the production of calcium chloride only sulphides dominates. Even in production of sulphides only mercury, silver, copper, bismuth, lead, zinc, nickel, cobalt, iron, do dominate., calcium is particularly absent. The sulphides produced favour further reduction of pH value. In the absence of required mixing of water masses the water body continues to remain in anaerobic condition with low pH. Again this condition favours low strength soil.

TRANSPORTATION

Soil is nothing but rock on its way to ocean. Weathered products of rock forming minerals travel, calcium gets many opportunities for deposition. Calcium is fixed in lime stone shale sequences. Not much is available to reach ocean. In other words calcium is re-deposited quickly when conditions are favorable.

Calcium Chloride and Expansive Clay

Many researchers have done research and published many papers in the last few decades involving various additives to expansive clays [1] [2] [3].

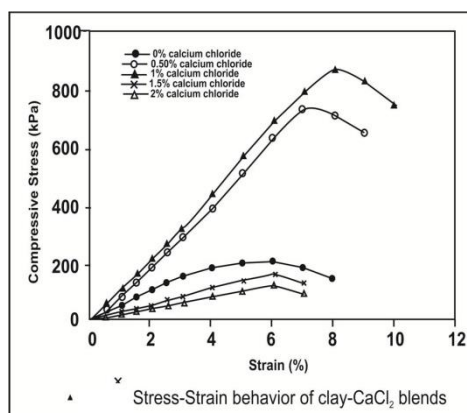


Fig. 1 Effect of Calcium Chloride(CaCl_2) Stress – Strain Behaviour of Expansive Clays. [4]

Fig 1. shows the effect of calcium chloride on stress-strain behavior of expansive clay specimens in unconfined compression test. The figure shows the stress-strain behaviour of the untreated expansive clay specimen in comparison with that of calcium chloride (CaCl_2) treated expansive clay specimens with the (CaCl_2) content varying as 0,0.5,1,1.5, and 2%. The untreated expansive clay specimen failed at a stress of 200 kPa and at a strain of 6%. However with the addition of calcium chloride, the failure stress, and the failure strain of the specimens increased initially. It was observed that the failure stress and the failure strain at 0.5% calcium chloride were 725 kPa and 7% respectively showing an increase of 263% in failure stress and 16.7% in failure strain 1% calcium chloride, however, the failure stress and failure strain were maximum at 856 kPa and 8%, respectively, showing a significant increase of 328% in stress and 33% in strain. This means that there was considerable improvement in the engineering behaviour of clay calcium chloride mixes when the calcium chloride content was 1%. However, the failure compressive strength decreased considerably when the calcium chloride content was increased to 1.5 and 2% indicating that 1% was the optimum calcium chloride content.

SODIUM CARBONATE AND CALCIUM CARBONATE AND CLAYS

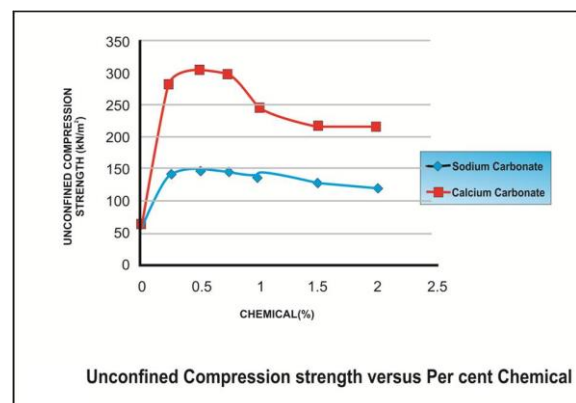


Fig.2 Unconfined Compression strength versus Percent chemical [5]

In Fig. 2 the variation of unconfined compression strength with per-cent calcium carbonate is also shown. The upper curve corresponds to calcium carbonate where the lower curve corresponds to sodium carbonate. The maximum improvement in unconfined compression strength occurs at 0.75% when the soil is admixed with either Na_2CO_3 or CaCO_3 . It is nearly five fold in case of CaCO_3 whereas it is nearly two fold in case of Na_2CO_3 .

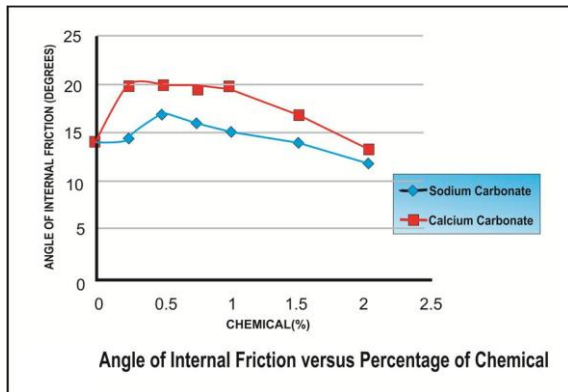


Fig. 3 Angel of Internal Friction versus percentage of chemical [5]

Fig 3. depicts the variation of angle of internal friction with per cent chemical. The upper curve corresponds to CaCO_3 whereas the lower curve corresponds to Na_2CO_3 . The maximum improvement in angle of internal friction value is about 21% and 43% when the soil is admixed with Na_2CO_3 and CaCO_3 respectively and is observed at 0.5% for Na_2CO_3 and 0.75% for CaCO_3 of the chemical in both cases.

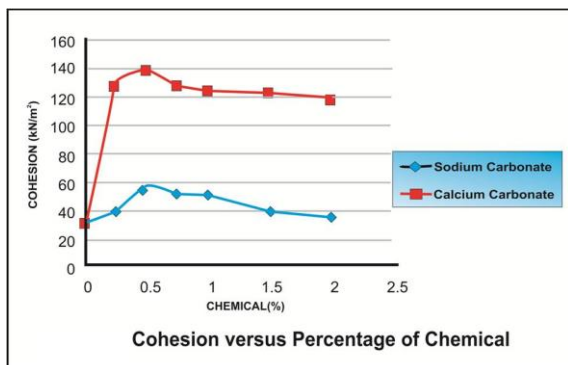


Fig.4 Cohesion versus Percentage of chemical [5]

In fig.4. the variation of cohesion with per-cent chemical is shown . It is seen from the plot that the upper curve corresponds to CaCO_3 whereas the bottom one corresponds to Na_2CO_3 . The maximum improvement in cohesion is about 77% for the soil admixed with Na_2CO_3 which occurs at 0.50% of the chemical CaCO_3 and its value is about 330% . From the aforesaid discussion it is concluded that 0.75%, 0.50% of the chemical by weight of the soil is sufficient in improving the unconfined compressive and tri-axial compression strength for both Na_2CO_3 and CaCO_3 .

Ocean Environment and CCD(Calcium Compensation depth) and Sediment Movement.

Facts about CCD: [6]

1. CaCO_3 shells (tests) sink from surface waters.

2. Tests may reach a depth where water is significantly under-saturated with respect to CaCO_3 .
3. At this depth, called lysocline, shells begin to dissolve.
4. In the modern oceans, there is also a depth at which there is no longer any free CaCO_3 .
5. This depth is called the Carbonate compensation depth (CCD) = -4km.
6. CaCO_3 tests accumulate only if they settle on seafloor above CCD.

Four Stages of Sediment Movements.(Fig 5)

1. Before crossing CCD. 2. When crossing lysocline zone. 3. When crossing the CCD. 4. After Crossing CCD.

Sediment Movements Before Crossing CCD.

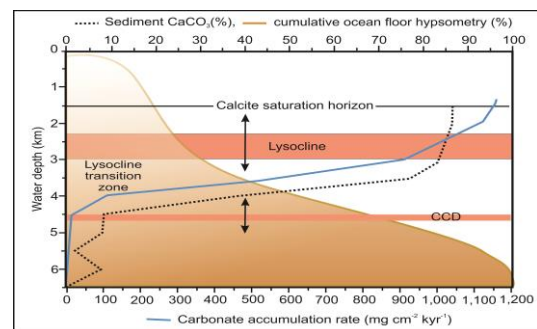


Fig.5 Carbonate Compensation Depth

The Turbidity current progressively filled by a well graded or otherwise, sediment load generates the momentum in addition to other factors like slope, water depth and other obstacles on its way to Abyssal plain. When conditions are favourable the Turbidity current picks up all particles picks up all particles including Carbonate particles (in any form) and the shear strength increases with distance.

Sediment Movements when crossing Lysocline Layer.

The Calcium Carbonate and other Carbonates slowly dissolve. The proportional decrease in particle to particle contact mechanism decreases shear strength of the Turbidity current. But still the Turbidity Current is mobile and penetrates lysocline layer to reach the CCD.

When Sediment Movements crossing CCD:

The dissolution CaCO_3 the current weakens because of the following reasons.

1. The unit weight or density of CaCO_3 is 2.7/ gm/cm³.
2. CaCO_3 is a good binding material for other particles.

3. The Saline Sea water is modified because of the dissolution of CaCO_3 .

Under these conditions the ambient fluid which encloses Turbidity current dominates and Turbidity Current loses height, inorganic load (CaCO_3 Particles load) and momentum and broadens, trying to spread horizontally.

Sediment movement after crossing CCD.

The last leg of transport of the sediment through Turbidity current is geo-technically important. In Abyssal plain the slope is less than 5° in most of the areas. The unaffected clay moves along with mud and by spreading the sediments create abyssal fans, similar to fans of a river. At this stage the Turbidity Current merges with Saline water after depositing all the particles. The reduced shear strength $\tau = c + \sigma \tan \phi$ is a function of c and ϕ . The cohesion C represents coaxial component of shear strength and represents non coaxial component of shear strength. The shear strength (τ) is a combination of pure shear (c) and simple shear (τ). The sediment just moves to and fro in the space of stillness which is the environment of Abyssal plain and different from the coastal and restless environment.

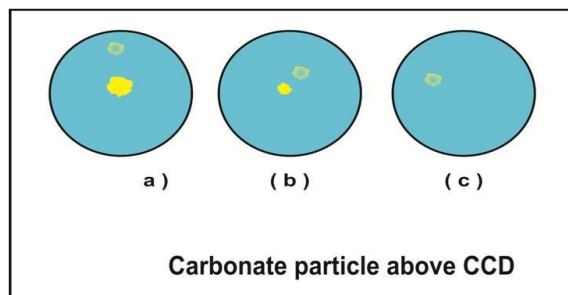


Fig.6 Carbonate Particles and CCD

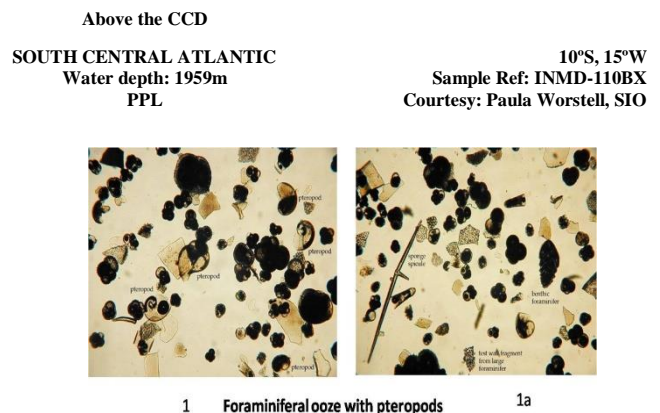
Fig.6a Carbonate particle above CCD.
Fig.6b Carbonate dissolving in lysocline depth
Fig 6c. Carbonate particle completely dissolved. (Cal-gone)

The lysocline is the depth in the ocean below which the rate of dissolution of calcite increases dramatically. Shallow marine waters are generally supersaturated in calcite, CaCO_3 , so as marine organisms (which often have shells made of calcite or its polymorph, aragonite) die, they will tend to fall downwards without dissolving. As depth (i.e., pressure) increases within the water columns, the corresponding calcite saturation of seawater decreases and the shells start to dissolve. The reaction involved, though more complex, can be thought as: $\text{CaCO}_3(\text{s}) + \text{H}_2\text{O}(\text{l}) + \text{CO}_2 \rightarrow \text{Ca}^{2+}(\text{aq}) + 2\text{HCO}_3^-(\text{aq})$. At the lysocline the rate of dissolution increases dramatically. Below this there exists a depth known as the *carbonate compensation depth*

(CCD) below which the rate of supply of calcite equals the rate of dissolution, such that no calcite is deposited. This depth is the equivalent of a marine snow-line, and averages about 4,500 meters below sea-level. Hence, the two are not equivalent. The lysocline and compensation depth occur at greater depths in the Atlantic (5000-6000 m) than in the Pacific (4000-5000 m) and at greater depths in equatorial regions than in polar regions.

The depth of the CCD varies as a function of the chemical composition of the seawater and its temperature. Specifically, it is the deep waters that are under-saturated with calcium carbonate primarily because its solubility increases strongly with increasing pressure and salinity and decreasing temperature. Furthermore, it is not constant over time, having been globally much shallower in the Cretaceous through to Eocene. If the atmospheric concentration of carbon dioxide continues to increase, the CCD can be expected to rise, along with the ocean's acidity.

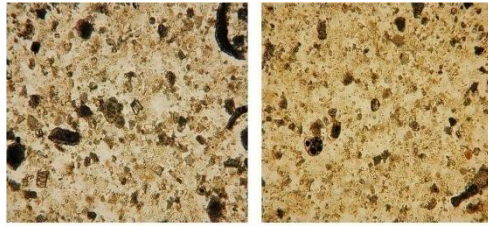
Available Documented Photographic Evidences of the Carbonate Compensation Depth Environment : [7] plates 1 to 7



Abundant whole foraminifer tests (some opaque due to size and presence of air bubbles within test chambers), foraminifer fragments from larger foraminifera and pteropods comprised of calcium carbonate and aragonite indicate a sample from well above the CCD. Benthic foraminifera and sponge spicules are also present. The foraminifera are in the size range 0.05-0.10 mm.

Partway down to CCD

EASTERN NORTH PACIFIC
Water depth: 2845m
PPL
10°N, 109°W
Sample Ref: BNFC-44P, 1cm
Courtesy: Paula Worstell, SIO



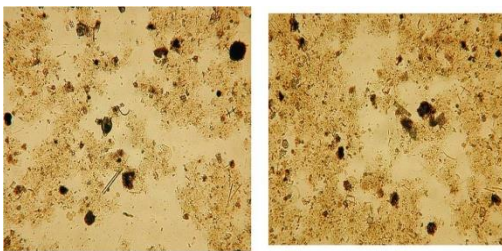
2 Calcareous ooze 2a

At deeper water depths the calcareous ooze consists mainly of fragmented foraminifera tests; complete foraminifera tests are rare. The sediment is still highly calcareous and larger fragments are in the size range 0.05-0.10 mm.

Approaching the CCD

EASTERN NORTH PACIFIC
Water depth: 3891m
PPL

12°N, 110°W
Sample Ref: BNFC-53P, 6cm
Courtesy: Paula Worstell, SIO



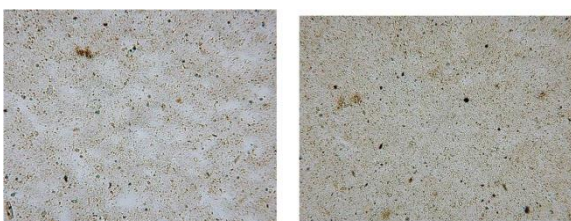
3 Clayey calcareous ooze 3a

At water depths approaching the CCD, foraminifers are mostly dissolved; only very small calcareous fragments remain. Siliceous microfossils are not dissolved. Fragments of siliceous radiolarians are present. The larger grains are of the order of 0.05 mm in size.

Below the CCD

NORTH PACIFIC, EAST OF
HAWAII
Water depth: 5365m
PPL

27°N, 147°W
Sample Ref: ZETES-38G, 64cm
Courtesy: Paula Worstell



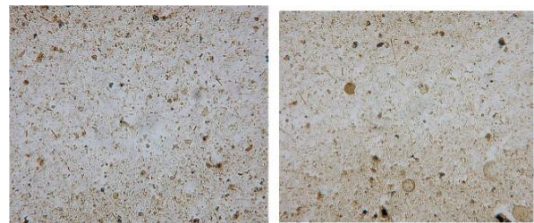
4 Deep sea red clay 4a

Below the CCD calcium carbonate is dissolved. Although calcareous microfossils may be living in the water column, their tests are not preserved in sediments on the sea floor. Seen here is a barren, fine-grained clay. Reddish-brown grains and irregular flecks of iron oxides are present together with clay- and very fine silt- grade mineral particles. Individual grains are under 4 μ m (0.004 mm) in size.

Below the CCD

NORTH CENTRAL PACIFIC
Water depth: 5530m
PPL

33°N, 174°W
Sample Ref: JYN-4G, 27cm
Courtesy: Paula Worstell, SIO



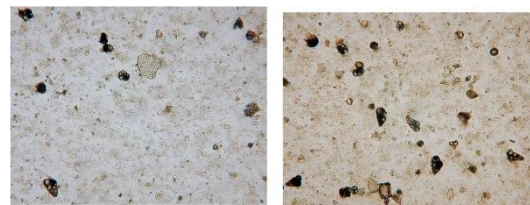
5 Deep sea red clay 5a

Deposited below the CCD, this fine-grained deep-sea clay contains some diatoms and siliceous spicules. Because the calcareous components are dissolved, siliceous microfossils are often concentrated in sediments deposited below the CCD. Diatoms are in the size range 10-100 μ m (0.01-0.1 mm) and individual clay grains are under 4 μ m (0.004 mm) in size.

Rapid burial, below CCD

SW PACIFIC, SAMOAN PASSAGE
Water depth: 5763m
PPL

17°S, 168°W
Sample Ref: CATO-29PG,
25cm
Courtesy: Paula Worstell,
SIO



6 Foraminifer nanno fossil ooze 6a

An unusual occurrence of a foraminifer nannofossil ooze recovered from well below the CCD. A turbidity current transported these calcareous sediments from a nearby topographic high. Rapid burial protected the calcareous microfossils from dissolution. The small planktonic foraminifers are in the size range of 0.05-0.10mm. Fragments of larger foraminifera are also present.

The CCD in the Pacific Ocean

CENTRAL PACIFIC
Water depth: 5060m
PPL

23°N, 153°W
Sample Ref: HILO-7G, 5cm
Courtesy: Paula Worstell, SIO



The CCD in the Pacific Ocean lies between 4200-4500 meters. This barren fine-grained red clay was recovered at a water depth of 5060m, well below the CCD in the central Pacific. Reddish-brown grains and irregular flecks of iron oxides are present, together with clay- and very fine to fine silt-grade mineral particles. Large grains are about, or under, 0.01 mm in size.

Summary

Rivers dump lot of sediments to ocean. In rainy season the hyper-pycnal flow forces many sediments into the ocean. When these sediments accumulate in continental shelf submarine slumps take place and the sediments move to continental slope. Here the minerals (CaCO_3 , CaCl_2 and other cementing minerals) and sediments gather momentum and Turbidity cement is developed. But Calcium Carbonate and Calcium Chloride continue to strengthen the sediments. The effect of Calcium Chloride, Calcium Carbonate and Sodium Carbonate in imparting strength is discussed in detail. These are related to the “Association” of environmentally significant minerals in producing strength (Shear Strength) to the sediments.

The sediments after gathering momentum flow towards abyssal plains. Turbidity currents generate the required force and momentum to the sediments. When sediments reach in the vicinity of carbonate compensation depth they undergo dramatic change in their behavior. Here only Calcium Carbonate dominates. Calcium and Sodium Carbonate play only a minor or no role at all with the movement of sediments.

The “dissociation” starts and the calcium Carbonate in solid particle form goes into solution and the sediment movement slows down. At last

Clay and silt are only that are present in the abyssal plains. The shear strength of the sediments is lost. The slope is less than 5° and only oozes and clays (red clays) are found. Minerals are responsible for this geomorphologic process that starts from Coastal areas to abyssal plains.

Critical Review of the paper

- 1) The results and concepts of laboratory experiment always do not match with the field variations. In Marine environment the problem leads to complexity and confusion. Only multi-disciplinary approach to the problems with reasoning will find a good solution.
- 2) Taking the basic shear strength equation for a soil sample, $\tau = c + \sigma \tan \phi$, when applied to marine environment will modify the results. The laboratory Test results are not directly applicable to marine environment.
- 3) Generally σ , the Pressure is low and Temperature is high in Coastal areas and in deep sea, the σ , the Pressure is extremely high and the Temperature is very low. In Coastal Areas the CaCO_3 Particles as Solid contributes for Angle of Internal Friction ϕ and the Clay contributes for Cohesion. In this condition (Coastal Areas to Continental Slope Areas) the Shear Strength is more. But in Calcium Carbonate Compensation Depth, there is noticeable Paradigm Shift in Soil Behaviour. For the same Equation ($\tau = c + \sigma \tan \phi$) due to Marine Environment. (Where c is Cohesion, ϕ = Angle of Internal Friction, σ = Normal Stress.)

The Geotechnical implications are:

- 1) CaCO_3 is saturated in Warm Shallow Waters and can form Sediments (as Solid particles CaCO_3). At Deeper Cooler Waters CaCO_3 is not saturated, so does not form deposit after a Certain Depth. Average CCD is 4500 m, below 5000 m Calcareous Ooze is not found. Since CaCO_3 Particles vanish (Cal Gone) ϕ is drastically reduced.
- 2) The LysoCline is the depth at which the rate of dissolution of Calcite begins to increase dramatically, but as the depth and pressure increase and the Temperature decreases, the Solubility of Calcite increases.
- 3) The Geo-Technical results achieved and conclusions arrived at in a controlled limited uncertainty are not directly applicable to marine Geo-Technical

behavior of soils in a complex marine environment. The paradigm shift observed in the Geo-Technical behavior of minerals (soils) in marine environment are not contradictory to laboratory based experiments, but only a logical expected Geo-Technical behavior which is only complementary to laboratory results.

- 4) The Pacific has lower pH and is cooler than the Atlantic. Thus the Ocean Acidification is such a major issue., in Modern Oceanography. The Industrial Revolution has tilted the Carbon Cycle. By increasing CO_2 in Atmosphere. We have also increased the amount of CO_2 in the Ocean. This increase of CO_2 increases H^+ ions present. Let us hope that CCD will absorb problems associated with CO_2 at least for some more decades.
- 5) It is expected that in the long run CCD Research will help to solve Carbon Sequestration, Global Warming and act as natural Carbon Sink.

CONCLUSION

In coastal area to continental slope end association of minerals (their Geochemistry) imparts strength. In abyssal plains the “dissociation” of minerals cause loss of strength to sediments, due to change in sediment behavior when they cross Carbonate Compensation depth.

REFERENCES

- [1] Katti, R.K., Patwardhan, S.K. and Thorat S.S. Some Engineering properties of Electro-chemically treated Bombay marine clay, Saturation Symposium on soft clay, Bangkok, Thailand, 1977, pp 663-664.
- [2] Katti, R.K. Stabilization of marine clay with various inorganic additives, Second Southeast Asian Conference on Soil Engineering, Singapore, 1970. pp 589-599.
- [3] Pavate, T.V Study on electrochemical hardening of marine clay, thesis (Ph.D), Indian institute of Technology, Bombay. 1974
- [4] Radhey S.Sharma., . R.Phanikumar. and VaraPrasada Rao Engineering Behaviour of a Remolded Expansive Clay Blended with lime, Calcium Chloride, and Rice-Husk Ash, Journal of Materials in Civil Engineering(C)ASCE., August 2008 pp 505-515
- [5] P.Ramesh., A.V.Narasimha Rao., N.Krishnamurthy. Efficacy of Sodium Carbonate and Calcium Carbonate in stabilizing a Black Cotton Soil. International Journal of Emerging Technology and Advanced Engineering. October 2012 pp 197-201.
- [6] Nature International Weekly Journal of Science . 2012 ofl 488 issue 7413
- [7] Under-Water Images. BOSCORF. British Ocean Sediment Core Research Facility. National Environmental Research Council. National Oceanography Centre.

CFD IMPACT OF AIR POLLUTION AND ITS MULTIFARIOUS ADVANTAGES (CASE: SUDIRMAN-THAMRIN STREET, JAKARTA)

Heidy Octaviani Rachman¹ and Lita Sari Barus²

^{1,2}School of Strategic and Global Studies, University of Indonesia, Indonesia

ABSTRACT

Jakarta is one of the most polluted cities in the world. The Jakarta Government led the Car-Free Day for the first time in 2007, with aims to reduce the pollution and uses of the public transportation. For the last 10 years, CFD Sudirman-Thamrin has been successful to invites thousands of people down to the street. People start to engage this initiative week by week that caused increasing of CFD spot in other places such as the administrative city of Jakarta and another city in Indonesia. CFD has successfully decreasing the level of air pollution than non-CFD time. More than that, CFD has become one of the recreational area, profitable area in the sight of participant. Even some people still uses of the private car, CFD has forced them to walk to their purposes area. Based on the high participation of citizen, CFD can be a potential initiative to engage car-free life and become a solution to reduce pollution. First of all, the evaluation of CFD impact will be doing by knowing the effect to environment and participant, based on Governor Regulation of Jakarta. Deeper understanding of the problem get by observing the CFD Sudirman-Thamrin, tracking the phenomenon and doing in-depth interview to participant. To complete the data about level of air pollution, we use the data from The Environmental Agency of Jakarta that contains PM¹⁰, SO₂, CO, O₃, and NO level from the last 3 years. Understanding three main issues of CFD can be lead into improvement at planning and policy implementation, there are environmental effect; transportation choices, and the multifarious effect. Analysis pattern of participant behavior will help to know how to change their perception about CFD without side effect such as decreasing amount of participant.

Keywords: Car-Free Day, Evaluation, Air Pollution, Environment, Public Transportation

INTRODUCTION

Car Free Day is held for 3 main purposes those are to minimalize usage of the private vehicle, campaign for public transportation and improve the air quality. There has been a lot of literature focusing on CFDs air quality, but still rare to discuss CFDs in terms of significant transportation preferences and people behavior. There are many factors that influence people to use public transportation such as comfort level, security, affordability from origin site and destination, cost and time-travel effectiveness. So also with the use of private vehicles, such as the pride of having their own vehicle, feel more secure and comfortable. Private vehicle restrictions have been made on programs such as ERP, higher vehicle tax but not significant. In addition to determining the macro scale program, CFD can be maximized for a very significant purpose to the city.

Car-free program was first initiated in mainland Europe under the name "No Car Day" in 1997 [2]. Within 3 years, this program has been adapted by various countries in Europe. Starting the early 21st century, CFDs began to be implemented in various cities in Asia. Indonesia itself first adapted this program since 2007 in Jakarta.

Car Free Day is held to socialize the impact of dependence on private vehicles and their impact on

air quality and traffic congestion; encourage policymakers to consider integrated transportation policies and the importance of public transport systems for the community. (Rahadi et al., 2012) In the implementation of CFDs, regional governments usually cooperate with environmental agencies to calculate the impact of CFD implementation on air quality in the environment. The calculated air aspect includes CO, NO, NO₂, NO_x, O₃, SO₂, benzene, toluene, ethylbenzene, -o, -m and PM₁₀ (Masiol, Agostinelli, Formenton, Tarabotti, & Pavoni, 2014). The data obtained is then chemically analyzed and calculated the risks to human health, especially carcinogenic elements or human cancer moisturizers. Air quality calculations are so sophisticated that they can be counted every hour with sophisticated equipment.

Jakarta is one of the highest pollution cities in the world. The highest pollution source in Jakarta is caused by the use of motor vehicles [1]. Since 1970, the government has issued macro-micro environmental policies to minimize the negative impact of air pollution in the capital. One example of macro programs is the Langit Biru program to control and prevent air pollution. The Langit Biru Program reviews air pollution levels in cities across provinces in Indonesia. A macro program or policy cannot run on its own, it needs to be supported by

micro scale programs that contact directly with the community. One example of a micro scale program is the Car Free Day Program. The program was inaugurated in 2007 in Jakarta with limited intensity at some point only because it is still in the stage of habituation. The Car Free Day program has been adopted at some places in Jakarta, even in other cities in Indonesia.

The Car Day Program is held in several places in Jakarta and centered on Jalan Sudirman-Thamrin. CFDs located on Jalan Sudirman-Thamrin (Fig.1) are held every Sunday from 06.00 a.m. to 11.00 a.m. On that day, along the protocol roads are closed for private vehicles, TransJakarta buses are still allowed to pass through special lanes. Each week, this event was attended by participants from various regions in Jabodetabek.

CFDs aim to train or provide an overview to people to get used to switching from private transportation to public transport, as well as reducing pollution levels in the Area. The program is rated as an effective means of introducing pedestrian-friendly cities. Since the beginning of this program in Jakarta in 2007, the program has a positive response, judging by the participation of the people present at the CFD. When the program is implemented, along Sudirman-Thamrin Road has been transformed into a public space where people interact in which trade interactions can be found, between street vendors and buyers; as well as the artist interaction with the audience. These activities make people more interested to visit the CFD location even though it comes from a distant location, and good for sports, health, and psychological reasons.

The activities of the CFD also affect the people who move along Jalan Sudirman-Thamrin and residents outside the Area who have an interest to pass through the road. One of the perceived disadvantages is the accumulation of vehicles on roads around Jalan Sudirman-Thamrin.

CFD Sudirman-Thamrin is held along the 6.7KM, from the Arjuna Wiwaha Horse Statue (Jln MH Thamrin) to the Build Youth Statue (Jl Sudirman). Along the way is full of tall buildings with office designation, retail malls, hotels and some embassies. Transportation facilities available along Jln Sudirman-Thamrin include Commuter Line Railway Train, Transjakarta Bus, Airport Train, Local Bus and MRT in 2019. There is a point on Jln Sudirman that is potential to be developed with TOD style. (kenapa penting)

The implementation of CFDs involves many government institutions, one of the most significant being the presence of Dinas Perhubungan. They began to close Sudirman-Thamrin road at 06.00 a.m. by using patrol cars, motorcycle, siren, installation of traffic cones and portable notice boards. Quickly, street vendors have started to fill the sidewalks. The

densest time visited by participants is at 07.00-09.30 a.m. The CFD line is reopened for private vehicles at 10.55 a.m. Before the road access is opened, cars and motorbikes are already packed arterial roads, in order to access Jln Sudirman-Thamrin as soon as possible after the track is opened. Even at 10:55 a.m, the streets are not sterile yet. The last person left on the streets of CFD is usually the security officers, janitors, and merchants who still clean up their merchandise. There are even willing to wait up to 1 hour and there is congestion around the arterial segment before the opening of the CFD line. This shows that people still prefer private transportation as the primary choice, even when its use is limited.

Therefore paper is important because to know which activity held in CFD need to improve and to find how CFD can be more effect people behavior in choosing public transportation.

METHODS

To know how significant the effect of CFD to people behavior, we have to evaluate this program trough the main aims. In evaluating the success rate of CFDs, researchers used direct observation visual methods at point A, B, C and D.

Researchers follow the CFD activity from start to finish like other CFD participants. The result of the observation is poured in the map which will become the reference for the preparation of public temporal-spatial planning strategy. To complement the accuracy of the data, researchers conducted in-depth interviews with some CFD participants who could be considered representative of the population. Types of participants who will be interviewed include street vendors (PKL), participants who exercise, cycling, do the environmental campaign and art participants. Interviews were conducted by asking open questions to enable participants to answer according to their preferences without being limited by the researcher's opinion. After getting answers on the participants' perceptions of CFDs, researchers will cross-check other participants. The significance of the information from each participant will be summed up into conclusions points which can then be developed as a formula for the arrangement of public temporal space.

To see how the CFD really works from the government side, researchers interviewing Environmental Agency, Transportation Agency and Cooperation and Small and Medium Enterprises Agency.



Fig. 1 The maps of Air Control Station in Jakarta.
Source: Dinas Lingkungan Hidup, DKI Jakarta, 2018.

RESULT ANALYSIS

Air Pollution Impact

Air quality measurement has become the duty of the Environment Agency (Dinas Lingkungan Hidup). The measurements are using the automatic ambient air quality station, the data obtained is valid for the last 24 hours. In Jakarta there are 5 air quality measurement points, the point closest to the CFD is at Bundaran HI, DKI 1 (Fig.1). Air parameters measured include particulate matter (PM10), carbon dioxide (CO), sulfur dioxide (SO₂), nitrogen dioxide (NO₂) and ozone (O₃). From the data, the pollution in Sudirman-Thamrin at CFD is decreasing when weekends. But is it will impact to another roads, because people trying to reach someplace with another road than Sudirman-Thamrin. Even if we had the data from other place (DKI2, DKI3, DKI4 and DKI5), we can not relate if the air pollution was increasing in other place because people lack of the roads.

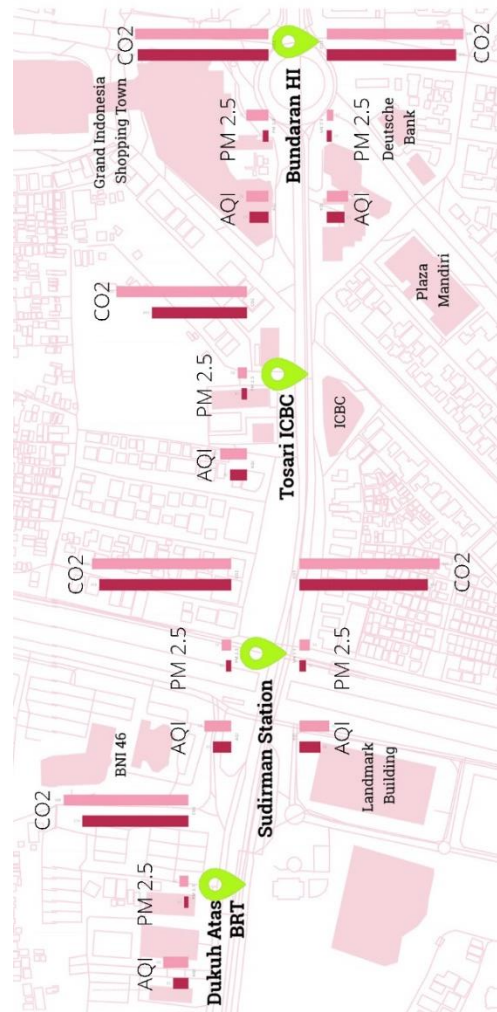


Fig. 2 Air pollution at the CFD area on weekdays (the pink one) and during CFD (the red one) .
Source: Eco-City Lived Project, 2018.

Multiflier Effect Of CFD Activities

A lot of people joining the CFD makes CFD more attractive than what its planned. People come with their family to CFD even their home not in neighborhood scale to the CFD area. Some of them take public transportation while the other still uses their private car and park it somewhere near the Sudirman-Thamrin Street.

When it comes demand, it will raised supply. Many street vendors are born in CFD. Its because the policy difference from previous and current governors regarding the presence of street vendors.

In the weekdays, the street vendors are trade everywhere with portable cart, mostly in Tanah Abang, near the CFD route. Some merchants who rent a place usually have better jobs on weekdays, selling at CFDs just for as a means of promotion for their business. Some of them have their own stores or have major work such as interior design/freelance. The perceived benefits for a five-time trader are the

easy access for street vendors to trade in CFDs without the need for permits and rent. While the losses are in the street vendors who rent the place because it is often obstructed by new vendors coming. From a survey of some street vendors, sales profit on CFDs rose 80-200%.

CFD traders who rent tents expect CFDs to be more rigid, while merchants who do not rent space feel fine and there is no need for change.

Implementation of CFD cannot be separable from the lifestyle of urban community (Prasetyo, 2017). The loose government role of the participants invites unauthorized street vendors to join the streets that should be filled by sports activities or environmental campaigns. At different points, CFDs can be interpreted differently by the participants themselves because of the dominance of activities that are not the main purpose. CFDs initially aimed at achieving environmental resilience and increasing public awareness of transportation, but then it provided a space to consume a variety of food provided by street vendors.

CFD is one example of placemaking that involves people to take to the streets. (LeGates & Stout, 2011) Community participation is very meaningful in placemaking. Similarly, on the contrary, the arrangement of the temporal public space should be based on the patterns that occur in the field to maximize the results to be achieved. Structuring with the bottom-up method will minimize the anomaly of the inherited impact. Research using the bottom-up method can be a recommendation for an academic review for regional government policy.

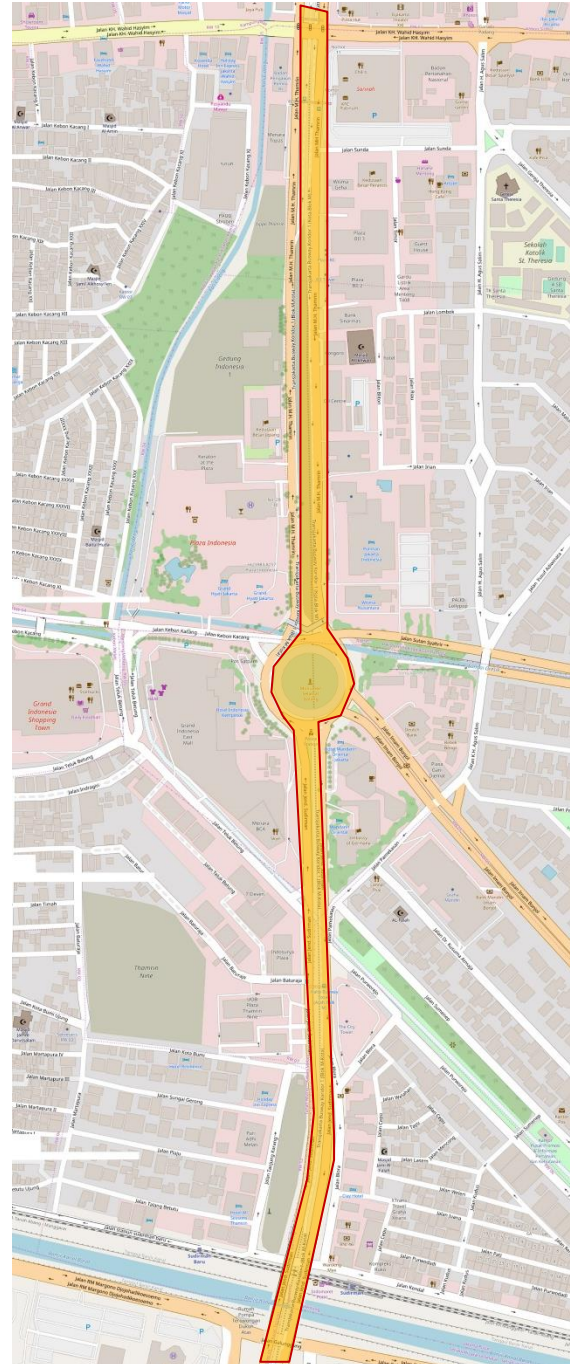


Fig. 3 The red bordered line are CFD Sudirman-Thamrin route, continuously 5KM to the south. This picture representative as the most denses people on CFD. Source: openstreetmap.org, 2018.

Based on the research result, it can be concluded that the street vendors in the area of car-free day (CFD) program in Sudirman - Thamrin is one of the informal sector workers. The economic income for street vendors in the car-free day (CFD) program in the Sudirman - Thamrin region gets significant benefits. This is different from the income they earn on a typical day that cannot meet their daily needs and for family savings.

Participation of street vendors to sell on car free day (CFD) program is very high. This is because of the enthusiasm of people who visit the CFD program is very high. Activities of community activities on Sunday around the Sudirman - Thamrin area, such as at the Hotel Indonesia and Grand Indonesia roundabout to make street vendors selling in the area.

The presence of street vendors will not be a problem because their presence also invites many participants to come to the CFD, even street vendors could be one reason why participants want to come to the CFD. This should be utilized by the management office, to be more active in campaigning for environmental awareness. In addition, there is a need to control the number and location of street vendors not to block the main purpose of the CFD. Thus the implementation of CFD in Sudirman Thamrin will become more harmonious and also economically beneficial for participants.

CONCLUSION

CFDs in Sudirman-Thamrin function more as a result of Placemaking, rather than an environmental program. But that does not mean the program is bad. This program has its own advantages in the eyes of Jakarta citizen. While the selection of transportation modes is also influenced by public transportation facilities. The tendency to use private vehicles is also a reaction to the inconvenience of road facilities and is somewhat influenced by social demands for the upper middle class. Routine micro-scale programs should be integrated with macro programs, in order to create a more comfortable and mutually supportive city between programs.

ACKNOWLEDGEMENTS

Thank you to Departement of Architecture Universitas Indonesia, CU Master of Eco-City student and Engineering student for the discussion for the several month about CFD and its problem. Mrs, Lita Sari Barus for a lot of the advice and brainstorming. Ahmad Safrudin, Direktur KPBB for the information about CFD Sudirman Thamrin since it first held on 1998. This article is part of Grant of International Publications for Student Final Project of Universitas Indonesia (Hibah PITTA): Analysis and Evaluation of Urban Community Behavior on Urban Transport Facilities and Policies.

REFERENCES

- [1] Ahmad Safrudin., Status dan Roadmap Pengendalian Udara di Indonesia, public discussion, 2018.
- [2] City of Seattle's CarSmart, 2001. *A Guide to Organizing Car-Free Day*, Seattle: Thinksmall.org.
- [3] Dieter Evers-Hans, Korff Rudiger. 2002. *Urbanisme di Asia Tenggara, Makna dan Kekuasaan dalam Ruang-ruang Sosial*. Yayasan Pustaka Obor Indonesia. Jakarta
- [4] LeGates, R. T., & Stout, F. (2011). *The City Reader. Routledge urban reader series* (6th ed.). New York: Routledge.
- [5] Masiol, M., Agostinelli, C., Formenton, G., Tarabotti, E., & Pavoni, B. (2014). Thirteen years of air pollution hourly monitoring in a large city: Potential sources, trends, cycles and effects of car-free days. *Science of the Total Environment*, 494–495, 84–96. <https://doi.org/10.1016/j.scitotenv.2014.06.122>
- [6] Mia Amalia, B. P. R. & J. B., 2013. The Consequences of Urban Air Pollution for Child Health: What does Self Reporting Data in the Jakarta Metropolitan Area Reveal?. *Working Papers in Trade and Development*, 09.
- [7] Rahadi, R. A., Hapsariniaty, A. W., Sarasvati, S. L., Kania, S., & Paramitha, T. P. (2012). Turning Road to a Public Place : Case Study of Car Free Day Phenomenon in Bandung, 37–46.
- [8] Rusdy, S., 2008. *Sustainable Transportation and the Promotion of Car Free Day Events*, Washington: University of Washington.
- [9] Sierra Club of Canada Eastern, 2001. *How to Stage CFD in Your Community?*. [Online] [Accessed 2018].
- [10] Wildsmith, Diane V., 2018. Eco-City Lived Project 2018. Departement of Architecture: Jakarta. (Unpublished work)

SPATIO-TEMPORAL ANALYSIS OF RICE FIELD PHENOLOGY USING SENTINEL-1 IMAGE IN KARAWANG REGENCY, WEST JAVA, INDONESIA

Supriatna¹, Rokhmatuloh¹, Adi Wibowo¹, Iqbal Putut Ash Shidiq¹, Glen Putra Pratama¹ and Laju Gandharum²

¹ Department of Geography, Faculty of Mathematics and Natural Sciences, Indonesia; ² Agency for The Assessment and Application of Technology, Indonesia

ABSTRACT

The *Oryza Sativa*, sp (or Paddy) is an important food crop for Indonesian people. It has become the primary staple food and the most gradually increased crop in terms of its productivity. It is recorded in 2015 that national production for paddy field was 71,766,496 tons, where 15.13% was produced by West Java province. With the national food security issues, monitoring in rice field growth becomes important to give some baseline information regarding the provision of staple food. Rice phenology is an essential information to ensure food security. The phase begins when the rice is planted in the ground and ends when the rice is ready for harvesting. Rice phenology divided into 5 classes, namely, land preparation, early vegetative, late vegetative, generative, and harvesting. One of the effective ways in monitoring is through rapid measurement using remote sensing system. The Indonesian National Institute of Aeronautics and Space (LAPAN) has applied the remote sensing technology to monitor paddy field growth (phenology). This study used Synthetic Aperture Radar (SAR), an active remote sensing system to monitor rice field phenology. The objective of this study is to implement Sentinel-1 SAR image in spatio-temporal analysis of the rice field phenology. Sentinel-1 Synthetic Aperture Radar images at the C-Band are capable of monitoring rice phenology. Then, this study aims to provide a spatial and temporal assessment of rice phenology in Karawang using Sentinel-1 images. As results, in northern irrigation area the paddy is grows quickly even it receive water last compared to southern and middle Karawang irrigation areas. Moreover, we found that the rice phenology phase distribution in Karawang not follow the irrigation pattern. Rice in northern irrigation areas have the lowest backscatter values. Temporal analysis shows that rice reaches harvesting stage quicker in dry season compared to rainy season with the same backscatter values.

Keywords: Rice field, phenology, Sentinel-1, spatio-temporal analysis, Karawang

INTRODUCTION

Rice phenology is defined as the changes that occur within the rice from the moment rice is planted in the ground and proceeds to fully grow during the harvesting stage [1]. According to the Agency for the Assessment and Application of Technology Indonesia, rice phenology is divided into five stages which are land preparation, early vegetative, vegetative stage, generative, and harvesting. The information of rice phenology can assist the rice planting farmers in their decision-making process, especially in the period where climate change affects the production of rice. Rice crop monitoring is always important, but there is a challenge in understanding the dynamics of phenological stages and providing accurate and timely information due to the large farming area [2, 3]. The costly, time wasting and labor consuming issues in this study can be addressed using remote sensing technology. Remote sensing imagery is useful in many applications, especially for obtaining

land-cover information in lower cost and lesser time [4, 5, 6].

Information on plant's phenology is related with biophysical and biochemical attribute of the plant. Those attributes were affecting the reflectance spectrum of the plant and changes in spectrum can be detected by remote sensing imagery [7]. Both optical sensors such as MODIS [3], Landsat [8], and SPOT [9], and radar sensor such as RADARSAT [10], ALOS PALSAR [11] and TanDEM-X [12] were useful to detect biophysical attribute and monitor phenology of the rice crop. The Synthetic Aperture Radar (SAR) image has been widely used to identify rice phenology due to the capability to provide a cloud free data. [13] find that three different dual *polarimetric* SAR image shows similar behavior in rice phenology monitoring. Sentinel-1 *polarimetric* images in the C-Band are capable of monitoring rice phenology [1, 14, 15, 16]. Then this research used the Sentinel-1 *polarimetric* image for identified the Rice Phenology.

The backscatter classification method is used to

classify rice phenology according to backscatter values. Karawang regency is chosen as the study area because it is one of the top rice producers within the West Java Province. West Java province is the largest rice producer in Indonesia, especially Karawang Regency. Based on national statistic report, in 2014-2015, rice production has been reduced from 11.085.544 to 10.856.438 tons from [17]. From the report, it is possible to acknowledge that efforts to maintain food security in West Java Province are necessary. Northern, Middle, and Southern Karawang areas are observed using spatial analysis according to the irrigation pattern [18]. Temporal analysis observes the rice phenology during the dry season and the rainy season. This research aims to provide a spatial and temporal assessment of rice phenology in Karawang according to Sentinel image analysis.

METHODS

Study Area

Karawang regency is located on $107^{\circ} 2' - 107^{\circ} 40'$ east and $5^{\circ} 56' - 6^{\circ} 34'$ south. It is an administrative region located in coastal area, adjacent to the Java sea especially in the north part. Karawang regency is chosen as the study area because it is one of the top rice producers within the West Java Province. According to the statistical data of West Java Province, the production of paddy field in Karawang reached 1,180,817 tons in 2015. It was the second largest production after Indramayu regency (1,233,785 tons).

Rice paddies observed in this study are rice paddies planted in rice fields that grow in a cycle of three main periods which are planting period, growing period, and harvesting period. Five classes were taken from these three main periods according to literature study on Sentinel-1 backscatter values which are land preparation, early vegetative, late vegetative, generative, and harvesting/ripening. Spatial analysis approach is used to achieve spatial pattern of rice growth phase and temporal analysis is used to achieve a temporal pattern of rice growth phase. Figure 1 explains the main conceptual framework in this research.

Image masking was performed on both Sentinel-1 images to separate rice fields from other landcover types in Karawang Regency. Pre-processing of Sentinel-1 SAR images includes radiometric calibration to adjust pixel values so that they represent backscatter, radiometric terrain flattening to smoothen rough surfaces caused by topographic differences, speckle filtering to remove image noise that causes spatial patterns that are not uniform, and geometric terrain correction to register geographic coordinates on the Sentinel-1 image. Decibel values are used to create samples for phenology classes

based on literature study which are then validated using field survey.

Maximum likelihood classification is then used to classify the Sentinel-1 image into five classes. Reference data which consists of gps coordinates and field photos are used to create training areas of each rice phenology for the maximum likelihood classifier. Each phenology has 1 point with a size of 1 pixel used to create a training area and the total number of points collected in this research are 78 points meaning the number of pixels used to create training areas for both Sentinel-1 images are 78 pixels. List of data used in this research can be seen in Table 2 below.

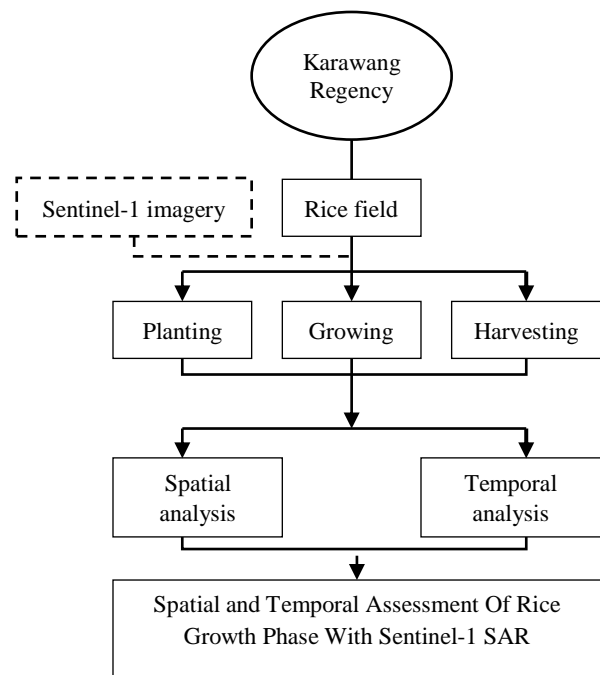


Fig. 1 Conceptual framework of this study.

Table 1 Rice phenology backscatter values in Indramayu Regency.

No.	Acquisition Date	Backscatter Value VH Polarisation	Rice Phenology
1	7 February 2016	-18	Land Preparation
2	19 February 2016	-19	Land Preparation
3	02 March 2016	-22	Early Vegetative
4	14 March 2016	-21	Vegetative
5	26 March 2016	-17	Late Vegetative
6	25 May 2016	-13	Generative and Harvesting
7	30 June 2016	-19	Land Preparation

8	24 July 2016	-20	Vegetative
---	--------------	-----	------------

Source: Agency for the Assessment and Application of Technology Indonesia (BPPT), 2016

Table 2 Data used in this study.

Information	Data Format	Source
Sampling area for rice phenology	Field photos and GPS coordinate	Field Survey (22 June 2017 and 13 November 2017)
Rice phenology	Planting calendar (2016-2017)	Tabular data from Ministry of Agriculture
	Sentinel-1 SAR Image	European Space Agency
Spatial pattern of rice planting	Area Survey Sampling (June 2017)	Agency For The Assessment And Application Of Technology (BPPT)
	Standard Rice Crop Field Map (2012)	Ministry Of Agriculture

RESULTS AND DISCUSSION

Backscatter classification of 22 June and 13 November 2017 Sentinel-1 SAR images produced five classes of rice phenology which are land preparation, early vegetative, late vegetative, generative, and harvesting. Land preparation phase has the lowest area percentage in Karawang rice field with 14% of area in 22 June. Harvesting phase during 22 June shows the highest percentage of area which is 57% in Karawang rice field. Rice phenology during 13 November 2017 has a lowest area percentage of 17% for late vegetative, and harvesting phase as the highest with 31% of area. Spatial information of rice phenology in Karawang regency can be seen in Figure 2.

Based on research conducted by [18] Karawang Regency has an irrigation pattern that starts from southern Karawang near Jatiluhur Dam and ends at the northern parts of Karawang. Rice crops in Southern Karawang Regency receive water ahead of middle and northern parts of Karawang Regency. Sentinel-1 Classified Rice Phenology maps show that northern areas of Karawang reach harvesting stage quicker than middle and southern areas of Karawang Regency. Rice in middle areas of Karawang reach harvesting stage second quickest after Northern Karawang. Southern areas of Karawang have rice which reaches harvesting stage at the slowest rate after northern and middle areas of Karawang Regency.

According to backscatter values in Southern Karawang irrigation areas, the pattern shows that

backscatter is at it's highest in land preparation phase and reduces in early vegetative phase. After early vegetative phase, backscatter values increase to -16 dB in late vegetative phase, drops to -15 dB in generative phase and rises up to -13.3 dB when rice reaches harvesting stage. Backscatter pattern of rice phenology in Southern Karawang irrigation areas can be seen in Figure 3 below.

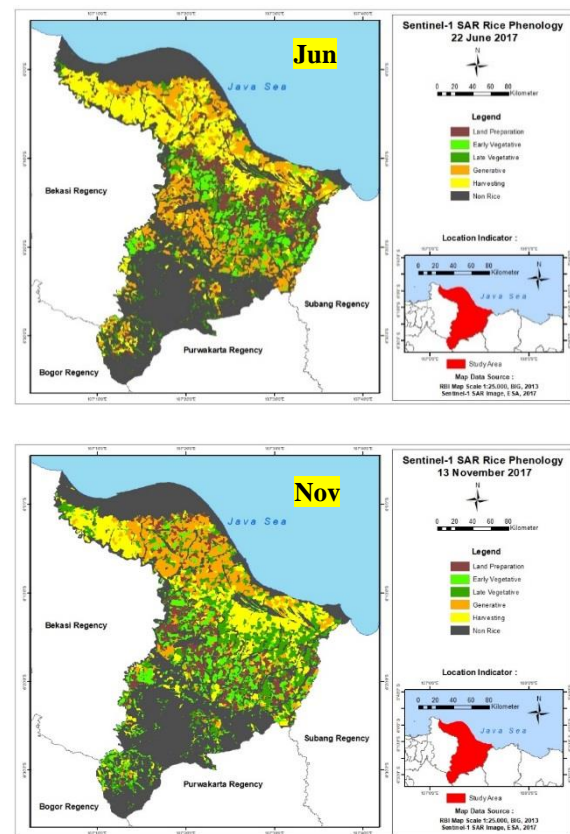


Fig. 2 Maximum likelihood classification for rice planting stages in 22 June and 13 November.

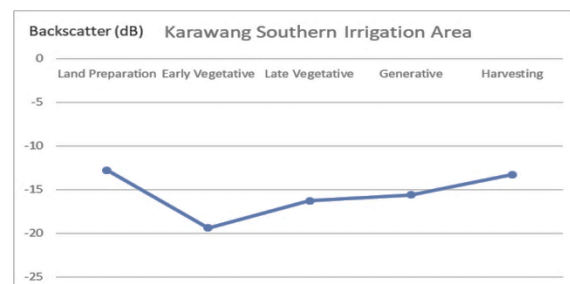


Fig. 3 Backscatter for each stage in Southern Karawang irrigation area.

Backscatter values of middle Karawang irrigation areas show a pattern where backscatter is at it's lowest when the rice plant is being prepared, and increases to -14 dB when the rice grows to early vegetative stage. After the early vegetative stage,

rice phenology backscatter drops to -17 dB in late vegetative phase, increases in generative phase and reaches its peak at -11 dB when rice reaches harvesting stage. Backscatter pattern of rice phenology in middle Karawang irrigation areas can be seen in Figure 4 below.

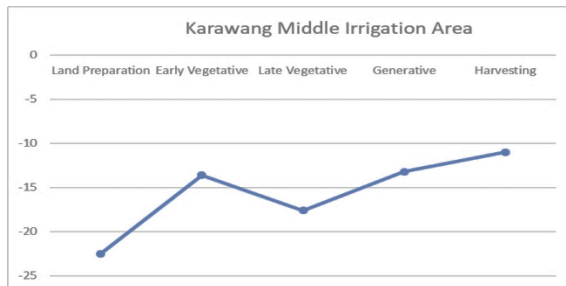


Fig. 4 Backscatter for each stage in Middle Karawang irrigation area.

Backscatter pattern of northern irrigation areas show that backscatter starts from -15.4 dB at the land preparation stage which then drops to -18.7 dB when rice reaches the early vegetative stage. Rice backscatter continues to drop when reaching the late vegetative stage and increases when rice reaches the generative stage. Backscatter values decrease from -15 to -16.2 when rice is ready for harvesting. Backscatter pattern of rice phenology in northern Karawang irrigation areas can be seen in Figure 5 below.

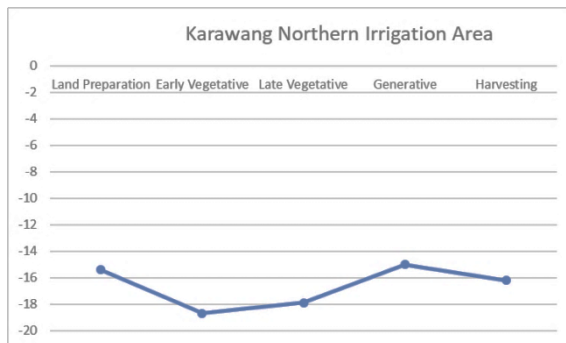


Fig. 5 Backscatter for each stage in Northern Karawang irrigation area

The result on three observed area of Karawang regency shows different backscatter pattern and value in each rice phenology phase. Although our results differ slightly from those of [1, 19, 20], it could nevertheless be argued the site dependency factor giving significant effect. This limitation became the underline issue when a SAR image based method would like to be proposed for large targeted area. Then a representative sample is obviously need to achieve a good result.

Backscatter comparisons between dry season and rainy season show similar backscatter values from late vegetative phase to the harvesting phase. Differences in backscatter values are seen in land preparation and early vegetative stage. Backscatter values are higher for land preparation stage in the rainy season compared to dry season. Backscatter values are higher for the early vegetative stage in dry season compared to rainy season. Comparison between backscatter values in dry season and rainy season can be seen in Figure 6.

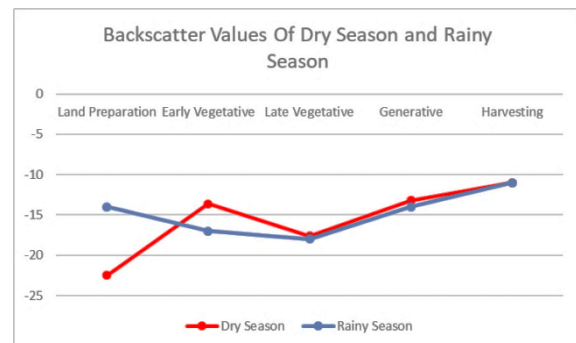


Fig. 6 Rice Phenology Backscatter Comparison Between Dry Season and Rainy Season

CONCLUSION

Rice phenology spatial pattern shows that northern irrigation areas grow rice which reaches harvesting stage quicker compared to middle and southern irrigation areas. Backscatter values are the lowest for harvesting stage rice in northern irrigation areas and the highest in middle irrigation areas. Rice growth phase spatial pattern does not follow irrigation pattern. Temporal pattern shows that rice reaches harvesting stage quicker in the dry season compared to rainy season with the same backscatter values. These findings add to a growing body of literature on to our understanding of rice phenology identification using SAR image.

ACKNOWLEDGEMENTS

This study is supported by the Ministry of Research and Higher Education, under the Penelitian Dasar Unggulan Perguruan Tinggi (PDUPT) or the Basic Primary Research for Higher Education grant.

REFERENCES

- [1] Nguyen, D. B., Gruber, A., & Wagner, W. (2016). Mapping rice extent and cropping scheme in the Mekong Delta using Sentinel-1A data. *Remote Sensing Letters*, 7(12), 1209-1218.
- [2] Atzberger, C. (2013). Advances in remote sensing of agriculture: Context description,

- existing operational monitoring systems and major information needs. *Remote Sensing*, 5(2), 949-981.
- [3] Onojeghuo, A. O., Blackburn, G. A., Wang, Q., Atkinson, P. M., Kindred, D., & Miao, Y. (2018). Rice crop phenology mapping at high spatial and temporal resolution using downscaled MODIS time-series. *GIScience & Remote Sensing*, DOI: 10.1080/15481603.2018.1423725.
- [4] Ismail, M. H. & Jusoff, K. 2008. Satellite data classification accuracy assessment based from reference dataset. *International Journal of Computer and Information Science and Engineering* 2: 96-102.
- [5] Shidiq, I. P. A., & Ismail, M. H. (2016). Stand Age Model for Mapping Spatial Distribution of Rubber Tree Using Remotely Sensed Data in Kedah, Malaysia. *Jurnal Teknologi*, 78(5), 239-244.
- [6] Shidiq, I. P. A., Ismail, M. H., Ramli, M. F., & Kamarudin, N. (2017). Combination of ALOS PALSAR and Landsat 5 Imagery for Rubber Tree mapping. *The Malaysian Forester*, 80(1), 55-72.
- [7] Kuenzer, C., & Knauer, K. (2013). Remote sensing of rice crop areas. *International Journal of Remote Sensing*, 34(6), 2101-2139.
- [8] Dong, J., Xiao, X., Kou, W., Qin, Y., Zhang, G., Li, L., ... & Liu, J. (2015). Tracking the dynamics of paddy rice planting area in 1986–2010 through time series Landsat images and phenology-based algorithms. *Remote Sensing of Environment*, 160, 99-113.
- [9] Upadhyay, G., Ray, S. S., & Panigrahy, S. (2008). Derivation of crop phenological parameters using multi-date SPOT-VGT-NDVI data: A case study for Punjab. *Journal of the Indian Society of Remote Sensing*, 36(1), 37.
- [10] Choudhury, I., & Chakraborty, M. (2006). SAR signature investigation of rice crop using RADARSAT data. *International Journal of Remote Sensing*, 27(3), 519-534.
- [11] Zhang, Y., Wang, C., Wu, J., Qi, J., & Salas, W. A. (2009). Mapping paddy rice with multitemporal ALOS/PALSAR imagery in southeast China. *International Journal of Remote Sensing*, 30(23), 6301-6315.
- [12] Rossi, C., & Erten, E. (2015). Paddy-rice monitoring using TanDEM-X. *IEEE Transactions on Geoscience and Remote Sensing*, 53(2), 900-910.
- [13] Watanabe T, Izumi Y, Tetuko J, Sumantyo S. Comparison of three compact-SAR mode through rice phenology monitoring. In *Antennas and Propagation (ISAP), 2017 International Symposium on* 2017 Oct 30 (pp. 1-2). *IEEE*.
- [14] Lopez-Sanchez, J.M., Vicente-Guijalba, F., Ballester-Berman, J.D. and Cloude, S.R., 2014. Polarimetric response of rice fields at C-band: Analysis and phenology retrieval. *IEEE Transactions on Geoscience and Remote Sensing*, 52(5), pp.2977-2993.
- [15] Chen, C.F., Son, N.T., Chen, C.R., Chang, L.Y. and Chiang, S.H., 2016. Rice crop mapping using Sentinel-1A phenological metrics. *International Archives of the Photogrammetry, Remote Sensing and Spatial Information Sciences*, 41, p.B8.
- [16] Mansaray, L.R., Huang, W., Zhang, D., Huang, J. and Li, J., 2017. Mapping rice fields in urban Shanghai, southeast China, using Sentinel-1A and Landsat 8 datasets. *Remote Sensing*, 9(3), p.257.
- [17] BPS – Agency for Statistic. 2015. Rice production report. *Annual Report*.
- [18] Semedi., Siregar., Sanjaya. 2012. Rice Crop Spatial Distribution and Production Estimation Using MODIS EVI Case Study of Karawang, Subang, and Indramayu Regency. Bogor: Institut Pertanian Bogor.
- [19] Yang H, Pan B, Wu W, Tai J. Field Based rice classification in Wuhua county through integration of multi-temporal Sentinel-1 and Landsat-8 OLI Data. *International J. Application Earth Obs Geoinformation*. 69 (2018) 226-236.
- [20] Tian, H., Wu, M., Wang, L. and Niu, Z., 2018. Mapping Early, Middle and Late Rice Extent Using Sentinel-1A and Landsat-8 Data in the Poyang Lake Plain, China. *Sensors*, 18(1), p.185.

DEVELOPMENT OF GREEN INFRASTRUCTURE IN URBAN CATCHMENT AREA (CASE STUDY: TANJUNG BARAT SUB-DISTRICT, SOUTH JAKARTA)

Dimas Ario Nugroho¹, Jachrizal Soemabrata^{2*}, Hendricus Andy Simarmata¹, Dwinanti Rika Marthanty²
¹Urban Development Studies, University of Indonesia; ²Faculty of Engineering, University of Indonesia

ABSTRACT

The rapid urbanization of the city of Jakarta has resulted in the decreasing of the hydrological function of the city due to the increase of impervious land cover and the reduced water catchment area. Water conservation efforts are needed by increasing water infiltration and reducing surface water runoff with the Low Impact Development approach with green infrastructure (GI) implementation in the urban catchment area. This research takes a case study in Tanjung Barat Sub-district, South Jakarta, which acts as one of water catchment area of Jakarta. The aims of this study is to determine the placement of GI in accordance with the criteria of land suitability, and analyze the effectiveness of its application. The method used in this research is the modeling of GI placement by using BMP Siting Tools module on the SUSTAIN program and ArcGIS. And its effectiveness analysis with the calculation of flow coefficient and flow of runoff. The study result showed some of GI types that suitable to be implemented are bioretention and rain barrel. Based on the calculation of flow coefficient and runoff flow, it is known that GI application is effective in lowering the flow coefficient and reducing runoff discharge by 26.25%.

Keywords: Urbanization, Low Impact Development, Water Conservation, Land Suitability, Effectiveness Analysis

1. INTRODUCTION

Rapid development of urban areas characterized by increasing population and settlement expansion led to increased impervious area and urban activity. This has an impact on the disruption of hydrological cycle balance in urban areas, due to increased water runoff during rainfall and decreasing water absorption [1].

The city of Jakarta as one of the most rapidly growing urban areas in Indonesia [2] experienced problems related to the decreasing of the city's hydrological function due to the higher percentage of built-up areas and the reduced water catchment area [3]. This is exacerbated by conventional urban drainage systems, climate change and inadequate provision of water infrastructure so that there are still many people who use groundwater [4]. As a result, Jakarta is difficult to get rid of problems related to the decline of hydrological functions, such as floods, water crisis, land subsidence, and sea water intrusion [3].

Water conservation efforts are needed to restore hydrological functions in urban areas, particularly those in catchment areas. This can be done by increasing the capacity of water infiltration, thereby increasing groundwater levels [5]

One of the water conservation methods is the Low Impact Development (LID) approach, with the application of green infrastructure (GI) [6]. GI is the best practice implementation based on LID

approach in the stormwater management by holding for as long as possible stormwater in an area to enlarge the infiltration flow into groundwater [5]. GI serves to increase water absorption capacity by reducing the impact of surface water flow by retaining and absorbing water runoff to the soil, thus protecting the city from floods and droughts [6, 7]. The form of GI can be a natural, semi-natural, and artificial network of multifunctional ecological systems located within or within urban areas on all spatial scales [8]. Examples of GI include bioretention or rain garden, green roof, rain barrels or cisterns, infiltration trench, vegetated swales, wetland, retention pond, porous pavement, etc [9].

The application of GI has been successful in providing both direct and indirect benefits such as drainage system cost efficiency, decreasing rainfall runoff, reducing pollution, increasing green open space, improving climate comfort as well as quality of life in an environment [4, 10]. However, in order to apply the GI more optimally and effectively in accordance with its function, it is necessary to further study in determining the suitability of the site or location of the placement of GI in accordance with the character and function of each GI [1].

This study aims to obtain modeling related to the type and location of GI implementation based on suitability analysis and its effectiveness. The research took place in the Tanjung Barat subdistrict, South Jakarta, which is one of the areas

that became water catchment area for the city of Jakarta.

The result of modeling of suitability analysis is map of GI placement according to land suitability criteria based on physical criterion, such as soil type, groundwater level, drainage area, land slope, head, land cover, road network, water body, and the percentage of impervious [12]. Then to know the effectiveness of the placement of GI that has been modeled, can be analyzed with the calculation of flow coefficient and runoff discharge.

2. METHOD

There are two stages in this research: (1) map of GI placement modeling; and (2) hydrological analysis to determine the effectiveness of GI placement.

2.1 Map of GI Placement Modeling

At this stage, it is done using suitability analysis method, assisted by BMP Siting Tools (BST) module on the SUSTAIN Model, that is embedded in ArcGIS 10.1 software. BST is software that can assist in choosing the appropriate location for each GI that refers to the method of LID [9].

Table 1. Data Format for BMP Siting Tool

ArcGIS Layer	Format
DEM (Digital Elevation Model)	Raster file
Land use	Raster and Table file
Percent impervious	Raster file
Urban Land use	Shape file
Road	Shape file
Stream	Shape file
Soil	Shape and Table file
Groundwater Table Depth	Shape file
Land Ownership	Shape file

The data requirement in this study, according to the criteria specified in the BST is a thematic map, both in raster and shape format, for the data layer in ArcGIS. The thematic maps needed in the data layer include contour, land use, built-up land, land tenure, soil, road and river network maps, and groundwater table depth [1].

Then, a suitability analysis is performed by setting criteria for the nine parameters considered appropriate for each type of GI. The criteria used in this study are primarily based on predetermined criteria derived from guidelines for the use of BST [11]. However, these criteria can be adjusted

according to preferences based on conditions, local knowledge, and rules at the study site [1].

2.2 Analysis of GI Effectiveness

The effectiveness analysis is done by comparison of the existing condition and after applied GI. So it can be analyzed the amount of flow coefficient or curve number (CN) which is used due to surface runoff potential. CN calculations on the existing conditions of all land cover at the study site, with the following formula [13] :

$$CN_C = \frac{CN_1 A_1 + CN_2 A_2 + \dots + CN_j A_j}{A_1 + A_2 + \dots + A_j} \quad (1)$$

Where : CN_C = CN Composite
 A_j = Area of land cover
 CN_j = CN of each land cover

Then calculation CN value of GI based on land connectivity to impervious area. CN in the impervious area is calculated by observing a direct relationship between the area and with the drainage system [14].

$$CN_{LID} = CN_p + \left(\frac{P_{imp}}{100}\right) \times (98 - CN_p) \times (1 - 0.5 R) \quad (2)$$

Where : CN_{LID} = CN GI
 CN_p = CN *pervious area*
 R = Ratio of impervious areas that are not connected to the drainage system of the total area
 P_{imp} = Percentage of *impervious area*

After that, the calculation of runoff flow volume, based on the value of the rainfall design, that becomes the input and the ability of the ground to retain or absorb water. Calculation of runoff flow using Soil Conservation Services (SCS) method calculation parameters [15] are:

$$Q = \frac{(P_2 - 0.2 S)^2}{P_2 + 0.8 S} \quad (4)$$

$$\text{with } S = \frac{1000}{CN} - 10 \quad (5)$$

Where : Q = Runoff flow (in/s)
 P_2 = Daily maximum rainfall of 2 years (in)
 S = Maximum retention potential of the land (in)

3. RESULT AND DISCUSSION

3.1 Study Area Description

The study location is located in Tanjung Barat Subdistrict, South Jakarta, which is one of the water catchment of Ciliwung River Basin located in DKI Jakarta province. It has a fairly high rate of land cover change, with percentage of 53.99% or 179.84 ha [16]. Whereas based on the guidance in the city plan [17] that in the area functioned as water catchment area, so that with high percentage of build area will reduce the hydrological function.

Geographically, Tanjung Barat Subdistrict is located at 06 ° 17'43.105 " - 06 ° 18'42.934" South Latitude and 106 ° 50 '27.077" - 106 ° 50'17.716 " East Longitude. The total area of Tanjung Barat Subdistrict is 366.8 ha. Based on the results of land use map processing, it is known that the housing occupies area of 125.71 ha or 34.27% of the total area. Water body consists of river, pond, and channel with an area of 14.12 ha (3.85%). Green open space consists of public and private open space, and also bare land, with an area of 113.61 ha (30.97%). The road consists of toll, national, provincial, arterial, and collectors with an area of 37.53 Ha (10.23%). Meanwhile, non-residential buildings consist of offices, commercials, and schools with an area of 10.41 Ha (2.84%).

Other physical conditions such as the slope of land in the village of Tanjung Barat Subdistrict is relatively flat with a slope of 0-8%. The hydrological soil group (HSG) in Tanjung Barat Subdistrict is included in group C which has soil conditions with medium runoff potential and low infiltration rate with infiltration rate 1-4 mm / day [13]. While the groundwater table depth is in the range of 3.53-9.81 m from the soil surface.

Table 2. Physical condition at Tanjung Barat Subdistrict

Physical Criteria	Value
Area	366.8 ha
Slope	0-8%
Build area	69.03%
Green open space	30.97
HSG	C
Groundwater table depth	3.53-9.81 m

3.2 GI Distribution

Based on the analysis using input data and criteria processed by BST, the resulting layer in the ArcGIS software shows the location for each type of GI and a composite map layer showing all the appropriate combinations of GI types in each location.

There are two types of GI that can be developed in accordance with the physical conditions in Tanjung Barat Subdistrict, namely bioretention and rain barrels. The distribution of location and type of GI from this suitability analysis is presented in Figure 1. The limitation of selected GI, is due to the criteria of the HSG, which in the Tanjung Barat Subdistrict is included with the HSG type C criteria. This causes the type of GI that serves to infiltrated such as infiltration basin, infiltration trench, and porous pavement can't be applied because the HSG required is criteria A or B. In addition, the limited land and regulations related to road, rivers and buildings borders cause the limited number of selected GI.

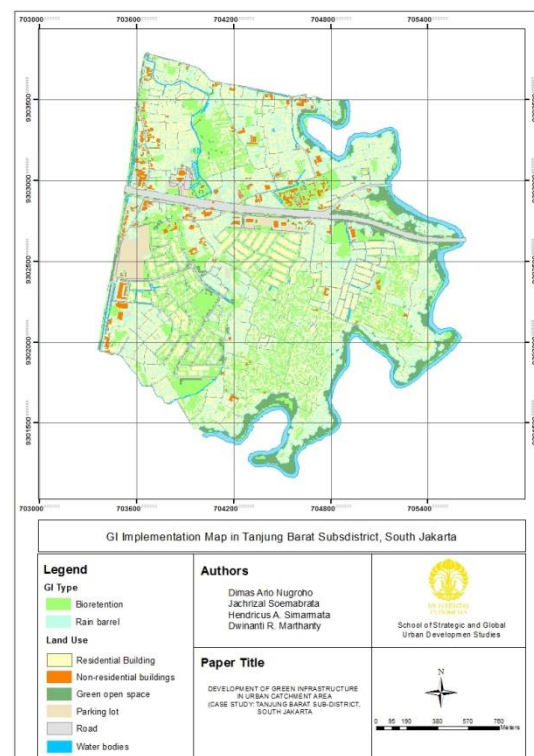


Fig.1 Map of distribution and type of GI in Tanjung Barat Subdistrict

Bioretention is selected because it does not require large land and can be used in any soil condition because there is soil treatment by bringing more fertile soil and greater infill capacity if needed. Rain barrel was also chosen because the criteria are not too tight, which is limited only by the criterion of the building border only.

The total area of bioretention that can be applied is 45.48 ha, and placed in the existing green open space both public and private. The application of bioretention is flexible, applicable in house yards, median road, sidewalks, parking lots, and in small alleys in densely populated housing

[18].

Bioretention becomes an additional feature in green open space in increasing infiltration capacity. It has a infiltration rate of 7 mm / h with a capacity of 6 inch [5]. It can be estimated that the volume of bioretention capacity is 69,130 m³.

Meanwhile for rain barrel, it can be used in rainwater harvesting as a reservoirs. It is useful to meet the needs of water outside drinking water, bathing and washing, such as watering plants, flushing toilets and other.

3.3 Analysis of GI Effectiveness

3.3.1 Flow coefficient (CN)

The flow coefficient or curve number (CN) is a number that shows the ratio between the extent of runoff to rainfall [15]. The calculation of the effectiveness of GI based on the flow coefficient can be assessed based on the comparison on the existing condition and after the applied of GI. So It can analyze the amount of flow coefficient used due to potential runoff. The flow coefficient analysis uses calculation parameters: (1) type of ground cover; (2) percentage of impervious area; (3) hydrological soil group; and (4) the hydrological condition (average humidity or runoff).

Tabel 3. CN Value of Existing Land Use in Tanjung Barat Subdistrict

Land Use	Area (km ²)	CN	CN*Area
Water bodies	0.141	0	0
Green open space	1.136	74	84.064
Parking lot	0.654	98	64.092
Road	0.375	98	36.750
Non-residential buildings	0.104	94	9.776
Residential buildings	1.257	90	113.130

The calculation of the value of the flow coefficient based on land use within the catchment area of Tanjung Barat Subdistrict is based on the coefficient value of each type of land cover based on the National Resources Conservation Service (NRCS) classification [13] as listed in table 3. The results obtained are:

$$CN_C = \frac{86.064 + 64.092 + 36.750 + 9.776 + 113.130}{3.667}$$

$$CN_C = 83.94$$

After known the placement of GI based on map modeling, it can be calculated CN value of GI based on land connectivity to impervious area. The CN in the impervious area is calculated by

observing a direct relationship with the drainage system [14].

Tabel 4. CN Value of GI implementation in Tanjung Barat Subdistrict

Land Use	Area (km ²)	CN	CN*Area
Water bodies	0.141	0	0
Green open space	0.681	74	50.394
Bioretention	0.455	61	27.450
Parking lot	0.654	98	64.092
Road	0.375	98	36.750
Non-residential buildings	0.104	94	9.776
Residential buildings	1.257	90	113.130

From table 4, calculations can be done to determine the percentage of impervious area (Pimp), and is equal to 65.176%. CN value of impervious land (CN_u) is 93.618 and CN land value of pervious area (CN_p) is 68.524. From the ratio of CN value on the impervious and pervious area are known ratio (R) of 1.37.

The results obtained from the calculation of the flow coefficient of the application of GI (CN_{LID}) are:

$$CN_{LID} = 68.524 + (65.176/100) \times (98 - 68.524) \times (1 - 0.5 (1.37))$$

$$= 74.57$$

In this calculation, bioretention becomes an additional feature in the green open space in increasing the infiltration capacity. Bioretention has a infiltration rate of 7 mm/h, so that an green open space with bioretention device has a soil condition with infiltration rate such as the HSG B condition, with a value of CN 61.

CN_{LID} value is lower than CN_C due to using GI. The purpose of applying GI is to increase the ability of infiltration and reduce or decide surface runoff from impervious area. So as to decrease the runoff coefficient and extend the concentration time. CN_C value of existing condition is equal to 83.94. Meanwhile the CN_{LID} value is 74.57. It showed significant decreases, which approached CN values on land cover in the form of green open space in good condition with soil hydrological group C (CN value 74). This indicates that the application of GI can reduce the negative impact of a region that is dominated by impervious area, especially related to the stormwater management. In this case in green open space with the use of bioretention more effective in reducing surface runoff compared to regular ones.

3.3.2 Runoff flow discharge

The calculation of runoff flow based on the value of the rain design that becomes the input and the ability of the soil to hold or infiltrated water. Since GI only works effectively in initiating direct runoff and channel protection from sedimentation and erosion, it is used two annual rain design [5]. Rainfall data is obtained from University of Indonesia (UI) Campus Station, Depok. From the calculation results with frequency analysis with normal distribution method, obtained the value of maximum daily rain return period of two annual average of 124.12 mm or 4.89 inches.

Tabel 5. Rainfall data from UI Campus Station 2008-2017

No	year	Rainfall Max (mm)
1	2008	152.00
2	2009	137.00
3	2010	109.00
4	2011	117.40
5	2012	128.20
6	2013	101.70
7	2014	151.50
8	2015	97.20
9	2016	141.50
10	2017	105.70

Calculation of runoff flow at existing condition, with value of CN_e at eksiting condition is equal to 83.94. So the results of the runoff flow calculation on the existing conditions are:

$$Q = \frac{(4.89 - (0.2 \times 1.9))^2}{4.89 + (0.8 \times 1.9)}$$

$$= 3.17 \text{ inch/s} = 80.6 \text{ mm/s} = 0.08 \text{ m/s}$$

$$\text{with } S = \frac{1000}{83.94} - 10 = 1.9 \text{ inch}$$

With the area of Tanjung Barat Subdistrict is 3.667 km² or 3,667,000 m², the peak discharge for the whole area under the existing condition can be calculated as follows:

$$Q_p = A \times Q = 3,667,000 \times 0.08 = 293,360 \text{ m}^3/\text{s}$$

Where :

$$\begin{aligned} Q_p &= \text{Peak discharge in an area (m}^3/\text{s)} \\ A &= \text{Area (m}^2\text{)} \\ Q &= \text{Runoff discharge (m/s)} \end{aligned}$$

Then on the runoff calculation on conditions after applied GI, with the CN_{LID} value of 75.58, the result of the runoff flow is as follows:

$$Q = \frac{(4.89 - (0.2 \times 3.41))^2}{4.89 + (0.8 \times 3.41)}$$

$$= 2.32 \text{ inch/s} = 58.93 \text{ mm/s} = 0.059 \text{ m/s}$$

$$\text{with } S = \frac{1000}{74.57} - 10 = 3.41 \text{ inch}$$

It can be known that the peak discharge for the whole area under the conditions of GI can be calculated as follows:

$$Q_p = A \times Q = 3,667,000 \times 0.059 = 216,353 \text{ m}^3/\text{s}$$

The peak discharge value in an area, in the existing condition has a greater value than the condition using GI. Application of bioretention increases the ability of land retention potential and decreases the value of the flow coefficient.

In accordance with the calculation that has been done, it is known that the peak discharge value at the existing condition is 293,360 m³/s. While the peak discharge value after applied bioretensi is equal to 216,353 m³/s. There is a difference of 77,007 m³/s of water discharges impregnated to the ground or accommodated in a GI. The efficiency rating of the flow rate reduction was 26,25%.

4. CONCLUSION

Based on the results of land suitability analysis model using BST, it is known that GI that can be applied in Tanjung Barat Subdistrict is bioretention and rain barrel. Meanwhile, from the results of the effectiveness analysis of the application of GI, it is known that the value of the flow coefficient (CN) on the existing conditions and after applied GI is 83.94 and 74.57 respectively. Then from the calculation of peak discharge at existing condition and after applied GI respectively equal to 293,360 m³/s and 216,353 m³/s, with efficiency value equal to 26.25%. So the application of GI is quite effective in increasing the infiltration capacity in Tanjung Barat Subdistrict.

There needs to be integration and equality of perceptions of all relevant stakeholders, of the importance of GI implementation. The location of bioretention that spreads in all green open spaces both public and private, and the provision of rain barrel in each building as an effort to rainwater harvesting needs to be supported and implemented by all stakeholders, both government agencies, private sector, and household.

5. ACKNOWLEDGEMENTS

This article is part of grant of International Indexed Publications For University of Indonesia

Student's Final Project, as part of superior research titled "A Water Sensitive Infrastructure Study to Achieve Sustainable Cities".

6. REFERENCES

- [1] Kesuma Warganda, T. and Sutjiningsih, D. 'Placement of BMPs in urban catchment area using SUSTAIN model: Case study at Universitas Indonesia Campus, Depok, West Java, Indonesia', MATEC Web of Conferences, 138. doi: 10.1051/mateconf/201713806007. 2017.
- [2] Soemabrata, J, Ahmad Z, Irene S, Esti S. Risk Mapping Studies of Hydro-Meteorological Hazard in Depok Middle City. *International Journal of GEOMATE*, Vol. 14, Issue 44, 2018, pp. 128-133.
- [3] Firman T, Indra M S, Ichzar C I, H A Simarmata. Potential climate-change related vulnerabilities in Jakarta : Challenges and current status. *Habitat International* Vol. 35, 2011, pp 372-278.
- [4] Baptiste, A.K., Foley, C., & Smardon, R. Understanding urban neighborhood differences in willingness to implement GI measures: a casestudy of Syracuse, NY. *Landscape and Urban Planning*, Vol. 136, 2015, pp 1-12.
- [5] Marthanty, Dwinanti R. *Uji Kelayakan Metode Infiltrasi Horton sebagai Alternatif Perhitungan Limpasan Hujan Metode SCS (Studi Kasus Sub-DAS Sugutamu, Kota Depok, Jawa Barat*. Master Thesis : Faculty of Engineering, Graduate Programe, University of Indonesia. Depok. 2008.
- [6] Dietz, Michael E. Low Impact Development Practices: A Review of Current Research and Recommendations for Future Directions. *Journal of Water, Air, Soil Pollution*. Springer Science and Business Media. 2007.
- [7] Herslund, Lisa et al. Condition and Opportunities for Green Infrastructure – Aiming for Green, Water-Resilient Cities in Addis Ababa and Dar es Salam. *Landscape and Urban Planning*. 2017.
- [8] Tzoulasa, K., Korpelab, K., Vennic, S., Yli-Pelkonenc, V., Kaźmierczaka, A., Niemelac, J., & Jamesa, P. Promoting ecosystem and human health in urban areas using Green Infrastructure: A literature review. *Landscape and Urban Planning*, Vol. 81, 2007, pp. 167-178.
- [9] Maryati, Sri, An Nissa S H, Putri A. Green Infrastructure Development in Cisangkuy Subwatershed, Bandung Regency : potential and problems. Procedia- Social and Behavioral Sciences Vol. 227, 2016, pp 617-622.
- [10] Cohen, Jeffrey P., R. Field, A. N. Tafuri, and M. A. Ports. Cost Comparison of Conventional Gray Combined Sewer Overflow Control Infrastructure versus a Green/Gray Combination. *Journal of Sustainable Water in the Built Environment*, American Society of Civil Engineers (ASCE). 2012.
- [11] Tetra Tech, Inc. *BMP Siting Tool: Step by Step Guide, ArcGIS 10.1 Service Pack 1*. Tetra Tech, Inc. Fairfax. 2013.
- [12] Shoemaker, Leslie, J Riverson, Khalid A, Jenny X Z, Sabu P, Teresa R. *SUSTAIN : A Framework for Placement of Best Management Practices in Urban Watersheds to Protect Water Quality*. USEPA. Cincinnati. 2009.
- [13] National Resources Conservation Service (NRCS). *Urban Hydrology for Small Watersheds TR-55*, USDA Natural Resource Conservation Service Conservation Engineering Division Technical Release 55. doi: Technical Release 55. 1986.
- [14] Prince George County. *Low Impact Development Manual*. Department of Environment Resources, Largo, Maryland. United States of America. 1999.
- [15] Asdak, Chay. *Hidrologi dan Pengelolaan Daerah Aliran Sungai*. Gadjah Mada University Press. Yogyakarta. 2014.
- [16] Aslinda, Nindy dan Syartinilia. Kajian Perubahan Lahan Menjadi Permukiman dan Karakteristiknya di Daerah Aliran Sungai (DAS) Ciliwung Bagian Hilir. *Jurnal Lanskap Indonesia*, Vol. 8 No. 1. 2016.
- [17] Jakarta Province. Local Regulation of Jakarta Province Number 1/2012 regarding Regional Spatial Planning of Jakarta 2030.
- [18] Zuma, Defri Satiya. *Kajian Simulasi Penerapan Bioretensi dan Kolam Retensi di DAS Ciliwung Hulu*. Master Thesis : Graduate School, Bogor Agricultural University. 2017.

REMOVAL OF ACID ORANGE II DYE BY GRANITIC NANO-ZERO VALENT IRON (nZVI) COMPOSITE

Nur 'Aishah Zarime¹, Wan Zuhairi Wan Yaacob² and Habibah Jamil³

Geology Programme, Faculty of Science and Technology, Universiti Kebangsaan Malaysia, Malaysia

ABSTRACT

The study highlights the effectiveness of nanoscale zero-valent iron (nZVI) composite in removing Acid Orange II dye. In this study, granitic residual soil has been used as supported material to stabilize the nanoscale zero-valent iron (nZVI) and to improve its adsorption capacity. The physical, chemical, mineralogical and morphological properties of the successfully synthesized granitic nano zero valent iron (Gr-nZVI) have been analyzed by Brunnaer–Emmett–Teller (BET) surface area, Field Emission Scanning Electron Microscopy (FESEM), X-Ray Diffraction (XRD) and X-ray Photoelectron Spectroscopy with Auger Electron Spectroscopy (XPS-AES). The batch adsorption tests for the granitic residual soil (Gr) and the granitic nano-zero valent iron (Gr-nZVI) on Acid Orange II have been conducted to determine the effectiveness of both materials in dye removal. The five effects analyzed in the Batch test are concentration, dose, pH, kinetic and temperature. The study found that Gr-nZVI has higher absorption capacity compared to Gr. The effectiveness of Gr-nZVI composite in dye adsorption is due to the dispersion of nZVI particles on granitic soil particles, consequently providing more sites for adsorption. The results suggest that Gr-nZVI has potential as low-cost adsorbent for Acid Orange II removal from synthetic dye wastewater.

Keywords: Granitic Residual Soil, Nano-Zero Valent Iron Composite, Batch Test

1. INTRODUCTION

Huge amount of residual dyes from textile, tannery, paper, printing, paints, rubber and plastic industries are released to the environment and it would contaminate water and soil due to its toxicity and degradability[1], [2]. Textile residual dye are highly resistant to light, pH and microbial attack render it existence in the environment for a longer period of time[3]. To overcome this environmental problem, material from nano zero valent iron (nZVI) are suggested to remove the residual dye. Recently, nZVI has been extensively studied for remediation and waste water treatment [4]–[7]. The nZVI are chosen due to its potential to decolorize azo-dyes rapidly without further treatments [8]. The nZVI also enhanced reactivity by increasing the surface area and volume ratios thus providing more reactive surface sites [4]. However, there are disadvantages of using nZVI because it has strong tendency to agglomerate into larger particles resulting in diminishing reactivity, and such condition in the treatment system are uneconomical due to the generation of secondary iron pollution [4]. To address this problem, composite nZVI has been proposed to stabilize the nZVI particles onto various supports. In this study, Gr-nZVI has been synthesized via chemical reduction method by using Ferric Chloride Tetrahydrate, $\text{FeCl}_3 \cdot 6\text{H}_2\text{O}$ and Sodium Borohidrat, NaBH_4 . The adsorption capacity of Gr-nZVI in by Batch test.

2. MATERIALS AND METHODS

2.1. Materials

The granitic residual soil (BGR) from Broga, Selangor was used in this study. Acid Orange II was supplied in solid state with high purity (wt.% 99.9%) from Tianjin Yuhua Co., China. Chemical such as Ferric Chloride Tetrahydrate, $\text{FeCl}_3 \cdot 6\text{H}_2\text{O}$ (Acros organics, 99 +%), Sodium Borohidrat, NaBH_4 (Acros organics, 98 +%) and Ethanol $\text{C}_2\text{H}_6\text{O}$ (Fisher Scientific, 99.4%) were used in this analysis.

2.2. Synthesizing nZVI Composite

The granitic nano zero valent iron (Gr-nZVI) composite was synthesized by using chemical reduction method [9], [10]. Ferric chloride solutions were prepared by mixing 4.38g ferric chloride tetrahydrate with 50 ml mixture of ethanol and deionized water (35ml ethanol + 15ml of deionized water). Granitic residual soil was added to ferric chloride solution and the mixture was shaken using ultrasonic shaker for 30 minutes. An amount of 6.091 g sodium borohydride were dissolved in 100 ml deionized water to produce NaBH_4 solutions. The NaBH_4 solutions were pipetted and were dropped (1 drop/ 2 seconds) into ferric chloride solution on a magnetic stirrer. The mixture was stirred for 20 minutes after the last

dropped of NaBH_4 . The black particles of Gr-nZVI composite were filtered and were washed three times with ethanol (50ml). The Gr-nZVI composite was oven dried at 50°C for approximately 12 hours.

2.3. Characterization of nZVI Composite

The physical characterization of granitic residual soil, Gr and Gr-nZVI composite were analyzed using Brunauer–Emmett–Teller by N_2 desorption method to determine the specific area of particles. Chemical characterization was conducted by means of X-ray photoelectron spectroscopy and Auger Electron Spectroscopy (XPS-AES) to measure the surficial chemical composition and elements valence of particles. The morphology and mineralogy of the particles were characterized by Field Emission Scanning Electron Microscope (FESEM) and X-ray Diffraction (XRD). FESEM was performed by using Merlin Compact Supra 55VP where it was utilized the sound pulses transmitted through a particle suspension to determine the properties of the suspended particles [11]. Besides, XRD patterns for Gr and Gr-nZVI composite were also determined by Bruker/D8 Advance with a high-power Cu-K α radioactive source at 40kV/40mA.

2.4. Batch Test

The test was performed to study the removal of Acid Orange II using nanoparticles (nZVI) composite. Batch test method was reported by [12]. Gr and Gr-nZVI were prepared by passing the materials through 63 μm sieve. Acid Orange II solution was prepared with 7 different concentrations, the 5 mg/L, 20 mg/L, 40 mg/L, 60 mg/L and 100 mg/L. To perform this test, 0.5 g of Gr-nZVI with 50 ml of Acid Orange II (1:100 ratio soil/solution) were mixed in centrifuge tubes. The mixture samples were shaken at 150 RPM for 3 hours to attain their equilibrium [13]. After shaking, mixture samples were centrifuged at 1500 RPM for 15 minutes and filtered through 45 μm nitrocellulose membranes. The solutions were analyzed using UV-VIS Spectrophotometer (UV1201).

There are 5 effects in Batch test were analyzed including concentration, dose, pH, kinetic and temperature. To determine the optimum dosage, different dosage of materials (0.03 g, 0.05 g, 0.07 g, 0.1 g, 0.3 g, 0.5 g, 0.7 g, and 1.0 g) was used. The materials with different dose were added to 50ml Acid Orange II (50 mg/L). For pH effect, different pH of Acid Orange II (pH2, pH4, pH6, pH8, pH10 and pH12) was used. Kinetic effect represented by shaking time (5 min, 10 min, 20

min, 30 min, 45 min, 60 min, 120 min, 180 min and 360 min) while for temperature effect, different temperature (30°C , 40°C , 50°C and 60°C) was used in this analysis. For all factor, the batch test analysis was carried out with the ratio 1:100.

The concentration of Acid Orange II absorbed by particles, q_e was calculated using the formula as follows;

$$q_e = \frac{(C_o - C_e)V}{M}$$

Where; C_o and C_e representing initial concentration and equilibrium concentration respectively (mg/L), V is volume of solution added (ml), M is mass of air-dried material (g)

3. RESULTS AND DISCUSSIONS

3.1. Characterization of Nanoparticles (nZVI) Composite

Table 1 showed the result of specific surface areas (BET) for Granite residual soil (Gr) and granitic nZVI composite (Gr-nZVI). Gr showed higher surface area (14.1724 m^2/g) compared to Gr-nZVI (6.7619 m^2/g). Gr also showed higher pore volume (0.0484 cm^3/g) compared to Gr-nZVI (0.0298 cm^3/g). The results indicated that pores in the granitic residual soil were filled with added nZVI particles [14], [15]. The larger surface area led to more uniform distribution of nZVI particles on the appropriate clay [16].

Table 1 Specific surface areas (BET) result for Granitic residual soil (Gr) and Granitic nZVI composite (Gr-nZVI)

Sampel	Gr	Gr-nZVI
BET Surface Area (m^2/g)	14.1724	6.7619
Pore Volume (cm^3/g)	0.0484	0.0298
Pore Size (\AA)	136.6348 (13.66348 nm)	176.0732 (17.60732 nm)

Figure 1 and Figure 2 showed the X-ray photoelectron spectroscopy and Auger Electron Spectroscopy (XPS-AES) spectrum of Gr and Gr-nZVI. As displayed in Figure 1(a), Fe, O, C, Si and Al were found on the Gr surface while Na, Fe, O, C, B, Si and Al were distributed on Gr-nZVI surface. Na and B were expected to be present as NaBH_4 was used to synthesize Gr-nZVI [9]. To confirm the occurrence of Fe, the XPS-AES

spectrum of the Fe 2p were displayed in Figure 1 and Figure 2(b). Figure 1(b) depicted the binding energy Fe 2p_{1/2} 722.5 eV while for Gr-nZVI (Figure 2(b)) depicted binding energy of Fe 2p_{1/2} 721.1 eV. Both peaks indicated the granitic surface as FeO. Granite (igneous rock) composed of various minerals including quartz, potassium and plagioclase feldspars, crystalline iron-bearing minerals (commonly amphibole and magnetite), and micaceous minerals [17]. According to [9], the peaks at 719.7 eV (Fe 2p_{1/2}) corresponding to zero valent iron.

The morphologies of Gr and Gr-nZVI described by SEM and FESEM. Figure 3 shows the SEM image for Gr where it contained kaolinite, illite and halloysite minerals. Kaolinite was indicated by its well sheet shape while illite has unorganized sheet shape. Halloysite was identified by rod shape overlaid kaolinite minerals. These results were in

1(b)

agreement with report by [18]. Figure 4 shows FESEM image where the existence of nZVI can be observed. The nZVI particles have spherical shapes and aggregated into a chain-like [19], [20] on granitic soil surface. According to [21], aggregations of nZVI were due to its huge interface energy and magnetic property. The nZVI particle sizes were in the range of 54.75 nm to 71.46 nm. The X-ray Diffraction (XRD) patterns for Gr and Gr-nZVI were presented in Figure 5. Gr in XRD pattern consisted of kaolinite, identified through peak of 2.55 Å and 3.55 Å. Illite was identified by the peak of 4.47 Å and halloysite was identified by 3.62 Å peak. Gr-nZVI showed that the kaolinite, illite and halloysite minerals were remained on the soil particles after synthesizing process. In Gr-nZVI, small peak at $2\theta = 44.9^\circ$ corresponded to the formation of zero valent iron [7], [9].

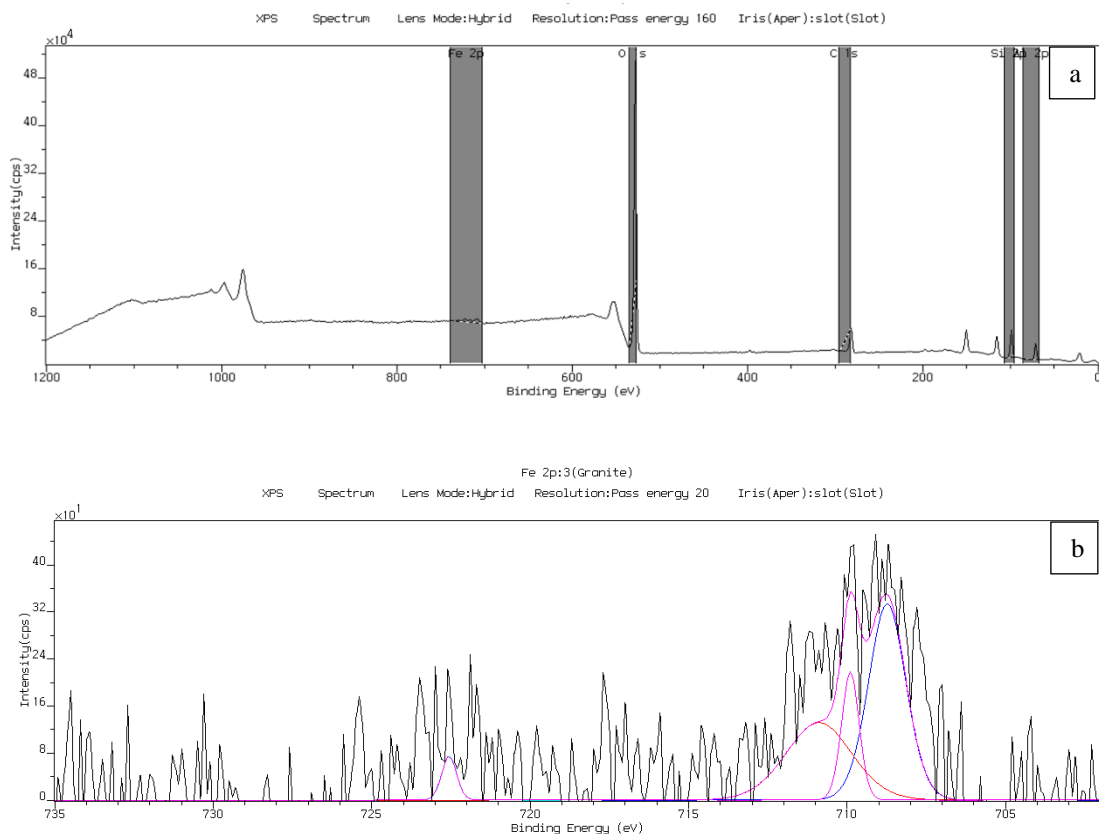


Figure 1 X-ray photoelectron spectroscopy and Auger Electron Spectroscopy (XPS-AES) result for granite, Gr (a) full Gr and (b) Fe 2p line

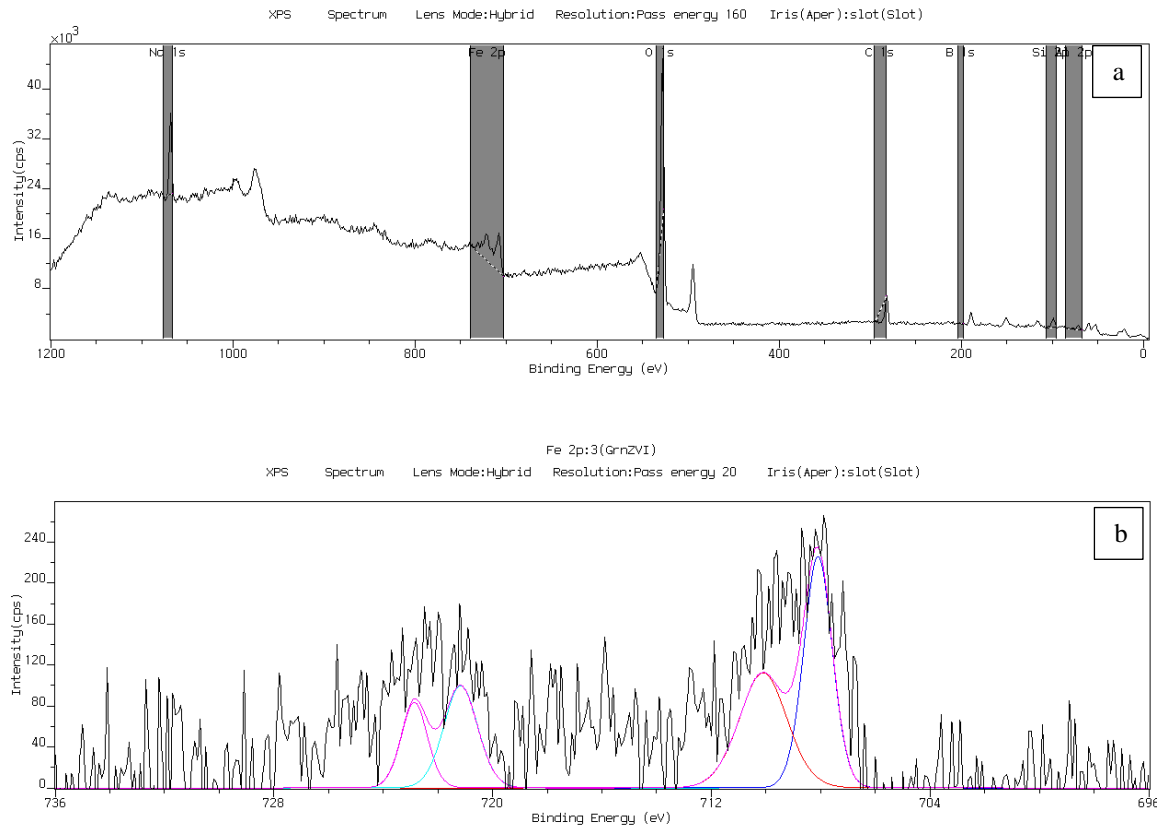


Figure 2 X-ray photoelectron spectroscopy with Auger Electron Spectroscopy (XPS-AES) result for Gr-nZVI, Gr (a) full Gr-nZVI and (b) Fe 2p line

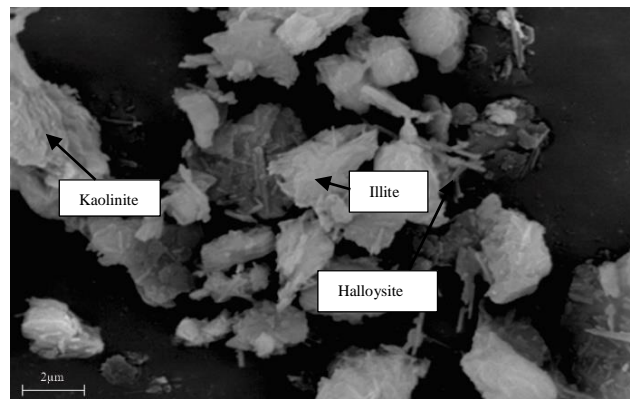


Figure 3 Scanning Electron Microscope (SEM) image with Mag=5000X for Gr sample.

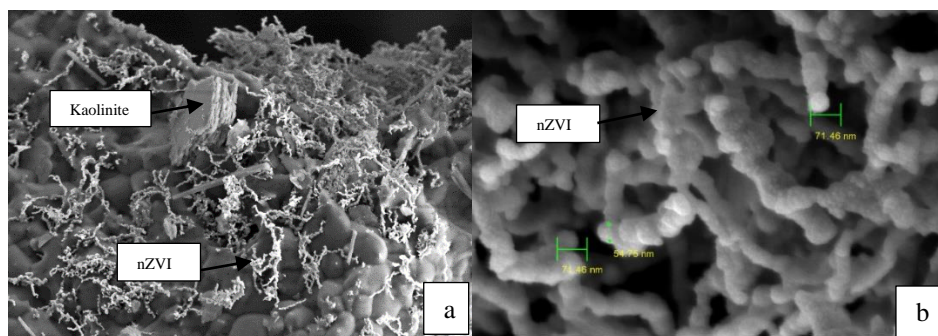


Figure 4 Field Emission Scanning Electron Microscope (FESEM) images for both Gr-nZVI (a) Mag=10000X and (b) Mag=100000X

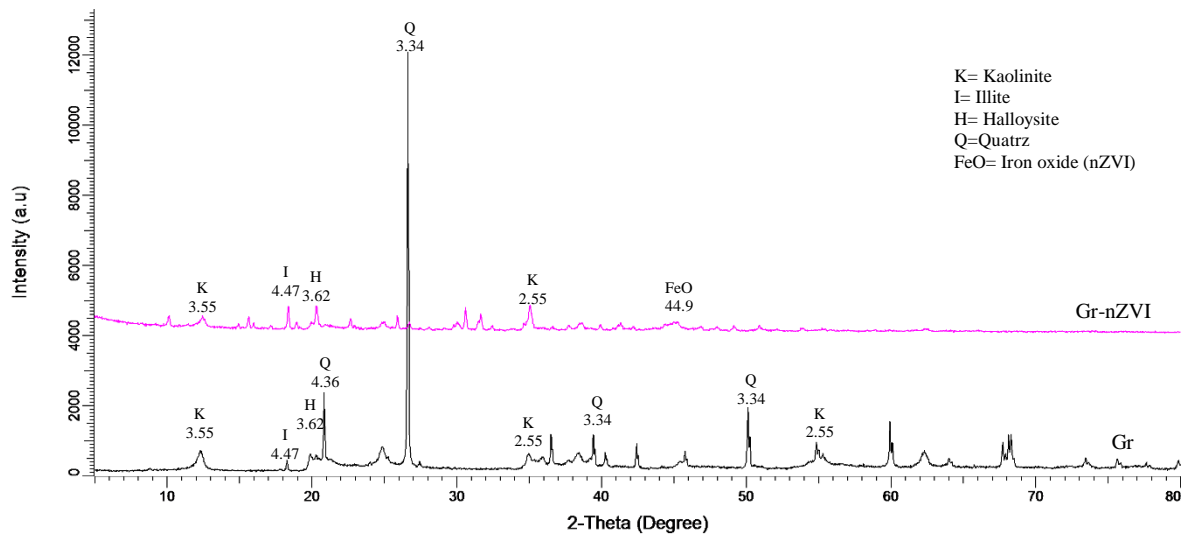


Figure 5 X-ray Diffraction (XRD) images for Gr and Gr-nZVI

3.2. Batch Test

Batch test was conducted to determine adsorption capacity of the materials (Gr and Gr-nZVI).

3.2.1 Dose Effect

Figure 6 showed the adsorption of Acid Orange II by absorbent materials (Gr and Gr-nZVI) in different dosage. The results showed that, the adsorption capacity for both materials (Gr and Gr-nZVI) were decreased with the increase of adsorbent materials. According to [22], such condition was due to the overlapping of adsorption sites, rendering it overcrowded with adsorbent particles. The curve also depicted the Gr-nZVI adsorbed more dye than Gr. The equilibrium concentration after adsorption for Gr-nZVI and Gr was 5.3284 mg/g and 3.3800 mg/g respectively. According to [9], [23], [24], higher adsorption capacity of Gr-nZVI was due to larger specific area and the availability of more adsorption sites to accelerate initial reaction. The optimum adsorbent dosages was 0.5 g and further experiments were carried out using this dose.

3.2.2 Concentration Effect

The effect of initial concentration of Acid Orange II was investigated in the ranged of 5 mg/L to 100 mg/L and was presented in Figure 7. Based on its higher adsorption capacity, the Gr-nZVI proved as better adsorbent compared to Gr. The result also showed that the adsorption capacity increased with the increasing of initial concentration until at one point it became constant although the initial concentration was increased.

For Gr-nZVI, at initial concentration of 40 - 100 mg/L, the graph was constant, indicating the saturated Gr-nZVI surface no more dye or metal ions can be adsorbed [25]. The optimum metal concentration was determined as 40 mg/L.

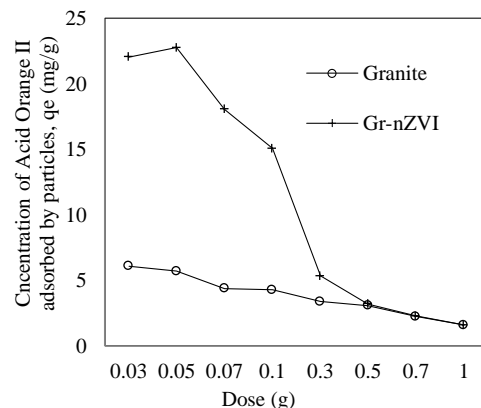


Figure 6 Effect of dosage in adsorption capacity of Gr and Gr-nZVI

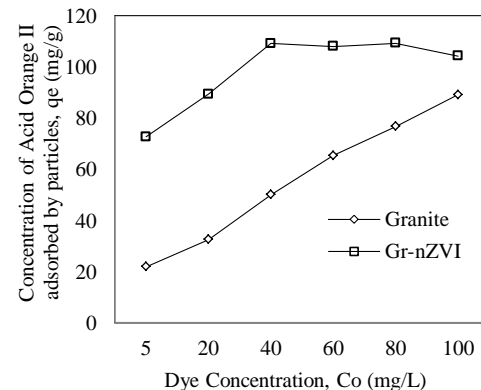


Figure 7 Effect of initial concentration of Acid Orange II in adsorption capacity of Gr and Gr-nZVI

nZVI

3.2.3 pH Effect

The effect of pH on the adsorption of Acid Orange II by Gr and Gr-nZVI were shown in Figure 8 with initial dye concentration of 50 mg/L and adsorbent dosage 0.5g. From the graph, in all pH conditions, Gr-nZVI showed higher adsorption capacity (q_e pH2= 5.3284 mg/g) compared to Gr (q_e pH2= 3.0288 mg/g). The Gr-nZVI graph was constant suggesting that its adsorption capacity was not affected by pH values. However, according to [26], the maximum adsorption for DR23 and DR80 (anionic dye) was at pH 2. This was due to the strong electrostatic attraction between positively charged surface of the adsorbent and the anionic dye. As pH of dye increased, negative charged sites were also increased. Negative charged on the adsorbent's surface site did not favored the adsorption of ionic dye due to electrostatic repulsion. Gr curve showed the decreased of adsorption capacity with the increased of pH values. At higher pH, there was competition adsorption between OH⁻ ions and anionic resulting lower adsorption capacity [26], [27].

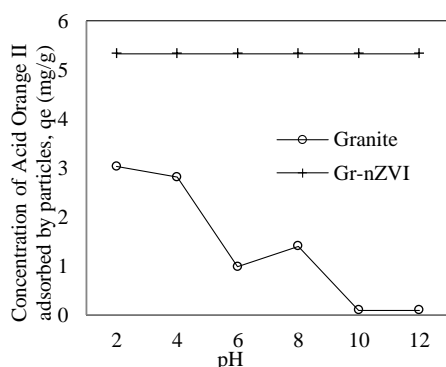


Figure 8 Effect of pH in adsorption capacity of Gr and Gr-nZVI

3.2.4 Kinetic Effect

Figure 9 shows the adsorption kinetics of Acid Orange II on Gr and Gr-nZVI. Both curves showed higher adsorption at the beginning and remained constant (reached equilibrium) after 5 minutes. A similar trend reported by [22]. According to [28], rapid phase was due to the presence of large number of vacant sites, which led to increase in concentration gradient between dye solution and adsorbent surface. The equilibrium time also depended on dye initial concentration. The lower dye initial concentration, the shorter the equilibrium time interval [28]. Gr-nZVI also showed better results in adsorbing Acid Orange II compared to Gr. Gr-nZVI provided both mineral and nZVI particle surfaces to adsorb dye. As

reported by [4], the core shell of nZVI possessed hydroxyl groups when it was interface with dye solution and it has their own capability to immobilize sorbate molecules by surface complexation. The nZVI core also formed an electron where it could reduce Acid Orange II.

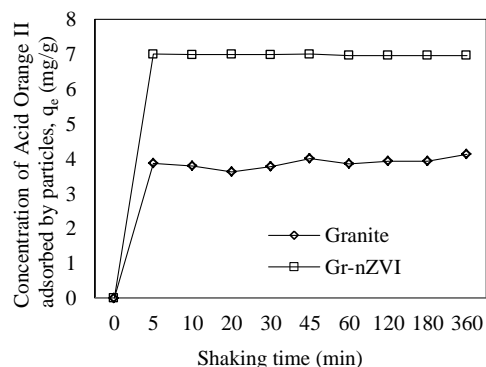


Figure 9 Effect of kinetic in adsorption capacity of Gr and Gr-nZVI

3.2.5 Temperature Effect

To understand the temperature effect of Acid Orange II on Gr and Gr-nZVI, the experiments were carried out at 30, 40, 50 and 60 °C with dye concentration of 50 mg/L and adsorbent dosage 0.5g. The results were displayed in Figure 10. Gr curve showed that dye adsorption capacity was increased with increasing of temperature. Similar results were reported by [23]. For Gr-nZVI, the curve was constant, and the adsorption capacity higher compared to Gr. The results showed that temperature effect did not give any significant effect on Gr-nZVI sample. Gr-nZVI provided both mineral and nZVI particles surfaces for greater adsorption sites compared to Gr. The findings suggesting the stability of Gr-nZVI towards temperature effects and proven as better materials for water treatment in the natural environment.

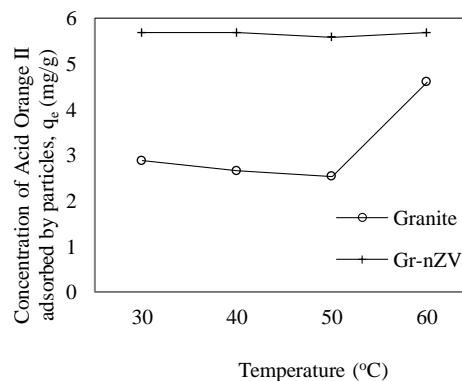


Figure 10 The effect of temperature in adsorption capacity of Gr and Gr-Nzvi

4 CONCLUSIONS

In this study, Gr-nZVI was proven as better materials in adsorbing Acid Orange II compared to Gr. Based on Batch test, Gr-nZVI was stable in all effects tested including concentration, dose, pH, kinetic and temperature effects. Since Gr was low-cost material and easily obtain remediation material to remove Acid Orange II and other anionic dyes in wastewater.

ACKNOWLEDGEMENTS

This research project was supported by Centre for Research & Instrumentation Management (CRIM), UKM with financial support Ministry of Education. Authors acknowledged Geology Program, Faculty of Science and Technology, Universiti Kebangsaan Malaysia (UKM), Malaysia for their assistance in conducting this research.

REFERENCES

- [1] Xi Y, Megharaj M., and Naidu R., Dispersion of zerovalent iron nanoparticles onto bentonites and use of these catalysts for orange II decolourisation. *Appl. Clay Sci.*, vol. 53, no. 4, 2011, pp. 716–722.
- [2] Zhang C., Zhu Z., Zhang H., and Hu Z., Rapid decolorization of Acid Orange II aqueous solution by amorphous zero-valent iron. *J. Environ. Sci.*, vol. 24, no. 6, 2012, pp. 1021–1026.
- [3] Selvanathan N., Subki N. S., and Sulaiman M. A., Dye Adsorbent by Activated Carbon. *J. Trop. Resour. Sustain. Sci.*, vol. 3, no. 1, 2015, pp. 169–173.
- [4] Luo S., Qin P., Shao J., Peng L., Zeng Q., and Gu J. D., Synthesis of reactive nanoscale zero valent iron using rectorite supports and its application for Orange II removal, *Chem. Eng. J.*, vol. 223, 2013, pp. 1–7.
- [5] Busch J., Meißner T., Potthoff A., Bleyl S., Georgi A., Mackenzie K., Trabitzzsch R., Werban U., Oswald S.E., A field investigation on transport of carbon-supported nanoscale zero-valent iron (nZVI) in groundwater, *J. Contam. Hydrol.* Vol. 181, 2014.
- [6] Huang D., Chen G., Zeng G., Xu P., Yan M., Lai C., Zhang C., Li N., Cheng M., He X and He Y., Synthesis and Application of Modified Zero-Valent Iron Nanoparticles for Removal of Hexavalent Chromium from Wastewater, *Water, Air, Soil Pollut.*, vol. 226, no. 11, 2015, pp. 375.
- [7] Al-Dokheily M. E. and Sadoon A. A.-B. J., Synthesis of Iron Nanoparticles and Applications in the Removal of Heavy Metals from Aqueous Solutions, *Chem. Process Eng. Res.*, vol. 34, 2015.
- [8] Shih Y., Tso C., and Tung L., Rapid degradation of methyl orange with nanoscale zerovalent iron particles. *J. Environ. Eng. Manag.*, vol. 20, no. 3, 2010, pp. 137–143.
- [9] Yaacob W. Z. W. and How H. K., Synthesis and Characterization of Marine Clay-Supported Nano Zero Valent Iron, *Am. J. Environ. Sci.*, vol. 11, no. 2, 2015, pp. 115–124.
- [10] Rashmi S., Madhu G., Kittur A., and Suresh R., Synthesis, characterization and application of zero valent iron nanoparticles for the removal of toxic metal hexavalent chromium from aqueous solution. *Int. J. Curr. Eng. Technol.*, 2013, pp. 37–42.
- [11] Jamei M. R., Khosravi M., and Anvaripour B., Soil Remediation Using Nano Zero-valent Iron Synthesized by an Ultrasonic Method, *Iran. J. Oil Gas Sci. Technol.* vol. 1, no. 1, 2012, pp. 1–12.
- [12] USEPA, Batch-Type Procedures for Estimating Soil Adsorption of Chemicals, EPA/530/SW- 87/006-F, 1992.
- [13] Antoniadis V. and Tsadilas C. D., Sorption of cadmium, nickel, and zinc in mono- and multimetal systems, *Appl. Chem.*, vol. 22, 2007, pp. 2375–2380.
- [14] Zhu H., Jia Y., Wu X., and Wang H., Removal of arsenic from water by supported nano zero-valent iron on activated carbon, *J. Hazard. Mater.*, vol. 172, no. 2–3, 2009, pp. 1591–1596.
- [15] Chen Z. X., Cheng Y., Chen Z., Megharaj M., and Naidu R., Kaolin-supported nanoscale zero-valent iron for removing cationic dye-crystal violet in aqueous solution, *Nanotechnol. Sustain. Dev.* First Ed., 2012 pp. 189–196.
- [16] Tomas'evic' D. D., Kozma G., Kerkez D. V., Dalmacija B. D., Dalmacija M. B., Bec'elic'-Tomin M. R., Kukovec A', Ko'nya Z., and Ronc'evic S., Toxic metal immobilization in contaminated sediment using bentonite- and kaolinite-supported nano zero-valent iron, *J. Nanoparticle Res.*, vol. 16, no. 8, 2014.
- [17] Jan Y., Wang T., Li M., Tsai S., Wei Y., and Teng S., Adsorption of Se species on

- crushed granite : A direct linkage with its internal iron-related minerals, *Applied Radiation and Isotopes*. vol. 66, 2008pp. 14–23.
- [18] Robertson I. D. M., Weathering of Granitic Muscovite to Kaolinite and Halloysite and of Plagioclase-Derived Kaolinite to Halloysite, *Clays Clay Miner.* vol. 39, no. 2, 1991, pp. 113–126.
- [19] Shi L., Zhang X., and liang Chen Z., Removal of Chromium (VI) from wastewater using bentonite-supported nanoscale zero-valent iron, *Water Res.* vol. 45, no. 2, 2011, pp. 886–892.
- [20] Kerkez D. V., Tomas'evic' D. D., Kozma G., Bec'elic'-Tomin M. R., Prica M. D., Ronc'evic' S. D., Kukovecz A., Dalmacija B. D., and Ko' nya Z. Three different clay-supported nanoscale zero-valent iron materials for industrial azo dye degradation: A comparative study, *J. Taiwan Inst. Chem. Eng.*, vol. 45, no. 5, 2014, pp. 2451–2461.
- [21] Han L., Xue S., Zhao S., Yan J., Qian L., and Chen M., Biochar supported nanoscale iron particles for the efficient removal of methyl orange dye in aqueous solutions, *PLoS One*, vol. 10, no. 7, 2015, pp. 1–15.
- [22] Hefne J. A., Mekhemer W. K., Alandis N. M., Aldayel O. A., and Alajyan T., Removal of Silver (I) from Aqueous Solutions by Natural Bentonite, vol. 22, no. 1, 2010, pp. 155–176.
- [23] Reddy M. C. S., Sivaramakrishna L., and Reddy V., The use of an agricultural waste material, Jujuba seeds for the removal of anionic dye (Congo red) from aqueous medium., *J. Hazard. Mater.*, vol. 203–204, 2012, pp. 118–27.
- [24] Shu H. Y., Chang M. C., Chen C. C., and Chen P. E., Using resin supported nano zero-valent iron particles for decoloration of Acid Blue 113 azo dye solution, *J. Hazard. Mater.*, vol. 184, no. 1–3, 2010, pp. 499–505.
- [25] Veli S. and Alyüz B., Adsorption of copper and zinc from aqueous solutions by using natural clay., *J. Hazard. Mater.*, vol. 149, no. 1, 2007, pp. 226–33.
- [26] Arami M., Limaee N. Y., Mahmoodi N. M., and Tabrizi N. S., Removal of dyes from colored textile wastewater by orange peel adsorbent: Equilibrium and kinetic studies, *J. Colloid Interface Sci.*, vol. 288, no. 2, 2005, pp. 371–376.
- [27] Shen D., Fan J., Zhou W., Gao B., Yue Q., and Kang Q., Adsorption kinetics and isotherm of anionic dyes onto organo-bentonite from single and multisolute systems, *J. Hazard. Mater.* vol. 172, no. 1, 2009, pp. 99–107.
- [28] Babazadeh H., Nazemi, A. H. and Manshouri, M., Isotherm and Kinetic Studies on Adsorption of Pb, Zn and Cu by Kaolinite, *Caspian J. Env. Sci*, vol. 9, no. 2, 2011, pp. 243–255.

INFLUENCE OF RAILINGS STIFFNESS ON WHEEL LOAD DISTRIBUTION IN THREE- AND FOUR-LANE CONCRETE SLAB BRIDGES

Ghassan Fawaz¹, Mohammad Abou Nough¹, Mounir Mabsout¹, and Kassim Tarhini²

¹Dept. of Civil and Environmental Engineering, Amer. Univ. of Beirut, Lebanon.

²Dept. of Civil Engineering, U.S. Coast Guard Academy, New London, CT 06320, USA.

ABSTRACT

The American Association of State Highway and Transportation Officials Load and Resistance Factor Design (AASHTO LRFD) do not account for the presence of railings in the analysis or design of highway bridges. This paper presents a follow-up parametric investigation of the influence of railing stiffness on the wheel load distribution in simply-supported, one-span, three- and four-lane reinforced concrete slab bridges using the finite-element analysis (FEA). A total of 48 bridge cases are modeled using refined 3D FEA and bridge parameters such as span lengths, slab widths, and railings that were varied within practical ranges. Various railings stiffness were considered to be built integrally with the bridge deck and placed on both edges of the concrete slabs. The FEA wheel load distribution and bending moments are compared with reference bridge slabs without railings as well as to the AASHTO design procedures. According to the FEA results, the presence of railings reduces the longitudinal bending moment in the concrete slabs by 25% to 60% depending on the stiffness of the railings in one- and two-lane reinforced concrete bridges. However, when considering three- and four-lane bridges, the presence of railings reduced the longitudinal bending moment in the concrete slab by a range of 10% to 32% depending on the stiffness of railings. The results of this investigation will assist bridge engineers in better evaluating the load carrying capacities of multi-lane concrete slab bridges using 3D FEA and account for the contribution of railings. The presence of railings can also be considered a possible alternative for strengthening existing concrete slab bridges.

Keywords: Concrete Slab Bridges, Multi-lane, Railings Stiffness, Finite-Element Analysis, AASHTO Procedures, Load-Carrying Capacity.

1. INTRODUCTION

According to the U.S.A. Federal Highway Administration's 2016 National Bridge Inventory data, approximately 22% of the nation's 603,620 bridges are structurally deficient or functionally obsolete as reported in Better Roads Magazine (November 2016). Highway Bridges that are either built using cast-in-place concrete or precast concrete panels form about 69% of all bridges (423,216). Single span reinforced concrete bridges represent about 150,000 and assuming 22% (33,000) of those bridges to be structurally deficient or functionally obsolete. It is also known that the average bridge age in the U.S.A. is 43 years old while most of the bridges were designed for a lifespan of 50 years. Therefore, an increasing number of bridges will soon need either major rehabilitation or replacement. However, this bridge inventory accounts for structures with span lengths greater than 6 m (20 ft), where the majority of the structurally deficient bridges are short spans, averaging less than 15 m (50 ft) in length. These deficient bridges are being recommended for weight-limit posting,

rehabilitation, or replacement. Thousands of such structures especially with span length are less than 6 m (20 ft) in every state and municipality may be ignored, not inspected, or not replaced on regular basis due to the lack of funding. This task is left up to each local government to maintain such structures that span less than 6 m (20 ft) without federal support.

Therefore, a significant number of highway bridges are short-span reinforced concrete slabs that are owned and maintained by local and state governments. The main advantage of concrete slab bridges is the ease of construction and the ability to field adjustment of the roadway profile during construction. The design of highway bridges in the United States conforms to the American Association of State Highway and Transportation Officials (AASHTO) Standard [1] or Load and Resistance Factor Design (LRFD) Bridge Design Specifications [2]. The current AASHTO procedures do not consider the effect of railings that are built integrally with bridge deck in the evaluation of the load-carrying capacity of bridges. Therefore, this study investigates the effect of railings and its stiffness in

resisting highway loading and by increasing the load-carrying capacity of reinforced concrete slab bridges.

A parametric study investigated straight, single-span, simply-supported reinforced concrete slab bridges using finite-element analysis (FEA) [10]. Results indicated that AASHTO Specifications overestimate the FEA bending moments for short spans, one-lane bridges and agreed with FEA moments for short spans in combination of two or more lanes. In addition, AASHTO Standard Specifications underestimates the FEA moments for longer spans. As for AASHTO LRFD procedure, it overestimates the FEA bending moments for all bridge cases. Several studies were conducted and reported in the literature that investigated the influence of sidewalks and railings on wheel load distribution in steel and prestressed girder bridges which was shown to increase the stiffness of the superstructure and improve the load-carrying capacity of these bridges [4]–[5]–[6]–[7]–[9].

Recently, a published investigation studying the influence of one standard railings size on concrete slab bridges was performed [8]. The results indicated that, placing two railings on straight concrete slab bridges, AASHTO Standard Specifications procedures overestimated the FEA moments by 100% for one-lane bridges, and by 20% for bridges with two or more lanes. AASHTO LRFD overestimated the FEA moments in all bridge cases by 150% for one-lane, 70% for two-lanes, and a 30% for three- and four-lanes when placing two railings on slab bridges. It is worth noting that the AASHTO procedures, which overestimated the FEA moments, did not consider the presence of side railings and the effect of their stiffness. Another study investigated the influence of railing stiffness in one- and two-lane reinforced concrete slab bridges [3]. The study showed that the presence of railings reduces the longitudinal bending moment in slabs or increase the load carrying capacity by a range of 25% to 60% depending on the stiffness of the railings.

This paper builds on the 3D FEA investigation studying the influence of railing stiffness in one- and two-lane bridges reported in [3]. The paper presents the results of a parametric study investigating the influence of railings stiffness in simply supported one-span, three- and four-lane bridges and how it will increase the load-carrying capacity of reinforced concrete slab bridges.

2. AASHTO BENDING MOMENTS

For simply-supported concrete slab bridges, AASHTO Standard Specifications (2002) suggest three approaches in determining the live-load bending moment but only one procedure is used in

this study that was compared with the finite-element analysis results.

$$M = 13,500S \text{ for } S \leq 15m \quad (1)$$

$$M = 1,000(19.5S - 90) \text{ for } S > 15m \quad (2)$$

Where:

S = span length (m)

M = longitudinal bending moment per unit width (N-m/m)

AASHTO LRFD Section 4.6.2.3 (2014) provides an equivalent strip width procedure to design reinforced concrete slab bridges that is comparable to procedures specified in the Standard Specifications. However, the AASHTO LRFD Section 3.6.1.2 requires the use of HL93 (addition of HS20 Truck plus lane loading) live loading. This approach is to divide the total bending moment by an equivalent width to obtain a statically design moment per unit width. The equivalent width “E” of longitudinal strips per lane for both shear and moment is determined using the following formulas:

The width for one lane loaded is

$$E = 250 + 0.42\sqrt{L1 \times W1} \quad (3)$$

while the width for multi-lanes loaded is:

$$E = 2,100 + 0.12\sqrt{L1 \times W1} \quad (4)$$

Where:

E = equivalent width of longitudinal strips per lane, “mm”

L1 = span length in “mm”, the lesser of the actual span or 18,000 mm

W1 = edge-to-edge width of bridge in “mm” taken to be the lesser of the actual width or 18,000 mm for multi-lane loading, or 9,000 mm for single-lane loading.

The AASHTO Standard Specifications and AASHTO LRFD equations above do not take into account the influence of side railing when analyzing or designing a concrete slab bridges. These equations will be used calculating the AASHTO bending moments that will be compared with 3D FEA results.

3. DESCRIPTION OF BRIDGE CASES

Building on the published investigations [3]–[8] typical simply-supported one-span, three-lane, and four-lane reinforced concrete slab bridge cases were selected and analyzed in this investigation. Four span lengths were considered in this parametric study: 7.2, 10.8, 13.8, and 16.2 m (24, 36, 46, and 54 ft) with corresponding slab thicknesses of 450, 525,

600, and 675 mm (18, 21, 24, and 27 inches), respectively. The concrete slab thicknesses were calculated using the AASHTO equations to control deflection. The overall slab widths were assumed to be: 10.8 m (36 ft) for three-lanes, and 14.4 m (48 ft) for four-lanes.

The base case for the standard railings size adopted from previous research was 200 mm (8 in) wide and 760 mm (30 in) high above slab [8]. Another parameter considered in this study was varying the railings stiffness, which is represented by the moment of inertia of the railing (I) computed at the bottom of the railing section.

$$I_{(bottom)} = I_{(center)} + Ad^2 = \frac{bh^3}{12} + bh\left(\frac{h}{2}\right)^2 = \frac{bh^3}{3}$$

$$\therefore I_{(bottom)} = 4I_{(center)}$$

Five stiffness factors are considered including X1, X2, X3, X4, and X0.5, along with X0 (reference case with no railings). Figure 1 shows the various railing sizes considered in this investigation.

Where:

- X0 No railing, reference case moment of inertia = 0
- X0.5 Half the base case moment of inertia = 2Ic
- X1 Moment of inertia of base case = 4Ic
- X2 Twice the base case moment of inertia = 8Ic
- X3 Triple the base case moment of inertia = 12Ic
- X4 Four times the base case moment of inertia = 16Ic

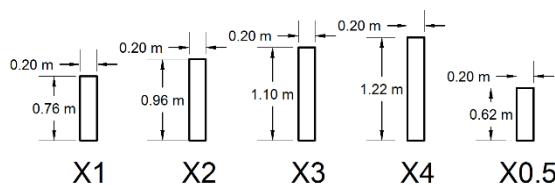


Fig. 1 Various railing sizes (X1, X2, X3, X4, X0.5).

Figure 2 shows a typical cross-section and plan-view of three-lane bridge cases with/without railings (base case, X1), with HS20 trucks placed transversely close to one edge of the slab deck with minimum spacing between trucks (Edge loading condition).

4. BRIDGE LOADING

The bridge cases considered in this study were subjected to AASHTO HS20 design trucks assuming to be traveling in the same direction when considering multiple lanes. AASHTO HS20 design trucks were placed longitudinally and transversely to produce maximum bending moments. The results of

a previous study indicated that the Edge loading condition is more critical than the Centered loading condition where trucks are centered transversally each in its own lane [8]. Therefore, only the Edge loading condition was adopted in this study. Figure 2 shows the Edge loading condition for the three-lane bridge case where the first design truck was placed close to one edge of the slab, such that the center of the left wheel of the left most truck is positioned at 0.3 m (1 ft) from the left edge of the slab, and the other trucks were placed side-by-side with a distance 1.2 m (4 ft) between the adjacent trucks in order to produce the worst live loading condition on the bridge.

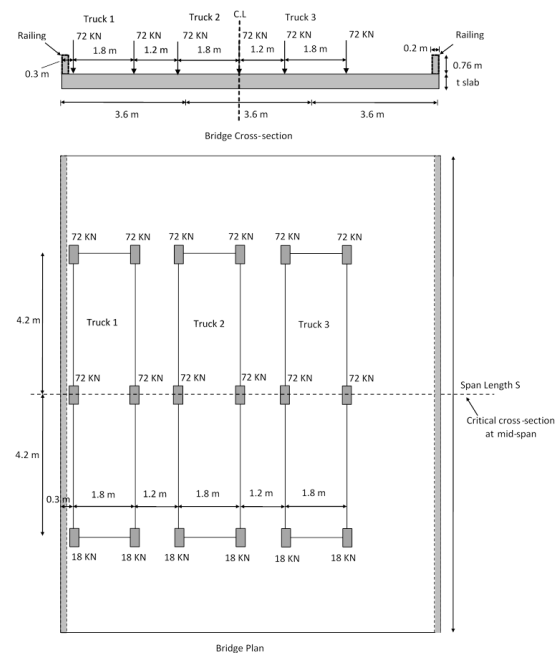


Fig. 2 Typical cross-section and plan-view of a three-lane bridge with base case railings (X1).

5. FINITE ELEMENT MODELING

A total of 48 slab bridge cases were investigated using the 3D FEA. The computer program SAP2000 (version 17) was used to discretize the bridge geometry into a convenient number of square four-node shell elements with six degrees of freedom at each node [11]. Railings could be modeled as shell elements placed orthogonally on top and along the edges of each slab, which represent a realistic but complex geometric model. A previous study showed that railings modeled as beam elements placed “eccentrically” along the slab edges with the moment of inertia calculated about its base, as described in Section 3, gave similar results for longitudinal moments than when modeled with shell elements [8]. Therefore, the simpler eccentric beam element was adopted to model the railings in this

study. Figure 3 illustrates a typical 3D finite element model with the corresponding longitudinal bending moment contours for a 10.8 m (36 ft) span, three-lane bridge, in the presence of two railings, and subject to HS20 Edge loading condition.

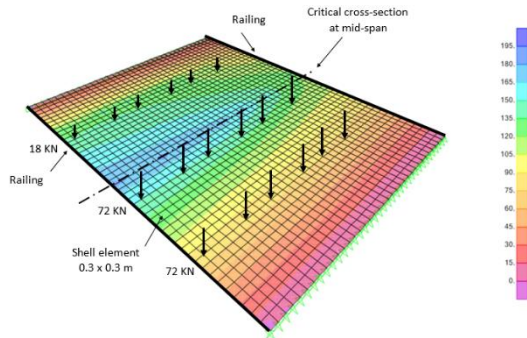


Fig. 3 3D-FEA model and longitudinal bending moments (KN-m/m) for a 10.8 m (36 ft), three-lane bridge, with base case railings (X1) on both edges of the slab.

6. FINITE-ELEMENT ANALYSIS RESULTS

The 3D-FEA results are reported in terms of the maximum longitudinal bending moments at critical locations in the concrete slab bridges. The FEA results for bridges with railings of different stiffness factors were compared with reference bridge cases without railings as well as with AASHTO Standard Specifications and LRFD procedures.

6.1. FEA RESULTS vs. AASHTO PROCEDURES

Figure 4 shows typical 3D-FEA longitudinal bending moments at the critical sections for all the three-lane bridge cases in combination with the four span lengths (S) and base case railings (X1). Figure 5 shows the bending moment variations at the critical section for all the three-lane bridges of 10.8 m (36 ft) span length, considering different railing stiffness (X0, X0.5, X1, X2, X3, X4), as compared with the AASHTO Standard Specifications and LRFD moments. The maximum 3D-FEA longitudinal moments in Figure 5 for the concrete slabs was defined as the first peak value occurring after the maximum value at the leftmost edge, the latter moment assumed to be resisted by the edge beam.

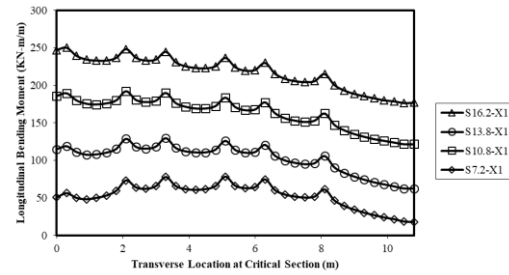


Fig. 4 3D-FEA longitudinal bending moments for three-lane bridges with all span lengths (S) and base case railings (X1).

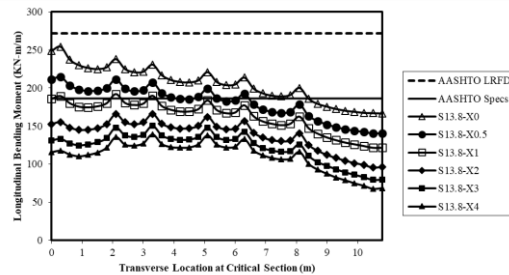


Fig. 5 3D-FEA longitudinal bending moments for 10.8 m (36 ft) span, three-lane bridge, and various railings stiffness.

Table 1 summarizes the increase or decrease in predicting bending moments in the concrete slabs when comparing the maximum FEA with the AASHTO Standard Specifications moments (Eq. 1 or 2) for all the bridge cases. Using Table 1, it can be observed that, for bridge cases with no railings (X0), for three and four lanes, AASHTO Standard Specifications generally tends to give similar moments for short-span bridges, or lower results (by about 20%) as compared to the FEA slab moments for spans longer than 10.8 m and either three- or four-lanes. When base case railings (X1) are present in a concrete slab, the FEA slab moments were off by about 10% of AASHTO moments in three- and four-lane bridges. In addition, as the stiffness factor of railings increases, the FEA moments decrease and a more significant AASHTO overestimation was observed to be about 10%.

With reference to Table 2, AASHTO LRFD overestimates the FEA slab moments in almost all bridge cases with or without railings. Assuming no railings on the bridge, AASHTO LRFD overestimates the FEA slab moments by about 15% for three-lane bridges, and by about 10% for four-lane bridges. This overestimation increases with the increase in railing stiffness. When base case railings (X1) are present, the AASHTO LRFD overestimation of the FEA slab moments reaching an average high of 40% in three-lane bridges or 30% in four-lane bridges. This overestimation is further increased as the railings stiffness factor increases

where it reaches 90% for three-lane bridges and around 60% for four-lane bridges with (X4) railings stiffness factor.

Table 1. Comparison of FEA Maximum Slab Longitudinal Bending Moments and AASHTO Standard Specifications Moments

Number of Lanes	Span Length (m)	FEA Maximum Longitudinal Moments (KN-m/m) and Percent Difference with AASHTO Specs						AASHTO Specs Moments (KN-m/m)
		Stiffness Factor						
		X0		X1		X2		
3	7.2	97.7	-1%	78.1	24%	75.0	30%	97.2
	10.8	168.7	-14%	129.4	13%	114.1	28%	145.8
	13.8	238.1	-22%	192.2	-3%	166.0	12%	186.3
	16.2	292.6	-23%	248.6	-9%	219.0	3%	225.9
4	7.2	100.3	-3%	86.3	13%	84.4	15%	97.2
	10.8	175.9	-17%	142.1	3%	131.5	11%	145.8
	13.8	248.5	-25%	207.4	-10%	185.6	0%	186.3
	16.2	304.7	-26%	266.5	-15%	239.5	-6%	225.9
3		X3		X4		X0.5		
	7.2	73.5	32%	72.7	34%	84.7	15%	97.2
	10.8	106.1	37%	101.4	44%	143.9	1%	145.8
	13.8	150.2	24%	139.0	34%	211.6	-12%	186.3
4	16.2	197.6	14%	182.3	24%	268.2	-16%	225.9
	7.2	83.6	16%	83.1	17%	88.7	10%	97.2
	10.8	126.0	16%	122.6	19%	152.7	-5%	145.8
	13.8	173.3	8%	164.4	13%	225.1	-17%	186.3
	16.2	221.3	2%	208.4	8%	283.7	-20%	225.9

Table 2. Comparison of FEA Maximum Slab Longitudinal Bending Moments and AASHTO LRFD Moments

Number of Lanes	Span Length (m)	FEA Maximum Longitudinal Moments (KN-m/m) and Percent Difference with AASHTO LRFD						AASHTO LRFD Moments (KN-m/m)
		Stiffness Factor						
		X0	X1		X2			
3	7.2	97.7	4%	78.1	30%	75.0	36%	101.7
	10.8	168.7	13%	129.4	47%	114.1	67%	190.4
	13.8	238.1	14%	192.2	41%	166.0	64%	271.8
	16.2	292.6	19%	248.6	40%	219.0	58%	347.0
4	7.2	100.3	-4%	86.3	12%	84.4	15%	96.8
	10.8	175.9	2%	142.1	27%	131.5	37%	180.0
	13.8	248.5	8%	207.4	30%	185.6	45%	269.1
	16.2	304.7	14%	266.5	30%	239.5	45%	347.0
3		X3		X4		X0.5		
	7.2	73.5	38%	72.7	40%	84.7	20%	101.7
	10.8	106.1	79%	101.4	88%	143.9	32%	190.4
	13.8	150.2	81%	139.0	96%	211.6	28%	271.8
4	16.2	197.6	76%	182.3	90%	268.2	29%	347.0
	7.2	83.6	16%	83.1	16%	88.7	9%	96.8
	10.8	126.0	43%	122.6	47%	152.7	18%	180.0
	13.8	173.3	55%	164.4	64%	225.1	20%	269.1
	16.2	221.3	57%	208.4	66%	283.7	22%	347.0

6.2. FEA RESULTS WITH RAILINGS vs. WITH NO RAILING

The maximum slab bending moments are summarized in Table 3 for all bridge cases in terms of ratios of FEA results for cases with various railing stiffness factors as compared to the corresponding cases without railings (reference case, X0). Table 3 shows that the presence of railings reduces the maximum longitudinal slab moment and this decrease is evidently more pronounced as the railings stiffness factor increases. For three-lane bridges, the slab moments reduced by about 20% when adding railing with stiffness factor (X1) as

compared to the same bridge which was reduced by 40% for (X4) railing stiffness factor. As for four-lane bridges, the slab moments reduced by about 15% with X1 railing stiffness factor, compared to about 30% with X4 railing stiffness factor. It is worth mentioning that the reduction in moments is higher in three-lane bridges than in the wide four-lane bridges; also the rate of the increase of the reduction decreases as the railing stiffness factor increases.

Table 3. Comparison of FEA Results of Railing Stiffness to Reference Case without Railing

Number of Lanes	Span Length (m)	Ratio of FEA Maximum Longitudinal Moment with Railings to Reference Case without Railings						Reference Moment X0
		Stiffness Factor						
		X0	X1	X2				
3	7.2	97.7	1.00	78.1	0.80	75.0	0.77	97.7
	10.8	168.7	1.00	129.4	0.77	114.1	0.68	168.7
	13.8	238.1	1.00	192.2	0.81	166.0	0.70	238.1
	16.2	292.6	1.00	248.6	0.85	219.0	0.75	292.6
4	7.2	100.3	1.00	86.3	0.86	84.4	0.84	100.3
	10.8	175.9	1.00	142.1	0.81	131.5	0.75	175.9
	13.8	248.5	1.00	207.4	0.83	185.6	0.75	248.5
	16.2	304.7	1.00	266.5	0.87	239.5	0.79	304.7
3		X3		X4		X0.5		
	7.2	73.5	0.75	72.7	0.74	84.7	0.87	97.7
	10.8	106.1	0.63	101.4	0.60	143.9	0.85	168.7
	13.8	150.2	0.63	139.0	0.58	211.6	0.89	238.1
	16.2	197.6	0.68	182.3	0.62	268.2	0.92	292.6
4	7.2	83.6	0.83	83.1	0.83	88.7	0.89	100.3
	10.8	126.0	0.72	122.6	0.70	152.7	0.87	175.9
	13.8	173.3	0.70	164.4	0.66	225.1	0.91	248.5
	16.2	221.3	0.73	208.4	0.68	283.7	0.93	304.7

7. SUMMARY AND CONCLUSIONS

AASHTO Standard Specifications and AASHTO LRFD empirical equations do not account for the presence of railings as integral parts of a bridge slab, and these elements are neglected during the design stage. Based on the 3D finite-element analysis, it is evident that the presence of railings increases the load-carrying capacity of the concrete slab bridges if they are modeled and constructed as integral parts of the slab. It was also found that the maximum longitudinal bending moment, due to the presence of standard railings placed integrally on both edges of the slab deck, reduced by about 40% for one-lane, 30% for two-lanes, 20% for three-lanes, and 15% for four-lane bridges. This reduction in the slab moment gets smaller with the increase in the number of lanes, and gets larger with the increase in the railing stiffness. Therefore, and to different extents, the presence of side railings therefore increases the load-carrying capacity of reinforced concrete slab bridges and the addition of stiffer railings can be used as an alternative strengthening technique to upgrade existing bridges that require rehabilitation or to allow permit vehicles on the bridge.

8. ACKNOWLEDGMENT

This research was supported by a grant from the University Research Board (URB) at the American University of Beirut to whom the authors are indebted and thankful.

9. REFERENCES

- [1] AASHTO (2002). *Standard specifications for highway bridges*, 17th Ed., American Association of State Highway and Transportation Officials (AASHTO), Washington, D.C.
- [2] AASHTO (2014). *LRFD bridge design specifications*, 7th Ed., American Association of State Highway and Transportation Officials (AASHTO), Washington, D.C.
- [3] Abou Nouh, M., Fawaz, G., Mabsout, M. and Tarhini, K. (2017). "Influence of railing stiffness on wheel load distribution in one- and two-lane concrete slab bridges." *Int. J. of GEOMATE*, Vol. 12, Issue 33, 134-138.
- [4] Akinci, N.O., Liu, J., and Bowman, M.D. (2008). "Parapet strength and contribution to live load response for super load passages." *J. Bridge Eng.*, 13(1), 55-63.
- [5] Chung, W., Liu, J., and Sotelino, E.D. (2006). "Influence of secondary elements and deck cracking on the lateral load distribution of steel girder bridges." *J. Bridge Eng.*, 11(2), 178-187.
- [6] Conner, S., and Huo, X.S. (2006). "Influence of parapets and aspect ratio on live-load distribution." *J. Bridge Eng.*, 11(2), 188-196.
- [7] Eamon, C., and Nowak, A. (2002). "Effects of edge-stiffening elements and diaphragms on bridge resistance and load distribution." *J. Bridge Eng.*, 7(5), 258-266.
- [8] Fawaz, G., Waked, M., Mabsout, M., and Tarhini, K. (2017). "Influence of railings on load carrying capacity of concrete slab bridges." *Bridge Structures*, IOS Press, Vol. 12, No. 3-4, pp. 85-96.
- [9] Mabsout, M., Tarhini, K., Frederick, G., and Kobrosly M. (1997). "Influence of sidewalks and railings on wheel load distribution in steel girder highway bridges." *J. Bridge Eng.*, 2(3), 88-96.
- [10] Mabsout, M., Tarhini, K., Jabakhanji, R., and Awwad, E. (2004). "Wheel load distribution in simply supported concrete slab bridges." *J. Bridge Eng.*, 9(2), 147-155.
- [11] SAP2000 (version 17). Computers and Structures Inc., Berkeley, California.

INFLUENCE OF DIESEL OIL CONTAMINANTS ON GGBS BLENDED WITH BENTONITE AND LATERITIC SOIL AS LINERS

Devarangadi Manikanta¹, Uma Shankar M², B.R. Phanikumar³

¹Research Scholar, ²Associate Professor, VIT University, India; ³Professor, SRKR Engineering College, India

ABSTRACT

The use of industrial waste as a liner in landfills replaces the conventional type of liners such as compacted clay liners, geo-membrane and geo-synthetic clay liners etc. GGBS (ground granulated blast furnace slag) is an industrial waste extracted from iron and steel industries. Based on an experimental work, this paper proposes GGBS blended with bentonite and lateritic soil mixtures as an alternative to a conventional liner. The various proportions used in the blend were 10% GGBS + 70% bentonite + 20% lateritic soil; 15% GGBS + 65% bentonite + 20% lateritic soil; 20% GGBS + 60% bentonite + 20% lateritic soil. The paper presents experimental data on *LL* (liquid limit), *FSI* (free swell index) and hydraulic conductivity for the above blends. The permeating fluids used in the blend were deionized water (DIW) and diesel oil contaminants (DOC). Diesel oil contaminants were procured from automobile and fuel testing manufacturers considered as spillage, an organic effluent contaminating groundwater. Permeating DOC evaluates the field conditions. Results obtained from the tests showed that *LL* and *FSI* decreased with increasing GGBS content. Hydraulic conductivity tests were also performed at OMC and MDD. OMC decreased and MDD increased with increase in GGBS content. And hydraulic conductivity decreased with increase in GGBS content on permeating with DIW and DOC. The hydraulic conductivity of the blends determined with DIW and DOC was less than 10^{-7} cm/sec conforming to the recommendation of the United States Environmental Protection Agency (USEPA). Based on the results obtained from the study, optimum percentage of GGBS content can be determined with which lateritic soil can be blended to prove as an alternative to the conventional type of a liner.

Key words: GGBS, Liquid limit, Free swell index, Hydraulic conductivity, Diesel oil contaminants

1. INTRODUCTION

In India slag production is estimated to be more than 10 million tonnes per annum [1]. Significant amount of slag is used to clinker in cement manufacturers and soil stabilization. Discarded slag pollutes soil and groundwater; hence it is imperative to effectively use the slag to prevent the contamination of soil and water.

Considerable research on landfill liners has been done with various industrial wastes such as fly ash, lime, gypsum, coal gangue, steel slag, waste wood ash, red mud and tailings. Three different types of fly ash has been examined and treated with 2% lime which resulted in lower permeability. Further, strength gain in due course of time was also observed [2]. Gypsum-treated lime-fly ash mixtures resulted in a lower hydraulic conductivity due to accelerated formation of cementitious compounds and hydration [3]. The feasibility of coal gangue as liner material was studied. Permeability, sorption and leaching behavior have been performed and it has been concluded that lower regulatory values have been observed [4]. Steel slag such as electric arc furnace slag and ladle slag was recommended and utilized for a top cover in sanitary landfill [5,6]. The waste

wood ash (WWA) with different proportions blended with lateritic soil was examined as a liner. The results showed that maximum percentage of 4% of WWA could be used as liner [7]. Fly ash mixed with red mud and tailings was examined as liner. Because of its lower hydraulic conductivity, it can be used as a seepage barrier [8]. Many research findings discussed the use of GGBS in stabilizing the lithomargic clay [9], marine soft clays [10], dispersive clays [11] and also treated as effective binder in reducing toxic hydrogen sulfide gas [12]. No research was so far done on the use of GGBS as a liner material. This paper suggests GGBS (ground granulated blast furnace slag), a by-product of iron ore as a liner in landfills.

The paper presents experimental data on *LL* (liquid limit), *FSI* (free swell index) and hydraulic conductivity of GGBS blended with bentonite and lateritic soil. Hydraulic conductivity was determined by permeating with DIW and DOC as influents. DOC is an organic substance which pollutes groundwater and soil due to spillages/leakage from automobile industries and oil containers. Furthermore, hydraulic conductivity tests with DIW and DOC was continued till a steady state was attained.

2. MATERIALS USED

Sodium based bentonite was used because of its high adsorption capacity and presence of montmorillonites which expand considerably with sodium, as the predominant exchangeable cation, resulting in swelling. The material was procured from Kolar district in Karnataka, India. GGBS was collected from cement industries near Chennai, TN, India. Lateritic soil was used in the test programme. It was highly pervious and crystalline in nature. It was collected at a depth of 1m from ground level at Vellore, TN, India. According to the Unified Soil Classification System, lateritic soil was classified as SM (silty sand). In this study, deionized water (DIW) and diesel oil contaminant (DOC) were used as permeating fluids. The viscosity of DOC was 10.542 centistokes (0.1054 cm²/sec), and its density was 843.075 kg/m³. Table 1 shows the Engineering properties of the lateritic soil, bentonite and GGBS.

Property	Lateritic soil	Bentonite	GGBS
Liquid limit (%)	-	410	38.6
Plastic limit (%)	-	65	-
Plasticity index	-	345	-
Coarse sand %	4.972	-	-
Medium Sand %	52.12	-	-
%	34.496	-	1
Fine sand %	8.142	100	99
Silt and Clay %	17.4	43	25.2
OMC %	1.67	1.230	1.568
MDD g/cm ³			
FSI %	-	510	-

Note: OMC is the optimum moisture content, MDD is the maximum dry density and FSI is free swell index.

3. MIX DESIGN

The various mixes used were A1: 10% GGBS + 70% bentonite + 20% lateritic soil; A2: 15% GGBS + 65% bentonite + 20% lateritic soil; A3: 20% GGBS + 60% bentonite + 20% lateritic soil. *LL* and *FSI*, compaction and hydraulic conductivity were determined for all the above blends. Hydraulic conductivity was determined at the respective OMC and MDD of the mixes. Based on the results obtained from compaction tests, void ratios of the blends were determined.

4. EXPERIMENTAL INVESTIGATION

4.1 Liquid limit (*LL*) and free swell index (*FSI*)

The *LL* test of the blends was performed according to ASTM D4318-00. And, the free swell index (*FSI*) test of the blends was determined as per ASTM D5890-02.

4.2 Compaction characteristics

Standard Proctor compaction tests for all the mixes were determined as per ASTM D698-07. The maximum dry density (MDD) and optimum moisture content (OMC) of the mixes are determined.

4.3 Hydraulic conductivity

Hydraulic conductivity tests were performed by falling head permeameter as per ASTM D5084-03. The mixes are compacted at their respective MDD and OMC. The permeant fluids used were DIW and DOC.

4.3.1 Preparation of sample for hydraulic conductivity

The specimens for hydraulic conductivity tests were prepared according to the mix proportion as shown in Section 3.1. Hydraulic conductivity tests were performed on GGBS blended with soil and bentonite in the standard falling permeameter equipment after compacting the blends in the test molds at their MDD and OMC. The influents used were DIW and DOC. Permeation of mixes with DIW and DOC was continued till a steady state was attained. Before the test, however, the samples were soaked in water for a minimum of 48 hours for complete saturation.

5. RESULTS AND DISCUSSION

5.1 Effect of GGBS content with DIW and DOC on liquid limit (*LL*)

The liquid limit (*LL*) of the mixes was determined with DIW and DOC. Table 2 gives the values of *LL* with DIW. *LL* decreased significantly with increasing GGBS content. *LL* depends on the particle size; the finer the particle size, the higher would be the values of *LL*. As the amount of finer particles present in bentonite are replaced with coarser particles present in the GGBS, *LL* decreases. Moreover, GGBS is a pozzolanic material, and on combination with soil and bentonite it induces hydration which causes flocculation by which the average particle size increases leading to a reduction in *LL* and plasticity [13]. The percentage change in *LL* from A1 to A3 was 19.19%. Plasticity tests done in presence of DOC indicated that the blends were rendered non-plastic.

5.2 Effect of GGBS content on free swell index (*FSI*)

FSI tests were on the blends with DIW and DOC. Table 2 presents the *FSI* values. *FSI*

decreased from 500% to 400% when the GGBS content increased from 105 to 20%. *FSI* decreases with increase in particle size. The finer the particle size, the higher the *FSI* would be. As bentonite is replaced with GGBS, the average particle size of the blend increases. Hence, *FSI* decreases with increase in GGBS content [13]. No swell was observed when mixes were permeated with diesel oil contaminants.

5.3 Correlation between *LL* and *FSI* of all the blends

Fig 1 shows the correlation of *FSI* and *LL* obtained for different mixtures. The figure depicts that, as *LL* decreases, *FSI* also decreases with increase in GGBS content. This is true for all the mixes. For example, when GGBS increased from 10% to 20%, *LL* decreased from 225.39% to 182.13%, and *FSI* decreased from 500% to 400% respectively.

Table 2. *LL* and *FSI* values

Mix no.	<i>LL</i> (%)	<i>FSI</i> (%)
A1	225.39	500
A2	199.34	480
A3	182.13	400

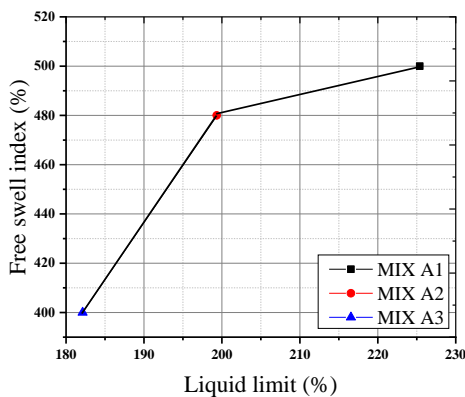


Fig.1 Correlation between *LL* and *FSI*

5.4 Compaction characteristics of different mixes

Fig. 2 shows the compaction curves for the mixes. As GGBS content increased, compaction curves shifted upwards, indicating an increase in dry density. MDD and OMC are tabulated in Table 3. Using Equation 1, void ratio (*e*) and specific gravity (*G_s*) were determined. As GGBS content increased in the blend, MDD increased and OMC decreased. For example: when GGBS increased from 10% to 20%, MDD increased from 16.255 to 16.775 kN/m³ and OMC decreased from 18.2 to 16% respectively. Increase in MDD can be

attributed to the flocculation triggered by GGBS. The reduction in OMC can be explained through the fact that larger clusters of particles form through flocculation which do not need higher amounts of water for compaction [14]. The void ratio decreased from 0.60 to 0.57 and specific gravity decreased from 2.695 to 2.668, when GGBS content increased from 10% to 20%.

$$e = \left(\frac{\gamma_d}{\gamma_w G_s} - 1 \right) \quad (1)$$

Equation (1) refers to void ratio (*e*), dry unit weight (γ_d), the unit weight of water (γ_w) and *G_s* is the specific gravity of mixtures.

Table 3. Proctor compaction results

Mix	Max. dry unit weight (kN/m ³)	OMC (%)	Void ratio (<i>e</i>)
A1	16.255	18.2	0.60
A2	16.529	17.2	0.59
A3	16.775	16	0.57

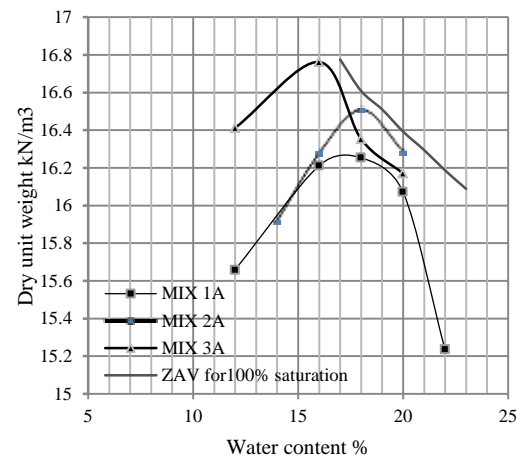


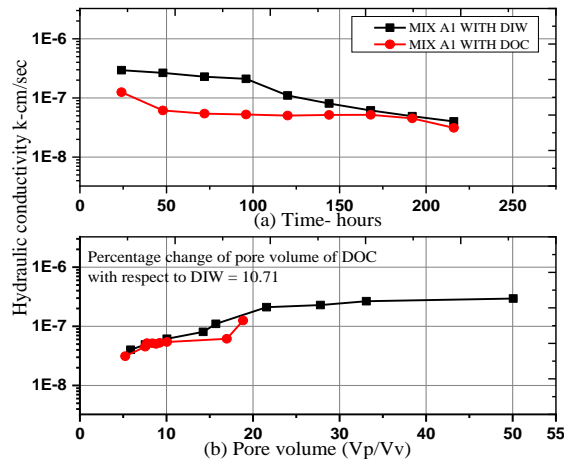
Fig. 2 Compaction curves

5.5 Hydraulic conductivity (*k*)

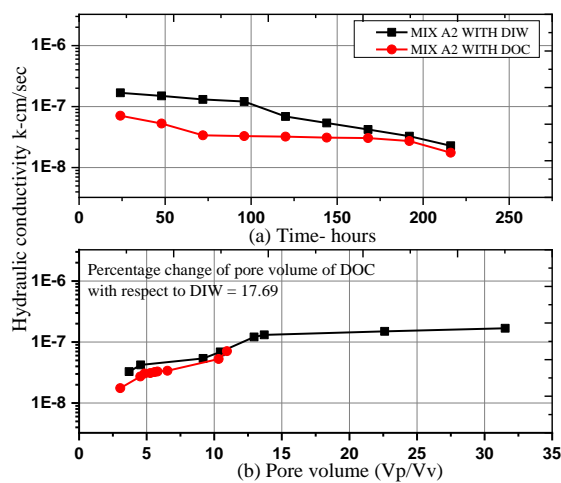
Hydraulic conductivity of the mixes was determined at their respective OMC and MDD. The permeant fluids used were DIW and DOC. Table 4 shows the hydraulic conductivity data. The hydraulic conductivity permeated with DIW and DOC for the mixes was found to be less than 10⁻⁷ cm/sec which is in accordance with USEPA. The pore volumes of the blends determined with DIW for the mixes A1, A2 and A3 were 5.87, 3.71 and 2.60 respectively. The pore volumes of the mixes permeated with DOC were 5.24, 3.05 and 0.87 respectively. The percentage change in pore volume of DOC with respect to DIW was 10.71% for A1. Similarly, for A2 and A3 the percentage of change was 17.69% and 66.67% respectively.

Table 4. Hydraulic conductivity data

Mix no.	k with DIW (cm/sec)	k with DOC (cm/sec)
A1	4.0121×10^{-8}	3.1223×10^{-8}
A2	2.2799×10^{-8}	1.7531×10^{-8}
A3	1.4963×10^{-8}	4.8406×10^{-9}



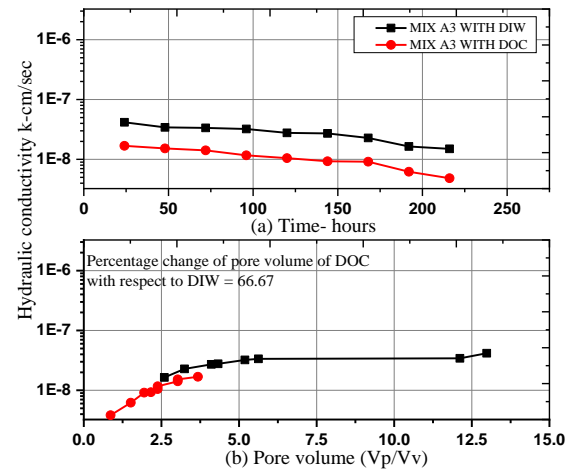
Figs. 3(a) and 3(b) variation of hydraulic conductivity with time and pore volume for A1



Figs. 4(a) and 4(b) variation of hydraulic conductivity with time and pore volume for A2

5.5.1 Effect of GGBS content on hydraulic conductivity

Figs. 3(a) and 3(b) show the variation of hydraulic conductivity for A1 permeated with DIW and DOC. Fig. 3(a) shows the variation of hydraulic conductivity with time. Hydraulic conductivity initially increased but decreased as time period increased. For example, k value was 2.9466×10^{-7} cm/sec at 24 hours, and within 240 hours, k value was 4.0121×10^{-8} cm/sec. As the pores of soil got saturated with increase in time k was decreased.



Figs. 5(a) and 5(b) variation of hydraulic conductivity with time and pore volume for A3

This was true for the mixes A1 A2 and A3 too. See Figs. 3(a), 4(a) and 5(a). A similar pattern was observed when the blends were permeated with DOC. For example, k value was observed to be 1.2497×10^{-7} cm/sec, at the end of 240 hours k value was 3.1223×10^{-8} cm/sec. The hydraulic conductivity test for all the blends were terminated till flow becomes steady. Most of the blends achieved steady state less than 240 hours (10 days). At the end of 240 hours the hydraulic conductivity k of DOC was found to be less than DIW. This is true for all the mixes. See Figs. 3(a), 4(a) and 5(a). For example, in A1 the hydraulic conductivity of DIW was observed to be 4.0121×10^{-8} cm/sec, where k value of DOC was 3.1223×10^{-8} cm/sec. This is because DOC is more viscous in nature compared to DIW. As a result when blend was permeated with DOC it clogs the pores of the blend.

Figs. 3(b), 4(b) and 5 (b) respectively show the variation of hydraulic conductivity for A1, A2 and A3 with pore volume permeated with DIW and DOC. Decrease pattern was observed, when permeated with DIW and DOC for A1. For example in case of Fig.3(b) the pore volume was observed to be in decrease trend i.e. from 50.06 to 5.87, when hydraulic conductivity decreases from 2.9466×10^{-7} to 4.0121×10^{-8} cm/sec. Similar pattern was observed when blend permeated with DOC, For example, 18.85 to 5.24 when hydraulic conductivity decreased from 1.2497×10^{-7} to 3.1223×10^{-8} cm/sec. This is true for all the blends (See Figs. 3b, 4b and 5b). The decrease in pore volume is due to the initial hydration of sample which has taken place for first 48 hours in saturation in which GGBS has potential cementitious reactivity [15]. The final hydration of the blend may be analyzed for the amount of fluid permeated from the burette stand to form the cementitious reactivity thus obtaining a gradual

decrease in fluid present in the burette for the less number of pores present in the sample. Hence, a lower hydraulic conductivity with less pore volume resulted.

6. CONCLUSIONS

LL and *FSI* determined with *DIW* decreased with increasing *GGBS* content. *LL* determined with *DOC* indicated non-plastic nature. There was a good correlation between *LL* and *FSI* which indicated that the higher the *LL*, the higher would be the *FSI*.

Hydraulic conductivity of *GGBS* blended with soil and bentonite and determined with *DIW* decreased significantly with increasing *GGBS* content. The hydraulic conductivity of *GGBS* blended with soil and bentonite and determined with *DOC* decreased significantly with increasing *GGBS* content. The permeation with *DOC* gave lower hydraulic conductivity when compared to *DIW* due to high viscosity of *DOC*.

Based on the results obtained, *GGBS* blended with bentonite and lateritic soil proved to be an alternative for a conventional liner. It can effectively prevent leachate migration into soil and water when permeated with organic fluids such as diesel oil contaminant.

7. REFERENCES

- [1] NVCA, "Yearbook 2017," *Pitchbook*, vol. 2017, no. 712, pp. 1–11, 2017.
- [2] J. P. Prashanth, P. V. Sivapullaiah, and A. Sridharan, "Pozzolanic fly ash as a hydraulic barrier in land fills," *Eng. Geol.*, vol. 60, no. 1–4, pp. 245–252, 2001.
- [3] P. V. Sivapullaiah and M. A. A. Baig, "Gypsum treated fly ash as a liner for waste disposal facilities," *Waste Manag.*, vol. 31, no. 2, pp. 359–369, 2011.
- [4] H. Wu, Q. Wen, L. Hu, M. Gong, and Z. Tang, "Feasibility study on the application of coal gangue as landfill liner material," *Waste Manag.*, vol. 63, pp. 161–171, 2017.
- [5] I. Herrmann, L. Andreas, S. Diener, and L. Lind, "Steel slag used in landfill cover liners: Laboratory and field tests," *Waste Manag. Res.*, vol. 28, no. 12, pp. 1114–1121, 2010.
- [6] L. Andreas, S. Diener, and A. Lagerkvist, "Steel slags in a landfill top cover - Experiences from a full-scale experiment," *Waste Manag.*, vol. 34, no. 3, pp. 692–701, 2014.
- [7] K. J. Osinubi, J. R. Oluremi, A. O. Eberemu, and S. T. Ijimdiya, "Interaction of landfill leachate with compacted lateritic soil – waste wood ash mixture," *Proc. Inst. Civ. Eng. - Waste Resour. Manag.*, vol. 170, no. 3+4, pp. 1–11, 2017.
- [8] H. Engineering and C. Author, "Experimental Study on Application of Industrial Waste in Landfill Liner Yating YANG 1 , Qingbo WEN 2 and Liming HU 3," *Control*, pp. 3881–3890, 2012.
- [9] D. C. Sekhar and S. Nayak, "SEM and XRD investigations on lithomargic clay stabilized using granulated blast furnace slag and cement," *Int. J. Geotech. Eng.*, vol. 6362, no. September, pp. 1–15, 2017.
- [10] Y. Yi, C. Li, S. Liu, and M. Asce, "Alkali-Activated Ground-Granulated Blast Furnace Slag for Stabilization of Marine Soft Clay," *J. Materail Civ. Eng.*, vol. 11, no. 4, pp. 246–250, 2010.
- [11] A. R. Goodarzi and M. Salimi, "Stabilization treatment of a dispersive clayey soil using granulated blast furnace slag and basic oxygen furnace slag," *Appl. Clay Sci.*, vol. 108, pp. 61–69, 2015.
- [12] C. W. W. Ng, M. Xie, and A. K. Leung, "Removal of hydrogen sulfide using soil amended with ground granulated blast furnace," *J. Environ. Eng. ASCE*, vol. 143, no. 7, pp. 1–8, 2016.
- [13] M. U. Shankar and B. R. Phanikumar, "Correlation studies on index properties of fly ash-stabilised expansive clay liners," *Geomech. Geoengin.*, vol. 7, no. 4, pp. 283–291, 2012.
- [14] E. Dale, M. C. Nobe, C. Clevenger, and J. Cross, "Icsdec 2012 © asce 2013 214," *Icsdec*, no. 2011, pp. 818–825, 2013.
- [15] K. V. Manjunath, L. Govindaraju, and P. V. Sivapullaiah, "Blast Furnace Slag for Bulk Geotechnical Applications," *Proc. Indian Geotech. Conf. December 15-17,2011, Kochi (Paper No.H-098.)*, no. December, pp. 401–404, 2011.

IS WATER AVAILABLE IN THE PUBLIC PLACES SAFE TO DRINK IN BANGLADESH?

Ijjaj Mahmud Chowdhury¹, Istiakur Rahman², Sk. Sadman Sakib³, Kazi Ismile Hossain⁴ and Shoumic Shahid Chowdhury⁵

^{1,2,3,4,5} Faculty of Engineering and Technology, Islamic University of Technology (IUT), Bangladesh

ABSTRACT

Access to safe drinking water has been a key development concern for the developing countries at national, regional and local level. Bangladesh being one of the most densely populated countries in the world, is struggling to provide safe drinking water facilities to the citizens. This paper focuses on the quality of drinking water available in the public places. The study was conducted in Gazipur city which is an industrial area and also the largest city corporation of Bangladesh in terms of area where more than 2.5 million people resides. Additionally, thousands of people travel to this area every day and a major portion of them belong to textile and readymade garment industry. The consumption of drinking water from public places mostly takes place during break time of the industry employees. A questionnaire survey was carried out to understand the perception of consumers towards drinking water quality. Altogether 14 physical, chemical and microbiological parameters were tested in the laboratory against the water samples collected from 29 different locations comprising of several sources to determine the current status of water quality. Presence of Total Coliform, Fecal Coliform and E. coli were found 97%, 90% and 79% respectively in relatively high concentrations than the recommended value and must be reduced to the allowable limit before consumption.

Keywords: Safe drinking water, Physico-chemical parameters, Microbiological parameters, Health effects

INTRODUCTION

One of the sustainable development goals is to provide clean water and sanitation through ensuring access to safe and affordable drinking water for all by 2030 universally [1]. Safe drinking-water means the water that does not represent any significant risk to health over a lifetime of consumption, including different sensitivities that may occur between life stages [2]. In 2015, according to WHO and UNICEF 2.1 billion people lack access to safely managed drinking water services [3]. Numerous studies have been done on the drinking water quality and its sources all over the world. Sakai [4] found that in Myanmar most of the sources of water (river, lake, dam, and well) were found to be generally good quality except arsenic and iron in groundwater. It was also found that highest microbial organisms were obtained from pot water followed by non-piped water, piped water and bottled water. Bacterial contamination can get into water in many ways; the presence of certain organisms in water may be an indication of either the corrosion of cast iron or the bio-deterioration of construction materials to form substances that support the growth of microorganisms. Nonmetallic materials such as plastics, rubber-jointing compounds, and pipe-lining materials

provide organic nutrients and thus encourage the growth of microorganisms [5], [6].

Like many other developing countries Bangladesh is also suffering from the widespread of microbial contamination of water especially with the vast presence of E.coli. In Bangladesh, about 80% of piped water and over 40% of all improved water sources is found to be contaminated with E. coli contamination [7]. As per WHO only 136 out of 300 municipalities provide piped water to the households having single or multi tap. As Bangladesh has recently met the graduation criteria to be a developing country from a least developed country the country needs to focus on its water infrastructure to make further economic development.

A Huge portion of country's working population in the industries mostly belongs to low income group and by nature of their job they have to stay outside home for more than 12 hours a day. As a result, this mass population has to consume water from workplace, roadside shops and tea-stalls which comes through piped water system or commercially supplied jar water from different unidentifiable sources except commercially produced bottle water. The shopkeepers who took part in the questionnaire survey revealed that the suppliers of jar water claimed the water to be pure but are often reluctant to talk

about the source and treatment procedure of the water. Moreover, most of the consumers usually drink water in different public places from jar water or sometimes even from non-filtered water as they cannot afford bottled water. A study on the quality of commercially supplied jar drinking water was carried out at Chattogram (previously known as Chittagong) in Bangladesh in 2018 and significant presence of total coliform and fecal coliform were observed [8]. Regarding the quality of drinking water, microbiological contamination is a primary concern of developing countries. In addition, inorganic contaminants, concerning both health and aesthetic aspects, can be present in the waters [9]. Though there has been several studies conducted on the household drinking water quality in Bangladesh, but information on public drinking water remains unclear as limited studies have been conducted in this study area. The quality of the water available in the public places in Gazipur is needed to be assessed to acquire more knowledge on overall quality and hygiene issues.

METHODOLOGY

Study Area and Sampling Sites

The location of the study area is Gazipur City Corporation (GCC), situated besides the capital city Dhaka. The GCC was created in January 2013 and is composed of 57 wards drawn from most of the previous Gazipur Sadar Unions and the entire former Tongi municipality. GCC is the largest city corporation of Bangladesh having an area of 329.53 square kilometer. The current population of Gazipur city is about 2.5 million. This city connects two major city Dhaka and Mymensingh through Dhaka-Mymensingh highway, one of the most commercially important highway. Six zones as shown in Figure 1 were selected within the GCC namely Gazipur Chowrasta, Bason, Sign Board, Board Bazar, Gazipura and Station Road from where the samples were collected. The location of sampling sites has been selected randomly across this highway near about industry or public gathering places e.g., bus stop, market etc. within the selected zones.

A total of 29 samples were collected from roadside shops (locally known as Tong) of which 11 are from commercially supplied jar water (locally known as filtered water), 6 are from piped water system and 13 are from non-piped water system mostly collected in large container (50 to 100 liter capacity) from nearby submersible sources. Fig. 2 shows how water is consumed / stored through different supply system. For most cases it has been observed that the container used for the storage is not well maintained.



Fig. 1 Location of the six zones from where samples have been collected



2(a)

2(b)



2(c)

Fig. 2 Typical supply system of drinking water available for public in of Gazipur city (a) collected water stored in large container (b) piped water (c) commercially supplied jar water

Parameters Measured

To determine the potability of the water available for consumers in the public spaces the collected samples were measured against the following 14

parameters shown in Table 1 which includes physical, of the survey is shown in Table 2.

Table 1 Water quality parameters and analytic method of determination

Parameter Type	Parameter	Method of Determination
Physical	Temperature	Instrumental (HACH Portable Meter)
	Color	Spectrophotometer DR 2800 (Pt. Co. Std. Method)
	Turbidity	APHA Standard Method- 2130 B
	Total Dissolved Solids (TDS)	APHA Standard Method- 2540
Chemical	pH	APHA Standard Method- 4500-H+ B
	Alkalinity	Titrimetric Method
	Hardness	EDTA Titrimetric Method
	Iron	Spectrophotometer DR 2800 (FerroVer Method)
	Manganese	Spectrophotometer DR 2800 (Periodate Oxidation Method)
	Chloride	Titrimetric Method
	Arsenic	Using Arsenic Kit
Microbiological	Total Coliform (TC)	Membrane Filtration Method
	Fecal Coliform (FC)	
	E. coli	

chemical, and microbiological parameters.

The result obtained from the lab tests were then analyzed to determine the quality of drinking water and to understand the level of pollutant concentration. The results were compared with the WHO guideline value (health based) and local standards. Different basic statistical parameters such as maximum, minimum, mean and standard deviation were also determined against the parameters.

Questionnaire Survey

A questionnaire survey was carried out to inquire the water consumption behavior in the public places. This survey was also aimed to understand the perception of consumers towards hygiene and water quality. A total of 123 individuals including consumers and shopkeepers participated in the survey. The socio economic status of the participants

RESULTS

29 drinking water samples (jar water, piped and non-piped water) were collected from different public spots and 11 physical and chemical parameters were tested as mentioned in Table 1. Out of these samples tested for water quality all were found to be within the permissible range of WHO and national guidelines except color and turbidity. The results obtained from laboratory tests are mentioned below in Table 3.

Microbiological analysis of the water reveals that almost all the samples were contaminated with TC or FC or E.Coli. Presence of TC was found to be highest (97%) followed by FC (90%) and E.Coli (79%). The results from microbiological analysis are also categorized in Table 4 according to different risk grade [10].

Table 2 Socio-economic condition of the respondent participated in the survey

		No. of people	%			No. of people	%
Gender	Male	97	78.9	Profession	Garments Worker	44	35.8
	Female	26	21.1		Officers/Executives/Managers	26	21.1
Age Group (years)	0-15	3	2.4		Students	9	7.3
	15-30	36	29.3		Rickshaw Puller and Day Laborer	21	17.1
	30-45	57	46.3		Bus/Truck Driver	12	9.8
	45-60	24	19.5		Shop keeper	11	8.9
	>60	3	2.4	Monthly Income (BDT)	<10000	41	33.3
Highest Education Level	Illiterate	33	26.8		10000-20000	52	42.3
	Primary	18	14.6		>20000	30	24.4
	Secondary	21	17.1				
	≥Higher Secondary	51	41.5				

Table 3 Test results for physical, chemical and microbiological parameters

Parameters	Unit	Range of Obtained Value	Mean \pm Std. Deviation	WHO Guideline Value (GV)	Bangladesh Standard (ECR 1997)	% exceeding GV (either WHO or local standard)
Temperature	$^{\circ}\text{C}$	17-24	21.3 \pm 2.2	--	20-30	0
Color	Pt. Co	2-50	13.28 \pm 11.28	--	15	27.6
Turbidity	NTU	0.47-5.56	1.75 \pm 1.24	5	10	10
pH	--	6.07-8.25	7.5 \pm 0.55	6.5-9.5	6.5-8.5	0
Total Dissolved Solids (TDS)	mg/L	139-660	239.62 \pm 100.18	1200	1000	0
Alkalinity	mg/L as CaCO_3	13-39	24.97 \pm 6.34	--	--	0
Hardness	mg/L as CaCO_3	25-120	57.45 \pm 23.37	500	200-500	0
Iron	mg/L	0-0.25	0.05 \pm 0.05	0.3	0.3-1	0
Manganese	mg/L	0.04-0.99	0.105 \pm 0.19	0.4	0.1	0
Chloride	mg/L	2-22.2	8.85 \pm 5.86	250	150-600	0
Arsenic	$\mu\text{g/L}$	nil	--	0.01	0.05	0
TC	Cfu/100 ml	0-50	25 \pm 14.7	0	0	97
FC	Cfu/100 ml	0-70	27 \pm 20.4	0	0	90
E.Coli	Cfu/100 ml	0-20	9 \pm 6.5	0	0	79

Table 4 Microbiological risk analysis

Risk Grade	Range of coliform (cfu/100 ml)	TC	FC	E. Coli
A (No risk)	0	3.45	10.34	20.69
B (Low risk)	1-10	17.24	10.34	34.48
C (High risk)	11-100	79.31	79.31	44.83
D (Very high risk)	101- >1000	--	--	--

Five different brands (including local and multinational) of commercial bottled water were also tested to determine microbial contamination. All of the five samples proved to be of no risk.

DISCUSSION

This study assessed the drinking water available in the public places against physico-chemical and microbiological parameters. The results show that pH, TDS, Hardness, Iron, Manganese, Chloride and Arsenic all fall under the guideline value provided by WHO or national authority.

If the pH value is low, water can be corrosive in nature and may damage the pipe system and the high

pH value adversely affects the disinfection process [9], [10]. In case of Iron, as there is no health based guideline available, a guideline developed on history based suggests that there is no noticeable change in taste if the concentration remains below 0.3 mg/L. While presence of manganese in drinking water becomes objectionable when it is deposited in water mains and causes discoloration. Chloride in drinking water typically originates from natural sources, sewage and industrial effluents. Chloride concentration above 250 mg/L can give detectable taste in water. Concerning about arsenic, the WHO guideline value is 0.1 $\mu\text{g/L}$ but when any source containing arsenic increased over 10 $\mu\text{g/L}$ concentration, this will be the dominant source of arsenic intake. A guideline value of 500 mg/L as CaCO_3 is recommended by WHO for hardness based on taste and household use considerations, although concentration above 200 mg/L as CaCO_3 may affect its acceptability to consumers depending on local considerations.

The study did not find any case where the above mentioned physico-chemical parameters show concentrations not satisfying WHO or national guidelines except color and turbidity. Though there are not any health based guideline value for color of water but higher value of color indicates the necessity for further investigation to determine the presence of colored organic matter or industrial wastes [5]. Like color, for turbidity there is also no health based guideline but less turbid water has a high range of acceptability to the consumers. Moreover, turbid

water possesses the potentiality to be contaminated microbiologically and constitute different health problems [9].

The results revealed from microbiological analysis indicate that all the samples irrespective of their supply type they were found microbiologically contaminated. Out of 29 samples 21 samples were found to be contaminated with TC, FC and *E. coli*, 6 samples with any two indicator organism and two samples with one indicator organism. In case of TC and FC almost 80% samples show high health risk potentiality whereas for *E. coli* it is around 45%. Drinking water contaminated with *E. coli* may responsible for urinary tract infection, pulmonary infection and can also cause diarrhea and water borne diseases [11].

Precautions can be taken to reduce microbial contamination through disinfection. Disinfection can be done both in the Point-of-Entry (POE) and Point-of-Use (POU) with appropriate dosage for water treatment due to microbial contamination. Chlorination can be a useful treatment process as chlorine effectively kills a large variety of microbial waterborne pathogens. Flocculant-disinfectant POU water treatment followed by filtration has a very high reduction rate against waterborne bacterial pathogens including salmonella typhi, vibrio cholera and specially *Escherichia coli*. In Western Kenya combined flocculant-disinfectant treatment reduced more than 90% of *E. coli* contamination along with high reduction efficiency against turbidity [12]. The POU water treatment product is composed of a coagulant, an alkaline agent, flocculation aids, a flocculent and a chlorine-based disinfectant. However this treatment method is expensive and requires government subsidy for implementation. It has also been observed in Nepal that regular cleaning of the water holding tanks subsequently reduce coliform counts greatly [13]. As it has been found from this study that most of the shopkeepers store water in a very unhygienic fashion, cleaning of water holding tanks regularly might provide some instant microbial reduction.

The contamination of microbiological organism into the water may be occurred due to old piping system and discontinuity of water supply in case of the samples which were collected from pipe network. In case of non-piped water collected in large container, 100% presence of microbial contamination indicates careless, dirtiness, unaware behavior of the shop-keeper. Surprisingly almost all the samples collected from commercially supplied jar water were also contaminated with any of the tested parameter. Even though the suppliers use ground water which may not be affected with microbial contamination but due to their irresponsible handling and unhygienic

practices the water may often get contaminated. The results are also an indication to the fact that the water is not treated properly or often supplied untreated. Literature suggests that the presence of indicator organisms is a severe threat to the community and this should be dealt with good manufacturing processes or techniques by the suppliers [8].

From the survey it was revealed that a random person consumes 0.5 L to 1 L drinking water in a day from public places and mostly from roadside shops (Tong). 58% of respondents would prefer commercially supplied jar water (filtered water) whereas 26% and 16% would prefer submersible (piped/non-piped) and bottled water respectively when they are outside of home and work place. The similar question was asked with a condition that what they would prefer if all of the water types (filter, submersible and bottled water) are available to them at same/subsidized price. The response was such that 77% would select bottled water, 23% would prefer filtered water and no one would like to consume water from piped/non-piped source.

CONCLUSION

This study finds that the overall quality of drinking water in public places is unsafe to drink as most of the samples are microbiologically contaminated and the people consuming this water are under threat of health risk associated with water related diseases. People who cannot afford bottled water are bound to drink from available options in the public places and the quality of that water is often compromised in the study area. Respective authority should be more proactive and ensure that the supplied water is complying with the national standard.

ACKNOWLEDGEMENTS

The laboratory tests were conducted at the environmental engineering lab of Department of Civil and Environmental Engineering of Islamic University of Technology. The authors acknowledge the support received from the university and thankful to the laboratory staff for their assistance in conducting the tests.

REFERENCES

- [1] Sustainable Development Goals, United Nations Development Program, 2016. Retrieved from <http://www.undp.org/content/undp/en/home/sustainable-development-goals/goal-6-clean-water-and-sanitation.html>
- [2] World Health Organization, Guidelines for drinking-water quality [electronic resource]: incorporating 1st and 2nd addenda, Vol.1,

- recommendations, 3rd ed. World Health Organization, 2008
- [3] Progress on drinking water, sanitation and hygiene: 2017 update and SDG baselines. Geneva: World Health Organization (WHO) and the United Nations Children's Fund (UNICEF), 2017.
- [4] Sakai H., Kataoka Y., and Fukushi K., Quality of Source Water and Drinking Water in Urban Areas of Myanmar, *The Scientific World Journal*, Vol. 2013.
- [5] World Health Organization, Guidelines for drinking-water quality, vol. Surveillance and control of community supplies, 2nd ed. World Health Organization, Geneva, 1997.
- [6] Agard L., Alexander C., Green S., Jackson M., Patel S., and Adesiyun A., Microbial Quality of Water Supply to an Urban Community in Trinidad, *Journal of Food Protection*, Vol. 65, No. 8, 2002, pp. 1297-1303.
- [7] World Bank, Reducing Inequalities in Water Supply, Sanitation, and Hygiene in the Era of the Sustainable Development Goals: Synthesis Report of the WASH Poverty Diagnostic Initiative, WASH Synthesis Report, World Bank, Washington, DC., 2017.
- [8] Mina S. A., Marzan L. W., Sultana T., and Akter Y., Quality assessment of commercially supplied drinking jar water in Chittagong City, Bangladesh, *Applied Water Science*, Vol. 8, Issue 1, 2018.
- [9] Sorlini S., Palazzini D., Sieliechi J. M., and Ngassoum M. B., Assessment of Physical-Chemical Drinking Water Quality in the Logone Valley (Chad-Cameroon), *Sustainability*, Vol. 5, Issue 7, 2013, pp. 3060-3076.
- [10] Drinking water quality assessment, Aryal J, Gautam B, Sapkota N., *J Nepal Health Res Council*, Vol. 10, Issue 22, 2012, pp. 192-196.
- [11] Suthar S., Chhimpa V. and Singh S., Bacterial Contamination in Drinking Water: A Case Study in Rural Areas of Northern Rajasthan, India, *Environmental Monitoring and Assessment*, Vol. 159, 2009, pp. 43-50.
- [12] Crump J. A., Okoth G. O., Slutsker L., Ogaja D. O., Keswick B. H., and Luby S. P., Effect of point-of-use disinfection, flocculation and combined flocculation-disinfection on drinking water quality in western Kenya, *Journal of Applied Microbiology*, Vol. 97, Issue 1, 2004.
- [13] Nicholson K. N., Neumann K., Dowling C., and Sharma S., *E. coli* and Coliform Bacteria as Indicators for Drinking Water Quality and Handling of Drinking Water in the Sagarmatha National Park, Nepal, *Journal of Environmental Management and Sustainable Development*, Vol. 6, Issue 2, 2017.

A STUDY TO IMPROVE THE WATER QUALITY PARAMETERS OF THREE MAJOR RIVERS SURROUNDING THE CAPITAL CITY OF BANGLADESH THROUGH COAGULATION

Istiaqur Rahman¹, Sk. Sadman Sakib², Md. Rezoan Khan Nafiz³, Shadman Alam⁴, Md. Rwanakul Islam Chowdhury⁵

^{1,2,3,4,5} Faculty of Engineering and Technology, Islamic University of Technology (IUT), Bangladesh

ABSTRACT

Dhaka, the capital city of Bangladesh is surrounded by the three major rivers Buriganga, Turag, and Dhaleshwari. A large number of people are dependent on these river's water for their daily use. Many industries have been located along these rivers because these rivers provide transportation and have been a convenient place to discharge waste. Chemical waste products which are discharged into these rivers have a significant effect on the water quality of these rivers. The purpose of this study is to improve the quality of polluted water of these rivers to use it for non-potable use with coagulation process. Aluminum Sulfate ($\text{Al}_2(\text{SO}_4)_3 \cdot 18\text{H}_2\text{O}$) is used as the coagulant as the market value of this coagulant is within the reach of residents living near these rivers and readily available in the local market. To find out the optimum dosage of the coagulant Jar test method has been used. Different physical, chemical and microbiological parameters (e.g. pH, Turbidity, Color, Total dissolved solids, Alkalinity, Total coliform, Fecal coliform and E. Coli) were tested in the laboratory against the water samples collected from the different location of these rivers. It has been shown that the application of different dosage (i.e. 0, 2, 4, 6, 8, 10 mg/L) of alum coagulant contributes to the improvement of water quality. The result has been compared with WHO guideline and ECR for Bangladesh 1997 guideline values. Results obtaining from the laboratory test will act as a guideline for improving water quality parameters through coagulation process using Aluminum Sulfate ($\text{Al}_2(\text{SO}_4)_3 \cdot 18\text{H}_2\text{O}$).

Keywords: Coagulation, Physico-chemical parameters, Microbiological parameters, Optimum alum dosage

INTRODUCTION

Water is essential and it is life to all living organisms. Without water life will be short-lived. The value of water is in both quality and quantity. Quality is important for maintaining good health. Poor quality water is subject to bring all types of health and disease problems. Quantity is equally important because if enough water is not available, a lot of functions of living organisms will cease to operate or function and that will result to death or loss of life. [1] Bangladesh, the ninth most populous country of the world, inhabited by 166 million people [2], is largely dependent on surface water sources such as rivers, ponds, canals, ditches, etc., for domestic water supply, especially in rural areas. [3]. The peripheral rivers of Bangladesh are the most important watershed and crucial source of water for irrigation as well as for heavy and light industries, aquaculture, animal farming, municipal supply and wastewater dilution. However, the surface water along these rivers is known to be polluted due to municipal and industrial untreated wastewaters that are discharged into these rivers directly [4-5] Development activities mostly depend on the rivers for the cleaning and disposal purposes. So, it urges a systematically

monitoring study to assess the status of pollution to suggest some management strategies. The seasonal variations along with the geographic and geomorphologic disparity also direct a fluctuation of pollution among the rivers of the country. [6] The main rivers flowing around Dhaka are Buriganga, Turag, Dhaleswari, Shitalakya and Bangshi. It is observed that around 40% industries of Bangladesh including tannery, textile and dyeing, chemical, plastic, fertilizer are located within greater Dhaka and surrounded by these rivers.[7] Bangladesh is one of those polluted countries, which currently holds 1176 industries that discharge about 0.4 million m^3 of untreated waste to the rivers in a day [8]. The increasing urbanization and industrialization of Bangladesh have negative implications for water quality where the industrial effluents directly dispose into the rivers without any consideration of the environment [9]. The existing tendency of industrialization and urbanization may contribute greatly to the poor quality of water through indiscriminate disposal of solid waste, industrial effluents and other toxic wastes which are the major environmental issues posing threats to the existence of human being [10]. The rivers are being polluted with wastewater of thousands of industrial units,

sewerage wastes and from agricultural practices which contain huge volume of toxic substances including heavy metals such as Cr, Cu, Pb, Ni, Mn, As, Cd, Fe, Hg and organic contaminants. [11-13]

A significant number of researches have been carried out to know the water quality of few rivers in Dhaka. [14-15] Due to rapid growth of textiles, tanneries, pharmaceuticals and other industries in the Konabari, a huge amount of industrial chemicals and wastes are generating daily which are directly discharging into the Turag River. [16] As a result, water used for human consumption, industrial purposes, land irrigation and fish production, is thought to be greatly contaminated by these toxic substances. The water quality of the River Buriganga, which receives domestic, industrial, agricultural and other wastewater discharges, is deteriorating due to the increasing pressure of urbanization and industrialization in Dhaka City. A considerable variation in the content of psychochemical and toxic elements in the studied river suggests input of pollution from different sources. Further, excess concentration of Fe, Al and K compared to WHO standard was observed in Turag, Pb, Fe, Al, Cr and K in Buriganga, Cd, Fe, K, Al and Cr in Shitalakya, Fe, Al and K in Bangshi and As in Dhaleswari river water. [17] A large number of tanneries (around 200) [18] located in the Hazaribug and Rayer Bazar areas of Dhaka, use more than 200 chemicals, including several types of acid, preservative, lime, sodium chloride, chromium, etc. [19] The Buriganga has been highly contaminated by the tanneries' effluent. Tannery effluent contains BOD levels between 0.07 g/l and 0.35 g/l [20]. Moreover, from the toxicity distribution pattern, it is seen that Buriganga > Shitalakya > Bangshi > Turag > Dhaleswari. [21] Demand for fresh water is ever on the increase for the people of this city. And to meet their demands, they turn to the above-mentioned rivers as the primary source of fresh water. But it is evident that the quality of the water from these rivers is far below the standards set for ideal fresh water parameters. For non-potable use of water from such sources, proper treatment of water is needed. There are various ways for treatment of water. Coagulation is mainly for particle removal by Sedimentation. Also, many studies showed that coagulation with Aluminum Sulfate ($\text{Al}_2(\text{SO}_4)_3 \cdot 18\text{H}_2\text{O}$) dosage can improve the water quality by reducing internal loading, turbidity, color, trihalomethanes (THM), dissolved organic matter (DOM) as well as microbial growth. The reduction in internal loading following alum addition is probably the most cost-effective of in-lake treatments for managing lake quality [22]. THM formation can be significantly reduced by alum treatment as the likely potential precursors such as aromatic components of DOM are preferentially removed by alum treatment. The results of this study suggest that compounds which inhibit microbial

growth are preferentially removed by alum treatment and/or microbial consortia composition changes after alum treatment [23]. In Myanmar, 20 stored drinking water samples from 50 control households and from 50 house-holds where alum treatment was used were tested for fecal coliform bacteria. Mean fecal coliform counts were similar in both households before the addition of alum but were lower in the treatment households 24 and 48 hours after alum was added [24]. So, coagulation with alum is not only being used for particle sedimentation but also for improving physical, chemical and biological parameters of the water. Although many other researches have been done previously, no such research has yet been done on coagulation technique as means for treatment in this region.

MATERIALS AND METHODS

Study Area

Water samples had been collected from Buriganga, Turag and Dhaleswari River. The Buriganga River is a tide- influenced river forming the western and southern boundaries of Dhaka City. Its catchment area is 253 km². Majority of the industries of Bangladesh are located by the riverbank. There are approximately 2,500 factories located on the river area surrounding Dhaka reported by different government agencies. Many industrial plants including tanneries are discharging untreated wastewater directly into the Buriganga. The Turag River is the upper tributary of the Buriganga. The Turag originates from the Bangshi River, the latter an important tributary of the Dhaleswari River, flows through Gazipur and joins the Buriganga at Mirpur in Dhaka District. The river Turag have been steadily experiencing complicated problems like pollution and encroachment that have almost suffocated the valuable lifelines of the city. This industrial area possesses a large amount of heavy industries. This cluster of industries of the capital city generates a lot of effluents daily, which contain lots of heavy metal. The Dhaleswari River is a distributary, 160 km long, of the Jamuna River in central Bangladesh. The uncontrolled dumping of industrial waste from the industries located along the banks of the river has greatly increased the river water pollution to a very dangerous level. The majority of the industries have made little effort to follow environmental law, and the water has become visibly discolored.

Sample Collection

A total of 30 samples were collected in sterilized containers with caps (500 mL) according to APHA method. They were thoroughly cleaned by rinsing with 20% HNO_3 and deionized water, followed by repeated washing with river water to avoid

contamination in the bottle. After sampling, the bottles were screwed carefully and marked with the respective identification number. Collected samples were promptly carried to the laboratory and almost all the physical and chemical properties were then determined. All possible efforts were made to minimize the time lag between collection and analysis, so that no significant change in the quality of the river water could occur. From each of the sampling points, at least ten raw samples were collected and analyzed. The average of the ten results was considered as the representative result. Samples were collected from March 2018 to May 2018, and the timing of collection were chosen randomly in day time. The point sources included numerous industries like textile, leather, dyeing industries and brick fields.

Co-ordinates of sample water collection from Buriganga river is $23^{\circ}42'00.3''\text{N}$ $90^{\circ}24'59.4''\text{E}$ while that of Turag river is $23^{\circ}52'55.0''\text{N}$ $90^{\circ}24'15.2''\text{E}$. Location of sample taken from Dhaleswari river is $23^{\circ}49'14.7''\text{N}$ $90^{\circ}14'54.4''\text{E}$ as shown in Fig 1.



Fig. 1 Image showing sampling location

Collected Samples were taken, analyzed and average values of parameters were taken from each point as the final result.

Methodology

The water sample was distributed among six jars containing 500 ml water each. Each of the jars were dosed with alum dosage of varying amounts such as 0g/500 mL, 1g/500mL, 2g/500mL, 3g/500mL, 4g/500mL, 5g/500mL respectively, and then the paddles of the jar testing apparatus were inserted inside the beakers. For flocculation initial speed was maintained at 100 rpm for 1 min, then the speed was

reduced to 40 rpm for 10 minutes to ensure even mixing. After that the beakers were allowed to settle down for 60 minutes. Similar actions were taken for all the water samples from different locations.

The water parameters that have been considered for this study are pH, color, turbidity, TDS, alkalinity, total coliform, fecal coliform and E. coli. It has been shown that the application of different dosage of alum coagulant contributes to the improvement of water quality. Thus, various tests of the mentioned parameters have been made before the application of dosage and also after application of alum and the results were compared. For testing the physical parameters, color has been tested determined using Spectrophotometer DR 2800 (Pt. Co. Std. Method), whereas turbidity was determined using APHA Standard Method- 2130 B. For determining chemical properties, pH was determined using APHA Standard Method- 4500-H+ B, alkalinity by Titrimetric Method and chloride by Titrimetric Method. Bacterial parameters like total coliform, fecal coliform and E.coli have been determined by Membrane Filtration Method

RESULTS AND DISCUSSION

The water quality of the three different rivers around Dhaka City (i.e. Turag, Buriganga, and Dhaleswari) revealed a high level of water pollution when compared with the ECR-1997 and WHO guideline recommended values as shown in Table 1. The result of this study shows that the inflowing river water treated with Alum may be an effective way to improve the water quality parameters that have been tested. After applying the different dosage of Alum following by coagulation process, a significant change has been found in Color, Turbidity, alkalinity, TDS and the biological parameters of specific river water. Figure 2 shows that the color of water varied within the ranges from 720 to 60 Pt-Co Unit after applying different dosage of alum (i.e. 0, 2, 4, 6, 8, 10 mg/L) for Turag, 16.7 to 7.08 Pt-Co Unit for Buriganga and 36 to 6 Pt-Co Unit for Dhaleswari river water. The optimum dosage for the color of these rivers was 2, 4 and 2 mg/L respectively. The removal efficiency of the color of Turag, Buriganga, and Dhaleswari was found to be 91.78%, 95.15%, 88.68% respectively in comparison with the raw sample as shown in Fig 3 at the specific optimum dosage of those river water. Alkalinity is a measure of a river's "buffering capacity," or its ability to neutralize acid. Alkaline compounds in the water such as bicarbonates, carbonates, and hydroxides remove H^+ ions and lower the acidity of the alkalinity of the respective rivers was found to be in the ranges from (34-50), (18-70), (4-16) mg/L as CaCO_3 , which is shown in Fig 4. The optimum dosage were 4, 4 and 2 mg/L. Alkalinity removal efficiencies in river Turag, Buriganga and Dhaleswari are found to be 46.88%,

Table 1 Water quality parameters of the rivers before co-agulation

Parameters	Obtained Values			WHO Guideline Std. value	ECR-1997 Std. Value
	Turag	Buriganga	Dhaleswari		
pH	7.49	7.48	7.56	6.5-8.5	6.5-8.5
Color (pt-Co)	730	146	53	15	15
Turbidity (NTU)	101.6	150	7.41	10	10
Alkalinity(mg/LasCaCO ₃)	64	83	32	-	-
TDS (mg/L)	92	482	132	1000	1000
TC (cfu/100 ml)	20	10	6	-	-
FC (cfu/100 ml)	350	5	1	-	-
E. Coli (cfu/100 ml)	400	388	60	-	-

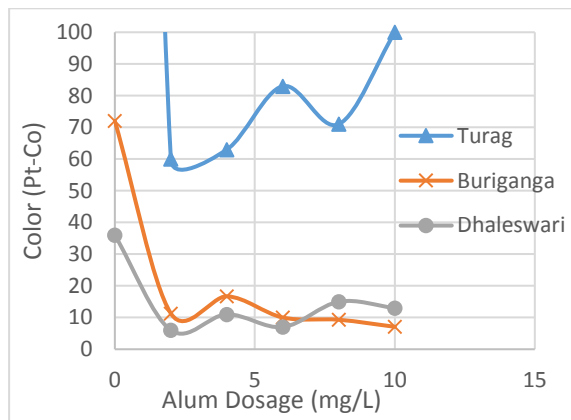


Fig. 2 Color of river water at different Alum dosage.

95.6), (36-104), (1.65-4.25) NTU respectively which

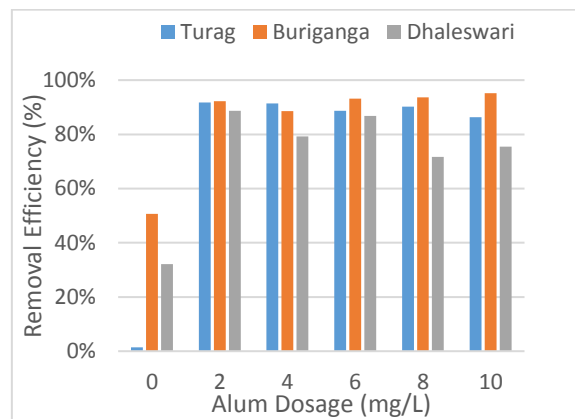


Fig. 3 Removal efficiency of color at different Alum dosage

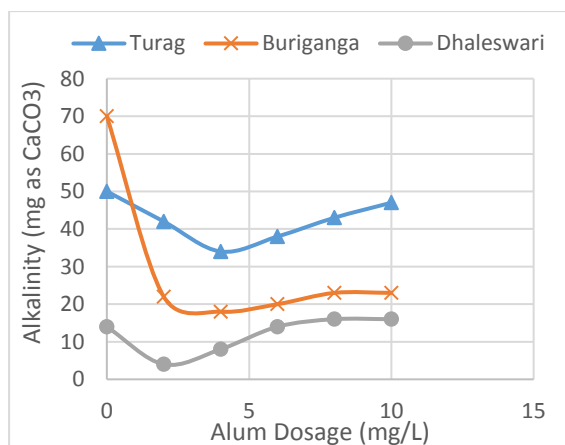


Fig. 4 Alkalinity of river water at different Alum dosage

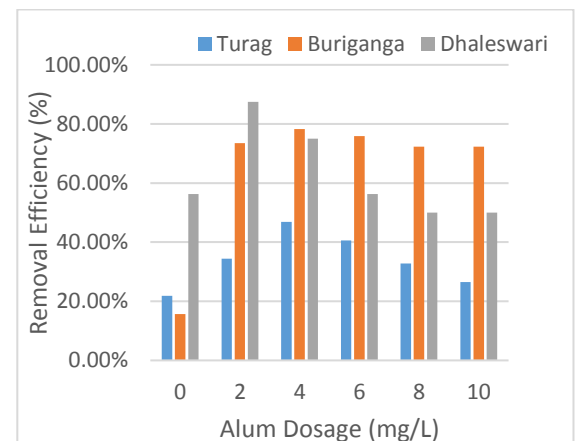


Fig. 5 Removal efficiency of alkalinity at different

78.31%, 87.50% respectively which is shown in Fig. 5. The turbidity of the river water of Turag, Buriganga, and Dhaleswari after applying alum dosage had changed significantly within the ranges from (4.85-

is shown in Fig 6. The optimum dosage for turbidity of the respective rivers was 4, 4, 2 mg/L. It has been observed that 95.23%, 76.00%, 87.50% turbidity removal efficiency for the respective rivers which is

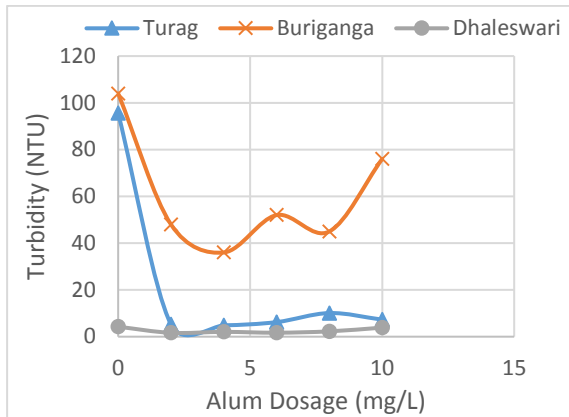


Fig. 6 Turbidity of river water at different Alum dosage

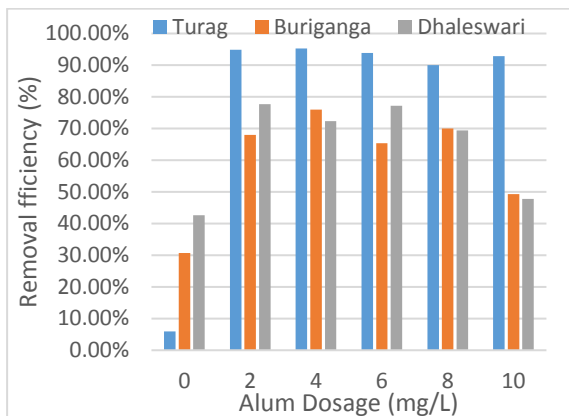


Fig. 7 Removal efficiency of Turbidity at different Alum dosage.

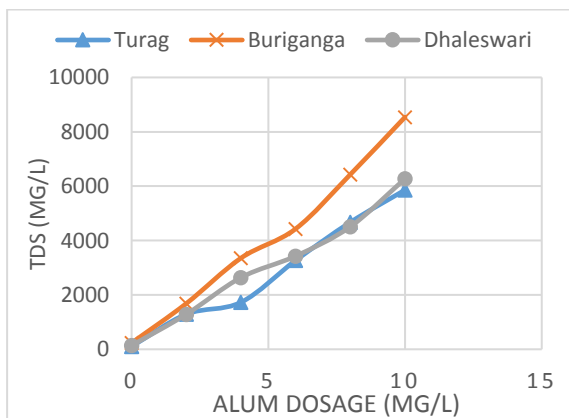


Fig. 8 Alkalinity of river water at different Alum dosage

shown in Fig 7. By applying this dosage Turbidity can be improved and came within the WHO and ECR-1997 range. The TDS value is the metallic substances in water that are in colloidal and dissolved conditions. The measured TDS values after applying alum dosage are shown in Fig 8. There is an increase

of TDS values in each of the rivers. This kind of scenario is responsible for the alum dosage which contributes to the metallic substances in water. The biological parameters such as TC, FC and E. Coli have a great impact on human body. Because the presence of these colonies in water that is being used by the human is hazardous to human health. The river water sample's TC, FC, and E.coli count before applying dosage are shown in Table 1. It is far beyond the recommended values. It has been seen that after applying alum dosage ranges between 2-10 mg/L has the effectiveness to remove all the microorganisms from water. The pH values found in the three rivers ranged from 6.9 to 7.9. All the pH value are within the range recommended by WHO guideline and ECR-1997 value.

It can be summarised from the study that water from these rivers can be used safely for non-potable domestic purpose after applying optimum alum dosage as a treatment method. For the large-scale usage, we can use the following equation,

$$Y = 0.5 (kX) \quad (1)$$

Refer to "Eq. (1),"

Y = total dosage of alum, (mg)

X= volume of water to be treated, (L)

K= is a variable that determined based on the optimum dosage usage of specific river (for this study it ranges from 2-4 mg/L)

CONCLUSION

Alum treatment for river water is substantially less expensive, longstanding and effective for non-potable uses. For potable uses further treatment is needed regarding the overall quality of the water. The results of these laboratory studies are promising and act as a guideline for treating river water by alum coagulation. This study is able to provide a hint to get the right amount of alum dosage for large-scale usage. However, treating inflows with alum has a number of challenges associated with seasonal variations of river water and solids management of the industries situated nearby. Further studies have to be done to find a complete guideline for alum coagulation of river water.

ACKNOWLEDGEMENTS

The authors are thankful to the Department of Civil and Environmental Engineering, Islamic University of Technology (IUT) for permitting and providing necessary facility to carry out present research work.

REFERENCES

- [1] E. j. Gereta, "THE IMPORTANCE OF WATER QUALITY AND QUANTITY IN THE

- TROPICAL ECOSYSTEMS, TANZANIA,” Norwegian University of Science and Technology, 2004.
- [2] Bangladesh Population. (2018-06-04). Retrieved 2018-06-09, from <http://worldpopulationreview.com/countries/bangladesh/>
- [3] K. Sohel, M. Chowdhury, and M. Ahmed, “Surface water quality in and around Dhaka City.,” *Aqua*, vol. 52, 2003, pp. 141–153. [5] S. K. Karn and H. Harada, “Surface water pollution in three urban territories of Nepal, India, and Bangladesh,” *Environ. Manage.*, vol. 28, no. 4, 2001, pp. 483–496.
- [4] V. Subramanian, Water quality in South Asia, *Asian Journal of Water, Environment and Pollution*, Vol. 1, No. 1 & 2, 2004, pp. 41-54.
- [5] S. K. Karn and H. Harada, “Surface water pollution in three urban territories of Nepal, India, and Bangladesh,” *Environ. Manage.*, vol. 28, no. 4, 2001, pp. 483–496.
- [6] Sikder, Md. Tajuddin; Yasuda, Masaomi; Yastiawati; Syawal, Suhaemi M.; Saito, Takeshi; Tanaka, Shunitz; Kurasaki, Masaaki, Comparative Assessment of Water Quality in the Major Rivers of Dhaka and West Java, *International Journal of Environmental Protection*, Vol 2, No 4, 2012, pp 8-1
- [7] Faisal, I., Shammin, R. and J. Junaid, Industrial Pollution in Bangladesh. World Bank Report. 2004
- [8] Rabbani, G. and Sharif, M.I., Dhaka City –state of Environment (SoE), 2005
- [9] BCAS (Bangladesh Centre of Advanced Studies), The state of Bangladeshi water, series 5, Bangladesh Centre of Advanced Studies, Bangladesh, 2004
- [10] Furtado, A. A. L.; Albuquerque, R. T.; Leite, S. G. F. and Pecanha, R. P., Effect of hydraulic retention time on nitrification in an airlift biological reactor, *Brazilian Journal of Chemical Engineering*, 1998
- [11] Sultana, Mahfuza S., Islam, M.S., Saha, R. and A.M.A. Mansur, Impact of the effluent of textile dyeing industries on the surface water quality inside D.N.D. embankment, Narayanganj. *Bangladesh J. Sci. Ind. Res.*, Vol 44 No 1, 2009, 65-80.
- [12] Moniruzzaman, M., Elahi, S.F. and M.A.A. Jahangir, Study on Temporal Variation of Physicochemical Parameters of Buriganga River Water through GIS (Geographical Information System) Technology. *Bangladesh J. Sci. Ind. Res.*, Vol 44, No 3, 2009 327-334.
- [13] Mohiuddin, K.M., Zakir, H.M., Otomo, K., Sharmin, S. and N. Shikazono . Geochemical distribution of trace metal pollutants in water and sediments of downstream of an urban river. *Int. J. Environ. Sci. Tech.*, Vol 7, No 1, 2010, pp. 17-28.
- [14] Ahmed, M.K., Das, M., Islam, M.M., Akter, M.S. and S. Islam. Physico-Chemical Properties of Tannery and Textile Effluents and Surface Water of River Buriganga and Karnatoli, Bangladesh. *World Applied Sciences Journal*, Vol 12, No 2, 2011, pp. 152-159.
- [15] Ali, M.N. and K. Alam, Ecological Health Risk of Buriganga River, Dhaka, Bangladesh. *Hydro Nepal*, 2008, pp. 325-28.
- [16] M. S. Islam, T. R. Tusher, M. Mustafa and S. Mahmud, Effects of Solid Waste and Industrial Effluents on Water Quality of Turag River at Konabari Industrial Area, Gazipur, Bangladesh, *J. Environ. Sci. & Natural Resources*, Vol 5, No 2, 2012, pp. 213 – 218.
- [17] Mahfuz S. Sultana, S. Rana, T. Imam, M. Aktaruzzaman and S. Yoshida, Evaluation of Suitability of River Water for Multipurposes by Assessing Various Indices, *Asian Journal of Water, Environment and Pollution*, Vol. 13, No. 3, 2016, pp. 45–54.
- [18] K. M.A. Sohel, M.A. I. Chowdhury and M. F. Ahmed, Surface water quality in and around Dhaka, *Journal of Water Supply: Research and Technology—AQUA*, 2003
- [19] JAPAN INTERNATIONAL COOPERATION AGENCY (JICA) & DWASA, The Study of the Upazila Governance and Development Project in the People’s Republic of Bangladesh, International Development Center of Japan Inc. KRI International Corp. 1998
- [20] Mohammad Kamrul Hasan, Md. Khalid Hasan And Anwar Hossain, A Comparative Study of Water Quality in The Peripheral Rivers Of Dhaka City, Department of Fisheries, University of Dhaka, Dhaka-1000, Bangladesh, *Dhaka Univ. J. Biol. Sci.*, Vol 22, No 2, 2013 pp. 145-154,
- [21] Mihir Lal Saha, Mahbubar Rahman Khan, Mohammad Ali and Sirajul Hoque, Bacterial Load And Chemical Pollution Level of The River Buriganga, Dhaka, Bangladesh, Laboratory of Microbiology, Department of Botany, University of Dhaka, Dhaka-1000, Bangladesh, *Bangladesh J. Bot.*, Vol 38, No 1, 2009, pp. 87-91.
- [22] Cooke, G. D., E. B. Welch, S. A. Peterson & P. R. Newroth, Lake and Reservoir Restoration. Butterworths, London, 1986.
- [23] D.W. Page, J.A. van Leeuwen, K.M. Spark, M. Drikas, N. Withers, D.E. Mulcahy, Effect of alum treatment on the trihalomethane formation and bacterial regrowth potential of natural and synthetic waters, *Water Research*, vol 36, 2002, pp 4884–4892.
- [24] Oo KN, Aung KS, Thida M, Khine WW, Soe, MM, Aye T. Effectiveness of potash alum in decontaminating household water. *J Diarrhoeal Dis Res.* 1993;11:172-174.

EXPERIMENTAL STUDY FOR EVALUATING THE SEISMIC PERFORMANCE OF RC FRAME STRUCTURE WITH PARTIALLY INFILLED BY BRICK MASONRY

Jafril Tanjung¹, Febrin Anas Ismail¹, Oscar Fithrah Nur¹, Maidiawati², Hamdeni Medriosa² and Mahli³

¹Engineering Faculty, Andalas University, INDONESIA; ²Padang Institute of Technology, INDONESIA

³Syiah Kuala University, INDONESIA

ABSTRACT

The responses of the brick masonry infilled reinforced concrete (RC) frame structures under seismic excitation were quite complex due to highly nonlinear of their composite behavior and interaction between RC frame structure and its brick masonry infill. The presence of the brick masonry infills can greatly improve the seismic performance of RC frame structures by increasing their lateral strength and stiffness, respectively. However, when the RC frame structure is only partially infilled with the brick masonry wall, the responses of the RC frame structure become completely different. In this study, a series of experiments was conducted to evaluate the seismic performance of RC frame structures with partially infilled by the brick masonry. Three of one-fourth scaled-down of RC frame specimens, i.e. a bare RC frame, a fully brick infilled RC frame and a partially brick infilled RC frame have been experimentally tested under lateral static reversed cyclic loading. Experimentally results have shown that existence of the partially brick masonry infilled in the RC frame structure plays a significant role in damaging of the RC column.

Keywords: RC building, Partial brick masonry, Seismic performance, Reversed cyclic loading

INTRODUCTION

The unreinforced burned clay brick masonry has been commonly used as the infills and/or partition walls in reinforced concrete (RC) frame structures in the seismic-prone area such as Sumatra Island, Indonesia. Post-earthquake observation after M8.5 and M7.9 Sumatra earthquake 2007 [1], M7.9 West-Sumatra earthquake 2009 [2] and M6.5 Pidie Jaya – Aceh earthquake 2016 [3] demonstrated the beneficial as well as the undesired effects of the brick masonry infill to the seismic performance of the RC frame structures. As it was investigated by Maidiawati and Sanada on the damaged of RC buildings after Sumatera earthquake 2007 [4] indicated that the significant contribution of the brick masonry infill to help the structure survive during this Sumatra earthquake 2007. Unfortunately, the brick masonry infills also caused the undesired effect on the seismic response of structures, the such as soft-story effect. The similar and identical phenomenon mentioned above was also clearly observed after West-Sumatra and Pidie-Jaya earthquakes [5] as well as Wenchuan-China earthquake 2008 and Lushan-China earthquake 2013 [6].

Indeed, recent decades, several research activities have been devoted to investigate how the effects of brick masonry infill to seismic performance of the RC frame structures. These research activities including the research work in the

field of experimental study and analytical study as well. Maidiawati, Sanada, Konishi and Tanjung [7] have tested the RC frame structures infilled by the exported brick masonry from survived-RC building in Padang city, Indonesia. The experimental studies have also been conducted by Tanjung and Maidiawati [8,9] using local brick masonries produced in West-Sumatra area. These experimental studies have concluded that the brick masonry infills increase the lateral strength and stiffness of the RC frame structure; delayed the failure of the structure; and unfortunately decrease the overall ductility of the structure. The presence of the brick masonry infills caused changes in the deformation behavior of structure, i.e. from initially follow the behavior of frame structure and thus changed to truss structure behavior. Others similar and comprehensive experimental researches have been well-documented by Al-Chaar [10]; Cavaleri and Trapani [11]; and Korkmaz and Taciroglu [12].

The studies of Cavaleri and Trapani [11]; and Maidiawati and Sanada [13] have been proposed the analytical method for describing the contribution of brick masonry infills to seismic performance of the RC frame structures. Their proposed methods were derived based on their experimental works. Cavaleri and Trapani applied the macro modeling approach by substituting the brick masonry infills with diagonal pin jointed struts. This approach has succeeded for simulating the nonlinear seismic responses of RC frame structure with brick masonry

infills subjected to lateral static reversed cyclic loading. Another method Maidiawati and Sanada have proposed the analytical model by replacing the brick masonry infill with the diagonal compression strut. This diagonal compression strut, indeed, represents the idealization of distributed compression transferred between RC frame structure and brick masonry infill interfaces. In their method, the equivalent strut width is evaluated by static equilibriums of the compression balance and lateral displacement compatibility at the frame-infill interfaces. This proposed analytical method has also succeeded when evaluating the seismic performance of the survived RC building during Sumatra earthquake 2007.

The studies activities resumed above are mostly focused on the investigation of the effects of fully brick masonry infills in the RC frame structures. The studies for the partially brick masonry infills are still very limited. One of them has been performed and reported by Pradhan et.al. [14]. Others researchers' studies, such as by Kakaletsis et.al. [15]; Surendran and Kaushik [16]; and Akhoundi, Lourenco and Vasconcelos [17] are the studies in the field of the brick masonry infills with central, door or window openings.

Based on the post-earthquake investigation after Pidie-Jaya, Aceh earthquake 2016 [4] has shown the different damaged pattern of the RC frame structure with partially infilled by brick masonry compare to fully infilled by brick masonry and bare frame as well. The series experimental study discussing in this paper was conducted to find the answer how the partially brick masonry infilled in RC frame structure influences the seismic performance of it structures.

EXPERIMENTAL PROGRAM

The experimental works describe in this paper was conducted by using the structural testing facilities at Structural and Construction Material Laboratory, Syiah Kuala University, Banda Aceh, Indonesia. The materials for constructing the tested specimens were collected from local markets in Banda Aceh. Three of 1:4 reduce-scaled one-bay and one-story RC frame specimens were prepared, i.e. a bare RC frame, a fully brick infilled RC frame and a partially brick infilled RC frame. The specimens represent the first story of commonly constructed low-rise RC frame structures in Indonesia. All the specimens were subjected to lateral static reversed cyclic loading.

Test Specimens

The typical geometry and reinforcement details used for all RC frame specimens are illustrated in Fig.1. The columns of the RC frame were detailed to

yield in flexure before shear failure. The dimension of the cross-section of columns was 125 mm x 125 mm and reinforced with 4D10 longitudinal bars and $\phi 4@50$ transverse hoops. The dimension of the cross-section of the columns and their reinforcements were designed considering the scale reduction. The clear height of the columns was 750 mm. The dimension of top-beam was 150 mm wide, 150 mm deep and 1550 mm long and reinforced with 4D13 longitudinal bars and $\phi 6@50$ transverse stirrups. The columns were then supported by the lower-beam which was fastened to the strong floor by using six post-tensioning rods. The dimension of the lower-beam was 700 mm wide, 150 mm deep and 1650 mm long and reinforced with 12D16 longitudinal bars and $\phi 6@50$ transverse stirrups.

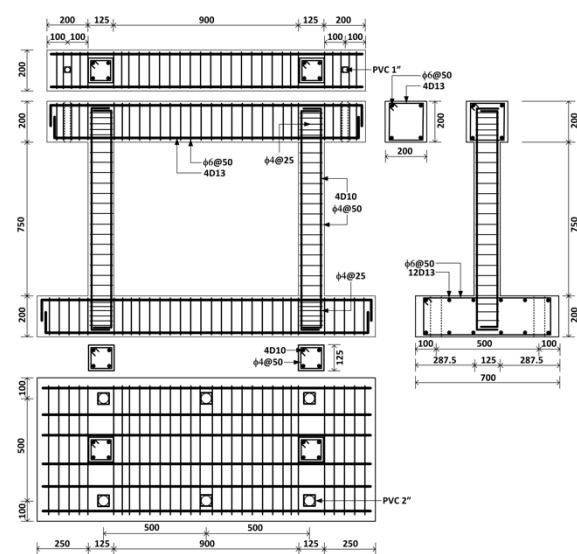
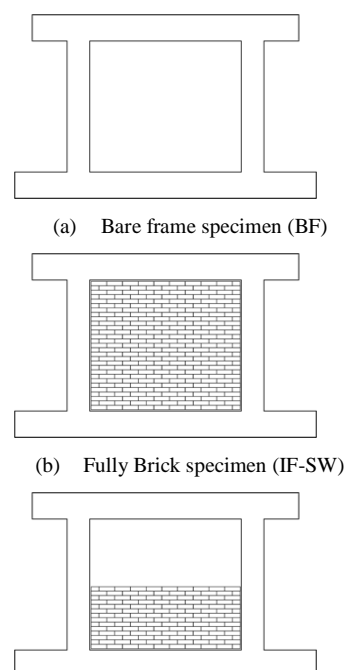


Fig. 1 Reinforcement Detail of Specimen.

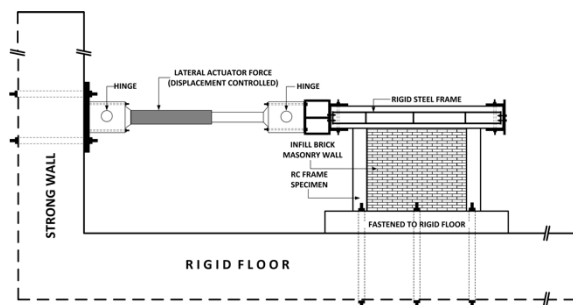


(c) Partially Brick specimen (IF-O4)

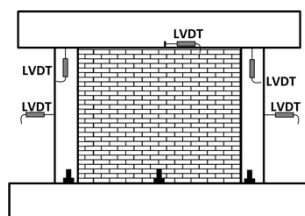
Fig. 2 Type of Specimens.

The schematic view of three RC frame specimens is shown in Fig. 2, i.e. the bare frame (BF) specimens, fully brick masonry infilled (IF-SW) specimen and partially brick masonry infilled (IF-O4) specimen. The infill area of IF-O4 specimen was approximately half of infill area of IF-SW specimen. The IF-SW and IF-O4 specimens were infilled by 1:4 reduce-scaled masonries of burnt clay brick with a dimension of 30 mm wide, 13 mm deep, 60 mm long. The mortar beds with the ratio of cement: water in 1:0.5 were used for assembling the brick masonry as infills. The infill was then covered by 5 mm thickness of mortar on it both surfaces. Noting that for all specimens, there were no shear connectors installed on the interface between column and infill.

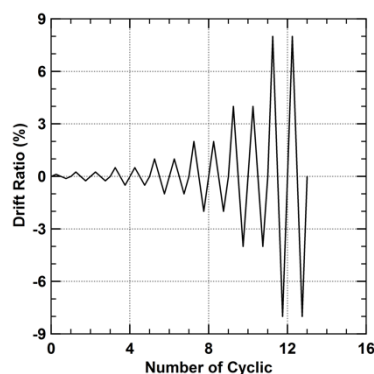
Test Setup and Instrumentation



(a) Cyclic Loading Test Setup



(b) LVDT Plan



(c) Cyclic Loading Procedure

Fig. 3 Test Setup and Instrumentation.

Figure 3.a shows a schematic image of the cyclic loading test setup plan for current experimental works. At first, the specimen was placed on the rigid floor. To keep the specimen remain in its place, the lower-beam was fastened to the rigid floor by using six post-tensioning rods. A double action lateral actuator force equipment was attached and fastened the strong wall by using four post-tensioning rods.

In order to prevent the applied force caused the out of plane deformation during testing, the top-beam was constrained by two horizontal steel beams. These two horizontal beams were connected to the actuator force, which mounted on the strong wall. The displacement transducers were installed at several points to measure the deformation as well as to be controlling the displacement point of the whole test, as shown in Fig. 3b.

The cyclic procedure applied in current works is following FEMA461 [18] as is given in Fig. 3c. The procedure began with a drift ratio 0.125% ($R=1/800$), 0.250% ($R=1/400$), and up to 8% ($R=1/12.5$); where R is the drift angle. This cyclic procedure was conducted in displacement control with loading speed of approximately 0.05 mm/s. Except for the first drift ratio, two cycles were applied for each drift ratio. Incremental of the applied lateral static load and the deformation of the specimen were monitored and recorded throughout the tests. In order to identify the failure mechanism of the specimen, the initial cracks and its crack propagation were marked on the specimen in every loading cycle.

EXPERIMENTAL RESULTS & DISCUSSION

Material Properties

The material properties used for constructing RC frame specimens, including their brick masonry infills, were obtained by standard material testing procedures. The compressive strength of concrete cylinder at 28 days after casting was 49.9 MPa, i.e. the sample of the concrete was cast to the RC frame specimens. The compressive strength of the brick masonry cube was 10.9 MPa. The nominal yield (tensile) strengths of the reinforcements, respectively for $\varnothing 4$, $\varnothing 6$, D10, and D13, were 390.2 (598.3) MPa, 346.8 (448.6) MPa, 462.0 (619.7) MPa, and 421.1 (582.4) MPa.

Loading-Deformation Curves and Crack Patterns

Bare-frame Specimen (BF)

Figure 4.a. shows the hysteretic loop of lateral loading-displacement for BF specimen. The ultimate lateral strength was reached at 51.3kN at 57.8 mm of lateral displacement, i.e. at the drift ratio of almost 8% ($R=1/12.5$). The initial flexural crack at the top

side of the tensile column was observed within drift ratio 0.25% ($R=1/400$); the lateral displacement was 1.2 mm. The initial shear crack appeared at the compressive column within the drift ratio 0.5% ($R=200$); the lateral displacement at that time was 3.8 mm. Within the last cycle of drift ratio 8% ($R=1/12.5$), the compressive column experienced shear failure at the lateral displacement of 57.8 mm, as is shown in Fig. 5.a. As we expected, the RC columns of the specimen exhibited the flexural failure before experienced the shear failure.

i.e. within the drift ratio 0.125% ($R=1/800$). Initial flexural and shear cracks of the tensile column were observed within the drift ratio of 0.25% ($R=1/400$) at the lateral displacement about 1.3 mm and 1.6 mm, respectively. The diagonal shear crack was observed at the center of brick masonry infill within the drift ratio 0.5% ($R=1/200$) when the lateral displacement about 3.4 mm. Within the drift ratio of 2% ($R=1/50$), the brick masonry infill experienced the shear failure, thus the lateral strength of the specimen started to significantly degradant. As soon as shear failure of

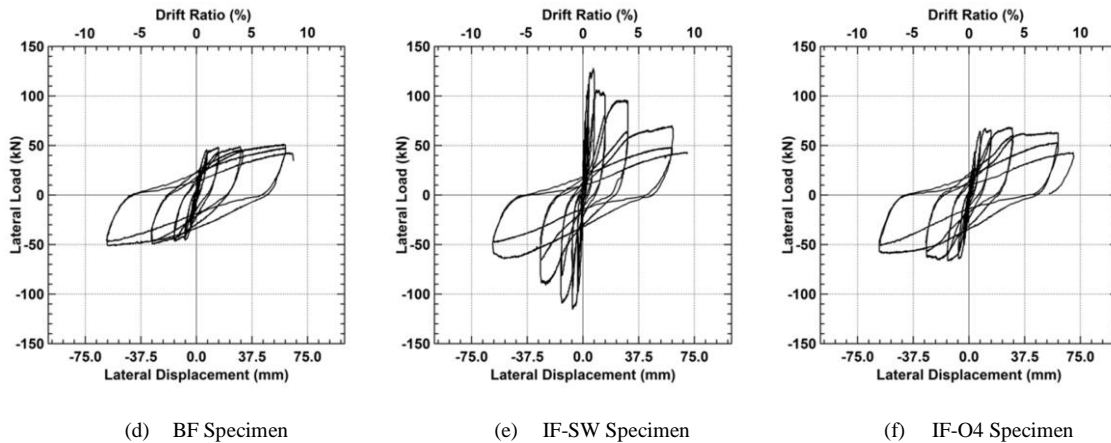


Fig. 4 Relation of Applied Lateral Loading and Displacement.

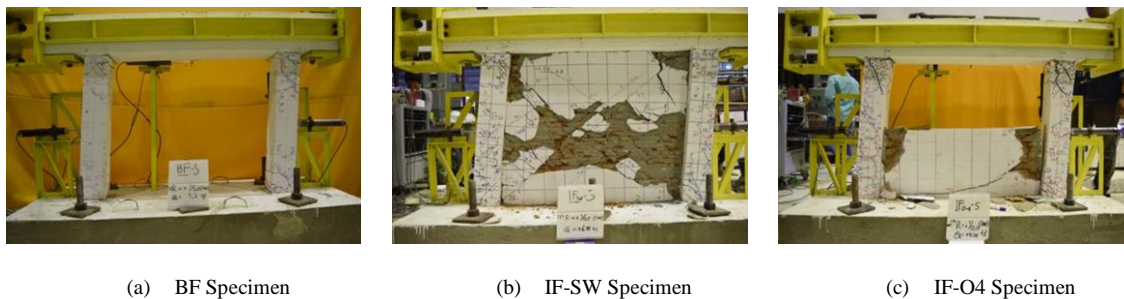


Fig. 5 Crack Patterns at Drift Ratio=8% ($R=1/12.5$).

Fully Brick Masonry Infilled Specimen (IF-SW)

The hysteretic loop of the relation between the lateral loading and displacement for IF-SW specimen is shown in Fig. 4.b. Its figure exhibits that the presence of brick masonry infill in RC frame significantly increased the lateral stiffness of the specimen. The increasing of the lateral stiffness was indicated by increasing of the lateral strength capacity of the specimen, i.e. 127.7kN at about 7 mm lateral displacement. Increase about 2.5 times compare to the capacity of the bare-frame BF specimen.

A separation crack has appeared between column and brick masonry infill at the beginning of loading,

the brick masonry infill, the strength of the specimen then now depends on the strength of the RC frame structure. Continued the lateral loading caused the boundary columns experienced the shear failure within the drift ratio of 8% ($R=1/12.5$) as is shown in Fig. 5.b.

Partially Brick Masonry Infilled Specimen (IF-OS)

For the IF-O4 specimen, the hysteretic loop of the lateral loading-displacement is shown in Fig. 4.c. The ultimate lateral strength of 68.5kN was reached at lateral displacement about 27.1 mm. Although the area of the brick masonry infill for IF-O4 specimen was half of IF-SW specimen, the increasing the lateral strength of IF-O4 specimen much less than

IF-SW specimen, compare to bare specimen BF. The lateral strength of IF-SW specimen increased about 148%, while the IF-O4 specimen increased only about 33%.

The failure pattern of the brick masonry infill in this specimen was dominated by the horizontal crack. Compare to IF-SW specimen, i.e. the major failure pattern was inclined diagonal shear cracks. The presence of this partially brick masonry infill made the stiffness of the RC columns specimen, where the partially brick masonry installed, relatively increase when was compared to other parts of these columns. As the consequence, the parts of the columns without brick masonry infill became the weak area of the RC frame structure. The observation during experimental works has shown that the failure of the current specimen was dominated by the shear failure at the area of columns without brick masonry infill as is shown in Fig. 5.c. This fact suggested that the partially brick masonry infill in RC frame structure has significantly played role in the damaged of the RC columns of the specimen.

CONCLUSIONS

The experimental work for evaluating the seismic performance of the partially brick masonry infilled RC frame structure has been conducted in this study. For this purpose, three of 1:4 reduced-scale one-bay one-story RC frame specimens have been tested subjected to lateral static reversed cyclic loading, i.e. bare RC frame, fully brick infilled RC frame and partially brick infill specimens, respectively. When comparing the BF to IF-SW specimens, the presence of the fully brick masonry in IF-SW frame directly adding the stiffness of the RC frame; resulting the increased of the lateral strength capacity of the RC frame. The presence of this full brick masonry has also delayed the collapse of RC columns in the IF-SW specimen; since the RC frame and brick masonry now in the composite when they were subjected to lateral loads. Unfortunately, for the IF-O4 specimen, although its lateral strength capacity has increased, compared to BF specimen, the presence of partially brick masonry infill caused the premature collapse of the RC column of the specimen. Therefore, when the RC frame is planned to partially infilled by the brick masonry, the reinforcement design of the column has to consider the additional shear force caused by the presence of its partially brick infills.

ACKNOWLEDGMENTS

This research work is financially supported by the Institute of Research and Community Development of Andalas University through the Research Grant of Program Penelitian Skim Klaster

Riset Percepatan Guru Besar (KRP2GB) with the contract number 13/UN.16.17/PPP.PGB/LPPM/2018. The authors also sincerely acknowledge to Professor Katsuki Takiguchi, Takiguchi Laboratory, Department of Mechanical and Environmental Informatics, Tokyo Institute of Technology, Japan; Dr. Abdullah, Civil Engineering Department, Syiah Kuala University; head and staffs of Structure and Construction Material Laboratory, Engineering Faculty, Syiah Kuala University, for supporting during prepared the specimens, provided the structural testing facilities and conducted the structural tests.

REFERENCES

- [1] https://en.wikipedia.org/wiki/September_2007_Sumatra_earthquakes.
- [2] https://en.wikipedia.org/wiki/2009_Sumatra_earthquakes.
- [3] https://en.wikipedia.org/wiki/2016_Aceh_earthquake.
- [4] Maidiawati and Sanada Y., Investigation and Analysis of Buildings Damaged during the September 2007 Sumatra, Indonesia Earthquakes, Journal of Asian Architecture and Building Engineering (JAABE), Vol 7 No 2, 2008, pp. 371-378.
- [5] Tanjung J., Post-earthquake Investigation Report of Damaged Reinforced Concrete Buildings after Pidie-Jaya Earthquake 2016, Civil Engineering Department, Andalas University, Unpublished Report, 2017.
- [6] Yuan F., Xiaobin W., and Shulu Z., Failure Modes of Masonry Infill Walls and Influence on RC Frame Structure Under an Earthquake, Tenth U.S. National Conference on Earthquake Engineering, Frontiers of Earthquake Engineering, 2014, Alaska.
- [7] Maidiawati, Sanada Y., Konishi D. and Tanjung J., Seismic Performance of Nonstructural Brick Walls Used in Indonesian R/C Buildings, Journal of Asian Architecture and Building Engineering (JAABE) Vol 10 No 1, 2011, pp. 203-210.
- [8] [Tanjung J. and Maidiawati, Studi Eksperimental tentang Pengaruh Dinding Bata Merah Terhadap Ketahanan Lateral Struktur Beton Bertulang, Jurnal Teknik Sipil ITB, Vol 23 No 2, 2016, pp. 99-106.
- [9] Tanjung J. and Maidiawati, The Experimental Investigation on Beneficial Effects of the Local Brick Masonry Infills to Seismic Performance of R/C Frame Structures in West Sumatera, International Journal of Civil Engineering and Technology (IJCIET), Vol 8, Issue 10, 2017, pp. 687-697.
- [10] Al-Chaar G., Evaluating Strength and Stiffness of Unreinforced Masonry Infill Structures, Research Report ERDC/CERL TR-02-1, U.S.

- Army Corps of Engineers, 2002.
- [11] Cavaleri L., Di Trapani F., Cyclic response of masonry infilled RC frames: Experimental results and simplified modeling, *Soil Dynamics and Earthquake Engineering*, Vol. 65, 2014, pp. 224-242.
- [12] Korkmaz H.H. and Taciroglu E., Experimental Investigation of Contribution of Brick Infill Walls to the Seismic Response of Reinforced Concrete Frames, *Proc. Of Int. Conf. on Structural Arch. and Civil Eng.*, Dubai, 2015, pp. 222-227.
- [13] Maidiawati and Sanada Y., R/C Frame–infill Interaction Model and Its Application to Indonesian Buildings, *Earthquake Engineering & Structural Dynamic*, Vol 46, 2017, pp. 221–241.
- [14] Pradhan P.M., Pradhan P.L, and Maskey R.K., Lateral Strength of Partial Masonry Infill Wall in Concrete Frame Under Static Load, *Journal of Civil Engineering (IEB)*, Vol 40 (1), 2012, pp. 67-77.
- [15] Kakaletsis D.J., Masonry Infills with Window Openings and Influence on Reinforced Concrete Frame Constructions, *Earthquake Resistant Engineering Structures VII*, WIT Press, 2009, pp. 445-455.
- [16] Surendran S. and Kaushik H.B., Masonry Infill RC Frames with Openings: Review of In-plane Lateral Load Behaviour and Modeling Approaches, *The Open Construction and Building Technology Journal*, Vol 6 (Suppl 1-M9), 2012, pp. 126-154.
- [17] Akhoundi F., Lourenço P.B. and Vasconcelos G., Numerically Based Proposals for the Stiffness and Strength of Masonry Infills with Openings in Reinforced Concrete Frames, *Earthquake Engineering & Structural Dynamics*, Vol. 45, Issue 16, 2016, pp. 869-891.
- [18] Interim Testing Protocols for Determining the Seismic Performance Characteristic of Structural and Nonstructural Component,” FEMA 461, 2007, pp. 21-25.

CORAL REEFS DEGRADATION PATTERN AND ITS EXPOSURE TOWARDS CLIMATE CHANGE IN BUNAKEN NATIONAL PARK

Nafil Rabbani Attamimi¹, Ratna Saraswati²

¹Department of Geography, Faculty of Mathematics and Natural Science, University of Indonesia, Indonesia; ² ¹Department of Geography, Faculty of Mathematics and Natural Science, University of Indonesia, Indonesia

ABSTRACT

Coral reef is one of many shallow water ecosystems that are found in Bunaken National park. The coral reefs ecosystem in Bunaken National Park are threatened by the impact of climate change, such as rising sea water temperature, Change in Salinity, and increase extreme meteorological events. This study will address the coral reefs condition and its pattern in Bunaken National Park, how are the water condition in Bunaken National Park changes in the timespan of 2002-2017, and what are the relations between the degradation pattern of the coral reefs and the sea water condition as an exposure towards the ecosystem Climate change in the context of this study is based on oceanographic variables such as sea surface temperature and sea water salinity. The methods that are used in this study is through meta-descriptive analysis to determine the exposure of the coral reefs, spatial-descriptive analysis to relate between climate change and coral reef conditions. The results showed that the degradation conditions of coral reefs from 2002 to 2013 have decreased, but the condition of the degraded coral reefs has increased by 2017. Based on the analysis of the conditions of the exposure and coral reefs show that, there is a correlation between the two.

Keywords: Coral Reefs, Climate Change, Exposure, and Shallow Water

INTRODUCTION

Coral Reefs and its Exposure

The existence of coral reefs has an important function for maintaining the morphological structure of a coastal body where coral reefs serve as destructive wave barriers that can lead to coastal abrasion [1]. In addition, coral reefs also have a variety of functions and use that can be utilized directly by human life economically, such as when humans can utilize flora and fauna on coral reef ecosystems [3]. Another usage on where coral reefs can be utilized by people, is through preserving them and using them as means for tourism [3].

Although coral reefs provide benefits for people and play an important role to support marine habitat, the coral reefs are one of an ecosystem that is very sensitive towards environmental change. This is because coral reefs are one of an ecosystem that needs a specific environmental condition for it to live and to develop properly. A slight condition change in the sea could impact the ecosystem severely. A coral reefs ecosystem must have a specific amount sea surface temperature, salinity, acidity, ocean current, as well as the amount of sunlight received [3].

The ecosystem of coral reefs can experience a different kind of challenges that could threaten its existence. Challenges faced by coral reefs such as challenges to coral reef ecosystem damage, pollution

from human waste, extreme weather events that can damage corals, or climate challenge experienced locally or globally that can disrupt growth and can be deadly for the coral reef ecosystem [4]. Climate change is one of the main disruptions faced by coral reef ecosystems. Basically, climate change can have an impact towards the condition of the sea, on which could affect atmospheric and marine conditions. Changes in the environmental condition could hinder the growth and productivity of the coral reefs, as well as threatened its existence [4].

Many previous studies have revealed that climate change greatly affects oceanic marine conditions, whether the conditions of ocean currents movement, physical, chemical, or biological conditions. Climate change globally can affect sea surface temperatures, ocean currents, salinity, seawater acidity, sea levels, and other variables [5]. Sea changes will have an impact on coral reef ecosystems, as coral reefs need to have very specific conditions to live to grow [6]. With climate change, the development and life of the coral reef ecosystem will be disrupted because there is a variable component of the sea undergoing slowly experienced changes [7].

Climatological factors and meteorological factors that can affect the condition of coral reefs among others are sea surface temperatures [2], salinity of sea water [2], and other extreme meteorological events [9]. The climate change exposure variables that will be used in this research are sea surface temperature, and salinity of sea water.

Coral Reefs Degradation

The degradation of coral reefs means that the condition of the reefs is damaged on which could not function properly as an ecosystem for marine habitats [10]. Degraded coral reefs could be considered that the reefs are bleached, deceased (dead), infected by a disease, as well as physically destroyed from human activity. In this research, the coral reefs that are being classified as degraded coral reefs are deceased coral reefs and bleached coral reefs, since those are the conditions that are mostly being affected by the environment in Bunaken National Park [11].

Coral Reefs in Bunaken National Park

Bunaken National Park is a national park located in the Celebes Sea that contains five islands (Bunaken Island, Manado Tua Island, Siladen Island, Mantehage Island, and Nain Island). Bunaken National Park is located in the northern part from Manado City, North Sulawesi Province, Indonesia

Bunaken National Park consists of various marine ecosystems, and coastal morphology. The ecosystems of Bunaken National Park are dominated by coral reef ecosystems, where there are various biotic, abiotic, flora, and fauna components in the area. In addition to the coral reef ecosystem, Bunaken national park also has other types of ecosystems such as seagrass beds, and mangroves [8]. Bunaken National Park has an area of 79 thousand hectares which consists of five islands (Bunaken Island, Manado Tua Island, Siladen Island, Mantehage Island, and Nain Island).

Bunaken National Park has more than 8 thousand hectares of coral reefs, spread around of the five islands of Bunaken National Park. The depth and distribution of coral reefs in the Bunaken National Park area vary greatly, where the range of depth of coral reefs in the bunaken national park ranges from 5 to 200 meters below sea level [8].

This research is done because climate change is a phenomenon that gives impact to coral reef ecosystem. The reason for this research was conducted in Bunaken National Park because coral reef ecosystem located in Bunaken National Park has very high economic function, such as used for tourism and as food availability for human [8]. The study is conducted to analyze how the degradation of coral reefs ecosystem in Bunaken National Park, relates with its exposure towards climate change.

The condition of the coral reefs within the national park is varied, on which there are coral reefs conditions that are healthy, bleached, and deceased [12]. One of the main reason why there are still plenty of healthy coral reefs in this national park is that this national park is still continually being conserved since its main purpose the national park was built is to conserve the ecosystem. Nevertheless,

there are still coral reefs that are deceased, and bleached. The degradation that happens to the coral reefs could be traced based on a lot of environmental factors. One of the factors that contribute the increasing susceptibility of the condition of the coral reefs is climate change, where the increase of the sea surface temperature, acidity, and the frequency of extreme weather is a strong contributing factor why the coral reefs are degraded in the national park [13]. Other factors that may increase the degraded and damaged coral reefs in the national park is because of human activity. Since the local people are dependent on the livelihood of the marine habitat in the national park it could provide a serious threat to the coral reefs ecosystem without a proper management program [11].

METHODS

Shallow Water Analysis

The first process is to analyze the shallow water ecosystem in Bunaken National Park to identify the distribution and the pattern of the benthic habitats in shallow water ecosystem in Bunaken National Park from a satellite image. The satellite image that is used in this study is a satellite image from Landsat 7 ETM+ and Landsat 8 OLI. It will analyze the shallow water ecosystem in Bunaken National Park in the year 2002, 2007, 2013, and 2017.

Shallow water analysis is a remote sensing method that uses reflectance radiance value in a satellite image to get an algorithm that will help to detect the shallow water column. In a more generic term, shallow water analysis is a supervised classifying method through an algorithm that can detect the ecosystem beneath the shallow water [14]. This method on this study will be done by using satellite image processing software. The value of the reflectance values is based on band number 1, 2, and 3 from the Landsat satellite imagery. The calculation of the algorithm formula (1, 2 and 3) is used three different times to retrieve red, blue, and green spectrum. The red spectrum is based on B1 and B2, the green spectrum is based on B1 and B3, and the blue spectrum is based on B2 and B3. The band of each equation is based on the first, second, and third Landsat image layer on each band.

$$Y = (\ln 1st B + (ki/kj) \ln 2nd B) \quad (1)$$

$$Ki/kj = a + (a^2+1)^{1/2} \quad (2)$$

$$a = (\text{Var}(1st B) - \text{Var}(2nd B)) / (2 * \text{Covar}(1st B * 2nd B)) \quad (3)$$

Y is the formula for the algorithm to be written in the band math, 1st B, and 2nd B is the 1st and the 2nd band formula based on the value of its reflectance radiance, ki/kj is a variant and covariant constant which is gotten from a. a is a value gotten from variant value of the 1st B and 2nd B divided by

its covariant. 1st B and 2nd B means the band number (B1, B2, or B3) depending on the color spectrum.

The calculation is done to identify the benthic ecosystem in the shallow water in Bunaken National Park. After the calculation through band math is finished, three different algorithms will be produced on which will display three different color spectrums. The three algorithms are inputted in the band math which will be selected based on the color spectrum in the order of red, green, and blue.

After calculating through band math for analyzing shallow water ecosystem, classification for each type of morphology is needed to distinguish between types of coral reefs. The types of classification that will be done is by distinguishing the healthy coral reefs, the degraded coral reefs (deceased coral reefs, and bleached coral reefs), and seagrass. To distinguish the habitats, collecting sample directly from the study region is necessary. 300 samples have been collected directly in the study region specifically from Bunaken Island, figure 1 shows the map of the distribution where the sample was collected in Bunaken Island.

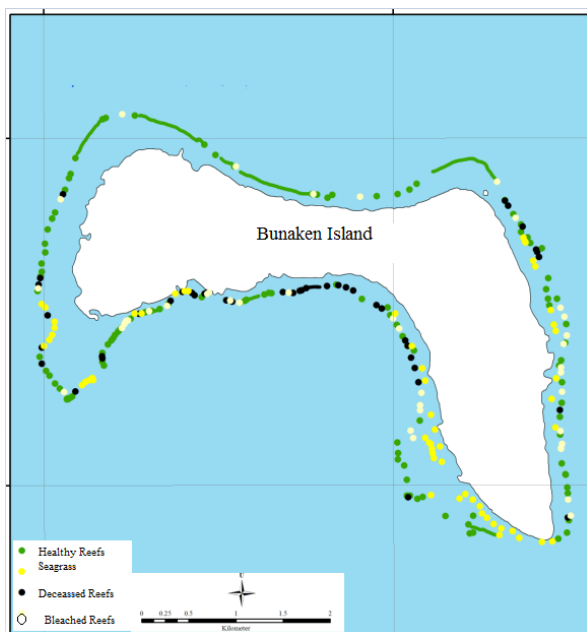


Fig. 1. Distribution of Sample-collection in Bunaken Island

The plotted sample will then be converted to a polygon so it can be used as the region of interest by using geographic information system (GIS) application. The region of interest that have been converted are inputted to the shallow water algorithm. The sample data will be used further to classify each shallow water ecosystem in the study area by using supervised classification. Supervised classification will classify the whole shallow water in the study region, based on the 300-sample data that have been collected. After conducting

supervised classification, it results a morphology of shallow water that shows healthy coral reefs, deceased coral reefs, bleached coral reefs, and seagrass beds. This analysis can be further done by converting file types into vector files, and performing geometric calculations to determine the area of healthy coral reefs, deceased coral reefs, bleached coral reefs, and seagrass beds in 2017. On which will result in a map that shows the whole study region based on the classification that has been inputted inside the shallow water algorithm.

Sea Surface Temperature (SST) Analysis

Surface temperature of sea water can be obtained by using the processed Landsat image [15] To obtain sea surface temperature data from Landsat image, it is necessary to pre-process the image where the image will be corrected based on the radiance value. The first thing to look for to identify sea surface temperatures is to identify the value of spectral radiance from an image that was previously still a digital number[18]. Digital number is a maximum radiance of band 10 on Landsat 8 or band 6 in Landsat 7. Radiance spectral obtained by using the formula:

$$L_x (\text{Landsat 7}) = 0.0370588 B_6 * \text{digital number} + 32 \quad (4)$$

$$L_x (\text{Landsat 8}) = 0.0003342 * b_{10} + 0.1 \quad (5)$$

Where L_x is the Radiance Spectral value

The radiance spectral formula will be inserted into the band math where the satellite image will calculate the value of the spectral radiance to obtain the sea surface temperature value. \ After obtaining the radiance spectral value, then the processed image can be used directly to determine its temperature using the formula:

$$T = K_2 / \ln (K_1 / L_\lambda + 1) \quad (6)$$

$$T (\text{Landsat 8}) = 1321.0789 / (\ln ((774.8853 / L_\lambda) + 1)) \quad (7)$$

$$T (\text{Landsat 7}) = 1282.71 / \log (666.09 / L_\lambda) + 1 \quad (8)$$

Where T is temperature, and K_1 / K_2 is the value of calibration constant at band 10 on Landsat 8 or band 6 on Landsat 7.

The T formula will be entered into the math band. After getting an image that has a temperature value, then the value needs to be changed in order to be the value of sea surface temperature, using the formula:

$$SST = (0.0684 * (\text{float } (B_1 - 3)) - (5.3082 * (B_{12})) + (137.59 * B_1) - 1161.2 \quad (9)$$

Where B_1 is the layer of T and SST is Sea Surface Temperature or Sea surface temperature (SST) [16].

The formula of the SST will be inserted into the math band to get the image layer showing the SST data. After getting the value of sea surface temperature, the map of sea surface temperature in Bunaken National Park area can be done by

classifying sea water to indicate which area which are optimal, less suitable, and not suitable according to the classification that is shown in table 1 [12].

Table 1: SST Suitability for Coral Reefs

Parameter	Optimal	Less Suitable	Not Suitable
SST	27-30 °C	<27 °C	>30 °C

Seawater Salinity Analysis

To identify the salinity of seawater, the type of image pre-processing performed in this analysis is by correction of radiometric and calibration of the reflectance type by performing calibration of the digital number reflectance. After image pre-processing, math band calculations will be performed using an algorithm. The algorithm used to identify marine salinity distribution is Cimandiri algorithm [17], where the algorithm has the formula: $\text{Salinity} = 29,983 + 165,047 (B2) - 260,227 (B3) + 2,609 (B4)$ (10)

Where:

B2: Blue Band

B3: Green Band

B4: Red Band

The image processing to obtain the value of seawater salinity is by inputting the formula input to the band math, on which the bands that are used in this analysis are band 2,3 and band 4 that shows true color. After obtaining the value of seawater salinity, the map of it can be obtained from the satellite image within the Bunaken National Park can be done by classifying sea water to indicate which region is are optimal, less suitable, and not suitable for coral reefs based on the classification as set out in Table 2 [9].

Table 2: Seawater Salinity Suitability for Coral Reefs

Parameter	Optimal	Less Suitable	Not Suitable
Salinity	30 – 36 PSU	>36 PSU	<30 PSU

RESULTS

Coral Reefs Ecosystem in Bunaken National Park

The results of the shallow water analysis algorithm, shallow water ecosystems in Bunaken National Park can be seen on the map in Figure 2. The map shows the condition of coral reefs along with the distribution of shallow water ecosystems in Bunaken National Park in 2002, 2007, 2013 and 2017. The classification used in the map that is shown in figure 2 shows healthy coral reefs,

deceased coral reefs, bleached coral reefs, seagrass, and other built-up area. These maps are based on the shallow water analysis algorithm that have been classified based on sample that are collected in Bunaken Island as shown in figure 1. Table 3 shows the area size of each type of shallow water ecosystem classification in Bunaken National Park from 2002 to 2017.

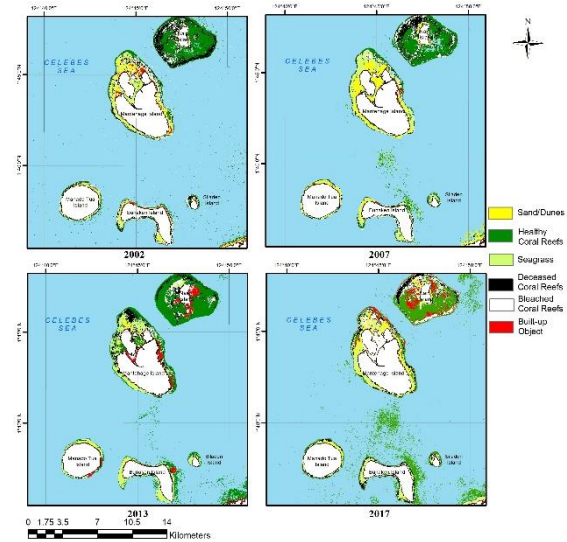


Fig. 2. Spatial Distribution and Its degradation pattern of Coral Reefs in Bunaken National Park (2002, 2007, 2013, and 2017).

Table 3: Area Size of Shallow water ecosystem in Bunaken National Park

Area (Ha)	2002	2007	2013	2017
Healthy Reefs	17,461,330.40	19,419,023.50	30,565,753.37	30,684,798.19
Deceased Reefs	10,405,567.22	7,180,707.11	6,237,082.12	7,015,449.40
Bleached Reefs	7,204,242.12	6,699,643.47	4,373,714.56	7,845,673.17
Seagrass	8,757,983.50	9,993,298.62	10,834,288.13	11,616,532.24

Sea Surface Temperature in Bunaken National Park

The result of SST analysis in Bunaken National Park can be seen on the map in figure 3. The map shows the condition of the sea surface temperature in Bunaken National park in 2002, 2007, 2013, and 2017. The classification that are being used in the map from figure 3 is based on what is shown from table 1.

Seawater Salinity in Bunaken National Park.

The result of Seawater salinity analysis in Bunaken National Park can be seen on the map in

figure 4. The map shows the condition of the seawater salinity in Bunaken National park in 2002, 2007, 2013, and 2017. The classification that are being used in the map from figure 4 is based on what is shown from table 2

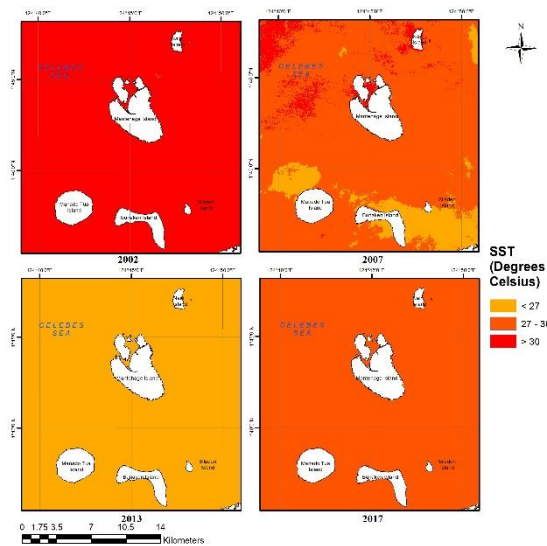


Fig. 3. Sea Surface Temperature in Bunaken National Park (2002, 2007, 2013, and 2017).

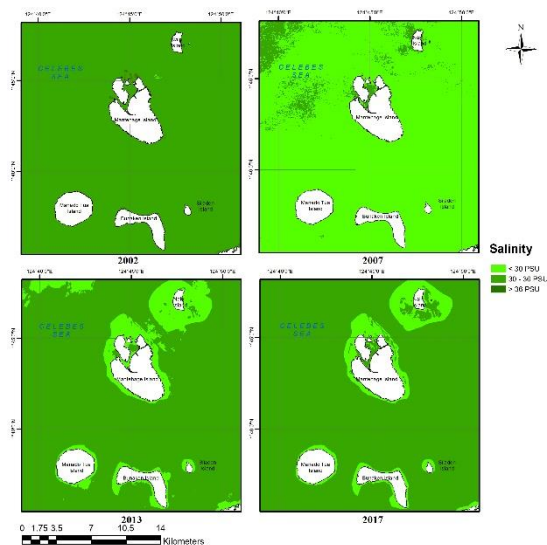


Fig. 4. Seawater Salinity in Bunaken National Park (2002, 2007, 2013, and 2017).

DISCUSSION

Coral Reefs Degradation Pattern

The coral reefs degradation pattern could be shown in figure 2 that shows the map of it. The map shows that the condition of the coral reefs in Bunaken National Park are vary in each year. The map shows that Nain Island have the largest shallow water ecosystem in the National Park. The spatial pattern of the coral reefs in Bunaken National Park are shown that the further away from the coastline,

the better the condition of the coral reefs. Almost the outermost layer of the shallow water ecosystem in Bunaken National Park consist of healthy coral reefs. The spatial pattern of deceased and the bleached coral reefs on the other hand are located mostly near the coastline of each island in Bunaken National Park.

The map shows that the worst condition of coral reefs degradation happened in 2002, where it has the largest area of deceased and bleached coral reefs combined compared to other years, on which could be seen in table 3. Based on table 3, it is shown that the area of deceased and bleached coral reefs from 2002 to 2013 have decreased in size, whereas the area of healthy coral reefs from 2002 to 2017 have increased. On the other hand, the area of degraded coral reefs from 2013 to 2017 have increased dramatically from the previous years on which have been steadily declined.

Coral Reefs Exposure towards Climate Change

Based on figure 3 and figure 4 that shows the map of sea surface temperature, and seawater salinity in Bunaken National Park in 2002, 2007, 2013, it shows that the sea surface temperature for the year 2002 are above 30 °C and the seawater salinity level in 2002 are 30-36 PSU. It shows that the year 2002 have an optimal seawater salinity condition for coral reefs, and not suitable SST condition for coral reefs. The SST condition could possibly the reason why there are large area of degraded coral reefs in Bunaken National Park since the SST of Bunaken National Park reach up to 36 °C in 2002 (based on table 3).

In 2007 and 2013 the SST condition in Bunaken National Park are quite vary. The SST condition have relatively been declining compare to 2002. The decline of the sea surface temperature could be a major factor why the number of degraded coral reefs have been declining from 2002 to 2013. The salinity level on the other hand, was relatively declining in 2007 and goes back incline in 2013.

In 2017 the Sea surface temperature are relatively optimal for coral reefs, where it has a temperature between 27-30 °C. Even though 2017 was the year where the degraded coral reefs were at an all-time high from the last 15 years. The reason of that was because the seawater salinity in 2017 around the shallow water ecosystem for every island in Bunaken National Park has the lowest salinity level (below 30 PSU down to 16PSU).

CONCLUSION

This study shows that the coral reefs in Bunaken National Park has a pattern on which the furthest away from the island, the better the condition of the coral reefs. Where degraded coral reefs are usually located closely from the island. The degrade coral reefs of Bunaken National Park from 2002-2013

were on a decline, where it came to incline once again in the year of 2017. This study shows that there are a correlation between the change of sea surface temperature and seawater salinity level and the area of degraded coral reefs, where the higher the temperature and the lower the salinity level of seawater the bigger the size area of the degraded coral reefs.

ACKNOWLEDGEMENTS

This research were sponsored by Hibah PITTA program from FMIPA Universitas Indonesia.

REFERENCES

- [1] Crabbe MJC. 2007. Global warming and coral reefs: Modelling the effect of temperature on *Acropora palmata* colony growth. *Computational Biology and Chemistry* 3.
- [2] Crabbe MJC. 2008. Climate change, global warming and coral reefs: Modelling the effects of temperature. *Computational Biology and Chemistry*..
- [3] Chen Ping-Yu, Chi-Chung Chen, LanFen Chu, Bruce McCarl. 2015. Evaluating the economic damage of climate change on global coral reefs. *Global Environmental Change*
- [4] Ateweberhan M, David A Feary, Shashank Keshavmurthy, Allen Chen, Michael H. Schleyer, Charles R.C. Sheppard (2013). Climate change impacts on coral reefs: Synergies with local effects, possibilities for acclimation, and management implications. *Marine Pollution Bulletin*.
- [5] Hoegh-Guldberg O (1999). Climate change, coral bleaching and the future of the world's coral reefs. *CISRO Publishing*.
- [6] Gibo C, Tiffany Letsom, dan Charley Westbrook (2012). Effects of Temperature, Salinity, pH, Reef Size, and *Tripterygion* on the distribution of *Montipora dilatata* in Kaneohe Bay. *University of Hawaii At Manoa Biol 403: Field Problems in Marine Biology*.
- [7] Gattuso, J.-P., Magnan, A., Billé, R., Cheung, W.W.L., Howes, E.L., Joos, F., Allemand, D., Bopp, L., Cooley, S.R., Eakin, C.M., Hoegh-Guldberg, O., Kelly, R.P., Pörtner, H.-O., Rogers, A.D., Baxter, J.M., Laffoley, D., Osborn, D., Rankovic, A., Rochette, J., Sumaila, U.R., Treyer, S., Turley, C., (2015). Contrasting futures for ocean and society from different anthropogenic CO₂ emissions scenarios. *Science* 349.
- [8] Mehta A (1999). Field Guide for Bunaken National Park National Park Natural History Book Field. Bunaken National Park Hall. (Indonesian)
- [9] Sparrow Leanne, Paolo Momiglianod, Garry R. Russa, Kirsten Heimanna (2017). Effects of temperature, salinity and composition of the dinoflagellate assemblage on the growth of *Gambierdiscus carpenteri* isolated from the Great Barrier Reef. *Harmful Algae* 65
- [10] Indonesian Ministry of Forestry (2008). Management of Bunaken Resort-Based Bunaken National Park. (Indonesian)
- [11] Indonesian Ministry of Forestry (n.d.). Building And Strengthening The Commitments Of The Parties In Managing The Bunaken National Park: "Lesson Learn".: "Lesson Learn". *NRM- EPIQ Programme. (Indonesian)*.
- [12] LIPI (2017). Status of Indonesian Coral Reef 2017. *Oceanographic Research Center – LIPI. (Indonesian)*.
- [13] Government of the City of Manado (2015). Vulnerability Assessment Of Climate Change In Manado City. (Indonesian).
- [14] Jaelani, L. M., Laili, N., dan Marini (2015). Pengaruh Algoritma Lyzenga dalam pemetaan Terumbu Karang Menggunakan WorldView-2, Studi Kasus: Perairan PLTU Paiton Probolinggo. *Jurnal Penginderaan Jauh*, Vol. 12 No. 2, 123-131. (Indonesian)
- [15] Kartikasari, F., Jaelani, L. M., dan Winarso, G. (2016). Analysis of Distribution of Concentration Sea surface temperature and pH of making duck grouper cultivation locations using Landsat-8 satellite imagery (Case Study: Teluk Lampung, Lampung). *ITS Technical Journal* Vol. 5). (Indonesian)
- [16] Trisakti, Bambang (2004). Study of Sea Surface Temperature (SST) using Landsat-7 ETM (In Comparison with Sea Surface Temperature of NOAA-12 AVHRR). *Remote Sensing Application and Technology Development Center – LAPAN. Research Gate*
- [17] Supriatna, L., Supriatna, J., dan Koetsoer (2016). Algorithm model for the Determination of Cimandiri Estuarine Boundary Using Remote Sensing. *AIP conference Proceedings*, 1729.020079 (2016); doi. 10.1063/1.4946982
- [18] Lyzenga (1981). Remote Sensing Of Bottom Reflectance And Water Attenuation Parameters In Shallow Water Using Aircraft And Landsat Data. *Int. 1. Remote sensing*, 1981, vol. 2, no. 1.

ROLE DIFFERENCE AMONG RIVERS AFFECTED BY VOLCANIC ACTIVITIES OF MT. ONTAKE FOR WATER QUALITY OF THE NIGORIGAWA RIVER

Akiko Usami¹, Yoshitaka Matsumoto², Megumi Nobori³, Akihiko Yagi¹ and Eiji Iwatsuki¹

¹Faculty of Engineering Aichi Institute of Technology (AIT), JAPAN,

²National Institute of Technology, Toyota College Department of Civil Engineering, Japan

³Mie Prefectural Center of Constructional Technology, JAPAN

ABSTRACT

To understand the influence of volcanic activities of Mt. Ontake on the Nigorigawa River, the distribution of elements contained in the water of the Nigorigawa were examined. The Nigorigawa has several tributaries such as the Akagawa River, the Shirakawa River, the Denjogawa River, and small streams. Sampling stations were located in the Nigorigawa and upstream rivers of it. These water samples were analyzed by the ICPE. The Akagawa and the Denjogawa show anomalous water quality. The amounts of elements in the water of the Akagawa are far more than those in other rivers (ex. S: 138 mgL⁻¹, Fe: 34 mgL⁻¹, Al: 33 mgL⁻¹). The water quality of the Akagawa shown above is consistent with characteristic features in the volcanic zone. In contrast, the water of the Denjogawa contains large amounts of Na (46 mgL⁻¹). It is likely due to dissolution from the sediment of Mt. Ontake, because the Denjogawa has a source in the Ontake Landslide, which was caused by the 1984 Nagano Prefecture Earthquake. It was found that the Akagawa and the Denjogawa play a role different from each other for forming the water quality of the Nigorigawa (the Akagawa: eruption, the Denjogawa: earthquake).

Keywords: distribution of elements, Nigorigawa River, Mt. Ontake, volcanic activity, Ontake Landslide

INTRODUCTION

Mt. Ontake (altitude 3,076m) is located across Nagano Prefecture and Gifu Prefecture. Mt. Ontake often has shown volcanic activities. Since recorded history, it erupted on a medium scale for the first time in 1979. Thereafter, small-scale eruptions occurred in 1991 and 2007, and a medium-scale eruption happened again in 2014 [1]. All of them were phreatic eruptions [2], [3]. Also, the Western Nagano Prefecture earthquake (M6.8) occurred in 1984, which caused the sector collapse at Mt. Ontake, i.e., the Ontake Landslide.

Mt. Ontake has several rivers, one of which is the Ohtakigawa River flowing in the southern side of it. Generally, it is known that volcanic activities affect water quality of the surrounding rivers and change their water quality [4]. Actually, the Ohtakigawa is reported to be affected by the eruption [5], [6]. In addition, it was found that in the Ohtakigawa after the junction with the Nigorigawa, pH was low, the electric conductivity was high, and biota was less [7]-[9]. Recently, Usami et al. [10] have progressed the above research and showed the formation process of anomalous water quality of the Ohtakigawa from a viewpoint of elements.

The previous works shown above have revealed that the water quality in the Ohtakigawa is significantly affected by the Nigorigawa. In order to

recover the Ohtakigawa environment damaged owing to the volcanic activities, however, we need more information to further comprehend the formation process of the water quality of the Nigorigawa.

In this work, to further approach the cause of the characteristic water quality of the Nigorigawa, we surveyed the upstream of the Nigorigawa. We observed elements in water of the Nigorigawa and upstream rivers of the Nigorigawa to clarify the relation between the rivers.

METHODS

Study site

Figure 1 shows a map of sampling stations. We selected ten stations as the sampling stations in tributaries of the Ohtakigawa River (the Nigorigawa River, the Shimokurosawa River, the Shirakawa River, and the Uguigawa River) and in upstream rivers of the Nigorigawa River (the Nigorisawagawa River, the Denjogawa River, the Akagawa River, the Shirakawa River, and branches of the Denjogawa and the Nigorisawagawa). Here, it is noted that the Ohtakigawa and the Nigorigawa have a different tributary with the same name "Shirakawa". Hereinafter we call the Shirakawa of the Ohtakigawa

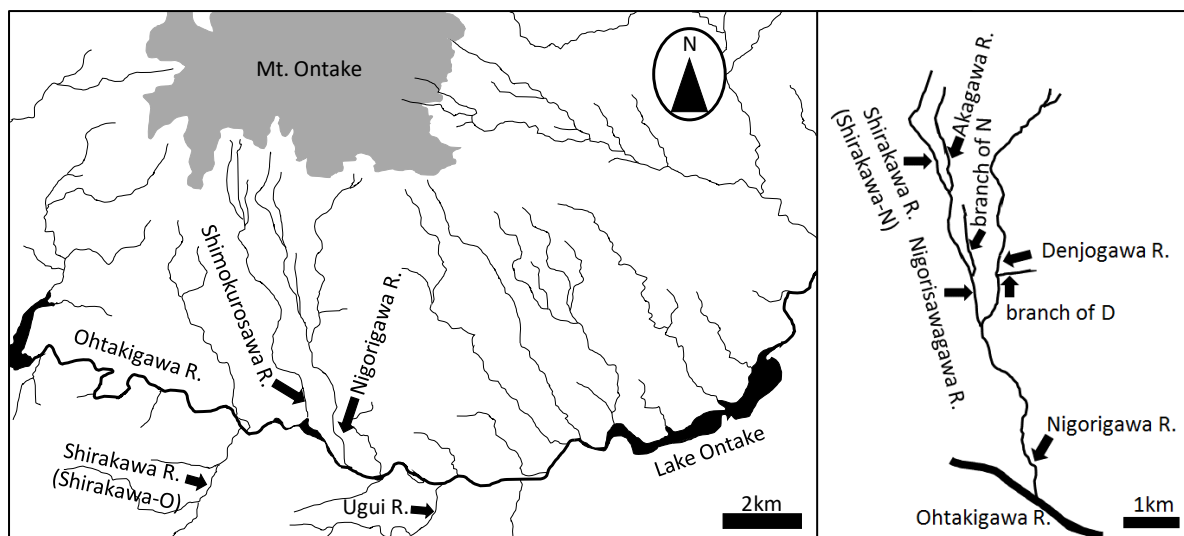


Figure 1 Sampling stations in the Ohtakigawa watershed. The left panel is a map which shows sampling stations in tributaries of the Ohtakigawa. The right panel is an enlarged map focusing on the Nigorigawa and upstream rivers of it, sampling stations in which rivers are displayed.

“the Shirakawa-O” and the Shirakawa of the Nigorigawa “the Shirakawa-N.”

Investigations were carried out from October 10, 2015 to November 25-26, 2017 as shown in Table 1.

Sampling and analysis

pH

Samples obtained from the survey on November 25-26, 2017 were brought back to the laboratory and pH was measured by using a pH meter (Mettler Toledo Portable pH Meter Pro2Go).

In the investigation from October 10, 2015 to November 4, 2017, pH of the sample was measured by a pH meter (RISEPRO ph-900).

Elements

Samples were filtered. Filtration was carried out with a teflon filter paper (PTFE, 0.5μm, φ 47mm), and the samples were separated into dissolved and suspended matters.

The filtrate samples were added to aqua regia (HNO₃: HCl=1:3), and the suspended particle matter on the teflon filter was decomposed in aqua regia. Elements contained in them were analyzed and 21 element species (Na, Mg, Al, Si, P, S, K, Ca, Ti, V, Cr, Mn, Fe, Co, Ni, Cu, Zn, As, Se, Mo, Sn) were measured by using the ICPE.

In this work, nine element species: Na, Mg, Al, Si, S, K, Ca, Mn and Fe, which generally are the main components of volcanic ejecta [11],[12], and actually demonstrated high concentrations, are exhibited in detail.

Table 1 Sampling stations and sampling dates. The circles indicate that water was sampled at the corresponding station and date. “Upstream rivers of the Nigorigawa” means the sampling stations in the Nigorisawagawa, the Denjogawa, the Akagawa, the Shirakawa-N, and branches of the Denjogawa and the Nigorisawagawa.

Sampling station	Upstream rivers of the Nigorigawa	Nigorigawa	Shirakawa-O	Shimokurosawa	Uguigawa
Oct. 10, 2015		○	○	○	
Sep. 17, 2016		○	○	○	○
Oct. 29, 2016		○	○	○	○
Mar. 4, 2017		○	○	○	○
May 6, 2017		○	○	○	○
Jun. 24, 2017		○	○	○	○
Aug. 5, 2017		○	○	○	○
Nov. 4, 2017		○	○	○	○
Nov. 25-26, 2017	○	○			
Investigation frequency	1	9	8	8	7

RESULT

Concentrations

The Nigorigawa

Figure 2 shows the concentrations of the nine element species at each sampling station. First, the

water quality of the Nigorigawa is overviewed; S, Na, Ca and Si have high concentrations (40, 32, 30 and 26 mgL^{-1} , respectively). In addition, the concentrations of all the nine elements are 6-158 times higher than those in other tributaries of the Ohtakigawa (the Shimokurosawa, the Shirakawa-O and the Uguigawa rivers). Thus, it is confirmed as reported by [10] that the water quality of the Nigorigawa is anomalous enough to dominantly affect the water quality of the Ohtakigawa.

The Nigorisawagawa and the Denjogawa

Next, the water quality of the Nigorisawagawa and the Denjogawa, into which the upstream of the Nigorigawa bifurcates, are compared. The concentrations of S, Al and Fe in the Nigorisawagawa (S: 67 mgL^{-1} , Al: 10 mgL^{-1} , Fe: 6 mgL^{-1}) shows quite high values compared with those in the Denjogawa (S: 7 mgL^{-1} , Al: 0 mgL^{-1} , Fe: 0 mgL^{-1}). In contrast, the concentration of Na in the Denjogawa (46 mgL^{-1}) is much higher than that in the Nigorisawagawa (19 mgL^{-1}). From these results, it is clearly seen that the high concentration of S in the Nigorigawa is caused by the Nigorisawagawa and the high concentration of Na in the Nigorigawa is due to effects of the Denjogawa.

The Akagawa and the Shirakawa-N

The upstream of the Nigorisawagawa further bifurcates into the Akagawa and the Shirakawa-N. First, let us discuss S, Ca and Si, which show high ratio in the Nigorisawagawa. The concentrations of S, Ca and Si are high both in the Akagawa and in the Shirakawa-N. It is consequently found that the high concentrations of S, Ca and Si in the Nigorisawagawa are caused by both of the Akagawa and the Shirakawa-N. Next, let us observe Al and Fe, whose concentrations in the Nigorisawagawa is much higher than those in other tributaries of the Ohtakigawa. The Al and Fe concentrations in the Akagawa are extremely high compared with those in the Shirakawa-N (16 times and 229 times higher, respectively). From this result, it is found that the high concentrations of Al and Fe in the Nigorisawagawa are almost due to the Akagawa.

Branches of the Denjogawa and the Nigorisawagawa

In branches of the Denjogawa and the Nigorisawagawa, the concentrations of the nine elements are sufficiently small as in other tributaries of the Ohtakigawa (Figure 2) and thus their influence on the Nigorigawa, can be ignored.

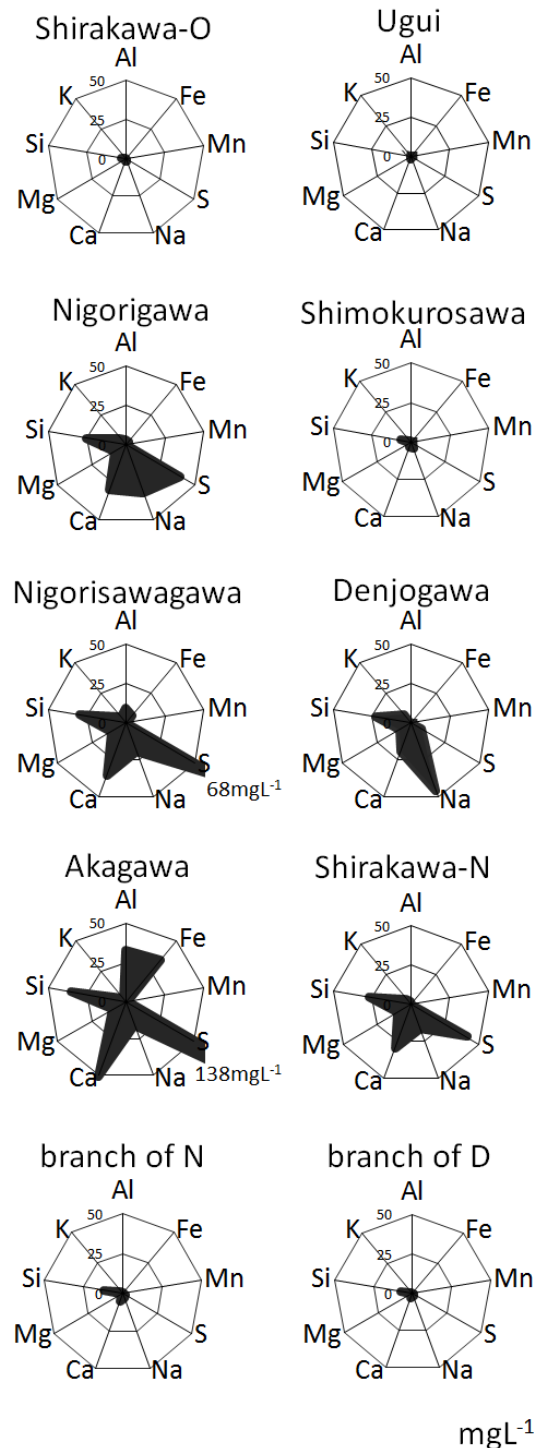


Figure 2 Concentrations of the nine element species at each sampling station.

Speciation

The speciation of S, Na, Ca and Si, which show high concentrations in the Nigorigawa, is investigated. They are in dissolved state in all the rivers including

the Nigorigawa. That is, they exist as sulfate ion, sodium ion, calcium ion and silicon oxide, respectively.

In addition, the speciation of Al and Fe, whose concentrations are high especially in the Akagawa, is shown in Figure 3. Rivers are arranged from the top panel to the bottom panel in ascending order of pH. Al and Fe have a property to dissolve in acid water. Indeed, Al and Fe exist as dissolved matters (aluminum ion and iron ion) in the Akagawa, where pH is 2.9. In the Nigorisawagawa (pH=3.7), the downstream of the Akagawa, 10% of Fe exists in suspended state, and in the Nigorigawa (pH=5.9), the downstream of the Nigorisawagawa, ratios of suspended matters of Al and Fe are 44 % and 28%, respectively. This implies that pH rises owing to the influence of other rivers, the Shirakawa-N and the Denjogawa, and the dissolved matters are gradually changed to the suspended matters.

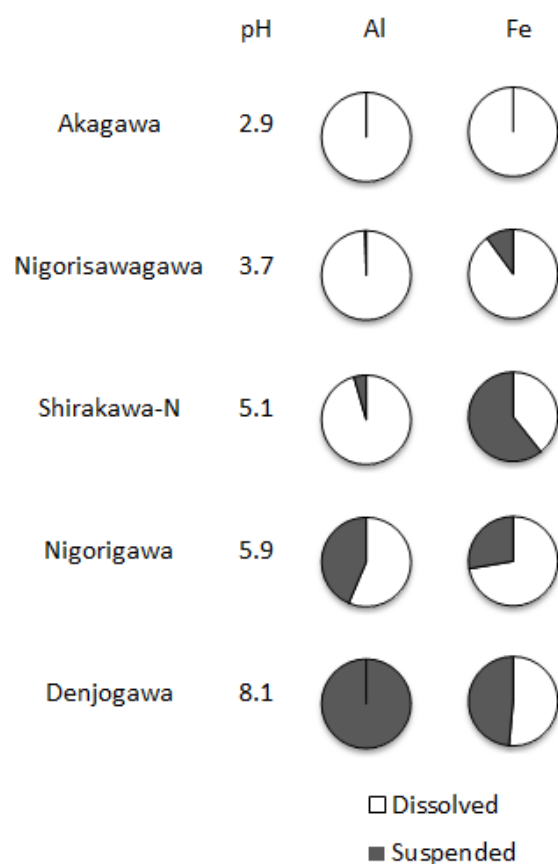


Figure 3 Speciation of Al and Fe in the Nigorigawa and upstream rivers of it.

Change in the two years

The Nigorigawa has been surveyed nine times during the two years from October in 2015 to November in 2017. It is noted that the surveys have been taken one year later the eruption on the September 2014. The concentrations of the nine element species at the nine surveys are shown in Figure 4. Each concentration does not have a clear tendency to change.

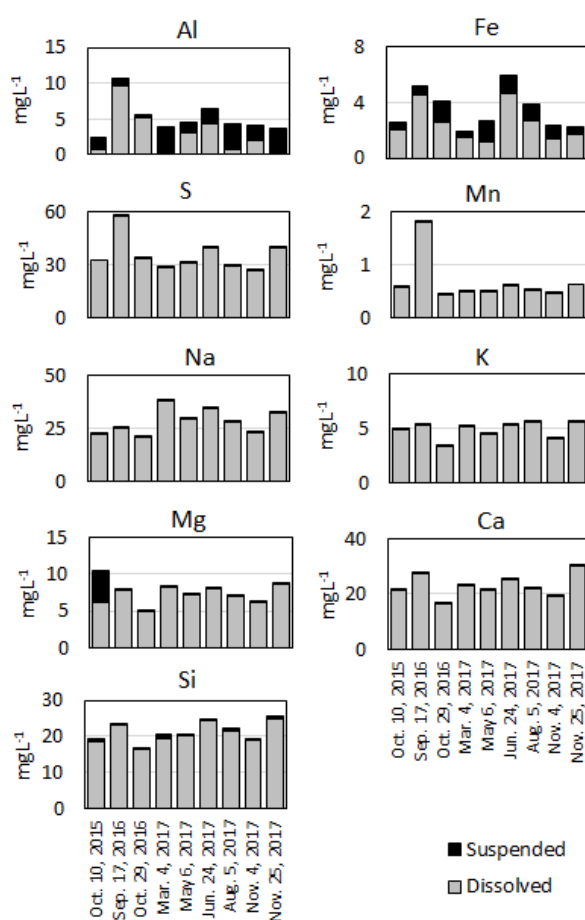


Figure 4 Concentrations of the nine element species at the nine surveys from October in 2015 to November in 2017

CONCLUSION AND DISCUSSION

In this work, it has been found that the characteristic water quality of the Nigorigawa is formed mainly by both of the Akagawa and the Denjogawa, which play different roles, respectively.

Here, it is discussed how the water quality is formed in the Akagawa and the Denjogawa,

respectively. First, we consider what causes the high concentrations of S, Al and Fe in the Akagawa. The Akagawa has a source in the vicinity of craters that erupted in 1979 and 2014 [13]. This implies that the water in the Akagawa is acidified by the solution of SO_2 contained in the volcanic gas and the oxidation of FeS contained in the volcanic ejecta [14]-[16], and consequently, Al and Fe contained in soil and rock are eluted in acid water. Next, we discuss the cause of the high concentration of Na in the Denjogawa. The Denjogawa has a source on the site of the sector collapse (the Ontake Landslide in 1986), where soil and rock are exposed. It is inferred that Na elutes from the soil and rock by weathering process [17], and inflows into the Denjogawa.

In the Akagawa, Al and Fe are in dissolved state. The speciation of Al and Fe is changed to suspended state as pH rises due to the influence of the Shirakawa-N and the Denjogawa. Through the process of the speciation change, the water quality of the Nigorigawa is formed.

Suspending Al and Fe has positive and negative aspects for living things there. A positive aspect is that these elements are removed from the river water by suspending process, because Al and Fe with high concentrations are poisonous to living things [18], [19]. On the other hand, a negative aspect is that the suspended elements eventually precipitate on the surface of the river bed, and adversely affects periphyton [20]-[22].

The change in the element concentrations in the Nigorigawa has not shown noticeable tendencies for the two years from 2015 to 2017. It is inferred that the Nigorigawa continues to affect the water quality of the Ohtakigawa. In addition, as described above, the Nigorigawa is affected mainly by the two upstream rivers, the Akagawa and the Denjogawa. Thereby, it is implied that the water quality of the Akagawa and the Denjogawa also does not significantly change.

ACKNOWLEDGEMENTS

The authors grateful to Kiso District Forest Office, Forest Agency of Japan for permission to use forest roads for the access to the study sites. They thank Kentaro NOZAKI of Sugiyama Jogakuen University, Takashi TASHIRO of Nagoya University, and Yukio ONODA of the Aqua Restoration Research Center for cooperation in the field survey and valuable suggestions. They thank students of Aichi Institute of Technology for their helping in this work. This research was supported by a Grant from the Water Research Environment Center (No.2017-05: representative: Takayoshi Matsumoto). The analysis in this work is performed on "ICPE-9000" (SHIMADZU) which supported by 2012 Ministry of Education Private University Research Facilities Maintenance costs subsidies.

REFERENCES

- [1] Tashiro T., Water environment of the Ohtaki River near Mount Ontake in the Kiso River System with particular references on natural disasters and water resources and hydropower development (in Japanese), Rikunomizu (Limnology in Tokai Region of Japan), Vol.74, 2016, pp. 5-11.
- [2] Sano Y., Kagoshima T., Takahara N. Nishio Y. Roulleau E., Pinti L. D. and Fischer P. T., Ten-year helium anomaly prior to the 2014 Mt. Ontake eruption, Scientific Reports Online Edition: 2015/08/19 (Japan time), doi:10.1038/srep13069.
- [3] Oikawa T., Yamaoka K., Yoshimoto M., Nakada S., Takeshita Y., Maeno F., Ishizuka Y., Komori J., Shimano T. and Nakano S., The 2014 Eruption of Ontake volcano, central Japan (in Japanese), Bulletin of the Volcanological Society of Japan, Vol. 60, Issue 3, 2015, pp.411-415.
- [4] Yamano M., Ossaka T., Oi T. and Ossaka J., Halide Ions in River Waters in the Kusatsu-Shirane Volcano Area, Gunma (in Japanese), The Chemical Society of Japan, Vol. 1997 Issue 3, 1997, pp.194-200.
- [5] Imamoto H., Andou M., Iki H. and Onoshima K., Measures Against the Predicted Degradations of Water Quality of Makio Dam Reservoir by the Volcanic Eruption of Mt. Ontake (in Japanese), Journal of Japan Society of Dam Engineers, Vol. 27, Issue 2, 2017, pp.133-140.
- [6] Asami K., Koderia K., Igari Y. and Horiuchi M., A study on the water environment of around Mt. Ontake after eruption (140927) (5) (in Japanese)", Book of abstracts in The Study Meeting of the Association of Japanese Geographers Spring 2017, p. 100107.
- [7] Nozaki K., Autumn and winter periphyton biomass in the Ohtakigawa River watershed 1 year after the 2014 eruption of Mount Ontake, central Japan, Rikunomizu (Limnology in Tokai Region of Japan), Vol.74, 2016, pp. 13-21.
- [8] Onoda Y. and Kayaba Y., Comparison of fish fauna in a river that received pyroclastic flow from the volcanic eruption of Mt. Ontake in 2014 with that in neighboring rivers, Rikunomizu (Limnology in Tokai Region of Japan), Vol.74, 2016, pp. 23-28.
- [9] Taniguchi T., Special feature: Effects of the 2014 Mount Ontake eruption on inland waters (in Japanese), Rikunomizu (Limnology in Tokai Region of Japan), Vol.74, 2016, pp. 1-3.

- [10] Usami A., Nobori M., Yagi A. and Iwatsuki E., Presence state of trace elements in the Ohtakigawa River watershed from the foot of Mt. Ontake, International Journal of GEOMATE, April. 2018 Vol.14, Issue 44, pp.15-19.
- [11] Yamada N. and Kobayashi T., Geology of the Ontakesan district. With Geological Sheet Map at 1: 50,000 (in Japanese), Geological Survey of Japan, 136p. 1988, pp. 122-127.
- [12] Sugiura T., Sugisaki R., Mizutani Y. and Kusakabe M., Geochemistry of volcanic ashes, thermal waters and gases ejected during the 1979 eruption of Ontake Volcano, Japan (in Japanese), Second series Bulletin of the Volcanological Society of Japan, Vol. 25, Issue 4, 1980, pp.231-244.
- [13] Sasaki H., Chiba T., Kishimoto H. and Naruke S., Characteristics of the syneruptive-spouted type lahar generated by the September 2014 eruption of Mount Ontake, Japan, Earth, Planets and Space, 2016, 68:141.
- [14] Tase N. and Sugihara S., Hydrological understanding of natural waters with unique characteristics. 2. Acid Rivers around Sugadaira area (in Japanese), Journal of Japanese Association of Hydrological Sciences, Vol. 41, Issue 2, 2011, pp.39-46.
- [15] Mori T., Hashimoto T., Terada A., Yoshimoto M., Kazahaya R., Shinohara H. and Tanaka R., Volcanic plume measurements using a UAV for the 2014 Mt. Ontake eruption, Earth, Planets and Space, 2016, 68:49.
- [16] Minami Y., Imura T., Hayashi S. and Ohba T., Mineralogical study on volcanic ash of the eruption on September 27, 2014 at Ontake volcano, central Japan: correlation with porphyry copper systems, Earth, Planets and Space, 2016, 68:67.
- [17] Yoshioka R., Koizumi N., Kusakabe M. and Chiba H., Chemical and isotopic compositions of natural water from an area of large-scale landslide caused by the Western Nagano Prefecture Earthquake (in Japanese), Annuals, Disas. Prev. Res. Inst., Kyoto Univ., No. 29 B-1, 1986, pp.379-390.
- [18] Ikuta K., Influence of acid rain on fish (in Japanese) [Translated from Japanese], Society of environmental conservation engineering, Vol.27, No.11, 1998, PP. 45-49.
- [19] Koshikawa M., Watanabe M., Koshikawa H., Komatsu K., Imai A., Inaba K. and Takamatsu T., Speciation of aluminum in Lake Kasumigaura, Japan (in Japanese), BUNSEKI KAGAKU (The Japan Society for Analytical Chemistry), Vol. 59, No.12, 2010, PP.1137-1142.
- [20] Sasaki A., Kariya H., Ito A., Kawaguchi H., Aizawa J. and Umita T., Influence of water quality and sediment on the growth of attached algae in the river Akagawa receiving effluent from an acid mine drainage treatment Plant (in Japanese), Environmental Engineering Research, Vol. 40, 2003, PP127-138.
- [21] Sasaki A., Ito A., Takahashi S., Aizawa J. and Umita T., Effect of metal hydrolytic products on the growth of attached algae (in Japanese), Environmental Engineering Research, Vol. 41, 2004, PP367-376.
- [22] Sasaki A., Tate N., Ito A., Aizawa J. and Umita T., Estimation of the effects of Al hydrolysis products on river ecosystems using attached algae as bioindicator (in Japanese), Environmental Engineering Research, Vol. 43, 2006, PP493-499.

COMPRESSIVE LOADING TEST OF STEEL PILE TOP FILLED WITH CONCRETE

Mutsuki Sato¹, Toshiharu Hirose² and Yoshihiro Kimura³

¹ Faculty of Engineering, Tohoku University, Japan; ² Japanese Technical Association for Steel Pipe Piles and Sheet Piles, Japan ³ New Industry Creation Hatchery Center, Tohoku University, Japan

ABSTRACT

In Japan, for real structures with the steel pile foundation, the steel pile top is filled with concrete in order to connect it to the RC footing beam rigidly [1]. From the point of view of the seismic design, concrete infill is expected to prevent the local buckling at the steel pile top and concrete filled steel pile may thereby have higher strength than the hollow steel piles. While bending moment is applied to the pile top, slips occur between the steel pile and the concrete infill due to member being partly filled. Therefore, despite of internal ring being attached to the steel pile top, the stress transfer mechanism between steel pile with internal ring and concrete infill has not took place. Bearing strength of internal ring for CFT was evaluated in the previous experiment, but ultimate strength due to local buckling has not been clarified yet. Therefore, in this paper, compression loading test of concrete filled steel pile with internal ring is carried out. According to the results of this experiment, the axial compressive strength of concrete filled steel pile top with internal ring is 20% higher than that of steel pile with no internal ring. The axial compressive strength of concrete filled steel pile top with no internal ring is slightly higher than that of that of hollow steel pile. Furthermore, this paper clarifies stress transfer mechanism between steel pile with internal ring and concrete infill, its compressive ultimate strength, and the plastic deformation capacity considering to local buckling behavior.

Keywords: Steel Pile, Compression Loading Test, Local Buckling Behavior, Pile Top Reinforcement

INTRODUCTION

In Japan, for the steel pile foundation, the steel pile top is filled with concrete to connect it to RC footing beam rigidly. Internal rings are attached to the steel pile top to transmit the stress between concrete infill and the steel pile. Steel piles filled with concrete at the top and typical concrete-filled steel tube (CFT) has different local buckling behavior, the ultimate strength, and the plastic deformation capacity due to the concrete infill and internal rings at the pile top. As a consequence, it is not valid to apply design equations of CFT members.

In addition, the stress transfer mechanism between the steel pile with the internal ring and concrete infill has not been clarified. In this paper, compression tests are performed with steel pile top filled with concrete and numerical analyses models of the steel pile top filled with concrete are modeled. In addition, the ultimate strength and plastic deformation capacity of the steel pile top filled with concrete is clarified with the numerical analyses. The stress transfer mechanism between the steel pile with internal rings and concrete infill is revealed as well.

AXIAL COMPRESSION LOADING TEST OF STEEL PILE TOP FILLED WITH CONCRETE

The test specimen and the location of

displacement gauges are shown in Fig. 1. The test specimens are steel piles of different cross-section with a concrete member at the pile top. For the steel pipe, the outside diameter and thickness of A-A section are 488 mm and 9 mm, and those of B-B section are 508 mm and 19 mm, respectively. Hereinafter, steel pile shown in A-A section is called as "tested part" and steel pile shown in section B-B is called as "load application part" Concrete is filled up to 488 mm from the bottom. In this paper, pile plate of A-A section is thicker than that of B-B section to clarify the local buckling behavior of the pile top filled with concrete. Internal rings are attached on the inside of the steel pile at 122 and 244 mm heights. Hereinafter, the internal ring at 122 mm is called as "lower ring" and the one at 244 mm is called as "upper ring".

In Fig. 1, d , t , and l represent outside diameter, thickness, and length of test part, respectively. D , T , and L denote the outside diameter, thickness, and length of load applied part. w and s represent width and thickness of internal rings. Strain gauges and displacement gauges are set up as described in Fig. 1(c).

Material properties are presented in Table 1. Here, σ_b , σ_t , and E_c denote the concrete ultimate compressive strength, tensile strength, and elastic modulus. σ_y , σ_u , ε_y , and E_s represent the steel yield strength, the steel ultimate strength, the steel yield strain, and the steel elastic modulus, respectively.

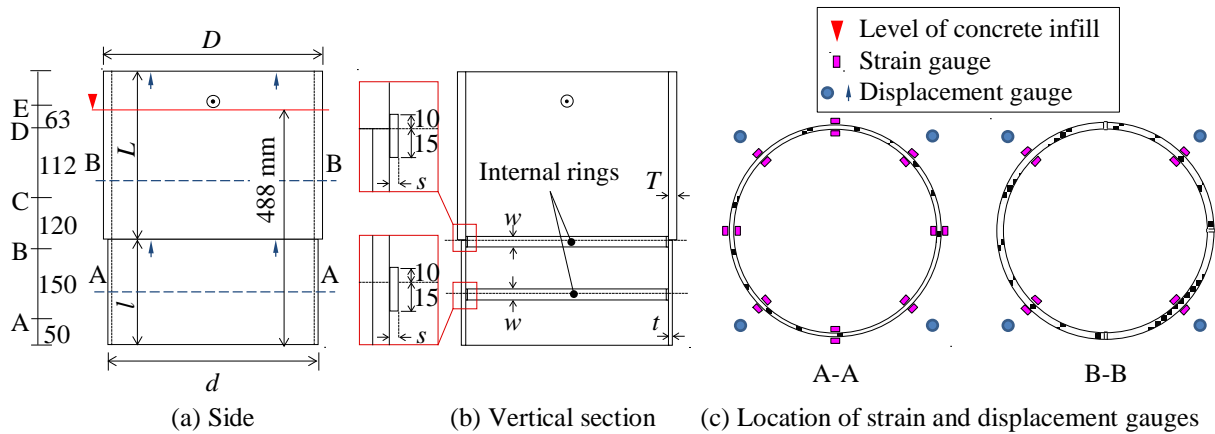


Fig. 1 Test Specimen and the location of displacement gauges

Table 2 presents the specimen parameters. Type A1 specimen has tested part whose length equals to $d/2$, and internal rings attached. Results of this specimen, stress transfer mechanism between internal rings and concrete infill, and ultimate strength under axial compression are clarified. Type A2 has same shape of Type A1, however, with no concrete infill. Type C is filled with concrete and does not have internal rings. Comparing Type C and Type A1, the magnitude of transferred stress between steel pile and concrete infill though the internal rings can be clarified. Unlike other specimens, for Type D with internal rings, the steel pipe length of the test part is set to 488 mm. Type D has the same cross section up to the height of the concrete infill in order to reproduce the pile top used in real structures.

NUMERICAL ANALYSES OF STEEL PILE TOP FILLED WITH CONCRETE

Numerical Models of Pile Top Filled with Concrete

The numerical analysis model, as shown in Fig. 2, defined using ABAQUS 6.14 [2] is utilized for these numerical analyses. Shell elements have been used in the steel pile, and solid elements have been used to model concrete infill and internal rings. The

Table 1 Material properties

Steel pile	E_s [MPa]	σ_y [MPa]	σ_u [MPa]	ε_y [%]
	2.07×10^5	301	431	0.148
Concrete	E_c [MPa]	σ_b [MPa]	σ_t [MPa]	
	2.45×10^4	27.7	3.7	

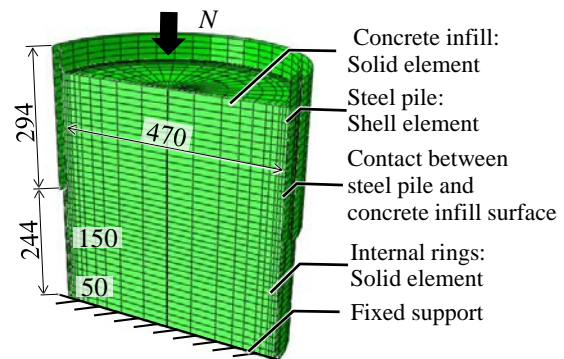


Fig. 2 Numerical analysis model

bottom end of steel pile and the vertical displacement of bottom end of concrete infill are fixed. The contact is defined with no coefficient of friction between steel pipe and concrete infill. Each dimension of the numerical analyses models is shown in Table 2.

Table 2 Specimen parameters

Specimens	Steel pile tested part				Steel pile load application part				Internal rings		Concrete
	Diameter d (mm)	Thickness t (mm)	d/t	Length l (mm)	Diameter d (mm)	Thickness t (mm)	d/t	Length l (mm)	Thickness s (mm)	Width w (mm)	
Type A1	488	9	54.2	244	508	19	26.7	294	6	25	Filled
Type A2									6	25	-
Type C									-	-	Filled
Type D				488				50	6	25	Filled

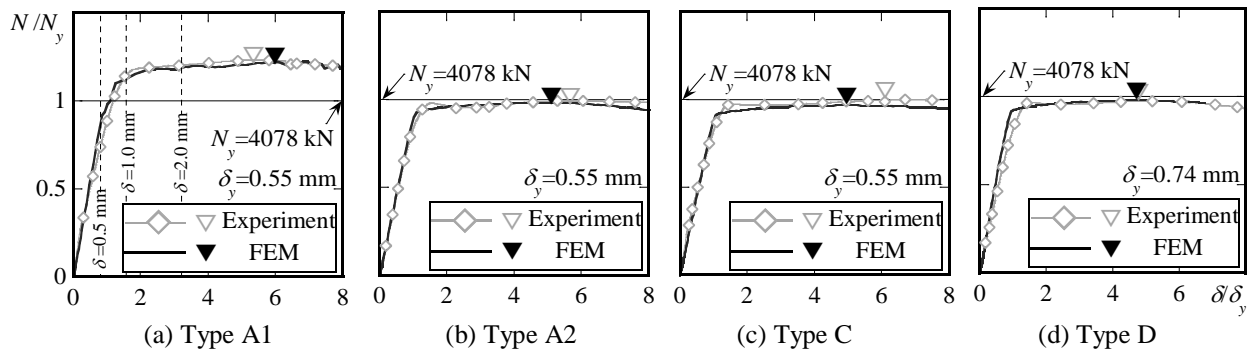


Fig. 3 Hysteresis curves results obtained from loading tests and numerical analyses

Results of Numerical Analysis

Fig. 3 compares the hysteresis curves results obtained from experimental and numerical analyses. N , N_y , δ , δ_y , the white triangle, and the black triangle denote compression load, the yield strength, vertical displacement of loading point, the steel yield displacement which is calculated from dividing N_y with steel pile's vertical stiffness, the ultimate strength of the loading tests, and numerical analyses, respectively. Although the results of the numerical analysis show higher elastic stiffness than that of loading test for Type D, the other results of analyses and loading tests are in good convergence. Based on these results, the validity of numerical analysis models is proven.

Fig. 4 shows the local buckling behavior of test specimens and numerical models. Here, the white triangle represents the peak of local buckling deformation of the steel pile. Since experimental and numerical results show good convergence, the validity of numerical analysis about characteristics of deformation results is proven. In the Type A1 local buckling occurs between upper and lower internal rings, and for Type A2 and Type C local buckling occurs in the area below lower internal ring, whilst in Type D local buckling occurs in the area upper internal ring.

STRESS TRANSFER MECHANISM BETWEEN STEEL PILE ATTACHED WITH INTERNAL RINGS AND CONCRETE INFILL

Behavior of Concrete near Internal Rings

Photo 1 shows the surface of concrete infill after the loading test. For Type A1, the concrete surface is crashed right under the upper ring, however, the concrete surface around the lower ring looks fine. Then, for Type C, D, the concrete infill surface is untouched.

Fig. 5 represents distributions of axial strain in

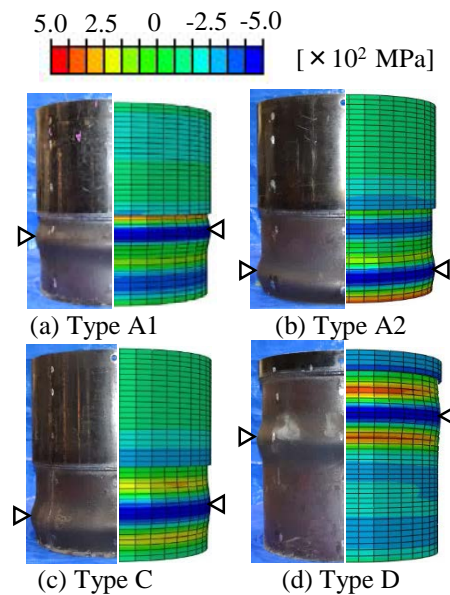


Fig. 4 Local buckling behavior of test specimens and numerical models

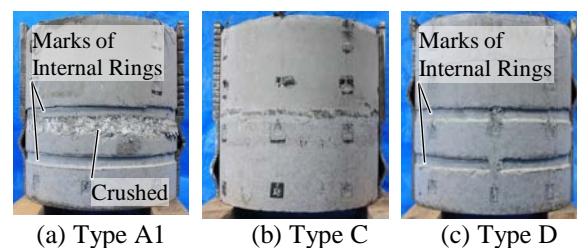


Photo 1 Surface of concrete infill

vertical section of concrete infill obtained from numerical models of Type A1 when $\delta=0.5$, 1.0, and 2.0 mm. Here, the solid triangles locate internal rings. Area colored in black or white represents where the strain exceeds that of compression or tensile strength; Crushing or cracking occurs in concrete infill. Tensile strain progresses in the

obliquely downward direction of the upper ring, and in the surface of concrete infill right under the upper ring strain is larger than compression strain. On the other hand, in the vicinity of the lower ring strain occurs scarcely.

It is clarified that axial force is transmitted from the steel pile to the concrete infill via the upper ring more than the lower ring from Photo 1(a) and Fig. 6.

Amount of Axial Force Transmitted through Internal Rings

Fig.6 shows the hysteresis curves of normalized axial forces N_A , N_B , and N_C by yield strength N_y , calculated from strains measured on the location A, B and C of respective specimens (Fig.1). Here, the perfect elasto-plasticity was adopted, and resulting strain-based estimated axial forces are called hereinafter as “calculated axial force.”

Fig.7 shows the premise of the calculation for transmitted axial forces through internal rings, shown in Fig. 8. Here, ΔN_{B-C} and ΔN_{A-B} represent the difference of calculated axial forces between the location B and C, A and B; $\Delta N_{B-C} = N_C - N_B$, $\Delta N_{A-B} = N_B - N_A$. N_{S-up} and N_{S-low} represent the axial forces transmitted through the upper and lower internal rings. To cancel axial forces transmitted via bonding effect between the concrete infill and the steel pile, shifts of calculated axial forces between corresponding locations in Type C (no internal rings) is used. Therefore, N_{S-up} is calculated by subtracting ΔN_{B-C} of Type C from that of Type A1, and N_{S-low} is also calculated by subtracting ΔN_{A-B} of Type C from that of Type A1.

Fig. 8 (a) and (b) show the hysteresis curves of the amount of axial forces transmitted from the steel pile to concrete infill through the internal rings obtained from the assumption of Fig. 7. N' ($=N_{S-up} + N_{S-low}$, N_{S-up} , and N_{S-low}) shows the axial force calculated from the assumption of Fig. 7, and n represents the ratios of N' and calculated axial force at location E (N_E). n_1 and n_2 are described in Eqs. (1) and (2).

$$n_1 = (N_A + N_{S-up} + N_{S-low}) / N_E \quad (1)$$

$$n_2 = (N_{S-up} + N_{S-low}) / N_E \quad (2)$$

The areas which are painted with gray and hatch pattern show the amount of transmitted axial force from steel pile to concrete infill through upper ring and lower ring. N_{S-down} become 0 near $\delta/\delta_y=1.5$ because N_A and N_B reach N_y around $\delta=1.5\text{mm}$ as

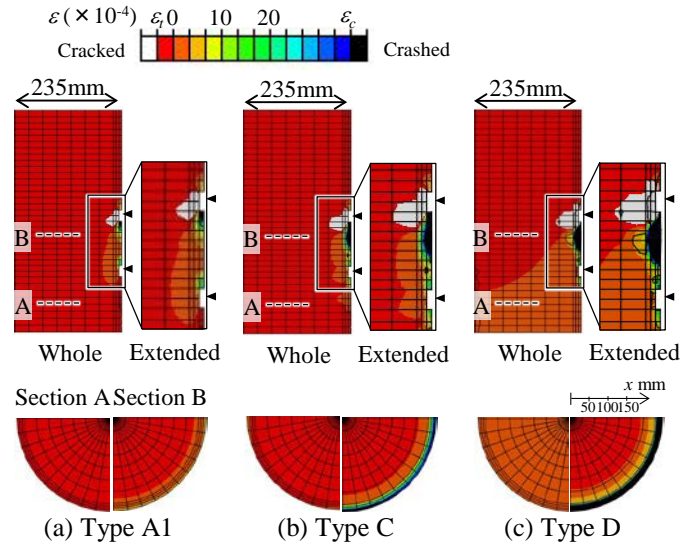


Fig. 5 Distributions of axial strain in vertical section of concrete infill

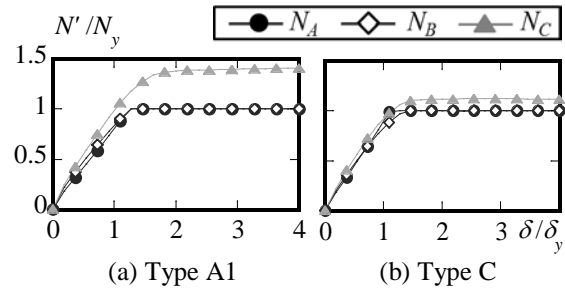


Fig. 6 Hysteresis curves of axial forces which affect steel piles

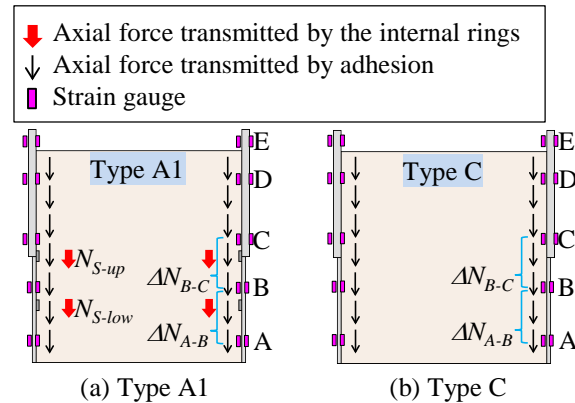


Fig. 7 Premise of calculation of axial forces transmitted through internal rings

shown in Fig. 6. Likewise, even in the experiment, the steel pile becomes plastic near the upper and lower cross section of the internal rings, and the axial force does not increase significantly. Furthermore, the gray area is larger than the hatch pattern area, which means that amount of the

transmitted axial force from steel pile to concrete infill through upper ring is dominant over the one transmitted by lower ring. That is why, as shown in Photo 1(a), it is considered that the surface of the concrete right under the upper ring is damaged.

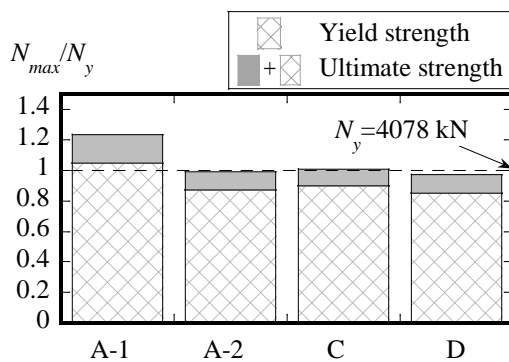
The hysteresis curve of increased strength by internal rings is shown in Fig. 9. Here, ΔN denotes the difference between the load applied on Type A1 and Type C at each same displacement. In this diagram, the gray area is corresponding to ΔN . P_{CU} is the concrete infill push-out strength which is shown in Eq (3). [3]. Here, A_c , A_r , and $\alpha_c (=5.05-0.053 \times (d/t))$ represent the section area of concrete, the projected area of internal rings, and the coefficient which depends on d/t .

$$P_{CU} = \alpha_c \cdot P_c \quad \therefore P_c = F_c \cdot (A_c \cdot A_r)^{0.5} \quad (3)$$

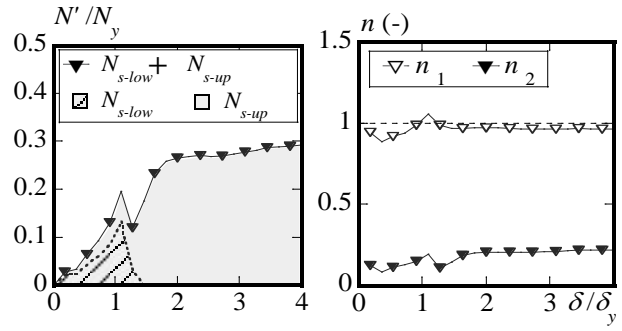
Under this experimental condition, it is shown that if internal rings are attached to steel pile, the compression strength is about 20% higher than in case of no internal rings. This amount of additional strength provided from internal rings is corresponding to about 30% of the concrete push-out strength. This result comes from the reason as shown below. In this experiment, steel pile carries the most of axial force because both bottom surface of the steel pile and the concrete infill are grounded. In addition, the shear stiffness of internal ring is too flexible to transmit the stress from the steel pile to the concrete before pile yielding.

STRUCTURAL CAPACITY OF STEEL PILE TOP UNDER AXIAL COMPRESSION

Fig. 10 (a) and (b) show the strength ratio, N_{max}/N_y , and ductility. Here, N_{max} denotes the ultimate strength of each specimen, yield strength denotes the strength when axial strain from strain gauge reaches yield stress for the first time. δ_{max} denotes the



(a) Strength ratio



(a) Amount of transmitted axial force

(b) n_1 and n_2

Fig. 8 Hysteresis curves of the amount of transmitted axial forces

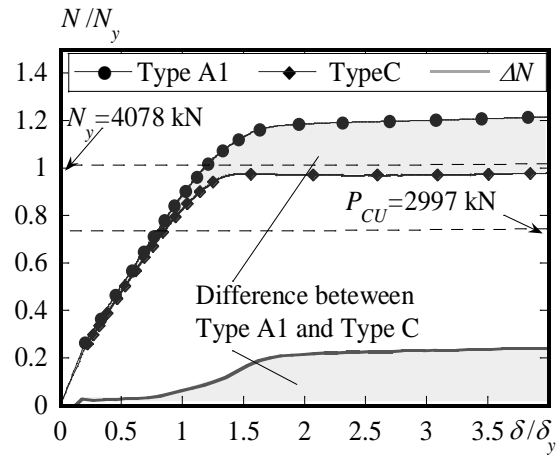
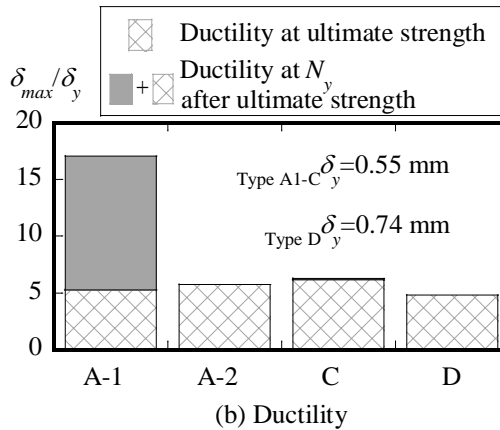


Fig. 9 Hysteresis curve of increased strength by internal rings

displacement at maximum strength. δ_y denotes the axial displacement at N_y decreased after ultimate strength which is obtained from dividing N_y by the stiffness of the steel pile obtained from elastic theory. Then, “Ductility at N_y after the Ultimate Strength” is



(b) Ductility

Fig. 10 Structural capacity of steel pile top under axial compression

not shown with the specimens whose ultimate strength does not reach N_y . Regarding the strength ratio, Type A1 has the largest maximum strength ratio and yield strength ratio. For all specimens except Type A1, the maximum strength ratio is almost the same, and yield strength ratio are also almost the same. Regarding the ductility, the ductility at the ultimate strength of Type C is the largest, however considering the ductility at N_y after the ultimate strength, the Type A1 is about three times larger than the other specimens.

CONCLUSION

Compression loading tests and numerical analyses were carried out to clarify the structural capacity of the steel pile top, the local buckling behavior and the stress transfer mechanism between steel pile and concrete infill through the internal rings. Results show the following.

- 1) The amount of the axial force transmitted from steel pile to concrete infill through upper ring is greater than that of the lower ring.
- 2) The stress from the steel pile is transmitted to the surface of the concrete infill.
- 3) From the results of the compression loading tests, it is shown that the strength is about 20% higher than in case of no internal rings.

- 4) Due to the difference in the loading condition with the concrete infill pushing-out test, the axial force transmission through the internal rings equals about 30% of the concrete infill push-out strength.
- 5) Although the ductility of Type C without internal rings is the largest of all four specimens at their ultimate strength. However, Type A1's ductility is three times larger than the other specimens in case of considering the ductility of N_y after ultimate strength.

ACKNOWLEDGMENTS

The authors appreciate the support of the Japan Iron and Steel Foundation and JSPS Grand-in-Aid for Scientific Research (A).

- [1] Architectural Institute of Japan, Recommendation for Design of Building Foundations, 2001. (in Japanese)
 - [2] Dassault Systèmes: ABAQUS/Standard User's Manual version 6.14-2, 2014.4
- Toshiaki MIYAO, Nobuyuki NAKAMURA, Takehiko SUGIYAMA, "Evaluation of Bearing Strength of Baking Rings for Concrete Filled Tube" AIJ J. Techno. Des. No. 4, 51-56, Mar., 1997

INFLUENCE OF FLOODS ON THE INCLINATION OF STUPAS IN AYUTTHAYA, THAILAND

Yuko Ishida¹, Ayaka Oya², Weerakaset Suanpaga³, Chalemnchai Trakulphudphong³, Chaweewan Denpaiboon⁴ and Ryoichi Fukagawa⁵

¹Research Organization of Science and Engineering, Ritsumeikan University, Japan;

²CTI Engineering Co., Ltd., Japan;

³Faculty of Engineering, Kasetsart University, Thailand; ³

⁴Faculty of Architecture and Planning, Thammasat University, Thailand;

⁵Department of Science and Engineering, Ritsumeikan University, Japan

ABSTRACT

The Ayutthaya Historical Park in Thailand contains many Buddhist temples and stupas. Many of the stupas are inclined; however the main causes of inclination are not completely understood. We hypothesized that the following were inclination influences: soil condition, groundwater fluctuation, and floods. When a flood occurred in Ayutthaya in 2007, the influence of the flood on cultural assets in the historical park area were surveyed by another group in a previous study. Their results showed that flooding was not the cause of inclination. We confirmed the transformation of the ground surface at the Wat Krasai temple, our study site out of the historical park area, by a flood in 2017. Therefore, we investigated the ground soil and analyzed the flood's influence using a finite element method. The Wat Krasai stupa inclines about two degrees to the northern side. In this study, the results indicated that the flood influence on the inclined Wat Krasai stupa was only modest in size. In addition, floods could not have inclined the Wat Krasai stupa to match the present condition.

Keywords: Flood, Consolidation settlement, 2D numerical analysis, Inclined stupa, Cultural property

INTRODUCTION

Natural disasters inflict serious damage on our society, e.g., loss of life and economic losses. Owners of cultural property are also concerned with possible damage from such disasters.

Thailand is highly exposed and vulnerable to natural disasters caused by hydrometeorological hazards, due to its geographical location. Floods are the most frequent natural disaster in Thailand. They have recently worsened, becoming more severe and devastating.

The catastrophic 2011 flood caused damage to 64 out of Thailand's 77 provinces, including the Ayutthaya Historical Park, and a total of 5,247,125 households or 16,224,304 people were affected. The death toll reached 1,026 people and the total economic damages and losses stood at 1.44 billion Baht (US\$ 45.7 billion, approximately). The 2017 flood impacted 44 provinces, including Ayutthaya, 302 districts, 1,724 sub-districts, and 14,105 villages, and affected 609,425 households and 1,898,322 people. Forty-four people were confirmed dead [1].

Ayutthaya is located in the central plain of the central part of Thailand, in the Chao Phraya River basin delta area, which lies very low on the sedimentary plain. Ayutthaya is about 100 km upstream from the mouth of the Chao Phraya River;

its altitude is only about 5 m, and the terrain gradient is very gentle, from 1 / 100,000 to 1 / 50,000. Additionally, the Pasac River, a Chao Phraya River tributary, joins the Chao Phraya River in Ayutthaya County [2]. Therefore, rainy-season flooding and urban flooding occur frequently in Ayutthaya.

In Ayutthaya, many historical properties have inclined and settled. We assumed that one of the causes is flooding. In this research, we will clarify the influence of floods on the stupas, a precious cultural asset of Ayutthaya, using two-dimensional numerical analysis.

PREVIOUS INVESTIGATION OF FLOOD DAMAGE OF CULTURAL PROPERTIES

In 2011, continuous heavy rain caused massive flooding over a broad area, including Ayutthaya, and many ruins sank in the water (Photo 1). Wittaya et al. analyzed the possible physical impact of floods on the cultural heritage in Ayutthaya. They surveyed 294 historical monument sites (HMS) located in Ayutthaya city / island and the buffer zone outside the island, and they assessed 84 HMS as damaged by flood in 2011 [3]. However, specific damage data were not provided.

In a separate investigation, experts from the Fine Arts Department of the Thai Ministry and the

2017 and observed the soil condition carefully. The surface soil was confirmed to soften easily, with low permeability in the rainy season and cracks occurring in the ground in the dry season (Photo 2). In addition, cracks and the expanding disconnection of masonry joints were also confirmed in the brick structure, which was made in 2013 (Photo 3). One cause of these phenomena was presumed to be the influence of a partial subsidence, due to the cyclic wet-dry condition of the soil.



Photo 2 Wet and dry conditions of the surface soil



Photo 3 Cracks of brick structures

Soil investigation and laboratory tests

Four standard penetration tests (SPTs) were carried out around the stupa at Wat Krasai to identify the ground composition (shown in Fig. 3). The government of Thailand conducted tests at the Bor-1 and Bor-2 sub-sites in March 2013. We measured the unit weight of the brick in January

2015, conducted SPTs and sampling at the Bor-3 and Bor-4 sub-sites in March 2016, and then carried out some laboratory tests. The thickness of the soil layers and the groundwater level at each point are presented in Table 1. The brick parameters are shown in Table 2.

ANALYSIS CONDITIONS

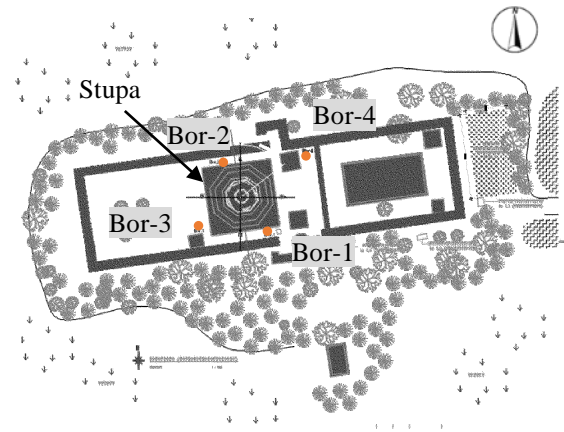


Fig. 3 Location of standard penetration tests

Table 1 Depth of soil layers and groundwater level (m)

	BH-1	BH-2	BH-3	BH-4
Layer 1	①0-3.0	①0-4.0	①0-2.5	①0-4.0
Layer 2	②3.0-6.5	②4.0-10.0	②2.5-4.0	②4.0-10.0
Layer 3	③6.5-10.0	③10.0-14.5	③—	③10.0-11.5
Layer 4	④10.0-19.0	④14.5-20.5	④4.0-19.0	④11.5-19.0
Layer 5	⑤19.0-25.95	⑤20.5-27.45	⑤19.0-21.45	⑤19.0-30.45
GWL	GL-3.2	GL-3.2	GL-2.0	GL-2.1

Table 2 Material property of bricks

material model	linear elasticity
density	1.546 g/cm ³
Young's modulus	5.0×10 ⁵ kN/m ²
Poisson ratio	0.07
unit weight	15.15kN/m ³

Modelization of the Wat Krasai stupa

Several types of stupa are present in the Ayutthaya Historical Park and surrounding area. These stupas appear to have been built in the era of the Ayutthaya dynasty (1351–1767 A.D.). Most of them are badly degraded and some of them are inclined. The stupa of Wat Krasai is also inclined. Restoration, which covered the lower part of the stupa, was carried out in 2013 to prevent further settlement. The stupa originally had an entrance; however, the entrance was completely covered by bricks as part of the restoration work. Therefore, we could not confirm what kind of basement it had. We tried to determine the basement characteristics by considering another stupa, Wat Langkhakhao, which has a similar appearance to the Wat Krasai stupa and

has an entrance (Photo 4). The entrance of the Wat Langkhakhao stupa, which was reached using stairs, was about 1 m high. We could not stay inside the stupa for very long because of the numerous bats inside. In the range that could be visually confirmed, blocks were laid on the edge of the foundation only near the entrance; the basement seemed to be covered with soil, as shown in Photo 5. We had guessed that the basement consisted of bricks, from the drawing and pictures of the Wat Krasai stupa before the restoration; hence, the condition with soil in the basement confused us. Eventually, since we could not obtain certain information on the stupa basement, it remained an indeterminate element of this analysis.

We created a model of the Wat Krasai stupa, shown in Fig. 4, based on the drawing and pictures of Wat Krasai. The stupa consists of several parts, including an eight-sided pyramid and a conical body



Photo 4 Wat Krasai and Wat Langkhakhao



Photo 5 Wat Langkhakhao basement

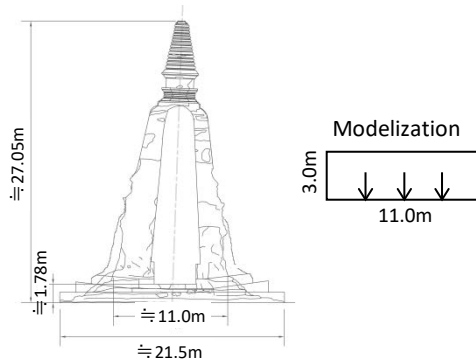


Fig. 4 Model of Wat Krasai

with a multi-layered structure. This entire structure is hollow, with an approximate height of 27.05 meters, and an approximate body diameter of 11.0 meters. Before the restoration work, the base part of the stupa was under the ground. This indicates that the stupa sank below the surrounding ground. The stupa foundation was excavated and the octagonal and bottom quadrangular bases were added, using a great many bricks for reinforcement. The distance from the ground level to the bottom of the hollow is approximately 1.78 meters, and the octagonal-base diameter is approximately 21.5 meters. The Wat Krasai stupa is modeled as a bar shape, which are 11.0 m in width simulates the stupa body, 3.0 m in height, and 1.0 m in depth for the two dimensional analysis. The weight of the stupa was calculated from the cross-section and the unit weight. The unit weight was converted to fit the model.

Soil-composition formula

A two-dimensional finite element method (FEM) analysis was performed using Plaxis, a commercially available geotechnical-engineering software package. The composition formula of the soil was applied using an elastic viscoplastic model by Sekiguchi · Ota, based on the cam clay model. The cam clay model is an elasto-plastic constitutive formula of the soil material aimed at expressing the behavior of saturated clay; it was remixed in the laboratory in a normal consolidated state under load. Sekiguchi · Ota extended the cam clay model for anisotropic normal compaction clay. The yield function f and viscoplastic strain-rate tensor were derived as shown below:

$$f = \frac{\lambda - \kappa}{1 + e_0} \ln \frac{p'}{p'_0} + D\eta^* \quad (1)$$

$$\eta^* = \sqrt{\frac{3}{2} \left(\frac{s_{ij}}{p'} - \frac{s_{ij0}}{p'_0} \right) \left(\frac{s_{ij}}{p'} - \frac{s_{ij0}}{p'_0} \right)} \quad (2)$$

$$f = MD \ln \frac{p'}{p'_0} + D\eta^* \quad (3)$$

$$\varepsilon_v^{vp} = \left\{ 1 - \exp \left(-\frac{v_p}{\alpha} \right) \right\} \left(\frac{\lambda - \kappa}{1 + e_0} \frac{p'}{p'_0} + D\eta^* \right) + v_0 \exp \left(\frac{f - v_p}{\alpha} \right) \quad (4)$$

in which λ is the compression index, κ is the swelling index, e_0 is the initial void ratio, p' is the average effective stress, p'_0 is the initial average effective stress, D is the dilatancy coefficient, s_{ij} is the deviator stress tensor, ε_v^{vp} is the viscoplastic strain-rate tensor, v_p is the plastic volume strain, v_0 is the initial volume strain velocity, and α is the secondary compression coefficient. Parameters, including the compression index, swelling index,

dilatancy coefficient, coefficient of earth pressure at rest, secondary compression coefficient, and irreversible ratio, were determined using a parameter-decision chart, based on comparing the FEM analysis results with actual measured values. Table 3 shows the input parameters.

Flood reproduction

In the analysis, two floods were reproduced. The groundwater level was set to 4.5 m underground, with reference to the value measured at Bor. 3 in October 2016.

The first flood assumed the following conditions:

1. The groundwater level starts to rise one year from the present time.
2. The water-level rise speed is set to 0.5 m / day.
3. The maximum water level is set to 2 m.
4. The maximum water level is maintained for 30 days.
5. The water-level falling speed is set to 0.5 m / day.
6. The water level was lowered to GL-4.5 m.

The second flood assumed the following:

1. The groundwater level starts to rise one year from step 6 in the first flood.
- 2.-6. Steps 2–6 are repeated.
7. The final step of the analysis was assumed to be one year after the second flood.

RESULTS AND DISCUSSION

The results are described below. A year after the initial state, a maximum displacement of 14.04 cm occurred, due to the consolidation process (Fig.5). The settlement amount was calculated to be larger on the left side (Southwest side) than on the right side (Northeast side) of the stupa model, and the

stupa was leaning to the left (Southwest) in this results. However, the actual stupa is inclined toward the north and east, which is not consistent with the analysis results. Before the analysis, we had considered that the second (thick) layer of very-soft to medium-stiff clay on the northeast side would become the key subsidence layer from the boring profile. However, the results of the laboratory soil tests indicated that the shear strength of the third to fourth layer of stiff-to-hard clay was smaller than that of the second layer of clay. The analysis result is considered to reflect the thickness of the weak shear-strength layer.

The displacement at 1 year later from initial state and transition of the groundwater level are shown in Table 4 and Fig. 5. First, we analyzed the amount of displacement during the first flood period. In the water-rising process (days 365–374) between the groundwater levels of -4.5 m and ground surface, the gap of unsaturated ground filled with water and the displacement amount (settlement amount) shrank.

As the water level changed from the ground surface to reach 2.0 m above the ground (days 374–378), the displacement amount decreased. During the 30 days when the water level was 2.0 m above the ground, the displacement slightly decreased (days 378–408). As the water level descended, the

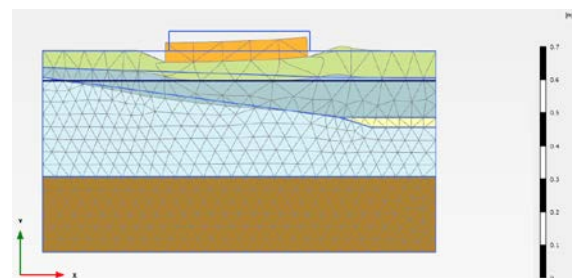


Fig. 5 Displacement one year later

Table 3 Soil parameters

		Layer 1	Layer 2	Layer 3	Layer 4	Layer 5
unsaturated unit weight γ_{unsat}	(kN/m ³)	19.20	16.60	19.20	15.30	18.13
saturated unit weight γ_{sat}	(kN/m ³)	19.37	19.79	20.48	18.10	21.07
liquid limit	(%)	54.86	60.50	-	44.35	-
plastic limit	(%)	36.45	29.35	-	21.30	-
compression index C_c		0.52	0.54	-	0.41	-
swelling index C_s		0.13	0.13	-	0.10	-
compression index λ^*		0.23	0.23	-	0.18	-
swelling index k^*		0.06	0.06	-	0.04	-
internal friction angle ϕ	(°)	19.00	15.00	25.00	11.00	35.00
critical state parameter M		1.10	1.09	0.98	1.18	1.20
secondary compression coefficient		0.0259	0.0268	-	0.0203	-
irreversible ratio		0.63	0.62	0.56	0.67	0.69
dilatancy coefficient		0.06	0.07	-	0.06	-
cohesion	(kN/m ²)	9.80	10.80	0.00	49.00	0.00
void ratio		0.64	0.62	0.51	0.95	0.43
hydraulic conductivity	(cm/sec)	2.813*10-9	4.071*10-9	5.0*10-6	4.372*10-9	1*10-5

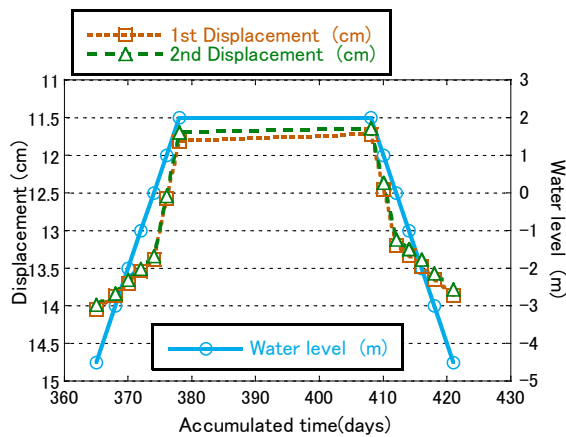


Fig. 6 Displacement transition

Table 4 Displacement transition

Accumrate time (day)	Water level (m)	Displacement (cm)	Accumrate time (day)	Water level (m)	Displacement (cm)
0	-4.5	0.00	786	-4.5	13.99
365	-4.5	14.04	789	-3.0	13.84
368	-3.0	13.87	791	-2.0	13.66
370	-2.0	13.70	793	-1.0	13.51
372	-1.0	13.54	795	0.0	13.34
374	0.0	13.38	797	1.0	12.54
376	1.0	12.57	799	2.0	11.70
378	2.0	11.81	829	2.0	11.64
408	2.0	11.72	831	1.0	12.37
410	1.0	12.45	833	0.0	13.12
412	0.0	13.20	835	-1.0	13.25
414	-1.0	13.33	837	-2.0	13.39
416	-2.0	13.47	839	-3.0	13.57
418	-3.0	13.65	842	-4.5	13.78
421	-4.5	13.86	1207	-4.5	13.94

displacement amount increased significantly, and when the water level fell to the ground surface (412 days, 13.20 cm), the displacement amount was almost the same as before the flooding (374 days, 13.38 cm). The difference of displacement amount at the final stage at which the groundwater level reached -4.5 m and the amount before the flood occurred was only 1.0 mm.

Next, we compared the results of the first and second floods. As the water level rose from before the flood to the ground surface, the displacement amounts of the first and second floods were almost the same. As the water level rose from the ground surface to 2.0 m above the ground, the displacement amount was larger in the first flood than the second flood. Even as the water level fell, the displacement amount of the first flood was larger than the second flood. One year after the second flood (1207 days, 13.94 cm), the displacement was almost the same as before the flood occurred (365 days, 14.04 cm). Additionally, the displacement increment during the flood was 2.40 cm at the maximum. We also analyzed the other model changed the width from

11.0 m to 21.5 m. The result of the displacement increment during the flood was 1.33 cm at the maximum. Therefore, the influence of the flood on the stupa inclination is considered to be small.

CONCLUSION

We modeled the inclined stupa and the ground profile, based on the SPTs of the surrounding Wat Krasai and the laboratory soil test, and conducted an FEM analysis for the cases of two floods. The displacement amount results differed from the actual settlement of the stupa. The shear strength of the third-to-fourth clay level might have been underestimated.

In addition, the maximum displacement at the time of flooding was 2.40 cm, and the amount of displacement before and after the flooding was almost unchanged. In conclusion, the flood had little influence on the stupa inclination.

ACKNOWLEDGMENTS

We would like to sincerely thank the Third Regional Office of Fine Arts and the Ayutthaya Historical Park for their cooperation and provision of information.

REFERENCES

- [1] Puntatip Srikwan, Thailand Country Report 2017, Asian Disaster reduction center, 2017.
- [2] JICA, The cooperation preparation survey report of flood control plan at eastern Pasac River in Ayutthaya district in Kingdom of Thailand, 2012, pp.2-8-2-9.
- [3] Wittaya Daungthima, Kazunori Hokao, Analysing the Possible Physical Impact of Flood Disasters on Cultural Heritage in Ayutthaya, Thailand, International Journal of Sustainable Future for Human Security, J-Sustain , Vol. 1, No.1, 2013, pp.35-39.
- [4] National Research Institute for Cultural Properties, Tokyo, Report on the investigations of the flood damage of cultural properties in the Ayutthaya Historical Park, Japan Center for International Cooperation in Conservation, National Research Institute for Cultural Properties, Tokyo, pp.9-47, 2012.
- [5] Noppadol Phienweij, Hiroyasu Otsu, Nutthapon Supawiwat, Kenji Takahashi, Land Subsidence Caused by Groundwater Pumpage in Bangkok, Soils and Foundation(in Japanese), Vol. 53, No. 2, Ser. No. 565, pp.16-18, 2005.

THE EFFECTS OF TRANSLUTHRIN AS THE ACTIVE SUBSTANCE OF ONE PUSH AEROSOL REPELLENT ON ORGANS DAMAGE OF MICE (*MUS MUSCULUS*) (CASE STUDY OF LUNG, LIVER, BLOODS, AND KIDNEY)

Unggul P. Juswono¹, Arinto Y. P. Wardoyo¹, Chomsin S. Widodo¹, and Johan A. E. Noor¹

¹Faculty of Mathematics and Natural Sciences, Brawijaya University, Indonesia

ABSTRACT

One push aerosol repellent used by the public contains an active substance called transluthrin. Transluthrin is mostly pyrethroid synthetic which has functions as neurotoxin substance. It may act as free radicals in the body due to the compounds which have one free electron that makes it reactive. The purpose of this study was to investigate the effects of transluthrin on mice organs. In this study, the experimental animals (Wistar mice) were put in an exposure chamber and exposed by one push aerosol repellent contains around 20-25% of transluthrin one time a day for 15 days. The damage of mice organs was identified by the microscopic picture (400x of magnification). The results showed that the expose of repellent contains about 20-25% of transluthrin on mice increase the damage of lung, liver, blood, and kidney cells from 13% to 24%, 12% to 27%, 9% to 69% and 22% to 55%, respectively.

Keywords: Transluthrin; Lung cells; Liver cells; Blood cells; Kidney cells

INTRODUCTION

Air as one of the natural resources which are the main need for a living thing and non-renewable. Air pollution has negative effects on human health. Substances that are often used in daily life and potentially as air pollutants (pollutants) are cigarette smoke [1], air freshener aerosol, and insecticide aerosol [2]. Increased concentrations of air pollutants are related to various diseases such as lung cancers, Parkinson, and many others [3-5].

Pollutants, both gaseous and particulates are very harmful to the health of the human body. Pollutants can pass through the body through respiration and oral processes. The presence of pollutants in the body will be able to disrupt the function of organs, including the kidney as the main organ in the excretory system [6,7], the lungs as respiratory organs [8], the liver that plays an important role in the process of detoxification and blood as the most fluid in the body [9,10].

The degree of an organ damage caused by particulate matters of pollutants is strongly influenced by particle size [11,12]. The size of the particulate matter varies greatly. Based on its size, the particles can be classified into three kinds, i.e. coarse particles, fine particles, and ultrafine particles. Ultrafine-sized particles give a greater effect than larger particles. The results showed that the fraction of ultrafine particles was the most damaging particulate matter [13].

One of the substances that are often used in daily life and potentially as a pollutant is one push aerosol

mosquito repellent. Indonesia is one country that has a tropical climate, where the tropical climate is very suitable for the breeding process of insects, especially mosquitoes. Mosquitoes themselves can cause various diseases. The effort to overcome the increasing number of diseases caused by mosquitoes is to use some chemicals insecticide-containing mosquito repellent.

For each type of a mosquito repellent contains different ingredients depending on the brand and their types. One of the most popular mosquito repellents in the market is the one-push aerosol which has a variety of content one of which is transluthrin chemicals. Transluthrin is one of the pyrethroid insecticides that produces a rapid reaction with low persistence. Pyrethroid insecticide has a very specific effect on insect nerve cells, so it needs a little amount to have the required effect [14].

One push aerosol mosquito repellent is mostly used in a closed room. The scent of mosquito repellent is an indication that the harmful compound of mosquito repellent is still spreading in the room as well as an indication of the residue in the room. This can disrupt the respiratory tract. If the particles enter the lung, it will flow in the blood so it will give certain effects such as inflammation of the sensitive organs [3,15]. The transluthrin active ingredients contained in one push aerosol can decrease the erythrocytes.

The pulmonary lung is the organ that first contacts directly with particles. Particles that enter the lungs will be carried by the blood and circulated throughout the body. The blood then goes to the

kidney for a filtering. The filtered residues will be detoxified by the liver. So that the potential organs affected by the active ingredients of the mosquito repellent are lung, blood, kidney, and liver.

Based on the description of the dangers of mosquito repellent and the potential impact on the organs, it is necessary to conduct a research to investigate the impact of mosquito repellent on organs. The purpose of this study was to investigate the damage level of the kidney, liver, lung and blood organ in mice exposed by the indoor aerosol one push mosquito repellent. This study will contribute to a better understanding of the pollutant impact on the anatomy, structure and work function of the organ.

MATERIALS AND METHODS

Experimental Animals and Treatments

We used 2-3-month-old male mice (Wistar) as the experimental animals that were divided into three groups: a control group, a treatment group A and a treatment group B. The control group was unexposed mice. The treatment group was sprayed with the different mosquito repellent. The group A and B were exposed by the transfluthrin content of 21.3% and 25% respectively. The exposure dose was given for five spray pushes. After the mice were sprayed, they were placed in the exposure chamber with the dimension of 20 cm x 20 cm x 30 cm for 20 minutes (Fig. 1). Then the chamber was opened to the mice breathed free air. After spraying for 15 days, the mice were dissected to take the organ: lungs, blood, kidneys, and livers.

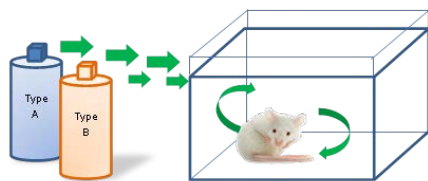


Fig. 1 Chamber of exposure to mice with mosquito repellent.

Preparation and Histological Examination

Kidneys, Livers, and Lungs

The mice from the control group and the treatment groups were sacrificed by a cervical dislocation. The kidneys, livers, and lungs were cleaned using NaCl (0.9%). They were fixed in a buffered formalin (10%) for a week and dehydrated in upgraded ethanol series. After being processed to the paraffinization, they were cut using a microtome

and were colored using HE (hematoxylin and eosin) [6].

Blood

The blood smears were placed onto the object glasses. They were fixed with 70% methanol solution and then covered with the cover glasses. When they came dried (± 5 minutes), they were stained using a Giemsa and buffer pro-Giemsa solution [10].

Histological Examination

The cells deformation was observed using a microscope (400x of magnification). The damage level of the observed organ was calculated using Eq. (1) [6]:

$$\text{Damage (\%)} = \frac{\sum \text{deformed cells}}{\sum \text{observed cells}} \times 100\% \quad (1)$$

RESULTS

Lung Damage

The microscopic picture of the lung treatment group mice is shown in Fig. 2.

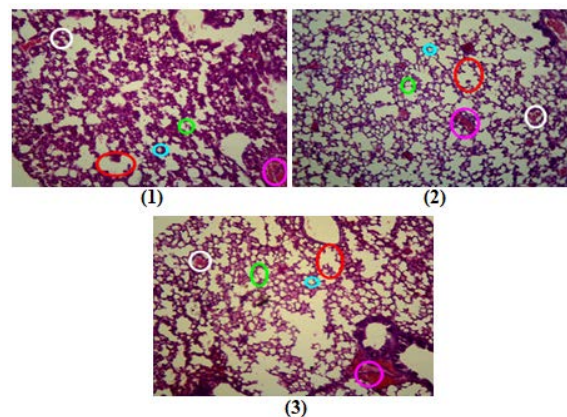


Fig. 2 Microscopic pictures of lungs of mice (1) control (without treatment), (2) type-A and (3) Type-B. The red, green, and grey circles show the emphysema, DSA, and edema, respectively. The pink circles indicate the bleeding.

Lung emphysema is a disease whose primary symptom is an airway obstruction because the air sacs in the lungs are excessively bulging and suffered extensive damage. Edema is characterized by the presence of fluid-filled alveoli and an increased laxity of the alveolar septum. Alveolar septal destructions (DSAs) are characterized by the thinning of the alveolar septum, atrophy, and in some parts a total damage of the alveolar septum

that spherical formed and may also be accompanied by enlargement of the ducts and alveolar sacs. For normal alveolar cells characterized by an almost spherical (poly) cell shape with a size of 4-5 μ m [8]. The lung damage is calculated by counting the normal cells and the damaged cells in five random fields to determine the cell deformation [16]. The percentage of the cell deformation is presented in Fig. 3.

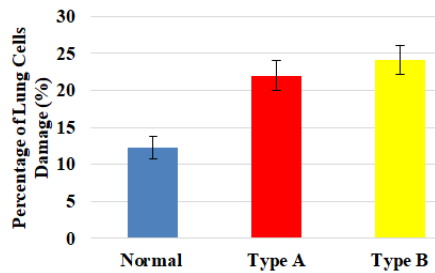


Fig. 3 Damage percentages of the mice lungs.

Red Blood Cells Damage

The microscopic picture and percentage of blood cells damage of red blood cells can be seen in Fig. 4.

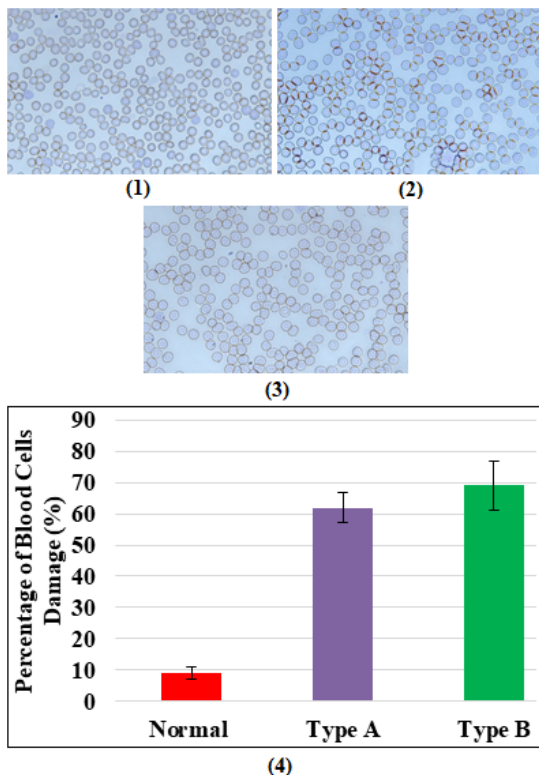


Fig. 4 Microscopic pictures of red blood cells of mice (1) control (without treatment), (2) type-A and (3) Type-B. The percentage of red blood cells damage (4).

The physical changes were determined by the comparison between the size and shape of normal cells and the abnormal cells [10]. The abnormal blood cells are classified into 9 types of cellular damage, i.e., cell target, teardrop, crystal, roll cell, polychromasia, sickle cell, stomatocyte and basophilic [17,18]. Cell targets are the blood cells that have erythrocytes that look like shoots or Mexican hats. Teardrop is a pear-shaped blood cell or like water droplets. Krista is a blood cell that has a straight or crooked or slightly square shape. Roll cell is a blood cell that holds each other. Sickle cell is a damage that has erythrocytes shaped crescents, stiff, and chronic hemolytic anemia. Stomatocyte is a type of blood cell that has erythrocytes in the form of a central pallor such as the mouth. Basophilic is a blood cell damage that has a slim/ rounded granule. Keratocyte is a blood cell damage that has a barrier shape.

Kidney Damage

The observation of the kidney cell damage was demonstrated by the microscopic images of the glomerular cells and tubules (Fig. 5) [6]. The results of the glomerular observation (green arrows) and kidney tubular mice showed that the pollutant exposure can cause the damage of the kidney structure that is known as the glomerulus and tubular damage. Glomerular damage is characterized by the widening of Bowman space [19,20]. Tubular damage is characterized by narrowing of the tubular lumen (orange circles). The increasing of the glomerular and tubular damage will cause necrosis or cell death called Acute Tubular Necrosis (ATN). ATN is caused by lack of oxygen (ischemic ATN) and the influence of toxic substances in cells (nephrotoxic ATN). Microscopically, there is a pigment of hemoglobin pigment scattered in the tubules. The percentage of the kidney cells damage is presented in Fig. 6.

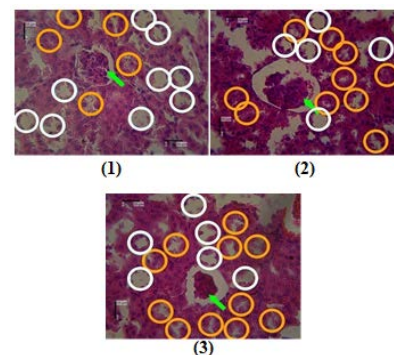


Fig. 5 Microscopic pictures of kidneys of mice (1) control (without treatment), (2) type-A and (3) Type-B. White circles show normal tubules.

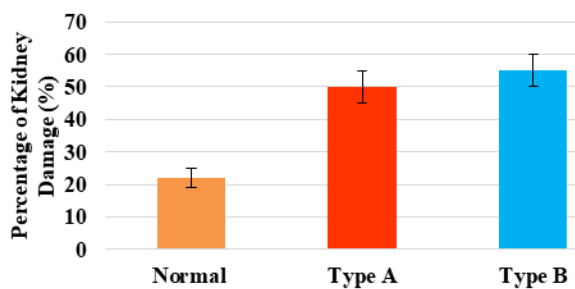


Fig. 6 Damage percentages of the mice kidneys.

Liver Damage

The changes in the mice liver include the central vein, hepatocyte cell form, and sinusoid blood vessel (Fig. 7) [9]. The centralist vein shape that is originally a spherical shape and unbroken. After receiving treatment, the vein began to break. Similarly, hepatocyte cells also had to change the shape. Meanwhile, the sinusoidal blood vessels became wider. The observation of liver cells showed that spraying of pollutant material in mice had the adverse effects on the liver organ of mice where the administration of these pollutants affected the shape and structure of mice liver cells. Dosage type B-type mosquito spray for high intensity can cause blood cells to get worse. At a spray dosage of 5 times obtained damage of liver cells reached 27.49%.

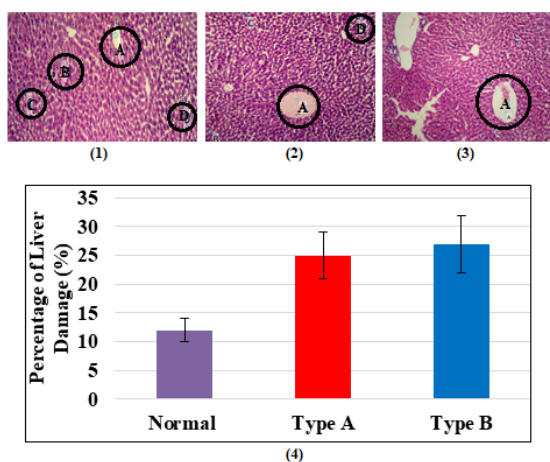


Fig. 7 Microscopic pictures of livers of mice (1) control (without treatment), (2) type-A and (3) Type-B. Captions: A = Vein Centralist, B = Normal Cell, C = Binucleus, D = Parenchymal Degeneration. The percentage of liver cells damage.

DISCUSSION

Insecticide one push aerosol is considered the most powerful in killing or eradicating mosquitoes. There are 5 ways insecticide work on the insect body

that affects the nervous system, inhibits energy production, affects the endocrine system, inhibits cuticle production and inhibits water balance. Transfluthrin contained in both types of mosquito repellents is a pyrethroid class II obtained from the synthesis of pyrethrin. Based on their toxicity and structure, pyrethroid is classified as type I and type II. Type I is a pyrethroid group that has no α -cyano group and type II has an α -cyano group.

The interaction between blood and transfluthrin occurs when the blood passes through the lungs. Blood contains hemoglobin which acts as an oxygen binder. With the transfluthrin entering the lungs, the hemoglobin will tend to bind transfluthrin rather than oxygen gas to be circulated throughout the body. The blood containing transfluthrin can affect other substances needed by the body such as nutrients, hormones, fats, sugars, and proteins. Pyrethroid is able to increase activation and prevent deactivation. The impact of the event resulted in the ion channel open longer. At the cellular level, pyrethroid interferes with nerve activity, membrane depolarization, and synaptic disorders [21]. The membrane of a protein affected by pyrethroid causes the change of the action potential of the cells.

Enzymes that hydrolyze ATP have been found to be sensitive to pyrethroid reactions. ATPase neural membrane is a target for pyrethroid in invertebrate insects, whereas in rats it is synaptosome. Pyrethroid joins the lipid bilayer layer to interfere with phospholipid conditions and cause instability in the membrane. The mechanism of neurotoxicity begins with an interruption in the activity of Ion Na^+ , K^+ and ATP ions and membrane instability.

Several types of pyrethroid are known to produce poisoning symptoms similar to poisoning due to cyanide and aldehyde. Pyrethroid is thought to be capable of generating free radicals and causing stress on cells. Pyrethroid manifold cypermethrin and fenvalerate have been known to produce oxidative stress and changes in antioxidant enzymes [22]. Oxidative stress is a condition where there is a disturbance of balance between the production of free radicals with antioxidants that cause tissue damage. Oxidative stress can be caused by a reduction in natural antioxidant levels in the body and increased free radical production [12]. Oxidative stress occurs due to the presence of reactive oxygen species (ROS) in cells more than the natural oxidant compounds in cells. Free radicals are substances, molecules, compounds that have highly cellular reactive properties. If radicals are not inactivated, their reactive characteristic can damage all types of cellular macromolecules such as carbohydrates, proteins, lipids, and DNA. Free radicals generally stand on their own, with very fast reactions with other atoms filling in the vacancy of an unpaired orbital. Transfluthrin is a free radical of the C atoms in the structure of benzene.

The kidneys function to produce urine from the body's metabolic processes. The kidney is the main path of toxic substances (toxins). The release of the substance is carried out by three (3) processes: filtration by the glomerulus, reabsorption by tubules and secretion by tubules. The kidneys also concentrate toxically on the filtrate and carry the toxic via tubular cells. Glomerular damage will lead to disruption of the filtration process in the glomerulus so that the ability to filter blood is reduced, the proteins and blood cells will accumulate in the tubules.

Tubules serve as a place of reabsorption and secretion in the process of formation of urine. Damage to the kidney tubules is characterized by the presence of tubular cells that swell due to fluid shift from outside the cell into the cell. This shift occurs because the toxic substances contained in ultrafine particles from pollutants cause changes in the surface charge of the tubule epithelial cells, the active transport of ions and organic acids, and the ability to concentrate from the kidneys that eventually lead to damaged tubules, impaired urinary flow, increased via tubular pressure. This cell swelling causes the tubular lumen to become narrowed until closure. If the tubule cell is damaged, it will interfere with the system of urine formation in the kidney, then the substance that is not needed by the body cannot be removed from the body, so it will be toxic (toxic) that can damage the kidney organ [23,24].

CONCLUSION

The results of the research have shown that there is damage to organ cells in mice due to the pollutant exposure. The transfluthrin active substances contained in one push aerosol affect the mice organ with the different damage degrees. The blood is the worst damage with the percentage of 69 %. Meanwhile, the lung is the least damage of 24 %. The organ damage depends on the transfluthrin content. In which more dose of transfluthrin caused more damage.

REFERENCES

- [1] Wardoyo A. Y. P., Santjojo D. J. D. H., Rahayu T., and Subagyo S., Influence of smoking rate on ultrafine particle emission of cigarette smoke. *J. Biol. Res.*, Vol. 23, 2018, pp.90–94.
- [2] Lü D., Zhang X., Wu W., and Jiang W., Measurement and statistic analysis of combustion heat of two kinds of household spray aerosols in China. *Procedia Eng.*, Vol. 45, 2012, pp.638–642.
- [3] Buonanno G., Giovinco G., Morawska L., and Stabile I., Lung cancer risk of airborne particles for Italian population. *Environ. Res.*, Vol. 142, 2015, pp.443–451.
- [4] Allen J. L., Liu X., Weston D., Conrad K., Oberdörster G., and Cory-Slechta D. A., Consequences of developmental exposure to concentrated ambient ultrafine particle air pollution combined with the adult paraquat and maneb model of the Parkinson's disease phenotype in male mice. *Neurotoxicology*, Vol. 41, 2014, pp.80–88.
- [5] Sioutas C., Delfino R. J., and Singh M., Exposure assessment for atmospheric ultrafine particles (UFPs) and implications in epidemiologic research. *Environ. Health Perspect.*, Vol. 113, 2005, pp.947–956.
- [6] Wardoyo A. Y. P., Juswono U. P., and Noor J. A. E., Varied dose exposures to ultrafine particles in the motorcycle smoke cause kidney cell damages in male mice. *Toxicol. Reports.*, Vol. 5, 2018, pp.383–389.
- [7] Passagne I., Morille M., Rousset M., Pujalté I., and L'Azou B., Implication of oxidative stress in size-dependent toxicity of silica nanoparticles in kidney cells. *Toxicology*, Vol. 299, 2012, pp.112–124.
- [8] Wardoyo A. Y. P., Juswono U. P., and Noor J. A. E., Comparison of lung damages due to petrol and diesel car smoke exposures: histological study. *Int. J. GEOMATE*, Vol. 15, 2018, pp.124–129.
- [9] Wardoyo A. Y. P., Juswono U. P., and Noor J. A. E., An observation of histological evidence on internal organ damages in mice caused by repeated exposures to motorcycle emissions, in *Proc. AIP Conf. Proc.*, 2017, pp.020007-1-020007-11.
- [10] Wardoyo A. Y. P., Juswono U. P., and Noor J. A. E., A study of the correlation between ultrafine particle emissions in motorcycle smoke and mice erythrocyte damages. *Exp. Toxicol. Pathol.*, Vol. 69, 2017, pp.649–655.
- [11] Yang H., Chang S., and Lu R., The effect of particulate matter size on cardiovascular health in Taipei Basin, Taiwan. *Comput. Methods Programs Biomed.*, Vol. 137, 2016, pp.261–268.
- [12] Upadhyay S., Ganguly K., and Stoeger T., Inhaled ambient particulate matter and lung health burden. *Eur. Med. J. Respir.*, Vol. 2, 2014, pp.88–95.
- [13] Oberdörster G., Maynard A., Donaldson K., Castranova V., Fitzpatrick J., Ausman K., Carter J., Karn B., Kreyling W., Lai D., and Olin S., Principles for characterizing the potential human health effects from exposure to nanomaterials: elements of a screening strategy. *Part. Fibre Toxicol.*, Vol. 35, 2005, pp.1–35.

- [14] Miao J., Wang D., Yan J., Wang Y., Teng M., Zhou Z., and Zhu W., Comparison of subacute effects of two types of pyrethroid insecticides using metabolomics methods. *Pestic. Biochem. Physiol.*, Vol. 143, 2017, pp.161–167.
- [15] Buonanno G., Stabile L., and Morawska L., Personal exposure to ultrafine particles: The influence of time-activity patterns. *Sci. Total Environ.*, Vol. 468–469, 2014, pp.903–907.
- [16] Wang T., Miao M., Bai M., Li Y., Li M., Li C., and Xu Y., Effect of sophora japonica total flavonoids on pancreas, kidney tissue morphology of streptozotocin-induced diabetic mice model. *Saudi J. Biol. Sci.*, Vol. 24, 2017, pp.741–747.
- [17] Almeida L. E. F., Wang L., Kamimura S., Wong E. C. C., Nouraie M., Maric I., Albani S., Finkel J., and Quezado Z. M. N., Rapamycin increases fetal hemoglobin and ameliorates the nociception phenotype in sickle cell mice. *Blood Cells, Mol. Dis.*, Vol. 55, 2015, pp.363–372.
- [18] Pretorius E., Mbotwe S., and Bester J., Erythrocytes and their role as health indicator: Using structure in a patient-orientated precision medicine approach. *Blood Rev.*, Vol. 30, 2016, pp.263–274.
- [19] Sarkar A., Das J., Manna P., and Sil P. C., Nano-copper induces oxidative stress and apoptosis in kidney via both extrinsic and intrinsic pathways. *Toxicology*, Vol. 290, 2011, pp.209–218.
- [20] Momeni H. R., Professor A., and Eskandari N., Effect of curcumin on kidney histopathological changes, lipid peroxidation and total antioxidant capacity of serum in sodium arsenite-treated mice. *Exp. Toxicol. Pathol.*, Vol. 69, 2017, pp.93–97.
- [21] Soderlund D. M., Molecular mechanisms of pyrethroid insecticide neurotoxicity. *Arch. Toxicol.*, Vol. 86, 2013, pp.165–181.
- [22] Akbar S. M. D., Sharma H. C., Jayalakshmi S. K., and Sreeramulu K., Effect of pyrethroids, permethrin and fenvalerate, on the oxidative stress of *Helicoverpa armigera*. *World J. Sci. Technol.* Vol. 2, 2012, pp.1–5.
- [23] Grigoryev D. N., Liu M., Hassoun H. T., Cheadle C., Barnes K. C., and Rabb H., The local and systemic inflammatory transcriptome after acute kidney injury. *J. Am. Soc. Nephrol.*, Vol. 19, 2008, pp.547–558.
- [24] Xu D., Chen M., Ren X., Ren X., and Wu Y., Leonurine ameliorates LPS-induced acute kidney injury via suppressing ROS-mediated NF- κ B signaling pathway. *Fitoterapia*, Vol. 97, 2014, pp.148–155.

DEVELOPMENT OF THE DEFORMATION MONITORING SYSTEM WITH WIRELESS SENSOR NETWORK AND EVALUATION OF MECHANICAL STABILITY FOR DAMAGED STONEWALLS BY HUGE EARTHQUAKE IN KUMAMOTO CASTLE

Yuuya KATSUDA¹, Satoshi SUGIMOTO¹, Yoichi ISHIZUKA¹, Shohei IWASAKI¹, Ryoma TAKAESU¹,
Koichiro YAMASHITA², Minoru YAMANAKA³

¹Faculty of Engineering, Nagasaki University, Japan;

² Fujitsu Laboratories Ltd., Japan; ³Faculty of Engineering, Kagawa University, Japan

ABSTRACT

Kumamoto Castle was constructed about 400 years ago, and now Cultural Affairs Agency of Japan treats as an important historical spot. The 2016 Kumamoto Earthquake was damaged a lot of stonewalls of this castle. Authors continue to investigate the deformation of unstable stonewalls by high accuracy laser module for measuring distance. And these stonewalls should be monitored continuously for evaluation of mechanical stability, so we developed and established the wireless network system for measuring the changing angle of some stonewalls surface in this castle. The characteristics of this system are low cost and low power consumption with small scale electric generation and a simple server.

Authors also carried out making simulation model and calculation for evaluation of stonewalls stability by the distinct element method under the several conditions of stonewall shape and interface of materials. The failure area of stonewalls and backfill are estimated by these results of simulation, and it is discussed that these areas should be reinforced under repair of damaged stonewalls.

Keywords: Kumamoto Castle, Stonewalls, Wireless sensor network, Numerical simulation

INTRODUCTION

The 2016 Kumamoto earthquake gave huge damage for several structures in Japan. Kumamoto Castle was also damaged on architectural structures, stone wall, embankment and so on. The number of damaged stone walls and embankment is over hundreds especially as shown in Fig. 1 [1][2]. Therefore, the evaluation method of stone wall and embankment stabilization is required from the view of geotechnical engineering quickly.

Kumamoto Castle was constructed about 400 years ago, and now Cultural Affairs Agency of Japan treats as an important historical spot. Authors continue to investigate the deformation of unstable stonewalls by high accuracy laser module for measuring distance [1][3][4]. And these stonewalls should be monitored continuously for evaluation of mechanical stability, so we developed and established the wireless network system for measuring the changing angle of some stonewalls surface in this castle. The characteristics of this system are low cost and low power consumption with small scale electric generation and a simple server [5][6][7].

Authors also carried out making simulation model and calculation for evaluation of stonewalls stability by the extended distinct element method under the several conditions of stonewall shape and interface of materials. The failure area of stonewalls

and backfill are estimated by these results of simulation, and it is discussed that these areas should be reinforced under repair of damaged stonewalls.



Fig. 1 Several damages of Kumamoto Castle

OVERVIEW OF MONITORING SYSTEM

Our research team tried to mount the deformation monitoring system for evaluation of stonewall stability in Kumamoto Castle. The proposed system for monitoring is named MIST, which stands for Maintenance solution for Infrastructure and Slopes with Telecommunication [7]. The proposed remote monitoring system, shown in Fig. 2, is using ZigBee which is an IEEE 802.15.4-based specification for a

suite of communication protocols. One of MIST is composed of (a) coordinator, (b) router and (c) end-device shown in Fig. 3. Each terminal has own ZigBee chip. Recently, with the spread of Internet of Things (IoT), various wireless communication standards are established. In the various standards, ZigBee has the feature like realizing over 60,000 connection and very low power consumption. Moreover, by using a sleep mode of Zigbee, it is possible to collect the necessary data and suppress the power consumption. Further, by wireless communication using multi-hop, it is possible to use a plurality of communication paths, the overall system flexibility, stability is improved. Therefore, ZigBee is suitable for such a sensor network which requires multiple terminals and connections, also powered by standalone energy supply [3]. The voltage value obtained by the sensors at end-devices is converted to 16bit data by ADC in the end devices. The data is transmitted to the coordinator (master unit) via some routers (repeaters). This action is happened in periodically, like once in 30 minutes. At the coordinator, which is tiny microcomputer (Raspberry Pi), all the data is transmitted to the remote host computer via the internet. The sensor devices are connected to end-devices with analog via ADC or digital via I2C. Each terminal is activated by own solar panel and Li-ion battery. Thus, the proposed MIST system can provide not only remote monitoring of long-distance location but also real time analysis. Also, the analyzed data or sensed raw data can be accessed via an internet. The actual screenshot is shown in Fig. 5.



Fig. 2 Image of Proposed System (MIST)

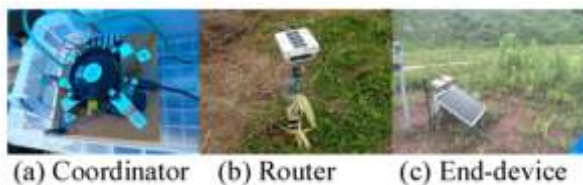


Fig. 3 Terminal Devices

Application of MIST system for Kumamoto Castle

The 2016 Kumamoto earthquake gave huge

damage for several earth structures in Kumamoto Castle. There are a lot of damage cases, for example, floating out of stonewalls, cracking of embankments as shown in Photo 1 & 2. These will be concerns in future on instability as earth structures. In this study, MIST system were constructed and operated on trial in the specific area of Kumamoto Castle for monitoring these damaged structures. Now some wireless sensors with gyroscope function were set on the top of damaged stonewalls, and it was confirmed that these apparatuses continued to work and collect displacement data stably.



Photo 1 Floating stonewall



Photo 2 Cracking embankment

Fig. 4 shows the installation positions of end devices, routers and coordinators installed in the unstable stonewall existing around Iida-maru and Takeno-maru in Kumamoto Castle. Here, routers for relaying communications are arranged as shown in this figure, in order to monitor the stone walls at 5 places in total at two locations separated by a single distance of about 100 m from the coordinator. Since it was considered that the distance between equipment based on the result of field intensity measurement at the site, the height difference, the surrounding stonewalls and the existence of trees were each considered to affect the stability of communication. We also installed two routers at the same spot to improve the relay stability of

communication. The first equipment installation in November 2017, the second installation in January 2018, and as of the end of this fiscal year, the equipment arrangement shown in Fig. 5 is adopted. In addition, an example of displaying the communication status on the web is shown in Fig. 6.

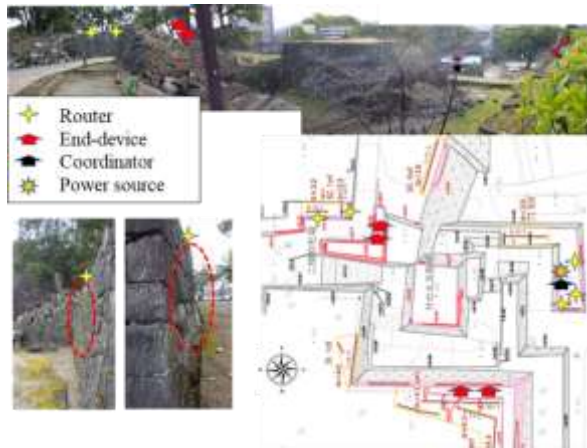


Fig. 4 Location of each monitoring devices in the test field



Fig. 5 Monitoring devices



Fig. 6 View of communication situation on web browser

During the measurement of about 3 months, environmental conditions such as sunshine and

outdoor temperature were bad conditions, and due to malfunction of power generation of the solar panel installed in each equipment and charging / discharging of the lithium ion battery Communication stoppage which is thought to have occurred. Therefore, as shown in Fig. 7, stable monitoring was not reached, but improvements will be made by increasing the solar panel and changing the battery type.

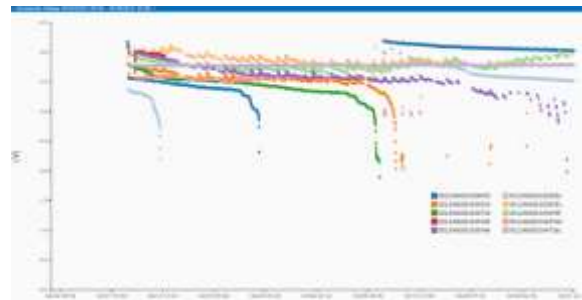


Fig. 7 View of output voltage process for two months

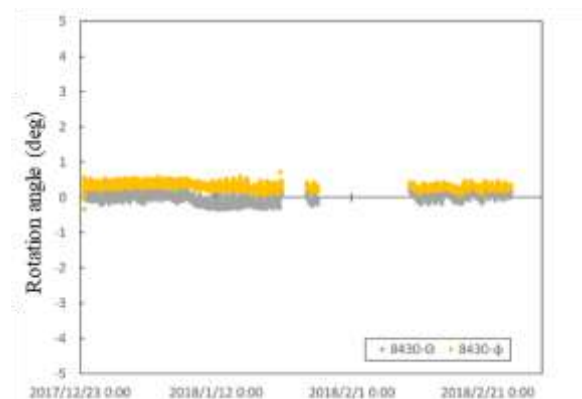


Fig. 8 Results of rotation angle of gyro sensor

It is possible to calculate the rotation angle of stone based on the output change of the gyro sensor mounted on the communication module. As an example of the monitoring result, Fig. 8 shows the change of the rotation angle of the module ID: 8430 where data was collected by relatively stable communication. The observation period is from 23 December 2017 to 24 February 2018, and the rotation angle in two directions is calculated from the beginning of the period. On the way, it can be confirmed that although there is data loss due to disruption of communication, it is almost unchanged in rotation angle. On the other hand, it is considered that the fact that the glass rod for confirming the occurrence of deformation occurred on the side of the stonewall from the current year does not occur at present has a stable condition as shown in Photo 3. In the future, we plan to continue validity of the output data of the module together with the result of regular fixed point observation of the stone wall section by the laser rangefinder.



Photo 3 Glass rods for monitoring displacement between stones



(a) Situation before the disaster



(b) Situation after the disaster
Fig. 9 Failure the stonewall of H323

THE STONE WALL MODELING AND CALCULATION BASED ON DYNAMIC NUMERICAL SIMULATION

Selection of target location for model

The model was selected from 60 stone walls which were targeted at the survey of the damage situation of

Kumamoto Castle. The selection terms are as follows. The first is that the height of the stone wall is 10 meters or more. The second is that collapse is occurring in the central part of the stone wall. Third, there is information on shape in past literature. Based on the above conditions, we selected part number H323 as the object of the model. Fig.9 show the model H323 before and after the disaster. The figure shows that H323 collapsed only at the central part of the stone wall. In H323 there was data of the shape before the earthquake in F.Kuwahara " The gradient of the stone walls in Kumamoto Castle "[8]. We created the shape of the model with reference to this literature.

Overview of model

Fig.10 shows the setting element condition of the model. The area of the back soil was set as an elasto-plastic element. The area of the stone and the bedrock were set as rigid elements. Between stone wall, between the stone wall and the back soil were set as joint elements.

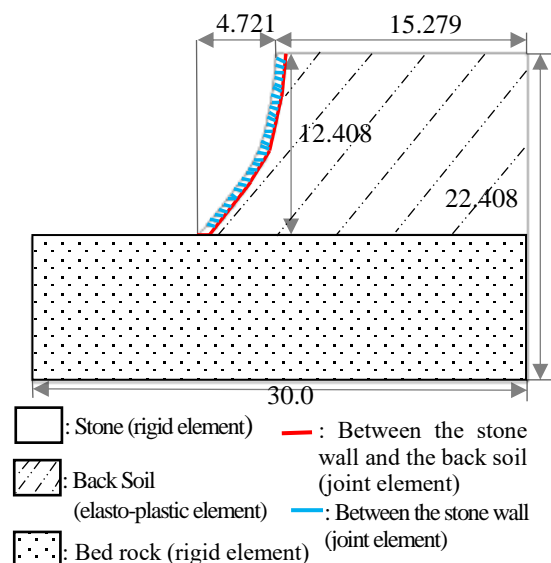


Fig.10 Element condition of the model (unit : meter)

The boundary condition of model

When doing dynamic numerical simulation, the important point is setting boundary conditions. In order to reproduce the seismic motion, we set the boundary condition shown in Fig.11. A dashpot was provided at the bottom of the model. The boundary surface becomes a viscous boundary by a dashpot. Below the boundary surface is expressed as semi-infinite ground by a viscous boundary. Semi-infinite ground absorbs the escaping wave energy. It is possible to input only the rising wave component of the seismic wave by absorbing the wave energy. We set free rock area on side of model. We set an energy

transfer boundary between the free rock area and the model. The energy transfer boundary transmits the escaping wave energy to the free rock area. The free rock area absorbs the escaping wave energy. By this effect, the side of boundary surface is expressed as semi-infinite ground.

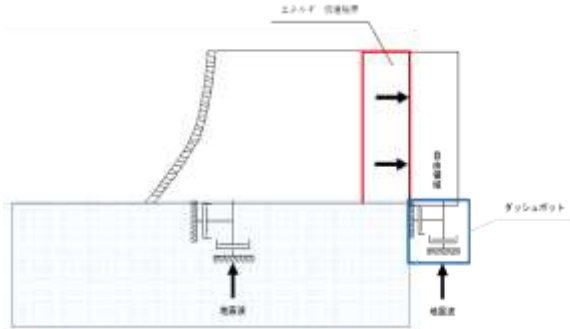


Fig.11 Overview of boundary condition

Setting up of model's characteristic value

Tab.1 shows the physical properties of stone and back soil in the model. Tab.2 shows the physical property value of joint element. Since the target model collapsed at the upper part of stone wall, it is considered that the stress in the vertical direction was small from the viewpoint of Mohr-Coulomb's failure criterion. Therefore, it is considered that the influence of the angle of shear resistance is small. On the other hand, it is considered that the influence of the cohesion of back soil is large. For the above reason, we divided the cohesion of back soil into 3 cases. (Tab.3)

Tab.1 Physical property value of block element

Item	Embankment	Stone
Density $\rho(\text{g/cm}^3)$	2.5	2.75
Elastic Coefficient $E(\text{MPa})$	55	5.5×10^4
Poisson's ratio ν	0.1	0.2
Cohesion $c(\text{KPa})$	Refer to Tab.3	7.0×10^2
Internal Frictional Angle $\phi(^{\circ})$	40	45
Tensile Strength $\sigma(\text{MPa})$	350	7.0×10^6

Tab.2 Physical property value of joint element

Item	The between embankment and stone	The between stone
Cohesion $c(\text{KPa})$	35	350
Internal friction angle $\phi(^{\circ})$	35	40
Tensile strength $\sigma_t(\text{MPa})$	350	35

Tab.3 Cohesion of embankment

Cohesion (KPa)	case1	case2	case3
	0.0	15.0	50.0

On the seismic velocity waveform applied to the model

When doing dynamic numerical simulation, it is necessary to input observed earthquake record. We used the main shock of the Kumamoto earthquake that occurred on April 16. The seismic wave characteristics of the main shock were obtained from "Kyoshin Net" (K-net) of National Research Institute for Earth Science and Disaster Resilience[9]. "KMM006 Kumamoto" was selected as an observed earthquake record. Fig.12 shows the observation point of "KMM006 Kumamoto".



Fig.12 Observation station

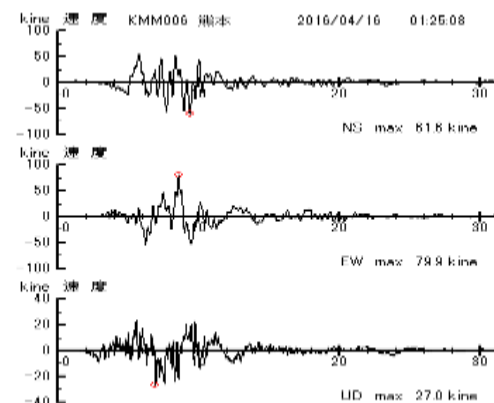


Fig.13 Seismic velocity waveform in Kumamoto

Fig.13 shows the velocity waveform of observed earthquake record. The maximum speed of the velocity waveform NS component is 61.6 kine(cm/sec). The maximum speed of the velocity waveform EW component is 79.9 kine(cm/sec). The maximum speed of the velocity waveform UD component is 27.0 kine(cm/sec). The NS component means the waveform in the north-south direction of

the seismic waveform. Similarly, the EW component means the waveform in the east-west direction, and the UD component means the waveform in the vertical direction.

In the model H323, the direction of the stone wall is the south direction. For that reason, the NS component was used as the velocity component in the shear direction. 0.0 to 15.0 seconds at which the maximum waveform is observed was used as the input waveform.

RESULT OF SIMULATION AND DISCUSSION

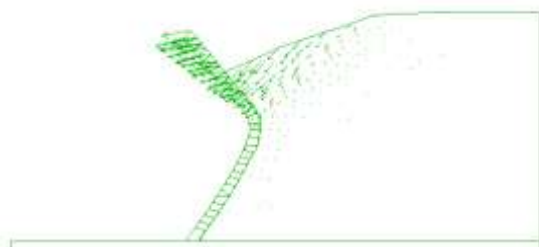
Displacement vector

Fig.14,15,16 shows the simulation results of displacement vector. The displacement to the outside of the stone wall was confirmed in all cases. In the case 1 (cohesion 0 KPa), the back soil of the upper part of stone wall collapses to stone wall side. The maximum displacement is 5.184 meters.

In the case 2 (cohesion 15 KPa), the back soil of the upper part of the stone wall is the largest displaced. But case 2 did not collapse. The maximum displacement is 0.1219 meters.

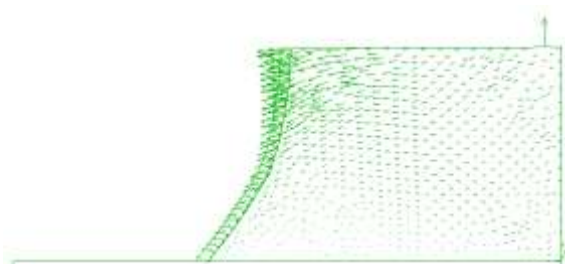
In the case3(cohesion50KPa), large displacement was not confirmed. However, the case 3 was larger displacement than the case 2. The maximum displacement is 0.1512 meters.

In Case 1, it is considered that the back soil caused plastic deformation at the time of gravity analysis. On the other hand, in case 2 and case3, the top of the back soil confirmed an upward displacement of 0 to 13 centimeters. It is considered that the top of the back soil has not set as a viscous boundary.



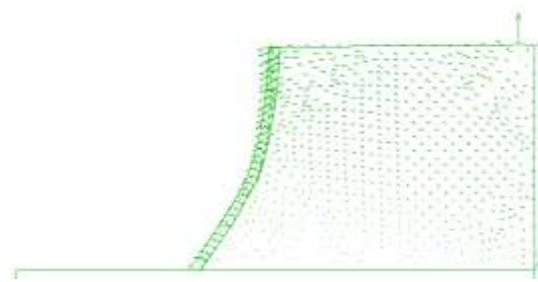
Maximum displacement 5.184m

Fig.14 Displacement vector of cohesion 0 (KPa)



Maximum displacement 0.1219m

Fig.15 Displacement vector of cohesion 15 (KPa)



Maximum displacement 0.1512m

Fig.16 Displacement vector of cohesion 50 (KPa)

Elastic fracture

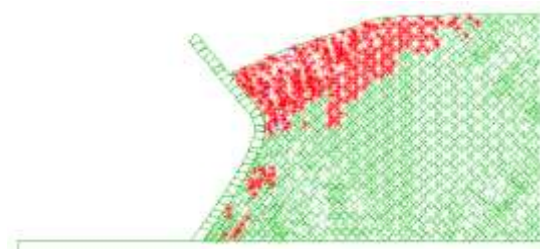
Fig.17,18,19 shows the simulation results of elastic fracture. The phenomenon shown in this figure expresses the collapse situation of the back soil which is the elastic plasticity model. Red is plasticity failure, purple is tensile failure, green is expressed as past failure points.

In the case 1 (cohesion 0KPa), the whole back soil was destroyed 1 second after the start of measurement. Plastic failure occurred in the back soil of the upper part of stone wall. After that, the back soil on the upper part of stone wall collapsed with tensile failure.

In the case 2 (cohesion 15KPa), The back soil surface has destroyed already in 1 second. It is considered that this cause is gravity analysis before the main simulation. Because the surface of the back soil received the load of the stone. After that, plastic failure gradually occurred from the back soil in the lower part of stone wall. In the end, tensile failure occurred in the back soil of the top of stone wall.

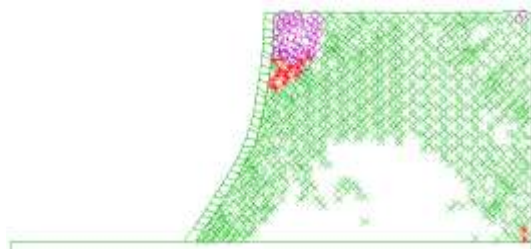
In the case 3 (cohesion 50KPa), it is found that the failure range is narrower than case 2. Plastic failure of the lower part of stone wall was later than Case 2. From this result, it is understood that the influence on the back soil is relatively small.

As a collapse mechanism inside the back soil, it was found that collapse progresses on the back soil surface due to plastic fracture. When exceeding a certain range of failure on the surface of the back soil, tensile failure occurs in the back soil of the upper part of the stone wall. As a result, active earth pressure occurred at the upper part of stone wall.



× : elastic destruction × : tensile destruction
× : past destruction

Fig.17 Elastic destruction of cohesion0(KPa)



× : elastic destruction × : tensile destruction
× : past destruction

Fig.18 Elastic destruction of cohesion15(KPa)



× : elastic destruction × : tensile destruction
× : past destruction

Fig.19 Elastic destruction of cohesion50(KPa)

CONCLUSION

In this paper, we described the construction and operation of a monitoring system aimed at evaluating the stability of the stone wall damaged by a huge earthquake and numerical calculation by the distinct element method. This monitoring system is realized by diverting and extending what the authors developed for evaluating the stability of the slope. The current situation has problems in securing communication stability and securing power supply. However, since measurement with a gyro sensor is realized, it is necessary to improve these problems.

In the analysis, the stone wall collapse was caused by the change in cohesion of the embankment, so it was found that the cohesion was one of the factors for the stone wall collapse mechanism. The factor for collapse that the elastic fracture of the embankment close to the stone wall surface and the tensile fracture on the ground surface of the embankment. When the maximum velocity waves for earthquake had passed, elastic and tensile fracture simultaneously occurred in the embankment of the stone wall, and active earth pressure was generated. Due to this collapse mechanism, the embankment began to be destroyed gradually from the ground surface. When destruction progresses had passed, a large displacement occurs as in adhesive. We presumed that the stone wall has collapsed due to the displacement of the back soil.

ACKNOWLEDGEMENTS

The authors gratefully appreciate a lot support and understanding for this investigation from all officers of Kumamoto Castle Survey and Research Center after shortly after the 2016 Kumamoto earthquake. And our gratitude extends to all cooperators of this investigation with several instruments and information.

REFERENCES

- [1] S. Sugimoto, M. Yamanaka, H. Maeda, N. Fukuda, Y. Katsuda: Research of damaged condition by the 2016 Kumamoto Earthquake and ground investigation on stone walls and earth structures in Kumamoto Castle, International Journal of GEOMATE, Vol.14, Issue 45, 2018, pp.66-72.
- [2] S. Sugimoto, M. Yamanaka: Reports of damaged earth structures in Kumamoto Castle, Proceedings of 54th Natural disaster and science symposium, 2017, pp.45-51. (in Japanese)
- [3] Y. Katsuda, Y.Jiang, K. Omine, S.Sugimoto: Research of damaged stone structures in Kumamoto Castle by the 2016 Kumamoto Earthquake, Proceedings of 72th JSCE conference (CD-ROM), 2017, pp.479-480. (in Japanese)
- [4] Y. Katsuda, S.Sugimoto, M. Yamanaka: Reports of survey on damaged stonewalls in Kumamoto Castle by the 2016 Kumamoto Earthquake, Proceedings of the Japan National Conference on Geotechnical Engineering, 2018, in submission. (in Japanese)
- [5] S. Sugimoto, T. Sasamura, J. Ishida, Y. Ishizuka, T. Fujishima, T. Fujimoto, S. Iwasaki, K. Yamashita, K. Kurihara: Development and application of slope monitoring system by wireless sensor network, Proceedings of 71th JSCE conference (CD-ROM), 2016, pp.27-28. (in Japanese)
- [6] H. Chang, J. Ishida, S. Sugimoto, Y.Jiang, K. Omine, Y. Ishizuka, T. Sasamura, S. Iwasaki: Application of slope monitoring system by wireless sensor network, Proceedings of 72th JSCE conference (CD-ROM), 2017, pp.67-68. (in Japanese)
- [7] Y. Nishikawa, T. Sasamura, Y. Ishizuka, S. Sugimoto, S. Iwasaki, H. Wang, T. Fujishima, T. Fujimoto, K. Yamashita, T. Suzuki, K. Kurihara: Design of Stable Wireless Sensor Network for Slope Monitoring, Proceedings of 2018 IEEE Topical Conference on Wireless Sensors and Sensor Networks(CDROM), TU3P-18, 2018, pp.8-11.
- [8] F. Kuwahara: The gradient of the stone walls in Kumamoto Castle, Report of researches / Nippon Institute of Technology, 14-2, 1984, pp.59-74.

- (in Japanese)
- [9] National Research Institute for Earth and Disaster Resilience “K-NET”, <http://www.kyoshin.bosai.go.jp/kyoshin/>, 2017.

GEOMATE 2019

9th International Conference on
Geotechnique, Construction Materials & Environment
Tokyo, Japan

Invitation to participate

- The "International Journal of GEOMATE" is a Scientific Journal of the GEOMATE International Society that encompasses a broad area in Geotechnique, Construction Materials and Environment.
- The key objective of this journal is to promote interdisciplinary research from various regions of the globe.
- The editorial board of the journal is comprised of extensively qualified researchers, academicians, scientists from Japan and other countries of the world.
- It is peer-reviewed Journal that is published quarterly till 2015 and now monthly. All articles published in this journal are available on line.
- Contributors may download the manuscript preparation template for submitting paper or contact to the Editors-in-Chief

[editor@geomatejournal.com]

ISSN: 2186-2990

DOI: <http://dx.doi.org/10.21660/geomate>



Scopus

EBSCO

CENGAGE

GIF

doi

crossref

VOLUME 00

Issue 00

Month, Year

International Journal of GEOMATE

(Geotechnique, Construction Materials and Environment)



THE GEOMATE INTERNATIONAL SOCIETY

Tsu, Japan

<http://www.geomatejournal.com/>